

ASNR 56th Annual Meeting Proceedings

Monday, June 4, 2018
10:30AM - 12:00PM

Parallel Paper Session: Stroke Treatment Strategies

O-01

10:30AM - 10:37AM

Endovascular Treatment for Acute Ischaemic Stroke in Routine Clinical Practice: Results from the MRCLEAN Registry

I Jansen¹, M Mulder², R Goldhoorn³, W Schonewille⁴, J Martens⁵, B van der Worp⁶, G Lycklama a Nijeholt⁷, Y Roos¹, R van Oostenbrugge³, A van der Lugt², W van Zwam³, D Dippel², C Majoie¹
¹Academic Medical Center, Amsterdam, North-Holland, the Netherlands, ²Erasmus University Medical Center, Rotterdam, South-Holland, the Netherlands, ³MUMC, Maastricht, Limburg, the Netherlands, ⁴St. Antonius Hospital, Nieuwegein, Utrecht, the Netherlands, ⁵Rijnstateziekenhuis, Arnhem, Gelderland, the Netherlands, ⁶UMCU, Utrecht, the Netherlands, ⁷Haaglanden Medisch Centrum, Leidschendam, South-Holland, the Netherlands

Purpose

Endovascular treatment (EVT) for acute ischaemic stroke is currently being implemented as standard of care. Whether efficacy and safety in routine clinical practice are comparable to previous randomised clinical trials of EVT for acute ischaemic stroke is yet unknown. The aim of this study was to determine efficacy and safety of EVT in routine clinical practice.

Materials and Methods

The MR CLEAN Registry is an ongoing, prospective, observational study in all centers that perform EVT in the Netherlands. Data were analyzed from patients treated between March 2014 and June 2016. Primary outcome was the modified Rankin Scale score (mRS), ranging from 0 (no symptoms) to 6 (death). Outcomes and safety parameters were compared to the MR CLEAN trial intervention and control arms.

Results

From the MR CLEAN Registry, we included 1488 patients who were treated within 6.5 hours from onset of symptoms. There was a significant shift towards better functional outcome compared to the MR CLEAN trial intervention arm (acOR= 1.33 (95% CI: 1.04-1.71); p=0.02) and the MR CLEAN trial control arm (acOR= 1.95 (95% CI: 1.54-2.47); p<0.01). The reperfusion rate, defined as a score of 2B-3 on the extended Thrombolysis in Cerebral Infarction (eTICI) score, was 59%, the same as in the MR CLEAN trial patients. The duration from onset to start of endovascular treatment was almost 1 hour shorter in the MR CLEAN Registry patients: 208 versus 260 minutes. In 5.8%, a symptomatic intracranial haemorrhage occurred, compared to 7.7% in the MR CLEAN intervention arm, and 6.4% in the MR CLEAN trial control arm.

Conclusions

In routine clinical practice, EVT for patients with acute ischaemic anterior circulation stroke due to intracranial proximal artery occlusion, is at least as effective and safe as in the trial setting.

O-02

10:37AM - 10:44AM

Impact of Endovascular Recanalization in Patients with Low Initial ASPECTS Score on Edema Formation and Clinical Outcome in Acute Anterior Circulation Strokes

G Broocks¹, F Flottmann¹, T Faizy¹, M Schoenfeld¹, U Hanning¹, H Leischner¹, S Gellissen¹, J Fiehler¹, A Kemmling²

¹University Medical Center Hamburg-Eppendorf, Hamburg, Germany, ²University Medical Center Schleswig-Holstein, Luebeck, Germany

Purpose

In patients with acute ischemic strokes, endovascular treatment improves functional outcomes and reduces mortality. However, a possible clinical benefit of mechanical recanalization for patients presenting with a low initial ASPECTS remains unclear. We hypothesize that in these patients, successful recanalization leads to an improvement in mortality and degree of disability by reducing edema formation and malignant mass effect.

Materials and Methods

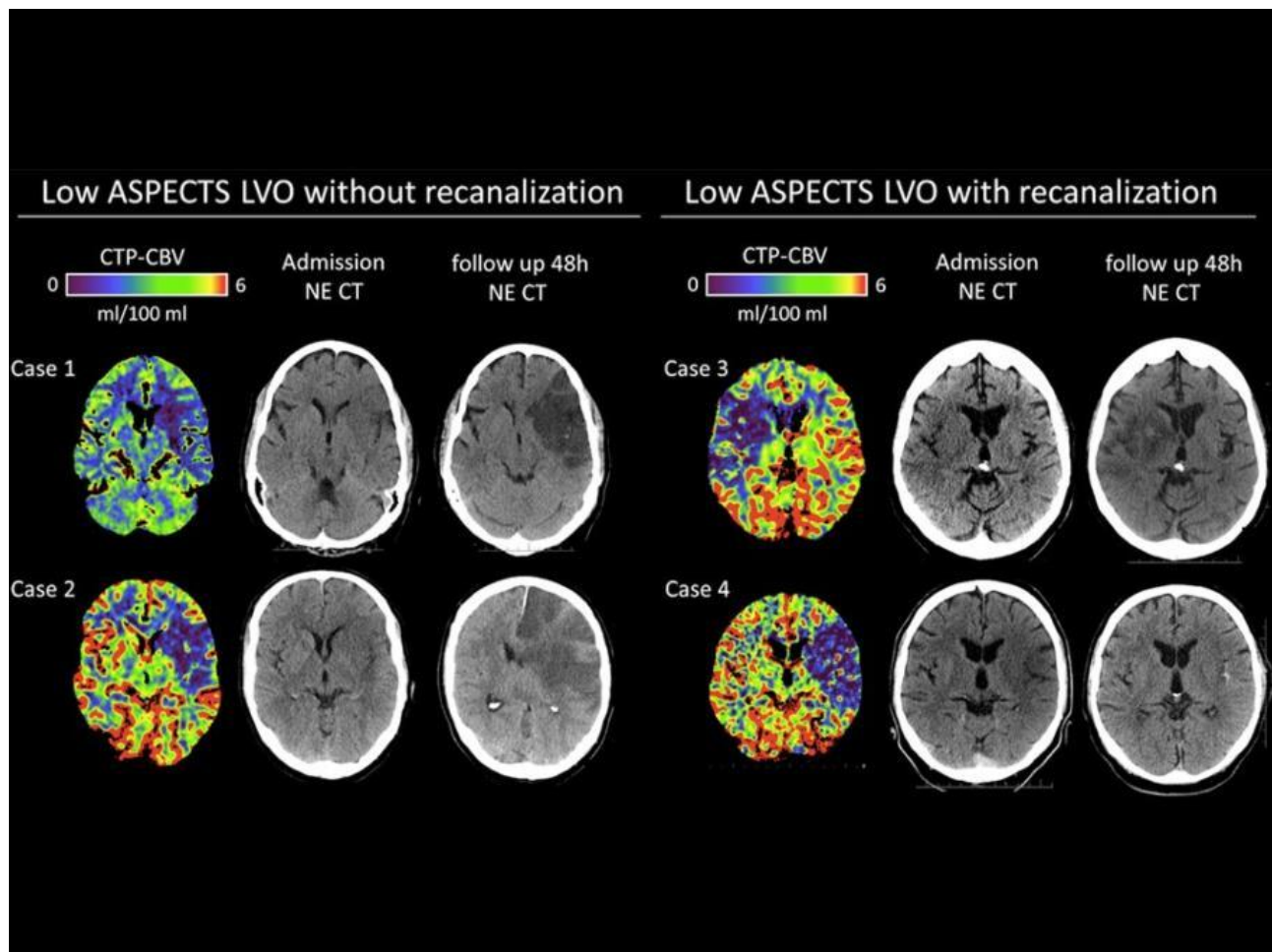
All patients with an acute ischemic stroke due to a large vessel occlusion in the anterior circulation and an ASPECTS score of 5 or less were analyzed (admitted 01/2015-08/2017). The patients were assembled into two groups: successful endovascular recanalization (TICI 2b/3) or no endovascular recanalization (no endovascular procedure, TICI 0-2a). To quantify edema formation after therapy, net water uptake was calculated based on relative hypoattenuation in follow-up CT and compared to initial water uptake in the admission CT. The occurrence of malignant infarctions and secondary parenchymal hemorrhage (PH) was documented. Furthermore, modified Rankin scale (mRS) score was assessed (latest available score).

Results

We included 95 patients, of which 34 received successful endovascular recanalization. The mean percent net water uptake in the follow-up CT was 27% ($\pm 7,3\%$) for patients without endovascular recanalization versus 17% ($\pm 5,8\%$) in recanalized patients. The prevalence of malignant infarctions was 45,9% versus 29,4% in favor for the patients with endovascular recanalization. The mean mRS score was 5.1 (± 0.9) in patients without recanalization versus 3.1 (± 1.8) in patients with recanalization. There was no significant difference for secondary PH in both groups ($p=0.5$).

Conclusions

In this cohort, successful recanalization in patients with low initial ASPECTS score resulted in a significant reduction of edema formation and was associated with a decreased prevalence of malignant infarctions and an improvement of clinical outcome.



(Filename: TCT_O-02_FIG_ASPECTS_ASNR.jpg)

O-03

10:44AM - 10:51AM

Thrombus Perviousness in Endovascular and Intravenous Treatment for Acute Ischemic Stroke: Analysis of the HERMES Collaboration Data.

M Kappelhof¹, M Tolhuisen¹, K Treurniet¹, B Dutra¹, H Alves¹, S Brown², K Muir³, Y Roos¹, A Demchuk⁴, B Campbell⁵, A van der Lugt⁶, P White⁷, M HILL⁴, D Dippel⁶, M Goyal⁴, H Marquering¹, C Majoie¹

¹Academic Medical Center, Amsterdam, the Netherlands, ²Altair Biostatistics, St. Louis Park, MN, ³Queen Elizabeth University Hospital, Glasgow, Scotland, ⁴University of Calgary, Foothills Medical Centre, Calgary, Alberta, Canada, ⁵Royal Melbourne Hospital, Melbourne, Australia, ⁶Erasmus University Medical Center, Rotterdam, the Netherlands, ⁷Newcastle University, Newcastle Upon Tyne, Newcastle, England

Purpose

Thrombus perviousness estimates thrombus permeability based on radiological single-phase images, to assess residual blood flow through a clot. Previously, two studies described an association of thrombus perviousness with favorable functional outcome after acute ischemic stroke (1, 2). This association was present both among patients treated by intravenous tissue plasminogen activator (IV-tPA) and endovascular treatment (EVT). We aimed to investigate possible treatment modification effect of

Oral Presentations & Excerptas

thrombus perviousness in intervention and control arm patients of the pooled HERMES-collaboration dataset.

Materials and Methods

We included 393 patients with thin-slice noncontrast CT (NCCT) and CT angiography (CTA) available. Thrombus density was measured on coregistered NCCT and CTA to calculate thrombus attenuation increase (TAI) as a measure for perviousness. Control arm patients received IV-tPA if eligible. Intervention consisted of EVT preceded by IV-tPA if indicated. Multivariable regression analyses with multiplicative interaction terms were performed to determine treatment effect modification, and association of TAI with functional outcome (modified Rankin scale score; mRS), chance of favorable outcome (mRS 0-2), mortality, reperfusion (mTICI-score 2b-3), and final infarct volume (FIV).

Results

Median TAI was 3.5HU (IQR:-4.3-11.8). Increased thrombus perviousness was associated with improved ordinal mRS, with a significant treatment effect modification ($p=0.005$). For control arm patients, aOR for a 1-step mRS improvement was 1.22 (95%CI 1.11-1.35) per 5HU increase in TAI. In the intervention arm no significant association was found. Among controls, increased perviousness was associated with a higher chance of favorable outcome (aOR 1.33; 95%CI 1.14-1.56; Figure 1); FIV decreased with 13% (95%CI 7-18) per 5HU TAI increase. Increased perviousness was associated with a lower chance of mortality in the overall population. For intervention arm patients, perviousness was not significantly associated with favorable functional outcome, reperfusion, or FIV.

Conclusions

Thrombus perviousness measured on acute-phase NCCT and CTA is associated with improved functional outcome, mortality, and FIV. Increasing perviousness is associated with increasing IV-tPA benefit.

mRS 0-2 by TAI, adjusted

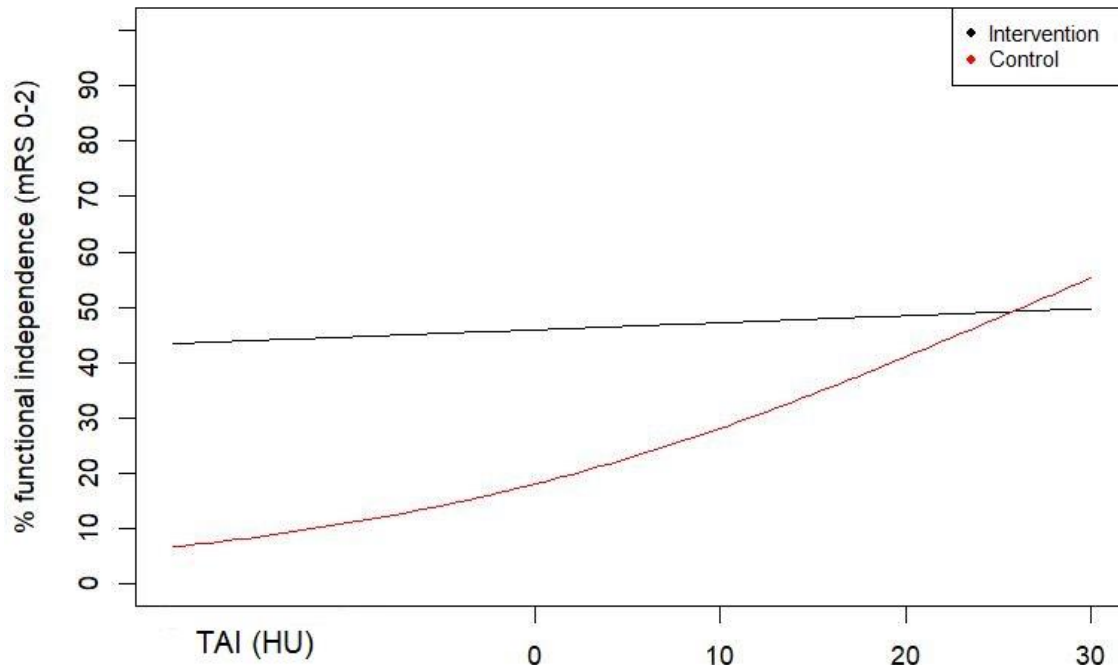


Figure 1 - Adjusted probability of favorable outcome as a function of TAI for control (IV-tPA if eligible) and intervention (EVT with preceding IV-tPA if eligible) patients.

TAI=thrombus attenuation increase, HU=Hounsfield Units, IV-tPA=intravenous tissue plasminogen activator.

(Filename: TCT_O-03_Fig1_ProbabilitiesTAI_mRS02_highres.jpg)

O-04

10:51AM - 10:58AM

Endovascular management of acute stroke in the elderly: A systematic review and meta-analysis.

C Hilditch¹, P Nicholson¹, W Brinjikji¹

¹*Toronto Western Hospital, Toronto, Ontario, Canada*

Purpose

We present the results of a systematic review and meta-analysis examining clinical, procedural and radiological outcomes of endovascular therapy (EVT) for acute stroke in patients aged older than 80 years.

Materials and Methods

We searched Pubmed, Medline and Embase from 1992 through to week 35 of 2017 for studies evaluating EVT for acute stroke in the elderly. Two independent reviewers selected studies and abstracted data. The primary endpoint was good functional outcome at 3 months defined as modified Rankin Scale ≤ 2 . Data were analyzed using random-effects meta-analysis.

Results

Seventeen studies reporting on 860 patients were included. The rate of good functional outcome at 3 months was 27% (95% CI=21%-32%). Mortality at 3 months was 34% (95% CI=23%-44%). Successful recanalization was achieved in 78% of patients (95% CI=72%-85%). Procedure related complications occurred in 11% (95% CI=4%-17%). The incidence of intracranial hemorrhage was 24% (95% CI=15%-32%) and for symptomatic intracranial hemorrhage it was 8% (95% CI=5%-10%). Mean time to groin was 251 minutes (95% CI=211-239). Procedure time was 99 minutes (95% CI=55-135mins).

Conclusions

Good functional recovery in octogenarians treated with EVT for acute stroke is inferior to that reported for younger patients despite comparable rates of recanalization and symptom to revascularization times. However, at least one in four older patients treated with EVT for acute stroke had a good functional outcome.

O-05

10:58AM - 11:05AM

Drip-and-Ship vs. Mothership: Conditional Probability Modelling for Patients with Suspected Large Vessel Occlusion

J Holodinsky¹, T Williamson¹, A Demchuk¹, H Zhao², L Zhu¹, F Malik¹, M GOYAL³, M HILL³, N Kamal¹

¹*University of Calgary, Calgary, Alberta, Canada*, ²*Royal Melbourne Hospital, Parkville, Victoria, Australia*, ³*Foothills Medical Centre, Calgary, Alberta, Canada*

Purpose

For patients with suspected large vessel occlusion (LVO) stroke should we bypass alteplase treatment at primary stroke centres (PSC) in favor of endovascular therapy (EVT) at comprehensive stroke centres (CSC) (mothership) or transport the patient to the PSC for alteplase and then transfer to the CSC for EVT (drip-and-ship)? This is complicated by the inability to definitively diagnose LVO stroke without imaging.

Materials and Methods

The efficacy decay of alteplase and EVT over time [derived from clinical trials (1, 2)] and the accuracy of the Los Angeles Motor Scale (LAMS) LVO screening tool were combined with various treatment times to predict the probability of good outcome (mRS 0 – 1 at 90 days) for both drip-and-ship and mothership transport strategies for patients with LAMS ≥ 4 . Models were generated for two efficiency scenarios (A:

efficient PSC and CSCs and B: inefficient PSCs, efficient CSCs) and two different transport times between PSC and CSCs (60 and 120 minutes).

Results

The results are shown in the Figure. If the patient is closest to the CSC mothership is always superior. If treatment is efficient at both centres drip-and-ship is superior if the centres are far apart and the patient must travel past a PSC to get to a CSC, when the centres are closer together the strategies are near equivalent (Panel A). Slow treatment at the PSC increases the area where mothership is superior and eliminates the area where drip-and-ship is clearly superior unless the time from onset to alteplase administration exceeds 4.5 hours in the mothership scenario (Panel B).

Conclusions

Due to the uncertainty in patient diagnosis both transport options are nearly equivalent in most scenarios. A triaging tool with greater positive predictive value would increase the size of the mothership areas. However, even with diagnosis uncertainty the importance of fast treatment times is illustrated.

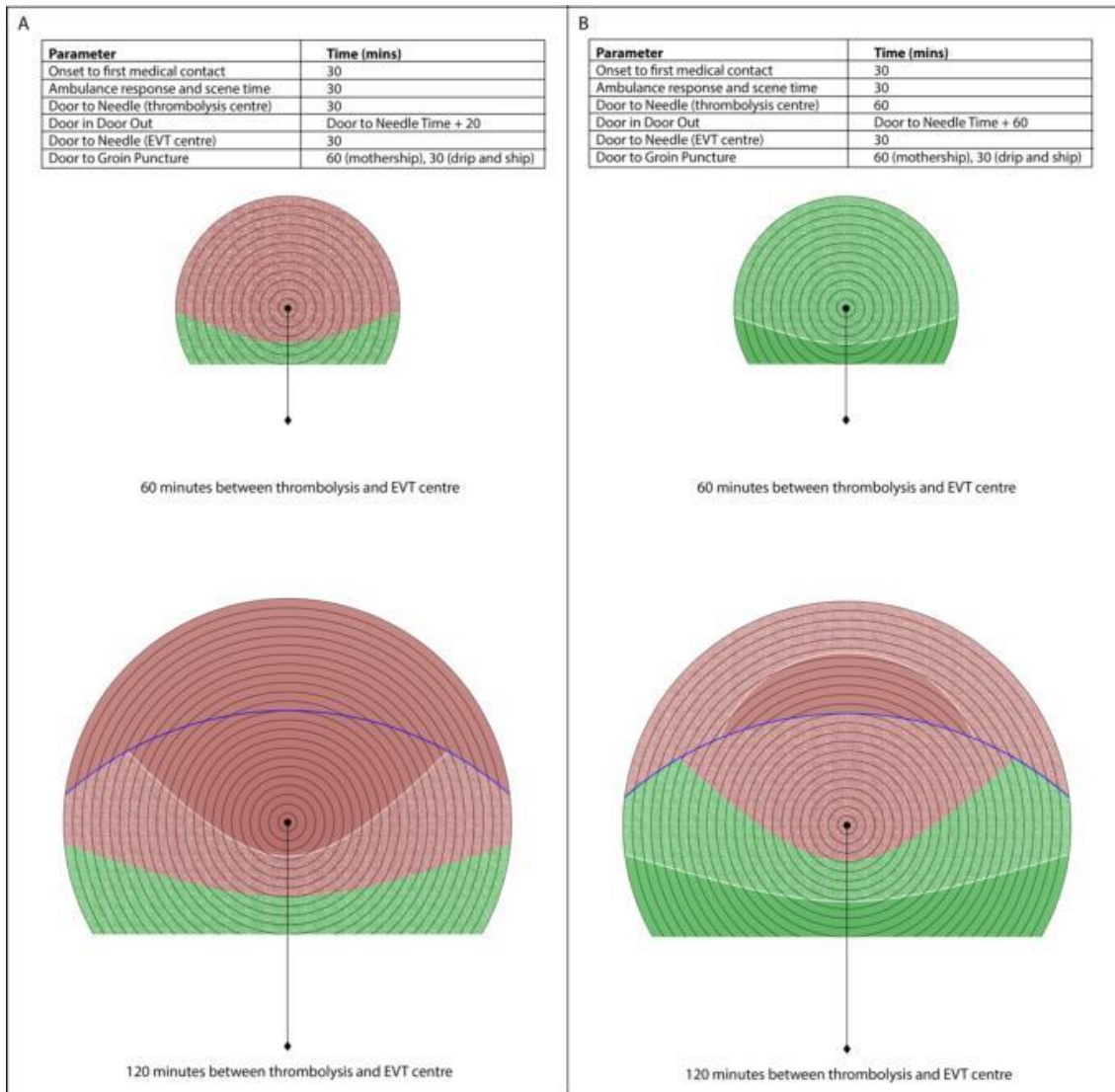
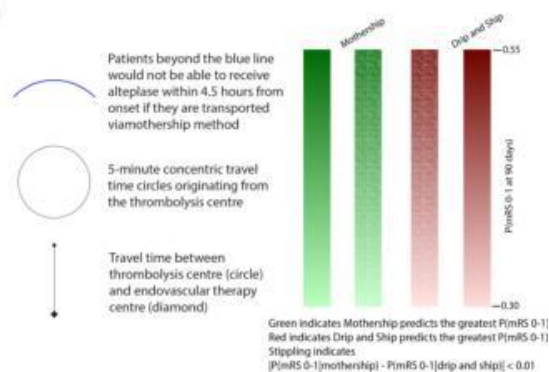


Figure. Two dimensional temporal spatial diagrams depicting transport decision making for patients with suspected ischemic stroke with large vessel occlusion, defined as Los Angeles Motor Scale Score ≥ 4 , in two different efficiency scenarios. The diagrams depict a single thrombolysis center in the middle of the figure, depicted with a circle, and an endovascular therapy center, depicted by a diamond, at two different travel times (60 and 120 minutes) below it. There are 5 minute concentric travel time circles radiating from the thrombolysis center. Red indicates areas where drip and ship predicts the greatest probability of excellent outcome and green indicates areas where mothership predicts the greatest probability of excellent outcome. White stippling indicates areas where the optimal transport method supersedes the other by 1% or less. Area where the patient is closest to the endovascular therapy center is not shown as the mothership option is always best in this scenario. The degree of color saturation reflects the value of the probability of excellent outcome. The blue line represents the point where the onset to needle time in the mothership scenario is > 270 minutes.



(Filename: TCT_O-05_ASNR_Abstract1_figure.jpg)

O-06

11:05AM - 11:12AM

Drip-and-Ship vs. Mothership: A Comparison of Two Different Conditional Probability Models

J Holodinsky¹, T Williamson¹, A Demchuk¹, H Zhao², M Francis¹, M Goyal³, M Hill³, N Kamal¹
¹University of Calgary, Calgary, Alberta, Canada, ²Royal Melbourne Hospital, Parkville, Victoria, Australia, ³Foothills Medical Centre, Calgary, Alberta, Canada

Purpose

There is uncertainty about the best treatment method for patients with suspected large vessel occlusion (LVO) stroke. The drip-and-ship [alteplase at a primary stroke centre (PSC) and then transfer to a comprehensive stroke centre (CSC) for endovascular therapy (EVT)] and mothership (bypassing the PSC in pursuit of EVT at a CSC) transport methods have been proposed. Earlier, these two methods were evaluated for patients with assumed known LVO (1, 2). However, as LVO cannot be definitively diagnosed in the field (without imaging) we present an update for patients with suspected LVO using the Los Angeles Motor Scale (LAMS) screening tool.

Materials and Methods

Conditional probability models were created using the expected distribution of LVO, non-LVO occlusions (nLVO), intracranial hemorrhages (ICH), and stroke mimics (SM) for patients with LAMS \geq 4 and time dependent probability of good outcome for alteplase (for LVO and nLVO) and EVT (3, 4), and probability of good outcome for ICH and SM to create conditional probability models for drip-and-ship and mothership scenarios. Results were mapped in the state of California, USA and compared with the previous model.

Results

For patients with LAMS \geq 4 drip-and-ship and mothership predict nearly equivalent outcomes in many areas (Figure – Panel A-1). Drip-and-ship is most relevant at PSCs that are far from CSCs. Increasing door-to-needle time (DNT) decreases the size of drip-and-ship areas (Figure – Panel B-1). This contrasts with the prior model, which assumes known LVO, (Figure – Panel A-2) where mothership is more dominant especially as DNT increases (Figure – Panel B-2). The absolute probability of good outcome is higher in the previous model due to the assumptions made in the prior model (high TICI 2b-3 rate and fast door to reperfusion times) (1, 2). This is diluted in the updated model due to diagnostic uncertainty and emphasis on onset to treatment rather than reperfusion times.

Conclusions

Modelling patients with suspected LVO as compared to confirmed LVO introduces important differences in modelling patient transport. This uncertainty in diagnosis decreases the relative difference between the probabilities of good outcome for the two transport options.

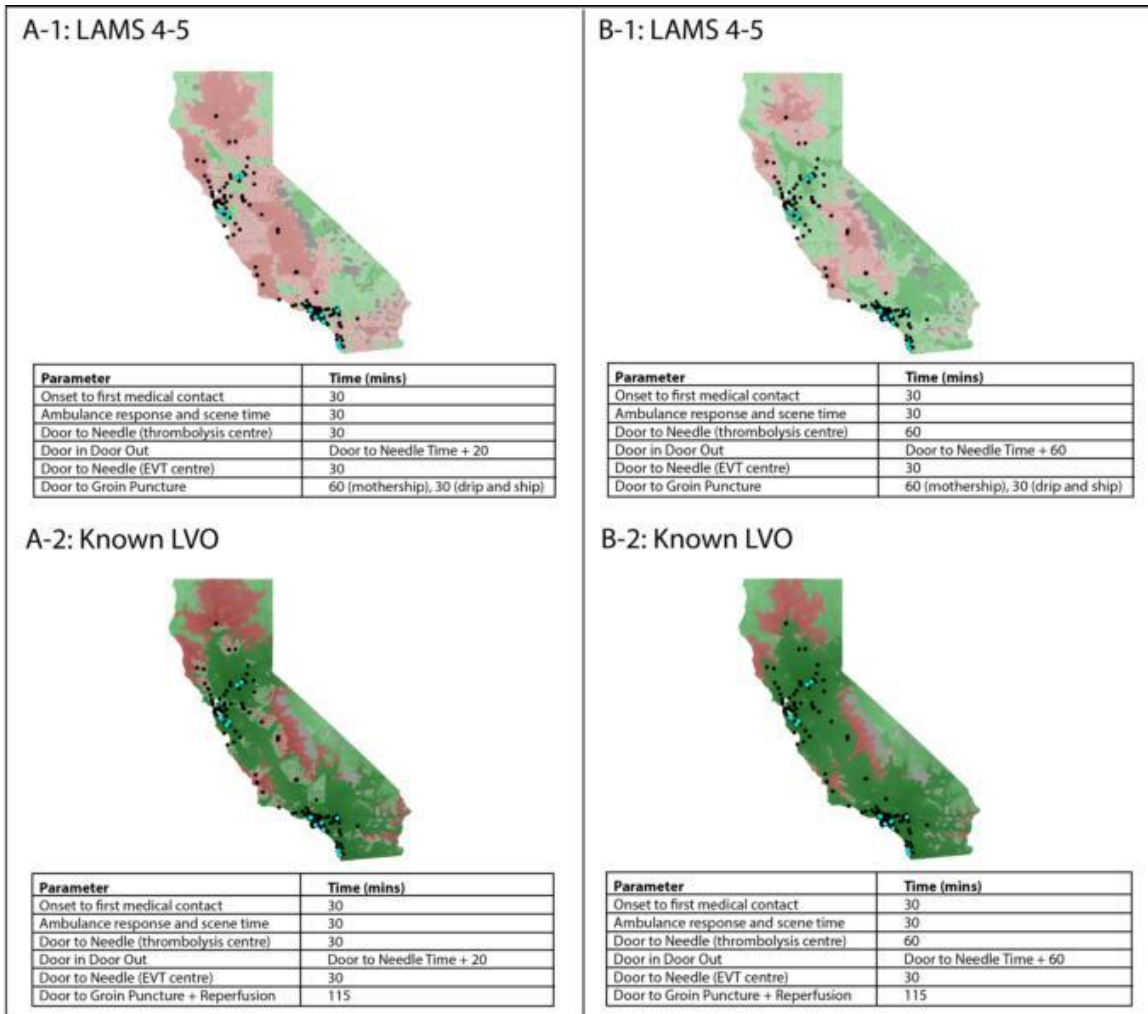
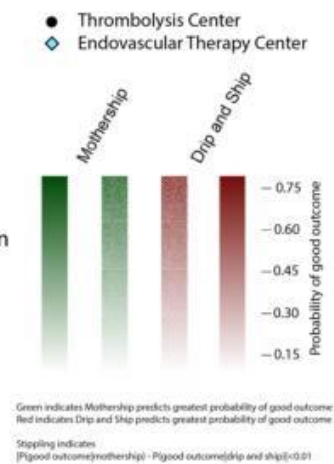


Figure. Maps depicting the probability of good outcome and best predicted transport strategy for patients with suspected ischemic stroke with large vessel occlusion, defined as Los Angeles Motor Scale Score ≥ 4 (A-1 and B-1), and patients with known large vessel occlusion (A-2 and B-2) in the state of California, USA. In the maps thrombolysis centers are depicted by black dots and endovascular therapy centers are depicted by blue diamonds. Panel A displays a system with optimized treatment times. Panel B displays a system with fast treatment at endovascular therapy centers but slow treatment at thrombolysis centers. Red indicates areas where drip-and-ship predicts the greatest probability of excellent outcome and green indicates areas where mothership predicts the greatest probability of excellent outcome. White stippling indicates areas where the optimal transport method supersedes the other by 1% or less. The degree of color saturation reflects the value of the probability of excellent outcome. Grey areas indicate a lack of road infrastructure data thus transport times and therefore optimal transport method could not be determined.



(Filename: TCT_O-06_ASNR_Abstract2_figure.jpg)

O-07

11:12AM - 11:19AM

Drip-and-Ship vs. Mothership: The Effect of Large Vessel Occlusion Screening Tools on Conditional Probability Modelling

J Holodinsky¹, T Williamson¹, A Demchuk¹, H Zhao², L Zhu¹, F Malik¹, M Goyal³, M ill³, N Kamal¹
¹University of Calgary, Calgary, Alberta, Canada, ²Royal Melbourne Hospital, Parkville, Victoria, Australia, ³Foothills Medical Centre, Calgary, Alberta, Canada

Purpose

Ischemic stroke with large vessel occlusion (LVO) cannot be definitively diagnosed without imaging. Clinical screening tools to help identify LVO in the field have variable positive predictive value (PPV). The accuracy and PPV of a clinical screen tool for LVO impacts transport decisions.

Materials and Methods

Using conditional probability modelling, we estimated the effect of screening tool diagnostic properties for LVO. The PPV of various screening tools [generated from a prospective study of suspected stroke patients (1)], were combined with the efficacy decay of alteplase and EVT over time (2, 3) to predict the probability of good outcome (mRS 0 – 1 at 90 days) for the drip-and-ship [alteplase at a primary stroke centre (PSC) and then transfer to a comprehensive stroke centre (CSC) for endovascular therapy (EVT)] and mothership (bypassing the PSC in pursuit of EVT at a CSC) transport strategies.

Results

The results are shown in the Figure. As the PPV of the tool increases, the areas where mothership predicts the best outcome increases. At longer treatment times at the PSC the drip-and-ship area also decreases as PPV increases. The absolute probability of good outcome also decreases as PPV increases because more LVO strokes, with inherently poorer outcomes than most false positives, are identified.

Conclusions

The PPV of the screening tool impacts transport decision-making. Due to the efficacy of efficacy of EVT for LVO stroke as PPV increases so does the area where mothership predicts the greatest probability of good outcome.

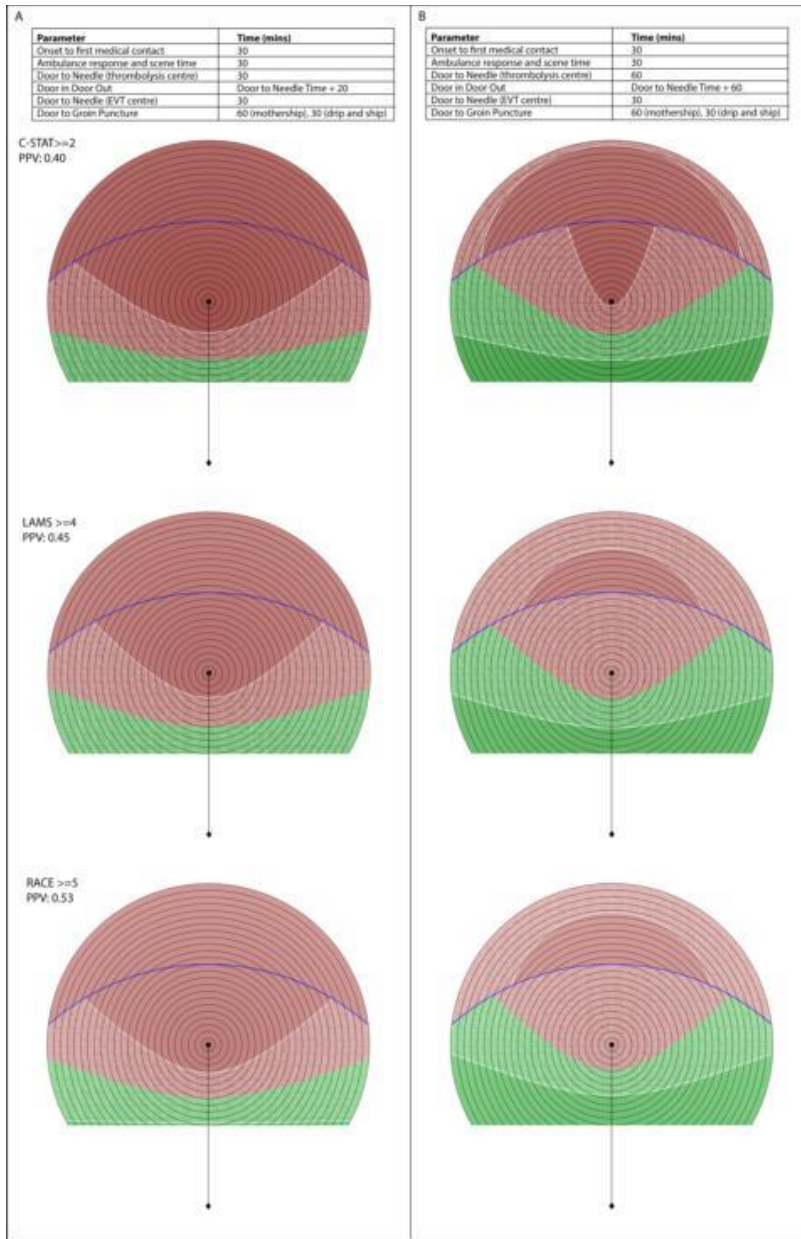
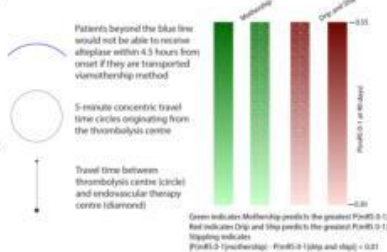


Figure. Two dimensional temporal spatial diagrams depicting transport decision making for patients with suspected ischemic stroke using various large vessel occlusion screening tools in two different efficiency scenarios. The diagrams depict a single thrombolysis center in the middle of the figure, depicted with a circle, and an endovascular therapy center, depicted by a diamond, 120 minutes below it. There are 5 minute concentric travel time circles radiating from the thrombolysis center. Red indicates areas where drip and ship predicts the greatest probability of excellent outcome and green indicates areas where mothership predicts the greatest probability of excellent outcome. White stippling indicates areas where the optimal transport method supersedes the other by 1% or less. Area where the patient is closest to the endovascular therapy center is not shown as the mothership option is always best in this scenario. The degree of color saturation reflects the value of the probability of excellent outcome. The blue line represents the point where the onset to needle time in the mothership scenario is > 270 minutes.



(Filename: TCT_O-07_ASNR_Abstract3_figure.jpg)

O-08

11:19AM - 11:26AM

Drip and Ship versus Direct Transfer to Comprehensive Stroke Center: A Modelling Based Analysis

Oral Presentations & Excerpts

X Wu¹, B Geng¹, K Seifert², V Kalra³, D Gandhi⁴, P Sanelli⁵, A Malhotra²

¹*Yale University School of Medicine, New Haven, CT*, ²*Yale New Haven Hospital, New Haven, CT*, ³*Orlando Health, Tampa, FL*, ⁴*University of Maryland School of Medicine, Baltimore, MD*, ⁵*Northwell Health, Manhasset, NY*

Purpose

The success of thrombectomy trials for acute ischemic stroke create 2 options for prehospital decision-making: (1) transport the patient to the nearest endovascular capable center (ECC) even though this may mean bypassing a closer non-ECC (mothership model), or (2) transport to nECC for intravenous thrombolysis and then transfer the patient to the nearest ECC for endovascular therapy (drip-and-ship model).

Materials and Methods

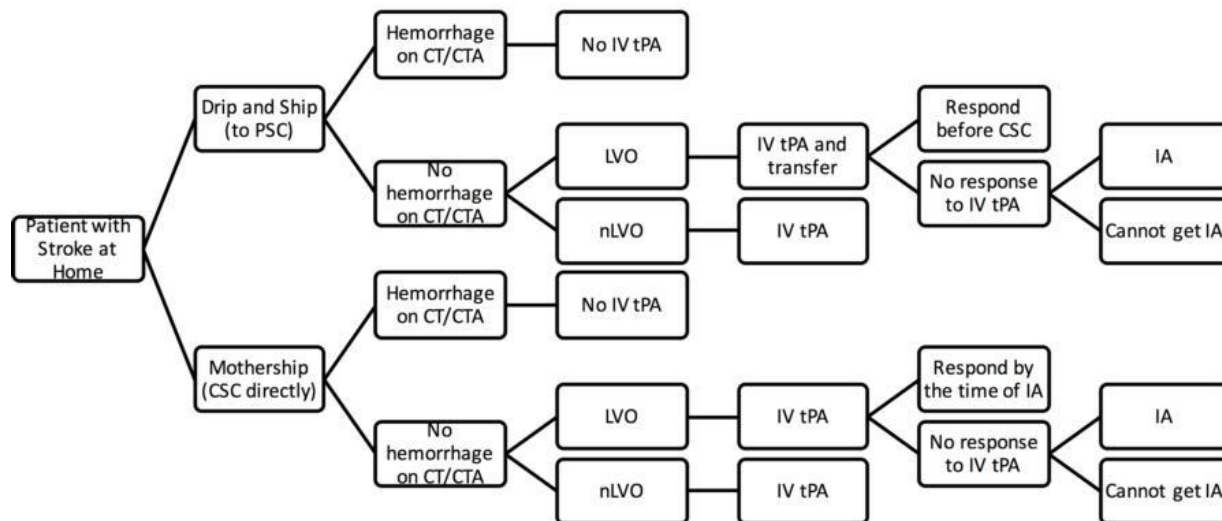
A decision-analytical modelling study was constructed to simulate a 50-year-old man with acute stroke being evaluated by EMS, with the closest healthcare facility being a nECC. Input probabilities were derived from recent literature with thrombectomy data and outcomes from the highly effective.

Results

In the base case calculation using HERMES data, we found Mothership to be the better strategy. We performed extensive two-way sensitivity analyses varying the additional time it would take to ECC and the transfer time between nECC to ECC at different settings. The results show when time to nECC is 30 min, Mothership is the better strategy until the time to ECC exceeds 93 min, or when it takes less than 126 min to transfer patients from nECC to ECC. As the time to nECC increases, the thresholds on additional time to ECC and transfer time lowers. When the time to nECC is 90 min, drip-and-ship becomes the better strategy regardless of the additional time to ECC and the transfer time.

Conclusions

We have used decision-analysis, modelling-based technique to address the problem of acute stroke triage from a population-based perspective. By feeding in the time to the nearest ECC and nECC, the EMS and stroke team can make the most appropriate decision on where to transfer the patient for the best outcomes based on the currently available data.



(Filename: TCT_O-08_ASNRgraph.jpg)

O-09

11:26AM - 11:33AM

House Calls: New Generation Mobile Stroke Unit Brings CT into the Field Reducing Time to Diagnosis

E Nyberg¹, J Cox¹, R Kowalski¹, D Vela Duarte¹, B Schimpf¹, W Jones¹

¹University of Colorado, Aurora, CO

Purpose

Each 30-minute delay in thrombolytic therapy may result in a 20% decrease in treatment effect and likelihood of a positive outcome in patients with acute ischemic stroke (1). Our Mobile Stroke Unit (MSU) is a new-generation ambulance with on-board CT and teleneurology capability which can facilitate diagnosis and tPA delivery in the field. This study demonstrates the impact of the MSU on imaging expediency, including time from EMS dispatch to image acquisition and from dispatch to radiologist report.

Materials and Methods

IRB approval was obtained. We reviewed our prospectively maintained stroke alert database at our comprehensive stroke center for stroke patients presenting during 2016 via the MSU and controls imaged through the conventional in-hospital pathway. Controls were matched for prehospital status, geographic region and time of day. We collected the EMS dispatch time, imaging time (time images available in PACS), and report time (time of verbal report to the stroke neurologist). Group comparisons of time

intervals between MSU patients and controls were compared using student's t-tests. Benchmark metrics were compared using Fisher's exact tests.

Results

There were 97 patients included, including 47 MSU patients and 50 controls. Mean dispatch to imaging times were 21 vs. 44 minutes in MSU and control groups, respectively ($p < 0.001$) (Table 1). Mean dispatch to report times were 34 vs. 54 minutes in MSU and control groups, respectively ($p < 0.001$) (Table 2). The MSU pathway was significantly more likely to get images to PACS within 30 minutes and to provide a report within 60 minutes compared with controls ($p < 0.001$) (Figures 1 and 2).

Conclusions

The MSU reduces times from dispatch to image acquisition and communication of findings to the stroke neurologist. MSU reduced time to report by 22 minutes and was significantly more likely to provide a report within the 'golden hour' since EMS dispatch. This has the potential to substantially impact the delivery and effectiveness of thrombolytic treatment.

O-10

11:33AM - 11:40AM

Modelling the Impact of Multiple Mobile Stroke Unit Surrounding a Metropolitan Area

J Holodinsky¹, N Kamal¹, C Zerna¹, L Zhu¹, M Hill², M Goyal³

¹University of Calgary, Calgary, Alberta, Canada, ²Foothills Medical Centre, Calgary, Alberta, Canada

Purpose

The mobile stroke unit (MSU) has brought stroke imaging and alteplase administration to the field, shortening onset to needle time for acute ischemic stroke patients in some situations. In areas with widespread urban sprawl, having multiple MSUs stationed in the community may improve patient outcomes. For patients with suspected large vessel occlusion (LVO) using the Los Angeles Motor Scale (LAMS) we compare the probability of good outcome for patients taken direct to comprehensive stroke centre (CSC) (mothership) vs. utilizing multiple MSUs surrounding the CSC.

Materials and Methods

The efficacy decay of alteplase and EVT over time [derived from clinical trials (1, 2)] was combined with the accuracy of the Los Angeles Motor Scale (LAMS) LVO screening tool in a conditional probability model to predict the probability of good outcome (mRS 0 – 1 at 90 days) for both mothership and MSU transport strategy. Three scenarios were generated where four MSUs are placed at 30, 60, and 120 minutes away from the CSC respectively.

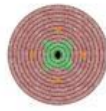
Results

The results are visualized using temporal-spatial diagrams with one CSC and four MSUs stationed at various distances from the CSC with each MSU covering one quarter of the city. In a small geographic area (MSUs placed 30 minutes away from the CSC) both the MSU and mothership approach predict nearly equivalent outcomes. However, as the MSUs are placed further from the CSC the MSU predicts the best patient outcomes in the geographic area close to where the MSU is stationed, especially in areas where the door-to-needle time would exceed 270 minutes if mothership transport was used.

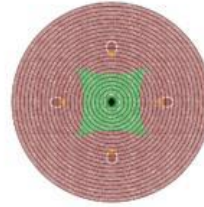
Conclusions

From a patient-outcomes perspective, multiple MSUs stationed far away from the CSC may improve patient outcomes over a strict mothership approach. This in addition to the individual environment and cost-effectiveness should be taken into context when deciding the best place to house future MSUs.

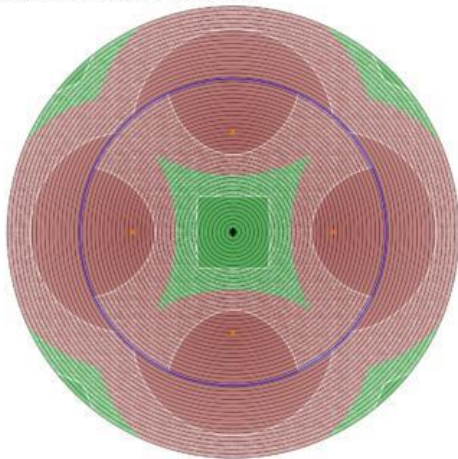
Scenario A.
60 minute radius from Comprehensive Stroke Centre
4 Mobile Stroke Units housed 30 minutes away from the Comprehensive Stroke Centre
Each Mobile Stroke Unit covers one quarter of the city



Scenario B.
120 minute radius from Comprehensive Stroke Centre
4 Mobile Stroke Units housed 60 minutes away from the Comprehensive Stroke Centre
Each Mobile Stroke Unit covers one quarter of the city



Scenario C.
270 minute radius from Comprehensive Stroke Centre
4 Mobile Stroke Units housed 120 minutes away from the Comprehensive Stroke Centre
Each Mobile Stroke Unit covers one quarter of the city



Parameter	Time (mins)
Onset to first medical contact	30
Ambulance response time	7
Ambulance scene time	20
Mobile Stroke Unit scene time	30
Door to Needle (Mobile Stroke Unit)	20
Door in Door Out (Mobile Stroke Unit)	Door to Needle Time + 15
Door to Needle (EVT centre)	30
Door to Groin Puncture	60 (mothership), 30 (transfer from MSU)

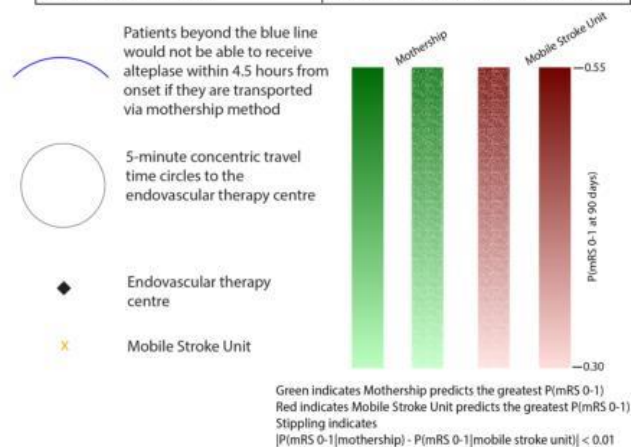


Figure. Two dimensional temporal-spatial diagrams depicting optimal transport and treatment decisions for patients with Los Angeles Motor Scale Score ≥ 4 . The diagrams depict a single comprehensive stroke centre (black diamond) in the middle of the figure with mobile stroke units (orange x) placed at varying distances from it. The concentric circles radiating from the comprehensive stroke centre represent 5 minute travel times to the comprehensive stroke centre. Red indicates the mobile stroke unit has the best predicted probability of good outcome, green indicates the mothership model has the best predicted probability of good outcome, and the white stippling indicates the two options are near equivalent (± 0.01). The degree of saturation indicates the value of the probability of good outcome. The blue line represents the point where onset to needle time in the mothership scenario is > 270 minutes.

(Filename: TCT_O-10_ASNR_MSU_abstract2_figure.jpg)

O-11

11:40AM - 11:47AM

When does having a Mobile Stroke Unit make sense in a metropolitan area from a patient outcome perspective?

J Holodinsky¹, N Kamal¹, C Zerna¹, L Zhu¹, M Hill², M Goyal²

¹University of Calgary, Calgary, Alberta, Canada, ²Foothills Medical Centre, Calgary, Alberta, Canada

Purpose

The mobile stroke unit (MSU) has brought stroke imaging and alteplase administration to the field, and as

Oral Presentations & Excerptas

such the possibility to shorten onset to needle time for acute ischemic stroke patients. However, onset to groin puncture times may be lengthened due to additional travel time incurred by the MSU for patients needing endovascular therapy (EVT). We compare the probability of good outcome for patients taken direct to comprehensive stroke centre (CSC) (mothership) and patients utilizing the MSU for patients with suspected large vessel occlusion (LVO) using the Los Angeles Motor Scale (LAMS).

Materials and Methods

Using conditional-probability modelling the efficacy decay of alteplase and EVT over time [derived from clinical trials (1, 2)] was combined with the accuracy of the Los Angeles Motor Scale (LAMS) LVO screening tool to predict the probability of good outcome (mRS 0 – 1 at 90 days) for both mothership and MSU transport strategy. Two treatment time scenarios are considered: one where door to groin puncture time at the CSC is shortened for patients transferred from the MSU (A) and one where door to groin puncture time is unaffected (B).

Results

The results are visualized in a small metropolitan area with one CSC and one MSU which is housed at the CSC. In this scenario both transport options predict near equivalent outcomes. In Scenario A if the MSU can reach the patient in <10 minutes the MSU predicts the greatest probability of good outcome; however, this probability is still nearly equivalent to that predicted by the mothership scenario. If the MSU does not lead to time savings when the patient arrives at the CSC this area disappears.

Conclusions

From a patient-outcomes perspective in a system where a single MSU is housed at a single CSC there are no areas where the MSU shows clear benefit over the mothership approach. As near equivalent outcomes are predicted individual environment and cost-effectiveness should be taken into context when deciding the best transport strategy.

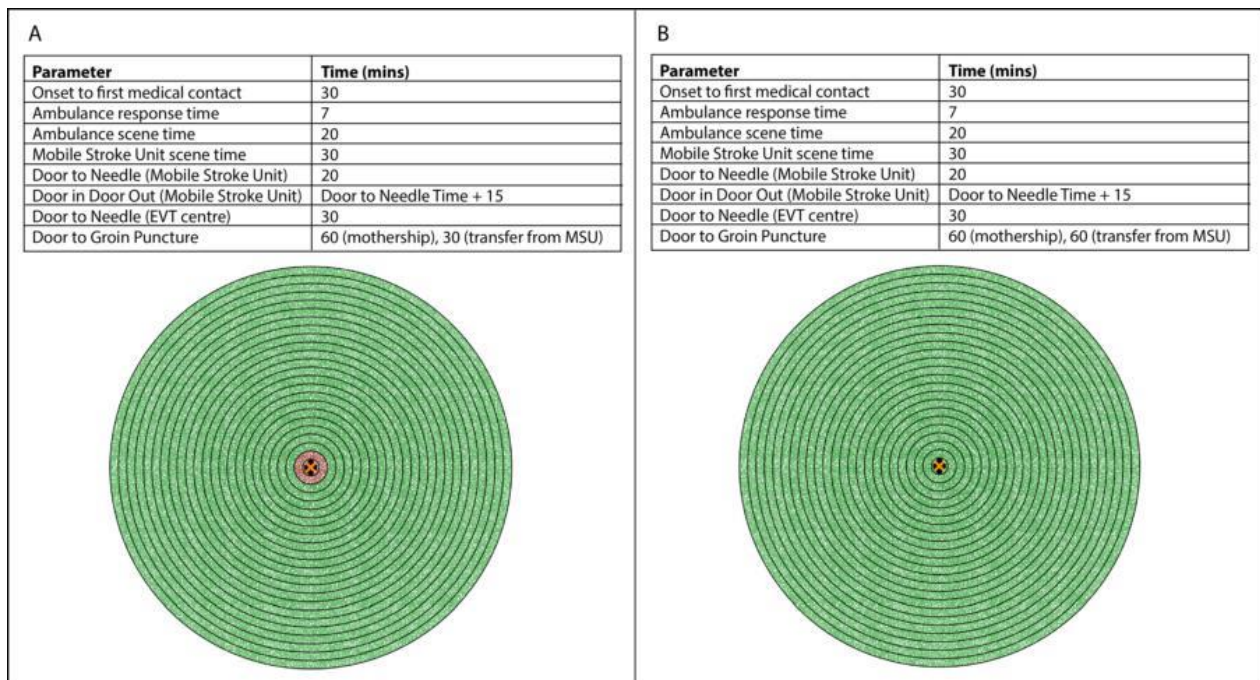
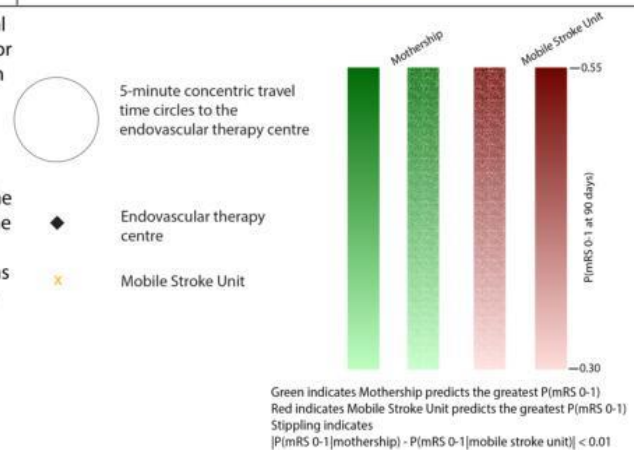


Figure. Two dimensional temporal-spatial diagrams depicting optimal transport and treatment decisions for patients with Los Angeles Motor Scale Score ≥ 4 . Two scenarios are depicted, one where door to groin puncture time at the comprehensive stroke centre is shorter for transferred patients (Panel A) and one where door to groin puncture time is unaffected by patient transfer status (Panel B). The diagrams depict a single comprehensive stroke centre (black diamond) in the middle of the figure with a mobile stroke unit (orange x) housed at the comprehensive stroke centre. The concentric circles radiating from the comprehensive stroke centre represent 5 minute travel times to the comprehensive stroke centre. Red indicates the mobile stroke unit has the best predicted probability of good outcome, green indicates the mothership model has the best predicted probability of good outcome, and the white stippling indicates the two options are near equivalent (± 0.01). The degree of saturation indicates the value of the probability of good outcome.



(Filename: TCT_O-11_ASNR_MSU_abstract1_figure.jpg)

O-12

11:47AM - 11:54AM

Modelling the Impact of Mobile Stroke Unit Dispatcher Accuracy on Patient Outcomes

J Holodinsky¹, N Kamal¹, C Zerna¹, L Zhu¹, M Hill², M Goyal²

¹University of Calgary, Calgary, Alberta, Canada, ²Foothills Medical Center, Calgary, Alberta, Canada

Purpose

Ischemic stroke with large vessel occlusion (LVO) cannot be definitively diagnosed without imaging. The Mobile Stroke Unit (MSU) has brought this capability (along with alteplase administration) to the field. In areas with widespread urban sprawl, having MSUs stationed in the community may improve patient outcomes. However, this is also dependent on how accurately dispatch can assess suspected stroke with LVO over the phone. We compare the probability of good outcome for patients taken directly to comprehensive stroke centre (CSC) (mothership) vs. utilizing a MSU at varying levels of dispatcher accuracy in identifying ischemic stroke with suspected LVO.

Oral Presentations & Excerptas

Materials and Methods

Conditional probability models for patients with suspected stroke with LVO for the mothership and MSU scenarios were generated. The positive predictive value (PPV) of dispatcher screening was varied from 25% to 75%. The efficacy decay of alteplase and EVT over time [derived from clinical trials (1, 2)] were combined in a conditional probability model to predict the probability of good outcome (mRS 0 – 1 at 90 days) for both mothership and MSU transport strategy.

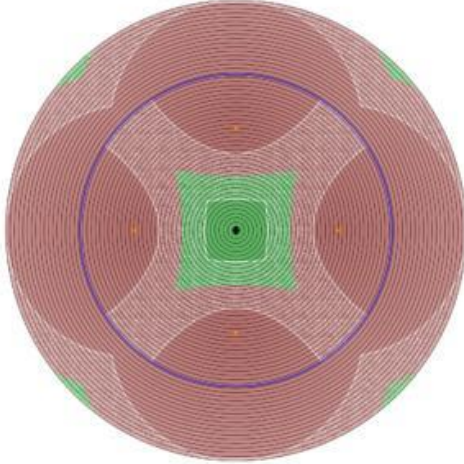
Results

The results are visualized using temporal-spatial diagrams with one CSC and four MSUs stationed around the CSC with each MSU covering one quarter of the city. If dispatcher accuracy is poor more non-LVO strokes will be picked up and the area where the MSU predicts best outcomes is large as these patients will benefit from fast alteplase. However, as the accuracy of the dispatcher in identifying stroke with LVO increases the areas where the MSU predicts the best patient outcomes decreases as the MSU would impose delays for patients with LVO in receiving EVT.

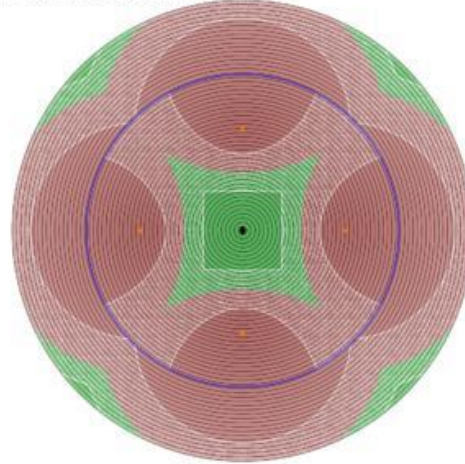
Conclusions

The ability to accurately dispatch the MSU to patients with suspected LVO impacts transport decision-making and the radius where using a MSU predicts best patient outcomes over a strict mothership approach. This should be considered when designing a stroke system containing a MSU.

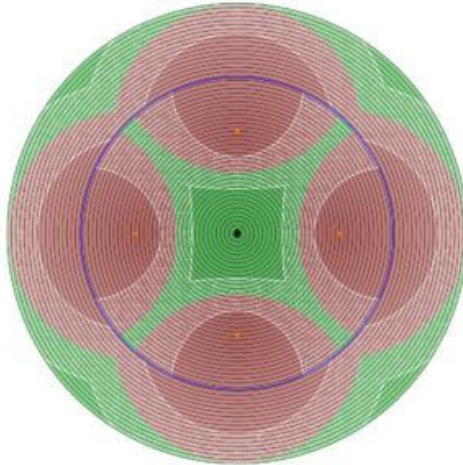
Scenario A.
 Dispatcher PPV: 0.25
 4 Mobile Stroke Units housed 120 minutes away from the Comprehensive Stroke Centre
 Each Mobile Stroke Unit covers one quarter of the city



Scenario B.
 Dispatcher PPV: 0.50
 4 Mobile Stroke Units housed 120 minutes away from the Comprehensive Stroke Centre
 Each Mobile Stroke Unit covers one quarter of the city



Scenario C.
 Dispatcher PPV: 0.75
 4 Mobile Stroke Units housed 120 minutes away from the Comprehensive Stroke Centre
 Each Mobile Stroke Unit covers one quarter of the city



Parameter	Time (mins)
Onset to first medical contact	30
Ambulance response time	7
Ambulance scene time	20
Mobile Stroke Unit scene time	30
Door to Needle (Mobile Stroke Unit)	20
Door in Door Out (Mobile Stroke Unit)	Door to Needle Time + 15
Door to Needle (EVT centre)	30
Door to Groin Puncture	60 (mothership), 30 (transfer from MSU)

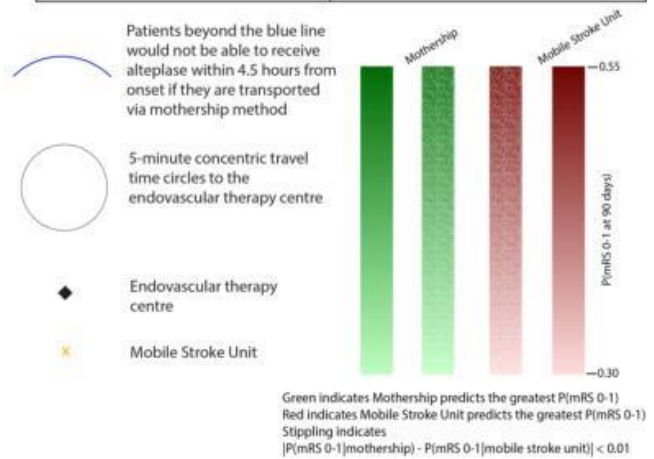


Figure. Two dimensional temporal-spatial diagrams depicting optimal transport and treatment decisions for patients using varying dispatcher accuracy in identifying ischemic stroke with large vessel occlusion. The diagrams depict a single comprehensive stroke centre (black diamond) in the middle of the figure with mobile stroke units (orange x) placed 120 minutes travel time from it. The concentric circles radiating from the comprehensive stroke centre represent 5 minute travel times to the comprehensive stroke centre. Red indicates the mobile stroke unit has the best predicted probability of good outcome, green indicates the the mothership model has the best predicted probability of good outcome, and white stippling indicates the two options are near equivalent (± 0.01). The degree of saturation indicates the value of the probability of good outcome. The blue line represents the point where onset to needle time in the mothership scenario is > 270 minutes.

(Filename: TCT_O-12_ASNR_MSU_abstract3_figure.jpg)

Monday, June 4, 2018
 10:30AM - 12:00PM

Parallel Paper Session: Advanced Techniques in Brain Tumor Imaging I

Revised nomogram combining advanced MR imaging radiomics, clinical parameters, and genomics in patients with newly diagnosed glioblastoma: improved prognostication over established clinical model

J Park¹, H Kim¹, Y Heo², J Kim¹, S Kim¹

¹*University of Ulsan College of Medicine, Asan Medical Center, Seoul, Republic of Korea*, ²*Busan Paik Hospital, Inje University, Busan, Republic of Korea*

Purpose

To develop and validate a nomogram combining clinical parameters, genomics, and advanced magnetic resonance (MR) imaging radiomics for individualized prognostication in patients with newly diagnosed glioblastoma

Materials and Methods

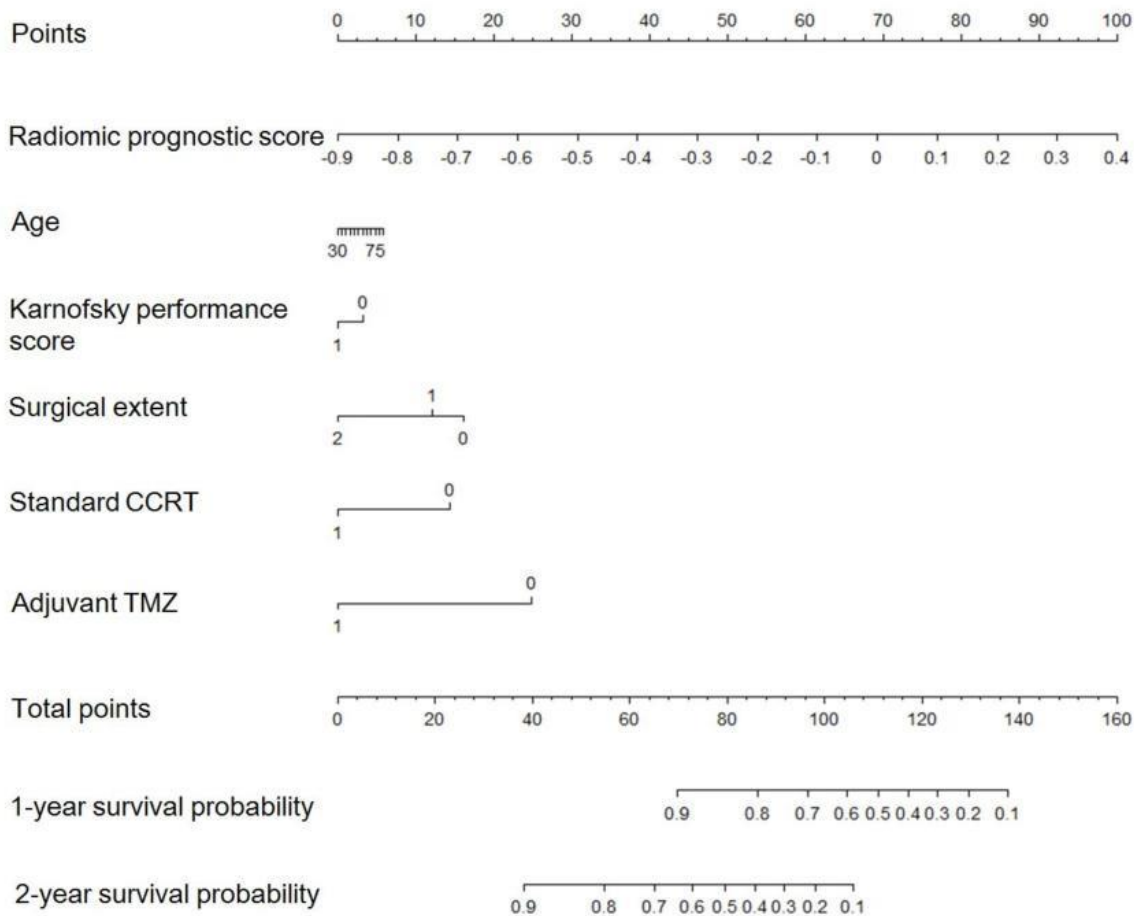
The prognostication model was developed in 158 patients with newly diagnosed glioblastoma from March 2012 to November 2016. A total of 6472 radiomic features were extracted from contrast-enhanced T1-weighted imaging, fluid-attenuated inversion recovery, diffusion-weighted imaging, and dynamic susceptibility contrast imaging. After radiomic feature selection using LASSO regression, individualized radiomic score was calculated. The nomogram was built incorporating radiomic score, O6-methylguanine-DNA-methyltransferase (MGMT) gene methylation status, and clinical predictors. The model performance was assessed using the C-index and integrated Brier score (IBS) and calibrated. The model was externally validated in 58 patients with different imaging scheme.

Results

A radiomic score with 6 selected multiparametric MR features significantly discriminated overall survival in the training (C-index, 0.691; IBS, 0.169) and the validation set (C-index, 0.617; IBS, 0.196). The nomogram was significantly better at predicting OS compared to the radiomic score ($P = .002$), or baseline clinical predictors and MGMT ($P = .035$). The nomogram showed good discrimination in both training (C-index, 0.78; IBS, 0.149) and validation (C-index, 0.68; IBS, 0.158) sets with good calibration.

Conclusions

This revised glioblastoma nomogram including advanced MR imaging radiomics may potentially improve individualized prognostication compared to established clinical models.



(Filename: TCT_O-13_Fig4B.JPG)

O-14

10:37AM - 10:44AM

Hypermutated gliomas exhibit a unique MRI-based radiomic-texture phenotype

I Hassan¹, A Kotrotsou², C Kamiya Matsuoka³, K Alfaro-Munoz³, N Elshafeey⁴, N El Shafei⁵, P Zinn⁶, J de Groot⁷, R Colen²

¹The University of Texas - MD Anderson Cancer Center, Houston, TX, ²MD Anderson Cancer Center, Houston, TX, ³Md Anderson cancer center, HOUSTON, TX, ⁴MD Anderson cancer center, HOUSTON, TX, ⁵National Research Centre, Giza, Giza, ⁶Baylor College of Medicine, Houston, TX, ⁷Md Anderson Cancer Center, HOUSTON, TX

Purpose

Hypermutation is the extensive increase in DNA mutations in cancer cells; it has been reported in various types of cancers including low- and high-grade gliomas [1]. Incidence of hypermutation in gliomas is more frequently seen at time of recurrence following exposure to alkylating chemotherapy such as temozolomide [2]. Hypermutation occurs mainly because of a disruption of DNA repair machinery, due to mutations in the mismatch repair genes (MMR), as well as disruption of DNA fidelity, due to mutation of DNA polymerase genes (POLE and POLD) [3]. Hypermutated tumors are usually associated with

better response to immune checkpoint inhibitors, and recently, multiple endeavors are directed towards testing immune checkpoint inhibitors in hypermutated gliomas [4]. Herein, we sought to identify a predictive imaging-based signature for hypermutated gliomas using a radiomics-based approach.

Materials and Methods

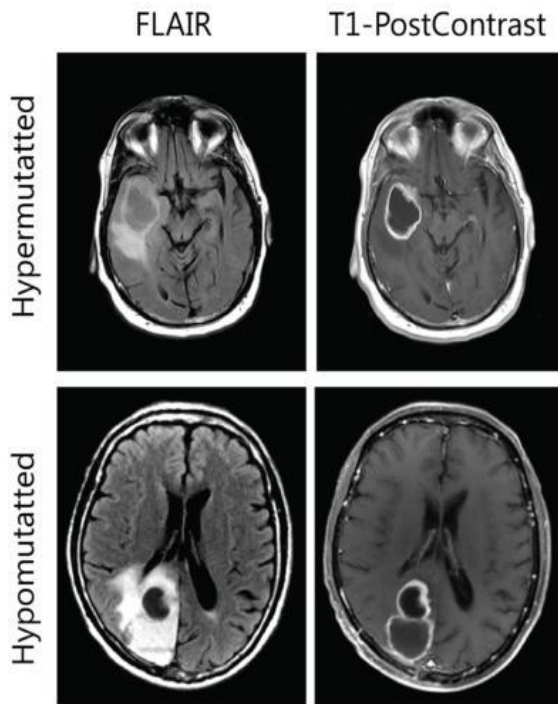
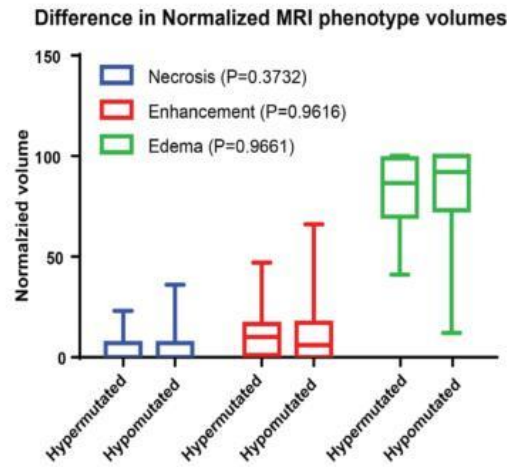
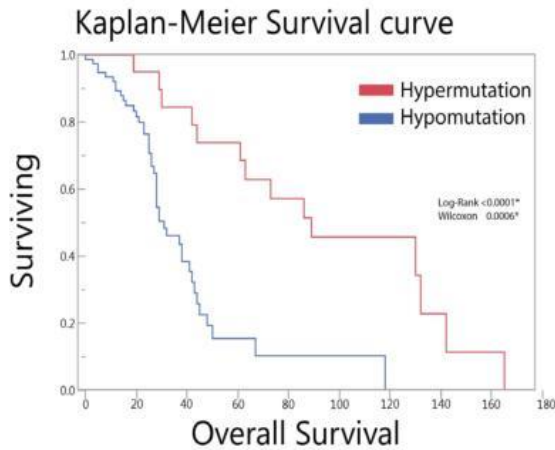
In this IRB-approved retrospective study, we analyzed a total of 101 patients with primary gliomas from the University of Texas MD Anderson Cancer Center. Next generation sequencing (NGS) platforms (T200 and Foundation 1) were used to determine the Mutation burden status in postbiopsy (stereotactic/excisional) tumor samples. Patients were dichotomized based on their mutation burden; 77 hypomutated (<30 mutations) and 24 hypermutated (≥ 30 mutations or <30 with MMR gene or POLE/POLD gene mutations). Radiomic analysis was performed on the conventional MR images (FLAIR and T1 postcontrast) obtained prior to tumor tissue surgical sampling; and a total of 2480 rotation-invariant radiomic features were extracted using: (i) the first-order histogram and (ii) grey level co-occurrence matrix. The Maximum Relevance Minimum Redundancy technique was used to select the most relevant radiomic features. ROC analysis and leave-one-out cross validation (LOOCV) were used to assess the performance of the Support Vector Machine (SVM) classifier as and AUC, Sensitivity, Specificity, and p-value were obtained.

Results

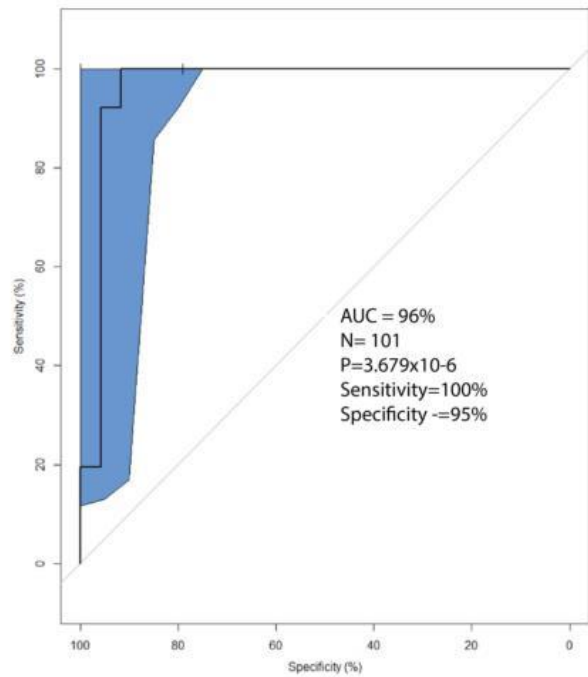
We used mRmR to select the top 100 most relevant radiomic features, then we used selected radiomic features to build our predictive model using support vector machine (SVM) algorithms. Then, we validated the model using leave-one-out cross validation (LOOCV). Our predictive model showed high significance, accuracy as well as sensitivity and specificity as follows: 96% Accuracy (95%CI: 0.90-1) ($P=3.679 \times 10^{-6}$), 100% sensitivity and 95% specificity.

Conclusions

MRI-extracted radiomic-texture features can be used to identify hypermutated gliomas with high accuracy, sensitivity and specificity. Upon further validation, this signature can be implemented in future clinical trials for patient selection.



ROC -Curve for Top 100 Texture features



(Filename: TCT_O-14_Figure1A.jpg)

O-15

10:44AM - 10:51AM

Development and External Validation of Diffusion and Perfusion MR Radiomics Model as a Diagnostic Biomarker for Differentiating between Pseudoprogression and True Progression in Patients with Newly Diagnosed Glioblastoma

J Kim¹, J Park¹, H Kim¹, S Jung¹, S Choi²

¹Asan Medical Center, Seoul, Republic of Korea²Seoul National University Hospital, Seoul, Republic of Korea

Purpose

To develop and externally validate a multiparametric MR radiomics model in a multicenter setting to facilitate the differentiation between pseudoprogression and early tumor progression (ETP) in newly diagnosed glioblastomas.

Materials and Methods

The model was developed using 6472 radiomic features from the enlarging contrast-enhancing portions of 61 glioblastoma patients (26 patients with pseudoprogression and 35 patients with ETP) after standard treatment. Patients underwent multiparametric MR examinations including conventional (contrast-enhanced T1-weighted imaging and fluid-attenuated inversion recovery), diffusion-weighted, and dynamic susceptibility contrast perfusion imaging. The Least Absolute Shrinkage and Selection Operator logistic regression model was applied to select the features. The diagnostic performances using different combinations of MR imaging were compared via the area under the receiver operating characteristics curve (AUC) and cross validated. The model was externally validated (n = 34) with different imaging protocols.

Results

Twelve significant radiomic features (3 from conventional, 2 from diffusion and 7 from perfusion MR imaging) were utilized to construct the model. The multiparametric approach (AUC 0.90) showed significantly better performance compared to conventional (AUC 0.76, P=.012), diffusion (AUC 0.78, P=.014), or combined conventional and diffusion radiomics (AUC 0.83, P=.043). Adding perfusion to conventional MR radiomics showed similar diagnostic performance (AUC 0.90) to multiparametric approach. This trend was maintained in the validation cohort, with an AUC of 0.85 using the multiparametric MR radiomics model, thus demonstrating robustness.

Conclusions

The multiparametric MR radiomics model showed improved diagnostic performance for identifying pseudoprogression and has the potential to augment the role of advanced MR imaging in multicenter studies of glioblastoma.

O-16

10:51AM - 10:58AM

Radiogenomics Analysis of Tumor Hemodynamic Characteristic in Patients with Newly Diagnosed Glioblastomas: Combination with TCIA Database

X Liu¹, R Mangla², R Jain³

¹University of Rochester Medical Center, Rochester, NY, ²SUNY Upstate, Syracuse, NY, ³New York University School of Medicine, New York, NY

Purpose

Tumor angiogenesis is very important for survival outcome in patients with glioblastomas; however, the radiogenomics association of hemodynamic changes, beyond VEGF, remains unclear. The purpose of this study is to investigate the association between MR perfusion abnormalities and genomic biomarkers in newly diagnosed glioblastomas.

Materials and Methods

MR dynamic susceptibility contrast perfusion-weighted imaging (DSC-PWI) examinations of 41 new diagnosed glioblastomas (mean age is 62.32±12.09) were enrolled in University of Rochester Medical Center (URMC), the genomics biomarkers of TP53, Ki-67 labelling index, isocitrate dehydrogenase (IDH), mammalian target of rapamycin (mTOR), and epidermal growth factor receptor (EGFR) were evaluated. Forty-five glioblastoma cases with MR DSC-PWI and U133 array gene expression in The Cancer Imaging Archive (TCIA) were reviewed for comparison. The mean and maximal rCBV ratio of the enhancing tumor (rCBV_{mean} and rCBV_{max}) were measured in all cases, maximal rCBV ratio of peri-enhancing tumor area (rCBV_{peri-tumor max}) and mean rCBV ratio of peri-enhancing tumor area (rCBV_{peri-tumor mean}) were measured in two groups respectively. The correlation analysis, and Cox

Oral Presentations & Excerpts

regression were performed. Additional 483 glioblastoma cases with U133 array gene expression archived in the Cancer Genome Atlas Research Network (TCGA) were used to identify the detected radiogenomics associations between MR DSC-PWI parameters and genomic biomarkers.

Results

The rCBV ratio of peri-enhancing tumor area was found to be the strongest predictor of overall survival (OS) in both groups, (hazard ratio= 1.29 and 1.16 respectively). The correlation analysis found difference of radiogenomic association in enhancing and peri-enhancing areas in both groups. In URM group, the rCBVmax correlated with mTOR and the rCBVperi-tumor max had significant association with mTOR after adjustment of gender and EGFR. In TCIA group, the rCBVmax correlated with AKT2 and the rCBVperi-tumor mean had significant correlation with FOXO3. AKT2 and FOXO3 had significant association with mTOR ($p < 0.05$). The gene expression analysis in 483 glioblastoma cases identify this gene network.

Conclusions

The difference of radiogenomic associations in enhancing and peri-enhancing areas and gene network may suggest PI3K/Akt/mTOR signaling pathway plays important role in different moderation of angiogenesis in glioblastomas. The implication of rCBVperi-tumor will promote future development of new targeting therapies aiming to tumor proliferation and vasculature infiltration.

O-17

10:58AM - 11:05AM

Quantitative radiomics and machine learning to distinguish true progression from pseudoprogression in patients with GBM

H Akbari¹, S Bakas¹, M Martinez-Lage², M Nasrallah¹, M Rozycki¹, S Rathore¹, G Shukla³, S Mohan⁴, R Wolf⁵, M Bilello¹, C Davatzikos¹

¹University of Pennsylvania, Philadelphia, PA, ²Massachusetts General Hospital, Boston, MA, ³Thomas Jefferson University, Philadelphia, PA, ⁴University of Pennsylvania School of Medicine, Philadelphia, PA, ⁵Hospital of the University of Pennsylvania, Philadelphia, PA

Purpose

We seek multiparametric MRI (mpMRI) markers in treated glioblastoma (GBM) to distinguish true progression (TP) from pseudoprogression (PsP). We hypothesize that integrative analysis of comprehensive radiomic features, encapsulating the complete imaging phenotype of biological properties, can be associated with underlying pathology of apparent progression.

Materials and Methods

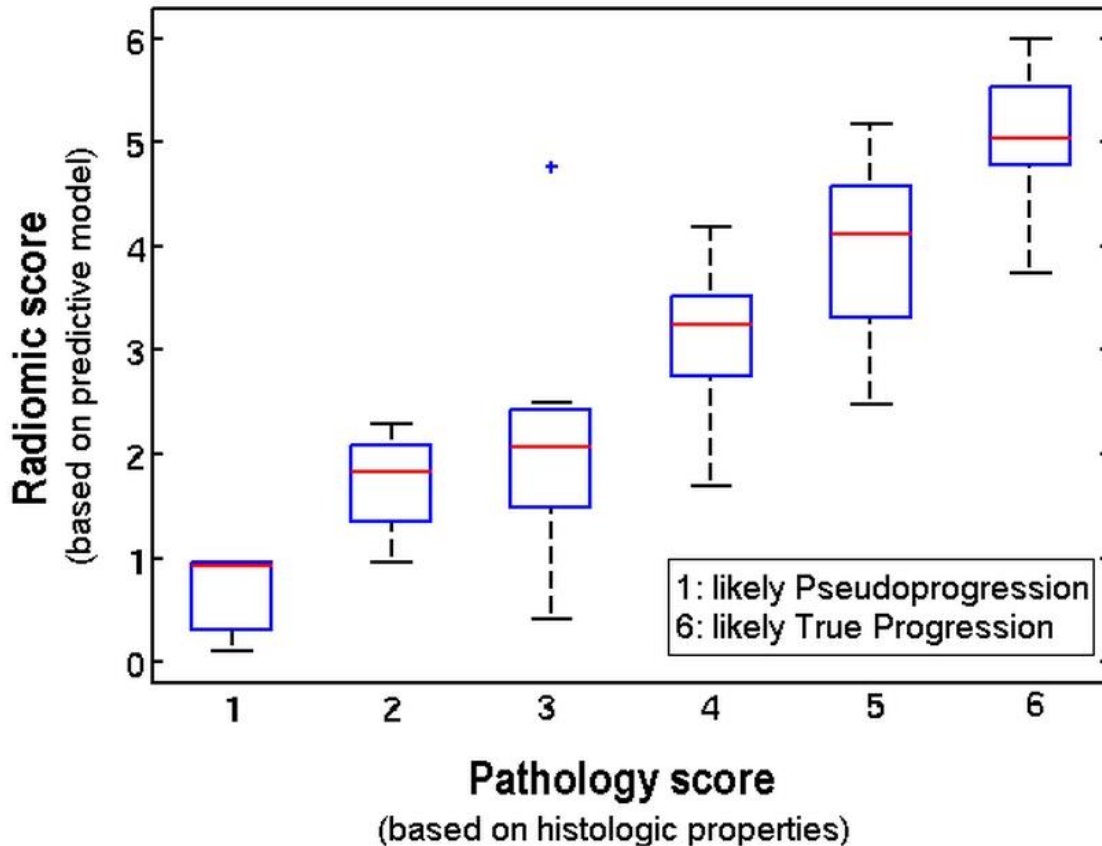
We retrospectively analyzed 50 GBM patients, who underwent a second resection due to radiographic diagnosis of progression, with comprehensive preoperative mpMRI data, i.e., T1, T1Gd, T2, FLAIR, DSC, DTI. Specimens were blindly assessed and scored from 1-6 (1=likely PsP, 6=likely TP) based on various histologic properties by a neuropathologist. We conducted a radiomic analysis based on 'isolated' (IF) and 'encapsulated' (EF) features extracted from all mpMRI from the regions of apparent progression. The IF describe intensity statistics and momentary hemodynamic features, e.g. rCBV. The EF describe the complete 1) intensity distributions and 2) perfusion dynamic signal, both summarized by principal component analysis (PCA), hence encapsulating the complete 1) imaging phenotype and 2) hemodynamic profile, respectively. We modeled progression using Support Vector Regression with a linear kernel, while optimizing features through sequential selection. Leave-one-out cross-validation was used to evaluate the performance and generalizability of the predictive model on unseen data.

Results

Pearson correlation between radiomic and pathology scores is 0.86 ($p = 5 \times 10^{-16}$). The top-ranked features, based on sequential selection, were the EF of FLAIR and DSC signals, and 37 of the 40 most important were also EF.

Conclusions

Quantitative radiomic analysis of comprehensive mpMRI data, optimally integrated into a signature via machine learning, distinguishes GBM TP from PsP with high correlation to pathological validation. This study introduced EF of imaging phenotypes and hemodynamic profile. Feature interpretation reveals TP associated with higher angiogenesis (i.e., increased rCBV) and cellularity (i.e., decreased ADC), but lower water concentration (i.e., decreased FLAIR, T2), when compared to PsP.



(Filename: TCT_O-17_PsP_ASNR.jpg)

O-18

11:05AM - 11:12AM

Genome-wide copy number abundance correlation with imaging phenotype and survival in IDH mutated astrocytomas

R Jain¹, C Wu², L Poisson³, I Littig¹, L Nunes¹, S Patel⁴, D Placantonakis¹, S Patel¹, J Golfinos¹, M Snuderl¹, A Chi¹

¹New York University School of Medicine, New York, NY, ²Taipei Veterans General Hospital, School of Medicine, National Yang Ming University, Taipei, Taiwan, ³Henry Ford Health System, Detroit, MI, ⁴University of Virginia Health System, Charlottesville, VA

Purpose

There is variability in survival within IDHmut gliomas determined by chromosomal events and it has been reported that copy number variation (CNV) abundance is associated with survival in low-grade

glioma. The purpose of this study was to correlate the extent of genome-wide CNV in IDHmut gliomas with specific MR imaging features including tumor blood-volume estimates and patient survival.

Materials and Methods

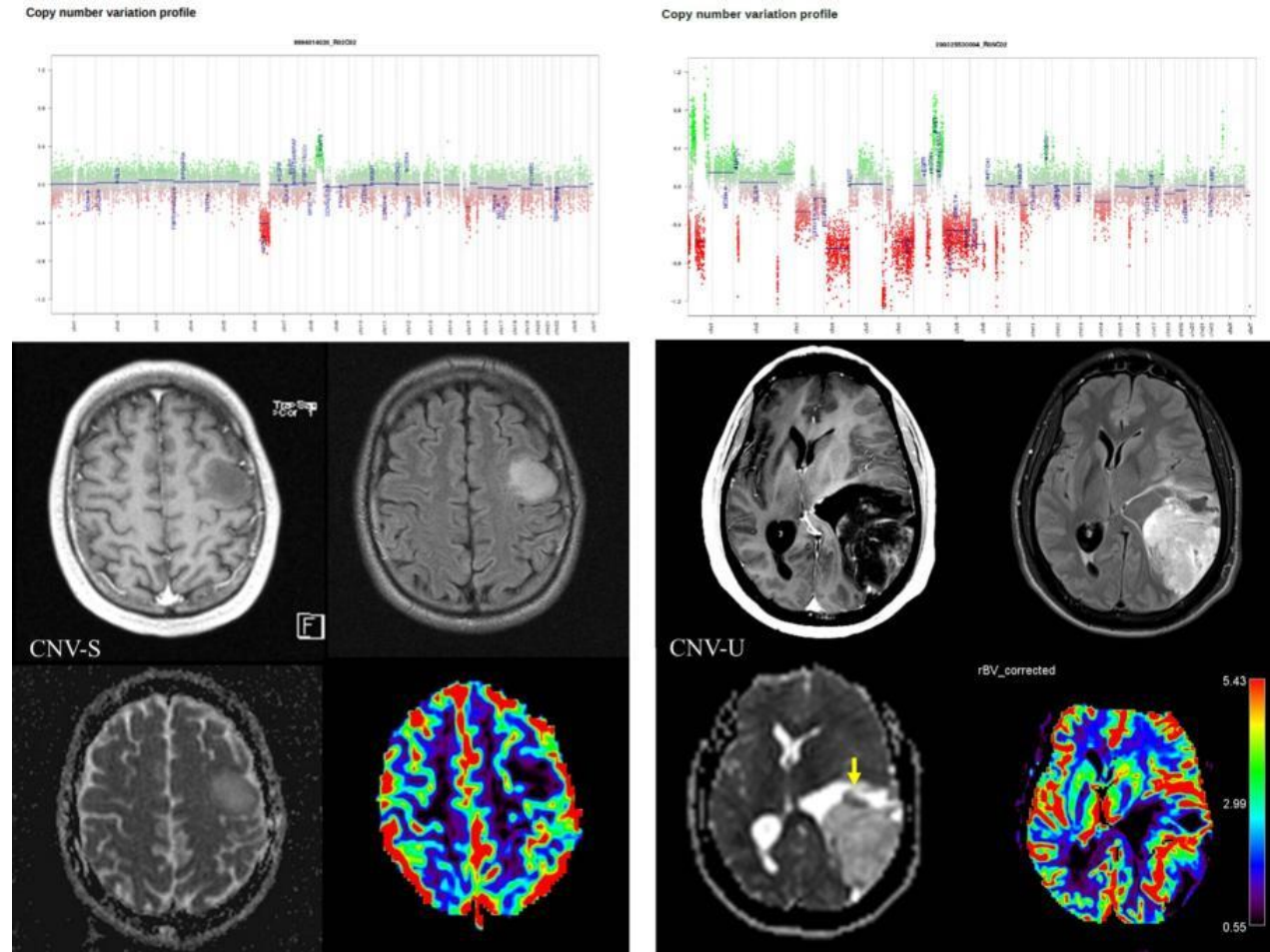
A discovery cohort of 22 cases of IDHmut 1p/19q noncodel glioma (WHO grade II-IV) with preoperative MRI were included from our institute. We reviewed CNV plots obtained with Illumina 850k EPIC DNA methylation arrays from these tumors. Gliomas were divided into two groups based on the degree of genome-wide CNV abundance into CNV stable (CNV-S) with <3 chromosomal gains or losses and lack of focal gene amplifications and CNV unstable (CNV-U) with >3 large chromosomal gains/losses and/or focal amplifications. MR morphological features modified from VASARI dataset were reviewed by two neuroradiologists. Tumor blood volume estimates (rCBV) were obtained using DSC T2* perfusion analysis. Our analysis assessed the association between imaging features, CNV and progression free survival. A validation cohort of 23 IDHmut 1p/19q noncodel gliomas with genomic, perfusion and survival data from TCGA was also analyzed.

Results

There were 16 (72.7%) CNV-U and 6 (27.3%) CNV-S IDH-mutated gliomas. Necrosis was significantly more prevalent in CNV-U (5/6, 83.3%) than in CNV-S gliomas (2/16, 12.5%; $P = 0.004$). Mean tumor size and maximum diameter based on FLAIR was significantly larger in CNV-U IDH-mutated gliomas ($77.3 \pm 12.6\text{mm}$, $42.6 \pm 6.2\text{mm}^2$) than in CNV-S ($54.8 \pm 19.2\text{mm}$, $23.2 \pm 3.6\text{mm}^2$, $P = 0.016$ and 0.013 , respectively). CNV-U gliomas were more likely to have foci of signal intensities lower or equal to contralateral normal-appearing white matter on ADC map than CNV-S gliomas ($P = 0.006$). CNV-S gliomas demonstrated significantly lower mean rCBV (1.4 ± 0.4) than CNV-U gliomas (4.0 ± 1.1 , $P = 0.009$). There were no significant differences of the remaining MR features and CNV sub-groups. Tumors in CNV-U group tended to have shorter time to progression than those in CNV-S group, although no statistically significance was observed ($P = 0.081$).

Conclusions

MRI features, including the presence of necrosis, larger tumor size/maximum diameter, foci of restricted diffusion and higher rCBV, were seen more frequently in IDH-mutated gliomas with unstable genome-wide CNV (CNV-U), suggesting that imaging features usually associated with more aggressive tumors can help differentiate CNV-U astrocytomas from CNV-S astrocytomas.



(Filename: TCT_O-18_CNV.jpg)

O-19

11:12AM - 11:19AM

Can preoperative seizures predict IDH mutation?

P Lee¹, M Liu¹, A Lignelli¹, S Jambawalikar¹, F Iwamoto¹, E Garcon¹

¹Columbia University Medical Center, New York, NY

Purpose

Mutant isocitrate dehydrogenase 1 (IDH1) produces D-2-hydroxyglutarate (D2HG), a molecule which mimics the activity of the excitatory neurotransmitter glutamate on the NMDA receptor. WHO grade II-IV gliomas with IDH mutation are reported to be associated with higher rates of seizures compared to IDH wild type. In this study, we evaluated the use of preoperative clinical history of seizures as a predictor of 2HG peak on MR spectroscopy in glioma patients.

Materials and Methods

We performed a retrospective study of 28 randomly selected patients less than 60-years-old with gliomas who underwent preoperative 2HG MR spectroscopy. All patients subsequently underwent surgical resection and have known IDH1/2 mutation status determined by immunohistochemistry or gene sequencing. The cohort included four astrocytomas, nine anaplastic astrocytomas, eight oligodendrogliomas, and seven glioblastomas. Patient charts were reviewed for any history of preoperative seizure. MRI and MRS were performed on two different scanners: GE Medical 3T Excite

HD and Philips 3T Achieva using an 8-channel head coil. For 2HG MRS we used a point resolved spectroscopy sequence with the following parameters: number of excitations 256-384, spectral window 2500, number of samples 2048, TE/TR 97/2000, TE1/TE2 were 26/71 ms for the GE scanner and 32/65 for the Philips scanner (de la Fuente). Voxels are prescribed as 8mL(2cmx2cmx2cm) unless inhomogeneities force the use of a smaller voxel. Raw data was transferred to a separate workstation and analyzed with LCModel software. Basis sets provided by LCModel for TE 97 including the 2HG metabolite were used. Water unsuppressed data was used for water scaling of metabolite concentrations. CRLB less than 30% and SNR>10 was used as a threshold for confidence of presence of 2HG peak.

Results

Preoperative seizure occurred in 17/28 patients (61%). A 2HG peak was seen on MR spectroscopy in 12/28 patients (43%). IDH mutation was found by immunohistochemistry or gene sequencing in 22/28 patients (79%). Fisher exact test demonstrated no statistically significant association between preoperative seizure and either 2HG peak on MR spectroscopy ($p=1.0$) or IDH mutation ($p=0.65$).

Conclusions

Although IDH mutation has been reported to be associated with higher rates of preoperative seizure compared to IDH wild type, we found that preoperative seizure is not a good predictor of 2HG peak on MR spectroscopy or IDH mutation.

O-20

11:19AM - 11:26AM

Prediction of 1p/19q codeletion status in IDH-mutant low grade gliomas – how accurate can the neuroradiologist be?

P Batchala¹, D Schiff¹, C Fadul¹, K Mrachek², T Eluvathingal Muttikkal¹, R Jain³, S Patel¹

¹University of Virginia Health System, Charlottesville, VA, ²University of Virginia, Charlottesville, VA, ³New York University School of Medicine, New York, NY

Purpose

The 2016 WHO classification of CNS tumors segregates lower-grade gliomas (LGGs) harboring isocitrate dehydrogenase gene (IDH) mutations into two subgroups based on the presence or absence of codeletion in chromosome arms 1p and 19q: 1) Oligodendroglioma, IDH-mutant and 1p/19q codeleted; 2) Diffuse astrocytoma, IDH-mutant (and 1p/19q noncodeleted). Several studies describe imaging features that correlate with codeleted and noncodeleted LGGs [1-5], but no prior studies have evaluated how reproducibly and accurately neuroradiologists predict codeletion status using those features. Our purpose was to determine neuroradiologist performance in differentiating between IDH-mutant subtypes.

Materials and Methods

From our institution, 108 IDH-mutant grade II/III LGGs with preoperative MRI and known 1p/19q status (50 codeleted, 58 noncodeleted) were selected. Two independent blinded neuroradiologists predicted 1p/19q codeletion status based on the preoperative MRI scan using published features that correlate with 1p/19q codeletion status (differences in tumor margins, texture, calcification, T2-FLAIR mismatch sign, and location (Figure)). Inter-reader agreement was calculated, and discordant results were resolved in consensus. Reader findings were compared with known 1p/19q status. The same procedure was undertaken on a validation set of 144 grade II/III IDH-mutant gliomas (49 codeleted, 95 noncodeleted) available through The Cancer Genome Atlas (TCGA).

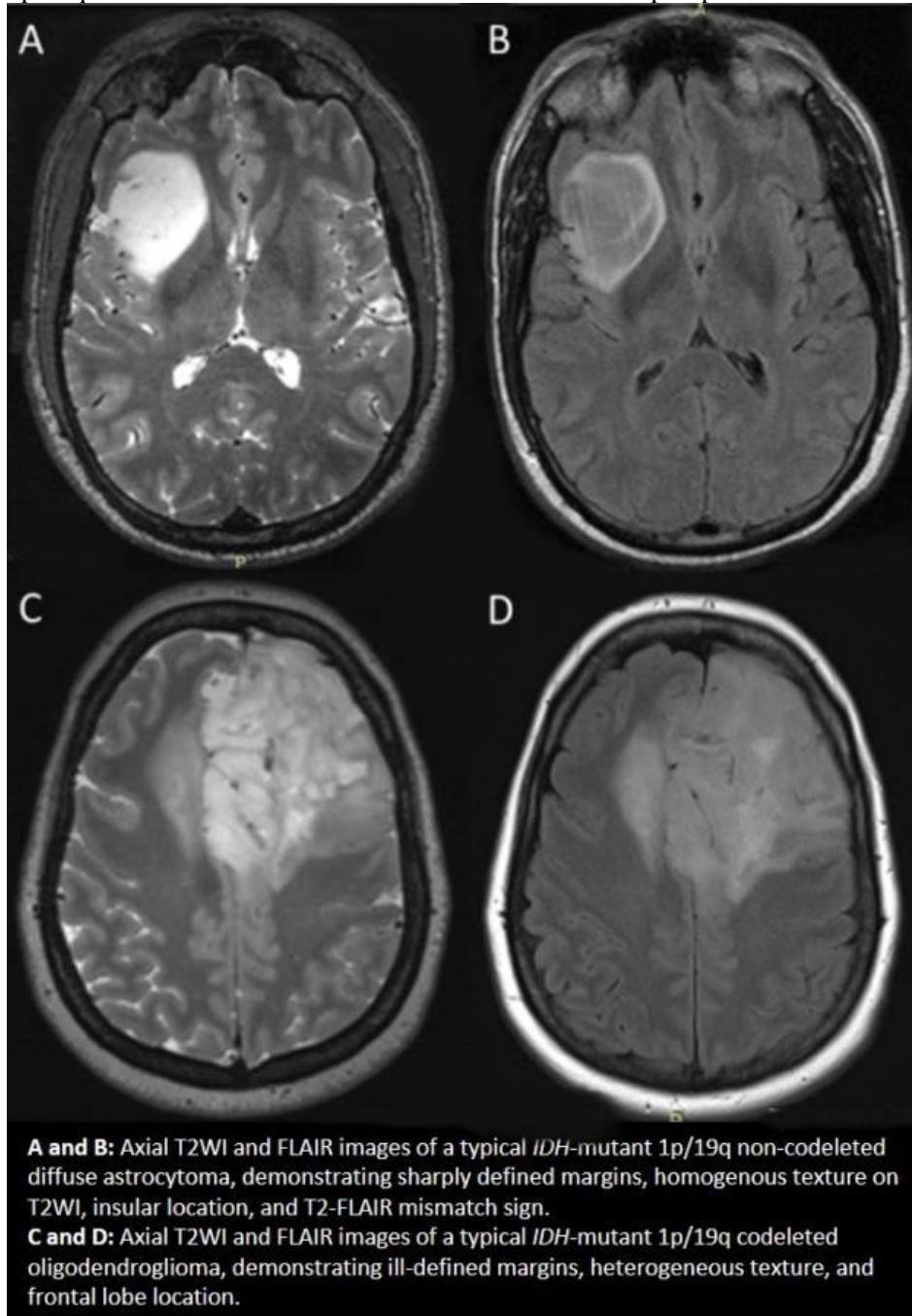
Results

Review of institutional cases yielded substantial inter-reader agreement ($\kappa = 0.635$). A 1p/19q codeletion status was correctly predicted on the basis of MRI in 86.2% ($p<0.0001$). Review of the validation set of TCGA cases also yielded substantial inter-reader agreement ($\kappa = 0.631$), and correct prediction of 1p/19q status in 85.4% of cases ($p<0.0001$). Among TCGA cases, reader confidence, on a scale from 1-3, was significantly higher among concordant versus discordant judgments with 1p/19q molecular status (2.24 versus 1.62, $p = 0.0002$).

Oral Presentations & Excerptas

Conclusions

Neuroradiologists demonstrate substantial agreement and moderate (~85%) accuracy in determining 1p/19q codeletion status in IDH-mutant LGGs based on preoperative MRI.



(Filename: TCT_O-20_Figure1.jpg)

O-21

11:26AM - 11:33AM

Identification of IDH Mutant Glioblastomas by Using Diffusion and Perfusion MR Imaging

S Chawla¹, S Wang¹, S Mohan¹, A Nabavizadeh¹, M Nasrallah¹, S Brem², H Poptani³

Oral Presentations & Excerptas

¹Perelman School of Medicine at the University of Pennsylvania, Philadelphia, PA, ²Hospital of the University of Pennsylvania, Philadelphia, PA, ³University of Liverpool, Liverpool, England

Purpose

Accurate identification of IDH-mutation is clinically important. Using sophisticated MR spectroscopy sequences, some studies (1, 2) have identified low-grade gliomas harboring IDH mutation by detecting 2-hydroxyglutarate (2-HG). However, not all IDH mutant gliomas show neomorphic activity of 2-HG production. (3) Therefore, it is essential to develop alternative imaging biomarkers to distinguish IDH-mutant from IDH-wild-type gliomas. These biomarkers may also provide insights into the tumor microenvironment that may eventually assist in emergent of targeted therapeutic agents. Anecdotal studies (4, 5) have employed MR diffusion and perfusion imaging techniques to differentiate these two genotypes in low-grade gliomas. Although incidence of IDH mutation in glioblastomas (GBMs) is only 10%, it is equally important to develop imaging biomarkers to understand their tumor microenvironment and to discriminate their IDH profiles. Therefore, present study was performed to investigate the potential of diffusion-tensor imaging (DTI) and dynamic-susceptibility contrast perfusion-weighted imaging (DSC-PWI) in differentiating IDH-mutant from IDH-wild-type GBMs.

Materials and Methods

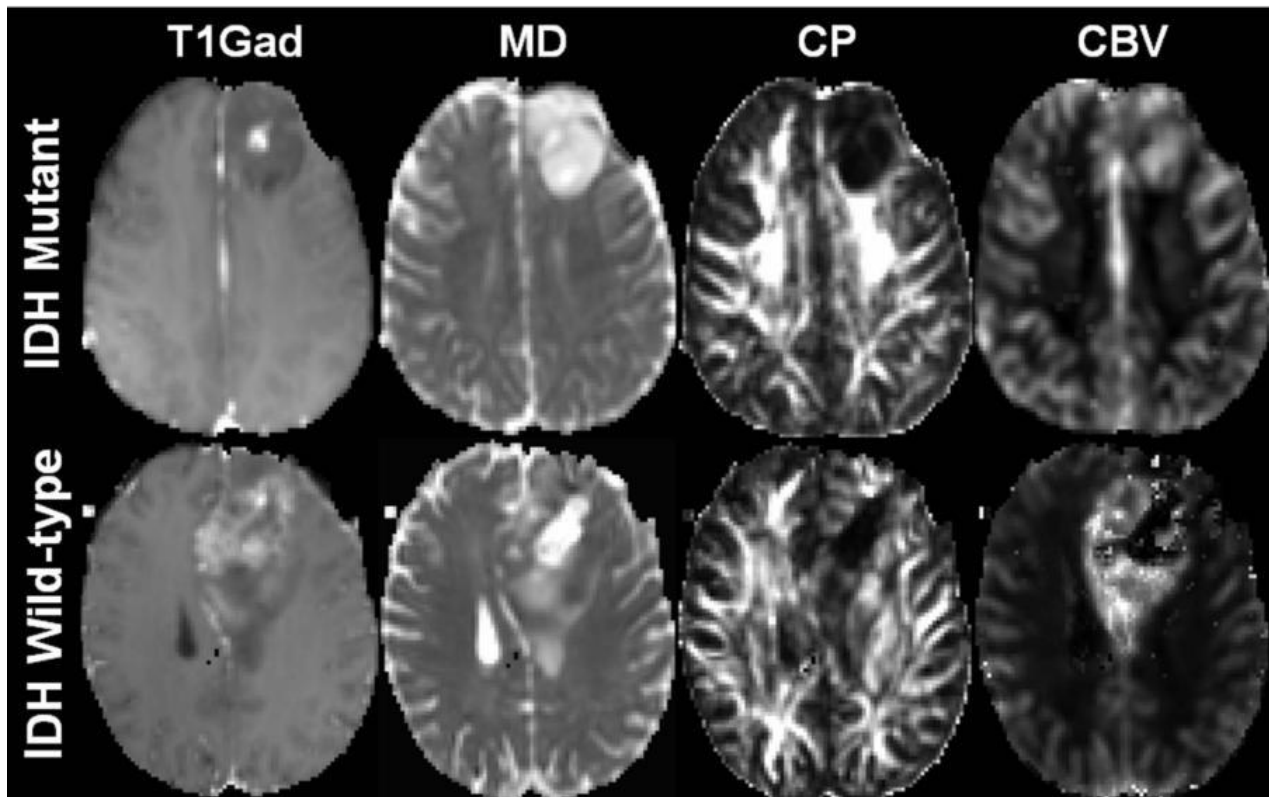
A cohort of 22 treatment naïve patients with IDH-mutant (n=12) and IDH-wild-type (n=10) GBM underwent DTI and DSC-PWI on 3T MR system. Image processing included coregistration and segmentation of contrast-enhancing/solid regions of neoplasms. Median values of DTI parameters [mean diffusivity (MD), fractional anisotropy (FA), coefficient of linear (CL) and planar anisotropy (CP)] and relative cerebral blood volume (rCBV) besides 90th percentile of rCBV (rCBVmax) were computed from enhancing/solid regions and were compared between IDH-mutant and IDH-wild-type GBMs using Mann-Whitney tests.

Results

Representative anatomical images, MD, CP and CBV maps are shown in Figure 1. From DTI, significantly higher MD ($1.5 \pm 0.3 \times 10^{-3}$ vs. $1.1 \pm 0.1 \times 10^{-3} \text{mm}^2/\text{s}$, $p=0.02$), and diminished CP (0.06 ± 0.01 vs. 0.09 ± 0.03 , $p=0.04$) were observed in IDH-mutant than in IDH-wild-type GBMs. Additionally, there were trends of higher FA and CL in IDH-wild-type GBMs. From DSC-PWI, reduced rCBV (1.78 ± 0.84 vs. 4.03 ± 1.01 , $p=0.03$) and rCBVmax (2.85 ± 1.06 vs. 6.43 ± 2.06 , $p=0.02$) were observed in IDH-mutant compared to IDH-wild-type GBMs.

Conclusions

DTI and DSC-PWI may be useful in distinguishing IDH-mutant from IDH-wild-type GBMs.



(Filename: TCT_O-21_Figure_Final.jpg)

O-22

11:33AM - 11:40AM

Imaging Prediction of Isocitrate Dehydrogenase (IDH) Mutation in Patients with Glioma: A Systematic Review and Meta-Analysis

C Suh¹, H Kim¹, S Kim¹

¹Asan Medical Center, Seoul, Republic of Korea

Purpose

To evaluate the imaging features of IDH mutant glioma and to assess the diagnostic performance of magnetic resonance imaging (MRI) for prediction of IDH mutation in patients with glioma

Materials and Methods

A systematic search of Ovid-MEDLINE and EMBASE up to October 10, 2017 was conducted to find relevant studies. The search terms combined synonyms for 'glioma', 'IDH mutation', and 'MRI'. Studies evaluating the imaging features of IDH-mutant glioma and the diagnostic performance of MRI for prediction of IDH-mutation in patients with glioma were selected. The pooled summary estimates of sensitivity and specificity and their 95% CIs were calculated using a bivariate random-effects model. The results of multiple subgroup analyses are reported.

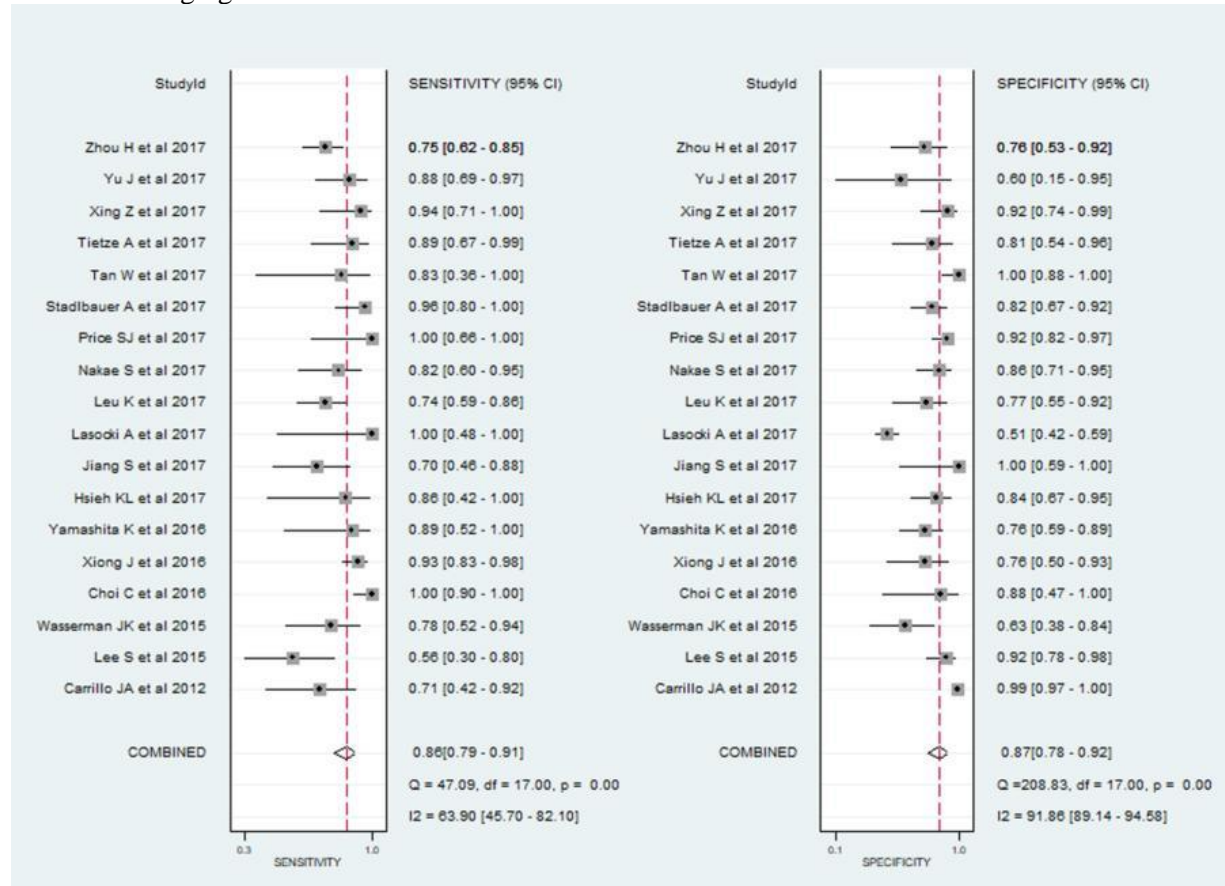
Results

Twenty-eight original articles in a total of 2146 patients with glioma were included. IDH-mutant glioma showed frontal lobe predominance, less contrast enhancement, well-defined border, high ADC value, and low rCBV value. For the meta-analysis that included 18 original articles, the summary sensitivity was 86% (95% CI, 79%–91%) and the summary specificity was 87% (95% CI, 78–92%). In a subgroup analysis, the summary sensitivity of 2-hydroxyglutarate magnetic resonance spectroscopy (MRS) (96% [95% CI, 91–100%]) was higher than the summary sensitivities of other imaging modalities.

Oral Presentations & Excerptas

Conclusions

IDH-mutant glioma consistently demonstrated less aggressive imaging features than IDH-wild-type glioma. Despite the variety of different MRI techniques used, MRI showed the potential to noninvasively predict IDH mutation in patients with glioma; 2-hydroxyglutarate MRS shows higher pooled sensitivity than other imaging modalities.



(Filename: TCT_O-22_Figure.jpg)

O-23

11:40AM - 11:47AM

Radiogenomic Analysis of TERT Promoter Mutation Status in IDH wildtype Glioblastoma: Assessing Differences in Imaging Phenotype and Quantitative Apparent Diffusion Coefficient

M Lum¹, J Ivanidze¹, I Kovanlikaya¹, R Magge¹, R Ramakrishna¹, H Fine¹, G Chiang²

¹New York Presbyterian Hospital - Weill Cornell, New York, NY, ²Weill Cornell Medical College, New York, NY

Purpose

Mutations in the telomerase reverse transcriptase (TERT) promoter occur commonly in glioblastoma (GBM) and portend a worse prognosis. Increased TERT activity has been reported to preserve telomeres, allowing tumors to avoid induction of senescence. Phenotypic and apparent diffusion coefficient (ADC) correlates of TERT mutation status have not been reported.

Materials and Methods

This IRB-approved retrospective pilot study included 30 patients with IDH1/2-negative GBM (14 TERT-negative, 16 TERT-positive). All patients underwent a standard-of-care preoperative MR imaging

Oral Presentations & Excerptas

protocol with ADC maps available for 25 patients. Histogram analysis of whole tumor ADC values was performed on enhancing tumor volumes-of-interest, and differences between TERT-negative and TERT-positive tumors were assessed using Mann-Whitney-U tests. Imaging phenotypes associated with TERT mutation status were evaluated using the Visually Accessible Rembrandt Images (VASARI) feature set by two neuroradiologists, with differences assessed with Pearson chi-squared tests.

Results

A higher proportion of TERT-negative tumors demonstrated nonenhancing tumor that crossed midline (35.7% versus 0%, p-value 0.014). There was no statistically significant difference between groups in the other VASARI features. Of the tumors with ADC data, there was no significant difference in mean or median ADC values, although there was a trend towards less ADC skew (coefficient -0.77, $p = 0.058$) and less ADC kurtosis in the TERT-positive tumors (coefficient -3.99, $p = 0.058$).

Conclusions

Our pilot study demonstrated some evidence of phenotypic and diffusion differences associated with TERT promoter mutations in GBM. Further work in a larger sample is needed to confirm these findings.

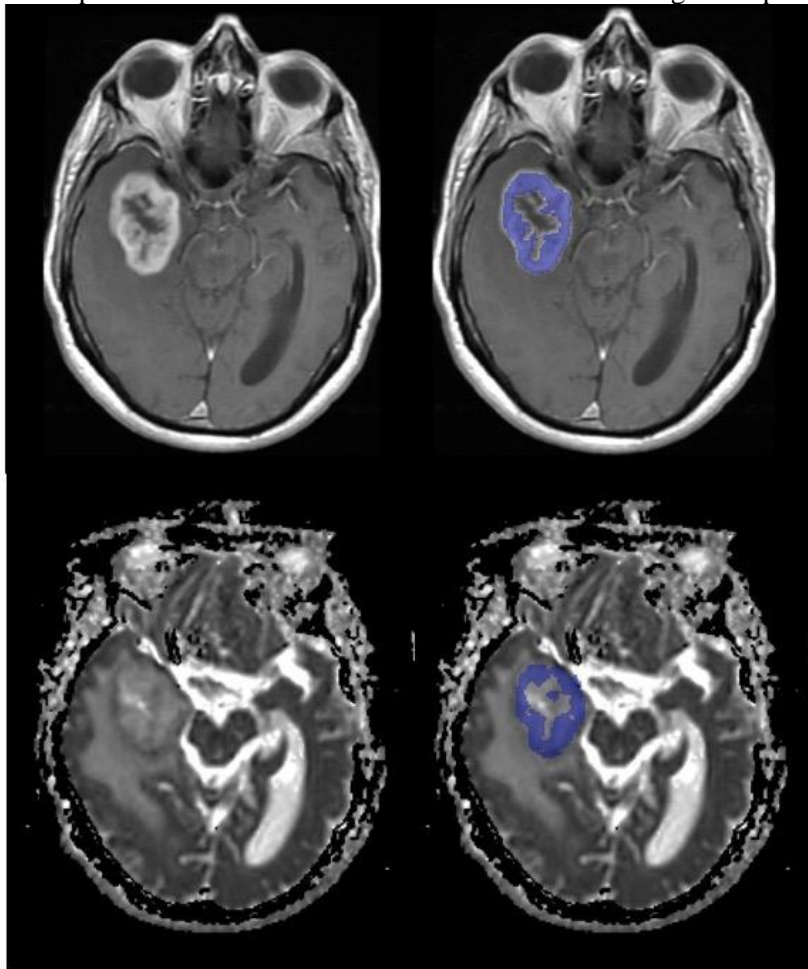


Figure 1. Enhancing tumor volumes-of-interest were delineated on postcontrast T1-weighted images and overlaid on co-registered ADC maps for histogram analysis.

(Filename: TCT_O-23_ASNRCaption300dpi.jpg)

O-24

11:47AM - 11:54AM

Radiogenomic analysis of TCGA-LGG dataset and automatic MRI segmentation illuminates biologically distinct molecular subsets and pathways

S Yamamoto¹, J Villanueva-Meyer¹, S Cha¹

¹University of California San Francisco, San Francisco, CA

Purpose

Assess the feasibility of radiogenomic analysis to integrate the molecular landscape and imaging of grade III gliomas using fully automated MRI segmentation software, gene expression, RNA sequencing, DNA sequencing, copy-number variation, and DNA methylation data.

Materials and Methods

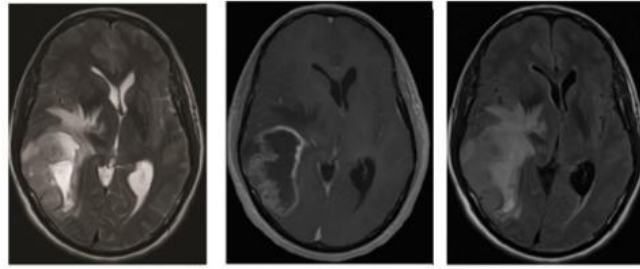
Patients with histologically verified grade III gliomas (oligodendroglioma, oligoastrocytoma, and astrocytoma) were manually curated from the TCGA-LGG database based on full availability of preoperative MR imaging, molecular, and clinical data (age and recurrence-free survival). For imaging, pre/postcontrast T1, T2, and FLAIR sequences were required for Brain Tumor Imaging Analysis (BraTumIA), a fully automated segmentation software which quantifies volume of unaffected tissue, nonmass-like FLAIR/T2 (NMLF), and abnormal tissue (represents a combination of nonenhancing, enhancing, and necrotic components). Molecular data consisting of whole-genome sequencing, RNA sequencing, DNA copy-number, single-nucleotide polymorphism, gene-expression, and DNA methylation arrays were downloaded from TCGA. All data were quantified and analyzed by the Broad Institute FireBrowse portal, with all data points quantified accordingly to their respective type of analysis. To create a radiogenomic map, unsupervised hierarchical clustering was performed to create clusters of patients using only imaging and clinical phenotypes. After distinct clusters were defined, univariate analysis determined differences in their molecular landscape against each respective group. Finally, Kaplan-Meier survival curves were generated, and the log-rank test was used to assess statistical difference in progression-free survival (PFS).

Results

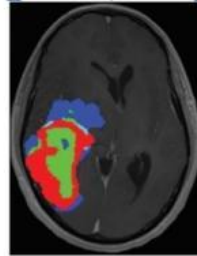
Clustering of imaging features and clinical variable (age) revealed four unique unsupervised groups: high NMLF tumor (n=20, imaging cluster 1), older patients with low NMLF (n=16, cluster 2), younger patients low NMLF (n=14, cluster 3), and patients with increased abnormal tissue (n=10, cluster 4). Statistically significant difference in PFS was found among the four clusters (p<0.01), with the largest difference between the longest PFS (seen in younger patients with increased abnormal tissue (group 4), versus the shortest PFS in patients with older patients with low NMLF (group 2). Deeper look into each cluster's molecular landscape revealed a series of markers that define each group. Imaging cluster 1 consisted of highly methylated MGMT (18/20, 90%), concentration of IDH mutants (20/20, 100%), and increased trend in DNA copy-number loss. Cluster 2 was most enriched in unmethylated MGMT (6/16, 38%), IDH wildtypes (14/16, 88%), TERT mutants (13/16, 81%), chromosome 7 gain/10 loss (10/16, 63%), classical molecular subtype (9/16, 56%), and increased trend in DNA copy-number gain. Cluster 3 showed proneural molecular subtypes (8/14, 57%), 1p/19q codeletion (14/14, 100%), and ATRX mutants (8/14, 57%). Lastly, cluster 4 was represented by methylated MGMT (9/10, 90%), IDH mutants (8/10, 80%), 1p/19q codeletion (9/10, 90%), frame shift/nonsense P53 mutations (7/10, 70%), high G-CIMP (7/10, 70%), and low trend in DNA copy-number loss.

Conclusions

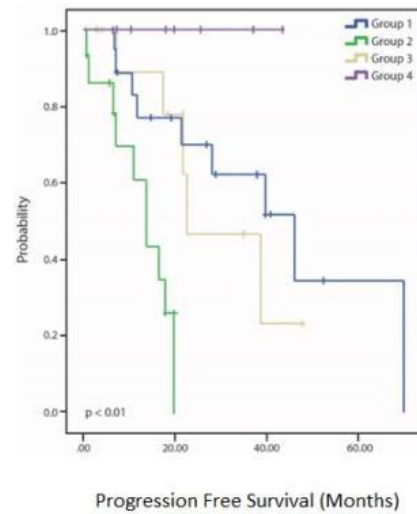
Radiogenomic analysis combining automated MRI segmentation, clinical, and molecular information may have the ability to discover distinct groups of grade III gliomas with varying molecular landscapes and clinical outcomes.



Example segmentation



Imaging Cluster	1	2	3	4
Table 1. Clinical Characteristics of the Sample Set Arranged by Imaging Cluster				
Clinical				
Histology (n)				
Astrocytoma	8	6	8	4
Oligoastrocytoma	2	6	4	4
Oligodendroglioma	10	2	4	2
Gender				
Male	8	11	5	5
Female	12	3	11	5
Age				
Median (range)	45 (30-74)	31 (22-48)	60 (46-75)	45 (29-66)
Ethnicity				
Caucasian	17	19	15	9
African American	2	0	1	1
Asian	1	0	0	0
NA	0	1	0	0
KPS				
<70	1	1	1	1
70-80	2	0	4	0
90	7	7	6	2
100	2	1	0	2
Unknown	8	5	4	5
Followuptime				
Median	21.1	8.1	10.3	8.4
TranscriptomeSubtype				
Proneural	10	8	0	5
Mesenchymal	2	1	1	1
Neural	5	1	4	0
Classical	0	2	8	1
NA	5	3	3	3



(Filename: TCT_O-24_Untitled1.jpg)

Monday, June 4, 2018

10:30AM - 12:00PM

Excerpta: Adult Brain: Degenerative and Inflammatory, Infectious Disease

E-1

10:30AM - 10:34AM

Rare Case of Autoimmune GFAP Astrocytopathy Encephalomyelitis

L Eisenmenger¹, M Shah¹, C Glastonbury¹

¹University of California, San Francisco, San Francisco, CA

Purpose

Glial fibrillary acidic protein (GFAP) astrocytopathy is a rare immunotherapy-responsive autoimmune CNS disorder, sometimes associated with a paraneoplastic cause (1). This entity is an important, treatable cause of rapidly progressive dementia. It is therefore important for the neuroradiologist to recognize the typical imaging findings of this disorder. Our purpose is to present a case of confirmed autoimmune GFAP astrocytopathy encephalomyelitis.

Oral Presentations & Excerptas

Materials and Methods

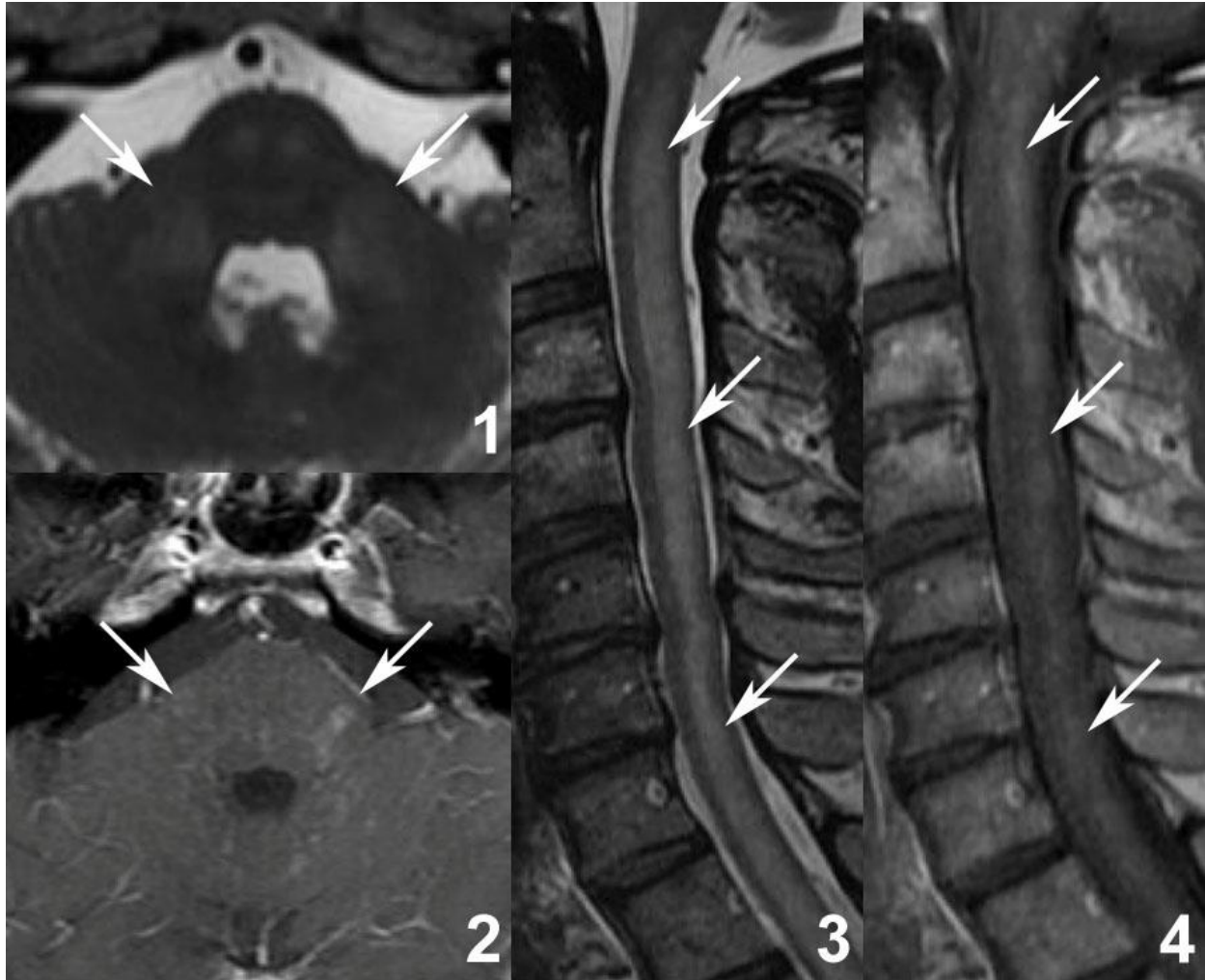
A 66-year-old man with a history of depression and remote polysubstance abuse initially presented in August 2017 with subacute cognitive and motor decline since January 2017. On neurologic examination, he was disoriented and inattentive, abulic but not aphasic, and had quadriparesis with findings consistent with myelopathy. His outpatient workup was notable for CSF lymphocytic pleocytosis and elevated CSF protein, positive serum VGKC antibodies, and abnormal MR imaging. He was treated with recurrent courses of pulse steroids, which was associated with transient improvement, but overall continued to decline with persistent deficits across multiple domains. He was admitted in late October 2017 for expedited workup, and additional CSF testing was positive for GFAP receptor antibody, which was confirmed by GFAP α -IgG cell-based assay at the Mayo Clinic Neuroimmunology Laboratory. No primary malignancy was found in this case. The patient was treated initially with IVIG and pulse dose steroids, subsequently discharged on a prolonged prednisone taper resulting in progressive memory and gait improvement.

Results

On the brain MRI, there were extensive confluent areas of supra and infratentorial T2/FLAIR hyperintensity with involvement of the periventricular white matter, bilateral brachium ponti (image 1), the medulla, and the pons including the root entry zone of both trigeminal nerves. Some of these areas demonstrated punctate, nodular parenchymal/perivascular enhancement, most notably in periventricular white-matter and bilateral brachium ponti (image 2). There was additional diffuse abnormal T2/FLAIR hyperintensity throughout the cervicothoracic cord (image 3) with associated subtle, patchy enhancement (image 4), similar to the enhancement pattern of brain parenchyma. Imaging findings GFAP astrocytopathy have previously been described as linear, perivascular radial gadolinium enhancement extending outward from the ventricles with the enhancement sometimes being more punctate in appearance (1). Those patients with cord involvement typically have longitudinally extensive transverse myelitis (greater than or equal to three vertebral segments long).

Conclusions

Glial fibrillary acidic protein (GFAP) astrocytopathy is a rare but immunotherapy-responsive autoimmune CNS disorder with unique neuroradiology findings making it essential for early recognition and appropriate treatment.



(Filename: TCT_E-1_ashnr.jpg)

E-2

10:34AM - 10:38AM

Capecitabine Induced Leukoencephalopathy

M Manganaro¹, D Miller¹, E Gu¹, F Boucher¹, Z Wilseck¹, J Kim¹

¹University of Michigan, Ann Arbor, MI

Purpose

This case report illustrates sequela of Capecitabine, an oral fluoropyrimidine chemotherapeutic agent used primarily in the treatment of colorectal and breast cancer. There are some case reports documenting Capecitabine-induced leukoencephalopathy, but none demonstrate this degree of white matter restricted diffusion involving the corpus callosum and all of the fibers of the bilateral corticospinal tracts.

Materials and Methods

A 55-year-old female with recently diagnosed rectal cancer presented to the emergency department with dysphasia, confusion, and severe ataxia. The neurology specialist was contacted immediately and the physical exam findings were concerning for acute stroke vs. a new metastatic brain lesion. The patient was admitted to the neurology service and an MRI of the brain with and without contrast was ordered revealing significant areas of restricted diffusion involving the bilateral centrum semiovale, corpus callosum, and posterior limb of internal capsule. Upon review of history the patient had initiated

chemotherapy with Capecitabine approximately five days prior to presentation. Capecitabine was stopped and the patient's symptoms improved over the next three days; she was discharged in good health with no residual deficits.

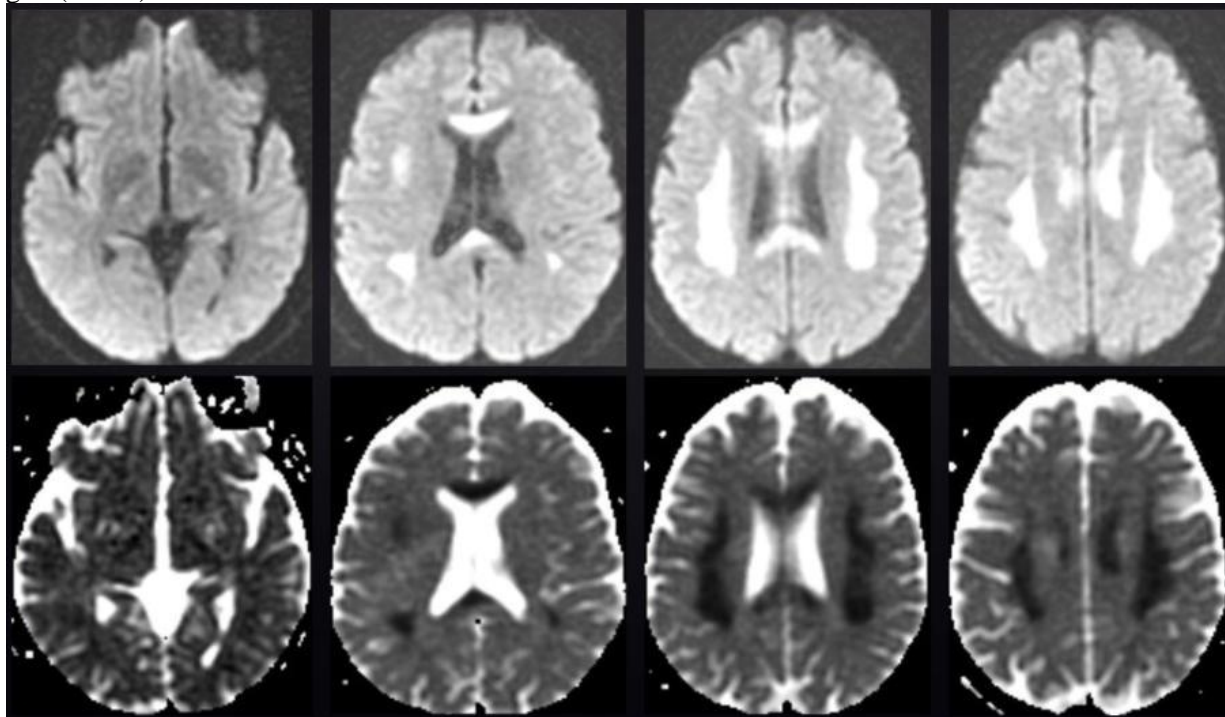
Results

MRI of the brain revealed extensive areas of restricted diffusion involving the bilateral centrum semiovale, corpus callosum, and posterior limb of internal capsule. These locations contain densely myelinated white matter tracts including the bilateral corticospinal tracts explaining the patient's ataxia and confusion. Follow-up MRI one month later was unremarkable with no signal abnormality.

Conclusions

Although Capecitabine-induced leukoencephalopathy has been previously described, the extensive signal abnormality in this case is unique. It truly highlights the spectrum of toxic effects of Capecitabine. The teaching point is that when you see bilateral symmetric think about toxic/metabolic etiologies.

Capecitabine is an oral fluoropyrimidine chemotherapeutic agent used primarily in the treatment of colorectal and breast cancer. Capecitabine-induced leukoencephalopathy was first described by Niemann et al. in 2004 and to date 12 cases of this disease with associated MRI findings of leukoencephalopathy reported. Although the exact mechanism of capecitabine neurotoxicity is not well understood, it is known that during its conversion to 5-FU it crosses the blood brain barrier and is found preferentially in the white matter tracts. This results in a wide spectrum of symptoms depending on the location of involvement making diagnosis difficult. Radiological findings in this condition typically include signal changes in the cerebral white matter seen on MRI, specifically restricted diffusion and/or increased signal intensity on T2/FLAIR sequences. There appears to be a strong propensity for involvement of the corpus callosum and densely myelinated white matter tracts in the periventricular, posterior parietal, and anterior thalamic regions. Capecitabine-induced leukoencephalopathy is treated by the cessation of capecitabine chemotherapy. Excellent recovery upon cessation of capecitabine with no or minimal residual deficit has been reported to occur within several days in all reported cases. Radiological differential diagnosis of leukoencephalopathy involving the bilateral corticospinal tracts, which would include amyotrophic lateral sclerosis (ALS), primary lateral sclerosis (PLS), hypoglycaemic coma, X-linked adrenoleukodystrophy (ALD), Wilson disease as well as adult-onset leukoencephalopathy with axonal spheroids and pigmented glia (ALSP).



(Filename: TCT_E-2_CapcitabineInducedLeukoencephalopathy.jpg)

E-3

10:38AM - 10:42AM

MDMA (3,4-methylenedioxymethamphetamine) overdose causing anoxic-ischemic encephalopathy

M Manganaro¹, F Boucher¹, D Miller¹, E Gu¹, Z Wilseck¹, J Kim¹, A Anderson¹

¹*University of Michigan, Ann Arbor, MI*

Purpose

Carbon monoxide is a classic cause of ischemia and anoxic injury in the bilateral globus pallidi; however, MDMA (3,4-methylenedioxymethamphetamine) is another etiology that can have a similar imaging appearance.

Materials and Methods

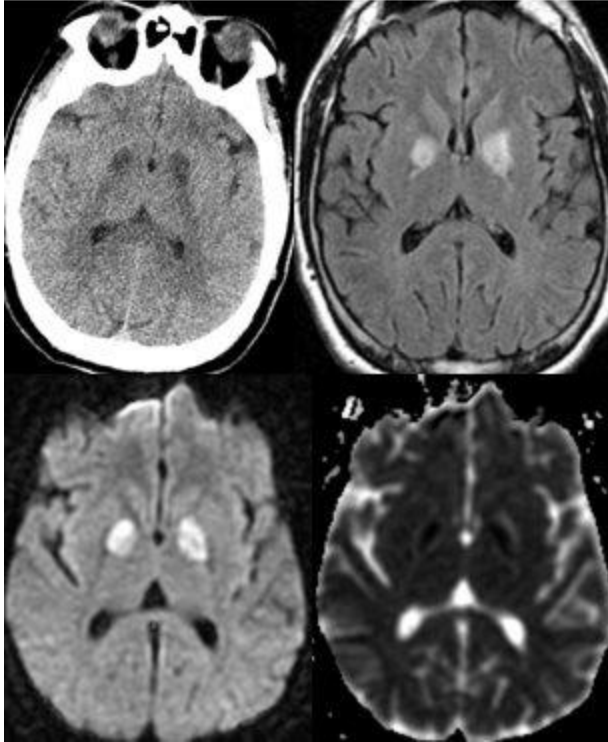
A 28-year-old male was found unconscious and rushed to the emergency department where he was stabilized and a CT head was performed revealing hypodensities in the bilateral basal ganglia. MRI demonstrated restricted diffusion corresponding to the hypodensities on CT consistent with ischemia. The patient was intubated and further work-up revealed a toxicology screen positive for MDMA (3,4-methylenedioxymethamphetamine), which can result in ischemic changes of the deep white-matter structures including the Globus pallidi in a similar pattern to that seen in CO poisoning. Following aggressive rehydration and temperature cooling the patient awoke with no visible neurological deficits. After counseling he was discharged in good health.

Results

CT: hypo-densities in the bilateral Globus pallidi MRI: FLAIR hyper-intensity and restricted diffusion in the bilateral Globus pallidi

Conclusions

Carbon monoxide is a classic cause of ischemia and anoxic injury in the bilateral globus pallidi; however, MDMA (3,4-methylenedioxymethamphetamine) is another etiology that can have a similar imaging appearance. The mechanism of action includes rapid release of 5-hydroxytryptamine, which is one of the most potent vasoconstrictors in the brain, which stimulates the 5-HT_{2A} receptors in small vessels leading to prolonged vasospasm with necrosis in the involved regions of the brain. The highest concentration of these receptors is in the globus pallidi and occipital cortex, which accounts for these neuroimaging findings.



(Filename: TCT_E-3_Methoverdose.jpg)

E-4

10:42AM - 10:46AM

CT and MRI Findings in Two Siblings with Pompe's Disease

J Hodgson¹, T Moritani², A Capizzano¹

¹University of Iowa Hospitals and Clinics, Iowa City, IA, ²University of Michigan, Ann Arbor, MI

Purpose

Late-onset Pompe's disease has been associated with intracranial arteriopathies due to arterial intimal and smooth muscle lysosomal glycogen accumulation. In this report, we present two sibling cases that demonstrate characteristic radiologic findings of Pompe's disease. The purpose of this report is to emphasize the importance of fully evaluating the etiology of stroke in patients with Pompe's disease.

Materials and Methods

Patient One: A 41-year-old male with late-onset Pompe's disease presented with several weeks' duration of intermittent diplopia and left facial paralysis. Patient Two: The patient's brother, a 37-year-old male with late-onset Pompe's disease, was subsequently evaluated and found to have mild vertebral artery ectasia and wall thickening. He was treated with enzyme replacement therapy.

Results

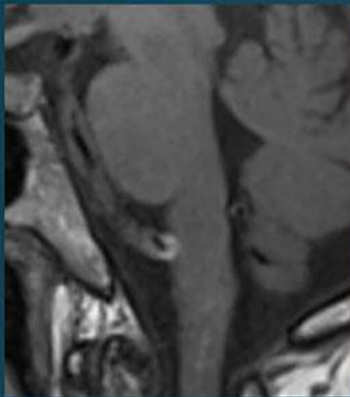
Initial MRI revealed an acute stroke in the right cerebellum and cerebellar peduncle. Further investigation revealed the cerebellar infarcts were secondary to dissection of the vertebrobasilar artery. Two month follow-up MRI and MRA including pre- and postcontrast T1 SPACE and T2 SPACE (3-D Black Blood Imaging) revealed multifocal dissection and intramural hematoma of the vertebrobasilar artery. Arterial wall thickening with enhancement is thought to be due to lysosomal glycogen accumulation with associated vessel wall injury. CT angiogram (CTA) demonstrated vertebral artery dissection and stenosis of the vertebrobasilar artery. The patient was treated with aspirin, statin, and enzyme replacement therapy but progressively worsened on follow-up CTA and MRI/MRA.

Conclusions

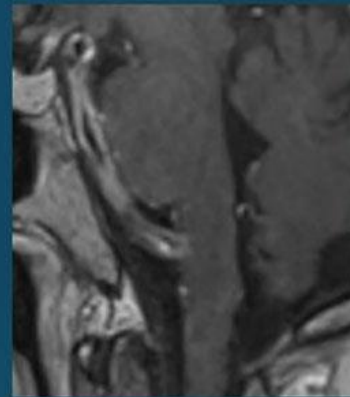
We illustrate characteristic vascular imaging findings and stress the importance of evaluating intracranial arteriopathies in patients with late-onset Pompe's disease, as they are at increased risk of developing vertebrobasilar artery dissection and stroke.

A 41-year-old male with late-onset Pompe's disease presented with several week duration of intermittent diplopia and left facial paralysis.

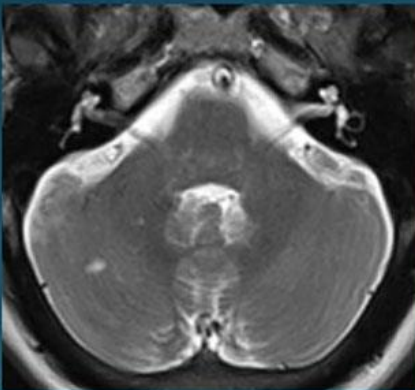
Sag T1 SPACE



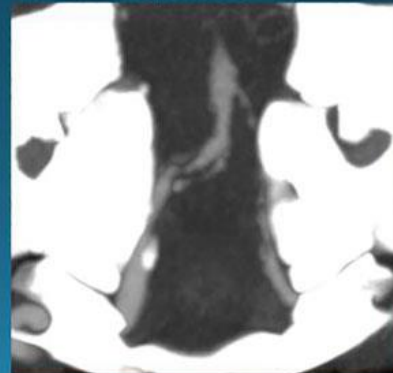
Sag CE T1 SPACE with contrast



T2 Ax



CTA coronal MPR



(Filename: TCT_E-4_Pompephoto1ASNR28229.jpg)

E-6

10:50AM - 10:54AM

Case report- A 53 year-old female with history of diabetes mellitus presents with involuntary movements

D Luu¹, J Greenstein¹, L Voutsinas¹, S Serras¹, J Hwang¹, M Raden¹, D Klein¹

¹Staten Island University Hospital, Northwell Health, Staten Island, NY

Purpose

Hemichorea-hemiballism syndrome (HHS) is a rare cause of unilateral chorea usually seen in diabetic patients presenting with nonketotic hyperglycemia. This case report discusses a 53-year-old female patient who presented to our ED with characteristic clinical presentation and imaging findings of HHS.

Materials and Methods

A 53-year-old female with a history of diabetes mellitus presented to the emergency department with

Oral Presentations & Excerptas

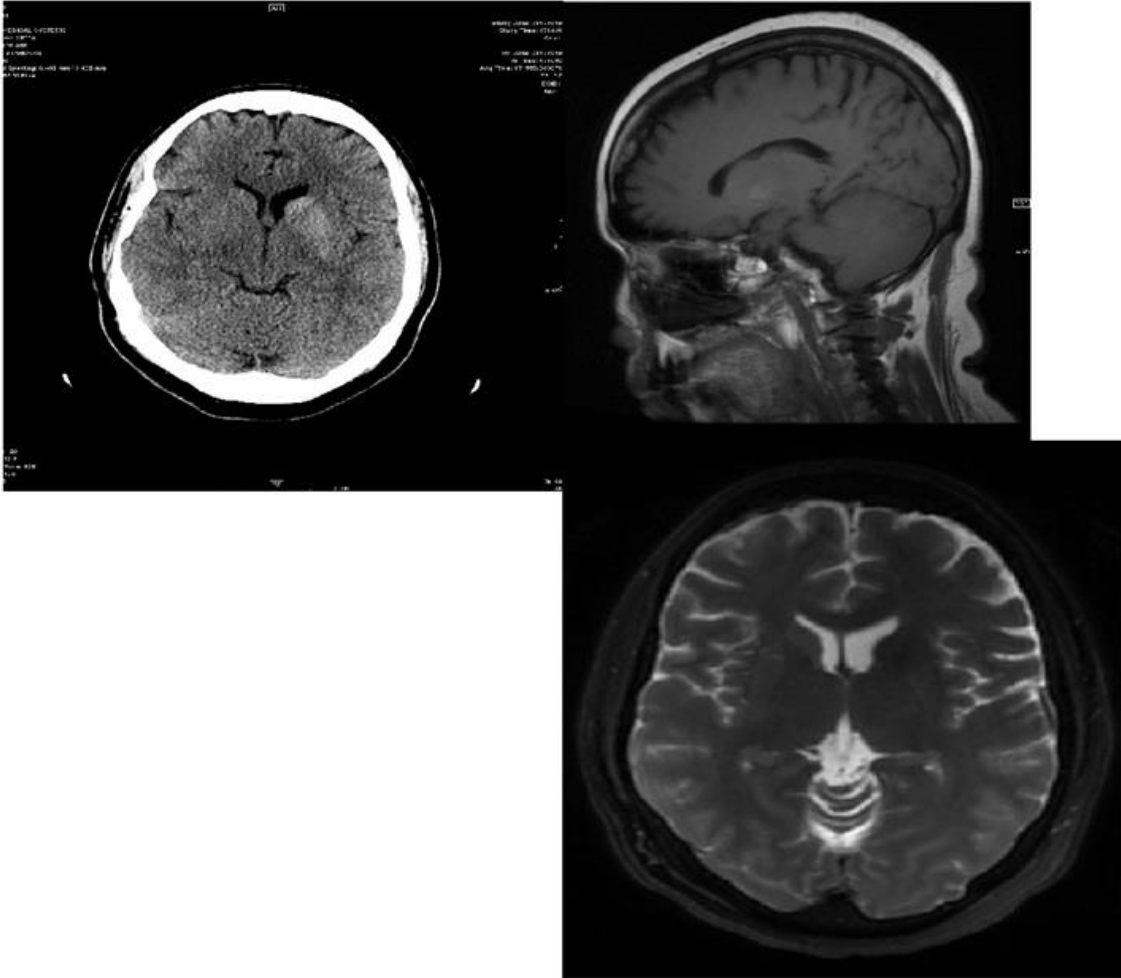
involuntary choreiform-like movements to her right upper and lower extremities. She reports that the movements started two days ago and were not associated with recent trauma, new medications, or focal weakness. Laboratory analysis demonstrated an elevated blood plasma glucose >600, with an arterial pH greater than 7.30, and undetectable serum ketones. A noncontrast CT of the head was obtained initially and a MRI of the brain two days later.

Results

Noncontrast axial CT of the head demonstrates a nonexpansile uniform hyperdensity of the left caudate head and putamen without mass effect or adjacent edema. MRI of the brain without contrast shows increased T1 signal and decreased T2 signal noted in the left caudate head and the left putamen.

Conclusions

Hemichorea-hemiballism syndrome (HHS) is a rare cause of unilateral chorea usually seen in diabetic patients presenting with nonketotic hyperglycemia. It is considered to be one of the neurological complications of nonketotic hyperglycemia, along with nonketotic hyperosmolar coma and nonketotic hyperglycemic seizures. The pathogenesis is not completely understood, but is believed to be due to hyperglycemia-induced disruption of the blood-brain barrier, along with perfusion changes to the contralateral striatum, and ischemic excitotoxicity of GABAergic neurons and reactive astrocytes. Symptoms are involuntary, poorly coordinated movements of the extremities which improve while asleep, and can be either unilateral or bilateral. The diagnosis is made clinically based on the presence of choreiform movements in the setting of uncontrolled hyperglycemia. However, typical imaging findings can help supplement assurance for the diagnosis. MRI of the brain is the modality of choice for assessing possible nonketotic hyperglycemia hemichorea and typically demonstrates signal changes particularly in the putamen and/or caudate. Hyperintensity on T1WI sequence is the most consistent finding of the disease. T2/Flair sequence may be variable but generally demonstrates hypointensity in the area and DWI will show restricted diffusion. CT of the head may be initially normal, but later it can demonstrate hyperdensity in the striatal region. Treatment consists of aggressive glycemic control and symptomatic management of choreic movements with either benzodiazepines or typical neuroleptics such as Haldol or risperidone. The prognosis is excellent, but depends on the prompt identification and management of hyperglycemia. The imaging findings have been found to gradually resolve after glycemia correction. However, they tend to return to baseline more slowly than the clinical findings.



(Filename: TCT_E-6_ASNR2018.jpg)

E-7

10:54AM - 10:58AM

CNS Findings of Secondary Hemochromatosis in β Thalassemia

M Clement¹, N Wilson¹

¹*Boston University Medical School, Boston Medical Center, Boston, MA*

Purpose

Imaging findings of secondary hemochromatosis related to multiple prior blood transfusions in a patient with β Thalassemia will be reviewed.

Materials and Methods

A 44-year-old female from Ecuador with beta thalassemia intermedia presented with mild tremors (right arm > left arm), arthralgias and ataxia. She has a past medical history of hypothyroidism, osteoporosis, and is status post cholecystectomy. Her last blood transfusion was one year ago. Her laboratory studies were remarkable for hyperferritinemia; mild but consistently greater than 1000 ng/mL. Brain MRI was obtained to evaluate the source of her movement disorder which demonstrated findings suggestive of secondary hemochromatosis. Subsequently, MRI of the abdomen was obtained with additional findings

consistent with secondary hemochromatosis. The patient will start chelation therapy with Jadenu 1400mg daily for a short period of time to treat iron overload. Her tremor is improving on Propanolol.

Results

Brain MRI demonstrated susceptibility artifact (Images 1-2) and T1 hypointensity (Image 3) in the bilateral caudate, left greater than right. Dentate nuclei (Image 2), red nuclei and substantia nigra demonstrated blooming artifact on susceptibility weighted sequence (Fast Field Echo). There was also the suggestion of blooming artifact in the choroid plexus. The bone marrow was diffusely T1 hypointense (Image 3). MRI of the abdomen (Image 4) demonstrated diffuse T1 hypointense signal within the liver and spleen on T2-weighted imaging. There was loss of signal throughout the liver on in phase imaging. Splenomegaly was present and the bone marrow was diffusely T1 hypointense. In addition, iron quantification demonstrated iron level of 6 ± 1 mg iron/mg dry-weight tissue (normal range: 0.2 - 2.0 mg iron / mg dry-weight tissue). Findings are consistent with secondary hemochromatosis.

Conclusions

Recognition of the constellation of CNS findings in secondary hemochromatosis can both provide the initial diagnosis of iron overload and substantially guide clinical management. Often serum ferritin levels are unreliable. MRI susceptibility weighted sequences are an invaluable biomarker for characterizing the extent of iron overload and monitoring disease progression.

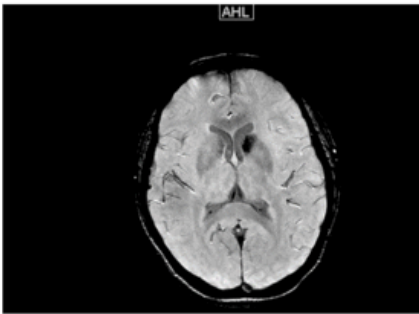


Image 1. Axial Fast Field Echo (FFE) Brain MRI

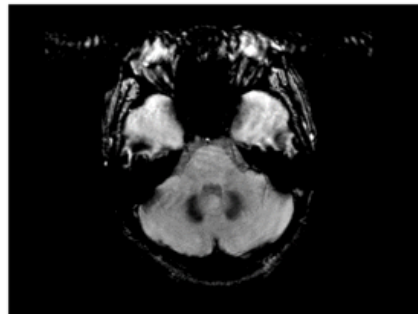


Image 2. Axial FFE Brain MRI

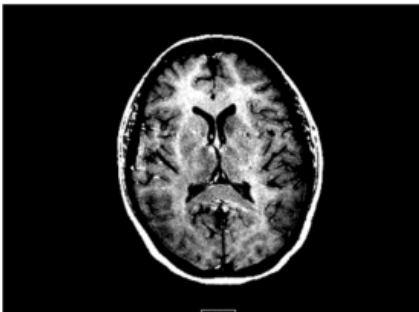
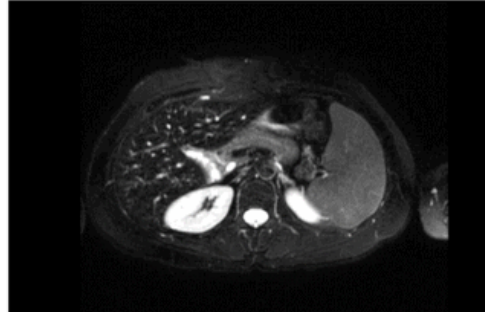


Image 3. T1 Non-Contrast Spin Echo Brain MRI

(Filename: TCT_E-7_ThalGraphics.gif)



T2 Axial Abdomen MRI

E-8

10:58AM - 11:02AM

Wallerian Degeneration of the Splenium of the Corpus Callosum: MRI Findings and Symptoms

D Quiñones Tapia¹, A Castellaccio², F Gilo Arrojo¹

¹Hospital del Rosario, Madrid, Spain, ²Università degli Studi di Sassari, Sassari, Sardinia, Italy

Purpose

Wallerian degeneration (WD) of the corticospinal tract is a well known imaging finding on MRI. But,

Oral Presentations & Excerptas

when it affects other white-matter tracts both imaging and associated symptoms are not as common. We present a case where a delayed lesion of the corpus callosum occurred months after occipital lobe infarct. The patient was symptomatic and complained demanding further studies and MRI. We bring attention to delayed symptoms in the setting of Wallerian degeneration in the splenium.

Materials and Methods

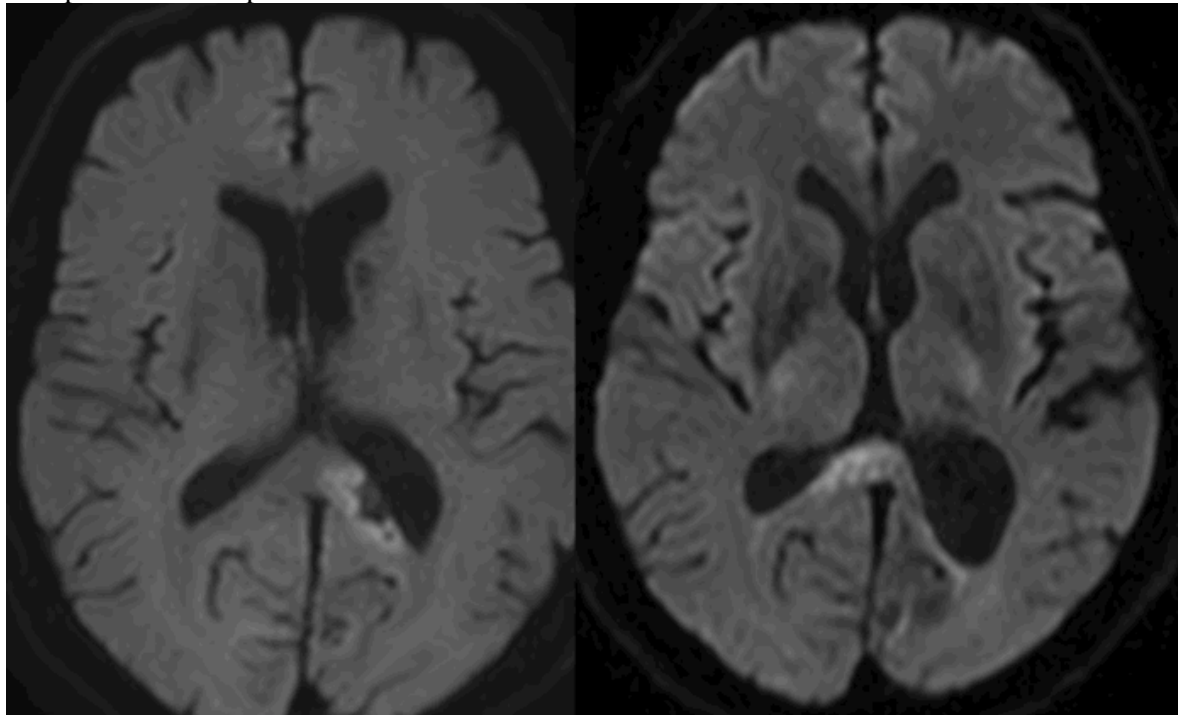
A 59-year-old right-handed male with multiple vascular risk factors had a left internal carotid artery endarterectomy and an embolic arterial occlusion of the right leg two months before. On examination he had no motor deficit and right hemianopia. MRI revealed a small medial left occipital infarct and a subependymal white-matter lesion of the left posterior corpus callosum. Six months later he complains of dizziness and cognitive and intellectual disturbances. He has prosopagnosia and right hemianopia persists. He demands MRI which was obtained 11 months after initial infarct, demonstrating progressive left occipital lobe atrophy and a new lesion in the splenium. This lesion perdured three more months and progressed to the right side.

Results

- Axial DWI (b 1000), FLAIR and T2*, sagittal T1, and sagittal 3D T2 - 3T MRI 2 months after stroke: subacute vascular lesion affecting the subependymal left atrium white matter with restricted diffusion. No mass effect or hemosiderin. Small medial occipital chronic cortical infarct. - 3T MRI at 11 months: chronic left PCA infarct with progressive atrophy and subependymal malacia. New lesion crossing the splenium with restricted diffusion, hyperintense on FLAIR and T2 and hypointense on T1, suggestive of Wallerian degeneration. - 1.5T MRI at 14 months: WD progresses to the right side.

Conclusions

The incidence of Wallerian degeneration in the corpus callosum after ischemia is unknown, but reported rarely. In the corticospinal tract a stereotypical imaging course of Wallerian degeneration is well known, but not when it affects the splenium. The patient had prosopagnosia and "felt strange" and his symptoms started months after initial vascular insult, perduring over months. Symptoms could be related to disrupted interhemispheric connection of visual areas.



(Filename: TCT_E-8_WD.gif)

E-9

11:02AM - 11:06AM

How about DaT? A Rare Case of Young Onset Parkinson Disease

V Yedavalli¹, Z Dymon², M Gabriel²

¹Advocate Illinois Masonic Medical Center, Chicago, IL, ²Loyola University Medical Center, Maywood, IL

Purpose

Parkinson disease is a debilitating neurodegenerative condition, most commonly affecting elderly white males with average age at diagnosis in the seventh decade. Although common overall, Parkinson disease has a rare subtype characterized by early manifestation of symptoms. This young-onset Parkinson disease subtype (YOPD) is seen in ages 21 to 49 with a prevalence of 12-40 per 100,000 cases. Moreover, given that the disease is masked by concomitant psychiatric conditions which are more commonly seen, this creates a diagnostic dilemma. We present a case of a 44-year-old male diagnosed with YOPD on DAT scan after an initial routine seizure workup.

Materials and Methods

We present a 44-year-old Caucasian male with acute seizures which was initially thought to be benzodiazepine withdrawal. The patient's past medical history was significant for clinical anxiety treated with benzodiazepines as well as cocaine and alcohol abuse. MR brain was subsequently performed and was negative for acute abnormality or abnormal enhancing lesion. EEG evaluation was also within normal limits without epileptiform activity. The patient then presented with a new onset left-sided fine postural tremor and mild rigidity with normal strength and sensation on physical examination. Thereafter, an I123 DaT scan was performed and demonstrated decreased activity in the right putamen, consistent with parkinsonian syndrome. After appropriate therapy, the patient's symptoms were controlled.

Results

Figure 1: A-B) DaT images demonstrating marked decreased uptake within the right putamen, consistent with Parkinson disease.

Conclusions

Parkinson disease is a debilitating neurodegenerative disease with multiple subtypes. The young-onset form (YOPD) is especially rare and often masked due to overlapping symptoms from more common psychiatric diseases, making the diagnosis challenging. If suspected, DaT scan can add value in early diagnosis of YOPD, allowing for appropriate therapy and management.

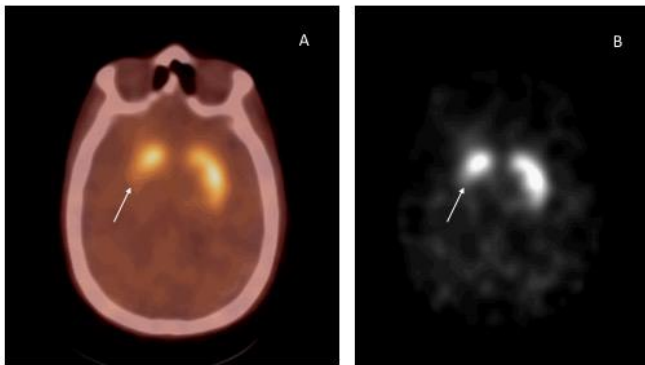


Figure 1: A-B) DAT images demonstrating marked asymmetric lack of uptake within the right putamen consistent with Parkinson's disease.

(Filename: TCT_E-9_YOPDDATscan.jpg)

E-10

11:06AM - 11:10AM

Unusual Imaging Findings in Chronic Hepatic Encephalopathy/ Acquired Hepatocerebral Degeneration

V Tsehmaster Abitbul¹, N Zakhari¹, E Portela de Oliveira¹, A Guarnizo¹, S Bravo-Grau², M dos Santos¹, C Torres¹

¹*The Ottawa Hospital, Ottawa, Ontario, Canada,* ²*P. Universidad Católica de Chile, Santiago, Chile*

Purpose

Acquired hepatocerebral degeneration is a rare clinical neurological syndrome, associated with chronic liver disease, characterized by cognitive dysfunction and motor disorders. We would like to review the clinical presentation and MRI findings of acquired hepatocerebral degeneration, and present key imaging findings associated with this rare neurological syndrome.

Materials and Methods

A 63-year-old woman who presented with a two year history of rapid cognitive decline, psychosis, parkinsonism, behavioral deficits, dysarthria, facial dyskinesia, tremor and gait ataxia. She had a past medical history of nonalcoholic steatohepatitis (NASH), diagnosed two years earlier.

Results

MRI at presentation showed subcortical, linear increased T2-weighted and FLAIR signal intensity in laminar distribution within bilateral precentral gyri, in addition to other frontal and parietal gyri with associated GRE blooming. Additionally, symmetric T2 hyperintensity was seen in bilateral putamen nuclei, as well as symmetrical susceptibility foci at bilateral globus pallidi. On follow-up MRI, two years later, the cortical abnormalities persisted, however appeared less conspicuous, and there had been interval resolution of findings in the putamen.

Conclusions

We present herein unusual imaging findings of laminar subcortical T2-weighted hyperintensities corresponding to pseudo laminar spongiform degeneration, in a patient with clinical chronic hepatic encephalopathy and acquired hepatocerebral degeneration. Similar findings have been described in the middle cerebellar peduncles and lentiform nuclei. (Example images would be shown on presentation). The cause of these white-matter changes is uncertain, but toxic and metabolic processes as well as osmotic changes associated with electrolyte disorders, related to liver disease have been proposed as underlying etiologies.

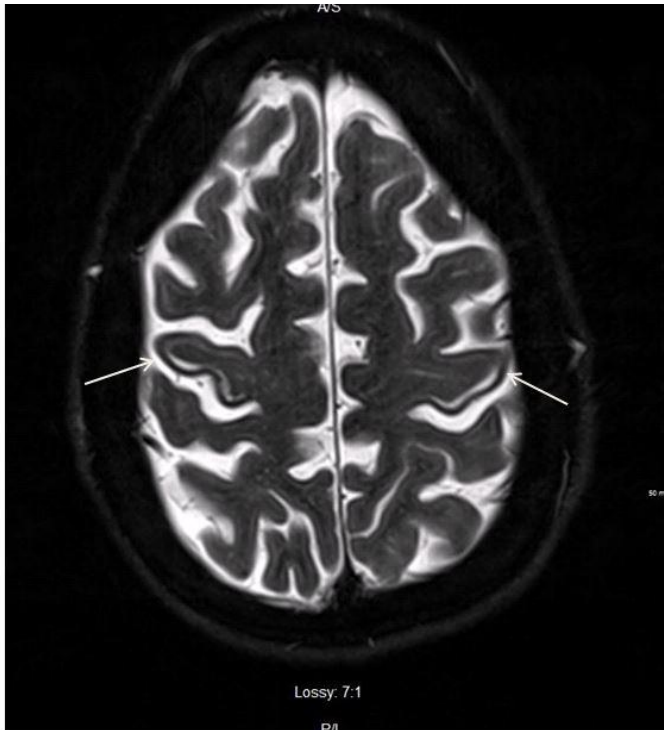


Figure 1: T2 weighted axial image showing linear subcortical high signal in laminar distribution in bilateral frontal and parietal gyri (arrows).

(Filename: TCT_E-10_Hepatocerebraldegenerationabstractimage.JPG)

E-11

11:10AM - 11:14AM

Beyond Dawson’s fingers: critical findings pointing to multiple sclerosis

M Juan¹, A Sidhu², R Kaakaji¹

¹St. Mary Mercy Hospital, Livonia, MI, ²Providence-Providence Park Hospital, Southfield, MI

Purpose

Since the coining of the term "Dawson's fingers" in 1916, periventricular white-matter lesions have been widely associated with multiple sclerosis (MS) (ref. 1). However, seldom known are various additional radiographic features, which are equally important and characteristic of the immune-mediated demyelinating disease. We present a case highlighting these findings.

Materials and Methods

A 63-year-old female presented with five-day history of loss of balance, weakness, upper extremity paresthesia and profound fatigue. Contrast-enhanced magnetic resonance imaging (MRI) of the brain and cervical spine were performed.

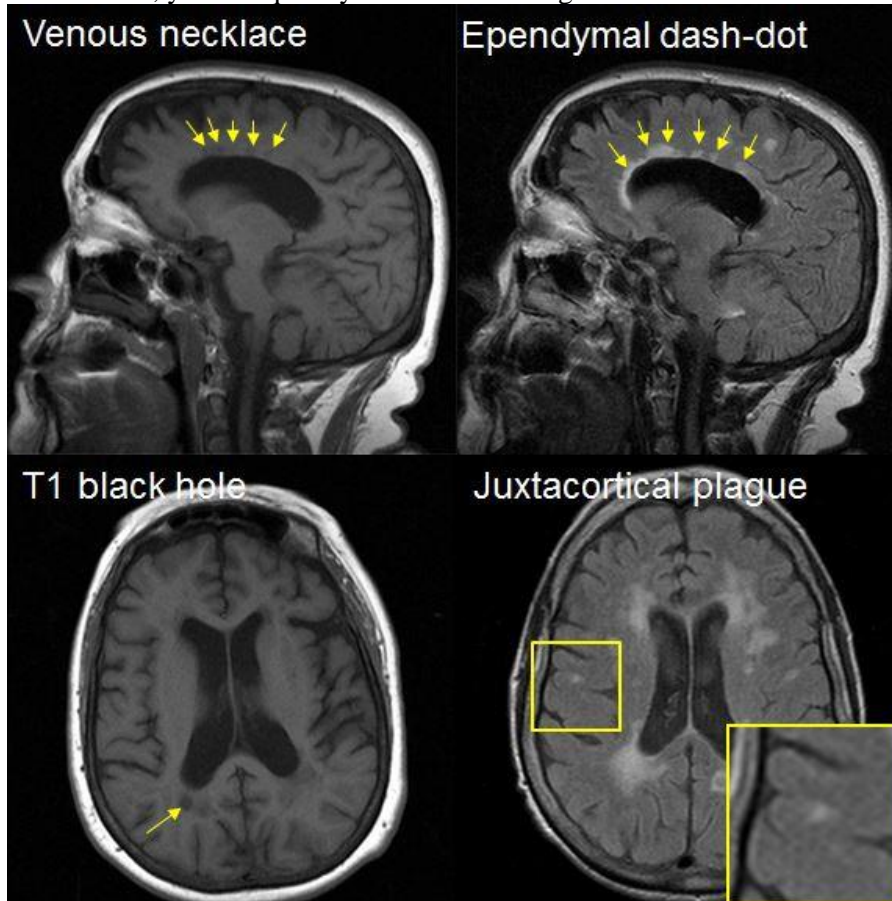
Results

MRI brain demonstrated moderate burden of patchy and confluent areas of abnormal T2/FLAIR hyperintense signal in the periventricular, deep, and subcortical cerebral white matter. Scattered iso to hypointense lesions (T1 black holes) and small nodular hypointensities in the calloseseptal interface (venous necklace) were seen on T1WI. FLAIR sequences showed small foci of hyperintensity along the calloseseptal interface (ependymal dot-dash sign) and juxtacortical plaques in the parieto-occipital region. MRI cervical spine demonstrated hyperintense signal within central and posterior paramedian spinal cord on T2WI at the level of C1-C2 interspace.

Oral Presentations & Excerptas

Conclusions

Based on the McDonald criteria, the diagnosis of MS requires evidence of lesions disseminated in time and space (ref. 2). Consequently, MRI plays a crucial role with its capability of detecting the locations of the demyelinating lesions (space dissemination) and tracking disease changes over time (time dissemination) offering objective data for the diagnosis of MS. Beyond Dawson's fingers, MS can be accompanied by a number of additional less well known MRI findings including venous necklaces, T1 black holes, juxtacortical plaques, and the ependymal dot-dash sign (ref. 2-4). The current case reviews the common, yet infrequently cited MRI findings of MS.



(Filename: TCT_E-11_BeyondDawsonsfingers_ASNR2018_MJuan.JPG)

E-12

11:14AM - 11:18AM

Ectopic Cerebellar Brain Parenchyma

R Hobohm¹, P Codd¹, J Voyvodic¹, M Malinzak¹
¹Duke University Medical Center, Durham, NC

Purpose

Although ectopic cerebellar brain parenchyma is an extremely rare entity, it is a diagnosis that can be made based on MRI findings in select cases, obviating the need for surgical intervention.

Materials and Methods

A 53-year-old male with no relevant past medical history presented with nine months of frontal headaches, left-sided tinnitus, and phonophobia. An outside MRI of the brain reported a right cerebellopontine angle meningioma, and the patient was referred for neurosurgical evaluation.

Oral Presentations & Excerptas

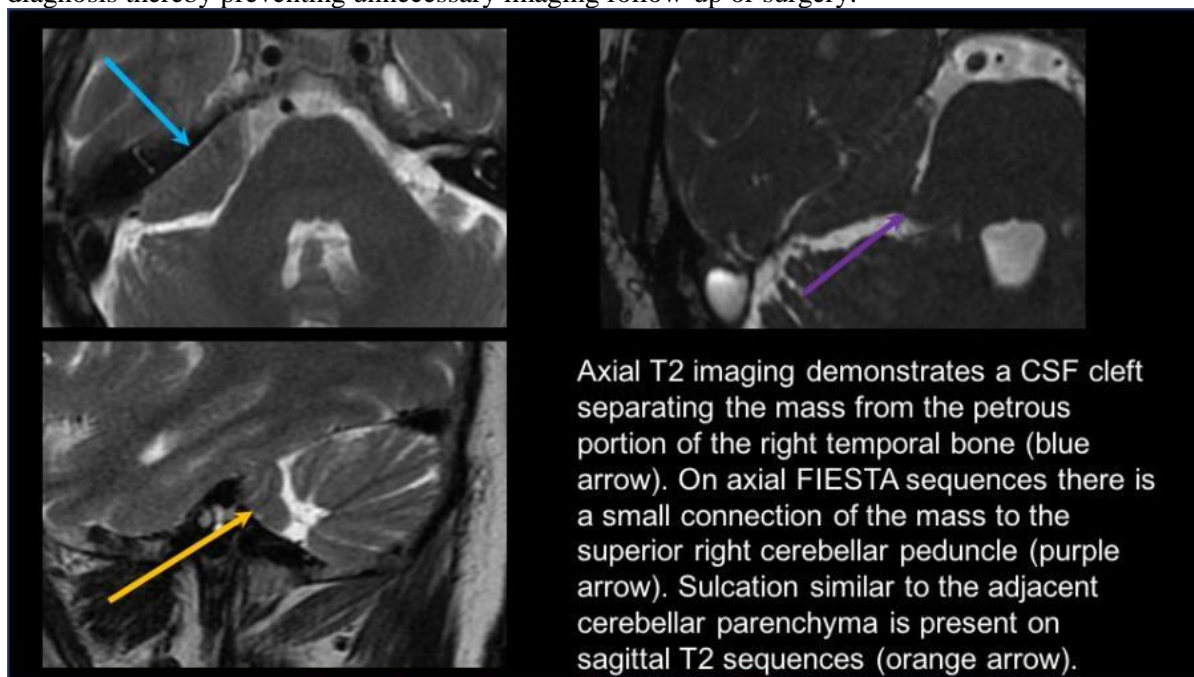
Neurological examination was normal except for decreased auditory discrimination on the right. Audiology examination revealed moderate to severe left (contralateral to the lesion) and mild right sensorineural hearing loss with excellent speech recognition.

Results

Repeat contrast-enhanced MRI with targeted imaging of the internal auditory canals was performed to better characterize the mass. This demonstrated an unchanged 3.4 x 1.9 x 1.4 cm mass lesion in the right cerebellopontine angle. The lesion demonstrated signal characteristics identical to brain parenchyma on all MRI sequences, with no restricted diffusion or appreciable contrast enhancement. T2-weighted images revealed a thin cleft of CSF between the mass and the right petrous temporal bone, which would not be expected for a meningioma. Moreover, the morphology of the mass was remarkable for surface undulations that appeared indistinguishable from the folia of the adjacent normal cerebellum, as well as for a narrow parenchymal stalk connecting the lesion to the right superior cerebellar peduncle. DTI and functional MRI analyses are scheduled but yet to be performed at time of submission.

Conclusions

The imaging findings of the right cerebellopontine angle mass lesion were not consistent with meningioma as suggested on outside imaging but rather most consistent with ectopic cerebellar brain parenchyma. This is a rare diagnosis, especially in the adult population, as a majority of the reported cases occurred in pediatric patients with additional central nervous system anomalies. The patient's right-sided ectopic cerebellar brain parenchyma is currently thought to be asymptomatic, as the complaints of headache and tinnitus are of recent onset and predominantly affect the contralateral side. Knowledge of ectopic cerebellar brain parenchyma and optimization of MRI sequence selection can help to establish the diagnosis thereby preventing unnecessary imaging follow-up or surgery.



(Filename: TCT_E-12_ASNRSubmission.jpg)

E-13

11:18AM - 11:22AM

Multifocal Calvarial Tuberculosis Mimicking Metastatic Tumor

S Kamalian¹, S Teoh¹, A Simeone¹, D Smoot¹, P Sasson¹, L Khorashadi¹

¹Mount Auburn Hospital, Cambridge, MA

Purpose

Tuberculosis (TB) continues to be of clinical concern in the highly developed countries, likely as a byproduct of ease of travel to and from the endemic areas. Although many patients are diagnosed and treated in early stages of the disease, there are a subgroup of patients who present with advanced stages of disease to the healthcare facilities due to different factors, such as cultural barriers or stigma, level of education and TB medication adherence due to side effects. Familiarity with the constellation of possible imaging findings in patients with late-stage TB is crucial for timely diagnosis, radiologists may play a crucial role in assisting the clinicians to arrive at the correct diagnosis.

Materials and Methods

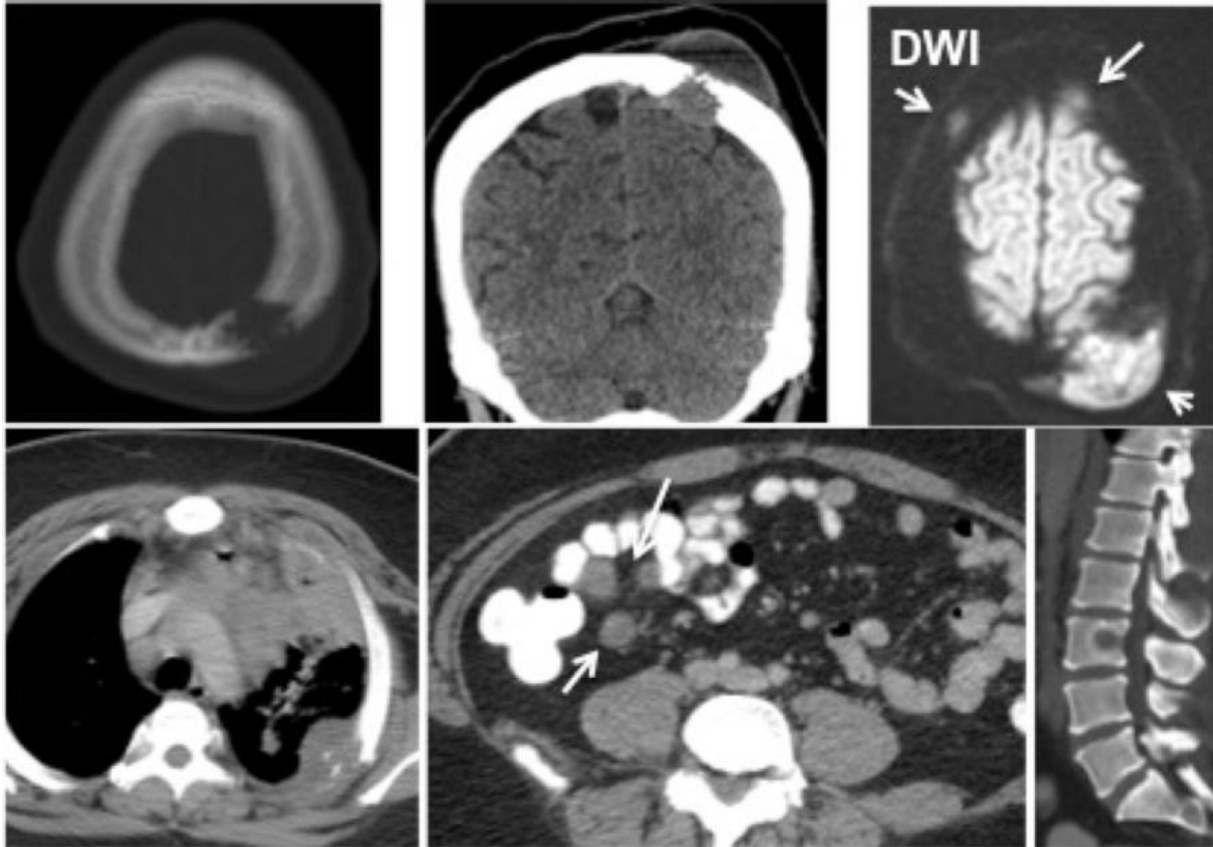
A 25-year-old man without significant past medical history presented to the emergency department with chief complaint of lump on his head, fatigue and unintentional weight loss. At presentation the remainder of the history was noncontributory. On physical exam, there was a prominent lump over the posterior aspect of the left parietal bone. Biopsy confirmed granulomatous inflammation with acid fast bacilli on gram staining. Further history which was later provided by the patient included father diagnosed with active tuberculosis two years ago, who was admitted to hospital and eventually completed proper TB treatment. Our patient refused the PPD test, but the rest of the family had negative PPD test. He also evaded all health care visits from the state while his father was being treated for TB.

Results

The initial head CT showed a 4.8 cm aggressive-appearing mass centered within the diploic space of the left parietal bone eroding the inner and outer tables with mass effect on the left parietal lobe. MRI of the brain showed multiple additional intradiploic, enhancing masses in the skull with dural extension. Metastatic work-up included a Torso CT showing left upper lobe consolidation and multiple lytic lesions in the left ribs. Additional lytic lesions in the lumbar vertebral bodies with mesenteric lymphadenopathy (figure), concerning for metastatic disease versus multifocal infections such as TB.

Conclusions

Familiarity with the constellation of possible imaging findings in patients with long-standing TB is essential for radiologists to guide the patient management.



(Filename: TCT_E-13_SkullTBJPEG.jpg)

E-14

11:22AM - 11:26AM

Neuro-Behcet's Disease Presenting with Mixed Parenchymal and Vascular Features.

M.Nguyen¹, V Phalke¹

¹*Oregon Health Science University, Portland, OR*

Purpose

Behcet's disease (BD) is a multisystem inflammatory disorder of unclear etiology, classically manifesting as aphthous oral and genital ulcers in conjunction with uveitis. Central nervous system involvement, known as Neuro-Behcet's disease (NBD), affects less than 10% of patients but accounts for the majority of morbidity and mortality associated with BD. Two categories of NBD – parenchymal and nonparenchymal – encompass our current understanding of the neurologic syndromes that develop in the course of systemic BD. Parenchymal NBD is characterized by intra-axial lesions with predilection for the brainstem and basal ganglia, and likely related to small vessel vasculitis. Nonparenchymal NBD, which targets the main cerebral vasculature in the form of aneurysm, thrombosis or hemorrhage, comprises far fewer cases. Both forms are rarely identified simultaneously in the same patient, as described here.

Materials and Methods

A 54-year-old female presents with complaint of progressively worsening headaches localized to the retro-orbital and parietal regions over the past several weeks. She describes approximately 12 years of near-daily migraines without aura, with pain typically generalized to the bioccipital regions. The patient also endorses a diagnosis of Behcet's disease given her history of relapsing noninfectious oral and genital aphthous ulcers over the past 17 years, although recent ophthalmoscopy did not confirm uveitis. She was recently initiated on treatment with azathioprine by her rheumatologist. Physical examination revealed

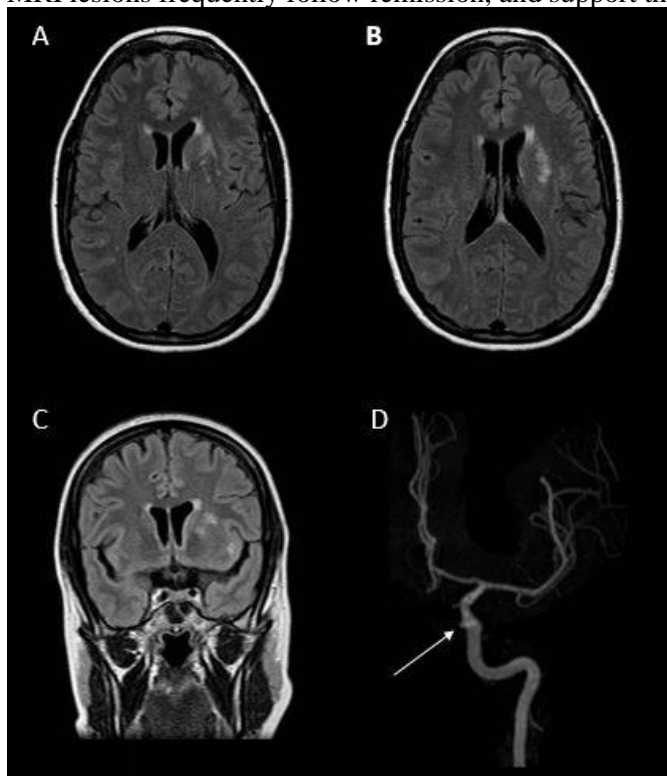
scattered ulcers in the oral mucosa and genital regions, and was otherwise unremarkable. Neurological examination did not reveal focal deficits. Gadolinium-enhanced magnetic resonance imaging of her brain revealed T2/FLAIR hyperintensities in the left putamen, and left greater than right extreme capsules. There was no associated mass effect, diffusion restriction or abnormal enhancement. Additional findings included a 2mm aneurysm in the medial wall of the left cavernous internal carotid artery. The patient was continued on azathioprine and reported improvement in her headaches and ulcers during subsequent follow-up at one and two months after the MRI exam.

Results

Axial FLAIR (figures A and B) and coronal FLAIR (figure C) gadolinium-enhanced brain MRI demonstrate high signal in the left putamen with involvement of the left greater than right extreme capsules. MR angiography (figure D, arrow) demonstrates a 2mm aneurysm in the medial wall of the left cavernous internal carotid artery.

Conclusions

To date, there are no validated criteria for definitive diagnosis of Neuro-Behcet's disease. The diagnosis is broadly defined as a neurologic syndrome with features of Behcet's disease that is supported by imaging, and no alternative explanation for neurologic complaints. Given the heterogeneous course of NBD, cautious exclusion of more common etiologies such as stroke, metastases and demyelinating disease takes precedence in narrowing the differential to NBD, particularly in patients over the age of 50 with or without ancillary features of systemic Behcet's disease. Our patient meets the International Study Group criteria for BD, and presents with longstanding neurological symptoms that initially developed in the typical 20 to 40 year age range. Imaging is the current gold standard for diagnosis, and necessary to distinguish between parenchymal and nonparenchymal forms of NBD in order to guide further management. Recent studies have advocated for subclassification of parenchymal NBD into acute and chronic-progressive types to further tailor treatment, although no evidence-based treatment strategy exists. Current treatment paradigms include high-dose steroids followed by prolonged taper in the acute setting, and long-term prevention with immunosuppressant and TNF agents. Decrease or resolution of MRI lesions frequently follow remission, and support the diagnosis.



(Filename: TCT_E-14_NBD.JPG)

Granulomatous Hypophysitis

J Scheibal¹, R Hebert¹, A Steven²

¹Ochsner Clinic Foundation, New Orleans, LA, ²Ochsner Health System, New Orleans, LA

Purpose

To report a rare case of granulomatous hypophysitis. The clinical presentation, imaging features, and management are reviewed and contrasted to other pituitary lesions.

Materials and Methods

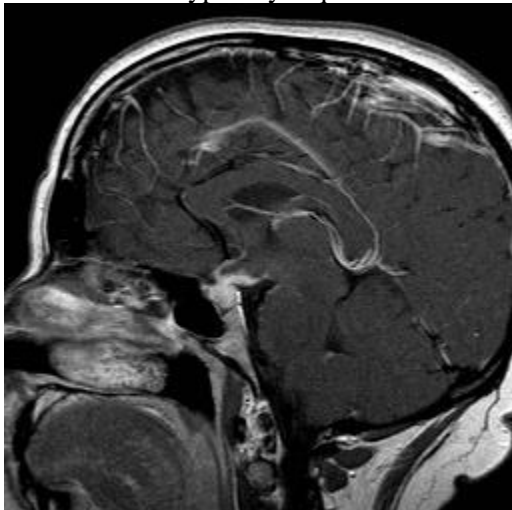
A 34-year-old female with history of Hashimoto's disease and irritable bowel syndrome presented from an outside institution with three days of acute onset, severe visual disturbance and one week history of recurrent migraine headaches, nausea and right-sided facial tingling. She denied any vomiting, fevers, or other acute complaint. Physical exam was positive for a bitemporal visual field deficit. MRI was performed revealing a homogeneously enhancing, thickened pituitary gland and pituitary infundibulum. Transsphenoidal biopsy and subsequent resection were performed revealing a granulomatous inflammatory process of the anterior and posterior pituitary glands, pathologic findings consistent with granulomatous hypophysitis.

Results

MRI brain demonstrates diffuse enlargement of the pituitary gland and infundibulum with intermediate signal intensity on T1- and T2-weighted images. There was diffuse homogeneous enhancement of the pituitary gland and stalk extending along the hypothalamus on postcontrast images. This lesion abutted the adjacent optic chiasm and there was additional thickening and peripheral enhancement of the optic tracts, chiasm and prechiasmatic optic nerves. Reported imaging characteristics of granulomatous hypophysitis include intense, homogeneous enhancement of the pituitary gland and infundibulum. Invasion of the adjacent sella turcica is rare. These imaging features overlap with several other more common inflammatory and neoplastic conditions including lymphocytic hypophysitis, Langerhans cell histiocytosis, tuberculous hypophysitis, neurosarcoidosis, CSF metastasis, and pituitary adenomas.

Conclusions

Granulomatous hypophysitis is a rare, chronic inflammatory disease of the pituitary gland. Patients most commonly present with headache, visual field deficits, and constitutional symptoms including low-grade fever, nausea, and vomiting. Imaging characteristics include diffuse enlargement of the pituitary gland and stalk with infiltrative postcontrast enhancement. While medical management is key, surgical intervention is typically required for both diagnostic and therapeutic purposes.



(Filename: TCT_E-16_1_1.jpg)

E-17

11:34AM - 11:38AM

Autosomal dominant TREX 1 angiopathy; imaging findings with histo-pathological correlation.

Y E Guindy¹, M Cornford¹, M Morrow¹, A Mlikotic¹

¹*Harbor University of California Los Angeles Medical Center, Torrance, CA*

Purpose

To discuss the imaging characteristics, clinical manifestation and genetic mutation associated with autosomal dominant TREX 1 angiopathy (aka CHARIOT, HRENS, CRV and RCVL), a rare form of central nervous system vasculitis

Materials and Methods

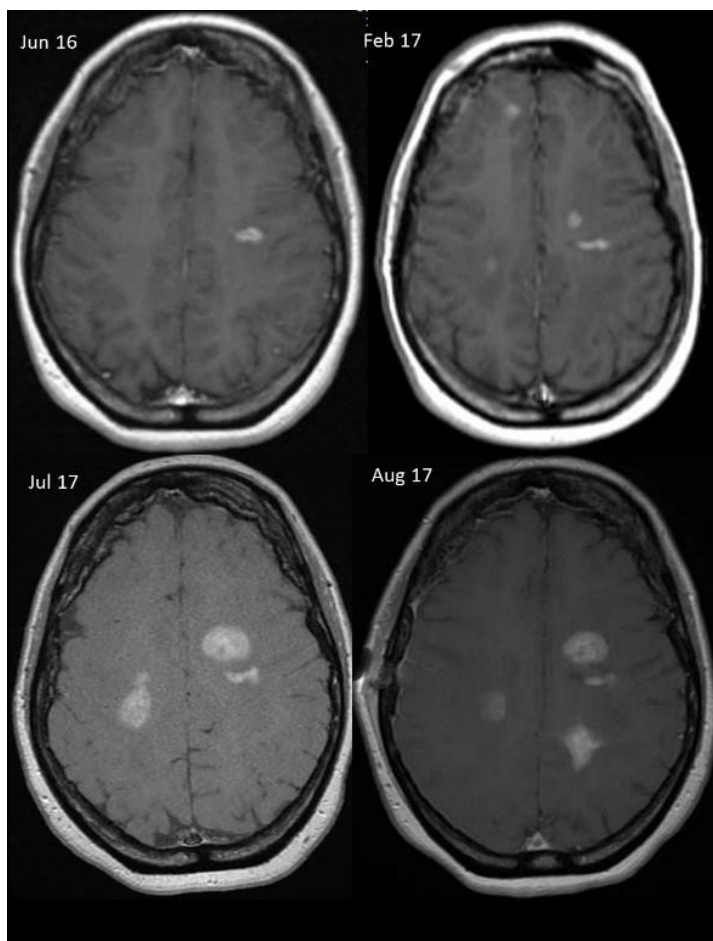
A 46-year-old woman, initially presented with bilateral vision loss, was diagnosed with vascular retinopathy. Family history included early death in several family members who were diagnosed with brain tumor or stroke. Sixteen months later she returned with dysarthria and word-finding difficulty and was found to have several (8) enhancing supratentorial white-matter lesions on MR imaging. Cerebrospinal fluid analysis yielded only oligoclonal bands, suggestive of a demyelinating process. The patient's clinical course remained stable; however, serial imaging demonstrated an increase in the size and number of parenchymal lesions and with an increasing degree of vasogenic edema. A biopsy of a temporal lobe lesion revealed perivascular inflammation. More recent imaging during admission for weakness and ataxia showed additional lesions and new development of infarcts. Genetic testing ultimately confirmed a TREX 1 mutation of chromosome 3.

Results

Serial MR imaging revealed a progressive course of linear and mass-like T2-FLAIR hyperintense, enhancing white matter lesions, some with diffusion restriction. Over time, lesions both increased in number and size with worsening degree of vasogenic edema. Later imaging showed further development of supratentorial and infratentorial arterial distribution infarcts.

Conclusions

Autosomal dominant TREX 1 angiopathy is a rare, inherited disorder that affects the basement membrane of the vascular endothelium. This entity should be considered in the differential for CNS vasculitides when characteristic CNS imaging and associated clinical findings are present.



(Filename: TCT_E-17_chariot.jpg)

E-18

11:38AM - 11:42AM

An Unusual Manifestation of Tuberculosis with Isolated Skull Base and Pachymeningeal Involvement

C Choi¹, J Cain², S Mathur²

¹Royal Preston Hospital, Manchester, England, ²Royal Preston Hospital, Preston, Lancashire, England

Purpose

A case report highlighting an unusual case of tuberculosis of the skull base with a protracted clinical course.

Materials and Methods

A 26-year-old male presented with a three-month history of persistent daily headaches and swallowing problems, but no focal neurological deficit on examination. Clinically he was diagnosed with myasthenia gravis which was subsequently well controlled with prednisolone and azathioprine. An MRI of the head was acquired at that time which was initially thought to be normal, but retrospectively demonstrated some subtle signal abnormality in the clivus. The patient was reassured and remained well on treatment until he re-presented three years later describing recurrent 'explosive' headaches that were worse on valsalva.

Results

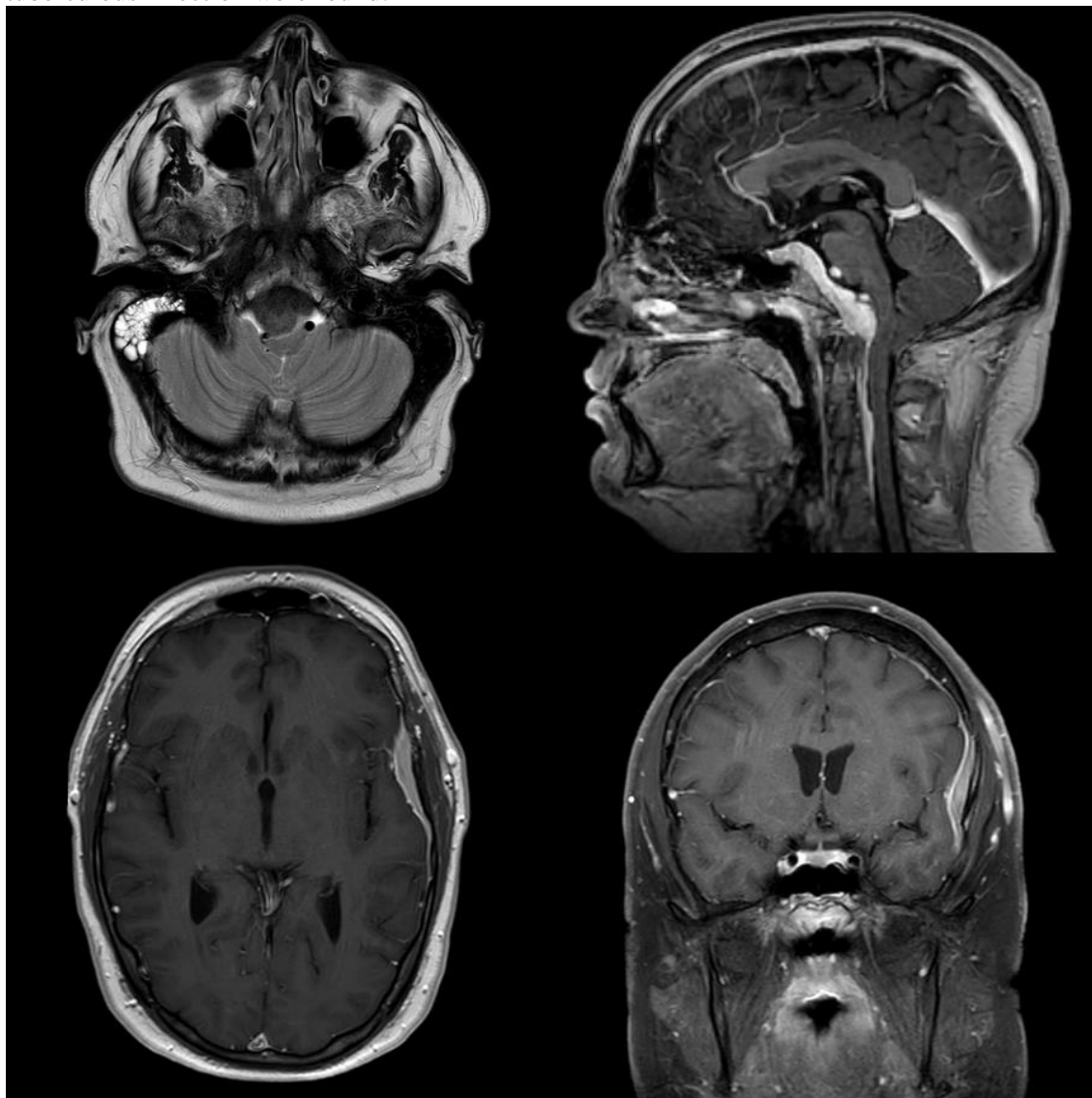
The initial MR demonstrates subtle abnormal T1 hypointensity in the clivus and nonspecific partial fluid opacification of the mastoid air cells bilaterally. The MR study from three years later shows a

Oral Presentations & Excerptas

homogeneously T2 hypointense extra-axial mass arising from the clivus causing kinking and compression of the brainstem. Prominent enhancement was demonstrated on postcontrast images both within the lesion and the clivus. Given the T2 signal, the primary differential was of inflammatory pseudotumour, possibly IgG4 related disease. Histology of this lesion revealed only inflammatory cells. Further imaging two months later demonstrated no change in the primary lesion, but did reveal a new left convexity dural based lesion. Biopsy of this lesion found no features of IgG4 disease; however, it did identify acid-fast bacilli. Early follow-up MRI after commencement of antituberculous treatment has shown a reduction in size of both lesions.

Conclusions

Tuberculosis is notorious for its protean clinical presentation and imaging findings (1). Approximately 5% of cases involve the CNS (1); however, this figure is higher in immunocompromised patients and involvement of the clivus is rare (2, 3). Although tuberculosis is an important rare differential for a hypertrophic pachymeningitis, this case is unusual its initially indolent course. No other signs of systemic tuberculous infection were found.



(Filename: TCT_E-18_TB.jpg)

E-19

Multimodality Imaging of Ipilimumab-Induced Hypophysitis in the Treatment of Metastatic Melanoma

M Flores¹, J Dennison¹, J Murray¹, G Felsberg¹, S Messina¹

¹*Florida Hospital Orlando, Orlando, FL*

Purpose

Melanoma incidence has risen over the past 30 years, with a projected incidence of 87-110 new cases in 2017.¹ The first drug therapy to demonstrate improved overall survival in grade III and IV metastatic melanoma was Ipilimumab (Ipi), an immune checkpoint inhibitor (monoclonal antibody). (2-4) Ipi successfully promotes immune antitumor activity by inhibiting cytotoxic T-lymphocyte antigen-4 (CTLA-4), which subsequently increases T-cell activation and proliferation. (4) Immune activation may result in multiple side-effects termed immune-related adverse events (irAEs). (2,4) During clinical trials, hypophysitis with hypopituitarism was the most common irAE reported involving the endocrine system. Ipilimumab-induced hypophysitis (IH) has a reported incidence of up to 15-17%. (2,4) The majority of patients who develop IH experience deficiencies involving multiple anterior pituitary hormones, significantly contributing to patient morbidity. (4)

Materials and Methods

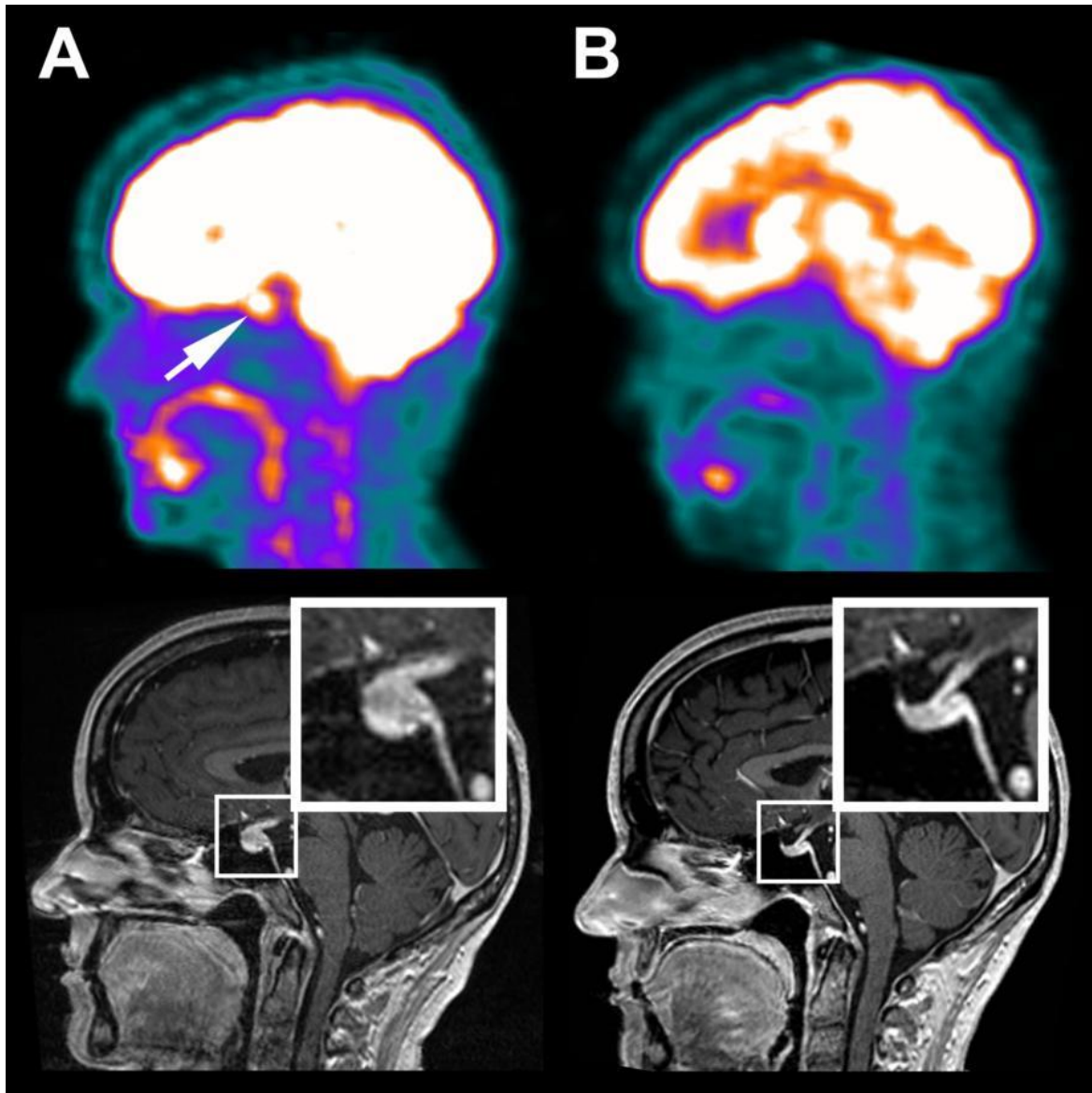
A 48-year-old female with metastatic melanoma was started on Ipilimumab therapy. Three months later she developed fatigue, loss of appetite, and joint pain. PET imaging demonstrated abnormal activity involving the pituitary gland, concerning for IH. Correlation with labs revealed a TSH of 0.42 (0.4-4.5 mIU/L) and free T4 of 2.9 (0.58-1.64 ng/dL). Imaging (5) and clinical findings were consistent with central hypothyroidism secondary to IH. Patient was started on Levothyroxine and hydrocortisone with a positive response.

Results

Initial staging MRI demonstrated normal pituitary with no corresponding hypermetabolic activity on PET/CT. Three month follow-up PET/CT revealed new hypermetabolic activity localizing to the pituitary gland (A, arrow). MRI was recommended which demonstrated diffuse enlargement/enhancement of the pituitary gland, measuring up to 13mm craniocaudal (A), previously 7mm pretreatment. After treatment for IH, imaging demonstrated resolved pituitary hypermetabolic activity on PET/CT and normalization of pituitary size (B).

Conclusions

Patients undergoing Ipilimumab therapy for metastatic melanoma may develop hypermetabolic activity involving the pituitary gland on PET/CT with corresponding enlargement/enhancement on MRI. Findings should prompt consideration of Ipilimumab-induced hypophysitis and discussion with the clinical team.



(Filename: TCT_E-19_Fig1.jpg)

E-20

11:46AM - 11:50AM

Neurosarcoidosis Mimicking Malignant Tumor on Conventional MR and Multiparametric Advanced Brain Imaging with Long Term Follow Up

B Wang¹, L Ketonen¹

¹MD Anderson Cancer Center, Houston, TX

Purpose

To illustrate the imaging findings of a case of neurosarcoidosis mimicking malignant tumor on advanced tumor imaging, which to our knowledge has not been reported in the literature. Our purpose is to raise awareness of the neuroradiology community concerning this imaging finding.

Materials and Methods

Patient is a 34-year-old female who presents to the emergency center with gait problem and visual field

Oral Presentations & Excerptas

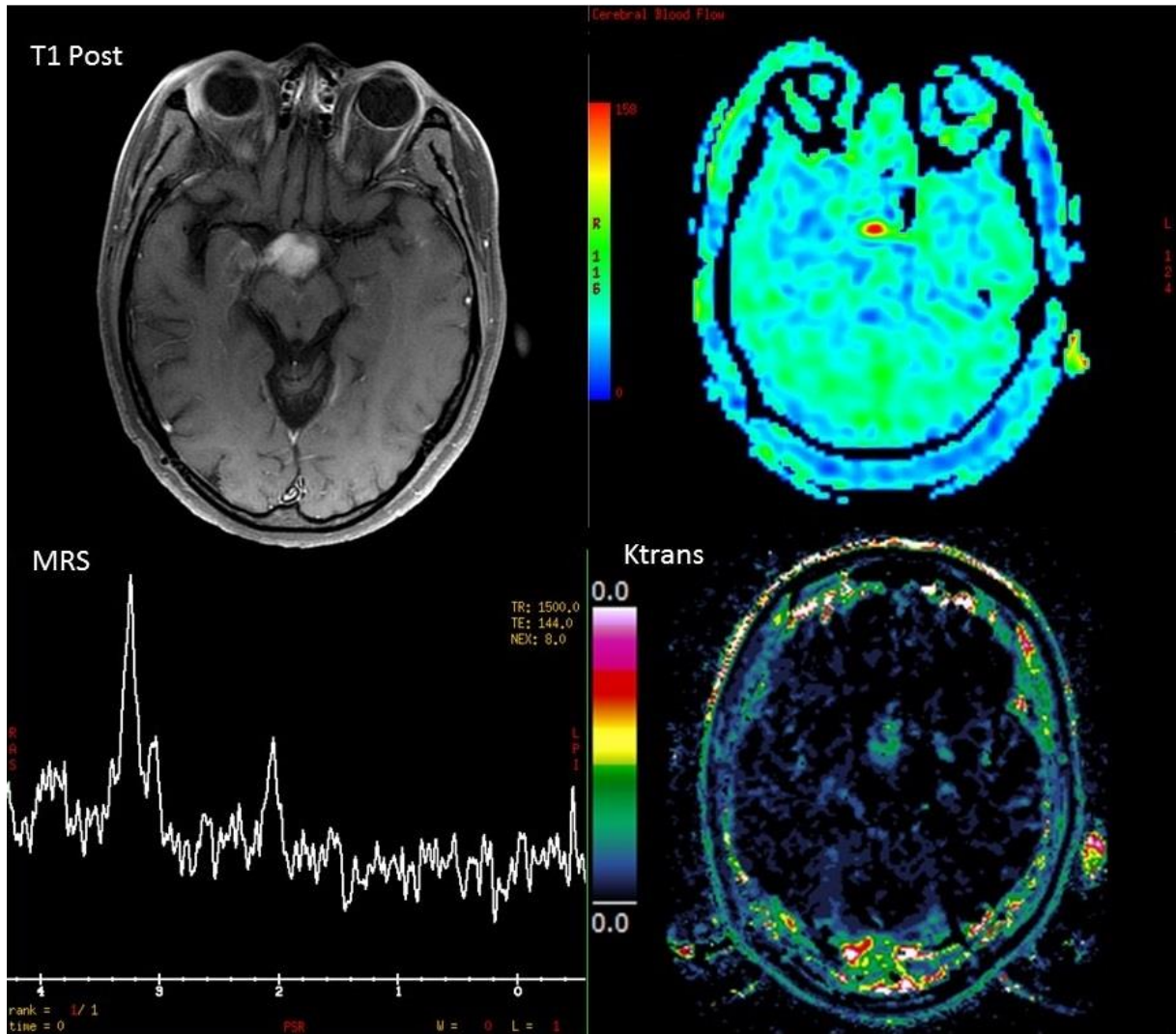
change. The patient is oriented $\times 1$. History is obtained from outside facility records. She has a reported history of brain aneurysm status post coiling. Patient reported to an outside facility for management of confusion. She was thought to be hyponatremic. She had been experiencing polyuria polydipsia. In the emergency center her sodium was noted at 115. She was admitted for further evaluation and management. Imaging of the brain revealed a brain mass for which she was transferred here for further evaluation and management.

Results

On CT, there appears to be a mass in the hypothalamic region, suggestive of underlying tumor. MRI demonstrates a 2 cm enhancing lesion in the hypothalamic region with associated patchy enhancement along the margin of third ventricle extending into the sublenticular regions with associated T2 FLAIR hyperintensity. Extension of enhancement into lining of the ventricle suggests possible subarachnoid seeding. DWI demonstrates no restricted diffusion within the lesion. MRI with advanced brain tumor imaging (ABTI) four days later shows an infiltrative mass in the hypothalamus with perivascular and leptomeningeal extension, progressed since prior exam. Arterial spin labeling demonstrates focal increased cerebral blood flow within the mass centered in the hypothalamus. There is increased K trans and cerebral blood volume at the site. Single voxel spectroscopy of the hypothalamic mass exhibits a decreased NAA peak with marked inversion of the choline to creatine ratio (>2). ABTI features favor a neoplasm such as high grade glioma.

Conclusions

Sarcoidosis is a multisystem noncaseating granulomatous disease of unknown cause. Neurosarcoidosis has been reported in approximately 5% of patients with sarcoidosis in clinical studies. Neurologic involvement can range from peripheral or cranial neuropathy to central nervous system (CNS) disease. Neurosarcoidosis may have a poor natural prognosis, and even patients who receive treatment may be severely ill and at risk of death mainly due to the CNS involvement. We illustrated the imaging findings of a case of neurosarcoidosis mimicking malignant tumor on advanced tumor imaging. To our knowledge this has not been systematically evaluated in the radiological literature. Long-term imaging follow-ups are also provided after various treatments including steroids, infliximab, and CellCept. Neuroradiologists should be aware of the imaging appearance on ABTI and consider it in the differential diagnosis when the characteristic features are encountered. The knowledge gained may potentially impact patient management, especially in inoperable cases and in locations where it is risky to perform a biopsy.



(Filename: TCT_E-20_NeurosarcoidosisASNR2018ImageFileSubmit.jpg)

E-21

11:50AM - 11:54AM

A Rare Case of Nonfatal Powassan Encephalitis in Northern New Jersey

N Dholakia¹, D Choe¹, L Gesner¹, R Pawar¹
¹*Saint Barnabas Medical Center, Livingston, NJ*

Purpose

The Powassan virus is a rare North American RNA arbovirus which can cause rapidly progressive and eventually fatal encephalitis at a rate about 4-5 times higher than all other tickborne viruses causing encephalitis (10-15% case fatality rate overall). Here, we report a case of nonfatal Powassan encephalitis where acute radiographic presentation did not correlate with the patient's clinical course.

Materials and Methods

A 40-year-old male presented to the ED several weeks after known tick bites in upstate New York with a three-day history of progressively worsening fever, nausea, headache, diplopia and gait disturbances but no focal neurologic/motor deficits. Lumbar puncture demonstrated leukocytosis and elevated total protein, and subsequent fungal/viral serologies revealed positive IgM assay for Powassan virus. The

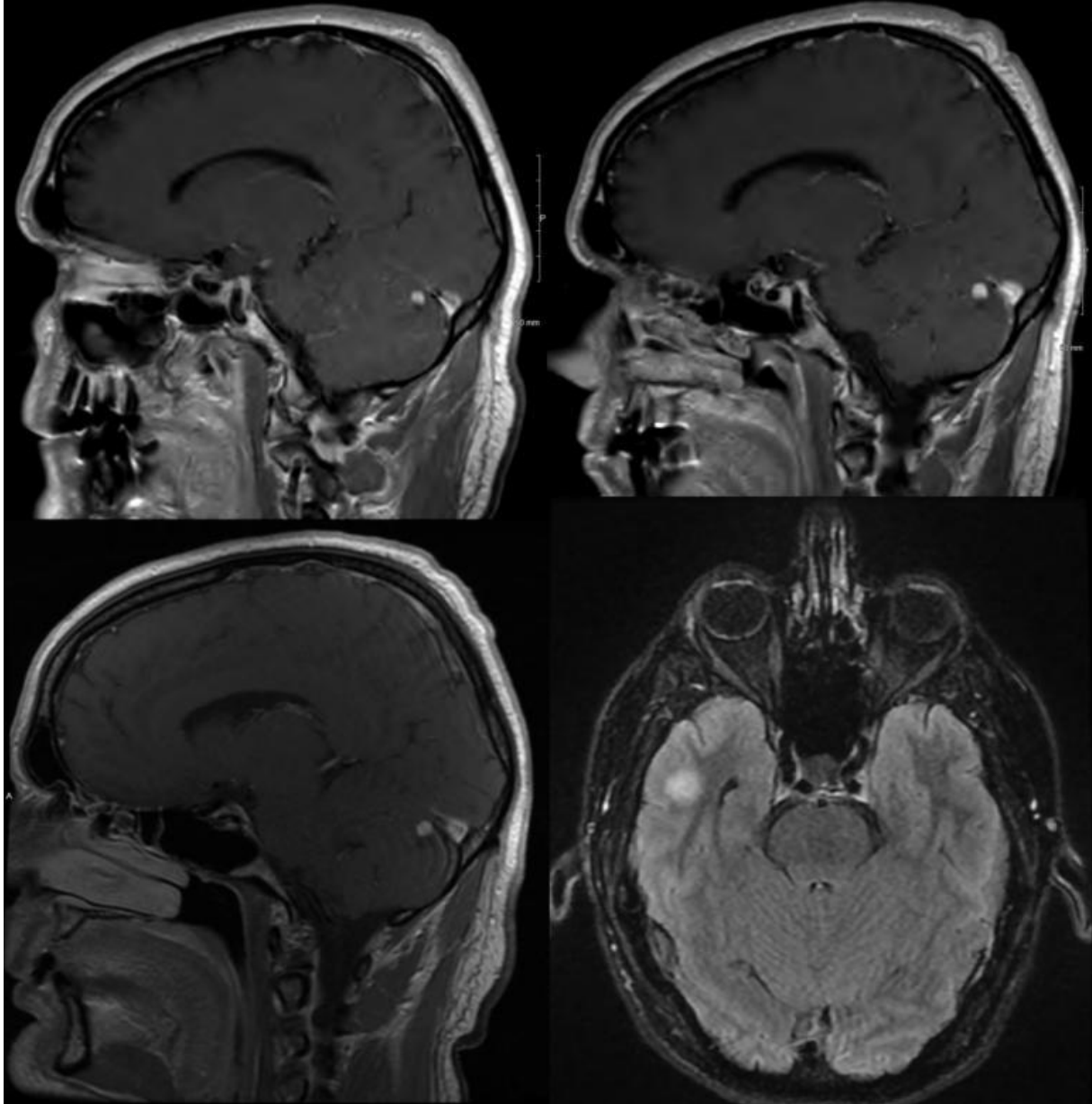
patient improved with intravenous steroid therapy and was discharged without signs of clinical relapse on multiple interval follow-up examinations.

Results

Initial noncontrast head CT showed no hemorrhage or mass effect. MRI demonstrated an 8 x 5 mm lesion in the superomedial left cerebellum of low T1 and increased T2 signal intensity with a halo of vasogenic edema extending inferiorly. The lesion displayed solid avid enhancement and no restricted diffusion. Repeat MRI three weeks later (prior to discharge) demonstrated no change in enhancement properties, size or degree of edema. Follow-up outpatient MRI done eight weeks after discharge showed the left cerebellar lesion to be unchanged; however, a new right temporal lobe T2/FLAIR hyperintense lesion with surrounding edema was evident. The new lesion did not exhibit any mass effect or restricted diffusion.

Conclusions

Powassan encephalitis is a rare but commonly fatal disease for which no targeted treatment or vaccine currently exists. Imaging findings are variable across limited reported cases and may not correlate to clinical symptoms. Further research is necessary to characterize pathognomonic radiographic features distinguishing this disease from other tickborne encephalitides.



[Top left] T1 post-contrast sagittal reconstruction at the time of admission shows an enhancing lesion in the superior cerebellum which is unchanged at the time of discharge [top right]. When the patient returns for a routine follow up examination, a repeat MR demonstrates the stable cerebellar lesion [bottom left] as well as a new T2/FLAIR hyperintense lesion in the right temporal lobe [bottom right].

(Filename: TCT_E-21_ImageCompositeHiRes.jpg)

Monday, June 4, 2018
10:30AM - 12:00PM
Parallel Paper Session: Education and Training

Oral Presentations & Excerptas

O-25

10:30AM - 10:37AM

Radiology Resident Boot Camp: Simulating the On-Call Experience Utilizing An Open-Source Web-Based Platform-Independent DICOM Viewer

R Javan¹, L Shu², T Mithug³, A Yepuri⁴, T Kim¹, M Taheri⁵, R Zeman³

¹George Washington University Hospital, Washington, DC, ²George Washington University School of Medicine, Washington, DC, ³George Washington University, Washington, DC, ⁴George Washington University Hospital, Washington, DC, ⁵George Washington University, Washington, DC, DC

Purpose

Evaluation of radiology resident call preparedness is often limited to still image interpretation during objective structured clinical examination (OSCE) or knowledge-based multiple-choice questions, such as in-service examinations. Our goal was to create a more realistic, tailored and active learning experience for junior residents preparing for call, using a low-cost widely available system.

Materials and Methods

We utilized an open-source web-based PACS named "Weasis", which we integrated with a reporting system. MySQL database programming language, JBOSS application server, MyEclipse development environment and JAVA language were utilized. We used WADO (Web Access to DICOM Object) to achieve web client DICOM image access with full PACS functionality. Students were tasked to provide impression points for each of the reviewed studies using a voice recognition system or a keyboard. During the time the trainees were reviewing the exams, an online automated calling system, Voicent, was implemented to intermittently direct specific calls to the trainee's phone with questions pertaining to either study results or appropriate protocols for the provided clinical histories. The length of time a trainee requires to complete the assigned tasks was automatically recorded.

Results

A total of 100 neuroradiology examinations with diagnoses ranging from normal to those requiring urgent medical management were collected. Anonymized complete DICOM studies were seamlessly sent from the hospital PACS to a shared secure server on the hospital network. Trainees on any computer, PC or Mac, connected to the shared hospital network, could access cases without the need for occupying a dedicated radiology workstation. An attending radiologist was later able to review the accuracy and efficiency of their performance and provide individualized feedback.

Conclusions

Weasis and a custom add-on reporting system, a real-time and easy-access freeware platform-independent image database can be used to simulate a real-world PACS. This system provides a novel opportunity for radiology programs to prepare residents for call.

O-26

10:37AM - 10:44AM

Beyond Static Pictures for Teaching Medical Imaging in the Age of Digital - Online Stroke Education and ASPECTS Training Website Revisited

N Kashani¹, A Al Sultan¹, B Menon¹, A Demchuk¹, M Hill¹, M Goyal¹

¹University of Calgary - Foothills Medical Center, Calgary, Alberta, Canada

Purpose

Computer-based learning or "e-learning," has been playing an increasingly important role in healthcare education (1). With the proliferation of electronic devices, ubiquitous use by students and learners around the world, and the ever increasing performance and capabilities of our electronic devices, there is a great opportunity for learner engagement on the web. There is consensus amongst the radiology community that web-based methods of information dissemination can enhance learner experience and an effective

Oral Presentations & Excerptas

strategy as deemed by a panel that met during the RSNA on education (2). Teaching and learning of medical imaging specially given its visual nature can hence be enabled by web-based technologies and creation of online resources. Stroke imaging, relying on detection of subtle areas of grey/white loss on complete image sets of the brain, as well as vascular imaging necessitating depiction of small structures is not well depicted on static single images. Scrollable sets with additional features such as window, level, zoom, pan, and reformats are needed in order to adequately view and interpret all the images stimulating the learner to detect the abnormal images amongst the rest. Until now, such a capability has been limited by the large size of imaging data sets, speed of transmission over the web, and the file format DICOM specific to medical imaging, making this only possible on select workstations within the hospital environment but not outside or on personal learning devices. Using some of the advances in web-based technologies and image display, we set out to create an online system which leverages some of these emerging capabilities. Focusing on stroke education and vascular imaging, we have created a teaching file system with fast scrollable complete image sets without the need for any additional plugins or preinstalled software on the web. We hope this would serve as a highly available resource creating a more stimulating learning environment.

Materials and Methods

Using open source web standards and languages such as HTML 5, JavaScript, PHP, CSS, and leveraging the organizational power of content management systems (CMS), we created a web-based system for display and classification of cases related to vascular imaging and acute stroke. Leveraging cloud computing and solid state servers for delivery of content and information at scale, with added deployment of a content distribution network (CDN) for improved delivery to a global audience, we created a scalable system that would maintain its speed and performance worldwide. Using new standards in medical image transmission such as DICOMWeb and RESTful APIs, we created a fully scrollable study library containing full image set and series, with ability to display full resolution, lossless images, right in the browser natively without the need to use any plugins. Using components from each imaging study, topic specific training modules related to each area such as noncontrast CT, CT angiography, multiphase CTA, CT perfusion, MRI, and conventional angiography, as well as ASPECTS and collateral scoring were created and available for training on the website.

Results

We successfully created an online web-based system using open source tools and technologies leveraging some of the latest advances. Full scrollable Image sets provide a more realistic training environment with tools for image manipulation without the need for any additional software. Creation of topic-based quizzes and modules on stroke imaging, process of validation using expert opinion, methodologies used in calculating passing score, and statistical analyses of preliminary results will be discussed at the meeting.

Conclusions

Creation of online content and web-based teaching material could greatly improve access to information and serve as a reference point for medical trainees, residents, fellows, continual education, and those interested in learning more about different aspects of stroke and vascular imaging. Such system would allow for sharing of learning points and tips and tricks on interpretation and technique of imaging in acute stroke. Emerging web technologies have enabled seamless delivery and processing of large data sets such as medical images, and this improvement in performance and speed could be leveraged in radiology education online. Allowing for richer content delivered right on personal devices available at all times and when convenient for the learner, we hope these additional resources and tools would create a more realistic, enriching and engaging training environment. Our hope is to continually update the site as more practice points and examples becomes available and create dynamic content for learners of different training levels, interests, and skill sets.

ASPECTS HOME | mCTA COLLATERALS HOME | Contact | In the Media | Login

ASPECT SCORE in Acute Stroke



UNIVERSITY OF
CALGARY

Home | EdModules | CasePACS | EdPACS | Education | Projects | Publications | Lab

CasePACS - Latest Acute Stroke Cases

Clinical Vignettes and Discussion on Imaging of Acute Stroke

Distal occlusion, use of mCTA

44 year old male with acute onset speech difficulty.

LastSeenNormal (LSN) 2 hours. NIHSS<5

Baseline imaging: NCCT - 09:02 am



[Read more...](#)

Stroke or Mimic?

64 year old gentleman presenting with word finding difficulties and Wernekie's aphasia.

Baseline CT Scan was Performed



[Read more](#)

[Rate the ASPECT Score](#)

(Filename: TCT_O-26_Capturejpg.jpg)

O-27

10:44AM - 10:51AM

Development of a Customized Pediatric Neuroradiology Curriculum for Neuroradiology and General Pediatric Radiology Fellows using an LMS (Learning Management System)

K Shekdar¹, J Reid¹

¹Children's Hospital of Philadelphia, Philadelphia, PA

Oral Presentations & Excerptas

Purpose

Both neuroradiologists, and general pediatric radiologists require a unique set of skills to confidently manage pediatric neuroradiology cases either in a community or primary-care setting, as well as complex cases in a specialized pediatric tertiary-care hospital. The purpose of this study is to address the specific needs of both sets of trainees by developing a customized pediatric neuroradiology curriculum.

Materials and Methods

This presentation will focus on the sequential steps involved in the planning and development of the pediatric neuroradiology curriculum over a period of two years using our Learning Management System (LMS) including the needs assessment, goals and objectives, knowledge and skills content and method for delivery.

Results

Through a brief demonstration of its breadth and functionality on the LMS, we will demonstrate the utility of this system and the potential of this LMS for extension in other fields of neuroradiology and general radiology education.

Conclusions

Pediatric neuroradiology is a niche subspecialty of neuroradiology. The goal of pediatric neuroradiology education is to help both the neuroradiology and general pediatric radiology trainees to develop skills to confidently manage pediatric neuroradiology cases in a community or primary-care setting as well as in a specialized pediatric tertiary-care setting.

O-28

10:51AM - 10:58AM

Current Status of Training Environments in Neurointerventional Practice

M Nawka¹, J Spallek², J Buhk¹, J Fiehler¹, A Frölich¹

¹University Medical Center Hamburg-Eppendorf, Hamburg, Germany, ²Technical University Hamburg-Harburg, Hamburg, Germany

Purpose

There are several different training environments for practicing neurointerventional procedures in silico, in vitro and in vivo. We seek to replace animal-based training with suitable alternatives. In an effort to determine present training model distribution and preferences, we interviewed European interventional neuroradiologists about their experience in different training environments.

Materials and Methods

A voluntary online LimeSurvey comprising 23 questions concerning the different training facilities was designed and electronically conducted with the members of the European Society for Minimally Invasive Neurological Therapy. Questions were designed by the authors.

Results

Seventy-one physicians with an average experience of 11.8 (+/-8.7) years completed the survey. All queried interventional procedures have been performed at least once as first operator. The majority of participants had experience with performing interventional procedures in animal-based training (e.g. stroke intervention: 36; 50.7%). Overall, animal-based training was rated as the most suitable environment to practice coil embolization (23; 32.4%), flow diverter placement (27; 38%) and stroke intervention (26; 36.6%). In-vitro training before using a new device in patients was supported by most participants (35; 49.3%). Additionally, preferred training models showed to be dependent on the years of experience with more experienced physicians rating animal-based training as less suitable to learn and to improve operator skills than inexperienced operators.

Conclusions

This survey discloses the preferred training modalities in European neurointerventional centers. The majority of interviewed physicians support the general concept of in-vitro training, most suitable training

modalities being dependent on procedure and experience. As animal-based training is still common, alternate artificial environments meeting these demands must be established.

O-29

10:58AM - 11:05AM

The Unseen AJNR Twitter Impact: A “Silent” but Active Twitter Following

C Tomblinson¹, V Wadhwa², E Latimer², C Gauss², K Mason³, J McCarty²

¹Mayo Clinic, Phoenix, AZ, ²University of Arkansas for Medical Sciences, Little Rock, AR, ³American Journal of Neuroradiology, Oak Brook, IL

Purpose

Twitter continues to be an active social media platform for radiologists and academic organizations. While many of the interactions are visible to the public (retweets, likes, and replies), some of the more important metrics for content engagement are not (URL clicks). The American Journal of Neuroradiology (AJNR) has a Twitter account (@theAJNR) that posts each online case and published article with a unique URL link to the corresponding AJNR webpage. We hypothesized that case views and article readership resulting from Twitter posts (indicated by the number of URL clicks) exceeds the number of visible engagements, implying a "silent" Twitter following and educational outreach far greater than meets the eye.

Materials and Methods

Twitter analytics were obtained from the AJNR Twitter account for tweets published from November 2016 - October 2017. The difference between URL clicks and retweets and between URL clicks and likes was computed for each tweet of each type (AJNR article, case, or other). Both difference response variables were analyzed separately using a one-way analysis of variance.

Results

Analyzed were 874 tweets. There was sufficient evidence to suggest that at least two of the population mean differences were statistically significantly different ($p < 0.0001$) for the difference between URL clicks and retweets and between URL clicks and likes. For all three types of tweets (AJNR article, case, or other), the mean number of URL clicks was statistically significantly greater than the mean number of retweets ($p < 0.0001$) and likes ($p < 0.0001$).

Conclusions

The AJNR Twitter account has an ever-present silent following with a far broader audience reach than previously recognized. This study suggests that the impact should not be measured by likes and retweets of AJNR cases and articles alone. Rather, the number of URL clicks, an engagement not visible to the public, is more representative of the viewership of AJNR online content and outnumbers both retweets and likes.

O-30

11:05AM - 11:12AM

Clinical, Demographic and Technical Predictors of Neuroradiological MRI Exam Duration

G Avey¹, D Belden², R Zea¹, J Yu¹

¹University of Wisconsin, Madison, WI, ²University of Wisconsin School of Medicine, Madison, WI

Purpose

Efficient resource utilization increases patient access to imaging and contributes to significant gains in imaging capacity, patient throughput, and increased patient satisfaction. Despite these benefits, however, little is known regarding which nontechnological factors contribute to the wide variances in the duration of MRI examinations. The purpose of this study is to identify potential associations that can contribute to variances in MRI exam length.

Oral Presentations & Excerptas

Materials and Methods

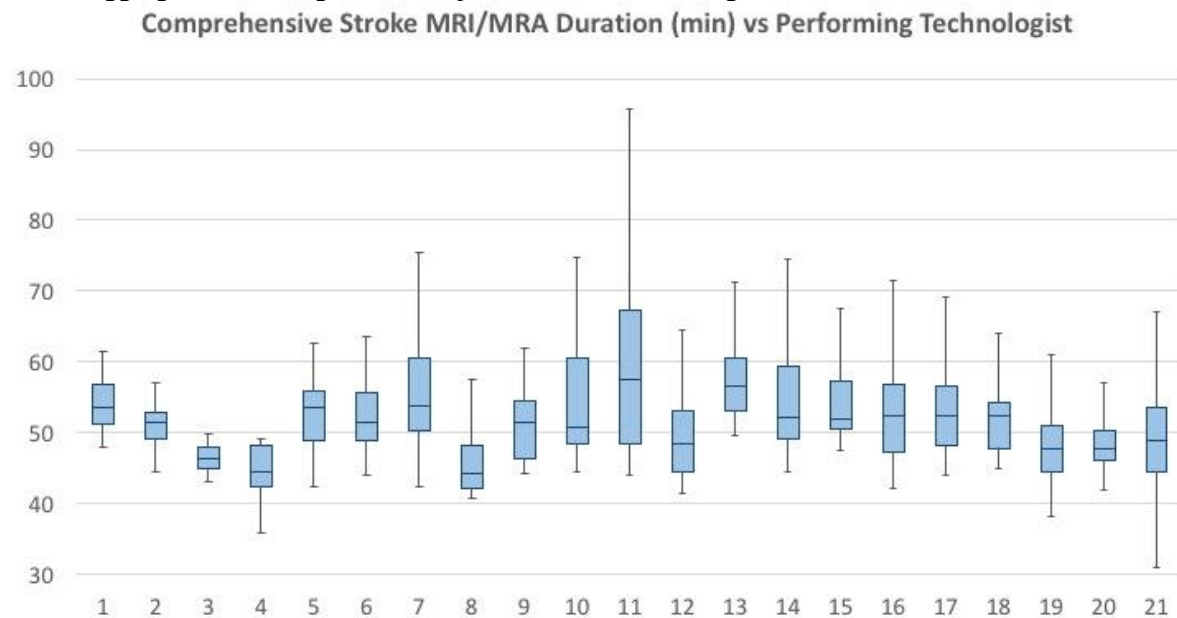
Consecutive standard MRI examinations of the cervical spine without contrast, comprehensive stroke exams, and comprehensive brain examinations from June 30, 2016 through June 30, 2017 were included in this study. Linear models for patient age, gender, performing technologist, patient location, field strength, use of sedation, and the time of day were constructed for each individual variable for each exam type. A multivariate mixed model was then generated.

Results

A total of 2705 MRI records were retrieved including 850 cervical spine exams, 1336 comprehensive brain exams, and 519 comprehensive stroke exams. Exams for male patients were longer in duration (1.7 minutes, $P < 0.001$). Inpatient vs. outpatient status was also significant, with ED patients requiring approximately 1.2 minutes longer than outpatients on average, and inpatients 3.0 minutes longer than outpatients. The multivariate model found that male gender, inpatient/ER/outpatient status, and the performing technologist were all significant residual predictors of MRI exam length. The standard deviation associated with the technologist component was 2.6 minutes ($p < 0.001$). Patient age, day of the week, and magnetic field strength were not predictive of MRI exam length.

Conclusions

Patient gender, inpatient/ED/outpatient status, and the performing technologist were all predictive of MRI exam length. In particular, the performing technologist had a significant contribution to the variance in exam time. These individual effects represent 5% to 10% of the median exam time within this sample, and in aggregate have a significant impact on MRI scheduling and utilization.



(Filename: TCT_O-30_Techvsstrokeexamduration.jpg)

O-31

11:12AM - 11:19AM

Fluoroscopically Guided Lumbar Puncture : Evaluation of the Cytological Diagnosis

F Thibault¹, R Hadjeres¹, A Maietta¹, J Sirois¹, D Landry¹, C Bard¹

¹University of Montreal, Montreal, Quebec, Canada

Purpose

Obtaining a specimen for cytology is a common request in the radiology department. A good diagnostic

Oral Presentations & Excerptas

yield is desired to ensure adequate patient management. The purpose of our study was to assess the success rate of fluoroscopically guided lumbar puncture (FGLP) in our hospital - assessing the percentage of specimens which were adequate and representative for cytological diagnosis.

Materials and Methods

In collaboration with the pathology department, the cytology analysis of 100 patients who had had a FGLP and of 100 patients who had had a bedside lumbar puncture (BLP) between January 2014 and December 2015 was reviewed. In the FGLP group, the indication for the procedure, the needle type, and the delay between sampling and handling of the specimen in pathology were noted. In view of the large number of unrepresentative specimens in both groups, changes were made: filling the entire tube with fixative immediately after sampling, adding Cytospin Collection Fluid (Shandon, Inc.) to the specimen once in pathology, and putting a cap on the tube to minimize evaporation during centrifugation. The cytology analyses were then reviewed for all patients (110) who had had a FGLP or a BLP between March 24 and October 11, 2017.

Results

In the FGLP group, 31% of the specimens were considered unrepresentative because of cellular degeneration, compared to 32% in the BLP group ($p > 0,05$). In the FGLP group, 47% of the specimens were collected for a diagnostic purpose, 37% for a therapeutic purpose, and 16% for both. Thirty-eight specimens (60,3%) were collected with a 22-gauge (G) spinal needle, 13 (20,7%) with a 25G spinal needle, and 12 (19%) with a 24G round tip needle ($p > 0,05$). The delay between sampling and handling in pathology was 0-2 days for 67 specimens (73,6%), and 3-5 days for 24 specimens (26,4%) ($p > 0,05$). After changes were made in the preparation, 11% of the specimens were considered unrepresentative ($p < 0,01$), representing a 20% improvement of our success rate.

Conclusions

Our results suggest that the success rate of cytological analysis is equivalent for FGLP and BLP in our hospital. In the FGLP group, the needle type and the delay between sampling and handling in pathology did not show a statistically significant difference in performance. Optimization of the preparation of the specimens was decisive in obtaining adequate and representative cytological diagnosis, improving patient care.

O-32

11:19AM - 11:26AM

Role of Spinal Imaging in the care-pathway of patients with Angiogram-Negative Spontaneous Subarachnoid Hemorrhage. Single-center experience.

A Aladi¹, S Jabbar¹

¹*Keele University, Stoke-on-Trent, Staffordshire, United Kingdom*

Purpose

To evaluate the diagnostic yield of Magnetic Resonance Imaging (MRI) for the spinal column in searching for a spinal etiology for angiograph-negative spontaneous subarachnoid haemorrhage (AN-SAH)¹

Materials and Methods

In this single-center retrospective review, all adult patients admitted with nontraumatic, angiographically negative SAH to the Walton Centre, Liverpool, United Kingdom, between June 2009 to December 2015 were included. Patients with SAH due to trauma or defined vascular causes were excluded. Outcomes reviewed included utilization rate, diagnostic yield and median time of the spinal MRI and MRA imaging test during initial hospital admission and in postadmission period from hospital discharge date until 180 days.

Results

Three-hundred patients were included in this study. The proportion of male was 65.6% (mean age 42.1), while female proportion was 43.3% (mean age 53.4). Whole spinal axis by standard T1- and T2-weighted

MR imaging was done in 51 patients (17%) during the initial admission, while a follow-up spinal MRI and MRA were done in 20 patients (6.6%). Cervical T1- and T2-weighted MR imaging offered to 86 patients (28.7%) during initial hospital admission, while after hospital discharge, 30 patients (10%) had a repeat cervical MRA. In all patients, no further information related to the bleeding sources were added after delayed follow-up MR imaging for spinal axis.

Conclusions

In spontaneous nonaneurysmal SAH patients, MR imaging of the spinal axis has a very low diagnostic yield, and routine radiological investigation of the spinal axis in nonaneurysmal SAH patient's care pathway is therefore not recommended.

Monday, June 4, 2018

1:15PM - 2:45PM

Parallel Paper Session: Advanced Techniques in Brain Tumor Imaging II

O-33

1:15PM - 1:22PM

A Comparison of Low Flip-Angle, No-Preload DSC-MRI to Intermediate Flip-Angle, Preload-Based DSC-MRI as a Reference Standard

J Boxerman¹, C Quarles², M Prah³, K Schmainda³

¹Rhode Island Hospital, Providence, RI, ²Barrow Neurological Institute, Phoenix, AZ, ³Medical College of Wisconsin, Milwaukee, WI

Purpose

DSC-MRI using preload, intermediate flip-angle (60°), and postprocessing leakage correction has gained traction as standard methodology. [1] Based upon preliminary simulations, [2] we hypothesized that low flip-angle (30°) DSC-MRI without preload yields rCBV estimates practically equivalent to the reference standard.

Materials and Methods

Patients with high-grade glioma or brain metastases and clinically indicated MRI were considered for inclusion in this IRB-approved, two-institution study. Two successive DSC-MRIs (3T, single-dose gadobutrol, gradient-echo, TE=30-35ms, TR=1.2-1.5s) were performed for each patient: "low flip-angle" DSC-MRI (no preload [P-], 30° flip-angle) provided preload (P+) for "intermediate flip-angle" DSC-MRI (60° flip-angle). Standardized rCBV (sRCBV) [3] maps were generated, with (C+) and without (C-) postprocessing leakage correction. Mean rCBVs were extracted from coregistered segmented contrast-enhancing lesion volumes (CELV). Postprocessing was performed in OsiriX-MD (Pixmeo) using IBNeuro and IBDeltaSuite plugins (Imaging Biometrics). Percent error, Lin's concordance correlation coefficient (LCCC), and Bland-Altman plots were calculated across all subjects for CELV sRCBV obtained with 30°/P-/C-, 30°/P-/C+ and 60°/P+/C- protocols relative to the reference standard (60°/P+/C+).

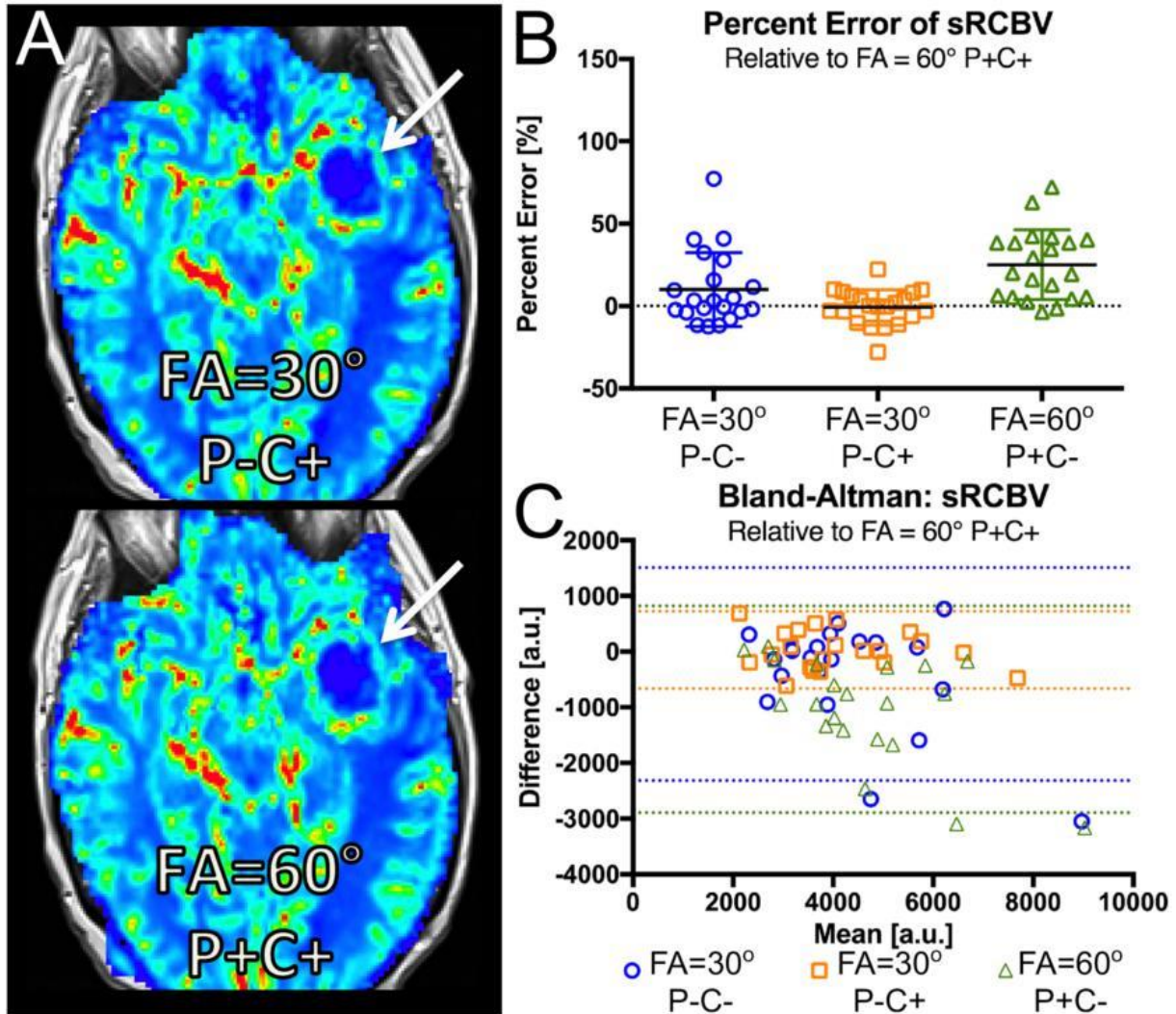
Results

Twenty-one patients with >1cc CELV were included. SRCBV maps were qualitatively similar for 30°/P-/C+ and 60°/P+/C+ protocols (Fig. 1A). Bias ($\mu=-0.8\%$) and mean magnitude (7.9%) of error were lower compared to reference (60°/P+/C+) sRCBV for 30°/P-/C+ than for 30°/P-/C- (10.0%, 15.4%) and 60°/P+/C- (25.1%, 25.6%) protocols (Fig. 1B). Compared to reference (60°/P+/C+), LCCC was 0.97 for 30°/P-/C+, with poorer performance for 30°/P-/C- (0.80) and 60°/P+/C- (0.70) protocols. On Bland-Altman analysis (Fig. 1C), 30°/P-/C+ yielded improved limits of agreement without bias or dependence

on underlying sRCBV compared to 30°/P-/C- and 60°/P+/C- protocols. Normalized rCBV analysis provided similar results.

Conclusions

RCBV measured with low flip-angle, no-preload DSC-MRI using postprocessing leakage correction strongly agrees with rCBV obtained with intermediate flip-angle, preload-based, leakage-corrected technique. Low flip-angle DSC-MRI may provide an attractive alternative methodology for measuring tumor rCBV without need for preload contrast administration.



(Filename: TCT_O-33_AbstractFig.jpg)

O-34

1:22PM - 1:29PM

Dual Iron and Gadolinium Contrast Enhanced MRI Specifically Diagnoses Glioblastoma Pseudoprogression

R Barajas¹, D Schwartz¹, H McConnell¹, B Hamilton¹, D Pettersson¹, J Jaboin¹, P Ambady¹, J Firkins¹, A Horvath¹, C Varallyay¹, J Prola¹, C Kubicky¹, R Fu¹, L Muldoon¹, W Rooney¹, E Neuwelt¹

¹Oregon Health and Science University, Portland, OR

Purpose

In patients with newly diagnosed glioblastoma, maximal safe resection, temozolomide (TMZ)-based chemoradiotherapy (CRT) and maintenance TMZ is the standard of care and first-line treatment (1). In a subset of patients, CRT may lead to the radiographic phenomenon known as pseudoprogression, which manifests as enlarging enhancement on gadolinium-based contrast agent (GBCA) T1-weighted magnetic resonance imaging (MRI) examinations (2). Pseudoprogression is relevant as patients will stabilize or resolve their enhancing lesion without intervention, unlike patients with tumor recurrence, and may experience an overall improved survival benefit (3). The origins of pseudoprogression are hypothesized to be neuroinflammatory in nature, and may be related to CRT (4). At the cellular level, mutated forms of the isocitrate dehydrogenase-1 (IDH-1) protein may contribute to pseudoprogression incidence. Furthermore, the ionizing radiation from radiotherapy elicits a robust innate immune response, which creates a reactive oxygen species rich environment that promotes cellular oxidative damage in tumor cells. Currently, there is no biologically specific MRI biomarker that can differentiate neuroinflammation-induced pseudoprogression from recurrent glioblastoma following CRT. Both recurrent tumor growth and neuroinflammation mediated pseudoprogression demonstrate increased enhancement on T1-weighted gadolinium contrast-enhanced MRI. Preclinical ultrasmall superparamagnetic iron oxide (USPIO) nanoparticle ferumoxytol based imaging models of brain tumor associated neuroinflammation have shown promise in specifically localizing neuroimmunity (5). Unlike GBCAs, USPIO is phagocytosed by tumor-associated macrophages, which are known to infiltrate the tumor microenvironment during CRT-induced neuroinflammation. Therefore, we hypothesized that the addition of USPIO enhanced MRI may serve as a specific biomarker of glioblastoma pseudoprogression when compared to GBCA alone.

Materials and Methods

In this IRB-approved retrospective study, we analyzed patients with a diagnosis of glioblastoma treated with maximal safe resection and TMZ-based CRT who underwent gadolinium contrast-enhanced MRI (gadoteridol, Bracco; GdCE) followed by USPIO-enhanced MRI for suspected disease progression on 3T clinical scanner (Philips Healthcare). IDH1 mutational status was characterized by exome sequencing. USPIO enhanced MRI was performed with T1-weighted spin-echo sequence (TR/TE=900ms/10ms, field of view(FOV)=180×240mm, imaging matrix=192x256, 44 mm² thick contiguous sagittal slices, in-plane resolution=.9375 mm²) 24 hours following the intravenous administration of 4 to 8 mg/kg Ferumoxytol. All gadolinium contrast-enhanced MRI examinations were performed within 48 hours before Ferumoxytol administration. The sum of products diameter (SPD) was calculated according to RANO criteria (5) for both contrast agents in a blinded manner using commercially available software (IMPAX 6.5.5; Agfa Corporation) by an attending radiologist with an American Board of Radiology certificate-added qualification in neuroradiology. Enhancement mismatch was calculated as the natural log (Ln) of the USPIO to GBCA SPD ratio. The Ln of the contrast mismatch ratio was utilized to normalize the SPD data so that weighting differences between lesions of markedly different size were minimized. Student's T-test assessed for differences in mismatch ratios between groups. Receiver operator curve (ROC) analysis provided an optimal cutoff value allowing for the determination of sensitivity and specificity. P-value less than .05 was considered to indicate a significant difference.

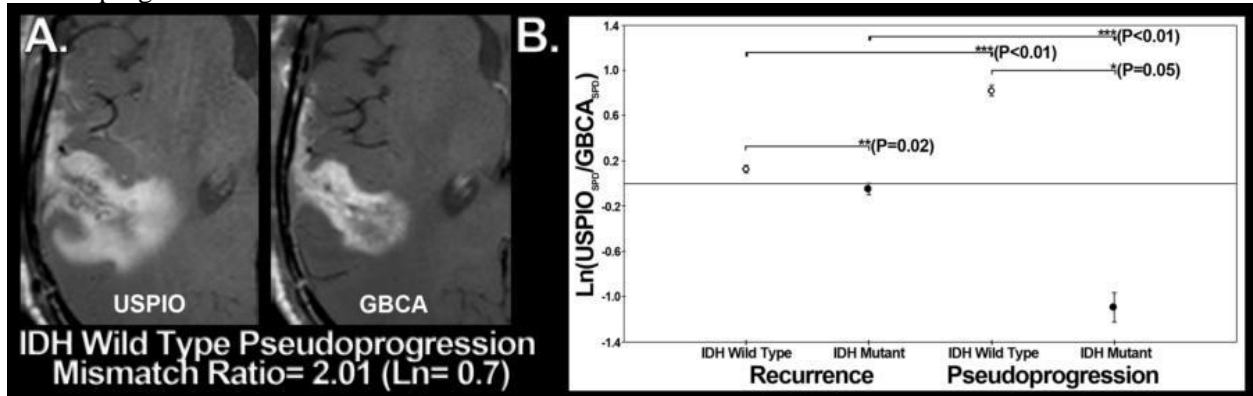
Results

Between January 2012 and January 2017, 430 patients were imaged with USPIO at OHSU. Among this cohort, 148 (34%) had a diagnosis of glioblastoma and 42 (10%) met study inclusion criteria. Thirty-six patients had a diagnosis of IDH-1 wild-type glioblastoma (25 recurrent disease/11 pseudoprogression). Six patients had a diagnosis of IDH-1 mutated glioblastoma (four recurrent disease/two pseudoprogression). Within the IDH-1 wild-type patients the USPIO/GBCA enhancement mismatch was significantly elevated at time of pseudoprogression (mean ± standard deviation (of log ratio)); 0.82 ± 0.15) when compared to disease progression (0.13 ± 0.17); $P < 0.01$; Figure 1). Patients with IDH-1 mutation demonstrated significantly reduced USPIO/GBCA enhancement mismatch with the development of pseudoprogression (-1.06 ± 0.19) when compared to disease progression (-0.05 ± 0.10); $P < 0.01$; Figure 1). There was no significant difference between USPIO and GBCA SPD measurements (as defined by RANO) in patients subgrouped by IDH-1 status, disease status, or as a cohort. Receiver

operating characteristic curve analysis identified USPIO/GBCA enhancement mismatch threshold values of 1.74 ($L_n = 0.56$) for IDH-1 wild-type and 0.41 ($L_n = -0.89$) for IDH-1 mutated patients as optimal cutoff values for the diagnosis of pseudoprogression; 100% sensitivity and specificity in this cohort.

Conclusions

Our results reveal the first clinical evidence that the ratio of USPIO to GBCA enhancement on MRI, but not SPD, is a highly sensitive and specific marker for the differentiation of pseudoprogression from disease recurrence in patients with glioblastoma. This suggests that the proposed USPIO and GBCA enhancing MR imaging paradigm uniquely characterizes CRT induced neuroinflammation. Contrast-enhanced MRI provides a means to explore therapeutic response in patients with glioblastoma. However, GBCA-enhancement on T1-weighted MR images is only indicative of a disrupted blood-brain barrier and cannot distinguish between tumor recurrence and the radiographic phenomenon known as pseudoprogression. Unlike GBCA, USPIO is phagocytized by infiltrating monocytes or resident microglia that are stimulated by chemotactic signals and traffic to the site of inflammation, thereby allowing visualization of neuroinflammation on MRI. USPIO enhancement at these sites is specific, does not occur unless neuroinflammation is present, and does not occur outside of the lesion or in the contralateral hemisphere. As such, USPIO and GBCA enhancement mismatch observed in our study is hypothesized to be a marker of TAM-associated USPIO accumulation within the inflamed post-CRT environment in patients with wild-type glioblastoma. Although, the imaging findings are counter intuitive than the previously described incidence of pseudoprogression occurring in IDH-1 mutated patients. If prospectively validated as a biologically specific measure of neuroinflammation, the combined utilization of USPIO and GBCA enhanced MR imaging could impact treatment strategy, timing and method of disease monitoring, and potentially the clinical outcome of patients with glioblastoma through the improvement of endpoint sensitivity in clinical trials by correctly differentiating pseudoprogression from disease progression.



(Filename: TCT_O-34_ASNRFigure3Submitted.jpg)

O-35

1:29PM - 1:36PM

Utility of Percent Signal Recovery and Average Baseline Signal in DSC-MRI Optimized for rCBV Measurement for Differentiation of GBM, Metastasis, Lymphoma and Meningioma

M Lee¹, L Bell², G Baird³, C Quarles², J Boxerman³

¹Alpert Medical School, Brown University, Providence, RI, ²Barrow Neurological Institute, Phoenix, AZ, ³Rhode Island Hospital, Providence, RI

Purpose

Percentage signal recovery (PSR) in nonleakage-corrected (no preload, high flip-angle, intermediate TE) DSC-MRI differs significantly for GBM, metastasis, and lymphoma. [1] Since PSR is pulse-sequence

Oral Presentations & Excerptas

dependent, [2] we investigated whether PSR in DSC-MRI optimized for rCBV accuracy (pre-load, intermediate flip-angle, low TE)[3,4] can still differentiate intracranial neoplasms.

Materials and Methods

We retrospectively analyzed preop DSC-MRI of treatment-naïve, pathology-proven GBMs (n=36), lymphomas (n=12), metastases (n=28), and meningiomas (n=18) treated between January 2015 September 2017. DSC-MRI protocol (1.5T/3T, single-dose gadobutrol bolus, gradient-echo, TR≈1.5s, 120 time-points, 50-point baseline) was selected for rCBV accuracy (¼-dose preload, 60° flip-angle, TE=30-35ms). PSR ($[S1-Sm]/[S0-Sm]$, 10-point average baseline S0, tail S1; minimum Sm) maps were generated without postprocessing leakage correction using Matlab. Mean PSRs were extracted from co-registered segmented contrast-enhancing lesion volumes (CELV) generated using OsiriX-MD and IBDeltaSuite (Imaging Biometrics), avoiding necrosis and susceptibility artifacts. Average signal-time curves, SI(t), were constructed by averaging across CELV voxels. Using SAS/GLIMMIX, 95% confidence intervals for mean PSR and baseline SI(t) by tumor pathology were calculated using generalized mixed modeling with sandwich estimation, mean observations nested within-subject, and Tukey adjustment ($\alpha=0.05$).

Results

Mean PSR differed significantly between GBM (105.2 [95% CI 98.3–111.9]) and lymphoma (141.8 [118.0–165.5], $p=0.019$); GBM and meningioma (84.3 [75.5–93.1], $p=0.0013$); lymphoma and metastasis (103.8 [91.0–116.5], $p=0.029$); and lymphoma and meningioma ($p<0.0001$); but not between GBM and metastasis ($p=0.99$) or metastasis and meningioma ($p=0.065$). Mean baseline SI(t) differed significantly between GBM (647.5 [608.2–686.8]) and metastasis (543.5 [498.1–588.8], $p=0.0038$); metastasis and meningioma (443.06 [387.5–498.6], $p=0.031$); and all other pairwise comparisons except GBM and lymphoma (666.3 [598.3–734.3], $p=0.97$).

Conclusions

Similar to results for DSC-MRI acquired without preload, PSR for preload-based, intermediate flip-angle DSC-MRI significantly differs for most pairwise comparisons of GBM, metastasis, lymphoma, and meningioma, except for GBM versus metastasis. However, mean baseline SI(t), reflecting preload extravasation and a "snapshot" of dynamic contrast enhancement, may help differentiate GBM from metastasis.

O-36

1:36PM - 1:43PM

Quantification of DSC-MRI Derived Fractional Tumor Burden (FTB) is Predictive of Survival in Newly Diagnosed Glioblastoma Following Concomitant Chemo-radiotherapy

M Prah¹, J Connelly¹, S Rand¹, K Schmainda¹

¹Medical College of Wisconsin, Milwaukee, WI

Purpose

DSC-MRI derived fractional tumor burden (FTB) maps provide a spatial means to distinguish between tumor and treatment effect (TE). [1] We hypothesized that the degree to which FTB-classified tumor is present will prove useful as a surrogate marker of outcome in newly diagnosed glioblastoma following chemoradiotherapy (CRT).

Materials and Methods

Consent was obtained from all participants in this retrospective IRB-approved study. Consecutive subjects with primary, newly diagnosed glioblastoma were included if DSC-MRI (GRE-EPI, TE/TR=31ms/1.48s, using a 0.1 mmol/kg preload [2]) was performed within 90d following CRT completion and enhancing lesion volume (ELV) was >1cc. Leakage-corrected, normalized relative cerebral blood volume (nRCBV) maps [2,3] were created and coregistered with T1+C. Postprocessing was performed using OsiriX-MD and Imaging Biometrics software. FTB maps were generated using the previously reported nRCBV threshold (1.13) for distinguishing glioblastoma from TE [1]. PFS and OS

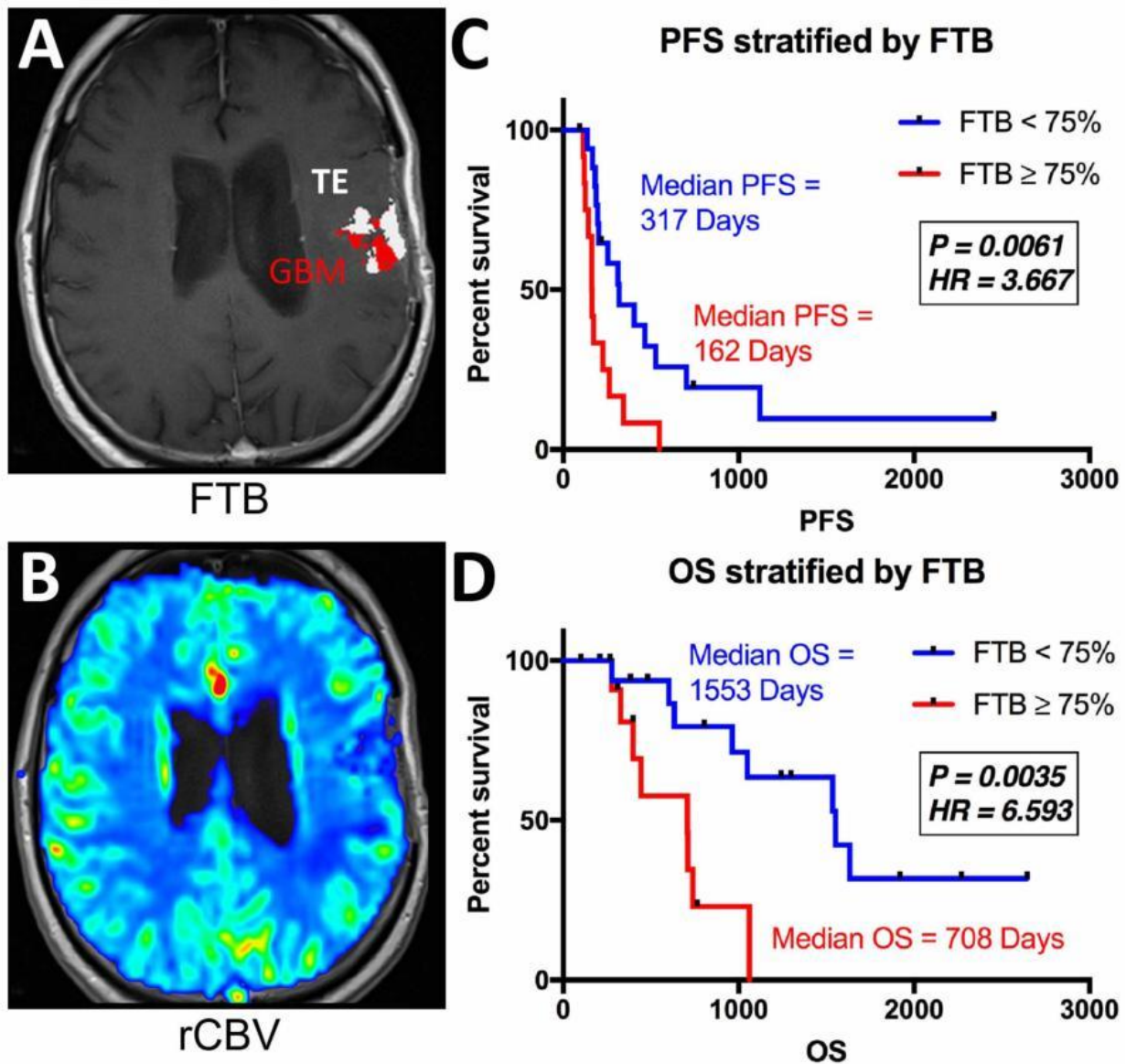
were determined from date of surgical diagnosis. Kaplan-Meier survival analysis was performed to assess the ability of FTB, mean nRCBV within ELV [4], and tumor methylation status [5] to predict PFS and OS with groups separated by the median for nRCBV or empirically at 75% for FTB.

Results

Thirty subjects (16m/14f; median age=58y) met inclusion. Example nRCBV and FTB maps are given in Fig1 A-B. Improved PFS ($p=0.0061$; HR=3.667; 317d vs. 162d) and OS ($P=0.0035$; HR=6.593; 1553d vs. 708d) were observed for FTB <75% (Fig1B-C). No significant differences in either PFS ($P=0.25$) or OS ($P=0.48$) were found for median nRCBV. Surprisingly, no significant advantages in PFS ($P=0.13$) or OS ($P=0.62$) were observed in patients who were methylated. Interestingly, the subject with the lowest FTB (17%) had the longest PFS, despite being unmethylated.

Conclusions

In this study, FTB was predictive of both PFS and OS, providing both spatial and quantifiable information with potential for use as a surrogate maker of response within the 90d pseudoprogression window following CRT.



(Filename: TCT_O-36_Fig1.jpg)

O-37

1:43PM - 1:50PM

“Overshoot”-Induced Underestimation of MR-DSC PWI rCBV Without Contrast Leakage Correction in Post-treatment Evaluation of Patients With Malignant Cerebral Tumors

X Liu¹, W Tian¹, A Hussain¹, H Wang¹

¹University of Rochester Medical Center, Rochester, NY

Purpose

MR dynamic susceptibility contrast (DSC) perfusion-weighted imaging (PWI) has been widely used in the treatment response evaluation in patients with malignant cerebral tumors after chemoradiation treatment. The first-pass effect in MR DSC-PWI leads to decrease of T2* signal intensity followed by recovery after the peak. In most of brain tumors, the T2* signal intensity could recover back close to the base line. The phenomenon that T2* signal intensity recovers higher than the base line is defined as "overshoot". In this study, we compared the relative blood volume (rCBV) values without and with contrast leakage correction in such patients with "overshoot", using FDA-approved MR DSC-PWI programs.

Materials and Methods

We retrospectively reviewed 75 MR DSC-PWI examinations in the patients with malignant cerebral tumors after chemoradiation treatment, including 53 patients with high-grade gliomas and 22 patients with brain metastasis. 50 cases with pathology-confirmed recurrent or progressive tumors. The rCBV maps without and with contrast leakage correction were generated using FDA-approved GE BrainStat and NordicICE programs. Two neuroradiologists measured the rCBV values in the same localized ROIs with "overshoot", and the difference of rCBV values without and with contrast leakage correction were assessed.

Results

The interoperator analysis between two neuroradiologists showed that the intraclass correlation coefficient (ICC) was 0.917. The mean rCBV value of GE BrainStat and NordicICE rCBV without contrast leakage correction was 0.31 ± 0.17 , ranged from 0.16 to 0.72. The mean value of NordicICE contrast leakage corrected rCBV was 2.26 ± 1.83 , ranged from 1.77 to 3.44. The mean NordicICE rCBV values with contrast leakage correction in the regions with "overshoot", were significantly higher than rCBV values without contrast leakage correction, $p < 0.001$.

Conclusions

The "overshoot" can cause underestimation of rCBV change in such treatment response evaluation of the patients with malignant cerebral tumors after chemoradiation treatment. Therefore, careful interpretation of post-treatment hemodynamic changes is necessary and important.

O-38

1:50PM - 1:57PM

Spatial correlation of different DCE perfusion markers in high grade gliomas

N Anzalone¹, U Zanolini¹, G Conte¹, M Caulo², M Grimaldi³, A Bizzi⁴, A Falini¹, A Castellano²

¹San Raffaele Hospital, Milan, Italy, ²University of Chieti, Chieti, Italy, ³Istituto Clinico Humanitas, Rozzano, Milano, Italy, ⁴Istituto Neurologico Besta, Milan, Italy

Purpose

DCE-MRI (Dynamic Contrast-Enhanced MRI) can provide markers of blood volume (Vp), volume transfer constant (K_{Trans}, considered an estimate of BBB permeability) and extravascular-extracellular volume (V_e) by the application of a bicompartimental model. Scarce data are available on their quantitative and spatial correlation within the same lesion. This study aims at determining the spatial and

quantitative variation of the different DCE markers within glioblastomas to understand if they provide different information that may possibly impact on biopsy planning.

Materials and Methods

Thirty-eight patients with surgically proved glioblastoma WHO IV were studied at 3T with conventional MRI and DCE perfusion. Parametric maps of Ktrans, Vp, Ve were calculated using Olea software (Olea Sphere, Olea Medical Solutions, France) and analyzed by two operators. By hotspot analysis, the colocalization of highest values from different maps was determined and their values compared using Wilcoxon test. After lesion segmentation, a voxel-by-voxel Spearman rank correlation was also performed.

Results

In most of 60% of cases the highest value from each parametric map of DCE did not colocalize (34/38 Vp-Ve; 28/38 Vp-Ktrans; 25/38 Ktrans-VE). The Wilcoxon test resulted to be highly significant ($P < 0.05$) between the hotspot values and the ROI measured in the rest of the lesion. Strong correlations were found both in hotspots and voxel-by-voxel analysis between Ve and Ktrans ($\rho = 0.754$; $\rho = 0.823$), Ktrans and Vp ($\rho = 0.820$; $\rho = 0.774$) and Vp and Ve ($\rho = 0.525$; $\rho = 0.638$), respectively.

Conclusions

Despite the intrinsic glioblastoma heterogeneity, confirmed by the majority of noncolocalization of hotspots from different markers of vascularization, our data showed a high correlation among different DCE values, thus suggesting that each map can be equally representative to define and quantify tumor regions of neoangiogenesis.

O-39

1:57PM - 2:04PM

Concordance of published FDG PET and DCE MR perfusion cutoffs in detecting recurrent high-grade glioma using hybrid PET-MRI

L Seligman¹, I Kovanlikaya², D Naeger¹, R Magge³, R Ramakrishna³, S Pannullo², H Fine³, G Chiang²
¹University of California San Francisco, San Francisco, CA, ²Weill Cornell Medical College, New York, NY, ³NewYork-Presbyterian Hospital - Weill Cornell, New York, NY

Purpose

Both 18F-fluorodeoxyglucose (FDG) positron emission tomography (PET) and MR perfusion (MRP) techniques are used to differentiate recurrent glioma from treatment-related change. Published cutoff values for these techniques have not been validated, despite wide use of these techniques clinically. Our study aimed to assess the concordance and reproducibility of these cutoffs in our cohort of post-treatment high-grade gliomas.

Materials and Methods

This IRB-approved retrospective study included 41 consecutive patients who underwent hybrid PET-MRI for post-treatment high-grade gliomas (21 grade 3 astrocytomas, 20 glioblastomas). Published cutoffs for FDG-PET and MRP were used to assess accuracy in the whole cohort and separated by tumor grade. Whole tumor volumes-of-interest and regions-of-interest were delineated manually with Olea and Siemens Syngo software to obtain maximum, mean, and histogram values for plasma volume (Vp), permeability (Ktrans), and FDG uptake (SUV).

Results

The maximum accuracy, sensitivity, and specificity obtained by FDG-PET and MRP cutoffs were similar: 76% accuracy (FDG-PET 34-76%, MRP 32-76%), 94% sensitivity (FDG-PET 25-94%, MRP 22-94%), 67% specificity (FDG-PET 11-67%, MRP 0-67%), although lower than previously published. Accuracy was higher when separated by tumor grade (up to 80% for glioblastoma and 81% for grade 3 astrocytoma). Percent agreement between FDG-PET and MRP cutoffs ranged from 34 to 83%, with 80% agreement between the best performing PET and MRP cutoffs.

Conclusions

Our study finds that FDG-PET and MRP have similar accuracy in differentiating recurrent tumor from post-treatment change, although accuracy is lower than previously published. Concordance rates varied significantly, and different cutoffs achieved greatest sensitivity or specificity. Further work is required to optimize imaging modalities for diagnosis of recurrent high-grade glioma, and current clinical use of these techniques should be guided by tumor grade and clinical goals.

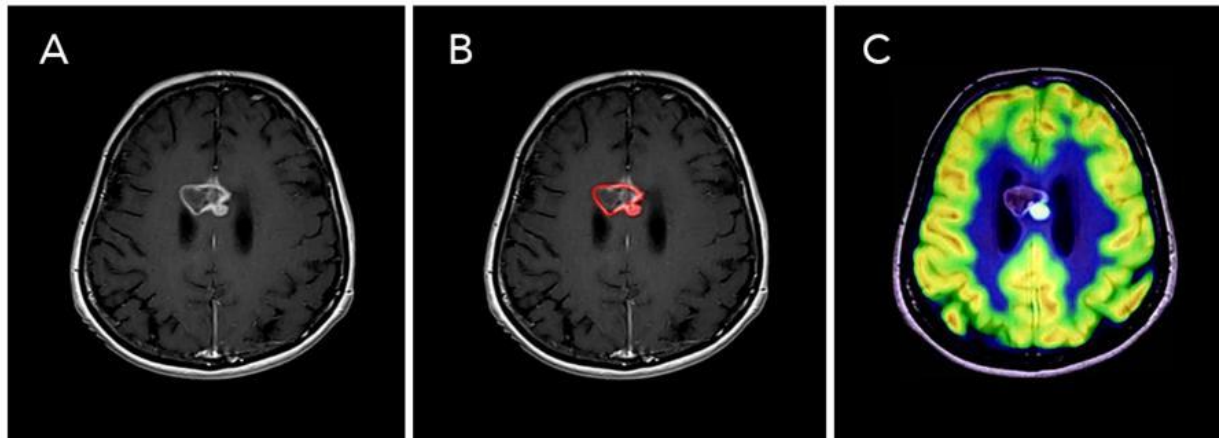


Figure 1A: Postgadolinium axial T1-weighted MR image in a representative patient.

Figure 1B: Enhancing tumor volume-of-interest (highlighted in red).

Figure 1C: Hybrid PET-MR image of the same patient showing FDG avidity in the solid tumor nodule.

(Filename: TCT_O-39_PETMRfigure.jpg)

O-40

2:04PM - 2:11PM

The Use of MRI Arterial Spin Labelling Blood Flow Over Four Years to Characterize Intra Cranial Metastasis Blood Flow and the Value of Obtaining Base Line Data to Distinguish Between Tumor Recurrence and Radiation Change in the Enlarging Lesion Following Gamma Knife SRS.

s_holmes¹, E Lambert²

¹Hawaii Advanced Imaging Institute, Honolulu, HI, ²St. George's University of London, London, United Kingdom

Purpose

The use of ASL has been reported to be more accurate than PET and SPECT in characterizing post-SRS brain metastasis as either recurrent tumor or radiation necrosis, and specifically elevated flow indicated recurrent tumor, but the patients in that paper did not have baseline ASL data. We have performed ASL in over 300 patients over four years and our data indicates that up to 30+% of nontreated metastasis have relatively low flow at baseline, and therefore we propose that baseline ASL data on all pre-SRS patients should be obtained. Those tumors with low flow prior to SRS would not be expected to have elevated flow post treatment, and not having this data will lead to elevated false negative ASL conclusions.

Materials and Methods

We have performed pseudocontinuous dual-delay ASL at both 1.5 and 2.5 seconds on all the pre and post Gamma Knife patients for over four years now, with data on over 300 patients. This was added to the routine MRI exam, which also included DSC MR gadolinium perfusion on many of these same patients. All of the patients that were not lost to follow-up had routine every three month follow-up MRI using these same sequences.

Results

Whereas elevated flow using ASL does indeed indicate recurrent tumor, over 30% of the metastasis had

Oral Presentations & Excerptas

relatively low flow at baseline, and these patients would not be expected to manifest elevated flow with tumor recurrence. Certain hypervascular tumors, such as renal cell carcinoma consistently had elevated flow and when present, allowed the use of ASL to characterize lesions in follow-up in those patients with renal failure or who could not receive Gadolinium.

Conclusions

ASL is a reliable and easily performed sequence to establish pre- and post-GK flow analysis on intracranial metastasis 10 mm or larger, and in smaller metastasis in certain hypervascular tumors such as renal cell carcinoma. A significant percentage of intracranial metastasis have relatively low flow at baseline, and this should be factored into the post-GK analysis when using this data to distinguish between recurrent tumor and radiation change in the enlarging lesion. This data can also be used in the hypervascular metastasis for reliable characterization in those patients with significant renal dysfunction and when Gadolinium can not be administered.

O-42

2:18PM - 2:25PM

Can Perfusion Imaging Predict CyberKnife Treatment Response in Cerebral Metastatic Disease?

S GhaderiNiri¹, M Amsbaugh², M Yusuf³, S Woo³, J Gaskins³, R Bert¹

¹University of Louisville, Louisville, KY, ²MD Anderson Cancer Center, Houston, TX, ³University of Louisville, James Graham Brown Cancer Center, Louisville, KY

Purpose

Of cancer patients 26% develop a CNS metastasis. Many patients are treated with stereotactic radiosurgery. While many lesions demonstrate a complete response to stereotactically-delivered focal radiation, a significant proportion of lesions are resistant. Imaging biomarkers predicting treatment failure would be important for prognosis and treatment planning. There has been a paucity of such studies for CNS metastatic disease. As the hypoxic model has been useful in predicting response to radiotherapy, we hypothesized that perfusion-weighted imaging would be a useful tool in predicting treatment failure for cyberknife therapy.

Materials and Methods

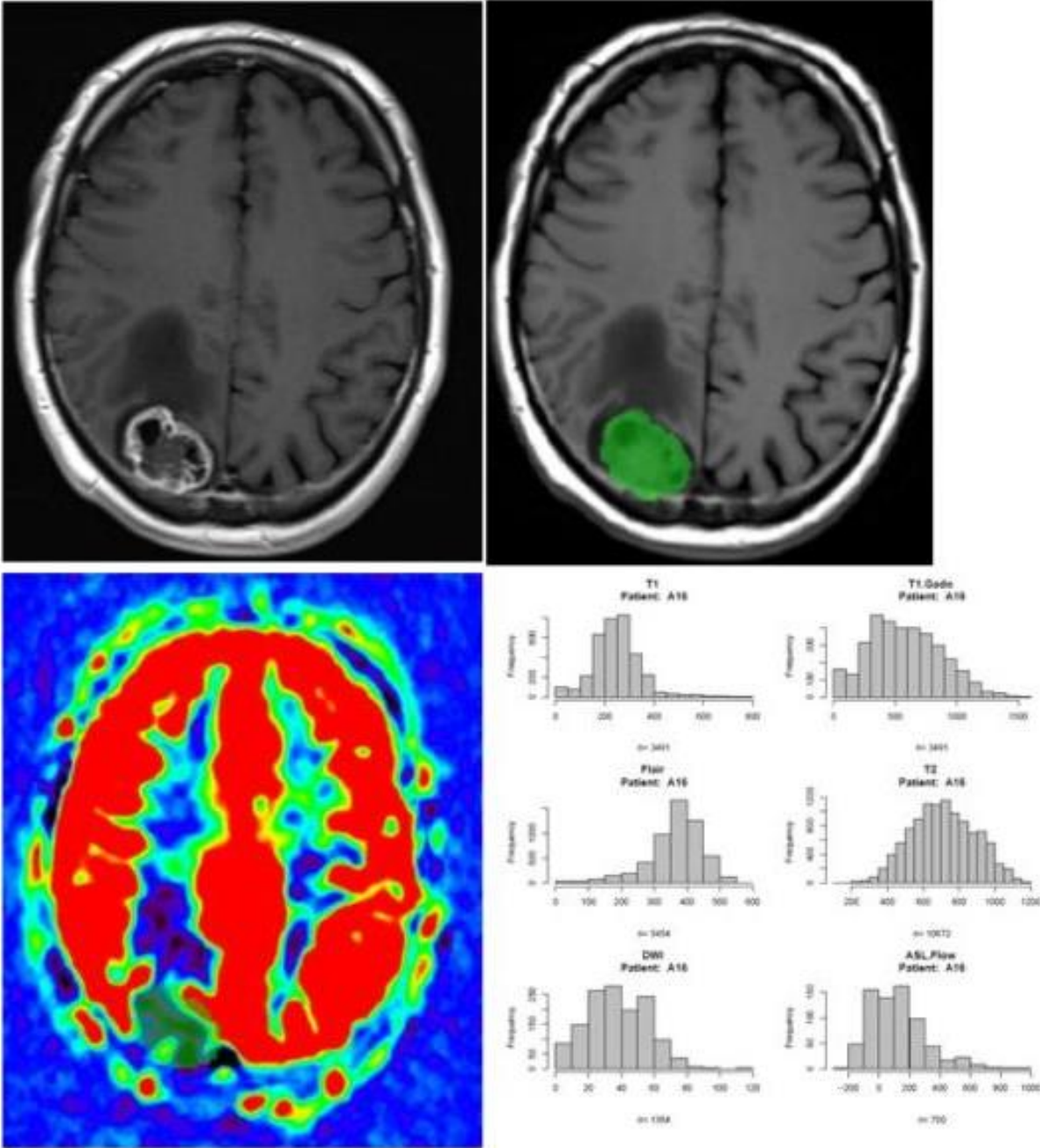
A total of 33 patients were selected from the radiation oncology database that had received cyberknife treatment for CNS brain metastases and had received DSC or ASL perfusion-weighted 1.5T or 3T MRI prior to treatment, along with conventional pulse sequences. Lesion ROI were hand drawn by a trained resident on all slices containing a lesion greater 5mm. Fifty-seven lesions were retrospectively analyzed using commercial software with downloadable signal intensity CSV files for ROI voxels. Downloaded data were then statistically analyzed with statistical software after normalization of ROI values to normal white matter using standard C/N.

Results

Results were somewhat contradictory between ASL CBF and DSC CBV using our available imaging. ASL had a modest result using our current imaging package (Siemens/PASL). If 93% of voxels showed C/N>1, there was a 78% chance of treatment response. Overall S/S was 78/56. For DSC, CBV mean was the best predictor with 100% of the failed lesion having average C/N>0.89. Overall S/S was 100/73.

Conclusions

PWI may be a usable biomarker for predicting treatment response to stereotactic radiosurgery but will require further prospective analysis with larger data samples. Further analysis, additional biomarkers and other statistical parameters are ongoing and will be updated at the meeting.



(Filename: TCT_O-42_Presentation22.jpg)

O-43

2:25PM - 2:32PM

MR Perfusion and Diffusion Imaging in the Follow-Up of Recurrent Glioblastoma Treated With Programmed Death (PD)-1 Immunotherapy

A Kravitz¹, A Hormigo², P Belani², C Hadjipanayis², A Doshi², B Delman², K Nael²

¹Charles E. Schmidt College of Medicine at Florida Atlantic University, Boca Raton, FL, ²Icahn School of Medicine at Mount Sinai, New York, NY

Purpose

By blocking programmed cell death (PD)-1 signaling pathways, Nivolumab results in significant inflammatory response and progressive enlargement and enhancement of the treated glioblastoma (GB). We aimed to describe the sequential quantitative changes of MR perfusion and diffusion in a cohort of patients with GB who were treated with Nivolumab- immunotherapy.

Materials and Methods

Patients with diagnosis of recurrent GB who had MR perfusion and diffusion before and after Nivolumab treatment were evaluated. Using coregistered images, mean values of the ADC, Ktrans and CBV were calculated from a volume-of-interest of the enhancing tumor in pre and postimmunotherapy scans. For ADC and CBV, ratios were obtained by normalizing to the contralateral hemisphere. Patients were assigned as stable/improved vs. progressed using follow-up clinical and imaging findings according to RANO criteria. The trend of imaging biomarkers was compared between stable and progressed patients.

Results

Seven patients (4M, 3F, mean age 67.4) met inclusion criteria. Interval time between two MRI studies was 2.79 ± 1.07 months (Mean \pm SD). The mean \pm SD of enhancing tumor volumes were 6.29 ± 9.16 mL and 13.79 ± 10.86 mL in pre- and post-Nivolumab scans. Five of seven patients were classified as stable/improved after Nivolumab treatment. Four of these patients showed interval increase in the tumor volume (pseudoprogression). The mean \pm SD of rCBV, Ktrans and rADC values in pre-/post-Nivolumab therapy were $(2.15 \pm 1.07/2.64 \pm 0.81)$, $(0.12 \pm 0.06/0.21 \pm 0.13 \text{ min}^{-1})$, $(1.35 \pm 0.46/1.86 \pm 0.56)$ respectively.

Conclusions

In Nivolumab-induced pseudoprogression, there is interval increase in rADC, rCBV and Ktrans. Interval increase in rCBV and Ktrans are contradictory to what has been described in cytotoxic (temozolomide)-induced pseudoprogression. This highlights a potentially different mechanism and pathophysiology for pseudoprogression caused by PD-1-mediated immunotherapy (Nivolumab).

O-44

2:32PM - 2:39PM

Simultaneous Imaging of Brain Tumor Cellularity and Perfusion Using MR Neuro-Immune Imaging

Q Wang¹, G Guzman Perez-Carrillo², Y Wang¹, P LaMontagne¹, S Dahiya¹, T Benzinger¹

¹Washington University in St. Louis, St. Louis, MO, ²University of Arizona- Banner Medical Center, Tucson, AZ

Purpose

Brain tumors are heterogeneous, and usually contain different grades of tumor cells, and/or abnormal vascular structures. Conventional anatomical magnetic resonance imaging (MRI) without contrast enhancement is very limited in evaluating heterogeneity. We developed a new diffusion MRI-based method, neuroimmune imaging (NII), to simultaneously image and quantify tumor cells of different grades (based on cellularity) and capillary blood perfusion for each voxel within the tumor, which cannot be achieved using conventional diffusion MRI techniques.

Materials and Methods

Seven adult patients having known or suspected brain gliomas were included in this preliminary study.

Oral Presentations & Excerpts

Patients underwent clinical brain tumor MRI protocol including MPRAGE, T2 FLAIR, dynamic susceptibility contrast (DSC) perfusion imaging and NII on the Siemens 3.0 Tesla PET/MR scanner prior to planned standard-of-care surgical resection and/or stereotactic biopsy. NII was acquired with multi-b value scheme ($b_{max} = 2000s/mm^2$ and 74 directions). NII expanded the diffusion basis employed in original DBSI [1, 2] to model the sub-voxel cellularity components and the capillary blood perfusion effects that has been used in intravoxel incoherent motion imaging [3]. Tumor cell fraction (TCF) maps for different tumor grade were generated using NII and compared to coordinate-guided biopsy or surgical resection results. ADC cutoffs for tumor grade based on previous literatures [4, 5]. The association between NII-generated perfusion fraction (PF) and DSC-derived cerebral blood volume (CBV) was investigated.

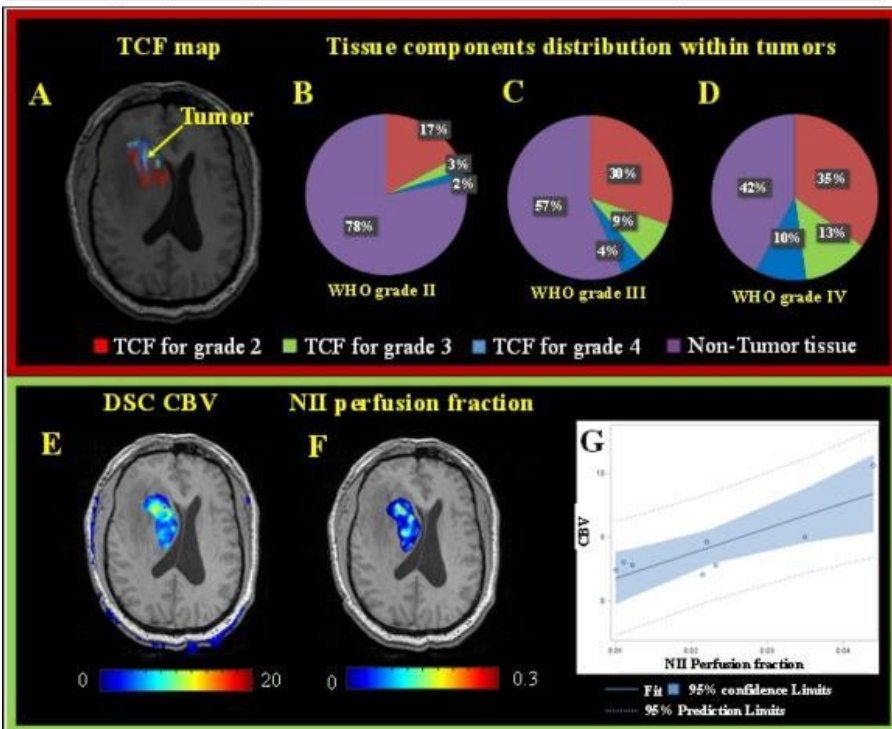
Results

NII detected tumor grades were consistent with biopsy assessment (Table 1). With the increasing of WHO tumor grades, TCF for each tumor grade (II-IV) kept increasing and the nontumor components kept decreasing (Figure 1A-D). Another important finding in this study was the NII detected PF highly correlated with DSC CBV ($r=0.83$ (95% confidence interval [0.39, 0.96]) (Figure 1E-G).

Conclusions

NII can simultaneously characterize brain tumor heterogeneity, including various grades of tumor cells and capillary blood perfusion without using contrast agents or radioactive tracers. NII measurements are consistent with pathology assessments from biopsy tissues and clinical perfusion measures. Larger studies will be needed to further establish NII's clinical role.

Table 1. Characteristics of patients and the tumor grades detected by biopsy and NII				
Patient #	Age	Gender	Tumor pathology	NII-tumor grade
#1	64	Female	<u>Oligoastrocytoma</u> WHO grade II	2
#2	36	Female	<u>Oligodendroglioma</u> WHO grade II	2
#3	38	Male	Anaplastic astrocytoma WHO grade III	3
#4	30	Male	Diffuse astrocytoma WHO grade II	2
#5	33	Female	<u>Oligodendroglioma</u> WHO grade II	2
#6	47	Male	<u>Oligodendroglioma</u> WHO grade III	3
#7	62	Male	<u>Glioblastoma</u> WHO grade IV	4



(Filename: TCT_O-44_Figure_table.jpg)

Monday, June 4, 2018

1:15PM - 2:45PM

Parallel Paper Session: Epilepsy Imaging Techniques

O-45

Oral Presentations & Excerptas

Clinical Utility of FDG PET/MR Imaging in Mesial Temporal Sclerosis (MTS): Correlations with Disease Severity

R Gupta¹, P Sharma², R Matthews³, K Yaddanapudi³, D Franceschi³, L Bangiyev³

¹Mount Sinai Hospital, New York, NY, ²Mount Sinai Beth Israel, New York, NY, ³Stony Brook University Hospital, Stony Brook, NY

Purpose

MTS can be difficult to diagnose on imaging and there is a paucity of data on hippocampal metabolism and its correlation with morphology and clinical severity. The purpose of this study is to illustrate the added value of FDG PET/MR imaging in MTS.

Materials and Methods

Twenty-two patients with clinically diagnosed epilepsy underwent simultaneous FDG PET/MR imaging (Siemens Healthcare mMR biograph) with 3T MRI. Patients were included if they had findings consistent with unilateral MTS diagnosed through MRI and FDG PET. MRI seizure protocol was followed and MIM software was used for image fusion. A neuroradiologist and a nuclear radiologist interpreted the exams in consensus. Both hippocampi were contoured and analyzed in all patients with MTS.

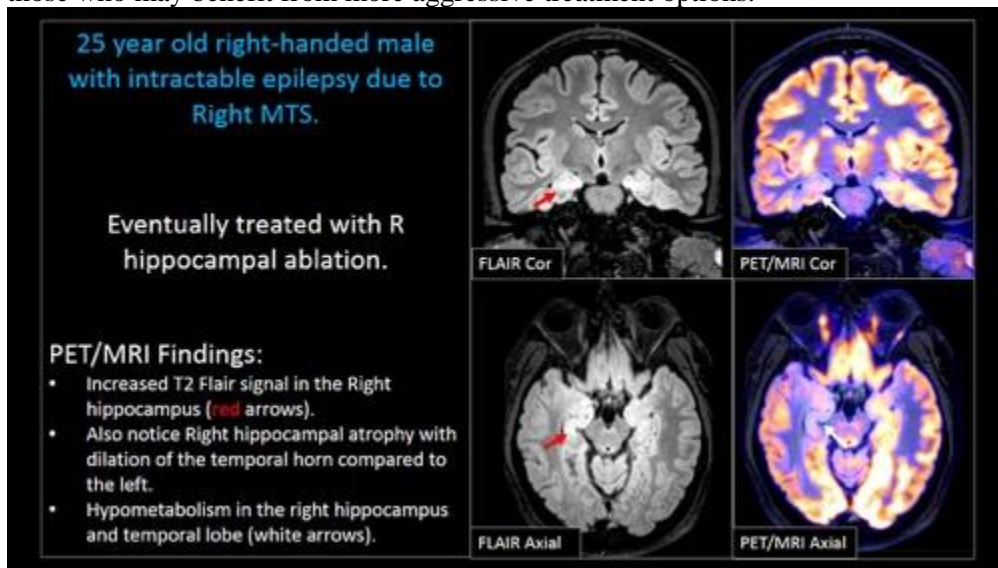
Quantitative morphometric and metabolic parameters were correlated with each other as well as with an epilepsy severity index for each patient based on clinical factors.

Results

Five patients (3 M, 2 F, avg age: 48 ± 15 yrs) with unilateral MTS were included. The affected hippocampus had a significantly smaller volume (0.8 ± 0.2 vs 1.8 ± 0.2 cm³, $p = 0.0008$); higher signal intensity (195 ± 15 vs 181 ± 14 , $p = 0.006$); and lower metabolic activity (SUVmax 5.9 ± 0.6 vs 7.9 ± 1.5 , $p = 0.02$), compared to the contralateral side. A weak correlation was observed between the difference in volume and difference in intensity ($r = 0.1$) as well as difference in metabolic activity ($r = 0.3$) between the two hippocampi in each patient. The difference in hippocampal metabolic activity, between the affected and normal side, had a moderate correlation with that patient's epilepsy severity index ($r = 0.5$).

Conclusions

FDG PET/MR imaging can quantitate hippocampal hypometabolism in MTS patients and help identify those who may benefit from more aggressive treatment options.



(Filename: TCT_O-45_MTS.jpg)

O-46

Epileptogenic Pathologies of the Temporal Lobe Prompt Distinct Changes in the Functional Language Connectome

O Foesleitner¹, K Nanning¹, S Bonelli¹, E Patarai¹, D Prayer¹, G Kasprian¹

¹*Medical University of Vienna, Vienna, Austria*

Purpose

Temporal lobe epilepsy (TLE) is most commonly caused by mesiotemporal sclerosis (MTS) or low-grade tumors (ref. 1). In some cases no structural lesion can be detected on MRI (nl-TLE). TLE is associated with language deficits (ref. 2). Functional language networks (summarized as language connectome) can be analyzed with functional MRI (fMRI). Our aim was to investigate whether different epileptogenic pathologies of the temporal lobe show distinct changes in the functional language connectome.

Materials and Methods

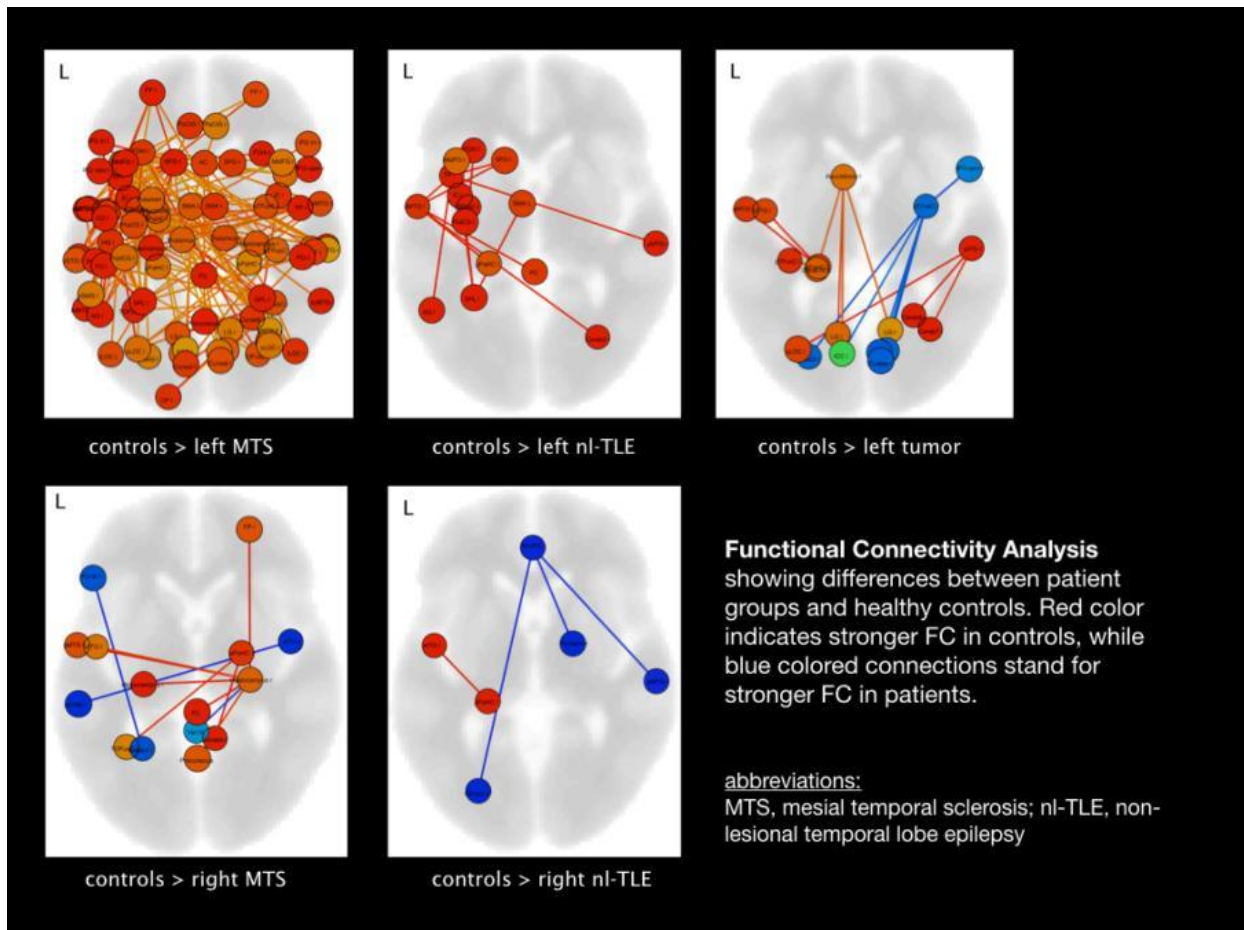
We retrospectively included 99 patients with TLE (left/right: 22/22 MTS, 25/20 nl-TLE, 10 left mesiotemporal low-grade tumors) and 21 healthy controls. All participants performed a 5-min verb generation task on the same 3T fMRI scanner. Functional connectivity (FC) was analyzed using all time points after task regression (CONN toolbox 17.f). Significance levels were set at <0.05 FDR-corrected. Clinical parameters were considered as covariates.

Results

There was no significant difference between any group regarding age at MRI, sex, age at seizure onset, or in-scanner motion parameters (all $p > 0.05$). Left temporal pathologies were associated with more severe changes of the language connectome than right temporal pathologies. Left MTS showed the most widespread decreases in FC including multiple regions in both hemispheres. Left nl-TLE was accompanied by predominantly left lateral temporal decreases in FC. In tumors FC was decreased locally but increased in the contralateral hemisphere.

Conclusions

Different epileptogenic pathologies in the temporal lobe prompt distinct changes in the functional language connectome. Significantly more decreased functional connections can be found in left than right temporal pathologies. Mesiotemporal sclerosis leads to severe intra and interhemispheric alterations, while nonlesional TLE and mesiotemporal tumors have a more local impact on the functional language connectome.



(Filename: TCT_O-46_fcpath.jpg)

O-47

1:29PM - 1:36PM

Paravascular Spaces as a Potential Neuroimaging Biomarker for post-traumatic seizures

G Barisano¹, D Duncan², Y Shi², M Sarabi², A Toga², M Law¹

¹Department of Radiology, Keck Medical Center of University of Southern California, Los Angeles, CA, ²Stevens Neuroimaging and Informatics Institute, University of Southern California, Los Angeles, CA

Purpose

Paravascular spaces (PVSs), also known as Virchow-Robin spaces, are tubular cerebrospinal fluid-filled structures that surround blood vessels penetrating the brain parenchyma. In recent years, many studies have suggested that PVSs may play an important role both in the clearance of metabolic waste products from the brain and in neuroinflammation. Specifically, PVSs may be involved in the recruitment of macrophages across the blood-brain barrier, and their impairment could explain the altered macrophage activity resulting in seizure onset and formation of seizure foci (1–3). The relationship between epilepsy and the presence of enlarged or reduced PVSs is still not well understood (4). We aim to investigate the relationship between PVSs and both traumatic brain injury (TBI) and the development of seizures as a neuroimaging biomarker for post-traumatic epilepsy.

Materials and Methods

We analyzed PVS in 11 subjects (age range: 12-68 years old) who suffered a TBI using data collected in the Epilepsy Bioinformatics Study for Antiepileptogenic Therapy (EpiBioS4Rx). Healthy subjects (age

range: 20-62 years old) were used as controls. MRI scans were performed 14 days after trauma using 3T MRI. Enlarged PVSs were rated according to published methods (5).

Results

We found a significant asymmetric distribution of PVSs in six subjects: In their MRI both the total number and the mean caliber of PVS resulted significantly decreased in the hemisphere affected by the trauma compared to the contralateral side and compared with control subjects. Moreover, all patients experienced at least one episode of seizure within the first month after the trauma, while the subjects with normal PVSs did not develop post-traumatic seizures in the same period of time.

Conclusions

Microstructural brain alterations are important for the development of seizures. PVSs distribution and quantification may be considered a potential noninvasive biomarker to predict the risk of seizures after TBI and to localize the suspected seizure onset area. These results may have important therapeutic implications as there are potential therapeutic targets for improving CSF clearance. This research was supported by the National Institute of Neurological Disorders and Stroke of the National Institutes of Health under Award Number U54NS100064.

O-48

1:36PM - 1:43PM

Pseudo-continuous Arterial Spin Labeling in Epilepsy: A Case Review.

J Lally¹, E Friedman¹

¹*The University of Texas Health Science Center at Houston, Houston, TX*

Purpose

In epilepsy, identification of structural lesions on conventional MR imaging can be challenging. In some cases, differentiation between the types of structural lesions may be important. For example, the presence of neoplasia may alter the surgeon's extent of resection and affect patient prognosis. The purpose of this case review is to examine, evaluate, and discuss our recent experience with arterial spin-labeling (ASL)-MR perfusion in patients with structural lesions.

Materials and Methods

Cases were identified and presented at our institutional neurosurgery tumor board and/or epilepsy conference for multidisciplinary evaluation and treatment planning. Patients included underwent conventional MRI and pseudocontinuous ASL (pCASL) perfusion. If appropriate, surgical histopathology and genetics were also reviewed.

Results

Cases include etiologies such as glial tumors, skull-base meningoencephalocele, focal cortical dysplasia, mesial temporal lobe sclerosis, and encephalomalacia. For all patients, pCASL images were evaluated and lesional perfusion was qualitatively compared to the contralateral, uninvolved white matter and cortex. If obtained, additional advanced imaging findings on fluorodeoxyglucose-positron emission tomography (FDG-PET), proton magnetic resonance spectroscopy (MRS) and dynamic susceptibility contrast MR (DSC) were also described.

Conclusions

ASL is useful in the identification and delineation of structural lesions, potentially amenable to surgical resection. As a noninvasive perfusion technique dispensing the need for intravenous contrast, ionizing radiation, and radiotracer administration, pCASL will become increasingly utilized in epilepsy.

O-49

1:43PM - 1:50PM

Image Processing for Detection of Mesial Temporal Sclerosis in Adults: A Case-Control Study.

F Dahi¹, M Parsons², D Vaswani³, A Sharma⁴

Oral Presentations & Excerpts

¹Washington University in Saint Louis, Saint Louis, MO, ²Mallinckrodt Institute of Radiology, Saint Louis, MO, ³Mallinckrodt Institute of Radiology, Saint Louis, MO, ⁴Mallinckrodt Institute of Radiology, Saint Louis, MO

Purpose

Detection of Mesial temporal sclerosis (MTS) patients with intractable epilepsy is important. We tested an image-processing algorithm that aims to facilitate detection of MTS on MRI.

Materials and Methods

This retrospective, IRB-approved study included 33 patients with histologically established diagnosis of MTS and 32 controls without seizure history. A blinded coinvestigator processed coronal FLAIR images from these patients using a custom image-processing algorithm (Correlative Image Enhancement, CIE), saving processed images as a separate DICOM series. The algorithm markedly increased the hippocampal signal intensity if it detected baseline differences between the intensities of the hippocampus and the normal gray matter. Three blinded readers (one neuroradiologist with >10 years of experience, one neuroradiology fellow, and one radiology resident) rated baseline and processed series separately for signal intensity of each hippocampus and presence of MTS on a 5-point scale ranging from 1 (definitely normal) to 5 (definitely abnormal), and indicated whether they detected marked hyperintensity resulting from processing. Effect of processing on sensitivity, specificity, positive predictive value and negative predictive value of each reader were assessed.

Results

Sensitivity of detecting MTS-related hippocampal signal abnormality increased following image processing from 54.5% to 81.8% for reader 1, from 60.6% to 84.8% for reader 2, and from 75.7% to 81.8% for reader 3. While there was minimal decrease in specificity from 100% to 98.4% for reader 1, specificity improved from 95.3% to 98.4% for reader 2, and from 98.4% to 100% for reader 3. Of note, decreased specificity for reader 1 was due to a false positive rating assigned to a control hippocampus that was left unaltered by the processing.

Conclusions

By markedly increasing signal intensity of many MTS-affected hippocampi, CIE improved sensitivity of MTS detection without any significant detriment to specificity. This benefit was seen for all readers, much more so for inexperienced readers.

O-50

1:50PM - 1:57PM

Automated and Manual Diffusion Tractography in Presurgical Diagnostic of patients with Temporal Lobe Epilepsy

I Orosz¹, V Patel¹, H Yokota¹, D Woodworth¹, N Salamon³

¹David Geffen School of Medicine at University of California Los Angeles, Los Angeles, CA, ²University of California Los Angeles, Los Angeles, CA

Purpose

Diffusion-tensor imaging (DTI) studies have demonstrated microstructural white-matter alterations in epileptogenic regions. Nevertheless, DTI methods are not yet routinely used in the the diagnostic of individual patients with epilepsy. The purpose of our case series study was to assess whether tractography techniques could aid in presurgical epileptogenic zone (EZ) localization in individual patients with temporal lobe epilepsy (TLE).

Materials and Methods

We retrospectively evaluated the DTI images of two adult patients with TLE and compared these with the results of their preoperative epilepsy diagnostic evaluation. Seizure onset zone (SOZ) was defined by intracranial electroencephalography (iEEG). Two age- and-gender matched healthy controls were also included. We applied: 1) automated whole brain probabilistic tractography in native space with TRActs

Oral Presentations & Excerptas

Constrained by UnderLying Anatomy (TRACULA) and 2) manual deterministic tractography seeded from intracranial electrode sites using TrackVis. Fractional anisotropy (FA) of the tracts was measured as the DTI outcome parameter.

Results

Using manual tractography we found that the mean FA of the electrode sites located in the SOZ were lower compared to the non-SOZ sites within both patients. Using TRACULA we detected decreased FA of the entire superior longitudinal fasciculus (slf) ipsilateral to the SOZ in case 1 of unilateral neocortical TLE and frontal opercular SOZ. In case 2 of unilateral mesial TLE and extensive bilateral seizure spread the temporal bundle of the slf tract in both hemispheres and the forceps minor of the corpus callosum showed markedly decreased FA compared to the control. Increased FA of the cingulum contralateral to the SOZ was found in both patients compared to controls.

Conclusions

DTI alterations seemed to correspond to the patients' EZ and seizure spread as delineated by the multimodal presurgical diagnostic evaluation. Future studies should focus on prospective application of fast and reproducible automated tractography tools in preoperative epilepsy evaluation to standardize tractography methods in order to incorporate DTI into the clinical routine.

O-51

1:57PM - 2:04PM

Simulation of Implantation of EEG Electrodes, Strips and Grids Utilizing 3D Printing of Mesh-Like Cerebral Cortex and Deep Brain Structures

R Javan¹, D Shields¹, M Koubeissi¹, P Heidari¹, B Patel¹

¹George Washington University Hospital, Washington, DC

Purpose

The aim of this project was to develop a 3-D printed simulation system for mimicking the placement of EEG electrodes, strips and grids, which could also potentially be used for patient-specific preprocedural planning.

Materials and Methods

The "Split" function along with the basic segmentation tools of Materialise InPrint 2.0 was used to remove the calvarium and osseous skull base from the brain parenchyma in a DICOM dataset of a T1-weighted 3-D FSPGR MRI brain. The result was exported as a Stereolithography (STL) file into Autodesk 3-D Studio Max, where using the "Pro Optimizer" modifier, the number of polygons were decreased by 60% and the "Lattice" modifier was applied in order to create a mesh-like brain surface. Deeper brain structures, i.e. the deep gray nuclei, were graphically designed and added, also with a mesh-like surface. The final model was then 3-D printed as a cerebral hemisphere with polyamide material using selective laser sintering technology through an online commercial service.

Results

The purpose of the mesh-like nature of the surface of the brain and deep structures is three-fold. Not only the surface anatomy can be fully appreciated and taught, but also the deep structures can be visualized through the surface. Additionally, electrodes can be passed through the model to reach the deep structures numerous times without damaging the model. The final model is light and durable and can be placed in a hemi-calvarium 3-D printed from CT head data, with gypsum-based material, which would also allow for drilling of burr holes.

Conclusions

Knowledge of the brain surface anatomy and the approach to reach deep brain structures with electrodes is important for both neurosurgeons and epileptologists. This relatively low-cost technique can also be implemented for interdisciplinary preprocedural planning for patients requiring intracranial EEG monitoring.

Diffusion Tensor Tractography and Magnetic Resonance Guided Focused Ultrasound Modeling in the Treatment of Mesial Temporal Sclerosis: A Proof of Concept Study

E Weidman¹, R Uribe¹, C Hoffman¹, J Chazen¹

¹*New York-Presbyterian Hospital/Weill Cornell Medical Center, New York, NY*

Purpose

Mesial temporal sclerosis is a common cause of medically refractory epilepsy. Surgical treatment is highly effective but associated with postoperative deficits, including disruption of the optic radiations [1]. Transcranial magnetic resonance guided focused ultrasound (MRgFUS) is a minimally invasive technique that allows targeted thermal ablation through an intact skull [2]. It is FDA-approved for the treatment of essential tremor [3, 4]. MRgFUS requires precise target localization and adequate availability of elements (>800) to reach the selected target. This study evaluates the feasibility of mapping the fornix-fimbriae with diffusion-tensor imaging (DTI) and modeling MRgFUS ablation for seizure treatment.

Materials and Methods

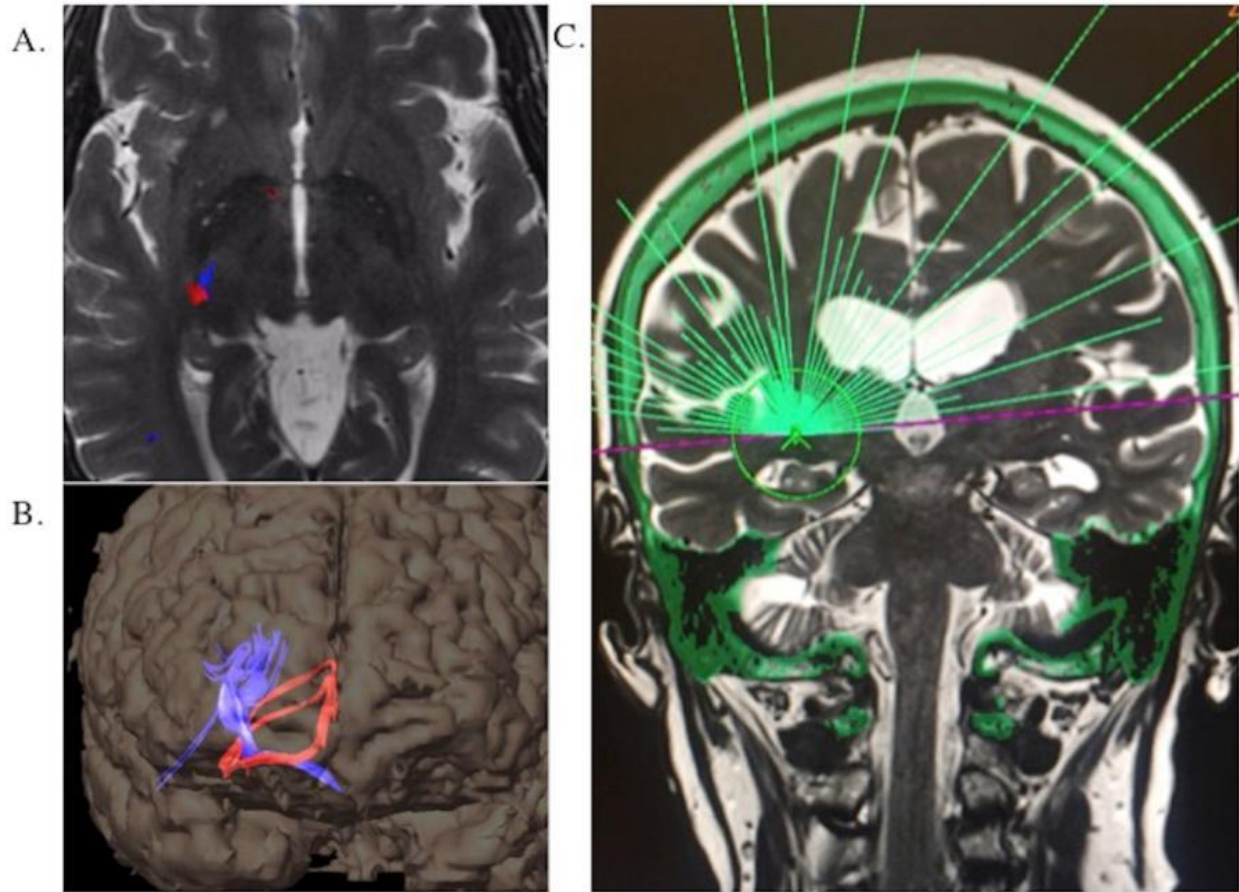
Retrospectively reviewed were 3 Tesla MRI examinations with DTI. Patients with essential tremor who underwent CT and MRI prior to MRgFUS were included. The fornix-fimbriae tract and optic radiations were mapped using Brainlab iPlanNet Cranial v3.0. Fractional anisotropy threshold and minimum fiber length were manually adjusted by a neuroradiologist to optimize tractograms. The ablation target was selected in collaboration with a neurosurgeon to target the fornix-fimbriae posterior to the optic radiations. The MRgFUS procedure was then modeled using the same methods as in clinical ablation cases. Briefly, a CT-MR fusion was performed. Frontal sinuses and intracranial calcifications along the treatment path were blocked as no-pass regions using the Insightec® surgical planning software. The ablation site was marked and a theoretical helmet angulation was prescribed. The number of available elements from the 1024-array were calculated.

Results

The fornix-fimbriae were successfully fiber tracked in seven of 19 patients. For patients with tracked fornix-fimbriae, >900 (more than adequate) elements were available to target the prescribed ablation site.

Conclusions

MRgFUS may provide a minimally invasive option for treatment of medically refractory epilepsy in a subset of patients. This theoretical modeling is important as it establishes groundwork for future clinical trials. Optimization of DTI parameters will be necessary to assist in target localization.



(A) Axial T2 image at the level of the anterior commissure-posterior commissure and (B) frontal 3D rendered tractography with brain overlay demonstrating close approximation of the right fornix-fimbriae (red) and optic radiation (blue). (C) Fused coronal CT/MR demonstrating available US arrays for theoretic ablation target on MRgFUS model.

(Filename: TCT_O-52_ASNRfinalfigure.jpg)

O-53

2:11PM - 2:18PM

Efficacy of 7T Neuroimaging of Epilepsy Lesions

S Jones¹, I Wang¹, T Emch¹, V Hill¹, M Larvie¹, J Lee¹, P Ruggieri², S Statsevych¹, M Lowe¹

¹Cleveland Clinic, Cleveland, OH, ²Cleveland Clinic Foundation, Cleveland, OH

Purpose

We propose to investigate the clinical utility of in vivo structural 7T MRI to identify focal cortical dysplasia (FCD), using a cohort of 70 drug-resistant epilepsy patient with a large array of epileptogenic pathologies. We report initial results of the impact of 7T visual and postprocessing analyses on clinical care, as well as confirmation of the epileptogenicity and pathology of 7T findings by ICEEG and surgery.

Materials and Methods

This study was approved by the Cleveland Clinic IRB. Patients were imaged at 7T if they had a clear or equivocal lesion on 3T MRI, or had negative 3T MRI but clinical and other imaging data strongly suggested focal epilepsy. A 7T protocol included an anatomic MP2RAGE sequence, axial FLAIR, axial coronal and axial T2*. Postprocessing of all T1W MP2RAGE sequences was performed using the morphometric analysis program (MAP) in MATLAB SPM (Figure 1). Two substudies were then

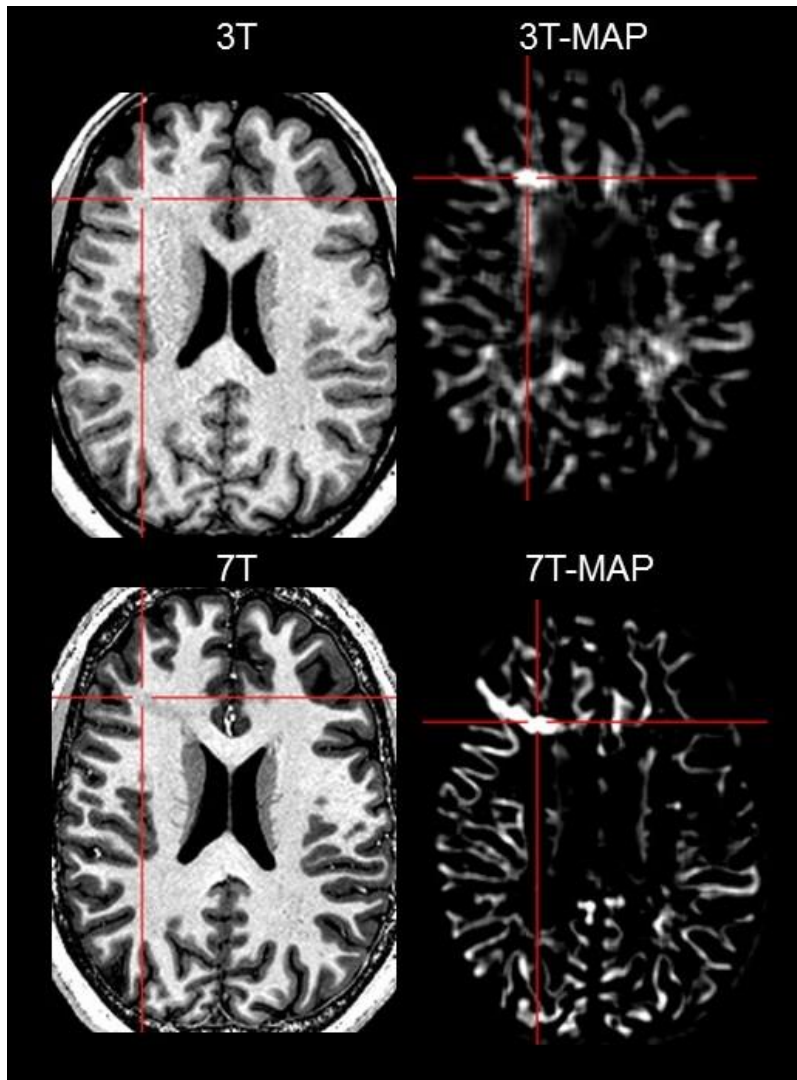
conducted: 1. One experienced neuroradiologist performed initial assessment based on visual and MAP analysis of 7T images. Positive findings were communicated to the clinical patient management team and interpreted in the context of other presurgical evaluation data. Concordance between 7T findings, ICEEG and surgical resection was then assessed. All available microscopic slides from surgical resections were reviewed by a dedicated neuropathologist. Seizure outcome was classified according to Engel's class. 2. Lesion conspicuity between 7T and 3T images was scored independently within a group of seven clinical neuroradiologists. Scoring included independent conspicuity of lesions at 3T and 7T; relative of conspicuity of 3T to 7T; demarcation of the lesion boundary; lesion diagnosis; and which sequences were the most useful.

Results

A total of 70 epilepsy patients were included, comprising three groups: 26 patients with nonlesional lower-field MRI; 13 patients with equivocal lesions on lower-field MRI; and 31 patients with definite lesional lower-field MRI. In the nonlesional group, visual analysis revealed additional findings in seven patients, and MAP identified subtle FCD in an additional nine patients. In the 10 patients who had positive 7T findings (either visual and/or MAP) and ICEEG, good concordance was observed in nine (7 concordant, two concordant-minus. In all the patients who had positive 7T findings (visual and/or MAP) and underwent surgery, eight underwent complete resection of the abnormality, and had favorable seizure outcomes (7 class I, 1 class II); two had partial or no resection of the abnormality, and had class III outcome. The subtle lesional group mostly included patients with suspected MTS and FCD. In only two patients, the suspected lesion (FCD) was confirmed. MAP yielded additional FCD in two patients. In the lesional group, the majority of cases had no additional information generated by 7T; however, in four patients with extensive cortical abnormalities, visual analysis of 7T showed improved delineation of lesion extent, which is important for resection. In two patients, additional FCD was identified by visual analyses of 7T. MAP did not generate additional findings in this group. Histopathology work is ongoing. An example of an epileptogenic lesion in the right frontal lobe at both 3T and 7T is shown in the accompanying figure. In addition is the corresponding VBM at each field strength. The main weakness of this investigation included imaging artifacts associated with field inhomogeneity, motion and pulsation. The evaluation of 3T vs. 7T lesion conspicuity by a group of neuroradiologists is now complete, analysis underway, and results will be presented.

Conclusions

Our initial experience showed that 7T MRI is useful to: (1) detect subtle FCD lesions in 3T-negative patients; (2) confirm or refute suspicious equivocal findings on 3T scans; and (3) delineate the extent of pathology in the presence of 3T-visible lesions. Results of a 3T vs. 7T lesion conspicuity evaluated by a group of seven neuroradiologists will be presented.



(Filename: TCT_O-53_ASNR-7T-EpilepsyFigures.jpg)

O-54

2:18PM - 2:25PM

Identification of Epileptogenic Lesions using Ultrafast 7T EEG-fMRI and 3D Paradigm-Free Modeling

S Jones¹, C Caballero-Gaudes², A Crawford¹, B Krishnan¹, S Oh¹, W Shin¹, M Lowe¹

¹Cleveland Clinic, Cleveland, OH, ²Basque Center of Cognition, Brain and Language, San Sebastian, Spain

Purpose

There is great clinical utility for any noninvasive MRI technique guiding neurosurgeons to identify focal epileptogenic lesions. We propose to use well known EEG-fMRI techniques, but extend the traditional current method in three ways: apply 7T to increase intrinsic BOLD signal; use increased temporal resolution (TR 300ms) from multiband techniques to separate primary from secondary epileptogenic zones; and use paradigm-free mapping to identify interictal spikes obtained during long scans. We test this methodology using isolated finger taps as a surrogate for epileptogenic spikes. Close correspondence

between conventional event analysis and paradigm free mapping suggests epileptogenic spikes can be reliably detected if their HRF is similar to a single finger tap.

Materials and Methods

One healthy control subject was scanned twice on different days at 7T (Siemens) using a 32-channel receive transmit coil (QED, Cleveland, OH). A volumetric MP2RAGE was acquired for anatomy (WIP900). On the first day, the protocol consisted of a simultaneously multislice excited (SMS) EPI (WIP770B) collected at TR=2800ms (1.2x1.2x1.5mm, MB factor=3) and 500ms (iso-3mm, MB factor=3). On the second day, EPI data was collected at TR=500ms and 300ms (iso-3mm, MB factor=4). During scanning, finger tapping was performed in a block designed ON and OFF paradigm with 45-second cycles (see Figure 1). For the first six minutes, a single finger tapping from the right index finger to the right thumb was performed. For the remaining four minutes, the subject was instructed to repeat the same finger tapping sequentially 10 times. Data were analyzed in two different ways. A standard GLM analysis was performed with the tapping categorized as events. Additionally, a data driven, paradigm-free method was employed (1). Data were first corrected for motion using SLOMOCO2 and then detrended using 3dDetrend. Brain extraction was performed to create a mask using FSL BET. Executed was 3dPFM using the LASSO algorithm along with the Bayesian Information Criterion for deconvolution, and the SPM canonical HRF was used as the hemodynamic model. Finally, these same techniques were applied to data from 12 epilepsy patients where EEG-fMRI was simultaneously collected using the same protocol as day 1 of the finger tapping. The new method was then recently applied to 7 epilepsy patients that underwent 7T EEG-fMRI studies, which included TRs ranging from 300 msec to 2800 msec.

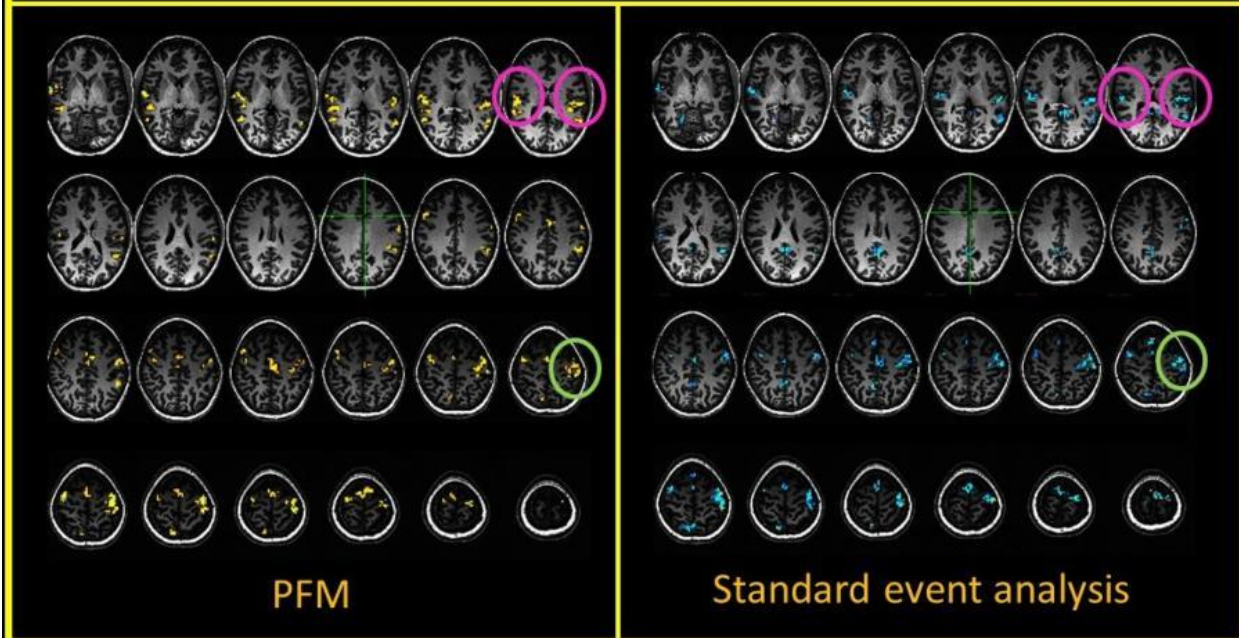
Results

BOLD activation maps are readily generated using standard 7T EEG-fMRI techniques (TR=2.8 sec) using single finger taps as a surrogate for epileptogenic spikes, either with models using known time-points, or data-driven techniques using paradigm free models. BOLD maps are also readily generated at either TR=0.5 sec or TR=0.3 sec. Statistical parametric maps using these two independent methods generate similar maps, suggesting that a paradigm-free method could successfully detect epileptogenic spikes assuming the resulting BOLD HRF is similar to that assumed in the model, here the canonical HRF for a single finger tap. The attached figures are derived from the same data set at TR=0.5 sec with the subject performing single fingertaps immediately after an auditory cue. The left panel uses a paradigm-free model with no other input information, whereas the right panel used a standard GLM analysis that relies on the known timing of the auditory cue as an input. The patterns are closely similar, with the green circles showing expected activation in the hand motor control area, and pink circles showing expected activation in the bilateral Heschl's gyrus of primary auditory cortex. Early results applied to epilepsy patients support this hypothesis, as confirmed with correlations to MEG and postoperative outcome following resective surgery.

Conclusions

This work advances current EEG-fMRI techniques for the identification of epileptogenic lesions in three ways: (1) 7T for increased SNR and BOLD contrast; (2) shorter TR (300 msec) using multiband techniques for increased temporal identification; and (3) analysis using data-driven techniques of paradigm-free mapping, which extend limitations currently based on EEG spike identification.

Using finger tapping to test 7T EEG-fMRI method: Paradigm-free method vs standard analysis



(Filename: TCT_O-54_7T-EEG-fMRI-Erlangen-2017.jpg)

O-55

2:25PM - 2:32PM

Association of DVA location and metabolic activity with EEG localization of epilepsy

J Lazor¹, J Stein¹, J Schmitt², K Davis³, A Nabavizadeh²

¹The Hospital of the University of Pennsylvania, Philadelphia, PA, ²University of Pennsylvania, Philadelphia, PA, ³University of Pennsylvania, Swarthmore, PA

Purpose

Developmental venous anomalies (DVA) are generally considered to be incidental variants of normal venous drainage. [1] However, studies involving 18F-FDG-PET and perfusion imaging have demonstrated DVAs to be vascular lesions with abnormal physiologic features. [2, 3] The clinical significance of this altered physiology remains uncertain. This study correlates location and metabolic activity of DVAs in patients with epilepsy with the site of seizure focus on ictal and/or interictal EEG.

Materials and Methods

A retrospective search was performed for epilepsy patients with DVAs who underwent 18F-FDG-PET and MRI brain imaging. MRI and PET images were coregistered and analyzed for DVA size, location, associated structural findings and qualitative and quantitative measurement of 18F-FDG uptake in DVA drainage territory. The EMR was reviewed for each subject to determine seizure semiology and ictal/interictal EEG seizure localization.

Results

Twenty-seven DVAs in 25 patients were included. Thirteen (48%) DVAs demonstrated regional metabolic abnormality on 18F-FDG-PET. There was no association between DVA site and seizure focus on interictal or ictal EEG ($p=0.085$ and $p=0.085$, respectively). DVA location was concordant with EEG

Oral Presentations & Excerptas

seizure focus only in three subjects, and all of these DVAs demonstrated regional hypometabolism. However, in this concordant group, one DVA was associated with cavernoma, and another patient underwent resection of the anterior temporal lobe which contained the DVA without decrease in seizure frequency. Furthermore, there was no significant relationship between DVA metabolic activity and DVA-EEG lobar or laterality concordance ($p=1$ and $p=0.61$, respectively).

Conclusions

DVAs frequently demonstrate hypometabolism on 18F-FDG-PET imaging; [3] however, we found no significant association between location of DVA and site of seizure focus, and hypometabolism within the DVA drainage territory was not predictive of EEG/DVA co-localization. Given the high prevalence of DVAs and the increasing use of 18F-FDG-PET for localization of epilepsy, knowledge of this poor association is important to avoid diagnostic confusion and potentially unnecessary surgery in epilepsy patients.

O-56

2:32PM - 2:39PM

Automatic detection of Fiducial markers in MRI images using 2D - Convolutional Neural Networks for MEG coregistration

C Bangalore Yogananda¹, G Murugesan², E Davenport³, B Wagner⁴, C Whitlow⁵, J Maldjian²
¹UT Southwestern Medical Center, Arlington, TX, ²University of Texas Southwestern, Dallas, TX, ³UT Southwestern Medical Center, Dallas, TX, ⁴University of Texas Southwestern, 5323 Harry Hines Blvd. , TX, ⁵Wake Forest University School of Medicine, Winston-Salem, NC

Purpose

The purpose of this study is to describe a method for automated fiducial marker detection in magnetic resonance imaging (MRI) images. Fiducials are used to register MRI images to Magnetoencephalography (MEG) data.

Materials and Methods

MRI data from 130 male football players as part of the iTAKL study 1 of subconcussive impacts including 110 high school (14-18 years) and 20 youth (9-13 years) players were used. T1-weighted MRI images were manually labelled for (a) slices with fiducial markers and (b) the center of the marker. Two-D Convolutional Neural Networks (2-D CNNs) were constructed to recognize and predict the local structures for fiducial markers in the images. A binary classifier MRI-Bnet was developed using the 2-D CNNs. MRI-Bnet recognized and learned the local structures for fiducial markers in these T1-weighted images. The output of the classifier is the slices which contained fiducial markers. These slices were Image thresholding to obtain the center of the fiducial markers. The classifier was trained using the labelled data from 100 high school subjects. Thirty data sets, apart from the training, were used for testing the classifier's performance (10 high school and 20 youth subjects).

Results

MRI-Bnet performed well in detecting the total number of slices in a brain volume that had fiducial markers with an accuracy of 97.2% and detecting at least one slice per fiducial location with an accuracy of 97%. Accuracy for predicting the fiducial's center was 99% (Table 1).

Conclusions

We demonstrate that MRI-Bnet predicted the number of slices with fiducial markers with an accuracy of 97.2%, was 97% accurate in predicting at least one slice per marker and had an average accuracy of 99% in predicting the fiducial's center. This work allows for automatic fiducial-based registration of MRI and MEG images and automation of a critical manual step in MEG analysis workflows.

	NAS sag	NAS cor	NAS axi	LPA sag	LPA cor	LPA axi	RPA sag	RPA cor	RPA axi
Mean Difference between labelled and predicted locations (Voxels)	-0.51042	-2.544	-1.3312	0.5611	0.2233	1.1833	-1.0166	-0.8011	-1.2862
Location predicting Accuracy	0.99	0.98	0.98	0.996	0.999	0.986	0.994	0.995	0.985

CTF Coordinate system :
 NAS – Nasion
 LPA – Left Pre-auricular Point
 RPA – Right Pre-auricular point

PLANES :
 Sag – Sagittal
 Axi – Axial
 Cor – Coronal

Table 1: Summary of location prediction accuracy

(Filename: TCT_O-56_Capture.jpg)

Monday, June 4, 2018

1:15PM - 2:45PM

Parallel Paper Session: Imaging Neurodegenerative Diseases

O-57

1:15PM - 1:22PM

Allopregnanolone as a regenerative therapeutic for Alzheimer's Disease: Phase 1B/2A MRI outcomes and interactions with APOE4 genotype

M Law¹, Y Shi², D Aydogan³, J Gahm³, N Kono³, K Rodgers⁴, W Mack³, G Barisano², C Lopez⁴, R Irwin³, G Hernandez⁵, C Solinsky³, L Schneider³, R Brinton⁴

¹Keck Medical Center of USC, Los Angeles, CA, ²University of Southern California, Los Angeles, CA, ³USC Keck, Los Angeles, CA, ⁴University of Arizona, Tucson, AZ, ⁵University of Arizona, Los Angeles, CA

Purpose

Phase 1b/2a double-blind placebo-controlled multiple ascending dose clinical trial of allopregnanolone (ALLO) administered IV using a regenerative regimen for 12 weeks to establish MRI-based indicators of regeneration such as hippocampal volume, gray- and white-matter volumes, multishell diffusion MRI and possible interactions with APOE4 genotype. ClinicalTrials.gov Identifier: NCT02221622.

Materials and Methods

Double-blind placebo-controlled multiple ascending dose clinical trial design. MRI and cognitive objectives included feasibility and impact of ALLO on MRI indicators of regeneration and cognition. A human connectome/ADNI MRI protocol was used pre and post 12 weeks of IV ALLO. Freesurfer was used to determine hippocampal and subfield volumetrics as well as gray/white-matter volumes. FOD (fiber orientation density) DTI was used to determine white-matter changes from multishell DTI and fornix bundle reconstruction from FOD-based analysis.

Results

Twelve-week exposure of up to 10 mg of ALLO once per week resulted in no detectable adverse effects including ARIA E or ARIA H (amyloid-related imaging abnormalities) on MRI. Structural analysis of MRI-based indicators of gray-matter volume were consistent with regeneration in select brain regions, in particular the hippocampus and dentate gyrus with a significant slowing of volume loss compare with controls. Evaluation of the fornix bundle with Allo therapy will also show the structural connectivity of the fornix bundle. Cogstate indicators were consistent with improvement. Subjects with one or two APOE4 allele demonstrated more of an effect to ALLO than those that did not and controls.

Conclusions

Allopregnanolone is a first-in-class regenerative therapeutic for MCI and Alzheimer's disease that targets

endogenous neural stem cells and disease modifying mechanisms. Phase 1b/2a clinical trial data indicate safety and potential efficacy but also demonstrated some improvement in the MRI metrics above with particular interaction with APOE4 genotype. These MRI metrics will be included as primary end points for Phase 2. Research supported by National Institute on Aging U01AG031115 to RDB; U01AG047222 to RDB; UF1AG046148 to RDB & LS; Alzheimer Drug Discovery Foundation to RDB. ASNR Boerger Research Fund for Alzheimers Disease and Neurocognitive Disease to ML

O-58

1:22PM - 1:29PM

Allopregnanolone as a regenerative therapeutic for Alzheimer's Disease: Phase 1B/2A MRI outcomes and interactions with APOE4 genotype has been submitted to the ASNR Abstract Submission Site by: Meng Law, Keck Medical Center of USC, Los Angeles, CA, United States, meng.law@usc.edu. I am co-author

L. Schneider¹

¹*USC Keck, Los Angeles, CA*

Purpose

Disclosure

Materials and Methods

see abstract

Results

see Law's abstract

Conclusions

Allopregnanolone as a regenerative therapeutic for Alzheimer's Disease: Phase 1B/2A MRI outcomes and interactions with APOE4 genotype has been submitted to the ASNR Abstract Submission Site by: Meng Law, Keck Medical Center of USC, Los Angeles, CA, United States, meng.law@usc.edu. As a co-author, you are required to disclose before the abstract can be finalized. The primary/submitter will be notified when your disclosure has been completed.

O-59

1:29PM - 1:36PM

Spatial Patterns of Correlation between Regional Cortical Amyloid and Cortical Thickness in a Cohort of Alzheimer's Patients.

S Jones¹, M Larvie¹, A Crawford¹, J Leverenz¹, J Cummings¹, J Pillai¹

¹*Cleveland Clinic, Cleveland, OH*

Purpose

We investigated the regional correlations between cortical amyloid deposition and regional cortical thickness in a cohort of 31 patients with Alzheimer's disease (AD) who had both concomitant structural MRI and amyloid PET scans. We hypothesized that a linear relationship between amyloid burden and cortical thickness would be clearly noted in all neocortical regions.

Materials and Methods

A cross-sectional study comprised 31 patients with early AD with both positive amyloid brain PET imaging, and structural MRI including a volumetric T1W sequence permitting segmentation by FreeSurfer. Patient data included age, education and gender. Cognitive status was measured using the Montreal Cognitive Assessment (MOCA), and were divided into two groups by a score of 16. PET images were coregistered to MRI images using FSL, and PET images were corrected for partial volume effects. For each of 34 FreeSurfer cortical parcellations the mean cortical thickness and mean amyloid burden was measured. A linear correlation was obtained for each parcellation, across the 31 patients, and

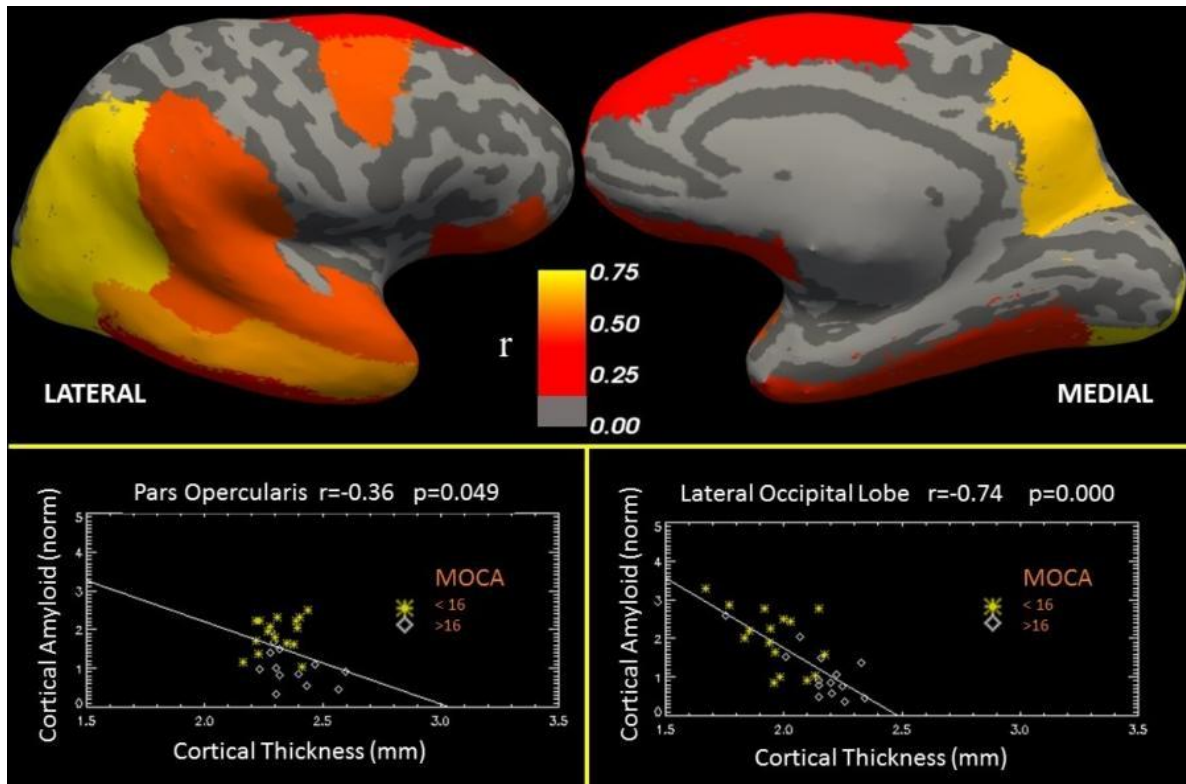
the correlation coefficients were spatially mapped onto a semi-inflated brain surface. For multiple comparisons of the 34 FreeSurfer regions, a false discovery rate of 0.1 was used, with a Benjamini Hochberg P-value of 0.085.

Results

Among neocortical regions with a statistically significant correlation, the linear relationship between amyloid and cortical thickness was always inverse, such that increased cortical amyloid correlates with decreased cortical thickness. The neocortical regions of highest correlation involve the precuneus and lateral occipital lobes, followed by middle temporal gyrus, then superior temporal gyrus, inferior parietal lobules, orbitofrontal convexities, and inferior prefrontal lobe. The correlation was notably poor in some neocortical regions (e.g. superior parietal, fusiform, lingual) even as the amyloid burden was not different. Additionally, there was lack of the above linear relationship in allocortical regions known to be affected early in AD (entorhinal, parahippocampal) and neocortical regions affected late in AD (primary sensory cortices). When patients were classified according to high and low MOCA scores: those with higher MOCA scores had thicker cortex and less amyloid, whereas subjects with lower MOCA scores had thinner cortex and increased amyloid burden. Among regions with reduced linear correlation between amyloid and cortical thickness, differences in amyloid burden were more notable than differences in cortical thickness. These patterns suggest a temporal evolution, such that amyloid accumulation precedes cortical thinning. Most strikingly in this cohort of AD patients, the linear relationship extended to the lateral occipital lobe, with a statistically significant $r = -0.74$, and the frontal lobe pars opercularis, with marginally significant $r = -0.36$. The attached figure shows a semi-inflated brain, whose colored overlay represents the magnitude of the correlation coefficient r between cortical thickness and cortical amyloid. Regions are only color-coded if the correlation shows a false discovery rate of 0.1. An additional 49 patients have now been scanned at the time of this writing, and their additional results will be presented.

Conclusions

A linear relationship between amyloid burden and cortical thickness was identified involving some but not all neocortical regions among clinically symptomatic AD patients. Strikingly, the variation in the relationship between amyloid and cortical thickness is notable even within cortical parcellations within temporal, frontal and parietal regions commonly thought be affected in the clinical stage of AD.



(Filename: TCT_O-59_Figuresfor2018ASNRv2.jpg)

O-61

1:36PM - 1:43PM

Which Reference Regions are Suitable for Sodium Signal Intensity Normalization in the Evaluation of Early Alzheimer's Disease at 3T MRI?

E Lui¹, V Venkatraman², T Li³, C Steward¹, B Sutton⁴, S Kolbe², B Moffat², C Kokkinos⁵, S Salinas², P Desmond¹

¹Royal Melbourne Hospital, University of Melbourne, Melbourne, Australia, ²University of Melbourne, Melbourne, Australia, ³Karolinska University Hospital, Stockholm, Sweden, ⁴University of Illinois at Urbana-Champaign, Urbana, IL, ⁵Epworth Hospital Richmond, Melbourne, Australia

Purpose

Signal intensity (SI) normalisation is one of the methods used in quantitative sodium ²³Na-MRI, with potential application in early Alzheimer's disease (AD) [1]. However, the suitability of various reference regions (ROI_{ref}) for normalizing target regions-of-interest SI (ROI_{target}) has not been studied. We aim to assess which ROI_{ref} may be suitable for ²³Na-MRI evaluation of early AD.

Materials and Methods

Forty-three cognitively normal subjects (74±6years; 54% female) underwent 3T MRI (Trio, Siemens). Acquired was ²³Na-MRI using the FlexTPI sequence [2] with a dual-tuned 1H/²³Na birdcage head coil (Rapid Biomedical) at nominal 5mm isotropic resolution (TR=160ms, TE=0.3ms, FA=90deg). Volumetric 1mm isotropic T1 was segmented and parcellated with Freesurfer6.0 and FSLv.5. B0B1-corrected and partial volume-corrected were ²³Na-images [2, 3]. ROI SI were extracted from ²³Na images after a neuroradiologist checked ²³Na co-registration with T1 and T2 images. ROI_{ref} [Table1] were short-listed for being least likely to be affected by white-matter disease and AD pathology. Normalized SI were calculated, $SI_{normalized} = SI_{target} / SI_{ref}$. Statistics were performed on SPSSv24.

Oral Presentations & Excerptas

Results

Lateral ventricle was the only SIref associated with age ($p < 0.01$). Only cerebellar WM SIref was significantly related ($p < 0.01$) to gender. Standard deviation (SD) of SIref was highest for lateral ventricle, and similarly low for all other SIref [Table.1]. Postcentral GM ROIref had the lowest coefficient-of-variation (CoV) for parahippocampal, cingulate, precuneus and superior parietal SInormalized. Midbrain ROIref yielded the lowest hippocampal SInormalized CoV, although CoV was only 1% higher using postcentral GM ROIref. Precentral GM ROIref yielded the lowest SInormalized CoV for the middle frontal gyrus, but CoV from postcentral GM ROIref was only 2% higher. Combined pre and postcentral GM ROIref yielded a CoV 1-6% higher than the best CoV for each ROItarget. Lateral ventricle ROIref had the highest CoV for all ROItarget, CoV 250% to 1120% higher than the best CoV of each ROItarget [Table.1]. None of the brain ROItarget SInormalized showed a significant association with age using GM, midbrain and cerebellar WM ROIref, expected for $^{23}\text{Na-SI}$ in cognitively normal subjects [4]. Combined pre and postcentral GM ROIref had the lowest correlation coefficient (0.028-0.150) for all brain ROItarget. Lateral ventricular SInormalized remained significantly associated with age ($p < 0.001$) [Table.2].

Conclusions

For quantitative $^{23}\text{Na-MRI}$ evaluation of AD using SI normalization method, postcentral GM, precentral GM, combined pre and postcentral GM, and midbrain appear suitable. Lateral ventricle is shown to be unsuitable.

Table 1. Summary of Normalized SI for Target Regions

		Pre-normalize		REFERENCE REGIONS (ROI _{ref})															
				Cerebellar WM		Midbrain		Pre- and Post Central Gyrus (grey matter)		Precentral Gyrus (grey matter)		Precentral Gyrus(white matter)		Postcentral Gyrus (grey matter)		Postcentral Gyrus (white matter)		Lateral Ventricle	
				SI	CoV	SI	CoV	SI	CoV	SI	CoV	SI	CoV	SI	CoV	SI	CoV	SI	CoV
TARGET REGIONS (ROI _{target})	Hippocampus	0.43 (0.07)	0.16	1.15 (0.19)	0.17	0.98 (0.12)	0.12	1.15 (0.16)	0.14	1.18 (0.19)	0.16	1.29 (0.24)	0.18	1.12 (0.14)	0.13	1.19 (0.21)	0.18	0.46 (0.14)	0.30
	Parahippocampal Gyrus	0.41 (0.07)	0.17	1.10 (0.22)	0.20	0.94 (0.14)	0.15	1.10 (0.19)	0.17	1.11 (0.17)	0.15	1.25 (0.45)	0.36	1.05 (0.15)	0.14	1.17 (0.43)	0.36	0.43 (0.26)	0.61
	Cingulate Gyrus	0.38 (0.07)	0.18	1.04 (0.22)	0.21	0.89 (0.15)	0.17	1.02 (0.11)	0.11	1.04 (0.11)	0.11	1.16 (0.24)	0.21	0.98 (0.10)	0.10	1.07 (0.21)	0.20	0.39 (0.26)	0.67
	Middle Frontal Gyrus	0.35 (0.06)	0.17	0.95 (0.20)	0.21	0.81 (0.15)	0.19	0.93 (0.09)	0.10	0.95 (0.05)	0.05	1.06 (0.18)	0.17	0.90 (0.06)	0.07	0.98 (0.17)	0.17	0.36 (0.18)	0.50
	Precuneus	0.39 (0.07)	0.18	1.06 (0.21)	0.20	0.90 (0.14)	0.15	1.05 (0.10)	0.10	1.06 (0.10)	0.09	1.26 (0.31)	0.25	1.00 (0.09)	0.09	1.10 (0.21)	0.19	0.39 (0.26)	0.67
	Superior Parietal Gyrus	0.40 (0.08)	0.20	1.07 (0.21)	0.20	0.90 (0.14)	0.16	1.04 (0.11)	0.11	1.07 (0.08)	0.07	1.20 (0.23)	0.19	1.10 (0.06)	0.05	1.11 (0.21)	0.19	0.43 (0.24)	0.56
	Lateral Ventricle	0.99 (0.20)	0.20	2.67 (0.61)	0.23	2.30 (0.58)	0.25	2.74 (0.82)	0.30	2.78 (0.85)	0.31	2.99 (0.66)	0.22	2.63 (0.81)	0.38	2.77 (0.65)	0.23	-	-

SI represented as Mean(SD), CoV = SD/Mean. # Median(IQR), CoV = IQR/Median

Table 2. Correlation of Age and Normalized SI of Target Regions for all Possible Reference Regions

		Pre-normalize		REFERENCE REGIONS (ROI _{ref})							
				Cerebellar WM	Midbrain	Pre and Post central Gyrus (gray matter)	Precentral Gyrus (grey matter)	Precentral Gyrus (white matter)	Postcentral Gyrus (grey matter)	Postcentral Gyrus (white matter)	Lateral Ventricle
TARGET REGIONS (ROI _{target})	Hippocampus	-0.132		-0.209	-0.239	0.057	-0.071	-0.213	-0.078	-0.196	-0.353*
	Parahippocampal Gyrus	-0.215		-0.267	-0.293	-0.063	-0.121	-0.245	-0.133	-0.216*	-0.295**
	Cingulate Gyrus	-0.225		-0.259	-0.282	-0.150	-0.157	-0.272	-0.189	-0.265	-0.273*
	Middle Frontal Gyrus	-0.235		-0.249	-0.244	-0.085	-0.155	-0.315*	-0.159	-0.297	-0.261*
	Precuneus	-0.171		-0.216	-0.225	-0.028	-0.039	-0.150	-0.067	-0.209	-0.243*
	Superior Parietal Gyrus	-0.198		-0.248	-0.076	-0.083	-0.028	-0.265	-0.134	-0.254	-0.230*
	Lateral Ventricle	0.398**		0.315*	0.319*	0.358**	0.337*	0.277	0.338*	0.284	-

Kendall's tau-b test; *: p<0.05; **: p<0.01

(Filename: TCT_O-61_ASNR2018_Na_Norm_table.jpg)

O-62

1:43PM - 1:50PM

Machine Learning of Quantified Volumetric MR Imaging for Diagnostic Delineation of Alzheimer's Dementia and Mild Cognitive Impairment in the Alzheimer's Disease Neuroimaging Initiative

C Raji¹, S Meysami², J Ahdidan³, D Merrill²

¹University of California San Francisco, San Francisco, CA, ²University of California Los Angeles Medical Center, Los Angeles, CA, ³Brainreader, Horsens, CA

Purpose

Alzheimer's disease (AD) is the most common cause of dementia (1). Recommended clinical use of

Oral Presentations & Excerptas

imaging has been limited to visual evaluations of brain MRI for ruling out "organic" causes of dementia such as stroke or tumor (2). No role of imaging currently exists for identifying mild cognitive impairment (MCI), a proposed prodromal phase of AD (3). Development of FDA cleared quantitative software allows for quantification of multiple brain regions (4). We evaluated discriminative ability of a newer program for identifying AD from MCI and controls.

Materials and Methods

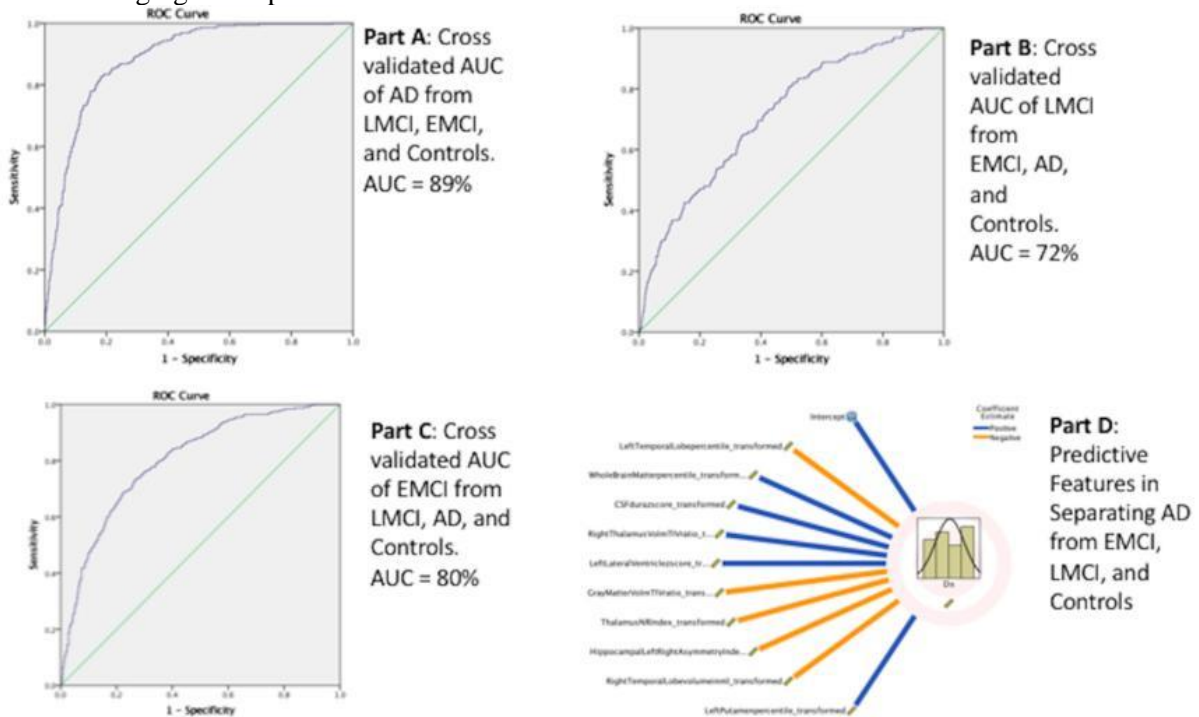
Volumetric 1.5 and 3.0T MRI brain scans (n = 1143 with mean age 74.6 years) were obtained from the the Alzheimer's Disease Neuroimaging Initiative (ADNI) using standard protocols (5). This cohort consisted of controls (n = 261), early mild cognitive impairment (EMCI, n = 310), late mild cognitive impairment (LMCI, n = 223), and AD (n = 349). Neuroreader™ (Brainreader ApS, Horsens, Denmark) was used to compute brain volumes. Machine learning was done using cross-validated discriminant analysis algorithm in IBM SPSS Modeler (v. 18, Armonk, NY). Area under the curve (AUC) was generated for AD and MCI subgroups to evaluate diagnostic performance. Automated linear regression was used to identify predictive regions.

Results

Regionally quantified volumetric MR imaging data separated AD from non-AD groups with AUC of 89%, 85% sensitivity, and 79% specificity (Figure 1A). Automated volumetrics delineated LMCI from other groups with AUC of 72%, 70% sensitivity, and 62% specificity (Figure 1B). EMCI was distinguished from LMCI, AD, and controls groups with AUC of 80%, 76% sensitivity, and 70% specificity. Figure 1D shows predictive regions delineating AD from MCI subgroups and controls including total CSF volume, hippocampal asymmetry, and temporal lobe

Conclusions

Machine-learning analysis of quantified brain regions on MR imaging provides good diagnostic delineation of AD from MCI subgroups and normal controls. Overlap between LMCI and AD and EMCI and controls may partially account for reduced diagnostic performance in MCI. Future studies will utilize longitudinal imaging for improved delineative outcomes.



(Filename: TCT_O-62_Figure_1_BR.jpg)

1:50PM - 1:57PM

3-D Convolutional Neural Networks for Classifying Brain MRIs from Alzheimer's Disease, Mild Cognitive Impairment and Normal Subjects

R Gorniak¹, A Flanders¹, P Lakhani¹

¹Thomas Jefferson University, Philadelphia, PA

Purpose

Alzheimer's disease (AD) is the most common form of dementia. Patients with mild cognitive impairment (MCI) have a less severe decline in cognitive ability and are at increased risk for developing AD. While the diagnosis of AD/MCI is primarily clinical, imaging can be a supportive biomarker in the early diagnosis. To potentially aid in interpreting MRIs in this setting, two 3-D convolution neural networks were trained to classify brain MRIs as from patients with Alzheimer's disease or mild cognitive impairment or as normal controls.

Materials and Methods

Volumetric T1 images of the brain of individuals clinically classified as AD, MCI or normal were obtained from the Alzheimer's Disease Neuroimaging Initiative (ADNI), Open Access Series of Imaging Studies (OASIS) and Minimal Interval Resonance Imaging in Alzheimer's Disease (MIRIAD) data sets. Used were 3500 MRIs. FSL was used to extract the brain from the whole head images. The images were cropped to 140x190x140 voxels. The images were split into training and validation sets of 3000 and 500 MRIs, respectively. Two models were used to perform a three-way classification. One model is based on a 3-D modified version of the VGG architecture which uses multiple layers of 3x3x3 convolutions and pooling, ending in fully connected layers. The other architecture was based on a 3-D modified version of SqueezeNet with simple bypass which uses 1x1x1 and 3x3x3 convolutions and pooling but no fully connected layers. Keras with Tensorflow backend was used to construct and train the models for 200 epochs on a system utilizing a single NVIDIA GeForce Titan X graphics processing unit with 12 gigabytes of memory.

Results

On the validation set, the SqueezeNet model achieved a 95.2% accuracy and the VGG model achieved a 96.5% accuracy.

Conclusions

Three-D convolution neural networks can be trained to differentiate T1 MRIs from AD, MCI or normal subjects with a high level of accuracy. Both model architectures performed with similar accuracy. Additionally, as these models were constructed from a large number of MRIs from multiple sources, they may be useful as pretrained models that can be used for transfer learning in other brain diseases.

O-64

1:57PM - 2:04PM

Myeloperoxidase PET Imaging Mapping Neuroinflammation in Alzheimer's Disease

C Wang¹, M Zeller¹, G Wojtkiewicz¹, J Wang¹, S Schmidt¹, J Chen¹

¹Massachusetts General Hospital, Boston, MA

Purpose

Neuroinflammation plays key roles in Alzheimer's disease (AD). Myeloperoxidase (MPO), a key inflammatory enzyme, is associated with beta-amyloid (A β) in both animal models and in AD patients. We aimed to develop a PET probe to image MPO activity and report on neuroinflammation in AD.

Materials and Methods

Experimental protocol was approved by the institutional animal care committee. Radiolabeled was 18F-bis-5-dihydroxytryptamide (FBHT) using an automated synthesizer. Specificity of the 5-hydroxytryptamide moiety for MPO activity had been previously established in MPO-deficient mice. In

Oral Presentations & Excerptas

the first experiment, naïve wild-type (WT) mice were injected with ~500 μCi of either FBHT or 18F-FLT to assess whether FBHT can cross the intact blood-brain barrier. In the second experiment, 7-8 months old 5xFAD mice (AD) or age-matched nontransgenic litter mates (WT) were used ($n=4$ per group) to test if FBHT can report on MPO activity in the AD mouse brain. Mice were intravenously injected with ~500 μCi FBHT and then imaged on a PET-CT scanner (Siemens) three hours after FBHT injection. Images were analyzed by a neuroradiologist blinded to the group assignment. Statistical significance was evaluated by the Mann-Whitney test.

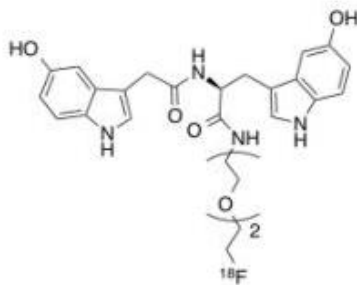
Results

We found that there was increased uptake of FBHT (A) in the brain that is three times higher than 18F-FLT, consistent with FBHT crossing intact blood-brain barrier (B). Correspondingly, there was (C) ~70% increased FBHT uptake ($p=0.029$) in the brains of AD mice (1.91 ± 0.17) compared to the brains of non-AD WT mice (1.12 ± 0.14), noninvasively demonstrating increased MPO activity and inflammation in the AD mouse brains but not in the non-AD mouse brains.

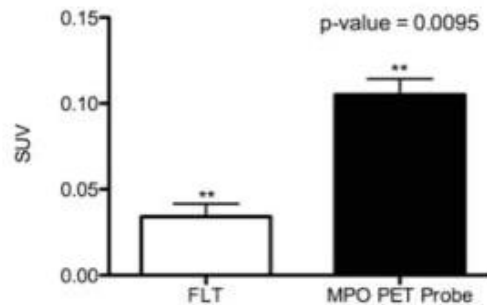
Conclusions

Once translated, FBHT, a PET agent targeting MPO activity, can be a useful noninvasive tool to image and track MPO activity and neuroinflammation in Alzheimer's disease patients.

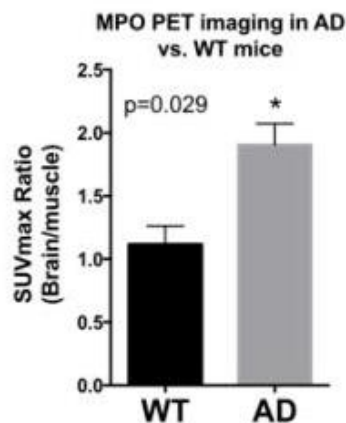
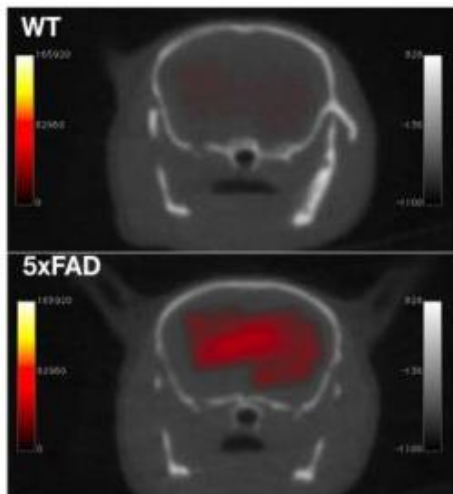
A Structure of FBHT



B FBHT can cross blood brain barrier



C PET/CT imaging of AD and WT mice



(Filename: TCT_O-64_asnrimage001.jpg)

O-65

2:04PM - 2:11PM

Diagnostic and Prognostic Value of the Entorhinal Cortex Atrophy (ERICA) Score in Mild Cognitive Impairment

S Enkirch¹, A Traschütz¹, C Widmann¹, E Hattingen², M Heneka¹, H Schild²

¹University Hospital Bonn, Bonn, Germany, ²University Clinic Bonn, Bonn, Germany

Purpose

To validate the novel entorhinal cortex atrophy (ERICA) MRI rating scale--which we introduced at ASNR 2017--regarding diagnosis, biomarker status, neuropsychological profile and dementia risk in mild cognitive impairment (MCI).

Materials and Methods

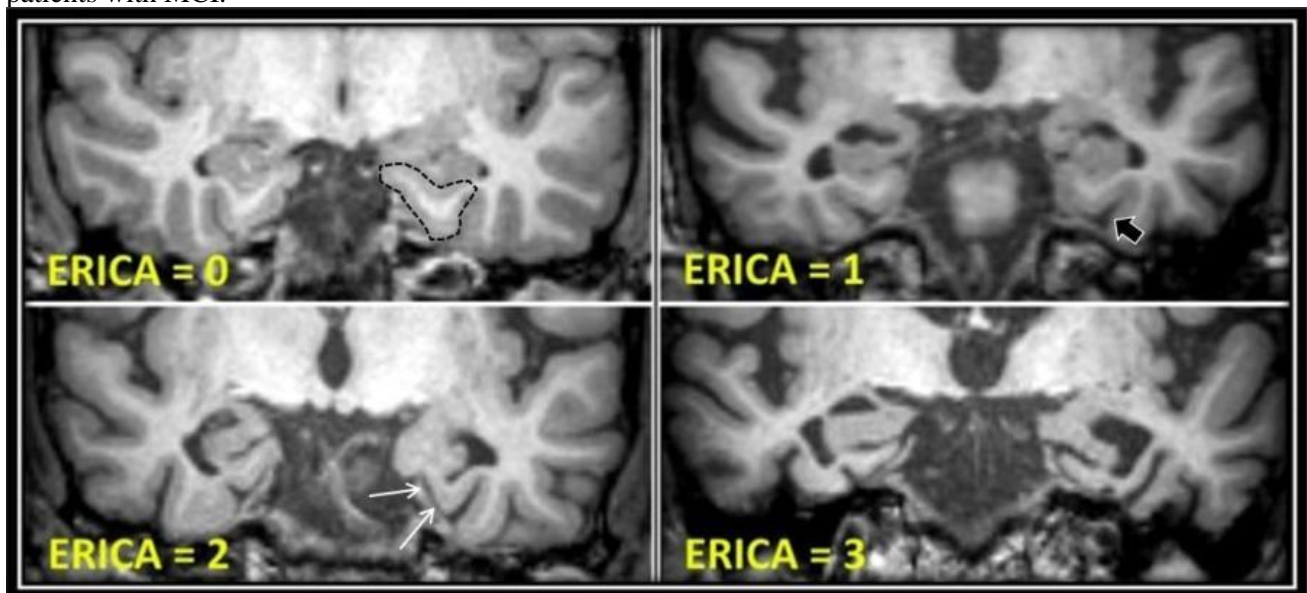
ERICA (Figure 1) and medial temporal lobe atrophy (MTA) scores were retrospectively compared regarding their discrimination of MCI (n = 80) from subjective cognitive decline (n = 60) and Alzheimer's disease (AD) dementia (n = 60), and their sensitivity, specificity and predictive values for cerebrospinal fluid amyloid/tau status as well as conversion to AD dementia (median follow-up 28 months) were evaluated. Associations with neuropsychological tests were explored by correlation and multivariable linear regression analysis.

Results

The ERICA score with 'tentorial cleft sign' achieved 97% positive predictive value for the presence of MCI, and was superior to the MTA score in discriminating MCI from AD dementia. Like the MTA score, the ERICA score was not predictive of amyloid status, but was superior to the MTA score in predicting tau positivity. The ERICA score was specifically associated with measures of verbal learning and memory after adjusting for age, sex, education and global cognitive level. Unlike the MTA score, the ERICA score was also associated with cued verbal recall. Sensitivity to predicting conversion to Alzheimer's disease dementia was 53%, but 83% specificity yielded a positive predictive value equivalent to tau status (83%). The ERICA score achieved 90% positive and 100% negative predictive value when combined with tau status and verbal recall, respectively.

Conclusions

The ERICA score is both a simple and valuable tool to establish clinical diagnosis and prognosis in patients with MCI.



(Filename: TCT_O-65_ERICA score.jpg)

O-66

Concordance of Quantitative SUVR with Visual Assessment of [18F]-AV-1451 tau PET/MRI and Relation to Off-target Sites

A Zaza¹, C Mejias², B Gordon¹, Y Su², B Ances², T Benzinger²

¹Washington University in Saint Louis, School of Medicine, Saint Louis, MO, ²Washington University in Saint Louis, Saint Louis, MO

Purpose

Although the quantitative Standardized Uptake Value Ratios (SUVRs) for AV-1451 (aka flortaucipir) tau PET have been used so far in studying tauopathies, this technique requires sophisticated software processing which might not be available in future clinical workflows. We developed a visual scoring system for AV-1451 PET/MRI images, and compared these results to an established quantitative classification method.

Materials and Methods

One-hundred-seventy adults (20 with Clinical Dementia Rating [CDR] above zero) underwent [18F]-AV-1451 positron emission tomography (PET). Seven were participants in Dominantly Inherited Alzheimer Network (DIAN). For quantitative analyses, as previously reported (Mishara et. al., 2017) data were processed using region-of-interest (ROI) approach with FreeSurfer. Regional data were partial volume corrected and converted to SUVRs normalized to whole cerebellum. AV-1451 SUVR cutoff of 1.25 was used to define high tau. For visual assessment, PET and MRI images were fused using MIM (Cleveland, Ohio) and interpreted by two readers. Visual scoring scale was developed based on the degree of tracer uptake in regional and spatial distribution within frontal, parietal, temporal and occipital lobes (0: uptake similar, 1: mildly greater, 2: markedly greater than background). The off-target sites including basal ganglia, thalamus, midbrain, choroid plexus, and bone marrow were visually scored separately.

Results

Visual assessment was generally concordant with quantitative approaches (93%). Visual/quantitative discordance was greater in few scans with high tau SUVRs. Nine participants (5%) had high tau on SUVRs while visual score was 0. Conversely, four participants (2%) have low tau on SUVRs while visual score has a range (1-2) in at least one region, excluding off-target sites.

Conclusions

Visual/quantitative discordance can be secondary to AV-1451 tau uptake in adjacent off-target sites and may result in falsely high tau SUVR. Conversely, asymmetrically increased uptake in one region might result in falsely low tau SUVR. Combination of visual and quantitative tools for AV-1451 tau uptake might be necessary in clinical practice.

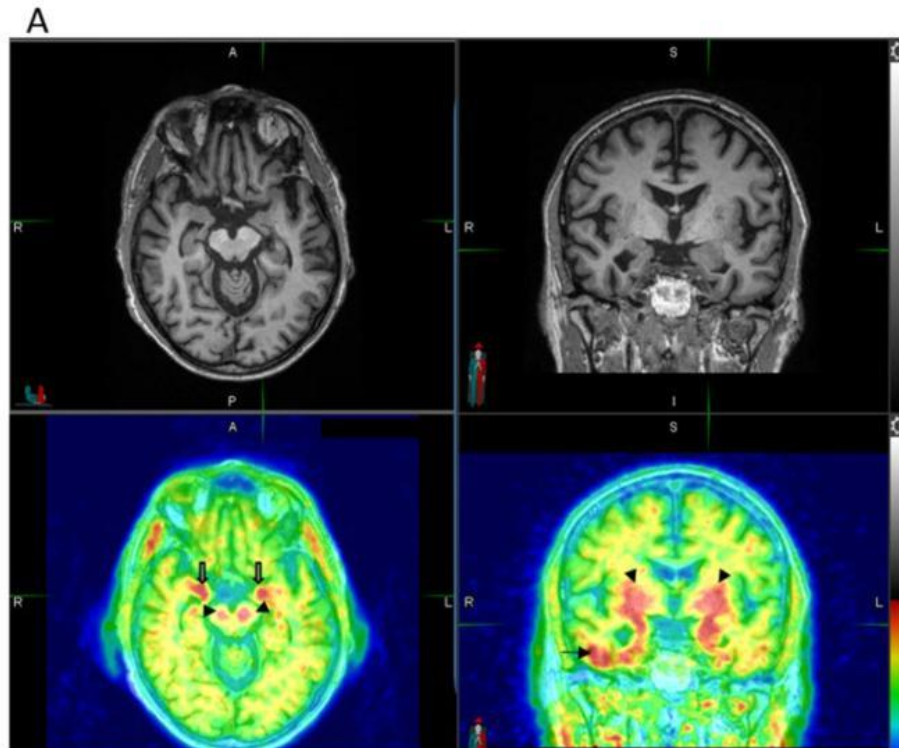


Fig. A: Top: T1 weighted images and bottom: AV-1451 PET/MR fused images for a 90-year-old male with CDR=0. The calculated partial volume corrected SUVR is 1.15; below the cut-off for high tau. Visual score within frontal=0, parietal=0, temporal=2, asymmetric (arrows on right) including amygdala (arrows on left)=2 and occipital lobes=0 consistent with discordance. Off-target sites: Visual score within basal ganglia=2 (arrow heads on right), = and mid brain=2 (arrow heads on left)

(Filename: TCT_O-66_graphicfile.jpg)

O-67

2:18PM - 2:25PM

The Associations Among Physical Frailty, Cognitive Impairment, and Brain Structural Alteration in Patients with Parkinson Disease

Y Chen¹, H Chen¹, C Lu¹, M Chen¹, K Chou², N Tsai¹, C Yu¹, P Chiang³, W Lin⁴

¹*Kaohsiung Chang-Gung Memorial Hospital, Kaohsiung, Taiwan*, ²*Institute of Neuroscience, National Yang-Ming University, Taipei, Taiwan*, ³*Kaohsiung Chang Gung Memorial Hospital, and Chang Gung University College of Medicine, Taiwan, Kaohsiung, Taiwan*, ⁴*Kaohsiung Chang Gung Memorial Hospital, Kaohsiung, Taiwan*

Purpose

Physical frailty describes a state of increased vulnerability to stressors due to decreases in functions and reserve across multiple physiologic systems and is associated with increased mortality and other adverse outcomes. Physical frailty is associated with cognitive impairment that may be explained by their shared common pathophysiologies such as systemic inflammation and increased oxidative stress. It was recently found that physical frailty is associated with brain structural alterations in the normal aging population. In this study we aimed to investigate the structural changes of the brain that correlate with physical frailty and cognitive impairments in Parkinson's disease (PD) patients. We hypothesized that there would be

distinct but overlapping patterns of physical frailty-associated and cognitive impairment-associated structural changes in the brains of PD patients due to shared pathophysiologies.

Materials and Methods

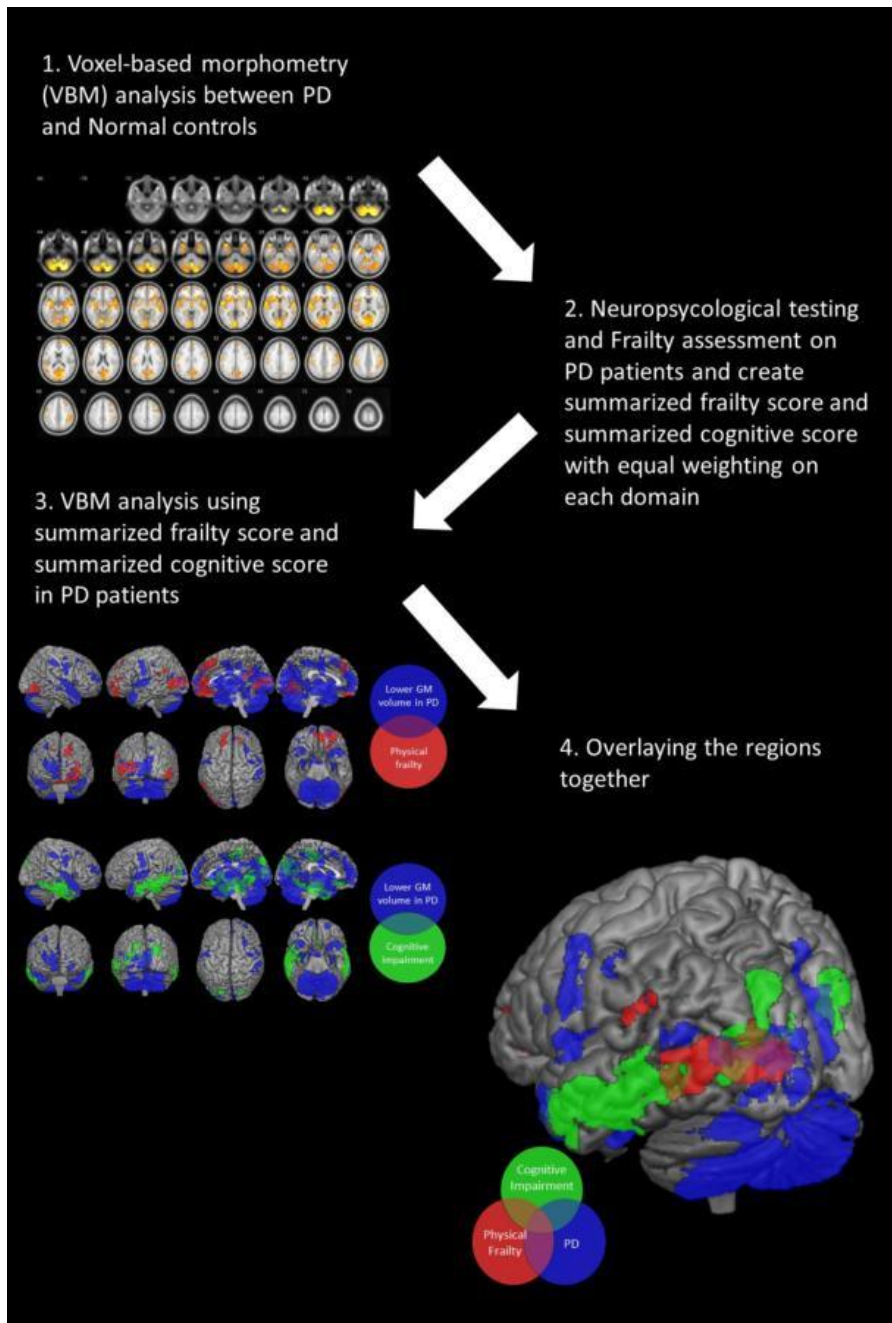
Sixty-one PD patients and 59 age- and sex-matched healthy controls were enrolled. Frailty assessment by Fried's criteria and comprehensive neuropsychological testing by Wechsler Adult Intelligence scale-III and Cognitive Ability Screening Instrument were done. Structural brain MR imagings were acquired under 3.0T whole body GE Signa MRI system. T1 structural images were preprocessed and analyzed using Statistical Parametric Mapping software (SPM12) running on Matlab R2012a for voxel-based morphometric analysis.

Results

Exploratory group-wise comparison of gray-matter volume revealed that the PD patients exhibited diffuse gray-matter volume (GMV) reductions. Voxel-wise multiple linear regression showed that physical frailty-related decreases in GMV were mostly observed in the bilateral frontal and occipital cortices, while cognitive impairment-related decreases in GMV were mostly observed in the bilateral frontal, occipital, and temporal cortices. These regions overlap in the lateral occipital cortex. When different cognitive domains were analyzed separately, the overlap in lateral occipital cortex were consistent across every cognitive domain.

Conclusions

Physical frailty and cognitive impairments in PD patients are common. The identification of these conditions is important and may alter the treatment plan for a given patient. Our results suggest the role of structural changes to the lateral occipital cortex as a potential imaging biomarker for identifying such conditions.



(Filename: TCT_O-67_ASNRfig.jpg)

O-68

2:25PM - 2:32PM

Optimized Imaging at 3.0 T of the Rostral Zona Incerta (rZI) for Deep Brain Stimulation (DBS) in Parkinson's Disease (PD)

A Thaker¹, K Reddy¹, D Kern¹

¹University of Colorado Anschutz Medical Campus, Aurora, CO

Purpose

Deep-brain stimulation (DBS) of the subthalamic nucleus (STN) is an effective treatment for Parkinson's

Oral Presentations & Excerptas

disease (PD); however, unwanted, adverse effects may occur. Recently, the rostral zona incerta (rZI) has been proposed as a potential alternative DBS target for the treatment of PD. This structure is not reliably imaged with routine DBS protocols preventing direct neurosurgical targeting. In this study, we present pilot data of an optimized 2-D coronal gradient echo (GRE) sequence which allows consistent visualization of the rZI in both control and PD populations at 3.0 Tesla, not previously reported in the literature.

Materials and Methods

Eleven PD patients had conventional T1 and T2 MRI sequences performed for DBS evaluation. Six of these patients had additional optimized 2-D coronal GRE sequences performed to visualize the rZI. Four healthy control subjects also underwent GRE imaging. Imaging of all 15 patients was reviewed independently and blinded by a neuroradiologist and a movement disorder neurologist, utilizing a 3-point Likert scale rating bilateral rZI visualization (0-nonvisualized, 1-partially visualized, 2-clearly visualized).

Results

In healthy control subjects (n=4), bilateral rZI visualization on optimized coronal GRE imaging was rated at 2/2 with complete interrater agreement. In PD patients who underwent traditional DBS imaging (n=5), bilateral rZI visualization was rated 0/2 with complete interrater agreement. In PD patients who underwent optimized coronal GRE imaging (n=6), bilateral rZI visualization was rated at a mean Likert score of 1.3 with high interrater agreement.

Conclusions

In a small pilot series of patients, we demonstrate promising initial data suggesting that an optimized coronal 2D GRE sequence can consistently image the rZI at 3.0 Tesla in PD patients. Prior short reports have successfully imaged this small structure in healthy controls at 7.0 Tesla. Improved visualization will allow direct targeting of the rZI for electrode placement during DBS.



Optimized coronal GRE sequence at 3.0 Tesla in a healthy control subject demonstrates the rostral zona incerta (rZI), globus pallidus externa (GPe), globus pallidus interna (GPi), subthalamic nucleus (STN), and substantia nigra (SN)

(Filename: TCT_O-68_ASNRfigure.gif)

O-222

2:32PM - 2:39PM

Effectiveness of Brain Volumetric Software as an Objective Tool for Determining Patient Risk for Normal Pressure Hydrocephalus

S Omar¹, T Tran¹, W Caton², K King¹

¹Huntington Medical Research Institutes, Pasadena, CA, ²Huntington Hospital, Pasadena, CA

Purpose

Normal Pressure Hydrocephalus (NPH) is an underdiagnosed yet potentially treatable condition that may account for up to 10% of dementia cases. Subjective interpretation of ventricle enlargement in disproportion to sulci is used to assess risk for NPH on imaging but may contribute to ambiguity based on its subjective nature. FDA-approved software to quantify brain volumes are available, but have yet to see widespread application in clinical practice. We sought to identify objective markers for patients referred to our center for advanced workup of NPH based on clinical and radiologic criteria from those evaluated for memory loss without suspicion of NPH using NeuroQuant (CorTech Labs).

Oral Presentations & Excerptas

Materials and Methods

Scanning was performed on a 1.5T GE MRI system for eight patients referred for advanced NPH workup and nine patients referred for memory loss by a neurologist and neurosurgeon, each with 30+ years of experience. T1 3D FSPGR was obtained per NeuroQuant recommendations. We evaluated lateral ventricular (LV) volume adjusted for intracranial volume (ICV), LV normative percent for age, and LV * cortical gray matter (for ventricle-atrophy concordance as sulci volume not available) as predictors. Groups were compared using a standard t-test with significance at $p < 0.05$.

Results

LV/ICV ($p=0.001$), LV normative for age ($p=.03$) and LV volume cortical gray-matter volume ($p=0.0004$) were all significantly larger for NPH compared with memory loss patients (Figure 1).

Conclusions

NeuroQuant lateral ventricle volume and lateral ventricle cortical gray-matter volume significantly differed among those identified as at risk for NPH. NeuroQuant may provide objective data to assist risk assessment for this condition. It is worth noting that all patients referred for NPH were at or above the 95th percentile of LV volume for age (Figure 1C) and this may be a useful initial screening tool for NPH prompting expert neuroradiology consultation.

Figure 1. T-test analysis for patients at risk for Normal Pressure Hydrocephalus (NPH) patients ($N=8$) and patients referred for memory loss only ($N=9$).

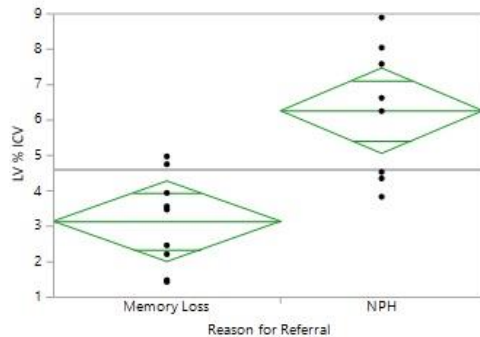


Figure 1A. Lateral Ventricle Volume reported as Percentage of Intracranial Volume (%ICV). Values represent the distribution of data of NPH patients ($6.25 \pm 0.57\%$, $N=8$) and memory loss patients ($3.13 \pm 0.53\%$, $N=9$). $p = 0.0004$

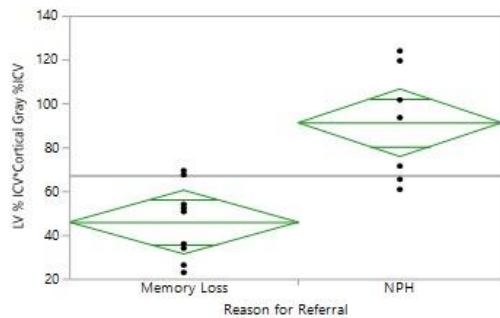


Figure 1B. Ratio of Lateral Ventricle and Cortical Gray Matter Volume. Values represent the distribution of data for NPH patients ($91.2 \pm 7.2 \text{ cm}^6$) and memory loss patients ($45.9 \pm 6.8 \text{ cm}^6$). $p = 0.001$

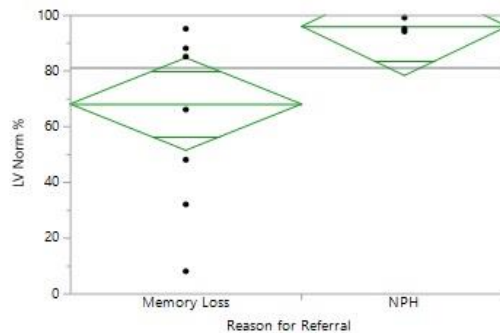


Figure 1C. Normative Percentile for Lateral Ventricle Volume. Values represent the distribution of data for NPH patients ($96 \pm 8.3\%$) and memory loss patients ($68 \pm 7.8\%$). $p = 0.03$

(Filename: TCT_O-222_Figure.jpg)

MRI of the Relationship between White Matter Hyperintensities, Hemosiderin Deposition and Paravascular Spaces for a Possible Mechanism of Brain Injury in Vascular Cognitive Impairment and Alzheimer's Disease

G Barisano¹, A Montagne², S Ma³, M Sarabi³, D Wang³, Y Shi³, B Zlokovic², A Toga³, M Law¹

¹*Department of Radiology, Keck Medical Center of University of Southern California, Los Angeles, CA,* ²*Zilkha Neurogenetic Institute, University of Southern California, Los Angeles, CA,* ³*Stevens Institute of Neuroimaging and Informatics, University of Southern California, Los Angeles, CA*

Purpose

Considerable overlap exists between cerebral small vessel disease (SVD), Alzheimer's disease (AD), and vascular cognitive impairment and dementia (VCID) [1], but the pathophysiological mechanisms leading to white-matter hyperintensities (WMH) and demyelination is not well understood. We hypothesize that a decrease in cerebral blood flow due to arterial aging and stiffness coupled with disrupted blood-brain barrier (BBB) results in the passage of blood-derived neurotoxic proteins (including fibrin and hemosiderin) into the paravascular spaces (PVSs) or Virchow-Robin spaces. This leads to obstruction, enlargement, and dysfunction of these CSF clearance pathways [2]. Ultimately, this leads to tissue injury, astrogliosis and demyelination of surrounding white matter [3].

Materials and Methods

We studied 76 subjects with vascular risk factors from the USC ADRC. Young and old healthy subjects were used as controls. MRI scans were performed on both a GE HDxT 3T and Siemens Prisma 3T. In all 76 subjects, we calculated the degree of WMH using the Fazekas scale (1 to 3 points) and the degree of hemosiderin deposition (HD) in the basal ganglia using a similar 3-point scale. Enlarged paravascular spaces were rated according to the published methods [4]. Spearman's correlation coefficient was used for correlation between PVS, WMH, and HD.

Results

We found that patients with enlarged PVS demonstrated larger volumes of periventricular and deep WMH and more HD in the basal ganglia (p-value = 0.013 and 0.028, respectively).

Conclusions

By accurately imaging and quantifying PVS, we can add this novel, poorly understood MRI finding for characterizing SVD, AD, and VCID. This may be a biomarker for CSF clearance which is closely affected by cerebral blood flow and BBB permeability. This will be important in characterizing cohorts for drug clinical trials and may also provide an understanding for drug and mechanical therapy for AD where improved CSF regulation and clearance has been shown to improve memory [5]. Research reported in this abstract was supported by the National Institute of Biomedical Imaging and Bioengineering of the National Institutes of Health under Award Number P41EB015922. The content is solely the responsibility of the authors and does not necessarily represent the official views of the National Institutes of Health. #ML partially funded by NIH/NIA P50-AG05142, NIH P01AG052350, NIH P01AD06572. ASNR Boerger Research Fund for Alzheimers Disease and Neurocognitive Disease to ML.

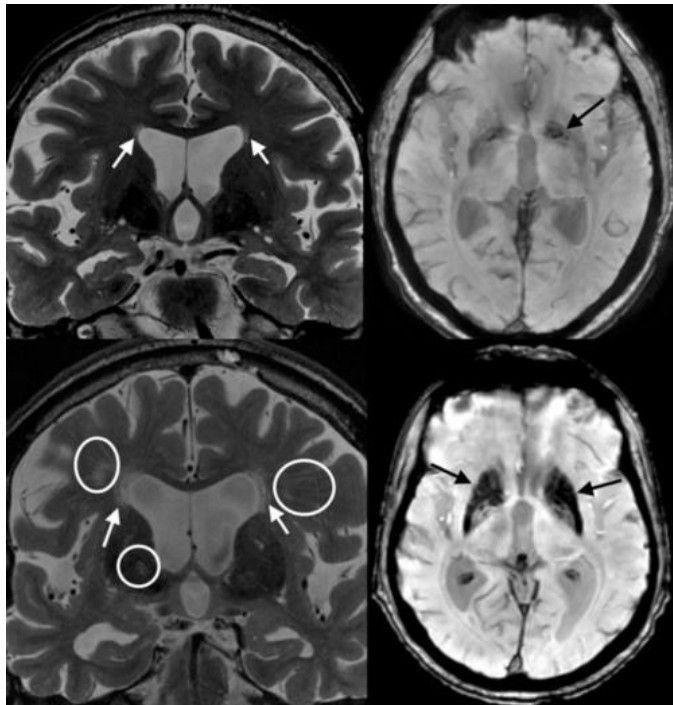


Figure 1: T2WI (left) and SWI (right) at 3T showing a patient with Fazekas grade 1 WMH (white arrows), low grade of hemosiderin deposition (black arrow) and no enlarged PVSs.

Figure 2: T2WI (left) and SWI (right) at 3T showing a patient with Fazekas grade 3 WMH (white arrows), high grade of HD (black arrows) and many enlarged PVSs (white circles). This causes neurotoxic proteins to leak in to the adjacent white matter resulting in loss of myelin, axons and oligodendrocytes.

(Filename: TCT_O-60_FIGUREABSTRACT.jpg)

Monday, June 4, 2018

3:00PM - 4:30PM

Parallel Paper Session: New Findings in Multiple Sclerosis

O-69

3:00PM - 3:07PM

Hyperintensity in Deep Brain Structures on Unenhanced T1-Weighted MR in a Large Cohort of Patients with Secondary Progressive Multiple Sclerosis: Relationship with Dose and Ionization of Linear Gadolinium-Based Contrast Agent.

H Kang¹, M Hii¹, M Le¹, R Tam¹, A Riddehough¹, A Traboulsee¹, S Kolind¹, D Li¹

¹University of British Columbia, Vancouver, British Columbia, Canada

Purpose

To confirm if more frequent gadolinium-based contrast agents (GBCA) administrations are associated with higher signal intensity (SI) changes in deep-brain structures on unenhanced T1-weighted MR images. Secondly, to compare SI differences between ionic and nonionic linear GBCA.

Materials and Methods

Patients with secondary progressive multiple sclerosis originally enrolled in a multicenter, two-year clinical therapeutic trial of MPB8298 (clinicaltrials.gov #NCT00869726 and ISRCTN98373474) were studied retrospectively. Ethics committees at each site approved the study and all subjects signed written informed consent. Eighty patients (frequent cohort), per protocol, received nine GBCA injections (30 patients nonionic, 50 ionic) between week -4 and year one and an additional injection by year two. One-hundred-fifteen patients (infrequent cohort), per protocol, received 2 GBCA injections (40 patients nonionic, 75 ionic) between week -4 and year one and an additional injection by year two. SI was

Oral Presentations & Excerptas

measured by placing regions of interest in the dentate (DN), globus pallidus (GP), caudate (CD), thalamus (TH), pons and white matter (WM). The SI was normalized by calculating the following SI ratios: DN/pons, GP/WM, CD/WM, and TH/WM.

Results

Between week -4 and year one in the frequent cohort, there were significant increases in all SI ratios while only the DN/pons showed a significant increase in the infrequent group, as indicated by paired t-test (Table 1 and 2). Between year one and year two, when both cohorts received only one additional GBCA injection, no significant changes were observed. Significantly greater SI ratio changes were observed in subjects that received linear nonionic GBCA than those receiving linear ionic GBCA (Table 3).

Conclusions

High signal-intensity changes in deep-brain structures on unenhanced T1-weighted images from gadolinium deposition are related to the frequency and type of GBCA (linear nonionic GBCA greater than linear ionic GBCA) administrations.

	Δ Week -4 to Year 1	p-value	Δ Year 1 to Year 2	p-value	Δ Week -4 to Year 2	p-value
L. DN	0.04±0.09 (4%)	0.0002	0.01±0.09 (1%)	NS	0.05±0.09 (5%)	<0.0001
L. GP	0.05±0.09 (5%)	<0.0001	-0.02±0.11 (-1%)	NS	0.03±0.10 (3%)	0.005
L. CD	0.03±0.08 (3%)	0.0004	0±0.11 (0%)	NS	0.03±0.09 (3%)	0.005
L. TH	0.03±0.09 (3%)	0.01	0±0.11 (0%)	NS	0.03±0.09 (3%)	0.01

Table 1. Absolute and Relative Increase in SI Ratios for the Frequent Cohort. Data are mean±SD (% increase). Not Significant (NS)

	Δ Week -4 to Year 1	p-value	Δ Year 1 to Year 2	p-value	Δ Week -4 to Year 2	p-value
L. DN	0.05±0.17 (5%)	0.003	0±0.20 (0%)	NS	0.04±0.15 (4%)	0.003
L. GP	0.01±0.09 (1%)	NS	0±0.17 (0%)	NS	0±0.18 (0%)	NS
L. CD	0.01±0.09 (1%)	NS	0±0.22 (0%)	NS	0±0.21 (0%)	NS
L. TH	0±0.09 (0%)	NS	0.01±0.18 (1%)	NS	0.01±0.19 (1%)	NS

Table 2. Absolute and Relative Increase in SI Ratios for the Infrequent Cohort. Data are mean±SD (% increase) Not Significant (NS)

	Δ Week -4 to Year 2				Nonionic vs. Ionic
	Linear Nonionic	p-value	Linear Ionic	p-value	p-value [#]
L. DN	0.08±0.09 (8%)	<0.0001	0.03±0.09 (3%)	0.01	0.02
L. GP	0.06±0.06 (6%)	<0.0001	0.02±0.11 (2%)	NS	0.05
L. CD	0.03±0.06 (3%)	0.03	0.03±0.10 (3%)	0.04	NS
L. TH	0.04±0.06 (4%)	0.001	0.02±0.10 (2%)	NS	NS

Table 3. Absolute and Relative Increase in SI Ratios Between Week-4 to Year 2 for Linear Nonionic and Linear Ionic Patients. Data are mean±SD (% increase)

[#] Comparison of Nonionic versus Ionic GBCA regarding the Degree of SI ratio Increase.

(Filename: TCT_O-69_tables3.jpg)

O-70

3:07PM - 3:14PM

MRI Identification of Central Vein Sign in Radiologically Isolated Syndrome: Perivenous White Matter Pathology in Asymptomatic Individuals

S Suthiphosuwana¹, P Sati², D Reich², A Bharatha¹, J Oh¹

¹*St. Michael's Hospital, University of Toronto, Toronto, Ontario, Canada,* ²*National Institutes of Health, Bethesda, MD*

Purpose

Radiologically isolated syndrome (RIS) describes asymptomatic individuals with incidental radiologic abnormalities highly suggestive of multiple sclerosis (MS). [1] Recent evidence suggests a significant proportion of MS white-matter lesions have radiologically visible central veins within, called the "central vein sign" (CVS), which is indicative of inflammatory demyelination, and may differentiate MS from mimics and have predictive value in specific clinical settings. [2,3] To date, CVS in RIS has not been evaluated. We aimed to determine whether CVS is present in white-matter lesions of RIS subjects.

Materials and Methods

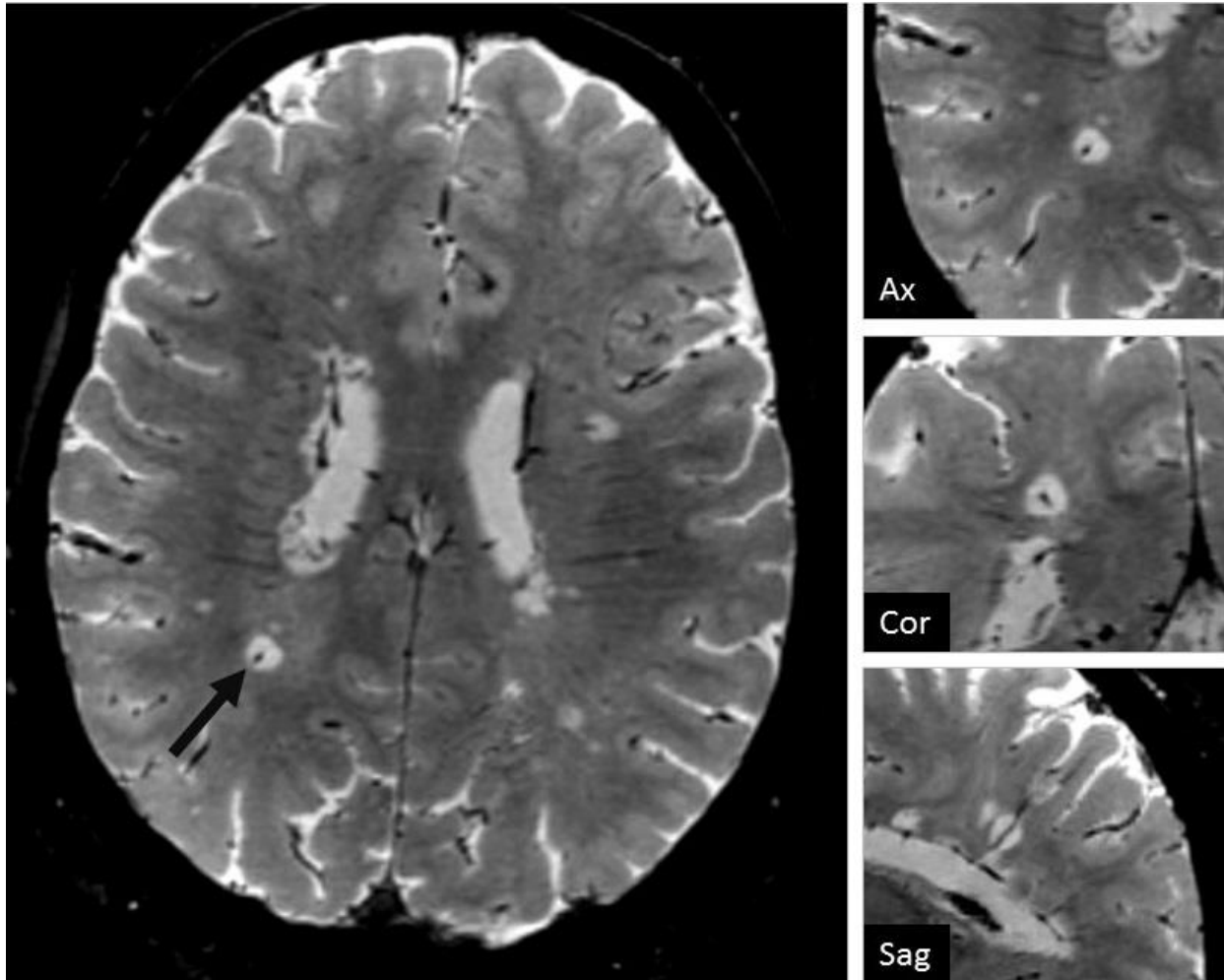
Thirteen subjects with RIS (10 females, 3 males; mean age, 42.85 years) underwent 3.0-T brain MRI using 3-D fluid-attenuated inversion recovery (FLAIR) and 3-D T2*-weighted multishot echo-planar imaging sequence. White-matter lesions were detected and analyzed for number, size, location, and a presence of CVS.

Results

A total of 427 white-matter lesions in the brain were identified. Mean number of lesions per person was 33 (range 9-87). According to recently published CVS criteria [2], 260 lesions (61%) were excluded from the analysis. Evaluated were 167 remaining brain lesions (39%) to assess the presence of CVS. The mean proportion of lesions with CVS per person was 88% (range 67%-100%), which meets the "40 percent" threshold that has been proposed to distinguish MS from other white-matter disorders. [3]

Conclusions

Individuals with RIS have a large proportion of white-matter lesions with MRI-identified CVS, similar to what has been reported in MS. This finding suggests that RIS subjects harbor perivenous inflammatory demyelinating pathology similar to what is observed in MS, which may have prognostic implications. Prospective follow-up of this cohort is planned, which will be helpful to better understand the predictive value of the CVS in RIS.



(Filename: TCT_O-70_Abstract_image_CVS_RIS.jpg)

O-71

3:14PM - 3:21PM

Conventional MRI imaging features and histogram analysis of new T2 lesions correlates with outcome in Multiple Sclerosis patients.

F Moron¹, K Wang¹, D Guffey¹, J Carlton¹, G Hutton¹

¹Baylor College of Medicine, Houston, TX

Purpose

The aim of this study is to evaluate the value of ADC and FLAIR histogram analysis (HA) of new T2 lesions in 1) discriminating new acute demyelinating (ADL) white-matter lesions and new nonacutely demyelinating (N-ADL) lesions without the use of gadolinium; and 2) in predicting outcomes in patients with multiple sclerosis (MS).

Materials and Methods

Thirty patients with clinically definite MS and available brain MRIs were reviewed. A new ADL is defined as an enhancing lesion. A new N-ADL was defined as a new nonenhancing lesion absent on a prior MRI performed <1 year. Discrete lesions were selected for optimal region-of-interest (ROI) placement. Mean, maximum, minimum, 10th, 25th, 50th, 75th, and 90th percentile values were calculated. A second ROI was drawn in the contralateral normal-appearing white matter for

Oral Presentations & Excerptas

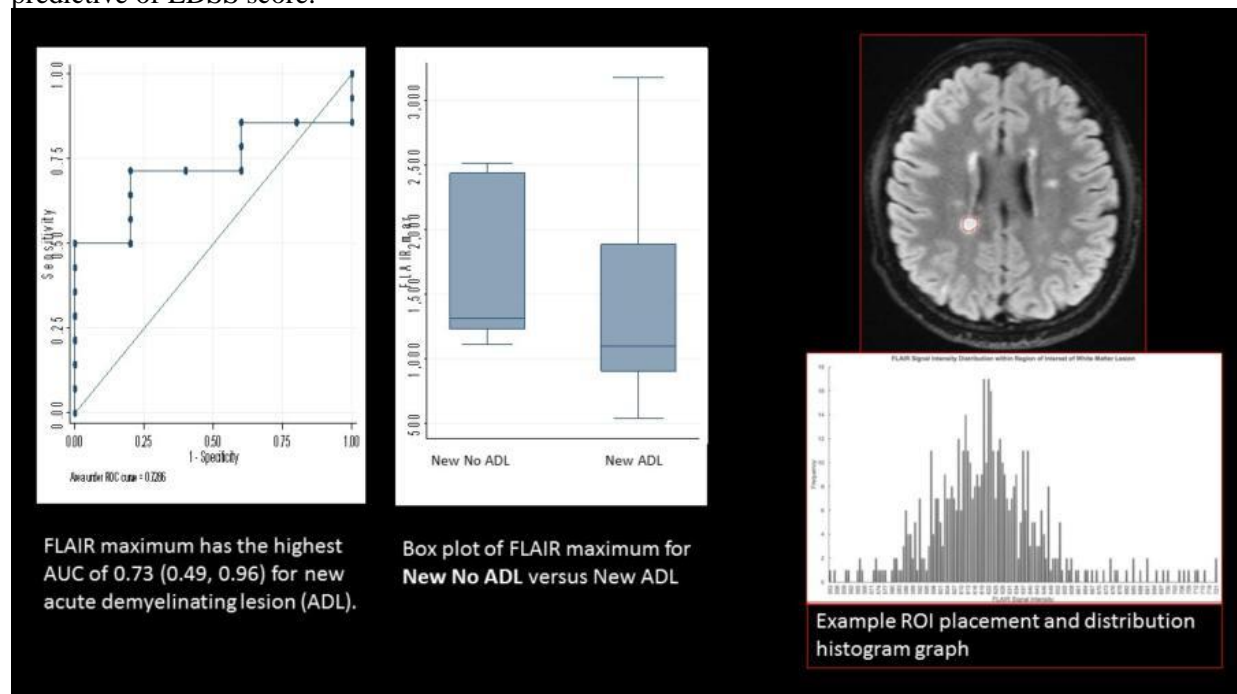
normalization. A ratio was obtained by dividing lesion by contralateral WM value (ADC_r and FLAIR_r). Chart review of demographic, clinical, and outcome data including EDSS score and annual relapse rate were collected. Simple and multivariate linear regression analysis assessed the association between imaging parameters and outcome measures. Receiver operating characteristic (ROC) analysis evaluated discriminatory power of imaging parameters.

Results

In discriminating between N-ADL and ADL, area under the curve (AUC) was highest for the maximum FLAIR (0.73) and the minimum FLAIR_r (0.70). After adjusting for ADL and N-ADL, logistic regression demonstrated min, mean, 10th through 75th percentile FLAIR values were inversely significantly associated with EDSS score ($p < 0.05$); as FLAIR HA increases, EDSS decreases. The log-transformed min, mean, max, 10th and 25th percentile FLAIR_r were inversely significantly associated with EDSS score ($p < 0.05$). No significant associations were found with ADC values or annualized relapse rate.

Conclusions

The absolute FLAIR SI and FLAIR_r may both discriminate between ADLs and N-ADLs and is also predictive of EDSS score.



(Filename: TCT_O-71_Slide1.JPG)

O-72

3:21PM - 3:28PM

Contrast Enhancement Does Not Increase Sensitivity in Detecting New Multiple Sclerosis Lesions in Routine Follow-up MRI.

P Eichinger¹, S Schön¹, H Wiestler², H Zhang¹, V Pongratz¹, J Kirschke¹, C Zimmer¹, B Wiestler¹
¹Klinikum Rechts der Isar, Technical University Munich, Munich, Bavaria, Germany, ²Isar-Amper-Klinikum München-Ost, Haar, Bavaria, Germany

Purpose

The routine administration of contrast agent in follow-up MRI scans of patients with multiple sclerosis (MS) is considered necessary to maximize sensitivity in detecting new lesions [1]. We hypothesized that this does not longer hold true if 3-D images and sophisticated image postprocessing are used.

Oral Presentations & Excerptas

Materials and Methods

We analyzed 507 follow-up scans of 361 patients with clinically isolated syndrome or MS including 3-D FLAIR, 3-D T2, 3-D double inversion recovery (DIR) and 3-D T1 +/- gadolinium. Additionally, we calculated a longitudinal subtraction map for the DIR images [2] that depicts differences between the baseline and the follow-up image and thus helps to directly visualize new lesions. The nonenhanced images along with the DIR subtraction maps were analyzed for new or enlarging lesions. In an independent read, the contrast-enhanced T1 was analyzed for contrast-enhancing lesions (CEL).

Results

In 264 of 507 scans new lesions were detected with a total of 1992 new lesions. A total of 207 CEL were detected in 69 of 507 scans. Four of those CEL were missed in the nonenhanced images and only retrospectively identified as new lesions. This corresponds to 0.20% of all new lesions. However, the three patients in whom these CEL were missed showed a high number of both CEL and new lesions that had been correctly detected. Hence, evaluation of the general presence of new lesions with or without contrast agent did not differ in a single patient.

Conclusions

Our study suggests that contrast agent is dispensable for detecting new lesions if 3-D images along with subtraction maps are used. In light of recent findings regarding intracranial gadolinium depositions [3] our data question the routine use of contrast agent in follow-up scans of patients with multiple sclerosis.

O-73

3:28PM - 3:35PM

Gadolinium Enhancing White Matter lesions on Follow-up MR Imaging in Patients with Multiple Sclerosis: Is Contrast Always Necessary?

R Mattay¹, K Davtayan¹, M Bilello¹, A Mamourian¹

¹*University of Pennsylvania, Philadelphia, PA*

Purpose

Patients with MS routinely have MR imaging with contrast every 6-12 months to assess response to medication (1). The use of contrast adds cost to the exam and multiple recent studies provide evidence of tissue deposition of MR contrast agents (2-5). The goal of this retrospective image-analysis study is to determine if contrast could be reserved for only those patients that show new MS lesions on follow up exams. To maximize sensitivity to any new lesions, we used a previously described computerized image comparison software to evaluate for stability or progression of MS lesions on each scan and correlated those findings with evidence of any contrast enhancing lesions.

Materials and Methods

Temporally sequential brain follow-up MR studies of 67 patients with a diagnosis of MS (20 Male, 47 Female, mean age = 50 years +/- 13.6 years) were reviewed on PACS. All included postprocessed images using the department's unique computer assisted detection software, which superimposed the current and previous FLAIR sequences and marked in color any new, enlarging, or resolving MS lesions. Two investigators independently recorded any changes in the number or size of previously identified lesions and the presence of enhancing lesions. Any disagreements between these two investigators' assessments were resolved by a senior neuroradiologist.

Results

Sixteen scans showed an increase in lesion burden, 50 scans showed stable lesion burden, and one scan showed a decrease in lesion burden. Of the 16 scans that showed an increase in lesion burden on noncontrast images, eight demonstrated enhancing lesions. In only one instance among the 67 patients did we see enhancement of a stable sized pre-existing lesion but in that case there were also new enhancing lesions.

Conclusions

All patients with enhancing lesions had evidence of progression on noncontrast imaging. These results

support the concept that contrast enhancement could be reserved for those MS patients who demonstrate new lesions on follow-up MR scans. While this may require calling back a small subset of patients to establish enhancing disease, it would substantially decrease the cost of imaging in this group of patients while decreasing their risk to the known and unknown risks of MR contrast agents.

O-74

3:35PM - 3:42PM

Functional Network Connectivity and Clinical Phenotypes of Multiple Sclerosis: the CONNECTIMS Study

J Puig¹, G Blasco², A Alberich-Bayarri³, C Biarnes¹, M Marti-Navas¹, M Rivero⁴, J Gich⁴, C Figley⁵, K Nael⁶, C Leiva-Salinas⁷, S Pedraza², L Ramio-Torrenta⁴

¹Diagnostic Imaging Institute, IDI-IDIBGI, University Hospital Dr Josep Trueta, Girona, Spain, ²Imaging Research Unit, IDI-IDIBGI, Hospital Dr Josep Trueta, Girona, Spain, ³La Fe Health Research Institute, Valencia, Spain, ⁴IDIBGI, University Hospital Dr Josep Trueta, Girona, Spain, ⁵University of Manitoba, Winnipeg, Manitoba, Canada, ⁶Icahn School of Medicine at Mount Sinai, New York, NY, ⁷University of Missouri, Columbia, MO

Purpose

Reliable imaging biomarkers could help in characterizing and monitoring patients with MS. Functional connectivity both increases and decreases over disease stages. The impact of functional plasticity mechanisms on clinical phenotype remains unclear. To determine functional connectivity changes in disease stages (clinical phenotype), we investigated resting-state functional connectivity abnormalities in a cohort of multiple sclerosis (MS) patients.

Materials and Methods

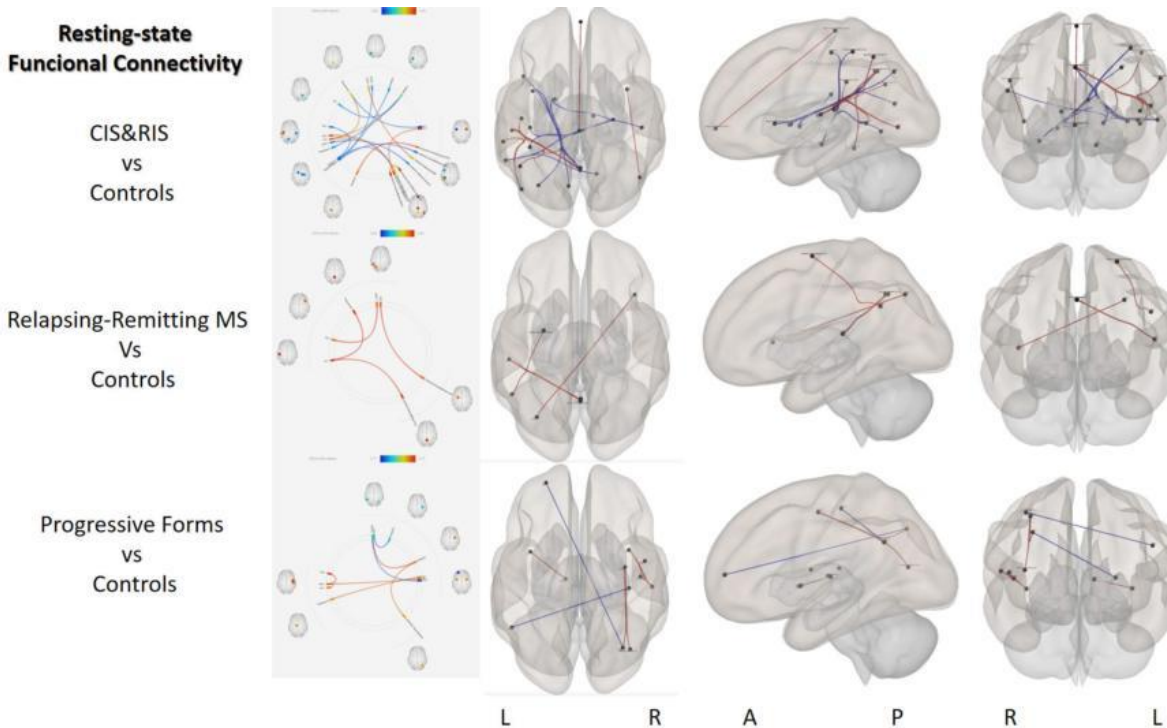
In this cross-sectional analysis, 82 patients with clinically or radiologically isolated syndrome (CIS/RIS) (n=23; 18 female; age 35±9.1 years), relapsing-remitting MS (n=24; 16 female; mean age 43.9±11.3 years), or primary or secondary progressive MS (n=35; 19 female; age 53.5±7.2 years) and 30 matched healthy controls (18 female; age 41.4±10.9 years) underwent 1.5T MRI. We calculated volumes of total white matter, gray matter, and lesions (Olea Sphere 3.0 [La Ciotat, France]). We used CONN v17 (Functional Connectivity SPM toolbox, McGovern Institute of Brain Research, MIT) to analyze connectivity abnormalities by graph theory, using age, sex, lesion volume, and schooling as covariates.

Results

Interhemispheric connectivity was altered in all MS clinical phenotypes (Figure), being decreased in patients with relapsing-remitting MS and increased in those with primary or secondary progressive MS. Intra-hemispheric connectivity was decreased in patients with relapsing-remitting MS and in those with progressive MS. Regional network properties in patients with CIS/RIS differed from those in healthy controls. The modification of regional network properties contributed to phenotypic variability of MS.

Conclusions

Decreased and increased functional connectivity contributes to phenotypic variability in MS. These findings are likely due to a deficit of integration of connectivity at a global network level.



(Filename: TCT_O-74_FigureMSrsfunctionalconnectivity.jpg)

O-75

3:42PM - 3:49PM

Predicting Conversion from Clinically Isolated Syndrome to Multiple Sclerosis - A MRI Feature Based Machine Learning Approach

H Zhang¹, E Alberts², V Pongratz¹, M Mühlau¹, C Zimmer¹, P Eichinger¹, B Wiestler¹

¹Klinikum Rechts der Isar, Technical University Munich, Munich, Bavaria, Germany, ²Technical University Munich, Munich, Bavaria, Germany

Purpose

MR imaging is a routinely used diagnostic tool in patients presenting with a Clinically Isolated Syndrome (CIS) [1] as it may demonstrate brain lesions suspicious of an inflammatory cause. We hypothesized that studying imaging features of these lesions such as shape and brightness in the baseline MRI may allow predicting conversion into MS.

Materials and Methods

We performed a retrospective single-center study including scans of 84 patients who presented with CIS and were followed-up for a minimum of three years. Conversion into definite MS was defined according to the 2010 McDonald criteria, i.e. encompassed both clinical and radiological criteria. MRI scans included 3-D FLAIR and 3-D T1 images in which lesions were segmented semiautomatically. Shape and brightness features were automatically generated from these masks and input into an oblique random forest machine learning model. Prediction accuracies were validated through a three-fold cross-validation.

Results

Of 84 patients, 66 converted to MS. Conversion/nonconversion was predicted correctly in 71 of 84 patients in a random forest model based on shape features. Including brightness features did not contribute to improving the model's performance. This predictor was significantly more accurate than predicting conversion with Barkhof's criteria [2] ($p < 0.001$, McNemar's test) with a sensitivity of 94%

and specificity of 50% (85% and 28%, respectively for Barkhof's criteria). The corresponding contingency tables are given in Figure 1.

Conclusions

As patients who convert to definite MS benefit from early treatment [3, 4], an early available classification model would be highly desirable. Our study shows that shape parameters of lesions can contribute to predicting the future course of CIS patients more accurately.

Predictive Model	CIS	MS
Predicted CIS	9	4
Predicted MS	9	62

Barkhof's Criteria	CIS	MS
Predicted CIS	5	10
Predicted MS	13	56

(Filename: TCT_O-75_Figure1.jpg)

O-76

3:49PM - 3:56PM

Automatic Detection of New MS Lesions on Longitudinal Subtraction Images

B Wiestler¹, P Eichinger¹, H Wiestler², H Zhang¹, V Pongratz¹, C Zimmer¹, M Mühlau¹, J Kirschke¹, S Albarqouni³

¹Klinikum Rechts der Isar, TU München, Munich, Bavaria, Germany, ²Isar-Amper-Klinikum München-Ost, Haar, Bavaria, Germany, ³Computer Aided Medical Procedures, Garching, Bavaria, Germany

Purpose

MRI plays a central role in the diagnosis and management of Multiple Sclerosis (MS) patients. Several studies have, however, shown that detecting new lesions on follow-up imaging is subject to relevant interobserver variability. We have therefore aimed to develop a software for automatic detection and segmentation of new or enlarged MS lesions in longitudinal subtraction images [1].

Materials and Methods

In a first step, the software marks candidate lesions on both DIR and T1 subtraction images [1], using simple constraints on shape and intensity. Next, several image features pertaining to shape, intensity and neighborhood of these features are extracted from each lesion, and an oblique random forest (RF) classifier was trained on a discovery cohort of 42 patients to distinguish true new lesions from noise. The resulting classifier was then validated in 22 previously unseen patients.

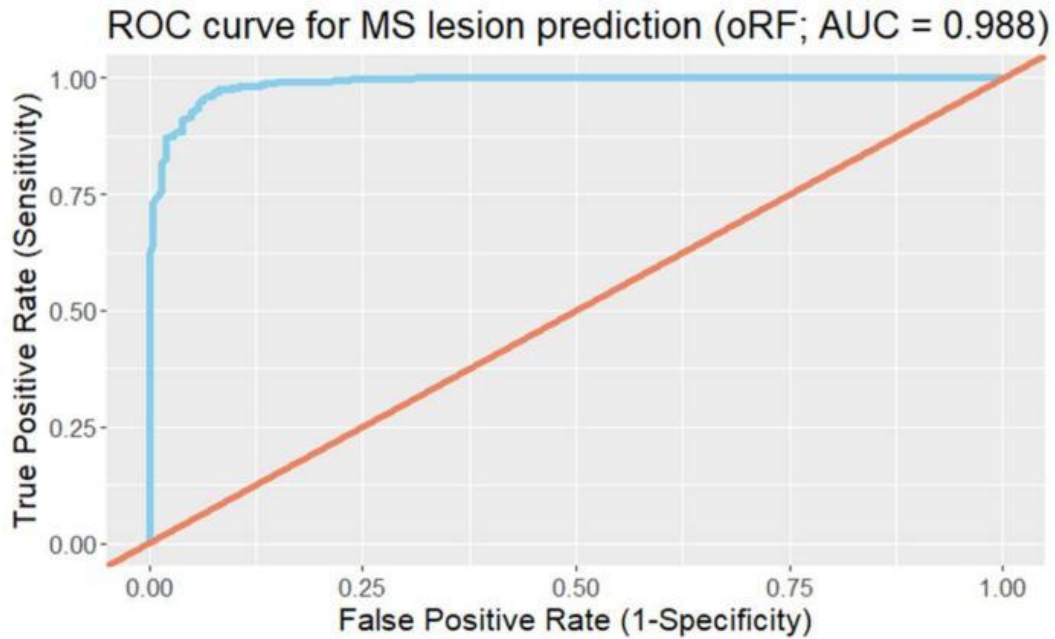
Results

The software marked 866 candidate lesions in the discovery cohort, of which 207 were true lesions. Eight true lesions were missed in this step, mostly because of their small size (detection rate 96.2%). Using features from these lesions as input, the RF classifier for separating noise from true lesions reached a total accuracy of 95.3% (Figure 1A), detecting 192 of 207 marked lesions (92.7%, Figure 1B). Intriguingly, the software additionally detected nine MS lesions which have previously been overlooked by two neuroradiologists who generated the reference standard. The software therefore correctly labelled 192/215 new lesions (detection rate 89.3%).

Conclusions

A software exploiting the high lesion-background contrast of subtraction images combined with a machine learning classifier based on simple image features can detect new or enlarged MS lesions with a compelling detection rate of 89%, which is well within the range of human readers in contemporary trials. Further underlining the potential of such approaches to computer-assisted radiology, the software also identified lesions which have been overlooked by two neuroradiologists.

1A)



1B)

	Noise	True Lesion
Predicted „Noise“	633	15
Predicted „True Lesion“	26	192

Figure 1. ROC curve of the RF classifier for separating noise from true new MS lesions (A). Contingency table with the classification results in the 22 previously unseen validation patients (B).

(Filename: TCT_O-76_Figure1.jpg)

O-77

3:56PM - 4:03PM

Multiple Sclerosis, Cannabis, & Clinical Disability: A Molecular Imaging Study with ¹⁸F-FDG Positron Emission Tomography

J Honce¹, J Kindred², J Kwak¹, T Rudroff²

¹University of Colorado, Aurora, CO, ²Colorado State University, Fort Collins, CO

Purpose

[¹⁸F]-Fluorodeoxyglucose (FDG) Positron Emission Tomography (PET) imaging has shown that healthy regular cannabis users have lower regional glucose uptake at rest compared to nonusers. Relative to healthy controls, lower brain glucose uptake has also been observed in patients with multiple sclerosis (PwMS), and this decrease is associated with physical and cognitive impairments. The primary aim of this study was to measure resting-brain glucose uptake in PwMS regularly using and not using cannabis. Our secondary aim was to determine if users and nonusers performed differently on standard clinical assessments of disability and if these differences were associated with altered brain glucose uptake.

Materials and Methods

Sixteen PwMS: eight cannabis users (mean 49.6-years, 6 female) and eight nonusers (mean 50.8-years, 6 female), underwent FDG PET-CT imaging and a battery of standard clinical/cognitive disability measures. PwMS with relapses within three months, concurrent neurologic disorders or hyperglycemia were excluded. Standardized Uptake Value images were created and whole brain voxel-wise and regional analyses were performed with SPM12.

Results

PwMS using ingested cannabis an average of 2.3 times per day and 6.9 days per week. Regular cannabis users demonstrated greater glucose uptake in small areas throughout the frontal and temporal lobes, bilaterally. Functional variables were mostly similar between groups ($P > 0.16$), except for decreased information processing speed ($P = 0.02$) and hand grip strength ($P = 0.02$) in cannabis users. These group differences were not explained by resting-brain glucose uptake in any of the examined brain regions; however, across all participants, greater glucose uptake was associated with less fatigue, disability, spasticity and pain.

Conclusions

Our findings indicate that regular cannabis use may not negatively affect brain glucose uptake in PwMS. However, cannabis should be used under medical supervision with a focus on monitoring cognitive function and muscle strength for possible negative effects induced by cannabis use.

Table 1. Demographics and performance test values

	Non-users	Users	<i>P-value</i>
Sex (M/F)	2 / 6	2 / 6	
Age	50.8 (13.2)	49.6 (15.0)	0.875
Disease Duration	14.9 (8.3)	8.4 (7.4)	0.121
Ht. (m)	1.7 (0.1)	1.7 (0.1)	0.186
Wt. (kg)	79.0 (25.5)	75.7 (20.0)	0.521
Alcohol (drinks / week)	1.5 (2.4)	1.7 (2.5)	0.880
HG (Dom)	36.9 (9.2)	27.1 (3.8)	0.015*
HG (Non)	27.1 (3.8)	24.5 (3.1)	0.064
25Ft Walk Test (sec)	6.2 (4.8)	5.8 (2.1)	0.855
PT (Dom)	23.1 (6.6)	24.2 (9.4)	0.798
PT (Non)	22.7 (5.1)	24.7 (7.8)	0.570
PASAT	43.5 (8.8)	31.8 (8.6)	0.018 *
TUG	12.1 (14.3)	9.7 (4.1)	0.644
ABC	78.5 (18.6)	69.5 (26.1)	0.437
BDI	12.6 (7.1)	14.1 (6.1)	0.657
FSS	4.9 (2.3)	5.3 (1.3)	0.690
PES	13.9 (6.8)	16.1 (6.4)	0.506
NRS	3.6 (4.0)	1.9 (1.8)	0.282

PT = 9 hole peg test, Dom = Dominant, Non = Non-Dominant, PASAT =Paced Auditory Serial Addition Test, TUG = Timed up and go, ABC = Activities of Balance Confidence, BDI = Beck's Depression Inventory, FSS = Fatigue Severity Scale, PES = Pain Effects Scale, NRS = Numerical Rating Scale of Spasticity.

(Filename: TCT_O-77_Table1.JPG)

O-78

4:03PM - 4:10PM

Longitudinal assessment of the microstructural substrates underlying Gad-enhancing lesions in MS using multi-shell Neurite Orientation Dispersion and Density Imaging (NODDI).

S Sacco¹, E Caverzasi¹, T Gundel², G Rush², S Bastianello³, R Henry¹, " EPIC Investigators "²
¹University of California San Francisco, San Francisco, CA, ²Weill Institute for Neurosciences, University of California San Francisco, San Francisco, CA, ³ University of Pavia, Pavia, Italy

Purpose

DTI is sensitive in detecting loss of integrity in MS lesions and normal appearing white matter (NAWM). Nonetheless, DTI lacks specificity since different histopathological processes may determine overlapping patterns of metrics changes. NODDI models neurite density (NDI) and its orientation dispersion (ODI), an extracellular compartment including nonneurite contributions (VECVF), and an isotropic CSF like compartment (VISO). We aim to assess, for the first time, NODDI metrics longitudinally in MS gad-enhancing lesions (GEL) and NAWM.

Materials and Methods

Twenty-two MS patients (mean age 36.5+/-8.6, 18 female, 16RR 4CIS 2PP, EDSS 2.6+/-1.6) underwent two serial enhanced 3T MRIs 12.6+/-9 months apart with NODDI acquisitions. WM lesions were segmented on FLAIR and 140 GEL on postcontrast MPRAGE. NAWM masks were generated by

subtracting lesions from SIENAX WM masks. NODDI fitting was performed with the NODDI Matlab Toolbox and DTI using DiPy. Mean values of NODDI and diffusion metrics were extracted at both time-points within the total NAWM as well as in the GEL mask and differences were assessed by parametric test.

Results

All GEL were nonenhancing at follow-up. GELs showed similar isoVF and ODI, but decreased NDI and increased VECVF values compared to NAWM, possibly related to inflammatory changes. The longitudinal evaluation showed that the resolution of enhancement was associated with a progressive decrease in the VECVF/NDI ratio. Consistent with the literature non-GEL demonstrated lower ODI compared with NAWM [1, 2] as well as with GEL, possibly as result of reduced tissue complexity.

Conclusions

We demonstrate for the first time a serial assessment of multishell NODDI in MS. NODDI allows the detection of specific microstructural changes occurring in MS brain. Longitudinal changes in GEL likely represent a progressive resolution/decrease in inflammatory changes and accumulation of structural damage.

O-79

4:10PM - 4:17PM

Cortical or Juxtacortical Lesion? Evaluation of Phase Sensitive Inversion Recovery sequence in characterization and follow up of Multiple Sclerosis Patients

M Lima¹, G Furlin¹, A Kupske¹, K Nunes¹, M Longo², B Valentini¹, F Aesse¹, J Muller¹, M Caneda¹, M De Vecino¹

¹Hospital Moinhos de Vento, Porto Alegre, Rio Grande do Sul, Brazil, ²Massachusetts General Hospital, Boston, MA

Purpose

Multiple Sclerosis (MS) is a demyelinating process that affects not only white matter, but also cortical gray matter. Cortical plaques can be classified by location and pathologic substract. Juxtacortical lesions remain part of the differential diagnosis of cortical lesions, since the imaging differentiation can be challenging with the standard Magnetic Resonance (MRI) sequences. However, new pulse sequences have demonstrated better results in detection and differentiation of this lesions, like Double Inversion Recovery (DIR) and Phase Sensitive Inversion Recovery (PSIR), which shows accuracy 4-5 times greater than DIR in some studies. The study aims to assess the performance of PSIR in detection and differential diagnosis of cortical plaques in patients with diagnosis of MS, in comparison with FLAIR.

Materials and Methods

We retrospectively evaluated patients with diagnosis of MS confirmed by McDonald criteria (2010) who underwent MRI examination in our service between March 2016 and April 2017 and were studied with the sequences FLAIR and PSIR in 3T equipment. The images were evaluated by two radiologists that quantified the number of lesions detected first in FLAIR sequence and after in PSIR sequence. After, they estimated how many lesions were reclassified using PSIR sequence. The incoherences in the first evaluation were solved by a third radiologist.

Results

Included were 71 patients, with mean age of 45.4 years and average of 12.7 years of disease evolution. Fifty-two patients (73.2%) presented with juxtacortical lesions. Of these, 43 (82.7%) had lesions that were reclassified as leucocortical or cortical using PSIR, with a median number of 2.55 lesions per patient. Thirty-eight patients (54.3%) presented supratentorial lesions identified only in PSIR, with a median number of 1.44 lesions per patient. Twenty-three patients (32.9%) presented infratentorial lesions identified only in PSIR, with a median number of 1.43 lesions per patient. PSIR sequence showed better detection performance than FLAIR in identifying MS lesions either in supratentorial and infratentorial

compartments ($p < 0.001$ for both), detecting an average of 1.5 more lesions in supratentorial and 0.42 more lesions in infratentorial compartment.

Conclusions

The evaluation of MS lesions with PSIR shows greater performance for diagnosis and classification in comparison with FLAIR sequence, either in supratentorial or infratentorial compartment and its use should be encouraged in the clinical practice.

O-80

4:17PM - 4:24PM

Quantitative Myelin Water Imaging detects age-dependent demyelinating alterations of the Cerebral White Matter Microstructure - A multiparametric MRI study

T Faizy¹, G Broocks¹, D Kumar², J Sedlacik¹, F Flottmann¹, H Leischner¹, U Hanning¹, M Grosser¹, S Jan-Patrick¹, A Kemmling³, J Fiehler¹, S Gellissen¹

¹University Medical Center Hamburg-Eppendorf, Hamburg, Germany, ²University of Pennsylvania, Philadelphia, PA, ³University Medical Center Schleswig-Holstein, Luebeck, Germany

Purpose

Age-related microstructural changes of the cerebral white matter (WM) may be evaluated using quantitative MRI techniques. Advanced sequences such as diffusion-tensor imaging (DTI) are sensitive to the effects of aging, but lack the specificity to determine the underlying pathophysiological mechanisms, especially those related to demyelination. Other advanced MRI techniques, such as Myelin Water Imaging (MWI) or Magnetization Transfer Imaging (MTI) may be more sensitive to demyelinating WM processes during aging. The purpose of this study was to evaluate age-dependent microstructural changes of the cerebral WM utilizing a new 3-D MWI approach.

Materials and Methods

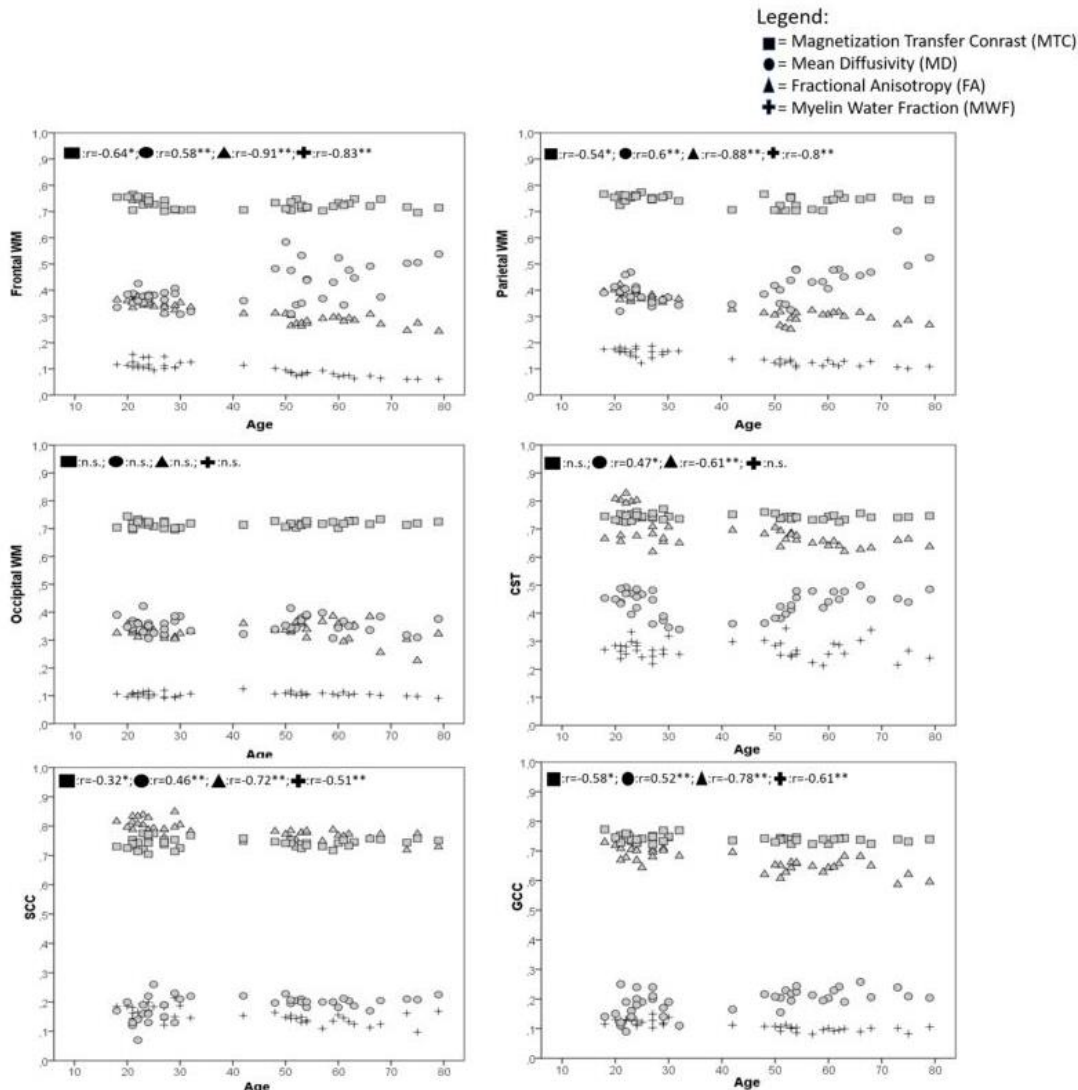
Multiparametric MRI data from DTI, MTI and a novel 3-D MWI algorithm were acquired from 41 healthy subjects (aged 18-79 years). All multiparametric MRI maps were processed with a series of linear and nonlinear registrations, and region of interest (ROI)-based age-associated correlations were assessed for each calculated quantitative map. Also, mixed effect models were computed to investigate an interdependence between age and each measure derived from the multiparametric MRI sequences.

Results

Fractional Anisotropy (FA) showed the strongest negative correlation with age in all assessed ROIs paralleled by an increase of mean diffusivity (MD). Myelin Water Fraction (MWF) and Magnetization Transfer Contrast (MTC) measures correlated well with age, predominantly in frontal and parietal brain regions. All investigated measurements showed the strongest alterations in frontally located brain areas, whereas measurements derived from posterior brain regions (occipital WM) did not show any significant differences with age, reflecting an anterior-posterior gradient of microstructural brain changes in the cerebral white-matter pattern. (Please also refer to the attached figure).

Conclusions

Diffusion metrics remain the most sensitive markers for age-dependent microstructural alterations. Declines of MWF measurements indicate demyelination and may reflect a portion of age-related demyelinating processes occurring in the cerebral WM pattern.



(Filename: TCT_O-80_Figure_cross.jpg)

Monday, June 4, 2018
 3:00PM - 4:30PM
 Parallel Paper Session: Pediatric Imaging

O-81

3:00PM - 3:07PM

Segmentation of Pediatric Hindbrain at 7 Tesla: First Steps Toward Developing a Hindbrain Atlas

M Barkovich¹, D Xu¹, R Desikan¹

¹University of California, San Francisco, San Francisco, CA

Purpose

There is growing awareness of the role of the hindbrain in pediatric neurodevelopmental and psychiatric

Oral Presentations & Excerptas

diseases. Currently there are no automated methods for quantitative evaluation of hindbrain structures on clinical or research MRI exams, although probabilistic atlases have been developed in adults. An automated method of pediatric hindbrain segmentation using training data from expert cerebellar segmentation and a priori information from ultra high-field hindbrain imaging could aid in the evaluation of abnormal hindbrain morphometry.

Materials and Methods

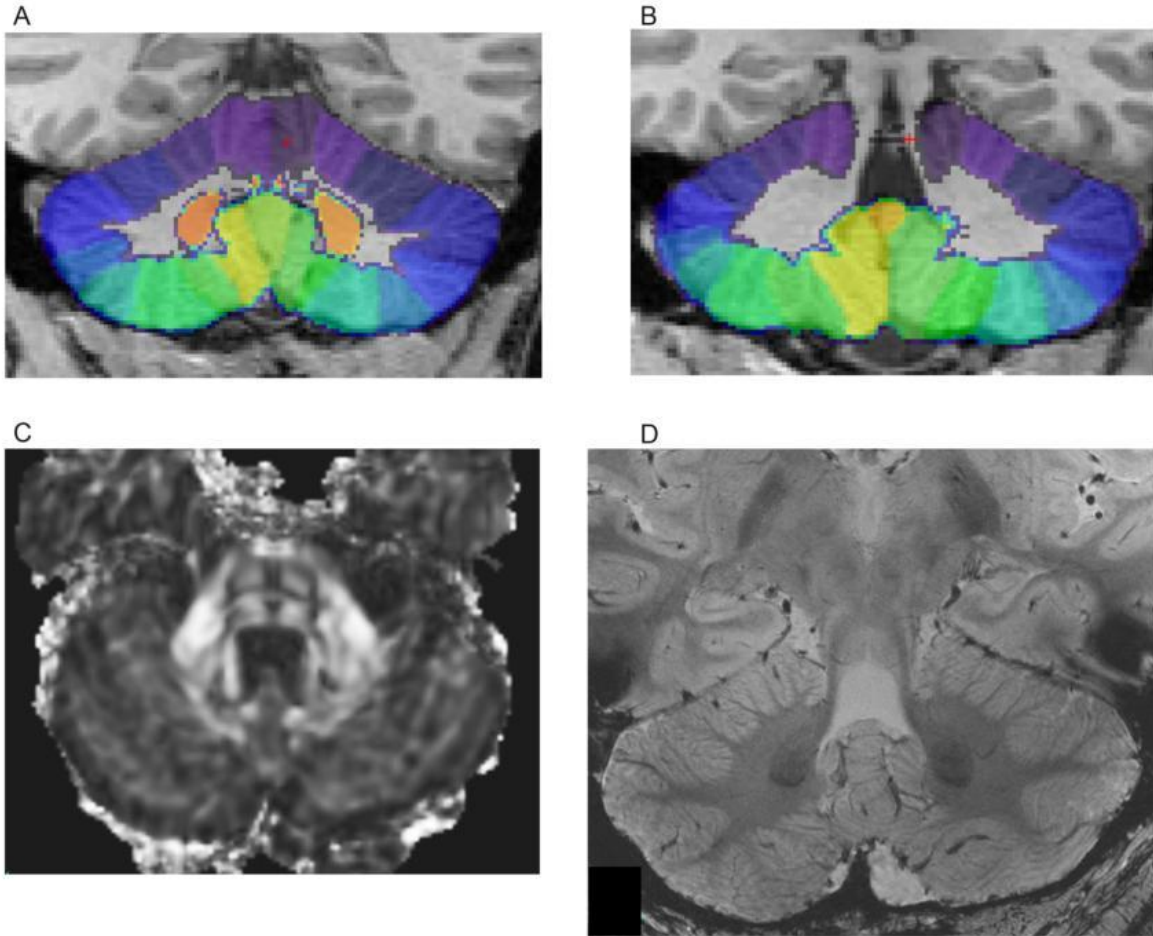
The pediatric hindbrain was manually segmented into 62 regions, 23 of which are paired, in the brainstem and cerebellum on 3 Tesla T1-weighted MRI scans of normal, volunteer, children. Obtained were 7 Tesla gradient recalled echo (GRE) anatomic imaging and diffusion tensor imaging (DTI) of the hindbrain in five normal pediatric volunteers and the iron containing nuclei on GRE images and white-matter tracts on DTI were manually segmented.

Results

Successful 62 region segmentation of the pediatric hindbrain on standard 3 Tesla clinical MRI, with registration of ultra high-field anatomic images and DTI to the 3 Tesla T1-weighted volumetric acquisitions.

Conclusions

These detailed pediatric hindbrain segmentations, registered to ultra high-field imaging, will comprise an atlas which can be used for subsequent automated pediatric hindbrain segmentation on standard clinical MRI.



Cerebellar segmentation on 3T anatomic images is shown in panes A and B, with A highlighting the dentate nuclei (orange). 7 Tesla MRI of the hindbrain (C and D) with an axial DTI image (C) showing the horizontally oriented tracts in the middle cerebellar peduncles. Oblique coronal GRE image of the cerebellum (D) shows the hypointensity of the iron containing dentate nuclei nicely.

(Filename: TCT_O-81_Fig.jpg)

O-82

3:07PM - 3:14PM

Quantitative Assessment of Regional Brain Myelination during Development using Synthetic MRI

J Guerin¹, P Naidu¹, J Leach¹, B Jones¹, H West¹, A McAllister², J Dudley¹, S Serai³

¹Cincinnati Children's Hospital Medical Center, Cincinnati, OH, ²Nationwide Childrens Hospital, Columbus, OH, ³Children's Hospital of Philadelphia, Philadelphia, PA

Purpose

Previous methods for quantitative intracranial myelin assessment typically require long scan times and complex processing limiting clinical use. Synthetic MRI is a method in which a short (six-minute) multiple-spin echo saturation recovery sequence (QMAP) is used with four saturation recovery times and two echoes in conjunction with postprocessing software (SyMRI, < 1 minute) to create absolute R1, R2 and PD relaxivity maps. SyMRI infers the presence of myelin based upon its effect on intra and extracellular water (magnetization exchange), alterations in local R1, R2 and PD, and application of these values in multiparametric space to estimate myelin partial volume (as part of a multicomponent partial

Oral Presentations & Excerptas

volume model) in each acquisition voxel [1]. Prior studies have evaluated whole brain normative segmentation values during development, including myelin, with this technique [2]. The current study aims to more specifically define myelin fraction (MY%) in specific brain regions during early development (0-5y) using this technique and preliminarily assess its clinical utility.

Materials and Methods

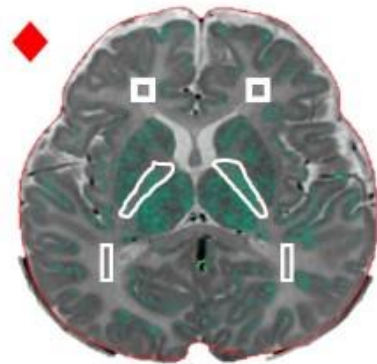
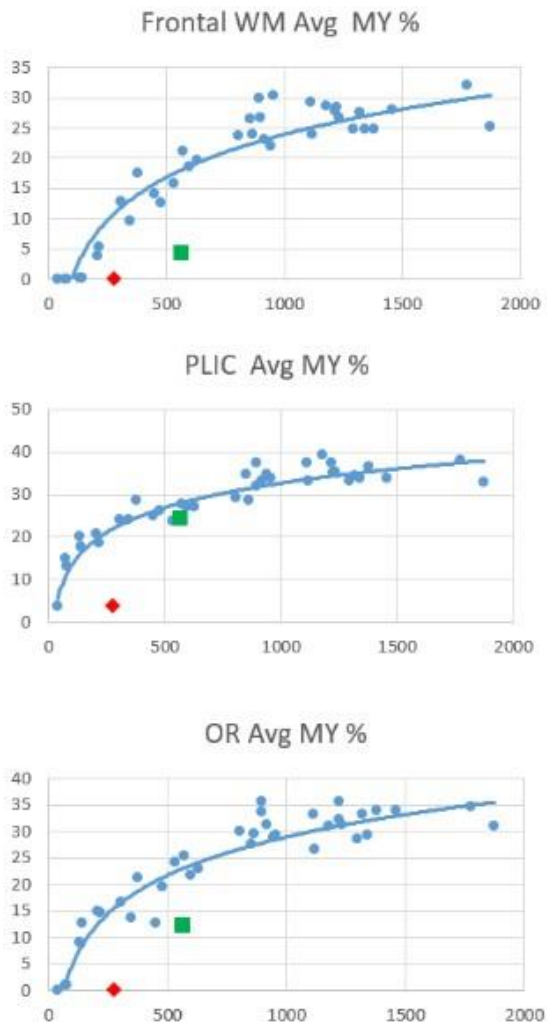
An institutional review board-approved retrospective review was performed of all brain MR imaging examinations during a 54-month period in which the QMAP sequence was performed (1082 exams). Of 246 MRI examinations with a normal radiology report, 65 were excluded (clinical and technical) leaving 181 normal exams. Of these subjects 37 were younger than 5y forming the study cohort (mean age: 2y; 39d – 4.9y). All were performed at 3T. The exams were quantitatively analyzed using SyMRI software (Synthetic MRI v8.0). MY% was calculated in key regions of interest (ROI) (the genu and splenium of the corpus callosum, caudate head, putamina, thalami, anterior limb of the internal capsule (ALIC), posterior limb of the internal capsule (PLIC), optic radiations (OR) and frontal lobe white matter (WM) at the level of the foramen of Monro, frontal, perirolandic, and parietal WM at the level of the corona radiata, pons, temporal WM, occipital WM, medulla, brachium pontis, and cerebellar WM) and plotted versus age. Mean values were utilized in each ROI with paired structures averaged. Selected abnormal exams were compared with these normative curves.

Results

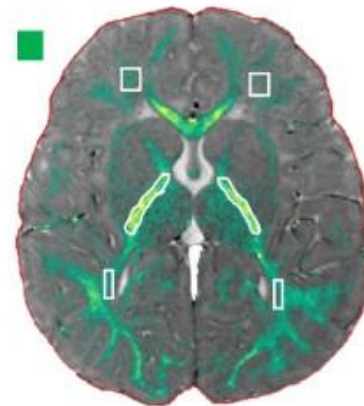
Myelin fraction curves within regions of interest are similar in morphology to previously published curves using alternative techniques, demonstrating rapid linear increase in MY% during the first 12-18 months and subsequent slowing of myelination beyond this age [3]. Regional differences in myelination were identified. Patients with pathologic myelin content can be identified quantitatively by comparing individual values to the normative curves. In some cases specific disease processes may be suggested. Figure 1 demonstrates abnormally decreased MY% in the PLIC, frontal WM, and OR in a 9mo with Pelizaeus-Merzbacher disease compared with normative curve. In another subject with Alexander disease, decreased MY% is most pronounced in frontal WM, less pronounced in the OR, and essentially normal in the PLIC consistent with the known distribution of altered myelination in this condition.

Conclusions

Regional quantitative analysis of myelination in young children is possible using a single six-minute sequence, rapid software analysis and manual ROI placement and correlates with previously published data. Regional abnormalities of myelination in pathologic conditions can be identified.



9 mo M PMD



18 mo M Alexander

(Filename: TCT_O-82_abstractfigure.jpg)

O-83

3:14PM - 3:21PM

Quantitative Assessment of Regional Brain T1, T2, and PD values During Development using Synthetic MRI

P Naidu¹, J Guerin¹, J Leach¹, B Jones¹, H West¹, A McAllister², J Dudley¹, S Serai¹

¹Cincinnati Children's Hospital Medical Center, Cincinnati, OH, ²Nationwide Childrens Hospital, Columbus, OH

Purpose

Synthetic MRI (SyMRI) is a newer technique in which a six-minute sequence (QMAP, which utilizes a multislice, multiecho, and multidelay acquisition) is used to obtain quantitative parameters of the brain. The sequence allows for calculation of absolute voxelwise R1 and R2 relaxivity and PD values via SyMRI software (< 1 minute processing time) yielding T1, T2, and PD maps. We analyzed the values of specific brain regions on MRIs obtained in a normal pediatric population using SyMRI in order to

evaluate trends in absolute T1, T2, and PD in early development (0-5 years) and compared these values to the published literature.

Materials and Methods

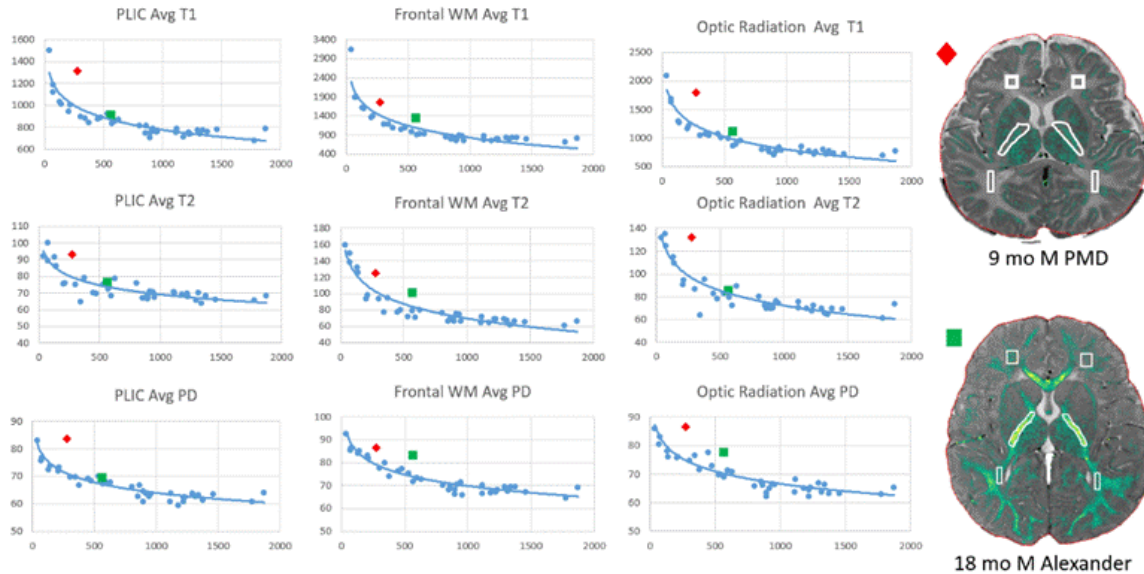
An institutional review board approved retrospective review was performed of all brain MR imaging examinations during a 54-month period in which the QMAP sequence was performed (1082 exams). Of 246 MRI examinations with a normal radiology report, 65 were excluded (due to clinical and technical reasons), leaving 181 normal exams. Of these subjects 37 were younger than five years old, forming the study cohort (mean cohort age: 2 years; range: 39 days – 4.9 years). All exams were performed at 3T and quantitatively analyzed with SyMRI software (Synthetic MR, version 8.0). T1, T2, and PD values were calculated in key regions of interest (the genu and splenium of the corpus callosum, caudate head, putamina, thalami, anterior limb of the internal capsule [ALIC], posterior limb of the internal capsule [PLIC], optic radiations [OR], frontal lobe white matter at the level of the foramen of Monro, frontal, perirolandic, and parietal white matter at the level of the corona radiata, temporal white matter, occipital white matter, medulla, pons, brachium pontis, and cerebellar white matter). Mean values were utilized in each ROI, with paired structures averaged. Values were plotted relative to age. Example pathologic cases were assessed using the same ROIs to assess clinical utility.

Results

T1, T2, and PD values for various regions of interest showed predictable and regionally different changes with age related to ongoing myelination and brain maturation. Logarithmic curve fitting of T1 and T2 values for each region of interest versus patient age was excellent; these curves are very similar in configuration to those previously published [1, 2], although the absolute values of both were somewhat less than in prior reports using different techniques. Quantitative information was useful when assessing pathologic cases. Figure 1 demonstrates abnormally prolonged T1, T2 and PD in the PLIC, frontal WM, and OR in a 9 month-old with Pelizaeus-Merzbacher disease (PMD) compared with normative curves. In another subject with Alexander disease, the T1, T2, and PD prolongation is most pronounced in the frontal WM, with relatively normal values in the OR and PLIC consistent with the known distribution of disease in this condition.

Conclusions

SyMRI allows for quantitative assessment of T1, T2, and PD in the developing brain using a short (six minute) sequence and rapid processing using simple ROI placement in standard anatomic regions. T1 and T2 values progressively shortened in the setting of ongoing myelination, although the absolute values for both were consistently lower than previously reported values. Potential reasons for this difference include different methods for assessing T2 (rapid and longer components), scanner eddy current issues, or other factors. Despite these differences, comparing SyMRI derived quantitative T1, PD and T2 values in standardized ROIs was useful in differentiating normal and pathologic states.



(Filename: TCT_O-83_FigureT1T2.gif)

O-84

3:21PM - 3:28PM

MR Venography predicts increased intracranial hypertension in children with hydrocephalus

A Rohr¹, F Knerlich-Lukoschus², M Heran³, J Shewchuk⁴, O Jansen⁵

¹Vancouver General Hospital and University of British Columbia Hospital, Vancouver, British Columbia, Canada, ²Asklepios Kinderklinik Sankt Augustin, Sankt Augustin, Nordrhein-Westfalen, Germany, ³Vancouver General Hospital, Vancouver, British Columbia, Canada, ⁴University of British Columbia, Vancouver, British Columbia, Canada, ⁵University Hospital Schleswig-Holstein, Kiel, Schleswig-Holstein, Germany

Purpose

Head imaging with CT or MRI is often requested in children with hydrocephalus who are unwell with a suspicion of intracranial hypertension/presumed shunt failure. The finding of significant hydrocephalus may result in invasive procedures such as shunt revisions to prevent a life-threatening situation. Clinical signs and symptoms are, however, mostly nonspecific and the presence or absence of hydrocephalus does not reliably predict or exclude intracranial hypertension in these patients (1). This is especially true when no previous images are available from a time when the child was well. Dural-sinus narrowing in the presence of intracranial hypertension has been reported in three cases of shunt patients with slit-ventricles (2) and is known to be correlated with idiopathic intracranial hypertension in adults (3). We investigated whether dural-sinus narrowing as seen on MR venography occurs in children shunted for hydrocephalus and if this finding is more reliable in detecting intracranial hypertension than the imaging finding of ventriculomegaly.

Materials and Methods

N=24 cranial MRIs of n=12 consecutive children with hydrocephalus were retrospectively included from a database of our institution if MR imaging was available at two points of time: a) when the child was well and there was no evidence of intracranial hypertension and b) when there was definitive intracranial hypertension as retrospectively proven by follow-up evaluation and intraoperative results of shunt revisions (gold standard). The group consisted of seven boys and five girls, age 0 - 18 years. All scans included regular T2w axial and coronal images and phase-contrast venography on a 1.5 T MRI using a VENC of 15 cm/sec. Two criteria were compared: 1) "Hydrocephalus" and 2) "Significant Dural-Sinus

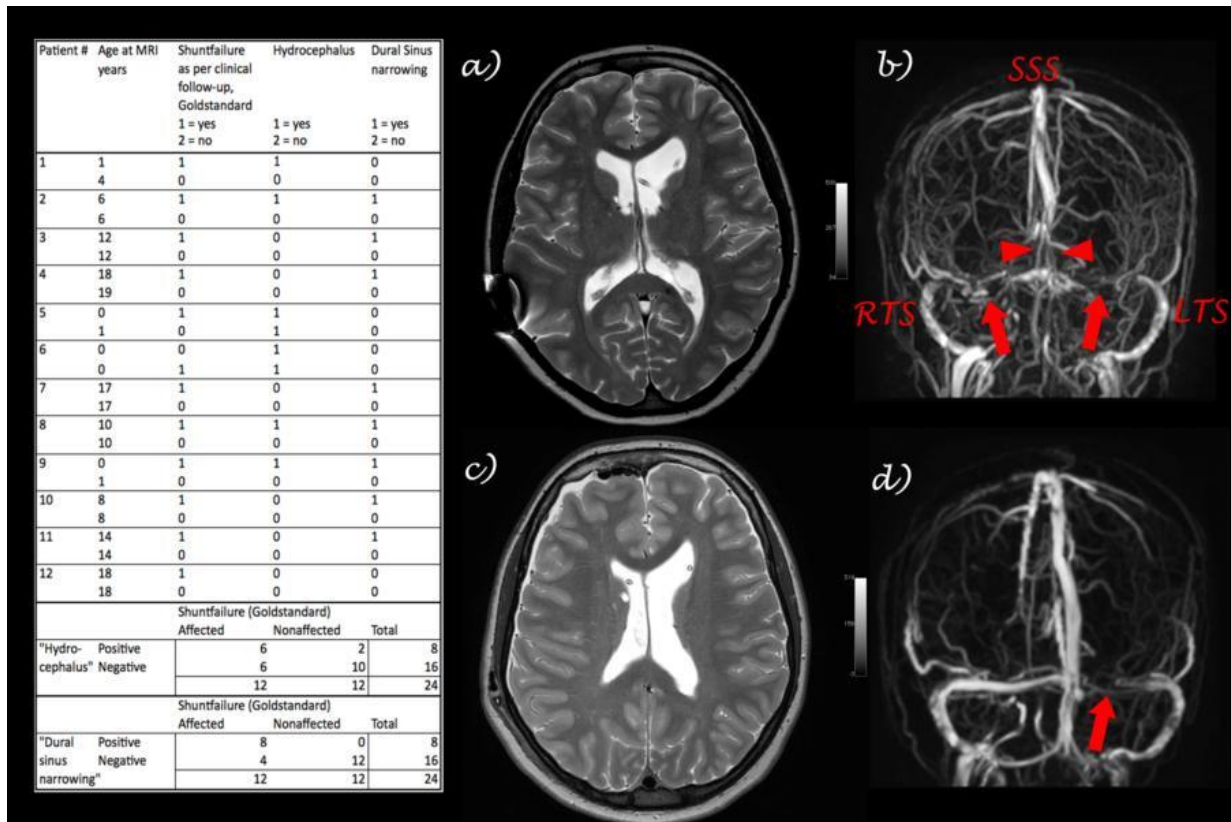
Narrowing". First, a neuroradiologist with more than 10 years experience in MRI and pediatric neuroimaging (AR) assessed T2w images with regard to the presence or absence of hydrocephalus. Second, abnormalities of the superior sagittal and the right and left transverse sinuses were noted as follows: Narrowing was defined as a focal reduction in diameter to $\leq 50\%$ compared to the normal appearing adjacent sinus or when flow signal was absent or severely compromised within the sinus. To be significant, all three sinuses had to be affected. Otherwise, MR venography was considered to be normal. The reader was blinded with respect to patient data and time of imaging and T2w images were interpreted separately from venous imaging. Results were analyzed as per two-by-two contingency tables and significant difference between methods were assessed using the paired Cochran Q test. Significance was assumed with $p < 0.05$.

Results

Narrowing of all three dural sinuses was seen in eight of 12 cases with intracranial hypertension/shunt failure with no false positives (table). Significant dural-sinus narrowing was never seen in cases when children were well. There were four false negatives. This resulted in sensitivity of 0.67 and specificity of 1.0. Significant hydrocephalus as subjectively assessed was seen in six of 12 cases with intracranial hypertension/shunt failure and there were two false positives. Ventricle size was normal or small in 10 of 12 cases when children were well, but ventricle size was also normal or small in six cases when intracranial hypertension was present. This resulted in a sensitivity of 0.5 and specificity of 0.83. PPV and NPV were 1.0 and 0.75 for "Significant Dural-Sinus Narrowing" and were 0.75 and 0.63 for "Hydrocephalus", respectively. Results differed significantly between the test methods ($p = 0.01$). If we considered significant dural sinus narrowing to be present when 2 or more sinuses were narrowed as opposed to all three sinuses, sensitivity increased from 0.67 to 0.92, but specificity decreased from 1.0 to 0.67. An example is given in the figure: 17-year-old girl with a history of posthemorrhagic hydrocephalus and two ventriculo-peritoneal shunts inserted. A first MRI is done on an urgent basis when she presents with severe headache and vomiting. Ventricle size is within normal limits (a). MR venography (b) shows severe narrowing of the inferior aspect of the superior sagittal sinus (SSS, arrowheads) and of the left and right transverse sinuses (LTS, RTS, arrows) with almost no flow-signal. This is considered significant dural-sinus narrowing. After shunt revision and improvement of symptoms, ventricle size has not changed significantly (c). MR venography demonstrates normalization in the appearance of the SSS and RTS. Residual narrowing is seen within the LTS (d).

Conclusions

Dural-sinus narrowing in children with hydrocephalus on phase-contrast MR venography more reliably predicted intracranial hypertension/shunt failure than the presence of hydrocephalus. Dural-sinus narrowing as a diagnostic criterion has, to our knowledge, never been systematically investigated in this group of patients, but is known to correlate with idiopathic intracranial hypertension in adults. In the routine imaging of shunted hydrocephalus, MR venography can easily be added to the imaging protocol and might significantly add to the value of MRI in children (and adults) who are critically at risk. The study is limited by retrospectivity and the number of cases.



(Filename: TCT_O-84_ASNRpicturefile.jpg)

O-85

3:28PM - 3:35PM

Time dependent changes in extra-axial structures of term newborns: A prospective single center transfontanelle ultrasound study.

M Adin¹, M Soyoral

¹Tatvan Can Hospital, Turkey, Batman, Turkey

Purpose

The purpose of this prospective transfontanelle ultrasound study was to demonstrate normal values of CSF-filled extra-axial spaces (subarachnoid space) and ventricles of term newborns that were born via normal vaginal delivery and have had no history of comorbid pathologies or an abnormal course of pregnancy in order to help in distinguishing mainly from hydrocephalus, and thus preventing unnecessary interventions and imaging studies.

Materials and Methods

One hundred newborn subjects born via normal vaginal delivery (NVD) and normal for gestational ages (born at >37 and < 42 weeks of gestation), uneventful prenatal course and no maternal predisposing factors and/or family history of hydrocephalus or serious genetic disorders were recruited. Subjects were scanned in their first week of life, mostly on the first few days. Body weight (at the time of birth and ultrasound examination), length, and head circumference were measured. Ultrasound examinations were performed in supine position with examinee's face positioned in midline with help of assistant health personnel, to grant a virtual line passing through nose and mid sternum. The same radiologist performed all ultrasound evaluations using the same machine and transducer (Hitachi Medical Systems, Tokyo, Japan). A transverse scan through anterior fontanel with 5–13 MHz linear transducer (Hitachi Medical

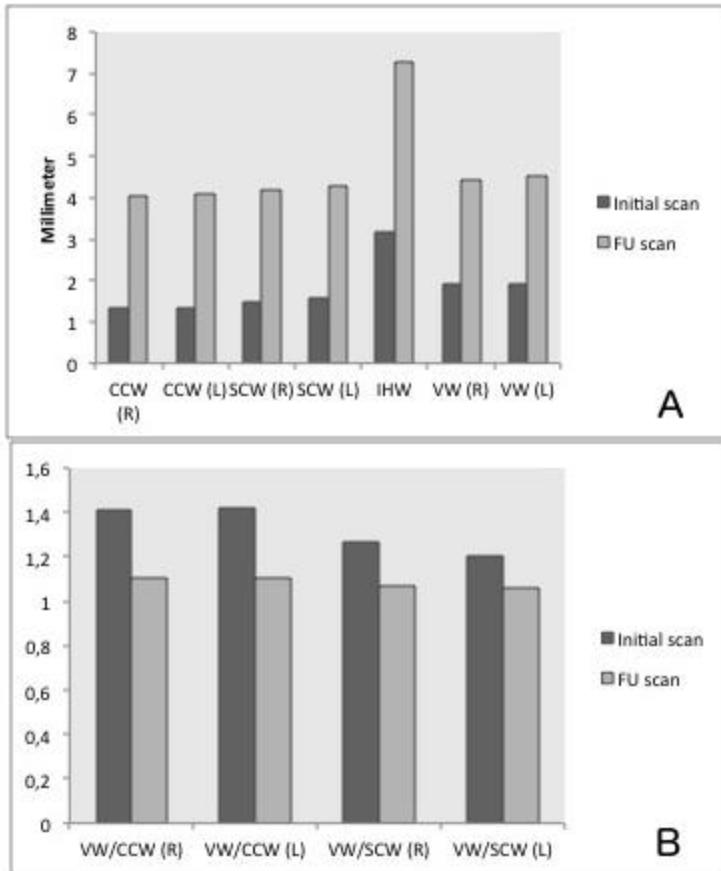
Systems, Tokyo, Japan) obtained through the level of foramen Monroe. On coronal plane, calipers were placed to measure sagittal sinus to cortex distance (SCW), cortex to cranium distance (CCW) and interhemispheric distance (IHW). These were repeated on both sides. Widths of frontal horns of lateral ventricles were also noted. Subjects were rescanned after two months for the measurement of the same metrics. Statistical analyses were performed using Student's t tests for testing differences in means of both genders, and right and left sides of the same individual. The relationship between subjects' age, height, weight and head circumference and width of the subarachnoid spaces and ventricle widths were determined using linear regression analyses.

Results

Included were 46 female and 54 male subjects in the study (all caucasian). Mean age at initial scan was 4.9 days (range: 1-25, Std Dev: 6.2). Mean values for head circumference, weight, and height were, 34.5 cm (range: 33-38, Std Dev: 1.14), 3.4 kg (range: 2.5-4.2 Std Dev: 0.45), 50.3 (range: 48-56 Std Dev: 1.95), respectively. At the follow-up scan, the same measurements were respectively as following; 38.6 cm (range: 33-43, Std Dev: 5.91), 5.7 kg (range: 3.2-8 Std Dev: 0.95), 58.3 (range: 52-64 Std Dev: 3.11). Sonographic intracranial measurements are shown in Figure 1A to better reflect the time-dependent changes in the widths of subarachnoid spaces. There was no statistically significant difference between measurements of subarachnoid widths in both genders (p value: 0.22). Also statistical analysis showed no difference between widths of right and left sides (p value: 0.42). Linear regression analysis showed significant time depended positive correlation between increase of weight, height and head circumferences and that of subarachnoid space measurements. Among the measured subarachnoid spaces, CCW showed the highest proportional increase while IHW had the least proportional increase during the follow-up period. The changes in ratios of VWs to CCWs and SCWs are presented in Figure 1B. At the follow-up scan, there was a consistent decreasing ratio of VWs to CCWs and VWs to SCWs. No statistically significant difference found between interval decrease in the ratios for right and left sides. A decreasing trend of these ratios over time may show a slower acceleration in ventricle size increase over time when compared with other extra-axial CSF space widths.

Conclusions

In conclusion, we presented the normal metrics of extra-axial CSF space measurements of term newborns with normal pregnancy course and no comorbidities or family history of pertinent disorders. In our present study, the ratio of ventricle widths to other measured CSF spaces was consistently decreasing over time, and these ratios may be used in determination of abnormal entities of these anatomical regions like hydrocephalus (1-3).



(Filename: TCT_O-85_Figure_1.jpg)

O-86

3:35PM - 3:42PM

Structural MRI Brain Findings in a Group of Typically-Developing Adolescents Enrolled in the Adolescent Brain Cognitive Development (ABCD) Cohort

Y Li¹, R Desikan¹, T Jernigan², R Dougherty³, L Sugrue¹

¹University of California San Francisco, San Francisco, CA, ²University of California San Diego, San Diego, CA, ³Stanford University, Stanford, CA

Purpose

To catalog the incidence of various findings, both normal variants and pathologic conditions, on structural MRIs of volunteer, typically developing, children without significant intellectual or behavioral disabilities, enrolled in a longitudinal study on brain development.

Materials and Methods

We evaluated 4250 structural brain MRIs of normal, healthy adolescent children age 9-11. Studies consisted of 3-D T1 and 3-D T2 sequences, reformatted in three plans, and were anonymized to patient demographics. One of three board certified radiologists rated each study on a scale of 0-4: 0 – Study cannot be read; 1- No abnormal findings; 2 – Normal anatomic variant or common incidental finding; 3 – Consider routine referral; 4 – Consider immediate referral. For all categories 2-4, comments were provided regarding the details and significance of the abnormality.

Results

Of the 4250 studies, 51 were classified category 0 (1.2%); 3560 category 1 (83.8%); 475 category 2 (11.1%); 155 category 3 (3.6%); and 9 category 4 (0.2%). Common category 2 findings included pineal

cysts, arachnoid cysts, developmental venous anomalies, mastoid effusions and significant sinus disease. Common category 3 findings included larger pineal cysts or cavum vellum interpositum cysts at risk for causing hydrocephalus, periventricular nodular heterotopias (PVNH), findings concerning for demyelinating disease or low grade gliomas. Overall, 36 cases of PVNH were identified, constituting an incidence of 0.8% in this population of typically developing children. Category 4 lesions included large thalamic or suprasellar masses, hydrocephalus, diffuse white-matter abnormality, and craniocervical junction instability.

Conclusions

Through the evaluation of structural brain MRIs of typically developing adolescents without significant intellectual or behavioral abnormalities, we have determined the incidence rate of various findings in a large cross-sectional population of normal individuals. Of particular interest, we identified PVNH in 0.8% of these subjects, a surprisingly high incidence of this developmental abnormality of neuronal migration whose incidence in the general population was previously unknown.

O-87

3:42PM - 3:49PM

CNS Involvement in Patients with Overgrowth Syndromes

M Jurkiewicz¹, F Lu¹, A Pollock¹, T Feygin¹

¹*Children's Hospital of Philadelphia, Philadelphia, PA*

Purpose

Numerous entities, which may manifest as a paraspinal lesion, include a spectrum of sporadic overgrowth neurocutaneous disorders, rare congenital diseases of unclear etiology with highly variable phenotypes. The classification of these disorders is not complete and the literature, describing this pathology, mainly arises from pathology/plastic surgery fields. These paraspinal lesions usually consist of a combination of lipomatous and vascular (arterial, venous and lymphatic vessels) tissue, and occasionally of peripheral nerves hypertrophy. They may severely compromise the cord. Currently, the prognosis for a child with these lesions depends on age at diagnosis and symptoms severity, with earlier detection and earlier treatment resulting in better outcomes. We review clinical presentation and imaging features of these diseases in patients of different ages, ranging from fetus to adult. The illustrated cases include Congenital Lipomatous Overgrowth, Vascular Malformations, Epidermal Nevis, Spinal/Skeletal Anomalies/Scoliosis (CLOVES) (1), Epidermal Nevus Syndrome (ENS) (2), and Parkes Weber Syndrome (3).

Materials and Methods

Prenatal (when available) and postnatal MRI as well as clinical information in patients with suspected overgrowth syndromes were reviewed.

Results

Eight patients with CLOVES, two patients with ENS and one patient with Parks Weber syndromes presenting with paraspinal masses and some degree of hemihypertrophy were identified. The age at presentation was in a range from 26 weeks of gestational age to 37 years. Variable degrees of compression of the spinal cord, conus medullaris, and/or cauda equina were identified secondary to vascular enlargement, soft tissue encroachment, neuronal hypertrophy or epidural lipomatosis in seven patients. Four patients had no encroachment on the spinal canal.

Conclusions

Familiarity with imaging and clinical features of overgrowth syndromes will allow the radiologist to raise this as a potential diagnosis, help initiate appropriate workup, and direct and monitor treatment. Spine MRI should be performed in all patients with overgrowth syndromes due to the potential for spinal cord compromise.

O-88

3:49PM - 3:56PM

Oral Presentations & Excerpts

Abnormal foramen magnum as a novel imaging feature in Joubert syndrome

M Shapira Rootman¹, C Raybaud¹, P Shannon², G Yoon¹, D Chitayat², S Blaser¹

¹*The Hospital for Sick Children, Toronto, Ontario, Canada*, ²*Mount Sinai Hospital, Toronto, Ontario, Canada*

Purpose

Primary ciliopathies are heterogeneous disorders resulting from primary cilia dysfunction. Primary cilia are microtubule-based organelles projecting from the cell surface and known to be involved in key developmental pathways. The prototype is Joubert syndrome, whose distinctive imaging feature is the 'molar tooth' (Fig. a) configuration of the brainstem. Keyhole-shaped foramen magnum results from persistent midline opisthion cleft due to incomplete fusion of the supraoccipital bone ossification centers. This morphology is described in the rare ciliopathy hydroletharus syndrome. Defects of the posterior foramen magnum arc are also present in Meckel-Gruber syndrome. To the best of our knowledge, abnormal foramen magnum is only rarely described in Joubert. The main purpose of this study is to evaluate the shape of the foramen magnum in Joubert ciliopathy. Potentially, the coexistence of this feature could assist in the radiological identification of these patients, including the fetus.

Materials and Methods

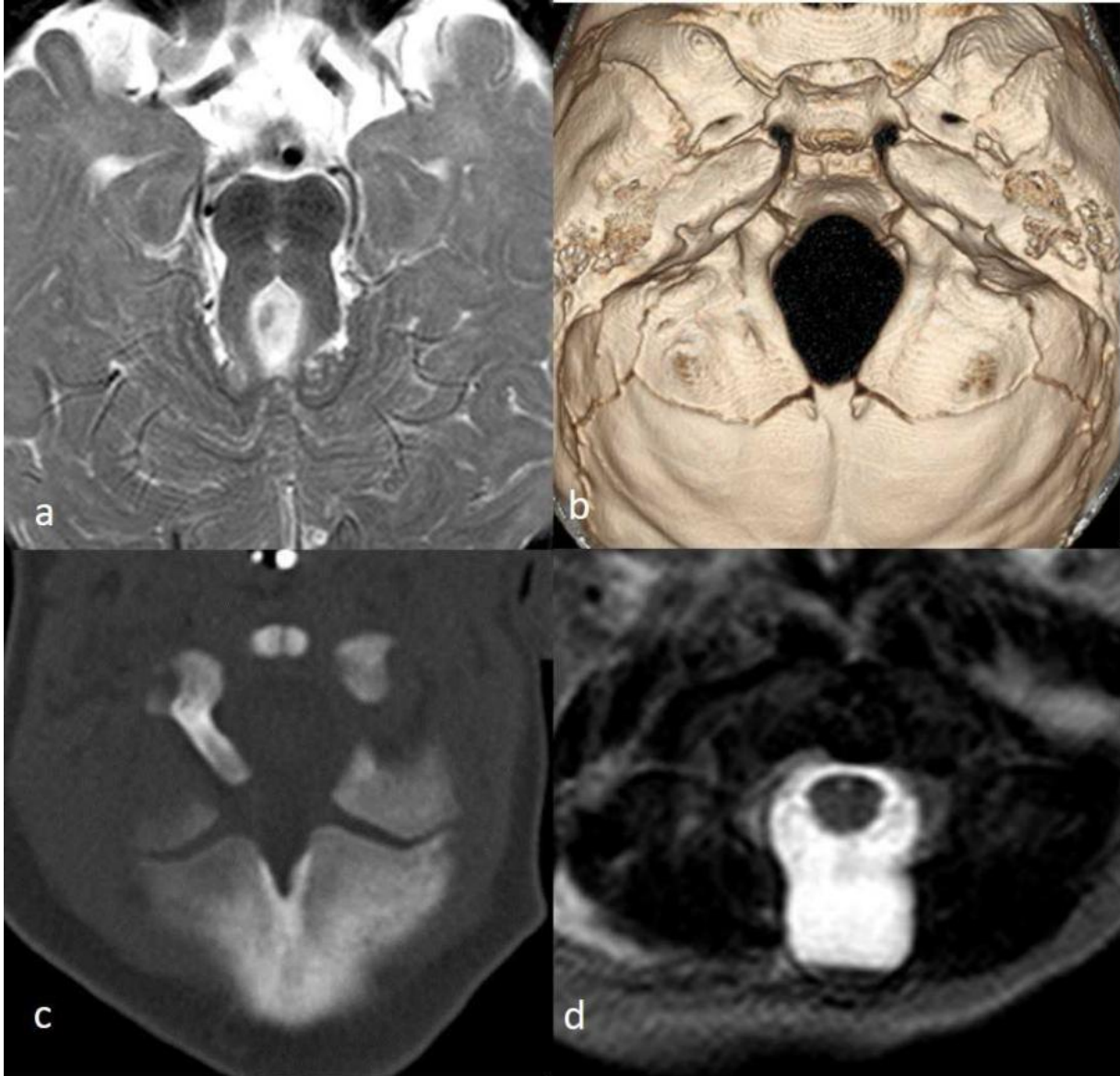
Serial CT and MRI scans of patients with confirmed molar tooth deformity were identified and imaging (+/-) genetic testing were reviewed. Foramen magnum in each was evaluated by two pediatric neuroradiologists (in consensus) and categorized as 'normal' ("shield" shaped, Fig. b) or abnormal ("keyhole" Fig. c, "diamond/rhomboid" or foramen magnum meningocele, Fig. d). The prevalence of foramen magnum abnormalities in patients with molar tooth deformity was calculated.

Results

To date, MR and CT scans of 61 patients including six fetal cases with molar tooth deformity were reviewed. Of these, 24 patients (39%) exhibited shield configuration of the foramen magnum, 17 (28%) had a diamond/rhomboid shaped foramen magnum, 12 (20%) had keyhole configuration and six (10%) had foramen magnum meningocele. Two cases were indeterminate due to chosen imaging parameters (slice thickness).

Conclusions

Abnormal configuration of the foramen magnum represents a novel imaging finding in Joubert syndrome. It was noted to be particularly useful in increasing confidence in the diagnosis in fetal cases prior to genetic testing.



(Filename: TCT_O-88_foramenmagnumjoubert.jpg)

O-89

3:56PM - 4:03PM

T2 Hypointensity Can Reliably Identify the Primary Motor and Somatosensory Cortices in Children

M Jurkiewicz¹, W Gaetz¹, T Roberts¹, E Schwartz¹
¹Children's Hospital of Philadelphia, Philadelphia, PA

Purpose

Reliable identification of eloquent cortices, including the perirolandic regions, is crucial for presurgical planning and prognosis in patients with epilepsy, neoplasia and vascular malformations. Perirolandic cortex has been consistently shown to be T2 hypointense in the normal brains of neonates and infants up to the age of six months (1, 2) as well as adolescents and adults (3). The changes in signal intensity in the perirolandic gyri are thought to reflect the degree of myelination as well as more advanced development

of the neurons (2). We set out to determine if primary motor and somatosensory cortices could be consistently identified in children based on signal from T2-weighted imaging.

Materials and Methods

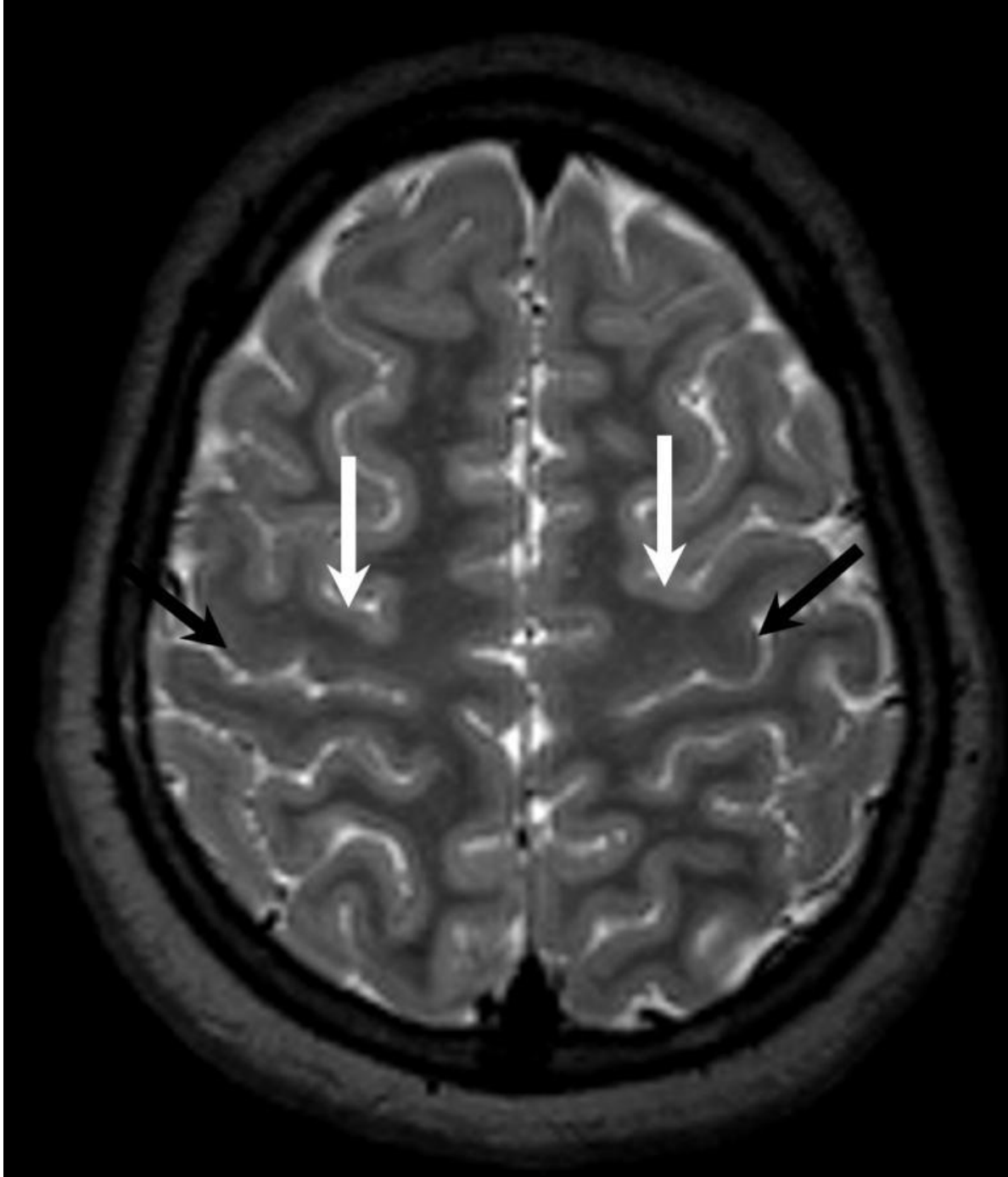
Retrospective review of 78 patients (37 female, ages: 5 months-18 years) referred for clinical magnetoencephalography (MEG), including functional mapping of the primary motor and/or somatosensory cortex. MEG functional localizations were correlated with axial T2-weighted brain images. Signal intensity of each perirolandic cortex, as identified by gyral morphology and functional mapping results, was graded with respect to signal of the cortex lining the ipsilateral precentral sulcus (hyper, iso, or hypointense).

Results

Studied were 144 hemispheres in 73 patients. Of those, 139 hemispheres showed clear perirolandic T2 hypointensity: 71/74 (96%) in the right hemisphere and 73/75 (97%) in the left hemisphere (black arrows on Figure 1 compared to white arrows denoting cortex of other regions).

Conclusions

Hypointense cortex on T2-weighted imaging in the perirolandic regions can reliably identify these eloquent regions in children of all ages undergoing clinical brain MRI and T2 signal assessment is a valuable addition to morphologic evaluation for localizing primary motor and somatosensory cortices.



(Filename: TCT_O-89_Bilat2warrows.jpg)

O-90

4:03PM - 4:10PM

Abnormal Cortical and Subcortical Cerebral Morphology in Neurofibromatosis Type 1: A Potential Novel Biomarker for Disease Pathophysiology and Progression

M Barkovich¹, C Tan¹, L Sugrue¹, R Desikan¹, A Barkovich¹
¹University of California, San Francisco, San Francisco, CA

Oral Presentations & Excerptas

Purpose

Characteristic T2 hyperintensities in the deep grey nuclei and brainstem in children with Neurofibromatosis Type 1 (NF1) are a minor diagnostic criteria for the disease and usually resolve by the second decade; their etiology remains poorly understood. Quantitative evaluation of changes in NF1 brain morphometry may reveal other imaging manifestations of the disease and provide biomarkers for alterations in NF1 associated molecular pathways at different developmental stages.

Materials and Methods

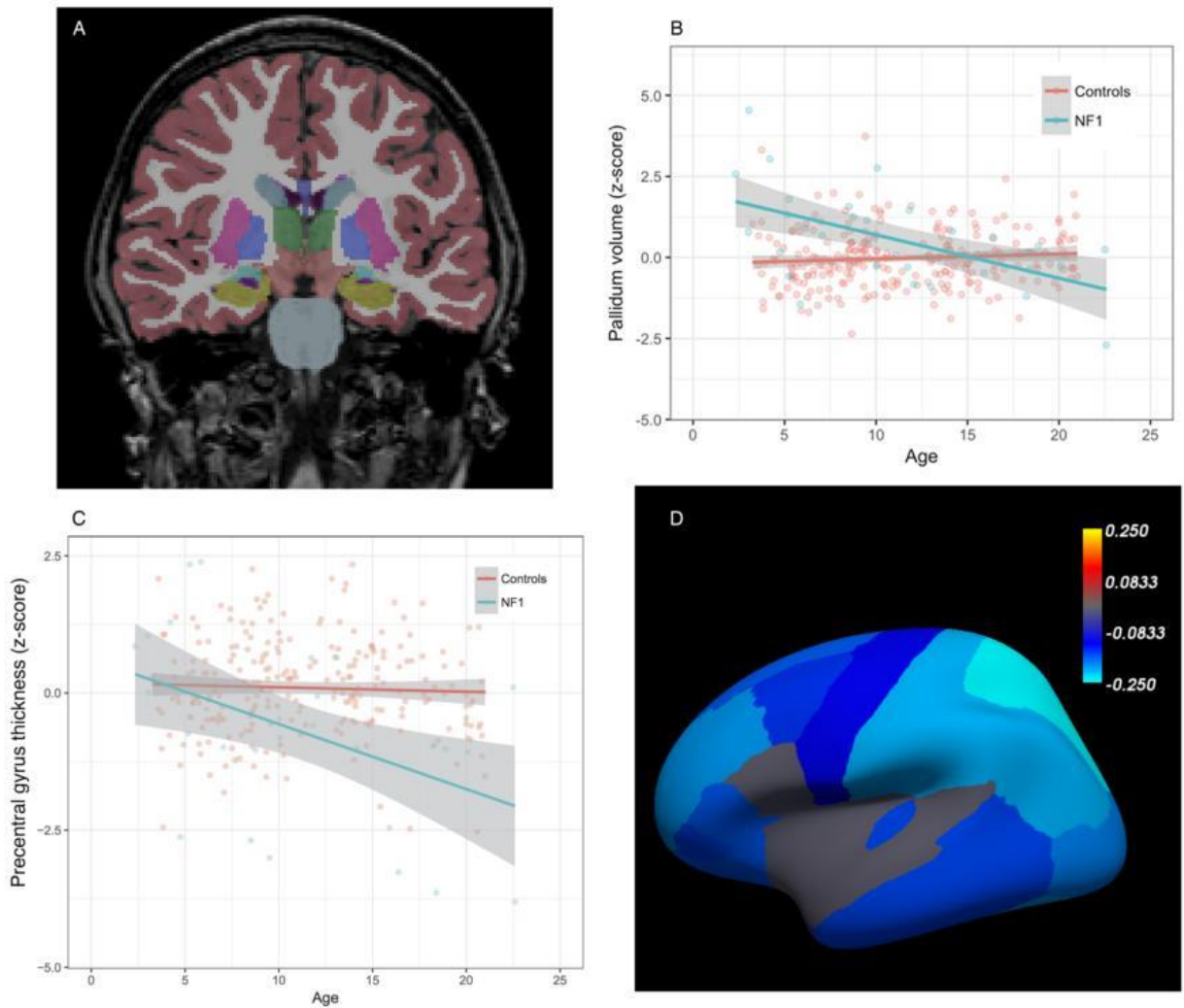
Subcortical volumes and cortical thicknesses were quantitatively assessed in 32 children with NF1 and in 245 age- and sex-matched normal controls across 10 subcortical and 34 cortical regions of interest (ROIs). Using linear models and correcting for intracranial volume, quantitative differences between subcortical volumes and cortical thicknesses in NF1 patients and controls were assessed, covarying for age and gender and correcting for multiple comparisons. Regional associations in cases and controls were further assessed using hierarchical cluster analysis and partial correlations.

Results

NF1 patients have larger subcortical volumes, most notably of the hippocampi, amygdalae, ventral diencephalon and thalami. In the thalami and pallida, subcortical volumes appear to decrease with increasing age. NF1 patients have significantly thicker cortices in the occipital lobe and significantly thinner cortices in portions of the frontal lobe. In 22 cortical ROIs, cortical thickness in NF1 patients decreases with increasing age. In hierarchical cluster analysis, cortical thickness and subcortical volume have a distinct pattern of regional spatial correlation in NF1 patients relative to controls.

Conclusions

Children with NF1 have robustly larger volumes of the same subcortical regions where characteristic NF1 signal abnormalities occur and these volume differences, like the signal abnormalities, may also be age dependent. In addition, NF1 children display significant, apparently age-dependent, regional differences in cerebral cortical thickness, with thinner frontal cortices and thicker occipital cortices. These morphologic differences could provide a biomarker for disease pathophysiology, but further study of the temporally dynamic manifestations of NF1 is needed.



Subcortical volumes (B) and cortical thickness (C) in NF1 patients with increasing age. Heat map of slope of age versus cortical thickness in NF1 patients (D) painted over a semi-inflated surface rendering of the brain (showing the lateral surface). Regions without significant effects are grey. Note that the slopes are all negative.

(Filename: TCT_O-90_fig.jpg)

O-91

4:10PM - 4:17PM

Neurofibromatosis type 1 patients with optic pathway gliomas: Accuracy of non-contrast MR in imaging surveillance

M Shapira Rootman¹, P Krishnan¹, N Singh², S Gerrie², L Figueiredo Nobre², M Shroff¹

¹The Hospital for Sick Children, Toronto, Ontario, ²N/A, N/A

Purpose

Neurofibromatosis 1 (NF1) patients are at risk for developing intracranial low-grade tumors, most notably optic pathway gliomas (OPG). Early detection of OPG could improve visual outcomes. Serial MR Studies with contrast material is the standard protocol to monitor these patients. Recent concerns related to gadolinium deposition in the central nervous system have been discussed extensively in recent literature. In this context, alternative MR imaging strategies aimed at reduced usage of contrast material are being

Oral Presentations & Excerptas

actively sought, especially in the pediatric population. The aim of the study is to evaluate the relative diagnostic accuracy of serial noncontrast MR studies for imaging surveillance of OPG in NF1 patients.

Materials and Methods

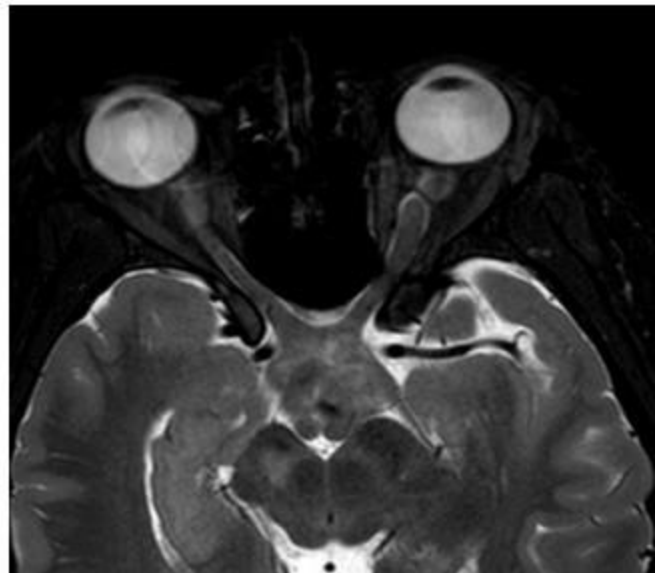
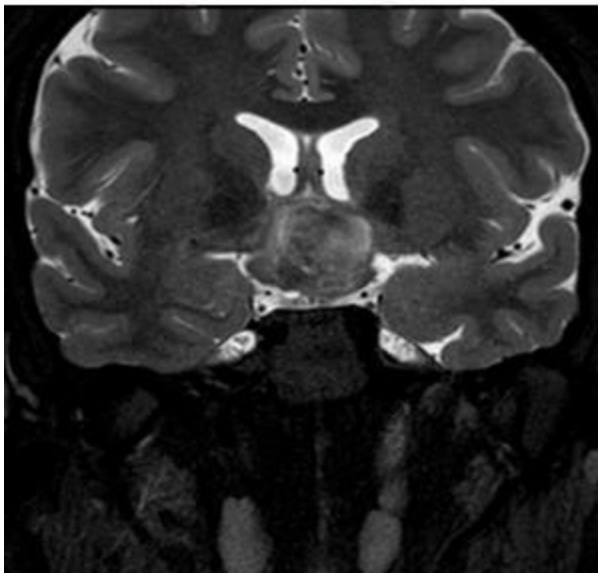
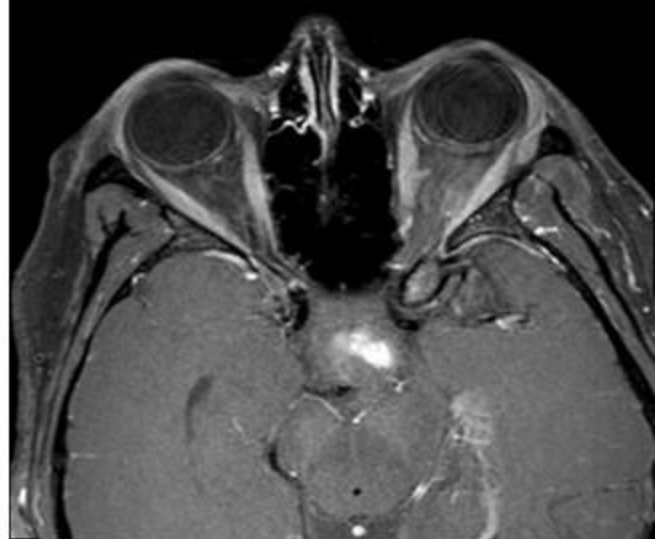
In this retrospective study of 102 NF1 patients with OPG, serial MR studies of the brain and orbits were reviewed by two readers. For each patient, first baseline MR in addition to three consecutive most recent follow-up studies were analyzed. One reader was blinded to the postcontrast MR sequences. Each lesion was evaluated for its location, size and interval alteration (stable, reduced or progression) according to both the RANO criteria and the reader's subjective assessment. Statistical analysis was performed to evaluate the diagnostic yield of noncontrast MRI as a reliable tool in the follow-up studies of OPG.

Results

One-hundred-two patients with NF1 with OPG were included in the study. The optic pathway glioma involved the optic nerves in 95 cases (93%), optic chiasm in 59 cases (57%) and optic tract in 42 cases (41%). There was a high degree of concordance (80%) between both the readers evaluating the overall data set using RANO criteria and subjective analysis with 100 % agreement for assessing progression in the subset.

Conclusions

Our data suggests noncontrast serial MRI studies are a reliable substitute with high degree of accuracy for imaging surveillance and disease follow up of NF1 patients with OPG.



(Filename: TCT_O-91_abstractimage.jpg)

O-92

4:17PM - 4:24PM

Subependymal Giant Cell Astrocytoma Size Measurement In Tuberous Sclerosis Complex: Non-Contrast versus Contrast-Enhanced 3D T1-Weighted MRI

B Hill¹, J Gadde², V Allen³, D Wolf², S Palasis²

¹Emory University, Atlanta, GA, ²Emory University and Children's Healthcare of Atlanta, Atlanta, GA, ³Children's Hospital of Atlanta, Atlanta, GA

Purpose

The 2012 International Tuberous Sclerosis Complex Consensus Group recommended MRI with and without contrast every 1-3 years until age 25 years for all tuberous sclerosis complex (TSC) patients. However, the added value of intravenous contrast in this setting is not clear; according to the consensus group, all growing subependymal lesions should be considered subependymal giant cell astrocytoma (SEGA).

Oral Presentations & Excerptas

Materials and Methods

Thirty-nine MRI examinations from 12 established TSC patients with known SEGA were retrospectively reviewed for all caudothalamic groove lesions greater than 1 cm. Lesions were measured in two planes on noncontrast axial 3-D T1WI and postcontrast 3-D T1WI in a randomized fashion by two attending pediatric neuroradiologists. Differences in lesion measurement were compared to zero using a one sample t-test.

Results

Comparing noncontrast to contrast-enhanced 3-D T1-weighted MRI, reader A measured lesions approximately 1 mm larger in long axis without contrast; there was no difference in long axis measurements for reader B. Both readers measured lesions approximately 0.5 mm larger in short axis without contrast. Comparing reader A to reader B, reader A measured lesions approximately 1-2 mm larger than reader B without contrast, and approximately 0.5-1 mm larger with contrast. All results were statistically different from zero ($p < 0.05$).

Conclusions

Caudothalamic groove lesions may appear minimally larger on noncontrast 3-D T1WI when compared to contrast-enhanced 3-D T1WI. Resulting differences in lesion measurement may not be clinically meaningful, however, especially given interobserver variability. Benefits of noncontrast MRI include decreased study acquisition time and decreased parental concerns of gadolinium deposition.

Monday, June 4, 2018

3:00PM - 4:30PM

Parallel Paper Session: Spine Interventions

O-93

3:00PM - 3:07PM

CT Guided Percutaneous Synovial Cyst Rupture Using a 11G Jamshidi Needle: Early Experience and Results of a Novel Therapeutic Technique.

S Islam¹, D Johnson²

¹Imperial College London, London, United Kingdom, ²St. Georges NHS Foundation Trust, London, United Kingdom

Purpose

Synovial cysts of the lumbar spine are an increasingly reported cause of radiculopathy, lower back pain, and neurologic deficits. Percutaneous treatment offers a minimally invasive alternative to potentially high-risk surgery. Percutaneous techniques involve imaging to guide a small calibre needle into the facet joint. In our experience this leads to a high rate of reoccurrence requiring further surgical intervention. We have recently tried a novel approach using a large bore needle under CT guidance in the hope of achieving increased disruption of the fibrocartilaginous wall and reducing recurrence. The purpose of the study was to review the early results of percutaneous synovial cyst treatment using a 11G Jamshidi needle.

Materials and Methods

Nine patients (4M, 5F; mean age 68.2 years) underwent percutaneous lumbar synovial cyst rupture through a translaminar approach using a 11G Jamshidi needle under CT guidance. Following rupture as demonstrated by contrast injection, 80mg Depomedrone + 1ml 0.5% Bupivacaine were injected locally into the rupture bed. The procedure was performed under sedation (Midazolam and Pethidine). Patients were followed up for six months post procedure.

Oral Presentations & Excerpts

Results

At short term follow up (six weeks), 8/9 patients had satisfactory relief of symptoms, with only one patient requiring surgery. At long-term follow-up (six months), five patients remained asymptomatic. Three patients required a single repeat percutaneous procedure, of which two went on to have surgery. There were 0 overnight stays, and 0 complications related to the procedure.

Conclusions

There is currently no gold standard technique for percutaneous synovial cyst treatment and the previously published outcome data is based on using small 20/22G needles. The number of patients requiring future surgery in these studies varies from 10-55% (1). This is the first time a large bore needle has been used to achieve cyst rupture/disruption. In our small patient cohort, we have demonstrated that cyst rupture using a large bore needle is safe and effective.

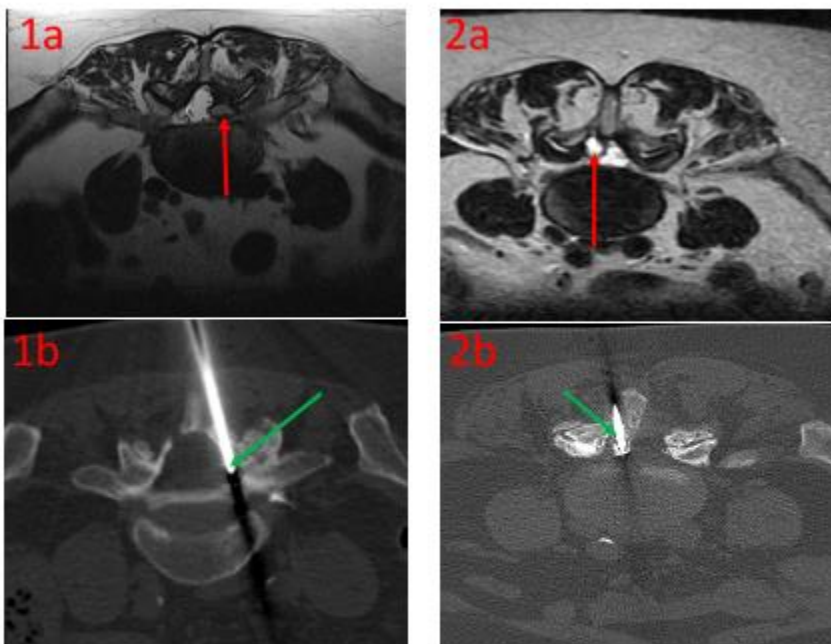


Figure 1- 64 YO female, with a large left L4/L5 synovial cyst with impingement on the left lateral recess and theca (a). The cyst was ruptured through a translaminar approach using a 11G Jamshidi needle with no recurrence of symptoms at 6 months (b).

Figure 2- 66 YO female with a right L4/L5 synovial cyst causing neural impingement (a). This was ruptured using a 11G Jamshidi needle (green arrow).

(Filename: TCT_O-93_ASNR.jpg)

O-94

3:07PM - 3:14PM

Implementation of Evidence-based Appropriateness Guidelines for Epidural Steroid Injection for Patients with Chronic Low Back Pain

L Shah¹, T Hutchins¹, S Johnson², Y Anzai¹

¹University of Utah, Salt Lake City, UT, ²University of Utah School of Medicine, Salt Lake City, UT

Purpose

Chronic low back pain (LBP) is a common problem and has resulted in rapidly increasing referrals for epidural steroid injections (ESI) at our affiliated Veterans' Administration hospital. This mirrors trends

elsewhere, particularly with the opioid epidemic as referring clinicians seek alternative means of pain management. No single treatment is a panacea for LBP, and ESI, which is not without risk, may be over-utilized without appropriate management with more conservative methods. In order to better serve the population that would benefit from ESIs, decrease unindicated referrals, and minimize adverse outcomes, we implemented evidence-based guidelines for spine injection referral.

Materials and Methods

Multidisciplinary evidence-based guidelines were implemented in 2014, including first-line six-weeks of physical therapy and oral medications. Two spine interventionalists reviewed each patient's imaging and clinical history prior to scheduling to determine the appropriateness of the requested procedure. If patients still had pain after a trial of three ESIs in the same location in one year, they were referred to Physical Medicine and Rehabilitation (PM&R) or Spine Surgery for further evaluation. Data was collected from before and after implementation and patient-level changes in BMI, opioid use, and multispecialty care referral patterns were compared.

Results

Before protocol implementation, approximately 1500 ESIs were performed per year (2014). ESIs decreased to 1350 in 2015 (10% reduction) and to 550 in 2016 (63% reduction). Frequency of injections decreased in 72% of patients. Referrals to PM&R and Neurosurgery increased (11.7%, $p=0.003$ and 2.6%, $p=0.04$, respectively). PT referral increased 77% for those who had not received it prior to 2014. Among patients on opioids, 69% decreased or discontinued use. BMI decreased in 64% of patients.

Conclusions

Implementation of an evidence-based protocol for ESI referral resulted in a significant decrease in inappropriate spine procedures, more comprehensive pain management, and standardized care for patients with chronic LBP.

Frequency of injections	Number of patients	Percent (%)
Decrease	54	72
No change	10	13
Increase	11	15
Total	75	100

Change in physical therapy	After 2014	
Before 2014	No (%)	Yes (%)
No (%)	5 (23)	17 (77)
Yes (%)	16 (30)	37 (70)
Total (%)	21 (28)	54 (72)

Opioids	Discontinued (%)	Decreased dose (%)	Same (%)	Increased dose (%)
No	8 (11)	0 (0)	6 (8)	0 (0)
Yes	29 (39)	13 (17)	16 (21)	3 (4)
Total	37 (50)	13 (17)	22 (29)	3 (4)

(Filename: TCT_O-94_UpdatedESItablesv2.jpg)

O-96

3:21PM - 3:28PM

Can RF Ablation followed with PMMA augmentation for Osteolytic Spine Metastasis provide both Pain relief and Structural stability?

S Lee¹, N Oren¹, S Ali¹, E Ramos², S Pitroda¹, J Patel¹

¹*The University of Chicago, Chicago, IL*, ²*University of Chicago Medical Center, Chicago, IL*

Purpose

Radiofrequency Ablation and Vertebral Augmentation (RFVA) has been regarded as a reasonable option for painful spinal metastatic lesions for symptomatic relief. However, the role of the RFVA for spinal structural stability, especially in osteolytic metastatic vertebral lesions has rarely been evaluated.

Materials and Methods

A retrospective analysis of 25 vertebral bodies in 21 patients (M:F=11:10, mean age=61.4 years) who were treated with RFVA due to painful osteolytic metastatic vertebral compression fractures was performed. Pre and postprocedure pain degree was recorded using visual analog score (VAS). Preprocedure Spine instability Neoplastic Score (SINS) per index vertebra was calculated. Postprocedure structural stability was evaluated by assessing for worsening height loss or osseous retropulsion of the index vertebrae on follow-up imaging studies.

Results

Etiologies of metastases included multiple myeloma (n=5/21, 23.8%), breast cancer (n=4/21, 19%), nonsmall cell lung cancer (n=3/21, 13%), renal cell carcinoma (n=3/21, 13%), and others histologies (n=6/21, 29%). Involved vertebral bodies were seen from T7 to S2 with the most frequent location of T12 (n=6, 24%). The mean degree of compression fracture and mean SINS were 36.9% and 9.84 (range: 8 to 14), respectively. Postprocedure pain reduction was seen in 85.7% (n=18/21) and the mean degree of pain reduction was 60.31%. Follow-up imaging (median=144 days, range=21 to 540 days) was available in 13 patients (n=21, 62%). Postprocedural vertebral stability was seen in 11 patients (n=11/13, 84.6%). The remaining two patients showed progressive retropulsion due to local tumor growth, one of which required decompression surgery to relieve unilateral nerve root compression.

Conclusions

RFVA demonstrated postprocedural pain reduction and structural stability in vast majority of patients. RFVA could be considered as an alternative option in patients with painful osteolytic spinal metastasis with indeterminate stability based on the SINS.

O-97

3:28PM - 3:35PM

When is too long? Time course for enhancement in post discectomy patients.

L Mitchell¹, T Biega²

¹*Tripler Army Medical Center, Honolulu, HI*, ²*Landstuhl Regional Medical Center, APO AE, Germany*

Purpose

To establish a time-line for how long after discectomy patients may have enhancement

Materials and Methods

Retrospective review of all MRI of the lumbar spine with and without gadolinium from a single institution RIS over the past five years. All studies reviewed by a board-certified radiologist with certification of additional qualification in neuroradiology. Enhancement scored as present at operative site or absent.

Results

RIS review yielded 563 possible studies. After excluding studies with surgical hardware, unknown operative date, or performed for infection work up, 274 studies included in assessment. Range from

surgery to postoperative imaging included studies performed one month or less up to 13 years 3 months. All studies (n=163) performed one year following surgery or sooner demonstrated enhancement. Thirty-seven of 39 of cases performed between one and two years post operative demonstrated enhancement. Twenty-eight of 29 cases performed between two and three years post operative demonstrated enhancement. All studies (n=16) performed between three and four years post operative demonstrated enhancement. Nineteen of 22 cases performed between four and five years post operative demonstrated enhancement. Four of five cases performed five years after surgery demonstrated enhancement.

Conclusions

Following discectomy, gadolinium enhanced studies should be performed in the first five years to improve specificity. Data suggests that scar will enhance longer than five years post operative; however, further investigation is needed to determine how long and how significant it is in the interpretation of postoperative spines.

O-98

3:35PM - 3:42PM

Efficacy of a vertebral augmentation system used for bone remodelling as treatment of vertebral fractures

S Marcia¹, E Piras¹, A Spinelli¹, S Marini¹, L Saba²

¹ATS Sardegna, Cagliari, Italy, ²AOU Cagliari, Cagliari, Italy

Purpose

The aim of this study was to evaluate the effectiveness and safety of a bone remodelling system in the treatment of painful vertebral compressive fractures (VCFs).

Materials and Methods

Thirty consecutive patients with painful vertebral compressive fractures underwent the bone remodelling (Tektona®, SpineArt, CH) procedure. Patients had been previously evaluated by clinical examination and X-ray, CTms and MRI-T2wSTIR. All the procedures were executed with local anaesthesia and a bilateral approach under digital fluoroscopic guidance. In total, 37 vertebrae were treated. Clinical evaluation and assessment of pain using a 11-point visual analogue scale (VAS, 0–10) were performed at baseline, immediately after the procedure, at six and 12 months; disability and health status by means of ODI and SF36 were also evaluated. Vertebral height (VH) restoration by vertebral body volume (VBV) calculation with CTms was assessed before (pre) and immediately after the procedure (post), as well as vertebral heights (anterior, middle and posterior VHs) and the local (LK) and regional (RK) kyphosis angles.

Results

We obtained a progressive reduction of the pain in all the patients we evaluated at 6-m (30 patients) and at 12-m (21 patients) (VAS pre: 7.6, post: 2.8, 6M: 2.1, 12M: 2.7), improvement of functions (ODI pre: 55.5, 6M: 22.3, 12M: 27) as well an average improvement of 15% in SF- 36 Physical Health score (PHs pre: 40.6%, 6M: 55.6%) at 6-m and of 2% (PHs at 12M: 42.5%) at 12-m. We observed a good height restoration (middle VH pre: 13.8mm, post: 15.4mm, 12M: 14.4mm, difference: 1.6mm – 0.6mm), a good increase in the volume of the vertebral bodies (VBV pre: 21.6cm³, post: 23.08cm³, 12M: 22.13cm³, difference: 1.4cm³ – 0.53cm³). The correction of local kyphosis have been checked immediate postoperatively and at 12-m and the kyphosis correction was confirmed, as follows: an average LK decrease of 1.57° and an average RK decrease of 2.6°. No major complications arose.

Conclusions

From our study, the use of bone remodelling system was found to be safe and effective in the treatment of painful vertebral fractures, providing pain relief and anatomical restoration.

O-99

3:42PM - 3:49PM

Recent Imaging of Vertebral Compression Fractures is Beneficial in Pre-Operative Planning for Vertebral Augmentation

X Yang¹, X Chin¹, J Deutsch¹, A Arneja¹, A Aggarwal², A Doshi²

¹Mount Sinai Hospital, New York, NY, ²Icahn School of Medicine at Mount Sinai, New York, NY

Purpose

Vertebral compression fractures are a common source of chronic back pain and morbidity. Percutaneous vertebral augmentation is a minimally invasive procedure for treating vertebral compression fractures with the potential to alleviate pain and reduce reliance on pain medications [1]. Patients usually undergo evaluation with diagnostic imaging with MRI or CT scanning prior to vertebral augmentation. However, interval changes of the fracture or formation of new fractures can change procedural management [2]. We investigate the impact of timing of preprocedural imaging and changes in vertebral compression fractures prior to augmentation.

Materials and Methods

Patients who received percutaneous vertebral body augmentation at Mount Sinai Hospital between September 2013 and September 2017 were identified utilizing PACS query. Cases with cross-sectional imaging (MRI/CT) within four weeks and prior to four weeks of the vertebral augmentation procedure were included. Cases that did not demonstrate the augmented vertebral compression deformity on the initial scan were excluded. A detailed retrospective review of the included cases was conducted, assessing for new fractures, increased vertebral body height loss, new retropulsion, and changes in STIR signal between imaging sets.

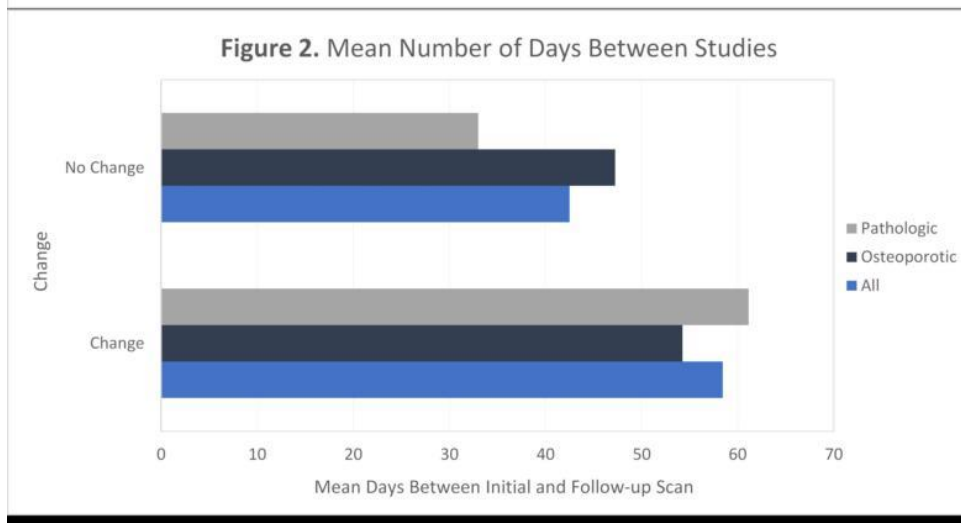
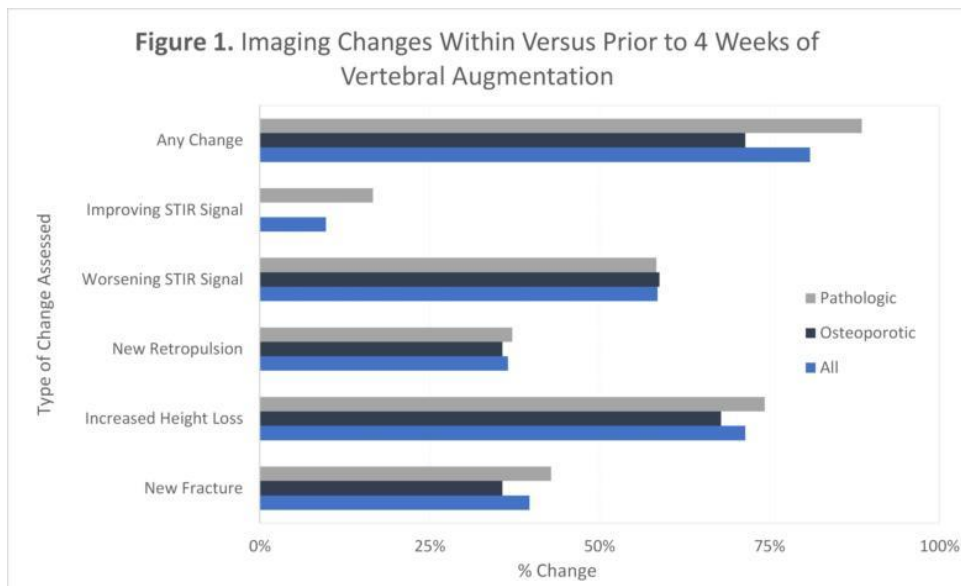
Results

A total of 63 vertebral compression fracture cases were included (28 osteoporotic, 35 pathologic). When considering all cases, 81.0% demonstrate change between initial and follow-up imaging studies.

Analyzing osteoporotic and pathologic fractures separately, 71.4 % and 88.6% exhibit change ($p=0.04$), respectively. The most frequent source of change between studies is increasing vertebral compression fracture height loss (71.4% all cases; 67.9% osteoporotic cases; 74.3% pathologic cases). The mean number of days between studies with and without change are respectively 58.4 and 42.5 (all cases; $p=0.04$), 54.3 and 47.3 (osteoporotic cases; $p=0.29$), and 61.1 and 33.0 (pathologic cases; $p=0.02$).

Conclusions

Recent cross-sectional imaging within four weeks of potential percutaneous vertebral augmentation often detect change in vertebral compression fractures that could affect procedural management. This outcome is seen in both osteoporotic and pathologic compression fractures, but is most pronounced with pathologic fractures.



(Filename: TCT_O-99_Figures.jpg)

O-100

3:49PM - 3:56PM

Efficacy of Euthermic Discolysis with Ho Laser in treatment of radicular pain

S Marcia¹, E Piras¹, A Spinelli¹, S Marini¹
¹ATS Sardegna, Cagliari, Italy

Purpose

The aim of this study is to provide the efficacy of Euthermic Discolysis with Ho Laser in the treatment of disc protrusions by means of pain relief and functions.

Materials and Methods

Fifty-six patients (35 males, 21 females, av. Age: 51.2) with cervicobrachia or sciatic pain due to cervical or lumbar contained discal herniation (Pfirmann grade 1-3) were selected for treatment with percutaneous disc decompression by means of Ho LaserYAG Discolux® (Techlamed, ITA). Diagnosis was confirmed by MRI and EMG in all patients. All procedures were performed under fluoroscopic guidance and with local anesthesia. Eighteen-gauge Chiba needles were used to insert the laser fiber.

Oral Presentations & Excerptas

Clinical evaluation, assessment of pain by means of a 11-point visual analogue scale (VAS, 0-10) and of functions by means of the Oswestry disability scale (ODI 0- 50) was performed at baseline and at six months after the procedure. The use of painkillers was also evaluated.

Results

A total of 59 intervertebral discs (35 cervical, 24 lumbar) on 56 patients were treated. Baseline pain was 7.54 ± 1.4 , baseline ODI was 58.4%. At six months, pain was 2.8 ± 2.3 ($p < 0.01$), while ODI was 19.3%. No complications arose. Of the patients, 75% stopped painkillers, 20% reduced the uptaking, 5% were still on analgesic drugs.

Conclusions

From our preliminary study, the treatment of contained discal herniation with Euthermic Discolysis with Ho Laser is an optimal therapy for symptomatic patients showing a good reduction of pain and a good increase of functions.

O-101

3:56PM - 4:03PM

Motion Characteristics of the Functional Spinal Unit during Lumbar Disc Injection

W Bartynski¹, V Agarwal², A Khan³

¹Duke University, Durham, NC, ²University of Pittsburgh Medical Center, Pittsburgh, PA, ³University of Pittsburgh School of Medicine, Pittsburgh, PA

Purpose

While lumbar discography has been used for decades to identify discs considered responsible for a patient's low back pain (LBP), the biomechanical effects on the 'Functional Spinal Unit (FSU)' during discography have received little attention. This study assesses the biomechanical characteristics of the FSU during disc injection.

Materials and Methods

Lateral projection FSU motion was retrospectively evaluated at 78 lumbar disc levels in 31 patients where superimposition of the inferior endplates and facets on routine pre- and postinjection images could be achieved. Motion of the anterior element (superior endplate [EP]) and posterior element (PostEl: pedicle, facet, foramen) components of the FSU was visually evaluated by 'dynamically' alternating between pre- and postinjection images. Anterior segment motion (EP elevation/rocking) and posterior segment motion (pedicle/facet motion, foramen enlargement) were subjectively graded (prominent motion, intermediate motion, questionable motion, no motion).

Results

Twenty-nine levels appeared normal and 49 demonstrated disc degeneration (Adams criteria). In normal discs, prominent EP motion was identified in 27/29 (93%) with prominent PostEl motion identified in 23/27 (85%) and questionable motion in 4/27. Intermediate EP motion encountered in 2/29 (intermediate PostEl motion identified: 1, questionable motion: 1). In degenerative discs, prominent EP motion was identified in 29/49 (60%) with prominent PostEl motion in all 29. Intermediate EP motion was identified in 11/49 (22%) with intermediate PostEl motion identified in 9 and questionable motion in 2. No EP or PostEl motion was identified in 8/49 and irregular motion was encountered in 1. Overall, PostEl motion consistent with visualized EP motion was identified in 62/78 (79.5%) disc levels.

Conclusions

Both disc-related and posterior element motion occur during disc injection at lumbar discography. Injection of the disc should be considered a study of the FSU, not disc alone. Potential superimposed contribution of facet-related LBP must be clarified in order to understand the pain response encountered at 'Discography'. This observation might also relate to the anesthetic response of painful discs encountered at lumbar discography.

O-102

Oral Presentations & Excerptas

Whether vertebroplasty based on clinical plus imaging (MRI with or without bone scan) selection criteria is related to higher efficacy on pain scale among patients with painful osteoporotic vertebral compression fractures anywhere in the world- A systematic review and Metanalysis

J Shankar¹, R Merdad¹, R Parker¹

¹*Dalhousie University, Halifax, Nova Scotia, Canada*

Purpose

Vertebral compression fractures (VCFs) are the most common type of osteoporotic fracture associated with significant rates of morbidity and mortality. When pain relief is not achieved with nonsurgical techniques, percutaneous vertebral augmentation (PVA) (vertebroplasty) is often used. Imaging (bone scan and/or MRI) shows bone marrow edema and helps select patients for PVA. The purpose of our study is to synthesize evidence on efficacy of PVA in VCF patients, and to assess whether trials that selected patients based on clinical examination plus imaging showed better pain outcomes compared to trials that selected patients based on clinical examination only.

Materials and Methods

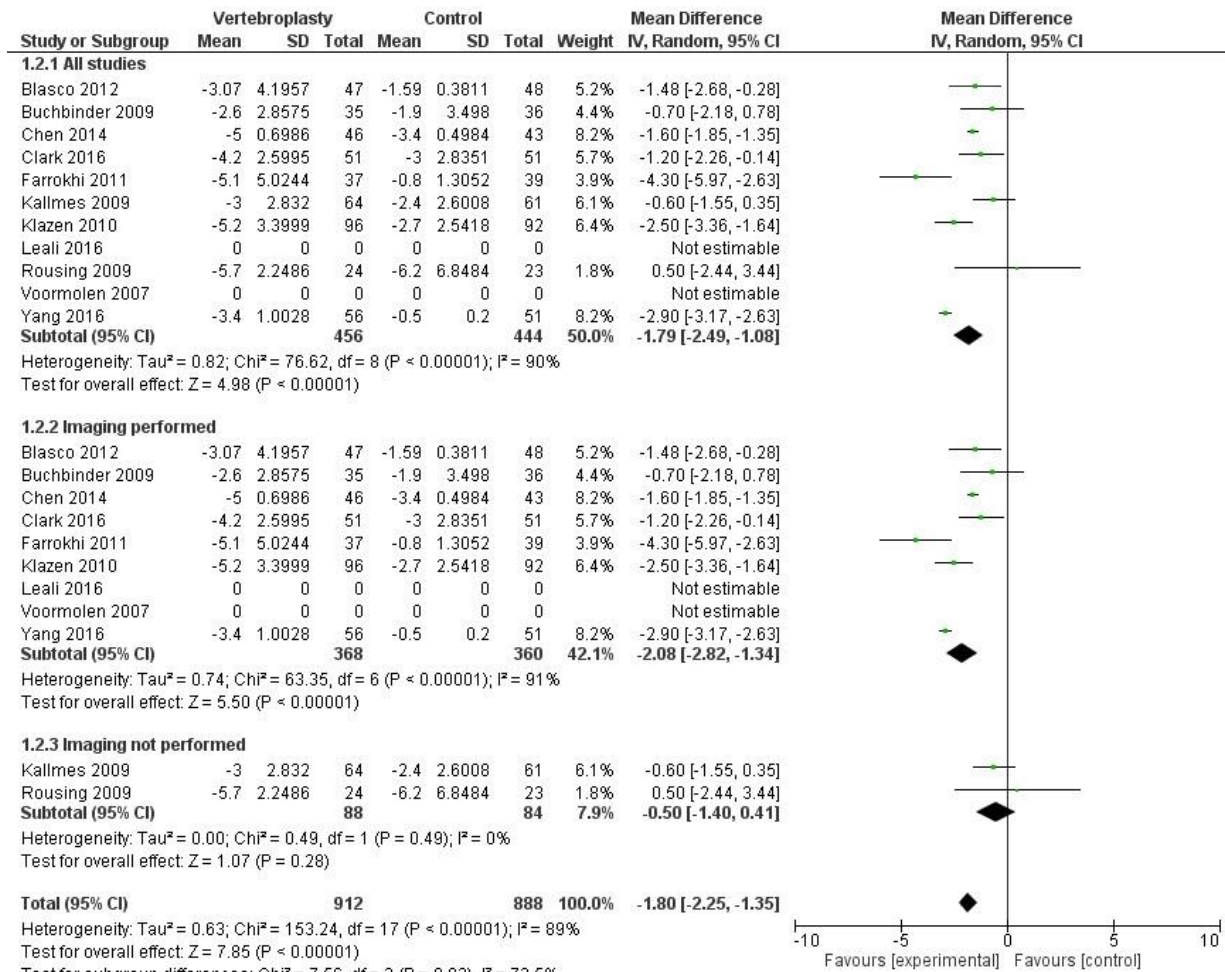
We performed a systematic review and meta-analysis. PubMed, Embase and Cochrane Library databases were searched to identify randomized controlled trials (RCTs) that met a prespecified inclusion criteria including reporting a visual analog scale (VAS) pain score. A pooled estimate of mean differences (MDs) in pain with 95% CIs was utilized to express the efficacy of vertebroplasty. Subgroup analysis was performed to compare between trials that used imaging to confirm findings of edema prior to patient enrollment and those that did not.

Results

A total of 11 RCTs with 900 participants were included in the review and analysis. Nine studies used imaging to confirm the presence of bone edema as an inclusion criteria prior to enrollment. Of these 9, 8 studies showed evidence of effectiveness of PVA in reducing pain. The two studies that did not include imaging confirmation of edema as a prerequisite for patient inclusion did not show evidence of effectiveness of PVA in reducing pain. The results of the meta-analysis including 11 trials (900 participants) shows a MD of -1.79 [95% CI -2.49 to -1.08, $p < 0.001$] in pain intensity when comparing PVA to conservative management. The MD from trials that used imaging (728 participants) was -2.08 [95% CI -2.82 to -1.34, $p < 0.001$] and from trials that did not use imaging (172 participants) was -0.50 [95% CI -1.40 to 0.41, $p = 0.28$].

Conclusions

Vertebroplasty results in improvement in pain from osteoporotic compression fracture compared to conservative management. Efficacy of vertebroplasty significantly improved when patients were selected based on imaging confirmation of marrow edema.



(Filename: TCT_O-102_Forestplot.jpg)

O-103

4:10PM - 4:17PM

Initial single center experience: New Generation of Radiofrequency Heat Ablation Device and Kyphoplasty in Spinal Metastases Treatment

F Massari¹, A Puri¹, D Rex¹, K de Macedo Rodrigues¹, A Kühn¹, M Howk¹, W Ajay K¹

¹University of Massachusetts, Worcester, MA

Purpose

The aim of the current study was to evaluate the safety and the efficacy in coupled use of the new generation of RadioFrequency Thermal Ablation devices (Osteocool™) and Kyphoplasty for the palliative treatment of spinal osteolytic metastases.

Materials and Methods

Hybrid treatment was used in pain management in terminally ill or patients not a candidate for resective surgery with spinal bone metastases. Patients referred to our institution for symptomatic malignant fractures treatment with RFA and Kyphoplasty, from March 2016 to November 2017, were retrospectively reviewed. Bipolar RFA was performed (Osteocool RF ablation system, Medtronic) reaching a constant temperature of 70 C° over 7 to 15 minutes followed by cement injection. Clinical outcomes were evaluated by review of the electronic medical record (EMR) and clinical visit F/U. Pre- and postprocedural pain scores were documented in order to determine the degree of pain relief.

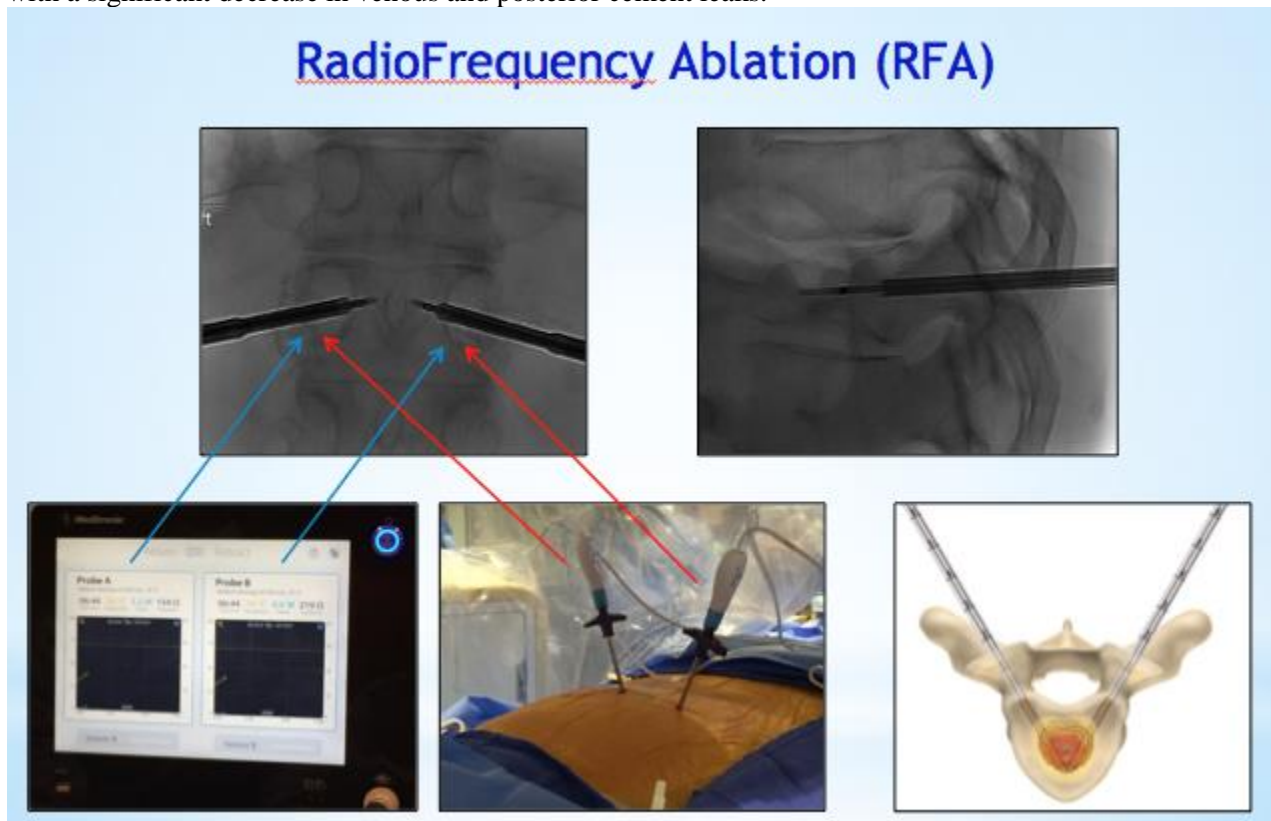
Oral Presentations & Excerptas

Results

Twenty-six patients in the study were treated with the RFA assisted technique. These contributed to 61 KP levels. All were technically successful without morbidity or mortality. There was a significantly reduced rate of posterior and venous cement leaks when RFA was used prior to KP. Pain scores in the RFA assisted group decreased significantly post procedure with no unanticipated neuropathic events.

Conclusions

The new generation of RadioFrequency Thermal Ablation devices (Osteocool™) using a bipolar device + Kyphoplasty have demonstrated an increased efficacy in achieving pain relief and VB stabilization in spinal metastases management, allowing a controlled injection of cement into a preformed thermal cavity with a significant decrease in venous and posterior cement leaks.



(Filename: TCT_O-103_Image1.JPG)

O-104

4:17PM - 4:24PM

Efficacy of Lumbosacral Spine Phantom in Improving Trainee Proficiency and Confidence in CT-guided Spine Procedures

Y Li¹, Z Li¹, S Ammanuel¹, D Gillan¹, V Shah¹

¹University of California San Francisco, San Francisco, CA

Purpose

To evaluate the efficacy of using a realistic 3D-printed lumbosacral spine phantom in improving trainees' proficiency in performing CT-guided facet joint injections

Materials and Methods

A lumbosacral spine phantom was 3D-printed, based off a real patient CT lumbar spine. The model was printed using calcium sulfate, allowing for visibility under CT, and subsequently embedded in a clear

Oral Presentations & Excerptas

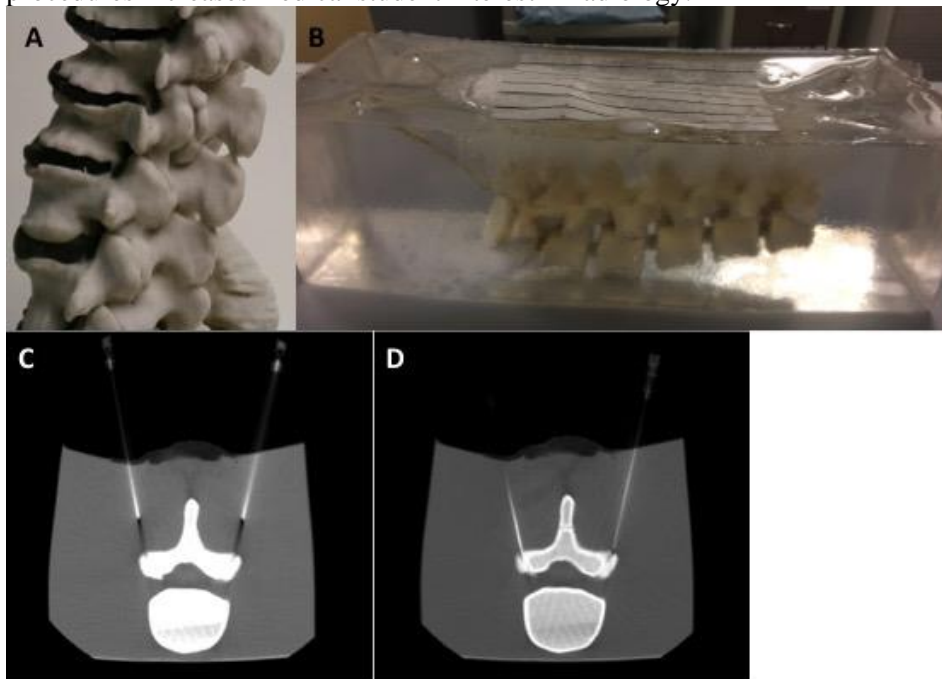
gelatin mixture that mimics the consistency of soft tissue. A total of 12 medical students with no prior exposure to CT-guided lumbar spine procedures were divided into two groups. Both groups received an introductory didactic lecture, as well as identical pre- and post-test written assessments. The questions tested level of interest in radiology, confidence in performing CT-guided facet blocks, common sources of adult back pain, and identification of spine anatomy on axial CT images. Group 1 (7 students), the experienced group, received two separate training sessions using the simulation model. Group 2 (5 students), considered the novice group, received only 1 training session. Student t-test was used to assess for statistically significant differences in test answers and number of needle readjustments between the experienced and novice groups.

Results

There was no statistically significant difference in baseline knowledge on pretest answers between the experienced and the novice groups ($p=0.57$). The experienced group demonstrated a trend toward better performance during the last simulation session, compared with the novice group, with fewer needle readjustments ($p=0.07$). For all students, the post-test demonstrated a trend toward increased "interest in radiology" ($p=0.27$) and a significant increase in "confidence in ability to perform CT-guided spine procedures" ($p=0.00001$).

Conclusions

Training using a realistic 3D-printed lumbosacral spine model helps novices to acquire the skills and confidence to perform CT-guided spine procedures. Early hands-on exposure to radiology-guided procedures increases medical student interest in radiology.



- A. 3D-printed lumbosacral spine model with realistic spondylosis, including degenerative facet joints.
- B. Spine model embedded in gelatin mold, with overlying grid in preparation for CT-guided procedure.
- C. Axial CT image from CT-guided facet injection with needles headed in the trajectory of bilateral facet joints.
- D. Axial CT image from CT-guided facet injection with needles advanced into bilateral facet joints.

(Filename: TCT_O-104_spinefigure1.jpg)

Monday, June 4, 2018

3:00PM - 4:31PM

Parallel Paper Session: Cerebral Aneurysms Management and Treatment

O-105

3:00PM - 3:07PM

Management of Unruptured Intracranial Aneurysms in the Elderly: A Cost-Effectiveness Analysis

X Wu¹, B Geng¹, K Seifert², V Kalra³, D Gandhi⁴, P Sanelli⁵, A Malhotra²

¹*Yale University School of Medicine, New Haven, CT*, ²*Yale New Haven Hospital, New Haven, CT*, ³*Orlando Health, Tampa, FL*, ⁴*University of Maryland School of Medicine, Baltimore, MD*, ⁵*Northwell Health, Manhasset, NY*

Purpose

Unruptured intracranial aneurysms (UIAs) are relatively common, with a significant proportion in patients above 65 years of age. This study evaluates the cost-effectiveness of five different management strategies for UIAs in elderly patients: annual magnetic resonance angiography (MRA) screening, biennial MRA screening, MRA screening every 5 years, coiling and follow-up and, no treatment or preventive follow-up.

Materials and Methods

A decision-analytic model-based cost-effectiveness analysis was done using inputs from the medical literature. A Markov decision model was constructed from a societal perspective starting with patients 65-years-old on average, with incidental detections of UIA and no prior history of subarachnoid hemorrhage. Clinical, cost, and outcome parameters were extracted from medical literature specific to the elderly population. Probabilistic, one-way, and two-way sensitivity analyses were performed.

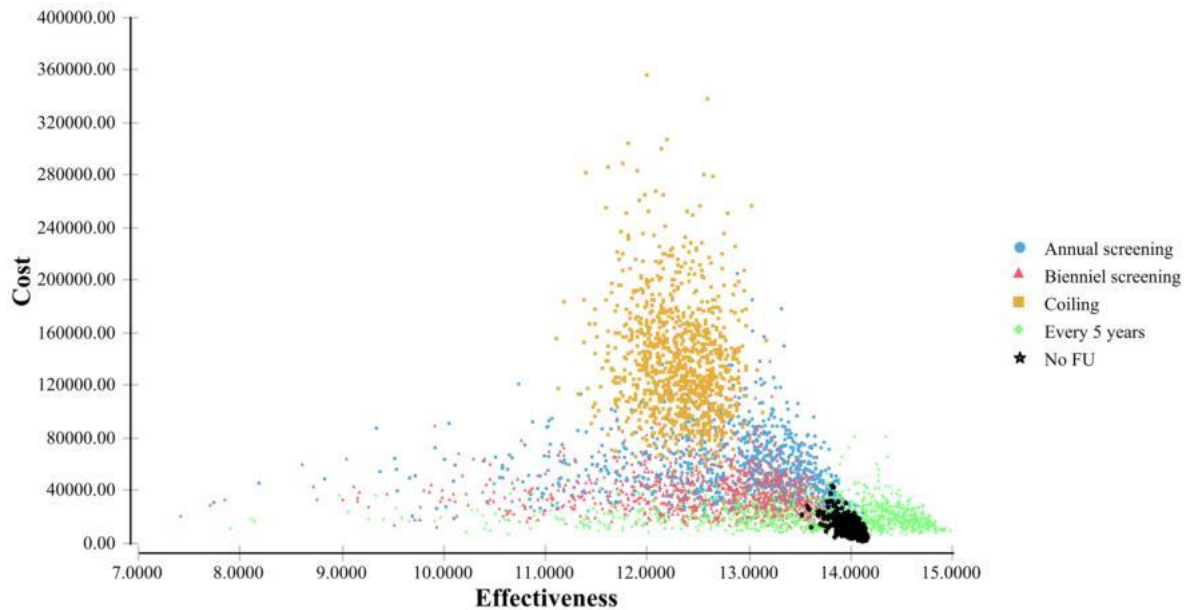
Results

The base-case calculation shows no preventive follow-up to be the most cost-effective strategy (cost: \$10,838, health benefit: 14.01 QALYs), showing lower costs and higher effectiveness. Among the imaging follow-ups, MRA every 5 years is the most cost-effective. The conclusion remains robust in probabilistic and one-way sensitivity analyses. In 10,000 simulations performed in probabilistic sensitivity analysis shows no follow-up in 84.65% of the iterations. No routine follow-up remains the optimal strategy when the annual growth rate, and rupture risk of growing aneurysms are varied from 0 to 30%. If imaging has to be considered, the best imaging strategy is 5-year follow-up when the rupture risk of growing aneurysms is < 37.7%. When the annual rupture risk of nongrowing UIAs is <5.3%, no follow-up is the optimal strategy. If annual rupture risk is >5.3%, coiling should be performed directly.

Conclusions

Given the current literature, routine preventive treatment or periodic, close imaging follow-up is not a cost-effective strategy in all elderly patients with unruptured intracranial aneurysms. More aggressive management strategies might be more appropriate in selected patients at high risk for rupture.

Cost-Effectiveness Scatterplot



(Filename: TCT_O-105_CEScatterplot.jpg)

O-106

3:07PM - 3:14PM

Screening for intracranial aneurysms in patients with Adult Polycystic Kidney Disease: A Cost Effectiveness analysis

X Wu¹, H Forman¹, C Matouk¹, D Gandhi², P Sanelli³, A Malhotra⁴

¹Yale University School of Medicine, New Haven, CT, ²University of Maryland School of Medicine, Baltimore, MD, ³Northwell Health, Manhasset, NY, ⁴Yale New Haven Hospital, New Haven, CT

Purpose

Adult polycystic kidney disease (ADPKD) is one of the most common hereditary diseases with a high prevalence (10%) of intracranial aneurysms (IAs). Although screening for IAs is recommended in ADPKD patients, the age, frequency of screening and management of detected IAs are not defined. We conducted a cost-effectiveness analysis to determine the optimal screening and management strategy for IAs in ADPKD patients.

Materials and Methods

We constructed a Markov model from a societal perspective starting with an ADPKD patients at the age of 30. The strategies included were: 1) no screening, 2) one-time screening and annual follow-up if a IA is detected, 3) every-5-year screening and endovascular coiling is a IA is detected, 4) every-5-year screening and annual follow-up, and 5) every-5-year screening and biennial follow-up. Various sensitivity analyses were performed to assess the robustness of the conclusion.

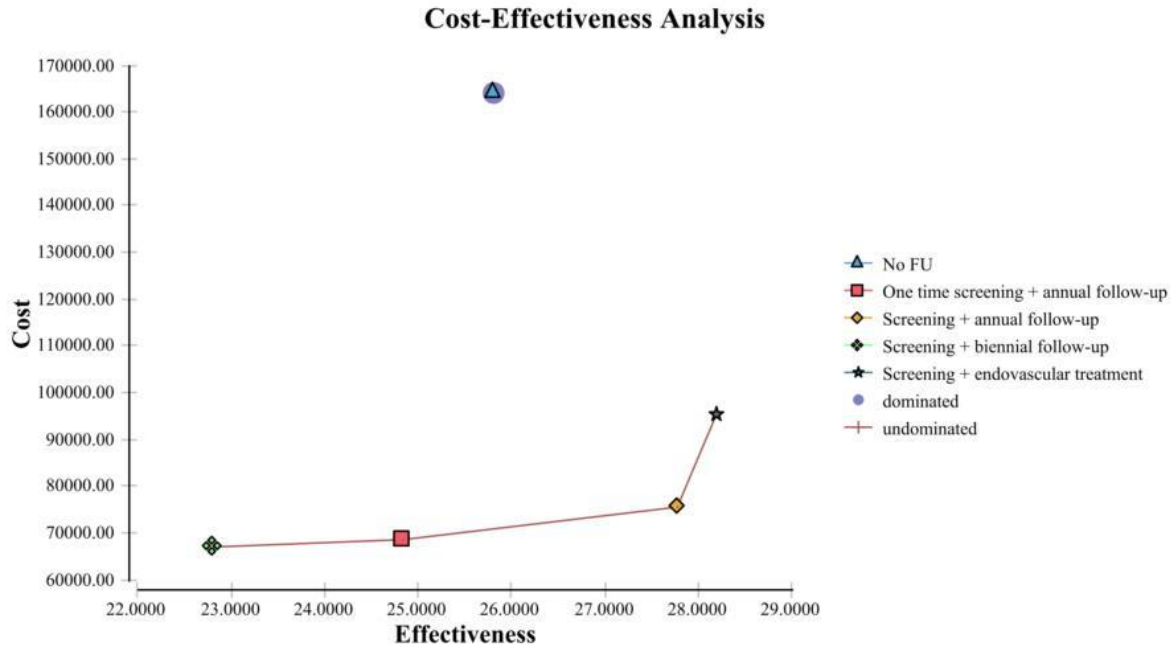
Results

In the base-case calculation, no screening is shown to be the least favorable strategy, and every-5-year screening + endovascular coiling is the optimal one, with every-5-year screening + annual follow-up being the second most favorable strategy. In the probabilistic sensitivity analysis, screening + endovascular coiling is the better strategy as compared to every-5-year screening + annual follow-up in 6,392 of 10,000 simulations. When the overall rupture risk is <0.22%, 0.22%-1.54%, and <1.54% annually, no follow-up, every-5-year screening + annual follow-up, every-5-year screening + endovascular treatment are the respective optimal strategies. Screening every 5 years + endovascular

Oral Presentations & Excerpts

coiling is the most cost-effective when the probability of moderate disability from coiling is lower than 12.54%. When the probability is higher than 12.54%, screening every 5 years + annual follow-up becomes the optimal strategy. The risk of moderate disability from SAH has no effect on the conclusion.

Conclusions
 Screening for IAs is cost-effective in ADPKD patients. The optimal strategy is screening every 5 years and treatment of detected aneurysm, resulting in the best health outcome and lowest cost.



(Filename: TCT_O-106_ASNR.jpg)

O-107

3:14PM - 3:21PM

Impact of Early Endovascular Aneurysm Treatment on Clinical Outcome in Subarachnoid Hemorrhage

S Rawal¹, J Fang², J Victor², R Macdonald¹, G Rinkel³, T Krings¹, M Kapral¹, A Laupacis¹

¹University of Toronto, Toronto, Ontario, Canada, ²Institute for Clinical Evaluative Sciences, Toronto, Ontario, Canada, ³University Medical Center Utrecht, Utrecht, the Netherlands

Purpose

Rapid aneurysm treatment following subarachnoid hemorrhage (SAH) is intended to prevent rebleeding, which can have devastating effects on outcome. While management guidelines recommend that aneurysm occlusion occur "as early as feasible", (1) there is currently no consensus on when exactly treatment should occur, and whether earlier treatment actually improves outcome. (2)

Materials and Methods

A retrospective population-based cohort study was performed to assess the impact of early endovascular aneurysm treatment on clinical outcome using provincial stroke registry and health administrative data from Ontario. The cohort included adult patients with a confirmed diagnosis of aneurysmal SAH who underwent endovascular aneurysm treatment. Aneurysm treatment was defined as early (<1 calendar date of symptom onset) versus late. The outcomes assessed were poor functional status (modified Rankin scale >=3), death at discharge, discharge disposition, and 30-day case fatality. Risk adjustment for predictors of outcome in SAH (age, sex, SAH severity, comorbidities, and aneurysm features) was performed through

multivariable logistic regression models for each outcome. Potential clustering at the hospital level was accounted for by generalized estimating equations.

Results

Included in the study cohort were 1047 patients. Univariate analysis showed no significant impact of treatment timing on outcomes; older age and indicators of increased SAH severity were predictors of worse outcome. Multivariable analyses accounting for clustered data showed no significant impact of treatment timing on outcomes; older age, ventriculostomy placement and mechanical ventilation were significant predictors of poor functional outcome and case fatality on discharge and at 30 days.

Conclusions

In this large cohort of SAH patients, there was no significant impact of early endovascular aneurysm treatment on outcome. This evidence supports current clinical practice of nonemergent management of ruptured aneurysms in the endovascular setting.

O-108

3:21PM - 3:28PM

Factors influencing confidence of diagnostic rating and retreatment recommendation in coiled aneurysms

M Ernst¹, J Buhk¹, J Fiehler¹

¹*University Medical Center Hamburg-Eppendorf, Hamburg, Germany*

Purpose

Angiographic occlusion and retreatment of coiled aneurysms are commonly used as surrogate endpoint in clinical trials. We aimed to evaluate the influence of aneurysm, patient and rater characteristics on the confidence of visual evaluation of aneurysm coiling and on retreatment decision.

Materials and Methods

There were 26 participants of the Advanced Course in Endovascular Interventional Neuroradiology of the European Society of Neuroradiology asked to evaluate digital subtraction angiography of patients that had received endovascular coiling by determining the grade of aneurysm occlusion, the change between immediate postprocedure and follow-up angiogram, their level of confidence, the technical difficulty of retreatment and the best therapeutic approach. Experience, knowledge, and skills of each participant were assessed. Influence of rater and case characteristics on indicated confidence in diagnostic rating and retreatment recommendation were analyzed.

Results

Interrater reliability was moderate with regard to the assessment of aneurysm occlusion grade (ICC=.581), excellent with regard to change (ICC=.776). Overall confidence in diagnostic rating was high (median "very certain"). Confidence was statistically significantly higher in cases that were generally rated as "worse". The odds of recommending retreatment were significantly higher in cases that were generally rated with higher mean confidence.

Conclusions

Though overall confidence in diagnostic rating was high, our study confirms the suboptimal interrater reliability of visual assessment of aneurysm occlusion as well as retreatment recommendations, rendering both as primary outcome measure questionable. Beside recurrence status, recommendation of retreatment is significantly influenced by patient age, aneurysm neck width, as well as characteristics of the therapist.

O-109

3:28PM - 3:35PM

Customizable 3D Printed Simulation Model of Aneurysms in the Circle of Willis: A Step Closer to Reality

F Farhadi¹, R Javan¹, C Gragnaniello¹, A Yepuri¹, F Razjouyan², U Igbaogi², N Greek²

¹George Washington University Hospital, Washington, DC, ²George Washington University, Washington, DC

Purpose

The aim of this project was to construct a low-cost customizable simulation system of aneurysms in the circle of Willis and its branches.

Materials and Methods

DICOM images from an MRA head were used to create a Stereolithography model of the circle of Willis using Materialise InPrint. A desktop 3-D printer utilizing fused deposition modeling technology was used for 3-D printing. A water-soluble synthetic polymer, polyvinyl alcohol (PVA), was used as the printing material for the arterial network. Two different concentrations of silicone in solvent were applied to the outer layer of the model, with the more flexible silicone applied to a desired area, such as the basilar tip, which would lead to development of aneurysm. Immersing the final product in water dissolved PVA, leaving a hollow elastic vascular model with thin walls. The designated open ends of the model were connected to a pressure-adjustable closed-circuit liquid circulation pump in order to simulate blood flow.

Results

The wall of the vascular system developed in this current technique allows for a more realistic simulation when compared to models where the flexible vessel walls are directly 3-D printed with PolyJet technology. This is due to the ability to create thinner walls as well as the ability to create larger and more complex vascular anatomy since no support material is needed for the long hollow tubular structure with overhanging edges. Furthermore, the aneurysms are the result of true wall protrusion with a tensile force developed in the walls of the aneurysm.

Conclusions

The hollow vascular system can be embedded in a soft model of brain parenchyma created through molding techniques to allow neurosurgical trainees to practice clipping of aneurysms that are truly the result of bulging of the vascular wall as opposed to the traditional directly 3-D printed thick-walled static aneurysms.

O-110

3:35PM - 3:42PM

Creation of Different Size of Aneurysms by Adjusting the Position of Sheath during Elastase Incubation

Y Ding¹, S Asnafi¹, D Dai¹, D Kallmes¹, R Kadirvel¹

¹Mayo Clinic, Rochester, MN

Purpose

Different sizes of aneurysms are required for varied topics of research. The purpose of the study was to determine whether adjusting position of sheath during elastase incubation can result in different sizes of elastase induced aneurysms (smaller or bigger) in rabbits.

Materials and Methods

Aneurysm volume of 18 elastase-induced aneurysms were retrospectively analyzed along with sheath position during creation in New Zealand white rabbits. Two groups were classified according to the distance (DIS) between the tip of sheath to the origin of right common carotid artery (RCCA): Group 1 (DIS < 7 mm, n = 9) in which the vascular sheath was put near the origin of RCCA (short arrow in Figure A); Group 2 (DIS > 16 mm, n = 9) in which the vascular sheath was put far from the origin of RCCA (long arrow in Figure C). Follow-up digital subtraction angiography (DSA) was done 3 weeks after aneurysm creation. Aneurysm sizes (neck diameter, width, height, and volume) in the two groups were measured and calculated. Comparison of aneurysm volumes between the two groups was compared using the Student's t test.

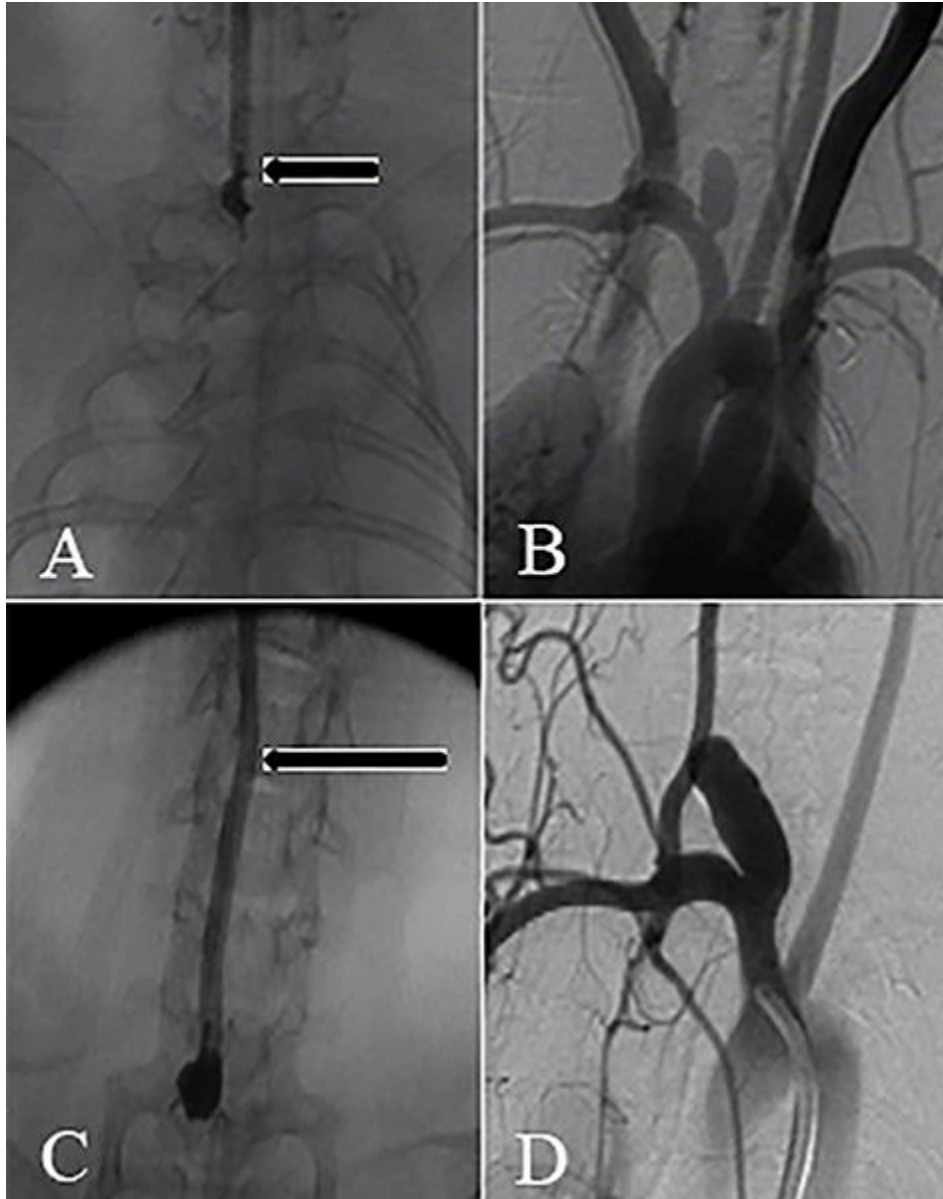
Oral Presentations & Excerptas

Results

The mean aneurysm neck, width, and height for Group 1 were 2.3 ± 0.9 mm, 3.1 ± 0.7 mm, and 7.1 ± 2.3 mm, respectively (Figure B). Mean aneurysm neck, width, and height in Group 2 were 4.2 ± 1.7 mm, 4.1 ± 1.1 mm, and 10.1 ± 2.2 mm, respectively (Figure D). Mean aneurysm volume in Group 1 was 53 ± 20 mm³, which was smaller than that (152 ± 102 mm³) in Group 2 ($p = .01$).

Conclusions

Different volume of aneurysms can be created by adjusting the position of sheath during elastase incubation.



(Filename: TCT_O-110_Figure13inhalf.jpg)

O-111

3:42PM - 3:49PM

The Use of Flow Diverters To Treat Small and Very Small Ruptured, Saccular Aneurysms

P Bhogal¹, H Henkes¹, H Bänzner¹

Oral Presentations & Excerptas

¹*Klinikum Stuttgart, Stuttgart, Germany*

Purpose

The use of flow diverter stents (FDS) is well documented; however, there is limited literature available on their use to treat acutely ruptured intracranial aneurysms. We sought to evaluate the effectiveness of FDS to treat small (≤ 5 mm) and very small (≤ 3 mm) ruptured aneurysms.

Materials and Methods

We performed a retrospective review of our prospectively maintained database to identify all patients presenting to our center with acute subarachnoid haemorrhage with small and very small (≤ 5 mm) aneurysms and treated with FDS between January 2013 and December 2017.

Results

We identified 15 patients (8 female) with average age 59.2 ± 9.8 years (range 48-80). The average aneurysm fundus size was 2.9 ± 1.3 mm (range 1-5mm), the average neck width was 2.8 ± 1.0 mm (range 1-5mm) with average aspect ratio 1.1. The majority of aneurysms were located in the anterior circulation (n=11) with 6 aneurysms located on the clinoidal or supraclinoidal segment of the ICA, 2 aneurysms located at the A1/A2 junction, 1 aneurysm on the anterior communicating artery (AcomA), 1 aneurysm on the pericallosal artery, and 1 aneurysm located on the posterior communicating artery (PcomA). In the posterior circulation 2 aneurysms were located on the basilar artery, 1 aneurysm on the superior cerebellar artery, and 1 aneurysm on the posterior cerebral artery. Four of the aneurysms had previously been treated, two with coils, one with microsurgical clipping and one with both clipping and coils. In terms of clinical presentation, 4 patients presented with Hunt Hess grade 1, 4 patients with Hunt Hess grade 2, 6 patients with Hunt Hess grade 3, and 1 patient with Hunt Hess grade 5 subarachnoid haemorrhage. Four patients had endoventricular drains (EVD's) inserted and one patient had a lumbar drain inserted. There were no cases of haemorrhage secondary to drain insertion or following initiation of antiplatelet medication. Delivery of the flow diverter was feasible in all cases. The p64 was used in 14 cases and the PED was used in 1 patient. In 3 patients 2 FDS were deployed. The average time from ictus to treatment was 8.7 days (range 1-22 days) and there were no cases of repeat rupture prior to treatment. There were no cases of intraoperative aneurysm rupture. Angiographic follow-up was available in 11 patients. At initial follow-up performed on average at 3.1 months after the procedure, 7 aneurysms (64%) were completely occluded (RRC 1), 2 aneurysms showed small remnants (RRC 2) and two aneurysms were unchanged. Overall adequate occlusion was achieved in 82% of cases.

Conclusions

The use of FDS to treat small and very small ruptured saccular aneurysms is feasible and has good radiographic and clinical outcomes. Although the use FDS should not be considered first-line treatment it represents a potential alternative treatment option when standard endovascular coiling or neurosurgery may not be feasible.

O-112

3:49PM - 3:56PM

Long-Term Visual Outcome in Patients Treated by Flow Diversion for Carotid-Ophthalmic Aneurysms

R Touzé¹, V Touitou¹, E Shotar¹, J Gabrieli¹, B Mathon¹, N Sourour¹, F Clarençon¹

¹*Pitié-Salpêtrière Hospital, Paris, France*

Purpose

Flow-diverter stents (FDSs) are a major upgrade in the treatment of intracranial aneurysms. While promoting the aneurysm's sac thrombosis, these devices are supposed to preserve the patency of the branches covered by the stent's mesh. However, complications involving these covered branches have been reported, especially the ophthalmic artery (OA). The purpose of our study was to evaluate long-term (i.e. > 2 years) ophthalmic complication rate of carotid-ophthalmic aneurysms (COA) without visual

pathways compression, treated by a FDS covering the OA by performing a systematic exhaustive ophthalmic examination.

Materials and Methods

Retrospective analysis of a single-center database screening the patients treated from October 2009 to April 2015 for an intracranial aneurysm with a FDS. The patients treated for a noncompressive COA with coverage of the OA by the device were studied (n = 30; 32%). Among, these patients, 15 (50%) were excluded. The remaining 15 patients (50%) underwent a systematic and extensive ophthalmic examination at least two years after the stent placement by two ophthalmologists.

Results

Ninety-four patients treated with a FDS for intracranial aneurysm were identified. Fifteen patients with 16 CAOs treated with a FDS were included. Mean follow-up was 4.1 ± 2 years. Six of these patients (40%), presented ophthalmic complications, including three fugax amauroses (18.8%) and four significant visual field defects (25%). After comparing each eye visual field's patients, we observed a statistically significant difference between the eye on the FDS side compared to the contralateral eye, with a mean deviation of -1.68 dB versus -0.89 dB respectively ($p = 0.004$). Visual acuity was preserved in all patients.

Conclusions

Patients treated by FDS for COA have overall a good long-term clinical ophthalmic outcome. However, extensive ophthalmic examination shows a high percentage of minor modifications such as small visual field defects. Interventional neuroradiologists should be aware of these possible complications when choosing to treat these aneurysms with FDS.

O-113

3:56PM - 4:03PM

Parent Artery Occlusions Following Use of SILK Flow Diverters for Treatment of Intracranial Aneurysms

I Macdonald¹, J Shankar¹

¹Dalhousie University, Halifax, Nova Scotia, Canada

Purpose

SILK flow diverters (SFD) are an important tool in the treatment of complex intracranial aneurysms. The efficacy of SFDs in the management of cerebral aneurysms has been established; however, the risk of complications in particular parent artery occlusion has yet to be fully elucidated. The purpose of our study was to analyze our single-center database of intracranial aneurysms treated with SFDs and assess for rates and potential risk factors for parent artery occlusion.

Materials and Methods

Between September 2010 and September 2017, 35 patients were treated for intracranial aneurysms using SFDs at a Canadian institution by an experienced interventional neuroradiologist. This database was retrospectively analyzed for frequency of parent artery occlusions and then for potential contributing factors such as patient demographics, aneurysm characteristics, and technical aspects of the procedure. t-Test and chi-squared tests were performed using SPSS.

Results

Following treatment with SFDs, average clinical and imaging follow-up was 31 and 22 months, respectively. Aneurysms were located in the anterior circulation in 28 patients and in the posterior circulation in 7 patients with a mean diameter of 13.76 mm (range- 4-25 mm). Parent artery occlusions were identified in 22.8% (8/35) of patients, were all associated with anterior circulation aneurysms ($p=0.107$), and predominantly resulted in asymptomatic internal carotid artery occlusion. Of these, 50% (4/8) had a fusiform shape compared with only 18% (5/27) in nonoccluded patients ($p=0.074$). In those with parent artery occlusion, 62.5% (5/8) were asymptomatic upon clinical follow-up. Notably, the

presence of clinical symptoms at the time of initial SFD intervention was significantly associated with parent artery occlusion (p=0.012).

Conclusions

The risk of parent artery occlusion, in intracranial aneurysms treated with SFD, was high, but most remained asymptomatic with this complication. Aneurysms that were symptomatic at time of initial intervention demonstrated higher risk of parent artery occlusion.

O-114

4:03PM - 4:10PM

Flow diversion for the treatment of basilar apex aneurysms

A Dmytriw¹, N Adeeb², P Foreman³, C Griessenauer², A Kumar⁴, C Ogilvy², K Phan², H Shallwani⁵, N Limbucci⁶, S Mangiafico⁶, C Michelozzi⁷, T Krings⁸, V Pereira⁹, C Matouk¹⁰, Y Zhang¹¹, M Harrigan³, H Shakir⁵, A Siddiqui⁵, E Levy⁵, L Renieri⁶, C Cognard¹²

¹University of Toronto, Toronto, ON, ²Beth Israel Deaconess Medical Center, Harvard Medical School, Boston, MA, ³University of Alabama, Birmingham, AL, ⁴St. Michael's Hospital, Toronto, Ontario, ⁵State University of New York at Buffalo, Buffalo, NY, ⁶University of Florence, Florence, Italy, ⁷Michallon Hospital, La Tronche, Tououse, ⁸University of Toronto, Toronto, Ontario, ⁹Toronto Western Hospital and University Health Network, Toronto, Ontario, ¹⁰Yale University School of Medicine, New Haven, CT, ¹¹Toronto Western Hospital, University Health Network, Toronto, Ontario, ¹²University Hospital of Toulouse, Toulouse, Toulouse

Purpose

Flow diversion for posterior circulation aneurysms constitutes an increasingly common off-label use. Certain basilar apex aneurysms are daunting lesions that present a significant treatment challenge. This is the largest study of basilar apex aneurysms treated with flow diversion to date.

Materials and Methods

A retrospective review of prospectively maintained databases at eight academic institutions was performed from the years 2009 to 2016 to identify patients with basilar apex aneurysms treated with a flow diverter. Clinical and radiographic data were analyzed with emphasis on occlusion and complication rates.

Results

Sixteen consecutive patients (median age 54.5 years, male:female ratio of 1:2.2) underwent 18 procedures to treat 16 posterior circulation aneurysms with either Pipeline Embolization Device or Flow Redirection Endoluminal Device. Except for 1 patient, all other aneurysms resulted in some symptomatology. Five procedures (31.3%) were performed in the setting of aneurysmal subarachnoid hemorrhage, with 4 for saccular and 1 for blister morphology. At a median follow-up of 6 months, complete (100%) and near-complete (90-99%) occlusion was noted in 68.8% of aneurysms. The rate of partial (<90%) occlusion was higher in patients treated with flow-diversion alone (42.9%) compared to flow-diversion with coiling (22.2%). There was no difference in mRS at follow-up between those with adjunctive coiling and those without. Patients with partial occlusion were significantly younger compared to those with near complete occlusion and complete occlusion (54.2±4.6 vs 67.3±5.6 vs 59.4±8.7 years, P=0.016). Retreatment with an additional flow-diverter occurred in patients with larger aneurysm necks (8 and 15 mm) and adjunctive coiling, but had no other attributes in common. Major complications (≥ 2 points in mRS change) occurred in one patient (6.3%), who experienced PCA and cerebellar strokes as well as SAH after placement of a single flow diverter. Minor complications occurred in 2 additional patients (12.5%). Symptomatic thromboembolic and hemorrhagic complications occurred in 11.1% of procedures each, all of which were immediate. One procedure resulted in development of perianeurysmal edema and mass effect (5.6%), the only minor complication which affected mRS. Aneurysms with intraluminal thrombus had higher complication rates even though similar in size. At 6 latest follow-up, 87.5% of patients had either an improved or comparable mRS to presentation.

Oral Presentations & Excerpts

Conclusions

Flow diversion for the treatment of basilar apex aneurysms results in acceptable occlusion rates in highly selected cases. Both primary flow diversion and rescue after failed clipping or coiling resulted in mRS that was either equal or better than at presentation and the technology represents a viable alternative or adjunctive to these techniques.

O-115

4:10PM - 4:17PM

Multiparametric MRI Follow-up of Intracranial Aneurysms Treated with the Woven EndoBridge (WEB): a Case of Faraday's Cage?

M Nawka¹, J Sedlacik¹, A Frölich¹, M Bester¹, J Fiehler¹, J Buhk¹

¹*University Medical Center Hamburg-Eppendorf, Hamburg, Germany*

Purpose

To evaluate multiparametric initial and six months' follow-up MRI both including noncontrast and contrast-enhanced morphological and angiographic techniques of intracranial aneurysms treated with the single-layer Woven EndoBridge (WEB) embolization system applying simultaneous DSA as reference of standard.

Materials and Methods

We retrospectively identified all patients with incidental and acute ruptured intracranial aneurysms treated with a WEB device (WEB SL and WEB SLS) between March 2014 and June 2016 in our neurovascular center with early (within seven days) postinterventional multiparametric MRI as well as midterm (5-8 months) follow-up MRI and DSA available. Occlusion rates were recorded both in DSA and MRA. In MRI, signal intensities within the WEB as well as in the occluded dome distal to the WEB, if present, were measured by region-of-interest analysis.

Results

Twenty-five patients fulfilled the inclusion criteria. Rates of complete/adequate occlusion at mid-term F/U were 84% (same in MRA and DSA). There was no significant difference between initial and follow-up MRI comparing the region of interest (ROI) inside the WEB in both noncontrast ($p=0.946$) and contrast-enhanced imaging ($p=0.377$), although a hyperintense thrombus in the not WEB-carrying dome was repeatedly observed.

Conclusions

MRA is consistent with DSA with regard to short and midterm follow-up after WEB-embolization of intracranial aneurysms. However, signal intensity measurements suggest that neither CE MR angiography nor morphological sequences are capable of revealing reliable information on the WEB lumen, presumably due to RF shielding. Performing at least one DSA exam for follow-up is highly recommended.

O-116

4:17PM - 4:24PM

Aneurysm Remnants after Flow Diversion: Clinical and Angiographic Outcomes

T Madaelil¹, B Howard¹, C Cawley¹, F Tong², D Haussen¹, J Grossberg¹

¹*Emory University, Atlanta, GA*, ²*Emory University School Of Medicine, Atlanta, GA*

Purpose

Flow diversion is an established method to treat aneurysms not amenable to microsurgical clipping or coil embolization. However, long-term imaging and clinical data with respect to aneurysm remnants after flow diversion remain sparse. Our goal was to evaluate the longitudinal angiographic and clinical outcomes of aneurysm remnants after flow diversion.

Materials and Methods

A prospectively-maintained institutional database of patients treated with pipeline embolization device was searched from inception until October 2017 for patients that demonstrated residual filling on follow-up imaging. Patient-level information regarding aneurysm characteristics, procedural details, and clinical follow-up were all collected into an electronic database. These data points included patient characteristics of age, sex, familial history of aneurysms, tobacco use; aneurysm characteristics include type, size, and location; procedural details such as number of devices used, use of adjunctive devices during PED placement, and clinical outcome with duration of both clinical and radiographic follow-up. Incomplete occlusion status was defined as class A-C based on O'Kelly-Marotta (OKM) grading scale for assessment of aneurysms treated by flow diversion after independent retrospective review of follow-up imaging by a fellowship trained neuroradiologist who did not participate in the initial procedure. Complete occlusion was defined as class D based on OKM grading scale. The association between demographic and clinical risk factors on incomplete occlusion, as well as long-term clinical outcome for patients with incomplete occlusion versus patients with complete occlusion was evaluated using Fisher's exact and two-tailed t tests for categorical and continuous variables, respectively. The threshold of statistical significance was $\alpha=0.05$. All statistical analyses were performed using SPSS V22 (IBM Corp, Armonk, NY, USA) and Excel 2007 (Microsoft Corp, Redmond, Washington, U.S.).

Results

During the study period 296 interventions were performed in 283 patients in order to treat 294 distinct aneurysms. Overwhelmingly, 87% of the patients treated were female with a median patient age of 55 years (IQR 47-65 years). Minimum six-month follow-up imaging was available in 84.5% (239/283) patients which included both DSA (86.2%; 206/239) and MRA (13.8%; 33/239). At six months, 61.5% (147/239) of aneurysms demonstrated complete occlusion (class D-OKM scale), 23.8% (57/239) of aneurysms had entry remnant (class C-OKM scale), and 13.4% (32/239) aneurysms had subtotal filling (class B-OKM scale). In patients with available late surveillance imaging at a median duration of 16 months (IQR 12-24 months), progressive complete occlusion was observed in 40.5% (17/42) aneurysms (class D-OKM scale). Higher rates of progressive complete occlusion were observed in aneurysms with remnant necks (44.4%, 12/27; class C-OKM scale) as opposed to aneurysms with subtotal filling (33.3%, 5/15; class B-OKM scale), although this trend was not statistically significant ($p=0.53$). Procedural characteristics and aneurysm morphology played an important role on aneurysm occlusion on midterm (6 month) imaging follow-up. The presence of adjunctive coil during initial PED placement did result in higher rates of complete occlusion at 6 months (73.9%, 34/46 vs. 58.6%, 99/169)($p=0.06$). On-label use of PED was associated with higher rate of occlusion (73.0%, 54/74) than off-label use (58.5%, 93/159) ($p=0.04$). In addition, the use of more than one device during the procedure resulted in higher rates of complete occlusion at 6 months (79.5%, 31/39) versus a single device (58.9%, 116/197) ($p=0.02$). There was no correlation between wide necked aneurysms ($>4\text{mm}$) or diameter ($>10\text{mm}$) and the rate of occlusion ($p=0.29$, $p=0.52$). Of the aneurysm remnants 25 available for clinical analysis based on last known follow-up imaging, none had delayed rupture with a median clinical follow-up of 31 months.

Conclusions

Aneurysm remnants after flow diversion are infrequent with minimal clinical impact. When appropriate, the presence overlapping devices and on-label usage may result in higher rates of complete occlusion.

O-116a

4:24PM - 4:31PM

A Deep Learning Approach to Automated Cerebral Aneurysm Detection on Magnetic Resonance Angiograms

J Stember¹, P Chang¹, J Grinband², C Filippi³, M Liu¹, S Marfatia¹, P Meyers², A Lignelli¹, S Jambawalikar¹

¹Columbia University Medical Center, New York, NY, ²Columbia University, New York, NY, ³Hofstra Northwell School of Medicine, New York, NY

Oral Presentations & Excerpts

Purpose

Convolutional neural networks (CNNs) have become widely recognized as the best performing method in various image analysis challenges. We seek to demonstrate that a CNN can automatically detect cerebral aneurysms from magnetic resonance angiographic (MRA) images.

Materials and Methods

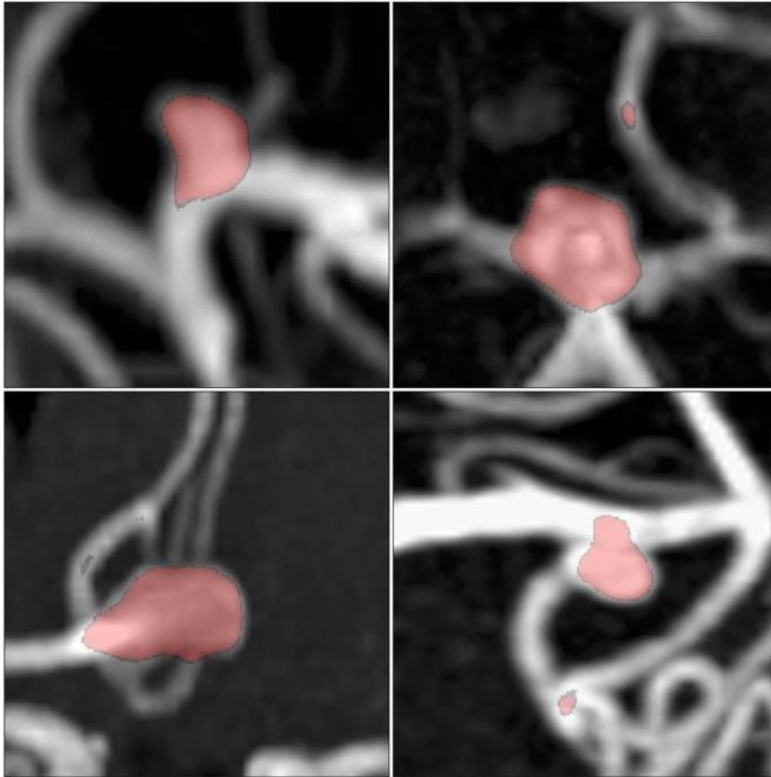
Three-hundred-thirty-six MRA maximum intensity projection (MIP) images of aneurysms at least 3 mm in maximum dimension were obtained from the PACS database. Images were normalized via z-score standardization (mean=0, S.D.=1). Aneurysms were manually localized by an approximate polygonal ROI. A 21-layer CNN based on the U-net architecture [1] was used for aneurysm detection. Extensive real-data augmentation included: (1) random left-right and up-down image flips, (2) random image rotation by 0 to 360 degrees, (3) random affine transformations, (4) random displacement by -10 to +10 voxels in row and column directions, (5) random scaling by 75 to 150%.

Results

The proposed CNN successfully identified presence and location of aneurysm in 85/86 (98.8% of) test cases, with a receiver operating characteristic (ROC) area under the curve value of 0.87. The higher true positive rate region of the ROC curve is felt to be more clinically useful, since the goal is high sensitivity in bringing possible aneurysms to the radiologist's attention. Examples of test image aneurysm localization are shown in Figure 1.

Conclusions

The deep-learning approach shows promise as a method to automatically predict and detect cerebral aneurysms. Here we have built on our prior work with conventional angiograms [2] to demonstrate proof-of-principle for MRA images. Future applications will focus on fully three-dimensional MRA and CTA data sets. Additional training data, along with three-dimensional representations, are expected to permit more accurate identification of smaller and more subtle aneurysms. The approach can be used as a second reader to improve accuracy of radiologist interpretation, or to bring potential aneurysms to the radiologist's attention for contrast-enhanced MRIs in which the primary clinical concern is not related to vessels. Another application is for triage of images with a high likelihood of containing aneurysms for expedited radiologist interpretation.



(Filename: TCT_O-116a_figurePanel.jpg)

Monday, June 4, 2018

3:00PM - 4:30PM

Excerpta: Adult Brain: Infectious Disease/Vascular Diagnosis and Neoplasms

E-22

3:00PM - 3:04PM

Leptomeningeal Inflammation in Multiple Sclerosis as a Link to Cortical Pathology: An Unfamiliar Entity to Many Radiologists

R Kurtz¹, K Learned², S Chawla³, S Mohan⁴

¹Hospital of the University of Pennsylvania, Philadelphia, PA, ²University Pennsylvania Health System, Philadelphia, PA, ³Hospital of the University of Pennsylvania, Wallingford, PA, ⁴University of Pennsylvania, Philadelphia, PA

Purpose

While accumulating evidence suggests an important role for cortical and subpial pathology in patients with multiple sclerosis (MS), little is known about their incidence, natural history, treatment response, or prognostic value because they are difficult to detect on conventional MRI. We discuss image acquisition techniques and appearances of leptomeningeal inflammation and enhancement on high-resolution MRI, with the aim to expose more radiologists to the presence of this recently described entity.

Oral Presentations & Excerptas

Materials and Methods

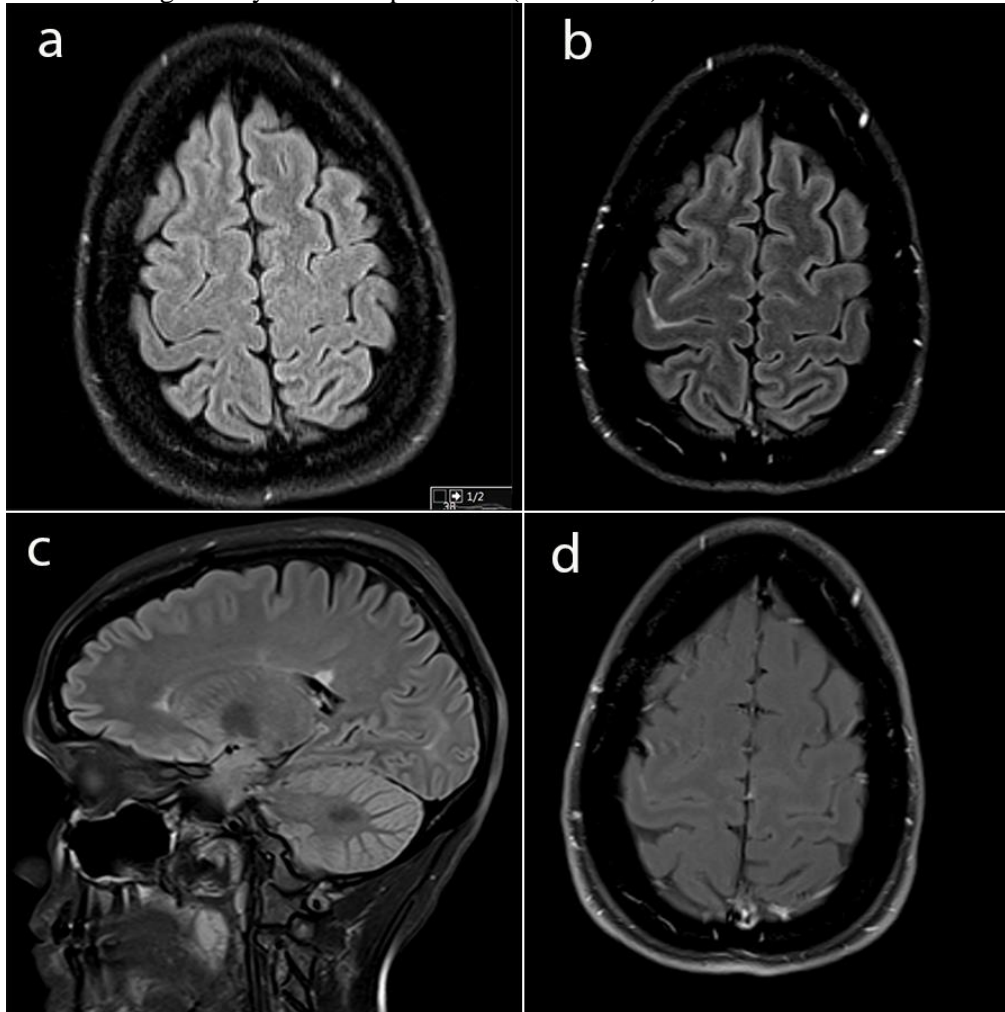
A 34-year-old female presented with multiple sclerosis for over 10 years, currently being treated with peginterferon beta-1a. No other significant past medical history and with a stable neurological exam.

Results

Multiple scattered white-matter lesions in the periventricular and juxtacortical white matter as well as within the corpus callosum and spinal cord (image c), consistent with history of MS. Linear and nodular areas of sulcal abnormality were seen on the postcontrast FLAIR sequence along bilateral frontal convexities, more prominent on the right (image b). These were not seen on the noncontrast FLAIR image (image a) but potentially faintly visualized on the postcontrast T1 image (image d).

Conclusions

It is often felt that the presence of leptomeningeal enhancement on MRI should lead to consideration of alternate diagnoses other than demyelinating disease. However, high-resolution delayed postcontrast FLAIR images cannot only detect leptomeningeal enhancement but may also be a useful biomarker for meningeal inflammation and cortical demyelination in patients with MS (references 1 and 2). The optimal MRI approach to define and detect leptomeningeal enhancement requires further research, with potential increased diagnostic yield of 7T platforms (reference 3).



(Filename: TCT_E-22_4imageswithletters.jpg)

E-23

3:04PM - 3:08PM

Hyperintense CSF on FLAIR imaging after previous gadolinium administration

Oral Presentations & Excerptas

A Postma¹, A Stadler^{21/sup>}

¹MUMC+, Maastricht, the Netherlands

Purpose

MR imaging of the brain, often with i.v. gadolinium for detection of blood-brain-barrier disruption, is standard of care in patients suspected of intracerebral pathology. There is an ongoing discussion regarding NSF with linear contrast agents in patients with kidney failure and more recently the deposition of gadolinium in the brain. We present two patients with kidney failure, in whom enhancement of the CSF and eyes was present at imaging of the brain one and two days after a previous gift of i.v. macrocyclic gadolinium.

Materials and Methods

Patient 1 Clinical history A 64-year-old male patient with NSCLC developed renal failure and was diagnosed with renal infarcts at CT. No fever, no headache were present. Lab findings demonstrated an eGFR of 15.7 mL/min/1.73m. No signs of infection were found. He underwent contrast-enhanced MRA of the renal arteries under the suspicion of renal artery thrombosis, which was read as normal. A total of 15 cc gadovist was administered. The next day (22 hours later) he underwent MRI of the brain to rule out cerebral metastasis. Precontrast T1-weighted images showed hyperintensity of the choroid plexus and cerebral vessels. FLAIR images (fig) demonstrated (a) high signal intensity in the peripheral CSF (nonsuppressed), (b) high signal intensity in the Virchow robin spaces, (c) increased signal in the corpus vitreum and (d) high signal intensity in the anterior chamber of the eye, as well as increased signal intensity in the perilymphe of the inner ear (e). There was normal suppression of the intraventricular CSF. Because at first this was interpreted to be an artifact with insufficient suppression of fluid, the patient was rescanned with additional inversion times and at a different scanner. However, the high signal intensities persisted. **Patient 2** A 50-year-old male with a history of systemic lupus erythematosus and with known renal failure underwent an MRI of the spine with administration of 10 cc gadovist, to rule out spondylodiscitis. He was on dialysis and eGFR was 12.6 mL/min/1.73m. Two days later he underwent an MRI of the brain because of seizures. Hyperintensity of the peripheral CSF at FLAIR imaging was noted. Moreover, there was an increased signal intensity of the eye vitreum and the anterior eye chamber, as well as the perilymphe at the inner ear.

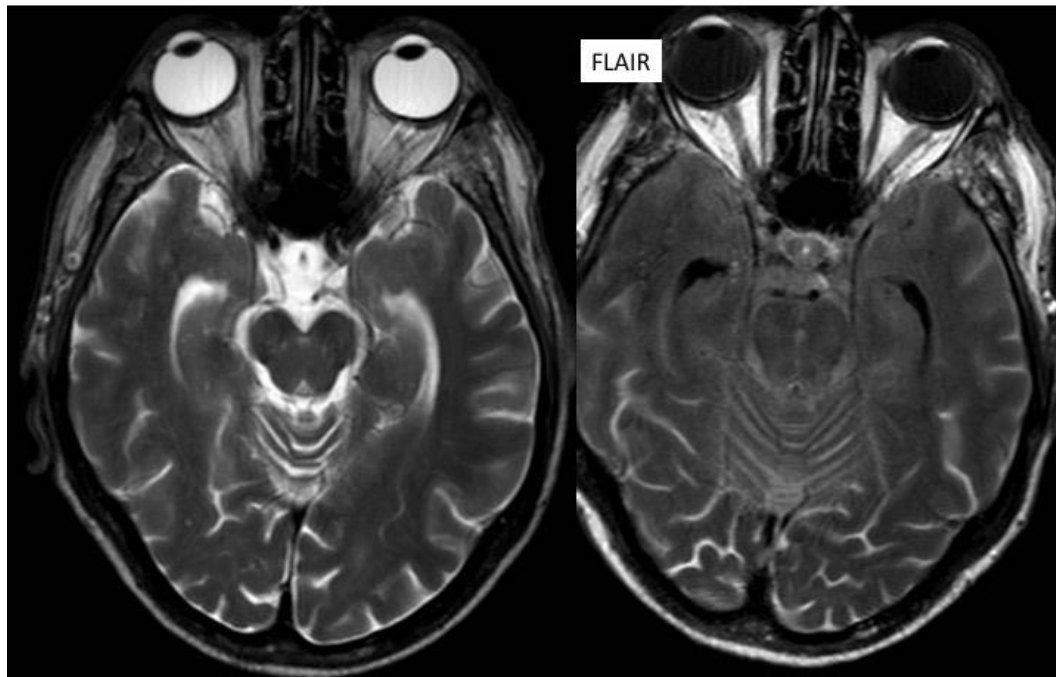
Results

Described at the case

Conclusions

Hyperintensity of CSF after i.v. administration of gadolinium on T1-w images is seen in case of meningitis or leptomeningeal metastasis, due to the T1 effect of FLAIR. In case of meningitis or hemorrhage, the elevated protein content can let CSF appear hyperintense on nonenhanced T1-w images. This can be mimicked in patients who underwent general anaesthesia shortly before being scanned, caused either by oxygen administration or medication. However, neither of the two patients showed clinical evidence for meningitis or subarachnoid hemorrhage nor did they have an altered mental status, underwent general anaesthesia prior to the MRI or were in need of oxygen. The phenomenon of CSF hyperintensity days after administration of i.v. gadolinium chelates was already described in 2000. In 2007 Morris et. al. observed the same effect in 11 patients between one and six days post gadolinium. To rule out hemorrhage or meningitis, most of the patients underwent lumbar puncture, without abnormalities at CSF analysis. They stated that the hyperintensity of peripheral CSF could be explained by the prolonged presence of gadolinium in the serum in patients with impaired kidney function. Pietsch et al. stated that small gadolinium molecules could leave the vessels of the choroid plexus into the interstitium, getting into the CSF and with the flow from the ventricles into the subarachnoid space. There, they accumulate, whereas they would be transported via the venous system to the kidneys to be cleared. Gadolinium administration received a lot of attention, initially in the context of NSF and more recently with deposition in the brain after repeated administrations. The phenomenon of the presence of gadolinium in the CSF and other structures in patients with renal failure has been described long ago, but

is not widely known. Radiologists should be aware of this phenomenon and keep this differential in mind when encountering patients with high CSF signal.



(Filename: TCT_E-23_FlairhyperintensityperipheralCSF.jpg)

E-24

3:08PM - 3:12PM

Reversible Sulcal FLAIR Hyperintensity on MRI in a Patient with Migraine with Aura

E Portela de Oliveira¹, V Tsehmaister Abitbul¹, M Kontolemos¹, R Glikstein², C Torres¹

¹University of Ottawa - The Ottawa Hospital, Ottawa, Ontario, Canada, ²University of Ottawa, Ottawa, Ontario, Canada

Purpose

Migraine is a neurologic disorder that affects roughly 10%–15% of the general population characterized by paroxysmal attacks of unilateral throbbing headache and autonomic nervous system dysfunction. Approximately one-third of patients with migraine experience transient neurological symptoms known as auras, which characterize a variant known as migraine with aura. More recent investigations in patients with aura also demonstrated volumetric changes in gray- and white-matter regions, leptomeningeal postgadolinium enhancement, cortical swelling, or cortical hyperintensity in fluid-attenuated inversion recovery (FLAIR), sequence. A rare entity that has been described in the literature affecting patients with aura is the Reversible Sulcal Hyperintensity. To the best of our knowledge, there are only two case reports in the literature describing reversible MRI hyperintensity involving the sulci. Herein, we present a patient with transient sulcal hyperintensities on (FLAIR) images during a migraine attack.

Materials and Methods

We present a case of a 66-year-old, right-handed woman with acute bilateral frontal headache and visual changes characterized as migraine with aura. The woman was diagnosed with migraine with aura four months previously when she presented symptoms of headaches, vertigo and right-sided numbness. The patient's medical history was negative for hypertension and seizure disorder. She denied a family history of migraine and has been recently diagnosed with paroxysmal atrial fibrillation. In this current acute

Oral Presentations & Excerpts

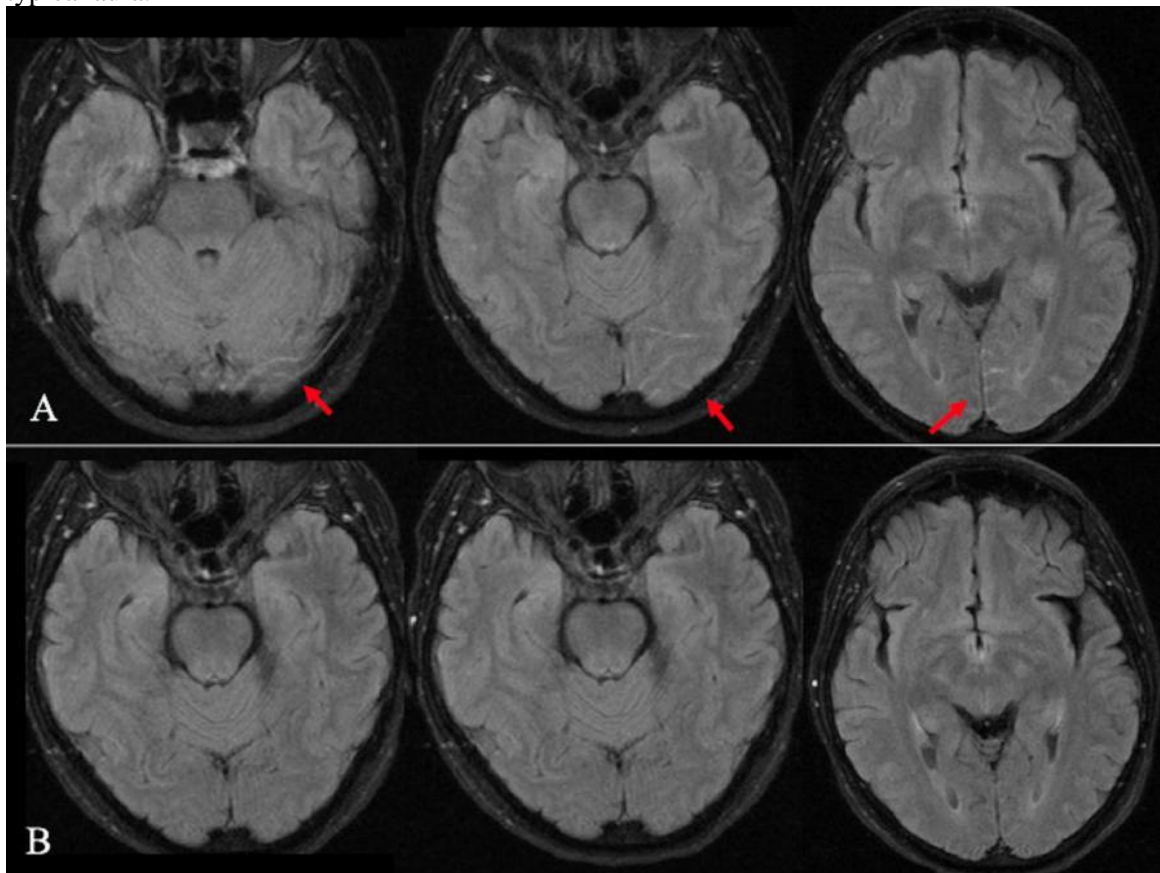
episode of headache, she presented the emergency department with reversible visual changes characterized by sparkling lights in the periphery of her vision lasting up to 20 min. An MRI was performed.

Results

1.5T MRI brain showed T2-FLAIR hyperintensity within some of the cerebral sulci in the occipital lobes. (Fig. 1A) There was no associated abnormal enhancement or restricted diffusion. GRE sequences did not demonstrate areas of hemorrhage. Follow-up MRI 4 weeks after treatment demonstrated resolution of the sulcal hyperintensities in the occipital lobes. (Fig. 1B)

Conclusions

A rare entity that has been described in the literature affecting patients with aura is the Reversible Sulcal Hyperintensity. This abnormality demonstrated on MRI could be due to increased leptomeningeal vascularity with plasma extravasation and increased protein concentration. The proper clinical setting and the reversibility of imaging abnormalities suggest a neuronal inflammatory pathology in migraine with typical aura.



(Filename: TCT_E-24_Fig1.jpg)

E-25

3:12PM - 3:16PM

4D Flow MRI Shows Vascular Flow and Waveform Responses to Stereotactic Radiosurgery (SRS) for Brain Arteriovenous Malformations (AVMs) As Early As 2 Months Post Treatment

T Retson¹, C Li¹, J Hattangadi-Gluth¹, J Handwerker¹, R Karunamuni¹, A Hsiao¹, N Farid¹

¹University of California San Diego, La Jolla, CA

Purpose

To pilot 4-D Flow MRI assessment of early physiologic changes in cerebrovascular flow volume and waveforms after definitive stereotactic radiosurgery (SRS) for arteriovenous malformations (AVMs). We examine flow waveforms prior to, and within the first three months after SRS, providing the earliest noted evidence of treatment response.

Materials and Methods

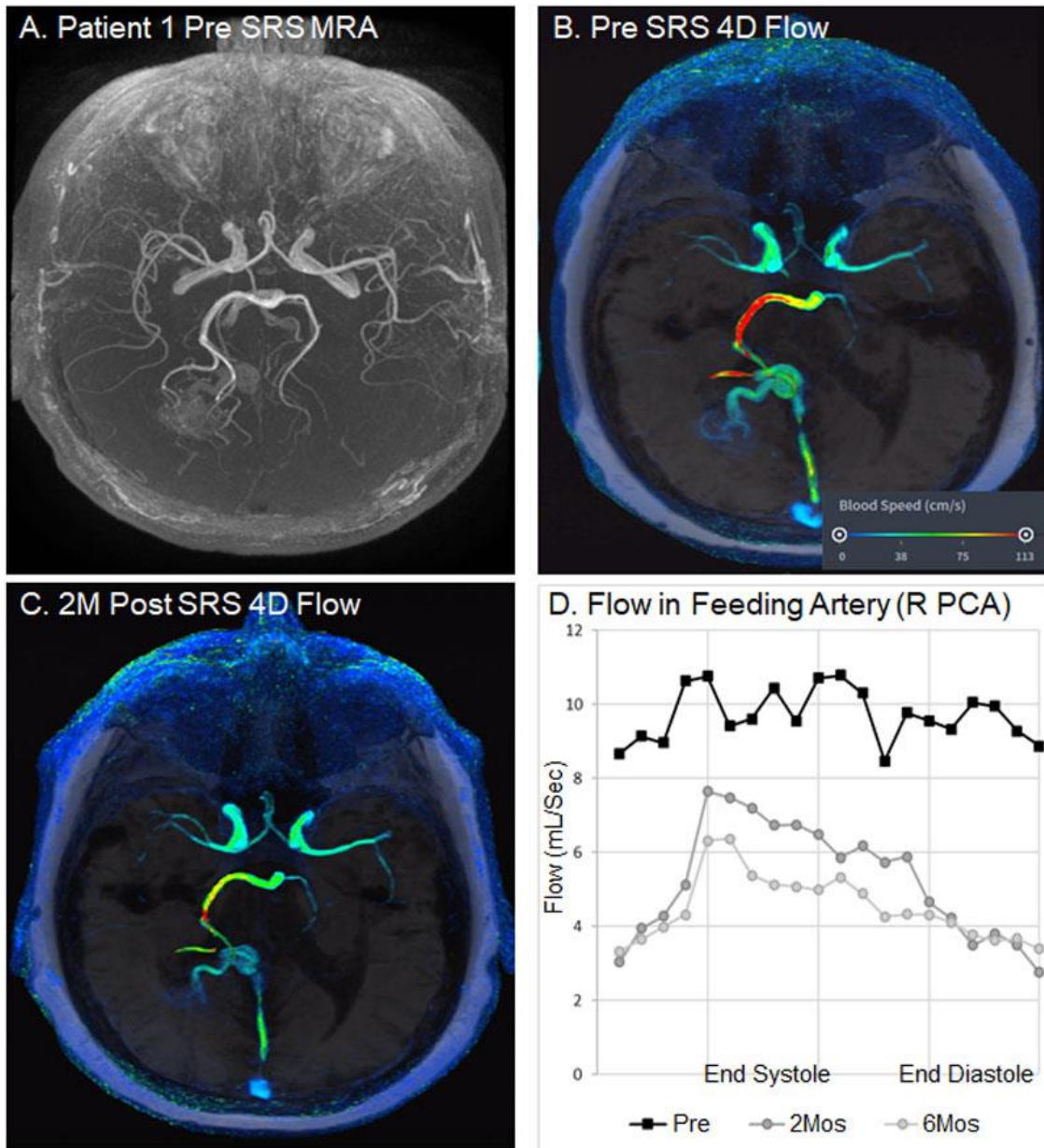
Findings are reported from two patients with temporal/occipital Spetzler-Martin grade 4 AVMs. Patient 1 is a 31-year-old male who underwent SRS (20Gy x 1), and Patient 2 is a 33-year-old female who underwent SRS (22Gy x 1).

Results

We previously presented a single case illustrating hemodynamic changes measured by 4-D Flow as early as six months after SRS (1). Here, MRI with 4-D Flow was performed before SRS and at follow up of two and six months (Patient 1), or three months (Patient 2). For Patient 1 (shown in the figure), two-month follow-up noted only subtle nidus change, and at six months there was a slight decrease in size of the nidus and draining vein. When examined with 4-D Flow, at two months there was a 54% reduction in flow of the supplying artery (PCA), and a 57% reduction in flow of the draining vein. Further, flow in both vessels changed from a consistent monophasic waveform to pulsatile. At six months change in PCA flow was stable while the draining vein decreased by an additional 19%. In Patient 2, at three-month follow-up the nidus had minimally decreased by 2mm; however, 4-D Flow showed a 58% flow reduction in the feeding artery and a 67% reduction in the draining vein.

Conclusions

In this study 4-D Flow is used to show physiologic changes occurring as early as two months after SRS in both the AVM feeding arteries and draining veins. Alterations in flow dynamics further reveal early remodeling not previously shown, and illustrate the potential for 4-D flow to assess and quantify SRS treatment response much earlier than with conventional imaging.



(Filename: TCT_E-25_ASNRFig.jpg)

E-26

3:16PM - 3:20PM

Primary Angiitis of the Central Nervous System: Lymphocytic Type.

A Guarnizo¹, V Tsehmaster Abitbul¹, N Zakhari¹, C Torres¹

¹University of Ottawa - The Ottawa Hospital, Ottawa, Ontario, Canada

Purpose

1. To review the clinical presentation, epidemiology and prognosis of lymphocytic vasculitis of the central nervous system
2. To discuss the imaging findings of the lymphocytic subtype of primary angiitis of the central nervous system

Materials and Methods

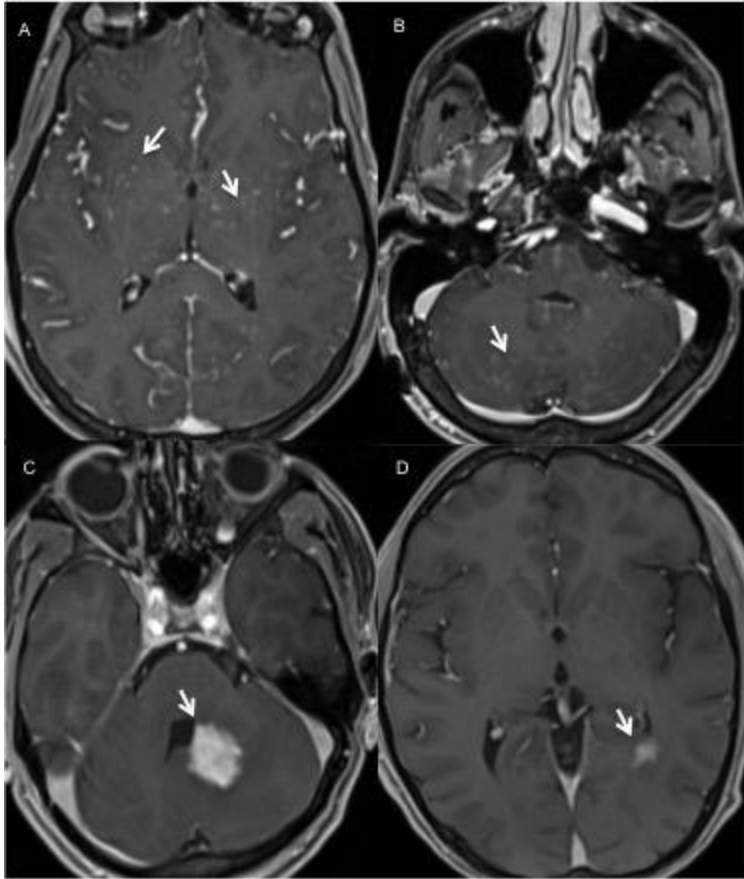
Previously healthy 24-year-old man presented with one week history of dizziness, vertigo, fatigue and confusion. On physical exam, he presented difficulty standing and difficulty with tandem gait walking. CSF cytology showed increased cellularity with many lymphocytes and monocytes. Cultures were negative for viruses, mycobacteria and fungus. Cytology was negative for malignancy. Brain and dura-mater biopsy showed chronic inflammation in the arachnoid space and perivascular topography, predominantly in the white matter, multiple infarcts of different ages involving both the cortex and the white matter with perivascular inflammation and mild gliosis. There was also fibrosis of the vessel walls with intramural lymphocytes. A second case of a 33-year-old man with one-month history of decreased coordination initially diagnosed as a vertigo will be presented as well. His symptoms included significant gait ataxia, decreased fine motor coordination of the left hand and associated paresthesias in both arms. On physical exam he presented with dysidiadochokinesia of left upper limb and prominent gait ataxia. The CSF cytology showed lymphocytes, monocytes and plasmacytoid cells. Cytology was negative for malignancy. The biopsy from a left cerebellar lesion showed changes highly suggestive of angiitis of the lymphocytic type associated with parenchymal mixed inflammatory infiltrate. It did not show features of neoplasm.

Results

Case 1. Axial T1W sequences post gadolinium (A and B) show multiple punctate enhancing foci in the cerebellum, in the pons and in the bilateral basal ganglia (arrows). Case 2. Axial T1W sequence post gadolinium shows an intra-axial avidly enhancing mass centered in the left cerebellar hemisphere causing partial effacement of the fourth ventricle (C). Axial T1W sequence post gadolinium (D) shows an irregular enhancing lesion in the left peritrial white matter.

Conclusions

Lymphocytic vasculitis is the second most common type of primary central nervous system angiitis. This rare inflammatory disorder affects small and medium size vessels of the brain and meninges. The diagnosis is challenging due to variable and nonspecific symptoms. The most common symptoms include headache, stroke, transit ischemic attacks, focal neurological deficits and altered cognition. Although brain biopsy is the gold standard, MRI of the brain with a sensitivity of 90% is a suitable modality to suggest the diagnosis. The prognosis of these patients is poor, with less than 50% survival, if left untreated, which makes an early diagnosis and prompt treatment imperative.



(Filename: TCT_E-26_LV.jpg)

E-27

3:20PM - 3:24PM

High Resolution Vessel Wall Imaging and Vasculopathy related to Herpes Zoster Ophthalmicus

J Song¹, S Ojeda¹, P Schaefer¹, J Romero¹

¹Massachusetts General Hospital, Boston, MA

Purpose

Varicella zoster virus (VZV) is a common viral infection with over 50% of patients over the age of 80 years infected. VZV reactivation can result in highly morbid complications related to vasculopathy. We show that high-resolution vessel-wall magnetic resonance imaging (HR-VWI) can aid in the diagnosis of vasculopathy related to herpes zoster ophthalmicus.

Materials and Methods

A 91-year-old male presented with a rash and burning facial dysesthesias over the left V1 distribution. He was diagnosed with herpes zoster ophthalmicus and treated with IV acyclovir. Three weeks later, he developed left cranial nerve 3 and 6 palsies. A MRI of the brain was negative. Cerebrospinal fluid was negative for VZV PCR but showed elevated VZV IgM and IgG. He was treated with another course of IV acyclovir for a diagnosis of VZV reactivation. Three months later, he returned with right facial droop and weakness and dysarthria. A brain MRI revealed acute infarcts in the left basal ganglia and corona radiata (Fig. A). A computerized tomography angiography (CTA) of the head revealed severe left ICA terminus stenosis extending into the left M1 MCA (Fig. B). HR-VWI revealed concentric thickening and enhancement of the left ICA terminus (Fig. C-D). Taken together with the clinical history and laboratory serologies, the findings were consistent with VZV vasculitis.

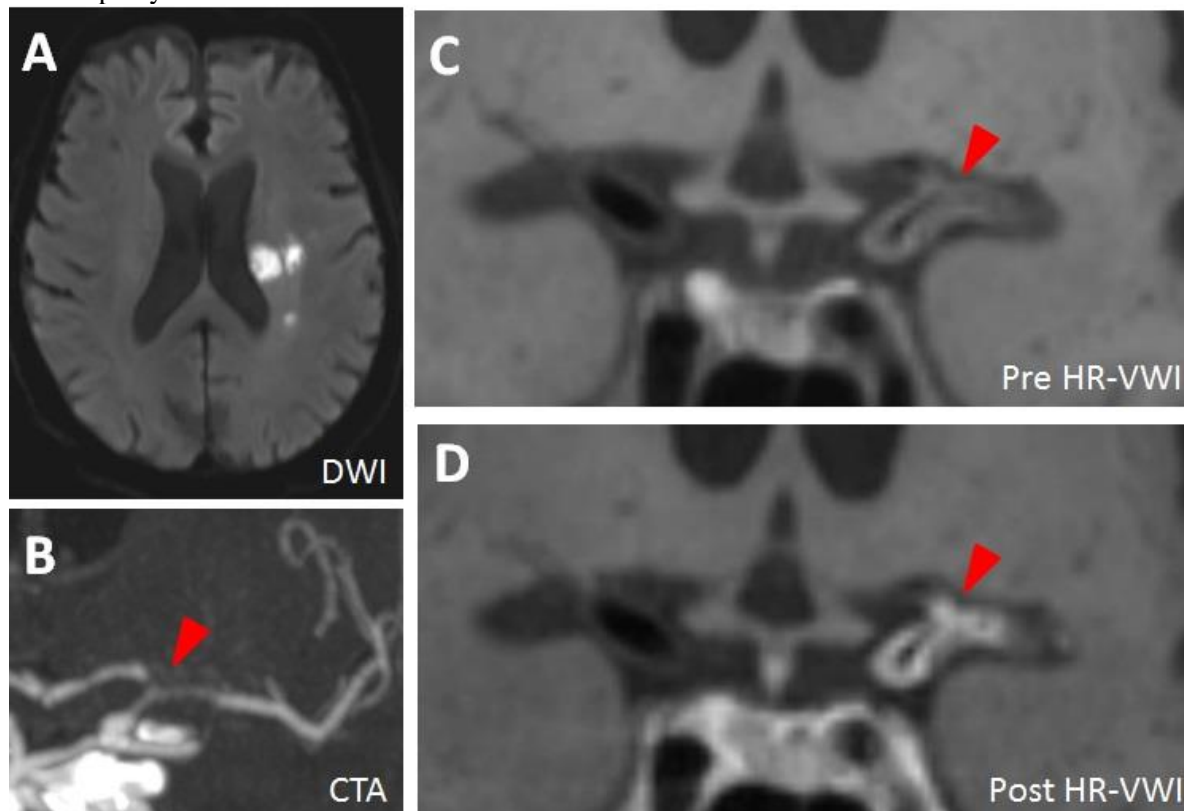
Oral Presentations & Excerptas

Results

(A) A MRI Brain (DWI and ADC maps) shows acute infarcts extending into the left corona radiata. (B) Coronal 3-D MIP CTA head image shows severe left ICA terminus stenosis. (C) Pre and (D) postcontrast HR-VWI shows wall thickening and enhancement of the left ICA terminus.

Conclusions

Given the high prevalence of latent VZV infection, awareness of the risk of stroke is critical for the clinician for an expedient diagnosis and treatment plan. HR-VWI can aid in the diagnosis of VZV vasculopathy.



(Filename: TCT_E-27_Figure.jpg)

E-28

3:24PM - 3:28PM

Moyamoya type Occlusion of the Left Internal Carotid Terminus Related to Neuro-Behcet's Vasculitis

F Boucher¹, M Manganaro², J Griauzde³, R Lobo², C Centonze²

¹University of Michigan, Ann Arbor, MI, ²University of Michigan, Ann Arbor, MI, ³University of Michigan health System, Ann Arbor, MI

Purpose

Demonstrate a rare cause of Moyamoya pattern in a patient presenting with new onset left leg weakness

Materials and Methods

A 16-year-old male with NFK B1A gene variant immunodeficiency, disseminated mycobacterial avium complex infection, currently undergoing treatment, prior ulcerating small and large bowel disease, previously diagnosed as Crohn's and recurrent mouth ulcerations presents with new onset left lower extremity weakness. MRI/MRA were ordered; findings later confirmed with conventional cerebral angiography.

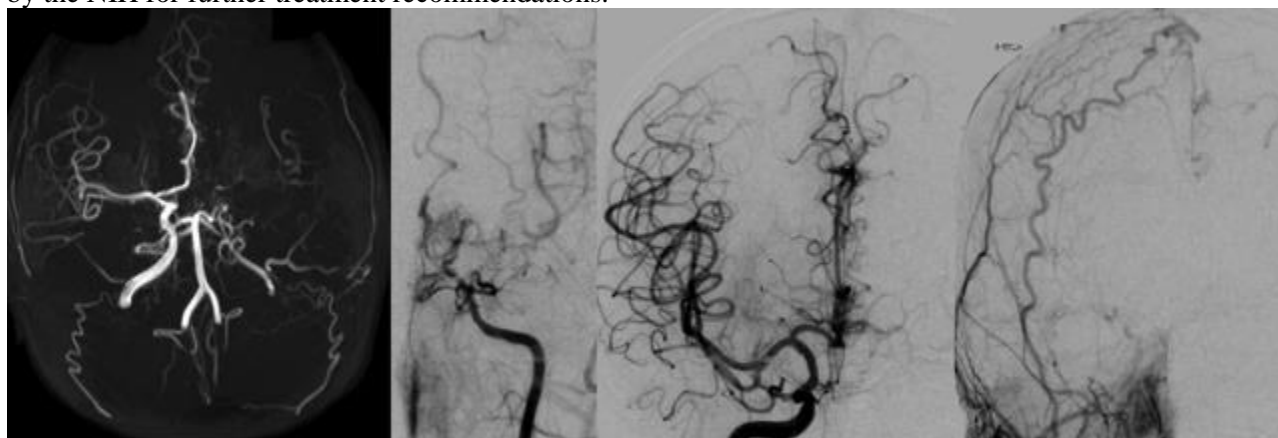
Oral Presentations & Excerptas

Results

Multislab 3-D TOF MIP images demonstrate no flow-related enhancement of the left internal carotid terminus, A1 or M1 segments of the anterior and middle cerebral arteries, respectively. There is flow-related enhancement in prominent left lenticulostriate vessels. Diffusion-weighted sequences (not shown) reveal no signal abnormalities in these same vascular distributions. There are, however, foci of restricted diffusion, predominantly within the supratentorial right cerebral hemisphere, correlating with the patient's symptoms. The above findings are supported on subsequent conventional angiography. Additional findings demonstrating collateral flow to the left internal carotid vascular territories via right and left external carotid and left anterior cerebral arteries. Lumbar puncture to assess for various markers of vasculitis vs. infectious etiologies demonstrated pleiocytosis and mildly elevated CSF protein, but no other signs of infection.

Conclusions

Lengthy discussion of the patient's clinical course, imaging and laboratory findings between Pediatric Rheumatology, Pediatric Infectious Disease and Pediatric Neurology favored Neuro-Behcet's given the history of Crohn's-like illness, small and large bowel ulcers, recurrent mouth ulcerations, history of epididymitis and CNS pleiocytosis without additional signs of infection. Neurosurgery was consulted because of the Moyamoya type findings; surgical intervention was deferred in the absence of symptoms ipsilateral to the left internal carotid artery findings. The patient's symptoms improved with high-dosed oral prednisone, with only left foot drop persisting at discharge. Further treatment of presumed Neuro-Behcet's disease, such as biologic monotherapy, Rituxumab, was deferred at the time of discharge given the patient's ongoing therapy for disseminated Mycobacterial Avium Complex. The case is to be reviewed by the NIH for further treatment recommendations.



(Filename: TCT_E-28_MoyaMerged.jpg)

E-29

3:28PM - 3:32PM

Cerebellopontine Angle Cistern Arteriovenous Malformations – Understanding the Distinctive Angioarchitecture of a Unique and Challenging Entity

P Morden¹, H Marin¹, S Patel¹, B Griffith¹

¹Henry Ford Health System, Detroit, MI

Purpose

Cerebellopontine angle cistern AVMs are specific lesions that can cause neurovascular compression syndromes as well as intracranial hemorrhage. While increasingly recognized in the literature, these lesions remain challenging to treat due to their unique pathophysiology and angioarchitecture. This excerpt presents four such cases collected over the past seven years at a single institution and discusses lesion architecture, presentation, and treatment.

Oral Presentations & Excerptas

Materials and Methods

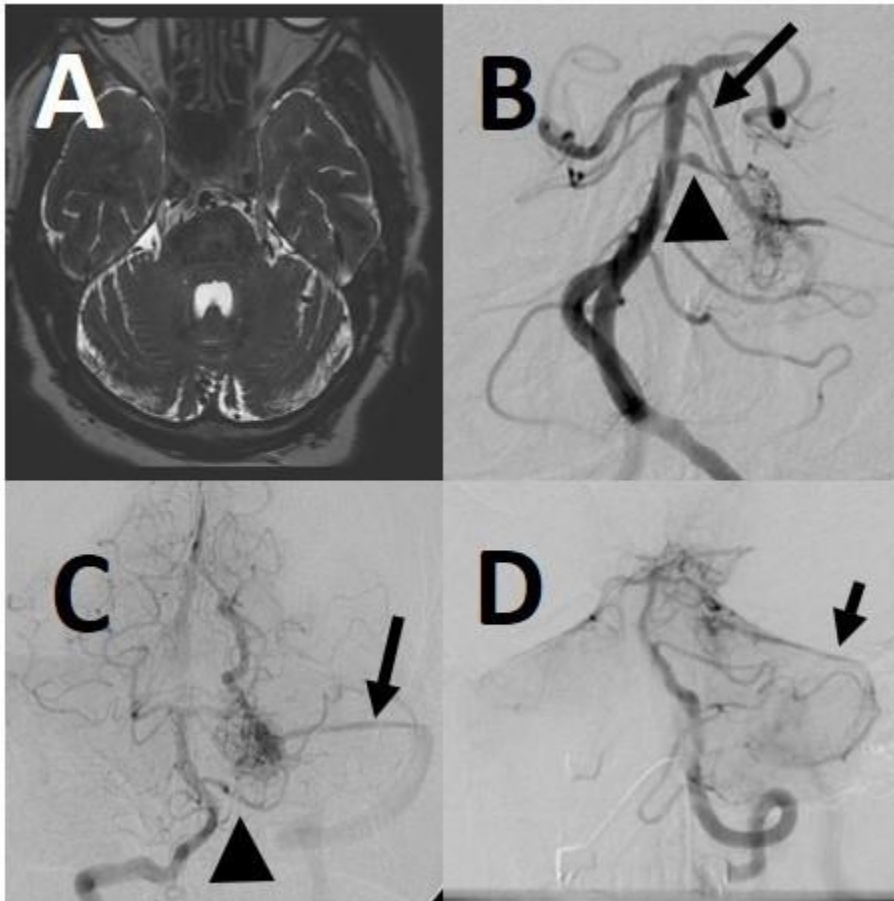
Cases 1 and 2: 57-year-old and 62-year-old males presenting with trigeminal neuralgia Cases 3 and 4: 46-year-old female and 63-year-old male presenting with headache with subarachnoid hemorrhage diagnosed on initial CT imaging All patients underwent MRI and digital subtraction angiography (DSA) prior to intervention.

Results

Thin-slice, heavily T2-weighted axial sequence demonstrates prominent, asymmetric flow voids surrounding the proximal left fifth cranial nerve in Case 1 (Figure 1A). Figures 1B, C, and D are DSA images of vertebral artery injections in Cases 1, 2, and 4, respectively. Intrinsic pontine arteries are seen to feed the nidi: superior cerebellar and pontine circumferential arteries in Figure 1B (arrow and arrowhead, respectively) and the anterior-inferior cerebellar artery in Figure 1C (arrowhead). Drainage of the nidi is via the superior petrosal sinus (Figures 1C, 1D arrows). There was a small aneurysm proximally within a feeding circumferential pontine artery in Case #1 (Figure 1B, arrowhead).

Conclusions

We present four cases of cerebellopontine angle cistern AVMs. In all four cases, the AVMs were fed by intrinsic pontine arteries and drained by the superior petrosal sinus. Two cases presented with trigeminal neuralgia and two with subarachnoid hemorrhage. The literature does not offer a clear-cut consensus on optimal treatment and strategies, which may be patient-dependent. Our institution has experienced complications with both surgical and endovascular approaches, including brainstem infarct and hemorrhage. Understanding the unique angioarchitecture of these lesions is essential to planning the appropriate treatment strategy.



(Filename: TCT_E-29_CPAngleAVMs.jpg)

Thyroid Storm Presenting with Moyamoya Syndrome

J Kang¹, F Torres¹

¹*Kaiser Permanente Los Angeles Medical Center, Los Angeles, CA*

Purpose

Moyamoya syndrome is a cerebral vasculopathy characterized by progressive stenosis of the internal carotid arteries (ICA), and formation of extensive collateral vessels. This syndrome has been reported to be associated with Graves' Thyrotoxicosis. We present an interesting case in which a patient presented with severe thyrotoxicosis and was found to have numerous watershed infarcts due to underlying Moyamoya syndrome. We will discuss the epidemiology, pathogenesis, salient imaging findings, and treatment options for this disease entity.

Materials and Methods

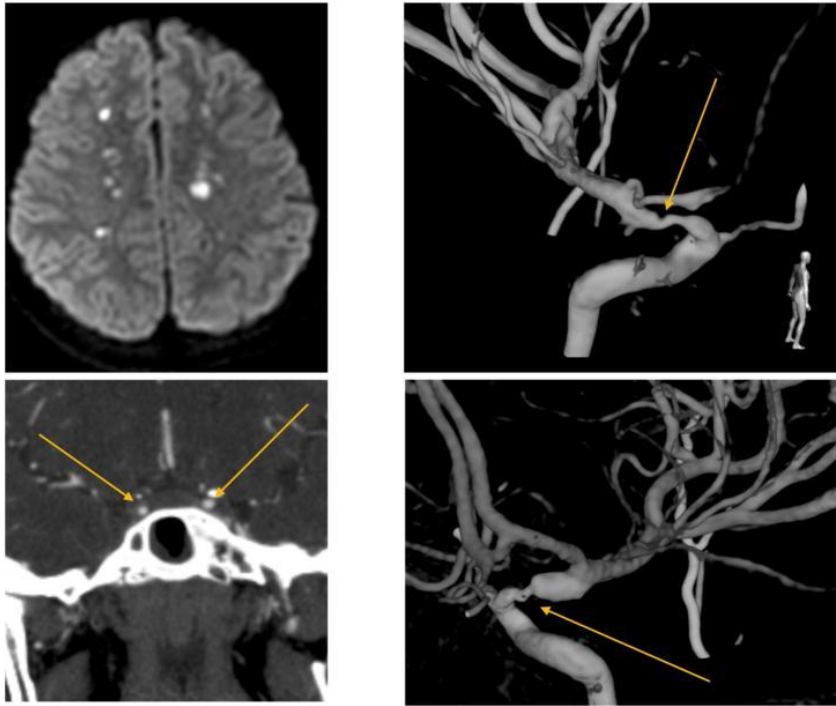
A 21-year-old female with Graves disease presented with acute altered mental status, found to be yelling, flailing, and thrashing her limbs upon waking up. Initial exam revealed profound neurological deficits including absent brainstem reflexes necessitating intubation and absent reflexive responses to noxious stimuli. Lab work was consistent with thyroid storm. On imaging, she was found to have bilateral watershed infarcts with a Moyamoya-like pattern of the cerebrovasculature. After systemic control of her thyrotoxicosis she had remarkable neurologic recovery.

Results

Initial MRI revealed numerous punctate infarcts in a watershed distribution in bilateral hemispheres. On angiogram, severe stenosis was seen in the bilateral supraophthalmic segments of the intracranial internal carotid arteries. Additionally, there was irregular narrowing of the proximal bilateral MCA, and the proximal bilateral ACA. There were posterior cerebral artery collaterals to the ACA and MCA branches.

Conclusions

Moyamoya syndrome associated with severe thyrotoxicosis is rare presentation of uncontrolled Graves' disease. The exact pathoetiologic linkage is unknown. Definitive treatment may be achieved through superficial temporal artery–middle cerebral artery anastomosis combined with encephalomyosynangiosis or encephaloduroarteriosynangiosis.



(Filename: TCT_E-30_MoymoyaImages.jpg)

E-31

3:36PM - 3:40PM

Persisting Embryonal Infundibular Recess

C Toh¹, T Siow¹, M Castillo²

¹Chang Gung Memorial Hospital at Linkou, Taoyuan, Taiwan, ²University of North Carolina at Chapel Hill, Chapel Hill, NC

Purpose

To report the imaging features of persistent embryonal infundibular recess (PEIR) on three-dimensional (3-D) constructive interference in steady state (CISS), which could readily distinguish PEIR from other pituitary cystic lesions

Materials and Methods

A 38-year-old woman was referred for evaluation of a pituitary cystic mass. MRI revealed a 10.2 mm cystic mass in an enlarged sella turcica. 3-D high-resolution MRI using constructive interference in steady-state sequence clearly delineated a communicating tract between the third ventricle and the sellar cyst through pituitary stalk (Figure 1). A final diagnosis of PEIR was made. The patient was successfully managed with conservative treatment and the lesion was in stationary condition over a five year follow-up period.

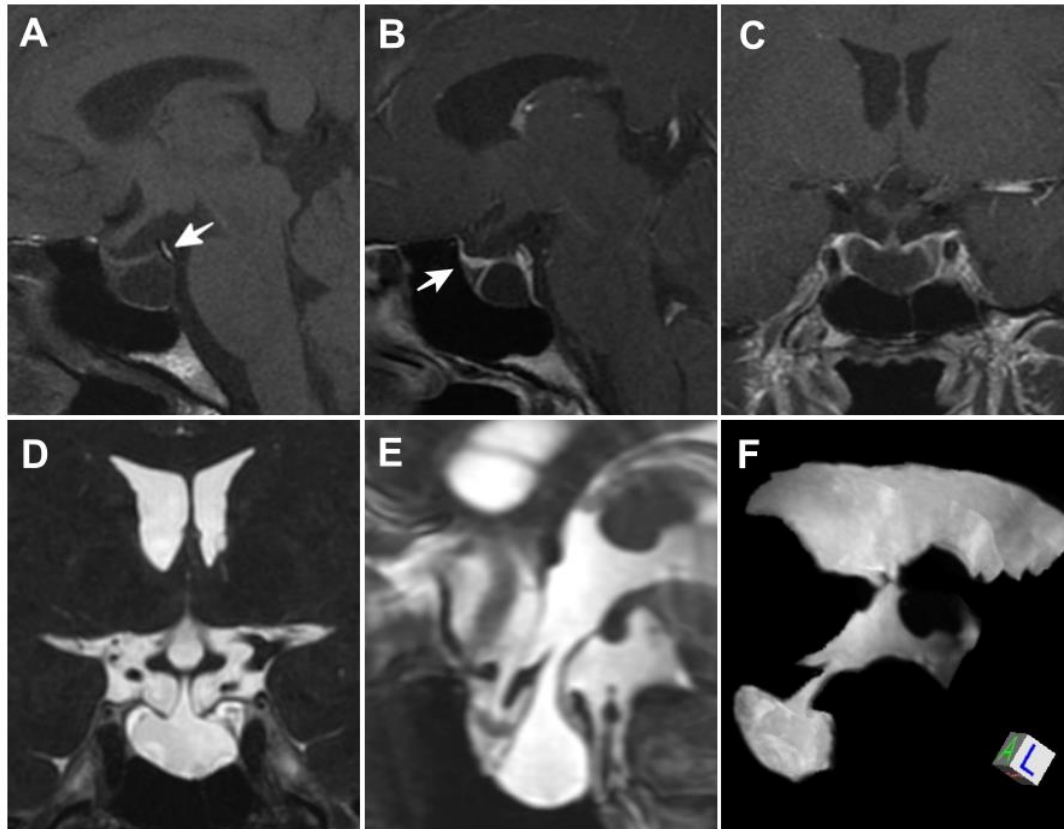
Results

Figure 1. MRI showing cystic expansion of the sella. Sagittal unenhanced T1-weighted image (A) and gadolinium-enhanced MRI (B) show superior displacement of both the posterior (arrow in A) and anterior lobes (arrow in B) of pituitary gland. Coronal gadolinium-enhanced MRI (C) shows that the pituitary stalk was in midline position. Coronal (D) and sagittal (E) 3-D CISS MRI clearly demonstrate a communicating tract between third ventricle and the cyst through pituitary stalk. The maximal intensity projection of sagittal 3-D CISS (F) clearly displays the relation of PEIR with ventricular system.

Oral Presentations & Excerptas

Conclusions

This is the first case report demonstrating imaging features of PEIR in 3-D high-resolution MRI. Although PEIR is a rare anomaly, imaging diagnosis of this entity is important since confusion with other pituitary cystic lesions and the attempt of surgical removal may lead to serious complications.



(Filename: TCT_E-31_01.jpg)

E-32

3:40PM - 3:44PM

Primary leptomenigeal medulloblastoma; First reported case of desmoplastic/nodular medulloblastoma without a discrete parenchymal mass

M Hanna¹, M Hanna², A Aggarwal¹, P Belani¹

¹Icahn School of Medicine at Mount Sinai, New York, NY, ²Memorial Sloan Kettering, New York, NY

Purpose

Medulloblastoma is the most common CNS embryonal tumor of childhood. It classically presents as a midline mass of the posterior fossa. There have been five reported patients with "primary" leptomenigeal medulloblastoma, without an identifiable mass lesion. In all reported cases, the patients all died within approximately two months of diagnosis. Histologically, there are four subgroup groups, with the desmoplastic/nodular subgroup having a more favorable outcome in adolescents than other variants of medulloblastoma. MR findings classically demonstrate a cerebellar mass, which may extend to the leptomeninges. To our knowledge, this is the first case of primary leptomenigeal desmoplastic/nodular medulloblastoma (WHO Grade IV) without a discrete parenchymal mass and such atypical presentation should be considered in the differential diagnosis of nodular leptomenigeal disease.

Materials and Methods

A 21-year-old male presented with a second episode of unresponsiveness in two weeks in the setting of

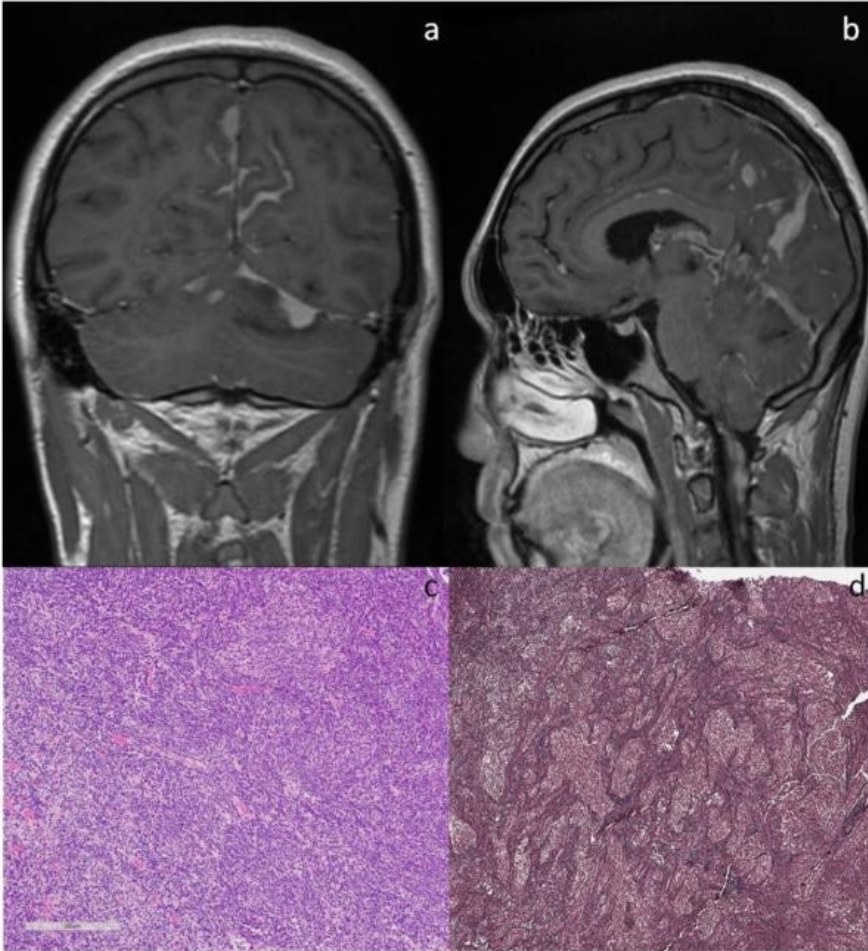
traumatic brain injury while playing football. Unresponsiveness with leg shaking was concerning for a possible seizure, which warranted MRI imaging with contrast.

Results

An MRI with contrast demonstrated extensive FLAIR hyperintensity and nodular enhancement throughout the leptomeningeal spaces of the cerebrum and cerebellum but no discrete parenchymal mass. A thick rind of enhancement was also seen along the dorsal leptomeningeal aspect of the upper cervical cord. The findings were consistent with diffuse leptomeningeal disease. The patient underwent a right frontal brain biopsy with pathology results showing a desmoplastic/nodular medulloblastoma (WHO Grade IV) with Sonic Hedgehog mutation. The tumor was characterized by a nodular architecture with pale circumscribed nodules composed of bland, streaming cells surrounded by extranodular hypercellular atypical cells. The tumor showed GAB1 expression, but was negative for p53 and MYC by immunohistochemistry, which was consistent with a desmoplastic/nodular medulloblastomas with activation of the sonic hedgehog pathway.

Conclusions

Medulloblastoma typically presents as a mass in the posterior fossa. In this case, however, there were atypical radiographic features where instead of a discrete mass, the findings were that of diffuse nodular leptomeningeal disease. Since being diagnosed 3 months ago, the patient has undergone chemotherapy treatment and will be continually followed. This subtype, as primary leptomeningeal disease, may have a similar prognostic profile compared to other medulloblastoma subtypes in this setting.



Radiology and Pathology Imaging

a, Coronal T1 post contrast; b, Sagittal T1 post contrast; There is extensive nodular enhancement throughout the cerebral and cerebellar hemispheres with involvement along the dorsal aspect of the cervical cord. c, H&E medium magnification; d, reticulin stain medium magnification. The reticulin stain shows characteristic reticulin-free (pale areas) and reticulin-rich (extranodular areas) foci.

(Filename: TCT_E-32_DesmoplasticNodularMedulloblastoma.jpg)

E-33

3:44PM - 3:48PM

Assessment of Radiation Treatment Response of a Skull Base Meningioma Using Arterial Spin Labeling

P Manning¹, A Sung¹, A Simon², R Lee³, T Liu², J Hattangadi-Gluth², N Farid¹

¹University of California, San Diego, San Diego, CA, ²University of California San Diego, La Jolla, CA, ³University of California San Diego/VA Medical Center, San Diego, CA

Oral Presentations & Excerptas

Purpose

To determine whether arterial spin labeling (ASL) can assess treatment response after radiotherapy for skull-base meningioma

Materials and Methods

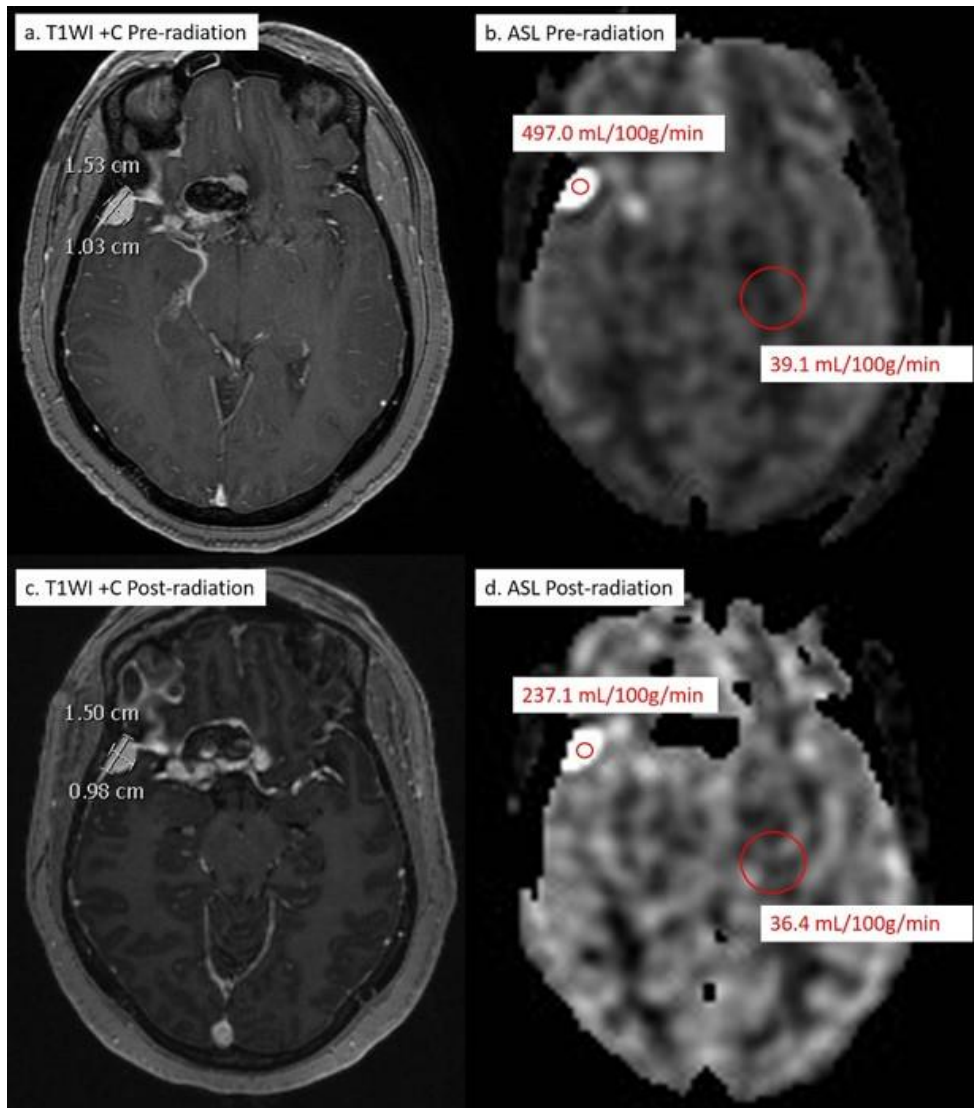
A 52-year-old woman with a large en plaque meningioma abutting several critical structures was treated with definitive intensity modulated radiation therapy (IMRT) to 54 Gy over 30 fractions. MRI, including ASL perfusion, was performed 2 weeks prior to initiation of radiotherapy as well as eight weeks and 36 weeks after completion of radiotherapy.

Results

Preradiation MRI showed an extensive en plaque meningioma involving the right middle cranial fossa, planum sphenoidale, and the right cavernous sinus with complete encasement of the cavernous ICA. Prior to radiation therapy, a dominant nodule along the anterior temporal convexity measured 1.5 x 1.0 cm with its cerebral blood flow (CBF) measuring 497.0 mL/100g/min (control 39.1 mL/100g/min). Repeat MRI 8 weeks after radiation showed stable size of the nodule, but with reduced CBF measuring 295.3 mL/100g/min (control 39.8 mL/100g/min). Follow-up MRI 36 weeks after radiation again showed stable size of the nodule but with further reduction of CBF, now measuring 237.1 mL/100g/min (control 36.4 mL/100g/min) (Figure 1).

Conclusions

Classically, treatment response after radiation is evaluated by comparing pre and post-treatment tumor size on contrast-enhanced MRI. Typically, however, these measurements do not change in meningiomas after radiotherapy. Furthermore, complex tumor morphology and enhancement related to radiation treatment effect can confound these measurements [1, 2]. To address these limitations, perfusion MRI has emerged as a useful adjunct to evaluate treatment response [3, 4]. With current concerns over deposition of gadolinium-based contrast agents in the brain, ASL perfusion is particularly appealing as it can be performed without contrast [5]. In this patient with a skull base meningioma treated with radiation, ASL showed 40% decrease in CBF at eight weeks postradiotherapy with further reduction at 36 weeks, although tumor size remained stable, suggesting that ASL may serve as a better biomarker of treatment response.



(Filename: TCT_E-33_ASNRMeningiomaFigure.jpg)

E-34

3:48PM - 3:52PM

Dural Inflammatory Pseudotumor from Combination Immunotherapy for Metastatic Melanoma

L Bahoura¹, R Lukas¹, C Horbinski¹, S Chandra¹, J Chandler¹, B Liu¹
¹Northwestern University Feinberg School of Medicine, Chicago, IL

Purpose

As immunotherapies for cancer become increasingly available to patients, clinicians and radiologists face a major challenge in evaluating treatment response. We present a case of a patient with melanoma metastatic to the right frontal lobe who developed a new dural-based lesion shortly after beginning the first course of combination ipilimumab/nivolumab, which significantly decreased in size and essentially resolved on follow-up imaging without altering treatment. Our purpose is to show the evolution of this finding and discuss immune-related response in the setting of immunotherapies.

Materials and Methods

A 56-year-old female with melanoma. Two years after the initial diagnosis, she was found to have a large

Oral Presentations & Excerptas

right frontal lobe metastasis, which was treated with resection and stereotactic radiosurgery. Follow-up imaging in the subsequent six months demonstrated increasing nonspecific enhancement along the margins of the resection cavity, and the patient began immunotherapy with combination ipilimumab/nivolumab. Follow-up imaging 17 days later, after two cycles of immunotherapy, showed similar, nonspecific enhancement along the margins of the resection, a new 2 cm dural lesion in the right frontal region, and new enlargement of the pituitary gland, suspicious for immune-modulated hypophysitis. The immunotherapy was continued, with the addition of a short course of steroids, and follow-up imaging 20 days later showed significant decrease in size in the dural lesion, immediately prior to planned surgery. Pathology from re-resection of the right frontal resection cavity enhancement showed no tumor; however, granulomas were found in the sample. A subsequent postoperative follow-up study one month later demonstrated complete resolution of the dural-based enhancement.

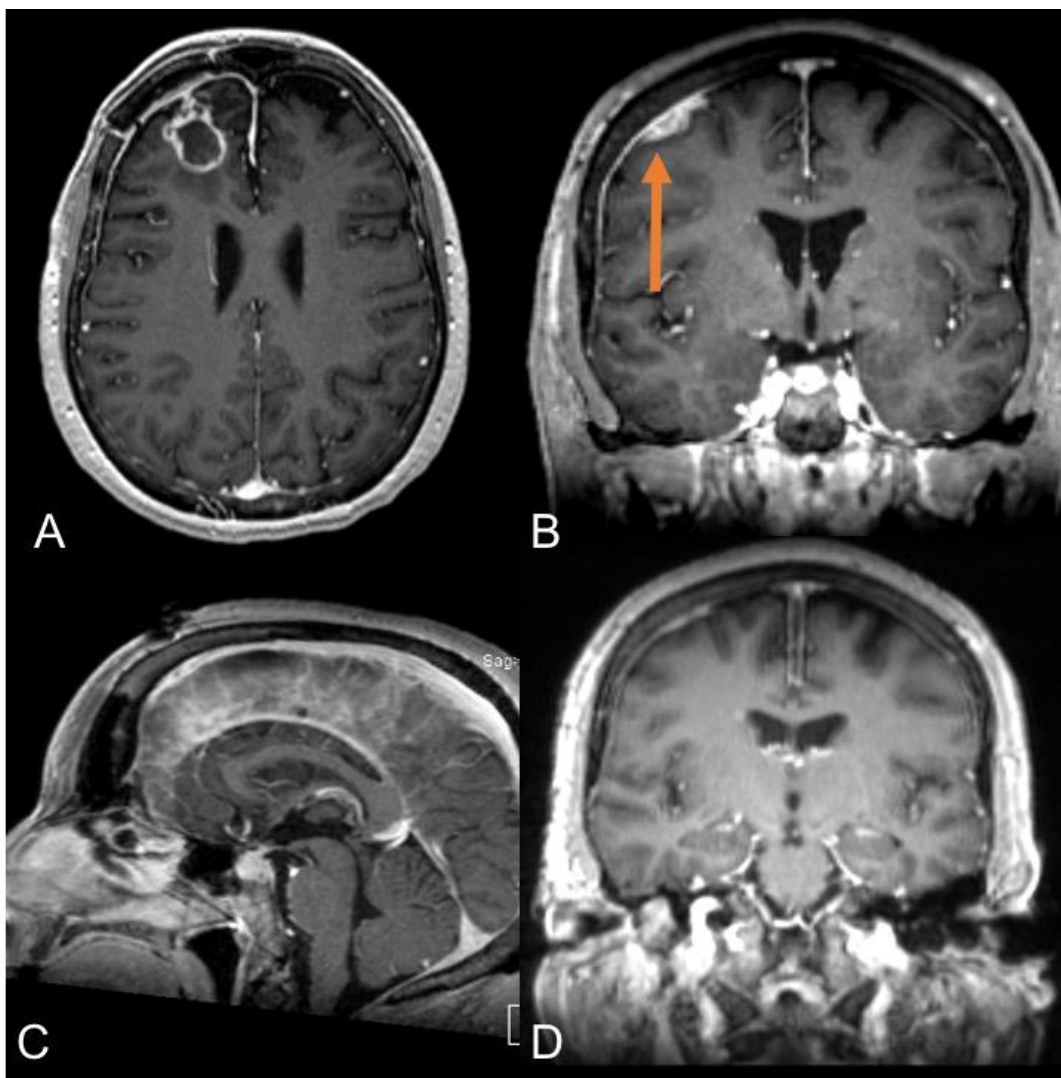
Results

A. Axial T1 postcontrast image from a follow-up brain MRI after resection of a right frontal lesion reveals increasing enhancement along the margins of the resection cavity. There was no dural-based lesion at that time, just prior to the initiation of combination ipilimumab/nivolumab. B. Coronal T1 postcontrast image from a follow-up brain MRI after 17 days of immunotherapy reveals a new right frontal dural lesion measuring 2 cm (arrow). C. Sagittal T1 postcontrast image demonstrates new enlargement of the pituitary gland. D. Coronal T1 postcontrast image from a follow-up brain MRI 20 days later reveals significant decrease in size, near complete resolution, of the enhancing dural lesion.

Conclusions

This case illustrates the importance of recognizing immune-related responses to tumor treatment, which can often complicate imaging findings and lead to premature or incorrect diagnosis of tumor progression. We speculate that the new dural-based lesion which presented shortly after immunotherapy initiation likely represents an inflammatory pseudotumor comprised of a lymphocytic infiltrate rather than melanoma tumor cells, especially given the concurrent immune-modulated hypophysitis. Alternatively, the possibility of pseudoprogression of an occult dural micro-metastasis which subsequently improved with continued treatment was also considered, but this was felt to be much less likely given the rapid development and resolution of the finding. The classic criteria for defining tumor progression are becoming less reliable with evolving treatments, especially immunotherapy medications.

Pseudoprogression from immunotherapy drugs, followed by tumor shrinkage, has been reported with use in the setting of metastatic melanoma and metastatic nonsmall cell lung cancer. Radiologists should be aware of this phenomenon and other immune-related responses, and further research is necessary to fully understand these various responses to treatment in order to provide meaningful interpretation of imaging.



(Filename: TCT_E-34_ASNR-LB.jpg)

E-35

3:52PM - 3:56PM

An Interesting Case of Gorham-Stout Disease with Craniofacial Involvement

C Choi¹, J Cain², S Mathur²

¹Royal Preston Hospital, Manchester, England, ²Royal Preston Hospital, Preston, United Kingdom

Purpose

A case presentation highlighting the clinical and radiological features of a rare case of histologically confirmed Gorham-Stout disease (progressive massive osteolysis) involving the skull base

Materials and Methods

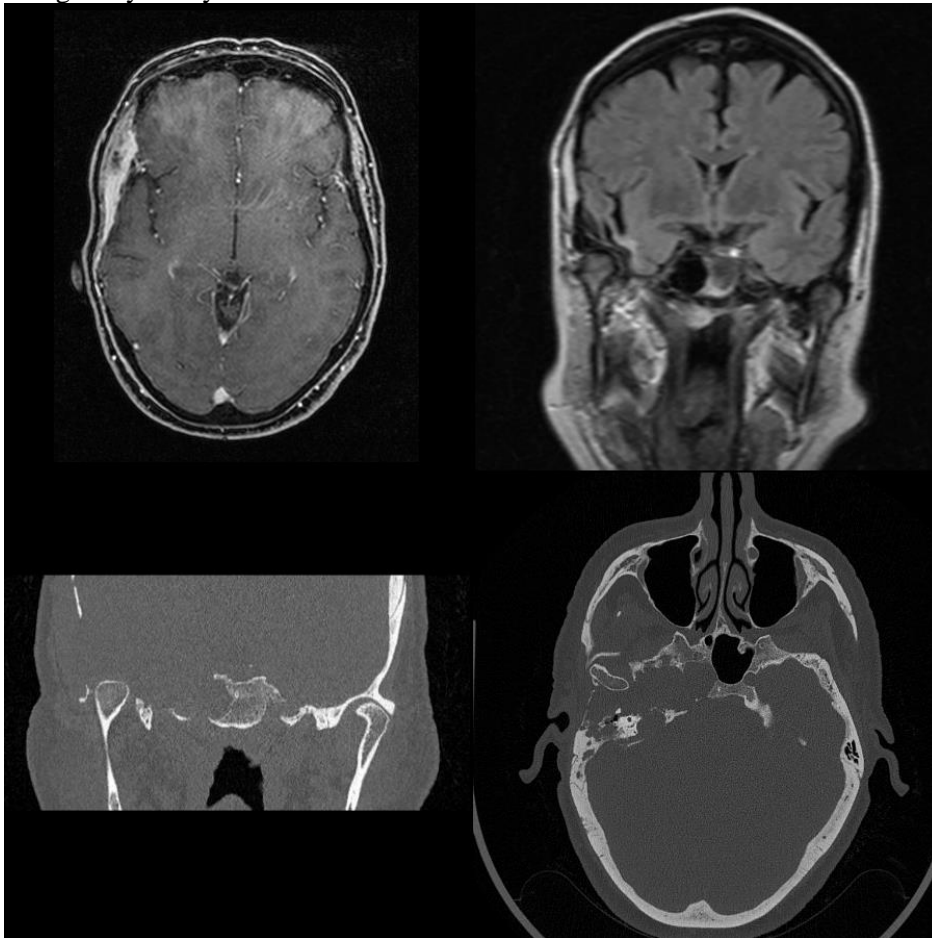
A 64-year-old female presented to primary care complaining of pain involving the right side of the head and face. She also described a sensation that the bones of the face on the right side were 'collapsing' and intermittent swelling behind the ear. Her past medical history included treated pulmonary and spinal tuberculosis 32 years prior. She was otherwise well and was referring directly for a CT.

Results

The initial CT demonstrated extensive patchy osteolysis involving the right skull base and frontotemporal convexity with abnormal soft tissue thickening in the region of the temporalis muscle. Intracranially, there was marked right temporal volume loss. The subsequent MR revealed abnormal T2 hyperintense soft tissue expanding the temporalis muscle overlying the convexity bone loss that enhanced avidly on postcontrast images. There was right temporal encephalomalacia and asymmetrical positioning of the mandibular condyle. A dedicated CT of the temporal bones and a reformatted coronal oblique image better delineate the protrusion of mandibular condyle into the middle cranial fossa and the extent of osteolysis.

Conclusions

Gorham-Stout disease is a rare nonmalignant condition of unknown aetiology first described in 1838 (1). It is characterized by progressive local bone resorption and the presence of angiomatous tissue on biopsy (2, 3) in the absence of other causes. Involvement of the skull has been described (4), however this case is particularly interesting due to the involvement of the skull base and damage to the temporal lobe, presumably due to repetitive microtrauma associated with mastication. Histology in this case revealed exaggerated osteoclastic activity and a vascular lesion characteristic of Gorham-Stout with no evidence of malignancy or mycobacterial infection.



(Filename: TCT_E-35_Gorhams.jpg)

E-36

3:56PM - 4:00PM

Subependymal Giant Cell Astrocytoma Arising in the Absence of Tuberous Sclerosis Complex

C Stuart¹, P Rabiei¹, L Ocasio², M Syed¹, R Riascos¹, M Patino¹

¹The University of Texas Health Science Center at Houston, Houston, TX, ²Memorial Hermann, Houston, TX

Purpose

To illustrate a rare case of subependymal giant cell astrocytoma arising in the absence of tuberous sclerosis complex

Materials and Methods

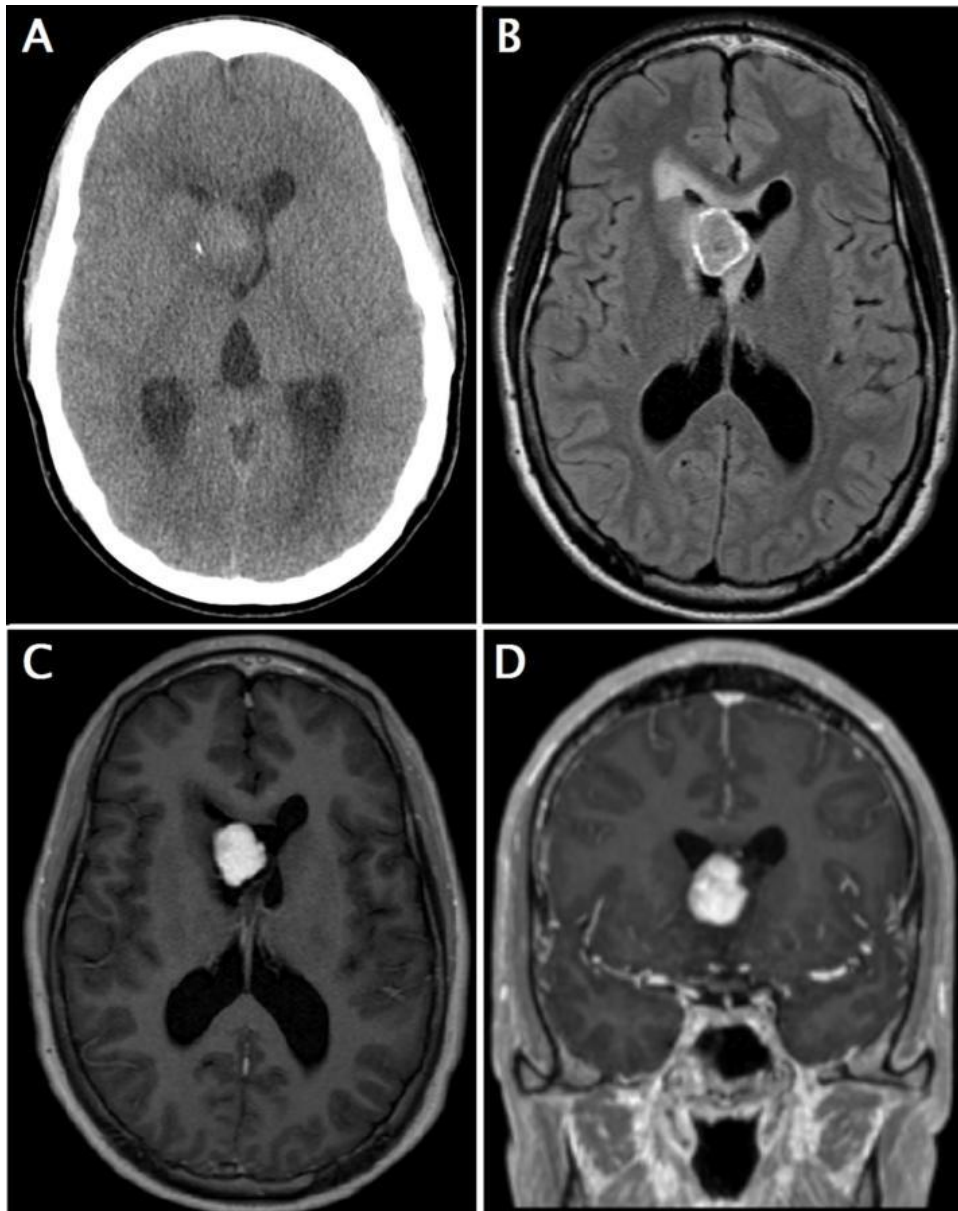
A 24-year-old male presents with a five-month history of episodic generalized headaches lasting 2-5 hours. For the past two weeks he complains of progressively worsening headaches, episodic blurry vision, and right peripheral vision loss. Imaging demonstrated a ventricular mass and hydrocephalus. He subsequently underwent a right frontal transcortical transventricular approach gross total resection of the intraventricular mass using the Stealth navigation system. Pathology revealed a subependymal giant cell astrocytoma (SEGA), WHO grade I. Genetic testing for TSC1 and TSC2 was negative, and there were no other intracranial or extracranial stigmata of TSC.

Results

A. Noncontrast CT demonstrates a partially calcified mass at the foramen of Monro causing hydrocephalus. B. MR FLAIR imaging reveals a 2.5 cm T2 hyperintense mass in the right lateral ventricle at the foramen of Monro with surrounding vasogenic edema. C. Postcontrast MR imaging demonstrates avid homogeneous enhancement of the mass. D. Postcontrast coronal view confirms the location of the mass at the foramen of Monro.

Conclusions

Subependymal giant cell astrocytoma (SEGA) is an enlarging foramen of Monro mass which is only typically seen in patients with tuberous sclerosis complex (TSC). This case is particularly unique as the patient had no other findings of TSC as well as negative genetic testing. TSC has two known distinct genetic loci which are mutated in the disease: TSC1 is found on chromosome 9q and TSC2 is found on chromosome 16p. It is inherited in an autosomal dominant pattern with high penetrance. There is a large degree of phenotypic variability. However, only 50% of patients have a known family history. The remainder of the cases arise from de novo mutations.



(Filename: TCT_E-36_SEGA_700dpi.jpg)

E-37

4:00PM - 4:04PM

Cerebellopontine Angle Glioblastoma

B White¹, A Jaster¹, M Pinho¹

¹*University of Texas Southwestern Medical Center, Dallas, TX*

Purpose

This brief presentation will describe a cerebellopontine angle mass with an atypical appearance that may suggest a rare diagnosis.

Materials and Methods

A 41-year-old pregnant female presented with three months of right-sided hearing loss and underwent noncontrast MR imaging of the internal auditory canals (IAC), which demonstrated a right

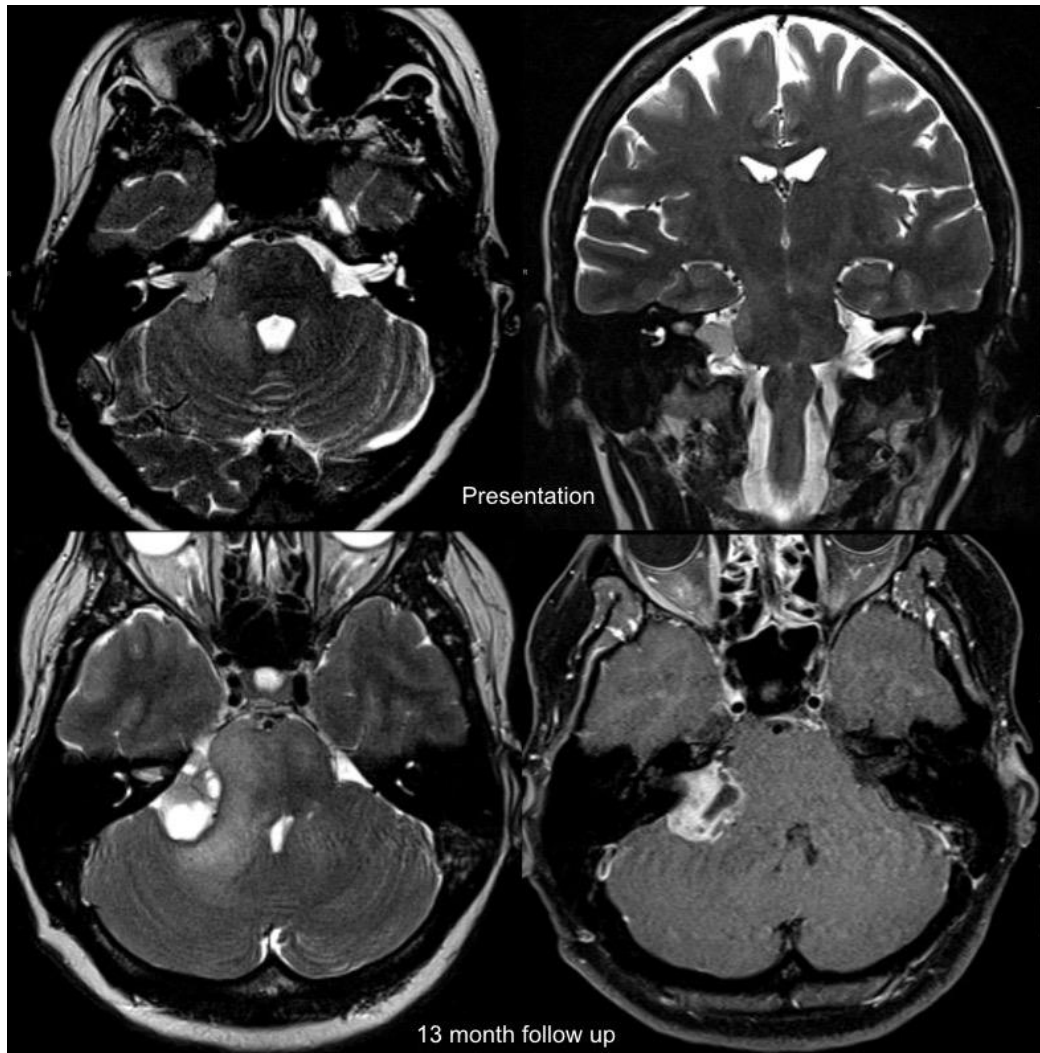
cerebellopontine angle (CPA) mass that was felt most likely to represent a vestibular schwannoma. Subsequent imaging for hand tingling demonstrated an expansile intramedullary cervical spinal cord mass. The patient was lost to follow-up for 13 months until worsening symptoms prompted repeat imaging, which demonstrated significant enlargement of both masses. The patient underwent partial resection of the CPA mass yielding a pathologic diagnosis of glioblastoma. Both the brain and spine lesions progressed rapidly in spite of radiation and medical therapy, and the patient passed away two years after initial symptom onset.

Results

Axial and coronal T2 images at presentation demonstrate a right CPA extra-axial mass involving the IAC with disproportionately large peritumoral T2 signal within the pons, middle cerebellar peduncle, and cerebellum. Axial T2 and T1 postcontrast images 13 months later demonstrate marked interval enlargement of the now partially cystic avidly enhancing mass with increased mass effect as well as progressive expansile hyperintense T2 signal in the adjacent brainstem and cerebellum.

Conclusions

Glioblastomas of the cerebellopontine angle (CPA) are exceedingly rare and are thought to originate from the brainstem and project exophytically. When glioblastomas do present in this location, they are commonly misdiagnosed as more typical benign tumors, such as schwannomas or meningiomas, since both radiological features and clinical symptoms may overlap. There are, however, some important distinguishing features, particularly a disproportionate degree of peritumoral T2/FLAIR hyperintensity within the brainstem/cerebellum relative to the size of the CPA mass, blurring of the tumor/brainstem interface, and rapid progression.



(Filename: TCT_E-37_CPAGBM.jpg)

E-38

4:04PM - 4:08PM

Brainstem Leptomeningeal Pseudoprogression in Glioblastoma Following Radiation Therapy

N Kinger¹, M Hoch², H Shu¹, B Weinberg²

¹Emory University School of Medicine, Atlanta, GA, ²Emory University Hospital, Atlanta, GA

Purpose

Standard glioblastoma treatment consists of maximal debulking followed by focal radiation with concurrent and adjuvant temozolomide. MRI is used for treatment monitoring and to guide therapeutic decision-making, but early radiation effects (pseudoprogression) and tumor progression can both have worsening enhancement and edema. Parenchymal pseudoprogression is well documented, but worsening leptomeningeal enhancement due to treatment effect has not been widely described. The purpose of this excerpt is to demonstrate a case of brainstem leptomeningeal enhancement after the chemoradiation phase of therapy which improved on follow-up and likely represented treatment effect.

Materials and Methods

A 40-year-old man presented with seizures and on imaging was diagnosed with a bifrontal enhancing mass consistent with glioblastoma. He underwent debulking surgery followed by radiation and concurrent

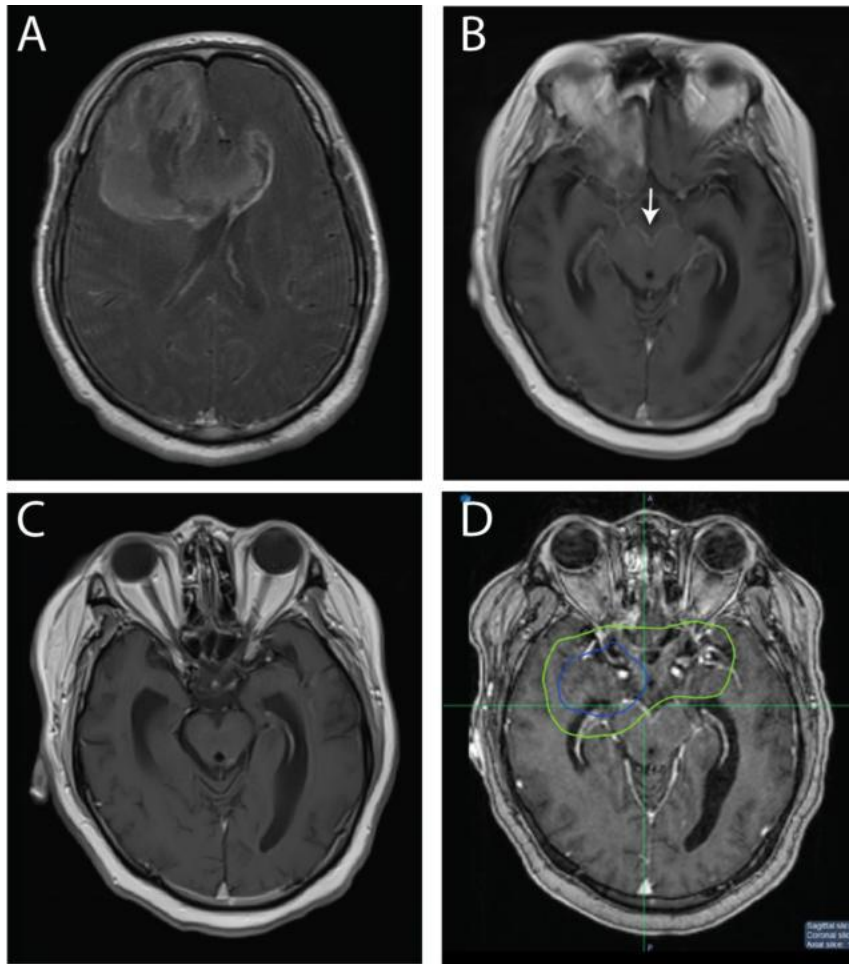
temozolomide. One month after completing chemoradiation, the patient was clinically stable and underwent MRI, which was suspicious for distant disease progression. Additional follow-up imaging was performed one month later.

Results

Initial imaging demonstrated a large bifrontal enhancing tumor crossing the midline through the genu of the corpus callosum. On one month post-treatment imaging, the patient had increasing enhancement in the tumor bed thought most likely to represent pseudoprogression. However, new leptomeningeal enhancement was noted distant from the tumor along the midbrain and was concerning for disease progression. Follow-up MRI one month later demonstrated near complete resolution of leptomeningeal enhancement, likely representing self-limited radiation effect. Radiation dose maps demonstrated radiation in the 40-50 Gy range to the affected region. Further follow-up brain MRIs have not demonstrated return of abnormal enhancement in the leptomeninges or brainstem.

Conclusions

In glioblastoma patients, awareness of pseudoprogression after chemoradiation is important in evaluating treatment response and minimizing unnecessary changes to therapy. Parenchymal pseudoprogression has been well documented. However, worsening leptomeningeal enhancement following therapy may also represent treatment effects which can resolve spontaneously. If distant leptomeningeal enhancement occurs, correlation with radiation dose maps may be useful in guiding interpretation.



(A) Heterogeneously enhancing mass within the right frontal lobe extending along the anterior corpus callosum into the left frontal lobe compatible with glioblastoma. (B) New leptomeningeal enhancement along the midbrain 1 month after completing chemoradiation. (C) 2 month post-treatment follow up demonstrating resolution of leptomeningeal enhancement. (D) Radiation dose overlay demonstrating radiation dose to the brainstem. Blue = 50 Gy, Green = 40 Gy. Dose at the green marker intersection was 44 Gy. (Filename: TCT_E-38_asnrfigure_v2.jpg)

E-39

4:08PM - 4:12PM

Intracranial Lipoma with Associated Cortical Calcification and Leptomeningeal Enhancement – A Rare Variant of Sturge-Weber Syndrome Type 3?

P Morden¹, B Griffith¹, J Corrigan¹, S Patel¹
¹Henry Ford Health System, Detroit, MI

Purpose

Intracranial lipoma is a rare finding in itself (<1% intracranial tumors), particularly when located along the cerebral hemispheric surface. The association of cortical calcification and leptomeningeal enhancement along with a hemispheric lipoma, but in the absence of associated physical abnormalities, appears to be exceptionally rare: a review of the literature found two articles describing three cases with

similar findings. This excerpt describes the unusual presentation of a parietal convexity lipoma with associated cortical calcification and leptomeningeal enhancement and briefly reviews the existing literature regarding this rare entity and its potential pathogenesis.

Materials and Methods

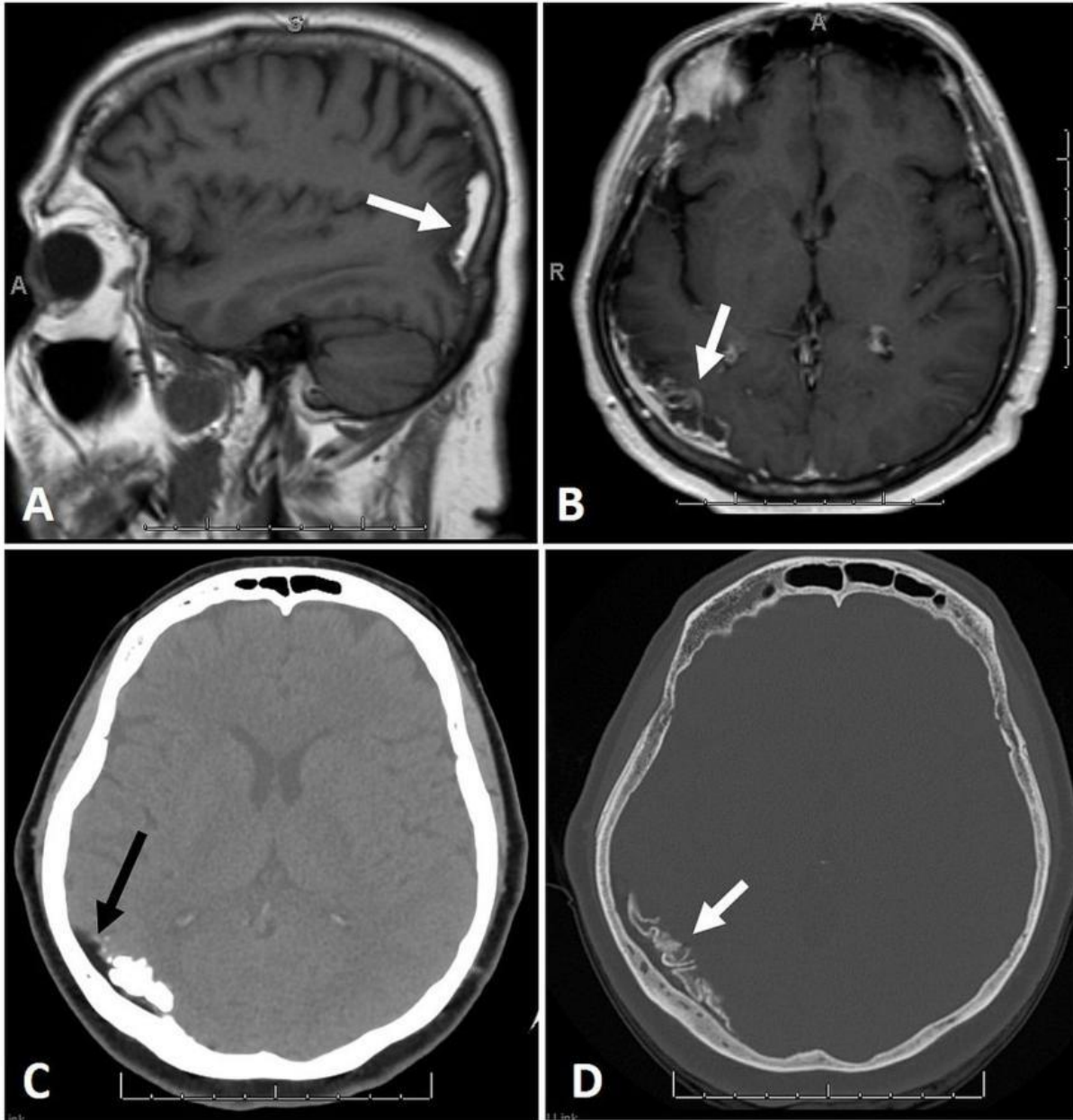
We present a case of intracranial parietal convexity lipoma with associated focal cortical calcification and leptomeningeal enhancement found incidentally in a 62-year-old female presenting with dizziness. The patient had no additional intracranial abnormalities and no findings of an underlying neurocutaneous disorder on physical examination.

Results

T1-weighted sagittal sequence demonstrates an extra-axial hyperintense lesion overlying the right parietal convexity with signal isointense to subcutaneous fat (Fig. 1A). Axial postcontrast T1-weighted image demonstrates leptomeningeal enhancement underlying the lesion (Fig. 1B). Noncontrast axial CT images demonstrate a fat containing extra-axial lesion (Fig. 1C) along the right parietal convexity with focal gyriform calcifications in the underlying cortex (Fig. 1D).

Conclusions

Intracranial lipoma with associated focal cortical calcification and leptomeningeal enhancement is an exceptionally rare constellation of findings with only three cases reported in the literature. One previous report of similar cases noted some overlapping features with Sturge-Weber and Haberland (Encephalocraniocutaneous lipomatosis) syndromes and posited that this entity may be a rare presentation along the same spectrum of neurocutaneous disorders. Alternatively, it may be that meningeal circulation modification is the root cause of the distinctive cortical calcification pattern seen in Sturge-Weber and that a meningeal lipoma may occasionally mimic this process and appearance.



(Filename: TCT_E-39_Intracraniallipoma.jpg)

E-40

4:12PM - 4:16PM

Malignant Melanoma as a Coalescent Tumor within Intracerebral Epidermoid – A Rare Case Report.

M Syed¹, M Patino², C Sitton², R Riascos², R Patel², M Bhattacharjee¹, A Kamali²

¹University of Texas at Houston, Houston, TX, ²University of Texas Health Science Center at Houston, Houston, TX

Purpose

To illustrate a rare case of primary malignant melanoma existing as a coalescent tumor within a recurrent intracerebral epidermoid

Materials and Methods

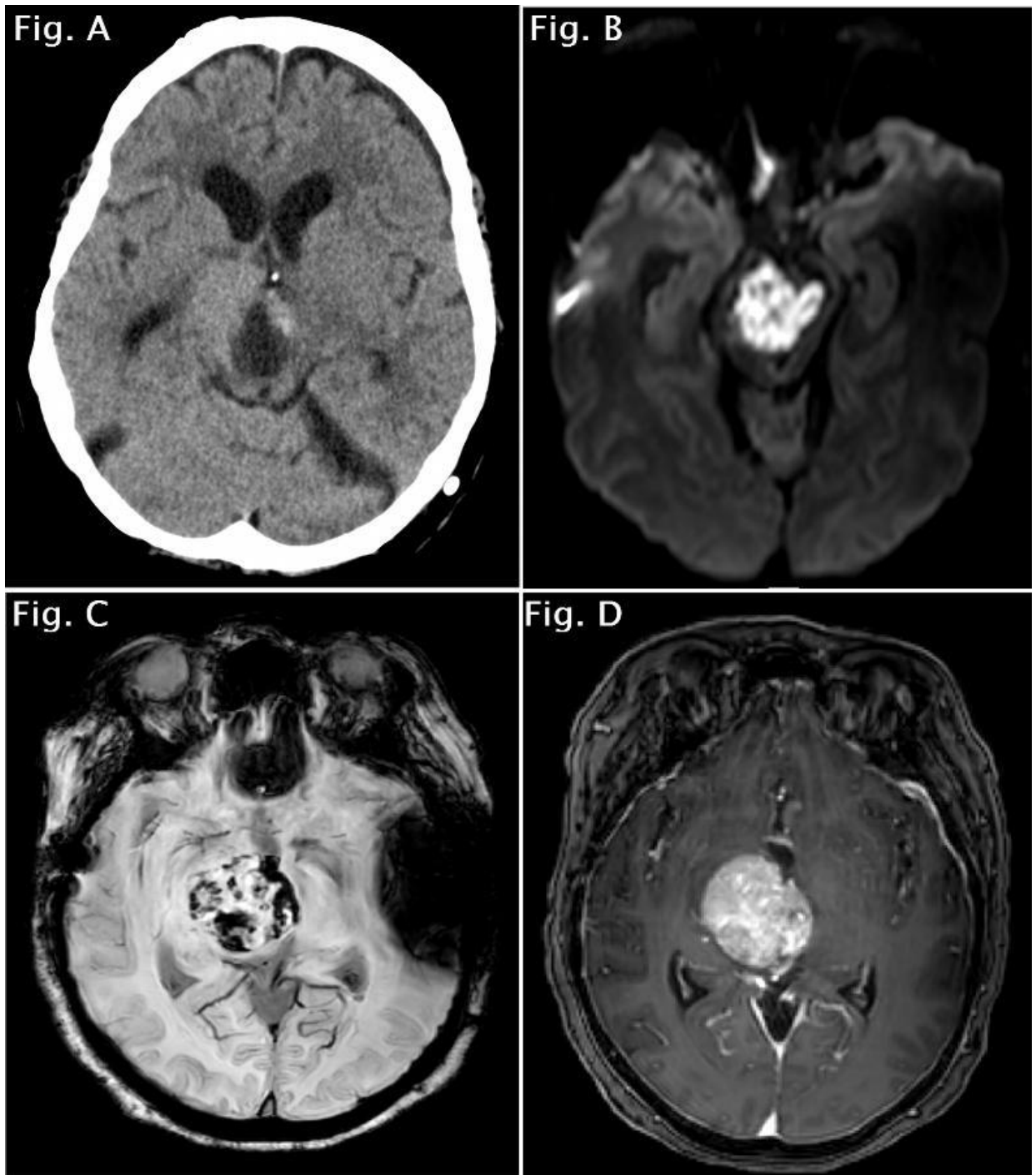
A 55-year-old female presented with altered mental status. The patient's family reported a history of prior epidermoid resection in 2003. The patient is wheelchair bound and with right CN III palsy since prior surgery. On initial imaging (CT), patient was found to have a right thalamic mass with associated mass effect upon third ventricle and obstructive hydrocephalus. Patient underwent external ventricular drain (EVD) placement and biopsy. Pathology revealed malignant melanoma coexisting with epidermoid. Subsequent whole body PET-CT and dermatologic exam showed no evidence of cutaneous melanoma. Patient underwent gamma knife treatment and subsequent suboccipital craniotomy for resection of the tumor.

Results

Noncontrast CT demonstrates hyperdense mass in the right thalamus (Fig. A) with a hypodense component inferiorly extending into the midbrain. There is mass effect upon the third ventricle with associated obstructive hydrocephalus. MRI brain demonstrates avidly enhancing (Fig. D) right thalamic mass with internal areas of increased susceptibility (Fig. C). Inferiorly the mass demonstrates diffusion hyper intensity (Fig. B) and extends into the midbrain. DWI hyperintensity extends into the prepontine cistern.

Conclusions

Epidermoid tumors are uncommon benign lesions, representing 0.3% to 1.8% of all primary intracranial neoplasms. They are derived from the ectopic inclusions of epithelial cells during the closure of the neural tube between the third and fifth week of fetal development. Malignant transformation of intracranial epidermoid is very rare. Of the reported cases, almost all have been malignant transformation into squamous cell carcinoma. To the best of our knowledge, this is the first reportable case of malignant transformation of epidermoid into melanoma. Malignant transformation of the trapped melanocytes within the ectopic inclusions of epithelial cells during embryogenesis is thought to be the likely etiology of this coalescent tumor.



(Filename: TCT_E-40_Mumtaz_final.jpg)

E-41

4:16PM - 4:20PM

Rare Case of Cavernous Sinus Hemangioma and Unique Application of Tc-99m Labeled RBC Scan in Diagnosis

D Noblett¹, J Chang¹, A Toussi¹, B Dahlin¹, K Shahlaie¹

¹University of California, Davis, Sacramento, CA

Oral Presentations & Excerptas

Purpose

The purpose of this project is to demonstrate the usefulness of Tc-99m RBC nuclear medicine imaging in diagnosing cavernous sinus hemangiomas.

Materials and Methods

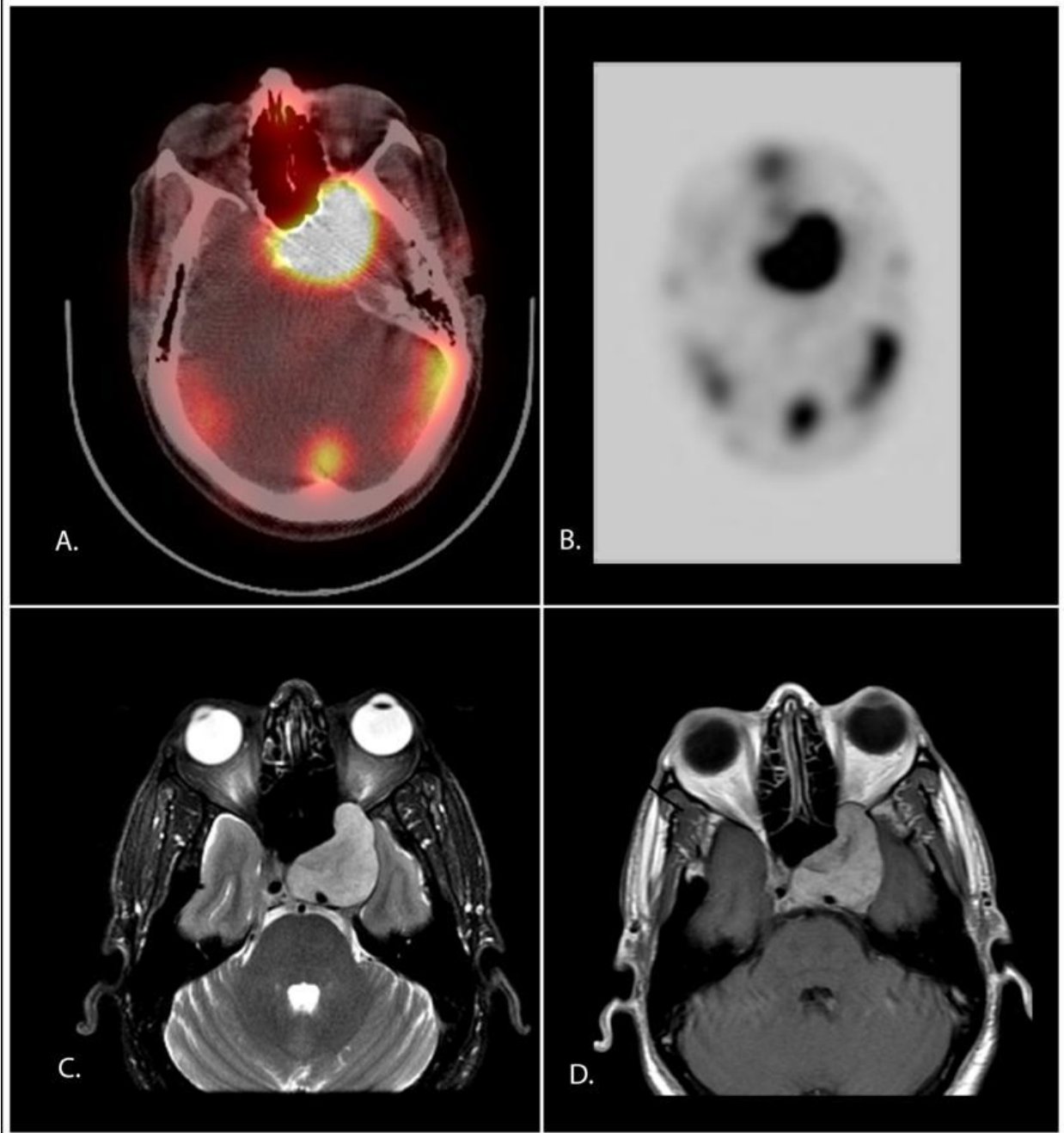
A 57-year-old man with progressive blurry vision and headache over seven months. He was found to have left-sided ptosis, lid lag, and diplopia with upward gaze on exam. Detailed eye exam demonstrated inferior visual field defect afferent pupillary defect in left eye. Surgical tumor debulking and biopsy demonstrated nonspecific fibrovascular, focally cellular tissue. Immunohistochemistry was noncontributory.

Results

MRI demonstrated a left parasellar mass, which was iso/hyperintense on T2-weighted imaging with heterogeneous enhancement. The mass extended into the cavernous sinus and encased the left internal carotid artery. Conventional angiography demonstrated scant delayed vascularity. The patient underwent nuclear medicine scintigraphy, with administration of Tc-99m RBC, an imaging modality generally used in identifying gastrointestinal bleeds and liver hemangiomas. Scintigraphy and SPECT localization demonstrated significant Tc-99m RBC delayed blood pool activity within the left cavernous sinus mass, a finding consistent with a cavernous sinus hemangioma.

Conclusions

Cavernous sinus hemangiomas are rare extra-axial tumors that account for approximately 3% of benign cavernous sinus masses and are more common in middle-aged women. Symptoms are generally secondary to mass effect and are nonspecific. MRI is imaging modality of choice and typically appear hypo- to isointense on T1-weighted imaging and hyperintense on T2-weighted imaging. In our case, the MRI findings were not specific and surgical biopsy was also inconclusive, prompting the utilization of a positive tagged RBC scan. One should consider exploiting this imaging technique where the diagnosis of cavernous sinus hemangioma is unclear and requires confirmation for surgical planning or definitive radiosurgical treatment.



(Filename: TCT_E-41_ASNRHemangiomaImage.jpg)

E-42

4:20PM - 4:24PM

Primary Cerebral Histiocytic Sarcoma

A Guarnizo¹, T Nguyen¹, R Glikstein², C Torres¹

¹The Ottawa Hospital, University of Ottawa, Ottawa, Ontario, Canada, ²University of Ottawa, Ottawa, Ontario, Canada

Purpose

1. To describe the imaging findings of histiocytic sarcoma of the brain on CT and MRI 2. To review the histopathological features of primary cerebral histiocytic sarcoma

Materials and Methods

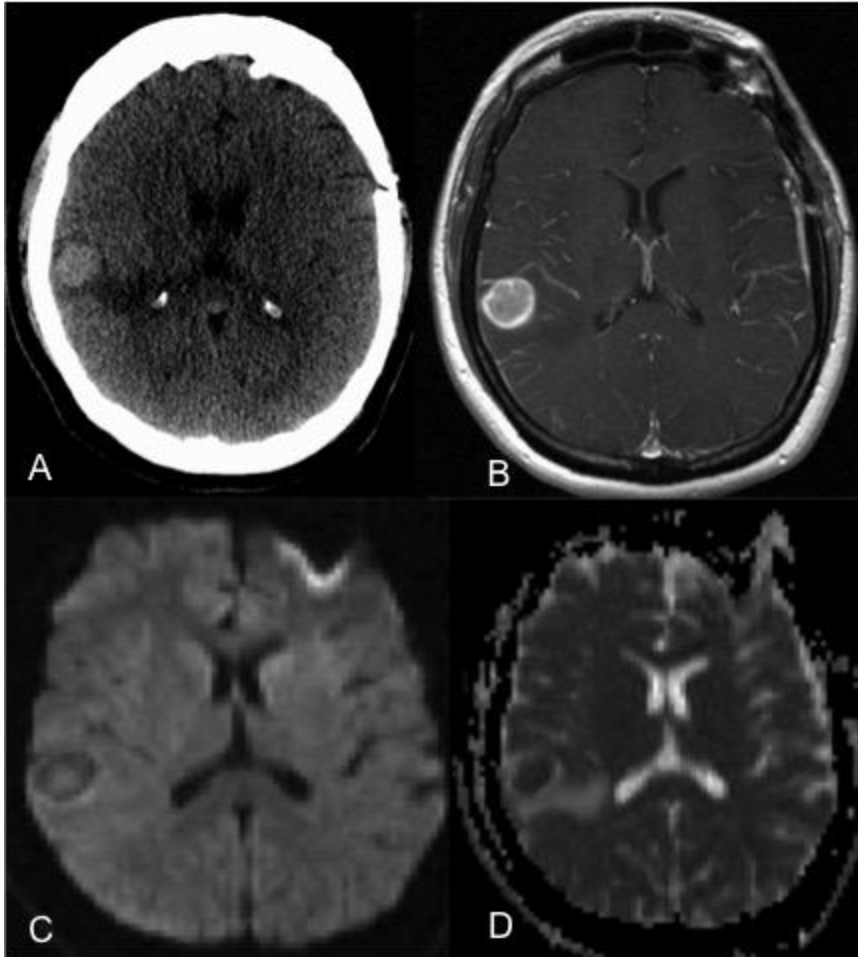
A 38-old-year woman with previously clipped left paraophthalmic aneurysm presented with three-day history of headaches and nausea. Physical examination was unremarkable. Head CT showed a right temporal hyperdense lesion with surrounding edema. MRI of the brain showed a T2 hypointense enhancing lesion with restricted diffusion in the right temporal lobe with surrounding edema. The patient had a microsurgical resection of the lesion. The pathology showed atypical giant cells positive for CD68, S100, CD163 markers and to a lesser extent CD1A. The lesion was defined as a Langerhans' cell sarcoma with low proliferation fraction and circumscribed margins.

Results

Axial image of head CT (A) shows a hyperdense lesion in the right temporal lobe with surrounding edema. Axial T1W sequence with gad; (B) DWI and ADC map (C and D) show an enhancing right temporal lesion with restricted diffusion.

Conclusions

Histiocytic sarcoma of the brain is a rare neoplasm of hematopoietic origin. The imaging findings are not well established; most of the cases present with a single focal hyperdense lesion on CT due to high nuclear to cytoplasmic ratio, without hemorrhage or calcification. On MRI, these lesions are well circumscribed with surrounding edema and heterogeneous enhancement; some cases have shown multiple lesions or leptomeningeal extension. Symptoms include headache, dizziness, weakness and loss of consciousness. The differential diagnosis includes lymphoma, infectious process, primary brain neoplasm, metastatic disease and autoimmune disease. Prognosis is poor due to the rapid progression and poor response to therapy.



(Filename: TCT_E-42_HS.jpg)

E-43

4:24PM - 4:28PM

Suprasellar Osteolipoma: A Rare Entity

S Koenig¹, C Bazan¹

¹University of Texas Health Science Center at San Antonio, San Antonio, TX

Purpose

Intracranial osteolipomas are rare benign neoplasms consisting of fat and calcified and/or ossified tissue, felt to be congenital in nature. They are distinguished from other simple intracranial lipomas by an arrangement of central adipose tissue and peripheral osseous tissue. They typically occur in the midline within the suprasellar region, tuber cinereum, interpeduncular region, or rarely within the hypothalamus. While frequently asymptomatic, this neoplasm can be associated with several clinical symptoms including headaches, vision changes, precocious puberty, facial numbness or weakness, eyelid depression, epilepsy, behavioral disturbances, or pituitary dysfunction. Additionally, osteolipomas may be associated with other intracranial malformations such as corpus callosal agenesis. It is important to recognize this congenital neoplasm as a benign entity as most are found incidentally on imaging. However, it is also important to know that these lesions may be associated with several clinical symptoms, which could warrant surgery or resection. We present a case of an osteolipoma of the suprasellar region found

incidentally in a trauma patient, as well as a review of the imaging findings, embryology, pathogenesis, and management of these lesions.

Materials and Methods

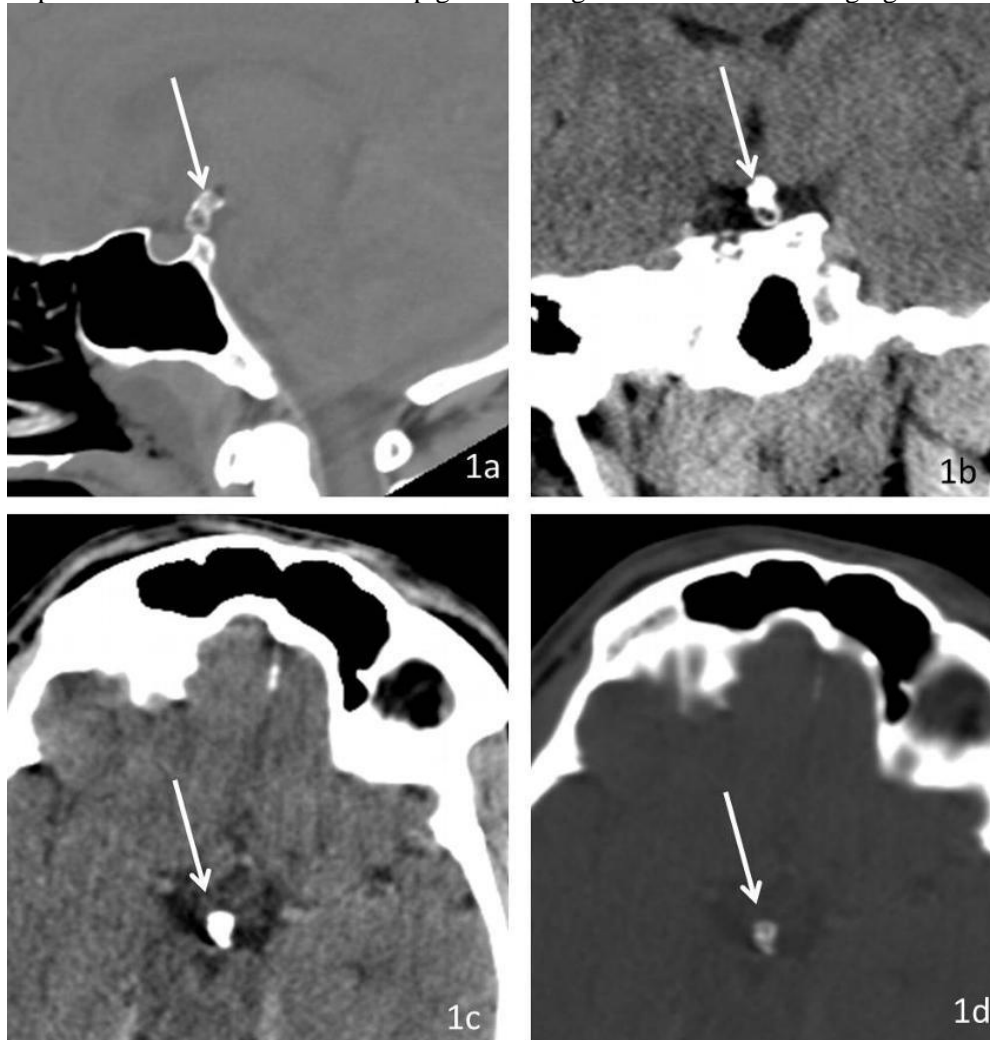
A 40-year-old male presented for imaging after a motor vehicle crash. A noncontrast CT of the head demonstrated a subcentimeter, fat containing, and partially calcified suprasellar lesion immediately superior to the dorsum sellae in the midline. The internal attenuation of the lesion was -38 Hounsfield units. No surrounding cerebral edema, hemorrhage, or fracture of the skull base was present. Upon review of the patient's clinical chart, the patient appeared to be asymptomatic from the lesion, and it was incidentally noted.

Results

Figure 1a through 1d demonstrate a subcentimeter lesion (arrows) in the suprasellar region with central fat and peripheral calcification/ossification consistent with an osteolipoma. Central attenuation measures -38 HU. No other findings to suggest fracture or intracranial trauma are present.

Conclusions

Intracranial osteolipomas are rare benign congenital entities typically found incidentally on imaging. While management is often conservative, it is also important to recognize the potential clinical implications of these lesions to help guide management and further imaging recommendations.



(Filename: TCT_E-43_Picture5.jpg)

LGII Encephalitis – A Newly Understood Autoimmune Encephalitis

P Rodriguez¹, R Kurtz¹

¹*Hospital of the University of Pennsylvania, Philadelphia, PA*

Purpose

Review the clinical and imaging characteristics of anti-LGII encephalitis and how to differentiate this diagnosis from other forms of limbic encephalitis

Materials and Methods

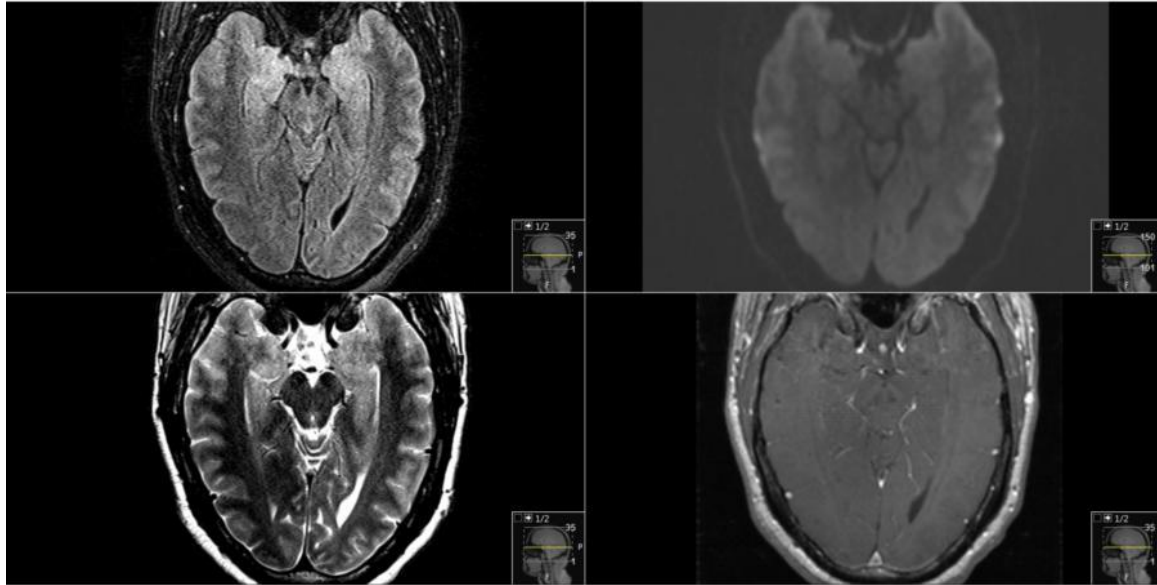
A 39-year-old white male without past medical history was in his usual state of health until one month prior to presentation, when he began to experience difficulty completing sentences and had new onset of psychosis. He initially would stop midsentence and could not recall his thoughts. This further deteriorated to the point that he could only speak in single syllable words. The family reported a subsequent rapid decline in memory function. He would hallucinate and would experience panic attacks. He began to experience nocturnal seizures described by his mother as foaming of the mouth, with bilateral arm and leg stiffening and with postictal confusion. It was noted that he had a new "jittery" feeling in his jaw that lasted seconds with feeling like he was being defibrillated at times. He was admitted with altered mental status. EEG showed right temporal sharp waves at F4. MRI was ordered. Testing revealed anti-LGII antibodies. He was treated with steroids and rituximab.

Results

There is mildly hyperintense signal on the T2 and FLAIR sequences in the bilateral medial temporal lobes, with amygdala involvement. There is no restricted diffusion or abnormal enhancement in these areas.

Conclusions

The constellation of clinical, MRI, and lab tests are consistent with the diagnosis of anti-LGII encephalitis. Previously thought to be an autoimmune response against voltage-gated potassium channels, anti-LGII encephalitis has recently been characterized instead as a rare autoimmune disease to the synaptic protein leucine-rich, glioma-activated 1 (LGII) (reference 1). The median age of diagnosis is 60 and patients present with subacute memory loss, seizures and hyponatremia. The described transient fascio-brachial dystonic seizures are characteristic for this disease but other types of seizures can occur (reference 2). Patients tend to respond to steroids and other immune-modulating therapy. The primary differential considerations for limbic encephalitis are autoimmune, paraneoplastic and infectious causes.



(Filename: TCT_E-15_Case2_ASNR.jpg)

Monday, June 4, 2018

3:00PM - 4:30PM

Parallel Paper Session: Brain: New and Advanced Techniques

O-117

3:00PM - 3:07PM

The Ability of Compressed SENSE MR Imaging to Evaluate the Brain Relative to Conventional Fully Acquired MR Imaging: A Prospective Evaluation.

J Vranic¹, N Cross¹, Y Wang², D Hippe¹, M Mossa-Basha¹

¹University of Washington, Seattle, WA, ²University of Washington, Philips MR Clinical Science, Seattle, WA

Purpose

The purpose of this prospective imaging study is to qualitatively evaluate the clinical performance of accelerated acquisition compressed SENSE sagittal FLAIR and axial SPGR magnetic resonance imaging sequences in evaluating the brain relative to conventional fully acquired sagittal FLAIR and axial SPGR magnetic resonance imaging sequences.

Materials and Methods

All patients were prospectively recruited from January 1, 2016 through September 1, 2017 and were over the age of 18; were able to undergo a 3T MRI examination; and were able to receive intravenous gadolinium contrast. In cases where these criteria were not met, the patient was excluded. Enrolled patients received a clinically warranted brain MRI as part of their routine diagnostic evaluation. For each imaging study, the patient received either a fully sampled sagittal FLAIR and accompanying compressed SENSE sagittal FLAIR imaging sequence (FOV 24 cm; matrix size 215x215mm; TR/TE 4800/288 ms; slice thickness 1 mm) or a fully sampled axial SPGR and accompanying compressed SENSE axial SPGR imaging sequence (FOV 24 cm; matrix size 224 x 224; TR/TE 25/3.5 ms; slice thickness 2 mm) with all scans being performed at 3T. For each compressed SENSE imaging sequence, incoherent undersampling of k-space was performed with image reconstruction that enforced sparsity constrained by data

Oral Presentations & Excerptas

consistency to allow for accurate image reconstruction. Following image acquisition, 2 neuroradiologists blinded to imaging sequence type, reviewed the above-mentioned MRI sequences in a randomized order. Overall image quality was rated on a 4-point scale with 1 point corresponding to nondiagnostic image quality and 4 points corresponding to optimal image quality. SNR and artifact prominence ratings were performed on a 5-point scale, with 1 point corresponding to poor performance and 5 points corresponding to excellent performance. Finally, brain parenchymal lesion clarity and gray-white matter sharpness were rated on a 3-point scale with 1 point corresponding to poor quality and 3 points corresponding to excellent quality. Average differences in rater scores were calculated for each metric as part of the statistical analysis. Variable dichotomization was performed in several instances to aid with rating comparison. A p-value <0.05 was considered statistically significant.

Results

Thirty-five patients underwent a total of 35 fully sampled sagittal FLAIR and 35 compressed SENSE sagittal FLAIR MR scans (70 scans total), whereas 31 patients underwent a total of 34 fully sampled axial SPGR and 34 compressed SENSE SPGR MR scans (68 scans total). There were no statistically significant differences between the combined rater scores for each imaging metric of the fully acquired sagittal FLAIR sequences and the combined rater scores for each imaging metric of the compressed SENSE sagittal FLAIR sequences. The lowest p-value between these two imaging sequences was found to be $p=0.36$ and corresponded to the evaluation of gray-white matter boundaries. There were no statistically significant differences between the combined rater scores for each imaging metric of the fully acquired axial SPGR sequences and the combined rater scores for each imaging metric of the compressed SENSE axial SPGR sequences. The lowest p-value between these two imaging sequences was found to be $p=0.15$ and corresponded to the evaluation of optimal image quality.

Conclusions

In this prospective imaging study, accelerated compressed SENSE sagittal FLAIR and axial SPGR imaging sequences perform well for the evaluation of the brain relative to conventional fully acquired sagittal FLAIR and axial SPGR imaging sequences. Despite requiring data acquisition that utilizes incoherent k-space under-sampling, these novel imaging sequences on average do not significantly degrade image quality relative to their conventional imaging sequence correlates, as based on the imaging metrics evaluated for in this study.

O-119

3:14PM - 3:21PM

Improved T2-weighted 3D FLAIR from a compact 3T scanner with high-performance gradients

J Huston¹, N Campeau¹, J Trzasko¹, Y Shu¹, E Gray¹, T Foo², M Bernstein¹

¹Mayo Clinic, Rochester, MN, ²GE Global Research, Niskayuna, NY

Purpose

This NIH-funded initiative has designed and built a high-performance, low-cryogen, compact 3T MRI system with gradients capable of 80 mT/m and 700 T/m/s. The initial clinical goal of the project was to show parity with a whole body system in terms of image quality and acquisition time.

Materials and Methods

Under an IRB-approved protocol, 25 clinical patients receiving a head MRI examination were scanned both on a standard whole-body MRI system (GE Discovery MR750, GE Healthcare) and the compact 3T. The sagittal T2-weighted 3D FLAIR parameters were as follows: 256×256 matrix, $24 \times 24 \times 18.2$ cm field-of-view, 7600 ms TR, 93.0 ms effective TE and 2025 ms TI on the whole-body system, 91.3 ms TE and 206 ms TI on the compact system, with an echo spacing (ESP) of 4.88 ms on the whole-body and 3.77 ms on the compact system. The exams were reviewed by two board-certified neuroradiologists and graded on a five-point ordinal scale from -2 to +2, with +2 indicating strong preference for the compact system and -2 indicating strong preference for the whole-body system. Each pair of images was

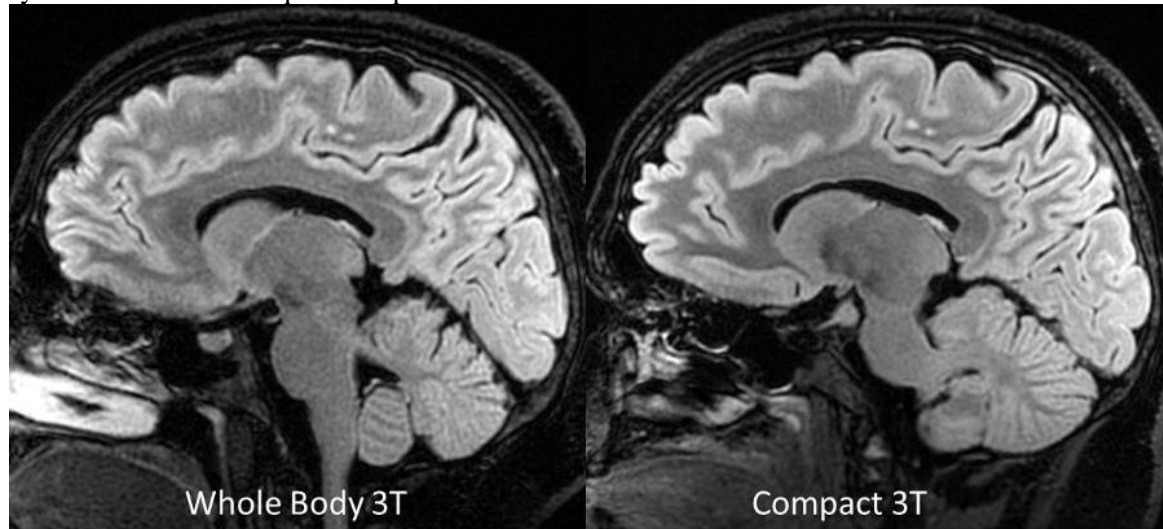
comparatively evaluated using the following attributes: signal-to-noise ratio (SNR), lesion conspicuity, motion artifact, gray/white matter contrast, cerebellar folia conspicuity, and overall exam quality.

Results

A one-sided Wilcoxon Sign-Rank was used to generate p-values and the results indicate that the compact 3T outperformed the whole-body system in terms of SNR ($p < 0.001$), lesion conspicuity ($p < 0.001$), gray-white matter contrast ($p = 0.008$), and overall quality ($p < 0.001$) (Figure). Furthermore, two-sided test results indicate that the compact 3T system performed comparably to the whole-body system with respect to motion artifact ($p = 0.312$) and cerebellar folia conspicuity ($p = 0.883$).

Conclusions

There is strong statistical evidence that the compact 3T provides equal or better image quality with the 3D FLAIR sequence and the higher slew rate gradient system allows an ESP reduction of 25% compared to the whole-body system. The unchanged incidence of motion artifact also suggests that the compact system offers at least equivalent patient comfort.



(Filename: TCT_O-119_C3TASNR.jpg)

O-120

3:21PM - 3:28PM

Age-Related Measurements of the Myelin Water Fraction derived from 3D multi-echo GRASE reflect the Cerebral White Matter Microstructure

T Faizy¹, D Kumar², G Broocks¹, C Thaler¹, F Flottmann¹, H Leischner¹, S Hewera¹, D Kutzner¹, D Dotzauer¹, S Jan-Patrick¹, R Reddy², J Fiehler¹, J Sedlacik¹, S Gellissen¹

¹University Medical Center Hamburg-Eppendorf, Hamburg, Germany, ²University of Pennsylvania, Philadelphia, PA

Purpose

Myelin Water Fraction (MWF) measurements derived from quantitative Myelin Water Imaging (MWI) may detect demyelinating changes of the cerebral white-matter (WM) microstructure. Here, we investigated age-related alterations of the MWF in normal aging brains of healthy volunteers utilizing two fast and clinically applicable 3-D gradient and spin echo (GRASE) MWI sequences with 3mm and 5mm isotropic voxel size.

Materials and Methods

In 41 healthy subjects (age range: 18-79 years), distinct regions of interest (ROI) were defined in the cerebral WM and corticospinal tracts on both brain hemispheres. ROIs were double-checked for accuracy.

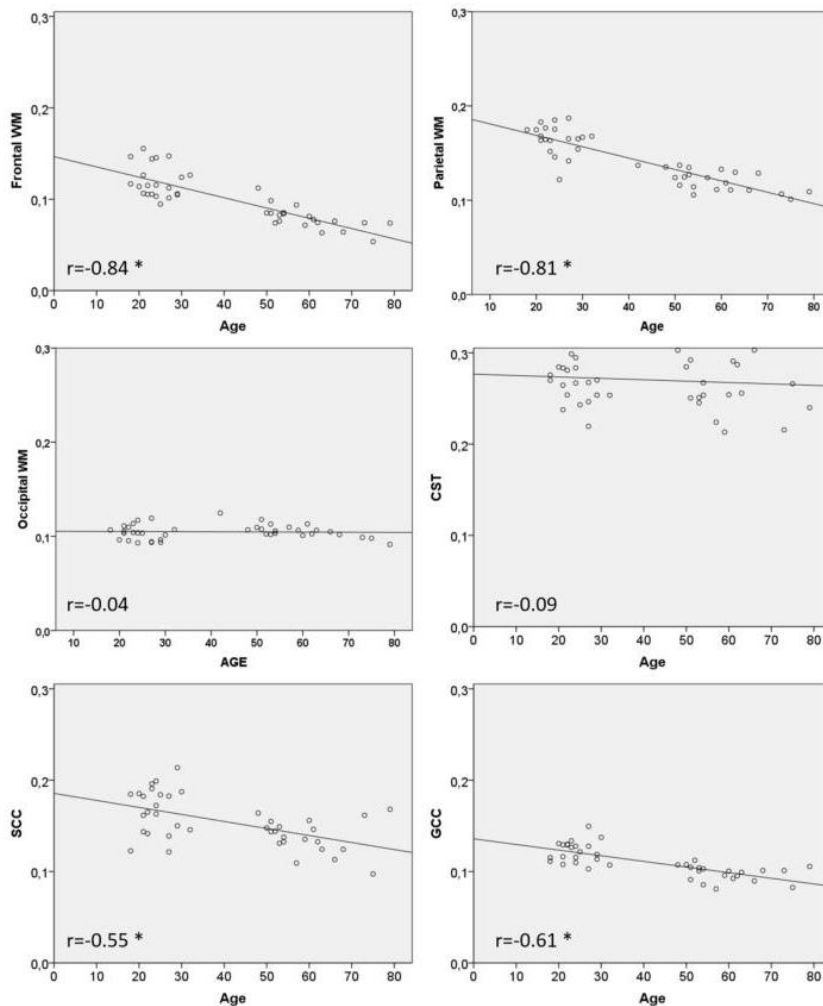
Subsequently, MWF values were obtained for each ROI and region based correlations and linear mixed models were applied to investigate age dependencies of regionally selective MWF measures.

Results

For the 3mm sequence, significant correlations of the mean MWF with age were found for most ROIs ($r > -0.8$ for WM ROIs; $r = -0.55$ for splenium corporis callosi; $r = -0.75$ for genu corporis callosi; $p < 0.001$ for all ROIs). Similar correlations with age were found for the ROIs of the 5mm sequence. No significant correlations were found for the corticospinal tract and the occipital WM ($p > 0.05$). Mean MWF values obtained from the 3mm and 5mm sequences showed a strong positive correlation ($r > 0.89$ for all ROIs, $p < 0.001$).

Conclusions

The applied 3-D GRASE MWF sequences seem to be sensitive for age-dependent demyelinating changes of the cerebral WM microstructure. The here reported MWF values might be of substantial use as reference for further investigations in patient studies.



(Filename: TCT_O-120_Figure2.jpg)

O-121

3:28PM - 3:35PM

Measures of Tissue Coherency in Clinical MRI Reflect Myelin Integrity in Multiple Sclerosis Patients

Y Zhang¹, S Sharma¹

¹*University of Calgary, Calgary, Alberta, Canada*

Purpose

Quantitative assessment of tissue pathology using MRI has important implications in many neurological disorders such as multiple sclerosis (MS). We have developed a method for assessing tissue integrity by quantifying the coherency of MRI voxels (1). The goal here was to determine the pathological correlates of this method using postmortem brain MRI.

Materials and Methods

T2-weighted MR images were acquired from 10 fresh postmortem brain specimens with MS using a 1.5T scanner. Immediately following MRI, the specimens underwent histological examination that included luxol fast blue staining for myelin. Three types of regions were identified in MRI and matched to the coregistered histological images: normal appearing white matter (NAWM), diffusely abnormal white matter (DAWM) and focal lesions. Tissue coherency in a MRI area was evaluated using a Fourier transform-based method. The steps were: 1) calculation of Fourier transform and power spectrum; 2) spectrum normalization and thresholding; and 3) polar conversion of the power spectrum. This yielded a distribution of spectral density at different aligning angles, from which we derived the dominant orientation, orientation strength, and angular entropy (complexity) of the spectrum. The coherency of myelin tissue in histological images was calculated using a method called structure tensor analysis (2).

Results

In total, we examined 46 brain regions, 11 from NAWM, 12 from DAWM and 23 from lesions. Angular entropy was significantly higher in lesions ($p < 0.05$) than DAWM and NAWM in both MRI and myelin images. Between these two imaging types, there were also significant correlations in angular entropy ($r = 0.7958$, $p < 0.05$), dominant orientation ($r = 0.8896$, $p < 0.05$), and orientation strength ($r = 0.6258$, $p < 0.05$). Measures of DAWM did not differ significantly from that of NAWM.

Conclusions

Our results suggest that spectral density measures in standard clinical MRI is a potential marker of myelin integrity in MS patients. Further verification is warranted.

O-122

3:35PM - 3:42PM

T1 Mapping Does not Lead to Significant Differences in an eTofts model parameters for brain DCE-MRI

M Cai¹, K Nael¹, N Swinburne¹

¹*Icahn Sinai School of Medicine at Mount Sinai Hospital, New York, NY*

Purpose

Quantitative brain dynamic contrast-enhanced MR imaging (DCE-MRI) can be performed to generate brain perfusion parameters by using a pharmacokinetic model. Parameter values are estimated using T1 dynamic enhancement intensity measured in individual voxels. T1 maps are generated from precontrast sequences to increase the estimation accuracy of the model by allowing for conversion of enhancement intensity into a contrast concentration. These precontrast sequences add scan time, processing time, and errors associated with coregistration. This study aims to compare DCE analysis using T1 maps generated with a multiple flip angle (MFA) approach to DCE analysis without the use of T1 mapping to determine if the generated kinetic parameter values are significantly different.

Materials and Methods

After IRB approval, retrospective review was performed on glioblastoma (GBM) patients who underwent radiation therapy. Further inclusion criteria required the patients to undergo post-treatment DCE-MR imaging and pathology of the treated lesion to confirm radiation necrosis versus GBM recurrence.

Oral Presentations & Excerpts

Volume-of-interests (VOI) were created using contrast-enhanced T1 sequences. DCE analysis was performed using an extended Tofts pharmacokinetic model both with and without the generation of MFA T1 maps. Using coregistered images, signal intensity histograms for all VOI voxels were measured for the following DCE-derived kinetic parameters: K_{trans}, KEP, VP, and VE. From these histograms, mean, 90th percentile, and kurtosis values were extracted. A paired T-test was used to compare each value for each kinetic parameter extracted from the histogram first as a generation population and then in separated groups by pathology. Direction comparison between radiation necrosis patients and recurrent tumor was made using a two-value T-test assuming unequivocal variance.

Results

For the included 15 patients in the sample population, pathology demonstrated 7 patients with radiation necrosis and 8 patients with recurrent tumor, 7 females and 8 males. Assuming a 95% confidence interval, there was no significant difference in DCE-derived mean values for K_{trans} (p=0.15), KEP (p=0.65), VP (p=0.05), and VE (p=0.12). For the 90th percentile value, there was no significant difference for K_{trans} (p=0.26), KEP (p=0.19), VP (p=0.28). There was no difference in kurtosis regarding K_{trans} (p=0.43), KEP (p=0.45), VP (p=0.38). There was a significant difference between the with and without T1 mapping groups for the 90th percentile value of VE (p<0.04) and for VE kurtosis (p<0.05). Comparing T1 mapping to no T1 mapping DCE-MRI after stratification into radiation necrosis and recurrence groups also yielded no significant difference except for the 90th percentile values for Ve in the radiation necrosis group (p=0.3). Direct comparison between the radiation necrosis group and tumor recurrence group yielded no difference for each parameter both with and without T1 mapping with a mean p-value across all groups of 0.68 (minimum p-value of 0.16 when comparing radiation necrosis against tumor recurrence with T1 mapping for VP).

Conclusions

With the exception of the 90th percentile and kurtosis values for VE, there were no statistical difference in the population of signal intensities generated by DCE analysis for the 15 patients. Kurtosis values suggest a tight distribution of signal intensities across all parameters for DCE both with and without T1 mapping (see fig. 1) as the lowest kurtosis value was still above 3, which would represent a normal distribution curve. A larger cohort would provide more powerful results; however, this initial study shows promise that DCE-MRI may be performed without MFA T1 mapping, which would allow for faster scan times and faster processing.

O-123

3:42PM - 3:49PM

Properties of Path Tracing (Cinematic) Rendering for Medical Imaging

A Davis¹

¹*New York University Langone Medical Center, New York, NY*

Purpose

Three-dimensional post-processing software (PPS) for medical imaging is based upon ray casting; a single ray of simulated light is passed through a region of interest and projected onto a 2-D surface. PPS algorithms use sets of rules to produce the final appearance termed volume rendering technique (VRT). VRT is modified by parameters affecting field of view and voxel opacity, lighting, shading and color. VRT provides improved spatial comprehension but has been criticized for unrealistic appearance as compared with real human visual experience. This is secondary to simplistic single-ray interrogation of imaging data. Path-tracing VRT is a new technique allowing for complex secondary interactions of light between voxels, due to reflection and resorption, creating a photorealistic appearance. While visually realistic, questions remain whether this is diagnostically advantageous. This study investigates individual optical characteristics of the path tracing method, their affect on image quality and compares results with ray-casting VRT using parameters widely accepted as fundamental to image interpretation.

Materials and Methods

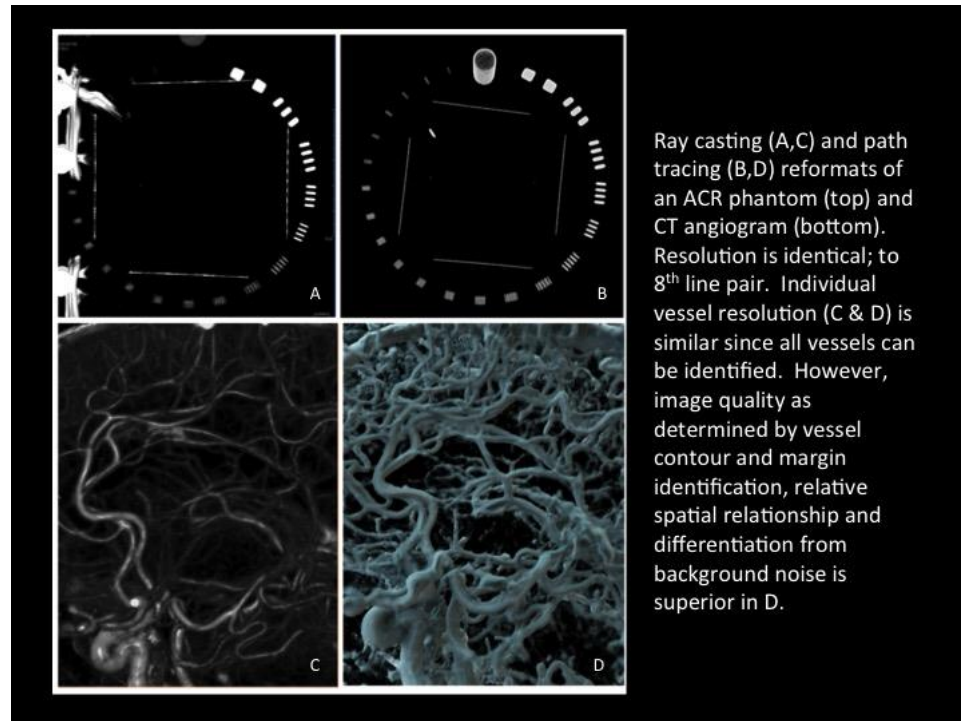
All images obtained on a 128 detector CT. An ACR phantom and CT angiograms segmented to visualize only the anterior cerebral artery were utilized. Images were reconstructed utilizing both ray-casting and path-tracing technique. Reconstruction parameters common to both techniques were equilibrated as best possible including field of view, brightness - exposure, color, opacity, direction and ambiance of lighting, specularity, background noise windowing. Final images presented on identical monitors and windowing performed to bring background noise to first barely perceptible level. Narrowly defined visual characteristics customarily accepted as essential to diagnostic image quality were used. Final images were redacted of identifying postprocessing information and presented in pairs of ray casting and path tracing in a blinded fashion to four nonradiologist expert evaluators (three postprocessing technologists with four to 15 years experience and one CT physicist with 10 years experience). Resolution was determined by smallest line pair visible on ACR phantom and smallest vessel identified on CTA. Image quality of CTA scored by selection of image with best presentation of small structures determined by identification of vessel morphology including contour and margin, relative spatial position and conspicuity from background.

Results

Resolution determined by smallest ACR line pairs was identical between techniques for all evaluators. Similarly identification of smallest vessels on CTA was identical for both techniques though for ray-casting technique it was thought to be mostly due to the brightness of specular reflection. All evaluators rated path-tracing technique superior for all image pairs presented with regard to identification of vessel morphology, including contours and margins, relative spatial position and differentiation from background noise.

Conclusions

This study demonstrates with both phantom and clinical cases that resolution per se is not different between ray-casting and path-tracing techniques. However, conspicuity and morphology of small structures judged by interpretation of contours and margins, relative spatial position of vessels and differentiation from background noise is improved with path tracing technique, particularly when object size is close to native CT resolution. Findings indicate path tracing VRT may be superior to traditional 3-D reconstruction methods.



O-124

3:49PM - 3:56PM

Motion Artifact Detection with Gradient Entropy

M Hoff¹, C Hall¹, J Andre¹

¹*University of Washington, Seattle, WA*

Purpose

Motion artifacts arising from patient motion during MR examinations frequently yield suboptimal image quality that can negatively impact radiological interpretation [1, 2]. A quantitative and standardized metric for assessing motion artifacts could permit assessment of patient motion prevalence during clinical scanning to enable clinical decision-making. Gradient entropy is a potential metric of motion artifacts [3]. Here the gradient entropy is measured and correlated with radiological motion artifact assessment to generate reliable motion artifact quantification.

Materials and Methods

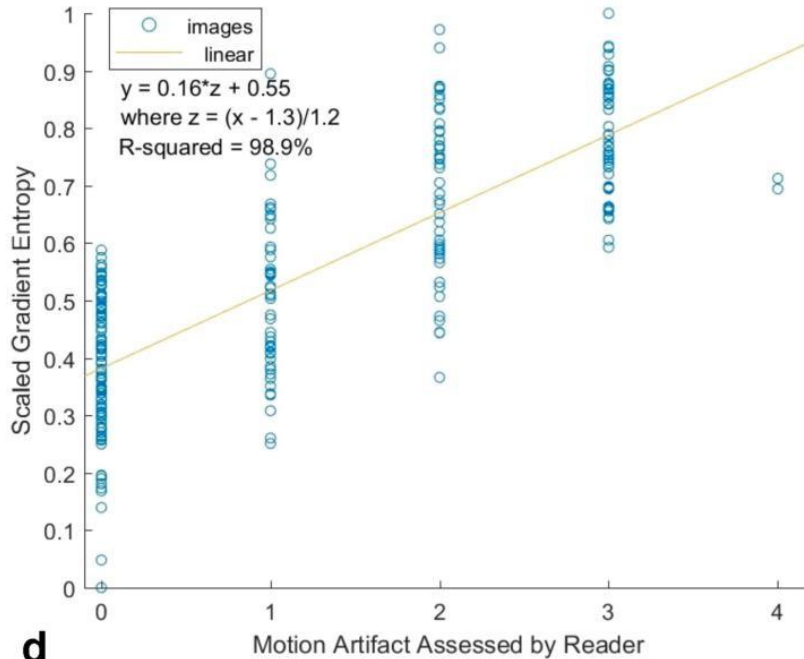
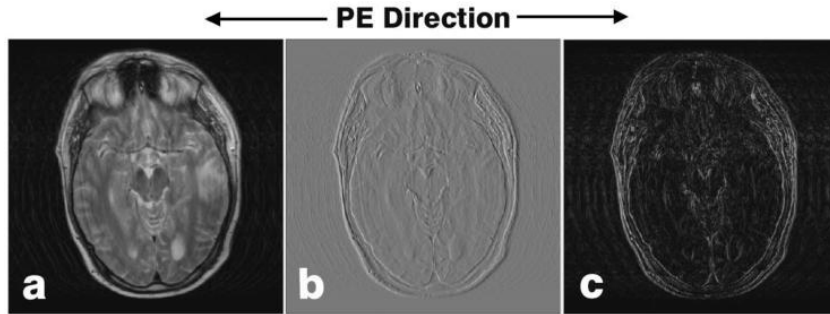
Magnitude images from consented T2-weighted 2-D spin-echo brain scans were acquired and anonymized. An experienced neuroradiologist identified 115 artifact-free images, and 2-12 pixel translational and 1.0°-2.5° rotational motion artifacts were artificially simulated and added. These simulated-artifact images (Fig. a) were intermingled with the original artifact-free images in blinded fashion for evaluation by an experienced neuroradiologist using a previously defined clinical five-point modified Likert scale (0: no artifact, 4: severe motion artifact) [2]. The gradient entropy for each image was calculated as previously described [3], where intermediate steps of the single-pixel gradient along the phase encoding direction is shown in Fig. b and a gradient entropy map is shown in Fig. c.

Results

Fig. d depicts the gradient entropy values computed as a function of the radiologist likert-scale evaluation. The data shows a strong correlation, with R-squared = 98.9%, inferring that we should see higher gradient entropy for increases in observed MRI motion artifact. Gradient entropy computation in larger datasets could ultimately be used to detect/quantify motion artifacts in order to improve clinical decision-making, workflow, and efficiency.

Conclusions

Gradient entropy is a robust identifier of MRI motion artifacts, and holds promise as a competent metric for motion artifact quantification.



(Filename: TCT_O-124_imagedoc4.jpg)

O-125

3:56PM - 4:03PM

Relationship between Cough-associated Changes in CSF flow and Disease Severity in Chiari I Malformation: an Exploratory study using Real-time MRI

A Bezuidenhout¹, R Bhadela¹

¹Beth Israel Deaconess Medical Center, Boston, MA

Purpose

To correlate disease severity in patients with Chiari I malformation (CMI) with cough-associated changes in CSF flow as measured with real-time MRI

Materials and Methods

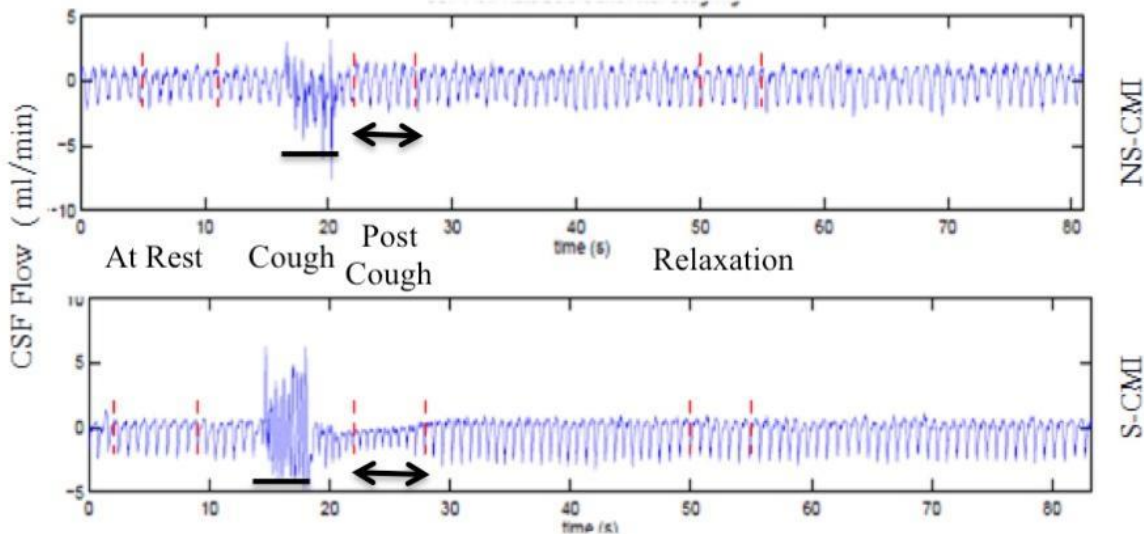
Thirteen CMI patients (tonsillar herniation ≥ 5 -mm) were prospectively studied. A real-time, flow-sensitized pencil-beam MRI scan was used to measure CSF stroke volume (SVCSF) during rest and immediately following coughing and relaxation periods (total scan time 90-seconds). Multiple posterior fossa and cranio-cervical anatomic measurements were also obtained. Patients were classified into two groups by neurosurgeons blinded to MRI measurements: (1) Nonspecific CMI (NS-CMI; 5/13): CMI with nonspecific symptoms like noncough related or mild occasional cough-related headache, neck pain, dizziness, paresthesias and/or trouble swallowing; (2) Specific-CMI (S-CMI; 8/13): CMI patients with

specific symptoms and/or objective findings like severe cough-related headache, myelopathy, syringomyelia, and muscle atrophy. Spearman correlation was used to determine correlations between MRI measurements and disease severity and both groups were also compared using a Mann-Whitney test.

Results
There was a significant negative correlation between percent change in SVCSF (resting to postcoughing) and CMI disease severity ($R=0.59$; $p=0.03$). Mann-Whitney comparisons showed percent change in SVCSF (resting to postcoughing) to be significantly different between patient groups ($p=0.04$). No other SVCSF or anatomic measure was significantly different between the groups.

Conclusions

Our exploratory study indicates that assessment of CSF flow response to a coughing challenge may be a valuable objective noninvasive test for clinical assessment of CMI patients.



(Filename: TCT_O-125_Figure3.jpg)

O-126

4:03PM - 4:10PM

Preoperative Evaluation of Intracranial Tumor Stiffness and Adhesion using MR Elastography

J Huston¹, Z Yin¹, J Hughes¹, K Glaser¹, A Manduca¹

¹Mayo Clinic, Rochester, MN

Purpose

Knowledge of brain tumor consistency and adhesion can be important to surgical outcome but has been reliably assessed only during surgery. MR elastography (MRE) is a form of MRI designed to evaluate tissue stiffness. A recently developed component of MRE, slip interface imaging (SII), has the ability to evaluate the adherence at the tumor-brain interface. The purpose of this study was to evaluate the use of MRE and SII in predicting tumor stiffness and adhesion during intracranial tumor resection.

Materials and Methods

Fifty patients with intracranial extra-axial tumors who underwent tumor excision were enrolled (vestibular schwannoma: $n=14$; meningiomas: $n=36$). Mechanical vibrations were introduced into the brain using a soft, pillow-like brain driver placed under the head, and 3-D motion was measured with spin-echo echo-planar-imaging MRE sequences. MRE-measured stiffness, and SII-derived octahedral shear strain (OSS) and normalized OSS (NOSS) were determined from wave displacement measurements. Neurosurgeons evaluated the stiffness of the tumors and the degree of tumor-brain adhesion during surgery.

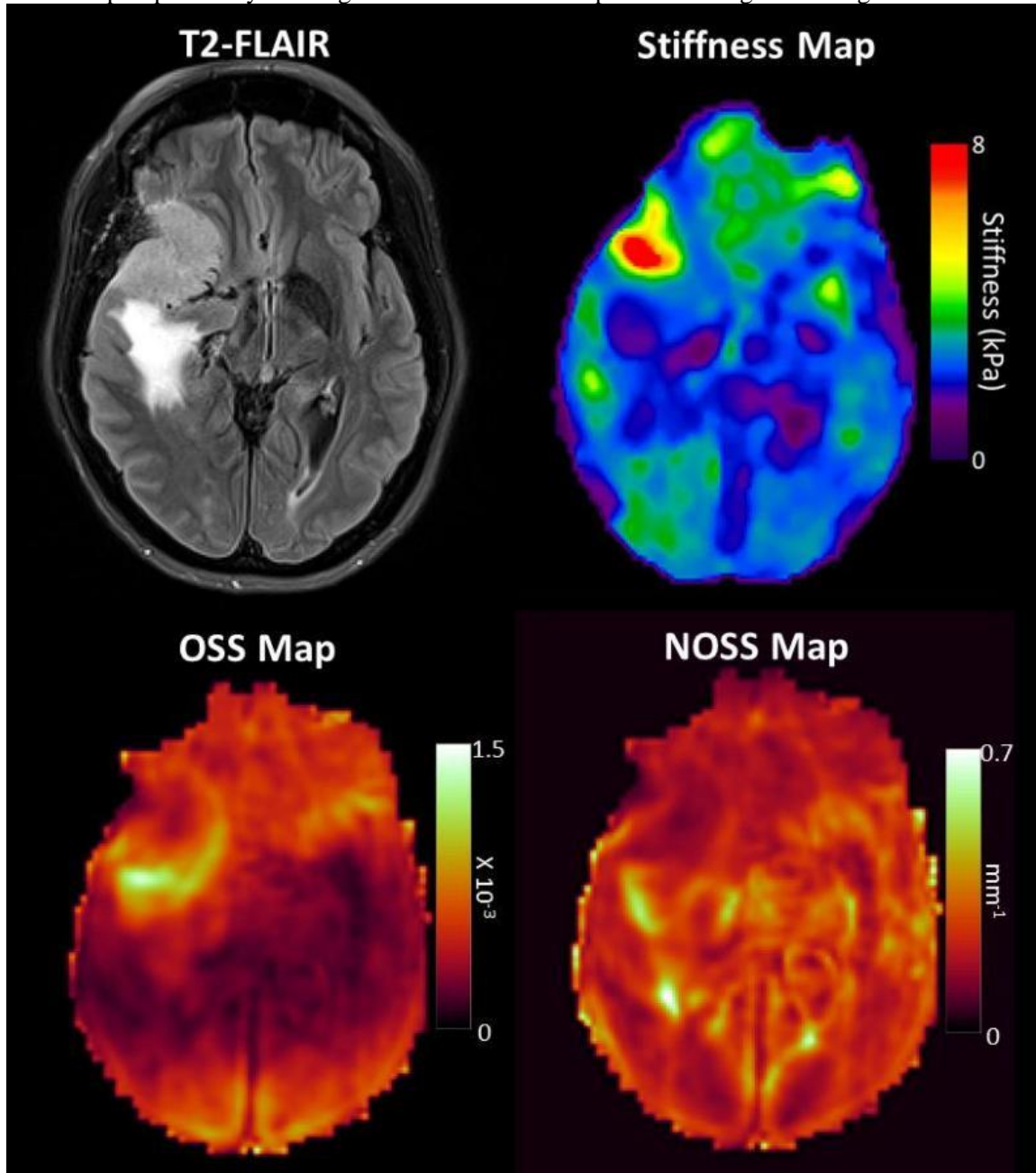
Oral Presentations & Excerptas

Results

MRE-measured stiffness and SII-derived NOSS strongly correlated with intra-operative surgical findings of tumor consistency and adhesion for both categories of tumors. Heterogeneity of tumor consistency was demonstrated with higher frequency, and higher resolution of MRE. NOSS provided a more accurate prediction of tumor-brain adhesion in the presence of peritumoral edema compared to OSS. As shown in a meningioma example (Figure), MRE predicted a firm tumor (higher values on stiffness map) with no separation between the tumor and brain (lack of slip interface at the tumor-brain interface on NOSS map), consistent with the surgical findings.

Conclusions

Initial results demonstrate that MRE and SII can noninvasively determine intracranial tumor stiffness and adhesion preoperatively offering a better assessment of procedure length and surgical risk.



(Filename: TCT_O-126_figureASNR.jpg)

Partial Volume Correction is Important for Quantitative Sodium ^{23}Na -MRI Brain at 3T

E Lui¹, V Venkatraman², T Li³, C Steward¹, B Sutton⁴, S Kolbe², B Moffat², C Kokkinos⁵, S Salinas², P Desmond¹

¹Royal Melbourne Hospital, University of Melbourne, Melbourne, Australia, ²University of Melbourne, Melbourne, Australia, ³Karolinska University Hospital, Stockholm, Sweden, ⁴University of Illinois at Urbana-Champaign, Urbana, IL, ⁵Epworth Hospital Richmond, Melbourne, Australia

Purpose

Quantitative ^{23}Na -MRI has potential clinical applications in neurodegenerative brain diseases [1, 2], but the importance of partial volume correction (PVC) has not been evaluated at 3T. We aim to assess the magnitude of signal intensity (SI) change from PVC on various brain regions using a PET-derived point-spread-function-based hybrid method previously evaluated [3].

Materials and Methods

Thirty-nine subjects (mean age=76±6years; female=66%) underwent 3T MRI (Trio, Siemens). ^{23}Na -MRI was acquired using a dual-tuned $^1\text{H}/^{23}\text{Na}$ birdcage head coil (Rapid Biomedical) at nominal 5mm isotropic resolution (FlexTPI sequence, TR=160ms, TE=0.3ms, FA=90degrees, NEX=2, TA=8minutes with data for B0 & B1 correction [4]). Volumetric isotropic 1mm T1 and T2 images were also acquired using 12-ch Siemens head coil. Data processing: (i) An automated Matlab pipeline [4] generated B0 and B1 corrected whole-brain sodium images (ii) Region-of-interest (ROI) and tissue probability maps were segmented on MPRAGE using Freesurfer 6.0 and FSLv.5 (iii) Sodium was coregistered with T1 and T2 using ANTS (iv) Registration and segmentation were visually inspected by a neuroradiologist (v) Hybrid geometric-transfer-matrix (GTM) and region-based voxel-wise (RBV) PVC [3] applied at FWHM=18mm (vi) Pre-PVC and post-PVC sodium SI of each ROI compared (vii) statistics performed on Excel.

Results

[Table1] summarizes the SI change of various ROIs post-PVC. CSF ROIs showed the largest expected SI increase (up to 88%, $p<0.001$). All grey-matter (GM) ROIs had expected SI decrease ($p<0.01$), between 10-23%, with hippocampi, parahippocampal, cingulate and precuneus GM by 18-23%. Pons and midbrain also showed expected decrease, but of a lesser magnitude ~10% ($p<0.001$). White matter (WM) had the least SI change, with 13/16 ROIs changing by <3.5%, cerebellar WM least (0.5%, $p=0.25$). SI ratios also improved post-PVC towards physiological CSF:brain sodium ratios [Table 2], similar to post-GTM-PVC ratios of a younger cohort (mean age=26yrs) at 7T 3mm resolution and superior to their ratios pre-PVC [5].

Conclusions

PVC is important for quantitative ^{23}Na ROI analysis at clinical 3T resolution and should be applied prior to using GM or CSF SI for quantification or normalization.

Table 1: Signal Intensity Change pre and post-PVC in various ROIs

	Pre-PVC SI		Post-PVC SI		Diff	% Difference
	Mean	SD	Mean	SD		
Supratentorial CSF	0.48	0.06	0.90	0.20	0.42	88.1***
Lateral Ventricle	0.80	0.10	1.07	0.19	0.27	34.1***
Cerebral GM[#]	0.42	0.03	0.33	0.11	-0.09	-21.1***
Basal Ganglia	0.43	0.04	0.38	0.04	-0.05	-11.9***
Thalami	0.48	0.06	0.40	0.07	-0.08	-15.8***
Hippocampi	0.50	0.04	0.41	0.05	-0.09	-17.8***
Parahippo [^] GM	0.49	0.04	0.39	0.07	-0.10	-20.8***
Cingulate GM	0.47	0.04	0.36	0.08	-0.11	-22.7***
Precuneus GM	0.46	0.03	0.37	0.07	-0.09	-18.7***
PreCentral GM	0.41	0.04	0.36	0.07	-0.04	-10.7***
PostCentral GM	0.42	0.04	0.38	0.07	-0.04	-9.5**
MFG ^{^^} GM	0.38	0.04	0.35	0.07	-0.04	-9.5**
Supr parietal GM	0.43	0.04	0.39	0.09	-0.04	-9.6**
Supramarginal GM	0.41	0.03	0.36	0.07	-0.05	-13.0***
Cerebral WM^{##}	0.38	0.03	0.38	0.05	0.01	1.8
Frontal WM	0.35	0.03	0.35	0.05	-0.01	-2.1
Occipital WM	0.38	0.03	0.39	0.04	0.01	3.4*
Parietal WM	0.38	0.03	0.37	0.05	-0.01	-1.8
Temporal WM	0.38	0.03	0.39	0.05	0.01	2.3
Parahippo WM	0.46	0.04	0.44	0.06	-0.01	-3.1*
Cingulate WM	0.45	0.04	0.41	0.06	-0.04	-8.6***
Corpus callosal WM	0.54	0.05	0.45	0.06	-0.08	-15.6***
Precuneus WM	0.40	0.03	0.40	0.05	-0.01	-2.1
Precentral WM	0.35	0.03	0.34	0.05	-0.01	-2.2
Postcentral WM	0.38	0.03	0.37	0.05	-0.01	-2.6
MFG WM	0.34	0.04	0.33	0.05	-0.01	-2.7*
Supr parietal WM	0.37	0.03	0.37	0.05	-0.01	-1.6
Supramarginal WM	0.37	0.03	0.36	0.04	-0.01	-2.6*
Cerebellum WM	0.38	0.05	0.38	0.05	0.00	-0.5
Midbrain	0.48	0.03	0.43	0.04	-0.05	-10.9***
Pons	0.42	0.03	0.38	0.04	-0.04	-9.2***

[^]Parahippocampal ^{^^}Middle frontal gyrus [#]Grey matter ^{##}White matter

* p<0.05, **p<0.01, ***p<0.001 (2-tail paired t-test)

Table 2: Signal Intensity ratios pre and post-PVC*

Resolution (mm)	SI ratios	
	Lat vent:GM	Lat vent:WM
Pre-PVC 3T	1.9	2.1
Pre-PVC 7T [*]	1.8	2.1
Post-GTM-RBV-PVC 3T	3.2	2.8
Post-GTM-PVC 7T [*]	2.9	3.4

*published values⁵ ; Physiological sodium CSF:brain ~3-3.7

(Filename: TCT_O-127_ASNR_PVC_submission.jpg)

O-128

Z Effective and Electron Density Values of Structures of the Brain and Head, Derived From Spectral CT

E Ben-David¹, Z Romman², I Leichter¹, J Sosna¹, J Gomori¹

¹*Hadassah Hebrew University Medical Center, Jerusalem, Israel*, ²*Philips Healthcare, Haifa, Israel*

Purpose

In an effort to evaluate intrinsic physical properties using dual-energy CT rather than kVp dependent Hounsfield Units, our purpose was to determine average effective atomic number (Z_{eff}) and electron-density (ED) values, relative to water, of tissues of the brain and head, using spectral CT data.

Materials and Methods

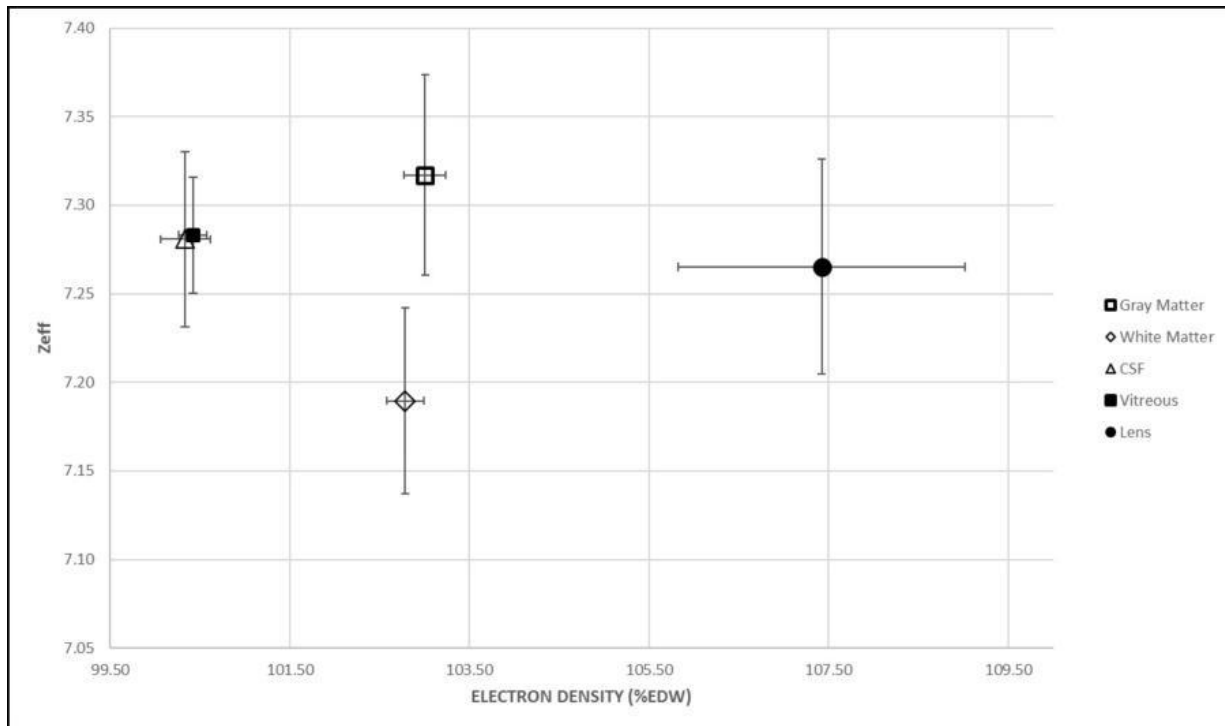
Scans of 33 patients who underwent noncontrast-enhanced head CT (IQon, Philips Healthcare, Eindhoven, Nederland) between February and September 2017, with no radiological findings were retrospectively reviewed. Noncontrast enhanced series were performed at 120 kVp on a detection-based dual-energy system. Z_{eff} and ED images were retrospectively reconstructed directly from the scanner spectral acquisition. Pixel values were received from ROIs of 3 gray-white matter pairs, CSF, vitreous, optic lens and retro-buccal fat. Paired t-test was used to assess the significance of the difference of measurements between gray and white matter and between CSF and vitreous.

Results

Marked were 330 ROIs, resulting in 21328 pixels of gray and white matter, 3579 pixels of CSF, vitreous and fat, and 2583 pixels of the lens. Average ROI area was $8.5 \pm 1.5 \text{ mm}^2$ for the lens and $24.9 \pm 0.4 \text{ mm}^2$ for all other structures. Z_{eff} for gray matter, white matter, CSF, vitreous, lens and fat were 7.32 ± 0.06 , 7.19 ± 0.05 , 7.28 ± 0.05 , 7.28 ± 0.03 , 7.27 ± 0.06 , and 5.92 ± 0.24 , respectively. ED for these structures was 103.01 ± 0.23 , 102.79 ± 0.21 , 100.34 ± 0.28 , 100.43 ± 0.16 , 107.42 ± 1.6 , and 92.88 ± 0.6 %EDW, respectively (Figure). P-value for comparison of gray and white matter Z_{eff} and ED were <0.001 . P-value for comparison of vitreous and CSF was 0.78 for Z_{eff} and 0.07 for ED.

Conclusions

Some tissues of the brain and head evaluated in this study have unique Z_{eff} and ED values, allowing for definition based on physical properties rather than Hounsfield Units that are kVp dependent.



(Filename: TCT_O-128_ZeffED.jpg)

O-128a

4:24PM - 4:30PM

Optimizing Resources for Endovascular Clot Retrieval for Acute Ischemic Stroke Using a Discrete-Event Simulation model

S Huang¹, J Maingard², H Kok³, C Barras⁴, V Thijs⁵, R Chandra⁶, D Brooks², H Asadi⁷

¹Australian National University Medical School, Canberra, ACT, ²Deakin University, Melbourne, Australia, ³Guy's and St Thomas' NHS Foundation Trust, London, United Kingdom, ⁴The South Australian Health and Medical Research Institute, Adelaide, Australia, ⁵University of Melbourne, Melbourne, Australia, ⁶Monash Health and Monash University, Clayton, Victoria, ⁷Monash University, Melbourne, Australia

Purpose

Endovascular Clot Retrieval (ECR) is the standard of care for acute stroke due to a large vessel occlusion. It is a time critical and complex process involving many specialized care providers and resources. Maximizing patient benefit while minimizing cost of this service requires optimization of human and physical assets. The aim of this study was to develop a computer simulation of an ECR service designed to optimize resource allocation.

Materials and Methods

Using Simmer—an R-based Discrete Event Simulation (DES) package— as frequently employed in complex logistical operations, we have developed a comprehensive computational model that closely mimics the environment of an ECR service from presentation to emergency department to the angio suite. This model was tested using real data collected from a quaternary institution with ECR service.

Results

Our model assesses the impact of available services, and aids optimization of resource distribution and access, allowing comparison of various competing strategies. In this simulation, the numbers of different human or capital resources such as stroke physicians, neuro-interventionists, and angiography equipment

can be varied to assess the impact on efficiency and availability of service delivery. Other factors and variables such as equipment breakdown, servicing or times taken during components of an individual stroke management pathway can also be integrated, to identify sources of systemic delay and cost-points, with a view to service improvement.

Conclusions

A novel computer simulation is proposed to assess resource allocation, directed at optimizing the timely, effective and equitable application of human and physical resources. This model can provide clinically important data to help existing ECR services, in targeting optimum service delivery and best patient outcomes.

Monday, June 4, 2018

4:45PM - 6:15PM

Parallel Paper Session: Spine: New Findings

O-129

4:45PM - 4:52PM

The Normal Lumbosacral Disc Herniation: incidence of vertebral anatomic variants and Nomenclature 2.0

L Hahn¹, S Rothman¹, M Shiroishi¹, C Liu¹, A Lerner²

¹University of Southern California Keck School of Medicine, Los Angeles, CA, ²University of Southern California, Los Angeles, CA

Purpose

The first comprehensive article defining the terms used in describing the anatomy and pathology of the lumbar disc "Nomenclature and Classification of Lumbar Disc Pathology" was published in 2000 by the ASNR, the ASSR, and the NASS. (1) This created a lexicon for describing the anatomy and pathology of the disc as seen on imaging studies. It was not meant to be a series of "pathologic" diagnoses. Although that treatise was quickly accepted, some issues of controversy remained. In 2002, the document was reviewed and ultimately revised and accepted by NASS, ASSR and ASNR and after 10 years of negotiations, published as "Nomenclature 2.0". (2) There remains one issue that was not satisfactorily resolved. What should be done about the "normal" herniated or bulging disc? The broad definition of "herniated disc" includes nucleus, cartilage fibrous tissue and bone projecting beyond the margins of the attached bones. What is to be done when the normal disc projects beyond the vertebral bony edges, which occurs frequently at the lumbosacral junction? In his classical book, Farfan has documented the anatomic variations of the lumbar vertebrae and discs. (3) He proved that the shape and size of the vertebral endplates defined the pattern of internal degeneration of the disc. Vertebra whose posterior edges were convex towards the spinal canal developed central annular fissures and central nuclear herniation and those with convex vertebral bodies developed lateral fissures and herniations. Consequently, if the adjacent endplates of the sacrum and L5 were of different sizes or shapes then the disc which attaches the 2 structures must extend between the 2 bones and therefore project beyond the shorter endplate. According to Nomenclature 2.0 this normal anatomic variant must be called a "disc herniation". The purpose of this study is to determine the incidence of this normal "disc bulge or herniation" at the lumbosacral junction as seen on Sagittal MRI scans.

Materials and Methods

For this study, we reviewed the list of patients who underwent MR lumbar spine imaging from April 16, 2017 to November 9, 2017 based on our institution's RIS-PACS database. Only 18- to 35-year-old patients were included. We identified 128 patients in this age group with MRI lumbar spine.

Oral Presentations & Excerptas

Subsequently, we reviewed clinical records and MRI scan reports, in our electronic medical record and excluded all patients with neurofibroma, scoliosis, diffuse osseous or meningeal metastatic disease, prior lumbar spine surgery, spondylolysis, and limbus vertebra at L5-S1. For the purposes of this study, we defined the normal L5/S1 disc as one with an intact annulus and normal intradiscal signal. A normal but aging disc was defined as one with an intact annulus and slight signal reduction in signal in the posterior portion of the disc. An abnormal disc was defined as one showing generalized reduction in intradiscal signal with or without outer annular disruption, high-intensity zone (HIZ), bulging, or herniation. All cases were reviewed by 2 experienced attending neuroradiologists. Endplate lengths were measured at the inferior endplate of L5 and superior endplate of S1 on sagittal T2 images. The shape of the endplates was determined on the axial T2 images as concave, convex, beaked, or flat. P-value was calculated by using the chi-square test comparing the groups with normal and abnormal disc herniation with the control group (no disc herniation or abnormal disc signal).

Results

Total 92 patients (51 females (55.4%), and 41 males (44.6%)) fulfilled the inclusion criteria. Thirty-six patients (39.1%) demonstrated normal L5-S1 disc and 56 patients (60.9%) demonstrated L5-S1 disc herniation. Of those with disc herniation, 16 patients (28.6%) demonstrated normal "disc herniation", 38 patients (67.9%) with abnormal disc signal, and 2 (3.6%) patients had indeterminate signal (discordant description by 2 reviewers). Figure 1 is a thin slice of an intrinsically normal L5/S1 disc and Figure 2 is a corresponding T2WI sagittal MR image of similar disk at L5/S1. This normal disc projects 5 mm beyond the sacrum and would be considered a normal "disc herniation". Incongruent length of the endplates is seen in both cases. Total of 27 patients (29.3%) demonstrated incongruent endplates length. Out of those with normal disc herniation, 5 (31.3%) patients had incongruent endplate length ($p=0.003$). Out of those with abnormal disc herniation, 20 (52.6%) patients had incongruent endplate length (<0.001). Only 1 patient with normal L5-S1 disc demonstrated incongruent endplates length (2.8%). One out of 2 patients with indeterminate disc signal also had incongruent endplates length (2.8%). Total of 22 patients (23.9%) demonstrated incongruent endplates shapes. Out of those with normal disc herniation, 3 (18.8%) patients had incongruent endplate shape ($p=0.08$). Out of those with abnormal disc herniation, 10 (26.3%) patients had incongruent endplate shape. Eight patients with normal L5-S1 disc demonstrated incongruent endplates shape (22.2%) ($p=0.17$).

Conclusions

Our results indicate that 28.6% of our 18- to 35-year-old patients demonstrated "normal disc herniation" at L5/S1 without any generalized reduction in intradiscal signal, outer annular disruption, or high-intensity zone (HIZ). According to Nomenclature 2.0, these patients fall under the category of "disc herniation", although the finding clearly represents a normal anatomic variant. Our results also show that patients with normal disc herniation at L5-S1 demonstrate a higher percentage of incongruent endplate length at L5/S1 compared with patients without "disc herniation" (31.3% vs 2.8%, $p=0.003$). This finding supports the hypothesis that incongruent sizes of the adjacent endplates of the L5 and S1 vertebra may cause the disc attached to these structures to project beyond the shorter endplate. Although we have also hypothesized that incongruent endplate shapes at S1 and L5 would also cause the intervertebral disc to extend beyond one endplate, our results show that there is no correlation between the incongruent endplate shapes and normal "disc herniation". In summary, normal "disc herniation" is a common variant at L5/S1 level and is associated with incongruent endplate lengths of L5 and S1 vertebra. A new, revised nomenclature incorporating this variant is needed to avoid miscommunication and over diagnosis of disc herniations at the L5-S1 level.

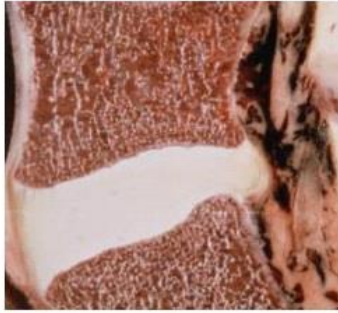


Figure 1

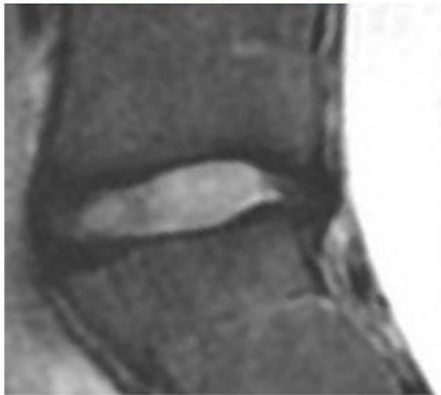


Figure 2

(Filename: TCT_O-129_ASNRfigure1and2.jpg)

O-130

4:52PM - 4:59PM

Radiologists Agree More on Assessment of Change Than Degree of Stenosis on Follow-up Cervical Spine MRIs

J Costello¹, M Peckham¹, L Shah¹, T Hutchins¹

¹University of Utah, Salt Lake City, UT

Purpose

Follow-up MR imaging of the cervical spine is often ordered to evaluate change from baseline pain. Multiple studies have shown considerable variability with only fair inter-rater agreement between radiologists when reporting severity of spinal canal and foraminal stenosis using standard systems of grading. This may result in an unclear or misleading report that can have important clinical or medico-legal ramifications. To date, studies have not evaluated radiologists' concordance in evaluating change on cervical MR. We hypothesized that radiologists have better agreement in assessing change than in rating stenosis severity on these follow-up exams.

Materials and Methods

Initial and follow-up cervical MRIs performed for neck pain were retrospectively reviewed by two radiologists blinded to imaging reports. For each patient, spinal canal and bilateral neural foramina from C1-C2 to C7-T1 were compared and narrowing rated as "increased", "decreased", or "unchanged." Concordance between blinded readers was calculated with prevalence and bias adjusted kappa. The MRI reports were then reviewed and differences in severity assessment (mild, moderate, severe), as well as whether or not the report specifically mentioned change/no change, were documented for each level.

Results

A total of 420 cervical regions were assessed for change. Concordance between two blinded radiologists for assessment of change was 87% for spinal canal, 91% for left neural foramina and 88% for right neural

Oral Presentations & Excerptas

foramina. After evaluation of follow-up reports, it was noted that the severity scale (mild, moderate, severe) was reported in 98% of cervical regions, but interval change was only specifically assessed in 68% of cervical levels. At approximately 30 cervical levels, the severity scale language differed in the follow-up report, but no mention of interval change was present. In follow-up reports containing an assessment of change, nonconcordant language was present where the severity grading scale was noted to be different but the examination was ruled as unchanged in 10% of cervical levels.

Conclusions

Blinded radiologists had excellent agreement when assessing for change on follow-up cervical MRIs. Despite the known variability between radiologists in grading stenosis, many follow-up reports preferentially focused on severity rather than assessment of change, which may be more clinically important. Also, discordant language related to inter-rater variability implied change in several patients when it was not truly present. For clarity and consistency in reporting, we recommend focusing on change assessment in follow-up cervical spine MRIs for neck pain.

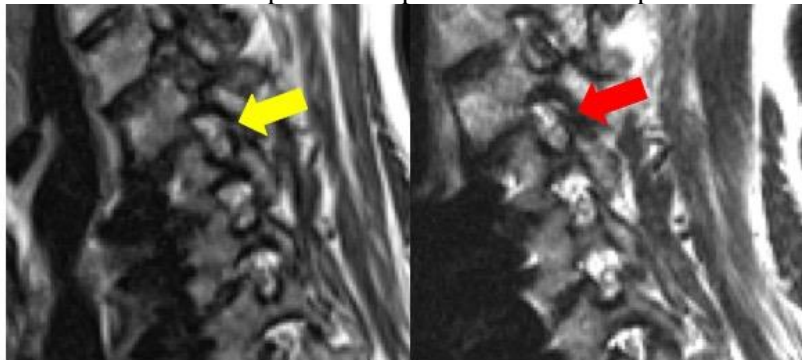


Figure: Potential misleading report. Sagittal oblique images of the right neural foramina. Narrowing at the C4-C5 neural foramina was reported as moderate (yellow arrow), indicating an increase from the prior MRI exam (red arrow). There was no mention of change in the report. Both blinded radiologists agreed there was no change at this level.

(Filename: TCT_O-130_Figure.jpg)

O-131

4:59PM - 5:06PM

Radiologists Agree More on Assessment of Change Than Degree of Stenosis on Follow-up Lumbar Spine MRIs.

M Peckham¹, J Costello¹, L Shah¹, T Hutchins¹

¹University of Utah, Salt Lake City, UT

Purpose

Follow-up MR imaging of the lumbar spine is often ordered to evaluate change from baseline pain. Multiple studies have shown considerable variability with only fair inter-rater agreement between radiologists when reporting severity of spinal canal and foraminal stenosis using standard systems of grading. This may result in an unclear or misleading report that can have important clinical or medico-legal ramifications. To date, studies have not evaluated radiologists' concordance in evaluating change on repeat lumbar MR. We hypothesized that radiologists have better agreement in assessing change than in rating stenosis severity on these follow-up exams.

Materials and Methods

Initial and follow-up lumbar MRIs performed for low-back pain were retrospectively reviewed by two radiologists blinded to imaging reports. For each patient, spinal canal and bilateral neural foramina from L1-2 to L5-S1 were compared and narrowing rated as "increased", "decreased", or "unchanged."

Concordance between blinded readers was calculated with prevalence and bias adjusted kappa. The MRI reports were then reviewed and differences in severity assessment (mild, moderate, severe), as well as whether or not the report specifically mentioned change/no change, were documented for each level.

Results

Forty-nine lumbar MRIs with follow-up studies were evaluated with a total of 735 regions assessed for change. Concordance between two blinded radiologists for assessment of change was excellent (0.85 for spinal canal, and 0.95 and 0.96 for neural foramina). After evaluation of follow-up reports, it was noted that the severity scale (mild, moderate, severe) was reported in 88% of patients and 76% of regions, but interval change was only specifically assessed in 61% of patients and 38% of regions. In approximately 132 regions spanning 25 patients, the severity scale language differed in the follow-up report, but no mention of interval change was present. In follow-up reports containing an assessment of change, nonconcordant language was present where the severity grading scale was noted to be different but the examination was ruled as unchanged in 40% of subjects and 13% of regions.

Conclusions

Blinded radiologists had excellent agreement when assessing for change on follow-up lumbar MRIs. Interestingly, despite the known variability between radiologists in rating stenosis, follow-up reports preferentially focused on severity rather than assessment of change which may be more clinically important. Furthermore, discordant language from inter-rater variability implied change in several patients when it was not truly present. For clarity and consistency in reporting, we recommend focusing on change assessment in follow-up lumbar spine MRIs for back pain.

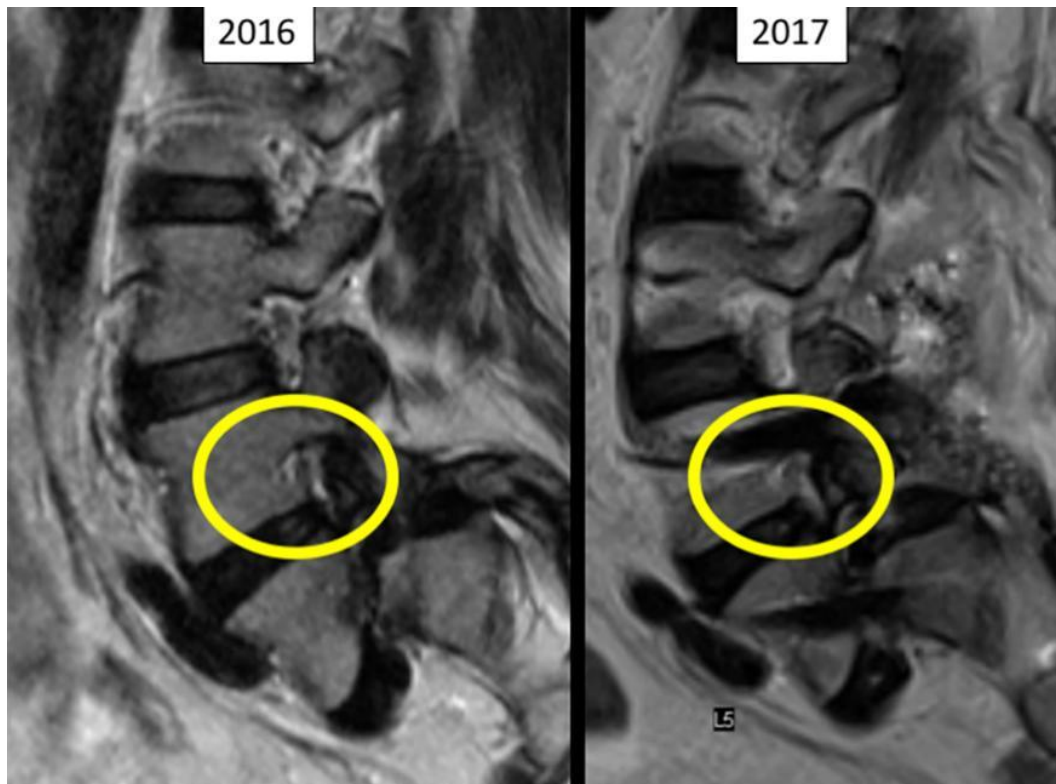


Figure: Two sagittal T2 images through the level of the left L4-5 neural foramen (yellow circle) before and after posterolateral fixation. The severity description differed between both studies, rated as mild preoperatively in 2016, and moderate postoperatively in 2017. The follow-up 2017 MRI report did not include an assessment of change, though it was implied by discordant severity language. Blinded readers agreed that narrowing was unchanged.

(Filename: TCT_O-131_Assessmentfigure.jpg)

O-132

5:06PM - 5:13PM

Posterior spinal cord indentation: imaging findings and clinical outcome

N Zakhari¹, S Chakraborty¹, T Nguyen¹

¹The Ottawa Hospital, Ottawa, Ontario, Canada

Purpose

Posterior spinal cord indentation can be seen with dorsal arachnoid web, spinal cord herniation and arachnoid cyst. With increased awareness of the arachnoid web and the scalpel sign, more subtle indentations are identified, and guidelines are required to direct management. Our purpose is to identify the imaging findings, associated with worse clinical outcome.

Materials and Methods

Retrospective review of 91 MRI from April 2009 to March 2016 with key words "cord herniation" and "web" were identified. Imaging follow up and clinical data were recorded. Two neuroradiologists blinded to the clinical data separately assessed multiple imaging findings including degree of indentation and

signal abnormality and each provided his diagnosis. Differences and association of imaging and clinical findings were assessed via t-test and Fisher exact and Chi-squared tests for continuous and categorical data. Inter-rater agreement was calculated.

Results

Included were 73 patients, 65 were clinically stable, or the finding was incidental and 8 had clinical worsening or required surgery. There was significant difference in % of cord diameter decrease between the 2 clinical groups [$p = 0.013$, reader 1; $p = 0.027$ reader 2] and between those with worsening versus stability on imaging follow up ($p=0.04$; $p=0.03$). The clinical course was significantly associated with subjective cord indentation depth assessment ($p = 0.03$ reader 1) and presence of syrinx ($p=0.017$ reader 2) on original MR and worsening on imaging follow up ($p=0.03$). The interrater agreement was good for cord signal abnormality ($k=0.64$; 95% CI 0.45-0.82) and moderate for syrinx ($k=0.58$; 95% CI:0.25-0.91). There was only fair agreement for scalpel sign classification and in the final diagnosis ($k=0.35$ 95% CI 0.15-0.55) and ($k=0.279$; 95% CI:0.14-0.42).

Conclusions

The degree of cord indentation, presence of syrinx and worsening of imaging findings are associated with worse clinical course and can be useful in guiding management and directing subspecialty referrals.



Fig. 1: Depth of posterior cord indentation: Sag. T2WI showing (A)mild (18%), (B) moderate (40%) and (C) severe (70%) posterior cord indentation.

(Filename: TCT_O-132_CORD_HERNIATION_Final-JPG.jpg)

O-133

5:13PM - 5:20PM

Bone Mineral Density in Opportunistic Quantitative Computed Tomography is the Main Predictive Factor of One-year Reoperation after Posterior Lumbar Instrumentation

M Loeffler¹, N Loreck¹, C Zimmer¹, Y Ryang¹, J Kirschke¹

¹Klinikum rechts der Isar, Technical University Munich, Munich, Bavaria, Germany

Purpose

Vertebral bone mass is believed to be an important determinant of outcome after instrumented spinal surgery. Previously, bone mineral density (BMD) was identified as a predictive factor for screw loosening [1]. Therefore, we investigated the association of BMD with the rate of reoperation within the first year after posterior lumbar fixation.

Materials and Methods

We included 293 patients (median age 72, range 27-94 years) who received lumbar spinal fixation for degenerative spine disease, infection or vertebral body fracture either by a rigid, semirigid, or additionally cement-augmented rigid pedicle screw-rod system, in the years 2010 to 2014. Overall 27 patients had reoperation within one year. Lumbar BMD was assessed on preoperative CT scans by opportunistic quantitative computed tomography (qCT) [1-4]. In a multivariate logistic regression model we predicted one-year reoperation by BMD and other surgery related factors. In ROC analysis the performance of BMD as a classifier for occurrence of reoperation was tested and optimal thresholds were determined.

Results

Patients' prevalence of osteoporosis was 37.5% ($BMD < 80 \text{ mg/cm}^3$). Among all factors, BMD was the main predictor for the risk of reoperation (odds ratio = .972 for 1 mg/cm^3 change, $p < .001$; Table 1). Patients with reoperation and cement-augmented fixations had lower BMD values ($41.7 \pm 13.9 \text{ mg/cm}^3$) than nonaugmented fixations ($73.8 \pm 35.8 \text{ mg/cm}^3$; Figure 1), which didn't reach statistical significance due to limited number of reoperations. Whether reoperation occurred within one year after noncement-augmented surgery could be predicted by a $BMD < 79.2 \text{ mg/cm}^3$ (specificity 78.6%).

Conclusions

These results show that $BMD < 79.2 \text{ mg/cm}^3$ is the major risk factor for surgery failure within the first year following nonaugmented posterior lumbar fixation. Including this quantitative measure in surgical planning would be easily feasible by means of opportunistic qCT without additional radiation exposure or costs.

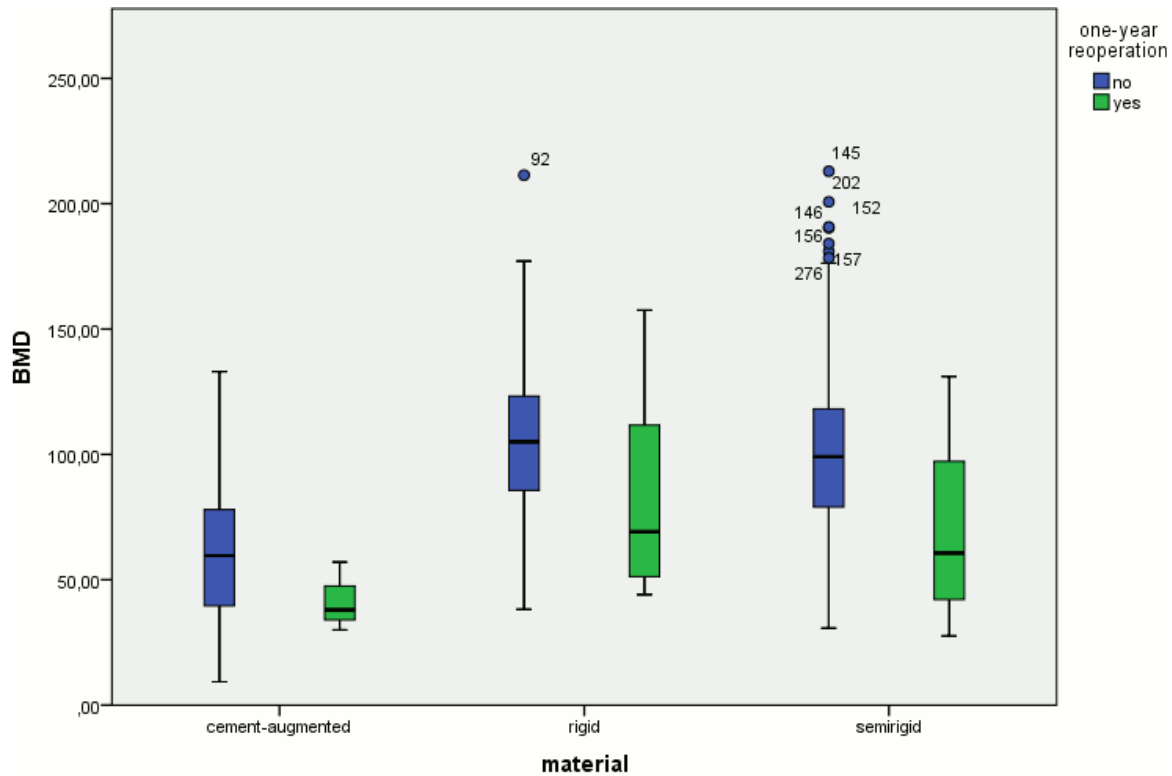


Figure 1

Table 1

	Wald	Logit	Odds ratio	95% CI	p-value
age	.282	-.012	.988	.945-1.033	.596
indication	4.202				.122
infection vs. degeneration	.014	.111	1.117	.183-6.836	.905
fracture vs. degeneration	4.137	1.947	7.010	1.073-45.783	.042
BMD	12.000	-.028	.972	.956-.988	.001
surgery duration	8.924	.624	1.867	1.240-2.812	.003
no. of instrumented segments	7.993	-.827	.438	.247-.776	.005
material	9.358				.009
rigid vs. cement	4.532	1.856	6.400	1.159-35.351	.033
semirigid vs. cement	9.341	2.677	14.539	2.612-80.921	.002

(Filename: TCT_O-133_FigureAbstract.gif)

O-134

5:20PM - 5:27PM

Magnetic Resonance Guided High Intensity Focused Ultrasound for the Treatment of Facetogenic Pain.

L Shah¹, M Peckham¹, H Odeen², T Hutchins¹, S Miller², A Payne²

¹University of Utah, Salt Lake City, UT, ²Utah Center for Advanced Imaging Research, Salt Lake City, UT

Purpose

Low back pain (LBP) is the most common pain symptom experienced by Americans, and although there is myriad of etiologies, up to 52% is facetogenic in origin with studies supporting the medial branch of

the spinal dorsal ramus, which supplies the facet joint and multifidus muscle, as the potential pain generator. Facetogenic LBP is frequently treated with steroid injections and radiofrequency ablation (RFA). Recent studies have demonstrated feasibility of spine applications of MR-guided focused high intensity ultrasound (MRgHIFU), which enables noninvasively targeting the medial branch nerve. MRgHIFU does not require skin puncture or radiation and can be precisely targeted to form discrete thermal lesions along a nerve. We demonstrate our pilot work in a direct comparison of MRgHIFU and RFA.

Materials and Methods

RFA was performed on the lumbar spines of two swine specimens at four levels, directly followed by MRgHIFU on the contralateral side with multiple diagnostic MRI sequences obtained concurrently. Each swine was reimaged seven days after the treatments. MRgHIFU was performed in a 3T Prisma MRI. A preclinical MRgHIFU system was used with a custom pig holder that positioned the animal oblique/supine above the ultrasound transducer. A 5-channel RF MRI coil was integrated into the animal trough to provide improvement of signal-to-noise-ratio. The animal was positioned obliquely and the transducer was tilted 30-40° to the vertical in order to best access the lumbar medial branch nerve. The transducer was coupled to the animal's skin with degassed water. Ablation was performed at 110 acoustic watts. Necropsy was performed one week post treatment.

Results

HIFU imparted greater energy per area (~1145.9 J/cm²) as compared to RFA (~107.4 J/cm²). The burn lesion created by MRgHIFU had an approximately 4 x 10 mm cylindrical size while RFA created 20 mm radius lesion. T1 and T2 sequences demonstrated adequate localization of the MRgHIFU burn in the region of the medial branch, with an arc-like configuration of edema and enhancement along the groove formed by the transverse process and the lateral aspect of the superior articular process. Adequate localization for RFA was also demonstrated, with enhancement/edema extending to the region of the medial branch; however, the edema and necrosis were noted more distant from the medial branch groove on several levels. On follow-up MRI, both RFA and MRgHIFU treated levels demonstrated acute denervation changes of the multifidus muscle. Histology demonstrated necrosis in the region of the medial branch nerve as well as muscle edema, necrosis and inflammation on both RFA and MRgHIFU treatment sides, though slightly greater on the RFA side.

Conclusions

Preliminary studies support MRgHIFU as a promising noninvasive technique for ablation of the medial branch of the dorsal ramus nerve, with imaging and histology demonstrating accurate localization comparable to RFA and potentially less adjacent tissue trauma.

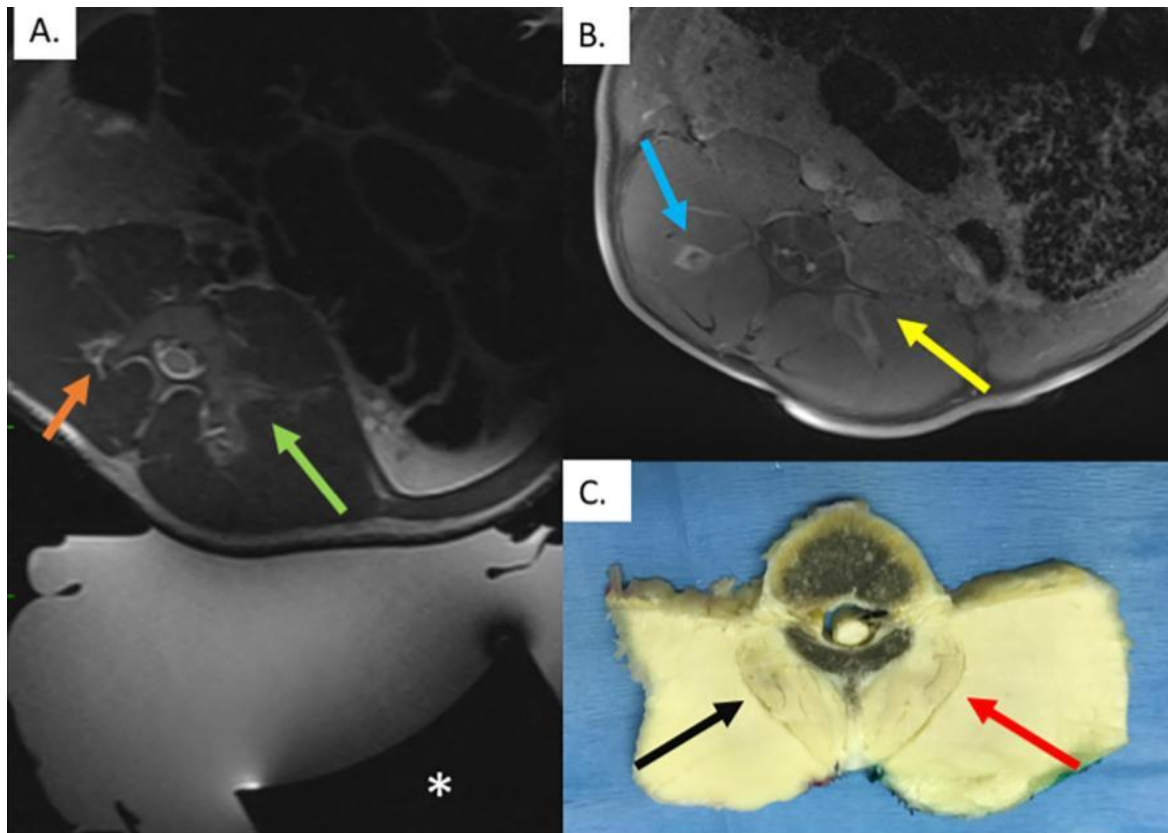


Figure: MRI T2-weighted sequence demonstrates edema in the region of the medial branch from both RFA (a, orange arrow) and MRgHIFU (a, green arrow) treatments. The transducer can be seen directed towards the subject (asterisk). T1 post-contrast fat saturated (b) sequence demonstrates enhancement on both RFA (blue arrow) and MRgHIFU (yellow arrow) treated sides. The largest area of necrosis on the RFA side is slightly posterior to the region of the medial branch when compared to the MRgHIFU side which demonstrates an arc-like region of enhancement along the medial branch osseous groove. Necropsy specimen of the L1 level (c) demonstrates slightly more hemorrhagic products on the RFA treated side (black arrow) when compared to the MRgHIFU treated side (red arrow).

(Filename: TCT_O-134_HIFU_presentation4.jpg)

O-135

5:27PM - 5:34PM

Clinical Utility of a Novel Ultrafast T2 Weighted Sequence for Spine Imaging

J Becker¹, B Winegar¹, M Saranathan¹, m Keerthivasan¹

¹University of Arizona, Tucson, AZ

Purpose

TSE-based T2WI of the spine suffers from long scan times. This work proposes a fast imaging protocol using variable refocusing flip angles, optimized for blurring and specific absorption rate.

Materials and Methods

A variable refocusing flip angle echo train was optimized for the spine to improve point spread function and minimize specific absorption rate, yielding images with improved spatial resolution and SNR compared to the constant flip angle sequence. Data was acquired from 50 patients (20 lumbar, 14 cervical and 16 whole-spine) using conventional TSE and the proposed sequence, with a single-shot variant for whole-spine. Noninferiority analysis was performed to evaluate efficiency of the proposed technique.

Oral Presentations & Excerptas

Results

The proposed sequence resulted in a 2x shorter scan time with more than 1.5x lower specific absorption rate. The variable flip angle sequence was noninferior to the conventional TSE ($p < 0.025$) for all criteria except signal-to-noise for the lumbar spine protocol. The cervical spine exams had a mean score ≥ 4 for all criteria but showed noninferiority only for a subset of the criteria. However, concordance analysis showed high agreement ($>80\%$) between the proposed method and the TSE for all the clinical criteria, indicating its diagnostic utility.

Conclusions

We present a fast and motion robust T2-weighted spine protocol using variable refocusing flip angles, including a single-shot variant. The sequences have better point spread function behavior than their constant flip angle counterparts and, being a faster scan, are less sensitive to patient motion, often seen in the longer TSE scans.

O-136

5:34PM - 5:41PM

Epidural Fat Distortion Sign: Tool for Localizing Spinal Canal Pathologies

H KIM¹, S Dilmaghani², F Berkowitz¹, A Sayah¹

¹Medstar Georgetown University Hospital, Washington, DC, ²Georgetown University Medical School, Washington, DC

Purpose

Differential diagnosis and treatment approach differ based on the location of pathology within the spinal canal. Distortion of epidural fat pad may be useful in localizing a spinal pathology to the epidural space, although never fully investigated in the literature. Our study aims to assess the efficacy of evaluating epidural fat involvement in the localization of epidural versus nonepidural pathologies through a large-scale retrospective imaging review.

Materials and Methods

Our study is a HIPAA-compliant, IRB-approved, retrospective evaluation of MRI studies of spine with description of epidural, subdural, or intradural spinal canal pathologies performed from November 1, 2015 to July 5, 2017 at MedStar Georgetown University Hospital. Exclusion criteria were present in more than one spinal canal pathologies, minimal extent of pathology, epidural lipomatosis, and incomplete or nondiagnostic quality studies. Selected studies were independently analyzed by two neuroradiologists in terms of whether epidural fat surrounding a lesion was involved ("epidural fat distortion sign") or spared. The results were compared to the gold standards, which were determined by a combination of original radiologic interpretation and clinical data (e.g., pathology or operative report). Statistical analysis, including Cohen's kappa for inter-observer reliability, was performed.

Results

Among 4041 MRI studies of spine screened, 172 studies were selected for review based on the inclusion and exclusion criteria (129 epidural; 4 subdural; 39 intradural). Sensitivity and specificity of localizing spinal canal pathology using the epidural fat distortion sign by two neuroradiologists were 95-98% and 92-93%, respectively. Positive predictive value and negative predictive value were 98-98% and 83-93%, respectively. Inter-observer reliability for applying epidural fat distortion sign was 0.88 (near perfect agreement).

Conclusions

Preliminary results of our study demonstrate that the epidural fat distortion sign is a highly sensitive and specific tool for localizing spinal canal pathology with a high degree of inter-observer reliability.

O-137

5:41PM - 5:48PM

The Spinal Lines that Divide: Imaging, Identification, and localization of Collections and Leaks of the Spine with focus on Digital Subtraction Myelography Technique

N Kashani¹, Z ASSIS¹, M Eesa¹, M Joshi¹, W Hu¹

¹*University of Calgary Foothills Medical Center, Calgary, Alberta, Canada*

Purpose

Identification of dural lines on spinal imaging is useful for localization of abnormal intraspinal collections and leaks (1). Result of dural, vascular, or arachnoid tears, detection of these collections using both diagnostic and myelographic techniques is important for determining the compartmentalization, exact location, and guided treatment of the underlying etiology. Accurate localization on imaging is key as nontargeted therapy or surgical approach may not provide relief in a substantial number of patients (2). Hence radiologic and myelographic findings can aid in accurate detection, localization, and targeted treatment. We will review the initial detection of these leaks on conventional CT and MRI imaging presenting case examples of collections in each of the epidural, subdural, and subarachnoid spaces. We will highlight useful features and signs to determine the compartmentalization of these collections using intrathecal contrast on CT or MRI. Digital Subtraction Myelography (DSM), a technique used to more accurately localize the exact site of these dural dehiscences and tears utilizing the high spatial resolution of radiography will be discussed. We will cover useful tips during the intervention for better identification and visualization of these often subtle and variable tears. In this case review study we hope to highlight useful practice examples for better detection, localization, and guided management of collections and leaks of the spine.

Materials and Methods

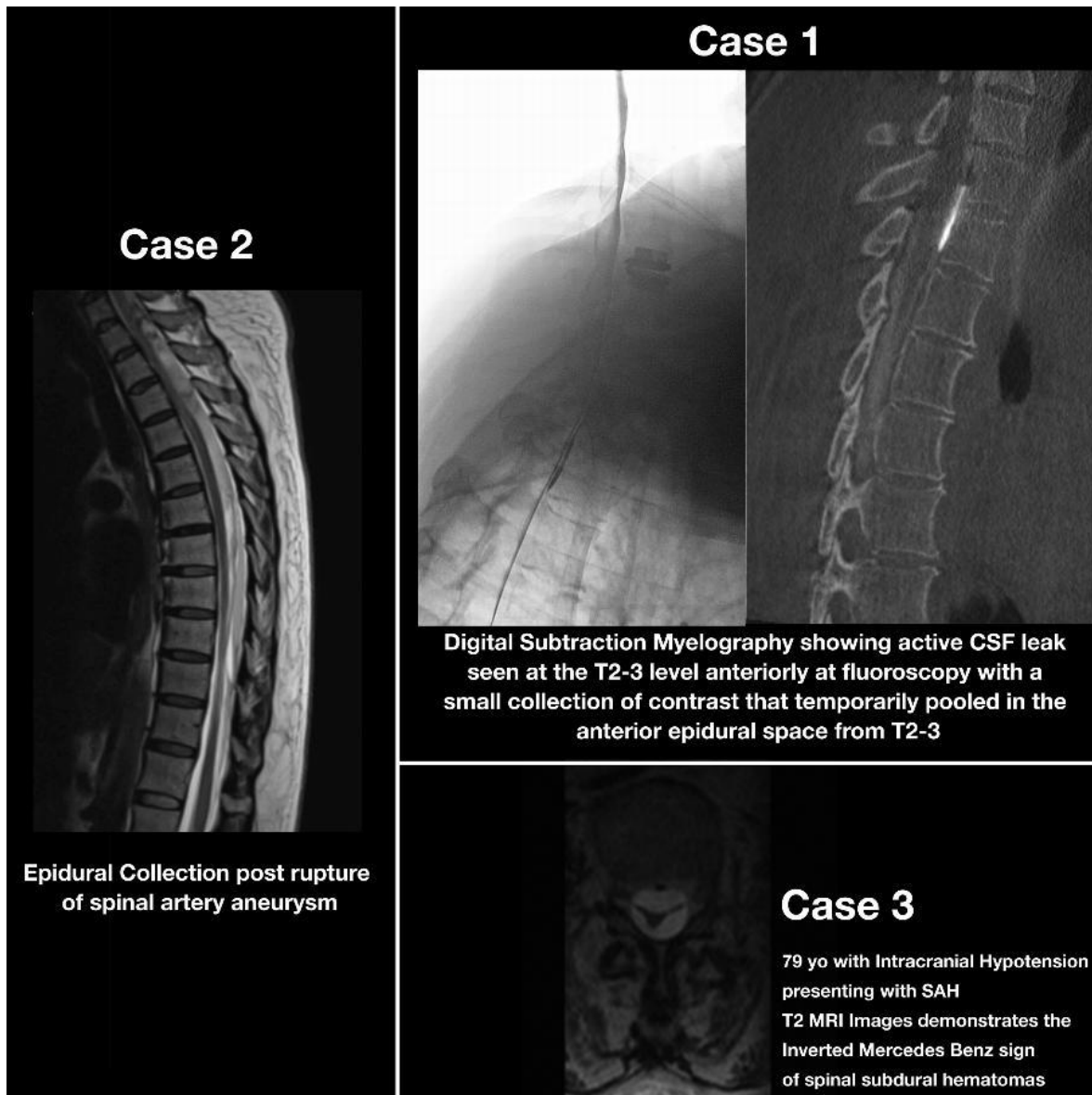
A case series of 12 patients presenting with spinal collections and CSF leaks detected on initial CT or MRI imaging over the past 3 years at our institution were reviewed. Subsequent fluoroscopic or CT myelographic studies were obtained and reviewed. Imaging features were compared across the cohort. Digital subtraction myelography (DSM) was a technique used to monitor passage of intrathecal contrast material along the spinal canal in real time to pinpoint the exact source of a high-flow CSF leak (3) was employed in the angio suite. Multimodality images acquired will be shared in a scrollable format in the presentations.

Results

The results of this series will be presented in a case-based format and discussed qualitatively as imaging features and findings, practice examples, tips, and pointers on procedural myelographic techniques. Digital subtraction myelography technique and its role to pinpoint the exact source of a high-flow CSF leak will be discussed and a case demonstrated. We will discuss implications for treatment in cases where a defect was identified on imaging, and how that guided management in the studied case series.

Conclusions

Detection of intraspinal collection and leaks on conventional CT and MRI studies requires further investigation with intrathecal contrast injection and myelographic studies to determine the compartmentalization and localization. Imaging features can be helpful in distinguishing which of the spinal compartments is involved, and can help guide additional imaging and investigations. Digital subtraction myelography (DSM) is an effective technique for identification of the precise location of dural tears and high-flow CSF leaks. Accurate localization of dural tears and dehiscences can help guide more effective targeted therapy with either blood patch or surgical intervention in cases of CSF leaks.



(Filename: TCT_O-137_spinefewcases.jpg)

O-140

6:02PM - 6:09PM

Comparison of radiation doses imparted during multidetector CT-scanners and cone beam computed tomography for the postoperative, spinal fusion assessment

N Guberina¹, M Forsting², A Ringelstein³

¹Institute of Diagnostic and Interventional Radiology and Neuroradiology, Essen, Germany, ²Institute of Diagnostic and Interventional Radiology and Neuroradiology, University Hospital Essen, Essen, Germany, ³MariaHilf Kliniken Mönchengladbach, Mönchengladbach, NRW, Germany

Purpose

To assess and compare radiation doses imparted during various, multidetector, single and dual-source CT scanners (MSCT) as well as cone beam computed tomography (CBCT) for the postoperative examination of spinal fusion of the lumbar spine.

Oral Presentations & Excerptas

Materials and Methods

Radiation doses were assessed during standardized lumbar spine CT protocols at different MSCT ((I) single-source CT scanner Somatom Definition AS+, (II) 2nd generation of dual-source CT scanner Somatom Definition Flash in single source technique, (III) 2nd generation of dual-source CT scanner Somatom Definition Flash in dual-source technique (all Siemens Healthcare, Erlangen, Germany)) and at the CBCT Ziehm Vision RFD 3D (Ziehm Imaging GmbH, Nürnberg, Germany) (IV) (a) RFD-3D (Standard) and (b) RFD-3D (L-D). Image quality was examined independently by evaluating various important parameters (pedicle placement, quality control of spinal fusion surgery, and the evaluation of the lumbar spine in case of complications) determined on real patients' examinations. Wilcoxon signed rank test was used to determine statistically significant differences ($p < 0.05$).

Results

In MSCT setting following radiation doses were assessed (CTDI_w; DLP): (I) 8.9 mGy; 96.8 mGycm; (II) 14.2 mGy; 153.4 mGycm; (III) 22.0 mGy; 236.2 mGycm; in the CBCT setting radiation doses were distributed as follows: (IV) (a) 17.2 mGy; 187.0 mGycm; (b) 13.0 mGy; 143.1 mGycm. Overall, image quality, was evaluated as good for both, MSCT and CBCT examinations.

Conclusions

Dual-source MSCT scanning involves considerable radiation dose for the postoperative examination of spinal fusion of the lumbar spine. Radiation doses are markedly lower during CBCT and single-source MSCT compared to dual-source MSCT lumbar spine examinations while maintaining sufficient image quality.

O-95

6:09PM - 6:15PM

Spread of Injectate During Cervical Interlaminar Epidural Steroid Injections: Reassessing Ventral Epidural and Craniocaudal Spread with Axial Imaging

T Amrhein¹, E Bozdogan¹, S Vekaria¹, P Patel¹, P Kranz¹

¹Duke University Medical Center, Durham, NC

Purpose

Cervical interlaminar epidural steroid injections (CILESI) are commonly performed for treatment of cervicalgia. However, in 18-32% of cases patients do not experience symptom relief. [1, 2] Prior studies have examined the extent of contrast spread during conventional fluoroscopy-guided CILESI and have determined that there is successful spread of contrast to several vertebral body levels away from the location of the inserted needle ranging from approximately 3.1 - 3.8 vertebral bodies. [3, 4] For this reason, previous authors have purported that medication can successfully be delivered to the superior cervical spine (e.g. C1/2 or C2/3) via an inferior cervical spine ILESI (e.g. C6/7 or C7/T1). However, since these prior studies were done under conventional fluoroscopy guidance and only lateral and frontal images were acquired (i.e. no axial imaging was available), they were not able to assess for the extent of spread to the ventral epidural space or to the neuroforamen. Delivery of medication to these locations is critical for the treatment of disc origin pain or pain referable to nerve root compression. The purpose of this study was to determine the extent of contrast spread to these locations during CILESI.

Materials and Methods

We retrospectively reviewed consecutive CT fluoroscopy-guided CILESI performed at a single institution from June 2016 to December 2017. In all cases the same volume of steroid (2 mL) and contrast (3 mL) was injected and a postprocedure scan was obtained to assess for extent of injectate spread. These images were reviewed by two neuroradiology fellows and the following was recorded: injection level, contrast flow extent (VES, ipsilateral neuroforamen [ILNF], contralateral neuroforamen [CLNF] see Figure). Disagreements were adjudicated by a board-certified neuroradiologist with six years of CTFG-ILESI experience.

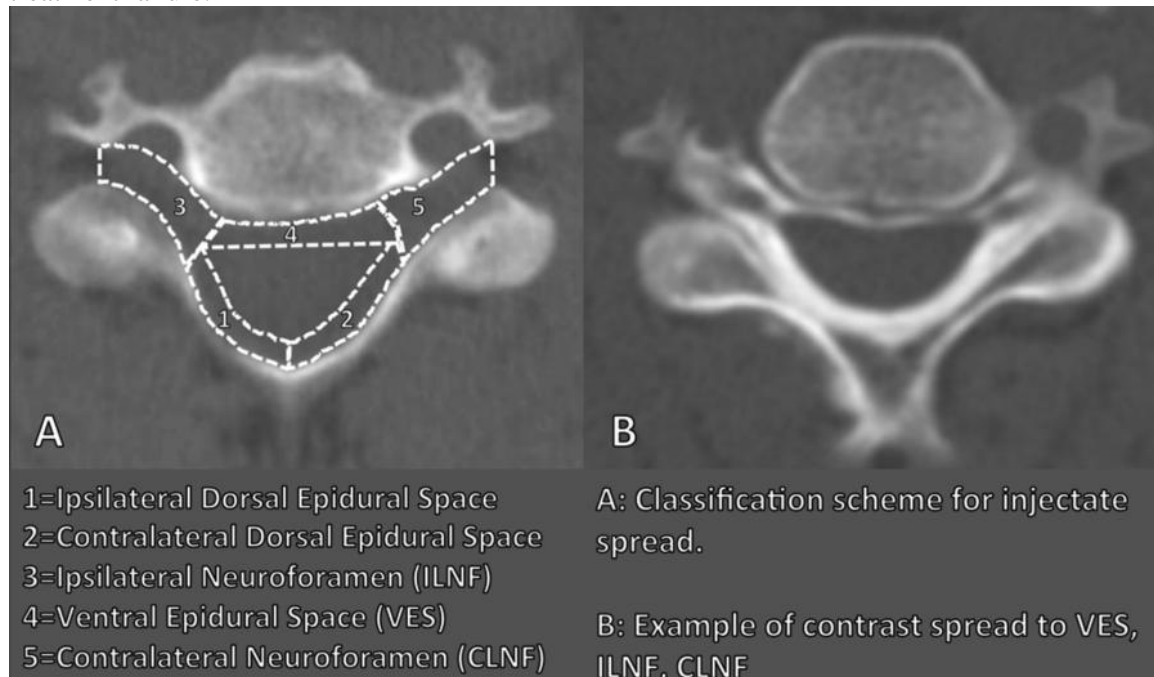
Oral Presentations & Excerptas

Results

Forty-three cases were identified. Needle placements occurred from C3/4 to C7/T1. Eighteen cases (41.9%) demonstrated no spread to VES at any level. The average spread of contrast (number of vertebral bodies) was: VES (0.58 cranial, 0.6 caudal), ILNF (2.4, 1.3), CLNF (2.3, 1.2).

Conclusions

We found that in nearly 42% of cases injectate did not spread to the VES, which could result in suboptimal delivery of steroid to ventral pain generators and thereby may be a potential source of treatment failure.



(Filename: TCT_O-95_FigureAJNR2017.jpg)

Monday, June 4, 2018

4:45PM - 6:15PM

Parallel Paper Session: Interventional: Aneurysms, AVMs and Tumors

O-141

4:45PM - 4:52PM

Factors influencing confidence of treatment recommendation of unruptured intracranial aneurysms and estimated risk of procedure-related neurological complications

M Ernst¹, J Buhk¹, J Fiehler¹

¹University Medical Center Hamburg-Eppendorf, Hamburg, Germany

Purpose

The endovascular treatment options for unruptured intracranial aneurysms have increased substantially in recent decades. Little is known about the agreement and confidence of neurointerventionalists in their treatment recommendation. We aimed to assess the interrater reliability and to evaluate factors influencing the confidence of treatment recommendation. Especially the estimation of procedure-related neurological complications might have a high influence on treatment recommendations. We aimed to

Oral Presentations & Excerptas

assess the ability of neurointerventionalists to predict procedure-related neurological complications compared to a recently developed score to quantify individual patient risk. Moreover, we analyzed factors influencing the ability of risk prediction.

Materials and Methods

Twenty-six participants of the Advanced Course in Endovascular Interventional Neuroradiology of the European Society of Neuroradiology 2017 were asked to evaluate digital subtraction angiography of patients with unruptured cerebral aneurysms by determining the best therapeutic approach, their level of confidence in their treatment recommendation, and the risk of procedure-related neurological complications. Knowledge and experience in endovascular treatment of aneurysms of each participant were assessed. Based on cerebral ischemic comorbidities, size, and core areas the recently developed 3-point S-C-C risk score was determined for each case. The ability of the participants to predict procedure-related neurological complications was compared to the predictive quality of the S-C-C risk score. Influence of participant and case characteristics on treatment recommendation, indicated confidence in treatment recommendation and ability of predicting procedure-related neurological complications were analyzed. Moreover the interrater reliability in treatment recommendation and in the estimation of risk of complications was calculated.

Results

Treatment recommendation: Interrater reliability was moderate with regard to any treatment recommendation (ICC=0.49), high with regard to recommendation of clipping (ICC=0.72), moderate with regard to coiling (ICC=0.61) and WEB device (ICC=0.59), low regarding to Flow Diverter (ICC=0.33) and stent assisted coiling (ICC=0.34). The recommendation of clipping was less likely with more experience in endovascular treatment of aneurysms and more likely with increasing knowledge. Odds of recommending WEB device were lower with more experience in endovascular aneurysm treatment, higher in patients with multiple aneurysms and increasing neck width. The recommendation of stent-assisted coiling was more likely with increasing neck width, when cerebral ischemic comorbidities were present, and when the aneurysm was located in the posterior circulation. Confidence in treatment recommendation: Confidence in treatment recommendation varied statistically significantly according to recommended treatments with highest confidence for flow diverter and coiling, followed by clipping, WEB device, and stent-assisted coiling. Estimation of risk of complications: The S-S-C risk score had a moderate predictive quality (AUC of 0.686, 95% CI 0.451 to 0.920). At average, the participants were significantly worse than the S-C-C risk score (mean AUC of 0.529, 95% CI of the mean 0.482 to 0.575) and not better than random guess in predicting procedure-related neurological. However, some of them were good (best participant AUC: 0.807), but some were even worse than random guess (worse participant AUC: 0.318). Neither knowledge nor experience in endovascular aneurysm treatment was statistically significantly associated with the participants' ability to predict procedure-related neurological complications (as measured by the AUC). Interrater reliability was low with regard to the estimation of risk of complications (ICC=0.38).

Conclusions

Our study shows a moderate interrater reliability of treatment recommendations of unruptured intracranial aneurysms. Confidence in treatment recommendation varied statistically significantly according to recommended treatments with highest confidence for flow diverter and coiling. Overall performance in predicting procedure-related neurological complications was worse than the S-C-C risk score and not better than random guess.

O-142

4:52PM - 4:59PM

Increased Rupture Risk of Intracranial Aneurysms Associated with Methamphetamine Use

D Noblett¹, J Chang¹, B Dahlin¹

¹University of California, Davis, Sacramento, CA

Purpose

Ruptured intracranial saccular aneurysms are a common cause of atraumatic subarachnoid hemorrhage (SAH) and are associated with significant morbidity and mortality. Small aneurysms, less than 7mm in diameter are associated with lower risk of spontaneous rupture and are less commonly treated with endovascular intervention. Methamphetamine use is a growing problem in the United States and recent studies suggest poor outcomes for methamphetamine users with SAH secondary to ruptured aneurysms. We sought to characterize the size, morphology, and location of ruptured and unruptured intracranial aneurysms in methamphetamine users and to suggest whether intracranial aneurysms in this patient population may be at higher risk of rupture at a smaller size.

Materials and Methods

Clinical characteristics and patient data were collected via retrospective chart review of patients with intracranial aneurysms and history of methamphetamine use. Data included measuring aneurysm size(s), taken as the largest diameter; morphology, including saccular or fusiform; and location within the circle of Willis. Aneurysm rupture was determined by the presence of subarachnoid hemorrhage in the setting of an intracranial aneurysm.

Results

A total of 62 eligible patients were identified with at least one intracranial aneurysm and history of methamphetamine use, which yielded 73 intracranial aneurysms studied (n=73). The average largest diameter of unruptured aneurysms (n=44, mean 5.1, median 4.5, StdDev 2.6) was smaller than that of ruptured aneurysms (n=29, mean 6.3, median 5.5, StdDev 2.5) (p=.024), and the average of both groups was less than 7mm.

Conclusions

Based on our data, methamphetamine use may be a risk factor for intracranial aneurysmal rupture at a smaller size. These patients may benefit from early endovascular intervention, as the risk of aneurysmal rupture and subarachnoid hemorrhage may exceed risk of intervention for these small aneurysms.

O-143

4:59PM - 5:06PM

To Study the Factors Predicting Aneurysms Regrowth Following Endovascular Treatment

R Kamble¹, N Khandelwal¹, V Gupta¹, A Kumar¹, C Ahuja¹, S Gupta¹, N Singla¹

¹*Postgraduate Institute of Medical Education and Research, Chandigarh, India*

Purpose

Aneurysm regrowth following endovascular treatment is a frequent challenge for the neurointervention team. There are number of already proven but still debated factors predicting aneurysm regrowth following coiling. This study is to understand and foster them further and address the additional factors.

Materials and Methods

It was a retrospective study design which included the cohort of both ruptured and unruptured saccular aneurysms treated with stand-alone coiling, balloon-assisted and stent-assisted coiling with total of 181 patients having 199 aneurysms. We excluded aneurysms treated with flow diverters and nonsaccular aneurysms. Adequacy of aneurysm occlusion at immediate postprocedure and follow-up was graded according to Modified Raymond-Roy occlusion Classification(MRRC). Follow-up evaluation was done with both MR angiography and conventional angiography.

Results

There were 181 patients with 199 saccular aneurysms. Among these 199 aneurysms, 155 (78%) were ruptured and 39 (20%) were unruptured. Ruptured status was not known in five aneurysms. Out of 199 aneurysms 104, 42 and 53 were treated with stand-alone coiling, balloon-assisted and stent-assisted coiling respectively. Initial aneurysms occlusion grade is as follows: Forty-one MRRC-I, 57 MRRC-II, 73 MRRC-IIIa and 28 MRRC-IIIb. All the 41 aneurysms with initial MRRC-I had successful outcome at follow-up. Seven out of 57 aneurysms with MRRC-II, 30 out of 73 aneurysms with MRRC-IIIa and 27

Oral Presentations & Excerptas

out of 28 aneurysms with MRRC-IIIb had recanalization at follow-up. In our study MRRC-IIIa group was further studied to know the implication of duration of contrast stasis within coil interstices in predicting aneurysms recanalization. Our study identifies larger size, greater volume, larger neck size, lower packing density, incomplete initial occlusion, rapid-contrast washout among MRRC IIIa aneurysms and coiled aneurysms in hypertensive patient among univariate analysis and incomplete initial occlusion and rapid-contrast washout in MRRC IIIa aneurysms among multivariate analysis were significantly associated with aneurysm recurrence. In addition to multiple factors already proven, we found another significant factor in the form of early-contrast washout from the coil interstices in predicting aneurysms regrowth.

Conclusions

There are multiple factors already proved but still debated regarding their association in aneurysm regrowth. "Present study confirms the already known factors predisposing to regrowth of aneurysm and gives an additional factor, i.e., the early washout of contrast as a significant factor predicting regrowth".

O-144

5:06PM - 5:13PM

Management of Small Unruptured Intracranial Aneurysms- a survey of neuroradiologists

X Wu¹, B Geng¹, L Tu¹, V Kalra², D Gandhi³, P Sanelli⁴, A Malhotra⁵

¹Yale University School of Medicine, New Haven, CT, ²Orlando Health, Tampa, FL, ³University of Maryland School of Medicine, Baltimore, MD, ⁴Northwell Health, Manhasset, NY, ⁵Yale New Haven Hospital, New Haven, CT

Purpose

There is a lack of clarity in guidelines for management of patients with small or tiny unruptured intracranial aneurysms (UIAs). We performed this study to determine current practice pattern on management of UIAs, especially regarding imaging surveillance for conservatively managed patients.

Materials and Methods

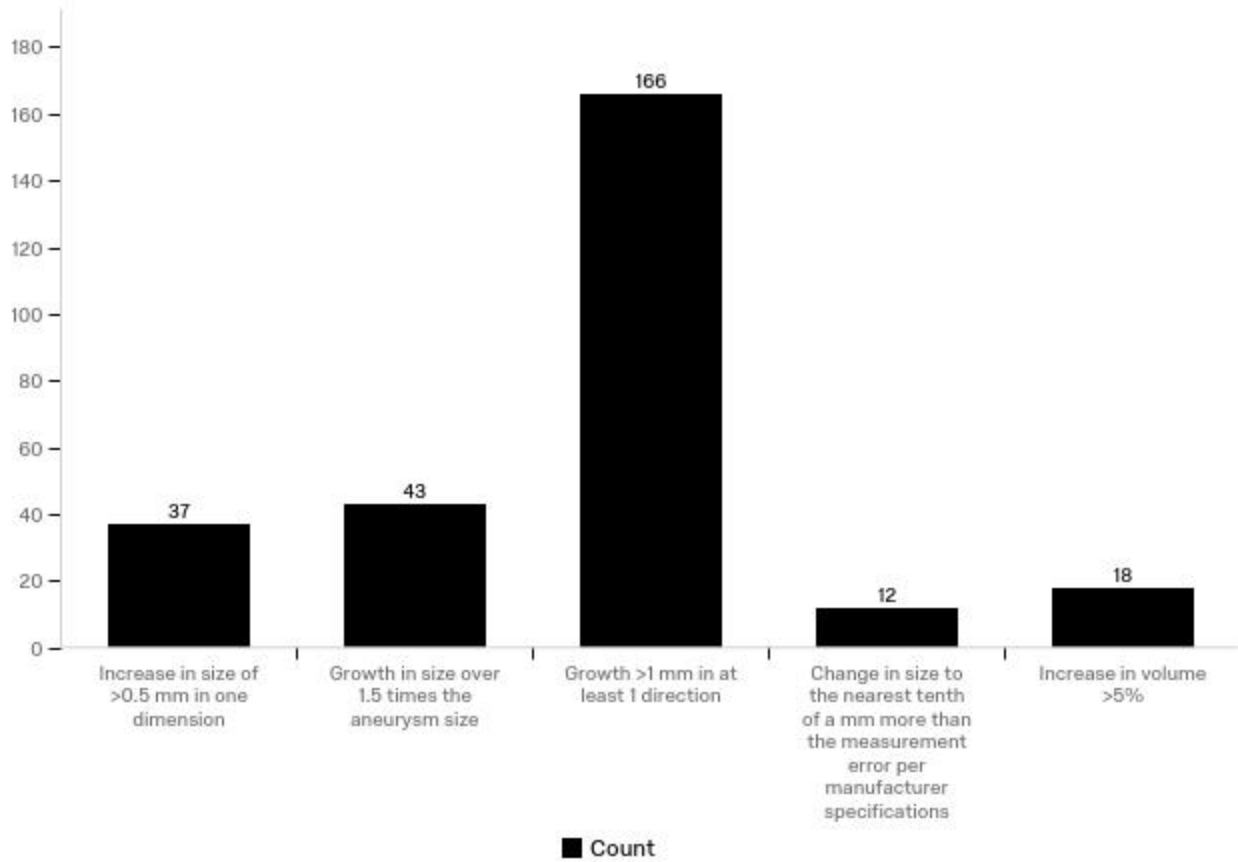
An online survey was designed to examine physician practice and preference regarding the management of small UIAs (≤ 7 mm in diameter). The survey was circulated to members of the American Society of Neuroradiology (ASNR) 2017. Participation was voluntary and all responses were anonymous. The responses from diagnostic neuroradiologists and neurointerventional radiologist/endovascular surgeons were compared using the χ^2 test.

Results

A total of 227 individual survey responses were obtained and included in the analysis with 54.6% (124/227) from diagnostic neuroradiologists (practicing $>50\%$ neuroradiology) and one-third (29%) were neurointerventional radiologists. There were 173/227 who responded that routine, periodic imaging surveillance would be appropriate for conservatively managed UIAs and 84% respondents recommend surveillance frequency of at least once a year. There were 59% that favored indefinite, life-long follow-up for small UIAs and similar number of respondents favored noncontrast MR angiography for follow-up. Significant heterogeneity was found in size measurements used to assess aneurysms, and criteria used to define growth on surveillance imaging. Change in size, change in morphology, and complex morphology were the criteria most frequently selected for the decision to treat UIAs. A statistically significant proportion of neurointerventional radiologists/endovascular neurosurgeons chose age and smoking history as compared to diagnostic neuroradiologists as part of their decision to treat UIAs.

Conclusions

The survey results show significant heterogeneity in practice even amongst neuroradiologists and underlies the need to standardize imaging practice. Further studies are needed to assess the optimal frequency and duration of surveillance imaging for UIAs. The criteria used to measure aneurysms and define growth on imaging also need to be standardized.



(Filename: TCT_O-144_ASNRfigure.jpg)

O-145

5:13PM - 5:20PM

Technical feasibility of the use of the PulseRider implant for wide neck bifurcation aneurysm endovascular treatment - ionInitial experience.

K de Macedo Rodrigues¹, P Kan², A Kühn¹, D Rex¹, F Massari¹, W Ajay K³, A Puri¹

¹University of Massachusetts, Worcester, MA, ²Baylor College of Medicine, Houston, TX, ³University of Massachusetts Medical School, Worcester, MA

Purpose

To demonstrate initial technical feasibility of the use of a new self-expanding nitinol implant recently made commercially available in the United States to assist in endovascular embolization of wide-neck bifurcation aneurysms.

Materials and Methods

We retrospectively reviewed performance on four consecutive procedures on patients (3 females) with age ranging from 52 – 67-years-old in 2 centers. Patients underwent endovascular elective embolization of unruptured cerebral aneurysms with the use of the PulseRider nitinol implant (Pulsar Vascular, Los Gatos, California) in addition to detachable embolization coils. Three wide-neck basilar tip aneurysms and one anterior communicating artery aneurysm were treated. The PulseRider implant was delivered through a 021 microcatheter. Two "Y" shape and 2 "T" shape devices were utilized. Patients were placed in dual antiplatelet therapy for 5 days prior to the procedure. Immediate follow-up angiograms and clinical evaluation were analyzed.

Oral Presentations & Excerptas

Results

Successful deployment of the PulseRider was achieved in all 4 patients. Two patients necessitated device shape exchange which was possible as the implant is retrievable. A Raymond II occlusion was attained immediately after finishing embolization procedure. No periprocedural or immediate postprocedural complications ensued.

Conclusions

We demonstrate the technical feasibility of the use of a newly commercially available intracranial device to assist in endovascular embolization of wide-neck bifurcation aneurysms. Limitations of this case series include small sample size and absence of imaging follow-up or long-term clinical follow-up.

O-146

5:20PM - 5:27PM

High Prevalence of Venous Outflow Stenosis in Brain AVM: Is It a Cause or Result?

Y Kikuchi¹

¹*Kameda Medical Center, Kamogawa City, Japan*

Purpose

Brain AVM has been considered a congenital arteriovenous shunt lesion. Stenosis on the vein in AVM has been described and considered secondary lesion. With the advancement of 3-D DSA, veins close to the dural sinus are demonstrated without overlapping of the nearby large dural sinuses. This study was conducted to elucidate the prevalence of venous outflow stenosis of brain AVM with 3-D DSA.

Materials and Methods

Cerebral DSAs in the last ten-year period in our institution were reviewed with special attention to the venous outflow segments on 3-D DSA.

Results

Twenty-three pial AVMs with good quality 3-D DSA were identified. Among these, there was a tight stenosis at the venous outflow in 14 cases (60%). In 9 cases, stenosis was not found or equivocal.

Conclusions

With the advancement of 3-D imaging of the cerebral vessels, it became possible to recognize stenosis at the veins close to the large dural sinuses. The high prevalence (60%) of the venous outflow stenosis found in this study suggests that this may not be the incidental finding or secondary lesion but the primary abnormality of the AVM. AVM could be a lesion of venous collaterals with arteriovenous shunt secondary to the venous outflow stenosis. Neuroradiologists should pay close attention to the venous outflow segment of the AVM on 3-D DSA.

O-147

5:27PM - 5:34PM

Feasibility of Intra-arterial Chemotherapy for Retinoblastoma: Experiences in a Large Single Center Cohort Study

E Stenzel¹, S Zülw¹, A Radbruch², C Mönninghoff³

¹*University Hospital Essen, Essen, Germany*, ²*German Cancer Research Center, Heidelberg, Germany*, ³*Institute of Diagnostic and Interventional Radiology and Neuroradiology, Essen, Northrhine-Westfalia, Germany*

Purpose

In the last 10 years intra-arterial chemotherapy (IAC) has been increasingly used in the clinical management of retinoblastoma. It is reported to provide tumor control even in advanced stage disease that might have previously required enucleation. In clinical practice, IAC can be impossible mostly due to three reasons: 1) significant collaterals to meningeal arteries, 2) technical failure of ophthalmic artery

catheterization, or 3) retina blood supply from collaterals different to the ophthalmic artery. In the current study we assessed the failure rate of AIC due to the three above-named issues depending on the age of the examined children.

Materials and Methods

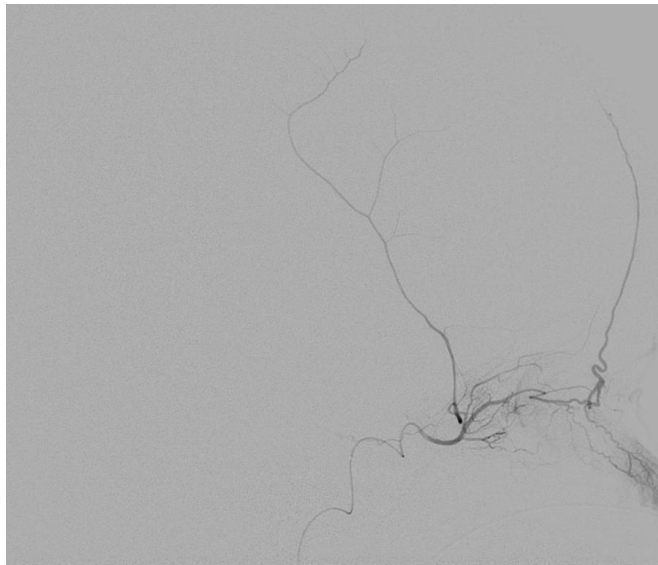
All patients admitted for IAC in our hospital were retrospectively assessed by chart review. Failure rates of IAC were assessed and classified according to the three above-mentioned criteria.

Results

Ninety-eight patients (median age 21.4 months, range 5.3 months – 10.5 years) were identified. IAC was performed in 69 (70.4%) patients and failed in 12 (12.2%) cases because of meningeal collaterals (Fig. 1), in eight because of technical failure to cannulate the ophthalmic artery and in nine because of alternative blood supply of the retina.

Conclusions

The rather defensive approach that is pursued in our center resulted in an overall failure rate of AIC around 30%. The relatively high probability of failure needs to be addressed adequately in the patient conversation prior to the procedure. The technical failure rate of 9% might be reduced by the application of more vigorous therapeutic approaches such as balloon occlusion of the internal carotid artery. More research is finally needed to determine if existing meningeal collaterals should be regarded as valid exclusion criterion.



(Filename: TCT_O-147_ASNRBild.jpg)

O-148

5:34PM - 5:41PM

Clinical and Angiographic Features of NonInvoluting Congenital Hemangiomas (NICH).

A Patel¹, J Fifi², J Mocco³, R De Leacy³

¹Stanford University, Palo Alto, CA, ²Mount Sinai Hospital, New York, NY, ³Icahn School of Medicine at Mount Sinai, New York, NY

Purpose

While infantile hemangiomas are very common, congenital hemangiomas are rare and less understood. Congenital hemangiomas are present at birth. They fall into two major categories: rapidly involuting congenital hemangioma (RICH) and noninvoluting congenital hemangioma (NICH). NICH is the rarer of the two entities. If not recognized and treated appropriately, NICH can lead to significant morbidity. There is a paucity of literature regarding NICH. In this paper, we will outline our experience with this

Oral Presentations & Excerptas

condition, focusing on clinical and angiographic features. We will also present the largest case series on endovascular embolization and direct percutaneous treatment for this condition to date. Our case series is the first to demonstrate that effective embolization or percutaneous sclerotherapy can obviate the need for resection in select cases.

Materials and Methods

Case Selection: Ten patients with noninvoluting hemangiomas were identified from the period of January 1990 to May 2017 for this retrospective IRB approved study. All cases were patients who had been referred for endovascular embolization and/or direct percutaneous sclerotherapy. Lesion location, clinical scenario, patient age, angiographic features, embolization technique, postembolization angiography, need for multiple treatments (if applicable), and long-term clinical follow-up were recorded. When possible, we accessed pathology reports confirming GLUT-1 negativity. Angiography and Endovascular

Embolization: For patients undergoing angiography and embolization, the right common femoral artery was accessed. A 4F sheath was placed. A 4F Berenstein catheter and/or Prowler 10 microcatheter was used to superselect the vessel of interest. Superselective injections with the microcatheter along the arcade of the vascular lesion would be done to confirm angiographic appearance of NICH. Embolization was performed once distal catheterization was achieved and it was determined that the patient's lesion was suitable for treatment. In most cases we used NBCA 0.7 cc of 25% NBCA for injection. Direct

Percutaneous Sclerotherapy: Patients presenting with very large hemangiomas undergoing direct percutaneous sclerotherapy were also reviewed. Under direct fluoroscopic monitoring, direct percutaneous puncture of the lesion of interest at multiple locations were done. Following establishment of blood flow a small excision of contrast material was done to confirm the intravascular location of our angiocath. Subsequently, sclerosis with progressive small injections of 98% ethanol were done. Many cases utilized multiple, separate puncture sites in which ethanol was injected followed with 5 cc or so of Avitene suspension for hemostasis. Sclerotherapy would involve the venous portion of the hemangioma.

Results

We identified a total of ten patients who underwent 25 total treatments. Most of our patients presented between ages 2 and 8 years of age. Seven patients were male and 3 were female. Many patients presented with a bluish discoloration and spongy mass that was not regressing with conservative treatment. In some cases GLUT-1 testing was provided prior to referral. Our cases highlight several important points. One, noninvoluting congenital hemangiomas have the same angiographic features throughout the body. A NICH we treated in the anterior chest wall shows the same features as facial NICH, including a arterial-capillary web, no arteriovenous shunting, and draining veins. This lesion was initially treated with Quadraspheres and did not significantly involute. The lesion was subsequently successfully treated with ethanol. Figure 1 attached of a right facial NICH is a representative case and highlights key angiographic features of NICH which include: an arteriocapillary web, no arteriovenous shunting, and identifiable draining veins. Another important observation from our experience is that both endovascular embolization and direct percutaneous sclerotherapy are effective. Six cases demonstrate successful endovascular embolization of lesions demonstrating angiographic and clinical features of NICH. Direct percutaneous sclerotherapy is another technique that can be utilized. Our group's experience is that this technique works as well in select cases. Contrary to previous reports, our experience shows that in some cases endovascular embolization or direct percutaneous sclerotherapy can obviate the need for a surgical resection. Six of our cases demonstrate that effective endovascular embolization and/or direct sclerotherapy can entirely obviate the need for a resection. In an additional three cases, preprocedure embolization considerably decreased intraoperative bleeding.

Conclusions

Our study is the largest case series of embolization and/or direct sclerotherapy for NICH and most thorough evaluation of angiographic features associated with these lesions. NICH have distinguishing angiographic and clinical features. Endovascular and/or direct percutaneous embolization is an effective treatment in many cases.

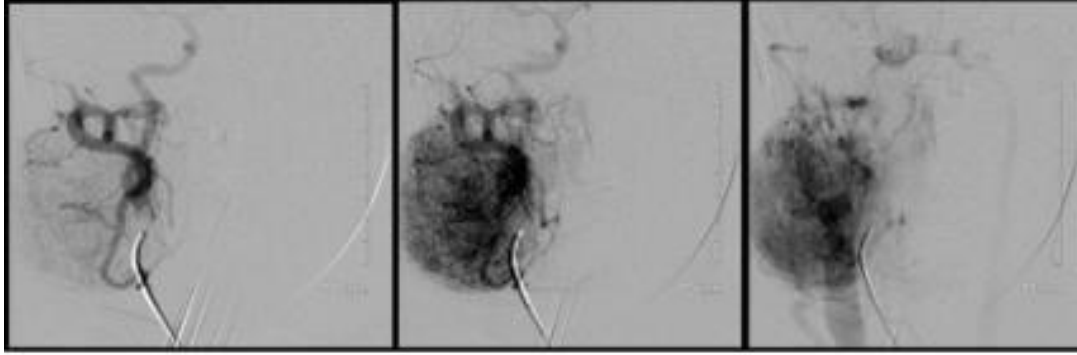


Figure 1. Right ECA injection of a right facial NICH. There is a discrete angiographic appearance involving an arteriocapillary web, no arteriovenous shunting, and identifiable draining veins. This lesion was treated successfully with PVA particles.

(Filename: TCT_O-148_figure1.jpg)

O-391a

5:55PM - 6:02PM

Imaging of infectious intracranial aneurysms- a report of 8 cases

A Gupta¹, K Bhattacharya², H PENDHARKAR³, C Prasad⁴

¹National Institute of Mental Health and NeuroSciences (NIMHANS), Bangalore, Karnataka, ²National Institute of Mental Health and Neurosciences, India, Bangalore, Karnataka, ³NATIONAL INSTITUTE OF MENTAL HEALTH & NEUROSCIENCES, BANGALORE, KARNATAKA, ⁴National Institute of Mental Health & NeuroSciences (NIMHANS), Bangalore, Karnataka

Purpose

To study the intracranial aneurysms associated with systemic or local infection and their imaging features.

Materials and Methods

Cross sectional imaging and/or digital subtraction angiograms of 8 patients who presented with infectious intracranial aneurysms between 2013 to 2016 were reviewed. The clinical features, associated significant medical, surgical and treatment history were analysed.

Results

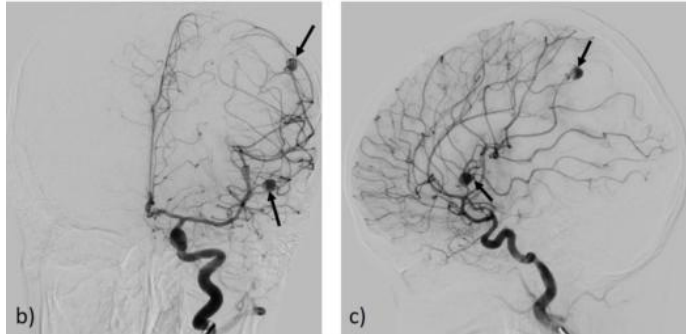
Five of the 8 patients were male and 3 were female. A total of 11 aneurysms were noted in 8 patients. Bacterial source (*Streptococcus viridans*) was identified as the source of infection in 3 of these cases, angioinvasive fungus in 1 case, and tuberculous meningitis was seen in another patient. In rest of the 3 cases, no definite infectious organism was identified from blood culture as they were already on antibiotic therapy. Rheumatic heart disease was noted in 2 patients, cranial trauma and skull base injury in 2 patients and immunocompromised status in 2 patients. Two of these aneurysms were observed in the posterior circulation (involving the basilar trunk) and rest were in the anterior circulation. Majority of the aneurysms (8/11) were less than 1 cm in size and located distally on cortical branches of anterior and middle cerebral arteries. Rest of the aneurysms (2 located on basilar artery and 1 in the cavernous segment of the left internal carotid artery) were large (>2cm in size). The small aneurysms were medically managed on antibiotics/ antitubercular drugs. In two of the larger aneurysms endovascular management was done and in the last case patient succumbed to brain death due to extensive infarcts and brain edema.

Conclusions

Infectious intracranial aneurysms are a rare but important cause of aneurysmal subarachnoid hemorrhage. Identification and timely medical and/ or surgical/ endovascular management will be lifesaving.



a) CT scan axial section of patient 14, known case of Rheumatic heart disease who presented with sudden onset severe headache showing an acute left parietal lobe hematoma with intraventricular extension.



b) and c) AP and lateral view of left internal carotid artery injection showing aneurysms in the cortical branches of the left middle cerebral artery (arrows).

(Filename: TCT_O-391a_Aneurysm_Gupta.jpg)

O-391b

6:02PM - 6:09PM

Results of long term outcome of flow diverter placement – a single institutional experience

A Gupta¹, S Das², H PENDHARKAR³, A HR⁴, C Prasad⁵, J Saini⁶, A Deepesh⁷, K Bhattacharya⁸
¹National Institute of Mental Health and NeuroSciences (NIMHANS), Bangalore, Karnataka, ²National Institute of Health and Neurosciences, BANGALORE, Karnataka, ³NATIONAL INSTITUTE OF MENTAL HEALTH & NEUROSCIENCES, BANGALORE, KARNATAKA, ⁴National Institute of Mental Health And Neuro Sciences, Bengaluru, Karnataka, ⁵National Institute of Mental Health & NeuroSciences (NIMHANS), Bangalore, Karnataka, ⁶National Institute of Mental Health & NeuroSciences, Bangalore, Karnataka, ⁷National Institute of Mental Health And Neuro Sciences, Bangalore, Karnataka, ⁸National Institute of Mental Health and Neurosciences, India, Bangalore, Karnataka

Purpose

The aim of this study was to evaluate the efficacy of flow diverters and clinical outcome of intracranial aneurysm patients treated with flow diversion at least 6 months after the procedure.

Materials and Methods

The present study is a retrospective-prospective, hospital based study conducted on 31 patients managed with flow diversion in the Department of NIIR, NIMHANS, Bangalore from September 2013 to November 2017. On follow up clinical assessment and cerebral angiogram was done at least 6 months after the procedure. The modified Rankin score was used for clinical assessment. Poor clinical outcome was defined by modified Rankin score >2 after 6 months. The O'Kelly-Marotta (OKM) grading scale was used to grade residual aneurysm filling on angiogram. Efficacy was defined as 100% occlusion of the aneurysm without significant stenosis (defined as $\leq 50\%$ stenosis) of the parent artery.

Results

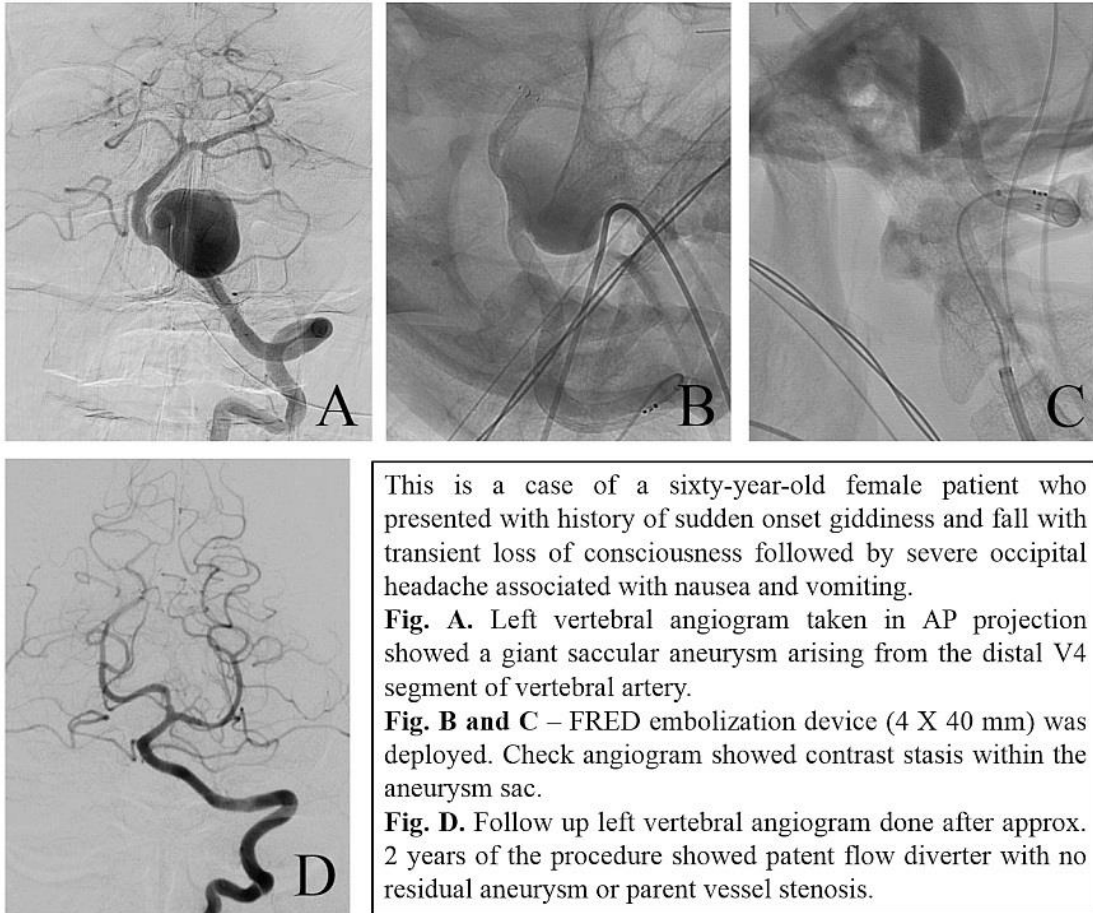
Following are the salient findings in our study – • Clinical follow up was available in 27 cases. All cases of posterior circulation had good clinical outcomes (MRS 0 or 1); 75% of the anterior circulation cases had good clinical outcome (MRS 0), one case had MRS score of 5 and 4 patients had MRS score of 6. •

Oral Presentations & Excerptas

Angiographic follow up was available in 15 cases, 11 cases of anterior circulation aneurysms, and 4 cases of posterior circulation aneurysms. There was no residual aneurysm in 75% of both anterior and posterior circulation cases. There was <50% parent vessel stenosis in 90.9% of the anterior circulation cases, and all cases of posterior circulation aneurysms.

Conclusions

Flow diversion is a reasonably safe and effective treatment option for properly selected cases of intracranial aneurysms and offers good result with acceptable rate of complications.



(Filename: TCT_O-391b_FlowDiverters_Gupta.jpg)

Tuesday, June 5, 2018

8:00AM - 9:00AM

Parallel Paper Session: Computer Assisted and Deep Learning Methods in Stroke Imaging

O-149

8:00AM - 8:07AM

Comparison of CT Grayscale versus Colorized ASPECTS in Patients with Emergent Large Vessel Occlusion Stroke

S Beck¹, D Hoss¹, S Harder¹, U Oyoyo², J Jacobson¹

¹Loma Linda University Medical Center, Loma Linda, CA, ²Loma Linda University, Loma Linda, CA

Oral Presentations & Excerptas

Purpose

The middle cerebral artery (MCA) accounts for most intracranial large vessel occlusions (LVOs) and is the most frequently intervened upon. The ASPECTS (Alberta Stroke Program Early CT Scoring) system is commonly accepted for identifying infarcts, with MR diffusion-weighted imaging (DWI) utilized for estimating acute infarct size. ASPECTS utilizes high-contrast grayscale images, but research shows using color palettes can improve contrast perception. This study was initiated to determine if colorized ASPECTS images improve accuracy in detecting acute MCA territory infarcts, and if they can function as a teaching tool for trainee radiologists.

Materials and Methods

Informed consent and IRB waiver of consent were obtained as necessary. Adult stroke-protocol CTs and MRIs between January 2013 and August 2017 were reviewed for diagnosis of LVO and no intracranial hemorrhage. Eighty patients (42 female, 38 male) remained after excluding for time between CT and DWI acquisition exceeding 75 minutes. Grayscale CT, colorized CT, and DWI ASPECTS scores each were obtained by two attending radiologists. Four radiology resident volunteers provided CT ASPECTS scores and a 5-point confidence level response for each reading. Statistical analysis was performed including Wilcoxon signed rank, Kappa, and Mann Whitney U tests.

Results

No statistically significant confidence level difference was seen between the gray and colorized modalities. Residents overall had statistically significant higher accuracy with grayscale images ($p < 0.05$), with no significant difference for the attendings. Resident kappa values for accuracy were highest in the insular cortex (0.61), followed by the M2 region and lentiform nucleus. The M4-6 regions showed the least accuracy.

Conclusions

Colorized ASPECT images did not improve user confidence for resident radiologists, and grayscale imaging read accuracy was greater. Attendings showed no accuracy difference between CT imaging types. Traditionally earlier infarcting regions (insular cortex and lentiform nucleus) were more accurately detected than typical penumbra regions (superior MCA distribution).

O-150

8:07AM - 8:14AM

Detection of early infarction signs with a computer-aided assessment of the Alberta Stroke Program Early CT score (ASPECTS) in the clinical routine

N Guberina¹, A Radbruch², U Dietrich¹, C Deuschl¹, M Forsting¹, A Ringelstein¹, C Mönninghoff¹
¹*Institute of Diagnostic and Interventional Radiology and Neuroradiology, Essen, Germany*, ²*German Cancer Research Center, Heidelberg, Germany*

Purpose

New software solutions emerged to support radiologists in image interpretation and to enhance clinical decision-making in the acute ischemic stroke setting. The study aimed to verify a computer-aided assessment of the Alberta Stroke Program Early CT Score (ASPECTS) for detecting signs of early infarction.

Materials and Methods

The ASPECTS scores were determined for 120 CT scans of patients with middle cerebral artery stroke in the acute ischemic stroke setting (within 6h of onset). Patient collective was differentiated according to (I) normal brain, (II) advanced leukoencephalopathic changes, (III) old infarcts and (IV) atypical parenchymal defects (multiple sclerosis, metastasectomy, aneurysm coiling, etc.). ASPECTS assessments were automatically provided by the software package e-ASPECTS (Brainomix®, Oxford, UK) (A). Subsequently, three neuroradiologists (B), (C) and (D) examined independently and, blinded to the definite infarction, altogether 2400 brain regions (caudate, putamen, internal capsule, insular cortex, M1-

Oral Presentations & Excerptas

6). Intermodality comparison was performed with the definite infarct core as reference standard after best medical care (thrombolysis and/or thrombectomy).

Results

Intermodality comparison reveals higher correlation coefficient of (B) 0.71; (C) 0.76; (D) 0.80 with definite infarct core compared to (A) 0.59 for ASPECTS assessment in the acute ischemic stroke setting. While (B), (C) and (D) showed an excellent correlation for individual patient groups (I), (III), (IV), except for (II), (A) was not significant in patient groups with pre-existing changes (II), (III), (IV). The following sensitivity, specificity, PPV, NPV, and accuracy are achieved (in %): (A) 83; 57; 55; 82; 67; (B) 74; 76; 69; 83; 77; (C) 80.8; 85.2; 76; 84; 80; (D) 63; 90.7; 82; 79; 80.

Conclusions

For assessment of ASPECTS score the examined software may provide valid data in case of the normal brain. However, overall performance of experienced neuroradiologists is still superior to automated computational performance, particularly in patient groups with pre-existing cerebral changes.

O-151

8:14AM - 8:21AM

Impact of CT ischemic lesion location on modified Rankin Scale score in patients with acute ischemic stroke – a voxel-based approach

M Ernst¹, H Marquering², C Majoie², A Boers², N Forkert³, S Gellissen¹, J Fiehler¹

¹University Medical Center Hamburg-Eppendorf, Hamburg, Germany, ²Academic Medical Center, Amsterdam, the Netherlands, ³University of Calgary, Calgary, Canada

Purpose

Previous studies indicated that ischemic lesion volume can be useful as a surrogate marker for functional outcome but should be considered in the context of lesion location. In contrast to previous studies using the region-of-interest approach, this study aims to measure the impact of ischemic lesion location on functional outcome using a more precise voxel-wise-approach.

Materials and Methods

Datasets of acute ischemic stroke patients from Multicenter Randomized Clinical Trial of Endovascular Therapy for Acute Ischemic Stroke in the Netherlands (MR CLEAN) were used. Primary outcome was functional outcome as assessed on the modified Rankin Scale (mRS) three months after stroke. Ischemic lesion volume was determined on CT scans 3-9 days after stroke. Voxel-based lesion symptom mapping techniques including covariates that are known to be associated with functional outcome were used to determine the impact of ischemic lesion location for outcome.

Results

Out of the 500 patients of the MR CLEAN trial, 216 were included for analysis. Lesion-symptom mapping with inclusion of covariates revealed that especially left-hemispheric lesions in the deep periventricular white matter and adjacent internal capsule showed large influence on functional outcome (Figure 1).

Conclusions

Our study confirms that infarct location has an important impact on outcome of stroke patients and should be considered in prediction models. Even after adjusting for covariates the left-hemispheric cortico-subcortical fiber tracts seem to have a high impact on functional outcome.

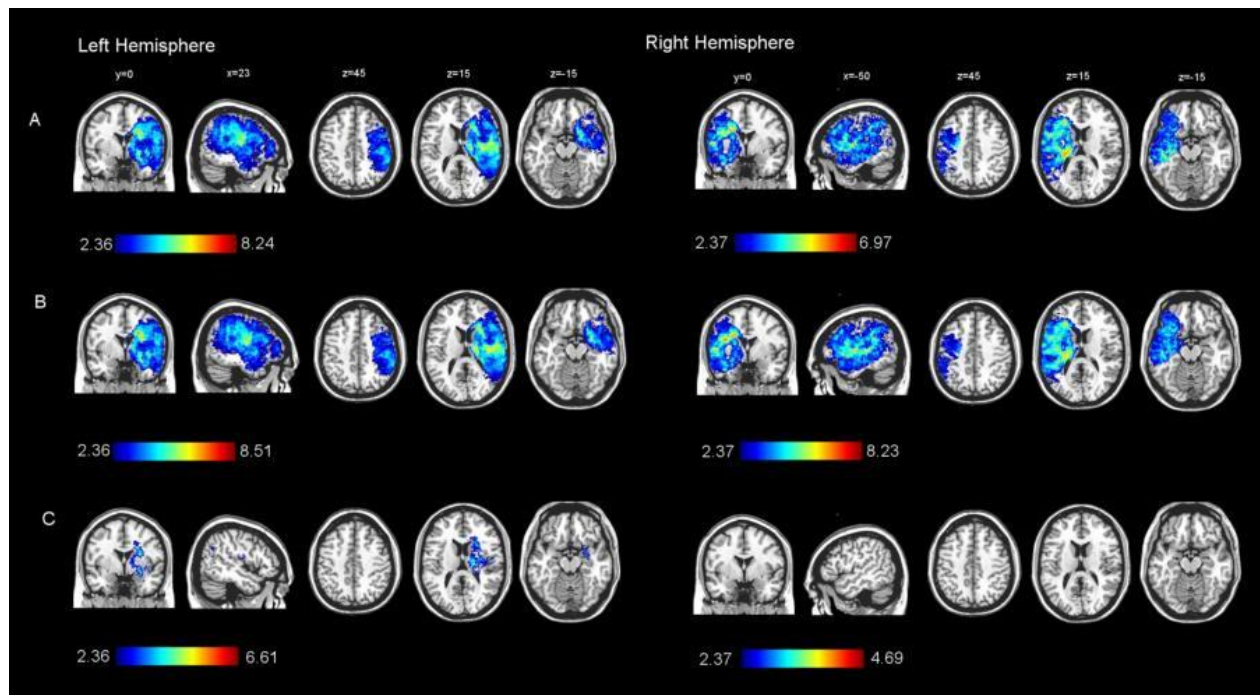


Figure 1. Voxel-based lesion symptom mapping of lesion impact on modified Rankin Scale (mRS) calculated separately for each hemisphere (right side, n=94; left side, n=122) using (A) no covariates, (B) sex and age as covariates, (C) sex, age, and ischemic lesion volume as covariates. The color range indicates t-scores resulting thresholded at 1% false discovery rate. Higher t-scores (red) indicate areas associated with worse clinical outcome (mRS).

(Filename: TCT_O-151_Figure1.jpg)

O-152

8:21AM - 8:28AM

Differentiation of Infarct Core, Penumbra and Normal Brain on Non-Contrast CT in Acute Stroke Using Texture Analysis

V Tsehmaster Abitbul¹, N Zakhari¹, R Thornhill¹, W Shabana¹

¹The Ottawa Hospital University of Ottawa, Ottawa, Ontario, Canada

Purpose

Early identification of acute ischemia and tissue at risk (i.e. penumbra) plays an important role in treatment and recovery of stroke patients. Currently, differentiation of penumbra from infarct core and normal brain can be assessed using CT perfusion (CTP). However, CTP is not widely available, requires IV contrast administration and is associated with higher radiation dose compared with noncontrast CT (NCCT). Our objective is to determine if texture analysis of NCCT alone, could differentiate between normal brain tissue, core infarct and penumbra.

Materials and Methods

Retrospective review of acute stroke patients who underwent a NCCT and CTP between June 1, 2016 to July 1, 2017. We identified areas of core infarct, penumbra and normal tissue on the CTP maps. Regions-of-interest (ROI) were placed on corresponding areas on the NCCT images and saved for subsequent texture analysis. We extracted textural features related to the grey-level histogram, grey-level co-occurrence (GLCM) and run-length matrix (RLM) for each ROI. Within subjects differences among core infarct, penumbra, and normal ROIs were assessed using repeated measures ANOVA with posthoc Bonferroni correction.

Results

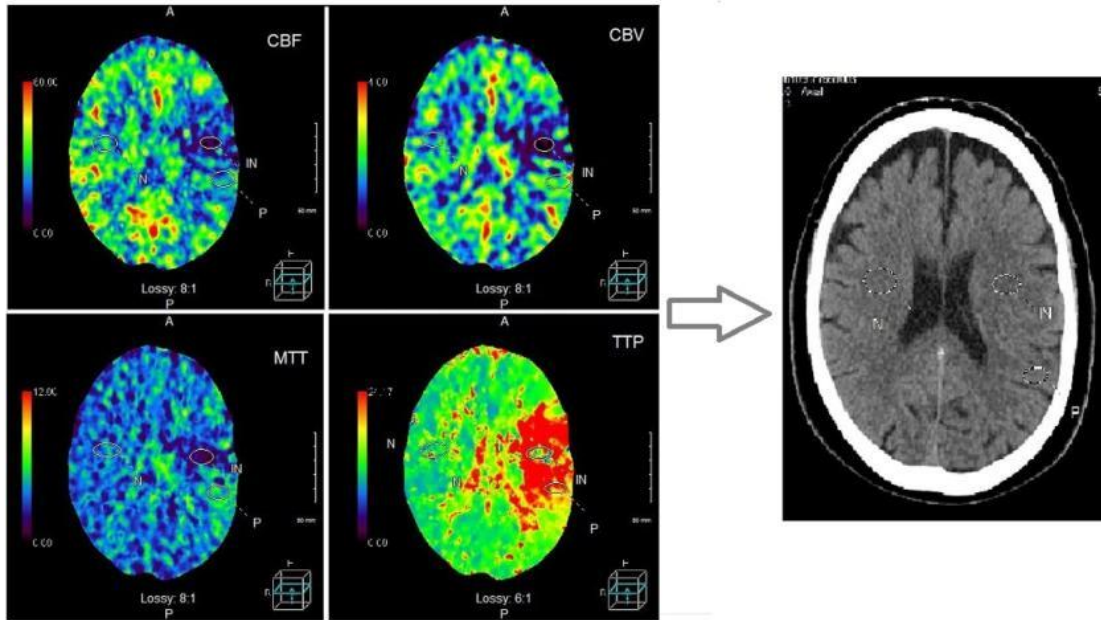
Forty-nine patients were included in this study. The grey-level histogram mean values associated with infarct core ROIs were significantly lower than both normal and penumbral regions ($P < 0.0001$ for each

Oral Presentations & Excerptas

comparison); grey-level mean histogram values associated with penumbral regions were significantly greater than normal regions ($P=0.01$). Infarct core grey-level skewness values were greater than the penumbra ($P=0.04$). Infarct core grey-level kurtosis values were higher than both normal ($P=0.001$) and penumbral regions ($P=0.001$). Penumbral run-length nonuniformity and grey-level nonuniformity values were lower than the infarct core and normal brain values ($P \leq 0.03$ for each comparison).

Conclusions

Texture analysis features can be useful in differentiating infarct core, penumbra and normal brain on NCCT in the acute stroke setting.



(Filename: TCT_O-152_27CTP-IMAGE.jpg)

O-153

8:28AM - 8:35AM

Artificial Intelligence Detection of Cerebrovascular Large Vessel Occlusion – VIZ Algorithm Diagnostic Accuracy and Clinical Notification Times in a Retrospective Evaluation

A Chatterjee¹, C Johnson¹, A Harvin¹, P Mullin¹

¹Medical University of South Carolina, Charleston, SC

Purpose

In acute stroke, rapid evaluation for cerebrovascular large vessel occlusion (LVO) amenable to endovascular thrombectomy is crucial for improved patient outcomes. The VIZ algorithm utilizes artificial intelligence (AI) to process CT angiography (CTA) studies, identify LVOs, and notify treating physicians using a completely automated platform. We retrospectively evaluated prospectively acquired CTA studies using the VIZ platform to determine its diagnostic accuracy and notification times versus our institution's standard-of-care workflow.

Materials and Methods

Fifty-four patients with acute stroke CTA studies were identified from our institution acquired over 60 days. Thirty-four patients had internal carotid artery terminus (ICAT), MCA M1 segment, or MCA M2 segment occlusions confirmed with conventional angiography that were amenable to endovascular thrombectomy. Twenty had no LVO. The CTA studies were submitted to the VIZ algorithm for LVO identification and the total processing time was recorded. These VIZ results and processing times were compared against the time between acquisition and clinician notification for each study.

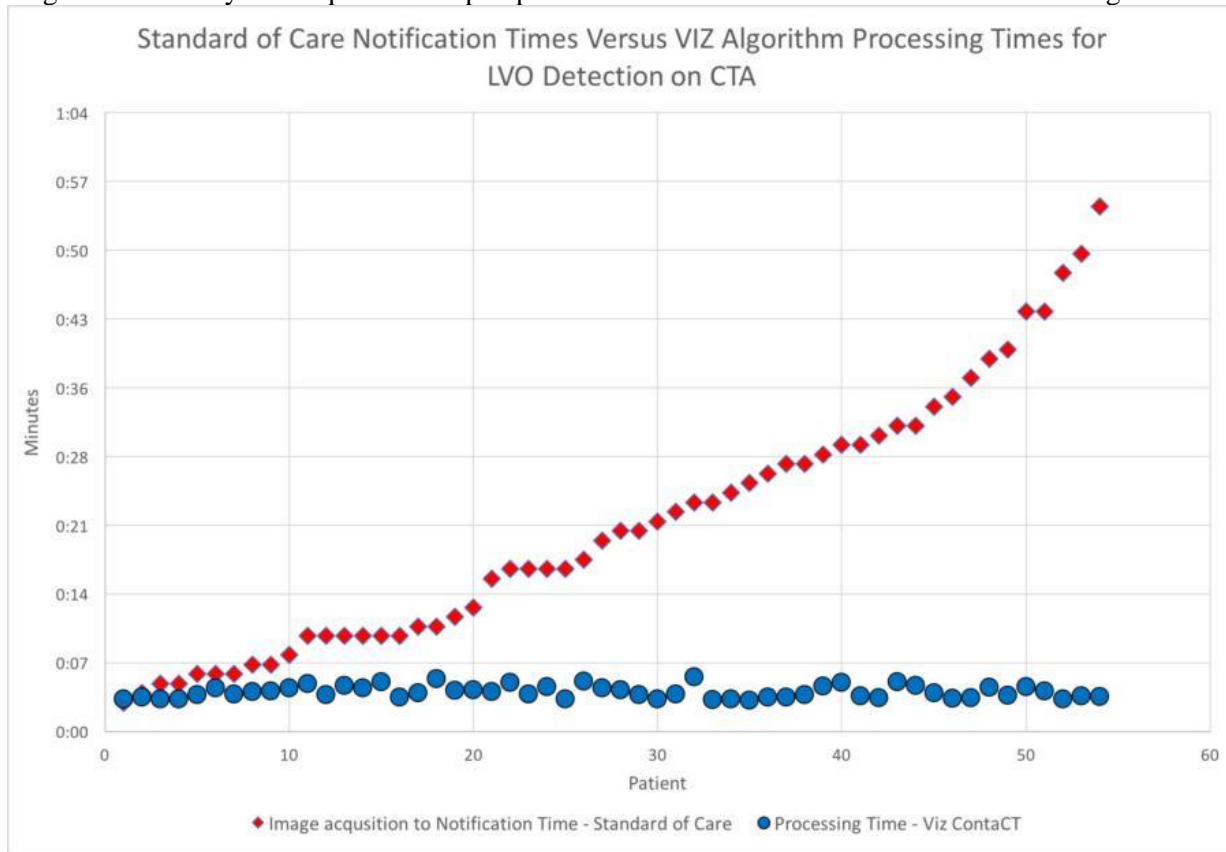
Oral Presentations & Excerptas

Results

The VIZ algorithm demonstrated a 91% sensitivity (31/34) and 85% specificity (17/20) for detection of LVO. Summary statistics for standard-of-care notification times in minutes were a mean of 21, standard deviation of 13, minimum of 3, and maximum of 55. Summary statistics for VIZ algorithm processing times in minutes were a mean of 4, standard deviation of 0.5, minimum of 3, and maximum of 5. (Figure 1)

Conclusions

VIZ algorithm AI evaluation of CTA in acute stroke has good diagnostic accuracy and consistently short processing time for detection of LVO. This may serve as a powerful adjunct enabling radiologists to more rapidly identify ICAT and MCA LVOs in a patient population where early diagnosis is critical for improved outcomes. As this is an evolving field, we can expect continued advances and improvements in diagnostic accuracy that require future prospective evaluation in a clinical stroke-center setting.



(Filename: TCT_O-153_2017_12_15Graph.jpg)

O-154

8:35AM - 8:42AM

Prediction of the Final Infarct from Acute Stroke Neuroimaging Using Deep Learning

E Gong¹, T Thamm², J Guo¹, G Zaharchuk¹

¹Stanford University, Stanford, CA

Purpose

Predicting the final infarct of an acute ischemic stroke using magnetic resonance imaging (MRI) is valuable for triage and prognosis assessment. We developed and tested a deep learning model to predict

the final stroke lesion from acute stroke multi-contrast MR images, using a deep learning architecture with improved designs for multi-scale and patch-based learning.

Materials and Methods

Compared with traditional CNN networks, our proposed model has three main contributions and features:

1. A three-dimensional CNN was implemented which utilizes available 3D spatial information more effectively.
 2. Our patch-wise approach uses small 3D patches taken from the original images/volumes as inputs to focus on local voxel information. Training on patches also prevents over-fitting by extracting from each image thousands of samples.
 3. The multi-scale structure learns the lesion prediction from patches with different resolutions to fuse information at various scales with both local and global contextual information.
- To validate, our proposed 3D CNN model was trained and tested using the MICCAI ISLES 2017 challenge dataset with 43 cases with acute DWI-ADC and PWI maps registered to the annotated final infarct segmentation at day 90th. The Dice Score Coefficient (DSC) was used as the major quality metric to evaluate the model's segmentation performance.

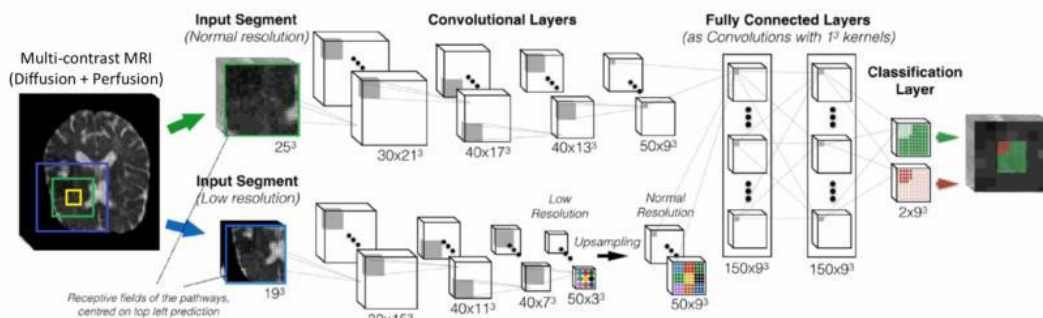
Results

We achieved a mean DSC of 0.35 (with 0.20 STD) on the testing set. Our model performs better on test dataset samples with large stroke lesions, reaching a DSC around 0.70, significantly improved from winning entries in ISLES 2016. Our proposed method is the top entry in the ISLES 2017 public leaderboard.

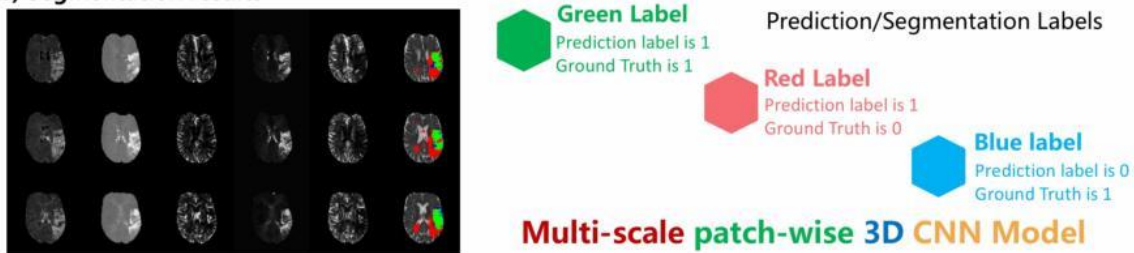
Conclusions

We demonstrated that a deep learning approach with an advanced network architecture can predict the final stroke lesion accurately based on acute diffusion and perfusion MRI. Given its inherent speed, high performance, and capacity for further improvement, deep learning is a promising method for MRI-based stroke outcome prediction.

a) Network Structure



b) Segmentation results



(Filename: TCT_O-154_network.jpg)

O-155

8:42AM - 8:49AM

Deep Learning Quantification of Parenchymal Hemorrhage Volume Correlates With Patient Clinical Outcome

E Kuoy¹, M Daun², J Pao², P Chang³, D Chow⁴

Oral Presentations & Excerptas

¹UC Irvine, Orange, CA, ²UC Irvine Health, Orange, CA, ³University of California San Francisco, San Francisco, CA, ⁴University of California, Irvine, Irvine, CA

Purpose

Recent advances in deep learning will soon yield tools for precise measurement of various radiographic abnormalities, including automated quantification of intraparenchymal hemorrhage (IPH) volume. However, the clinical utility of these tools remains unclear. In this study, we investigate whether IPH quantification can be used to predict patient clinical outcome.

Materials and Methods

After IRB approval, an institutional database was queried for IPH cases between October 2013 and October 2015. Patients were limited to those with available baseline clinical status including Glasgow Coma Scale (GCS), age, and sex. Quantification of IPH volume was performed using a fully automated deep learning tool on initial noncontrast head CT exam. The tool was previously validated on a separate large cohort of 358 manual annotations with Pearson correlation of 0.999 by two radiologists. Patients were divided into cohorts based on modified Rankin scale (mRS) <= 3 at discharge, and development of pneumonia, nonpulmonary infection, or seizure. Differences in baseline clinical status and IPH volume between cohorts were determined using a two-sample t-test. A logistic regression model combining clinical status and IPH volume was created to predict clinical outcome.

Results

A total of 279 IPH patients were identified. Mean IPH volume was calculated as 22.8 cm3 (range 0.12 cm3-173 cm3). IPH volume was significantly different when stratifying cohorts by mRS (p < 0.001), as well as development of pneumonia (p = 0.0042) and nonpulmonary infection (p = 0.022); however, no significant relationship was seen in development of seizure (p = 0.95). The differences in hemorrhage volume were more significant than any other clinical markers (Table 1). A logistic model combining clinical markers (GCS, age, sex) and IPH volume could predict mRS score (0.81), pneumonia (0.82) and nonpulmonary infection (0.79) with reasonable accuracy.

Conclusions

Precise IPH quantification facilitated by emerging automated deep learning tools can be used as a novel biomarker for prediction of clinical outcome.

Table 1. Summary of Results

Summary of results comparing cohort differences based on two-sample *t*-tests. For modified Rankin score, pneumonia and non-pulmonary infection, deep learning quantification of IPH volume is the most significant difference.

	IPH	GCS	age	sex
<i>mRS ≤ 3</i>	p-val < 0.0001 t-score = 4.15	p-val = 0.0014 t-score = -3.29	p-val = 0.00026 t-score = 3.78	p-val = 0.95 t-score = -0.053
<i>pneumonia</i>	p-val = 0.0042 t-score = -2.93	p-val = 0.43 t-score = 0.77	p-val = 0.88 t-score = -0.15	p-val = 0.60 t-score = 0.52
<i>other infection</i>	p-val = 0.022 t-score = -2.32	p-val = 0.086 t-score = 1.73	p-val = 0.12 t-score = -1.55	p-val = 0.20 t-score = -1.27
<i>seizure</i>	p-val = 0.95 t-score = 0.063	p-val = 0.70 t-score = -0.38	p-val = 0.038 t-score = 2.093	p-val = 0.35 t-score = -0.92

Key: mRS = modified Rankin score; IPH = intraparenchymal hemorrhage volume; GCS = Glasgow Coma Scale

(Filename: TCT_O-155_Abstract2_Clinical.jpg)

O-156

Oral Presentations & Excerptas

Hybrid 3D/2D Convolutional Neural Network for Hemorrhage Detection on Head CT

P Chang¹, E Kuoy², J Pao², M Daun², D Chow²

¹University of California San Francisco, San Francisco, CA, ²University of California Irvine, Irvine, CA

Purpose

In recent years, deep learning through convolutional neural networks (CNN) has emerged as a powerful technique for image pattern recognition [1]. This study evaluates a fully automated CNN customized for the detection of intraparenchymal (IPH), subarachnoid (SAH), and epidural/subdural (EDH/SDH) hemorrhages on noncontrast CT (NCCT).

Materials and Methods

After IRB approval, all NCCTs acquired between January 1, 2017 and July 31, 2017 at a single institution were downloaded. Using natural-language processing and visual inspection, cases of IPH, SAH or EPH/SDH were identified. Manual 3-D annotations were generated for IPH (voxel-level segmentation masks) and SAH/EPH/SDH (coarse region-of-interest). A custom hybrid 3-D/2-D CNN (Figure 1) was created for voxel-level classification of hemorrhage whereby slice-wise prediction was dependent on contextual information from the five immediate slices surrounding the region-of-interest.

Results

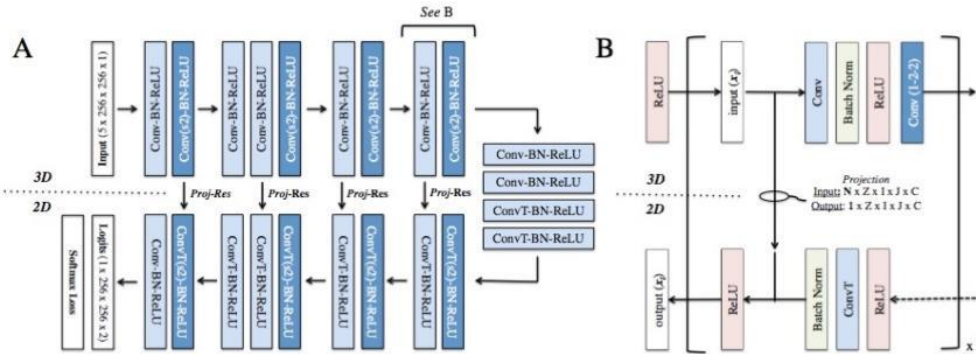
A total of 10,159 NCCTs were identified, 901 (8.9%) of which contained hemorrhage including IPH (n=358; 3.5%), SAH (n=319; 3.1%) and EPH/SDH (n=224; 2.2%), yielding a total of 512,598 images. Upon five-fold cross-validation, the overall algorithm accuracy was 0.971 with AUC, sensitivity, specificity, PPV and NPV of 0.974, 0.971, 0.975, 0.793 and 0.997 respectively. In total 26/901 (2.9%) of hemorrhages were missed. Further stratification of results by hemorrhage type are shown in Table 1. For IPH, quantification of hemorrhage volume demonstrated a Dice score of 0.942 and Pearson correlation of 0.999 with human experts. Average prediction time for a single patient from raw unprocessed DICOM images was on average 0.089 seconds.

Conclusions

This study demonstrates feasibility of deep learning for accurate detection of hemorrhage on NCCT. A prospective trial is currently ongoing to utilize the algorithm as a triage tool to identify positive hemorrhage cases, assessing potential reduction in turnaround time and improved patient outcomes.

Figure 1. Network Architecture and Summary of Results

(a) Hybrid 3D-contracting and 2D-expanding fully convolutional CNN architecture for prediction of hemorrhage. The contracting arm is composed predominantly of $1 \times 3 \times 3$ convolutions at stride 1 (light blue), with an occasional 3D $2 \times 3 \times 3$ convolution at stride 2 to decrease the feature map to 25% of the original (dark blue). The expanding arm is composed entirely of 2D $1 \times 3 \times 3$ convolutional transpose operations. (b) Connections between the contracting and expanding arm are facilitated by residual addition operations between corresponding layers. 3D layers in the contracting arm are mapped to 2D layers in the expanding arm by projection operations. (c) Table summarizing results stratified by hemorrhage type.



C

	IPH	SAH	EDH/SDH	Negative	Total
Positive	353	311	211	229	1,104
Negative	5	8	13	9,029	9,055
Total	358	319	224	9,258	10,159

Key: IPH = intraparenchymal hemorrhage; SAH = subarachnoid hemorrhage; EDH = epidural hemorrhage; SDH = subdural hemorrhage

(Filename: TCT_O-156_Abstract1_Hemorrhage_Detection.jpg)

Tuesday, June 5, 2018

8:00AM - 9:00AM

Parallel Paper Session: Brain: Traumatic Injury

O-157

8:00AM - 8:07AM

Computed Tomography findings and their correlation to Glasgow Coma Score and other risk factors.

C Martins¹, C Assuncao²

¹Universidade Federal do Parana, Curitiba, Panama, ²Hospital Angelina Caron, Curitiba, Panama

Purpose

The study was focused at correlating Glasgow Coma Scale, and risk factors such as sex, age and tracheal

Oral Presentations & Excerptas

intubation with the cranial computed tomography findings in patients with traumatic brain injury in a major Brazilian hospital.

Materials and Methods

A prospective, cross-sectional study was developed with 89 patients who were admitted at the local trauma center and given a Glasgow coma score, and who also were submitted to computed tomography at the first eight hours following admission.

Results

The mean age of the population was 34.75 ± 19.70 years, with prevalence of males (75.2%). The most common causes of traumatic brain injury were: traffic accidents (62.7%), household injuries (16.2%), second level falls (12.6%), victims of aggression/violence (4.3%) and same level falls (4.3%). In the present study, 72.3% of patients had traumatic brain injury rated as mild, 6.3% as moderate and 21.4% as severe. Tomographic findings such as hematomas, hemorrhages, skull fractures and contusions were observed in 79.42% of patients. Most of the findings of severe traumatic brain injury were observed in the patients above 45 years old (95.4%) and in this group, all the patients required tracheal intubation.

Conclusions

Statistical significant results were observed for correlations between the Glasgow Coma Scale, age below 45 years, need for tracheal intubation and the presence of CT findings ($p < 0.05$).

O-158

8:07AM - 8:14AM

Utility of CT Angiography in Patients with Acute Subdural Hematoma

B Geng¹, X Wu¹, L Tu¹, K Seifert², D Gandhi³, P Sanelli⁴, A Malhotra²

¹Yale University School of Medicine, New Haven, CT, ²Yale New Haven Hospital, New Haven, CT, ³University of Maryland School of Medicine, Baltimore, MD, ⁴Northwell Health, Manhasset, NY

Purpose

To determine the utility of computed tomography angiography (CTA) in patients with acute subdural hemorrhage Subdural hematomas (SDH) are not uncommon, especially in elderly population who may not have a history of significant trauma. Other predisposing causes such as use of anticoagulation also increase the risk, even with minor trauma. Rarely they can be caused by aneurysmal rupture. Aneurysm rupture with a subdural hemorrhage component has been reported to be associated with a poorer prognosis than aneurysm rupture associated with subarachnoid hemorrhage (SAH).

Materials and Methods

We retrospectively reviewed 411 consecutive patients with SDH that underwent CTA at our institution between January 1, 1999 and June 30, 2016. We excluded patients with prior histories of aneurysms, intracranial hemorrhage, as well as those who underwent CTA postoperatively to check for aneurysm treatment outcome. A total of 233 reviewed patients were included in the study and assessed for aneurysm detection as well as presence of concurrent SAH.

Results

The average age of patients included in the study was 54.2 ± 22.7 years with a male to female ratio of 1.84:1. CTA imaging revealed 15 aneurysms in 15 patients; of those 15 aneurysms, 9 were felt to be incidental aneurysms that did not explain the patient's intracranial hemorrhage. The cause of intracranial hemorrhage in 6 patients (2.6%) was a ruptured aneurysm. All of those 6 patients presented with concurrent SAH. Thus the percentage of intracranial aneurysm rupture presenting as pure SDH without SAH at our institution was 0% (95% CI: 0-1.57%).

Conclusions

Intracranial aneurysm rupture is reported in the literature to cause SDH without concurrent SAH. However, we did not find any positive cases for aneurysms in institutional retrospective review of SDH patients without associated SAH. Patients presenting with isolated subdural hemorrhage without SAH may have a low yield on CTA.

Oral Presentations & Excerpts

Contrast extravasation on CTA in acute head trauma.

A Eran¹, I Varaganov¹, R Shreter²

¹*Rambam Health Care Campus, Haifa, Israel*, ²*Hillel Yaffe Medical Center, Hadera, Israel*

Purpose

In head trauma, neck/head CTA are indicated when there is concern for occult vascular injury. Prior studies showed that contrast extravasation (CE) on CTA might have prognostic and treatment implications; however, data is scarce and opposing. In this study we sought to retrospectively characterize the implication of acute contrast extravasation on clinical outcome and care in a large patients' cohort.

Materials and Methods

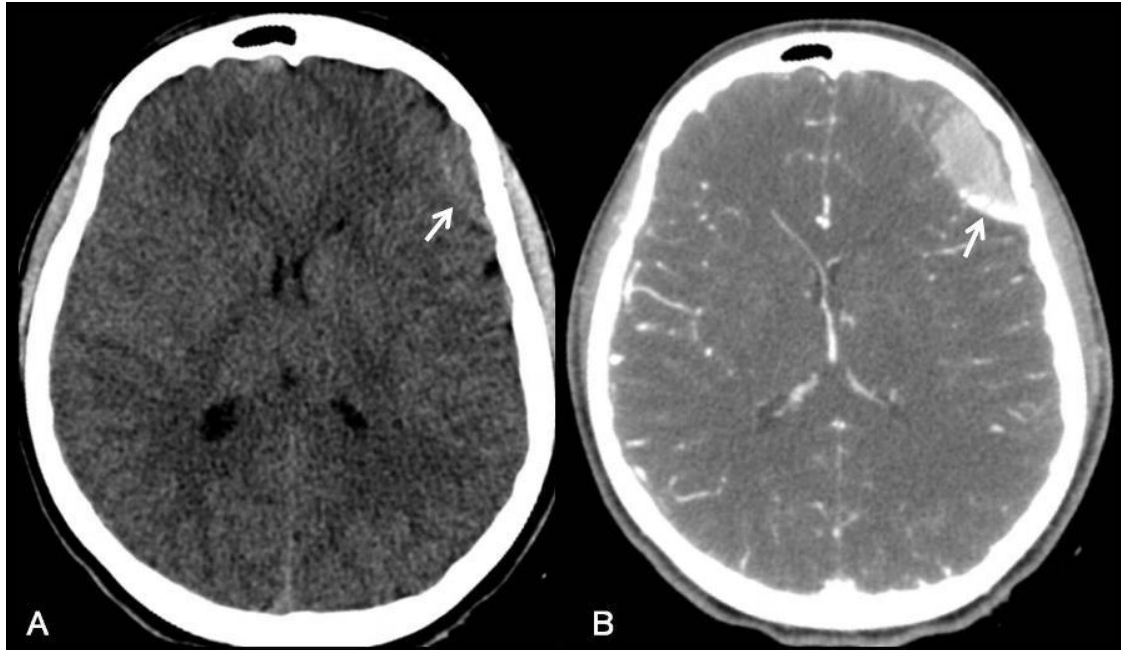
Identified were 244 cases that matched the following search criteria: (a) acute trauma victims, (b) had NCCT at arrival and early follow-up CT up to 48 hrs, (c) had CTA upon arrival, and (d) had intracranial traumatic findings. CE was defined as intrahematoma pooling of contrast, outside a vessel with density greater than 120 HU and of any shape or size. Image review for CE was blinded to patients' outcome. Outcome was graded using Glasgow Coma Outcome Score (GCOS) upon discharge, based on patient's electronic record.

Results

Upon hospital arrival 57 patients (23.3%) had CE on CTA. Hematoma types associated with CE were epidural hematoma, subdural hematoma and cortical contusion. On univariate analysis, patients with CE were significantly more likely to be intubated on arrival, had lower GCS on arrival, showed higher rates of hematoma growth, had intraoperative active bleed, had longer hospitalization stay and had significantly higher rate of GCOS 1 (death). Patients without CE were significantly more likely to be treated conservatively and had higher rates of GCOS 5 (no or minimal neurologic injury). Perhematome type analysis showed that in patients with subdural hematoma and CE the prognostic effect of CE was retained and they were significantly more likely to have GCOS 1 ($p=0.006$). In patients with epidural hematoma and cortical contusion this association was not shown. Multivariate analysis for arriving at a good vs. bad outcome showed that the presence of any type of extravasation reduces the chance of arriving at good outcome ($p=0.02$, $OR=0.389$, $95\% CI=0.1760.862$).

Conclusions

CE on CTA in acute head trauma settings is an important imaging finding that might have a prognostic significance. The prognostic effect is mostly apparent in patients with subdural hematoma.



(Filename: TCT_O-159_fig1-AB.jpg)

O-160

8:21AM - 8:28AM

Role of Brain MRI in Evaluation of Trauma Patients

W Malak¹, D Adran¹, C Farris¹, R Khan², C Takahashi¹, A Mian³

¹Boston University Medical Center, Boston, MA, ²University of Arizona Medical Center, Tucson, AZ, ³Boston University/Boston Medical Center, Boston, MA

Purpose

To characterize significant intracranial pathology detected on Brain MRI (bMRI) in trauma patients not detected on initial head CT (HCT) and to evaluate indications for bMRI in trauma patients to determine which indications are associated with new positive findings detected on bMRI. The goal of this work is to develop guidelines for which trauma patients should undergo bMRI after initial HCT.

Materials and Methods

This HIPAA compliant, IRB approved study retrospectively identified all admitted trauma patients at our level I trauma center that underwent bMRI between 8/2008 and 2/2011 based on review of the institutional trauma registry and PACS (n=137). Reports in PACS and the EMR were reviewed to determine the indication for each bMRI and to determine the significant findings detected on bMRI not initially detected by HCT on admission. Indications for ordering studies were categorized as clinical indication only, indication based on findings on initial HCT, or both. The percentage of bMRIs showing significant additional findings for each clinical indication were determined.

Results

Brain MRI detected significant intracranial pathology in 45.3% of patients undergoing bMRI not detected on initial HCT. The most common findings detected by bMRI were Diffuse Axonal Injury (DAI) (51.6%) and infarct (19.4%). The indication for ordering a bMRI was based on clinical findings alone in 70.8%, imaging findings on initial HCT alone in 22.6%, and both in 6.6% of patients. The most common clinical indications for obtaining a bMRI were altered mental status (AMS), seizure or seizure-like activity, and focal neurologic deficit. Studies ordered for AMS had the highest percentage of positive studies, 63.3%, of all indications alone.

Oral Presentations & Excerpts

Conclusions

In the trauma setting and based on initial imaging and clinical findings, bMRI can yield important additional information after HCT when there is strong clinical suspicion for other significant injury not detected by HCT.

Table 1. Significant New Findings Detected on Brain MRI Not Seen on CT Head		
Significant Finding	Percentage of Cases with New Finding on MRI Brain	Number of Cases with New Finding on MRI Brain (Cases with Specific Finding/All Cases with New Finding on MRI)
Diffuse Axonal Injury	51.6%	32/62
Infarct	19.4%	12/62
Other	29.0%	18/62

Table 2. Indications for Brain MRIs		
Indication for Scan	Percentage of Brain MRIs	Number of Brain MRIs Performed (For Indication/Total)
Based on Clinical Findings	70.80291971	97/137
Based on Head CT Findings	22.62773723	31/137
Based on Both	6.569343066	9/137

Table 3. Most Common Specific Clinical Indications for Brain MRI Examinations		
Clinical Indication	Percentage of Cases with Clinical Indication	Number of Cases with Clinical Indication (Number of Cases with Specific Indication/Total Cases with Clinical Indication)
Altered Mental Status	46.3%	48/106
Seizure or Seizure-like Activity	23.6%	25/106
Focal Neurologic Deficit	36.8%	39/106

*Note that some cases had more than one clinical indication.

Table 4. Percentage of Postive Studies Based on Clinical Indication		
Clinical Indication	Percentage of Cases with Clinical Indication that had a Significant New Finding on Brain MRI	Number of Cases with Clinical Indication that had a Significant New Finding on Brain MRI (Number with Clinical Indication with New Finding/Total Cases with Clinical Indication)
Altered Mental Status Alone	63.30%	19/30
Seizure or Seizure-like Activity Alone	5.90%	1/17
Focal Neurologic Deficit Alone	41.70%	10/24
Altered Mental Status + Focal Neurologic Deficit	66.60%	8/12
Altered Mental Status + Seizure or Seizure-like Activity	40%	2/5
Seizure or Seizure-like Activity + Focal Neurologic Deficit	0%	0/2
Altered Mental Status + Focal Neurologic Deficit + Seizure or Seizure-like Activity	100%	1/1

(Filename: TCT_O-160_ASNR2018Tables.jpg)

O-161

8:28AM - 8:35AM

MRI findings in patients with a clinical diagnosis of post-concussion syndrome: Toronto neuroimaging criteria for post-concussion syndrome

J Panwar¹, C Hsu², C Tator³, D Mikulis⁴

¹University Health Network, University of Toronto, Toronto, Ontario, Canada, ²St. Michael's Hospital, Toronto, Ontario, Canada, ³University of Toronto and Toronto Western Hospital, Toronto, Ontario, Canada, ⁴Toronto Western Hospital, Toronto, Ontario, Canada

Purpose

In a large prospective cohort we analyze the nature and frequency of structural brain lesions on MRI to establish a neuroimaging criteria for postconcussion syndrome (PCS).

Materials and Methods

A total of 117 patients (mean age=33, male:female ratio of 1.6) with a clinical diagnosis of PCS (Zurich guidelines 2012) were prospective enrolled from Jan 2013 to Dec 2015. All patients underwent neuropsychiatric examination and MRI brain performed on a 3 Tesla MRI platform (GE Medical Systems; Signa HDxt). MRI protocol includes FSPGR 3D T1 (TR/TE= 7.00/2.50 ms; 1 mm³ voxels), FLAIR (TR/TE/TI= 11,000/150/2250 ms; 0.86 x 1.33 x 3 mm voxels) and EPI GRE axial (TR/TE= 2000/25 ms; 0.83 x 0.86 x 4 mm voxels). Two neuroradiologists reviewed the studies independently with final agreement on consensus. Neuroimaging findings documented include extra-axial hemorrhage, contusions (site and number), encephalomalacia (site and number), cerebral microbleeds (numbers), cortical siderosis, number of white-matter hyperintensities (WMH) (0-5, 5-10, 10-20 and > 20), brain atrophy and clinically relevant incidental findings.

Results

Only two patients (1.7%, 2/117) had positive findings compatible with traumatic etiology with a single microbleed seen in one patient and orbitofrontal contusion in the other patient. Twenty-eight patients (24%, 28/117) had nonspecific WMH (12% 0-5 lesions, 5% 5-10 lesions, 4% 10-20 lesions and 2.5% > 20 lesions) which was not significantly increased when compared to age-matched control derived from the published data (Hopkins et al, 2006). Incidental findings include developmental venous anomaly (8.5%, 10/117) and arachnoid cyst (1.7%, 2/117).

Conclusions

Traumatic structural lesions in PCS were exceedingly rare. Based on our prospective data we proposed the 'Toronto MR Imaging Criteria for Postconcussion Syndrome' which includes no extra-axial hemorrhage, no contusion, no microbleed on either blood productive sensitive GRE sequence, no generalized or pattern specific atrophy and WMH irrespective of number is not an exclusion.

O-162

8:35AM - 8:42AM

Correlation of Cavum Septum Pellucidum and Cavum Vergae In Fighters to Neuropsychiatric Scores and Brain Volumes

J Lee¹, J Wu¹, J Bullen¹, M Modic¹, C Bernick², S Banks², P Ruggieri³, S Jones¹

¹Cleveland Clinic, Cleveland, OH, ²Cleveland Clinic, Las Vegas, NV, ³Cleveland Clinic Foundation, Cleveland, OH

Purpose

Repetitive traumatic brain injury in the sports realm has been a topic of increasing interest, with many studies investigating the clinical and/or imaging characteristics of athletes involved in contact sports. However, linking imaging and clinical findings has been rarely reported in the literature, especially with respect to combat sports. In fighters, there have been correlations between decreased SPECT perfusion and abnormal psychometric testing, decreased deep gray structure volumes with increased impulsiveness, and smaller thalamic volumes with slower processing speed. This study examines the relationship between the presence and size of cavum septum pellucidum (CSP) and cavum vergae (CV) in professional fighters, various neuropsychiatric scores, and different brain volumes.

Materials and Methods

Evaluated were 476 professional fighters (boxers and mixed martial arts) with conventional 3T MRI and neuropsychiatric testing for CSP and CV, and combined length of the CSP and CV as cavum septum pellucidum vergae (CSPV). A linear regression model was used to test the hypothesis that neuropsychiatric scores and various brain volumes such as supratentorial volumes and deep gray structure volumes are different for fighters with CSPV than fighters without CSPV, after accounting for age and

Oral Presentations & Excerpts

education as covariates. Resulting p-values were adjusted for multiple comparisons using Holm's step-down procedure.

Results

Included were 476 fighters (440 male, 36 female) whose mean age was 30 years (sd: 8, range: 18-72). The mean number of years of education was 13 (sd: 3, range: 2-25). Of the fighters, 239 had a CSP (50%) and 63 (13%) had a CV. After adjusting for age and education, fighters with more professional fights were more likely to have CV (odds ratio associated with each additional fight: 1.02, $p = 0.033$) and increases in CSPV size (increase associated with each additional fight: 0.16 mm, $p = 0.010$). After adjusting for age and education, fighters with CV had significantly lower psychomotor speed (PsychoS, $p < 0.001$), processing speed (PSS, $p = 0.024$), and lower volumes in the supratentorium ($p = 0.009$), thalamus ($p = 0.004$), corpus callosum ($p < 0.001$), caudate ($p < 0.001$), putamen ($p = 0.012$), hippocampus ($p = 0.012$), and amygdala ($p = 0.012$) compared to fighters without CV. Additionally, increases in CSPV size were associated with lower PSS ($p = 0.017$) and PsychoS ($p < 0.001$) scores. Lastly, increases in CSPV size was associated with lower volumes in the supratentorium ($p < 0.001$, each 1mm increase in CSPV size associated with -1595 in supratentorial volume), thalamus ($p < 0.001$, each 1mm increase in CSPV size associated with -26 in thalamic volume), corpus callosum ($p < 0.001$, each 1mm increase in CSPV size associated with -11 in corpus callosal volume), caudate ($p < 0.001$, each 1mm increase in CSPV size associated with -18 in caudate volume), putamen ($p = 0.003$, each 1mm increase in CSPV size associated with -18 in putaminal volume), hippocampus ($p = 0.004$, each 1mm increase in CSPV size associated with -10 in thalamic volume), amygdala ($p = 0.00$, each 1mm increase in CSPV size associated with -6 in thalamic volume).

Conclusions

This study shows that the previously published finding of increased CSP and CV in fighters also correlates with their impaired neuropsychomotor testing, specifically decreased psychomotor speed and processing speed, and decreased various brain volumes after adjusting for age and education. While CSP and CV are commonly seen even in normal patients, presence of CV in particular in patients with repetitive trauma may be an indicator of brain injury on conventional MRI and should not be summarily dismissed as a normal finding.

O-163

8:42AM - 8:49AM

5-Year Arterial Spin Labeling MR Perfusion evaluation of concussive blast injury with associated neuropsychological measures

J Andre¹, S Rane¹, J Barber¹, N Temkin¹, C Mac Donald¹

¹University of Washington, Seattle, WA

Purpose

Following concussive blast mild traumatic brain injury (cbTBI), conventional imaging only sparsely identifies radiological findings associated with clinical outcome and more sensitive methods are needed. We sought to assess perfusion status in active-duty US military and veterans previous exposed to cbTBI in combat.

Materials and Methods

Participants with cbTBI were recruited directly in Afghanistan or following medical evacuation to Landstuhl Regional Medical Center in Germany, following diagnosis of head injury by trained medical personnel working in the TBI clinics in Afghanistan or Germany. This 5-year follow-up prospective study was performed in subjects comprised of 29 individuals (aged 28 ± 6 years, 27 M) who sustained cbTBI during deployment (between 2008-2013); 34 individuals (aged 31 ± 8 years, 30 M) without history of blast exposure and no diagnosis of prior brain injury from deployment served as controls. MRI performed at 3T comprised: sequential 3D T1-weighted images (T1WI) and a pseudocontinuous arterial spin labeling (pCASL) preparation. Calculated cerebral blood flow (CBF) maps were derived, based on

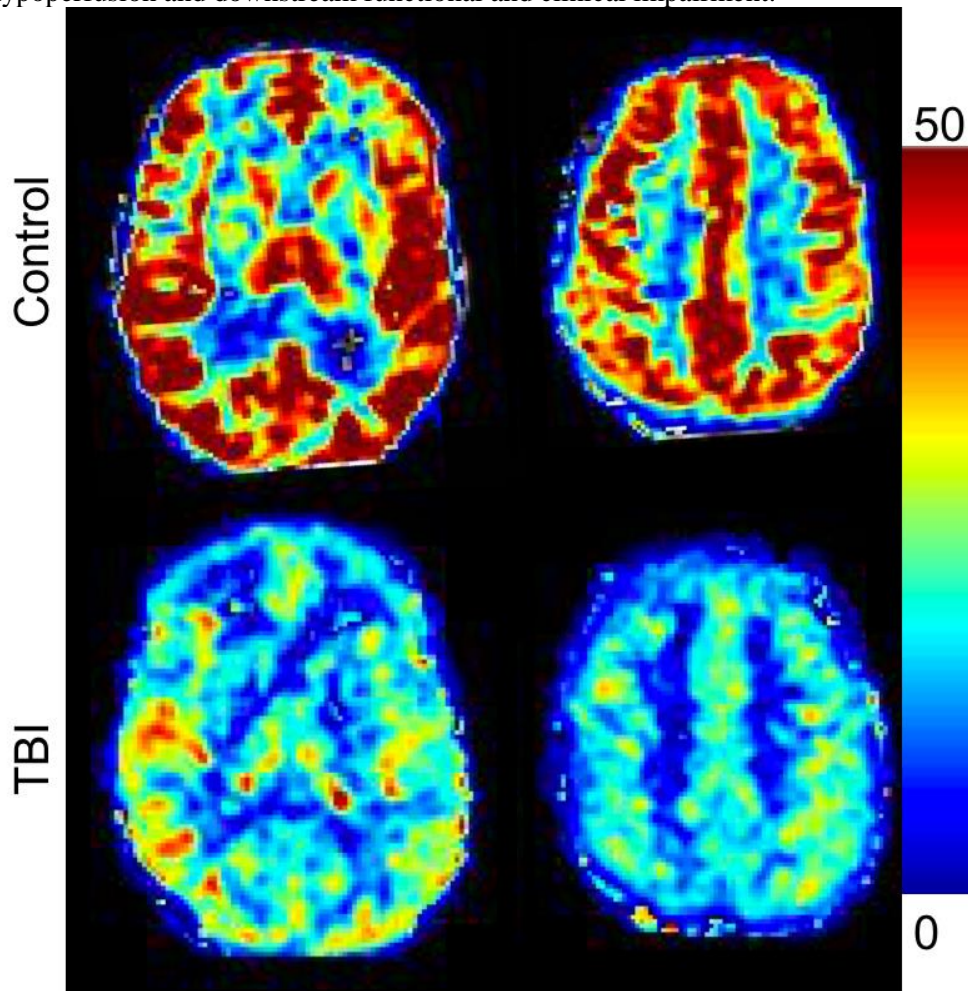
current expert recommendations [1], registered to corresponding T1WIs, compared between injured and control groups using a 2-sided t-test, and corrected for multiple comparison using Bonferroni adjustment (p -value for significance = $0.05/48 = 0.001$). Clinical evaluation included structured neurobehavioral interviews, a neuropsychological battery, and structured psychiatric evaluations.

Results

In cbTBI subjects, cross-sectional analysis identified significant hypoperfusion in 4 of 48 cortical regions of interest (central, parietal, and frontal opercular cortices, and inferior temporal gyrus), compared to combat-deployed controls. Additionally, 69% (20/29) of cbTBI subjects were found to have 2 or more regions of hypoperfusion ($p = 0.001$; Fischer's Exact Test; Odds ratio 3.6). Logistic regression on the dichotomized number of hypoperfused regions (0-1 vs. 2 or more) identified TBI diagnosis and 5-year performance on measures of motor coordination, verbal memory, and executive function as the top model (AUC = 0.85).

Conclusions

Service members who sustained cbTBI in combat exhibit sustained regional hypoperfusion 5 years postinjury compared to combat-deployed controls, with suggested association between chronic, regional hypoperfusion and downstream functional and clinical impairment.



(Filename: TCT_O-163_ASNRFigure2018TBI.jpg)

O-164

8:49AM - 8:56AM

Dynamic Contrast-enhanced MR Imaging for Quantitative Assessment of Blood-brain Barrier Disruption in Mild Traumatic Brain Injury Patients with Post-concussion Syndrome

R Yoo¹, S Choi¹

¹Seoul National University Hospital, Seoul, Republic of Korea

Purpose

To explore the utility of dynamic contrast-enhanced (DCE) MR imaging for quantitative analysis of blood-brain barrier disruption in mild traumatic brain injury (mTBI) patients with postconcussion syndrome (PCS).

Materials and Methods

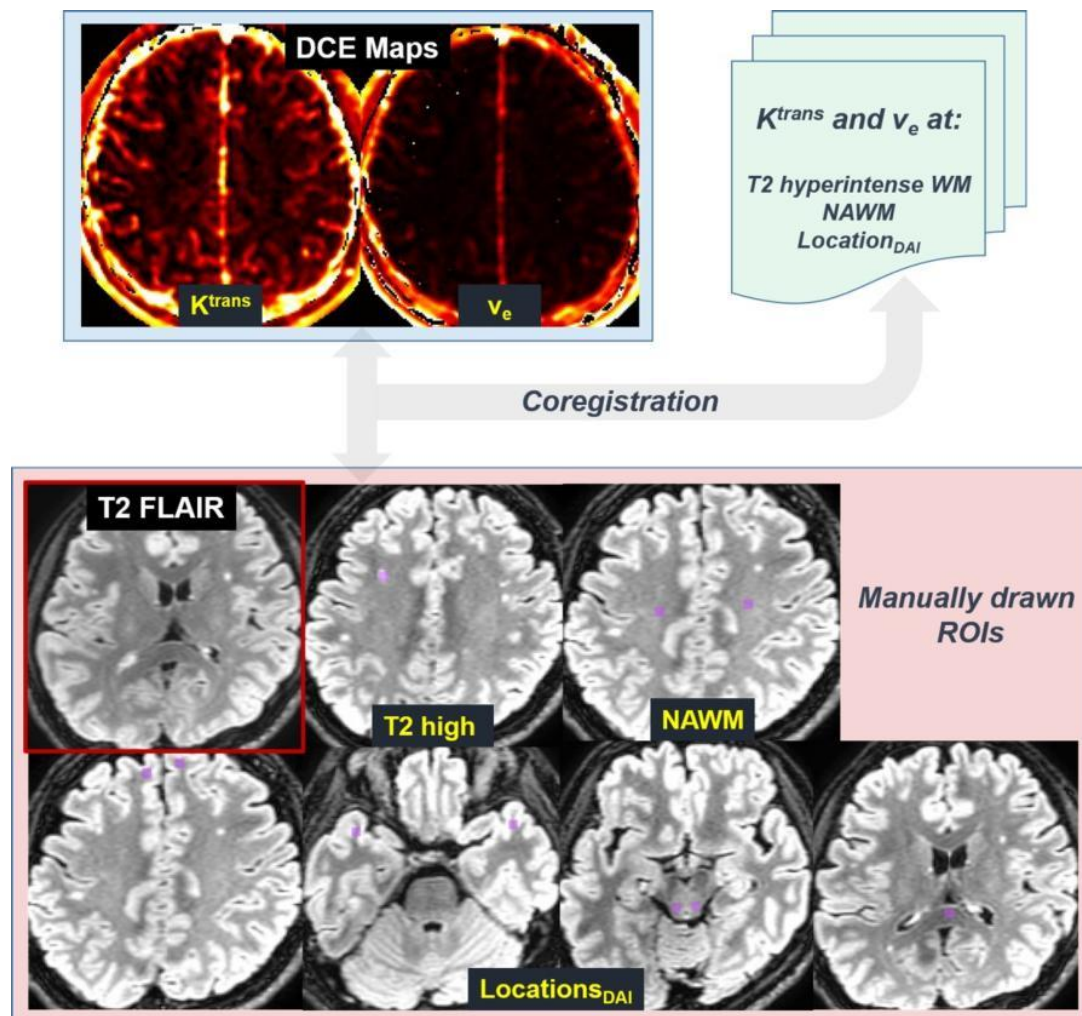
Forty-four consecutive patients with PCS after mTBI and 32 controls, who had undergone MR imaging including DCE MR imaging at our institution between October 2016 and September 2017, were included in this retrospective study. K_{trans} and v_e were analyzed at contrast-enhancing lesions, T2 hyperintense white-matter (WM) lesions, normal appearing white matters (NAWM), and predilection sites for diffuse axonal injury (LocationDAI). Mann-Whitney U-test was performed to compare the parameters between mTBI patients and controls and between patients with average or good performance and those with atypical performance.

Results

T2 hyperintense WM lesions were found in 21 patients. Median v_e of the T2 hyperintense WM lesions in mTBI patients was higher than that of NAWM in controls ($P=.027$). Both median K_{trans} and v_e at NAWM were also significantly higher in mTBI than in controls ($P=.023$ and $P=.029$, respectively). In addition, mTBI patients had higher K_{trans} and v_e at LocationDAI than controls ($P=.008$ and $P=.015$, respectively). The median v_e at LocationDAI was significantly higher in patients with atypical performance in digit span test (forward) than in those with average or good performance ($P=.043$).

Conclusions

mTBI patients with PCS had higher K_{trans} and v_e values than controls not only at T2 hyperintense WM lesions but also at NAWM and LocationDAI.



(Filename: TCT_O-164_Fig1.jpg)

Tuesday, June 5, 2018

8:00AM - 9:00AM

Parallel Paper Session: Imaging Brain Metastases

O-165

8:00AM - 8:07AM

Texture Features as a Biomarker for Melanoma Brain Metastasis Response to Immune Checkpoint Inhibitors

M Birger¹, A Bhatia², H Um², A Bialczak³, T Yang², R Malani², A Shoushtari², R Young²

¹Columbia University College of Physicians and Surgeons, New York, NY, ²Memorial Sloan Kettering Cancer Center, New York, NY, ³Memorial Sloan Kettering Cancer Center, New Hyde Park, NY

Purpose

Brain metastases in patients with melanoma are frequent and associated with a poor prognosis. Immune checkpoint inhibitors (ICI) are associated with responses in a subset of patients with melanoma brain

Oral Presentations & Excerptas

metastases; however, the relationship between radiographic features and response to ICI is poorly understood. We hypothesized that texture analysis of contrast T1-weighted magnetic resonance images (MRI) could be used as a biomarker to predict response to ICI in melanoma brain metastases.

Materials and Methods

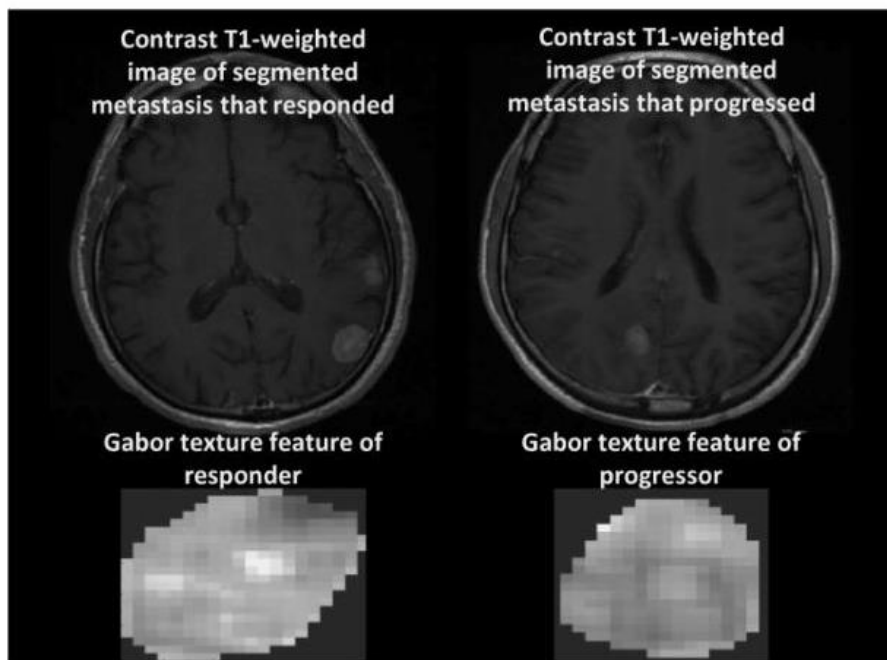
Between 2010 and 2017, we retrospectively reviewed patients with measurable malignant melanoma brain metastases on pretreatment contrast T1-weighted MRI who received ICI (n=138). Volume-of-interests were drawn around up to 5 metastases per patient (242 metastases in total), and first-order, Haralick, and Gabor texture features were extracted for each lesion. A neuro-oncologist and neuroradiologist determined clinical and radiographic progression for each metastasis according to modified RANO-BM criteria. Cox regression analysis was run to determine the hazard ratios associated with the texture features, with each metastasis categorized as a progressor or a responder.

Results

Initial analysis of lesions demonstrating clear progression (n = 17) or clear response (n=10) revealed that increased energy was associated with decreased risk of progression (p=0.031). Correlation trended towards increased risk of progression (p=.34). Gabor texture and remaining Haralick features did not demonstrate an association with response to ICI.

Conclusions

Preliminary results suggest specific MRI texture features are associated with varying response to immune checkpoint inhibition in melanoma metastases. Further research is required to better understand these associations and their potential clinical utility.



(Filename: TCT_O-165_AbstractfigBW.jpg)

O-166

8:07AM - 8:14AM

Location of Brain Metastases from Breast Cancer Depending on the HER2 Receptor Status

M Bechstein¹, T Schneider¹, M Schoenfeld¹, J Fiehler¹, S Gellissen¹

¹University Medical Center Hamburg-Eppendorf, Hamburg, Germany

Purpose

The prognosis of HER2-positive breast cancer is significantly worse compared to HER2-negative breast cancer. This is the first study comparing the location and volume of brain metastases dependent on the HER2 receptor status of the primary breast cancer.

Materials and Methods

This monocentric and retrospective study includes 45 patients with breast cancer who were diagnosed with brain metastases between 02/2008 – 12/2016 by 1.5T or 3T MRI. ROI-based mapping and metastases volumetry was performed on 3D-CE-T1w images.

Results

There was no significant difference in the location of brain metastases in HER2-negative and HER2-positive breast cancer patients. The most frequent location of brain metastases in HER2-negative cancers was the frontal lobe (26,4 % of all metastases), followed by the cerebellum (25,8%) and the parietal lobe (12,3%). Brain metastases in HER2-positive cancers were predominantly found in the cerebellum (42,3 %), followed by the frontal lobe (17,9%) and the parietal lobe (12,9%). The mean volume of brain metastases in HER2-negative cancers was 9,84 ml (median 4.10 ml, IQR 0.47 – 19,16 ml), in HER2-positive cancers 15,36 ml (median 10,12 ml, IQR 0,90 – 19,57 ml).

Conclusions

This preliminary data indicates that predominant site of metastasation in the brain is not linked to the HER2-receptor status of breast cancer tissue. Further analysis will focus on differences in the volume of brain metastases in specific subregions of the brain.

		location		
		1st (%)	2nd (%)	3rd (%)
HER2-neg.	24 patients n brain metastases = 341	frontal (26)	cerebell. (26)	parietal (12)
HER2-pos.	21 Patients n brain metastases = 319	cerebell. (42)	frontal (18)	parietal (13)

(Filename: TCT_O-166_brain_mets_location.jpg)

O-167

8:14AM - 8:21AM

Metastatic Brain Cancer: Insights from Mathematical Modeling of Tumor Size and Growth Patterns.

M Buller¹, K Chapple¹, R Bird¹

¹Barrow Neurological Institute, Phoenix, AZ

Purpose

Metastases in patients with metastatic brain cancer vary widely in size and number. We sought to determine whether the size of these metastases follows a normal or non-Gaussian distribution.

Materials and Methods

We retrospectively reviewed brain magnetic resonance imaging (MRI) reports dated between February 1, 2016, and July 1, 2017, that contained the terms metastases or multiple metastases. Studies were excluded for patients with <3 metastases, previous treatment (via surgery or radiosurgery), and dural metastases. Sixty patients were identified who had 3–53 brain metastases. The diameter of each tumor was measured, and the volume of individual tumors was calculated using 1-mm or 2-mm slice thickness contrast-enhanced spoiled-gradient MRI. For each patient, tumors were numbered in descending order based on volume, and the data for each patient were analyzed separately using regression curve fit analysis across 12 distributions. R-squared values were generated for each patient to determine goodness of fit, with

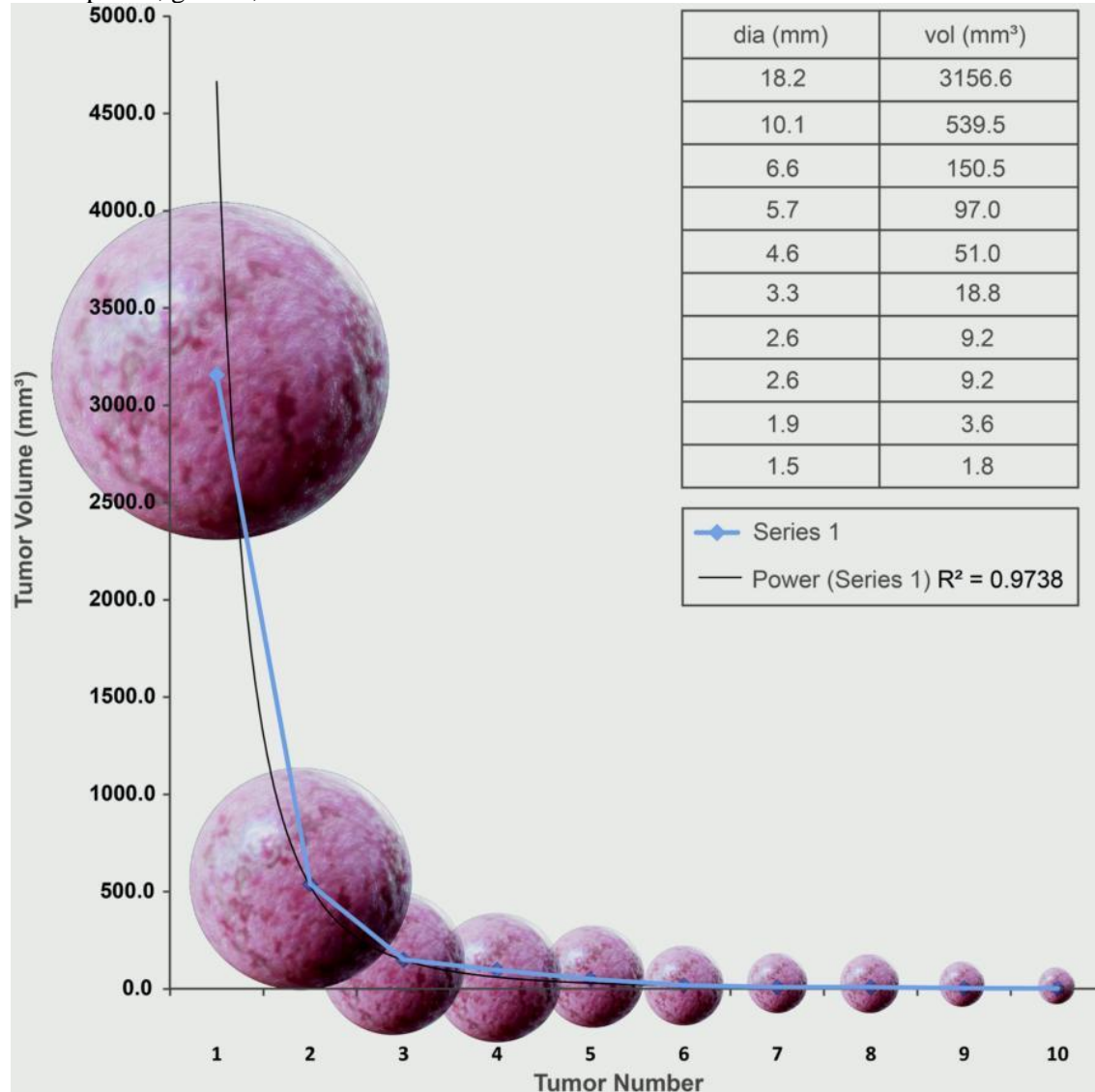
those values approaching 1 reflecting better fit. Model P-values were reviewed to assess the fit of the intercept-only model in comparison to each distribution. Values of $P < .05$ were considered significant.

Results

Regression analysis best fit with a power law distribution (see figure for example). The mean R-squared value using a power law model was 0.910 across all patients (0.902–0.918, 95% CI). Fifty of the 60 patients had significant results ($P < 0.05$). All 10 patients without significant results had < 5 metastases (n=2 with 4 metastases, n=8 with 3 metastases).

Conclusions

In this series, the size of brain metastases best fits a power law distribution in patients with ≥ 5 lesions, which implies that a common set of fundamental processes and systemic constraints (interdependence) governs the size of brain metastases (1). This observation suggests a foundation for future research on the development, growth, and treatment of brain metastases.



(Filename: TCT_O-167_ASNR2018Figure.jpg)

O-168

8:21AM - 8:28AM

Response Patterns of Brain Metastases Following Immunotherapy

F Jiang¹, S Goldberg¹, H Kluger¹, V Chiang¹, A Mahajan¹
¹*Yale School of Medicine, New Haven, CT*

Purpose

Pembrolizumab is a monoclonal antibody that blocks the interaction of programmed death-1 receptor (PD-1) on T cells with its ligands. This trial was specifically aimed to study the effect of immune therapy with pembrolizumab in patients with brain metastases.

Materials and Methods

Patients with melanoma or nonsmall cell lung cancer (NSCLC) and brain metastases were enrolled for a phase 2 trial. Patients had at least one brain metastasis on MRI between 5-20 mm untreated or unequivocally progressing after radiation therapy. Patient received 10 mg/kg pembrolizumab intravenously every two weeks. Treatment continued until disease progression, drug toxicity, development of comorbidities, withdrawal from study or death. Contrast-enhanced MRI was performed at baseline, four weeks following initiation of treatment for patient safety purposes, and then every eight weeks, until two years on treatment, to assess therapy efficacy.

Results

Data from 32/36 evaluable patients in the study were analyzed. Following patterns were observed: 1. Complete response with all lesions resolved (seven patients) 2. Partial response with significant decrease in lesion size and/or some lesions resolved (three patients) 3. Progressive disease - Lesions continued to increase in size (16 patients) - Decrease in size of preexisting lesions with new leptomeningeal disease (one patient) - Decrease in size of some preexisting lesions with increase in others (three patients) - Resolution of preexisting lesions with new lesion(s) emerging during the trial, some of which resolved, while others remained unchanged in size (one patient) 4. Stable disease (one patient)

Conclusions

Our clinical trial is the first study to show intracranial activity of immunotherapy in metastatic melanoma and NSCLC. A wide range of radiologic response patterns were seen, which may reflect the complexity of inducing a tumor-directed immune response and individual patient's immune system and tumor. The myriad of responses reflect the complexity of the biology of brain metastases, thus underscoring the need for close follow-up of patients with a multidisciplinary team of neurosurgeons and oncologists.

O-169

8:28AM - 8:35AM

Volumetric analysis of brain metastases treated with laser interstitial thermal therapy (LITT) and correlation with clinical outcome

D Bastos¹, J Loree¹, V Kumar¹, K Shah¹, G Rao¹, J Weinberg¹, S Prabhu¹
¹*MD Anderson Cancer Center, Houston, TX*

Purpose

Describe and analyze the volumetric responses of metastatic brain tumors treated with LITT and how changes correlate with local recurrence (LR)

Materials and Methods

We retrospectively reviewed a series of 63 consecutive patients with 82 lesions treated with LITT for metastatic tumors to the brain. These lesions included both untreated and previously treated but progressive lesions (prior SRS, WBRT or both). Tumor and edema volumes were quantified using MRI with contrast-enhanced T1-weighted (T1C+) and fluid-attenuated inversion recovery (FLAIR) sequences before and after treatment using the iPlan Software and volumes between slices is calculated following Cavalieri's Principle. Spider and scatter plots for tumor and edema volume were created to analyze volumetric changes after ablation with Locally Weighed Scatterplot Smoothing (LOWESS) used to smooth scatter plots. Patients were compared using Chi-square tests and odds ratios (OR) calculated.

Oral Presentations & Excerpts

Results

Visualase Thermal Therapy System (MedTronic, Minneapolis, MN) was used from December 2012 to August 2015 in 23 patients, 38 lesions (46%). The Neuroblate System (Monteris Medical Corporation, Plymouth, MN) was used from September 2015 to January 2017 in 40 patients, 44 lesions (54%). Mean tumor volume was 4.84cm³, mean edema volume was 43.86cm³ and the mean ablation volume was 8.09cm³. Mean edema volume at first follow-up (between 3-6 weeks) was 32.21cm³, with mean tumor volume of 9.25cm³. For tumor volume, the LOWESS showed an initial increase in the first month, followed by steady decrease in the following months. Tumor edema shows a plateau or a slight increase in the first month, followed by a steady decrease in the subsequent months. Patients with LR showed an increase in the edema in the first 60 days, whereas tumor volume tended to remain stable, increasing in size after the third/fourth month. We established 60 days as our reference for analyzing LR. We found that if edema volume is above baseline (pre-LITT) or shows an increasing size from nadir on the first scan after day 60, there is an increased risk of LR (OR 4.22; 95% CI 1.50-11.89, P=0.0053). Likewise, tumor volume above baseline ablation volume or increasing from a nadir on the first scan after day 60 had an increased risk of recurrence (OR 3.46; 95% CI 1.23-9.71, P=0.0016). If both edema and tumor volume are above baseline or increasing after day 60, there is also an increased risk of LR (OR 4.00; 95% CI 1.41-11.36, P=0.0077).

Conclusions

If either edema or tumor volume fail to fall below baseline or show an increasing trend on the first scan after day 60 post LITT, patients have an increased risk of LR. Qualitatively edema was the first feature observed in LR followed by increase in tumor volume.

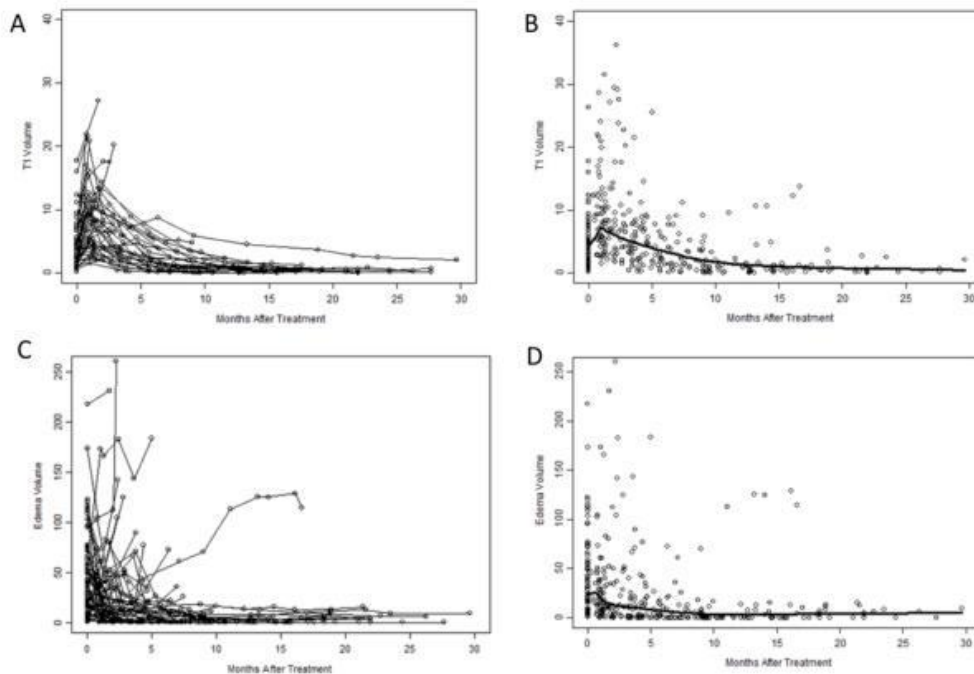


Figure 1. A. Spider plot of tumoral volume in all lesions B. Scatter plots of tumoral volume in all lesions using LOWESS smooth line; C. Spider plot of perilesional edema in all lesions; D. Scatter plots of perilesional edema in all lesions using LOWESS smooth line

(Filename: TCT_O-169_Figure1.jpg)

O-170

8:35AM - 8:42AM

Precision imaging of metastatic and primary brain tumors after radiation with 18F-FDOPA hybrid PET-MRI is feasible and cost effective

M Aboian¹, R Barajas², V Ravanfar¹, E Bahroos¹, E Tong¹, J Taylor¹, S Braunstein¹, M Hernandez Pampaloni¹, S Cha¹

¹University of California San Francisco, San Francisco, CA, ²Oregon Health and Science University, Portland, OR

Purpose

Postradiation changes in the brain can mimic tumor recurrence on MRI, requiring multiple short-term follow-ups to differentiate tumor progression from radiation necrosis. We propose combining functional and anatomic imaging with FDOPA PET tracer in hybrid PET-MRI to improve detection of tumor recurrence.

Materials and Methods

Eight adult patients treated with radiation therapy were identified--four with metastatic disease from breast and lung cancer and four with primary brain glioma (IDH wildtype glioblastoma). Patients were scanned on hybrid PET-MRI (GE Healthcare) with clinical MRI brain sequences and dynamic FDOPA uptake. Dynamic FDOPA uptake within these tumors over 45 minutes after tracer injection was analyzed and compared to ADC histogram analysis.

Results

Eight patients had successful [18F]FDOPA PET and clinical quality MRI on hybrid PET-MRI. Significant cost savings were achieved in batch scanning of patients with first group including three patients and second five patients. Only two batches of [18F]FDOPA were prepared and total cost of scanning was \$13,200 as compared to \$28,800 if patients were scanned separately. This resulted in savings of \$15,600. Successful dynamic FDOPA uptake within the tumor was seen in all patients and ratio of tumor to contralateral ROI were found to range from 1.8-4.5. While raw SUV values did not differentiate between recurrent tumor and radiation changes, tumor/contralateral SUVmax ratios were elevated to 4.5 in recurrent glioblastoma, 2.5 in hypoxic treated glioblastoma, and 1.8 in nonrecurrent metastatic breast cancer after gamma knife treatment.

Conclusions

Batch imaging of patients with [18F]FDOPA PET-MRI is feasible and cost effective. MRI imaging characteristics are critical for interpretation of dynamic [18F]FDOPA uptake within the tumor and FDOPA uptake within 3D tumor predicts patient outcomes at six months.

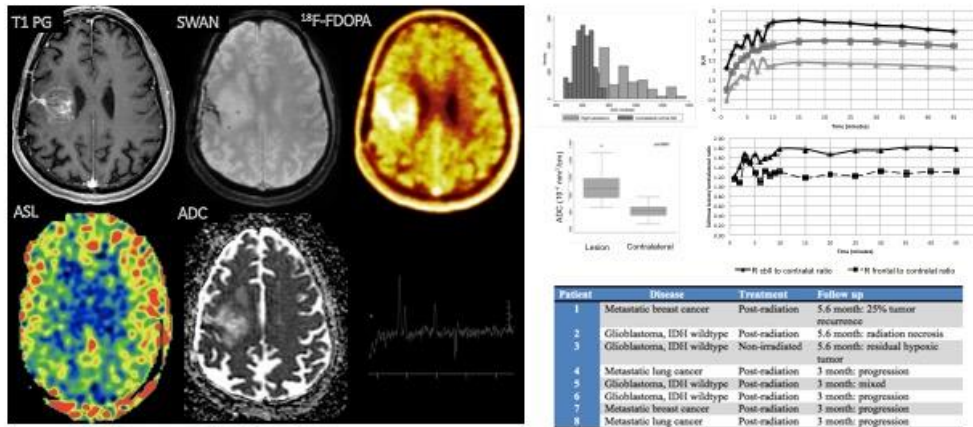


Figure 1: [¹⁸F]FDOPA PET-MRI imaging in patient with glioblastoma (IDH1 wildtype) demonstrated low SUVmax/contralateral uptake within the first 10 minutes of scan time after administration. This patient was found to have good response to therapy with no evidence of progression at 2 months follow up. (A) Clinical quality MRI demonstrates ill defined enhancement within the tumor that does not demonstrate increased cerebral blood flow or reduced diffusion. (B) Dynamic raw [¹⁸F]FDOPA uptake within the lesion and ratio of lesion to contralateral ROI over time of 45 minutes after intravenous infusion. Quantitative analysis of diffusion within the lesion using ADC histogram analysis. (C) Patient characteristics and follow up in all of the patients scanned to date.

(Filename: TCT_O-170_PETMRIfigure.jpg)

O-171

8:42AM - 8:49AM

Imaging of Laser Interstitial Thermal Therapy (LITT) for the Treatment of Brain Metastasis and Radiation Necrosis: A review of 82 treated lesions at our institution.

D Bastos¹, S Prabhu¹, G Rao¹, J Weinberg¹, R Colen¹, S Calle², D Schomer¹, K Shah¹, V Kumar¹
¹MD Anderson Cancer Center, Houston, TX, ²The University of Texas Health Science Center at Houston, Houston, TX

Purpose

Laser interstitial thermal therapy (LITT) is a safe and effective alternative to neurosurgical resection of brain metastasis and progressive radiation necrosis. Our purpose is to review the pre-LITT, intraoperative LITT (iMRI) and post-LITT MR imaging findings of brain metastasis and radiation necrosis treated with LITT, in order to establish which characteristics may be helpful in predicting success or failure postlaser ablation.

Materials and Methods

A retrospective review was made of patients status post-LITT for the treatment of brain metastasis or radiation necrosis between December 2012 to January 2017 who had received prior whole brain radiation therapy (WBRT) and/or stereotactic radiosurgery (SRS), with the exception of 5 de novo/untreated brain metastasis. A total of 82 lesions were treated in 63 patients. The lesions selected for LITT either represented recurrent metastasis/new metastasis vs. progressing radiation necrosis and were subdivided based on conventional and advanced MR imaging (MRS, ASL, DCE, DSC). Of note, the lesions could not be biopsied at the time of LITT due to risk of hemorrhage or introduction of air which would impede lesion ablation. The lesion size, tumor histology and location of the lesion were recorded. Follow-up imaging studies were reviewed to determine whether there was stability/treatment response or lesion recurrence. The LITT procedure was performed using the Visualase Thermal Therapy System (MedTronic, Minneapolis, MN) or the NeuroBlate System (Monteris Medical Corporation, Plymouth, MN). The extent of ablation was calculated using subtraction imaging by superimposing the manually

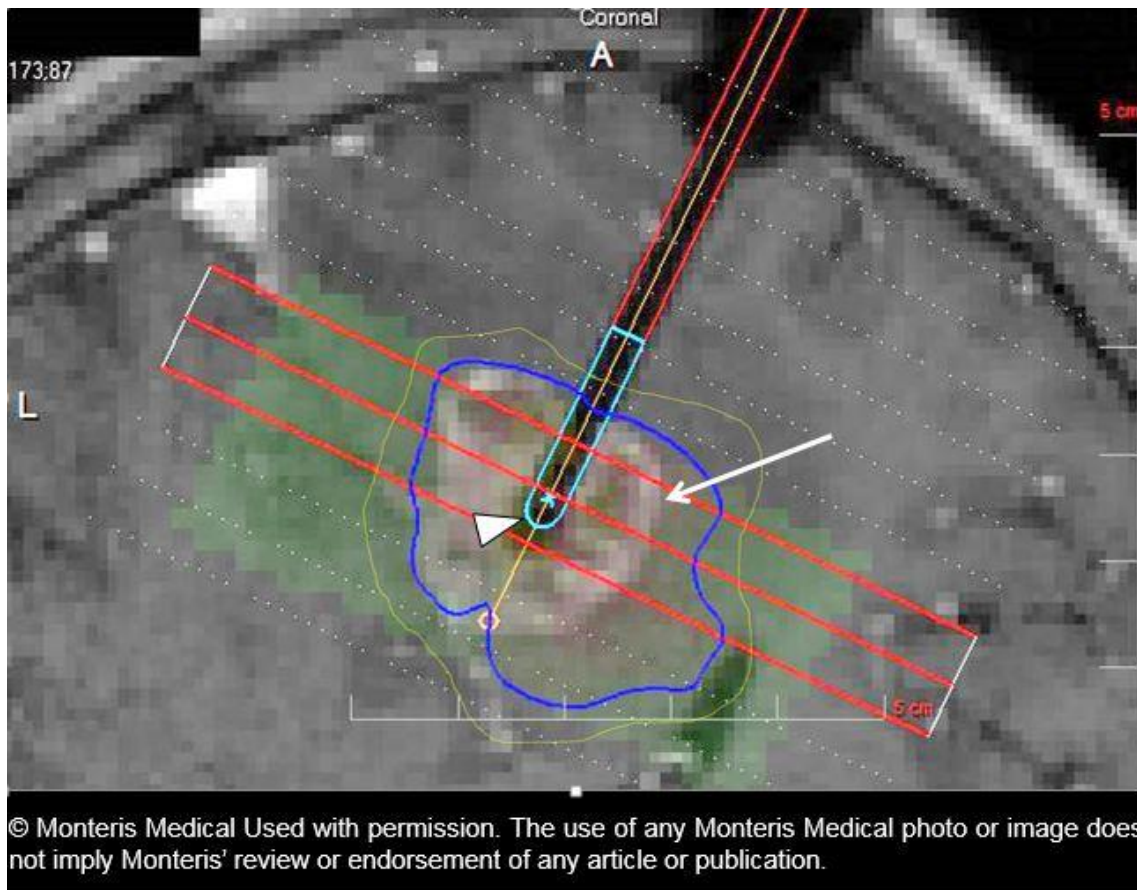
segmented lesion contours on T1C+ pre-LITT with the T1+C post-LITT images. Residual nodular contrast enhancement on intraoperative subtraction imaging was defined as an incomplete lesion ablation.

Results

The mean time from SRS to LITT was 12 months. The mean patient age at the time of LITT was 57-years-old. The mean lesion progression free survival (PFS) was 11 months. The mean treated lesion volume was 4.84 cm³. Lesions larger than 6 cm³ had a shorter progression-free survival (PFS) with a mean of 12 months; compared to 17 months in smaller lesions (p=0.033). Dural-based lesions also showed a worse PFS (mean 9 months) when compared to nondural-based lesions (mean 18 months) (p=0.001). Completely ablated lesions had a mean PFS of 19 months when compared to 8 months for incompletely ablated lesions (p<0.001). Lesions favoring radiation necrosis on advanced MR imaging had a better PFS following LITT, when compared to lesions favored to be tumor (p=0.017). The PFS based on the histology of the ablated tumors was not statistically different; however, after 15 months of follow-up, a trend was observed where NSCLC and breast cancer histology had a worse PFS in comparison with melanoma and other histology. Imaging features unique to LITT include: high T1 intensity in the ablation area immediately following therapy, which is representative of coagulation necrosis. Immediately after LITT, contrast leakage around the ablated lesion can be observed due to presumed break down of the blood brain barrier. In addition, a distinct zonal architecture (concentric rings) of the ablated lesion can be seen a few days to months following ablation.

Conclusions

This study represents the largest series on brain metastasis and radiation necrosis treated with LITT. Dural-based lesions had a higher recurrence rate compared to nondural-based lesions. Lesions that had incomplete ablations had a shorter PFS and tumors larger than 6 cm³ were associated with a greater number of incomplete ablations. Lesions with advanced MR imaging features favoring recurrent metastatic tumor, had a higher rate of local failure and a worse PFS when compared to lesions classified as radiation necrosis. Knowledge of factors relevant to lesion recurrence may enable improved patient selection for LITT.



(Filename: TCT_O-171_LITTprobe2.JPG)

O-172

8:49AM - 8:56AM

Accuracy of T2- weighted images for detection of intracranial meningioma growth – towards lowering gadolinium administration

A Postma¹, R van den Dool², M Anten¹

¹MUMC+, Maastricht, the Netherlands, ²University of Maastricht, Maastricht, the Netherlands

Purpose

To study the accuracy of T2-weighted images, compared to contrast-enhanced T1-weighted (CE-T1W) images for growth detection in the follow-up of meningiomas. Meningiomas account for 13-26% of all primary intracranial tumors and are benign in 90% of cases (1, 2). The prevalence of confirmed meningiomas is 97.5 in 100.000 persons in the United States. Meningiomas can clinically manifest themselves by several symptoms and signs, including focal or generalized epilepsy and neurological deficits (2). However, these tumors are often found incidentally. Imaging is useful for diagnosis and follow-up of meningiomas. Administration of gadolinium often plays an important role in diagnosing and frequent follow-up of meningioma. However, accumulation of gadolinium in the brain is reported after frequent injections (3). Although no clinical consequences are reported so far, it remains unclear if this presents a health risk for patients. If follow-up with T2w images would suffice, repeated gadolinium administration could be reduced.

Materials and Methods

In this retrospective study, patients with an intracranial meningioma at MR-examination in 2012-2015

were identified. When at least one follow-up scan, with a minimum of 11 months' interval, was present, patients were included. Skull base meningioma and fully operated meningioma were excluded. The meningiomas were measured at T2w and 3D-CE-T1w. Measurements at 3D-CE-T1w were considered gold standard. Tumor growth was defined as an increase of $\geq 10\%$ of the longest diameter of the tumor over one year.

Results

A total of 81 patients were included. Tumor growth was detected in 12 patients at T2w and 8 patients at CE-T1w. The sensitivity of the T2w measurements compared to the reference standard CE-T1w was 100%. The specificity was 94,5%. Positive predictive value (PPV) was 66,7% and negative predictive value (NPV) was 100%.

Conclusions

A high diagnostic accuracy was shown for the detection of growth of intracranial meningioma at T2w images, compared to CE-T1w images. This could imply that gadolinium may be withdrawn from the initial follow-up of known meningioma. When in doubt, or when therapy is indicated additional contrast-enhanced imaging then can be added. This could have large impact on gadolinium use in follow-up of meningioma patients.

Tuesday, June 5, 2018

8:00AM - 9:00AM

Parallel Paper Session: Brain: New Findings

O-173

8:00AM - 8:07AM

Using Diffusion Tensor Tractography to Evaluate Cortical Spinal Tracts in Patients with Supratentorial Intracerebral Hemorrhage with and without Evacuation in the Acute to Early-Subacute Stage

M Hirano¹, C Kellner², J Scaggiante², D Lefton²

¹Mount Sinai Beth Israel, New York, NY, ²Mount Sinai West, New York, NY

Purpose

To examine the utility of diffusion-tensor imaging (DTI) tractography in evaluating fiber characteristics of the ipsilateral and contralateral cortical spinal tracts (CST) in patients with acute intracerebral hemorrhage (ICH) with and without minimally invasive endoscopic evacuation. We believe it is feasible to measure quantitatively the fractional anisotropy (FA) of the CST, data which may assist in determining whether early evacuation will improve future outcome.

Materials and Methods

This prospective cohort consists of 12 patients (mean age=65, range=47-85) with radiographically proven supratentorial, intra-axial ICH. A bleed volume of 15cc was the major determining factor for whether to perform evacuation. Within 24 hours of admission 8/12 patients underwent endoscopic evacuation. DTI was performed within 24 hours of admission and 7-13 days post hemorrhage with or without evacuation. One patient was unable to obtain the DTI at admission. Streamline tractography was performed on acquired DTI. The contralateral and ipsilateral CSTs were evaluated with region of interests placed at the cerebral peduncles and the posterior limb of the internal capsule. Mean FA (mFA) ratios (ipsilateral/contralateral mean FA) and statistics including the paired sample t-test were calculated.

Results

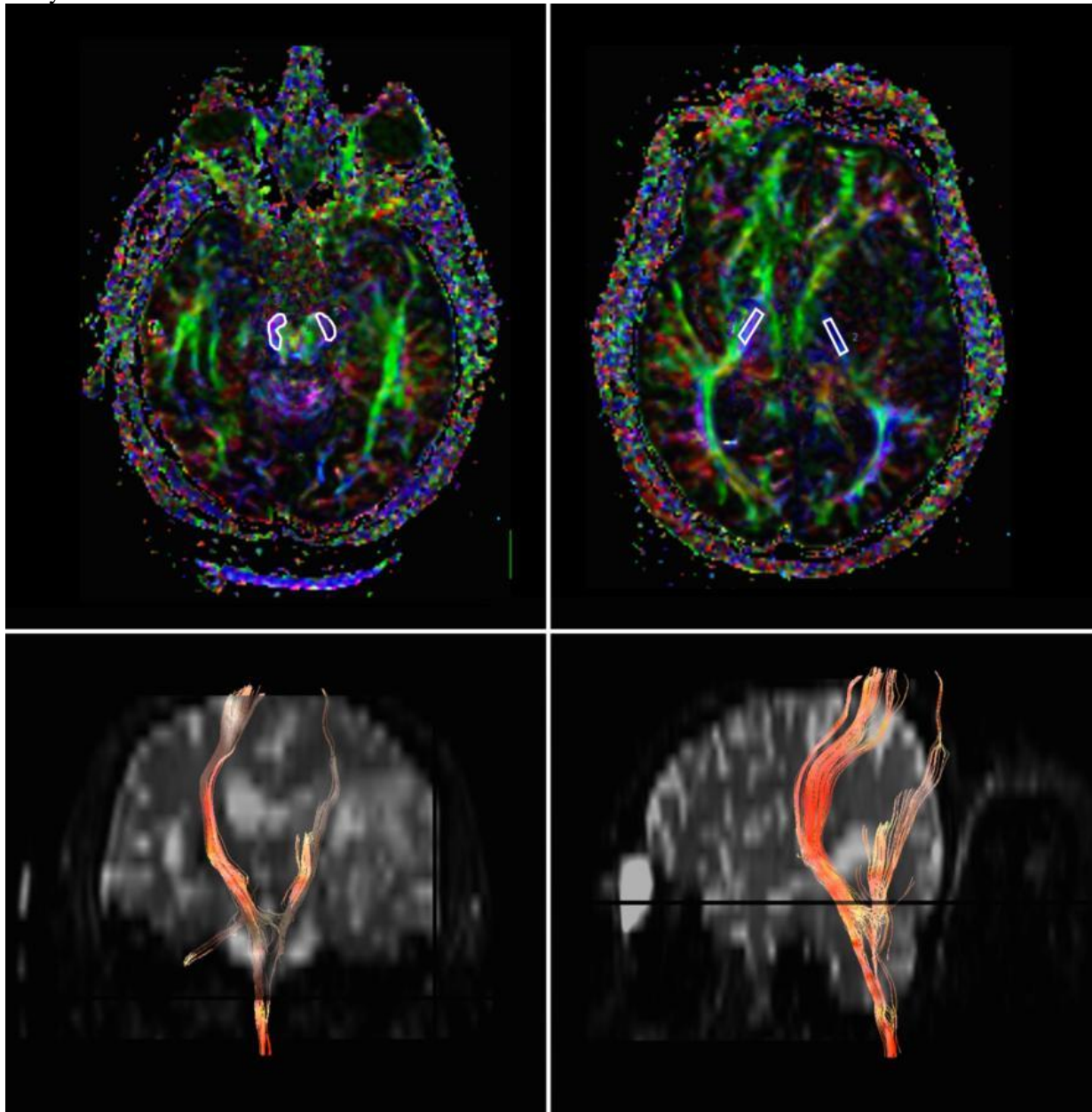
In the neurosurgical candidates at admission, the mFA ratios averaged 91% (n=7, range=76-98%, p=0.03). The mFA ratios averaged 87% (n=8, range=71-97%, p=0.005) 7-13 days post evacuation. In the

Oral Presentations & Excerpts

nonsurgical candidates at admission, the mFA ratios averaged 92% (n=4, range=86-99%, p=0.06). 7 days post bleed, the mFA ratios averaged 89% (n=2, range=86-91%, p=0.12).

Conclusions

On admission and short-term follow-up, the neurosurgical candidates demonstrated a significant difference in the mFA of their CSTs compared to the nonsurgical candidates. These findings may illustrate the significance of ICH volume in the resulting structural alteration on DTI tractography. This prospective study demonstrates the ability to measure and quantify a degree of disruption and potential recovery in future follow-up. A larger cohort and long-term follow-up will supplement this ongoing pilot study.



(Filename: TCT_O-173_asnrabstractmh1.jpg)

O-174

8:07AM - 8:14AM

A Chemobrain Study: Clinical, Genetic and Imaging Evaluation of the Cognitive Effects of Chemotherapy in Patients with Colorectal Cancer

M Sales¹, D Da Conceição², E Amaro², V Serrao¹, D Apolinário¹, C Suemoto¹, R Riechelmann¹
¹Instituto do Câncer do Estado de São Paulo, São Paulo, Brazil, ²Faculdade de Medicina da Universidade de São Paulo, São Paulo, Brazil

Purpose

Cognitive dysfunction may occur after chemotherapy in cancer survivors, especially in those treated for breast cancer. (1-3) The frequency and to which extent such toxicity develops in colorectal cancer (CRC) survivors is unknown. This prospective study evaluated the effects of adjuvant chemotherapy on the cognitive performance of patients with localized CRC in comparison with a control group who did not receive chemotherapy.

Materials and Methods

Consecutive patients with localized stages II and III CRC completed neuropsychological assessments, self-reported cognitive complaints questionnaires, and depressive symptoms evaluation before starting fluoropyrimidine-based adjuvant chemotherapy (t1) and after 12 months (t2). Blood was collected for apolipoprotein E (APOE) genotyping. Diffusion tensor imaging (DTI) data was acquired from a smaller group of participants at both time-points. DTI data was processed using DTI-toolkit registration software and standard FSL tract-based spatial statistics (TBSS) pipeline. (4, 5)

Results

In a two-year period, 85 patients were recruited: 59 received chemotherapy (CTh+) and 26 did not (CTh-). No difference was found on cognitive performance between the two groups during the follow-up, considering the global composite score (p=0.38), attention (p= 0.84) or memory (p= 0.97). However, there was a significant difference on executive function domain, after adjustment for age, sex, education, and depressive symptoms at baseline (p=0.04). The presence of the E4 allele did not influence the cognitive performance of patients. In patients that underwent MRI, tract-based spatial statistics (TBSS) did not show voxelwise significant differences in structural brain connectivity at baseline and during follow-up.

Conclusions

After adjusting for confounding factors, patients with CRC who received adjuvant fluorouracil with or without oxaliplatin presented cognitive decline on executive function after 12 months in comparison to patients with localized disease that did not receive chemotherapy. The neural substrate of the executive decline demonstrated in this work remains to be uncovered with further multimodal neuroimaging studies.

Table. Association between cognitive function and chemotherapy use during the follow-up

	Simple		Multiple*	
	β (95% CI)	p	β (95% CI)	p
Global Composite Score	-0.64 (-1.93; 0.66)	0.33	-0.61 (-1.88; 0.66)	0.34
Memory	-0.06 (-2.17; 2.06)	0.96	0.03 (-2.08; 2.15)	0.97
Attention	0.29 (-1.83; 2.41)	0.79	0.22 (-1.89; 2.33)	0.84
Executive function	-1.88 (-3.58; -0.18)	0.03	-1.80 (-3.50; -0.11)	0.04

*Linear mixed models adjusted for age, sex, education, and depressive symptoms at baseline.

(Filename: TCT_O-174_Table.jpg)

O-175

8:14AM - 8:21AM

A CT-Based Diagnostic Index to Differentiate Between Progressive Supranuclear Palsy and Parkinson's disease for DaT-SPECT/CT.

Oral Presentations & Excerptas

R Gupta¹, C Huang², R Matthews³, B Balgobin³, V Tatineni⁴, R Reinsel⁵, D Franceschi³, T Duong², G Schwartz³

¹Mount Sinai Hospital, New York, NY, ²Stony Brook Medicine, Stony Brook, NY, ³Stony Brook University Hospital, Stony Brook, NY, ⁴Stony Brook University, Stony Brook, NY, ⁵Stony Brook University Hospital, *, NY

Purpose

I123 Ioflupane is a radiopharmaceutical used in the diagnosis of parkinsonian syndromes to detect the dopamine transporter (DAT) in the terminal boutons of substantia nigra pars compacta neurons. Using a CT-based diagnostic index we sought to differentiate progressive supranuclear palsy (PSP) from idiopathic Parkinson's disease (PD) using the low-dose CT scan acquired with DAT-SPECT/CT.

Materials and Methods

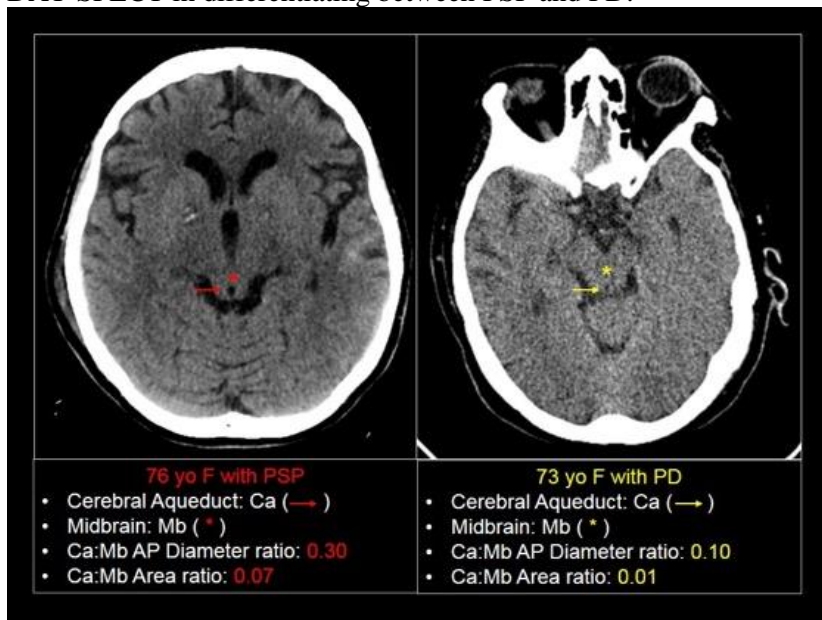
We identified six patients with a clinical diagnosis of PSP who had a DaT-SPECT/CT. Patients were age and gender matched with PD patients who had a DaT-SPECT/CT. CT component was acquired on a 6-slice SPECT-CT using a low dose protocol for attenuation correction. Using axial display, three readers were blinded and performed AP diameter and area measurements of the Sylvian aqueduct and midbrain on the CT portion of the DaT-SPECT/CT. Low-dose CT was compared to dedicated brain MRI and CT for each patient.

Results

Average AP diameter of the Sylvian aqueduct in PSP patients was trended to be larger than in PD patients, measuring 4.4 vs. 3.0 mm ($p < 0.07$). Average aqueduct area was significantly larger in PSP patients, 11.9 vs. 5.1 mm² ($p=0.009$). Differences in midbrain diameter and area were not statistically significant between the two groups ($P > 0.05$). Patients with PSP had a smaller average corrected midbrain/aqueduct diameter ratio compared to PD patients, 2.8 vs. 4.4 ($p=0.015$). The corrected midbrain/aqueduct area ratio was also smaller in PSP patients, with an average ratio of 15.5 vs. 32.0 ($p=0.015$). The intra-class correlation coefficient to determine inter-reader reliability between the three readers was 0.7 for both the diameter and area ratio. Leave-one-out cross-validation provided the highest predictive accuracy for the area ratio, calculated at 83%..

Conclusions

CT-based ratios of the midbrain and Sylvian aqueduct using a low-dose CT protocol further complements DAT-SPECT in differentiating between PSP and PD.



Comparison between task activation and resting-state connectivity maps in the motor and language networks for presurgical planning

G Shah¹, S Peltier², Y Wang³

¹University of Michigan, Ann Arbor, MI, ²University of Michigan Health System, Ann Arbor, MI, ³Sichuan Provincial People's Hospital, Chengdu, China

Purpose

Functional MRI is used to map eloquent cortex in presurgical planning, offering a noninvasive alternative to electrophysiological or Wada testing. Task fMRI allows probing of a single neural system in compliant subjects, while resting-state fMRI can evaluate multiple functional networks at once, with less burden on subjects, and can be used to monitor physiological changes in the short, medium, and long term [1]. Recent clinical work has demonstrated concordance between task activity and resting state maps in the motor network during tumor presurgical planning, with better correspondence at 3T as compared to 1.5 T [2]; while another study has shown discordance between the hand-motor activity as determined by resting-state, task, and anatomical MR imaging [3]. However, these studies used a priori seed regions, and there has been limited work examining presurgical planning using data-driven resting-state fMRI analysis in the language network. In this study, presurgical patients with brain tumors were imaged. Task activation and resting-state ICA maps for both motor and language networks were generated for each subject and compared for spatial overlap.

Materials and Methods

Subjects: 28 subjects undergoing presurgical planning were included in this study (18M/10F; 53 (\pm 15) years-old; heterogeneous pathologies, grade IV glioblastoma most common). **MRI Acquisition:** Task and resting-state fMRI scans were collected using a 3T Philips Ingenia MR scanner. **Resting-state EPI Parameters:** TR/TE/FA = 2s/28ms/90, 64x64 matrix, 3.75x3.75x3.5 mm, 39 slices, 300 timepoints. **Resting-state data** were collected with eyes closed on all subjects. A single finger-tapping motor task and a verb generation task were acquired for functional activation localization in the motor and language networks, respectively. **Preprocessing:** Slice-time correction and spatial smoothing were implemented using SPM8. Low-pass filtering (cut-off of 0.08 Hz) was then applied in MATLAB to restrict the MR signal to the frequency band of interest, and remove higher frequency noise sources 5. **Data Analysis:** Motor and language task activation maps were generated using DynaSuite Neuro software (InVivo Diagnostic Imaging), thresholded at 0.05 significance. Resting-state network maps were generated using FastICA [4]. For each subject, the ICA maps with highest spatial correlation with the task activation map were selected as winning network, with secondary components also inspected, for both motor and language. The percent spatial overlap of the activation maps with the resting state networks was calculated. The Dice coefficient of spatial similarity was also calculated, defined as: $\text{Dice} = 2|X \cap Y| / (|X| + |Y|)$, where X and Y are the thresholded task activation and resting state maps, respectively.

Results

Visual inspection demonstrated resting state maps show good definition of the motor network, in agreement with the task activation maps (Figure 1). Additionally, the second ICA component in some subjects added additional motor network information. In Figure 2, the first ICA component has a larger extent on the side of the pathology, while the second ICA component adds in the contralateral side. The calculated motor task activation overlap with the resting state network was high across all subjects (0.73 ± 0.14), but the Dice coefficient was low (0.29 ± 0.14), indicating the resting-state networks contain the majority of task activation, but also extend farther spatially. The same analysis was done for the language networks; Figure 3 shows typical results. The resting-state language ICA network has a high spatial overlap with the verb task activation (0.83 ± 0.17).

Conclusions

In this study, we investigated using resting-state fMRI to identify coherent brain networks using a data-driven analysis in presurgical tumor patients. Both motor and language networks were identified from a single resting-state scan, and the resulting network maps compared well to corresponding task activation maps, with a high percent of spatial overlap, without requiring an external task.

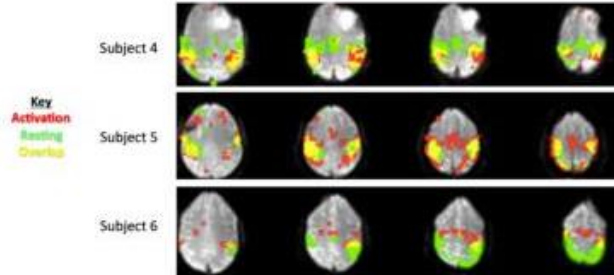


Figure 1. Task activation and resting-state ICA maps for the motor network in typical subjects.

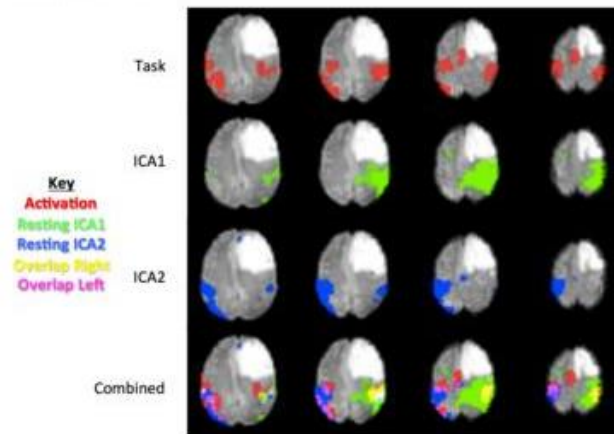


Figure 2. Task activation and resting-state ICA maps for the motor network for a subject with multiple motor components.

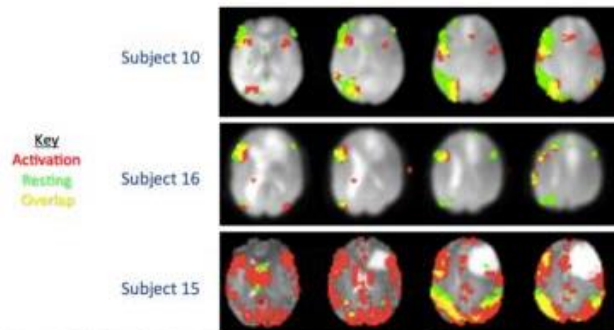


Figure 3. Task activation and resting-state ICA maps for the language network in typical subjects.

(Filename: TCT_O-176_asnr_figures_2017_bettysize3.jpg)

O-177

8:28AM - 8:35AM

A voxel-based analysis of cerebral blood flow abnormalities in obsessive-compulsive disorder using pseudo-continuous arterial spin labeling MRI

D Momosaka¹, O Togao¹, A Hiwatashi¹, K Yamashita¹, H Tomiyama¹, H Honda¹

Oral Presentations & Excerptas

Purpose

Previous studies have investigated gray- and white-matter volume abnormalities in patients with obsessive-compulsive disorder (OCD) using voxel-based morphometry (VBM) methods; however, they lacked evaluation of regional cerebral blood flow (CBF). Therefore, the purpose of this study was to clarify the CBF alterations in OCD patients by comparing CBF acquired by pseudocontinuous arterial spin labeling (pCASL) in OCD patients with that in healthy controls with a voxel-based analysis.

Materials and Methods

This retrospective study was approved by our institutional review boards, and written informed consent was waived. Subjects comprised 25 patients with OCD and 64 healthy control subjects. Structured clinical interviews for DSM-IV-TR (SCID) were administered to confirm the inclusion criteria of OCD. Healthy control subjects were recruited and assessed using the SCID to exclude any concurrent or lifetime history of DSM-IV Axis I disorders. Imaging was performed on a 3T scanner. Quantitative CBF maps generated from pCASL images and M0 images were coregistered with the 3D T1-weighted images, spatially normalized to an anatomical template of East Asian brains, and smoothed with 12-mm full width at a one-half maximum. A voxel-by-voxel analysis of covariance was computed to detect regional differences in CBF between OCD patients and normal control subjects with SPM12. The significance level was set at the p-value of less than 0.05 with the family-wise error rate correction for multiple comparisons.

Results

There were significant CBF reductions in the right globus pallidus, the right operculum, and the left posterior cingulate cortex in the patients with OCD compared with the controls.

Conclusions

The result of the present study is in line with some previous studies showing decreased gray-matter volume in the same areas. CBF reduction in patients observed in the present study shed light on the pathophysiology of OCD from a different perspective.

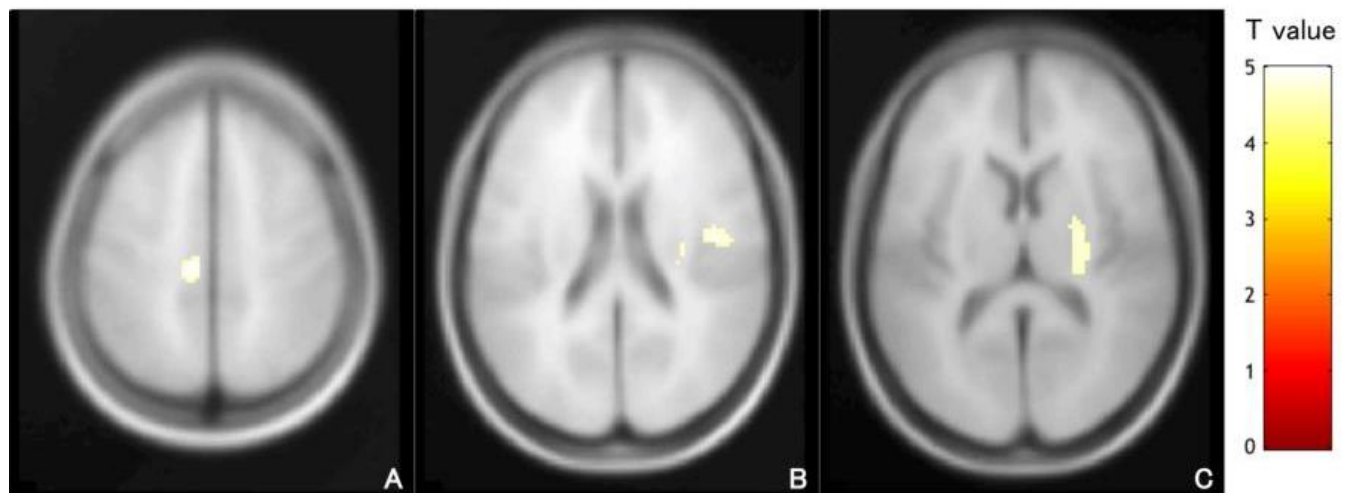


Fig. There were foci of significantly decreased CBF in OCD patients relative to normal control subjects ($P < 0.05$ family-wise error) in the left posterior cingulate cortex (A), the right frontal operculum (B), and the right globus pallidus (C).

(Filename: TCT_O-177_OCDfig.jpg)

O-178

8:35AM - 8:42AM

Deep seated intracranial hemorrhages; when is angiographic imaging required?

Oral Presentations & Excerptas

S Jacobs¹, A Bharatha²

¹University of Toronto, Toronto, Ontario, Canada, ²St. Michael's Hospital, University of Toronto, Toronto, Ontario, Canada

Purpose

Deep-seated spontaneous intracranial hemorrhages are often thought to be due to hypertension particularly in older patients with known history of hypertension. Current guidelines suggest vascular imaging in younger patients, those without hypertension, or those with atypical bleed patterns to detect possible macrovascular causes. The purpose of this study is to determine the incidence of macrovascular causes of hemorrhage in deep-seated ICH in younger patients and those without known hypertension compared to older patients with known hypertension.

Materials and Methods

A retrospective study was conducted of all patients presenting with acute nontraumatic ICH of unknown etiology on CT from 2005 to 2016. Deep intracerebral hemorrhage was defined as basal ganglia/thalamus, brainstem or cerebellum. Patients with lobar hemorrhage and subarachnoid hemorrhage with aneurysmal pattern were excluded.

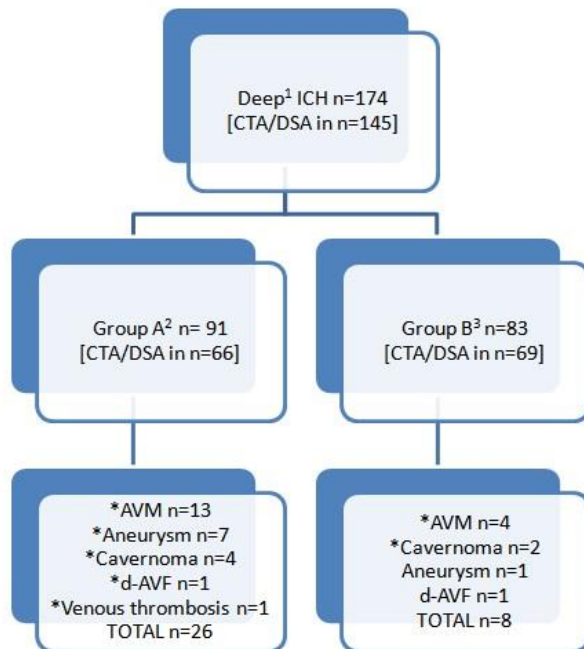
Results

In patients <45 and patients ≥45 without hypertension (Group A), 91 were identified with deep-seated ICH of which 66 had CTA and/or DSA. A macrovascular cause was identified in 26 (39%). In patients ≥45 with hypertension (Group B), 83 were identified with deep-seated ICH of which 69 had CTA and/or DSA. A macrovascular cause was identified in eight patients, 12% (see table 1). The frequency of macrovascular causes for ICH was lower in Group 2 compared to Group 1 (p<0.05).

Conclusions

In younger patients and those without history of hypertension, macrovascular causes for deep-seated ICH are more common than in older patients with known hypertension. However, even the latter group had a notable 12% incidence of macrovascular etiologies for hemorrhage. Our study suggests that noninvasive vascular imaging should be performed in all patients with spontaneous ICH, including older hypertensive patients with deep-seated ICH.

Table 1: Research Design



¹ Deep = Basal ganglia/thalamus, brainstem or cerebellum

² Group A = patients <45 with or without hypertension and patients ≥45 without hypertension

³ Group B = patients ≥45 with hypertension

(Filename: TCT_O-178_Table1.jpg)

O-179

8:42AM - 8:49AM

The Visual Cortex Sign in Anoxic Brain Injury

D Martin¹, B Hoffman², M Oswood²

¹Stanford University, Stanford, CA, ²Hennepin County Medical Center, Minneapolis, MN

Purpose

To identify patterns of MR imaging findings in patients who have suffered anoxic brain injury

Materials and Methods

In this IRB-approved retrospective study, we identified patients with a suspected clinical diagnosis of anoxic brain injury between 2011 and 2016 who subsequently underwent MRI. Patients were excluded when clinical and/or imaging findings established an alternative diagnosis. Cases of neonatal hypoxic/ischemic injury were also specifically excluded. In total, 61 patients were identified who underwent 66 MR scans. Images were reviewed by two neuroradiologists and findings were correlated with clinical data including the cause of the anoxic insult, comorbidities such as hypertension, diabetes, and coronary artery disease, the use of therapeutic hypothermia, and in-hospital mortality.

Results

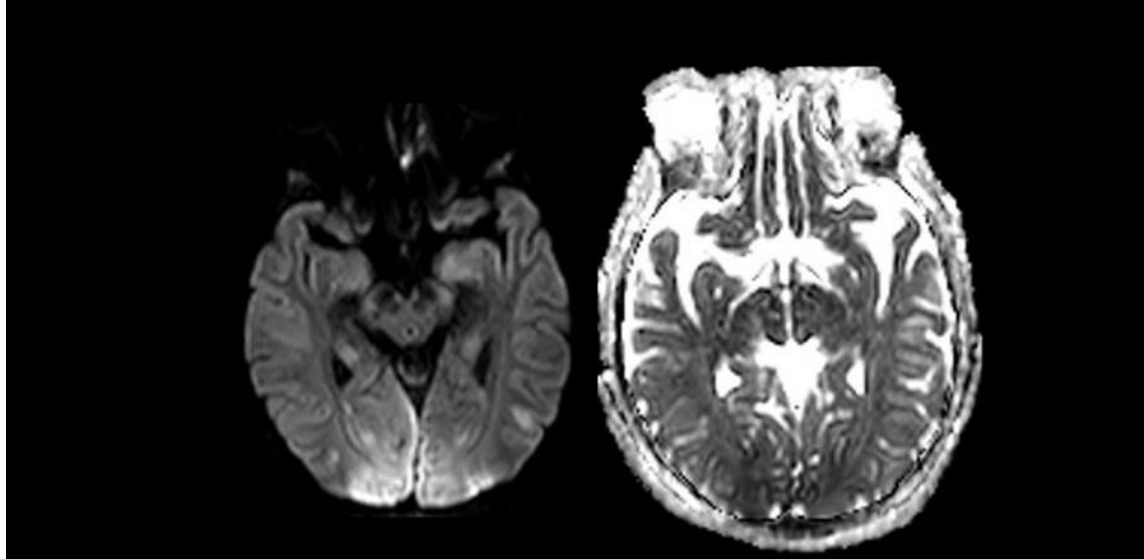
Abnormal restricted diffusion was present in 96% of patients. Evidence of cortical-restricted diffusion showed in 85% and 63% involved the deep gray nuclei, with smaller proportions showing restricted diffusion in the cerebellum and hippocampus (47% and 34%, respectively). Within those patients with cortical-restricted diffusion, we observed a subset of patients (45%) with a marked posterior predominance of ischemia, particularly involving the primary visual cortex in the medial aspect of the occipital lobes. We term this pattern the visual cortex sign. Among this subset of patients, there was no significant difference in in-hospital mortality, magnet strength, or the use of therapeutic hypothermia.

However, this group of patients was scanned sooner on average following their anoxic insult (3.4 days versus 5.2 days, $p=0.04$).

Conclusions

We have observed a novel marker of anoxic brain injury, the visual cortex sign. While this phenomenon has not previously been observed in the adult population, it is plausible that differences in autoregulation in the posterior circulation or the metabolic rate could predispose this region to anoxic injury. The visual cortex sign may be a leading indicator of cortical ischemia in patients who have suffered anoxic injury.

DWI and ADC images showing visual cortex sign in 32 year old woman scanned 4 days after cardiac arrest



(Filename: TCT_O-179_visualcortexsign-2.jpg)

O-180

8:49AM - 8:56AM

Invisible cortex sign: a new and highly-accurate feature to localize the inferolateral central sulcus

S Su¹, N Yang², F Gaillard¹

¹Royal Melbourne Hospital, Melbourne, Victoria, Australia, ²Austin Hospital, Melbourne, Victoria, Australia

Purpose

The central sulcus is an important landmark on MRI brain, but its inferolateral portion can be difficult to identify using existing techniques/signs. (1) We observed that the cortex abutting the central sulcus appears isointense to the adjacent white matter on diffusion-weighted imaging (DWI) and evaluated whether this "invisible cortex sign" could be used to identify the inferolateral central sulcus.

Materials and Methods

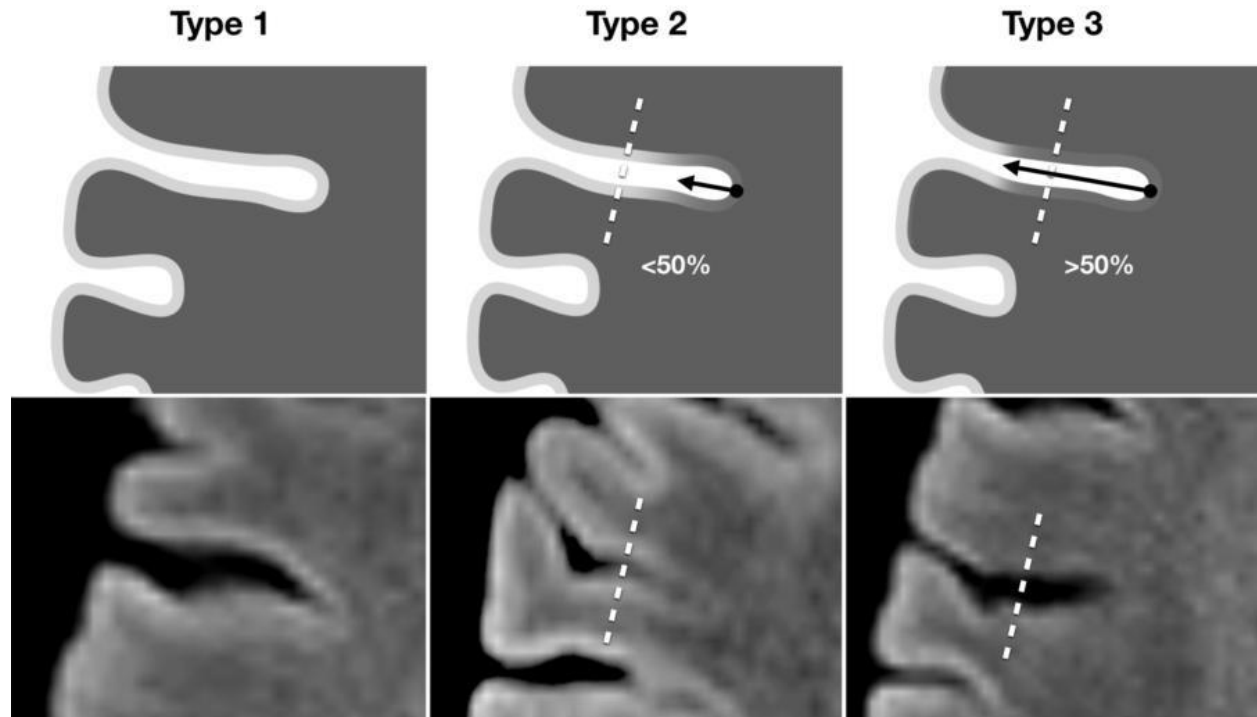
Single axial DWI images, just above the subcentral gyrus such that it included the most inferolateral portion of the central sulcus, were obtained from 108 consecutive "normal" MRI brain studies. Ten readers then marked the central sulcus based on the presence of the "invisible cortex sign". Their accuracy was compared against the central sulcus as identified by the principal investigators on tri-planar T1 volumetric MRI sequences. The appearance of the cortex was also categorized into three types (Figure 1): normal cortical hyperintensity seen around all parts of the sulcus (Type 1), lost in the deepest parts of the sulcus (<50% depth, Type 2), or lost in the majority of sulcus (>50% depth, Type 3).

Results

The central sulcus was correctly identified in 95.5% of cases ($\sigma=3.7\%$; range 89.4% to 99.1%). Older individuals had more Type 3 invisible cortices. Statistically significant differences between the ages of patients in the different types of invisible cortices was demonstrated by one-way ANOVA ($F(2, 429) = 74.9, p < 0.0005$). Dunnett T3 posthoc test showed statistically significant differences in the mean age of Type 1 vs Type 2 invisible cortices ($p=0.025$), Type 1 vs. Type 3 invisible cortices ($p < 0.0005$), as well as Type 2 vs. Type 3 invisible cortices ($p < 0.0005$).

Conclusions

The "invisible cortex sign" is a highly accurate method of identifying the inferolateral central sulcus on axial slices, and this sign tends to involve >50% of the sulcus in older patients.



(Filename: TCT_O-180_Figure2.jpg)

Tuesday, June 5, 2018

8:00AM - 9:00AM

Parallel Paper Session: Pediatric: Advanced Techniques I

O-181

8:00AM - 8:07AM

DTI Assessment of Regional White Matter Changes in the Cervical and Thoracic Spinal Cord in Pediatric Subjects

S Saksena¹, D Middleton¹, L Krisa¹, M Alizadeh¹, C Conklin¹, A Flanders¹, F Mohamed¹, S Faro²
¹Thomas Jefferson University, Philadelphia, PA, ²Johns Hopkins School of Medicine, Baltimore, PA

Purpose

Measurements of water diffusion within the spinal cord (SC) after an injury, including in regions distant

Oral Presentations & Excerptas

from the injury site, may provide valuable insight into the severity of injury. Prior adult studies have shown that diffusion-tensor imaging (DTI) allows for noninvasive assessment of the severity of spinal cord injury (SCI). (1, 2) During chronic SCI, the extensive longitudinal spreading of the lesions creates changes in the SC morphology. Changes in the diffusivity associated with these structural changes makes it possible to identify the rostral and caudal extent of the lesion using DTI. The aim of this study was to determine whether DTI at sites cephalad and caudal to the injury provides measures of injury severity in pediatric subjects with chronic SCI. We compared these data with the normative DTI data of the typically developing (TD) pediatric subjects.

Materials and Methods

A total of 10 TD (mean age, 12.0 ± 2.93 years) without evidence of SCI or pathology and 9 subjects with chronic SCI (mean age, 12.48 ± 3.17 years) were included in the study. SCI subjects underwent a neurological evaluation based on ISNCSCI and consisted of AIS A (n=7) and B (n=3). They had both cervical and thoracic injuries. Written informed assent and consent was obtained under the protocol approved by IRB. Imaging: Subjects underwent scans using 3T Verio MR scanner. The protocol consisted of conventional T1- and T2-weighted scans and axial DTI scans based on the inner field of view sequence 3 to cover the cervical (C1 upper thoracic region) and thoracic (upper thoracic region-L1) SC. The imaging parameters included: 20 diffusion directions, 6 b0 acquisitions, $b=800$ s/mm², voxel size= $0.8 \times 0.8 \times 6$ mm³, axial slices=40, TR=7900ms, TE=110ms, and TA=8:49min. Data analysis: After motion correction 4 and tensor estimation 5, ROIs were manually drawn to extract information from the whole cord and SC white-matter (WM) areas: ventral, dorsal, and both right and left lateral regions by a board certified pediatric neuroradiologist (Fig. 1). DTI parameters; FA, MD, AD and RD were quantified at each intervertebral disk level and at the midvertebral body level of the cervical and thoracic SC in these subjects. For each SCI subject, the regions relative to injury were identified. First, the level of injury was identified using the conventional MR images. The cephalad region was defined as the region above the level of MR injury and caudal region was defined as region below the level of MR injury. We chose to separate the cephalad and caudal regions into distal third, middle third and proximal third cephalad and caudal to the level of injury. DTI parameters for each WM region were measured at these three levels cephalad and caudal relative to injury. Statistical analysis: A t-test was performed to assess the differences between TD and SCI in the regions cephalad and caudal to injury.

Results

FA, MD, AD and RD showed significant changes in ventral WM in SCI subjects compared to TD at distal levels cephalad to the injury (Table 1). MD and AD were significantly lower in whole cord, ventral, dorsal, right and left lateral WM in SCI subjects compared to TD at middle levels cephalad to the injury (Table 2). AD was significantly lower in dorsal, right and left lateral WM in SCI subjects compared to TD at middle levels caudal to the injury (Table 2). FA was significantly lower in all the WM regions and whole cord in the SCI subjects at proximal levels caudal to the injury compared to TD (Table 3). MD and AD also showed significant changes in dorsal, right and left lateral WM at proximal levels caudal to the injury (Table 3).

Conclusions

We demonstrated changes in FA and AD in WM regions at levels both cephalad and caudal to the injury site. In contrast, conventional MRI showed no cord signal abnormalities. This suggests that FA and AD has the potential to be sensitive marker of true extent of cord injury and might be useful in detecting remote injuries.

Table 1: Summary of means of FA, MD, AD and RD in whole cord and white matter areas of the spinal cord cephalad and caudal (distal) to the level

of MR injury in TD pediatric subjects and subjects with chronic SCI.

		Cephalad_Distal				Caudal_Distal			
		DTI Parameters				DTI Parameters			
		FA	MD	AD	RD	FA	MD	AD	RD
Whole Cord	TD	0.557±0.063	1.172±0.179	1.944±0.258	0.786±0.163	0.445±0.051	0.942±0.217	1.408±0.315	0.709±0.173
	SCI	0.565±0.111	1.101±0.230	1.845±0.267	0.728±0.254	0.431±0.081	0.943±0.241	1.387±0.359	0.721±0.199
Ventral WM	TD	0.398±0.096	1.590±0.452	2.274±0.524	1.248±0.434	0.416±0.085	0.946±0.252	1.367±0.327	0.736±0.224
	SCI	0.446±0.143	1.283±0.388	1.675±0.319	0.962±0.338	0.373±0.142	1.032±0.237	1.401±0.297	0.804±0.242
Dorsal WM	TD	0.578±0.105	1.057±0.279	1.794±0.347	0.688±0.269	0.405±0.106	1.035±0.257	1.484±0.365	0.816±0.260
	SCI	0.571±0.145	1.089±0.357	1.825±0.407	0.727±0.381	0.434±0.107	0.946±0.306	1.412±0.475	0.713±0.245
Right_Lateral WM	TD	0.612±0.108	1.026±0.251	1.814±0.300	0.635±0.254	0.422±0.057	0.919±0.218	1.354±0.349	0.702±0.164
	SCI	0.572±0.129	1.074±0.353	1.907±0.441	0.707±0.362	0.445±0.096	0.915±0.273	1.364±0.415	0.691±0.222
Left_Lateral WM	TD	0.568±0.137	1.297±0.361	2.175±0.421	0.858±0.372	0.473±0.118	1.231±0.373	1.897±0.478	0.896±0.345
	SCI	0.554±0.143	1.340±0.377	2.110±0.418	0.907±0.406	0.477±0.148	1.065±0.453	1.617±0.584	0.789±0.403

Bold indicates that the DTI value is significantly different in subjects with SCI compared to the TD subjects.

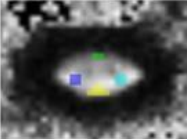


Figure 1: Regions of interest of DTI on the axial image of grayscale FA map at the different spinal cord white matter areas are shown in green (ventral region), yellow (dorsal region), dark and light blue (right and left lateral region) respectively.

Table 2: Summary of means of FA, MD, AD and RD in whole cord and white matter areas of the spinal cord cephalad and caudal (middle) to the level

of MR injury in TD pediatric subjects and subjects with chronic SCI.

		Cephalad_Middle				Caudal_Middle			
		DTI Parameters				DTI Parameters			
		FA	MD	AD	RD	FA	MD	AD	RD
Whole Cord	TD	0.544±0.068	1.161±0.136	1.925±0.187	0.778±0.142	0.527±0.087	1.121±0.314	1.784±0.395	0.790±0.289
	SCI	0.501±0.072	1.091±0.169	1.753±0.201	0.760±0.102	0.457±0.065	1.047±0.225	1.583±0.337	0.778±0.184
Ventral WM	TD	0.405±0.121	1.624±0.398	2.343±0.396	1.265±0.423	0.448±0.110	1.072±0.274	1.600±0.352	0.808±0.264
	SCI	0.363±0.109	1.376±0.325	1.926±0.371	1.102±0.332	0.324±0.115	1.173±0.250	1.569±0.293	0.976±0.256
Dorsal WM	TD	0.531±0.098	1.107±0.226	1.815±0.284	0.754±0.230	0.503±0.130	1.298±0.500	2.020±0.600	0.937±0.472
	SCI	0.554±0.123	0.960±0.194	1.622±0.266	0.629±0.207	0.449±0.102	1.135±0.346	1.702±0.420	0.852±0.325
Right_Lateral WM	TD	0.554±0.102	1.071±0.211	1.802±0.267	0.705±0.219	0.527±0.142	1.170±0.414	1.872±0.458	0.818±0.407
	SCI	0.534±0.107	0.970±0.189	1.610±0.264	0.650±0.189	0.481±0.147	0.978±0.313	1.519±0.469	0.707±0.307
Left_Lateral WM	TD	0.549±0.115	1.396±0.320	2.320±0.377	0.934±0.328	0.495±0.154	1.448±0.595	2.226±0.704	1.060±0.557
	SCI	0.490±0.097	1.272±0.235	2.038±0.331	0.889±0.232	0.477±0.102	1.165±0.406	1.815±0.574	0.841±0.341

Bold indicates that the DTI value is significantly different in subjects with SCI compared to the TD subjects.

Table 3: Summary of means of FA, MD, AD and RD in whole cord and white matter areas of the spinal cord cephalad and caudal (proximal) to the level

of MR injury in TD pediatric subjects and subjects with chronic SCI.

		Cephalad_Proximal				Caudal_Proximal			
		DTI Parameters				DTI Parameters			
		FA	MD	AD	RD	FA	MD	AD	RD
Whole Cord	TD	0.507±0.080	0.967±0.231	1.647±0.314	0.722±0.150	0.522±0.082	1.180±0.314	1.891±0.454	0.824±0.261
	SCI	0.466±0.074	1.048±0.182	1.616±0.279	0.764±0.157	0.376±0.064	1.039±0.299	1.469±0.393	0.828±0.289
Ventral WM	TD	0.408±0.095	1.076±0.377	1.693±0.411	0.900±0.282	0.425±0.104	1.184±0.331	1.737±0.410	0.908±0.317
	SCI	0.337±0.101	1.351±0.387	1.833±0.437	1.109±0.381	0.329±0.098	1.119±0.410	1.517±0.570	0.920±0.344
Dorsal WM	TD	0.505±0.104	0.968±0.273	1.688±0.382	0.738±0.224	0.502±0.136	1.297±0.479	2.038±0.602	0.926±0.442
	SCI	0.478±0.129	0.953±0.201	1.488±0.292	0.688±0.197	0.383±0.093	1.041±0.309	1.453±0.383	0.836±0.298
Right_Lateral WM	TD	0.529±0.116	0.957±0.254	1.658±0.381	0.688±0.209	0.513±0.133	1.271±0.435	2.018±0.567	0.898±0.401
	SCI	0.487±0.107	0.983±0.195	1.544±0.252	0.700±0.196	0.366±0.102	1.034±0.316	1.437±0.380	0.833±0.300
Left_Lateral WM	TD	0.482±0.121	1.174±0.382	1.992±0.479	0.916±0.304	0.496±0.128	1.472±0.598	2.208±0.783	1.055±0.525
	SCI	0.443±0.095	1.225±0.281	1.960±0.396	0.907±0.258	0.396±0.099	0.988±0.313	1.421±0.419	0.772±0.275

Bold indicates that the DTI value is significantly different in subjects with SCI compared to the TD subjects.

(Filename: TCT_O-181_ImageFile.jpg)

O-182

8:07AM - 8:14AM

Comparison of Arterial Spin Labeling (ASL) and 18F Fluorodeoxyglucose Positron Emission Tomography (FDG-PET) in Localization of Epileptogenic Focus for Pre-surgical Evaluation of Intractable Epilepsy.

R Nikam¹, V Kandula¹, A Choudhary¹, H Chugani¹
¹A I duPont Hospital for Children, Wilmington, DE

Purpose

To evaluate concordance of arterial spin labeling (ASL) and FDG-PET findings in localization of epileptogenic focus for presurgical evaluation

Materials and Methods

Sixty consecutive pediatric patients with intractable epilepsy, underwent standardized evaluation with concurrent structural MRI including ASL and FDG-PET studies for presurgical evaluation. Imaging data was acquired on 3T-GE Signa PET-MRI scanner.

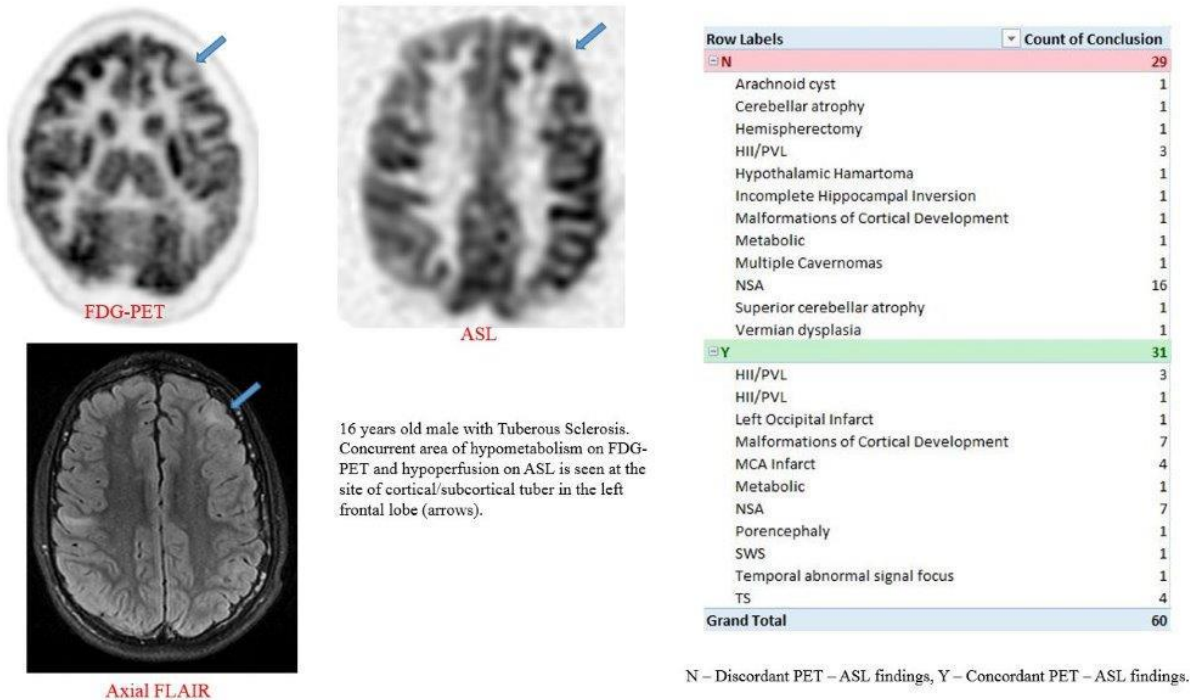
Results

Out of the 60 patients (female: 28, male: 32, mean age: 8.5 years, SD: 5.7 years), 37 patients had structural abnormality on MRI, amongst which concordant ASL and PET findings were identified in 24 patients (64.86 %). Extremely high concordance was identified with structural abnormalities such as malformations of cortical development of 87.5% (7/8), tuberous sclerosis (4/4, 100 %), and arterial infarcts (5/5, 100 %). Out of 23 patients with structurally normal MRIs, only 7 had ASL findings concordant with PET data (30.43%), amongst which 6 demonstrated normal perfusion and glucose metabolism, while one showed multifocal abnormalities on ASL and PET. Amongst remainder of 16 patients from this cohort with discordant ASL-PET findings, normal perfusion with abnormal glucose metabolism was seen in 10 (62.5%). Three patients depicting abnormal perfusion on ASL, showed normal glucose metabolism, while 3 patients demonstrated abnormalities on PET localized to contralateral hemisphere or different lobes. None of the 11 patients demonstrating hypometabolism in unilateral or

bilateral temporal lobes demonstrated abnormal perfusion. Also, there was limited evaluation of cerebellum with only one (amongst 11 FDG-PET detected abnormal metabolism) demonstrated abnormal perfusion on ASL. Overall the concordance between ASL and PET in our study is 51.67% (31/60).

Conclusions

Arterial spin labelling perfusion imaging may be helpful in localization of epileptogenic focus in patients with structural abnormalities, but fares poorly in patients with no structural abnormality, in temporal lobe epilepsy and in depiction of posterior fossa abnormalities.



(Filename: TCT_O-182_ASLEPET.jpg)

O-183

8:14AM - 8:21AM

Alternating Hemiplegia of Childhood: Voxel-Based Analysis at 3T Exploring Ictal and Interictal Disease Mechanisms

M Severino¹, D Tortora¹, L Pisciotta¹, G Morana¹, A Zicca¹, E De Grandis¹, A Rossi¹
¹Istituto Giannina Gaslini, Genova, Italy

Purpose

Alternating Hemiplegia of Childhood (AHC) is a very severe and intractable disorder, characterized by a combination of paroxysmal movement disorders and permanent neurological features. Despite the recent discovery of ATP1A3 mutations in 75% of cases, there is little knowledge about the disease pathophysiology. We aim to evaluate white-matter microstructural changes and gray-matter volume in patients with AHC and correlate them with clinical features.

Materials and Methods

Eight genetically confirmed AHC patients (6 males, 2 females, age range 10-24 years) recruited through the Italian Biobank and Clinical Registry for AHC (www.ibahc.org), and 13 controls, underwent 3T MRI with 3D T1 and diffusion-weighted imaging (64 directions). Data obtained with tract-based spatial statistics (TBSS) and voxel-based morphometry (VBM) analysis were correlated with dystonia and ataxia rating scales.

Results

Compared with the control group, patients with AHC exhibited significant volume decrease in several gray- and white-matter regions, including the frontal lobes, thalami, cerebral peduncles and cerebellum ($P=.031$). Patients with AHC presented lower fractional anisotropy (FA) values in multiple regions compared to controls ($P<.001$): centrum semiovale, corona radiata, internal and external capsules and optic radiations. Patients also demonstrated significantly lower radial diffusivity (RD) and mean diffusivity (MD) values, and increased axial diffusivity (AD) values in the same white-matter areas and at level of the corpus callosum. These findings correlated with the motor scores ($P=.02$).

Conclusions

White-matter microstructural changes and morphological alterations in the frontal regions, thalami, and cerebellum might contribute to the pathogenic mechanism of motor dysfunction in patients with AHC.

O-184

8:21AM - 8:28AM

Impaired Structural Connectivity of Frontal-Eye-Field and Posterior Parietal Cortices with Pulvinar Mediates the Impact of Prematurity on Adult Perceptual Organization

M Berndt¹, J Bäuml¹, A Menegaux¹, D Hedderich¹, C Zimmer¹, P Bartmann², M Daamen², A Wohlschläger¹, C Sorg¹

¹*Klinikum rechts der Isar, Technical University of Munich, Munich, Germany*, ²*University Hospital Bonn, Bonn, Germany*

Purpose

Premature birth impacts on adult cognitive performance including perceptual organization (PO), which depends on frontal eye field and posterior parietal cortices of the dorsal attention network (DAN). Furthermore, prematurity causes lasting changes in thalamo-cortical structural connectivity (1). We tested the hypothesis that structural connectivity between thalamus and DAN is impaired in premature born adults and mediates the impact of prematurity on PO.

Materials and Methods

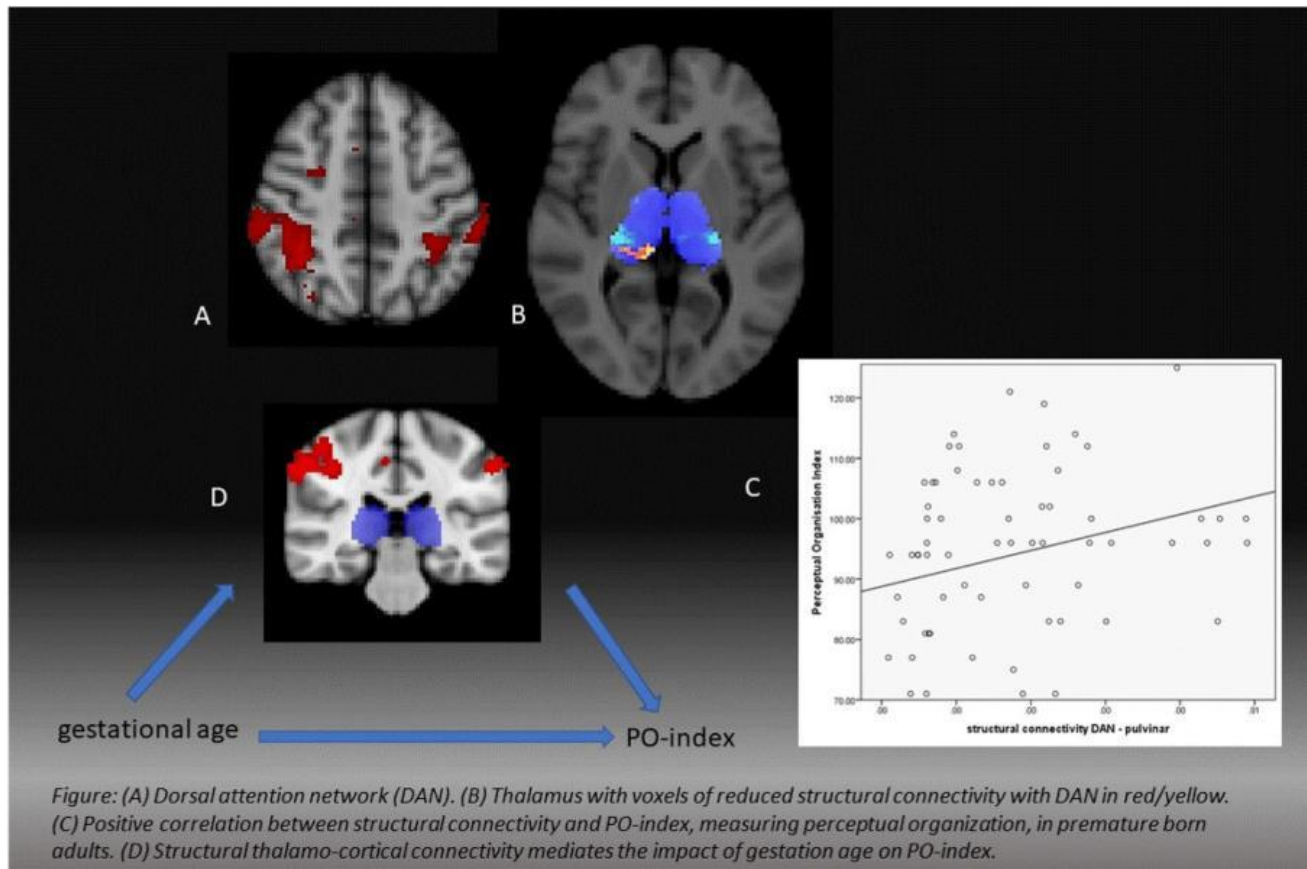
As part of the prospective Bavarian Longitudinal Study (BEST), diffusion-tensor imaging and cognitive assessment data (PO-index subscale of Wechsler Adult Intelligence Scale-III) of 70 very preterm and/or very low birth weight (male: 41; mean age: 26.6 years) and 57 term born young adults (male: 35; mean age: 26.5 years) were analyzed. The individual cortical ROI (dorsal attention network) was derived from an independent component analysis of resting-state fMRI data. Applying a probabilistic tractography algorithm, connectivity maps between DAN and thalamus were generated and compared between premature and term born adults using voxelwise t-tests. Connectivity differences were studied in relation to PO-measures for mediating effects.

Results

Premature born adults showed a significantly reduced structural connectivity between pulvinar and DAN ($p<0.05$, FWE corrected, see figure). Aberrant structural connectivity was associated with a reduced PO-index ($r = 0.27$, $p = 0.030$). In a path analytic model, thalamo-cortical connectivity significantly mediated the association between gestational age and PO.

Conclusions

We provide evidence for long-term effects of premature birth on structural thalamo-DAN connectivity in adulthood, mediating the effect of prematurity on PO. Therefore, DAN-thalamus connectivity might be a relevant target for developing specific prognostic and therapeutic concepts for premature born children's perceptual deficits.



(Filename: TCT_O-184_Figure.jpg)

O-185

8:28AM - 8:35AM

Quantitative Susceptibility Mapping (QSM) and Diffusion Kurtosis Imaging (DKI) for Detection of Early Radiation-Induced White Matter Injury in Children with Primary Brain Tumors

S Palasis¹, J Wu², D Aguilera¹, D Qiu²

¹Children's Healthcare of Atlanta, Atlanta, GA, ²Emory University School of Medicine, Atlanta, GA

Purpose

Children with brain tumors are commonly treated with whole-brain radiation therapy. However, radiation therapy can lead to several adverse effects, including neurocognitive decline. White matter has been reported to be predisposed to radiation-induced injury, which may be a major cause of neurocognitive deficits. Quantitative susceptibility mapping (QSM) and diffusion-kurtosis imaging (DKI) are techniques sensitive to microstructural changes. In this study, we aimed to evaluate the early changes of radiation-induced white-matter injury using QSM and DKI.

Materials and Methods

Seven patients with primary brain tumors (age, 12 ± 3.32 years; 3 females) requiring whole-brain radiation were included in the study. The patients underwent MR examinations before and after radiotherapy at multiple time points on a Philips Ingenia 3T scanner (Philips Healthcare, Best, the Netherlands) with a 32-channel head array coil. QSM images were acquired using a 3-D multiecho gradient-echo (GRE) sequence: FOV = 230 x 230 mm², matrix = 256 x 256, slice thickness = 1.5 mm, 108 slices, TR = 35.26 ms, first TE = 7.2 ms, 5 echoes, echo spacing = 6.2 ms. The phase image from each echo was first unwrapped using a Laplacian method followed by spherical mean filtering to remove

Oral Presentations & Excerpts

the background field to generate the filtered field map. The filtered field maps from each echo were then averaged to increase the signal-to-noise ratio. An L1-norm optimization-based method was used to reconstruct susceptibility map. DKI images were obtained. Acquired spatial resolution 2.50 x 2.55 x 2.50 (reconstructed at 2.50 isotropic), FOV: 240 x 240 x 129, 48 Slices, SENSE = 2, TR/TE = 6500/95, 64 directions, B=0, 1000, 2500. Image processing was performed using a software package developed in-house. The conventional images were reviewed blindly by two pediatric neuroradiologists. Neurocognitive testing was performed prior to radiation and at one year post radiation.

Results

The FLAIR, DWI, and SWI images were evaluated by two pediatric neuroradiologists in double-blind fashion. There was agreement that no definite radiation injury to white matter could be detected qualitatively on conventional MR imaging. On the QSM analysis, susceptibility changes could be detected as early as 6 months after radiation therapy. There were changes noted on DKI analysis but these were variable. Changes were detected on neurocognitive evaluation at one year post treatment.

Conclusions

By using QSM, we have successfully detected susceptibility changes in white matter following radiation therapy in children with brain tumors. Susceptibility in white matter increased after radiation therapy as compared to the baseline visit, possibly due to demyelination. QSM therefore could be utilized as a valuable biomarker for radiation-induced white-matter damage.

O-186

8:35AM - 8:42AM

Machine learning analysis of edge density imaging for identification of children with sensory over-responsivity

S Payabvash¹, E Palacios¹, D Cuneo¹, M Gerdes¹, A Brandes-Aitken¹, J Harris¹, J Owen¹, M Wang¹, E Marco¹, P Mukherjee¹

¹*University of California at San Francisco, San Francisco, CA*

Purpose

Sensory over-responsivity (SOR) – the destructive negative response to typically non-noxious stimuli – is currently part of the diagnostic criteria for Autism Spectrum Disorder. However, SOR is also reported in children with Attention Deficit/Hyperactivity Disorder, anxiety, and those without additional comorbid conditions. SOR is estimated to affect more than 1 in 20 children and leads to deficits in learning as well as disruption of the home and school community. There is growing interest in understanding the neural underpinnings of SOR. We use Edge-density Imaging (EDI) to evaluate structural connectomic changes in children with SOR. Then, we apply machine-learning algorithms for differentiation of children with and without SOR based on the tract-specific average Edge Density (ED) as a diagnostic imaging biomarker.

Materials and Methods

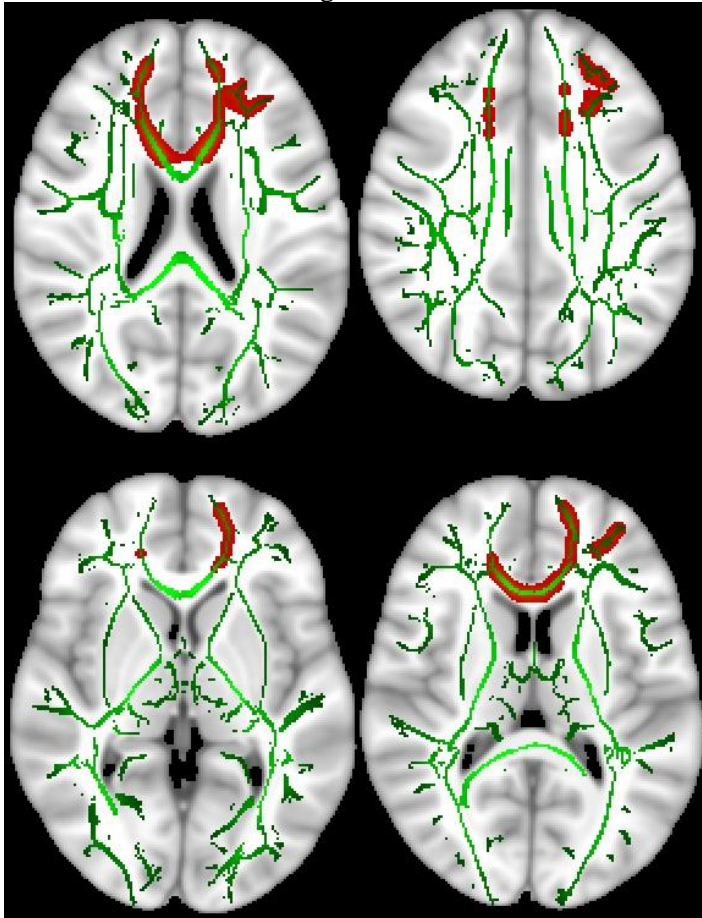
The clinical and imaging data were extracted from the Sensory Processing Disorders Consortium dataset. The ED maps were developed using DTI and high-resolution T1 scans. Tract-based Spatial Statistics (TBSS) was used for registration of post-processed ED maps onto the standardized brain space, followed by voxel-wise comparison of ED between patients with SOR versus typically developing children (TDC). Then, using the JHU ICBM-DTI-81 atlas, the average ED of each tract was calculated. Three different machine-learning methods were applied for differentiation of SOR from TDC using tract-based average ED values: support vector machines (SVM) with "linear" and "polynomial" kernels; and random forest algorithms. For all models, the cohort was randomly split into training and validation data set in a 4:1 ratio, preserving the SOR-to-TDC proportion. The random sampling was repeated 1000 times for each model and the accuracy was tested on the validation data set. In addition, we applied 10-fold cross-validation in all models.

Results

Of a total of 39 children included in our study, 15 had auditory SOR, and were compared to matched children without auditory SOR (n=24). All children were male with age range of 9 to 14. On voxel-based TBSS, children with SOR had lower ED in the anterior corpus callosum body and genu compared to TDC (Figure). Notably, there was no significant difference in distribution of the autism clinical features between the SOR and TDC groups (p=0.185). Using receiver operating characteristic (ROC) analysis, the ED of the left and right parahippocampal gyrus (ventral cingulum) could best differentiate SOR from TDC with area under curve of 0.71 (95% CI: 0.53-0.89, p=0.028), and 0.70 (95% CI: 0.52 - 0.88, p=0.035), respectively. For machine learning analyses, the training datasets included 19 TDC and 12 SOR; and validation datasets included 5 TDC and 3 SOR. The averaged accuracy for the random forest model, SVM with "linear" kernel, and SVM with "polynomial" kernel were 81%, 77%, and 73%, respectively.

Conclusions

Reduced number of connectome edges in the anterior body and genu of corpus callosum is an imaging hallmark of SOR compared to TDC. The machine-learning algorithms integrating tract-based average ED can devise accurate differentiation models for identification of children with SOR. With confirmation in larger cohorts, such connectomic imaging biomarkers can supplement clinical tools for timely diagnosis and effective treatment triage of SOR children.



(Filename: TCT_O-186_picASNRfin.jpg)

O-187

Multi-Modality PET-MRI Image Joint Reconstruction

8:42AM - 8:49AM

Oral Presentations & Excerptas

Y Xiao¹, Y Liang¹, Y Chen¹, X Ye², R Fang¹

¹University of Florida, Gainesville, FL, ²Georgia State University, Atlanta, GA

Purpose

With the recent advances in medical imaging technologies which allow simultaneous acquisition of multiple imaging modalities such as PET-CT, PET-MRI, multimodality imaging reconstruction can combine strength of different modalities for clinical diagnosis.

Materials and Methods

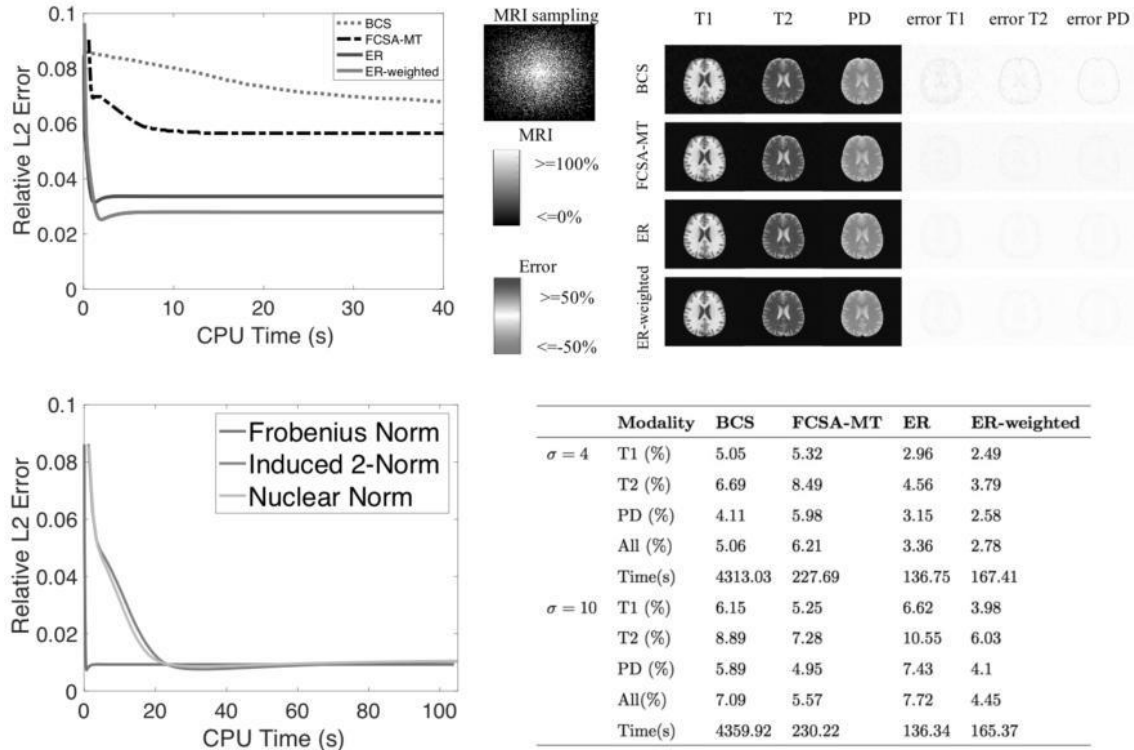
We propose a multimodality joint-edge image reconstruction method that integrates the strengths of different edge information for PET-MRI imaging. For the consideration of highly correlated images from different imaging modalities, we reformulate the standard total-variation (TV) regularization function into a vectorial total-variation (VTV) function by introducing three types of matrix norm: Frobenius norm, Induced 2-norm, and Nuclear norm. Instead of reconstructing the images directly, we reconstruct the gradient of the images for faster convergence time and lower computation complexity. Through our experiments on the clinical data, this method reduces the edge (gradient) restoration computational complexity while preserves high-image fidelity at different noise levels.

Results

The experiment compares four different reconstruction methods: Bayesian Compressed Sensing (BCS), Fast Composite Splitting Algorithm for Multicontrast MRI (FCSA-MT), the proposed Edge Reconstruction (ER), and the proposed Edge Reconstruction Weighted by Covariance (ER-weighted). Figure 1 demonstration of the benefits of the proposed method regarding the relative l2 error over CPU time with noise level $\sigma=4$. Figure 2 shows the comparison between 3 norm methods. Figure 3 visualizes the reconstructed images as well as the errors for different methods when $\sigma=4$. Table 1 presents the overall quantitative results. All these results confirm the advancement of the reconstructing the edges in the gradient space.

Conclusions

Our suggested method produces a critical decrease in processing speed and a significant reduction in relative error. Therefore, this is an efficient and high-fidelity image reconstruction method for multimodality data.



(Filename: TCT_O-187_figure.jpg)

O-188

8:49AM - 8:56AM

Comparing efficacy of different paradigms utilized for language mapping in pediatric functional MRI studies

K Shekdar¹, R Golembski¹, D Zarnow¹, A Vossough¹, E Schwartz¹, T Roberts¹
¹Children's Hospital of Philadelphia, Philadelphia, PA

Purpose

To compare the efficacy of different paradigms utilized for language mapping in pediatric functional MRI studies

Materials and Methods

We retrospectively reviewed clinical fMRI studies performed at our institute from 2008 to November 2017 for language mapping. The commonly used paradigms for language mapping included picture naming, verb generation, auditory decision task (ADT) often called 'semantic decision task', categorization, reading, and passive listening tasks. Activation was determined with the general linear model. Task performance was monitored by the MRI technologist using button box recording and direct observation, and it was confirmed that the patient performed the task appropriately. Areas of BOLD activation in response to the various tasks were analyzed. Significance testing was performed to assess differences in reliability between different fMRI testing paradigms. All fMRI studies were performed on a 3T Siemens Verio™ scanner. Primary fMRI post processing was done on Siemens Leonardo postprocessing workstation. A commercially available postprocessing software with augmented motion correction/GLM capabilities was also used in conjunction.

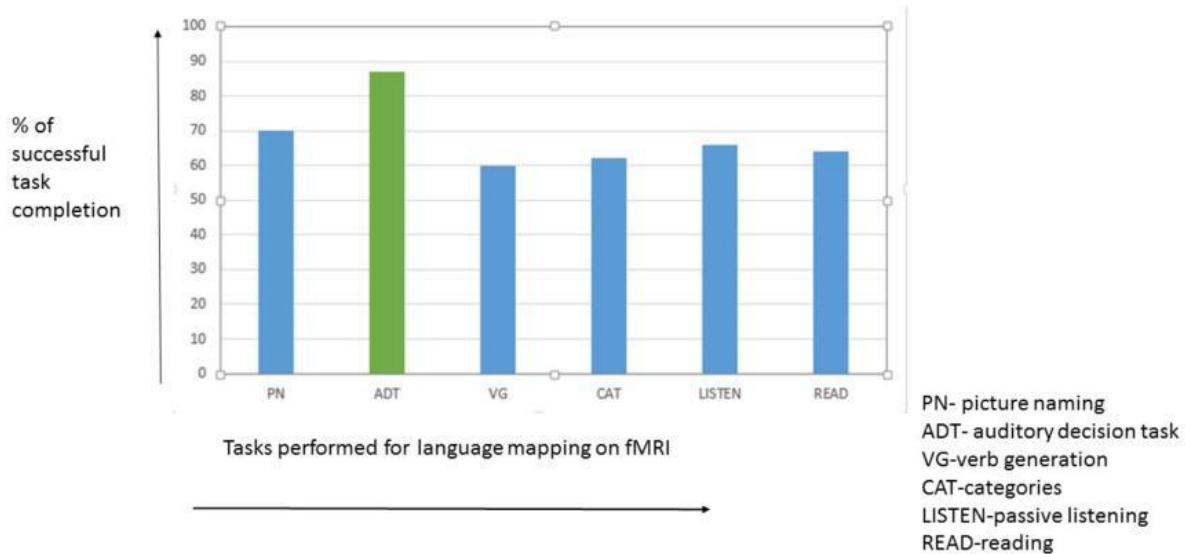
Results

A total of 39 clinical fMRI studies were referred for language localization in the time period of the study. Of the 39 studies 18 were for mass lesions, predominantly tumors, and six were for vascular lesions. The

other main indication was medically refractory epilepsy being considered for surgery. Qualitative BOLD response analysis in response to the various tasks for language localization revealed consistently robust activation to ADT testing. The relative utility of each test on the panel used for language mapping is shown in the accompanying graph. ADT - 'auditory decision task', often called 'semantic decision task' had highest utility. PN - picture naming scored better in patients with developmental delay. The patients above 10 years of age consistently did better on ADT.

Conclusions

A panel of tasks is recommended to reliably identify language localization and various components of language function in children. However, in our experience the utility of ADT in the panel of tests had consistent information qualitatively and quantitatively and PN was useful in the subset of patients with developmental delay. Performing fMRI studies in pediatric patients presents a unique set of challenges and limitations. The high yield of ADT and PN tasks merit a higher chronological order in the language test panel.



(Filename: TCT_O-188_fMRIgraph.jpg)

Tuesday, June 5, 2018

10:30AM - 12:00PM

Parallel Paper Session: Policy and Quality

O-189

10:30AM - 10:37AM

Contemporary National Trends for Head CT use in Emergency Department: Insights from National Hospital Ambulatory Medical Care Survey (NHAMCS) 2007-2014

P Dubey¹, A Saxena², J Weintraub³, G Moonis³, A Lignelli³, a khandji⁴, K Nasir²

¹Scarsdale, NY, ²Baptist Health South Florida, Coral Gables, FL, ³Columbia University Medical Center, New York, NY, ⁴Columbia Presbyterian Medical Center, Rye, NY

Oral Presentations & Excerpts

Purpose

There is increasing computed tomography (CT) utilization in emergency departments (ED) over the years. (1) Head CT is one of the highly utilized modalities, raising concerns regarding cost and radiation exposure. However, recent trends, disparities and primary determinants of utilization for head CT use in ED are not well understood. In this study, we aim to describe contemporary nationwide trends associated with head CT use among patients presenting to ED settings.

Materials and Methods

We undertook an analysis of the 2007-2014 National Hospital Ambulatory Medical Care Survey (NHAMCS), a nationally representative survey of U.S. ED encounters, with a primary goal to assess the rate of ED visits, factors and leading reasons for head CT use.

Results

The NHAMCS database is a cross-sectional survey of ED visits ranging from 35,490 in 2007 to 23,844 in 2014, representing 117 million and 141 million ED visits in respective years. Head CT represented 48.4% (95% CI: 46.0-50.9%) of all CT performed in ED in 2007; the respective proportions were 48.2% (95% CI: 46.0-50.5%) in 2014. The 2007 annual head CT rates among all ED visits were 6.7% (95% CI: 6.1-7.3%) that peaked at 8.0% (95% CI: 7.4-8.5%) in 2010 and decreased to 7.1% (95% CI: 6.4-7.8%) in 2014. A higher head CT rate utilization in ED was noted in the elderly, non-Hispanic whites, non-Medicaid patients, midwest/south region and urban hospitals. In 2007, the 3 leading reasons for visits among patients receiving head CTs in the ED were trauma (20.9%; 95% CI: 18.5 - 23.4), headache (13.1%; 95% CI: 11.3 - 14.9), and dizziness/syncope (9.6%; 95% CI: 7.9-11.2), which was responsible for 47% head CT's in 2014.

Conclusions

In summary, head CT is performed in nearly 1 in 14 of all ED visits representing 50% of all CT performed in these settings. Overall utilization rates have remained relatively stable from 2007 to 2014 with injuries, headache and dizziness/syncope responsible for nearly half of all head CT's. These insights will support pragmatic discussion among policy makers for facilitating evidence-based use of head CT in appropriate candidates.

	Y2007	Y2008	Y2009	Y2010	Y2011	Y2012	Y2013	Y2014
TOTAL ED VISITS (MILLIONS)	117.00	127.00	136.00	130.00	136.00	131.00	130.00	141.00
TOTAL ED VISITS WITH ANY CT PERFORMED IN ED (MILLIONS)	16.20	18.10	19.50	21.30	21.50	20.10	20.20	21.00
TOTAL ED VISITS WITH HEAD CT PERFORMED IN ED (MILLIONS)	7.80	9.00	9.70	10.30	10.60	9.30	9.40	10.00
PROPORTION OF ED VISITS WITH HEAD CT PERFORMED % (95% CI)	48.4% (46, 50.9)	49.6% (47.5, 51.7)	49.6% (47, 52.2)	48.6% (46.6, 50.6)	49.1% (47.1, 51)	46.4% (44.1, 48.7)	46.5% (44.4, 48.6)	48.2% (46, 50.5)

(Filename: TCT_O-189_ASNRNHMACSheadCT2.jpg)

Trends on Head CT and MRI Use in Emergency Department Visits for Stroke and Transient Ischemic Attack: Insights from National Hospital Ambulatory Medical Care Survey (NHAMCS) 2007-2014

P Dubey¹, A Saxena², J Weintraub¹, G Moonis², A Lignelli², A Khandji³, K Nasir²

¹*Columbia University Medical Center, New York, NY*, ²*Baptist Health South Florida, Coral Gables, FL*, ³*Columbia Presbyterian Medical Center, Rye, NY*

Purpose

Head computed tomography (CT) is a critical component of stroke/transient ischemic attacks (TIA) evaluation in emergency departments (ED). In addition, recently there has been increasing emphasis on added utility of MRI. Neuroimaging remains a cornerstone towards meeting regulatory requirements for comprehensive stroke center certification. However, despite well-defined guidelines for neuroimaging use in Acute Stroke evaluation, there is wide variability in utilization, which is not fully understood. In this study, we aim to comprehensively detail contemporary national utilization rates and disparities for head CT/MRI in routine emergency department stroke care.

Materials and Methods

We undertook an analysis of National Hospital Ambulatory Medical Care Survey (NHAMCS), a nationally representative survey of U.S. ED encounters representing 1,045 million ED visits for the 2007-2014 time period. We analyzed all stroke/TIA visits for patients 18 years or older identified using the ICD-9-CM (Reference One) codes of 433.XX-436.XX. For both head CT and MRI rates, we report proportions of use for each interval after pooling the survey data into 6 two-year intervals (2007-08, 2009-10, 2011-12, 2013-14).

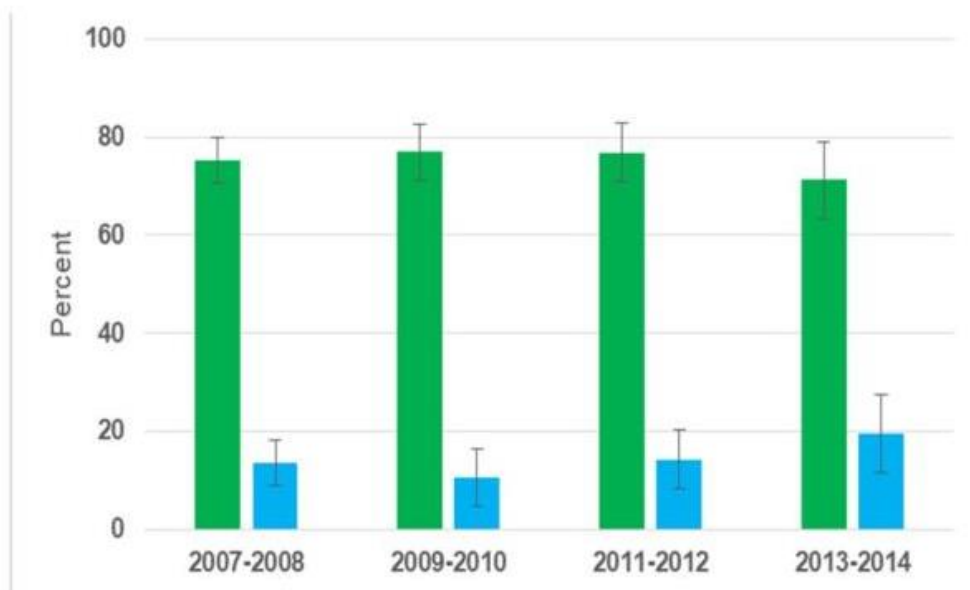
Results

We identified 1,045 million ED encounters for the 2007-2014 time period. Once in the ED, for stroke/TIA, head CT was performed in 75.2% (95% CI: 72.3-78.1) with rates ranging from 75.3% (95% CI: 70.6-79.9%) in 2007-08 to 71.3% (95% CI: 63.4-79.1%) in 2013-14 among stroke patients. Conversely rate of head MRI increased significantly over the time period from 13.5% (7.8-19.1%) to 19.6% (95% CI: 13.6-25.5%). Majority of those head MRI also received head CT (61% in 2007-08 vs 74% in 2013-2014). In adjusted analysis private insurance was independently associated with a higher head CT use, whereas urban hospitals and western U.S. regions were independently associated with higher MRI rates in ED setting patients presenting with stroke/TIA.

Conclusions

In summary, utilization of head CT seen in nearly three quarters of ED visits among stroke/TIA patients has remained stable in recent years. Conversely, MRI utilization for stroke/TIA has increased to nearly 1 in 5 patients in 2014. These insights provide opportunities to standardize care processes to enhance efficiency of existing stroke care in ED settings.

HEAD CT AND MRI RATES AMONGST STROKE/TIA PATIENTS , NHAMCS (2007-2014)



(Filename: TCT_O-190_ASNRStrokeRate2.jpg)

O-191

10:44AM - 10:51AM

Clinical Utility of a Brain MRI After a Negative Head CT in the Emergent Setting

J ALchammas¹, K Tech²

¹Beaumont Hospital, Royal Oak, MI, ²Beaumont Health at Royal Oak, Royal Oak, MI

Purpose

Obtaining a brain MRI (BMRI) after a negative head CT (HCT) in the Emergency Room (ER) setting is time consuming, expensive and often not clinically helpful. Based on clinical experience, many of the BMRI ordered after a negative HCT are not needed, as the BMRI is often negative. No data is available on this topic from a PubMed literature search.

Materials and Methods

Retrospective review of an institutional database of 27,792 patients who underwent either a HCT or BRMI in the ER from November 2015 to November 2017 yielded the records of 1,272 patients (4.6%) who underwent a BRMI after a negative HCT. A negative HCT was defined as a stable old finding(s) from prior HCT/BMRI, sinus disease or senescent changes. The most common indications for ordering a BRMI after a negative HCT was for altered mental status, headache, stroke-like symptoms and dizziness, which constituted 1008 patients (79%). Imaging findings and patient demographics were obtained from the electronic medical record.

Results

The study age range was 18-89 year-olds, and the mean patient age was 64 years. The 1,023 patients (80%) that had a negative HCT did not have positive correlate on the BMRI. The remaining 249 patients (20%) had a negative HCT finding but a positive finding on BMRI. A positive finding on the BMRI was defined as an acute/subacute stroke, new brain lesion, venous thrombosis or a cerebral arterial aneurysm. Within these 249 patients, 82 patients (33%) had an emergent finding such as an acute/subacute stroke or a venous thrombosis. The remaining 167 patients (67%) had nonemergent finding(s) such as small cerebral arterial aneurysm.

Oral Presentations & Excerpts

Conclusions

Obtaining a BMRI after a negative HCT in the ER setting is often not clinically helpful as 80% of these patients had no significant finding on the BMRI after a negative HCT. Therefore, a stringent criterion should be developed to determine who should get a BMRI after a negative HCT to ensure appropriate use of healthcare resources.

O-192

10:51AM - 10:58AM

Effective and Ineffective Tools in Increasing Referring Providers' Utilization of Radiology Clinical Decision Support

M Keiper¹, D Moore¹, C Harvey¹, S Osborn¹, J Pelz¹

¹*University of Nebraska Medical Center, Omaha, NE*

Purpose

To determine the baseline utilization of radiology decision-support software by referring clinicians, and demonstrate potential effective tools in improving mandated use of decision-support software

Materials and Methods

Clinical decision support (CDS) was provided for referring providers over a one-year period. Initially, providers were permitted to either utilize a discrete clinical support indication or bypass CDS by manually entering a free text indication for the imaging study. Percent utilization of CDS indications vs. free text indications was recorded over an initial 3-month period and subdivided by ordering type (All Users, Provider, and Nonprovider). Percent utilization of CDS indications was also recorded after two separate time-intensive medical center wide educational interventions encouraging providers to use discrete CDS indications at 6 months and 9 months after offering CDS. Subsequent to these interventions, an updated abridged set of discrete CDS indications were released significantly streamlining and decreasing the number of indication options from which to select. In addition, the free text option was removed and replaced with an "other" field, which required an additional mouse click to provide pertinent history and potential free text indications. Percent utilization of discrete CDS indications was recorded after this final intervention.

Results

Percent utilization of discrete CDS indications was approximately 30% for all providers six months after initiation of the program. After the medical center-wide educational interventions to referring providers, percent utilization remained at 30%. After the final interventions of generating more streamlined discrete CDS indications, removing the free text field and increasing the steps necessary to enter free text indications, percent utilization of discrete CDS indications improved to approximately 50% based on initial short-term results.

Conclusions

Utilization of discrete CDS indications by referring providers will likely remain low despite time and labor intensive educational programs promoting its use. Streamlining the process of using CDS software for referring clinicians while limiting the access to free text indications will likely be an effective tool in increasing the mandated use of CDS while still providing useful communication of pertinent patient history to the radiologist.

O-193

10:58AM - 11:05AM

Steering the Course to Success in Outpatient Imaging and Inpatient Throughput in a Large Academic Medical Center

M Keiper¹, J Pelz¹, C Harvey¹, D Moore¹, S Osborn¹

¹*University of Nebraska Medical Center, Omaha, NE*

Oral Presentations & Excerptas

Purpose

To demonstrate the utility and effectiveness of steerage of outpatient imaging to underutilized ambulatory imaging centers in order to improve overall equipment utilization and decrease delays in inpatient imaging in an academic medical center

Materials and Methods

All outpatient ambulatory imaging was actively directed to three outpatient imaging centers and away from the main campus of an academic medical center over a six-month period. Emphasis on steerage was on CT and MRI patients but involved all imaging modalities. Patients and referring clinicians were given the option to remain at the main campus for imaging but were strongly encouraged to schedule at outpatient centers. Concurrent with steerage, scheduling of inpatient exams with reserved imaging time slots at the main campus was instituted in order to guarantee timely access for inpatient imaging. Change in utilization of outpatient imaging centers and wait times for inpatient imaging were measured for all modalities.

Results

Steerage of outpatient imaging to outpatient imaging centers at the time of scheduling was highly successful with increase in overall utilization of the outpatient centers by a mean of 80% with a range of 21-200% over a six-month period. Corresponding decreases in utilization were also noted on the main campus but not to a similar degree. Dedicated scheduled time slots for specific inpatients within the outpatient schedule at the main campus was accomplished. The decreased imaging utilization and institution of patient specific scheduled time slots at the main campus for inpatients resulted in a mean decrease in waiting time for a radiology exam of approximately seven hours for inpatients.

Conclusions

Active steerage of outpatient imaging in a large academic medical center can be a highly effective manner in which to increase utilization and profitability of free-standing imaging centers. By improving imaging availability on the main campus of the medical center and actively scheduling inpatients in specific time slots, a significant decrease in imaging delays of inpatients may also be realized and lead to improved patient care and bed management at a large medical center.

O-194

11:05AM - 11:12AM

Results of the Second Comprehensive Survey of the United States' Neuroradiology Workforce

J Chen¹

¹*San Diego VA/University of California San Diego Medical Center, La Jolla, CA*

Purpose

To report the results of the second comprehensive survey of the neuroradiology work environment and its effects in the setting of continued increases in workload within the U.S.

Materials and Methods

A voluntary online survey was sent to the U.S. membership of the ASNR consisting of 45 questions relating to the neuroradiology work environment. Measures included type of work and call, length of workday, self-reported burnout symptoms, participation in teaching, mentoring, research/publications, and other nonclinical activities. Trends in compensation, perceived interpretation and report quality, communication of abnormal results, and intention of early retirement or career changes were also surveyed.

Results

Partial results reported for space: 412 practicing neuroradiologists (80% male) responded to the survey, with a broad range of respondents in years of practice; 56% reported teaching responsibilities with trainees; 48% reported full subspecialty neuroradiology practice; 67% reported increased RVU workload, while 50% reported longer workdays; 71% reported reading more cases per hour. Regarding interpreting

Oral Presentations & Excerpts

cases faster than optimal, largest percentage of respondents responding frequently or always was in the mid-Atlantic region (49%), greater in later career (42%), and greater in women (49%); 31% never or rarely signed reports faster than needed for optimal clarity; 57% sometimes, frequently or always made errors due to productivity pressures. Symptoms of burnout ranged between 45-76% across four measures. Mean scores on burnout were least in the West (56%). For teaching, mentoring, research/publications, a mean of 82% reported significant cutbacks. For practice-building activities, 69% reported significant cutbacks; 37% reported intention to retire early as somewhat or very likely.

Conclusions

Workload demands have had negative effects on the quality of the work environment, the ability and desire of radiologists to perform key clinical, academic or practice-building duties and the symptoms of burnout with variability based on geographic location, gender, practice type and location.

O-195

11:12AM - 11:19AM

Influences for Gender Disparity in Academic Neuroradiology

M Ahmadi¹, K Khurshid¹, P Sanelli², S Jalal¹, T Chahal³, M Castillo⁴, F Khosa¹

¹Vancouver General Hospital, Vancouver, British Columbia, Canada, ²Northwell Health, Manhasset, NY, ³University of British Columbia Faculty of Medicine, Vancouver, British Columbia, Canada, ⁴University of North Carolina at Chapel Hill, Chapel Hill, NC

Purpose

In this study, our aim was to quantify sex representation in neuroradiology faculty rankings and determine any related factors that may contribute to any such disparity.

Materials and Methods

We evaluated the academic and administrative faculty members of neuroradiology divisions for all online listed programs in the U.S. and Canada. After excluding programs that did not fulfill our selection criteria, we generated a short list of 85 U.S. and eight Canadian programs. We found 465 faculty members who met the inclusion criteria for our study. We used Elsevier's SCOPUS for gathering the data pertaining to the publications, H-index, citations, and tenure of the productivity of each faculty member.

Results

Sex disparity was insignificant when analyzing academic ranks. There are more men working in neuroimaging relative to women ($X^2 = 0.46$; $P = .79$). However, sex disparity was highly significant for leadership positions in neuroradiology ($X^2 = 6.76$; $P = .009$). The median H-index was higher among men faculty members (17.5) versus women faculty members (9). Women faculty members have odds of 0.84 compared with men faculty members of having a higher H-index, adjusting for publications, citations, academic ranks, leadership ranks, and interaction between sex and publications and sex and citations (9).

Conclusions

Neuroradiology faculty members follow the same male sex predominance seen in many other specialties of medicine. In this study, issues such as mentoring, role models, opportunities to engage in leadership/research activities, funding opportunities, and mindfulness regarding research productivity are explored.

Table 1: Description of baseline characteristics for neuroimaging faculty in North America

Variables	Men	Women	Total Available Numbers
Total population, no. (%)	358 (76.9)	107 (23.01)	465 (100)
Academic ranks, no. (%)			
Assistant professors	169 (75.11)	56 (24.89)	225 (100)
Associate professors	95 (76.61)	29 (23.39)	124 (100)
Professors	77 (78.57)	21 (21.43)	98 (100)
Leadership, no. (%)			
Heads, chiefs, chairs, and directors	56 (91.8)	5 (8.2)	61 (100)
Second in Command: Associate chiefs, vice chairs, deputy directors	7 (63.6)	4 (36.36)	11 (100)
Citations	USA	Canada	
Assistant professors	n = 110	n = 29	n = 139
Median	103.5	53	96
Range	0–4935	2–4507	0–4935
Associate professors	n = 71	n = 23	n = 94
Median	292	376	301.5
Range	0–15039	4–7871	0–15039
Professors	n = 61	n = 19	n = 80
Median	2065	1081	1745
Range	22–21708	0–9548	0–21708
Publications			
Assistant professors	n = 128	n = 34	n = 162
Median	12	12.5	12
Range	1–144	2–245	1–245
Associate professors	n = 80	n = 24	n = 104
Median	23	28.5	23.5
Range	2–349	2–177	2–349
Professors	n = 70	n = 20	n = 90
Median	81.5	55	72
Range	5–460	3–285	3–460

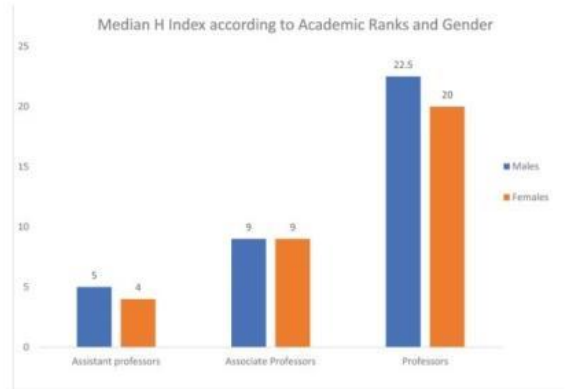


FIG 1. Distribution of median H-index according to academic ranks and sex.

(Filename: TCT_O-195_Table.jpg)

O-196

11:19AM - 11:26AM

LONGEVITY AS THE MEASURE OF HEALTHCARE BENEFIT COMPARING THE CANADIAN VERSUS UNITED STATES (US) HEALTH CARE SYSTEMS: COST, COMPLEXITY, INSURANCE COVERAGE AND NUMBER OF CT AND MRI UNITS INSTALLED: AN INCOMPLETE TRUTH?

H Valand¹, O Chohan², S Chu³, R Tu⁴

¹American University of Integrative Sciences, Toronto, Ontario, Canada, ²Christiana Care Health System, Newark, DE, ³Vancouver General Hospital, Bellevue, WA, ⁴The George Washington University, Washington, DC

Purpose

To compare uninsured rates, cost, intensity and availability of radiology resources and outcomes in Canada versus the U.S.

Materials and Methods

Population and utilization of radiology services data was obtained through publicly available sources such as Organization for Economic Cooperation and Development, Center for Disease Control, Stats Canada and National Institute of Health.

Results

In the U.S., there are 28.2 million uninsured, which is nearly equivalent to the entire population of Canada. Canada offers a health care system accessible to all though associated with prolonged wait time for diagnostic imaging studies, especially MRI. In 2015 there were 9.48 MRI units: 1,000,000 people in Canada, versus 38.96 MRI units: 1,000,000 in the U.S. In Canada 55 MRI scans per 1000 inhabitants versus 96 scans per 1000 inhabitants in the U.S. were completed (see table).

Conclusions

U.S. and Canadian health care systems are a topic of heightened discussion, particularly as the U.S. is reassessing coverage for the un- and under-insured. The differences between the uninsured, cost, MRI and CT units and utilization versus outcome are discordant with longevity. Clearly there are other variables such as population, case mix and social determinants of health that must be considered in the discussion between the two systems. Though life expectancy may be viewed as the measure of effectiveness of a

system, cost, availability and radiology resource use intensity are at first glance discordant. Considerations as immigration rates and composition, firearm associated injuries, narcotic overdose and other social determinants of health must be included in any discussion for an accurate comparison between the two systems.

COMPARISON OF COMPUTED TOMOGRAPHY (CT) SCANNER UTILIZATION IN CANADA VS USA				
		Scans	Canada	USA
Total CT Usage (Hospital + Ambulatory + Other)		Total Number (M)	5.68	82
		Per 1000 people	156.6	253.8
		Per Scanner	10561.9	6062.8
CT Usage	CT Exams in Hospitals Setting	Total Number (M)	5.61	65.7
		Per 1000 people	154.4	203.3
		Per Scanner	8973.8	7373.7
	CT Exams in Ambulatory Care Setting	Total Number (M)	79,261	16.3
		Per 1000 people	2.2	50.4
		Per Scanner	2735.3	3532

COMPARISON OF MAGNETIC RESONANCE IMAGING (MRI) SCANNER UTILIZATION IN CANADA VS USA				
		Scans	Canada	USA
Total MRI Usage (Hospital + Ambulatory + Other)		Total Number (M)	2.03	39
		Per 1000 people	55.9	120.7
		Per Scanner	5946.9	3287
MRI Usage	MRI Exams in Hospitals Setting	Total Number (M)	1.8	16.5
		Per 1000 people	49.4	51.1
		Per Scanner	6485.6	3064.1
	MRI Exams in Ambulatory Care Setting	Total Number	234308	22.5 M
		Per 1000 people	6.5	69.6
		Per Scanner	3170.9	3471.2

M = in Million

(Filename: TCT_O-196_Canada-Vs-US-Table-1.jpg)

O-197

11:26AM - 11:33AM

SOCIAL DETERMINANTS OF HEALTH (SDH): AN ESSENTIAL ELEMENT IN THE MEASURE OF BENEFIT VERSUS COST OF NEURORADIOLOGY IN CANADA VS UNITED STATES (US).

H Valand¹, O Chohan², S Chu³, R Tu⁴

¹American University of Integrative Sciences, Toronto, Ontario, Canada, ²Christiana Care Health System, Newark, DE, ³Vancouver General Hospital, Bellevue, WA, ⁴The George Washington University Hospital, Washington, DC

Purpose

To define, compare and account for the social determinants of health influencing health care, cost vs. outcomes between Canada and the U.S.

Materials and Methods

Population and utilization of radiology services data was obtained through publicly available sources such as Organization for Economic Cooperation and Development, Stats Canada, National Institute of Health, Department of Justice, Canada and Global Health Data Exchange.

Results

1. Immigration: 90% vs. 68% immigrants from countries with little/no health care comparing the U.S. vs. Canada (see table). 2. Resources: Magnetic resonance (MR) units per million people increased from 1.4 to 9.5 in Canada, compared to 10.5 to 39 in the U.S. The number of computed tomography (CT) units per

Oral Presentations & Excerptas

million people in Canada increased from 8 to 16, compared to an increase from 24 to 41 in the U.S. (see table). 3. Selected Social Determinants of Health: 2,458 opioid-related deaths per year in Canada vs. 33,091 in the U.S.; 604 homicide-related deaths in Canada per year vs. 13,455 in the U.S.; 179 firearm-related deaths per year in Canada vs 9,616 in the U.S.

Conclusions

The U.S. and Canadian health care differences between the number of un- and under-insured citizens, geography, heritage, language, and culture are well known. Canadians access a publicly funded universal healthcare system, whereas, U.S. patients access a complex multipayer system with care generally provided through either employer-sponsored private insurance or a government income- (Medicaid) or age- (Medicare) based system. Each country has a differing number of MR and CT installed units and utilization. At first glance Canadians paradoxically live slightly longer compared to their U.S. neighbor. The apparent discrepancy between resources, spending and outcome is accountable by adjusting for Social Determinants of Health (SDH), defined by the World Health Organization as conditions in which people are born, grow, live, work and age. Differing SDH variables as immigration rates, immigrant composition, firearm-related injury and drug-related death account for the benefit of radiology services, health care costs and health outcomes (life expectancy). Our work is the first to introduce the term "Social Determinants of Health" in the narrative of health policy and the radiology literature. SDH is an essential variable to include in an accurate comparison of Canadian vs. U.S. health care.

Vital & Economic Statistics		
	Canada	US
Population (million) ^a	35.8	320.9
Uninsured (% of population) ^b	0	9
Average Life Expectancy (years) ^c	82.1	78.7
Per Capita Health Care Spending (in US\$) ^{d,e}	4,734	9,990
Total Health Care Spending (in US\$) ^{d,e}	170 billion	3200 billion
Total Health Care Spending (% of GDP) ^{d,e}	11.4	17.8
Selected Social Determents of Health		
Number Opioid Related Deaths ^{f,g}	2,458	33,091
Total Death by Homicide ^{h,i}	604	13,455
Homicide by Firearm ^{h,i}	179	9616

a. https://data.worldbank.org/indicator/SP.POP.TOTL?end=2016&locations=US-CA&start=1960&view=chart&year_high_desc=false. Accessed Dec. 7, 2017.

b. [https://www.kff.org/other/state-indicator/total-population/?dataView=1&activeTab=graph¤tTimeframe=0&startTimeframe=3&selectedDistributions=uninsured&sortMModel=%7B%22colId%22:%22Location%22,%22sort%22:%22asc%22%7D](https://www.kff.org/other/state-indicator/total-population/?dataView=1&activeTab=graph¤tTimeframe=0&startTimeframe=3&selectedDistributions=uninsured&sortModel=%7B%22colId%22:%22Location%22,%22sort%22:%22asc%22%7D). Accessed Dec. 7, 2017.

c. <https://data.worldbank.org/indicator/SP.DYN.LE00.IN?locations=CA-US>. Accessed Dec. 7, 2017.

d. <https://www.cihi.ca/en/national-health-expenditure-trends#data-tables>. Accessed Dec. 7, 2017.

e. National Center for Health Statistics. Health, United States, 2016: With Chartbook on Long-term Trends in Health. Hyattsville, MD. 2017.

f. <https://www.canada.ca/en/health-canada/services/substance-abuse/prescription-drug-abuse/opioids/national-report-apparent-opioid-related-deaths.html>

g. <https://www.cdc.gov/mmwr/volumes/65/wr/mm655051e1.htm>

h. <http://www.statcan.gc.ca/tables-tableaux/sum-som/101/cst01/legal01-eng.htm>

i. https://ucr.fbi.gov/crime-in-the-u.s/2015/crime-in-the-u.s.-2015/tables/expanded_homicide_data_table_7_murder_types_of_weapons_used_percent_distribution_by_region_2015.xls

(Filename: TCT_O-197_SDH-Table1.jpg)

O-198

11:33AM - 11:40AM

Low Back Pain and Cancer: Are We Imaging in a Timely Manner?

Oral Presentations & Excerptas

P Dougherty¹, L Gold¹, P Heagerty¹, D Kallmes², K James¹, K Sherman³, P Luetmer², E Meier¹, B Griffith⁴, D Nerenz⁴, J Friedly¹, A Avins⁵, R Deyo⁶, J Jarvik¹

¹University of Washington, Seattle, WA, ²Mayo Clinic, Rochester, MN, ³Kaiser Permanente Washington, Seattle, WA, ⁴Henry Ford Health System, Detroit, MI, ⁵Kaiser Permanente Northern California, Oakland, CA, ⁶Oregon Health Sciences, Portland, OR

Purpose

Low back pain is a frequent reason why patients visit primary-care providers (PCP). Obtaining imaging for lower back pain (LBP) is usually not indicated in the first 6 weeks. However, most guidelines recommend not delaying imaging for patients with a history of cancer. Our aim is to determine the timing of imaging for primary-care patients with a cancer history who present with a new episode of care for LBP.

Materials and Methods

Using patients enrolled in the Lumbar Imaging with Reporting of Epidemiology (LIRE) study, we retrospectively identified patients with a prior diagnosis of cancer who developed LBP after at least six months without a LBP-related visit. Using Current Procedural Terminology (CPT) codes we determined whether PCPs obtained lumbar spine imaging within two and six weeks after visits with International Classification of Diseases (ICD), 9th and 10th editions, indicating LBP.

Results

Of the 238,232 LIRE patients, 5740 had a history of cancer with at least six months without a LBP related visit. Subsequently, 4854 then had a LBP visit. Of these, 801 (17%) were not imaged within two weeks and 447 (9%) were not imaged at six weeks. Younger patients (P=0.008) and women (P=0.02) were less likely to be imaged early.

Conclusions

Most patients with histories of cancer appropriately received early imaging for their LBP; however, a sizable number of individuals did not. One limitation of our study was our ability to ascertain symptom chronicity.

	NO imaging within 2 weeks n=801 (17%)	Imaging within 2 weeks n=4053 (83%)	Chi-Square p-value	NO imaging within 6 weeks n=447 (9%)	Imaging within 6 weeks n=4407 (91%)	Chi-Square p-value
Site						
1	77 (24%)	247 (76%)	0.002	41 (13%)	283 (87%)	0.06
2	587 (16%)	3066 (84%)		332 (9%)	3321 (91%)	
3	72 (14%)	427 (86%)		36 (7%)	463 (93%)	
4	65 (17%)	313 (83%)		38 (10%)	340 (90%)	
Image Modality (Column percent)						
X-ray	--	3406 (84%)		--	3625 (82%)	
CT	--	85 (2%)	--	--	108 (2%)	--
MRI	--	537 (13%)		--	641 (15%)	
PET-CT	--	7 (0.2%)		--	11 (0.3%)	
Bone Scan	--	18 (0.4%)		--	22 (0.5%)	
Male	345 (16%)	1861 (84%)		180 (8%)	2026 (92%)	0.02
Female	456 (17%)	2192 (83%)	0.14	267 (10%)	2381 (90%)	
Race						
Black	86 (18%)	380 (82%)		44 (9%)	422 (91%)	
White	624 (16%)	3169 (84%)	0.38	349 (9%)	3444 (91%)	0.98
Other	91 (15%)	504 (85%)		54 (9%)	541 (91%)	
Hispanic Ethnicity	87 (18%)	396 (82%)	0.35	51 (11%)	432 (89%)	0.28
Non-Hispanic Ethnicity	714 (16%)	3657 (84%)		396 (9%)	3975 (91%)	

(Filename: TCT_O-198_AbstractTable.jpg)

O-199

11:40AM - 11:47AM

Effect of a standardized reporting tool on the rate and concordance of management recommendations for incidental thyroid nodules on CT and MRI.

M Buller¹, L Alhilali¹

¹Barrow Neurological Institute, Phoenix, AZ

Purpose

To assess the effect of the implementation of a standardized reporting tool on the rate of appropriate management recommendations for incidental thyroid nodules (ITNs).

Materials and Methods

In June 2015, our institution implemented a standardized reporting tool for ITNs. The reporting radiologist first selects the tool from a toolbar above the report. The radiologist then selects the

Oral Presentations & Excerpts

appropriate category of thyroid nodule from a list, which automatically inserts the appropriate recommendation into the report. The categories are derived from the different management branch points of the ACR Incidental Thyroid Findings Committee white paper (1) and a short description defining the category is provided in the selection list. CT and MRI radiology reports with management recommendations for thyroid nodules were retrospectively reviewed between November 1, 2014 and October 1, 2017. Scans performed for known or suspected thyroid pathology were excluded. The proportion of appropriate recommendations, as per the ACR white paper, were compared between reports completed before and after template implementation using a chi-squared test. Subgroup analysis was performed according to patient age and nodule size.

Results

Identified were 73 reports before template implementation and 296 were identified after. Overall template usage was 24.3% (72/296). There was no significant difference in the proportion of appropriate recommendations for young patients (<35 years) regardless of nodule size (100% vs 66%, $p=.3607$ and 100% vs 100%, $p=1$) or for older patients (≥ 35 years) with nodules larger than 1.5 cm (94% vs 96.5%, $p=.4317$). In older patients with small nodules (<1.5 cm), the proportion of appropriate recommendations increased significantly (10% vs 53.9%, $p=0.0003$). Of the inappropriate recommendations in this group prior to template implementation, 100% were for unnecessary ultrasound.

Conclusions

Implementation of a standardized reporting tool significantly increased the appropriateness of recommendations in older patients with small thyroid nodules resulting in fewer recommendations for unnecessary follow-up examinations.

Tuesday, June 5, 2018

10:30AM - 12:00PM

Excerpta: Neoplasms, Stroke and Interventional

E-44

10:30AM - 10:34AM

Multiple Meningiomas Confined to the Right Cerebral Hemisphere with a Third Ventricular Meningioma Causing Acute Obstructive Hydrocephalus

N Eickstaedt¹, F Diehn¹, A Burrows¹, M Link¹, T Kaufmann¹

¹Mayo Clinic, Rochester, MN

Purpose

To present a case of multiple meningiomas confined to the right cerebral hemisphere which presented as acute obstructive hydrocephalus secondary to a third ventricular mass

Materials and Methods

A 57-year-old female was referred from an outside institution for a headache and multiple intracranial masses. The patient described two months of intermittent headaches, increasing in severity and frequency over the last week, without nausea or vomiting. She also endorsed intermittent blurry vision but was otherwise neurologically intact. Imaging findings were consistent with meningiomatosis confined to the right cerebral hemisphere including a third ventricular meningioma which caused acute obstructive hydrocephalus. The third ventricular tumor and a 3.4 cm right frontal parasagittal tumor were resected. Both were atypical meningiomas (WHO Grade II). The patient declined genetic testing for insurance reasons. The patient then underwent stereotactic radiosurgery of the remaining intracranial masses. The third ventricle is an unusual location for intraventricular meningioma, with the lateral ventricle being the most common site. Only one other case of meningiomatosis confined to a single cerebral hemisphere has

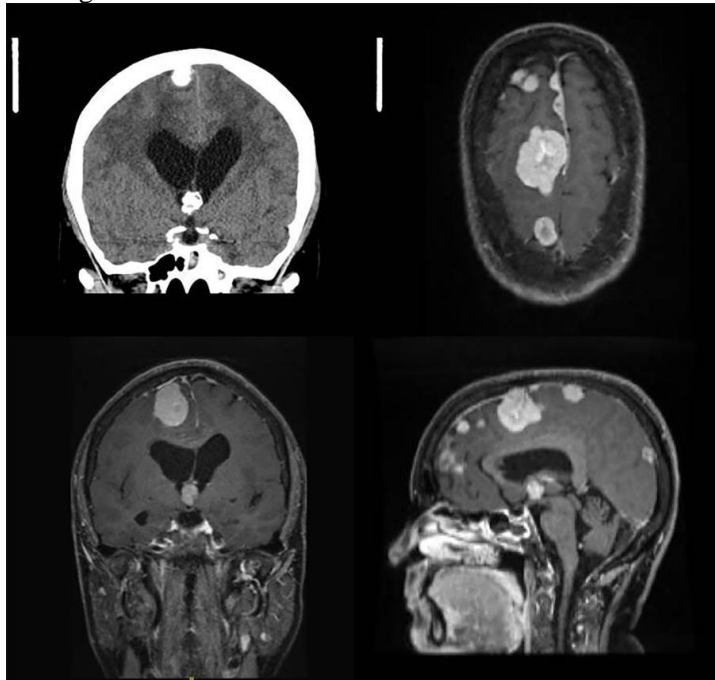
been reported in the literature, which also presented with acute neurological symptoms. Meningiomatosis itself is not a risk factor for rapid tumor growth or acute decompensation, as the tumor growth rate of solitary versus multiple meningiomas is not significantly different. However, it was uncertain if this current case represented diffuse intracranial metastatic spread of grade II meningioma on presentation vs. de novo growth of multiple meningiomas/meningiomatosis.

Results

Noncontrast CT depicted 12, mostly calcified, dural-based masses varying in size and confined to the right cerebral hemisphere (convexity and parafalcine), but also a 1.2 cm calcified mass within the anterosuperior aspect of the third ventricle in the region of the foramina of Monro which caused obstructive hydrocephalus. Subsequent MRI depicted the masses to be variable in signal intensity, related to calcification, and avidly enhancing.

Conclusions

We present an unusual case of multiple meningiomas confined to a single cerebral hemisphere, including an uncommon third ventricular atypical meningioma which caused obstructive hydrocephalus. This could represent metastatic spread of meningioma, vs. a very unusual case of unilateral cerebral hemispheric meningiomatosis.



(Filename: TCT_E-44_MeningiomatosisASNR.jpg)

E-45

10:34AM - 10:38AM

Intraventricular Glioblastoma with Neuronal Component

J Rees¹, I Tuna², M Rahman², J Gregory², J Kresak²

¹University of Florida, Sarasota, FL, ²University of Florida, Gainesville, FL

Purpose

To present unusual imaging features of a rare intraventricular glioblastoma multiforme (GBM) with neuronal component (NC), which is a newly described WHO 2016 brain tumor, and to discuss its histogenesis

Materials and Methods

None

Oral Presentations & Excerptas

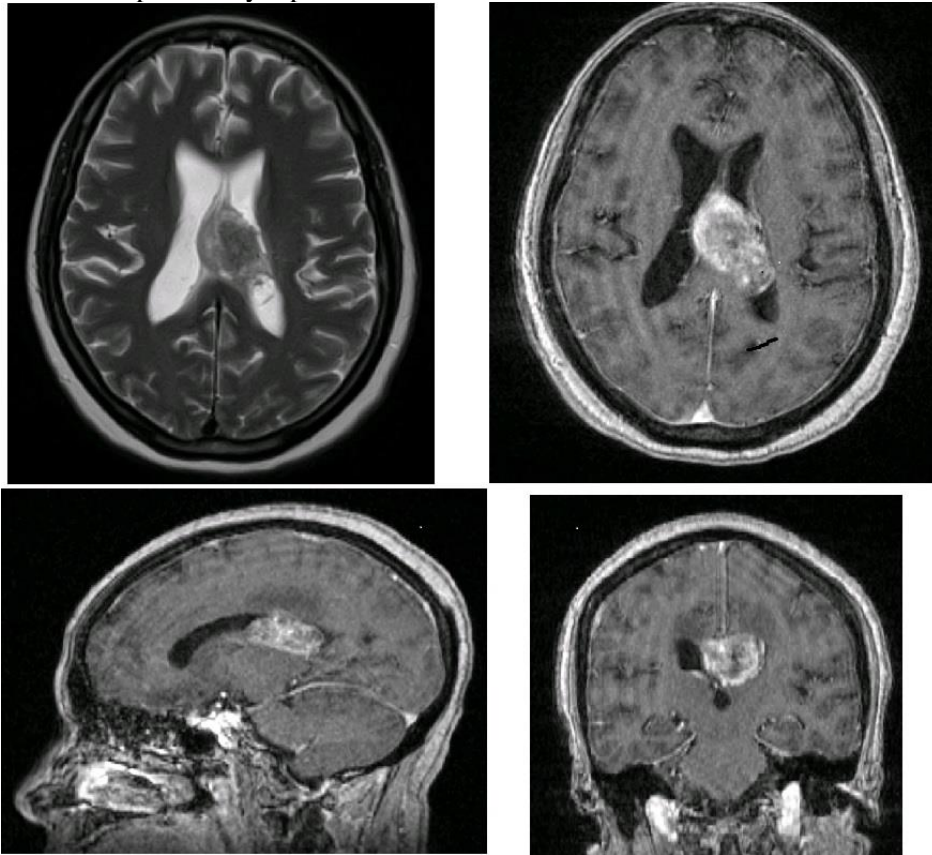
Results

In preoperative imaging, we see a large heterogeneous mass which may have grown exophytically from the left thalamus into the lateral ventricle. On pathologic examination, this tumor displays a biphasic histology, with a larger component staining strongly positive for synaptophysin a neuronal marker, without any glial fibrillary acidic protein GFAP positivity, suggesting purely neuronal lineage, and the other smaller component staining only faintly with GFAP as well as synaptophysin indicating mixed glial and neuronal precursors.

Conclusions

In early embryologic development, ectoderm divides into peripheral ectoderm which becomes skin, and central or neural ectoderm, and subsequently neural ectoderm divides into epidermoblasts and neuroblasts. epidermoblasts differentiate into the various glial cell lines: astrocytes, ependymal cells, oligodendroglia, and microglia. neuroblasts differentiate into the different types of neurons: pyramidal cells, betz cells, purkinje cells and others. The dual histology of this tumor suggests its cell of origin must have arisen before complete differentiation of neural ectoderm into glial and neuronal precursors.

Although it displays near total neuronal differentiation, under WHO 2016 it is still considered a variant of GBM and is expected to display similar behavioral and prognostic features. Intraventricular GBMs of any type are quite unusual and the presentation of this rare histologic variant as an intraventricular mass has never been previously reported.



(Filename: TCT_E-45_GBmwNeuronalComponentComposite.jpg)

E-46

10:38AM - 10:42AM

Collision Tumor: A Rare Case of Metastatic Breast Carcinoma Invasion into a Skull Base Meningioma

B Diegman¹, P Kim², E Velez¹, K Hurth³

¹USC+LAC, Los Angeles, CA, ²Keck School of Medicine of University of Southern California, La Crescenta, CA, ³University of Southern California, Los Angeles, CA

Purpose

Present a rare case of collision tumor of a skull-base meningioma and metastatic breast carcinoma in a patient with a confusing clinical picture. Discuss the imaging findings on CT and MRI, and illustrate the histopathologic correlation.

Materials and Methods

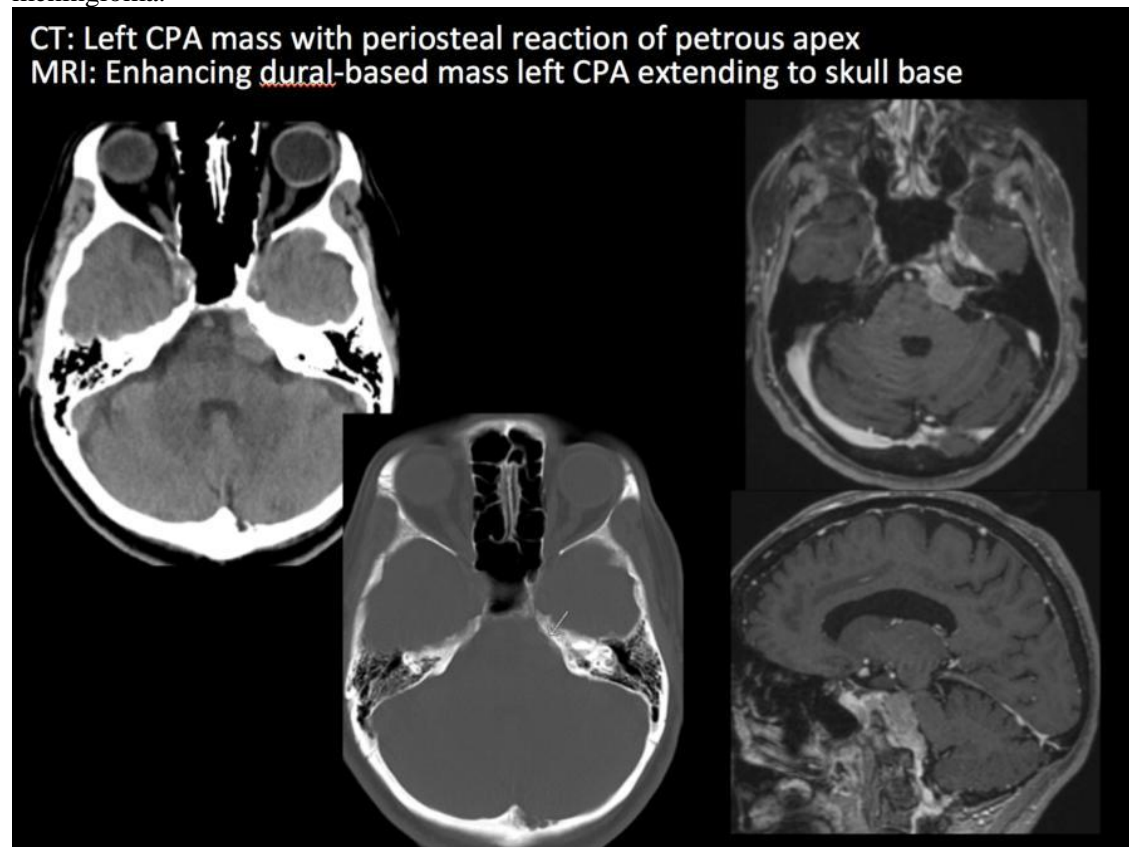
A 75-year-old female with a remote history of melanoma status postexcision presented with left-sided facial numbness, diplopia, and hearing loss. Initial CT demonstrated a left CPA mass. Subsequent MRI demonstrated an enhancing dural-based mass in the left CPA. Initial diagnosis favored meningioma. Patient fell down a few weeks later and was found to have a pathologic femur fracture. Bone biopsy revealed metastatic breast carcinoma. Patient's symptoms worsened, and another MRI was obtained 6 weeks after the initial MRI, which showed interval growth of the dural-based mass. Differential diagnosis was now metastasis vs. meningioma. Patient underwent surgical biopsy.

Results

Hyperdense CPA mass on CT with adjacent periosteal reaction. Homogeneously enhancing dural-based CPA mass extending along the skull base on MRI. Short-term follow-up MRI showed interval growth of mass over six weeks. Histopathologic analysis of the tumor demonstrated mixed meningioma and carcinoma of the breast.

Conclusions

Collision tumor is a rare entity more commonly described in the literature with adrenal adenomas. In the brain, meningioma is the most common collision tumor, being a slow growing and hypervascular tumor. This rare diagnosis should be considered when unexpected rapid growth is seen in a suspected meningioma.



Two Unusual Cortical Based Tumors of a Common Entity: Clinical, Imaging and Histopathological Correlation

S Aziz¹, P Rabiei¹, S Khanpara¹, M Bhattacharjee¹, A Kamali¹, E Bonfante¹, R Riascos¹, R Patel¹
¹*The University of Texas Health Science Center at Houston, Houston, TX*

Purpose

Ependymomas account for approximately 5% of all neuroepithelial tumors and 10% of all pediatric brain tumors. The majority of ependymomas are infratentorial. Of the supratentorial tumors, 50% are extraventricular, with the majority located within the vicinity of the ventricular margins. Remote cortical extraventricular ependymomas with no connection to the ventricular lining are extremely rare. With more advanced neuroimaging protocols, these lesions can be more easily characterized. We describe two educational cases of such extraventricular ependymomas to discuss their clinical, imaging and histopathological findings.

Materials and Methods

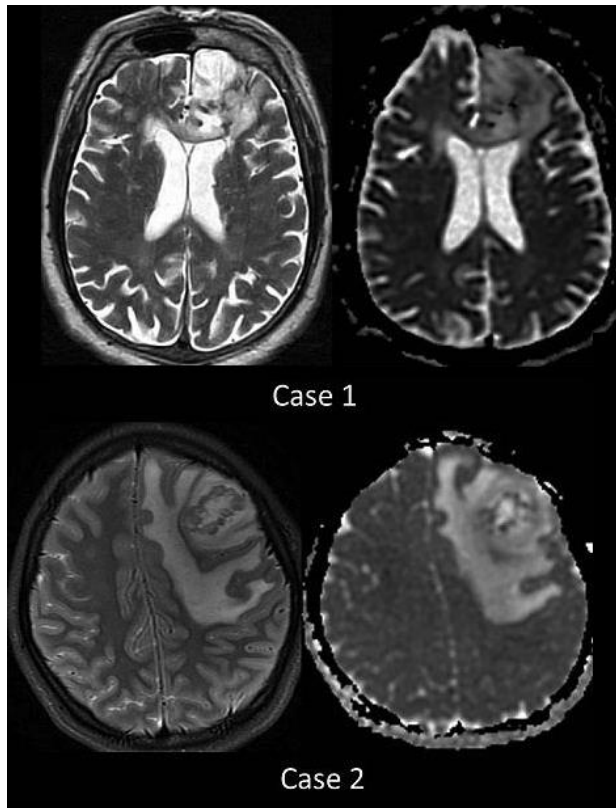
A 19-year-old female presented with a two-month history of seizures and visual disturbances with CT revealing a 4cm partially cystic left frontal mass with mass effect. Contrast MRI was obtained with a multiparametric advanced neuroimaging protocol including MR spectroscopy, MR perfusion and DTI (Figure 1). Patient underwent total resection of the mass, with histopathological examination revealing giant cell ependymoma. A 62-year-old male presented with a two-week history of worsening lethargy and headaches, with CT revealing a focal area of L frontoparietal cerebral edema. Contrast MRI with multiparametric sequences was obtained (Figure 1). Patient underwent frontal craniotomy and resection of tumor, with histopathological examination revealing clear cell ependymoma.

Results

Case 1 (Clear Cell Ependymoma): Heterogeneously enhancing mass on T2 spin echo (left) with diffusion restriction on ADC (right) and small foci of low signal susceptibility and internal T2 signal suggesting hemorrhage and central necrosis. Case 2 (Giant Cell Ependymoma): Infiltrative mass involving L frontal lobe and anterior corpus callosum, with extensive hemosiderin deposition and focal areas of contrast enhancement within the lesion.

Conclusions

Although supratentorial extraventricular presentations of ependymoma are often reported, a remote cortical presentation is extremely rare. With development of advanced multiparametric neuroimaging protocols, these lesions can be more easily characterized.



(Filename: TCT_E-47_Images3copy.jpg)

E-48

10:46AM - 10:50AM

Acutely Hemorrhagic Meningioma with "Spot Sign" on CT Angiogram

S Aziz¹, R Riascos¹, A Simonetta¹

¹University of Texas Health Science Center - Houston, Houston, TX

Purpose

Although hemorrhagic meningiomas have been reported in the literature, active extravasation within a meningioma on a CT angiogram has not been reported. We present a unique case of a hemorrhagic meningioma with active extravasation, mimicking a more vascular type lesion on initial impression.

Materials and Methods

A 42-year-old female presented with one week of progressive headaches, nausea and dizziness with a three-day history of right upper extremity numbness. CT without contrast demonstrated a hematoma in the left parietal parasagittal region, and CT angiogram and MRI were subsequently obtained (Figure 1). Patient underwent resection of mass with histopathology revealing hemorrhagic meningioma. The patient recovered mild function of her right upper extremity.

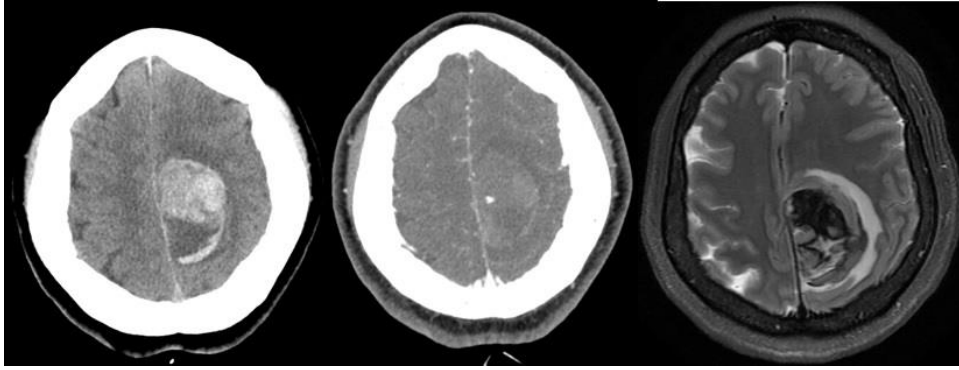
Results

CT without contrast (left) revealed a large round hemorrhagic lesion in the left parasagittal region with surrounding vasogenic edema. CT angiogram (middle) revealed the classical "spot sign" of active extravasation within the hemorrhagic lesion. MRI (right) revealed a hematoma with different stages of bleeding and heterogeneous enhancement post contrast.

Conclusions

We present a unique exhibit of acutely hemorrhagic meningioma with the "spot sign" pathognomonic for active extravasation on CT angiogram.

Oral Presentations & Excerptas



(Filename: TCT_E-48_img.jpg)

E-49

10:50AM - 10:54AM

Cerebral Venous Air Embolism

M Manganaro¹, J Kim¹, J Ross¹

¹*University of Michigan, Ann Arbor, MI*

Purpose

Use of lung windows may aid in detection of cerebral venous air embolism, a rare finding on CT that is difficult to detect due to the rapid absorption of air, but can have catastrophic outcomes.

Materials and Methods

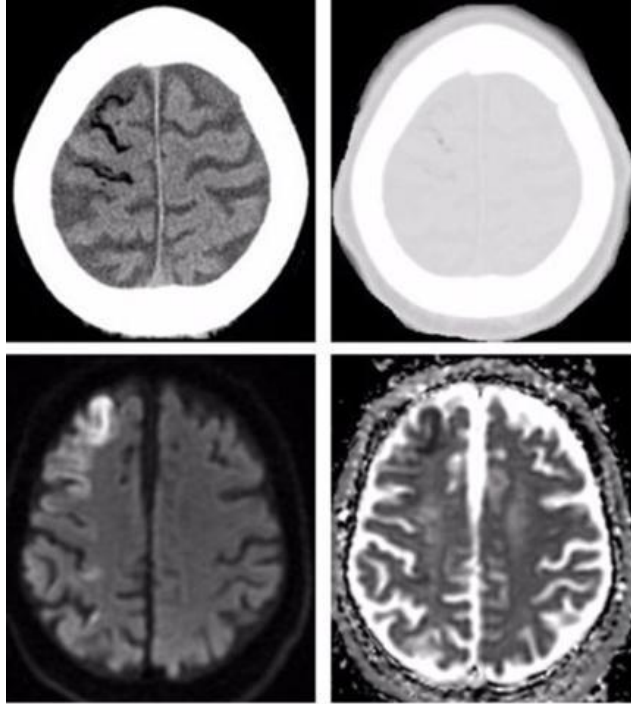
A 66-year-old obese male with history of severe peripheral arterial disease who underwent a right fem-pop bypass graft six hours prior was found to have acute left hemiplegia. Head CT was ordered showing air following the distribution of the cortical veins in the right frontal lobe suspicious for venous air embolism. The patient was immediately placed in Trendelenburg position and placed on high flow oxygen. Subsequent MRI two days later was performed showing corresponding gyriform cortical ischemia in the right frontal lobe. The patient did well after the supportive treatment measures and had minimal deficits after the venous air embolism.

Results

CT: abnormal low attenuation follows the distribution of the cortical veins MRI: gyriform cortical ischemia in the right frontal lobe corresponding to the CT findings

Conclusions

Cerebral air embolism can be arterial or venous and is often iatrogenic in cause. Cerebral air embolism is rare but can be fatal as the air emboli can act like thrombotic emboli and cause occlusion and ischemic stroke. Presentation is often varied and nonspecific but includes confusion, motor weakness, decreased consciousness, seizure and vision loss. CT may only be diagnostic in the acute setting as gas is absorbed rapidly and the use of lung windows may help increase detection. Treatment is supportive, but high-flow oxygen, hyperbaric oxygen therapy, and placing the patient in Trendelenburg position all have documented efficacy for the treatment of cerebral venous air embolism.



(Filename: TCT_E-49_Cerebralembolism.jpg)

E-50

10:54AM - 10:58AM

Direct puncture and percutaneous nBCA embolization of a traumatic head and neck pseudoaneurysm

D Volders¹, J Shewchuk², M Heran²

¹University of British Columbia, Vancouver BC, British Columbia, Canada, ²Vancouver General Hospital, Vancouver, British Columbia, Canada

Purpose

To demonstrate how a combination of direct percutaneous puncture and nBCA embolization can be used as a safe, effective and fast treatment method of head and neck pseudoaneurysms

Materials and Methods

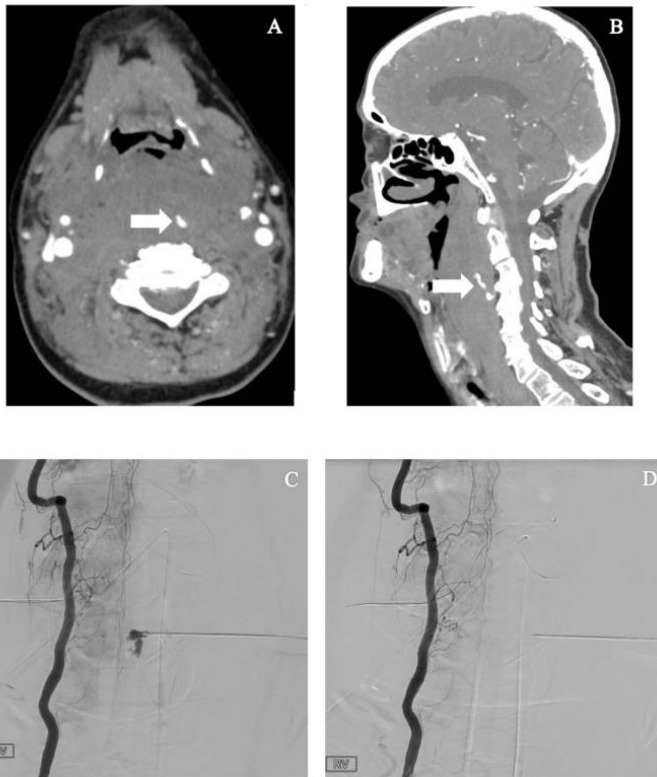
A 91-year-old male presented in our emergency department with progressive neck swelling and associated dysphagia after direct neck trauma due to a fall a day earlier.

Results

An early arterial and venous neck CT scan demonstrated an extensive C1-C5 prevertebral hematoma, as well as a small C3-C4 pseudoaneurysm without obvious parent vessel in the midline of the prevertebral soft tissues (panel A and B). The patient was brought to the neuroangiography suite for an emergency cerebral angiogram and embolization. A selective right vertebral artery angiography demonstrated the pseudoaneurysm arising from a small vertebral muscular branch at C3-C4. A rotational CT angiography was performed for better delineating the pseudoaneurysm and for planning treatment via direct percutaneous puncture using Xper Guide technique. Using target and progress view of the Xper Guide, a 22 gauge 3-1/2" length spinal needle was advanced into the pseudoaneurysm. Curative embolization was achieved by injection of 1.5 mL of a 1:1 mixture of Lipiodol and n-butyl cyanoacrylate (nBCA) while performing right vertebral artery control angiography (panel C and D).

Conclusions

A ruptured head and neck pseudoaneurysm can be a life-threatening condition requiring urgent or emergent treatment. Most often these lesions are embolized transarterially; however, vessel tortuosity, anatomic variants, prior intervention, or surgery and inflammation may render an endovascular approach sometimes impossible. We report a case of an extensive expanding head and neck hematoma due to a bleeding vertebral muscular branch pseudoaneurysm which was successfully treated using a combination of direct percutaneous puncture and nBCA embolization. This approach can offer a safe, effective and fast alternative pseudoaneurysm treatment when transarterial embolization is challenging or impossible.



(Filename: TCT_E-50_Figureexcerpta.gif)

E-52

11:02AM - 11:06AM

Glue embolization of artery of Adamkiewicz pseudoaneurysm with active extravasation following MDMA abuse

D Volders¹, J Nugent², M Fatehi², M Heran²

¹University of British Columbia, Vancouver BC, British Columbia, Canada, ²Vancouver General Hospital, Vancouver, British Columbia, Canada

Purpose

Spinal subarachnoid hemorrhage due to isolated spinal artery dissection or aneurysm rupture is a rare event and there is no standardized approach to its treatment. All four patients with Adamkiewicz artery dissection or aneurysm rupture reported in the literature in the past decade have been observed with only conservative therapy. We report the first endovascular embolization of the Artery of Adamkiewicz.

Materials and Methods

A 42-year-old male presented to care following 3,4-methylenedioxy-N-methylamphetamine (MDMA)

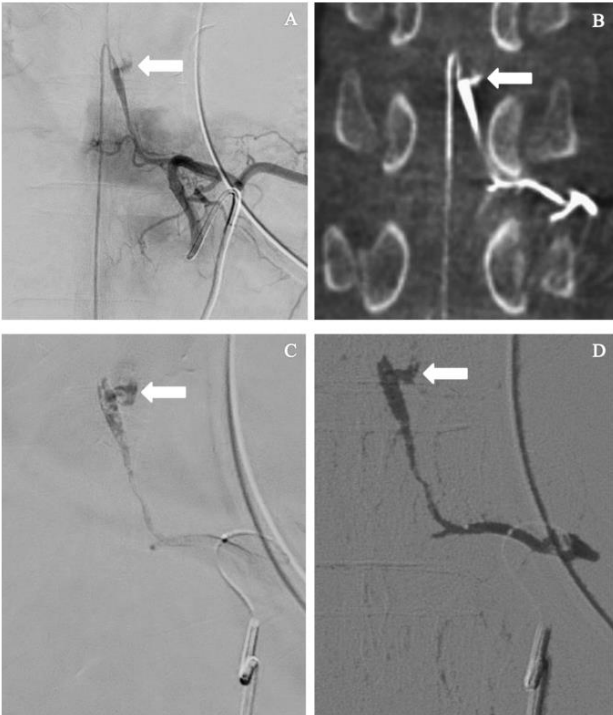
abuse with extensive intracranial and spinal subarachnoid hemorrhage due to dissections of the Artery of Adamkiewicz and left vertebral artery. Due to the patient's paraplegia and active extravasation, it was decided that an endovascular approach was necessary to prevent further neurologic deterioration.

Results

A spinal angiogram demonstrated a pseudoaneurysm of the Adamkiewicz artery with active extravasation (white arrow) after injection of the left T10 costal artery (Panel A). Corroborating findings on rotational CT angiography were observed (Panel B). Panel C shows entry of glue into the dissecting aneurysm and occlusion of the site of active extravasation. Digital subtraction angiography demonstrates glue has occluded the posterior branch of the intercostal artery, the Adamkiewicz Artery, and the origins of the ascending and descending limbs of the anterior spinal artery (Panel D). Three months later the patient was walking with hiking poles, and at six months had 5/5 strength bilaterally in the extremities with a conus and cauda mixed syndrome.

Conclusions

Spontaneous dissection of the Artery of Adamkiewicz represents an extremely rare cause for spinal and intracranial subarachnoid hemorrhage, and may require emergent endovascular management. The clinical outcome of vessel sacrifice cannot be predicted on imaging.



(Filename: TCT_E-52_Images.gif)

E-53

11:06AM - 11:10AM

Dual Pathology: Coexistence of Calcifying Pseudoneoplasm of the Neuraxis(CAPNON) and Primary Intracranial Mesenchymal Chondrosarcoma

R Sezer¹, M Ağıldere¹, Ö Işıksaçan Özen¹, E Sönmez¹, N Altınörs¹, A Terzi¹

¹Baskent University Faculty of Medicine, Ankara, Turkey

Purpose

Our aim is to present CT and MRI findings of a very rare dual pathology of the brain which is coexistence of malignant brain mesenchymal tumor and calcifying pseudoneoplasm of the neuraxis.

Oral Presentations & Excerptas

Materials and Methods

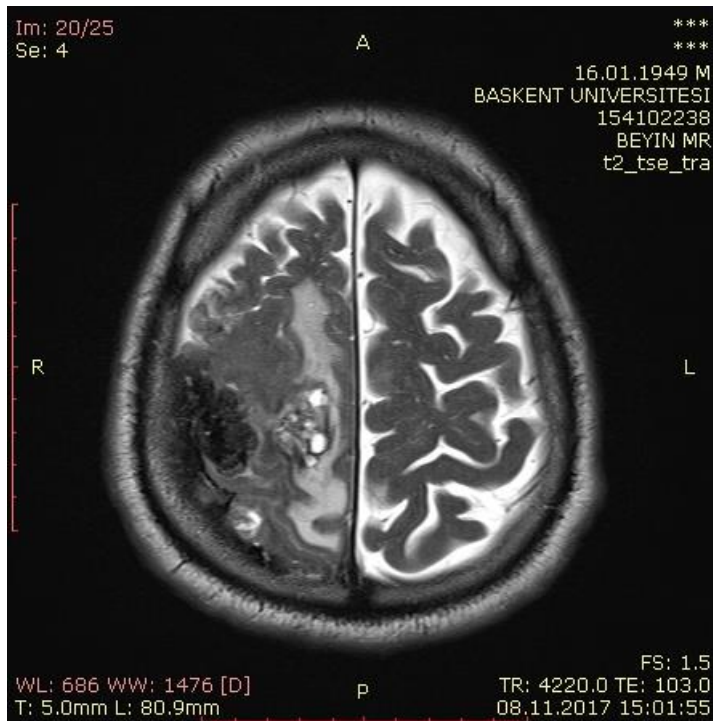
A 68-year-old man with prostate carcinoma diagnosed for right parietal calcified mass while he was being investigated for staging of cancer with brain CT and MRI at outside hospital. He underwent radical prostatectomy a year ago. Two months after his operation he presented with seizure. The patient underwent nonenhanced brain CT scan. There was a calcified right parietal mass as seen before on CT and MRI. He received antiepileptic drugs for his seizure. After a month he presented with left hemiparesis that was involving the upper extremity. This time there were focal parenchymal hematoma with peripheral edema at the right precentral gyrus and also right parietal calcified mass which was seen before. After ten days brain CT scan repeated. Hematoma was resolved but vasogenic edema was insistent. During this period the patient received physical therapy for his hemiparesis and antiepileptic treatment for his seizure. Nine months after his first seizure he was consulted by our radiology department with his CT and MRI images which were performed at outside hospital. Brain CT and MRI were repeated once more because of the new neurological symptoms. There were a right parietal dura-based calcified mass and also new heterogeneous enhancing mass at the right precentral gyrus with large peripheral edema. During this period the patient's clinical status was getting worse; therefore, neurosurgeons decided to operate. After craniotomy two separate masses were totally resected by using navigation and pathological diagnoses were made after immunohistochemical staining. Vimentin, S100 were positive for the precentral gyral mass determining mesenchymal chondrosarcoma. EMA, GFAP were positive parameters for the dura-based calcified right parietal mass determining pseudoneoplasm of the neuroaxis (CAPNON) as final diagnosis.

Results

Nonenhanced brain CT scan revealed right parietal dura-based calcified mass with irregular margins measured about 7x2.3 cm at the longest diameter had irregular margins with effacement of the right parietal cortical sulci. Brain CT demonstrated after developing hemiparesis, intraparenchymal hematoma with edema close to calcifying dural-based mass. Follow-up brain CT demonstrated resorption of hematoma but insistent clinical findings deserved follow-up MRI. Follow-up brain MRI demonstrated T1 hypo, T2 hyperintense, heterogeneous enhancing intraparenchymal masses with large edema next to the calcified mass. Calcified dural-based lesion demonstrated T and T2 hypointense area with limited enhancement.

Conclusions

Calcifying pseudoneoplasm of the neuroaxis (CAPNON) and primary intracranial mesenchymal chondrosarcoma both are very rare lesions of the central nerve system (CNS) and also coexistence of them is also extremely rare. To our knowledge there's no reported case for this dual pathology in the literature. CAPNON is a non-neoplastic calcified lesion of the CNS and it can be seen intra-axial or extra-axial region of the spine or brain and mostly dural-based. On CT images CAPNON is classically hyperdense and on MRI images it tends to be hypointense both on T1- and T2-weighted sequences because of dense calcification. Surrounding vasogenic edema is not common. CAPNON can contain variable amounts of fibrous stroma, bone, palisading spindle and epithelioid cells and a chondromyxoid-like matrix. Radiologic appearance depends on the histologic content. It's difficult to distinguish a meningioma from a CAPNON lesion because both lesions are dural-based and calcified. The theory for CAPNON's etiology depends on the perilesional granulomatous inflammation which refers to reactive process. Intracranial mesenchymal chondrosarcoma is a very rare and a high-grade malignant neoplasm which can be seen in the intra-axial or extra-axial region. It has a slightly female preponderance and is usually seen in the second and third decade of life. These tumors have a high tendency to be locally aggressive, with recurrence; it is the most malignant subtype of chondrosarcomas. The origin of the tumor is still unclear. The most agreed-upon theory for the origin of these tumors is the multipotent mesenchymal cells in the dura or arachnoid. On CT, the tumor margins can be well-defined or lobulated, and it can be hypodense or isodense to muscle. On MRI lesion characterisation is hypo to isointense on T1WI, iso or hyperintense on T2WI and intense enhancement after contrast media injection. Radical surgical resection of the tumor is the best treatment of choice.



(Filename: TCT_E-53_IMG-0003-00001.jpg)

E-54

11:10AM - 11:14AM

Complex revascularisation angioplasty in a patient with a combined type A aortic dissection and hemispheric hypoperfusion syndrome

D Volders¹, R Cook¹, M Heran²

¹University of British Columbia, Vancouver, British Columbia, Canada, ²Vancouver General Hospital, Vancouver, British Columbia, Canada

Purpose

Aortic dissection involving the brachiocephalic and right common carotid arteries can present significant and unique challenges in management. We present a patient with an aortic dissection and right hemispheric hypoperfusion syndrome who was treated via a combination of percutaneous right common carotid access and transfemoral arterial approaches.

Materials and Methods

A 73-year-old male presented with asymmetric blood pressure and right hemispheric syndrome.

Results

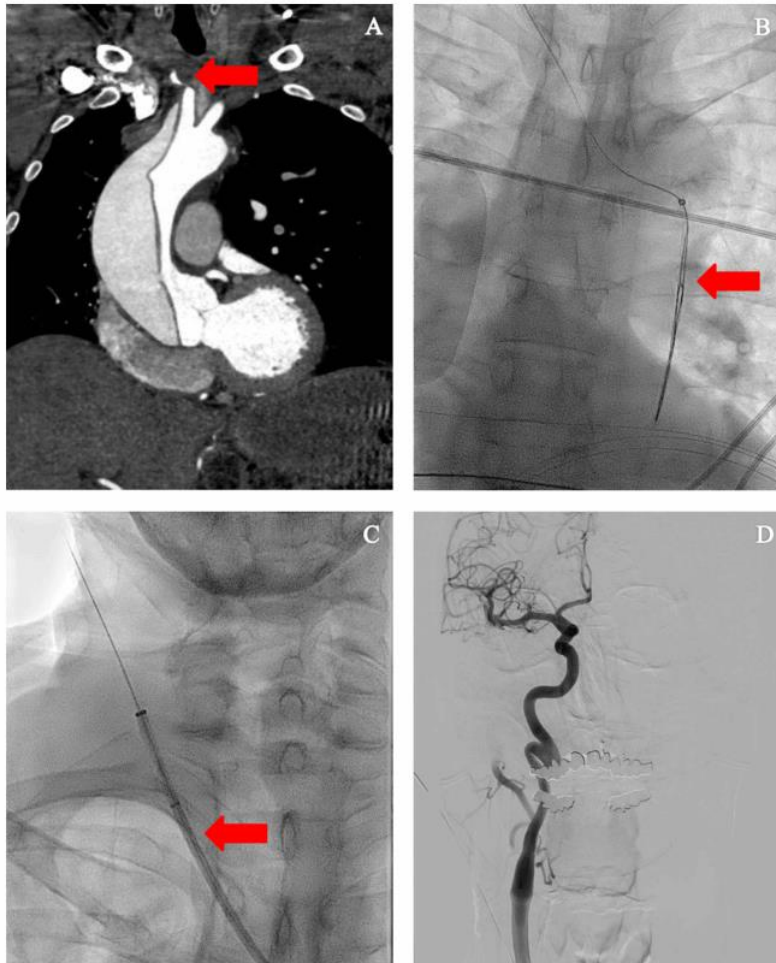
CT angiography demonstrated a type A aortic dissection with extension to brachiocephalic trunk and right common carotid artery (Panel A). This resulted in profound flow limitation into the downstream carotid circulation, with the patient's symptoms accounted for by intracranial hypoperfusion. Percutaneous ultrasound-guided access to the true lumen of the right common carotid artery beyond the dissection flap was performed, directed in a retrograde fashion, with a 2-French micropuncture cannula placed. A V-18 wire was advanced through the dissection, into the aortic arch, with a 7-French Ensnare advanced from the right femoral arterial access to snare and pull the V-18 wire through the femoral sheath for "through-and-through" access (Panel B). A Penumbra Neuron Max guide sheath was advanced over the V-18 guide wire into the true right common carotid artery lumen (Panel C). A Medtronic Visi-Pro 10 mm x 37 mm balloon expandable stent was deployed successfully across the dissection flap, with profound flow

Oral Presentations & Excerptas

improvement through the brachiocephalic and right common carotid arteries, with normal right cerebral hemisphere flow return (Panel D). The patient demonstrated immediate clinical improvement, with complete recovery of his strength and neglect. He subsequently went on to have uneventful open repair of his Type A aortic dissection.

Conclusions

We demonstrate a unique percutaneous carotid arterial access as an aid for transfemoral arterial stenting for treatment of a hypoperfusion syndrome of the right cerebral hemisphere due to complex type A aortic dissection.



(Filename: TCT_E-54_Image.gif)

E-55

11:14AM - 11:18AM

Anterior cerebral artery vasospasm and infarction secondary to pituitary tumor apoplexy

E Velez¹, B Diegnan¹, A Rajamohan¹, J Bakhsheshian², G Zada², J Acharya¹

¹LAC+USC, Los Angeles, CA, ²University of Southern California, Los Angeles, CA

Purpose

To illustrate a rare, but serious complication of pituitary apoplexy

Oral Presentations & Excerptas

Materials and Methods

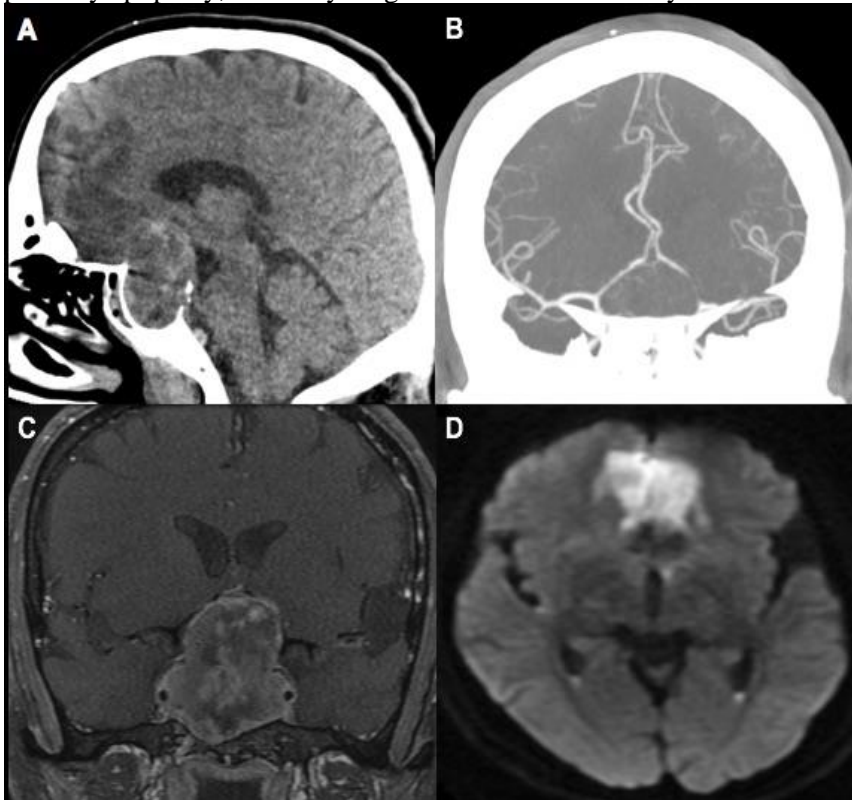
A 42-year-old man with one month of worsening headaches and blurry vision presented with five days of bilateral vision loss, a fixed and dilated right pupil, and stupor. In the emergency department he became bradycardic and unresponsive, requiring intubation. A CT scan was performed demonstrating a 4.5 cm sellar and suprasellar mass with areas of hemorrhage and loss of gray-white matter differentiation in the bilateral frontal lobes. CTA demonstrated vasospasm of the bilateral anterior cerebral arteries and MRI demonstrated acute infarction in the corresponding ACA territories. Additionally, the MRI demonstrated blood product of varying age, suggesting that the macroadenoma hemorrhaged multiple times. The patient underwent emergent transsphenoidal craniotomy to resect the tumor, which was shown to be a 4.6 cm pituitary adenoma with extensive hemorrhage and necrosis.

Results

Image A: Initial noncontrast head CT demonstrates a 2.9 cm x 3.6 cm x 4.5 cm bilobed heterogeneous sellar and suprasellar mass with internal hemorrhage. Also noted is confluent hypodensities in the bilateral inferior frontal lobes extending along the anterior cerebral artery distribution. Image B: CT angiography maximum intensity projection images demonstrates stretching and narrowing of the bilateral distal cavernous ICAs and A1 segments. Image C: T1-weighted postcontrast imaging demonstrates a heterogenous enhancing mass with areas of necrosis and internal hemorrhage consistent with pituitary apoplexy. Image D: Diffusion-weighted imaging demonstrates bilateral ACA territory infarcts, involving the bilateral gyrus recti and medial aspects of both frontal lobes.

Conclusions

Pituitary apoplexy can cause vasospasm of the bilateral anterior cerebral arteries, leading to cerebral ischemia. Early recognition, diagnosis, and treatment of pituitary apoplexy is paramount to avoid complication and clinical decline in these patients. Vasospasm is a rare, but described complication of pituitary apoplexy, and early diagnosis is crucial for early treatment.



(Filename: TCT_E-55_pituitaryapoplexyimage.jpg)

E-56

Lymphomatoid Granulomatosis: Case report of a challenging presentation of a rare entity

E Neufeld¹, K Salzman¹, J McNally¹, C Palmer¹

¹University of Utah, Salt Lake City, UT

Purpose

A 67-year-old male presented with cognitive decline and neurologic deficits. MRI demonstrated ependymal enhancement and periventricular masses. Postmortem pathology returned as lymphomatoid granulomatosis (LG), unusual as he had isolated CNS disease. LG and its manifestations are presented with the goal of raising awareness of this entity.

Materials and Methods

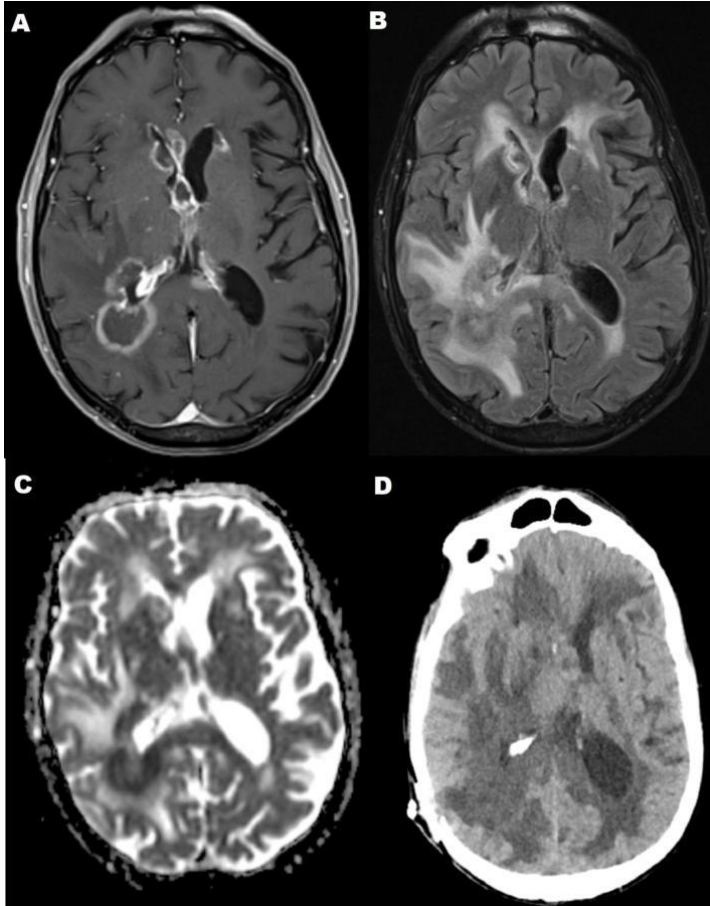
Initial workup of the patient with lumbar puncture returned elevated protein and lymphocytic pleocytosis. Infectious/autoimmune workup was negative. MRI showed nodular ependymal enhancement suggesting infectious ventriculitis. Ventricular biopsy was done with pathology returning "mass-like proliferation of atypical B-cells." He declined and developed ring enhancing lesions on MRI despite antifungals. Open biopsy of a lesion was performed without evidence of fungal infection. Aggregates of atypical B-cells positive for EBV with angioinvasion were shown, confirming LG.

Results

A. T1 post: nodular ependymal enhancement. Discrete rim-enhancing periventricular masses communicating with the ventricular system. B. FLAIR: signal abnormality in the periventricular white matter and centrum semiovale. Mass effect with partial effacement of the right lateral ventricle. C. ADC: Enhancing components feature restricted diffusion, notable along the right peritrial white matter. D. CT performed 3 weeks later: Increase in white-matter hypoattenuation and midline shift. Interval right parietal biopsy changes.

Conclusions

LG is a lymphoproliferative reaction to EBV and occurs almost entirely in immunosuppressed patients. It is most commonly systemic with skin and pulmonary involvement dominating. CNS involvement occurs in 1/3, with isolated CNS involvement being rare. MRI findings occur along the perivascular spaces and ependyma. Enhancement may be punctate, linear, or be discrete enhancing masses in 1/3 of patients. Nodular leptomeningeal and cranial nerve enhancement can be seen. Spine involvement is rare. Pathology demonstrates polymorphic lymphoid infiltrates, angiitis, and granuloma formation. Our case demonstrates an uncommon presentation of this rare disease. Awareness of LG may prevent the misdiagnosis of infection and direct management appropriately.



(Filename: TCT_E-56_ExcerptaImages.jpg)

E-57

11:22AM - 11:26AM

Cerebral Air Embolism Due to Atrioesophageal Fistula – A Rare but Devastating Complication of Catheter Ablation for Atrial Fibrillation

A Heilala¹, J Corrigan¹, S Patel¹, B Griffith¹

¹Henry Ford Health System, Detroit, MI

Purpose

Catheter ablation is increasingly offered to patients with recurrent, symptomatic, drug-refractory paroxysmal atrial fibrillation. Atrioesophageal fistula is a rare but catastrophic complication of these procedures, which can occur due to thermal esophageal injury caused by radiofrequency energy delivered to the adjacent left atrium. This excerpta describes a case of cerebral air embolism in a patient with atrioesophageal fistula following catheter ablation.

Materials and Methods

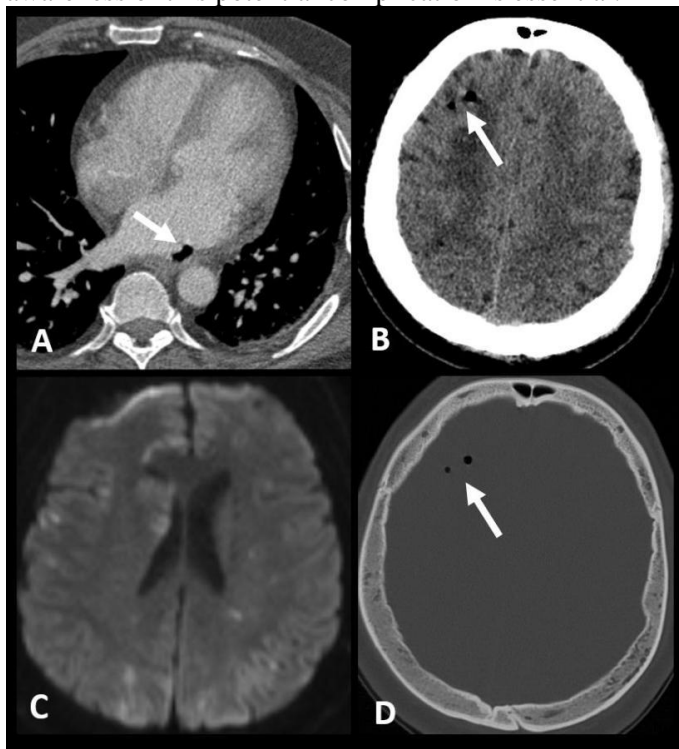
We present the case of a 42-year-old male with atrial fibrillation who presented to an outside institution one month following left atrial radiofrequency ablation. The patient had experienced dysphagia since the ablation, but presented more acutely with altered mentation, bilateral upper extremity weakness and GI bleeding. Initial CT and MRI showed multiple areas of acute and subacute infarct and CT chest was concerning for atrioesophageal fistula. Following transfer to our facility, the patient went into V-fib arrest at which time CT head demonstrated cerebral air emboli.

Results

CT chest (Fig. 1A) shows a focus of air within the posterior wall of the left atrium concerning for atrioesophageal fistula. Noncontrast CT head shows multiple air emboli and developing areas of embolic infarct (Fig. 1B, D). MRI of the brain demonstrates multiple foci of restricted diffusion compatible with embolic infarcts. Postcontrast images (not shown) also demonstrated enhancing foci compatible with areas of subacute infarction.

Conclusions

Cerebral air embolism is a rare cause of ischemic infarct. Oftentimes, the source is difficult to identify and appropriate clinical history is needed to establish the diagnosis. Atrioesophageal fistula, a potential complication of catheter ablation, is one potential cause. Although rare, given the increasing frequency of catheter ablation in the treatment of atrial fibrillation, it is becoming more likely that neuroradiologists will encounter this in practice. As early diagnosis and treatment are critical to improving outcome, awareness of this potential complication is essential.



(Filename: TCT_E-57_AtrioesophagealFistula.jpg)

E-58

11:26AM - 11:30AM

Adult-Onset Atypical Teratoid/Rhabdoid Tumor in the Sellar Region – A Distinct Variant of an Exceptionally Rare Tumor?

P Annigeri¹, B Griffith¹, J Corrigan¹, S Patel¹

¹Henry Ford Health System, Detroit, MI

Purpose

Atypical teratoid/rhabdoid tumor (AT/RT) is a highly aggressive tumor of the central nervous system, most commonly affecting young children. AT/RT is rarely found in adults, most commonly occurring in the cerebral hemispheres. To date only 14 cases of sellar-region AT/RTs have been reported.

Interestingly, recent literature suggests that these sellar region tumors may, in fact, represent a distinct

variant of AT/RT. This excerpt describes a case of sellar region AT/RT in an adult patient and reviews the recent literature regarding this entity.

Materials and Methods

We report the case of a 63-year-old female who presented with worsening headaches, diplopia, polydipsia and nausea. Initial imaging revealed a sellar/suprasellar region lesion, which was complicated by further hemorrhage of the lesion leading to obstructive hydrocephalus and subsequent surgery. Excisional biopsy was performed and pathology was compatible with AT/RT (SMARCB1/INI1 deficient tumor).

Results

Initial head CT demonstrated a hyperdense sellar/supresellar region mass (Fig 1A). Sagittal T1-weighted pre and postcontrast sequences (Fig 1B, D) demonstrate a T1 isointense, heterogeneously enhancing sellar/suprasellar lesion (solid arrow) with a second component or additional lesion at the anterior floor of the third ventricle (dotted arrow). Axial FLAIR sequence (Fig 1C) demonstrates the suprasellar component (dotted arrow) and optic tract edema (solid arrows).

Conclusions

AT/RT is a highly malignant tumor most commonly occurring in young children. While rarely occurring in adults, it is most commonly found in the cerebral hemispheres. To date, only 14 cases of sellar region AT/RT have been described in the literature. Interestingly, all reported cases occurred in females, as in our case, which is in contrast to the male predominance of pediatric and nonsellar region adult AT/RTs. In conclusion, sellar-region AT/RT may represent a distinct variant of an already rare tumor and should be considered in the differential diagnosis of sellar/suprasellar lesions in adult female patients.



(Filename: TCT_E-58_ATRT.jpg)

E-59

11:30AM - 11:34AM

Multifocal Symptomatic Intracranial Plaque Enhancement, Is There an Underlying Systemic Inflammatory Process?

J Ormsby¹, S Prabhakaran¹, M Hurley¹, A Shaibani¹, S Ansari¹

¹Northwestern University, Feinberg School of Medicine, Chicago, IL

Purpose

To suggest that systemic inflammation may influence destabilization of multifocal intracranial atherosclerotic disease (ICAD) and related ischemic strokes

Materials and Methods

A 63-year-old man with medical history of hypertension, hyperlipidemia, diabetes mellitus type II, and

Oral Presentations & Excerptas

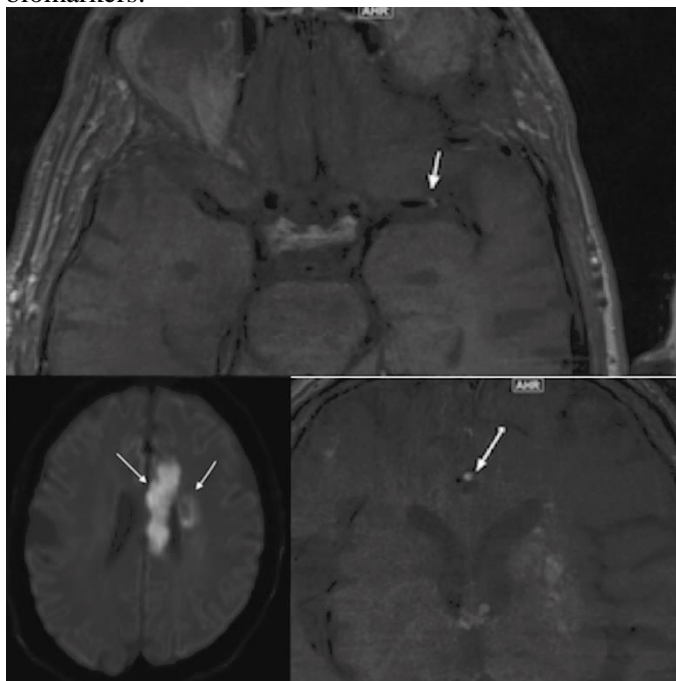
peripheral vascular disease presented with dysarthria, dysphagia and left-sided hemiplegia. Magnetic resonance (MR) imaging showed an acute infarct in the left basal ganglia-caudate and lentiform nucleus. Approximately one month later, he returned with new onset right-sided weakness and repeat MR imaging demonstrated new subacute infarcts of the left middle cerebellar peduncle with enhancement as well as new acute infarcts within the left anterior cerebral artery (ACA) territory. High-resolution MR vessel wall imaging (VWI) was also performed at this time with findings as described below. All other imaging and laboratory evaluations including cerebral spinal fluid analysis, cardioembolic etiology, and hypercoagulable panel were unrevealing, thus the infarcts were favored to be due to ICAD.

Results

On MR VWI there were multiple intracranial atherosclerotic plaques as defined by eccentric vessel wall/plaque enhancement including within the left M1 middle cerebral artery (MCA), left anterior inferior cerebellar artery (AICA), and proximal left A2 ACA correlating with high grade stenoses and the multifocal distribution infarcts. On serial MR diffusion and perfusion-weighted imaging (DWI/PWI), the patient demonstrated sequential areas of diffusion restriction in a pattern of thromboembolic ischemic strokes within each of these territories over the course of approximately 1-2 months. There was no significant elevated transit time in the left MCA distribution on MR PWI consistent with a thromboembolic perforator occlusion mechanism. Although elevated transit time was noted in the left ACA distribution, MR VWI also confirmed a thromboembolic stroke mechanism with A2 segment left ACA occlusion distal to intracranial stenosis. The patient returned 2 months later with recurrent left MCA thromboembolic infarct compatible with an unstable atherosclerotic plaque refractory to medical management.

Conclusions

Several studies have postulated that enhancing ICAD plaques may represent "vulnerable" lesions which are susceptible to rupture, and vary physiologically from stable plaques. Our patient demonstrated multiple enhancing, unstable intracranial plaques that became symptomatic over a short time interval suggesting an underlying systemic inflammatory process rather than local inflammatory destabilization. It has been hypothesized that plaque instability may be triggered by an exogenous process such as an infection or inflammatory trigger. Further investigation into the triggers of intracranial plaque instability will be required in a larger cohort of stroke patients utilizing new imaging techniques and serum biomarkers.



(Filename: TCT_E-59_VWIcombined.jpg)

Tumefactive Demyelination Coexisting with Primary Central Nervous System Lymphoma

L Ocasio¹, J Lally¹, L Ballester¹, R Riascos¹

¹*University of Texas HSC - Houston, Houston, TX*

Purpose

Multifocal tumefactive demyelinating lesions (TDL) have rarely heralded the subsequent diagnosis of primary central nervous system lymphoma (PCNSL), even after negative biopsy. Described is a rare case of these entities coexisting with discordant preliminary and final histopathology.

Materials and Methods

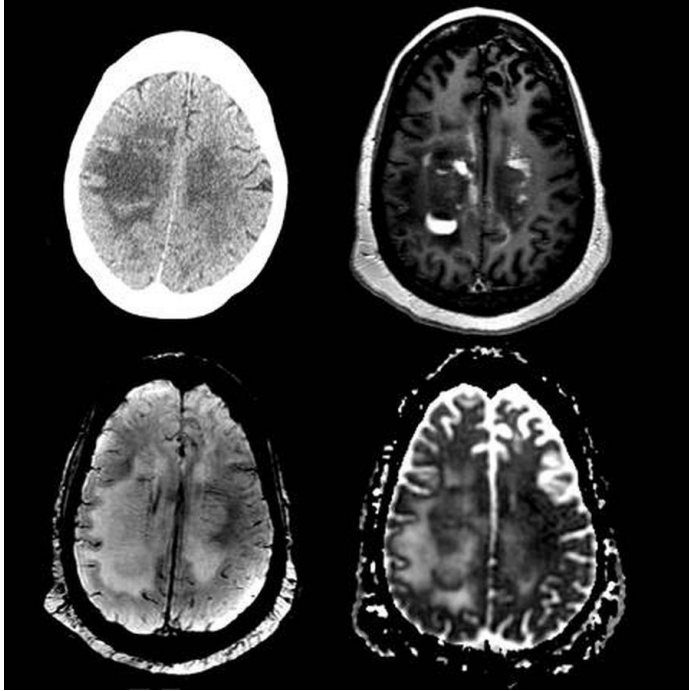
A 53-year-old immunocompetent woman with altered sensorium was transferred to our facility after initial imaging showing multifocal periventricular lesions suspicious for "brain cancer." Clinically, the patient presented after one month of progressive weight loss, postural imbalance, and left-sided weakness. The patient reported previous symptomatic episodes occurring 8 and 36 months prior. Cerebrospinal fluid was negative for oligoclonal bands, but protein and lymphocytes were mildly elevated. On imaging, the primary diagnostic consideration was multifocal TDL, with PCNSL and glioblastoma thought much less likely. Ultimately, brain biopsy was pursued. Initial frozen section showed Creutzfeldt astrocytes and macrophage infiltration favoring TDL. Final histopathology confirmed demyelination but revealed a population of large pleomorphic lymphocytes, establishing a concurrent diagnosis of diffuse large B-cell CNS lymphoma.

Results

Noncontrast CT showed heterogeneously dense bihemispheric lesions crossing the corpus callosum with a suggestion of lesional hyperdensity (Fig. 1a, top left). On MRI, postcontrast T1-weighted images show lack of mass effect, open ring enhancement, and burned out right centrum semiovale and left frontal lobe T1 hypo-intense lesions (Fig. 1b, top right). Periventricular vein architecture was preserved on susceptibility-weighted images (Fig. 1c, bottom left). ADC maps showed scattered areas of restricted diffusion (Fig. 1d, bottom right).

Conclusions

This case report highlights the challenging nature of radiologically discriminating TDL from PCNSL. Further muddying the waters, are several case reports showing multifocal sentinel demyelination preceding the diagnosis of PCNSL, even after initial biopsy [1-4]. This case may represent this point of transition. While previously reported, a distinct and causative relationship between these two entities is yet to be established.



(Filename: TCT_E-60_Excerpta-Final.jpg)

E-61

11:38AM - 11:42AM

Granulocytic Sarcoma (Chloroma) Presenting as Multifocal Intraparenchymal Masses

N Solomon¹, S Calle¹

¹*The University of Texas Health Science Center at Houston, Houston, TX*

Purpose

Granulocytic sarcomas, also known as chloromas due to the lesion's typical green color caused by high levels of myeloperoxidase in immature cells, are rare lesions seen in the setting of myelogenous leukemia and other myeloproliferative disorders. These masses are more common in acute myelogenous leukemia and occur in approximately 2.5-9.1% of patients with this condition [1]. In the central nervous system, granulocytic sarcomas typically appear as extra-axial masses. We present a case of granulocytic sarcoma presenting as multifocal intraparenchymal masses, an atypical imaging manifestation of this disease.

Materials and Methods

A 44-year-old female with chronic myelogenous leukemia on Sprycel (dasatinib) presented with altered mental status. She was found to have a blast crisis and CT of the head showed a left parietal lobe lesion. Chemotherapy was initiated with complete resolution of the brain lesion verified by imaging. She was discharged home awaiting bone marrow transplantation. Four months later, the patient presented again with new onset seizures. Her neurological exam was concerning for herniation with dilatation and fixation of her pupils. CT of the head showed multifocal parenchymal lesions involving the right temporal lobe and left frontal lobe with extension into the genu of the corpus callosum and left basal ganglia. Pathology of the resected right temporal lobe mass showed leptomeningeal and parenchymal involvement by myeloid leukemia. Immunohistochemical staining confirmed the cells to be positive for myeloperoxidase and negative for GFAP, concordant with diagnosis of brain involvement by myeloid leukemia.

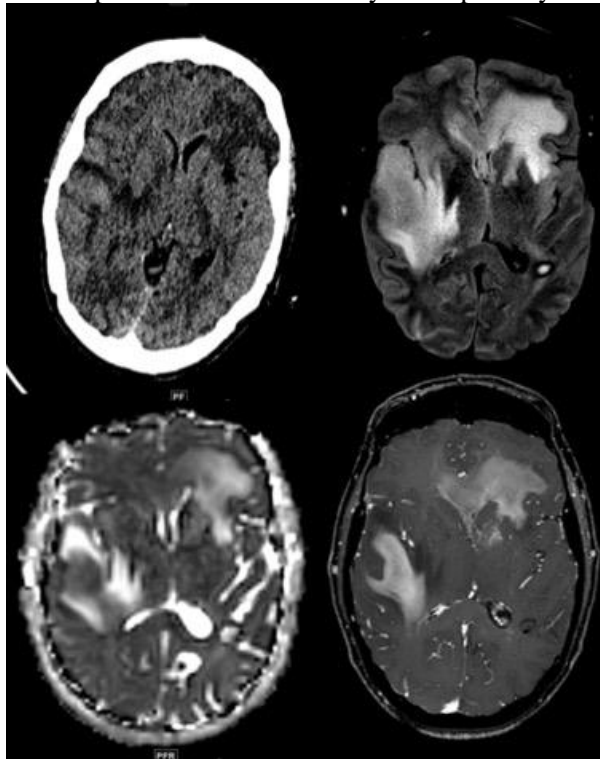
Results

On CT, a hyperdense lesion in the right temporal lobe is seen with surrounding vasogenic edema. Left frontal lobe vasogenic edema is also identified. MRI with and without contrast (Philips Ingenia 3T)

demonstrates almost complete resolution of the previous left parietal mass with associated volume loss and no contrast enhancement. New infiltrative multifocal lesions with a predominantly solid enhancement are now seen in the left periventricular frontal lobe, left anterior insula, genu of corpus callosum, and anterior septum pellucidum. A second dominant component in the right temporal lobe with central necrosis and surrounding T2 hyperintensity is also noted. There are patchy low ADC values throughout the infiltrative multifocal process.

Conclusions

Granulocytic sarcomas may develop as the presenting feature or at any point during the diagnosis of myelogenous leukemia. Their tissue of origin is thought to be the extra-axial veins located in the meninges and ependyma. This entity typically manifests as solitary or multiple extra-axial masses that demonstrate hyperdensity on noncontrast CT. MRI generally shows low to intermediate signal intensity on T1-weighted images, intermediate to high signal intensity on T2-weighted images and homogeneous enhancement following contrast administration. A separate imaging presentation has been described as patchy leptomeningeal involvement which can be difficult to distinguish from leptomeningeal carcinomatosis and infectious meningitis, among others. Rarely are granulocytic sarcomas seen to present as intraparenchymal masses. The characteristics on CT and MRI are similar to their extra-axial counterparts and clinical history is the primary indication of this pathology.



(Filename: TCT_E-61_Picture1.jpg)

E-62

11:42AM - 11:46AM

Angry Looking Textiloma Mimicking Recurrent Glioblastoma on Conventional MR and Multiparametric Advanced Brain Tumor Imaging

A Elakkad¹, N Elshafeey¹, A Kumar¹, B Wang¹

¹MD Anderson Cancer Center, Houston, TX

Purpose

Intracranial retained surgical materials (gossypiboma or textiloma) are uncommon incidents and are usually asymptomatic. In patients with resected glioblastoma (GBM), confusion with recurrent tumor or radiation necrosis remains the main challenge. Thus, it is important to consider textiloma as one of the possible differentials for this patient group. We present the imaging findings on both conventional magnetic resonance (MR) and multiparametric advanced brain tumor imaging (ABTI) in a pathologically proven textiloma mixed with radiation necrosis that mimics recurrent glioblastoma.

Materials and Methods

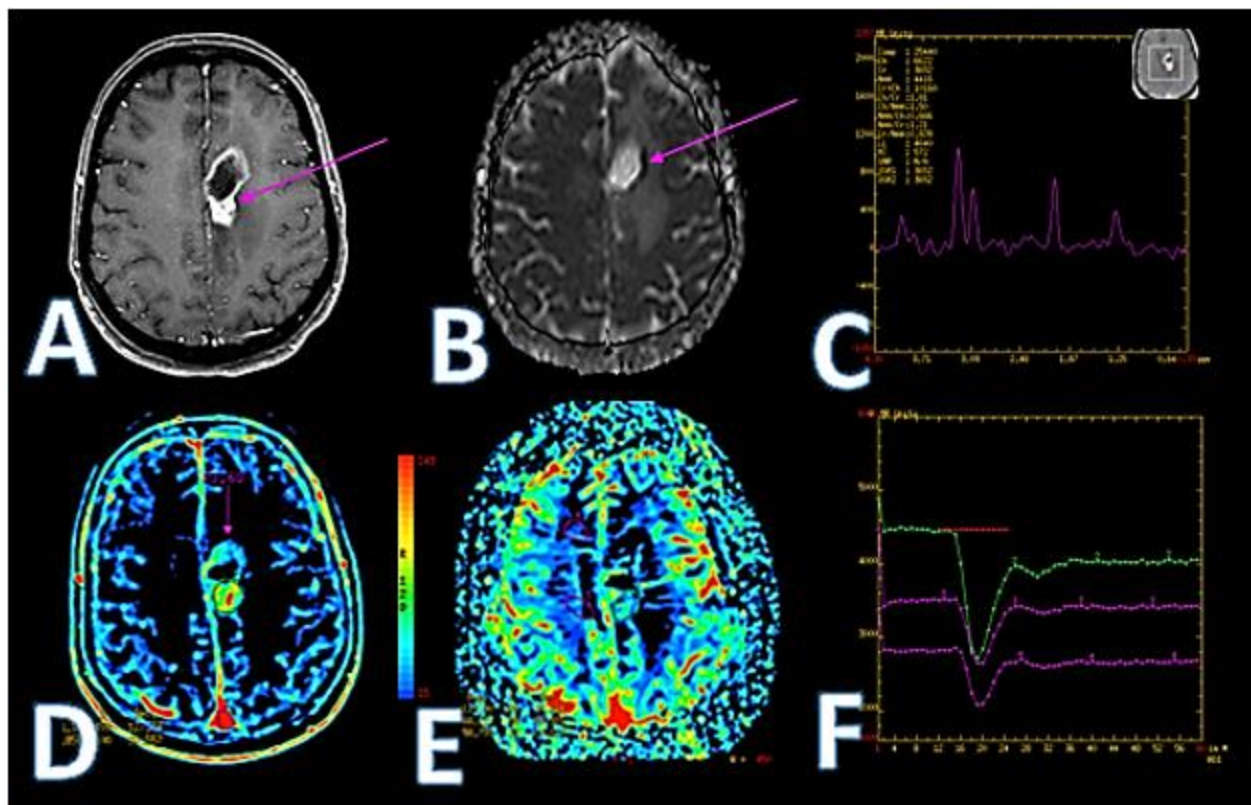
A right-handed 60-year-old female patient was asymptomatic until she developed a seizure activity focal to her right arm. Imaging showed a left frontal lobe lesion. She had a gross total resection and pathology was grade IV GBM. This was followed by six weeks of chemoradiation with concurrent Temodar. Several months later, follow-up MRI findings were worrisome for tumor recurrence around the resection cavity. Advanced brain tumor imaging (ABTI) was concordant with the conventional MRI findings. A redo-resection was planned and pathology revealed textiloma in a background of radiation necrosis. No viable tumor was identified.

Results

Conventional MR imaging showed a solid nodular enhancement posterior to the resection cavity. Also the solid peripheral enhancement around the resection cavity displayed restricted diffusion on apparent diffusion coefficient (ADC map). Magnetic resonance spectroscopy demonstrated an elevated choline to creatine ratio over the area of nodularity with a ratio of >1.8 . Dynamic susceptibility contrast (DSC) showed mild increase in relative cerebral blood volume (rCBV); however, on the time signal curve a rapid steep drop of signal intensity (SI) was shown with a percentage of signal recovery (pSR) of about 60%, findings worrisome for tumor recurrence. Dynamic contrast enhancement (DCE) demonstrated increased capillary permeability keeping with viable tumor.

Conclusions

To our knowledge, we are presenting the first report of pathologically proven textiloma mixed with radiation necrosis that mimics recurrent GBM on both conventional MR and ABTI. Conventional MR findings of solid nodular enhancement in the setting of high perfusion metrics in different MR perfusion parameters that are usually seen in high grade gliomas can also be encountered in textilomas. Also, spectroscopic findings can demonstrate elevated choline to creatine ratio resembling tumor recurrence. Although textilomas are not common, it is essential to include it in the list of differential, as it will highly impact the treatment plan in GBM patients.



Axial T1 post contrast (figure A) showing a solid nodular enhancement at the posterior aspect of the resection cavity (purple arrow). ADC map (figure B), axial image demonstrating a rim of restricted diffusion corresponding to the peripheral enhancement seen in the conventional images (purple arrow in figure B). MRS (figure C) showing elevated choline:creatine ratio of >1.8 . DCE and K-trans image (figure D) with high capillary permeability in the area of solid nodular component at the posterior aspect of the resection cavity. The peak enhancement integral 3, 60 value is elevated at approximately 22% which is suspicious for malignancy (pink arrow in figure D). DSC and rCBV map (figure E) showing mildly elevated relative cerebral blood volume at the green ROI, however on the time signal curve (figure F) a rapid steep drop of signal intensity (SI) was shown with a percentage of signal recovery (pSR) of about 60% favoring viable tumoral tissue at this area.

(Filename: TCT_E-62_Textiloma.jpg)

E-5

11:46AM - 11:50AM

Critical Illness-Associated Cerebral Microbleeds Related to Heat Stroke

M Thompson¹, A Hasso¹

¹University of California Irvine, Orange, CA

Purpose

Critical illness-associated unique pattern of cerebral microbleeds have recently been reported in the literature; however, no cases have been related to a history of heat stroke, which makes our case unique. Additionally, neuroimaging findings related to heat stress is rarely reported in the literature and is therefore important to discuss.

Materials and Methods

A 46-year-old male construction worker without significant past medical history had a witness collapse and "shaking episode" while at work. Upon arrival to the emergency department he was found to have a rectal temperature of 109.2F, hypotension, acute respiratory failure, and encephalopathy, compatible with

Oral Presentations & Excerptas

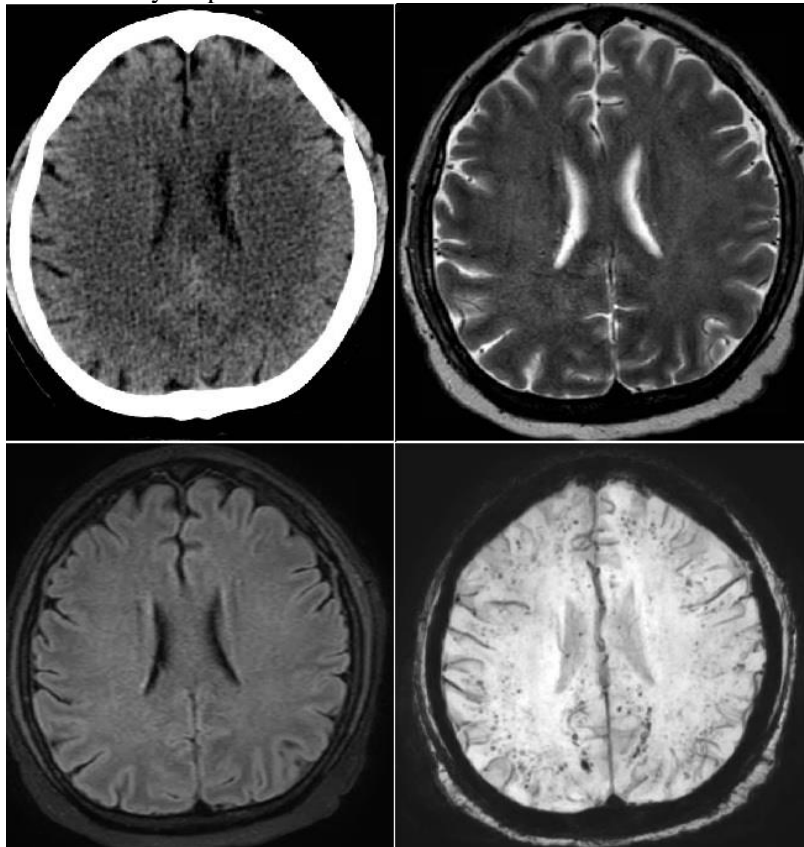
the diagnosis of heat stroke. In the weeks to follow, he developed acute liver failure, disseminated intravascular coagulation, acute renal failure, and ventilator-associated pneumonia. After eight weeks, his severe encephalopathy had failed to improve. After repeated negative workups for other potential causes of his encephalopathy, his family discussed with an ethics committee and decided for end-of-life care.

Results

Noncontrast CT of the head demonstrates no abnormality. MRI of the brain without and with contrast was performed. No abnormality is detected on the T1, T2, FLAIR, or postcontrast sequences. However, susceptibility-weighted images (SWI) demonstrates profound bilateral cerebral microbleeds in a pattern which involves particularly the juxtacortical white matter and corpus callosum, while uniquely sparing the periventricular and deep white matter and gray matter.

Conclusions

Microbleed patterns distinct from hypertension, amyloid, and diffuse axonal injury are important to recognize and may be the only neuroimaging abnormality detected in critically ill patients with encephalopathy, as with our case. This particular microbleed pattern is likely the result of a common end-pathway related to damage to the blood-brain barrier which can be due to hypoxia, heat stress, or inflammatory response.



(Filename: TCT_E-5_Figure1.jpg)

E-115

11:50AM - 11:54AM

Tumor Regurgitation: A Dramatic and Rare Presentation

Z Bhatti¹, K Hammoud²

¹University of Michigan, Ann Arbor, MI, ²Tufts Medical Center, Cambridge, MA

Purpose

To discuss a rare case of hypopharyngeal lipoma presenting with regurgitation into the mouth resulting in airway compromise

Materials and Methods

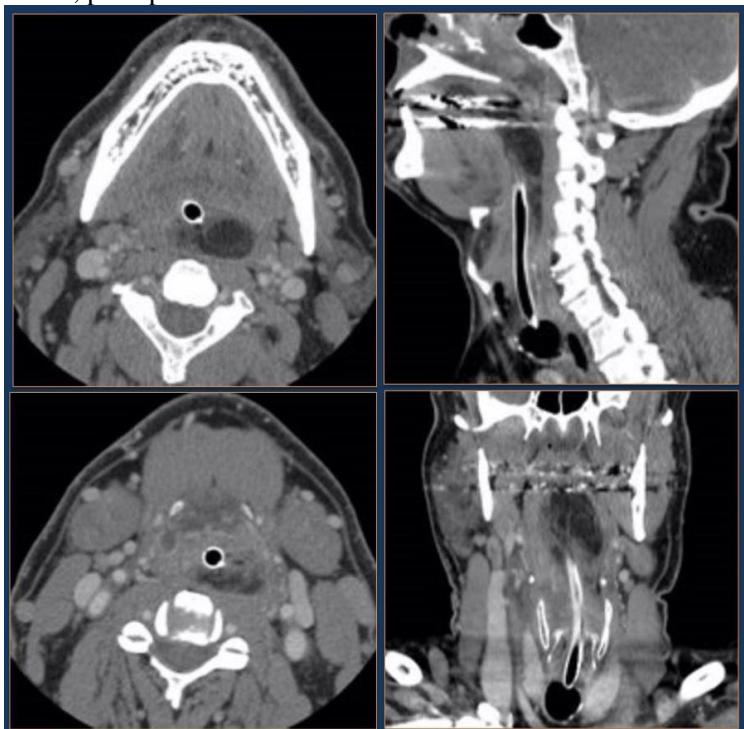
A previously healthy patient presented with acute onset coughing after eating, complicated by bleeding from the mouth and difficulty breathing. Physical examination revealed a soft mass in the mouth without apparent attachment to the oral cavity or oropharynx. The patient was emergently intubated and CT scan was performed, revealing a large mass in the oral cavity completely effacing the aerodigestive tract. Endoscopy and surgical resection were subsequently performed, which revealed a polypoid pedunculated mass arising just proximal to the upper esophageal sphincter. Pathology was consistent with a lipoma. Pedunculated lipomas of the hypopharynx are very rare, and the clinical presentation was very dramatic in this case.

Results

CT scan of the neck revealed a well defined, large, hypodense fat-attenuation mass lesion in the oral cavity, oropharynx, and hypopharynx completely effacing the aerodigestive tract.

Conclusions

Pedunculated lipomas of the hypopharynx and proximal esophagus are very rare, and retrograde prolapse into the oral cavity can be an emergency. Regurgitation into the mouth carries the risk of asphyxiation, hence, prompt removal is indicated.



(Filename: TCT_E-115_ASNRCasimages.JPG)

Tuesday, June 5, 2018

10:30AM - 12:00PM

Parallel Paper Session: Pediatric: Developmental and Congenital

O-201

10:30AM - 10:37AM

Oral Presentations & Excerptas

Volumetric Analysis of the Gray and White Matter of Patients with Allan-Herndon-Dudley Syndrome During Childhood

M Busch¹, C McGill¹, K Holden², L Bonilha¹, M Matheus¹

¹Medical University of South Carolina, Charleston, SC, ²Greenwood Genetic Center, Greenwood, SC

Purpose

Allan-Herndon-Dudley syndrome (AHDS) is a rare X-linked neurogenetic disorder. It occurs due to a mutation in the monocarboxylate transporter 8 gene encoding a thyroid hormone transporter. The affected boys present early in life with significant neurodevelopmental delays, hypotonia, and involuntary movements, most often dystonia. The characteristic imaging finding associated with this syndrome is delayed myelination. We propose to assess the gray matter (GM) and white matter (WM) total volume in pediatric patients with AHDS using brain MRI to evaluate brain growth pattern.

Materials and Methods

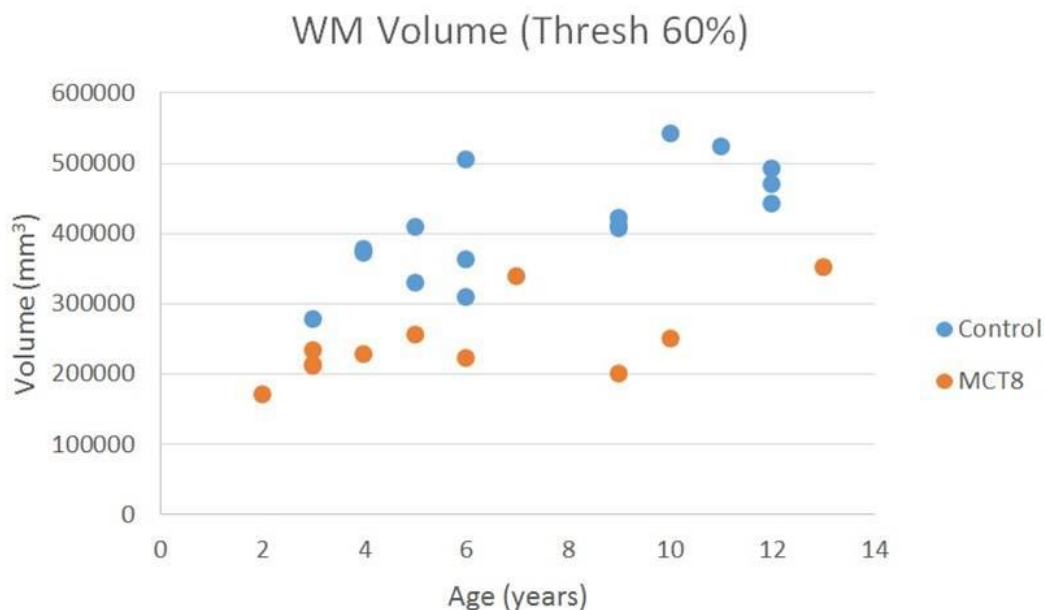
Pediatric patients with AHDS (n=11), age 2-13 years, were recruited with an almost symmetrical distribution to reflect 12 years of childhood. Age- and gender-matched normal controls were also recruited (n=16). Volumetric T1-weighted brain MRI images were acquired. The gray and white matter were segmented, measured, and compared.

Results

Regression analysis of the segmented GM total volume shows a slow progressive growth curve during childhood with minimal differences between subjects and control patients. AHDS GM volume is smaller than controls by a small but consistent margin. The WM volume analysis reveals a similar growth pattern, but with more pronounced differences between AHDS patients and controls, again by a consistent margin throughout development.

Conclusions

The results presented here reveal that the GM and WM volume of patients with AHDS is smaller than normal subjects at the same age by a consistent margin throughout development, but demonstrate a similar growth rate pattern during childhood as compared to normal subjects. WM appears to be more affected than GM. The growing pattern of the AHDS brain does not show degenerative/progressive characteristics during childhood.



(Filename: TCT_O-201_WM_1.jpg)

O-202

10:37AM - 10:44AM

Textural Analysis of Ambulatory and Non-ambulatory Children with Muscle Disorders using T1 Weighted MRIs of the Mid-calf and Mid-thigh

C Yip¹, P Tang², J Allen¹

¹Duke-NUS Medical School, Singapore, Singapore, ²KK Women's and Children's Hospital, Singapore, Singapore

Purpose

Textural analysis has the potential to characterize muscle abnormalities that are not visible to the human eye, and may have a higher sensitivity in the diagnosis of early disease when changes are subtle. It may be a useful quantitative tool to monitor disease progression and treatment response in clinical trials of drug treatments for muscular disorders. This study seeks to determine if textural analysis can distinguish between ambulatory and nonambulatory patients with muscle disorders.

Materials and Methods

This study uses the statistical filtration-histogram approach to perform textural analysis. The textural parameters studied were mean, standard deviation (SD), entropy, mean of positive pixels (MPP), skewness and kurtosis. The sample population consists of six subjects with muscle disorders, three ambulant and three nonambulant. All subjects were scanned with a 3T MRI scanner with similar imaging parameters in KK Women's and Children's Hospital. Textural analysis was performed with TexRAD with regions of interest (ROIs) in the anterior and posterior compartments of the mid thigh and mid calf outlined by a single operator on T1-weighted images. The software suite SAS was used for statistical analysis.

Results

In the mid thigh, the textural parameters standard deviation (SD), entropy, mean of positive pixels (MPP), skewness and kurtosis showed significant difference between the muscles of ambulant and nonambulant patients and the greatest Cohen's d value was exhibited by entropy (6.18) followed by SD (3.58) and MPP (3.36). In the mid calf, the textural parameters standard deviation (SD), entropy, mean of positive pixels (MPP), and skewness showed significant difference between the muscles of ambulant and nonambulant patients and the greatest Cohen's d value was exhibited by SD (4.06) followed by MPP (2.66) and entropy (2.63).

Conclusions

Texture analysis shows differences in the mid thigh and mid calf muscles of ambulant and nonambulant patients with muscle disorders. The top three textural parameters with the greatest Cohen's d values are entropy, SD and MPP.

Table 1. Textural Parameters Compared between Ambulant and Non-Ambulant Patients in the Mid-Thigh at SSF 2 (n = 6)

Textural Parameter	Estimate		Mean difference	95% CI	Cohen's <i>d</i>	<i>P</i> value
	Ambulant	Non-Ambulant				
Mean	-10.99 ± 10.70	-71.66 ± 62.54	-60.66	-22.68, -98.65	1.35	0.43
SD	85.89 ± 18.18	683.14 ± 234.91	597.25	738.31, 456.20	3.58	* < 0.01
Entropy	5.31 ± 0.31	7.08 ± 0.26	1.77	2.01, 1.53	6.19	* < 0.01
MPP	48.43 ± 22.45	505.07 ± 191.01	456.64	571.78, 341.50	3.36	* < 0.01
Skewness	-0.33 ± 0.66	0.10 ± 0.35	0.43	-0.88, 0.02	0.81	* < 0.01
Kurtosis	4.19 ± 1.90	0.51 ± 0.91	-3.68	-2.42, -4.94	2.47	* < 0.01

*denotes *P* value < 0.05. Differences were tested with ANCOVA adjusted for age and gender.

Note: SD = Standard Deviation, MPP = Mean of Positive Pixels

Table 2. Textural Parameters Compared between Ambulant and Non-Ambulant Patients in the Mid-Calf at SSF 2 (n = 6)

Textural Parameter	Estimate		Mean difference	95% CI	Cohen's <i>d</i>	<i>P</i> value
	Ambulant	Non-Ambulant				
Mean	-23.73 ± 14.98	-137.09 ± 153.80	-113.36	-20.85, -205.87	1.04	0.80
SD	128.33 ± 23.30	726.46 ± 207.19	598.14	782.57, 413.7	4.06	* < 0.01
Entropy	5.47 ± 0.08	6.56 ± 0.58	1.09	1.44, 0.75	2.63	* < 0.01
MPP	60.63 ± 18.62	466.014 ± 214.44	405.39	534.25, 276.53	2.66	* < 0.01
Skewness	-0.72 ± 0.62	-0.16 ± 0.31	0.56	0.98, 0.14	1.14	* < 0.01
Kurtosis	2.51 ± 1.15	0.85 ± 1.02	-1.66	-0.74, -2.58	1.53	0.70

*denotes *P* value < 0.05. Differences were tested with ANCOVA adjusted for age and gender.

Note: SD = Standard Deviation, MPP = Mean of Positive Pixels

(Filename: TCT_O-202_MuscleTable.jpg)

O-203

10:44AM - 10:51AM

Comparison of MR Scoring Systems in Predicting Neurologic Outcomes in Neonates with Hypoxic-ischemic Encephalopathy: Deep Gray Injury Associated Best with Seizures

C Toensing¹, S Harder¹, A Achiriloaie¹, J Jacobson¹, U Oyoyo¹, P Kim¹

¹Loma Linda University Medical Center, Loma Linda, CA

Purpose

Hypoxic-ischemic encephalopathy (HIE) is the most common cause of death among the neonatal population. The ability to provide prognostic information can aid in diagnosis and management of these patients. This study was undertaken to evaluate three commonly accepted imaging scoring systems (National Institute of Child Health and Human Development [NICHD]), Barkovich et. al., Rutherford et. al.) for HIE and to investigate which region was best associated with neurologic outcomes.

Materials and Methods

IRB waiver of consent was obtained. MRI scans of a cohort of 98 consecutive pediatric patients with the clinical diagnosis of HIE were retrospectively reviewed and scored using each scoring system. Each patient's chart was reviewed by an experienced pediatric neurologist (PP) to determine the presence or absence of EEG-confirmed seizures, used as a surrogate for neurologic outcomes. Statistical analysis was performed, including Mann-Whitney U test, with odds ratios calculated.

Results

Patient mean age was 10 days +/- 4.5 with 52 males. Forty-six neonates had EEG-proven seizures. The basal ganglia (BG) score under the Barkovich scale and basal ganglia and thalamus score (BGT) under the Rutherford scale were associated with seizure (*p* = 0.05 and *p* = 0.02). The watershed score under the

Barkovich scale, and the white matter and cortical involvement scores under the Rutherford scale were not associated with seizure. The odds of seizure with a moderate-severe BG score (2-4) and BGT score (2-3) were 3.91 [95% CI: 1.4-11.1] and 7.77, [95% CI: 1.6-37]. The odds of seizure with a moderate-severe NICHD score (2A, 2B and 3) were 3.27 [95% CI: 1.2-8.9].

Conclusions

Moderate-severe BG, BGT and NICHD scores all reflect moderate-severe abnormal signal in deep-gray structures. This study shows that moderate-severe abnormal signal in deep grey structures is best associated with EEG-proven seizures during hospitalization, suggesting these findings correlate with worse neurologic outcomes.

O-204

10:51AM - 10:58AM

Perfusion and Diffusion Imaging in Distinguishing Pilocytic Versus Pilomyxoid Astrocytomas Above and Below the Tentorium

C Ho¹, V Seit², N Supakul¹, M Groswald¹, J Cardinal³, S Kralik²

¹Indiana University School of Medicine, Indianapolis, IN, ²Indiana University, Indianapolis, IN, ³TRA Medical Imaging, Tacoma, WA

Purpose

Pilomyxoid astrocytoma (PMA) is more aggressive and has a higher likelihood of leptomeningeal dissemination, leading to worse outcome compared to pilocytic astrocytomas (PA). Furthermore, genetic differences have been found between supratentorial versus infratentorial PAs. Perfusion- and diffusion-imaging were utilized to assess for differences between PMAs and PAs as well as supratentorial (ST) versus infratentorial (IT) tumors.

Materials and Methods

This retrospective, IRB exempt study included consecutive patients from 2011 to 2016 with histologically diagnosed PA or PMA with dynamic susceptibility contrast perfusion and diffusion MR imaging. Solid tumor volumes (VOI) were manually traced on commercially available software (Olea Shere 3.0, Olea Medical, La Ciotat, France) using T1+C or T2 imaging registered to computed ADC, rCBV, K2 leakage, and MTT maps. The resulting data were evaluated with Student's and Welch's T-tests.

Results

Forty-nine subjects (mean age 6.7, 1-15 years, 24 females) met inclusion criteria. There were 30 IT PAs, 8 ST PAs, 5 IT PMAs, and 6 ST PMAs. No significant differences were found between the means of the VOIs between all ST versus IT tumors, ST PAs versus IT PAs, ST PMAs versus IT PMAs, or between all PAs and PMAs for ADC, K2 and MTT. Significant difference for Student's t-tests but not Welch's t-tests were seen in rCBV between all ST (2.60 ± 0.63 95CI) and all IT (2.06 ± 0.18) tumors ($p=0.02$ vs 0.1), as well as between ST PAs (2.53 ± 0.68) and IT PAs (2.04 ± 0.19) ($P=0.04$ vs. $P=0.14$).

Conclusions

PAs and PMAs, as well as supra- and infratentorial locations cannot be distinguished by ADC, K2, or MTT parameters. There is a trend toward a higher perfusion difference in supratentorial tumors versus infratentorial tumors.

O-205

10:58AM - 11:05AM

Synthetic MRI in Tuberous Sclerosis: Quantitative Assessment of Parenchymal and CSF Volumes and of Lesional T1, T2 and PD values

B Jones¹, J Leach², H West¹

¹Cincinnati Children's Hospital, Cincinnati, OH

Purpose

Synthetic MRI (SyMRI) is an MR imaging method in which a multiple spin echo saturation recovery sequence utilizing four saturation delays and two echoes (QMAP) is used to obtain quantitative parameters of the brain [1]. The sequence allows for calculation of absolute voxel-wise R1 and R2 relaxivity and PD values via SyMRI software yielding T1, T2 and PD maps. It also can perform quantitative brain segmentation, allowing for rapid assessment of regional and global volumes of CSF, gray matter, and white matter. Tuberous Sclerosis (TS) is a genetic disorder caused by mutations in the TSC1 or TSC2 gene, resulting in the development of benign tumors in multiple organs, with a substantial burden of disease manifest in the brain. Brain lesions in this condition are found in the ependymal lining of the ventricles, white matter, and cortical gray matter. Imaging characteristics of the lesions can evolve over time, and some lesions can become more aggressive. We analyzed a large population of patients with TS utilizing SyMR in order to identify and quantify characteristic alterations in brain parenchymal and CSF volume compared to age-matched normal values, and to analyze the various parenchymal lesion types in regard to their absolute T1, T2, and PD values compared to normal-appearing regions of the brain.

Materials and Methods

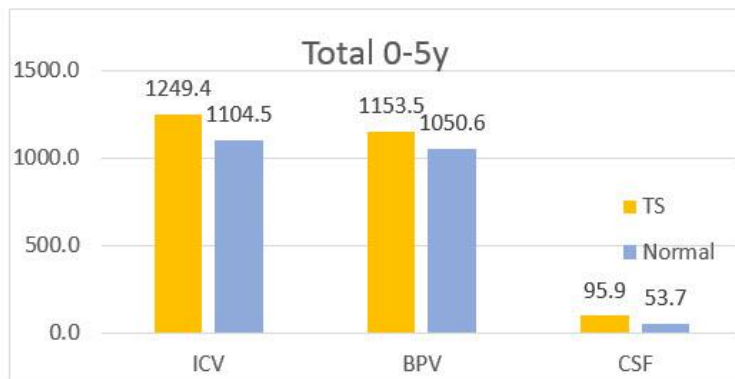
An institutional review board-approved retrospective review was performed of all brain MR imaging examinations acquired over a 47-month period on patients with a confirmed diagnosis of TS in which the QMAP sequence was performed. A total of 96 studies in 89 subjects were identified and reviewed; seven of the subjects had two studies each. SyMRI was used to calculate intracranial volume (ICV), brain parenchyma volume (BPV), and global CSF volume in each case. Regions of interest (ROI) were drawn around characteristic cortical, white matter, ventricular, and cerebellar lesions (when present) in each case, and absolute T1, T2, and proton density values were recorded for each lesion. Similar ROIs were created in normal-appearing gray matter and white matter for each case.

Results

In subjects 0-5 years of age, intracranial volumes were increased relative to normal values, with increases in both CSF and brain parenchyma volumes. These differences lessened in older subjects. For cortical lesions, there was no difference in absolute T1, T2, or PD values between lesion and normal appearing cortex ROIs, but there were substantial differences in these values for white matter lesions and their normal appearing comparison ROIs.

Conclusions

SyMRI volumetric analysis of subjects with tuberous sclerosis yields insight into differences in brain development compared to normal populations. Analysis of specific lesion characteristics indicates that imaging abnormalities primarily result from white matter, rather than gray matter, alterations. These findings have the potential to increase understanding of the relationship between the underlying lesion pathology and imaging phenotype in this disorder, and may increase understanding of the imaging manifestations of related pathologies such as focal cortical dysplasia and low grade glioma.



Intracranial volumes in TS v normal

(Filename: TCT_O-205_2017-12-15_8-29-33.jpg)

O-206

11:05AM - 11:12AM

FAST MRI FOR SHUNTED CHILDREN: SINGLE SEQUENCE AXIAL FAST T2 COULD REPLACE CURRENT PROTOCOLS

S Subramanian¹, J Ly², T Elizabeth¹, V Lee¹, A Panigrahy¹, G Zuccoli¹

¹Children's Hospital of Pittsburgh, Pittsburgh, PA, ²University of Pittsburgh Medical Center, Pittsburgh, PA

Purpose

Evaluation for VP shunt malfunction in children is assessed by FAST MRI using axial, coronal and sagittal plane SSFSE/HASTE and axial GRE sequences. This approach is currently considered the gold standard evaluation in shunted patients. However, usefulness has never been tested.

Materials and Methods

A retrospective 12-years IRB approved review of 350 cases of FAST MRI obtained to evaluate shunt malfunction in a large U.S. third-level pediatric center. The utility of axial plane, coronal plane and sagittal plane was tested to assess ventricular caliber compared to prior studies by using a qualitative 3-points score assessment. Diagnostic confidence of axial; axial and coronal; axial, coronal and sagittal sequences was evaluated by two radiologists independently. Student T test for reader 1 and reader 2 was assessed.

Results

The assessment of change in ventricular caliber on the axial plane only was comparable between reader 1 and reader 2 with a p value of 0.84 and 0.68. The assessment of interval changes in ventricular caliber only on axial and coronal planes was similar for reader 1 and reader 2 with p values of 0.31 and 0.52 (not statistically significant). The diagnostic confidence (p value) for the axial plane vs. axial and coronal plane for reader 1 was 0.31 and for reader 2 was 0.28. The diagnostic confidence (p value) for the axial and 3-planes MRI was 0.31 and 0.057, respectively.

Conclusions

One plane SSFSE compared to multiple plane is adequate to assess ventricular size assessment.

O-207

11:12AM - 11:19AM

Radiation Dose Reduction Strategies for Intrathecal Spinraza (Nusinersen) Administration in Spinal Muscular Atrophy

I Ikuta¹, A Mustafa², M Johnson¹

¹*Yale University School of Medicine, New Haven, CT*, ²*Yale University, New Haven, CT*

Purpose

Spinraza (nusinersen) is the only treatment for spinal muscular atrophy (SMA) approved by the United States Food and Drug Administration. Its administration route is intrathecal. Given the drastic changes in spine morphology of SMA patients (scoliosis, surgical hardware, etc), image-guided lumbar puncture is typically requested. While radiation exposure from medical imaging is always as low as reasonably achievable (ALARA), this principle is highly relevant to the pediatric patients with SMA given the increased radiosensitivity of pediatric soft tissues. A low radiation exposure is also desired for each administration given the necessity for lifelong treatment with nusinersen. We provide our experience with intrathecal nusinersen administration as an initial radiation exposure benchmark, and to highlight the tips and pitfalls in this radiation dose optimization process.

Materials and Methods

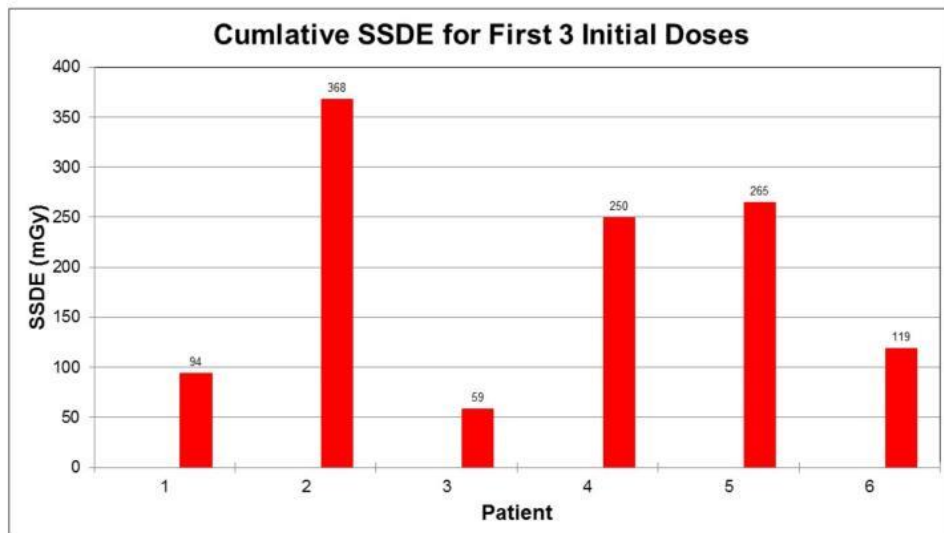
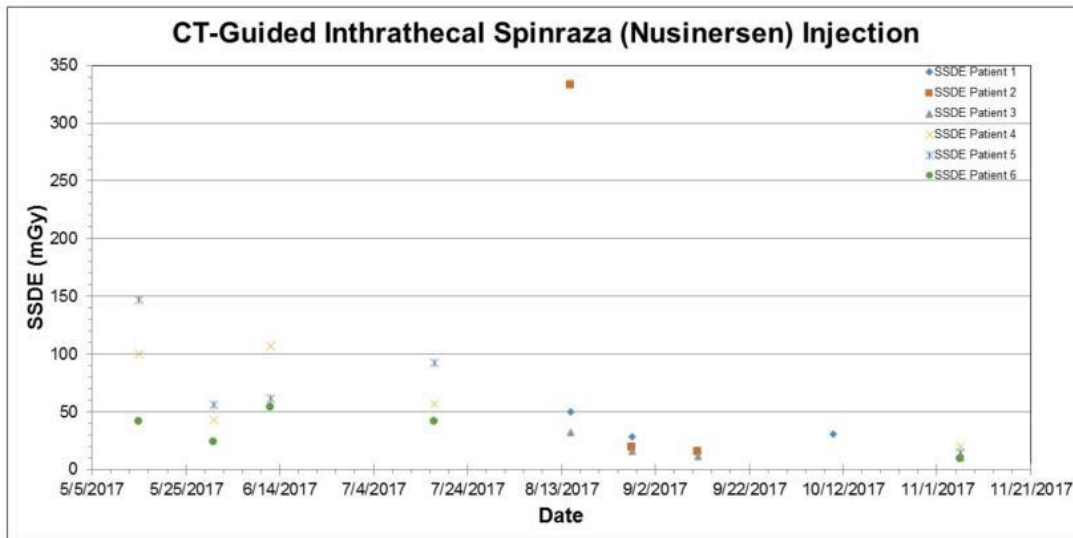
Institutional review board approval was obtained for this Health Insurance Portability and Accountability Act-compliant study, with waiver of informed consent. The study was performed at a tertiary care academic hospital. Patients with SMA underwent CT-guided lumbar puncture with intrathecal nusinersen injection by an interventional neuroradiologist from May 15, 2017, through November 6, 2017. The CT x-ray tube output metrics were recorded for each administration, including kVp, mA, slice thickness, number of passes, and CTDIvol. The geometric mean of the patient's cross-sectional diameter was determined from the axial anteroposterior and lateral diameters, and applied to the CTDIvol to produce a size-specific dose estimate (SSDE) for each encounter. Injections were given on initial day 1, day 14, day 28, day 58, and day 178, prior to indefinite injections every 4 months. Cumulative SSDE was summated for each patient.

Results

Six patients have been enrolled for treatment with ages ranging from 4-19 years. The SSDE for initial day 1 ranged from 11-333 mGy. While the 5th dose (day 178) SSDE data is available for only three patients due to staggered start times, the SSDE decreased and ranged from 9-20 mGy. Data for all six patients is available through three doses (day 28), with cumulative SSDE ranging from 59-368 mGy. Overall, there was a downward trend in SSDE. The scan length was variable, which limits radiation exposure estimates at the extremes of the scanned anatomy, but should be accurate for the central regions of the scan. An outlier (patient 2) had a larger initial Day 1 SSDE due to more extensive initial planning and error in marking the initial table position. Strategies which demonstrated persistent efficacy in radiation exposure reduction included: 1. allowing for increased noise in order to lower the kVp 2. disabling the automated exposure current and fixing the mA 3. allowing for decreased contrast resolution in order to lower the mA 4. forgoing spinal needle-tip imaging confirmation in the thecal sac in the case of spontaneous return of CSF Decreasing scan length after the initial planning scan reduces the radiation exposure, but does not factor into the calculation of SSDE.

Conclusions

Through a combination of preprocedure planning, reducing the number of CT scan passes, optimizing CT scanner x-ray tube output metrics, and finding acceptable noise and contrast levels, we were able to systematically reduce the radiation exposure for patients undergoing CT-guided lumbar puncture for intrathecal nusinersen therapy for patients with spinal muscular atrophy.



(Filename: TCT_O-207_ASNR18fig_prelim.jpg)

O-208

11:19AM - 11:26AM

Radiographically Occult Tethered Cord in Pediatric and Adult Patients

A Baker¹, J Boxerman², P Klinge², G Baird², J Rogg²

¹Brown University, Providence, RI, ²Rhode Island Hospital, Providence, RI

Purpose

Tethered cord syndrome (TCS) is identified by a clinical spectrum including neurologic, urologic, and orthopedic signs and symptoms. [1, 2] MRI has traditionally played an important diagnostic role, demonstrating signs of spinal cord tethering including low-lying conus and thickened or lipomatous filum. [3] The goal of this study was to assess the sensitivity of MRI in patients with "occult" TCS in children and adults.

Oral Presentations & Excerptas

Materials and Methods

Two board-certified neuroradiologists (NR) retrospectively reviewed lumbar MRI for 55 subjects (4-56 years-old, mean 31). Twenty-eight patients clinically diagnosed with TCS by a specialized pediatric and adult neurosurgeon without concordant preoperative MRI findings ("radiographically occult") were compared to 27 age-matched controls imaged for "back pain". All TCS patients demonstrated clinical response to surgery at 1,3 year postoperative evaluation by objective assessment. Fifty-four patients were scanned at 1.5T or 3T. Protocol included axial and sagittal T1, T2-weighted sequences. Axial T1 performed in 44 patients, 24 with TCS and 20 controls. All cases were independently and randomly presented to each NR for review of criteria for tethered cord: conus position at or below lower L2 and fatty or thickened filum. Diagnostic performance was evaluated using generalized mixed modeling, assuming a binary distribution with sandwich estimation, where observations were nested within radiologist.

Results

NR1 diagnosed 0 of 28 TCS patients as having positive MRI findings for tethered cord. NR2 called a tethered cord when it was clinically tethered; this radiologist also called a tethered cord when it was not clinically tethered. Sensitivity 3.5%, specificity 96%, $p=0.99$, ROC: 0.50.

Conclusions

This study confirms absence of classic tethered cord MRI findings in a population of patients with TCS. Further quantification with a larger patient population is the next step to refine a threshold for conus position associated with TCS.

Tuesday, June 5, 2018

1:15PM - 2:46PM

Parallel Paper Sessions: Skull Base and Sinus

O-209

1:15PM - 1:22PM

Magnetic Resonance Imaging-Based Evaluations of Olfactory Bulb Atrophy in Patients with Olfactory Dysfunction

M Chung¹, J Kim², Y Choi², J Lee²

¹Chung-Ang University Hospital, Seoul, Republic of Korea, ²Asan Medical Center, Seoul, Republic of Korea

Purpose

We aimed to evaluate the utility of visual olfactory bulb atrophy and neuropathy analyses using MRI in patients with olfactory dysfunction.

Materials and Methods

Thirty-four patients who presented with subjective olfactory loss between March 2016 and February 2017 were included. Patients underwent a nasal endoscopic examination, olfactory testing with the Korean Version of the Sniffin' Sticks Test, and MRI. All patients completed the Sino-nasal Outcome Test and Questionnaire of Olfactory Disorders. Olfactory bulb atrophy and neuropathy were evaluated on MR images by two head and neck radiologists.

Results

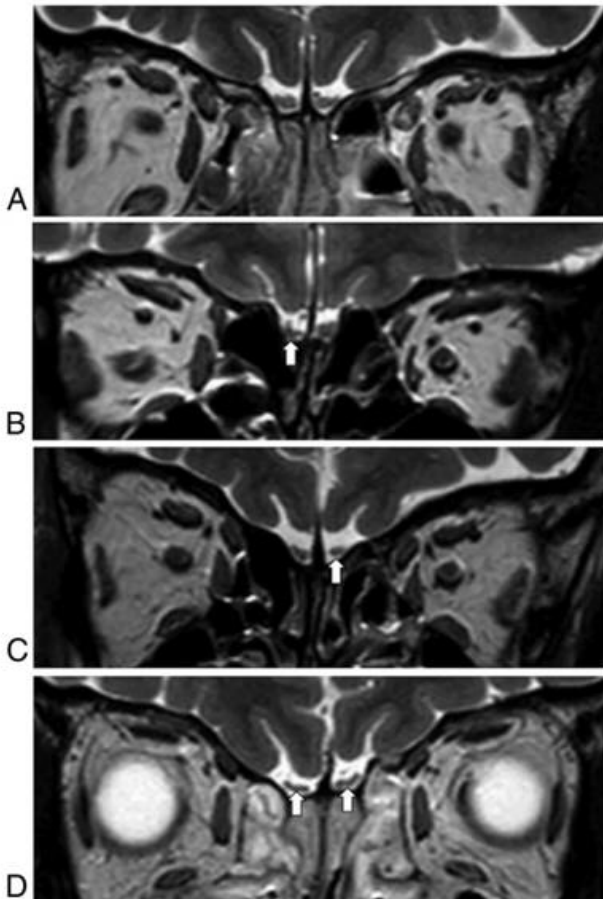
The etiology of olfactory loss was chronic rhinosinusitis with/without nasal polyps in 15 (44.1%) patients, respiratory viral infection in seven (20.6%), trauma in two (5.9%), and idiopathic in 10 (32.3%) patients. Although 10 (29.4%) of the 34 patients were normosmic according to the Sniffin' Sticks Test, their scores on the other tests were not different from those of patients who were hyposmic/anosmic according to the

Oral Presentations & Excerptas

Sniffin' Sticks Test. However, the detection rate of olfactory bulb atrophy was significantly higher in hyposmic/anosmic patients than it was in normosmic patients ($p = 0.002$). No difference in olfactory bulb neuropathy was identified between normosmic and hyposmic/anosmic patients ($p = 0.395$).

Conclusions

MRI evaluations of olfactory bulb atrophy can be used to objectively diagnose olfactory dysfunction in patients with subjective olfactory loss.



Atrophy of olfactory bulb. A. normal, B. atrophy in right olfactory bulb, C. atrophy of left olfactory bulb, and D. atrophy of both olfactory bulb

(Filename: TCT_O-209_fig.jpg)

O-210

1:22PM - 1:29PM

Prospective evaluation of Blood-Brain-Barrier Dysfunction in Patients with Aneurysmal Subarachnoid Hemorrhage - Correlation with Clinical Outcomes in a Pilot Cohort.

P Sharma¹, R Ferraro¹, G Askin¹, A Segal¹, A Gupta¹, P Sanelli², J Ivanidze¹

¹New York Presbyterian Hospital - Weill Cornell Medical College, New York, NY, ²Northwell Health, Manhasset, NY

Purpose

CT Perfusion (CTP) allows quantitative assessment of blood-brain-barrier (BBB) permeability parameters, including PS (flow across the vessel wall to the extravascular extracellular space (EES)), Ktrans (plasma flow per unit tissue volume), KEP (EES-to-IVS contrast washout rate), VP (plasma volume) and VE (EES volume). BBB disruption is thought to play a role in the pathophysiology of aneurysmal subarachnoid hemorrhage (SAH) complications. The purpose of this study was to prospectively evaluate BBB dysfunction in the clinical setting and to correlate BBBP with clinical outcomes in patients with SAH.

Materials and Methods

In this prospective IRB-approved pilot study, 10 patients with SAH underwent CTP imaging early in the post aneurysmal rupture period (0-3 days) as part of clinical standard-of-care. CTP data were postprocessed into quantitative parametric maps, including PS, kTrans, KEP, VE, and VP, using Olea 2.3 software. Patients were stratified into good clinical outcomes (mRS 0-2, N =6) and poor outcomes (mRS 3-4, N=4). Descriptive statistics were calculated for the entire dataset. The two-sample t-test or Wilcoxon rank-sum test, as appropriate, was used to assess the associations between CTP parameters and mRS category at discharge and at one-month follow-up. Statistical analyses were performed with R Version 3.3.1.

Results

BBBP parameters were evaluated in patients categorized as having moderate/high disability (MRS 3-4, N = 4) compared with patients with low/no disability (mRS 0-2), N =6). BBBP parameter data in the stratified subgroups are provided in the accompanying table.

Conclusions

Given the pilot character of this study, our data did not reach statistical significance. However, there was a trend for increased BBB dysfunction, reflected in higher PS, higher VE, lower KEP, and higher VP, in patients with poor mRS compared to patients with good mRS at discharge and at one-month follow-up, respectively. Future work will focus on validating this pilot data in a larger patient cohort, laying the foundation for the validation of BBBP evaluation with CTP as a prognostic biomarker in SAH.

Bivariate associations by MRS category (0-2, 3-4) at discharge				
	moderate/high disability	no/low disability	p. overall	N
	N=4	N=6		
PS	30.0	28.5	0.854	10
VE	0.15	0.10	0.403	10
Ktrans	0.14	0.14	0.868	10
KEP	1.07	1.52	0.386	10
VP	0.25	0.22	0.707	10
F	199	179	0.741	10
E	0.23	0.14	0.145	10

Bivariate associations by MRS category (0-2, 3-4) at 1-month follow-up				
	moderate/high disability	no/low disability	p. overall	N
	N=4	N=6		
PS	35.9	27.1	0.620	10
VE	0.16	0.09	0.317	10
F	204	184	0.818	10
E	0.2	0.18	0.660	10
Ktrans	0.15	0.14	0.855	10
KEP	1.07	1.32	0.505	10
VP	0.29	0.22	0.604	10

(Filename: TCT_O-210_ASNR2018_PS_JI.jpg)

O-211

1:29PM - 1:36PM

Automatic Detection of Cerebral Microbleeds (CMBs) using Strategically Acquired Gradient Echo (STAGE) imaging

Y Chen¹, S Xia², L Wang³, S Sethi³, M Fawaz¹, S Liu¹, E Haacke¹

¹The MRI Institute for Biomedical Research, Bingham Farms, MI, ²Tianjin First Central Hospital, Tianjin, China, ³Magnetic Resonance Innovations Inc., Bingham Farms, MI

Purpose

To automatically detect and segment cerebral microbleeds (CMBs) using Strategically Acquired Gradient Echo (STAGE) imaging

Materials and Methods

STAGE imaging employs multiple double-echo gradient echo acquisitions providing whole brain-covered T1WE, T1W, PDW, T1 map, PD map, R2* map, SWI, tSWI, QSM, MRV and MRA in just 10 minutes [1-3]. In this study, sixty-five subacute stroke subjects were scanned using STAGE at Tianjin First Central Hospital China on a clinical 3T scanner (Siemens Trio) approved by the local IRB. A total of 27 subjects had CMBs reported by the participating radiologists. The PDW image (TE=7.5ms, FA=6deg) shows both CMBs and a few veins as hypointense on the magnitude images but not small veins.

However, both large and small veins and CMBs are shown in the SWI and QSM data [4, 5]. To detect CMBs using STAGE data we propose the following algorithm: 1) apply a threshold on the QSM data to segment high susceptibility structures including veins, CMBs and deep gray matter; 2) apply another

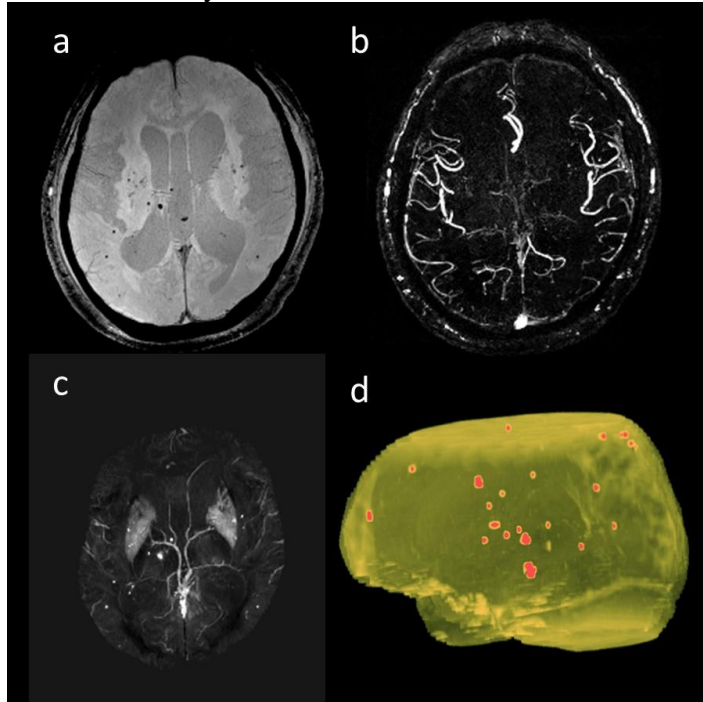
threshold on the low FA magnitude images to segment predominantly CMBs with only a few false positives from larger veins remaining; 3) apply a mask to the MRV data denoting all blood vessels [3]; and 4) generate a product mask incorporating all the above steps.

Results

CMBs were detected successfully on 22 of the 27 subjects. Three data sets had false negatives which represented tiny CMBs. Two data sets had false positives. The figure shows one of the subject's data including: a) minimum intensity projection of PDW; b) maximum intensity projection (MIP) of MRV; c) MIP of QSM; and d) 3-D rendering of the detected CMBs overlaid on the magnitude images.

Conclusions

Preliminary results show that STAGE data can be used for detecting CMBs in a clinical environment. The current sensitivity with these limited number of cases is 94.6% and the specificity is 95.0%.



(Filename: TCT_O-211_figure1.jpg)

O-212

1:36PM - 1:43PM

Volumetric Brain MRI and Neonatal Neurobehavioral Correlates in Infants of Zika-infected Mothers

S Ghosh¹, J Riotti², A Ramachandran², E Bandstra¹, J Hofheimer³, F Reyes Avila¹, E Crep¹, C Bauer¹, S Andreansky¹, I Gonzalez¹, V Govind¹, G Saigal⁴

¹University of Miami, Miami, FL, ²Jackson Memorial Hospital, Miami, FL, ³UNC Health, Chapel Hill, NC, ⁴University of Miami/Jackson Memorial Hospital, Miami, FL

Purpose

Congenital Zika syndrome (CZS) comprises a unique pattern of devastating birth defects including microcephaly in infants prenatally infected with Zika virus (ZIKV). Unlike the visibly noticeable microcephaly in ZIKV-infected infants, a significant proportion of ZIKV-exposed children (89-94%) appear phenotypically normal without microcephaly at birth. However, recent reports [1] indicate that some of these infants subsequently show lagging trajectories in brain growth and development. Thus, the objective of this study is to measure and compare the brain-tissue, CSF and total intracranial volumes in

Oral Presentations & Excerptas

ZIKV-infected, ZIKV-exposed, and healthy control infants from MR imaging, and associate these measures with neurobehavioral measures.

Materials and Methods

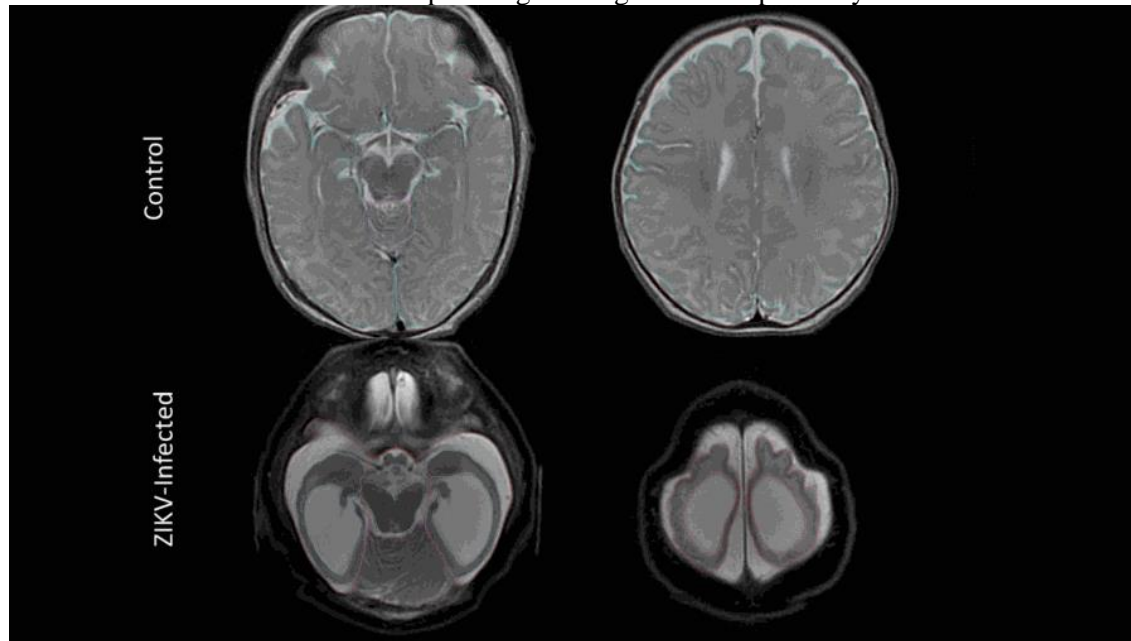
The study population consists of nine ZIKV-exposed infants whose mothers had laboratory evidence of ZIKV infection during pregnancy, one with CZS and microcephaly, and one control. T2-MRI acquired at 3T (without sedation and contrast) were used to manually trace and calculate the total whole-brain volume (TWV), CSF and total intracranial volume (TIV) using MultiTracer [2]. The NICU-Network-Neurobehavioral-Scale (NNS) was administered at full-term equivalent gestation and the 13 subscale scores were calculated and categorized [3].

Results

Preliminary results show that 60% of the 10 infants with gestational ZIKV-exposure or infection demonstrated neurobehavioral deficits on at least three NNS subscales, including either high (40%) or low (50%) arousal, poor focused attention (30%), poor self-regulation (30%), lethargy (30%), and hyper or hypotonicity (20% each). The infant with CZS showed neurobehavioral deficits on hypertonicity, asymmetric reflexes, stress, and handling needs. Volumetric MRI analysis of exposed infants (n=5) demonstrate lower TIV, and substantially lower TWV (supratentorial structures, cerebellum and brainstem), and larger component of CSF compared to normal control (TWV 441 mL in exposed versus 549 mL in control), see Figure 1. Additionally, there is substantial difference between ratio of whole brain to CSF in exposed infants compared to normal control (1.56 in exposed infants, compared to 6.53 in control).

Conclusions

Despite lack of gross microcephaly, the majority of Zika-exposed infants demonstrated functional neurobehavioral deficits and subtle pathologic changes in brain parenchymal structures.



(Filename: TCT_O-212_Contouringexamplefinalgif.gif)

O-213

1:43PM - 1:50PM

Multiparametric Quantitative and Functional Magnetic Resonance Imaging in Differentiation of Central Nervous System Tuberculoma and Neurocysticercosis

R Ghosh¹, P Singh¹, S Vyas¹, N Khandelwal¹, P Singhi¹, N Sankhyan¹, S Dhawan¹

¹Postgraduate Institute of Medical Education and Research, Chandigarh, India

Oral Presentations & Excerptas

Purpose

Tuberculoma and neurocysticercosis (NCC) are two most common intracranial infections in developing countries (1, 2). They are often difficult to differentiate on neuroimaging and in absence of typical imaging features cause significant diagnostic dilemmas. Differentiation is extremely important particularly to avoid empirical use of antitubercular medications. The aim of this study was to better characterize and differentiate CNS tuberculoma and NCC by using quantitative and functional MRI.

Materials and Methods

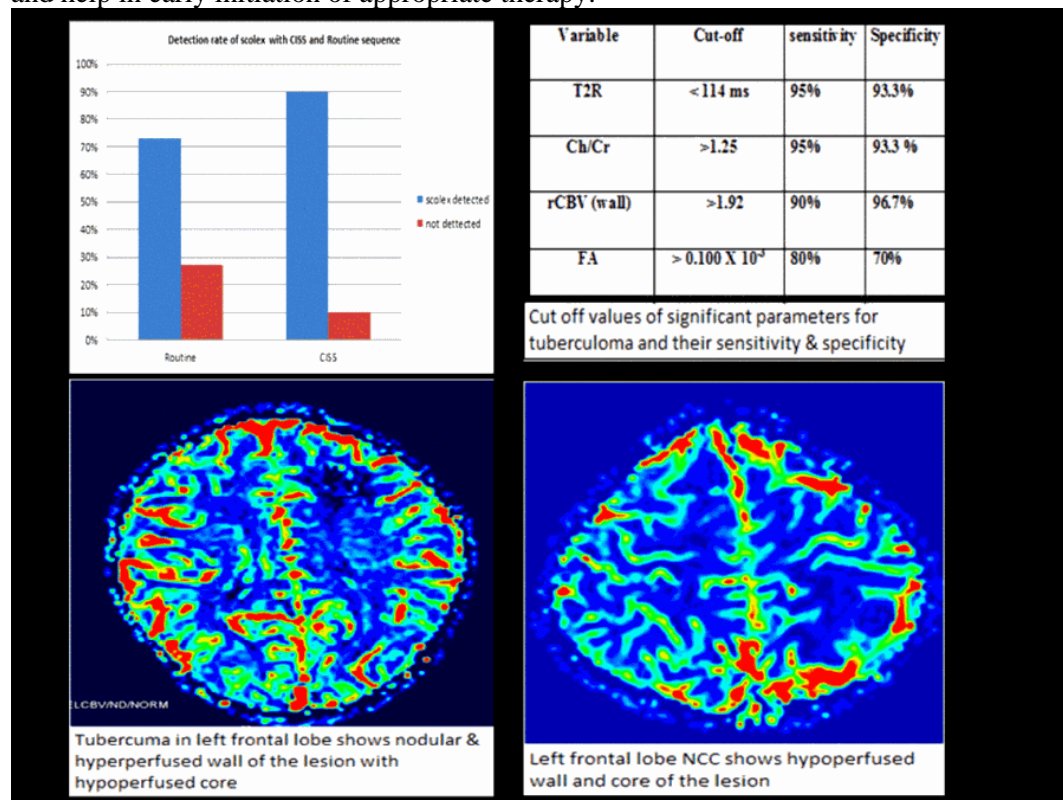
Fifty newly diagnosed patients (20 tuberculoma and 30 NCC) were evaluated by using conventional and advanced sequences such as CISS, SWI, DTI, T2 Relaxometry (T2R), perfusion and spectroscopy. rCBV, FA, T2R values and metabolite ratios were calculated from various parts of lesion and normal parenchyma. Diagnosis was confirmed by typical biochemical, microbiological and imaging features.

Results

CISS was most useful sequence for scolex detection (90% on CISS vs. 73% on routine sequences). SWI showed higher scolex detection ability. Mean values of FA, T2R from core and rCBV from wall of lesion were significantly different in tuberculoma and NCC ($P < 0.05$). Mean values of rCBV, FA and T2R for tuberculoma and NCC were (3.36 vs 1.3), (1.09×10^{-3} vs 1.4×10^{-3}), (0.13×10^{-3} vs 0.09×10^{-3}) and (88.65 ms vs 272.3 ms) respectively. T2R was most significant sequence in differentiation. Cutoff values have been proposed for each significant parameter. Tuberculoma showed higher Choline/Creatinine ratio than NCC ($P < 0.001$) on MRS.

Conclusions

Quantitative MRI in combination with conventional sequences can better characterize and differentiate similar appearing tuberculoma and NCC, and may be incorporated in routine protocol for this purpose. Advanced sequences may be a problem-solving tool in indeterminate cases which will avoid brain biopsy and help in early initiation of appropriate therapy.



(Filename: TCT_O-213_graphicfinal.gif)

Relationship between Pineal Cyst Size and Aqueductal CSF Flow Measured by Phase Contrast MRI

A Bezuidenhout¹, R Bhadelia¹

¹*Beth Israel Deaconess Medical Center, Boston, MA*

Purpose

Most patients with pineal cysts referred for neurosurgical consultation have no specific symptoms or objective findings except for pineal cyst size to help in management decisions. Our purpose was to assess the relationship between pineal cyst size and aqueductal CSF flow using PC-MRI.

Materials and Methods

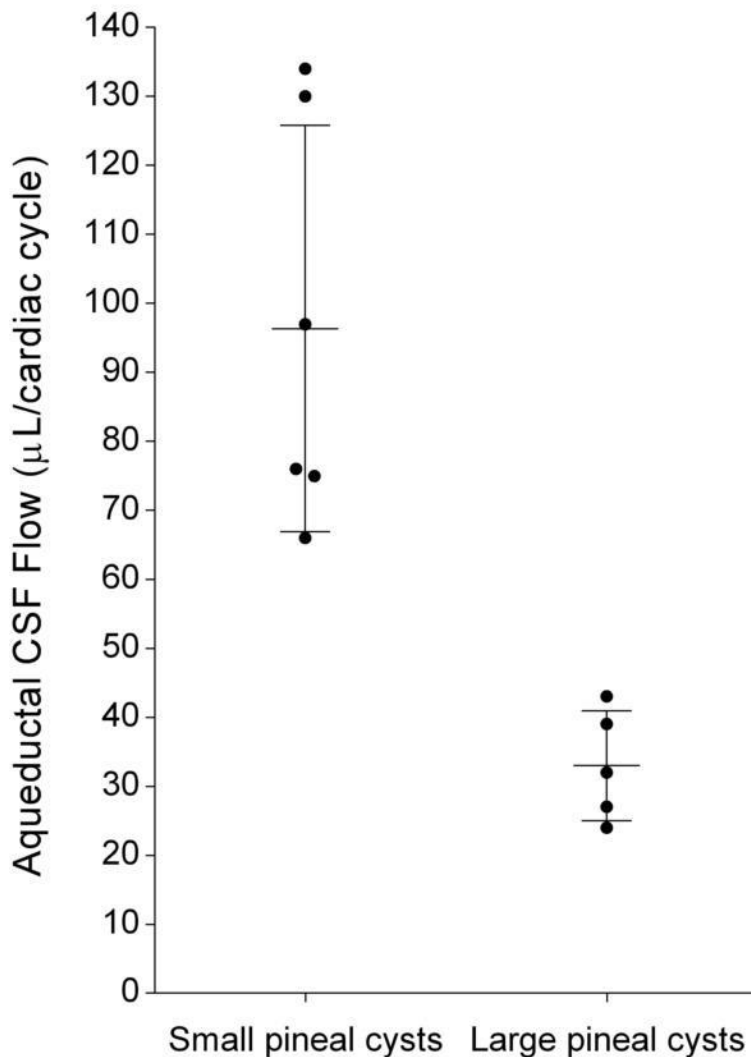
Eleven adult patients with pineal cysts (> 1-cm in size) referred for neurosurgical consultations were included. Cyst volume was calculated using 3-D T1 images. PC-MRI in axial plane with velocity encoding of 5 cm/sec was used to quantitatively assess CSF flow through the cerebral aqueduct to determine the aqueductal stroke volume, which was then correlated to cyst size using Pearson's correlation. Pineal cysts were grouped by size into small (6/11) and large (5/11) using the median value to compare aqueductal stroke volume using Mann-Whitney test.

Results

Patients were 39 ± 13 years (mean \pm SD) of age, and 10/11 (91%) were female. There was significant negative correlation between cyst volume and aqueductal stroke volume ($r=0.74$; $p=0.009$). Volume of small cysts (4954 ± 2157 mm³) was significantly different compared to large cysts (13752 ± 3738 mm³; $p=0.008$). The aqueductal stroke volume of patients harboring large cysts 33 ± 8 μ L/cardiac cycle was significantly lower than that of patients with small cysts 96 ± 29 μ L/cardiac cycle ($p=0.008$).

Conclusions

Aqueductal CSF flow appears to decrease with increasing pineal cyst size. Our preliminary results provide first evidence that even in the absence of objective neurological findings or hydrocephalus, larger pineal cysts already display decreased CSF flow through the cerebral aqueduct.



(Filename: TCT_O-214_FIGURE3.jpg)

O-215

1:57PM - 2:04PM

Prospective Evaluation of Blood-Brain-Barrier Integrity and Cerebrospinal Fluid Lipocalin-2 Protein Levels in Aneurysmal Subarachnoid Hemorrhage: Correlation with Disease Severity.

J Ivanidze¹, R Ferraro¹, A Segal¹, A Gupta¹, P Sanelli²

¹New York Presbyterian Hospital - Weill Cornell Medical College, New York, NY, ²Northwell Health, Manhasset, NY

Purpose

Lipocalin-2 (LCN2), has experimentally been shown to activate CNS inflammatory mediators and promote acute brain injury; however, it has not previously been evaluated in the clinical setting. Blood-brain-barrier (BBB) integrity has been hypothesized to correlate with CNS inflammation. Our purpose was to prospectively correlate cerebrospinal fluid (CSF) LCN2 levels with clinical disease severity and BBB permeability.

Oral Presentations & Excerptas

Materials and Methods

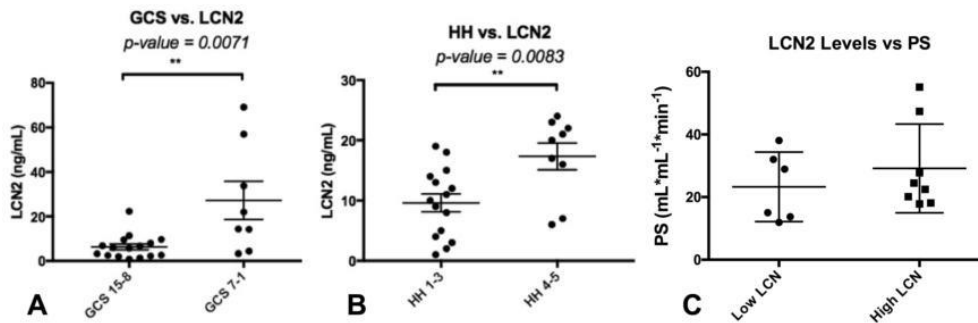
In this prospective IRB-approved study, CSF was collected from SAH patients via ventriculostomy catheter. CSF LCN2 protein levels were measured using ELISA technique. Patients were stratified by admission Glasgow Coma Scale (GCS) and Hunt Hess Scale (HH) into severe (GCS 1-7; HH 4-5) versus mild-moderate (GCS 8-15; HH 1-3) categories. CTP data were postprocessed into quantitative parametric maps, including PS, kTrans, KEP, and VP, using Olea 2.3 software. BBBP parameters were used for further stratification. Statistical analysis was performed using Mann-Whitney tests.

Results

Twenty-four patients met inclusion criteria. LCN2 levels were significantly elevated in the severe GCS group (N = 8) compared to the mild/moderate GCS group (N = 16) (median, 18.2 versus 5.9 ng/mL, $p = 0.0071$). LCN2 levels were significantly elevated in the severe HH group (N = 9) compared to the mild/moderate HH group (N = 15) (median, 21.9 versus 6.7 ng/mL, $p = 0.0083$). There was a trend for higher LCN2 levels in patients with BBB dysfunction (High PS group, mean LCN2 11.39, Low PS group, mean LCN2 4.438); however, this did not reach statistical significance ($p = 0.28$).

Conclusions

We prospectively evaluated BBB dysfunction using CTP and inflammation using LCN2 CSF protein analysis in SAH patients and correlated these findings with clinical disease severity. We found significant correlation between clinical scores of SAH disease severity and CSF LCN2 levels. Our findings lay the groundwork for future studies of LCN2 and BBB integrity as a multimodal prognostic biomarker in the assessment of disease severity and clinical outcomes in SAH.



LCN2 Correlates with Disease Severity in Patients with SAH. Patients stratified by GCS (A) and HH (B) demonstrated statistically significant differences in LCN2 CSF protein expression levels. Furthermore, patients with higher LCN2 CSF protein levels demonstrated a trend for higher PS as measured by CT-Perfusion (C).

(Filename: TCT_O-215_ASNR2018BBBPLCN.jpg)

O-217

2:11PM - 2:18PM

Scan-rescan Repeatability of Hippocampal Volume Measurements in Patients with Low-grade Glioma: Comparison of Automated Software Packages

D Barboriak¹, S Woodring¹, S Panta¹, E Lipp¹, F McSherry¹, J Herndon¹, A Desjardins¹, D Randazzo¹, H Friedman¹, K Peters¹

¹Duke University Medical Center, Durham, NC

Purpose

Although direct quality of life measures are useful for following psychosocial outcomes in patients with brain tumors, the development of an imaging biomarker would be helpful to better understand the biological underpinning of successful survivorship in these patients. Hippocampal volume (HV) has been

associated with both cognitive and other functional performance and can be measured from volumetric T1-weighted MRI using automated software. We compared repeatability of HV measurement for four software packages.

Materials and Methods

We used Bland-Altman repeatability coefficients (RC) and intraclass correlation coefficients (ICC) to compare 0- and 10-minute scan-rescan reproducibility of HV measurements in 26 patients with WHO grade II gliomas not involving the hippocampi at baseline and after six months using four software packages: FSL/FIRST, FreeSurfer, HippoSeg and NeuroQuant.

Results

Patients were a median age of 42 (range 22-68), 54% male, 61.5% had KPS \geq 90, 65.4% had a gross total resection, and 58% had no prior progressions. Thirteen patients (50%) had no prior treatment (surgery, chemotherapy or radiotherapy). For total HV, the RC in mm³ with 95% confidence intervals was 490 (386-671), 743 (586-1019), 896 (706-1228) and 907 (714-1242) at baseline and 496 (391-680), 589 (464-807), 1107 (872-1517) and 547 (431-750) at six months using FSL/FIRST, FreeSurfer, HippoSeg and NeuroQuant, respectively. Differences in HV within time point were not significant; mean HV was 8083, 6032, 6945 and 8416 mm³ at baseline and 8179, 6000, 7001 and 8653 mm³ at six months, respectively. The ICC was 0.977 (0.957-0.988), 0.881 (0.784-0.936), 0.841 (0.716-0.913) and 0.956 (0.918-0.977) for baseline and 0.979 (0.960-0.989), 0.922 (0.857-0.959), 0.852 (0.736-0.920) and 0.985 (0.971-0.992) at six months, respectively.

Conclusions

FSL/FIRST showed lower RC than HippoSeg and NeuroQuant at baseline and higher ICC than FreeSurfer and HippoSeg at both baseline and six months. This data is useful to inform software choice and sample-size calculations for studies of HV in this patient group.

O-218

2:18PM - 2:25PM

Spinal imaging findings of open spinal dysraphism on fetal and postnatal MRI

U Nagaraj¹, K Bierbrauer¹, C Stevenson¹, J Peiro¹, B Kline-Fath¹

¹Cincinnati Children's Hospital Medical Center, Cincinnati, OH

Purpose

To examine spinal imaging findings in fetuses with open spinal dysraphism and compare with postnatal imaging features

Materials and Methods

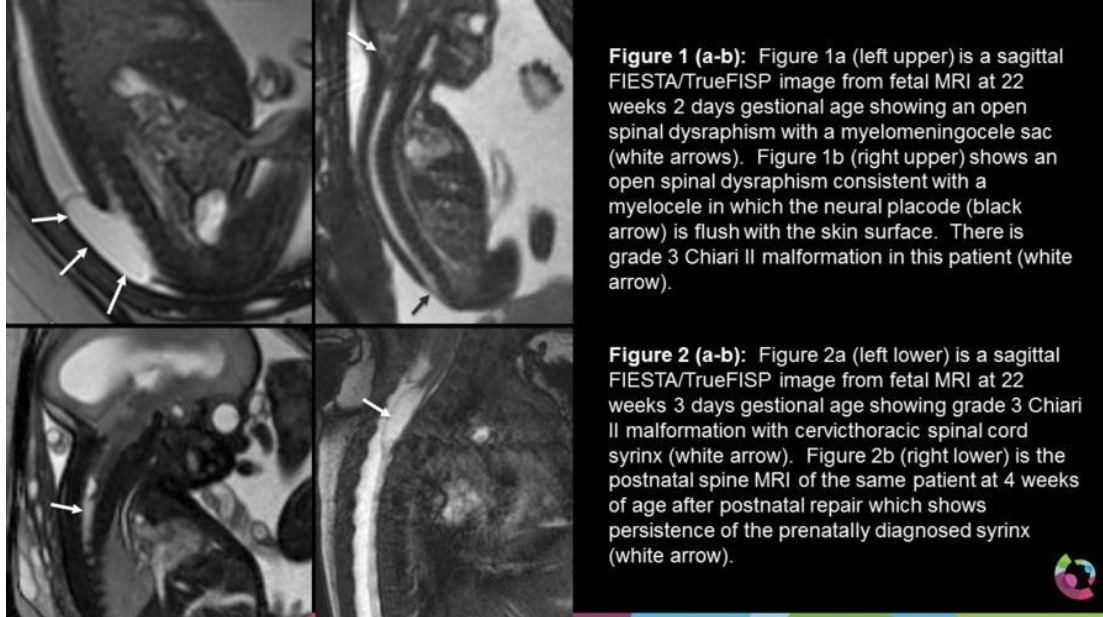
A single-center HIPPA compliant IRB approved retrospective analysis was performed of fetal MRIs with open spinal dysraphism from January 2004 through October 2016 with available diagnostic postnatal spine MRI. Images were reviewed by two board certified fellowship-trained pediatric neuroradiologists. Corresponding obstetrical ultrasound and clinical/operative reports were reviewed.

Results

Included were 119 fetal MRIs of open-spinal dysraphism with available postnatal spine MRI and clinical/neurosurgical follow-up. Average gestational age at fetal MRI was 23.9 ± 3.6 weeks. Of these, 29% (35/119) had myeloceles; the remainder had myelomeningoceles. All myeloceles (35/35) had grade 3 (severe) Chiari II malformation; however, only 74% (62/84) of myelomeningoceles (62/84) had grade 3 Chiari II malformation. Of fetuses 5% (6/119) had focal kyphosis, all (6/6) with grade 3 Chiari II malformation. The level of the osseous defect between fetal and postnatal MRI was concordant in 43% (51/119) of cases, and was one level different in 39% (47/119) of cases. Syrinx was noted in 3% (4/119) of prenatal studies, all cervical, all confirmed on postnatal MRI; however, fetal MRI was performed after the second trimester in 3/4 of these patients. Of postnatal spine MRIs 39% (47/119) had evidence of spinal cord syrinx, of which 30% (14/47) had undergone prenatal repair.

Conclusions

We present our experience of spinal imaging findings on pre and postnatal MRI in patients with open spinal dysraphism. Of fetuses 100% imaged with myelocoele or kyphosis had severe Chiari II malformation. Concordance within one level of the osseous defect was seen in 82% (98/119) of patients between pre and postnatal MRI, an important factor in counseling and determining candidates for prenatal surgery. Though rare, fetal MRI had a high specificity for detecting cervical spinal cord syrinx.



(Filename: TCT_O-218_ASNRChiariSpine.jpg)

O-219

2:25PM - 2:32PM

Measuring Thalamic Lesion Extent Following Focused Ultrasound Thalamotomy

J Druzgal¹, J Patrie², J Elias¹, M Wintermark³

¹University of Virginia, Charlottesville, VA, ²University of Virginia Health System, Charlottesville, VA, ³Stanford University, Stanford, CA

Purpose

Unilateral MR-guided focused ultrasound thalamotomy has recently been FDA-approved for treatment of essential tremor. The target of the thalamotomy is the ventral intermediate (VIM) nucleus, a structure estimated to measure 6mm x 4mm x 4mm. Despite clinical approval for the technique, the extent of the lesion made in humans remains relatively unknown. We hypothesized that longitudinal volumetric measurements of the thalamus could be used to approximate the actual lesion size.

Materials and Methods

A retrospective analysis was performed on 56 patients who underwent unilateral thalamotomy under study protocols for either essential tremor or tremor-dominant Parkinson's disease. All patients had pretreatment MPRAGE MRI performed. Post-treatment MPRAGE scans were available at post-treatment days 1 (N=14), 2-10 (N=15), 11-50 (N=40), 51-100 (N=15), and 101-433 (N=32). All MPRAGE scans were processed through Freesurfer to obtain thalamus volumes ipsilateral and contralateral to the side of unilateral thalamotomy. Longitudinal changes in ipsilateral and contralateral thalamic volumes were tested, referenced to each patient's baseline thalamic volumes.

Results

The ipsilateral thalamic volume increased at post-treatment days 1 (466 mm³, p<0.001), 2-10 (580 mm³,

p<0.001), and decreased at post-treatment days 11-50 (-104 mm³, p=0.046), 51-100 (-188 mm³, p=0.010), and 101-433 (-286 mm³, p<0.001). The contralateral thalamic volume was unchanged at post-treatment days 1, 2-10, 11-50, 51-100, and decreased at post-treatment days 100-433 (-100 mm³, p<0.001). The change difference between the ipsilateral and contralateral thalamus is at least 186 mm³ at the time points more than 50 days post-treatment.

Conclusions

Increases in thalamic volume within 10 days of thalamotomy likely reflect edema related to the treatment, confounding estimates of lesion size. Tissue loss from thalamotomy maximizes by post-treatment days 51-100 and remains relatively consistent at days 101-433. The amount of tissue lost exceeds estimates of VIM nucleus volume, suggesting that other thalamic structures are affected, either through direct effects of the thalamotomy or subsequent Wallerian degeneration.

O-220

2:32PM - 2:39PM

Leptomeningeal Enhancement on FLAIR Imaging in Patients with Cerebral Aneurysms Treated with Endovascular Therapy

Y Li¹, D Simpson², C Funk¹, A Ahmed², D Dawkins¹, J Yu²

¹University of Wisconsin Hospitals and Clinics, Madison, WI, ²University of Wisconsin, Madison, WI

Purpose

The effects of endoluminal manipulations and intra-arterial medications on the downstream cerebrovascular structures after endovascular therapy remain largely unknown. Imaging biomarkers of cerebrovascular dysfunction after endovascular therapy have been reported presuming intra-arterial contrast administration and sudden changes in cerebral hemodynamics as the underlying etiologies; however, rigorous characterization of postcontrast (pc) FLAIR following endovascular treatment for intracranial aneurysms has not been reported. We report, to the best of our knowledge, the first description of abnormal leptomeningeal enhancement on pcFLAIR MRI following endovascular aneurysm treatment and suggest pathophysiologic correlates to clinically observed cerebrovascular dysfunction following endovascular therapy.

Materials and Methods

From July 2012 to November 2017 patients harboring intracranial aneurysms were treated with flow diverting stents. Patients subsequently underwent postoperative MR imaging within 24 hours of the procedure. In a single-center retrospective study, we reviewed these patient demographics and imaging findings.

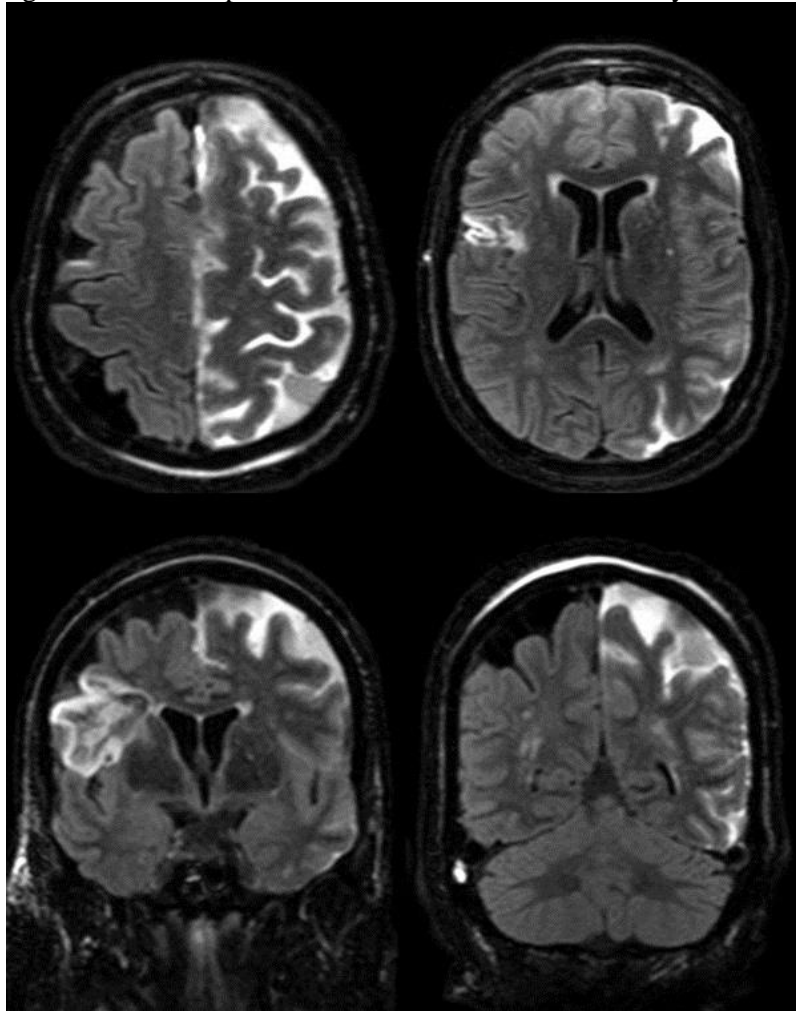
Results

We identified 80 patients (8 males) who underwent endovascular flow diversion treatment of 84 intracranial aneurysms between July 2012 and November 2017. The mean age was 56.8 ± 13 years. In our cohort 69 out of 80 (86%) patients developed abnormal leptomeningeal enhancement (LME) on postoperative pcFLAIR imaging within the ipsilateral circulation. Of the 12 patients who had both pre and pcFLAIR imaging, LME was absent on precontrast imaging and seen exclusively on pcFLAIR in all cases. A total of 35 (44%) patients also underwent CT imaging immediately postprocedure. Subarachnoid contrast was observed in 11 of 35 patients (31%) all of whom also had pcFLAIR LME. The presence of subarachnoid contrast in patients with pcFLAIR LME was 11 of 31 (35%). There was no statistically significant relationship between the presence of LME and age, sex, presence of DWI lesions, hypertension, smoking, or aneurysm size.

Conclusions

We report a novel imaging finding of LME on pcFLAIR imaging observed in 86% of patients undergoing endovascular treatment of intracranial aneurysms. The extent to which this imaging finding correlates with cortical dysfunction, manifesting as transient neurological deficits or electroencephalography changes, remains to be explored. Future research is required to identify risk factors for development of

LME after endovascular therapy. Further elucidation of the pathophysiology of pcFLAIR LME may shed light on the development of PRES and cerebrovascular dysfunction seen after endovascular therapy.



(Filename: TCT_O-220_Figure1.jpg)

O-221

2:39PM - 2:46PM

Added Value of Arterial Spin Labeling Perfusion in the Emergency Department: A 6 month Institutional Experience

G Cruciata¹, F Pacheco², P Pawha³, J Schefflein³, A Doshi³, J Puig⁴, K Nael³, P Belani³

¹Mount Sinai Hospital, Brooklyn, NY, ²Santa Casa de São Paulo School of Medicine, São Paulo, Brazil, ³Icahn School of Medicine at Mount Sinai, New York, NY, ⁴Diagnostic Imaging Institute (IDI), IDIBGI, University Hospital Dr JosepTrueta, Girona, Spain

Purpose

Utilization of arterial spine labeling (ASL) perfusion has been exponentially increased due to improved and faster acquisition time and ease of postprocessing. We aimed to investigate the added value of ASL imaging to a routine unenhanced brain MRI scan for patients referred to our Emergency Department.

Materials and Methods

In this retrospective study, the MRI scans of consecutive patients who presented to our emergency department from October 2016 to March 2017 were reviewed independently by two board-certified

Oral Presentations & Excerptas

neuroradiologists. ASL sequence (PCASL, TR/TE: 4000/20, four-minute acquisition time) (1) was added to our routine brain MRI. The readers were asked to interpret the ASL cerebral blood flow maps in order to 1) identify any hypoperfusion or hyperperfusion and 2) determine whether ASL abnormality had added value to the conventional MR imaging in each patient. Final diagnoses were extracted from patients' discharge summary and patients were categorized to two groups: infarction and noninfarction. Interobserver agreement was calculated by Kappa test and percentages of ASL abnormalities were calculated and subdivided in each category.

Results

Out of 385 MRI exams reviewed, ASL abnormalities were identified in 150 (38.9%) patients. Among these, 92 (61%) had a final diagnosis of acute infarction and 58 (39%) had other neurologic processes (noninfarction). In patients with infarction, ASL demonstrated an ischemic penumbra in 31%, luxury perfusion indicating reperfusion of the infarction in 36%, and matched perfusion-diffusion deficit in 33%. In noninfarction group, ASL showed nonterritorial hyperperfusion in patients with seizure (15.5%), relevant hypoperfusion in patients with transient ischemic attack (46.5%) and hyperperfusion in other processes (38%) such as hypervascular masses, Wernicke's, and other encephalopathies. Interobserver agreement was $k=0.70$, 95% CI=0.60 to 0.80.

Conclusions

Addition of a four-minute ASL sequence to routine brain MRI in the emergency setting showed an approximately 39% added value to conventional brain MRI. This added value extends beyond patients with infarction and helps in identifying other important neurological processes such as seizure, TIA and encephalopathies.

Tuesday, June 5, 2018

1:15PM - 2:45PM

Parallel Paper Session: Fetal Brain Imaging

O-223

1:15PM - 1:22PM

Accuracy of MRI for Determining Extent of Perineural Tumor Spread at the Skull Base: A Radiology-Pathology Correlation Study

B Hill¹, S Cantrell¹, C Solares¹, K Magliocca¹, P Hudgins¹, A Aiken¹

¹*Emory University, Atlanta, GA*

Purpose

Increasing utilization of image-guided skull-base surgery has allowed for resection of more advanced head and neck malignancies. Accurate preoperative assessment of perineural spread (PNS) extent is imperative to determining potential resectability. Previous studies evaluating the accuracy of MRI for detection of PNS have shown high accuracy for overall detection; however, accuracy in characterizing the extent of PNS at the skull base is less well elucidated. The purpose of this study is to compare both initial clinical MRI interpretation and blinded re-review to pathology (from directed biopsy/resection) to evaluate the accuracy of MRI for delineation of PNS extent.

Materials and Methods

As part of a quality improvement process, we retrospectively identified 12 cases of H&N cancer with (A) positive PNS at the skull base reported on the initial MRI impression and (B) subsequent resection/biopsy of at least one radiological site of interest. Initial study interpretation and blinded re-review were performed by dedicated H&N radiologists with re-review conducted by two dedicated H&N radiologists (CAQ, three and 12 years). Preoperative MRI reports were compared with postoperative/postbiopsy

Oral Presentations & Excerpts

pathology reports. On re-review, skull base sites of interest were rated as positive, indeterminate or negative, using the following modified criteria: asymmetric nerve enlargement on at least two sequences AND central/internal nerve enhancement were considered positive for PNS. The presence of only one of these criteria were classified as indeterminate.

Results

Initial MRI interpretations correctly determined the extent of PNS in 6/12 patients (50%), overestimated PNS in 5/12 (42%), and underestimated PNS in 1/12 (8%). Most false positives (5/6) had prior treatment (surgery/XRT). Using modified imaging criteria for PNS, MRI correctly determined extent of PNS in 10/12 patients (83%), overestimated extent in 2/12 (17%), and underestimated extent in 0/12 (0%). Of the two persistent false positives, both had prior craniofacial radiation.

Conclusions

MR imaging is sensitive for the detection of PNS in the skull base, but may overestimate extent of disease, particularly in the post-treated patient; this may unnecessarily preclude resection at some centers. The specificity of MRI for determining extent of PNS can be improved by using strict criteria.

O-224

1:22PM - 1:29PM

The Rostral Migratory Stream in the Human Fetal Brain: Postmortem MRI, Correlation with Histology and Preliminary Results with in Utero Fetal MRI

C Mitter¹, P Brugger¹, G Gruber¹, D Bettelheim¹, D Prayer¹, G Kasprian¹

¹Medical University of Vienna, Vienna, Austria

Purpose

The rostral migratory stream (RMS) projects along an extension of the lateral ventricle to the olfactory bulb and constitutes the main migration pathway of neural progenitor cells from the subventricular zone to the olfactory bulb (Ref.1). It has been extensively researched in the rodent brain due to its implication in adult neurogenesis and has also been described in histological studies of both the adult (2) and fetal (3) human brain. The purpose of our study was to investigate the MRI appearance of the RMS in the human fetal brain using postmortem 3T MRI and to correlate our imaging findings with histology in identical subjects. In addition, we performed a preliminary analysis on the potential of in vivo fetal MRI to visualize the RMS in utero.

Materials and Methods

We included 10 human fetuses between 16 and 25 gestational weeks without gross cerebral malformations. Postmortem MR imaging was performed within 24h after fetal demise as part of routine virtual autopsy examinations. The RMS was delineated on orthogonal T2w sequences. Neuropathological autopsy was available in 6/10 cases, which enabled correlation of imaging findings with histology. To investigate the potential of fetal MR to visualize the RMS in utero we analyzed 20 fetal MR examinations of fetuses without cerebral malformations between 20 and 25 gestational weeks and rated the visibility of a hypointense RMS on T2w images.

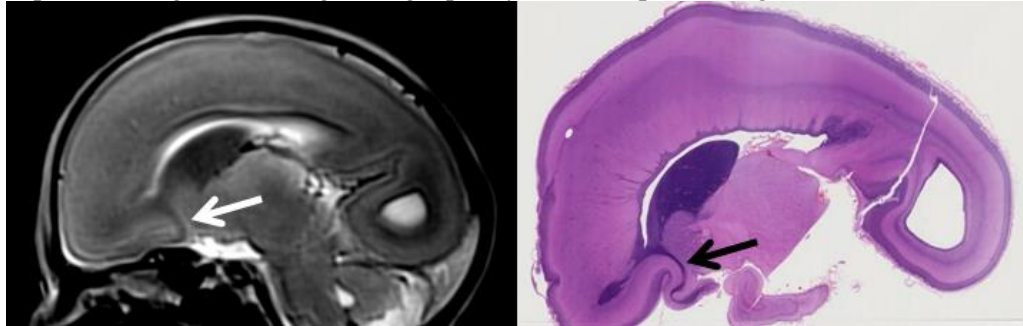
Results

The RMS was identified in all 10/10 subjects as a T2-hypointense extension of the ganglionic eminence. It was found to project as a flattened structure rostral of the caudate nucleus from the bottom of the anterior horn of the lateral ventricle ventrocaudal towards the base of the olfactory peduncle where it angulated rostral into the horizontal plane to continue into the olfactory bulb. Histological sections at multiple levels confirmed the postmortem MR findings of a flattened RMS configuration, its projection path and its high cell density, as indicated by its low signal on T2w images. In 4/20 fetal MR examinations the RMS could be seen as tiny areas of decreased T2 signal intensity at locations corresponding to the RMS in postmortem MR and histology.

Conclusions

The RMS is a prominent structure in the second trimester human fetal brain and can be reliably depicted

as a T2-hypointense extension of the ganglionic eminence on 3T postmortem MRI due to its high cell density. The postmortem MR anatomy of the RMS may be of value as a reference for in vivo studies. Preliminary results suggest that visualization of the RMS in utero with fetal MR is possible, but may be dependent on gestational age, image quality and slice positioning.



(Filename: TCT_O-224_Untitled.jpg)

O-225

1:29PM - 1:36PM

Feasibility and applicability of FLAIR-EPI in the evaluation of the fetal brain

M Diogo¹, G Kasprian², G Gruber², P Brugger², D Bettelheim², D Prayer²

¹Medical University of Vienna, Lisbon, Portugal, ²Medical University of Vienna, Vienna, Austria

Purpose

T2WI provide limited depiction of brain lamination, particularly after gestational week (GW) 26, faring worse than US and postmortem MR. By subtracting the subplate's water signal, FLAIR images have potential advantages in visualization of lamination. It's applicability has not been tested in in-vivo fetal MRI. This paper aimed to study the applicability of FLAIR in routine fetal MRI and compare qualitatively, T2-SSFSE and FLAIR images in assessment of fetal brain structures.

Materials and Methods

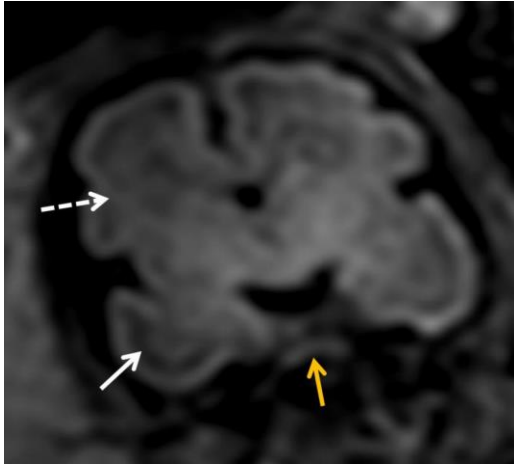
Retrospectively review of fetal MRIs acquired from 01.2014 to 11.2017, for singleton pregnancies, with T2-SSFSE and FLAIR sequences over the brain in equivalent orthogonal planes. Images were evaluated by two neuroradiologists with fetal MR experience. Cases were assessed for image quality, type and severity of artifacts, and visualization of predetermined cranial structures (qualified in three grades of visibility), and findings compared between T2 and FLAIR sequences. Interrater agreement was calculated.

Results

A total of 524 studies were included, with a mean gestational age of 26.4 GW (18-38). Overall, there was no significant difference in presence or severity of artifacts between T2 and FLAIR; FLAIR sequences were more affected by artifacts on 3T ($p=0.032$). Interrater agreement was 0.95 in evaluation of FLAIR images and 0.83 on T2. Lamination was better identified on FLAIR ($p<0.001$) throughout gestation; there was no difference in lamination visualization on fetuses ≤ 23 GW at 3T. Small structures (like septum pellucidum, optic nerves) were better identified on T2WI ($p=0.012$).

Conclusions

FLAIR can be successfully used in the majority of routine fetal MRI of the brain. It provides a better depiction of fetal brain lamination throughout gestation than T2WI, especially in visualization of the SP.



(Filename: TCT_O-225_Apresentao1.jpg)

O-226

1:36PM - 1:43PM

Fetoscopic Repair of Myelomeningocele as an Alternative to Open Fetal Surgery: Neuroimaging analysis with pre- and post-treatment MRI from Center for Fetal Therapy at the Johns Hopkins Hospital

A Tekes¹, J Miller¹, E Ahn², A Baschat³, T Huisman¹

¹Johns Hopkins University, Baltimore, MD, ²Johns Hopkins University School of Medicine, Baltimore, MD, ³Johns Hopkins Hospital, Baltimore, MD

Purpose

The Management of Myelomeningocele (MMC) Study showed that prenatal repair of MMC with hysterotomy lowers the risk of hydrocephalus and improves motor outcomes at 30 months of age. However hysterotomy is associated with maternal fetal risks: uterine rupture/dehiscence, transfusion, placenta accreta for future pregnancies, preterm labor, and prematurity. Fetoscopic repair is a minimally invasive technique, which aims to minimize/eliminate aforementioned risks. We report our preliminary results with preprocedure and postprocedure fetal neuroimaging and postnatal neuroimaging findings.

Materials and Methods

Fetuses with MMC had fetoscopic repair using a two-port approach with carbon dioxide insufflation before 26 gestational weeks. Preprocedure and six-week postprocedure MRI was obtained at 1.5 T following institutional protocol. All neonates had head ultrasound (HUS) at day of life one.

Neuroimaging findings were evaluated with MRI before and after fetoscopic repair: morphology of the MMC, craniocaudal (CC) and transverse diameter of the dysraphic defect, severity of Chiari II, hindbrain herniation, ventricular size/biparietal head diameter (also evaluated in postnatal HUS).

Results

Five enrolled fetuses had preprocedure fetal MRI; 4/5 had postprocedure fetal MRI and 1/5 had postprocedure MRI postnatally due to preterm labor. All MMCs were in the lumbosacral, 2/5 were in-level, 3/5 were raised morphologically. CC and transverse diameter of MMC ranged between 0.7 cm and 3.42 cm, and 0.52 cm and 1.16 respectively. All MMCs were successfully closed, and one had a minor residual dysraphic defect that did not require an additional procedure. Four-fifths had severe Chiari II malformation which significantly improved, one persisted. Hindbrain herniation ranged between 0.52 and 1.72 cm in preprocedure MRI and completely resolved in 4/5. Ventricular size/biparietal head diameter decreased in 2/5, and remained stable in 2/5 fetuses in postprocedure MRI and in postnatal head US.

Conclusions

Fetoscopic MMC repair is technically feasible with markedly improved hindbrain herniation.

Effect of Isolated Congenital Heart Disease on Fetal Brain Maturation

C Jaimes¹, C Stopp¹, A Gholipour¹, S Warfield¹, E Yang¹, C Rollins¹

¹Boston Children's Hospital, Boston, MA

Purpose

To determine if isolated congenital heart disease (CHD) affects fetal brain maturation

Materials and Methods

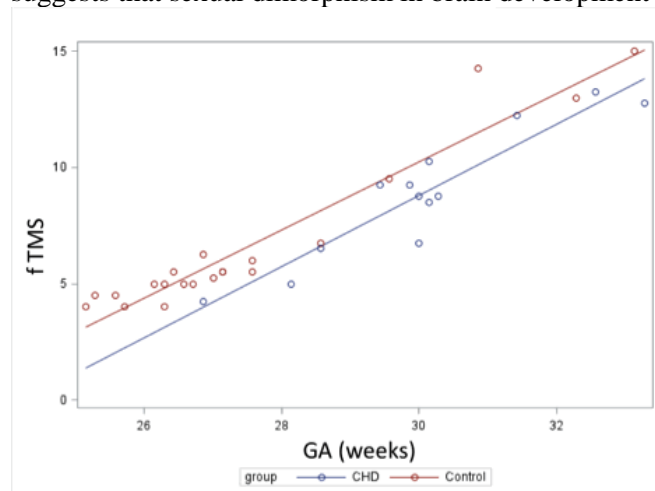
This prospective study was IRB approved and HIPAA compliant. Thirteen fetuses with isolated CHD (four female, nine male; median gestational age [GA]: 30w, range: 26w 6d-33w 2d; five with transposition of the great arteries [TGA], eight with hypoplastic left-heart syndrome [HLHS]) and 21 healthy controls were included in the analysis (11 female, 10 male; median GA: 26w 6d, range: 25w 1d-33w 1d). For all subjects, super-resolution volumetric reconstructions were created from multiplanar 2D T2-SSFSE images (Gholipour A, IEEE Trans Med Imaging [2010]). Two radiologists blinded to the clinical data reviewed the reconstructed brain images independently and assigned scores according to a validated fetal total maturation score (fTMS) that evaluates sulcation, myelination, and involution of germinal matrix (Vossough A, Radiology [2013]). Interrater reliability was estimated by Pearson correlation. Scores from both radiologists were averaged for every subject and averaged fTMS was used in multivariate linear regression to evaluate the relationships between clinical variables and fTMS.

Results

The CHD group had significantly lower fTMS than the controls (β -estimate [95% CI]: -1.5 [-2.3 to -0.7], $p < 0.001$; Fig 1) after adjusting for GA. The difference between groups was observed in the individual scores of both readers ($p < 0.001$ each). Both groups were found to be developing at similar rates (GA and fTMS interaction $p = 0.75$). After adjusting for group and GA, female fetuses had significantly higher fTMS scores (0.70 [0.03 to 1.37], $p = 0.04$) though this finding was driven by the scores of one reader. The Pearson correlation between the scores of the two readers was 0.97 (CHD: 0.94 ; control: 0.99).

Conclusions

The fTMS shows evidence of delayed brain maturation in fetuses with TGA and HLHS as early as the second trimester of pregnancy. Higher fTMS in female fetuses after correcting for group-related effects suggests that sexual dimorphism in brain development arises in utero.



(Filename: TCT_O-227_Untitled.gif)

1:50PM - 1:57PM

Brain Volumetry in Fetuses with Congenital Diaphragmatic Hernia based on fetal MRI - a Pilot Study

F Prayer¹, D Bettelheim¹, M Weber¹, G Gruber¹, G Kasprian¹, D Prayer¹, P Brugger¹

¹*Medical University of Vienna, Vienna, Austria*

Purpose

Reduced brain volume has been demonstrated in fetuses with congenital heart disease (CHD), which exhibit similar pathophysiology to fetuses with congenital diaphragmatic hernia (CDH) (1). In both CHD and CDH fetuses, left ventricular hypoplasia and reduced cerebral perfusion have been described (2, 3). Furthermore, neurodevelopmental impairment in CDH survivors has been reported, yet the impact of CDH on fetal brain growth remains unresolved. The purpose of this study was to perform manual fetal MRI-based segmentation and volumetry of the brain in fetuses with CDH.

Materials and Methods

Routine fetal MRI data of 24 fetuses with CDH and 24 normal age-matched fetuses were used to perform manual segmentation and volumetry of the brain and intracranial liquor spaces. Furthermore, manual fetal MRI-based lung segmentation and volumetry were performed in CDH cases. Manual segmentations and volumetric measurements were obtained using ITK-Snap (4). Brain and liquor volumes of CDH and normal fetuses were compared using paired t-test. Pearson's correlation of brain and lung volumes of CDH fetuses was performed.

Results

Fetal MRI-based brain volumetry revealed that brain volume is significantly reduced in CDH fetuses compared to normal fetuses (mean: -8.35cm³; 95% CI: -15.53cm³ to -1.17cm³, SD: 19.23cm³, p = 0.024). Brain and lung volumes in CDH fetuses showed significant correlation (r=0.617; p<0.001). There was no significant difference in intracranial cerebrospinal fluid volume between CDH and normal fetuses (p=0.192).

Conclusions

Brain volume in CDH fetuses is significantly smaller than in normal fetuses. While further research to clear up the underlying pathophysiology and impact on neurodevelopment is needed, it is evident that brains of CDH fetuses are not suitable for the establishment of reference values for normal fetal brain growth.

O-229

1:57PM - 2:04PM

Fluid-attenuated inversion recovery sequences in the diagnosis of lissencephaly on fetal MRI

M Diogo¹, G Kasprian², G Gruber², G Dovjak², D Bettelheim², D Prayer²

¹*Medical University of Vienna, Lisbon, Portugal*, ²*Medical University of Vienna, Vienna, Austria*

Purpose

Lissencephaly is a malformation of cortical development secondary to abnormal neuronal migration. Early prenatal detection is extremely challenging. The aim of this paper is to investigate the added value of FLAIR sequences in the diagnosis of lissencephaly using fetal MRI.

Materials and Methods

Cases of lissencephaly with T2-single shot fast spin echo (SSFSE) and FLAIR sequences over the fetal brain were searched in a fetal MRI database. An age-matched group of 12 patients with normal brains was added to avoid reading biases. Each sequence was evaluated by two foetal-MRI-experienced neuroradiologists blinded to clinical information except gestational age (GA). Images were reviewed at two different time points: all T2WI alone, and T2WI and FLAIR images together. Visualization of

lamination and gyration were assessed, and adequacy to GA determined, as well as its degree of certainty (0-5).

Results

Twelve cases fulfilled inclusion criteria. Mean gestational age was 28.6 gestational weeks (range 24-32). A total of 5.2 T2-SSFSE and 2.1 FLAIR sequences were obtained over each fetal brain. In 92% (11/12) of cases, brain lamination was better visualized on FLAIR. Gyration patterns were better assessed on T2WI in all cases. Using both T2WI and FLAIR images, the positive predictive value of MRI improved from 89% to 100% and negative predictive value from 75% to 96%; sensitivity from 66.7% to 95.8% and specificity from 90.1% to 100%. The degree of certainty increased from 3 to 4.8.

Conclusions

FLAIR sequences over the fetal brain may help in the diagnosis of migrational disorders leading to lissencephaly.

O-230

2:04PM - 2:11PM

Magnetic Resonance Morphological Signs of Fetal Inflammatory Response Syndrome as Potential Biomarkers of Cytomegalovirus Infection

V Pfahler¹, M Diogo², S Stoecklein³, D Bettelheim², G Gruber², P Brugger², G Kasprian², D Prayer⁴
¹Klinikum d. Universität München Institut für Klinische Radiologie, Munich, Germany, ²Medical University Vienna, Vienna, Austria, ³Ludwig-Maximilians University Munich, Munich, Germany

Purpose

Cytomegalovirus (CMV) is the most frequent congenital virus infection worldwide. Manifestations of intrauterine CMV infection may not always involve the brain. However, morphological or functional cerebral impairment may be present even in case of a normal fetal brain. The objective was to retrospectively examine fetal MRIs for cerebral and extracerebral findings in cases of maternal primary CMV infection during pregnancy.

Materials and Methods

The fetal MRI database was retrospectively searched for congenital CMV infections. Forty cases of primary CMV infection during pregnancy were included; three cases had a follow-up MRI performed between six days to 10.5 weeks after the first examination. Images were reviewed by one neuroradiologist and one radiology resident for placental and fetal extracerebral and intracerebral findings, blinded to the MR and US reports. The findings were later compared with the clinical MR report for missed findings.

Results

The mean gestational age was 29.8 weeks with a maximum of 38 weeks and a minimum of 21 weeks. In seven cases (17.5%) no abnormalities in either the brain, the body or the placenta were found. In 18 cases (45.0%) brain abnormalities were found. Twenty-six cases (65.0%) showed abnormalities in the body, mainly involving the fetal liver, and 25 cases (62.5%) in the placenta. Two of three cases with follow-up didn't show significant changes in the second examination, with one case showing aggravation of the brain and placental changes, as well as new body abnormalities.

Conclusions

In the course of a FIRS associated with CMV extracerebral findings are very common, in fetuses with maternal primary CMV infection during pregnancy, and could potentially be used as an MR biomarker for this disease, initiating further monitoring of fetal and postnatal brain development in these cases.

O-231

2:11PM - 2:18PM

Taking the Dental out of Incidental: Prevalence and Reporting Rates of Incidental Dental Disease on Head CT Examinations

K Hammoud¹, M Lanfranchi², D Adams³, W Mehan⁴, H Bedi⁵

¹Tufts Medical Center, Cambridge, MA, ²Tufts Medical Center, Boston, MA, ³University of Washington, Seattle, WA, ⁴Massachusetts General Hospital, Boston, MA, ⁵St. Elizabeth's Medical Center, Wellesley, MA

Purpose

Dental disease is prevalent and may lead to an increase in patient morbidity and mortality, especially if left untreated. Although dedicated head computed tomography (CT) examinations should exclude the level of the teeth, often times the teeth are inadvertently included in the study. Therefore, dental pathology may be incidentally seen or overlooked on head CT examinations performed for various indications other than dental complaints. The purpose of this study is to examine the prevalence of clinically significant dental disease incidentally present and missed on head CT exams, and to determine the effect of the institution of a dental disease field/macro in a standardized head CT dictation template on the rate of reporting dental disease.

Materials and Methods

Head CT examinations over a one-year period at our institution were randomly selected until the following criteria were filled: Fifty studies were collected which included the level of the teeth within the six months prior to the implementation of a dental field/macro in our institution's head CT report template, and 50 studies were collected including the level of the teeth within the six months following the implementation of the dental macro. Dental findings were recorded from the initial finalized report. Exam images were subsequently reviewed for the presence of dental disease by two neuroradiologists who were blinded to the original report and each other's findings.

Results

Of 6,445 head CT examinations performed at our institution over one year, 307 studies were randomly selected in order to obtain a preset total goal of 100 head CT examinations with teeth included in the field of view (33%). Dental disease was determined by two neuroradiologists blinded to the original radiologic reports to be present in 40-41% of the cases, while only 11% of the initial radiologic reports mentioned dental disease ($p < 0.01$). The addition of a dental disease field in the dictation template resulted in no significant difference in reporting dental disease (14% vs. 8%, $p = 0.371$).

Conclusions

Although the level of the teeth should not be included on routine head CT examinations, they often are, posing a potential blind spot for the radiologist who may be interpreting the study for other indications. Despite its prevalence and potentially serious consequences, dental disease is often overlooked/underreported on routine head CT examinations. Inclusion of a passive dental disease field/macro in a standardized template did not significantly improve the rate of reporting dental disease.

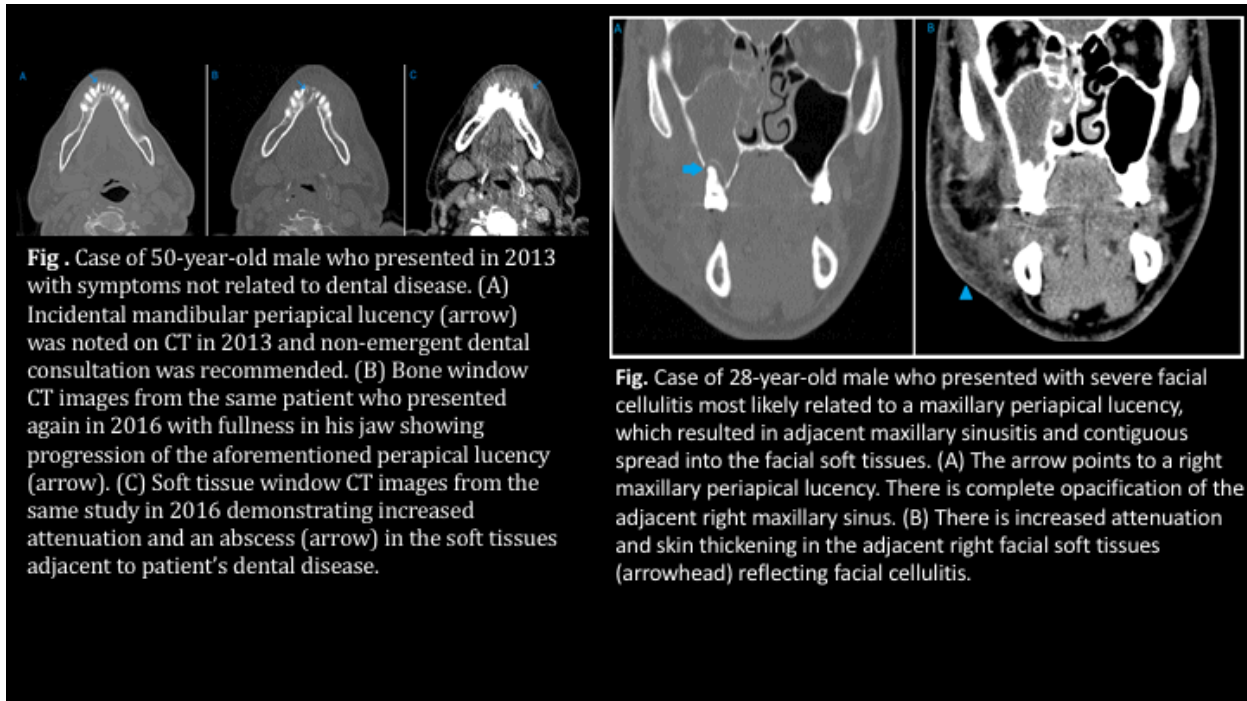


Fig . Case of 50-year-old male who presented in 2013 with symptoms not related to dental disease. (A) Incidental mandibular periapical lucency (arrow) was noted on CT in 2013 and non-emergent dental consultation was recommended. (B) Bone window CT images from the same patient who presented again in 2016 with fullness in his jaw showing progression of the aforementioned perapical lucency (arrow). (C) Soft tissue window CT images from the same study in 2016 demonstrating increased attenuation and an abscess (arrow) in the soft tissues adjacent to patient’s dental disease.

Fig. Case of 28-year-old male who presented with severe facial cellulitis most likely related to a maxillary periapical lucency, which resulted in adjacent maxillary sinusitis and contiguous spread into the facial soft tissues. (A) The arrow points to a right maxillary periapical lucency. There is complete opacification of the adjacent right maxillary sinus. (B) There is increased attenuation and skin thickening in the adjacent right facial soft tissues (arrowhead) reflecting facial cellulitis.

(Filename: TCT_O-231_Slide1.gif)

O-232

2:18PM - 2:25PM

Comparison of T2 single shot fast spin echo and FLAIR sequences in assessment of fetal ventriculomegaly

M Diogo¹, G Kasprian², G Gruber², D Bettelheim², D Prayer²

¹Medical University of Vienna, Lisbon, Portugal, ²Medical University of Vienna, Vienna, Austria

Purpose

Although ventriculomegaly is the most common referral for fetal brain MRI, it still poses a diagnostic and prognostic challenge. Assessment of brain lamination an essential part of exclusion of associated migrational disorders, but is limited after gestational week (GW) 26 on T2WI. The aim of this study is to assess the additional information provided by FLAIR sequences in fetuses with ventriculomegaly.

Materials and Methods

Retrospective evaluation of fetal MRI studies with ventriculomegaly and FLAIR and T2SSFSE images over the fetal brain in equivalent orthogonal planes. The study criteria was met by 114 cases. Each sequence was analyzed for identification of the subplate by lobes, ventricle size, and brain anomalies. Raters (two) were asked whether FLAIR images provided additional information to the FSE T2WI in either confirming the lesion or excluding pathology.

Results

The mean GA, was 28.2 gestational weeks (range 19-36). There was a statistical significant difference (p<0.001) in subplate identification in all lobes in favor of the FLAIR sequence. Most additional brain anomalies were at least partially identifiable on FLAIR images (91%), although better depicted on T2 on 29.2% (vs 17.5% on FLAIR). FLAIR provided additional information in brain lesions in 49.3% of patients, and in excluding lesions in 81.3%.

Conclusions

FLAIR images can provide additional information in cases of fetal ventriculomegaly, particularly in the assessment of lamination.

O-216

2:25PM - 2:32PM

Vascular disruption: a possible underlying mechanism for fetal brain “malformation”

D Prayer¹, M Diogo¹, D Covini², G Gruber¹, P Brugger¹, G Kasprian¹

¹*Medical University of Vienna, Vienna, Austria*, ²*Hospital Italiano de Buenos Aires, Buenos Aires, Argentina*

Purpose

The majority of fetal brain pathologies detected on prenatal imaging studies is thought to be of malformative origin. However, there is growing evidence of the (in-utero) acquired nature of these lesions, namely due to vascular disruption (1). Schizencephaly, septum pellucidum agenesis (SPA), polymicrogyria, and hydranencephaly have been described as consequences of a vascular disruption sequence (VDS) (2). The aim of this study was to investigate whether fetal MRI could provide additional information regarding the etiology of these fetal brain anomalies.

Materials and Methods

In this retrospective review a database consisting of 5400 fetal MRI's performed between 18 and 39 gestational weeks was screened for schizencephaly, SPA, and hydranencephaly without referred vascular or hemorrhagic findings on ultrasound. Forty-seven cases fulfilled the inclusion criteria. Images were reviewed by a fetal imaging-dedicated radiologist and two neuroradiologists for brain findings, signs of blood degradation products and placental assessment. A prescreened age-matched control group of 25 patients was used to compare incidence of placental events. Studies were performed on 1.5T or 3T magnets, and included a minimum of T1, T2 and susceptibility-weighted sequences covering the fetal brain and the placenta.

Results

Of the 47 cases collected, there were 27 cases (57.4%) of schizencephaly, 14 (29.7%) of SPA and six hydranencephalies (12.8%). Mean gestational age was 29.6 (range 23-36) GW. There were signs of placental hemorrhage or brain blood degradation products in 61.7% of cases. None of the SPA cases presented signs of hemorrhage. When SPA was excluded from analysis, there were findings of VDS in 96% of cases (32/33). Placental findings (40.4%) were also significantly different from the control group (6%). Associated cortical changes were present in 42.4% of cases.

Conclusions

Congenital brain pathologies may be acquired secondary to vascular events. MRI is a valuable tool in the identification/confirmation of fetal anomalies, but more importantly in providing clues to their vascular origin, and hence guiding prognostic and etiological investigations.

Tuesday, June 5, 2018

3:00PM - 4:30PM

Parallel Paper Session - Head and Neck: New (Techniques) and Deep (Spaces)

O-233

3:00PM - 3:07PM

Dual-Layer CT-derived Virtual Non-Contrast Images: Could Both Intrinsic and Extrinsic Thyroid Glandular Iodine Be Successfully Suppressed?

Y Lee¹

¹*Korea University Ansan Hospital, Ansan-si, Gyeonggi-do, Republic of Korea*

Oral Presentations & Excerptas

Purpose

Thyroid gland, known as an intrinsically iodine-concentrated organ, usually shows the more avid enhancement than other neck structures after contrast-media injection. To evaluate the efficacy of dual-layer CT-derived virtual noncontrast (VNC) technique, we compared the thyroid glandular CT attenuation on both VNC images reformatted before and after contrast enhancement.

Materials and Methods

We retrospectively enrolled 128 patients (M:F=17:111, age= 48.0±10.4 yr) who consecutively underwent both ultrasound and neck CT examination due to their thyroid nodule during the recent 12 months (October 2016 to September 2017). After obtaining both true unenhanced (TUE) and true contrast-enhanced (TCE) scanning using an IQon CT (Philips Healthcare) scanner at 120 kVp, additional two sets of VNC images were created from TUE and TCE series. On the TUE, TCE and both VNC images, attenuation measurements were done by drawing an identical region of interest at the thyroid parenchyma sonographically devoid of nodule at the same axial level. Statistical analysis was performed by paired t-test.

Results

The mean attenuation values of thyroid gland were 102.9±18.0HU, 219.6±35.8HU for TUE and TCE, respectively. Although a pairwise comparison revealed the significant difference in the measured attenuation values of VNC images from both TUE and TCE images (2.0±5.7HU, $p<0.001$; 61.2±7.8HU vs 59.2±8.1HU), their discrepancies ≤ 5 HU, $5 < \leq 10$ HU, and $10 < \leq 15$ HU were 61.7%, 27.3%, and 10.9% of all measurement.

Conclusions

VNC technique of dual-layer CT could successfully suppress both inherently tissue-containing and extrinsically administered iodine of thyroid parenchyma.

O-234

3:07PM - 3:14PM

Optimal Adaptive Statistical Iterative Reconstruction Settings for the Evaluation of the Neck Using Low-Energy Dual-Energy CT Virtual Monochromatic Images

G Romero-Sanchez¹, R Forghani¹

¹*Jewish General Hospital and McGill University, Montreal, Quebec, Canada*

Purpose

Dual-energy CT (DECT) low-energy virtual monochromatic images (VMIs) have been shown to improve visibility of head and neck cancers and the tumor-soft tissue boundary. However, the higher image noise on these reconstructions may represent a relative barrier to more widespread adoption and subjective acceptance. In this study, we evaluated the optimal iterative reconstruction settings for reducing image noise and improving quality of low energy VMIs.

Materials and Methods

DECT scans from 10 consecutive patients were evaluated. All subjects were scanned with a 64-section scanner with fast kVp switching and low-energy VMIs at 40 keV reconstructed using different Adaptive Statistical Iterative Reconstruction (ASIR) settings (no ASIR, 20%, 40%, 60%, 80%, 100%). Image quality and noise was evaluated quantitatively and subjectively by evaluating normal tissues at different levels in the neck. This consisted of muscles at six different levels as well as different glands (parotid, sublingual, submandibular, and thyroid). Quantitative analysis was performed using three circular ROIs per structure. Standard deviation (SD) was used as a measure of image noise and signal to noise ratios were calculated by dividing the CT attenuation (in Hounsfield units) by the SD.

Results

A total of 1800 ROIs were evaluated, with an average ROI area of 9.59 mm². There was no significant difference in muscle or gland attenuation using different ASIR settings. On the other hand, there was a

Oral Presentations & Excerptas

decrease in image noise and increase in SNR with increasing ASIR settings, with the best quantitative results obtained with an ASIR setting of 100. Although quantitatively the SNR progressively increased with increasing ASIR, subjectively, the best image quality was achieved at ASIR settings between 20 and 40%.

Conclusions

Forty keV VMIs reconstructed using an ASIR setting between 20 and 40% decrease image noise, increase SNR, and improve subjective image quality in the neck.

O-235

3:14PM - 3:21PM

A CAD System to Track Cervical Adenopathy on CT over Time

I Oguz¹, M Bilello¹

¹*University of Pennsylvania, Philadelphia, PA*

Purpose

The task of comparing a current CT neck to a prior one to detect changes in cervical adenopathy in patients with thyroid cancer is both tedious and prone to error for the neuroradiologist. The difficulty comes essentially from the different angulation of the images at different time points, as well as from volume averaging. We propose a computer-aided detection (CAD) system to monitor cervical adenopathy. This system relies on advanced registration methods, as global rigid registration is likely to fail because of the deformable nature of the neck.

Materials and Methods

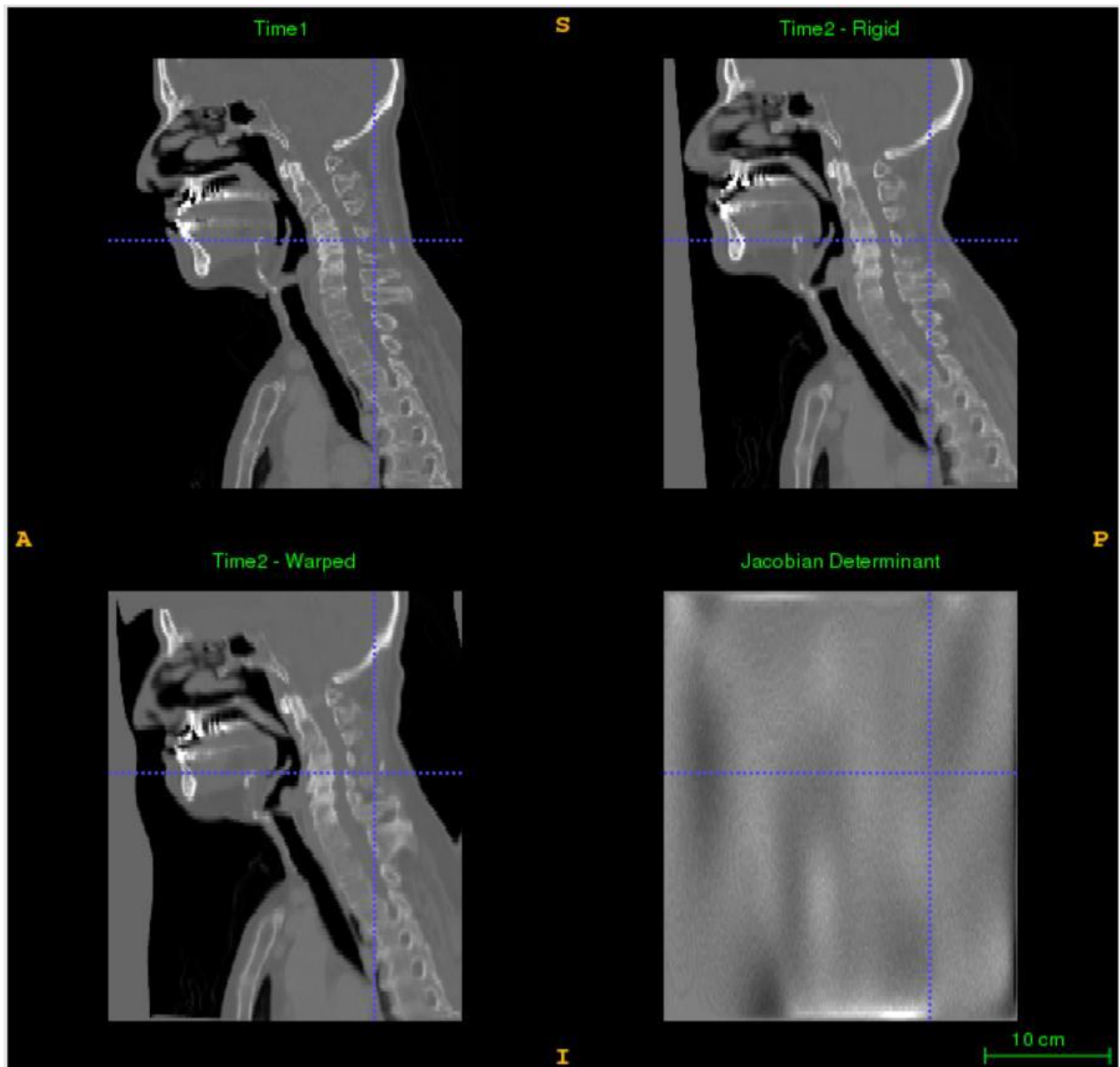
Given two images from different time points, a rigid registration is first performed on the whole image to capture global motion. Next, a piecewise-rigid registration is performed to capture the differences in patient pose (head tilt, etc.), using five vertical partitions to represent the image. These piecewise transformations are combined and smoothed to reduce interpolation artifacts at the seams between the partitions. Finally, a deformable registration is performed to capture any residual motion, using a very smooth deformation model. The normalized cross-correlation similarity metric was used for all steps. All registration steps were performed using the publicly available greedy package [1,2]. The determinant of the Jacobian matrix of the total deformation was computed at each voxel.

Results

We applied the proposed method to pairs of images from five patients. The registration quality was visually inspected. The proposed workflow resulted in substantially more accurate alignment than global rigid registration. The Jacobian determinant allows the identification of areas of compression/expansion (dark/bright areas in figure).

Conclusions

This preliminary work demonstrates the feasibility of a CAD system to monitor changes in cervical adenopathy on CT neck. This work will have applications in other imaging modalities and disease processes, e.g., MR neck follow-up for head and neck cancer, and follow-up of cord disease in MR spine for multiple sclerosis.



(Filename: TCT_O-235_asnr-figure.jpg)

O-236

3:21PM - 3:28PM

DSA-like bone subtraction iodine imaging using area detector CT for evaluation of skull base invasion by nasopharyngeal carcinoma

T Hiyama¹, H Kuno¹, K Sekiya¹, K Tatsushi¹, M Kusumoto¹
¹National Cancer Center Hospital East, Kashiwa, Chiba, Japan

Purpose

Digital subtraction angiography (DSA)-like bone subtraction iodine (BSI) imaging using area detector CT enables evaluation of iodine distribution in the bone marrow (1-3). The purpose of this study was to assess the clinical usefulness of BSI imaging for evaluation of skull-base invasion in patients with nasopharyngeal carcinoma.

Oral Presentations & Excerptas

Materials and Methods

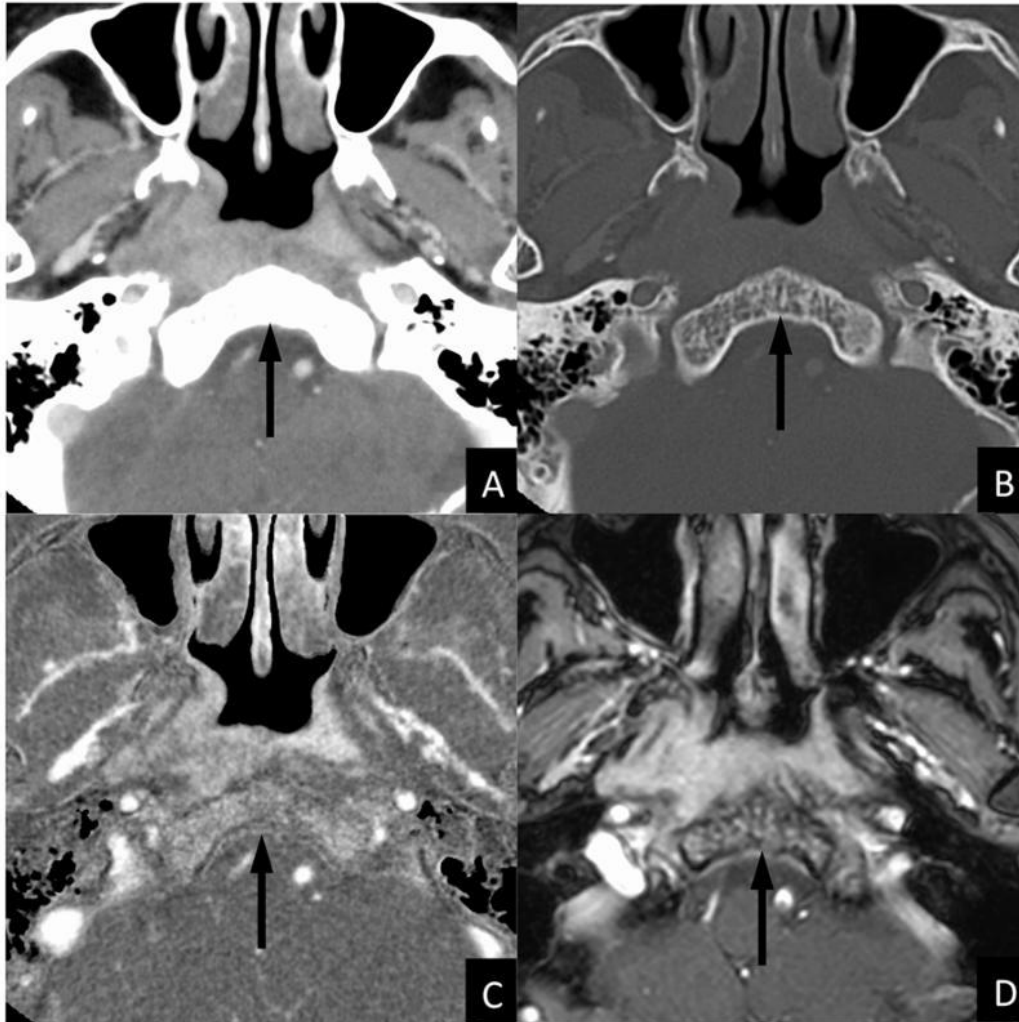
Forty-four consecutive patients (28 men, 16 women; age 18–79 years, median age 60 years) who underwent contrast-enhanced CT using 320-row area detector CT and 3.0T-MRI for nasopharyngeal carcinoma staging, between April 2012 and November 2017, were enrolled in this IRB-approved study. DSA-like BSI image was generated by subtracting the pre and postcontrast volume scans using a high-resolution deformable registration algorithm. Two blinded observers evaluated skull-base invasion at different subsites (sphenoid body, clivus, bilateral base of the pterygoid process, and petrous bone) according to a five-point scale using only conventional CT (soft tissue and bone window) or a combination of conventional CT and BSI. A combination of MRI and CT features observed by an experienced neuroradiologist was used as the reference standard for evaluating sensitivity, specificity and the areas under the ROC curve (AUC) for skull-base invasion. Sensitivity and specificity were compared by McNemar's test and generalized estimating equations to account for clustering.

Results

Twenty-six patients (59%) with 84 subsites showed skull-base invasion. CT-BSI images showed higher sensitivity (92.9% vs. 77.4%, $P=.01$) and specificity (96.1% vs. 85.6%, $P=.004$) compared to conventional CT images alone for evaluating skull-base invasion. The AUC of the CT-BSI images was significantly larger (AUC = 0.976, $P<.001$) than that of the conventional CT images alone (AUC = 0.892).

Conclusions

CT-BSI has a higher diagnostic potential than conventional CT for assessment of skull-base invasion in patients with nasopharyngeal carcinoma and may help to improve accuracy in radiotherapy treatment planning.



Tumor invasion into the clivus is undetectable on contrast-enhanced CT (A, B; ↑), but obvious on BSI imaging (C; ↑) and postcontrast fat-suppressed T1-weighted image (D; ↑).

(Filename: TCT_O-236_Figure.jpg)

O-237

3:28PM - 3:35PM

Sonographic Features of Melanoma Nodal Metastasis in the Head and Neck

S Ahmed¹, B Chen², T Vu¹, J Stewart¹, D Schomer¹, K Shah¹

¹The University of Texas MD Anderson Cancer Center, Houston, TX, ²University of Texas McGovern, Houston, TX,

Purpose

Ultrasonography is used for surveillance of regional nodal basins in patients with melanoma of the head and neck at our institution. Contrast-enhanced CT and PET-CT are used for surveillance at other institutions, as ultrasound is operator-dependent and challenging to standardize. The purpose of our study is to compare the sonographic features of biopsy-proven cervical nodal melanoma metastasis versus biopsy-proven benign lymph nodes with atypical imaging features.

Materials and Methods

Hospital pathology database was queried for cases of cervical lymph node FNA with indication of melanoma between 2012 and 2017. Demographic data and patient history were obtained via chart review. Sonographic images of the lymph nodes sampled were reviewed by two CAQ'd neuroradiologists, each with greater than 10 years of experience in head and neck imaging including ultrasound. The following features were documented for each node: margins, echogenicity of cortex, hilum, cystic contents, calcification, vascular flow, and posterior acoustic enhancement.

Results

The first 50 consecutive lymph nodes with FNA=melanoma, and the first 72 consecutive nodes with FNA=benign were selected for review. Seven of these 122 nodes were excluded as it was not clear which node had been biopsied. Of the 115 nodes in our review, benign=67 and melanoma=48. Patient age range from 27 years to 87 years (mean=59.7, median=62). Total number of patients=87 (male=66, female=21), with some patients having more than one node sampled. See attached table for results.

Conclusions

Irregular margins ($p=0.0007$), absent or obscured hilum ($p=0.001$), hypoechogenicity of the cortex ($p=0.02$), absent or disorganized vascular flow ($p=0.0005$), and posterior acoustic enhancement ($p<0.0001$) are more commonly seen in cervical lymph nodes with FNA=melanoma than with FNA=benign. The presence of cystic change ($p=0.57$) and calcification ($p=0.17$) was not statistically significant between the two groups. Knowledge of these imaging features is helpful when performing sonographic surveillance for melanoma in the head and neck.

	FNA Pathology		P-value
	Benign	Melanoma	
Margin			
Smooth	65	36	0.0007
Irregular	2	12	
Echogenicity			
Hypoechoic	14	20	0.02
Isoechoic or hyperechoic	53	28	
Hilum			
Normal	43	16	0.001
Obscured or absent	24	32	
Cystic			
Yes	66	46	0.57
no	1	2	
Calcification			
Yes	0	2	0.17
no	67	46	
Posterior acoustic enhancement			
Yes	9	25	<0.0001
no	58	23	
Vascular flow			
Hilar (normal)	26	5	0.0005
Absent or disorganized	38	42	

(Filename: TCT_O-237_ResultstableASNR.jpg)

O-238

3:35PM - 3:42PM

Differential Diagnosis of Necrotic Cervical Lymphadenopathy: Tree Analysis

S You¹, B Kim¹, B Kim¹, N Lee¹

Oral Presentations & Excerptas

Purpose

To establish a differential diagnosis tree for patients with necrotic lymphadenopathy on contrast-enhanced neck CT using imaging and clinical findings

Materials and Methods

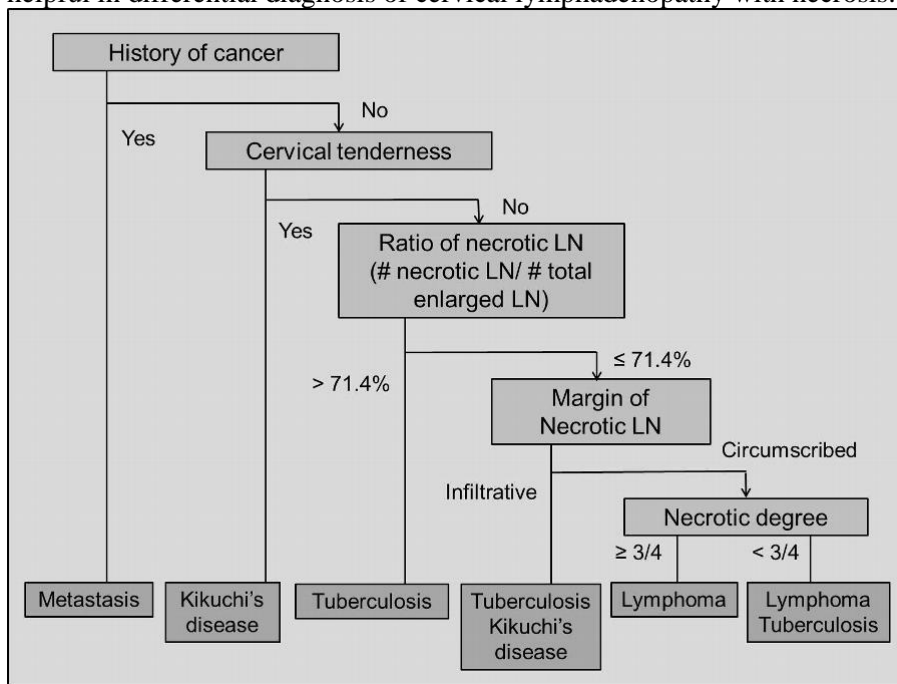
This retrospective study included 151 patients (68 men and 83 women; mean age, 44.2 ± 18.5 years; range, 10-91 years) with pathologically confirmed tuberculosis (n = 50), metastasis (n = 35), lymphoma (n = 28), and kikuchi's disease (n = 38). All patients underwent contrast-enhanced neck CT, and imaging findings (shape and margin of necrotic lymph node [LN], shape, margin, location and density of necrotic portion in necrotic LN, ratio of necrotic LN = number of necrotic LN/number of total enlarged LN, necrotic degree, perinodal infiltration) of necrotic lymph nodes were analyzed. Clinical findings including body temperature, WBC count, cervical tenderness, history of underlying cancer were collected. Using imaging and clinical findings, the diagnostic tree was established. The diagnostic performance of that was evaluated.

Results

Five factors were adopted in tree analysis (history of cancer, $P < .001$; cervical tenderness, $P < .001$; ratio of necrotic LN, $P < .001$; margin of necrotic LN, $P = 0.003$; necrotic degree, $P < .001$). The diagnostic tree based on those factors showed excellent overall diagnostic performance (overall accuracy [95% confidence level], 0.914 [0.857-0.953]; tuberculosis, accuracy = 0.961, sensitivity [Sn] = 0.921, specificity [Sp] = 1.000; metastasis, accuracy = 0.983, Sn = 1.000, Sp = 0.966; lymphoma, accuracy = 0.881, Sn = 0.786, Sp = 0.976; kikuchi's disease, accuracy = 0.961, Sn = 0.921, Sp = 1.000).

Conclusions

A simple diagnostic tree using CT findings of the necrotic lymph node and clinical information may be helpful in differential diagnosis of cervical lymphadenopathy with necrosis.



(Filename: TCT_O-238_Fig1.jpg)

O-239

3:42PM - 3:49PM

The Utility of FDG-PET Scanning in Head and Neck Cancer Patients: Search for the Unknown Primary

Oral Presentations & Excerptas

A Levitt¹, D Ginsburg², J Bello³, K Shifteh¹

¹Montefiore Medical Center, New York, NY, ²Bronx, NY

Purpose

To determine whether fluoro-deoxy-glucose positron emission tomography (FDG-PET) imaging alone can identify a primary source for patients who present with adenopathy due to metastatic head and neck squamous cell carcinoma, when diagnostic CT fails to reveal a primary malignancy.

Materials and Methods

Over a ten-year period, we encountered 34 patients with histologically proven metastatic squamous cell carcinoma of unknown primary origin despite full clinical and endoscopic evaluation. Patients without pretreatment PET-CT imaging were excluded from the study. Twenty-eight of 34 patients had pretreatment contrast computed tomography (CT) studies to search for a primary lesion. The other six patients did not have any pretreatment CT imaging of the neck.

Results

PET-CT studies failed to reveal a primary malignancy in all but one case in which the primary was suggested in the right tonsil, but not definitively called. In all 28 patients evaluated with contrast-enhanced CT scanning, no primary malignancy was detected. In retrospect, there was streak artifact obscuring evaluation of the right tonsil. In 13 of the 34 patients, PET-CT demonstrated abnormal extranodal uptake but these abnormalities were not found to represent malignancy on subsequent evaluation.

Conclusions

The utility of FDG-PET alone in identifying a primary source for metastatic head and neck squamous cell carcinoma may not be as clearly evident as suggested in the literature. In our study when diagnostic CT failed to reveal a primary malignancy, FDG-PET also failed except in one equivocal case.

O-240

3:49PM - 3:56PM

Retrospective Analysis of Strangulation/Hanging Injuries via CT Angiography

C Hazen¹, J Heymann¹

¹University of Texas Medical Branch, Galveston, TX

Purpose

To investigate the appropriateness of using CT angiography (CTA) in screening for potential carotid dissection after a strangulation or hanging and to evaluate the incidence of these injuries.

Materials and Methods

Retrospective chart review of all CTAs was performed for patients presenting to our institution's ED after a strangulation or hanging between September 2007 and April 2017. Relevant data acquired from a thorough chart review included demographic information, mechanism of injury, physical examination findings, any associated neurological deficits or loss of consciousness (LOC), pre-existing risk factors, and incidental findings on radiologic examination.

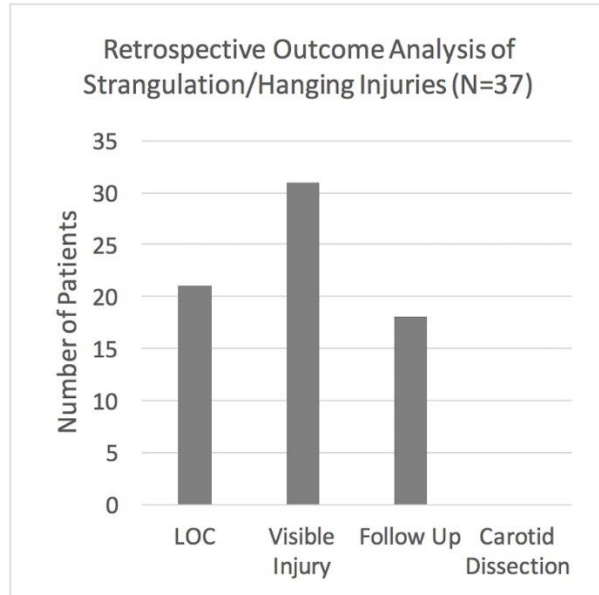
Results

A total of 37 patient charts were evaluated based on demographics, physical exam findings, short-term follow-up if available, and imaging findings. Patients were assessed for LOC based on self-report or objective evaluation, with 21 patients experiencing LOC, 14 retaining consciousness, and two who were unsure. On physical examination, 31 patients had visible injuries on the neck or face with or without associated neck pain, three experienced mild neurological deficits, and three had an unremarkable exam. Upon review of short-term outcomes of these 37 patients, 19 patients did not return for follow-up examination but were discharged in stable condition, six returned within the next several years for

recurrent suicidal ideations, and 12 presented sometime after for unrelated concerns. After evaluation by CTA, all patients were negative for carotid dissection or injury.

Conclusions

As carotid dissections can lead to stroke or death, ordering CTAs for strangulation and neck trauma victims has become standard. However, true carotid injury is rare and usually due to blunt-force trauma such as motor vehicle accidents. In our population isolated to strangulation or hanging, the incidence of carotid injury was zero. This study calls into question the utility of CTA in strangulation or hanging, especially in the absence of neurological symptoms.



(Filename: TCT_O-240_finalimagejpeg.jpg)

O-241

3:56PM - 4:03PM

Acute Ischemic Optic Neuropathy- Value of High-Resolution Diffusion Imaging for Optic Nerve Lesions

A Agarwal¹, V Nguyen¹

¹University of Texas Southwestern Medical Center, Dallas, TX

Purpose

To illustrate the MR imaging findings in a case of acute ischemic optic neuropathy and discuss the role of high-resolution diffusion imaging for evaluation of optic nerves

Materials and Methods

A 72-year-old male presented at an outside facility for evaluation of subacute vision loss of the left eye and acute vision loss of the right eye. He had already undergone a significant workup at the outside hospital including temporal artery biopsy which was negative for giant-cell arteritis (GCA) and MR of the orbits and brain which was read as unremarkable. He received high-dose steroids at the outside facility and had no improvement in his vision prior to arrival. He was admitted to the neurology service at our Institution after a couple of days. Ophthalmology evaluation done was unremarkable without evidence of retinitis or ischemic retinal change and a normal fundoscopic exam. Though the differential for his vision loss included Neuromyelitis optica (NMO) and giant-cell arteritis (GCA), pulse-dose steroids were not given as he had failed to improve on them prior to admission. Repeat MRI of the orbits with high-resolution diffusion imaging revealed areas of restricted diffusion involving bilateral intraorbital segments

Oral Presentations & Excerpts

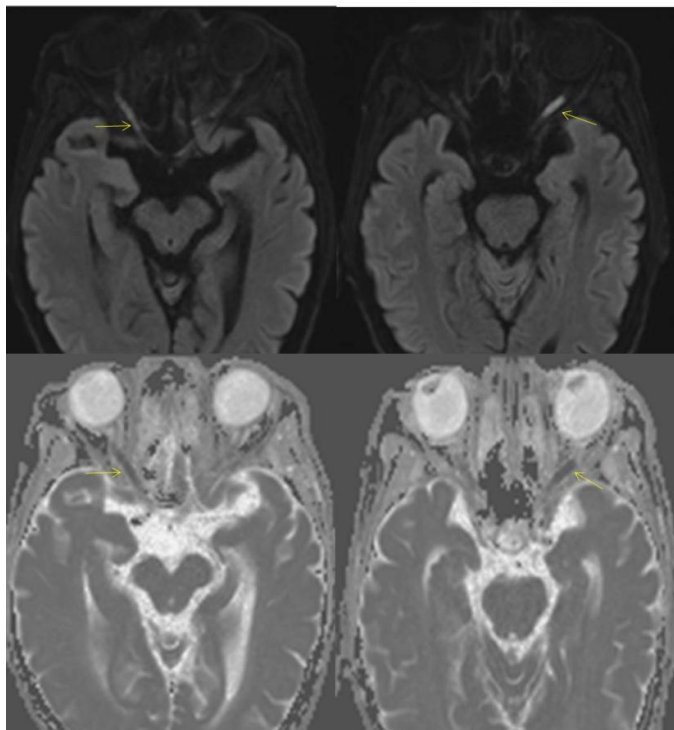
of the optic nerves with markedly low ADC values. Mild enhancement was also seen in this segment of the optic nerve. Imaging diagnosis of Acute Ischemic Optic Neuropathy (ION) was made. The patient had complete vision loss even after three weeks. The top of the differential remained GCA during this admission; however, it was felt that steroids would be unhelpful as he had already lost his vision. It was hypothesized that his lack of positive biopsy for GCA was secondary to his immunodeficiency.

Results

MRI of the orbits done at an outside facility on the day of admission was read as being unremarkable. MRI orbits done subsequently (day two after admission) at our facility (Figure 1 below) with high-resolution diffusion imaging, revealed linear areas of restricted diffusion involving the intraorbital segments of bilateral optic nerves with markedly low ADC values. Mild enhancement was also seen in this segment of the optic nerves.

Conclusions

This exhibit illustrates a case of acute ischemic optic neuropathy with the purpose of highlighting the role of dedicated high-resolution DW imaging for acute optic-nerve pathology.



(Filename: TCT_O-241_ION.jpg)

O-242

4:03PM - 4:10PM

Negative Predictive Value of MRI Following Resection of Pituitary Macroadenoma

J McCloskey¹, A Weyer¹, B Branstetter¹, M Hughes¹

¹University of Pittsburgh Medical Center, Pittsburgh, PA

Purpose

The goal of this study is to determine the negative predictive value (NPV) of MRI following resection of pituitary macroadenoma and whether a negative MRI decreases the need for additional imaging surveillance.

Materials and Methods

Consecutive patients from our skullbase surgical database were selected who underwent expanded

Oral Presentations & Excerpts

endonasal approach surgery for pituitary macroadenoma. Patients were excluded if they had prior pituitary surgery or fewer than two surveillance MRIs. A score of 1 (negative), 2 (probably negative), 3 (probably recurrent), or 4 (definitive MRI evidence of recurrent tumor) was assigned to each MRI report. The NPV was then calculated for a single negative surveillance MRI and for two consecutive negative surveillance MRIs. Any follow-up MRI performed after the immediate postoperative exam was considered a surveillance study. Disease absence was defined as lack of clinical and/or imaging evidence of recurrent disease for a minimum of one-year follow-up.

Results

Twenty-one patients met inclusion criteria. Mean follow-up time was 36 months (range 9-57) and patients underwent an average of three surveillance MR exams. Of the 21 patients, 17 had at least one negative surveillance exam and 15 patients had two consecutive negative surveillance studies. The NPV of a single negative surveillance MRI was 94% (16/17). The NPV of two consecutive negative surveillance exams was 100% (15/15). Fifty additional patients have been identified that will ultimately improve the statistical power of this analysis.

Conclusions

In patients who have undergone resection of pituitary macroadenoma, a single negative surveillance MRI has NPV 94%, but this increases to 100% in patients with two consecutive negative surveillance MRIs. This obviates the need for additional surveillance MRIs in the absence of clinical recurrence.

O-243

4:10PM - 4:17PM

Utility of Dual Energy CT Iodine Material Decomposition Maps and Low Energy Virtual Monochromatic Images for Detection of Perineural Spread in Head and Neck Malignancy

G Romero-Sanchez¹, A Perez-Lara², R Forghani¹

¹*Jewish General Hospital and McGill University, Montreal, Quebec, Canada,* ²*Hospital General de Malaga, Malaga, Spain*

Purpose

Dual-energy CT (DECT) has been shown to improve evaluation of head and neck cancer but its utility for the detection of perineural spread of tumor (PNS) is currently unknown. In this study, we investigated whether DECT low-energy virtual monochromatic images (VMI) and iodine-water material decomposition maps (IW) can improve delineation and detection of PNS in head and neck cancer.

Materials and Methods

A total of 15 cases of PNS affecting different segments of cranial nerves V or VII nerves were evaluated. All subjects were scanned with a 64-slice dual-energy scanner with fast kVp switching. All cases were pathology-proven based on biopsy or surgery, or had a complementary MRI proving the presence of perineural spread. The imaging appearance on 65 keV VMI (typically considered equivalent to a conventional 120 kVp single energy CT), 40 keV VMI, and IW maps were compared.

Results

Subjectively, addition of 40 keV VMIs and IW maps improved visualization of PNS and extent of PNS compared to the use of 65 keV VMIs alone. These reconstructions seem particularly useful in more subtle cases of PNS. Both the 40 keV VMIs and IW maps were found to be useful for PNS detection.

Conclusions

Advanced DECT reconstructions such as low-energy VMIs and IW maps may be useful for characterization and detection of perineural spread. This may be particularly useful in cases of early or subtle PNS.

O-244

4:17PM - 4:24PM

Correlation of pretreatment SUV-derived quantitative FDG-PET indices of Head and Neck Adenoid Cystic Carcinoma with pathologic grade and metastatic potential; preliminary results

Y Koksels¹, M Gencturk¹, W Yue¹, F Li¹, Z Cayci¹

¹*University of Minnesota, Minneapolis, MN*

Purpose

To determine whether quantitative FDG/PET parameters including maximum standardized uptake value (SUVmax), total metabolic tumor volume (TMTV) and total lesion glycolysis (TLG) of the primary tumor on pretreatment imaging correlate with the tumor pathological grade and with the distant metastatic potential in patients with adenoid cystic carcinoma (ACC) of the head and neck.

Materials and Methods

Pathology database for the June 2007 to August 2017 period was reviewed for detection of cases with adenoid cystic carcinoma of the head and neck region. Detected were 36 patients. Of these 36 patients, 21 had PET/CT before surgery. These PET/CTs were reviewed and quantitative parameters for quantification analysis were calculated. One-way analysis of variance is performed to test the correlation of PET parameters and the histopathological grading. Multivariate analysis was performed using the Cox proportional hazard regression model.

Results

Of the 36 patients, there were six (17%) patients with grade 1, 12 (34%) patients with grade 2 and 18 (50%) patients with grade 3 tumors on surgical pathology. Distant metastasis was present in nine (25%) patients. Of these nine, four had grade 3, four had grade 2 and one had grade 1 tumor. There was statistically significant correlation between TLG and histopathologic grade ($p=0.01$). The SUVmax and TMTV did not correlate with the tumor grade. Multivariate analysis demonstrated that the TLG was the only predictor of distant metastasis.

Conclusions

Pretreatment primary head and neck ACC TLG correlates with histopathological grading and is a predictor of distant metastasis.

Tuesday, June 5, 2018

3:00PM - 4:30PM

Parallel Paper Session: Pediatrics: New Findings

O-245

3:00PM - 3:07PM

Perfusion Abnormalities at 3D ASL in Patients with Acute Encephalopathy with Biphase Seizures and Late Reduced Diffusion

H Uetani¹, M Kitajima¹, T Sugahara², Y Muto², K Hirai², H Kikuchi², Y Kuroki², M Tateishi¹, Y Yamashita¹

¹*Kumamoto University, Kumamoto, Japan*, ²*Japanese Red Cross Kumamoto Hospital, Kumamoto, Japan*

Purpose

Acute encephalopathy with biphase seizures and late reduced diffusion (AESD) is the most common encephalopathy subtype in Japanese children. (1) The syndrome is characterized by a prolonged febrile seizure as the initial neurologic symptom with no abnormalities on conventional MR images at day 1, followed by secondary seizures with reduced diffusion in subcortical regions at days 3–6. (2) Arterial spin labeling (ASL) is useful to evaluate the cerebral perfusion in acute encephalitis (3); however, the cerebral

Oral Presentations & Excerptas

perfusion in AESD using ASL has not been fully evaluated. The purpose of study was to evaluate perfusion abnormalities and its temporal changes at 3D ASL in patients with AESD.

Materials and Methods

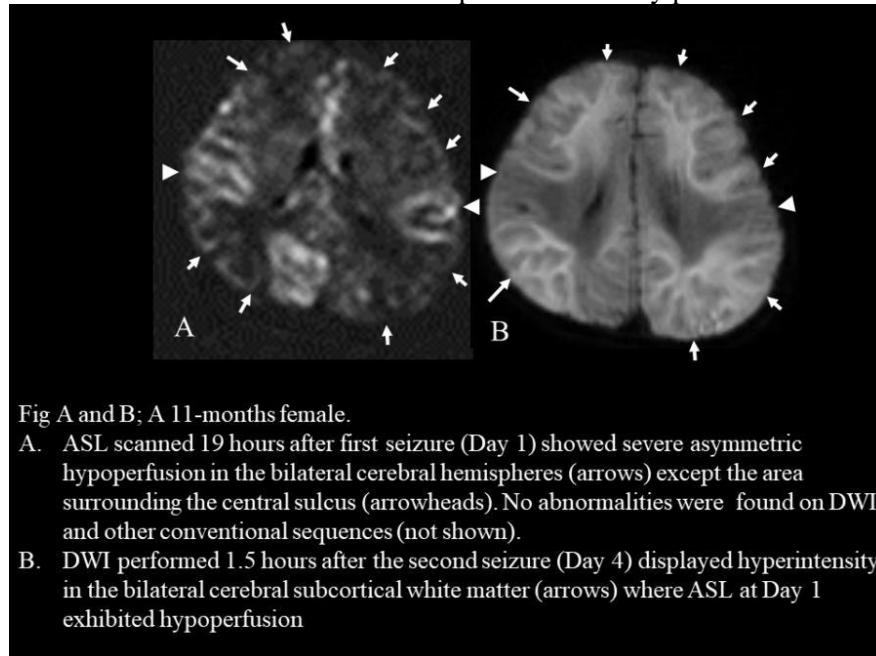
We evaluated seven patients with AESD (5 females, 2 males, mean age; 21 months) who underwent 3T or 1.5T MR including 3-D ASL, DWI, and conventional sequences. Abnormal perfusion on ASL was qualitatively evaluated using a 3-point grading system; hypoperfusion, normal, and hyperperfusion. In four patients who underwent follow-up MRI, the temporal change of the perfusion abnormality was assessed. Additionally, we compared ASL findings with other sequences.

Results

Both patients scanned less than 24 hours after the first seizure showed hyperperfusion. Hyperperfusion was found in four patients who were scanned less than 24 hours after the second seizure. Three patients displayed hypoperfusion, and one patient showed normal perfusion at one month after the onset. In four patients who underwent follow-up MR examinations, perfusion abnormalities changed with time. MR imaging findings on DWI and other sequences were normal when the patients were scanned less than 24 hours after the first seizure, while, DWI hyperintensity in subcortical white matter appeared in all patients who were scanned after the second seizure.

Conclusions

ASL can detect the disturbed cerebral perfusion in early period of AESD and its temporal changes.



(Filename: TCT_O-245_2018ASNRAESD.jpg)

O-247

3:07PM - 3:14PM

A CAD System to Track Brain White Matter Lesions of Multiple Sclerosis in Pediatric Patients on MRI Over Time

M Jurkiewicz¹, M Bilello², K Shekdar¹

¹Children's Hospital of Philadelphia, Philadelphia, PA, ²University of Pennsylvania, Philadelphia, PA

Purpose

Multiple sclerosis (MS) is the most important immune-mediated demyelinating disease of the human beings (1). Although the incidence of MS in pediatric patients is much less than adults it is among the

Oral Presentations & Excerptas

most common acquired white-matter disease in children. MRI is the most important para-clinical tool for diagnosing and monitoring MS (2), with the geographic and chronologic distribution of T2/FLAIR hyperintense lesions essential for diagnosis (3, 4). Interpreting serial brain MRI studies can be a tedious and error-prone task for the neuroradiologist, in both qualitative and quantitative assessment of change in white-matter lesion load. Especially in patients with MS, it is critical to report response to treatment and identify new lesions accurately, highlighting the need for a computer-aided detection (CAD) system to detect and quantify changes in brain white-matter lesions over time. A CAD system has been successfully used in the adult population for monitoring MS lesions (5). The purpose of our study was to assess the feasibility of this CAD system to track brain lesions of MS in the pediatric patients on MRI over time.

Materials and Methods

Brain MRI images were acquired from four patients with known multiple sclerosis who were undergoing treatment, for a total of 14 cases including current and prior studies. The age of these patients with MS ranged from 17 to 19 years and followed over the course of up to 2.5 years. The system applies a preprocessing pipeline to the T2/FLAIR sequences of both prior and current studies, including coregistration, skull-stripping, and intensity normalization. The program then generates forward and backward difference maps on each modality, highlighting interval increase or decrease in lesion load on T2/FLAIR. Detected changes are color-coded and displayed on subtraction maps. The program takes two to three minutes to run on a desktop Linux workstation. Performance, including sensitivity and rate of false-positive detection, was assessed by comparison with a human expert.

Results

Results demonstrate a sensitivity around 95% for new/progressed areas of abnormal T2 signal on T2/FLAIR and 95% for resolved/improved areas of abnormal T2 signal on T2/FLAIR. Additionally, the CAD identified new lesions 60% of cases and improved/resolved lesions in 20%, that were not detected by the human reader. False positives occurred mainly in the parenchymal structures such as skull base, orbits, CSF, and calvarium, which were easily discarded.

Conclusions

This preliminary work demonstrates the feasibility of a CAD system to monitor changes in T2/FLAIR hyperintense brain lesions in pediatric patients with MS. A CAD system that helps monitor temporal changes in brain white-matter lesions of MS in pediatric patients on MRI would improve clinical care through increased reproducibility and accuracy, and shorter turn-around time over human-only interpretation.

O-248

3:14PM - 3:21PM

Evaluation of brain's viscoelasticity in children using MR-elastography

F Macruz¹, M Kurt¹, E Ozkaya², H Lv¹, M Wintermark¹

¹Stanford University, Stanford, CA, ²Stevens, Hoboken, NJ

Purpose

Magnetic resonance elastography (MRE) is a quantitative imaging technique that allows characterization of the mechanical properties of a tissue, throughout the application of a mechanical stress on it, imaging of the consequential shear-waves and calculation of the tissue properties based on the mathematical inversion of the shear-waved image. The relation between the mechanical properties and the microstructural composition and organization of neural tissue has brought the attention to this imaging method as an important biomarker of many neurological conditions and a reflector of cognitive function. However, because it is a recently described method, brain MRE studies on children and adolescents have only just begun to be described.

Materials and Methods

Cerebral elastography was performed in 27 healthy children and adolescents with age range from 7 to 17 years old (mean age of 11.7 years old). The exam was performed in a 3T machine (GE) and FLAIR, 3-D

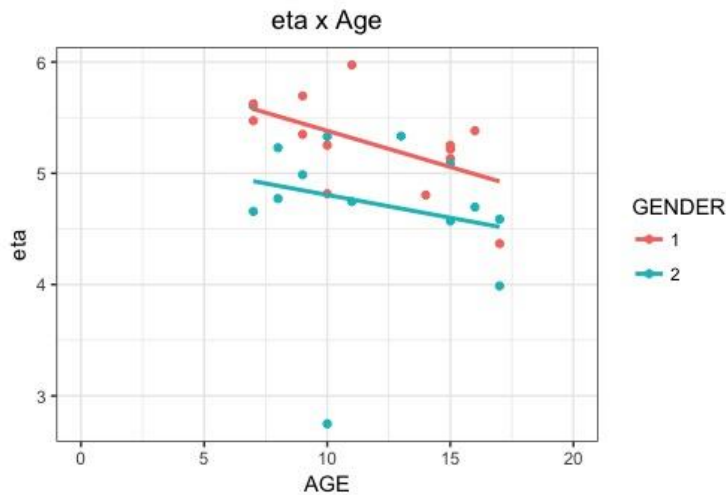
BRAVO and spin-echo EPI MRE sequences were evaluated by two neuroradiologists. MRE operating frequencies of 40 Hz, 60 Hz and 80 Hz were chosen and the images coregistered to MRI images. Then calculation of the storage and loss of the whole brain, in the respective frequencies, were performed, with obtainment of frequent independent parameter (E1, E2 and eta). A final stiffness was estimated and its variance according to brain volume, volunteer age and gender was analyzed.

Results

Our results show a tendency of decrease in the storage and loss values in lower frequencies according to the age. Interestingly, no significant differences were observed in higher frequency (80 Hz), reflecting differences in brain performance according to the frequency of acquisition. In regard to the frequent independent parameter, we have found that stiffness parameters (E1 and E2) and the viscosity parameter (η) decrease with age. The most significant relation was between stiffness and gender, with women (group 1) showing lower values of E1 and higher of E2 and η than men (group 2). Although an increase in the volume according to age was observed, no relation between stiffness and cerebral volume was identified.

Conclusions

Viscoelasticity of the brain tissue can be measured using MR and viscous properties (loss and storage modulus) can be extracted from the MRE data collected at different frequencies. Frequency independent parameter, generated from the original loss and storage maps can also be obtained, with both information reflecting the final stiffness of the tissue. In children, we verified that the stiffness changes with age and gender, but not with volume. According to our results, it is safe to affirm that the brain gets softer between ages of 7 and 17 years old.



(Filename: TCT_O-248_Childrenwholebrainetaxage.jpg)

O-249

3:21PM - 3:28PM

Pediatric Brain and Whole Spine CSF Flow Imaging using Phase Contrast Cine for New Clinical Application

B Wang¹, P Hou¹, L Ketonen¹

¹The University of Texas MD Anderson Cancer Center, Houston, TX

Purpose

Before infusion of therapeutic agent into surgically placed ventricular access device (VAD) into the fourth ventricle in the brain, demonstration of free CSF (cerebrospinal fluid) flow from the fourth ventricle to the lumbar spine is essential to avoid locally too high concentration of chemotherapy. Until now nuclear medicine studies have been utilized to assess for blockage of CSF prior to intraventricular

Oral Presentations & Excerptas

chemotherapy infusions. MRI cine phase-contrast (PC) flow studies can be performed simultaneously with a standard diagnostic brain and spine MRI to assess disease burden. We will illustrate PC MRI sequences we created to assess CSF flow from fourth ventricle down to sacrum, which to our knowledge has not been reported in literature. Factors important to the success of CSF imaging will be discussed.

Materials and Methods

Phase contrast image is highly sensitive to field homogeneity and gradient strength, especially at low velocity encoding (VENC) value. Regional shimming helps to reduce noise. A cardiac or peripheral gating is mandatory to catch synchronized slow CSF flow imaging. This is a critical step, clinically a failed CSF flow study is most likely due to failed gating. A straight midsagittal plane from central upper to lower spinal cord is selected so that the whole spine CSF flow is imaged. Velocity encoding is applied in all three directions for the brain, single direction for the spine. VENC of 5cm/sec will help increase SNR for slower CSF flow. A thick anterior saturation pulse is added to block cardiac motion artifacts. Typical parameters: 256x192, FOV of 24 cm (brain), 28 – 36 cm (spine), slice thickness 5 -10 mm, TR of 25 – 30 msec, TE of 4 – 6msec, 2 averages, results in total scan time of 5 – 6 minutes. Eighteen pediatric patients with recurrent malignant posterior fossa tumors underwent implantation of VAD into the fourth ventricle with simultaneous maximal safe surgical resection if resectable tumor was in operative field. Prior to infusing therapeutic agents into the VAD, cine MRI PC CSF flow sequences of the brain and total spine were performed. Velocity encoding (VENC) of 5 cm/sec and 10 cm/sec was used to confirm CSF flow from the fourth ventricular outlets to the lumbosacral spine. Qualitative CSF flow was characterized by neuroradiologists as present or absent.

Results

Eighteen patients have received fourth ventricle infusions to date; they all had progressive disease at the time of MRI examination despite prior surgery, radiation therapy and various chemotherapy agents. None had neurological toxicity following therapy. CSF flow study was successful on every patient and confirmed CSF flow through the spinal canal, and therefore nuclear medicine CSF flow studies were not required in any of the patients. Factors important to success of CSF imaging include low VENC, regional shimming, cardiac gating, and midsagittal plane selection.

Conclusions

We describe a new indication and method for PC CSF flow study from fourth ventricle outlets to distal spinal canal to be used in patients that are in need for local therapeutic treatment delivery into the fourth ventricle of the brain via VAD, in order to avoid locally too high concentration of the chemotherapy. Of the 18 pediatric patients who have received infusions after using this MR technique to date, none have had neurological toxicity. CSF flow including the fourth ventricle and the total spine can be assessed noninvasively and expediently with PC MRI sequences during routine diagnostic brain and spine MRI. Advantages over nuclear medicine studies include eliminating an invasive procedure and avoiding radiation exposure.



(Filename: TCT_O-249_CSFFlowabstractASNR2018Imagejpeg.jpg)

O-250

3:28PM - 3:35PM

Time-STAMP and Time-SLIP CSF Imaging in Pediatric Patients and Adult Volunteers

Oral Presentations & Excerpts

M Borzage¹, J Kwak¹, T Wu¹, S Ponrartana², B Tamrazi², W Gibbs³, M Law³, M Nelson², J McComb⁴, S Bluml²

¹*Fetal and Neonatal Institute, University of Southern California, Los Angeles, CA*, ²*Children's Hospital Los Angeles and University of Southern California Keck School of Medicine, Los Angeles, CA*, ³*University of Southern California Keck School of Medicine, Los Angeles, CA*, ⁴*Children's Hospital Los Angeles, Los Angeles, CA*

Purpose

To demonstrate that a novel tag-based CSF imaging methodology offers improved contrast when compared with a commercially available implementation. Therefore, we compared the quantitative performance of tag-based CSF imaging techniques. Time-Spatial Labeling Inversion Pulse (Time-SLIP) uses an arterial spin-labeling technique to tag CSF as an endogenous tracer but creates variation in background signal that decreases contrast. Time Static Tagging And Monocontrast Preservation (Time-STAMP), is similar in general to Time-SLIP but minimizes the variations in background signal to improve contrast. We tested both tag-based sequences (Time-SLIP and Time-STAMP) in healthy adults to compare the contrast from each sequence, and tested Time-STAMP in pediatric patients with cerebrospinal fluid (CSF) abnormalities to assess its general applicability in clinical practice.

Materials and Methods

We recruited 10 healthy adults (5 male, 5 female, 36 ± 18 years) and acquired both Time-SLIP and Time-STAMP images for them. We also recruited 19 pediatric patients (12 male, 7 female, 1 month to 13 years) with CSF abnormalities, and acquired Time-STAMP images for them. Abnormalities for these patients were mainly congenital and acquired hydrocephalus requiring surgical intervention; etiologies included tumors, arachnoid cysts and webs, posthemorrhagic changes and structural malformations. We used two different clinical 3T MR scanners. We imaged healthy adults on a Titan 3T (Toshiba, Irvine, CA), and pediatric patients on a 3T Achieva (Philips, Best, the Netherlands). For healthy adults on the Toshiba MR: the tag-based techniques used a single-shot half-Fourier fast spin-echo sequence: repetition time = 13450ms, echo time 80ms, flip angle = 90 degrees, acquisition matrix 224x224, voxel resolution=1.0x1.0x5.0mm³. For Time-SLIP, we acquired 20 cardiac-gated with delay times of 1700, 1800...3600ms. Cardiac and respiration rates were monitored to trigger the Time-SLIP sequences. Time-STAMP acquisitions were identical to Time-SLIP except: we used a quasi-constant delay time of 2500-2590ms and physiological gating was omitted. Images were analyzed in Matlab (Mathworks Natick, MA), ROIs were placed in the parenchyma (brainstem), tagged CSF (fourth ventricle) untagged CSF (lateral ventricle) and flowing CSF (third ventricle and aqueduct). For pediatric patients on the Philips MR, Time-STAMP was implemented via a single-shot half-Fourier fast spin-echo sequence with repetition time = 8000ms, echo time 7ms, acquisition matrix 256x161, voxel resolution=0.9x1.4x4.0mm³ and a fixed delay of 2500ms. Physiological gating was omitted. Due to time limitations we acquired fewer dynamic images (median=9). Pathologies lead to alternative tag placements, and CSF ROIs included the lateral, third, and fourth ventricles, prepontine and interpeduncular cistern and cisterna magna.

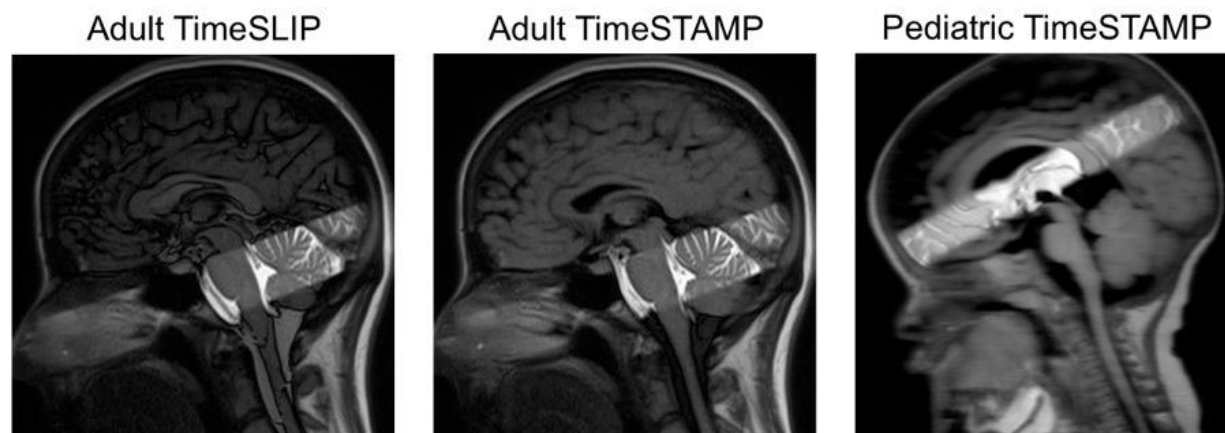
Results

Representative Time-SLIP and Time-STAMP images from one healthy adult, and Time-STAMP images from one pediatric patient (Figure 1), demonstrate CSF flow and contrast. We graphed the ROI intensities for each exam (not shown). For Adults, for whom we acquired both Time-SLIP and Time-STAMP images, we were able to assess differences in contrast via a two-way repeated measures analysis of variance (ANOVA) and Tukey's multiple comparison correction. Time-STAMP had better contrast than Time-SLIP ($p < 0.0001$) for all comparisons. Time-STAMP contrast was 14000 ± 1500 , Time-SLIP contrast of 9800 ± 1500 , in arbitrary units. The improvements, in contrast, were highest between dark untagged static CSF and parenchyma. Using the average contrast between the pair of ROIs for this comparison, Time-STAMP was 24% to 135% higher (mean= $44 \pm 33\%$) than Time-SLIP. In pediatric patients, only the Time-STAMP contrasts were available. We assessed Time-STAMP for tagged and untagged CSF was 3900 ± 1500 , in arbitrary units. It is noteworthy the fast readouts of Time-STAMP provided useful images even in cases where significant patient motion was present. For patients with

various levels of sedation and compliance with imaging instructions, this is an improvement in usability over phase-contrast MR images, which while excellent at quantifying flow, are inherently highly sensitive to head motion.

Conclusions

Untagged CSF in Time-STAMP has nearly constant delay time and hence less variable contrast as demonstrated in healthy adults. In our population of pediatric patients, the images were able to depict CSF flow and as part of our clinical workflow were successful even in patients with significant head motion. Therefore, Time-STAMP appears to provide useful improvements of contrast in a sequence that is practical for clinical use.



(Filename: TCT_O-250_Picture1.jpg)

O-251

3:35PM - 3:42PM

Impact of iterative model reconstruction combined with low dose on the image quality of head and neck CT angiography for pediatric patients

B Cheng¹, X Chen¹, Y Guo¹, G Ning¹

¹West China Second University Hospital, Sichuan University, Chengdu, Sichuan Province, China

Purpose

The radiation safety and the risk for special diseases increase attention [1]. As for children, the radiation safety is amplified due to children being more sensitive to the effects of ionizing radiation [2]. Therefore, a better strategy to reduce radiation dose and contrast media (CM) intake in pediatric patients yield the top priority. This study aims to evaluate the imaging quality of head and neck computed tomographic angiography (hnCTA) in pediatric patients at lowered radiation dose by combining Iterative model reconstruction (IMR) with low-voltage scan.

Materials and Methods

One hundred pediatric patients were enrolled and randomly divided into two groups. Group A (n=50) was scanned with 100kV, 50 ml contrast agent, combined with the filtered back projection (FBP), and Group B (n=50) was scanned with 70kV, 30 ml contrast agent, combined with IMR. Mann-Whitney U test was used to compare the enhanced CT value of arteries, image noise, signal noise ratio (SNR), contrast noise ratio (CNR), the score of image quality, effective radiation dose (ED) and iodine intake of contrast agent between two groups.

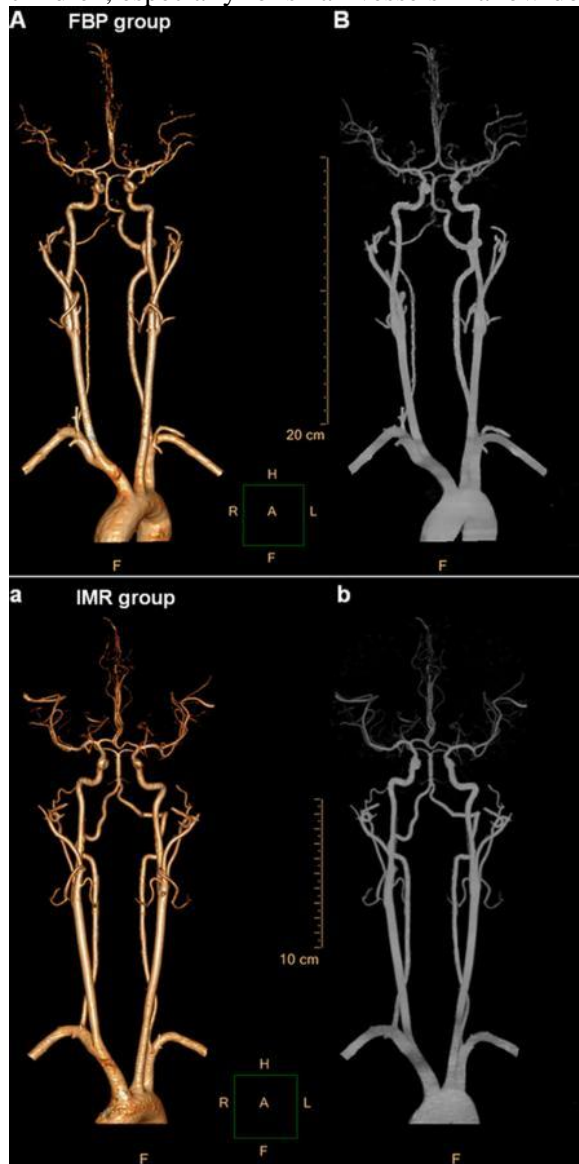
Results

The mean ED and iodine intake of Group B were reduced by 70.4% and 43.2% of Group A. The mean CT values of the arteries in Group B were significantly higher than in Group A, whereas the image noises of Group B were significantly lower than Group A. Group B exhibited a better image quality score and higher mean CNR/SNR than Group A.

Oral Presentations & Excerptas

Conclusions

Compared to FBP algorithm, the knowledge-based IMR technique in hnCTA enables significant reduction of patient radiation dose while preserving diagnostic image quality. Thus, the combination of low-tube voltage scanning with IMR algorithm provided an excellent solution for imaging vessels of children, especially for small vessels in a low-dose scanning situation.



(Filename: TCT_O-251_Figure.jpg)

O-252

3:42PM - 3:49PM

Radiation Dose and Image Quality in Pediatric Neck CT: Findings Before and After a Quality Improvement Project

D Patel¹, S Tipnis¹, S Stalcup¹, M Matheus¹, M Spampinato¹

¹Medical University of South Carolina, Charleston, SC

Purpose

To evaluate the image quality of pediatric neck CT studies before and after the implementation of low radiation dose protocols

Materials and Methods

We retrospectively reviewed 208 pediatric neck CT studies, 96 before and 112 after the implementation of low-dose protocols, performed in children aged 0-16 years. We obtained CT scanning parameters, CT dose index (CTDI_{vol}), and dose-length product (DLP) from the Picture Archiving and Communication System. A quantitative assessment of image quality was performed by measuring the background noise (BN) and calculating signal-to-noise ratio (SNR) on the axial CT image through the true vocal folds. Three neuroradiologists assessed the image quality of the same CT image using a 5-point scoring system, where 1 = nondiagnostic and 5 = excellent diagnostic quality, and scores equal to or greater than 3 indicated satisfactory diagnostic quality. We compared CTDI_{vol}, DLP, average image quality ratings, and SNR of studies conducted at baseline and with low-dose protocols using the Mann-Whitney test. Results were considered statistically significant when $p < 0.05$.

Results

CTDI_{vol} and DLP were significantly lower in studies performed using the low-dose protocols than at baseline ($p < 0.001$ for both variables), but there was no significant change in image quality and SNR (respectively $p = 0.335$ and $p = 0.064$).

Conclusions

Following the implementation of low radiation dose pediatric neck CT protocols, we observed no degradation of diagnostic image quality. Our initial results suggest that there may be an opportunity for further radiation dose reduction without compromising diagnostic image quality.

Table

	mAs*	DLP	CTDI _{vol}	SNR	Image Quality score
Baseline protocol	222.1 (70.9)	340.9 (246.88)	13.4 (7.4)	17.7 (5.7)	3.9 (0.6)
Low dose protocol	159.8 (83.1)	204.7 (178.1)	7.7 (6.1)	15.7 (8.9)	3.8 (0.4)

*Average (standard deviation)

(Filename: TCT_O-252_AbstractTable.jpg)

O-253

3:49PM - 3:56PM

Synthetic MRI in Children: Relationship between Automated Intracranial Volumetrics and Head Circumference

K Gertz¹, J Leach¹, B Jones¹, A McAllister¹, H West¹, S Serai¹

¹Cincinnati Children's Hospital Medical Center, Cincinnati, OH

Purpose

Synthetic MRI (SyMRI) can be used to determine intracranial volume (ICV), brain parenchymal volume (BPV) and volumes of other intracranial compartments such as white matter, gray matter, and cerebrospinal fluid (CSF) utilizing a rapid MRI sequence and immediate post processing. This study aimed to use SyMRI as a tool to determine a precise relationship between ICV as determined by SyMRI and clinical and MRI determined head circumference (HC). Additionally, the utility of SyMRI in evaluation of patients with abnormal clinical HC was explored.

Materials and Methods

Evaluated were 181 normal SyMRI scans and 96 abnormal scans. HC was calculated by MRI for each of these scans ($n = 277$) using a previously validated method (1). The HC and ICV were compared with linear regression in the 181 normal scans alone as well as all 277 scans consisting of both normal and

Oral Presentations & Excerptas

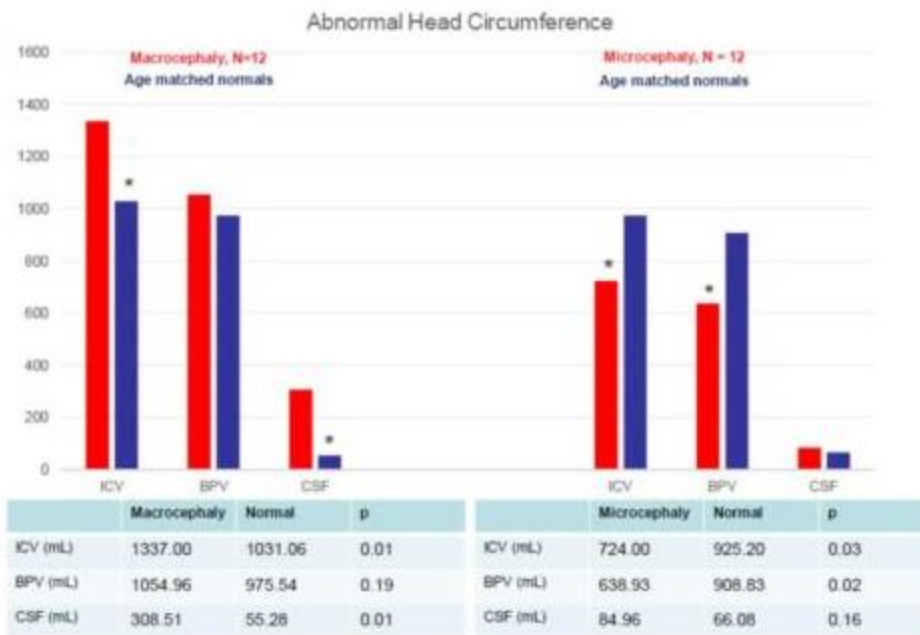
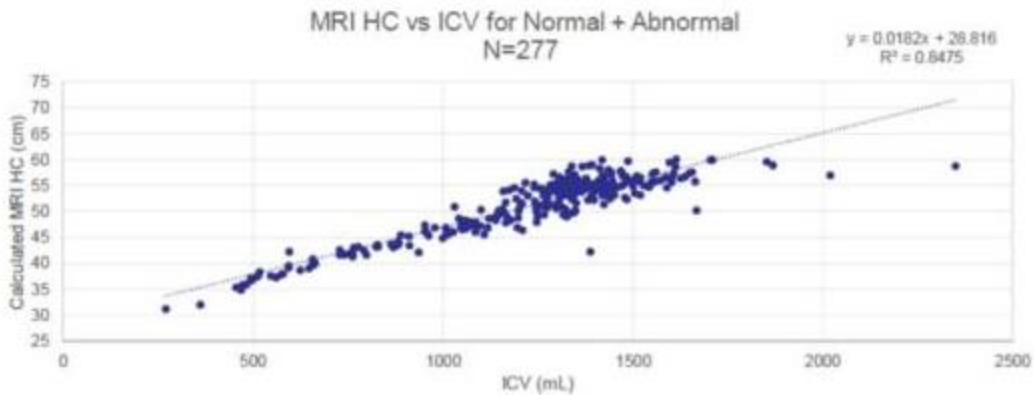
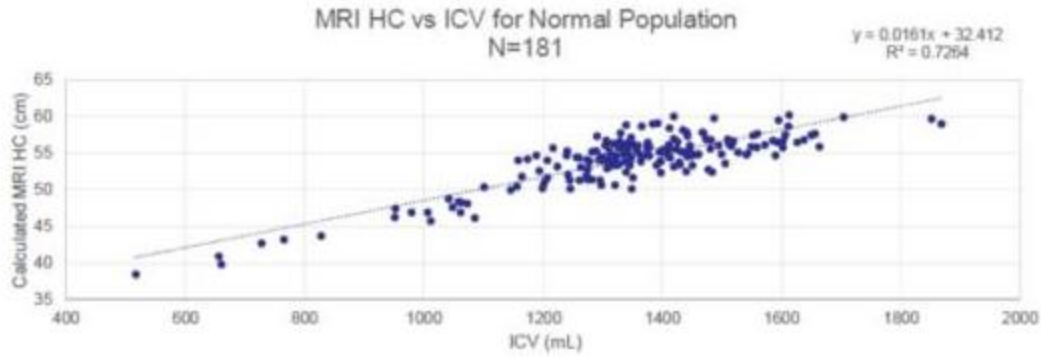
abnormal studies. A comparison of ICV, BPV, and CSF volume was then made between 12 macrocephalic children (>95% CDC percentile for HC), 12 microcephalic children (<5% CDC percentile for HC) and 12 age-matched controls for each group.

Results

There was a linear relationship between HC and ICV for both the 181 normal scans ($y = 0.0161x + 32.412$, $R^2 = 0.7264$) and the 277 scans that were comprised of normal and abnormal studies ($y = 0.0182x + 28.816$, $R^2 = 0.8457$). Macrocephalic patients showed a significant difference in ICV ($p = 0.01$) and CSF volume ($p = 0.01$), while not showing any significant difference in BPV ($p = 0.19$) when compared with age-matched controls. Microcephalic patients showed a significant difference in ICV ($p = 0.03$) and BPV ($p = 0.02$) but not in CSF volume ($p = 0.16$) compared with controls.

Conclusions

This study shows a linear, predictable relationship between HC and ICV as determined by SyMRI for both normal and abnormal populations. These findings suggest that accurate estimates of HC may be estimated from ICV as derived from SyMRI, a potentially useful tool for clinical scan assessment. SyMRI was also able to discriminate whether abnormal cranial volume was driven primarily by increases in CSF, as in the case of macrocephaly, or by decreases in BPV, as in the case of microcephaly. Based on these findings, the etiology of abnormal HC in children may be more clearly delineated with SyMRI.



(Filename: TCT_O-253_ASNR2018Graphics1200dpi.jpg)

O-254

3:56PM - 4:03PM

Brain Iron Deposition After Ferumoxytol-enhanced MRI: A Study of Porcine and Pediatric Brains

M Iv¹, A Theruvath², K Shpanskaya², L Pisani³, O Lenkov², H Daldrup-Link², K Yeom⁴

Oral Presentations & Excerptas

¹Stanford University Medical Center, Stanford, CA, ²Lucile Packard Children's Hospital/Stanford University, Palo Alto, CA, ³Stanford University, Stanford, CA, ⁴Stanford Hospital, Stanford, CA

Purpose

While it is known that gadolinium deposits in brain after contrast-enhanced MRIs (1), it is unknown if iron oxide nanoparticles deposit in brain after intravenous injection. In this study, we investigate if there are detectable amounts of intracranial iron deposition after multiple ferumoxytol administrations.

Materials and Methods

This is an IRB-approved retrospective case-control study of nine pigs and 12 pediatric patients who received ferumoxytol (5 and 3 mg/kg, respectively). Whole porcine brains were imaged ex vivo at 7T, with acquisition of T2* maps. Pediatric patients who had at least two ferumoxytol-enhanced MRIs at 3T with quantitative susceptibility mapping and R2* maps were included (2-3). For pigs, regions of interests (ROIs) were placed in the caudate, lentiform, dentate nuclei, and thalami bilaterally. For humans, ROIs were placed in the caudate, globus pallidus, putamen, dentate nucleus, thalamus, and substantia nigra. Statistical analyses included independent-samples t-test, paired-samples t-test, and Pearson correlation.

Results

In pigs, there were no significant differences in R2* of brain regions in ferumoxytol-exposed vs. control ($P>0.05$) and no significant correlation between ferumoxytol dose and R2* in any of the brain regions. In humans (age, mean +/- std dev: 12.3 +/- 5.4 years; 7 females, 5 males), mean time of follow-up MRI was 14.67 months. R2* and susceptibility in all brain regions did not significantly differ from baseline ($P>0.05$), except for slightly increased R2* in the dentate and globus pallidus at follow-up ($P=0.013$ and $P=0.019$, respectively). No significant correlation was found between ferumoxytol dose and R2* and susceptibility values in any brain region.

Conclusions

No significant differences were found in R2* and susceptibility values in pediatric or porcine brains after ferumoxytol-enhanced MRIs except for slightly increased R2* in the dentate nucleus and globus pallidus in pediatric brains at follow-up, suggesting that exogenous ferumoxytol-iron administration results in minimal brain iron deposition.

O-255

4:03PM - 4:10PM

Gadolinium Deposition in the Pediatric Brain: No Increased Intrinsic T1-Weighted Signal Intensity within the Dentate Nucleus Following the Repeated Administration of the Macrocyclic Agent Gadobutrol

J Young¹, J Qiao², I Orosz², N Salamon², M Franke², H Kim², W Pope²

¹University of California Davis School of Medicine, Sacramento, CA, ²David Geffen School of Medicine at University of California Los Angeles, Los Angeles, CA

Purpose

To determine whether repeated administration of the macrocyclic gadolinium-based contrast agent (GBCA) gadobutrol in children is associated with the development of increased intrinsic T1-weighted signal intensity within the cerebellar dentate nucleus, an imaging surrogate for gadolinium deposition

Materials and Methods

With IRB approval for this HIPAA-compliant retrospective study, we identified a cohort of eight patients under the age of 18 years without posterior fossa disease who underwent at least four gadobutrol-enhanced MR examinations of the brain from 2013-2017 and who had not had prior exposure to any other GBCA. For comparison, we identified a cohort of 19 patients under the age of 18 years who underwent at least four gadopentetate dimeglumine-enhanced MR exams from 2013-2017. For each examination, both dentate nuclei were manually contoured on unenhanced images; the mean dentate-to-pons signal intensity (DN-P SI) ratio was calculated. The DN-P SI ratios from the first and last MR exams were compared

Oral Presentations & Excerptas

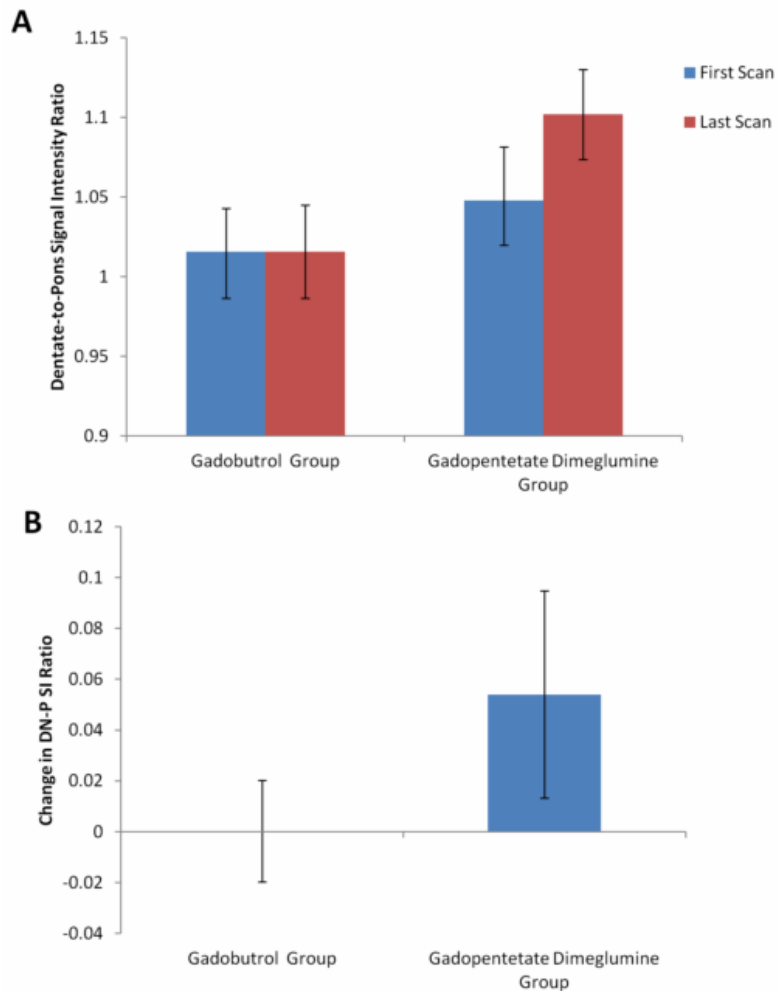
using paired t-tests. The change in DN-P SI ratio was compared using t-tests. Ordinary least squares regression was performed to assess the effect of the type of GBCA on the change in the DN-P SI ratio while controlling for potentially confounding variables.

Results

In the gadobutrol cohort, there was no significant change in the mean DN-P SI ratio from the first to the last scan (1.02 vs. 1.02, $p=0.98$, Panel A). In the gadopentetate dimeglumine cohort, there was a significant increase in the mean DN-P SI ratio from the first to the last scan (1.05 vs. 1.10, $p=0.01$, Panel A). The change in the DN-P SI ratio from the first to the last scan was significantly lower in the gadobutrol cohort than in the gadopentetate dimeglumine cohort (0.00 vs. 0.05, $p=0.02$, Panel B). After controlling for the number of doses of gadolinium received, patient age, patient diagnosis, history of chemotherapy, and history of radiation, the change in DN-P SI ratio from the first to the last scan was significantly lower for patients in the gadobutrol group than for patients in the gadopentetate dimeglumine group (coefficient=-0.08, $p=0.04$). Additionally, for direct comparison with the eight patients in our gadobutrol subcohort, we identified an age-matched subcohort of eight patients who received an equivalent number of doses of gadopentetate dimeglumine. In these age-matched and gadolinium dose-matched subcohorts, the change in the DN-P SI ratio from the first to the last scan was significantly lower in the gadobutrol subcohort than in the gadopentetate dimeglumine subcohort (0.00 vs. 0.08, $p=0.03$).

Conclusions

Repeated administration of the macrocyclic GBCA gadobutrol in children was not associated with increased intrinsic T1-weighted signal intensity within the dentate nucleus, while the repeated administration of the linear GBCA gadopentetate dimeglumine was associated with increased intrinsic T1-weighted signal intensity within the dentate nucleus, presumably due to gadolinium deposition. Thus, macrocyclic GBCAs may be less likely than linear GBCAs to deposit within the pediatric brain, consistent with prior published studies in adults.



(Filename: TCT_O-255_ASNR2018Figure.gif)

O-256

4:10PM - 4:17PM

Thalamic and Dentate Nuclei Abnormalities in Children with Gaucher Disease

S Culleton¹, F D'Arco², S Stagliano³, J Davison², G Perucca⁴, B Soares⁵

¹National Hospital for Neurology and Neurosurgery, London, United Kingdom, ²Great Ormond Street Hospital for Children, London, United Kingdom, ³Fondazione Policlinico Universitario A. Gemelli, Rome, Italy, ⁴Regina Margherita Children's Hospital, Turin, Italy, ⁵Johns Hopkins University School of Medicine, Baltimore, MD

Purpose

Gaucher Disease (GD) is the commonest of the lysosomal storage disorders (1). A wide range of neurological abnormalities occur in GD; however, the findings on cerebral imaging to date have been described as nonspecific or normal. We report previously undescribed image finding on MRI brain imaging in a small group of children with GD.

Materials and Methods

On review of cases with confirmed diagnosis of GD and brain imaging in two tertiary pediatric centres we found signal abnormalities in the thalami and/or dentate nuclei in three patients. A literature search did

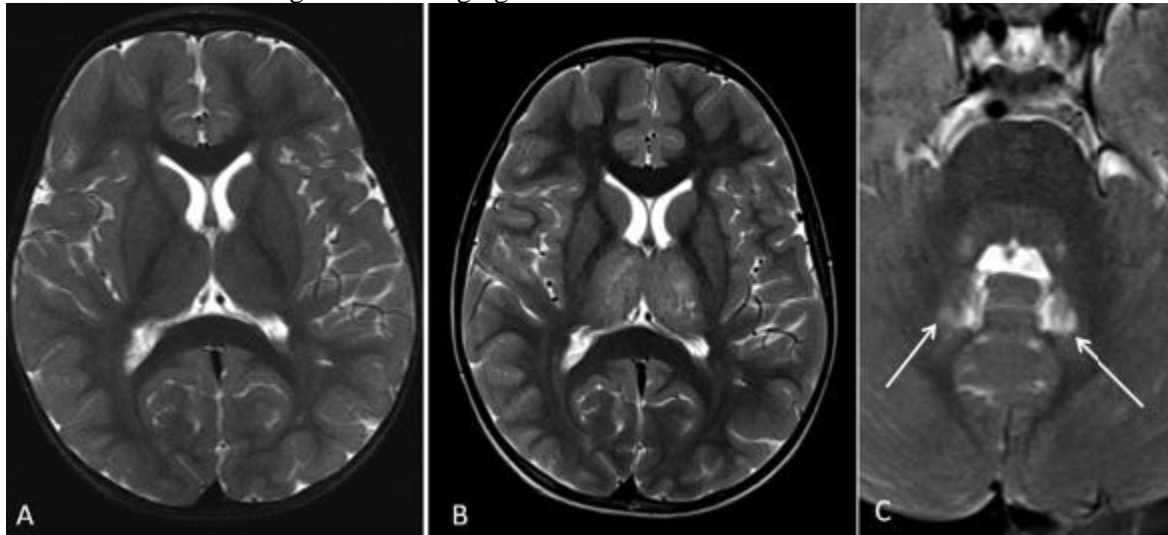
not show specific image features reported in GD nor have these findings been described in the current literature to the best of our knowledge.

Results

MRI findings of three children with GD are described. The first case described is a 10 year-old-boy with bilateral swelling in the thalami and dentate nuclei (Figure 1). Case 2 is an 8-year-old boy with signal changes in the dentate nuclei. Case 3 is an 11-year-old boy with swelling of the thalami and caudate nuclei and associated diffusion restriction. We speculate that diffusion restriction may be due to excitotoxic damage and intramyelinic edema.

Conclusions

The correlation between image findings in GD and associated neurological impairment or treatment efficacy remains unknown at present. We conclude that the thalami and dentate nuclei warrant particular attention when reviewing cerebral imaging of children with GD.



(Filename: TCT_O-256_Figure1GD.jpg)

O-246

4:17PM - 4:24PM

Differentiation of Pediatric-onset Neuromyelitis Optica from Acute Disseminated Encephalomyelitis on Brain Magnetic Resonance Imaging

E BULUT¹, M Levy², j Karakaya¹, T Huisman², I Izbudak²

¹Hacettepe University, Ankara, Turkey, ²Johns Hopkins University, Baltimore, MD

Purpose

To investigate brain MRI features that may help to differentiate pediatric-onset neuromyelitis optica (NMO) from acute disseminated encephalomyelitis (ADEM)

Materials and Methods

We retrospectively examined initial brain MRI studies of 10 patients with pediatric-onset NMO (F/M: 7/3) and 10 patients with ADEM (F/M: 2/8). The mean age of the patients at the time of MRI was 10.3 ± 5.6 and 8.7 ± 5.3 years, respectively. Brain lesions were evaluated with respect to location, extent, expansion, T1 hypointensity, contrast enhancement/pattern and associated restricted diffusion. Fisher's exact test was performed to compare MRI findings between pediatric-onset NMO and ADEM patients. Results with p-values < 0.05 were considered to be statistically significant.

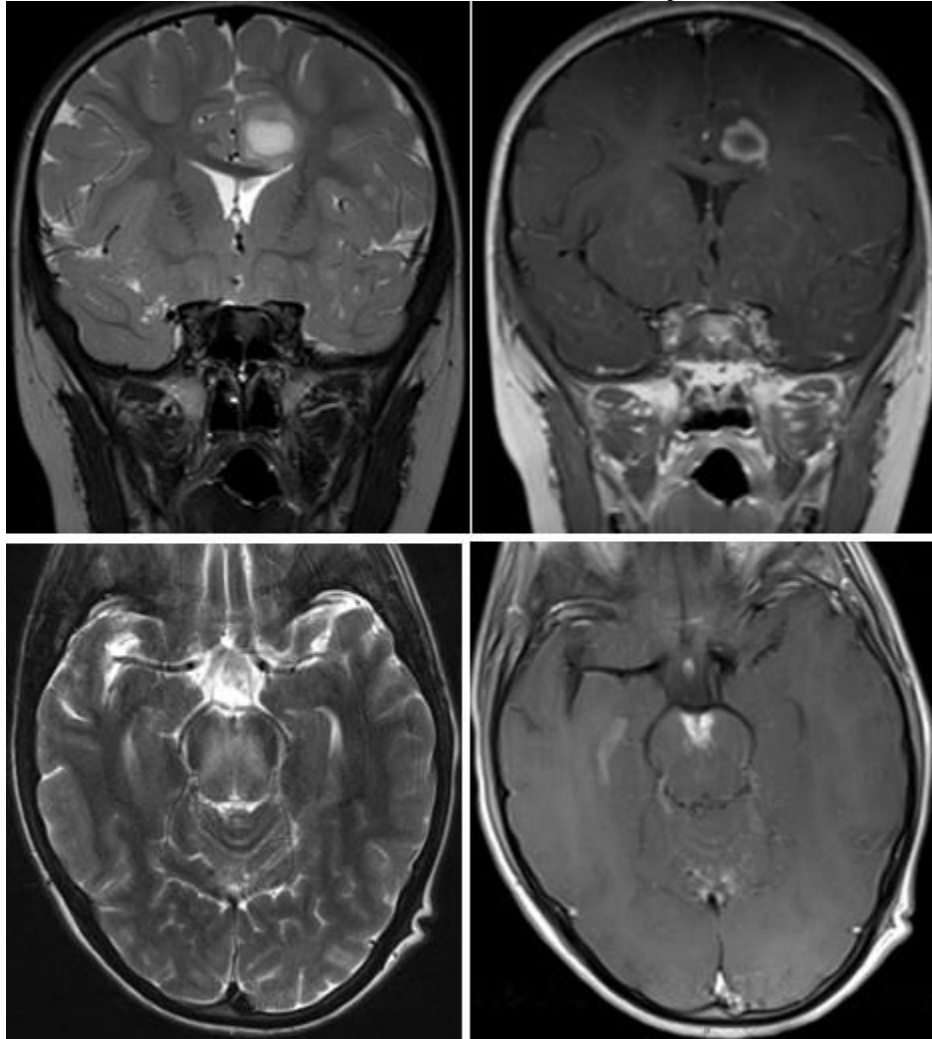
Results

Cerebral subcortical±juxtacortical and pons± middle cerebellar peduncle were most frequent locations involved in both NMO (n=5 and n=4, respectively) and ADEM (n=9 and n=7, respectively). Thalamic

involvement was also frequent in ADEM (n=7), whereas detected only in one patient with NMO (p=0.020). None of the patients with NMO had hypothalamic, internal capsule or cortical involvement contrary to patients with ADEM. The internal capsule involvement was found to be significantly different between groups (p=0.033). There was no significant difference in terms of extent, expansion, T1 hypointensity, contrast enhancement and diffusion characteristics. Contrast enhancement was frequent in NMO patients (n=8), most common patterns were patchy parenchymal (n=5) and leptomeningeal enhancement (n=3).

Conclusions

Although there is a considerable overlap in brain MRI findings, thalamic and internal capsule involvement could be used to differentiate ADEM from pediatric-onset NMO.



(Filename: TCT_O-246_pediatric-onsetNMO.jpg)

Tuesday, June 5, 2018
3:00PM - 4:30PM
Parallel Paper Session: Spine: Advanced Techniques

O-257

3:00PM - 3:07PM

MRI Predictors of Recurrence after an Acute Transverse Myelitis of Unidentified Etiology

E Bulut¹, T Shoemaker², j Karakaya¹, M Mealy², M Levy², I Izbudak²

¹*Hacettepe University, Ankara, Turkey*, ²*Johns Hopkins University, Baltimore, MD*

Purpose

To identify spinal MRI findings predictive of relapse in patients with acute transverse myelitis of unidentified etiology

Materials and Methods

Spinal MRI examinations of 77 patients (mean age: 36.1±19.9 years) who were diagnosed with acute transverse myelitis from January 1, 2005 to January 1, 2017 were evaluated retrospectively. Only the patients whom the underlying cause of myelitis could not be identified initially (at least three months) were included in study. Initial spinal MRI of patients with unidentified acute myelitis were examined in terms of length, location and distribution of involvement, extension to brain stem, cord expansion, T1 signal of lesion, contrast enhancement, extension to pial surface, and signs of owl's eyes and bright spotty lesions. The relapse rates at least one year (1-14 years) after myelitis attack were also recorded for recurrent myelitis. Associations of MRI findings with relapse rates were studied with univariate associations and binary log-linear regression. Differences were considered significant for p values <0.05.

Results

Twenty-five patients (32%) eventually developed recurrent symptoms. Logistic regression revealed three main MRI criteria as risk factors for relapse: presence of enhancement (odds ratio [OR] 5.93, 95% confidence interval [CI] 1.52–23.17), bright spotty lesions (odds ratio [OR] 4.31, 95% confidence interval [CI] 1.35–13.81) and expansion (odds ratio [OR] 3.19, 95% confidence interval [CI] 0.87–11.70). A significant correlation could not be found between length, location and distribution of involvement, extension to brain stem, T1 signal of lesion and signs of owl's eyes.

Conclusions

The MRI findings of lesion enhancement, cord expansion and presence of bright spotty lesions could be used as early predictors of relapse in patients with acute transverse myelitis of unidentified etiology. Collaborative studies with larger number of patients are required to validate these findings.



(Filename: TCT_O-257_idiopathictransversmyelitis.jpg)

O-258

3:07PM - 3:14PM

Volumetric Analysis of the Cervical Cord in Neuromyelitis Optica and Multiple Sclerosis.

M Peckham¹, C Johnson¹, T Hutchins¹, L Shah¹

¹University of Utah, Salt Lake City, UT

Purpose

Neuromyelitis optica spectrum disorder (NMOSD) and multiple sclerosis (MS) are demyelinating diseases of the central nervous system that can be clinically and radiographically challenging to discriminate. NMOSD commonly presents as a long segment cervical myelitis, which can be seen concurrently with, or have a history of, chronic relapsing optic neuropathy. MS, on the other hand, presents more often with brain lesions and shorter segment spinal cord lesions. While studies of NMOSD in the cervical cord have focused on its propensity for gray matter because of abundant Aquaporin-4 antigen, recent postmortem as well as diffusion-tensor imaging studies have demonstrated that NMOSD frequently and extensively affects white matter as well as gray matter in the cord. Quantitative volumetric analysis of the cervical cord in patients with these conditions has not been reported.

Materials and Methods

Quantitative analysis of cervical MRIs of retrospectively identified subjects with clinically confirmed MS, NMO, and normal controls was performed using the Spinal Cord Toolbox, Version 3.1 (SCT; <https://www.nitrc.org/projects/sct/>). Inclusion criteria included a sagittal T2 sequence (3.0 cm thk/3.3 cm gap) of the cervical cord. Scans with extensive motion artifact and surgical hardware were excluded. Volumetric analysis was performed of the cervical cord, with probabilistic volumes also obtained of gray- and white-matter regions after registration to standardized PAM50 template.

Results

Five subjects with NMO (average 49 y/o, 2 females), 7 with MS (average 34 y/o, 4 females) and 16 normal controls (average 43 y/o, 10 females) were evaluated. The NMO group showed overall higher cord volume at affected levels (1946.7 mm³) than MS (1518.9 mm³, p=.0035), NMO values higher than control subjects (1340.4 mm³, p=.0039). MS cord volumes were not statistically different than controls (p=.253). NMO also demonstrated a trend of higher volume of gray matter in affected levels (408.3 mm³) than MS (351.7 mm³, p=.225) and controls (361.6 mm³, p=.491), as well as higher white-matter volumes (1404.1 vs 1176.4 mm³ in MS, p=0.0495). NMO showed similar gray/white-matter ratio in affected regions (0.28) compared to MS (0.30), p=.544 and controls (0.27), p=.626.

Conclusions

NMOSD demonstrates overall higher cord volume, gray-matter expansion, and white-matter expansion than MS using volumetric analysis of the cervical cord, corresponding with recent studies showing that NMOSD frequently affects both regions. Quantitative volumetric analysis is a promising technique for elucidating the pathophysiology of these spinal cord disease states.

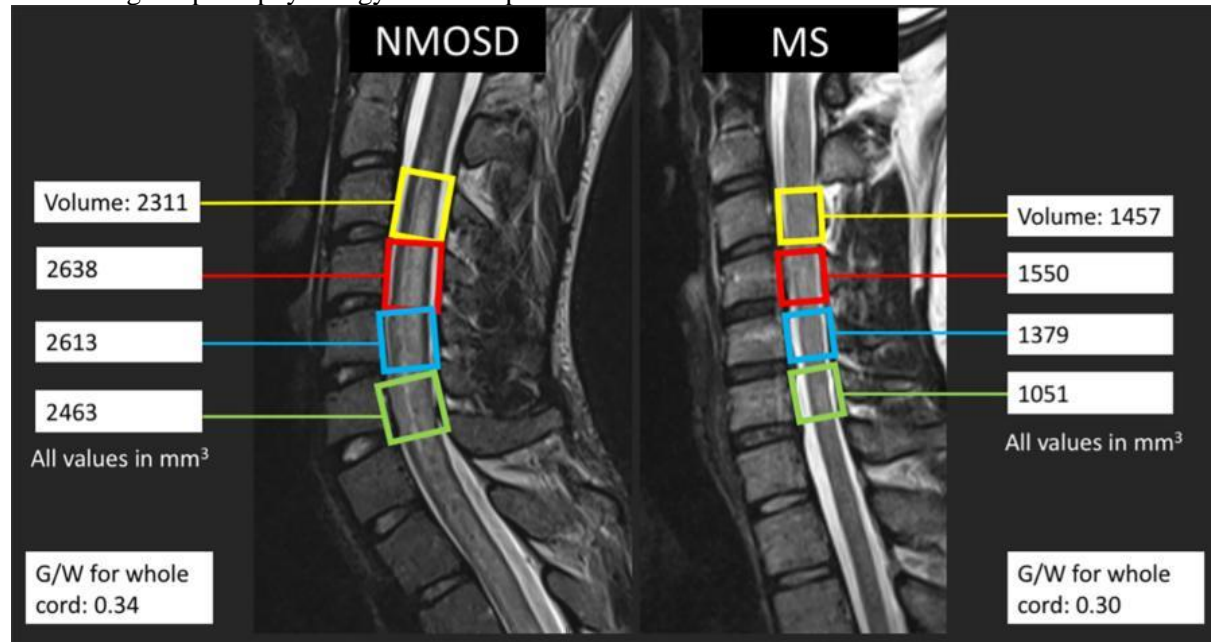


Figure: Subjects with NMOSD and MS above both demonstrate holocord involvement of demyelinating disease, with the NMOSD subject demonstrating overall higher volume (gray and white matter) than MS. Both disease states demonstrated similar gray to white matter ratios, supporting that NMOSD affects both regions.

(Filename: TCT_O-258_NMO_MSfigure.jpg)

O-259

3:14PM - 3:21PM

Variations in Fluid Movement in a Syring With Changes in Syring Size, Heart Rate and CSF Velocity

V Vinje¹, V Haughton², K Mardal¹, M Rognes¹

Oral Presentations & Excerptas

¹*Simula Research Laboratory, Fornebu, Norway,* ²*University of Wisconsin School of Medicine and Public Health, Oconomowoc, WI*

Purpose

The cerebrospinal fluid (CSF) flow profile seen in Chiari patients may be important for syrinx development [Lloyd, 2017]. Magnetic resonance imaging (MRI) reveals rapid fluid movement within a syrinx during the cardiac cycle [Honey, 2017]. However, less is known about the velocities of this flow. We used computational fluid dynamics to study syrinx velocities as a function of syrinx size, cycle rate and CSF flow profile.

Materials and Methods

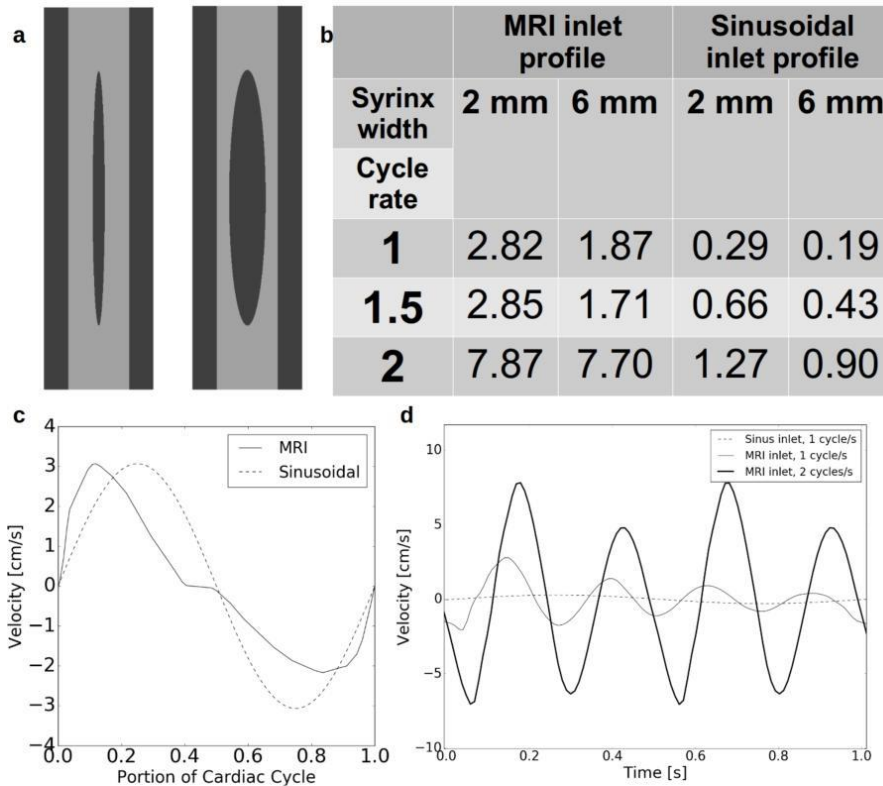
We created an idealized model of the upper spinal cord and subarachnoid space (Fig.a). The CSF, spinal cord and syrinx was modeled as a fluid-structure interaction problem. [Vinje, 2016]. Two CSF inlet profiles were tested, one sinusoidal, and one extracted by MRI in a Chiari patient having 44% shorter systole duration (Fig.c). Furthermore, we used three different rates of 1, 1.5 and 2 cycles/second. Finally, we tested syrinx widths of 2 and 6 mm.

Results

High-frequent oscillatory motion, up to four cycles/second was observed within the syrinx (Fig. d). Maximal syrinx velocities varied between 0.19 and 7.87 cm/s and was larger in the small syrinx (Fig.b). With the MRI inlet profile, the relationship between cycle rate and syrinx velocity is nonlinear, with a substantial increase at two cycles/second (Fig.b). A sinusoidal inlet profile, drastically reduced syrinx velocity (Fig.b) and cycle rate (Fig. d).

Conclusions

Syrinx velocities at resting cycle rate (1 cycle/second) was predicted to be close to those previously reported [Brugières, 2000]. The CSF flow profile may not only be important for syrinx development [Lloyd, 2017]. In particular, we found the 44% decrease in systole duration to increase syrinx velocity by a factor of 10, also introducing a nonlinear relationship between CSF cycling rate and syrinx velocity.



a) Computational domain. **b)** Maximal syringe velocities (cm/s) in all test cases. **c)** Inlet velocities used. **d)** Syringe velocities with a 2 mm syringe under varying conditions.

(Filename: TCT_O-259_MultifigureBWtextWithSin.jpg)

O-260

3:21PM - 3:28PM

Spinal Arachnoid Webs – Multimodality Imaging with Focus on Intra-operative Spinal Ultrasound.

R Thakkar¹, V Nayar¹, F Berkowitz¹, A Sayah¹

¹Medstar Georgetown University Hospital, Washington, DC

Purpose

Arachnoid webs are rare intradural lesions causing spinal cord compression or alteration of cerebrospinal fluid (CSF) dynamics with/without syringomyelia. Clinically patients present with myelopathy. MRI is used to diagnose the level of cord compression. We aim to demonstrate the use of intraoperative ultrasound during spinal surgery for web resection as a useful adjunctive diagnostic imaging tool.

Materials and Methods

A retrospective review of seven cases with MRI diagnosis of arachnoid web/cysts causing cord compression. Of these, three patients demonstrated cord signal abnormalities. All 7/7 patients had thoracic laminectomies at the level of cord compression. Intraoperative ultrasound using a high-frequency linear probe was performed twice in the same surgery, prior to durotomy and after microsurgical excision of adhesions.

Results

In all seven patients, intraoperative ultrasound demonstrated multiple echogenic septations within the dorsal spinal canal causing cord compression. Additionally, ultrasound demonstrated regional dampening of normal CSF pulsations. Cysts within the cord were found in 3/7 patients as evaluated on preoperative

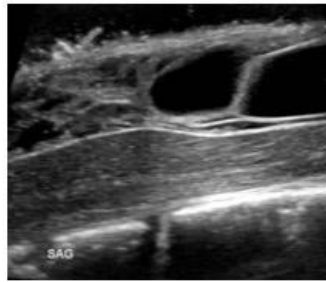
MRI, consistent with syrinx. Following microsurgical resection of adhesions, intraoperative ultrasound confirmed complete resection of adhesions with improvement in cord compression and CSF dynamics. In three patients with additional surgical fenestration of syrinx, ultrasound demonstrated smaller cysts within the cord. Following surgery all patients had significant clinical improvement, with postoperative MRI findings demonstrating resected arachnoid web/cysts, marked improvement in cord compression, and with reduction in presyrinx/syrinx.

Conclusions

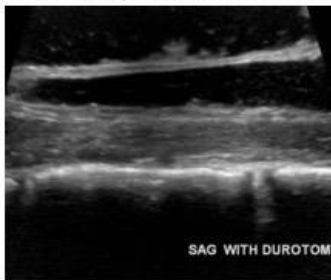
Intraoperative ultrasound can be a useful adjunct imaging tool during spine surgery for arachnoid web/cyst. Specifically, it confirms 1) adequate exposure of pathology prior to durotomy, 2) MR diagnosis demonstrating echogenic septations and regional dampening of CSF pulsations, and 3) adequate resection of adhesions and relief of cord compression. It can also distinguish syrinx versus presyrinx edema, which may lead to myelotomy in cases of necessary syrinx fenestration.



Pre-op MR – Arachnoid web causing focal anterior compression of the cord



Intra-op US - multiseptated echogenic adhesions causing cord compression



Post resection intra-op US confirms complete resection of adhesions with improvement in cord compression.



Post-op MR – significant improvement in cord displacement

(Filename: TCT_O-260_Slide1.jpg)

O-261

3:28PM - 3:35PM

Differences in Velocity Distributions in Supine vs. Prone CSF Pulsations in the Cervical Spinal Canal Support Local Arterial Contributions to CSF Pulsatilities

R Bert¹, D Muddasani¹, M Negahdar¹, B Wellman¹, M Boakye¹

¹University of Louisville, Louisville, KY

Purpose

Cine MRI CSF flow patterns in the cervical spine have been characterized in the supine position and local velocity profiles evaluated. Prone positioning changes the distribution of the free subarachnoid space and should therefore change the regional velocity distributions. If CSF pulsations are generated only in the

Oral Presentations & Excerptas

cranial vault, the velocity distributions should obey Pascal's law. We have tested the hypothesis by comparing supine and prone CSF flow and velocity profiles in the cervical spine with contradictory results.

Materials and Methods

Eight studies, four prone, four supine, were obtained from four healthy volunteers aged 23 – 35 years (2 female, 2 male) using retrospective external peripheral pulse gating (PPG). Scanner and parameters: 3T Scanner (Siemens Skyra); TE/TR=6.5/59.7ms/FA=7°/slice thickness=6mm/FOV=160mm/20=phases. VENCs customized to: 10/15/20/90/100cm/s to avoid aliasing. Transverse scans were performed at the foramen magnum, C2-3, C4 and C7-T1. Data were analyzed using custom software based on Matlab. The average maximum, minimum, mean, delta, absolute velocities, area of the ROI and net flow of the CSF were calculated at each region.

Results

Cohort average flow and pulsatility curves for the analyzed octants from C4 are shown in the figures below. Correlation of CSF octants with internal carotid artery (ICA), common carotid artery (CCA), vertebral artery (VA) and internal jugular vein (IJV) are shown in the table. Both flow and velocity waveforms changed with position, decreasing or increasing with cross-sectional area of the subarachnoid space. Lateral flow changed variable at different levels. Arterial waveform correlations were unchanged but venous correlation increased with prone positioning.

Conclusions

Differences in velocity profiles are not explainable by Pascal's law but support local contributions to flow pulsations with variable venous contributions.

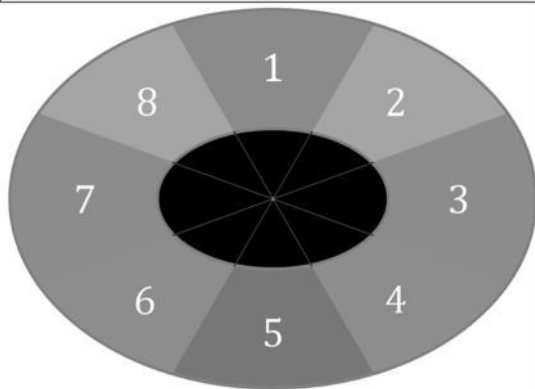
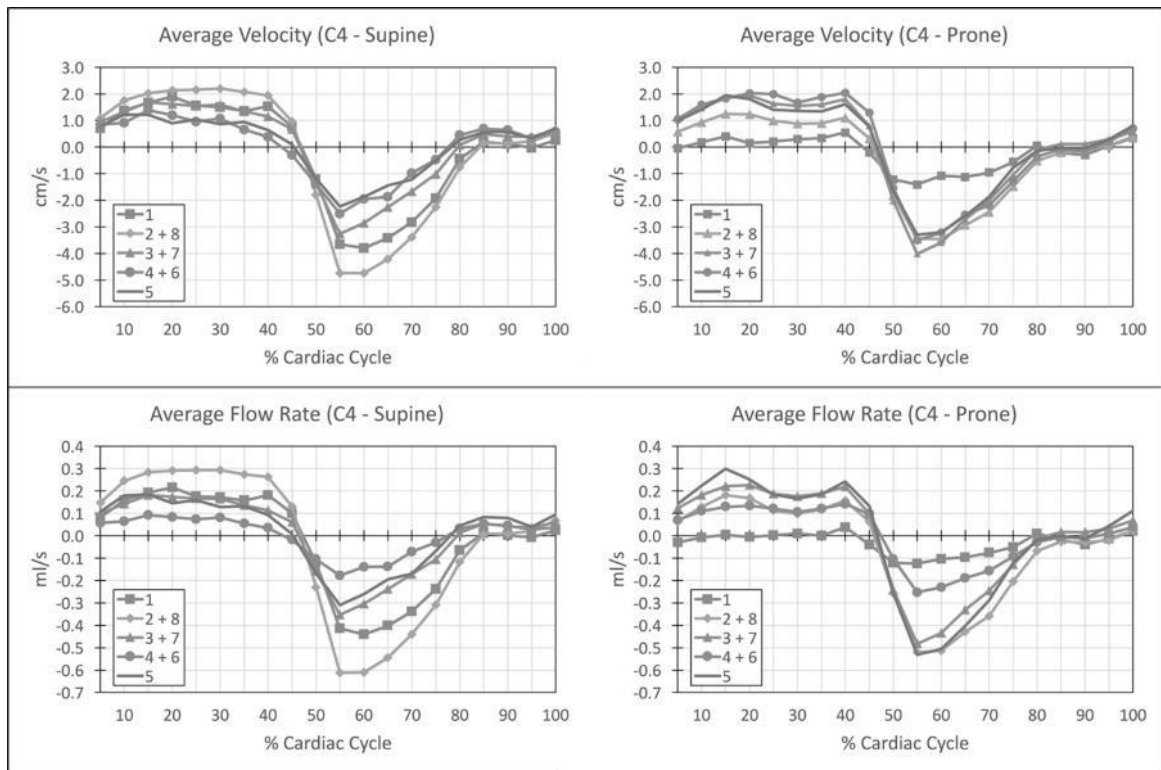


Table: Averaged Correlation Coefficients

		Supine				Prone			
		CCA	ICA	VA	IJV	CCA	ICA	VA	IJV
Systole + Diastole	Foramen	0.713	0.941	0.834	0.453	0.701	0.929	0.766	0.624
	C2-C3	0.612	0.894	0.765	0.500	0.648	0.905	0.749	0.664
	C4	0.550	0.863	0.713	0.498	0.656	0.900	0.754	0.628
	C7-T1	0.602	0.846	0.736	0.447	0.615	0.873	0.732	0.694
Diastole	Foramen	0.943	0.923	0.932	0.043	0.876	0.937	0.868	0.173
	C2-C3	0.869	0.909	0.910	0.104	0.835	0.830	0.812	0.107
	C4	0.821	0.873	0.823	0.031	0.797	0.819	0.798	0.043
	C7-T1	0.887	0.832	0.868	0.029	0.834	0.784	0.822	0.056
Systole	Foramen	0.787	0.934	0.848	0.169	0.789	0.947	0.791	0.473
	C2-C3	0.701	0.880	0.796	0.261	0.791	0.958	0.809	0.495
	C4	0.697	0.886	0.792	0.223	0.832	0.973	0.841	0.459
	C7-T1	0.711	0.880	0.785	0.188	0.721	0.921	0.752	0.602

(Filename: TCT_O-261_ASNR_2018.jpg)

O-262

3:35PM - 3:42PM

The diagnostic performance of ADC in the differentiation of Acute Spinal Cord Ischemia Syndrome (ASCIS) from other causes of acute non-compressive myelopathies

A Belay¹, T Sasaki², T Moritani³

¹University of Iowa Hospitals and Clinics, Iowa City, IA, ²University of Iowa, Iowa City, IA, ³University of Michigan, Ann Arbor, MI

Purpose

To evaluate the diagnostic performance of ADC in the differentiation of Acute Spinal-cord Ischemia Syndrome (ASCIS) from other causes of acute noncompressive myelopathies

Materials and Methods

IRB approval was obtained. A search for the word 'spinal-cord infarct' was performed on the radiology

reports of patients who had MRI of the spine (cervical, thoracic and/or lumbar) at the University of Iowa Hospitals and Clinics between March 2006 and September 2016 resulting in 193 patients. After applying appropriate exclusion criteria, data on 39 patients (25 males and 14 females, mean age 58 years) with clinical suspicion of acute arterial spinal-cord infarction were analyzed. Twenty patients were found to have acute arterial spinal-cord infarction and 19 patients were found to have other etiology. Spinal-cord abnormality was localized on other MR sequences including T2-weighted images and DWI and correlated with the ADC map. An experienced neuroradiologist and a radiology resident measured the ADC of a representative region of spinal-cord abnormality by placing a region of interest (ROI) on the ADC map in consensus fashion. ROI sizes were constrained between 10 and 20 mm². The average and minimum ADC values and standard deviation were recorded. Average and minimum ADC values of normal spinal cord were measured in the same fashion. Normal spinal cord was chosen as a representative area of spinal cord without any signal (and adjacent bony) abnormalities in other MR sequences and correlated with the ADC map. Interobserver concordance was measured using the intraclass correlation coefficient (ICC) for all measured variables. ADC_{min}, ADC_{mean}, ADC_{min} ratio (ADC min of abnormal cord/ADC_{mean} of normal cord), and ADC_{mean} ratio (ADC mean of abnormal cord/ADC_{mean} of normal cord) for the acute arterial infarction group and other causes group were analyzed using independent student's T test. Using clinical diagnosis as the reference standard, the diagnostic performances of ADC_{min} ratio, ADC_{mean} ratio, ADC_{min}, and ADC_{mean} values were calculated by plotting receiver operating characteristics curves. Area under the curve was calculated for each of these parameters.

Results

The interobserver agreement score of the two readers was 0.72-0.80, high enough for further evaluation.

(i) Nonischemic causes of diffusion restriction in the spinal cord had generally higher absolute ADC values and ratios than acute spinal-cord ischemia syndrome, $p < 0.05$. (ii) The area under the curve was maximized at ADC mean of 0.89×10^{-3} mm²/s, ADC min 0.63×10^{-3} mm²/s, ADC ratio mean 0.68, ADC ratio min 0.5 with sensitivity and specificity of 0.8 and 0.9, 0.7 and 0.9, 0.8 and 0.95, and 0.7 and 0.9 respectively. ADC mean ratio 0.68 had the highest specificity of 95 % with the likelihood ratio of 15 for the diagnosis of acute spinal-cord ischemia syndrome. (iii) Diagnostic accuracy of ADC was best with a mean ADC absolute value 0.87×10^{-3} mm²/s and mean ADC ratio of 0.68.

Conclusions

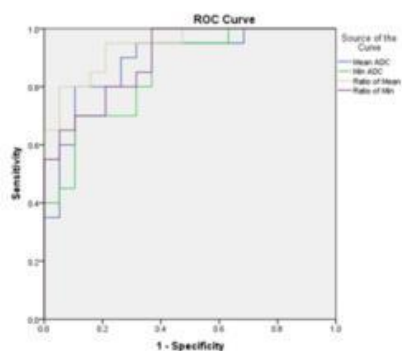
(i) Nonischemic causes of diffusion restriction in the spinal cord had generally higher absolute ADC values and ratios than acute spinal-cord ischemia syndrome, $p < 0.05$. (ii) ADC mean ratio less than or equal to 0.68 had the highest specificity (95 %) with a positive likelihood ratio of 15 for the diagnosis of acute spinal-cord ischemia syndrome. (iII) Benchmark ADC values and ratios can be a valuable tool to the clinician/radiologist in including/excluding ASCIS when the differentiation of ASCIS from other causes of acute noncompressive myelopathies is difficult clinically and by other imaging criteria.

	Infarction	Non-Infarction	P value
Number	20	19	
Mean ADC in lesion ($\times 10^{-3}$ mm ² /s)	0.742 +/- 0.164	1.04 +/- 0.173	<0.001
Min ADC in lesion ($\times 10^{-3}$ mm ² /s)	0.559 +/- 0.207	0.852 +/- 0.191	<0.001
Mean ADC in normal spinal cord as a reference ($\times 10^{-3}$ mm ² /s)	1.22 +/- 0.0889	1.17 +/- 0.207	0.269
Ratio of mean ADC to reference	0.606 +/- 0.128	0.903 +/- 0.153	<0.001
Ratio of min ADC to reference	0.456 +/- 0.165	0.744 +/- 0.175	<0.001

Table 1: Comparison between spinal cord infarction and non-infarction using a paired t test

	Mean ADC	Min ADC	Ratio mean ADC	Ratio min ADC
AUC [95% CI]	0.889 [0.786, 0.993]	0.853 [0.736, 0.970]	0.939 [0.871, 1.00]	0.897 [0.804, 0.991]
P value	<0.001	<0.001	<0.001	<0.001
Cutoff value	0.872 $\times 10^{-3}$ mm ² /s	0.633 $\times 10^{-3}$ mm ² /s	0.677	0.497
Sensitivity	0.800	0.700	0.800	0.700
Specificity	0.895	0.895	0.947	0.895
Positive LR	7.62	6.67	15.09	6.67
Negative LR	0.22	0.34	0.21	0.34

Table 2: ROC analysis for predicting spinal cord infarction



(Filename: TCT_O-262_Figurefinal.jpg)

O-263

3:42PM - 3:49PM

Curved planar reformation images from neck CTA used for screening blunt cerebrovascular injury

L Ocasio¹, R Riascos², E Bonfante², J Lally², N Solomon², M Syed³, C Stuart², P Rabiei², C Sitton²

Oral Presentations & Excerptas

¹Memorial Hermann, Houston, TX, ²The University of Texas Health Science Center Houston, TX, ³University of Texas, Houston, TX

Purpose

To evaluate the effectiveness of curved planar reformation from neck CTA as a screening technique for early detection of high-grade blunt cerebrovascular injuries (BCVIs)

Materials and Methods

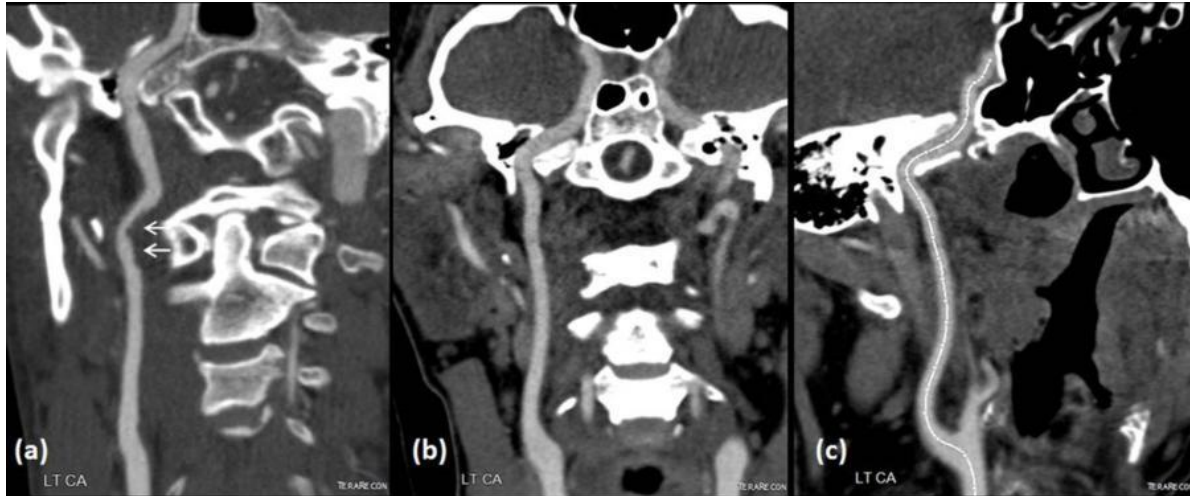
We identified cases of BCVI through searching a database of radiology reports using the key terms "CTA neck" and "grade 2, 3 and 4". Twenty-six patients with high grade BCVI (fig.a) and 26 age- and sex-matched controls (fig.b) with normal reports were identified in the period from 2016 to 2017. All cases were acquired using multidetector CT, and were postprocessed using Terarecon software with APS (advanced preprocessing server) to auto-generate vessel centerlines in the carotid (fig.c) and vertebral arteries from origin to intracranial termination. Visual inspection and manual corrections were performed by an experienced operator (L.O.). Twelve rotational projections of each vessel were created, with an average postprocessing time of 20 minutes/case. Images were transferred to our clinical PACS station, and blinded review was performed by two experienced neuroradiologists (25 years in practice) and three neuroradiology fellows. Each reviewer evaluated two unique sets of 26 cases containing equal numbers of abnormal and control patients. Each vessel was individually graded according to the BIFFL scale and the total time of reading each set was recorded. Responses were considered correct if they concurred to the prior report.

Results

A total of 10 sets of patients with a number of 1,032 vessels were evaluated. Overall specificity and sensitivity of using CPR for detection of BCVI was 88.4 % and 96.5% respectively for both sets, with a PPV of 87.5% and a NPV of 96.5%. The average reading time was 1.30 minutes per case, and 36 minutes per set. Sensitivity and specificity for reading the first set was 87.6%, and 97% respectively with a PPV of 90%, and NPV of 96%. On the second reading set, we found a sensitivity of 89.2%, a specificity of 96%, PPV 85% and NPV of 97%. four of the five readers improved their sensitivity on the second set compared to the first set. Overall, a higher number of false positive results were found when evaluating the vertebral arteries. A different distribution was observed for false negative results where carotid arteries had a higher number on the first set, and vertebral arteries on the second set. Data for all trials is represented in figure (d).

Conclusions

The ability of our readers to duplicate the results from the original report varied significantly with sensitivities varying 72-100%. Specificity varied less, ranging between 93-100%. There was a trend toward improvement in sensitivity from the first to the second set. This study utilized 96 images per case compared to an average of 872 used in the original interpretation, with an average reading time of 1.5 minutes per case. Giving an opportunity for readers to become more familiarized with this technique, this approach shows promise for improving the efficiency of CTA BCVI screening in a high-volume practice without sacrificing accuracy.



FIRST READ														
READER	TIME	TP	FP	FP LOCATION		TN	FN	FN LOCATION		SENSITIVITY	SPECIFICITY	PPV	NPV	TOTAL VESSELS
				Carotid	Vertebral			Carotid	Vertebral					
A	41'35"	19	3	2	1	76	2	1	1	90	96	86	97	100
B	30'33"	22	1	0	1	77	4	2	2	84	98	95	95	104
C	34'13"	25	3	0	3	74	2	1	1	92	96	89	97	104
D	25'25"	18	1	0	1	73	7	5	2	72	98	94	91	100
E	49'30"	27	4	2	2	73	0	0	0	100	95	87	100	104
				4	8			9	6	87.6	97	90	96	512
SECOND READ														
A	40'56"	19	4	2	2	80	0	0	0	100	95	83	100	104
B	30'04"	17	0	0	0	85	2	0	2	89	100	100	98	104
C	25'50"	18	3	1	2	82	1	0	1	95	96	86	99	104
D	29'28"	16	6	2	4	77	5	2	3	76	93	73	94	104
E	44'26"	18	4	2	2	79	3	2	1	86	95	82	96	104
(d)				7	10			4	7	89.2	96	85	97	520

(Filename: TCT_O-263_CPRASNR_600dpi.jpg)

O-264

3:49PM - 3:56PM

Perineural Spread from Metastatic Prostate Cancer Identified on MR Neurography with Quantitative ADC

C Raji¹, C Chin¹, V Shah¹

¹University of California San Francisco, San Francisco, CA

Purpose

Prostate cancer is one of the most common malignancies with perineural invasion to the lumbosacral plexus occurring with prevalence of 7-44% (1) but metastases to the lumbosacral plexus is rare. The purpose of this work was to better characterize the role of MR neurography in perineural spread from prostate cancer (2-5) augmented with quantitative diffusion MR imaging.

Materials and Methods

The PACS at the University of California San Francisco, Department of Radiology and Biomedical Imaging was queried using Montage (Nuance, Burlington, MA). The search terms "lumbosacral plexus, prostate" and "biopsy" were used to determine cases with possible perineural spread from prostate cancer.

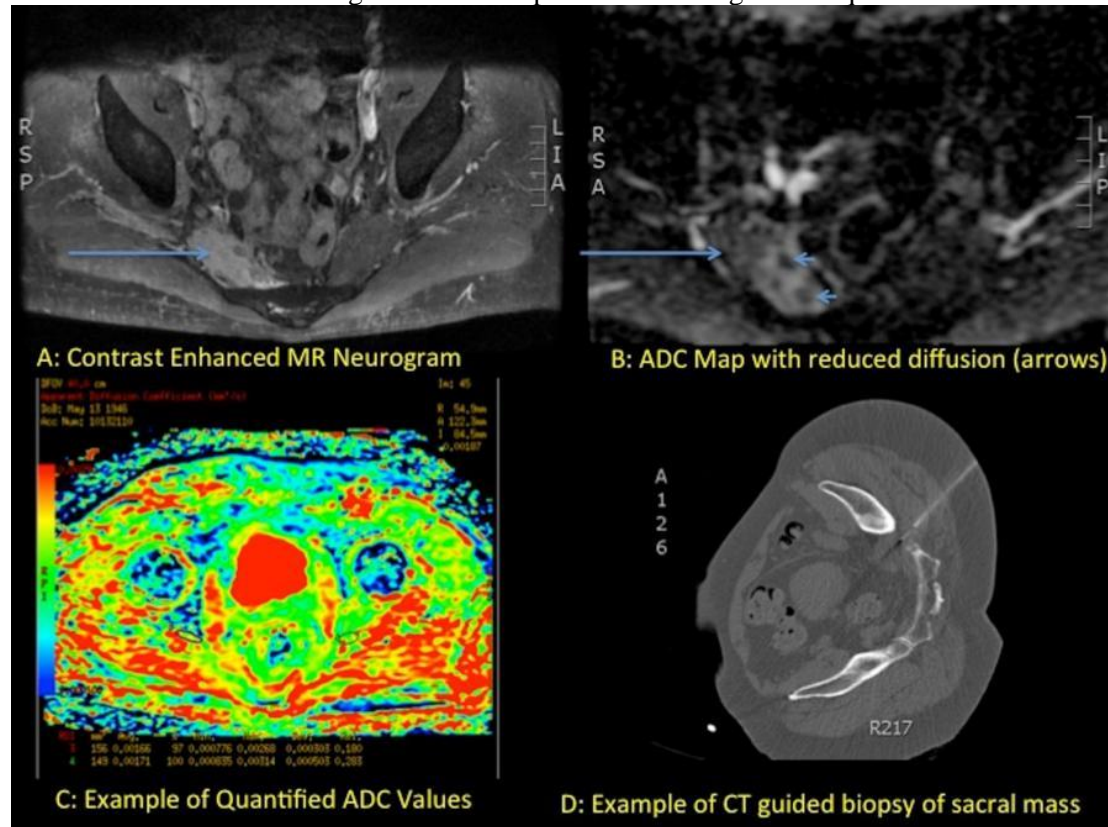
Results

A total of 107 radiology reports were yielded from the Montage search. Of these, four patients (mean age 67; all male) were identified as having abnormal lumbar neurograms in relation possible perineural spread from prostate cancer. Of these, 75% received radiation treatment for prostate cancer. Imaging findings of perineural spread were nodular asymmetric abnormal contrast enhancement on MR neurography (Figure

1A, arrows). All cases of perineural spread had reduced diffusion on ADC maps. In two nonbiopsy confirmed cases, the suspected side of perineural spread had quantified ADC values less than $0.9 \times 10^{-3} \text{ mm}^2/\text{s}$ with low ADC also visually apparent in the sciatic (Figure 1B, long arrow) and sacral nerves (Figure 1B, arrowheads). In one patient, subsequent radiation resulted in normalization of ADC values to $1.4\text{-}1.7 \times 10^{-3} \text{ mm}^2/\text{s}$ (Figure 1C). CT-guided sciatic nerve biopsy confirmed perineural spread in two cases (Figure 1D).

Conclusions

This case series demonstrates the potential of contrast-enhanced lumbosacral neurography with quantitative diffusion MR imaging to identify perineural spread and distinguish it from radiation plexitis. With perineural spread, asymmetric mass like contrast enhancement along with low ADC values was noted while with perineural spread and these values subsequently normalized following radiation therapy. Future studies will utilize larger numbers of patients with longitudinal quantified diffusion MR imaging.



(Filename: TCT_O-264_Figure_1_VS.jpg)

O-265

3:56PM - 4:03PM

Dynamic Contrast-Enhanced MRI in Evaluation of Treated and Untreated Vertebral Tumors

V Sundaram¹, A Su¹, A Aggarwal¹, A Doshi¹, K Nael¹, P Pawha¹

¹Icahn School of Medicine at Mount Sinai, New York, NY

Purpose

Dynamic contrast-enhanced (DCE) MR imaging has been applied extensively in the evaluation of brain tumors, but its potential utility in spine imaging has received less attention. We aimed to describe quantitative values of DCE-MRI in vertebral tumors including both treated and untreated lesions.

Materials and Methods

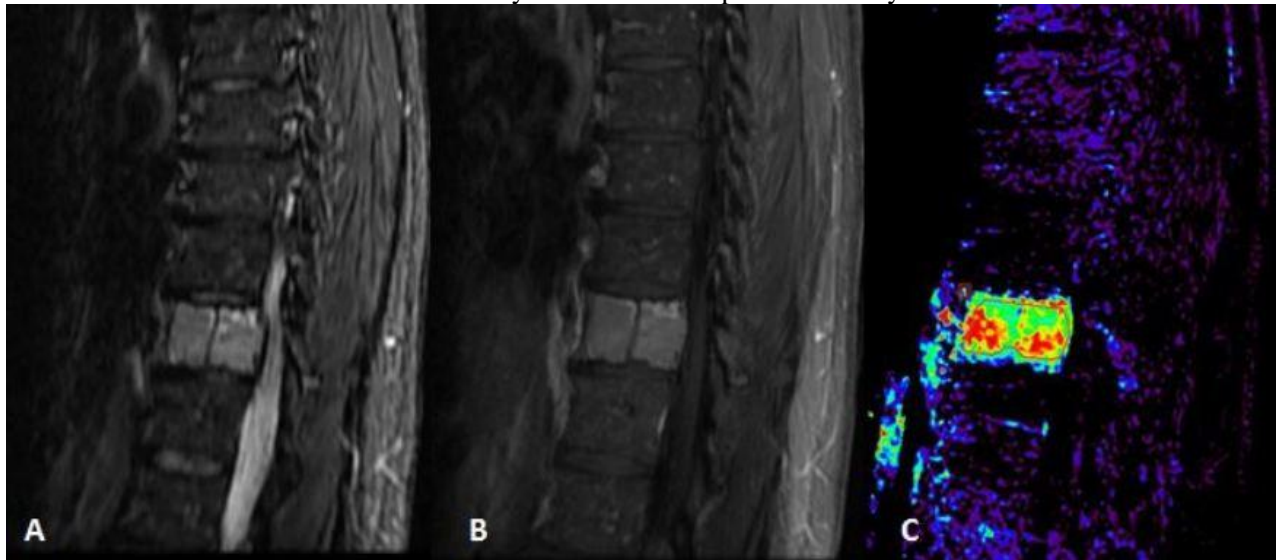
So far, 10 lesions were identified in eight patients with metastasis or myeloma who underwent DCE MR imaging of the spine. A total of six lesions were imaged prior to treatment and four lesions were imaged after radiation therapy. Postprocessing of the DCE sequences was performed using an FDA approved software (Olea Sphere, Olea Medical) to obtain transfer constant (Ktrans), peak enhancement, and plasma volume (VP) parametric maps. Quantitative analysis was obtained from ROIs that were placed on the lesion and also on normal appearing vertebral marrow to calculate normalized ratios. Calculations of mean, median, and standard deviation for each parameter were obtained for all lesions, as well as subgroups of treated and untreated lesions.

Results

Compared to normal marrow (internal control), all untreated and treated lesions yielded significantly higher values for maximum Ktrans, mean and maximum peak enhancement, and mean and maximum VP ($p < 0.05$). Mean Ktrans values trended lower for treated than untreated lesions (0.15 vs 0.36). Mean VP normalized ratios trended lower for treated than untreated lesions (4.1 vs 16.6). Mean peak enhancement normalized ratios trended lower for treated than untreated lesions (2.6 vs 5.3).

Conclusions

Quantitative DCE MR can distinguish vertebral neoplasm from normal vertebral marrow. DCE MR can potentially aid in discriminating untreated from treated vertebral lesions. These findings suggest that DCE MR has potential utility for following the post-treatment course of osseous spine metastases. These data trends can be further clarified with the analysis of additional patients as they become available.



(Filename: TCT_O-265_SagSTIR-T1FLAIRPOST-PEAKENHFINAL2.JPG)

O-266

4:03PM - 4:10PM

Role of Whole Body MR Diffusion Imaging in Identifying Active Myeloma Lesions: Comparative Analysis with Histopathology

P Tang¹, K Nael², A Doshi², P Pawha², P Belani², A Aggarwal²

¹Mount Sinai Hospital, New York, NY, ²Icahn School of Medicine at Mount Sinai, New York, NY

Purpose

Whole body diffusion-weighting imaging (WB-DWI) has become an accepted standard in the evaluation of disease burden in multiple myeloma [2]. Quantitative analysis of ADC values has been used to determine the bone marrow cellularity and in assessment of treatment response in myeloma [1-3]. In

Oral Presentations & Excerptas

patients undergoing treatment, targeted biopsies of suspicious lesions are performed for genomic analysis, which often alters treatment regimen. This study aims to assess the potential utility of ADC in predicting lesions that are likely to yield a positive biopsy result.

Materials and Methods

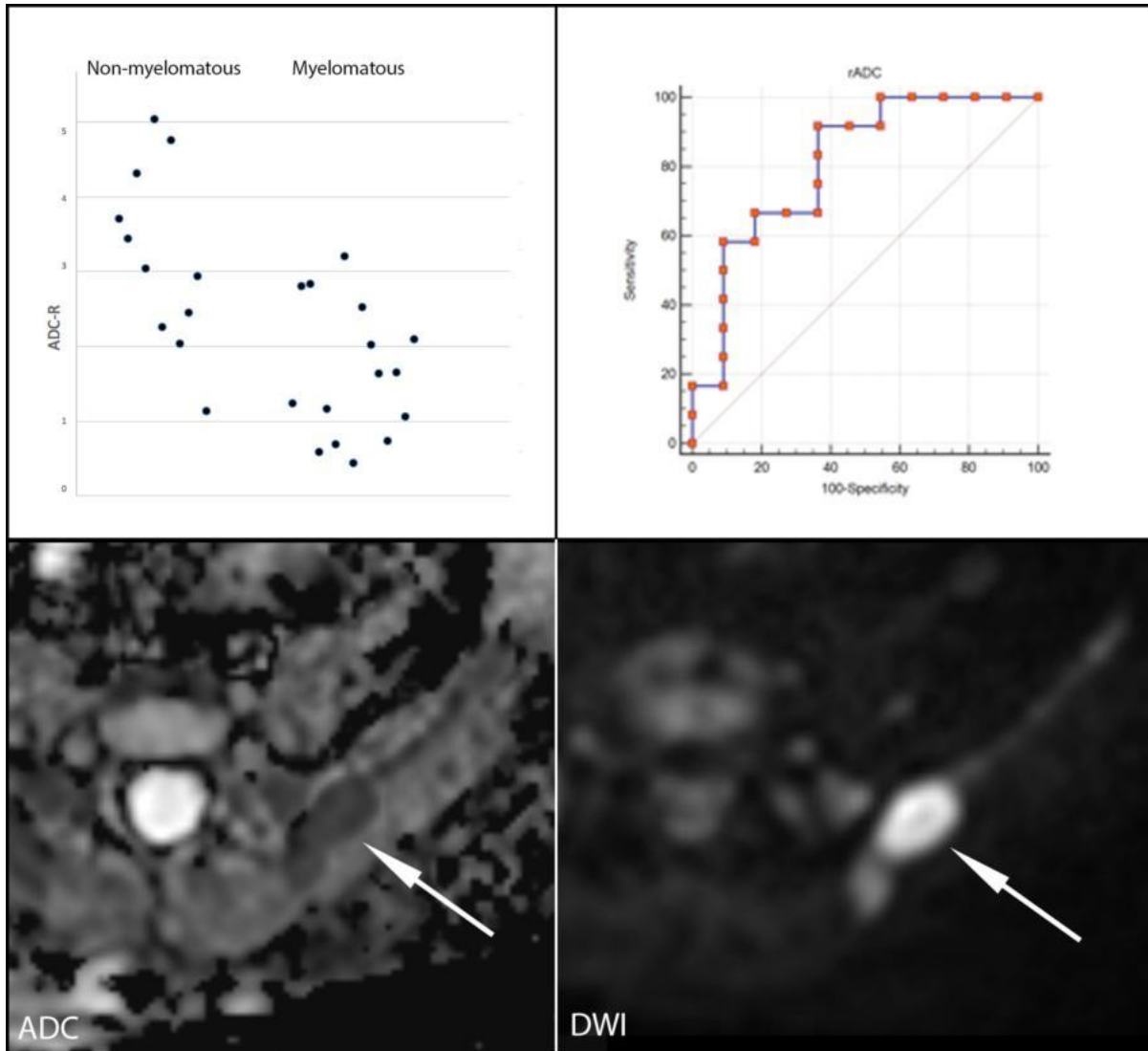
In this retrospective single-institution study, digital charts of patients with multiple myeloma were reviewed from January 2016 to November 2017. Patients were included if they had undergone WB-DWI and a subsequent bone biopsy within four weeks of imaging. Using STIR and T1, the biopsy site was triangulated with reference to CT acquired during biopsy. Average ADC values were obtained from the targeted lesion on the concurrent WB-DWI by drawing a region of interest (ROI). As a standardization reference, additional ROIs were drawn on normal, uninvolved equivalent tissue of the contralateral side, or in the case of vertebral bodies, an adjacent level. The relative ADC (rADC) was calculated as the lesion ADC divided by reference ADC values. Lesions were classified to active myeloma or nonmyeloma based on the results of histopathology following biopsy. Statistical analysis was performed using univariate and receiver operating characteristic (ROC) analysis.

Results

A total of 23 biopsied lesions in 18 patients (mean age \pm SD: 60 ± 11.7 , 11 males, 7 females) were included. The majority were axial osseous lesions (87%, 20/23), with the remainder in the appendicular skeleton (13%, 3/23). The average rADC values (mean \pm SD) were 3.19 ± 1.2 and 1.9 ± 0.79 in nonmyeloma vs. myeloma lesions respectively ($p= 0.005$). ROC analysis showed an area under curve [AUC] = 0.81. Using a threshold of 2.8 resulted in a sensitivity of 91.67%, specificity of 63.64% and an overall diagnostic accuracy of 77.6%.

Conclusions

rADC value derived from WB-DWI is promising in identifying active myeloma lesions with an overall diagnostic accuracy of 77.6%. This finding may serve as a useful marker in guiding clinical decision-making when choosing a target lesion to biopsy, particularly in the post-treatment setting.



(Filename: TCT_O-266_DWIBfigure1.jpg)

O-267

4:10PM - 4:17PM

Imaging Findings in Spinal Neurosarcoidosis at Presentation: A Review of Thirteen Cases

G BATHLA¹, P Watal², N Soni³, T Moritani⁴, A Capizzano⁴

¹University of Iowa hospitals and Clinics, IOWA CITY, IA, ²University of Iowa hospitals and Clinics, iowa city, IA, ³UIHC, iowa, IA, ⁴University of Iowa Hospitals and Clinics, Iowa City, IA

Purpose

The aim of the study was to determine the incidence of spinal imaging findings in patients with Neurosarcoidosis [NS] at presentation.

Materials and Methods

Retrospective review of the MR imaging findings was performed in NS patients who presented to a single tertiary care center over a 15-year period [2002-17]. This yielded a total of 49 patients with NS [Per Zajicek criteria, 11 patients were definite, 34 were 'probable', while four patients were 'possible']. Of these 18 patients had spinal imaging at presentation, either at a 1.5 or a 3T system. Eight patients had whole

spine MRI studies, while an additional 10 patients had some spine imaging at presentation (four with cervical and thoracic spine imaging, three with thoracic and lumbar spine imaging and three had only cervical [2] or thoracic [1] spine imaging). Except for one patient, all studies were with contrast. Images were coanalyzed by two fellowship trained neuroradiologists.

Results

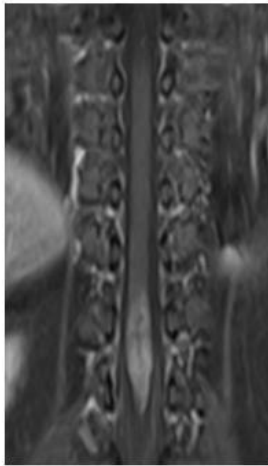
Spinal cord involvement was noted in 10 patients [56%], with the cervical segment involved most frequently [90%], followed by the thoracic segment [70%]. The involvement was often long segment and had a propensity for the dorsal surface. Two patients had exclusive leptomeningeal involvement and one patient only had dural involvement. One of the patients with spinal involvement also had bony involvement of the vertebral column. One patient had isolated spinal NS without concurrent brain involvement. In total, about 72% [13/18] of the patients showed some form of spinal involvement.

Conclusions

Spinal involvement in NS was previously considered uncommon but is increasingly recognized with widespread use of MR imaging. The cervical and thoracic segments are more commonly involved with cord involvement seen in greater than half of the cases. Isolated spinal involvement is rare and occurs in less than 2% of NS patients.



Two different patients with cervical cord involvement



Conus involvement



Bony and meningeal involvement

(Filename: TCT_O-267_ASNRabstractimages-3.jpg)

O-268

4:17PM - 4:24PM

Fluoroscopically Guided Lumbar Punctures to Evaluate for Meningitis: An Institutional Review of Incidence and Factors associated with Positive Results

M Ro¹, J Tanabe², A Jensen³

¹University of Colorado, Evergreen, CO, ²University of Colorado School of Medicine, Aurora, CO, ³University of Colorado, Aurora, CO

Purpose

Fluoroscopically guided lumbar punctures (LP) are in high demand in the workup for meningitis. Reasons include procedural difficulty, provider inexperience, patient preference, and local practice. Compared to a

Oral Presentations & Excerptas

bedside LP, fluoroscopically guided LPs consume more resources, result in radiation exposure and may delay diagnosis. Understanding the diagnostic sensitivity and factors associated with "positive" results may inform processes to improve patient care.

Materials and Methods

Fluoroscopically guided LPs ordered between 2014 and 2016 were identified via a search of our institution's electronic medical system database. A neuroradiology fellow (MR) reviewed orders and recorded all variables. Inclusions: orders for meningitis. Exclusions: orders for leptomeningeal carcinomatosis, opening pressure only, or oligoclonal bands. Fluoroscopically guided LPs that failed to yield CSF were excluded. A study was considered positive if it met any of the following criteria: positive gram stain, bacterial/fungal culture, or viral PCR. Variables of interest included self-reported altered mental status, temperature, serum white count, and time between administration of antibiotics and procedure. Associations between variables and positive CSF were analyzed with logistic regression.

Results

Out of 141 patients, 27 were excluded. Of the remaining 114 patients (age 53.7 (18.9) years, 45% male, 91 inpatient), 82 (72.6%) received antibiotics on average two (3.7) days prior to the LP. Ten of 114 were positive (six gram stains/bacterial or fungal cultures and four viral PCRs), for a yield of 9.6%. There were no significant associations between variables and positive CSF.

Conclusions

Fluoroscopically guided LPs resulted in a relatively low positive diagnostic yield (9.6%). Our data suggests that classic symptoms of meningitis are not significantly associated with a positive yield; however, a larger sample size will be needed to test a true predictive relationship. Given the resource utilization, radiation exposure for both patients and staff, and low yield, future research should investigate the effect of a negative result on patient management.

Tuesday, June 5, 2018

3:00PM - 4:30PM

Parallel Paper Session: Interventional: Stroke Trials

O-269

3:00PM - 3:07PM

Endovascular Treatment Correlated with Clinical and Imaging Outcome in the DEFUSE 3 Study

M Marks¹, J Heit², M Lansberg³, G Albers³

¹Stanford University, Stanford, CA, ²Stanford University Hospital, Stanford, CA, ³Stanford, Stanford, CA

Purpose

DEFUSE 3 is a prospective randomized Phase III multicenter controlled trial evaluating endovascular therapy for patients with acute ischemic anterior circulation strokes due to large artery occlusion treated between 6-16 hours of stroke onset. The study hypothesized that endovascular therapy improved functional outcome and imaging outcomes in this patient population. The aim of this study is to correlate the angiographic findings in the endovascular therapy group with functional outcome and imaging performed pre and post treatment.

Materials and Methods

Endovascular therapy was performed with FDA approved thrombectomy devices and suction thrombectomy catheters used alone or in combination. If tandem lesions were present cervical angioplasty with or without stent placement could be performed. Patients undergoing endovascular therapy had core lab adjudication of the primary arterial occlusive lesion (AOL), and pre and post-treatment Thrombolysis in Cerebral Infarction (TICI) score. The modified TICI scoring system was used (TICI 2B = 50-99%

Oral Presentations & Excerptas

reperfusion and TICI 3 = 100% reperfusion). These angiographic results were correlated with functional outcome (assessed with 90-day modified Rankin Score) and baseline vessel imaging and perfusion data from CTA/CTP or MRA/MRP as well with 24-hour follow-up MR DWI/PWI/MRA assessed for infarct volume growth and reperfusion.

Results

Enrolled in the DEFUSE 3 study were 182 patients and 92 were randomized to endovascular therapy. Patients arrived 9.28 +/- 2.63 hours (mean +/- SD) after stroke onset. The endovascular group had femoral access at 11.26 +/- 2.63 hours after stroke onset and reperfusion was at 46 +/- 25 minutes after femoral access. The results of the analyses that correlate endovascular treatment with clinical and imaging outcome are under embargo and will be presented.

Conclusions

To be presented.

O-270

3:07PM - 3:14PM

External Validation of DAWN: Benefit Seems Similar But Restrictive Selection Criteria Might Omit Potential Responders.

C Ducroux¹, N Khoury², A Leclerc³, R Blanc⁴, M Piotin⁴, R Fahed⁵

¹Saint-Antoine Hospital, Paris, Ile-de-France, ²HSHS Neuroscience Center, Hospital Sisters Health System St. John's Hospital, Springfield, IL, ³Fondation Rothschild, Paris, France, ⁴Fondation Rothschild Hospital, Paris, Ile-de-France, ⁵Montreal University Hospital Center (CHUM), Montreal, Canada

Purpose

We aimed to conduct an external validation of the selection criteria of the diffusion-weighted imaging or computerized tomography-perfusion assessment with clinical mismatch in the triage of wake-up and late-presenting strokes undergoing Neurointervention with Trevo (DAWN) trial 1, 2 in a cohort of unknown onset stroke (UOS) patients treated with thrombectomy.

Materials and Methods

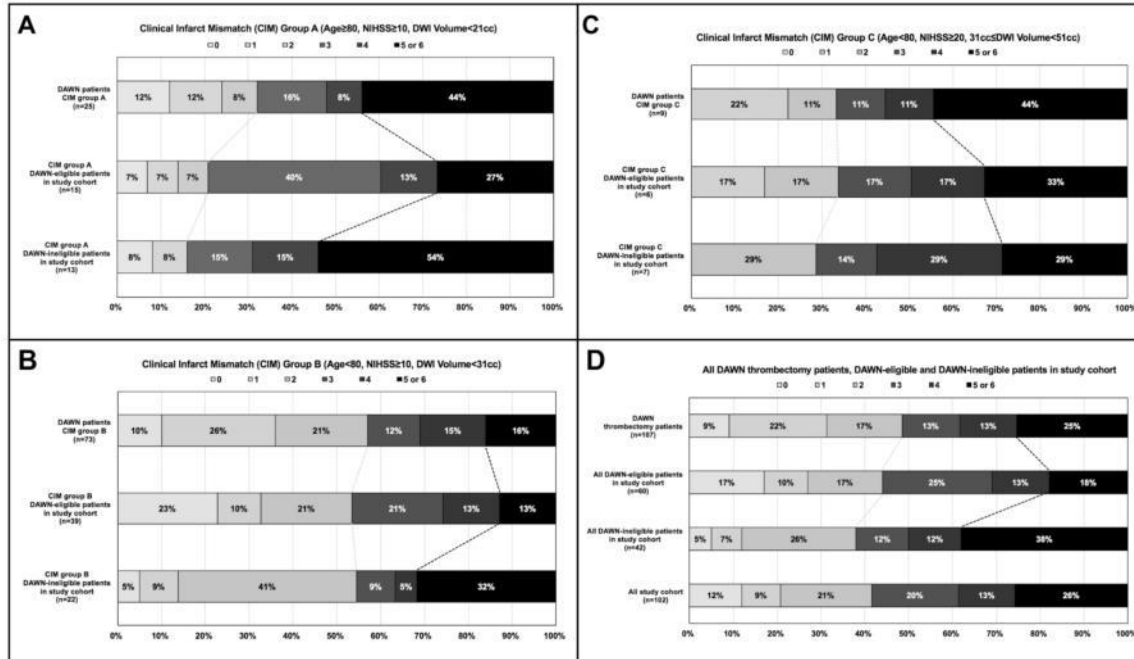
A study cohort of UOS patients was selected from a prospectively collected thrombectomy database to match the inclusion criteria of DAWN. Patients were stratified according to DAWN Groups A/B/C. Group A criteria identified patients ≥ 80 years old with a NIHSS ≥ 10 + DWI volume < 21 cc; Group B: patients < 80 years old with a NIHSS ≥ 10 + DWI volume < 31 cc; and Group C: patients < 80 years old with a NIHSS ≥ 20 + DWI volume ≥ 31 and < 51 cc. We compared proportions of patients with a modified Rankin Scale (mRS) ≤ 2 at three months follow-up between DAWN-eligible patients and the study cohort and the DAWN trial thrombectomy group.

Results

Out of 102 patients, 60 (59%) were defined as DAWN-eligible. Among these, 26 patients (43%) reached a mRS ≤ 2 at three months follow-up (vs. 52/107 patients [49%] in the DAWN trial thrombectomy group; $P=0.52$). The proportion of DAWN-ineligible patients for Groups A/B/C with a mRS ≤ 2 were 2/13 patients (15%), 12/22 patients (55%), and 2/7 patients (29%), respectively (Figure 1).

Conclusions

The results of the DAWN trial were externally validated in a UOS cohort where the trial's selection criteria identified a similar proportion of responders to thrombectomy. Additional trials are needed to address benefit in patients with larger infarct volumes who were not eligible for DAWN.



(Filename: TCT_O-270_Figure1.jpg)

O-271

3:14PM - 3:21PM

Endovascular Technique and Patients Outcomes Following Mechanical Thrombectomy for Acute Ischemic Stroke Treatment

J Heit¹, D Marcellus², B Martin², R Dodd², H Do², M Lansberg³, G Albers³, M Marks²

¹Stanford University Hospital, Stanford, CA, ²Stanford University, Stanford, CA, ³Stanford, Stanford, CA

Purpose

Endovascular mechanical thrombectomy (EMT) is an effective treatment for acute ischemic stroke (AIS) caused by large vessel occlusion (LVO). We determined how EMT technical variations influence patient outcome.

Materials and Methods

We performed a retrospective cohort study of all patients undergoing EMT for AIS treatment at our neurovascular referral center from January 2014 to August 2017. Patient demographic, treatment, imaging, and outcome data were determined by electronic medical record review. Primary outcome was a good clinical outcome (90-day modified Rankin Scale score of ≤ 2). Secondary outcome measures were mortality and symptomatic hemorrhage.

Results

Identified were 146 patients who underwent EMT; 123 patients (68 females; 55%; $p=0.30$) had clinical follow-up and were analyzed. There were no differences in medical comorbidities or time since last seen normal to treatment between patients with a good clinical outcome compared to those with a poor outcome. Univariate analysis found younger age ($p=0.01$), LVO location to the M1 MCA segment ($p=0.05$), fewer thrombectomy attempts ($p=0.0001$), higher TICI score ($p<0.05$), successful reperfusion (TICI IIB/III; $p=0.04$), and shorter procedure time ($p=0.009$) to be predictors of a good outcome. Multivariate regression analysis of these six variables found young age ($p=0.01$), LVO location to the M1 MCA segment ($p=0.03$), fewer thrombectomy attempts ($p=0.03$), and successful reperfusion (TICI IIB/III; $p<0.0001$) to be predictors of a good outcome after treatment. Increased age ($p=0.01$), increased number of thrombectomy attempts ($p=0.001$) and unsuccessful reperfusion (0.02) were correlated with

mortality. Increased number of pulls was also correlated with reperfusion parenchymal hemorrhage (p=0.05).

Conclusions

Good outcome after AIS treatment EMT is more likely in younger patients, LVO location in the M1 MCA segment, fewer thrombectomy attempts, and TIC1 IIB/III reperfusion. Increased age, increased thrombectomy attempts, and unsuccessful reperfusion predict mortality.

O-272

3:21PM - 3:28PM

Single Institution Experience with Endovascular Versus Medical Therapy for Large-Vessel Occlusive Strokes Presenting with Mild Symptoms

D Wolman¹, D Marcellus², M Marks², R Dodd², H Do², B Martin², M Lansberg³, G Albers³, J Heit⁴
¹Stanford University, San Francisco, CA, ²Stanford University, Stanford, CA, ³Stanford, Stanford, CA, ⁴Stanford University Hospital, Stanford, CA

Purpose

The benefit of endovascular mechanical thrombectomy (EMT) for the treatment of acute ischemic stroke (AIS) due to large-vessel occlusion (LVO) with mild symptoms (NIHSS≤6) is unknown (1). We determined whether AIS patients with core-mismatch profiles and NIHSS ≤6 benefit from EMT (2-5).

Materials and Methods

We performed a retrospective cohort study of consecutive patients with acute ischemic stroke evaluated for EMT at our neurovascular referral center from 2011-2017. Inclusion criteria were: LVO of the internal carotid, M1, or M2 MCA segment, core infarct <70mL, core-mismatch profile on perfusion-weighted imaging (PWI), and NIHSS≤6. Patients were grouped into those who underwent EMT and those who underwent medical therapy (MT) only. Primary outcome was NIHSS shift (difference between discharge and admission scores). Secondary outcomes were a good outcome at 90-days (modified Rankin Scale [mRS] score ≤2), mortality, and reperfusion hemorrhage.

Results

Twenty-five patients (13 MT and 12 EMT) were included. There were no differences in patient demographics, medical comorbidities, intravenous tPA administration, LVO location, presentation NIHSS, or mismatch volume between the two groups. Among EMT patients, 75% achieved TIC1 IIB/III reperfusion. There was no difference in NIHSS shift between MT or EMT patients (mean -1.7 vs. -1.7; P=0.55; 95% CI -2.53 to 2.54). A trend toward decreased length of stay (2.8 versus 4.3 days; P=0.098) and increased discharge to home was seen among MT (69%) versus EMT patients (33%; P=0.088). Two EMT patients died in hospital (17%) compared to zero MT patients (P=0.08). EMT patients were more likely to develop a reperfusion hemorrhage (58% versus 0% in MT; P<0.001). At 90 days, eight MT patients (62%) and five EMT patients (42%) were lost to follow-up. Among those with follow-up, a good outcome was achieved in 60% (MT) and 86% (EMT; P=0.178).

Conclusions

EMT may present an unfavorable risk-benefit ratio over MT for patients presenting with mild stroke symptoms despite a LVO and core-mismatch profile.

O-273

3:28PM - 3:35PM

Thromboaspiration Of Downstream And New Territory Emboli Using The 3MAX Catheter During Mechanical Thrombectomy Of Large Vessel Occlusions

F Settecase¹

¹Hoag Memorial Hospital, Newport Beach, CA

Purpose

Higher angiographic revascularization scores are correlated with improved outcomes after mechanical thrombectomy (MT) of large-vessel occlusion (LVO) acute ischemic stroke. Further improvements in LVO patient outcomes may be achieved with more aggressive treatment of distal emboli (DE) and emboli to new territory (ENT). The feasibility and safety of endovascular therapy for DE and ENT during MT, however, is unknown.

Materials and Methods

After institutional review board approval, we retrospectively identified and reviewed a series of 10 patients presenting to our institution with acute ischemic stroke due to a LVO treated with MT, initially by either thromboaspiration or stentriever and developed DE and/or ENT. Each patient was treated with subsequent aspiration thrombectomy of DE or ENT using the 3MAX reperfusion catheter. Demographic and clinical characteristics as well as procedural and angiographic data were collected for each patient.

Results

The results are summarized in Table 1. Thromboaspiration of DE or ENT was successful in 8/10 patients (80%). Final mTICI score was improved over the initial mTICI after LVO MT in all five successful DE 3MAX thromboaspirations. All ENT (4/4) were successfully removed. No complications related to 3MAX aspiration catheter use were noted.

Conclusions

Use of the 3MAX catheter for treatment of DE or ENT is feasible and efficacious; however, further evaluation in larger prospective studies is necessary.

Case	Baseline LVO location	baseline mTICI	# LVO passes	initial LVO device(s) used	initial mTICI	DE or ENT	DE/ENT Location	# 3MAX passes	Adjunct to 3MAX	Final mTICI score	3MAX success?	ASPECTS	SAH or IPH
1	Proximal R M2 MCA	2A	2	Stent-retriever	2B	DE	Distal M2 and M3 MCA branches	2	1 mg tPA x2 prior to each aspiration	2B	N	9	N
2	L M1 MCA	2B	0	none	2B	DE	distal M2	2	1 mg tPA and 2 mg tPA prior to each aspiration	2B	N	10	N
3	R M1 segment MCA	0	1	ACE68	2B	DE and ENT	distal M2 and pericallosal	1, stent-retriever in M2	none	3	Y	10	N
4	L ICA terminus	0	1	ACE68	2B	DE	M3	1	none	2B	Partial (converted to M4)	10	N
5	R ICA terminus	0	4	ACE64	3	ENT	pericallosal basilar and P1 PCA	2	2 mg tPA into pericallosal	3	Y	8	N
6	Basilar	0	4	stent-retriever x3, CAT6 x1	1	DE	basilar and P1 PCA	1	none	3	Y	n/a	N
7	R M1 segment MCA	2A	1	ACE64	2A	DE and ENT	M2 MCA segment and pericallosal	1 for pericallosal, 3 for M2 branches	tPA 1 mg and verapamil 2 mg	2B	Y	6	N
8	L M1 MCA	1	1	ACE68	2B	DE	M2 MCA	2	none	3	Y	10	N
9	L ICA	0	3	5MAXACE	3	ENT	LA2 ACA	1	none	3	Y	10	N
10	Basilar	0	0	IV TPA	2B	DE	R P1 PCA	3	none	3	Y	n/a	N

mTICI – modified Treatment In Cerebral Ischemia; SAH – subarachnoid hemorrhage; IPH – intraparenchymal hemorrhage; MCA- middle cerebral artery; ICA – internal carotid artery

(Filename: TCT_O-273_Table1abstract.gif)

O-274

3:35PM - 3:42PM

Management of tandem occlusions in acute ischemic stroke - Intracranial versus extracranial first and extracranial stenting versus angioplasty alone: A systematic review and meta-analysis

M Wilson¹, M Murad², T Krings³, J Rempel¹, W Brinjikji²

¹University of Alberta, Edmonton, Alberta, Canada, ²Mayo Clinic, Rochester, MN, ³Toronto Western Hospital, Toronto, Ontario, Canada

Purpose

Optimal technical approaches of large-vessel anterior circulation acute ischemic strokes with concomitant

Oral Presentations & Excerptas

extracranial internal carotid artery tandem occlusions is controversial. The purpose of this systematic review and meta-analysis was to evaluate: 1) the overall outcomes of patients with tandem occlusions treated with second generation mechanical thrombectomy devices, 2) differences in outcomes of extracranial versus intracranial first approaches, and 3) differences in outcomes of extracranial stenting at time of procedure versus angioplasty alone.

Materials and Methods

We searched MEDLINE, EMBASE, and the Web of Science through September 2017 for studies evaluating patients presenting with acute tandem occlusions of the extracranial ICA and intracranial ICA and/or proximal MCA treated with second generation mechanical thrombectomy devices. Outcomes of interest were: 1) mRS \leq 0-2 at 90 days, 2) mortality at 90 days, 3) procedure related complications, 4) technically successful rates of carotid revascularization, 5) TICI IIb/III, 6) TICI III, 7) symptomatic ICH, and 8) NIHSS at 90 days. Outcomes were pooled across studies using the random-effects model and expressed as cumulative incidence (event rate) and 95% confidence interval (CI).

Results

Thirty-three studies were included in analysis. Overall mRS \leq 0-2 at 90 days was 47% (95% CI 42-51%). No statistical difference was seen in 90-day mRS \leq 0-2 for patients treated with extracranial versus intracranial first approaches, 53% (95% CI 44-61%) vs 49% (95% CI 44-57%) (p=0.58). No statistical difference was seen in 90-day mRS \leq 0-2 for patients treated with extracranial stenting versus angioplasty alone, 49% (95% CI 42-56%) vs 49% (95% CI 33-65%) (p=0.39). No other statistical differences in outcome or safety were identified.

Conclusions

Nearly half of all tandem occlusion patients treated with mechanical thrombectomy have good neurological outcomes. No statistical differences in outcome are identified between extracranial first versus intracranial first approaches, nor extracranial stenting versus angioplasty alone.

O-275

3:42PM - 3:49PM

Complications During Thrombectomy For Acute Ischemic Stroke: Results From the MR CLEAN Registry

K Treurniet¹, K Compagne², I Jansen¹, R Goldhoorn³, P van Doormaal², R van den Berg¹, D Dippel², Y Roos¹, A van der Lugt², W van Zwam³, C Majoie¹, A van Es²

¹Academic Medical Center, Amsterdam, North Holland, the Netherlands, ²Erasmus University Medical Center, Rotterdam, the Netherlands, ³MUMC+, Maastricht, Limburg, the Netherlands

Purpose

Reduction of periprocedural complications is necessary to further improve clinical outcome after endovascular therapy (EVT) for acute stroke caused by a proximal anterior circulation occlusion. However, complication rates reported in clinical trials vary and likely do not reflect those in routine clinical practice. [1] We report the incidence of procedural complications and their association with functional outcome in patients who underwent thrombectomy in the MR CLEAN Registry.

Materials and Methods

All EVT centers in the Netherlands contribute to the ongoing, prospective MR CLEAN Registry. Data collected from March 2014 to June 2016 were analyzed. Thrombectomy was performed in 1308 (86%) of the total 1513 patients with digital subtraction angiography (DSA) images available. Six readers assessed available DSA images and reported dissection, perforation, evidence of embolization in a new territory (ENT) or other complications. The association of any of these complications with functional outcome (modified Rankin Scale (mRS) at approximately 90 days after stroke onset) was assessed with ordinal logistic regression, with and without adjustment for possible confounders.

Results

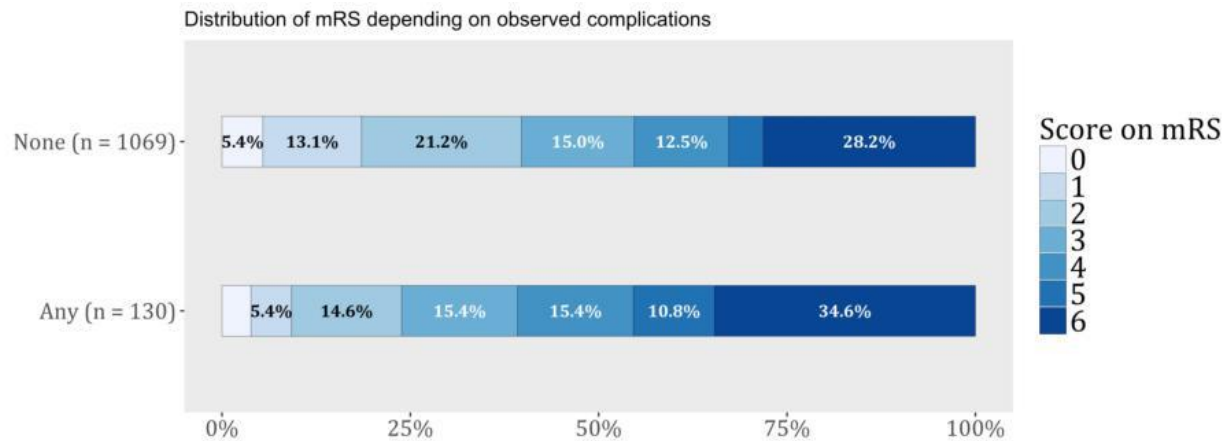
Complications were observed in 139 of 1308 patients (10.6%). In 32 patients (2.4%) a dissection was

Oral Presentations & Excerpts

observed, in 24 patients (1.8%) a perforation and in 75 patients (5.7%) an ENT. In 11 cases (0.8%), other complications were found. In figure 1, the mRS distribution of patients with and without any observed complication is shown. The occurrence of periprocedural complications was associated with worse functional outcome (common odds ratio: 0.59, 95% CI 0.44-0.81, adjusted common odds ratio 0.55, 95% CI 0.40-0.75).

Conclusions

Periprocedural complications are observed on DSA in over one-tenth of all patients in whom thrombectomy is performed in routine clinical practice in the Netherlands, and have an adverse effect on functional outcome.



(Filename: TCT_O-275_anycompplot.jpg)

O-276

3:49PM - 3:56PM

Emergency conversion to general anesthesia during mechanical thrombectomy

F Flottmann¹, H Leischner¹, L Watermann¹, T Faizy¹, M Deb-Chatterji¹, G Thomalla¹, C Brekenfeld¹, J Fiehler¹, S Gellissen¹

¹University Medical Center Hamburg-Eppendorf, Hamburg, Germany

Purpose

Optimal airway management during thrombectomy of acute stroke patients is controversial. Patients are either treated under general anesthesia (GA) or conscious sedation (CS). Nevertheless, some CS patients require emergency conversion to GA during mechanical thrombectomy, for example due to severe agitation. The aim of this study was to 1) investigate possible reasons and predictors of emergency conversion and 2) to compare angiographic and clinical outcome of patients with emergency conversion to regular CS patients.

Materials and Methods

We retrospectively analyzed 198 consecutive patients in whom mechanical thrombectomy was initiated under CS. The cohort was divided in patients who were converted to GA and patients who remained under CS during the whole procedure. We compared age, sex, pre-existing diseases, cardiac parameters, initial NIHSS and ASPECTS score, location of occlusion, times between symptom onset/admission/imaging/groin puncture/flow restoration, TICI score after thrombectomy, number of retrievals, complications during the procedure, and NIHSS and mRS scores during and after hospitalization.

Results

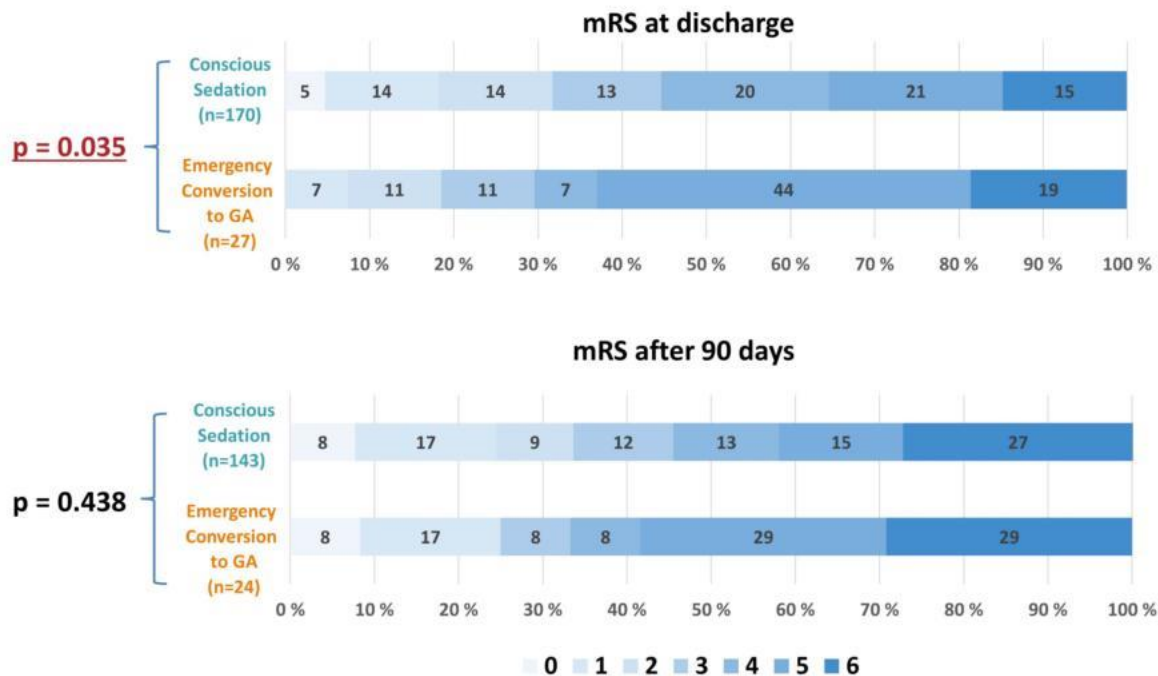
Of 198 patients in whom treatment was initiated under CS, 27 (14%) were converted to GA by emergency intubation during thrombectomy. Due to severe agitation 25 of these 27 patients were intubated. Upon admission to the hospital, patients with later emergency conversion to GA had significantly higher

systolic blood pressure values (mean 170 mmHg vs. 157 mmHg, $p=0,017$) and higher NIHSS scores (mean 17 vs. 14, $p=0,032$). Time from groin puncture to recanalization was longer (median 64min vs 49min, $p=0,009$). Their mRS at discharge was higher (median 5 vs. 4, $p = 0,035$), while no differences in angiographic outcome or mRS 90 were found ($p>0.05$).

Conclusions

A significant amount of thrombectomy patients under CS suffered from severe agitation and required emergency conversion to GA during the procedure. These patients might be identified by increased systolic blood pressure and NIHSS upon admission. Although time from groin puncture to flow restoration was prolonged, emergency conversion to GA was safe and not associated with a difference in disability after 90 days.

**Emergency conversion to general anesthesia during mechanical thrombectomy:
mRS difference at discharge, but not after 90 days**



(Filename: TCT_O-276_asnr_intubation.jpg)

O-277

3:56PM - 4:03PM

Mechanical Thrombectomy in Acute Ischemic Stroke: Does Patient Selection by MRI Improve Patient Outcomes Over Patient Selection by CT?

J Pace¹, S Dekker¹, C Glenn¹, T Ostergard¹, H Liu¹, N Bambakidis¹, Y Hu¹

¹University Hospitals Cleveland / CWRU, Department of Neurological Surgery, Cleveland, OH

Purpose

Mechanical thrombectomy is the standard-of-care treatment in acute ischemic stroke (AIS) due to large-vessel occlusion. We compared outcomes of patients selected for thrombectomy based on magnetic resonance imaging (MRI) vs. computed tomography (CT) screening.

Materials and Methods

A retrospective study of a prospectively maintained stroke registry was conducted. Patients were screened with MRI unless contraindicated. Patients with previous infarction, multiple large vessel occlusions, or those treated beyond eight hours from symptom onset were excluded.

Results

Evaluated were 86 patients (31 CT and 55 MRI) who underwent mechanical thrombectomy for AIS. There was no significant difference between the time of arrival to image acquisition between CT (89.24 ± 46.2 min) and MRI (109.36 ± 37.57 min; $p = 0.11$), or time to revascularization (4.37 ± 2.24 hours (CT) vs. 3.96 ± 2.27 hours (MRI); $p = 0.58$). The CT group had better ASPECT scores (8.68 ± 0.97 vs. 8.13 ± 0.89 , $p = 0.02$), but higher preprocedure NIHSS (18.10 ± 3.50 vs. 15.35 ± 5.14 ; $p = 0.01$). The modified Rankin Score was similar between CT and MRI at both baseline (0.45 ± 1.06 vs. 0.29 ± 0.76 ; $p = 0.58$), and 90 days (2.92 ± 2.08 vs. 2.59 ± 1.80 ; $p=0.55$). There was no difference in symptomatic hemorrhage rates (6.45% vs. 10.91%; $p = 0.49$), number of serious complications (16.13% vs. 9.09%; $p = 0.32$), or good radiographic outcomes (74.2% vs. 70.9%; $p = 0.32$), between the CT vs. MRI group.

Conclusions

The use of MRI screening for thrombectomy in AIS resulted in acceptable rates of recanalization and good long-term outcome. While the visualization of stroke volume was improved with MRI, the use of this screening modality did not result in improved patient selection for thrombectomy as equivalent outcomes were observed in each group.

O-278

4:03PM - 4:10PM

Worse Endovascular Recanalization Results for Patients with In-hospital Onset Acute Ischemic Stroke

S Mönch¹, M Lehm¹, C Maegerlein¹, D Hedderich¹, M Berndt¹, T Boeckh-Behrens¹, S Wunderlich¹, C Zimmer¹, B Friedrich¹

¹*Klinikum rechts der Isar, Technical University Munich, Munich, Bavaria, Germany*

Purpose

Strokes with onset inside the hospital account for approximately 2-17% of all acute ischemic strokes. The few existing studies addressing these in-hospital strokes lack a thorough analysis of patients which underwent endovascular mechanical thrombectomy [1, 2]. In this study we comparatively assessed in-hospital vs. out-of-hospital onset strokes treated with endovascular mechanical thrombectomy.

Materials and Methods

In a single-center case-control study a propensity score-matched analysis in a 1:2 ratio with the covariates sex, age, type of occluded large vessel, i.v. thrombolysis, and National Institutes of Health Stroke Scale prior to endovascular mechanical thrombectomy was performed. All identified in-hospital stroke patients between 2010 and 2017 were matched to consecutive out-of-hospital stroke patients.

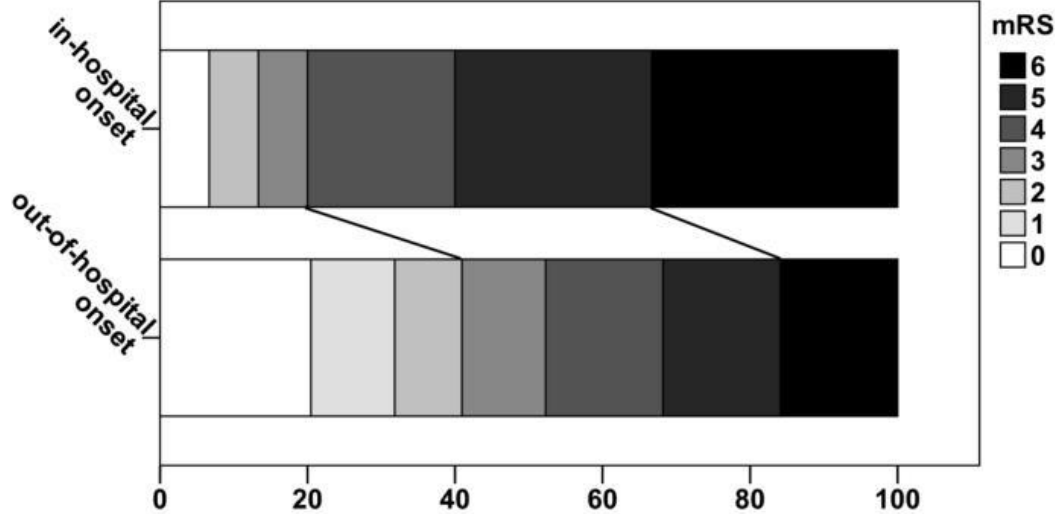
Results

Twenty-seven in-hospital strokes were compared to 54 out-of-hospital strokes. After PS matching, the baseline characteristics were well balanced between groups. The times for symptom onset to alarm, symptom onset to brain imaging, symptom onset/alarm to start of recanalization and symptom onset to final recanalization respectively were significantly faster in in-hospital stroke patients. In contrast to that, the recanalization procedure itself took significantly longer in in-house patients and had a significantly lower rate of technical success (69.9% vs. 88.9%, $p=0.001$) resulting in significantly worse clinical outcome (mRS 0-2: 7% vs. 33%; $p=0.026$).

Conclusions

The recognition, assessment and preinterventional procedures of patients with in-hospital stroke symptom onset seem to be favorable compared to patients with out-of-hospital stroke onset. Nevertheless, in-

hospital stroke patients display inferior recanalization results and substantially poorer clinical outcomes, making them a highly vulnerable subgroup of stroke patients. The reasons for this will be discussed.



(Filename: TCT_O-278_mRSin-hospitalvsoutofhospitalstroke.jpg)

O-279

4:10PM - 4:17PM

Impact of CTA Collateral Status and Treatment Delay on Functional Outcome after Endovascular Stroke Treatment: Results from the MR CLEAN Registry

I Jansen¹, M Mulder², R Goldhoorn³, J Martens⁴, W Schonewille⁵, G Lycklama a Nijeholt⁶, D Liebeskind⁷, R van Oostenbrugge³, Y Roos¹, A van der Lugt², W van Zwam³, D Dippel², I van den Wijngaard⁶, C Majoie¹

¹Academic Medical Center, Amsterdam, North-Holland, the Netherlands, ²Erasmus University Medical Center, Rotterdam, South-Holland, the Netherlands, ³MUMC, Maastricht, Limburg, the Netherlands, ⁴Rijnstateziekenhuis, Arnhem, Gelderland, the Netherlands, ⁵St. Antonius Hospital, Nieuwegein, Utrecht, the Netherlands, ⁶Haaglanden Medisch Centrum, Leidschendam, South-Holland, the Netherlands, ⁷University of California Los Angeles, Los Angeles, CA

Purpose

The precise role of CTA collateral status for endovascular treatment (EVT) patient selection in acute ischaemic stroke is unclear. We investigated the association of CTA collateral status and time to treatment with functional outcome in patients treated with EVT.

Materials and Methods

The MR CLEAN Registry is an ongoing, prospective, observational study in all centres performing EVT in the Netherlands. Data between March 2014 and June 2016 were analyzed. Functional outcome was measured on the modified Rankin Scale score (mRS) at 90 days. CTA collateral status was graded from 0 (absent) to 3 (good). We assessed the associations of both CTA collateral status and time to treatment on mRS with ordinal logistic regression, and determined EVT effect modification by comparing to the MR CLEAN trial control group.

Results

In total, 1413 patients were analysed. Collateral status on CTA was significantly associated with mRS at 90 days (acOR 1.5 [95% CI 1.4 – 1.7]). Good functional outcome (mRS 0-2) was achieved in 13% of patients with grade 0, 27% in grade 1, 46% in grade 2 and 53% in grade 3. CTA collateral status significantly modified the effect of EVT (p=0.025), but not the relationship with time-to-treatment

($p=0.67$). Better collateral grades corresponded to lower mortality ($p<0.001$), but not to differences in symptomatic intracranial haemorrhage ($p=0.14$).

Conclusions

In routine clinical practice, CTA collateral status was associated with functional outcome after EVT. Within the six-hour time window, patients with absent and poor collaterals may still benefit from EVT.

O-280

4:17PM - 4:24PM

Acute Thrombectomy in the Ageing Population: A retrospective analysis of radiological and clinical outcomes in acute thrombectomies performed in patients over 80 years with an intention to treat analysis

E Cora¹, V Demetriou², F Essbairhen¹, H AlQahtani¹, B Drake¹, H Lesiuk¹, P White³, D Iancu¹

¹The Ottawa Hospital, Ottawa, Ontario, Canada, ²Royal Victoria Infirmary, Newcastle Upon Tyne, Newcastle, England, ³Newcastle University, Newcastle Upon Tyne, England

Purpose

The incidence of ischemic stroke is higher in the older population and there is a higher mortality (1). With increasing life expectancy worldwide, the elderly population who will present with clinical signs and symptoms of acute ischemic stroke and who may potentially be considered for acute thrombectomy is likely to increase in the next few years. Recent studies have demonstrated clinical benefit when performing an acute thrombectomy for patients presenting with acute ischemic stroke secondary to large vessel occlusion (2, 3). However, the safety and clinical outcomes in this age group are not yet clear. The aim of this pragmatic, retrospective study performed in two centers is to provide further data from clinical practice and to assess the safety and efficacy of endovascular thrombectomy in this age group.

Materials and Methods

This study retrospectively reviewed all consecutive patients referred for thrombectomy procedure at our institutions with modern thrombectomy devices, either performed with stent-retrievers, aspiration devices or a combination of both. We collected data on thrombectomies performed from January 1, 2015 to September 1, 2017 on patients who were 80 years or older at the procedure date. We collected demographic data, risk factors, clinical and radiological findings, as well as treatment details. The primary outcome measures were recanalization rates (mTICI score), NIHSS score at 24 hours and 90 day mRS.

Results

We identified 83 patients; however, we only had complete data for 75 patients (50 females and 25 males) with a median age of 84 which were included. Atrial fibrillation was present in 61% (46/75) of our patients compared to 33% (209/634) in the HERMES study. The other baseline clinical characteristics are similar to previous studies. The most commonly occluded vessel was the M1 MCA in 49% (37/75). Tandem occlusions were present in 15% (11/75) which is more than the 11% (61/561) present in the HERMES meta-analysis. Within 103 minutes from symptoms onset, 67% (50/75) of patients received IV tPA, a similar time-frame to other major international trials. Good reperfusion as assessed by mTICI 2b or 3 score was achieved in 60% (45/75) patients, lower than the 71% achieved in the HERMES study across all age groups. Reperfusion was achieved in 224 minutes versus 285 minutes in the HERMES meta-analysis. A good functional outcome with mRS 0-2 at 90 days was achieved in 31% (23/75) patients, similar to 30% reported by the HERMES meta-analysis. The rate of symptomatic intracranial hemorrhage at 5% is similar to the rate of 4.4% in the HERMES data. The 90-day mortality rate 35% (26/75) is slightly higher than in the HERMES meta-analysis for this subgroup of patients reported at 28%. This may be due to the fact that our patient group had more comorbidities and tandem occlusions.

Conclusions

Our study adds valuable evidence to the limited available published data regarding both the safety and clinical outcomes in patients 80 years of age and older who undergo thrombectomy for ischemic stroke due to large vessel occlusion. Overall, our findings support the data from clinical trials and confirm that

mechanical thrombectomy can be performed safely and in a timely fashion outside of trials with similar results.

Basic Demographics	Study Population (n=75)	HERMES Data – Intervention Population (n=634)
Median Age (years)	84 (81 - 89)	68 (57–77)
Men	25 (33%)	330 (52%)
Women	50 (67%)	304 (48%)
Past Medical History		
Hypertension	49 (65%)	352 (56%)
Diabetes Mellitus	11 (15%)	82 (13%)
Atrial Fibrillation	46 (61%)	209 (33%)
Smoking (recent or current)	10 (13%)	194 (31%)
Clinical Characteristics		
Baseline NIHSS score	17 (12 - 22)	17 (14–20) [†]
Baseline glucose (mmol/L)	6.7 (5.9 - 8.2)	6.6 (5.9–7.8) [‡]
Imaging Characteristics		
ASPECTS at baseline	9 (8-10)	9 (7–10) [‡]
Intracranial Occlusion Location		
ICA	13 (17%)	133 (21%)
M1	37 (49%)	439 (69%)
M2	7 (9%)	51 (8%)
Tandem	11 (15%)	11% (61/561) [†]
Basilar	5 (7%)	0%
Other	2 (3%)	11 (2%)
Collateral Status		
Good	47 (63%)	N/A
Moderate	16 (21%)	N/A
Poor	12 (16%)	N/A
Treatment Details and Process Times		
Treatment with intravenous alteplase	50 (67%)	526 (83%)
Process times (min)		
Onset to IV rt-PA	103 (75 - 135)	100 (75–133) ^{**}
Onset to Reperfusion	224 (148 - 253)	285 (210–362)
Anesthesia details		
CS (conscious sedation)	60 (80%)	N/A
GA (general anesthetic)	9 (12%)	N/A
CS transformed to GA during case	6 (8%)	N/A
Reperfusion (mTICI)		
0	14 (19%)	
1/2a	16 (21%)	168/570 (29%)
2b/3	45 (60%)	402/570 (71%)
Outcomes		
NIHSS at 24 hours	11 (6-16)	8 (3 – 16) [‡]
mRS 0-2 at 90 days	23 (31%)	30% [‡]
mRS 3-6 at 90 days	52 (69%)	70% [‡]
Safety outcomes at 90 days		
Asymptomatic intracranial hemorrhage	8 (11%)	5.1% (32/629)
Symptomatic intracranial hemorrhage	4 (5%)	4.4% (28/634)
Mortality	26 (35%)	28% [‡]
Data are median (IQR), n(%), or mean (SD). NIHSS=National Institutes of Health Stroke Scale. ASPECTS=Alberta Stroke Program Early CT Score. mTICI=modified Thrombolysis in Cerebral Infarction.		
[†] Tandem lesions percentage from supplemental HERMES data.		
[‡] Data for patients of age >=80 from supplemental HERMES data.		
[‡] n=631		
[‡] n=620		
^{**} n=598		
[‡] n=615		

(Filename: TCT_O-280_Table.jpg)

Tuesday, June 5, 2018
3:00PM - 4:30PM
Parallel Paper Session: Deep Learning Techniques and Methods

O-281

3:00PM - 3:07PM

Deep Learning for Automated Differentiation of Head CT Protocols

J Pao¹, M Daun¹, E Kuoy¹, D Chow¹, P Chang²

¹*University of California Irvine, Irvine, CA*, ²*University of California San Francisco, San Francisco, CA*

Purpose

Determination of CT acquisition protocol such as presence of contrast, orientation and reconstruction status are critical for full automation of image analysis techniques including emerging deep-learning tools which are typically optimized for specific imaging parameters. Obtaining this information from DICOM headers is tedious and prone to error. We propose an approach using deep learning to identify CT protocols directly from raw imaging data.

Materials and Methods

After IRB approval, noncontrast and contrast-enhanced head CT exams obtained in January 2017 at a single institution were identified. All series for all exams were downloaded and separated into the following three categories: presence of contrast (without or with); orientation (axial, coronal or sagittal reconstruction); reconstruction algorithm (soft-tissue or bone). Annotation was performed using a combination of natural-language processing of DICOM headers and visual inspection. A custom 3-D convolutional neural network based on residual architecture (Figure 1) was created to map an input 8 x 256 x 256 volume into a prediction for each of the three protocol categories.

Results

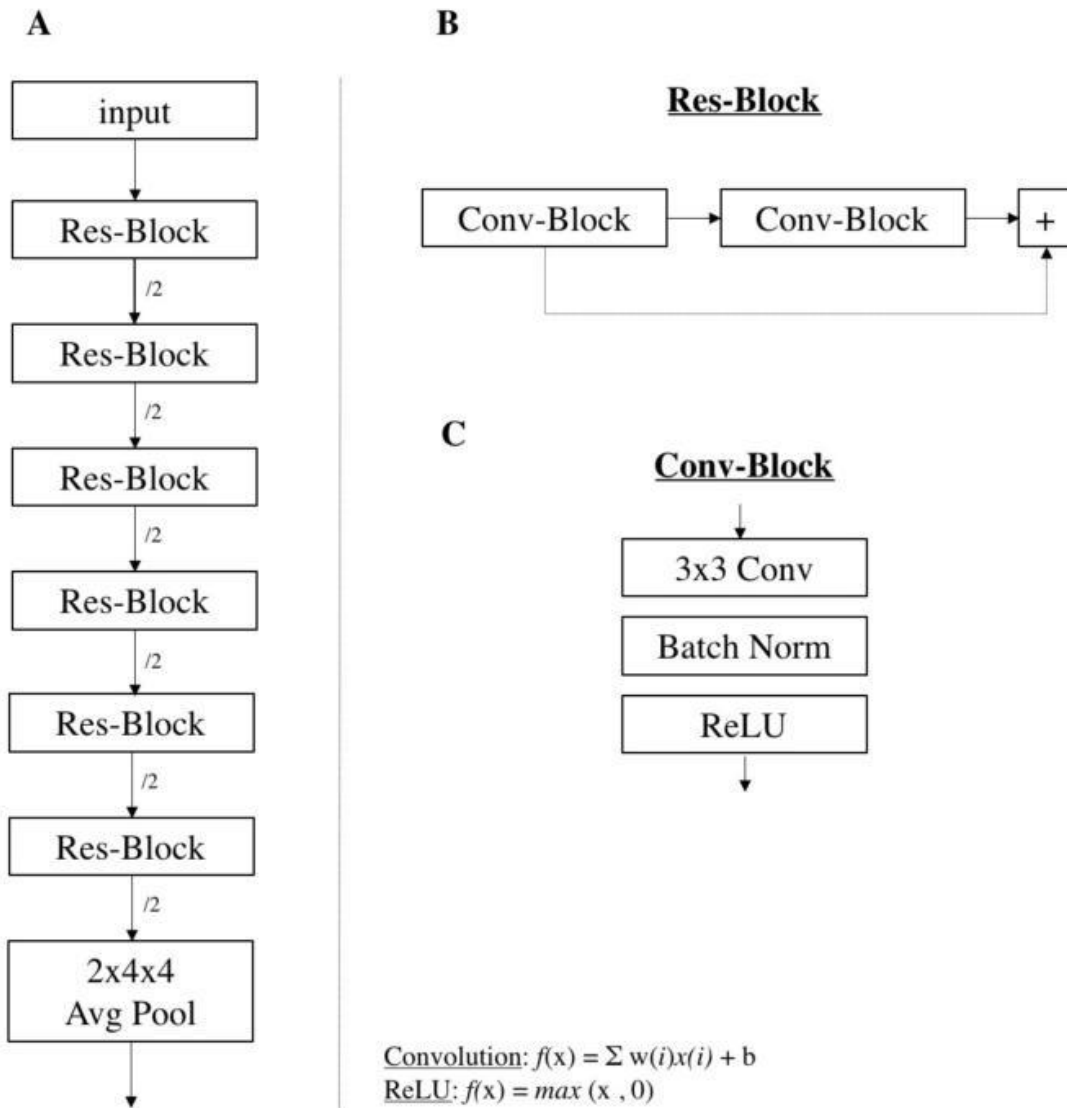
A total of 1,000 head CT exams were identified yielding a total of 5,623 different series, including: 2,412 noncontrast, 3,192 contrast-enhanced; 3,472 axial, 1,075 coronal, 1,076 sagittal; 2,378 soft-tissue, 3,245 bone reconstructions. Upon five-fold cross validation, accuracy was high for differentiation of presence of contrast (0.991), orientation (0.998) and reconstruction technique (0.994). Using DICOM headers alone, accuracy was slightly lower for all categories including presence of contrast (0.981), orientation (0.931) and reconstruction technique (0.946).

Conclusions

An automated deep-learning tool can determine acquisition parameters directly from image data with high accuracy, facilitating full end-to-end deployment of image analysis tools. The same technology can be used to improve reliability of hanging protocols across all vendors and institutions by removing reliance on underlying DICOM headers.

Figure 1. Network Architecture

(a) Summary of residual neural network architecture. A total of six residual blocks are used, subsampling the feature map six times through 2x3x3 convolutions with a stride of 2 in the XY-direction and valid padding in the Z-direction (demarcated by /2 in the figure). (b) Each residual block consists of two serial 1x3x3 convolutional blocks, the latter of which is mapped to the former via an addition operation. (c) Each convolutional block consists of a 1x3x3 convolution, batch normalization and a ReLU nonlinearity.



(Filename: TCT_O-281_Abstract3_Protocols.jpg)

O-282

3:07PM - 3:14PM

Improved Hemorrhage Detection on Non-Contrast Head CT Using a Robust Artificial Intelligence Pipeline

B Odry¹, B Georgescu¹, K Adinarayan², B Lou¹, K Stoltman³, R Goyal³, T Tong³, A Hoang², M Nadar¹, P Sanelli², D Comaniciu¹

¹Siemens Healthineers, Princeton, NJ, ²Northwell Health, Manhasset, NY, ³Hofstra Northwell School of Medicine, Manhasset, NY

Purpose

Noncontrast CT (NCCT) is the most commonly prescribed imaging study in the emergency evaluation of acute stroke and traumatic brain injury to rule out hemorrhage and guide urgent treatment decisions. Recent advances in deep learning technologies show improvements in several medical imaging problems [1, 2]. Here, we propose a full 3-dimensional (3-D) artificial intelligence (AI) pipeline that standardizes and automates steps for accurate and importantly fast hemorrhage detection, which, as a direct consequence, would improve efficiency in treatment guidance in the emergency setting.

Materials and Methods

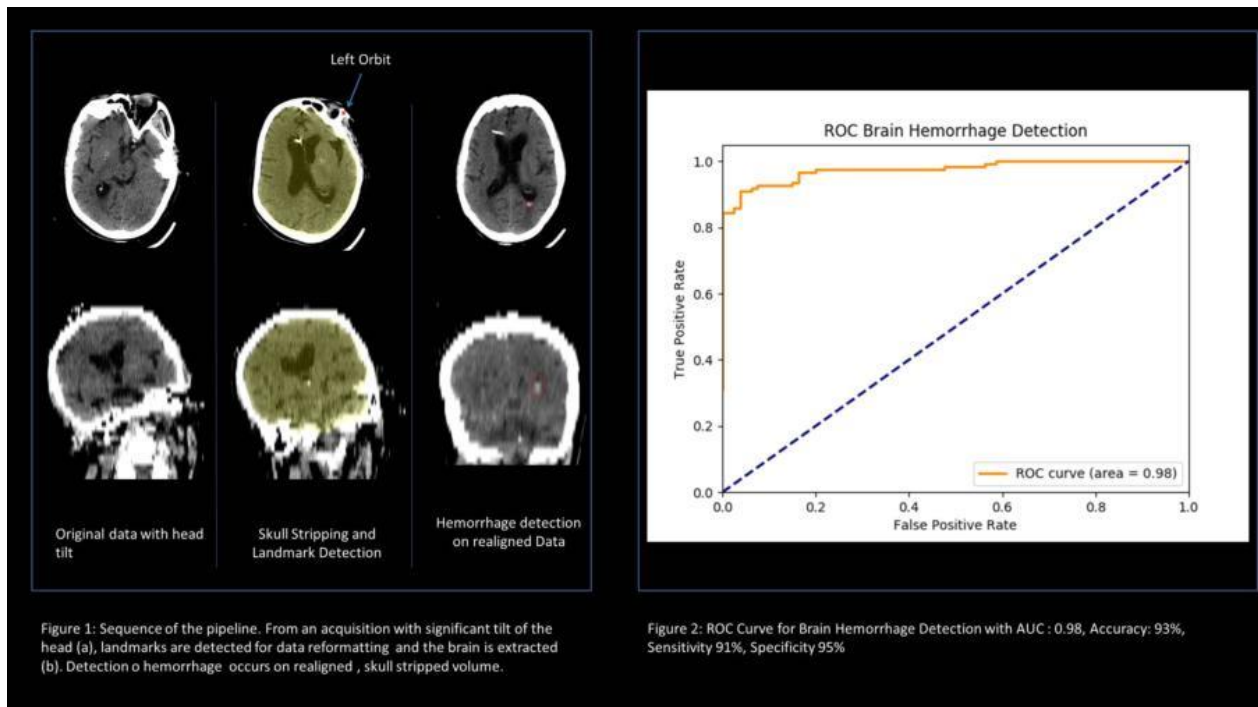
We obtained scans from 1,940 retrospective patients from our acute stroke database. Axial, sagittal, coronal acquisitions were used for the purpose of this study. Field of view was acquired using a 512x512x34 matrix at 0.5x0.5x5mm. Overall, we had 2,210 exams, with 55% diagnosed with hemorrhage. IRB approval was granted for this study. We developed a 3-D AI pipeline comprised of three main steps. First, we trained an agent via multiscale deep reinforcement learning [3] to identify five anatomical landmarks (Bregma, Crista Galli, External Occipital Protuberance, Left and Right Orbital Bones) and estimate brain orientation along the midsagittal plane, hence, reducing variability in head position at acquisition time [Figure 1]. Second, we used an image-to-image convolutional network trained with an adversarial network to extract the brain [4] and exclude strong features (from skull, eyes) that could deceive the detection process. Third, we trained a 3-D fully convolutional dense network [5] with a brain window to detect hemorrhage on 68,000 images (2,000 exams) with augmentation (random rotation, translation, and noise added at each training iteration). The presence of hemorrhage, irrespective of hemorrhage type (intracerebral, subdural, epidural, subarachnoid, microhemorrhage), described on the dictated reports was used as ground truth, with no annotation of images.

Results

Testing of the 3-D AI pipeline was performed on a separate cohort from our acute stroke database. The testing cohort was comprised of 7,410 images (210 NCCT exams) with the same data acquisition and parameters as the cohort used for the development phase in the methods. Again, the ground truth was the presence of hemorrhage (irrespective of type and location) dictated in the final reports. Receiver operating characteristic (ROC) analysis [Figure 2] revealed that our full AI pipeline achieves an area-under-the-curve (AUC) of 0.98 with accuracy of 93%, sensitivity of 91% and specificity of 95%, or false negative rate of 5% and false positive rate of 2.3%.

Conclusions

Our 3-D AI pipeline can detect hemorrhage on NCCT with 93% accuracy and very low false positive/negative results. Implementation of this 3-D AI pipeline in the clinical setting has the potential to accurately detect hemorrhage in an automated and expedited manner to assist radiologists in rapid decision-making for patients with neurologic emergencies, particularly acute stroke and traumatic brain injury. This feature is based on research, and is not commercially available. Due to regulatory reasons, its future availability cannot be guaranteed.



(Filename: TCT_O-282_ASNR_Odry_figures.jpg)

O-283

3:14PM - 3:21PM

Real-time decision support for cerebral vasospasm detection on conventional angiograms using deep learning

M Maros¹, A Förster¹, M Alzghoul¹, E Neumaier-Probst¹, C Cho¹, J Böhme¹, C Groden¹, H Wenz¹
¹University Medical Center Mannheim, Medical Faculty Mannheim of University Heidelberg, Mannheim, Baden-Württemberg, Germany

Purpose

Cerebral vasospasm (VP) is a life-threatening condition with highly increased risk of death or permanent disability. VP detection on conventional angiographic (DSA) images requires multiple years of training and expert-level knowledge. Here, we investigated the applicability of deep-learning-based image classifier for VP detection.

Materials and Methods

A retrospective cohort of 91 patients (57F; 34M) mean age 57 years (range: 23-86 yrs) undergoing cerebral DSA was retrieved from local database. Angiograms were reassessed by two independent blinded neuroradiologists. The single most representative ap series of internal carotid artery (left/right or both) were selected (n=140) and categorized as VP positive (n+=50) or negative (n-=90). The angiograms were randomly divided into training (112; 80%) and test sets (28; 20%). We retrained and custom modified a deep convolutional neural network (CNN) pretrained on ImageNet[1] with rectified linear units (ReLU) and a fully connected dense block using softmax activation [2].

Results

The deep CNN showed (Fig. 1): 1. an overall training accuracy of 87.5% (98/112) with a corresponding test accuracy of 85.7% (24/28); 2. a specificity of 100% (18/18) correctly identifying all VP negative cases in the test set; 3. a sensitivity of 60% (6/10) for VP positive test cases; 4. a precision of 100% (6/6) as all predicted VP positive cases were indeed true positives. It achieved these results, despite using only a single DSA image and no comparison to baseline or previous imaging of that same patient. Using this

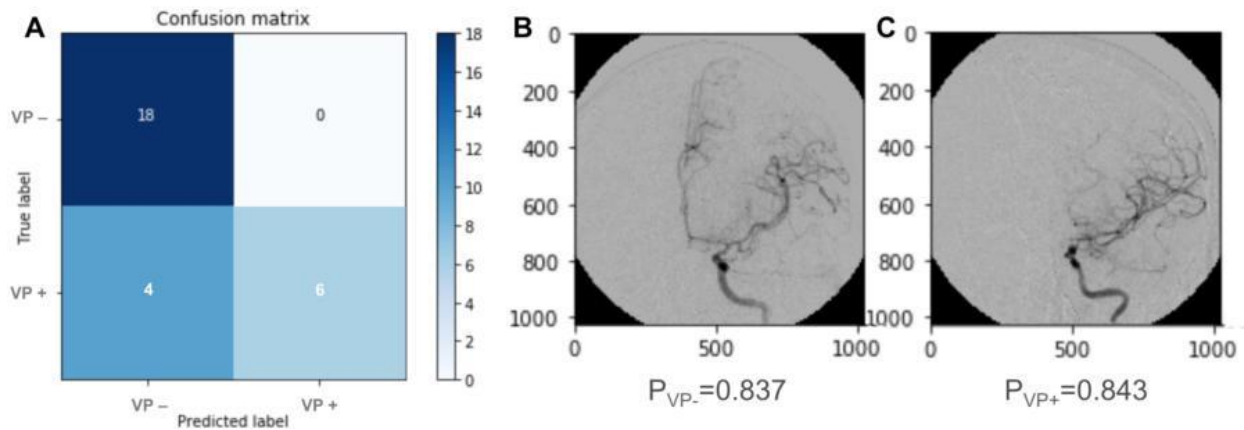
Oral Presentations & Excerptas

expert-driven lightweight approach the pretrained model could be batch fitted in 1-2s on the whole test set using consumer level graphics cards.

Conclusions

Deep-learning-based cerebral vasospasm detection using expert selected angiographic images might be a feasible real-time assistive technology to increase diagnostic accuracy.

Figure 1. (A) Confusion matrix of test set performance; (B) correctly classified VP negative-, (C) VP positive cases with corresponding probabilities



(Filename: TCT_O-283_20171215-ASNR-2018-MarosME-Abstract-Nr1661-Figure.jpg)

O-284

3:21PM - 3:28PM

Disease Detection in Resting State fMRI with Unsupervised Deep Learning Trained on Normal Subjects

M Cekic¹, N Salamon²

¹University of California Los Angeles Medical Center, Los Angeles, CA, ²University of California Los Angeles, Los Angeles, CA

Purpose

A major problem in the development of algorithms for automated classification of neurological disease with resting-state functional magnetic resonance imaging (rfMRI) is paucity of patient data, as most available data is that of normal subjects. Here we develop an unsupervised algorithm for classification of disease states trained on only normal data and attempt to extract latent features of the patient data sets.

Materials and Methods

We developed unsupervised deep neural network algorithms for anomaly detection in multivariate rfMRI data using the open-source libraries for deep-learning Keras and TensorFlow. We apply several approaches including deep recurrent layers in order to account for the temporal dependencies in the data as well as convolutional architectures for the analysis of functional connectivity. We train the models using only data from normal subjects and calculate the reconstruction error obtained from our test sets in order to differentiate disease from control. We apply our model to the well-established preprocessed rfMRI databases Autism Brain Imaging Data Exchange (ABIDE I) and ADHD-200. We then train our models on open-source data obtained from the Human Connectome Project and 1000 Functional Connectomes Project and apply the algorithms to patient data from our institution.

Results

We demonstrate the feasibility of training a deep unsupervised neural network model on only normal data by being able to classify disease states at a rate greater than chance on the ABIDE and ADHD-200 data set. Although we do not match the state-of-the-art classification obtained with supervised models, we demonstrate the feasibility of training an unsupervised neural network with only normal data and still

being able to perform greater than chance classification of rfMRI data. Our model is also able to extract latent features of the data such as resting state networks.

Conclusions

We develop an unsupervised deep-learning paradigm for detection of anomalous rfMRI data. To our knowledge, this is the first attempt to perform classification of functional imaging data using a deep unsupervised anomaly detection paradigm. This is a more general approach to classification than the supervised method and may be useful both for detection of novel disease and improving our understanding of resting-state fMRI and its role in neurological disease processes.

O-285

3:28PM - 3:35PM

Building a Predictive Analytics Foundation to Assess Radiologically-Identifiable Encephalopathies

H Huang¹, Y Koksels¹, Z McKinney¹, J Rykken¹, A McKinney¹

¹*University of Minnesota, Minneapolis, MN*

Purpose

Encephalopathies arise from various causes. In theory, a more rapid diagnosis in an obtunded patient could be obtained as the probability of being positive increases as more information is provided. Thus, predictive algorithms could be generated based on patient status (inpatient/outpatient) and history/symptoms. This study intended to determine the likelihood (probability) of radiologically identifiable encephalopathies using the EHR's patient "status" and "reason for exam" (RFE) fields.

Materials and Methods

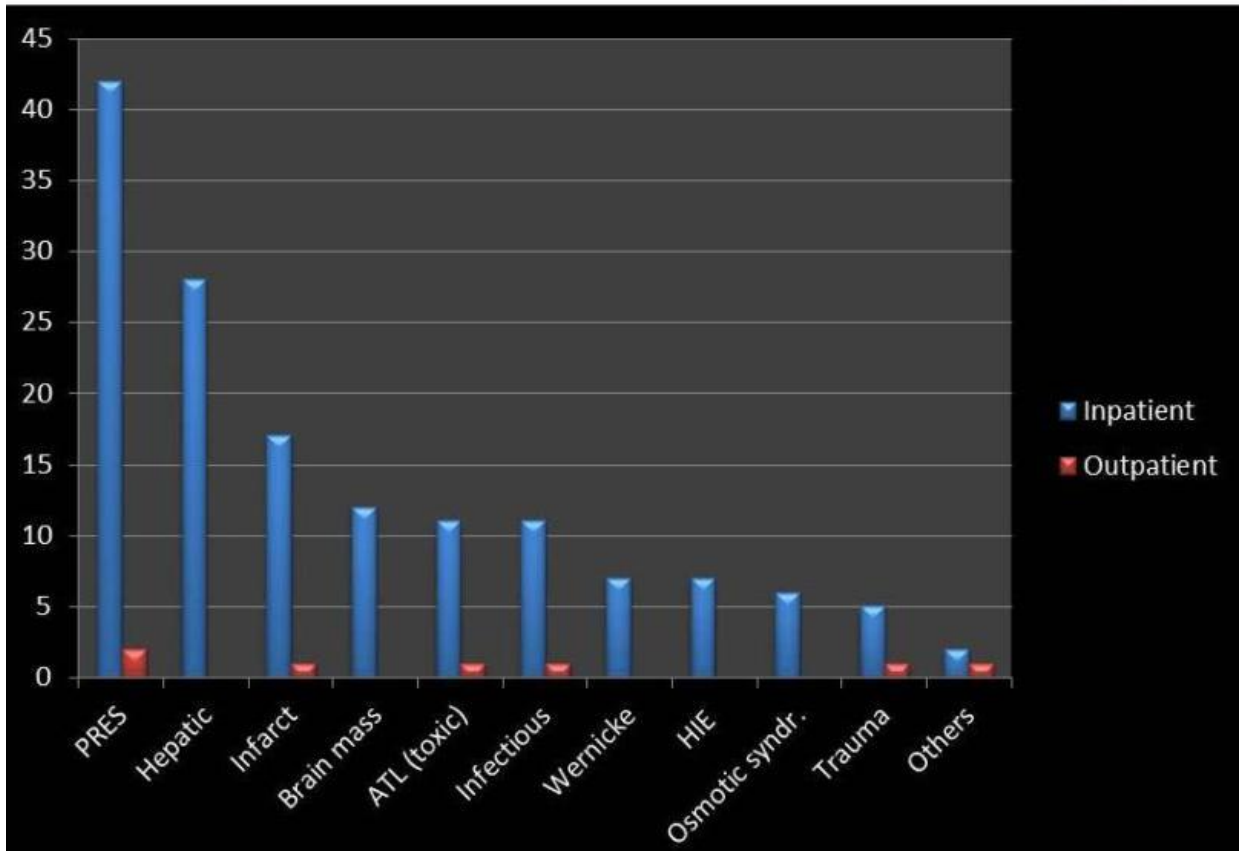
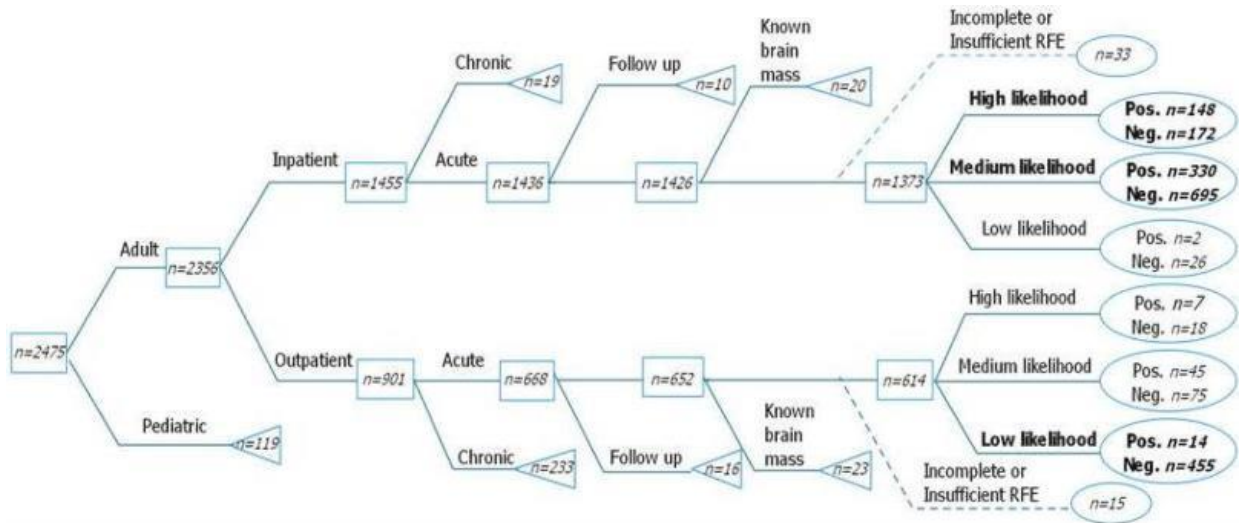
Using report search software (VITREA Intelligence, Canon, Minnetonka, MN, U.S.), 2475 brain MRI reports over 3.5 years were identified by the RFE for: "altered mental status", "confusion", "obtunded", and "encephalopathic", as they imply an encephalopathy. Before ascribing likelihoods, the software denoted patients as {inpatient vs. outpatient} and {adult vs. pediatric} (children excluded given potential neonatal insults, n=119). Based on the RFE, also excluded were terms implying chronicity, follow-up of known MRI abnormalities, or known brain mass (n=321 total). The remaining 2035 RFE's were graded by two radiologists (blinded to the report itself) as a "likelihood" for a radiologically identifiable syndrome: 1) "high", 2) "medium", or 3) "low" likelihood, based on various terms that increase the probability of there being an identifiable syndrome (e.g. "hypertension", "liver failure", "r/o PRES", etc.).

Results

Of included adult inpatients' MRI reports (n=1406), 513 (36.5%) were radiologically positive for an encephalopathic syndrome, 893 (63.5%) being negative. Of these 513 positives, 320 were HL (62.4%), where 46.3% of the HL RFE's (n=148) were radiologically positive (Figure). In contrast, of outpatients' (n=629), 87% were negative, 72.3% being classified as LL. This implies that such an algorithm is highly sensitive (99.6%) in inpatients with HL or ML, while having a high NPV in LL outpatients (97.0%). The most commonly identified syndrome was posterior reversible encephalopathy (n=44).

Conclusions

Patient status (inpatient vs. outpatient) and provided history (ROE) are important harbingers of eventual imaging findings in encephalopathic patients, and could be used to develop predictive algorithms.



(Filename: TCT_O-285_ASNR2018EncephalopathPA1.jpg)

O-287

3:42PM - 3:49PM

Predicting Glioblastoma Tumor Recurrence vs Pseudoprogression Utilizing Convolutional Neural Networks

S Mutasa¹, W Genestine¹, G Zanazzi¹, N Delgado¹, F Iwamoto¹, A Lassman¹, P Chang², P Canoll¹, J Bruce¹, A Lignelli¹

Oral Presentations & Excerptas

¹Columbia University Medical Center, New York, NY, ²University of California San Francisco, San Francisco, CA

Purpose

A novel convolutional neural network (CNN) can employ small data sets to predict tumor recurrence versus treatment effect in glioblastoma patients utilizing a brain MRI data set.

Materials and Methods

An IRB-approved retrospective review from January 2010 to July 2017 identified 49 patients [Age 20-78(56), Sex 35M/14F] with glioblastoma who underwent standard treatment of primary resection with adjuvant temozolomide/radiation therapy. Patients selected underwent both postoperative MRI surveillance and subsequent rebiopsies for possible recurrence. Seventy-five MRI data sets were then categorized into two groups: biopsy-proven predominantly recurrent tumor (54) versus either biopsy-proven predominantly treatment effect (9) or stable surveillance MRI (12), average minimum six months post resection without progression for subsequent 12 months. T1 postcontrast enhancement was manually segmented and a patch-based approach was utilized to generate 25340 32x32 pixel 2-D slices cropped from different tumor sections. On average, 314 boxes of each tumor were created. A 21-layer residual CNN was designed. Four-fold cross validation was utilized and performance measured on a per-volume basis.

Results

The CNN achieved an AUC, sensitivity and specificity of 0.76 ± 0.13 , 0.88 ± 0.14 and 0.64 ± 0.19 respectively in predicting recurrent tumor versus treatment effect in a small single-institution data set.

Conclusions

Preliminary results demonstrate that deep learning through novel CNNs can be designed to utilize small 3-D data sets to predict tumor recurrence from treatment effect in this cohort of glioblastoma patients with confounding post-treatment MRI signal changes on T1 postcontrast imaging. Research with a larger pathology-driven database to examine MRI T1 post/FLAIR/DWI signal changes as well as second-line treatment effects is ongoing.

O-288

3:49PM - 3:56PM

Evaluation of Dynamic Susceptibility Contrast MRI Perfusion Using Principal Component Analysis and Machine Learning to Detect Occult Infiltration of Glioblastoma

H Akbari¹, M Martinez-Lage², M Bilello¹, S Mohan³, R Wolf⁴, C Davatzikos¹

¹University of Pennsylvania, Philadelphia, PA, ²Massachusetts General Hospital, Boston, MA, ³University of Pennsylvania School of Medicine, Philadelphia, PA, ⁴Hospital of the University of Pennsylvania, Philadelphia, PA

Purpose

DSC-MRI perfusion contains rich information about the dynamics of blood perfusion beyond commonly extracted measures. This information can reveal complementary information to cerebral blood volume reflecting heterogeneity in perfusion dynamics, identified via principal component analysis (PCA) of the perfusion time-curves. We hypothesized that PCA would more accurately visualize and magnify subtle but important characteristics of tissue heterogeneity in patients with GBM, which capture aspects of the underlying tissue biology.

Materials and Methods

In a retrospective cohort of 40 de novo GBM patients, PCA was used to distill the DSC-MRI time series down to a few parameters (principal components) that capture the temporal dynamics of blood perfusion. In order to determine what information beyond the DSC-derived standard sequences was conveyed by the PCs, we calculated rCBV, peak height (PH), and percentage signal recovery (PSR) metrics. We built a support vector machine (SVM) to predict the location of recurrence, and built a support vector regression

Oral Presentations & Excerptas

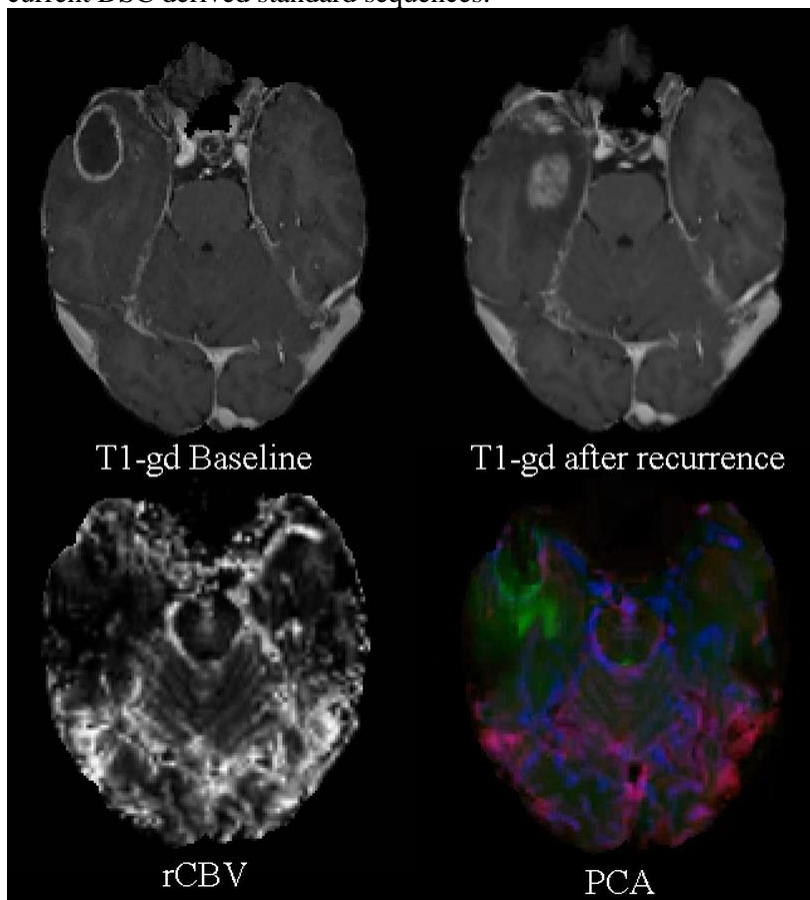
(SVR) model to estimate the ratio of true progression/pseudoprogression in each patient using PCs and compared with the standard sequences. The results were evaluated against regions of post-resection recurrence in follow-up studies based on pathology reports.

Results

Six principal components were sufficient to capture more than 99% of the variance in the perfusion signal for all tissue types. The areas that later demonstrated tumor recurrence were detected with 74% accuracy using PCs compared to 66% combining rCBV, PH, and PSR. Also, PCs derived SVR correlated ($r=0.71$) with the pathological score of true progression/pseudoprogression ratio while conventional sequences had lower correlation ($r=0.64$).

Conclusions

PCA is a novel comprehensive technique to summarize perfusion dynamics by evaluating the entire signal that facilitates visualization of the heterogeneity within the peritumoral region, which can potentially be utilized to gauge areas of likely tumor infiltration. This method provides information above and beyond current DSC derived standard sequences.



(Filename: TCT_O-288_PCA_ASNR_txt.jpg)

O-289

3:56PM - 4:03PM

Using Deep Learning technique to synthesize high quality cerebral full-dose Positron Emission Magnetic Resonance Images (PET-MRI) from low-dose ones

F Macruz¹, K Chen², E Gong², J Xu², M Khalighi², G Zaharchuk¹

¹Stanford University, Stanford, CA, ²Stanford, Stanford, CA

Oral Presentations & Excerptas

Purpose

Cerebral PET/MRI is a powerful imaging modality that allows simultaneous obtainment of anatomical and functional information of the brain. However, one of the major inconveniences of this modality is related to the need of the radiotracer and includes its risks, high cost, difficulty of manipulation and short half-life duration. Although several attempts have been made to reduce the injected dose of radiotracer, the simultaneous reduction on imaging quality is a constant challenge to a successful accomplishment of this goal. With that in mind, the purpose of this study was to predict standard high-quality PET images, resembling the ones acquired with full injected dose, from low-dose images (DRF= 4 or 75% dose reduction) combined with MRI images, using for that, deep-learning methods.

Materials and Methods

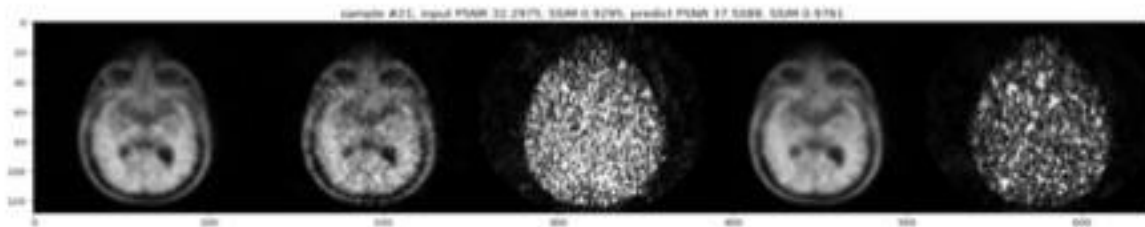
For the purpose of this study, we used Amyloid-PET and MRI images of 87 patients (mean age= 73.3; SV = 7.46), 45 with Alzheimer's disease (AD) and 42 normal controls, obtained from the Alzheimer's Disease Neuroimaging Initiative (ADNI) database (adni.loni.usc.edu). Only patients who had PET and MRI exams with less than one month apart from each other were selected. The Amyloid-PET and MRI images were selected from ADNI-2, ADNI-GO and ADNI-3 studies, regardless the use of 18F-florbetapir and 18F-florbetaben as radiotracers and the scanner manufacturer. The MRI images utilized were T1-weighted SPGR and T2-FLAIR images. A convolutional-deconvolutional DNN with the proposed structure (Figure 1) was trained, using the MR images (T1-weighted and T2-FLAIR) and the low-dose PET image as input and the full-dose PET image, as the ground truth. A five-fold cross-validation was used to prevent training and testing on the same subjects (65 subjects for training, 22 subjects for testing per network trained). Also, the FSL software was used to generate a brain mask derived from the T1 images of each subject, for voxel-based analyses.

Results

For each axial slice of the volumes, the synthesized PET image and the original low-dose PET images within the brain mask were compared to the original full-dose image. The metrics peak signal-to-noise ratio (PSNR), structural similarity (SSIM), and root mean square error (RMSE) were calculated. Qualitatively, the synthesized images show marked improvement in noise reduction, spatial resolution, cortical definition and grey-white matter differentiation, resembling a lot the ground truth image. Quantitatively, the images synthesized have a higher PSNR, a higher SSIM and a lower RMSE in all subjects.

Conclusions

Deep learning can potentially reconstruct high-quality Amyloid PET images from low-dose ones, with only 25% of the regular radiotracer dose. In order to do that, we combined spatial information from PET and MR scan done one month apart, to preserve local details and structure. This promising result changes the perspective on dose reduction PET/MRI exams and hopefully will allow safer and more efficient PET scans in the future.



(Filename: TCT_O-289_PET_low_dose_images.jpg)

O-290

4:03PM - 4:10PM

Improving Workflow by Using Deep Learning to Label Brain and Spine MRI Sequences

Oral Presentations & Excerptas

J Tang¹, J Seah², F Gaillard³

¹Royal Melbourne Hospital, Parkville, Victoria, Australia, ²Alfred Health, Prahran, Victoria, Australia, ³Royal Melbourne Hospital/University of Melbourne, Parkville, Victoria, Australia

Purpose

MRI reading protocols help to improve efficiency in everyday reporting. Most picture archiving and communication system (PACS) reading protocols rely on DICOM tags to identify sequences. Intervendor and interinstitution variability of the Digital Imaging and Communications in Medicine (DICOM) tags can result in inaccurate hanging of sequences. The purpose of this study is to develop a deep-learning algorithm which automatically detects MRI brain and spine sequences and labels the sequence with a DICOM tag. The DICOM tag can then be incorporated into a script which creates reading protocol files that may be incorporated into a local PACS.

Materials and Methods

Divided by case into training were 348,953 MRI brain and spine slices from Radiopaedia.org, validation and testing sets in a ratio of 8:1:1. All images were scaled to 256 x 256. The ResNet, Inceptionv3 and VGG architectures were trained and validated. Accuracies were compared between the architectures for different sequences.

Results

The best per slice validation accuracy of 94% was achieved using the Inceptionv3 architecture. The ResNet and VGG architectures achieved a similar accuracy of 93%. The Inceptionv3 architecture was most accurate for coronal T1 slices, with a testing accuracy of 98%. The lowest performance was 87% for contrast enhanced axial T1 slices.

Conclusions

The deep-learning algorithm can accurately determine MRI sequence. This algorithm would be useful in ensuring consistent labelling of MRI sequences across vendors, which in turn will ensure that reading protocols integrated into PACS systems open correctly and therefore improve daily workflow.

O-291

4:10PM - 4:17PM

Image Super-Resolution and Radiation Reduction via Deep Learning

Y Xiao¹, P Sanelli², R Fang¹

¹University of Florida, Gainesville, FL, ²Northwell Health, Manhasset, NY

Purpose

Cerebral Computed Tomography Perfusion (CTP) scanning will produce excessive X-ray radiation exposure to patients, which raises the public's concerns about the associated risks such as cancer. Researchers are devoted to reducing such unnecessary radiation.

Materials and Methods

We propose a deep-learning method by reducing the CTP scanning time to minimize the radiation exposure. It is a convolutional neural network (Figure 1) adopted from VDSR [1] for image super resolution that combines spatial and temporal cross-sections to reconstruct high-resolution images. The experiments conducted on CTP sequences of 22 patients with size 512x512x119, with two spatial dimensions and one temporal dimension, denoted as X, Y, and T. The combination of X, Y, and T results in three cross-sections: XY, XT, and YT. We add D, the diagonal of X and Y dimensions, and combine D with T into another cross-section DT. The proposed network takes the downscaled four cross-sections into its four single directional branches to get the intermediate high-resolution images, then combine and pass those results into a cascaded convolutional neural network to reconstruct the final high-quality CTP slices.

Results

We down-scale the input cross-sections from both spatial and temporal directions into 1/3 of the original

Oral Presentations & Excerptas

size. After obtaining the final slices, we calculate the Cerebral Blood Flood (CBF) and Cerebral Blood Volume (CBV) for all results in different stages. We measure the images quality by the peak signal-to-noise ratio (PSNR) and structural similarity index measure (SSIM). The comparison results in Table 1 show our proposed method achieves the best performance of 26dB and 23dB for PSNR on CBF and CBV, which is around 25% higher than the bicubic low-resolution images.

Conclusions

Our method can maintain the image quality with only 1/3 of the original scanning time. Therefore, it is an efficient method and a possible solution for radiation reduction.

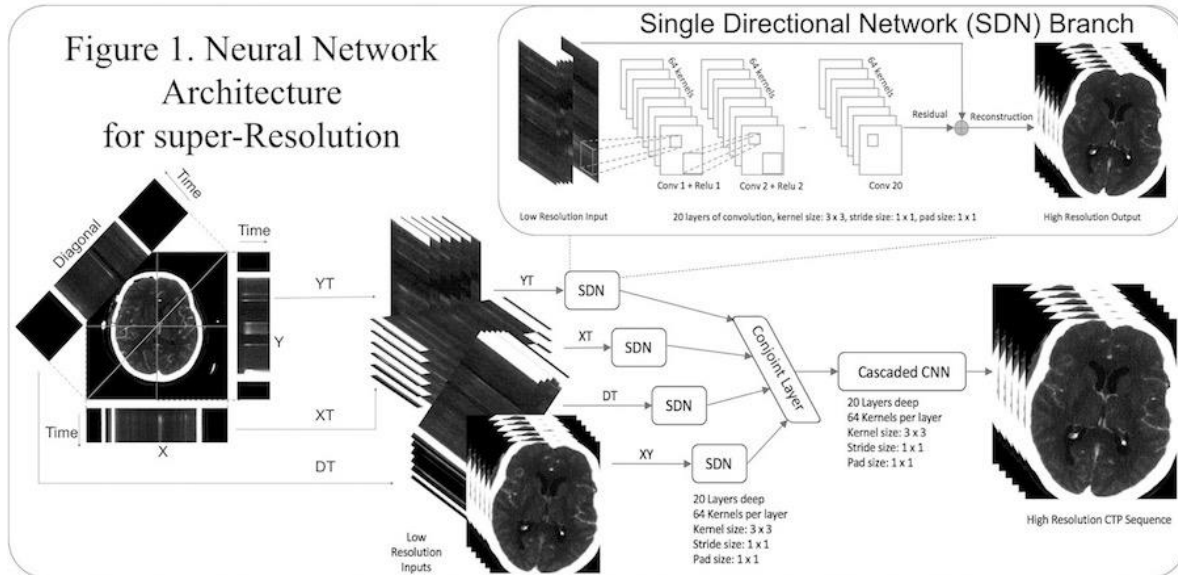


Table 1	CBF		CBV	
	PSNR	SSIM	PSNR	SSIM
sSVD				
Bicubic	19.271	0.901	18.909	0.880
Spat-SDN	22.311	0.946	21.203	0.925
Temp-SDN	24.919	0.974	21.730	0.945
STAR	26.131	0.978	23.003	0.955

(Filename: TCT_O-291_Figure.jpg)

O-292

4:17PM - 4:24PM

Machine Learning-based Iterative Image Reconstruction Algorithm Allows Significant Reduction in Brain MRI Scan Times

L Tanenbaum¹, W Gibbs², B Johnson³, I Varaganov⁴, J Gomori⁵, A Pais⁶, T Aharoni⁶, R Shreter⁷
¹RadNet, Inc., New York, NY, ²Keck School of Medicine, University of South California, Los Angeles, CA, ³Center for Diagnostic Imaging, St. Louis Park, MN, ⁴Rambam Health Care Campus, Haifa, Israel, ⁵Hadassah Hebrew University Medical Center, Jerusalem, Israel, ⁶Medic Vision Imaging Solutions Ltd., Tirat-Carmel, Israel, ⁷Hillel Yaffe Medical Center, Hadera, Israel

Purpose

To evaluate image quality, grey-white (GW) matter differentiation and overall diagnostic sufficiency of brain MRI images acquired with reduced scan time protocols, processed with a novel 3-D image enhancement algorithm ("iQMR" by Medic Vision Ltd.) compared with images from sites' routine protocols

Materials and Methods

Under IRB approval, 37 subjects (mean age 48 \pm 15 years) were scanned on three 1.5T scanners (Ingenia-Philips, n=18; Aera-Siemens, n=9; Signa-HDx-General Electric, n=10), at three different sites using the site's routine clinical brain protocols as well as time-reduced variants (30% shorter, in average, than the sites' routine brain exam). The short scans were prescribed by changing conventional acquisition parameters, such that the revised setting traded scan time reductions for decreased signal to noise ratio. After offline processing with iQMR, images were compared with the original unprocessed images (155 scans) and with the corresponding routine protocols (153 scans). Independent, blinded, side-by-side comparisons of diagnostic quality, visual image quality, GW-matter differentiation and presence of artifacts were performed by six neuroradiologists using a 5-point Likert-scale (3= equal, >3 processed image is superior).

Results

Reviewer assessments exhibited superiority of the processed images over the original unprocessed images for diagnostic quality (median=3, mode=3, mean=3.29 \pm 0.56), visual image quality (median=4, mode=4, mean=3.7 \pm 0.63), GW-matter differentiation (median=3, mode=3, mean 3.26 \pm 0.61) and artifacts' appearance (median=3, mode=3, mean=3.29 \pm 0.59) (n=850 reads). Additionally, the processed time-reduced images demonstrated equality for diagnostic quality (median=3, mode=3, mean=2.94 \pm 0.39), visual image quality (median=3, mode=3, mean=2.83 \pm 0.69), GW-matter differentiation (median=3, mode=3, mean=2.91 \pm 0.46) and artifacts' appearance (median=3, mode=3, mean=2.91 \pm 0.54) (n=614 reads). Figure 1 shows comparable T1- and T2- weighted imaging of conventional and processed short protocols from a normal brain.

Conclusions

iQMR processing can reduce routine brain exam scan time by 30% without adversely affecting image quality. These findings may have substantial applications in the routine clinical practice by potentially enabling reduced scan time, decreased motion artifacts and a lesser need for repeat scans.

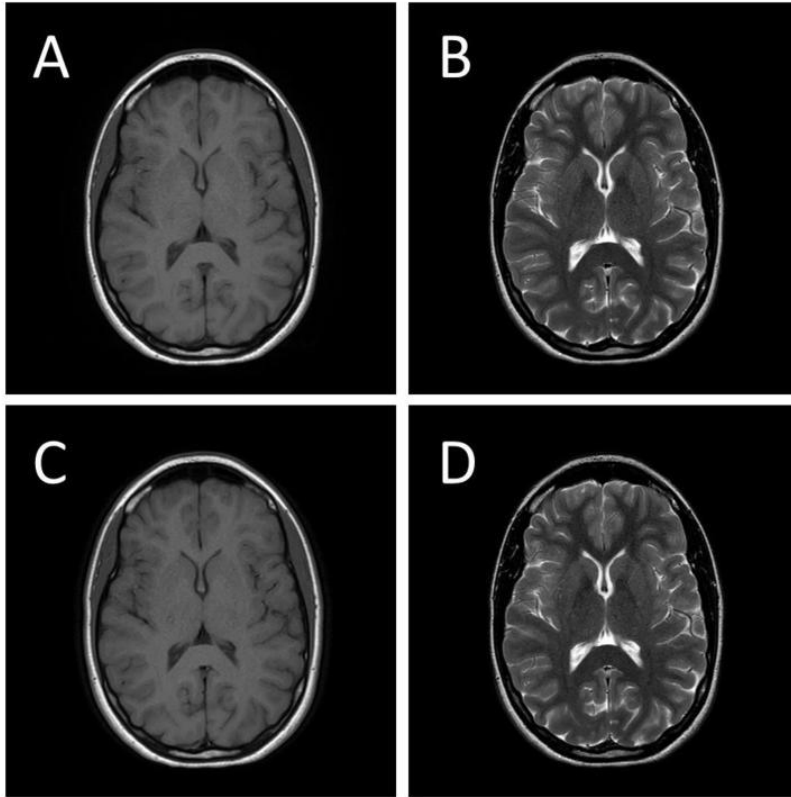


Figure 1. Axial conventional and processed-short protocols 1.5T imaging of normal brain. Conventional (upper row) T1-weighted imaging (A) and T2-weighted imaging (B) and the corresponding processed-shorter protocol variants imaging (lower row, C-D) demonstrating comparable image quality and diagnostic suitability. Scan time of variants was reduced by 37% for T1 and by 50% for T2.

(Filename: TCT_O-292_Figure1_asnr.jpg)

Tuesday, June 5, 2018

3:00PM - 4:30PM

Parallel Paper Session: Brain Tumor Imaging: New Findings

O-293

3:00PM - 3:07PM

Distinguishing True Progression from Pseudoprogession in Glioblastoma Patients Treated with Immunotherapy Using Standard MRI Sequences

W Tom¹, C McDonald², N Bahrami², N Farid¹

¹University of California, San Diego, San Diego, CA, ²University of California, San Diego, La Jolla, CA

Purpose

Assessing immunotherapy response in glioblastoma is complicated by pseudoprogession--the phenomenon of worsening imaging findings related to therapy in the absence of true tumor progression.

Oral Presentations & Excerptas

The purpose of this study is to identify MRI findings which can help distinguish true progression from pseudoprogression in glioblastoma patients receiving immunotherapy.

Materials and Methods

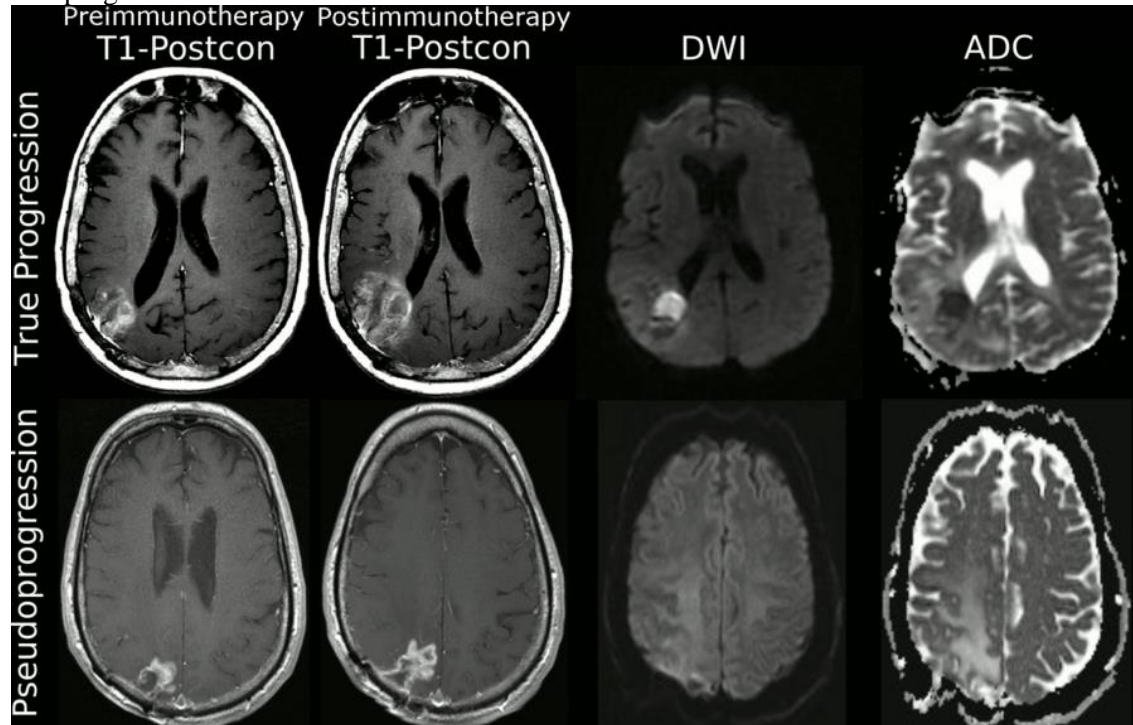
We retrospectively identified 25 glioblastoma patients treated with immunotherapy at our institution. The majority of the patients received an immunotherapeutic vaccine (i.e. DCVax-L, ICT-107, ICT-121, rindopepimut, or Sunovion WT1), while a few patients received an immune checkpoint inhibitor (i.e. nivolumab). Comparing the immediate preimmunotherapy scan and the first postimmunotherapy scan demonstrating imaging progression, a board-certified neuroradiologist categorized the change in area of contrast enhancement and FLAIR hyperintensity based on a qualitative assessment of the postcontrast and FLAIR sequences as follows: no change, up to 25% increase, greater than 25% and up to 75% increase, and greater than 75% increase. The presence or absence of new enhancing lesions and the presence or absence of restricted diffusion (i.e. hyperintense DWI signal and hypointense ADC signal) was also noted on the postimmunotherapy scan. The cases were classified as true progression if pathology demonstrated recurrent tumor or if death occurred within one year of the MRI demonstrating imaging progression. The remainder of the cases were classified as pseudoprogression.

Results

We classified 13 cases as true progression and 12 cases as pseudoprogression. True progression was associated with greater interval increases in the area of contrast enhancement ($P = .003$) and the presence of restricted diffusion in the postimmunotherapy MRI ($P = .02$). Interval increase in the area of contrast enhancement exceeding 25% had a sensitivity of 92% (95% CI, 64%-100%) and a specificity of 58% (95% CI, 28%-85%) for true progression. The presence of restricted diffusion had a sensitivity of 69% (95% CI, 39%-91%) and a specificity of 83% (95% CI, 52%-98%) for true progression. Development of new lesions ($P = 1$) and interval increase in the area of FLAIR hyperintensity ($P = .19$) were not statistically different between the two groups.

Conclusions

In glioblastoma patients treated with immunotherapy, interval increase in the area of contrast enhancement exceeding 25% in the postimmunotherapy MRI is sensitive (92%) but not specific (58%) for true progression, while the presence of restricted diffusion is specific (83%) but not sensitive (69%) for true progression.



(Filename: TCT_O-293_ASNRfigure3.gif)

O-294

3:07PM - 3:14PM

Evaluation of Therapeutic Response of Glioblastoma to Insulin-like Growth Factor Receptor Type 1 (IGF-1R) Antisense Treatment Protocol, using Dynamic Susceptibility Contrast (DSC) Perfusion Imaging.

R Nikam¹, K Talekar², K Atsina², A Flanders²

¹A I duPont Hospital for Children, Wilmington, DE, ²Thomas Jefferson University Hospital, Philadelphia, PA

Purpose

Antisense agents are novel immunotherapeutic agents, currently being assessed to stimulate the immune system to combat certain neoplasms including glioblastomas. The purpose of this preliminary investigation is to evaluate therapeutic response of glioblastomas treated with antisense agents using serial DSC perfusion imaging.

Materials and Methods

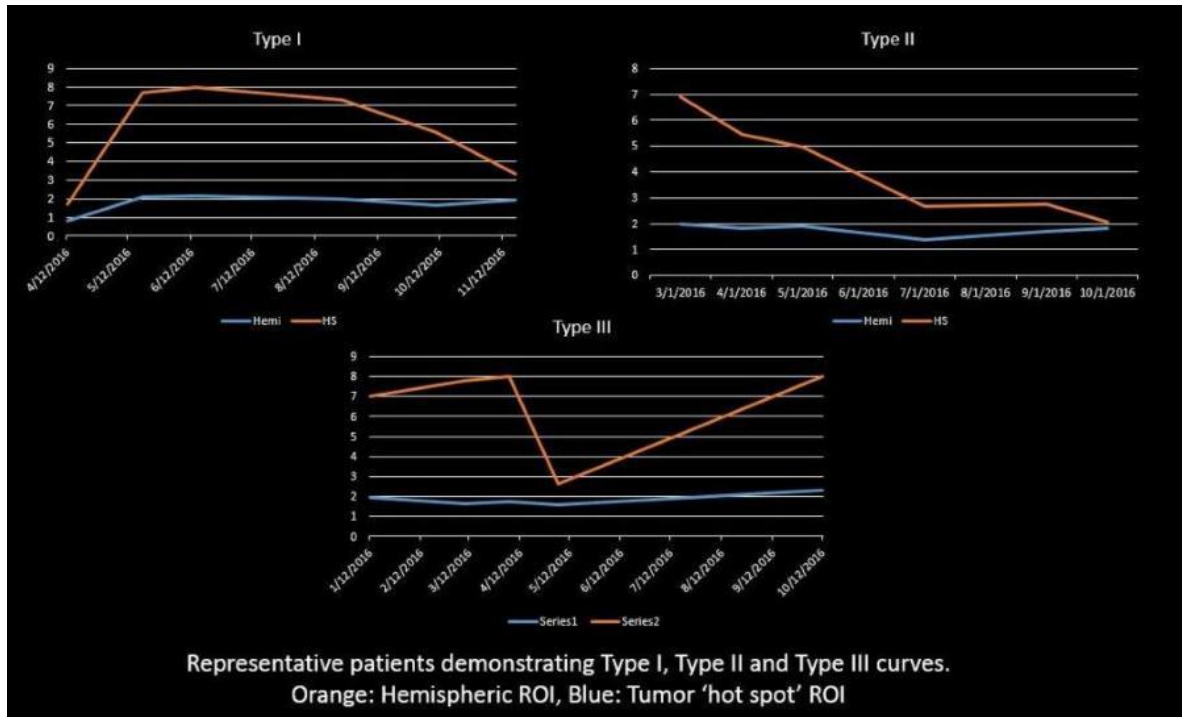
As a part of phase I-II immunotherapy trial at a single institution, serial DSC perfusion data were acquired for eight patients with GBM treated using an antisense DNA regimen. All patients underwent protocol surgery for tumor resection/debulking. A "vaccine" was created using recently harvested GBM tissue from the patient and antisense DNA. Semipermeable biodiffusion chambers were filled with sterilized and irradiated autologous tumor cells and implanted into the patient's rectus sheath for 24 hours and then removed. Baseline and serial, conventional MRI and DSC perfusion imaging was performed at regular time intervals. rCBV was calculated by dividing either hemispheric regions of interest (ROIs) or tumor "hot-spot" ROIs with ROIs from contralateral normal appearing white matter. Serial clinical assessment included Karnofsky performance scale and multiplex cytokine assays to assess immune response.

Results

Based on the serial perfusion data, and our experience from a previous phase-1 trial, we describe three types of perfusion curves. Type I curve is characterized by initial increase in rCBV at eight to 12 weeks post vaccination, followed by gradual decline. Out of eight patients, five demonstrated type I pattern. We hypothesize that this transient paradoxical elevation of rCBV probably reflects pseudoprogression, and may reflect an immune mediated inflammatory response post vaccination. Type II curve is characterized by progressively declining rCBV values. From our cohort, two patients demonstrated this type II pattern. We hypothesize that both types I and II curves represent favorable post-treatment effect. The difference between these two subgroups is that the patients with type-I response had partial debulking of the tumor at protocol surgery while the patients demonstrating type-II curves had gross total resection of the tumor during protocol surgery. Type III curve is characterized by progressively increasing rCBV values and suggests tumor progression. One patient demonstrated type III pattern. This is a preliminary investigation with 32 patients enrolled in this study, and further analysis is underway to test our hypothesis.

Conclusions

Therapeutic response of glioblastoma to novel antisense agents can be characterized into three patterns, with type III curve suggesting a significantly poorer outcome than type I and II. Paradoxical elevation in rCBV (type I pattern) probably reflects pseudoprogression, and most likely suggests an immune-mediated inflammatory response post vaccination.



(Filename: TCT_O-294_FigAntisense.jpg)

O-295

3:14PM - 3:21PM

ADC-map-based Classification of Glioma-Subtypes in diffusion-weighted MR-Imaging

N Nuessle¹, J Hempel¹, J Schittenhelm¹, U Klose¹

¹University Hospital Tuebingen, Tuebingen, Germany

Purpose

Gliomas are the most common primary cerebral tumors and are almost always associated with an extremely poor overall survival and more years of life lost than any other tumor. So far, postinterventional histopathological examinations are the gold-standard procedure for final diagnosing. An accurate preinterventional diagnosis is necessary to offer the patients a fast and promising therapy. Diffusion-weighted imaging (DWI) and estimation of diffusion coefficient and kurtosis values within the tumor seem to be a promising way for such a differentiation. The purpose of this study was to assess the diagnostic and predictive performance of ADC-values from two b-value measurements in the preinterventional in vivo assessment of gliomas following the WHO 2016 integrated diagnosis scheme and to compare this method to the previously described method of mean kurtosis (MK) and mean diffusivity (MD) based evaluation.

Materials and Methods

Ninety-seven patients with suspected glioma who provided written informed consent were retrospectively assessed between January 2014 and September 2017 from a prospective trial approved by the local institutional review board. All patients underwent preinterventional MRI examination including diffusion-weighted imaging with b-values of 0 (b0), 500 (b500), 1000, 1500, 2000 and 2500 s/mm² and two averages and six directions per b-value. Signals were averaged over all directions. Tumor volume was drawn in by hand on the basis of T2-FLAIR signal alterations as full tumor volume on multiple slices. MK- and MD-maps were calculated from all acquired data. Nine different ADC-maps from pairs of two b-values were calculated (five using b0 and four using b500 as a reference). ADC-, MK- and MD-maps

Oral Presentations & Excerptas

were interpolated to the matrix points of the FLAIR images, VOIs were subsequently transferred from the FLAIR images to the ADC-, MK- and MD-maps and mean values of the tumor subtypes were compared. One-way ANOVA with posthoc Games-Howell correction was used to compare ADC, MD and MK between 2016 CNS WHO-based tumor grades. Postinterventional histopathological tumor grading was realized on a molecular basis using the molecular markers IDH-mutation, 1p/19q- and ATRX-loss.

Results

MK-analysis delivered best results using all six measured b-values, as shown in previous studies ($p < 0.001$). Results of the MD evaluation were significant, when leaving out the b-value of 0 s/mm² ($p < 0.01$). Two b-value dependent ADC-map based evaluation showed great potential in separating the three diagnosis groups and statistically highly significant differences between the groups were demonstrated ($p < 0.001$). ADC values of astrocytomas appeared to be significantly higher than those of the oligodendrogliomas and GBM in all b-values. ADC values of oligodendrogliomas were significantly higher than those of GBM. Best discrimination was achieved when calculating the ADC-maps with b-values of 500 s/mm² and 2500 s/mm², avoiding the perfusion influence included in the b₀ measurement. Discovered findings underline the hypothesis, that different glioma subtypes seem to show differences in diffusion-weighted MR imaging.

Conclusions

Measurement of only two b-values compared with ADC-based assessment could be sufficient for preinterventional diagnosing. This corresponds to a reduction of acquisition time by 66% (two instead of six minutes), while results remained comparable to the MK evaluation and were better than in the MD-based analysis. Apparently, perfusion-based influence in DWI and DKI needs to be considered in the discrimination of different glioma subtypes. Looking at MK maps, glioblastomas, known to have higher perfusion, present higher MK values which intensify the measurable differences. In MD and ADC maps, higher graded gliomas present lower MD or ADC values; therefore perfusion based influence in lower b-value measurement impair the results. Therefore, ADC map-based evaluation of glioma in DWI provides great potential in accurate preinterventional diagnosing of glioma subtypes. The proposed technique is time-saving (66% reduction of acquisition time) and consists of a relatively simple postprocessing method. Therefore it is an important step to introduce preinterventional glioma grading in routine clinical practice. Further investigations, using higher b-values, may provide even higher diagnostic accuracy.

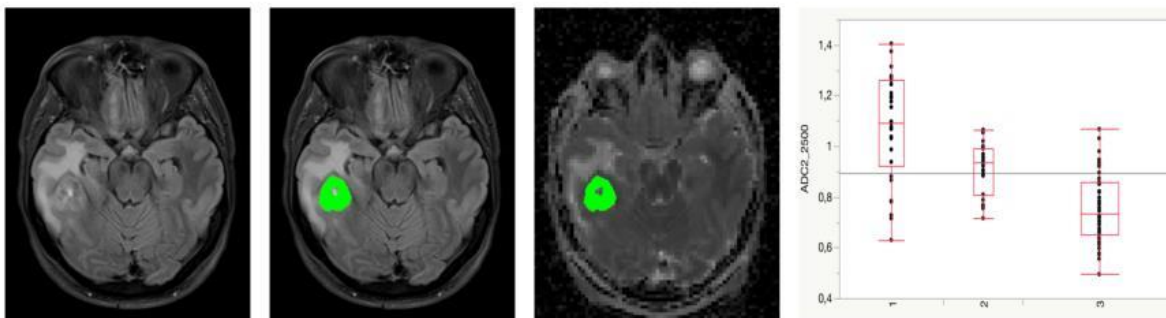


Fig. 1-3: FLAIR- and DW-Images of histopathologically confirmed GBM-patient. Unmodified FLAIR, FLAIR with drawn in tumor region and DWI, fitted to the matrix of the FLAIR-images, with transferred tumor region.

Fig. 4: Distribution of the mean ADC-values using b-values of 500 s/mm² and 2500 s/mm², classified to the three groups (1=Astrocytoma, 2=Oligodendroglioma, 3=GBM).

(Filename: TCT_O-295_Fig_ASNR.jpg)

O-296

3:21PM - 3:28PM

Simultaneous pH- and oxygen-weighted metabolic MRI of human gliomas at 3T

B Ellingson¹, J Yao², A Chakhoyan², A Lai², N Salamon², P Nghiemphu², W Pope¹, T Cloughesy²
¹David Geffen School of Medicine at University of California Los Angeles, Los Angeles, CA, ²University of California Los Angeles, Los Angeles, CA

Purpose

Abnormal metabolism (1) is a hallmark of cancer. The chemical exchange between amine and amide protons in bulk water has been shown to be pH dependent using CEST imaging (2). R2', the reversible transverse relaxation rate, has been shown to correlate with oxygen extraction (3-6) and has been used to explore oxygen metabolism in brain tumors (5, 7). In the current study we present a technique for fast pH- and oxygen-weighted MR imaging contrast using multiecho amine proton chemical exchange saturation transfer echo spin-and-gradient echoplanar imaging (CEST-SAGE-EPI) on a clinical 3T system.

Materials and Methods

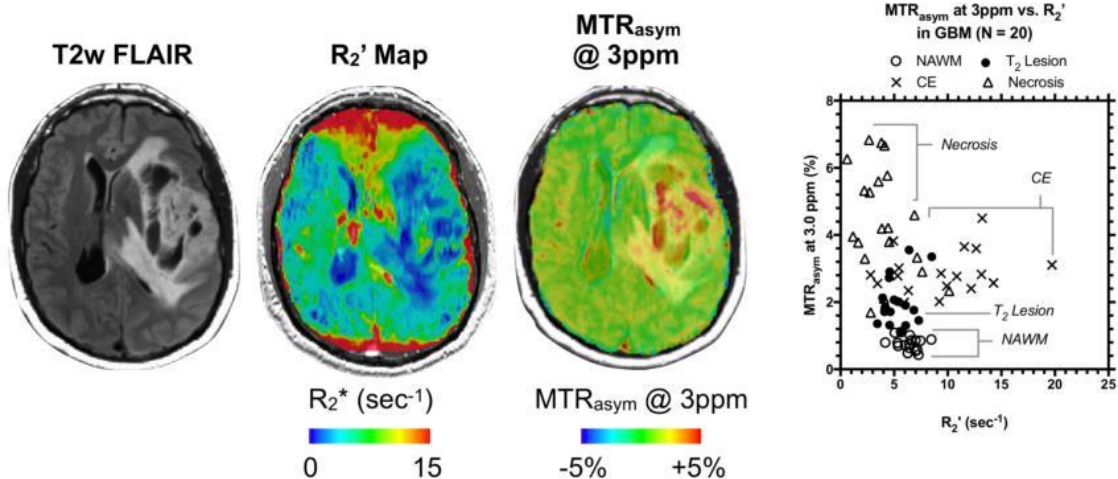
Relaxometry measures of R2, R2*, and R2' were performed using CEST-SAGE-EPI and standard techniques in a series of glutamine phantoms with combinations of varying pH and gadopentetic acid concentration. All experiments were repeated twice and compared to simulations. Forty-seven histologically proven glioma patients (WHO IV, N=20; WHO III, N=14; WHO II, N=13) who signed IRB informed consent were also scanned prior to initial surgical resection or at first recurrence.

Results

In phantom samples containing varying concentration of Gd-DTPA, CEST-SAGE-EPI estimates of R2, R2*, and R2' varied linearly with concentration and matched standard measurements. T2 hyperintense lesions in all patients exhibited heterogeneous areas of elevated MTR_{asym} at 3ppm (acidity) and R2' (hypoxia) T2 hyperintense lesions exhibited a significantly lower R2' (4.8±0.2 sec⁻¹) compared with NAWM (6.2±0.2 sec⁻¹; P<0.0001) and did not vary significantly across tumor grade (P=0.0537). In glioblastoma, differences in R2' across tissue types were observed (P=0.0001). MTR_{asym} within T2 hyperintense lesions (1.7±0.1%) were significantly higher than NAWM (0.8±0.03%; P<0.0001) and varied across grade (P=0.0297).

Conclusions

The current study presents a new CEST-SAGE-EPI sequence for obtaining high-speed, whole-brain pH- and oxygen-sensitive image contrasts for brain tumor evaluation. Results in tumors showed a high degree of spatial heterogeneity and measurements were consistent with known cancer biology.



(Filename: TCT_O-296_Fig1001.jpg)

O-297

3:28PM - 3:35PM

Development of an Automatic Tumor Detection and Segmentation Algorithm using Multi-contrast MR and Linear Discriminant Analysis

A Hasse¹, Y Jeong², S Ansari³, T Carroll¹

¹University of Chicago, Chicago, IL, ²Northwestern University, Chicago, IL, ³Northwestern University, Feinberg School of Medicine, Chicago, IL

Purpose

To devise an accurate, automatic algorithm to detect and segment glioblastoma multiforme lesions in multicontrast MR images

Materials and Methods

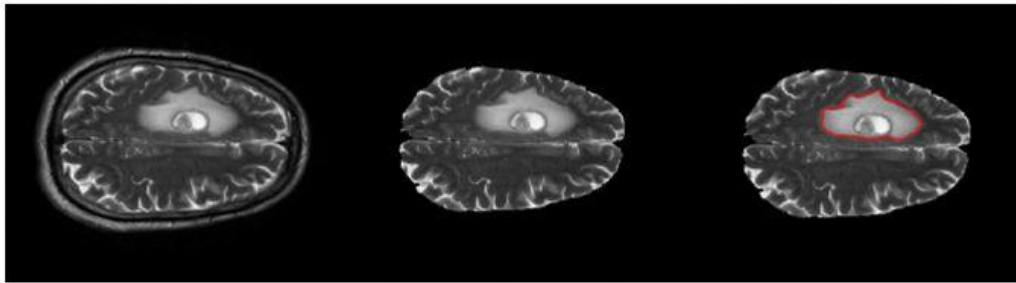
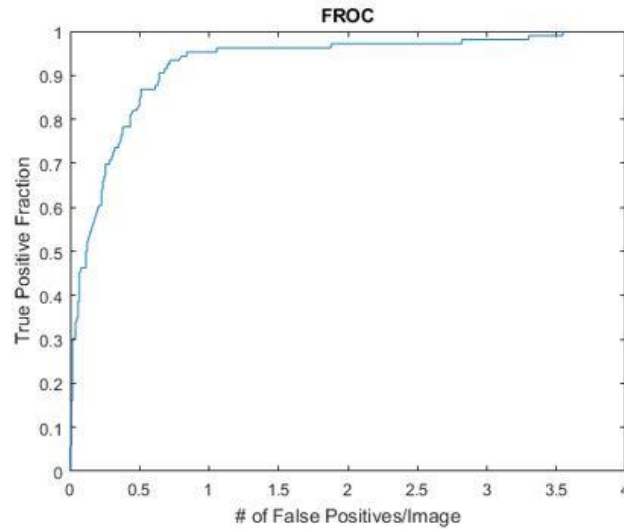
Using a previously acquired data set containing MR images of patients diagnosed with glioblastoma multiforme (GBM), an automatic segmentation algorithm was developed in MATLAB. This algorithm utilizes four standard MR sequences, T1-weighted precontrast, T1-weighted postcontrast, T2-weighted, and T2-weighted with fluid attenuated inversion recovery (FLAIR), to determine possible candidates for GBM lesions in a registered image set. Classification of skull and fat was completed using Statistical Parameter Mapping (SPM12) and removed from the image to allow for lesion segmentation to be performed on only the brain. Normalized gray-level thresholding was applied on each sequence, with priority given to candidates appearing on multiple sequences. Linear discriminant analysis (LDA) was chosen as an initial classifying algorithm, resulting in a feature vector that maximized the ratio of between-class distance to within-class variation. The candidates then passed through the pretrained (n=10) LDA algorithm to classify whether each possible lesion was a region of interest, defined as a region with abnormal features caused by GBM lesions and including active tumor sites, or was not a region of interest.

Results

Figure 1 shows a free-response receiver operating characteristic (FROC) curve resulting from the training set. To achieve a true-positive fraction of 0.95 using this training set and algorithm, an average of 0.84 false positives per image would be required. Figure 2 shows an example set of T2-weighted images, beginning with the initial slice (left), then to the segmented brain (middle), and finally ending with the contoured tumor that was detected and segmented with this algorithm (right).

Conclusions

An accurate and automatic GBM lesion segmentation was developed using gray-level thresholding of T1-weighted precontrast, T1-weighted postcontrast, T2-weighted, and T2-weighted FLAIR images, along with LDA to classify regions of interest.



(Filename: TCT_O-297_FROC_segment_combo.JPG)

O-299

3:42PM - 3:49PM

Histological validation of glioblastoma radiomic profiles at autopsy

S Hurrell¹, S McGarry¹, J Connelly¹, P LaViolette¹

¹Medical College of Wisconsin, Milwaukee, WI

Purpose

Radiomic profiles (RPs) are coded combinations of intensity-segmented radiographic contrasts from multiparametric magnetic resonance imaging. A previous experiment in de novo glioblastoma patients found five RPs associated with poor prognosis, prior to therapy (1). This study histologically validates these RPs at autopsy to determine the underlying pathology associated with each.

Materials and Methods

Radiomic profiles were calculated for five patients on the final MR images acquired prior to death. A region of interest (ROI) was used to mask the images by the FLAIR hyperintensity. Within this mask, the T1, T1+C, FLAIR, and ADC images were intensity segmented into three bins (bright, medium, and dark) and assigned numerical values (3, 2, 1). Assigning a 4-digit code to each voxel then combined these segmentations. For example, a code of 3-3-3-3 indicates high intensity on T1, ADC, FLAIR and T1+C respectively. Whole brain samples from five patients were sliced axially at autopsy using custom patient specific 3-D printed slicing jigs to orient slices according to the patient's MRI scan. Tissue samples were taken from regions aligned with RPs present on imaging that are associated with poor outcome. The digitized histology was then computationally segmented into tissue types including cellularity, cytoplasm, and extracellular fluid. RPs were then compared voxel-wise to the high resolution magnified H&E stained

tissue samples. Segmentation values were averaged over all five patients for each RP. Patient clinical factors such as overall survival, treatment, and time from MRI to death were factored into conclusions.

Results

RP 1-1-3-3 corresponded to coagulative necrosis in the majority of regions tested. RP 1-2-1-3 had the high levels of extracellular fluid and heightened cellularity. Visual inspection showed active cell death and treatment effect, which aligns with segmented findings. RP 1-2-3-3 was dominated by pseudopallisading necrosis, while RP 2-1-3-3 corresponded to hypercellularity and malignant growth. Finally RP 3-1-3-3 had the lowest levels of fluid with the highest levels of cytoplasm and cellularity, which visually showed endothelial proliferation and general malignant growth.

Conclusions

This study finds that RPs associated with poor prognosis, are all dominated by different heterogeneous characteristics of aggressive glioblastoma. Further study is needed in larger patient populations at different stages of treatment.

O-300

3:49PM - 3:56PM

Involvement of the Olfactory Apparatus by CNS Glial Tumors

X Wu¹, Y Li², C Glastonbury², S Cha²

¹Emory University, Atlanta, GA, ²University of California, San Francisco, San Francisco, CA

Purpose

The olfactory tracts and bulbs are central nervous system white matter tracts maintained by central neuroglia. Thus, glial tumors can originate from and metastasize to the olfactory apparatus. The goal of this project is to characterize the range of imaging findings of glial tumors that would affect the olfactory bulbs and tracts.

Materials and Methods

A HIPAA-compliant retrospective search was conducted through the institutional teaching files, identifying patients with olfactory nerve masses. The search was refined for patients with known history of glial tumor or pathologically proven gliomatous involvement of the olfactory nerve, while excluding pathologically proven nongliomatous masses. The cases were then reviewed and their clinical and imaging findings synthesized.

Results

The search yielded 12 cases. One primary pilocytic astrocytoma arising from the olfactory nerve presented as a well demarcated enhancing mass. Two diffuse anaplastic oligodendroglioma cases presented as nonenhancing mass-like FLAIR signal abnormality in the olfactory tracts. Two astrocytomas, one diffuse and one anaplastic, presented as nonenhancing olfactory nerve mass-like FLAIR signal abnormalities. One case of diffuse midline glioma presented with nonenhancing olfactory nerve involvement. Six glioblastomas presented as enhancing masses of the olfactory nerves (4) or nonenhancing infiltrative lesions (2).

Conclusions

As CNS white-matter tracts, the olfactory tracts and bulbs could be affected by a range of primary and metastatic glial tumors, including pilocytic astrocytoma, anaplastic oligodendroglioma, diffuse and anaplastic astrocytomas, diffuse midline glioma, or glioblastoma. This involvement may present as well defined, focal enhancement or infiltrative, masslike FLAIR hyperintensities involving the olfactory tract/bulb. Familiarity with the imaging findings of gliomatous involvement of the olfactory nerves is important in order to distinguish them from other disease processes and accurately identify malignant disease progression.

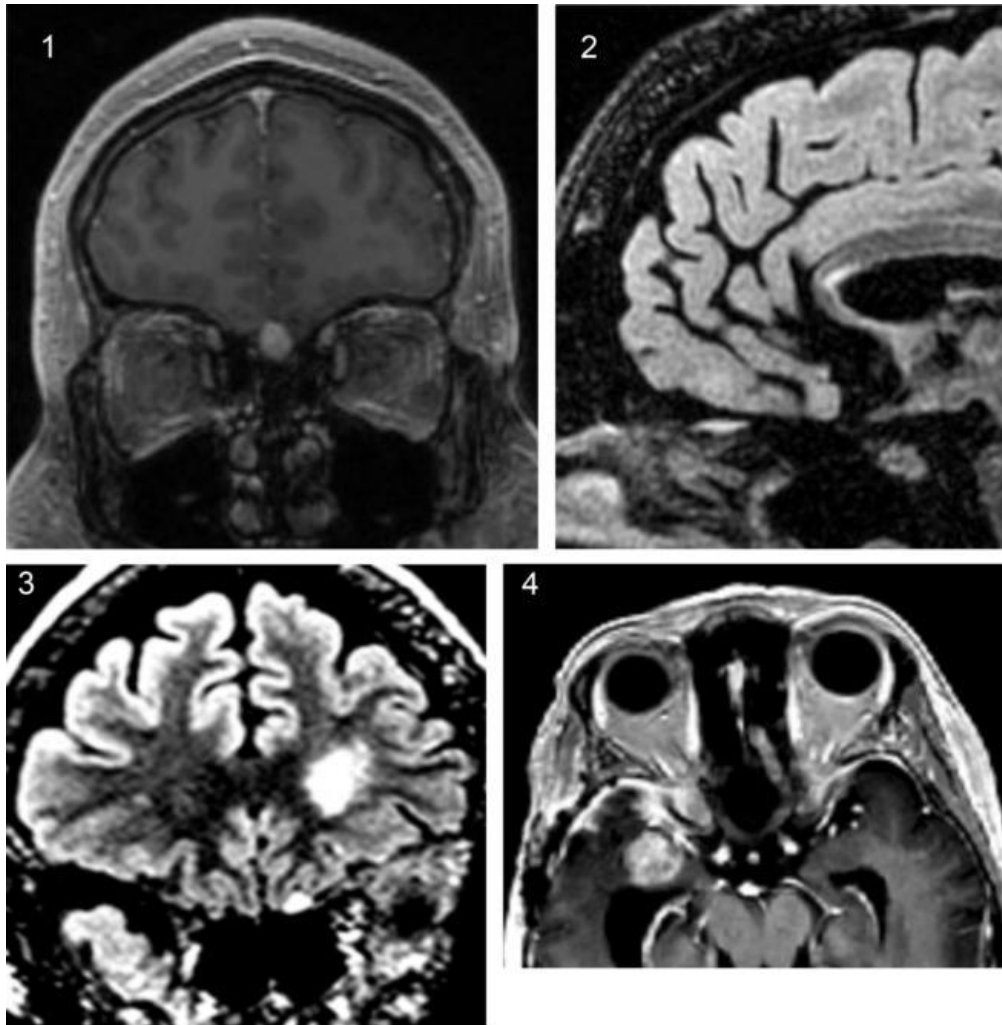


Fig. 1: Primary pilocytic astrocytoma of the olfactory nerve in a 27-year-old man.

Fig. 2: Recurrent diffuse astrocytoma. Nonenhancing asymmetric mass like FLAIR signal abnormality in the left olfactory nerve reflecting disease recurrence/progression in 51 year old patient 12 years after subtotal resection of diffuse astrocytoma in the inferior left frontal lobe.

Fig. 3: Recurrent oligodendroglioma. Nonenhancing masslike FLAIR signal abnormality in the left olfactory nerve in a 54 year old patient with anaplastic oligodendroglioma.

Fig. 4: Recurrent glioblastoma, IDH1 wildtype, MGMT unmethylated, EGFR amplified with enhancing mass-like FLAIR hyperintensity along the left olfactory nerve in a 61 year old woman.

(Filename: TCT_O-300_Figures.jpg)

O-301

3:56PM - 4:03PM

Correlation between von Willebrand factor antigen plasmatic levels (VWF:Ag) and dynamic contrast-enhanced (DCE) ktrans in grade IV gliomas (GBM): preliminary results

F Doniselli¹, G Marfia², S Navone², P Summers², R Campanella², A Costa²

¹University of Milan, San Donato Milanese, MI, ²IRCCS Ospedale Maggiore Policlinico, Milano, MI

Oral Presentations & Excerptas

Purpose

The proangiogenic values of VWF:Ag is known since decades (1) and its role in brain tumor has been recently confirmed (2). Aim of this retrospective study is to investigate the correlation of VWF:Ag and MRI-perfusion parameters (dynamic susceptibility contrast DSC and DCE) in patients with grade IV glial tumours (GBM).

Materials and Methods

We reviewed a series of 26 patients with biopsy-proved GBM who underwent preoperative DCE-MRI and DSC-MRI (males/females: 18/8; median age: 63 years). VWF:Ag were analyzed from preoperative collected plasma sample (expressed as IU/dL). We measured mean and maximum values of DSC-derived relative cerebral blood flow (rCBF) and volume (rCBV), and their ratios with contralateral normal side, DCE-derived volume transfer constant (K_{trans}), plasma volume (V_p) and reflux rate constant between fractional volume of the extravascular space and blood plasma (K_{ep}). Nonparametric Mann-Whitney test was used.

Results

The median overall survival was seven months (interquartile range=5-12). The distribution of vWF:Ag was bimodal, for which the median value (247 IU/dl) was used to separate the patients into two equally sized groups: a low vWF group (vWF:Ag < 248 IU/dl; median = 165 IU/dl, IQR=137-201 IU/dl) and a high vWF group (vWF:Ag > 248 IU/dl; median = 410 IU/dl, IQR = 329-528 IU/dl). When we compared the two groups, median follow-up duration was 10 months (IR= 7-15) and six months (IR= 3-7.5), respectively (p=0.02). Median K_{trans} values were 0.31 min⁻¹ (IR= 0.16–0.50) and 0.53 min⁻¹ (IR= 0.34–1.19), respectively (p=0.02). Median K_{ep} values were 1.79 min⁻¹ (IR= 1.23 – 2.70) and 3.89 min⁻¹ (IR= 2.42–7.15), respectively (p=0.005). No significant differences in overall survival or correlation with vWF:Ag were found for other parameters.

Conclusions

These preliminary findings in a small group of patients suggest a role for VWF:Ag, K_{trans}, and K_{ep} as a prognostic indicator of postoperative survival of patients with GBM.

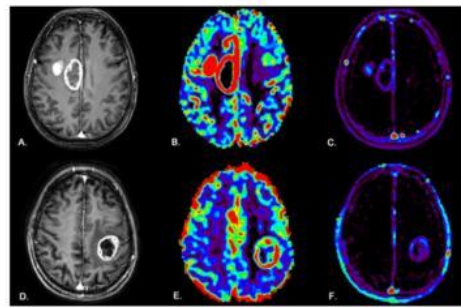
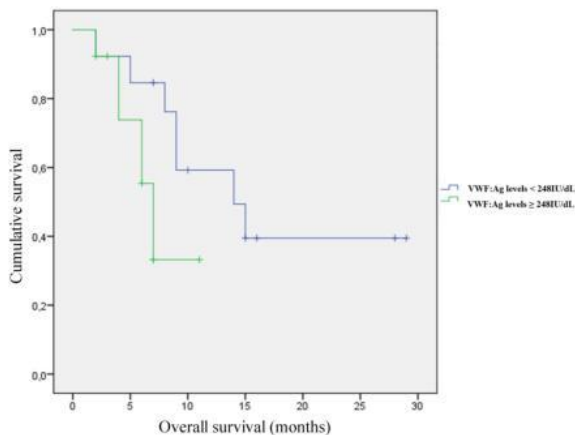
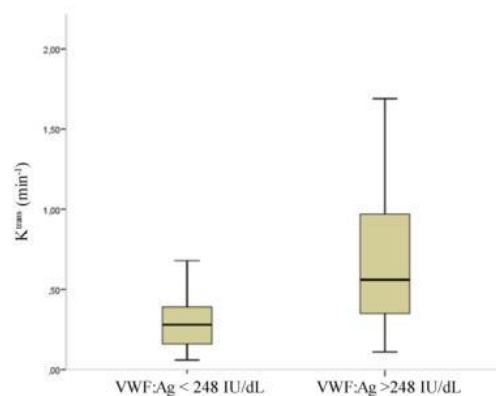
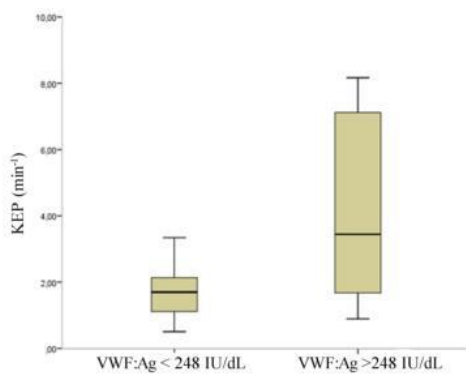


Image examples of a high and a low VWF:Ag plasmatic level GBM patient. MRI Images of GBM patient with low (< 248 IU/dl, A, B, C) and a high (> 248 IU/dl, D, E, F) VWF:Ag plasmatic level. (A, D) T1-W1 post contrast, (B, E) rCBV maps, (C, F) Ktrans maps.



(Filename: TCT_O-301_graphics.jpg)

O-302

4:03PM - 4:10PM

Visually accesable rembrandt images assessment features predict recurrent gbM prognostic outcomes

X Du¹

¹Daping Hospital, Chongqing, China

Purpose

To estimate Visually AcceSAbLe Rembrandt Images Assessment (VASARI) features in predicting recurrent GBM (rGBM) prognostic outcomes

Materials and Methods

Patients clinical and MRI data were collected retrospectively. VASARI features, prognostic outcomes contained time to recurrence (TTR) and recurrent patterns were analyzed. Features' correlations with TTR were evaluated using Spearman correlation analysis and COX proportional hazards regression model. Univariate and multivariate analysis was used to estimate significant predictor for recurrent patterns.

Results

Sixty-five patients were involved, 30 VASARI features and two recurrent patterns (local and distant) were defined. Four VASARI features including multifocal, enhancing tumor crosses midline, satellites and lesion size correlated with TTR (r=-0.326, -0.264, -0.383, 0.425, respectively, P<0.05) and multivariate analysis confirmed satellites as a significant indicator for shorter TTR (OR=0.281, P=0.014), independent of age, KPS and chemoradiotherapy. Univariate analysis revealed significant differences of

proportion necrosis, definition of the nonenhancing, cortical involvement between two recurrent patterns ($Z=-2.337, -2.235, -2.350$, respectively, $P<0.05$). On multivariate regression analysis, proportion necrosis was an independent predictor for "distant" recurrence ($OR=0.461, P=0.034$).

Conclusions

VASARI features associated with recurrent GBM patterns and TTR and could be potential predictors for recurrent GBM prognostic outcomes.

O-303

4:10PM - 4:17PM

Use of Quantitative Diffusion-Weighted MR Imaging in Differentiating Between Glioblastoma and Primary Central Nervous System Lymphoma

C Stuart¹, P Rabiei¹, M Syed¹, L Ocasio², R Riascos¹, R Patel¹, C Cai¹, A Kamali¹

¹The University of Texas Health Science Center at Houston, Houston, TX, ²Memorial Hermann, Houston, TX

Purpose

In patients presenting with newly diagnosed brain tumors, it is important to differentiate between glioblastoma and primary central nervous system (CNS) lymphoma on initial imaging because the treatment regimen is markedly different. Our aim was to examine the role of quantitative diffusion-weighted imaging (DWI) in distinguishing these two entities.

Materials and Methods

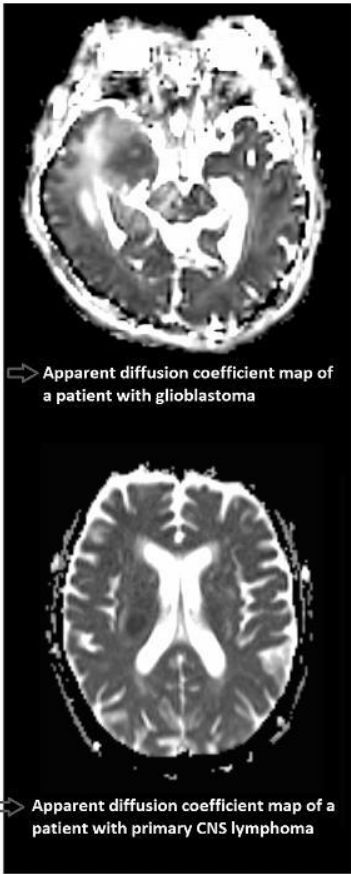
This retrospective study examined two groups: 42 patients with pathology proven glioblastoma and 30 patients with pathology proven primary CNS lymphoma referred to Memorial Hermann hospital at the Texas Medical Center from 2014-2017. The intratumoral foci with the greatest degree of restricted diffusivity underwent quantitative apparent diffusion coefficient (ADC) measurement by region of interest (ROI) placement in Centricity by two blinded interpreters. The ROIs were placed to avoid volume averaging with necrotic, cystic, or hemorrhagic components of the tumor utilizing complementary MR sequences (T1WI, T1WI-postcontrast, SWI, and T2WI). Median ADC values were compared with the Wilcoxon Rank-Sum Test. Patient ages and genders in the two groups were compared with two-sample t-test and Chi-square test, respectively. ROI areas between the interpreters were compared with the Wilcoxon Rank-Sum Test.

Results

Between the two groups there was no statistically significant difference in patient age (p -value=0.37) or gender (p -value=0.06). Between the two interpreters there was a significant difference in ROI area which did not impact the results. The median ADC values (averaged between two interpreters) in the primary CNS lymphoma group was significantly lower than the median ADC value in the glioblastoma group (p -value<0.0001). The median ADC values (lower quartile-upper quartile) were 582 (511-687) for the lymphoma group and 789 (734-896) for the glioblastoma group.

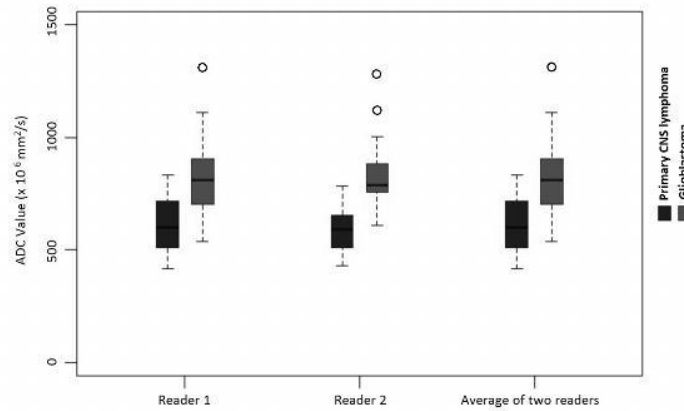
Conclusions

Quantitative diffusion-weighted MR imaging can aid diagnostic accuracy when attempting to differentiate glioblastoma and primary CNS lymphoma.



(Lower Quartile-Upper Quartile), Median (x10 ⁶ mm ² /s)		Primary CNS lymphoma	Glioblastoma	P-Value*
Reader 1	Min ADC	(461-662), 574	(640-811), 719	P<0.05
	Avg ADC	(510-718), 599	(705-904), 811	
Reader 2	Min ADC	(458-580), 525	(708-784), 751	P<0.05
	Avg ADC	(508-654), 589	(758-881), 789	
Average of 2 Reads	Min ADC	(471-614), 558	(678-802), 733	P<0.05
	Avg ADC	(511-687), 582	(734-896), 789	

⇒ Comparison of intra-tumoral ADC values between glioblastoma and primary CNS lymphoma
* Wilcoxon Rank-Sum Test



⇒ Distribution of ADC values(Avg.) in glioblastoma vs primary CNS lymphoma

(Filename: TCT_O-303_Graphic_File_GBM_vs_LYM_700dpi.jpg)

O-304

4:17PM - 4:24PM

ADC edge metrics in the differentiation of PCNSL from GBM

S Mills¹, M Jenkinson²

¹The Walton Centre NHS Foundation Trust, Liverpool, Merseyside, England, ²University of Liverpool, Liverpool, Merseyside, England

Purpose

Primary central nervous system lymphoma (PCNSL) has an incidence of 0.5 per 100,000 people. Radiologically it can be difficult to distinguish from glioblastoma multiforme (GBM) on conventional sequences. ADC measures are thought to reflect a surrogate of tumor cellularity. PCNSL and GBM both have increased tumor cellularity but GBM tumor edges are more ill-defined histologically with tumor cells extending way beyond the contrast-enhancing edge seen on imaging. The aim of this study was to assess the role of ADC measurement at the tumor edge in distinguishing GBM from PCNSL.

Materials and Methods

Patients were identified retrospectively from the histology database. Preoperative diffusion-weighted images from 20 patients with biopsy proven PCNSL and 20 patients with biopsy proven GBM were reviewed. For each patient, four adjacent ADC measures were made across the enhancing edge of the tumor border were made; two within the enhancing component and two within the peri-tumoral region (Figure 1). The gradient of the ADC transition (the ADC transition coefficient, ATC) was measured. An unpaired t test was performed to compare this metric between GBM and PCNSL.

Results

Mean ATC for PCNSL (230.07, range 60.5 to 407.5, SEM 23.011) was significantly higher than those with GBM (29.495, range -365.2 to 188.1, SEM 31.72), $t = -5.118$ and $p < 0.001$ (Figure 2). There was no difference in age or sex distribution between the two groups ($p=0.368$ and 0.731 respectively).

Conclusions

Evaluating the edge of the enhancing tumor with ADC using ATC, shows potential as a metric for differentiating GBM from PCNSL.

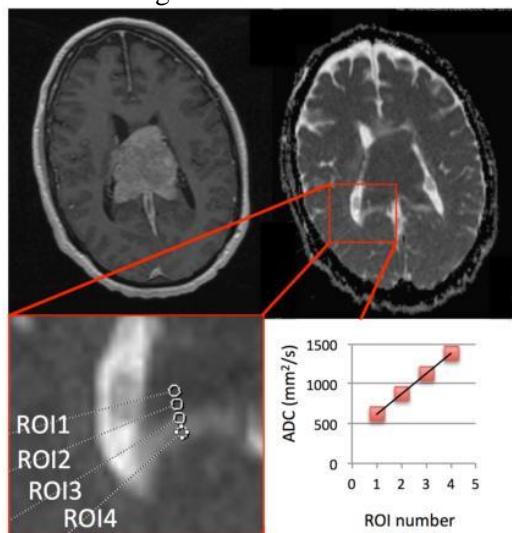


Figure 1. Post gadolinium contrast T1 weighted imaging and ADC maps with regions of interest distributed across the edge. Enlarged image from the ADC map showing the separate ROIs. Example measures of single PCNSL case calculation of ATC (ADC transitional coefficient - slope of the plotted line).

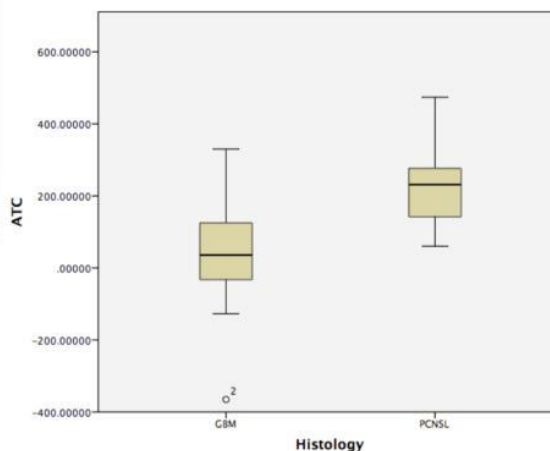


Figure 2. Box and whisker plot of ATC measures for GBM and PCNSL.

(Filename: TCT_O-304_PCNSL_ATC_ASNR2018.jpg)

Tuesday, June 5, 2018

3:00PM - 4:30PM

Parallel Paper Session: Brain: Inflammatory and Infectious Diseases

O-305

3:00PM - 3:07PM

Cerebrovascular Manifestations in Neurosarcoidosis at Presentation and Follow up: An Under-recognized Spectrum of the Imaging Manifestation.

G BATHLA¹, P Watal², N Soni³, A Capizzano⁴, T Moritani⁴

¹University of Iowa hospitals and Clinics, IOWA CITY, IA, ²University of Iowa hospitals and Clinics, iowa city, IA, ³UIHC, iowa, IA, ⁴University of Iowa Hospitals and Clinics, Iowa City, IA

Purpose

To determine the occurrence of ischemic and hemorrhagic events in patients with Neurosarcoidosis at presentation and on follow-up

Oral Presentations & Excerptas

Materials and Methods

We retrospectively reviewed the MR imaging findings in Neurosarcoidosis [NS] patients who presented to a single tertiary care center from 2002 through 2017, with emphasis on cerebrovascular events [CVE]. The study was IRB approved. Images were coanalyzed by two fellowship-trained neuroradiologists with greater than 15 years of experience in neuroimaging.

Results

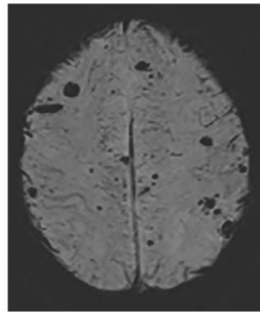
A total of 49 patients were analyzed. There were 32 females and 17 males. All patients had MRI brain study at presentation, either at a 1.5 or a 3T system. Per Zajicek criteria, 11 patients were definite, 34 were 'probable', while four patients were 'possible' NS. Ischemic events occurred in four patients at presentation while parenchymal hemorrhages occurred in three patients. The combined occurrence of CVE at presentation was 14% [8% for ischemic events, 6% for hemorrhagic events]. On follow up, three additional patients developed ischemic infarcts, of which, one patient had parenchymal hemorrhage at presentation. Additionally, one patient also developed new parenchymal hemorrhages. In total, 10 patients in current cohort developed CVE, either at presentation or on follow up [seven with ischemic events and four with hemorrhagic events, of which one patient had both ischemic and hemorrhagic events]. All patients with parenchymal hemorrhages had subcortical involvement with sparing of the basal ganglia. Patients with CVE had a higher incidence of perivascular enhancement that NS patients without CVE.

Conclusions

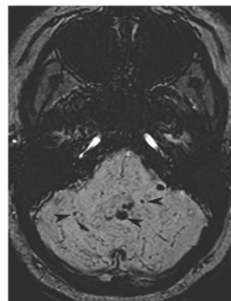
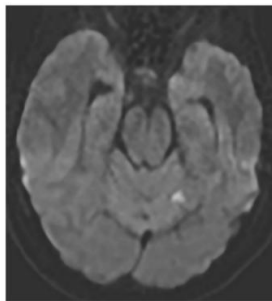
CVE occurs in a significant number of patients with NS but continues to be a less well appreciated manifestation of NS. The likely reason is less prevalent use of MR imaging in the previously described studies, lack of awareness and improvement in imaging techniques over the years. These should be actively sought in patients with NS, given the higher morbidity in such cases.



Pt-1 with infarct



Pt -2 with bleeds



Pt-3 with infarcts and bleeds

(Filename: TCT_O-305_ASNRabstractimages-1.jpg)

O-306

3:07PM - 3:14PM

Imaging Findings in Neurosarcoidosis at Presentation: Looking at the Bigger Picture

G BATHLA¹, P Watal², N Soni³, A Capizzano⁴, T Moritani⁴

Oral Presentations & Excerptas

¹University of Iowa hospitals and Clinics, IOWA CITY, IA, ²University of Iowa hospitals and Clinics, iowa city, IA, ³UIHC, iowa, IA, ⁴University of Iowa Hospitals and Clinics, Iowa City, IA

Purpose

The aim of the study was to determine the incidence of various imaging findings in patients with Neurosarcoidosis [NS] at presentation.

Materials and Methods

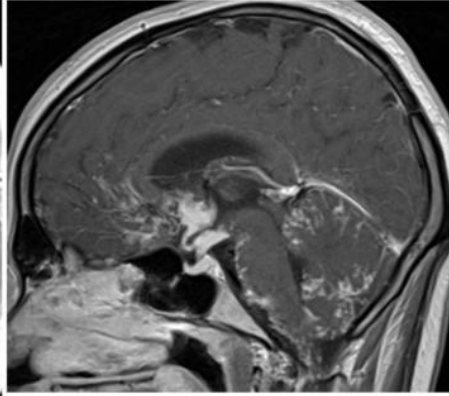
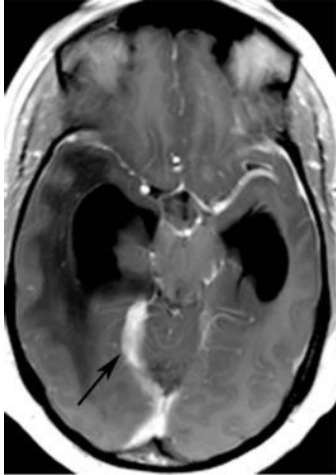
We retrospectively reviewed the MR imaging findings in Neurosarcoidosis [NS] patients who presented to a single-tertiary care center from 2002 through 2017. Images were coanalyzed by two fellowship trained neuroradiologists with greater than 15 years of experience in neuroimaging.

Results

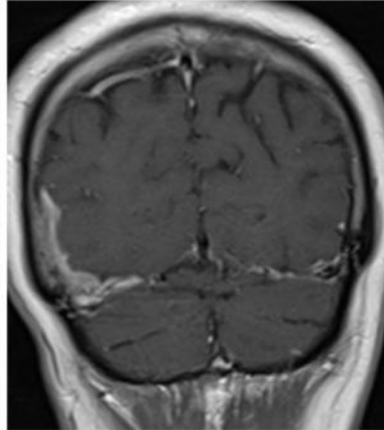
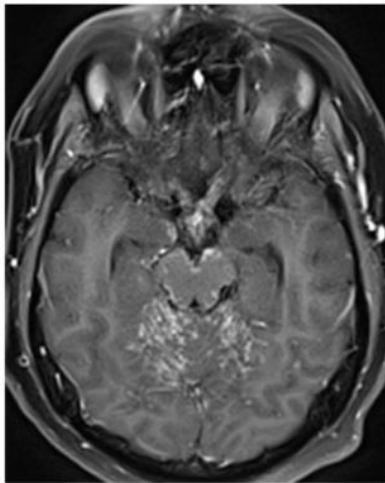
A total of 49 patients were evaluated. All patients had MRI brain study at presentation, either at a 1.5 or a 3T system. Eight patients had whole spine MRI studies, while an additional 10 patients had some spine imaging at presentation. The mean age at presentation was 46 years (Age range 14-75) with 17 males and 32 females. Per Zajicek criteria, 11 patients were definite, 34 were 'probable', while four patients were 'possible' NS. Most of the patients had evidence of extra-CNS involvement (81%), while nine patients (19%) had isolated CNS involvement. Positive imaging findings on MRI of the brain were noted in 82% of patients. In order of decreasing frequency, following imaging manifestations were noted: Periventricular WM changes [49%], meningitis [41%], cranial nerve involvement [41%], pachymeningeal involvement [31%], parenchymal granulomas [20%], cerebrovascular events [14%], bone involvement [10%], HPA axis involvement [10%], hydrocephalus [8%] and choroid plexus involvement [4%]. Involvement of the spinal cord was noted in over half [56%] of the patients who underwent spinal imaging at presentation.

Conclusions

The imaging findings in NS are often nonspecific but are seen in a large proportion of patients. Some of these were not well recognized previously [cerebrovascular events, bone and choroid plexus involvement] while some were underestimated [spinal involvement, WM lesions], likely due to less frequent use of MR imaging in the previously described studies. The imaging spectrum in NS continues to expand.



Hydrocephalus and dural inv
HPA axis involvement



Dural involv
Meningeal and CN involv

(Filename: TCT_O-306_ASNRabstractimages-2.jpg)

O-307

3:14PM - 3:21PM

Brain Imaging in Serology Positive Dengue Cases with Neurological Symptoms – a Clinico-radiological Correlation.

H Vanjare¹, P Mannam¹, S Mani¹

¹Christian Medical College and Hospital, Vellore, Vellore, Tamil Nadu, India

Purpose

Dengue is the second most common mosquito borne arboviral disease (1). There is recent surge in dengue cases and it has been reported from more than 100 countries (2). Fifty-million cases are estimated to occur globally per year (1). Neurological involvement in dengue infection is uncommon [4-5%] (3-5) and there is inadequate imaging literature in this field. The aim of the study was to describe brain imaging findings in cases with dengue infection having neurological symptoms and assess predictors for poor outcome.

Materials and Methods

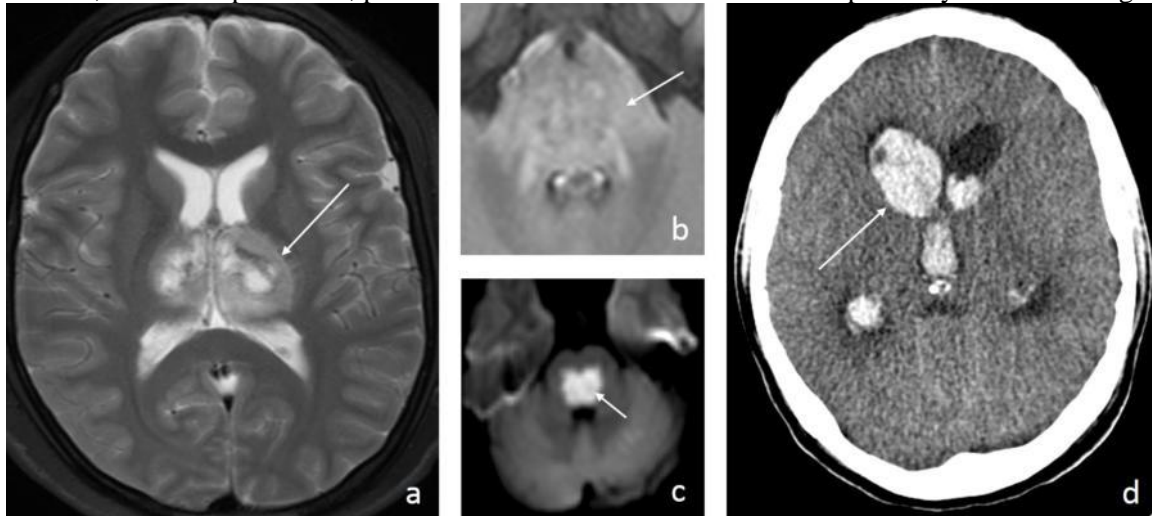
A single-center retrospective chart review was done with the cases identified using the radiology department's case database. Thirty-five cases with acute dengue infection with symptoms suggestive of CNS involvement undergoing imaging of the brain were included in the study (duration 2006 to 2017). Clinical, laboratory and imaging parameters were assessed and correlated for poor outcome.

Results

GCS less than or equal to 12 at presentation, WHO (2009) classification of dengue into severe type and presence of acute renal failure had significant association for poor outcome (p-value 0.04, 0.02 and 0.03 respectively). Imaging parameters which had significant association for poor outcome were thalamic involvement (p-value 0.005, image a), cerebellar peduncle involvement (p-value 0.01, image b), presence of diffusion restriction (p-value 0.01, image c) and presence of hemorrhage (p-value 0.003, image d).

Conclusions

Although accurate identification of dengue infection related brain changes cannot be made purely based on imaging findings; the differential diagnosis can be significantly reduced. With the additional input of typical clinical presentation, thrombocytopenia and local prevalence of the disease, one can not only suggest the possibility of dengue infection but can also help in prognosis based on involvement of thalami, cerebellar peduncles, presence of diffusion restriction and intraparenchymal hemorrhage.



(Filename: TCT_O-307_Harshaddengue.jpg)

O-308

3:21PM - 3:28PM

Alterations in BBB Permeability in Antineuronal Antibody-Positive Lupus Patients.

J Ivanidze¹, M Mackay², B Diamond², B Volpe², A Hoang³, P Sanelli³

¹New York Presbyterian Hospital Cornell, New York, NY, ²Donald and Barbara Zucker School of Medicine at Hofstra/Northwell, Manhasset, NY, ³Northwell Health, Manhasset, NY

Purpose

Cognitive impairment occurs in systemic lupus erythematosus (SLE), associated with antineuronal antibodies targeting NMDA receptors (DNRAb), which cross the blood brain barrier (BBB). Changes in BBB permeability (BBBP) appear to precede structural changes and clinical deterioration in SLE. In view of our prior work that demonstrated abnormal brain metabolism on FDG-PET involving the hippocampi and frontal cortex which correlated with cognitive decline in SLE, we hypothesized that alterations in BBBP are also seen in these same brain regions.

Materials and Methods

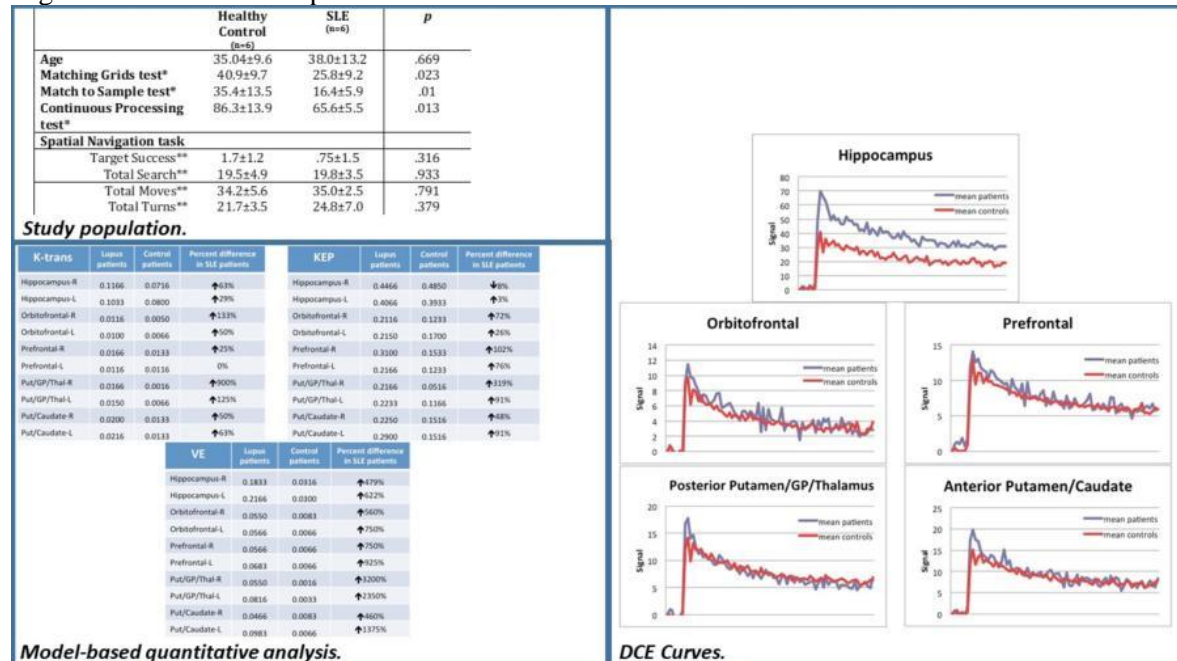
IRB-approved recruitment of SLE patients and healthy controls to undergo neuropsychiatric testing and DCE-MRI on a 3T Siemens magnet. Standardized postprocessing into BBBP parameters (K-trans, KEP, VE) was performed using Olea Sphere software (Tofts and Kermod model). ROI sampling the hippocampus, orbitofrontal and prefrontal cortex, posterior putamen/globus pallidus/thalamus, and anterior putamen/caudate was performed. Demographic and testing differences between the SLE and HC groups were calculated using the Student's t-test. Descriptive statistics were calculated for SLE patients and controls for each region and each BBBP parameter. The percent difference between SLE patients and controls was computed.

Results

Six SLE and six control subjects were enrolled. No significant group differences for age; however, SLE patients performed significantly worse than the controls on the cognitive testing (Table 1). Though not statistically significant, SLE patients also performed worse on the spatial navigation task. DCE-MRI demonstrates increased hippocampal permeability in SLE patients (Figure 1). Additional model-based quantitative analysis revealed consistently elevated K-trans, KEP and VE in almost all of the brain regions in SLE patients (Figure 2).

Conclusions

DCE-MRI demonstrated increased permeability in the hippocampus, frontal cortex and deep gray matter in SLE with cognitive impairment, compared to controls, representing the same regions of abnormal metabolism on FDG-PET. Further investigations will explore the role of BBBP in the pathophysiology of cognitive decline in SLE patients.



(Filename: TCT_O-308_Lupus-Figures.jpg)

O-309

3:28PM - 3:35PM

White matter cellularity change and its association with CSF β -amyloid in preclinical and early symptomatic AD

Q Wang¹, Y Wang¹, J Shimony², B Ances¹, C Sutphen¹, A Fagan¹, C Cruchaga¹, T Benzinger¹

¹Washington University in St. Louis, St. Louis, MO, ²Washington University School of Medicine, Saint Louis, MO

Purpose

Innate immune cells, particularly microglia and astrocytes, have been reported to mediate the inflammatory response in Alzheimer disease (AD) and are considered a significant contributor to AD pathogenesis. In the AD brain, A β deposition and neurofibrillary tangles provide obvious stimuli for neuroinflammation [1]. This study aims to investigate the relationship between the CSF β -amyloid (A β 42) (a marker of A β deposition) and white-matter cellularity change (reflecting immune cell activation) in presymptomatic and early symptomatic AD using neuroimmune imaging (NII) based on previous success of diffusion-basis spectrum imaging (DBSI) in neurodegenerative diseases [2, 3].

Materials and Methods

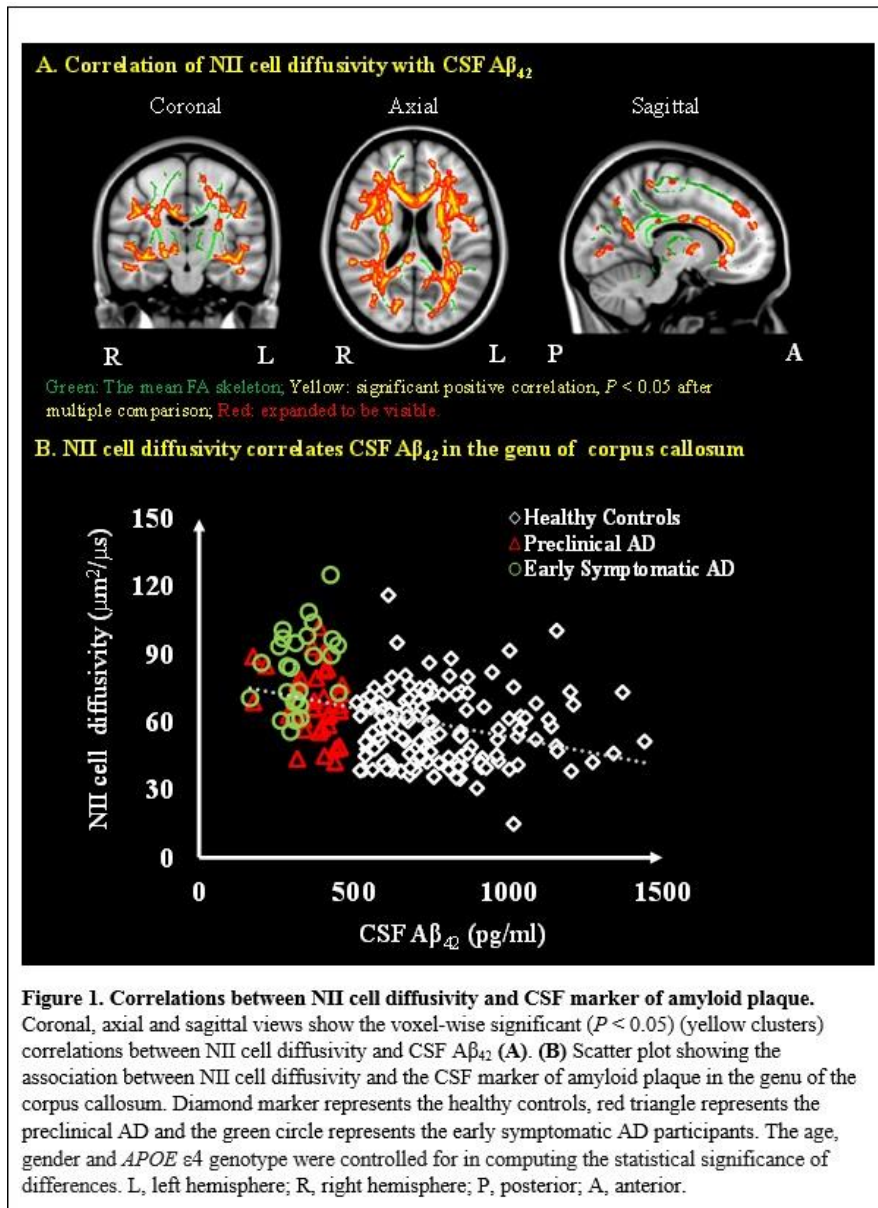
We used cerebrospinal fluid (CSF) biomarkers (for β -amyloid plaques and neuronal injury) and NII to evaluate three groups of preclinical and early symptomatic AD patients: (1) 140 cognitively normal healthy controls who were biomarker-negative by A β 42 and total tau (t-tau); (2) 34 cognitively normal participants with preclinical AD who were biomarker-positive by CSF A β 42; and (3) 26 cognitively impaired participants who were biomarker-positive by CSF A β 42. NII was acquired with multi-b value scheme (bmax =1400s/mm² and 23 directions). NII cell diffusivity (reflecting inflammatory cell activation) was quantified by solving the NII model.

Results

NII cell diffusivity in major WM tracts was negatively correlated with CSF levels of A β 42 (Fig. 1) when analyzed across all groups. The mean NII cell diffusivity from the cluster located in the genu of corpus callosum were extracted. As an estimate of effect size, partial correlations were also examined between the NII imaging marker and CSF A β 42. When controlling with age, gender and APOE ϵ 4 genotype, the partial correlation with CSF A β 42 was $r_{\text{partial}} = -0.39$ ($P < 0.001$) for NII cell diffusivity.

Conclusions

The significant negative correlation between NII cell diffusivity and CSF A β 42 suggests NII may be used to track the activation of microglia associated with abnormal β -amyloid accumulation. NII holds promise to noninvasively study the role of inflammation during AD progression and the effect of treatments targeting immune response.



(Filename: TCT_O-309_Figure1.jpg)

O-310

3:35PM - 3:42PM

Brain Microstructure Changes Revealed by Diffusional Kurtosis Imaging and Cognitive Impairment in Cirrhotic Patients without Overt Hepatic Encephalopathy

H Chen¹

¹Fujian Medical University Union Hospital, Fuzhou, Fujian, China

Purpose

Brain morphological abnormalities have been well identified in cirrhotic patients, whose condition concomitantly involves gray matter (GM) and white matter (WM). Diffusion-tensor imaging (DTI) is the most frequently used MR diffusion-weighted technique for evaluating cirrhosis-related changes in the

Oral Presentations & Excerptas

cerebral microstructure. Notably, all of these previous studies were based on the conventional DTI technique, which assumes the water diffusion to be a Gaussian distribution. As a natural extension of diffusion-tensor imaging, the diffusional-kurtosis imaging (DKI) method employs multiple b-values to quantify non-Gaussian diffusion by estimating the excess kurtosis of the displacement distribution, in which both standard DTI parameters and kurtosis parameters--including mean kurtosis (MK), axial kurtosis (K_{\parallel}), and radial kurtosis (K_{\perp})--could be obtained. Thus, by taking into account the fundamentally non-Gaussian property of water diffusion in biological tissue, DKI can function as a complementary technique to the conventional DTI to more fully depict the characterization of brain tissue microstructure. The kurtosis metrics are believed to reflect the heterogeneity of the intravoxel diffusion environment and are thus indicators of microstructural complexity. Moreover, DKI permits the characterization of microstructural integrity in both GM and WM. Thus, DKI provides an opportunity for not only WM region exploration, as in previous DTI studies, but for whole-brain exploration of microstructural abnormalities in cirrhosis. DKI is thought to exhibit improved sensitivity and specificity in detecting changes in neural tissues. Thus, the goal of the present study was to employ DKI to investigate the changes in both GM and WM microstructure in cirrhotic patients using a voxel-based analysis. The relationship between brain microstructural abnormalities and cognitive performance was also examined.

Materials and Methods

This study included 18 cirrhotic patients without overt hepatic encephalopathy (HE) and 17 healthy controls who underwent diffusion imaging. There were no significant differences between control and patient groups, in terms of age (50.1 ± 11.9 years vs. 52.7 ± 9.9 years, $P = 0.487$), sex (14 males and 3 females vs 16 males and 2 females, $P = 0.658$), or education level (9.9 ± 3.8 years vs 8.8 ± 2.8 years, $P = 0.293$). Cognition was measured using Psychometric Hepatic Encephalopathy Score (PHES). Whole-brain voxel-based analyses (VBA) were performed to investigate between-group differences in DKI-derived parameters, including MK, K_{\parallel} , and K_{\perp} . The global GM and WM DKI-metrics were computed for each cirrhotic patient. Spearman correlation analyses were performed to measure the relationships between the DKI variables and cognitive performance in cirrhotic patients.

Results

The cirrhotic patients had worse performance in all five PHES subtests and lower PHES score than the healthy controls (-3.3 ± 4.8 vs 0.6 ± 1.6 , $P = 0.004$), indicating cognitive impairments. The cirrhotic patients had significantly lower global MK, K_{\parallel} , and K_{\perp} in GM and WM. VBA showed that cirrhotic patients had decreased MK, K_{\parallel} , and K_{\perp} in diffuse GM regions (particularly in cingulate cortex, precuneus, insular cortex, frontal areas, basal ganglia, hippocampus/parahippocampal gyrus, supramarginal gyrus and angular gyrus, postcentral and precentral gyrus, and cerebellum) and WM regions (particularly in corpus callosum, internal capsule, frontal regions, parietal regions, occipital regions, and cerebellum). The correlation analysis showed that the average GM MK ($r = 0.474$, $P = 0.047$), K_{\parallel} ($r = 0.470$, $P = 0.048$), and K_{\perp} ($r = 0.495$, $P = 0.039$) were positively correlated with PHES score in cirrhotic patients. Also, the mean WM MK ($r = 0.581$, $P = 0.011$), K_{\parallel} ($r = 0.501$, $P = 0.034$), and K_{\perp} ($r = 0.615$, $P = 0.007$) were significantly correlated with PHES score.

Conclusions

The present study outlined whole-brain microstructural abnormalities in cirrhotic patients without overt HE, which were diffusely distributed in both GM and WM regions. Lower diffusional kurtosis parameters suggest decreased brain microstructural complexity in cirrhotic patients. The altered microstructural properties of both GM and WM were correlated with the cognitive performance of patients, suggesting the potential of these metrics to serve as biomarkers for early diagnosis of HE. DKI can provide supplementary information for characterizing brain structural abnormalities in cirrhosis.

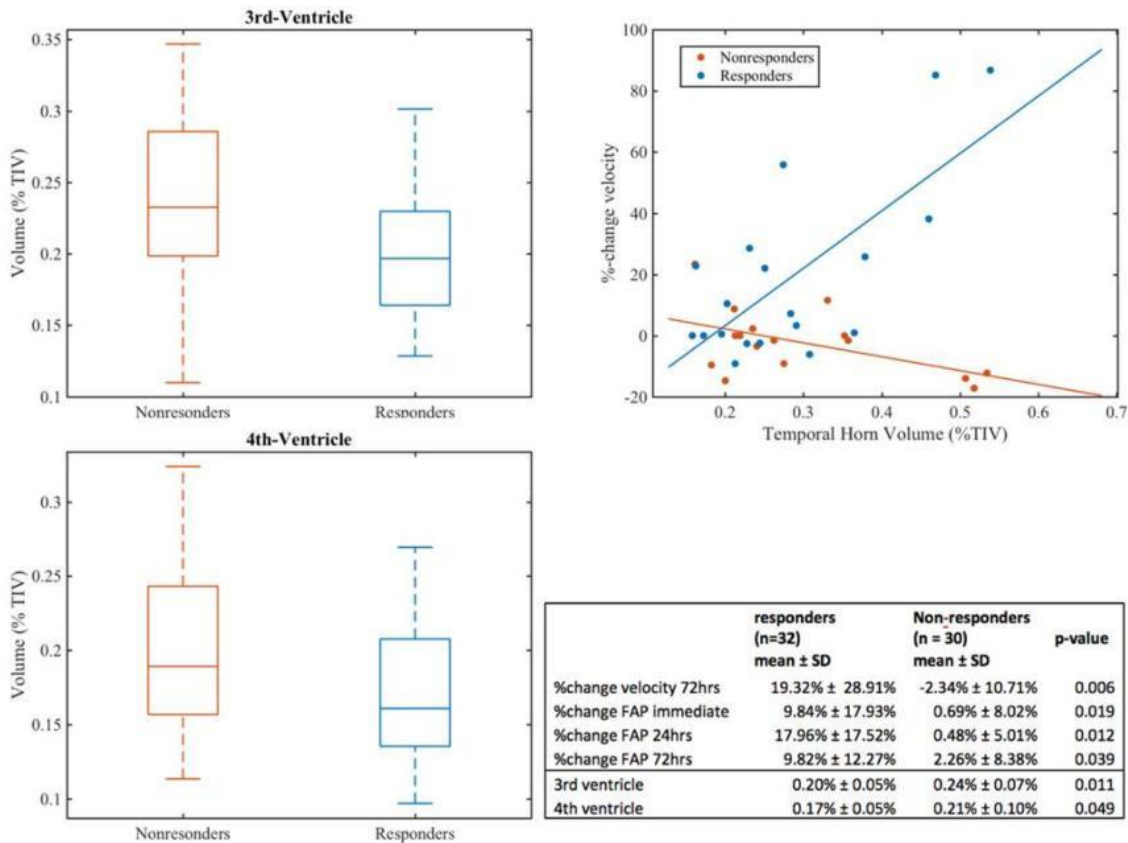


Figure legend: left). Box-plots demonstrating significant differences in third and fourth ventricle volumes between responders and non-responders. Right-top). Linear regression plot showing correlations between % velocity change (y axis) and temporal horn volume (x axis) in responders versus non-responders. Right-bottom) table providing means and p-values for t-test results.

(Filename: TCT_O-311_ASNRfinalfigure.jpg)

O-314

4:03PM - 4:10PM

Multimodal MRI Staging Improves Clinico-Imaging Correlations in sJCD.

S Sacco¹, E Caverzasi¹, M Paoletti², A Staffaroni¹, I Allen¹, G Marx¹, J Kramer³, S Bastianello⁴, R Henry¹, H Rosen³, M Geschwind³

¹University of California San Francisco, San Francisco, CA, ²Institute of Radiology, University of Pavia, Pavia, Italy, ³University of Pavia, Pavia, Italy, ⁴University of Pavia, Pavia, Italy

Purpose

We have shown that focal change in mean diffusivity (MD) over time in sporadic Jakob-Creutzfeldt disease (sJCD) follows J-shaped curve, with initial gray-matter (GM) MD reduction, followed by a progressive MD increase. [1] This pattern might be related to changes in the vacuole size and/or atrophy. To test this hypothesis and to better track MRI changes in sJCD, we developed a model combining MD and volume loss (Volume-MD staging) and tested its correlation with clinical deficits.

Materials and Methods

Using HARDI and high-resolution T1 imaging, average MD and volume for GM regions of interest (ROIs; Desikan atlas) were extracted in 37 sJCD cases. MD and Volume Z-scores were computed using 30 age/gender-matched healthy controls to classify sJCD ROIs as involved or not (statistical threshold MD +/- 2SD, Volume -2SD). ROIs were Volume-MD staged as: 0=no abnormalities; 1=decreased MD

only; 2=decreased MD and volume; 3=normal "pseudo-normalized" MD, decreased volume; 4=increased MD, decreased volume. We correlated Volume, MD and Volume-MD stage with clinical scales at total, cortical, subcortical and cerebellar GM level, as well as with clinical signs/symptoms using prespecified ROIs.

Results

ROI volume loss generally correlated with lower MMSE and lower Barthel, but did not correlate with any specific signs/symptoms. Increasing MD correlated with worse MMSE and Barthel in cortical and cerebellar GM, but decreasing subcortical MD correlated with worse neuropsychiatric symptoms and contralateral extrapyramidal symptoms, and decreasing primary sensory cortex MD correlated with higher-level cortical sensory deficits (astereognosis and asterographia). More advanced Volume-MD stages generally correlated better than Volume or MD alone with lower MMSE and lower Barthel and also showed correlations with pyramidal, higher cortical sensory, executive and visual-spatial deficits.

Conclusions

A Volume-MD staging overall correlated better with clinical deficits than MD or volume alone. Models tracking sJCD progression should account for both changes in MD and volume loss.

O-315

4:10PM - 4:17PM

Acute Toxic Leukoencephalopathy: Etiologies, Imaging Findings and Outcomes in 100 Patients

C Ozutemiz¹, S Khanipour Roshan¹, N Kroll², J Rykken¹, M Oswood³, L Zhang⁴, A McKinney¹

¹University of Minnesota, Minneapolis, MN, ²University of Minnesota, School of Medicine, Minneapolis, MN, ³Hennepin County Medical Center, Minneapolis, MN, ⁴Clinical and Translational Science Institute, University of Minnesota, Minneapolis, MN

Purpose

To further describe causes of ATL, and to evaluate differences in imaging severity and clinical outcomes amongst different etiologies of acute toxic leukoencephalopathy (ATL)

Materials and Methods

Based on searching MRI reports between June 2002 - June 2017, 100 ATL patients were included with: 1) an MRI <three weeks of presentation and 2) DWI/FLAIR with ADC. The MRI severity on DWI and FLAIR was jointly graded by two neuroradiologists (previously described system). The clinical outcome was assessed via both the modified Rankin scale (mRS) and ATL outcome score (ATLOS). Etiologic subcategories composed of n>6 patients were identified for statistical comparison, to compare between subgroups regarding the DWI and FLAIR severity, mRS and ATLOS, as well as to correlate between DWI and FLAIR severity with both mRS and ATLOS.

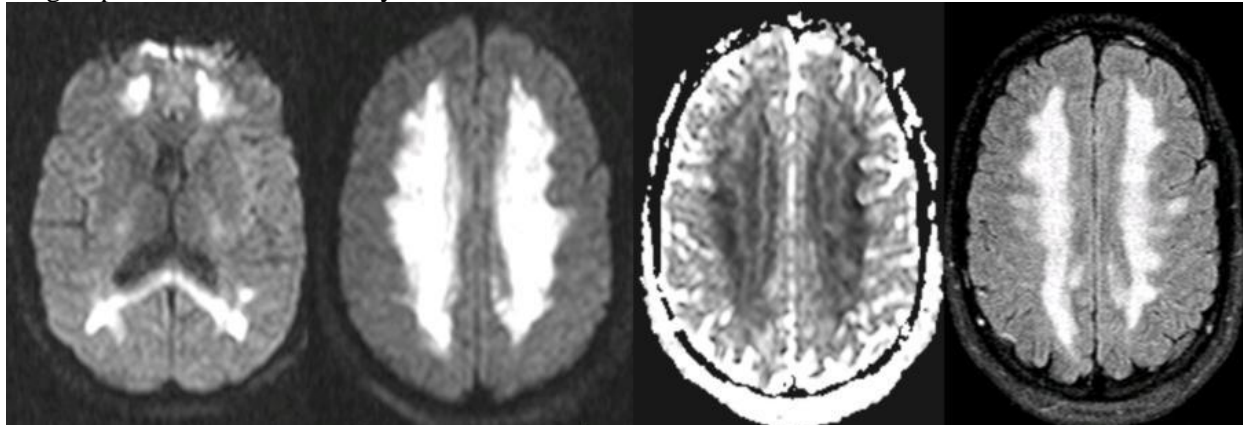
Results

Of 100 patients, the ATL subcategories having n>6 were chemotherapy (n=35), opiates (n=19), acute hepatic encephalopathy (AHE, n=14), and immunosuppressants (n=11). Other etiologies were carbon monoxide (n=3) and other various or idiopathic causes (n=18 total). Regarding MRI severity, the opiates subgroup was overall significantly more severe on DWI versus the immunosuppressant (p=0.003) and AHE (p=0.003) subgroups, while being more severe on FLAIR versus the AHE (p=0.003) and chemotherapeutics (p=0.006) subgroups. Regarding outcome, there were significant differences between chemotherapeutics and immunosuppressants for the mRS and ATLOS scores (p=0.004-0.006), and between opiate and immunosuppressant subgroups regarding the mRS only (p=0.007); the remaining comparisons between subgroups did not have significant differences in outcomes (each p>0.05). For all 100 patients, both DWI and FLAIR severities correlated with outcomes (rho=0.289-0.350, each p<0.01), with the opiates subgroup having the strongest correlation (rho=0.473-0.609, p<0.01).

Conclusions

Chemotherapeutic toxicity seems the most common and reversible ATL etiology. In contrast, the opiates

subgroup has relatively more severe MRI findings, and has the strongest correlations of the ATL subgroups between MRI severity and outcomes.



(Filename: TCT_O-315_Picture1.jpg)

O-316

4:17PM - 4:24PM

Insoluble Gd salts may increase T1 signal in deep brain nuclei and other tissues

T Anderson¹, K Maravilla¹, J Gatenby¹
¹University of Washington, Seattle, WA

Purpose

Since Kanda first described T1 signal increase (T1SI) in deep-brain nuclei of patients receiving multiple injections of linear Gd-based contrast agents (GBCA), there has been much interest regarding the form(s) of Gd responsible. Studies from Xia and McDonald have demonstrated insoluble deposits of GdPO₄ in such patients' surgical or autopsy brain tissues, respectively. Multiple investigators have rejected this species of Gd as a possible cause of T1SI. The purpose of this study was to determine if Gd salts could result in T1SI. We postulated that solid inorganic Gd salts would lead to T1SI due to water interaction with Gd at the crystal surface.

Materials and Methods

GdPO₄ was suspended in buffered 5% agarose at concentrations between 0.032-3.2 $\mu\text{mol Gd/cc}$ (5-500 $\mu\text{g Gd/cc}$) simulating concentrations of Gd found in skin of NSF patients and in deep-brain nuclei of patients with T1SI. Similar concentrations of gadoteridol (ProHance®) in buffered 5% agarose were prepared, along with control samples of water, aqueous buffer, and buffered 5% agarose. Average particle size was measured for each Gd salt using laser diffraction. Samples were imaged at 3T with IR SE images at varying inversion times (≥ 10 inversion times for each sample, ranging from 50-300 ms). R1 ($1/T1$) was calculated for each Gd and gadoteridol concentration and relaxivities ($r1$, $\text{L}\cdot\text{mM}^{-1}\cdot\text{sec}^{-1}$) were calculated from R1 values. Signal intensities of samples at 50 $\mu\text{g Gd/cc}$ were measured and compared to buffered 5% agarose to calculate a percent signal enhancement.

Results

Samples containing GdPO₄ showed significant T1SI compared to controls, indicating an enhancement effect from water interacting with Gd at the surface of the salt crystal. The percent enhancement for GdPO₄ measured 47%. Average particle size of our GdPO₄ samples was 4.8 μm and $r1$ value was 0.43 $\text{L}\cdot\text{mM}^{-1}\cdot\text{sec}^{-1}$. By comparison, our calculated $r1$ for gadoteridol was 4.23 $\text{L}\cdot\text{mM}^{-1}\cdot\text{sec}^{-1}$, which agrees well with literature values.

Conclusions

Solid GdPO₄ with particle size $\sim 5 \mu\text{m}$ leads to significant T1SI when suspended in buffered 5% agarose, with 47% enhancement. In vivo, much smaller particle sizes of $\leq 1 \mu\text{m}$ have been reported and are

therefore expected to demonstrate even greater enhancement . Thus, Gd salts formed from transmetalation of linear GBCA may be contributing to T1SI in deep-brain nuclei of patients who have undergone multiple GBCA-enhanced MRI scans.

Tuesday, June 5, 2018

4:45PM - 6:15PM

Parallel Paper Session: Advanced Diagnostic Techniques in Cerebral Aneurysms and AVMs

O-317

4:45PM - 4:52PM

How Good is CTA in Detecting Blood Blister Aneurysms? Our 12 Years Experience.

R Ashmawy¹, T Marotta², L Noël de Tilly²

¹University of Toronto and St. Michael's Hospital, Toronto, Ontario, Canada, ²St. Michael's Hospital, Toronto, Ontario, Canada

Purpose

Blood-blister aneurysms (BBAs) pose diagnostic and therapeutic challenges due to wall friability, unusual morphology, and location. Interventions used for management of BBAs are evolving and vary by institution. Due to poor natural history of BBAs, prompt diagnosis on the initial computed tomography angiography (CTA) is of utmost importance to guide the management. Previous utility of CTA was presented in a publication of only a small number of BBAs (six cases) and they were all on internal carotid arteries (ICA).

Materials and Methods

We searched our databases for the term "blister aneurysm" for 12-year period. The cases that were included had the following criteria: at least one CTA before the performance of the digital subtraction angiography (DSA), the aneurysm did not arise at a branching point, and it had a wide neck and shallow dome. The CT reports (if available) were reviewed to assess whether the diagnosis was indicated prospectively. If not, the study was assessed retrospectively for the diagnosis. All cerebral angiograms were reviewed by two trained neuroradiologists to confirm blister configuration of the BBAs.

Results

Seventeen cases were included; 12 of the BBAs were in the supraclinoid ICA, three in the anterior communicating artery, one in a middle cerebral artery, and one in an anterior cerebral artery. Of these 17 cases, 15 CTA reports were available and the diagnosis was made prospectively in 13 cases and retrospectively in one. For the two studies with no available report, the BBAs was also seen on the CTA.

Conclusions

BBAs are uncommon but serious cause of subarachnoid hemorrhage. Its diagnosis on CTA is achievable in most cases with careful review of the CTA in multiple planes as well as with 3-D reconstructions. The diagnosis of BBAs on CTA provides a clear road map for the next step of management.

O-318

4:52PM - 4:59PM

An Ultrafast Contrast Enhanced MRA for Grading Residual Aneurysm After Treatment: Comparison to Time-of-Flight (TOF) MRA and Digital Subtraction Angiography (DSA).

R Gupta¹, P Belani¹, R De Leacy¹, J Mocco¹, J Fifi², A Doshi¹, K Nael¹

¹Icahn School of Medicine at Mount Sinai, New York, NY, ²Mount Sinai Hospital, New York, NY

Purpose

Using Differential Subsampling with Cartesian Ordering (DISCO), an ultrafast high-spatial resolution head MRA has been introduced. We aimed to determine the diagnostic performance of DISCO-MRA in grading residual aneurysm in comparison to TOF-MRA and DSA in patients with treated intracranial aneurysms (IA).

Materials and Methods

The inclusion criteria were patients with IA who were treated with coil-embolization, and had DISCO-MRA, TOF-MRA and follow-up DSA. DISCO-MRA was performed using a gradient-echo sequence (TR/TE: 3.24/1.4 ms, FA 12°) and DISCO undersampling strategy (variable density k-space undersampling and view-sharing). 3D voxel-size of 0.75 x 0.75 x 1 mm³ was obtained during 6 sec acquisition covering the entire head. TOF-MRA was obtained with voxel size of 0.5 x .05 x 1 mm³ during six-minute acquisition time. TOF-MRA and DISCO-MRA were reviewed in two separate sessions by a neuroradiologist. DSA images were evaluated by a neuroradiology-trained interventionalist blinded to MRA data. Residual aneurysm was determined by using a Modified Raymond–Roy Classification (MRRC): Class I – complete obliteration, II – residual neck, IIIa – contrast in coil interstices, and IIIb – contrast along wall. Statistical analysis was performed using Kappa coefficients and the Chi-squared test.

Results

A total of 31 treated IAs in 29 patients (24 F, 5 M, average age of 58 ± 12 years) were included. The intermodality agreement (k, 95% CI) were: k =0.54, 95% CI 0.25 to 0.82 for DISCO vs. TOF; 0.57, 95% CI 0.30 to 0.84 for DISCO vs. DSA; and 0.23, 95% CI -0.028 to 0.48 for TOF vs. DSA. MRRC grading scores matched DSA scores in 20/31 for TOF-MRA (Chi-squared: 13.9, p = 0.03) and 25/31 when DISCO-MRA was used (Chi-squared: 39.0, p < 0.001).

Conclusions

In patients with treated IA, DISCO-MRA provides superior diagnostic performance in comparison to TOF-MRA for a more accurate delineation of residual aneurysm and in a fraction of the time.

O-319

4:59PM - 5:06PM

Efficacy of Virtual Reality for Clinical Education to Improve Detection of Intracranial Aneurysms

M Bayona¹, A Eastaway², C Sturge¹, S Banerjee¹, T Hutchins¹, J Cramer³, C Kilburg¹, P Tausky¹, E Quigley¹

¹University of Utah, Salt Lake City, UT, ²University of Utah, Sandy, UT, ³University of Nebraska Medical Center, Omaha, NE

Purpose

Increasing sophistication coupled with decreased cost of immersive head-mounted display technology such as Oculus and Vive VR systems, or even low-cost systems like Google Cardboard, have opened a new avenue for teaching residents and fellows about complicated anatomy and pathology. This technology has the added benefit that it is easily shared between academic institutions, allowing for widespread dissemination of rare pathology for education. This pilot study seeks to examine if virtualization of intracranial aneurysms is an effective and rapid way to improve resident ability to detect intracranial aneurysms.

Materials and Methods

An IRB-approved retrospective review of radiology studies with intracranial aneurysms was performed to determine the most common locations of aneurysms at our institution. Next, a high-quality model of a normal skull base, circle of Willis (COW), and brain were segmented using Mimics software. Using 3Matics and Meshmixer, simulated aneurysms were added, including creation of virtual pterional views of multilobular MCA aneurysms. Resident and medical student volunteers were randomly separated into two groups. After a pretest, the first group then underwent conventional didactic instruction regarding aneurysms. The second group was given an instructional session with the virtual models of aneurysms.

Oral Presentations & Excerpts

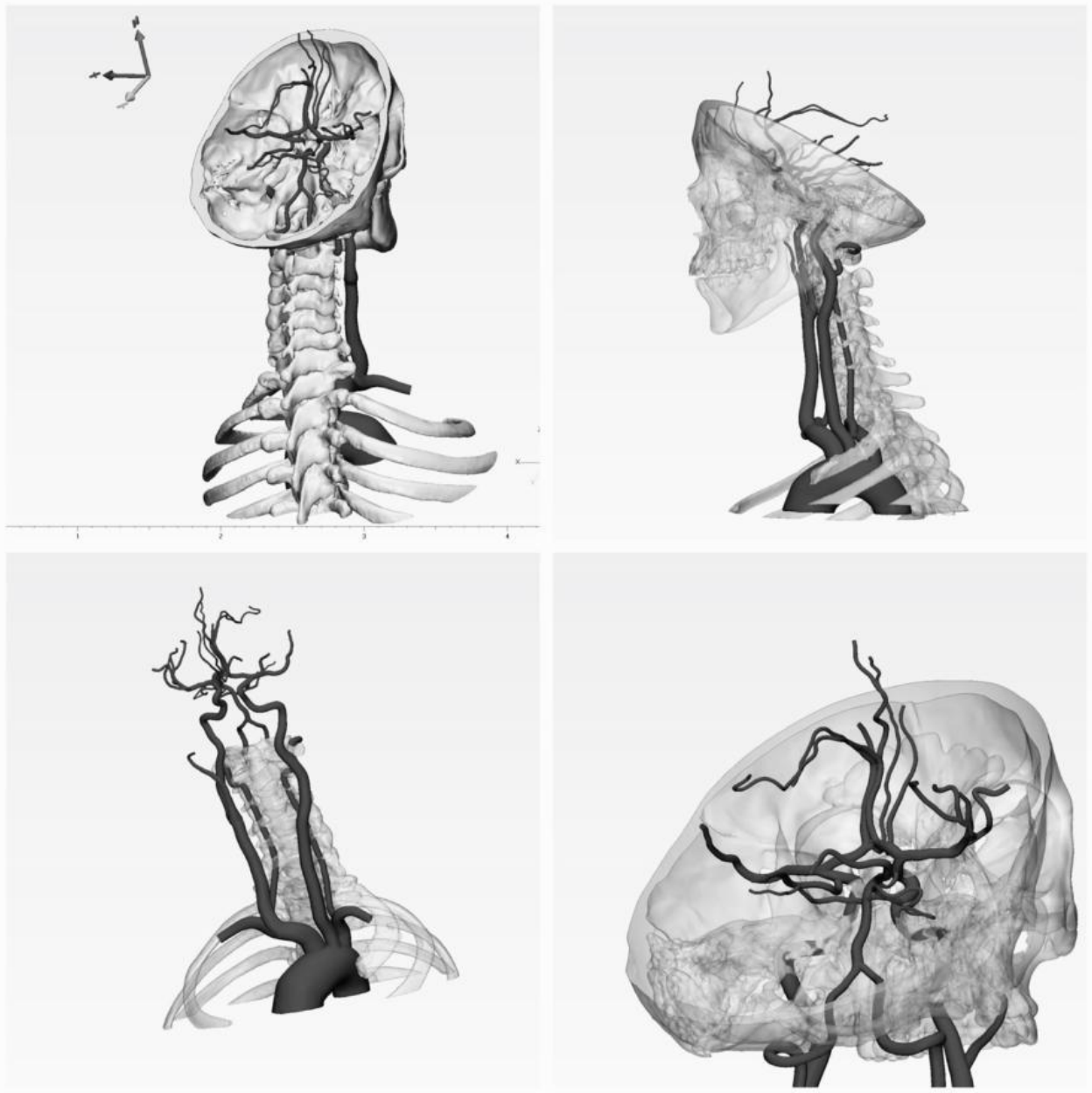
Both groups completed multiple-choice tests to identify a variety of aneurysms on cross-sectional imaging both before and after the educational sessions and their scores were compared.

Results

Pretest and post-test scores of residents undergoing the virtual training demonstrated improvement in the ability of both groups to detect and correctly localize a variety of intracranial aneurysms on cross-sectional imaging. Added benefits for neurosurgical operators included increased comfort for surgical or endovascular treatment. The project generated several high-quality 3-D models of intracranial aneurysms which will soon be available as open source for other academic institutions to download for virtualization and/or three-dimensional printing.

Conclusions

Virtual visualization of complex anatomy or pathology is an effective method of rapidly teaching trainees that has the added benefit of facilitating dissemination of unique and complex cases to other academic institutions.



O-320

5:06PM - 5:13PM

Relative Pressure Measurements Acquired Using 4D-Flow MRA Compared With Intravascular Catheter Measurements in Patients with Cerebral Aneurysms

W Chang¹, M Loecher¹, J Chiang¹, A Chien¹, D Ennis¹, J Villablanca¹

¹*University of California Los Angeles, Los Angeles, CA*

Purpose

Elevated blood pressure has long been associated with risk of intracranial aneurysm rupture. Investigators have generally operated under the assumption that intraaneurysmal pressure is correlated with mean arterial blood pressure. Further, some groups have observed that small variations in pressure throughout the cardiac cycle may be associated with aneurysm growth and rupture, while other groups have examined the correlation of blood pressure and heart rate on hemodynamics within aneurysms and that noted flow morphology can affect aneurysmal dome pressure. However, direct in-vivo intra-aneurysmal pressure measurements are generally invasive. Therefore, noninvasive relative pressure measurements may have value in the evaluation of intracranial aneurysms. In this study, we use 3T 4D flow MRA to estimate relative pressure measurements within aneurysms and parent arteries, and compare the results to direct in-vivo contemporaneous digital subtraction catheter-based measurements (DSA).

Materials and Methods

Two patients with three aneurysms (female, ages 77, 50) were scanned on a 3T MRI scanner (Prisma, Siemens) using 4D flow phase contrast MRA at 0.5 mm isotropic spatial resolution. Scan time was 12 minutes. Venc was 40 cm/s, and FOV was 220 x 220 x 52 mm. The aneurysms measured 6.5, 8.9, and 6.9 mm in largest dimension on DSA. These patients subsequently underwent digital subtraction angiography and parent vessel and intra-aneurysmal pressure measurements were performed before and after endovascular treatment. A 7F sheath was placed in the common carotid artery with Navien 58 and Echelon 10 microcatheters (internal lumen diameter of 0.017) which were used to obtain parent artery and intra-aneurysmal measurements, respectively. Relative pressure maps were created from 4D flow data using a custom Matlab environment. Pressure drops were calculated from pressure within the aneurysm sac relative to pressure within the cavernous ICA at the point where catheter-based pressure measurements were acquired on the DSA.

Results

Measured systolic blood pressures within the aneurysms on DSA were 164, 78, and 134 mm Hg, respectively, where the parent vessel pressures on DSA were 169, 79 and 109 mm Hg. The pressure drops from the cavernous internal carotid artery to the aneurysm at the areas sampled on the DSA as calculated from velocity data from 4D flow MRA were 5, 4, and 8 mm Hg, respectively, compared to pressure drops of 5, 1, and 25 mm Hg from catheter-based measurements from the patients.

Conclusions

Noninvasive intra-aneurysmal pressure measurements may have some prognostic value in certain flow conditions, but have been difficult to acquire to date, due to low spatial resolution. Several studies have been performed using 4D flow MRA in canines which demonstrated promising results. In this study, we present our initial clinical experience of intra-aneurysmal relative pressure measurements in two human patients with three aneurysms. The sample size is too small for statistical significance; however, the initial results are promising as a proof of concept.

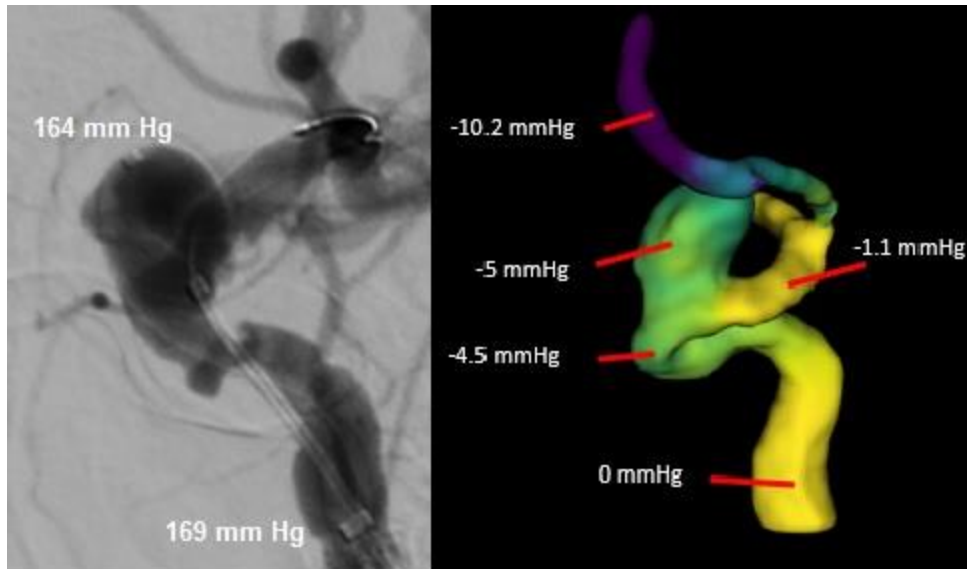


Figure 1: a) left: DSA of an internal carotid artery aneurysm showing catheter-based pressure measurements in the cavernous ICA and in the aneurysm sac. **b) right:** Pressure map from 4D Flow showing 5 mm pressure drop from the cavernous ICA to the aneurysm sac.

(Filename: TCT_O-320_pressureasnrfig.jpg)

O-321

5:13PM - 5:20PM

Biomechanical Changes of Intracranial Aneurysms Using 4D Flow and Vessel Wall Imaging: A Comparative Analysis Between Evolving Vs. Stable Aneurysms

K Nael¹, T Shogan¹, A Bakhshinejad², M Fung³, R De Leacy¹, J Fifi⁴, J Mocco¹

¹Icahn School of Medicine at Mount Sinai, New York, NY, ²University of Wisconsin, Milwaukee, WI, ³GE Health Care, New York, NY, ⁴Mount Sinai Hospital, New York, NY

Purpose

Hemodynamic factors and arterial wall remodeling may play an important role in the initiation and growth of intracranial aneurysms (IA) (1-2). We sought to characterize and compare these biomechanical changes in a cohort of patients with stable vs. evolving aneurysms using 4D-flow MRI and vessel wall Imaging (VWI).

Materials and Methods

From our institution registry of untreated IA, 10 patients who had evolving aneurysm (defined as interval change in size or morphometry, i.e. new lobulation, daughter sac, irregular wall) and 10 patients whose aneurysms remained entirely stable during their sequential surveillance were identified. These patients underwent a dedicated 3T MR imaging protocol encompassing MRA, VWI, and 4D-flow. 4D-flow data was processed using Arterys software (San Francisco, CA) and hemodynamic parameters including flow velocity, peak wall-shear stress (WSS), flow eccentricity and flow-jet angle in each aneurysm were obtained. Patient-specific Computational Fluid Dynamics (CFD) model was generated using proper orthogonal decomposition-ridge regression (POD-RR) algorithm to minimize the noise and enhance the resolution. The associations of flow parameters with commonly used risk factors and morphometric features were assessed using univariate and multivariate analyses.

Results

The age, sex, IA-size, aspect-ratio and size-ratio were not significantly different between two groups. The

mean follow-up time was comparable (43 ± 39 vs. 51 ± 44.2 months, $p=0.58$). The frequency of IA wall enhancement was higher in evolving IAs (70%) than stable IAs (30%), without statistical significance ($p=0.09$). The mean \pm SD of flow parameters in evolving vs. stable IAs were: peak-WSS: 68.1 ± 18.3 cPa vs. 49.2 ± 17.2 cPa, $p=0.04$; flow eccentricity: 0.27 ± 0.13 vs. 0.15 ± 0.05 , $p=0.03$; and flow-jet angle: $76.9 \pm 13.4^\circ$ vs. $61 \pm 17.5^\circ$, $p=0.05$. Multivariate regression analysis identified Peak-WSS and flow eccentricity as independent predictors of evolving IAs.

Conclusions

4D-flow MRI-derived peak WSS and flow eccentricity may be able to identify evolving from stable IAs independent of commonly used size and morphometric features.

O-322

5:20PM - 5:27PM

Intracranial Aneurysms at Higher Clinical Risk for Rupture Demonstrate Increased Wall Enhancement on Vessel Wall MRI.

J Hartman¹, H Watase¹, J Sun¹, D Hippe¹, L Kim¹, M Levitt¹, L Sekhar¹, T Hatsukami¹, C Yuan¹, M Mossa-Basha¹

¹University of Washington, Seattle, WA

Purpose

To evaluate if intracranial vessel wall MRI (VWI) aneurysm characteristics correlate with clinical risk factors for aneurysm rupture

Materials and Methods

After IRB approval, 46 patients with 66 intracranial aneurysms were prospectively consented, recruited, and underwent VWI between April 6, 2016 and August 29, 2017. The 3-D VWI protocol included 3-D T1 space (0.56 mm^3 resolution) pre and post contrast, together with MRA and 3-D T2 space (0.5 mm^3 resolution). Two independent raters evaluated each individual aneurysm while blinded to clinical information. Aneurysms were evaluated in a plane perpendicular to the aneurysm lumen, with the aneurysm wall divided into four equivalent quadrants circumferentially. The raters evaluated each quadrant for the presence of wall enhancement, intensity of enhancement relative to the infundibulum (0=none, 1=less than infundibulum, 2=equal or greater than infundibulum), and qualitative presence of wall thinning. PHASES score (Population, Hypertension, Age, Size, Earlier subarachnoid hemorrhage, Site) for risk of rupture was calculated for each individual aneurysm. The analyses from the two raters were pooled for data analysis. Exploratory univariate analysis was performed comparing VWI aneurysm characteristics between aneurysms at higher clinical risk for rupture (PHASES score greater than 3) and lower clinical risk for rupture (PHASES score ≤ 3) using logistic regression with generalized estimating equations to account for correlation between multiple ratings per patient.

Results

The median PHASES score for aneurysms was 4 (range 0-12). There were 27 aneurysms (54 ratings) with PHASES score ≤ 3 (41%) and 39 aneurysms (78 ratings) with PHASES score >3 (59%). Aneurysms with a PHASES score >3 demonstrated significantly higher maximum intensity ratings (mean: 0.6 vs. 0.4, $p=0.042$) and more quadrants with enhancement (mean: 1.1 vs. 0.6, $p=0.054$) compared with aneurysms with a phases score of ≤ 3 (table 1).

Conclusions

This preliminary data suggests aneurysms at higher risk of rupture may demonstrate more diffuse enhancement and increased intensity of enhancement.

Table 1. Univariate associations between PHASES score and VWI features of aneurysms.

Variable	PHASES Score*		Univariate Model	
	0-3 (N=54)	>3 (N=78)	OR (95% CI)	P-value
Any enhancement	16 (29.6)	32 (41.0)	1.7 (0.8, 3.9)	0.19
No. of quadrants with enhancement (0-4), per 1-quadrant increase	0.6	1.1	1.4 (1.0, 1.9)	0.054
Maximum intensity of enhancement (0-2), per 1-level increase	0.4	0.6	1.8 (1.0, 3.0)	0.042
Any appreciable wall thinning	5 (9.3)	11 (14.1)	1.7 (0.4, 6.4)	0.47

OR = odds ratio; *Values are no. (%) or mean.

(Filename: TCT_O-322_IVWITable1.jpg)

O-323

5:27PM - 5:34PM

Correlating Wall Shear Stress and Permeability of Intracranial Aneurysms

M Pan¹, P Vakil², T Carroll³, M Markl², S Schnell², S Ansari⁴

¹Northwestern University Feinberg School of Medicine, Chicago, IL, ²Northwestern University, Chicago, IL, ³University of Chicago, Chicago, IL, ⁴Northwestern University, Feinberg School of Medicine, Chicago, IL

Purpose

Rupture risk assessment of intracranial aneurysms using noninvasive MRI is an active area of research, particularly in the realm of intra-aneurysmal flow modeling with 4D flow MRI and imaging of wall tracer uptake and permeability using DCE-MRI. While several studies have examined these parameters independently, no study has thus far examined them simultaneously in the same patient. In this work we report the comparison of intra-aneurysmal hemodynamic parameters with wall permeability modeling within the same patient.

Materials and Methods

With IRB approval we acquired 4D flow phase contrast MRI data and DCE-MRI in eight consecutive, angiographically confirmed saccular cerebral aneurysms. We quantified contrast agent leakage rate (Ktrans) through the aneurysm wall using Tofts's model using a previously reported method [1]. Images were postprocessed using in-house software to calculate hemodynamic parameters wall shear stress (WSS) [2], and permeability parameter Ktrans. Mean WSS and Ktrans were cross-sectionally compared across all aneurysms. We further used linear regression to compare hemodynamic and wall-permeability parameters.

Results

The results of our regression analysis are shown in figure 1. We found no statistically significant correlation between mean WSS and Ktrans ($R^2 = 0.0012$, $p = 0.93$). Similarly there was no correlation between mean velocity and Ktrans ($R^2 = 0.020$, $p = 0.73$), as well as aneurysm diameter and Ktrans ($R^2 = 0.0050$, $p = 0.87$).

Conclusions

In this study we did not find significant correlation between intra-aneurysmal hemodynamics and wall permeability. Their lack of intercorrelation suggests they may contribute unique information about aneurysm risk profile and serve as independent markers of rupture risk.

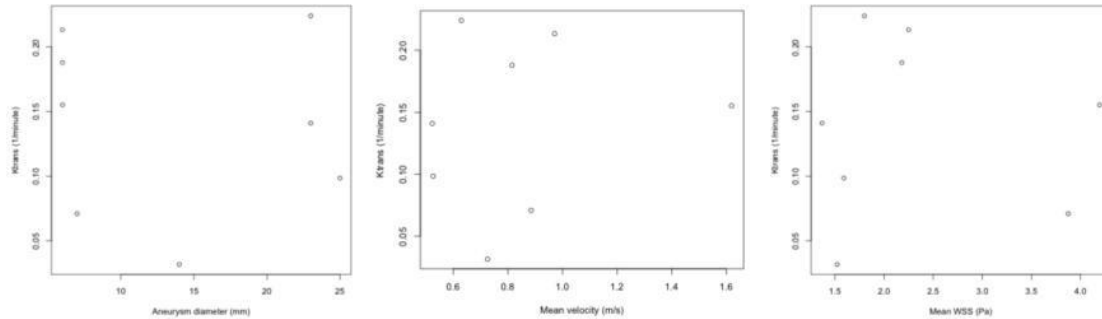


Figure 1. K^{trans} correlation analysis

(Filename: TCT_O-323_ASNRabstractfigure1.jpg)

O-324

5:34PM - 5:41PM

Efficacy of an AVM Classification System that Directs Endovascular Therapies Accurately

W Yakes¹

¹The Yakes Vascular Malformation Center, Englewood, CO

Purpose

To determine if AVM angioarchitecture characteristics can be predictive and direct specific curative endovascular procedures accurately and consistently to treat high-flow malformations

Materials and Methods

Angiographic analysis of high-flow vascular malformations determined four major angioarchitectures. Type I: direct arterial/arteriolar to vein/venule connection; e.g., as commonly seen in pulmonary AVF, congenital renal AVF, etc. Type II: arterial/arteriolar connections to a "nidus" that then have several out-flow veins with no intervening capillary beds in any of the vascular interconnections Type IIIa: arterial/arteriolar connections to an aneurysmal vein ("nidus" is the vein wall) that drains into a dominant out-flow vein with no intervening capillary bed in these connections Type IIIb: same angioarchitecture as Type IIIa, except that there are more than one (several) out-flow veins Type IV: "Infiltrative" form of AVM whereby innumerable microarteriolar branches fistulize through a tissue (e.g., ear) totally infiltrating it, shunting into multiple out-flow veins. Capillary beds also exist in the tissue and are mixed with the innumerable AVFs. Without the capillaries the tissue could not be viable, therefore must be present.

Results

Type I: can be effectively treated with mechanical devices; e.g., coils, Amplatzer Plugs, etc. Type II: can be effectively treated with ethanol embolization Type IIIa: can be effectively treated by transcatheter ethanol, retrograde vein catheter access or direct puncture access of the aneurysmal vein and treatment with ethanol and coils, or even by coils alone Type IIIb: can be effectively treated as above, but can be more challenging by the vein route as more veins (not a single out-flow vein) require closure Type IV: can be effectively treated by transcatheter or direct puncture of the innumerable microfistulous AVFs by embolization with 50% -50% ethanol nonionic contrast mixture

Conclusions

This never-before reported classification system has a direct impact on determining the curative endovascular and direct puncture embolization procedures and also determines the embolic agents that will successfully treat complex AVMS in the body.

O-325

Angiogram negative spontaneous subarachnoid hemorrhage: The yield of repeated angiogramA Aladi¹¹*Keele University, Stoke-on-Trent, Staffordshire, England***Purpose**

To evaluate the revenue, utilization rate and diagnostic yield of the repeated angiogram imaging tests to identify the secondary vascular causes in patients with nonaneurysmal SAH (NA-SAH) 1

Materials and Methods

A retrospective assessment for the data of all adult patients admitted to the Walton Centre, Liverpool, United Kingdom with angiographically negative SAH, between June 2009 to December 2015 was done. Patients with SAH due to trauma or defined vascular causes were excluded. The outcomes studied includes: utilization rate, diagnostic yield and median time for the initial and postadmission imaging test to the following: in-hospital DSA and CTA, and follow-up DSA and CTA (from 0 to 180 days post discharge).

Results

Three-hundred patients with NA-SAH were included in the study. In 200 (66.66%), the blood distribution was perimesencephalic in 150 (75%), nonperimesencephalic 36(18%), and superficial in 12(6%). In 42(28%) of the perimesencephalic SAH patients and in 10(27.77%)of the diffuse SAH undergo a repeated DSA under high suspicion of underlying pathology. The time frame was between 90-180 days after the initial negative angiography. None of the repeat angiograms showed an underlying aetiology for the SAH in the perimesencephalic group. Only one pericallosal aneurysm was discovered in the diffuse group, and another patient died from cardiac arrest in the RCU. At six-months' follow-up, 99.33% patients of PM-SAH and 83.33% of diffuse-SAH had mRS of 0.

Conclusions

After negative initial angiograms (CTA and /or DSA), repeat angiogram is not essential in the follow-up care pathway of patients with perimesencephalic SAH, and these patients tend to have a better prognosis. The diffuse pattern of the bleed is associated with more chances of an underlying pathology and a repeated angiogram is recommended.

O-326**Transradial Diagnostic Cerebral Angiography: Feasibility and Safety in a Community Hospital Setting**T Peebles¹¹*Radiology Associates of the Fox Valley, Neenah, WI***Purpose**

The primary purpose of this study was to assess the feasibility and safety of a single operator performing diagnostic cerebral angiography via transradial access as the primary access route in a community hospital setting and compare to prior published reports from academic centers. The secondary purpose was to compare the transradial procedure parameters of case duration, fluoroscopy time, fluoroscopy dose, contrast dose, major and minor complication rates with a similar number of prior cases done through femoral access.

Materials and Methods

Over a 14-month period 217 consecutive patients presenting for diagnostic cerebral angiography at three community hospitals were considered for primary access via the radial artery. All transradial cases were included from the outset of learning the technique. Institutional review board waivers were obtained from each of the hospital systems where patients were treated. All procedures were performed by a single

fellowship trained neurointerventional radiologist. A total of 54 patients were excluded and underwent primary femoral access because of contraindications to the radial access route due to poor collateral circulation (Barbeau test result C or D), acute intracranial hemorrhage, venous access or trauma preventing access to the desired radial artery, if multiple bilateral subclavian branch selection was anticipated or if there was previous knowledge of anatomic configuration that would preclude successful transradial selection of target vessels. One-hundred-sixty-three patients underwent transradial diagnostic cerebral angiography. Procedure reports were reviewed and the diagnostic success rate, radial to femoral conversion rate, major and minor complications at the time of procedure and delayed follow-up were tabulated. Follow-up for delayed complications was obtained by direct patient follow-up in clinic or hospital, or by reviewing electronic medical records for call backs and referring provider office notes. Procedure report data including patient age, gender, number of vessels injected, procedure duration, fluoroscopy time, fluoroscopy dose, contrast dose and 3-D acquisition for each case were tabulated. Conversion rate from radial to femoral access was calculated and compared to prior published reports and to cardiology literature. A comparison was made to a matched set of consecutive transfemoral diagnostic cerebral angiograms performed by the same operator during the preceding 14 months.

Results

There was 100% diagnostic success for transradial cases. There were no major periprocedure or delayed complications. There were two minor periprocedure complications: one with forearm swelling and bruising treated with elevation and application of blood pressure cuff and another with side-branch radial artery injury managed by temporary placement of longer sheath during the procedure that was subsequently removed. There were four delayed minor complications: two patients described numbness and tingling in the thumb and index finger that lasted 24 hours then resolved. Two patients presented on day two and the other day five post procedure with forearm swelling and bruising. Both had normal neurovascular exams and both underwent US evaluation showing patent radial artery, no pseudoaneurysm or dissection and were managed conservatively. Ten (6%) patients undergoing transradial angiography were on anticoagulation with either Warfarin or Eliquis. None of the patients undergoing transfemoral angiography were on anticoagulants. The transradial and transfemoral groups were compared. There were 60% females in the transradial group and 58% in the transfemoral group. Of patients 64% in the transradial group underwent 3-D acquisition vs. 27% in the transfemoral group. The right side was accessed in 90% of radial and 91% of femoral cases. Student t Test was used to compare the procedure data for transradial and transfemoral cases. The procedure averages (transradial vs. transfemoral) are: case duration 28.6 vs 22.3 minutes ($p < .001$), fluoro time 8.6 vs 5.7 min ($p < .001$), vessels injected 3.2 vs. 4.1 ($p < .001$), fluoro dose 277 vs. 262 mGy ($p = 0.566$), contrast dose 61 vs. 64 mL ($p = 0.669$). The radial to femoral conversion rate was 5%. There was one major complication in the transfemoral group caused by entrapment of a micropuncture sheath that was inadvertently placed through an existing Starclose device that required surgical cut down for extraction.

Conclusions

Transradial cerebral angiography is feasible and safe in a "real world" community hospital setting even accounting for the learning curve associated with the technique. The procedure was 100% successful with a low conversion rate. In this series, 75% of all diagnostic cerebral angiograms were done using a transradial access from the outset of learning the technique with no major complications. Compared to transfemoral cerebral angiography the technique adds slightly to overall procedure duration but the fluoroscopy dose and contrast dose were not significantly different. The transradial access route for cerebral angiography should be considered primarily due to lower bleeding risk, patient preference and avoidance of reversing anticoagulation for patients requiring cerebral angiography.

O-327

5:55PM - 6:02PM

Utility of Follow-up Imaging in Isolated Perimesencephalic Hemorrhage: an Updated Metaanalysis

B Geng¹, X Wu¹, L Tu¹, D Gandhi², P Sanelli³, A Malhotra⁴

¹*Yale University School of Medicine, New Haven, CT*, ²*University of Maryland School of Medicine, Baltimore, MD*, ³*Northwell Health, Manhasset, NY*, ⁴*Yale New Haven Hospital, New Haven, CT*

Purpose

To evaluate the evidence for use and utility of repeat angiographic imaging after a negative computed tomography angiography (CTA) in patients with perimesencephalic subarachnoid hemorrhage (pSAH). Isolated pSAH is an uncommon, distinct subtype of subarachnoid hemorrhage (SAH) with a more benign prognosis. A negative CTA has been shown to be reliable in excluding aneurysmal rupture as the underlying etiology of pSAH. However, there is debate on the utility of digital subtraction angiography (DSA) and subsequent angiographic imaging in determining a vascular cause in pSAH.

Materials and Methods

Retrospective institutional analysis of patients with pSAH was performed from 2014 to 2017 for number and types of follow-up angiographic imaging studies. Patients with a history of trauma were excluded. Updated search of literature was performed by a medical librarian from 2014 to 2017 to assess the utility of follow-up imaging after a negative initial angiographic study. The abstracts of 211 studies were screened by two reviewers for relevance using the Cochrane screening tool Covidence. Review articles, case reports, papers that were included in the previous analysis and full articles or presentations that were unavailable in English were excluded.

Results

The institutional review revealed no utility of additional imaging after a negative CTA in six patients with isolated, nontraumatic pSAH. Out of 211 screened abstracts, 13 full-length texts met inclusion criteria. These 13 reports included 686 patients with an average age of 53.32 and a male to female ratio of 57.0:43.0. Of these 686 patients, 588 with initially negative angiography had follow-up imaging with DSA, CTA or both. A vascular etiology underlying the pSAH was found in three patients from a single study--two aneurysms and one patient with vasculitis--for a detection rate of 0.10% (95% CI: 0.00% - 0.81%).

Conclusions

Use of repeat angiographic imaging after a negative CTA for pSAH patients remains not uncommon; however, the utility is questionable. In patients with a strictly defined pSAH pattern and clinical picture consistent with pSAH, an initial negative CTA should be adequate and repeated follow-up studies can be avoided.

O-328

6:02PM - 6:09PM

Utility of Angiography for Etiology of Primary Intraventricular Hemorrhage

K Seifert¹, X Wu², L Tu¹, A Malhotra¹

¹*Yale New Haven Hospital, New Haven, CT*, ²*Yale University School of Medicine, New Haven, CT*

Purpose

Primary intraventricular hemorrhage is rare, accounting for approximately 3% of intracranial hemorrhage. It has been previously reported that an underlying etiology can easily be diagnosed by angiography, with the most common causes including vascular malformations, moyamoya disease, aneurysm, arterial dissection, and dural arteriovenous fistulas. Often, angiography with CT or MR, or conventional angiography is performed after the diagnosis of intraventricular hemorrhage to help evaluate for these causes. However, results are often inconclusive, with no underlying structural abnormality causing the hemorrhage identified. Further angiography studies are often ordered in an attempt to detect an abnormality that may have been previously missed. We evaluated the utility of ordering initial and repeat angiography studies on patients with primary intraventricular hemorrhage.

Materials and Methods

We performed a retrospective review of patients who presented with intraventricular hemorrhage, who

received angiography imaging with CT, MR, or conventional angiography. Patients with concurrent subarachnoid or parenchymal hemorrhage at presentation were eliminated from this study. Imaging studies were reviewed for etiology of patient's hemorrhage. Additional medical information was obtained by chart review, including demographics and comorbidities, as well as clinical course.

Results

As primary intraventricular hemorrhage is rare, we included all patients in our database that presented with isolated intraventricular hemorrhage, which spanned the following dates: June 1993 to November 2017. The most common underlying abnormalities included vascular malformations, aneurysms, moyamoya disease, recent infarct, and trauma. The average number of angiography studies each patient received was three. Of patients 14% had known structural abnormalities thought to be responsible for their hemorrhage, with no additional findings on angiography. Of patients 23% had structural abnormalities that were diagnosed on their first angiography study. Despite finding a cause on the initial study, these patients often received follow-up angiography examinations; however, no additional abnormalities were detected on the subsequent studies. In patients with an initial negative angiogram who received repeat angiography studies, a cause was detected in only 5% of patients on the second study. No abnormalities were detected on further ensuing angiograms.

Conclusions

Intraventricular hemorrhage is a rare subset of intracranial hemorrhage, which can result from a structural abnormality in some patients. Our results show that the abnormalities are most commonly detected on the first angiography study performed. Repeat evaluation only detected a small number of abnormalities not initially diagnosed and did not provide any additional information for patients who already had an identified cause. Thus, repeat angiography does not provide significant additional clinical benefit.

Tuesday, June 5, 2018

4:45PM - 6:15PM

Excerptas: Pediatric Head & Neck

E-63

4:45PM - 4:49PM

Coronoid Process Hyperplasia: A rare disorder masquerading as temporomandibular joint disease.

E Schneble¹, R Moore¹, A Bonde¹, A Batouli¹, B Hamilton¹, D Pettersson¹, R Barajas¹

¹*Oregon Health and Sciences University, Portland, OR*

Purpose

Increase awareness of coronoid hyperplasia and the central role of CT in diagnosis and surgical planning

Materials and Methods

Bilateral mandibular coronoid-process hyperplasia is a rare condition causing a painless progressive reduction in mouth opening. Given its insidious onset, a missed or delayed diagnosis can occur. We report a case of coronoid hyperplasia in a young child that was initially misdiagnosed as a TMJ disorder. The discussion emphasizes the central role of CT in initial diagnosis and surgical planning of this rare entity. A healthy 4-year-old male presented to his dentist for care of multiple dental caries. The dentist was unable to treat the caries because of a restricted range of motion of the jaw. The patient was given a presumptive diagnosis of TMJ dysfunction and referred to oral surgery. Physical exam by the oral surgeon demonstrated a maximum incisal opening of 15 mm. CT imaging revealed abnormal elongation of the coronoid process extending above the level of the zygomatic arches. Operative plan included bilateral coronoidectomies with repeat perioperative CT under anesthesia immediately prior to surgery with 2-D and 3-D multiplanar reconstructions for planning purposes. Surgery was performed and the

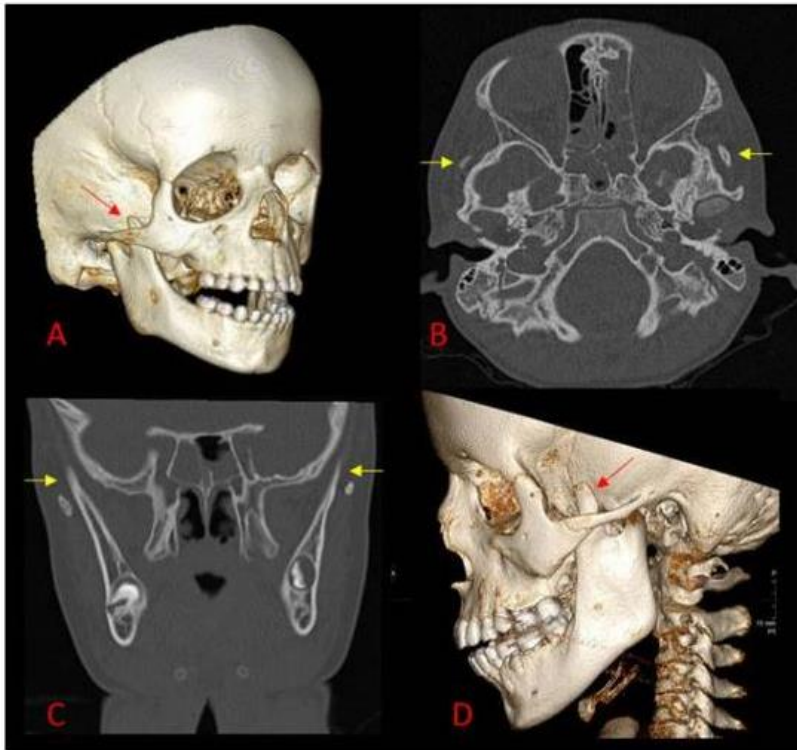
incisal opening distance improved to 25 mm. Four years later, oral range of motion had returned to its preoperative level with a maximal incisal opening of 15 mm. Repeat CT imaging with 3-D reconstructions revealed recurrent and progressive coronoid hyperplasia with temporalis muscle ossification. Given the young age at presentation, temporary surgical success may be secondary to immaturity of the patient. Repeat surgical intervention is currently delayed until the patient can fully engage in postoperative physical therapy. Coronoid hyperplasia is a rare condition of unknown etiology that may be missed without three-dimensional radiographic imaging, as in this case. Also demonstrated is a young age at presentation, a mean age at initial diagnosis of 23 years having been previously cited.

Results

Volume-rendered 3-D image from the patient's preoperative CT shows the tip of the right coronoid process extending above the level of the mandibular condyles (A). Axial (B) and coronal (C) CT images shows the bilateral coronoid processes extending above the level of the zygomatic arches. Four years postoperatively, the patient's limited range of mandibular motion returned and repeat CT was performed. A volume-rendered 3-D image from that CT shows progressive elongation of coronoid process projecting superior to the zygomatic arch (D).

Conclusions

Coronoid hyperplasia as a cause of limited mouth opening remains relatively unknown and often misdiagnosed. A rare, often painless, non-neoplastic condition, coronoid hyperplasia is unfamiliar to many clinicians with significant potential for under-reporting. Characterized by restricted mouth opening due to impingement of the coronoid processes on the zygomatic arches, it is a cause of significant morbidity with the potential to be corrected with appropriate diagnosis and treatment. The elongated coronoid processes are formed of histologically normal bone closely associated with the anterior portion of the zygomatic bone, thus limiting mouth opening. Coronoid hyperplasia occurs in both unilateral and bilateral forms, the unilateral form often associated with trauma or other pathological condition. Given an often progressive and insidious onset, misdiagnosis of TMJ dysfunction often occurs initially. Multiple etiologies have been proposed to include mandibular hypomobility or hypoplasia, temporalis muscle disorder, TMJ dysfunction, and genetic inheritance. Jacob's disease is a separate pathology when coronoid process hyperplasia forms a pseudocartilaginous joint with the zygomatic process. Bilateral presentation is associated with a 3.3:1.0 male to female predominance. Although initial detection may occur with panoramic radiograph, CT is useful to delineate morphology and extent of involvement. Protocols may include axial and sagittal CT reformats in the open position. A coronoid/condyle ratio of <1.0 has been proposed of as indication of normal anatomy. Multiplanar reformats (MPR) and 3-D rendering are fundamental surgical planning tools for oral surgeons. Postoperatively, MRI is useful to assess for fibrotic reaction of the temporalis muscle at the coronoidectomy site. Although further surgery may be required to treat limited opening, prognosis of coronoid hyperplasia is excellent with adequate treatment.



(Filename: TCT_E-63_CoronoidHyperplasia_images.jpg)

E-64

4:49PM - 4:53PM

Spontaneous Lateral Sphenoid Sinus Cephalocele Presenting after a Big Sneeze!!

A Krishnan¹, K Tran², L Bahoura³

¹Beaumont Health, Royal Oak, Royal oak, MI, ²Oakland University William Beaumont School of Medicine, Royal Oak, MI, ³Northwestern Memorial Hospital, Chicago, IL

Purpose

To report the unusual presentation and imaging of a 55-year-old woman who noticed fluid draining from her nose shortly after strong sneezing, and was found to have a fluid collection in the sphenoid sinus with herniation of brain into the sinus on imaging. Findings were consistent with a lateral sphenoid sinus cephalocele.

Materials and Methods

A 55-year-old woman experienced clear fluid draining from her nose after "the strongest sneeze of her life". She was evaluated, her nasal fluid tested positive for beta-2-transferrin, consistent with a CSF leak, and was sent in for brain MRI to assess for anterior skull base defect. She denied any recent trauma but had a history 20 years earlier of traumatic injury to the spine and head. She was imaged 3 weeks after her clinical symptoms started. In addition to routine sequences, high resolution imaging of the sinuses including (CISS) Constructive Interference in Steady State, T2 SPACE (Sampling Perfection with Application optimized Contrasts using different flip angle Evolution) were performed. The sphenoid sinus was fluid-filled and a portion of the left medial temporal lobe was found to be herniated into the sphenoid sinus. These findings were not present on a head MRI performed 12 years earlier and the sphenoid sinus at that time was well pneumatized and clear. A CT of the sinuses was performed for presurgical planning. It confirmed a defect in the left lateral wall of the sphenoid sinus through which the temporal lobe had

Oral Presentations & Excerptas

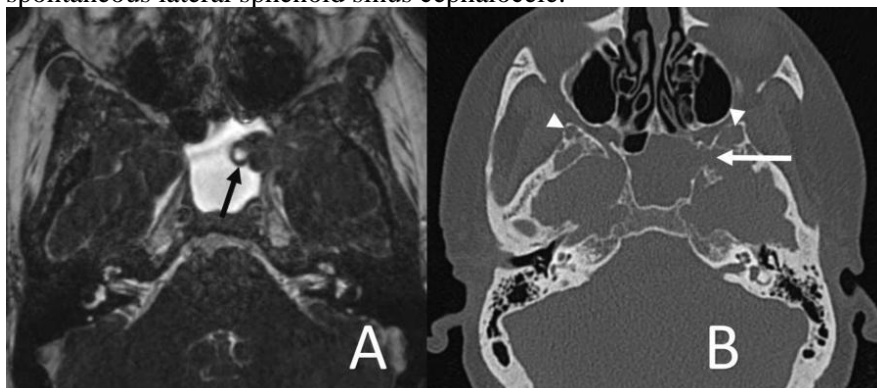
herniated. Additionally, multiple areas of focal thinning or defects (pits) were seen along the walls of the middle cranial fossa bilaterally, particularly along the greater wing of the sphenoid bone. These were also seen on a head CT performed 9 years earlier suggesting that they were chronic findings.

Results

MRI imaging (Figure 1a axial CISS with herniated brain depicted with black arrow) demonstrated the near totally opacified sphenoid sinus with the left temporal lobe herniating (cephalocele) into the sphenoid sinus through a defect in the inferior left lateral aspect of the sinus. The intrasinus brain tissue was contiguous with the left temporal lobe but appeared gliotic with a cyst within it. This morphology of the brain was best seen on the high resolution CISS sequence and SPACE T2 3D sequence, which depicted the defect very well. There was faint rim-like enhancement around the involved brain. CT imaging (Figure 1b axial CT of the sinuses) also revealed the extensive presumed arachnoid pits (arrowheads) with thinning diffusely of multiple osseous structures along the middle cranial fossa. A defect (white arrow) in the left lateral wall of the sphenoid sinus was also seen.

Conclusions

Spontaneous lateral sphenoid sinus cephaloceles are a subset of cephaloceles and are now believed to be an acquired condition occurring from a combination of underlying anatomic factors and superimposed physiologic conditions. Primarily, abnormal thinning of the bones in the middle cranial fossa, from aberrant arachnoid granulations (responsible for the imaged pits in the bones) that scallop the bones are believed to predispose to final disruption of the wall of the sphenoid sinus and herniation of brain. One postulated reason for the extensive arachnoid pits is the possibility of underlying intracranial hypertension in these patients. Our patient did not carry this diagnosis but fit the demographics and had a long standing history of headaches. What was unusual was her presentation after a bout of sneezing. While an earlier head MRI exam did not show a cephalocele, there were multiple arachnoid pits present on older head CTs raising the possibility that she had over the years weakened the walls of the sphenoid sinus and the sudden elevation in pressure resulted in a dural tear and CSF leak. The gliotic appearance of the cephalocele suggested that the herniation may have occurred over some time. Sneezing while often considered to be trivial has been associated with serious events including rupture of intracranial aneurysms (and which coincidentally occurred at our institution about a month before this patient presented). We hope with this case to make neuroradiologists aware of an unusual presentation of a spontaneous lateral sphenoid sinus cephalocele.



(Filename: TCT_E-64_ASNRsubmittedpicture.jpg)

E-65

4:53PM - 4:57PM

Liposarcoma of the retropharyngeal space

E Velez¹, M Lee¹, J Acharya¹, B Su², B Diegman¹, A Rajamohan¹

¹LAC+USC, Los Angeles, CA, ²University of Southern California Los Angeles David Geffen School of Medicine, Los Angeles, CA

Purpose

To illustrate a rare primary tumor of the retropharyngeal space

Materials and Methods

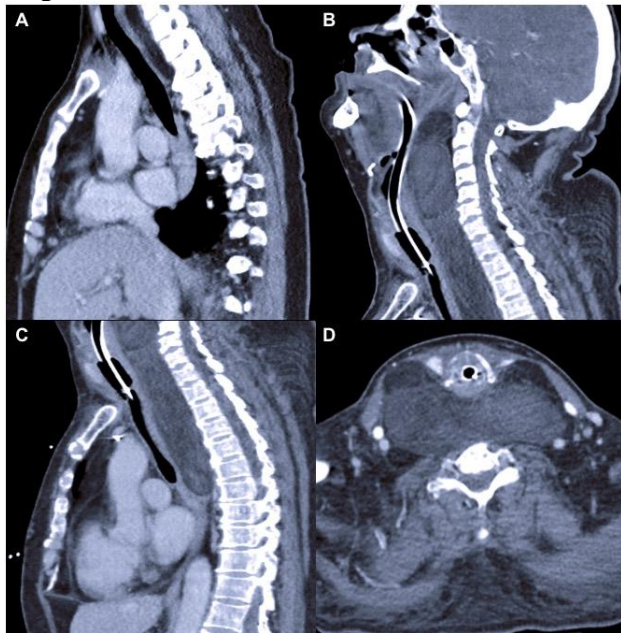
A 73-year-old woman with a remote history of lymphoma presented from an outside hospital with a 6-year history of a retropharyngeal mass and 1-year history of dysphagia. A screening CT performed 6 years previously reported a 3.3 cm fatty area near the thoracic inlet, thought to be a lipoma. One year prior to presentation she developed dysphagia, and underwent a repeat CT showing significant enlargement of the mass. Endoscopic biopsy results were consistent with pleomorphic spindle-cell lipoma; at that time the mass was deemed unresectable. She presented to the emergency department with shortness of breath and stridor requiring intubation. Subsequent CT demonstrated further enlargement of the mass. After initial stabilization she underwent a bilateral modified radical neck dissection, tracheostomy, and retropharyngeal mass excision with complete resection of the tumor. Pathology revealed a 21.6 cm well-differentiated liposarcoma with negative lymph nodes. Her postoperative course was complicated by prolonged ventilator requirements, ventilator associated pneumonia, and tracheal stenosis. She was discharged to a long-term acute-care facility on postoperative day 23, and remains disease-free 1 year out.

Results

Image A: initial contrast-enhanced CT, 6 years prior to presentation, demonstrates a 7.2 cm x 5.2 cm x 1 cm fat-density retropharyngeal mass Image B/C/D: contrast-enhanced CT at presentation demonstrates a 20 cm x 9 cm x 6 cm soft-tissue mass with areas of enhancement and fat extending from the retropharyngeal neck into the posterior mediastinum from the C1 to T7 level, concerning for liposarcoma. The mass completely obstructs the oropharynx and causes anterior displacement of the esophagus and trachea.

Conclusions

Liposarcomas of the retropharyngeal space can enlarge quickly, resulting in significant morbidity and mortality. Early recognition, diagnosis, and treatment is crucial to avoid complications and more complex surgeries.



(Filename: TCT_E-65_retropharyngealmass.jpg)

E-66

4:57PM - 5:01PM

Giant Cell Tumor of the Carotid Sheath

J Huang¹, J Newman¹, B Pukenas¹, M Husson¹, L Bagley¹

¹University of Pennsylvania Health System, Philadelphia, PA

Purpose

To report the first case of giant cell tumor of the carotid sheath

Materials and Methods

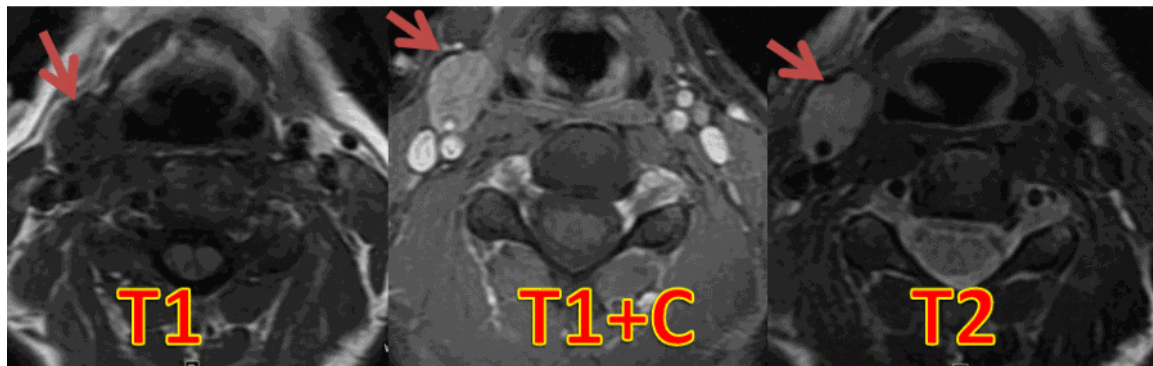
We report a case of a 38-year-old woman who noticed a right-side neck mass which was painless and asymptomatic. The patient had no relevant medical history and physical examination revealed a palpable mass in the right neck which was described as a firm, semimobile 1cm pulsatile mass. US of the neck revealed a hypoechoic, vascular solid nodule measuring 2 x 1.3 x 2cm in the right neck at level II/III. MRI of the neck revealed a well circumscribed, homogenous, T1 hypointense, T2 hyperintense, enhancing mass anterior to the carotid bifurcation, contacting and possibly encasing the right external carotid artery just beyond its origin. Despite some atypical features, a diagnosis of paraganglioma was entertained, and the patient subsequently underwent angiography and embolization of the vascular mass. Of note, the mass was located anterior to the common carotid artery bifurcation, and supply was from the superior thyroidal artery, not the ascending pharyngeal artery. Surgical excision of the mass was performed and pathology revealed spindle cells with scattered giant cells. Immunohistochemical staining revealed CD68 activity in the multinucleated giant cells supporting the diagnosis of giant cell tumor of soft tissue. The patient suffered no ill effects from the operation and is recurrence-free 30 months following excision. Primary carotid sheath neoplasms typically have a fairly narrow differential diagnosis including carotid body tumors (CBT), glomus vagale, nerve sheath tumors including schwannomas and neurofibromas as well as metastatic lymphadenopathy and lymphoma. Therefore the diagnosis of giant cell tumor of the soft tissue (GCTST) on pathology was highly unexpected and novel in this region

Results

Ultrasound: solid, hypoechoic, vascular nodule measuring 2 x 1.3 x 2cm in the right neck at level II/III. This was just anterior to the carotid bifurcation. MRI: well-circumscribed, homogenous, T1 hypointense, T2 hyperintense, enhancing mass anterior to the carotid bifurcation, contacting and possibly encasing the right external carotid artery just beyond its origin. Conventional Angiography: frontal and lateral views of the neck obtained during injection of the left common carotid artery again demonstrated a rounded, moderately vascular mass lesion anterior medial to the right common carotid artery bifurcation, mildly displacing the right external carotid artery posteriorly with supply via multiple branches of the superior thyroidal artery.

Conclusions

Giant cell tumor of the soft tissue can occur in the carotid sheath and should be considered as a potential, albeit rare, diagnosis in tumors of this area.



(Filename: TCT_E-66_Figures1.gif)

Proximal Tracheal Recurrence in HPV-positive Squamous Cell Carcinoma of the Base of Tongue: a Rare Occurrence

M Chen¹, N Gross¹, L Ginsberg¹

¹*MD Anderson Cancer Center, Houston, TX*

Purpose

To present 2 rare cases of tracheal recurrence from HPV positive squamous cell carcinoma of the base of tongue

Materials and Methods

A 58-year-old man, never smoker with an exophytic T2N2b left base of tongue HPV-positive squamous cell carcinoma (SCC) underwent biopsy and subsequent treatment with induction chemotherapy followed by transoral robotic surgery. Histologically, the patient had a complete response to chemotherapy. Approximately 13 months after the initial biopsy, the patient developed recurrence in the anterior, proximal tracheal wall. The second patient is a 75-year-old man with a history of smoking and an exophytic T2N0 right base of tongue HPV-positive SCC. The patient underwent biopsy and subsequent transoral robotic surgery as single modality therapy. Approximately 8 months after initial biopsy, the patient developed radiologically detectable recurrence in the anterior, proximal tracheal wall. Both patients underwent endotracheal intubation for biopsies and surgeries.

Results

Contrast-enhanced CT of the first patient demonstrated a nodule along the anterior wall of the trachea that grew over a 5-month period and was biopsy proven HPV-positive recurrence. The patient was treated with local therapy and has been free of recurrence, but subsequently developed lung metastases. Contrast-enhanced CT in the second patient showed a slightly bulkier nodule along the anterior wall of the proximal trachea, biopsy proven HPV-positive SCC. This patient underwent local therapy and remains in surveillance.

Conclusions

Proximal tracheal recurrence from HPV-positive SCC is a rare entity. The pathophysiology in these cases is unknown but seems likely to be related to seeding from intubation during biopsy or surgery and may be more likely to occur if the primary tumor is exophytic, as in our 2 cases. The trachea can be overlooked by the radiologist, and awareness for the potential seeding pattern of endotracheal intubation, particularly along the anterior tracheal wall is helpful in the detection for recurrences.

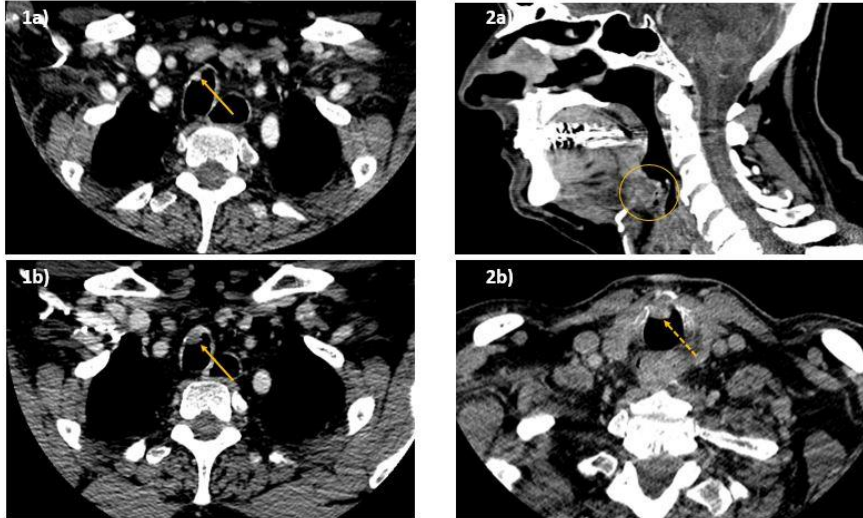


Figure 1: Contrast enhanced axial CT from the first case demonstrated a nodule (arrow) along the anterior wall of the trachea (a) that enlarged over a 5 month period (b). Figure 2: Prior to treatment, imaging (a) demonstrated a bulky exophytic mass in the right base of tongue (circle). Approximately 12 months after initial biopsy and therapy, the patient developed a nodule (dashed arrow) in the anterior wall of the subglottic trachea, biopsy proven HPV SCC.

(Filename: TCT_E-67_Trachealmet.JPG)

E-69

5:09PM - 5:13PM

Spontaneous Salivary Gland Hemorrhage after Anticoagulation for Acute Bilateral Carotid Arterial Thrombosis in a Pregnant Female with Antiphospholipid Syndrome

C Pluguez-Turull¹, K Clark¹

¹University of Texas Health Science Center at San Antonio, San Antonio, TX

Purpose

To present the very rare case of spontaneous salivary gland hemorrhage in an anticoagulated patient. Spontaneous hemorrhages in this region can rapidly progress to compromise the upper airways. Familiarity with this clinical entity should be suspected in all anticoagulated patients presenting with acute neck fullness and pain, specially at treatment (opposed to prophylactic) doses.

Materials and Methods

This is a rare case of bilateral submandibular gland and right tonsillar hemorrhage after heparin initiation for acute bilateral carotid arterial thrombosis in a 38-year-old 6-week pregnant female with antiphospholipid syndrome presenting with acute right blindness. Only a few reports have been described regarding spontaneous salivary gland hemorrhage in an ubiquitous anticoagulated patient population. The imaging characteristics are suggestive, but the rare occurrence might sway the diagnosis to infection/abscess formation, unless there is clear evidence of a sharply acute occurrence (evidenced on short-interval imaging) in a patient with risk factors, as in this case.

Results

Interval hypodense and heterogeneous appearance of the bilateral submandibular glands with adjacent fat stranding, likely represents acute hemorrhage given the change from comparison CT one day prior and the provided history of anticoagulation therapy at treatment doses. Interval hypodensity in the right tonsil likely represents hemorrhage as well. Neck CTA demonstrates complete occlusion of the right common carotid artery at its midportion extending distally throughout the cervical ICA and intracranial ICA and a nonocclusive filling defect in the distal left common carotid artery.

Conclusions

This is a rare case of spontaneous salivary gland hemorrhage in a young pregnant female with

antiphospholipid syndrome after anticoagulation treatment for acute bilateral carotid arterial thrombosis. Very few case reports have documented this complication. The imaging characteristics could suggest inflammation/infection, particularly given the absence of trauma, unless there is clear evidence of a sharply acute occurrence (evidenced on short interval imaging) in a patient with risk factors. Salivary gland spontaneous hemorrhages can rapidly progress and compromise the upper airways. Familiarity with this clinical entity should be suspected in all anticoagulated patients presenting with acute neck fullness and pain, specially at treatment doses.

E-70

5:13PM - 5:17PM

Erdheim Chester isolated to the skull base.

J Bykowski¹, M Shroads¹

¹*University of California at San Diego, San Diego, CA*

Purpose

Erdheim Chester disease is a rare non-Langerhans cell histiocytosis that classically presents in middle age, affecting the long bone diaphysis and metaphyses; however, it can affect all organs and the skin. Central nervous system involvement has been described, including infiltration of the hypothalamus-pituitary axis, cerebellum, or brainstem with meningeal involvement less frequently. This case presents an unusual isolated presentation in the skull base.

Materials and Methods

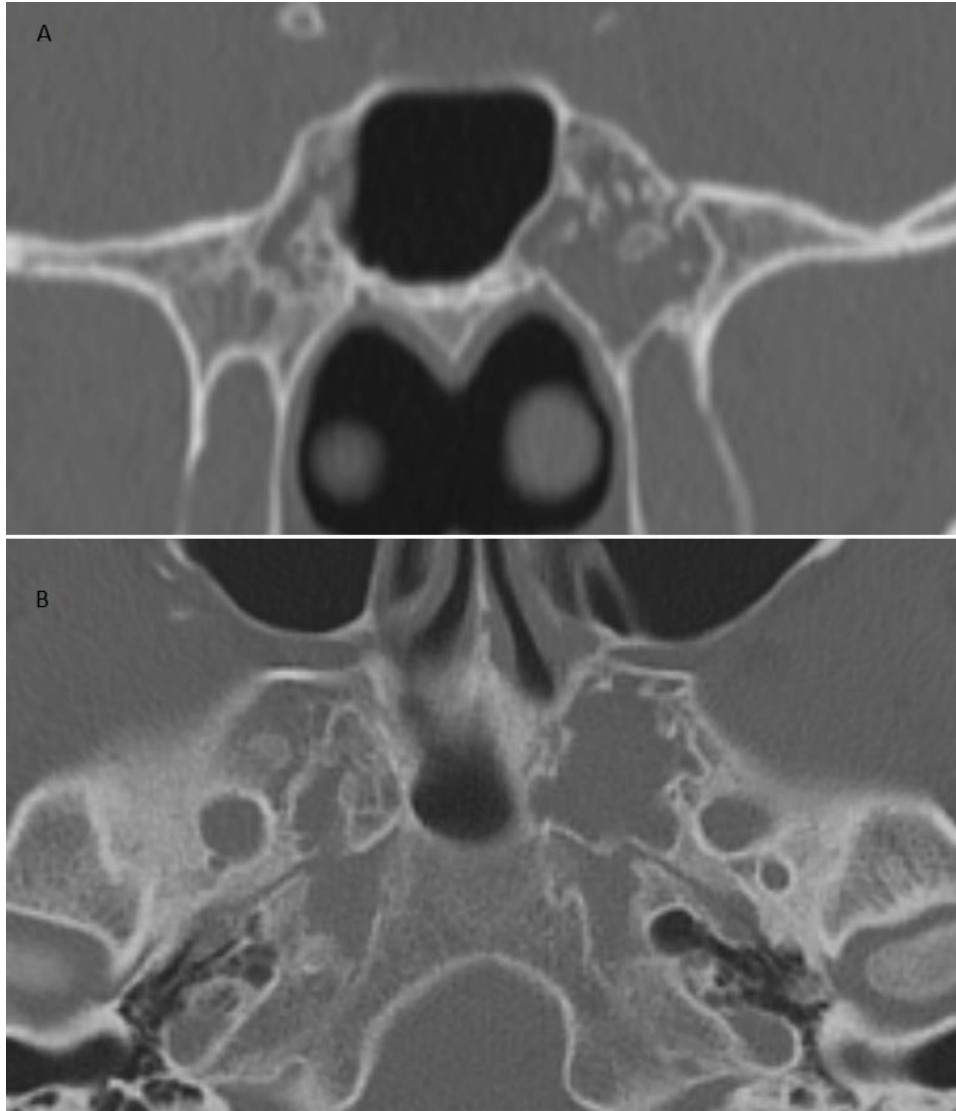
A 32-year-old man presented to outside facility with chronic sinus symptoms and new left facial numbness. CT was performed and revealed lucent areas within the sphenoid bilaterally with sclerotic margins. Subsequent MRI confirmed mild internal enhancement in the marrow, with no visible enhancement of either cranial nerve V2 in foramen rotundum or the vidian nerves. Given the progressive cranial neuropathy, endoscopic biopsy was performed revealing Erdheim Chester disease, which classically uses the RAS-RAF-MEK-ERK pathway. This tumor was BRAF V600E negative. He was treated with Peg-interferon alpha, but had to discontinue due to transaminitis. However, two months post cessation he is now asymptomatic.

Results

Coronal CT (A) reveals central lucency within the sphenoid bone with peripheral sclerosis bilaterally, left more than right. The bone of the vidian canals and foramina rotundum were intact within the resolution of CT. Axial CT (B) reveals the irregular margin, approaching but not involving foramina ovale bilaterally.

Conclusions

The skull base is a common location for benign fibro-osseous lesions; however, in the setting of a new or progressive cranial nerve symptom more aggressive entities must be considered. The radiologist can be of assistance helping to identify endoscopic targets, both to confirm diagnosis and to assist with molecular profiling.



(Filename: TCT_E-70_ECD.jpg)

E-71

5:17PM - 5:21PM

Bisphosphonate-induced Inflammation of the Orbit

D Treister¹, C Hess¹, C Glastonbury¹, J Villanueva-Meyer¹

¹University Of California San Francisco, San Francisco, CA

Purpose

While infectious orbital cellulitis is well recognized among clinicians and radiologists, orbital inflammation related to bisphosphonate use is much less frequently encountered. A causal link between oral and intravenous bisphosphonates and inflammation of the globe and periorcular structures has been suggested by case series and in vitro studies, the latter of which have demonstrated potential mechanisms of inflammation by activation of T-cells and release of proinflammatory mediators. (1-3) We report two patients presenting with ocular symptoms after receiving intravenous zoledronic acid.

Materials and Methods

Case 1 is a 71-year-old male who presented with progressive right eye swelling and retro-orbital pain 7 days after initial treatment with intravenous zoledronate. Case 2 is a 56-year-old male presenting with bilateral eye swelling and pain beginning 3 days after intravenous zoledronate.

Results

Case 1: Contrast-enhanced MRI of the orbits demonstrated mild right proptosis, diffuse right orbital edema and abnormal enhancement of the intraconal and extraconal fat, and hyperenhancement of the optic nerve sheath. There was no inflammatory involvement of the optic nerve or extraocular muscles and no significant disease in the paranasal sinuses. Case 2: Contrast-enhanced MRI of the orbits revealed focal orbital inflammation and abnormal enhancement in the superolateral left orbit and inferolateral right orbit with involvement of the adjacent extracocular muscles. Inflammatory changes extended lateral to the orbits to the soft tissues of the face.

Conclusions

Orbital inflammation is an unusual side effect following the administration of bisphosphonates with varied clinical and radiographic manifestations. Bisphosphonate-related orbital inflammation should be considered when patient history indicates recent drug administration, particularly in the absence of additional findings to suggest infection such as paranasal sinus disease.

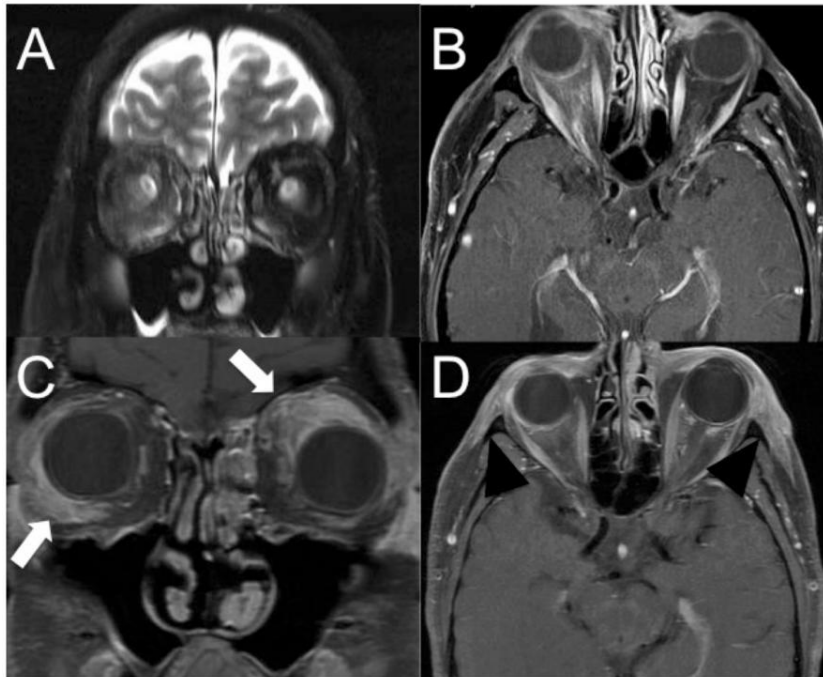


Figure 1. Case 1: Coronal fat saturated T2 (A) and axial T1 post-contrast (B) MR images show edema and abnormal enhancement throughout the right intraconal and extraconal fat. Case 2: Coronal (C) and axial (D) post-contrast MR images show abnormal enhancement in the inferolateral right and superolateral left orbits (white arrows) and inflammation in the periorbital soft tissues of the face (black arrowheads).

(Filename: TCT_E-71_ASNR_bisphosphonate_orbits.jpg)

E-72

5:21PM - 5:25PM

Phosphaturic Mesenchymal Tumor: An uncommon entity with an interesting presentation

K Memon¹, D Pechersky², A Karagianis³, S Ansari³, A Korutz³, B Liu³

¹Northwestern University, Chicago, IL, ²Northwestern Memorial Hospital, Chicago, IL, ³Northwestern University, Feinberg School of Medicine, Chicago, IL

Purpose

To report the clinical presentation, extensive diagnostic workup and imaging manifestations of a rare clinical entity called Mesenchymal Phosphaturic Tumor in the head and neck region

Materials and Methods

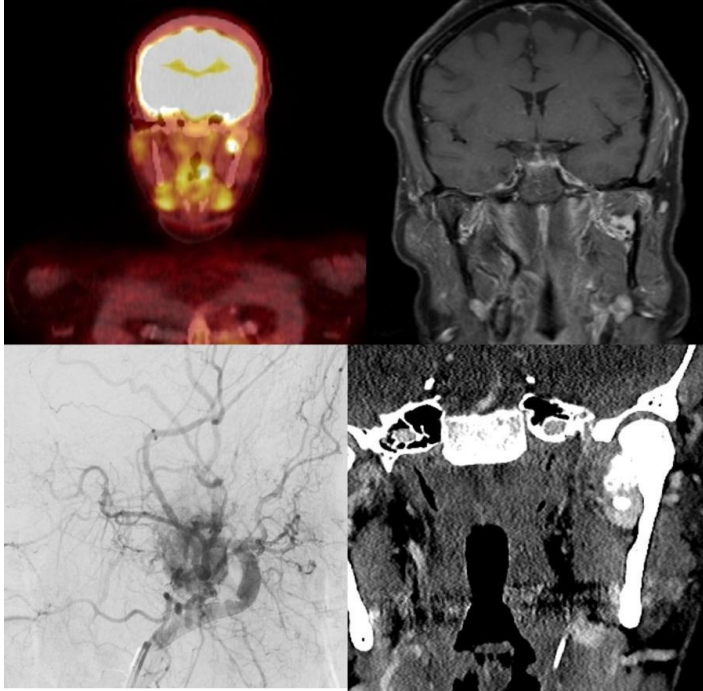
48-year-old previously healthy African-American female presented to her primary care physician approximately eight years ago for altered gait and leg pain, and was referred to endocrinology for high parathyroid hormone levels, normal serum calcium and hypophosphatemia. An underlying metabolic bone disease was suspected and patient was started on calcium and vitamin D supplementation. In 2010 she developed a nondisplaced fracture of the greater tuberosity of the left humerus. In 2013, she developed bilateral femoral stress fractures which were managed conservatively. Due to increasing pain and incomplete healing, the fractures were surgically repaired in 2015. She was reevaluated by endocrinology given continued hypophosphatemia. A PET scan was done to evaluate for occult malignancy which demonstrated a focal hypermetabolic focus with calcifications adjacent to the left mandibular condyle. A CT neck subsequently confirmed the findings of an osseous focus arising from the medial cortex of the left mandibular condyle. However, given its appearance and extension along the fibers of the lateral pterygoid muscle, this was attributed to possible chronic avulsion injury. A subsequent MRI demonstrated abnormal T2 hyperintense signal and enhancement in the region of calcification and a biopsy was recommended. Subsequently, venous samples were obtained from the external jugular, internal jugular and brachiocephalic veins bilaterally, which were unrevealing. An octreotide scan was also performed which did not demonstrate any occult malignancy in the chest, abdomen and pelvis but redemonstrated increased uptake adjacent to the left mandibular condyle. Subsequently, the left mandibular condyle mass was biopsied which demonstrated the lesion to be a phosphaturic mesenchymal tumor, for which she underwent embolization and resection recently. Follow-up evaluation demonstrated improvement in serum phosphorus level.

Results

PET Scan: A focal hypermetabolic finding is noted corresponding to calcific changes adjacent to the left mandibular condyle on CT. These findings were thought to be related to post-traumatic changes, but are of uncertain etiology. A follow-up diagnostic CT imaging of the neck was recommended for further evaluation. **CT Neck:** Osseous focus arising from the medial cortex of the left mandible condyle without associated soft tissue component, corresponding to abnormal hypermetabolic activity on the prior PET/CT. Given its appearance and extension along the fibers of the lateral pterygoid muscle, this finding was thought to be related to chronic avulsion injury with subsequent new bone formation of the inferior head of the lateral pterygoid muscle in the setting of hyperparathyroidism, with osteochondroma as a differential consideration (not shown). **MR Neck:** Abnormal enhancement (with T2 hyperintense signal, not shown) corresponding to the region of mineralization noted along the medial aspect of the left mandibular condyle. The signal characteristics of this lesion were not those expected for a densely ossified mass, and was given a differential diagnosis that included both benign or low-grade malignant chondroid lesions or a reactive bone-forming process related to a chronic avulsion injury. **CTA Neck:** A 2.3 cm partially calcified mass arising from the medial margin of the left mandibular condyle/condylar neck, increased in size compared to prior CT neck. The left ECA terminal branches bifurcate just posterior to the left condylar neck/neoplasm. Maxillary artery runs through the tumor, to the pterygopalatine fossa. **Angiogram:** Hypervascular tumor blush involving the left mandibular condyle/ramus supplied predominantly from a proximal left internal maxillary artery.

Conclusions

Phosphaturic mesenchymal tumors represent a rare etiology of tumor-induced osteomalacia syndrome resulting in renal phosphate wasting and decreased bone mineralization. In our case report, the final diagnosis was obtained approximately eight years from the initial symptom onset. This is likely due to a combination of atypical presentation and difficulty in localization of the tumor by imaging. Although rare, phosphaturic mesenchymal tumor should be considered in any patient who presents with hypophosphatemic osteomalacia.



(Filename: TCT_E-72_Picture2.jpg)

E-73

5:25PM - 5:29PM

An atypical case of progressive biparietal thinning

I Mark¹, R Watson¹, C Rydberg¹, G Miller¹, V Lehman¹
¹Mayo Clinic, Rochester, MN

Purpose

To review the image findings of biparietal thinning and present an unusual case of progressive thinning

Materials and Methods

A 77-year-old female with a history of osteopenia, rheumatic heart disease, and long-term anticoagulation for a mitral valve replacement. The patient's imaging history includes a normal head CT in 2009, mild biparietal thinning in 2013, and progressive biparietal thinning with overlying soft tissue thickening in 2016. The marked progression raised concern for Gorham's disease and a bone biopsy of the left parietal bone was performed.

Results

Normal biparietal region in 2009. Mild biparietal flattening in 2013. In 2016, new thinning of the diploe with loss of the outer table and overlying soft tissue thickening. Intact inner table. Follow-up CT 4 months later demonstrated resolution of the soft tissue thickening with stable biparietal thinning.

Conclusions

Benign biparietal thinning is an uncommon finding on imaging and can be mistaken for a more sinister process. Chronic findings are benign and do not warrant further follow-up. We presented an atypical case, with marked progression of bilateral thinning with associated soft tissue thickening.

E-74

5:29PM - 5:33PM

Granulomatous invasive fungal sinusitis. Back to visit... after 25 years

P Naval Baudin¹, P Puac², F Grippi², H Sa e Silva³, R Alvarez², C Zamora², M Castillo²
¹Hospital Universitari de Bellvitge, Barcelona, Spain, ²University of North Carolina at Chapel Hill, Chapel Hill, NC, ³Hospital Pedro Hispano, ULSM, Porto, Portugal

Purpose

The spectrum of fungal sinonasal disease is wide and ranges from noninvasive forms in immunocompetent patients to invasive acute and chronic forms in immunocompromised individuals. Granulomatous invasive sinusitis (GIFS) is a rare chronic mass-forming infection usually caused by *Aspergillus flavus*. We present a case of GIFS that recurred 25 years after initial presentation.

Materials and Methods

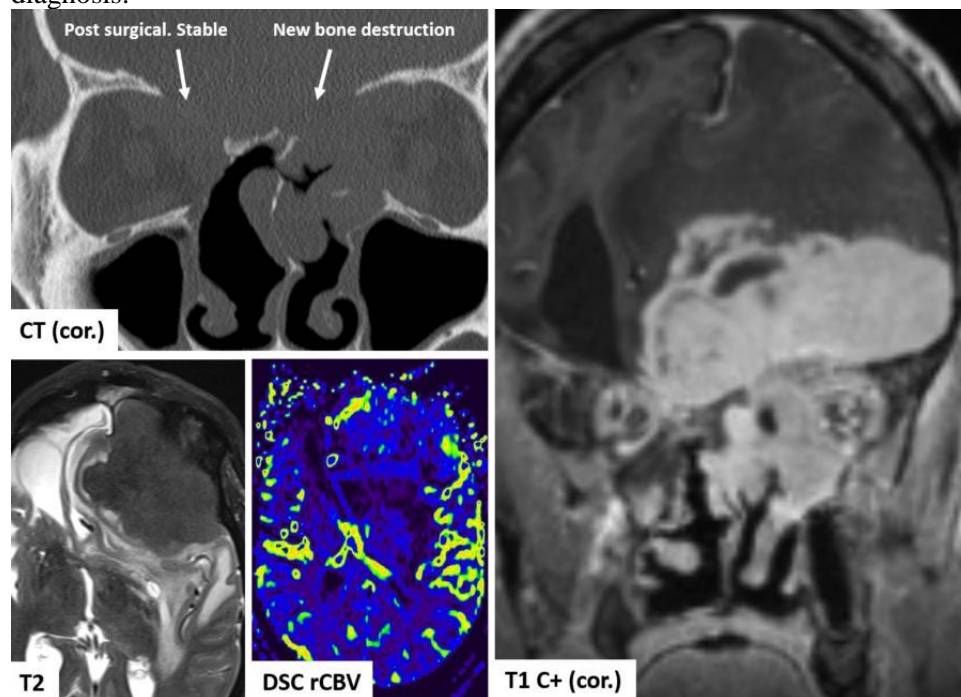
A 48-year-old immunocompetent male with history of surgically resected fungal mass 25 years earlier presented with complaints of vision loss and headaches. Sinus-CT 7 years prior demonstrated postsurgical changes without evidence of relapse. Imaging studies from his most recent admission showed a sinonasal mass with intracranial extension which was surgically resected. Pathology revealed marked chronic inflammation and fungal forms with culture yielding *Aspergillus flavus*.

Results

CT demonstrated postsurgical changes on the right with new osseous destruction on the left and a soft tissue mass extending into the left naso-ethmoidal cavity and orbit. MRI showed an avidly enhancing mass with large intracranial mass effect. There was markedly low T2, DWI and ADC signal probably representing a T2 blackout effect, as well as dot-like foci of paramagnetic artifact on SWI. DSC-perfusion map showed decreased rCBV. The appearance was very similar to the fungal mass that had been resected 25 years prior.

Conclusions

GIFS is a rare form of mass-forming fungal disease that can be mistaken for malignancy. Certain imaging findings such as low T2-signal, paramagnetic deposits, and decreased perfusion may suggest the diagnosis.



(Filename: TCT_E-74_imagen300.jpg)

E-75

5:33PM - 5:37PM

On the nose diagnosis: a case of nasal extranodal NK/T cell lymphoma.

A Goldman-Yassen¹, A Levitt¹, D Ginsburg¹, J Burns¹, T Miller¹, J Bello¹, K Shifteh¹
¹*Montefiore Medical Center, Bronx, NY*

Purpose

To describe a case and review the clinical and imaging findings of extranodal NK/T cell lymphoma of the nasal cavity

Materials and Methods

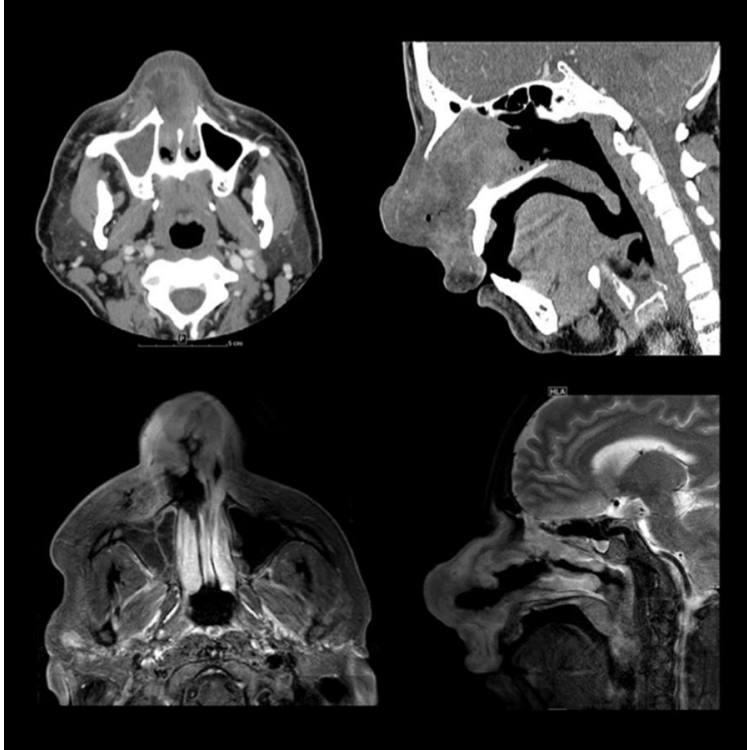
A 32-year-old Hispanic man without significant past medical history presented with nasal pain and swelling, progressive over 6 weeks. He had been hospitalized previously for the same problem at an outside hospital and treated with antibiotics, without improvement. Since that hospitalization, the swelling extended to his upper lip and he developed difficulty swallowing, headache, and nasal drainage. On presentation, he was afebrile, without leukocytosis. Physical examination demonstrated diffuse swelling and tenderness of the nose with honey-colored crusting extending to above his upper lip. With a presumed diagnosis of a severe sinonasal infection he underwent bedside incision and drainage without much purulence noted. He was taken to the operating room, where the nasal cavities were found to be filled with necrotic debris, without recognizable landmarks and a large anterior septal perforation was present. Biopsy demonstrated atypical angiocentric/angiodesructive NK/T cell proliferation. Epstein-Barr virus (EBV) encoded ribonucleic acid in situ hybridization (EBER) was diffusely positive. Together, these findings supported the diagnosis of extranodal NK/T cell lymphoma, nasal type. Bone marrow biopsy was normal. Staging F18-FDG PET/CT demonstrated multiple FDG avid cervical lymph nodes. He was started on dexamethasone, etoposide, ifosfamide and carboplatin (DeVIC regimen) with concurrent radiation therapy.

Results

Contrast-enhanced computed tomography demonstrates marked soft tissue swelling and fullness with abnormal enhancement involving the nasal cavity, including bilateral nasal ala, with areas of necrosis and emphysema. There is no significant bony erosion or associated soft tissue calcification. Magnetic resonance images obtained following bedside debridement demonstrate the soft tissue fullness, isointense to muscle on T1-weighted images and hyperintense on T2-weighted images, with fairly homogenous enhancement of the solid component on gadolinium-enhanced T1-weighted images. There is no intracranial or intraorbital extension of disease.

Conclusions

Extranodal NK/T-cell lymphoma of the nasal type is uncommon in the United States and Europe, more often diagnosed in patients from Asia and Central and South America. The nose is the most frequently involved extranodal tissue; other primary extranodal sites include the palate and upper airway, with rare nodal involvement. The course is aggressive and the prognosis poor. Angiocentric/angiodesructive histology is typical of extranodal NK/T cell lymphoma and invasion of vascular walls causes occlusion of the lumen, resulting in prominent ischemic necrosis of both tumor cells and normal tissue, as was seen in this case. It is highly associated with Epstein-Barr viral infection. Most lymphomas that originate from the nasal cavity or ethmoid sinus are T-cell in origin, which have a worse prognosis than lymphomas that originate from the maxillary sinus, which are more commonly B-cell lymphomas, with a better prognosis. CT and MR imaging appearances are nonspecific; other nasal cavity tumors such as squamous cell carcinoma and nonneoplastic conditions such as necrotizing fasciitis and granulomatosis with polyangiitis may have a similar imaging appearance. More specific imaging findings include preferential involvement of the nasal cavity with diffuse mucosal/submucosal infiltration and tumor extension with little bone destruction, as demonstrated in this case.



(Filename: TCT_E-75_Slide1.jpg)

E-76

5:37PM - 5:41PM

Masticator Space Mass in a Two Year Old

R Fullerton¹, A Levitt¹, D Ginsburg¹, J Bello¹, K Shifteh¹
¹Montefiore Medical Center, Bronx, NY

Purpose

To describe a case and to review the clinical and imaging findings of extra cranial germ-cell tumors of the head and neck

Materials and Methods

Patient is a 2-year-old female with no past medical history who presents with 1 week of decreased oral intake and left-sided cheek swelling. The patient's father took her to the dentist, where she was given a course of azithromycin for a presumed dental abscess. After completing her course of antibiotics, the patient's swelling had not subsided, and the patient was referred to oral and maxillofacial surgery for further management. A biopsy and contrast enhanced MRI and CT of the lesion were obtained.

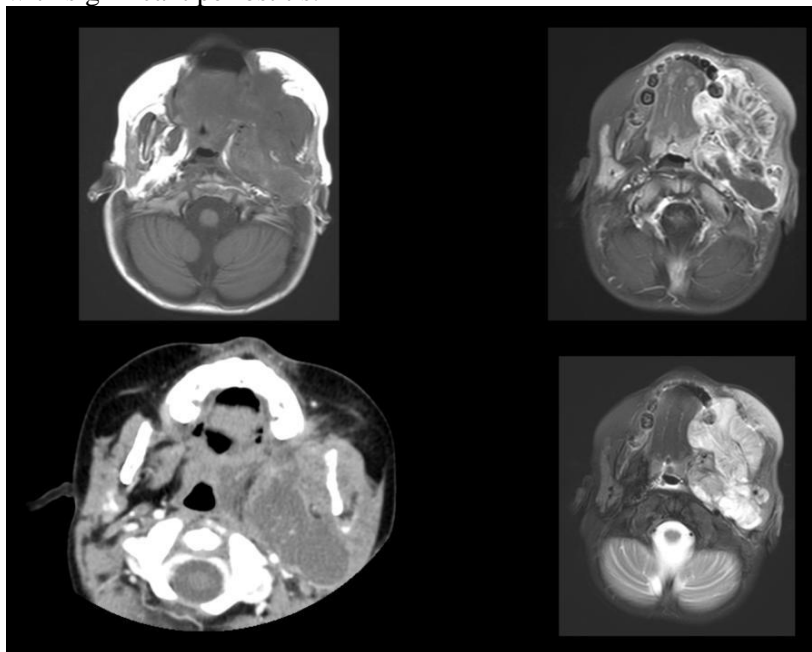
Results

CT demonstrates a multiloculated hypoattenuating lesion centered in the left masticator space with peripheral enhancement and erosion of the adjacent mandibular cortex. MRI demonstrates an irregular, lobulated, heterogenous mass involving the left masticator, buccal, parapharyngeal, and submandibular spaces. The lesion is isointense to muscle on T1-weighted images and is hyperintense on T2-weighted images. There are enhancing septations with a nonenhancing portion along the posterior aspect of the mass. There is extension into the left foramen ovale.

Conclusions

Germ cell tumors can be found outside of the gonads, with the most common extragonadal sites including the anterior mediastinum, central nervous system, and sacrococcygeal region. However, extracranial head

and neck germ cell tumors are rare. Germ cell tumors can be generally broken down into four categories: seminomatous, nonseminomatous, teratomas, and mixed. Seminomatous tumors are homogenous and lobulated on CT and MR with enhancing fibrovascular septa. Nonseminomatous tumors are heterogeneously enhancing with areas of hemorrhage and necrosis. Areas of hypoattenuation on noncontrast CT can be seen, as well as focal areas of T1 hyperintensity. These masses have irregular borders, with invasion of adjacent structures. Teratomas are cystic, usually contain gross fat, and are benign appearing. Other malignant lesions that can occur in the masticator space include rhabdomyosarcoma, Ewing sarcoma of the mandible, and metastatic neuroblastoma. Rhabdomyosarcoma is usually isointense to muscle on T1 images and demonstrates moderate, homogenous enhancement. Bony and perineural invasion may also occur. Ewing sarcoma will demonstrate a permeative destructive lesion with a soft-tissue component. The lesion is usually hypointense on T1 and hyperintense on T2, with the classic "onion skin" periosteal reaction rare in head and neck Ewing sarcoma. Metastatic neuroblastoma to the mandible is rare but reported. These soft-tissue lesions are usually partially calcified with significant periostitis.



(Filename: TCT_E-76_germcelltumorimageshires.jpg)

E-77

5:41PM - 5:45PM

Epstein Barr Virus Associated Smooth Muscle Tumor in the Head & Neck

W Mallon¹, A Levitt¹, D Ginsburg¹, J Lee¹, S Slasky², J Bello¹, K Shifteh¹

Montefiore Medical Center, New York, NY, ²Rutgers-New Jersey Medical School, Newark, NJ

Purpose

To describe the imaging features of a rare case of Epstein-Barr Virus smooth muscle tumor in the head and neck

Materials and Methods

The patient is a 36-year-old male with a history of multiple prior hospital admissions related to severe immunocompromise from poorly controlled HIV/AIDS and resultant CMV retinitis, disseminated histoplasmosis as well as perianal fistula/abscess. An MRI of the brain was performed for altered mental

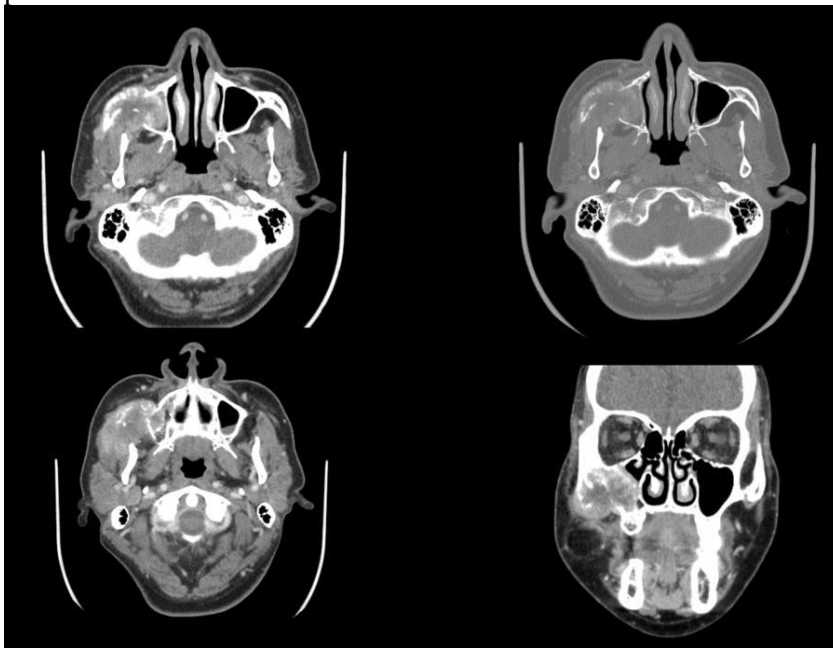
status in the midst of a 4-month long hospitalization and a right masticator space lesion was incidentally seen. A dedicated CT of the neck was performed at this time.

Results

Contrast enhanced CT of the neck demonstrates a soft tissue mass centered in the right maxillary sinus with infiltration into the adjacent soft tissues and erosion of the adjacent bones.

Conclusions

The pathogenesis of EBV-SMT is thought to be related to the infection and neoplastic transformation of smooth muscle cells by EBV with clonal expansion. These tumors have a propensity to arise in virtually any anatomical location. A review of 64 published cases of EBV-SMT published in the English language demonstrated EBV-SMT tumors to be relatively more common in the CNS (20%) and soft tissues (18%) with only 9% of cases arising in the head and neck. A unique feature of EBV-SMT in AIDS patients is their frequent multifocal involvement (more than 50% cases) which is not typically seen in immunocompetent individuals. This finding was true in this immunocompromised patient, who developed an additional EBV-SMT in his left thigh. The differential diagnosis of a spindle-cell neoplasm arising in the setting of HIV infection includes Kaposi sarcoma, osteosarcoma, squamous cell carcinoma and metastatic disease. Kaposi sarcoma is a vascular tumor that more typically involves the skin although mucosal involvement with bone invasion may be seen. Osteosarcoma more commonly involves the mandible although it can present in the maxilla with aggressive osseous destruction and periosteal reaction as in this patient. Squamous cell carcinoma presenting in the masticator space typically originates from the oral cavity, oropharynx or CN V3, none of which were seen in this case. Metastatic disease may also cause aggressive bony destructive changes but typically without significant periosteal reaction or peritumoral calcification.



(Filename: TCT_E-77_EBVsmoothmuscleumorhires.jpg)

E-78

5:45PM - 5:49PM

Uncommon Appearance of Peritonsillar Abscess

F Boucher¹, Z Bhatti¹, D Quint¹, O Khan¹

¹University of Michigan, Ann Arbor, MI

Purpose

Demonstrate an atypical appearance of a peritonsillar abscess, in a pediatric patient, and suggest that the atypical appearance may be due to the specific causative organisms

Materials and Methods

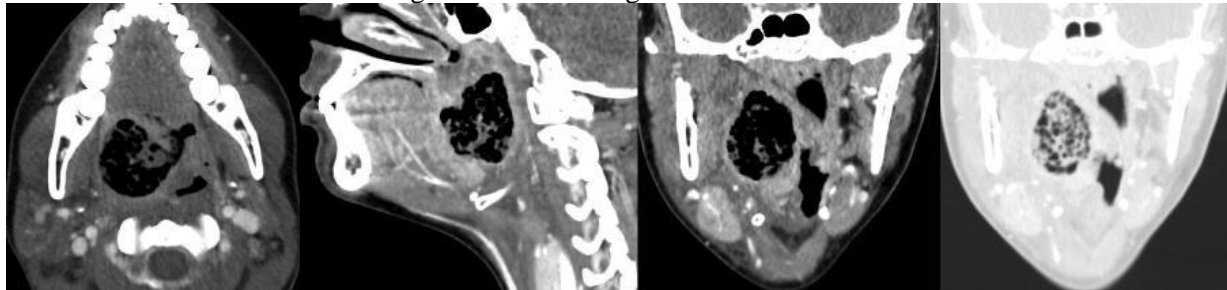
A 14-year-old female patient presented to the emergency department with fever, odynophagia, and hematemesis. Contrast-enhanced CT of the neck was performed.

Results

Contrast-enhanced CT demonstrated a large right peritonsillar gas and fluid collection, effacing much of the oropharynx. The appearance was somewhat atypical given the predominant gaseous component. Vascularity surrounding the abscess was patent. Inquiry to the primary team confirmed that no manipulation or instrumentation had been performed. Interrogation of the electronic chart revealed that the patient is immune-compromised with neutropenia due to aplastic anemia, additional significant laboratory finding of thrombocytopenia. The patient was medically optimized and underwent tonsillectomy with pharyngeal debridement.

Conclusions

Cultures grew multiple microorganisms, including *Fusobacterium necrophorum*, an obligate anaerobic gram negative bacteria which is the causative agent in Lemierre's syndrome (not present in this case). It was possible that the predominantly gaseous component of this patient's peritonsillar abscess was due to gas production from anaerobic organisms, especially given the lack of prior instrumentation at the time of imaging. The patient received intravenous Piperacillin/tazobactam for several days. She was eventually transitioned to an oral antibiotic regimen and discharged home.



(Filename: TCT_E-78_Abscessmerged.jpg)

E-79

5:49PM - 5:53PM

Stop and Smell the Rosai: Sinonasal Rosai-Dorfman Disease Presenting with Isolated Nasal Obstruction

D Josifoski¹, P Morden¹, S Patel¹, H Marin¹, J Craig¹, B Griffith¹

¹Henry Ford Health System, Detroit, MI

Purpose

Rosai-Dorfman disease (RDD) is a rare histiocytic proliferative disorder typically characterized by massive painless cervical lymphadenopathy in children or young adults. Extranodal involvement, however, is not uncommon and has been reported in 43% of cases, with the head and neck the most common site of occurrence. While less common, nasal cavity and paranasal sinus involvement has been reported in 11% of cases. This excerpt describes a case of sinonasal RDD, highlighting the important imaging characteristics and differential diagnosis.

Materials and Methods

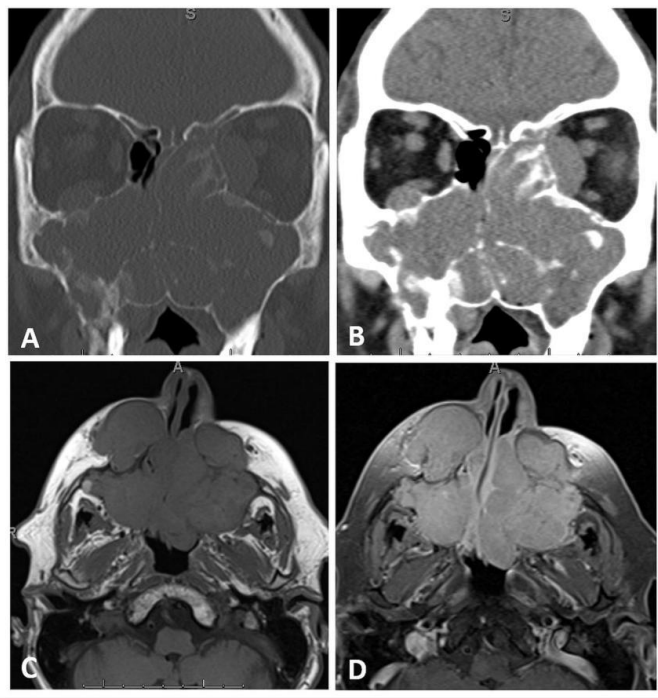
This is a case of a 67-year-old female presenting with a 2-year history of bilateral nasal obstruction, gradually worsening diplopia, and a gradually enlarging right cheek bulge. Nasal endoscopy revealed a polypoid mucosalized mass filling both nasal cavities. Biopsy of the mass was consistent with RDD.

Results

CT demonstrated bulky homogeneous soft tissue density filling all of the paranasal sinuses and bilateral nasal cavities, with erosion of some of the orbital walls and anterior walls of the maxillary sinuses. There was also extension of the tumor into the orbits and premaxillary soft tissues. MRI revealed a T1 isointense soft tissue mass with diffuse homogeneous gadolinium enhancement.

Conclusions

Rosai-Dorfman disease typically presents in childhood or early adulthood with involvement of the cervical lymph nodes. When extranodal, the head and neck region is most commonly involved, with involvement of the nasal cavity and paranasal sinuses reported in 11% of cases. Given its rarity, sinonasal RDD poses a significant diagnostic challenge. Additionally, treatment is also challenging due to a lack of high-quality clinical studies. This case highlights the importance of including RDD in the differential diagnosis of sinonasal masses.



(Filename: TCT_E-79_RDD.jpg)

E-80

5:53PM - 5:57PM

Styloid Process Osteoradionecrosis

A Elakkad¹, L Ginsberg¹

¹MD Anderson Cancer Center, Houston, TX

Purpose

Radiation therapy is a mainstay of head and neck cancer therapy. Osteoradionecrosis (ORN) is a known side-effect of radiation affecting 5-22% of treated patients. Although the mandible is the most common site of ORN, any bone within the radiation field can be affected. We present the imaging findings of styloid process osteoradionecrosis in 2 patients.

Materials and Methods

Patient 1: A 69-year-old male patient with squamous cell carcinoma (SCC) of the right glossopharyngeal sulcus was treated to a dose 70Gy. He presented 20 months following XRT with right-sided facial pain, trismus and dysphagia. Imaging was initially regarded as negative, but after two months of symptom

Oral Presentations & Excerptas

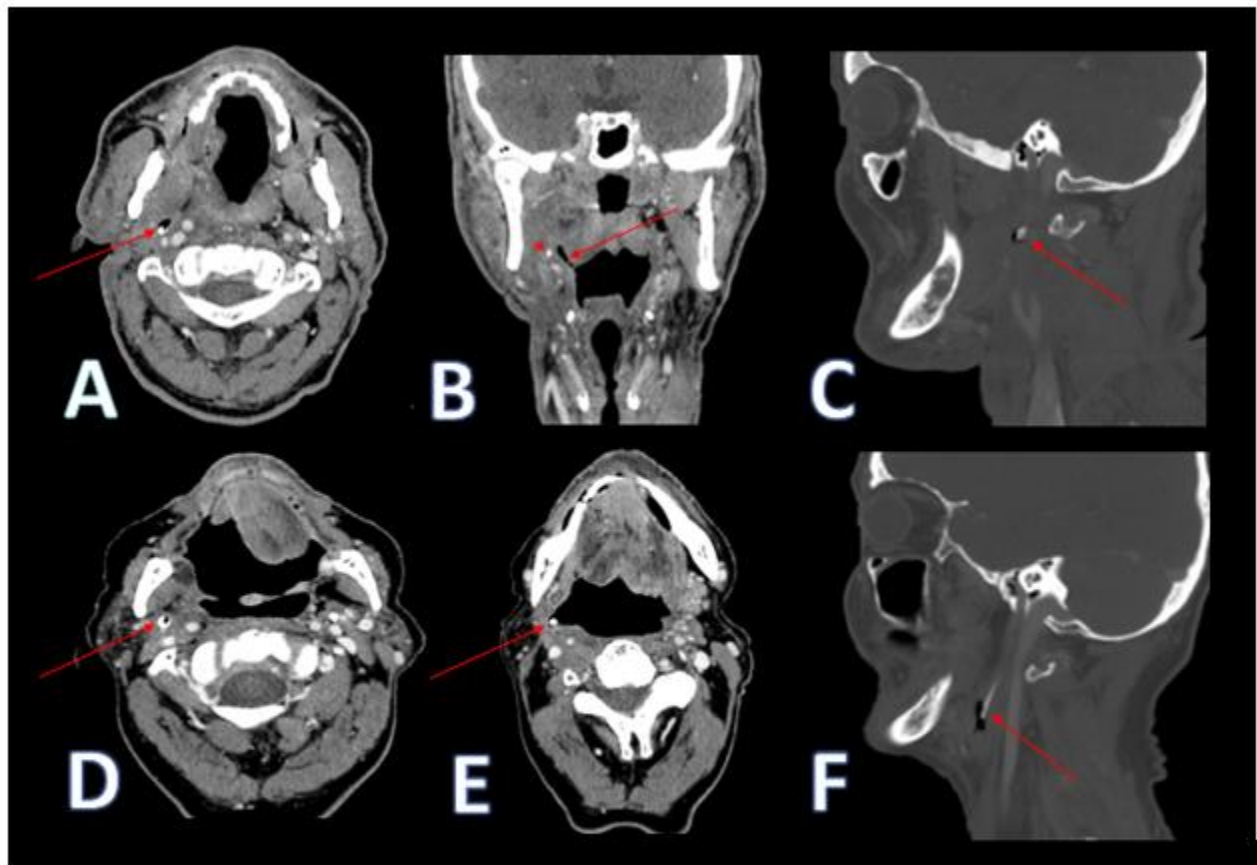
progression, CT revealed a small pharyngeal mucosal defect leading to an exposed right styloid process with intraosseous air, findings evident in retrospect on the earlier exam. Patient 2: A 65-year-old male patient with right tonsillar SCC was treated with 66Gy XRT and 8 years later presented with worsening right throat pain, dysphagia and severe right otalgia. CT showed a debris-filled pharyngeal ulcer, and an exposed styloid with intraosseous air. Relentless symptoms necessitated composite resection including partial pharyngectomy, styloid resection, and free flap reconstruction.

Results

Both cases share common imaging findings of mucosal defects directly in contact with or leading to a styloid process surrounded by and itself containing intraosseous air.

Conclusions

To our knowledge, we are presenting the first radiology report of styloid process ORN in imaging literature. We presume that styloid process ORN to be rare, given the limited available data on this entity. Patients likely have one or more of following symptoms: throat pain, dysphagia, or trismus, symptoms also typical of mucosal ulceration, which in our two patients was also present. CT is a valuable tool in diagnosis of styloid process ORN. CT is ideal in detecting the mucosal defects, styloid findings and would also be useful in the case of infectious complication.



Case 1 (Figures: A-C) Exposed right styloid process with surrounding air (arrows in A&C). Figure B shows a mucosal defect (arrow) leading to the styloid process (red asterisk). Case 2 (Figure D-F) shows the right styloid process with intraosseous air (arrow in D) and ulceration of the right pharyngeal wall with extrusion of the styloid process into the lumen (arrows in E &F).

(Filename: TCT_E-80_Capture.jpg)

Tuesday, June 5, 2018

4:45PM - 6:15PM

Parallel Paper Session: Brain Tumors: New Diagnostic Considerations I

O-329

4:45PM - 4:52PM

The status of the MGMT promoter is associated with magnetic resonance imaging characteristics and prognosis in glioblastomas

R Wang¹

¹*The Affiliated Hospital of Guizhou Medical University, Guiyang, China*

Purpose

The Glioblastoma (GBM) is the most malignant and lethal tumor, whose prognosis is very poor. It used to appear mostly in the older generations because brain cells decline with age. Once confirmed, the five-year survival rate no more than 5%. The O6-methylguanine-DNA-methyltransferase (MGMT) promoter methylation is closely tied to a better prognosis in GBM patients and is sensitive to chemotherapy such as temozolomide(TMZ). It is important to confirm MGMT promoter genotype in GBM. If we comprehend the status of the MGMT promoter, we will work out a personalized program for patients, treatment.

Materials and Methods

In this study with 43 GBM patients enrolled who had MGMT status measured, the research mainly investigated the relationship between the status of the MGMT promoter and magnetic resonance imaging (MRI) characteristics and prognosis. These include 24 patients who were MGMT promoter methylation and the others were not. The clinical data were related to the methylation status by Kaplan-Meier analyses.

Results

The results showed that the mass effect was severe for MGMT promoter methylation which often appeared in right temporal. The larger the tumor volume and the degree of edema more severe, the worse the prognosis. Karnofsky Performance(KPS) Scores greater than 70 show longer overall survival.

Conclusions

The patients who received radiotherapy, chemotherapy and surgery treatment their overall survival will be longer than the others. The results of the study revealed that patients who are with MGMT promoter methylation will prolong their lives.

O-330

4:52PM - 4:59PM

Differentiation primary central nervous system lymphoma from glioblastoma: probabilistic analysis using voxel-based morphometry

K Yamashita¹, A Hiwatashi¹, O Togao¹, D Momosaka¹, H Honda¹

¹*Kyushu University, Fukuoka, Japan*

Purpose

MR imaging is a main noninvasive technique to assess the intracranial tumor locations preoperatively. Our purpose was to evaluate the diagnostic feasibility of probabilistic analysis using voxel-based morphometry (VBM) in differentiating primary central nervous system lymphoma (PCNSL) from glioblastoma (GBM).

Materials and Methods

We retrospectively studied 118 patients with GBM (M: F = 57:61; mean age \pm SD = 56.9 \pm 19.3 years old, median = 61 years old) and 52 patients with PCNSL (M: F = 37:15; mean age \pm SD = 62.0 \pm 13.3

Oral Presentations & Excerptas

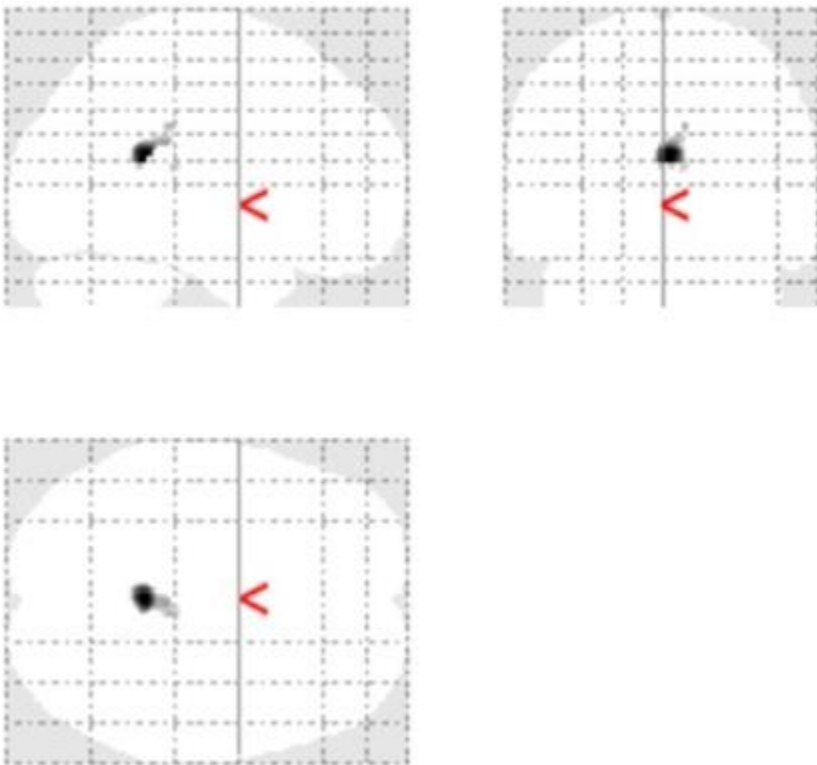
years old, median = 66 years old). Each patient underwent preoperative postcontrast T1-weighted images with a 1.5 or 3 T MR scanner. Postcontrast T1-weighted images were coregistered and spatially normalized using MNI152 template. Subsequently, a region of interest (ROI) was placed in the center of enhancing tumor in the normalized images with 1mm isotropic resolution. The identical ROI between normalized and MNI152 template images was set up using ROI manager function with ImageJ software. Then, spherical volume of interest (VOI) of radius 10mm was manually determined. Each VOI was removed from the MNI152 template images for subsequent VBM analysis. To compare the differences of preferential occurrence site between PCNSL and GBM, VBM analysis was performed using SPM 12 software, and the default setting was chosen.

Results

VBM analysis revealed significantly higher frequency of occurrence in the splenium of corpus callosum in PCNSL than in GBM patients ($p < 0.05$; family-wise error correction). Frequency map demonstrates that GBM has a tendency to be situated in deep white matter.

Conclusions

Probabilistic analysis using VBM provides useful information for differentiating PCNSL from GBM.



(Filename: TCT_O-330_2.jpg)

O-331

4:59PM - 5:06PM

A Move Towards Structured Reporting for Post Treatment Glioma Response

A Gore¹, M Hoch¹, B Weinberg¹

¹Emory University Hospital, Atlanta, GA

Purpose

Assessment of post-treatment glioma response remains challenging, particularly differentiating tumor progression from treatment effects. The lack of standardized reporting adds to the complexity and

Oral Presentations & Excerpts

variability in interpretations. We identify areas of improvement needed in the current reporting system at our institution.

Materials and Methods

A comprehensive 22 question survey designed to obtain feedback on current MRI brain tumor reports was sent to various specialists, including: neurooncologists, neurosurgeons, pathologists, radiologists, and radiation oncologists at our institution. All specialists participated in the care of brain tumor patients. The survey was divided into multiple sections with emphasis on the quality of current MRI brain tumor reports, areas of improvement/structured formatting, trust in radiology reports to guide management, and overall satisfaction in brain tumor reporting.

Results

A total of 53 participants including 27 radiologists and 26 nonradiologists responded to the survey and multiple areas of concern were identified (Table 1). Both groups noted a lack of consistency between reports with radiologists less satisfied with consistency. Both groups also recognized significant ambiguity within a single report regarding brain tumor response and felt the current reporting system has disadvantages compared to structured reporting. Current reporting only sometimes promoted clear communication between patients and physicians and between radiologists and referring physicians. Additionally, there was a strong consensus that patients were only sometimes satisfied with their brain tumor MRI reports. Among both radiologists and nonradiologists, there was a strong desire for developing reports with structured findings and impression sections tied to management that would aid clinical decisions in brain tumor care.

Conclusions

Our survey recognizes the needed improvement in the current reporting system in patients with brain tumors. We aim to develop a standardized reporting system to better assist clinicians with management decisions and improve value-based care.

Table 1 Opinions regarding current brain tumor surveillance MRI reports

	All	Radiologist	Non-Radiologist	p-value
How well do the current radiology reports				
Clearly communicate the relevant findings	3.85	3.67	4.04	0.0587
Maintain consistency	3.43	3.22	3.65	0.0841
Refrain from ambiguity	3.15	2.93	3.38	0.0979
Promote clear communication between patient and physician	3.42	3.11	3.73	0.0078
Promote clear communication between radiologist and ordering physician	3.77	3.48	4.08	0.0020
Facilitate decision-making for treatment	3.60	3.30	3.92	0.0042
Match your practice patterns	3.68	3.41	3.96	0.0062
Facilitate research	3.08	2.52	3.65	0.0000
Facilitate trainee (resident and fellow) education	3.60	3.30	3.92	0.0086
Promote confidence in report findings	3.51	3.19	3.85	0.0057
How strongly do you agree with the following statements				
Finding sections should adhere to a structured format	4.23	4.33	4.12	0.3785
Impression sections in radiology reports should adhere to a structured format	4.42	4.44	4.38	0.7733
It would be helpful if report impressions provided categories which corresponded to suggested management decisions	4.26	4.59	3.92	0.0035
Overall satisfaction				
Overall, how satisfied are you with the primary brain tumor MRI reports?	3.74	3.48	4.00	0.0264
Overall, what is your perception of patient satisfaction with brain tumor MRI reports?	3.38	3.13	3.63	0.0378
What is your overall level of trust in the information contained in radiology reports for MRIs on brain tumor patients?	3.92	3.70	4.15	0.0345

Values are based on a 5 point Likert scale (1-Never, 2-Rarely, 3-Sometimes, 4-Often, 5-Always). Values in red are less than 3.5 and in green are greater than 4. p-values are for comparison between radiologists and non-radiologists ($p < 0.05$ is significant; red).

(Filename: TCT_O-331_Table1.jpg)

O-332

5:06PM - 5:13PM

Visually AcceSable Rembrandt Images Assessment features predict recurrent GBM prognostic outcomes

X Du¹

¹Daping Hospital, Chongqing, China

Purpose

To estimate Visually AcceSable Rembrandt Images Assessment (VASARI) features in predicting recurrent GBM (rGBM) prognostic outcomes

Materials and Methods

Patients' clinical and MRI data were collected retrospectively. VASARI features, prognostic outcomes contained time to recurrence (TTR) and recurrent patterns were analyzed. Features' correlations with TTR were evaluated using Spearman correlation analysis and COX proportional hazards regression model. Univariate and multivariate analysis was used to estimate significant predictor for recurrent patterns.

Results

Sixty-five patients were involved, 30 VASARI features and two recurrent patterns (local and distant)

were defined. Four VASARI features including multifocal, enhancing tumor crosses midline, satellites and lesion size correlated with TTR ($r=-0.326, -0.264, -0.383, 0.425$, respectively, $P<0.05$) and multivariate analysis confirmed satellites as a significant indicator for shorter TTR ($OR=0.281, P=0.014$), independent of age, KPS and chemoradiotherapy. Univariate analysis revealed significant differences of proportion necrosis, definition of the nonenhancing, cortical involvement between two recurrent patterns ($Z=-2.337, -2.235, -2.350$, respectively, $P<0.05$). On multivariate regression analysis, proportion necrosis was an independent predictor for "distant" recurrence ($OR=0.461, P=0.034$).

Conclusions

VASARI features associated with recurrent GBM patterns and TTR could be potential predictors for recurrent GBM prognostic outcomes.

O-333

5:13PM - 5:20PM

Usefulness of turbo spin-echo diffusion-weighted imaging for evaluating various pituitary lesions

M Azuma¹, Z Khant¹, Y Kadota¹, M Enzaki¹, T Watanabe¹, K Yokogami¹, H Takeshima¹, T Hirai¹

¹*University of Miyazaki, Miyazaki, Japan*

Purpose

To determine the usefulness of turbo-spin echo diffusion-weighted imaging (TSE-DWI) in the evaluation of various pituitary lesions compared with echo planar (EP) DWI

Materials and Methods

We included consecutive 22 patients with pituitary lesion who underwent conventional pre and postcontrast MR imaging (MRI) and TSE- and EP-DWI at 3T. They included 12 pituitary adenomas (PA), six Rathke's cleft cysts (RCC) and four craniopharyngiomas (CR). Among them, 10 PA and two CR were surgically confirmed. On sagittal DWI and apparent diffusion coefficient (ADC) maps, two radiologists evaluated the visualization of the optic chiasm, pituitary gland and pituitary stalk and the spatial relationship between the lesion and its normal surroundings compared with contrast-enhanced T1-weighted sagittal images, and the whole image quality. For quantitative study, ADC values and signal-to-noise ratio (SNR) were evaluated. For statistical analysis, Wilcoxon signed-rank test, Cohen's kappa coefficient and Pearson's correlation coefficients were used.

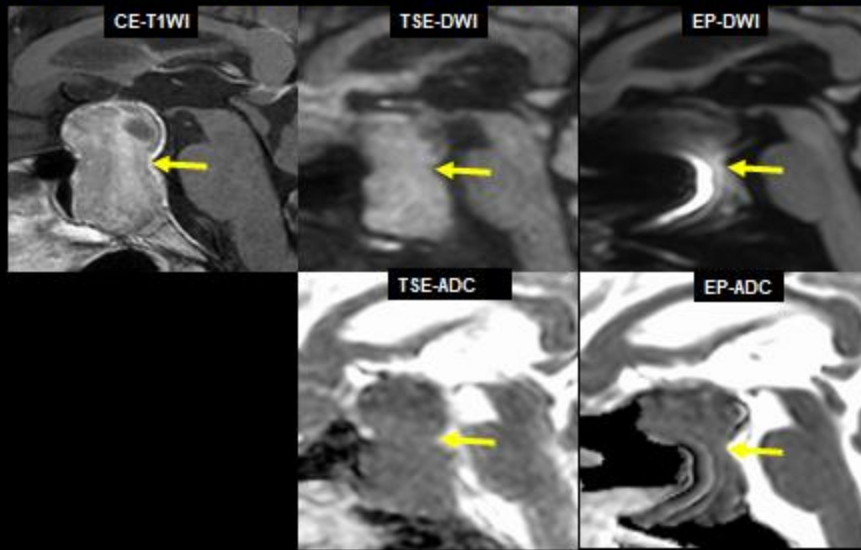
Results

On both DWI and ADC maps, the whole image quality and the visualization of the pituitary gland and the spatial relationship between the lesion and its normal surroundings were significantly better for TSE than EP sequences ($P < 0.05$). There was moderate to very good interobserver agreement for the qualitative evaluations ($\text{kappa} = 0.46 - 1.0$). In ADC values measured on TSE- and EP-ADC maps, there was a significant correlation ($r = 0.64, P < 0.05$). In SNR, there was no significant difference between the two types of DWI ($P > 0.05$).

Conclusions

In the evaluation of pituitary lesions, TSE-DWI is more useful than EP-DWI.

A 78-y.o. woman with pathologically proven pituitary adenoma



(Filename: TCT_O-333_Fig.jpg)

O-334

5:20PM - 5:27PM

White Matter Matters: Consequences of ROI Misplacements in MR Perfusion Analysis Pretreatment Primary Brain Tumor

B Matos¹, F Nascimento¹, M Camargo¹, R Soares¹, S Malheiros¹, A Barbosa¹, E Amaro¹
¹Hospital Israelita Albert Einstein, São Paulo, São Paulo

Purpose

Cerebral white matter is known to have inhomogeneous rCBV values and knowing the mean values and the variability of its different regions can help make a more accurate analysis of tumor perfusion which can impact directly in clinical decisions.

Materials and Methods

We analyzed 46 patients diagnosed with primary brain tumor (10 low/36 high grade) before treatment. We used routine software processing tools (ADW-Server - GE, U.S.) for rCBV calculation and ROI-based MR-perfusion evaluation with 5mm circular ROIs positioned in eight different contrasting areas of each lesion and compared the rCBV values in relation to ROIs positioned in white matter regions (30 ROIs standardized locations: 24 subcortical, two semioval center, four periventricular) and to eight automatically placed homologous regions (symmetrical and contralateral) to the tumor ROIs. We measured each ROI variability and the relationship between tumor ROIs and various control ROIs as described above. Statistical analysis including median and mean rCBV values, standard deviation and coefficient of variation were calculated.

Results

The rCBV values based on 46 patients for the three white-matter (WM) regions are different ($p < 0,001$; Mann-Whitney) (see table). Periventricular WM regions showed highest rCBV and the semioval center has lowest rCBV. In 9% of cases (four cases), tumor ROI rCBV/white matter rCBV relationship crossed

changed from above or below 1,75 criteria (Law et al, AJNR 2003) according to the location of the control ROI. All discordant cases were observed in low grade tumors.

Conclusions

Our initial results highlight the relevance of standard placement of ROIs in white-matter region as control regions for primary brain tumor. Depending on control ROI placement, rCBV relation can be higher or lower than 1,75 and this could indicate changes the clinical management.

ID	av_SubcorticalWM	av_SemiovalcenterWH	av_PeriventricularWM
Number of values	46	46	46
Minimum	24,77	24,1	28,79
25% Percentile	42,39	34,16	45,83
Median	49,32	42,29	57,89
75% Percentile	58,35	49,72	71,33
Maximum	79,39	78,02	89,79
Mean	50,5	44,04	58,75
Std. Deviation	12,66	12,24	15,8
Std. Error of Mean	1,867	1,805	2,329
Lower 95% CI of mean	46,74	40,41	54,06
Upper 95% CI of mean	54,25	47,68	63,44
95% CI of median			
Actual confidence level	97.41%	97.41%	97.41%
Lower confidence limit	44,86	36,23	47,36
Upper confidence limit	56,01	45,98	67,92
Coefficient of variation	25.07%	27.79%	26.89%
Skewness	0,3276	0,937	0,141
Kurtosis	0,2482	0,4921	-1,002
Sum	2323	2026	2703
D'Agostino & Pearson normality test			
K2	1,278	7,206	5,354
P value	0,5278	0,0272	0,0688
Passed normality test (alpha=0.05)?	Yes	No	Yes
P value summary	ns	*	ns
Shapiro-Wilk normality test			
W	0,9723	0,9319	0,9683
P value	0,3375	0,0099	0,2385

(Filename: TCT_O-334_table.jpg)

O-335

5:27PM - 5:34PM

Assessment of early Wallerian degeneration using synthetic MRI and MR fibrography

O Sakai¹, V Andreu¹, M Chapman¹, M Horn¹, H Jara¹

¹Boston Medical Center, Boston University School of Medicine, Boston, MA

Purpose

Wallerian degeneration represents antegrade axonal degeneration after an insult to the cell body. Signal abnormalities on DWI within the corticospinal tract are a marker of underlying parenchymal atrophy, gliosis, and myelin loss, and a predictor of poor outcome. MR fibrography is a recently developed

Oral Presentations & Excerptas

imaging technique based on synthetic MRI with which the global wiring of the brain, or connectome, can be rendered in three dimensions at high spatial resolution and with the unrivaled anatomic accuracy of the turbo-spin echo (TSE) pulse sequence. The purpose of this study was to assess early Wallerian degeneration using synthetic MRI with WMF in patients with acute infarct.

Materials and Methods

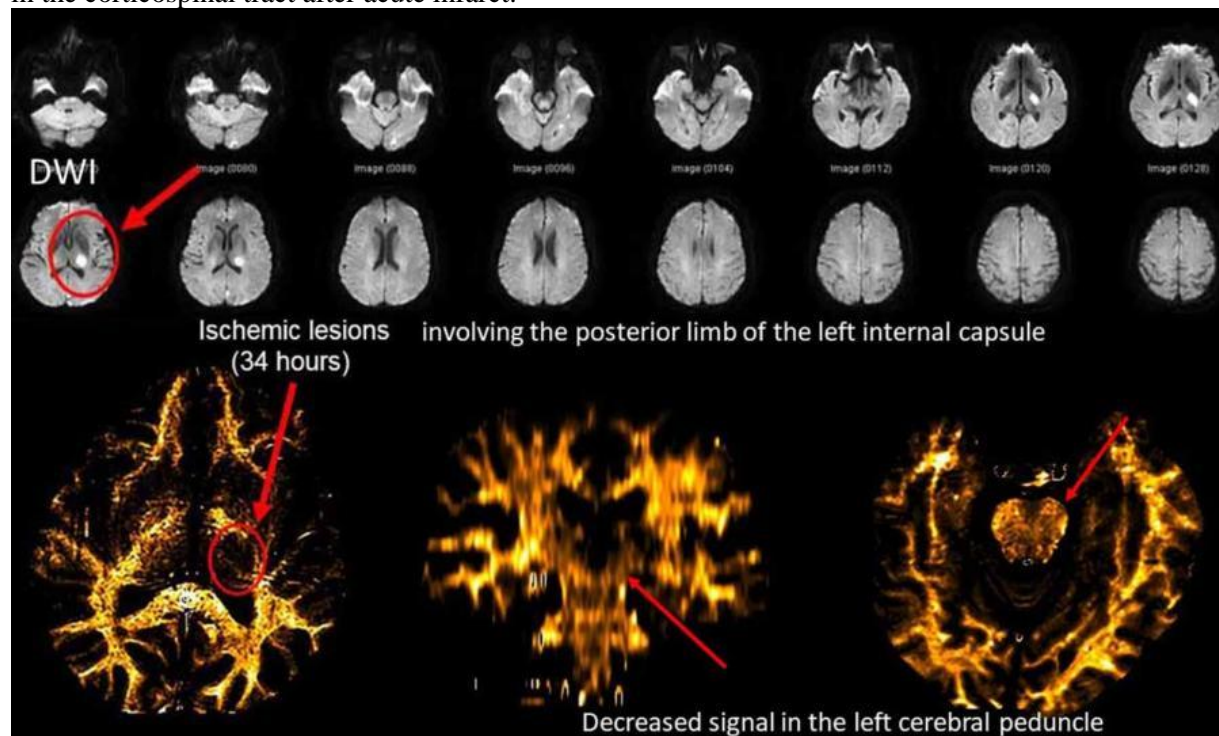
In this IRB approved retrospective study, the Tri-TSE 3T-MRI scans of 15 patients with acute infarct were processed with a synthetic-MRI program that allows for creating weighted images of the four principal qMRI parameters: proton-density (PD), correlation time diffusion coefficient (Dct), T1, and T2. Imaging parameters: 36 contiguous slices, voxel=0.5 x 0.5 x 5 mm³, TRs=475&3500ms, TEs=10&90ms. Areas of acute infarcts were first identified as hyperintensities on diffusion-weighted images and then compared to the raw images of the heavily 1/T1 weighted synthetic images of the connectome.

Results

Decreased signal and loss of white-matter fiber integrity was seen on MR fibrography within the corticospinal tract in addition to the area of acute infarct in patients with acute infarct confirmed by DWI (Figure).

Conclusions

MR fibrography is sensitive to loss of myelin water and could be used to identify early secondary changes in the corticospinal tract after acute infarct.



(Filename: TCT_O-335_Presentation1.jpg)

O-336

5:34PM - 5:41PM

Robustness of multi-parametric and multi-regional MRI derived radiomics features in GBM

X Du¹

¹Daping Hospital, Chongqing, China

Purpose

To compare the robustness of multiparametric and multiregional MRI features and optimize the application of these features in GBM

Materials and Methods

One hundred GBM patients confirmed by pathology were included and presurgical MRI data were collected. ROIs were defined manually by three experienced radiologists and radiomics features were extracted. Features' robustness was analyzed using intraclass correlation coefficient (ICC) and their differences were compared.

Results

ROIs were defined as "edema", "necrosis", "contrast", "tumor", "ADC", "SWI" and "anatomy" areas and three feature categories, containing "intensity", "texture" and "shape", were extracted. Out of 401 features 54 belonged to intensity, 331 belonged to texture and 16 to shape. Average robustness of all features was "high" (ICC= 0.9233±0.1105). "Voxel size" has the highest robustness (ICC=1.000), with "-333-4MaxProbability" in "necrosis" area the lowest (ICC=0.1700). Mean ICC in all seven areas showed significant difference (F=265.3, P<0.001) with ICC in edema was the lowest (ICC=0.8532±0.1210). Shape's ICC was the lowest in "SWI", "anatomy", "ADC" and "contrast" areas (F=122.1, 53.84, 28.66 and 32.27, P<0.001, respectively) and intensity was the highest in "edema" and "necrosis" (F=11.00 and 7.675, P<0.001, respectively).

Conclusions

Robustness of radiomics feature in different ROIs derived from multiparametric and multiregional MRI was comparable. This indicated that otherness of feature robustness in different ROIs should be taken into consideration to optimize radiomics application in clinic.

O-337

5:41PM - 5:48PM

Robustness of multi-parametric and multi-regional MRI derived radiomics features in GBM

X Du¹

¹*Daping Hospital, Chongqing, China*

Purpose

To compare the robustness of multiparametric and multiregional MRI features and optimize the application of these features in GBM

Materials and Methods

One hundred GBM patients confirmed by pathology were included and presurgical MRI data were collected. ROIs were defined manually by three experienced radiologists and radiomics features were extracted. Features' robustness was analyzed using intraclass correlation coefficient (ICC) and their differences were compared.

Results

ROIs were defined as "edema", "necrosis", "contrast", "tumor", "ADC", "SWI" and "anatomy" areas and three feature categories, containing "intensity", "texture" and "shape", were extracted. Out of 401 features 54 belonged to intensity, 331 belonged to texture and 16 to shape. Average robustness of all features was "high" (ICC= 0.9233±0.1105). "Voxel size" has the highest robustness (ICC=1.000), with "-333-4MaxProbability" in "necrosis" area has the lowest (ICC=0.1700). Mean ICC in all seven areas showed significant difference (F=265.3, P<0.001) with ICC in edema was the lowest (ICC=0.8532±0.1210). Shape's ICC was the lowest in "SWI", "anatomy", "ADC" and "contrast" areas (F=122.1, 53.84, 28.66 and 32.27, P<0.001, respectively) and intensity was the highest in "edema" and "necrosis" (F=11.00 and 7.675, P<0.001, respectively).

Conclusions

Robustness of radiomics feature in different ROIs derived from multiparametric and multiregional MRI

was comparable. This indicated that otherness of feature robustness in different ROIs showed be taken into consideration to optimize radiomics application in clinic.

O-338

5:48PM - 5:55PM

Identification of thalamic Substructures in high b-value DWI

N Nuessle¹, B Bender¹, U Klose¹

¹*University Hospital Tuebingen, Tuebingen, Germany*

Purpose

In recent years, deep-brain stimulation (DBS) was discovered for treatment of various neurological and psychological diseases. Primarily used in treatment of Parkinson patients, the options nowadays include primary dystonia, epilepsy, depression and others. New targets, especially different thalamic nuclei, have been identified as target regions for DBS. Implantation of modern stimulation devices requires precise structural information of the human brain fitted to patients' individual anatomy. Planning of DBS implantation is usually performed by conventional MRI or CT scans combined with stereotactical anatomical atlases based on postmortem images. Stereotactical data have to be applied to the patients' brain. Therefore, it would be helpful and lead to an increased accuracy of DBS implantation to identify intrathalamic substructures, such as the different thalamic nuclei in preinterventional MR imaging.

Various approaches have been proposed during the last years. The purpose of this study was to evaluate the capability of high b-value DWI in separating and identifying intrathalamic substructures and to compare these images with postmortem histological stereotactical atlases of the human brain. Finally, to introduce a measurement protocol that could allow the preinterventional and individual stereotactical planning of DBS implantations

Materials and Methods

Seven healthy probands (4 male, 3 female) were recruited in a prospective MRI study, approved by the local institutional review board of our university hospital. All probands provided written informed consent, had to be healthy without any cerebral illnesses or injuries, never underwent surgical intervention in the brain region and didn't receive steroid therapy at that time. No contrast medium was used. Measurements were performed on a 3T-MRI scanner, able to obtain relatively high b-values with acceptable noise and vibration levels. MPRAGE 3-D sequence was used to reconstruct anatomically correct images of the probands' brain and to plan acquisition of diffusion-weighted images (DWI) in AC/PC orientation. Spin-echo echo-planar imaging DWI sequence with b-values of 0 (b0) and 5000 s/mm² (b5000) was used and diffusion was encoded in 64 directions. For b0, two and for b5000, five averages were measured. DWI acquisition was not performed as full-brain imaging but we focused on the thalamic and subthalamic region. Following to the MRI scan, images were denoised using total generalized variation. The images were evaluated on a Linux-Fedora-workstation and seven intrathalamic substructures (Pulvinar, Nuclei centrales, Nucleus medialis, Nuclei ventrointermedii, Nuclei ventrocaudales, Nuclei ventrorales and Nucleus lateropolaris thalami), defined prior to the evaluation, were identified and drawn in by hand in the slice 4 mm above the AC/PC line. Later, the defined substructures were compared to a histological stereotactical atlas of the brain.

Results

In all probands, all seven intrathalamic substructures could be identified due to different signal variations. Nuclei, which were drawn in based on DWI, corresponded very well with the histological data from the atlases. In addition, high concordance between the drawn in nuclei in the different probands could be shown. No movement artefacts could be seen on the images and no noise and vibration problems were declared by the patients.

Conclusions

Various techniques for identification of intrathalamic nuclei have been reported previously.

Unfortunately, they are often associated with long acquisition time and complicated postprocessing

procedures. High b-value DWI seems to present a new and simple way to separate different thalamic substructures in preinterventional MR imaging. Acquisition time of 17 minutes may provide problems due to movement artifacts when applied in patients. However, in healthy probands, no movement artifacts were found. Reduction of measured directions could reduce acquisition time while capability of identification remains consistent. In conclusion, high b-value diffusion-weighted imaging shows great potential in determining thalamic substructures. Therefore, as it allows individual mapping of the thalamic nuclei in preinterventional MRI, it could lead to better planning of DBS implantation in neurological and psychiatric patients. Further investigations, trying to reduce the needed acquisition time, may provide sequences that are more easily applicable to patients.

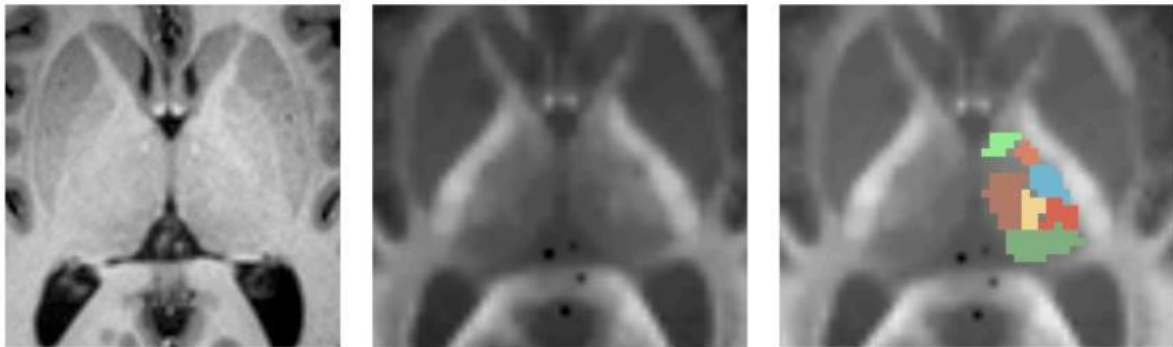


Fig. 1: MRI-scan of the thalamic region. T1 MPRAGE, DWI at 5000 s/mm² without and with drawn in nuclei. (Green = pulvinar, light Brown = Nucleus medialis, Brown = Nuclei centrales, Blue = Nuclei ventrointermedii, Red = Nuclei ventrocaudales, Orange = Nuclei ventroorales and light Green = Nucleus lateropolaris thalami)

(Filename: TCT_O-338_Fig_Thalamus_ASNR.jpg)

O-339

5:55PM - 6:02PM

Long-Term Stability of Microbleeds in Susceptibility Weighted Imaging and Quantitative Susceptibility Mapping.

M Kozoriz¹, M Jarrett¹, C Kames¹, J Mosion², D Lang¹, T Vertinsky³, M Heran³, A Barr¹, W Honer¹, A Rauscher¹

¹University of British Columbia, Vancouver, British Columbia, Canada, ²Ludwig-Maximilians-Universität München, München, Germany, ³Vancouver General Hospital, Vancouver, British Columbia, Canada

Purpose

Susceptibility Weighted Imaging (SWI) is a MRI technique routinely used in clinical practice to detect brain parenchymal microbleeds. Quantitative Susceptibility Mapping (QSM), a postprocessing technique using the phase data of the SWI scan to map the spatial distribution of local tissue magnetic susceptibilities, is a recently developed technique. The clinical applicability of QSM is currently under investigation by our group. Subjectively, QSM offers improved lesion detection due to better contrast between microbleeds and background tissue and vasculature, and discrimination between blood products and calcium. We examined microbleeds with SWI and QSM on serial MRIs over an seven-year period to determine lesion presence and stability over time.

Materials and Methods

We retrospectively examined MRIs obtained from the HOTEL study (1), a population of low-income single-room housing occupants. In this study, there were 283 participants with good quality MRI scans (2). Of this group, serial MRIs from 29 participants were selected for review. A qualified radiologist

examined the MRIs to determine the presence of a microbleed. Once identified, lesion QSM values and lesion volumes were quantified using a lesion quantification software tool.

Results

Of the 29 patients reviewed, 15 subjects had at least one microbleed on their initial baseline scan. Three of 29 patients developed a new microbleed within the follow-up period. In one case, a lesion was detected on the QSM images but was not initially detected on the SWI images. This lesion was identifiable in retrospect. On both SWI and QSM imaging, lesions persisted throughout the time interval (up to seven years). In addition, there was no significant change in lesion volume with time using both techniques. QSM values were also not significantly changed with time.

Conclusions

Microbleeds do not significantly change in size or magnetic susceptibility over at least a seven-year period.

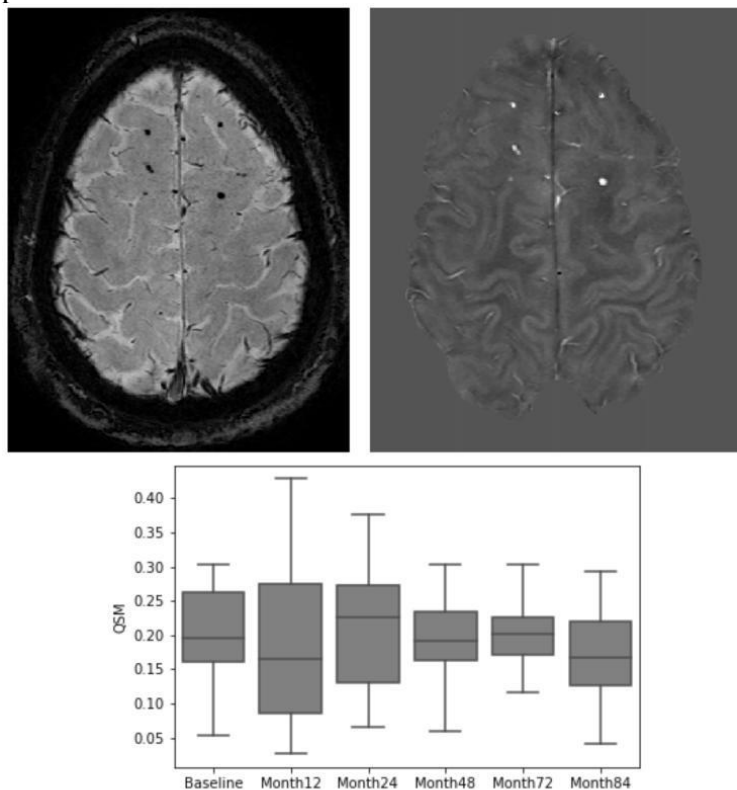


Figure 1: Example images demonstrating bilateral frontal lobe microbleeds on both SWI (left) and QSM (right) imaging. There was no significant change in lesion QSM value over a 7 year period (bottom).

(Filename: TCT_O-339_Slide1.jpg)

O-340

6:02PM - 6:09PM

Comparison of the MR Signal Intensities of Iodinated Contrast Agents Mixed with Normal Saline and That Mixed with Blood: Phantom Study

S You¹, B Kim¹, B Kim¹, N Lee¹

¹Korea University Anam Hospital, Seoul, Republic of Korea

Purpose

It is difficult to differentiate contrast staining from hemorrhagic transformation immediately after intra-

Oral Presentations & Excerpts

arterial (IA) thrombolysis on CT. The purpose of our study was to compare the MR signal intensity (SI) of iodinated contrast agents mixed with normal saline (IODNS) and that mixed with blood (IODBL) for differentiating those via MR imaging.

Materials and Methods

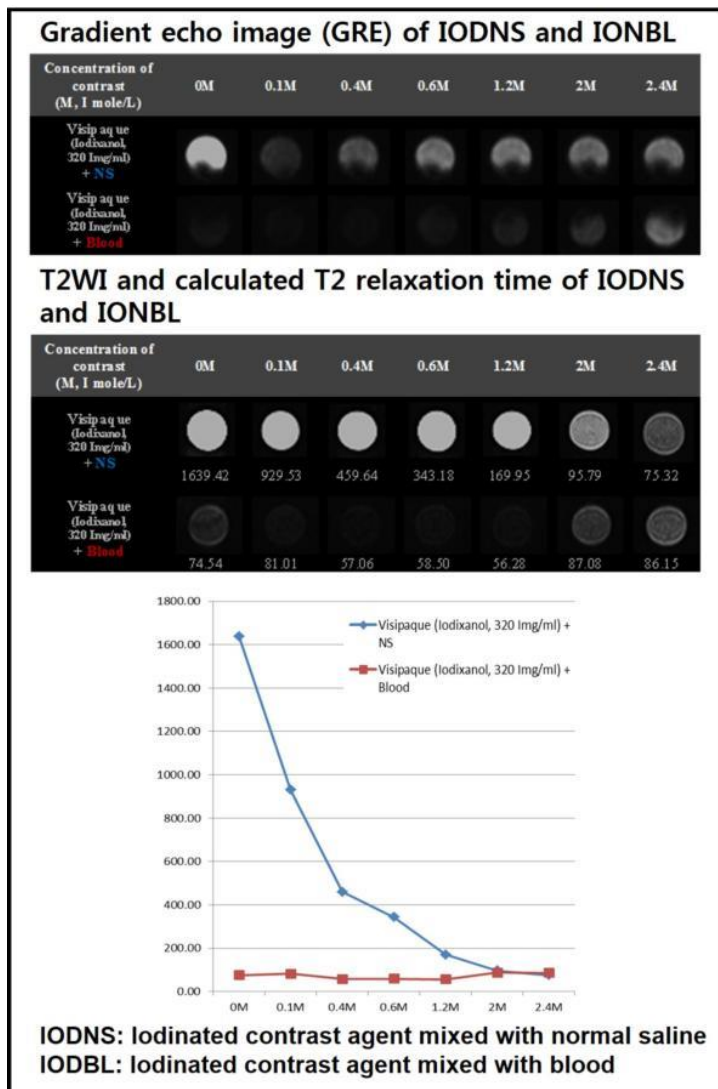
MRI studies of the phantom were performed using 3.0 T MR imaging scanners with a 32-channel head coil. The MRI protocol included T1-weighted image (T1WI), T2-weighted image (T2WI) and gradient echo sequence (GRE). The phantom which is consisted of 42 cells (6X7, [five different kinds of iodinated contrast agent mixed with normal saline and one of the iodinated contrast agent with blood] X [seven different concentrations (0, 0.1, 0.4, 0.6, 1.2, 2, 2.4 M, I mole/L)]). For IODBL column, Visipaque (iodixanol, 320 Img/ml) was mixed with arterial blood obtained within six hours. The signal intensities of each cell were compared visually and quantitatively by calculating the T1- and T2- relaxation time.

Results

IODNS showed T1 and T2 shortening effect. With increases in the concentration of contrast agents, the effect of T1 and T2 shortening becomes more powerful. IODBL showed more dark signal intensity than that of IODNS on T2WI. On GRE images, IODNS showed intermediate SI, but IODBL showed dark SI.

Conclusions

On 3T MRI, IODNS could be distinguished from IODBL on T2WI and GRE image. MRI, especially T2WI and GRE could be a good tool for differentiating hemorrhagic complication from contrast staining immediately after IA thrombolysis.



(Filename: TCT_O-340_Fig1.jpg)

Wednesday, June 6, 2018

8:00AM - 9:00AM

Parallel Paper Session: Cerebrovascular Imaging: New Applications

O-341

8:00AM - 8:07AM

Arterial Spin Labeling Perfusion MRI can Indicate Early Development of Moyamoya-like Vasculopathy in Neurofibromatosis Type I Patients

A Vossough¹

¹Children's Hospital of Philadelphia, University of Pennsylvania, Philadelphia, PA

Purpose

Neurofibromatosis type 1 (NF-1) is a common phakomatosis with many CNS and extra-CNS

Oral Presentations & Excerptas

manifestations, including mesodermal dysplasia. Development of moyamoya-like vasculopathy is an uncommon manifestation of NF-1 that may present with or eventually lead to catastrophic outcomes. Among children with NF1, those developing moyamoya syndrome are clinically indistinguishable from those without moyamoya. The purpose of this paper is to assess whether arterial spin-labeling perfusion MRI can indicate or predict early development of moyamoya vasculopathy in NF-1 patients, as these patients do not routinely undergo dedicated vascular imaging with MRA at all follow-up time-points.

Materials and Methods

All patients were evaluated at a single institution. Fifty known NF-1 patients were evaluated at multiple follow-up time-points with pulsed arterial spin-labeling perfusion MRI. Imaging parameters were constant for all studies in all patients. Inversion time was 1900ms for all patients and no crusher gradients were used in order to assess intravascular transit time artifacts. Ten patients developed moyamoya vasculopathy. Cerebral blood flow in the gray matter was measured on ASL perfusion imaging in bilateral anterior circulation and posterior circulation territories. Given that there may potentially be bilateral moyamoya and also potential posterior circulation transit and labeling artifacts on this type of ASL imaging, relative CBF ratios were also evaluated. A three-grade simple scoring for assessing degree of intravascular transit time effects was also performed. Prediction of development and presence of early moyamoya vasculopathy was assessed using these parameters as predictors compared to patients who were not later diagnosed with moyamoya.

Results

Ten patients developed moyamoya syndrome. Gray matter ASL CBF was lower (54 mL/min/100g vs. 88mL/min/100g, $p < 0.01$) in those who were diagnosed with moyamoya compared to control NF-1 patients when MRA was later performed. Relative CBF ration of < 0.52 provided best tradeoff between sensitivity and specificity. Arterial transit time artifact score of three had sensitivity of 100, but specificity of 85. A composite model was able to distinguish those with moyamoya with area under the curve of $AUC = 0.95$.

Conclusions

Arterial spin-labeling perfusion imaging was able to accurately predict early development of moyamoya vasculopathy in the subset of NF-1 patients who develop the disease. This can have clinical importance given the potential poor outcome associated with moyamoya, the fact that these patients are otherwise clinically indistinguishable with those who do not develop moyamoya syndrome, and that MRA is not routinely performed at all follow-up time-points in most institutions.

O-342

8:07AM - 8:14AM

CT Perfusion in Pediatric Patients: a Single Center 10 Year Experience

A Harvin¹, D Roberts-Wolfe², M Spampinato², A Chatterjee²

¹Medical University of South Carolina, 29425, SC, ²Medical University of South Carolina, Charleston, SC

Purpose

MRI has been increasingly utilized in children with stroke-like symptoms, due to concerns about radiation effects and the low pretest probability of ischemic stroke in children with focal neurological deficit. Here, we retrospectively assessed the sensitivity, specificity, and clinical utility of pediatric CT perfusion (CTP).

Materials and Methods

We retrospectively reviewed 30 CTP exams performed in 25 patients (age 0-18, median 14) at our institution over 10 years. CTP was compared against available follow-up MRI or CT studies for the diagnosis of cerebral infarction. The clinical value of CTP was subjectively rated as high, intermediate or low, based on unique information provided by CTP that influenced clinical management.

Results

CTP demonstrated specificity of 92% and sensitivity of 72% for the detection of acute cerebral infarction. Sensitivity of CTP was limited in cases of small vessel infarction or symmetric perfusion defects. CTP displayed high clinical utility for ruling out stroke in 9 of the 30 cases. Diagnoses from these 9 cases included hemiplegic migraine, ruptured aneurysm, subarachnoid hemorrhage, glioma and postinfectious Guillain-Barre syndrome. CTP did not demonstrate clinical utility in seven cases performed for either initial or follow-up evaluation of known chronic vascular disease. The clinical utility of CTP was indeterminate or of limited value for the remaining 15 cases. There were no cases where unique information influencing clinical management that would not have been provided by MRI.

Conclusions

CTP is feasible for ruling out acute ischemic infarction in conjunction with CT angiography of the head and neck. In our small series, CTP proved useful primarily to rule out ischemic stroke in pediatric patients with non stroke-related neurological deficit. Although timely access to MRI remains limited outside of tertiary centers, MRI should be favored over CTP given its greater accuracy in the work-up of stroke-like symptoms in children.

O-343

8:14AM - 8:21AM

MRI brain injury and neurodevelopmental outcomes in neonatal hypoxic-ischemic encephalopathy treated with therapeutic hypothermia. Does early treatment affect the outcome?

E Miller¹, J Davila¹, M Guillot¹, S Redpath¹, M Philippe², N Ben Fadel¹, N Barrowman¹, B Lemyre¹
¹Children's Hospital of Eastern Ontario, Ottawa, Ontario, Canada, ²University of Ottawa, Ottawa, Ontario, Canada

Purpose

Therapeutic hypothermia (TH) is the standard-of-care treatment for newborns with moderate to severe hypoxic-ischemic encephalopathy (HIE). While preclinical studies support starting TH within six hours of life, little clinical data exists that evaluates earlier initiation of TH. The objective of this study was to determine if initiation of TH three hours within the six hour window period makes a difference in the MRI pattern of brain injury and neurodevelopmental outcomes.

Materials and Methods

This retrospective cohort included neonates with HIE treated with TH at a level three neonatal intensive care unit between 2009 and 2016. Babies were grouped into early TH (started ≤ 3 hours of life) or late TH (started > 3 hours of life). Two pediatric neuroradiologists evaluated the severity and pattern of brain injury on MRI using the National Institute of Child Health and Human Development (NICHD) and Modified Barkovich scoring system. Neurodevelopmental outcomes were evaluated at four, 10, 18 and 48 months.

Results

Ninety-four patients (median gestational age 39 weeks; median birth weight 3.3 kg) were eligible. Based on Sarnat score at birth, the early TH group included more patients with severe HIE than the late TH group (32.7% vs 10.3%, $p=0.01$). Eighty-three neonates had a brain MRI (47 in the early TH group). No statistical difference was observed between the two groups with respect to the pattern and severity of brain injury in MRI. Both groups had more neonates with grades 0, 1A, 1B in the MRI NICHD scoring system (72% < 3 hours, 75% > 3 hours). With the modified Barkovich scoring system, both groups demonstrated less severe injury in the basal ganglia (score 0, 1: 80.9% < 3 hours, 80.6% > 3 hours). In the late cooling group, there was a trend towards more severe watershed (WS) injury (m-Barkovich WS score ≥ 3 ; 17% < 3 hours vs 30.6% > 3 hours, $p=0.19$). There was no difference in the neurodevelopmental outcomes between the two groups ($p=0.92$).

Conclusions

TH initiated before the first three hours of life was neither associated with a difference in brain injury on

MRI nor better neurodevelopmental outcomes in comparison with TH initiated after the first three hours of life.

O-344

8:21AM - 8:28AM

Number of Cerebral Microhemorrhages Correlates with Worse Long-term Neurologic Outcomes Among Pediatric Patients after Cardiopulmonary Bypass

C Toensing¹, S Harder¹, P Pichon¹, B Nasman¹, J Jacobson¹, S Hwang¹, U Oyoyo¹, P Kim¹

¹*Loma Linda University Medical Center, Loma Linda, CA*

Purpose

Children with congenital heart disease (CHD) often require cardiac transplantation with cardiopulmonary bypass (CPB). Neurological complications after CPB are a known risk of these procedures. Mechanisms often include gaseous microemboli, reperfusion syndrome, hypothermic circulatory arrest, and low-flow CPB. It has previously been shown that cerebral microhemorrhages (MHs) are frequently detected in patients after CPB. This study was undertaken to evaluate for correlation between the presence of cerebral MHs and neurologic outcomes as determined by the Pediatric Cerebral Performance Category (PCPC) score in patients with a history of cardiac transplantation and CPB.

Materials and Methods

IRB waiver of consent was obtained. MRI scans of a cohort of 128 consecutive pediatric patients who underwent cardiac transplantation and CPB were retrospectively reviewed for MH(s). A subgroup of 32 patients who obtained MRIs after CPB was selected who met selection criteria. Patients were imaged at a mean age of four years +/- SD 3 (18 males; 11 cyanotic heart disease). The number of cerebral MH on SWI was counted by an experienced neuroradiologist (SH). Each patient's PCPC score was determined by an experienced pediatric neurologist (PP) who reviewed the patient's chart. Statistical analysis was performed to evaluate for correlation between the number of MHs and PCPC score (Spearman's Rho).

Results

The median number of cerebral MHs was 51 [IQR 9.5, 51]. The average age at follow-up was 12 years +/- SD 3. The median PCPC score was 2 [IQR 1, 6]. The number of microhemorrhages correlates with the patient's PCPC score (correlation coefficient 0.387, $p = 0.032$).

Conclusions

Number of cerebral microhemorrhages correlates with worse long-term neurologic outcomes among pediatric patients after cardiopulmonary bypass.

O-345

8:28AM - 8:35AM

Resistive Index Values Measured by Head Ultrasound Can Predict Impaired Autoregulation in Cooled Neonates for Hypoxic Ischemic Injury (HII)

E Snyder¹, R Chavez-Valdez¹, J Perin¹, F Northington¹, T Huisman¹, J Lee-Summers¹, A Tekes-Brady¹

¹*Johns Hopkins University School of Medicine, Baltimore, MD*

Purpose

The purpose of this study is to evaluate whether resistive index (RI) values measured by transfontanelar head ultrasound (HUS) is associated with 1) brain injury using conventional MRI and diffusion-tensor imaging (DTI), and 2) with dysfunctional blood pressure autoregulation using near infrared spectroscopy (NIRS).

Materials and Methods

Neonates who underwent therapeutic hypothermia (TH) for HII were included (2010-2015). HUS was performed at the initiation (HUS-1) and at the end of TH (HUS-2). RI was sampled in the anterior

cerebral artery (ACA). NIRS was used to determine the hemoglobin volume index (HVx) to assess autoregulation during TH, rewarming and normothermia. Brain MRI with DTI was performed after cessation of cooling (day of life 4-9). ADC scalars were measured by region-of-interest analysis in bilateral centrum semiovale, basal ganglia, thalamus, PLIC, pons, cerebellar white matter. APGAR score at 10-minutes, cord pH, and base deficit/excess were recorded.

Results

Seventy-five neonates were included in the study. Higher APGAR scores at 10 min was associated with a higher RI values on HUS-1 ($p < 0.05$). After controlling for PPHN, ventilator support, inotrope use and significant PDA, lower RI values on HUS-1 were associated with greater qualitative MRI injury as determined on conventional sequences in central gyrus, white matter, thalamus, PLIC and brainstem. Lower RI values on HUS-2 were associated with 1) lower ADC values (worse injury) in all measured brain regions ($p < 0.05$), and 2) greater maximum HVx during normothermia and average and maximum HVx during rewarming ($p < 0.01$) suggesting worse blood pressure autoregulation.

Conclusions

Lower RI in the HUS correlated with worse brain injury as seen on qualitative MRI analysis and DTI, as well as impaired blood pressure autoregulation on NIRS. RI measurements and autoregulation monitoring are temporally related. Low RI values can serve as a marker of brain injury during cooling to guide optimization of blood pressure targets as adjuvant therapy.

O-346

8:35AM - 8:42AM

Hypoxic-Ischemic Injuries in Abusive Head Trauma

E Orru¹, T Huisman¹, I Izbudak¹

¹*Johns Hopkins Hospital, Baltimore, MD*

Purpose

Hypoxic-Ischemic Injuries (HII) are an important but relatively less understood and studied feature of nonpenetrating abusive head trauma (AHT). Diffusion-weighted imaging (DWI) is the most sensitive modality to assess presence and extent of such lesions. The purpose of this study is to determine the frequency of HII in children victims of AHT and to describe the most common DWI patterns.

Materials and Methods

This retrospective, IRB-approved study included all patients aged less than five years diagnosed with nonpenetrating AHT in a period of eight years. At our Institution AHT patients routinely receive MR imaging, including diffusion-tensor imaging, at or shortly after admission. Images and medical records were retrospectively reviewed in consensus to determine the presence of DWI abnormalities and to assess whether they were compatible with HII. HII was defined as presence of diffusion restriction in a nonvascular distribution not justified by the traumatic mechanism. Patients with known cervical or intracranial vascular injuries were excluded. The different patterns of HII were described and divided in subtypes when applicable. Correlation with clinical outcomes was performed when there was available data.

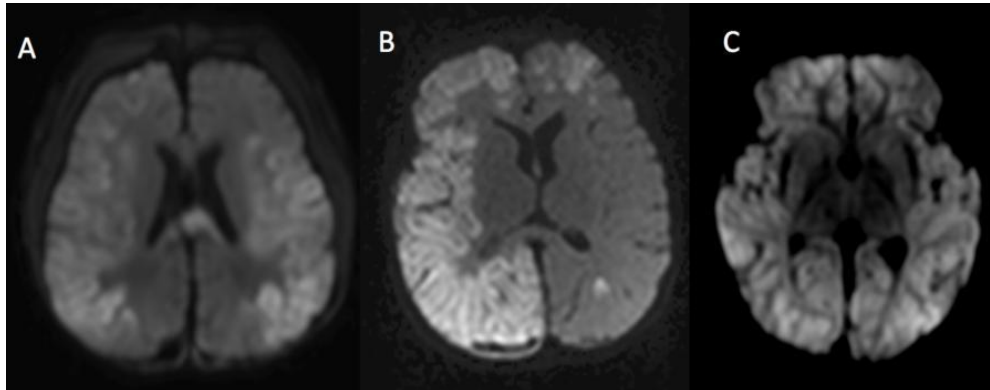
Results

The study population included 57 patients (20 females). DWI abnormalities were present in 29 subjects (50.9%) and 21 of these patients (36.8%) met the above specified criteria for HII. Of these, 14 (66.7%) had a predominantly cortical distribution, while seven (33.3%) had diffuse both cortical and deep gray/white-matter distribution. The cortical lesions were predominantly asymmetric (10, 71.4%). Six out of 57 patients (10.5%) died, and all of them showed evidence of HII on MRI. A total of 43 patients (75.4%) had SDH. Of these, 15 had HII. Six out of 21 patients with HII had no SDH. There is no significant correlation between the presence of SDH and that of HII ($p = 0.6$).

Conclusions

HII was present in slightly more than 1/3 of patients with AHT, and was seen in a cortical (either

symmetric or asymmetric) or diffuse brain distribution. Most of the times the diagnosis of AHT is difficult, as the radiological stigmata are not always present. Radiologists should be aware of the relatively high prevalence of HII in AHT and should raise the suspicion especially in unclear trauma cases.



(Filename: TCT_O-346_HIIintraumaImage1.jpg)

O-347

8:42AM - 8:49AM

Brain and Cerebrovascular Response to Jugular Compression: Preliminary Evaluation of a Novel Intracranial Protective Mechanism

J Leach¹, J Dudley¹, A McAllister², S Serai³

¹Cincinnati Children's Hospital Medical Center, Cincinnati, OH, ²Nationwide Childrens Hospital, Columbus, OH, ³Children's Hospital of Philadelphia, Philadelphia, PA

Purpose

Jugular vein compression via a passive collar device (CD) is a promising strategy for mitigating brain injury in collision sports and other impact-prone activities [1, 2]. Despite documentation of a moderating intracranial effect on impact-related DTI and fMRI metrics [1, 2], the mechanism of action of the device remains theoretical. Prior studies have demonstrated a potential intracranial mechanistic response of increased brain stiffness with neck compression [3]. To further investigate these theoretical constructs we employed TOF magnetic resonance venography (MRV), Phase contrast flow sequences (PC), brain MR elastography (MRE), and brain Synthetic MRI (SyMRI) in a small group of subjects to investigate the effects of the CD on venous volumes in the neck and head, venous flow in the neck, intracranial volumes of CSF and brain parenchyma (BPV), and brain stiffness.

Materials and Methods

Four volunteer subjects (3M:1F; ages 26-34; JVC 01-04) were scanned at 3T (GE750w) both without and with placement of a fitted CD (Q30 innovations, Westport, Connecticut) during a single session. Identical scan protocols were performed without and with collar placement and included: T1 volumetric brain images, TOF neck MRV at and above the location of the CD, Intracranial TOF MRV, PC flow sequence in the neck at the level of the CD, Brain MRE (20 Hz), and intracranial SyMRI. Volumetric analysis of the MRV data was performed in BrainLab iplan v3.0, PC flow data in Medis Suite Qflow v3.0, SyMRI data in SyMRI v8.0, and MRE data using a previously described method [ref] to obtain whole brain stiffness maps. MRE magnitude images were coregistered to T1 volume images and voxelwise percent change maps calculated. Percent change in venous volume, flow, CSF, BPV and brain stiffness with application of the CD were calculated.

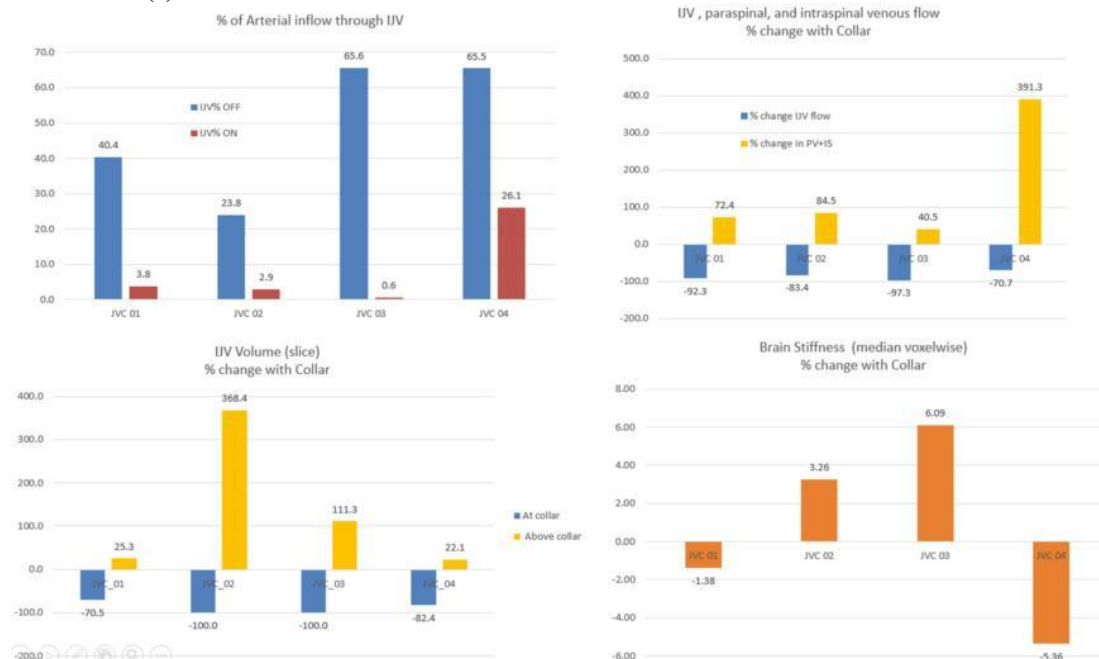
Results

At baseline percent IJV flow (as a percent of carotid and vertebral inflow) was variable (24-66%) and with CD placement decreased. Jugular vein slice volume and flow markedly decreased in the neck at the

location of the CD (-70.5 to -100%; and -70.7 to -97.3% respectively). IJV size variably increased superior to CD application between 22 and 368%. Recruitment of nonjugular venous pathways (intraspinal, ISV; paraspinal, PSV) after CD placement was also variable ranging from a 18.8 to 320% increase in size and 40.5 – 391% increase in flow after CD placement. Intracranial venous volume (TOF MRV) increased in 3/4 subjects. Brain stiffness showed variable response to CD application. The subject with the most marked increase in brain stiffness (+6%, JVC_01) had the largest percent IJV flow at baseline, the most marked percent decrease in IJV flow and volume after CD placement, and modest recruitment of alternative pathways for drainage. The subject with the most marked decrease in brain stiffness (JVC_04) had the least decrease in IJV flow and volume after CD placement, and the most robust increase in alternative pathways for drainage. Intracranial CSF interestingly increased the most in JVC_03, suggesting CSF displacement or conceivably overproduction.

Conclusions

Jugular vein compression via CD alters intracranial brain stiffness. In this preliminary investigation of a small number of subjects, variability in the local and intracranial effects of the CD could be demonstrated. Subject with the most preserved IJV flow and greatest recruitment of alternative pathways had a decrease in brain stiffness, whereas the subject with the largest decrease in IJV flow and smallest recruitment of alternative pathways had the largest increase in brain stiffness. CSF and intracranial venous volume effects were more variable, and potentially below the reproducibility of the techniques utilized. As this study was performed supine we could not assess the effect of posture on venous drainage pathways which could be significant. Further research is necessary to more fully elucidate the potential protective mechanism(s) of the CD.



(Filename: TCT_O-347_figure.jpg)

O-348

8:49AM - 8:56AM

Establishing Dominance: Incidence of Vertebral Artery Dominance in the Pediatric Population.

K Gwal¹, J Edgar², R Ichord², E Schwartz²

¹Children's Hospital of Philadelphia/University of California Davis Health System, Sacramento, CA, ²Children's Hospital of Philadelphia, Philadelphia, PA

Purpose

In adults, the vertebral arteries are commonly asymmetrical in size, with similar vertebral artery diameters present approximately 25% of the time. An association has been suggested between vertebral artery hypoplasia and posterior circulation stroke, in particular ipsilateral posterior inferior cerebellar artery (PICA) infarction or lateral medullary infarction. Clinical experience at our institution has suggested that dominance of one of the vertebral arteries is less commonly seen in the pediatric population. The present study evaluates the presence or absence of vertebral artery dominance in the pediatric population as a function of age from the neonatal period through 20 years.

Materials and Methods

A retrospective review of intracranial MRA (1.5 or 3T, 3D TOF noncontrast, 0.5-mm) (n=300; age range: birth to 20 years). The subjects were selected from the group of patients who underwent a noncontrast TOF intracranial MRA between January 1, 2010 and December 15, 2015. The patients were arranged into six age groups (<1 year, 2-4, 5-7, 8-10, 11-15, and 16-20 years) with 50 subjects in each age group. The vertebral arteries were evaluated for caliber and dominance, if any. A vertebral artery was considered dominant if visually doubled or more in caliber compared to the contralateral vessel. Age group comparison was performed with chi-square analysis.

Results

Overall, only 6.67% (20/300) of the subjects had a dominant vertebral artery across the age groups. Comparing children < 5 years to those \geq 11 years demonstrates a significant difference in the incidence of dominant vertebral arteries, < 5 years = 4/100, \geq 11 years of age = 16/100 ($p < 0.05$). All patients < 5 years of age who had a dominant vertebral artery were female (4/100). No statistically significant laterality prevailed.

Conclusions

The incidence of dominant vertebral arteries is less frequent in the pediatric population when compared with historical adult data. The present study demonstrates a statistically significant increase in the presence of dominant vertebral arteries as a function of age in children. The overall prevalence of vertebral artery dominance may have implications for catheter angiography vascular selection, may affect assessment for dissection, and may have a correlation with posterior circulation ischemic risk.

Wednesday, June 6, 2018

8:00AM - 9:00AM

Parallel Paper Session: Spine: Fluoroscopy-Guided Techniques

O-349

8:00AM - 8:07AM

Imaging Evaluation of Spontaneous Intracranial Hypotension

S Kim¹, M Hoch², S Patel¹, J Allen¹, B Weinberg²

¹Emory University, Atlanta, GA, ²Emory University Hospital, Atlanta, GA

Purpose

Spontaneous intracranial hypotension (SIH) is a treatable cause of persistent postural headache. Despite the range of diagnostic imaging studies available today, identifying the CSF leak site remains challenging. The purpose of this study was to determine which imaging modality was best used to diagnose leaks and to identify common anatomical sites of CSF leak.

Materials and Methods

Chart review of patients diagnosed with SIH and treated with blood patch at a single institution from January 2015 to December 2016 was performed. Patients' clinical symptoms and imaging findings were

Oral Presentations & Excerpts

recorded. CSF leaks were categorized into "definite leaks" and "suspected leaks" according to the confidence expressed in the radiology report.

Results

Thirty patients treated for SIH were identified; 20/30 (66%) patients were female, 21/30 (70%) patients were Caucasian, and 9/30 (30%) patients were African American. Mean age was 54 years old. A definite leak was identified in 11/30 (37%) patients. Of the 11 definite leaks, CT myelogram was the first modality to identify the leak 8/11 (73%), MRI spine in 2/11 (18%), and MRI myelogram in 1/11 (9%) patients. A suspected leak was identified in 14/30 (47%) SIH patients. Of the 14 suspected leaks, CT myelogram was the first modality to identify the leak 9/14 (64%), MRI spine in 4/14 (29%), and MRI myelogram in 1/14 (7%) of patients. The most common sites of definite and suspected CSF leak were C7-T1, C5-C6, and T10-T11 in decreasing order.

Conclusions

Identifying spinal CSF leaks in patients with SIH remains a diagnostic challenge. When leaks are found, CT myelogram is the most common modality with MR myelography as a troubleshooting tool. Given the most common sites of leak, empiric blood patch at C7-T1 or the thoracolumbar junction should be considered if no leak is identified.

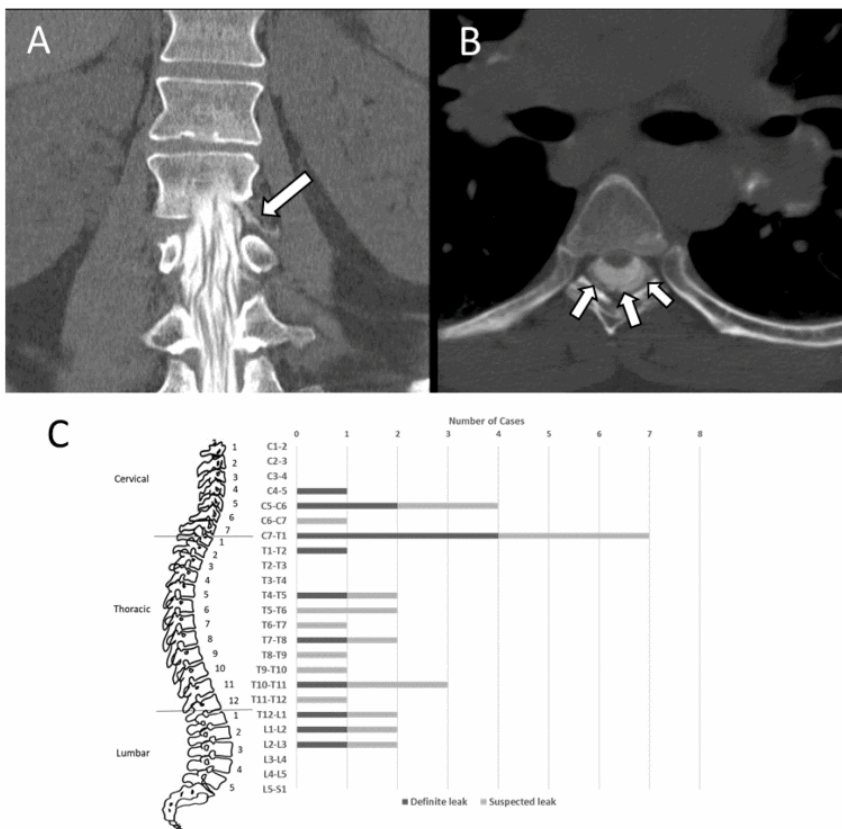


Figure 1. (A) Coronal images from a CT myelogram showing contrast extravasating along the course of the left L2 nerve root, called a definite CSF leak. (B) Images from a CT myelogram showing a contrast collection in the dorsal spinal canal. The collection extended over a long segment and was suspicious for being near a site of leak. (C) Histogram showing distribution of definite and suspected leak sites by spinal level.

(Filename: TCT_O-349_3by3DXASNRfigure_v2.gif)

O-350

8:07AM - 8:14AM

Treatment of Spontaneous Intracranial Hypotension

Oral Presentations & Excerptas

S Kim¹, M Hoch², S Patel¹, J Allen¹, B Weinberg²

¹Emory University, Atlanta, GA, ²Emory University Hospital, Atlanta, GA

Purpose

Spontaneous intracranial hypotension (SIH) is a cause of persistent postural headache most frequently associated with CSF leak in the spine. Epidural patch with autologous blood or fibrin is the most common treatment, although patients may require multiple treatment sessions and sites. The goal of this study is to assess the range of spinal procedures performed to treat SIH.

Materials and Methods

Chart review of patients diagnosed with and treated for SIH at a single institution from January 2015 to December 2016 was performed. Patients were categorized by certainty of spinal CSF leak based on CT and MR myelography. Treatment dates, injection location, amount of blood/fibrin injected, and whether injection was performed at leak site ("targeted") or empirically performed in a patient with clinical SIH but no leak site ("nontargeted") were recorded.

Results

Thirty patients treated for SIH were identified. All patients underwent at least one CT-guided blood patch, with 25/30 (83%) receiving targeted patches. Patients averaged 2.3 procedure sessions, 3.4 injection sites, and 7.8 mL of blood per site. More blood was injected at lumbar spine locations compared to cervical ($p=0.002$) and thoracic ($p=0.01$) sites. Of patients 8/30 (27%) underwent fibrin glue injection, averaging 2.0 sessions, 3.4 injection sites, and 3.7 mL of fibrin per site. Four patients required ≥ 6 treatment sessions and six patients required ≥ 6 injection sites.

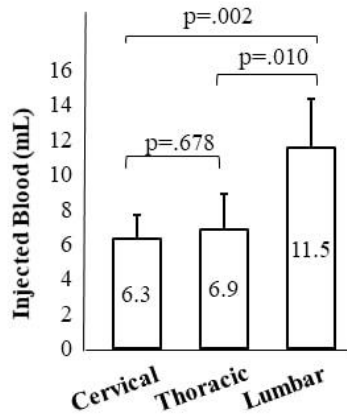
Conclusions

Patients without a myelographic leak averaged a single procedure, while patients with a suspected or confirmed leak required multiple treatment sessions and injection sites. Patients with suspected leaks received injections at more sites, probably reflecting uncertainty about the best treatment location. More blood was injected at lumbar sites, likely due to greater potential space in the spinal canal. Physicians should be aware of the potential need for repeat treatments for SIH and counsel patients accordingly, as persistence is needed to achieve complete response.

A

Definite Leak (n=11)		Suspected Leak (n=14)		No Leak (n=5)	
Average Number		Average Number		Average Number	
Procedures	Injections Sites	Procedures	Injections Sites	Procedures	Injections Sites
3	2.9	2.9	4.5	1	1.2

B



C

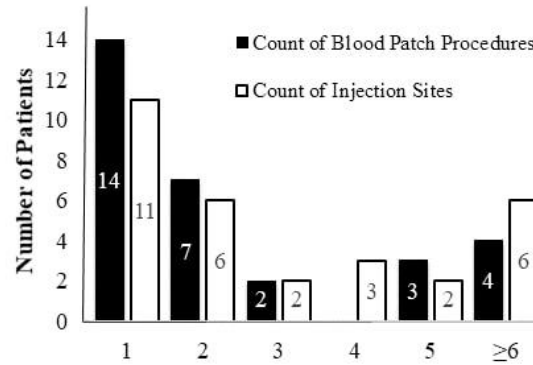


Figure 1. (A) Table showing the average number of procedures and injection sites according patients' leak site characteristics. (B) Histogram showing the average amount of blood used in cervical, thoracic, lumbar blood patches, and the paired t-test results. (C). Histogram showing a count of patients by the number of blood patch procedures and injection sites.

(Filename: TCT_O-350_TxDiagramswithupdatedC_bw3.jpg)

O-351

8:14AM - 8:21AM

Blood Patch Rates Following Lumbar Puncture with Whitacre Versus Quincke Needles: A Randomized Comparative Trial

D Cantrell¹, T Shokuhfar², A Muzaffar¹, M Czosek¹, M Hurley², A Shaibani², S Ansari²

¹Northwestern University, Chicago, IL, ²Northwestern University Feinberg School of Medicine, Chicago, IL

Purpose

Lumbar puncture (LP) is a critical diagnostic tool for the triage of patients with a broad spectrum of neurological diseases, and this procedure is increasingly performed by radiologists using fluoroscopic guidance. Review of medicare billing claims has demonstrated that radiologists performed 11.3% of LPs in 1991, 46.6% of all LPs in 2011, and are now the dominant provider group for this procedure [1]. The most common complication of LP is a postural postdural puncture headache, which is worse when upright and relieved when the patient is in the supine position. Persistent drainage of CSF created by the needle is the accepted mechanism for a postdural puncture headache exceeding two days in duration. For headaches that do not resolve with conservative measures, epidural blood patch is offered as a safe and effective intervention. Prior research has suggested that the use of pencil-tipped Whitacre needles during lumbar puncture can decrease the severity of postdural puncture headache and can reduce the number of patients that require subsequent epidural blood patch [2]. The purpose of this research is to compare the

incidence of epidural blood patch following lumbar puncture performed under fluoroscopic guidance with Whitacre versus Quincke spinal needles.

Materials and Methods

A randomized comparative trial is currently underway in which all patients referred to our radiology department for LP are randomized to either a 22-gauge Quincke bevel-tip needle or a 22-gauge Whitacre pencil-tip needle. Patient recruitment began October 3, 2016, and randomization was determined according to the day of the week. Lumbar punctures were performed by multiple operators each day including radiology residents, neuroradiology fellows, midlevel providers, and attending neurointerventionalists. The needle utilized for LPs was documented in the procedure dictation. Following departmental protocol, patients were required to lay flat for 2 hours after the procedure. Upon discharge, patients were further instructed to notify the neurointerventional service should they experience moderate or severe postural headaches, or any headache that persisted longer than two days. After routine clinical evaluation, epidural blood patch was offered to patients with persistent and/or severe postural headache that was felt to be the result of a CSF leak secondary to the dural puncture. Interim analysis was performed after achieving a threshold enrollment.

Results

From October 13, 2016 to December 1, 2017, a total of 1,133 lumbar punctures were performed for therapeutic and diagnostic purposes. Four hundred total lumbar punctures were performed with a Whitacre needle, and four of these patients required an epidural blood patch for the treatment of postdural puncture headache, yielding a 1.0% incidence of CSF leak requiring epidural blood patch following an LP with a Whitacre needle. A total of 733 lumbar punctures were performed with Quincke bevel-tip needles, 13 of which required epidural blood patch, yielding a 1.8% incidence for CSF leak. Although the trend suggests that Whitacre needles decrease the risk for CSF leak, this has not yet reached significance (Chi-squared p value = 0.3), and patient recruitment will continue. At the conclusion of the study, regression analysis will be utilized to risk adjust for confounding variables.

Conclusions

Interim analysis of a large volume randomized comparative trial suggests that performing lumbar puncture with a Whitacre needle can reduce the risk for CSF leak requiring epidural blood patch when compared to bevel tipped Quincke needles. However, this trend has not yet reached statistical significance, and continued patient recruitment is expected to yield further insight.

O-352

8:21AM - 8:28AM

A Randomized Pilot Study with Fluoroscopy Guided Lumbar Puncture: Post-Lumbar Puncture Headache Incidence According to Needle Type

C Bard¹, J Rioux-Beaupré¹, J Raymond¹, F Guilbert¹, L Létourneau-Guillon¹, D Landry¹

¹*University of Montreal Hospital Centre, Montreal, Quebec, Canada*

Purpose

According to previous study, pencil-point spinal needles (PPN) that reduce the incidence of postlumbar puncture headache (PLPH). PPN are expensive; clinicians are reluctant to use them and the outcome on fluoroscopy-guided post-lumbar puncture headache (FGPLPH) is unknown. This pilot study explores the incidence of FGPLPH according to needle type.

Materials and Methods

In this single-center study, between 2012 and 2017, 172 blinded patients scheduled to receive a FGLP were randomly distributed between a cutting-edge needle gauge 25 group (CEN) and a gauge 24 PPN group. Compared on FGPLPH were 168 patients (including intensity and duration) and Intervention failure (IF). BMI, age and gender were recorded.

Results

Results show total incidence of 17% of PLPH with almost double the incidence in the CEN group as

compared to the PPN group (20.2% vs 12.7%, $p = 0.189$). Approximately 810 participants would need to be accrued to identify a statistically significant difference ($\alpha = 0.05$, $p = 0.8$). Total incidence of IF was 7.7% with almost double the incidence in the PPN group than the CEN group (10.1% vs 5.6%, $p = 0.275$). The occurrence of other symptoms did not differ between groups (12.4% vs 11.5%; $p = 0.87$). In the patients with PLPH, there was no difference in intensity (scale 1-10; $\bar{x} = 5.1$ vs 5.8; $p = 0.442$) nor duration (in hours; $\bar{x} = 60.1$ vs 67.0; $p = 0.727$).

Conclusions

Our result shows no evidence but a trend towards a reduction in FGPLPH and toward an increase in IF using PPN. It is questionable that a larger, preferably multicenter study could motivate a change in practice

O-353

8:28AM - 8:35AM

Fluoroscopy Guided Epidural Blood Patch: Success Rates

C Ozutemiz¹, J Rykken¹, Y Koksel¹, H Huang²

¹University of Minnesota, Minneapolis, MN, ²University of Minnesota, School of Medicine, Minneapolis, MN

Purpose

Fluoroscopy-guided epidural blood patch (FGEBP) is performed to treat spontaneous/iatrogenic CSF leakage. The success rate of FGEBP has not been well studied.

Materials and Methods

All fluoroscopy-guided lumbar punctures (FGLP) and FGEBPs between January 2014 and May 2017 were retrospectively evaluated. Information regarding age, sex, BMI, previous LP before FGEBP, LP-FGEBP interval, LP level, patient position, LP needle, opening pressure, FGEBP level, FGEBP needle, administered blood volume, and FGEBP outcome were collected. The outcome was classified into three categories as "complete response", "partial response" and "unsuccessful". Comparison analysis between patients with/without previous LP was performed. Patients with "complete response" were compared to the combined group of "unsuccessful" and "partial response" patients, named "incomplete response". Two-sample/Fisher's exact (continuous/categorical variables) tests were used ($p < 0.05$).

Results

Sixty-seven FGEBPs were performed in 63 patients (female/male, 36/27; mean age/BMI 38/28.2). Fifty-six were referred following an LP; 31 were performed by radiologists. Our FGEBP rate was 1.78% over 3.5-years following FGLP. The mean LP-FGEBP interval was 4.8 days. FGEBP was unsuccessful in four procedures (6%). In two (3%) patients, blood patch was repeated. "Complete response" was achieved in 56 patients (85%). Average applied blood volume was 16 cc (range 5-30cc). No difference was found between "complete response" and "incomplete response" groups regarding age, sex, BMI, LP level/position, LP needle, FGEBP level, FGEBP needle and administered blood volume ($p > 0.05$). Patients with a prior LP had success rate of 89%, while patients without a prior LP had a success rate of 60% ($p = 0.04$). CSF opening pressure during the prior LP was higher in the "complete response" group vs the "incomplete response" group (30.3 ± 13 vs. 21.5 ± 2.1 cm CSF, $p = 0.03$).

Conclusions

The success rate of FGEBP is high, especially in the setting of previous LP and elevated CSF opening pressure.

O-354

8:35AM - 8:42AM

Transforaminal Lumbar Puncture. A Novel Technique in Patients with Challenging Access

D Nascene¹, C Ozutemiz¹, H Estby², A McKinney¹, J Rykken¹

¹University of Minnesota, Minneapolis, MN, ²University of Minnesota, School of Medicine, Minneapolis, MN

Purpose

Standard interlaminar lumbar puncture (LP) and cervical puncture (CP) may not be feasible in certain conditions. Recently, we have started to use transforaminal approach for those situations. To our knowledge, this method is not described previously. Our purpose is to describe this technique and our initial experience.

Materials and Methods

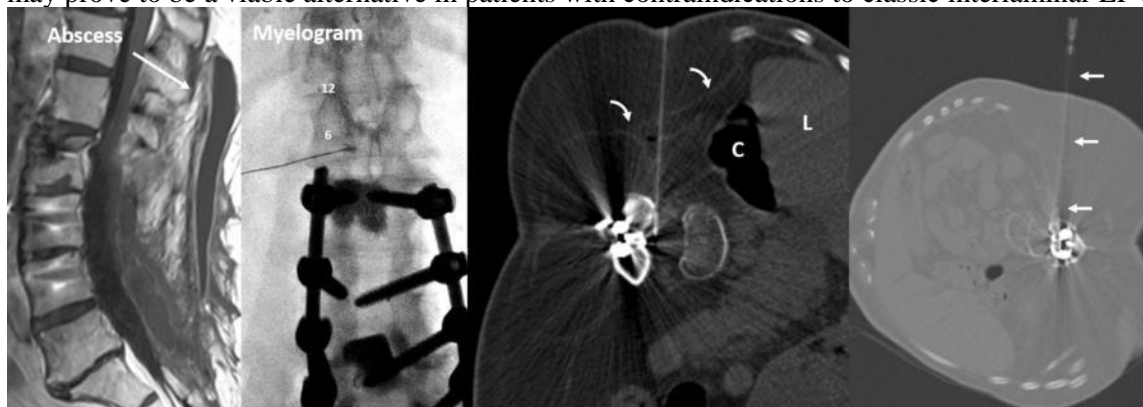
Between March 2016 and December 2017, 26 transforaminal lumbar punctures (TFLP) were performed in nine different patients, with 25 using CT and one using fluoroscopy guidance. Information pertaining patients age, sex, BMI, postprocedural complications, puncture level, needle size was collected.

Results

A total of 26 TFLP was performed in seven females and two males. Mean age was 39.6 (min:31 max:68). Mean BMI was 21.9 (min:12.6 max:40). Seven patients had spinal muscular atrophy and were referred for intrathecal Nusinersen (Spinraza®) administration. Preprocedural evaluation revealed extensive complete osseous fusion of posterior elements, accompanying some degree of hip flexion contractures and severe scoliosis, precluding proper positioning needed for CP. In two patients, CT myelography was performed via TFLP due to presence of possible abscess in the lower back and patients were unable to tolerate CP. All procedures were performed using 22 G Quincke needles, 3.5" in 10 procedures, 5" in 14, and 7" in two. L1-2 level was used in two, L2-3 in 10, L3-4 in 12 and the L4-5 level in two procedures. Post-LP headache was observed in five occasions, which were conservatively managed without any blood patch. In one case, patient felt heat and pain in the injection site which resolved spontaneously within hours. One patient had radicular pain after third injection which resolved with conservative treatment.

Conclusions

Although more evidence is necessary to determine the relative safety of TFLP, transforaminal approach may prove to be a viable alternative in patients with contraindications to classic interlaminar LP or CP.



(Filename: TCT_O-354_asnrabstractfig.jpg)

O-355

8:42AM - 8:49AM

A Multi-Layer Realistic Tiered Fluoroscopy-Guided Lumbar Puncture Phantom Utilizing 3D Printing with Tactile Feedback

R Javan¹, J Gibby², J Maclaughlan³, A Rao⁴, P Heidari¹, N Greek², M Taheri⁵

¹George Washington University Hospital, Washington, DC, ²George Washington University, Washington, DC, ³George Washington University School of Medicine and Health Sciences, N/A, ⁴George Washington University School of Medicine, Washington, DC, ⁵George Washington University, Washington, DC, DC

Purpose

The purpose of this project was to develop an advanced realistic simulation phantom for performing fluoroscopy-guided lumbar procedures. The realism goal is both with respect to the appearance under fluoroscopy as well as the soft tissue tactile feedback.

Materials and Methods

CT images of three different lumbosacral spines were imported into Materialise InPrint. Each of the three imported cases represented progressively more advanced degree of degenerative changes. The final composite, which extended from T12 to the midsacrum, consisted of two levels from each spine cut horizontally and exported in STL format. The images were subsequently imported into Autodesk 3-D Studio Max, where the structures were manual merged. Gypsum-based 3-D printing was used to create the radiodense hollowed bony anatomy with cortical thicknesses ranging from 2 to 5 mm to allow for visualization of the intricate anatomy. A fluid-filled rubber tube was inserted in the spinal canal to recreate the CSF filled dura, with one end sealed and connected to a pressured syringe. The osseous model was immersed in three different consistencies of silicone rubber to recreate muscle, fat and skin.

Results

A tiered multi-layer realistic phantom was developed using commercially available low-cost 3-D printing technology along with molding techniques for the purpose of teaching and practicing fluoroscopy-guided lumbar punctures and facet joint injections. This phantom simulates five distinct tissues. Several fluoroscopy-guided lumbar punctures and access of facet joints were attempted with success being marked by gaining access to the fluid-filled thecal sac and through tactile feedback respectively.

Conclusions

The fluoroscopic appearance of the model, the life-like tactile sensation of the soft tissues along with advancing degree of complexity of this model provides a great tool to introduce and improve trainees' procedural skills.

O-356

8:49AM - 8:56AM

Time to Switch Sides: A Retrospective Comparative Analysis of Fluoroscopic-Guided Lumbar Puncture in the Lateral Decubitus Versus the Routine Prone Position.

R Mangla¹, D Bakrukov², J Rozell³

¹SUNY Upstate, Syracuse, NY, ²Ross University, DeWitt, NY, ³Baystate Medical Center, Springfield, MA

Purpose

Fluoroscopic-guided lumbar puncture (LP) is more generally performed in the prone position; however, it is also performed in the lateral decubitus position though usually in cases which aim to more accurately measure opening pressure. We sought to determine the feasibility of performing all LPs in the lateral decubitus position rather than for just assessing opening pressure by investigating patient outcomes following procedures performed in the prone position versus those performed in the lateral decubitus position. Patient outcomes are determined on a number of factors such as fluoroscopy time, radiation dose, and procedure failure rate.

Materials and Methods

Retrospective chart analysis was performed on pertinent cases performed at a single institution from 2013 to present. Cases were assigned into two groups: Group A if performed in prone, and Group B if performed lateral decubitus. Data for each group collected includes fluoroscopy time, room time, dose area product (DAP), spinal level, needle size, patient tolerance, and procedure failure. Exclusion criteria includes trainee performed procedures (i.e., resident), placement of epidural blood patch, intrathecal chemotherapy, and reports with unknown LP level. Mean fluoroscopy time, room time, DAP, and procedure failure rate were calculated for both groups.

Results

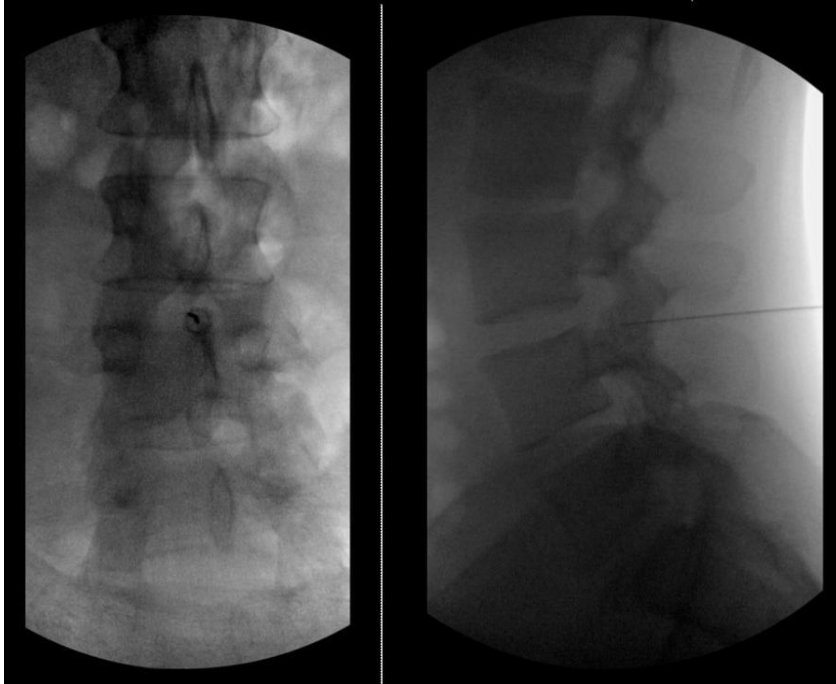
Mean fluoroscopy time of Group A was 1.05 minutes (SD 1.03, CI: 0.74 – 1.40) compared with Group B

Oral Presentations & Excerpts

at 0.97 minutes (SD: 1.26, CI: 0.76 – 1.18) [p = 0.83]. Mean DAP for group A was 42.65 mGy (SD: 59.46, CI: 23.16 – 60.97) compared with Group B at 47.99 mGy (SD: 111.89, CI: 23.32 – 72.67) [p=0.32]. Mean room time of Group A was 77.77 minutes (SD: 38.19, CI: 64.47 – 89.79) compared with Group B at 64.46 minutes (SD: 31.01, CI: 58.76 – 70.33) [p=0.29]. Overall failure rate was 8% in Group A and 5% in Group B.

Conclusions

Our data shows there is slightly decreased room time and fluoroscopy time as well as statistically significant decreased failure rate for procedures performed in the lateral decubitus position. Although there is mild though not significantly increased DAP, the decreased room time and decreased overall failure rate warrant a more universally accepted use of fluoroscopically-guided LPs in the lateral decubitus position.



(Filename: TCT_O-356_LP2.jpg)

Wednesday, June 6, 2018

8:00AM - 9:00AM

Parallel Paper Session: Vessel Wall Imaging: Advanced Techniques

O-357

8:00AM - 8:07AM

Evaluation of Vessel Wall Magnetic Resonance Imaging In Differentiation of Intracranial Vasculopathies: A New Brick in the Wall?

M Lima¹, M Longo², R Menegatti¹, B Valentini¹, F Aesse³, J Muller¹

¹Hospital Moinhos de Vento, Porto Alegre, Rio Grande do Sul, Brazil, ²Massachusetts General Hospital, Boston, MA, ³Hospital Moinhos de Vento, Porto Alegre, Brazil

Purpose

High-resolution magnetic resonance vessel-wall imaging is a relatively new and in-building technique,

Oral Presentations & Excerptas

with great potential to redefine the imaging diagnostic criteria in vasculopathies. This technique allows specific evaluation of the vessel wall, which previous and standard techniques were incapable of doing. Its ability to differentiate vascular diseases based on imaging aspects, and the clinical and prognostic applicability of this findings still need further acknowledgement. The purpose of this study is to evaluate the performance, sensibility, specificity, positive predictive value and negative predictive value of vessel-wall imaging in differentiating intracranial atherosclerosis, central nervous system vasculitis and reversible cerebral vasoconstriction syndrome in patients who underwent examination for intracranial vascular disease suspicion.

Materials and Methods

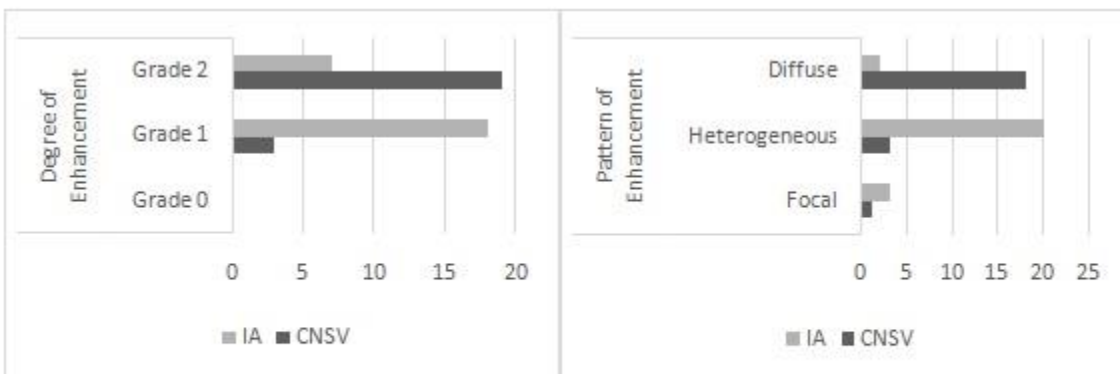
Review of magnetic resonance imaging vessel-wall studies performed between 2015 and 2017 at our institution in 29 patients suspected of having intracranial vasculopathy, through a cross-sectional study. The exams were performed in a 3,0 T equipment and images were analyzed in consensus by two board-certified neuroradiologists blinded for clinical information. The diagnostic imaging results were correlated with clinical findings, which were used as our gold standard.

Results

Of the 29 patients included, 58 vessels were studied. Twenty-two vessels were characterized as central nervous system vasculitis, 25 as intracranial atherosclerosis and 11 as reversible cerebral vasoconstriction syndrome. We found significant differences between the occurrence of parietal thickening and enhancement in cases of vasculitis and atherosclerosis in comparison with reversible cerebral vasoconstriction syndrome. Regarding the enhancement aspects, diffuse pattern and grade 2 (enhancement stronger than the pituitary stalk) enhancement were more frequent in vasculitis vessels, whereas heterogeneous pattern and grade 1 (enhancement similar or less than the pituitary stalk) enhancements were more common in intracranial atherosclerosis vessels. We also found high values of sensitivity, specificity, positive predictive value, negative predictive value and accuracy to this characteristics in association with the studied diseases, especially regarding diffuse pattern in vasculitis (S = 81.8%, E= 92%, PPV = 90%, NPV = 85.2%, ROC area = .869) and heterogeneous pattern in atherosclerosis (S = 80%, E = 86.4%, PPV = 87%, NPV = 79.2%, ROC area = .832).

Conclusions

High-resolution magnetic resonance vessel-wall imaging showed great results in differentiating the studied neurovascular diseases, demonstrating the characteristics of enhancement with high accuracy. Our findings are in accordance with recent studies published in medical literature regarding this subject.



Graphic. Graphics showing frequency of degree and pattern of enhancement. Note: The differences between degree and pattern in IA and CNSV presented with $p < 0.001$.

(Filename: TCT_O-357_Fig_4.jpg)

O-358

8:07AM - 8:14AM

Intracranial Vessel Wall Imaging and Etiologic Classification of Ischemic Stroke: Analysis of the First 205 Patients at the Toronto Western Hospital

D Mandell¹, J Schaafsma¹, C Jaigobin¹, J Coutinho², D Mikulis³, F Silver⁴

¹University Health Network, University of Toronto, Toronto, Ontario, Canada, ²Academic Medical Center, University of Amsterdam, Amsterdam, the Netherlands, ³Toronto Western Hospital, Toronto, Ontario, Canada, ⁴University of Toronto, Toronto, Ontario, Canada

Purpose

To determine the impact of using intracranial vessel-wall MRI (VW-MRI) on the etiologic classification of ischemic stroke

Materials and Methods

We studied all patients with stroke or transient ischemic attack referred on a clinical basis for 3-Tesla intracranial contrast-enhanced VW-MRI over an eight-year period at a single institute. A stroke neurologist (blinded to VW-MRI) reviewed the clinical records and conventional imaging reports for each patient and categorized stroke etiology using a modified TOAST classification system (1). A neuroradiologist categorized intracranial disease on VW-MRI using a pre-existing interpretive framework (2). The neurologist then reviewed the initial classification along with the VW-MRI results and confirmed or reclassified stroke etiology. We calculated the proportion of patients who were reclassified, and calculated the proportion of patients in each stroke category based on the workup incorporating VW-MRI versus conventional workup alone. We compared proportions using two-sided McNemar's tests.

Results

There were 205 patients, mean age 55 years (IQR 44-67), 52% (106/205) women. Median time between symptom onset and VW-MRI was 14 days (IQR 5-120). Etiologic classification incorporating VW-MRI differed from classification based on conventional workup alone in 53% (109/205) of patients. The proportion of patients with stroke etiology of intracranial atherosclerotic disease was higher with VW-MRI than with conventional workup alone: 55% (112/205) versus 25% (52/205) ($p < 0.001$). The proportion of patients categorized as intracranial arteriopathy not otherwise specified was lower with VW-MRI than with conventional workup alone: 6% (12/205) versus 33% (68/205) ($p < 0.001$). The proportion of patients categorized as cerebral small vessel disease was lower with VW-MRI than with conventional workup alone: 0% (1/205) versus 4% (8/205) ($p = 0.023$).

Conclusions

When patients are referred for intracranial VW-MRI based on clinical uncertainty regarding stroke etiology, using the existing interpretive framework for VW-MRI, a substantial proportion of patients are likely to have stroke etiology modified. This has diagnostic and therapeutic implications for institutes choosing to implement this newer technique.

O-359

8:14AM - 8:21AM

Reproducibility of 3D High-resolution Intracranial Vessel Wall Magnetic Resonance Imaging for Intracranial Atherosclerotic Disease

H Watase¹, J Sun¹, D Shibata¹, D Hippe¹, T Hatsukami¹, C Yuan¹, M Mossa-Basha¹

¹University of Washington, Seattle, WA

Purpose

The objective of this study was to evaluate the reproducibility of 3-D high-resolution intracranial vessel-wall magnetic resonance (MR) imaging for the identification of intracranial atherosclerotic disease (ICAD).

Materials and Methods

As part of the Intracranial Vessel Wall Imaging study (prospective NIH-funded observational cohort

Oral Presentations & Excerpts

study of ICAD), subjects with two or more risk factors for atherosclerosis, intracranial arterial irregularity on luminal imaging and no clinical evidence of other intracranial vasculopathies were recruited. After multiple training sessions, four reviewers with up to eight years of intracranial vessel wall MR imaging review experience evaluated individual intracranial arterial segments (cavernous and supraclinoid carotid, A1, M1, P1, basilar, V4, A2, M2, P2 arterial segments) using pre and postcontrast 3-D high-resolution T1-weighted intracranial vessel wall MR imaging and 3-D time-of-flight MR angiographic sequences. Reviewers specified whether a plaque was present and its location within each segment. Two pairs of reviewers independently evaluated images with consensus and interpair reproducibility of identifying plaques were calculated. Segments without sufficient image quality and coverage were excluded. Reproducibility was calculated with percentage (%) agreement and κ statistics.

Results

Three-hundred-and-fifteen artery segments in 19 subjects were evaluated. Overall interpair reproducibility was good (% agreement= 90.7%, $\kappa = 0.79$). Proximal anterior circulation segments including A1, M1, and P1 showed good reproducibility (% agreement=90.7%, $\kappa = 0.75$). Distal anterior circulation segments including A2, M2, and P2 showed moderate to good reproducibility (% agreement= 95%, $\kappa = 0.60$).

Conclusions

3-D high-resolution intracranial vessel-wall MR imaging detected ICAD with good to moderate reproducibility in both proximal and distal segments by four reviewers with different levels of experience.

O-360

8:21AM - 8:28AM

Correlation of 3D Time-of-Flight MRA and High Resolution Vessel Wall Magnetic Resonance Imaging in the presence of Vessel Wall Enhancement

J Song¹, S Rafla¹, S Ojeda², P Schaefer¹, J Romero¹

¹Massachusetts General Hospital, Boston, MA, ²Massachusetts General Hospital, New York City, NY

Purpose

Prior studies evaluating 3-D time-of-flight (TOF) magnetic resonance angiography (MRA) for evaluating cervical internal carotid arteries suggest 3-D TOF MRA may be inaccurate for assessing stenotic vessels. Given the even smaller caliber of intracranial segments compared to cervical segments, we hypothesized that 3-D TOF MRA may overestimate the luminal diameter compared to diameters measured by high-resolution vessel-wall magnetic resonance imaging (HR-VWI) in the presence of wall enhancement. To investigate this, correlations between the intradural vertebral artery diameters by 3-D TOF MRA and HR-VWI were evaluated.

Materials and Methods

Twenty-four subjects who underwent intracranial 3-D TOF MRA and a MRI brain with HR-VWI sequences were retrospectively identified. Six cases were excluded due to motion. All subjects were imaged for an indication of intracranial vasculopathy. Vessel-wall enhancement was graded from 0 to 2. Grade 0 indicated no enhancement, and grade 1 and 2 indicated enhancement less or greater than the pituitary infundibulum, respectively. Cross-sectional diameters of the intradural vertebral arteries (inner-to-inner wall) were measured at the same level on both exams. Statistical analyses were performed by SPSS v19.

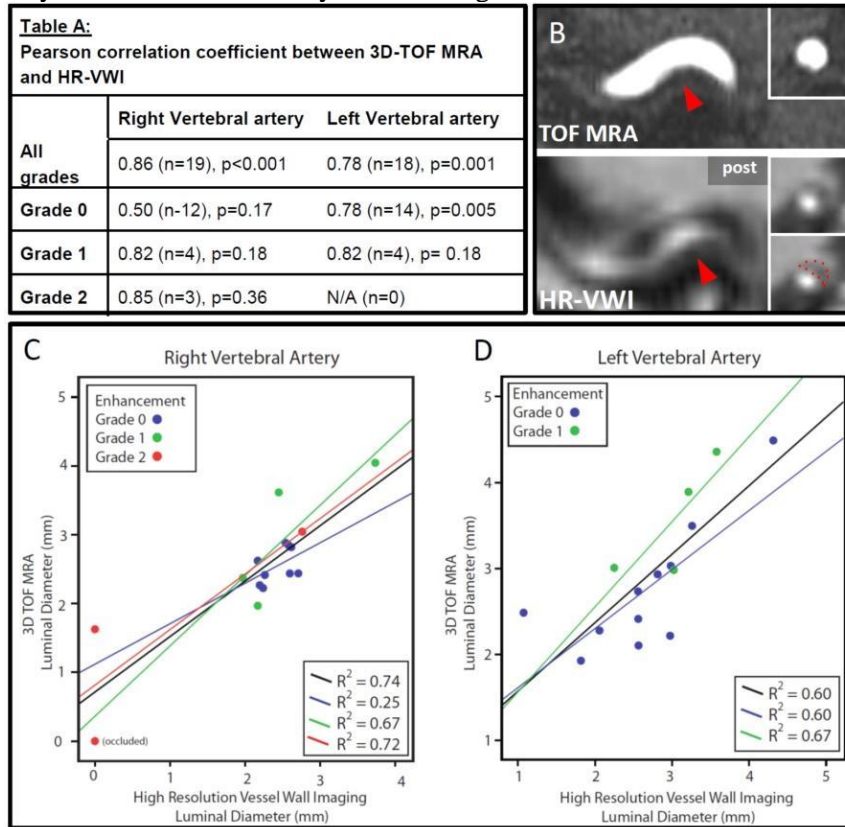
Results

Nineteen subjects with a mean age of 55 years met the inclusion criteria. Table A shows the number of vertebral artery segments by grade. In one subject, the left vertebral vessel wall enhancement grade could not be assessed as it was excluded from view. Statistically significant correlations between 3-D TOF MRA and HR-VWI of the bilateral vertebral arteries emerged ($p \leq 0.001$). When taking into account wall enhancement, moderate to strong correlations emerged but were not statistically significant ($p = 0.18-0.36$). In the presence of vessel-wall enhancement, 3-D TOF MRA appeared to show a slight overestimation of

the luminal diameter compared to HR-VWI. Fig. B illustrates sagittal and orthogonal views of a left vertebral artery by both exams; the dotted red line in the Fig. B inset highlights the luminal diameter seen by HR-VWI with a focus of eccentric wall enhancement. This contrasts with the apparent wider caliber seen by 3-D TOF MRA. Figs. C-D are scatterplots illustrating the correlations of the diameters.

Conclusions

In the presence of vessel-wall enhancement, 3-D TOF MRA overestimates the intradural vertebral artery luminal diameter compared to HR-VWI. Pathologies that manifest with vessel-wall enhancement (e.g., atherosclerosis or vasculitis) should be interpreted with caution when only using 3-D TOF MRA, which may decrease the sensitivity for detecting stenosis.



(Filename: TCT_O-360_Fig.jpg)

O-361

8:28AM - 8:35AM

Systemic Redox Status and Carotid Intraplaque Hemorrhage

B Liang¹

¹Emory University, Atlanta, GA

Purpose

MRI-detected carotid intraplaque hemorrhage (IPH) is a marker of vulnerable plaque and is associated with acute stroke and recurrent stroke risk despite standard medical therapy.(1) Carotid IPH is often centered at the bifurcation, an area predisposed to oscillatory shear stress and elevated endothelial reactive oxygen species (ROS). (2) Furthermore, carotid IPH is highly associated with low vitamin D, (3) and vitamin D status has been linked with redox status. (4) Currently, the relationship between systemic redox state and carotid IPH is unknown. The goal of this study was to examine the relationship between systemic thiol/disulfide redox status and carotid IPH.

Oral Presentations & Excerptas

Materials and Methods

In this IRB-approved prospective cross-sectional study, 100 patients undergoing neurovascular consultation for known carotid disease were recruited for carotid MRI and redox state analysis. IPH was detected with the Magnetization Prepared Rapid Acquisition Gradient-recalled Echo (MPRAGE) sequence. Cardiovascular risk factors were recorded as potential confounders, including male (93%), age (mean=71 years, S.D.=9, range 41,88), BMI (mean=29 kg/m², S.D.=5, range 20,45), eGFR (mean=67 mL/min/1.73 m², S.D.=18, range 23,121), current smoking (20%), prior smoking (45%), hypertension (81%), hyperlipidemia (74%), diabetes (40%), and medications including antiplatelet agents (77%), anticoagulation (8%), antihypertensives (75%) and statins (76%). Recent stroke was also recorded (50%). Immediately prior to MRI, blood draws were performed for vitamin D, angiotensin II, hsCRP, and redox status analysis. Plasma glutathione (GSH) and its oxidized form (GSSG) were measured by HPLC and GSH/GSSG was expressed as a redox potential described by the Nernst equation ($E_{GSSG} = -264 + 30 \cdot \log(1000[GSSG]/[GSH]^2)$ in mV) with a more positive value representing a more oxidized state. (5) Similarly, cysteine (Cys) and its oxidized form (CySS) were measured and E_{CySS} was calculated. Linear regression was used to determine the influence of redox state on carotid IPH volume and determine clinical determinants of systemic oxidative stress. Backwards elimination was performed at a threshold $p < 0.20$ to determine essential predictors.

Results

Patients with recent stroke had significantly higher carotid IPH volume compared to asymptomatic patients (279 mm³ vs. 158 mm³, $p=0.036$). A more oxidized E_{CySS} was significantly associated with carotid IPH volume on linear regression (coeff=6.9, $p=0.045$). Other factors in the final model included total CySS ($p=0.178$), hsCRP ($p < 0.001$), low vitamin D ('<30 ng/mL' $p=0.004$, 'continuous' $p=0.113$), smoking ('current' $p=0.008$, 'prior' $p=0.145$), age ($p=0.051$) and BMI ($p=0.164$). E_{GSSG} was eliminated from the final model after backwards elimination at threshold $p < 0.20$. Predictors of a more oxidized E_{CySS} included statin use (coeff=6.0, $p=0.002$), current smoking (coeff=6.1, $p=0.10$), and anticoagulant use (coeff=7.7, $p=0.023$), whereas GFR (coeff=-0.2, $p=0.002$) and diabetes (coeff=-2.5, $p=0.186$) indicated a more reduced E_{CySS} .

Conclusions

Carotid IPH volume was associated with a more oxidized cysteine redox state, suggesting that systemic oxidative stress may be a contributing factor to vulnerable plaque. This may represent a potential treatment target in patients with carotid IPH.

O-362

8:35AM - 8:42AM

Validation of quantitative vessel size imaging (VSI) in human gliomas using image-guided stereotactic biopsies

A Chakhoyan¹, R Harris¹, K Leu¹, M Dehghan Harati², N Salamon³, A Lai⁴, P Nghiemphu⁴, T Cloughesy⁴, B Ellingson¹

¹*UCLA-Department of Radiological Science, BTIL Lab, Los Angeles, CA*, ²*UCLA-Department of Pathology and Laboratory Medicine, Los Angeles, CA*, ³*UCLA-Department of Radiological Science, Los Angeles, CA*, ⁴*UCLA-Department of Neurology, Los Angeles, CA*

Purpose

Angiogenesis is critical for brain tumor development and malignant transformation, influencing both prognosis and response to therapy. The "vessel size imaging" (VSI) (2) is a quantitative technique that estimates the mean diameter of vessels by using multiecho spin-and-gradient-echo (SAGE) dynamic susceptibility contrast (DSC) perfusion MRI. In the current study we compared VSI to histology-equivalent estimates of vessel diameter using stereotactic image-guided biopsies.

Materials and Methods

A total of 30 image-guided biopsies were obtained in 11 glioma patients (five low-grade gliomas (LGG))

Oral Presentations & Excerptas

and six high-grade (HGG)). MRI examinations were acquired prior to surgery on a 3T MRI, including multiecho SAGE DSC perfusion (2x gradient echo, 1x asymmetric echo, and 1x spin-echo). One to four biopsy targets (5mm radius) were defined and stereotactically biopsied (Figure-A). Relative cerebral blood volume (rCBV) was calculated (3) using DSC data from a single gradient echo. VSI was quantified as $VSI_{\mu m} = 0.867(ADC \cdot rCBV)^{(1/2)} \cdot ((\Delta R2^*) / ((\Delta R2)^{(3/2)}))$ where ADC is the apparent diffusion coefficient (mm²/s), $\Delta R2^*$ and $\Delta R2$ are transverse relaxation rates. Histologically estimates of VSI were obtained as previously modeled. (4)

Results

A relatively low median vessel density was quantified by histology in LGG (79mm⁻²) compared to HGG (86mm⁻²). Median VSI was 12.91 μ m in LGG, while for HGG, the VSI was 11.28 μ m. We observed no significant correlation between VSI quantification by MRI and histology for LGGs (Figure-B) (11.60 \pm 3.66 μ m vs. 12.11 \pm 2.76 μ m, p=0.51); however, a strong association was observed in HGG (Figure-C, r=0.44, p<0.05).

Conclusions

MR measures of VSI exhibit a strong relationship to histological measures of vessel diameter in HGG.

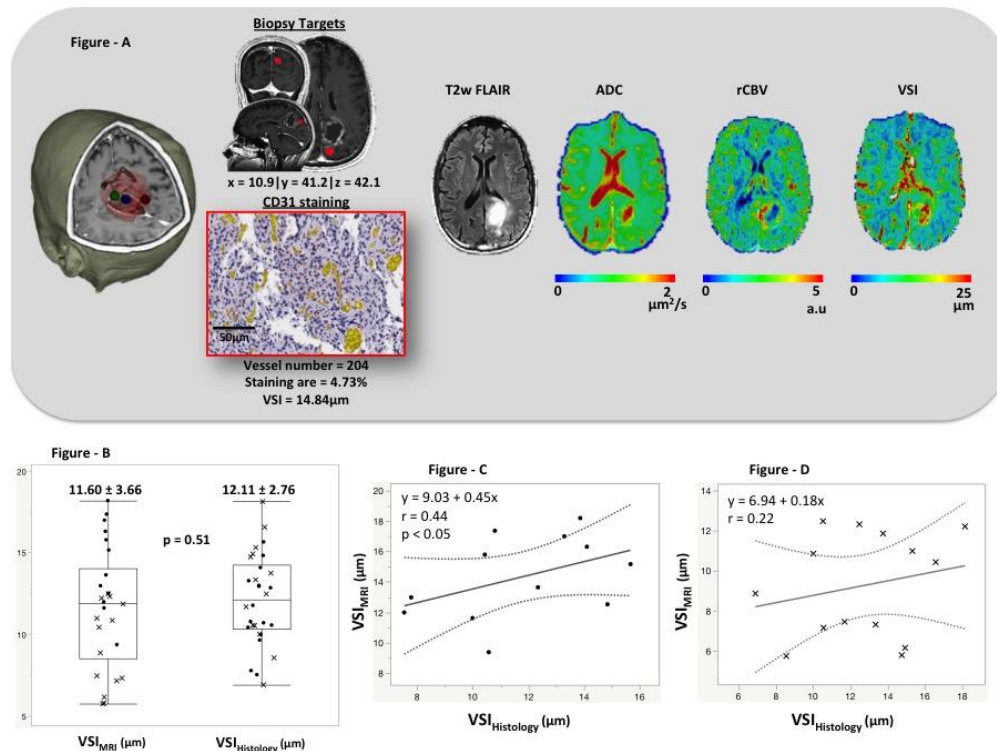


Figure: Example HGG patient with biopsy targets, CD31 staining, T2w-Flair, ADC, rCBV and VSI (A). Comparison of VSI between MRI and histology (B). Linear correlation of VSI quantified with MRI and histology in both HGG (C) and LGG (D).

(Filename: TCT_O-362_Figure.jpg)

O-363

8:42AM - 8:49AM

3D Vessel Wall Imaging of Scalp Arteries: Feasibility and Normal Appearance

B Kwan¹, T Chen², K Misquitta², A Naheed², D Mikulis², D Mandell¹

¹University of Toronto, Toronto, Ontario, Canada, ²Toronto Western Hospital, Toronto, Ontario, Canada

Purpose

Interpretation of high-resolution vessel-wall MRI (VW-MRI) relies on evaluation of the arteries of interest in both longitudinal and cross-sectional axes. But scalp vessels such as the superficial temporal arteries have a tortuous course, so they are difficult to study using orthogonal two-dimensional (2-D) vessel-wall sequences. The purposes of this study are to assess the feasibility of evaluating the scalp arteries using 3-D VW-MRI, and to characterize the range of normal appearances of the scalp arterial wall.

Materials and Methods

Patients scheduled for a gadolinium-enhanced brain MRI for reasons unrelated to vascular disease were recruited for the addition of scalp vessel-wall sequences to their clinical exam. On a 3-T MR system we performed a time-of-flight MRA covering from the C2 level to the vertex, and an optimized fat-suppressed, T1-weighted, 3-D VW-MRI CUBE sequence with the same coverage before and after intravenous injection of gadolinium contrast. Two neuroradiologists graded the quality of visualization of each extracranial carotid artery branch on a 3-point scale, and recorded the degree of enhancement of the arterial wall of each branch on a 3-point scale.

Results

This study is currently underway with high-quality imaging obtained in five patients in the last month (Figure 1). We will present our preliminary results (which we anticipate will include approximately 20 patients at the time of the upcoming ASNR meeting) including qualitative and quantitative descriptions for the normal appearances of the scalp arteries. Additionally, we will discuss the technical aspects of this imaging method and how to implement it in the clinical setting.

Conclusions

High-resolution 3-D VW-MRI may be a useful technique for visualization of external carotid artery branches in the scalp and aid in the diagnosis of conditions such as giant cell arteritis.

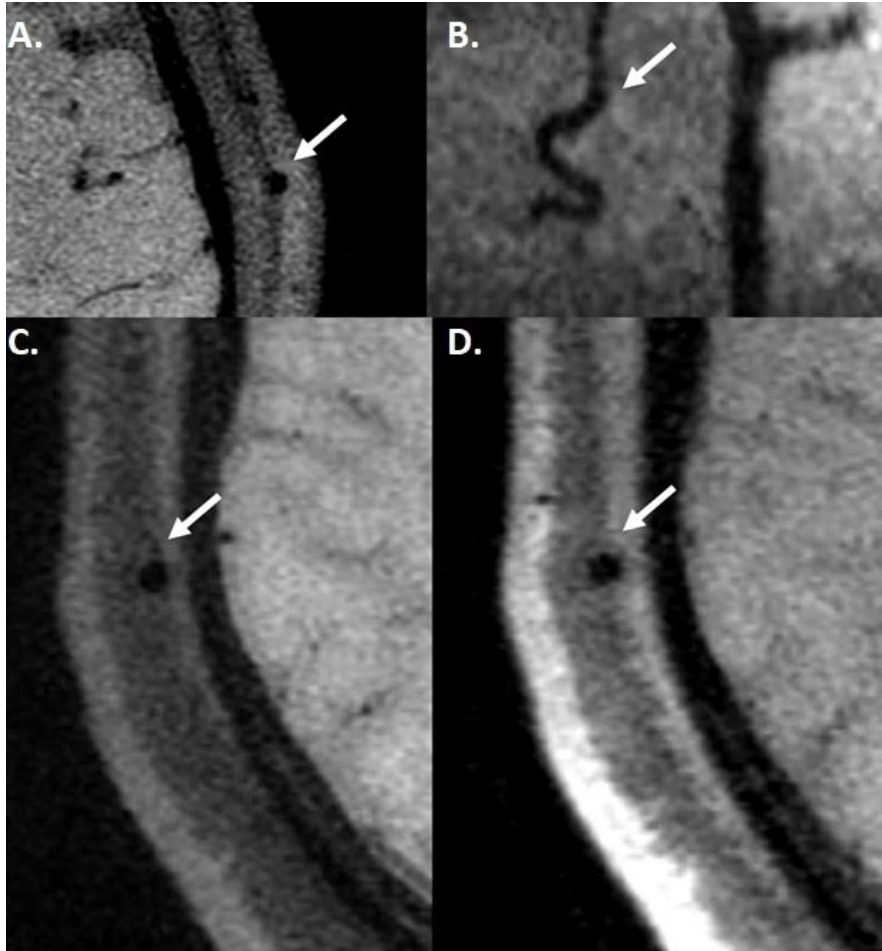


Figure 1. A. and B. demonstrate axial and sagittal images of the superficial temporal artery on T1 weighted fat suppressed 3D CUBE arterial wall imaging. Note the exquisite detail of the vessel. C. and D. demonstrate pre- and post-gadolinium T1 weighted fat suppressed 3D CUBE arterial wall imaging. Note there is no abnormal enhancement of the vessel wall on D. (Filename: TCT_O-363_Figure1-300dpi.jpg)

O-364

8:49AM - 8:56AM

Utility of High Resolution Vessel Wall Imaging in Hypertensive Angiopathy

J Song¹, M Gurol¹, P Schaefer¹, J Romero¹
¹Massachusetts General Hospital, Boston, MA

Purpose

Hypertensive small vessel strokes comprise nearly one third of all strokes. Small vessel arteriolosclerosis resulting in fibrinoid necrosis leading to lacunar infarcts and intraparenchymal hemorrhage is a challenge to identify by conventional vessel imaging techniques. High-resolution vessel wall magnetic resonance imaging (HR-VWI) may be able to highlight intracranial atherosclerosis with vessel-wall enhancement serving as a biomarker for symptomatic intracranial plaque.

Materials and Methods

A 66-year-old female with a medical history of essential hypertension and arthritis presented with severe headaches and dysarthria. Her medication included 325 mg of aspirin daily. Upon presentation, her blood pressure was 156/86. A head CT (A) revealed intraparenchymal hemorrhage centered in the right basal

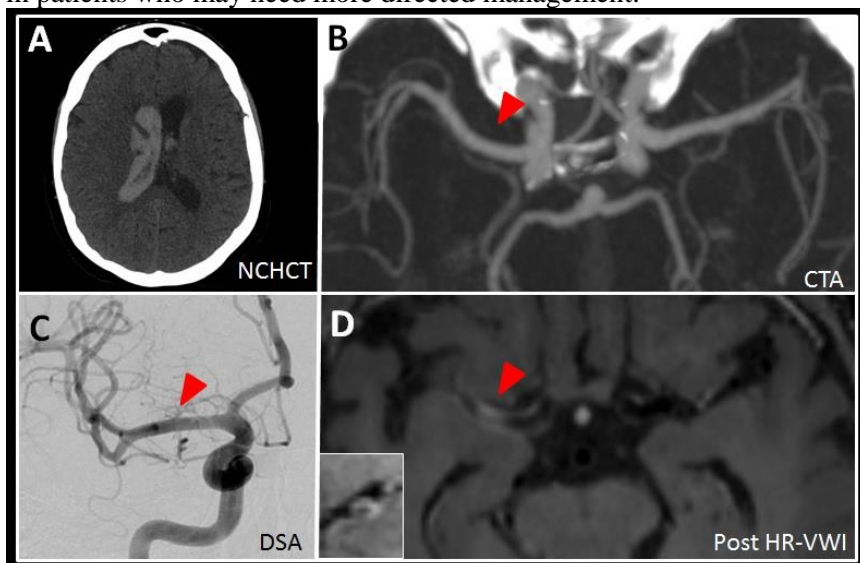
ganglia with intraventricular extension. Computed tomography angiogram (CTA) of the head (B) and cerebral angiogram (C) were unremarkable. A brain MRI with HR-VWI sequences revealed eccentric vessel-wall enhancement involving the right M1 middle cerebral artery (MCA) segment in the region of the lenticulostriate vessel origins. Taken together, these studies suggest an added utility for HR-VWI sequences in identifying symptomatic atherosclerosis, which may not be readily apparent by other conventional vessel imaging modalities.

Results

(A) Head CT in the axial plane shows a right basal ganglia intraparenchymal hemorrhage with intraventricular extension. (B) Axial 3-D MIP image from a CTA and (C) right internal carotid artery cerebral angiogram reveals no abnormality involving the right M1 MCA. (D) Postcontrast HR-VWI reveals eccentric wall enhancement of the right M1 MCA; the inset shows an orthogonal view of the M1 MCA, illustrating the eccentric wall enhancement.

Conclusions

HR-VWI may be able to highlight symptomatic atheromatous plaque in intracranial arteries that are otherwise not visible by other conventional methods of vessel imaging. HR-VWI may thus be an invaluable noninvasive tool, with added diagnostic utility, for identifying symptomatic intracranial plaque in patients who may need more directed management.



(Filename: TCT_O-364_Figure1.jpg)

Wednesday, June 6, 2018

8:00AM - 9:00AM

Parallel Paper Session: Carotid Artery Stenosis Imaging

O-365

8:00AM - 8:07AM

Systemic Oxidative Stress and MRI-Detected Carotid Intraplaque Hemorrhage

J McNally¹, S Kim¹, M Alexander¹, A DeHavenon¹, B Liang², D Jones², G Treiman¹, D Parker¹

¹University of Utah, Salt Lake City, UT, ²Emory University, Atlanta, GA

Purpose

MRI-detected carotid intraplaque hemorrhage (IPH) is a marker of vulnerable plaque and is associated

Oral Presentations & Excerptas

with acute stroke and recurrent stroke risk despite standard medical therapy. (1) Carotid IPH is often centered at the bifurcation, an area predisposed to oscillatory shear stress and elevated endothelial reactive oxygen species (ROS). (2) Furthermore, carotid IPH is highly associated with low vitamin D, (3) and vitamin D status has been linked with redox status. (4) Currently, the relationship between systemic redox state and carotid IPH is unknown. The goal of this study was to examine the connection between systemic thiol/disulfide redox status and carotid IPH.

Materials and Methods

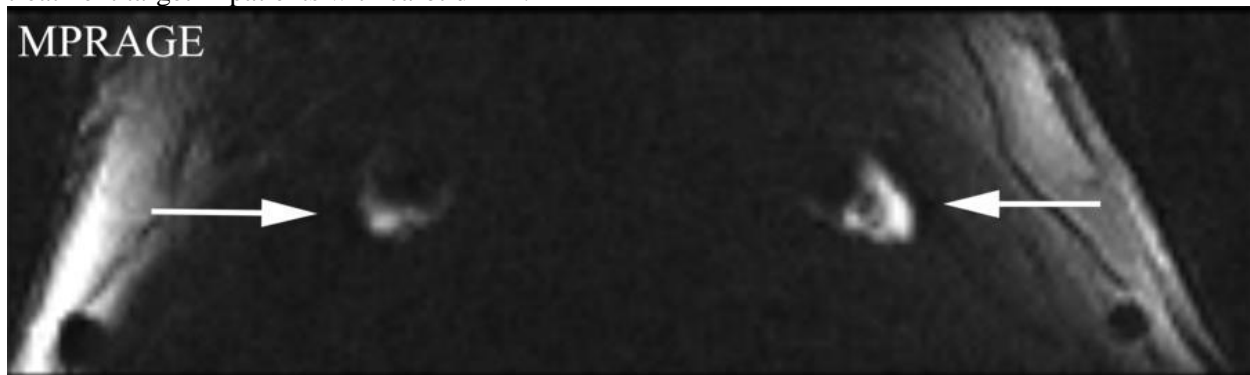
In this IRB-approved prospective cross sectional study, 100 patients undergoing neurovascular consultation for known carotid disease were recruited for carotid MRI and redox state analysis. IPH was detected with the Magnetization Prepared Rapid Acquisition Gradient-recalled Echo (MPRAGE) sequence. Cardiovascular risk factors were recorded as potential confounders, including male sex (93%), age (mean=71 years, S.D.=9, range 41,88), body mass index (BMI, mean=29 kg/m², S.D.=5, range 20,45), estimated glomerular filtration rate (eGFR, mean=67 mL/min/1.73m², S.D.=18, range 23,121), current smoking (20%), prior smoking (45%), hypertension (81%), hyperlipidemia (74%), diabetes (40%), and medications including antiplatelet agents (77%), anticoagulation (8%), antihypertensives (75%) and statins (76%). Recent stroke as defined by the AHA was also recorded (50%). Immediately prior to MRI, blood draws were performed for vitamin D, angiotensin II, high sensitivity C-reactive protein (hsCRP), and redox status analysis. Plasma glutathione (GSH) and its oxidized form (GSSG) were measured by HPLC and GSH/GSSG was expressed as a redox potential described by the Nernst equation ($E_{hGSSG} = -264 + 30 \cdot \log(1000[GSSG]/[GSH]^2)$ in mV) with a more positive value representing a more oxidized state. (5) Similarly, cysteine (Cys) and its oxidized form (CySS) were measured and E_{hCySS} was calculated. Linear regression was used to determine the influence of redox state on carotid IPH volume and determine clinical determinants of systemic oxidative stress. Backwards elimination was performed at a threshold $p < 0.20$ to determine essential predictors.

Results

Patients with recent stroke had significantly higher carotid IPH volume compared to asymptomatic patients (279 vs. 158 mm³, $p = 0.036$). A more oxidized E_{hCySS} was significantly associated with carotid IPH volume on linear regression (coeff=6.9, $p = 0.045$). Other factors in the final model included total CySS ($p = 0.178$), hsCRP ($p < 0.001$), low vitamin D ('<30 ng/mL' $p = 0.004$, 'continuous' $p = 0.113$), smoking ('current' $p = 0.008$, 'prior' $p = 0.145$), age ($p = 0.051$) and BMI ($p = 0.164$). E_{hGSSG} was eliminated from the final model after backwards elimination at threshold $p < 0.20$. Predictors of a more oxidized E_{hCySS} included statin use (coeff=6.0, $p = 0.002$), current smoking (coeff=6.1, $p = 0.10$), and anticoagulant use (coeff=7.7, $p = 0.023$), whereas eGFR (coeff=-0.2, $p = 0.002$) and diabetes (coeff=-2.5, $p = 0.186$) indicated a more reduced E_{hCySS} .

Conclusions

Carotid IPH volume was associated with a more oxidized cysteine redox state, suggesting that systemic oxidative stress may be a contributing factor to vulnerable plaque. This may represent a potential treatment target in patients with carotid IPH.



(Filename: TCT_O-365_BilateralcarotidIPHforASNR121517copy.jpg)

Carotid Plaque Beta Amyloid Precursor Protein Expression Correlates with Inflammation and MRI-Detected Intraplaque Hemorrhage

J McNally¹, D Miller², S Kim¹, A Sakata¹, M Alexander¹, A DeHavenon¹, G Treiman¹, D Parker¹
¹University of Utah, Salt Lake City, UT, ²University of Utah, Murray, UT

Purpose

Beta amyloid precursor protein (bAPP) is the amyloidogenic protein present in the amyloid deposits of Alzheimer's disease and cerebral amyloid angiopathy. (1, 2) Its native function and activity is not fully understood, however bAPP is known to be expressed in platelets and has been implicated in vascular inflammation and atherosclerosis. (3) Furthermore, platelet aggregation is an early sign prior to amyloid plaque development in Alzheimer's disease mouse models. (4) In carotid plaque, macrophage expression has been shown to correlate with markers of plaque inflammation including intraplaque hemorrhage (IPH). MRI-detected carotid intraplaque hemorrhage (IPH) has been shown to be associated with acute stroke and recurrent stroke risk despite standard medical therapy. (5) The goal of this study was to examine the relationship between carotid plaque bAPP expression with imaging markers of vulnerable plaque including MRI-detected carotid IPH, plaque thickness and stenosis.

Materials and Methods

In this IRB-approved prospective cross-sectional study, patients scheduled for carotid endarterectomy were recruited for preoperative carotid MRI and postoperative bAPP expression analysis. A total of 53 carotid plaques were available for MRI and immunohistochemistry correlation. IPH was detected with the Magnetization Prepared Rapid Acquisition Gradient-recalled Echo (MPRAGE) sequence. Cardiovascular risk factors were recorded, including male sex (98%), age (mean=70 years, S.D.=7, range 56,84), body mass index (BMI, mean=27 kg/m², S.D.=4, range 20,40), estimated glomerular filtration rate (eGFR, mean=68 mL/min/1.73m², S.D.=17, range 23,97), current smoking (26%), prior smoking (34%), hypertension (75%), hyperlipidemia (70%), diabetes (34%), and medications including antiplatelet agents (81%), anticoagulation (4%), antihypertensives (74%) and statins (79%). Recent ipsilateral stroke as defined by the AHA was also recorded (47%). Carotid endarterectomy specimens were formalin fixed and decalcified prior to routine processing. H&E and elastic (EVG) stains were performed to allow for characterization of plaques and features of instability (e.g. carotid IPH). Immunoperoxidase staining for bAPP (DAKO clone 6F/3D) was also performed. bAPP expression was scored by semiquantitative staining intensity (0=negative, 1=weak, 2=positive). Regression analysis was used to determine the correlation between bAPP expression and carotid markers of plaque vulnerability.

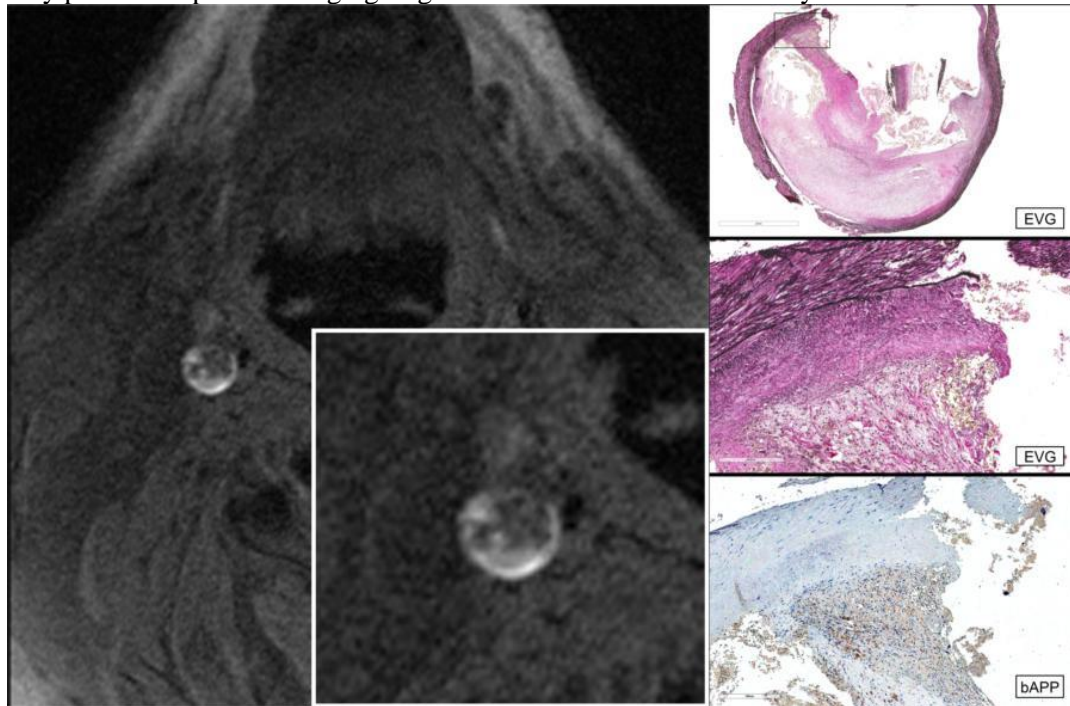
Results

bAPP staining was limited to macrophages in a coarse granular cytoplasmic pattern consistent with previously described macrophage phagocytosis of platelets expressing bAPP. In the figure, a representative patient with carotid IPH underwent endarterectomy and positive bAPP staining was found in and around a ruptured fibrous cap containing carotid IPH. In pooled imaging data, bAPP expression correlated with total MRI-IPH volume ($r=0.38$, $p=0.005$) and maximum plaque thickness ($r=0.30$, $p=0.03$), but not with stenosis measured by NASCET ($r=0.13$, $p=0.36$) or mm-stenosis ($r=-0.09$, $p=0.51$). Furthermore, for pathologically determined unstable plaques, mean semiquantitative bAPP score was 1.9 and for stable plaques it was 0.6 ($p<0.0001$). Correlation coefficients were also determined for semiquantitative bAPP scoring versus histologically determined percent soft/necrotic plaque ($r=0.57$, $p<0.0001$), fibrous cap thickness ($r=0.14$, $p=.31$), and cap inflammation ($r=0.34$, $p=0.012$).

Conclusions

This study is the first to show accumulation of bAPP within carotid plaques and demonstrate an association with specific features of plaque instability. These data show that bAPP expression is linked with MRI-detected carotid IPH and histologic markers of inflammation. By uncovering the links between

carotid IPH and inflammation, these results may have important implications for translational science and may provide important imaging targets to monitor treatment efficacy and discover new therapies.



(Filename: TCT_O-366_bAPPASNRfigure121517copy.jpg)

O-367

8:14AM - 8:21AM

Identification of Patients with Carotid Stenosis using Natural Language Processing

X Wu¹, Y Zhao², A Malhotra³, D Radev²

¹Yale University School of Medicine, New Haven, CT, ²Yale University, New Haven, CT, ³Yale New Haven Hospital, New Haven, CT

Purpose

The highly structural nature of medical reports may make it feasible for large-scale patient identification using computer modeling. This study aims to develop a natural language processing (NLP) model to retrospectively retrieve patients with a presence or history of carotid stenosis (CS) using their ultrasound reports.

Materials and Methods

The phrase "carotid stenosis" was used to retrieve ultrasound reports from our institution between January 2016 and December 2016. A total of 1,594 patients were included and labeled with whether the patient had past or present CS manually. To process the text data, we developed a parser to divide the raw text into the following fields: history/indication, comparison, findings, impression, as well as to extract the numerical values at each velocity measurement. For baseline method, we use bag of ngrams and TF-IDF (for each text field) as the features and use linear classifiers. Convolution neural network (CNN) is applied to the data set to improve the classification accuracy. In addition, we developed a novel convolution neural network, field-aware CNN, to leverage the parser we developed early, which achieves the best classification results.

Results

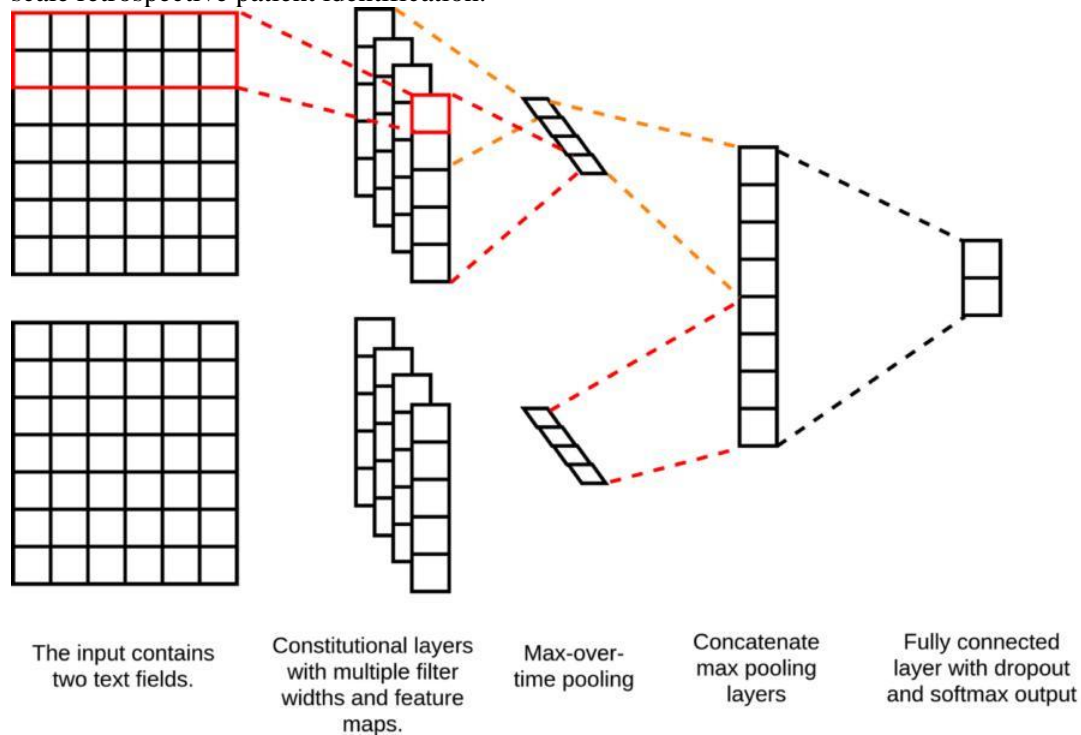
Among the 1,594 patients, 355 had a past history of CS and 405 had CS when the ultrasound was taken. In the baseline model, logistic regression yields an accuracy of 88% (sensitivity=73%, specificity=95%)

Oral Presentations & Excerptas

in predicting past CS, and an accuracy of 93% (sensitivity=88%, specificity=94%) in predicting present CS. Traditional CNN can predict past CS with an accuracy of 90% (sensitivity=82%, specificity=94%), and present CS with an accuracy of 97% (sensitivity=91%, specificity=95%). Field-Aware CNN has the best performance, with an accuracy of 92% for past CS (sensitivity=86%, specificity=95%), and an accuracy of 95% (sensitivity=99%, specificity=95%).

Conclusions

Through this study, we have developed a parser to automatically segment the report text into different sections and extract the key velocity measurements. We have proposed a novel neural network architecture taking advantage of the parsed texts, which is shown to be an efficient approach for large-scale retrospective patient identification.



(Filename: TCT_O-367_ASNRfigure.jpg)

O-368

8:21AM - 8:28AM

More than morphologic stenosis and hemodynamic impairment: Machine Learning Enables Digital Subtraction Angiography to Define the Clinical Impact of Carotid Stenosis

C Lin¹, S Ho², S Hung¹, W Guo¹, F Chang¹, C Luo¹

¹Taipei Veterans General Hospital; School of Medicine, National Yang Ming University, Taipei, Taiwan, ²National Chiao Tung University, Hsinchu, Tawan

Purpose

The study is aimed to explore the feasibility of using machine learning in digital subtraction angiography (DSA) to define the clinical impact of carotid stenosis on causing symptoms and infarcts as compared with morphologic stenosis and hemodynamic impairment related to the stenosis.

Materials and Methods

One-hundred-fifteen patients who received stenting for carotid stenosis were retrospectively recruited for analysis. Demographic data of patients such as age, gender, laterality of stenosis, comorbidity were used as clinical features. Stenotic degree, collateral condition, and distal stenosis, as well as quantitative time

Oral Presentations & Excerpts

density curve analysis on DSA were used as imaging features. Symptomatic stenosis were defined as those caused any episodes of stroke, transient ischemic attack, or amaurosis fugax in 180 days prior to DSA; prior MR infarcts were defined as any infarcts in the corresponding territory of stenotic site seen on presenting MR. Classifying models were established by inheritable bi-objective combinatorial genetic algorithm (IBCGA). The diagnostic accuracies between the variables and IBCGA model were compared.

Results
The accuracy was 89.6% to detect symptomatic carotid stenosis, and 91.3% to detect prior MR infarcts by IBCGA model. The area under curve (.887) of receiver operating characteristic curve of IBCGA model was larger than those of cerebral circulation time (CCT) (.637) and stenotic degree (.581) in detecting symptomatic patients. The area under curve of IBCCA (.929) in detecting prior MR infarcts was also larger than those of CCT (.49) and stenotic degree (.255).

Conclusions

Machine learning successfully improved the diagnostic value of DSA in identifying symptomatic carotid stenosis as well as cerebral infarcts on MR. This adjunctive real-time analysis of DSA provides feasibility in optimizing treatment strategy for carotid stenosis.

O-369

8:28AM - 8:35AM

Preventive Effect of Residual Stenosis on Hyperperfusion Syndrome after Carotid Artery Stenting not Followed by Balloon Dilatation

T Mori¹, Y Tanno¹, S Kasakura¹, N Nakai¹, K Yosioka¹

¹Shonan Kamakura General Hospital Stroke Center, Kamakura, Kanagawa, Japan

Purpose

Cerebral hyperperfusion syndrome (CHS) probably occurs after carotid artery stenting (CAS) of an extremely high-grade carotid artery stenosis (ex-CS) probably coupled with cerebral hemodynamic failure. The aim of our retrospective study was to investigate whether or not residual stenosis (rS) after CAS not followed by balloon dilatation (bD) had relation to prevention of CHS.

Materials and Methods

We included in our study patients with an ex-CS who underwent elective CAS not followed by bD from January 2016 to October 2017. We defined an ex-CS as a stenosis of more than NASCET 70% which caused delayed filling of contrast material in an internal carotid angiogram (CA) compared to an external CA and reduced signal intensity (ratio of less than 0.9) of the ipsilateral middle cerebral artery (MCA) compared to the contralateral MCA on 3-dimensional time-of-flight magnetic resonance angiography (MRA), and defined a significant residual stenosis (rS) as angiographic stenosis of more than NASCET 30% indicating area stenosis of more than 50%, or peak systolic velocity (PSV) of more than 80 cm/s by Doppler ultrasonography because significant stenosis caused PSV to increase. We evaluated patients' baseline characteristics, rS just after CAS and incidence of CHS.

Results

During the study period, we performed 93 elective CAS and 14 CAS of them matched our inclusive criteria. Their age was 73.5 (70.8-79) years (median, IQR) and carotid stenosis was NASCET 81.2% (77.8-90.9). Signal intensity ratio of the ipsilateral MCA compared to the contralateral side was 0.78 (0.68-0.84). Five patients (35.7%) had symptomatic CS. Median PSV before and just after CAS was 304 and 71.5 cm/s (p<0.0001). Median stent diameter stenosis was 33.4% (23-40) and area stenosis was 55.6% (40.6-63.5). Eight patients (57.1%) had angiographic rS. Five patients (35.7%) had PSV of more than 80 cm/s. Totally nine (64.3%) patients (44%) had significant rS. No CHS occurred in 14 patients with an ex-CS.

Conclusions

CAS not followed by bD resulted in significant rS in many patients with an ex-CS. It was probably associated with no CHS.

Oral Presentations & Excerptas

Carotid Webs: Survey of Current Clinical Practices

K Wojcik¹, G Vidal², J Tarsia², J Milburn², A Steven²

¹*The University of Queensland School of Medicine, Ochsner Clinical School, New Orleans, LA*, ²*Ochsner Clinic Foundation, New Orleans, LA*

Purpose

Carotid webs are thick, fibrous intimal bands which appear as intraluminal shelf-like defects on vascular imaging at the carotid bifurcation. Associated imaging findings can be subtle and overlooked as lesions are not commonly associated with significant vascular stenosis. Carotid webs have gained attention as potential underrecognized causes of "cryptogenic" ischemic stroke. (1–4) Despite increasing recognition, there is a paucity of published research on morbidity of such lesions with no available evidence-based treatment guidelines. The goal of this survey was to assess the state of current clinical practice.

Materials and Methods

An eight-question MCQ style survey of neurologists and radiologists assessed familiarity with this disease entity, preferred imaging modalities, and management strategies for asymptomatic and symptomatic (producing stroke) carotid webs. Responses were collected through SurveyMonkey software via anonymous responses to a posted survey link on the SNIS website in addition to anonymous emails.

Results

With data collection ongoing (currently over 70 responses), reported incidence and familiarity was higher among specialists (55% reported webs as routine or extensive clinical practice) vs. generalists (20%). Identification of carotid webs was consistent: CTA most frequently identified webs (67% of responses) while catheter-based DS angiogram was preferred to confirm the presence (67%). There was less consensus on management. Preferred therapy in acute strokes varied greatly with eight different management plans recorded, the most common being dual antiplatelet therapy (24% responses). Recurrent strokes due to webs garnered more invasive treatment plans including stenting (38%) and endarterectomy (22%).

Conclusions

Carotid webs represent an under recognized etiology for stroke, particularly cryptogenic strokes in younger patients without typical stroke risk factors. Recently, increased awareness and improved vascular imaging techniques have increased diagnostic capabilities. Continued advocacy is required particularly among nonspecialists. Certain practice patterns are evident despite an absence of established guidelines while others (treatment of webs in acute stroke) remain controversial. Continued research is necessary to validate these practices.

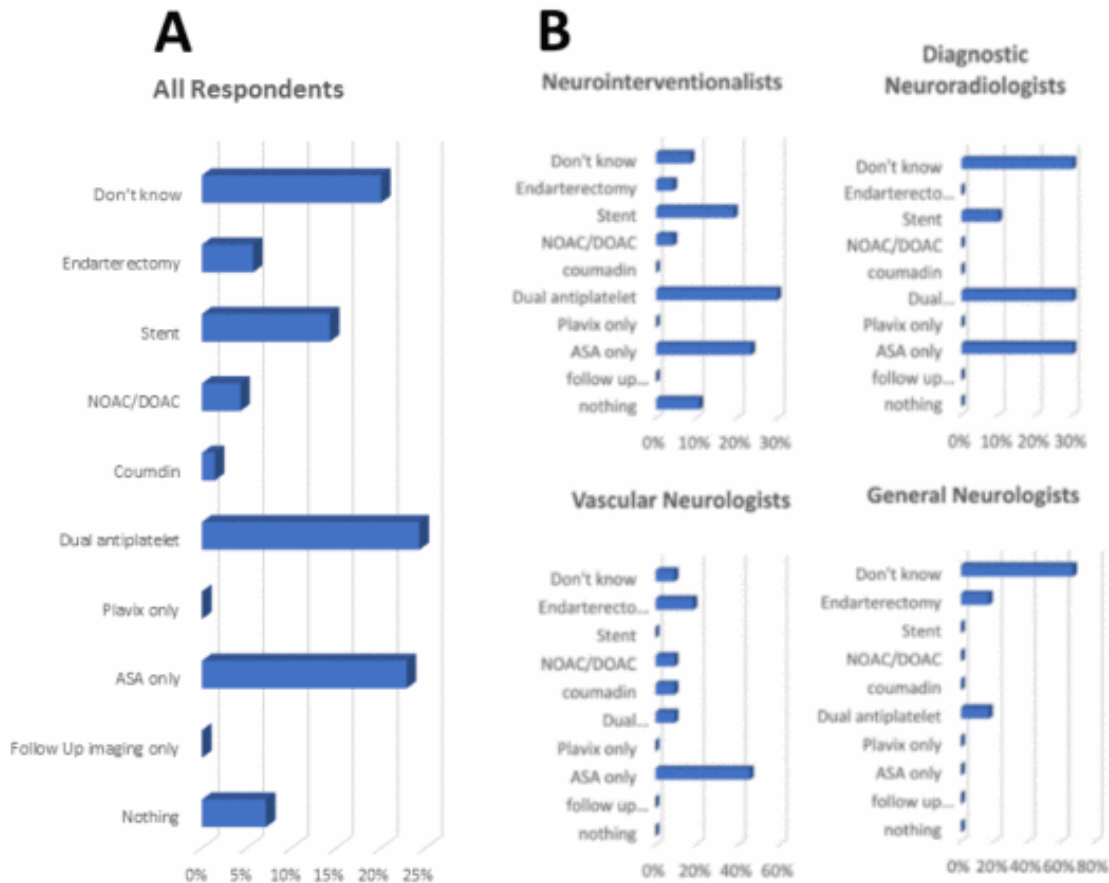


Figure 1: Preferred treatment of a carotid web in the setting of acute (ischemic) stroke survey responses for (A) all respondents and (B) responses per specialist.

(Filename: TCT_O-370_Slide1.GIF)

O-371

8:42AM - 8:49AM

Imaging of Spontaneous and Traumatic Cervical Artery Dissection: Comparison of Typical CT-Angiographic Features

U Hanning¹, T Niederstadt², M Raschke², R Dittrich², G Broocks³, M Schoenfeld¹, H Leischner³, F Flottmann³, J Fiehler³, W Heindel², P Sporns²

¹University of Hamburg-Eppendorf, Hamburg, Germany, ²University of Muenster, Muenster, North Rhine Westfalia, Germany, ³University Medical Center Hamburg-Eppendorf, Hamburg, Germany

Purpose

Cervical artery dissection (CAD) is an important etiology of ischemic stroke and early recognition is vital to prevent patients from the major complication cerebral embolization by administration of anticoagulants. Etiologies differ and can either be spontaneous or traumatic. Even though the historical gold standard still is catheter angiography, recent studies suggest a good performance of CT angiography (CTA) for detection of cervical artery dissection. We conducted this research to evaluate the variety and

frequency of possible imaging signs of spontaneous and traumatic cervical artery dissection and to guide neuroradiologists' decision-making.

Materials and Methods

Retrospective review of the database of our multiple injured patients admitted to the Department of Trauma, Hand, and Reconstructive Surgery of the University Hospital Muenster in Germany (a level 1 trauma center) for patients with traumatic cervical artery dissection (tCAD) and of our stroke database (2008-2015) for patients with spontaneous cervical artery dissection (sCAD) and admitted CT/CTA on initial clinical workup. All Images were evaluated concerning specific and sensitive radiological features for dissection by two experienced neuroradiologists. Imaging features were compared between the two etiologies.

Results

Included in our study were 145 patients (99 men, 46 female; 45 ± 18.8 years of age), consisting of 126 dissected arteries with a traumatic and 43 with spontaneous etiology. Intimal flaps were more frequently observed after traumatic etiology (58.1% tCADs, 6.9% sCADs; $p < 0.001$); additionally multivessel dissections were much more frequent in traumatic patients (3 sCADs, 21 tCADs) and only less than half (42%) of the patients with traumatic dissections showed cervical spine fractures.

Conclusions

Neuroradiologists should be aware that intimal flaps and multivessel dissections are more common after traumatic etiology. In addition, it seems important to conduct a CTA in a trauma setting, even if no cervical spine fracture is detected.

Wednesday, June 6, 2018

8:00AM - 9:00AM

Parallel Paper Session: Gadolinium Effects in the Brain

O-373

8:00AM - 8:07AM

Prior Scans and Intravenous Gadolinium: Radiologists' Friend or Foe?

R Mattay¹, D Leake², S Mohan¹, R Bryan¹

¹University of Pennsylvania, Philadelphia, PA, ²Austin Radiological Association, Austin, TX

Purpose

With the ever-increasing availability of imaging modalities and the number of diagnostic imaging studies being performed (1) along with the steadily declining reimbursements for imaging procedures (2), there is an increasing pressure on radiologists to read more and more scans. To this end, in this observational study we gathered information related to the variability in the time required to generate brain MRI reports based on whether there was a previous comparison scan and whether intravenous contrast was administered. The purpose of this study is to build a detailed benchmark for future reference.

Materials and Methods

We gathered observational data from attending radiologists interpreting 102 brain MRIs over three months, and measured the total amount of time taken for interpreting each study. The time taken for the following five activities performed during this period was measured: image viewing, obtaining clinical data, report transcription, education of trainees and/or clinicians, and 'other'. Additionally, for each scan, we recorded whether IV contrast was administered and whether there were prior/s for comparison.

Results

The total interpretation times of MRI scans that included a prior study and IV contrast were significantly longer than total times of MRI scans without either ($p < 0.001$). A linear regression model shows contrast

Oral Presentations & Excerptas

administration has a positive relationship with observation times ($p=0.007$). Additionally, prior studies had a positive relationship with clinical history ($p<0.001$), report transcription ($p=0.001$), and total times ($p<0.001$). See Table for mean timing values.

Conclusions

Our results demonstrate that a prior study is a better predictor of longer total times to generate a report than contrast injection. This is expected as prior studies tended to be other brain MRIs (203-278 images), while contrast injection only added ~ 75 additional images (axial and coronal postcontrast T1-weighted sequences) to the exam. These results provide a detailed benchmark for future reference, to aid in the development of new tools and techniques designed to improve the efficiency of radiologists to read brain MRI scans and generate reports.

	Observation	Clinical History	Transcription	Education	Total-Other
Mean (Total) N=102	2.15 +/- 0.83	0.56 +/- 0.67	1.39 +/- 1.27	0.00 +/- 0.00	4.29 +/- 2.18
Mean (No Previous) N=32	1.99 +/- 0.89	0.11 +/- 0.24	0.71 +/- 0.87	0.00 +/- 0.00	2.92 +/- 1.69
Mean (Previous) N=70	2.23 +/- 0.80	0.77 +/- 0.71	1.70 +/- 1.30	0.00 +/- 0.00	4.92 +/- 2.10
Mean (No Contrast) N=23	1.78 +/- 0.75	0.39 +/- 0.65	1.28 +/- 0.62	0.00 +/- 0.00	3.62 +/- 1.57
Mean (Contrast) N=79	2.26 +/- 0.79	0.61 +/- 0.70	1.43 +/- 1.30	0.00 +/- 0.00	4.49 +/- 2.20
Mean (Contrast + Previous) N=55	2.31 +/- 0.74	0.83 +/- 0.72	1.73 +/- 1.32	0.00 +/- 0.00	5.09 +/- 2.08
Mean (No contrast + no previous) N=8	1.52 +/- 0.75	0.10 +/- 0.19	0.65 +/- 0.60	0.00 +/- 0.00	2.38 +/- 1.19

All values are displayed in format Mean +/- Standard Deviation in minutes.

(Filename: TCT_O-373_ContrastTableASNR2018.jpg)

O-374

8:07AM - 8:14AM

Assessment of Adverse Neurologic Effects from Intracranial Gadolinium Deposits Following Intravenous Gadolinium Based Contrast Administration in a Preclinical Animal Model.

R McDonald¹, J Ayers-Ringler¹, C Fisher¹, D Kallmes¹, J McDonald¹

¹Mayo Clinic, Rochester, MN

Purpose

Concerns over the neurotoxic potential of retained gadolinium (Gd) in brain tissues following intravenous gadolinium-based contrast agent (GBCA) administration have led to dramatic changes in clinical practice worldwide, yet the clinical implications and symptoms associated with Gd deposition remain undefined. In the current study, we sought to determine if intracranial Gd retention results in detectable neurologic/cognitive symptoms in rats exposed to various commercially available GBCAs at differing supratherapeutic dose levels.

Oral Presentations & Excerptas

Materials and Methods

Male Wistar rats exposed to 20 intravenous injection administered over four weeks of 2.5 (80 human equivalent doses, HED) or 0.6 (20 HED) mmol Gd/kg GBCA (gadobenate dimeglumine, gadodiamide, gadopentetate dimeglumine, gadoxetate disodium, gadobutrol, gadoterate meglumine, and gadoteridol) were compared to saline injected controls. Unenhanced MRI, cognitive, mood and motor coordination behavior tests, and postnecropsy inductively coupled plasma mass spectrometry (ICP-MS) and transmission electron microscopy (TEM) were performed at six and 34 weeks post injection to assess the stability and neurotoxic potential of intracranial Gd deposits.

Results

GBCA exposure was not associated with significantly different locomotor, cognitive/memory, mood, or coordination function relative to controls ($p > .05$). There were no significant differences in neurologic function between linear and macrocyclic exposed groups ($p = .79$) or between 80 and 20 HED exposure groups ($p = .91$) despite significant differences in Gd tissue concentrations between controls, linear, and macrocyclic agents at common timepoints ($p \leq .003$).

Conclusions

In this rat model, there was no clinical evidence of neurotoxicity from chronic Gd exposure using tests targeted to assess the neurologic function of the neuroanatomic regions where Gd deposition is highest, using both 20 and 80 human dose equivalents and at six and 34 week time points. These results suggest that retained Gd foci are clinically silent and may not be harmful to brain parenchyma. Further tests are needed to assess the biological activity of these Gd foci.

O-375

8:14AM - 8:21AM

Detection of Chelated GBCA in Human Postmortem Brain and Bone Tissue; Distribution by different chelate species

M Hasegawa¹, D Ellisor², K Maravilla¹, L Gonzalez-Cuyar¹, D Roberts³

¹University of Washington, Seattle, WA, ²National Institute of Standards and Technology, Charleston, NC, ³Medical University of South Carolina, Charleston, SC

Purpose

To determine if intact chelates of Gd-based contrast agents (GBCA) are present in autopsy tissues from decedents exposed to different GBCA during life.

Materials and Methods

Tissue samples from 11 autopsy cases (eight with GBCA exposure, three controls naïve for GBCA) were collected from multiple anatomic sites including brain (globus pallidus, dentate nucleus, white matter), bone and skin. Electronic medical records were thoroughly searched to identify the types of GBCA administered along with dose, number and dates of injections. Tissue samples were homogenized and underwent a gentle acetonitrile/water extraction. The gentle extraction was necessary to ensure the Gd remained chelated to the contrast agent. Extracts were filtered through a 3kDa filter to remove macromolecular species. The filtrates were dried, reconstituted and hydrophilic interaction liquid chromatography (HILIC) was performed on all sample extracts to detect and identify intact chelated gadolinium forms. ICP-MS was performed to quantify the Gd content.

Results

Among the eight study cases there were three single agent exposures (1 ProHance, 2 Gadovist) while five received a mixture of various agents. The HILIC method detected chelated forms of GBCA in eight out of eight study cases and 0 of three controls. Recovery categorized by the contrast agent used was: Prohance 5/5, Gadovist 3/3, Multihance 1/2, Omniscan 1/2, Optimark 0/1, Magnevist 0/3. Both macrocyclic and linear contrast agents were detected in their chelated forms in various brain and bone tissue. Although not quantifiable, the levels of macrocyclic GBCA recovered appeared to be higher than linear agents.

Oral Presentations & Excerpts

Conclusions

HILIC was able to identify GBCA in chelated form in human brain and bone samples after exposure to GBCA. All macrocyclic exposures of GBCA were detected and, in addition, linear and macrocyclic agents were able to be detected and identified in cases of exposure to multiple GBCAs.

O-376

8:21AM - 8:28AM

Gadolinium deposition in the brain: Quantitative T1 brain changes measured using a modified MOLLI technique in patients receiving 2 doses of gadolinium (MultiHance).

J Becker¹, T Hinkel², V Patel¹

¹University of Arizona, Tucson, AZ, ²Midwestern University, Glendale, AZ

Purpose

Changes in T1 signal intensity have been shown to occur following administration of Gadolinium-based contrast agents (GBCAs). This study uses a Modified MOLLI T1 mapping technique adapted from cardiac use to precisely measure T1 values before and after administration of single doses of GBCA (MultiHance, gadobenate dimeglumine 529mg/ml at 0.1mmol/kg) during two MRI examinations.

Materials and Methods

Thirteen patients were included in the study and had T1 mapping performed using the Modified MOLLI technique. None had intracranial pathology in the regions of the brain evaluated. All received single doses of MultiHance at 0.1mmol/kg on two separate occasions at a time interval of one day to six weeks. Age range was 13 -70 years.

Results

Statistically significant changes in T1 values were seen following both episodes of gadolinium administration. These were maximal in the globus pallidus, followed by the dentate nucleus and putamen. T1 changes were seen at baseline for the second study when compared to the first, although this was not statistically significant.

Conclusions

The Modified MOLLI technique is a useful biomarker for measuring changes in T1 values following gadolinium administration. Although changes are seen in baseline T1 values at time intervals of up to six weeks following gadolinium administration, this was not found to be statistically significant.

O-377

8:28AM - 8:35AM

MRI Assessment of diffusion tensor imaging (DTI) parameter changes within fiber tracts traversing the globus pallidus and dentate nucleus related to deposition of Gadolinium following administration of a linear gadolinium based contrast agent (GBCA) gadolinium dimeglumine (MultiHance).

J Becker¹, V Patel¹, L MacKinnon¹, T Hinkel²

¹University of Arizona, Tucson, AZ, ²Midwestern University, Glendale, AZ

Purpose

The recent discovery of Gadolinium deposition in micromolar quantities of the brain following administration of GBCAs has alarmed the imaging community. Gadolinium has been found in all areas of the brain in nine postmortem specimens, following administration of all GBCAs with deposition most severe in the globus pallidus (GP) and dentate nucleus (DN). The chemical state of this gadolinium is unknown, important as free Gadolinium is highly toxic to neurons, but chelated gadolinium is relatively safe. There are currently no known neurological sequelae of Gadolinium deposition, but no large studies have been performed. DTI is a useful in vivo imaging biomarker for assessment of microstructural

Oral Presentations & Excerptas

changes within neurons, due to neuronal injury and has been previously used in only a small series to assess changes in neuronal integrity in tumors following gadolinium administration. This study correlates DTI changes with absolute changes in T1 values of the brain due to gadolinium deposition using a novel T1 mapping sequence in 10 patients.

Materials and Methods

All patients underwent DTI at 3T before and 10 minutes after administration of Gadolinium (MultiHance, gadobenate dimeglumine 529mg/ml.) Quantitative changes in T1 values were measured using a Modified MOLLI technique adapted from cardiac use and shown to have near perfect correlation with calculated gadolinium concentrations as measured in a phantom. T1 measurements were made bilaterally in the globus pallidus and dentate nucleus, and correlated with changes in tensor measurements in fibre tracts traversing these regions

Results

Significant T1 changes have been observed in both the globus pallidus and dentate nucleus in both hemispheres. At the time of submission of this abstract, our DTI imaging analysis is not complete, but we have observed changes in FA and RD following contrast administration.

Conclusions

This is a novel study showing changes in FA and RD in fibre tracts traversing the globus pallidus and dentate nucleus following gadolinium administration. DTI is an imaging biomarker that can be further used study of the effects of gadolinium deposition in the brain.

O-378

8:35AM - 8:42AM

Actively Demyelinating Disease May Predispose to Increased Gadolinium Deposition in the Globus Pallidus and Dentate Nucleus

S Moum¹, A Nemeth¹

¹*Northwestern University Feinberg School of Medicine, Chicago, Illinois*

Purpose

Evidence has emerged that repeated administration of gadolinium-based contrast agents (GBCA) results in brain gadolinium deposition. This pilot study aims to assess whether disease severity as measured by blood-brain-barrier breakdown results in brain gadolinium deposition and can help identify at-risk populations.

Materials and Methods

This single-center, retrospective pilot study was approved by the institutional review board and is HIPAA compliant. The authors identified seven adult patients with relapsing-remitting multiple sclerosis receiving natalizumab therapy who underwent three consecutive GBCA-enhanced MR brain examinations with gadopentetate dimeglumine and were imaged at 6-10 month intervals during treatment. Subjects were subdivided based on the presence or absence of abnormal parenchymal enhancement on imaging. The signal intensity (SI) in the globus pallidus, thalamus, dentate nucleus, and pons was measured on unenhanced axial T1-weighted MR images, consistent with published techniques. Measurements were performed by two readers in consensus. Dentate nucleus-pons and globus pallidus-thalamus SI ratios as well as relative percentage change of SI ratios were calculated and compared between subgroups, consistent with published techniques. The qualitative degree of demyelinating disease as seen on T2/FLAIR MR imaging was assigned to a 5-point Likert scale. Patient age, gender, relative gadolinium dose, and mean time between GBCA-enhanced MR examinations were also evaluated.

Results

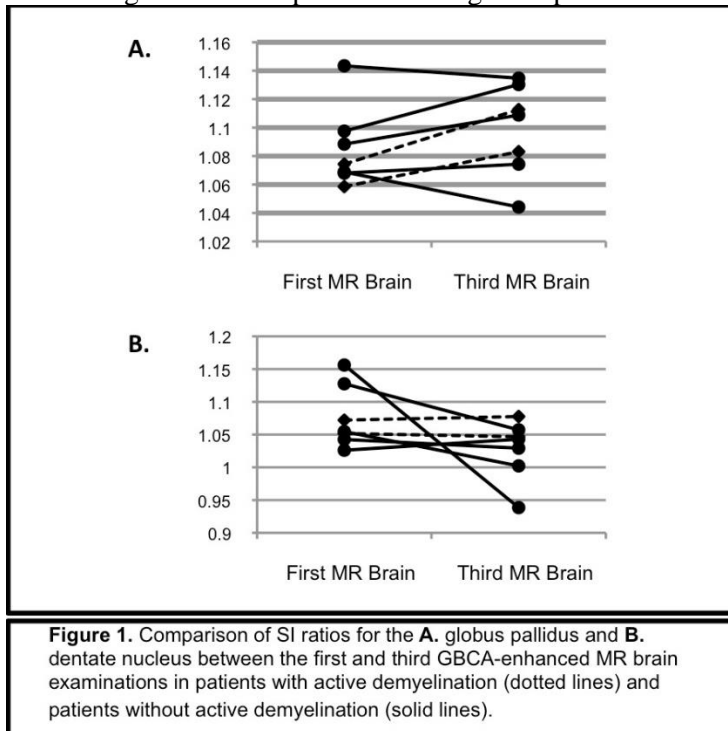
We identified seven patients who met the study inclusion criteria (2 M: 5 F, mean age 46.4 ± 10.8 , age range 32-62). Two patients were identified with abnormal parenchymal enhancement, compatible with active demyelination (0 M: 2 F, mean age 45.5 ± 9.2 , age range 39-52, mean interval between MR exams $226 \text{ d} \pm 65$, mean accumulated gadolinium dose $27 \text{ mL} \pm 4.2$). Five patients did not have active

Oral Presentations & Excerpts

demyelination (2 M: 3 F, mean age 46.8 ± 12.4 , age range 32–62, mean interval between MR exams $201 \text{ d} \pm 54.4$, mean accumulated gadolinium dose $34.4 \text{ mL} \pm 4.8$). The mean relative percentage change of globus pallidus–thalamus SI ratios was 0.48 ± 2.10 in patients without active demyelination and 2.95 ± 0.88 in patients with active demyelination (Figure 1A), suggesting a trend for increasing globus pallidus SI with increasing gadolinium exposure, particularly in the setting of active demyelination. In contrast, mean relative percentage change of dentate nucleus–pons SI ratios was -5.94 ± 7.85 in patients without active demyelination and 0.02 ± 0.69 in patients with active demyelination (Figure 1B).

Conclusions

In this pilot study, we observe a trend that actively demyelinating disease may predispose patients to increased gadolinium deposition in the globus pallidus and dentate nucleus.



(Filename: TCT_O-378_ASNR_Graphic_Final.jpg)

O-379

8:42AM - 8:49AM

Manganese-Enhanced MRI (MEMRI) of the Brain in Humans

D Sudarshana¹, G Nair², J Dwyer², B Dewey², S Steele², I Cortese², A Koretsky², D Reich²

¹Cleveland Clinic Lerner College of Medicine of Case Western Reserve University, Cleveland, OH, ²National Institute of Neurological Disorders and Stroke, National Institutes of Health, Bethesda, MD

Purpose

Manganese has been used as an MRI contrast agent to study neuronal function in animal models.¹ Teslascan® (mangafodipir) is a chelated Mn-based contrast agent which is FDA-approved for imaging in humans.² Manganese is released from Teslascan to enable enhancement of tissue.³ In this study, MEMRI of the brain was studied in healthy volunteers and individuals clinically diagnosed with MS.

Materials and Methods

Healthy and MS participants provided informed consent. Mangafodipir was administered at a rate of one ml/min for total dose of five $\mu\text{mol/kg}$ body weight. Participants completed a baseline history/physical

Oral Presentations & Excerptas

exam, MRI, and blood work. MRI (3T) was performed at various timepoints, ranging from four hours to seven days postmangafodipir administration.

Results

Nine healthy (6 male/3 female; median age 43 years) and two MS (both female, RRMS, EDSS of 2 and 3) volunteers underwent mangafodipir infusion with MRI scans at timepoints ranging from immediate post infusion to three months. Enhancement of the anterior pituitary and choroid plexus was seen in all subjects as early as one hour post administration with enhancement persisting up to one and seven days, respectively (Figure). Enhancement of the exocrine glands (parotids, submandibular, sublingual, thyroid and lacrimal) was noted as early as four hours post administration. Four healthy volunteers had exocrine gland enhancement lasting >one month that resolved by the three-month timepoint. No enhancement was noted in any of the stable white-matter lesions in the two MS participants.

Conclusions

Mangafodipir was well tolerated and did not result in any clinically relevant changes in laboratory values during the study. The study demonstrates that manganese released from Teslascan is readily taken up in brain and extracranial structures that lack a blood-brain barrier. We are planning to extend this study into additional MS cases with active and suspected chronic active lesions to study their impact on neuroaxonal function.

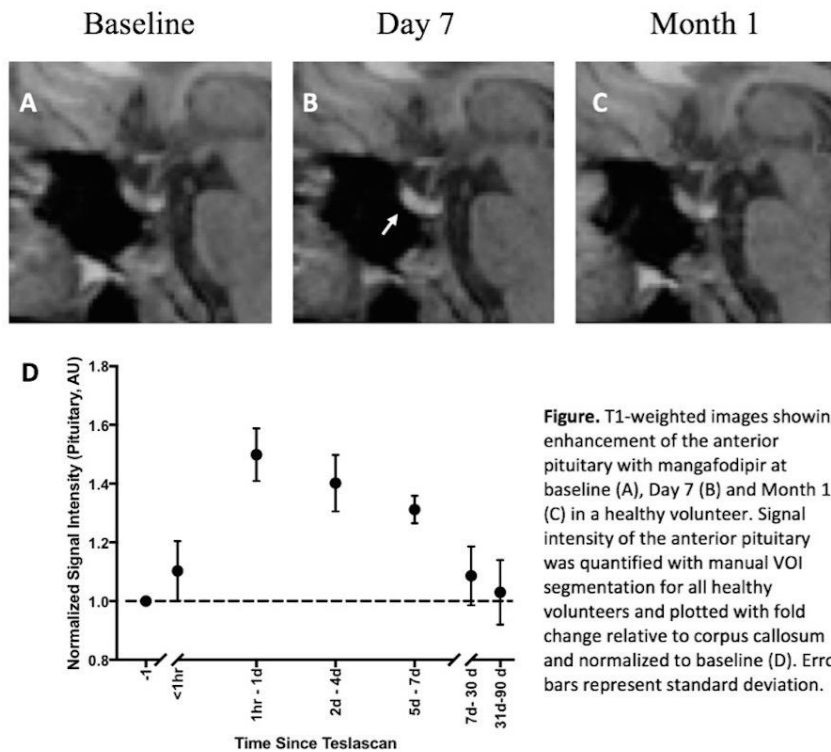


Figure. T1-weighted images showing enhancement of the anterior pituitary with mangafodipir at baseline (A), Day 7 (B) and Month 1 (C) in a healthy volunteer. Signal intensity of the anterior pituitary was quantified with manual VOI segmentation for all healthy volunteers and plotted with fold change relative to corpus callosum and normalized to baseline (D). Error bars represent standard deviation.

(Filename: TCT_O-379_Abstract_Figure1.jpg)

O-380

8:49AM - 8:56AM

Intravenous Iron Compound Contrast Effects on MR Imaging

M Wangsgard¹, L Gesner¹, B Carpenter¹, R Pawar¹

¹Saint Barnabas Medical Center, Livingston, NJ

Oral Presentations & Excerpts

Purpose

Intravenous iron compounds and the enhancing effects they produce are not widely documented. Incidentally encountering an MR scan of a patient receiving certain compounds creating the appearance of a postcontrast image can result in a disrupted workflow. The purpose is to expand awareness of the effects of parenteral iron therapy on MR imaging.

Materials and Methods

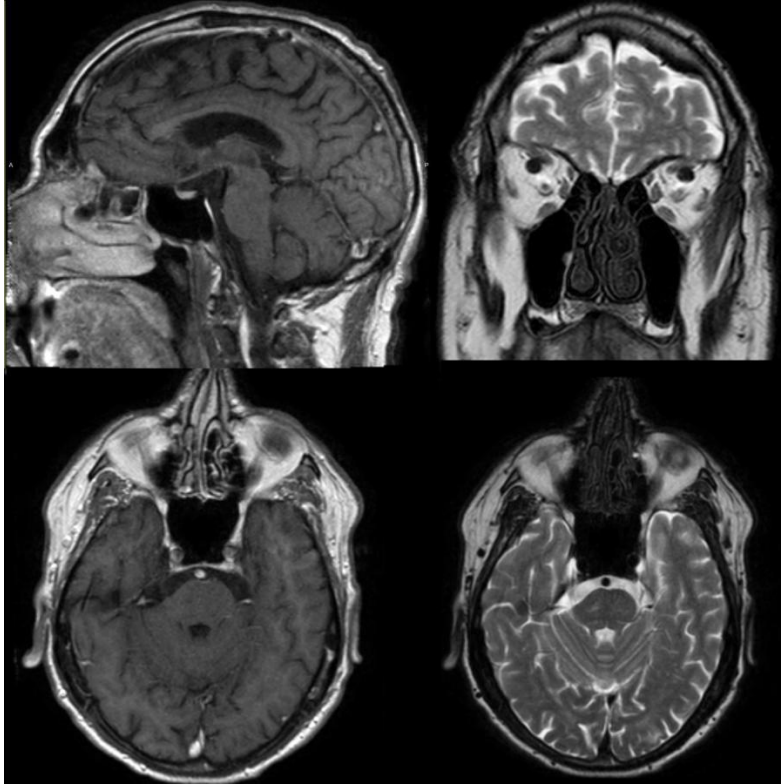
A 72-year-old male with a history of hereditary hemorrhagic telangiectasia presented due to double vision and fatigue. The patient receives twice weekly infusions of iron sucrose (Venofer) for iron deficiency due to chronic anemia and failure of conventional oral iron therapy. The patient was scanned on an open high field 1.0 Tesla unit.

Results

Noncontrast sequences demonstrate increased signal within the nasal mucosa and intracranial vessels on T1 weighted imaging. T2 images demonstrate decreased signal of the nasal mucosa, pituitary and turbinates and blooming of the vessels on gradient sequences. After excluding other causes of T1 shortening effects, such as recent gadolinium injections at outside institutions or mislabeled images, the cause was determined after careful review of the patient's medication list. Two days (51 hours) prior to the MR examination the patient had received an intravenous infusion of iron sucrose. This is a complex macromolecule composed of sucrose molecules with iron at the center which demonstrated intravascular and extravascular paramagnetic effects over two days after injection. This shortens both T1 and T2 relaxation times similar to gadolinium. Unlike gadolinium this creates T2 shortening at therapeutic levels on nonechoplanar sequences, explaining the decreased T2 signal in the nasal mucosa.

Conclusions

Certain newer medications can have a profound effect on MR signal intensity potentially confounding interpretation. Through an understanding of how these medications behave within the blood stream, misinterpretation by the radiologist can be avoided. Furthermore, because of the long vascular retention and reticuloendothelial clearance of these compounds they are being evaluated as potential contrast agents at a time when there is much attention focused on the uncertain biological effects of gadolinium deposition in the body. A similar IV iron product, ferumoxytol (Feraheme), was issued a patent for use as an MR contrast agent in 2014, although use as a contrast is limited due to low tolerability by patients.



(Filename: TCT_O-380_Venofer3.jpg)

O-380a

8:56AM - 9:00AM

Retinography based on fast axonal transport of TTc-488 in a rodent glaucoma model

L Le Roux¹, X Qiu¹, M Jacobsen¹, V Datar¹, D Piwnica-Worms¹, D Schellingerhout²

¹UT, MD Anderson Cancer Center, Houston, TX, ²UT, MD Anderson Cancer Center, Houston, TX

Purpose

The goal of this study is to use a fluorescent molecular nerve imaging probe based on the fast axonal transport of the non-toxic, C-fragment of Tetanus Toxin to visualize and quantitate retinal axon and retinal ganglion cell neural uptake in an established glaucoma model. The long term goal is to extend this animal model to the clinic with specific focus on the development of glaucoma-induced neuropathy and therapies as it pertains to neural transport.

Materials and Methods

Excitotoxic glaucoma was induced in Norwegian brown rat (n=5) eyes by injecting NMDA (N-methyl-D-aspartic acid, 80 nmol/2.5 μ L) into the vitreous of one eye and PBS into the contralateral eye as a control. This model is known to induce apoptosis in retinal ganglion cells. Forty-eight-four hours after the NMDA injection, the fluorescently labeled neural imaging probe based on the non-toxic, C-fragment of Tetanus Toxin (TTc-488) was injected into the vitreous of both the glaucomatous and control eyes (8 μ g TTc-488/2 μ l PBS). In vivo imaging of the distribution of TTc-488 was performed using confocal-scanning laser ophthalmoscopy (Heidelberg Retinal Angiograph II). Both eyes and associated neural tissues were harvested at 3 hours after TTc-488 injections. Whole retinal flat mount images for ex-vivo imaging was done on a high resolution, epi-fluorescent, zoom microscope (Zeiss AxioZoom16) followed by confocal imaging (Olympus FV1000). Retinal flat mount, fluorescent immuno-histology with antibodies serving as markers for retinal axons (anti-SMI32) and retinal ganglion cells (anti-RBPMS) were performed. Retinal

Oral Presentations & Excerptas

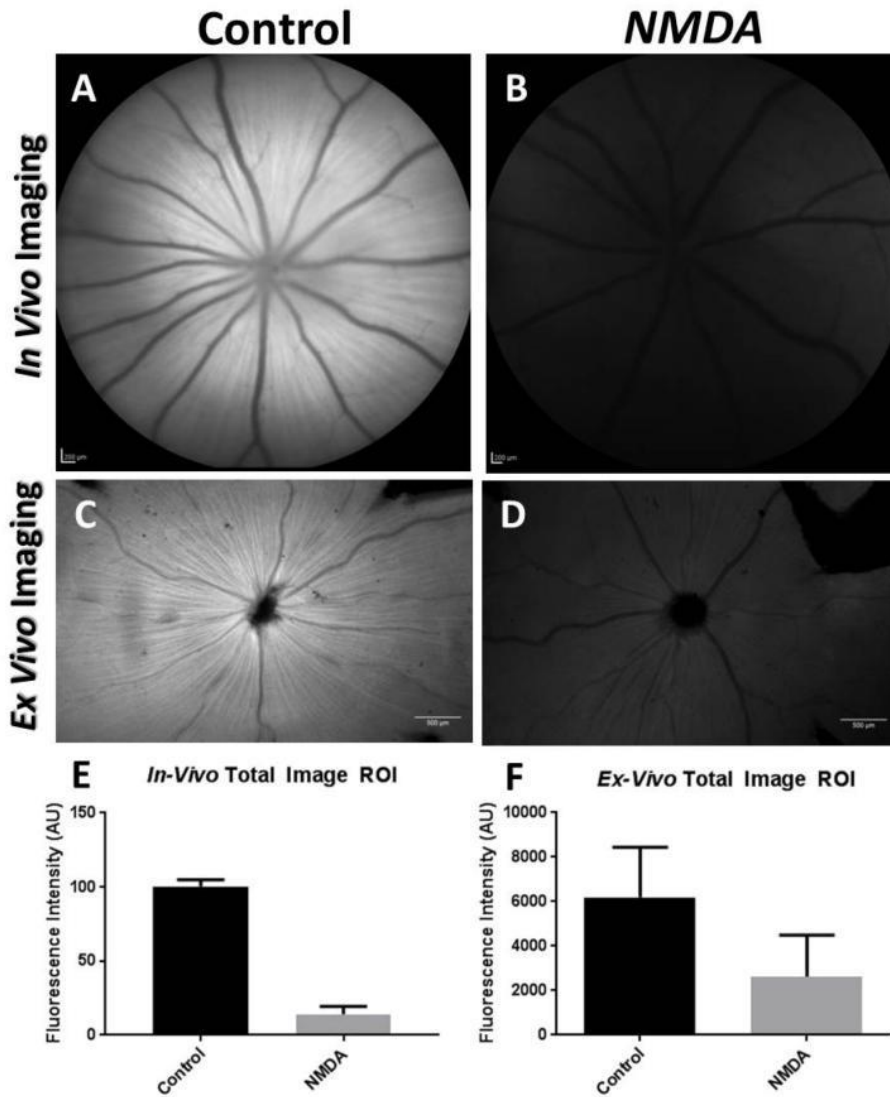
transect analysis was used to demonstrate the difference in the number axonal strands observed between control and treated groups using Matlab software and followed by two-tailed, paired t-test in GraphPad Prism.

Results

The in-vivo uptake and localization of the neural probe, TTc-488, to the retinal axons was illustrated with a clinical confocal-scanning laser ophthalmoscope within 3 hours of an intravitreal eye injection in rats. Ex-vivo imaging conformed that the neural probe, TTc-488 localized to the projecting retinal axons, dendritic inputs and the neuronal cell bodies of the retinal ganglion cells, as well as the bipolar cell axons in the outer synaptic layer. Fluorescent immuno-histology, demonstrated the co-localization of TTc in the retinal axons with the neurofilament marker, anti-SMI32. The presence of TTc in the retinal ganglion cell cytoplasm was confirmed with anti-RBPMS. The NMDA-induced model of glaucoma showed greatly reduced uptake and transport of TTc, demonstrated in both in living animals and excised tissues. The retinal transect analysis demonstrates a highly significant reduction in the number of TTc-488 stained axonal strand crossings in the retinas of glaucomatous eyes (365 +/- 41.46) in comparison with the abundance of axonal strands in the control eyes (479 +/-48.41), p=0.003.

Conclusions

A novel, fluorescently labeled nerve imaging probe, TTc-488, allows the in-vivo visualization and quantitation of retinal axons with a clinical confocal-scanning laser in both the normal and diseased states. Glaucoma decreases neuronal uptake and transport of TTc in a rodent glaucoma model, a condition in which the hallmark pathology is the loss of retinal axons and retinal ganglion cells.



(Filename: TCT_O-380a_Innvivo_exvivoretina_12_15_17.jpg)

Wednesday, June 6, 2018
 10:30AM - 12:00PM
 Parallel Paper Session - Jaw, Neck and Orbit

O-381

10:30AM - 10:37AM

Differentiating Non-Syndromic and Syndromic Odontogenic Keratocysts Using CT Texture Analysis

M Oda¹, V Andreu¹, M Qureshi¹, B Li¹, P Staziaki¹, M Chapman¹, O Sakai¹
¹Boston Medical Center, Boston University School of Medicine, Boston, MA

Oral Presentations & Excerptas

Purpose

Odontogenic keratocysts (OKCs) are commonly encountered developmental odontogenic cysts. OKCs are known for their high recurrence rate, aggressive behavior, and association with nevoid basal cell carcinoma syndrome (NBCCS) also known as Gorlin-Goltz syndrome, particularly when there are multiple OKCs. The majority of NBCCS patients have OKCs. The differences in pathological findings and recurrence rates between nonsyndromic and syndromic OKCs have been reported; however, there is no previous literature describing the difference in CT imaging findings between these two groups. The purpose of this study was to evaluate CT texture features to distinguish syndromic OKCs from nonsyndromic OKCs.

Materials and Methods

This retrospective study was approved by our IRB. Thirty-seven nonsyndromic OKCs (37 patients) and 20 syndromic OKCs (eight patients) who underwent noncontrast enhanced MDCT were enrolled. The lesions were manually contoured without including osseous walls and septa. CT texture features of the lesions were measured using an in-house developed Matlab-based texture analysis program. Histogram, gray-level co-occurrence matrix (GLCM), gray-level run-length (GLRL), gray-level gradient matrix (GLGM), Law's features, and the chi-square features were extracted from each segmented volume. Those parameters were tested with Mann-Whitney U test. Differences were considered significant at $p < 0.05$.

Results

Statistical analysis revealed that two histogram features (standard deviation [$p=0.027$], fourth moment [$p=0.013$]), 2 GLCM features (entropy [$p=0.021$], energy [$p=0.040$]), 3 GLRL features (short-run high gray-level emphasis [$p=0.025$], long-run low gray-level emphasis [$p=0.030$] and long-run high gray-level emphasis [$p=0.024$]) showed significant differences between nonsyndromic and syndromic OKCs.

Conclusions

CT texture analysis may have the potential to prove morphologic feature differences between nonsyndromic and syndromic OKCs.

Table. Statistically significant parameters differentiating between non-syndromic OKC and syndromic OKC

Texture parameters	Non-syndromic OKC		Syndromic OKC		P value
	Mean	SD	Mean	SD	
Histogram features					
SD	17.5	5.1	24.5	12.8	0.027
Fourth moment	7.76e5	1.42e6	4.2e7	1.69e8	0.013
GLCM features					
Entropy	1.14	0.41	0.90	0.27	0.021
Energy	0.00496	0.00193	0.00677	0.00362	0.040
GLRL features					
SRHGE	573.6	406.5	347.4	200.1	0.025
LRLGE	612.4	435.2	376.6	218.6	0.030
LRHGE	502.0	366.9	301.6	169.3	0.024

SD indicates standard deviation; GLCM, gray-level co-occurrence matrix; GLRL, gray-level run-length features; SRHGE, short-run high gray-level emphasis; LRLGE, long-run low gray-level emphasis; LRHGE, long-run high gray-level emphasis.

(Filename: TCT_O-381_NSOKCvsSOKCabstractfig.jpg)

O-382

10:37AM - 10:44AM

Using CT Texture Analysis to Differentiate Cystic and Cystic-Appearing Odontogenic Lesions

M Oda¹, P Staziaki¹, M Qureshi¹, B Li¹, V Andreu¹, M Chapman¹, A Wang¹, O Sakai¹

¹Boston Medical Center, Boston University School of Medicine, Boston, MA

Purpose

Many cystic or cystic-appearing odontogenic lesions demonstrate similar CT imaging findings. Although the relationship of the lesion to the tooth root or crown is often a clue to the etiology, accurate diagnosis may be difficult. The purpose of this study was to evaluate the use of texture features to distinguish common cystic or cystic-appearing lesions of the jaw such as dentigerous cysts (DC), odontogenic keratocysts (OKC), and ameloblastomas (AM).

Materials and Methods

This retrospective study was approved by our IRB. Ninety-eight pathologically proven cystic or cystic-appearing lesions of the jaw were included; DCs (n=42), OKCs (n=37) and AMs (n=19). Following manual segmentation, an in-house-developed Matlab-based texture analysis program extracted 41 texture features from each segmented volume. Kruskal-Wallis nonparametric analysis of variance and Steel-Dwass-Critchlow-Fligner multiple comparison procedures were performed for comparing all pairs of three types of lesions. Differences were considered significant at $p < 0.05$.

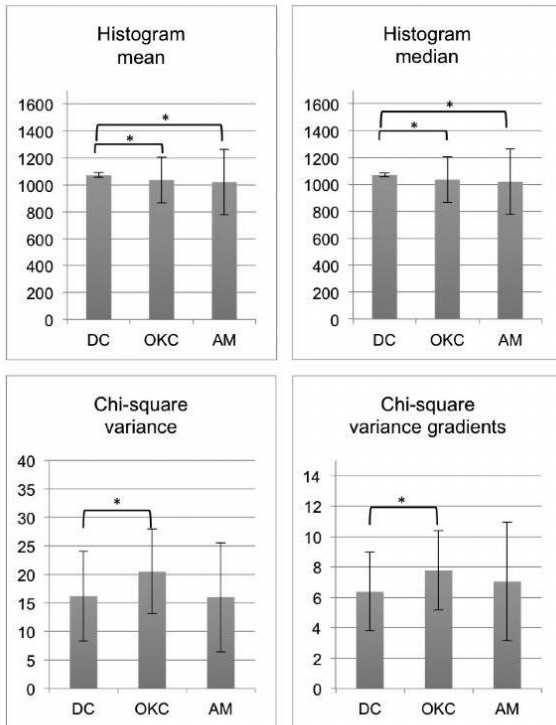
Results

Pairwise analysis revealed that eight histogram features (mean [$p=0.026$], median [$p=0.021$], SD [$p=0.018$], SD5 [$p=0.033$], geometric mean [$p=0.025$], harmonic mean [$p=0.026$], interquartile range [$p=0.004$], fourth moment [$p=0.029$]), 1 GLCM feature (entropy [$p=0.012$]), 3 GLRL features (short-run high gray-level emphasis [$p=0.009$], long-run low gray-level emphasis [$p=0.012$], long-run high gray-level emphasis [$p=0.013$]), 2 Low's features (L1 [$p=0.024$], L4 [$p=0.033$]), 4 GLGM features (mean gradients [$p=0.016$], variance gradients [$p=0.027$], skewness [$p=0.006$] and kurtosis [$p=0.007$]) and 2 chi-square features (chi-square variance [$p=0.026$], chi-square variance gradients [$p=0.031$]) showed significant differences between DC and OKC. Four histogram features (mean [$p=0.035$], median [$p=0.033$], geometric mean [$p=0.040$], harmonic mean [$p=0.040$]) showed significant differences between OKC and AM.

Conclusions

Some texture features demonstrate statistically significant differences between DC and OKC and between OKC and AM. Texture analysis may be considered as an adjunct to the evaluation and diagnosis of cystic or cystic-appearing odontogenic lesions.

Fig. Differences of texture parameters among three type of lesions



*Statistically significant ($p < 0.05$)

(Filename: TCT_O-382_AMvsOKCvsDCabstractfig.jpg)

O-383

10:44AM - 10:51AM

Utility of Likert Scale (Deauville Criteria) and The Value of Quantitative PET Parameters in Assessment of Radiochemotherapy Response of the Primary Oropharyngeal SCC; Preliminary Results

Y Koksels¹, M Gencturk¹, A Spano¹, M Reynolds¹, S Khanipour Roshan², Z Cayci¹

¹University of Minnesota, Minneapolis, MN, ²Drexel University College of Medicine, Philadelphia, PA

Purpose

The aim of this study is to determine whether Likert scale (Deauville Criteria) can be used accurately to categorize oropharyngeal SCC patients as responders or nonresponders following radiochemotherapy (RCT) on FDG-PET/CT scan and also to compare the performance of different methods used in interpretation of post-treatment PET/CT scans i.e. the Likert scale, SUVmax, Ratios of SUVmax primary site to mediastinal blood pool (P/M) and SUVmax primary site to liver (P/L) in predicting response to treatment.

Materials and Methods

One-hundred-one biopsy-proven patients with oropharyngeal cancer were retrospectively evaluated. FDG PET/CT Scans 8-12 weeks after RCT were assessed by Deauville Criteria, a five-point Likert Scale previously used in lymphoma studies. In addition, SUVmax of primary tumor, ratios of SUVmax P/M and P/L of first follow-up PET (PET2) were measured and calculated. The scores of 1, 2, 3 were

considered as "responders" and of 4 and 5 were considered as "nonresponders" according to Deauville Criteria. Clinical and imaging follow-up, and pathology results were used as a reference.

Results

Sensitivity, specificity, PPV and NPV of Likert scale (Deauville Criteria) were found as 80% (CI 44.4-97.5%) 89.5% (CI 79.6- 95.7%), 53.3% (CI 34.6- 71.1%) and 96.7% (CI 89.6-99%) respectively. When quantitative PET parameters were evaluated, statistically significant difference was seen between responders and nonresponders in SUV (max) and ratios with a cutoff 3.9 for SUVmax and 1.6 for ratios of SUVmax.

Conclusions

According to this study, Likert scale adequately categorized patients as responders and non responders. Since the NPV was found to be high and qualitative interpretation and scoring is simple and reproducible, Likert scale use can be used in interpretation of post-treatment PET scans in OSCC patient.

O-384

10:51AM - 10:58AM

Age-Related Prevalence of Calcification in the Cartilaginous Eustachian Tube

J Cheng¹, T Watkins¹, C Hsu¹

¹*Princess Alexandra Hospital, Brisbane, Queensland, Australia*

Purpose

Calcification of the cartilaginous Eustachian Tube (ET) is a rarely reported phenomenon and little is known of its incidence or clinical relevance. To our knowledge this is the largest study to investigate the prevalence and age-related incidence of ET calcification on computed tomography (CT) head scans in the adult population at a tertiary hospital.

Materials and Methods

This was a retrospective study of patients undergoing plain CT head scans at our tertiary hospital between January to December 2014 for patients aged 50 and above. A total of 5181 patients (2811 male and 2370 female; mean age of 70) had their respective CT head studies reviewed. Two radiologists evaluated each study independently for calcification in the cartilaginous portion of the ET on standardized soft tissue (W350 : L50) and bone windows (W800 : L450). Laterality and morphology of the calcifications were documented according to a predetermined visual scoring system on the bone window: (0= absence of calcification, 1 = calcification <3mm, 2 = calcification 3-7 mm, 3 = calcification >7 mm).

Results

ET calcification was observed in 1.93% of patients (100/5181), of which 40% (40/100) were bilateral and 60% (60/100) were unilateral; 37% (22/60) left and 63% (38/60) right. A significant positive correlation between calcification and age was evident on binary logistic regression $B=0.044$, $SE = 0.009$, $Wald = 26.534$ ($p<0.001$) with the estimated odds ratio favoring an increase of 4.5%, $Exp(B) = 1.045$, 95% CI (1.028,1.063) for each year of age above 50. Subgroup analysis of positive cases with calcification also showed increasing age correlated with higher grades of calcification, $r_s = 0.385$ ($p<0.001$).

Conclusions

ET calcifications are rare with an overall prevalence of only 1.93% above the age of 50. Also, it is likely an ageing phenomenon with both presence and severity demonstrating a significant positive correlation with patient age.

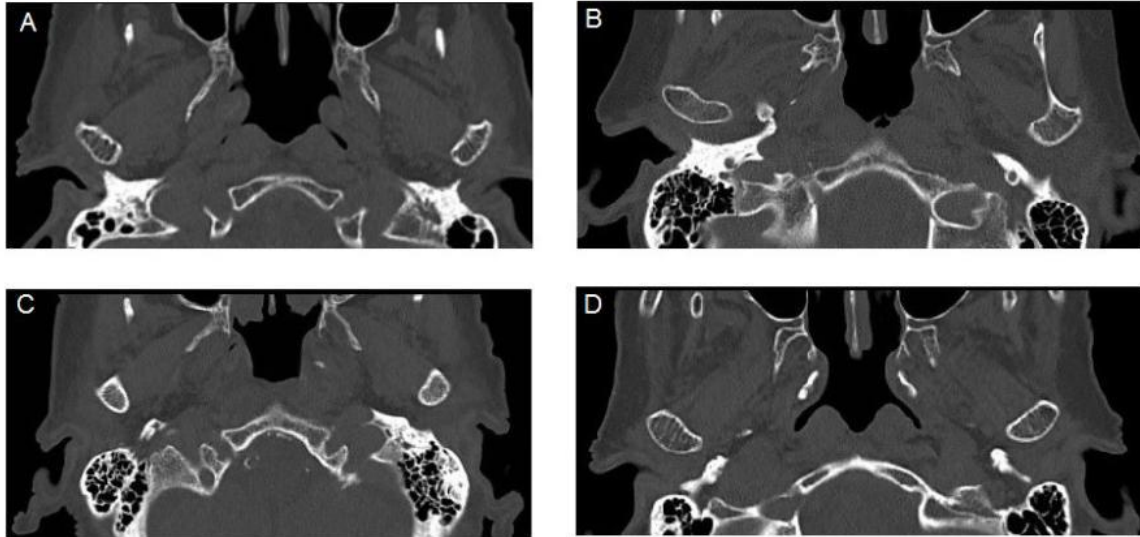


Figure 1: Grades of eustachian tube calcification as seen on bone algorithms. Grade 0 or no calcification (A), right-sided grade 1 calcification (B), left-sided grade 2 calcification (C) and bilateral grade 3 calcification (D).

(Filename: TCT_O-384_ETCalcificationFigureASNR.jpg)

O-385

10:58AM - 11:05AM

Negative Predictive Value of NI-RADS Category 2 First Post-treatment FDG PET/CT in Head and Neck Squamous Cell Carcinoma

P Wangaryattawanich¹, B Branstetter¹, M Hughes¹, D Clump II¹, D Heron¹, T Rath¹

¹University of Pittsburgh Medical Center, Pittsburgh, PA

Purpose

FDG PET/CT has a high negative predictive value in patients with head and neck squamous cell carcinoma (HNSCC) who respond completely to nonoperative therapy. However, the treatment failure (TF) rate in patients with a partial but incomplete response (IR) is unclear. The purpose of this study is to investigate the negative predictive value (NPV) of the first post-treatment FDG PET/CT in HNSCC patients with an IR interpreted as Neck Imaging Reporting and Data System (NI-RADS) Category 2.

Materials and Methods

We retrospectively identified HNSCC patients who were treated with curative chemoradiation therapy (CRT) or radiation therapy (RT) only in our institution between 2008 and 2016. We included patients whose first post-treatment FDG PET/CT was interpreted as showing marked improvement of locoregional tumor, but had only mild residual tumor mass or FDG activity in either the primary tumor bed or regional lymph nodes (NI-RADS category 2). The NPV of FDG PET/CT was calculated, including 95% confidence intervals using Newcombe's method. Two-year disease-free survival was the reference standard.

Results

Seventeen out of 110 patients (15%) experienced locoregional TF within two years of completing CRT or RT, yielding a negative predictive value (NPV) of 85% (95% confidence interval = 77 – 90%). The most common location of locoregional recurrence was cervical lymph nodes (59%). The median time interval between completion of therapy and local TF was 9.6 months (range: 4 – 24 months).

Conclusions

In patients with IR after treatment of HNSCC, the NPV of the first post-treatment FDG PET/CT is 85%,

which is lower than the 91% NPV of FDG PET/CT in patients with an initial complete response. Patients with an incomplete response should undergo more frequent clinical and imaging surveillance than patients with a complete response.

O-386

11:05AM - 11:12AM

Quantitative T2 Mapping and Fat Fraction Measurements of Extra-ocular Muscles in Thyroid Eye Disease

T Das¹, R Murthy¹, P Meyer¹, M Graves¹

¹Cambridge University Hospitals NHS Foundation Trust, Cambridge, United Kingdom

Purpose

Assessment of extraocular muscle (EOM) inflammation in Thyroid Eye Disease (TED) relies on clinical evaluation supported by imaging. Currently, the only means of TED activity quantification is clinical activity scoring (CAS). Accurate quantification would be useful to select appropriate treatment modalities and monitor treatment response. Longer T2 relaxation times correlate with greater EOM inflammation, but signal from fat can be confounding. The purpose of this study is to establish whether T2 mapping with fat fraction (FF) measurements of the EOMs could provide a robust quantitative measure of disease activity.

Materials and Methods

Thirty patients with TED and six healthy controls had MRI of the orbits on a 1.5T scanner including coronal Short- τ Inversion Recovery (STIR), T2 multiecho fast spin echo and multiecho fast gradient echo sequences. 11 patients were rescanned following treatment. STIR signal intensity ratios (SIR), T2 relaxation times and percentage FF were measured for inferior, medial and superior rectus muscles bilaterally in all individuals. Mean values for T2, SIR and FF were compared between TED and normal groups and between pre and post-treatment examinations.

Results

Although T2 and SIR correlated, mean T2 for each rectus muscle category, but not mean SIR, differed significantly between TED and normal groups ($p < 0.001$) and between pre and post-treatment examinations. Mean FF was greater in TED than in healthy controls ($p = 0.021$), with substantial variability in the mean FF for each muscle in the patient group.

Conclusions

Quantification of T2 relaxation times clearly differentiates abnormal from normal populations, as well as pretreatment from post-treatment status. This appears to be a reliable measure of disease activity, allowing assessment of individual muscles. We demonstrate feasibility of measuring FF in EOMs, thereby estimating the relative contributions of fat and water to the T2 signal. Radiological assessment of inflammation occasionally contradicted CAS, raising questions about the validity of clinical scoring of disease activity.

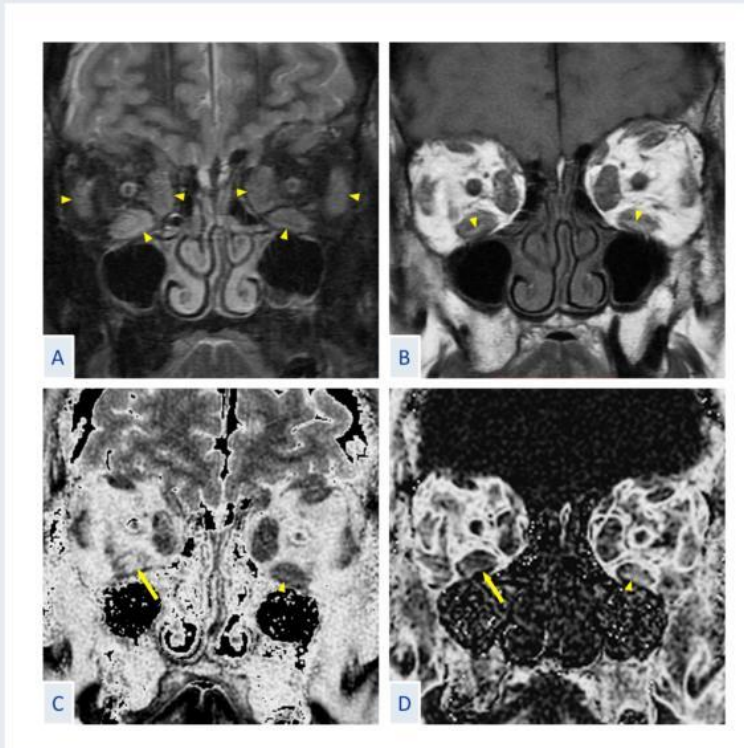


Fig 1. Images of the orbits of a patient with thyroid eye disease. A) Coronal STIR - enlargement and heterogeneous hyperintensity of extraocular muscles (arrowheads). B) Coronal T_1 - areas of T_1 hyperintensity within the muscles consistent with fatty change (arrowheads). C) T_2 relaxation map. Note longer T_2 relaxation in the right inferior rectus muscle (arrow) compared to the left (arrowhead). D) Fat Fraction map. Note higher fat fraction in the left inferior rectus muscle (arrowhead) compared to the right (arrow).

(Filename: TCT_O-386_TEDabstractimage.jpg)

O-387

11:12AM - 11:19AM

Hyperintensity of the Optic Nerve on 3D-FLAIR Imaging is a Sensitive and Specific Sign of Papilledema in Patients with Idiopathic Intracranial Hypertension

E Golden¹, R Krivochenitser¹, N Mathews¹, C Longhurst¹, Y Chen¹, J Yu², T Kennedy³

¹University of Wisconsin School of Medicine and Public Health, Madison, WI, ²University of Wisconsin-Madison, Madison, WI, ³University Of Wisconsin Hospital, Madison, WI

Purpose

High-diffusion signal of the optic nerve (ON) and the optic nerve head (ONH) on diffusion-weighted imaging (DWI) is associated with papilledema in patients with idiopathic intracranial hypertension (IIH). However, no studies to date have examined the potential for 3-D Fluid Attenuated Inversion Recovery (FLAIR) sequences to sensitively detect papilledema in IIH patients. The purpose of this study is to evaluate whether hyperintensity of the ON and ONH on 3-D FLAIR imaging is associated with papilledema in patients with IIH.

Materials and Methods

In this Institutional Review Board approved study, a retrospective chart review from December 2010 through December 2015 was performed. Consecutive patients with known IIH, as diagnosed by fundoscopic exam by a staff ophthalmologist, with concurrently performed contrast-enhanced (CE) MR

imaging with postcontrast 3-D FLAIR sequences were included in this single-institution study. Two CAQ-neuroradiologists blinded to clinical data independently reviewed each MRI. Each ON on CE 3-D FLAIR was evaluated and graded independently on a scale of 0-3: 0=normal ON; 1= hyperintensity within the nerve without involvement of the ONH; 2=hyperintensity within the ON with mild inversion of the ONH; and 3=hyperintensity within the ON with significant inversion of the ONH. Descriptive statistics were then calculated.

Results

Fifty-one patients (3 males, 48 females, mean age 29, SD=10.7) with known papilledema and 61 age- and sex-matched control patients (5 males, 56 females, mean age 30.9, SD=11.6) with normal MRIs were included in this study. For reader one, hyperintensity of at least one ON was 85.3% sensitive (95% CI 76.6-91.3) and 100% specific (95% CI 96.2-100) for presence of papilledema. For reader two, hyperintensity of at least one ON was 76.5% sensitive (95% CI 66.8-84.0) and 87.7% specific (95% CI 80.2-92.7) for the presence of papilledema. Inter-reader reliability was assessed using kappa values and was 0.8894 (95% CI 0.833-0.946).

Conclusions

We present the first application of CE 3-D FLAIR imaging towards the detection of papilledema. We demonstrate that hyperintensity of the ON on 3-D FLAIR imaging is sensitive and specific for detection of papilledema in patients with IHH, allows for high inter-reader agreement, and may outperform DWI in the detection of papilledema. CE 3-D FLAIR imaging is a feasible neuroimaging technique for the detection of papilledema and demonstrates how neuroimaging can both supplement and complement the funduscopic exam.

O-388

11:19AM - 11:26AM

3D Printing and Visualization of Orbital Trauma: New Tools in Education

L Eisenmenger¹, R Lobo², B Winegar³, J Cramer⁴, C Johnson⁵, M Bayona⁵, A Crum⁵, R Wiggins⁵, E Quigley⁵

¹University of California San Francisco, San Francisco, CA, ²University of Michigan, Ann Arbor, MI, ³University of Arizona, Tucson, AZ, ⁴University of Nebraska Medical Center, Omaha, NE, ⁵University of Utah, Salt Lake City, UT

Purpose

To create an open-source, downloadable library of anatomically accurate virtual and 3-D printed orbital fracture models to provide surgeons and trainees with visual and tactile simulations. This project applies open source software and commercial solutions for interacting with virtual models in our 3-D printing and visualization workflow. Image fusion of different modalities is compared across virtual reality, augmented reality, and stereoscopic display systems.

Materials and Methods

De-identified CT and MR DICOM data of complex orbital fracture cases were used to make virtual and 3-D printed models. Materialise Mimics (Plymouth, MI, U.S.), TeraRecon (Foster City, CA, U.S.), and Slicer (Boston, MA, U.S.) were used for segmentation. Next, a fused filament fabrication 3-D printer (Ultimaker 2+, Ultimaker 3, or Fusion3-D) was used to create poly lactic acid (PLA) models of complex orbital fractures. We compared open source software and commercial solutions to interacting with virtual models in our 3-D printing workflow. We applied Google Cardboard, Oculus virtual reality system, and stereoscopic pseudoholographic systems. Image fusion of different modalities were compared between immersive display systems. Two neuroradiologists evaluated the virtual and 3-D printed models for anatomic fidelity. Oculoplastic, ENT surgeons, and neuroradiologists evaluated models for applications in patient education, assigning fracture classification, improving anatomic understanding of fractures, preoperative simulation, and to determine which features of the models were the most helpful.

Results

Neuroradiologists confirmed the anatomic accuracy of the virtual and 3-D printed models compared to the DICOM data. Oculoplastic and ENT staff noted that both the virtual and 3-D printed orbital fracture models aid trainee education, improve anatomic understanding of the fractures, and facilitate preoperative simulation. Virtual sizing and placement of plate reconstruction was highly valued. Neuroradiologists also found that having virtual and physical examples of common fracture patterns allowed better education of radiology trainees.

Conclusions

Virtual and 3-D printed orbital fracture models can be used for trainee and patient education, improved anatomic understanding and classification of the fractures, and preoperative simulation. Trainees and consultants find interaction with virtualized models aid in the understanding of anatomy, pathology, and treatment options. Future prospective research is needed to evaluate for decreased operative times and improved patient outcomes with the use of 3-D printed orbital fracture simulators.



(Filename: TCT_O-388_LEEQORBITBW300DPI.jpg)

O-389

11:26AM - 11:33AM

Reproducibility of Globe Temperature Measurement using Diffusion Based Thermometry

J Derakhshan¹, L Loevner¹, F Wehrli¹

¹University of Pennsylvania, Philadelphia, PA

Purpose

Temperature measurement in the eye is important and challenging (1). The apparent diffusion coefficient can be used to measure temperature in nonrestricted fluids (2). Histogram methods have been used to determine temperature in the lateral ventricles, to derive a core brain temperature (3). More recently the technique has been applied to retrospective measurement of temperature in the globes using clinical diffusion weighted images (DWI) (4, 5). The goal of this study was to test the reproducibility of the measurement in vivo in human subjects.

Materials and Methods

Normal volunteers were placed in a 1.5T Siemens Avanto scanner (n=4). Repeated DWI images were obtained. The ADC images were imported into Matlab and the globe was manually segmented. A histogram of globe temperature was fit to a polynomial and T_{min}, T_{mean} and T_{peak} and T_{max} were calculated. The mean and standard deviation of the characteristic temperatures were obtained for each eye. A paired T-test was performed of temperature difference between the eyes and the data from the eyes were combined. Confidence intervals of 95% for each characteristic temperature were obtained and a T-test was performed between T_{peak} and T_{mean}.

Results

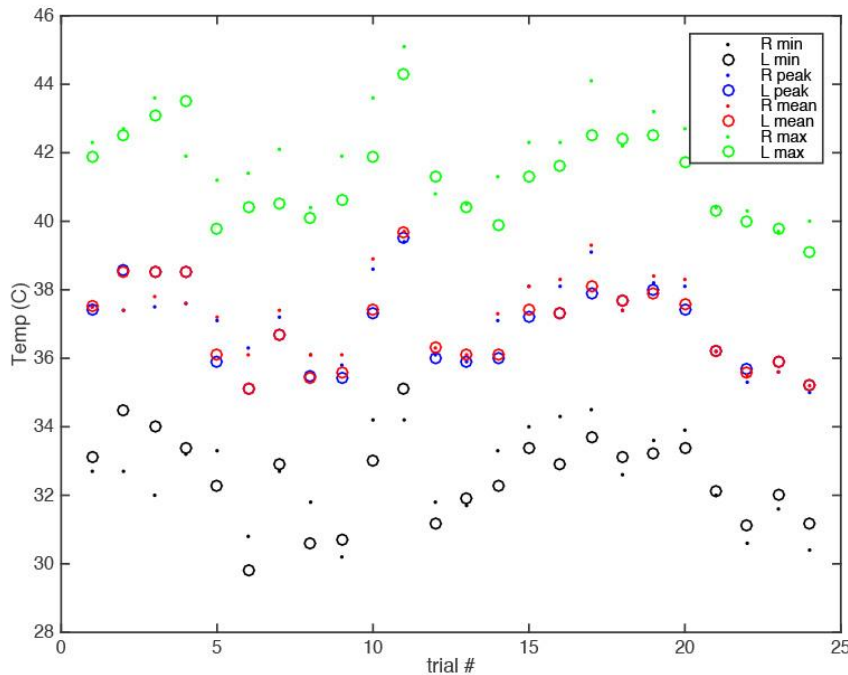
Characteristic temperatures from n=24 trials are plotted in the figure for one subject. There was no statistically significant difference between the right and left eyes for any of the temperatures.

Oral Presentations & Excerptas

Characteristic temperatures are as follows: $T_{min} = 32.6 \pm 1.3^{\circ}\text{C}$ with 95% confidence interval = [32.1,33.1], $T_{peak} = 37.0 \pm 1.2$ [36.5,37.5], $T_{mean} = 37.1 \pm 1.2$ [36.6,37.6] and $T_{max} = 41.6 \pm 1.4^{\circ}\text{C}$ [41.0,42.2]. There was no significant difference between peak and mean temperature ($p=0.70$).

Conclusions

Prospective repeated temperature measurement in the globe has been performed using diffusion-based thermometry. Mean globe temperature is $37.0 \pm 1.2^{\circ}\text{C}$ and mean globe temperature has been determined to be 37.0°C to within 1° precession.



(Filename: TCT_O-389_ASNR2018fig.jpg)

O-390

11:33AM - 11:40AM

Diagnostic Yield of MRI for Investigation of Sensorineural Hearing Loss

Y Amoako-Tuffour¹, J Shankar¹

¹Dalhousie University, Halifax, Nova Scotia, Canada

Purpose

Gadolinium-enhanced Magnetic Resonance Imaging (GdMRI) of the head is a common investigation for sensorineural hearing loss (SNHL). The yield of these studies is perceptibly low and seemingly at odds with the aims of wise resource allocation and risk reduction within the Canadian health care system. The purpose of this study was to quantify the diagnostic yield of GdMRI for SNHL and to identify characteristics that may be leveraged to improve the yield and optimize resource utilization.

Materials and Methods

We retrospectively reviewed 500 consecutive patients with GdMRI head for SNHL between 2011-2016 and categorized them with relevant, positive, findings and those without. Demographics, symptoms, interventions, responses, and investigations performed prior to GdMRI study were extracted and tabulated under each category. Chi-squared testing and T-testing were employed to compare proportions and means between the two groups.

Oral Presentations & Excerptas

Results

Total of 324 patients met inclusion criteria with a 6.2% positive detection rate on GdMRI. Only 7.3% (22) in GdMRI negative group underwent testing beyond audiometry compared with 35% (7) in GdMRI positive group. There was a 21% ($p < 0.05$) increased likelihood of abnormal Auditory Brainstem Response (ABR) in GdMRI positive patients compared to those without.

Conclusions

The yield of GdMRI for investigation of SNHL is very low. This yield may be increased by including audiometry with ABR in the triaging system for scheduling MRI for SNHL. GdMRI remains a valuable tool for investigation of SNHL. The small number of positive events limited the authors' ability to provide guidance for when GdMRI should be performed. However, it is recommended that referral sources be narrowed down to otolaryngologists exclusively, and that a standard battery of tests be performed prior to GdMRI. These changes will gradually help to develop a decision tree that will reduce the number of unnecessary studies.

Table 2: Summarized findings

	Total Number Included (n=324)	
	Relevant Positive Findings on MRI (n=20) n (%)	Negative/Incidental Findings on MRI (n=304) n (%)
Physician Referral		
ENT	20 (100)	281 (92.4)
Neurology	0	5 (1.6)
General Practitioner (Family Physician)	0	5 (1.6)
Internal Medicine	0	4 (1.3)
General Surgery	0	1 (0.3)
PMR	0	1 (0.3)
Ophthalmology	0	1 (0.3)
Orthopedic Surgery	0	1 (0.3)
Neurosurgery	0	1 (0.3)
Anesthesiology	0	1 (0.3)
Psychiatry	0	1 (0.3)
Emergency Medicine	0	1 (0.3)
Nurse Practitioner	0	1 (0.3)
Non-Imaging Testing: ABR and/or VEMP		
Abnormal ABR/VEMP Testing	7 (35)	19 (6.3)
Normal ABR/VEMP		3 (1)
Untested/Unspecified	13 (65)	282 (92.8)
Interventions		
Symptom Resolution with Prednisone	1 (5)	12 (4)
No Symptom Resolution with Prednisone	1 (5)	8 (2.6)
Unspecified (Or did not receive)	18 (90)	284 (93.4)
Age		
Mean	54	56.4
Median	52	58.5
Range	28 – 79	18 – 86
Gender		
Male	13 (65)	164 (54)
Female	7 (35)	140 (46)
Symptoms		
Vestibular (Disequilibrium, Vertigo)	8 (40)	60 (19.7)
Tinnitus	8 (40)	68 (22.4)
Neurological Deficits (aphasia, weakness, auditory verbal hallucinations)	1 (5)	6 (2)
Pain (Otagia, Headache)	2 (10)	9 (3)
Average Duration of Symptoms (where recorded) (years)	3.84	2.48

Table footnote: Participants are presented in two columns – one containing those with findings on MR and the other containing those without findings on MR. Rows correspond to the number (and percentage) of subjects in the group possessing a given characteristic. Characteristics collected include: referral source; non-imaging testing such as basic audiometry, Auditory Brainstem Response (ABR), Vestibular Evoked Myogenic Potential (VEMP); medical interventions such as the administration of steroids and/or SERC (Betahistine). ENT represents Otolaryngology Head and Neck Surgery/Ear Nose Throat. PMR represents Physical Medicine and Rehabilitation.

(Filename: TCT_O-390_Table2-SummarizedFindings.jpg)

O-392

11:47AM - 11:54AM

Evaluation of Flow within the Sigmoid Sinus in patients with Intracranial Hypertension before and following Lumbar Puncture using 4D flow and 2D Velocity-Encoded Phase Contrast MRI.

R Khangura¹, A Wright¹, D Saloner¹, H Haraldsson¹, E Kao¹, L Cao¹, N Jani¹, J Leach², M Amans¹
¹UCSF, San Francisco, CA, ²UCSF, San Francisco, CA

Purpose

Intracranial hypertension is often associated with dural venous stenosis near the sigmoid-transverse sinus junction. Additionally, many patients with intracranial hypertension present with pulsatile tinnitus as a primary symptom. Symptom relief can may be provided with therapeutic lumbar tap or intracranial dural venous stenting in such patients. 2-D and 4-D MRI may provide insight into changes in flow following therapeutic lumbar tap. Our IRB-approved study aims to quantify the flow within the sigmoid/transverse sinus before and following therapeutic lumbar tap and search for casual relationship to improvement of pulsatile tinnitus symptoms.

Materials and Methods

IRB-approved study enrolled 18 patients to participate in our study with suspected intracranial hypertension and symptoms of pulsatile tinnitus. Enrolled patients were scanned on a Siemens 3T MRI prior to lumbar puncture, immediately followed by a lumbar puncture/tap in the MRI scanner in the lateral decubitus position. Opening pressure and total volume of CSF removed was recorded. The patient was then positioned in the supine position and immediately reimaged in the same session. Clinical intake of their pulsatile tinnitus symptoms were evaluated before and after the lumbar puncture. 2-D flow and 4-D flow images were reviewed with ROI selected in the bilateral sigmoid/transverse sinuses, with resultant numerical flow values recorded. Pre and postlumbar puncture flow values within the sigmoid/transverse sinuses was then evaluated by two board-certified neuroradiologists.

Results

Eighteen patients were evaluated. In patients with an opening pressure greater than 25 mm H₂O (6), patients found to have relief of pulsatile tinnitus symptoms were associated with increased flow through the dominant sigmoid/transverse sinus, quantified by 2-D and 4-D flow ROI values.

Conclusions

In patients with clinical diagnosis of intracranial hypertension with an opening pressure greater than 25 cm H₂O, increased 2-D/4-D MRI flow within the dominant sigmoid sinus was noted upon following therapeutic lumbar puncture. Plan for future analysis includes evaluating streamline CFD and 4-D images to characterize change in CFD pattern and vortexes.

Wednesday, June 6, 2018

10:30AM - 12:00PM

Excerpta: Spine

E-81

10:30AM - 10:34AM

Oxyx Embolism: A Feared Complication of Neck Tumor Devascularization

J Kang¹, G Wu¹, L Feng¹

¹Kaiser Permanente Los Angeles Medical Center, Los Angeles, CA

Purpose

Onyx (Medtronic, Minneapolis MN), also known as ethylene vinyl alcohol, is a liquid embolic agent with unique nonadhesive characteristics that distinguish it from other available embolic agents. We will review the properties that make Onyx unique, the expanding indications for its use, as well as possible complications and management.

Materials and Methods

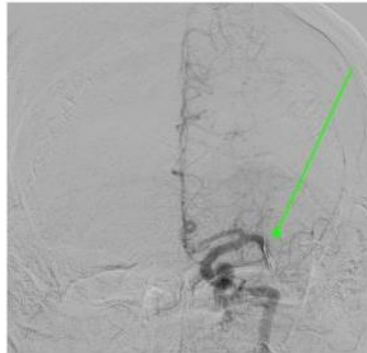
A 62-year-old male presented to us for preoperative embolization of a carotid body tumor with Onyx. Shortly after tumor resection, the patient had cardiac arrest from respiratory failure. After successful resuscitation, the patient had acute-onset aphasia and right-sided weakness. Angiography later confirmed this was due to an Onyx embolus to the left middle cerebral artery. A combination of snaring and aspiration techniques were utilized to remove the migrated cast. On follow-up, the patient showed near full neurologic recovery.

Results

Axial noncontrast CT head demonstrated edema in the left middle cerebral artery distribution consistent with infarction. A dense, almost metallic-density in the distal left middle cerebral artery was also noted, later confirmed to be an Onyx embolus. Intraoperative selective angiogram of the left internal carotid artery demonstrates occlusion of the left middle cerebral artery near the terminus as well as filling defects within the left anterior cerebral artery. There were Onyx emboli, presenting as a radio-opaque densities causing occlusions.

Conclusions

Onyx is a liquid embolic agent with unique, nonadhesive properties. Indications for Onyx use are arteriovenous malformations, Type I and II endoleaks, and preoperative embolization of hypervascular tumors. Complications of Onyx include reflux and migration of embolysate into anastomotic vessels and cranial nerve dysfunction. In the rare case of distal migration of Onyx emboli, snaring and aspiration techniques can be utilized to remove the migrated cast.



(Filename: TCT_E-81_OnyxImages.jpg)

544

10:30AM - 12:00PM

Serous Atrophy of the Bone Marrow in Anorexia Nervosa

E-82

10:34AM - 10:38AM

A Novel Percutaneous Approach to Retrieve an Ingested Extra-Esophageal Foreign Body using Advanced Interventional Radiology Techniques.

D Volders¹, M Heran²

¹*University of British Columbia, Vancouver BC, British Columbia, Canada,* ²*Vancouver General Hospital, Vancouver, British Columbia, Canada*

Purpose

Migration of an ingested foreign body to an extra-esophageal location is a very rare, but life-threatening complication. Retrieval of these objects is challenging and normally would require an open surgical approach. We want to describe a new and minimally invasive percutaneous method of retrieval.

Materials and Methods

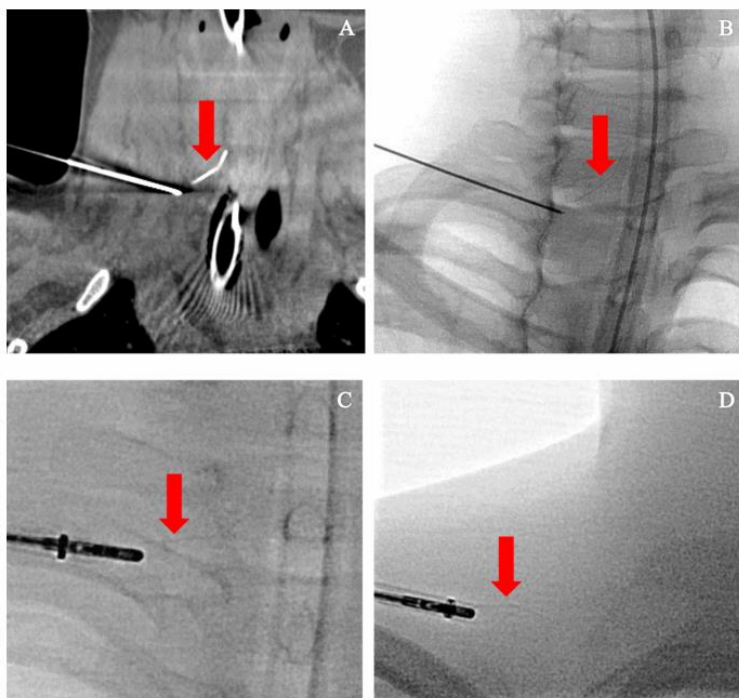
A previously healthy 8-year-old male presented to our emergency department with a history of odynophagia after eating barbecue steak that night. Chest x-ray and CT confirmed a radioopaque bristle-shaped foreign body in the esophagus. Unfortunately, this foreign body migrated extra-esophageal during a flexible esophagoscopy retrieval attempt in the operating suite.

Results

A fluoroscopic and ultrasound-guided percutaneously inserted needle allowed for subsequent 7 French sheath placement which was positioned immediately adjacent to the foreign body. The fluoroscopic technique was aided by rotational cone beam CT acquisition and subsequent needle guidance using Xper Guide (Panel A and B). This sheath was utilized as a port through which an endourology alligator forceps was used to retrieve the ingested barbecue bristle that had migrated laterally into the extra-esophageal space, medial and deep to the right carotid and jugular vessels (Panel C and D). The foreign body (red arrow) was retrieved successfully with the alligator forceps, without damage to vital structures in the surrounding area. The patient was monitored overnight and discharged the following day in good health and maintained on antibiotics as a precaution against potential infection.

Conclusions

We describe a novel previously unreported percutaneous retrieval procedure with the aid of advanced imaging techniques. This procedure may be considered as a minimally invasive option to retrieve foreign bodies in the neck and elsewhere in the body.



(Filename: TCT_E-82_picture-Exterpa-2.gif)

E-83

10:38AM - 10:42AM

Image Guided Percutaneous Drainage of Epidural Abscess

J Stephenson¹, S Forseen², B Gilbert²

¹Medical College of Georgia at Augusta University, Augusta, GA, ²Augusta University, Augusta, GA

Purpose

The purpose of this presentation is to discuss the procedure and technique of CT-guided percutaneous minimally invasive approach for epidural abscess drainage, as an alternative to the standard practice of open surgical drainage.

Materials and Methods

Patient presented three weeks status post total laparoscopic hysterectomy/bilateral salpingo-oophorectomy with worsening back/leg pain. Patient was febrile with leukocytosis. MR imaging revealed ventral epidural abscess. Neurosurgery determined no acute surgical intervention warranted at that time. Neuroradiology consulted for epidural abscess drainage.

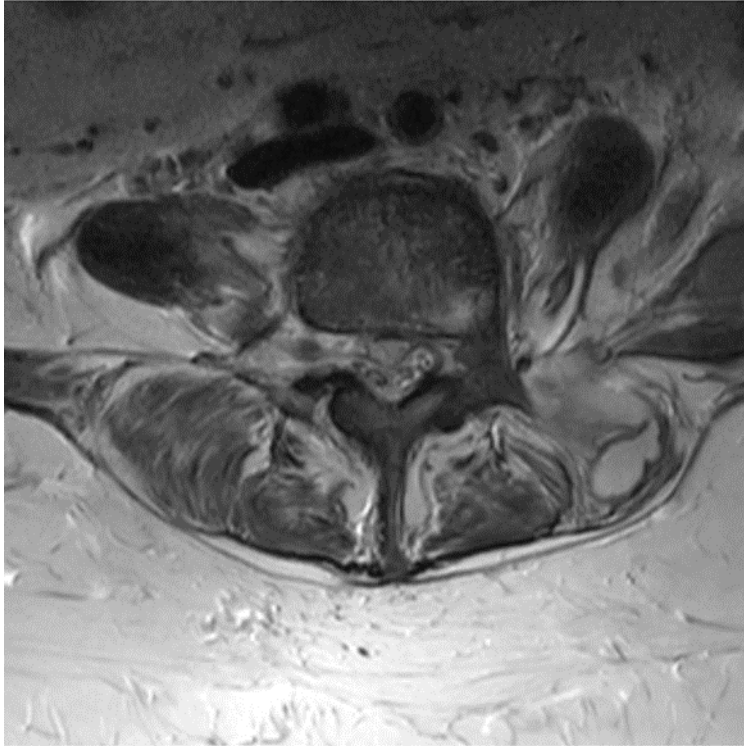
Results

MR lumbar spine T2 axial image demonstrates ventral epidural abscess. MR lumbar spine T1 post contrast Sagittal image demonstrates ventral epidural abscess, with dorsal displacement of distal spinal cord/conus medullaris. Intraprocedure CT axial image demonstrates coaxial biopsy needle placement in the ventral epidural space with fluid collection.

Conclusions

The standard of care for management of spinal epidural abscess (SEA) has long been IV antibiotic therapy, along with open surgical decompression, such as decompressive laminectomy when there is neurologic deficit. In the setting of significant patient comorbidity, an open surgical decompression may add substantial risk to a patient's outcome. As an alternative to open decompression, our institution will perform CT-guided percutaneous drainage of SEA, which is less invasive for the patient as compared

with open surgical decompression, and can provide an alternative option in patients who are determined to be poor surgical candidates. In select patients, imaging guided percutaneous SEA drainage is a viable alternative to open surgical decompression.



(Filename: TCT_E-83_Images.gif)

E-84

10:42AM - 10:46AM

Sacral Insufficiency Fracture as Complication of Palliative Radiotherapy to Lumbosacral Spine

S Fung¹, K Hsiao¹, H Wang¹, B Butler¹, B Teh¹

¹*Houston Methodist Hospital, Houston, TX*

Purpose

Insufficiency fracture (IF) is a potential complication of radiotherapy (RT). We present a case of sacral IF in a patient treated with palliative RT for multiple lumbosacral osseous metastases from breast cancer. She did not develop low back pain from sacral IF until four years after RT, but retrospective review showed evolving sacral alar changes beginning 1-2 years prior.

Materials and Methods

A 61-year-old woman diagnosed with left breast cancer, status post mastectomy and axillary lymph node dissection with pathologic stage T1cN3aM0, received adjuvant chemotherapy, RT, and hormone therapy. She was disease free until eight years after initial diagnosis when she developed low back pain and was found to have multiple osseous metastases to lumbosacral spine. Palliative RT (30 Gy in 10 fractions) was given to L2-sacrum including bilateral sacroiliac joints and medial ilium using single PA portal and 18 MV photons. After palliative RT, the patient reported improvement of her low back pain until four years post RT, when she developed worsening back pain that radiated down her right buttock to her toes.

Results

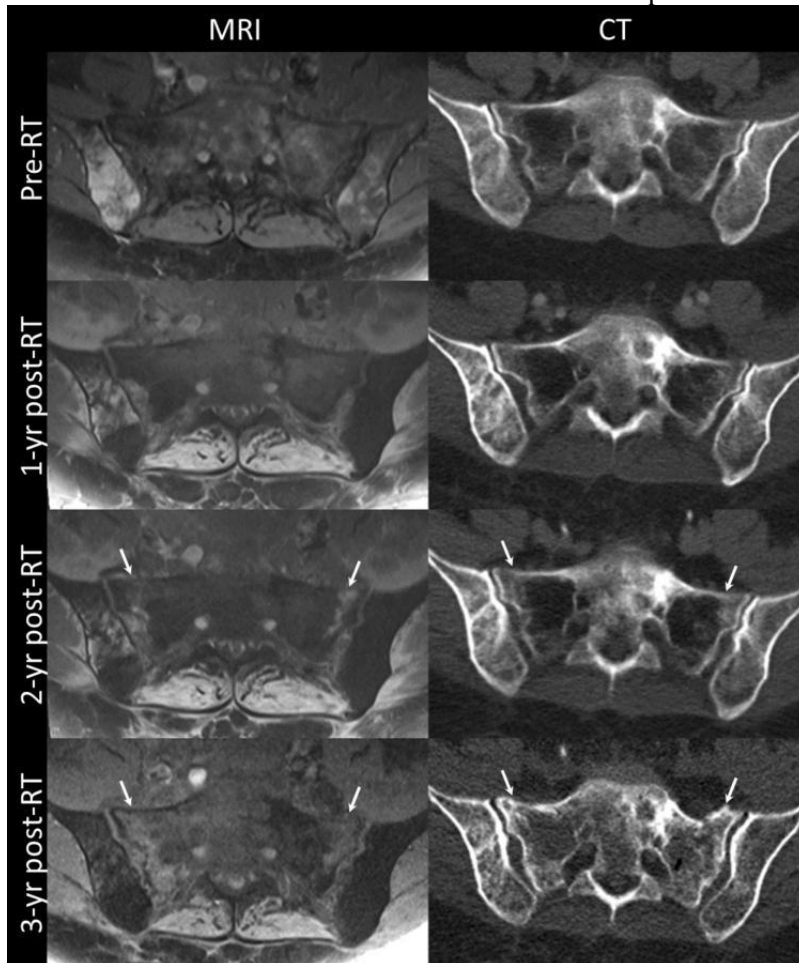
Lumbar spinal MRI prior to RT shows multiple enhancing osseous metastases involving the sacrum and bilateral ilium, which on CT are mixed osteoblastic and osteolytic. One year after RT, imaging shows

Oral Presentations & Excerptas

treatment response with resolving enhancing osseous metastases on MRI and increasing sclerosis of some of the treated metastases on CT. Two years after RT, first signs of developing sacral IF is seen on MRI with irregular linear enhancement and edema in the left sacral ala and mild diffuse enhancement and edema in the right sacral ala, which on CT shows corresponding developing sclerosis but no cortical disruption. Three years after RT, there is further evolution of sacral IF with increasing diffuse enhancement and edema in bilateral sacral ala on MRI. CT shows disruption of the left sacral alar cortex and buckling of the right sacral alar cortex. No new metastasis. Sacroplasty was subsequently performed for pain management.

Conclusions

Spinal osseous metastasis is the most common cause of pain in up to 70% of patients with advanced cancer. Palliative RT is able to relieve 50-80% of bone pain. However, a complication of RT is inducing IF, which is a type of stress fracture occurring under normal or physiological stress such as weight-bearing to weakened demineralized bone. RT substantially increases the risk of IF by hazard ratio of 1.65-3.16. IF can occur anywhere within the RT field, most commonly the sacrum after pelvic RT since the sacrum is a major weight-bearing structure of the body. Pain from sacral IF can be severe and may be confused clinically with spinal metastasis in cancer patients; therefore, knowledge and clinical suspicion of sacral IF is essential in the evaluation lumbosacral spine after RT.



(Filename: TCT_E-84_FungetalASNR2018AbstractFigure.jpg)

E-85

10:46AM - 10:50AM

Giant Collapsible Intraspinial Varix Mimicking an Epidural Enhancing Mass

J Kang¹, E Nguyen¹, M Lewis¹, G Radner¹, A Wong¹

¹*Kaiser Permanente Los Angeles Medical Center, Los Angeles, CA*

Purpose

Symptomatic epidural varices are an uncommon entity with the incidence ranging from 0.07% to 1.3%. Epidural varices are often mistaken for other mass lesions in the spine. Radiological diagnosis is important to prevent unnecessary invasive procedures, including biopsy. We present a case of an epidural mass initially presumed to be a neoplasm, but for which subsequent imaging yielded clues supporting a diagnosis of varix, later confirmed at surgery. We will discuss the epidemiology, postulated pathogenesis, salient imaging findings, and treatment options for this rare entity.

Materials and Methods

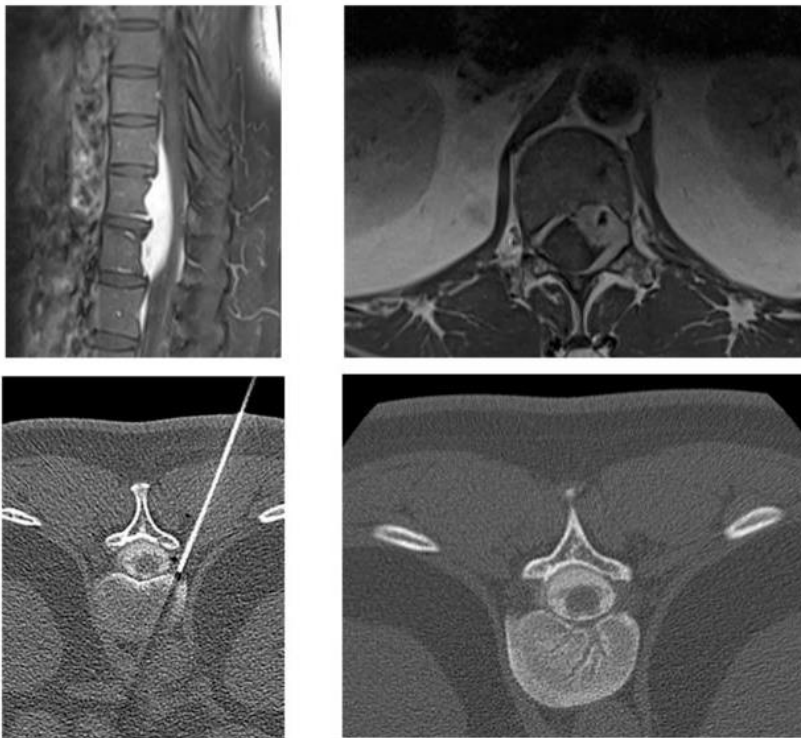
A 35-year-old female presented with a large enhancing epidural lesion in the thoracic spinal canal that had been detected incidentally on MRI for an unrelated indication. The lesion caused thecal sac compression. It was initially thought to represent an unusual peripheral nerve sheath tumor or lymphoma. Subsequently, a CT-myelogram guided percutaneous biopsy in the prone position showed marked decrease in lesion size and biopsy did not reveal neoplasm. On MRI follow-up, there was unexpected rebound to its original size. Detailed review of all imaging then revealed clues that supported a vascular etiology rather than neoplasm. Open surgical biopsy confirmed the lesion to be a large epidural varix.

Results

The CT and MR imaging features supporting varix in this case include: benign bony remodeling of the abutting vertebral cortex, intralesional flow void, dilated vascular channels in the adjacent vertebral body, and dynamic changes in the size of the lesion due to positioning (i.e., decreased size with prolonged prone positioning during the first biopsy procedure).

Conclusions

This unusual case illustrates the appearance and diagnostic clues of an epidural varix that can be used in distinguishing it from mimics, such as epidural neoplasms, with the potential to minimize unnecessary invasive workup.



(Filename: TCT_E-85_VarixImages.jpg)

E-86

10:50AM - 10:54AM

Unusual Case of Intradural Extramedullary Cervical Spine Hemangioblastoma

A komaraju¹, R Samant¹, R Ramakrishnaiah¹, M Gokden¹, J McCarty¹, E Angtuaco¹, S Geppert¹, R Vanhemert¹, M Kumar¹

¹University of Arkansas for Medical Sciences, Little Rock, AR

Purpose

To present an unusual case of intradural-extramedullary, undulating mobile hemangioblastoma: MRI and catheter angiographic findings

Materials and Methods

A 41-year-old, right-hand dominant, male presented with neck pain and bilateral upper extremity numbness, left arm radiculopathy, worse in the morning for several months. His motor examination demonstrated 5/5 power throughout bilateral lower extremities and 4/5 in upper extremities. Sensation is intact throughout. Reflexes 3+ symmetric with no hyperreflexia. No history of trauma was present. He had history of controlled hypertension on medication. No history or clinical findings to support von Hippel Lindau were present. MRI study and catheter angiogram study were performed. A hypervascular mass lesion was seen in the anterior intradural extramedullary space at C3-C4 level. Surgical resection of the lesion was performed with posterior decompression and cervical laminectomy from C3-C5 and posterior segmental fixation from C2-C6 was performed using lateral mass, screws, and posterolateral arthrodesis using autograft bone from C2-C6 level. Pathological specimen showed a vascular neoplasm composed of intervening sheets of cells with vacuolar cytoplasm. Reticulin stain demonstrates alternating cellular and reticular areas. Immunohistochemically, the specimen was strongly positive for vimentin and

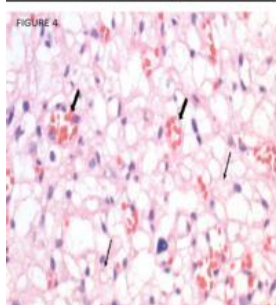
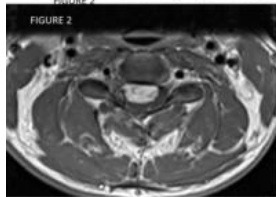
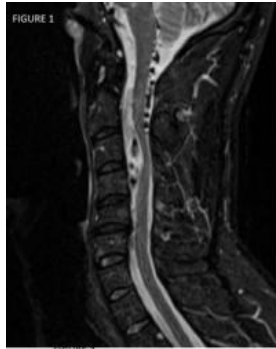
inhibin. Pancytokeratin, CK8/18, EMA, GFAP, PAX-8, RCC-Ma were negative supporting the diagnosis of hemangioblastoma.

Results

Preoperative MRI study of the cervical spine demonstrated a T2 hyperintense, heterogeneous, vascular, anterior intradural extramedullary lesion at C3 and C4 levels, with multiple flow voids on the T2 sequence. Differential diagnosis was a vascular malformation versus a hypervascular tumor. Catheter angiogram demonstrated a hypervascular pedunculated intradural tumor with a central tumor blush supplied by C1-2 and C3-4 pedicular branches of the right vertebral artery, with drainage into the epidural venous plexus. The real time fluoroscopic images/cine loops showed a freely mobile pedunculated mass with to and fro motion. No anterior spinal artery tumor feeders, intracranial pathology or additional malformations were seen. The rest of the spine, brain and retina (orbits) did not show any lesions. Legends for images under images/tables section: Figure 1: Image above is mid-sagittal T2 image. Heterogeneous T2 lesion with flow voids causing severe cord compression is noted. Flow voids are also noted posterior to the spinal canal at C1-2 levels. Figure 2: Image above is an axial T1 post contrast image demonstrates avidly enhancing extramedullary intradural lesion causing mass effect and severe cord compression. Figure 3: Image above is an angiographic image demonstrating a hypervascular pedunculated intradural tumor supplied by branches of the right vertebral artery showing early arterial filling in of the lesion. Figure 4: Pathology-microscopic image - The Neoplastic cells have variable vacuolated or foamy cytoplasm (arrows). Many blood vessels (block arrows) with erythrocytes are also seen.

Conclusions

Hemangioblastoma is a hypervascular, avidly enhancing lesion, which may present as a solid/nodular lesion, a cyst with a nodule appearance, or a predominantly cystic appearance. In addition to MRI study, which demonstrates the previously mentioned characteristics of the lesion, angiogram studies may show early enhancement, arterial feeders, and/or draining veins, in addition to the vascular blush. Evaluation of the brain and rest of the spine is essential. In addition to clinical history and exam, evaluation of chest, abdomen and pelvis to look for syndromic association like Von-Hippel Lindau is essential. Surgical resection is usually curative; however, some larger lesions may benefit from presurgical embolization. Appropriate follow-up postsurgically to evaluate for any recurrence and residual tumor must be performed. Other possible differentials include vascular malformations, medulloblastoma, astrocytoma, metastasis, ependymoma.



(Filename: TCT_E-86_GRAPHICFILEASNR.jpg)

E-87

10:54AM - 10:58AM

Dialysis-Related Amyloidosis of the Spine – A Mimic of Osseous Metastatic Disease

T Li¹, S Patel¹, H Marin¹, B Griffith¹

¹Henry Ford Health System, Detroit, MI

Purpose

Dialysis-related amyloidosis is a disease caused by the accumulation and tissue deposition of amyloid fibrils. Osteoarticular amyloidosis, which invariably occurs in long-standing hemodialysis, occurs as a result of beta-2 microglobulin deposition in periarticular tissues, synovium, and bone. The imaging findings are nonspecific, but can demonstrate lytic bone lesions and as a result can be mistaken for

Oral Presentations & Excerpts

multiple myeloma or metastatic disease. This excerpt describes a case of dialysis-related amyloidosis masquerading as numerous lytic lesions, briefly discussing important imaging characteristics and differential diagnoses.

Materials and Methods

We present the case of a 71-year-old male with a history of end-stage renal disease requiring hemodialysis and hepatocellular carcinoma presenting with generalized neck pain and new lower extremity numbness. The history of malignancy and new symptoms prompted imaging of the spine to exclude metastatic disease. The patient also had a previous lytic lesion involving the humerus, which was biopsied and found to be consistent with dialysis-related amyloidosis.

Results

MRI of the cervical spine (Fig. 1A) demonstrates a T1 hypointense lesion (arrow) involving the odontoid process. Subsequent CT of the cervical spine (Fig. 1B, C) demonstrates osteolytic lesions throughout the entire cervical spine (arrows), although most numerous within C1, C2, and the odontoid process (circle). Coronal CT and MRI of the right shoulder (Fig. 1D) demonstrates a large lytic and T1 hypointense lesion involving the right humeral head (arrow).

Conclusions

Dialysis-related amyloidosis occurs secondary to deposition of β 2-microglobulin and predominantly involves the osteoarticular system. It is characterized by a variety of imaging appearances, but can present with radiolucent lesions, which confounds the diagnosis as other etiologies, particularly multiple myeloma and metastatic disease, can have a similar appearance. Remembering to include amyloidosis as a potential cause of lytic bone lesions in patients on hemodialysis is important for ensuring appropriate patient workup.



(Filename: TCT_E-87_Amyloidosis.jpg)

E-88

10:58AM - 11:02AM

Unusual Location of a Well-Known Entity for Radiologists: Extensive Cervical Paraspinal Tumoral Calcinosis in Scleroderma.

M Smith¹, J Chang¹, A Ozturk¹, M Bobinski¹, N Pham¹

¹*University of California-Davis Medical Center, Sacramento, CA*

Purpose

To present a rare case of extensive cervical tumoral calcinosis (TC) in a patient with scleroderma

Materials and Methods

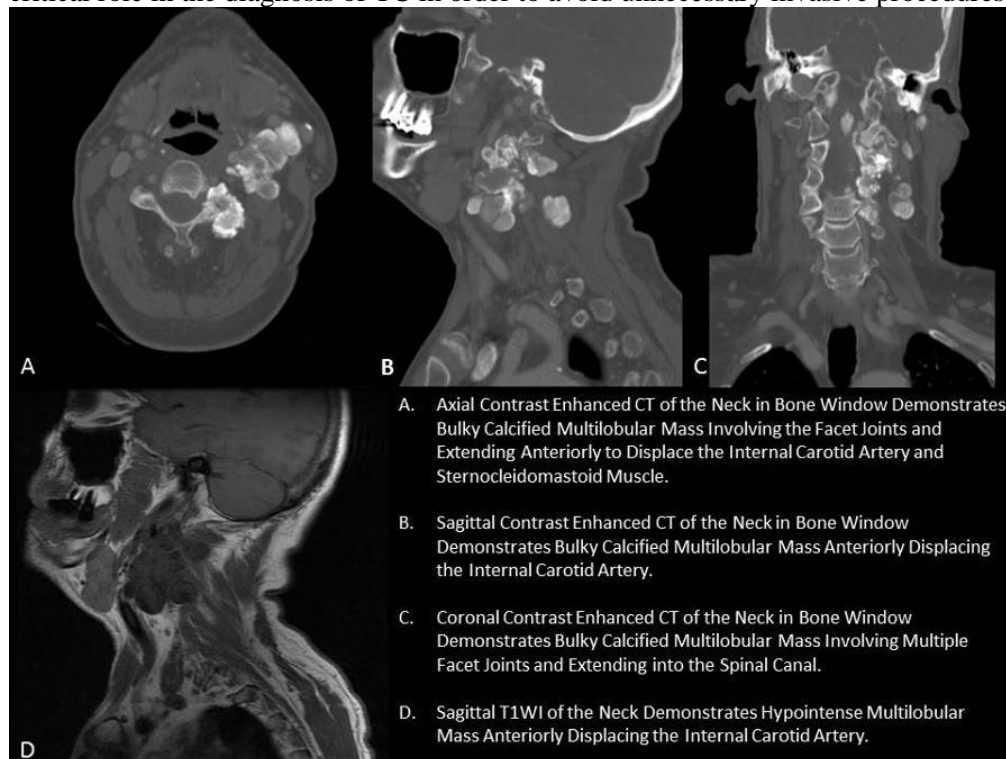
A 60-year-old man with a history of scleroderma diagnosed in 2015 presented to our institution for progressive neck pain, deformity, and worsening functional disability. Cervical spine computed tomography (CT) demonstrated multiple, calcified soft tissue masses within the left neck. The patient subsequently underwent surgical reduction of the anterior portion of the mass to alleviate his symptomatology. The excised calcified mass was pathologically confirmed to be TC.

Results

Cervical spine CT demonstrated a large calcified, multilobular mass extending along the left paraspinal soft tissues from C1 to C5 with involvement of the left-sided facet joints and atlanto-axial articulation. The mass displaced the left internal carotid artery and sternocleidomastoid muscle anteriorly. MRI of the cervical spine showed a hypointense mass on T1WI, T2WI, and STIR images without evidence of contrast enhancement. Massive periarticular calcification involved the C1-C5 facet joints with extension into the left C2 transverse foramen and left aspect of the spinal canal. However, there was no evidence of spinal cord compression.

Conclusions

Soft tissue calcifications are closely related to scleroderma which is usually characterized by small calcifications within sites of repetitive trauma, such as the hips, elbows, fingers, and forearms. Classical presentation of TC is of multiple mass-like lobulated deposits of dense calcifications within the periarticular regions of the appendicular skeleton, whereas the spine is much less commonly affected (1). In a described series of 21 patients with tumoral calcinosis, only one patient had scleroderma (2). TC in the cervical spine can be clinically symptomatic, extensive, and voluminous (as in our case), and may demonstrate aggressive features that can mimic a neoplastic or infectious process. Radiologists have a critical role in the diagnosis of TC in order to avoid unnecessary invasive procedures.



(Filename: TCT_E-88_TC.jpg)

E-89

11:02AM - 11:06AM

Avoiding a Bloody Mess: Keys to the Imaging Diagnosis of Intraosseous Hemangioblastoma

M Uzee¹, G Liebo¹, F Diehn¹, C Wood¹, J Morris¹, L Eckel¹

¹*Mayo Clinic-Rochester, Rochester, MN*

Purpose

Sporadic intraosseous hemangioblastoma is extremely rare, with only five cases previously described in the English literature. We present a case, along with several companion cases from our institution and the literature, to highlight key imaging findings that help distinguish it from more common lesions of bone and to guide optimal planning for diagnosis and management.

Materials and Methods

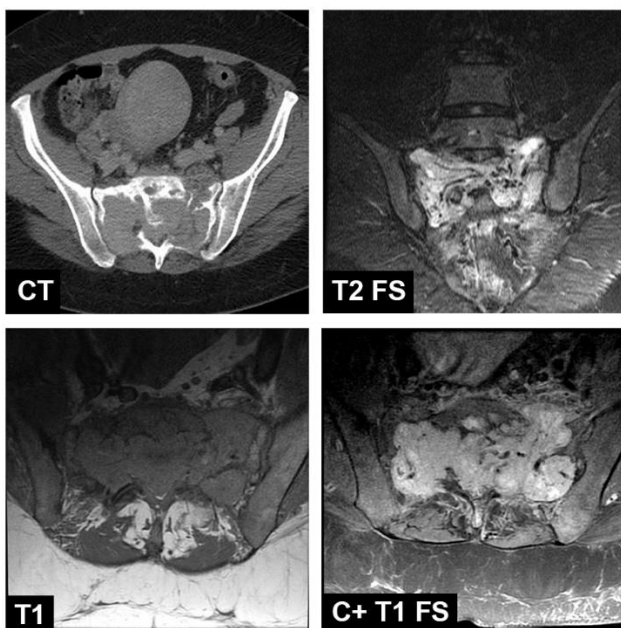
A 54-year-old female presented with sudden onset of severe buttock pain and bilateral lower extremity radiculopathy after bending down. Physical exam demonstrated absent ankle reflexes bilaterally and decreased light touch over the lateral aspect of the left foot. Laboratory values were significant for polycythemia. During CT guided biopsy, the lesion was found to be very vascular, soft, and somewhat vacuous. Following biopsy, the patient underwent preoperative embolization and surgical debulking. Postoperative course was complicated by severe pain and limited mobility, prompting further embolization, cryoablation, and posterior instrumented fusion.

Results

Lumbar spine MRI demonstrated an avidly enhancing, locally invasive, T2-hyperintense mass replacing the majority of the sacrum with numerous tortuous flow voids. Extrasosseous extension involved the epidural space, L5-S2 sacral neural foramina, and presacral space, effacing the sacral canal and engulfing the lumbosacral nerve roots. The lesion was purely lytic on CT. This combination of imaging findings is not expected when imaging other lesions of this region, such as aggressive hemangioma, chordoma, or hypervascular metastasis.

Conclusions

Primary extramedullary CNS hemangioblastomas are rare, particularly those centered in bone. Differentiation of hemangioblastoma from more common mimics on imaging is important as it can change both diagnostic and treatment approaches. Multiple tortuous flow voids, a lytic appearance on CT, and locally advanced tissue invasion are key imaging features of hemangioblastoma. Hemangioblastomas generally require presurgical embolization to prevent intraoperative bleeding complications during biopsy or resection. In addition, extramedullary hemangioblastomas tend to be more vacuous, potentially requiring a more invasive biopsy strategy.



(Filename: TCT_E-89_Composite_Hemangioblastoma.jpg)

E-90

11:06AM - 11:10AM

Diffuse Large B- and T-cell Neurolymphomatosis Preceding Systemic Symptoms of Lymphoma

M Tominna¹, K Patel¹, A Krishnan², A Wang²

¹Oakland University William Beaumont School of Medicine, Royal Oak, MI, ²Beaumont Health System, Royal Oak, MI

Purpose

Neurolymphomatosis is a rare, but frequently under-recognized type of lymphoma. Lymphoma is known as the "great-mimicker". It is important to be aware of this rare presentation of lymphoma which can involve nerve roots, cranial or peripheral nerves, or a nerve plexus. Diagnosis is often delayed and may be diagnosed postmortem in a majority of cases. Reviewed cases in the literature show that more than half of autopsy cases of neurolymphomatosis also had systemic involvement. Patients may have a complicated medical history and have underlying medical conditions which the clinician may attribute to the underlying cause of the patient's pain or symptoms. An astute radiologist can suggest this as a diagnosis which can result in an earlier diagnosis for appropriate treatment and prevent more invasive treatment such as surgery. Neurolymphomatosis is most commonly described with diffuse large B-cell lymphomas, but can also occur with T-cell lymphomas and we will present a case of each for review. Rarely, this entity also occur with leukemias.

Materials and Methods

The first patient a 40-year-old who presented with relentless severe radicular pain of the right foot fourth and fifth digits, as well as severe weakness of the right leg. The patient was initially thought to have sciatica or restless leg syndrome and was treated conservatively. Symptoms did not resolve and the patient went on to have a lumbar MRI at an outside facility. An enhancing and enlarged right S1 nerve was seen and felt to represent a schwannoma. The patient was taken to surgery due to persistent pain. The tumor was unable to be separated from the nerve root and an epidural lesion was also found. T-cell lymphoma was subsequently diagnosed on histopathology. A PET scan followed and revealed FDG uptake in the unresected right S1 nerve root, as well as a few FDG avid soft tissue masses seen

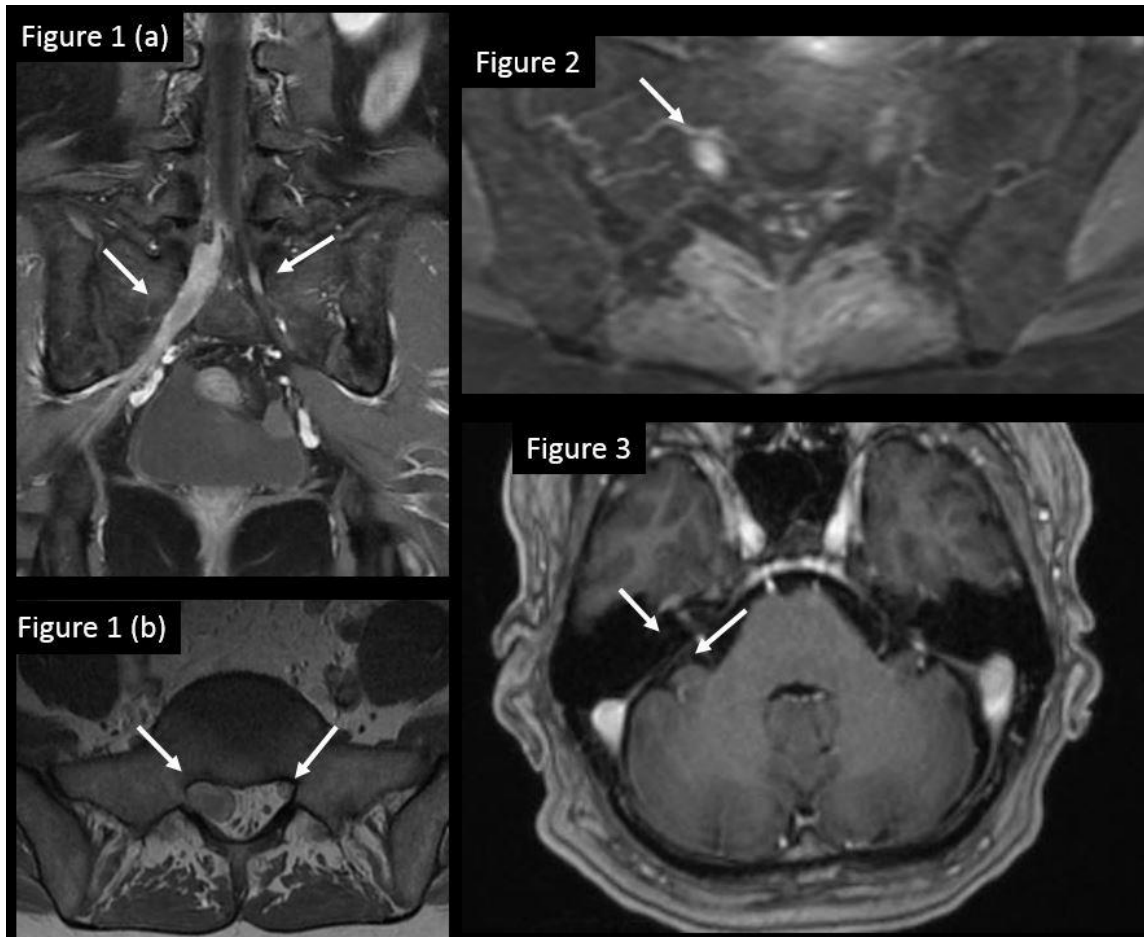
throughout body wall. The patient was started on systemic chemotherapy and intrathecal methotrexate. The second patient is a 64-year-old with a several month history of painful radiculopathy and weakness of the right lower extremity. Conservative management only helped temporarily. Initial lumbar MRI revealed disc extrusion at L5-S1 compressing the right S1 nerve root. This finding was concordant with the patient's symptoms and due to persistent pain, patient underwent lumbosacral decompression surgery. The patient's symptoms resolved after surgery, but returned a couple months later and were more severe. Repeat MRI exams showed enhancement of the right S1 nerve root, which was thought most likely related to postoperative change from scarring. New symptoms of facial droop occurred. CSF analysis was performed through lumbar puncture, which revealed lymphoma cells and diffuse large B-cell was diagnosed.

Results

The MR findings of the first case are shown in Figure 1 (a) and (b). The right S1 nerve root demonstrated fusiform enlargement with homogeneous contrast enhancement and was thought to represent a schwannoma. On review of the outside MRI exam, in retrospect there was also enhancement of the left S1 nerve root, though not appreciably enlarged, and may have been a clue to an alternative diagnosis. The MR findings of the second case are shown in Figures 2 and 3. In addition to postdecompression changes, there was enhancement of the S1 nerve root. Additional subtle enhancing foci were seen along the cauda equina and L4 nerve root. Inflammatory and neoplastic etiologies were suggested based on the enhancement. The MRI of the brain performed for right facial droop revealed enhancement of the right seventh cranial nerve and geniculate ganglion.

Conclusions

Neurolymphomatosis is a rare and commonly under-recognized form of lymphoma. In both cases of neurolymphomatosis, the neurologic symptoms were the initial presentation. While neither patient demonstrated systemic symptoms of lymphoma, following pathological diagnosis of lymphoma of the nerves, further investigation led to discovery of other sites of disease. Neurolymphomatosis can have different clinical manifestations. This includes painful polyradiculopathy or neuropathy, painless neuropathy, cranial neuropathy or mononeuropathy. Some clinical clues that can assist in the diagnosis may include rapid progression, extreme pain, and an asymmetric distribution. Both cases demonstrated painful radiculopathy, and the second case also had cranial neuropathy. On imaging, one would expect to see enlargement/enhancement of the nerve. The findings are nonspecific and could be seen in the setting of inflammatory neuropathies and other benign neoplasms. However, identification of other involved nerves may indicate the underlying condition is more widespread. Thus, it is imperative that the radiologist keeps neurolymphomatosis as a differential when evaluating nerve root enlargement or enhancement especially when multiple. The radiologist may be the first one to raise the possibility of this diagnosis. This can facilitate early systemic investigation and diagnosis of lymphoma.



(Filename: TCT_E-90_images.JPG)

E-91

11:10AM - 11:14AM

Osteosclerotic Multiple Myeloma

S Sharma¹, R Samant², R Ramakrishnaiah¹, J MCCARTY¹, R Van Hemert², E Angtuaco², M Kumar²
¹University of Arkansas for Medical Sciences, Little Rock, AR, ²UAMS, LITTLE ROCK, AR

Purpose

To include multiple myeloma among the differential diagnosis for diffuse osteosclerosis on imaging
Materials and Methods

A 60-year-old female presented with fatigue, shortness of breath and was found to have anemia with a Hb of 7.9, WBC of 6.5 and platelets of 206. She was transfused two units of pRBCs. Investigations for anemia included evaluation of bone marrow which was difficult to aspirate and a BM biopsy which revealed a 95% cellular marrow with 50% plasma cells, which were light chain restricted. No M-protein was present in urine. A diagnosis of IgG-kappa multiple myeloma was made. The patient was treated with BM transplant and VRD (Bortezomib-Lenalidomide-Dexamethazone) regimen. She achieved complete remission on this therapy and follow-up BM biopsy was negative.

Results

Initial bone survey with PET-CT and MRI demonstrated increased bone density and PET-CT showed diffuse sclerosis of the axial and appendicular skeleton (Fig. A) with no lytic lesions and no foci of increased FDG uptake. MRI demonstrated diffusely hypointense marrow on T1W images (Fig. C).

Subsequent follow-up scans post therapy demonstrated substantial improvement of bony sclerosis with restoration of normal marrow density on CT and corresponding normal hyperintense marrow signal on T1W images (Fig. B and D respectively).

Conclusions

Multiple myeloma can rarely present with sclerotic osseous disease instead of the more common lytic and osteopenic appearance. Diffuse osteosclerotic multiple myeloma can mimic other causes of bony sclerosis. Common adult etiologies for diffuse bony sclerosis include myelofibrosis, sickle cell disease, renal osteodystrophy, infiltrative tumors like lymphoma and leukemia, osteoblastic metastases like breast and prostate cancer. Paget's disease and fluorosis include some of the less common causes. Serum and urine assays, bone marrow examination and whole-body PET-CT and MRI of the spine and pelvis are utilized for the diagnosis and follow-up of multiple myeloma patients.



(Filename: TCT_E-91_Picture2.jpg)

E-92

11:14AM - 11:18AM

Phosphaturic Mesenchymal Tumor of the Cervical Spine

A Guarnizo¹, T Nguyen¹

¹*The Ottawa Hospital - University of Ottawa, Ottawa, Ontario, Canada*

Purpose

1. To describe the imaging findings of the phosphaturic mesenchymal tumor 2. To discuss the histopathological features of oncogenic osteomalacia secondary to phosphaturic mesenchymal tumor

Materials and Methods

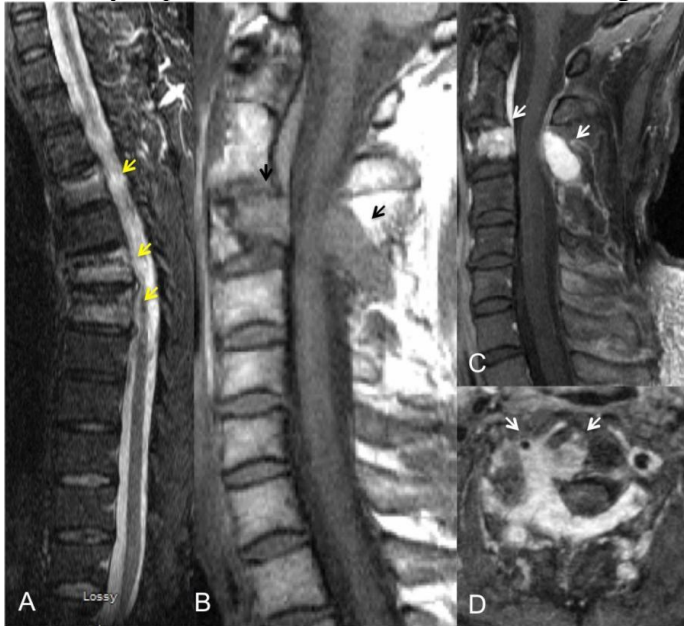
A 50-year-old man presented with two years of back pain associated with decreased mobility and difficulty functioning. The spine MRI showed generalized osteopenia, multilevel wedge compression fractures in the thoracic spine and a well-defined enhancing mass in the C3 vertebral body. The thorax and abdomen CT showed multiple rib fractures and sacral fractures. The work-up for multiple myeloma was negative. Serum phosphate and vitamin D levels were low. The fibroblast growth tumor (FGF)-23 levels were high. The patient underwent C3 corpectomy and C2 to C5 fusion. The pathology showed an epithelioid tumor with cartilaginous and myxoid features. The elevated FGF-23 levels and the induced tumor osteomalacia favored to be a phosphaturic mesenchymal tumor.

Results

Sagittal STIR image of the thoracic spine (A) showed T2, T4, T6 superior endplate compression fractures. Sagittal T1W without (B) and with gadolinium (C) and axial T1 with gadolinium (D) sequences show a mass within the right side of the C3 vertebral body with extension to the posterior elements and homogeneous enhancement.

Conclusions

Phosphaturic mesenchymal tumor is a rare benign neoplasm associated with oncogenic osteomalacia related to over secretion of fibroblast growth factor 23 (FGF-23) and secondary hypophosphatemia. Patients usually present with multiple pathological fractures, bone pain and muscle weakness. The imaging findings include an enhancing well defined mass that usually affects the extremities followed by the sinonasal cavities. The nonspecific imaging findings make the clinical evaluation, histopathology and laboratory important factors to make the definite diagnosis.



(Filename: TCT_E-92_PMTcopy.jpg)

E-93

11:18AM - 11:22AM

Osteitis Fibrosa Cystica of the Spine, Imaging Features and Clinical Presentation

T Huynh¹, S Kumar¹

¹Baylor College of Medicine, Houston, TX

Purpose

Spinal brown tumor can mimic metastatic disease. The purpose is to review the imaging features and clinical presentation of spinal brown tumor to prevent the diagnostic pitfall of calling it metastatic disease.

Materials and Methods

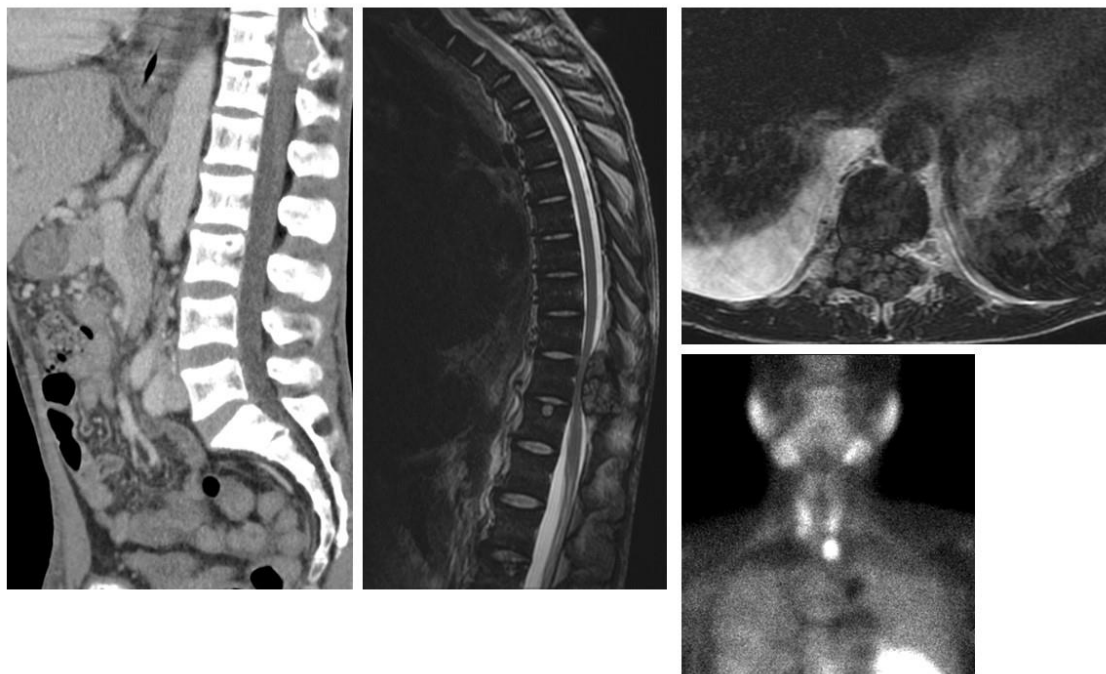
A 32-year-old male with end-stage renal disease presented with stabbing lower back pain. Abdominal CT and MRI showed an extradural mass centered in the posterior element of T11, resulting in cord compression. Abdominal CT also showed multiple lytic lesions in the sacrum, ilium and left femur. Metastatic disease was considered as working diagnosis due to multifocality and given history of autosomal dominant polycystic kidney disease. Biopsy indicated giant cell proliferation consistent with brown tumor of hyperparathyroidism. Parathyroid hormone (PTH) level was 1231 pg/mL (normal 8.7-77.1). Retrospective review of the patient chart showed that he had a sestamibi scan performed 19 months prior which showed a parathyroid adenoma. The patient underwent resection of the spinal mass and parathyroidectomy. Post op PTH value decreased to 133 pg/mL.

Results

Sagittal contrasted enhanced CT showed a 4 cm enhancing mass centered in the posterior elements of the T11 vertebrae without associated calcification or hemorrhage. T2-weighted sagittal and axial MRI showed a 4 cm, well circumscribed, expansile, multilobulated, extradural mass centered in the posterior element of T11 with suggestion of fluid/fluid level. The mass compressed the spinal cord and resulted in severe spinal canal stenosis. Sestamibi scan showed large focal radiotracer uptake inferior to the left thyroid lobe and small focal radiotracer uptake inferior to the right thyroid lobe.

Conclusions

Brown tumor of the spine causing cord compression is a rare entity. It is a locally aggressive lesion and mimics metastatic disease. Differential diagnosis includes multiple myeloma, lymphoma and giant cell tumor. Diagnosis of brown tumor depends on clinical, biochemical, radiological and pathological factors.



(Filename: TCT_E-93_asnrcase.jpg)

E-94

11:22AM - 11:26AM

**Utility Of Spine Steady State Fast Filled Echo (FFE) Sequence In The Diagnosis Of Chordoma
Non-Enhancing Leptomeningeal Drop- Metastases**

Oral Presentations & Excerptas

J Ortiz Jimenez¹, M Cortes Nino¹

¹McGill University - Montreal Neurological Hospital, Montreal Quebec, Canada

Purpose

To describe the utility of FFE sequence in detecting nonenhancing drop metastases in a patient with recurrent clivus chordoma with leptomeningeal intracranial and spinal metastases

Materials and Methods

A 26-year-old female with history of clivus chordoma treated with multiple surgeries and proton beam radiotherapy. Nine years later the patient developed lower cranial nerves symptoms.

Results

MRI with gadolinium demonstrated communicating hydrocephalus as well as recurrent chordoma invading the left orbit and pterygoid fossa. Abnormal areas of enhancement were not identified. A posterior fossa FFE sequence was performed showing tumor recurrence with cerebrospinal fluid (CSF) seeding involving the lateral and fourth ventricles, which were not detected in conventional T1 sequence with gadolinium. These findings led us to perform spinal imaging using T1 with gadolinium as well as FFE. The latter revealed multiple leptomeningeal drop metastases, not seen on T1 with gadolinium.

Conclusions

Chordoma CSF seeding has been described as a very unusual metastatic pattern, expected to enhance on T1 with gadolinium. Our case is unusual in that enhancement did not occur, prompting us to use FFE. Therefore, we propose that steady state FFE is a valuable sequence for the investigation of CSF seeding.

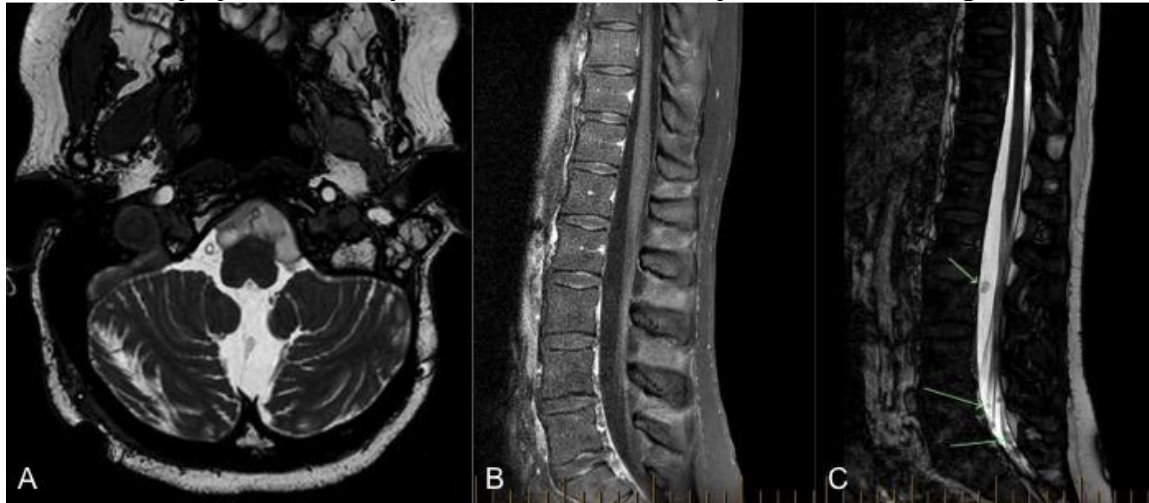


Fig. 1 Twenty six year old female with recurrent clivus chordoma. A, Posterior fossa FFE demonstrates recurrent tumor occupying the premedullary cistern. B, L-spine Sagittal T1 with gadolinium does not show enhancing lesions. C, L- Spine Sagittal FFE demonstrates multiple drop metastases along the cauda equina (arrows).

(Filename: TCT_E-94_Recurrentchordomanon-enhancingdrop-metastases.jpg)

E-95

11:26AM - 11:30AM

Organizing Hematoma Mimicking Spinal Cord Neoplasm after Transplantation of Olfactory Ensheathing Cells

C Zamora¹, J Aristizabal², M Castillo¹

¹University of North Carolina, Chapel Hill, NC, ²University of Antioquia, Medellin, Colombia

Purpose

An estimated 2.5 million people live with spinal cord injury worldwide. Stem cell transplantation may be performed experimentally in an attempt to stimulate neurite formation and promote recovery. Olfactory ensheathing cells (OEC) are capable of neuroregeneration through secretion of neurotropic factors. However, there are reports of teratoma formation and overgrowth of transplanted cells given their pluripotency. Our purpose is to present a case of an organizing hematoma mimicking neoplasm after spinal cord stem cell transplantation.

Materials and Methods

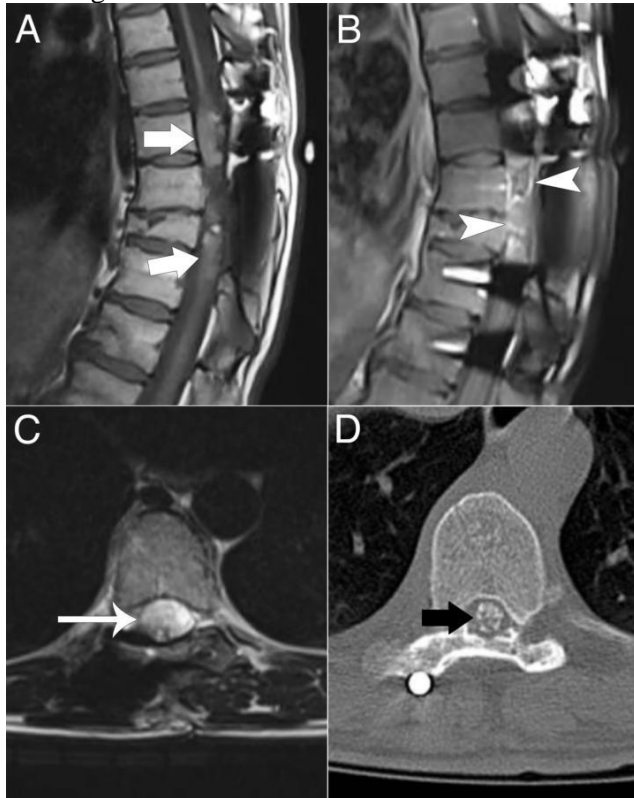
A 37-year-old female had an incomplete spinal cord injury at T10 from a motor vehicle accident which led to paraplegia with bowel and bladder incontinence. She underwent transplantation of autologous OECs into the spinal cord and regained some neurologic function. Fifteen years after initial injury she presented with progressively worsening back pain and decreasing neurologic function. MRI showed an intramedullary mass-like lesion at the level of injury (Figure). The patient underwent biopsy due to concern for neoplasm and histology revealed necrotic debris and an organizing hematoma but no evidence of malignancy.

Results

Sagittal pre (A) and postcontrast (B) T1 MR images show postsurgical changes as well as two expansile and mildly hyperintense lesions in the thoracic cord (white arrows) with peripheral contrast enhancement (arrowheads). Axial T2 (C) shows one of the lesions to be bright, expansile, and well-circumscribed (thin white arrow). There is coarse calcification on CT (black arrow, D).

Conclusions

Stem cell transplantation is promising but carries a risk of teratoma formation and cell overgrowth. However, in cases such as this one, organizing hematomas can mimic masses and pose a diagnostic challenge.



(Filename: TCT_E-95_composite1.jpg)

E-96

Serous Atrophy of the Bone Marrow in Anorexia Nervosa

M Patel¹, R Jain²

¹New York University Langone Health, New York, NY, ²New York University School of Medicine, New York, NY

Purpose

To present a case of serous atrophy of the bone marrow in a patient with anorexia nervosa, which was incidentally detected on an MRI of the cervical spine obtained to evaluate for trauma following a syncopal episode. Awareness of the imaging findings of this uncommon entity can prevent further unnecessary imaging.

Materials and Methods

A 26-year-old female was brought to the ED by emergency medical services after a syncopal episode while running on the treadmill. She was obtunded on arrival, and her vital signs were notable for bradycardia and hypothermia. A head CT was performed, which was within normal limits. A CT of the cervical spine demonstrated demineralized bones and vertically-oriented lucencies through the C7 and T1 spinous processes with sclerosis along the margins, suggestive of chronic fractures. There was no overlying soft tissue swelling, and the patient did not exhibit midline tenderness. An MRI was subsequently performed, which again showed chronic-appearing spinous process fractures. The MRI was also notable for a diffuse decrease in marrow signal on T1, as well as diffuse hypointense signal in the adjacent subcutaneous fat. On the STIR sequence, there was increased signal throughout the bone marrow and adjacent fat. Clinical findings relevant to the diagnosis were hypoglycemia and hypokalemia. The patient had a medication bottle in her possession containing a white powder, which she stated was a laxative. She also reported having a rigorous exercise regimen. Given the imaging and clinical findings, the patient was diagnosed with serous atrophy of the bone marrow in the setting of anorexia nervosa.

Results

Figure 1. Sagittal CT image of the cervical spine demonstrates decreased osseous mineralization in the visualized bones. There are irregular, vertically oriented lucencies through the C7 and T1 spinous processes (yellow arrows) with sclerosis along the margins, suggestive of chronic fractures. There is no overlying soft tissue swelling. Figure 2. Sagittal MR images of the cervical spine demonstrate mild, diffuse decrease in marrow signal on T1 relative to the intervertebral discs, as well as diffuse hypointense signal in the adjacent subcutaneous fat. On the STIR sequence, there is abnormal increased signal throughout the bone marrow and the adjacent fat. Figure 3. Axial gradient echo image of our patient's spine (A) demonstrates abnormal increased signal within the fat surrounding the paraspinal musculature. An image of a normal spine (B) is shown for comparison, with normal dark signal within the fat.

Conclusions

Serous atrophy of the bone marrow, also known as gelatinous transformation of the bone marrow, is characterized by atrophy of fat cells, loss of hematopoietic cells, and replacement by extracellular gelatinous substances. It is associated with a wide variety of underlying conditions including anorexia nervosa, alcoholism, HIV/AIDS, malignancy, and cytotoxic drugs. It confers an increased risk of fractures and infection and has characteristic findings on MRI. It is important to be aware of this diagnosis, as the abnormal marrow signal is often misinterpreted as technical error and leads to unnecessary repeat imaging.



Figure 1

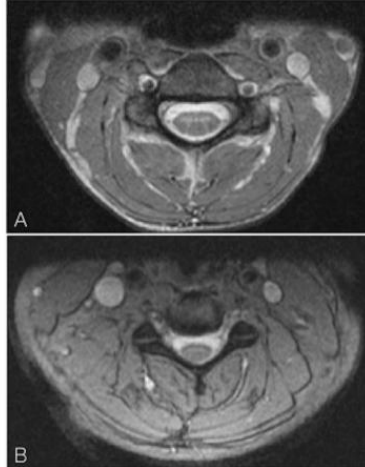


Figure 3

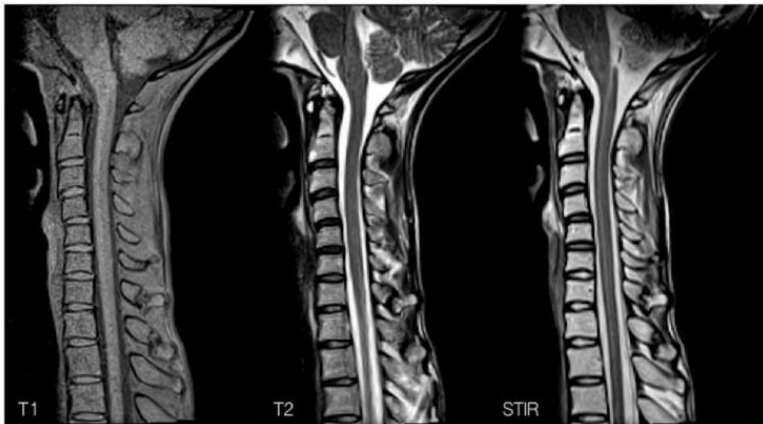


Figure 2

(Filename: TCT_E-96_Images.jpg)

E-97

11:34AM - 11:38AM

Subarachnoid and Intraventricular Fat Emboli Secondary to a Sacral Fracture Through a Perineural Cyst.

M Kozoriz¹, M Harmon², M Marangoni³, J Chew¹, J Shewchuk³

¹University of British Columbia, Vancouver, British Columbia, Canada, ²Burnaby General Hospital, Vancouver, British Columbia, Canada, ³Vancouver General Hospital, Vancouver, British Columbia, Canada

Purpose

Extra-axial fat is an uncommon finding and is usually secondary to a ruptured dermoid tumor. There are limited reports in the literature of transthecal fat emboli post fracture (1, 2). We present a case of intracranial fat emboli secondary to a sacral fracture with a suspected dural tear through a perineural cyst.

Materials and Methods

This previously well 43-year-old male presented to the emergency department shortly after sustaining a fall on his back while snowboarding. His symptoms on presentation consisted of increasing headache, nausea and vomiting. Beyond tenderness in the lower back, the neurological physical exam was unremarkable. The initial head CT was reported as normal. There was clinical concern for a CSF leak and MRI of the head and spine was subsequently performed. A suspected post-traumatic dural tear site was identified and this was successfully treated with a blood patch.

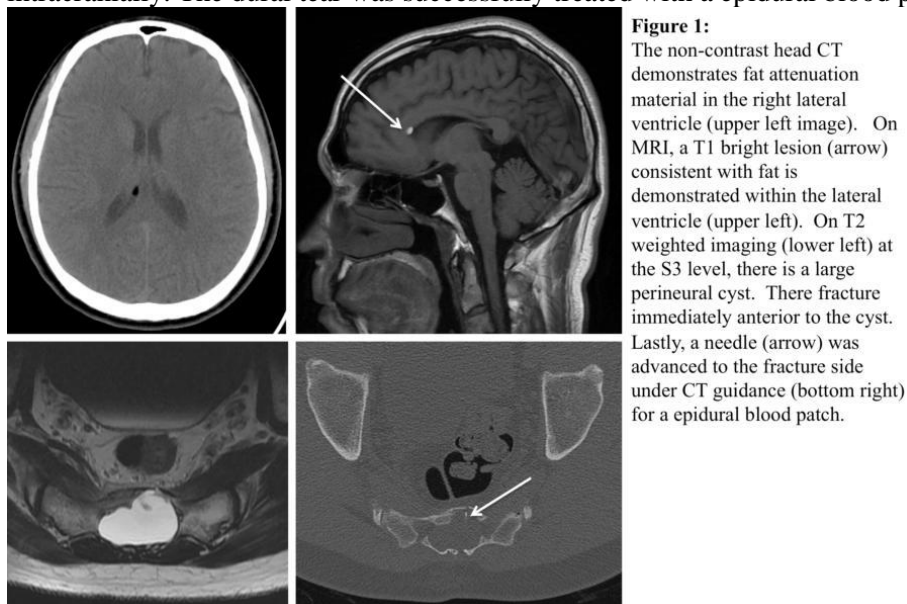
Oral Presentations & Excerptas

Results

On CT imaging, several foci of subarachnoid and intraventricular fat were retrospectively identified (Fig. 1). MRI (Fig. 1) demonstrates T1 hyperintense material within the extra-axial spaces, consistent with fat. On evaluation of the spine, an anterior sacral fracture at S3 was demonstrated. There was also bony remodeling of the underlying sacral neural foramen due to a large perineural cyst. Using a posterior approach, a needle was advanced through the perineural cyst to the site of fracture where an epidural blood patch was performed.

Conclusions

We report a rare case of a sacral fracture causing a perineural cyst dural tear with fat emboli extending intracranially. The dural tear was successfully treated with an epidural blood patch.



(Filename: TCT_E-97_Slide1.jpg)

Wednesday, June 6, 2018

1:15PM - 2:45PM

Parallel Paper Session: Advanced Techniques in Quantitative Imaging

O-393

1:15PM - 1:22PM

Pre-clinical Detection Based Spectral CT Scanner Produces Improved Intracranial Vascular Enhancement and Gray-White Matter Differentiation with Virtual Monoenergetic Reconstructions Compared to Conventional CTA.

A Jaster¹, W Moore¹, S Abbara¹, Y Xi¹, M Pinho¹

¹University of Texas Southwestern Medical Center, Dallas, TX

Purpose

To analyze quantitative image quality measures from initial brain CTA data collected from a preclinical detection-based spectral CT scanner (IQon, Philips Healthcare) to confirm the improvement in gray- and white-matter SNR and CNR and vascular enhancement demonstrated on prior studies utilizing alternative dual-energy technology. We evaluated the performance of quantitative image quality metrics of

Oral Presentations & Excerpts

intracranial vascular enhancement on several spectral virtual monoenergetic (VME) levels compared to conventional polychromatic images and compare quantitative measures of brain parenchymal image quality and gray-white matter differentiation on VME and polychromatic images as well. We hypothesized that VME spectral images would be significantly improved in all metrics.

Materials and Methods

In this IRB-approved, HIPPA-compliant, retrospective analysis 12 brain CTA scans were acquired with a preclinical detection-based spectral CT scanner (IQon, Philips Healthcare). The imaging data was reconstructed at VME energy levels from 40 to 90 keV at 5 keV increments and then from 90 to 140 keV at 10 keV increments. In addition, standard polychromatic conventional images were also reconstructed from the same acquisition. Five vascular regions of interest (ROI), which included the bilateral supraclinoid internal carotid arteries (ICAs), the M1 segments of the bilateral middle cerebral arteries (MCAs), and the basilar artery, three gray matter (GM) ROIs, and three white-matter (WM) ROIs were obtained at each VME energy level and on the conventional images at identical locations through colocalization techniques [total of 2,376 ROI measurements were made in this study]. The ROI measurements of CT attenuation were then analyzed with standard quality measures including: vascular signal-to-noise ratio (SNR), vascular-brain contrast-to-noise ratio (CNR), GM and WM SNR, and GM-WM CNR. Mean values from the conventional images were compared to the respective mean values on the VME images at each energy level via ANOVA with Dunnett adjustment for multiple comparison.

Results

We observed a progressive increase in the mean attenuation of GM, WM, and vascular structures from higher to lower VME energy levels with maximum GM, WM, and vascular attenuation obtained at 40 keV (Figure 1). Maximum GM SNR was observed at 40 keV with a progressive increase from 140 keV to 40 keV, but maximum WM SNR was seen at 65 keV; although, it should be noted that the WM SNR had a negligible slope across all energy levels. Maximum GM-to-WM CNR was observed at 40 keV with a progressive increase from 140 keV to 40 keV. Maximum vascular SNR and vascular-to-brain parenchyma CNR was observed at 40 keV with a progressive increase from 140 keV to 40 keV. VME had significantly better GM SNR relative to conventional images at energy levels 40-85 keV (all adjusted p values < 0.05). VME had significantly better WM SNR relative to conventional images at all energy levels (all adjusted p values < 0.0001). VME had significantly better GM-WM CNR relative to conventional images at energy levels 40-70 keV (all adjusted p values < 0.01) but statistically worse GM-WM CNR relative to conventional images 100-140 keV (all adjusted p values < 0.01). VME had significantly better vascular SNR relative to conventional images at energy levels 40-75 keV (all adjusted p values < 0.005) but significantly worse vascular SNR relative to conventional images at energy levels 100-140 keV (all adjusted p values < 0.005). VME had significantly better vascular CNR relative to conventional images at energy levels 40-70 keV (all adjusted p values < 0.001) but significantly worse vascular CNR relative to conventional images at energy levels 110-140 keV (all adjusted p values < 0.05).

Conclusions

The lower keV (40-70 keV) virtual monoenergetic reconstructions of brain CTA utilizing a preclinical detection-based spectral CT scanner created significantly better vascular enhancement differentiation and gray-white matter differentiation compared to conventional polychromatic images on the basis of all measured quality metrics, including GM SNR, WM SNR, GM-to-WM CNR, vascular SNR, and vascular-to-brain parenchyma CNR.

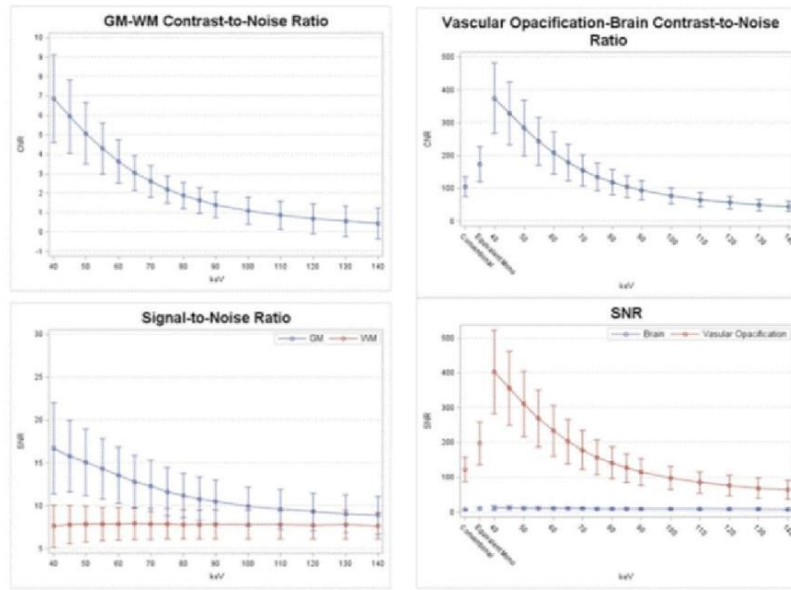


Figure 1: Graphs of quantitative metrics obtained from conventional polychromatic enhanced brain CTA and across multiple energy levels reconstructed from pre-clinical detection based spectral brain CTA. GM-WM metrics in the left column and vascular opacification-brain metrics in the right column.

(Filename: TCT_O-393_Figureabstractrevised.jpg)

O-394

1:22PM - 1:29PM

Dual Energy CT Iodine Markers for Assessment of Intracranial Hematoma Expansion Risk

C Tan¹, S Lam¹, D Kuppens², B Parameswaran³, R Forghani⁴, R Hu⁵, L Daftari Besheli⁶, J Goldstein¹, J Thrall⁷, M Lev⁸, J Romero⁷, R Gupta⁷

¹Massachusetts General Hospital and Harvard Medical School, Boston, MA, ²University of Twente, Enschede, N/A, ³Imaging Associates, Victoria, N/A, ⁴Jewish General Hospital & McGill University, Montreal, Quebec, ⁵Emory University, Atlanta, GA, ⁶University of Texas Health San Antonio, San Antonio, TX, ⁷Massachusetts General Hospital, Boston, MA, ⁸Massachusetts Gen'l Hosp./Harvard Med. Schl., Boston, MA

Purpose

While the spot sign on conventional single-energy CT is highly specific for hematoma expansion, its test characteristics are not optimal (Del Giudice et al., 2014; Du et al., 2014). In this study, we assessed the utility of dual-energy CT (DECT) and quantitative analysis of iodine extravasation for improving the diagnostic accuracy of CT in the prediction of hematoma expansion.

Materials and Methods

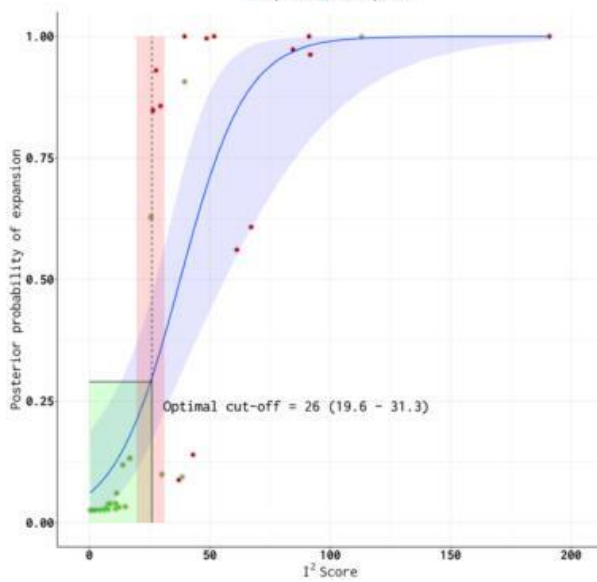
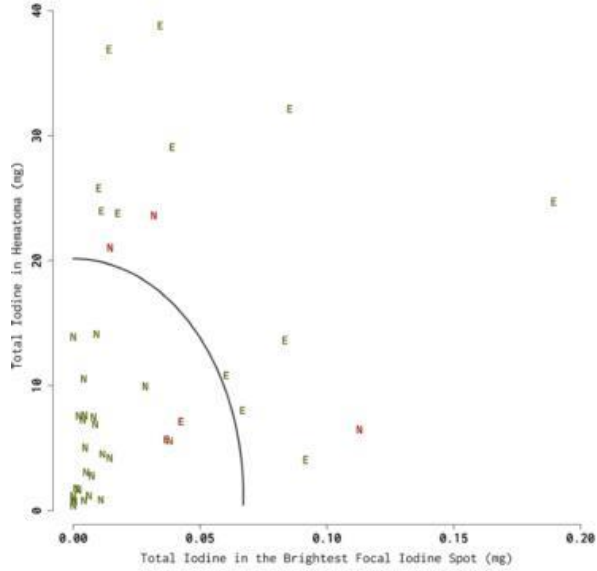
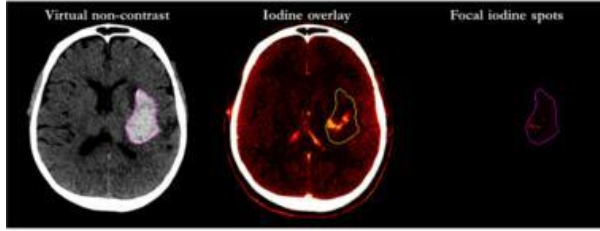
In 42 patients referred for DECT assessment of intracerebral hemorrhage (ICH) between October 2014 and January 2017, we used a machine-learning approach to automatically identify the hematoma and quantify iodine extravasation within the hematoma. Selected parameters of iodine extravasation were then used to predict the risk of hematoma expansion (Figure, upper panel). Specificity and sensitivity of these parameters were then prospectively validated on 25 new patients referred from February 2017 through June 2017.

Results

Our approach identified two features of iodine extravasation – total iodine concentration in the hematoma and iodine in focal iodine "spots" within the hematoma – as the most robust predictors of expansion (Figure, middle panel; E: expander, N: nonexpander, solid curve: boundary of classification). A score derived from these two variables, "I2 score", provided a measure of the probability of hematoma expansion on a case-by-case basis (Figure, lower panel). The optimal threshold for classification was $I_2=26$ (20 – 30; 95% C.I.), which lead to the correct identification of 37 (88.1%) of the cases (0.80 sensitivity and 0.86 specificity; area under the ROC curve 0.94 [0.87–1.00; 95% C.I.]) in the original data set, and 80% of the cases (0.80 sensitivity and 0.80 specificity; area under the ROC curve 0.86) in the prospective independent test data.

Conclusions

Our study describes and prospectively validates two novel markers of iodine extravasation on DECT imaging. When used together, these markers can help predict the risk of ICH expansion and thus help select patients for targeted therapy.



(Filename: TCT_O-394_ASNR2018_abstract_DECT_figure.jpg)

O-395

1:29PM - 1:36PM

Dual-energy CT Angiography-derived Virtual Non-contrast Images in Patients with Surgically Clipped Aneurysms

Y Heo¹, H Jeong¹, J Baek¹

Oral Presentations & Excerptas

¹*Inje University Busan Paik Hospital, Busan, Republic of Korea*

Purpose

CT angiography has been used in the evaluation of aneurysms after surgical clipping. However, repeated CT studies are associated with increased radiation hazards. The virtual unenhanced images (VNC) are reconstructed from dual-energy CT (DE-CT) angiography without additional radiation dose. The purpose of our study was to evaluate image quality and diagnostic performance of VNC and compare with true nonenhanced images (TNE) in the patients with surgically clipped aneurysms.

Materials and Methods

Ninety-two patients who underwent unenhanced CT and DE-CT angiography after surgical clipping for intracranial aneurysms were included (8 ACA, 11 A-com, 49 MCA, 15 distal ICA, 9 multiple). For quantitative analysis, image noises were measured on both VNC and TNE images in centrum semiovale, cerebellum and pons. For qualitative analysis, image noise, image quality (1: excellent, 2: sufficient, 3: insufficient), diagnostic confidence (1: nondiagnostic, 2: poor, 3: moderate, 4: good), level of acceptance (1: complete, 2: with restriction, 3: not acceptable), presence of artifact and severity of clip artifact (1: extensive, 2: moderate, 3: minimal, 4: no artifact) were measured. The CT dose index and dose-length product were recorded for the radiation dose analysis.

Results

Contrast-to-noise ratio of VNC was higher than those of TNE in centrum semiovale, cerebellum, pons ($p=0.000$). The image quality of VNC was excellent in 77.1% and sufficient in 20.7%. The diagnostic confidence of VNC was good in 76.0% and moderate in 21.7%. Level of acceptance of VNC was complete in 87.2% and with restriction in 22.8%. However, the addition of contrast-enhanced images from DE-CT increases the level of acceptance 97.8%. The clip artifacts were significantly lower in VNC than TNE. The CT dose index and dose-length product were markedly reduced without acquisition of TNE images.

Conclusions

VNC showed lower image quality and more image noise than TNE images, but it has advantages of reducing clip artifact and radiation dose. It has a potential to replace TNE images in follow-up of patients with surgically clipped aneurysms.

O-396

1:36PM - 1:43PM

Longitudinal Analysis of Quantitative Brain MRI in Astronauts Following Microgravity Exposure

R Riascos¹, A Kamali¹, L Kramer¹, P Rabiei¹, K Hasan¹

¹*The University of Texas Health Science Center at Houston, Houston, TX*

Purpose

To retrospectively evaluate the effects of microgravity on the brains of astronauts by obtaining and analyzing macro and microstructural measures using quantitative magnetic resonance imaging (qMRI), before and after microgravity exposure. We hypothesize that subtle structural change, manifested by alterations in diffusion-tensor imaging (DTI) metrics including fractional anisotropy and mean diffusivity, will affect regions involved in visual function.

Materials and Methods

Quantitative MRI data sets in 19 astronauts were acquired before the flight and repeated after completion of each mission. Both anatomical (volumetric) and microstructural (diffusion-tensor imaging-based) measures were analyzed. Paired t-tests were used to compare pre and postflight measures. Pearson correlation coefficient and linear regression were used to test the association of qMRI measures with age of the astronauts.

Results

An overall increase in lateral ventricular volume in the postflight scans was found. The volume of

Oral Presentations & Excerptas

thalamus proper showed some reduction predominantly on the right side. The fractional anisotropy was reduced in the right posterior thalamic radiation. An increased mean diffusivity in the occipital cortex on the right side, mostly seen in the fusiform gyrus was noted. There was also cortical thinning involving the bilateral fusiform gyri and right occipital lobe. The changes of the cortical thickness in the fusiform gyri were independent of the crew members' ages.

Conclusions

Our findings could be secondary to microgravity-induced intracranial hypertension, intracranial fluid redistribution, brain volume loss, microanatomic changes, rearrangement of the white matter or psychological stress during space flight. This study may provide neuroanatomical evidence of brain dysfunction or neuroplasticity in microgravity conditions and may offer an improved understanding of the mechanisms involved in intracranial pressure elevation and vision changes in a subset of crewmembers (1). Further research is still needed to corroborate some of the mechanisms proposed in this study.

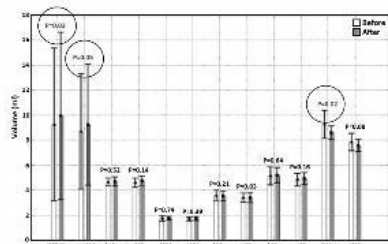


Figure 1. Post-flight volumetric data compared with the pre-flight baselines

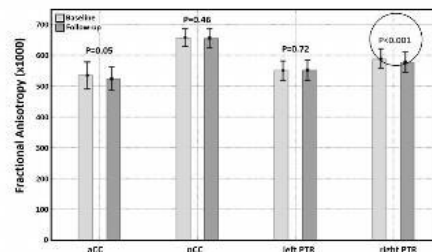


Figure 2. Fractional anisotropy of selected white matter regions

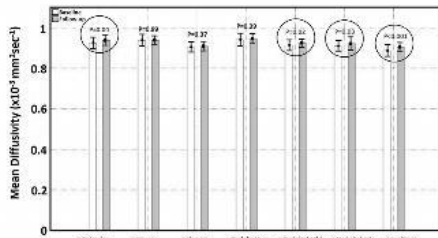


Figure 3. Mean diffusivity in the right occipital cortical domains

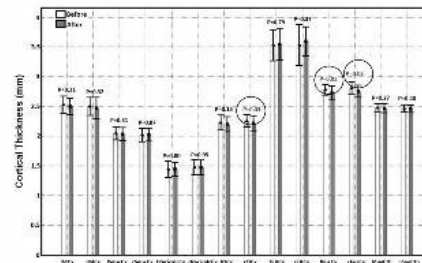


Figure 4. Post-flight vs. pre-flight total and regional cortical thickness

- LVCSF= lateral ventricular CSF, HC=hippocampi, AM=amygdalae, CN=caudate nuclei, PT=putamina, THP= thalamus proper, aCC= anterior corpus callosum, pCC=posterior corpus callosum, PTR= posterior thalamic radiation
- Fusiform= fusiform cortex, Motor= motor cortex, Sensory= sensory cortex, Pericalcarine=peri-calcarine cortex, Occipital= occipital cortex, ERCh=entorhinal cortex, AvgCth=average of hemispheric cortical thickness
- "r" and "l" before the name of the brain regions are referring to the right and left respectively

(Filename: TCT_O-396_dti-BW_700dpi.jpg)

O-397

1:43PM - 1:50PM

Utility of Minimum and Maximum Intensity Projection Images From 3D Volumetric Sequences For Detection of Focal Cortical Dysplasias

D Martin¹, B Yoon¹, M Penta¹, M Iv¹
¹Stanford University Medical Center, Stanford, CA

Purpose

Focal cortical dysplasias (FCD) are a rare but important source of epilepsy. These lesions are often subtle and can be missed on MRI. Given the numerous images associated with 3-D volumetric sequences

Oral Presentations & Excerptas

typically acquired in epilepsy protocol MRIs, we investigate the utility of overlapping maximum and minimum intensity projections (MIP and MinIP, respectively) of high-resolution sequences for the detection of FCDs.

Materials and Methods

In this IRB-approved retrospective case-control study, 10 patients with a clinikoradiologic or pathologic diagnosis of FCD and 10 normal controls were identified. Each patient had an epilepsy protocol MRI containing 3-D T1-weighted IR-SPGR/BRAVO and 3-D CUBE T2-FLAIR images. Five mm (slice thickness) x three mm overlapping axial MIPs of the CUBE T2-FLAIR and MinIPs of the T1 IR-SPGR/BRAVO images were created, and both the reconstructions and source images were reviewed by two neuroradiologists. For each pair of image types, time of interpretation was recorded and analyzed with a paired t-test. Confidence scores were assessed using a 5-point Likert scale. Interrater agreement for the presence of FCD was assessed with Cohen's kappa, and diagnostic accuracy was assessed with receiver operating characteristic (ROC) curve analysis.

Results

Time of interpretation was decreased significantly for the MIP and MinIP reconstructions in comparison to source images for both readers (60 vs. 122 seconds for reader 1, 28 vs. 45 seconds for reader 2, both $p < 0.001$). The sensitivity, specificity, and accuracy were unchanged for the reconstructions compared to the source images (0.9, 1.0, and 0.95 respectively). Interrater agreement for the presence of FCD was very high ($\text{kappa} = 0.8$). The confidence score for both readers was high (mean=4).

Conclusions

The use of MIP and MinIP reconstructions of 3-D volumetric sequences provided equivalent diagnostic accuracy with significant time savings for the detection of FCDs when compared to the high-resolution source images.

O-398

1:50PM - 1:57PM

On the potential role of fast multispectral qMRI and synthetic MRI in ischemic stroke patients with unknown time of onset

O Sakai¹, V Andreu¹, M Chapman¹, K Onoue¹, M Horn¹, H Jara¹

¹*Boston Medical Center, Boston University School of Medicine, Boston, MA*

Purpose

More than 25% of the patients with infarct are excluded from thrombolysis due to unknown time of onset. Standard MRI brain stroke protocols include DW-SE-sshEPI images that are sensitive for demonstrating the earliest (hyperacute) changes as restricted diffusion, and T2w-FLAIR images can demonstrate subsequent (acute) changes as decreased T2 dephasing. It is known that a large proportion of nocturnal stroke patients with unknown time of onset have a DW-FLAIR mismatch suggesting a more recent stroke onset than "last known well time." A question is if T2w-FLAIR is the most informative companion to DW-SE-sshEPI scan. Multispectral (MS) qMRI probes multiple parameters simultaneously -T1, T2, proton-density (PD), and correlation time diffusion coefficient (Dct)- with the same spatial resolution of T2w-FLAIR. MS-qMRI also has the potential of showing ischemia related changes in the pure parameter maps and can be used to synthesize T2w-FLAIR images. The purpose of this study was to assess potential benefits of MS-qMRI in the context of stroke onset time estimation.

Materials and Methods

This is an IRB-approved retrospective study. MR images of 20 patients with acute or subacute infarct were qMRI processed with T1, T2, PD, and Dct algorithms (Mathcad, PTC, Needham, MA). MRI was performed at 1.5T with the Tri-turbo spin echo (Tri-TSE) pulse sequence: concatenation of single- and dual-echo TSE.

Results

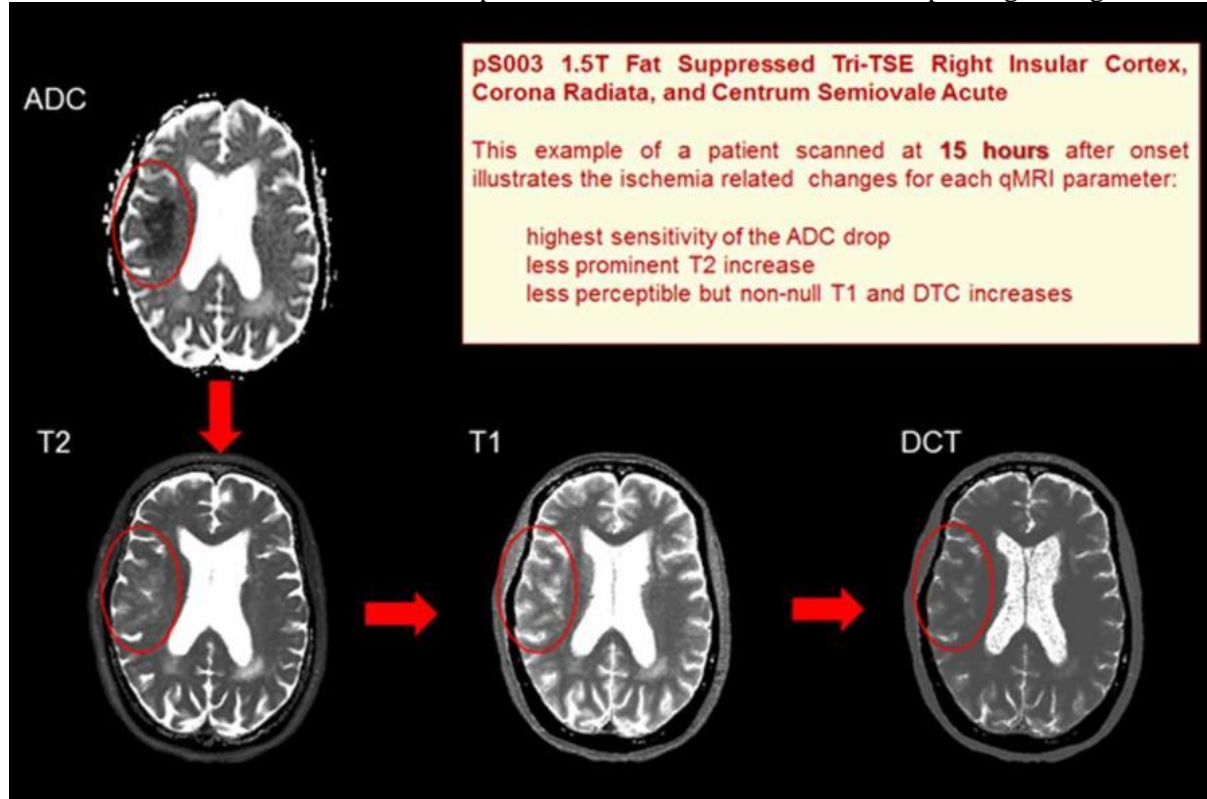
MS-qMRI maps and synthetic FLAIR images revealed the same lesions as the directly acquired T2w-

Oral Presentations & Excerptas

FLAIR. In addition, the following temporal trend was observed from early to late: ADC, then qT2 thus explaining the sensitivity of T2w-FLAIR, and later (qT1 and Dct) which are interrelated and appear to be the least sensitive to early molecular changes resulting from ischemia (Figure).

Conclusions

Fast MS-qMRI with the Tri-TSE pulse sequence or variants could provide crucial time-of-onset information for the evaluation of stroke patients and therefore contribute to improving management.



(Filename: TCT_O-398_Untitled-1.jpg)

O-399

1:57PM - 2:04PM

Comparison of Velocity-selective and Pulsed ASL Perfusion MRI in Patients with Suspected Cerebral Cortical Ischemia

D Bolar¹, B Rosen², P Schaefer¹

¹Massachusetts General Hospital, Boston, MA, ²Athinoula A. Martinos Center for Biomedical Imaging, Charlestown, MA

Purpose

Traditional pulsed ASL (PASL) suffers from arterial transit delay (ATD) effects, often resulting in inaccurate perfusion measurements in cerebral ischemia and steno-occlusive disease (Figure 1) (1). Velocity selective ASL (VSASL) is a newer ASL variant that accurately measures perfusion independent of ATD, since the magnetic label is created within the imaging slab and delivered immediately to target microvasculature (2). The purpose of this study is to compare VSASL and PASL perfusion in patients with suspected cerebral cortical ischemia.

Materials and Methods

Subject selection: Forty-two patients with suspected cerebral cortical ischemia scanned with an ASL protocol were considered for this IRB-approved study. Fifteen were excluded due to motion, leaving a

Oral Presentations & Excerptas

total of 27 patients (ages 7–90; 15M, 12F). Fifteen of these patients had subsequent CT or MR neuroimaging. Acquisition/image processing: MR imaging included VSASL, PASL, and conventional DWI, FLAIR, and susceptibility sequences. VSASL-specific parameters were $V_{\text{cutoff}}=2.1\text{cm/s}$ and $TI=1100\text{ms}$ (3). PASL-Q2tips specific parameters were $TI_1=800\text{ms}$, $TI_{1,\text{stop}}=1600\text{ms}$, $TI_2=2000\text{ms}$, and label width=150mm. PASL parameters were chosen based on ASL white-paper recommendations for patients (4). Most scans were acquired with a 2-D-EPI module: $TE/TR=13/3000\text{ms}$, $3.5\times 3.5\times 5.0\text{mm}^3$ voxels, 16 slices, $BW=2365\text{Hz/pixel}$, scan time=3.1m. A few scans were acquired with a 3-D-GRASE module: $TE/TR=21/3000\text{ms}$, $3.2\times 3.2\times 4.0\text{mm}^3$ voxels, 24 slices, $BW=2440\text{Hz/pixel}$, scan time=3.3m. Data Analysis: Two neuroradiologists (a second year fellow and senior attending) independently graded the ASL perfusion maps, considering five cortical vascular territories per hemisphere: ACA, frontal MCA, temporal MCA, parietal MCA, and PCA. A territory received a "0" for a perfusion deficit or "1" for normal perfusion without deficit. A Kappa statistic was calculated to assess interrater agreement. The territories were also evaluated for significant ischemia-related abnormalities on 1) concurrently performed conventional sequences and 2) subsequent MR/CT imaging (if available) or by clinical assessment.

Results

Table 1 summarizes ASL grading, abnormalities on concurrent conventional imaging, and new abnormalities by subsequent imaging and/or clinical assessment. Normal PASL and VSASL cortical perfusion had nearly perfect negative predictive value for current or subsequent ischemic changes. Abnormal PASL perfusion, however, had a high false-positive rate (25% to 35%) for associated ischemic changes and 100% of the PASL false positives had normal VSASL perfusion. Conversely, VSASL demonstrated ~0% false-positive rate. Substantial agreement and almost perfect agreement was found between raters for PASL ($K=0.68$) and VSASL ($K=0.86$), respectively. Figure 2 provides a representative example of a patient with significant PASL abnormality, but with preserved VSASL and normal DWI, FLAIR, and susceptibility imaging. Figure 3 provides data from the one case noted to have a matched PASL/VASL abnormality and associated susceptibility findings, with a matching clinical syndrome.

Conclusions

Normal VSASL and PASL perfusion have a high negative predictive value for current and future ischemia in this small population with suspected cerebral cortical ischemia. PASL, however, has a very high false-positive rate for ischemia, likely due to ATD errors. VSASL demonstrates ~0% false positive rate for ischemia, and these preliminary data suggest that VSASL deficits may correlate with ischemic changes on conventional imaging.

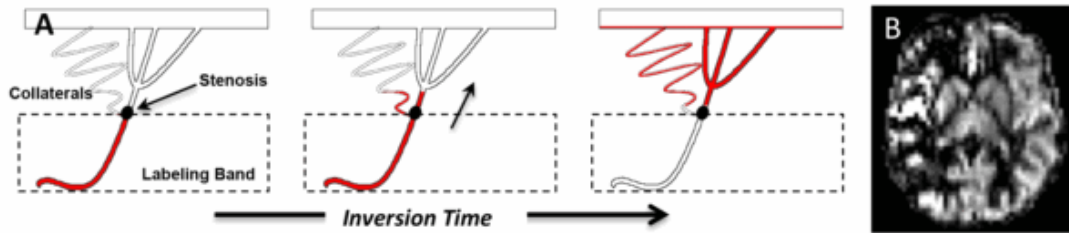


Figure 1. Standard ASL can result in inaccurate perfusion measurement in settings of arterial transit delays (ATD), since the magnetic label fails to reach the imaging slice during the inversion time (A). This manifests in apparent perfusion deficits and large-vessel artifacts (on the right in this example) (B).

<i># of cortical vascular territories across 27 patients with:</i>				
<i>Rater</i>	PASL deficit	<i>Within deficit: Abnormality on conventional imaging</i>	<i>Outside of deficit: Abnormality on conventional imaging</i>	<i>New abnormality on f/u imaging or by clinical assessment</i>
1	72/270	4/72	0/198	0
2	93/270	4/93	0/173	0
VSASL deficit				
1	4/270	3/4	1/267	0
2	3/270	3/3	1/266	0

Table 1. Number of territories with PASL or VSASL deficit, number of associated conventional imaging abnormalities within the deficit and outside of the deficit, and number of new abnormalities on follow-up imaging or by clinical assessment.

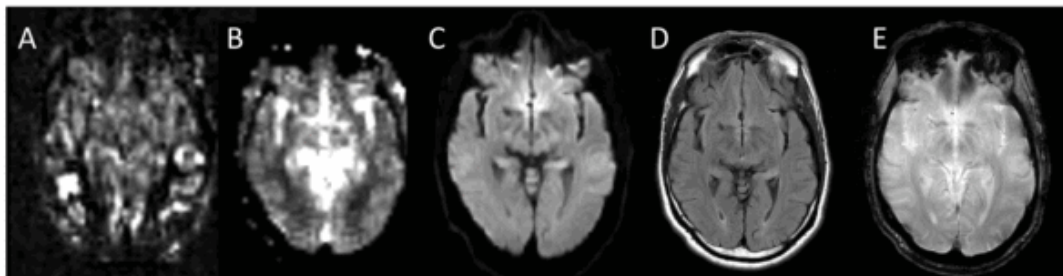


Figure 2. Patient with impaired PASL MCA perfusion (A), but with normal VSASL perfusion (B) and no abnormalities on DWI (C), FLAIR (D), and susceptibility (E) imaging.

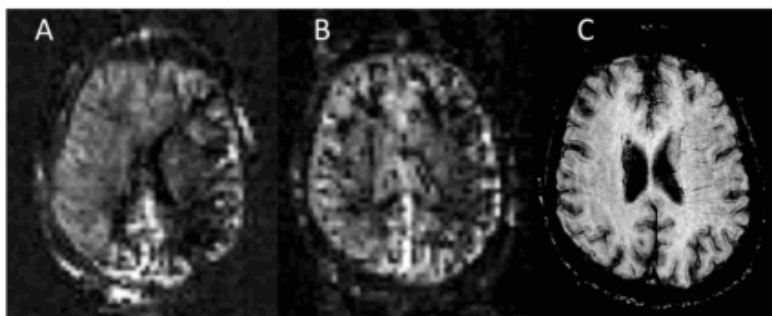


Figure 3. Patient with left MCA PASL (A) and VSASL (B) perfusion deficits and exaggerated left-sided vessels on susceptibility imaging (C) suggestive of increased oxygen extraction secondary to hypoperfusion. The patient exhibited blood-pressure-dependent left-sided weakness (without frank infarct).

(Filename: TCT_O-399_CroppedFig1.gif)

Quantitative Susceptibility Mapping of Intracranial Calcification and Hemorrhage: Preliminary Results from a Human Trial

M Jacobsen¹, K Hwang¹, L Le Roux¹, D Cody¹, D Schellingerhout¹

¹University of Texas MD Anderson Cancer Center, Houston, TX

Purpose

Intracranial lesions presenting with susceptibility effects on T2*-weighted Gradient Recalled Echo (T2* GRE) may be either calcific (diamagnetic, negative susceptibility) or hemorrhagic (paramagnetic, positive susceptibility). The purpose of this trial was to classify intracranial susceptibility lesions into these categories.

Materials and Methods

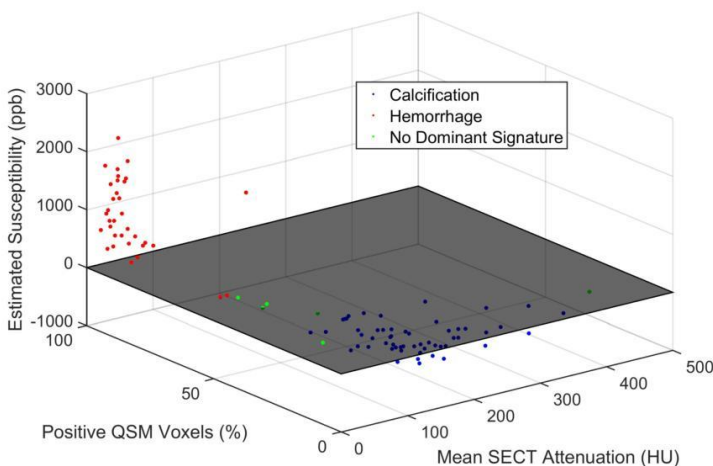
Fifteen patients with susceptibility lesions on T2* GRE were recruited into this IRB-approved trial. Patients underwent both CT and MRI with 3-D T1-weighted Fast Gradient Echo and 3D Multiecho Fast GRE (MFGRE) to perform Morphology-Enabled Dipole Inversion (MEDI) Quantitative Susceptibility Mapping (QSM). All images were coregistered and lesions were segmented on the first echo of the MFGRE (TE = 4.5 ms). Regions-of-interest were applied to the QSM and CT images, and mean susceptibility (ppb) and Hounsfield Unit (HU) were recorded for each lesion. Lesions were classified as calcific on MR when greater than 60% of voxels on QSM were negative and hemorrhagic if greater than 60% of voxels on QSM were positive, with no dominant magnetic signature otherwise. The presence of calcification was confirmed by SECT (mean HU > 100), with hemorrhage assumed otherwise.

Results

Ninety-six susceptibility lesions were identified. By QSM, 56 lesions were classified as calcifications (-121 +/- 89 ppb), 34 as hemorrhage (877 +/- 533 ppb), and six lesions had no dominant signature (76 +/- 156 ppb). Two lesions without dominant magnetic signatures were classified as calcifications on both SECT and had a negative mean susceptibility (118 HU and 438 HU; -23.8 ppb and -117 ppb), and three were classified as hemorrhage by SECT and mean susceptibility. The last lesion had discordant classifications between the modalities. QSM-defined calcifications featuring dominant magnetic signals had HUs as low as 67 HU.

Conclusions

QSM and CT agreed on the classification of known calcific lesions, and may allow for imaging-based classification of susceptibility lesions of calcifications below the SECT threshold of 100 HU.



(Filename: TCT_O-400_QSM3Dsuscept_perposQSM_MeanSECT.jpg)

O-401

2:11PM - 2:18PM

Axonal water fraction (AWF)-based corpus callosum registration for voxel-wise analysis: a diffusion study

S Chung¹, Y Lui¹

¹*New York University School of Medicine, New York, NY*

Purpose

The corpus callosum (CC) is the largest commissural fiber bundle, connecting two hemispheres. It is composed of many different anatomic white-matter (WM) tracts; larger axonal density with smaller fibers in the anterior CC, lower axonal density with larger fibers near the posterior body, and larger axonal density with mixed fibers in the posterior CC (Fig.1A). (1) However, changes of these fiber composition may not be well-aligned in the standard space by using conventional fractional anisotropy (FA)-based registration approaches because FA is inherently a nonspecific measure affected by multiple different microstructural features. (2) These measurements over slightly mismatched areas can lead to less accurate results during a voxel-wise analysis, especially along the CC. Here, we present a new registration approach, specifically for the CC regions, based on axonal water fraction (AWF)³ which is known to sensitive to axonal volume/density (Fig.1B).

Materials and Methods

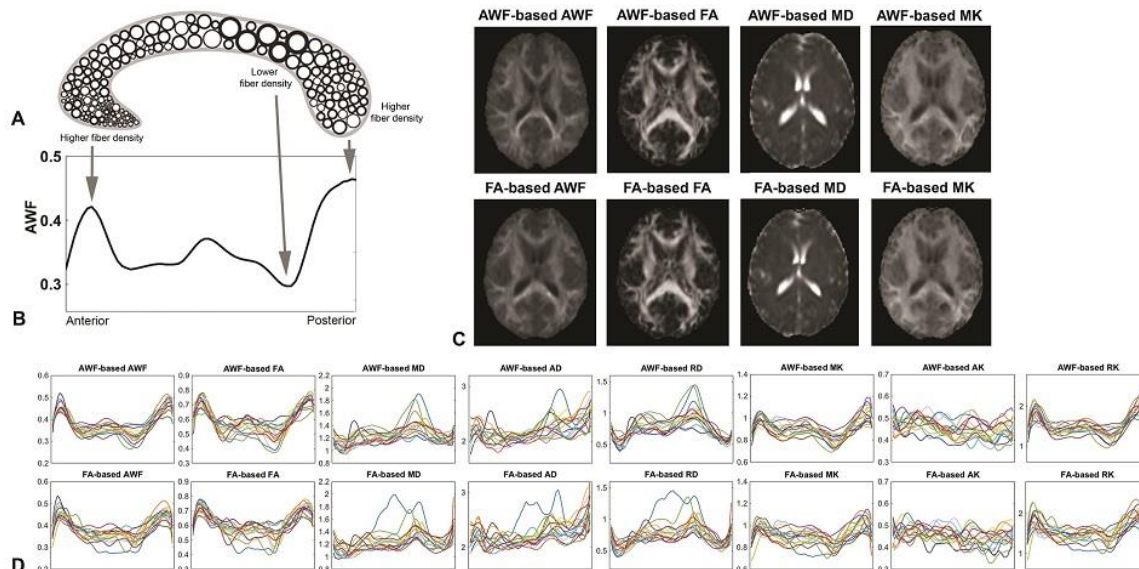
We studied 15 normal controls (31 ± 7 , 19-45 yrs; 7 males). Multishell diffusion imaging was performed on a 3T MR scanner (Skyra, Siemens) with five b-values (upto $2.5 \text{ms}/\mu\text{m}^2$, 60 directions). AWF was derived from a WM modeling. (3) Seven diffusion (FA,MD,AD,RD) and kurtosis (MK,AK,RK) metrics were tested. Subject's diffusion maps were registered to a standard space by using FA and AWF maps. Mean values on midsagittal regions (six slices) along the CC were calculated in a standard space, for comparison.

Results

Fig.1C shows AWF-based (top) and FA-based (bottom) maps in a standard space. Fig.1D shows plots of mean values of AWF-based (top) and FA-based maps (bottom) along the CC. The most different regions between two approaches were anterior and posterior body of the CC.

Conclusions

AWF has a potential to be used as a new registration approach specifically for the CC since AWF reflects underlying axonal volume/density. Better aligned diffusion maps would improve accuracy of voxel-wise analysis for the CC regions.



(Filename: TCT_O-401_figure1.jpg)

O-402

2:18PM - 2:25PM

Reversing the Frequency Encoding Direction in Brain MRI Mitigates Susceptibility Ghost Artifact caused by Dental Metal.

C McNair¹, A Huang¹, N Kagetsu¹

¹Mount Sinai St. Luke's West, New York, NY

Purpose

To investigate the frequency of dental metal induced brain MRI susceptibility ghost artifact. To determine the effect of reversing the frequency encoding direction on this artifact's negative impact on image quality and interpretation.

Materials and Methods

We retrospectively reviewed brain MRI cases in patients over age nine performed during the month of June 2016 at four hospitals within one hospital system. We determined the percentage of studies that showed dental metal induced susceptibility ghost artifact. A metal clip was mounted on an ACR head phantom to replicate susceptibility ghost artifact on an Optima MR450w 70cm 1.5T MR (Vendor A). Axial T2 FSE, T2 FLAIR, and T1 FLAIR images were acquired using both standard and reverse frequency encoding direction protocols. This same procedure was implemented on an MR Systems Ingenia 1.5 High Field Magnet (Vendor B).

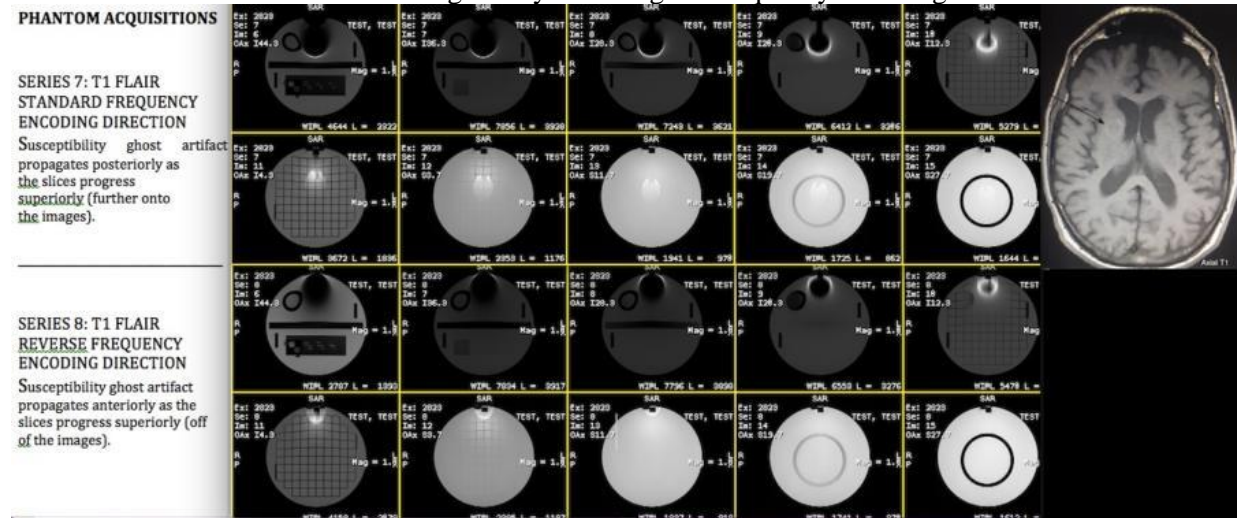
Results

Susceptibility ghost artifact was present in 2.8% of 144 total brain MRI studies (Standard Error= 0.0137, 95% CI = 0.000936 to 0.0546). Artifact was apparent on T1-weighted images in 100% of the positive studies, on T2 FLAIR in 75%, and on T2-weighted images in 75%. On phantom acquisitions using both machines, susceptibility ghost artifact was appreciated on T1 FLAIR and T2 FLAIR. Using standard frequency encoding direction propagated the artifact posteriorly as the slices progressed superiorly, causing the artifact to progress from anterior to posterior (onto the brain). Reversing frequency encoding direction propagated the artifact anteriorly as the slices progressed superiorly, causing the artifact to travel off of the region of interest.

Conclusions

Susceptibility ghost artifact from dental metal has been described previously. The ability to reverse

frequency encoding direction is a relatively new feature that is potentially underused. We show how artifact from dental metal can be mitigated by reversing the frequency encoding direction.



(Filename: TCT_O-402_ASNRJPEGImageDentalArtifact.jpg)

O-403

2:25PM - 2:32PM

A Novel Computer Vision Voxel Based Imaging Tool for Surgical Planning in Skull Base Tumors

A Davis¹, A Brunswick¹, K Drysdale², M Wong¹

¹New York University Langone Medical Center, New York, NY, ²Surgical Theatre, Brooklyn, NY

Purpose

Parasellar skull-base lesions present formidable surgical challenges. Often, these lesions reside within surgical blind spots obscured by vasculature, cranial nerves or bony structures, necessitating additional bony removal and/or mobilization of these structures. The choice of surgical approach plays a pivotal role in maximizing the extent of resection and minimizing morbidity. An optimal approach allows for a trajectory that eliminates or minimizes the volume of a lesion within a surgical blind spot, and decreases the degree of mobilization of soft tissue structures at the skull base. Prior studies have compared different surgical approaches to the parasellar region. They concluded that there is no significant difference in these parameters between the commonly used skull-base approaches. This study introduces an imaging-based, computer-aided protocol that seeks to customize the surgical approach for a given middle skull-base lesion. Imaging-based volumetric analysis of the relationship of the lesion to its adjacent bony and soft tissue structures allows for the comparison of the amount of lesion that would occupy surgical blind spots via different surgical approaches. This knowledge will aid preoperative planning by providing the surgeon with a well defined and customized anatomic approach to a given lesion, potentially minimizing surgical morbidity and diminishing the chance of subtotal resection. Three commonly used transcranial surgical approaches to the parasellar region were compared: pterional, supraorbital and midline subfrontal. A volumetric analysis of the parasellar region and its contents was performed. This analysis allows for a direct comparison of the volume of the surgical blind spot resulting from each surgical approach and demonstrates their precise anatomic location. In this way the different surgical approaches can be compared.

Materials and Methods

In the first phase of the study, three surgical approaches were compared using four cadaver specimens, functioning as an anatomically normal control group. For each specimen, a high-resolution volumetric T2-weighted image of the whole brain, as well as a high-resolution CT were acquired. The T2 and CT

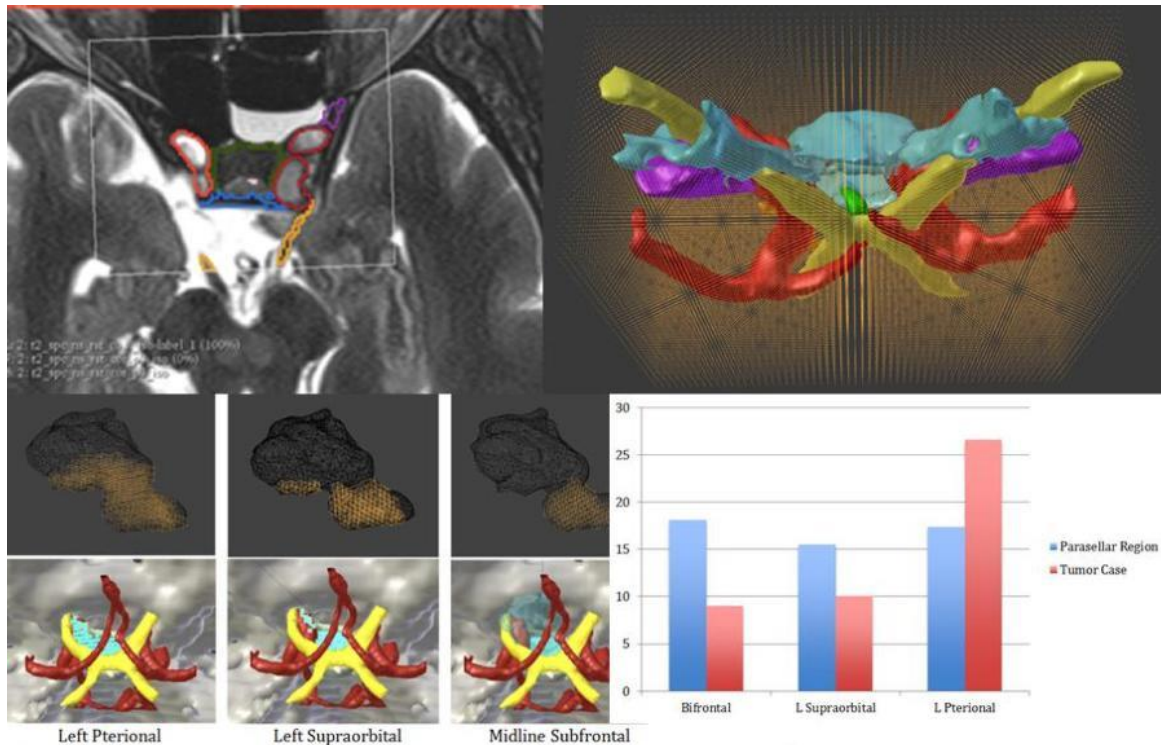
data sets for each specimen were coregistered using the Transformation module in 3D Slicer, based upon the sella turcica and surrounding osseous structures as landmarks. Once aligned, a 3-D representation of the specimen was generated using the volume rendering module in 3-D Slicer. A 3-D target region of interest (ROI) surrounding the parasellar area was created using standardized anatomical landmarks and the relevant skull-base structures within this ROI were manually segmented by a neuroradiologist using the Editor module in open-source 3-D Slicer software version 4.6.2 (Boston, MA). The ROI and critical structures created from both the MR and CT data were exported as .OBJ file formats and imported into the open-source software Blender version 2.78 (Amsterdam, Netherlands) software for the remainder of the analysis. Blender was used to create a 3-D map of every voxel within the ROI described above, along with the included segmented structures. This allowed the individual voxels that were not visible to be selected and used to calculate the volume of the surgical blind spot. This was repeated for each of the three approaches and compared. For the clinical tumor case the same imaging analysis was utilized. Only the tumor voxels were mapped in the Blender model. The same postprocessing analysis was used to select the tumor voxels that were not visible within a given approach. These voxels were both calculated and displayed and the three surgical approaches were then compared.

Results

Both the cadaver and the clinical case demonstrated the feasibility of image-based computer-determined surgical guidance. Location and volume of blind spots created by bone and critical structures could be easily demonstrated and compared via numerical and volumetric display. For the cadaver case, the left supraorbital approach yielded the best overall access to the selected parasellar region, followed by the left pterional approach and lastly the midline subfrontal approach. For the clinical tumor case the midline subfrontal approach yielded the fewest tumor voxels within a surgical blind spot, followed by the supraorbital approach and lastly the left pterional approach. The relative volume of tumor voxels within surgical blind spots is demonstrated in Table 1.

Conclusions

This study demonstrates using both cadaver and a real clinical case the feasibility of preoperative image-based computer-aided analysis to determine the optimal surgical approach customized for any individual parasellar skull-base lesion. Volume and location of surgical blind spots can be demonstrated by volume rendering in a graphical style or compared numerically. Surgical simulation may help to maximize surgical benefit and reduce surgical morbidity. The technique in this study was applied to complex skull-base tumors but is applicable to any intracranial lesion. While this study was based only on CT and MRI anatomy, the potential benefit of incorporating other imaging information including DTI and functional MRI is clear.



Segmentation of structures by T2 imaging (top left). Voxel map of parasellar region from cadaver; each dot representing the epicenter of a 1mm³ region (top right). Voxel maps showing tumor that lies within surgical blind spots with each surgical approach (bottom right). Percentage of tumor voxels that lies within the surgical blind spot from both cadaver case (blue) and tumor case (red) (bottom right).

(Filename: TCT_O-403_FigureforImageBasedSurgicalGuidanceJPEG.jpg)

O-404

2:32PM - 2:39PM

Texture Analysis Utilization for Differentiating Pituitary Adenomas and Normal Pituitary Gland

V Tsehmaster Abitbul¹, R Thornhill¹, R Glikstein²

¹The Ottawa Hospital University of Ottawa, Ottawa, Ontario, Canada, ²University of Ottawa, Ottawa, Ontario, Canada

Purpose

Pituitary adenomas account for approximately 90% of the pathology affecting the pituitary gland. Although MRI of the sella turcica is considered the standard of care for evaluating pituitary adenomas, there are cases when the MRI results remain equivocal. Quantitative texture analysis has shown considerable promise for characterizing intracranial neoplasms. Our purpose was to evaluate the performance of quantitative textural features for differentiating pituitary adenomas from normal glandular tissue.

Materials and Methods

This retrospective study included 48 patients with pathologically and/or laboratory-proven pituitary adenomas diagnosed between January 2013 and December 2015. The control group consisted of 35 patients who underwent MRI of the sella, which were assessed to be negative for pituitary pathology. Pituitary adenomas (lesions) and normal glands (control) were manually segmented and saved as regions-of-interest (ROI) for subsequent texture analysis. We extracted textural features related to the grey-level histogram, grey-level co-occurrence (GLCM) and run-length matrix (RLM) for each ROI. Stepwise

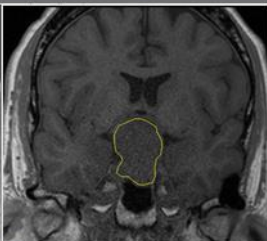
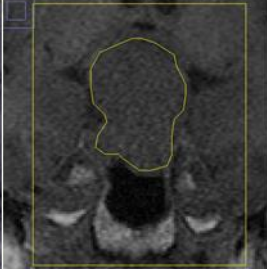
logistic regression analysis identified feature sets that would discriminate between the two groups (area under the ROC curve (AUC) significantly greater than 0.5, P).

Results

Representative ROIs and textural feature values for adenomas and normal glands are provided in Figure 1. The logistic regression model generated using grey-level mean, angular second moment (GLCM feature 'f1'), entropy (GLCM feature 'f9'), and grey-level nonuniformity (RLM feature) resulted in an AUC of 0.91 (SE=0.03; P< 0.0001). The SVM classifier trained on these features achieved a postcross validation accuracy of 79% for identifying pituitary adenomas.

Conclusions

Quantitative MRI texture shows potential for differentiating between normal glandular tissue and pituitary adenomas. The introduction of texture analysis opens a new perspective for pathologies affecting the CNS that may be not visible, even to the trained eye. This could prove particularly helpful for pituitary gland lesions that are notoriously difficult to diagnose.

	Normal Gland	Adenoma
ROI selection		
400% Magnification		
<i>Histogram Mean (<66.8)^a</i>	93	56
<i>f1 (<0.008)^a</i>	0.010	0.004
<i>f9 (>2.16)^a</i>	2.06	2.51
<i>GLNU (>9.7)^a</i>	6.0	101.3
<small>^a Cut-off associated with the Youden index for each textural feature for the identification of adenomas</small>		

(Filename: TCT_O-404_Pituitarytextureanalysisimage.jpg)

Wednesday, June 6, 2018

1:15PM - 2:45PM

Parallel Paper Session - Decision Support, Value, and Safety

O-405

1:15PM - 1:22PM

Implementation of Imaging Clinical Decision Support - Does CDS lead to appropriate use of imaging order?

Oral Presentations & Excerptas

Y Anzai¹, T Hutchins¹, R Wiggins²

¹University of Utah, Salt Lake City, UT, ²University of Utah Health Sciences Center, Salt Lake City, UT

Purpose

Under continuously rising health care costs, the efforts to reduce inappropriate imaging utilization led to the legislative approval of PAMA (Protecting Access to Medicare Act). PAMA mandates ordering providers to consult imaging CDS mechanism for advanced imaging and the furnishing providers (radiologists) to submit documentation of the CDS consultation on the Medicare claims reimbursement. The purpose of the study is to share the initial experience in implementing imaging CDS in a single academic institution.

Materials and Methods

We implemented the imaging CDS (National Decision Support Company) in late January of 2017 in preparation for the PAMA mandate. The CDS mechanism has deployed institution-wide through our EMR (EPIC) for all advanced imaging orders (CT, MR, cardiac imaging, and PET imaging) for all patient types.

Results

In the first four months, 70% of the orders were coded as "no score" in part due to free text entry by ordering providers, for which the CDS mechanism was not able to provide the appropriate scores. The free text entry was disabled in May of 2017, which reduced "no score" category to 42%. The vast majority of the remaining "no score" category was due to lack of appropriate use criteria (AUC), 55% of which were related to nuclear medicine studies, and 33% were related to imaging-guided procedures. CDS erroneously coded a noncontrast CT study inappropriately when patients had renal failure or contrast allergy, or contrast-enhanced spine MR inappropriately where patients with low back pain had a history of cancer.

Conclusions

Implementation of CDS mechanism requires engagement of radiologists in order to guide appropriate imaging use for higher value care. Automated extraction of medical information such as GFR or ICD 10 diagnosis from EMR facilitates the proper ordering and scoring.

O-406

1:22PM - 1:29PM

Use of Radiology Support, Communication and Alignment Network to Improve Lumbar Spine MRI Appropriateness for Low Back Pain: A 2-Year Follow-Up

K Wang¹, I Chong¹, C Yen¹, M Chen², B Reed¹, M Wintermark³, C Lincoln¹

¹Baylor College of Medicine, Houston, TX, ²MD Anderson, Houston, TX, ³Stanford University, Stanford, CA

Purpose

Radiology Support, Communication and Alignment Network (R-SCAN) was created by the American College of Radiology (ACR) as an informatics-based approach to leverage the collaboration between radiologists and referring physicians to improve the imaging appropriateness (1). We report our institutional experience on the long-term impact of R-SCAN in improving lumbar spine MRI appropriateness for low back pain approximately two years following education at three county-affiliated family medicine clinics.

Materials and Methods

Educational presentations were given at three county-affiliated clinics in April/May of 2016 highlighting the American College of Physicians and Choosing Wisely Campaign imaging guidelines using a case-based approach. A second education was given in November 2017; each of the three clinics received a different intervention (refresher presentation, guideline dissemination, none [control]). Baseline referral

Oral Presentations & Excerptas

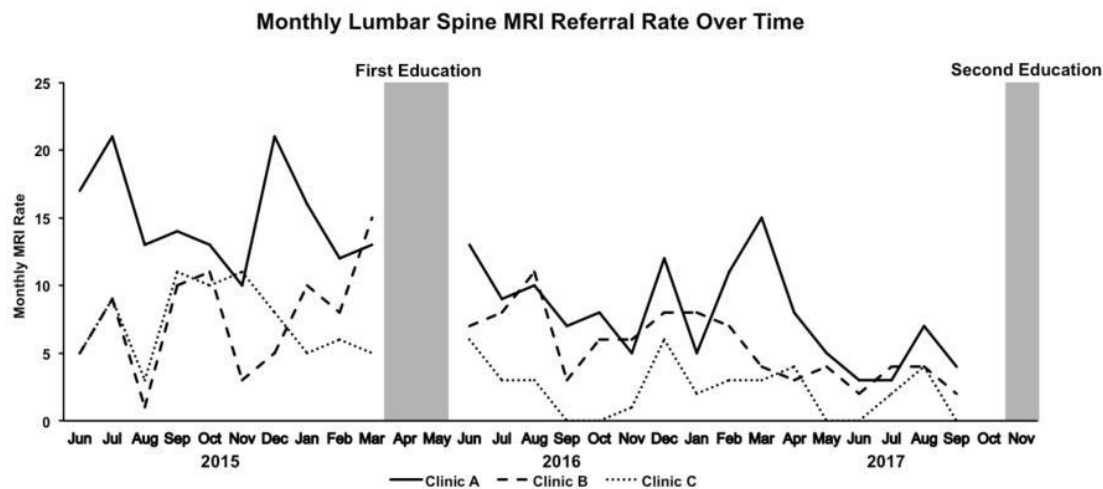
data were collected from June 1, 2015 to March 31, 2016. Data following first education were collected from June 1, 2016 to September 31, 2017. Data following second education will be collected from December 1, 2017 to March 31, 2018. Mann-Whitney test was used to compare monthly lumbar spine MRI referral rate before and after educations. Two independent samples' t-test was used to compare the ACR appropriateness criteria rating before and after educations.

Results

Monthly referral rate of Clinic A ($p < 0.001$), Clinic B ($p < 0.001$), and the combined average of all three clinics ($p < 0.0001$) was significantly lower during the 16-month period following first education when compared to the 10-month period before (Figure). Mean ACR appropriateness criteria rating was significantly higher following first education for Clinic B (4 vs. 5.5, $p = 0.025$), Clinic C (3.8 vs. 6.4, $p = 0.009$), and when combined (4.7 vs. 5.7, $p = 0.014$). Statistical comparisons for the second education are pending data collection through March 31, 2018, which will be approximately two years in elapsed time since the first education.

Conclusions

The impact in the use of R-SCAN to improve imaging appropriateness may be long-lasting and sustainable, and has resulted in significant improvement in imaging utilization and appropriateness of lumbar spine MRIs for at least 18 months following implementation at our institution.



(Filename: TCT_O-406_FFigure.jpg)

O-407

1:29PM - 1:36PM

Deleterious Effects of Poor Histories on Emergency MRI Neuroimaging

G Weinstein¹, M Lev², W Mehan¹

¹Massachusetts General Hospital, Boston, MA, ²Massachusetts General Hospital/Harvard Medical School, Boston, MA

Purpose

The utilization of MRI in emergency neuroimaging has increased with wider accessibility of MRI units in emergency departments. Based on the efficiency demands inherent in busy emergency departments, MRI exams are often protocolled based on the history provided in the order requisitions alone. Improper protocols can lead to misdiagnosis due to suboptimal imaging and wasted hospital resources secondary to repeat imaging. Our goal was to assess the frequency of studies protocolled improperly due to deficient or erroneous order requisition histories, and to assess possible factors that contributed to incorrect protocoling.

Oral Presentations & Excerpts

Materials and Methods

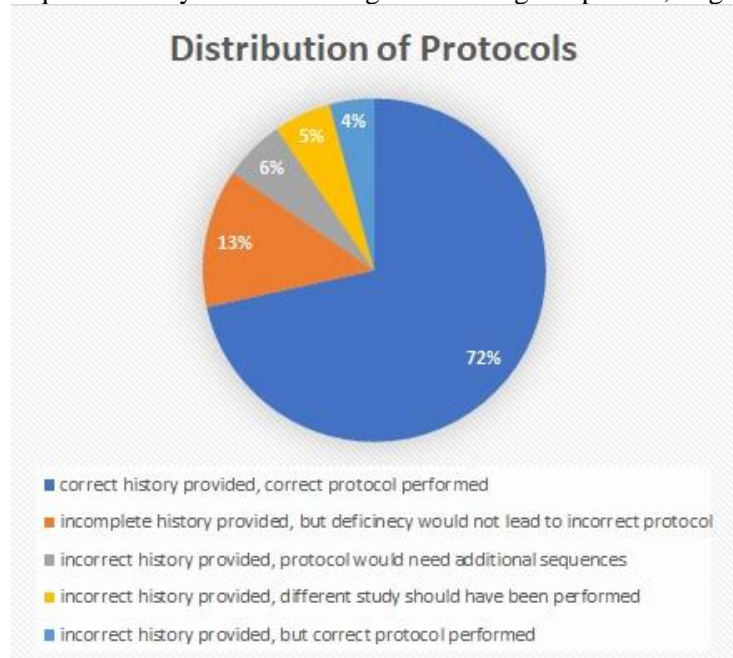
We retrospectively reviewed our radiology database for adult neuroimaging MRIs performed in our ED from August 30 to September 27, 2017. The exam indication and patient history listed in the order requisition ("provided history") was compared to the patient history detailed in the ED provider notes ("actual history"). The appropriateness of the selected exam protocols was evaluated in light of the actual and provided histories.

Results

Out of 260 total studies performed, 29 (11.2%) were suboptimally protocolled. Of these, 15 would have required additional sequences (such as SWI in the setting of trauma), and 14 would have required different studies performed (such as a contrast-enhanced study rather than a noncontrast study). We then subdivided the requisitions into those that had manually written-in provided history versus those that only had provided history selected from a prepopulated pick list. Studies that only had provided history in the form of a pick-list entry had a higher rate of improper protocol (15.8% versus 10.0%), although this was not statistically significant ($p=.13$).

Conclusions

Eleven percent of emergency adult neuro MRI exams performed at our institution were suboptimally protocolled due to erroneous or incomplete histories. Accurately provided histories in the order requisition may reduce misdiagnoses through improved, targeted protocols.



(Filename: TCT_O-407_piechart.jpg)

O-408

1:36PM - 1:43PM

Effectiveness of a Hospital System Intervention for Cord Compression: Are We Casting Our Net Too Wide?

R Thakkar¹, R Makipour¹, A Islam¹, A Jay¹

¹MedStar Georgetown University Hospital, Washington DC

Purpose

In 2015, our hospital system rolled out a two-part intervention focusing on recognizing cord compression: a SiTEL module and an electronic health records (EHR) generated Order Prompt that cues clinicians to

Oral Presentations & Excerptas

consider cord compression in patients. The aim of this pilot study was to evaluate whether the implementation of these two efforts has resulted in the over utilization of the "Stat Cord Compression" (SCC) MRI protocol.

Materials and Methods

A retrospective review of our EHR from 2015-2017 was conducted. The total number of SCC studies ordered before and after the implementation of the intervention was pulled from the database. For the feasibility of the pilot study, 100 patients in the "after intervention" group were evaluated. The SiTEL module laid out certain "red flags" that should cue clinicians that there is a concern for cord compression, including extremity weakness, incontinence, etc. All information was obtained from our system EHR.

Results

Before the intervention, there was a total of 114 cord compression (CC) studies ordered across our eight-hospital system. Of these, 11 cases (10%) were positive for CC. After the intervention was implemented, there was over a four-time increase in the number of SCC studies ordered to 472. Of the 100 cases we evaluated in this pilot study, 10 (10%) of patients were positive for CC. Of patients 49/100 had Order Prompt pop-up on admission and, 5/10 patients of the positive group. Of the 18 SiTEL red flags given in the module, only five were found to be clinically significant: extremity weakness ($p=0.029$), paresthesia ($p=0.005$), abnormal gait ($p=0.04$), bowel/urinary incontinence ($p=0.04$), and known cancer ($p=p.01$).

Conclusions

There has been more than 400% increase in number of SCC studies ordered by emergency department after implementation of SiTEL module and Order Prompt pop-ups without any significant increase in positive cases as interpreted by MRI.

O-409

1:43PM - 1:50PM

Computed Tomography Perfusion Aides in the Prognostication of Comatose Post-Cardiac Arrest Patients

J Shankar¹, A Quraishi¹, S Brandie¹, R Vandorpe¹

¹*Dalhousie University, Halifax, Halifax, Nova Scotia, Canada*

Purpose

Recent advances in emergency medicine and resuscitation management such as mild therapeutic hypothermia have improved the number of survivors of cardiac arrest. However, early assessment of the potential for neurological recovery in comatose cardiac arrest patients (CCAP) have been a challenge despite significant evolution in the imaging techniques. As resuscitation management techniques evolve, it is essential to identify patients who are most likely to achieve a good neurological outcome. The purpose of study was to see if the use of CT perfusion (CTP) in comatose cardiac arrest patients (CCAP) is feasible and if this technique can predict the likelihood that CCAP will have a devastating outcome, such as death or severe dependency, at hospital discharge.

Materials and Methods

The study was approved by the institutional research ethics board. We prospectively enrolled 10 newly admitted comatose adults (≥ 18 years old) who have suffered an out-of-hospital cardiac arrest and were treated with standard therapeutic hypothermia protocols. Informed consent was obtained. Patients underwent CTP of the head using our previously published brain death CTP protocol within six hours after finishing therapeutic hypothermia treatment. 'Matched defect' in the brainstem on CTP was considered to be predictive of devastating outcome. The imaging findings were compared with that from clinical assessment as well as the Modified Rankin score (mRS) at hospital discharge. Sensitivity, specificity, positive (PPV) and negative predictive values (NPV) for CTP were calculated in order to predict clinical outcome.

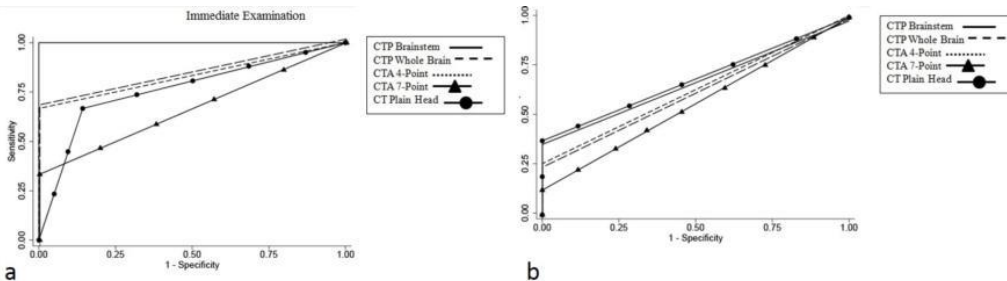
Results

Eight patients had mRS of ≥ 5 and two had mRS of ≤ 2 at hospital discharge. CTP predicted a good clinical

outcome in both patients with a mRS ≤ 2 . The AUC for plain CT head, CTA four-point scale, CTA seven-point scale, CTP whole brain and CTP brainstem only for predicting results of immediate clinical assessment were 0.76, 0.83, 0.67, 0.83 and one and that for predicting outcome at discharge were 0.69, 0.63, 0.56, 0.63, 0.63 and 0.69 respectively.

Conclusions

Our pilot study showed that CTP is feasible and had very high AUC in predicting the results of immediate clinical assessment in CCAP.



(Filename: TCT_O-409_Fig2.jpg)

O-410

1:50PM - 1:57PM

Analysis of MRI report quality in patients with painful osteoporotic vertebral compression fractures

R Bordia¹, A Ortiz¹

¹New York University Winthrop Hospital, Mineola, NY

Purpose

The purpose of this study is to analyze the quality of MRI reports with respect to documented description of vertebral compression fractures (VCFs).

Materials and Methods

Patients who underwent vertebral augmentation procedures between January 2015 and November 2017 were identified from the PACS archive. Patients were included in the study if spine MRI was performed prior to the procedure and images and reports of these studies were available for review. The following report elements were considered as being relevant for adequate patient surgical management: 1. Use of prior imaging for comparison, 2. Fracture level(s), 3. Fracture morphology (wedge, impaction, biconcave, burst), 4. Height loss (mild, moderate, severe or percent), 5. Kyphosis, 6. Fracture edema, 7. Cleft, 8. Fracture line, 9. Vertebral endplate injury, 10. Intervertebral disc injury, 11. Spinal canal compromise, 12. Posterior element injury, 13. Paraspinal edema, 14. Fracture acuity, and 15. Correlation with history. A retrospective blind review of these MR images was performed by a neuroradiologist and these characteristics were recorded. The final MRI reports were reviewed and scored for each feature – score of 1 was assigned when the feature was addressed in the report and 0 if it was not addressed or incorrectly reported. Report quality was classified as adequate (score > 7) or inadequate (≤ 7).

Results

Included in the study were 36 patients with 24 females and 12 males with the mean age of 78.5 years (range – 56-99). The element most underreported was disc injury (not mentioned in 88% reports). Other underreported elements include clefts, fracture lines, endplate fracture, posterior element injury and paraspinal tissue edema. None of the reports addressed correlation with patient's symptoms. Only two reports out of 36 addressed more than 10 elements. Most reports addressed fracture acuity (29 out of 31). Of reports 33% mentioned seven or fewer features and were grouped as inadequate.

Conclusions

A large proportion of MRI reports are inadequate with respect to description of VCF features that affect

their operative management. MRI report quality requires improvement with respect to VCF description in order for these reports to have utility in influencing subsequent surgical management with possible vertebral augmentation.

O-411

1:57PM - 2:04PM

Transverse Venous Sinus Stenosis in the Setting of Idiopathic Intracranial Hypertension: Are We Under-reporting and Can Education Improve Its Identification?

K Tran¹, A Krishnan¹, R Silbergleit¹

¹*Oakland University William Beaumont School of Medicine, Royal Oak, MI*

Purpose

Transverse sinus (TS) stenosis on magnetic resonance venogram (MRV) has previously been shown to be a sensitive imaging finding for idiopathic intracranial hypertension (IIH). However, this finding is often not assessed as MRV is ordered for exclusion of thrombosis and findings if present are often downplayed due to confusion with perceptions of anatomic variability, resulting in under-diagnosis of IIH. The aim of this study was to evaluate whether focused assessment of venous sinus stenosis following education resulted in an increase in the diagnostic sensitivity of TS stenosis. In addition we aimed to determine the accuracy of detection of IIH at our large tertiary care center and evaluate variables that may be responsible for under-diagnosis of this condition.

Materials and Methods

This IRB-approved study involved a search of our radiology report database for prior MRV examinations performed from the years 2014 to 2017 in patients in whom the diagnosis of IIH was established by the Modified Dandy Criteria. MRV exams were performed with postcontrast 2-D TOF technique on various scanners. Forty-two IIH patients meeting this criteria were randomized with a control group of 44 patients without IIH, and their MRV examinations after anonymization were independently reviewed by two neuroradiologists, who had received education on recognition of TS stenosis. The reviewers were asked to evaluate each case for TS stenosis and categorically state whether they were "normal/abnormal" for IIH, as well as to evaluate each transverse sinus individually for degree of narrowing based on a numerical scoring scale. The original MRV radiology reports for IIH patients were reviewed to assess the prior rate of reporting TS stenosis. Other variables such as presence of hypoplastic sinus morphology, timing of lumbar puncture relative to MRV examination, and planes of acquisition of MRV were reviewed. Statistical analysis was performed using univariate analysis.

Results

The two reviewers (following consensus read with original discordance in two patients) reported MRV findings consistent with IIH in 28 of 42 IIH patients and in one of 44 of controls, corresponding to a sensitivity of 67%, and a specificity of 98%. This was significantly improved compared to the 24% in IIH patients on the original radiology reports ($P < 0.001$). The identification of TS stenosis was not considerably different between patients that underwent MRV before or after lumbar puncture. A large number of false negative examinations were found to be associated with unilateral sinus abnormalities. In a few cases, the sagittal plane of MRV did not include the edges of the transverse sinus limiting assessment to axial MRV images.

Conclusions

Education with focused assessment for venous sinus stenosis was associated with higher detection rates of TS stenosis on MRV relative to original reporting. The overall incidence of TS stenosis on MRV in IIH patients in our center was however lower than 93% as previously reported in literature. As readers were asked to categorically state if findings were consistent with IIH or not, one potential source for the difference may have been from readers considering hypoplastic or unilateral stenosis as normal variants. MRV technique may have also played a part as different centers adopt various techniques.

O-412

2:04PM - 2:11PM

Utility of Routine Neck MRA in a Pediatric MRI Stroke Protocol

N Stence¹, A Baltensperger¹, D Mirsky¹, J Maloney¹, L Fenton¹, I Neuberger¹, T Bernard¹

¹*Children's Hospital Colorado, Aurora, CO*

Purpose

Cervical arterial dissection is a not infrequent cause of pediatric arterial ischemic stroke. (1) Out of concern over missing cervical arterial dissection in patients where pediatric stroke is suspected, our tertiary children's hospital added postcontrast 3-D neck MR angiography to every MRI ordered for a pediatric stroke workup, with the option to limit the examination to only a DWI and MRA circle of Willis (COW) if an acute stroke was seen and administration of TPA was considered. To ensure best practices, we undertook a retrospective quality improvement project to determine if the routine use of neck MRA in our MRI stroke protocol was indeed necessary, specifically in the subset of children where the DWI, SWI/GRE or MRA COW from the brain MRI were reported as normal.

Materials and Methods

The institutional PACS database was searched using Montage (Montage Healthcare Solutions, Philadelphia, PA) for stroke protocol MRIs that included DWI, GRE or SWI, circle of Willis MRA and 3-D postcontrast neck MRA in patients less than 18 years of age and with examinations performed between September 2010 and June 2017. Reports were reviewed for mention of any abnormalities on the DWI, SWI/GRE, MRA COW, and MRA neck portions of the examination.

Results

The search results yielded 1147 examinations in 888 unique patients (522 male, average age 10.8 years). In only a single case (a 15-year-old female with unusual history of episodic cervical ICA vasospasm) were the DWI, SWI/GRE or MRA COW all separately reported as normal and the MRA neck reported as abnormal for a cervical arterial abnormality.

Conclusions

In this large series, the addition of a routine neck MRA to our pediatric stroke MRI protocol was of extremely low yield when DWI, SWI/GRE and MRA COW were all normal. The routine use of neck MRA in pediatric stroke workups could be limited to cases where abnormalities are initially detected on these routine brain sequences or when cervical arterial abnormalities are still strongly suspected clinically.

O-413

2:11PM - 2:18PM

Does Including Neck CTA Imaging for the Work-up of Suspected Intracranial Hemorrhage Add Value?

S Raymond¹, C Stapleton¹, W Mehan¹

¹*Massachusetts General Hospital, Boston, MA*

Purpose

Neck CT angiography (CTA) is frequently performed in conjunction with head CTA in patients presenting with clinical signs and symptoms concerning for acute intracranial hemorrhage, despite relatively low ACR appropriateness (ACR criteria 4-5). This decision is sometimes justified by suggesting that CTA neck findings are useful in planning diagnostic or therapeutic catheter angiography. We investigated the utility of neck CTA in patients with suspected acute intracranial hemorrhage.

Materials and Methods

We searched our institutional database for ER patients undergoing CTA head and neck for the indication of hemorrhage or headache over a 12-month period. Trauma and ischemic stroke patients were excluded. A total of 109 patients met these criteria. Radiology reports were reviewed for significant findings

Oral Presentations & Excerptas

including severe stenosis, dissection, and any finding resulting in recommendation for additional imaging (incidental). CTA neck images were reviewed by two neurointerventionalists, a radiologist and neurosurgeon, to address the following questions: 1) Would findings on the CTA be helpful in performing catheter angiography or change the technical approach? 2) Would not having the CTA likely add more than 10 minutes to a standard four-vessel diagnostic angiogram? Statistical analysis was performed using R.

Results

Significant radiological findings including severe stenosis and dissection were present in 16%. Findings helpful for performing catheter angiography were seen in on average 21% (15-25%, Cohen kappa 0.63), and included anatomical arch variants such as a bovine arch, direct vertebral artery arch origin and aberrant subclavian artery. Findings that might substantially prolong angiography (> 10 minutes) if unknown occurred in < 4% (3-4%, Cohen kappa 0.85).

Conclusions

Although CTA neck can be helpful for planning of catheter angiography, it rarely uncovers findings that would significantly prolong the angiographic procedure (< 4% of cases). Reflexive ordering of neck CTA in patients with clinical concern for acute intracranial hemorrhage therefore subjects patient to an unnecessary test.

O-414

2:18PM - 2:25PM

Instituting a Protocol for MRIs in Patients with Cardiac Devices: Promote Patient Safety and Billing Compliance.

M Antonucci¹, M Spampinato¹, E Ritenour¹

¹*Medical University of South Carolina, Charleston, SC*

Purpose

Implantable cardiac devices traditionally precluded magnetic resonance imaging (MRI). However, several recent studies (1, 2), including 1500 MRIs in MagnaSafe registry patients (1), document relative safety in this setting. Given the prevalence of these devices, including 1.8 million patients in the United States alone (3), neuroradiologists should proactively design protocols to address safety parameters and billing compliance. While not widely known, regulations currently render many such scans noncovered services (4, 5). We demonstrate how a comprehensive protocol can be rapidly instituted and illustrate approaches to billing compliance.

Materials and Methods

We review the design and implementation of a comprehensive protocol for MRIs in patients with FDA-labeled "conditional" and "nonconditional" devices. We also review proactive and retroactive steps we instituted to prevent noncompliant billing.

Results

We established a protocol for MRIs in patients with cardiac devices. This entailed: 1. Multidisciplinary meetings with radiologists, physicists, MR technologists, and electrophysiologists 2. Establishing criteria for "conditional" labeling (e.g. each implanted component must be conditional) 3. If "conditional," MRI is expedited with structured reporting templates for compliant billing (see figure) 4. For "nonconditional" devices, radiology subspecialty representatives identified scenarios for approving MRI. We established parameters for cardiology approval, informed consent, scan supervision, low SAR technique, and documentation. Nonconditional MRIs are typically not billable, and: - The clinician/patient are informed of possible out-of-pocket expense. - Covered alternative modalities are reviewed. - Financial counseling is offered prior to MR. - Nonconditional status is documented to facilitate coding and avoid inappropriate billing (see figure). - The billing records of previously performed scans were reviewed and payments made under inadvertent noncompliant billing were reimbursed. Using this protocol, we safely performed 39 MRIs in five ICD and 34 pacemaker patients in 2016-2017.

Oral Presentations & Excerptas

Conclusions

Our institutional experience can serve as a template for others who scan patients with cardiac devices. A comprehensive protocol, ensuring patient safety and compliant billing, can be established rapidly and efficiently.

NON-CONDITIONAL CARDIAC DEVICE:

The patient has an intracardiac [*insert device type: pacemaker/ICD*], which is **NOT** FDA approved for MRI scanning under manufacturer specified conditions (MRI unsafe): [*insert manufacturer and specific model*]. It was implanted on [*insert date*].

The study was approved by the cardiology and radiology departments. Informed consent was obtained from the patient prior to the MRI. The study was performed under the supervision of the radiology department physicist. Electrophysiology staff was present for the duration of the examination and interrogated the device before, during and after the procedure. Cardiology assessed the patient prior to the scan with physicist and cardiology EP present during the scan.

Total SAR (specific absorption rate) remained below [(whole body averaged specific absorption rate (SAR) ≤ 2.0 W/kg, head SAR ≤ 3.2 W/kg)]. See PACS [*insert series number*] where details regarding the scan, pacemaker, and SAR values are reported.

CONDITIONAL CARDIAC DEVICE:

The patient has an intracardiac [*insert device type*], which is FDA approved for MRI scanning under manufacturer specified conditions (MRI conditional): [*insert manufacturer and specific model*]. It was implanted on [*insert date*].

The conditional nature of the device was confirmed by the cardiology service and the study was approved by radiology. Informed consent was obtained from the patient prior to the MRI. The patient's device was interrogated prior to the examination and reprogrammed following its completion by the electrophysiology service. The scan was acquired according to manufacturer specifications and total SAR (specific absorption rate) remained below appropriate threshold levels.

(Filename: TCT_O-414_mritemplatefigure.JPG)

O-415

2:25PM - 2:32PM

Integrative neuroradiology medical physics curriculum enhances resident education

M Khy¹, J Pao², M Helmy¹, D Chow³

¹University of California, Irvine, Orange, CA, ²UC Irvine Health, Orange, CA, ³University of California, Irvine, Irvine, CA

Purpose

Physics is a major component of the American Board of Radiology (ABR) core exam, comprising 15-20% of questions. In 2013, the ABR changed the core exam to assimilate physics throughout the tested subspecialties, including neuroradiology. Despite the importance of medical physics to both clinical practice and the core exam, it is often an area in which residents struggle with limited resources and where the education is modeled after physics topics rather than clinical application. The goal of this abstract is to describe our institution's experience with an integrative physics curriculum, using neuroradiology as a model.

Oral Presentations & Excerpts

Materials and Methods

This study was performed for the purposes of education and was exempt from IRB approval. A physics curriculum was devised, including topics in MR and CT that were outlined by the ABR Core Exam Study Guide. Residents at our program took a 13-question pretest MR exam from the RSNA resident physics modules, including: Basic Principles of Nuclear Magnetic Resonance, Image Formation, Image Characteristics, Pulse Sequences, Instrumentation, Image Artifacts, Special Acquisition Methods, and Quality/Bioeffects/Safety. Residents were randomly divided into two groups where Group One completed the traditional RSNA physics modules and Group Two completed the integrative physics course. A t-test was performed between the two groups to assess for statistical differences.

Results

Twenty-four residents were included in this study. The average score on the pretest exam was 48.5% (6.3/13, range 2-12). For PGY2/3 and PGY4/5, the average pretest scores were 36.9% (4.8/13) and 60.0% (7.8/13), respectively. Post test, the average score for Groups One and Two was 71.5% (9.3/13), which was significantly improved over the pretest exam mean score ($p < 0.05$). The mean scores of Group One and Group Two were and 61.5% (8/13) and 84.6% (11/13), respectively ($p < 0.05$).

Conclusions

An integrative medical physics curriculum demonstrates greater improvement in physics scores compared to a traditional module-based physics course.

O-416

2:32PM - 2:39PM

Acute adverse reactions following gadolinium-based contrast agent administration; A single-center review of 281,945 injections.

J McDonald¹, R McDonald¹, C Hunt¹, A Kolbe¹, J Schmitz¹, R Hartman¹, D Kallmes¹

¹Mayo Clinic, Rochester, MN

Purpose

To examine and compare rates of acute allergic-like and physiologic reactions between the four most commonly used GBCAs (gadodiamide, gadobutrol, gadobenate dimeglumine, and gadoterate meglumine) at our institution.

Materials and Methods

All intravenous GBCA injections for MR exams performed at our institution from June 1, 2009 – May 9, 2017 were identified. At our institution, all patients are monitored during and after GBCA-enhanced MR exam for the presence of any acute reactions. Reaction events were identified by reviewing MR technologist and MR nursing staff notes, radiologist reports, and any emergency department admission notes and subsequent provider visit notes. Reactions were classified into allergic-like or physiologic types and into mild, moderate, and severe categories using ACR criteria.

Results

A total of 281,945 GBCA injections (140,645 gadodiamide, 94,109 gadobutrol, 39,138 gadobenate dimeglumine, and 8,053 gadoterate meglumine) were included in the study. Allergic-like reactions occurred at an overall rate of 0.16% (n=440), with significantly higher rates observed with gadobenate dimeglumine (0.33%, n=129) and gadobutrol (0.20%, n=185) compared to gadodiamide (0.09%, n=122) and gadoterate meglumine (0.05%, n=4). Physiologic reactions occurred at an overall rate of 0.13% (n=376), with significantly higher rates observed with gadobenate dimeglumine (0.18%, n=71) and gadobutrol (0.16%, n=155) compared to gadodiamide (0.10%, n=144) and gadoterate meglumine (0.07%, n=6). Six severe allergic-like reactions (three gadobutrol, three gadobenate dimeglumine) occurred requiring hospitalization.

Conclusions

Gadobenate dimeglumine and gadobutrol were associated with significantly higher rates of allergic-like

and physiologic reactions compared to gadodiamide and gadoterate meglumine. No severe reactions were observed with gadodiamide and gadoterate meglumine administration.

Wednesday, June 6, 2018

1:15PM - 2:45PM

Parallel Paper Session - Head and Neck: Congenital, Salivary, and Temporal Bone

O-417

1:15PM - 1:22PM

The Spectrum of Stylohyoid Anomalies with Embryologic Considerations

J Rees¹, I Tuna¹, R DeJesus¹

¹*University of Florida, Gainesville, FL*

Purpose

To study the spectrum of anatomic variations in the stylohyoid (SLH) apparatus and to correlate the presence of SLH ossification with other developmental anomalies of the hyoid bone, and to relate these findings to their embryologic origins.

Materials and Methods

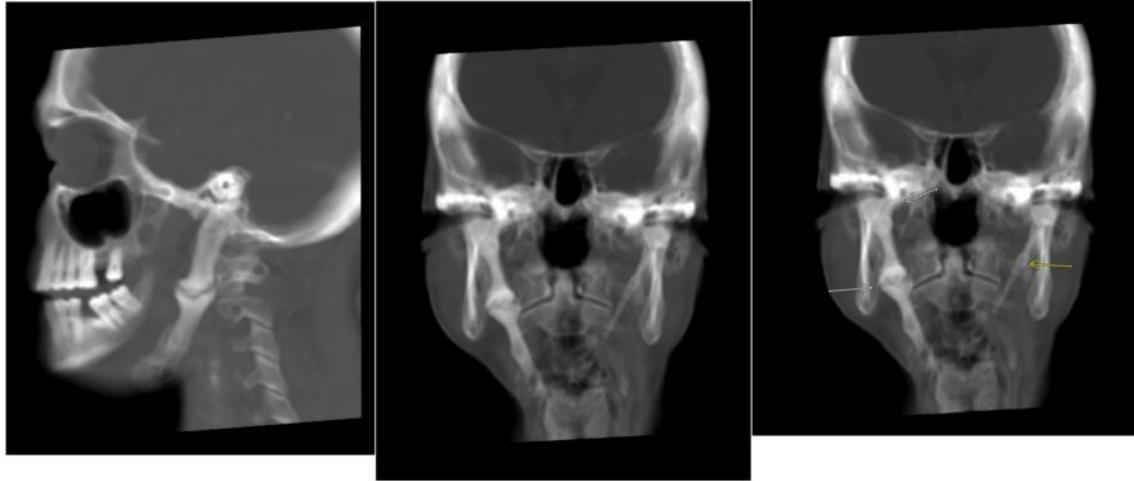
We identify and study 26 cases of complete SLH ossification and hyoid variations over two years. SLH ossification is analyzed and categorized for symmetry, morphology, thickness, patient age and clinical symptoms. Hyoid variations were described and catalogued individually. Literature review and study were targeted on the embryology of these structures in the attempt to understand and explain the findings observed with particular attention to the neural crest and molecular signaling.

Results

We find a wide range of SHL ossification which is often asymmetric in thickness, and size of the apparent marrow cavity. Hyoid anomalies are much less frequent but appear to be associated with greater thickening and anomaly in the styloid ligament. In several cases there appear to be pseudoarthrosis, or articulations along the course of the ossified stylohyoid ligament and when present, these are more commonly associated with substantial hyoid variance including thickening and atypical morphology. In one case (attached), the proximal thickened and ossified SLH is seen to form the back wall of the temporomandibular fossa and the anterior inferior bony external auditory canal suggesting a more extensive molecular miscommunication affecting the entire second pharyngeal arch.

Conclusions

The stylohyoid complex arises from the 2nd and 3rd pharyngeal arches which are composed of layers of mesodermal and neural crest elements. There is a complex interplay between cellular constituents and balanced molecular signaling which gives rise to the typical anatomic features in the upper neck and skull base. Our observed association between greater degrees and complexity of stylohyoid ligament ossification and greater hyoid variance, when interpreted in conjunction with the developing body of knowledge about the role of the neural crest elements and the molecular mechanisms which are in play, suggests that these findings represent a spectrum of developmental anomalies related to varying degrees of imbalance in opposing molecular signals.



(Filename: TCT_O-417_Stylohyoidanomalycomposite.jpg)

O-418

1:22PM - 1:29PM

Quantitative Evaluation of Imaging Quality and Diagnostic Performance PROPELLER Diffusion-weighted MR Imaging in Parotid Gland Tumors

C Juan¹, Y Liu², Y Lee², K Chien², J Chan¹, C Wang¹, J Lee¹, Y Chu¹, H Hsu¹

¹National Defense Medical Center and Tri-Service General Hospital, Taipei, Taiwan, ²Feng Chia University, Taichung, Taiwan

Purpose

To quantitatively evaluate the imaging quality, ADC, and diagnostic performance in distinguishing parotid pleomorphic adenomas (PMAs) from Warthin's tumors (WTs) of PROPELLER DWI (PROP-DWI) as compared to echo-planar DWI (EP-DWI).

Materials and Methods

This study comprised a total of 60 parotid tumors, including 30 pleomorphic adenomas (PMAs) and 30 Warthin tumors (WTs). All patients received prospectively designed PROP-DWI and EP-DWI for head and neck tumors in our hospital. Imaging quality including signal-to-noise ratio (SNR), contrast-to-noise (CNR), and tumor distortion was quantitatively analyzed. Tumor distortion of EP-DWI and PROP-DWI was evaluated by Dice similarity coefficient (DC), which was defined by the following equation: $DC = \frac{2|X \cap Y|}{(|X| + |Y|)}$, by comparing to the fast spin echo T2-weighted images as standard after image registration, respectively. Test-retest reliability and interobserver agreement for calculations of Dice coefficient were evaluated by Bland-Altman plots and intraclass coefficient (ICC). Apparent diffusion coefficient (ADC) of each parotid tumor was calculated after manually contouring the tumor on each pulse sequence. Relationship between the Dice coefficient and ROI size was evaluated by linear regression analysis. Nonparametric analysis including Wilcoxon signed-rank test and Mann-Whitney U test was used for group comparison. Diagnostic performance was evaluated by ROC curve analysis. $P < 0.05$ was considered statistically significant.

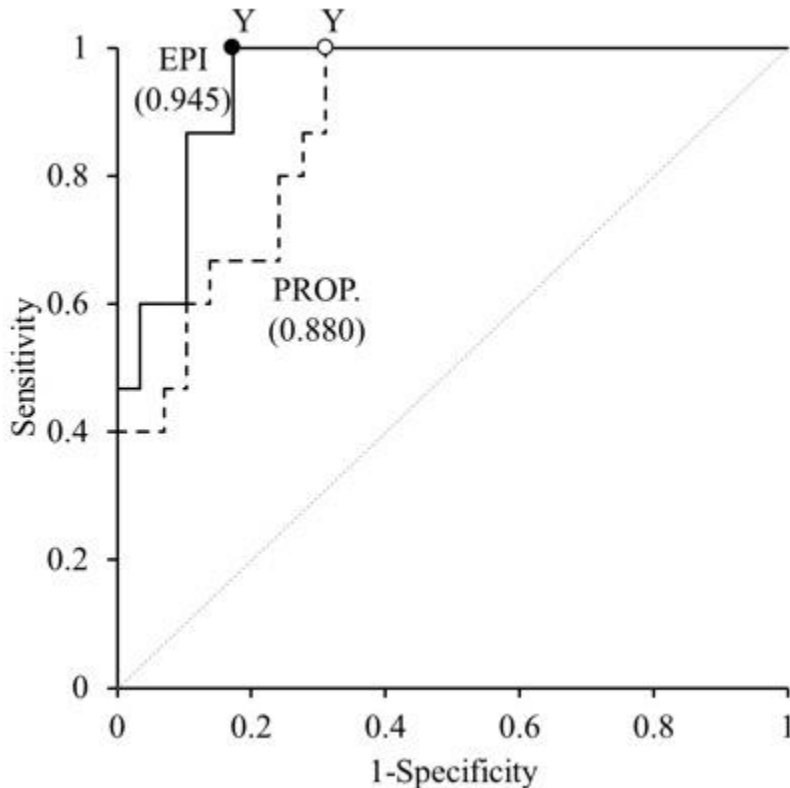
Results

Both PROP-DWI and EP-DWI showed excellent test-retest reliability and interobserver agreement with all ICC higher than 0.85. Linear regression analysis displayed that the Dice coefficient was positively associated with ROI size on both PROPELLER-DWI ($R^2 = 0.2496$, slope = 0.0195, $P < 0.001$) and EP-DWI ($R^2 = 0.2023$, slope = 0.0692, $P < 0.005$) significantly. PROP-DWI had significantly higher Dice coefficient than EP-DWI for both PMAs and WT ($P < 0.005$). PROP-DWI showed significantly lower

SNR, CNR, and higher ADC than EP-DWI ($P < 0.005$). WTs had significantly lower Dice coefficient than PMAs on EP-DWI only ($P < 0.005$). PMAs had significantly higher ADC than WTs in both PROP-DWI and EP-DWI ($P < 0.005$). The sensitivity, specificity, positive predictive value, negative predictive value, and accuracy in diagnosing PMAs was 100%, 69.0%, 62.5%, 100%, and 79.5%, respectively, using a cutoff ADC of $1.319 \times 10^{-3} \text{ mm}^2/\text{sec}$ for PROP-DWI, and, was 100%, 82.8%, 75%, 100%, and 88.6%, respectively, using a cutoff ADC of $1.036 \times 10^{-3} \text{ mm}^2/\text{sec}$ for EP-DWI. PROP-DWI showed significantly lower AUC (0.880) of than EP-DWI (0.945) in distinguishing PMAs from WTs ($P < 0.05$).

Conclusions

PROP-DWI provides less distorted images than EP-DWI with lower SNR and CNR for parotid gland tumors. It allows excellent diagnostic performance in distinguishing PMAs from WTs with lower AUC than EP-DWI.



(Filename: TCT_O-418_ROC.jpg)

O-419

1:29PM - 1:36PM

Assessing abnormal FLAIR signal changes in the cochlea pre- and post- hearing preservation surgery.

B Diegnan¹, N Tu², J Go¹

¹LAC/USC Medical Center, Los Angeles, ²University of Southern California, Los Angeles, CA,

Purpose

To evaluate the change in magnetic resonance imaging (MRI) T2-weighted cochlear fluid attenuation inversion recovery (FLAIR) signal intensity in vestibular schwannoma patients undergoing hearing preservation surgery.

Materials and Methods

All vestibular schwannoma patients who underwent resection of their tumor either via the middle fossa

craniotomy (MF) approach or retrosigmoid (RS) craniotomy from January 2013 to June 2017 were identified. Inclusion criteria included availability of FLAIR sequences on both preoperative and one year postoperative MRI scans, and availability of pre and post-operative audiograms. Nine MF and 26 RS patients were included in this study. Serviceable hearing was defined as Gardner-Robertson Grade 1 or 2. Hearing preservation was defined as retained serviceable hearing postoperatively. Mean signal intensity of the affected cochlea was evaluated by an operator-determined region-of-interest technique delineating the middle and apical turns of the cochlea and normalized against the contralateral cochlea. Percent change in FLAIR signal intensity was calculated for each patient.

Results

There was no difference in preoperative cochlear FLAIR signal intensity between hearing preserved and nonpreserved groups (1.92 vs 2.01, $p=0.38$). Postoperative cochlear FLAIR signal intensity was lower in the hearing preserved group, but did not reach statistical significance (1.45 vs 1.73, $p=0.13$). The hearing preserved group also demonstrated greater percent decrease than the nonpreserved group (-19.4% vs 0.8%, $p=0.19$), but also did not reach statistical significance. Hearing preservation rates were 89% (8/9) for MF, and 27% (7/26) for RS.

Conclusions

In patients undergoing successful hearing preservation vestibular schwannoma surgery, there is a trend toward greater improvement in cochlear FLAIR signal than in patients whose hearing is not preserved. This may have potential implications in determining the timing of surgical intervention for vestibular schwannoma patients.

O-420

1:36PM - 1:43PM

Audiometric Implications of Isolated Internal Auditory Canal Diverticula

D Mihal¹, Y Feng¹, M Kodet¹, M Carlson¹, J Lane¹

¹Mayo Clinic, Rochester, MN

Purpose

Previous studies have identified that bony internal auditory canal (IAC) diverticula (Figure 1) are relatively common, ranging from 5-10% of the population (1, 2). Further associations with otosclerosis and sensorineural hearing loss (SNHL) have also been proposed (1). The objective of this study is to analyze the association between IAC diverticula and SNHL in a large cohort of patients.

Materials and Methods

A retrospective review of all temporal bone CT scans obtained over a three-year period was performed by a single neuroradiologist with more than 20 years of experience. Scans were performed on Siemens CT scanners with a 64-, 128-, or 192-slice detectors. The presence of IAC diverticula, their anteroposterior (AP) depth, and radiological evidence of otosclerosis were reviewed. One patient with postoperative changes and nine patients without audiometric data were excluded from further analysis. Audiometric data consisted of air conduction, bone conduction, word comprehension, calculated pure tone averages, air bone gap, and a final assessment of sensorineural hearing loss, conductive hearing loss, mixed hearing loss, or normal hearing.

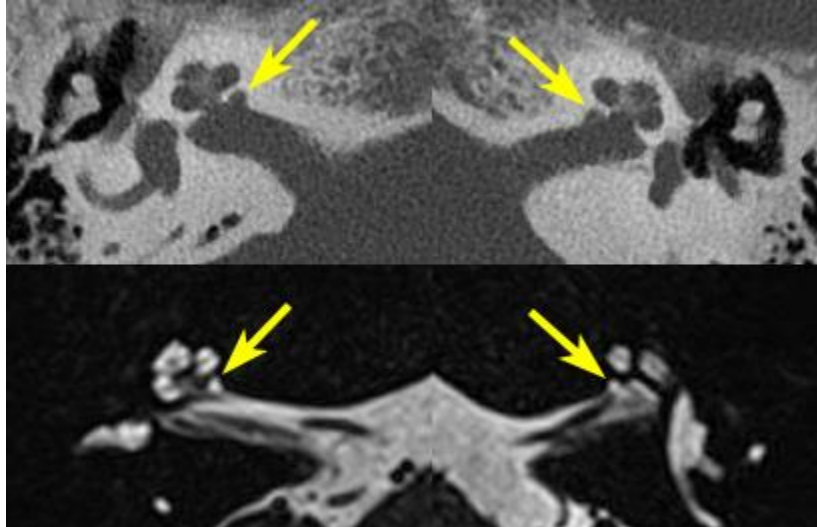
Results

A total of 1765 patients were scanned over the study interval, and 86 (4.8%) had either unilateral (17/35; 49% left-sided) or bilateral (51/86; 59%) IAC diverticula. The coincidence of otosclerosis and IAC diverticula was 1.64% (29/1765). Among all cases, the mean age was 51 years (range 1-91 yrs), and 43% occurred in women. In order to assess the implications of an isolated IAC diverticulum on SNHL, patients with concomitant otosclerosis and/or cases with bilateral diverticula and those without audiometric data were excluded, leaving 24 cases. In these cases, audiometric data for the ear with a diverticulum was compared to the contralateral "normal" ear – the latter serving as an internal control to adjust for the inherent selection bias of having hearing loss in cases where a temporal bone CT was ordered. Within this

subset, 13 ears with a diverticulum had SNHL [six with MHL and seven with pure SNHL], compared to 12 ears in the control side [four with MHL and eight with pure SNHL] ($P=0.75967$). The air conduction mean pure tone average in the diverticulum ear was 32 dB HL, compared to 25 dB HL in the control ear ($t\text{-value} = -0.9215$, $p\text{-value} = 0.361599$) and the mean word recognition score in the diverticulum ear was 88%, compared to 90% in the control ear ($t\text{-value} = 0.39351$, $p\text{-value} = 0.696086$).

Conclusions

Isolated bony IAC diverticula are not associated with a higher incidence or severity of SNHL compared to control ears. This finding most likely represents a normal anatomical variant in ears without otosclerosis.



(Filename: TCT_O-420_COMPOSITE-CT-T2-07-25-2017-03946011.jpg)

O-421

1:43PM - 1:50PM

A Color-Coded 3D-Printed Modular Puzzle of the Temporal Bone As A Novel Conceptual Anatomy Teaching Tool

R Javan¹, A Salman², M Yang³, F Farhadi¹, S Smilanich⁴, H Narayanan⁴

¹George Washington University Hospital, Washington, DC, ²GWU, Germantown, MD, ³George Washington University School of Medicine and Health Sciences, N/A, ⁴George Washington University, Washington, DC

Purpose

The purpose of this exhibit is to utilize 3-D printing in simplifying the understanding of the complex three-dimensional anatomy of the middle ear with its surrounding communications and neurovascular connections through a novel color-coded multipiece conceptual 3-D puzzle.

Materials and Methods

The middle ear along with its contents and anatomical landmarks is represented as a cube-shaped room and its communications as hallways, doors and windows. A color-coded 3-D printed model is then created which is deroofed and has multiple parts, which must be assembled. Each wall with its corresponding structures is a unique color. This approach simplifies the 3-D understanding, by providing an alternative method of visualization from within the cavity itself and breaking down the complex anatomy into smaller divisions. Graphics design software, Autodesk 3-D Studio Max, was used to create volumetric meshes of the conceptualized middle ear and surrounding structures. These include the ossicles, scutum, chorda tympani nerve, facial canal, tensor tympani, cochlear promontory, round and oval windows, tympanic membrane, carotid canal, jugular foramen, tympanic canaliculus, aditus ad

antrum, facial recess, sinus tympani, pyramidal eminence and inner ear elements. All of the structures are available individually, which can be properly assembled into a final model similar to pieces of a puzzle.

Results

A unique color-coded physical 3-D puzzle of the temporal bone was created with individual structures portrayed conceptually for the specific use of teaching complex anatomy based on the unique color of each wall of the middle ear. The model is 3-D printed with polyamide and every set of structures for each wall is spray painted a unique color.

Conclusions

An alternative approach to learning the intricate anatomy of the middle ear and its communications was designed, which may help trainees commit to memory this detailed anatomy and serve as a bridge between textbook knowledge base and detection on cross-sectional imaging.

O-422

1:50PM - 1:57PM

Effectiveness of a Conceptual 3D Printed Model of the Middle Ear in Teaching Complex Neuroanatomy

R Javan¹, A Yepuri², M Salehi Sadaghiani³, A Salman⁴, T Kim¹, Z Qazi⁵

¹George Washington University Hospital, Washington, DC, ²GEORGE WASHINGTON UNIVERSITY, WASHINGTON, DC, ³University of Pennsylvania, Philadelphia, PA, ⁴GWU, Germantown, MD, ⁵George Washington University, Washington, DC

Purpose

The purpose of this project was to evaluate the effectiveness of a conceptual 3-D printed model of the middle ear in teaching its complex neuroanatomy of the middle ear and its surroundings at an advanced level to radiology trainees.

Materials and Methods

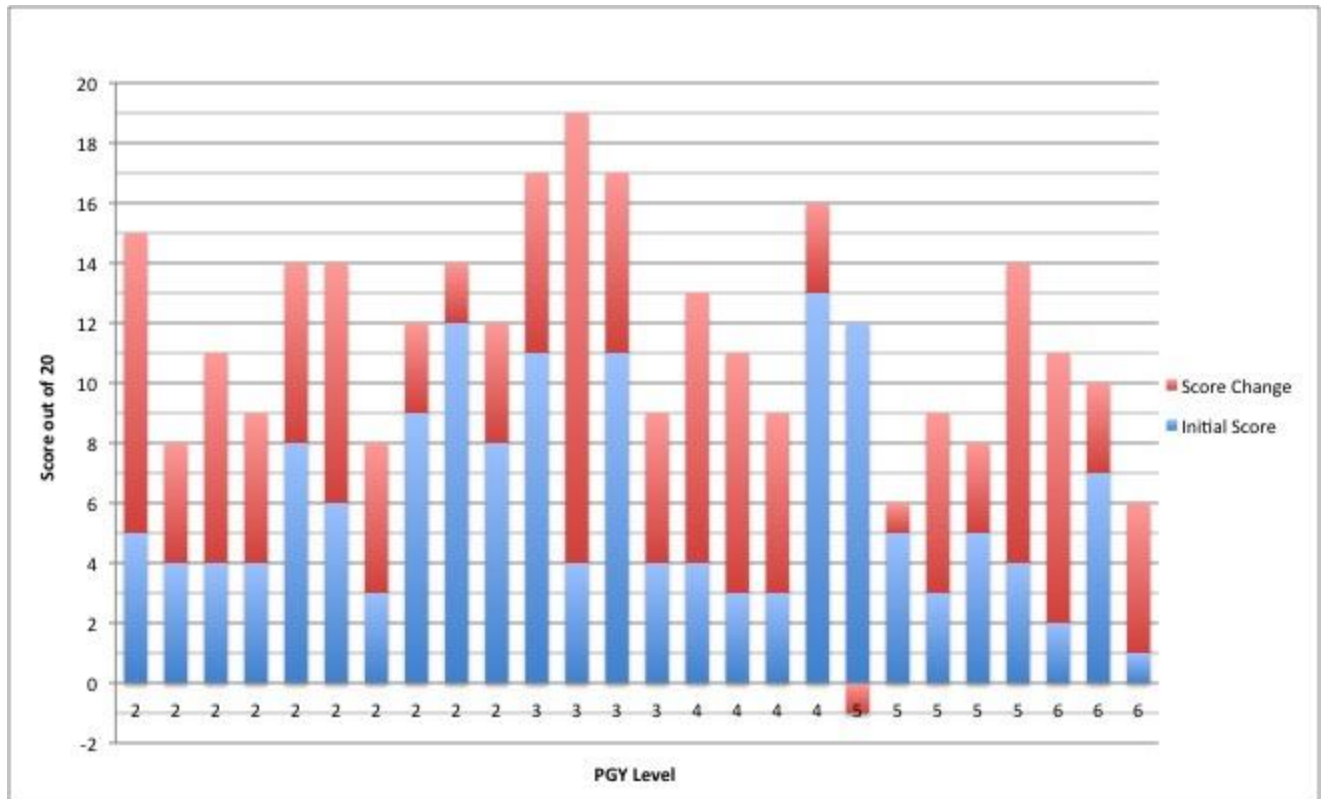
The middle ear is represented as a room with each of its components and surrounding structures assigned to a wall in order to simplify their three-dimensional understanding. A conceptual 3-D model was graphically designed using Autodesk 3D Studio Max. Subsequently, 3-D printing was performed using polyamide material. Twenty-seven radiology trainees embarked on taking part in the study, 26 of which completed the entire process. A set of 20 questions were developed based on advanced level knowledge of temporal bone, including relationship between structures as well as cross-sectional images. Each trainee completed the exam before and 5-7 days after a 20-minute small-group teaching session by a neuroradiology attending using the 3-D printed model. Each group consisted of 3-4 individuals. A 10-question survey was also provided.

Results

The range of scores prior to the training session was 5-65% (average of 29.8%), and after the session 30-95% (average of 58.3%). The improvement in the average scores was 28.5% (standard deviation of 16.6%). The highest improvement between different postgraduate year levels was the PGY3 level, followed by PGY2 and PGY4-PGY6 respectively. Highest improvement was 75% and one individual did worse by 5%. Survey results were highly positive.

Conclusions

Breaking down the anatomy of the middle ear structures into subgroups may help with understanding the three-dimensional relationships and subsequently lead to better detection on cross-sectional imaging. Furthermore, visualizing and physically holding a 3-D model may help with committing this information to memory. Randomized case-control studies, a larger sample population, as well as more controlled and standardized teaching scenarios are needed to evaluate the true effectiveness of this technique.



(Filename: TCT_O-422_MiddleEarData.jpg)

O-423

1:57PM - 2:04PM

Characterizing Enhancement in the Internal Auditory Canal on Post-Contrast Radial VIBE

K Munawar¹, E Raz¹, Y Lui²

¹New York University Langone Medical Center, New York, NY, ²New York University School of Medicine, New York City, NY

Purpose

The radial volume interpolated breath hold examination (VIBE) is a 3-D gradient-echo sequence that uses a radial-stack-of-stars sampling scheme to acquire k-space information along rotated spokes, offering a fat-suppressed sequence with increased spatial resolution. The purpose of this study is to evaluate and characterize normal physiologic enhancement within the internal auditory canal observed on the radial VIBE sequence to help differentiate it from pathological entities.

Materials and Methods

This retrospective study was approved by the institutional review board. We reviewed the clinical and radiology records of 450 consecutive patients who underwent an MRI brain with special attention to the internal auditory canal (IAC) performed on 3T magnets at our institution over a period of 18 months. The only exclusion criterion was an IAC with history of prior surgery or known mass. The patient population consisted of 280 females and 196 males (median age 56; mean age 54 years; age range, 7-88 years). We reviewed patient demographics, clinical presentation, and features of IAC enhancement. MRI sequences reviewed include postcontrast radial VIBE, postcontrast spin echo T1-weighted fat saturated (T1 FS+), and fluid sensitive Sampling Perfection with Application-optimized Contrasts by using different flip angle Evolutions (SPACE).

Oral Presentations & Excerptas

Results

Over the inclusion period of 18 months, 952 IACs were evaluated on 476 studies from 450 unique patients. Excluded were 228 IACs because of prior surgery or known neoplasm. Forty-one IACs (5.7%) showed a blush of enhancement in the fundus of the IAC without corresponding enhancement on postcontrast T1 FS+ or nodularity on SPACE sequences. Thirty-three (80.4%) of these had no clinical correlate related to the side of enhancement. Follow-up MRI was available in 11 of 41 with average follow-up time of 265 days, and showed no change.

Conclusions

Advances in imaging such as radial VIBE offer many desirable features for evaluating the IAC. Here we describe physiologic enhancement that can be seen in the fundus of the IAC which likely represents normal circumneural arteriovenous plexus enhancement. This finding can be seen in up to 5.7% of people. This characteristic enhancement without correlate on SPACE should be differentiated from pathologic enhancement such as from schwannoma, meningioma or neuritis.

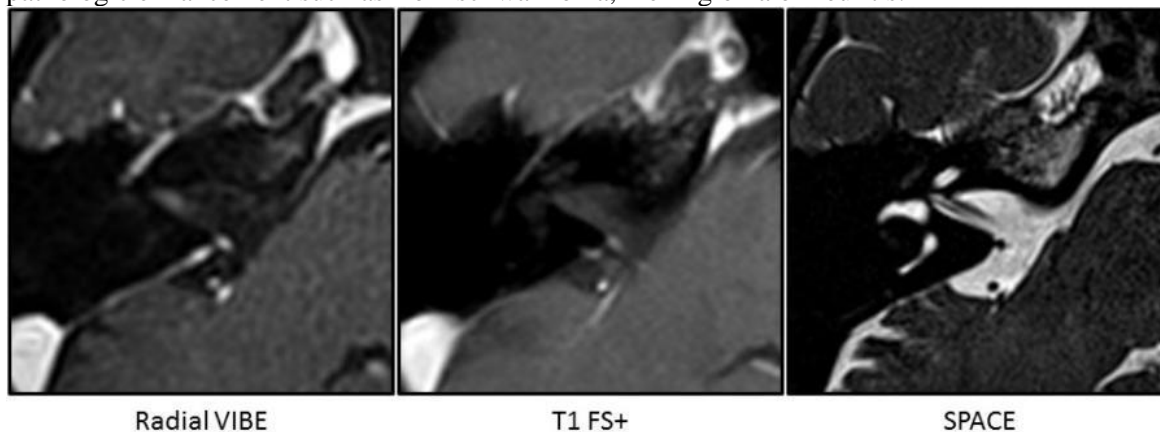


Figure demonstrates a blush of enhancement in the fundus of the IAC on the post-contrast radial VIBE sequence. There is no corresponding enhancement or nodularity on the conventional post-contrast T1 FS and fluid sensitive SPACE sequences, respectively.

(Filename: TCT_O-423_Figure.jpg)

O-424

2:04PM - 2:11PM

Pre- and Post-Flight Size Comparison of the Major Dural Venous Sinuses in Astronauts

P Rabiei¹, A Kamali¹, K Hasan¹, L Kramer¹, R Riascos¹

¹The University of Texas Health Science Center at Houston, Houston, TX

Purpose

Intracranial hypertension can alter the configuration of anatomic structures of the central nervous system. Astronauts have shown signs of increased intracranial pressure after returning from space flights (1). We aimed to determine if there is a statistically significant difference in the size of transverse and superior sagittal sinuses pre and post flight in astronauts.

Materials and Methods

Seventeen astronauts were scanned pre and post flight, using a 3Tesla Verio MRI (Siemens). 3-D isovolumetric T1-weighted images of their brains with isotropic voxel size of one mm were obtained in sagittal planes. The area of the sagittal sinus in the axial plane and the area of the left and right transverse

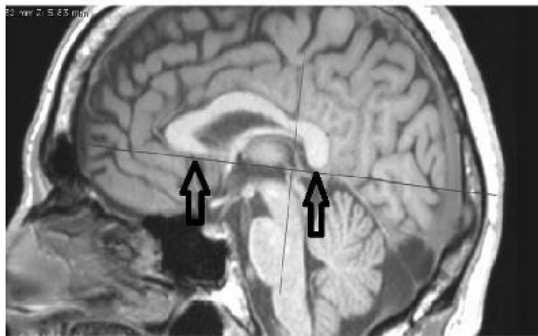
sinuses in the coronal plane were measured using MRIcron. The averages of pre and postflight areas of the transverse and superior sagittal sinuses were compared using paired t-test.

Results

MR images of 17 astronauts were evaluated with average age of 47.3 years and average time in flight of 82.7 days. Postflight average sizes of the right and left transverse venous sinuses were significantly decreased compared to preflight status, from 130.47 mm² and 128.59 mm² to 126 mm² and 124.12 mm² respectively (both p-values < 0.05). Although postflight superior sagittal sinus sizes also showed an average decrease (compared to pre-flight) from 108.29 mm² to 106.29 mm² in the astronauts, this decrease was not statistically significant (p-value = 0.139).

Conclusions

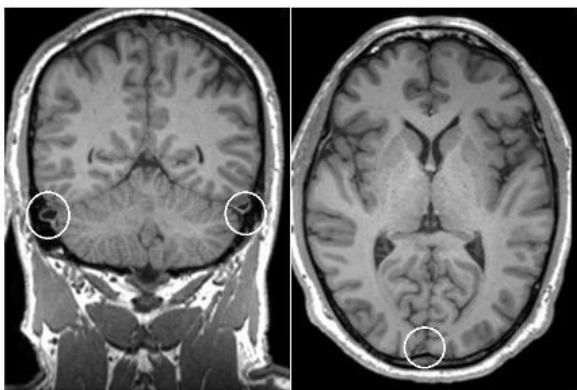
Our study showed postflight decrease in the size of the venous sinuses. These changes are similar to the ones described in patients with idiopathic intracranial hypertension. They can be attributed to structural brain changes in astronauts such as increase in size of the ventricles due to intracranial fluid redistribution or over production of CSF due to microgravity related dynamic changes. Further research, however, is still needed to prove some of the mechanisms proposed in this study.



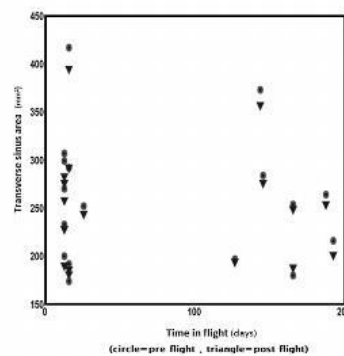
An axial plane was reconstructed that crossed the inferior aspect of the corpus callosum anteriorly and posteriorly.



A coronal plain, perpendicular to the axial plane that crosses through the opisthion was also obtained.



In the axial plane the area of the sagittal sinus and in the coronal plane, the area of the left and right transverse sinuses were also measured using MRIcron.



This diagram shows that most astronauts showed decreases in size of transverse sinus after being exposed to microgravity.

(Filename: TCT_O-424_venous-BW_700dpi.jpg)

O-425

2:11PM - 2:18PM

Ultra-High Resolution CT Scan of the Temporal Bone

K Yamashita¹, A Hiwatashi¹, O Togao¹, D Momosaka¹, H Honda¹

¹*Kyushu University, Fukuoka, Japan*

Purpose

Ultra High-Resolution CT (U-HRCT) provides better spatial resolution than conventional multidetector row CT (ConvCT) and could be expected to identify microstructures with its 0.25-mm collimation, 1792 channels and 160 detector rows, 0.4 × 0.5 mm focus-size, and a 1024 matrix. The purpose of the study was to evaluate key anatomic structures in temporal bone using U-HRCT comparing it to ConvCT.

Materials and Methods

A total of 30 patients (14 males and 16 females; age range, 8-82 years; median 49 years) underwent both U-HRCT and ConvCT. All CT images were obtained with 0.5-mm section thickness and a 512 × 512 matrix, and field of view of 80 mm. Transverse scans were acquired in a plane parallel to the orbitomeatal plane in the helical mode with 120 kV. Images of the 30 temporal bones of unaffected side were reviewed by two independent neuroradiologists who rated the visibility of key anatomic structures for both U-HRCT and ConvCT. The ratings between U-HRCT and ConvCT were compared using Wilcoxon matched-pairs signed rank test. The interobserver agreement on the rating of stapedius tendon was evaluated using weighted κ statistics.

Results

Excellent interobserver agreement was shown for U-HRCT ($\kappa = 0.920$), whereas good agreement was obtained for ConvCT ($\kappa = 0.733$). According to both observers, stapedius tendon was more clearly visualized using U-HRCT than ConvCT ($p < 0.0001$). All other anatomic structures were well visualized using both CT scanners.

Conclusions

The anatomy of temporal bone is more conspicuous on U-HRCT than on ConvCT because of its ultra high-resolution detector. U-HRCT may provide beneficial information for determining surgical indication or procedures.

O-426

2:18PM - 2:25PM

Three-Dimensional Printing the Intra- and Extra-cranial Segments of the Cranial Nerves Utilizing High-Resolution MRI and CT Co-Registration

A Rao¹, R Javan², P Heidari², K Uprety², C Gragnaniello², N Mostaghni³

¹*George Washington University School of Medicine, Washington, DC*, ²*George Washington University Hospital, Washington, DC*, ³*University of California, Irvine, Irvine, CA*

Purpose

Cranial nerves in their extracranial portions are difficult to study, given the intricate anatomy and technical difficulties in their visualization except when abnormal. In this study, we employed multiple imaging techniques to help outline the course of the cranial nerves in their intra and extracranial segments. Coupled with 3-D printing, this may allow for better understanding of their course as well as to help with preoperative planning of approaches to lesions involving these structures.

Materials and Methods

Skull base CT images of 0.6 mm thickness in bone kernel along with multiple high-resolution MRI sequences of the same skull base were imported as DICOM in Materialise Mimics and subsequently coregistered. The MRI sequences include axial SSFP images of the skull base acquired in 0.8 mm thickness. MR Neurography images of the entire head were acquired with 0.9 mm thickness and -0.45 gap, generating thin slices that are 3-D isotropic. Additionally, axial T1 postcontrast 3-D FSPGR images were also obtained. In Materialise Mimics, the 'Nerve Tracing' tool was utilized with 2 mm radius to

create the intra and extracranial segments by tracing the course either through actual visualization or using neural foramina, fissures and landmarks. The resulting 3-D meshes were then imported into Autodesk 3-D Studio Max where they were perfected and attached to a separate 3-D mesh of the brainstem from a previous project.

Results

An accurate 3-D printed model of the cranial nerves that includes the cisternal segments and parts of their extracranial segments, whether visible on imaging or deduced through known landmarks, was successfully created with polyamide material.

Conclusions

The complex neuroanatomy of the cranial nerves may better be understood and depicted using advanced 3-D printed models. This technique may also be of great use for the preoperative planning where delineation can impact the choice of surgical approach as well as improve outcomes.

O-427

2:25PM - 2:32PM

Importance of Scout Images in Cross Sectional Imaging

K Erbay¹, A Rahman², S Erbay²

¹University of Connecticut, Pittsburgh, PA, ²University Pittsburgh Medical Center, Pittsburgh, PA

Purpose

Scout images (SI) are the initial necessary step of cross-sectional imaging and may yield very valuable and relevant information for everyday radiologists. They identify the human body in space, localize the area of interest and visualize a larger part of the body with less image resolution than cross-sectional images. However, this poor visualization of larger part of the body can play a dangerous role in radiology (2, 3). Prior studies have suggested that significant number of unexpected radiologic findings in spinal CT studies may be visualized in scout images (4). Yet, well organized studies describing the incidence and prevalence of these unexpected findings (UF) in the scout images and comparing these across the different types of imaging studies and body parts are lacking. To our knowledge, no such data exists in the literature comparing unexpected findings seen in the scout images of spinal MRI versus CT studies. The purpose of the study is to better understand the distribution of reported unexpected findings between scout and cross-sectional images during spinal imaging as well as to generate a data comparing the distribution of reported unexpected findings in spinal CT and MRI studies. We have further explored the factors possibly affecting the detection rate of these unexpected findings in the spinal CT and MRI studies.

Materials and Methods

An institutional review board (IRB) approval was obtained prior to this retrospective record review of cervical, thoracic and lumbar spine CT and MRI studies, 500 cases for each modality. Spine CT and MRI studies must have clinical findings suggesting spinal diseases, planning and follow-up of spinal treatments. The reported imaging findings of these studies are then grouped into spinal versus nonspinal categories. The low dose frontal and lateral scan grams constitute the scout images (SI-CT) in spinal CT studies. The scout images of MRI (SI-MRI) studies were obtained in three orthogonal planes either as T1- or T2-weighted images or GRE. The report of each study and the imaging findings were reviewed by two board certified radiologists with each having over 10 years of clinical experience to identify and categorize reported imaging findings as spinal or nonspinal unexpected findings (UF). The UF's are further classified into three separate body parts: head-neck, chest including upper extremities and abdomen-pelvis including the lower extremities for CT and MRI studies. The statistical methods were descriptive statistics for the continuous variable, age, including mean, standard deviation (SD), median and the range for each subgroup, as well as a contingency table of counts and proportions for the nominal categorical variable, sex. For the continuous variable, a one-way analysis of variance (ANOVA) was conducted. For the nominal categorical variable, a Student chi-square test and Fisher's exact tests were

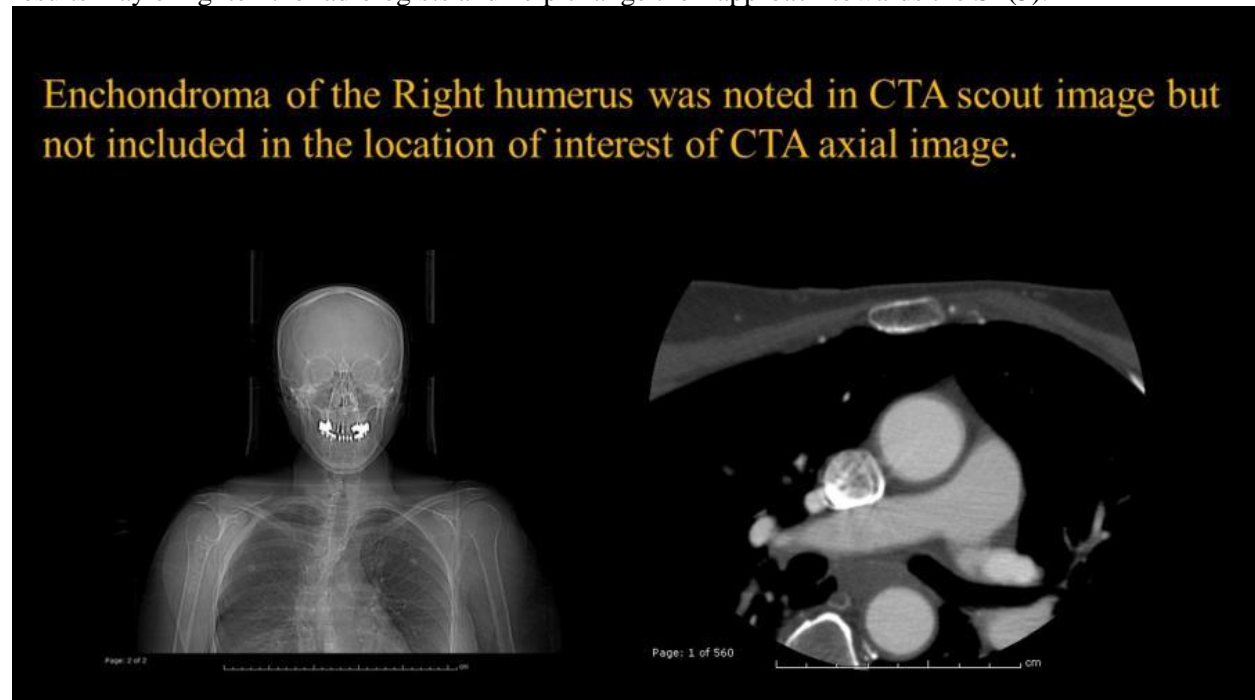
conducted. Two-sided p-values were reported, and the statistical significance was considered reached when $p < 0.05$. All analyses were conducted using R software version 2.15.1.

Results

There were total 81 UF in CT and 112 for MRI group; 20% of UF seen only in SI-MRI, which is statistically significant. This finding also highlights the importance of S-MRI. CSI-CT, compared to SI-CT, reported more UF (CSI 19, SI 2).

Conclusions

SI visualize a larger part of the body with less image resolution than cross-sectional images. This combination, coupled with the fact that radiology community may not invest too much time and effort to review these images, signifies the danger these images may pose. SI may harbor UF which may not be visualized or appreciated in CSI. Our results indicate that SI are important part of imaging studies and should be carefully reviewed for presence of SI. This is especially true for MRI studies of the spine. Our results may enlighten the radiologists and help change their approach towards the SI (5).



(Filename: TCT_O-427_Slide1.JPG)

O-428

2:32PM - 2:39PM

Craniocervical and Posterior Fossa Dimensions Can Affect Need for Decompressive Craniotomy In Posterior Fossa Hemorrhage

E Neufeld¹, L Shah¹

¹University of Utah, Salt Lake City, UT

Purpose

Posterior fossa hemorrhage (PFH) may require decompressive craniotomy due to hydrocephalus and/or herniation. Surgical literature shows that hematomata > 3 cm have higher likelihood of surgery, which is indicated for evidence of herniation or declining GCS. No evaluation of the effect of craniocervical junction (CCJ) and PF dimensions on the need for surgery exists. We evaluated validated CCJ/PF measurements in patients with PFH and correlated these measurements with need for decompression.

Oral Presentations & Excerptas

Materials and Methods

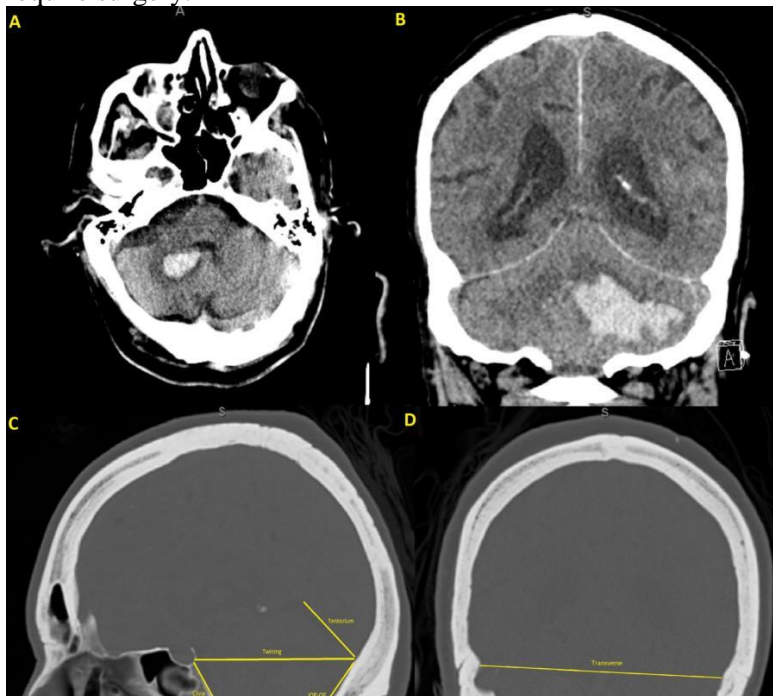
CT/MR examinations performed on adults with primary presentation of PFH were found. Cases with an underlying mass or concurrent supratentorial pathology were excluded. Hemorrhage size was measured in three dimensions and averaged. PF dimensions measured included: McRae's, clival line, Twining's, internal occipital protuberance to opisthion distance (IOP-OP), tentorium diameter, and transverse diameter of the PF as measured below the transverse-sigmoid junctions. Chart review for management details and patient disposition was performed. Values of the craniotomy group and nonsurgical, surviving group were compared using two tailed t-test.

Results

Included were 29 nonsurgical and 19 surgical cases. Statistically significant difference between hematoma diameter of the surgical (4.6 cm) and nonsurgical cases (2.9 cm) was found ($P<0.001$). Product of the clival length, Twining's, and transverse diameter was calculated. Statistically significant difference between mean of this measurement of the surgical (296.02 cm³) and nonsurgical cases (328.66 cm³) was found ($P=0.02$). A scaled score was made by dividing hematoma diameter by PF volume and multiplying by 1000. Statistically significant difference in the mean of scores of the nonsurgical and surgical patients was found ($P<0.01$). No nonsurgical patient scored >14 . No surgical patient scored <11 .

Conclusions

Our data indicates that smaller PF volumes were more likely to require surgery as determined by clinical standards, independent of hemorrhage size. Our data suggests that patients with scores 14 will likely require surgery.



(Filename: TCT_O-428_PFHImages.jpg)

Wednesday, June 6, 2018

3:00PM - 4:30PM

22D-Parallel Paper Session - Pediatric: Advanced Techniques

O-429

3:00PM - 3:07PM

Oral Presentations & Excerptas

Impact Exposure Threshold Changes in Gray Matter and Cerebrospinal Fluid Volumes in the Absence of Concussion

J Holcomb¹, G Murugesan¹, R Fisicaro¹, E Davenport², J Urban³, B Wagner¹, M Espeland³, C Whitlow³, J Stitzel³, J Maldjian¹

¹University of Texas Southwestern, Dallas, TX, ²University of Texas Southwestern Medical Center, Dallas, TX, ³Wake Forest University School of Medicine, Winston-Salem, NC

Purpose

The purpose of the study is to model the cumulative effects of head impacts on changes in global gray-matter volume (GMV) and global cerebrospinal fluid volume (CSFV) during a season of varsity high school football.

Materials and Methods

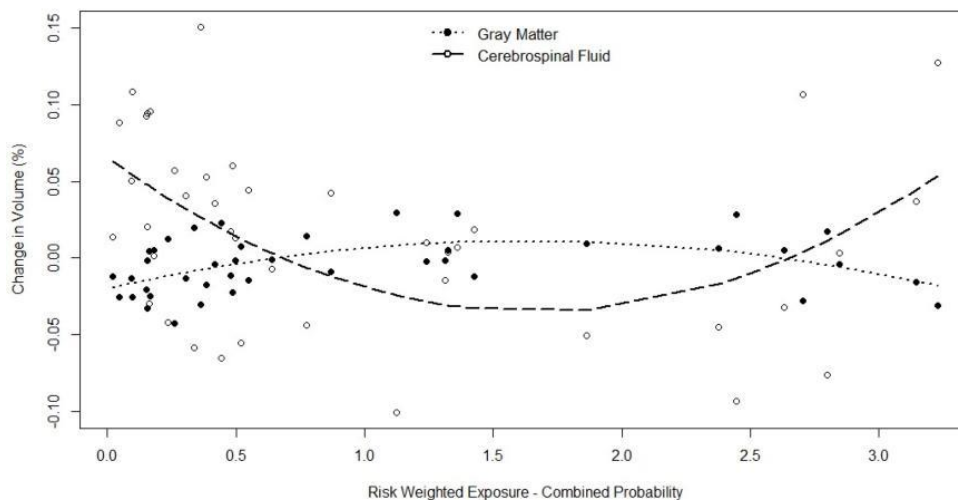
Forty-one high school players (mean age=17.12; no recent concussion hx) were instrumented with the Head Impact Telemetry System (HITS) during all football practices and games. HITS data were used to compute the combined probability risk-weighted cumulative exposure (RWECP) measure for each subject. (1) Each subject received a MRI before and after the season. GMV and CSFV were calculated using the vbm8 toolbox and SPM. To correct for changes in total intracranial volume (ICV) between scans, total GMV and total CSFV were divided by total ICV. Percent change in volume was then calculated. A quadratic model was created to test for interaction between changes in GMV and CSFV with the predictor regressors of RWECP, BMI, race, days between scans, and age.

Results

While controlling for BMI, race, days between scans, and age, RWECP was a significant quadratic predictor of changes in total GMV and CSFV ($R^2=0.2636$, $p\text{-value}=0.002988$; $R^2=0.2337$, $p\text{-value}=0.006359$ respectively). Further, global changes in GMV were significantly and inversely correlated with global changes in CSFV ($R^2=0.8117$, $p\text{-value}=1.01 \times 10^{-15}$).

Conclusions

This study provides evidence of an increase in GMV until a threshold value RWECP, with a decrease in GMV beyond that threshold. As gray-matter volumes are expected to decrease with time in adolescent populations (2), these findings may reflect compensation mechanisms which prevent normal gray-matter apoptosis below a threshold value of RWECP. Beyond that threshold, the ability for neural tissue to compensate through neuroprotective mechanisms may be eclipsed by trauma-induced atrophy, consistent with findings of gray-matter loss after concussion. (3) Evidence suggests inflammation may be involved in both outcomes. (4, 5)



(Filename: TCT_O-429_gm_csf_percent.jpg)

O-430

3:07PM - 3:14PM

Cerebral Peduncle White Matter Modeling Abnormalities Related to Head Impact Exposure After a Season of High School Football

R Fisicaro¹, E Davenport², J Holcomb¹, J Urban³, B Wagner¹, C Whitlow³, J Stitzel³, J Maldjian¹
¹University of Texas Southwestern, Dallas, TX, ²UT Southwestern Medical Center, Dallas, TX, ³Wake Forest University School of Medicine, Winston-Salem, NC

Purpose

The purpose of this study is to determine the relationship between changes in white-matter modeling (WMM) metrics and cumulative head impact exposure after a season of high school football in the absence of clinically diagnosed concussion. We expect cerebral peduncle tortuosity decreases and AWF increases based on previous findings related to inflammation and axonal swelling, respectively (1-3).

Materials and Methods

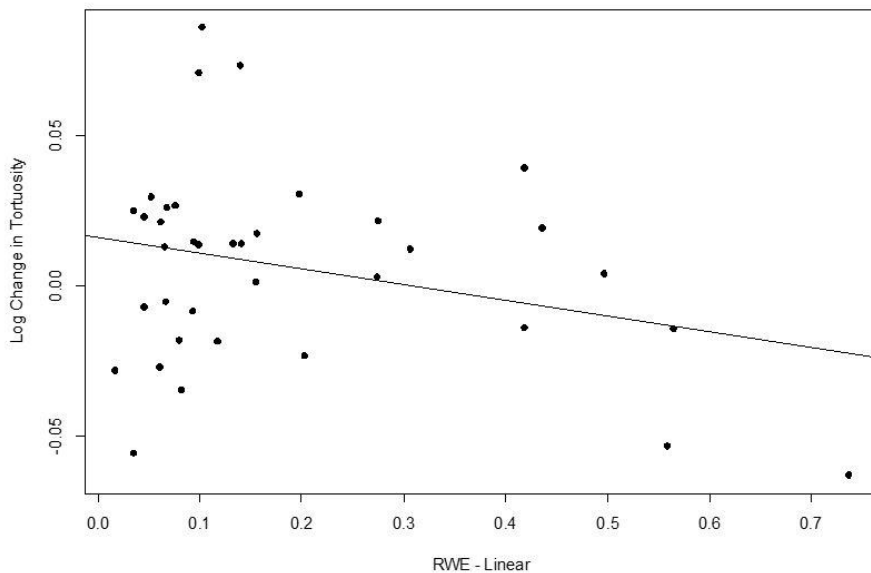
Thirty-seven football players from local high schools (age range 14.8-18.1) without significant medical history and no history of concussion within the past year were instrumented with the Head Impact Telemetry System (HITS) during all practices and games. Risk-weighted cumulative exposure (RWE) and its subcomponents combined probability (RWE_{cp}), linear (RWE_{lin}), and rotational (RWE_{rot}) were derived from the HITS data (4). MRI data were acquired pre and postseason. Images were normalized to MNI space and segmented into grey, white, and CSF using VBM8. The Johns Hopkins University (JHU) atlas was used to delineate the cerebral peduncle white matter region of interest. WMM metrics were calculated using the Diffusion Kurtosis Estimator (5). Linear regression analyses using R were conducted to study the relationship between WMM and RWE metrics. Age and BMI were used as regressors. To satisfy normality, log transformation was applied to WMM data.

Results

Regression analysis showed a significant, inverse relationship between RWE_{lin} and tortuosity ($p = 0.046$, $R^2 = 0.127$) and a trend towards significant, positive relationships between AWF and both RWE_{cp} and RWE_{lin} ($p=0.099$, $R^2=0.089$ and $p=0.118$, $R^2=0.081$, respectively). No other significant relationships were seen.

Conclusions

We demonstrate significant changes in tortuosity of the cerebral peduncle related to cumulative head impact exposure after a season of high school football in the absence of clinical concussion. Decreases in tortuosity suggest possible demyelination or extracellular inflammation while increases in AWF are suggestive of axonal swelling (2-3).



(Filename: TCT_O-430_Capture.JPG)

O-431

3:14PM - 3:21PM

MEG Measured Delta Waves Increase After Concussion

E Davenport¹, J Urban², B Wagner³, M Espeland², C Whitlow², J Stitzel², J Maldjian³

¹University of Texas Southwestern Medical Center, Dallas, TX, ²Wake Forest University School of Medicine, Winston-Salem, NC, ³University of Texas Southwestern, Dallas, TX

Purpose

The purpose of this study is to determine if delta waves, measured by magnetoencephalography (MEG), increase due to a sports concussion.

Materials and Methods

From a larger study on subconcussive impacts in high school football, five players were diagnosed with a concussion during the season (mean age=16.1). Subjects followed returned-to-play protocols. Eight minutes of eyes-open, resting-state MEG data were acquired for each subject and control using a 275 channel CTF whole-head system. Football players were scanned preseason, within 36 hours postconcussion, and postseason. Seven age- and gender-matched noncontact sports athletes (controls) were also recruited (mean age=16.2). Controls received baseline and follow-up scans four months later. Using Brainstorm1, MEG data were baseline corrected, band-stop filtered (60Hz), down-sampled to 250Hz, and band-pass filtered to 1-100Hz. Eye blinks, and muscle artifacts were removed using independent component analysis. The average whole-brain power of the delta frequency and total power was computed for each scan. The delta frequency power was normalized by the total power. In the concussed football players, preseason delta power was subtracted from concussion and postseason delta power. For the control subject, baseline delta power was subtracted from the four-month follow-up scan. T-tests were performed to compare the change in delta power of controls to the change in delta power of concussed football players at both concussion and postseason time points.

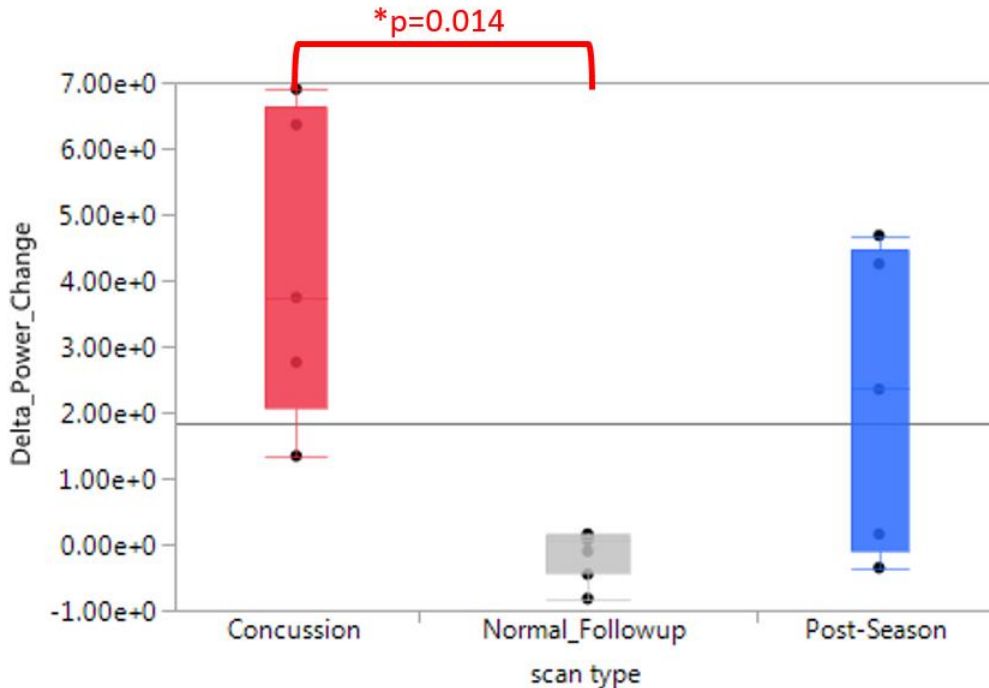
Results

The change in delta power following concussion was significantly different from controls ($p=0.0141$). There was no significant difference in the change in delta power at postseason compared to concussion

($p=0.2114$). Postseason, the football players did not show a significant difference from controls ($p=0.0834$).

Conclusions

We demonstrate that a single concussion can increase delta frequency power in MEG. However, the change in delta power normalizes after the players have followed returned-to-play protocols.



(Filename: TCT_O-431_box_plot.jpg)

O-432

3:21PM - 3:28PM

Diffusion Metric Variability in the Normal Pediatric Spinal Cord

B Reynolds¹, S Smith¹, S By², Q Weinberg², B Ramkorun², K Harrington², M Adams³, J Wellons³, A Bhatia³

¹Vanderbilt University Medical Center, Nashville, TN, ²Vanderbilt University Institute of Imaging Science, Nashville, TN, ³Monroe Carell Jr Children's Hospital at Vanderbilt, Nashville, TN

Purpose

The purpose of the study is to evaluate diffusion-tensor imaging (DTI) indices of the spinal cord (SC) in normal children based on age and cord level.

Materials and Methods

A retrospective analysis was performed on DTI acquired in a pediatric population at Vanderbilt Children's Hospital. Diffusion-weighted images (15 directions) were acquired on a 3.0T Philips Achieva in the cervical or thoracic/lumbar SC (By et al., 2016). Volumes of interest (VOI) were manually drawn for each axial slice to include whole cord, excluding CSF, conus, and brainstem. Mean DTI metrics (AD, RD, MD, and FA) were calculated across all voxels within each slice and across all slices containing cord (3-D VOI). For each patient, a representative slice (2-D VOI) was chosen based on location and data quality. 3-D VOI and 2-D VOI values were linearly correlated with the patients' ages.

Results

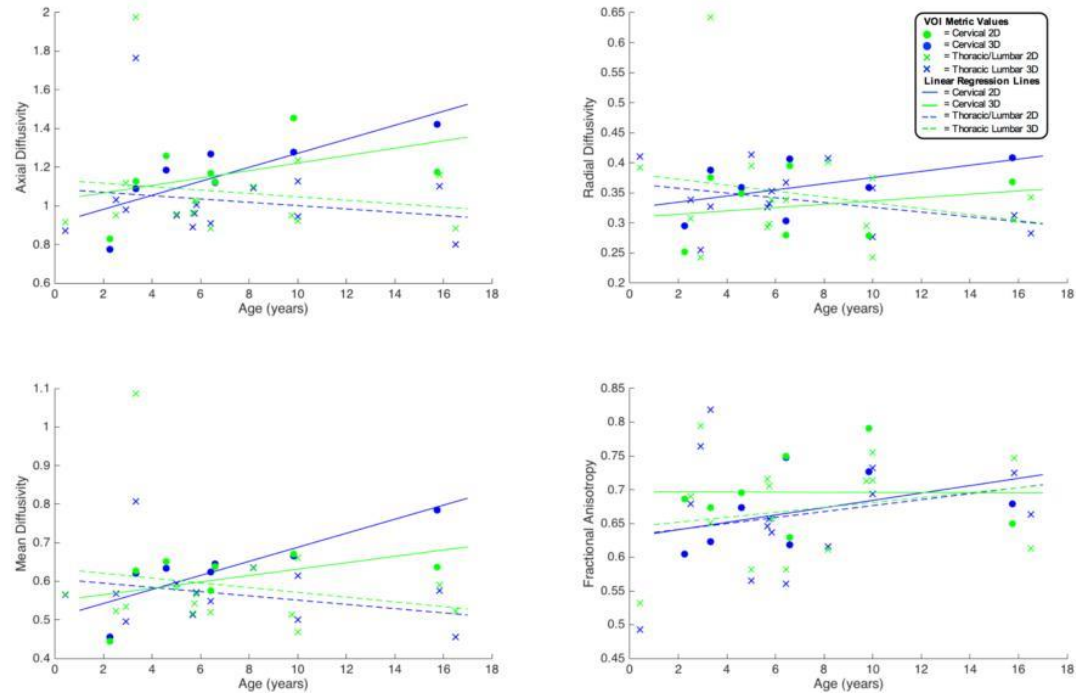
Twenty-two normal patients, seven within the cervical SC and 15 in the thoracic/lumbar SC, and ages

Oral Presentations & Excerptas

ranged from four months to 16-years-old. No diffusion metric showed a significant correlation with age using 2-D VOI. However, in 3-D VOI both AD and MD showed significant positive correlations with age in the cervical SC ($R=0.82$, $p=0.025$, and $R=0.86$, $p=0.012$) (Figure 1). Analyses also showed that rostral slices in the thoracic/lumbar SC have higher AD and MD than caudal slices (paired t-test, $p=0.001$, and $p=0.031$), and that the difference between rostral and caudal slices in the cervical SC increases with age for AD ($R=0.82$, $p=0.024$) and MD ($R=0.87$, $p=0.011$).

Conclusions

There is a correlation between age, cord level, and microstructural diffusivity in the pediatric spinal cord. Normal DTI indices during development must be defined in the pediatric spine before it can reach clinical utility in evaluating spinal pathology.



(Filename: TCT_O-432_Figure1.jpg)

O-433

3:28PM - 3:35PM

Volumetric Analysis of Pediatric Spinal Cord Structural MRI data using SCT

S Shahrapour¹, B De Leener², D Middleton³, A Flanders⁴, S Faro⁵, J Cohen-Adad², M Alizadeh³, L Krisa³, F Mohamed³

¹Temple University, Philadelphia, PA, ²Institute of Biomedical Engineering, Polytechnique Montreal, Montreal, QC, Canada, ³Thomas Jefferson University, Philadelphia, PA, ⁴Thomas Jefferson University Hospital, Philadelphia, PA, ⁵Johns Hopkins School of Medicine, Baltimore, MD,

Purpose

The purpose of this study is to investigate the age-related changes of the spinal cord volume in healthy pediatric subjects using a semiautomated and quantitative method implemented in the Spinal Cord Toolbox (SCT) [1] an open source software for processing spinal cord MR images.

Materials and Methods

A T2-weighted 3-D SPACE sequence from 20 typically developing (TD) pediatric subjects ranging in age from 6-16 years old subjects was acquired to cover C1-T12 in two slabs. The slabs were stitched to generate the entire cord using the vendor software on the scanner. The scans were performed using a 3.0T

Oral Presentations & Excerptas

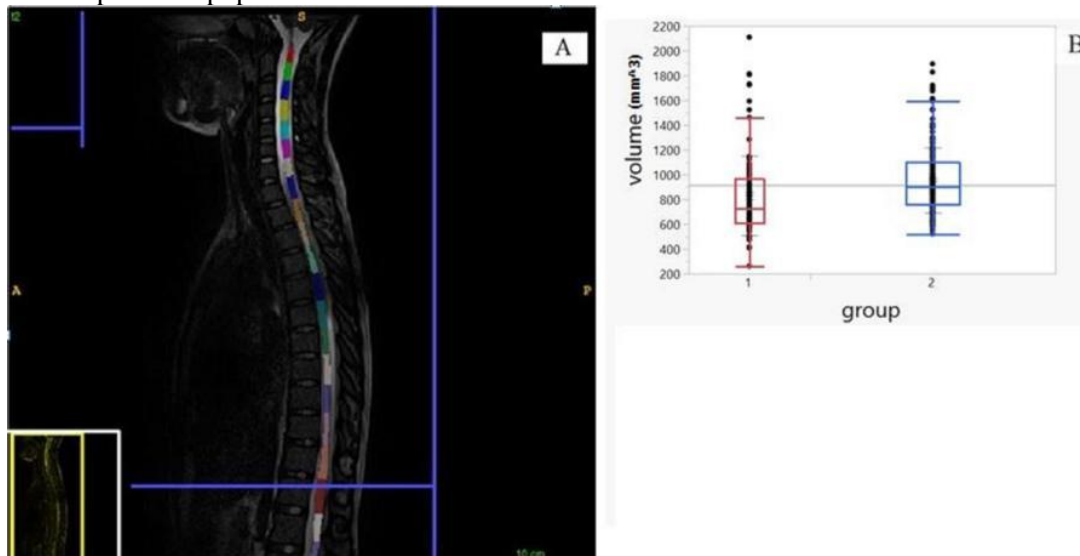
Siemens Verio MR scanner and the imaging parameters are: voxel size = $1 \times 1 \times 1 \text{ mm}^3$, TR=1500 ms, TE=122 ms and slice thickness=1 mm. The SCT pipeline involves segmentation of this stitched structural image [2] followed by vertebral level labelling as shown in Figure 1. The software then requires manual input of the first intervertebral disc and then continues a disc search along the entire cord (superior>inferior). Next the volume is calculated as the product of number of voxels at each disk level by voxel size. Volumes were then compared between two age groups (age group one=6–11 years (n=8) and age group two=12–16 years (n =12)). Standard least squared linear regression model based on restricted maximum likelihood (REML) method (JMP-13.0) was used to evaluate the relationship between age and cord volume.

Results

An increase in volume of spinal cord (group two= $956.173 \pm 264.673 \text{ mm}^3$, group one= $829.684 \pm 321.074 \text{ mm}^3$), were observed with age. Statistically significant differences were seen between the group volumes along the C1-T12 vertebral levels ($p < 0.001$, $r^2 = 0.77$) (Figure 1).

Conclusions

SCT is very effective in providing quantitative information from anatomical spinal cord with minimal user intervention. As expected, results of the study show that the spinal cord volume obtained in TD pediatric subjects was larger in older subjects, indicating impact of age on cord volume. Such automatic measurement of spinal cord might help the study of various pathological conditions affecting the spinal cord in pediatric populations.



A: Vertebral level labeling, B: Boxplot of cord volumes by age group

(Filename: TCT_O-433_Figure1.JPG)

O-434

3:35PM - 3:42PM

Single institution experience of intraspinal tumors presenting with leptomeningeal disease in the pediatric population

A Bhatia¹, J Ndolo¹, D Pastakia¹, S Pruthi¹, A Esbenshade¹

¹Monroe Carell Jr. Children's Hospital at Vanderbilt, Nashville, TN

Purpose

Intraspinal tumors in the pediatric population can infrequently present with leptomeningeal disease, resulting in hydrocephalus and making treatment options more challenging. A recent case out of our

institution of disseminated oligodendroglial-like leptomeningeal tumor of childhood presented with diffuse leptomeningeal disease. We reviewed our database to determine which tumors presented with imaging findings of leptomeningeal disease and describe the grading and imaging characteristics of the primary intraspinal tumor, such as size, location within the cord, and enhancement.

Materials and Methods

All spine tumors from our database at a single pediatric hospital were reviewed from 2005 to present (n=22). Initial MRI studies were reviewed of those presenting with leptomeningeal disease, based off postcontrast T1 sequences of the spine, and brain if available. The imaging characteristics of the primary tumor were described, including size, location, and enhancement. A review of the age, sex, and pathology was also performed.

Results

Seven out of 22 intraspinal tumors presented with leptomeningeal disease. Ages ranged from one month to 10 years of age with three males and four females. Largest dimension was used for size and ranged from 1.3 cm 7.3 cm. A majority were located in the cervical region, four out of seven patients with one centered at the T1 level. Three out of seven presented with hydrocephalus, two being low-grade tumors. All the tumors demonstrated enhancement with variable patterns. There was a mix of high-grade and low-grade tumors (four high-grade, three low-grade).

Conclusions

Primary intraspinal tumors presenting with leptomeningeal disease in the pediatric population may be low-grade or high-grade with variable imaging characteristics on MRI. This is consistent with literature, which has demonstrated those presenting with leptomeningeal disease are not more likely to be high-grade or low-grade.

O-435

3:42PM - 3:49PM

Driver mutations in pediatric diffuse gliomas with histone H3 K27M mutation

M Aboian¹, E Tong¹, S Cha¹

¹University of California San Francisco, San Francisco, CA

Purpose

Diffuse midline gliomas with histone H3 K27M mutation are aggressive tumors commonly found in children with similar imaging characteristics to histone wild-type diffuse midline gliomas. Driver mutations are common in these tumors and are presumed to play a critical role in tumorigenesis. We propose to evaluate imaging features of patients with different driver mutations such ACVR1, PPM1D, and p53.

Materials and Methods

We identified 212 pediatric patients (<21 years old) with high-grade gliomas with preoperative MRI imaging from tumor board review at our institution. Seven of these patients had 500 gene panel mutation testing and imaging characteristics of these tumors were evaluated. Gene expression patterns in normal brain were analyzed using Allen Brain Atlas.

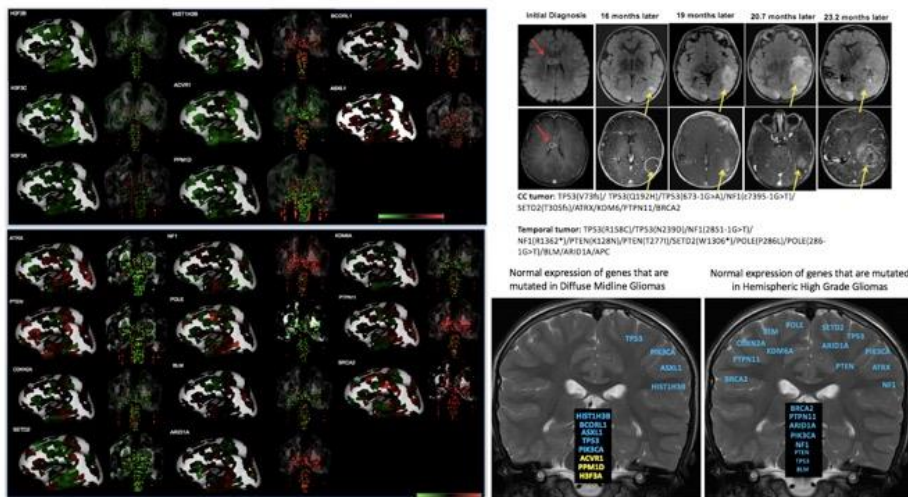
Results

Four of the patients had diffuse midline gliomas and three had hemispheric high-grade gliomas. Three of the diffuse midline gliomas had the K27M mutation in the tail of histone H3 protein. All of the patients undergoing 500 gene panel testing were found to have additional mutations in a variety of genes with most common being ACVR1, PPM1D, and p53. Midline gliomas did not have prominent enhancement while hemispheric gliomas with multiple mutations were found to have prominent enhancement. Gene expression analysis in normal brains based on Allen Brain Atlas demonstrated that genes mutated in midline gliomas were highly expressed along the midline brain structures with low expression within the cerebral hemispheres. On the other hand, genes mutated in hemispheric gliomas had high expression levels along the hemispheres.

Oral Presentations & Excerptas

Conclusions

Driver mutations are found in histone H3 K27M mutant and wild-type midline gliomas, while hemispheric high-grade gliomas are commonly hypermutated in genes that are normally expressed highly within the cerebral hemispheres. Hemispheric gliomas have lower ADC values as opposed to midline gliomas, while there is no significant difference in T2/FLAIR and postcontrast imaging characteristics between them.



(Filename: TCT_O-435_figure.jpg)

O-436

3:49PM - 3:56PM

Proliferative Index Influences Early Radiological Response Pattern Of Pediatric High-Grade Recurrent Gliomas Treated With HSV-1 G207 Oncolytic Immunovirotherapy

A Bag¹, R LI¹, D Osorio², J Hukin³, A Martin⁴, D Pastakia⁵, M Karajannis⁶, G Gillespie¹, J Markert¹, J Johnston¹, G Friedman¹

¹University of Alabama at Birmingham, Birmingham, AL, ²Nationwide Children's Hospital, Columbus, OH, ³University of British Columbia, Vancouver, BC, Canada, ⁴Johns Hopkins University School of Medicine, Baltimore, MD, ⁵Vanderbilt University Medical Center, Nashville, TN, ⁶Memorial Sloan Kettering Cancer Center, New York, NY

Purpose

Overall survival of pediatric high-grade gliomas is dismal, even with multimodality treatment approaches. Novel, targeted treatment strategies are being actively investigated to improve outcomes and lessen side effects. We are investigating the safety and tolerability and treatment response to intratumoral inoculation of genetically engineered oncolytic HSV-1 G207, which lacks genes essential for replication in normal brain. We report UNIQUE patterns of early radiographic response to this unique therapy.

Materials and Methods

After informed consent, patients underwent a biopsy to confirm viable tumor and then had up to four silastic catheters placed into enhancing areas of tumor. The following day, G207 was infused over six hours. Patients had an MRI prior to therapy, three days after, and at day 28-36 post-G207 infusion that included diffusion imaging, dynamic contrast-enhanced T1-weighted and susceptibility-weighted perfusion imaging, multiecho T2 imaging with tissue T2 calculation, in addition to 3-D T1- and T2-weighted imaging. Immunohistochemistry was performed on biopsy specimens and MIB-1% was calculated.

Oral Presentations & Excerptas

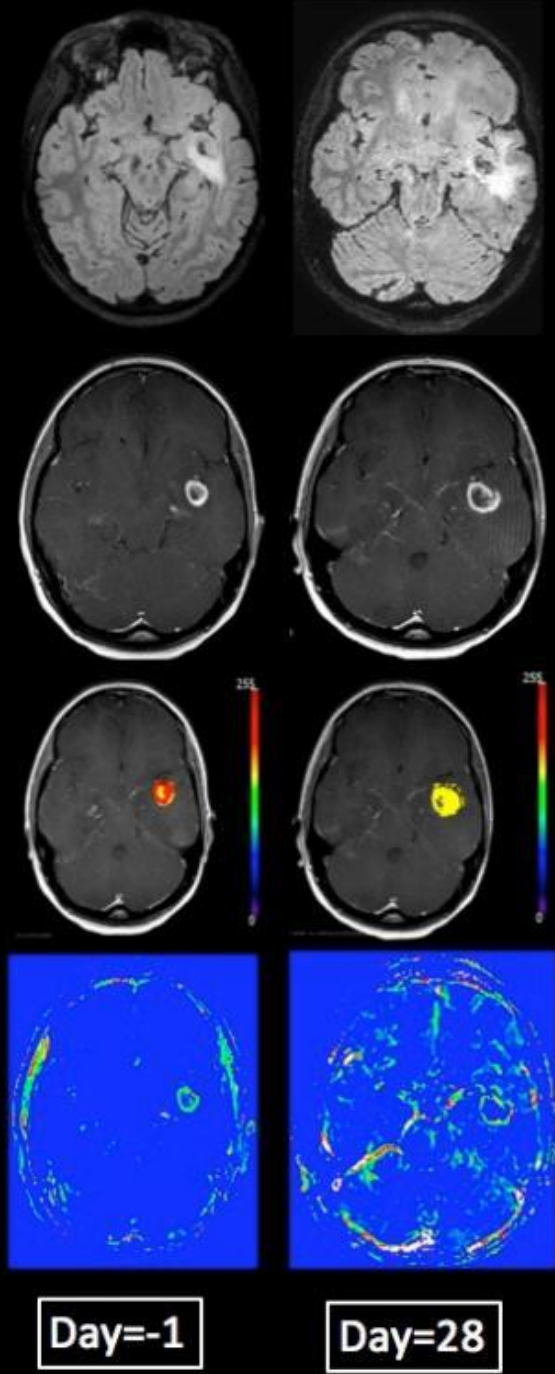
Results

Six high-grade gliomas (5 glioblastoma and 1 anaplastic astrocytoma) in five subjects were treated; one subject had multifocal disease with two foci treated. Three tumors had a high proliferation index (up to 70%) and three had a low proliferation index ($\leq 5\%$). Expected postoperative changes from the catheters was the only finding on the day three MRI for all patients. On the day 28-36 post-therapy MRI, tumors with high proliferation index either progressed (n=1) or demonstrated signs of pseudoprogression (n=2) including enlargement of the necrotic center with enlargement of enhancing component, worsening peritumoral T2 abnormal areas, increased mean apparent diffusion coefficient (mADC); and lowered mean relative cerebral blood volume (rCBV) and mean Ktrans. Except for mild increase in the mADC, tumors with low proliferation index (n=3) demonstrated no significant changes from the pretreatment MRI.

Conclusions

This data suggests that tumor proliferation index may influence early radiographic responses of pediatric high-grade gliomas to oncolytic HSV-1.

Tumor 2
Glioblasoma
MIB-1 index: high



(Filename: TCT_O-436_screenshot.jpg)

Textural Analysis of Posterior Fossa Pediatric Brain Tumors on T2 Weighted MRI Images

C Yip¹, P Tang², J Allen¹

¹Duke-NUS Medical School, Singapore, Singapore, ²KK Women's and Children's Hospital, Singapore, Singapore

Purpose

Pediatric brain tumors are the most common solid tumors and the second most common cancer in childhood with most occurring in the posterior fossa. Textural analysis can potentially give additional information to supplement visual inspection. This study seeks first to determine what textural parameters best distinguish normal brain from brain tumor in a pediatric population and if textural analysis is useful in distinguishing low-grade from high-grade tumors.

Materials and Methods

This study uses the statistical filtration histogram approach to perform textural analysis. The textural parameters studied were mean, standard deviation (SD), entropy, mean of positive pixels (MPP), skewness and kurtosis. The sample consists of 20 pediatric patients with brain tumors with MRI imaging available in DICOM format. Textural analysis was performed with TexRAD, with regions of interest (ROIs) drawn by a single operator on T2 axial slices, demarcating the brain tumors and normal brain tissue on the same axial slices. The software suite SAS was used for statistical analysis.

Results

Textural parameters of normal brain tissue in the groups of children with high-grade and low-grade brain tumors did not differ (all $p > 0.5$). The textural parameters mean, SD, entropy, MPP, skewness and kurtosis in both high-grade and low-grade brain tumors show significant difference compared to normal brain tissue (all $p < 0.01$). The textural parameters mean, SD, entropy, MPP, skewness and kurtosis were all greater in high-grade compared to low-grade brain tumors but statistical significance was only reached for SD, MPP and skewness.

Conclusions

The textural parameters mean, SD, entropy, MPP, skewness and kurtosis in brain tumors show significant difference compared to normal brain tissue. All of these texture parameters were also greater in high-grade compared to low-grade tumors on T2 MRI images, with statistical significance reached for SD, MPP and skewness.

Textural Parameters Compared between Normal Brain Tissue, High Grade Brain Tumors and Low Grade Brain Tumors at SSF 2 (n = 20)

Textural Parameter	Estimate				Normal Brain Tissue Compared in Children with Low and High Grade Brain Tumors	Normal Brain Tissue Compared Against Brain Tumors	Low Grade Compared Against High Grade Brain Tumors
	Normal Brain Tissue in Children with Low Grade Tumor	Normal Brain Tissue in Children with High Grade Tumor	Low Grade Tumor	High Grade Tumor			
Mean	2.79 ± 13.54	-2.94 ± 28.93	43.89 ± 27.13	63.66 ± 76.4	0.58	* 0.0002	0.19
SD	47.36 ± 25.08	53.41 ± 47.79	197.15 ± 89.71	341.32 ± 313.14	0.72	* 0.0002	* 0.02
Entropy	4.52 ± 0.53	4.56 ± 0.55	6.34 ± 0.55	6.58 ± 0.88	0.87	* < 0.0001	0.22
MPP	40.40 ± 19.43	43.72 ± 43.04	160.58 ± 68.17	271.46 ± 241.51	0.83	* < 0.0001	* 0.02
Skewness	-0.071 ± 0.42	-0.093 ± 0.56	0.32 ± 0.64	0.76 ± 0.9	0.92	* 0.0029	* 0.03
Kurtosis	-0.12 ± 0.57	0.034 ± 1.11	3.27 ± 4.77	4.24 ± 4.39	0.71	* < 0.0001	0.42

* Denotes P value < 0.05. Differences were tested with ANOVA.

Note: WHO Grade 1 Tumors are termed "Low Grade"; WHO Grade 4 Tumors are termed "High Grade". SD = Standard Deviation, MPP = Mean of Positive Pixels

(Filename: TCT_O-437_BrainTable.jpg)

Volumetry of Pediatric Low Grade Gliomas Compared to Linear Tumour Measurements.

S Culleton¹, F D'Arco², P O'Hare², A Lassaletta³, E Bouffet³, S Laughlin³

¹National Hospital for Neurology and Neurosurgery, London, United Kingdom, ²Great Ormond Street Hospital, London, United Kingdom, ³The Hospital for Sick Children, Toronto, Ontario, Canada

Purpose

Pediatric low-grade gliomas (LGGs) are a heterogeneous category of neoplasms. These LGGs consist most commonly of pilocytic astrocytomas with a favorable five-year survival rate, but with potential for recurrence, particularly in those incompletely resected (1). One of the major challenges is response quantification. This study is a retrospective comparison between bi-dimensional RANO (Response Assessment in Neuro-Oncology) criteria and manual volumetric segmentation (MVS) in pediatric low-grade gliomas.

Materials and Methods

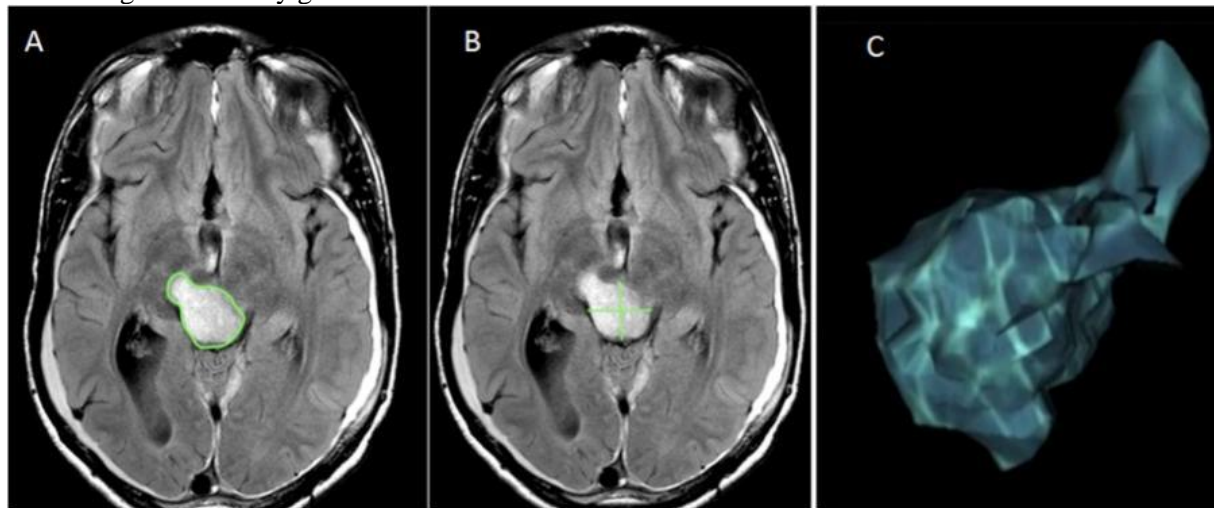
MRI FLAIR or T1 postcontrast images were used for assessment of tumor response. Seventy patients were included in this single center study. For each patient two scans were assessed ("time 0" and "end of therapy") and response to therapy was evaluated for both methods: 1) linear measurements according to RANO and 2) volumetry which was based on manual region of interest (ROI) placement (Figure 1). Figure 1 shows: examples of ROI delineation for volume calculation on FLAIR axial images (A) linear 2-D measurements on the same slice (B) 3-D volume rendering of the tumor (C) irregular structure of the tumor which makes assessment using linear measurements only inadequate. Inter-reader variability and average time for volumetric assessment were also calculated.

Results

Fourteen (20%) of the 70 patients had discordant results in terms of response assessment between the bi-dimensional measurements and MVS. All volumetric response assessments were in keeping with the subjective analysis of tumor (radiology report). Of the 14 patients, six had stable disease (SD) on MVS and progressive disease (PD) on 2-D assessment, five patients had SD on MVS and partial response (PR) on 2-D assessment, two patients had PD on MVS and SD on 2-D assessment, and one patient had PR on MVS and SD on 2-D analysis. The number of discordant results rises to 21 (30%) if minor response is integrated in the response assessment. MVS was relatively fast and showed good inter-reader concordance.

Conclusions

Our analysis shows that therapeutic response classification may change in a significant number of children by performing a volumetric tumor assessment. Furthermore MVS is not particularly time-consuming and has very good inter-reader concordance.



(Filename: TCT_O-438_Figure1.jpg)

O-439

4:10PM - 4:17PM

An Image Processing Algorithm to Aid Diagnosis of Mesial Temporal Sclerosis in Children: A Case-Control Study.

B Strnad¹, D Vaswani¹, A Sohn¹, M Parsons¹, A Sharma¹

¹Mallinckrodt Institute of Radiology, Saint Louis, MO

Purpose

In this retrospective case-control study, we aimed to assess the performance of an image-processing algorithm (Correlative Image Enhancement, CIE) for detection of MTS.

Materials and Methods

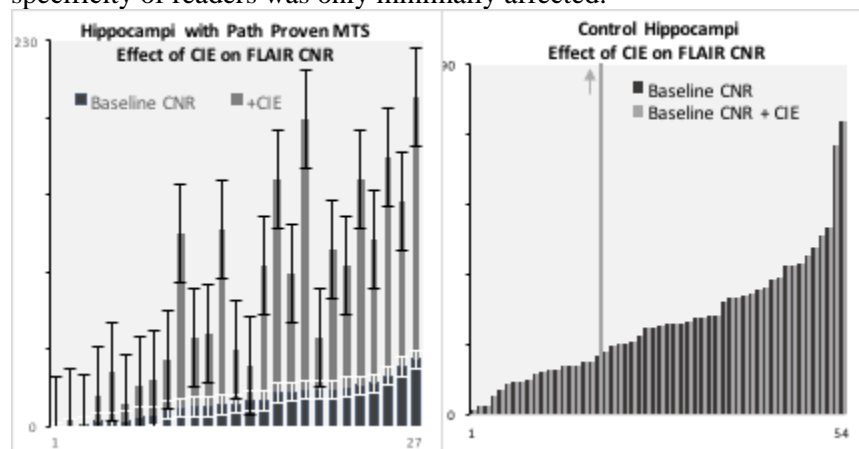
Identified were 27 cases with MTS (9 males, 18 females; mean age 16 years \pm SD 6.7) from a database of temporal lobectomies performed in children with refractory epilepsy. Identified by RIS search were 27 children without any history of seizures (9 males, 18 females; mean age 13.8 \pm SD 2.8 years) and with normal brain MRIs. A reviewer blinded to the disease status processed coronal FLAIR images using CIE, saving processed images as a new DICOM series. Using equivalent ROIs, another blinded investigator measured signal intensities of hippocampi, signal intensity of normal gray matter, and amount of noise in baseline and processed images. Two blinded reviewers rated these images for presence of hippocampal abnormality.

Results

CIE increased signal intensity and CNR in 26/27 hippocampi with pathologically confirmed MTS (sensitivity 96.3%) with an average CNR increase of 436% \pm SD 232% ($P < 0.001$, 2 sample t-test) from baseline. CIE increased CNR in 1/54 normal control hippocampi (specificity 98.2%), with an average CNR increase of 27.4% \pm SD 140% ($P = 0.326$, 2 sample t-test) from baseline. Following processing, sensitivity increased from 59.3% (95% CI, 38.8-77.6%) for reader 1, and from 81.5% (95% CI, 61.9-93.7%) for reader 2, to 96.3% (95% CI, 81-100%) for both readers. Specificity decreased from 100% (95% CI 93.4-100%) for reader 1, and increased from 92.6% (95% CI, 82.1-97.9%) for reader 2, to 98.2% for both readers (95% CI, 90.1-100%). Increased intensity following processing was reliably identifiable by both readers.

Conclusions

CIE significantly increased CNR of abnormal hippocampus with MTS, translating into a significant increase in reader sensitivities. With a false positive CNR increase seen in only 1.7% control hippocampi, specificity of readers was only minimally affected.



(Filename: TCT_O-439_ciefigs.gif)

O-440

4:17PM - 4:24PM

Image Processing to Allow Distinction of MTS-Affected and Normal Hippocampi In Children Undergoing Epilepsy Surgery.

Oral Presentations & Excerptas

A Sharma¹, S Tumuluru¹, H Orłowski², M Parsons¹, M Smyth²

¹Mallinckrodt Institute of Radiology, Saint Louis, MO, ²Washington University in St. Louis, St. Louis, MO

Purpose

Detection of mesial temporal sclerosis (MTS) in children undergoing epilepsy surgery is important. We assessed whether an image-processing algorithm (Correlative Image Enhancement, CIE) could facilitate differentiation between hippocampi with and without MTS in children undergoing epilepsy surgery.

Materials and Methods

Baseline coronal FLAIR images from brain MRIs of 27 children with epilepsy (15 males, 12 females; mean \pm SD] age: 12.1 \pm 6.2 years) who underwent hippocampal resection were processed using CIE. These included 19 hippocampi with MTS and eight normal hippocampi resected in conjunction with hemispherectomy. We assessed the effect of processing on contrast to noise ratio (CNR) between hippocampus and normal insular gray matter, and on assessment of hippocampal signal abnormality by two masked neuroradiologists.

Results

Processing resulted in a significant increase in mean CNR (from 3.9 \pm 5.3 to 25.3 \pm 25.8; $P < 0.0001$) for hippocampi with MTS, with a substantial ($>100\%$) increase from baseline seen 15/19 (78.9%) cases. Baseline CNR of 1.7 \pm 5.3 for normal hippocampi did not change significantly after processing (1.8 \pm 5.3; $P = 1$). For one reader, baseline sensitivity of 73.6% (95% CI: 48.8-90.8%) was unaffected but the specificity improved from 62.5% (95% CI: 24.5-91.5%) to 100% (95% CI: 63.1-100%). An increase in sensitivity from 73.6% (95% CI: 48.8-90.8%) to 78.9% (95% CI: 54.4-93.9%) and in specificity from 62.5% (95% CI: 24.5-91.5%) to 75% (95% CI: 34.9%-96.8%) was seen for the second reader.

Conclusions

In children with epilepsy, CIE-enhanced CNR for hippocampi proven to have MTS on histologic assessment but did not affect CNR for resected hippocampi that were normal. This facilitated more accurate categorization of hippocampi by both readers.

Wednesday, June 6, 2018

3:00PM - 4:30PM

Parallel Paper Session: Brain Tumors: New Diagnostic Considerations II

O-441

3:00PM - 3:07PM

Features of "Missed" Primary Brain Neoplasms: A Case-Control Study

M Maldonado¹, P Batchala¹, D Ornan², C Fadul³, D Schiff³, J Itri³, R Jain⁴, S Patel¹

¹University of Virginia Health System, Division of Neuroradiology, Charlottesville, VA, ²University of Virginia, Division of Neuroradiology, Charlottesville, VA, ³University of Virginia Health System, Charlottesville, VA, ⁴NYU School of Medicine, New York, NY

Purpose

To establish underlying features associated with cases of radiologically missed or misinterpreted primary brain neoplasms through a case-control study.

Materials and Methods

A retrospective case-control analysis of initially radiologically misinterpreted adult cerebral gliomas and lymphomas was performed. Cases of "missed" cerebral neoplasms were accrued from a PQI database maintained by the neuroradiology division at our institution. Controls of cerebral neoplasms that were

Oral Presentations & Excerpts

correctly diagnosed on initial imaging were randomly accrued from a CNS neoplasm database maintained by our neuroradiology division. Metrics recorded for cases and controls included features of the initial clinical presentation (patient demographics, symptoms, symptom onset, clinical setting, triage), initial imaging modality (CT, MRI, contrast administration), and imaging features of the tumor (location, size, mass effect, enhancement, necrosis, hemorrhage).

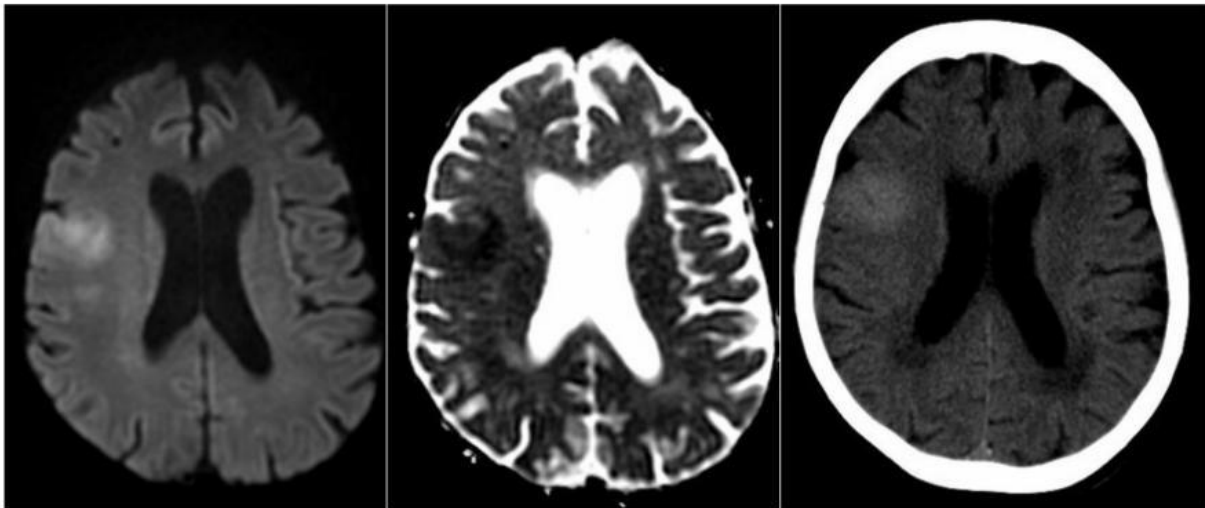
Results

There were a total of 12 initially "missed" brain neoplasms (10 diffuse gliomas, two lymphomas) and 36 controls (30 diffuse gliomas and six lymphomas). Among the 12 cases were five perceptual errors and seven interpretation errors. A nonsignificant trend was found between error type and initial imaging modality (perceptual errors associated with CT, interpretation errors associated with MRI, $p = 0.07$).

"Missed" cerebral neoplasms were more likely to undergo initial triage as a stroke workup (50% versus 8%, $p = 0.004$), undergo initial MRI without IV contrast (25% versus 3%, $p = 0.04$), and have less associated midline shift (mean of 0.8 mm versus 3.17 mm, $p = 0.018$) compared with controls.

Conclusions

Among cases of initially misinterpreted primary cerebral neoplasms, there are several clinical and imaging features which significantly differ from correctly diagnosed neoplasms. An understanding of such features may help radiologists avoid pitfalls when encountering such cases in clinical practice.



79 year old female with slurred speech and possible seizure presented to ER and underwent a stroke work up. The initial MRI showed focal diffusion restriction in the inferior right frontal lobe that was misinterpreted as acute infarct, but turned out to represent a GBM. A subsequently performed CT showed hyperdensity at the same site, indicating hypercellular neoplasm.

(Filename: TCT_O-441_AbstractFinalFigure.jpg)

O-442

3:07PM - 3:14PM

MR Fractal Analysis and Diffusion MR Metrics in Benign and Atypical Meningiomas: Multicenter Study

C Filippi¹, C Brogan², A El-Ali³, V Agarwal³, B Pramanik⁴, J Steinklein⁵, J Boockvar⁶, A Demopoulos⁷, D Chow⁸, P Chang⁹, R Watts¹⁰

¹Lenox Hill Hospital, New York, NY, ²Notre Dame University, Notre Dame, IN, ³University of Pittsburgh Medical Center, Pittsburgh, PA, ⁴Hofstra Northwell School of Medicine, New York, NY, ⁵Lenox Hill Hospital, New York, NY, ⁶North Shore Long Island Jewish Health System, New York, NY, ⁷North Shore Long Island Jewish Health System, Manhasset, NY, ⁸University of California Irvine, Irvine,

Oral Presentations & Excerptas

CA, ⁹University of California San Francisco, San Francisco, CA, ¹⁰University of Vermont Medical Center, Shelburne, VT

Purpose

Neurosurgical approaches to resection for an atypical meningioma (WHO II) are different compared to a benign, typical meningioma (WHO I), and there is no reliable way to make this distinction on preoperative MR imaging. Although the literature suggests that mean diffusivity may detect atypical meningioma, there are published cases where normal diffusion MR metrics are observed in atypical meningioma. There is an unmet need for neuroimaging to better characterize the potential for a meningioma to be atypical preoperatively. The purpose of this multicenter study was to use a fractal analysis approach to image interpretation which uses fully automated software to examine tumor texture in order to predict the propensity for atypia. Our hypothesis is that MR fractal analysis will be better than diffusion metrics for predicting atypical WHO II meningioma from benign typical WHO I meningioma.

Materials and Methods

This is a retrospective, multicenter study of 74 patients with meningioma (44 women, 30 men; mean age 59 +/- 11 years) that were seen in both Northwell Health and NY Presbyterian of New York and the University of Pittsburgh Medical Center from 2010 to 2017. Forty patients had WHO I benign meningioma and 35 patients had WHO II atypical meningioma. All patients had diffusion-weighted MR imaging performed with the following parameters: Single-Shot, Spin-Echo EPI sequence with TE/TR of 73/7000 msec and FOV 220 mm² with matrix size of 128 x 192 with contiguous 5mm slices no gap and b values of 0 and 1000 s/mm² and bandwidth of 1950 Hz/pixel. ADC values were generated by performance software (Functool Advantage Workstation, Version 4.6 GE Healthcare) for quantification of mean diffusivity. Fractal analysis with box-count method was performed on postcontrast T1-weighted MR images. Fractal dimension average (FDa) and maximum fractal dimension (FDm) were calculated using J1.9 MR fractal analysis software (NIH platform). Postcontrast T1 images are extracted and undergo threshold binarization (border of contrast-enhanced tumor on binarized image extracted by computing edges with the highest gradient magnitude) and box-count method used in which grid of known spacing (scale) is placed over the image so border pixels have a value of 1 and background pixels a value of 0. The number of boxes with non-zero pixels is counted; the process is repeated with multiple grids with increasing spacing and as tumor contour is divided into increasingly smaller boxes and the number of boxes of size (ϵ) required to cover the edge counted and indicated as $N(\epsilon)$. Fractal dimension (FD) is given by: $FD \lim_{\epsilon \rightarrow 0} [\log N(\epsilon)/\log(\epsilon)]$. As the scale increases, number of boxes containing objects decreases exponentially, and the exponent is equivalent to the fractal dimension, FD. Maximum spacing is set to 45% of diameter of the tumor border and minimum box size of two pixels.

Results

The FDm was 1.20 +/- .01 and FDa was 1.11 +/- .01 in WHO I meningioma, and the FDm was 1.33 +/- .02 and FDa was 1.24 +/- .02 in WHO II meningioma. The Mean Diffusivity was 1.00 +/- .04 in benign WHO I meningioma, and the mean diffusivity was 0.87 +/- .03 in patients with WHO atypical meningioma. Both the FDa and FDmax are significantly higher in patients with atypical WHO II meningioma ($p < .001$) and performed better than diffusion MR, but mean diffusivity is reliably lower in patients with atypical WHO II meningioma ($p < .03$). Qualitative signal on DWI (hyperintense signal) does not correlate significantly with atypical meningioma. AUC for the mean diffusivity was 0.658 +/- .063 but the AUC was better for both the FDavg at 0.848 +/- .045 and FDmax at 0.840 +/- .045. Both the FDmax and FDavg are highly correlated as expected with a Pearson coefficient of 0.931 and Spearman coefficient of 0.906. Mean diffusivity did not correlate with the FDavg and FDmax as expected, as these are fundamentally different quantitative metrics. With logistic regression analysis, MD (mean diffusivity) alone was about 62.7% accurate, FDavg alone was 73.7% accurate and FDmax alone at 70.7%. However, if all three metrics are combined, accuracy reaches 81.3% for prediction of WHO II meningioma from routine preoperative MR images.

Conclusions

Fractal dimension analysis on MR significantly correlates with atypical meningioma (WHO II) on

preoperative MR imaging and outperforms the standard mean diffusion metric on DWI. However, using both metrics (fractal analysis and diffusion MR) yields better results and more highly correlates with atypical histopathology on preoperative MR.

O-443

3:14PM - 3:21PM

Radiological-Pathological Correlations and Imaging Signatures for Gliomas

E Gates¹, J Lin¹, J Weinberg¹, J Hamilton¹, S Prabhu¹, J Hazle¹, G Fuller¹, V Baladandayuthapani¹, D Fuentes¹, D Schellingerhout¹

¹MD Anderson Cancer Center, Houston, TX

Purpose

To predict histological findings in untreated gliomas using imaging

Materials and Methods

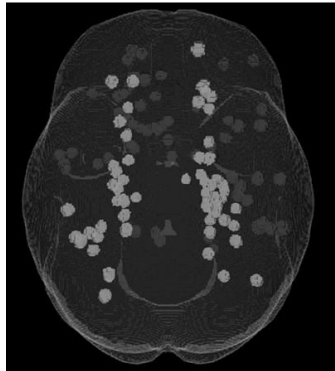
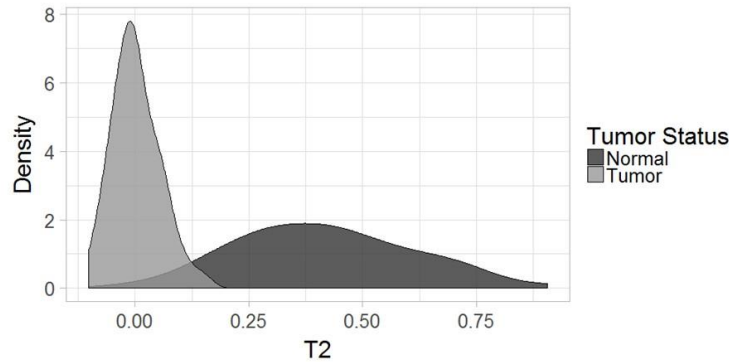
MR imaging was performed with anatomic, diffusion, permeability and perfusion sequences, followed by image-guided stereotactic biopsy prior to resection, in an IRB-approved trial. An imaging (23 parameters) and pathological description (six parameters) was developed for each biopsy, with virtual biopsies in normal-appearing brain balancing tumor over-representation. Machine learning models were built.

Results

Twenty-three patients had analyzable imaging-pathologic pairs, yielding 52 biopsy sites (2.26 biopsies/patient). The Random Forest method was the best algorithm tested. Tumor presence was predicted at 1.0 % error using four imaging inputs: T2, ADC, K2 and AUC. IDH1 mutation was predicted with 14.8% error using eight inputs. Using four inputs (T2, eADC, Ktrans, K2) increased the error to 18.2%. Tumor grade could be predicted at 6.2% error using 18 inputs. Using four inputs (T2, ADC, CBV and kep) increased the error to 6.8%. Ki67 (a proliferation marker) modeled best with four inputs (T2, FA, CBF, and kep), yielding a Pseudo R-squared=0.700 ± 0.188. ERG (erythroblast transformation-specific (ETS)-related gene, a vascularity marker) modeled best with eight inputs (Pseudo R-squared = 0.672 ± 0.103), but a four-variable input (T2, ADC, AUC, CBV) yielded Pseudo R-squared=0.647 ± 0.111. Cell Density modeled best with eight inputs (Pseudo R-squared = 0.746 ± 0.098), but a four-variable input (T2, FA, kep, K2) yielded Pseudo R-squared = 0.738 ± 0.094.

Conclusions

Pathologic features can be predicted to useful accuracies with clinical imaging data. This allows improving image-guided treatments for gliomas, and guides future imaging research. Confirmatory imaging trials are justified.



Top: Normalized histograms of average T2 weighted image intensity scaled between white matter (0) and CSF (1) for real and virtual biopsy sites. The separation between normal tissue and tumor supports the use of predictive modeling.

Bottom: Distribution of real biopsy sites (dark) and contralateral virtual biopsies (light) in a template brain.

(Filename: TCT_O-443_Fig1.jpg)

O-444

3:21PM - 3:28PM

Foretelling the Genotype: Predicting Lower-Grade Glioma Classification Based on the Pre-operative MRI

B Wiestler¹, E Alberts², G Tetteh², M Bieth², C Zimmer¹, B Menze²

¹Klinikum Rechts der Isar, TU München, Munich, Bavaria, Germany, ²TU München, Garching, Bavaria, Germany

Purpose

Recent advances in our understanding of the complex biology underlying gliomas have led to the identification of three biologically meaningful and clinically relevant groups of WHO grade II/III gliomas (LGG), based on isocitrate dehydrogenase (IDH) mutation and 1p/19q co-deletion [1], which has been incorporated into the recently updated WHO classification of brain tumors [2]. Hypothesizing that these biologically distinct tumors should be distinguishable in MRI, we aimed to develop a fully automated pipeline for image preprocessing, segmentation, feature extraction and genotype classification.

Materials and Methods

We collected 116 preoperative MRIs (FLAIR, T2, T1, T1ce) of LGG patients from the TCIA along with 450k methylation data to classify tumors molecularly. Fully automatic tumor segmentation of whole and active tumor was performed using a custom-developed algorithm [3]. From these regions, shape and texture features were extracted and used as input for machine-learning algorithms to predict genotype (n = 92; Figure 1a). Model performance was validated in a previously unseen cohort of patients (n = 24).

Results

All samples from this multicenter cohort could be successfully processed in our pipeline without the need for manual intervention. Best overall accuracy was seen with a Random Forest (RF) classifier using both shape and texture features (83% correctly classified in the validation set). Classifiers based on a Support

Vector Machine (SVM), multilayer perceptron (MLP) or logistic regression (LOG) tended to perform worse (67%, 42% and 71%, respectively; Figure 1b).

Conclusions

Our results indicate that a fully automated genotype prediction is feasible in lower-grade gliomas. We are currently collecting a second multicenter validation cohort to further validate our results. Given the prognostic and predictive relevance of molecular classification, analyses such as ours may in the future meaningfully complement pathological evaluation.

Figure 1a

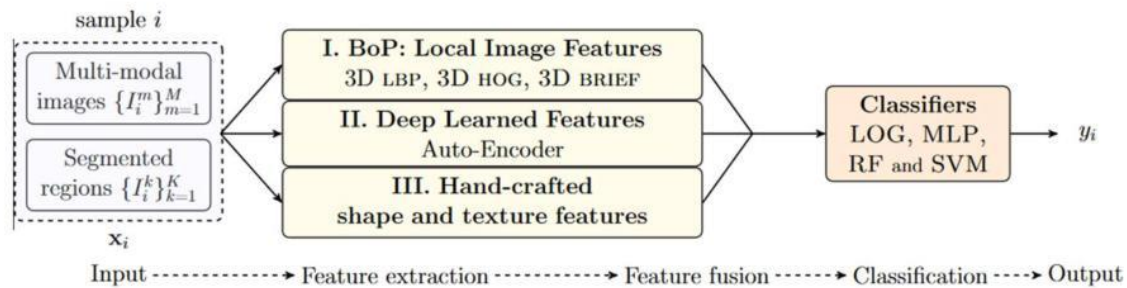


Figure 1b

Classifier	Discovery	Validation
LOG	1	0.71
MLP	0.63	0.42
RF	1	0.83
SVM	1	0.67

(Filename: TCT_O-444_Figure1.jpg)

O-445

3:28PM - 3:35PM

Quantification of Perihematomal Edema on CT in the Discrimination of Tumorous and Intracerebral Hemorrhage from Benign Causes

J Nawabi¹, C Thaler¹, G Broocks¹, U Hanning¹, J Fiehler¹, S Gellissen¹

¹University Medical Center Hamburg-Eppendorf, Hamburg, Germany

Purpose

Differentiation of tumorous intracerebral hemorrhage from benign etiology is critical concerning initial treatment plan and prognosis. Our aim was to investigate the diagnostic value of perihematomal edema characteristics in nonenhanced CT to discriminate tumorous and nontumorous causes of acute intracerebral hemorrhage (ICH).

Materials and Methods

This monocentric, retrospective study included 94 patients with acute intracerebral hemorrhage classified into six groups: primary intracerebral hemorrhage (Group 1), secondary intracerebral hemorrhage with vascular malformation (Group 2), or with amyloid angiopathy (Group 3), or unknown but nontumorous pathology (Group 4), with brain metastases (Group 5), or primary brain tumors (Group 6). The six groups were dichotomized into tumorous (Groups 5 and 6) and nontumorous intracerebral hemorrhage (Groups 1-4). To determine ICH and edema volume and density we performed manual segmentation for each patient (Analyze 12.0).

Oral Presentations & Excerptas

Results

Comparison of relative edema volume on nonenhanced CT showed a significant difference between the tumorous and nontumorous group. Absolute ICH volume, symptom time onset to CT and ICH localization showed no significant difference between the two groups. Receiver operating characteristic (ROC) analysis revealed the highest diagnostic performance for discriminating tumorous and nontumorous ICH for relative edema volume, adjusted for hematoma density as a covariate - with an area under the curve of 0,79 ($p < 0,0001$) with an optimal cutoff of $>0,013$ (optimal criterion with 58.8% sensitivity, 89.9% specificity).

Conclusions

Relative perihematomal edema, particularly adjusted for hematoma density of ICH, on nonenhanced CT might be useful for discriminating tumorous and nontumorous causes of acute ICH as an objective observer-independent imaging marker.

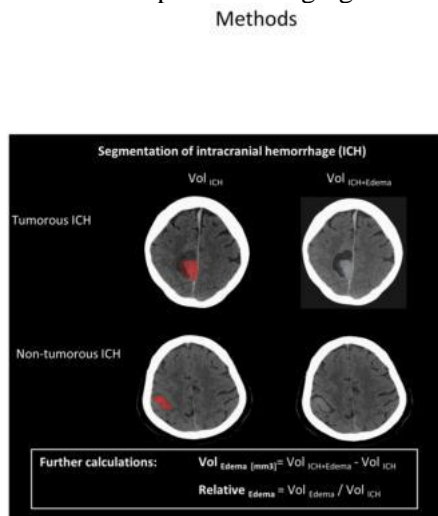


Figure 1: Representative cases of manual segmentation of tumorous and non-tumorous intracranial hemorrhage (ICH) using Analyze 12.0 (AnalyzeDirect, Overland Park, KS, USA) and calculation of perihematomal edema and relative edema volume, respectively.

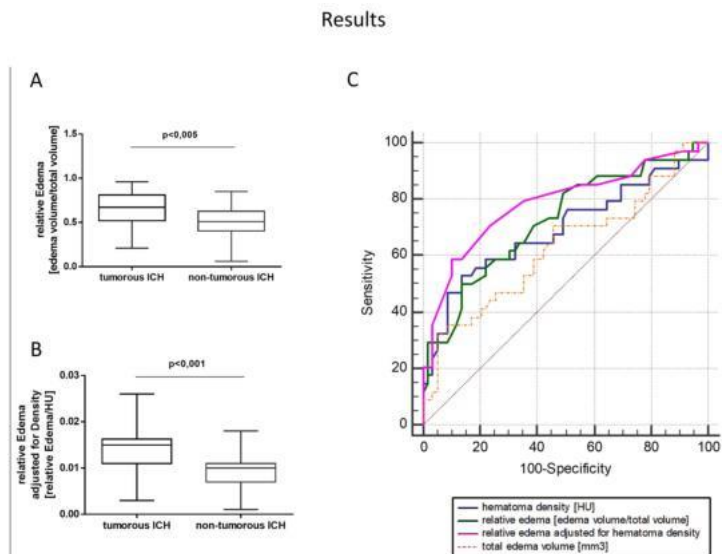


Figure 2: Difference among tumorous and non-tumorous intracerebral hemorrhage (ICH) in relative edema (A) and relative edema adjusted for ICH attenuation (hematoma density in HU) (B). Mann Whitney Test. Receiver operating characteristic curves of perihematomal edema parameters and ICH attenuation for discrimination of tumorous and non-tumorous ICHs (C).

(Filename: TCT_O-445_ASNR2018.jpg)

O-446

3:35PM - 3:42PM

Comparison of T1 Mapping and Fixed T1 Method in Quantification and Diagnostic Accuracy of Dynamic Contrast-Enhanced MRI Perfusion Biomarkers in Gliomas.

G Conte¹, L Altabella¹, A Castellano¹, A Falini¹, N Anzalone¹

¹Vita-Salute San Raffaele University and San Raffaele Hospital, Milan, Italy

Purpose

To compare dynamic contrast-enhanced (DCE) perfusion data in preoperative grading of gliomas using a fixed T1 value and a measured T1 obtained with variable flip-angle method.

Materials and Methods

We retrospectively reviewed 83 cases of histologically proven gliomas: 46 lower-grade gliomas (grade II and III) and 37 high-grade gliomas (grade IV). DCE-derived perfusion biomarkers maps of plasma volume fraction (Vp), extravascular extracellular volume fraction (Ve) and tracer transfer constant from plasma to tissue (Ktrans) were analyzed performing histogram analysis of the whole lesions. Perfusion maps were obtained using a fixed T1 value of 1500 ms and a measured T1 obtained with variable flip-

angle method. Each histogram parameter obtained in the two groups was compared in terms of quantification of perfusion parameters (Wilcoxon's test and Bland-Altman analysis) and diagnostic accuracy in glioma grading (ROC curves analysis).

Results

Perfusion parameters obtained with the fixed T1 value were significantly higher compared to those obtained with the variable flip-angle method. This difference seems to increase with increasing values of the perfusion parameters. As regards to diagnostic accuracy in glioma grading, there is no statistically significant differences between the two methods, except for the mean and median values of Vp obtained with the fixed T1 value, which prove better diagnostic accuracy.

Conclusions

In conclusion, perfusion data obtained with different T1 methods are significantly different, so they can't be grouped together as an homogenous group. Moreover, T1 measurement with variable flip-angle method doesn't seem to be necessary for glioma grading since the use of a fixed T1 value has proven equal diagnostic accuracy.

O-447

3:42PM - 3:49PM

3D high resolution post-contrast imaging at 3T for the delineation of enhancing brain tumors: a comparison of MPRAGE with SPACE and VIBE techniques.

L Danieli¹, D Distefano¹, E Prodi¹, E Ventura¹, G Riccitelli¹, M Reinert¹, A Kaelin-Lang¹, A Cianfoni¹, E Pravata¹

¹*Institute for Clinical Neurosciences of Southern Switzerland, Lugano, Switzerland*

Purpose

To prospectively investigate differences between the Magnetization-Prepared-Rapid-Gradient-Echo (MPRAGE) 3-D postcontrast T1-weighted technique (1) recommended by the modified RANO criteria (2), and two other available techniques [Sampling-Perfection-with-Application-optimized-Contrasts-using-different-flip-angle-Evolutions (SPACE) (3) and Volumetric-Interpolated-Brain-Examination (VIBE) (4)], in the assessment of contrast-to-noise-ratio (CNR), total volume (TV) and margins extent delineation (MED) of brain primitive tumors (pT) and metastases, potentially amenable to surgical and/or conformal radiotherapy treatment.

Materials and Methods

Fifty-four contrast-enhancing lesions (38 pT and 16 metastases) were detected in 37 patients using 3T MRI with 1-mm MPRAGE, VIBE and SPACE sequences acquired five minutes after 0.1ml/kg administration of gadobutrol, in random order. Lesions CNR and TV segmentation were performed by an experienced neuroradiologist using a validated semiautomated tool (SmartBrush, Brainlab) followed by manual refinement. For each combination of sequence pairs, MED mismatch was quantified using subtraction volumetric maps of the segmented lesions. Friedman repeated measures and paired-samples Wilcoxon nonparametric tests were used to investigate between-sequences discrepancies in CNR, TV and MED subtraction volumes.^[1]

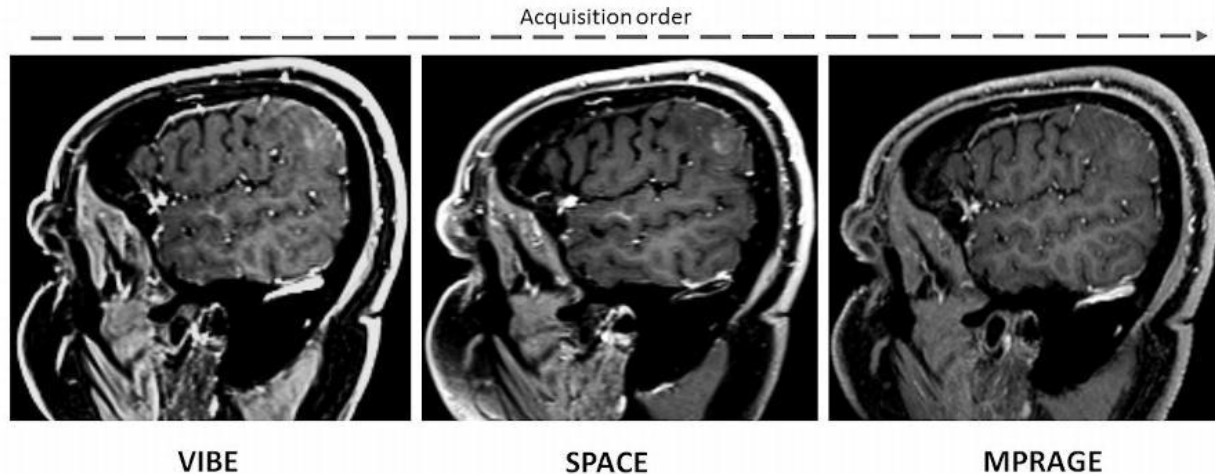
Results

In either pT and metastases, CNR was significantly higher in both SPACE and VIBE compared to MPRAGE (p<0.001 and p=0.001, respectively). Larger TVs were obtained with SPACE compared to MPRAGE in both pT (p=0.007) and metastases (p=0.003). Discrepancy in MED was also found, with SPACE significantly exceeding MPRAGE in both pT and metastases margins extent (p=0.008 and 0.01, respectively). An example of the technique-related effect on the enhancement conspicuity of a high-grade glioma is presented in Figure.

Conclusions

We found technique-related differences in crucial parameters for brain enhancing pT and metastases

delineation, when comparing MPRAGE to SPACE (CNR, TV and MED) and to VIBE (CNR only). These findings may be relevant for treatment planning and response assessment.^{[1][2]}



(Filename: TCT_O-447_Figure.jpg)

O-448

3:49PM - 3:56PM

White matter changes in patients with primary central nervous system lymphoma following high dose methotrexate treatment with or without rituximab

D Lin¹, F Estephan¹, X Ye¹, M Holdhoff¹

¹*Johns Hopkins University School of Medicine, Baltimore, MD*

Purpose

White-matter changes (WMC) can develop following systemic chemotherapy and may be associated with neurocognitive decline (1). High-dose methotrexate (HD-MTX) is the most commonly used chemotherapeutic agent for primary central nervous system lymphoma (PCNSL), and combination with rituximab (R)2 is common. We aimed to determine rate and grade of WMC in PCNSL patients treated with HD-MTX-R or HD-MTX.

Materials and Methods

MRI scans of patients with PCNSL treated with either HD-MTX-R or HD-MTX at Johns Hopkins were retrospectively reviewed for development of WMC. Patients had serial MRIs including a baseline and post-treatment exams. Severity of WMC on FLAIR MRI was assessed by a neuroradiologist blinded to treatment arm and clinical status. A WMC grade of 1-4 (minimal to severe) was assigned for each cerebral hemisphere and then summed (3).

Results

Forty-seven patients (mean age 66, range 33-84; 49% male) with newly-diagnosed PCNSL, treated with HD-MTX-R (n=34) or HD-MTX (n=13) were included. WMC were detected in 23 (68%) in the HD-MTX-R, and in six (46%) in the HD-MTX group. Among the patients who did develop WMC (n=29), these were detected in the MTX-R group at 4.6 months and in the MTX group 7.8 months following treatment initiation. Among these patients, the average WMC score was higher in HD-MTX-R compared to HD-MTX (4.7 vs. 2.5, respectively). Average WMC scores when first detected were 2.5 in HD-MTX-R and 1.6 in HD-MTX.

Conclusions

Development of WM changes in PCNSL patients treated with MTX and MTX-R is common. Based on this pilot study, these changes appear to be more frequent, occur earlier and are more extensive in patients

treated with HD-MTX-R compared to HD-MTX. The study is limited by small sample size particularly of the HD-MTX arm. Further analysis of the clinical correlation of these findings is ongoing.

O-449

3:56PM - 4:03PM

Third Ventricular Colloid Cysts: Correlation Of MRI Findings With Clinical Outcome

S Khanpara¹, R Riascos¹, P Rabiei¹, R Patel¹, O Arevalo¹, M Syed¹, K Westmark¹

¹*The University of Texas Health Science Center at Houston, Houston, TX*

Purpose

Colloid cysts are non-neoplastic lesions almost exclusively occurring within the third ventricle, typically near the foramen of Monro. In patients that present with symptoms from the cyst, there is a significant risk of sudden neurologic deterioration and death due to acute obstructive hydrocephalus. The purpose of this study is to investigate which imaging characteristics of the cyst and patient demographics are predictive of the cyst being or becoming symptomatic.

Materials and Methods

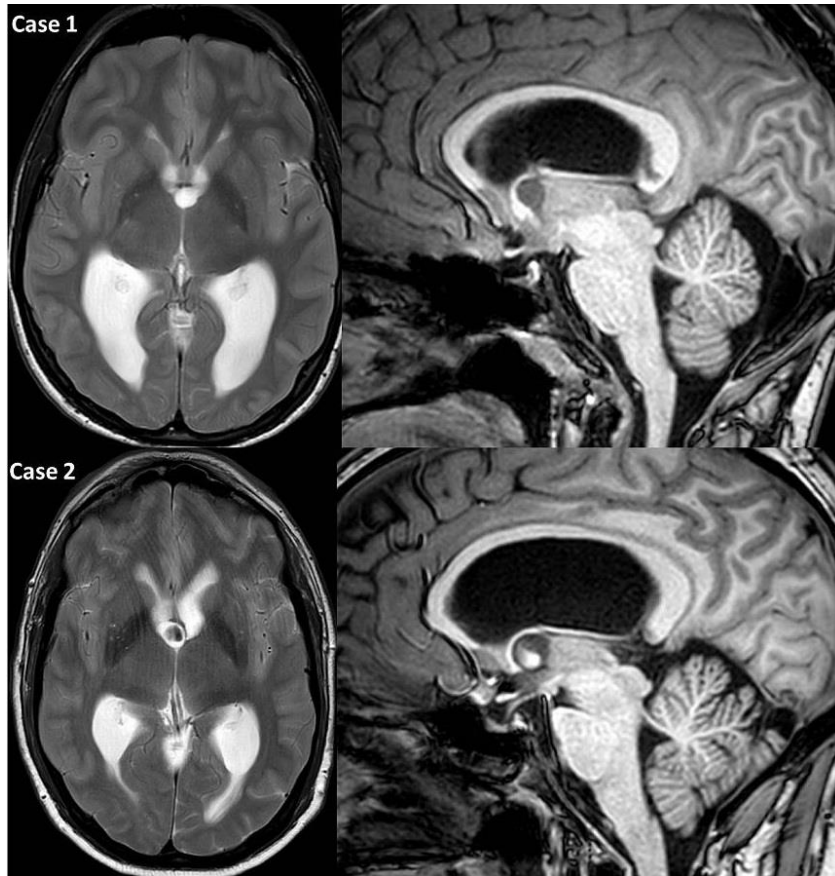
We retrospectively gathered clinical and MR imaging data of 62 colloid cyst patients at Memorial Hermann system of the greater Houston area from 2014 to 2017. Collected MRI scans of these patients were interpreted by a senior neuroradiologist and junior radiologist. Patients were divided into two groups: those who underwent surgery due to having symptomatic cysts, including acute obstructive hydrocephalus, and those who were asymptomatic with incidentally detected colloid cysts. Greatest axial dimension, volume measurements and localization of colloid cysts in relation to thalamic massa intermedia were obtained on axial and sagittal T1-weighted images or on CT.

Results

Maximum axial dimension, cyst volume and precise location of the cyst in the third ventricle relative to the massa intermedia correlated with the potential of the cyst to be symptomatic and result in obstructive hydrocephalus. We observed significant difference between the volume of the colloid cysts and hydrocephalus and the need for surgery with a p-value of 0.02 and 0.03 respectively. Patients with higher volumes were more likely to have hydrocephalus and go for surgery. We also noted a significant difference between occurrence of hydrocephalus and the position of the colloid cysts. Higher occurrence of hydrocephalus was associated with the cysts located anterior to thalamic massa intermedia (P=0.03). There were no sudden deaths in our study population.

Conclusions

Assessment of cyst size and precise location in the third ventricle can help determine which cysts are more likely to be or become symptomatic.



(Filename: TCT_O-449_CC.jpg)

O-450

4:03PM - 4:10PM

Pretreatment ADC values to predict response of vestibular schwannoma to gamma knife radiosurgery.

M Poturalski¹, C Karakasis¹, J Lee¹

¹*Cleveland Clinic Foundation, Cleveland, OH*

Purpose

Pretreatment tumor ADC values have been shown to be useful in predicting response of glioblastomas and vestibular schwannomas treated with radiation therapy. [1] Particularly, a prior study highlighted the minimum ADC of a pretreated vestibular schwannoma in predicting response. The purpose of the study is to validate the use of pretreatment ADC values in vestibular schwannomas as a predictor of response to gamma knife radiation therapy with a larger study population.

Materials and Methods

Search of an imaging database for patients with known vestibular schwannoma who received gamma knife radiosurgery at our institution was conducted. Included patients had a pretreatment MR allowing for measurement of tumor volume, adequate determination of an ADC value, and a follow-up MR of greater than 12 months from treatment, yielding 48 patients who were treated between June 2008 and August 2016. Three reviewers measured minimum, mean and maximum pretreatment ADC values from ROIs proportionate to tumor size. The pretreatment ADC values were standardized to white matter to compensate for differences in acquisition parameters and scanners in which MR examinations were performed. Pre and posttreatment tumor volumes were calculated through the summed areas of multiple

Oral Presentations & Excerptas

cross-sectional images through the tumor, and treatment response was defined as a decrease of 20% or more in total volume. [2] Follow-up MR examinations with mean time from treatment of 12 to 102 months were used to measure total tumor volume and determine change in size following treatment.

Results

Average age of the 48 patients included in the study was 63 years, with 20 males and 28 females. Average pretreatment tumor volume was 1.92cm³, and the average length of follow-up was 39 months. A multivariable linear regression analysis was performed to predict the percent tumor change due to gamma knife treatment based on the standardized ADC minimum, ADC mean, ADC maximum, length of follow-up and pretreatment tumor size. No significant regression equation was found between the variables and percent tumor size change ($F(5, 42)=1.072$, $p=0.390$, R^2 of 0.008). Individual variable predicted percent change was also not significant when correlated with ADCmin ($B=-0.423$, $p=0.351$), ADC mean ($B=0.545$, $p=0.563$), ADCmax ($B=-0.206$, $p=0.694$), follow-up months ($B=-0.671$, $p=0.094$), and pretreatment volume ($B=-4.215$, $p=0.413$). Additionally, when defining responders to treatment as 20% or more decrease in volume after gamma knife with the rest as nonresponders similar to a recent published article, an independent samples T-test was performed that showed no difference between the standardized ADC minimum ($p=0.369$), ADC mean ($p=0.945$), ADC maximum ($p=0.627$), and pretreatment tumor size ($p=0.917$) to differentiate between responders and nonresponders. The number of months of follow-up after treatment did significantly differentiate between responders and nonresponders ($p=0.004$), with responders having average follow up of 44.2 months and nonresponders having average follow up of 26.8 months.

Conclusions

This study demonstrates that lower pretreatment ADC values did not predict reduction in vestibular schwannoma size after gamma knife therapy. This study with a larger patient population is in contradistinction to previously reported findings.

O-451

4:10PM - 4:17PM

Delayed diagnosis worsens outcome in primary central nervous system lymphoma (PCNSL) - a single centre review

S Mills¹, M Jenkinson²

¹The Walton Centre NHS Foundation Trust, Liverpool, Merseyside, England, ²University of Liverpool, Liverpool, Merseyside, England

Purpose

The MRI appearances of PCNSL are of homogeneously enhancing tumor in a periventricular/CSF interface location. Radiological differential diagnoses include high-grade glioma or inflammation. Steroid treatment can cause lesions to 'disappear'. Current guidelines advise histo-pathological confirmation before commencing treatment. Repeat biopsy is warranted when the initial biopsy is either inconclusive, demonstrates nonspecific inflammation or there is remission due to steroid treatment. Without treatment, median survival is 1.5-3.3 months, improving to 10-20 months with treatment. The aim of this study was to evaluate the effect of time-to-diagnosis on overall survival in radiologically suspected PCNSL.

Materials and Methods

The audit sample was derived from radiology reports containing the terms "lymphoma"/"PCNSL" between 1 July 2007 to 1 November 2017. Imaging was reviewed to identify cases with parenchymal enhancement compatible with a radiological diagnosis of PCNSL. Time to histological PCNSL diagnosis from clinical presentation and overall survival for both histologically confirmed and no histological diagnosis was determined.

Results

Of patients 136 had parenchymal enhancement; 88 had surgery. Initial and repeat biopsy histology results are displayed in Tables 1 and 2; 55% had histological PCNSL. Time to histological confirmation was

Oral Presentations & Excerpts

delayed in patients requiring repeat biopsy compared to single biopsy ($p=0.038$). In four patients, steroid treatment resulted in delays of 99–347 days to first biopsy. Excluding these cases, initially inconclusive/inflammatory histology resulted in a significantly delayed diagnosis ($p=0.001$) but this did not affect survival ($p=0.756$). In contrast, patients with no biopsy or without a final histological diagnosis (with radiological appearances compatible with PCNSL) had significantly shorter survival ($p=0.001$, Figure 1).

Conclusions

Histological confirmation, either at initial or repeat biopsy, in radiologically suspected PCNSL is the key to better survival. Failure to biopsy or repeatedly inconclusive histology results in markedly reduced overall survival which suggest that this patient group may require a different management approach.

Histological Diagnosis	No Patients
unavailable	14
inconclusive	10
PCNSL	37
SCNSL	1
A (II)	1
AA (III)	4
O (II)	1
GBM	9
metastases	2
germinoma	1
inflammatory	4
granulomatous	2
PML	1
normal	1

Table 1. Detailing histology reports of 88 biopsied patients

Initial biopsy result	Repeat biopsy	No. patients
inflammatory	PCNSL	2
inflammatory	inconclusive	1
A (II)	PCNSL	1
inconclusive	PCNSL	3
inconclusive	demyelination	1
inconclusive	A (II)	1
inconclusive	inconclusive	2

Table 2. Detailing histology initial and subsequent histology reports of patients in whom repeat biopsy was performed

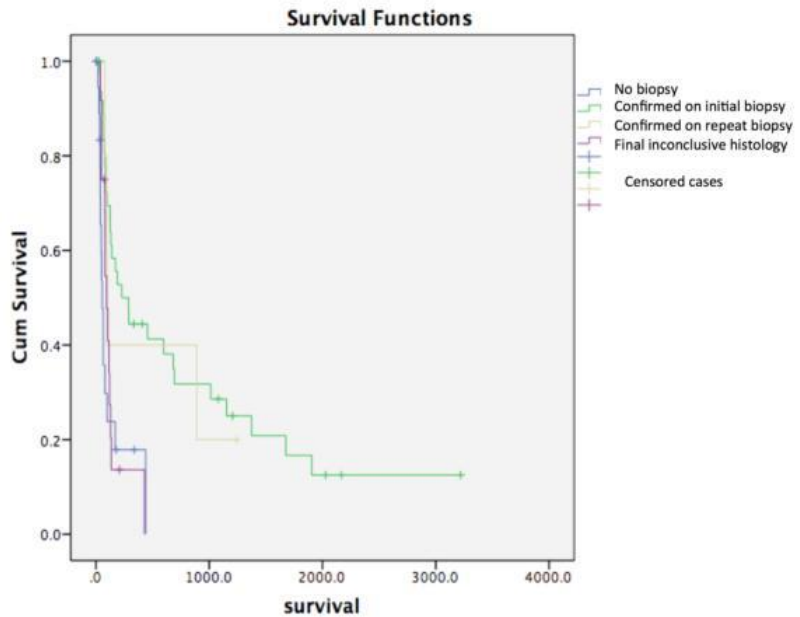


Figure 1. Survival curves of overall survival for patients with no biopsy (blue), formal histological diagnosis of PCNSL on initial biopsy (green) or repeat biopsy (yellow) and final inconclusive histology (purple)

(Filename: TCT_O-451_ASNR_2018_PCNSL_audit.jpg)

Wednesday, June 6, 2018

3:00PM - 4:30PM

Excerpta: Pediatrics and Head & Neck Cases

E-98

3:00PM - 3:04PM

Atlanto-axial instability with displacement of the dens behind the transverse ligament

E Bonfante¹, R Riascos¹, M Shah¹, S Fletcher¹

¹The University of Texas Health Science Center Houston, Houston, TX

Purpose

To report a case of traumatic atlantoaxial dislocation with entrapment of the dens behind the intact transverse ligament

Materials and Methods

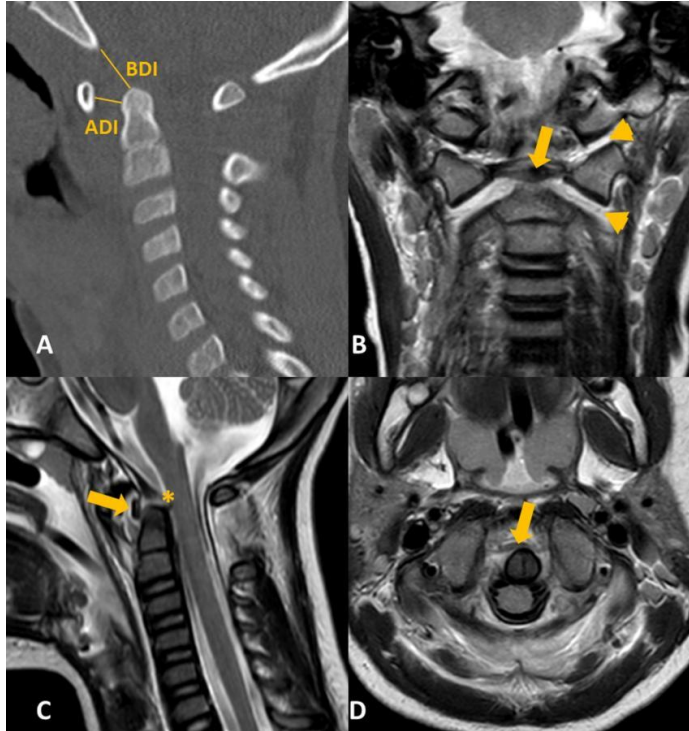
Patient is a three-year-old female restrained in the back seat of a stopped vehicle that was rear ended. The driver's chair broke and slid back into patient's knee. Patient had altered mental status and tachycardia on scene. Additional injuries included left open femur fracture, bilateral pulmonary contusions, small interhemispheric subdural hematoma, and cervical prevertebral space hematoma. CT of the cervical spine demonstrated widening of the atlantooccipital and atlantoaxial joints. MRI of the cervical spine demonstrated posterior dislocation of the dens behind an intact transverse ligament. Disruption of the tectorial membrane, widening of the atlantooccipital and atlantoaxial joints and intact cord were also shown. This unstable injury was managed with intraoperative reduction following placement of halo jacket under fluoroscopy. Post procedure radiographs showed improvement of the position of the dens with respect to the anterior arch of C1. The patient remained neurologically intact and will be reassessed in six weeks.

Results

A. Sagittal CT reformatted image demonstrates widening of the basion dental interval (BDI) and atlantodental interval (ADI). B. Coronal, C. Sagittal, and D. Axial, T2WI demonstrate an intact transverse ligament positioned anterior and superior to the dens (arrow). The atlantooccipital and atlantoaxial joints are widened (arrows). The cord is intact. The tectorial membrane is disrupted (star).

Conclusions

A pediatric patient sustained traumatic discoligamentous injury of the atlantoaxial and atlantooccipital joints, with posterior inferior dislocation of the dens behind an intact transverse ligament. This uncommon injury pattern is likely the result of longitudinal distraction of the atlantoaxial joint, followed by posterior translation of C2. This unstable injury is challenging due to the difficulty to reposition the dens in the ventral compartment of the atlas ring. The transverse portion of the cruciate ligament is one of the most important ligaments of the body. It is attached on either side to a tubercle in the inner ring of the atlas lateral mass and crosses from side-to-side in a dorsal convex arch to divide the atlas ring into a dorsal and ventral component. The ventral component contains the odontoid process and the dorsal component encompasses the spinal cord and the spinal accessory nerves.



(Filename: TCT_E-98_Fig1arrows.jpg)

E-99

3:04PM - 3:08PM

A Rare Case of Gallbladder Polyposis in Juvenile Subtype of Metachromatic Leukodystrophy: An MR, Spectroscopy, and US Correlation

V Yedavalli¹, V Kuttappan¹, V Pandey¹, J Samet²

¹Advocate Illinois Masonic Medical Center, Chicago, IL, ²Lurie Children's Hospital, Chicago, IL

Purpose

Metachromatic leukodystrophy (MLD) is a rare autosomal recessive genetic disorder characterized by deficiency of the arylsulfatase A enzyme, leading to accumulation of lipid-rich byproducts which causes demyelination. The juvenile subtype, seen in one out of 150,000 cases, is exceedingly rare. Studies have shown an association of gallbladder polyposis (GP) with MLD in up to 23% of patients, although literature is still scarce. We present a six-year-old female with behavior changes and worsening gait with a confirmed diagnosis of MLD after sonographic evaluation demonstrated GP.

Materials and Methods

We present a six-year-old female with worsening disorientation, unstable gait, and behavioral changes. The patient underwent an ultrasound for gallstones, which instead showed multiple polyps. Given the rarity of polyposis at this age, comprehensive evaluation for encephalopathy was performed, yielding low arylsulfatase A levels. Subsequent MRI with spectroscopy corroborated the lab values with imaging findings suggestive of an underlying leukodystrophy. The patient continued to exhibit neurological decline thereafter.

Results

Figure 1. A. Ultrasound demonstrates multiple intraluminal masses contiguous with the gallbladder wall compatible with polyposis. B. FLAIR images demonstrating confluent symmetric deep white matter disease with sparing of the subcortical U fibers compatible with a leukodystrophy. C. MR Spectroscopy demonstrates a decreased NAA/Cho ratio with elevated lactate peaks confirming MLD.

Conclusions

Juvenile MLD is an exceedingly rare autosomal recessive disease associated with GP. GP is often times found first before the diagnosis of MLD is confirmed. It is therefore crucial to undergo a comprehensive work-up for MLD if GP is found incidentally. With new promising therapies such as stem cell or bone marrow transplantation for MLD, accurate imaging diagnosis is essential for improved prognosis.

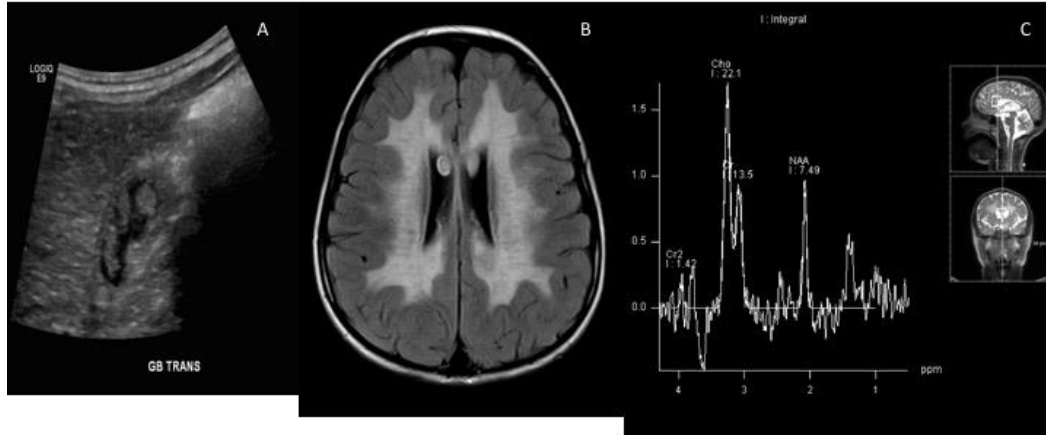


Figure 1. A) Ultrasound demonstrates multiple intraluminal masses contiguous with the gallbladder wall compatible with polyposis. B) FLAIR images demonstrating confluent symmetric deep white matter disease with sparing of the subcortical U fibers compatible a leukodystrophy. C) MR Spectroscopy demonstrates a decreased NAA/Cho ratio with elevated lactate peaks confirming MLD.

(Filename: TCT_E-99_MetachromaticLeukodystrophyGallbladderPolyposis.jpg)

E-100

3:08PM - 3:12PM

A Case of Parry-Romberg Syndrome With Abnormal Perfusion

A Mashhood¹, K Chan¹, S Harder¹

¹Loma Linda University Medical Center, Loma Linda, CA

Purpose

We describe a case of Parry Romberg syndrome (PRS) with associated intracranial findings, including focal perfusion abnormalities.

Materials and Methods

A 16-year-old female with an eight-year history of PRS, presented with symptoms of mild right hemifacial atrophy, localized morphea, and intractable catamenial epilepsy. Prior to admission, video-EEG monitoring revealed a right fronto-central seizure focus. MRI demonstrated diffuse T2 hyperintense signal in the right frontoparietal white matter with scattered foci of susceptibility hypointensity and contrast enhancement and regional impaired perfusion. There was focal thinning of the overlying right frontal scalp.

Results

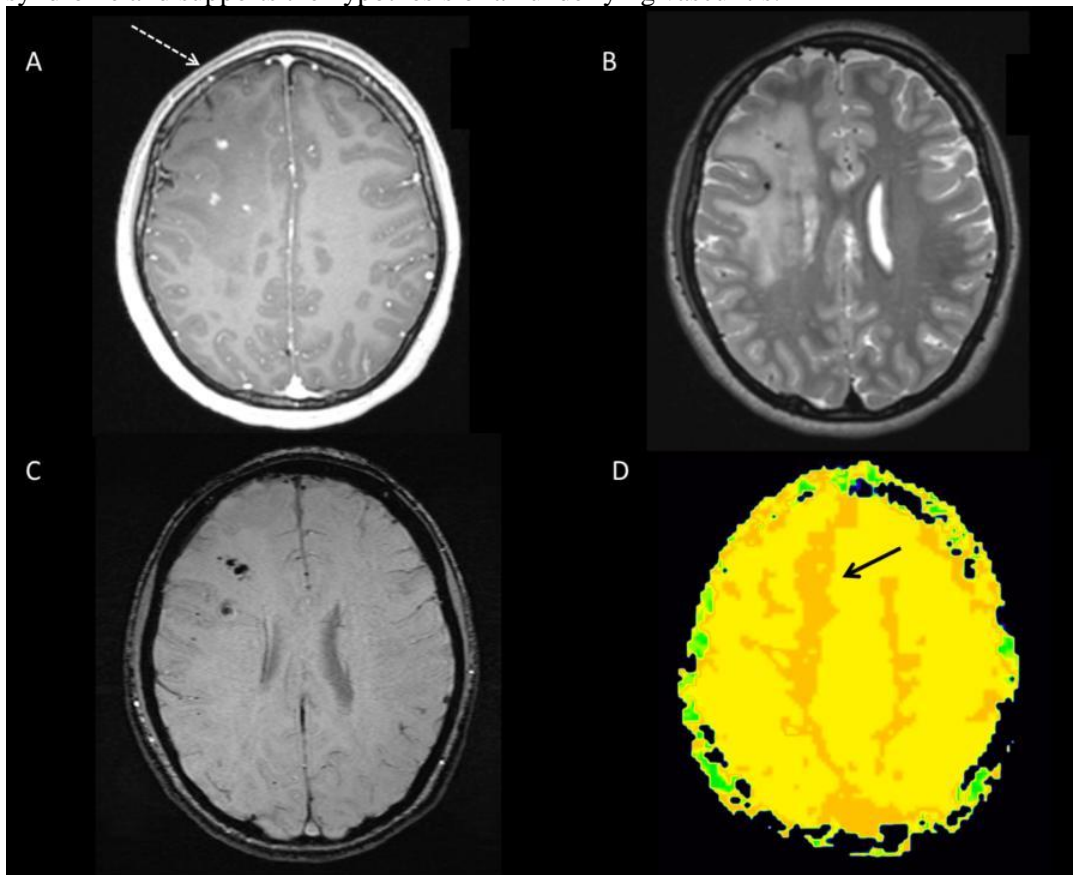
Axial postcontrast T1WI demonstrates focal thinning of the right frontal scalp (dashed arrow) with scattered foci of enhancement in the right frontal lobe (A). Axial T2WI shows hyperintensity in the right frontoparietal white matter (B) with scattered hypointense foci on the axial susceptibility weighted image (C). Perfusion weighted imaging demonstrates delayed time-to-peak perfusion in the parasagittal right frontoparietal region (black arrow) (D).

Conclusions

PRS is a disease characterized by progressive hemifacial atrophy, occasionally extending to other parts of the body (1). Intracranial abnormalities have been described, including T2 signal abnormalities ipsilateral

Oral Presentations & Excerptas

to the facial abnormality, and rarely, microhemorrhages and abnormal contrast enhancement (1). Advanced imaging findings of PRS have been reported including tractography, MRS and limited perfusion findings (2). The profound underlying intracranial findings in our patient are unusual, and the finding of impaired perfusion is not well-documented in the literature. While the pathophysiology of PRS is incompletely understood, one hypothesis suggests an underlying vasculitis, supported by clinical and laboratory findings, and response to anti-inflammatory therapy (1, 3). Cerebral biopsy has shown evidence of inflammation and abnormal vasculature (1, 4, 5). Impaired perfusion related to the region of abnormal signal in this patient adds to our understanding of the pathophysiology of Parry Romberg syndrome and supports the hypothesis of an underlying vasculitis.



(Filename: TCT_E-100_PRSfigure.jpg)

E-101

3:12PM - 3:16PM

"Mogging" Between NMO and MS : Can Anti-MOG Antibody Save Your Day?

N Shekhrjka¹, A Alter¹, W Vargas¹, A Lignelli²

¹New York Presbyterian Hospital, New York, NY, ²Columbia University Medical Center, New York City, NY

Purpose

Due to many overlapping features between Neuromyelitis Optica (NMO) and Multiple Sclerosis (MS), NMO was considered the subset of MS until the discovery of antibody that attacks a protein in astrocytes known as aquaporin-4 (Anti-AQP4) in 2005 for the diagnosis of NMO. Approximately 70% of the patients with NMO have positive Anti-AQP4 antibody. It could still be a challenge for the clinicians to classify the remaining 30% patients who are seronegative for Anti-AQP4 antibody into NMO or MS

Oral Presentations & Excerptas

categories due to overlapping clinical and imaging findings. Anti-Myelin oligodendrocyte glycoprotein (MOG) antibody has been found to be positive in many of the NMO patients who are seronegative for Anti-AQP4. This helps clinicians differentiate the disease from MS and also predict a better outcome compared to Anti-AQP4 positive NMO patients.

Materials and Methods

A 15-year-old female presents with headaches, neck pain and blurry vision after taking TB medication. Episode of LOC followed by difficulty speaking/left mouth weakness and seizure. Similar episode a year later. Symptoms resolved spontaneously over several months. Diagnosed with stroke and with migraine headaches at an outside hospital. Unknown outside neuroimaging. At 3rd presentation a year later: transient headaches, right neck pain, and right eye blurry vision. Hypercoagulability work-up was negative. MRI brain with left subcortical nonenhancing FLAIR-hyperintense lesions (Figure 1). At 4th presentation a year later: acute onset of left-sided headache with left eye pain and vision loss. Oligoclonal bands negative, IGg index normal, Anti-AQP4-antibody negative, myelin basic protein high at 9.97 (upper limit 5.50). MRI brain showed no new lesions. Orbital MRI showed enhancement of left optic nerve (Figure 2). C- and T-spine MRI without lesion. At 5th presentation 3 weeks later: left arm weakness followed by loss of consciousness consistent with focal seizure with secondary generalization. Right eye pain. MRI brain showed no new lesions. Orbital MRI showed new right optic neuritis. Infectious, hypercoagulability workup, paraneoplastic panel, connective tissue disease workup, Oligoclonal bands, IGg index, Anti-AQP4-antibody - negative. Anti-MOG antibody positive. Until this point patient was being treated with IV Methylprednisolone. On 6th presentation six weeks later: urinary hesitancy and urgency, bilateral leg paresthesias and left leg weakness. New spinal cord lesions on MRI T4 and T7-T8 (Figure 3A). Treated with IV Methylprednisolone and Rituximab. 7th presentation one month after completing rituximab treatment: dizziness, vomiting, bilateral hand/foot paresthesias, unsteady gait. MRI brain with new tumefactive supra and infratentorial lesions (Figure 4). MRI spine with new lesions in cervical (Figure 3B and 3C) and thoracic cord.

Results

At 3rd presentation: MRI brain with left subcortical nonenhancing FLAIR-hyperintense lesions (Figure 1) At 4th presentation a year later: MRI brain showed no new lesions. Orbital MRI showed enhancement of left optic nerve (Figure 2). C- and T-spine MRI without lesion (not shown). At 5th presentation three weeks later: MRI brain showed no new lesions. Orbital MRI showed new right optic neuritis (not shown) On 6th presentation six weeks later: new spinal cord lesions on MRI T4 and T7-T8 (Figure 3A) 7th presentation: MRI brain with new tumefactive supra and infratentorial lesions (Figure 4). MRI spine with new enhancing lesions in cervical (Figure 3B and 3C) and thoracic cord Features more consistent with NMO spectrum disorder than MS: 1. Back-to-back episodes of optic neuritis 2. Oligoclonal bands negative 3. Lack of "Dawson's fingers" appearance on MRI brain 4. MOG-antibody positivity Features less consistent with NMO spectrum disorder than MS: 1. None of the spinal cord lesions are long-segment. 2. Patient has tumefactive brain lesions. 3. By the 6th presentation patient was meeting McDonald criteria for MS (juxtacortical and spinal cord lesions).

Conclusions

Due to overlapping clinical and imaging features, differentiation between MS and NMO can be challenging particularly in patients who are negative for oligoclonal bands and anti-AQP4 antibodies. However, differentiating MS from NMO is of paramount importance as treatments for both the entities differ. In addition, treating patients with NMO with MS-specific therapies (e.g. beta-interferon or natalizumab) can actually lead to its exacerbation. With this interesting case overlapping features of MS and NMO are emphasized with a discussion of the clinical and imaging features differentiating both entities. The importance of oligoclonal bands, anti-AQP4 antibodies and anti-MOG antibodies will also be discussed.

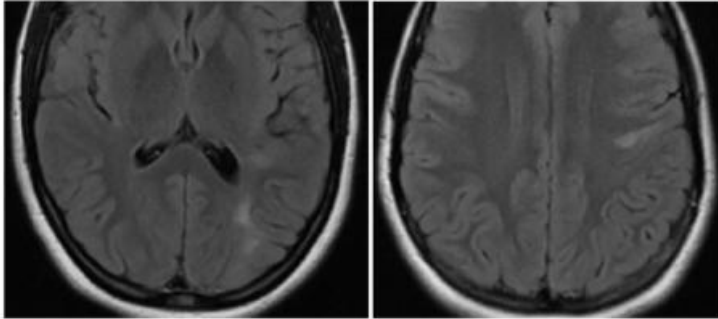


Figure 1: MRI brain at 3rd presentation. Axial FLAIR sequence demonstrates hyperintense subcortical lesions in the left parietal lobe.

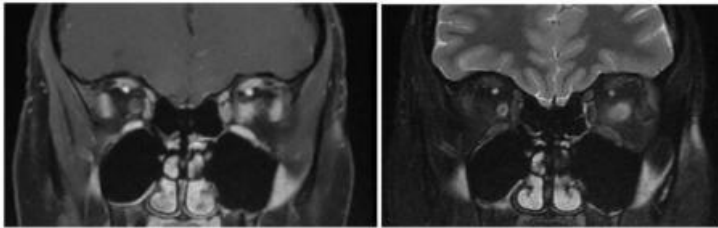


Figure 2: MRI orbits at 5th presentation. Coronal T1 Fat Sat with contrast (left) and Coronal T2 sequences through the intraorbital optic nerves shows enlarged T2 hyperintense left optic nerve with abnormal enhancement.

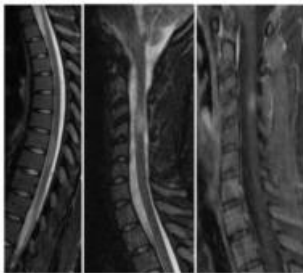


Figure 3:
 2a (left): At 5th presentation, Sagittal T2 sequence through thoracic cord shows T2 hyperintense lesion at T7-8 level.
 2b (middle): At 7th presentation, Sagittal T2 sequence through cervical cord shows T2 hyperintense lesion at C3-4 level.
 2c (right): At 7th presentation, Sagittal T1 Fat Sat with contrast sequence through cervical cord shows enhancing lesion at C3-4 level.

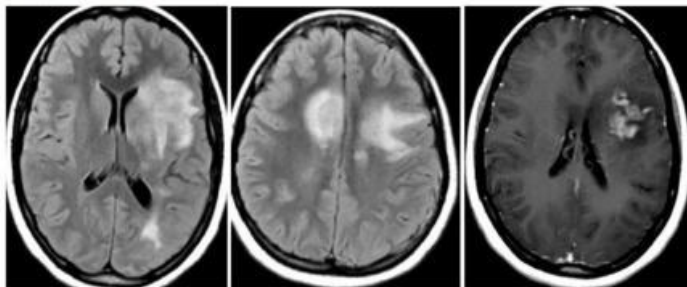


Figure 4: Axial FLAIR (left two) and Axial T1 post contrast images shows tumefactive white matter lesions in the supratentorial brain with contrast enhancement.

(Filename: TCT_E-101_MSvsNMO.jpg)

E-102

PML posterior fossa in a child

J Hunter¹

¹Texas Children's Hospital, Houston, TX

3:16PM - 3:20PM

Oral Presentations & Excerptas

Purpose

To acquaint the audience with salient imaging features of PML in the posterior fossa of an immunocompromised child

Materials and Methods

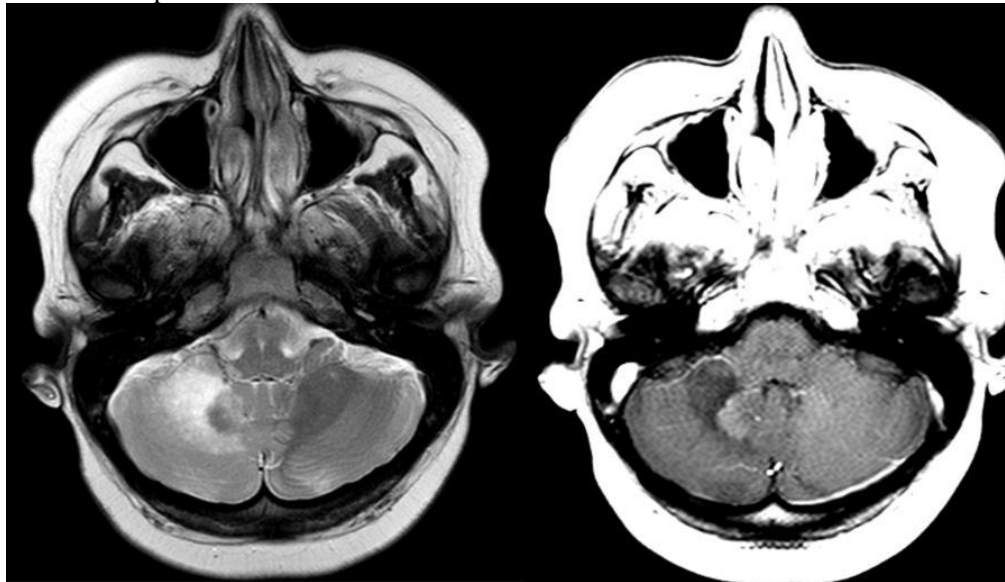
A 16-year-old female with pre-B cell ALL, currently in second remission, 15 months post bone marrow transplant complicated by hepatic graft vs. host disease. Treated for pancytopenia she now presents with confusion and balance changes. Subsequent lumbar puncture following MRI was positive for JC virus in the CSF with reactive lymphocytosis.

Results

Enhanced MRI examination of the brain demonstrated abnormal T2 hyperintensity returned from the right middle cerebellar peduncle and peridentate nuclear white matter with enhancement of the dentate nucleus following the administration of gadolinium chelate. There was no restricted diffusion abnormality or susceptibility. We had previously reported a case of PML presenting in the cerebellum in a seven-year-old male with perinatally acquired HIV infection carrying a diagnosis of AIDS with identical same imaging findings. Follow-up MR imaging three weeks later has demonstrated progression of T2 hyperintensity to involve the left cerebellum, medulla and pons.

Conclusions

There appear to be pathognomonic features of PML in the posterior fossa. The diagnosis on MRI was assisted by pattern recognition having previously reported a case of PML in the cerebellum of an immunocompromised child.



(Filename: TCT_E-102_pmlASNR.jpg)

E-103

3:20PM - 3:24PM

Cerebral mucormycosis mimicking a brain tumor

Y Liu¹, C Toensing², L Sande-Lopez¹, T Minasian¹, S Harder²

¹Loma Linda University Children's Hospital, Loma Linda, CA, ²Loma Linda University Medical Center, Loma Linda, CA

Purpose

We describe a case of intracranial mucormycosis in an immunocompetent child with perfusion features mimicking a brain tumor.

Oral Presentations & Excerptas

Materials and Methods

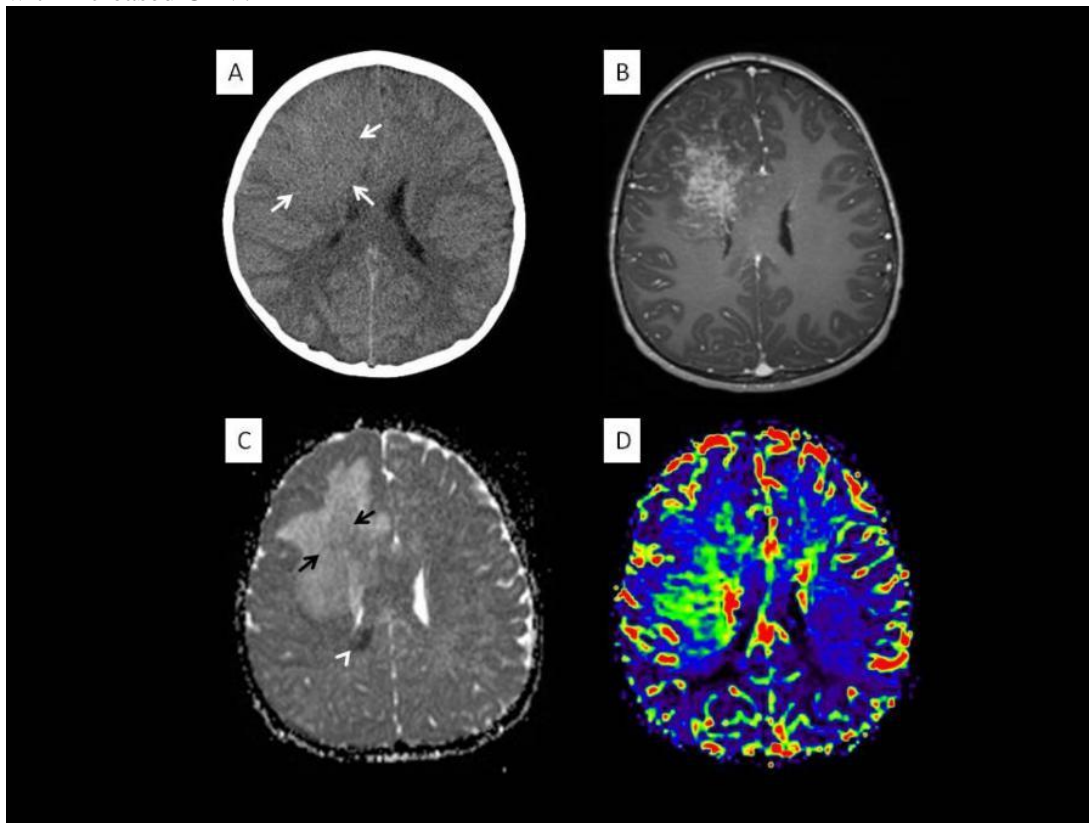
A four-year-old healthy male presented with intractable vomiting, worsening right frontal headaches for one month, and drowsiness for one day. Head CT demonstrated a large hyperdense right frontal lobe lesion. MRI showed a large, irregularly enhancing right frontal lobe lesion which involved the corpus callosum. Subtle associated diffusion restriction was noted with increased cerebral blood volume (CBV). A high-grade, hypercellular tumor was suspected although the enhancement pattern was unusual. A generous biopsy was performed given intraoperative pathology revealing granulomatous fungal encephalitis and the lesion being grossly ill-defined. Tissue culture confirmed growth of *Saksena* species. Extended work-up ruled out immunodeficiency and disseminated systemic fungal infection. He was treated with liposomal amphotericin B, posaconazole and terbinafine.

Results

Figure 1. Head CT (A) demonstrates a large, ill-defined, hyperdense region in the right frontal lobe (white arrows). Postcontrast T1-weighted image shows a large, ill-defined lesion with unusual curvilinear and nodular enhancement (B). The ADC map shows subtle associated diffusion restriction (black arrows) with surrounding facilitated diffusion. A small focus of more profound diffusion restriction is noted in the corpus callosum (white arrowhead) (C). Perfusion weighted imaging reveals increased cerebral blood volume throughout this region (D).

Conclusions

This is an unusual case of intracranial mucormycosis presenting in an immunocompetent patient as an intracranial mass lesion (1-3). *Saksena* species has previously been reported in immunocompetent patients (4). The source of the infection in our patient was unknown. The unusual curvilinear and nodular enhancement pattern in our case may reflect the angioinvasive nature of the organism, not previously reported. The finding of increased CBV is typically associated with neoplasms, with CNS infections typically demonstrating decreased CBV (5). This case demonstrates that fungal infection may present with increased CBV.



(Filename: TCT_E-103_Figure1CTandMRIfindingsoftherightfrontallobelesion.jpg)

Congenital Trigeminal Nerve Agenesis as a Cause of Childhood Neurotrophic Keratitis and Near Blindness.

M Smith¹, O Raslan¹, N Gandhi¹, A Ozturk¹, M Bobinski¹, J Chang¹, N Pham¹

¹*University of California, Davis Medical Center, Sacramento, CA*

Purpose

To the best of our knowledge, to report the first radiologically confirmed case of bilateral congenital trigeminal nerve agenesis as a cause of childhood neurotrophic keratitis and near blindness

Materials and Methods

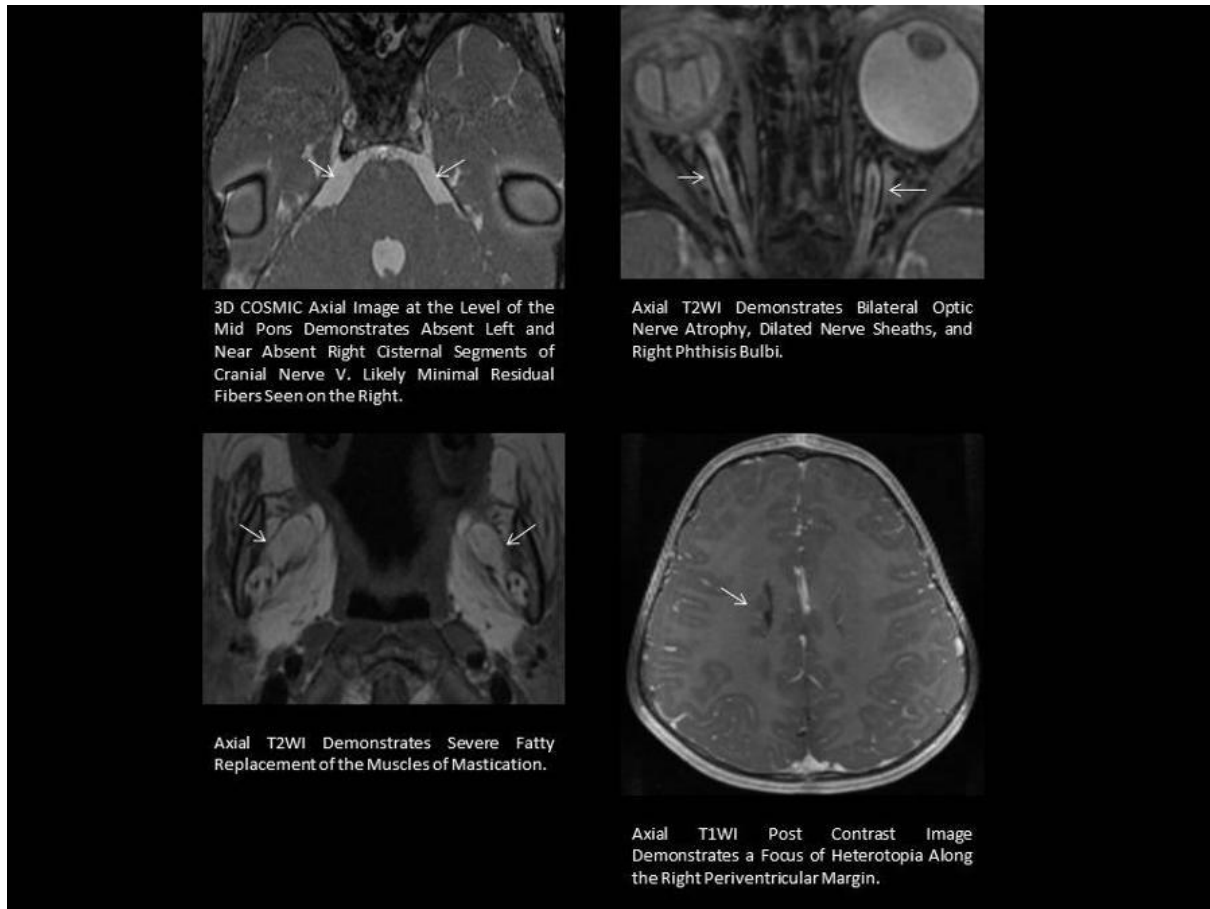
A girl of nine months of age with a past medical history significant for seizure and gastrostomy tube dependency was referred to our institution for presumed right infectious keratitis which progressed to bilateral keratitis by 11 months of age. Clinical testing for herpes simplex virus (HSV) was negative. Despite aggressive medical and surgical therapy including prophylaxis for presumed HSV keratitis, amniotic membrane grafting, tarsorrhaphy, and failed corneal transplant, rapid disease progression resulted in near bilateral blindness. Ophthalmoscopic evaluation noted possible corneal insensitivity. A subsequent MRI led to the diagnosis of trigeminal nerve agenesis on the left and near complete trigeminal agenesis on the right.

Results

MRI demonstrated absent left and nearly absent right trigeminal nerves. There was severe fatty atrophy of the muscles of mastication, hypoplasia of the optic nerves (presumed from absent visual stimulation), and right phthisis bulbi from failed corneal transplant. A small gray-matter heterotopia along the right periventricular margin likely represented an epileptogenic focus.

Conclusions

We present a rare case of bilateral trigeminal nerve agenesis, whereby the patient's clinical presentation, including bilateral keratitis (V1 division) and poor feeding from severe muscle of mastication atrophy (V3 division) requiring gastrostomy tube placement, could be retrospectively accounted for by trigeminal nerve agenesis (1,2). General facial anesthesia from all three divisions is difficult to assess in a patient of this age, but is suspected given repetitive motions targeted at the face. Radiologic confirmation of trigeminal agenesis allows for elimination of other diagnoses and identification of other intracranial abnormalities that may exist within a congenital syndrome (3,4). Whether this patient's constellation of findings is syndromic or isolated remains an ongoing investigation at our institution.



(Filename: TCT_E-104_Trigeminal2.jpg)

E-105

3:28PM - 3:32PM

Stroke-like Migraine Attacks after Radiation Therapy (SMART) Syndrome: Case Report of a Pediatric Brain Tumor Survivor Presenting 24 Years Following Radiation Therapy

M Fuortes¹, A Capizzano¹

¹University of Iowa Hospitals and Clinics, Iowa City, IA

Purpose

Stroke-like migraine attacks after radiation therapy is a rare late complication following radiation therapy typically presenting several years following treatment with rare cases reported developing decades later. The clinical presentation includes severe migraine headaches, seizures, and stroke-like neurological deficits which usually resolve over the course of a few weeks. During the acute symptomatic period patients characteristically have striking MRI findings with gyriform T2/FLAIR signal hyperintensity and leptomeningeal enhancement which have been reported most frequently in the temporoparietal and occipital lobes. The significantly delayed onset of clinical symptoms and imaging features of SMART syndrome following radiation therapy presents a unique diagnostic dilemma. We will present a recent case of SMART syndrome at our institution with a discussion of the clinical and imaging features that led to the diagnosis, followed by a brief review of the literature.

Materials and Methods

A 30-year-old male presented with severe migraine headaches and vision loss, which had progressively worsened over the past few weeks. He first noticed numbness in his right arm followed days later by

Oral Presentations & Excerpts

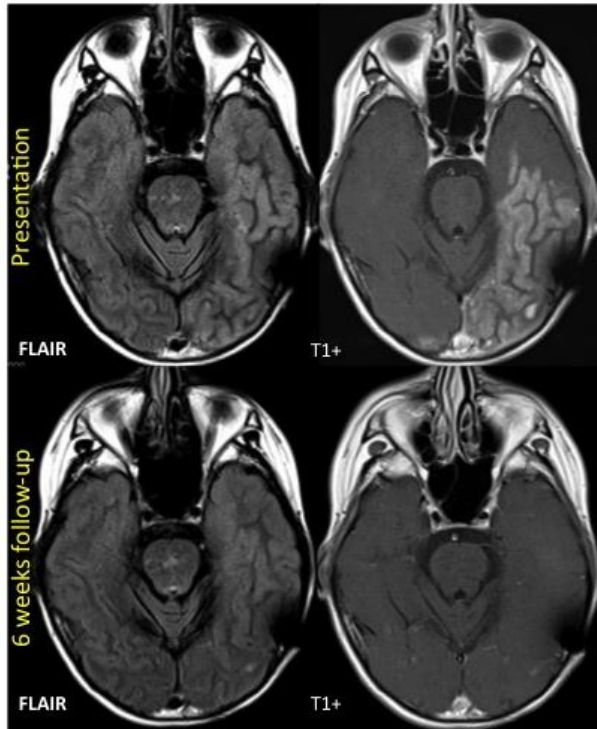
intense predominantly left-sided headaches. The patient has a past medical history significant for a medulloblastoma diagnosed at six years old that was successfully treated with surgical resection, chemotherapy and radiation therapy, and a ventriculoperitoneal shunt (VPS) placed around the time of his surgical resection. He was initially seen by his local neurosurgeon and at that time had a low-grade temperature of 100.5 degrees. CSF studies were obtained from a tap of the VPS reservoir and were normal with negative cultures. He was treated for migraine headaches without any noticeable improvement. The headaches continued to worsen and he subsequently developed blurry vision, language impairment and confusion at which point he presented to our emergency department. An MRI brain at this time demonstrated gyriform T2/FLAIR hyperintensities in the left temporoparietal and occipital lobes with corresponding postcontrast cortical and leptomeningeal enhancement. The patient was admitted to the hospital and electroencephalogram showed nonconvulsive status epilepticus with epileptiform discharges in the left parietal region. A wide differential diagnosis was considered including vascular or metabolic etiologies, infection, postictal changes, radiation necrosis and less likely malignancy. Lumbar puncture was repeated during his admission and was negative for bacterial or viral meningitis. He was treated with Keppra for his seizures and gabapentin for his headaches with significant improvement in his symptoms by the time of his discharge three days later. A follow-up MRI six weeks later showed minimal T2/FLAIR hyperintensities with complete resolution of the previously seen enhancement in the left temporoparietal and occipital lobes.

Results

MRI brain at time of admission showed marked T2/FLAIR hyperintensities in the cortex of the left temporoparietal and occipital lobes with sulcal effacement. The postcontrast images demonstrated intense gyriform enhancement in the affected areas with associated leptomeningeal enhancement. There were no significant signal changes on diffusion-weighted images. In addition, the patient has a left posterior parietal approach ventriculoperitoneal shunt which traverses the affected brain areas, and had no evidence of hydrocephalus. Notably, the patient has cerebellar volume loss and calcifications secondary to childhood radiation therapy, as well as multiple radiation-induced cavernomas. A follow-up MRI brain six weeks later showed marked improvement of the previous findings with minimal persistent T2/FLAIR hyperintensities in the left temporoparietal and occipital lobes and complete resolution of postcontrast enhancement.

Conclusions

We report a recent case of SMART syndrome at our institution that presented an initial diagnostic dilemma. Our patient was a pediatric brain tumor survivor who 24 years later developed severe migraines and focal neurological deficits characteristic of SMART syndrome. The delayed onset of symptoms and imaging findings following radiation therapy, and the rarity of the syndrome made it challenging to arrive at the diagnosis. By presenting the case with a brief review of the literature we hope to educate the audience about the syndrome and to aid in future diagnosis.



(Filename: TCT_E-105_SMARTsyndrome.jpg)

E-106

3:32PM - 3:36PM

Large Scalp Congenital Hemangioma with Internal Necrosis and Calcifications Masquerading Teratoma or Sarcoma: Four Illustrative Cases

F Lu¹, M Jurkiewicz¹, T Feygin¹

¹*Children's Hospital of Philadelphia, Philadelphia, PA*

Purpose

Congenital hemangioma (CH) is true vascular tumor that is fully developed at birth. It is different from the more commonly seen infantile hemangioma (IH) that is usually poorly discernable at birth and proliferates later. Several case series have reported the clinical course and histopathology of CH; however, description of imaging characteristics are limited, and particularly scant for large CH. Large CH poses a unique challenge to radiologists as it can demonstrate aggressive features, such as internal hemorrhage, necrosis and calcifications, masquerading teratoma or sarcoma. We present four cases of pathology-proven large scalp congenital hemangiomas. Fetal MR and ultrasound, postnatal CT and MR will be reviewed in detail.

Materials and Methods

Three fetal patients with large heterogeneous scalp mass were initially diagnosed at the gestational age ranging from 19 to 24 weeks. Prenatal and postnatal imaging and clinical information have been reviewed. In addition, imaging and clinical information were reviewed of a full-term newborn with a large scalp mass and congestive heart failure.

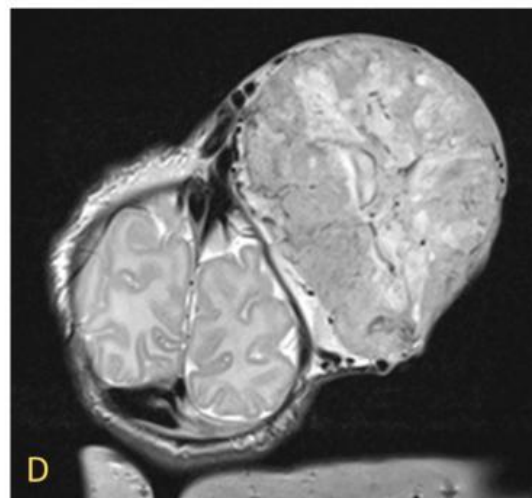
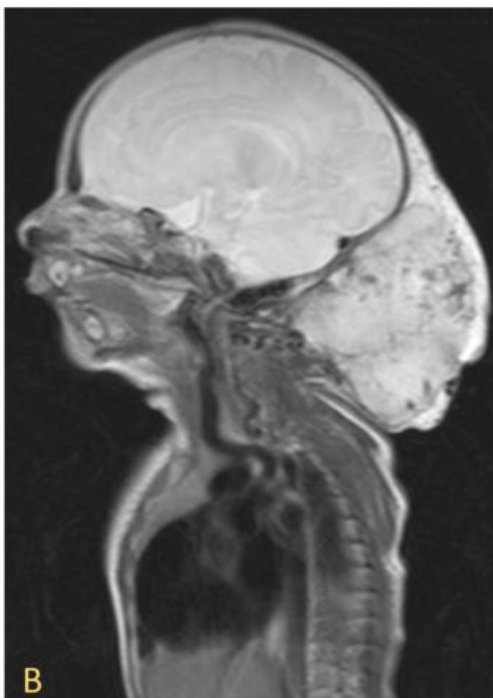
Results

All lesions were notable for similar imaging features of foci of internal hemorrhage, calcifications, necrosis and scalloping and mass effect upon the underlying bone. All cases showed no intracranial extension. The prenatally discovered lesions have been found to grow faster than the brain at full-term

birth. Although the radiologic findings were characteristic of congenital hemangiomas, the presence of internal hemorrhage and necrosis in conjunction with calcifications, peripheral predominance of perfusion and its significant mass effect concerned the clinicians for aggressive teratoma or sarcoma. All lesions were proved to be CH on pathology.

Conclusions

Large CH may have imaging characteristics that can be mistaken for aggressive teratoma or sarcoma. Familiarity with imaging and clinical features will aid the diagnosis and direct the treatment.



Patient One (A and B): Photo at time of birth and MR obtained one day after. The heart is enlarged and the left common carotid artery is engorged.

Patient Two (C and D): Fetal MR obtained at 24 week of gestation and MR obtained one day after birth. There is disproportionate growth of the large parietal scalp mass that demonstrates significant mass effect to the left hemicranium. The mass drains into a dilated superior sagittal sinus.

(Filename: TCT_E-106_ASNRCongenitalHemangioma.jpg)

E-107

3:36PM - 3:40PM

Hairy Polyp

Oral Presentations & Excerptas

M Manganaro¹, M Bazerbashi¹, J Bapuraj¹, D Miller¹, F Boucher¹, E Gu¹, Z Wilseck¹, J Kim¹, M Lee¹
¹University of Michigan, Ann Arbor, MI

Purpose

This case report illustrates an example of a congenital hairy polyp--a rare benign tumor representing the most common congenital nasopharyngeal mass.

Materials and Methods

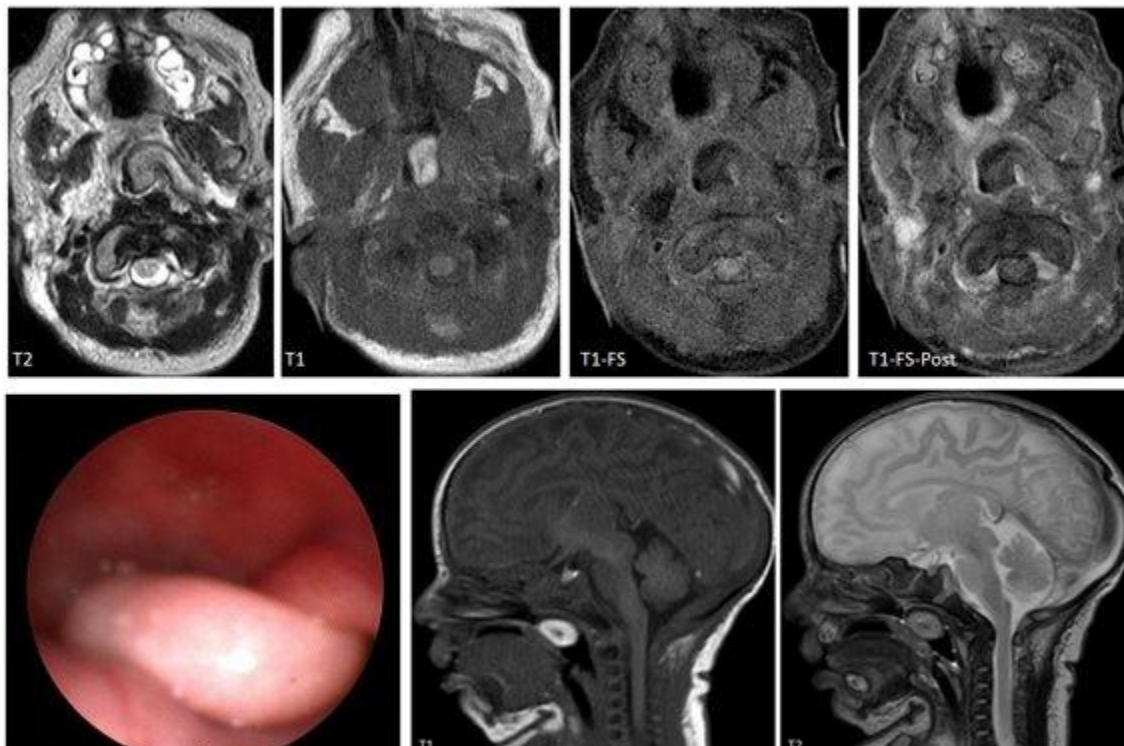
A full term healthy one-day-old baby boy was having intermittent choking and coughing with breast feeding as well as intermittent stridor. The father, a neurosurgeon, used a tongue depressor to look in baby #39's mouth and saw a mass at the back of the tongue. The baby was transferred to the NICU for airway evaluation and imaging to assess the mass. MRI revealed a pedunculated predominantly fat signal mass without associated contrast enhancement arising from the left Eustachian tube protruding into the posterior nasopharynx, which was confirmed during direct laryngoscopy. The mass was resected endoscopically and the gross pathology reveal a yellow-tan, glistening, fibrous fatty lesion containing large peripheral nerves consistent with hairy polyp. No teratomatous elements or glioneuronal tissue noted. After the resection the patient had an uneventful short postoperative stay in the hospital and was discharged home in good health.

Results

MRI of the skull base and neck revealed 1.8 cm pedunculated predominantly fat signal mass without associated contrast enhancement arising from the left Eustachian tube protruding into the posterior nasopharynx.

Conclusions

Hairy polyp is an unusual, but well-described entity that frequently presents during the first days after birth. Knowledge and recognition of this lesion is important as management with complete resection is curative.



(Filename: TCT_E-107_Hairypolyp.jpg)

MR Imaging and Spectroscopy in Adenylosuccinate Lyase Deficiency

C Pfeifer¹, S Castillo¹

¹University of Texas Southwestern Medical Center, Dallas, TX

Purpose

Adenylosuccinate Lyase Deficiency is a rare autosomal recessive disease of purine metabolism with only approximately 100 known cases, most commonly in Belgium and the Netherlands. Reports of neuroimaging findings are rare. The genetic and metabolic properties of this disorder are discussed in addition to imaging findings.

Materials and Methods

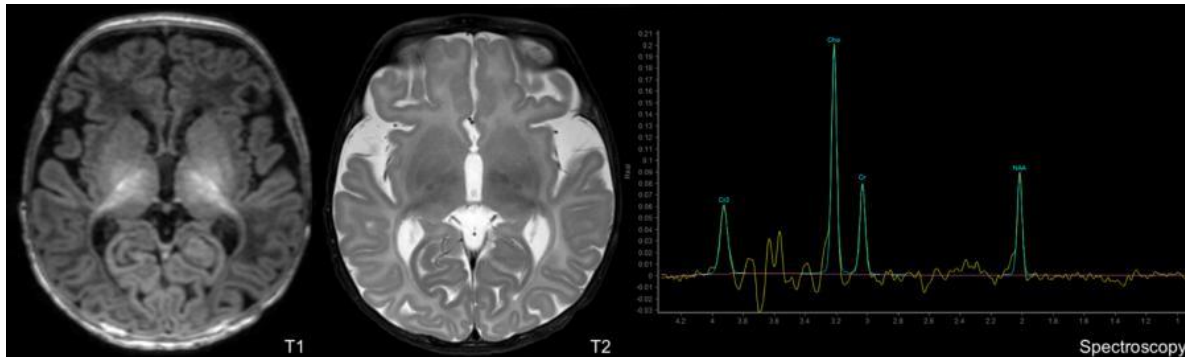
A term 3-month-old male presented with severe seizures and hypotonia since birth. As a result of increasing parental frustration, the child was transferred from an outside facility for advanced testing and 3.0 Tesla MRI. MRI of the brain performed at 3 months of age demonstrated a persistent newborn myelination pattern with generalized low parenchymal volume. MR Spectroscopy was also abnormal, prompting genetic and metabolic testing, which resulted in the diagnosis of adenylosuccinate lyase deficiency.

Results

MR findings were consistent with hypomyelination for age, with myelination confined to the bilateral posterior limbs of the internal capsules and peri-rolandic regions on T1-weighted images. On T2-weighted images, the white matter was diffusely hyperintense. The cortical sulci and ventricles were proportionally prominent in a pattern consistent with generalized low parenchymal volume. Magnetic Resonance Spectroscopy interrogation of a voxel of abnormal right parietal white matter performed at long TE revealed a decreased NAA peak and absent lactate peak.

Conclusions

The etiology of abnormal myelination in a newborn has a broad differential diagnosis. Given the very low incidence of adenylosuccinate lyase deficiency in the United States, clinicians should be aware of the possibility of this disorder in the setting of unexplained diffuse myelinopathy, as advanced testing is required to make the definitive diagnosis. The radiologist may be the first physician to suggest this condition.



(Filename: TCT_E-108_AS LTD1and2.jpg)

Rubinstein-Taybi Syndrome: A Case of Corpus Callosal Agenesis and Intracranial Diffuse B-Cell Lymphoma

S Koenig¹, C Bazan¹

Purpose

Rubinstein–Taybi syndrome (RTS), also known as broad thumb-hallux syndrome or Rubinstein syndrome, is a genetic disorder caused by a deletion on 16p13.3 and alterations of the CREBBP gene. The syndrome is characterized by short stature, mental retardation, distinctive facial features, broad thumbs with radial deviation, broad great toes, corpus callosal agenesis, and increased risk of both non malignant and malignant tumors including lymphoma and leukemia. We present a patient with known Rubinstein-Taybi syndrome to review the classic and clinical and imaging findings of this rare syndrome.

Materials and Methods

A 39 year old male with a known history of mental retardation and complete dependency for activities of daily living, as well as corpus callosal agenesis, presented with progressive left upper extremity weakness and altered mentation from baseline. Initial head CT images and MRI of the brain revealed a large enhancing right frontotemporal mass lesion involving the dura, as well as corpus callosal agenesis with colpocephaly. After biopsy of the mass, the patient was found to have intracranial diffuse B cell lymphoma. Genetic studies revealed findings consistent with Rubinstein-Taybi syndrome. Further imaging of the patient's left hand demonstrated a broad and shortened thumb with radial deviation. The mass was resected and chemotherapy was initiated with near resolution.

Results

Figure 1a is a radiograph of the left hand demonstrating a broad and radially deviated thumb which is a hallmark finding of Rubinstein-Taybi Syndrome. Figure 1b is an axial T1 post contrast imaging demonstrating an intensely enhancing right temporoparietal mass involving the dura which was found to be diffuse B-cell lymphoma in the same patient, as well as elongated and widely spaced lateral ventricles as seen in corpus callosal agenesis. Figures 1c and 1d are coronal T2 and sagittal T1 post tumor resection images demonstrating absence of the corpus callosum, as well as a high riding third ventricle.

Conclusions

Rubinstein-Taybi syndrome is a rare genetic syndrome with unique clinical and imaging findings. It is important to recognize the constellation of findings associated with the syndrome and the 16p13.3 micro deletion, as well as to recognize the strong correlation of the syndrome with both malignant and non malignant tumors.



(Filename: TCT_E-109_Picture1.jpg)

E-110

3:48PM - 3:52PM

Temporomandibular Joint Synovial Chondromatosis

M Manganaro¹, D Miller¹, E Gu¹, F Boucher¹, Z Wilseck¹, J Kim¹

¹University of Michigan, Ann Arbor, MI

Purpose

Synovial chondromatosis, also known as Reichel syndrome, is a benign monoarticular disorder of unknown origin that is characterized by synovial metaplasia and proliferation resulting in multiple intraarticular cartilaginous loose bodies of relatively similar size, not all of which are ossified. This is a common finding in an unusual place. Usually, the condition is monoarticular affecting any joint but the large joints are preferentially affected the knee (up to 70%), hip (20%), elbow, and shoulder.

Materials and Methods

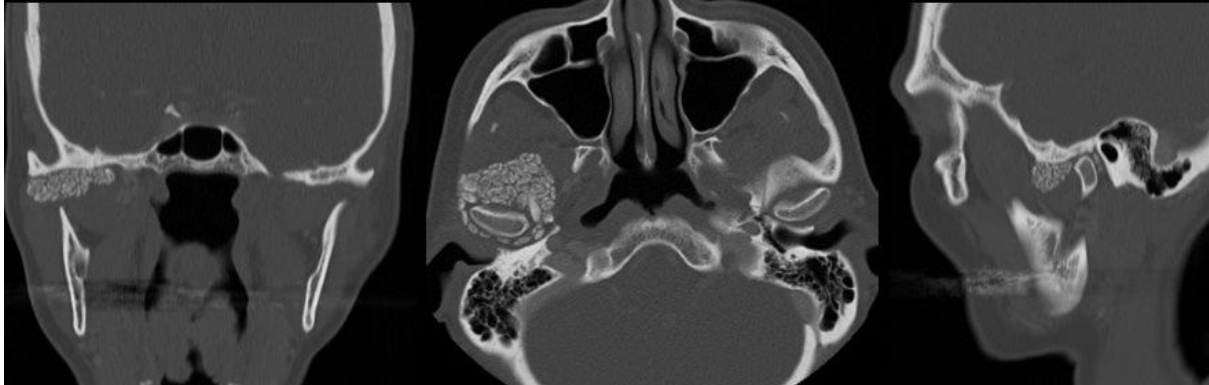
A 45-year-old healthy male presents to his dentist with increasing jaw pain with clicking noises when chewing. Suspecting TMJ pathology a maxillofacial CT was performed showing numerous tiny calcified rice bodies surrounding the right TMJ and the diagnosis of Synovial osteochondromatosis was made. The patient then underwent synovectomy with removal of the calcified intrarticular bodies. The patient is free of pain and the previously described clicking sensation.

Results

Numerous tiny calcified rice bodies surrounding the right TMJ

Conclusions

Primary synovial chondromatosis, also known as Reichel syndrome, is a benign monoarticular disorder of unknown origin that is characterized by synovial metaplasia and proliferation resulting in multiple intraarticular cartilaginous loose bodies of relatively similar size, not all of which are ossified. Hence, the term synovial chondromatosis is preferred over primary synovial osteochondromatosis. Secondary synovial chondromatosis is a degenerative. This is a common finding in an unusual place as the Temporomandibular joint is a synovial joint. Usually, the condition is monoarticular affecting any joint but the large joints are preferentially affected the knee (up to 70%), hip (20%), elbow, and shoulder. The age range of affected patients is wide, but most present in the 4th to 5th decade. Treatment of synovial chondromatosis usually consists of removal of the intra-articular bodies with or without synovectomy, but local recurrence is not uncommon.



(Filename: TCT_E-110_Synovialchondromatosis.jpg)

E-111

3:52PM - 3:56PM

Aneurysmal Bone Cyst within Fibrous Dysplasia: A Rare Association in the Sinuses

S Gupta¹, G Moonis¹

¹*Columbia University Medical Center, New York, NY*

Purpose

We present an extremely rare case of a presumed aneurysmal bone cyst arising from a sinonasal fibrous dysplasia lesion centered in the ethmoid sinuses in a 14-year-old male presenting with proptosis and eye pain.

Materials and Methods

A 14-year-old male presented to the emergency department of our institution with right eye proptosis first noticed one day before presentation and progressively worsening. An MRI of the brain and orbits with intravenous contrast administration and a CT of the sinuses were performed. Primary differential on both imaging studies was fibrous dysplasia with aneurysmal bone cyst. There was secondary proptosis and obstruction of the paranasal sinuses. A nasal endoscopy demonstrated a submucosal mass protruding from the right middle meatus. An excisional biopsy showed findings most consistent with fibrous dysplasia with psammoma-like spicules of bony condensation within the stroma.

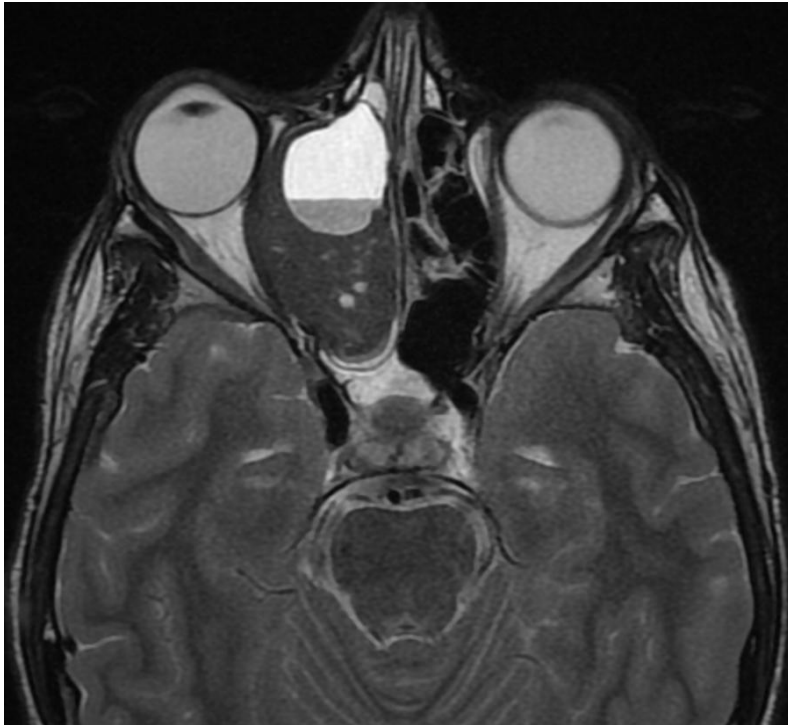
Results

An MRI of the brain and orbits showed an approximately 5 cm lesion of fibrous intensity centered in the right ethmoid sinus with an anterior 3 cm cystic component containing a fluid-fluid level, presumed to be hemorrhagic. The lesion extended into the nasal passages with obliteration of the right superior and middle turbinates. There was also secondary obstruction of the right frontal, maxillary and sphenoid sinuses. Mass effect was noted on the right globe with proptosis. There was also superior extension with erosion of the medial frontal calvarium. A CT of the sinuses demonstrated an approximately 5 cm

groundglass matrix lesion centered in the ethmoid sinuses with anterior well defined hemorrhagic cystic component. The primary differential of both studies was a sinonasal fibrous dysplasia lesion with hemorrhagic anterior aneurysmal bone cyst.

Conclusions

Fibrous dysplasia lesions and aneurysmal bone cysts are both benign entities and both demonstrate a predilection for the younger age group. We demonstrate an extremely rare case where they occur concurrently in a 14-year-old boy presenting with proptosis and mild eye pain. Although this lesion is extremely rare, it should be considered when classic imaging features such a fibrous matrix and fluid-fluid level are seen.



(Filename: TCT_E-111_AxialT2.jpg)

E-112

3:56PM - 4:00PM

Bilateral Cranial Nerve VI Palsy Secondary to Radiation Treatment of Nasopharyngeal Carcinoma: A Unique Cause of Diplopia.

J Pack¹, J Branchcomb², F Torres³, J Acharya⁴, C Liu¹, A Rajamohan¹

¹University of Southern California, Keck School of Medicine, Los Angeles, CA, ²LAC+USC Medical Center, Alhambra, CA, ³Kaiser Permanente, Los Angeles, CA, ⁴University of Southern California, Pasadena, CA

Purpose

Our goal is to provide insight into an uncommon entity in the United States which can be considered in a patient presenting with bilateral cranial nerve VI palsy and a history of prior radiation treatment.

Materials and Methods

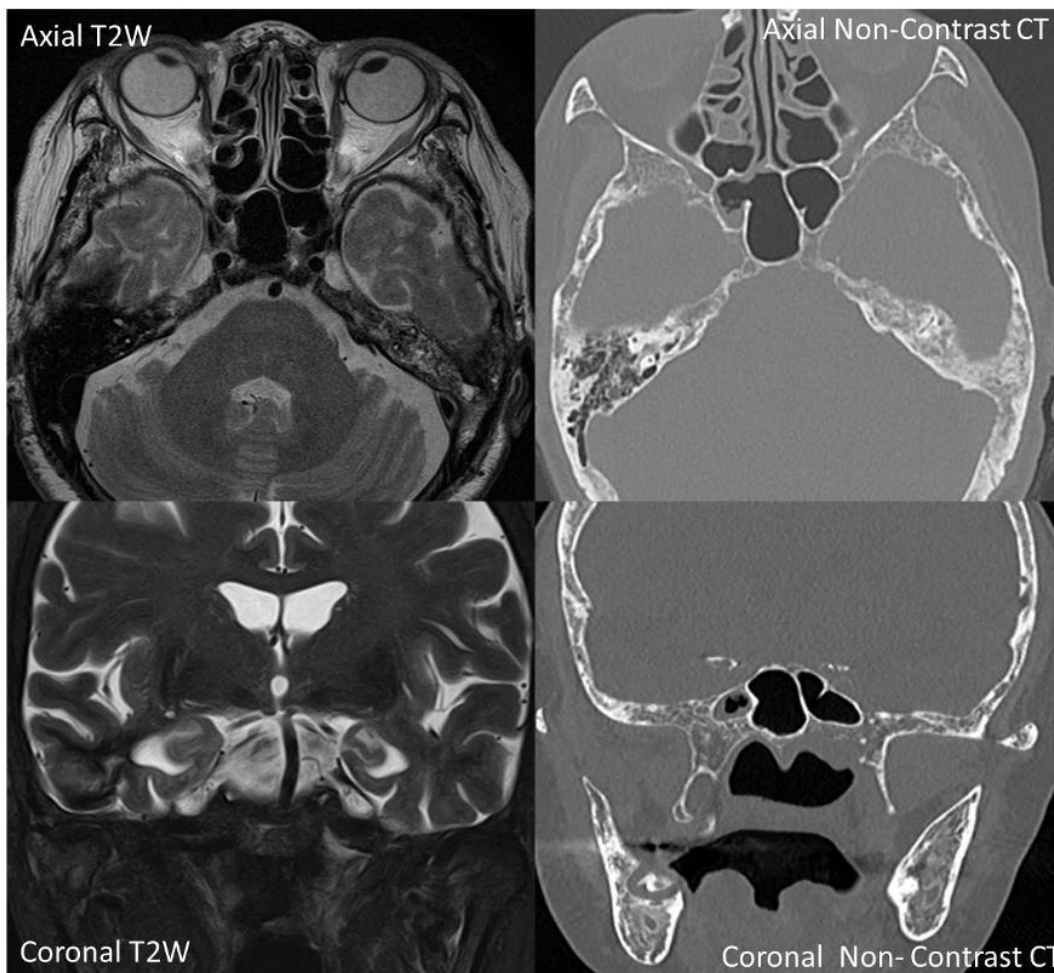
Our patient is a 66-year-old woman who presented to the neurology clinic with diplopia. She was found on clinical exam to have bilateral sixth cranial nerve palsy. The patient reports a remote history of nasopharyngeal carcinoma, status post prior radiation treatment in China.

Results

Initial evaluation of postcontrast T1W images showed no evidence of intracranial or perineural metastasis. No infarct or brainstem etiology for a CN VI palsy was present. Upon closer inspection, T2-weighted images demonstrated gliosis and chronic blood products within the temporal lobes compatible with radiation injury. Further examination of the skull base on prior CT demonstrates a striking, lytic and mottled appearance of the marrow compatible with osteonecrosis of the skull base and the mandible.

Conclusions

The differential diagnosis for a bilateral sixth nerve palsy, even in the setting of previously treated nasopharyngeal carcinoma is often focused on pontine lesions, destructive skull base lesions and leptomeningeal disease given that the adoption of IMRT (intensity-modulated radiation therapy) has significantly decreased the incidence of temporal lobe radiation necrosis and skull base osteoradionecrosis in this country. However, if a patient has received high dose radiation treatment in the past or in a foreign country, and there are findings suggestive of skull base osteoradionecrosis, radiation induced cranial nerve palsy should be considered.



(Filename: TCT_E-112_Radiation3.jpg)

E-113

4:00PM - 4:04PM

Temporal Encephalocele: an Uncommon Cause of Acute Otitis Media and Meningitis

Oral Presentations & Excerptas

S Sharma¹, N Gutta¹, R Samant², R Ramakrishnaiah¹, J MCCARTY¹, R Van Hemert², E Angtuaco², M Kumar²

¹University of Arkansas for Medical Sciences, Little Rock, AR, ²UAMS, LITTLE ROCK, AR

Purpose

To recognize the imaging features of temporal encephalocele and to identify it as a rare cause of otitis media and meningitis in adults

Materials and Methods

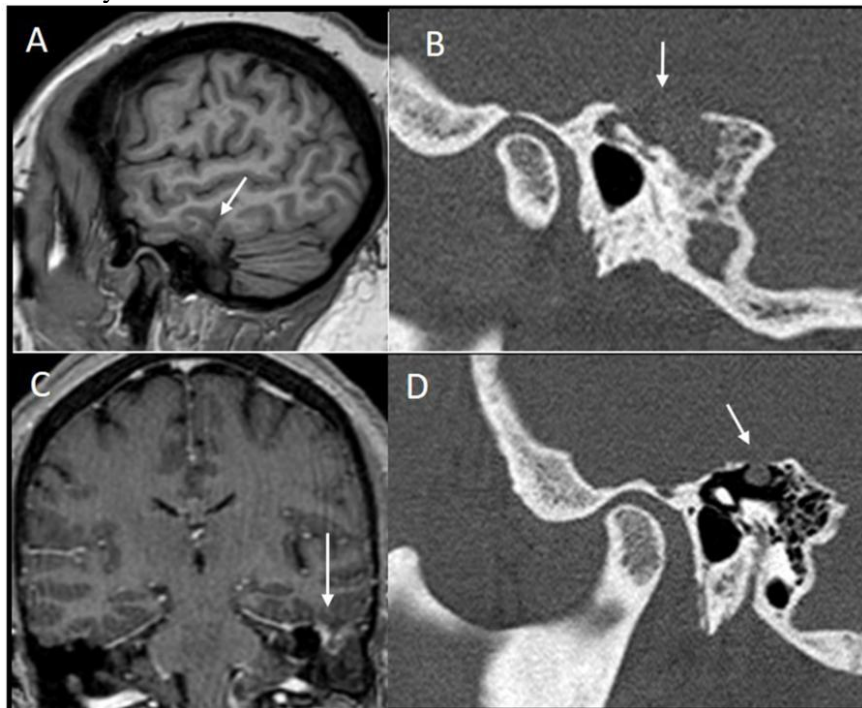
A 51-year-old female presented to the ED with fever and acute onset of confusion and left-side headache. The patient was also reported to have experienced a seizure for 20-30 seconds. She was admitted for workup of seizure and possible stroke. MRI brain was negative for stroke and demonstrated a left temporal encephalocele with otomastoiditis and meningitis. The subsequent exam was positive for otitis media and she was worked-up for the same. CSF evaluation demonstrated increased WBCs (19) with predominantly neutrophils (79%). No organisms were isolated and CSF cultures were negative. She was treated with vancomycin and meropenem for meningitis and encephalitis. After control of acute infection, she underwent elective tympanomastoid repair with cartilage graft placement.

Results

MRI brain demonstrated a focal posteroinferior temporal lobe encephalocele through a 1 cm defect in the roof of the mastoid antrum and tegmen tympani (Figs. A and C). Focal meningitis, encephalitis and mastoiditis were also present. A temporal bone CT was performed for better delineation of anatomy which better demonstrated these findings (Fig. B) and also detected two small right sided temporal encephaloceles (Fig. D).

Conclusions

Acute otitis media is usually associated with eustachian tube dysfunction which can result from upper respiratory tract infections, mucosal disease, craniofacial anomalies (cleft palate), mass lesions like nasopharyngeal tumors and adenoidal enlargement. Scarring resulting from radiotherapy can also predispose to eustachian tube dysfunction. Temporal lobe encephaloceles are uncommon and can rarely present as otomastoiditis and meningitis. Prompt identification and treatment can prevent severe morbidity.



(Filename: TCT_E-113_Picture3.jpg)

Riedel's Thyroiditis

A Levitt¹, D Ginsburg^{N/A}, R Zampolin², A Erdfarb², J Bello², K Shifteh²

¹Montefiore Medical Center, New York, NY, ²Montefiore Medical Center, Bronx, NY

Purpose

To describe a case of Riedel's thyroiditis, review its clinical and imaging findings and contrast them with thyroid cancer, lymphoma and thyroiditis

Materials and Methods

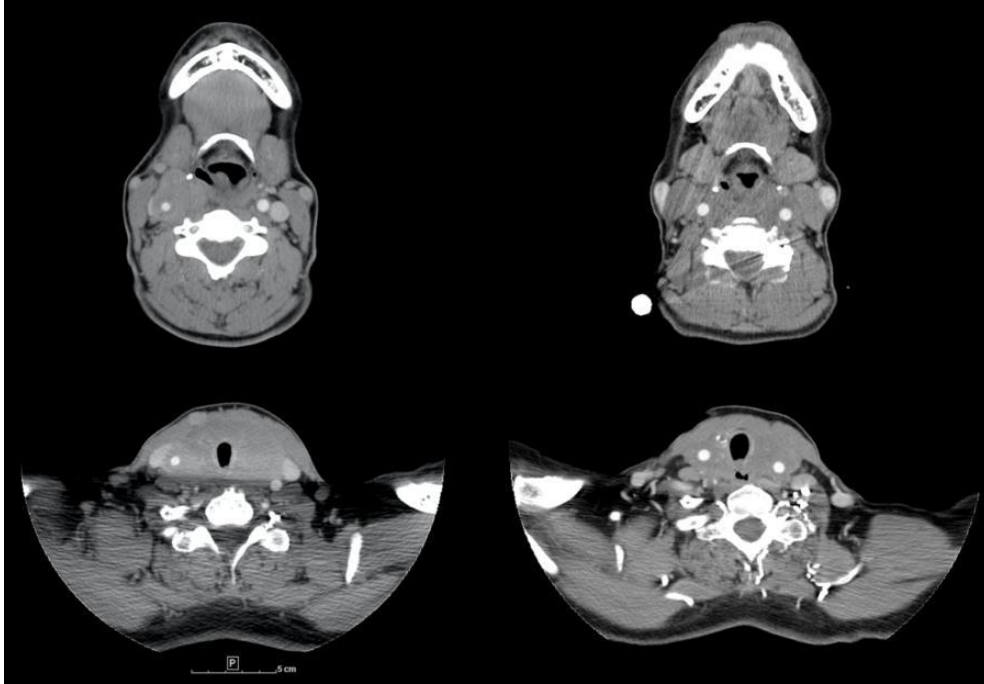
A 65-year-old female with no significant past medical history presented with sudden onset dyspnea and weakness. Further evaluation demonstrated dry skin, diffuse myalgias, constipation and hand paresthesias. Laboratory workup demonstrated an elevated TSH 64.5 and low free T4 of 0.12 consistent with hypothyroidism. Sonography demonstrated a diffusely enlarged and heterogeneous thyroid gland with multiple nodules. Core biopsy of the nodules was performed which failed to obtain sufficient cells for flow cytometry. Pathology did not demonstrate any thyroid tissue. At this point, a contrast-enhanced CT of the neck as well as multiple incisional biopsies were performed.

Results

Contrast-enhanced CT of the neck demonstrated an infiltrative hypodense mass centered in the thyroid with complete encasement of the right internal carotid artery. Extension into the right tracheoesophageal groove with right vocal cord paralysis was also demonstrated. Follow-up contrast enhanced CT of the neck demonstrated overall decreased extent of visceral space infiltration with new encasement of the left internal carotid artery and obliteration of the internal jugular veins.

Conclusions

Riedel's thyroiditis is a very rare inflammatory disease of the thyroid. It was seen in 37 patients over a 64-year period at the Mayo Clinic where over 56,000 thyroidectomies were performed and 3.5 million patients were registered. Case reports describe contrast enhanced CT findings of an enlarged and hypodense thyroid gland with infiltration into the adjacent soft tissues. MR imaging demonstrates thyroid hypointensity on T1- and T2-weighted images with minimal enhancement after the intravenous administration of gadolinium. The differential diagnosis includes Hashimoto's thyroiditis, anaplastic carcinoma of the thyroid and non-Hodgkin's lymphoma. Hashimoto's thyroiditis typically demonstrates enlargement without internal necrosis or calcification but is typically T2 bright and does not infiltrate surrounding soft tissues. Anaplastic carcinoma of the thyroid can have an enlarged and infiltrative appearance but is typically T2 bright, heterogeneously and avidly enhances and demonstrates internal hemorrhage and necrosis. Associated necrotic cervical lymphadenopathy is also frequently present. Non-Hodgkin's lymphoma can have an infiltrative appearance but is typically T2 bright, enhances avidly and is associated with non-necrotic cervical lymphadenopathy. Surgical pathology in this patient failed to demonstrate any normal thyroid tissue and a clinical diagnosis of Riedel's thyroiditis was made. The patient was placed on steroids and her hoarseness resolved. Due to facial swelling from the steroids, the patient was recently switched to tamoxifen).



(Filename: TCT_E-114_riedelsthyroiditisimageshires.jpg)

E-116

4:12PM - 4:16PM

Lobular Capillary Hemangioma of the Mandible

C Chan¹, M Iv², N Fischbein³, H Dahmouh¹

¹Stanford University Hospital, Stanford, CA, ²Stanford University Medical Center, Stanford, CA, ³Stanford University, Stanford, CA

Purpose

Lobular capillary hemangiomas are acquired benign vascular neoplasms which typically affect the skin and mucous membranes. While these lesions commonly involve the head and neck, particularly the oral cavity, there are no reports in the literature of lobular capillary hemangioma arising from the mandible. The diagnosis of such a rare entity can therefore be challenging, especially as it may mimic more aggressive lesions, including malignancy. We present a rare case of an 8-year-old male with a lobular capillary hemangioma of the mandible, highlighting its imaging features and discussing the differential diagnosis of primary mandibular lesions in the pediatric population.

Materials and Methods

An 8-year-old male presented to the emergency department with difficulty breathing and a rapidly growing left oral cavity lesion. On exam, a rubbery mass was palpated in the left retromolar trigone, with fibrinous maceration superiorly which was attributed to chewing. Contrast-enhanced CT of the neck demonstrated a large, lytic, expansile, and heterogeneously enhancing soft tissue mass centered in the left mandibular ramus that extended into the left retromolar trigone and masticator and buccal spaces. There was no aggressive periosteal reaction. MRI of the face showed a T1 isointense, T2 hyperintense mass centered in the medullary space of the left mandible. The mass contained numerous internal flow voids consistent with hypervascularity. No restricted diffusion was present to suggest hypercellularity or high nuclear-cytoplasmic ratio. The mass avidly enhanced after contrast administration. The differential diagnosis included Langerhans' cell histiocytosis, primary odontogenic lesions such as ameloblastoma, sarcoma, desmoplastic fibroma, vascular neoplasm, and venous malformation given the intensity of

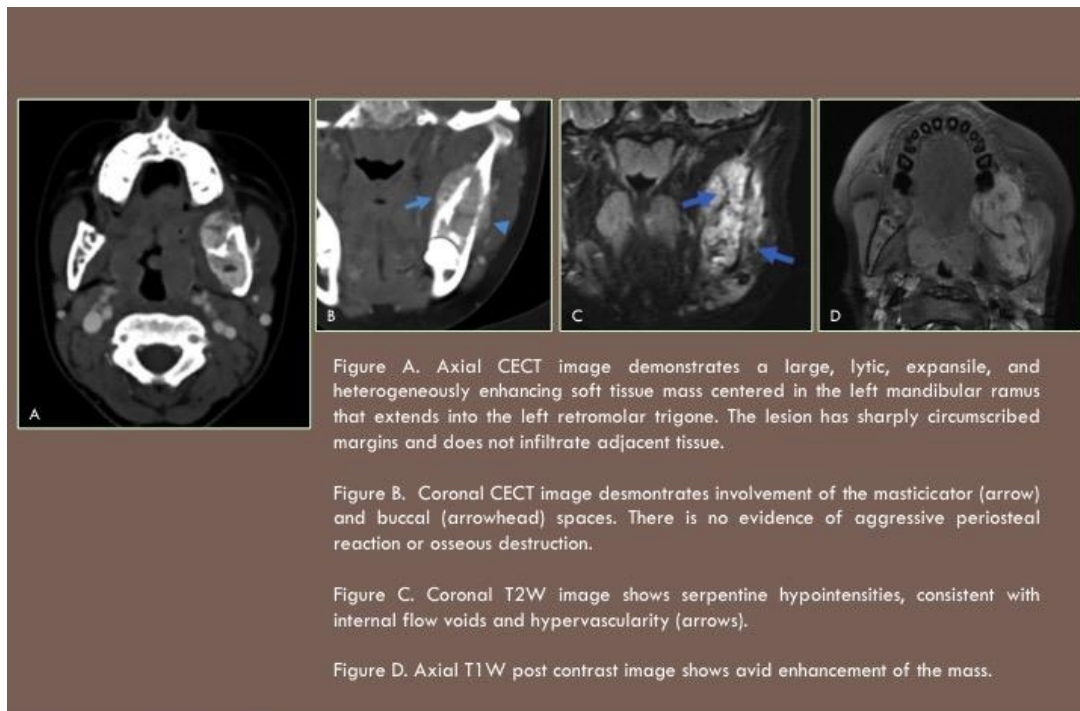
enhancement and the presence of large vessels within the mass. A CT-guided biopsy of the left mandibular mass showed cytologically bland spindle cells. The case was subsequently presented at head and neck tumor board. Given the clinical presentation, imaging findings, and initial pathology, it was felt that this lesion was most likely a benign vascular tumor. Embolization and resection were recommended, as it was felt unlikely that further biopsies would change the recommended treatment and would put the patient at an increased risk of bleeding given the hypervascular nature of the tumor. The patient ultimately underwent embolization and resection of the mass without complications. Final pathology was consistent with lobular capillary hemangioma. The remainder of the hospital course unremarkable; the patient was discharged in stable condition.

Results

The imaging features of a lobular capillary hemangiomas are nonspecific. Lobular capillary hemangiomas occurring in the oral cavity, especially those that are small in size, are often occult on imaging. In rare instances, localized alveolar bone resorption by large and long-standing gingival tumors can be seen. Dystrophic calcifications of variable appearance, ranging from punctate to large and irregular, may be also seen in the setting of long-standing lesions. Imaging findings in our case are similar to those described for lobular capillary hemangiomas that are found in the nasal cavity. On CT, those lesions appear as soft tissue masses with an iso- to hypo-attenuating cap of variable thickness, a feature which may help differentiate a lobular capillary hemangioma from other hypervascular tumors. Bony erosion may or may not be present. MR imaging findings include a T1-isointense and T2-hyperintense mass with a peripheral hypointense rim that may contain internal flow voids. There is no restricted diffusion as compared with more aggressive malignant processes. After contrast administration, these lesions often demonstrate avid enhancement. While CT and MRI features of this mass are often nonspecific, a lobular capillary hemangioma should be in the differential of mandibular masses in the pediatric population; this differential includes sarcoma such as rhabdomyosarcoma and osteosarcoma, Langerhans' cell histiocytosis, desmoplastic fibroma, primary odontogenic lesion such as ameloblastoma and central giant cell granuloma, and other vascular neoplasms and vascular malformations.

Conclusions

Lobular capillary hemangiomas are acquired benign vascular neoplasms of the skin and mucous membranes. They typically occur in the distal extremities and the head and neck, including the oral cavity. Oral lesions most commonly involve the gingiva. Extralingual involvement may also occur and involve the lips, tongue, buccal mucosa, palate, cheek, mucobuccal fold, and frenum. Involvement of the mandible has not been previously reported. While the highest incidence of oral lobular capillary hemangiomas is found in the second and fifth decades, these masses occur in patients of all ages. In the pediatric age group, this tumor typically occurs in early childhood, rarely in adolescents, and has a predilection for males. Clinical manifestations are nonspecific. Lobular capillary hemangioma may present as a compressible painless solitary red to purple cutaneous mass or swelling with rapid progression. Ulceration and hemorrhage may also occur. The etiology of lobular capillary hemangioma is unknown, although trauma, chronic local irritation, hormonal factors such as pregnancy or oral contraceptives, poor oral hygiene, and medications may play a role in the development of these lesions. Treatment often consists of conservative excision with or without preprocedure embolization to decrease risk of bleeding. Prognosis is excellent with complete excision of the tumor. However, in the setting of incomplete excision, failure to remove the inciting factor, and/or reinjury to the region, recurrence of oral lesions may occur at a rate of 3-23%. In summary, lobular capillary hemangiomas very rarely involve the mandible. Despite this rarity, it is important to suggest this diagnosis if the lesion demonstrates typical imaging findings such as hypervascularity and avid enhancement and an absence of malignant features. These findings, in combination with the clinical presentation and pathology, will help to guide appropriate management and treatment.



Lobular Capillary Hemangioma of the Maxilla

(Filename: TCT_E-116_Slide1.jpg)

E-117

4:16PM - 4:20PM

Reversible Hypoglossal Nerve Denervation: A Rare Diagnosis of Exclusion

M Chen¹, L Ginsberg¹

¹MD Anderson Cancer Center, Houston, TX

Purpose

To describe a case of reversible hypoglossal nerve denervation, a diagnosis of exclusion

Materials and Methods

A 71-year-old man with recurrent papillary thyroid carcinoma and diabetes underwent surveillance imaging. The patient was taking levatinib, a kinase inhibitor, for treatment of recurrent papillary thyroid carcinoma. Over the time course of imaging, there was no change in his medication dosing and no significant change in the disease burden of papillary thyroid carcinoma, centered primarily in his tracheoesophageal groove in the lower neck.

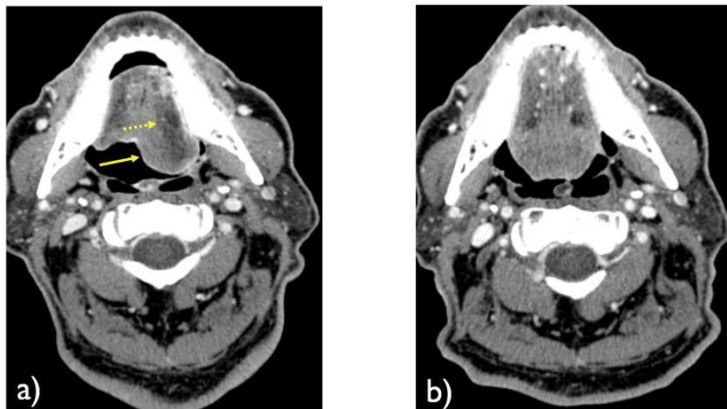
Results

Axial contrast-enhanced CT demonstrated posterior displacement of the left hemitongue with asymmetric hypoattenuation, findings consistent with hypoglossal paralysis. At the time of initial imaging, evaluation of the premedullary cistern, skull base, upper carotid space and sublingual space revealed no etiology. On follow-up imaging three months later, there was resolution of the findings associated with hypoglossal denervation with symmetric appearance of the tongue.

Conclusions

Reversible hypoglossal nerve denervation is extremely rare, with only case reports in the literature. A proposed mechanism is similar to a Bell's Palsy with underlying viral etiology. Reversible transient

denervation should be a diagnosis of exclusion, and other causes for hypoglossal denervation such as masses along the course of the nerve and carotid dissections must be excluded.



(a) Initial contrast enhanced axial CT neck demonstrated posterior displacement of the left hemitongue (arrow) and asymmetric hypoattenuation (dotted arrow). (b) 3 months later, follow up imaging show resolution of imaging findings with restored symmetry of the tongue

(Filename: TCT_E-117_graphic.jpg)

Wednesday, June 6, 2018

4:45PM - 6:15PM

Parallel Paper Session: Applications of Functional MR Imaging

O-453

4:45PM - 4:52PM

Feasibility of resting state functional magnetic resonance imaging (RS-fMRI) in localizing eloquent cortex in pretreatment planning in arteriovenous malformation.

rel daya¹, L Marple², J Shimony³, T Benzinger², M Miller-Thomas¹

¹Mallinckrodt Institute of Radiology, Saint Louis, MO, ²Washington University in St. Louis, St. Louis, MO, ³Washington University School of Medicine, Saint Louis, MO

Purpose

To evaluate the feasibility of resting-state functional magnetic resonance imaging (RS-fMRI) in detecting eloquent cortex including: language, somatomotor, and visual networks (when applicable) in patients with arteriovenous malformation (AVM) with comparison to task-based functional magnetic resonance imaging (TB-fMRI).

Materials and Methods

Initially 12 patients with arteriovenous malformation were identified as having RS-fMRI with or without TB-fMRI between August 2013 and October 2017. Of these, five patients had both RS-fMRI and TB-fMRI with TB-fMRI exams obtained on the same 3.0T scanner with dedicated task presentation system and processing software. Blood oxygen level dependent (BOLD) resting-state images were obtained and underwent seed-based correlation to establish areas of language activation using an in-house developed multilayer perceptron algorithm. Task-based images were obtained using finger-tapping, word generation, and visual stimulation paradigms. The BOLD sequence was registered to a 3D T1-weighted

Oral Presentations & Excerptas

magnetization-prepared rapid gradient-echo (MPRAGE) and was used to generate activation maps using dedicated commercial fMRI processing software. A neuroradiology fellow and attending evaluated the resting-state and task-based (when performed) images of all patients and determined the exams' technical success, ability to detect eloquent cortices (motor, language, and vision, when applicable), and ability to lateralize language dominance. In addition, concordance between RS-fMRI and TB-fMRI was evaluated in all five patients that had both exams.

Results

RS-fMRI was successfully acquired in 11/12 patients (91.6%). A single RS-fMRI failed the quality control assessment secondary to patient motion. TB-fMRI was obtained in five patients. RS-fMRI was successful in detecting the motor activation networks in both hemispheres in 11/11 patients (100%). Neurovascular uncoupling resulted in diminished, but present, somatomotor networks in 3/11 of RS-fMRI exams (27%), with all three cases demonstrating lesions in close proximity to the somatomotor network. RS-fMRI was successful in detecting language activation networks in 10/10 patients (100%, a single patient's language activation network was not processed). RS-fMRI was successful in detecting the visual activation network in 4/5 patients (80%) with lesions in close proximity to the visual cortex. RS-fMRI demonstrated excellent concordance with TB-fMRI, with concordance defined as touching of the activation networks on RS-fMRI and TB-fMRI. Concordance of the somatomotor activation network was noted in 4/5 patients (80%) in the hemisphere ipsilateral to the AVM and in 5/5 patients (100%) within the contralateral hemisphere. Concordance of Broca's area in the dominant language hemisphere was noted in 4/4 patients (100%). Concordance of Wernicke's area was noted in 2/4 patients (50%) secondary to lack of detection of Wernicke's area activation in 2 TB-fMRI exams. Concordance of the visual activation network was noted in 1/1 patient (100%) in both hemispheres. Neurovascular uncoupling resulted in lack of detection of somatomotor network ipsilateral to the AVM in one TB-fMRI (20%) and resulted in diminished activation of the somatomotor network in another case (20%).

Conclusions

RS-fMRI is feasible and accurate in localization of the language, motor and visual activation networks in patients with AVM with excellent concordance with TB-fMRI. RS-fMRI can serve as a reliable tool for pretreatment planning in AVM patients, particularly in instances when TB-fMRI cannot be obtained, such as impaired ability of the patient to cooperate with commands or patient claustrophobia, or when TB-fMRI is limited by technical factors.

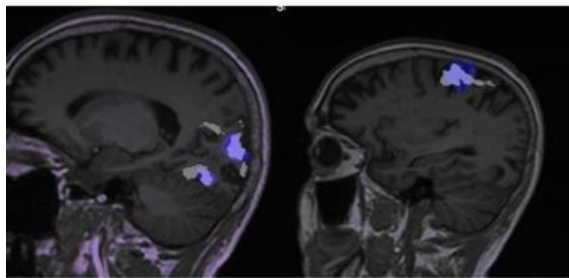


Figure 1A. Sagittal T1 MPRAGE demonstrates an occipital AVM within the expected visual cortex. Both RS-fMRI (gray) and TB-fMRI (blue) vision networks were successfully obtained and demonstrate concordance.

Figure 1B. Same patient demonstrates successful motor network activation on RS-fMRI (gray) and TB-fMRI (blue) with excellent concordance.

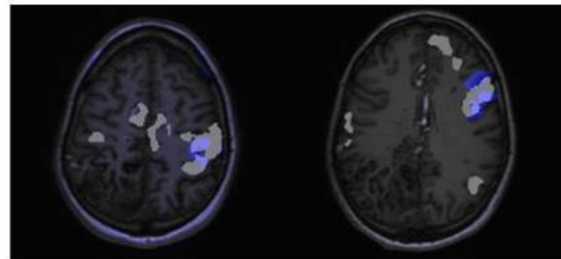


Figure 2A. Axial MPRAGE in a patient with right parietal AVM demonstrates diminished but present activation within the right somatomotor network on RS-fMRI (gray) with lack of activation on TB-fMRI. Both RS-fMRI and TB-fMRI were successful in detection of the somatomotor network on the contralateral side.

Figure 2B. Same patient axial MPRAGE demonstrates successful lateralization and detection of the language network on both RS-fMRI (gray) and TB-fMRI (blue) with concordance.

(Filename: TCT_O-453_NewMicrosoftPowerPointPresentation.jpg)

O-455

4:59PM - 5:06PM

Functional Outcome Following Temporal Lobe Surgery For Refractory Epilepsy Based on Memory Functional MRI

V Sawlani¹, K Kawsar¹, D Mccorry¹, A Hawkins¹, R Chelvarajah¹

¹*University Hospitals Birmingham NHS Foundation Trust, Birmingham, United Kingdom*

Purpose

fMRI for language has replaced the WADA test in the majority of epilepsy centers, and while WADA has been used as a test to predict memory outcome, the reliability and validity remains questioned (1). Within the Birmingham Epilepsy Surgery Program we use structural and functional techniques to examine the integrity of the contralateral temporal lobe; we wanted to examine fMRI memory to predict the postoperative memory outcomes. fMRI is a noninvasive technique that has substantial potential to lateralize memory functions and predict postoperative memory outcome in epilepsy patients undergoing temporal lobe epilepsy surgery (1, 2). Aim of the study is to testify the cognitive functional outcome of temporal lobe epilepsy surgery based on memory fMRI using the Home Town Walking Paradigm.

Materials and Methods

From January 2014 to December 2016, we performed memory fMRI in 26 refractory epilepsy patients. The memory fMRI was done by using 'Home Town Walking Paradigm' on epileptic patients who were being considered suitable for temporal lobe resection surgery. No WADA test was performed. fMRI was performed on 3T Siemens Vario MRI scanner. The fMRI is performed on two consecutive days with a block design, requiring mental navigation through one's hometown by using landmarks given by patients themselves. All the patients worked up for temporal lobe surgery undergo neuropsychometric assessment including memory functions before and 12 months after the surgery.

Results

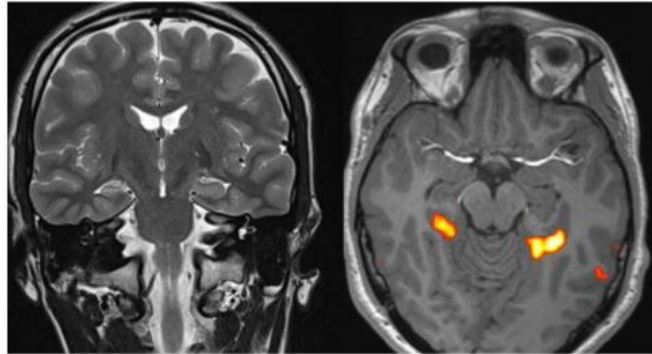
fMRI with Home Town Walking Paradigm showed reproducible and consistent results (Fig. 1) on two consecutive days. Of patients 9/26 were operated by anterior temporal lobectomy; 7/26 patients underwent insertion of vagal nerve stimulator. Among the operated patients, none reported a new cognitive memory deficit subjectively. Only three had detailed neuropsychometric assessment so far, while four are waiting to be done soon. Postoperative assessments showed auditory and visual memory index improved from preoperative status except the auditory memory index (AMI) in case 3 (Table 1).

Conclusions

Preliminary results of Memory fMRI using the Home Town Walking Paradigm seems helpful in predicting postoperative memory functions after temporal lobe surgery. We await reporting of further neuropsychometric assessment in other operated patients.

Figure 1.

Case 1. Right-sided hippocampal sclerosis: fMRI shows bilateral activation of parahippocampal gyri. Post-surgical neuropsychometric assessment at 12 months suggested a good clinical outcome.



Case 2. Left-sided hippocampal sclerosis: fMRI shows only left-sided activation. No surgery offered. Potentially high risk of memory deficit.

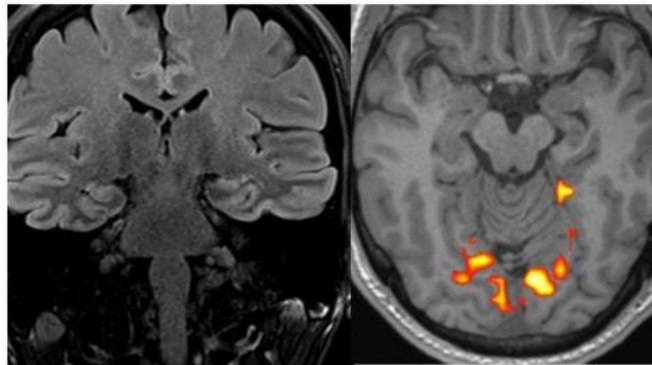


Table 1.

Patient	Pre-op (percentile)	Post-op
Case 1	AMI – 50 th , VMI – 25 th	AMI – 55 th , VMI – 50 th
Case 2	AMI – 53 rd , VMI – 1 st	AMI – 50 th , VMI – 7 th
Case 3	AMI – 34 th , VMI – 45 th	AMI – 21 st , VMI – 55 th

(Filename: TCT_O-455_Capture3.JPG)

O-456

5:06PM - 5:13PM

Correlation of Functional MRI with WADA Test and Surgical Outcomes for Hemispheric Language Lateralization in Refractory Epilepsy.

U Shafique¹, I Elhelf², N Soni¹, T Moritani³, A Capizzano¹

¹University of Iowa, Hospitals and Clinics, Iowa City, IA, ²University of Iowa, Iowa City, IA, ³University of Michigan, Ann Arbor, MI

Purpose

1. To correlate hemispheric language lateralization by functional MRI (fMRI) versus WADA test in patients with refractory epilepsy at presurgical evaluation 2. To determine incidence of postoperative language deficits in patients who underwent surgical excision of the epileptic focus

Oral Presentations & Excerptas

Materials and Methods

Institutional Review Board approval was obtained for this retrospective study. Of patients 35 with refractory epilepsy who underwent fMRI for language lateralization at preoperative evaluation were preselected. Patients with tumors or vascular malformations were excluded. Twenty-two were females and 13 were male with age range from 14 to 64 years with mean age of 29.8 years. Of patients 27 had temporal epilepsy, three had frontal epilepsy, 3 had frontotemporal epilepsy, 2 had parietal epilepsy. Twelve of the patients were treated with resective surgery of the epileptic focus. Fifteen of the patients had a WADA test done. fMRI was performed at 3 Tesla. Structural 3-D T1-weighted MPRAGE, B1 field map and DTI images of the brain were obtained in all cases followed by echo planar BOLD fMRI images with the task related block design. In-Vivo software was used to administer the paradigms through a MRI compatible projector, which consisted of the following verbal tasks: word generation, verb generation and sentence completion. Postprocessing was done in the Dynasuite workstation including motion and coregistration corrections as needed. Bonferroni correction was used to set up a statistical threshold of $p < 0.01$ before generating BOLD-structural T1-weighted fused images in the 3 planes. Assignment of language lateralization was defined on qualitative assessment of the significant BOLD activation voxels in language related cortical regions of each cerebral hemisphere. fMRI interpretation was done blinded from results of the Wada test in all cases. WADA test was performed by selective catheterization of the left and right internal carotid arteries. Digital subtraction angiography was used in multiple projections and neuropsychological testing of language and memory was performed during IV propofol injection. Records for surgical resection of epileptic focus and follow-up clinical exam information including any language deficit were accessed from the medical charts.

Results

Fourteen patients were right-handed and one left-handed (the latter with right language dominance). fMRI-based language lateralization was dominant on the left hemisphere in 11 cases and on the right in four cases. Two cases had significant bilateral BOLD activation but were assigned one case to the right and one to the left side based on consensus signal asymmetry. Language lateralization based on fMRI was in agreement with the WADA test in all of 15 patients. Seven patients had anterior temporal lobe resection for seizure management. Pathology showed hippocampal sclerosis in five and cortical dysplasia in two cases. One of the 12 patients who underwent surgical resection of the epileptic focus had speech difficulties after surgery which have been gradually improving. This patient had surgery of the same side as the fMRI defined language dominance. The rest of 11 operated patients did not have any postoperative language deficit. One of the patients who had a language deficit prior to surgery remained stable after surgery. Ten patients were followed from six months to three years post resection. Two patients have been followed for two months due to recent surgery. Eight patients were seizure free and four patients had decreased frequency of seizures which were well controlled with medication.

Conclusions

Language lateralization by functional MRI correlates with WADA test in nonlesional epilepsy patients and may replace WADA test for language lateralization. Further study is warranted, however, to assess memory functions with fMRI which typically display weaker BOLD signal as compared to language activation. There was no significant language deficit in patients who underwent surgical resection of the epileptic focus. Functional MRI is a noninvasive test when compared with WADA test. Additional benefits include decrease in potential complications, decreased procedure and recovery time, lack of radiation exposure and improved patient satisfaction.

O-458

5:20PM - 5:27PM

Effect of Sedation on Resting-State Functional Magnetic Resonance Imaging: A Single Center Experience

L Marple¹, rel daya², J Shimony³, T Benzinger⁴, M Miller-Thomas⁵

¹Washington University in St. Louis, St. Louis, MO, ²Mallinckrodt Institute of Radiology, Saint Louis, MO, ³Washington University School of Medicine, Saint Louis, MO, ⁴Washington University in St. Louis, Saint Louis, MO, ⁵Mallinckrodt Institute of Radiology, St. Louis, MO

Purpose

Resting-state functional magnetic resonance imaging (RS-fMRI) plays an important role in preoperative planning for multiple pathologies and its utilization continues to increase. A limitation for acquiring RS-fMRI is patients' ability to tolerate the MRI scan (pediatric population, altered mental status, claustrophobia, etc.). Sedation offers a potential method to acquire preoperative RS-fMRI exams in this subset of patients, but agents used for general anesthesia are known to disrupt spontaneous neural activity. The purpose of this work is to assess the feasibility of RS-fMRI in detection of motor and language activation networks for presurgical planning in sedated adult and pediatric patients.

Materials and Methods

A retrospective review of the clinical RS-fMRI exams performed between August 2014 and November 2017 identified 38 exams in 36 adult and pediatric patients (two patients had two exams each) who underwent clinical RS-fMRI exams under general anesthesia or monitored anesthesia care (MAC) monitored by a certified nurse anesthetist or anesthesiologist. Blood oxygen level dependent (BOLD) imaging and T1-weighted magnetization-prepared rapid gradient-echo (MPRAGE) images were obtained on a 3-Tesla scanner and resting-state analysis was performed using a previously trained machine-learning algorithm for identification of resting-state networks on an individual basis according to the method described by Hacker, et al. (2013). The quality control parameters generated by the processing software detailing patient movement, atlas registration, and resting-state network identification including default mode, somatosensory, and language networks were evaluated by a trained technician and neuroradiologist and graded as either passing or failing according to established parameters.

Retrospective review of all patients' anesthesia records was then performed to determine type of sedation (MAC or general anesthesia) and medications used to induce and maintain sedation.

Results

Performed were 38 sedated RS-fMRI exams for the following indications: 17 exams for preoperative planning for biopsy or resection of a mass-like brain lesion, seven exams for tuberous sclerosis treatment planning (TS, with or without subependymal giant cell astrocytoma), 11 exams for non-TS epilepsy management planning, and three exams for treatment planning for other etiologies such as arteriovenous malformation. All 38 sedation protocols used propofol for sedation induction with 18 exams using sevoflurane for sedation maintenance and 20 using propofol for sedation maintenance. Of RS-fMRI exams 24/38 (63%) were successful and 14/39 exams (37%) failed. None of the exams failed secondary to motion suggesting adequate sedation level. Of exams 9/14 (64%) failed secondary to atlas misregistration; 5/14 exams (36%) passed motion and atlas registration quality control steps, but failed to show resting-state network activation corresponding to the default mode, somatosensory, or language networks, with the cause of failure attributed to interference of sedation with BOLD imaging of neural networks. In total 5/38 exams (13%) failed secondary to presumed effect of sedation on BOLD imaging of neural networks. Of the failed sedated cases 3/5 received sevoflurane for maintenance of sedation (60%) and 2/5 cases received propofol for maintenance of sedation with no significant difference between the two groups (P value 0.259).

Conclusions

We demonstrated the feasibility of RS-fMRI in sedated patients with a failure rate of only 13%. It is worth noting that we observed an overall failure rate of 36% in sedated patients, but we only attributed the failure to anesthesia in 13% of cases. Our study demonstrates no significant difference in success rate across different sedation protocols.

	Passed exams	Failed exams	Percentage of passed exams
Total	25	14	62%
Mass-like lesions	13	5	72%
TS	2	5	29%
Non-TS Epilepsy	8	3	73%
Other	2	1	67%

Table 1. Breakdown of RS-fMRI success by pathology

	Total failed exams	Exams failed secondary to misregistration	Percentage of misregistration failure	Exams failed secondary to sedation	Percentage of sedation failure
Total	14	9	64%	5	36%
Mass-like lesions	5	4	80%	1	20%
TS	5	3	60%	2	40%
Non-TS Epilepsy	3	1	33%	2	67%
Other	1	1	100%	0	0%

Table 2. Breakdown of RS-fMRI failure causes by pathology

Sedation regimen	Total exams	Exams failed secondary to sedation	Percentage of sedation failure
Propofol alone	20	2	10%
Propofol and sevoflurane	18	3	17%

Table 3. Breakdown of failed exams by sedation regimen

(Filename: TCT_O-458_Sedation_Tables.jpg)

O-460

5:34PM - 5:41PM

Disrupted Resting-State Functional Connectivity in Patients with Traumatic Anosmia

M Park¹, J Chung², J Kim¹, Y Jeong², W Moon¹

¹Konkuk University Medical Center, Seoul, Republic of Korea, ²Korea Advanced Institute of Science and Technology, Daejeon, Republic of Korea

Purpose

Posttraumatic anosmia is not uncommon in up to 15% of patients with mild traumatic brain injury. Our aim was to investigate if traumatic anosmia alters functional connectivity in the resting brain and analyze the distribution of these changes.

Materials and Methods

From November 2012 to May 2014, 16 patients with traumatic anosmia (M:F = 11:5, 43.2 ± 10.2 years) and 12 healthy subjects ((M:F = 8:4, 26.8 ± 8.4 years) underwent resting-state fMRI using a 3T MRI

Oral Presentations & Excerpts

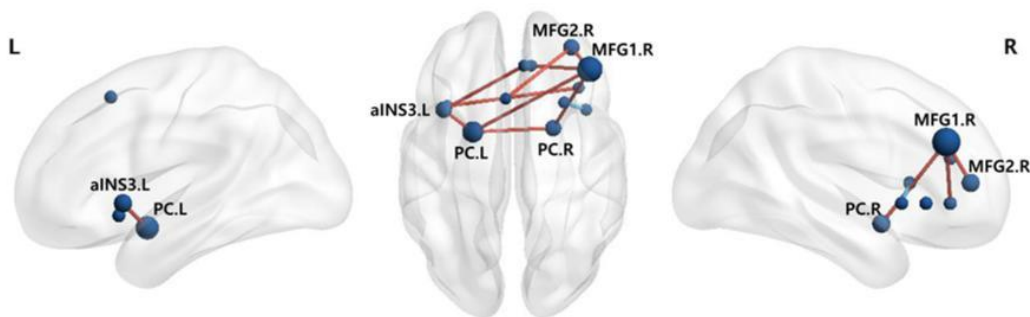
scanner. fMRI data were approached based on seed-based analysis, using the olfactory network as region of interest. Furthermore, both intranetwork and internetwork interactions were analyzed among six networks of brain, namely default mode network, salience network, attention network, visual network, sensory/somatomotor network and olfactory network.

Results

Patients had lower functional connectivity than healthy subjects within the olfactory network (FWE corrected $P < 0.0001$, adjusted for age) (Figure). On the whole brain analysis, intranetwork functional disruptions within the default mode network and salience network were detected in traumatic anosmia group (FWE corrected $P < 0.0001$, adjusted for age). Moreover, decreased internetworks functional connectivity was observed between sensory/somatomotor network and olfactory network (FWE corrected $P < 0.0001$, adjusted for age).

Conclusions

These results suggest that functional connectivity changes in the olfactory networks as well as other networks in traumatic anosmia patients and may help us to understand the neural mechanisms of traumatic anosmia.



(Filename: TCT_O-460_Figure.jpg)

O-462

5:48PM - 5:55PM

Segmentation of the Globus Pallidus Internus Using Probabilistic Diffusion Tractography for Deep Brain Stimulation Targeting in Parkinson's Disease

E Middlebrooks¹, I Tuna², S Grewal¹, L Almeida², K Foote², M Okun², V Holanda³

¹Mayo Clinic, Jacksonville, FL, ²University of Florida, Gainesville, FL, ³BP - A Beneficência Portuguesa de São Paulo, São Paulo, Brazil

Purpose

Although globus pallidus internus (GPi) deep-brain stimulation (DBS) is a widely accepted treatment for Parkinson's disease, there is persistent variability in outcomes that is yet to be fully understood. In this pilot study, we aimed to investigate the potential role of GPi segmentation using probabilistic tractography as an independent predictor of patient outcomes for use as a supplement to traditional targeting methods.

Materials and Methods

Eleven patients undergoing GPi DBS were included in this retrospective analysis. Using multidirection diffusion-weighted MRI, probabilistic tractography was performed at all individual GPi voxels. Each GPi voxel was then assigned to the one region-of-interest with the greatest number of propagated paths. Target regions included the globus pallidus externus (GPe), putamen, caudate, subthalamic nucleus (STN), substantia nigra, primary motor cortex (M1), supplementary motor area and premotor cortex (SMA/PMC), prefrontal cortex (PFC), thalamus, and pedunculo-pontine nucleus (PPN). Based on DBS programming settings, volumes of tissue activation were generated for each patient using a finite element

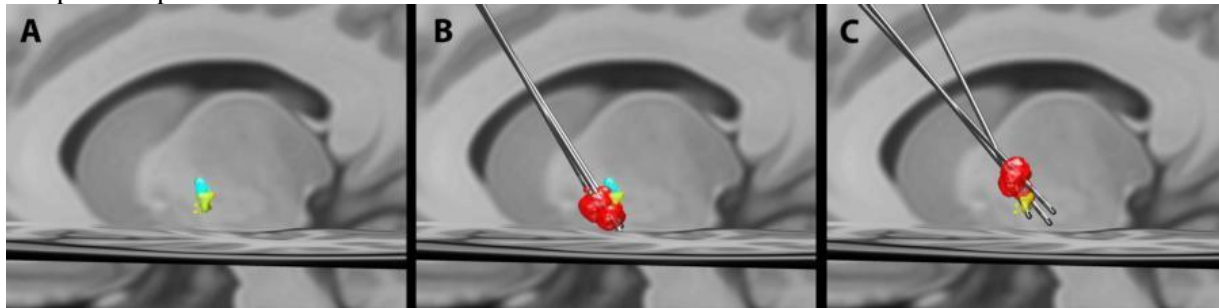
method solution. The volume of stimulation within each of the ten segmented GPi regions was calculated and compared to the change in Unified Parkinson Disease Rating Scale III (UPDRS III) score.

Results

Increasing volume of tissue activation was most strongly correlated with change in UPDRS III score for the primary motor region (Spearman's $r:0.74, P=0.010$), followed by the supplementary motor area/premotor cortex (Spearman's $r:0.47, P=0.15$).

Conclusions

In this study, we assessed a novel method of segmentation of the GPi based upon probabilistic tractography as a supplement to traditional targeting methods. We found that a higher volume of tissue activation in the somatosensory region of the GPi within our defined primary motor segment, and to a lesser degree the supplementary motor area/premotor cortex segment corresponded with greater improvement in six-month UPDRS III motor score. The results suggest our segmentation method is an independent predictor of functional outcome after GPi DBS in Parkinson's disease.



(Filename: TCT_O-462_Fig_3.jpg)

O-463

5:55PM - 6:02PM

Tracing ventral and dorsal language streams of the human brain using high resolution diffusion tensor tractography on 3T.

A Kamali¹, P Rabiei², O Arevalo³, R Patel², K Hasan⁴, R Riascos⁴

¹University of Texas, Health Science- Houston, Houston, TX, ²The University of Texas Health Science Center at Houston, Houston, TX, ³University of Texas health science center at houston, houston, TX, ⁴UTHSC-Houston, Houston, TX

Purpose

Based on an analogy between the visual and auditory systems, the following dual-stream model for language processing was suggested recently: A dorsal stream is involved in mapping sound to articulation, and a ventral stream in mapping sound to meaning. The ventral language stream includes the middle longitudinal fasciculus (MdLF) and arcuate fasciculus (AF). The dorsal language stream includes the superior longitudinal fasciculus (SLF) and the extreme capsule (ExC). Lack of adequate neuroimaging sensitivity and spatial resolution, so far, impeded depiction of small language pathways including the delicate fiber tracts of the SLF I or the SLF TP SPL (superior parietal lobule connection of the temporoparietal segment of the SLF) within the human brain. This work aimed to demonstrate for the first time the feasibility of in vivo quantification and visualization of the ventral and dorsal language streams using high-resolution DTI data on 3T.

Materials and Methods

Subjects: Fifteen healthy adults (age range 24-37 years) were studied and written informed consent was obtained from all subjects. **Conventional and DT-MRI Acquisition:** Data were acquired using a Philips 3.0 T Inera system using a SENSE receive head coil. Diffusion-weighted image (DWI) data were acquired axially using single-shot multislice 2-D spin-echo diffusion with the balanced Icosa21 tensor encoding scheme. The b-factor = 500 sec mm⁻², TR/TE = 14460/60 msec, FOV = 256 mm x 256 mm and

Oral Presentations & Excerpts

slice thickness / gap/ #slices = 1 mm / 0 mm / 120. The EPI phase encoding used a SENSE k-space undersampling factor of two, with an effective k-space matrix of 112x112 and an image matrix after zero-filling of 256x256. Fiber Tracking: We used the FACT algorithm (DTIStudio) to reconstruct language fiber tracts with a fractional anisotropy (FA) threshold of 0.22 and angle threshold of 60 degrees.

Results

The extreme capsule (ExC), the superior longitudinal fasciculus (SLF), the arcuate fasciculus (AF) and middle longitudinal fasciculus (MdLF) fiber tracts are clearly distinguishable in our results. Diffusion-tensor tractography is challenged by the signal-to-noise ratio (SNR) due to overestimation of anisotropy at low SNR and partial volume averaging upon using large voxel volumes. Using high-spatial resolution specially reduced slice thickness (1mm) in this study reduced the partial volume effect as well as incoherency due to fiber intercrossings within each voxel in highly crossing areas such as the temporal stem and periventricular white matter. This enabled us to reconstruct even the small trajectories such as the components of the SLF, AF and other language pathways using deterministic tractography approach.

Conclusions

To our knowledge, the current study is the first to present the entire ventral and dorsal language stream network using high spatial resolution DTI measurements on 3T.



(Filename: TCT_O-463_NewMicrosoftPowerPointPresentation.gif)

O-464

6:02PM - 6:09PM

Prediction of Remission to Pharmacotherapy in Late-Life Depression using Baseline and Single Dose Neural Activation

M Wang¹, H Karim², C Andreescu², D Tudorascu², J Karp², C Reynolds², H Aizenstein²

¹University of Pittsburgh School of Medicine and Carnegie Mellon University, Pittsburgh, PA, ²University of Pittsburgh, Pittsburgh, PA

Purpose

To determine if functional imaging collected before and after the first dosage of venlafaxine in a late-life major depressive treatment trial can be used to predict treatment efficacy

Materials and Methods

A total of 49 geriatric (age \geq 50) participants diagnosed with major depressive disorder completed an open-label 12-week venlafaxine treatment trial. Remission was defined by the Montgomery-Asberg depression

Oral Presentations & Excerptas

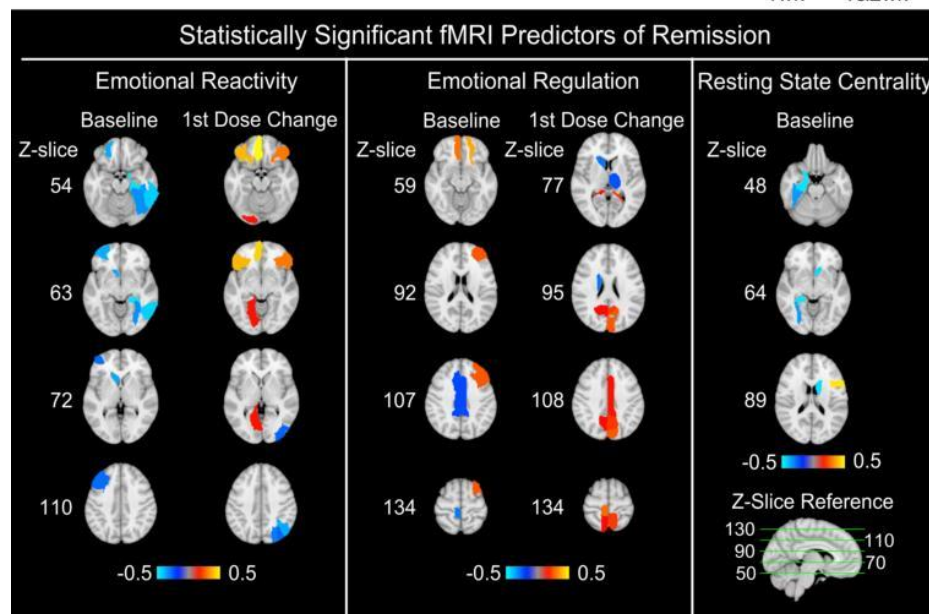
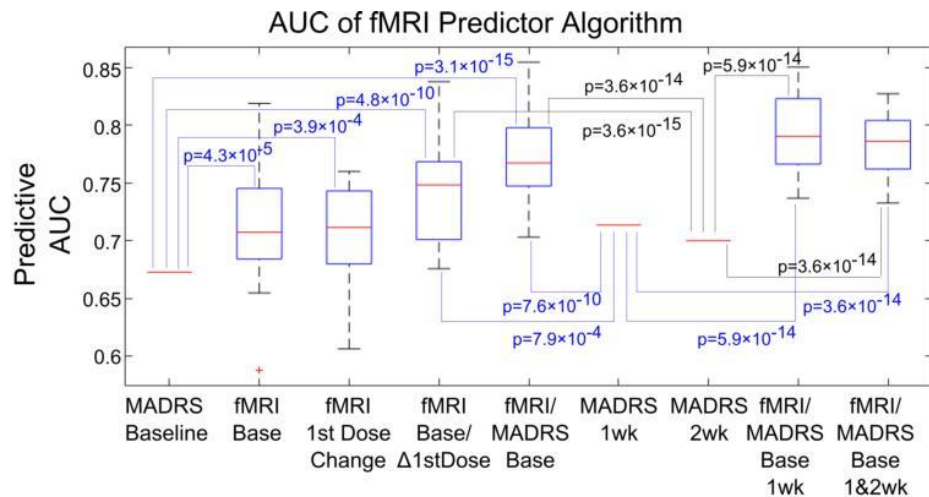
rating scale (MADRS) [1]. We collected fMRI data both at baseline and after a single dose (day) of venlafaxine during resting-state, an emotional regulation task, and an emotional reactivity task. Sequence parameters and data preprocessing steps are outlined in [2]. We employed principal components analysis, Tikhonov-regularized logistic classification, and least angle feature selection to predict remission by the end of the 12-week trial [3-4]. To assess predictive accuracy, we utilized ten-fold cross-validation and Receiver-Operator-Curves (ROC). Task-region pairs that significantly contributed to the algorithm's predictive power were identified via permutation testing (1000 trials).

Results

Figure 1 (top) illustrates the accuracy of the fMRI classification algorithm using the Area Under Curve (AUC) metric. Utilizing only the baseline MADRS and imaging collected at baseline and after the first dose (day), we found our classification algorithm yielded a sensitivity of 80% and a specificity of 63%, a 15% increase in accuracy over baseline clinical measures. For comparison, we also show the predictive power of the MADRS at one and two weeks (other clinical measures such as age, race, gender, etc. were nonpredictive). Figure 1 (bottom) shows the region/task pairs that passed permutation testing. Significant regions included the frontal cortex, hippocampus/parahippocampus, caudate and thalamus, medial temporal cortex, middle cingulate, and visual cortex.

Conclusions

Acute, dynamic trajectories of functional imaging metrics in response to a pharmacological intervention are a valuable tool towards predicting treatment response in late-life depression and elucidating the mechanism of pharmacological therapies in the context of the brain's functional architecture.



(Filename: TCT_O-464_Composite_FunctionalPredictiveAccuraciesSlices.jpg)

Wednesday, June 6, 2018

4:45PM - 6:15PM

Parallel Paper Session: Stroke Imaging: Diagnosis and Prognosis I

O-465

4:45PM - 4:52PM

Contralateral Cerebral Blood Flow Measured with Arterial Spin Labeling MRI Predicts Outcome in Acute Ischemic Stroke

T Thamm¹, J Guo¹, J Rosenberg¹, T Liang¹, S Christensen¹, M Marks¹, H Do¹, S Kemp¹, E Adair¹, I Eyngorn¹, M Lansberg¹, G Albers¹, G Zaharchuk¹

¹Stanford University, Stanford, CA

Oral Presentations & Excerptas

Purpose

Evaluating hemodynamics in the ipsilateral hemisphere is a common practice for selecting patients for intra-arterial treatment (IAT) in acute stroke. Arterial spin-labeling (ASL) can noninvasively measure quantitative cerebral blood flow (CBF). In this study, we hypothesized that contralateral CBF (cCBF) may identify patients with high collateral capacity and better outcome.

Materials and Methods

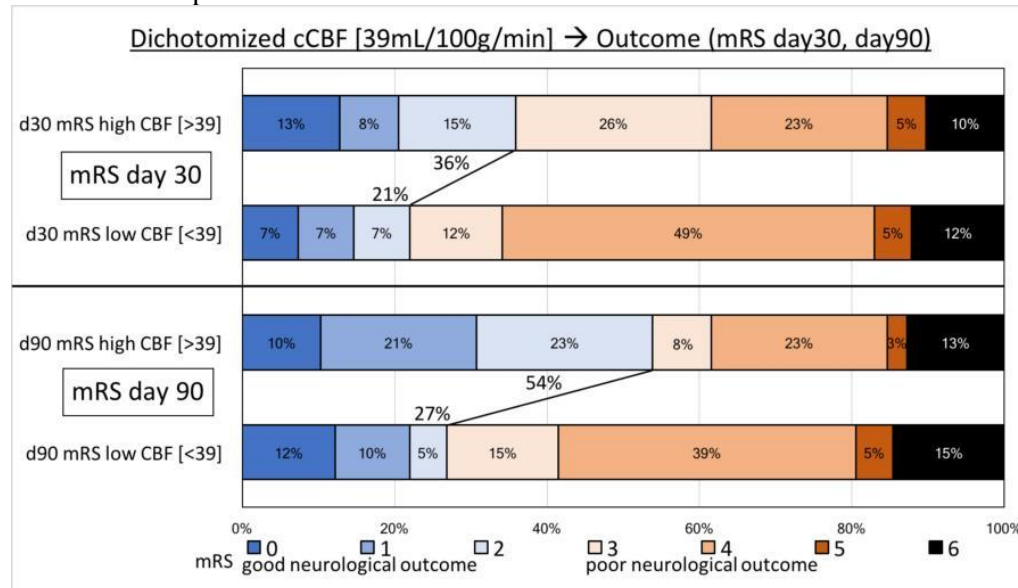
Patients were part of the prospective imaging the Collaterals in Acute Stroke (iCAS) study. Inclusion criteria were ischemic anterior circulation stroke, < 24 hours onset to imaging time [OIT], with imaging including DWI and pseudocontinuous ASL. cCBF was calculated in cortical ASPECTS ROIs in the contralateral hemisphere, and dichotomized into high and low groups based on the median cCBF of all subjects. Outcomes were assessed by NIHSS at baseline, day 1, and day 5; and mRS at days 30 and 90. Results are reported as medians with interquartile ranges [IQR]. Outcome differences were assessed with Wilcoxon (NIHSS) and Fisher's exact test (mRS).

Results

Eighty patients met the inclusion criteria: 44 females, age 66 [56-77] yrs, OIT 4.7 [3.4-7.6] hrs, baseline NIHSS 13 [9-20], 43 underwent IAT [34 with final TIC1>=2b], mean cCBF 39.0 [31.6-44.5] ml/100g/min. There was no difference between both groups in age, previous stroke, OIT, acute DWI lesion size, tPA treatment, or IAT. Baseline median NIHSS score was the same (13) for the low and high cCBF groups, but differed at day 1 (14 vs. 8, p=0.027) and day 5 (11 vs. 5, p=0.010). Patients with higher cCBF were more likely to be female (p=0.047) and to have better day 90 mRS (p=0.022).

Conclusions

Higher quantitative contralateral CBF measured by ASL is a significant predictor of good 90-day neurological outcome after stroke. This may reflect a better underlying capacity for collateral flow to the ischemic hemisphere.



(Filename: TCT_O-465_Figure1-ccbf-thammt-v2.jpg)

O-466

4:52PM - 4:59PM

Resting State Functional Connectivity MRI and Outcome after Acute Stroke

J Puig¹, G Blasco¹, A Alberich-Bayarri², C Biarnes¹, M Marti-Navas¹, M Rivero¹, J Gich¹, P Daunis-i-Estadella³, C Oramas-Requejo¹, J Serena¹, G Schlaug⁴, M Essig⁵, C Figley⁵, K Nael⁶, M Wintermark⁷, S Pedraza¹

¹IDIBGI, University Hospital Dr Josep Trueta, Girona, Spain, ²La Fe Health Research Institute, Valencia, IL, ³University of Girona, Girona, Spain, ⁴Beth Israel Deaconess Medical Center, Harvard Medical School, Boston, MA, ⁵University of Manitoba, Winnipeg, Manitoba, Canada, ⁶Icahn School of Medicine at Mount Sinai, New York, NY, ⁷Stanford University, Stanford, CA

Purpose

Physiological effects of stroke are best assessed over entire networks rather than just locally at the site of structural damage. Resting-state functional magnetic resonance imaging (rs-fMRI) can map functional-anatomic networks by analyzing spontaneously correlated low-frequency activity fluctuations across the brain, but its potential usefulness in predicting functional outcome after acute stroke remains unknown. We aimed to assess the ability of rs-fMRI to predict functional outcome.

Materials and Methods

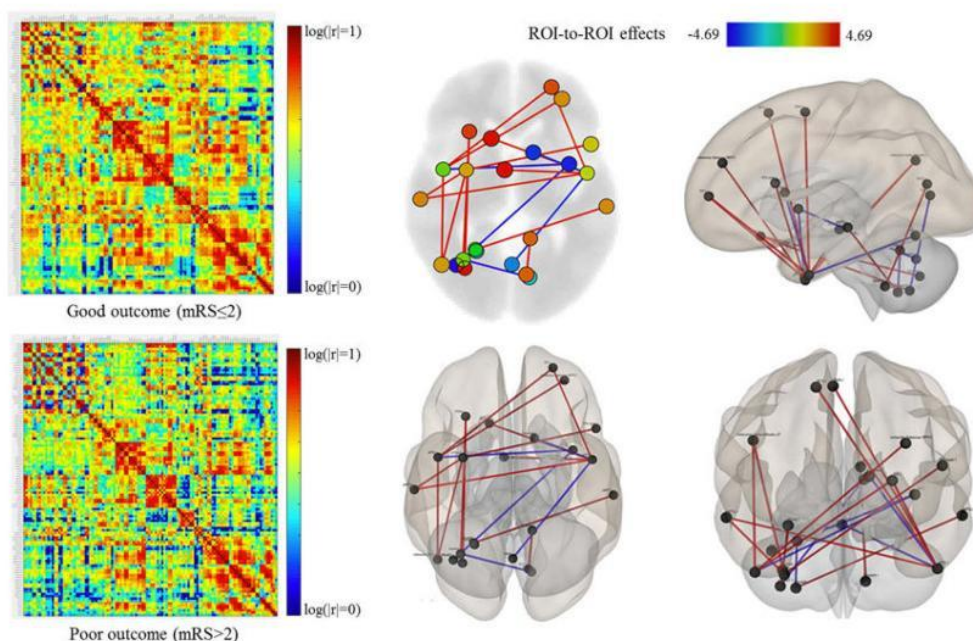
We scanned 37 consecutive reperfused stroke patients (age: 69 ± 14 years, 14 female, three-day National Institute of Health Stroke Scale [NIHSS] score: 6 ± 5) on day 3 after symptom onset. After imaging preprocessing, we used a whole-brain mask and the Harvard-Oxford probabilistic atlas to calculate the correlation coefficient matrices for paired brain regions. Functional outcome at 90 days was assessed with the modified Rankin Scale (mRS). We used region-of-interest analyses to explore the functional connectivity between regions and graph-computation analysis to detect differences in functional connectivity between patients with good functional outcome ($mRS \leq 2$) and those with poor outcome ($mRS > 2$).

Results

Patients with good outcome had greater functional connectivity than patients with poor outcome. Although three-day NIHSS score was the most accurate independent predictor of 90-day mRS (84.2%), adding functional connectivity increased accuracy to 94.7%. Preserved bilateral interhemispheric connectivity between the anterior inferior temporal gyrus (aITG) and frontal superior gyrus and decreased connectivity between the caudate and aITG in the left hemisphere had the greatest impact in favoring good prognosis.

Conclusions

These preliminary results suggest that rs-fMRI information about functional connectivity can complement early markers of stroke severity in predicting patients' 90-day stroke outcome and help stratify patients according to their chance of recovery. Understanding the network changes caused by stroke might enable rehabilitation interventions to be tailored to improve recovery.



Regions of interest (ROI)-based analysis for patients with good ($mRS \leq 2$) and poor ($mRS > 2$) functional outcome. Left panels display the correlation coefficients matrices for every pairwise region. The other panels display the graph visualization of the mean correlation coefficient weighted matrices for the group of patients with good outcome at 90 days, thresholded at $P < 0.05$, FEW corrected (5000 permutations).

(Filename: TCT_O-466_FigureRestingStrokeandOutcome.jpg)

O-467

4:59PM - 5:06PM

Impact of a Multidisciplinary Stroke Improvement Event, Post-processing Automation, and Standardized Radiologist Workflow on CT Perfusion Departmental and Radiologist Turnaround Time in Acute Stroke Evaluation

D Pozivilko¹, T Mulderink¹

¹Michigan State University, College of Human Medicine, Grand Rapids, MI

Purpose

Utilization of CT perfusion in acute stroke evaluation can aid in triaging patients to or away from endovascular therapy, but comes with the expense of additional time spent on image acquisition, postprocessing, and image interpretation. Recent introduction of automated quantitative postprocessing software including RAPID (Ischemaview, Redwood City CA) has the potential to streamline CT perfusion workflows in the setting of acute stroke. The purpose of this retrospective study was to measure the impacts of a weeklong multidisciplinary acute stroke improvement event, automation of CT perfusion postprocessing utilizing RAPID, and a standardized radiologist image review and communication workflow on departmental and radiologist turnaround time (TAT) in the setting of acute stroke.

Materials and Methods

A retrospective PACS query was performed to measure departmental and radiologist TAT for CT perfusion exams over four separate three-month time periods: baseline, following a stroke process improvement event, following implementation of RAPID, and following a pilot of standardized

radiologist workflows. Data was collected between April 2015 and October 2017. T-tests were used to determine statistically significant differences between parameters.

Results

Departmental turnaround time decreased 35% following the stroke process improvement event, and an additional 34% following RAPID. Radiologist turnaround time decreased 50% following the process improvement event and an additional 33% following RAPID. Two neuroradiologists participating in a workflow pilot decreased turnaround times 36% and 60% respectively. Radiologist TAT significantly decreased from 31.8 min (SD 38.8.9) at baseline to 10.6 min (SD 15.2) ($p < 0.005$) following RAPID implementation.

Conclusions

Automation of CT perfusion postprocessing with RAPID improved both departmental and radiologist TAT even after initial process optimization with a stroke process improvement event. Radiologist workflow standardization further improved TAT in a small pilot and may provide additional benefit beyond the aid of automated quantification in CT perfusion interpretation.

O-468

5:06PM - 5:13PM

DWI-ASPECTS and DWI-FLAIR Mismatch in Thrombectomy Candidates: an Interrater and Intrarater Agreement Study.

R Fahed¹, A Lecler¹, C Sabben¹, N Khoury², R Blanc¹, J Raymond³, M Piotin¹

¹*Fondation Rothschild Hospital, Paris, France*, ²*Neuroscience Center, Hospital Sisters' Health System St. John's Hospital, Springfield, IL*, ³*CHUM Centre Hospitalier de l'Université de Montréal, Montréal, QC, Canada*

Purpose

We aimed to study the intrarater and interrater agreement of clinicians attributing Diffusion-Weighted-Imaging-Alberta-Stroke-Program-Early-CT-Scores (DWI-ASPECTS) and DWI-Fluid-Attenuated-Inversion-Recovery (FLAIR) mismatch in acute ischemic stroke patients referred for mechanical thrombectomy.

Materials and Methods

Eighteen raters independently scored anonymized MRI scans of 30 participants from a multicenter thrombectomy trial, in two different reading sessions. Agreement was measured using Fleiss' and Cohen's kappa statistics.

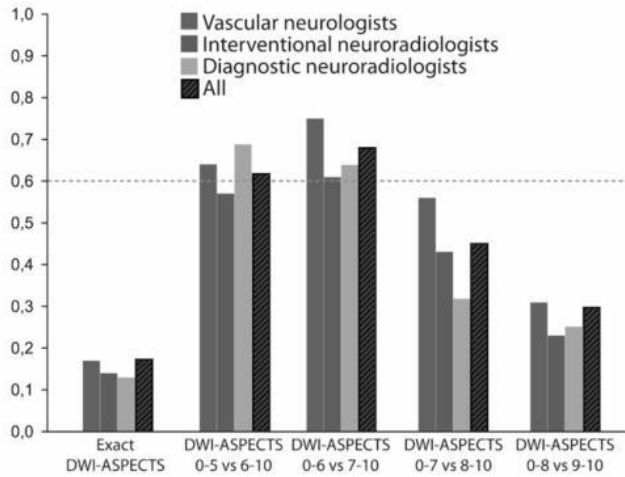
Results

Interrater agreement for DWI-ASPECTS was slight ($K = 0.17$ [0.14-0.21]) (figure 1A). Four raters (22.2%) had a substantial (or higher) intrarater agreement. Dichotomization of the DWI-ASPECTS (0-5 versus 6-10 or 0-6 versus 7-10) increased the interrater agreement to a substantial level ($K = 0.62$ [0.48-0.75]) and 0.68 [0.55-0.79], respectively) and more raters reached a substantial (or higher) intrarater agreement (17/18 raters [94.4%]). Interrater agreement for DWI-FLAIR mismatch was moderate ($K = 0.43$ [0.33-0.57]) (figure 1B); 11 raters (61.1%) reached a substantial (or higher) intrarater agreement.

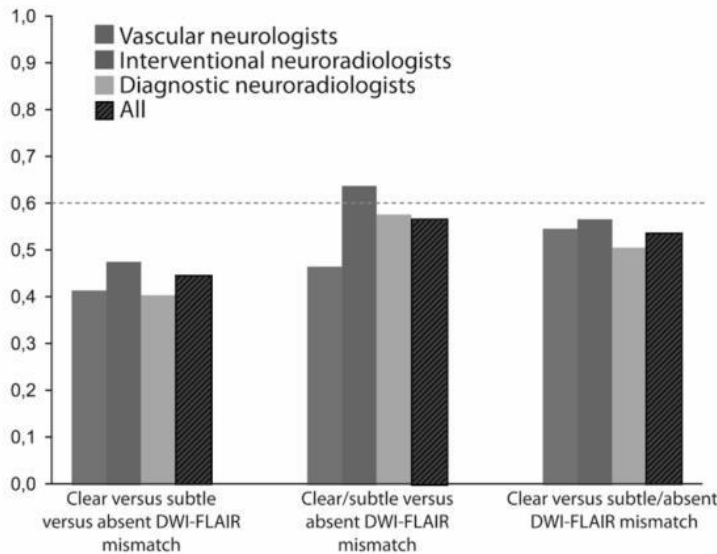
Conclusions

Agreement between clinicians assessing DWI-ASPECTS and DWI-FLAIR mismatch may not be sufficient to make repeatable clinical decisions in mechanical thrombectomy. The dichotomization of the DWI-ASPECTS (0-5 versus 0-6 or 0-6 versus 7-10) improved interrater and intrarater agreement, however its relevance for MT patients selection needs to be validated in a randomized trial.

A



B



(Filename: TCT_O-468_Figure1.jpg)

O-469

5:13PM - 5:20PM

DWI Prognostic Scores in Acute Basilar Artery Occlusion: a Literature Systematic Review and an Interrater and Intrarater Agreement Study.

R Fahed¹, C Ducroux², J Gabrieli³, N Khoury⁴, F Clarençon³

¹CHUM Centre Hospitalier de l'Université de Montréal, Montréal, Quebec, Canada, ²Saint-Antoine Hospital, Paris, Ile-de-France, ³Pitie-Salpetriere Hospital, Paris, Ile-de-France, ⁴Neuroscience Center, Hospital Sisters' Health System St. John's Hospital, Springfield, IL

Purpose

We aimed to systematically review the literature on diffusion-weighted imaging (DWI) scores for acute ischemic stroke (AIS) patients with acute basilar artery occlusion (BAO) and assess the interrater and intrarater agreement for each of the scores.

Oral Presentations & Excerptas

Materials and Methods

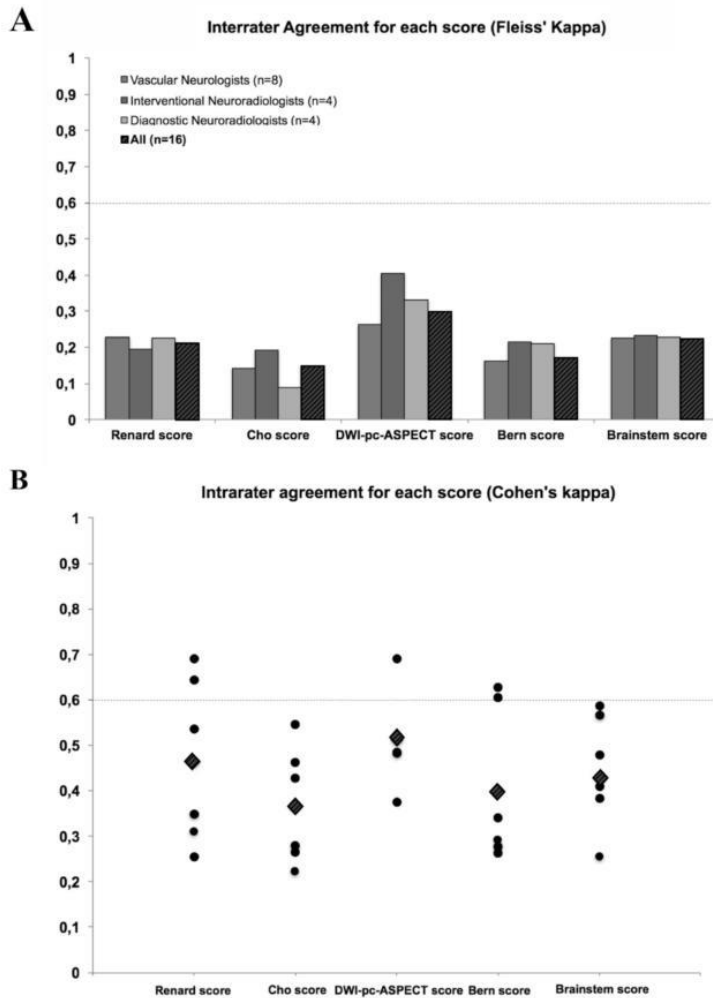
Studies describing a DWI score for AIS with BAO published from 2000-2017 were extracted. Sixteen raters (eight vascular neurologists, four interventional neuroradiologists, and four diagnostic neuroradiologists) graded anonymized MRI scans of 30 patients presenting with AIS due to BAO treated with mechanical thrombectomy using each of the scores. Six of these raters (one junior and one senior of each specialty) performed a second independent reading session to study intrarater agreement. Interrater and intrarater agreement were measured using Fleiss' Kappa statistics, and Cohen's unweighted kappa statistics, respectively.

Results

The review yielded five DWI scores, 1-5 and found no reliability assessment with kappa statistics for any of these scores. The agreement study showed that none of the scores reached a substantial interrater or intrarater agreement for all raters. The Diffusion-Weighted-Imaging-Posterior-Circulation-Alberta-Stroke-Program-Early-CT-Score (DWI-pc-ASPECTS) reached the highest interrater agreement for all raters (Kappa [95%CI] = 0.298 [0.237 – 0.383]) (figure 1A) and highest mean intrarater agreement (Kappa [95%CI] = 0.512 [0.404 – 0.619]) (figure 1B).

Conclusions

Five DWI scores are reported for the assessment of AIS due to BAO. Our agreement study did not show sufficient agreement for any of these scores to warrant their use in clinical practice.



(Filename: TCT_O-469_Figure_1_TIFF.jpg)

Relationship Between Infarct Growth and Collateral Status Assessed by Perfusion-CT and CT-Angiography

B Jiang¹, R Ball², Y Li¹, M Wintermark³

¹Stanford University School of Medicine, Stanford, CA, ²Stanford University, Palo Alto, CA, ³Stanford University, Stanford, CA

Purpose

Patient with major ischemic stroke caused by a large artery occlusion will lose 1.9 million neurons every minute without revascularization. Neuroimaging can be used to assess infarct growth and shows a very significant variability from patient to patient. The purpose of our study was to better understand the patient characteristics associated with this variability and its clinical relevance.

Materials and Methods

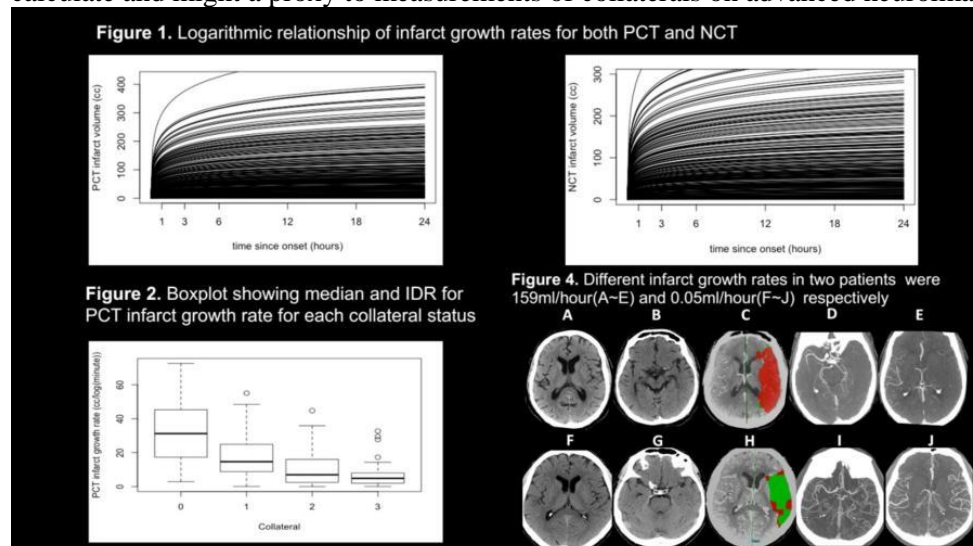
Using a registry of 878 patients, we identified the patients meeting the following inclusion criteria: acute infarct in the MCA territory, M1 occlusion with/without distal ICA/M2 involvement, time from symptom onset < 24h, PCT coverage at least 8 cm, baseline imaging workup including NCT, PCT, CTA and early recanalization CTA images (<72h). We extracted demographic and clinical information. On NCT, ASPECT score was assessed, the infarct was manually delineated and its volume calculated. PCT ischemic core and penumbra were automatically computed. The occlusion site, collateral score and recanalization status were evaluated on the baseline and early follow-up CTA images. Infarct growth rate for both PCT and NCT were calculated. We used an elastic net penalization likelihood method to identify patient characteristics associated with infarct growth rate and modified Rankin score at three months.

Results

Included in this study were 232 patients. The average infarct growth rate was 38.1 ml/hour. NCT and PCT infarct volumes and infarct growth rates were significantly correlated. Collateral status was the strongest predictor of infarct growth rates ($p < 0.001$).

Conclusions

Our study confirmed previous reports that there is a wide variability in terms of infarct growth rates. Poorer collaterals are associated with a faster infarct growth rate. Infarct growth is an easy parameter to calculate and might a proxy to measurements of collaterals on advanced neuroimaging.



(Filename: TCT_O-470_.jpg)

O-471

5:27PM - 5:34PM

Qualitative MR Diffusion and Perfusion Weighted Imaging Patterns in Symptomatic Intracranial Atherosclerotic Disease.

O Ansari¹, M Pan¹, A Al-Smadi¹, A Malani¹, P Vakil¹, S Prabhakaran¹, M Hurley¹, A Shaibani¹, T Carroll², S Ansari¹

¹Northwestern University, Feinberg School of Medicine, Chicago, IL, ²University of Chicago, Chicago, IL

Purpose

Symptomatic intracranial atherosclerotic disease (ICAD) is associated with ischemic stroke of three main etiologies: watershed infarction secondary to hypoperfusion related ischemia between two arterial distributions, perforator infarction from local plaque rupture and thrombosis leading to ischemia of small perforator arteries, and thromboembolic infarcts from unstable plaque related emboli to the distal vascular distribution. Specific diffusion-weighted imaging (DWI) patterns may allow characterization of ischemic stroke mechanisms in symptomatic ICAD. Perfusion-weighted imaging (PWI) via relative assessment of Mean Transit Time (MTT) and Cerebral Blood Volume (CBV) parameters can grossly stage hemodynamic failure. We sought to validate this approach by characterizing the distribution of stroke mechanisms across a symptomatic ICAD cohort using qualitative MR DWI pattern analysis and any associations with hemodynamic failure as observed with MR PWI.

Materials and Methods

From a prospective observational ICAD stroke registry since August 2012, we identified symptomatic ICAD patients that presented with acute infarcts downstream to a severe intracranial stenosis > 70% of the A1-A2 ACA, M1-M2 MCA, P1-P2 PCA, or supraclinoid ICA and received MR imaging with DWI and PWI. Two neuroradiologists qualitatively evaluated relative elevations in MTT and CBV color maps to grossly define stage 1 and stage 2 hemodynamic failure. MR DWI patterns were graded for watershed/hypoperfusion versus thromboembolic or perforator infarct patterns. Statistical analysis was performed for interobserver agreement in both DWI and PWI patterns and for any significant difference in increased MTT and/or CBV between the two infarct groups. P-value < 0.05 was considered significant.

Results

We identified 24 symptomatic ICAD patients with MR DWI, 22 patients with concomitant MR PWI. Interobserver agreement was excellent in both DWI and PWI qualitative analysis (Kappa > 0.7 both groups). Intracranial plaques were observed in 19 MCA, two ICA, two ACA, and one PCA locations. Of the 22 patients, 18 (79%) had thromboembolic and/or perforator infarcts and four (21%) had watershed hypoperfusion patterns of infarction. MTT was increased in 78% of vascular distributions associated with thromboembolic/perforator infarcts and 100% of watershed/hypoperfusion related infarcts (p=.010). In contrast, elevated CBV was increased in only 17% of vascular distributions with thromboembolic/perforator infarcts and 0% of watershed/hypoperfusion infarcts (p=.046).

Conclusions

Qualitative analysis of MR DWI and PWI characterized thromboembolic versus hypoperfusion mechanisms of ICAD related ischemic stroke with high interobserver agreement. Although the majority of symptomatic ICAD lesions presented with stage 1 hemodynamic failure (elevated MTT), the predominant mechanism of stroke was perforator and thromboembolic infarcts related to vulnerable, unstable plaques. Furthermore, severe stage 2 hemodynamic failure (elevated CBV) was rarely identified in our cohort, suggesting cerebrovascular failure may be relatively uncommon in ICAD, but pending quantitative analysis will be needed to confirm these preliminary findings.

O-473

5:34PM - 5:41PM

Imaging Predictors of Recurrent Ischemic Stroke: a Systematic Review and Meta-analysis

F Kauw¹, R Takx¹, H de Jong¹, B Velthuis¹, L Kappelle¹, J Dankbaar¹

¹*University Medical Center Utrecht, Utrecht, the Netherlands*

Purpose

To identify imaging predictors for recurrent ischemic stroke in patients with prior ischemic stroke by performing a systematic review and meta-analysis

Materials and Methods

A systematic search in PubMed, Embase, Cochrane Library and CINAHL was performed with the terms 'ischemic stroke' and 'predictors/determinants' and 'recurrence'. Quality assessment of the articles was performed and level of evidence was graded for the articles included in the meta-analysis. A weighted incidence rate with 95% confidence interval (CI) of recurrent ischemic stroke and a weighted mean of follow-up duration were calculated. Pooled odds ratios (OR) with 95% CIs and heterogeneity (I squared) were calculated using inverse variance random effect models.

Results

Out of 2,173 unique articles three articles analyzed imaging predictors and were included for the meta-analysis. The weighted incidence rate was 67 (95% CI 58-76) per 1000 person-years with a weighted mean follow-up duration of nine months. The following MRI findings were predictors of recurrent ischemic stroke with a moderate level of evidence: multiple lesions (pooled OR 3.0, 95% CI 2.1-4.4), multiple stage lesions (pooled OR 5.9, 95% CI 3.9-9.0), multiple territory lesions (pooled OR 3.5, 95% CI 2.2-5.5), chronic infarcts (pooled OR 1.8, 95% CI 1.2-2.5) and isolated cortical lesion (pooled OR 2.5, 95% CI 1.5-4.0). A limited level of evidence was present for the association between white matter lesions and recurrence of ischemic stroke (pooled OR 2.0, 95% CI 1.0-4.1). We found no studies using CT or ultrasound for the prediction of recurrent ischemic stroke.

Conclusions

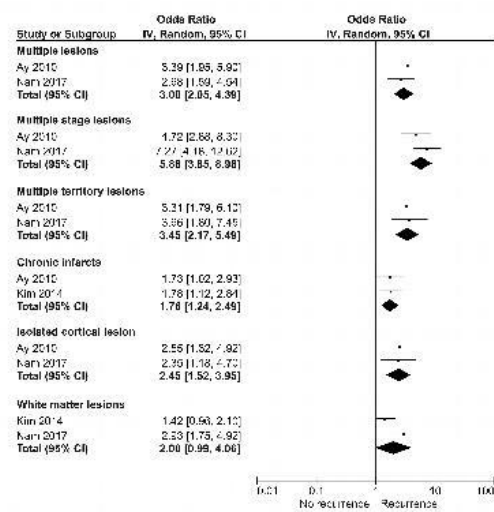
Limited evidence was present for imaging predictors of recurrent ischemic stroke. Predictors evaluated with MRI include multiple ischemic changes and isolated cortical lesions. Predictors concerning CT or ultrasound have not been published. Studies investigating imaging factors as predictors of recurrent ischemic stroke are warranted.

Table 1. Imaging predictors for recurrent ischemic stroke

Predictive factor	Study	Sample size, n	Variable definition	Factor prevalence	Follow-up duration	uv OR
Imaging factors (MRT)						
<i>Moderate level</i>						
Multiple lesions T=0%	Ay 2010	1458	Hypointense on DWI and hyperintense on ADC maps	40%	90 days	3.4 (2.0-5.9)
	Nari 2017	959	On DWI	39%	31 months	2.7 (1.6-4.54)
	Pooled					3.0 (2.1-4.4)
Multiple stage lesions T=3%	Ay 2010	1458	Multiple infarcts of different ages on ADC/FLAIR	11%	90 days	4.7 (2.7-8.1)
	Nari 2017	959	On DWI	11%	31 months	3.3 (1.2-12.6)
	Pooled					5.9 (3.9-9.0)
Multiple territory lesions T=0%	Ay 2010	1458	(sub)cortical infarct, anterior or posterior	10%	90 days	3.3 (1.8-6.1)
	Nari 2017	959	On DWI	6%	31 months	3.7 (1.8-7.5)
	Pooled					3.5 (2.2-5.5)
Chronic infarct T=0%	Ay 2010	1458	Hypointense on FLAIR and hyperintense on DWI	30%	90 days	1.7 (1.0-2.9)
	Kim 2014	2378	On MRT	15%	90 days	1.3 (1.1-2.8)
	Pooled					1.8 (1.2-2.5)
Isolated cortical lesion T=0%	Ay 2010	1458	-	9%	90 days	2.6 (1.3-4.9)
	Nari 2017	959	On DWI	9%	31 months	2.4 (1.7-4.7)
	Pooled					2.5 (1.5-4.0)
<i>Inconsistent</i>						
White matter lesions T=70%	Kim 2014	2378	FLAIR: Fazakas <2 vs >2	11%	90 days	1.1 (1.0-2.1)
	Nari 2017	959	FLAIR: Fazakas <2 vs >2	23%	31 months	2.9 (1.8-4.9)
	Pooled					2.0 (1.0-4.1)

*from prospective database
uv=univariable, OR=odds ratio, mv=multivariable, MRT=magnetic resonance imaging, DWI=diffusion weighted imaging, ADC=apparent diffusion coefficient, FLAIR=fluid-attenuated inversion recovery.

Figure 1. Forest plot of imaging predictors of recurrent ischemic stroke



Legend: IV: inversed variance, CI: confidence interval

(Filename: TCT_O-473_Figure_abstract2.jpg)

O-472

5:41PM - 5:48PM

Prediction of Recurrent Ischemic Stroke Using Baseline CT

F Kauw¹, R Takx¹, H de Jong¹, W Schonewille², L Kappelle¹, B Velthuis¹, J Dankbaar¹
¹University Medical Center Utrecht, Utrecht, the Netherlands, ²St. Antonius Hospital, Nieuwegein, Utrecht, the Netherlands

Purpose

To identify imaging (CT) predictors of recurrent ischemic stroke in patients with prior ischemic stroke or transient ischemic attack (TIA).

Materials and Methods

Patients with clinical features of cerebral ischemia < 9 hours were selected from two centers of the Dutch acute stroke trial (DUST). [1] Clinical and imaging data were collected prospectively. [1] Imaging data were based on noncontrast CT, CT angiography and CT perfusion maps. Variables included hyperdense vessel sign, the Alberta stroke program early CT score (ASPECTS), proximal intracranial occlusion, collateral score, significant stenosis of carotid or vertebrobasilar artery, perfusion deficit, penumbra/infarct core volume index and clot burden score. Primary outcome of the current investigation was recurrent ischemic stroke, which was extracted from medical records retrospectively. Hazard ratios (HR) with 95% confidence intervals (CI) were calculated for each baseline predictor using univariable and multivariable Cox regression models. Multivariable models were adjusted for the ABCD2 score. To investigate the influence of survival on the results, sensitivity analysis was performed for the group with more than three months of follow-up. The proportionality assumption was tested by using log minus log plots.

Oral Presentations & Excerptas

Results

Of the 490 patients with TIA or ischemic stroke 36 (7%) had recurrent ischemic stroke after a median follow-up of 23 months. The imaging predictor associated with recurrent ischemic stroke was ASPECTS >7 on MTT maps (adjusted HR 2.9, 95% CI 1.3-6.6). Sensitivity analysis of the group with more than three months of follow-up provided similar results. The proportionality assumption was not violated. Other imaging factors as determined by CT were not associated with recurrence in this study.

Conclusions

ASPECTS >7 on MTT maps, but no other imaging parameters are predictive of recurrent ischemic stroke.

O-475

5:55PM - 6:02PM

Predicting final infarct volume in stroke patients following endovascular treatment using dual-energy CT virtual non-contrast imaging

M Mentink¹, M Tijssen¹, W van Zwam¹, P Nelemans¹, A Postma¹

¹*University of Maastricht, Maastricht, the Netherlands*

Purpose

Endovascular treatment (EVT) for acute ischemic stroke has become standard-of-practice since MR Clean and other trials published their positive results. Imaging before and after EVT plays an important role in patient selection and follow-up. Hyperdensities on CT after EVT are frequently encountered. The ability of dual-energy CT (DECT) to differentiate between blood-brain-barrier breakdown (BBB) and intracerebral hemorrhage (ICH) is the main reason for DECT to become a preferred imaging modality after EVT in many clinics. Predicting final infarct volume, immediately after EVT is challenging. Mixed images of DECT after EVT were not able to accurately predict final infarct volume and demonstrated poor interrater reliability (previous study). Partly due to infarct growth in days following the acute stroke, partly because of the presence of parenchymal iodine enhancement due to BBB. DECT enables us to acquire virtual noncontrast (VNC) images in this early stage directly after EVT and thus eliminate the iodine enhancement. Hypodensity on VNC could therefore be more suitable to predict final infarct volume than mixed images. The aim of this retrospective study was to evaluate accuracy of infarct volume estimation on VNC images directly taken after EVT compared to CT taken at 24 hours and 5-7 days follow-up.

Materials and Methods

In a single-center retrospective study, 74 stroke patients that underwent EVT from July 2010 until December 2014 were included. DECT was performed following EVT using a Siemens SOMATOM Definition Flash. Simultaneous imaging at 80 kVp and 140 kVp was employed with standard calculation of mixed images. VNC images were calculated using a dedicated "brain hemorrhage algorithm". For assessing topographic infarct extension in the middle cerebral artery territory, the Alberta Stroke Program Early Computed Tomography Score (ASPECTS) was used, ranging from 0 (fully abnormal) -10 (normal) points. ASPECTS was scored on VNC images immediately after EVT and follow-up CT by a fellow neuroradiology and an experienced neuroradiologist. Volumes were acquired by segmentation of the hypodense areas with ITK-SNAP (www.itksnap.org). Agreement between raters and between images taken immediately after EVT and at early and later follow-up was assessed by 95% limits of agreement (95% LOA) according to Bland-Altman plots and by the intraclass correlation coefficient (ICC).

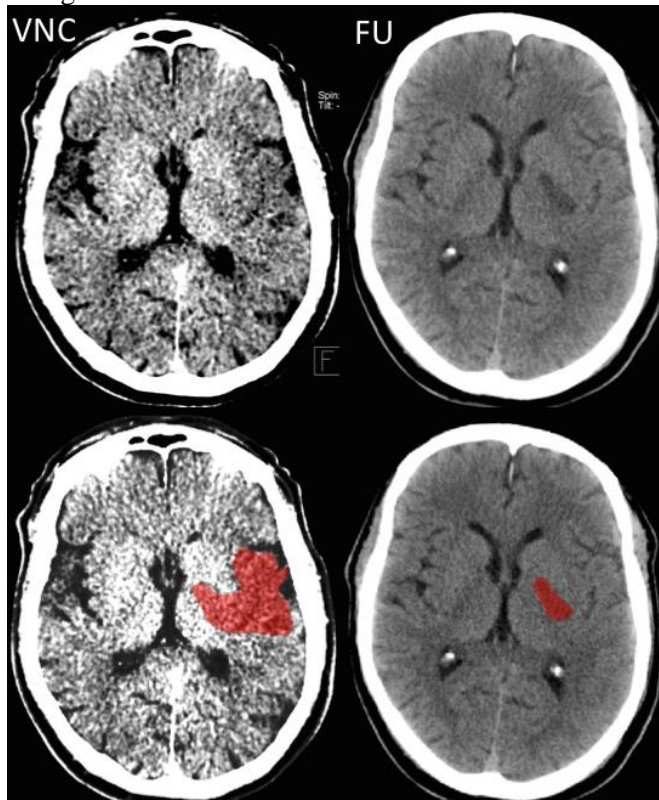
Results

Of 34 patients follow-up CT data at 24 hours were available and 25 patients of these had 5-7 days follow-up data available. For fellow and neuroradiologist ASPECT scoring the ICC was 0.73 for VNC imaging; 95% LOA ranged from 3.5 to -4.0 (mean difference -0.28). Analysis of agreement between VNC images and follow-up was performed with scoring data of the neuroradiologist, because of the broad LOA. Ninety-five percent LOA of ASPECTS between VNC images after EVT and 24 hours ranged from 5.3- -2.9 (mean difference 1.2) and at 5-7 days' follow-up from 6.9- -3.3 (mean difference 0.8). Median infarct

volumes were 44.6 mL (25-75 quartiles: 20.2-125.4 mL) at VNC images immediately after EVT, 50 mL (25-75 quartiles: 23.7-160.6 mL) at 24 hr follow-up, and 56.1 mL (25-75 quartiles: 22.6-170.6 mL) at 5-7 days follow-up.

Conclusions

ASPECT scoring of the VNC imaging showed a good interrater reliability. The use of VNC more reliably depicts infarct volume, if compared to mixed images alone. The subtraction of iodine enhancement improves delineation of the infarct. However, there is still a wide range. Prediction of final infarct volume using VNC of DECT immediately after EVT therefore remains difficult. This can be explained by poor to moderate demarcation of the hypodense areas in a scan with relative low SNR with ill-defined or indistinct margins of the infarcted region. Moreover, infarct growth can be still ongoing immediately after EVT due to ongoing metabolic cascades, or become smaller and better demarcated with decrease of vasogenic edema.



(Filename: TCT_O-475_asnrabstractmentink-postmaVNC.jpg)

O-476

6:02PM - 6:09PM

Individual Edema Correction in Early Follow-up CT Accurately Estimates Final Infarct Volumes after Ischemic Stroke

G Broocks¹, T Faizy¹, F Flottmann¹, U Hanning¹, G Schoen¹, H Leischner¹, M Schoenfeld¹, S Langner², J Fiehler¹, A Kemmling³, S Gellissen¹

¹University Medical Center Hamburg-Eppendorf, Hamburg, Germany, ²University Medical Center Greifswald, Greifswald, Germany, ³University Medical Center Schleswig-Holstein, Luebeck, Germany

Purpose

Final infarct volume is regularly used as end point in stroke trials; however, the reported volumes are most commonly derived from early follow-up imaging. Those volumes are significantly impaired by

Oral Presentations & Excerptas

ischemic edema, which causes an overestimation of the true final lesion volume. As water uptake can be quantified in computed tomography, we hypothesized that the final lesion volume can be better estimated by correcting the lesion volume in the early follow-up for the corresponding proportion of edema.

Materials and Methods

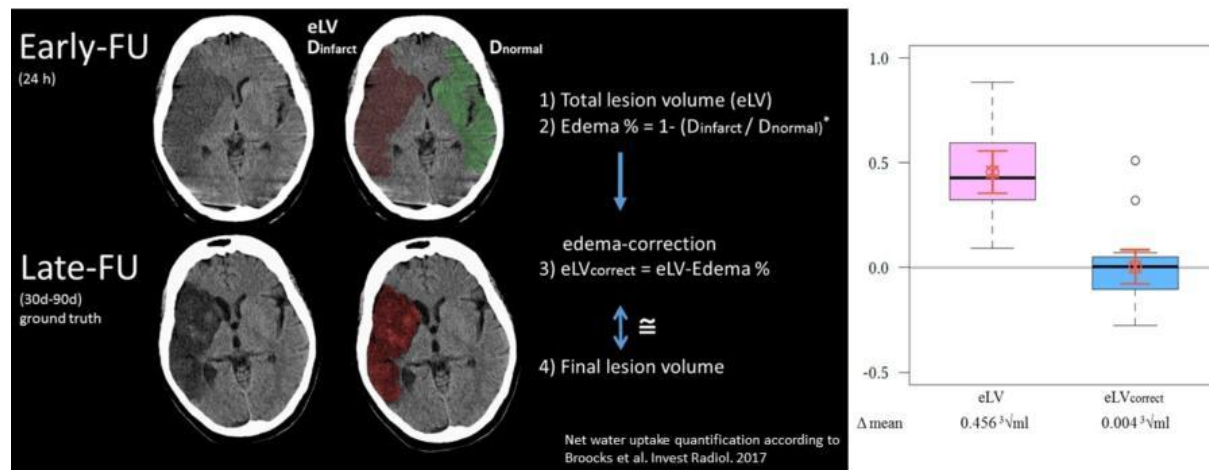
Twenty M1-MCA stroke patients with early and late follow-up CT (acquired after 30-90 days) were included. In the early follow-up 24 hours after onset, the proportion of edema contributing to the infarct lesion was calculated using net water uptake quantification based on relative density measurements and was subtracted from the total lesion volume to obtain edema-corrected lesion volumes. Finally, these corrected lesion volumes were compared to the final lesion volume on late follow-up serving as ground truth.

Results

The median lesion volume in the early follow-up was 115.1ml and significantly exceeded the median final lesion volume with 86.6ml ($p < 0.001$). The calculated mean proportion of edema was 25.8% ($\pm 5.9\%$) and was varying interindividually between 11.1% and 35.9%. The calculated median edema-corrected lesion volume measured after 24 hours was 87.1ml. The estimation of the final lesion volume based on the early follow-up was therefore improved by a mean of 31.4% ($\pm 2.1\%$) when corrected for the proportion of edema and did not differ significantly from the true final infarct volume ($p = 0.2$).

Conclusions

With edema correction, early follow-up lesion volumes were in close agreement with the actual final infarct volumes. CT-based edema correction improves the estimation of stroke outcomes based on early scans, which are in most cases more feasible and could especially be used to improve comparability and facilitate patient recruitment in clinical trials.



a) Edema correction based on net water uptake quantification

The proportion of edema of the total infarct lesion volume (1) in the early follow-up CT is calculated based on relative hypoattenuation (2) and deducted from the total lesion volume (3). The resulting (edema corrected) lesion volume is compared to the final lesion volume on late follow-up imaging (4).

b) The edema corrected volumes (blue) showed a high agreement to the true final infarct volume (grey, indicating the gold standard). In comparison, the uncorrected lesion volumes (eLV, pink).

(Filename: TCT_O-476_Fig_EC_ASNR18.jpg)

O-476a

6:09PM - 6:15PM

Evaluating the diagnostic value of different imaging modalities in cerebral venous thrombosis

O Shafaat¹, F Faeghi², A Bagheri², M Rabbani¹, K Jabbari¹, A Zandifar¹

¹Isfahan University of Medical Sciences, Isfahan, Iran, Islamic Republic of, ²Shahid Beheshti University of Medical Sciences, Tehran, Iran, Islamic Republic of

Purpose

Cerebral venous thrombosis (CVT) is a rare condition and has nonspecific symptoms. It can be potentially fatal if it remains undiagnosed and if the treatment is not started promptly. The combination of MRI and MRV is considered as the gold standard for evaluation of CVT. However, the sensitivity and specificity of MRI and MRV sequences are incomplete. Susceptibility weighted imaging (SWI) is one of the novel techniques in MRI and its contrast is based on the magnetic susceptibility differences between various tissues. This study was designed to compare different MRI sequences with SWI for visualization and evaluation of CVT.

Materials and Methods

Eighteen patients with CVT and eleven control patients without CVT were analyzed using different imaging modalities including MRI, SWI, and Phase contrast- magnetic resonance venography (PC-MRV). The MR sequences included T1-weighted spin echo (SE) imaging, T2-weighted turbo spin echo (TSE), T2-weighted SWI and three-dimensional phase contrast MRV.

Results

SWI showed the highest sensitivity, positive predictive value, and negative predictive value for the detection of cortical vein thrombosis (100%) and Specificity of all sequences in the diagnosis of cortical veins thrombosis was 100%. The sensitivity of PC-MRV, SWI, T2W, and T1W sequences in the diagnosis of venous sinus thrombosis were 100%, 75%, 50%, and 8.3% respectively. Specificity and positive predictive value of all sequences in the diagnosis of the venous sinus thrombosis were 100%. The negative predictive value of PC-MRV, SWI, T2W, and T1W sequences in the diagnosis of venous sinus thrombosis were 100%, 78.6%, 64.7%, and 50% respectively.

Conclusions

SWI had a high diagnostic value for diagnosing cortical vein thrombosis. PC-MRV was the superior MRI sequence for detecting venous sinus thrombosis. Besides PC-MRV, only SWI reached a sensitivity of over 50% for venous sinus thrombosis, followed by T2W, and T1W.

Thursday, June 7, 2018

8:00AM - 9:00AM

Parallel Paper Session: Imaging Utilization and Population Health Outcomes in Acute Stroke

O-483a

8:00AM - 9:00AM

Imaging Utilization and Population Health Outcomes in Acute Stroke

A Cote¹, K Adinarayan², A Hoang², P Sanelli², M Martinez³

¹Northwell Health Feinstein Institute for Medical Research, Manhasset, NY, ²Northwell Health, Manhasset, NY, ³-, Manhasset, NY

Purpose

Utilization of advanced imaging in addition to non-contrast head CT (NCCT) for acute stroke evaluation has shown benefit in providing additional treatment decision information. However, their routine clinical use has largely been bypassed due to the challenges of the 4.5 hour and 8 hour treatment windows for stroke interventions. We hypothesize that the use of advanced imaging such as MRI, benefits clinical outcomes when used as a decisional tool for intervention selection.

Oral Presentations & Excerptas

Materials and Methods

In this study we have amassed the imaging utilization for 669 acute stroke patients. Each was categorized by the most advanced brain imaging they received in the 8 hour treatment window from symptom onset, deemed the scan used to dictate treatment decisions, and their eventual treatment: No treatment, IV-tPA, or Endovascular. Each subgroup of imaging, within each treatment group, was then compared based on functional outcome, as measured by the modified Rankin Score (mRS) at time of discharge.

Results

Among the No Treatment group, 73.3 % received NCCT, 22.9% CTA, and 3.8% MRI as their most advanced imaging. No Treatment mean mRS NCCT = 2.2 (range 0-6), CTA = 2.6 (0-6), and MRI = 1.5 (0-6). Among IV-tPA treatment patients, 65.4% received NCCT, 30.3% CTA, and 2.6% MRI. The IV-tPA -NCCT group mean mRS = 2.5 (0-6), CTA = 2.9 (0-6), and MRI = 1.5 (0-4). Endovascular therapy-CTA mean mRS = 4.0 (4-5), MRI = 1.0 (1-1).

Conclusions

Within the No Treatment group, patients receiving MRIs displayed a lower mRS or superior functional outcome at discharge versus NCCT and CTA ($p < 0.21$ and $p < 0.054$ respectively). In the IV-tPA treatment group, MRI again showed better outcomes versus NCCT and CTA ($p < 0.31$ and $p < 1.7$). This suggests that MRI, while bearing a higher opportunity cost to perform, may lead to better overall outcomes when used to guide treatment in acute stroke.

Table 1: Utilization of imaging and treatment within 8 hour time window

Imaging Prior to Treatment Decision	Imaging Utilization- No Treatment (%) n=423	No Treatment- Age (mean, years) n=423	No Treatment- NIHSS (mean) n=388	IV-tPA (%) n=230	Endovascular therapy (%) n=16
NCCT	73.3	77	4.9	65.4	0.0
CTA	22.9	68	8.1	30.3	31.3
DSA	0.0	N/A	N/A	1.7	62.5
MRI	3.8	72	2.3	2.6	6.3

*IV-tPA includes IV-tPA administered outside of hospital

*13 subjects received both IV-tPA and endovascular therapy

Table 2: Functional outcomes (mRS scores) for each imaging strategy. Mean (range) of mRS scores are presented for each treatment group.

Imaging Type	No Treatment (n=362)	IV-tPA (n=213)	Endovascular Therapy (n=16)
NCCT	2.2 (0-6)	2.5 (0-6)	N/A
CTA	2.6 (0-6)	2.9 (0-6)	4.0 (4-5)
MRI	1.5 (0-6)	1.5 (0-4)	1.0 (1-1)
P-values (NCCT vs CTA)	7.0E-02	2.1E-01	N/A
P-values (NCCT vs MRI)	2.1E-01	3.1E-01	N/A
P-values (CTA vs MRI)	5.4E-02	1.7E-01	N/A

*N reduced due to missing mRS for specific subjects

(Filename: TCT_O-483a_CoteAbstractTable.GIF)

O-477

8:00AM - 8:07AM

Sensitivity and inter-rater reliability of stroke protocol CT in the early detection of stroke mimics

A Emira¹, A Schmitt¹, A Al busaidi¹, A Qureshi¹, R Jager²

¹Queen Square, London, United Kingdom, ²Institute of Neurology, Queen Square, London, United Kingdom

Purpose

Stroke mimics (SM) are common, especially at the earliest stages of the acute ischemic stroke (IS) pathway, occurring in up to a third of patients with clinically suspected IS. Computed tomography (CT) is a valuable early diagnostic measure that may demystify doubt over the clinical diagnosis of IS, though the added value of CT/CT angiogram (CTA) in identifying stroke mimics has not been measured. Our aim was to investigate the diagnostic benefit of CT/CTA in the early detection of stroke mimics by measuring its sensitivity and the interrater reliability.

Materials and Methods

A total of 86 patients who presented to accident and emergency with early stroke-like symptoms were recruited. The cohort comprised of patients with stroke (n= 22), stroke mimics (n=42), and patients without stroke or a mimic (n=22). The final clinical diagnoses were taken as the reference standard. Two neuroradiology fellows retrospectively reviewed the CT/CTA scans individually, blinded to the CT report findings and the final clinical diagnosis. The reviewers indicated their diagnosis (IS, SM or normal) and scored their diagnostic confidence of stroke on a scale of 1-5. The interrater reliability was also measured.

Results

The sensitivity of CT/CTA in detecting SM was 31%. The overall interrater reliability was moderate with a Kappa = 0.736 (95% CI 0.905 to 0.567), (P <0.001). The interrater reliability for stroke mimics was also moderate though lower with a Kappa= 0.634 (95% CI 0.465 to 0.803), (P <0.001). The total number of stroke mimics identified was 12 out of 42 (14%), with six cases identified by both readers.

Conclusions

Given the low sensitivity and the moderate interrater reliability, additional imaging such as MRI is recommended to ensure early and accurate diagnosis in cases where stroke is clinically doubtful or where a stroke mimic is suspected. Further studies comparing CT and MRI may illustrate the added value of a second modality.

O-478

8:07AM - 8:14AM

Hemorrhagic Transformation and Aspirin Prescription after Thrombectomy : an Interrater and Intrarater Agreement Study

A Guenego¹, R Fahed²

¹Toulouse University Hospital, Toulouse, France, ²Fondation Ophtalmologique Adolphe de Rothschild, Paris, France

Purpose

We aimed to systematically review the literature and assess the reliability of hemorrhagic transformation (HT) diagnosis and classification on brain computed tomography performed 22-36 hours after mechanical thrombectomy in acute ischemic stroke (AIS) patients with anterior circulation large vessel occlusion.

Materials and Methods

Studies assessing the reliability of HT diagnosis and/or ECASS classification were reviewed. Eighteen raters independently assessed twice 30 brain CT scans realized 22 to 36 hours after mechanical thrombectomy in patients included in a multicentric randomized trial. Agreement was measured with Fleiss' and Cohen's unweighted kappa statistics.

Oral Presentations & Excerptas

Results

The review yielded four studies reporting 19 measures of agreement. Populations, methods, analyses, and results were heterogeneous (moderate to excellent agreement), precluding a meta-analysis. In our study, interrater agreement for HT diagnosis was moderate for all raters ($\kappa=0.55$, 95%CI [0.41-0.68]) and each subspecialty. The interrater agreement for ECASS classification was fair for all raters ($\kappa=0.37$ [0.27-0.50]), but improved to a moderate level after dichotomization. Dichotomization of the ECASS classification also improved the number of raters to reach a substantial (or higher) intrarater agreement (from 7/18 [38.9%] to 14/18 [77.8%]). The interrater agreement for aspirin therapy decision was moderate for all raters ($\kappa=0.52$ [0.40-0.66]), and substantial among the vascular neurologists ($\kappa=0.70$ [0.57-0.84]).

Conclusions

The diagnosis and classification of HT according to ECASS criteria on brain CT scans performed 22 hours to 36 hours after thrombectomy might not be reliable among untrained physicians. Despite the lack of reliability, the interrater agreement for aspirin therapy decision among vascular neurologists was substantial.

O-479

8:14AM - 8:21AM

Predicting recanalization in acute stroke patients after intravenous thrombolysis

J Puig¹, G Blasco¹, P Daunis-i-Estadella², V Cuba¹, S Thio-Henestrosa², C Biarnes¹, M Marti-Navas¹, J Serena³, Y Silva³, M Terceño³, M Essig⁴, K Nael⁵, C Leiva-Salinas⁶, M Wintermark⁷, S Pedraza¹

¹Diagnostic Imaging Institute (IDI), IDIBGI, University Hospital Dr Josep Trueta, Girona, Spain, ²University of Girona, Girona, Spain, ³Hospital Dr Josep Trueta, IDIBGI, Girona, Spain, ⁴University of Manitoba, Winnipeg, Manitoba, Canada, ⁵Icahn School of Medicine at Mount Sinai, New York, NY, ⁶University of Missouri, Columbia, MO, ⁷Stanford University, Stanford, CA

Purpose

Intravenous thrombolysis (tPA) after ischemic stroke results in timely recanalization in only 50% of occluded arteries; the reasons for treatment failure are not fully understood. Being able to predict the success of tPA would probably help in choosing other recanalization strategies such as mechanical thrombectomy. Various studies have attempted to predict recanalization, some using clinical variables (e.g., time to treatment or stroke severity) and others using vascular risk factors. We evaluated clinical and imaging predictors to determine the best biomarkers of recanalization after intravenous tPA in patients with acute ischemic stroke.

Materials and Methods

Clinical and imaging data were prospectively collected in 630 patients treated with tPA within 4.5 hours of onset of acute ischemic stroke caused by middle cerebral artery occlusion. CT follow-up was performed at 24 hours. Patients referred for mechanical thrombolysis were excluded. Demographics, vascular risk factors, stroke severity (National Institutes of Health Stroke Scale [NIHSS] score), stroke origin, time to tPA, ASPECTS scores, thrombus characteristics (occlusion site, density, length, clot burden score [CBS]) (Olea Sphere 3.0, La Ciotat, France), and vascular recanalization (Thrombolysis in Myocardial Infarction criteria) after tPA were recorded. ROC curves selected optimal thresholds, and multivariate logistic regression analysis identified predictors of vascular recanalization.

Results

Of 630 patients, 550 met the inclusion criteria. Recanalization was successful in 209 (38%) patients. At admission, patients with persistent occlusion after tPA had higher NIHSS scores [18(13-21) vs. 13(9-19), $p<0.001$], ASPECTS scores [13(9-19) vs. 10(8;10), $p<0.001$], ischemic lesion volumes [32.3 mL (47.5-62.9) vs 14.9(2.8-40.8), $p=0.027$]; lower CBS [6(4-8) vs. 7(6-9), $p=0.043$]; and poorer collaterals. The best independent predictors of recanalization were NIHSS scores at admission (cut-off, 14; AUC, 0.644; $p<0.001$) and CBS (cut-off, 8; AUC, 0.634; $p=0.040$).

Oral Presentations & Excerptas

Conclusions

NIHSS scores at admission and the imaging-based CBS are useful markers for predicting recanalization after tPA administration.

O-480

8:21AM - 8:28AM

CTA Collaterals versus CT Perfusion CBF Maps for Core Infarct Volume Assessment in Patient Selection for Intra-Arterial Thrombectomy?

S McWilliams¹, S Kamalian¹, S Raymond², M Mansouri¹, R Hakimelahi³, P Schaefer¹, R Gonzalez¹, M Lev¹

¹Massachusetts General Hospital, Boston, MA, ²Massachusetts General Hospital, Cambridge, MA, ³Memorial Sloan Ketterin Cancer Center, New York, NY

Purpose

Since publication of the 2015 NEJM Intra-Arterial Thrombectomy (IAT) trial results and the more recent DAWN study results, there has been strong interest in determining optimal CT-based strategies for stroke patient treatment selection, when MR diffusion-weighted imaging (DWI) – the undisputed reference standard for "core" infarct volume assessment – cannot be obtained. Although specific volume thresholds vary slightly among centers, "small" infarct cores are considered "likely-to-benefit" from IAT and "large" cores "unlikely-to-benefit". Our goal was to compare the performance of visual CTA collateral assessment with that of CT perfusion cerebral blood flow maps (CTP-CBF) in making this determination.

Materials and Methods

Ischemic volumes of 62 acute anterior circulation occlusive stroke patients were visually segmented on DWI and compared with volume estimates from concurrent multiphase CTA collateral MIP projections and CTP-CBF maps. CTA collaterals ipsilateral to the occlusions were classified as having a "symmetric/hyperemic" or "reduced/malignant" pattern, versus the contralateral uninvolved hemisphere, per objective, well defined guidelines. CTP-CBF volumes were determined by both manual segmentation (using a previously determined 15% threshold) and in an automated fashion. Interrater reliability for three readers at different levels of training was assessed. Accuracy for identifying 100ml core infarct volumes was calculated.

Results

There were 13/62 patients with DWI core >100ml, 4/62 with DWI 70-100ml, and 45/62 with DWI <70ml. Sensitivity/Specificity for detection of >100ml and <70ml cores, respectively, were 92.3%/86.7% for visual collateral assessment, 92.3%/95.6% for manual CTP-CBF assessment, and 61.5%/100% for automated assessment. Interrater agreement for visual collateral assessment was very good to excellent.

Conclusions

Visual assessment of CTA collateral patterns in acute occlusive stroke patients compares favorably to CTP-CBF core volume estimates in stratifying patients as "likely-to-benefit" (core <70ml) versus "unlikely-to-benefit" (core >100ml) from IAT, relative to a DWI reference standard. CTP-CBF thresholds can be adjusted to maximize either sensitivity for "large" core or specificity for "small" core identification.

O-481

8:28AM - 8:35AM

Solving the Puzzle of Brain Infarction versus Stroke Mimics in Young Patients

B Martin¹, E Makariou¹, C Lee²

¹Georgetown University, Washington, DC, ²Medstar Georgetown University Hospital, Washington, DC

Purpose

The uncommon presentation of brain infarction in the younger patient should prompt a search for the underlying etiology with special consideration for stroke mimics. Here we evaluate the imaging findings for common etiologies responsible for brain infarction in younger patients while demonstrating how clinical presentation and imaging play a complementary, pivotal role in distinguishing brain infarction from stroke mimics.

Materials and Methods

Retrospective review of 48 patients between the age 15 and 35 diagnosed with brain infarction between January 2016 and August 2017. Patients were imaged by cross-sectional imaging to include MRI, MRA, CT or CTA as well as conventional cerebral angiography as indicated. Cases were grouped by etiology, with a special category and consideration given to mimickers of brain infarction.

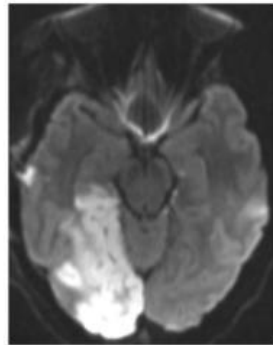
Results

In our experience over the last year, stroke mimics are slightly more common (17%) than any single etiology responsible for true brain infarction. Pathologies mimicking stroke included Mitochondrial encephalomyopathy, lactic acidosis, and stroke-like episodes (MELAS); acute lymphoblastic leukemia; neurosyphilis; lupus cerebritis; and paraneoplastic encephalitis. Intracranial cerebrovascular anomalies, including aneurysm and arteriovenous malformations, represent the most common culprit of brain infarction (15%), with infectious and cardiologic etiologies close behind (13% and 10%, respectively). Arterial dissection is commonly represented among cases (8%). Brain infarction as a complication of malignancy also represented a significant portion (6%) of cases. Additional etiologies include drug abuse, sickle-cell anemia, dural sinus thrombosis, carotid artery webs, complications related to labor and delivery or organ transplant, trauma and vasculitis.

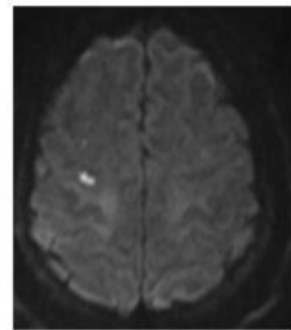
Conclusions

Discriminating between stroke mimic and true brain infarction, followed by narrowing possible etiologies for a true brain infarction, is critical in diagnosing and treating patients. Rapid recognition in some cases may facilitate treatment within a critical window or spare the patient from unnecessary procedures. Recognizing a mimic may be key to suggesting the next appropriate step in management. Reviewing the most common stroke etiologies and mimics in a particular institution's patient population is key to rapid diagnosis.

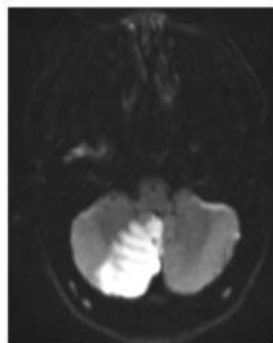
Diffusion Weighted Image of a 32 year old female patient with Small Cell Lung Cancer with Right PCA Distribution Infarction.



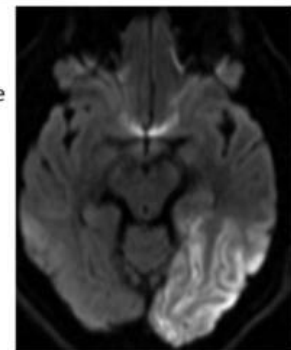
Diffusion Weighted Image of a 33 year old male patient with leukemic infiltration of the cerebrum mimicking embolic stroke.



Diffusion Weighted Image of a 23 year old male patient with embolic right PICA distribution infarction with known spongiform cardiomyopathy.



Diffusion Weighted Image of a 22 year old male patient with MELAS mimicking a left PCA distribution infarction.



(Filename: TCT_O-481_ImageMartin.jpg)

O-482

8:35AM - 8:42AM

The Influence of CT Perfusion on the Selection of Stroke Patients for Endovascular Therapy

J Ospel¹, K Grzegorz¹, K Blackham²

¹University Hospital Basel, Basel, Switzerland, ²University Hospitals Case Medical Center, University Heights, OH

Purpose

Determine whether CT perfusion (CTP) changes patient selection for interventional therapy in acute stroke patients compared to combined native CT and CT angiography (CTA) data.

Materials and Methods

Retrospectively evaluated in a blinded fashion were 286 consecutive acute stroke CT examinations (noncontrast CT, CTA, CTP) from patients who were examined within a 4,5 hours time window and received intravenous lysis. An experienced neurointerventionalist reviewed the cases first without and, after a month delay, with the CTP data (Syngo.via, Siemens Healthineers). Clinical information provided: NIHSS, age and side of neurologic deficit. Differences in detection rate of vessel occlusion and interventional decision were compared. Criteria for intervention on CTP included intervention on CTP included 1.2 mismatch ratio. Mann-Whitney-U test was used to detect differences in the detection rate of vessel occlusions.

Results

ASPECTS score was ≥ 7 in all cases. Detection rates of vessel occlusions and/or decision to intervene did not differ significantly between the two interpretive sessions (n = 165 in the reading without CTP vs. n = 171 when the additional CTP data was added, p = 0,315).

Conclusions

In the common scenario of an acute ischaemic stroke patient presenting within the 4.5 hour intravenous lysis window to a tertiary referral center, CTP is not adding significant value to triage. The decision to proceed with endovascular intervention should not be delayed by obtaining and processing CTP.

O-483

8:42AM - 8:49AM

Predicting Neurological Outcome After Cardiac Arrest Using Quantitative Diffusion Weighted Imaging Analysis

R Ward¹, J Mettenburg², N Siripong³, J Rittenberger²

¹University of Pittsburgh School of Medicine, Pittsburgh, PA, ²University of Pittsburgh Medical Center, Pittsburgh, PA, ³Clinical and Translational Science Institute, Pittsburgh, PA

Purpose

Following resuscitation from cardiac arrest, determining the prognosis of comatose patients can be challenging. Targeted Temperature Management (TTM) and standardizing postresuscitation care have significantly improved outcomes. However, early and accurate prognostic predictors are lacking in part due to sedation and TTM, which may confound the neurological examination. Quantitative analysis of apparent diffusion coefficient (ADC) maps may help to evaluate the extent and severity of brain injury in these patients. We predict that both whole brain anoxic injury and regional injury as represented by ADC are associated with functional outcome in comatose patients resuscitated following cardiac arrest (CA). Further, we hypothesize that injuries to cortical structures of the brain portend a worse prognosis than injuries to deeper structures of the brain.

Materials and Methods

From 2005 through 2010, diffusion-weighted MRI images were obtained from 116 patients who were resuscitated from CA. Mean ADC values were calculated for the whole brain, and the following regions: brainstem, caudate, cerebellum, frontal, insula, occipital, parietal, putamen, temporal, thalamus, and subcortical white matter. In addition to mean ADC values, subthreshold percentages were calculated in increments of 30 for ADC values of 600-900 $\times 10^{-6}$ mm²/sec in each region. (For instance, 45% of the voxels in a patient's occipital lobe have an ADC value < 630 ; 54% of the voxels in the patient's occipital lobe have an ADC value < 660 .) Magnetic resonance imaging was performed at 1.5T and ADC maps were derived from standard clinical diffusion-weighted imaging, using FSL. Images were registered to ICBM-452 T1 5th Order Polynomial Warps Atlas to create the segmented regions listed above. Upper and lower thresholds of 200 and 1000 $\times 10^{-6}$ mm²/sec were applied to eliminate noise and exclude cerebral spinal fluid, respectively. Clinical outcome, such as the patient's ability to follow commands, Cerebral Performance Category (CPC) scores, modified Rankin Scale scores (mRS), and discharge disposition were collected. A "good" outcome was defined as a CPC of 1-2, mRS of 0-3, or discharge to home or acute rehabilitation facility. To determine the largest distinguishing power between patients with good or poor outcomes, the difference in the proportion of voxels between good and poor outcomes was calculated for whole-brain and regions in each 30-point increment. We selected three ranges in each region that corresponded with the highest proportions. Independent t-tests were then calculated to determine whether the ranges with the largest differences in proportions were statistically significant. Because three ranges were compared for each region, we adjusted the p-values via Bonferroni correction to $p < .016$.

Results

Of the statistically significant values, we chose to report the ranges with the largest difference between means. The frontal ($d=6.84$, 95% CI [2.56, 11.12], $p=0.002$), parietal ($d=11.28$, 95% CI [5.19, 17.36], $p=0.001$), occipital ($d=12.50$, 95% CI [6.21, 18.80], $p=0.001$), temporal ($d=5.48$, CI 95% [1.30, 9.57], $p=0.011$), grey matter ($d=8.18$, 95% CI [3.48, 12.87], $p=0.001$), and white matter ($d=8.34$, CI 95% [3.52, 13.16], $p=0.001$) regions all demonstrated large differences between good and poor outcome patients at a voxel threshold of $< 600 \times 10^{-6}$ mm²/sec. The insula showed the largest difference between groups in the 780-810 range ($d=-1.77$, CI 95% [-2.75, -0.78], $p=0.001$). Finally, the caudate showed the largest difference in the 750-780 range ($d=-1.31$, CI 95% [-2.35, -0.27], $p=0.014$).

Conclusions

The largest differences between groups were in the $< 600 \times 10^{-6}$ mm²/sec range. The frontal lobe, parietal lobe, occipital lobe, temporal lobe, grey matter, and white matter all demonstrated large group differences in this range. The brainstem, caudate, and insula showed differences, albeit of smaller size, at higher ADC values. It is possible that these regions demonstrate low ADC values in most post-CA patients and, thus, the most profound differences occur at higher ranges. Moreover, these findings suggest that global, cortical and subcortical, injury portends the worse prognosis. One possible future direction is to determine why some patients with high percentages of sub 600 voxel regions demonstrate good neurological outcome, while the majority do not.

		Gender			
		Frequency	Percent	Valid Percent	Cumulative Percent
Valid	Male	55	47.4	49.1	49.1
	Female	57	49.1	50.9	100.0
	Total	112	96.6	100.0	
Missing	System	4	3.4		
Total		116	100.0		

		Rhythm			
		Frequency	Percent	Valid Percent	Cumulative Percent
Valid	Unknown	19	16.4	17.0	17.0
	VF/VT	49	42.2	43.8	60.7
	PEA	24	20.7	21.4	82.1
	Asystole	20	17.2	17.9	100.0
	Total	112	96.6	100.0	
Missing	System	4	3.4		
Total		116	100.0		

		Modified Rankin			
		Frequency	Percent	Valid Percent	Cumulative Percent
Valid	No symptoms at all	4	3.4	3.6	3.6
	No significant disability	4	3.4	3.6	7.1
	Slight disability	2	1.7	1.8	8.9
	Moderate disability	2	1.7	1.8	10.7
	Moderately severe disability	39	33.6	34.8	45.5
	Severe disability, bedridden	14	12.1	12.5	58.0
	Dead	47	40.5	42.0	100.0
Total	112	96.6	100.0		
Missing	System	4	3.4		
Total		116	100.0		

		Cerebral Performance Category			
		Frequency	Percent	Valid Percent	Cumulative Percent
Valid	Conscious and alert	9	7.8	8.0	8.0
	Conscious and alert w/ moderate disability	3	2.6	2.7	10.7
	Conscious with severe disability	44	37.9	39.3	50.0
	Comatose or persistent vegetative state	9	7.8	8.0	58.0
	Brain dead or death from other causes	47	40.5	42.0	100.0
	Total	112	96.6	100.0	
Missing	System	4	3.4		
Total		116	100.0		

(Filename: TCT_O-483_FINAL_WARD_VANCOUVER.jpg)

Thursday, June 7, 2018

8:00AM - 9:00AM

Parallel Paper Session: Interventional: Aneurysms and AVMs

O-484

8:00AM - 8:07AM

Non-Ischemic Cerebral Enhancing Lesions Secondary to Endovascular Aneurysm Therapy: A French National Registry

E Shotar¹, M Labeyrie², A Biondi³, S Velasco⁴, G Saliou⁵, G Boulouis⁶, O Naggara⁶, B Daumas Duport⁷, K Janot⁸, D Herbreteau⁸, C Michelozzi⁹, C Cognard¹⁰, H Redjem¹¹, N Bricout¹², J Pruvo¹², F Ricolfi¹³, F Di Maria¹⁴, N Sourour¹, F Clarençon¹

¹Pitié-Salpêtrière Hospital, Paris, France, ²Lariboisière Hospital, Paris, France, ³Besançon University Hospital, Besançon, France, ⁴University Hospital of Poitiers, Poitiers, France, ⁵Vaud University Hospital, Lausanne, Vaud, Switzerland, ⁶Saint Anne Hospital, Paris, France, ⁷Nord Laennec Hospital, Nantes, France, ⁸University Hospital of Tours, Tours, Indre et Loire, France, ⁹Michallon Hospital, La Tronche, Tououse, France, ¹⁰University Hospital of Toulouse, Toulouse, France, ¹¹Fondation Ophtalmologique Adolphe de Rothschild, Paris, France, ¹²Lille University Hospital, Lille, France, ¹³F. Mitterand Hospital, Dijon, France, ¹⁴Foch Hospital, Suresnes, Paris, France

Purpose

Delayed onset of nonischemic cerebral enhancing (NICE) lesions has been described after intracranial aneurysm endovascular therapy (EVT). The purpose of this study is to present the preliminary results of the NICE lesions retrospective French national registry.

Materials and Methods

A standardized questionnaire was sent to all French interventional neuroradiology departments (n = 37) under the aegis of the Société Française de Neuroradiologie (SFNR). Participating centers reported cases

Oral Presentations & Excerptas

of NICE lesions along with demographic, clinical and imaging data. Twenty-four centers responded to date, 16 of which encountered one or several cases of NICE lesions. Data regarding 20 patients treated for 21 aneurysms were collected. Data collection concerning another four cases is ongoing.

Results

Seventeen patients were females and three were males. Mean age at EVT was 46 ± 10 years. Five aneurysms were ruptured, one was compressive and 15 were incidental. Fifteen aneurysms were treated by regular or balloon assisted coiling, one by stent assisted coiling, four by flow diversion and another by flow disruption. Mean delay to NICE lesions onset was 8 ± 12 months (ranging from 1-50 months). Only 13 patients were symptomatic at time of discovery and two others developed symptoms secondarily. The most common symptom was cephalalgia, found in 11 patients. The last MRI examination, performed at 19 ± 14 months, demonstrated persistent contrast enhancement in 12 out of 18 patients.

Conclusions

NICE lesions are a rare complication of aneurysm EVT. This is the first nationwide registry of this complication.

O-485

8:07AM - 8:14AM

Embolization of dural cavernous fistulas via image guided superior ophthalmic vein access: report of 20 cases and review of literature.

D Volders¹, C Haw¹, J Shewchuk², M Heran²

¹University of British Columbia, Vancouver, British Columbia, Canada, ²Vancouver General Hospital, Vancouver, British Columbia, Canada

Purpose

Retrospective review of image-guided superior ophthalmic vein (SOV) access for carotico-cavernous fistula (CCF) treatment done at our institution. We wanted to assess the risks and benefits of this approach compared to similar control patients in literature who were treated with an inferior petrosal sinus (IPS) or surgical SOV access approach.

Materials and Methods

Between July 2012 and November 2017, 20 patients underwent endovascular treatment for CCF with transvenous embolization via the SOV. The patient group consisted of five male and 15 female patients aged 18 to 98 years (mean 61 years). In the majority of lesions (16/20), the feeders were from both the internal and external carotid arteries (Barrow's type D). In the majority of patients (16/20) the SOV could be accessed under ultrasound (US) (Panel A). In the remainder four patients where initial US access was unsuccessful, the SOV was accessed using Xper guide CT. Coil embolization of the cavernous sinus was performed in all cases (Panel B).

Results

In the majority of patients (14/20), the procedure went uneventfully. In four cases (20%), a procedural preseptal hematoma developed, which didn't require any further treatment. In two cases (10%), one with US and one with Xper guide CT access, a periprocedural retrobulbar hematoma developed, which required a postprocedural decompressive lateral canthotomy and inferior cantholysis. The visual symptoms relating to the CCF improved in all 20 patients. The two patients who developed a retrobulbar hematoma also had a normalization of their vision with no residual visual symptoms. (Table 1).

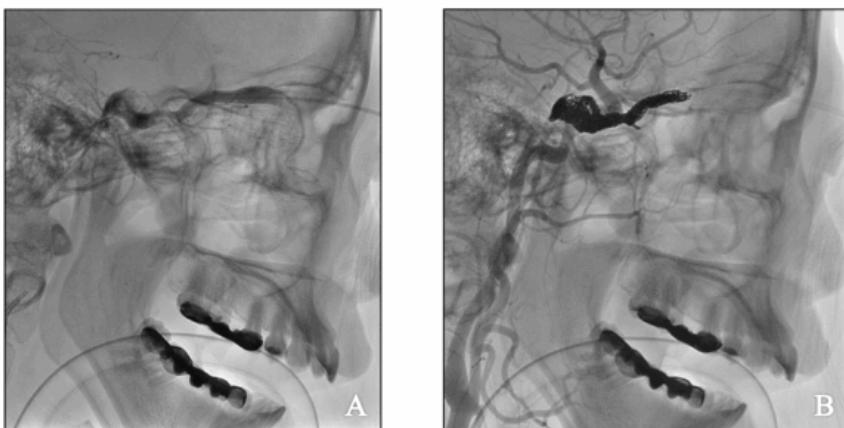
Conclusions

Direct image-guided percutaneous SOV access provides a relatively safe and time-saving alternative route for indirect CCF treatment compared to direct surgical access of the SOV in case of thrombosis of the IPS. To our knowledge, this is the largest case series of direct image-guided SOV access.

Table 1

No.	Sex/Age	Barrow Classification	IPS	SOV Access	Complications	Angiographic Result
1	F/67	D	trombosed	US	no	Complete remission
2	M/66	C	trombosed	US	no	Complete remission
3	M/59	D	trombosed	Xper CT	preseptal hematoma	Complete remission
4	F/18	C	trombosed	US	preseptal hematoma	Complete remission
5	F/59	D	trombosed	US	no	Complete remission
6	F/47	D	trombosed	US	preseptal hematoma	Complete remission
7	F/98	D	trombosed	US	no	Complete remission
8	F/77	B	trombosed	US	no	Complete remission
9	F/71	D	trombosed	US	no	Complete remission
10	M/70	D	trombosed	US	no	Complete remission
11	F/84	D	partial open	US	no	Complete remission
12	F/69	D	trombosed	Xper CT	preseptal hematoma	Complete remission
13	M/66	B	trombosed	US	retrobulbar hematoma	Complete remission
14	F/75	D	partial open	US	no	Complete remission
15	M/27	D	trombosed	US	no	Complete remission
16	F/67	D	trombosed	Xper CT	retrobulbar hematoma	Complete remission
17	F/76	D	partial open	Xper CT	no	Complete remission
18	F/82	D	trombosed	US	no	Complete remission
19	F/34	D	trombosed	US	no	Complete remission

Figure 1



(Filename: TCT_O-485_figureandtable.gif)

O-486

8:14AM - 8:21AM

Ear Arteriovenous Malformation Management

W Yakes¹

¹*The Yakes Vascular Malformation Center, Englewood, CO*

Purpose

To determine the efficacy of Ethanol Endovascular Repair of Ear Arteriovenous Malformation (AVMs)
Materials and Methods

Ten patients (7 female, 3 males; age range 6-39 years; mean age: 22 years) with ear AVMs presented for therapy. Two patients had failed prior embolizations (PVA/coils/nBCA/steroids) and two patients had other therapies (laser/excisions/grafting). All presented with a grossly enlarged painful ear, and five patients had intermittent bleeding. All patients underwent transcatheter and direct puncture ethanol treatments (86 procedures).

Oral Presentations & Excerptas

Results

All 10 patients were cured of their AVM at long-term follow-up (mean follow-up: 52 months). One patient had transient partial VII nerve palsy. Two patients had minor blisters and ear injuries that healed on the outer tragus.

Conclusions

Ethanol endovascular repair of Ear AVMs can achieve cures in this vexing lesion that previously was treated with resection of the ear and with high recurrence rates. This series documents long-term cures of AVMs of the ear and scalp that were not treatable by endovascular approaches as previously documented in the world's literature. Permanent treatment of the auricular AVMs is documented and no recurrence occurred in any patient. Only one article is published (group from Shanghai, China) emulating this technique, that I taught them.

O-487

8:21AM - 8:28AM

Mandibular AVM Diagnosis and Curative Endovascular Treatment

W Yakes¹

¹*The Yakes Vascular Malformation Center, Englewood, CO*

Purpose

To determine optimal management strategies for the treatment of mandibular AVM

Materials and Methods

Thirteen patients (10 females, 3 males, age 9 -14; mean age 10) underwent endovascular therapy to treat their mandibular AVMs. Nine patients had distinct intraosseous AVMs. Three had multiple facial and intramaxillary AVMs requiring treatment. Outside institutions recommended massive hemi-facial resections in these patients. Four patients had prior PVA and gel foam embolization; one patient had a lip graft; one had prior mandible surgery--all that had failed.

Results

All 13 patients have demonstrated MR and angiographic cure of their AVMs. One patient's therapy is not completed and is ongoing. The patient's mandibular AVM is cured, a third AVM in this patient in the infratemporal fossa is still undergoing treatment. The follow-up range is 11 months – 41 months, with a mean follow-up of 29 months. No complications were noted in treatment of mandibular AVMs. One patient required a minor gingival surgery after treatment of an additional intramaxillary AVM.

Conclusions

Endovascular approaches to manage mandibular AVM can be curative. The intraosseous variety is largely a fistula between artery and vein within the bone. All respond well to endovascular ethanol therapy alone. Surgery was not required in any patient. Surprisingly no complications were encountered in this patient series. Long-term cures are noted in this patient series with endovascular approaches alone. No massive surgical resections in any patient, even in patients with multiple AVMs of the soft tissues, mandible and maxilla, was required to effect cure. In patients who suffered hemorrhages from floating teeth, bone formed and stabilized the teeth and no further hemorrhages occurred. Ethanol sclerotherapy proved curative in mandibular intraosseous AVMs in patients who had additional facial soft-tissue AVMs and intramaxillary AVMs that were cured as well at long-term follow-up.

O-488

8:28AM - 8:35AM

Head and Neck Endovascular Repair of Vascular Malformations

W Yakes¹

¹*The Yakes Vascular Malformation Center, Englewood, CO*

Purpose

To determine the efficacy of ethanol embolotherapy of extracranial head and neck vascular malformations of all types, particularly after failure of other endovascular and surgical treatments

Materials and Methods

Presented were 166 patients (64 males, 102 females; mean age: 38 yrs) with extracranial arteriovenous malformations (AVMs) of the head and neck area. Over half of the patients had undergone previous failed therapies. All patients underwent ethanol embolotherapy under general anesthesia. Forty-five patients had AVMs and 121 patients had venous malformations (VM).

Results

Of 45 AVM patients, 36 patients are cured (mean follow-up 2 ½ years); of 121 venous malformation patients, 65 are at end-therapy (mean follow-up 4 ½ years). The remaining patients are not at end-therapy and are being treated for their residual malformations. In AVM follow-up, arteriography is the main imaging modality to determine cure or residual AVM as MR is less sensitive in the evaluation of residual AVM. In VM follow-up, MR is the main imaging tool, particularly with T-2 fat suppression and/or STIR imaging. All patients demonstrated improvement post therapy. Complications were 4.5%, to include bleeding (self-limited), partial 7th nerve palsy (with recovery), skin injury (not requiring skin grafts), infection, and pain.

Conclusions

Ethanol has proven its consistent curative potential at long-term follow-up for high-flow AVMs and low-flow VM lesions at long-term follow-up as lesions in the periphery. Complication rates remain low. The procedures are tolerated well by the patients and done on an out-patient basis. Prior surgery and embolization procedures can cause difficulty in lesion access, but does not obviate further ethanol endovascular treatment.

O-489

8:35AM - 8:42AM

Cost-Effectiveness of CT Angiography in Management of Tiny UIAs

X Wu¹, B Geng¹, K Seifert², V Kalra³, D Gandhi⁴, P Sanelli⁵, A Malhotra²

¹*Yale University School of Medicine, New Haven, CT*, ²*Yale New Haven Hospital, New Haven, CT*, ³*Orlando Health, Tampa, FL*, ⁴*University of Maryland School of Medicine, Baltimore, MD*, ⁵*Northwell Health, Manhasset, NY*

Purpose

Due to its noninvasive nature, high spatial resolution, speed, and availability, CTA makes an excellent modality for serial follow-up of known UIAs. However, increasing use of CTA raises radiation concerns as cumulative CT radiation exposure adds incrementally to baseline cancer risk. We performed this study to evaluate the cost-effectiveness of CTA for surveillance of tiny unruptured intracranial aneurysms (UIAs) and the impact of CTA radiation-induced brain tumor on the overall cost-effectiveness of CTA.

Materials and Methods

A Markov decision model was constructed from a societal perspective starting with patients 30, 40 or 50-year-old, with incidental detections of UIA ≤ 3 mm and no prior history of subarachnoid hemorrhage. Five different management strategies were assessed: annual CTA surveillance, biennial CTA, CTA follow-up every five years, coiling and follow-up and, no preventive treatment or routine follow-up. Probabilistic, one-way, and two-way sensitivity analyses were performed.

Results

The base case calculation shows no preventive follow-up to be the most cost-effective strategy in all age groups (cost: \$50,066, effectiveness: 24.40 QALY in 30 year-olds). No follow-up remains the dominant strategy when the annual rupture risk of nongrowing UIAs is smaller than 1.79%, or the rupture risk in growing aneurysms is $<25\%$. A two-way sensitivity analysis varying both the rupture risk of growing aneurysms and the proportion of them shows that when either the rupture risk of growing aneurysms is

lower than 4%, or its proportion is less than 1%, no follow-up is the optimal strategy regardless of the value of the other variable. When both risks are relatively high, annual follow-up is the most cost-effective. The radiation-induced brain cancer risk is relatively low and sensitivity analysis shows that the radiation-induced cancer risk does not influence the conclusions.

Conclusions

Given the current literature, aggressive treatment or routine surveillance imaging follow-up may not be the cost-effective strategy in all patients with aneurysms ≤ 3 mm.

Results of Base Case Calculation

	30 years of age at aneurysms discovery		40 years of age at aneurysms discovery		50 years of age at aneurysms discovery	
	Cost	Effectiveness (QALY)	Cost	Effectiveness (QALY)	Cost	Effectiveness (QALY)
No follow-up	\$50,066	24.40	\$39,726	22.27	\$28,705	19.38
Annual CTA follow-up	\$105,457	24.20	\$91,074	22.09	\$68,999	19.24
Biennial CTA follow-up	\$72,049	23.85	\$58,631	21.77	\$43,756	18.97
CTA every 5 years	\$61,969	23.54	\$50,270	21.81	\$37,524	19.36
Coiling	\$231,172	22.48	\$204,675	20.38	\$174,078	17.71

(Filename: TCT_O-489_ASNRtable.jpg)

O-490

8:42AM - 8:49AM

Comparison of Wall Shear Stress and Flow Morphology in a Patient with an Intracranial Aneurysm with Aneurysm Model of the Same Patient Generated Using 3D Printing

W Chang¹, N Kaneko¹, M Loecher¹, J Chiang¹, A Chien¹, D Ennis¹, J Villablanca¹

¹University of California Los Angeles, Los Angeles, CA

Purpose

Three-D printing is an emerging technology that has been used relatively sparingly in the medical field to date but has numerous potential applications, especially in radiology, since 3-D printed images can be readily generated from CT, MRI, or DSA data. While 3-D printed models of vascular malformations are generated with relative ease and have been shown to be excellent anatomic analogues of actual vessels, it is unclear if the models will replicate similar flow conditions to those obtained directly from actual patients. In this study, we compare data acquired using 4-D Flow MRA from a patient to that acquired using 4-D Flow MRA on a 3-D printed model of the same patient's aneurysm generated using data from 3-D rotational DSA.

Materials and Methods

A patient with a left internal carotid artery aneurysm was scanned on a 3T MRI scanner (Prisma, Siemens) using 4-D Flow Phase Contrast MRA at 0.5 mm isotropic spatial resolution. Scan time was 12 minutes, VENC was 40 cm/s, and FOV was 220 x 220 x 52 mm. The same patient underwent digital subtraction angiography and 3-D rotational angiography was performed. The STL data from the 3DRA was used to generate an acrylonitrile butadiene styrene vascular mold using a Mojo (Stratasys) 3-D

Oral Presentations & Excerpts

printer as a 1:1 replica (no magnification). Subsequently, the mold was smoothed by ABS solvent, then liquid silicone was applied to the mold and allowed to solidify. Subsequently, the ABS was dissolved using acetone leaving the silicone mold. The mold was then connected to a flow-pump and flow rates were matched to the time average flow rate from the 4-D MRA. Then a 4-D Flow MRA was performed using the same parameters used on the patient in the earlier acquisition. The data from the two acquisitions was postprocessed using a custom MATLAB environment and WSS data was calculated. WSS and streamline maps were generated of both models and are presented below.

Results

The flow phantom and patient demonstrated similar low wall shear stress measurements within the aneurysm dome, with a measurement of 0.37 N/m² for the flow phantom, compared to 0.44 N/m² for data acquired directly from the patient. Both the patient and flow phantom derived data results demonstrated elevated WSS at the aneurysm neck, with mean WSS of 4.14 N/m² for the flow phantom and 3.76 N/m² for the patient, and both the patient and flow phantom demonstrated somewhat lower WSS in the parent vessel, with WSS of 2.59 N/m² for the flow phantom and 2.42 N/m² for the patient. When observing the flow morphology shown on the WSS and streamline maps, both the patient and flow phantom demonstrated similar flow morphology, with elevated WSS in the aneurysm neck, and decreased WSS in the aneurysm dome, with a helical pattern of flow within the aneurysm sac in both cases.

Conclusions

We were able to successfully create a flow phantom using low-cost 3-D printing generated from data acquired from 3-D rotational angiography, which was successfully coupled with a flow pump and demonstrated similar WSS measurements and flow patterns compared to the actual patient when both the patient and flow phantom were scanned using 4-D Flow MRA. This technique demonstrates significant promise as these flow phantoms have myriad applications, including interventional device testing, sequence development without time constraints, testing of variable field strength, or SAR constraints, or generation of an endothelialized model with subsequent analysis of gene expression. The ability to generate flow phantoms with accurate flow properties quickly and easily using 3-D printing has high clinical utility. While this was a pilot study with only one example, we believe further investigation is warranted.

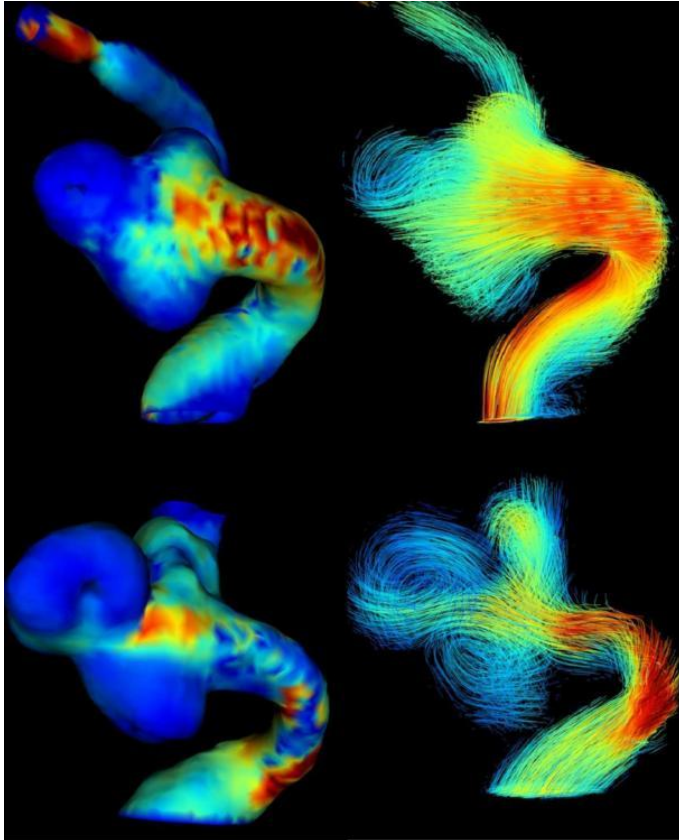


Figure 1: a) top left: WSS map of a flow phantom acquired using 4D Flow MRA showing low WSS in the aneurysm sac. b) top right: Streamline map of a flow phantom acquired using 4D Flow showing a helical flow pattern. c) bottom left: WSS map of the original patient showing low WSS in the aneurysm sac. d) bottom right: Streamline map of the original patient showing a helical flow pattern. (Filename: TCT_O-490_figure3dp.jpg)

O-491

8:49AM - 8:56AM

Angiogram-Negative Spontaneous Intracranial Subarachnoid Hemorrhage: A Multi-center Study of Rebleeding Rate and Pattern of Hemorrhage

G Sadigh¹, M Bhojak², A Aladi³, A Trofimova⁴, M Mossa-Basha⁵, L Wu⁵, S Dehkharghani⁶, A Derakhshani⁷, J Allen⁴

¹Emory University School of Medicine, Atlanta, GA, ²The Walton Centre, Liverpool, Merseyside, England, ³Keele University, Stoke-on-Trent, Staffordshire, England, ⁴Emory University, Atlanta, GA, ⁵University of Washington, Seattle, WA, ⁶Emory University Hospital, Atlanta, GA, ⁷New York University, New York, NY

Purpose

To assess the rebleeding rate in patients with angiographically-negative spontaneous subarachnoid hemorrhage (AN-SAH) stratified by pattern of hemorrhage at initial presentation

Materials and Methods

In this multicenter retrospective study, consecutive adult patients admitted with nontraumatic, AN-SAH to one of the five university hospitals between January 2010 and December 2015 were included. Patients with concurrent intraparenchymal, subdural, or epidural hematomas were excluded. Baseline clinical

Oral Presentations & Excerptas

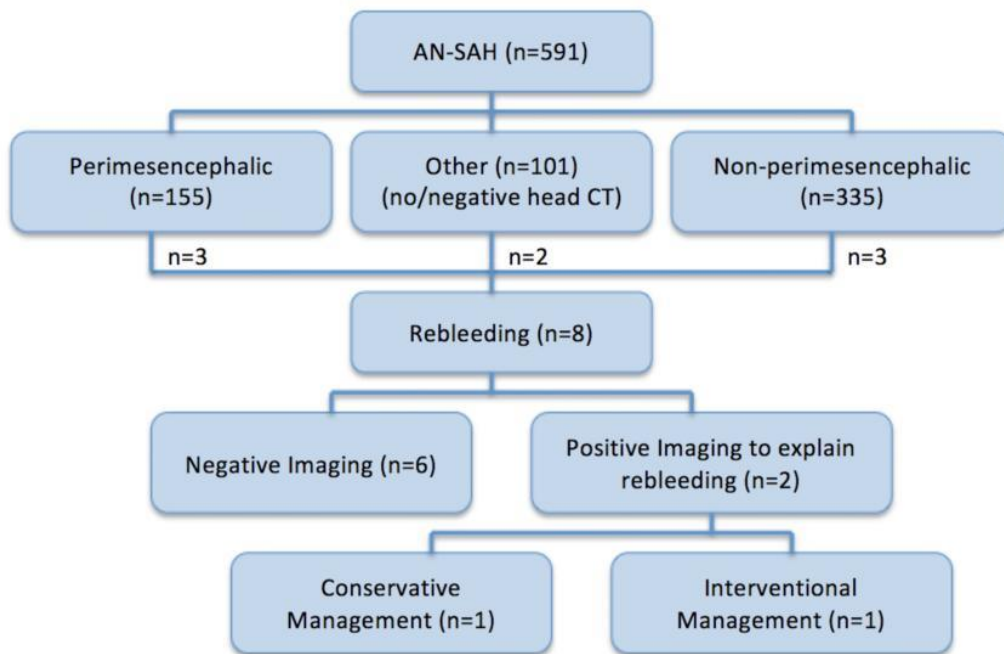
characteristics and posthospitalization outcomes for patients with at least one follow-up visit from date of diagnosis to October 2017 were collected. Pattern of hemorrhage on presentation noncontrast head CT (NCCT) and any recurrent SAH, identified from available follow-up records in the respective hospital system, was studied.

Results

Included were 694 patients (mean age, 54 year; 54% male). Mean (SD) Hunt and Hess and Fisher scores were 1.5 (0.9) and 2.7 (1), respectively; 85% (591/694) had at least one follow-up visit after discharge with their respective hospital system. Of these, 26% (155/591) had perimesencephalic patterns of hemorrhage, 57% (333/591) had nonperimesencephalic patterns, 17% (101/591) had no NCCT at presentation due to transfer from other hospitals, and 1% (8/694) had no hemorrhage on head CT (e.g. diagnosed by lumbar puncture). Only 1.3% (8/591) had documented rebleeding within median of four months of initial encounter discharge; 0.5% (3/591) had perimesencephalic and 0.5% (3/591) nonperimesencephalic hemorrhage at initial encounter and the remaining 0.3% (2/591) either did not have head CT at initial encounter or were diagnosed with lumbar puncture. A causative etiology for rebleeding was identified in 0.3% of patients (2/591), in both cases an aneurysm in patients with an initially nonperimesencephalic pattern at presentation.

Conclusions

Rebleeding rates in patients with AN-SAH is low (1.3%), regardless of pattern of hemorrhage. There is a need for standardized approach in radiologic management of these patients.



(Filename: TCT_O-491_Figure.jpg)

O-491a

8:56AM - 9:00AM

Application of the intracranial arterial pulsatility index for determination of lacunar infarct prognosis

A Zandifar¹, N Manouchehri¹, M Alizadeh², O Shafaat², E Zandifar³, F Khorvash³, M Saadatinia³

¹Isfahan University of Medical Sciences, Isfahan University of Medical Sciences, ²Isfahan University of Medical Sciences, Isfahan, Iran, Islamic Republic of, ³Isfahan University of Medical Sciences, Isfahan, Iran, Islamic Republic of

Purpose

Lacunar infarct is a subset of ischemic cerebrovascular accidents and has been shown to have a benign course; however long term follow ups have pointed to adverse neurological outcomes. In this study we aimed to investigate the usefulness of intracranial arterial pulsatility index (PI) as a determinant for arterial blood flow quality to assess the prognosis of lacunar infarcts.

Materials and Methods

50 patients with confirmed acute lacunar infarcts were enrolled in the study. Demographic and disease characteristics data was collected. A transcranial color coded sonogram was performed to assess the PI of bilateral ACA, MCA, PCA, vertebral and proximal internal carotid arteries. Patients' clinical status was assessed using a modified ranking scale (0-6). Patients were followed up for 6 months after discharge with regular visits for reevaluation of their clinical status

Results

The mean \pm SD of age was 64.1 \pm 9.07 and 57.1 percent of the patients were male. Upon discharge only 8.2% of the patients were ranked as 0 on the MRS; however after a 6-month follow up period this number grew to 49% of the patients. There were no significant differences between the left and right PI measurements in any of the assessed arteries. Patients with PIs over 1 on their primary assessment of the vertebral artery had significantly worse outcomes during the 6 months follow up. PIs from other arteries did not predict the prognosis.

Conclusions

Using sonogram assisted assessments of vertebral artery blood flow during the early stages of lacunar infarcts provides a reliable reference for estimation of prognosis.

Thursday, June 7, 2018

8:00AM - 9:00AM

Parallel Paper Session: Interventional: Advanced Techniques

O-492

8:00AM - 8:07AM

Sofia intermediate catheter and the SNAKE technique: safety and efficacy of the Sofia catheter without guidewire or microcatheter construct

J Heit¹, J Wong², A Moraff², N Telischak³, R Dodd², M Marks², H Do²

¹Stanford University Hospital, Stanford, CA, ²Stanford University, Stanford, CA, ³California Pacific Medical Center, San Francisco, CA

Purpose

Neurointerventional surgeries (NIS) benefit from supportive endovascular constructs. Sofia is a soft-tipped, flexible, braided single lumen intermediate catheter designed for NIS. Sofia advancement from the cervical to the intracranial circulation without a luminal guidewire or microcatheter construct has not been described. We valued the efficacy and safety of the new Sofia Non-wire Advancement technique (SNAKE) for advancement of the Sofia into the cerebral circulation.

Materials and Methods

Consecutive patients who underwent NIS using Sofia were identified. Patient information, SNAKE use, and patient outcome were determined from electronic medical records. Sofia advancement to cavernous

Oral Presentations & Excerptas

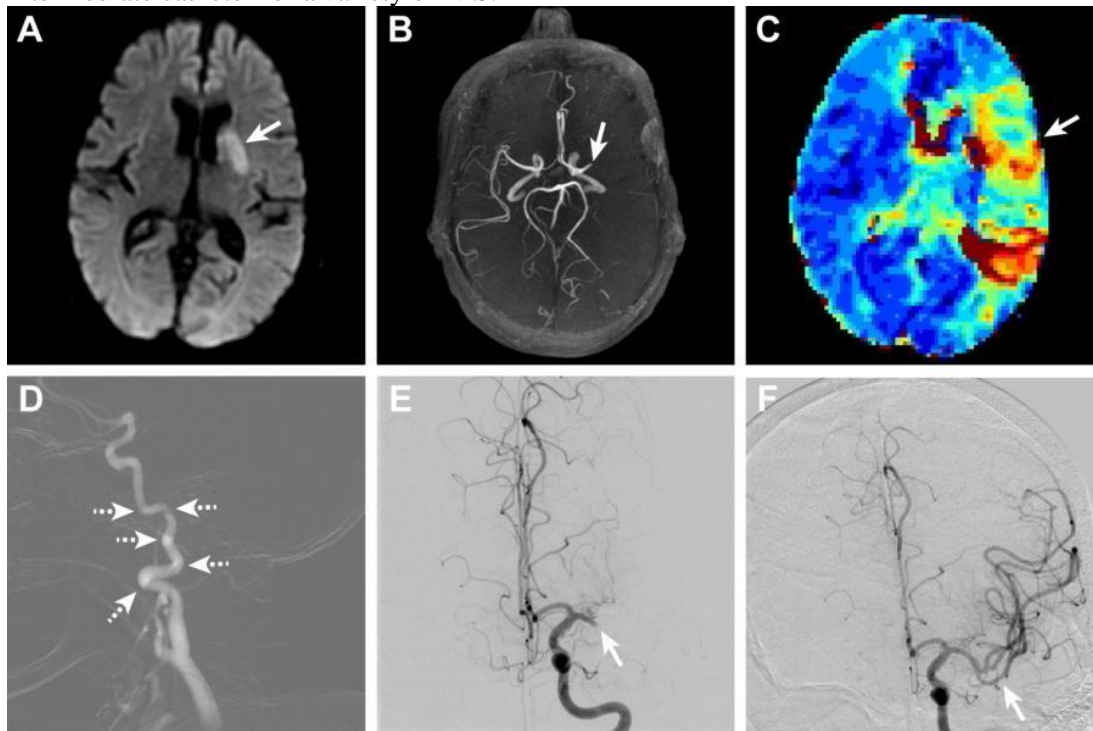
internal carotid artery or the V2/V3 segment junction of the vertebral artery was the primary outcome measure. Secondary outcomes included arterial vasospasm and arterial dissection.

Results

Identified were 263 patients (181 females, 69%) who underwent a total of 305 NIS using Sofia. SNAKE (SNAKE+) was used in 187 patients (61%). Technically successful were 292 procedures (96%), which included 184 SNAKE+ NIS and 109 SNAKE - NIS. Primary outcome was achieved in all SNAKE+ procedures, but not in five SNAKE- procedures (2%). No arterial dissections were identified among 305 interventions. In the intracranial circulation, a single SNAKE+ patient (0.5%) had nonflow limiting arterial vasospasm involving the petrous internal carotid. Three SNAKE+ patients (1.6%) and one SNAKE- patient (0.8%) demonstrated external carotid artery branch artery vasospasm during dural arteriovenous fistula or facial arteriovenous malformation treatment.

Conclusions

SNAKE is a safe and effective technique for Sofia advancement. Sofia is a highly effective and safe intermediate catheter for a variety of NIS.



(Filename: TCT_O-492_SNAKEFigure1.jpg)

O-493

8:07AM - 8:14AM

Endovascular management of severe stenosis of supra-aortic arteries in patients of Takayasu arteritis

S Chen¹, F Chang¹, C Luo¹, W Guo¹

¹Taipei Veterans General Hospital, Taipei, Taiwan

Purpose

To retrospectively evaluate the technical safety and outcomes of endovascular management of severe stenosis of the supra-aortic arteries in the patients of Takayasu arteritis (TA)

Materials and Methods

Between 2008 to 2016, six patients of TA with severe symptomatic stenosis of the supra-aortic arteries

Oral Presentations & Excerptas

accepted endovascular treatment in our institute. The indication of patient selection included more than 70% stenosis, with cerebral ischemic symptoms and without active disease (normal C-reactive protein [CRP]). All patients had pre and postprocedural MR evaluation, including three patients had high-resolution vessel wall imaging. We evaluate the technical safety (technical success, complication and ischemic lesions on postprocedural MRI) and outcome (stent-patency).

Results

All patients (100%) had successfully received stent placement or percutaneous transluminal angioplasty in the 23 treated arteries. They included 16 endovascular procedures performed in the six patients. The preprocedural CRP or erythrocyte sedimentation rate of these patients was 0.7 ± 0.9 mg/dL and 20.5 ± 21.3 mm/hr. The early postprocedural MRI in one week was available in 10 procedures and only two tiny silent acute infarcts were detected on DWI. No technical neurological complication was noted. The restenosis rate was 60.8% (14/23), which occurred in 11.5 ± 9.9 (5 to 45) months follow-up. All patients did not receive aggressive postprocedural immunosuppressing therapy. A case of repeated episodes of restenosis was successfully treated with a drug-eluting balloon (Ranger balloon, Boston Scientific) for angioplasty.

Conclusions

Endovascular treatment of TA was associated with high restenosis rate even in their inactive disease process. We suggest aggressive postprocedural medical treatment including dual-antiplatelet and immunosuppressive therapy and close follow-up to prevent the restenosis. Drug-eluting balloon angioplasty may be a promising option to treat in-stent restenosis.

O-494

8:14AM - 8:21AM

The pCANvas neck bridging device for the treatment of wide-necked bifurcation aneurysms – initial results

P Bhogal¹, H Henkes¹, P Lylyk², J Chudyk², C Bleise²

¹Klinikum Stuttgart, Stuttgart, Germany, ²ENERI-Clinica La Sagrada Familia, Buenos Aires, Argentina

Purpose

The pCANvas is a third generation aneurysm neck bridging device comprised of a laser cut electrolytically detached stent shaft with a distal crown of petals. Unlike the pCONus1 and pCONus2 devices the distal petals are covered in a biocompatible membrane that acts to both inhibit flow into the aneurysm as well as prevent coils being displaced into the parent vessel. Four radio-opaque markers are present on the distal crown to allow accurate placement of the membrane-covered crown at the aneurysm neck. This is the first neck bridging neurovascular device to incorporate this feature. The membrane is impermeable to blood flow; however, it can be easily punctured with standard microguidewires and microcatheters to allow additional coiling of aneurysms. We present our initial experience with the pCANvas device and present the technical success rate, complication rate, clinical and angiographic follow-up rate.

Materials and Methods

We performed a retrospective review of prospectively collected data to identify patients treated with the pCANvas device between February 2015 and February 2017.

Results

In all cases the pCANvas device was successfully deployed and there were no intraoperative complications. There were no intraoperative aneurysmal ruptures. At the end of the procedure angiography showed that 15 aneurysms had continued complete filling of the aneurysm (RRC 3) with two aneurysms showing only filling of the neck of the aneurysm (RRC 2). Early follow-up angiography was available for 16 patients at an average of 6.1 months (range 3-10 months) post procedure. Eleven aneurysms showed persistent and complete filling of (RRC 3) and five aneurysms showed complete occlusion of the aneurysm (RRC 1). Midterm angiographic follow-up was available for 14 patients at a

Oral Presentations & Excerptas

median of 18.2 months (range 7-38 months) post treatment. Three aneurysms showed complete filling of the aneurysm, three aneurysms had neck remnants and the remainder were completely occluded. To date, seven aneurysms have undergone repeat treatment with coiling of the aneurysms after the initial pCANvas procedure and follow-up angiography. In all cases this was because of a failure of the aneurysm to occlude after treatment with the pCANvas alone.

Conclusions

The pCANvas device is the first neck-bridging device to incorporate a membrane designed to alter intra-aneurysmal flow dynamics. Based on our initial experience the device appears safe; however, we recommend the device is used with adjunctive coiling of the aneurysm. Larger studies and long-term follow-up are required to assess the stability of aneurysm occlusion.

O-495

8:21AM - 8:28AM

The pCONus2 neck bridging device – early clinical experience and immediate angiographic results

P Bhogal¹, P Lylyk², H Henkes¹, J Chudyk², C Bleise²

¹Klinikum Stuttgart, Stuttgart, Germany, ²ENERI-Clinica La Sagrada Familia, Buenos Aires, Argentina

Purpose

Wide-necked aneurysms are challenging to treat for the interventional neuroradiologist. Recently, numerous devices dedicated to the treatment of these aneurysms have become available. We present our early experience of the pCONus2 and present the technical success rate, clinical outcome and immediate angiographic occlusion rates.

Materials and Methods

We performed a retrospective review of prospectively collected data to identify patients treated with the pCONus2 device between February 2015 and February 2017.

Results

We identified 12 patients treated with the pCONus2 device (10 female). The average of the patients was 56.6±15.8 years (range 13-71). The average dome width was 8.83±5.3mm (range 3.8-20mm), dome height 7.23±4.06mm (range 3.36-15mm) and neck width 5.88±2.92 (range 2.77-11mm). Angulation of the aneurysm to the parent vessel varied between 0 and 78°, mean average 32.2°. The aneurysms were located in the anterior circulation (n=10) and posterior circulation (n=2). At immediate post-treatment angiography 11 aneurysms showed mRRC grade I occlusion and one aneurysm mRRC grade II. There were no deaths or hemorrhagic complications. Three patients developed small thrombi during treatment all of which were successfully treated with glycoprotein IIb/IIIa antagonists. Six patients have early angiographic follow-up data, five of which show adequate aneurysm occlusion and one of which shows aneurysm recanalization.

Conclusions

The early results on the use of the pCONus2 suggest it can be used to assist in the treatment of wide-necked aneurysms; however, larger studies with longer-term follow-up data are required.

O-496

8:28AM - 8:35AM

Intrasaccular Flow Diversion for Bifurcation and Terminal Aneurysms: Buenos Aires Experience and Long Term Follow Up with pCANvas.

J CHUDYK¹, C Bleise¹, I LYLYK¹, P Lylyk¹

¹Instituto Médico ENERI - Clínica Sagrada Familia, Buenos Aires, Argentina

Purpose

pCANvas device is a new generation of flow diverter (FD), which is used inside the aneurysm sac and

creates a new concept of intrasaccular flow diversion. It's a stent-like device with a membrane at the distal part designed to modify the inflow in addition to coil support. It is planned for the treatment of bifurcation and terminal intracranial aneurysms (IA). We report our experience in a series of patients treated with this device, regarding the feasibility, safety and long-term follow-up.

Materials and Methods

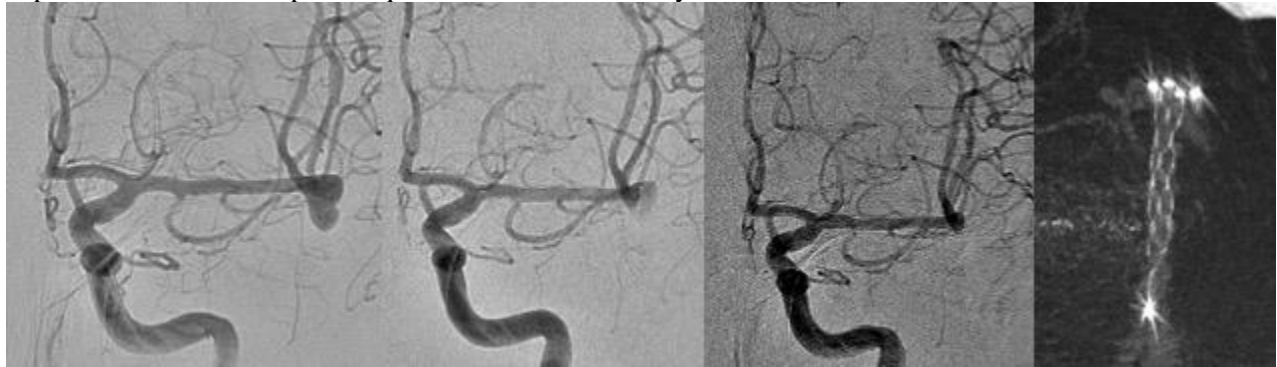
Between March 2014 and May 2017, pCANvas device was implanted in 33 patients with 33 IA. The device was used with or without coils according to each case. Located in anterior circulation were 29 IA. Middle cerebral artery (MCA) bifurcation was the most common location (15 IA). Clinical and angiographic controls were performed at three, six and every 12 months after the first year.

Results

The pCANvas device was successfully deployed in 91.6% of the cases. No hemorrhagic complications were observed; one (3%) patient presented thromboembolic complications. At six months, 50% of the aneurysms showed complete or near-complete occlusion and 84.4% at 24 months. Nine (27.3%) were treated without coils at the first session and required retreatment; mRS 0 in 32 (97%) of patients.

Conclusions

pCANvas device showed to be a safe alternative for the treatment of selected cases at bifurcation and terminal segments, with low rate of clinical complications and stable results over the time. More experience and follow-up are required to show its stability over time.



(Filename: TCT_O-496_pcanvas.jpg)

O-497

8:35AM - 8:42AM

Hydrophilic Polymer Coating Inhibits Platelet Adhesion In Vitro and In Vivo

H Henkes¹, M Aguilar Pèrez¹, E Henkes¹, P Lylyk²

¹Klinikum Stuttgart, Stuttgart, BW, ²ENERI-Clinica La Sagrada Familia, Buenos Aires, Argentina

Purpose

Platelets react to foreign body surfaces and induce blood coagulation. Therefore, during neurovascular interventions with implantation of stents and flow diverters the standard of care includes the dual antiplatelet therapy (DAPT) e.g. with ASA and clopidogrel, followed by antiplatelet monotherapy with ASA forever. Although the risk for stent thrombosis is reduced, the risk for hemorrhagic complications increases and there are patients for which DAPT is not suitable at all [1]. A potential solution for this dilemma is the application of an antithrombogenic coating on the device surface. Such a coating should reduce the thrombogenicity of the implant itself, hence making dual antiplatelet therapy obsolete. This would solve the problem of bleeding and reduce device-induced thrombosis as well. The purpose of this study was to develop and evaluate a new hydrophilic stent coating.

Materials and Methods

NiTi test plates and regular devices were coated with a hydrophilic polymer. Coating efficiency was analyzed using the Wilhelmy-Plate method. Platelet adhesion was examined during whole blood contact

Oral Presentations & Excerptas

in vitro. Uncoated NiTi test plates and devices served as control. Platelet adhesion was analyzed using SEM and CD61 immunofluorescence microscopy. In order to analyze tissue and healing response in vivo, coated and uncoated stents were implanted in nine New Zealand White Rabbits for 30 days. Cross sections of the vessels and stents were analyzed histologically. Coated braided flow diverter were then implanted in selected patients without DAPT.

Results

NiTi test plates and devices were coated homogeneously. After incubation with whole blood in vitro, uncoated NiTi plates were completely covered with platelets, whereas platelet adhesion on coated specimens was reduced significantly. Histology revealed no differences between coated and uncoated devices concerning tissue and healing response. Coated flow diverters were implanted in selected patients without DAPT successfully.

Conclusions

A new hydrophilic polymer coating was evaluated, which inhibits platelet adhesion in vitro. Preliminary clinical experience confirms its efficiency when applied on flow diverters and implanted in patients without DAPT.

O-498

8:42AM - 8:49AM

Clinico-Imaging Outcome of Dural Sinus Thrombectomy Using Fogarty Balloon – A Single Centre Experience

P Mannam¹, S Nidugala¹, S Mani¹, S Aaron¹, M Alexander¹

¹*Christian Medical College and Hospital, Vellore, Vellore, Tamil Nadu, India*

Purpose

Cerebral venous sinus thrombosis is a neurological disorder with a highly variable presentation and clinical course. The incidence of this disorder is variably reported in literature and is cited as being 13-15 cases per million per year (1, 2). Mechanical thrombectomy to expedite recanalization of cerebral venous sinuses is a procedure that is relatively underutilized; a total of 64 cases were reported to have undergone this procedure in published literature (3). In our institution, we have been performing local thrombectomy with a combination of balloon angioplasty, pharmacological agents and Penumbra (4) in the last few years. However, since March 2017, we performed the thrombectomy using Fogarty catheter with a transjugular access. We present this single-center experience of 20 patients who have undergone dural sinus thrombectomy.

Materials and Methods

Patients who underwent mechanical thrombectomy (duration: March - October 2017) were identified using the radiology department's case database. A retrospective analysis of these cases was done using the radiology database and the hospital information system. The individual cases were analyzed with respect to thrombus age on MRI and correlated with ease of guidewire transit at the time of mechanical thrombectomy, the results of the mechanical thrombectomy (satisfactory vs. unsatisfactory recanalization), immediate and delayed procedure-related complications, GCS at admission vs. GCS at 24 hours post procedure and duration of hospital stay.

Results

A total of 20 patients underwent Fogarty balloon-assisted mechanical thrombectomy; the recanalization rate was deemed satisfactory in all 20 patients with guidewire transit being achieved with moderate ease in all patients. Fourteen patients had superficial venous system thrombosis and six had a combination of superficial and deep venous system thrombosis. Preprocedure GCS ranged from 8/15 – 15/15; 18 patients had a GCS of 15/15 at discharge; one patient was discharged against medical advice with a 2T/15 GCS and worsening of parenchymal hemorrhage; and one patient had a GCS of 10T/15 at discharge (tracheostomy) and had worsened mass effect following the procedure. There were no immediate or delayed procedure-related complications.

Oral Presentations & Excerptas

Conclusions

Balloon-assisted mechanical thrombectomy using Fogarty balloon is a safe and effective procedure to reduce thrombus load and can be used in conjunction with medical management in patients with cerebral venous thrombosis. The transjugular access reduces the procedure time. The procedure is a cheaper alternative to expensive device-assisted procedures and improves the outcome of patients with cerebral venous sinus thrombosis.

O-499

8:49AM - 8:56AM

Novel Angiographic Phantom and Method for evaluating Spatial and Contrast Resolution of Digital Subtraction Angiography on Neuroangiographic Systems

J Mason¹, C Dodge², A Beardsley¹, G Benndorf¹

¹Baylor College of Medicine, Bellaire, TX, ²Texas Children's Hospital, Houston, TX

Purpose

Accurate visualization of small cerebral vessels during cerebral digital subtraction angiography (DSA) and neuroendovascular procedures is imperative for accurate diagnoses and avoiding adverse outcomes. Perforating arteries that supply crucial brain areas without collaterals, are at average 300 microns or less in diameter, and thus present a challenge for the resolution limits of neuroangiographic systems. Previous work comparing visualization performance of current state-of-the-art neuroangiographic systems using a calibrated model proved feasible for measuring contrast resolution (signal-to-noise ratios) of phantom vessels but lacked dose-rate monitoring, simulation of tissue attenuation, flow dynamics, and a method for measuring spatial resolution. In this study, angiographic imaging was performed using a novel 3-D printed angiographic phantom with a branching pattern, allowing for more realistic modeling of flow dynamics. Inner diameters ranging from 313 μm to 1000 μm were used to simulate the size of perforating arteries. The purpose of this experiment was to create and evaluate a novel angiographic phantom and method to calculate contrast and spatial resolution of cerebral DSA, and to use this data to compare visualization performance of different angiographic systems.

Materials and Methods

A novel 3-D printed angiographic phantom with a branching pattern was developed, which included: 1000 μm phantom vessels, 500 μm phantom vessels, and 313 μm phantom vessels. The phantom was made of Poly(methyl methacrylate) PMMA. Siemens Artis Zeego (Siemens Healthineers, Erlangen Germany) and Philips Allura Angiographic Systems (Philips Healthcare) were used to image the phantom. A novel cylindrical 3-D printed angiographic phantom was placed within a 16 cm PMMA head phantom to simulate tissue dose. Undiluted Omnipaque 300 was injected manually under 'blank road map' settings. Separate images were obtained under fluoro mode 1 and fluoro mode 2 settings for Phillips Allura, which were selected based on having similar dose rates to Siemens Artis Zeego settings used. Images were exported in 1024x1024 16bit DICOM format. ImageJ was used to extract 2-D plot profiles for each phantom vessel from 13 separate saved images from the injections. This data was then evaluated via Matlab; peak signal and full width at half maximum (FWHM) values from pixel DICOM data were extracted from the 13 separate images for each 1000, 500, and 313 μm phantom vessels using the findpeaks function. This data was then used to calculate FWHM averages as well as signal-to-noise ratios for each separate phantom vessel. SNR was calculated by mean peak signal divided by mean background peak signal. Both SNR data and FWHM were plotted against known phantom vessel sizes for Siemens Artis Zeego, Philips Allura mode 1, and Philips Allura mode 2 using local regression line smooth (LOESS) via matlab GRAMM script.

Results

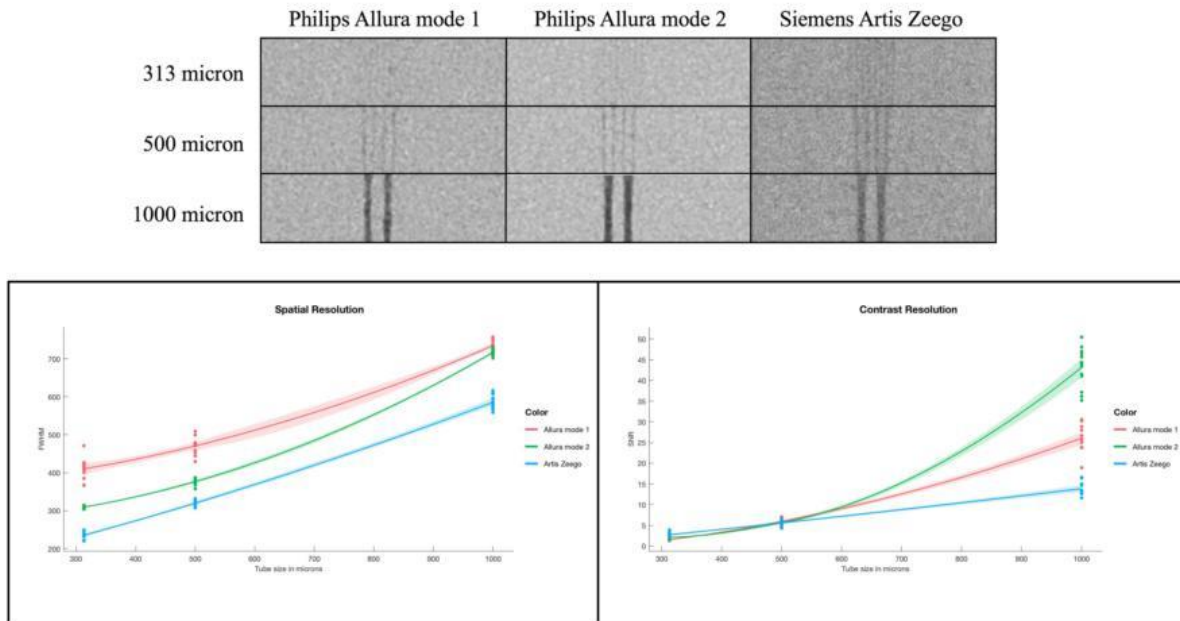
Roadmap Injections into the phantom consisted of the following settings, Dose Rates (mGy/min), KV and mA: Philips Allura mode 1 (10mGy/min, KV 90, mA 12), Philips Allura mode 2 (18mGy/min, KV 81, mA 14), Siemens Artis Zeego (12mGy/min; KV 78, mA 51). When spatial resolution was calculated from

Oral Presentations & Excerpts

DICOM measurements of FWHM (y-axis) and plotted against known phantom vessel sizes in μm (x-axis), Siemens Artis Zeego demonstrates the best spatial resolution for all phantom vessels, as measured by lower FWHM. Contrast resolution was measured by calculating SNR measurements (y-axis) and was plotted by known phantom vessels sizes in μm (x-axis). Both machines had similar contrast resolution at 500 microns; however, Philips demonstrates superior contrast resolution at 1000 microns (42.3 vs. 13.9) whereas Siemens had a slightly higher contrast resolution at 313 microns, as measured by SNR (2.7 vs 2.1).

Conclusions

Our study demonstrates the use of a novel 3-D printed angiographic phantom to simulate realistic vessel diameters and flow dynamics. We also establish a method to automatically calculate SNRs from peak signal values and to extract FWHM values of signals for each of the phantom vessel sizes. Lower FWHM correspond to better spatial resolution. We demonstrate that in this study Siemens Artis Zeego had superior spatial resolution compared to Philips Allura at 313 to 1000 microns, which correlates subjectively to the images. Additionally, Siemens Artis Zeego demonstrates superior contrast resolution at 313 microns compared with Philips Allura with lower dose rates (12mGy/min versus 18 mGy/min). However, Philips Allura demonstrated superior contrast resolution at 1000 microns compared with Siemens Artis Zeego. These calculations provide an objective measure of the spatial resolution and contrast resolution performance of angiographic systems. Furthermore, this phantom and method can be used together as a powerful tool to compare performance of angiographic systems for any liquid contrast or therapeutic agent with potential benefit for both research and clinical practice as part of quality control programs.



(Filename: TCT_O-499_updated.jpg)

Thursday, June 7, 2018
10:30AM - 12:00PM
Parallel Paper Session: Updates in Interventional Neuro

O-500

10:30AM - 10:37AM

Impact of Different Reconstruction Algorithms and Different Slice Thicknesses on an Automated Stroke Software Tool to Detect Early Ischemic Changes

F Austein¹, A Lebenatus¹, P Langguth¹, T Lindner¹, O Jansen¹

¹*University Hospital Schleswig-Holstein, Campus Kiel, Kiel, Schleswig-Holstein, Germany*

Purpose

Identifying differences of evaluation of the established 10-point quantitative topographic CT scan score (Alberta Stroke Program Early CT-Score [ASPECTS]) (1) for the detection of early ischemic changes by an automated computational software tool using different advanced reconstruction algorithms for brain CT (knowledge-based iterative algorithm [IMR] and standard iterative reconstruction [IR]) with different slice thicknesses.

Materials and Methods

We enrolled 50 patients with advanced CT (including native CT, CT angiography and CT perfusion) indicated by suspected acute stroke in the anterior circulation. We reconstructed axial images with IR and IMR using three different slice thicknesses. CT perfusion, follow-up scans and the evaluation of the radiologists served as ground truth to determine the definite infarct area. This retrospective study was approved by our ethics committee.

Results

The preliminary results showed that the automated ASPECT results were significantly influenced by reconstruction algorithms and slice thicknesses.

Conclusions

Automated stroke CT evaluation appears to be significantly influenced by the reconstruction algorithm and slice thickness which could lead to differences in therapeutic decision-making. Further research is necessary for standardization of reconstruction and optimal slice thickness to apply the automated stroke CT in more daily clinical use.

O-501

10:37AM - 10:44AM

Predicting final infarct volume in stroke patients following endovascular treatment using dual-energy CT mixed images

M Mentink¹, M Tijssen², W van Zwam², P Nelemans², A Postma²

¹*University of Maastricht, Maastricht, the Netherlands,* ²*Maastricht University Medical School, Maastricht, the Netherlands*

Purpose

Endovascular treatment (EVT) has become standard-of-care in acute stroke due to large vessel occlusion, after convincing evidence was provided for its effectiveness. Post-EVT CT, either with conventional single-energy CT or dual-energy CT (DECT) is used for evaluation of complications. DECT provides mixed images, which are considered equal to conventional single-energy CT. Additionally, virtual noncontrast (VNC) and iodine overlay images can be calculated for differentiation between contrast enhancement as a result of blood-brain-barrier breakdown (BBB) and hemorrhage. The ability of DECT to differentiate between BBB and bleeding could be a reason for DECT to become the preferred imaging modality after EVT. Follow-up CT is generally performed for treatment evaluation by estimation of final

infarct volume. Alberta Stroke Program Early Computed Tomography Score (ASPECTS) on pre-EVT CT scans can predict outcome in acute stroke patients, but is not predictive of final infarct volume. The ASPECTS quantifies CT changes in middle cerebral artery stroke, ranging from 0 (fully abnormal) -10 (normal) points. The aim of this retrospective study was to evaluate the accuracy of infarct volume estimation on mixed DECT images taken directly after EVT compared to CT taken at 24 hours and 5-7 days follow-up.

Materials and Methods

In this single-center retrospective study, 74 stroke patients that underwent EVT between July 2010 and December 2014 were included. DECT was performed immediately following EVT using a Siemens SOMATOM Definition Flash CT scanner. Simultaneous imaging at 80 kVp and 140 kVp was employed with calculation of mixed images. Patients with incomplete follow-up were excluded. ASPECTS was used for topographic quantification of the infarct of the middle cerebral artery territory. ASPECTS was scored on DECT mixed images and on follow-up CT by a fellow neuroradiology and an experienced neuroradiologist. Volumes were acquired by segmentation of the hypodense areas using ITK-SNAP (www.itksnap.org). Agreement between raters and between images taken immediately after EVT and at early or later follow-up was assessed by 95% limits of agreement (95% LOA) according to Bland-Altman plots and by the intraclass correlation coefficient (ICC).

Results

Of 34 patients follow-up CT data at 24 hours were available and 25 patients of these had 5-7 days follow-up data available. For fellow and neuroradiologist ASPECT scoring the ICC was 0.44 for hypodense infarcted areas on mixed images. Accordingly, 95% LOA ranged from 5.9 to -4.9 (mean difference 0.51). Because of poor interrater reliability, further analysis of agreement between mixed images and follow-up was performed with data of the neuroradiologist. Ninety-five percent LOA of ASPECTS between mixed images and 24 hours ranged from 8.0- -1.7 (mean difference 3.1) and at 5-7 days follow-up from 6.9- -1.3 (mean difference 2.8). Median infarct volumes were 8.6 mL (25-75 quartiles: 2.1-63.2 mL) at DECT mixed images immediately after EVT, 50 mL (25-75 quartiles: 23.7-160.6 mL) at 24 hr follow-up, and 56.1 mL (25-75 quartiles: 22.6-170.6 mL) at 5-7 days follow-up.

Conclusions

The interrater reliability of ASPECTS on post EVT DECT mixed images is poor. Final infarct volume or ASPECTS could not accurately be predicted from post-EVT hypodense areas on DECT mixed images immediately after EVT. Infarcts at follow-up showed lower ASPECTS and higher volume, with a wide range from smaller to larger infarcts. This could be explained by a lower dose scan and thus lower SNR in the mixed images. Probably more important, delineation of the infarcted area is less distinct in comparison with follow-up imaging, due to ill-defined boundaries and enhancement of parenchyma due to BBBB, leading to a higher level of uncertainty and less accurate estimate of infarcted area. Moreover, the ill-defined borders of hypodensity are obscured by enhancement due to BBBB. These areas of BBBB are probably part of the future infarction, and are not depicted as hypodense infarcted areas on mixed images due to parenchymal enhancement. Finally, infarct growth can still be ongoing immediately after EVT due to ongoing metabolic cascades, or be smaller and better demarcated with decrease of vasogenic edema. DECT provides the option to subtract iodine enhancement, in case of BBBB, by calculating VNC, which could improve prediction of final infarction volume.

O-502

10:44AM - 10:51AM

Failure of recanalization is more frequent in proximal ICA and multiple vessel occlusions

F Flottmann¹, H Leischner¹, T Faizy¹, M Deb-Chatterji¹, G Thomalla¹, C Brekenfeld¹, J Fiehler¹, S Gellissen¹

¹University Medical Center Hamburg-Eppendorf, Hamburg, Germany

Purpose

In acute ischemic stroke, mechanical thrombectomy (MT) allows flow restoration in a majority of cases of large artery occlusions. However, in up to 41% of cases, MT fails to achieve successful recanalization. We aimed at identifying predictors of failed recanalization.

Materials and Methods

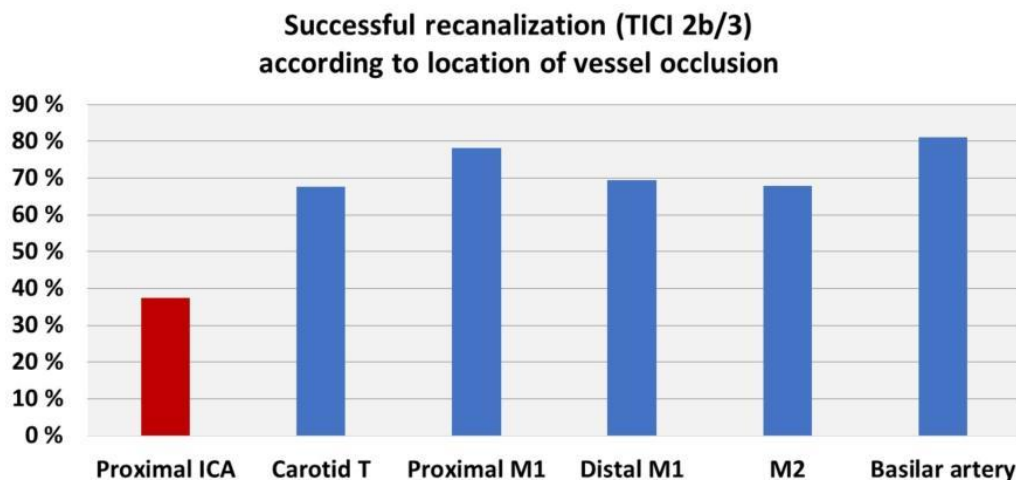
We retrospectively analyzed 287 ischemic stroke patients who received MT. We divided the cohort into patients with failed recanalization (TICI 0-2a) and successful recanalization (TICI 2b-3). Age, sex, comorbidities, NIHSS and ASPECTS score on admission, location of occlusion, number of affected vessels, iv-thrombolysis, times from symptom onset to admission/imaging/groin puncture and flow restoration, type of anesthesia, number of MT-retrievals and stroke etiology were compared.

Results

Failure of recanalization (TICI 0-2a) was significantly more frequently observed in proximal ICA occlusions (62.5% in proximal ICA vs. 25.9% across other locations of occlusion, $p < 0,001$), and when more than one vessel was occluded (47.7% in occlusions of multiple vessels vs. 26.2% in single vessels, $p = 0,004$). Failure of recanalization was associated with longer times from groin puncture to TICI (median 72min vs. 40min, $p < 0,001$).

Conclusions

Proximal ICA occlusions as well as occlusions of multiple vessels might require a different technical approach as opposed to intracranial occlusions of single vessels.



(Filename: TCT_O-502_asnr_failurereca.jpg)

O-503

10:51AM - 10:58AM

TICI 0/1 recanalization- analysis of reasons contributing to unsuccessful endovascular recanalization in stroke patients.

H Leischner¹, F Flottmann², G Broocks², T Faizy³, S Gellissen², M Deb-Chatterji¹, G Thomalla¹, J Fiehler², C Brekenfeld¹

¹University Medical Center Hamburg-Eppendorf, Hamburg, Germany

Purpose

Mechanical thrombectomy (MT) is the most effective therapy in patients suffering acute ischemic stroke due to large vessel occlusion (LVO). However, complete recanalization of the occluded vessel cannot be achieved in all patients, leading to significantly worse clinical outcome. In this study, we investigated the

underlying reasons which are associated with inefficient recanalization and discuss possible approaches to avoid unsuccessful recanalization.

Materials and Methods

Retrospectively analyzed were 648 consecutive stroke patients treated in the years 2010 to 2017 for an occlusion in the anterior circulation as well as none or minimal recanalization assessed according to the thrombolysis in cerebral infarction scale (TICI score of 0 and 1). The rate of patients in whom the aorta, the supraaortic cervical vessels or the intracranial vessels could be accessed was assessed. Furthermore, rate of successful thrombus passage by microguide and microcatheter was evaluated. Number of retrieval attempts, devices and techniques used, duration of the intervention and potential rescue methods were analyzed.

Results

In 72 of 648 consecutive patients, treatment with MT for LVO in the anterior circulation resulted in TICI 0/1. Patient characteristics with regard to age, sex and comorbidities, NIHSS at admission, and occlusion site did not differ between this group and those patients with recanalization (TICI 2a, 2b, and 3). The occlusion site could be reached by microcatheter or aspiration catheter in 79% of the cases. The main reason why the occlusion could not be reached were elongated cervical vessels. Passage of the occluding thrombus was achieved in 58% of the cases. Upon a successful passage, 20% of the cases showed a small degree of recanalization with immediate reocclusion during the intervention. The median number of retrieval attempts was 2 with median duration of angiography of 85 min. (IQR 55- 122). In 42% of the cases two or more devices/techniques were used. There was a significant difference with regard to the time of the procedure if three retrievals were conducted ($p=0,006$).

Conclusions

In patients with a TICI 0 or TICI 1 recanalization the thrombus can be reached in 79% and subsequently passed in 58% of the cases. In these patients rescue therapy (e.g. intracranial stent placement) might improve recanalization rate and clinical outcome. In patients with inaccessible intracranial vessels improved material (e.g. stiff guide catheters) as well as alternative puncture sites (e.g. carotid artery) might facilitate MT in the future.

O-504

10:58AM - 11:05AM

Influence of the time of day on the care of stroke patients undergoing endovascular stroke therapy.

H Leischner¹, F Flottmann¹, T Faizy¹, G Broocks¹, M Deb-Chatterji¹, C Brekenfeld¹, G Thomalla¹, J Fiehler¹, S Gellissen¹

¹*University Medical Center Hamburg-Eppendorf, Hamburg, Germany*

Purpose

The number of mechanical thrombectomies (MT) in patients with an acute stroke increased over the last couple of years. Admission and treatment of stroke patients is available 24 hours a day, i.e. during on-call duty (OC) or routine hours (RH). We hypothesized that the care and clinical outcome of stroke patients differs depending on treatment time during OC or RH.

Materials and Methods

Retrospectively analyzed were 194 consecutive stroke patients who underwent endovascular treatment. These patients were categorized into two groups according to their time of admission, RH-group treated weekdays from 8:00am-5:00pm, OC-group 5pm-8am and on weekends. Procedural aspects such as time "imaging to groin", "symptom to groin", "symptom to recanalization", TICI score, number of retrieval attempts and number of used devices were compared between the two groups. Further, patient characteristics as well as clinical outcome parameters such as score on the modified Rankin Scale (mRS) after 24hrs (mRSd1) and 90 days (mRSd90), NIH stroke scale score on day 1 after admission (NIHSSd1) and NIHSS on the day of discharge were investigated. In future steps of the project, more patients will be analyzed.

Oral Presentations & Excerpts

Results

The time "imaging to groin" ($p=0.019$), "symptom to groin" ($p=0.001$) and "symptom to recanalization" ($p=0.001$) was longer in the OC-group. In addition, the NIHSSd1 was significantly higher in the OC-group (median NIHSSd1 18) than in the RH-group (median NHSSd1 of 12). The same held true for the NIHSS on the day of discharge, which was significantly higher in the OC-group (median of 7) compared to the RH-group (median 10). No difference could be observed for the mRSd1 or mRSd90. With regard to the procedural parameters such as number of retrieval attempts, thrombolysis in cerebral infarction (TICI) scale score or other clinical characteristics, e.g. comorbidities, no significant difference ($p>0.05$) could be found.

Conclusions

Care of acute stroke patients undergoing MT during on-call duty appears to be more time-consuming and therefore could contribute to the inferior clinical outcome compared to patients who are treated during routine hours. Optimizing the on-call procedures and sensitizing the staff would be an improvement approach.

O-505

11:05AM - 11:12AM

Applicability of the SWIFT-PRIME inclusion criteria on an unselected patient population.

H Leischner¹, F Flottmann¹, G Broocks¹, T Faizy¹, C Brekenfeld¹, M Deb-Chatterji¹, G Thomalla¹, J Fiehler¹, S Gellissen¹

¹University Medical Center Hamburg-Eppendorf, Hamburg, Germany

Purpose

The results of the Solitaire with the Intention for Thrombectomy as Primary Endovascular Treatment (SWIFT-PRIME) trial have demonstrated the benefit of mechanical thrombectomy (MT) to acute stroke patients. Since the inclusion and exclusion criteria of SWIFT-PRIME are highly selective, we hypothesized that the SWIFT-PRIME results can only be applied to a very small group of patients treated in our institution.

Materials and Methods

Retrospectively analyzed were 185 consecutive acute stroke patients treated with MT and grouped according to their fulfilment of the inclusion and exclusion criteria of the SWIFT-PRIME trial (SP-pos and SP-neg). We compared the demographic and clinical characteristics (e.g. NIH stroke scale score on admission) as well as functional outcomes at 90 Days, according to the score on the modified Rankin scale (mRS90).

Results

Of the 186 patients, 18 (9,6%) met the inclusion and exclusion criteria of the SWIFT-PRIME study. With regard to the mRS at 90 days there was no significant difference between the SP-pos group (median 2) and the published data of the SWIFT-PRIME trial (median 2). The same could be observed with regard to the NIHSS on admission (median of 17 in both groups). The most frequent criteria that led to exclusion were i.v. lysis (70 patients), symptom to groin time >6hrs (87 patients) and ASPECTS>6 (82 patients). Within the next months, more patients will be included and we will also apply the criteria of the MrClean, ESCAPE and DAWN trial to our collective of unselected patients.

Conclusions

The results of SWIFT-PRIME only apply to a small group of patients presented to us in clinical routine. This is of importance when interpreting the clinical outcome of the patients who are treated in our institution.

O-506

11:12AM - 11:19AM

Degree of Conjugate Gaze Deviation on Computed Tomography Scan Predicts Proximal Vessel Occlusion and Expedite Candidates for Endovascular Therapy

n jiang¹, C Fong¹, D Sahlas¹, R Larrazabal¹
¹Hamilton Health Sciences, Hamilton, Ontario, Canada

Purpose

Recently trials have demonstrated superior outcomes with combination IV-tPA and endovascular therapy (EVT) within six hours of symptom onset in patients with proximal vessel occlusion (ICA, M1, proximal M2). The current gold standard of diagnosis is CT angiogram (CTA). Unfortunately, not all hospitals are equipped with CTA capability, and often the decision to transfer patient to tertiary center is based on nonenhanced CT. Conjugate gaze deviation (CGD) is associate with worse outcome in ischemic stroke and we predict that the more proximal the occlusion, the higher degree of CGD. Measuring degree of CGD can help expedite the transfer of patients to CTA/EVT capable facility.

Materials and Methods

A retrospective analysis was performed on 158 consecutive patients with acute ischemic stroke treated with IV-tPA at a tertiary center over 12-month period. Patients were categorized based on stroke location. Degree of CGD was measured. Demographics, ASPECT, National Institutes of Health Stroke Scale (NIHSS), modified Rankin Scales, length-of-stay, and mortality were collected.

Results

Of the 70/158 patients with +CGD, 66 (93%) patients have MCA strokes. Of the 70 MCA patients, 59 (84%) have proximal MCA stroke and seven (16%) have distal MCA stroke. The median degree of CGD is 16° in proximal and 2° in distal stroke. CGD is positively correlated with proximal stroke (p=0.011). Higher degree of CGD is demonstrated in proximal stroke as compared to distal MCA stroke.

Conclusions

Measuring the degree CGD may be a practical clinical tool in identifying patients with proximal occlusion in acute stroke evaluation and, therefore, expedite transfer of appropriate patients to a tertiary stroke facility for endovascular therapy.

Table 1

	Stroke type							Total
	Basilar	Internal Carotid	M1	M1/M2	MCA distal	None identified*	Vertebral	
gaze_deviation no	7	13	33	3	16	14	2	88
gaze_deviation yes	1	16	38	5	7	3	0	70
Total	8	29	71	8	23	17	2	158

* Small vessel occlusion or occlusion not identified on CTA

Table 2

Stroke type	N	Mean	95% Confidence Interval	
			Lower Bound	Upper Bound
Internal Carotid	29	16.190	11.928	20.451
M1	70	14.293	11.550	17.036
M1/M2	9	16.000	8.350	23.650
MCA distal	26	2.5385	.864	9.866
No identified*	19	4.184	-1.081	9.449
Vertebral	2	2.750	-13.478	18.978
Basilar	8	3.188	4.927	11.302

* Small vessel occlusion or occlusion not identified on CTA

Figure 1



Table 1: Presence of CGD and types of ischemic stroke

Table 2: Degree of conjugate gaze deviation and stroke types

Figure 1: Measuring Gaze Deviation as proposed by Coffman et al., 2015.

(Filename: TCT_O-506_TablesandFiguresASNR.jpg)

O-507

11:19AM - 11:26AM

Early Cerebral Vein After Endovascular Ischemic Stroke Treatment Predicts Symptomatic Reperfusion Hemorrhage

Oral Presentations & Excerptas

S Cartmell¹, R Ball¹, R Kaimal¹, N Telischak², M Marks¹, H Do¹, R Dodd¹, M Lansberg¹, G Albers¹, J Heit¹

¹Stanford University Hospital, Stanford, CA, ²California Pacific Medical Center, San Francisco, CA

Purpose

Symptomatic parenchymal hemorrhage (PH) after endovascular thrombectomy (EVT) of acute ischemic stroke (AIS) can lead to worse outcomes. Better clinical and imaging biomarkers of reperfusion PH are needed to identify at-risk AIS patients. We investigated clinical and imaging predictors of symptomatic PH following EVT with attention to early cerebral veins (ECV) on postreperfusion digital subtraction angiography (DSA).

Materials and Methods

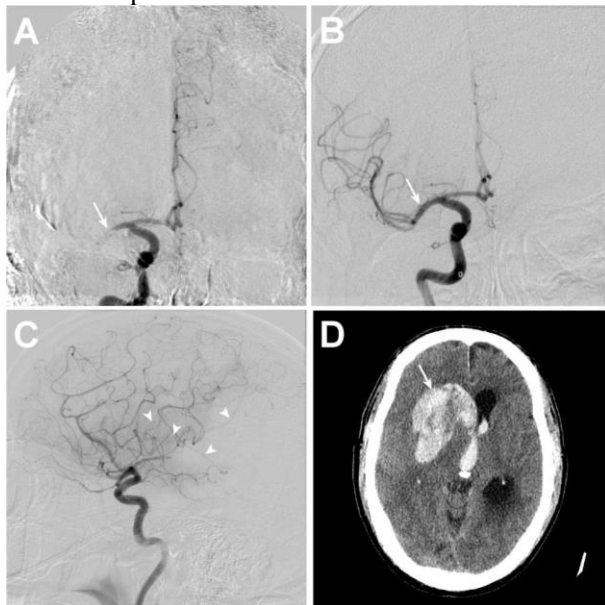
We performed a retrospective cohort study of consecutive anterior circulation large-vessel AIS patients undergoing EVT at our neurovascular referral center. Clinical and imaging characteristics were collected, and the random forest variable importance measure was used to identify the characteristics most predictive of symptomatic PH, defined as the appearance of ECASS PH1 or PH2 on post-treatment imaging with associated NIHSS change of ≥ 3 . Predictors of secondary outcomes, including 90-day mortality, 90-day functional independence ($mRS \leq 2$), and change in NIHSS score during the hospital stay were determined using the same methodology. Diagnostic test characteristics of ECV were determined using ROC analysis. Differences in characteristics between symptomatic PH +/- groups were assessed with the Fisher's exact test for categorical variables and the Wilcoxon rank sum (Mann-Whitney) test for continuous variables at the 0.05 significance level.

Results

Of 64 patients with anterior circulation large vessel (ICA or M1) occlusion included in this analysis, six (9.4%) developed symptomatic PH. ECV was the strongest predictor of subsequent hemorrhage, having approximately twice the importance of the next best predictor--male sex. Although ECV was also predictive of 90-day mortality and functional independence, other characteristics were more important than ECV for these outcomes. The sensitivity and specificity of ECV for subsequent hemorrhage were both equal to 83% with AUC of 0.83 with 95% confidence interval of [0.66, 1].

Conclusions

ECV on post-EVT DSA is highly diagnostic of subsequent symptomatic reperfusion hemorrhage. The appearance of this finding has important implications for post-treatment management of anticoagulation and blood pressure.



(Filename: TCT_O-507_Figure2DSAECV.jpg)

O-508

11:26AM - 11:33AM

Examination of radiation exposure imparted to adults undergoing various procedures in the neurointerventional setting

N Guberina¹, M Forsting², A Wetter³

¹*Institute of Diagnostic and Interventional Radiology and Neuroradiology, Essen, GA,* ²*Institute of Diagnostic and Interventional Radiology and Neuroradiology, University Hospital Essen, Essen, AZ,* ³*University Hospital Essen, Essen, Germany*

Purpose

The study aimed to examine radiation exposure in terms of diagnostic reference levels imparted to adults undergoing various neurointerventional procedures.

Materials and Methods

In a retrospective study design diagnostic reference levels (DRLs, 75th percentile of dose distribution) were examined for adults undergoing various standardized neurointerventional procedures after strict clinical and interdisciplinary indication as well as giving informed consent: (I) diagnostic interventional angiography; (II) mechanical thrombectomy; (III) inefficient mechanical thrombectomy; (IV) endovascular treatment of arteriovenous pathologies; (V) aneurysm coiling; (VI) endovascular angioplasty and stenting, (VII) vasospasm treatment. All neurointerventional procedures were performed on the flat panel angiography system Allura Xper (Philips Healthcare, Eindhoven, the Netherlands) at a large multicenter institute. Altogether, the data of 454 neurointerventional procedures were included in the time period from March 2016 - March 2017. Radiation doses were assessed with the help of dose monitoring software Radimetrics Enterprise Platform (Bayer Healthcare, Leverkusen, Germany).

Results

In detail, the following DRLs [mean value; standard deviation SD; dose range min.-max.] were assessed for the randomized patient collective: (I) diagnostic interventional angiography 25.8 Gy_{cm}² [24.8 Gy_{cm}²; 18.3; 11.2-85.4]; (II) mechanical thrombectomy 54.6 Gy_{cm}² [37.6 Gy_{cm}²; 44.3; 11.7-190.9]; (III) inefficient mechanical thrombectomy 73.3 Gy_{cm}² [46.5 Gy_{cm}²; 32.9; 13.8-101.1]; (IV) endovascular treatment of arteriovenous pathologies 162.0 Gy_{cm}² [103.7 Gy_{cm}²; 96.9; 12.7-206.1]; (V) aneurysm coiling 189.4 Gy_{cm}² [122.9 Gy_{cm}²; 70.6; 13.7-222.8]; (VI) endovascular angioplasty and stenting 78.1 Gy_{cm}² [43.0 Gy_{cm}²; 39.8; 11.7-118.3]; (VII) vasospasm treatment 50.9 Gy_{cm}² [33.7 Gy_{cm}²; 19.1; 11.3-68.7].

Conclusions

Determination of DRLs is the first step for dose optimization in the neurointerventional setting. Examination and monitoring of radiation exposure imparted to adult patients during various neurointerventional procedures is inevitable for a trans-institutional benchmarking.

O-509

11:33AM - 11:40AM

Percutaneous radial arterial approach as an alternative access for neurointerventional stroke treatment and coil embolization: report of 14 cases and review of literature.

D Volders¹, C Haw¹, M Heran²

¹*University of British Columbia, Vancouver, British Columbia, Canada,* ²*Vancouver General Hospital, Vancouver, British Columbia, Canada*

Purpose

As demonstrated in the Matrix Access Trial, radial as compared with femoral access reduces net adverse

Oral Presentations & Excerptas

clinical events, through a reduction in major bleeding and all-cause mortality in acute coronary syndrome patients undergoing invasive management. We want to demonstrate our radial access experience in neurointerventional thrombectomy and embolization procedures in this retrospective study.

Materials and Methods

Between December 2014 and November 2017, 14 patients underwent neurointerventional endovascular treatment using percutaneous ultrasound-guided radial arterial access. The patient group consisted of nine male and five female patients, aged 49 to 96 years (mean 73 years). In the majority (4/14), the procedure was performed for an acute basilar artery occlusion. The remainder was treated for recurrent vertebral artery emboli (3/14), posterior circulation aneurysms (2/14), dural arteriovenous fistulas (2/14) and high grade stenosis (2/14). One case was management of epistaxis due to bleeding internal maxillary artery pseudoaneurysm. In all cases, a preprocedural modified Barbeau test was performed. A Terumo radial access kit was used with 200 mcg of nitroglycerin, 2.5 mg of verapamil and 2000 units of heparin administered through the Slender sheath in order to optimize local perfusion while performing the neurointerventional procedure.

Results

Radial over femoral access was preferred due to hostile anatomy (vessel tortuosity, type III aortic arch) (13/14), and as an aid to management of critical supra-aortic stenosis (1/14). In the four thrombectomy and three aneurysm coiling cases of the posterior circulation, we were able to successfully place the guide catheter within the mean posterior circulation vessel 10 minutes from wrist puncture (Panel A + B). All procedures went uneventfully with no complications at the puncture site after sheath removal.

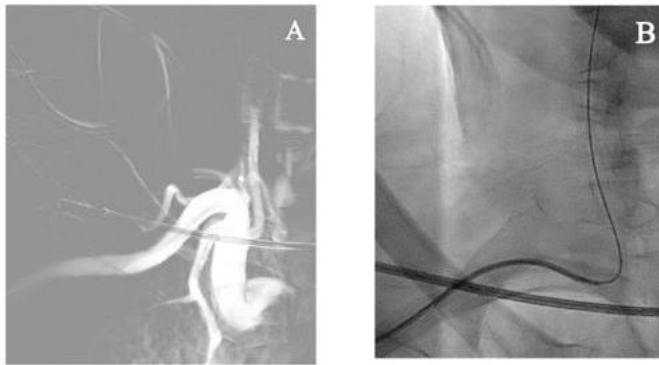
Conclusions

Radial access can be used as a safe and effective alternative to traditional transfemoral arterial approach for a variety of neurointerventional procedures, including thrombectomy and aneurysm management.

Table

Age/Sex	Pathology	Indication for Radial Access	Procedural Result	Complications
73/M	acute basilar artery occlusion	tortuosity	complete recanalization	no
51/M	acute basilar artery occlusion	tortuosity	complete recanalization	no
77/M	acute basilar artery occlusion	tortuosity + type III arch	complete recanalization	no
59/M	recurrent vertebral artery emboli	tortuosity	complete occlusion	no
79/M	recurrent vertebral artery emboli	tortuosity	complete occlusion	no
49/M	acute basilar artery occlusion	tortuosity	complete recanalization	no
83/M	high grade basilar artery stenosis	tortuosity	complete recanalization	no
83/F	internal maxillary pseudoaneurysm	tortuosity + type III arch	complete occlusion	no
96/F	posterior fossa dural AVF	tortuosity + type III arch	successful embolization	no
92/F	posterior fossa dural AVF	tortuosity	successful embolization	no
83/M	posterior circulation aneurysm	tortuosity	successful embolization	no
61/M	recurrent vertebral artery emboli	tortuosity	successful embolization	no
78/F	posterior circulation aneurysm	tortuosity	successful embolization	no
73/F	hemispheric hypoperfusion	critical stenosis	complete recanalization	no

Figure



(Filename: TCT_O-509_Images.jpg)

O-510

11:40AM - 11:47AM

Comparative Effectiveness Analysis of Pipeline Device versus Coiling in Unruptured Aneurysms <10 mm

X Wu¹, B Geng¹, L Tu¹, V Kalra², C Matouk¹, D Gandhi³, P Sanelli⁴, A Malhotra⁵
¹Yale University School of Medicine, New Haven, CT, ²Orlando Health, Tampa, FL, ³University of Maryland School of Medicine, Baltimore, MD, ⁴Northwell Health, Manhasset, NY, ⁵Yale New Haven Hospital, New Haven, CT

Purpose

Both endovascular coiling and the Pipeline Embolization device (PED) have been shown to be safe and clinically effective for treatment of small (<10 mm) aneurysms. We conducted a comparative effectiveness analysis to compare their utility in terms of health benefits.

Materials and Methods

A decision-analytical study was performed with Markov modeling methods to simulate patients with small unruptured aneurysms undergoing endovascular coiling versus PED for treatment. Input probabilities were derived from prior literature, and one-way, two-way and probabilistic sensitivity analyses were performed to assess model and input parameter uncertainty.

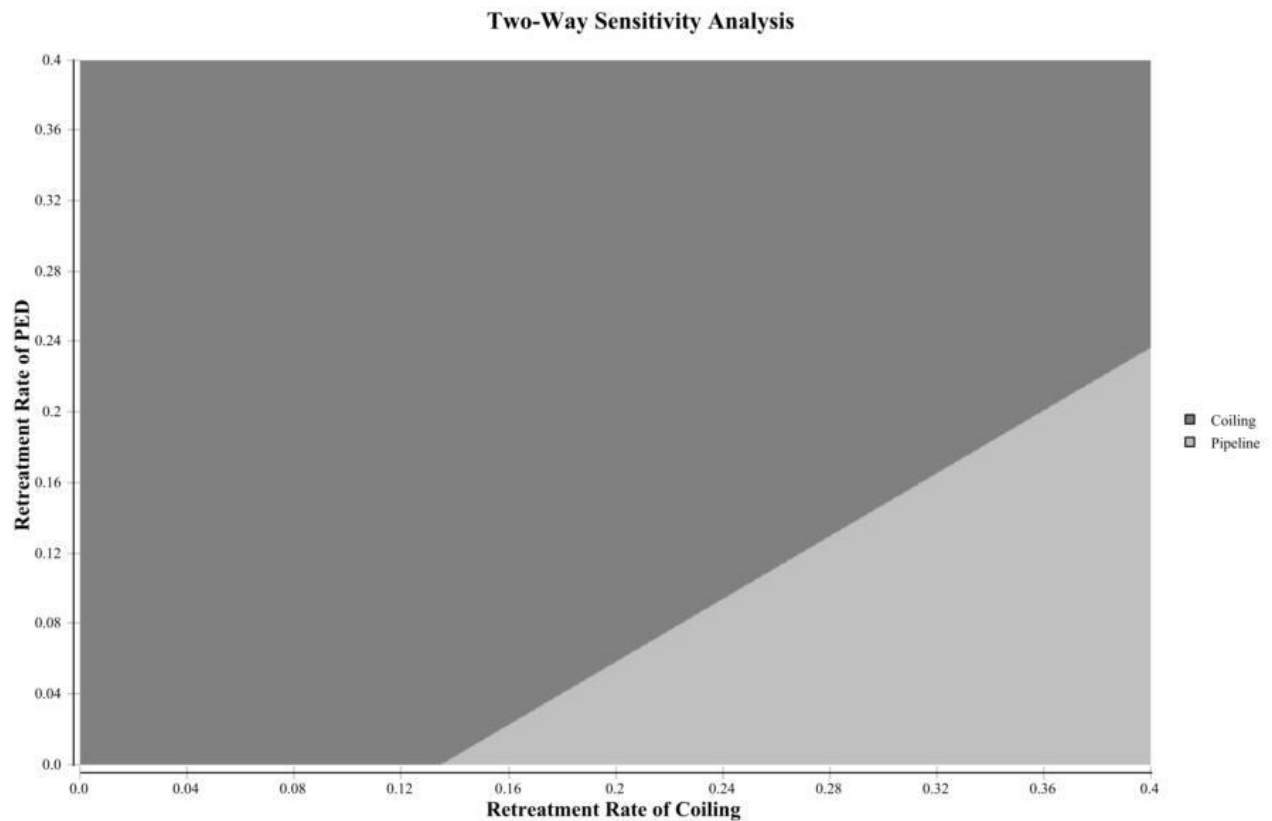
Oral Presentations & Excerptas

Results

The base case calculation for a 50-year old male reveals PED to have a higher health benefit (17.48 quality-adjusted life years [QALY]) than coiling (17.44 QALY). PED is the better option in 6,141 of the 10,000 iterations in probabilistic sensitivity analysis. When the retreatment rate of PED is lower than 9.53%, and the coiling retreatment is higher than 15.6%, PED is the better strategy. In the two-way sensitivity analysis varying the retreatment rates from both treatment modalities, when the retreatment of PED is approximately 14% lower than the retreatment of coiling, PED is the more favorable treatment strategy. Otherwise, coiling is more effective. The final conclusion is highly sensitive on the morbidity and mortality rates of PED and coiling, and PED remains the better strategy even when its morbidity and mortality rates are 7.6% higher than the base case values.

Conclusions

With the increasing use of PED for treatment of small unruptured aneurysms, our study indicates that PED may have higher health benefits, due to lower rates of retreatment. Longer follow-up studies are needed to document the rates of recurrence and retreatment after coiling and PED to assess cost effectiveness of these strategies.



(Filename: TCT_O-510_ASNRfigure.jpg)

Thursday, June 7, 2018

10:30AM - 12:00PM

Parallel Paper Session: Quantitative Imaging: Advanced Techniques and Methods

O-512

10:30AM - 10:37AM

Understanding impact of rotation of encoding vector during image pre-processing on tract specific diffusion metrics in deterministic tractography

P Lee¹, G Jindal², N Shekhrjka¹, G Banks¹, S Sheth¹, N Vanegas-Arroyave¹, S Jambawalikar³, A Lignelli³, P Dubey⁴

¹New York Presbyterian Hospital, New York, NY, ²Warren Albert School of Medicine, Brown University, Providence, RI, ³Columbia University Medical Center, New York, NY, ⁴Scarsdale, NY

Purpose

Echo planar imaging (EPI) is the commonly used readout format for diffusion weighting in standard clinical practice. Image preprocessing with rigid or nonrigid transformations are used to mitigate confounds related to EPI acquisitions, motion and eddy currents. However, preprocessing is often inconsistent in clinical settings, largely due to vendor specific variations. Most clinically available tractographic platforms do not account for rotational adjustment of B matrix after preprocessing. In this study we evaluate the variation induced by image preprocessing in tract specific quantification using deterministic approach.

Materials and Methods

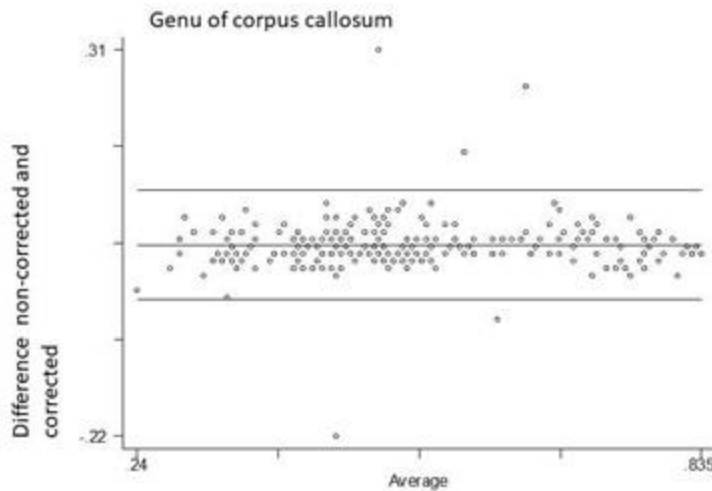
Five patients being evaluated for Deep Brain Stimulation were retrospectively analyzed for this study. Diffusion MRI images were acquired on a 3T GE signa MRI. Diffusion-tensor imaging (DTI) was performed for four patients with B value=1000 s/mm², 1 nondiffusion-weighted image and 64 diffusion encoding directions, isotropic voxel of 2 mm x 2 mm x 2 mm, TE=107.2, acquisition matrix=120x120. For the fifth patient, a nonisotropic voxel of 2.6 x 1.875 x 2.5 mm was used. Image analyses were performed using DTI studio software. For preprocessing, each diffusion-weighted image was registered to the nondiffusion-weighted image (B0) using rigid transformation. Manual inspection was performed for accuracy. Subsequently any rotation applied to the diffusion volume was also applied to the encoding vector (B matrix). Tensor calculation was performed using standard linear regression with and without image preprocessing. Three-D tractography was performed using FACT approach with FA threshold of 0.2 and angle threshold of 40 degrees. Left Corticospinal tract (CST) and Genu of corpus callosum (GCC) were reconstructed using previously published protocols. Fractional Anisotropy was measured as a function of length along CST and GCC. STATA version 11.2 was used for statistical analyses.

Results

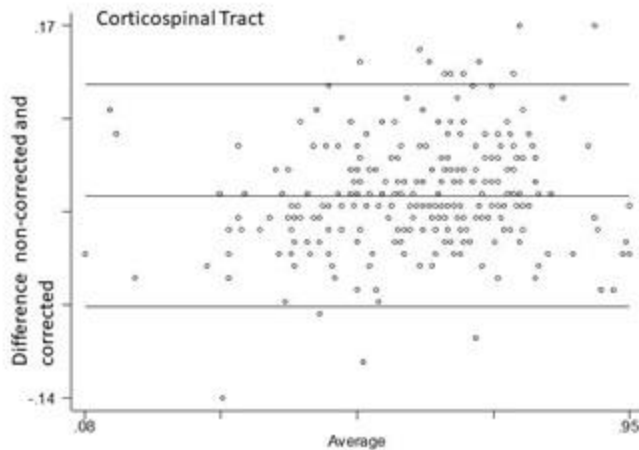
Mean FA measurements were obtained at each point along the length of CST and GCC across slices in axial and coronal planes respectively without and with image preprocessing including mirroring application of rotation of diffusion volume to the encoding vector. Bland Altman analyses showed a fixed bias between measurements made with and without correction including rotational adjustment of encoding vector. For CST noncorrected vs. corrected the mean difference was 0.029, and 95% CI was 0.023 to 0.034. For GCC, mean difference was 0.042 and 95% CI was 0.037 to 0.047. Analyses of variance shows a trend of higher variability with the noncorrected FA measurements, (p=0.1).

Conclusions

Our results show a significant impact of image preprocessing including rotational adjustment of encoding vectors on tract specific FA measurements in both CST and GCC. Significant differences in FA can affect both tract delineation and integrity of white-matter pathways. This suggests important implications for standardization of preprocessing protocols particularly when precision in tract-based quantitative measurements is clinically important.



Limits of agreement (Reference Range for difference): -0.033 to 0.117
 Mean difference: 0.042 (CI 0.037 to 0.047)
 Range : 0.240 to 0.835
 Pitman's Test of difference in variance: $r = 0.035$, $n = 237$, $p = 0.593$



Limits of agreement (Reference Range for difference): -0.064 to 0.122
 Mean difference: 0.029 (CI 0.023 to 0.034)
 Range : 0.080 to 0.950
 Pitman's Test of difference in variance: $r = 0.147$, $n = 274$, $p = 0.015$

(Filename: TCT_O-512_GCCandCSTnoncorrectedvscorrectd.jpg)

O-513

10:37AM - 10:44AM

Tract based fractional anisotropy as a function of tract length using deterministic 3D tractography

P Lee¹, G Jindal², N Shekhrajka¹, G Banks¹, S Sheth¹, N Vanegas-Arroyave¹, S Jambawalikar³, A Lignelli³, P Dubey⁴

¹New York Presbyterian Hospital, New York, NY, ²Warren Albert School of Medicine, Brown University, Providence, RI, ³Columbia University Medical Center, New York, NY, ⁴Scarsdale, NY

Oral Presentations & Excerptas

Purpose

Quantitative diffusion-tensor imaging (DTI) is commonly employed for assessment of structural integrity of white matter in research and clinical settings. Conventional summary estimates such as mean and median are used to quantify tract integrity. However, the within-tract heterogeneity of diffusion metrics based on morphologic organization of white matter is not adequately understood. In this study we evaluated variation in tract-based diffusion metrics as a function of tract length with 3-D reconstructions of corticospinal tract using deterministic tractography.

Materials and Methods

Five patients being evaluated for Deep-Brain Stimulation were retrospectively analyzed for this study. Diffusion MRI images were acquired on a 3T GE signa MRI. Diffusion-tensor imaging (DTI) was performed for four patients with B value=1000 s/mm², one nondiffusion-weighted image and 64 diffusion encoding directions, isotropic voxel of 2 mm x 2 mm x 2 mm, TE=107.2, acquisition matrix=120x120). For the fifth patient, a nonisotropic voxel of 2.6 x 1.875 x 2.5 mm was used. Image analyses were performed using DTI studio software. For preprocessing, each diffusion-weighted image was registered to nondiffusion-weighted image (B0) using rigid transformation. Manual inspection was performed for accuracy. Tensor calculation was performed using standard linear regression. Three-D tractography was performed using FACT approach with FA threshold of 0.2 and angle threshold of 40 degrees. Left corticospinal tract (CST) was reconstructed using previously published protocols. Fractional anisotropy was measured as a function of length along CST. STATA version 11.2 was used for statistical analyses.

Results

Mean FA measurements were obtained at each point along the length of CST in the axial plane. There was a significant variation of FA measurement along the length of the CST tract (p<0.0001). Further subdivision of tract length into four equal segments shows a significant nonlinear trend (p<0.0001), with greatest FA measurement corresponding to mid to lower tract segment (2nd quartile), followed by lowest (top quartile), and least in the upper tract segments (3rd and 4th quartiles). Anatomically, the mid to lower tract segment corresponds to the upper pons and midbrain and the lowest tract segment corresponds to lower pons and medulla.

Conclusions

Our results show significant variability of tract based FA measurement as a function of tract length. We found that the highest tract based FA estimates correspond to the midbrain and pons with a graded loss of FA more superiorly towards the cortex. These findings underscore the importance of location specific segmentation for FA analysis, often underestimated by the conventionally employed summary estimates such as mean or median.

O-514

10:44AM - 10:51AM

Neuroimaging Microglia: Development of a Quantitative Multi-Compartment Diffusion MRI Biomarker of Microglial Activation and Neuroinflammation

J Yu¹, S Yi¹, B Barnett¹, M Torres Velazquez¹, J Anderson¹

¹University of Wisconsin-Madison, Madison, WI

Purpose

Brain-immune interactions contribute to numerous acute and chronic disorders of the central nervous system (CNS) from ischemic stroke and traumatic brain injury to age-related dementia and Alzheimer's disease. Schizophrenia, major depression, and other neuropsychiatric disorders also exhibit hallmarks of neuroinflammation where peripheral cellular and humoral immunological abnormalities are more prevalent in psychiatric patients than in healthy controls. Genome-wide studies in schizophrenia have also revealed an association with markers in the major histocompatibility complex region (MHC) and postmortem studies have provided evidence of increased microglial populations and microglial activation

Oral Presentations & Excerpts

in patients with schizophrenia, depression, and other affective disorders. With a growing recognition of the role that microglial-mediated neuroinflammation plays in the neuropathogenesis of psychiatric disorders, there is significant interest in the development of new methodologies aimed at imaging neuroinflammation, microglial populations, and their distribution throughout the brain. However, many current imaging methodologies are encumbered by significant limitations including low specificity (diffusion-tensor imaging [DTI]), challenges to quantification (PET imaging of translocator protein [TSPO]), and low biocompatibility/toxicity (microparticles of iron oxide [MPIO]). Despite active research efforts to overcome these limitations, there remains no safe, widely accessible, or clinically viable neuroimaging methodology available for the in vivo study of neuroinflammation.

Materials and Methods

Microglial activation is induced in a rat model of peripheral inflammation via a single intraperitoneal (ip) injection of lipopolysaccharide (LPS). Briefly, male rats are injected with a single ip dose of LPS or vehicle (n=8, each group). Three hours post injection, all animals are transcardially perfused with PFA and brains cleanly dissected from the cranial vault. Brains are simultaneously imaged with a 4.7-T Agilent MRI system and a 3.5-cm diameter quadrature volume RF coil was used to acquire 10 nondiffusion-weighted images ($b=0 \text{ s}\cdot\text{mm}^{-2}$) and 75 diffusion-weighted images (25: $b=800 \text{ s}\cdot\text{mm}^{-2}$, 50: $b=2,000 \text{ s}\cdot\text{mm}^{-2}$). Following standard preprocessing, tensors are reconstructed, registered, and normalized to a population-specific template. In parallel, NODDI parameters were estimated using an ex-vivo fitting model and converted to volumetric parameter maps. Transformation fields from corresponding single-shell data registration were applied to NODDI data. NODDI data were then projected onto the previously defined white-matter skeleton that was created from single-shell diffusion tract-based spatial statistics (TBSS). TBSS were computed to evaluate whole-brain voxel-wise differences in standard diffusion indices and NODDI parameters between LPS and vehicle treated animals. Permutation test results for multiple comparisons and threshold-free cluster enhancement (TFCE) are implemented with FSL's Randomize and considered significant at the <0.05 level following family-wise error correction. Following imaging, brains were removed from their custom holders and were returned to ice-cold 4% PFA for 24 hours. After cryoprotection with 30% sucrose in 1X PBS, 40 μm coronal floating sections were collected in 1X PBS and stored at 4C until staining. Immunostaining and fluorescence quantification with Iba-1, NeuN, and GFAP were then performed per protocol.

Results

TBSS and ROI analysis reveals numerous clusters of significantly increased voxel-wise change in ODI three hours following intraperitoneal injection of LPS (Figure 1). Notably, no voxel-wise changes are seen in any scalar measures of the diffusion tensor (FA, MD, AD, RD) or in parametric measures of NDI thus confirming the unique sensitivity of ODI to morphometric changes in activated microglia in model of microglial activation. Concurrently performed quantitative immunofluorescence demonstrates significant changes in microglial populations in calculated imaging ROIs buttressing both the sensitivity and specificity of ODI to microglial populations.

Conclusions

Neuroinflammation underlies numerous neurologic and neuropsychiatric disorders and noninvasive biomarkers to detect and monitor microglial inflammation are needed. Multicompartment diffusion-tensor models such as NODDI allow for the direct biophysical interrogation of neurite density and orientation but also fortuitously permit the simultaneous interrogation of the extracellular compartment and the neuropathological changes that can occur within this space including changes related to microglia-mediated neuroinflammation. We will present the potentially groundbreaking application of NODDI to measure changes in the extracellular compartment to noninvasively detect and measure microglial burden in the brain. Ongoing work will determine the quantitative relationship between microglial density with parametric measures of NODDI with quantitative immunofluorescence and stereology. If successful, the validation of NODDI to detect and monitor microglial neuroinflammation would represent a major advance across a wide spectrum of neurologic and neuropsychiatric disorders with far reaching implications in clinical diagnosis, risk stratification, and therapeutic monitoring where a NODDI

biomarker of neuroinflammation could serve as a clinical endpoint assisting in the development of critically needed therapies.

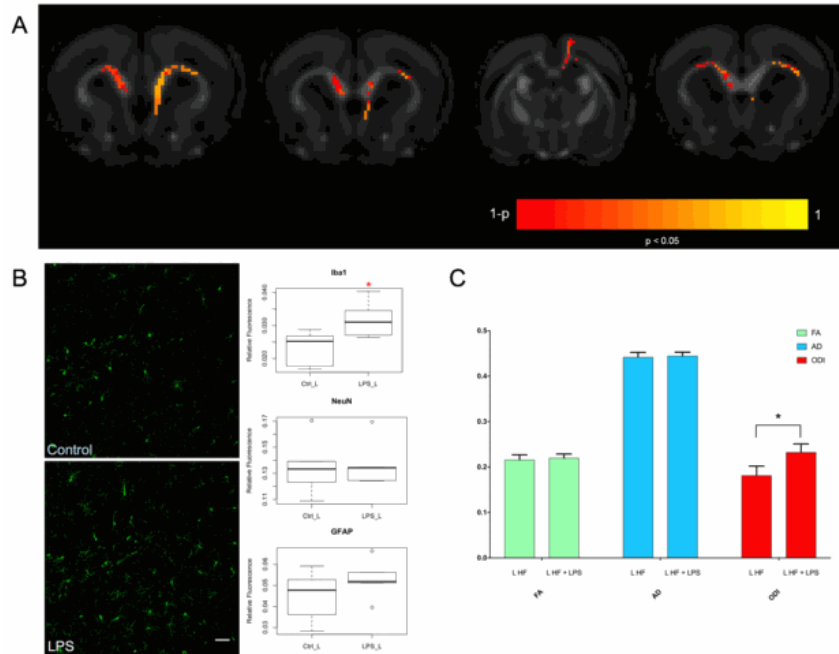


Figure 1:

(A) Tract-based spatial statistics (TBSS) analysis reveals voxel-wise changes in ODI in the rodent brain 3 hours following acute microglial activation following peripheral LPS administration with changes identified in the bilateral corpus callosum as well as in the left retrosplenial cortex (L-R, anterior-posterior) (n=6). No significant differences were identified in TBSS analyses of scalar measures of the diffusion tensor (FA, MD, AD, RD) or in parametric measures of NDI thus confirming the unique sensitivity of ODI to morphometric changes in activated microglia.

(B) Confocal microscopy of the dentate gyrus of the left hippocampus from vehicle (n=6) and LPS (n=6) treated rats 3-hours post-injection (scale bar, 40 μ m). Sections were stained with anti-Iba1 (microglia); anti-NeuN (neuron) and anti-GFAP (astrocyte) staining not shown here for clarity. Fluorescence signal from Iba1, NeuN, and GFAP were quantified and normalized to the area of hippocampus. A significant difference was found for Iba-1, consistent with microglial activation.

(C) DTI and NODDI region of interest analysis of the left dentate gyrus corresponding to the same area of quantitative immunofluorescence (qIF) performed in panel B. No significant differences were found in scalar measures of the diffusion tensor; a significant increase in parametric measures of ODI were identified between vehicle and LPS treated rats (n=6) corresponding to the significant increase in microglia demonstrated in our qIF data. The observed increase in ODI reflects the increased surface area and number of projections present in activated microglia and the predicted subsequent increase in hindered diffusion present within the extracellular compartment.

(Filename: TCT_O-514_ASNRAbstractFigure.gif)

O-515

10:51AM - 10:58AM

Diffusion Tensor Imaging to Investigate Diet-induced Changes in Neuronal Tissue Microstructure and Organization

M Torres Velazquez¹, M Meyerand¹, J Yu¹

¹University of Wisconsin-Madison, Madison, WI

Purpose

Alterations in gut microbiome composition have been associated with several neurodevelopmental and psychiatric disorders (1). In animal models, modifications of gut microbiome populations through dietary manipulation influence brain function and behavior, and have been shown to influence behavioral symptoms (2-3). The purpose of this research is to explore whether these behavioral changes are also accompanied by corresponding changes in neural tissue microstructure by employing diffusion-tensor imaging (DTI).

Materials and Methods

Male rats were assigned to one of four purified and irradiated diets: a control diet, a high-fat diet, a high-fiber diet, and a high-protein diet. Animals were fed the experimental diets immediately post weaning for a total of 21 days. At postnatal day (PND) 42, animals from each diet cohort (total n=20, n=5 per diet group, PRE) were sacrificed and brains dissected. The remaining animals (total n=24, n=6 per diet group, POST) were crossed over and remained on the control diet for an additional 21 days, whereupon the brains were isolated in a similar fashion. Brains were ex-vivo imaged and following standard preprocessing, tensors were reconstructed, registered, and normalized to a population-specific template. Tract-based spatial statistics (TBSS) were computed to evaluate whole-brain voxel-wise differences along standard diffusion-tensor indices; permutation test results were considered significant at the $\alpha < 0.05$ level after family-wise error correction.

Oral Presentations & Excerptas

Results

To uncover diet-induced changes in neural tissue microstructure, ex-vivo whole brain DTI was performed followed by a voxel-wise TBSS analysis on samples from both the PRE and POST diet groups. Figure 1 shows the TBSS experimental design; PRE diet group analysis (fig. 1a), POST diet group analysis (fig. 1b), and PRE-POST diet groups analysis (fig. 1c). Statistically significant differences in fractional anisotropy (FA), axial diffusivity (AD), radial diffusivity (RD), and trace (TR; trace: mean diffusivity [MD] x3) were identified. Figure 2 reveals substantial areas of differing FA, TR, and AD values for the high-fat diet group (B1:A1) principally concentrated in the neocortex and external capsule. Additionally, animals on the high-fiber diet (C1:A1) showed statistically significantly higher TR and AD in the hypothalamus, internal capsule, and brainstem, and statistically lower AD and RD values in the neocortex. Animals on the high-protein diet (D1:A1) demonstrated increased FA and RD in both the neocortex and cerebellum. TBSS analysis performed on POST animals also reveal widespread areas of increased FA, TR, AD, and RD in the high-fat group (B2:A2), which were found largely throughout the forebrain (fig. 3). Surprisingly, animals crossed over from the high-fiber diet (C2:A2) demonstrated tremendous changes in the diffusion tensor with widespread and global changes in the diffusion tensor with decreased FA, TR and AD, and increased RD that stand in stark contrast to the minimal changes seen in the high-fiber PRE group (C1:A1). While no significant differences in FA and AD were identified in the POST high-protein group (D2:A2), statistically significant decreased TR and RD values were observed throughout the brainstem. Lastly, results for PRE-POST diet groups (fig. 4) reveal areas with differing FA and RD values for the POST high-fat group (B2:B1), and significant TR, AD, and RD differences for both, high-fiber diet (C2:C1) and high-protein diet (D2:D1) groups.

Conclusions

The mechanism through which the gut microbiome exerts its effects on the central nervous system (CNS) is multifactorial (neural, endocrine, and immunologic) but is thought to largely occur via the generation of bacterial metabolites, which exert their physiologic effects both locally and systemically. Short-chain fatty acids (SCFA), produced by the bacterial fermentation of dietary carbohydrates, alter neuronal excitability and gut bacteria also manufacture a wide spectrum of neuroactive compounds that include dopamine, γ -aminobutyric acid, histamine, acetylcholine and tryptophan, a precursor in the biosynthesis of serotonin (4-5). The results of our work extend and build upon these findings by uncovering changes in white-matter structural integrity via differing DTI metrics that may be linked to diet-influenced gut microbiome populations. Our method for uncovering potential links between gut microbiome populations and brain structural changes can help guide important new experiments to study how these microbiome populations impact the CNS beyond transiently modulating the presence and flux of neuroactive molecules and compounds.

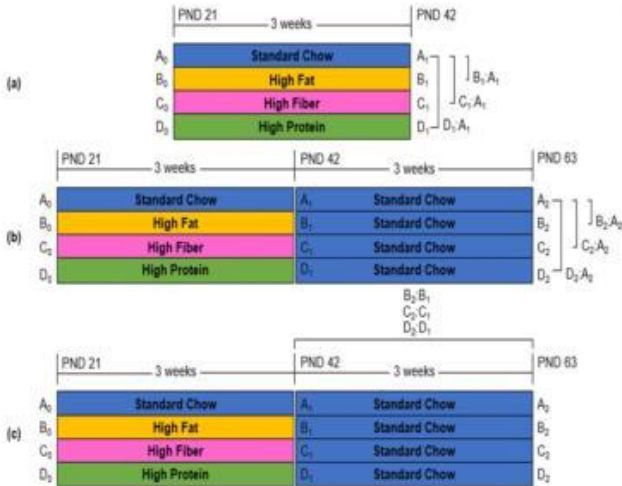


Figure 1. TBSS: Experimental Design.

Voxel-wise TBSS analysis was performed between animals on the control diet and those on either a high fat, high fiber, or high protein diet at (a) PND 42 (PRE-diet group) and (b) PND 63 (POST diet group). (c) In addition, a TBSS analysis was completed between animals on the PRE diet group (PND 42) and those on the POST diet group (PND 63).

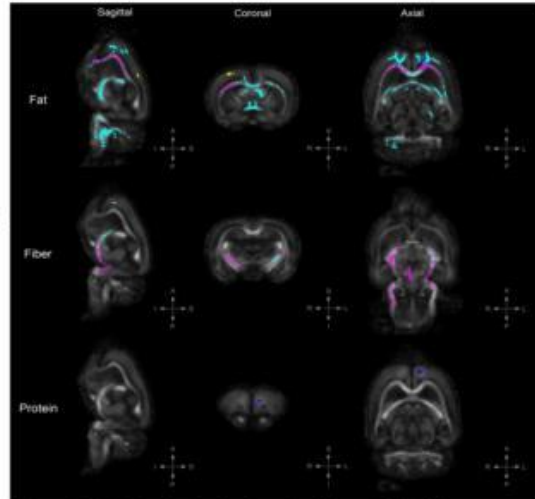


Figure 2. TBSS: Statistically significant DTI differences in PRE crossover diet group.

Statistically significant differences in fractional anisotropy (FA), axial diffusivity (AD), radial diffusivity (RD), and trace (TR; trace: mean diffusivity [MD] x3) between animals on the control diet and those on either a high fat, high fiber, or high protein diet (family-wise error corrected, $\alpha < 0.05$). Decreased FA= yellow, increased FA= blue, decreased AD= red, increased AD= light-blue, decreased RD= cooper, increased RD= green, increased TR= magenta.

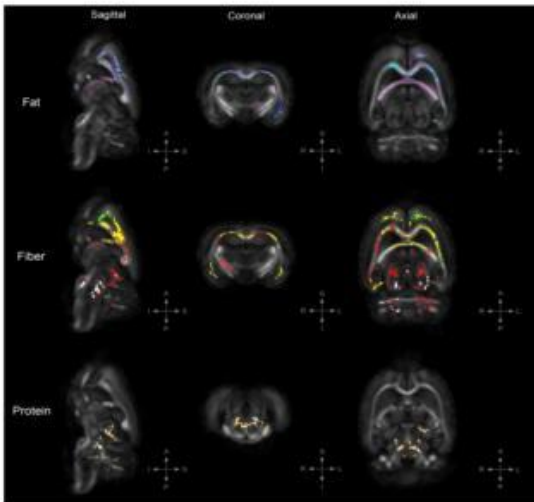


Figure 3. TBSS: Statistically significant DTI differences in POST crossover diet group.

Statistically significant differences in fractional anisotropy (FA), axial diffusivity (AD), radial diffusivity (RD), and trace (TR; trace: mean diffusivity [MD] x3) between animals on the control diet and those on either a high fat, high fiber, or high protein diet (family-wise error corrected, $\alpha < 0.05$). Decreased FA= yellow, increased FA= blue, decreased AD= red, increased AD= light-blue, decreased RD= cooper, increased RD= green, decreased TR= white, increased TR= magenta.

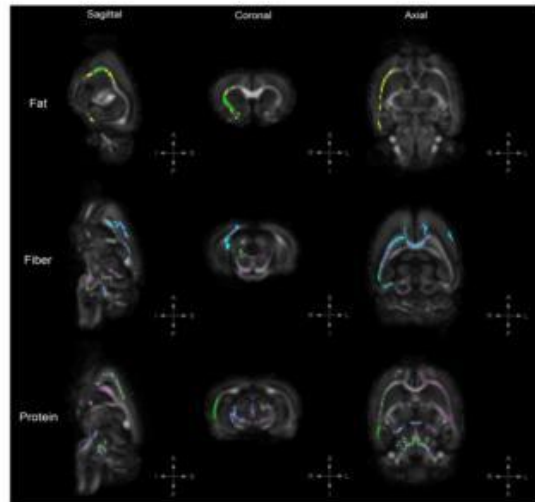


Figure 4. TBSS: Statistically significant DTI differences between PRE-POST diet groups.

Statistically significant differences in fractional anisotropy (FA), axial diffusivity (AD), radial diffusivity (RD), and trace (TR; trace: mean diffusivity [MD] x3) between animals on the PRE diet group and those on the POST diet group; either in a high fat, high fiber, or high protein diet (family-wise error corrected, $\alpha < 0.05$). Results are shown with respect to the POST diet groups; decreased FA= yellow, increased AD= light-blue, increased RD= green, increased TR= magenta.

(Filename: TCT_O-515_ASNR_2018_Abstract_Figures.jpg)

O-516

Track density imaging to visualize thalamolimbic fiber tracts at 3 Tesla

10:58AM - 11:05AM

Oral Presentations & Excerptas

J Böhme¹, M Maros¹, H Wenz¹, M Alzghoul¹, C Groden¹, A Förster¹

¹University Medical Center Mannheim, Medical Faculty Mannheim of University Heidelberg, Mannheim, Baden-Württemberg, Germany

Purpose

The limbic system consists of the limbic cortex, hippocampus, amygdala, septum and hypothalamus and is connected with numerous brain regions, e.g. the thalamus [1]. In this study, we investigated how well thalamolimbic fiber tracts can be identified by track density imaging (TDI) at 3 Tesla.

Materials and Methods

Diffusion-tensor imaging (DTI, a single-shot DWI spin echo–echo planar imaging acquisition [TR 9000 ms; TE 87 ms; 128 × 128 matrix; 2-mm isotropic resolution; 64 diffusion-weighted directions; b, 0 and 900 s/mm²; generalized autocalibrating partial parallel acquisition with factor 2; and 70 slices]) was performed in 18 healthy volunteers (10 females, 8 males; median age, 34.5 years; interquartile range, 31–44.5 years) on a 3-T MRI system (Magnetom Trio, Siemens, Erlangen, Germany), TDI generated from these datasets using the MRtrix software package, and compared to the published TDI [2] of a subject performed on a 7 Tesla MRI scanner to identify the thalamolimbic fiber tracts. The quality of the tract visualization was assessed on the basis of a 6-point Likert scale (5, excellent; 4, good; 3, moderate; 2, poor; 1, no adequate differentiation; 0, evaluation not possible) and a cumulative median calculated.

Results

All DTI data sets and calculated TDI were evaluable. Delineation of the cingulum (5) and fornix body (4.6) was rated as excellent, that of the anterior commissure (4.2), mamillothalamic tract (3.6), stria terminalis (3.6) and mamillotegmental fasciculus (3.5) was rated as good. Stria medullaris thalami (3.2), anterior thalamic radiation (2.9), superolateral medial forebrain bundle (2.9), inferomedial medial forebrain bundle (2.6), internal medullary lamina (2.9), septum pellucidum (3.0), posterior commissure (3.4), and superior frontooccipital fasciculus (3.3) were moderately identifiable. (For an example see Fig. 1).

Conclusions

Reliable visualization and delineation of thalamolimbic fiber tracts is possible with TDI at 3T.

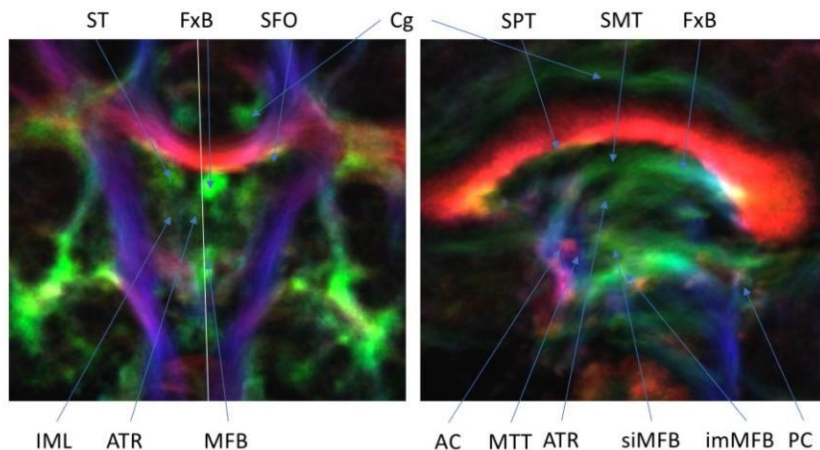


Figure 1: cingulum (Cg), fornix body (FxB), anterior commissure (AC), mamillothalamic tract (MTT), stria terminalis (ST), stria medullaris thalami (SMT), anterior thalamic radiation (ATR), superolateral medial forebrain bundle (slMFB), inferomedial medial forebrain bundle (imMFB), internal medullary lamina (IML), septum pellucidum tract (SPT), posterior commissure (PC) Superior frontooccipital fasciculus (SFO)

(Filename: TCT_O-516_TDI-Abbildungenglisch.jpg)

O-517

11:05AM - 11:12AM

Longitudinal Assessment of the Microstructural Integrity of the Superior Longitudinal Fasciculus in Head Injury Survivors with Language Disorders

D Grassi¹, D Da Conceição¹, C Leite²

¹Faculdade de Medicina da Universidade de São Paulo, Sao Paulo, Brazil, ²University Of Sao Paulo, Sao Paulo, Brazil

Purpose

Traumatic brain injury (TBI) is the number one cause of death and morbidity among young adults. Moreover, survivors are frequently left with functional disabilities such as language disorders during the most productive years of their lives. [1-3] The superior longitudinal fasciculus (SLF) is a major tract involved in human language processing, as it connects the Broca's area in the frontal lobe (speech production) with Wernicke's area in the temporal lobe (speech comprehension). The goal of the study is to evaluate the microstructural integrity of the SLF over time in TBI patients with diffuse axonal injury (DAI).

Materials and Methods

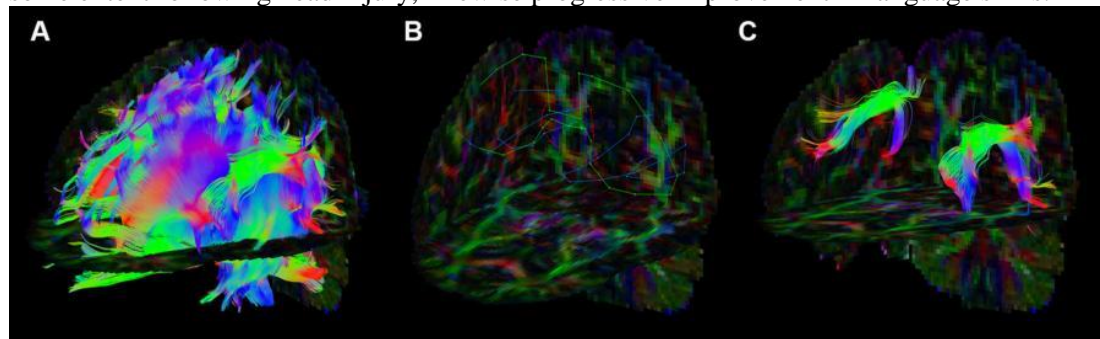
Twenty adults with moderate to severe TBI were evaluated at a 3.0T magnetic resonance imaging (MRI) scanner in the acute (t1, three months), subacute (t2, six months) and chronic stages (t3, 12 months) following trauma. Twenty matched controls were also recruited. DTI was obtained in the axial plane with 32 directions and b-values of 0 and 1000 s/mm². Preprocessing steps included correction of head motion and eddy current artifacts with ExploreDTI. The SLF was virtually dissected by the same rater with a deterministic streamline approach and a specific set of predefined rules based on a priori anatomical knowledge and the fiber assignment by continuous tracking (FACT) algorithm (Figure). [4] Language skills were also assessed with neuropsychological tests at all time-points. [5]

Results

There were significant changes of the SLF DTI metrics in TBI patients when compared to the healthy group. In comparison to t1, patients at t3 exhibited significant increases of diffusion anisotropy in the SLF. Patients' performances on language tests were suboptimal in all stages, but also improved over time.

Conclusions

Our study suggests that microstructural abnormalities in the SLF are not stationary and may reverse to some extent following head injury, likewise progressive improvement in language skills.



(Filename: TCT_O-517_Figure.jpg)

O-518

11:12AM - 11:19AM

Evaluation of the Glymphatic System with DTI in Idiopathic Normal Pressure Hydrocephalus

M Cekic¹, H Yokota², B Ellingson², M Linetsky², N Salamon³

Oral Presentations & Excerptas

¹University of California Los Angeles Medical Center, Los Angeles, CA, ²David Geffen School of Medicine at University of California Los Angeles, Los Angeles, CA, ³University of California Los Angeles, Los Angeles, CA

Purpose

Diagnosis of normal pressure hydrocephalus (NPH) is challenging based on structural imaging data alone. We use diffusion-tensor image analysis along the perivascular space (DTI-ALPS) to evaluate changes in the periventricular glymphatic system as an aid in the diagnosis of idiopathic normal pressure hydrocephalus (iNPH).

Materials and Methods

Twenty-four right-handed patients referred to our hydrocephalus clinic with imaging diagnosis of ventriculomegaly were included, with half (n = 12) diagnosed with iNPH and half (n = 12) without clinical signs of NPH (pseudo-iNPH; piNPH). Diffusivity maps in the direction of the x-axis (Dx, left-right), y-axis (Dy, antero-posterior), and z-axis (Dz, supero-inferior) were computed and coregistered to the ICBM DTI-81 atlas. Manual and atlas-based DTI-ALPS were computed and used to compare the diffusivity along the direction of the perivascular space (Dx) in the left periventricular white matter to that of projection and association fibers (Fig1). An ALPS-index was defined as: $ALPS\ index = \frac{\text{mean}(Dx_{proj}, Dx_{assoc})}{\text{mean}(Dy_{proj}, Dz_{assoc})}$, where Dx_{proj} and Dx_{assoc} are Dx values in the projection and association fiber areas, respectively. Evans index and callosal angle were also assessed in each case.

Results

ALPS-indices for control, piNPH, and NPH groups were 1.18 ± 0.08 , 1.08 ± 0.03 and 0.94 ± 0.06 , with significant differences between the groups (control vs. piNPH, $p = 0.003$; control vs. iNPH, $p < 0.001$; piNPH vs. iNPH, $p < 0.001$) (Fig2). Area under the curve (AUC) on receiver-operator characteristic (ROC) analysis was 0.92 for control vs. piNPH, 1.00 for control vs iNPH, and 1.00 for piNPH vs. iNPH. ALPS-index performed better than both Evans index (AUC = 1.00 vs. 0.84, $p = 0.028$) and callosal angle (AUC = 1.00 vs. 0.74, $p = 0.016$) in distinguishing between piNPH and iNPH.

Conclusions

ALPS index is able to distinguish reliably between iNPH, ventriculomegaly/pseudo-iNPH, and control groups and may be a helpful tool in imaging diagnosis and as a follow-up index of NPH.

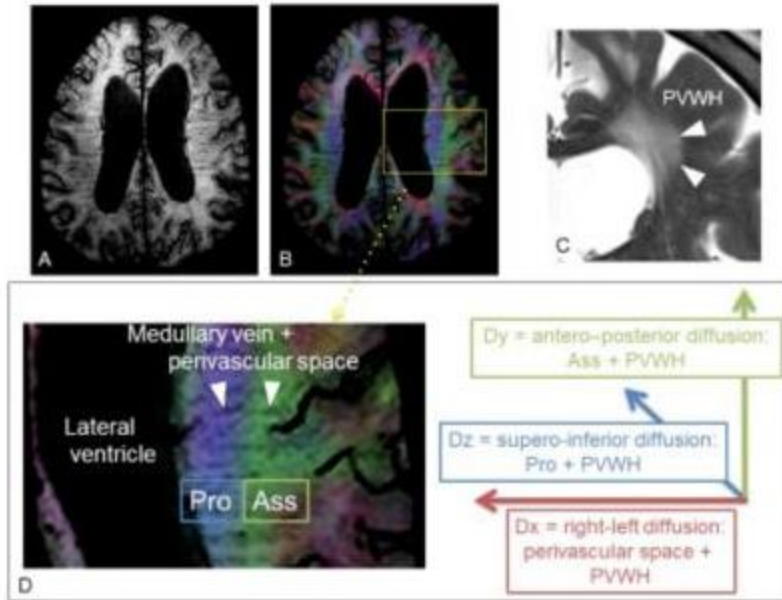


Fig 1

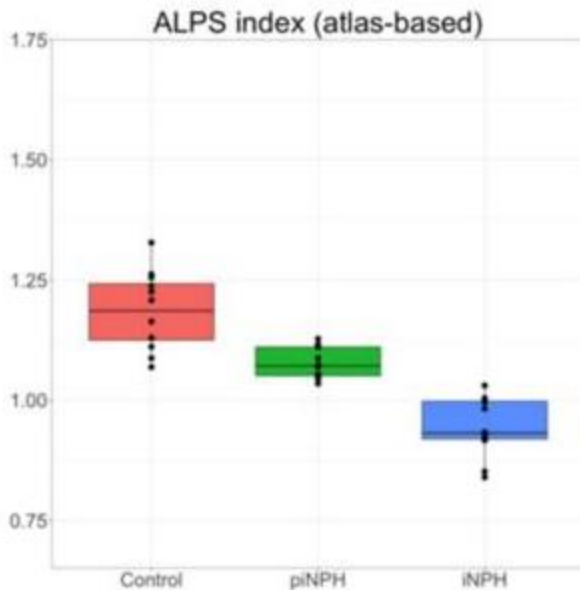


Fig 2

(Filename: TCT_O-518_NPHFigures.jpg)

O-519

11:19AM - 11:26AM

Methylene Blue Modulates Resting Functional Connectivity in the Healthy Elderly Human Brain

P Rodriguez¹, M Woolsey², M Polk², W Altmeyer², D Royall², F Gonzalez-Lima³, T Duong⁴

¹Hospital of the University of Pennsylvania, Philadelphia, PA, ²University of Texas Health San Antonio, San Antonio, TX, ³The University of Texas at Austin, Austin, TX, ⁴Stony Brook University School of Medicine, Stony Brook, NY

Purpose

Assess the effect of oral administration of methylene blue on resting functional connectivity over two and 12 weeks in the healthy elderly human brain compared to placebo and baseline.

Materials and Methods

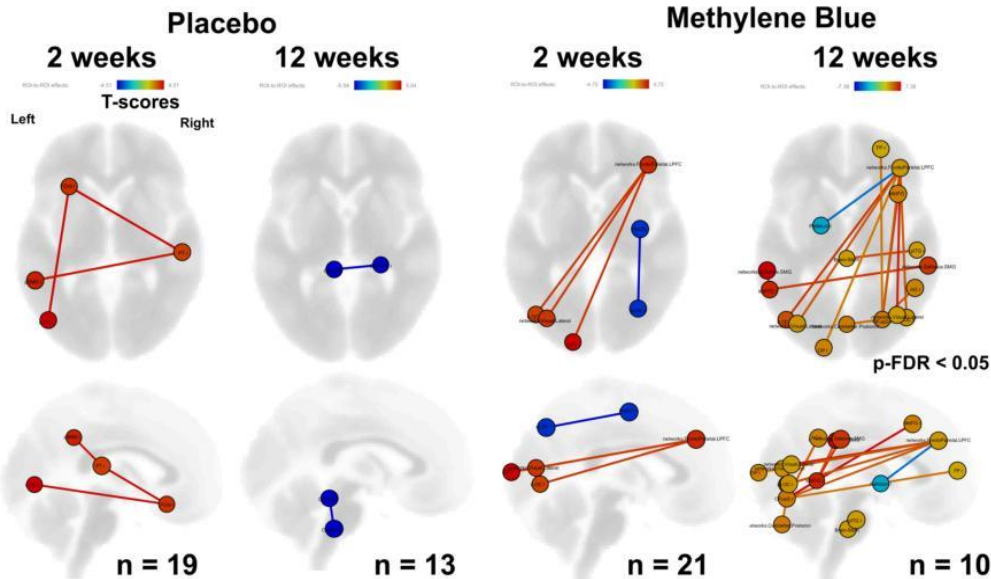
The institutional review board approved this prospective, HIPAA-compliant, randomized, double-blinded, placebo-controlled clinical trial and all subjects provided informed consent. USP grade methylene blue (94 mg three times daily, n=21, 70.2 years +/- 6.2 years) and placebo (n=19, 70 +/- 5.7 years) in combination with 97.5 mg phenazopyridine HCL daily was administered after a baseline 10-minute resting fMRI session in a 3T MRI scanner. Subjects returned at two weeks and 12 weeks for identical resting fMRI sessions. Functional connectivity analysis was conducted using the CONN toolbox (17.f) and Matlab (R2017a). Preprocessing using SPM and CONN included realignment and unwarping, structural segmentation and normalization, functional normalization, functional outlier detection (ART-based scrubbing), and spatial smoothing (8-mm FWHM). Principal components using segmented white matter, cerebral spinal fluid, motion realignment and scrubbing were used as denoising parameters using the CompCor method. Data were temporally band-pass filtered to 0.008Hz-0.09 Hz, and linear detrending and despiking after regression was also applied. A weighted GLM functional connectivity analysis using a hemodynamic response function weighting and bivariate correlation was used for ROI to ROI analysis. Signal was extracted from 10 mm regions of interest centered on 132 regions of the Automated Anatomical Labeling (AAL) atlas and centered on 32 cortical areas of the described networks derived from independent component analysis from the Human Connectome Project. Within-group analysis was observed over two and 12 weeks relative to baseline using an ROI to ROI analysis. Between-group contrasts were also generated. Multiple comparison correction was applied using two-sided thresholds. (seed-level threshold of $p < 0.05$ FDR corrected).

Results

The age, gender, handedness, years of education, baseline mini-mental status exam (MMSE), Montreal Cognitive Assessment (MoCA), Wechsler Memory Scale (WMS-IV), Geriatric Depression Scale (GDS), CLOX-1 and 2, and percent drug consumption over time did not differ between groups and both groups reported colored urine throughout the study. After two weeks of methylene blue intake, subjects had increased functional connectivity (FC) between the right lateral prefrontal cortex (node of the frontoparietal network) and the left lateral occipital cortex, left lateral visual network node and left occipital pole. After 12 weeks of methylene blue, using the same LPFC seed, there was persistent increased FC in the same areas but also increase in the right occipital fusiform gyrus, right visual network and right lateral occipital cortex. Additionally, a right frontal pole seed had increased FC with occipital fusiform gyrus, and a seed in the right salience network had increased FC with left middle temporal gyrus. Overall, the effects were very different from the placebo group (Figure 1), which showed only decreased FC between two cerebellar seeds at 12 weeks.

Conclusions

Methylene blue modulates cognitive task-positive networks and anatomical areas important for attention, working memory and visual perception, and these effects increased over 12 weeks.



(Filename: TCT_O-519_Figure1.jpg)

O-520

11:26AM - 11:33AM

Amide proton transfer imaging can reflect tissue acidosis and its reversal: demonstration with transient occlusion to permanent occlusion in a rat middle cerebral artery occlusion model

J Park¹, H Kim¹, J Kim¹, Y Heo², D Kim¹

¹University of Ulsan College of Medicine, Asan Medical Center, Seoul, Republic of Korea, ²Busan Paik Hospital, Inje University, Busan, Republic of Korea

Purpose

To assess amide proton transfer (APT) imaging in transient versus permanent rat middle cerebral artery occlusion (MCAO) models as a biomarker of tissue acidosis

Materials and Methods

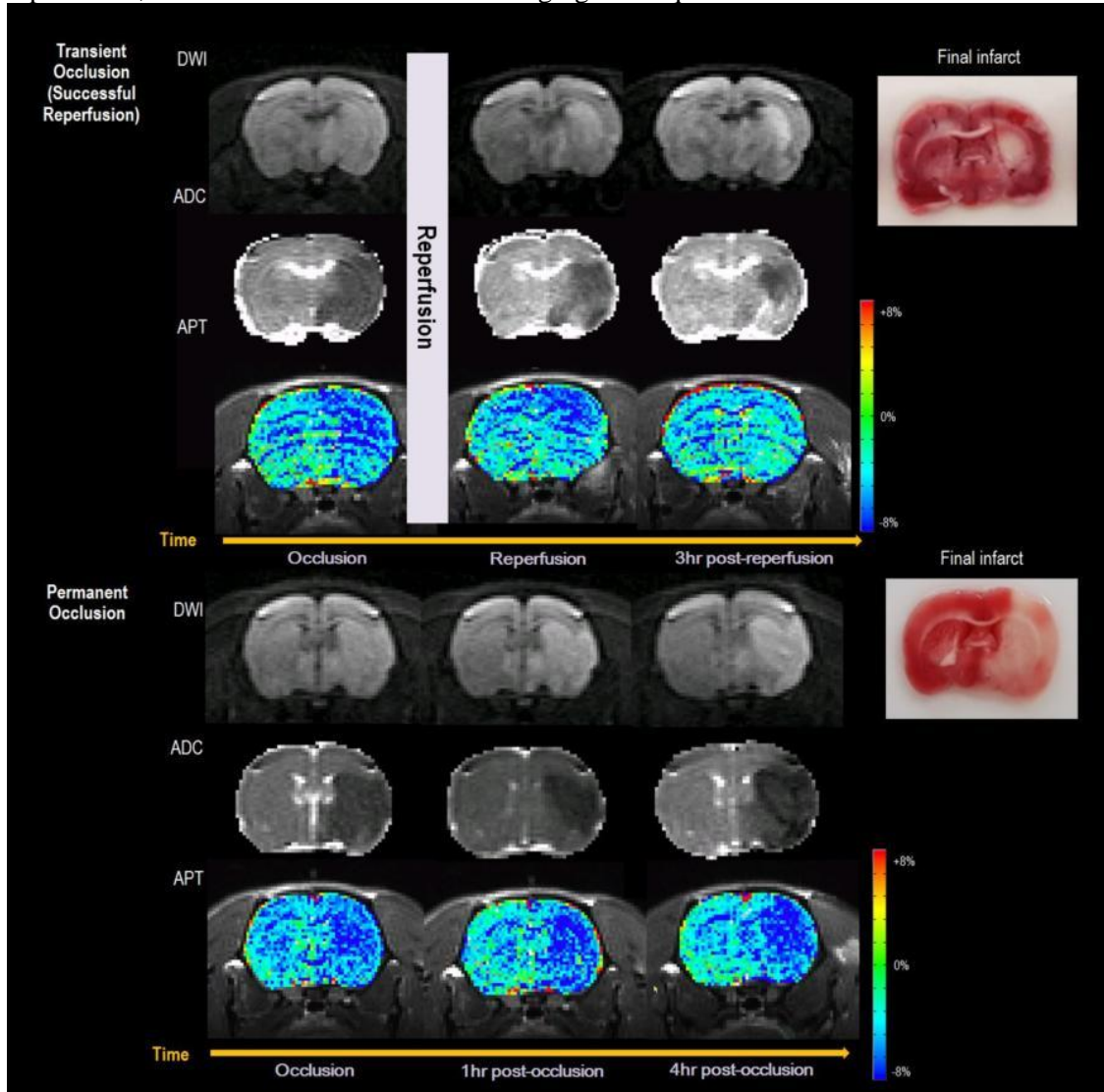
Twenty-four MCAO models (17 transient, seven permanent occlusion) were employed. APT asymmetry (APT_{asym}) from APT imaging, apparent diffusion coefficient (ADC) from diffusion-weighted imaging (DWI), cerebral blood flow (CBF) from arterial spin-labeling, and magnetic resonance (MR) spectroscopy were evaluated at three stages (immediate postocclusion, immediate postreperfusion or one hour postocclusion, and three hours postreperfusion or four hours postocclusion). The infarct area was based on DWI, ADC, and histological specimen. In transient occlusion, successful and unsuccessful reperfusion was determined by final infarct volume. Temporal changes in value and deficit areas of APT_{asym}, ADC, and CBF were compared for transient and permanent groups, and for successful and unsuccessful groups. APT_{asym} correlated with the lactate concentration.

Results

APT_{asym}, APT_{asym} deficit area, and CBF significantly increased in the immediate postreperfusion stage, but this was not demonstrated in the permanent occlusion (P = .002, .002, and .001). The APT_{asym} deficit areas were consistently smaller than the CBF deficit areas, but consistently larger than the ADC deficit areas. APT_{asym} showed a negative correlation with lactate concentration (r = -0.32, P = .02). In successful reperfusion, the APT_{asym} (P = .01) and APT_{asym} deficit reversed (P < .001); a significant change was not demonstrated in unsuccessful reperfusion.

Conclusions

APT imaging showed significant temporal reversal and negative correlation with lactate content after reperfusion, which could become a useful imaging technique to reflect tissue acidosis and its reversal.



(Filename: TCT_O-520_fig2.JPG)

O-521

11:33AM - 11:40AM

The Application of Dual-clustering Segmentation for Brain Hemorrhage and Edema Detection Using CT Images

A Mian¹, N Hua², C Takahashi³, J Shulman³, H Jara¹

¹Boston University/Boston Medical Center, Boston, MA, ²Boston University, Boston, MA, ³Boston Medical Center, Boston, MA

Purpose

Intracerebral hemorrhage (ICH) is associated with a high mortality rate of ~40%. It has been suggested that the volume ratio between the edema and the hemorrhage core is linked to disease outcomes. Clinically, such volumes are estimated on CT images using an ABC method (height x width x length/2),

Oral Presentations & Excerptas

which can be time-consuming and imprecise for lesions with irregular shapes. Our purpose is to develop a reliable, semi-automated segmentation method for estimating hemorrhage and edema volumes.

Materials and Methods

Under the approval of local IRB, a retrospective study was performed at our institution with 208 patients with hemorrhagic strokes. CT brain images were acquired using a single-source CT scanner (GE Healthcare). The sequential dual-clustering algorithm (see Figure 1) was programmed in Mathcad (Needham MA). Initially, the skull is stripped using an inverse mask method using automatic binarization. Second, the operator reduces the target volume to perform the dual-clustering segmentation. Dual-clustering method considers both geometric vicinity and intensity similarity between voxels. Hemorrhage was segmented first followed by the segmentation of edema. Corresponding volumes were obtained, and compared to ABC method accessed by two experienced radiologists. Statistical significance was defined as $P < 0.05$.

Results

The full algorithm was tested on patients with various sizes of hemorrhage, ranging 1.3~299.5 cm³ by ABC method, or 0.2~88.6 cm³ by dual-clustering segmentation. Dual clustering and ABC method showed a significant Pearson correlation in both hemorrhage ($r=0.878$, $p<0.001$) and edema ($r=0.881$, $p<0.001$) measurements. Linear regression showed ABC overestimated lesion sizes compared to dual-clustering method in (Figure 2).

Conclusions

The proposed dual-clustering algorithm can effectively segment hemorrhage and edema regions in brain CT images. Accurate segmentation of the affected region may help in the timely design of treatment plans, improve clinical outcome and facilitate future investigations of ICH.

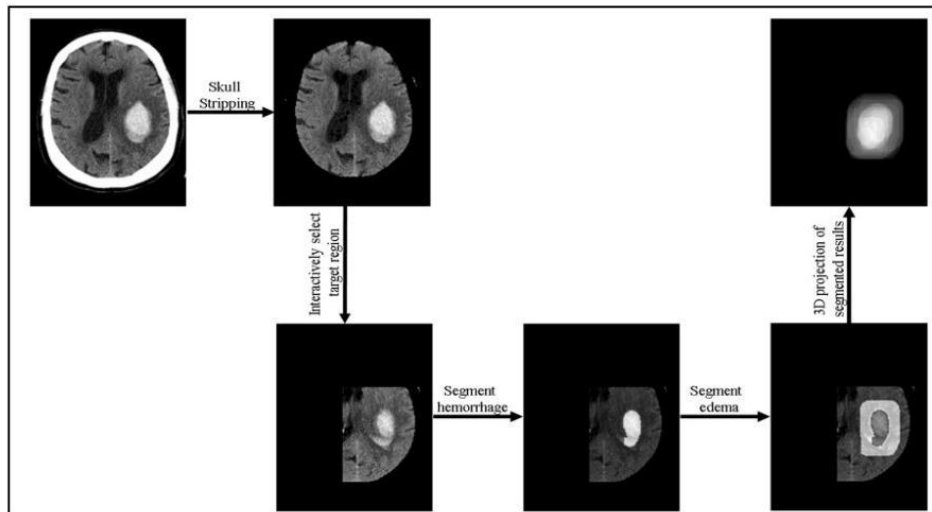


Figure 1. Illustration of the dual-clustering segmentation method.

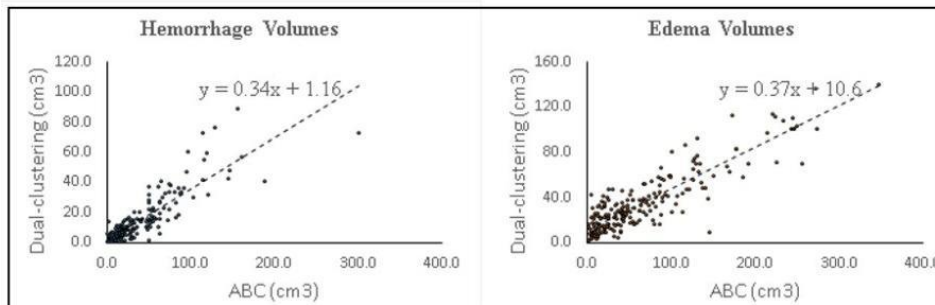


Figure 2. Linear regression of volumes obtained with the ABC and the dual-clustering method.

(Filename: TCT_O-521_asnr2018_figure1.jpg)

Intravoxel Incoherent Motion (IVIM) Perfusion Imaging to Predict the Post-treatment Cerebral Infarct Volume after Endovascular Reperfusion Therapy and Its Consistency with Routine Perfusion MR imaging: Initial Clinical Experience

G Zhu¹, C Federau², M Wintermark¹, J Heit¹

¹Stanford University, Stanford, CA, ²Centre Hospitalier Universitaire Vaudois, Lausanne, Vaud, Switzerland

Purpose

Intravoxel incoherent motion (IVIM) is a diffusion-weighted imaging (DWI) magnetic resonance imaging (MRI) technique that measures microvascular perfusion from a multi-b value acquisition. IVIM microvascular perfusion has not been directly compared to dynamic susceptibility contrast perfusion-weighted imaging (PWI) in the context of acute stroke. We determined the degree of correlation between gadolinium DSC and IVIM imaging penumbra and lesion size after endovascular reperfusion therapy in patients with acute ischemic stroke.

Materials and Methods

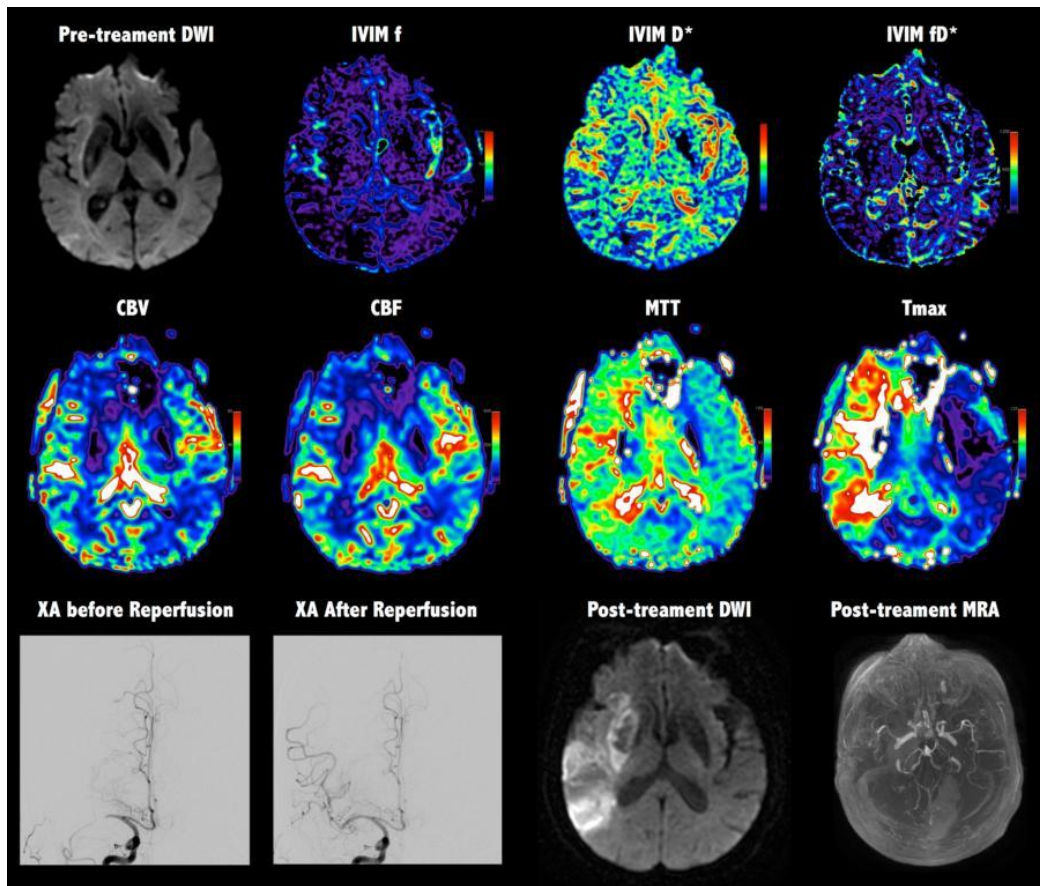
We performed a retrospective cohort study of acute ischemic stroke patients undergoing endovascular treatment triage by MRI. Inclusion criteria were: 1) internal carotid artery or M1 occlusion, 2) available IVIM and PWI, and 3) follow-up MRI within seven days. IVIM perfusion maps were derived using two-step fit of the IVIM bi-exponential equation voxel by voxel. Core infarction volume was determined by pre and post-treatment DWI. Ischemic penumbra volume was measured on PWI and IVIM by outlining of the perfusion deficit on PWI and IVIM maps. Pearson correlation analysis was used to determine the correlations between post-treatment infarct volume and other pretreatment imaging variables, including DWI, IVIM f, IVIM D*, IVIM fD*, PWI CBV, PWI CBF, PWI MTT, and PWI Tmax. Bland-Altman analysis was used to determine agreement among different perfusion variables. Significance level was set to $\alpha < 0.05$.

Results

Eleven patients (6 males, 55% ; mean age 67.1 ± 13.8 years) were included. Average pre and post-treatment core infarct volumes were 19.07 ± 23.56 ml and 37.73 ± 48.03 ml, respectively. Average pretreatment penumbra volumes on IVIM were 23.20 ± 25.63 ml (IVIM f), 14.01 ± 16.81 ml (IVIM D*), and 27.41 ± 40.01 ml (IVIM fD*). Average pretreatment penumbra volumes on PWI were 10.90 ± 13.33 ml (CBV), 24.83 ± 23.08 ml (CBF), 58.87 ± 37.85 ml (MTT), and 47.53 ± 26.78 ml (Tmax). Pre and post-treatment DWI core infarct volumes were well correlated ($r=0.959$, $R^2=0.919$, 95% CI : 0.864-0.988, $P<0.0001$). Pretreatment penumbra volume on PWI CBV was well correlated to post-treatment infarct core volume on DWI ($r=0.945$, $R^2=0.892$, 95% CI : 0.821-0.984, $P<0.0001$). Pretreatment penumbra volume on IVIM f showed the best correlation to post-treatment core infarct on DWI ($r=0.819$, $R^2=0.67$, 95% CI : 0.4883-0.944, $P=0.0006$). The best consistency among different perfusion variables was shown between IVIM fD* and CBF.

Conclusions

IVIM f best predicted post-treatment ischemic volume in patients with successful endovascular revascularization. IVIM fD* and DSC CBF showed excellent consistency. IVIM perfusion imaging is a promising alternative to gadolinium-based DSC to assess brain perfusion and predict final infarct volume.



(Filename: TCT_O-522_2018ASNR.jpg)

O-523

11:47AM - 11:54AM

Adaptive Statistical Iterative Reconstruction (ASIR) Improves Noncontrast Head CT Sensitivity to Detect lacunar Infarction Compared to Filtered Back Projection (FBP), Particularly in Neuroradiology Trainee/Early Career

M Mansouri¹, S Kamalian¹, L Roller¹, R Gupta¹, W Mehan¹, M Lev²

¹Massachusetts General Hospital, Boston, MA, ²Massachusetts General Hospital/Harvard Medical School, Boston, MA

Purpose

Studies have shown that noncontrast head CT (NCHCT) image reconstruction with ASIR improves image quality and low-contrast resolution compared to FBP. We sought to determine if ASIR would improve lacunar infarct detection and the overall image quality.

Materials and Methods

Selected were 29 consecutive adult patients who underwent NCHCT with MRI proven lacunar infarctions (LIs) for this retrospective study, HIPAA-compliant and IRB-approved. The NCHCT exams were performed on 64-slice MDCT and reconstructed with 100% FBP (Group A) and also 90% ASIR linearly blended with 10% FBP (Group B), at 5mm thickness. One neuroradiologist and one neuroradiology trainee reviewed both head CT image sets, blinded to the clinical/MRI findings. A second neuroradiologist reviewed the MRI images as the gold standard. LIs were categorized based on the acuity, laterality and involved region (caudate, globus pallidus, putamen, corona radiata, thalamus, pons, midbrain and cerebellum); 16 regions in each of 29 patients (n=464).

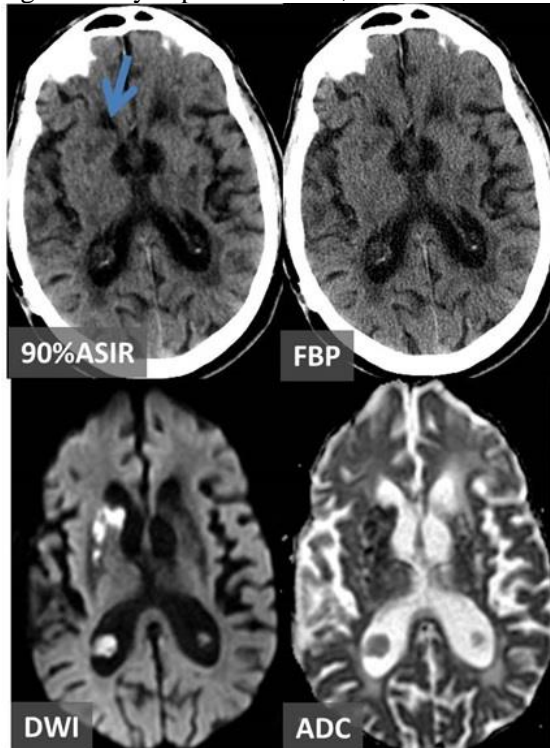
Oral Presentations & Excerptas

Results

Of 464, 95 (20%) regions had LIs, 20/95 (21%) were acute LIs and 49/95 (52%) were right-sided. The intraobserver agreement was excellent ($\kappa > 0.90$) for both 90% ASIR and FBP image sets; however, the interobserver agreement was moderate ($\kappa = 0.50$). For the trainee, 90% ASIR images significantly improved sensitivity (six more TP) to detect LIs (65% [62/95] vs. 59% [56/95], McNemar test $P = 0.03$) compared to the FBP images. For the neuroradiologist, 90% ASIR images showed an improved trend for sensitivity (five more TP) to detect LIs (62% [59/95] vs. 57% [54/95], $P = 0.06$) compared to the FBP images. However, the overall diagnostic accuracy of 90% ASIR was not significantly different compared to FBP images (trainee: 85% [396/464] vs. 86% [398/464], neuroradiologist: 83% [385/464] vs. 84% [388/464]), since 90% ASIR images introduced eight more FP for the trainee and nine more FP for the neuroradiologist evaluation. The overall image quality was significantly improved with 90% ASIR ($P < 0.01$).

Conclusions

ASIR significantly improved the neuroradiology trainee sensitivity to detect lacunar infarctions on NCHCT compared to FBP; however, for an experienced neuroradiologist ASIR images were not significantly superior to FBP, but there was an improved trend.



(Filename: TCT_O-523_ASIR90LacunarinfarctRSNAabstract.jpg)

Posters-Adult Brain

P-23

Aberrant Glioblastoma Neovascularization Patterns and Their Correlation with DCE-MRI-derived Parameters Following Temozolomide and Bevacizumab treatment

w xue¹

¹*The Third Affiliated Hospital, Army Medical University, Chongqing, China*

Purpose

To explore the effects of Temozolomide (TMZ) and Bevacizumab (bev) on neovascularization patterns and Dynamic Contrast-Enhanced MRI (DCE-MRI) features in glioblastoma

Materials and Methods

Orthotopic U87MG glioblastoma models were established and the mice were orally treated with TMZ (50 mg/kg for five consecutive days), intravenously BEV (15 mg/kg), and TMZ/BEV combined administration. MRI scanning and histological staining were performed on the first, third and sixth day after treatment. The changes of microvessel density (MVD) and neovascularization patterns in tumor region were investigated. The correlation between transfer coefficient (K_{trans}) derived from DCE-MRI and neovascularization patterns by histological analysis was analyzed.

Results

The amount of vascular mimicry (VM) significantly increased six days after BEV treatment. TMZ inhibited neovascularization at an early stage, but the microvessel density (MVD) and transfer coefficient (K_{trans}) derived from DCE-MRI increased six days after treatment. TMZ and BEV combination therapy slightly prolonged the inhibitory effect on tumor microvessels. Sprouting angiogenesis was positively correlated with K_{trans} in all treatment groups.

Conclusions

The increase in VM after BEV administration and the increase in MVD and K_{trans} after TMZ administration may be responsible for treatment resistance. K_{trans} holds great potential as an imaging biomarker for indicating the variation in sprouting angiogenesis during drug treatment for GBM.

P-07

Altered Resting State Functional Connectivity in Anterior Cingulate Cortex and Postcentral Gyrus After Autogenic Training

T Shizukuishi¹, O Abe², T Shinozaki³, Y Imamura³, M Okada⁴, Y Amano⁴

¹*Kawaguchi Municipal Medical Center, Kawaguchi, Saitama, Japan*, ²*The University of Tokyo, Bunkyo-ku, Tokyo, Japan*, ³*Nihon University School of Dentistry, Chiyoda-ku, Tokyo, Japan*, ⁴*Nihon University School of Medicine, Itabashi-ku, Tokyo, Japan*

Purpose

Autogenic training (AT) is a common and clinically used auto-hypnotic relaxation technique. It specifically aims at stress relieving, and also has a positive effect for chronic pain patients reportedly. Resting-state functional MRI (RS-fMRI) is able to evaluate the resting-state functional networks (RSNs) including salience network (anterior cingulate and insula cortex), sensorimotor network (primary and secondary sensorimotor cortex, supplementary motor area), and default mode network (precuneus, posterior cingulate and medial frontal cortex). Alterations of not only somatosensory network, but also salience and default mode network (DMN) reported in chronic pain patients may

underlie cognitive and affective processing problems. We investigated whether AT altered these resting state networks using RS-fMRI.

Materials and Methods

Ten healthy volunteers familiar with AT participated in this study. First, resting-state EPI scan (GE 3T MRI, slice thickness=3.8mm, TR=2000ms, 200 volumes) was acquired. Subsequently, participants conducted AT for 5 minutes in MR scanner, and resting-state EPI scan was acquired again. 3D T1-weighted anatomical images were also acquired for using anatomical data as preprocessing. The data were preprocessed using SPM12. And group independent component analysis (ICA) and seed-based functional connectivity analysis were implemented using Conn functional connectivity toolbox (v17b). The fMRI data were decomposed into 20 independent components, and group ICA was performed separately on each group (pre- and post- AT). ROI-to-ROI analysis was then performed using predefined ROIs where significant group difference was observed by group ICA as seeds. Then paired t tests were performed in both analyses. Significant clusters of activation were set at a peak voxel threshold of $P \leq 0.001$ and a cluster extent threshold of $P \leq 0.05$ with false discovery rate (FDR) correction for group ICA, and significant level was set at a $P \leq 0.05$ with FDR as seed level correction for ROI-to-ROI analysis.

Results

In group ICA analysis, post AT group revealed significant decreased resting-state activity in the anterior cingulate cortex (salience network), left postcentral gyrus (somatosensory network), left temporal fusiform gyrus and left lateral occipital cortex, while increased resting-state activity in the posterior cingulate cortex (DMN), left frontal pole, left lingual gyrus, and right lateral occipital cortex (Table 1). In ROI-to-ROI analysis, the functional connectivity of post AT group significantly increased in the anterior cingulate cortex, while it significantly decreased in the left postcentral gyrus (Table 2). The resting-state functional alterations of ACC and postcentral gyrus by AT were demonstrated in both ICA and ROI analysis, and those results consisted with resting-state functional alterations in chronic pain disease.

Conclusions

Conducting the autogenic training could have such positive effects not only to rebalance the automatic nervous system but also to alter the resting-state functional networks. Therefore, chronic pain could be relieved.

Table1 Maximum cluster locations of functional activity differences between pre and post AT groups in ICA.

Component #	Contrast	Clusters			Local maxima		
		Voxels	p-Value (FDR corrected)	Region	X (mm)	Y (mm)	Z (mm)
1	Post AT > Pre	66	0.0445	Left frontal pole	-40	44	10
4	Post AT > Pre	77	0.0294	Left lingual gyrus	-12	-50	4
5	Post AT > Pre	77	0.0283	Posterior cingulate cortex	-2	-16	30
9	Pre > Post AT	67	0.0289	Anterior cingulate cortex	-2	18	22
9	Pre > Post AT	109	0.0047	Temporal fusiform cortex	-36	-30	-30
12	Pre > Post AT	89	0.0198	Left lateral occipital cortex	-34	-62	16
13	Post AT > Pre	119	0.0027	Posterior cingulate cortex	-8	-18	28
19	Pre > Post AT	62	0.0481	Left postcentral gyrus	-40	-32	62
20	Post AT > Pre	102	0.0071	Right lateral occipital cortex	44	-74	26

Table2 Functional connectivity differences between pre and post AT groups in ROI analysis.

Seed region	Contrast	Target region	t-Value	p-Value (FDR corrected)
Anterior cingulate cortex	Post AT > Pre	Left inferior temporal gyrus	6.56	0.0144
Left postcentral gyrus	Pre > Post AT	Left anterior insula	4.35	0.0499
		Left pallidum	4.69	0.0499
		Right pallidum	5.51	0.0461
		Right putamen	4.41	0.0499

(Filename: TCT_P-07_ASNR2018_table.jpg)

P-06

Are You Puzzled When Credentialing Entities Ask You for Criteria for External Carotid Artery Stenosis? A Study Correlating Peak Systolic Velocities and Degree of External Carotid Artery Stenosis Based on CT Angiography

J Xu¹, S Rafla², M Pouria², D Root², S Lyons², J Romero²

¹Massachusetts General Hospital, Brookline, MA, ²Massachusetts General Hospital, Boston, MA

Purpose

External carotid artery (ECA) disease has been understated in the current literature [1], likely secondary to the lack of clinical significance of this diseased vessel. However, vascular ultrasound credentialing entities request the adoption of specific criteria for the assessment of the ECA [2]. Our purpose is to determine the ultrasound criteria for the detection of significant stenosis (>50%) using CT angiography (CTA) as the reference standard.

Materials and Methods

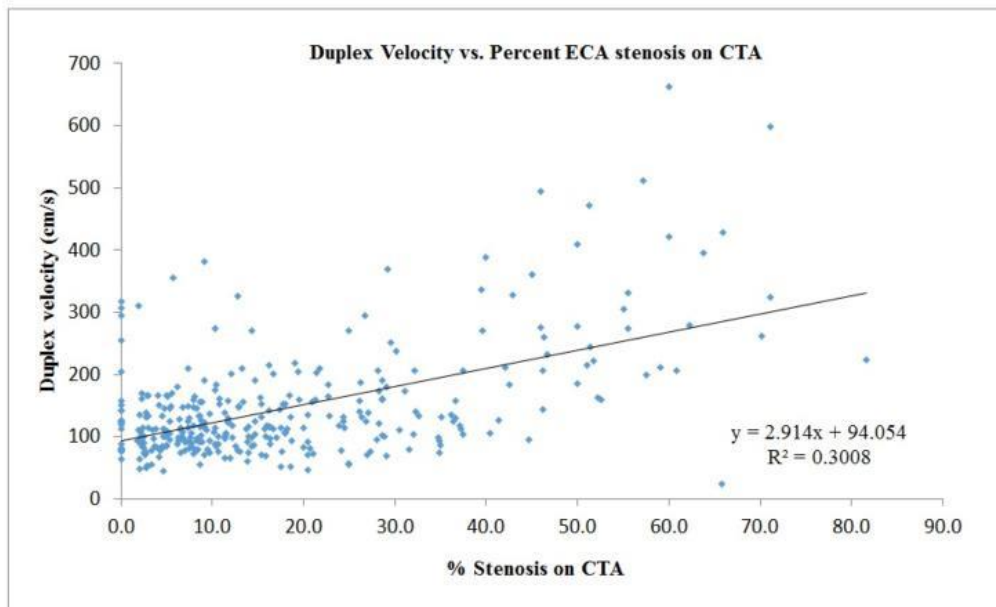
One-hundred-ninety-two patients who had a carotid ultrasound and a CTA of the neck performed within a 6-month period were included. Ultrasound measurements were reviewed for technical accuracy. CTAs were reassessed to determine the degree of stenosis of the bilateral ECAs using the NASCET criteria. Sensitivity, specificity, PPV, NPV and accuracy were calculated for different peak systolic velocity (PSV) cutoff points to determine the most sensitive PSV for >50% stenosis of the ECA.

Results

Of the 384 ECAs analyzed, 332 were included in the study. 52 ECAs were excluded because of non-diagnostic images, ipsilateral stent placement, and occlusion of the common carotid artery or internal carotid artery. A scatterplot was derived comparing PSVs and percent stenoses (Figure 1). Four PSVs were analyzed to determine the maximal operating point for >50% stenosis based on the CTA. 175 cm/s demonstrated a sensitivity of 92%, specificity of 84%, PPV of 0.33, NPV of 0.99 and accuracy of 0.85.

Conclusions

We determined that a PSV cutoff of 175 cm/s showed high sensitivity and specificity for detecting ECA stenosis of >50% based on CTA.



(Filename: TCT_P-06_ECAfigure1.jpg)

P-14

Arterial Spin Labeling (ASL) for Differentiation of Tumor from Post-treatment Changes in Patients with Cerebral Metastases Treated with Stereotactic Radiosurgery

M Hanna¹, A Bansal¹, M Bederson², I Germano¹, K Nael¹, A Aggarwal¹, P Belani¹

¹Icahn School of Medicine at Mount Sinai, New York, NY, ²University of Chicago, Chicago, IL

Purpose

Radiographic assessment of cerebral metastasis after stereotactic radiosurgery (SRS) remains a major challenge in neuroimaging. It is often difficult to distinguish viable tumor from post-treatment changes

Scientific Posters

(PTC) in this setting using conventional MR imaging, which can have major implications on patient management. The objective of this study is to evaluate the diagnostic yield of arterial spin labeling (ASL) for detecting tumor versus PTC after SRS.

Materials and Methods

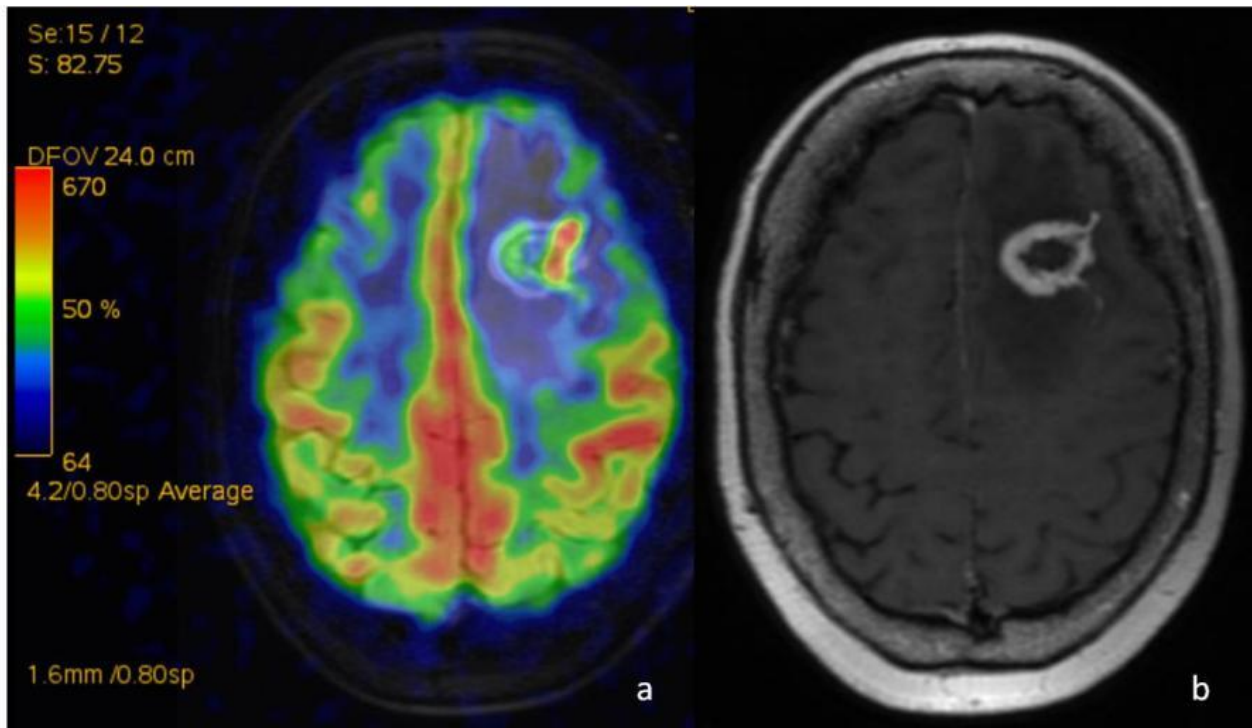
Patients with known brain metastases who had a new or enlarging enhancing lesion on ASL MR imaging within one year of SRS were retrospectively evaluated. For qualitative analysis, two fellowship trained neuroradiologists, who were blinded to the patients' outcomes, were asked to independently score the lesions on ASL postcontrast T1WI fusion images (postprocessed on a General Electric AW workstation) using the following grading system as it pertains to intensity of ASL in the enhancing lesion: 1. No demonstrable hyperintensity, 2. Mild hyperintensity or scattered hyperintense spots, 3. Diffuse moderate hyperintensity occupying $\leq 50\%$ of the tumor, and 4. Strong hyperintensity occupying $>50\%$ of the tumor. Reference was made to the contralateral uninvolved cerebral tissue. Scores were averaged for each patient. Mean scores were obtained for the tumor and PTC groups. Student's unpaired t-test was used to determine statistical significance between the two groups.

Results

Fourteen patients met the inclusion criteria. Seven patients (50%) had recurrent metastases and 7 patients (50%) had PTC based on histology or serial follow-up MR examinations demonstrating decreasing lesion size/enhancement. The tumor group demonstrated a statistically significant higher average score compared to the group demonstrating PTC (3.1 vs. 1.6, $p=0.001$).

Conclusions

In our series, ASL positivity (higher score) was associated with the pathologic diagnosis of tumor after SRS. Therefore, ASL may be useful in differentiating tumor from PTC. Validation of this finding in a larger series is warranted.



Arterial Spin Labeling (ASL) fusion map (a) demonstrates diffuse hyperintensity occupying more than 50 percent of the tumor in this patient with known brain metastasis from non small cell lung cancer. The corresponding post contrast T1W MR image of the brain (b) demonstrates a peripherally enhancing mass in the left frontal lobe. This was surgically resected and proven to be a metastatic lesion.

(Filename: TCT_P-14_ASLASNR121517.jpg)

P-17

Bickerstaff's Brainstem Encephalitis - Part of Anti-GQ1b Spectrum Disorder: Imaging Review of an Overlooked Diagnosis

N Sadiq¹, M Bowen¹, J Fazal¹, W Wali Muhammad¹, M Patel¹, S Jacob¹, V Sawlani¹

¹*University Hospitals Birmingham NHS Foundation Trust, Birmingham, United Kingdom*

Purpose

The brainstem is often a site of involvement in neoplastic, paraneoplastic, inflammatory, infective, vascular and metabolic disorders. Bickerstaff's Brainstem Encephalitis (BBE) is an overlooked imaging diagnosis. BBE is a rare disorder characterized by acute ophthalmoplegia, ataxia and altered sensorium (+/- long tract signs). It is now increasingly being recognized as an anti-GQ1b syndrome. (1,2) On retrospective review of our data, we found 11 confirmed cases of anti-GQ1b syndrome. Brainstem lesions pose a significant diagnostic challenge, having a wide differential diagnosis on conventional MRI. Multiparametric MRI can increase diagnostic accuracy by differentiating between neoplastic, inflammatory or vascular lesions. (3) BBE is a treatable cause with generally good prognosis especially if identified early.

Materials and Methods

Retrospective review of immunology lab database and online clinical records revealed 11 cases of anti-

GQ1b syndrome over the last 10 years. PACS was used to review the MRI head scans of these cases. Standard MRI brain examination included T2 axial, FLAIR axial, T1 sagittal, T2 coronal, DWI axial and postcontrast T1 sequences were available in all 11 patients. Multiparametric MRI was performed in one case presenting with brainstem swelling.

Results

Out of 11 cases of anti-GQ1b spectrum disorder, 55% (n=6) had Miller Fisher Syndrome (MFS), 36% (n=4) fulfilled BBE criteria and 9% (n=1) had Guillain-Barre Syndrome (GBS). Positive MRI findings of BBE were present in only one patient (9%). The patient with positive MRI findings had extensive brainstem involvement. MRI T2W sequence showed diffuse high signal in the pons. Diffusion MRI showed free diffusion, spectroscopy showed low MI/Cr, normal Cho/Cr, normal NAA/Cr and minimally raised glutamine and glutamate. Post-treatment follow up MRI showed complete resolution of the brainstem abnormality.

Conclusions

In brainstem lesions, BBE should be considered as a differential as diagnosing and treating this condition early can avoid significant morbidity and mortality. Positive MRI findings are often not present in patients with BBE. Even when present, the findings still have a wide differential. High resolution and multiparametric imaging can help to narrow the differential in the appropriate clinical setting to help avoid unnecessary brainstem biopsies.

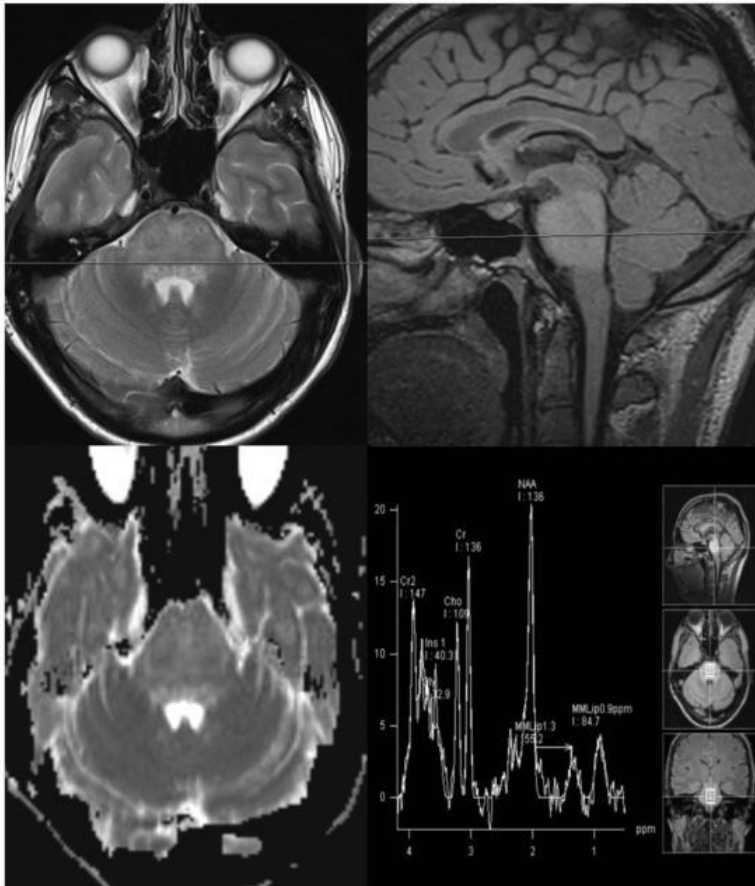


Fig. 1. Bickerstaff's Brainstem Encephalitis. Conventional MRI Findings: Axial T2W and sagittal FLAIR showed a diffuse high signal lesion in the pons. Multiparametric MRI: ADC showed free diffusion. MRS showed a normal myo-inositol (MI) and low MI/Cr ratio, a normal Cho/Cr ratio, a normal N-acetylaspartate/creatine (NAA/Cr) ratio and minimally raised glutamine and glutamate (2.3 ppm and 2.4 ppm). PWI (not shown) showed low rCBV compared to contralateral white matter.

(Filename: TCT_P-17_Capture3.JPG)

P-26

Clinical Application of Spiral 3D TFE-IR for Postcontrast Brain

H Friel¹, M McGranor², M Ooi¹, D Wang³, Z Li³, J Pipe³, J Fritz², N Pinter²

¹Philips Healthcare, Gainesville, FL, ²Dent Neurologic Institute, Amherst, NY, ³Barrow Neurological Institute, Phoenix, AZ

Purpose

Spiral MRI (1) has technical advantages vs. Cartesian MRI including higher SNR (2) and reduced flow,

motion and gradient distortion artifacts (3) and intrinsic Dixon fat suppression. This study provides a clinical overview of a prototype 3-D spiral TFE technique.

Materials and Methods

Sagittal prototype Spiral 3-D T1 TFE-IR (Spiral-TFE) was run in comparison to Cartesian 3-D T1 TFE-IR (Cart-TFE) postcontrast brain patients on a Philips 3.0T MR Ingenia scanner with standard hardware configuration. Spiral-TFE is an IR prepared gradient echo excitation, using a 2 TE-shifted stack-of-spiral readout with acquisition window ~ 10 ms. Reconstruction is performed online using a conjugate gradient algorithm for joint off-resonance deblurring and mDixon-based water/fat separation (4, 5) with reconstruction times of ~ 1 sec/slice. SNR measurements were performed using the Philips PIQT phantom. $SNR = [\text{signal mean}]/[\text{noise standard deviation}]$.

Results

Spiral-TFE had 50% more SNR than Cart-TFE with 25% shorter scan time (Table 1). Figure 1 shows 3mm sagittal and coronal reformats. Coherent ghost artifacts on Cart-TFE (arrows) are not seen on Spiral-TFE (image 1, 2). Grey/white brain contrast (stars) is better for Spiral-TFE (image 1, 2). Spiral-TFE shows uniform fat suppression and better visualization of orbit muscles (image 4).

Conclusions

Spiral-TFE enables broader clinical applications of 3-D T1 TFE IR with shorter scan time and higher SNR compared to Cart-TFE. Uniform mDixon based fat suppression is useful for orbit and head-and-neck applications and eliminate the need for additional fat suppression scans. Artifact reduction offers improved diagnostic accuracy and confidence for MR neurological imaging. Areas of further optimization include improvement of image sharpness and reduction of susceptibility artifacts.

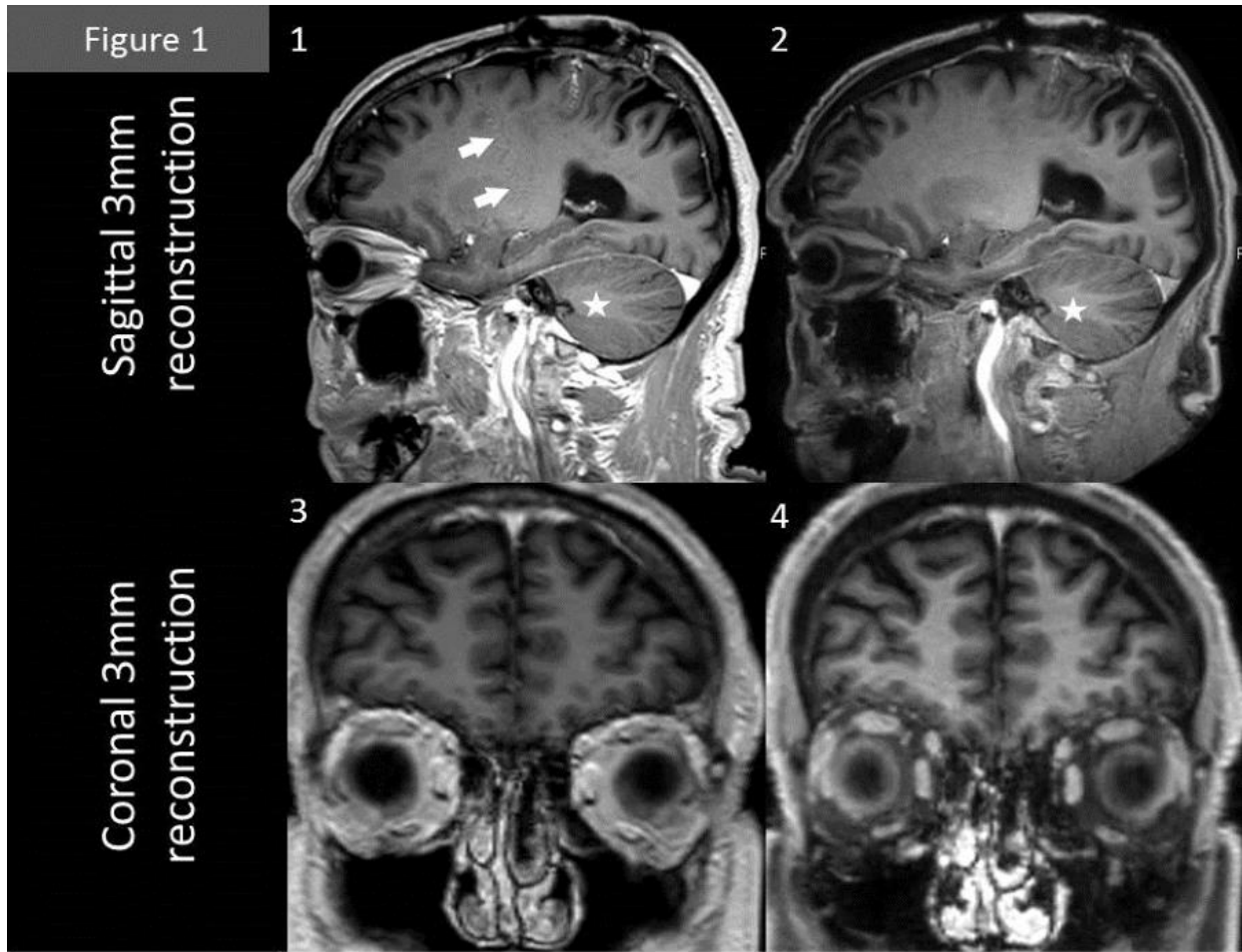


Table 1	Cart-TFE	Spiral TFE
TR/TE ₁ /TE ₂	5.8/2.6	17/1.48/2.63
Flip angle	8	10
Resolution	.94 x .94 x .94mm	.94 x .94 x .94mm
SENSE factor	2.4 slice direction	2.2 slice direction
Scan time	4:45min	3:30min
SNR	197	291

(Filename: TCT_P-26_ASNRSpiral3DTFEFINALgraphic.jpg)

P-20

Comparing Clinical and Radiographic Findings in Parinaud’s Syndrome With and Without Pineal Region Masses: A Better Understanding of a Poorly Defined Clinical and Radiographic Phenomenon

N Hura¹, A Lakraj², D Yousem¹, N Miller²

¹Russell H Morgan Department of Radiology Johns Hopkins University School of Medicine, Baltimore, MD, ²Wilmer Eye Institute, Baltimore, MD

Purpose

Parinaud's syndrome (PS) is characterized by the clinical triad of upgaze palsy, convergence retraction

nystagmus, and pupillary light-near dissociation. Though the classic etiology of PS was thought to be a pineal lesion, prior studies have suggested that pineal lesions may actually be less common than other brainstem pathologies (1, 2). While newer imaging modalities allow for detailed study of intracranial lesions resulting in PS, radiographic characterizations of PS remain poorly described. In this study, we aim to better understand the etiologies of PS and identify what imaging features are best predictive of PS.

Materials and Methods

After gaining IRB approval for this retrospective chart review, we searched our medical record database (Epic) and Radiology Information System (RIS) for patients with Parinaud's syndrome and pineal lesions from 1980 to 2017. The teaching file of one of the authors was used to identify additional cases of Parinaud's syndrome. All imaging reports and available studies were reviewed by a neuroradiologist.

Results

Of 93 patients with a clinical diagnosis of PS, only 21 had a pineal region lesion. Of the remaining 72, the most common pathology was vascular etiologies (24), including hemorrhage, ischemia, and vessel abnormalities, followed by other intracranial masses (14), hydrocephalus (12), trauma (6), and intracranial cysts (5). Based on a prior publication (3), we graded the degree of tectal plate displacement as greater than or less than 3 mm from its natural state. From imaging studies reviewed thus far, very few patients had compression of the tectal plate greater than 3 mm. This finding, combined with available imaging reports, suggests that displacement of the tectal plate may not be sufficient to diagnose PS.

Conclusions

We found that pineal masses cause a minority of cases of PS and that mere compression of the tectal plate was unlikely to elicit the classic triad without intrinsic brainstem signal abnormalities on MRI.

P-18

Contrast Enhancement of Intracranial Atherosclerotic Plaques on High- resolution Vessel Wall MRI is Not Predictive of Symptomatic Status

R Khabbaz¹, P Vakil², A Al-Smadi³, A ElMokadem⁴, A Shaibani³, M Hurley³, T Carroll⁵, S Ansari³
¹University of Illinois - Chicago College of Medicine, Chicago, IL, ²Northwestern University, Chicago, IL, ³Northwestern University Feinberg School of Medicine, Chicago, IL, ⁴Mansoura University, Mansoura, IL, ⁵University of Chicago, Chicago, IL

Purpose

Intracranial atherosclerotic disease (ICAD) accounts for 10-15% of ischemic stroke etiology. Imaging-based stratification to assess the vulnerability of intracranial plaques for ischemic complications may direct management. Studies have shown postcontrast intracranial plaque enhancement on high resolution vessel wall MRI (VWI) is sensitive to symptomatic ischemic presentations. However, its specificity remains poorly characterized. In this study, we compared patterns of postcontrast enhancement in concomitant symptomatic and asymptomatic high-grade intracranial plaques (1).

Materials and Methods

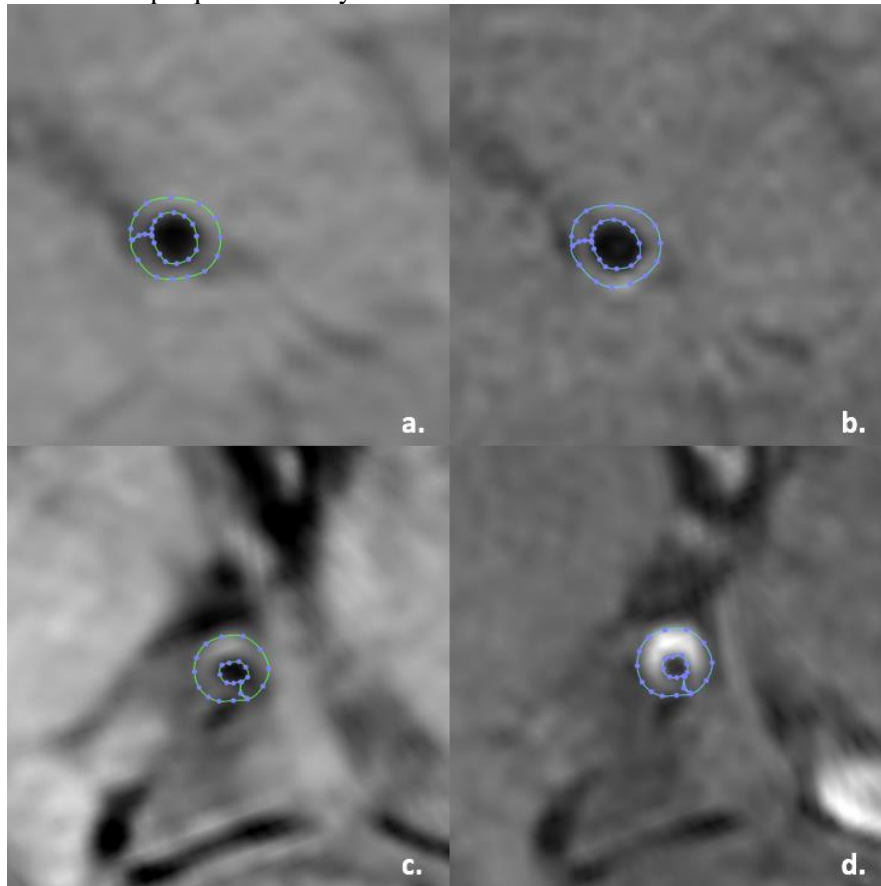
We retrospectively identified patients who presented with TIA or stroke and received high-resolution VWI with the 3D T1-SPACE protocol in addition to standard MRI/MRA brain protocols. All symptomatic or asymptomatic intracranial stenoses > 50% in a large intracranial artery as determined by two neuroradiologists using CT/MR angiography were included. Symptomatic plaques were defined as those presenting with a TIA/stroke in the corresponding vascular territory, based on either neurological exam and/or MR DWI. Severe (>70%) cervical carotid or tandem stenoses were excluded. Plaques were analyzed in orthogonal 1mm slices and segmented with ROIs drawn by neuroradiologists using OsiriX. Mean plaque signal intensity and postcontrast enhancement was measured using pre- and postcontrast images, as established in current literature (2,3). Qualitative analysis of plaque enhancement was performed independently by one neuroradiologist (4). Enhancement was compared using a two-sided t-test and chi-square test for quantitative and qualitative measures, respectively.

Results

We analyzed 26 patients with 40 plaques (22 asymptomatic and 18 symptomatic, age= 64.48yr \pm 11.36). In the qualitative enhancement analysis there was no significant association between plaque score and symptomatic status ($\chi^2=0.0265$, $p=0.8706$). Furthermore, our quantitative analysis demonstrated no statistically significant difference in mean enhancement between asymptomatic and symptomatic plaques (enhancement=0.4036 vs 0.4178 respectively, $p=0.8916$).

Conclusions

Our study demonstrates that plaque enhancement as quantified using HR MR VWI may not be a specific indicator of plaque instability.



(Filename: TCT_P-18_ScreenShot2017-12-15at21606PM.jpg)

P-05

Diagnostic Accuracy of Brain and Heart Spect in the Differential Diagnosis of Lewy Body Disease

M Yoshita¹

¹Hokuriku National Hospital, Nanto, Toyama, Japan

Purpose

The ^{99m}Tc-ethyl cysteinyl dimer (ECD) cerebral blood flow single photon emission computed tomography (SPECT), ^{123I}-2 β -Carbomethoxy-3 β -(4-iodophenyl)-N-(3-fluoropropyl) nortropane (^{123I}-FP-CIT) dopamine transporter (DAT) SPECT and ^{123I}-metaiodobenzylguanidine (MIBG) myocardial SPECT can be used to assist in the diagnosis of patients with Lewy bodies disease (LBD). We compared the diagnostic value of these three SPECT methods in differentiating LBD from non-LBD.

Scientific Posters

Materials and Methods

Patients with no-LBD (n=48) and patients with LBD (n=20) who underwent ECD SPECT, DAT SPECT and MIBG myocardial scintigraphy were enrolled. Patients with LBD consisted of dementia with Lewy bodies (n=33), Parkinson disease (n=7), Parkinson disease with dementia (n=4), and REM sleep behavior disorder (n=4). Patients with non-LBD consisted of Alzheimer's disease (n=9), progressive supranuclear palsy (n=3), multiple system atrophy (n=1), corticobasal degeneration (n=1), vascular dementia (n=1), essential tremor (n=1), sleep apnea syndrome (n=1), and normal (n=1). The sensitivity, specificity, and accuracy of those methods were calculated.

Results

The sensitivity and specificity of differentiating LBD from non-LBD were 73.0 and 90% by the MIBG heart uptake, 64.0 and 82.0% by the striatum uptake on DAT SPECT, and 76.0 and 53.0% by ECD SPECT, respectively.

Conclusions

These results suggested that using these methods is a useful and practical approach to differentiate LBD from non-LBD.

P-01

Diagnostic Reliability and Reproducibility of the Nigrosome-1 at 3 Tesla Magnetic Resonance Imaging in Daily Practice: A Multicenter Study

S Calloni¹, E Scola², S Sbaraini³, G Conte⁴, S Avignone⁵, A Vitucci⁶, G Sacilotto⁷, V Silani⁸, G Pezzoli⁷, F Triulzi⁹

¹University of Milan, Milan, MI, ²Fondazione irccs ca granda ospedale maggiore policlinico milano, Milan, Italy, ³Univeristy of Milan, Milano, MI, ⁴Fondazione Irccs Ca Granda Ospedale Maggiore Policlinico Milano, Milano, Italy, ⁵Fondazione Irccs Ca Granda Ospedale Maggiore Milano, Milano, Italy, ⁶Ospedale Maggiore Policlinico, IRCCS Ca' Granda, Milano, mi, ⁷Istituti Clinici di Perfezionamento, Milano, MI, ⁸IRCCS Istituto Auxologico Italiano, University of Milan, Milano, MI, ⁹Ospedale Maggiore Policlinico IRCCS Ca' Granda; Milan Italy, Milan, Italy

Purpose

Dorsolateral Nigral Hyperintensity (DNH) in substantia nigra pars compacta, depicted on susceptibility-weighted imaging (SWI), corresponds to Nigrosome-1 and is known to disappear in patients with Parkinson's disease (PD) and atypical Parkinsonian disorders (APDs). At present, the assessment of the DNH struggles to fit in the diagnostic work-up. Our aim is to assess the feasibility, the diagnostic value and the reproducibility of the loss of DNH on SWI images in a multicenter clinical setting in the diagnosis of PD and APDs.

Materials and Methods

We retrospectively and prospectively enrolled 154 patients with PD (n =48) or APD (n=28) and 78 controls. Subjects underwent MRI with axial SWI in two different institutes on two distinct MRI 3Tesla scanners: Group A (n=100) and Group B (n=54). Two blinded neuroradiologists reviewed the SWI. Images with movement artifacts were excluded. Inter-readers agreement was estimated. Sensitivity, specificity, positive predictive value (PPV) and negative predictive value (NPV) of the absence of the DNH in diagnosing PD and APD and in differentiating PD from APD were assessed.

Results

Only 5/154 patients were excluded from analyses for movement artifacts. Inter-rater agreement was high between raters (0.84). For the diagnosis of PD or APD, the consensus rating for the absence of the DNH showed an overall sensitivity of 96% and a specificity of 92%. A sensitivity of 97%, a specificity of 83%, a negative predictive value (NPV) of 93% was shown for group A. A sensitivity of 85%, a specificity of 95%, a NPV of 97 was shown for group B. In differentiating PD from APD a sensitivity of 96% and a specificity of 4% was shown.

Conclusions

The assessment of the DNH on SWI images is shown to be feasible, reproducible and with high diagnostic value in PD and APD patients, being a valid tool in daily practice.

P-25

Differentiation Between High-grade Gliomas and Metastatic Brain Tumors using Neurite Orientation Dispersion and Density Imaging of Peritumoral Region

H Uetani¹, M Kitajima¹, H Nakamura¹, T Yoneda¹, K Morita², M Tateishi³, A Mukasa¹, Y Yamashita¹
¹*Kumamoto University, Kumamoto, Japan,* ²*Kumamoto University Hospital, Kumamoto, Japan*

Purpose

Differentiation between high-grade glioma (HGG) and metastatic brain tumor (MET) is challenging by conventional MR images, especially when they exhibit atypical MR features. Neurite orientation dispersion and density imaging (NODDI) is a recently developed diffusion technique and provides brain microstructural information which cannot be obtained with previously reported MR imaging techniques. (1) The purpose of this study was to compare NODDI metrics and ADC of the peritumoral region between HGG and MET and determine whether NODDI can be used to differentiate HGG from MET.

Materials and Methods

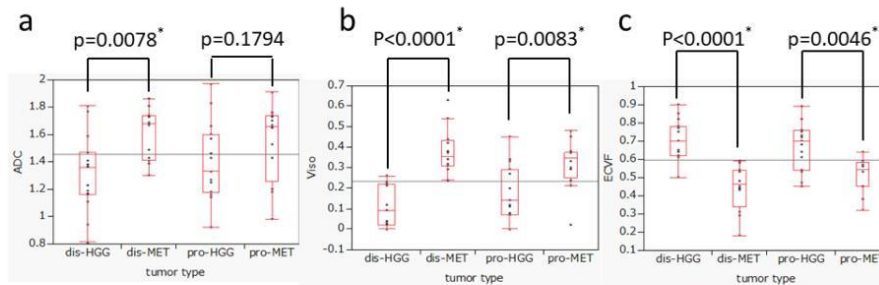
This study included 15 patients of HGGs and 12 patients of METs. At a 3T MRI unit, diffusion images were acquired using two diffusion weightings ($b = 1000, 2000 \text{ sec/mm}^2$) along 32 noncollinear directions, and 1 $b = 0 \text{ sec/mm}^2$ volume. For image processing of NODDI, we used a publicly available toolbox. Mean orientation dispersion index (ODI), intra-neurite volume fraction (ICVF), CSF volume fraction (Viso), extraneurite volume fraction (ECVF) and ADC of proximal and distal peritumoral region, defined as areas around the tumor with T2 hyperintensity and without contrast enhancement, were measured by manual ROI method. The statistical difference of the 5 metrics between the two tumor groups was tested by Mann-Whitney U test.

Results

The mean value of Viso and ADC in distal peritumoral region of METs were statistically higher than those of HGGs ($p < 0.0001$, $p = 0.0078$). Furthermore, Viso in proximal peritumoral region of METs was statistically higher than that of HGGs ($p = 0.0083$). ECVF in proximal and distal peritumoral region of METs was statistically lower than that of HGGs ($p = 0.0046$, $p < 0.0001$).

Conclusions

Our results indicate that Viso and ECVF in proximal and distal peritumoral region and ADC in distal peritumoral region are useful to differentiate between HGG and MET.



These graphs show that the mean value of ADC (a), Viso (b) and ECVF (c) in proximal and distal peritumoral area of high-grade gliomas (HGG) and metastatic brain tumors (MET).

*: Significant differences were noted in the peritumoral distal ADC, proximal and distal Viso and ECVF value between HGG and MET.

Viso: CSF volume fraction, ECVF: extra-neurite volume fraction,
 dis: distal, pro: proximal
 HGG: high-grade gliomas, MET: distal metastatic brain tumors*

(Filename: TCT_P-25_2018ASNR56thNODDI.jpg)

P-12

Diffusion-tensor Imaging of Intracranial Epidermoid Cysts

N Soni¹, T Moritani², A Capizzano¹, G Bathla¹, T Sasaki³

¹University of Iowa Hospitals and Clinics, Iowa City, IA, ²University of Michigan, Ann Arbor, MI, ³University of Iowa, Iowa City, IA

Purpose

Epidermoid cyst (EC) is one of the central nervous system masses showing characteristics high-signal intensity on DWI. Purpose of this abstract is to understand the predominant pattern of diffusion and microstructural pathology of epidermoid cysts using entire lesion diffusion tensor imaging (DTI) in comparison with the splenium of the corpus callosum (CC).

Materials and Methods

We retrospectively evaluated 19 patients with histologically proven intracranial epidermoid cysts using echo-planar DTI with 15 directions (TR-4100msec, TE-77msec, 2NEX, parallel imaging factor 2, slice thickness 5mm). Presurgical DTI data were analyzed with a region of interest (ROI) approach to include the entire lesion and a control ROI at the CC. For each lesion and CC, the following DTI parameters were calculated: fractional anisotropy (FA) and mean diffusivity (MD), axial diffusivity (AD), and radial diffusivity (RD). Statistical significance level was set at $p < .05$.

Results

The mean FA and AD were significantly lower in the lesion than in the CC ($P < .001$). The mean MD and RD were significantly higher in the lesion than in the CC ($P < .001$). Higher RD and lower AD in epidermoid cyst suggested preferential diffusion along a two-dimensional plane, which could be attributed to the parallel-layered arrangement of keratin filaments and flakes within these tumors in histopathology.

Conclusions

DTI derived parameters can provide information about the microstructural anatomy of epidermoid cyst and help in understanding the diffusion characteristics.

	Epidermoid (mean)	Splenium (mean)	p-value
FA	0.29	0.74	< .001
AD	1.21	1.64	< .001
MD	0.97	0.78	< .001
RD	0.85	0.363	< .001

(Filename: TCT_P-12_Table1.jpg)

P-10

DTI and NODDI Imaging in a Disc1 Genetic Model of Schizophrenia

B Barnett¹, M Torres Velazquez¹, S Yi¹, J Anderson¹, P Rowley¹, V Bakshi¹, J Yu¹

¹*University of Wisconsin-Madison, Madison, WI*

Purpose

Schizophrenia is a chronic and debilitating mental illness affecting perception, cognition, behavior, and social functioning and affects up to 1% of the worldwide population. Disc1 is a well-known genetic variant of large effect in the neuropathogenesis of schizophrenia first identified in a unique Scottish pedigree segregating with schizophrenia and influences neuronal migration and patterning in early neurodevelopment as well as corticogenesis in vivo. To further understand the contribution of Disc1 in the both the neurodevelopment and neuropathogenesis of schizophrenia, we utilized a novel biallelic CRISPR/Cas9 Disc1 rat knockout model and concurrently performed diffusion tensor imaging (DTI) and neurite orientation dispersion and density imaging (NODDI) to investigate the contribution of Disc1 to neural microstructure.

Materials and Methods

Using CRISPR/Cas9, the second coding exon of Disc1 was targeted for genome editing through the generation of nonsynonymous mutations. Genotyping of potential founders indicated the successful excision of the target, and genotyping of the resultant pups from the F1 generation identified two ideal loss-of-function alleles: Disc1[860] and Disc1[874]. Ex-vivo high-resolution magnetic resonance imaging of Disc1(-/-) and wild-type age- and sex-matched rats was performed. Brains were simultaneously imaged with a 4.7-T Agilent MRI system and a 3.5-cm diameter quadrature volume RF coil was used to acquire 10 nondiffusion-weighted images (b=0 s·mm²) and 75 diffusion-weighted images (25: b=800 s·mm², 50: b=2,000 s·mm²). Following standard preprocessing, tensors were reconstructed, registered, and normalized to a population-specific template. In parallel, NODDI parameters were estimated using an ex-vivo fitting model and converted to volumetric parameter maps. Transformation fields from corresponding single-shell data registration were applied to NODDI data. NODDI data were then projected onto the previously-defined white matter skeleton that was created from single-shell diffusion tract-based spatial statistics (TBSS). TBSS were computed to evaluate whole-brain voxel-wise differences in standard diffusion indices and NODDI parameters between Disc1(-/-) and control animals. Permutation test results for multiple comparisons and threshold-free cluster enhancement (TFCE) are implemented with FSL's randomize and considered significant at the <0.05 level following family-wise error correction.

Results

TBSS analysis revealed widespread perturbations in white matter structure and organization across all scalar measures of the diffusion tensor in Disc1(-/-) rats. Changes were most pronounced in neocortex and

corpus callosum, and unexpected changes in the hindbrain, including the cerebellum were demonstrated. This analysis also revealed voxel-wise changes in parametric measures of neurite density (NDI) and orientation dispersion (ODI) in the neocortex, corpus callosum, and cerebellum.

Conclusions

DTI and NODDI demonstrate the gene-specific contribution of *Disc1* in global measures of microstructural integrity. NODDI complements DTI by uncovering novel and previously occult regions of structural change and neurite organization and speaks to the utility of multi-shell diffusion studies in models of neuropsychiatric disease. These findings establish a platform for further exploration into molecular, behavioral, and neuroimaging features of this genetic model.

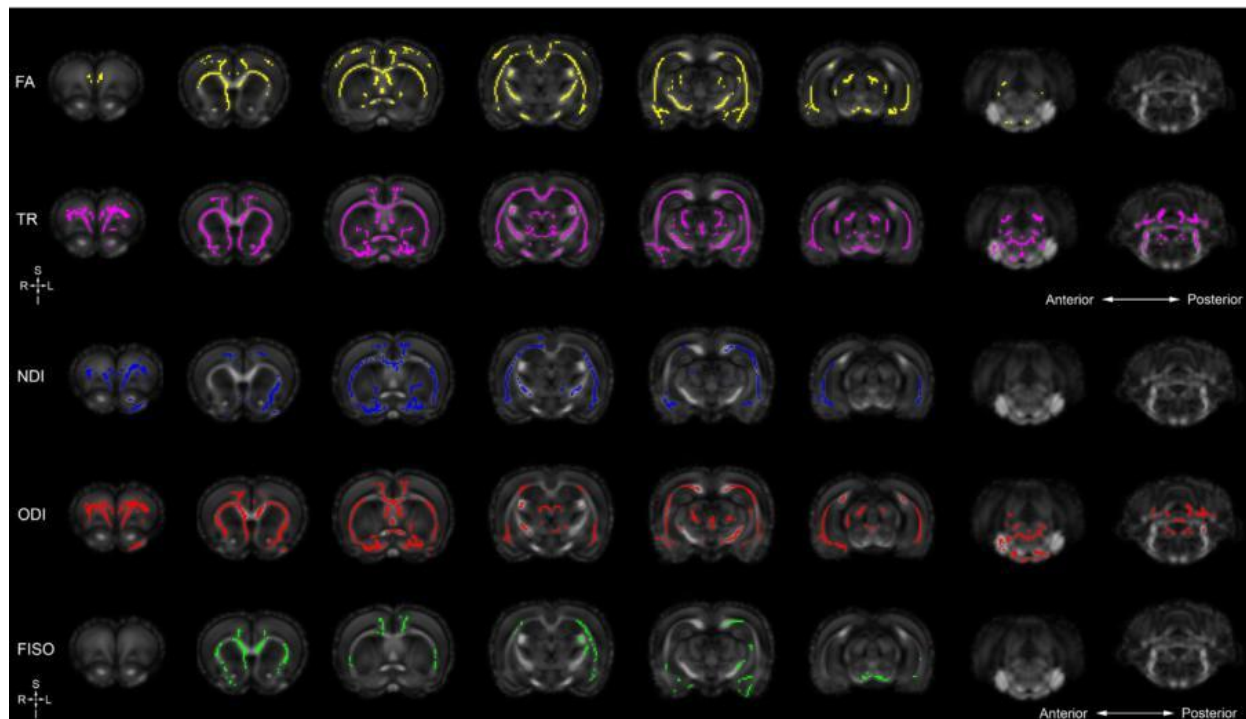


Figure 1: TBSS analysis revealed widespread perturbations in white matter structure and organization across all scalar measures of the diffusion tensor in *Disc1*(-/-) rats. Changes were most pronounced in neocortex and corpus callosum, and unexpected changes in the hindbrain, including the cerebellum were demonstrated. This analysis also revealed voxel-wise changes in parametric measures of neurite density (NDI) and orientation dispersion (ODI) in the neocortex, corpus callosum, and cerebellum.

(Filename: TCT_P-10_ASNR_Abstract_121517_Figure1.jpg)

P-29

Efficacy of High- Versus Low-dose Contrast for Brain MRI

N Anumula¹, A Miller¹, V Agarwal¹

¹University of Pittsburgh Medical Center, Pittsburgh, PA

Purpose

The optimization of MRI gadolinium-based contrast dosage is crucial to minimizing gadolinium deposition and potential long-term gadolinium-associated toxicity with the use of these agents. We analyze cases of both high- and low-dose contrast administration to determine if there is a statistically significant difference in diagnostic brain MRI studies.

Scientific Posters

Materials and Methods

MRI brain studies were retrospectively analyzed from our institution performed within the last year (9/1/16-9/1/17). Patients administered both high-dose Multihance (gadobenate dimeglumine) contrast agent defined as 21cc or greater and low-dose defined as 20cc or less were included in the study. A ratio of postcontrast enhancement to precontrast enhancement was calculated using regions of interest (ROIs) placed over the pituitary gland to generate a contrast enhancement ratio and compared for statistical significance. In one instance where this was not possible, dural venous sinus enhancement was measured.

Results

Fifteen patients were analyzed for both high- and low-dose contrast enhancement ratios. The mean of the high-dose contrast enhancement ratio was 2.25 with standard deviation of 0.89. The mean of the low-dose contrast enhancement ratio was 2.10 with standard deviation of 0.77. Using a paired t-test to compare the two groups, the p value was 0.4651 and considered not statistically significant.

Conclusions

There is no significant difference in using greater than 20cc Multihance contrast compared to using 20cc or less in MRI brain studies, and thus no added value in the administration of higher contrast doses.

P-16

Imaging Findings in Patients With Autoimmune Encephalitis - A Retrospective Review

N Sadiq¹, J Fazal¹, M Bowen¹, A Panayiotou¹, W Wali Muhammad¹, S Jacob¹, V Sawlani¹

¹University Hospitals Birmingham NHS Foundation Trust, Birmingham, United Kingdom

Purpose

Background: Autoimmune encephalitis constitutes 20% cases of patients presenting with an encephalitic picture (1). Neuroimaging findings may include normal MRI findings as well as limbic and extralimbic involvement. Prompt recognition allows early immunosuppression and improved outcomes. Objective: A retrospective review of the imaging findings in confirmed patients with autoimmune encephalitis at our institution in last five years

Materials and Methods

Retrospective review of immunology lab database and online clinical records to find confirmed cases of autoimmune encephalitis over the last five years. PACS system was used to review the MRI head scans. Standard MRI brain examination included T2 axial, FLAIR axial, T1 sagittal, T2 coronal and DWI axial sequences.

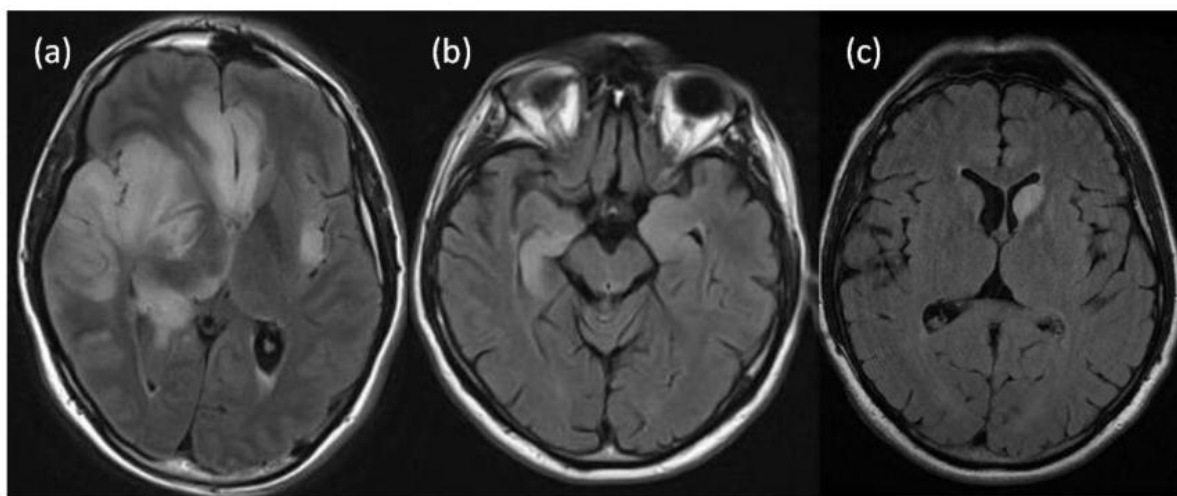
Results

We identified N-methyl-D-aspartate receptor (NMDAR) n=8, voltage gated potassium channel (VGKC) n=11, and leucine-rich glioma inactivated 1 (LGI1) n=11 encephalitis patients (Fig.1). One-eighth NMDAR encephalitis patients had abnormal MRI findings of T2 hyper-intense signal in right anterior temporal and bilateral frontal and left insular lobe. DWI sequence showed restricted diffusion. Four-elevenths with VGKC encephalitis had positive MRI findings. Two patients had limbic involvement while one also had involvement of basal ganglia. Two patients had modest cerebral atrophy. Four patients had normal MRI findings. MRI scan was not available for three patients. Five-elevenths patients with LGI1 encephalitis, had bilateral mesial temporal lobe changes. In one patient, MRI could not be done due to permanent pacemaker. Five patients had normal MRI findings.

Conclusions

In our series, 33% patients had abnormal MRI findings consistent with the diagnosis of autoimmune encephalitis. Individually, 12.5% NMDAR, 50% LGI1 and 36% of VGKC patients had positive MRI findings pointing towards the diagnosis. The MR positive rate in our setting is lower than reported in literature (2). Improvements in pickup rate can be achieved by utilizing high resolution FLAIR, T2 and DWI sequences on high field strength MRI.

Figure 1. Confirmed cases of: (a) NMDAR encephalitis (b) LGI1 encephalitis (c) Non-LGI1 VGKC encephalitis.



(Filename: TCT_P-16_Capture2.JPG)

P-31

Infarct Core Volume Measured by DWI in Hyperacute Stroke As a 90-day Predictor of Functional Outcome After Endovascular Reperfusion

P Diluca¹, G Maida¹, M Buezas¹, J Cirio¹, H Lambre¹, P Lylyk¹

¹*Clínica La Sagrada Familia, ENERI, Capital Federal, Buenos Aires, Argentina*

Purpose

Endovascular reperfusion is not recommended in ischemic strokes when core volume is bigger than 50 ml. All these patients without reperfusion had a 90-day modified ranking scale of 3-6, and 48% of mortality. In this study we evaluated the core volume measured on DWI as a functional predictor in large vessel occlusion (LVO) strokes of the anterior circulation, submitted to endovascular treatment (EVT).

Materials and Methods

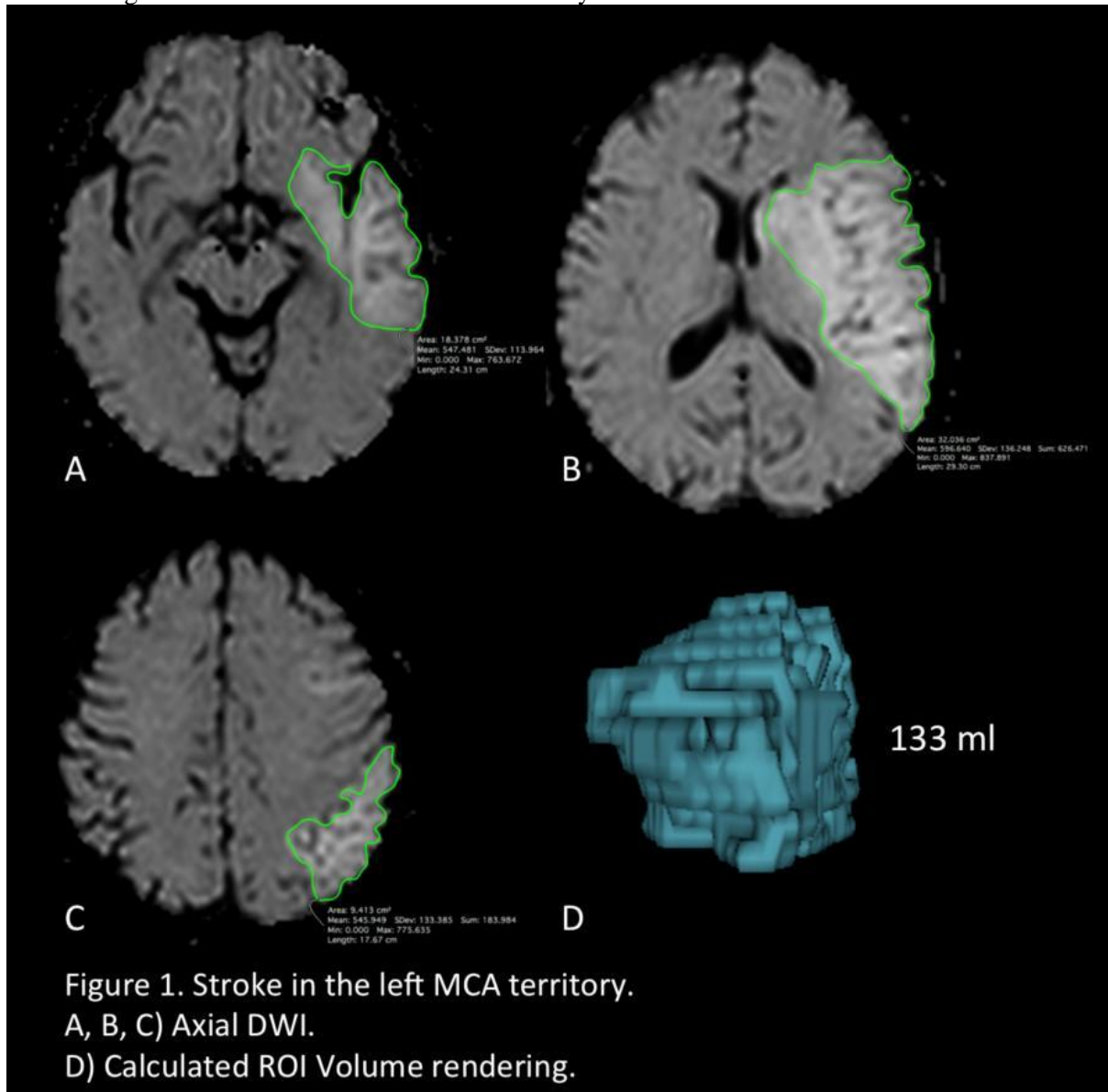
We retrospectively evaluated 80 LVO strokes pre-EVT. Core volume was manually calculated by a vascular neurologist and two neuroradiologists separately, using Osirix MD 7.5. Core volumes were grouped in A: less than 50 ml, B: between 51-70 ml and C: greater than 70 ml. Demographics data, NIHSS 0-24 hs, assistance metrics, grade of reperfusion by modified treatment In cerebral ischemia (mTICI), symptomatic intracranial hemorrhage (IH) and mRS at 90 days were also registered.

Results

Demographics data, risk factors, assistance metrics, TICIm and IH didn't show significant differences. In group A (n50), the DWI median and interquartile range was 10 ml (4-19), in group B (n11) 55 ml (53-63), and in group C (n19) 117 ml (86-152) p.0001. Group A had better outcome than group C in the mRS < 2 between 6 to 90 days (p.001 OR 7.3 IIC95% 1.8-28.5) (p.003 OR 0.14 IIC95% 0.03-0.59) respectively. There was no difference between groups A and B. The combination between groups A+B (<70 ml) didn't change the benefit in comparison with group C and the mRS < 2 between 6 to 90 days (p.0004 OR 5.88 IIC95% 1.5-22.3) (p.01 OR 0.22 IIC95% 0.06-0.75) respectively. Patients with DWI volume greater than 70 ml with EVT presented a nonstatistical significance benefit, in comparison to a group with similar characteristics without EVT.

Conclusions

The core volume measured in DWI lower than 70 ml in LVO strokes of the anterior circulation with EVT had a strong association with better outcome at 90 days.



(Filename: TCT_P-31_vol.jpg)

P-32

Long-term Changes in White Matter Microstructure During Recovery from mTBI in a Civilian Population

G Sultoti¹, E Palacios², N Nguyen², E Yuh², P Mukherjee²

¹Duke School of Medicine, Durham, NC, ²University of California, San Francisco, San Francisco, CA

Purpose

Diffusion-tensor imaging (DTI) has proven to be a useful biomarker of traumatic axonal injury (TAI) in

Scientific Posters

mild traumatic brain injury (mTBI). This study characterizes the time evolution of microstructural white matter injury in mTBI from the semi-acute to chronic phases, which white matter tracts are involved, and how the longitudinal trajectory of DTI metrics correlates with patients' evolving cognitive performance.

Materials and Methods

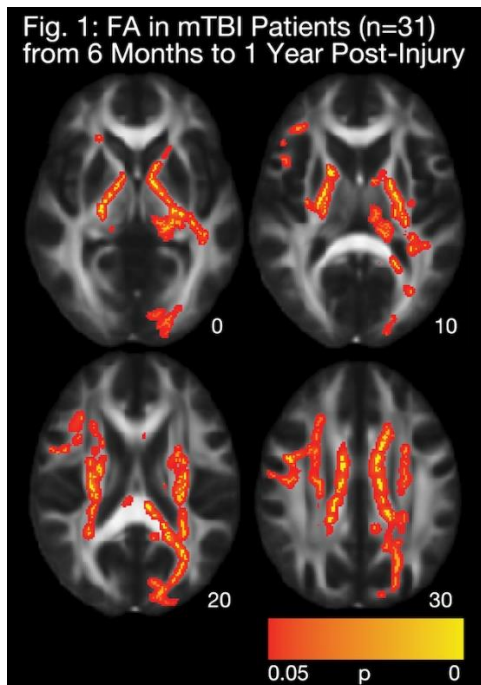
We acquired 3T DTI scans (55 directions, $b=1000$ s/mm², 1.8-mm isotropic resolution) and cognitive testing in 31 mTBI patients at 1 month, 6 months, and 1 year postinjury, employing a whole brain voxel-wise approach with tract-based spatial statistics (TBSS). Fractional anisotropy (FA), mean diffusivity (MD), axial diffusivity (AD), and radial diffusivity (RD) of the mTBI patients were compared to 36 healthy age- and gender-matched controls. Longitudinal analysis of changes in these 4 DTI metrics across the 3 time points was also conducted in the mTBI group. Voxelwise statistical comparisons were performed using permutation testing, with corrections for multiple voxelwise comparisons using threshold-free cluster enhancement (TFCE). Longitudinal changes in FA, MD, AD, and RD were then correlated to changes in cognitive testing results at each of the three time points.

Results

When compared to healthy control subjects, mTBI patients demonstrated an increased FA and decreased MD, AD, and RD at one year post injury in periventricular white matter tracts such as the corpus callosum – a supranormalization of chronic mTBI patients' DTI parameters relative to healthy controls. Longitudinally, an increase in FA from one month to one year post injury, especially noticeable after six months, and a decrease in MD, AD, and RD from one month to one year post injury were demonstrated in periventricular white-matter tracts such as the corpus callosum, the internal capsule, and the corona radiata (Fig. 1). These long-term longitudinal changes in DTI metrics, particularly in periventricular white-matter tracts, correlate with improvement in cognitive testing of attention, planning, calculation ability, auditory information processing speed, and dominant response inhibition as measured by the neurocognitive testing battery. Figure 1. Progressive increase of white matter fractional anisotropy (FA) from six months to one year after mild TBI. The red-yellow color scale depicts statistically significant increase of FA over time ($p<0.05$, corrected for multiple voxelwise comparisons).

Conclusions

Our results provide new evidence for the use of DTI as an imaging biomarker of cognitive outcome up to a year after mTBI, with much of the change in white-matter microstructure occurring after 6 months post injury, a time point that is typically used as the "long-term" outcome in mTBI studies. This continued evolution of DTI metrics beyond six months better captures the extent of recovery or deterioration in cognitive function after mTBI.



(Filename: TCT_P-32_ASNR_abstract_graphic_reduced.jpg)

P-04

Manual Segmentation to Assess the Effect of Physical Activity on Hippocampal Volume Loss Over Two Years in Elderly at Risk of Dementia

L Chau¹, E Lui², C Steward², V Venkatraman², K Cox³, N Lautenschlager¹, P Desmond²

¹University of Melbourne, Parkville, Victoria, Australia, ²Royal Melbourne Hospital, Parkville, Victoria, Australia, ³University of Western Australia, Perth, Western Australia

Purpose

Studies have demonstrated physical activity (PA) is protective against cognitive decline and dementia (1). We aim to assess the effect of PA on hippocampal volume loss in a cohort of older adults at risk of dementia who underwent a 2-year exercise program with 3T MRI (2) using manual segmentation.

Materials and Methods

This randomized controlled trial recruited participants from the Australian Imaging, Biomarkers and Lifestyle study (2, 3). The PA intervention was two years of moderate exercise; years of education and ApoE ϵ 4 status were also documented (2). Ninety-eight subjects had 3T MRI at baseline and two years, 48 (age 74.2 ± 5.7 , M=21, F=27) were allocated to the control arm, and 50 (age 72.2 ± 5.7 , M=22, F=28) to the exercise arm. Hippocampi were manually segmented using T1 weighted 1mm isotropic MPRAGE images (TR/TE/TI were 1900ms/2.13ms/900ms respectively, flip angle 9°) and based on anatomical landmarks defined previously (4) using ITK-SNAP. After ten segmentations, landmark consistency was assessed using a side-by-side comparison for each time-point. Automated intracranial volume (ICV) was obtained using FreeSurfer 6.0 (5) for head size correction. Change measure was calculated as volume difference at the two time-points divided by ICV. General linear models were performed using SPSS 24.0 (IBM, Chicago, IL). Significance defined < 0.05 .

Results

There was no difference between intervention and control group for left, right and total hippocampal volumes at two years ($p = 0.60, 0.51$ and 0.50 respectively) after adjusting for age, sex, education, ApoE

ε4 status, ICV and baseline hippocampal volume (Figure 1, Table 1). The change measure of hippocampal volume also showed no effect of the intervention on left, right and total hippocampal volume ($p = 0.54, 0.48$ and 0.45 respectively, Figure 2).

Conclusions

Our study found no group effect of the PA intervention on hippocampal volumes at two years using a manual segmentation method that focused on detecting subtle change.

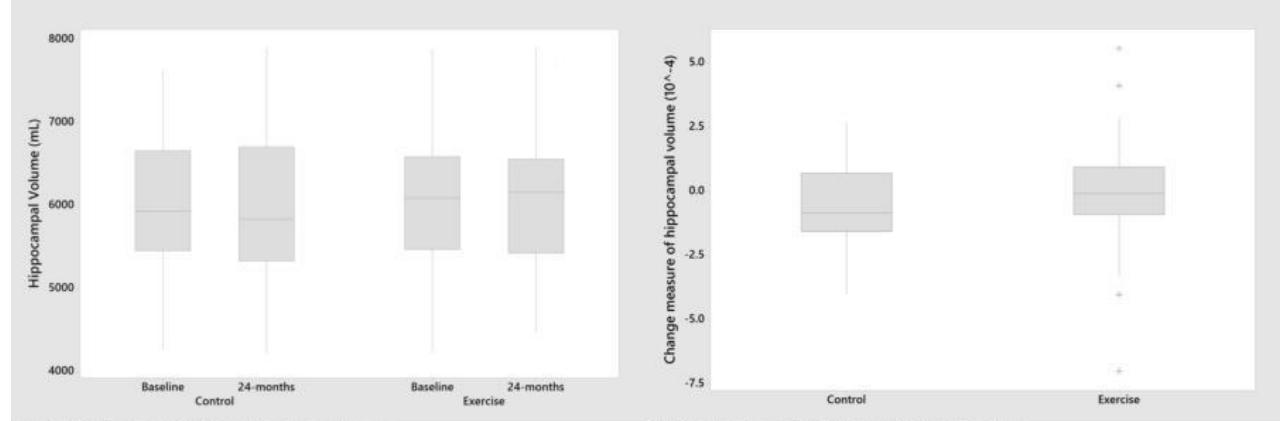


Figure 1. Effect of exercise on total hippocampal volume over two years.

Figure 2. Change measure of total hippocampal volume over two years.

Table 1. Regression results of hippocampal volume at two years predicting intervention.

	Left Hippocampus		Right Hippocampus		Total Hippocampus	
	β	p	β	p	β	p
Age	-0.071	0.050	-0.071	0.075	-0.074	0.035
Sex	-0.028	0.493	-0.032	0.487	-0.002	0.965
Education	-0.033	0.342	0.000	0.992	-0.016	0.636
ApoE status	-0.060	0.081	-0.058	0.138	-0.060	0.077
Baseline volume	0.929	0.000	0.907	0.000	0.926	0.000
ICV	0.011	0.812	-0.010	0.846	-0.001	0.984
Intervention	0.018	0.597	0.025	0.513	0.023	0.498

β and p -values from linear regression models adjusting for age, sex, years of education, ApoE ε4 carrier status, ICV, baseline hippocampal volume and the intervention.

(Filename: TCT_P-04_ASNR2018_Figures.jpg)

P-15

Microstructural Changes of the Trigeminal Nerve and White Matter Tracts in Patients with Trigeminal Neuralgia: An Evaluation with MR RESOLVE DTI

T Chen¹

¹Chi-Mei Medical Center/Graduate Institute of Medical Sciences, Chang Jung Christian University, Tainan, Taiwan

Purpose

Trigeminal neuralgia refractory to medical treatment can be managed with CyberKnife radiosurgery (CKRS) or radiofrequency ablation (RFA). It is also known that magnetic resonance imaging (MRI) with diffusion-tensor imaging (DTI) is capable of depicting microstructural changes of the trigeminal nerve. By means of DTI, we are able to detect subtle changes of the trigeminal nerve cisternal segment and the supratentorial/infratentorial white matter in patients diagnosed with trigeminal neuralgia.

Materials and Methods

We retrospectively enrolled 15 patients with refractory trigeminal neuralgia lasting for more than two years, who underwent CKRS or RFA as treatment. MRIs were done before treatment, including the sequences of three-dimensional T2-weighted sampling perfection with application-optimized contrast with different flip angle evolution (SPACE) imaging and readout segmentation of long variable echo-trains (RESOLVE) DTI with the generation of apparent diffusion coefficient (ADC), fractional anisotropy (FA), radial diffusivity (RD), axial diffusivity (AD) and mean diffusivity (MD) values in each voxel and

color-coded maps (orientation encoding). We analyzed the trigeminal nerve cisternal segment on the affected side and compared to the contralateral side after selecting a region of interest (ROI) manually. The application of tract-based spatial statistics (TBSS) was to depict supratentorial/infratentorial white matter changes.

Results

We observed decreased FA and increased RD and MD values of the affected side of trigeminal nerve cisternal segment, when compared to the contralateral side. Additionally, some differences were noted in supratentorial/infratentorial white matter in patients with trigeminal neuralgia.

Conclusions

DTI was useful in detecting microstructural changes in patients with trigeminal neuralgia, as demonstrated by FA, RD and MD differences in the trigeminal nerve cisternal segment. It also revealed supratentorial and infratentorial white-matter tracts abnormalities.

P-13

Occipital Hypoperfusion Measured with a Three-dimensional Stereotaxic ROI Template on 99mTc-ECD SPECT Correlates with Cardiac Uptake on 123I-MIBG Scintigraphy in Parkinson's Disease

T Nakatsuka¹, H Terada¹

¹*Toho University Sakura Medical Center, Sakura, Chiba, Japan*

Purpose

To assess whether occipital hypoperfusion measured with a three-dimensional stereotaxic ROI template (3DSRT) on 99mTc-ECD SPECT correlates with cardiac uptake on 123I-MIBG scintigraphy in the patients with Parkinson's disease (PD)

Materials and Methods

We retrospectively reviewed 23 patients (age, 66.6±7.4 years old; 9 males and 14 females) with clinically-diagnosed PD who had undergone 99mTc-ECD SPECT and 123I-MIBG scintigraphy for examining extrapyramidal signs. Regional cerebral blood flow (rCBF) in bilateral occipital lobes (OLs) and the occipital lobes-to-cerebellum (OLs/CBL) ratio of regional blood flow were measured with a 3DSRT. Cardiac uptake of 123I-MIBG was measured as the heart-to-mediastinum (H/M) ratio in planar images. Correlation analyses were performed between these parameters. We defined that $p < 0.05$ was statistically significant.

Results

Coefficients of correlation between rCBF in the OLs and the H/M ratios were 0.41 (early H/M ratio), 0.44 (delayed H/M ratio). Coefficients of correlation between the OLs/CBL ratio and the H/M ratios were 0.23 (early H/M ratio), 0.28 (delayed H/M ratio). The coefficient of correlation between rCBF in the OLs and the delayed H/M ratio was only statistically significant ($p = 0.03 < 0.05$).

Conclusions

Occipital hypoperfusion measured with a 3DSRT on 99mTc-ECD SPECT correlates the delayed H/M ratio on 123I-MIBG scintigraphy. Occipital hypoperfusion measured with the 3DSRT on 99mTc-ECD SPECT may predict the decrease in the delayed H/M ratio on 123I-MIBG scintigraphy.

P-03

Progressive Cerebral Atrophy as a Predictor of Patient Mortality

B Perry¹

¹*Maine Medical Center, Portland, ME*

Purpose

This study explores the correlation between rates of cerebral atrophy, as defined by change in bifrontal ratio, and five-year mortality. Bifrontal ratio is a metric that may be easily employed by the radiologist in day-to-day practice in interpretation of head CTs.

Materials and Methods

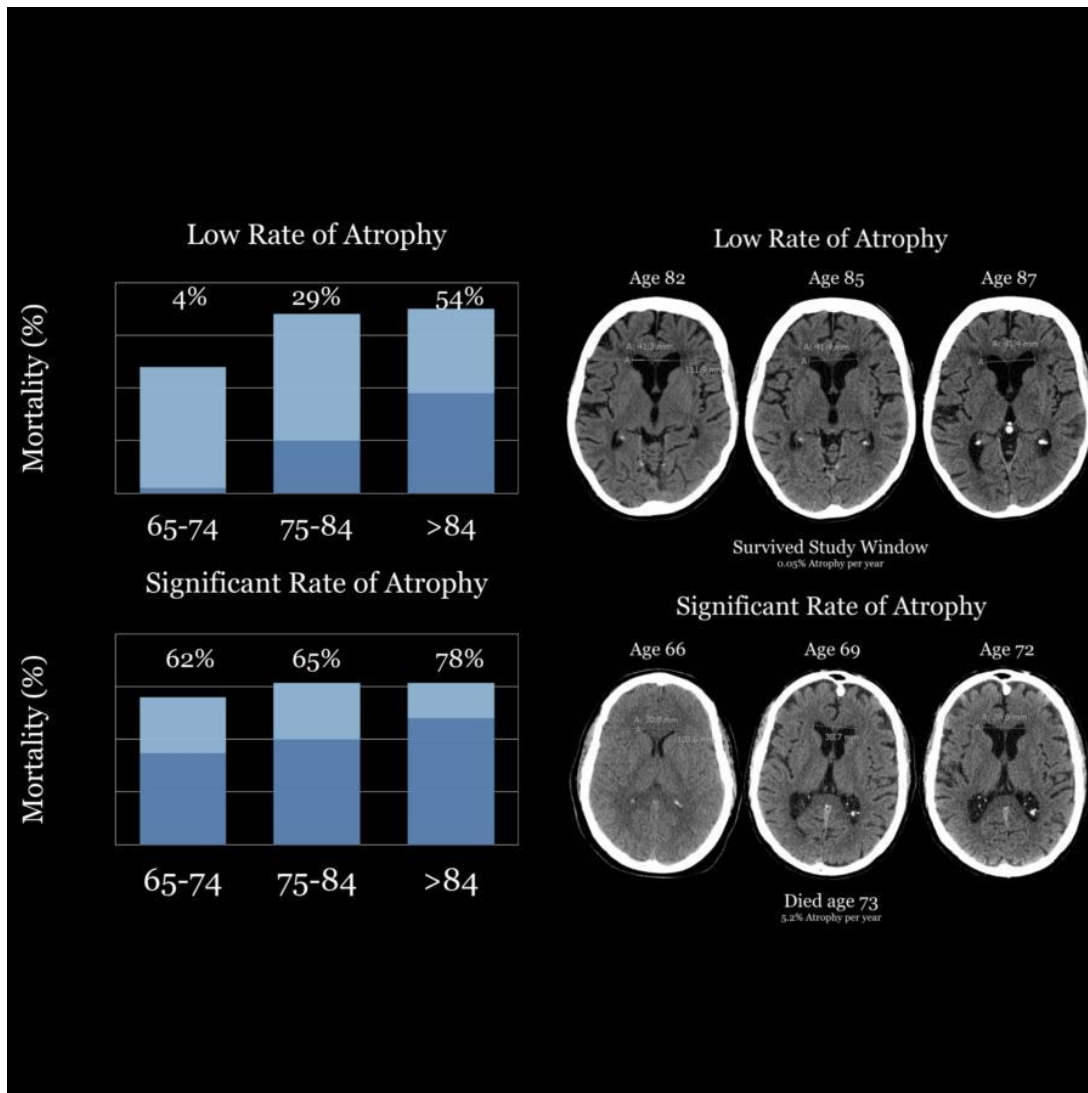
Noncontrast head CTs of patients 65 and over performed at Maine Medical Center (MMC) in the year 2010 were screened. Inclusion criteria included availability of at least two head CTs separated by at least 18 months and confirmation of five-year survival or mortality in the electronic health record. Exclusion criteria for any given scan included significant acute pathology. Bifrontal ratio was used to define degree and annual rate of atrophy. The primary endpoint was defined as either death or enrollment in hospice within five years of the initial scan.

Results

The study group contains 394 total patients, divided into three age cohorts: 65-74, 75-84, 85 and over. Patients with a significant rate of atrophy had 69% five-year mortality. From youngest to oldest cohorts, these numbers were 62%, 65%, and 78%. For patients with low rates of atrophy, five-year mortality rate for the youngest and oldest groups was 4% and 54% respectively.

Conclusions

There is a positive correlation between rate of cerebral atrophy and patient mortality. This correlation appears particularly pronounced at the extremes. Of the 27 patients in the study with more than 3% change in atrophy per year, only four of these were directly addressed in the imaging report as progressive atrophy. This data suggests that the identification and description of progressive atrophy - for which trend lines dating back several years are often essential - should become commonplace in the neuroradiologist's reporting.



(Filename: TCT_P-03_atrophyresearch.jpg)

P-02

Radiological Characteristics of MRI-guided Focused Ultrasound (MRgFUS) Thalamotomies for Essential Tremor (ET): Relevance to the Neuroradiologist

A Kapadia¹, A Boutet², G Elias², S Michael³, W Kucharczyk⁴, A Lozano²

¹University of Toronto, Toronto, Ontario, Canada, ²Toronto Western Hospital, University of Toronto, Toronto, Ontario, Canada, ³Sunnybrook Health Science Center, University of Toronto, Toronto, Ontario, Canada, ⁴Toronto General Hospital, Toronto, Ontario, Canada

Purpose

MRgFUS is a novel technique that uses high-intensity focused ultrasound to thermally ablate tissue to treat ET. As the number of patients undergoing MRgFUS increases, it is important for neuroradiologists to recognize the post-treatment appearance. The purpose of this study was to 1) define the temporal evolution of MRgFUS lesions on imaging, 2) evaluate the relationship of lesion appearance to treatment parameters, and 3) evaluate for predictive value of the MRI findings for clinical outcomes.

Materials and Methods

In this prospective study, 69 patients with medically refractory essential tremor underwent MRgFUS thalamotomy. Patients had MRIs and clinical evaluation using the Clinical Rating Scale for Tremor (CRST) score at one day, three months, and one year post procedure, with comparison to baseline. Patients were assessed for temporary and permanent side-effects. Statistical analysis and modeling was performed in R.

Results

The size of the MRI visible lesion on post-procedure day one varied depending on the pulse sequence. Average lesion volume (mm³) decreased with time (181.8 +/- 90.6 at day 1 and 28.4 +/-47.5 at 1 year). The degree of perilesional edema on day one as it appeared on FLAIR images varied and was associated with total energy deposited (p=0.047). Many patients demonstrated focal hyperintensity on FLAIR images persisting to one year. Characteristic zone II diffusion restriction was seen at day one, and resolved by three months. At day one nearly all lesions demonstrated intralesional haemorrhage. Postcontrast images demonstrated mild peripheral enhancement which persisted at one year. No association was demonstrated between MR imaging parameters and tremor score or adverse effects.

Conclusions

MRgFUS thalamotomy produces a characteristic lesion which decreases in volume over time. The perilesional edema seen early post treatment is associated with the amount of energy that is deposited. However, the basic imaging appearance is not predictive of treatment response or side-effects.

Table 1: Patient demographics.

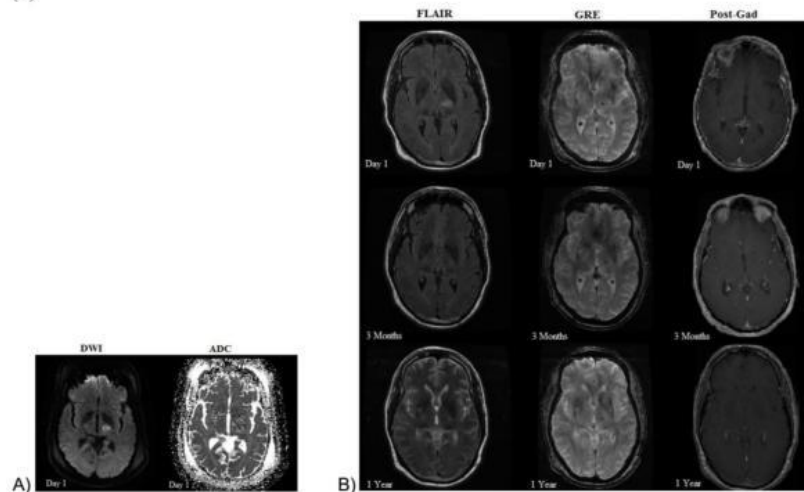
N	69
Age (years)	70.3 (+/-8.6)
Female (%)	29
Duration of Disease (Yrs)	31.1 (+/- 17.3)
Baseline CRST	59.5 (+/-17.5)

Table 2: Imaging appearance at day 1, 3 months and 1 year.

	Day 1	3 Months	1 Year
IMAGING			
FLAIR Edema (Day 1 Only)	100% (32 % Extensive, 68 % Limited)	N/A	N/A
Focal FLAIR			
Intralesional	N/A	41%	37%
Perilesional	N/A	15%	13%
Intralesional and Perilesional	N/A	18%	6%
None	N/A	26%	44%
Hemorrhage			
No	6%	N/A	N/A
Yes	94%	N/A	N/A
Zone II Diffusion Restriction	100%	N/A	N/A
Size Measurable	100%	79%	72%
Average Size (mm ³)	181.8 (+/- 90.6)	47.5 (+/-28.4)	28.4 (+/-47.5)
Clinical Outcome			
CRST Combined	59.5 (+/- 17.5)	34.8 (+/- 14.4)	39.3 (+/- 14.4)

Figure 1: Typical appearances of the thalamotomy lesion at day 1 on DWI (A) and day 1, 3 months and 1 year on evolution (B).

(B).



(Filename: TCT_P-02_Diagrams.jpg)

P-08

Regulated-convolutional Networks for Low-dose Cerebral CT Perfusion Restoration

P Liu¹, Y Li¹, M El Basha¹, P Sanelli², R Fang¹

¹University of Florida, Gainesville, FL, ²Northwell Health, Manhasset, NY

Purpose

Computed tomography perfusion (CTP) is a widely utilized imaging modality, especially for the brain region, owing to its high spatial resolution, wide availability, fast imaging, and low cost. However, its cine-scanning mode brings substantial concerns about the elevated radiation exposure. To reduce the

radiation dose in CTP, we propose a Regulated-Convolutional Neural Network (RC-Net) to restore the perfusion images from the low-dose data.

Materials and Methods

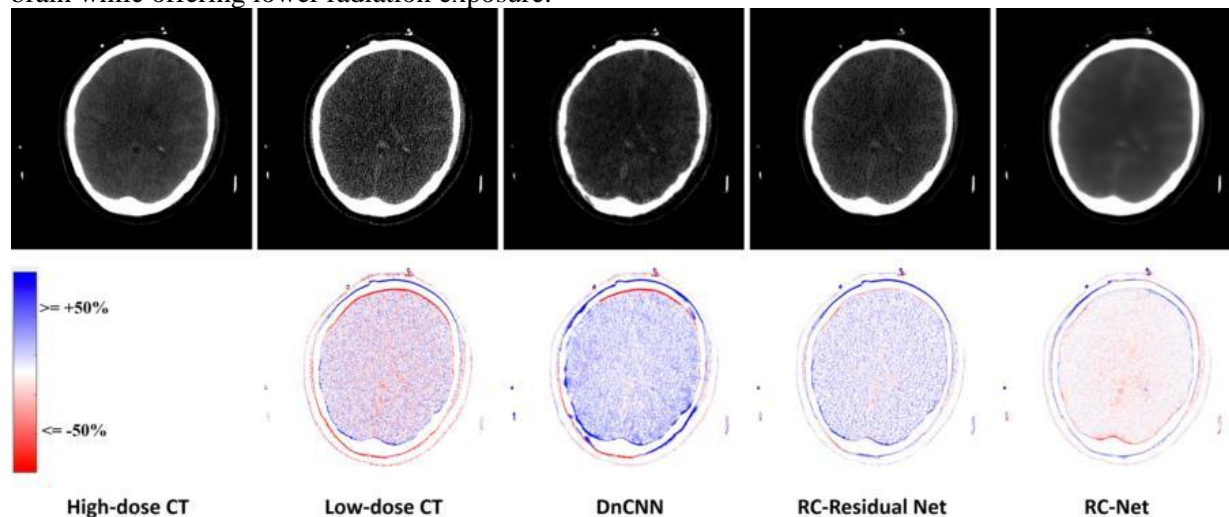
Preprocessing was performed on real CT images of human brains scanned at both low- (8 mAs and 20 mAs) and high-dose (160 mAs) from an IRB-approved HIPPA-compliant protocol on aneurysmal subarachnoid hemorrhage (aSAH) patients. The RC-Net structure is built by stacking multiple subnetwork blocks in a cascaded fashion. The organization of layers falls into three distinct functional sections: 1. the initial convolutional layer for feature-extraction 2. four regulated-convolution blocks for feature-mapping and transformations, each block containing a 1x1 convolutional layer, large 7x7 convolutional kernel followed by a smaller 3x3 convolutional kernel, with another 1x1 convolutional layer in between, cascaded by skip-connections 3. the image reconstruction layer

Results

RC-Net was trained with low/high-dose paired real whole brain CT scan patches from two patients. RC-Net, with restoration quality peak signal-to-noise ratio (PSNR) (dB)/structural similarity (SSIM) of 23.11/0.7300, out-performs state-of-art methods including DnCNN [1] of 22.52/0.7093. Differences between ground-truth and each methods DnCNN, RC-residual Net, RC-Net are shown visually in the following figure. Image restoration results (top) and Image difference results (bottom). Differences are shown in red-blue color bar. Red color correlates to the negative difference value between restoration and ground-truth while blue shows positive value. RC-Net shows better restoration result from low-dose CT.

Conclusions

A novel model RC-Net is developed and applied to restore low-dose cerebral CT perfusion scans. The model is capable of being trained to accurately perform image restoration while maintaining the option of being scalable with the proposed regulated-convolution block framework. High-quality cerebral perfusion maps produced from low-dose CTP data promises great potential for effective disease detection in the brain while offering lower radiation exposure.



(Filename: TCT_P-08_difference.jpg)

P-09

The Neural Connectivity Evaluation in Patient of Treatment Resistant Mood Disorders

C Chen¹, C Lin², J Chai¹, T Lan¹, H Chen¹

¹Taichung Veterans General Hospital, Taichung, Taiwan, ²Institute of Neuroscience, National Yang-Ming University, Taipei, Taiwan

Purpose

By using the resting-state fMRI (rsfMRI) to study the dynamic changes of brain connectivity in major depressive disorder (MDD) patients after repetitive transcranial magnetic stimulation (rTMS) therapy, we aimed to clarify the mechanism of rTMS therapy in MDD patients and its effects to brain connectivity between brain regions.

Materials and Methods

Patients with diagnosis of MDD and resistant to optimized treatment were referred to received TMS therapy over dorsolateral prefrontal cortex (DLPFC). Twenty-four patients were randomly assigned either to active TMS (n=14, 5 men, 9 women, age: 49.2±11.1 yr) or sham TMS (n=10, 5 men, 5 women, age: 45.4±7.7 yr) treatment group. The guided TMS was on a DLPFC target determined with resting-state functional connectivity (rsFC) and sham TMS was applied with coil tilted 90 degrees. All patients underwent 2 rsfMRI sessions using a Siemens 1.5T Aera system before (Pretest) and after (Post-test) the 2-week TMS intervention. Individual functional images were preprocessed and analyzed with statistical parametric mapping (SPM8) and Resting-State fMRI Data Analysis Toolkit (REST).

Results

This result inferred that combined rTMS with medicine had greater efficacy than monotherapy on alleviating the depressive symptom. We found the rTMS specifically highlighted connections in the cortico-limbic emotional regulation circuits, and the medication enhances the connections more related to default mode network and limbic pathways, while both groups showed improved default mode network and executive network connections, which inferred the general pattern of remission. Therefore, the results indicated that the local stimulation might mitigate depressive symptom through regulating the underlying neural circuitries rather than local effects.

Conclusions

The rsfMRI provided a noninvasive approach for the connectivity between brain regions beyond MDD more specifically. The treatment efficacy of combined rTMS and antidepressant seems to be better than monotherapy, but the subtle differences of the patient subtypes require further investigation.

P-30

Variability in At-risk Tissue Volumes in Patients with Proximal, Intracranial Large Vessel Occlusion In Acute Ischemic Stroke

S Dehkharghani¹, M Bowen²

¹New York University, New York, NY, ²Emory University School of Medicine, Atlanta, GA

Purpose

Proximal MCA occlusions have been reported to invariably compromise the entire MCA territory, producing a consistent hypoperfusion volume and penumbral volume varying only by infarction core size. Past studies may have been confounded by constrained spatial coverage and analysis limited to cortical tissues. The purpose of this study was to evaluate at-risk tissue volumes in MCA stroke by CTP using validated thresholds, hypothesizing significant heterogeneity of penumbral volumes in acute ischemic stroke (AIS).

Materials and Methods

AIS patients with MCA occlusion on CTA and pretreatment CTP were identified by review of a prospectively-enrolled endovascular therapy database. CTP were analyzed in a fully automated software environment (RAPID) including thresholding and lesion segmentation of CTP-produced core (rCBF<30%), hypoperfusion (Tmax>6s), and penumbral mismatch. Linear regression was performed to predict penumbral mismatch at each occlusion level based on known predictors, including core volume, time from onset to imaging, age, NIHSS, collateral score, and glucose. The residual error of the best-fit model was plotted against true, CTP-defined mismatch to assess for the presence of unaccounted variables influencing penumbral volume.

Scientific Posters

Results

Sixty-nine patients (age 64.6 ± 16 years, 40 women) met inclusion. MCA occlusions included: M1=50(72.5%) and M2=17(24.6%); 2(2.9%) had M3 occlusions and were not further analyzed. Mean(SD) symptom onset time to imaging was 372.2min(339.4). Mean(SD) infarction core and penumbral volumes were 27.0(48.6) and 134.1(80.3) cc among M1 occlusions, and 14.5(18.4) and 72.5(36.4)cc among M2, respectively. For M1 occlusions, the linear relationship between residual error and the true mismatch were $r^2=0.65$; for M2, $r^2=0.47$.

Conclusions

Penumbral volumes vary considerably in view of contemporary penumbral patient selection strategies. Importantly, heterogeneity in penumbral volumes amongst M1 and M2 occlusions is not simply accounted for by collateral score, core volume, and other known confounders, possibly reflecting subject-specific tissue-level collateral capacity not captured in collateral scoring. Given the wide variation in penumbral volume at point of occlusion, automated CTP characterization of tissue state may provide patient-specific profiles facilitating appropriate classification and treatment selection in AIS.

Posters-Head and Neck

P-35

Dual-energy CT Applications for the Evaluation of Soft Tissue Inflammation in the Neck

A Perez-Lara¹, G Romero-Sanchez², M Bayat³, R Forghani³

¹Hospital General de Malaga, Malaga, Spain, ²Jewish General Hospital, Montreal, Quebec, Canada, ³Jewish General Hospital and McGill University, Montreal, Quebec, Canada

Purpose

Currently, there is limited evidence pertaining to applications of dual energy CT (DECT) for the evaluation of inflammatory and infectious disease in neck. In this study, we evaluated whether DECT can be used to improve visualization of soft tissue inflammatory and phlegmonous changes and differentiation from normal tissues.

Materials and Methods

Fourteen patients with head and neck soft tissue abscess were selected. All patients underwent a DECT of the neck (64-slice dual-energy scanner with fast kVp switching) and the scans were retrospectively reconstructed at virtual monochromatic image (VMI) energy levels ranging from 40 to 140 keV in 5-keV increments. Quantitative evaluation was performed by placing three nonoverlapping ROIs in adjacent phlegmon and in the areas of nearby fat stranding, as well as in the normal subcutaneous fat and normal muscle as a reference. Spectral Hounsfield unit attenuation curves (SHUAC) and iodine concentration (IC) of phlegmon, cellulitic changes in adjacent fat, and of the normal subcutaneous fat and muscle were derived and compared. Percent relative attenuation differences were calculated to compare phlegmonous changes to normal reference tissue (muscle) and fat stranding to normal fat tissue.

Results

Evaluation of SHUACs of the enhancing part of the phlegmon demonstrated increasing density separation compared to normal muscle on low keV VMIs. The most striking difference was found at 40 keV ($P < 0.0001$, Mann-Whitney U test), and no significant attenuation differences were found on VMIs at 100 keV and higher. In addition, the SHUAC of the areas of fat stranding was found to be different compared normal fat at all energy levels ($P < 0.0001$, Mann-Whitney U test). The percent attenuation difference between phlegmon-muscle and fat stranding-normal fat was highest on 40 keV VMIs. There were significant differences in IC between phlegmon and muscle, with a cutoff of 1.02 mg/cm³ (100% specificity and sensitivity).

Conclusions

DECT may enable improved visualization and characterization of inflammatory changes and their extent, with optimal visualization of phlegmon on low energy VMIs at 40 keV.

P-36

Hemodynamic Segmentation of Digital Subtraction Angiography Using Independent Component Analysis

J Hong¹, Y Kao¹, F Chang², C Lin²

¹National Yang-Ming University, Taipei, Taiwan, ²Taipei Veterans General Hospital and National Yang-Ming University, Taipei, Taiwan

Purpose

Manual analysis of DSA images is time-consuming. We aimed to provide an automatic method for quantitatively analyzing DSA images for clinical application.

Materials and Methods

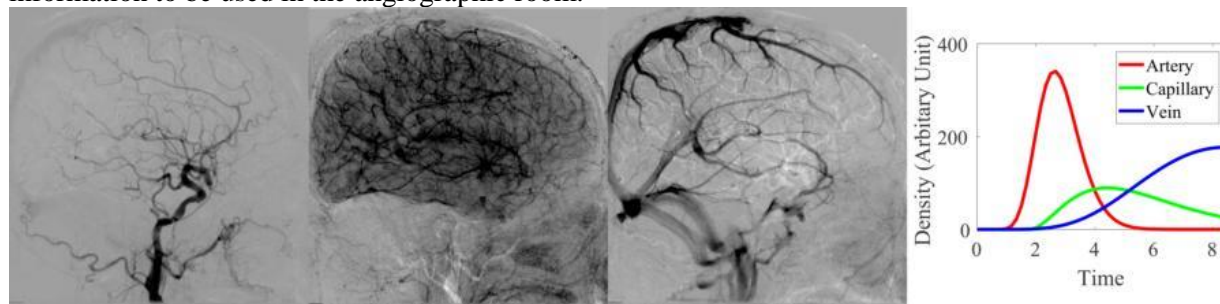
We retrospectively analyzed DSA images acquired from patients with carotid stenosis and underwent the stenting treatment. A registration process was applied to DSA images to reduce motion artifacts. The image sequence was segmented into three vasculatures, including the artery, capillary, and vein, using the independent component analysis. A thresholding method was utilized to generate masks of these three vasculatures. The time-density curves were measured from the three masks and seven hemodynamic parameters were measured from the time-density curve.

Results

The motion artifacts were effectively reduced after the registration process. Spatiotemporal information for the three vasculatures was successfully calculated from the segmentation procedure. Figure shows the three vasculatures and corresponding time-density curves. Time-density curves and corresponding hemodynamic parameters measured from the proposed automatic method correlated very well with that measured manually. The statistic outcome of t-test indicated the significant difference between some hemodynamic parameters measured before and after the stenting treatment.

Conclusions

The independent component analysis technique can automatically and effectively segment DSA images into the artery, capillary, and vein vasculatures. The automatically and manually measured hemodynamic parameters are very similar. The proposed automatic segmentation technique can provide useful information to be used in the angiographic room.



(Filename: TCT_P-36_Figure.jpg)

P-34

Imaging Spectrum of Infectious Thrombophlebitis of the Head and Neck (Lemierre Syndrome)

K Pippin¹, B Hamilton², H Harnsberger³, L Ledbetter⁴

¹University of Kansas Health System, Kansas City, KS, ²Oregon Health and Sciences University, Portland, OR, ³University of Utah, Salt Lake City, UT, ⁴University of Kansas, Kansas City, KS

Purpose

Lemierre syndrome is generally described as oropharyngeal infection secondary to *Fusobacterium necrophorum*, resulting in internal jugular vein (IJ) thrombosis and distant infectious metastases [1]. However, the clinical presentation and literature description of thrombophlebitis of the head and neck is variable [1-4]. This unclear definition of Lemierre syndrome can lead to confusion. The purpose of this project is to review cases of infectious thrombophlebitis of the head and neck, as well as review the literature regarding Lemierre syndrome.

Materials and Methods

Cases from three institutions were reviewed. Cases included head and neck infection resulting in thrombophlebitis, with or without distant septic emboli. In addition, a literature review was performed to identify cases described as Lemierre syndrome.

Results

Fifteen cases of infectious thrombophlebitis of the head and neck were identified. Patients were 15-63 years of age (median 22 years). IJ thrombosis was present in 9/15 patients (60%) with thrombosis of regional veins without IJ involvement in 6/15 patients (40%), including the pterygoid venous plexus, facial, mandibular, and external jugular veins. Sources of infection were pharyngitis, sialadenitis, mastoiditis, and masticator space abscess. Available culture results included three cases of *F. necrophorum* with other cases of *Prevotella* sp., MSSA, and *Streptococcus constellatus*. Distant spread included lungs as well as peripheral joints and cervical spine.

Conclusions

Lemierre syndrome is classically described as pharyngeal infection with *F. necrophorum*, IJ thrombosis, and pulmonary septic emboli. This case series demonstrates that infectious thrombophlebitis of the head and neck can originate outside of the pharynx, result from multiple organisms, cause thrombosis of any adjacent vein, and is not guaranteed to result in pulmonary septic emboli.



Figure 1: Left mandibular vein thrombosis (arrow) in a patient with tonsillar abscess. This patient also had pulmonary septic emboli (not shown).

(Filename: TCT_P-34_ASNR_image.jpg)

P-39

Predictive Measure of Sellar Tumor Morphology for Transsphenoidal Surgery

J Reese¹, J Campbell¹, J Han^{1/sup>}, K Lam¹, A Heffernan¹, G Day¹, S DeShields¹

¹*Eastern Virginia Medical School, Norfolk, VA*

Purpose

Endonasal transsphenoidal surgery is becoming the mainstay of treatment for sellar tumors. There are few studies that have evaluated the tumor size and extent on preoperative imaging to predict the rate of postoperative complications, but there is little data on the relationship between sellar tumor morphology and surgical outcomes.

Materials and Methods

Pre-operative MRI/CT scans from patients undergoing endoscopic sellar tumor resection from 2007 to 2017 were retrospectively evaluated. A neuroradiologist defined the sellar tumors by size, extension, and shape. The surgical difficulty, need for adjuvant treatment, rates of incomplete resection, and rates of postoperative complications were then stratified in relation to the predefined sellar tumor size, extension, and shape.

Results

Sellar tumors of 138 patients were classified from preoperative imaging into 6 characteristic morphologies: 1. Round (R), 2. Transverse oblong (T), 3. Vertical oblong (V), 4. Large lobulated (L), 5. Snowman (S), 6. Microadenoma (M). Specific tumor morphologies were significantly associated with incomplete tumor resections and the use of grafts for control of intraoperative cerebrospinal fluid leaks. Large lobulated (75%), snowman (35%), and transverse oblong (47%) tumors correlated with higher rates of residual tumor ($p < 0.001$). Large lobulated (50%), snowman (33%), and vertical oblong (23.5%) tumors more commonly required use of a graft to repair CSF leaks ($p < 0.012$).

Conclusions

Sellar tumors can be classified into characteristic morphologies on preoperative radiographic scans. Each characteristic morphology is associated with varying degrees of intraoperative surgical difficulty and complications. Utilizing tumor morphology may help aid surgeons in planning the extent of resection, need for complex closure, and patient counseling.

Table 1. Comparison of tumor shape to each type of complication

Variable	Tumor Shape						p-value ^a
	L	M	R	S	T	V	
Residual, n (%)							<0.0001
Yes	9 (21.4)	0 (0.0)	1 (2.4)	20 (47.6)	8 (19.1)	4 (9.5)	
No	3 (3.1)	9 (9.4)	25 (26.0)	37 (38.5)	9 (9.4)	13 (13.5)	
Recurrence, n (%)							0.1655
Yes	0 (0.0)	0 (0.0)	0 (0.0)	4 (57.1)	0 (0.0)	3 (42.9)	
No	12 (9.2)	9 (6.9)	26 (19.9)	53 (40.6)	17 (13.0)	14 (10.7)	
Re-Op, n (%)							0.1072
Yes	2 (15.4)	1 (7.7)	0 (0.0)	7 (53.9)	0 (0.0)	3 (23.1)	
No	10 (8.0)	8 (6.4)	26 (20.8)	50 (40.0)	17 (13.6)	14 (11.2)	
Adjuvant Tx, n (%)							0.0540
Yes	2 (40.0)	0 (0.0)	0 (0.0)	1 (20.0)	2 (40.0)	0 (0.0)	
No	10 (7.5)	9 (6.8)	26 (19.6)	56 (42.1)	15 (11.3)	17 (12.8)	
Dysosmia, n (%)							1.0000
Yes	0 (0.0)	0 (0.0)	0 (0.0)	1 (100.0)	0 (0.0)	0 (0.0)	
No	12 (8.8)	9 (6.6)	26 (19.0)	56 (40.9)	17 (12.4)	17 (12.4)	
Sinusitis, n (%)							0.9215
Yes	1 (14.3)	0 (0.0)	1 (14.3)	4 (57.1)	0 (0.0)	1 (14.3)	
No	11 (8.4)	9 (6.9)	25 (19.1)	53 (40.5)	17 (13.0)	16 (12.2)	
Meningitis, n (%)							0.1962
Yes	0 (0.0)	1 (14.3)	0 (0.0)	6 (85.7)	0 (0.0)	0 (0.0)	
No	12 (9.2)	8 (6.1)	26 (19.9)	51 (38.9)	17 (13.0)	17 (13.0)	
Vision Disturbance, n (%)							0.9386
Yes	1 (9.1)	0 (0.0)	2 (18.2)	4 (36.4)	2 (18.2)	2 (18.2)	
No	11 (8.7)	9 (7.1)	24 (18.9)	53 (41.7)	15 (11.8)	15 (11.8)	
Diabetes Insipidus, n (%)							0.2128
Yes	3 (10.3)	2 (6.9)	8 (27.6)	14 (48.3)	1 (3.5)	1 (3.5)	
No	9 (8.3)	7 (6.4)	18 (16.5)	43 (39.5)	16 (14.7)	16 (14.7)	
Presence of Complication, n (%)							0.0093
1 or more	11 (15.5)	3 (4.2)	9 (12.7)	33 (46.5)	9 (12.7)	6 (8.5)	
None	1 (1.5)	6 (9.0)	17 (25.4)	24 (35.8)	8 (11.9)	11 (16.4)	

^aFisher's Exact Test used

p < .05

Table 2. Comparison of graft/ID to each type of complication, tumor shape, tumor size, and tumor extension

Variable	Graft/ID		p-value
	Yes	No	
Tumor Shape, n (%)			0.0120 ^a
L	6 (50.0)	6 (50.0)	
M	2 (22.2)	7 (77.8)	
R	4 (15.4)	22 (84.6)	
S	19 (33.3)	38 (66.7)	
T	0 (0.0)	17 (100.0)	
V	4 (23.5)	13 (76.5)	
Tumor Size, mean (95% CI)			
Length (cm)	2.2 (1.9-2.5)	1.7 (1.6-1.8)	0.0014 ^b
Width (cm)	2.5 (2.1-3.0)	2.1 (2.0-2.3)	0.0355 ^b
Height (cm)	1.9 (1.5-2.3)	1.6 (1.5-1.8)	0.1939 ^b
S Length (cm)	2.1 (1.9-2.4)	1.4 (1.3-1.6)	<0.0001 ^b
S Width (cm)	2.3 (2.0-2.6)	1.4 (1.2-1.6)	<0.0001 ^b
S Height (cm)	1.6 (1.4-1.9)	1.0 (1.3-2.0)	<0.0001 ^b
Tumor Extension			
Suprasellar Extension (cm), mean (95% CI)	1.3 (1.1-1.5)	0.8 (0.7-1.0)	0.0006 ^b
Posterior Suprasellar Extension (cm), mean (95% CI)	0.5 (0.3-0.6)	0.4 (0.3-0.5)	0.3073 ^b
Anterior Suprasellar Extension (cm), mean (95% CI)	0.3 (0.2-0.7)	0.3 (0.2-0.5)	0.6100 ^b
Left Cavernous Sinus Extension (cm), mean (95% CI)	0.7 (0.5-0.8)	0.5 (0.4-0.6)	0.0556 ^b
Right Cavernous Sinus Extension (cm), mean (95% CI)	0.7 (0.5-0.8)	0.6 (0.5-0.7)	0.4610 ^b
Left Knosp, n (%)			0.5830 ^b
0	14 (21.2)	32 (78.8)	
1	6 (20.7)	23 (79.3)	
2	4 (23.5)	13 (76.5)	
4	5 (38.5)	8 (61.5)	
Right Knosp, n (%)			0.4166 ^b
0	17 (27.0)	46 (73.0)	
1	4 (12.9)	27 (87.1)	
2	4 (30.8)	9 (69.2)	
3	0 (0.0)	1 (100.0)	
4	6 (31.6)	13 (68.4)	

^aFisher's Exact Test used

^bTwo-tailed t-test assuming lognormal distribution used

^cMeans are reported as the geometric mean and 95% confidence interval

CI-Confidence Interval

p < .05

(Filename: TCT_P-39_GraphicFileTables.jpg)

P-41

Preoperative Consideration of Synchronous Thyroid Nodules in Patients with Papillary Thyroid Cancer: A Nodule-by-nodule Analysis Between Ultrasonography and Pathology

H Lee¹, H Lee¹, M Hahm¹

¹Kyungpook National University Hospital, Daegu, South Korea

Purpose

The purpose of this study was to evaluate the applicability of preoperative staging ultrasonography (PS-US) to the assessment of synchronous thyroid nodules in patients with PTC.

Materials and Methods

Two-hundred-ten patients diagnosed with PTC who underwent PS-US with more than a two-year follow-up were included. Synchronous nodules, divided into probably benign and suspicious nodules based on US, were correlated with pathologic results using a nodule-by-nodule analysis. We evaluated which clinical and US parameters were associated with contralateral thyroid cancer.

Results

Among 302 synchronous nodules in 129 patients, 83 (27.5%) synchronous nodules in 73 patients were diagnosed as malignant after surgery. The accuracy of US in differentiating malignant nodules from benign nodules was 71.5% (246/302). Ipsilateral probably benign nodules on PS-US were more likely to be malignant than were contralateral probably benign nodules (10.6% versus 2.0%, p = .015). But the malignancy rate of suspicious nodules according to location was not statistically different (55.1% versus 66.2%, p = .153). The presence of suspicious contralateral nodules and the number of synchronous nodules were significant factors related to contralateral cancer (p < .001 and .030).

Conclusions

If the indication for bilateral thyroidectomy was limited to suspicious contralateral nodules instead of contralateral nodules on US, the chances of performing thyroid-preserving surgery may be increased.

P-42

Quantitative Measurement of Heterogeneity on Ultrasonography in Patients with Diffuse Thyroid Disease: Value in Assessing Clinical Course of Disease (Pilot Study)

S Jeon¹, E Park²

¹Wonkwang University School of Medicine and Hospital, Iksan, Republic of Korea, ²Ulsan University Hospital, Ulsan, Republic of Korea

Purpose

To investigate the changes in thyroid heterogeneity during the course of the disease in patients with diffuse thyroid disease

Materials and Methods

A total of 29 subjects (10 Graves' disease, four Hashimoto's thyroiditis, 15 control group) who underwent initial ultrasonography (US) at the time of first diagnosis of diffuse thyroid disease and follow-up US after treatment were enrolled in this study. Thyroid ultrasound images were analyzed to evaluate inhomogeneity of parenchymal echogenicity by using MATLAB-based developed software, which calculate a coefficient of variation (CV) map of each pixel in free-hand region of interest on thyroid parenchyma. Difference of CV values between three groups (Grave's disease – initial US, Hashimoto's thyroiditis – initial US, control group) was assessed with Mann-Whitney U tests. In patients with diffuse thyroid disease, CV values of initial and follow-up US were compared by using paired t-test.

Results

The CV values of Graves' disease group and Hashimoto's thyroiditis group were significantly higher than control group (28.25, 28.86 vs 17.7, $p < 0.0001$). Of the 10 patients with Grave's disease, 5 patients underwent follow-up US during the therapy and 5 patients underwent follow-up US after relapse. While CV value of follow-up US was decreased compared to initial US in the former subgroup (32.17 vs 29.16), it was more increased in the latter subgroup (24.33 vs 30.80). But this change was not statistically significant in Graves' disease group ($p = 0.414$ in the former subgroup, $p = 0.105$ in the latter subgroup). In Hashimoto's thyroiditis group, CV value shows marginally significant difference between initial and follow-up US (28.86 vs 21.28, $p = 0.066$).

Conclusions

The CV value of diffuse thyroid disease group was higher than that of control group and it was affected by disease course in Hashimoto's thyroiditis. Our results suggest that quantification of thyroid heterogeneity using CV value could be used to assess clinical course of the disease in patients with diffuse thyroid disease.

P-40

Value of Labyrinthine Enhancement on 4-hour Delayed Enhanced 3D Fluid Attenuated Inversion Recovery MR Imaging in Idiopathic Sudden Sensorineural Hearing Loss

D Park¹

¹Hanyang University Guri Hospital, Guri, Gyeonggi-do, Republic of Korea

Purpose

This study aims to evaluate the initial and prognostic value of labyrinthine enhancement on four-hour delayed enhanced 3-D fluid attenuated inversion recovery (FLAIR) MR imaging in patients with idiopathic sudden sensorineural hearing loss.

Materials and Methods

This study comprised 216 patients who presented with unilateral sudden sensorineural hearing loss and underwent labyrinthine MR imaging, including pre-enhanced and four-hour delayed enhanced 3-D

FLAIR MR imaging. We analyzed labyrinthine enhancement on MR imaging and the correlation of labyrinthine enhancement with audiometric results.

Results

Ninety-one (42%) patients showed labyrinthine enhancement on four-hour delayed enhanced 3-D FLAIR MR imaging in the affected ear, which was classified as MRI+ group. The initial/final hearing loss levels in MRI+ group ($89\pm 32/67\pm 24$ dB) were significantly worse than those in the MRI- group ($64\pm 28/32\pm 15$ dB). The incidence of labyrinthine enhancement on 4-hours delayed enhanced 3-D FLAIR MR imaging was significantly higher (42 of 71, 59%) in 71 patients with initial profound hearing loss than in 145 patients with initial mild-to-moderate hearing loss (49 of 145, 34%). The rate of complete or partial recovery of hearing loss was significantly higher in the MRI- group (48%) than in the MRI+ group (11%).

Conclusions

Labyrinthine enhancement on four-hour delayed enhanced 3-D FLAIR MR imaging could be the sensitive MR image biomarker for the initial and the prognostic values assessing the hearing loss in patients with sudden sensorineural hearing loss. The initial and the prognostic status of hearing loss are worse in the MRI+ group than in the MRI- group according to the presence of labyrinthine enhancement on four-hour delayed enhanced MR imaging.

P-33

Where Is the Air Coming From? Nontraumatic and Unusual Etiology of Head and Neck Emphysema: A Pictorial Issue

A Wolosker¹, L Abreu Jr.¹, A Torres¹, M Borri¹

¹*Fleury Group, Hospital São Luiz - Rede D'Or, São Paulo, Brazil*

Purpose

Head and neck emphysema refers to the abnormal presence of air in the deep and superficial tissues of the head, face, orbit and neck. The goal of this study is to report many different cases of head and neck emphysema, of unusual etiology, with no evidence of fracture and discuss the most prevalent causes and its pathophysiology. A comprehensive search of the medical literature was performed vid PubMed.

Materials and Methods

The authors report cases of head and neck emphysema without any evidence of fracture, presented to the emergency department of São Luiz Rede D'Or Hospital in São Paulo - Brazil. All patients have confirmed diagnosis with computed tomography (CT) and also the demonstration of precise extension of gas dissection. The causes were confirmed by correlation with clinical history data. A comprehensive search of the medical literature was performed vid PubMed.

Results

Head and neck emphysema may occur with no evidence of trauma with fracture in a wide spectrum of conditions and is rare. It can arise when air is forced under pressure into the fascial spaces, dissecting the connective tissue and joining adjacent muscle planes. The medical literature cites as the most frequent causes: dental and otolaryngological procedures, tears in the pulmonary alveoli (increase alveolar pressure), tears in the gastrointestinal system, Valsalva manœuvre (sneezing, nose blowing, shouting or coughing) and high-pressure machine accidents (used in daily life) also identified in our cases. This study describes a series of cases of emphysema in head and neck not associated with fractures. Detailed anamnesis and careful physical examination are of paramount importance. Computed tomography is also useful to diagnose and to detect the precise extension of gas dissection. Most important, CT can evaluate the rare complications like infection, air embolism, visual loss and airway obstruction. In addition, it can guide clinical treatment decisions like the need for urgent tracheostomy or fasciotomy.

Conclusions

The management of head and neck emphysema is dependent on the extent and severity of the symptoms.

Careful history-taking and clinical examination, and the correct use of diagnostic imaging methods are paramount to diagnosing head and neck emphysema, extension and the main cause. Although head and neck emphysema rarely causes long-term morbidity, the early judicious administration of medicine or surgical treatment increases the likelihood of favorable outcomes for the patient.

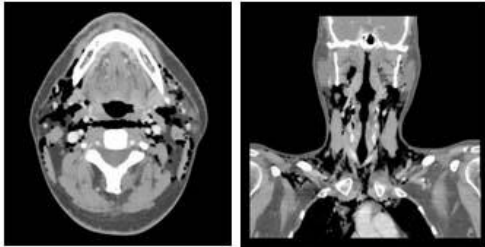


Fig 1. Axial and coronal CT scans show massive emphysema involving superficial and deep cervical spaces extending into the mediastinum after an episode of nonviolent coughing.

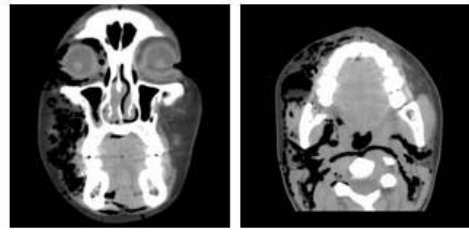


Fig 2. CT images showing diffuse emphysema dissecting cervical spaces after left dental procedure.

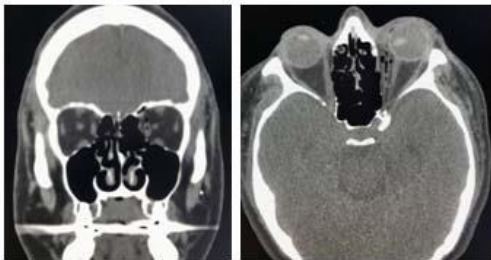


Fig 3. Axial and coronal CT scans showing orbital emphysema and gas in left medial rectus muscles after accident with high-pressure air instrument (used in daily life). Lens deslocation at left.

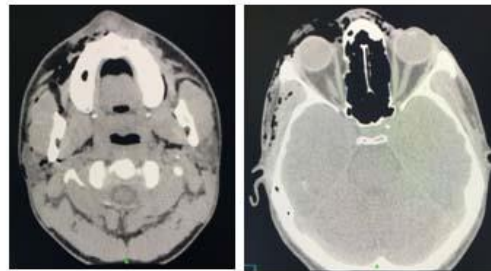


Fig 4. Computed tomography of the neck and face showing air in many cervical spaces after a strong sneeze.

(Filename: TCT_P-33_ASNR2018CORRETA.jpg)

Posters-Informatics

P-43

Radiomic Evaluation of Treatment Response in Patients with Glioblastoma: A Pilot Study

J Zhan¹, M Patel², K Natarajan², R Flintham², N Davies², P Sanghera², A Peet², G Cruickshank², I Ughratdar², V Duddalwar³, V Sawlani²

¹Qingdao University Hospital, Qingdao, Shandong, China, ²University Hospitals Birmingham NHS Foundation Trust, Birmingham, United Kingdom, ³University of Southern California, Los Angeles, CA

Purpose

Pseudoprogression of glioblastoma multiforme (GBM) following treatment occurs in 33-64% of patients (1). Conventional MRI cannot distinguish between pseudoprogression (psPD) and true tumor progression (tPD). Radiomic features could be used as predictors of treatment response. Our aim is to identify radiomic features that can be used to distinguish between psPD and tPD in patients with GBM.

Materials and Methods

For this pilot study, we retrospectively analyzed 20 MRI studies of patients with biopsy-proven GBM. Those who developed early progressive enhancing disease (ePD) at 4-6 weeks following standard chemoradiotherapy (CRT) treatment with temozolomide were included. Studies were labelled tPD or psPD from results of the follow-up scan at six-months post CRT. Tumor components on postcontrast T1W and T2W axial sequences were semiautomatically segmented (Fig. 1) by an experienced radiologist using ITK-SNAP (2) for enhancing disease, necrosis and oedema. Radiomic intensity, volume and texture (GLCM/GLRLM) features were calculated using CaPTK (3,4). Statistical analysis was performed using SPSS to determine the significance between means of both groups for each feature, and logistic regression analysis to produce an ROC curve for significant features.

Results

A total of 20 patients with 11 tPD (3 female, 8 male) and 9 psPD (7 female, 2 male) were included in this study. Mean age of patients with tPD was 54 years and 44 years for psPD. The most significant tumor features on pos-contrast T1W and T2W sequences were contrast, homogeneity, volume, grey level nonuniformity, and run length nonuniformity. The last three were also the most significant features for oedema on T2W sequences (Table 1).

Conclusions

In our pilot study, the limited volumetric and texture features extracted from standard postcontrast T1W and T2W images showed significant differences between the tPD and psPD groups on the first follow-up scan following CRT. With further validation through larger studies, these could prove to be useful radiomic features for earlier prediction of treatment response and prognosis.

Figure 1. Tumour segmentation. *Left:* Segmentation of contrast-enhancing tumour (red) and necrosis (blue) on post-contrast T1W sequences. *Right:* Segmentation of oedema on T2W sequences (yellow).

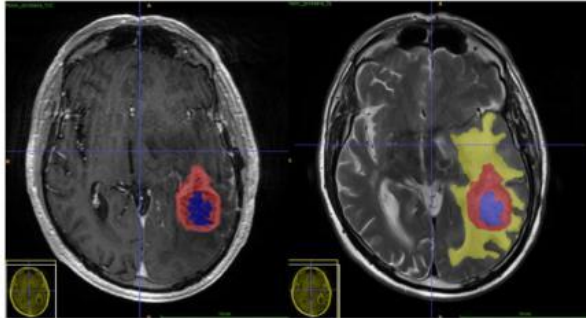


Table 1. Features showing significant differences between psPD and tPD groups.

ROI	Sequence		Features				
			Contrast	Homogeneity	Grey Level Non-Uniformity	Run Length Non-Uniformity	Volume
Contrast-Enhancing Tumour	Post-contrast T1W	tPD	2.81 ± 0.76	0.52 ± 0.04	3903 ± 2324	15127 ± 7014	27562 ± 13996
		psPD	4.27 ± 1.51	0.45 ± 0.08	1335 ± 797	6306 ± 2793	14992 ± 10237
		p-value	0.022*	0.014*	0.005*	0.002*	0.037*
Oedema	T2W	tPD			10735 ± 8384	28015 ± 11516	100730 ± 53446
		psPD			2646 ± 841	11914 ± 4189	37661 ± 18300
		p-value			0.010*	0.001*	0.003*

* significant at level $p < 0.05$

(Filename: TCT_P-43_Capture2.JPG)

P-44

Virtual Reality for Neuroradiology Education

S Ammanuel¹, B Rehani¹

¹University of California San Francisco, San Francisco, CA

Scientific Posters

Purpose

To introduce segmentation of radiologic image and making of 3-D models and implementation into virtual-reality software. This can be used as a technology platform for head-mounted stereoscopic displays to create 3-D immersive environments. To illustrate user interface design interactions such as gaze-controlled directional motion inside the virtual environment for immersive exploration of 3-D models.

Materials and Methods

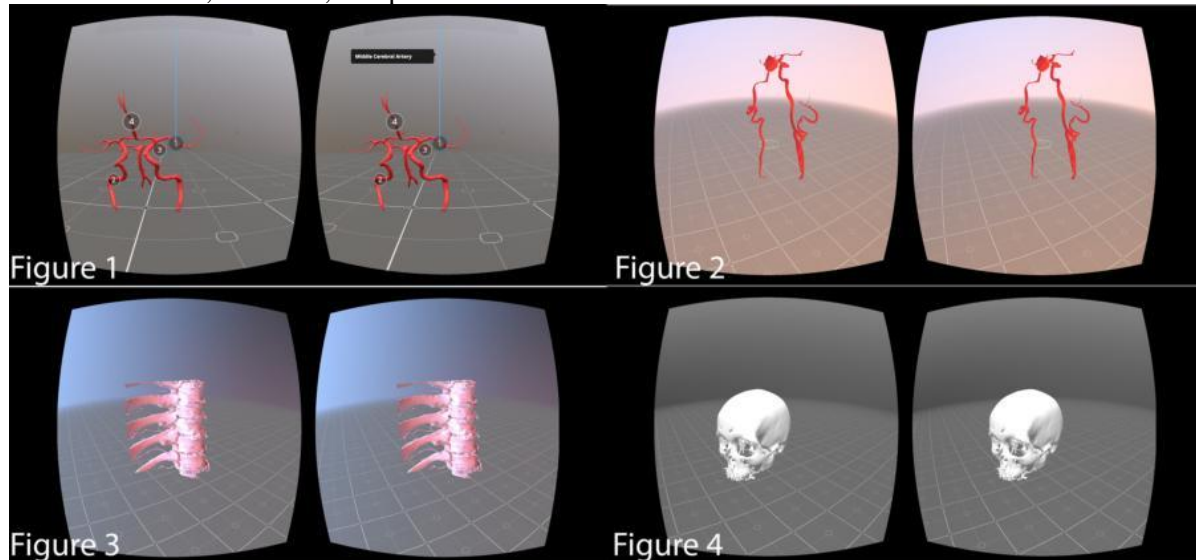
Raw DICOM images were downloaded from the OsiriX DICOM repository made freely available for research and teaching. DICOM datasets containing MR and CT of specific organs were processed using OsiriX region of interest and 3-D surface rendering. Blender and MeshMixer are free open-source software platforms for model editing. Models were imported into SketchFab, a website for publishing 3-D content into a virtual-reality interface, allowing rotational and transitional movement.

Results

Four anatomy modules are created with inputs to control the movement of 3-D models in the virtual space. Rotational and translational movements allow users to explore models by using head tilt and gaze input. Models of the Circle of Willis (Figure 1), Vertebral Aneurysm (Figure 2), Spine (Figure 3), Skull (Figure 4) are rendered in the user's field of view. To annotate anatomic structures in the virtual environment, any structure in the model can be numbered with a title and description. For example, we numbered the major vessels that are part of the Circle of Willis.

Conclusions

Virtual reality is constructed to have many uses in radiology education. Visualization of 3-D anatomic structures in a virtual environment gives another tool for teaching to students and patients. Four anatomy modules described here demonstrate user interaction patterns best suited for viewing contexts. Instead of viewing stacked 2-D images or 3-D models confined to desktop applications, virtual reality increases user interactivity. An understanding of anatomic structures in 3-D enhances the learning experience for medical students, residents, and patients.



(Filename: TCT_P-44_ASNRFigure.jpg)

Posters-Interventional

P-48

A Novel Morphologically Realistic Theoretical Model of Brain AVMs: Advanced Graphics Processing Unit Computing of a Massive Stochastic Network Ensemble Model for Simulating the Effects of Embolization on Intranidal Hemodynamics

M Jain¹, H Do², T Massoud¹

¹*Stanford University School of Medicine, Stanford, CA*, ²*Stanford University, Stanford, CA*

Purpose

Biomathematical models offer theoretical approaches to investigate complex intranidal AVM hemodynamics pre- and postembolization. Current AVM models are simple structures unrepresentative of clinically encountered AVMs. Recent advances in GPU computing only now permit construction of AVM models possessing extremely high vessel counts. We developed a more realistic AVM model that can replicate highly variable and complex nidus structures with vessel counts in the thousands, i.e. orders of magnitude greater than current models.

Materials and Methods

The AVM was a theoretical electrical circuit with a nidus described by a stochastic network ensemble model. We sampled and individually simulated 1,000 different nidus morphologies from this stochastic block model, together constituting an ensemble simulation of AVM hemodynamics. We modeled three nidus structures: purely plexiform, mixed plexiform and fistulous, and a fistula angioarchitecturally isolated from its adjacent plexiform nidus. We assigned appropriate biophysical values to all model vessels, and known values of mean intravascular pressure (P-mean) to extranidal vessels. We then used network analysis to calculate P-mean and volumetric flow rate within each nidus vessel. We derived an expression for rupture risk and conducted a parameter sensitivity analysis on the AVM model.

Results

Nidus networks had 60 nodes and an average of 1,000 vessels. Parameter sensitivity analysis showed that the model predicted realistic nidus flow rates (<900ml/min), P-mean, and rupture risks (mean: 41%, 0-98%). Purely plexiform nidi displayed reduced flow rates compared with mixed plexiform and fistulous models.

Conclusions

The propensity of brain AVMs to hemorrhage correlates with their hemodynamics. This biomathematical AVM model incorporates more realistic features, e.g. higher intranidal vessel counts and representation of many nidus morphologies, all allowed by parallel data processing using advanced GPU computing. This easy to implement model will serve as a useful tool for further theoretical investigations of AVM embolotherapy and its intra- and extranidal hemodynamic sequelae.

P-53

Effect of EMS Routing Paradigms on Patient-centered Outcomes in Acute Ischemic Stroke

M Zhou¹, A Kansagra²

¹*Washington University in St. Louis School of Medicine, St. Louis, MO*, ²*Washington University School of Medicine, St. Louis, MO*

Purpose

To compare performance of different emergency medical services routing paradigms for acute ischemic stroke using patient-centered clinical outcome metrics.

Materials and Methods

We develop a computerized simulation in Matlab (Mathworks, Natick, MA) to examine different paradigms for routing patients with acute ischemic stroke to hospitals of varying capability. Patients are treated in a system comprising one primary stroke center (PSC) and one thrombectomy-capable comprehensive stroke center (CSC), separated by a distance corresponding to urban, suburban, and rural

settings. In the Nearest Center paradigm, patients are sent to the nearest center; in CSC First, patients are sent to the CSC. In Rhode Island, patients with NIHSS \leq 7 are sent to the CSC, and all others are sent to the nearest center; in Distributive, patients with NIHSS \leq 7 are sent to the CSC, and all others are sent to the PSC. Additional system parameters are adapted from clinical trial data. Good clinical outcome is defined as 90-day modified Rankin Score of 0-2 and determined by treatment received and time to treatment. Clinical outcome distributions were compared using two-sample Kolmogorov-Smirnov tests, with a significance threshold of $\alpha=0.01$.

Results

In an urban setting, there is no statistically demonstrable difference between CSC First and Rhode Island ($p=1.00$), CSC First and Distributive ($p=1.00$), and Rhode Island and Distributive ($p=1.00$), but Nearest Center performs significantly worse than CSC First ($p<0.001$), Rhode Island ($p<0.001$), and Distributive ($p<0.001$). In a suburban setting, Nearest Center again performs significantly worse than CSC First ($p<0.001$) and Rhode Island ($p<0.001$), while CSC First and Rhode Island perform similarly ($p=1.00$). In a rural setting, there are statistically demonstrable differences between CSC First and Nearest Center ($p<0.001$), Rhode Island and Nearest Center ($p<0.001$), and CSC First and Rhode Island ($p<0.001$). The difference in median rate of good clinical outcome between the best and worst performing paradigm was 0.65% in the urban and 1.95% in the rural setting.

Conclusions

Paradigms that allow hospital bypass for at least some patients consistently produce better patient outcomes on a population level. Furthermore, differences in performance become more pronounced with increasing distance between centers, and therefore choice of paradigm may be most impactful in rural settings.

P-45

First Hungarian Results with PulseRider Device in Treating Broad-necked Bifurcational MCA Aneurysms with Branches Arising From the Sac

I Lazar¹, P Bartek²

¹*Borsod County University Teaching Hospital, Miskolc, Hungary,* ²*Petz Aladár University Teaching Hospital, Győr, Hungary*

Purpose

Adjunctive Neurovascular Support of Wide-neck aneurysm Embolization and Reconstruction trial (ANSWER) 10 months ago proved the safety and efficacy of PulseRider device in the endovascular treatment of patients with nonruptured bifurcational aneurysm. Since the study performed in the U.S. included only 34 patients and included only carotid terminus and basilar apex aneurysms we present our preliminary experiences our first consecutive five cases treated with MCA bifurcation aneurysms.

Materials and Methods

All procedures were carried out in MCA bifurcational aneurysms in four women and one man with the mean age of 51.4 years (40-63 years). All arising branches were partially or fully incorporated into the aneurysmal sac. Mean aneurysm neck widths were $\geq 5,5$ mm, and mean dome to neck ratio < 2 . All devices were Y shapes with 8 mm wide arches. Mean follow-up is 9.7 months.

Results

All procedures were technically successful with no loss of any branches. Immediate Raymond I or II occlusion was achieved in 100%. One patient developed contralateral hemiparesis of embolic origin after the procedure. She is mRS 2 at six months clinical control. All other patients are doing fine with a less than a year average follow-up. Follow-up imaging is available in three patients; the embolization results remained stable in all of them.

Conclusions

PulseRider seems to be a useful adjunctive device also in the treatment of MCA bifurcational aneurysms.

The main goal of its use in this territory seems to be avoiding any catheterization or stenting/ballooning of the arising branches, especially those with steep angulations.

P-52

Hemorrhagic Complications After Stent-retriever Thrombectomy in Patients with Acute Ischemic Stroke

W Yoon¹, S Kim¹, Y Lee¹, B Baek¹

¹*Chonnam National University Hospital, Gwangju, Republic of Korea*

Purpose

Hemorrhagic complications may occur after modern mechanical thrombectomy in patients with acute large vessel occlusions and can be serious. We sought to determine the predictors of intracranial hemorrhage (ICH) after stent-retriever thrombectomy in a large cohort of patients with acute large vessel occlusions.

Materials and Methods

We retrospectively reviewed clinical and radiologic data of 400 consecutive patients with acute ischemic stroke (341 anterior circulations and 59 posterior circulations) due to intracranial large arterial occlusions who underwent mechanical thrombectomy within eight hours from symptom onset. Logistic regression analyses were performed to determine the independent predictors of subarachnoid hemorrhage (SAH), hemorrhagic infarction (HI), and parenchymal hematoma (PH) after stent-retriever thrombectomy.

Results

A total of 165 patients (76 SAHs, 62 HIs, and 36 PHs) had ICH on follow-up CT scans after stent-retriever thrombectomy. Patients with longer procedure time (OR=1.019, 95% CI, 1.005-1.033, P=0.008) and MCA occlusion (OR=3.074, 95% CI, 1.672-5.650, P<0.001) had a higher incidence of SAH, while large artery atherosclerosis (OR=0.311, 95% CI, 0.144-0.672, P=0.003) was associated with lower risk of SAH. Patients with hypertension (OR=2.375, 95% CI, 1.063-5.310, P=0.035) had a higher risk of PH, while successful revascularization (OR=0.266, 95% CI, 0.100-0.708, P=0.008) and dyslipidemia (OR=0.284, 95% CI, 0.082-0.986, P=0.047) were associated with lower chance of PH. Only PH was associated with poor functional outcome at three months (OR=4.239, 95% CI, 1.051-17.097, P=0.042).

Conclusions

ICH was not uncommon after stent-retriever thrombectomy in patients with acute large vessel occlusions. Among various types of ICHs, only PH was associated with poor outcome at three months. Knowledge of the independent predictors and clinical results of each type of ICH is important to lead a better prognosis in these patients.

P-47

Intranidal Hemodynamic Compartmentalization of Brain AVMs: A Theoretical Three-dimensional Network Model Analysis of the Effects of Simulated Superselective Angiography

M Jain¹, H Do², T Massoud¹

¹*Stanford University School of Medicine, Stanford, CA*, ²*Stanford University, Stanford, CA*

Purpose

To develop a three-dimensional (3-D) biomathematical model of a brain arteriovenous malformations (AVMs) for theoretical investigations of intranidal regions of increased mean intravascular pressure (Pmean) or flow, representing hemodynamic compartments, upon simulated superselective angiography (SSA).

Materials and Methods

We constructed an AVM model consisting of a theoretical electrical circuit with four arterial feeders (AF1-AF4; AF3 being the largest), three draining veins, and a 3-D spatially-oriented nidus of 97 interconnecting plexiform and fistulous components. We assigned known values of P_{mean} to model vessels outside the AVM nidus and used network analysis to determine consequent P_{mean} and flow within each nidus vessel. We simulated SSA by increases in P_{mean} in each AF (with and without occlusion of all other AFs), and then established resulting increases in P_{mean} and flow within each nidus vessel. We analyzed shifts in hemodynamic compartments consequent to increasing injection pressures within the AFs.

Results

Total volumetric flow through the AVM was 678 mL/min, with an 8.6-fold increase through the intranidal fistula. SSA simulated by increases of 10mmHg in each of AF1, AF2, AF3, and AF4 resulted in dissipation of P_{mean} over 38%, 66%, 76%, or 20% of the nidus, respectively. A 30mmHg SSA injection pressure in each feeder with simultaneous occlusion of the other AFs produced further slight increases in spread of raised P_{mean} to 38%, 75%, 79%, and 26% of the nidus, respectively. Qualitative analysis of shifting intranidal compartments after these varying injection pressures was possible by mapping the hemodynamic changes onto the nidus network.

Conclusions

Differences in extent of nidus filling upon SSA injections provide theoretical evidence that hemodynamic forces help establish compartmentalization. Nidus compartments containing intranidal fistulas are larger than those formed only by plexiform vessels. This model should serve as a useful tool for further theoretical investigations of embolotherapy strategies for large AVMs.

P-46

Quantitative Arterial Tortuosity Reveals Evidence of Occult Arteriopathy in Pediatric Patients with Idiopathic Intracranial Arterial Aneurysms

A Chen¹, A Furthmiller², K Karani², B Zhang¹, J Taylor¹, J Leach¹, S Vadivelu¹, T Abruzzo³
¹Cincinnati Children's Hospital Medical Center, Cincinnati, OH, ²University of Cincinnati College of Medicine, Cincinnati, OH, ³Phoenix Children's Hospital, Phoenix, AZ

Purpose

Intracranial arterial aneurysms (IAA) are uncommon in the pediatric population. They occur more frequently in children with cerebral arteriopathy. Quantitative arterial tortuosity (QAT) has been reported as an imaging biomarker of arteriopathy. We sought to determine if alterations in QAT are associated with idiopathic IAA in children.

Materials and Methods

All cases were identified by retrospectively screening imaging reports, and confirmed by review of electronic medical records. Patients age 0-20 years who underwent cross-sectional vascular imaging of the head between January 1993 and July 2017 were eligible. Patients confirmed to have idiopathic IAA formed the study population. Patients without aneurysms or vascular risk factors formed the negative control population. Age- and sex-matched patients with known cerebral arteriopathies formed the positive control population. QAT of five cervicocerebral arterial segments was measured bilaterally using automated image processing software, and differences between groups analyzed.

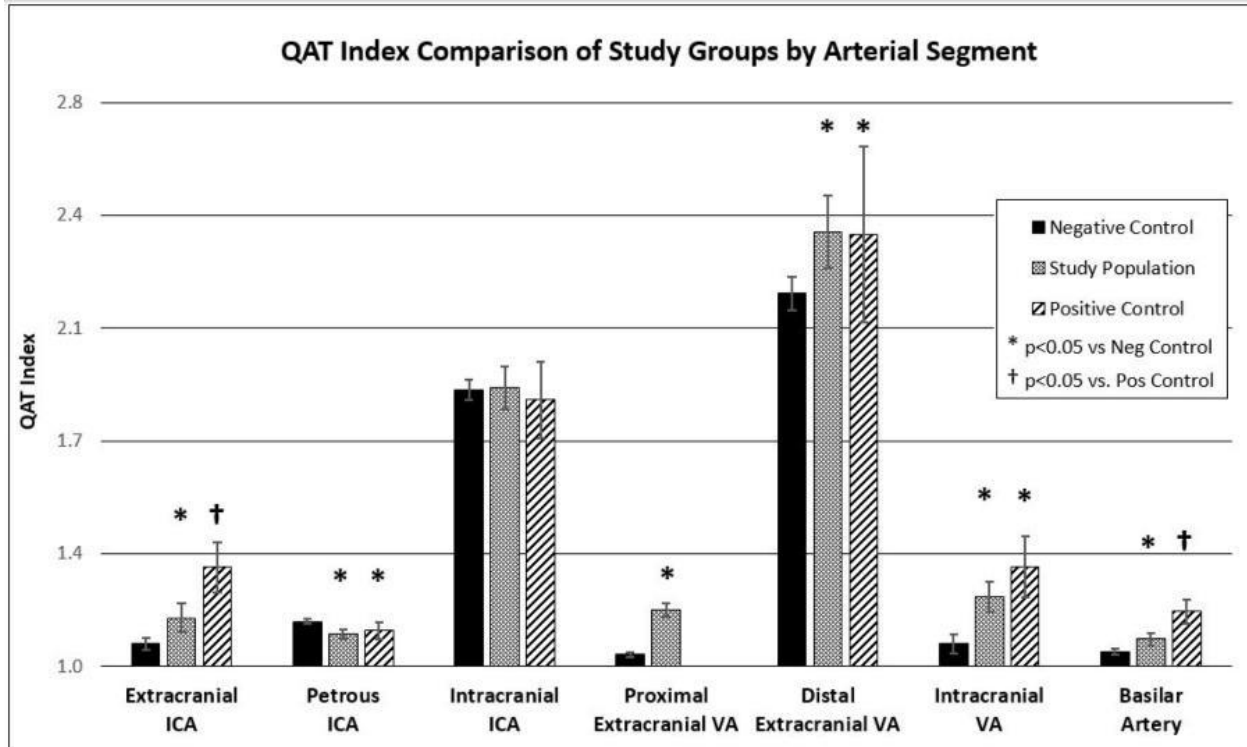
Results

There were 29 patients in the study group, 150 in the negative control group, and 179 in the positive control group. The positive control group comprised patients with sickle cell disease, neurofibromatosis type 1, Ehlers-Danlos, Loewy-Dietz, Alagille, Marfan, and PHACES syndromes. The mean QAT of the extracranial internal carotid artery, basilar artery, and all segments of the vertebral artery was significantly

greater ($p < 0.05$) in the study group than in the negative control group (Figure 1). Segmental QAT values in the study group closely matched those in the positive control group.

Conclusions

Children presenting with idiopathic IAAs frequently have abnormally increased cervicocerebral QAT, particularly in the posterior circulation. This finding suggests that otherwise occult arteriopathy may underlie the pathogenesis of IAA in this group.



(Filename: TCT_P-46_ASNRFigure.jpg)

P-51

Strategic Decisions when Embolizing Mixed Plexiform and Fistulous Brain AVMs: A Massive Stochastic Network Ensemble Biomathematical AVM Model Reveals a Higher Nidus Rupture Risk if Fistula Is Occluded First

M Jain¹, H Do², T Massoud¹

¹Stanford University School of Medicine, Stanford, CA, ²Stanford University, Stanford, CA

Purpose

High-flow fistulas isolated from a plexiform nidus are found in almost 40% of large brain arteriovenous malformations (AVMs). Although the usual approach to endovascularly occlude fistulas before plexiform nidus is considered safe, hemodynamically it remains unclear if consequent reduced hypertension in draining veins can result in greater flow through the plexiform component, thus theoretically raising its rupture risk. We used a novel biomathematical AVM model to investigate theoretical hemodynamic changes upon sequential embolizations of fistulous versus plexiform nidus components.

Materials and Methods

The AVM was a theoretical electrical circuit containing a nidus described by a massive stochastic network ensemble model with an average of 1,000 vessels. We sampled and individually simulated 1,000 different nidus morphologies that model an AVM with a fistula angioarchitecturally isolated from its

adjacent plexiform nidus. We then used network analysis to calculate mean intravascular pressure (P-mean) and volumetric flow rate within each nidus vessel; and used Monte Carlo analysis to assess overall risk of rupture when simulating fistula, plexiform, and fistula plus plexiform occlusions on each of the 1,000 different nidus morphologies.

Results

Risk of nidus rupture was elevated after occluding the fistula first. This higher risk was consistently observed in sample models with different network morphologies and vessel biophysical features, and when considering simultaneous alterations in P-mean within draining veins.

Conclusions

Initial occlusion of a fistula may theoretically raise the risk of rupture in an adjoining plexiform nidus component. This finding is at odds with the clinically observed known safety of empirically favoring fistula occlusion prior to plexiform nidus embolization. We will further analyze this discrepancy and determine whether, alternatively, it may be safer in selected AVMs to endovascularly occlude plexiform nidus before fistula; or, in the case that fistula occlusion must be performed first, embolizing plexiform simultaneously or shortly after occluding fistulous vessels.

P-49

Transvenous Coil Embolization for a Dural Arteriovenous Fistula with Angiographically Isolated Transverse-sigmoid Sinus: Multiple Microcatheter Technique via a Modern Triaxial System

T Mine¹, G Benndorf¹

¹*Rigshospitalet, København Ø, Copenhagen, Denmark*

Purpose

Dural arteriovenous fistulas (DAVFs) involving an "isolated" transverse-sigmoid sinus (TSS) with direct cortical venous drainage (CVD) have a high risk of intracranial hemorrhage [1]. Optimal endovascular strategy for definitive fistula closure has not been established. Transvenous approach is usually not considered due to expected technical challenges to navigate catheters into the isolated sinus portion. We present a case where transvenous catheter navigation through the "occluded" sinus allowed coil embolization for DAVFs with angiographically isolated TSS using a multiple microcatheter technique via a modern triaxial system.

Materials and Methods

A 69-year-old woman presented pulsatile tinnitus caused by DAVFs with isolated left TSS (Figure 1a). Via transfemoral venous approach, a triaxial system consisting of a 6Fr long sheath advanced into right jugular vein, a 6Fr guiding catheter advanced into the angiographically patent left transverse sinus, and microcatheters was established (Figure 1b). Two microcatheters were navigated through the thrombose segment into the isolated sinus and placed within the proximal and distal portion. Coil embolization was started with the proximal catheter to block the main draining cortical vein, and finalized with the distal catheter to block the drainage towards the deep venous system (Figure 1c).

Results

The affected sinus segment was tightly embolized and the fistula was completely occluded (Figure 1d). Pulsatile tinnitus disappeared immediately after the procedure.

Conclusions

Angiography reflects the main blood stream under the local blood pressure, hence it is not always equal to actual anatomical conditions. If there are potentially patent segments despite invisible in angiography, transvenous penetration could be less struggle and safer than transarterial liquid embolization. Multiple microcatheter approach could reduce the risk of unexpected moving of catheter tip during coil insertion and our triaxial system could provide the stable backup [2, 3]. Our procedure could be accomplished on the basis of the standard concept of the treatment for DAVFs and the new combination of recently advanced modalities.

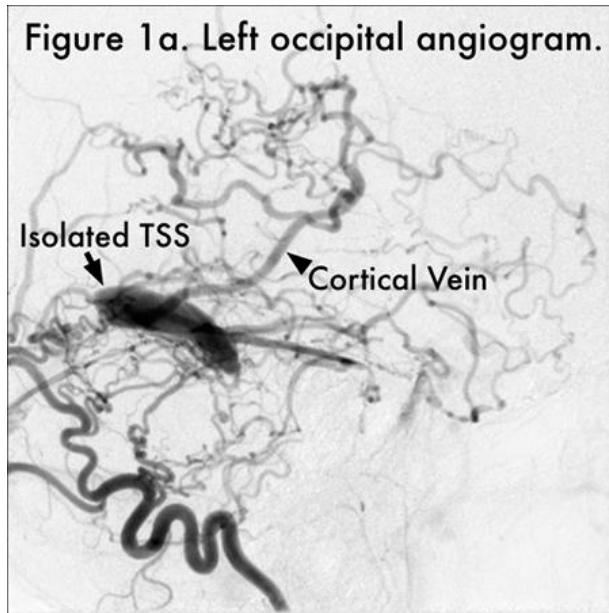
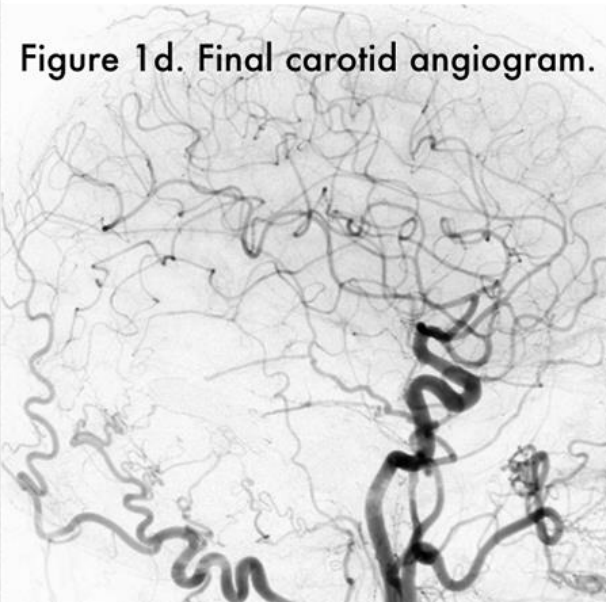
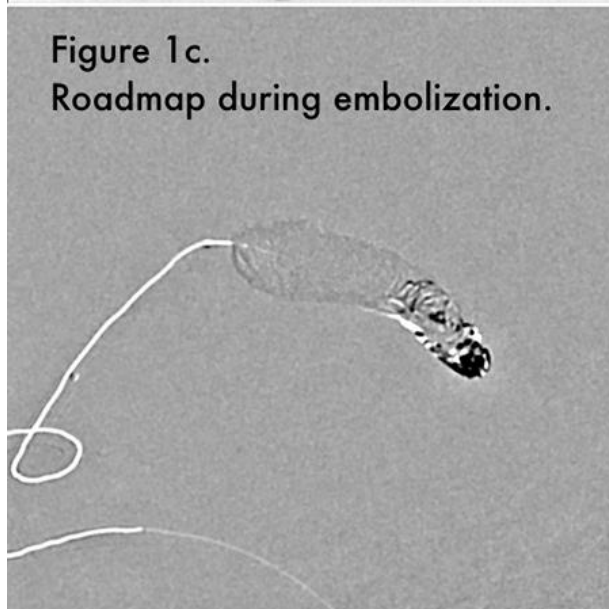
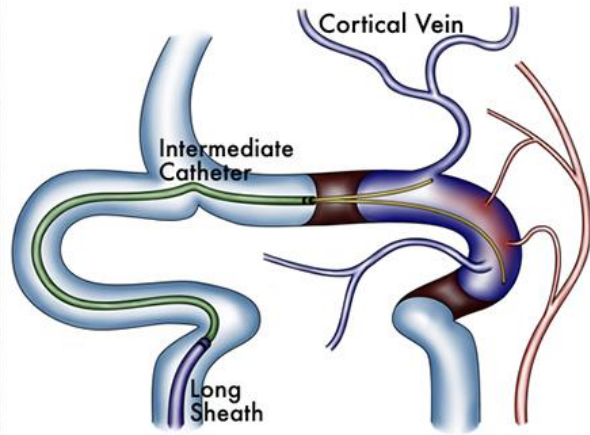


Figure 1b. Scheme of procedure.



(Filename: TCT_P-49_ASNRfigure1.jpg)

Posters-Pediatrics

P-65

Central Nervous System Imaging Spectrum and Evolution in Neurocutaneous Melanosis

K Jakchairoongruang¹, Y Khakoo², A Barkovich³

¹King Chulalongkorn Memorial Hospital, The Thai Red Cross Society, Bangkok, Thailand, ²Memorial Sloan-Kettering Cancer Center, New York, NY, ³University of California San Francisco-Benioff Children's Hospital, San Francisco, CA

Purpose

Neurocutaneous melanosis (NCM) is a rare neurocristopathy characterized by giant melanocytic cutaneous nevi and melanosis within the central nervous system (CNS). The prognosis of NCM patients with neurological manifestations is extremely poor. MRI is sensitive and specific for detection of CNS melanotic lesions. We describe the spectrum of CNS findings and evolutionary change in NCM patients on MRI over time.

Materials and Methods

Brain and spine MRI of 80 congenital melanocytic nevi patients (range from 1 day to 22 years) affiliated with Nevus Outreach from 1998 to 2017 were reviewed. CNS melanosis was diagnosed when T1 hyperintense parenchymal signal abnormalities were seen. Signal abnormality, enhancement, mass, CNS malformation and presence of cutaneous nevi were assessed. Follow-up MRIs were obtained in 9 patients to evaluate interval changes of signal abnormality or enhancement. Descriptive statistical analysis was used with $P < 0.05$ considered as significant.

Results

The most common locations of melanosis were the amygdala, pons, cerebellum and cerebral cortex. A strong association was found between hindbrain malformations and brain melanosis, which was seen best on T1 images prior to myelination (Table 1 and Figure 1,2). Reduced visibility (or loss of visibility) during patient growth may result from either of two postulated mechanisms: white matter myelination and melanin resorption by macrophages (Table 2 and Figure 1).

Conclusions

Brain and total spine MRI should be performed in all patients with giant congenital melanocytic nevi (who are at risk of development of neurocutaneous melanosis). We recommend initial imaging at 4 months of age to obtain greatest sensitivity for detection of melanosis before the white matter is fully myelinated with smallest risk from sedation. Presence of cerebellar hypoplasia in the setting of congenital melanocytic nevus with either presence or absence of brain melanosis is strongly suggestive of NCM and should raise a close search for other manifestations.

Findings	N (%)	Location (%)
Brain melanosis	33 (41%)	Amygdala (38%), brainstem (22%), cerebellum (13%), cerebral cortex (7%) and thalamus (5%) Size : few mm to 15 mm
Leptomeningeal enhancement with hydrocephalus	5 (6%) P=0.01*	Brain (5%) : Cerebellum and brainstem surface, cerebral sulci, basal cisterns Spine (6%) : Dorsal cervical and thoracic cord surface (6%) CSF loculations at dorsal thoracic level (3%) Clumped cauda equina (3%)
Hindbrain malformation	10 (12%) P=0.003*	Small pons and/or cerebellum (6%) Inferior vermian hypoplasia (1%) Dysmorphic, small cerebellar hemisphere with undersulcation (1%) Mega cisterna magna (3%)
Scalp and face cutaneous nevi	16 (20%) P=0.03#	Fourteen patients (17%) without brain melanosis

Table 1. Spectrum of CNS findings in patients with “at risk” congenital giant melanocytic nevus

* = positive association with melanosis, # = negative association with melanosis

	Interval from baseline study		N (%)
	1 month to 11 years		
Brain parenchymal melanosis			
No change	4 months to 11 years		6 (18%)
Smaller and fewer	4 months to 4 years		3 (9%)
Leptomeningeal enhancement and CSF loculations			
Increase	2 months and 2 years		1 (3%)
Decrease	9 and 16 months		1 (3%)

Table 2. Evolutional change of CNS findings in NCM patients

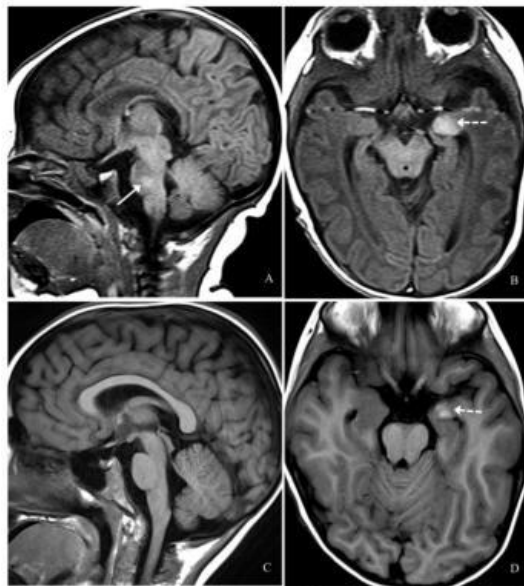


Figure 1. Less visible melanosis over time. Initial sagittal and axial T1WI at 21 days of age (A,B) and follow up at 4 years of age (C,D) showed smaller T1 hyperintensity at left amygdala (dashed arrows in B,D), while T1 hyperintensity in pons (arrow in A) became invisible in C.

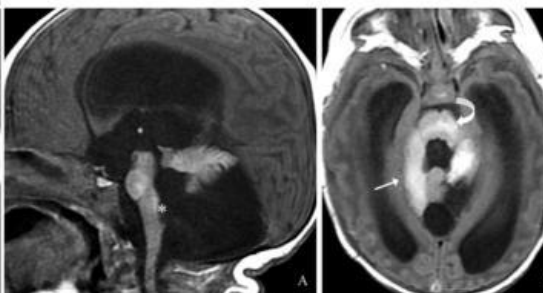


Figure 2. Cerebellar and pontine hypoplasia with parenchymal melanosis were seen in Sagittal (A) and axial (B) T1WI of a 20-day old infant. Extensive T1 hyperintensity throughout cerebellar hemispheres (arrows), pons (curved arrow) and medulla (asterisk). Severe communicating hydrocephalus was observed.

(Filename: TCT_P-65_FigureNCM.jpg)

P-54

Children with Sickle Cell Disease Treated with Hydroxyurea Show Increased CVR and White Matter Integrity: A Quantitative MRI Study

D Kapustin¹, J Leung², S Williams², A Kassner²

¹University of Toronto, Toronto, Ontario, Canada, ²The Hospital for Sick Children, Toronto, Ontario, Canada

Purpose

Sickle cell disease (SCD) is a monogenic blood disorder leading to chronic anemia, cerebral infarctions and impaired cognition [1,2]. These impairments have been linked to disruption in the white matter (WM) integrity in children with SCD [3]. Diffusion-tensor imaging (DTI) allows for microstructural analysis of WM by characterizing diffusion of water molecules. In SCD, widespread increases in WM mean diffusivity (MD), a primary DTI measure, have been observed and interpreted as demyelination and axonal injury [4]. We have previously demonstrated that cerebrovascular reactivity (CVR), a measure of vascular reserve, is diminished in children with SCD [5], and hydroxyurea (HU) therapy results in significant CVR improvement [3]. However, HU's impact on WM integrity is not established. We therefore assessed the relationship between WM CVR and MD parameters of pediatric SCD patients with and without HU therapy.

Materials and Methods

Twenty-three SCD patients were imaged using 3T MRI. Eleven patients were treated with HU (HU group) and 12 were not (non-HU group). In addition, 10 healthy controls were imaged. Imaging included structural T1, T2, diffusion-weighted sequences, and blood-oxygen level dependent (BOLD) CVR scans. MD histogram parameters (mean, median, skew, kurtosis, 5th, 25th, 75th, and 95th percentiles) were evaluated. Significant differences in histogram parameters and CVR measurements between groups were assessed.

Results

A significant WM CVR decrease was observed in HU and non-HU patients when compared to healthy controls. ANOVA revealed significant MD histogram skew and kurtosis elevation in non-HU subjects compared to controls and HU patients (Figure 1). WM CVR showed correlation with MD histogram skew and kurtosis in controls and non-HU patients (Figure 2).

Conclusions

The increased MD histogram skew and kurtosis in untreated patients may indicate widespread WM disruption across the brain. In contrast, HU-treated patients had MD histogram parameters that closer resembled those of healthy volunteers, suggesting a normalizing effect associated with treatment.

Figure 1

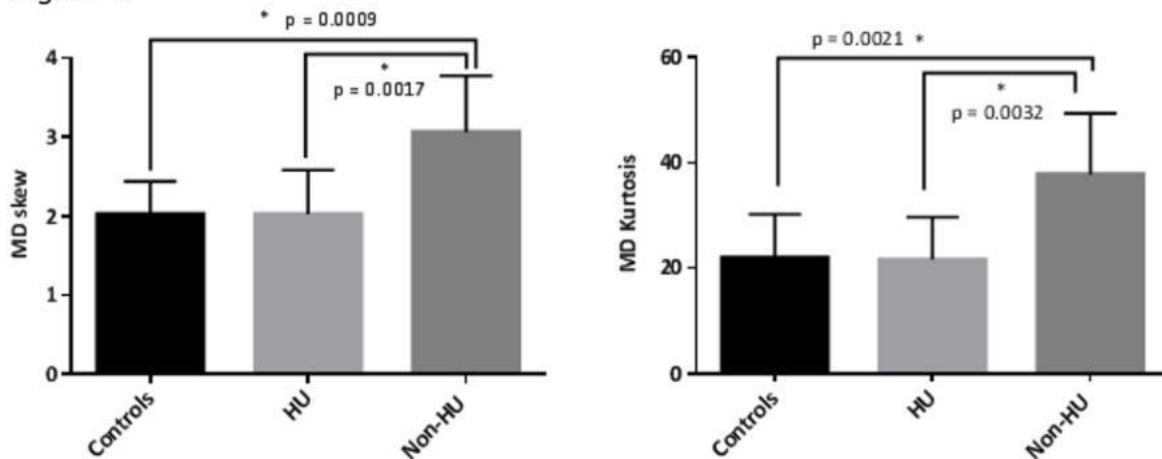
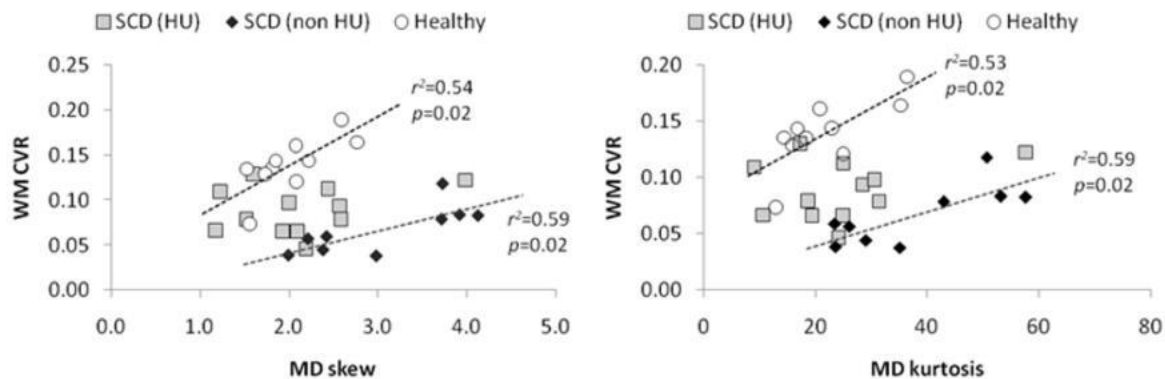


Figure 2



(Filename: TCT_P-54_PSMDFigureASNR.jpg)

P-63

Cine MRI Assessment of Carotid Artery Pulse Wave Velocity and Reflected Wave Amplitude in Children with Sickle Cell Disease

J Leung¹, D Goolaub¹, C Macgowan¹, L Cahill¹, J Sled¹, A Kassner¹

¹The Hospital for Sick Children, Toronto, Ontario, Canada

Purpose

In sickle cell disease (SCD), cerebral microvascular function is impaired resulting in an increased risk of hypoxic injury [1]. Such abnormalities in the microvasculature may be detectable within larger feeding arteries. By quantifying the blood flow and cross-sectional area of the common carotid artery (CCA) across a cardiac cycle, parameters such as pulse-wave velocity (PWV) and wave reflection coefficient (Γ) can be derived [2,3]. We used phase contrast MRI (PCMRI) to measure these properties in children with SCD and healthy controls. We hypothesize that the PWV and Γ in patients with SCD will be increased due to reduced vessel compliance and abnormalities in the microvasculature.

Materials and Methods

Six pediatric SCD patients (14.5 ± 2.3 years; 4F/2M) and 3 age-matched controls underwent imaging on a

3T clinical MRI system. The protocol included a PCMRI sequence derived from real-time cardiac imaging [4,5], consisting of a single-slice radial acquisition prescribed perpendicular to the CCA. Data analysis was performed using segment v2.0 (R5557; <http://segment.heiberg.se>) to define vessel boundaries and compute pulsatile flow volumes (Figure 1). PWV was calculated as the slope between area vs. flow during systole, and Γ was calculated as the ratio of backward to forward wave amplitude (Figure 2) [2]. Group averages of PWV and Γ were compared using Student's t-test, with statistical significance defined as $p < 0.05$.

Results

Mean PWV was found to be significantly greater in the SCD group compared to controls ($p = 0.017$). Mean Γ was also shown to be higher in SCD patients ($p = 0.027$). The results are graphed in Figure 3.

Conclusions

Using PCMRI, we could characterize the flow and reflection properties within the CCA and show significant differences between pediatric SCD patients and healthy controls. These parameters provide insight into the mechanical properties and vascular morphology of the cerebrovasculature in SCD patients and may aid in the clinical evaluation of children with cerebrovascular disorders.

Figure 1

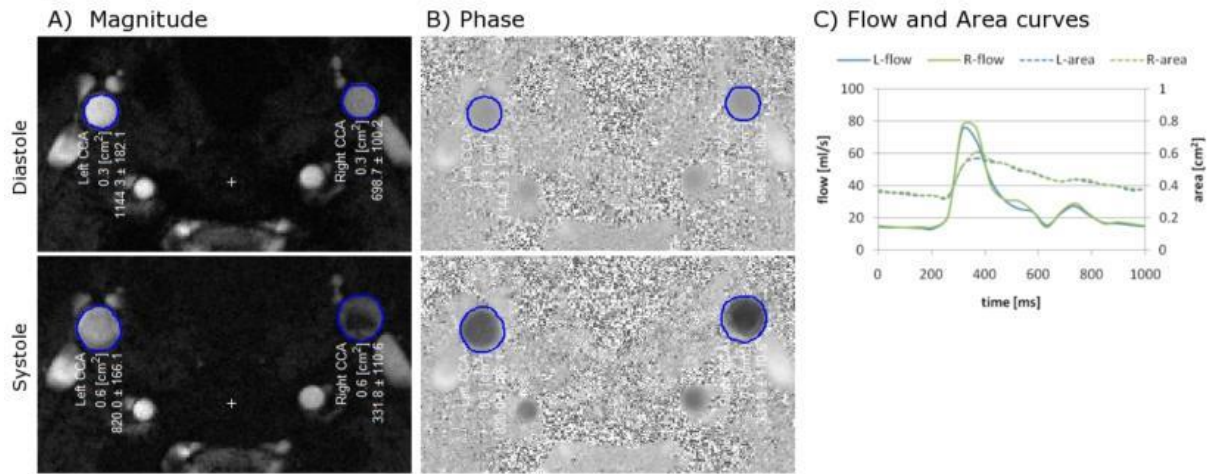


Figure 2

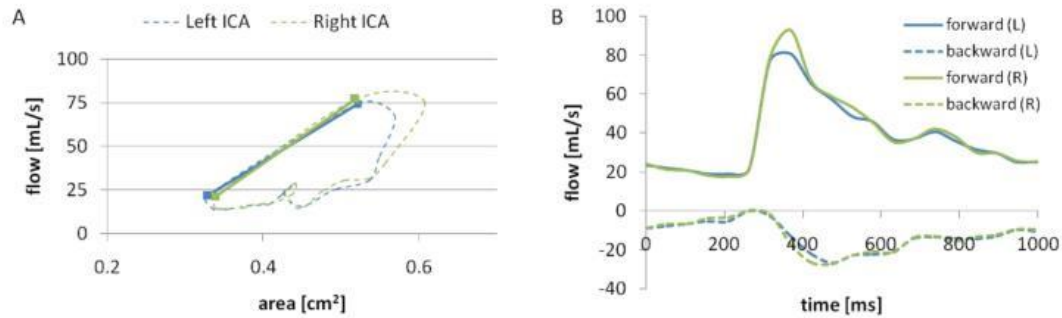
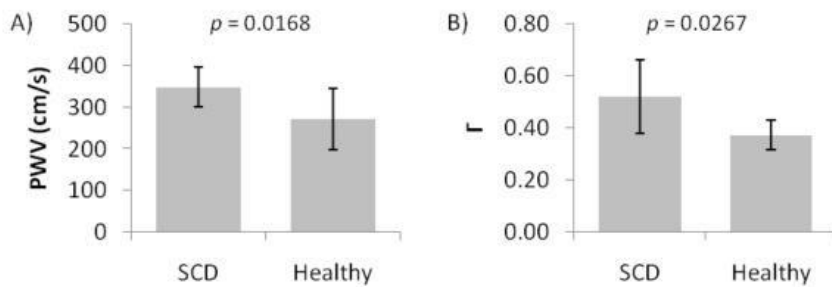


Figure 3



(Filename: TCT_P-63_ImpedanceFigureASNR.jpg)

P-62

Fast, Motion-robust, T1-weighted Neuroimaging with Single-shot Fast Spin Echo

D Litwiller¹, J Zhang², L Estkowksi³, D Rettmann⁴, E Bayram⁵

¹GE Healthcare, New York, NY, ²GE Healthcare, Vancouver, British Columbia, Canada, ³GE Healthcare, Menlo Park, CA, ⁴GE Healthcare, Rochester, MN, ⁵GE Healthcare, Houston, TX

Purpose

We present an enhanced single-shot fast spin echo-based method for the rapid acquisition of T1-weighted neuro images, which may be beneficial for fetal [1] and pediatric imaging, and for other imaging applications where patient motion and scan time present significant challenges.

Materials and Methods

For development purposes, adult volunteers were scanned on a 3.0T MRI scanner (Discovery MR750, GE Healthcare, Waukesha, WI) using a conventional T1-weighted FLAIR protocol, and a modified IR-prepared SSFSE pulse sequence with centric encoding and variable refocusing flip (vrf) angle [2] with similar parameters. The SSFSE inversion time (TI) of 600 ms was selected to provide gray-white tissue contrast that was comparable to the T1 FLAIR image (726 ms TI). For comparison, the acquired vrfSSFSE-IR data was subsequently reconstructed using conventional sum-of-squares and PSIR. The goal of PSIR image reconstruction is to enhance T1 contrast by preserving the otherwise discarded phase information [3,4].

Results

For 27 slice locations, and a TI of 600 ms, the vrfSSFSE-IR acquisition demonstrated a five-fold scan time advantage (of 2:07 vs. 0:25) due to the single-shot nature of the experimental pulse sequence. The imaging results summarized in Figure 1, demonstrate comparable gray-white tissue contrast between the T1 FLAIR (Figure 1c) and vrfSSFSE-IR (Figures 1a and 1b). Improved CSF suppression is obvious due to PSIR vs. magnitude-only image reconstruction (Figures 1c and 1b, respectively). Minor edge enhancement in the vrfSSFSE-IR image at the boundaries between gray matter and CSF may arise from the less selective slice profile characteristic of the SSFSE pulse sequence, warranting further investigation.

Conclusions

These results hold promise for T1-weighted neuroimaging, such as fetal and pediatric MRI, where speed and motion-robustness are critical. Clinical evaluation and further technical optimization, including further scan time reductions, will be considered in future work.

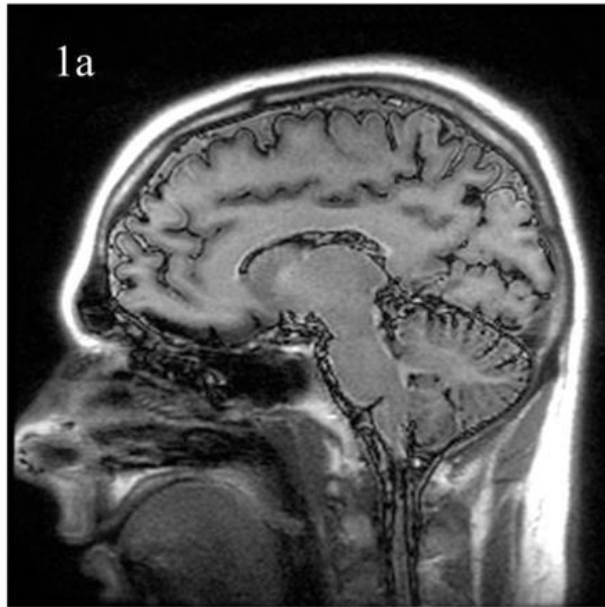
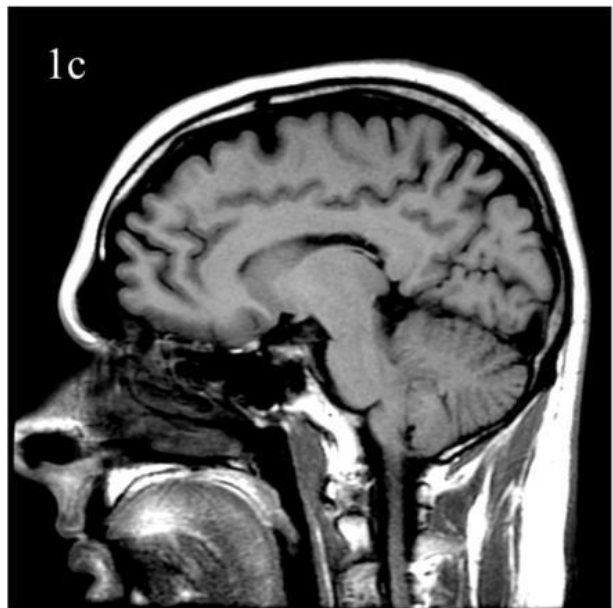
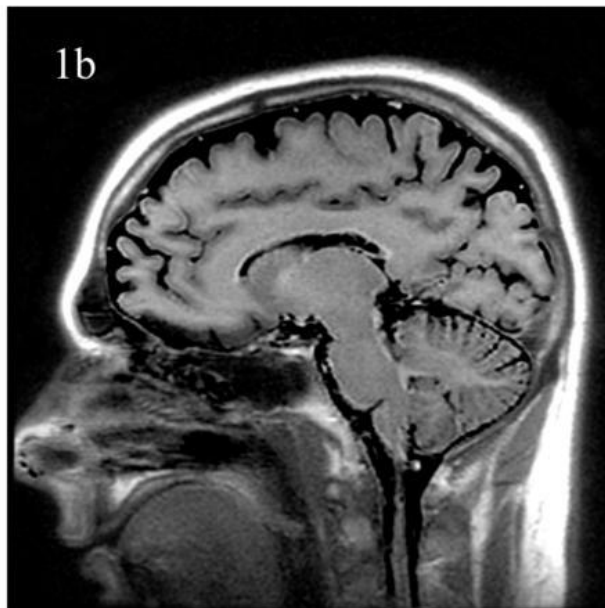


Figure 1:

1a. vrfSSFSE-IR (0:25)

1b. vrfSSFSE-IR +PSIR (0:25)

1c. T1 FLAIR (2:07)



(Filename: TCT_P-62_Figure1.jpg)

P-58

Longitudinal Concentration Change in the Developmental Rat Brain Using in Vivo Glutamate Chemical Exchange Saturation Transfer

W Paik¹, D Woo², H Kim²

¹Samsung Medical Center, Seoul, Republic of Korea, ²Asan Medical Center, Seoul, Republic of Korea

Purpose

Chemical exchange saturation transfer (CEST) is a novel enhanced molecular imaging technique that indirectly monitors neurochemicals in millimolar (mM) concentrations. The concentration of glutamate changes during the brain's developmental period, and the CEST imaging technique is useful for

Scientific Posters

measuring glutamate in the brain on the basis of the exchangeable protons in the amine group. The purpose of this study was to measure in vivo changes in glutamate level in five different regions of the developing healthy rat brain using the glutamate CEST (GluCEST) technique in a longitudinal study design.

Materials and Methods

MRI scans of six rats, including GluCEST, T2 mapping, and diffusion-weighted sequences, were acquired on a 7.0-T 160 mm small animal imaging system, every week, for two months from birth. Glutamate levels in five different regions (cerebral cortex, hippocampus, thalamus, basal ganglia, and amygdala) of the developmental rat brain were measured using GluCEST. The weekly values of T2, ADC, and GluCEST from the five different brain regions were compared with t-tests and Pearson's correlation analyses. These correlations were performed for three periods: all eight weeks, the first to the fifth week, and the fifth to the eighth week.

Results

An increase in GluCEST values was observed in the five different brain regions during the first five postnatal weeks. After the fifth postnatal week, the levels of glutamate in the five brain regions varied. As postnatal weeks went by, T2 and ADC values decreased. Negative correlations between glutamate concentrations and T2 or ADC values were found ($p < 0.0001$).

Conclusions

In rat brain, the fifth postnatal week is a possible time point for neurochemical developmental maturation, with the trends of glutamate concentration increase and T2 and ADC decrease, which are influenced by myelination and neuronal change, plateauing.

P-57

MRI Findings in Krabbe Disease: Systematic Review

D Guillen¹, G Zuccoli¹

¹*Children's Hospital of Pittsburgh of University of Pittsburgh Medical Center, Pittsburgh, PA*

Purpose

To report the brain findings in Krabbe disease in the first MRIs obtained

Materials and Methods

We reviewed all available original publications in Pubmed with the terms MRI, magnetic resonance imaging, Krabbe disease and Globoid Cell Leukodystrophy. We obtained the information of location of lesions and MRI sequence used to identify them and tabulated results from all the studies available. We did not analyze the studies that only reported DTI/Tractography or the results from magnetic resonance spectroscopy. We did not include studies that reported normal MRIs or only spine MRI findings.

Results

Forty-four publications were found with the search methodology. Six were excluded given that they did not report findings by location or met exclusion criteria. The total number of cases reported were 188. The most commonly reported sequence was T2/T2 FLAIR with 180 cases; the other eight did not specify the type of sequence. The most common locations were Periventricular white matter (64%), dentate nucleus in 43% of cases and parieto-occipital and cerebellar white matter both at 41% and 40% respectively.

Conclusions

The most frequent locations of MRI findings in Krabbe disease are the periventricular white matter, dentate nucleus, parieto-occipital and cerebellar white matter.

MRI findings in Krabbe disease by frequency of reported location		
Location	Cases reported	Frequency
Periventricular/Deep WM/Centrum Semiovale	111	64.2
Dentate	74	42.8
Parietal-Occipital	71	41.0
Cerebellar white matter	70	40.5
Pyramidal tracts	55	31.8
Corpus Callosum	54	31.2
Brainstem	51	29.5
Internal Capsule	49	28.3
Thalamus	37	21.4
Basal Ganglia/Deep gray matter	32	18.5
Optic nerve/Chiasm	28	16.2
Corona Radiata	24	13.9

(Filename: TCT_P-57_TableoffrequencyofMRIfindingsinKrabbedisease.jpg)

P-59

Normal MRI Appearances of the Pituitary Stalk in Infants: Correlation with Gestational Age, Postmenstrual Age and Chronological Age

T Okazaki¹, T Niwa¹

¹Tokai University School of Medicine, Isehara-shi, Kanagawa, Japan

Purpose

Neonatal pituitary gland is known to be hyperintense on T1-weighted image. We assessed the intensity of pituitary stalk in infants, correlated with gestational age, postmenstrual age and chronological age.

Materials and Methods

MR images of 90 infants (gestational age (GA), 25.3–41.4 weeks; postmenstrual age, 36.4–46.1; and chronological age, 3–141 days), who were screened at term-equivalent age, resulting in no abnormality on MRI, were analyzed. MR imaging was performed on a 3-T scanner. T1-weighted sagittal images were obtained using thin-slice inversion recovery 3D-turbo field echo sequence. For quantitative analysis, we rated the signal of the anterior lobe to that of pons by five-grade: 0: prominently lower – 2: iso-intensity – 4: prominently higher. For qualitative analysis, we measured signal intensities of the pituitary stalk and pons on midline T1-weighted sagittal images, and calculated signal ratio of the pituitary stalk to the pons. Visual scores and signal ratios were compared to GA, postmenstrual age and chronological age.

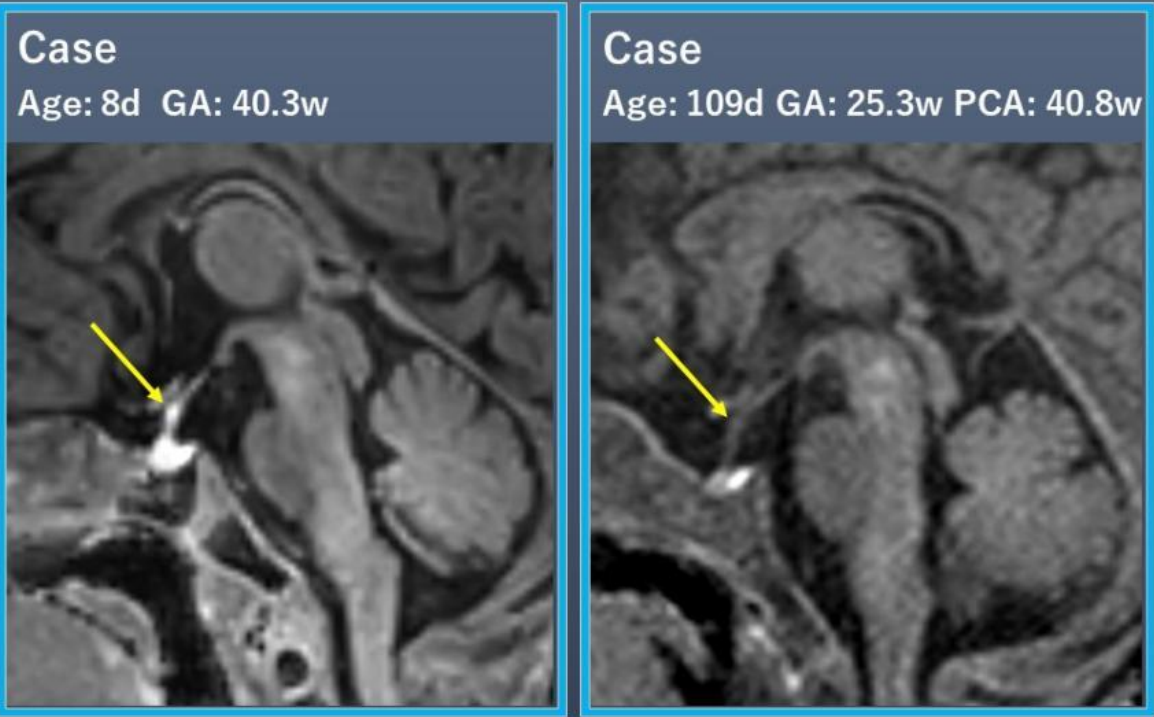
Results

Quantitative and qualitative analysis showed that intensities of pituitary stalk were negatively correlated with GA and chronological age. On the other hand, these data did not correlate with postmenstrual age.

Conclusions

The signal intensity of pituitary stalk on T1-weighted image may decrease along with postnatal growth in infants.

Signal intensity of the pituitary stalk



(Filename: TCT_P-59_NormalMRIappearancesofthepituitarystalkinnew.jpg)

P-64

Pediatric Head MRI: Clinical Value of Motion Correction Techniques in 7-14 Year-olds

R Watts¹, J Allison¹, A Arapovic², J Nickerson¹

¹Larner College of Medicine, University of Vermont, Burlington, VT, ²University of Vermont Medical Center, Burlington, VT

Purpose

Patient motion during MRI scans remains a substantial problem, resulting in reduced diagnostic value, repeat imaging, and the need for sedation for imaging of children. In addition to cost issues, concerns have been raised about pediatric anesthesia and neurotoxicity (1). The purpose of this prospective study was to compare conventional T2-weighted turbo-spin echo imaging with motion-insensitive PROPELLER techniques (2) with and without advanced reconstruction techniques (3) in pediatric head MRI.

Materials and Methods

Fourteen pediatric patients (mean age 9.7, range 7-14, 10 females) scheduled for head MRI were recruited for this IRB-approved and HIPAA-compliant study. Patients were scanned using a conventional turbo-spin echo technique, a PROPELLER-type technique (2) (Multivane, Philips HealthTech), and a more advanced PROPELLER technique that includes the use of SENSE acceleration, and rejection of blades corrupted by through-plane motion (3) (Multivane XD, Philips Healthtech). Multivane imaging protocols

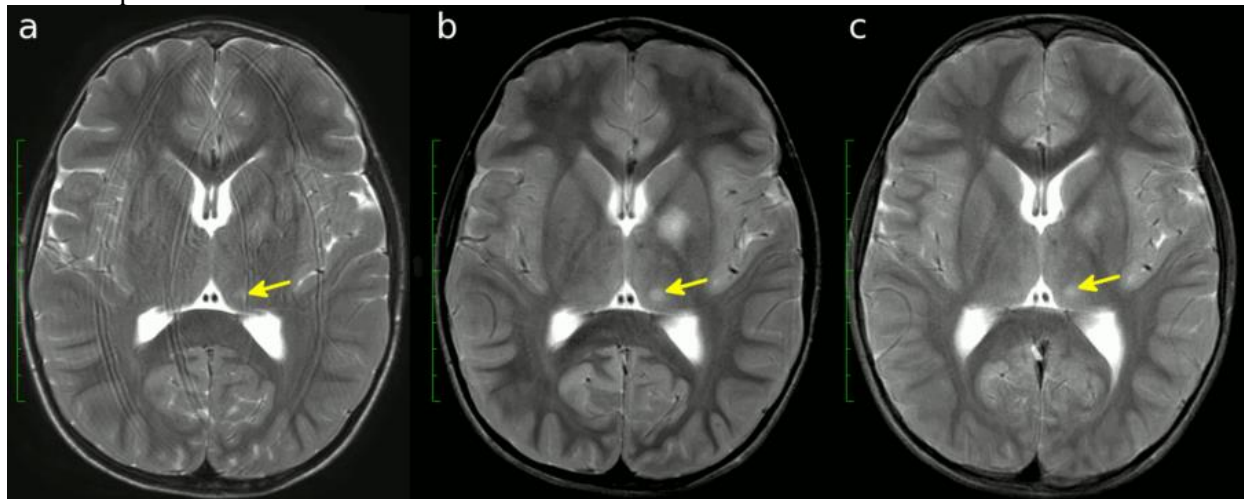
were modified to closely match the imaging resolution and TE of our conventional clinical T2-weighted imaging protocol (0.6mm in-plane acquired resolution, 4mm slice thickness). Due to the intrinsic oversampling of k-space with PROPELLER techniques, and the less aggressive use of SENSE, both the Multivane (SENSE not available, t=180s), and Multivane XD (SENSE 1.5, t=120s) scans were somewhat longer than the conventional T2-weighted scan (SENSE 2.2, t=86s). The scans were performed sequentially with randomized order, and assessed by two board-certified neuroradiologists who were blinded to the technique. Readers were asked to rate the images on a five-point scale, and rank their preference between the three techniques.

Results

An example of (a) conventional T2-weighted imaging, (b) Multivane, and (c) Multivane XD is shown in the Figure. For conventional T2-weighted imaging, 13/28 scan interpretations noted moderate artifacts with some impact on diagnostic value, and 1/28 was judged as having major artifacts with substantial impact on diagnostic value (see Figure a). No Multivane or Multivane XD scans were judged to have more than mild artifacts not impacting diagnostic value. These artifacts were mainly related to pulsatility (18/19) rather than patient motion. Both Multivane and Multivane XD demonstrated significantly higher ratings for diagnostic value than conventional T2 ($p < 0.002$, Wilcoxon Signed Rank test), but were not significantly ($p = 0.317$) different from each other. Both readers ranked the conventional T2 as being inferior to both Multivane and Multivane XD in all subjects ($p < 0.001$). Comparing Multivane XD to Multivane, one reader had a significant preference for Multivane XD ($p = 0.035$), and one had no significant preference ($p = 0.248$).

Conclusions

Both PROPELLER-type techniques resulted in increased diagnostic value compared to conventional T2-weighted imaging. While half of the conventional images were judged to have at least moderate artifacts, impacting diagnostic value, PROPELLER imaging resulted in only mild artifacts which did not impact diagnostic value. The use of Multivane required approximately doubling the scan time. For Multivane XD, the use of SENSE acceleration, along with improved reconstruction techniques, resulted in similar image quality to Multivane, but with only a modest (40%) increase in scan time over conventional imaging. In conclusion, PROPELLER-type motion correction techniques increase perceived diagnostic value for pediatric head MRI.



(Filename: TCT_P-64_Conv-MV-MVXD.gif)

P-60

Relative Cerebral Blood Flow in Pediatric Epilepsy Patients with EEG Abnormalities

P TANG¹, D Chan¹

¹*KK Women's and Children's Hospital, Singapore, Singapore*

Purpose

To measure cerebral perfusion using noninvasive arterial spin labelling (ASL) in pediatric epilepsy patients who have bilateral and unilateral EEG abnormalities

Materials and Methods

In this Institution Review Board approved prospective study, children with epilepsy and having abnormalities on EEG who were scheduled for MRI brain scans in KK Women's and Children's Hospital were recruited. Those who consented to participate had ASL performed during the MRI. The patients were all scanned on a 3T MR scanner with a 32-channel phased-array receive-only head coil. All individuals were scanned with 2D-pCASL and high-resolution anatomical images were acquired using sagittal 3D MPRAGE. ASL images were post processed by FMRIB Software Library (FSL, www.fmrib.ox.ac.uk/fsl) for motion correction and smoothing. Anatomical whole-brain mask was created for each subject to linearly and nonlinearly register MPRAGE to standard space (MNI152 template). Relative cerebral blood flow (CBF) image was registered to the MNI152 template through linear and nonlinear registration of the M0 image to MPRAGE using FSL. Custom Matlab scripts (Mathworks, MA, USA) were used to calculate the mean CBF. The cerebellum was excluded as 2D-pCASL had limited coverage.

Results

There were seven patients with unilateral abnormalities on EEG while four had bilateral abnormalities. Structural MRI showed normal brains in three, neuronal migration abnormalities in three, gliosis in two and nonspecific signal changes in three patients. The average relative CBF in those with unilateral EEG abnormalities is 53.1 +/-7.6 mls/100g/min compared to 62.9 +/-5.8 mls/100g/min in those with bilateral abnormalities (p=0.003). The right to left relative CBF ratios of those with unilateral EEG abnormalities is 1.0 and 1.1 in those with bilateral EEG abnormalities showing that the cerebral perfusion in these patients remains symmetrical.

Conclusions

Pediatric epilepsy patients with bilateral EEG abnormalities show increased relative CBF on ASL compared to those with unilateral EEG abnormalities.

Patient	EEG abnormality	Structural MRI abnormality	Relative CBF in Right cerebrum in mls/100g/min	Relative CBF in Left cerebrum in mls/100g/min	Ratio of Right to Left CBF
1	Left	Left subependymal nodules	50.75	49.56	1.02
2	Left	Bilateral cortical dysplasia	45.54	44.13	1.03
3	Left	Bilateral white matter hyperintensities	56.46	55.83	1.01
4	Right	Normal	57.44	54.82	1.05
5	Right	Right parietal heterotopia	71.59	63.86	1.12
6	Right	Bilateral subcortical hyperintensities	47.78	50.62	0.94
7	Right	Right temporal hyperintensity	45.73	49.56	0.92
8	Bilateral	Normal	69.26	68.12	1.02
9	Bilateral	Normal	64.37	59.02	1.09
10	Bilateral	Left parietal gliosis	61.23	51.12	1.20
11	Bilateral	Left cerebral gliosis	64.07	66.23	0.97

(Filename: TCT_P-60_TableASNRASLandepilepsy.jpg)

P-55

Treatment of Pediatric Intracranial Aneurysms: Case Series and Meta-analysis

A Kansagra¹, J Yasin², A Wallace³, T Madaelil³, J Osbun¹, C Moran¹, D Cross¹, D Limbrick⁴, G Zipfel¹, R Dacey⁵

¹Washington University in St. Louis School of Medicine, St. Louis, MO, ²University of Missouri-Columbia School of Medicine, Ballwin, MO, ³Mallinckrodt Institute of Radiology, St. Louis, MO, ⁴St. Louis Children's Hospital, St. Louis, MO, ⁵Washington University in St. Louis, St. Louis, MO

Purpose

To describe our institutional experience treating pediatric patients with cerebral aneurysms and to conduct a pooled analysis of available studies to provide the best current evidence on treatment-related outcomes.

Materials and Methods

We identified pediatric patients with cerebral aneurysms evaluated or treated at our institution using a comprehensive case log. We also identified studies to include in a pooled analysis through a systematic search of Pubmed, SCOPUS, EMBASE, and the Cochrane Database of Systematic Reviews. As part of both the local and pooled analyses, we recorded patient characteristics, aneurysm characteristics, management, and outcomes. Statistical analysis was performed using Fisher's exact test and the two-tailed Student's t-test, as appropriate.

Results

Forty-two pediatric patients with 57 aneurysms were evaluated at our institution, and treatment-specific

Scientific Posters

outcome data was available in 557 patients as part of our pooled analysis. The rates of favorable outcome with endovascular and surgical treatments were comparable in all children (87.8% versus 82.7%, respectively, $p=0.098$), children with ruptured aneurysms (73.8% versus 82.6%, respectively, $p=.256$), and children with unruptured aneurysms (96.2% versus 97.3%, respectively, $p=1.0$).

Conclusions

Endovascular and surgical treatment yield comparable long-term clinical outcomes in pediatric patients with cerebral aneurysms.

Posters-Socioeconomics

P-66

Incidental Renal Lesions on Lumbar Spine MRI: Who Needs Follow-up?

S Nelson¹, D Oettel¹, C Lisanti¹, R Schwoppe¹, V Timpone¹

¹*San Antonio Military Medical Center, San Antonio, TX*

Purpose

Incidentally discovered renal lesions on lumbar spine MRI are a common occurrence, with vast majority of lesions representing simple cysts. Many follow-up recommendations are generated by radiologists encountering renal lesions in an effort to more definitively characterize the finding as either a benign cyst, or more complex, potentially malignant lesion that would require further work-up or treatment. We hypothesized that careful analysis of the T2WI features of these incidentally discovered renal lesions could reliably identify complex renal lesions and that follow-up imaging may not be required for all cases.

Materials and Methods

Two independent readers retrospectively evaluated 149 renal lesions identified on noncontrast MR lumbar spine examinations in a consecutive patient population of 116 patients. Presence or absence of a complex renal lesion was determined using T2WI alone. Imaging features considered positive for complex renal lesion were lesion nodularity, septations, and T2 signal intensity darker than CSF. Using dedicated renal imaging cross sectional examinations as the reference standard, statistical analysis was performed to determine the accuracy of lumbar spine MRI in predicting a complex and potentially neoplastic renal lesion.

Results

Of 149 renal lesions, there were 115 simple cysts, and 34 complex renal lesions (20 Bosniak II cysts, nine renal cell carcinomas, three Bosniak IIF cysts, and two angiomyolipomas). Lumbar spine MR readers determined there was a simple cyst in 72/149 lesions, and complex renal lesion in 77/149. Reader sensitivity for detection of complex renal lesion on lumbar spine MR was 94% (95 CI: 80%-99%), specificity 63% (95 CI: 53%-72%), PPV 43% (95 CI: 37%-49%) and NPV 97% (95 CI: 90%-99%). Readers correctly identified all neoplastic and potentially neoplastic lesions (\geq BosniakIIF). Inter-reader agreement was excellent, kappa = 0.84.

Conclusions

Follow-up imaging may not be required in all cases of incidentally discovered renal lesions on lumbar spine MRI. T2WI on lumbar spine MRI appears to reliably rule out neoplastic and potentially neoplastic complex renal lesions. More judicious patient selection for follow-up recommendations on lumbar spine MRI can decrease the number of low diagnostic yielding follow-up exams and reduce associated healthcare costs.

P-67

Urgent Direct Access Brain MRI for Suspected Brain and CNS Cancers: Implementation of the NICE Guideline (NG12) - Nottingham Experience

A Evans¹, M Shah¹, T Aslam¹, J Shah¹

¹*Nottingham University Hospitals NHS Trust, Nottingham, United Kingdom*

Purpose

Background: The NICE guidance (NG12) published in June 2015 recommends urgent direct access MRI scan of the brain to be performed within two weeks to assess for brain or CNS cancer in adults with progressive, subacute loss of central neurological function. NICE used risk threshold of 3% positive predictive value to underpin the recommendations. Patients with new onset seizure have greatest PPV of 2.3% for a brain tumor (Hamilton 2007). At Nottingham we developed five specific criteria (corresponding to progressive, subacute loss of CNS function) under which patients may be referred directly from the primary care for urgent brain imaging and set up an urgent brain MRI pathway on 1st October 2016. **Objective:** To assess compliance and efficiency of the urgent direct access brain MRI pathway

Materials and Methods

All patients referred under the primary care direct-access pathway from 1st October 2016 to 28th February 2017 were reviewed. The clinical history and subsequent MRI findings were analyzed to determine the rate of positive findings. Referral, imaging and reporting times were reviewed to determine compliance with the pathway.

Results

Eighty-nine patients were referred under the pathway within the five-month period. Twelve patients breached the two week target for imaging either at patient request or due to administrative error; 87% patients had their reports within the agreed two weeks. Important findings from the pathway included 4 x metastasis, 1 x GBM, 1 x pituitary adenoma, 2 x subacute infarcts, 1 x bilateral subdural collection. The total brain tumor pickup from the pathway is 6.74% (6/89).

Conclusions

Using the Nottingham criteria for direct access brain MRI pathway the PPV is 6.7% which is higher than the threshold set by NICE and the PPV reported on prior studies. If optimized and well managed the direct access brain imaging pathway is efficient method for early detection of brain cancers.

Posters-Spine

P-75

Incidence and Clinical Significance of Blunt Cerebrovascular Injury in Trauma Pan Scans

P Albertine¹, M Mossa-Basha¹, K Linnau¹, K Sheehan²

¹*University of Washington, Seattle, WA*, ²*University of Washington, N/A*

Purpose

Prevalence of blunt cerebrovascular injuries (BCVI) has been reported to range from 0.08%-2.7%. It has been suggested that variation in prevalence may in part be related to screening. The goal of this study is to evaluate the impact of trauma 'Pan-Scans' in terms of overall detection of BCVI, rates of anticoagulation/antiplatelet therapy and post-BCVI infarction.

Materials and Methods

We retrospectively evaluated patients who presented to level I trauma center with history of major blunt traumatic injury (MVC, MCC, Fall >12 ft, car vs ped) between July 2011 and December 2013. Patients who presented prior to January 2013 received dedicated CTA head and neck only when there was concern

Scientific Posters

for BCVI (per Denver criteria). Patients who presented between January 2013 and December 2013 were imaged with trauma pan-scans and subsequent reformatted CTA head and neck were performed if there was suspicion for BCVI. Electronic medical records and electronic radiology files were reviewed to determine patient age (18-85), gender, grade of BCVI injury, TCD monitoring results, treatment, and rates of BCVI-related CVA.

Results

There were 1200 patients who presented to the ED between January 2011 and December 2013. Mean age 42.2 ± 17.4 years old, 64.4% of patients were male. Preliminary results show 14.4% incidence of BCVI in the trauma pan-scan group compared to 7.7% in the CTA head and neck group. Patients in the trauma pan-scan group had higher rates of treatment with anticoagulation (17.1% vs. 5.4%). Data analysis regarding overall outcome in relation to CVA post-BCVI is still under review.

Conclusions

In the setting of major blunt traumatic injury, patients who are screened for BCVI utilizing a trauma pan-scan rather than Denver criteria and dedicated head and neck CTA show higher rates of BCVI and higher rates of anticoagulation. Data analysis regarding rates of post-BCVI CVA is still under review.

P-71

It is Not Necessary to Discontinue Neurologic Medications Prior to Myelography

M Krupa¹, F Mihlon¹

¹*Eastern Virginia Medical School, Norfolk, VA*

Purpose

There is currently no consensus as to whether patients who are to undergo myelography should discontinue medications that could potentially lower their seizure threshold [1]. While early myelographic contrast agents did cause seizures in some patients, the non-ionic intrathecal contrast agent iohexol (Omnipaque) carries a very low risk of seizure [2] and there are only a few case reports of seizures associated with this agent [3,4]. Nonetheless, many radiology departments have patients temporarily discontinue many neurologic medications prior to myelography in an effort to decrease the perceived risk of myelography-induced seizure. This is often problematic for patients because they rely upon these medications to manage the daily manifestations of various chronic illnesses. In a survey of radiology departments published in AJR in 2005, approximately two-thirds of respondents reported screening for and temporarily discontinuing medications that could potentially lower seizure threshold, while one-third neither screened for nor discontinued these medications [5]. The purpose of this retrospective cohort study is to document our institution's experience performing myelography safely without screening for or discontinuing neurologic medications.

Materials and Methods

We performed a retrospective cohort analysis of all the myelograms done in 2016 at our institution, which does not screen for or discontinue potentially epileptogenic medications prior to myelography. All myelograms were performed with iohexol intrathecal contrast. A chart review of the patients who underwent myelography was performed, and the data retrieved was as follows: daily medications at the time of the procedure, contrast volume administered, type of myelogram (total spine, cervical, thoracic, or lumbar), and complications.

Results

A total of 143 patients underwent myelography during 2016 (39 whole spine, 40 cervical only, 3 thoracic only, and 61 lumbar only). Sixty-six patients (46%) were on at least one neurologic medication historically thought to lower seizure thresholds, and 13 (9%) were on two. The most common medications were duloxetine (15 patients), sertraline (14 patients), venlafaxine (9 patients), bupropion (8 patients), and amitriptyline (8 patients). Two patients had a documented history of epilepsy, and both were on

amitriptyline and venlafaxine. No patients were given benzodiazepines prior to the procedure for seizure prophylaxis. There were no seizures during or shortly following any of the 143 myelograms.

Conclusions

Intrathecal iohexol has very low epileptogenic potential. Patients undergoing myelography with iohexol do not need to be prescreened for medications that are historically thought to lower seizure threshold such as selective serotonin reuptake inhibitors (SSRIs) and tricyclic antidepressants (TCAs).

P-72

Reliability of CT Myelography Versus MRI for the Assessment of Spinal Epidural Disease

L Chen¹, K Peck¹, J Arevalo Perez¹, A Holodny¹, E Lis¹, Y Yamada¹, S Karimi¹, S Haque¹, J Lyo¹

¹Memorial Sloan Kettering Cancer Center, New York, NY

Purpose

MRI has largely replaced CT as the primary imaging modality for spinal metastases. However, CT myelography (CTM) is thought to provide better visualization of bony structures than MRI and can be directly correlated to electron densities necessary for radiotherapy treatment planning (1). We seek to investigate whether there continues to be merit in using CTM as it may provide greater inter- and intra-rater reliability in the assessment of spinal ventral epidural disease.

Materials and Methods

We retrospectively reviewed medical records for patients who received radiotherapy from 2009-2016. For patients with spinal ventral epidural disease who had MRI within seven days of CTM, four neuroradiologists independently assessed whether epidural disease could be diagnosed in both axial and sagittal projections and measured the maximum disease extension into the spinal canal. The interclass correlation coefficient (Krippendorff's alpha) was used to calculate inter- and intra-rater reliability.

Results

Forty-six sites of epidural disease from 31 patients were assessed. In the sagittal projection, inter-rater agreement was similar using CTM and T1-weighted MRI (Krippendorff's =0.63 and 0.66, respectively) and slightly greater than T2-weighted MRI (Krippendorff's =0.59). In the axial projection, inter-rater reliability was greater in CTM images (Krippendorff's =0.67) than in T1-weighted or T2-weighted MRI (Krippendorff's =0.56 and 0.57, respectively). Intra-rater reliability for each of the 4 raters was acceptable (Krippendorff's [0.57 to 0.75]).

Conclusions

On sagittal projections, CTM and T1-weighted MR are advantageous over T2-weighted MR for the measurement of ventral epidural disease extent. On axial projections, CTM provides slight advantage in the reliability of epidural disease measurement. Despite the more invasive nature of CTM, the ability of CTM to provide better visualization of the spinal cord and its mitigation of CSF pulsation effects compared to T2-weighted MRI (2) suggest that CTM should still be used in conjunction with MRI to assess ventral epidural disease and plan radiation therapy.

P-73

Spinal Cord Volume Is a Promising Parameter for Monitoring Multiple Sclerosis Activity in Patients with Higher Degrees of Disability

M Vaneckova¹, M Andelova¹, J Krasensky¹, L Sobisek², Z Seidl¹, T Hrebikova¹, T Uher¹, E Havrdova¹, B Benova¹, B Marechal³, T Kober³, D Horakova¹

¹Charles University In Prague, Prague 2, Czech Republic, ²University of Economics in Prague, Prague, Czech Republic, ³Siemens Healthcare, Lausanne, Switzerland

Purpose

To explore relationships between spinal cord volume (SCV), global and regional brain volumes (BVs), and disability in a large cohort of multiple sclerosis (MS) patients

Materials and Methods

We examined 1197 MS patients on a 3T MRI scanner (MAGNETOM Skyra, Siemens Healthcare). The MRI protocol consisted of 3D-T2W-Fat-Sat for SCV and 3D-MPRAGE for BVs. Cervical SCV was measured with a semiautomated edge-finding tool in 21 1 mm slices. Global and regional BVs were estimated by the fully automated MorphoBox prototype. Correlations between BVs and SCV were compared between gender-, age- and disease-duration matched patients with mild disability (EDSS 0-3) and relatively severe disability (EDSS ≥ 3.5). Uni- and multivariate generalized linear regression models were applied to identify best EDSS predictors.

Results

The strongest correlation was found between SCV and medulla oblongata ($\rho=0.67$), mesencephalon (0.60), pons (0.52), pallidum (0.49), putamen (0.47), whole brain (0.44). These correlations were weaker in patients with severe disability (oblongata 0.46, others less than 0.29). Overall, SCV and total BV (TBV) alone accounted for 11.3% and 12.1% respectively of EDSS variability. In the high-disability group, SCV alone explained 6.2% of EDSS variability, whereas in the lower disability group it was only 1.7%. TBV could explain similar percentage of variance of EDSS scores in both groups (6.6%, 6.0% respectively). Combining SCV and TBV in a multivariate model resulted in better predictive value (20.4%). Similar to univariate models, this combination explained better variance of EDSS scores ≥ 3.5 (12.4%) than of EDSS scores up to 3.0 (6.5%).

Conclusions

Lack of correlation in patients with severe disability suggests independent progression of spinal cord and brain pathology during the secondary progressive disease phase. Both SCV and TBV are strong EDSS predictors in patients with relatively severe disability. SCV might be a suitable MR marker for MS patients with progressive course.

P-68

Utility of Contrast in Postoperative Spine MRI for Failed Back Syndrome: When Should We Stop?

C Karakasis¹, J Lee¹, T Emch¹, V Hill¹, T Stultz², S Jones¹

¹Cleveland Clinic, Cleveland, OH, ²Cleveland Clinic, Brecksville, OH

Purpose

MRI is commonly obtained in evaluation of the postoperative spine, which frequently includes intravenous gadolinium contrast administration. There is a paucity of data to support contrast administration in this setting, and to our no knowledge no studies have evaluated the utility of contrast in these patients. The purpose of this research is to evaluate the role of postcontrast imaging in MRI evaluation of the postoperative spine, in patients who have been diagnosed with failed-back syndrome.

Materials and Methods

A retrospective study was performed of 70 patients who underwent MRI following single level lumbar surgery for discectomy. The study included the first follow-up examination for patients diagnosed with failed-back syndrome. Evaluation of the MRI examinations was performed by five separate readers with subspecialty training in neuroradiology for clinically significant findings, defined as recurrent disc, epidural fibrosis, infection, arachnoiditis, pseudomeningocele or other finding, on the precontrast and postcontrast imaging, and whether contrast was useful in the evaluation. Readers were blinded to the clinical history and the time since surgery. The null hypothesis was that the diagnostic yield of clinically significant findings after failed back surgery where contrast MRI is deemed helpful is not affected by the time since surgery. Logistic regression analysis was performed with Generalized Estimating Equations (GEEs) to account for the clustered data (i.e. five readers interpreting each image). The dependent

variable was the presence/absence of clinically useful information provided by contrast; the independent variables were reader and the time since surgery. A significance level of 0.05 was used. Secondary objectives include: 1. Estimate the yield of clinically significant findings on MRI without contrast as a function of time since surgery. Logistic regression analysis was used to assess the effect of time on yield before contrast. 2. Identify a cut-point in time since surgery where the yield of significant findings with contrast is too low to justify the use of contrast. Receiver Operating Characteristic analysis was used. 3. Re-analyze the primary analysis using a consensus score, defined as positive if three or more of the five readers identified the contrast images as helpful and negative if <three readers found the contrast images helpful.

Results

Seventy subjects were included, with imaging performed at a median of 0.83 years since surgery (range of one day to 11 years, with 25% of subjects imaged >2.5 years since surgery). In 64.3% of observations, readers reported clinically significant findings without contrast. Enhancement was recorded as present in 63.4% of cases and enhancement was found to be useful in 64.6% of cases. Enhancement was reported as very useful (score of 4/4) in 144 (64.9%). Marked variability between readers regarding presence/absence of clinically important nonenhancing findings related to surgery, with a range from 41.4% to 95.7% (kappa statistic = 0.220). There were also significant differences between readers in reporting the presence/absence of enhancement (range from 42.9% to 97.1%) (kappa statistic = 0.184), and in reporting the presence/absence of useful information with contrast (47.1% to 94.3%) (kappa statistic = 0.160). Time from surgery was a statistically significant predictor of the presence of useful information with contrast ($p < 0.001$). Useful information with contrast decreased at a rate of 34% per year (estimated odds ratio=0.66, 95% CI of [0.55, 0.80]). When scoring consensus is applied, the yield of postcontrast imaging decreases to less than 20% beyond five years. (Table 1, Figure 1). Time since surgery was a significant predictor of clinically important nonenhancing findings ($p < 0.001$). Useful information without contrast decreased at a rate of 29% per year (estimated odds ratio=0.71, with 95% CI of [0.60, 0.84]). Area under ROC curve was 0.70, indicating that time since surgery is a predictor of when contrast will be useful. Probability of useful information with contrast, as assessed by consensus of the five readers, is not constant over time ($p = 0.001$). Useful information with contrast decreased at a rate of 43% per year (estimated odds ratio=0.57, with 95% CI of [0.40, 0.79]). Estimated ROC area 0.768 (Figure 2).

Conclusions

Gadolinium contrast is frequently administered in MRI evaluation of the postoperative spine; however, in our experience this is frequently done in a nonstandardized fashion. Radiologists protocoling and interpreting the images, as well as clinicians ordering the examinations often question whether or not contrast should be administered in these patients. This study was undertaken in the attempt to improve understanding of the duration of time after surgery which contrast no longer adds clinical utility, as no such information is available in the medical literature. The study results suggest a continuous decrease in the yield of contrast for the identification of clinically significant findings on MR evaluation for failed-back syndrome, as a function of time since surgery. The yield begins to decrease after 1.5 years, and at 5+ years is less than 20%. The large interobserver variability in this study on the pooled data reflects the range of practice among neuroradiologists interpreting these examinations. The data becomes more consistent when a simple majority consensus was applied to the pooled data. This study provides an important initial inquiry into the role of contrast administration for the postoperative spine.

Table 1: Frequency of Helpful Information with Contrast as Function of Time Since Surgery

Time since surgery	Frequency where Contrast Useful (pooled over readers)	Frequency where Contrast Useful (consensus)
<6 months	83.3% (100/120)	91.7% (22/24)
7-11 months	63.1% (41/65)	76.9% (10/13)
1 – 1.9 years	60.0% (36/60)	83.3% (10/12)
2 – 2.9 years	60.0% (24/40)	62.5% (5/8)
3 – 4.9 years	42.9% (15/35)	42.9% (3/7)
5 – 6.9 years	40.0% (6/15)	33.3% (1/3)
7 – 11 years	26.7% (4/15)	0% (0/3)

Figure 1: Observed probability of clinically useful information over time (mid-point of time interval) with enhanced images based on readers' consensus.

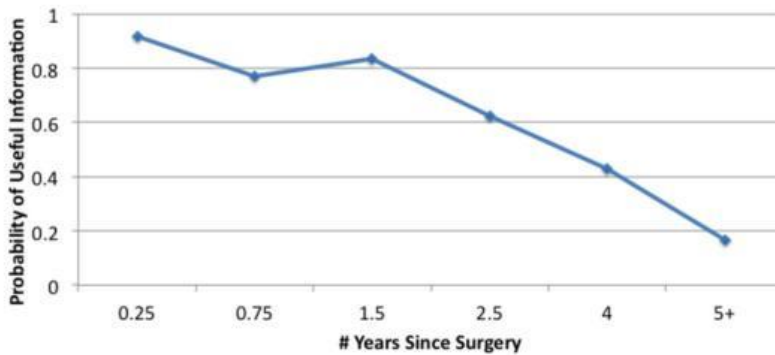
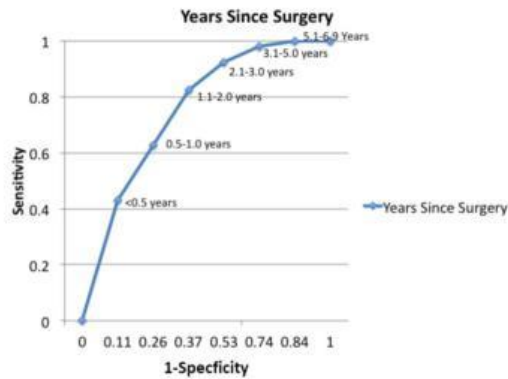


Figure 2: Empirical ROC curve of # years since surgery as a predictor of clinically useful information with enhancement, using readers' consensus as reference standard. The estimated ROC area is 0.768 with 95% CI of [0.632, 0.904].



(Filename: TCT_P-68_KarakasisetalFiguresandTablesASNR2018.jpg)

P-70

Utility of Diffusion-weighted Imaging in the Diagnosis of Epidural and Paraspinal Abscesses in Comparison with T2 and Postcontrast T1-weighted Images

A Belay¹, M Patel², T Sasaki², E Mastumoto¹, T Moritani³

¹University of Iowa Hospitals and Clinics, Iowa City, IA, ²University of Iowa, Iowa City, IA, ³University of Michigan, Ann Arbor, MI

Purpose

To compare the performance of diffusion, T2, and fat saturation postcontrast T1-weighted images in the diagnosis of epidural and paraspinal abscesses

Materials and Methods

IRB approval was obtained and informed consent was waived for this retrospective study. Cases were collected via a search utilizing several diagnosis codes. Out of 96 patients in total, after using exclusion criteria, 61 patients (39 males and 22 females, age range of 23-88 years) were analyzed. The 1.5 Tesla MRI scanners with axial single shot echo planar DWI with parallel imaging factor 2 or 3 were utilized for all of the reviewed exams. MRI studies were reviewed by two diagnostic radiology residents working in collaboration. The usefulness of diffusion, T2, and fat saturation postcontrast T1-weighted images in identifying and diagnosing epidural and paraspinal abscesses were graded on a scale of 1 to 5; 1 was given when the abnormality was not visualized in that sequence; 2 was given if the abnormality was visualized in that sequence but not helpful for diagnosis; 3 was given if the sequence was somewhat helpful for diagnosis; and 4 and 5 were given if the sequence was useful and very useful for diagnosis respectively. For ADC analysis, the ADC of a representative region of spinal cord abnormality was measured by placing a region of interest (ROI) on the ADC map in consensus fashion. ROIs were constrained between 0.1 to 22 mm². The average ADC values and standard deviation were recorded. Statistical analysis comparing the performances of T2 vs. DWI, DWI vs. post contrast, T2+ post contrast vs. DWI, T2+DWI vs. post contrast, DWI+post contrast vs. post contrast and T2+DWI+post contrast vs. DWI+post contrast was made using one tailed Student's t-test. The 1.5 T MRI scanners and Gadavist were utilized for all of the reviewed cases.

Results

In our subset of patients, methicillin susceptible staph aureus, followed by its methicillin resistant counterpart were the most frequently responsible organisms, accounting for three out of four epidural/paraspinal abscesses. We found no correlation between average ADC values and length of antibiotic treatment. DWI performed better than T2 but was inferior to postcontrast images for the diagnosis of epidural and paraspinal abscess (p values of 0.002 and 0.01 respectively). However, the performance of DWI combined with T2 did not show a statistically significant difference when compared with the performance of post contrast images alone in the diagnosis of epidural/paraspinal abscess (p value 0.39) (Figure 1). DWI+post contrast performed better than post contrast alone (P < 0.02) and there was no significant difference between the performance of T2+DWI+postcontrast sequences and DWI+postcontrast sequences. We think that DWI did not perform as well as postcontrast images due to its vulnerability to chemical fat saturation and diamagnetic susceptibility artifacts.

Conclusions

In comparing T2, DWI/ADC, contrast-enhanced sequences and their combinations for the diagnosis of epidural/paraspinal abscesses, while contrast-enhanced sequences performed better than DWI and T2 alone, the combination of DWI, postcontrast images and T2 as well as the combination of DWI and postcontrast images were found to have the most utility. DWI combined with T2 was found to have comparable performance to postcontrast sequences alone in the diagnosis of epidural/paraspinal abscess, and can be utilized when contrast cannot be given.

eP-60

Aqueduct Stroke Volume for Cerebrospinal Fluid Aqueduct Flow Quantification is More Robust than Peak Systolic Volume Using Different Clinical Workstation Software with and without Eddy Current Correction

W Wang¹, E Lui¹, P Desmond¹

¹Royal Melbourne Hospital, Parkville, Victoria, Australia

Purpose

Aqueduct stroke volume (ASV) [1, 2] and peak systolic velocity (PSV) [3] have been used to predict shunt responsiveness in NPH, but reported values have been variable [4]. We aim to compare the effect of two postprocessing workstations and eddy current correction (ECC) on ASV and PSV.

Materials and Methods

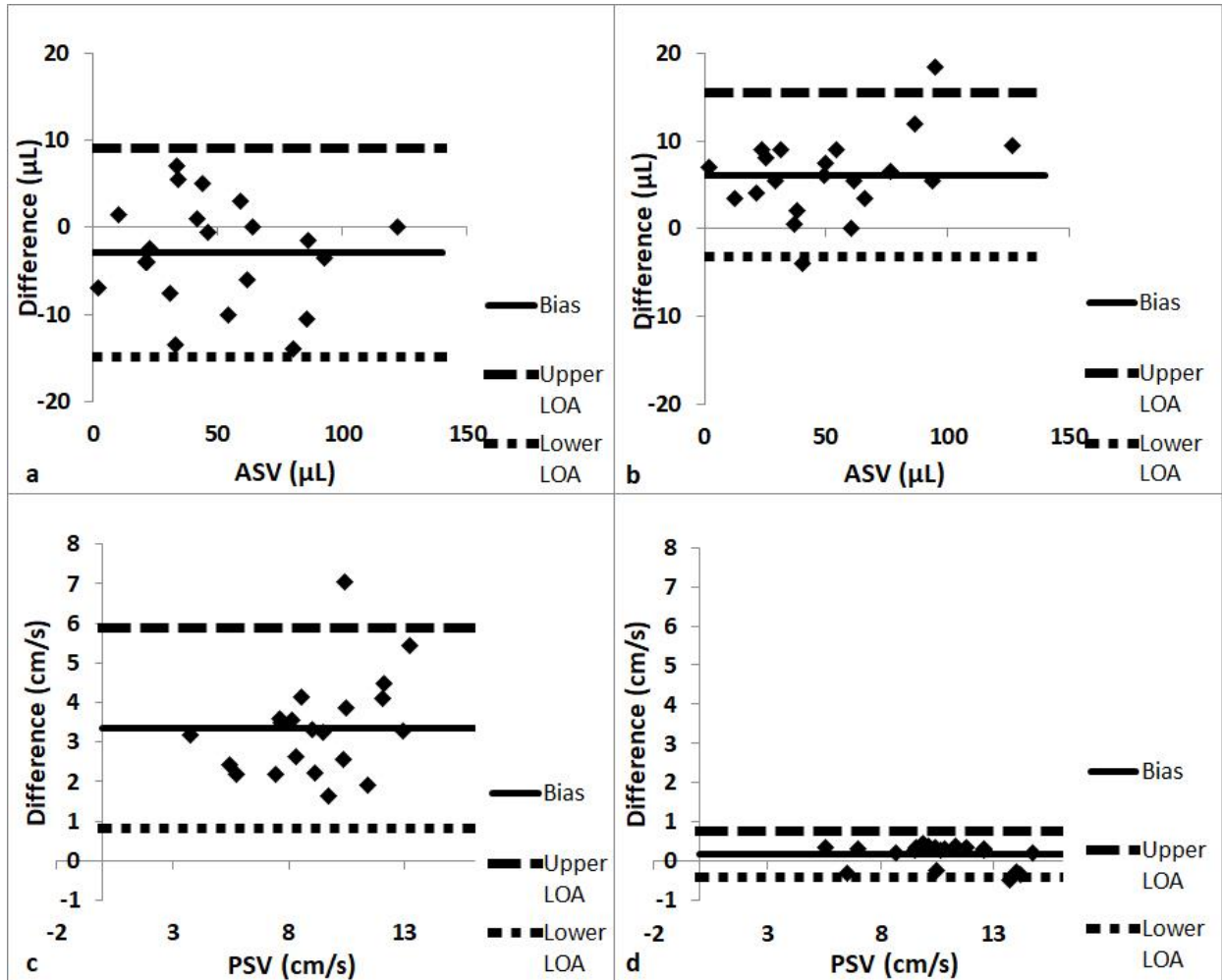
Twenty normal elderly subjects (age 65-82 years; 7 male) were prospectively recruited for 3T phase-contrast imaging through the cerebral aqueduct (VENC=20cm/s; matrix=192x256mm; slice thickness=4mm; TR=36.9ms; TE=6.08ms; flip angle 20 degrees). From this same dataset and using the same "fixed ROI" technique [5], ASV and PSV were obtained using Argus and Syngo-Via (Siemens) without ("Via") and with eddy current correction ("ViaECC"). Statistics were performed with SPSS.

Results

Argus, Via and ViaECC: (i)ASV (μ L, mean+SD) 51+31, 48+30 and 54+32 (ii)PSV (cm/s) 7.5+2.3, 10.9+2.8 and 11.0+2.7 respectively. Normal ASV and PSV are defined as \leq mean+2SD, with Argus-derived values 113 μ L and 12.1 cm/s respectively. Figure 1 shows Bland-Altman plots for ASV and PSV. ASV intraclass correlation coefficient (ICC) are all >0.98. PSV ICC comparing Via/Argus, ViaECC/Argus and with ViaECC/Via are 0.69, 0.66 and 0.99 respectively. Via and ViaECC ASV did not change classification from normal to abnormal using Argus derived cut off. Via and ViaECC PSV both changed classification to abnormal in 7/20 (35%). Figure 1: Bland-Altman plot for ASV and PSV (a)ASV Via vs Argus: mean difference -2.9 μ L (b)ASV ViaECC vs Via: mean difference 6.0 μ L. (c)PSV Via vs Argus: mean difference 3.4 cm/s (d)PSV ViaECC vs Via: mean difference 0.18 cm/s. Overall differences for ASV are small but for PSV are large. LOA: limit of agreement.

Conclusions

ASV is a more robust parameter for quantification of aqueduct CSF flow than PSV when using different clinical workstation software. Software ECC for both ASV and PSV did not affect results in a magnitude that was clinically significant for the evaluation of NPH.



(Filename: TCT_eP-60_BAplots.jpg)

eP-24

Assessment of Blood Brain Barrier (BBB) Perfusion Parameters in Tuberculous Meningitis (TBM) Using Dynamic Contrast Enhanced (DCE) Magnetic Resonance Imaging (MRI)

S Kumar¹, P Singh¹, S Vyas¹, M Modi¹

¹Postgraduate Institute of Medical Education and Research, Chandigarh, India

Purpose

To quantitatively evaluate BBB perfusion parameter changes in TBM patients using DCE MRI in comparison to healthy controls and evaluate whether it correlates with clinical staging of the disease.

Materials and Methods

Thirty confirmed patients of TBM fulfilling diagnostic criteria of Ahuja et al. were included in the study. Patients who met the inclusion criteria were divided into three groups on the basis of British Medical Research Council clinical criteria for the severity of TBM. DCE-MRI was used to measure BBB permeability in patients as well as 10 healthy controls. Postprocessing and detailed analysis of physiological indices was done on regions of interest (ROIs) placed in basal cisterns. Comparison of the mean permeability indices was done between the patients and controls. Correlation between permeability indices and clinical staging of the disease was also established.

Electronic Posters

Results

Permeability indices 'K trans mean' and 'Ve mean' were significantly higher (where $p < 0.01$) in basal cisterns of TBM patients when compared to healthy controls. The values were higher in cases showing larger exudates. Statistically significant positive correlation was also seen between clinical staging and Ve mean (where $P < 0.05$).

Conclusions

Our results emphasize the role of MRI in the quantitative measurement of BBB pathology in TBM, and correlates mean permeability indices with clinical staging of the disease. DCE derived permeability indices may be used as a marker for clinical staging of the disease, allowing prognostication of the patients with respect to clinical severity and optimizing therapeutic strategies.

eP-67a

Assessment of Extracranial-intracranial Bypass for Intracranial Major Trunk Stenoocclusive Lesions by Whole-brain Vessel Wall Imaging

K Tsuchiya¹, M Gomyo², S Hosoi¹, T Tahara¹

¹Saitama Medical Center, Saitama Medical University, Kawagoe, Japan, ²Kyorin University, Mitaka, Tokyo, Japan

Purpose

Whole brain vessel wall imaging (VWI) is recently used in the diagnosis of intracranial major artery stenoocclusive lesions. We applied the technique and black-blood MR angiography (BB-MRA) additionally obtained from its data to the diagnosis of patients who received extracranial (EC)-intracranial (IC) bypass. Our purpose of this study was to evaluate the value of the techniques in the assessment of stenoocclusive lesions and EC-IC bypass.

Materials and Methods

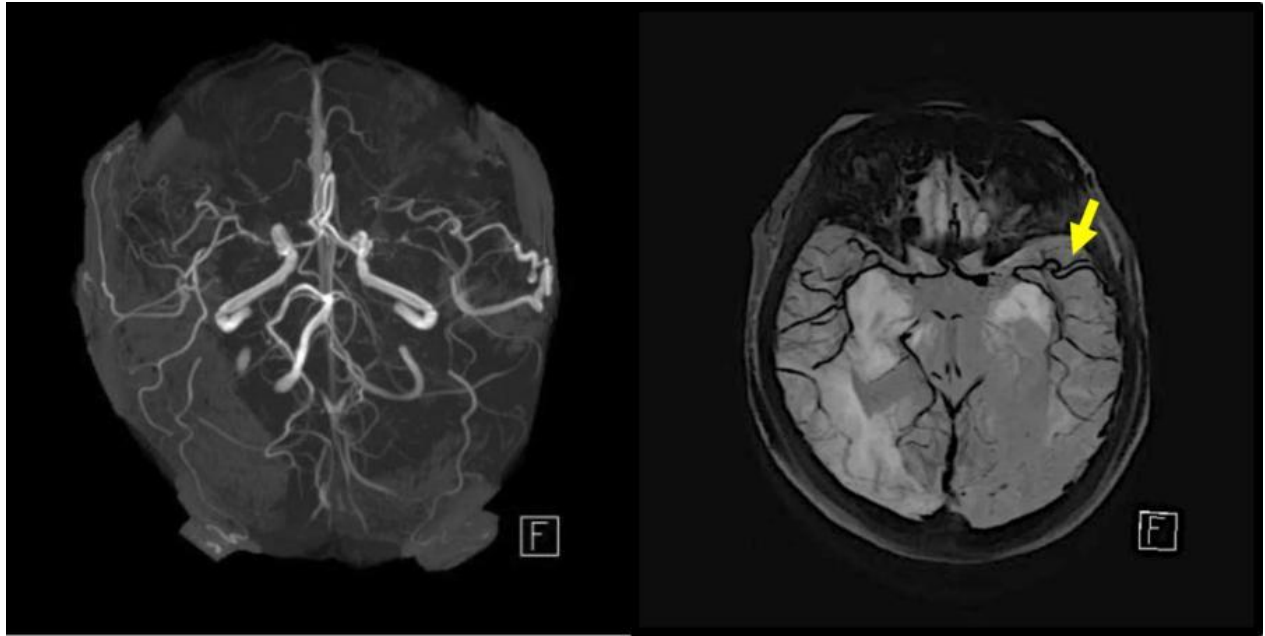
Using a 3-T imager (Siemens, Verio), we performed whole brain VWI employing a 3D T1-weighted SPACE sequence (FOV, 240 x 240 mm; matrix, 270 x 256; TR/TE, 540/11 msec; NSA, 1.6; GRAPPA factor, 2; turbo factor = 39, ETL, 31; # of slices, 192; slice thickness, 0.9 mm; scan time, 7:35) and afterwards generated axial BB-MRA images using a minimum-intensity-projection method (slice thickness, 30 mm; slice interval, 2 mm). Our study group comprised 23 patients (10 males and 13 females; age range: 5-76 years) after EC-IC bypass for occlusion or stenosis of the internal carotid or middle cerebral artery (n = 4) or moyamoya disease (n = 19). Two observers performed comparative visual assessments between 3D-TOF MRA including its source images and VWI regarding visualization of the stenoocclusive lesions as well as between 3D-TOF MRA and BB-MRA regarding visualization of the bypass using a three-point grading system.

Results

The VWI depicted stenoocclusive lesions better than 3D-TOF MRA in 20 of the 23 patients. The BB-MRA better visualized bypass recipient vessels in 14 of the 23 patients, although the two methods comparatively depicted anastomotic sites in 10 of the 23 patients.

Conclusions

Whole brain VWI and its applied BB-MRA could be techniques that effectively demonstrate intracranial major artery stenoocclusive lesions and status of EC-IC bypass, as the two techniques add detailed morphological information.



(Filename: TCT_eP-67a_Fig.jpg)

eP-45

Atypical Radiological Findings and Apparent Diffusion Coefficient (ADC) Values of Primary Central Nervous System Lymphoma (PCNSL): A Single Center Twelve-year Review

W Yu¹, I Khan¹, H Lee², X Lin¹

¹National Neuroscience Institute, Singapore, ²Tan Tock Seng Hospital, Singapore

Purpose

PCNSL classically manifests as single or multiple homogeneously enhancing lesions. Atypical findings like necrosis, irregular rim-like/absent enhancement, hemorrhage, calcification and cystic changes, have been reported, often leading to delayed diagnosis and treatment. Several studies have shown that ADC values from DWI imaging is significantly lower in lymphomas. We aim to characterize the atypical radiological features and ADC values of PCNSL in our local population.

Materials and Methods

We retrospectively reviewed all patients with histological diagnosis of CNS lymphoma at our tertiary center from 2005 to 2016. Patients with typical imaging findings of homogenous contrast enhancement without hemorrhage, calcification, necrosis and cystic changes, were excluded. Additional exclusion criteria included (i) relapsed PCNSL, (ii) secondary CNS lymphoma, and (iii) positive HIV. ADC values were computed by two methods (i) multiple ROIs (ROI1) in the non-necrotic enhancing tumor and (ii) whole tumor volume ROI (ROI2). ADC_{mean} and ADC_{min} values were measured for each lesion. Two independent raters scored the presenting MRI and CT scans.

Results

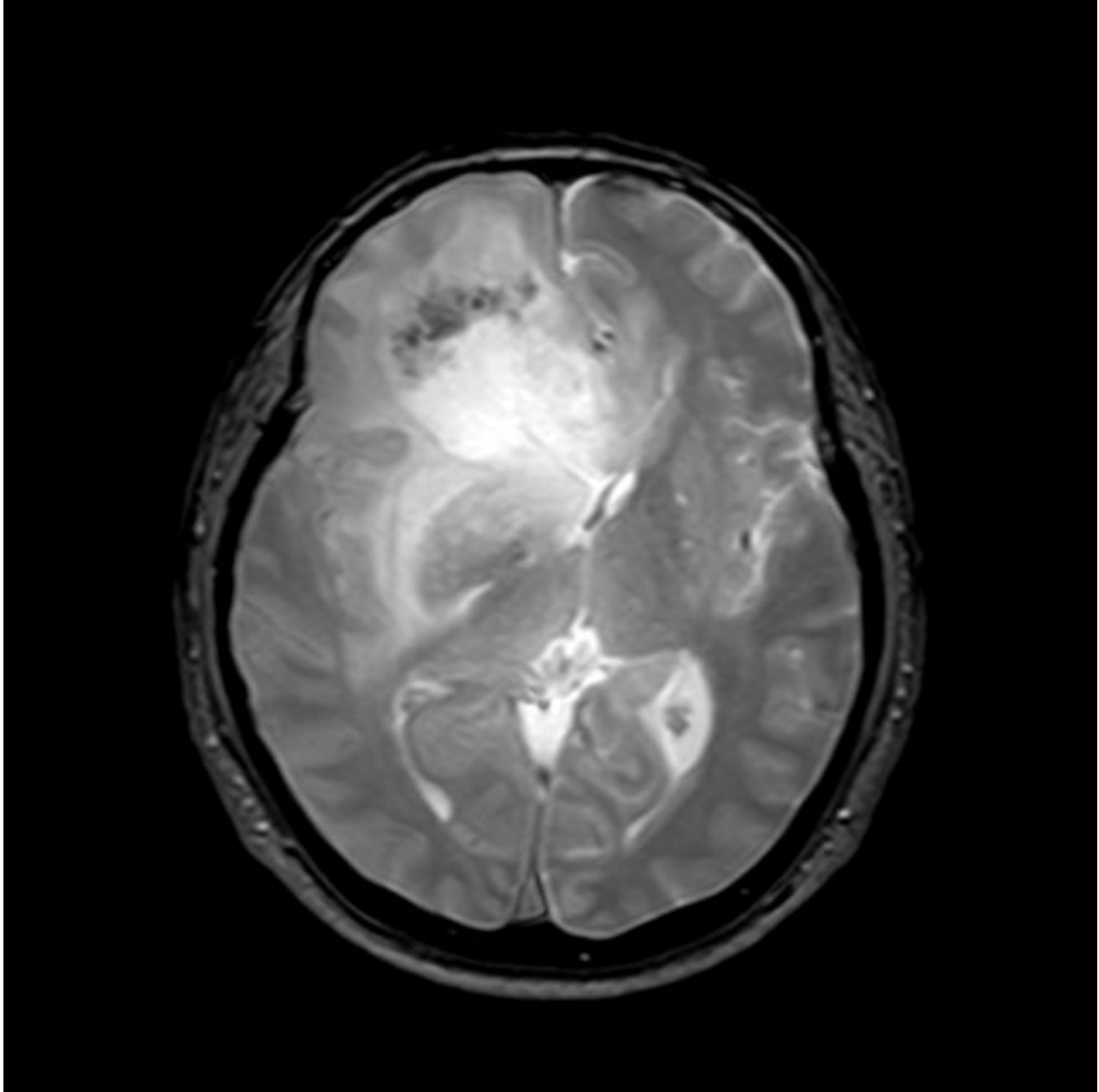
Sixteen patients (8 men, 8 women) were analyzed; median age was 61 (range 22-81) years. Histological diagnoses were DLBCL (n=14) and intravascular lymphoma (n=2). Fifteen (93%) patients had enhancing lesions (5 solitary; 10 multifocal); one had nonenhancing lesion. Most enhancing lesions had T1W hypointense (67%) and T2W mixed (53%) signal. Six (40%) had central nonenhancement and 9 (56%) had lesions with susceptibility. ADC_{mean} and ADC_{min} by both ROI methods was less than 0.98×10^{-3} mm²/sec. Lower ADC values were obtained by ROI2 method. Presurgical radiological diagnoses were

Electronic Posters

glioblastoma (n=9), demyelinating disease (n=2), malignant meningioma (n=1), vasculitis (n=1), and lymphoma (n=3).

Conclusions

PCNSL lesions may be nonenhancing, contain hemorrhage, calcification, cysts, necrosis, and mimic other CNS diseases. The use of ADC is an important adjunct to anatomical imaging and lymphomas demonstrate low ADC values, consistent with high tumor cellularity. A high index of suspicion is critical for early diagnosis.



(Filename: TCT_eP-45_GRE_lymphoma.jpg)

eP-25

Autoimmune Glial Fibrillary Acidic Protein (GFAP) Astrocytopathy presenting as Meningoencephalomyelitis: A Review of Two Cases from the UK

Electronic Posters

D White¹, M Patel¹, W Wali Muhammad¹, T Hayton¹, S Ramalingam¹, S Jacob¹, V Sawlani¹

¹University Hospitals Birmingham NHS Foundation Trust, Birmingham, United Kingdom

Purpose

Autoimmune Glial Fibrillary Acidic Protein (GFAP) Astrocytopathy is a relatively new category of immune-mediated disease involving the central nervous system that demonstrates a widely variable spectrum of clinical presentations, ranging from the relatively mild or subacute onset of cognitive impairment, seizures, encephalopathy, and meningeal symptoms to more complex forms of encephalomyelitis. GFAP α -IgG in CSF is highly specific for diagnosis of this entity (1).

Materials and Methods

We present a case review of two cases which were recently diagnosed in our institution with typical imaging findings (1). They presented with fever, meningoencephalitis and bilateral papilloedema. CSF antibody analysis (GFAP α -IgG) from Mayo Clinic confirmed the diagnosis of GFAP in both cases.

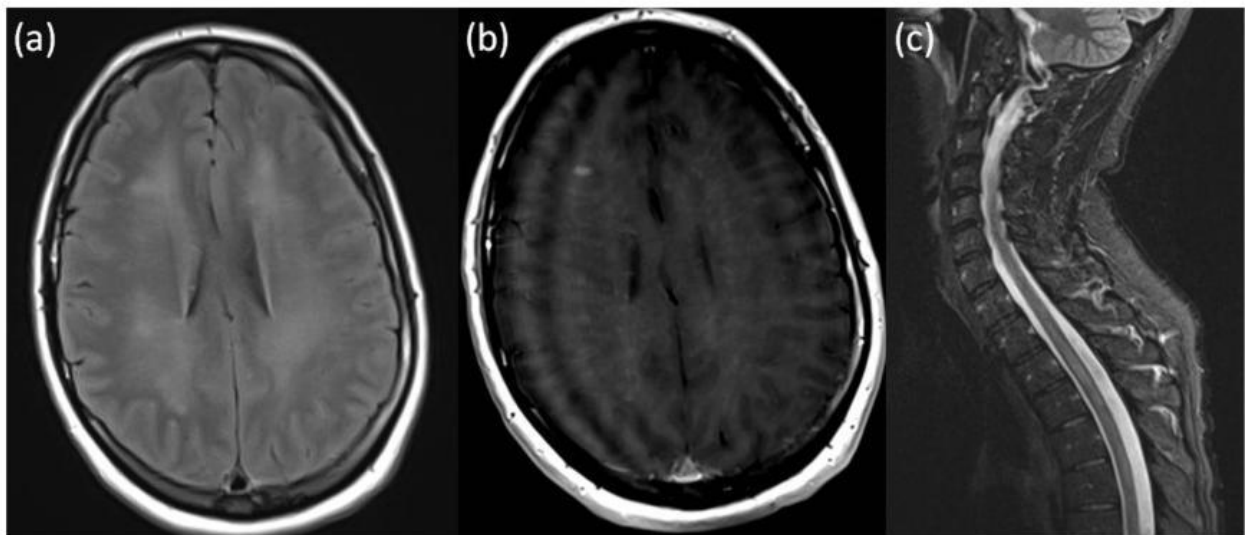
Results

The typical radiological findings in both of the cases were a radial pattern of enhancement in brain and longitudinally extensive myelitic lesions in the spinal cord. The first patient improved with immunosuppression treatment. The second patient had a significantly more severe clinical presentation with drug-refractory progression, who later died.

Conclusions

Patients presenting with subacute onset of cognitive impairment, meningoencephalomyelitis and papilloedema should raise the suspicion of GFAP. Though it is a relatively new disease entity for radiologists, the radial pattern of enhancement and long spinal cord lesions on imaging are striking and CSF and serum antibodies are highly specific.

Case 1. GFAP, (a) T2-FLAIR axial image shows diffuse leukoencephalopathic changes, (b) Post-contrast T1 axial image shows characteristic radial pattern of enhancement, (c) STIR sagittal sequence of the cervicothoracic spine shows long segment spinal cord lesion.



(Filename: TCT_eP-25_Image2.JPG)

eP-67b

Brain FDG PET and Its Role in Diagnosis of Various Dementia Syndromes Using Altered FDG Metabolisms

Electronic Posters

D Gandhi¹, P Sharma², N Gupta³, P Kochar⁴, Y Kumar⁵, T Olsavsky¹

¹St. Vincent's Medical Center, Bridgeport, CT, ²Yale New Haven Health System at Bridgeport Hospital, Milford, CT, ³Columbia University Medical Center, New York, NY, ⁴Yale New Haven Health Bridgeport Hospital, Bridgeport, CT, ⁵Basset Medical Center at Columbia University, Cooperstown, NY

Purpose

Few main different types of dementia syndromes are Alzheimer disease, frontotemporal dementia, dementia with Lewy bodies, and vascular dementia which needs to be diagnosed early in the development phase of the syndrome for better management of the patient. The patient may present with a significant decline in the cognition early in the course of the disease and routine clinical testing methods are not enough to diagnose dementia syndromes in the earlier course. It is also utmost important to differentiate different dementia syndromes accurately from each other due to the difference in the management from one another. Positron emission tomography with 2-[fluorine-18]fluoro-2-deoxy-d glucose biomarker is highly useful in differentiating between these dementia syndromes early in the course of disease via differentiating between various metabolic patterns in each dementia syndromes.

Materials and Methods

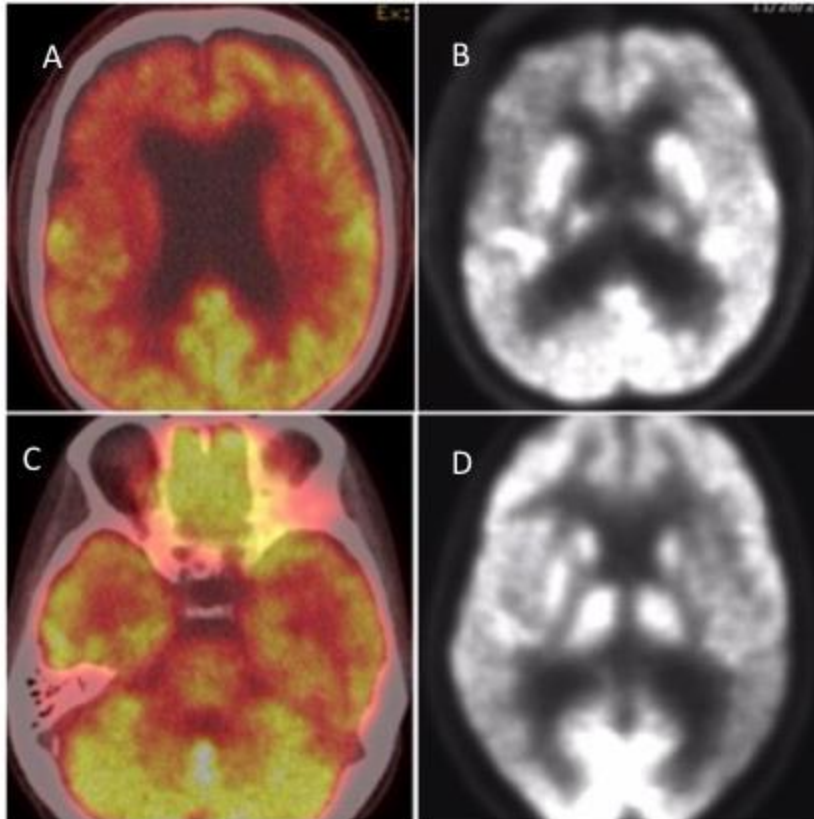
After four-hour fasting of all the patients, the injection of a standard dose of 5–10 mCi (185–370 MBq) of FDG via a peripheral vein has been given. Serum glucose levels were below 140 mg/dl in all nondiabetic patients. The glucose levels varied in diabetic patients but around or less than 140 mg/dl in most patients. All patients were well hydrated for better renal clearance of radioactivity. A thorough history including the reason for examination, prior surgical history, medications including benzodiazepines and barbiturates which can alter the biodistribution of FDG were taken into consideration. Patients were asked to remain quiet and calm with eyes open and not vocalize for standard cerebral uptake. According to literature, with closed eyes, there are chances of decreased uptake in occipital lobes which may misdiagnose DLB (Dementia of Lewy Body). Brain FDG PET was performed approximately 30 minutes after injection with image acquisition time for about 15 minutes. Nondiagnostic CTs have also performed in the same bed position as for PET which were used for anatomic correlation and correction of attenuation. Following the acquisition of nondiagnostic CT images, several postprocessing algorithms with color enhancement, scatter correction, resolution recovery, image reorientation and image reformation in three different planes (axial, coronal and sagittal) were performed which were helpful for visualization of subtle areas of hypometabolism.

Results

o Detailed descriptions of important dementia syndromes: - Pathophysiology - Epidemiology - Clinical presentation and diagnostic workup
o Role of FDG PET imaging in diagnosing these dementia syndromes including the different characteristic pattern of FDG uptake in each syndrome and how to differentiate between them with further recommendations. For example: - Markedly hypometabolic bilateral parietal lobes, and to lesser degree occipital cortices. Findings are nonspecific, but suspicious for Lewy body dementia. A DaTscan, a dopamine transporter (DAT) scan may be of benefit for further evaluation. - Decreased FDG uptake in the bilateral frontal and anterior cingulate gyrus suspicious for frontal predominant frontotemporal dementia. - Nonspecific bilateral temporal and parietal lobe hypometabolism. Findings are concerning for Alzheimer's disease. Beta-amyloid plaque imaging with F18-Florbetapir (Amyvid) may be of benefit for further evaluation.
o Types of important dementia syndromes with imaging examples.
o FDG PET imaging pitfalls, artifacts, and incidental findings.

Conclusions

FDG PET is helpful to differentiate between different patterns of metabolism in the brain in dementia syndromes. FDG PET is helpful for diagnosis of dementia syndromes in the earlier course even when dementia did not set in and only finding is cognition decline, which allows better prognosis in the patient. FDG PET imaging is used for further imaging recommendation like amyloid brain PET which typically used to exclude Alzheimer's dementia as a possible cause of dementia when negative.



Decreased FDG uptake in the bilateral frontal and anterior cingulate gyrus suspicious for frontal predominant frontotemporal dementia (A,B). Nonspecific bilateral temporal and parietal lobe hypometabolism concerning for Alzheimer's disease (C,D).

(Filename: TCT_eP-67b_Dementia1.jpg)

eP-67

Can Advanced Metal Detectors be Used for Clearing Patients with Retained Bullets for MR?: Ex Vivo testing.

A Mamourian¹

¹*University of Pennsylvania, Philadelphia, PA*

Purpose

Based on the perceived potential risk to patients with retained bullets if imaged with MR many sites limit access to MR for these patients. With the high and increasing incidence of gunshot injuries as well as ongoing wars with survivors returning with retained metal there is a need to determine who can have an MR safely. Based on the potential that advanced metal detectors that offer detection circuits can differentiate ferrous from non-ferrous metal, we tested the sensitivity of one such device using a realistic phantom for detection of commercially available ferrous and non-ferrous handgun bullets.

Materials and Methods

A dried human skull and its detachable skull flap were filled with a synthetic tissue analog, TX 151-

Electronic Posters

Balmar LLC, Lafayette LA, to simulate a patient brain and skull. Within the tissue analog multiple handgun bullet samples were placed in the approximate center of the skull to simulate a worst case for detection. We used a handheld advanced metal detector, PD 240CH-CEIA USA, OH, for all testing. Three types of .40 caliber bullets were used, an all lead cast bullet, a standard copper clad lead core bullet, and a readily available ferrous, soft steel clad -lead core bullet (both unfired and deformed).

Results

Using the "any metal" selection the unit detected the presence of all the bullets. Since the bullets were positioned in the center of the skull the activation occurred with multiple directions of approach. Using the "ferrous metal only" setting only the steel clad bullet activated the device. There were no false positives with the non-ferrous bullets. In some directions of approach the unit needed to be within 2cm of the surface for detection.

Conclusions

Using this advanced handheld unit ferrous bullets were consistently distinguished from non-ferrous bullets. The unit does need to be relatively close to the bullet but this testing indicates that it can detect the composition of a bullet that is within 9cm of the skin. Since any bullet away from the center of the skull will then be closer to one side or the other, all bullets in the skull should be accessible. These findings are promising for the use of advanced metal detectors for pre-MR screening of patients with retained bullets or similar sized metal fragments in the skull and likely spine, However, clinical utilization should remain a case by case decision and thoughtful use of these units is essential since any metal in the skull or surroundings, including the bed, will decrease their reliability.

eP-43

Combining Clinical Data and Vascular Pattern on MRI to Predict Survival in Newly Diagnosed Glioblastoma: A GLIOCAT Substudy

A Gimeno¹, G Blasco¹, C Biarnes¹, M Marti-Navas¹, P Daunis-i-Estadella², S Thio-Henestrosa², C Balana³, J Capellades⁴, A Alberich-Bayarri⁵, K Nael⁶, C Leiva-Salinas⁷, R Jain⁸, M Essig⁹, S Pedraza¹, J Puig¹

¹Diagnostic Imaging Institute (IDI), IDIBGI, University Hospital Dr Josep Trueta, Girona, Spain, ²University of Girona, Girona, Spain, ³Institut Català d'Oncologia, Germans Trias i Pujol University Hospital, Badalona, Barcelona, Spain, ⁴Hospital del Mar, Universitat Autònoma de Barcelona, Barcelona, Spain, ⁵La Fe Health Research Institute, Valencia, IL, ⁶sup>6Icahn School of Medicine at Mount Sinai, New York, NY, ⁷University of Missouri, Columbia, MO, ⁸New York University School of Medicine, New York, NY, ⁹University of Manitoba, Winnipeg, Manitoba, Canada

Purpose

MRI provides information on the physiologic properties of glioblastomas. Information about baseline risk and prognosis is crucial for assigning patients to optimized treatment regimens in clinical practice or to subgroups in clinical trials. In addition to established prognostic markers such as age, performance status, and extent of resection, increased vascularity on contrast-enhanced MRI is associated with shortened survival. We investigated whether glioblastoma vascular pattern (GVP-MRI), combined with clinical variables and other imaging features, could improve the predictive power of survival models.

Materials and Methods

From January 2012 through December 2016, 97 consecutive patients (62 men; mean age, 58±15 years) with histologically proven glioblastoma underwent 1.5T-MRI including anatomical, diffusion-weighted, first-pass DSC, and T1-weighted sequences after 0.1 mmol/kg gadobutrol (1 mm isometric voxel). We used Olea Sphere 3.0 software (La Ciotat, France) to analyze rCBV, rCBF, mean delay time, and apparent diffusion coefficient in volumes of interest for contrast-enhancing lesion (CEL), non-CEL, and contralateral tissue. Glioblastomas with >5 vessels seen within the lesion on postcontrast T1-weighted

images were considered hyper-GVP-MRI. Prognostic factors were evaluated by Kaplan-Meier survival, ROC analyses, and hazard ratios (HR).

Results

Glioblastomas were considered hyper-TVP-MRI in 58 (60.4%) patients. Patients with hyper-GVP-MRI glioblastomas were older, had higher volume CEL, increased rCBFCEL and poor survival. Combining Stupp protocol (HR:0.604; 95%CI:0.459-0.796), age (HR:0.163; 95%CI: 0.090-0.297), and TVP-MRI (HR: 1.481; 95%CI: 0.909-2.414) best predicted survival at 1 year (AUC 0.901, 83.3% sensitivity, 93.3% specificity, 96.2% PPV, 73.7% NPV).

Conclusions

Our preliminary data suggest that combining clinical parameters and vascular pattern on MRI improves survival prediction in newly diagnosed glioblastoma. Cross-validation studies in other populations are necessary to test the generalizability of our findings.

Survival prediction: summary of class performance

	Area under curve	Cut-off	Sensitivity	Specificity	Positive predictive value	Negative predictive value	Hazard Ratio (95% CI)	P-value	Likelihood P (multivariate)
<i>Univariate Analysis</i>									
Age	0.737	59.73	0.679	0.724	0.826	0.538	1.042 (1.022,1.063)	<0.001	
DMT _{NCEL}	0.697	-0.50	0.267	1.000	1.000	0.405	0.444 (0.232,0.852)	0.015	
ADC _{NCEL}	0.717	0.44	0.526	0.875	0.909	0.438	0.003 (0.648,9)	0.353	
Vessels number	0.709	6.94	0.696	0.621	0.780	0.514	1.029 (0.998,1.061)	0.033	
Thickness of enhancing margin	0.697	0.08	0.680	0.692	0.810	0.529			
Ependymal extension	0.612	0.09	0.800	0.423	0.727	0.524	1.694 (0.980,2.930)	0.059	
Vascular pattern	0.667	0.08	0.714	0.621	0.784	0.529	1.254 (0.788,1.998)	0.029	
Stupp protocol	0.778	0.97	0.625	0.931	0.946	0.562	0.163 (0.092,0.288)	<0.001	
<i>Bivariate Analysis</i>									
Age	0.859	58	0.867	0.733	0.867	0.733	1.042 (1.014-1.071)	0.002	<0.001
DMT _{NCEL}		- 0.48					0.560 (0.284-1.105)	0.095	
Age	0.850	54.8	0.714	0.897	0.930	0.619	1.026 (1.005-1.048)	<0.001	<0.001
Stupp protocol		2.0					0.213 (0.117-0.388)	0.015	
DMT _{NCEL}	0.844	0.508	0.833	0.800	0.893	0.706	0.414 (0.215-0.796)	0.008	0.009
Vascular pattern		1					1.820 (0.962-3.443)	0.040	
Vessels number	0.864	3	0.768	0.897	0.935	0.667	1.017 (0.987-1.048)	0.044	<0.001
Stupp protocol		2					0.170 (0.096-0.301)	<0.001	
Vascular pattern	0.850	-	0.625	0.931	0.946	0.562	1.265 (0.792-2.019)	0.042	<0.001
Stupp protocol							0.163 (0.092-0.288)	<0.001	
<i>Trivariate Analysis</i>									
Age							0.604 (0.459-0.796)	<0.001	<0.001
Stupp protocol							0.163 (0.090-0.297)	<0.001	
Vascular pattern	0.901	-	0.833	0.933	0.962	0.737	1.481 (0.909-2.414)	<0.045	

(Filename: TCT_eP-43_FigureClinicalandImaginginpredictingsurvivalGBM.jpg)

eP-04

Comparing Aqueduct Stroke Volume (ASV) and Peak Systolic Velocity (PSV) with Morphologic MRI Features in Idiopathic Normal Pressure Hydrocephalus (INPH)

W Wang¹, E Lui¹, S Su¹, P Desmond¹

Purpose

INPH is a potentially treatable cause of dementia but diagnosis can be difficult, with invasive diagnostic procedures often needed. MRI CSF aqueduct flow studies and various morphologic MRI signs have been described (1, 2, 3) to noninvasively aid the diagnosis of INPH, but to our knowledge have not been studied together. We aim to compare 2 aqueduct CSF flow parameters, ASV and PSV, between normal elderly subjects and INPH patients, and assess the frequency of various morphological imaging features for INPH.

Materials and Methods

Thirteen patients with a final clinical diagnosis of INPH (age 61-82, male=6) were compared to 40 elderly controls (age 65-83, male=13). 3T MRI phase contrast imaging was performed through the cerebral aqueduct with anatomical imaging including isotropic 1mm MPRAGE and high resolution CISS (Siemens). ASV and PSV using a previously described "fixed ROI" method (4) on Syngo-Via (Siemens) were obtained, and morphological features (Table 1) evaluated, with ROC curve analysis performed. Normal ASV and PSV were defined as \leq mean+2SD of the control group. Statistics were performed with SPSS.

Results

INPH patients vs. controls had mean ASV $142 \pm 87.7 \mu\text{L}$ and $51.2 \pm 30.6 \mu\text{L}$ ASV ($p < 0.001$), and PSV 11.5 ± 4.86 and $9.80 \pm 3.57 \text{ cm/s}$ ($p = 0.515$) respectively. The areas under the ROC curve for ASV vs PSV were 0.925 and 0.561 respectively. ASV Youden index was 71.5 μL (sensitivity 100%, specificity 75.6%, false-positive 22.5%). Ventriculomegaly, Evan's index and upward bowing of corpus callosum were present in 13/13 patients, while other frequently positive signs were abnormal ASV (12/13), upper midline profile sign (10/13), crowded gyri (9/13) and obliterated perihippocampal sulci (9/13) (Table 1).
Table 1 - Summary of imaging features of INPH patients. *Only 7 patients had the appropriate sequences for assessing the presence of aqueduct flow void.

Conclusions

ASV is more useful than PSV for measuring hyperdynamic CSF flow, and is also positive in more INPH patients than most morphological imaging features.

Feature	No. present (%)
Ventriculomegaly	13/13 (100%)
Evan's index positive	13/13 (100%)
Corpus callosal angle positive	7/13 (54%)
Crowding of gyri at the vertex	9/13 (69%)
Upward bowing corpus callosum	13/13 (100%)
Obliteration perihippocampal gyri	9/13 (69%)
Posterior cingulate sulcus sign	6/13 (46%)
Upper midbrain profile sign	10/13 (77%)
Aqueduct flow void	3/7* (43%)
Lateral ventricle temporal horn enlargement	5/13 (38%)
Periventricular white matter signal change	8/13 (62%)
ASV	12/13 (92%)
PSV	5/13 (38%)

(Filename: TCT_eP-04_INPHTable.jpg)

eP-08

Comparison of ASL Perfusion and SPECT Examination in Laterisation of Seizure Focus in Patients with Intractable Temporal Lobe Epilepsy

A Garg¹, K Bhullar¹, M Tripathi¹, M Tripathi¹

¹*All India Institute of Medical Sciences, New Delhi, India*

Purpose

The aim of present study is to compare the diagnostic performance of ASL perfusion and SPECT examination in laterisation of seizure focus in patients with intractable temporal lobe epilepsy.

Materials and Methods

Forty-three patients with intractable temporal lobe epilepsy underwent conventional MR examination on 3T scanner and ASL perfusion on 1.5 T scanner using 3D pseudocontinuous ASL. Interictal and Ictal SPECT were done, dye was injected within 20 sec of seizure for ictal SPECT. Ictal SPECT was substrated from interictal SPECT and overload on MR scan (SISCOM). The finding on conventional MR examination, ASL perfusion maps and SISCOM were noted to localize the seizure focus.

Results

Total 43 patients (M: 29, F-14, mean age 22.29 [range 4-50 yrs]) were included. On conventional MR imaging, 4 patients had normal MRI, 10 had isolated medial temporal sclerosis (MTS) (L-5, R-2 and B/l-3), MTS with focal cortical dysplasia (FCD) (7), MTS with perinatal insult (5), neoplasms (4), isolated Type 1 FCD (4), type 2B FCD (4) and other lesions (5). SPECT showed ipsilateral temporal lobe (22), contralateral temporal lobe (2), no localization (11) and extratemporal localization (8 patients). ASL perfusion was increased in 2 patients, decreased in 28 and normal in 13 patients. ASL perfusion maps showed ipsilateral temporal lobe (23), contralateral temporal lobe (1), no localization (13) and extratemporal localization (6 patients).

Conclusions

ASL perfusion maps are comparable of SPECT data in lateralising the seizure focus in patients with intractable temporal lobe epilepsy.

eP-59

Comparison of CT Angiography and High-resolution Time of Flight Magnetic Resonance Angiography for Intracranial Vessels Using Compressed Sense Technique

N Khandelwal¹, N Ray¹, P Singh¹, V Gupta¹, C Ahuja¹, M Modi¹, N Sankhyan¹, I Saha², K Rajendran³

¹*Post Graduate Institute of Medical Education and Research (PGIMER), Chandigarh, India,* ²*Philips Health Systems, Philips India Limited, Gurgaon, Haryana, India,* ³*Philips Health Systems, Philips India Limited, Chennai, Tamilnadu, India*

Purpose

CT angiography (CTA) is generally considered superior to time-of-flight (TOF) magnetic resonance angiography (MRA) - chiefly attributable to the comparatively lesser slice thickness achievable by CTA compared to TOF-MRA. Compressed-sensing MRI technique was combined with SENSE parallel imaging i.e., Compressed SENSE (C-SENSE), to develop high- resolution fast-imaging methodology for acquisition of TOF-MRA for intracranial vessels. (1-3) High-resolution TOF MRA was acquired using C-SENSE technique with a slice thickness comparable to CTA and with acquisition time comparable to conventional MRA and compared subsequently regarding image quality.

Materials and Methods

Twenty patients undergoing CT angiography of intracranial vessels on a 64-slice scanner for various indications were included in this instutional ethics committee approved study. Time-of-flight (TOF) MRA was acquired using the conventional technique and as well as C-SENSE technique. The slice thickness

Electronic Posters

and time required for CT angiography, conventional and C-SENSE TOF MRA were shown in Table-1. Two neuroradiologists, having 10 years and five years of experience of evaluating CTA and MRA, and blinded to the set of MRA they were evaluating, have evaluated the images regarding image quality on a predefined scale, based on visualization of different segments of major intracranial vessels, resolution, lesion conspicuity and artifacts and diagnostic confidence. The quantitative evaluation of image quality was done by comparing the image contrast ratio. Inter-rater agreement was assessed using κ test. The subjective visualization scores for each segment and the overall image contrast ratio were compared using the Wilcoxon signed-rank test and paired t test respectively.

Results

High interrater agreement was found regarding visualization of different intracranial arterial segments ($k=0.911$), resolution ($k=0.925$), lesion conspicuity ($k=0.918$), artifacts ($k=0.927$) and overall diagnostic confidence ($k=0.948$). The high-resolution MRA images acquired with C-SENSE were comparable to CTA with regards to all subjective parameters of image quality with statistically nonsignificant difference between the two, while conventional TOF MRA was found to be inferior to either CTA or high-resolution C-SENSE MRA. The image contrast ratio of MRA with C-SENSE technique was significantly better than conventional MRA; however, it was found to be inferior to CTA.

Conclusions

C-SENSE can be used as a tool for acquiring high-resolution MRA for intracranial vessels with a reduced slice thickness and acquired images can be comparable to CTA regarding image quality. Thus, high resolution C-SENSE TOF MRA can be used as an alternative to CTA particularly in paediatric populations or in patients requiring multiple follow-up imaging.

IMAGING TOOL		SLICE THICKNESS	TIME OF ACQUISITION	ACCELERATION FACTORS
CT ANGIOGRAPHY		0.6 mm	5-6 seconds	Not applicable
TOF MR ANGIOGRAPHY	CONVENTIONAL	3 mm	4 min 21 sec	2.5
	C-SENSE 1	0.9 mm	6 min 46 sec	4.5
	C-SENSE 2	0.9 mm	5 min 16 sec	5.3

(Filename: TCT_eP-59_TABLE1.jpg)

eP-34

Comparison of Intracranial Vessel Wall Imaging and 3D Time of Flight MRA for Arterial Stenosis and Atherosclerotic Plaque Detection

D Kim¹, J Huston¹, W Brinjikji¹, J Verdoorn¹, V Lehman¹

¹Mayo Clinic, Rochester, MN

Purpose

We compared the ability of intracranial high-resolution vessel-wall imaging (VWI) and 3-D time-of-flight (TOF) to detect and characterize arterial stenosis and atherosclerotic plaque.

Materials and Methods

All intracranial vessel wall imaging examinations at our institution using a commercially available 3-D SPACE technique with at least 1 imaging feature of atherosclerotic plaque performed within two months of a 3-D TOF examination were included. Any cases with a diagnosis of alternative cause of intracranial steno-occlusive disease or with significant motion were excluded. One radiologist with a CAQ in neuroradiology and one neuroradiology fellow scored all cases. In each case, 17 separate vessel segments were assessed for (1) presence of atherosclerosis, (2) diameter at maximal stenosis if present, (3) normal

Electronic Posters

diameter of the distal segment, on both noncontrast VWI and 3-D TOF at least 1 week apart blind to the other examination. The results were compared with the VWI and 3-D TOF exams considered as the reference standard for atherosclerosis and luminal diameter, respectively.

Results

Total of 286 segments in 17 patients were scored. Luminal diameter measurements for both normal and stenotic segments on VWI were similar to those on 3-D TOF examinations with a mean difference of 0.41mm, 0.38mm (staff, fellow) and 0.48mm, 0.56mm (staff, fellow) for normal and stenotic segments, respectively. Of stenotic segments 78%, 68% (staff, fellow) identified on 3-D TOF were also identified on VWI. Of atherosclerotic segments 55%, 46% (staff, fellow) seen in VWI were not seen with 3-D TOF.

Conclusions

Average luminal measurement differences between the two techniques were less than 0.6mm. Majority of segments with stenosis on VBI were also identified on VWI, suggesting that the presence and degree of stenosis may be roughly inferred when VWI is performed without concurrent luminal MRA. VWI demonstrated a considerably higher rate of detection of intracranial atherosclerosis compared to 3-D TOF.

eP-56

Comparison of Time of Flight Magnetic Resonance Angiography for Head and Neck Vessels Using Conventional and Compressed Sense Technique

N Ray¹, N Khandelwal¹, P Singh¹, V Gupta¹, C Ahuja¹, M Modi¹, N Sankhyan¹, I Saha², K Rajendran³
¹Postgraduate Institute of Medical Education and Research, Chandigarh, India, ²Philips Health Systems, Philips India Limited, Gurgaon, Haryana, India, ³Philips Health Systems, Philips India Limited, Chennai, Tamil Nadu, India

Purpose

This study uses the novel method of combining compressed sensing MRI technique with SENSE parallel imaging, i.e. Compressed SENSE (C-SENSE), to develop high-resolution fast imaging methodology for acquisition of time-of-flight (TOF) magnetic resonance angiography (MRA) for intracranial and extracranial vessels, by exploiting multi-element receiver coil sensitivity variation and sparsity constraining. (1-3)

Materials and Methods

Twenty patients undergoing MRA of head and neck vessels for various indications were included in this institutional ethics committee approved study. The time-of-flight (TOF) MRA was acquired using the conventional technique and C-SENSE technique, the latter being acquired with two different acceleration factors. The time required for conventional MRA and two C-SENSE sequences for intra and extracranial vessels are shown in Table 1. Two neuroradiologists, having 10 years and five years experience of evaluating MRI and blinded to the set of images, have evaluated the images independently regarding image quality on a predefined scale, based on visualization of different segments of major intra and extracranial vessels, resolution, lesion conspicuity and artifacts and overall diagnostic confidence. The quantitative evaluation of image quality was done by comparing the image contrast ratio. Interrater agreement was assessed using κ test. The subjective visualization scores for each segment and the overall image contrast ratio were compared using the Wilcoxon signed-rank test and paired t test respectively.

Results

High interrater agreement was found regarding all subjective parameters ($k=0.911$ and 0.924 for segmental vessel visualisation, $k=0.923$ and 0.918 for resolution, $k=0.907$ and 0.912 for artifacts, $k=0.930$ and 0.925 for lesion conspicuity and $k=0.935$ and 0.937 for overall diagnostic confidence for head and neck vessels respectively). Nonsignificant statistical difference was found regarding image quality between conventional MRI and C-SENSE using both the acceleration factors. The image contrast ratio difference between conventional and C-SENSE sequences were also equivalent with nonsignificant statistical differences between the two.

Electronic Posters

Conclusions

C-SENSE can be used as a potential tool for reducing acquisition time for intra- and extracranial MRA without compromising the image quality.

SEQUENCE		ACCELERATION FACTORS	TIME OF ACQUISITION	TIME REDUCTION
TOF-MRA INTRACRANIAL VESSELS	CONVENTIONAL	2.5	4 min 21 sec	Not applicable
	C-SENSE 1	3.0	3 min 48 sec	33 sec (12.6%)
	C-SENSE 2	4.5	2 min 34 sec	107 sec (40.5%)
TOF-MRA EXTRACRANIAL VESSELS	CONVENTIONAL	1.5	6 min 39 sec	Not applicable
	C-SENSE 1	2.25	4 min 35 sec	124 sec (31.1%)
	C-SENSE 2	2.0	5 min 08 sec	91 sec (29.5%)

(Filename: TCT_eP-56_TABLE1.jpg)

eP-28

Contrast Enhancement Characteristics of Treated Aneurysms on High Resolution Vessel Wall Imaging MRI

C Atkinson¹, P Naval Baudin², Y Lee¹, M Castillo¹

¹University of North Carolina, Chapel Hill, NC, ²Hospital Universitari de Bellvitge, L'Hospitalet de Llobregat, Barcelona, Spain

Purpose

The purpose of this exhibit will be to display the appearance of treated intracranial aneurysms using high-resolution vessel-wall MRI (HRVWI) and compare findings with conventional imaging modalities.

Materials and Methods

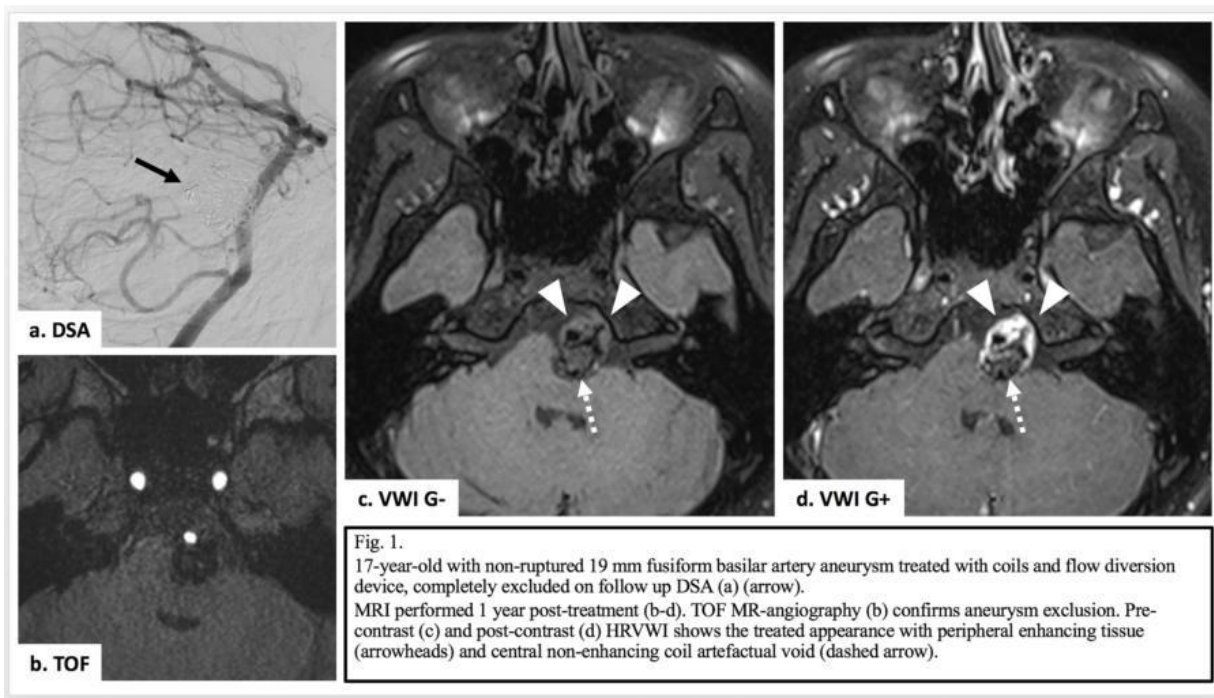
A retrospective study under IRB approval evaluated patients with known intracranial aneurysms using 1.5T or 3T MRI units and black blood high resolution pre and postcontrast vessel-wall imaging. Studies were reviewed by two board-certified neuroradiologists for presence or absence of vessel wall and or sac contrast enhancement and morphology of treated aneurysms. Differences were resolved by consensus. All aneurysms had angiographic correlation to confirm occlusion or patency.

Results

A total of 52 patients were examined using HRVWI. Thirty-one untreated aneurysms and 18 endovascular-treated aneurysms were evaluated. Aneurysms were treated as follows: six with Pipeline flow diversion device (FDD), 10 with coils, one with coils and pipeline FDD and one with coils and clipping. HRVWI was performed after a median of four years post treatment. Occluded aneurysms demonstrated complete or partial contrast enhancement within the excluded sac, a finding which may be potentially confusing and mimic patency (Figure 1). This contrast enhancement is likely due to granulation tissues within treated aneurysms as opposed to peri-aneurysmal inflammation or neovascularity which predominantly manifests at level of the vessel wall and is inseparable from it. Residual patent aneurysms and neck remnants did not demonstrate any internal enhancement.

Conclusions

Internal aneurysm contrast enhancement on HRVWI does not imply patency but correlated with occlusion in all of our patients with aneurysm sac exclusion.



(Filename: TCT_eP-28_abstractfigure.jpg)

eP-44

Correlation Between MRI Signs of Idiopathic Intracranial Hypertension and the Number of Arachnoid Granulations

B Patel¹, G Watane², D Brown³, M Taheri⁴

¹The George Washington University Hospital, Washington, DC, ²Brigham and Women's Hospital, Boston, MA, ³University of Texas Health Sciences Center, Houston, TX, ⁴George Washington University, Washington, DC

Purpose

In a recently published manuscript (PMID: 28937488), we proposed a compensatory mechanism of arachnoid granulations (AGs) in patients with idiopathic intracranial hypertension (IIH). In this paper, we showed a decreasing prevalence of "empty sella" appearance in IIH patients with increasing number of AGs. In addition, IIH patients with a higher number of AGs also tend to have a lower opening pressure. The relationship between other MRI findings of IIH and number of AGs was not fully explored. In this presentation, we tested the hypothesis that the prevalence of other typical MRI characteristics seen with increased intracranial pressure (ICP) are also inversely linked to the number of AGs in this patient population.

Materials and Methods

In a retrospective chart review study, 79 patients with a clinical diagnosis of IIH were studied to evaluate the prevalence of MRI findings related to increased ICP. An experienced neuroradiologist and neuroradiology fellow reviewed the brain MRI of these patients for the presence of typical findings of increased ICP, including transverse venous sinus stenosis, enlarged Meckels cave, and tortuosity of optic nerve. Statistical analysis was conducted to investigate an association of these imaging findings with number of AGs in IIH patient groups.

Results

The percentage of IIH patients with zero and two AGs and findings of tortuous optic nerves was 59% and

Electronic Posters

6%, respectively. The percentage of IIH patients with zero and two AGs and findings of enlarged Meckels cave was 61% and 9%, respectively. The percentage of IIH patients with zero and two AGs and findings of transverse sinus stenosis was 71% and 2%, respectively.

Conclusions

In concordance with our recently published data, there is an inverse correlation between the number of arachnoid granulations and prevalence of established imaging characteristics of IIH.

eP-02

Corticobasal Syndrome Variants: Is Functional Nuclear Imaging with FDG-PET or SPECT Pattern Capable of Predicting Clinical Features?

M Aranha¹, J Parmera¹, A Studart Neto¹, C Ono¹, C Buchpiguel¹, S Brucki¹, A Coutinho¹

¹University of São Paulo, São Paulo, SP

Purpose

Corticobasal syndrome (CBS) is an atypical parkinsonian syndrome first considered a primarily motor disorder but now recognized as a cognitive disorder associated with several cortical features. The term CBS denotes the phenotype of multiple pathologies, including corticobasal degeneration and Alzheimer's disease (AD). Accurate antemortem diagnosis of underlying pathology in CBS is challenging and new diagnostic methods are being developed to predict the pathology. The purpose of this study is to compare the clinical features of patients with probable CBS according to different individual brain functional patterns measured with FDG-PET (glucose metabolism) and SPECT (blood flow), exploring the potential role of these imaging techniques as diagnostic biomarkers.

Materials and Methods

Sixteen patients with clinical diagnosis of probable CBS were submitted to brain FDG-PET (14 patients) or SPECT with 99mTc-ECD (2 patients). They were first clinically diagnosed with CBS and investigated in relation to their movement disorders profile and cognitive symptoms. According to the FDG-PET or SPECT patterns, patients were distributed into an AD group (CBS likely related to AD) and a non-AD group (CBS likely unrelated to AD). Both groups were compared in relation to their clinical features and movement disorder profiles.

Results

At FDG-PET scan, two patients had an AD pattern and twelve patients presented with a non-AD pattern. At SPECT examinations, one patient had typical AD pattern and the other had non-AD pattern. Clinically, the most prevalent symptoms were akinetic-rigid parkinsonism (100%), limb apraxia (87,5%), myoclonus (56,3%), dystonia (56,3%) and aphasia (50%). Only dystonia demonstrated a significant difference between groups as 100% of individuals with this feature presented a non-AD pattern ($p=0,019$). Myoclonus showed a tendency to be related to the AD group ($p=0,069$) and apraxia of speech (31,8%) to the non-AD group, as 100% had a non-AD pattern ($p=0,181$). There were significant differences between the AD and non-AD groups on Addenbrooke's Cognitive Examination-Revised (ACE-R) (AD=4,00 +- 6,93 vs non-AD=32,50 +- 7,09 $p=0,001$), Mini Mental Score Examination (MMSE) (AD = 5,25 +- 7,54 vs non-AD = 15,02 +- 7,24 $p = 0,035$) and Hoehn and Yahr (HY) scale (AD = 1,75 +- 0,86 vs non-AD = 3,54 +- 1,45 $p = 0,015$). One of the subjects with an AD metabolic pattern tested positive for amyloid in a 11C-PiB-PET examination.

Conclusions

Dystonia and apraxia of speech were most closely related to a non-AD and myoclonus to an AD functional pattern of CBS. Individuals with an AD pattern presented with lower ACE-R and MMSE and higher HY scale scores. Functional nuclear imaging shows a potential to predict the different CBS variants while depicting their specific functional patterns.

eP-33

CT Negative Subarachnoid Hemorrhage with Negative Initial Follow-up Imaging: Meta-analysis and Management Recommendations

L Tu¹, K Seifert², X Wu¹, D Gandhi³, A Malhotra²

¹*Yale University School of Medicine, New Haven, CT*, ²*Yale New Haven Hospital, New Haven, CT*, ³*University of Maryland School of Medicine, Baltimore, MD*

Purpose

The purpose of this study is to synthesize the current literature into recommendations regarding the management of subarachnoid hemorrhage with normal head CT and xanthochromia on lumbar puncture (CT- LP+ SAH). A significant portion of these patients have a negative first angiographic/imaging study. We investigate the utility of additional imaging after the initially negative CTA.

Materials and Methods

PUBMED, EMBASE, SCOPUS and research meeting abstracts were searched up to March 2017 for studies of patients with spontaneous subarachnoid hemorrhage (SAH) and an initially negative angiographic/imaging study. Title/abstract and then full-text screening was performed by two independent reviewers. Study quality was assessed via the Cochrane Risk of Bias Tool (CRBT). Meta-analysis was conducted using random and fixed effects models.

Results

A total of 1936 studies were identified, of which 185 underwent full text review; 12 studies were included. Diagnostic methods for initial angiographic as well as follow-up studies were variable. Assessment of study quality by CRBT also showed variability; however, most studies had a low risk of bias. The meta-analysis revealed zero aneurysms among 125 patients. There were 2 cases of vasculitis, a single cervical AVM, and one case of a hemorrhagic pituitary adenoma. The yield for imaging after the first negative exam was low. A follow-up study after two consecutive negative angiographic/imaging exams was of no utility.

Conclusions

Spontaneous SAH may be categorized as perimesencephalic, diffuse/aneurysmal, peripheral (convexity, sulcal), or CT negative (detected only on lumbar puncture) based on the distribution of hemorrhage. The optimal management strategy for CT negative SAH detected on LP is not clearly defined, and practice patterns are variable. Our meta-analysis suggests that for most patients, no additional imaging is necessary after a negative initial CTA.

eP-63

Default Mode Network Connectivity Does Not Predict Functional Outcome after Acute Stroke

J Puig¹, G Blasco¹, A Alberich-Bayarri², C Biarnes¹, M Marti-Navas¹, M Rivero¹, C Oramas-Requejo¹, J Gich¹, J Serena¹, M Essig³, K Nael⁴, C Leiva-Salinas⁵, M Wintermark⁶, S Pedraza¹

¹*Diagnostic Imaging Institute (IDI), IDIBGI, University Hospital Dr Josep Trueta, Girona, Spain*, ²*La Fe Health Research Institute, Valencia, Spain*, ³*University of Manitoba, Winnipeg, Manitoba, Canada*, ⁴*Icahn School of Medicine at Mount Sinai, New York, NY*, ⁵*University of Missouri, Columbia, MO*, ⁶*Stanford University, Stanford, CA*

Purpose

Poststroke symptoms cannot always be explained by infarct location, being sometimes attributable to impairment of remote cortical regions. Remote effects might be due to the disruption of neuronal input vital to the function of those remote regions or of a certain network. The resting-state default mode network (DMN) comprises the medial temporal lobe, posterior cingulate cortex, medial prefrontal cortex, and bilateral parietal cortices. Growing evidence suggests that altered DMN correlates with cognitive

Electronic Posters

dysfunction in stroke patients; however, its usefulness in predicting functional outcome remains unknown. We investigated the usefulness of DMN alterations in predicting functional outcome 3 months after acute stroke.

Materials and Methods

Functional outcome at three months was assessed with the modified Rankin Scale (mRS). To detect differences in functional connectivity between patients with good functional outcome ($mRS \leq 2$) and those with poor outcome ($mRS > 2$), we used CONN v17 (Functional Connectivity SPM toolbox, McGovern Institute of Brain Research, MIT) to perform graph-theory analysis of brain networks. Covariates were age, territory of stroke, three-day NIHSS score, and infarct volume (Olea Sphere 3.0, La Ciotat, France). Results

Thirty-seven consecutive patients (age: 69 ± 14 years, 23 male, 3-day National Institute of Health Stroke Scale [NIHSS] score: 6 ± 5) were included on day three after stroke. The DMN connectivity network did not differ between patients with good vs. poor functional outcome; however, patients with good outcome had higher connectivity between the DMN and right hemisphere temporal fusiform cortex ($p = 0.0106$) (Figure).

Conclusions

These preliminary data suggest that connectivity within the DMN does not accurately predict functional outcome after stroke.

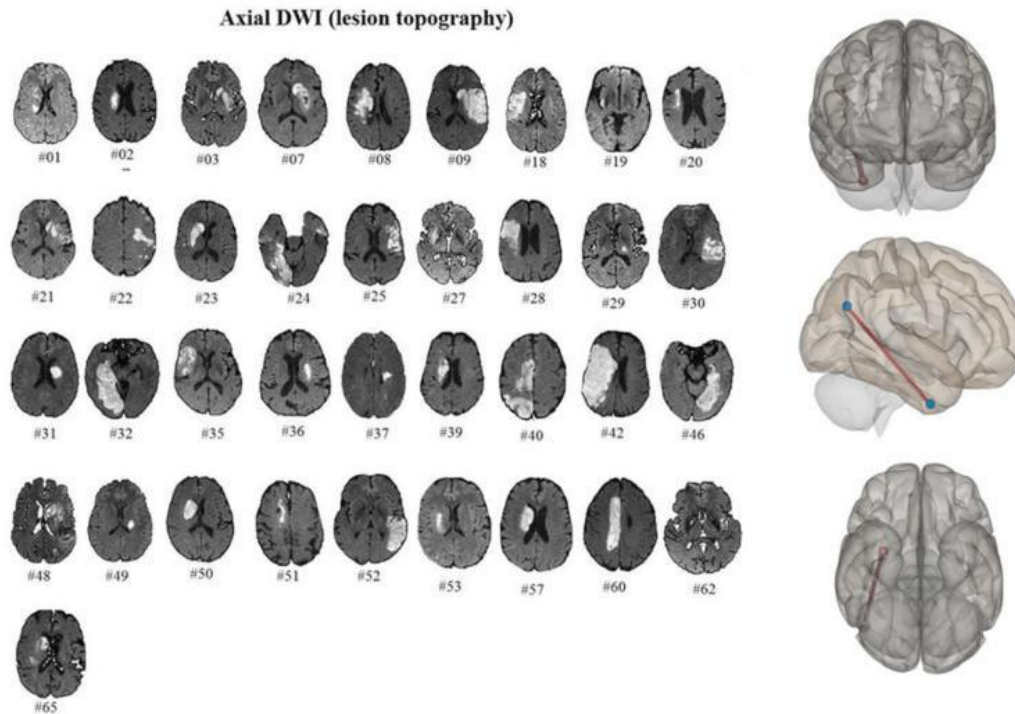


Figure. Infarct location on axial diffusion weighted imaging (left) and panels (right) display the graph visualization of the mean correlation coefficient weighted matrices for the group of patients with good outcome at 90 days.

(Filename: TCT_eP-63_FigureDMNstrokeoutcome.jpg)

eP-61

Delineation of the Central Sulcus by the Disappearing Central Sulcus Sign on Double Inversion Recovery (DIR) MRI

Electronic Posters

I Mark¹, C Rydberg¹, P Luetmer¹, R Witte¹, V Lehman¹

¹Mayo Clinic, Rochester, MN

Purpose

To identify the central sulcus by the disappearing central sulcus sign on double inversion recovery imaging

Materials and Methods

Forty-nine patients (98 hemispheres) were retrospectively reviewed by three CAQ neuroradiologists and one radiology resident. The central sulcus was identified on double inversion recovery (DIR) images by traditional landmarks and subsequently compared to the surrounding sulci (superior frontal, precentral, postcentral, pars marginalis) for subjective difference in signal intensity. Comparisons were made at the hand knob and operculum levels on axial images and on sagittal images where the inferior frontal sulcus terminates at the precentral sulcus, for a total of 294 locations. The comparison of signal intensity was further studied by the order of disappearance while decreasing the window level at a constant width. Sulci conspicuity was also analyzed with black/white inversion.

Results

Forty-nine patients were included (22 female, 27 male; average age 38.1 years). Relative to the surrounding sulci, the central sulcus was the first to disappear at all three levels with extremely high degrees of agreement: 100% agreement at the hand knob level, 100% agreement at the operculum level, and 99% agreement on sagittal images. All readers were also in >80% agreement that the central sulcus was more obvious with inversion of black and white. This agreement level includes 95.9% at the hand knob, 80.6% at the operculum level, and 95.8% on sagittal images.

Conclusions

The central sulcus can be identified by differences in signal intensity of the peri-rolandic cortex or superficial white matter compared to other cerebral regions. These differences are well seen on double inversion recovery, which is specifically designed and used to assess the grey-white junction and underlying white matter. Identification of the central sulcus was most prominent by the disappearing central sulcus sign, which was measured by decreasing the window level at a constant width.

eP-03

Detection of Subthreshold Wallerian Degeneration in Bilateral Cerebellar Hemispheres Following Pontine Stroke via Neuronal Density Modeling on DWI

O Kohannim¹, J Huang², G Hathout¹

¹University of California, Los Angeles, Los Angeles, CA, ²VA West Los Angeles, Los Angeles, CA

Purpose

Wallerian degeneration of pontocerebellar fibers secondary to pontine pathology has been well-documented in the literature (1). Imaging diagnosis most commonly entails detection of abnormal T2 signal in bilateral middle cerebellar peduncles. Here, we demonstrate detection of signal change on DWI within the cerebellum excluding the middle cerebellar peduncles via a two-compartment mathematical model of cell density on diffusion-weighted imaging (DWI).

Materials and Methods

In a retrospective feasibility study, deemed exempt by our institutional review board from review, we apply a biexponential model with intracellular and extracellular compartments to subacute and chronic DWI images of a patient with pontine infarction. DWI images comprise the three standard clinical beta values of 0, 500, and 1000. We exclude the middle cerebellar peduncles, which demonstrate visible abnormality on MRI (Figure 1a). At a voxelwise basis, we calculate intracellular and extracellular

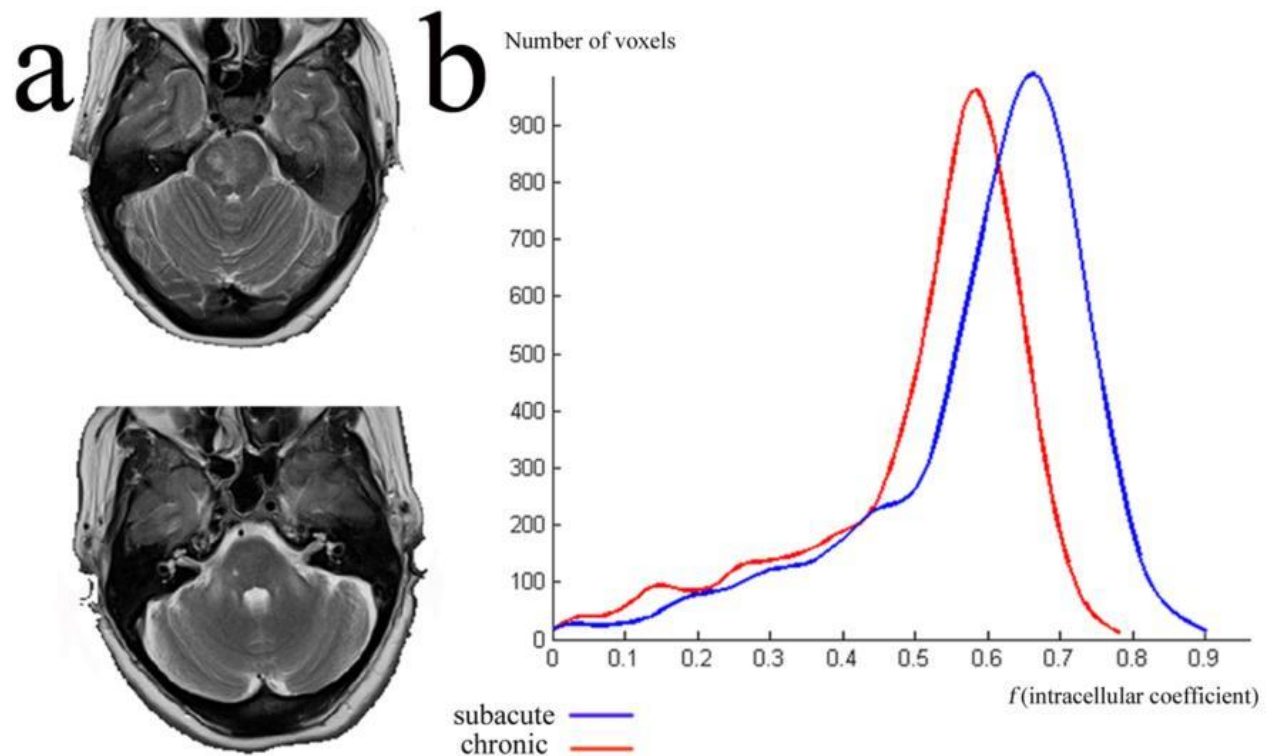
apparent diffusion coefficients for each side of the cerebellum, and compare the histograms of coefficients using the Mann-Whitney U Test.

Results

We find significantly reduced intracellular coefficients in the cerebellar cortex, excluding middle cerebellar peduncles, several months after the pontine stroke, when compared to several days after stroke ($p < 0.01$; Figure 1b). When we separately compare the right and left cerebellar hemispheres in the subacute phase to the corresponding hemispheres in the chronic phase, each hemisphere again demonstrates a reduced intracellular component in the chronic phase ($p < 0.01$).

Conclusions

Our two-compartment model allows detection of significant signal change, suggestive of reduced neuronal density presumably due to Wallerian degeneration, in bilateral, normal-appearing cerebellar hemispheres following pontine stroke. Previously, we showed the application of our model in detecting subthreshold signal change in cases of crossed cerebellar diaschisis. Our current study further validates the clinical utility of our model and its potential applications in diagnosis of subclinical neuropathology, including but not limited to neurodegeneration.



(Filename: TCT_eP-03_Fig1.jpg)

eP-50

Diagnostic Value of Multiphase Arterial Spin Labeling for the Prediction of Cerebrovascular Reactivity

H Choi¹

¹Bundang CHA Medical Center, Seongnam-si, Republic of Korea

Purpose

Cerebrovascular reactivity is a physiological characteristic of the brain that is related to the intrinsic ability of arteries to alter their diameters in response to a vasoactive stimulus, and this parameter is

Electronic Posters

important in cerebrovascular disease. In the present study, we evaluated the arterial transit time (ATT) in addition to the time corrected CBF (TCF) from the multiple postlabeling delay ASL as compared with basal/acetazolamide stress Technetium99-hexamethylpropylene amineoxime (99mTc-HMPAO) SPECT in prediction of the cerebrovascular reactivity.

Materials and Methods

TCF maps and ATT maps were acquired in 30 consecutive patients with unilateral ICA or MCA stenocclusive disease (severe stenosis or occlusion). Internal carotid artery territory-based ROIs were applied to both perfusion maps. Additionally, impairments in the CVR were evaluated according to both qualitative and quantitative analyses of the ROIs on basal/acetazolamide stress 99mTc-HMPAO SPECT using a previously described method. The ROIs were divided into three groups; group 0 included normal basal CBF and normal reactivity on acetazolamide challenge, group 1 included decreased CBF and impaired reactivity on acetazolamide challenge and group 2 included normal CBF and impaired reactivity on acetazolamide challenge. ANOVA test was performed to compare the ATT and TCF among three groups. Diagnostic decision tree was developed to differentiate among three groups.

Results

TCF showed significantly decreased in group 1 (45.8 ± 8.5 , 24.8 ± 12.5 and 44.1 ± 13.8 [ml/100 g/min] in group 0, group 1 and group 2, respectively, $P = .003$). ATT demonstrated significantly prolonged in group 1 and group 2 (1290.7 ± 204.1 , 1668.1 ± 207.3 and 1630.6 ± 269.0 [ms] in group 0, group 1 and group 2, respectively, $P < 0.001$). A cut-off value of TCF as 26 [ml/100 g/min] and ATT as 1527[ms], the three groups were differentiated 80.88% of accuracy.

Conclusions

Our results demonstrate that the ATT in addition to TCF based on ASL perfusion MRI can predict the cerebrovascular reactivity.

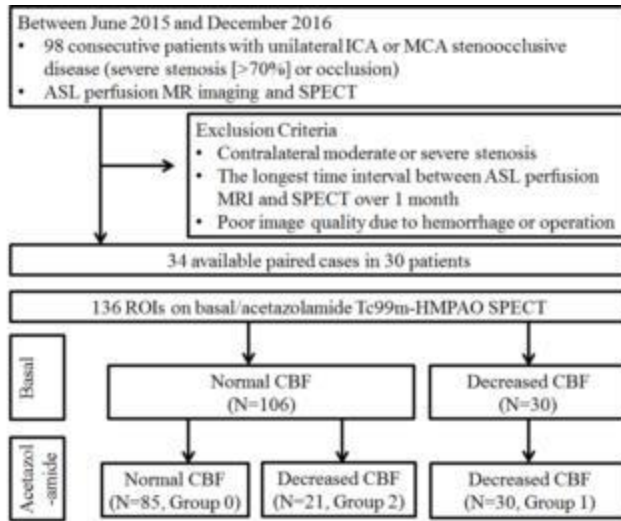
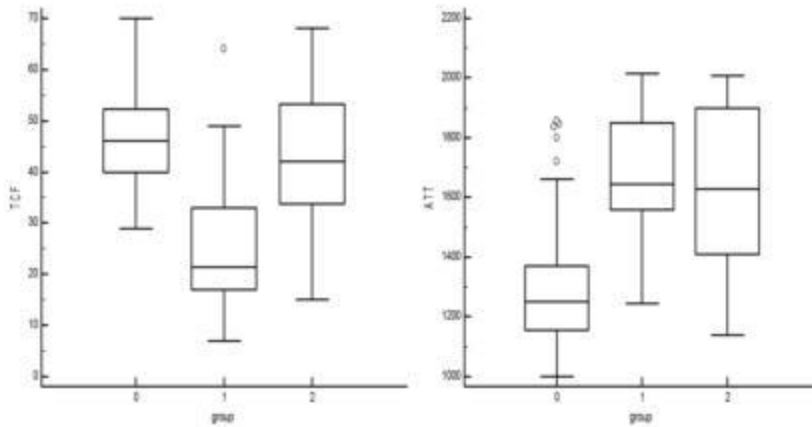


Fig 1. Flowchart of the study



A
B

Fig 2. Box and whisker plots show TCF and ATT values of ASL perfusion MRI in groups with basal and acetazolamide challenge CBF based on basal/acetazolamide Tc99m-HMPAO SPECT. A) Group 1 displayed decreased TCF compared to the other groups. B) Group 1 and group 2 demonstrated increased ATT values than group 1.

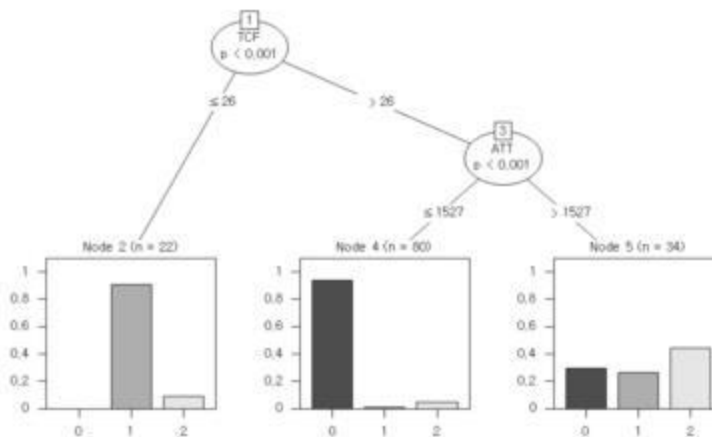


Fig 3. Diagnostic decision tree for differentiation of the impairment of cerebrovascular reactivity, especially normal basal CBF.

(Filename: TCT_eP-50_figASNR1214.jpg)

eP-23

Differential Diagnoses of Cerebral Aqueduct/Periaqueductal Lesions

M Bohanan¹, A Kamali², P Rabiei², O Arevalo², R Patel², R Riascos², K Hasan²

¹University of Texas Houston, Houston, TX, ²The University of Texas Health Science Center at Houston, Houston, TX

Purpose

The periaqueductal region is a major neuroanatomical component of the brainstem and has pivotal roles in autonomic functions, behavior, and cognition. We demonstrate differential diagnosis of cerebral aqueduct/periaqueductal lesions of the human brain by providing characteristic MRI imaging and clinical information.

Materials and Methods

We present 20 in-house interesting cases of following pathologies. 1) Aqueductal Stenosis, 2) Tectal Glioma, 3) Neurocysticercosis, 4) Multiple Sclerosis, 5) Enlarged Perivascular Spaces, 6) Diffuse Astrocytoma, Low Grade, 7) Encephalitis, 8) Interaventricular, 9) Hemorrhage, 10) Wilson Disease, 11) Metastasis, Parenchymal, 12) Wernicke Encephalopathy, 13) Behcet Disease, 14) Gliomatosis Cerebri, 15) Leigh Syndrome, 16) Alexander Disease, 17) Inflammatory Disease, 18) Other Demyelinating Diseases

Results

We demonstrate pictorial presentation of 20 interesting brain pathologies involving periaqueductal regions by providing adequate clinical information and characteristic imaging findings. We provide a take-home message from each case for the viewers.

Conclusions

Periaqueductal regions are prone to multiple pathologies, the differentiation of which is not easy all the time. We provide the imaging characteristics and clinical information for each pathology along with a take-home message which would be helpful to differentiate diseases from one another.

Diffuse Axonal Injury (DAI)

- Multifocal punctate hemorrhages at corticomedullary junction, corpus callosum, deep gray matter (GM) & upper brainstem (dorsolateral midbrain & pons)
- Multifocal hypointense T2*/GRE foci related to blood product susceptibility



(Filename: TCT_eP-23_NewMicrosoftPowerPointPresentation.gif)

eP-30

Diffuse Subarachnoid Hemorrhage with Negative Angiogram: Meta-analysis and Management Recommendations

L Tu¹, K Seifert², X Wu¹, D Ghandi³, A Malhotra²

¹*Yale University School of Medicine, New Haven, CT*, ²*Yale New Haven Hospital, New Haven, CT*, ³*University of Maryland School of Medicine, Baltimore, MD*

Purpose

The purpose of this study is to synthesize the current literature into recommendations regarding the management of diffuse subarachnoid hemorrhage with a negative first angiographic study. We will investigate the utility of additional imaging after an initially negative CTA, MRA, or DSA.

Materials and Methods

PUBMED, EMBASE, SCOPUS and research meeting abstracts were searched up to March 2017 for studies of patients with spontaneous subarachnoid hemorrhage (SAH) and an initially negative angiographic study (DSA, CTA, or MRA). Title/abstract and then full-text screening was performed by two independent reviewers. Study quality was assessed via the Cochrane Risk of Bias Tool (CRBT). Meta-analysis was conducted using random and fixed effects models.

Results

A total of 1936 studies were identified, of which 185 underwent full text review; 10 studies were included. Diagnostic methods for initial angiographic as well as follow up studies were variable. Assessment of study quality by CRBT also showed variability; however, most studies had a low risk of bias. The meta-analysis revealed 45 aneurysms among 452 patients. 3DRA (3-dimensional rotational angiography) was the most sensitive modality, more specific than 2D DSA. Additional repeat imaging is of highest yield when it is another 3DRA. There was heterogeneity in the delay before performance of the second angiographic study.

Conclusions

Spontaneous SAH may be categorized as perimesencephalic, diffuse/aneurysmal, peripheral (convexity, sulcal), or CT-negative (detected only on lumbar puncture) based on the distribution of hemorrhage. The optimal management strategy for diffuse SAH and an initial negative angiography is not clearly defined, and practice patterns are variable. Our meta-analysis suggests 3DRA as the optimal modality for follow up; 3D is preferred over 2D-DSA, CTA, and MRA. Should the second angiographic study also be unrevealing, additional imaging by repeat 3DRA is of highest sensitivity.

eP-47

Diffusion and Perfusion Magnetic Resonance Imaging Features in Predicting IDH Mutation Status in Glioblastomas

A Deepesh¹, j saini¹, C Prasad¹, M Bhat¹

¹*National Institute of Mental Health And Neuro Sciences, Bangalore, Karnataka, India*

Purpose

1. To predict the IDH mutation status of glioblastomas using conventional and advanced MR imaging characteristics 2. To correlate with histopathology, immunohistochemical and molecular parameters

Materials and Methods

Retrospective, hospital-based observational study. The study was approved by the institutional ethics committee and informed consent was waived off due to the retrospective nature of the study. Inclusion Criteria: Adults >18 years of age, whose CT and MRI has been suggestive of a high-grade hemispheric

Electronic Posters

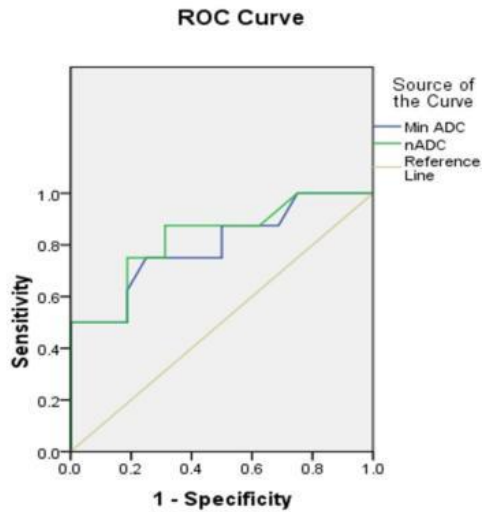
glioma, proved histopathologically, by immunohistochemistry (IHC) and molecular studies as glioblastoma as per the revised WHO 2016 classification of CNS tumors. Exclusion Criteria: Patients with solitary midline lesions, posterior fossa, brainstem lesions and extra-axial mass lesions. Imaging Methodology: MRI was performed on a 3.0 Tesla MR scanner with T2-weighted Turbo spin echo (FSE) axial and coronal images, T1-weighted spin echo axial images, T2-weighted fluid-attenuated inversion recovery (FLAIR), Venobold Images, 6 directions DTI, Postcontrast 3D T1 MPRAGE and Dynamic susceptibility contrast perfusion imaging. The MR data for the ADC maps and the perfusion raw data were digitally transferred from the picture archiving and communication system workstation system to and processed in Philips Intellispace Portal software version 9.0. For tumor apparent diffusion coefficient (ADC) values, multiple tumour ROI's of 30-40 mm² were drawn and the ROI with the lowest mean value was taken (min ADC) and normalized with the contralateral normal-appearing white matter to get the normalized ADC (n ADC). The ROIs were placed in the solid portions of the tumor avoiding obvious areas of necrosis, cysts, hemorrhage or blood vessels. For interpretation of the DSC-PWI data, whole brain CBV maps were generated by applying a single compartmental model with an arterial input function. The relative maximum CBV (r CBV) of the tumor was taken from ROI drawn and then the rCBV ratio was calculated by dividing the tumor CBV by the mean CBV of the contralateral unaffected white matter to minimize variances in rCBV values in each individual patient.

Results

There were nine cases of IDH mutant glioblastomas and 16 cases of IDH wild-type glioblastomas. Interpretation of Perfusion Parameters: The mean rCBV lesion of Grade IV IDH mutant glioblastomas was 16.3 and that of glioblastomas wildtype tumors was 45.84. The difference was statistically significant (P=0.006). The mean rCBV ratio of Grade IV IDH mutant glioblastomas was 4.7 while that of the wildtype glioblastomas was 7.6. The difference was not significant (P=0.136). Interpretation of Diffusion Parameters: The mean min ADC values of the IDH mutant glioblastomas was 0.9×10^{-3} mm²/s and that of the wildtype glioblastomas tumors was 0.718×10^{-3} mm²/s. The difference in mean min ADC between the two groups was statistically significant (P=0.019). The mean nADC values of the IDH mutant glioblastomas was 1.281×10^{-3} mm²/s and that of the wildtype glioblastomas was 0.954×10^{-3} mm²/s. The difference in mean NADC was highly significant between the two groups (P=0.009). The mean maximal lesional FA of the grade IV IDH mutant glioblastomas was 0.224 and that of the IDH wildtype glioblastomas was 0.328. The difference was statistically significant (P=0.013). ROC Curve Analysis: A cut-off value of <17.65 for rCBV of the lesion discriminates IDH mutant glioblastomas from the wildtype with a sensitivity and specificity of 71.4% and 93.75% respectively. The AUC is 0.884 with a p value of 0.004. A cut-off value of <3.35 for rCBV ratio discriminates IDH mutant glioblastomas from the wildtype with a sensitivity and specificity of 57.1% and 87.5% respectively. The AUC is 0.777 with a p value of 0.038. A cut-off value of <0.245 for lesion FA ratio discriminates IDH mutant glioblastomas from the wildtype with a sensitivity and specificity of 71.4% and 81.25% respectively. The AUC is 0.813 with a p value of 0.019.

Conclusions

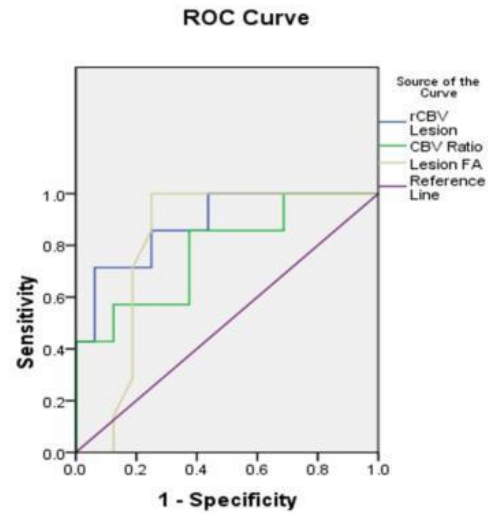
1. The IDH mutant tumors had higher minADC, nADC, and lower rCBV when compared to the wildtype tumors.
2. Combination of diffusion and perfusion-weighted imaging is useful to noninvasively predict the IDH mutation status of glioblastomas prior to surgery.
3. The IDH mutation status may be a noninvasive surrogate marker of prognosis and larger prospective clinical trials are warranted.



Diagonal segments are produced by ties.

	Area Under Curve	P-value	95% confidence intervals	
			Lower Bound	Upper Bound
Min ADC	.797	.020	.595	.998
nADC	.828	.010	.630	1.000

	Cut-off Value	Sensitivity	Specificity
Min ADC	>0.775	75%	75%
nADC	>1.138	75%	81.25%



Diagonal segments are produced by ties.

	Area Under Curve	P-value	95% confidence intervals	
			Lower Bound	Upper Bound
rCBV Lesion	.884	.004	.000	1.000
CBV Ratio	.777	.038	.563	.991
Lesion FA	.813	.019	.631	.994

	Cut-off Value	Sensitivity	Specificity
rCBV Lesion	<17.65	71.4%	93.75%
rCBV Ratio	<3.35	57.1%	87.5%
Lesion FA	<0.245	71.4%	81.25%

(Filename: TCT_eP-47_ASNRIDHJPEG.jpg)

eP-17

Diffusion Kurtosis Imaging with Tract-based Spatial Statistics Reveals White Matter Alterations in Children with Obstructive Sleep Apnea Syndrome

W Li¹, Y Liu¹, H Wen², H He³, Y Peng¹

¹Beijing Children's Hospital, Capital Medical University, National Center for Children's Health, Beijing, China, ²Research Center for Brain-Inspired Intelligence, Institute of Automation, Chinese Academy of Science, Beijing, China, ³The State Key Laboratory of Management and Control for Complex Systems, Institute of Automation, Beijing, China

Purpose

To understand the developmental cause of such changes, we investigated microstructural changes of WM in OSAS children by using diffusion kurtosis imaging (DKI) (1).

Materials and Methods

Ten children diagnosed with OSAS were recruited in the present study (age: 5.4±2.221 years, range: 4–10 years; 6 female). For each subject, T1-weighted imaging (T1 WI), T2-weighted imaging (T2 WI) and DKI were scanned. And on conventional MRI, the imaging appearances of all the cases were normal. For DKI dataset, conventional kurtosis related parameters such as: Axial diffusivity (AD), Radial diffusivity (RD), Mean diffusivity (MD), Fractional anisotropy (FA), Kurtosis fractional anisotropy (KFA), Axial kurtosis (Kax), Radial kurtosis (Krad), Mean kurtosis (Kmean), Mean kurtosis tensor

(MKT) were firstly computed for each subject. Then, Tract-Based Spatial Statistics (TBSS) was used to assess differences in WM between children with OSAS and normal controls (2).

Results

The white matter fibers with significant intergroup differences (FEW corrected $P < 0.05$) in DKI-derived kurtosis parameters are shown as bellows. The mainly involved region include bilateral corticospinal tract, inferior fronto-occipital fasciculus, inferior longitudinal fasciculus, posterior thalamic radiation (include optic radiation); right superior longitudinal fasciculus; left inferior frontal gyrus, brainstem, body of corpus callosum/forceps minor (Fig.1, Fig. 2).

Conclusions

DKI is more suitable than DTI for grasp tissue microstructure change, can better reflect the brain white matter changes in the microstructure. Children with OSAS showed significant functional alterations of the left Inferior longitudinal fasciculus, right Inferior fronto-occipital fasciculus and longitudinal fasciculus in children with OSAS.

■
Kurtosis fractional anisotropy (Kfa), degree of anisotropy of the kurtosis tensor

Controls > patients (cluster size >20):

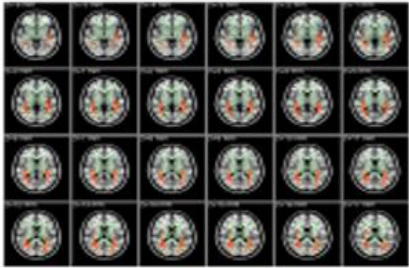


Figure 1. Skeleton clusters showing significantly decreased Kfa at $p < 0.05$

Axial kurtosis (Kax), the diffusional kurtosis in the direction of highest diffusion

Controls > patients (cluster size >20):

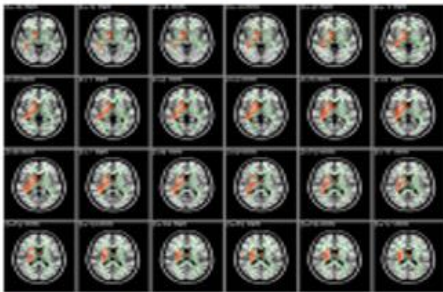


Figure 2. Skeleton clusters showing significantly decreased Kax at $p < 0.05$

In TBSS analysis of DKI parameters, Kfa values in the left Inferior longitudinal fasciculus, right Inferior fronto-occipital fasciculus were significantly positively correlated with duration time of the patient group, and negatively correlated with TS90 (the percentage of the total recorded time when the oxygen saturation below 90%) of the patient group (Figure3).

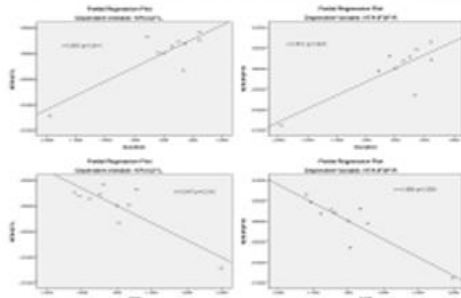


Figure3. Partial correlations between DKI parameters of abnormal WM ROIs and clinical

(Filename: TCT_eP-17_figures.jpg)

eP-16

Effects of Tumor Location on the Functional Integration of Resting State Networks in Glioma Patients

G Rajeev-Kumar¹, S Gohel², K Peck³, M Jenabi³, M Laino⁴, A Holodny³, B Vachha³

Electronic Posters

¹Icahn School of Medicine at Mount Sinai, New York, NY, ²Rutgers University School of Health Professions, Newark, NJ, ³Memorial Sloan Kettering Cancer Center, New York, NY, ⁴Catholic University of Sacred Heart-A.Gemelli Hospital, Rome, Italy

Purpose

Patients with gliomas report cognitive dysfunction suggestive of a global impairment of neural networks induced by tumor. We evaluate the functional heterogeneity of the posterior-cingulate-cortex (pCC) and medial-prefrontal-cortex (mPFC), key components of the default mode network (DMN) and assess their role in integrating information from additional resting state networks (RSNs). Proximity of tumors to these regions was hypothesized to alter connectivity not only within the DMN but also in other associated RSNs such as the dorsal attention network (DAN) and salience network (SN).

Materials and Methods

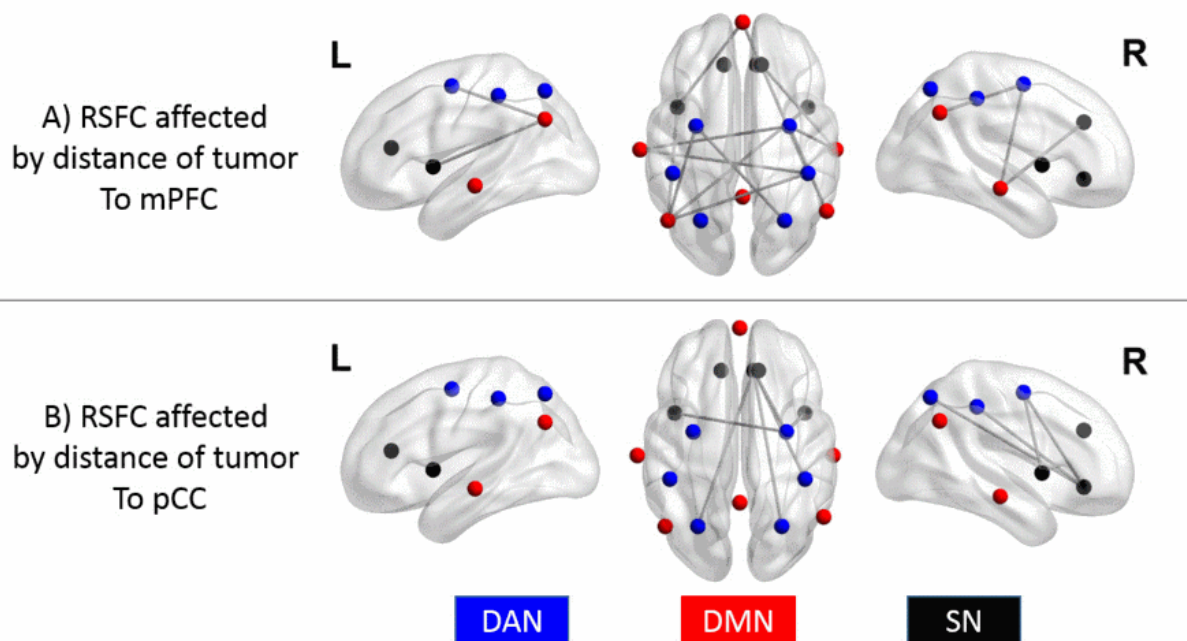
rsfMRI was obtained in 51 preoperative glioma patients. ICA was performed to identify DMN, DAN and SN networks. ROI masks were created and used to obtain subject specific functional connectivity matrices. Distance between tumor location and each of the ROIs was calculated for each subject. A linear regression based approach was used with functional connectivity between any two ROIs as dependent variable and the tumor distance from each of the ROIs as independent variables.

Results

A positive correlation between tumor distance from the mPFC and functional connectivity between the three networks was noted; the closer the tumor was to the mPFC, the weaker the connections were between the DMN and the other networks (Figure 1A). A negative correlation between tumor distance from the pCC and functional connectivity specifically between the DAN and SN was noted (Figure 1B) such that the connectivity between DAN and SN became stronger as the tumor distance decreased from the pCC.

Conclusions

The present study suggests specific functional differences between the two components of DMN and indicates a possible communication pathway connecting the RSNs. Results suggest that mPFC serves as the functional network modulator of the DMN while the pCC serves as the suppressor of the attention system when internal cognition is engaged.



(Filename: TCT_eP-16_Figure1AB.gif)

eP-19

Evaluation of Brain Tuberculosis and Metastases Using Arterial Spin Labeling Perfusion and Diffusion Tensor Imaging – A Prospective Comparative Study

N Soni¹, S Kumar², G Bathla¹

¹*University of Iowa Hospitals and Clinics, Iowa City, IA,* ²*SGPGIMS, Lucknow, Uttar Pradesh, India*

Purpose

To differentiate intra-axial tuberculosis (TB) from metastases on the basis of quantitative differences in the perfusion and diffusion indices of enhancing portion and nonenhancing perilesional edema using arterial spin labeling (ASL) and diffusion-tensor imaging (DTI)

Materials and Methods

Twelve patients with TB and 13 patients with metastases underwent conventional MRI including DTI and ASL sequences. The cerebral blood flow (CBF) values of enhancing portion (L) and perilesional edema (PE) were calculated, normalized (n) to the contralateral white matter (CWM) to obtain the nCBFL and nCBFPE ratios. Similarly, DTI data was processed to obtain fractional anisotropy (FA), mean diffusivity (MD), radial diffusivity (RD) and axial diffusivity (AD) values from the enhancing portion and PE.

Results

Out of 12 TB lesions, nine were conglomerate and two were nodular enhancing whereas four out of 13 metastases were nodular enhancing lesions with perilesional edema in all. The enhancing portion of metastases revealed statistically significant ($p=0.001$) high values of median nCBFL than TB and whereas the difference in the median nCBFPE was not statistically significant ($p=0.174$). The median FAL found to be higher in tuberculoma compared to metastases ($p=0.031$) whereas no statistically significant mean differences were found in FAPE ($p=0.587$) and in mean values of other diffusion parameters (MD, RD, and AD). Analysis by the ROC curve method revealed a cut-off value of >2.865 for nCBL and <0.073 for FAL in differentiating metastases from tuberculomas.

Conclusions

By measuring nCBFL and FAL using ASL perfusion and DTI technique, one can differentiate tuberculomas from metastases.

eP-05

Evaluation of Cerebral Microstructural Changes in Adult Patients with Obstructive Sleep Apnea by MR Diffusion Kurtosis Imaging

S Vyas¹, P Singh¹, N Khandelwal¹, V Govind², A Aggarwal¹, M Mohanty¹

¹*Postgraduate Institute of Medical Education and Research, Chandigarh, India,* ²*University of Miami, Miami, FL*

Purpose

Association between obstructive sleep apnea (OSA) and cognitive impairment is well-recognized, but little is known about neural deficits that underlie these sequelae. The purpose of this study was to evaluate the utility of diffusion kurtosis imaging (DKI) to assess microstructural tissue changes in the brain of patients with OSA.

Materials and Methods

This prospective study was conducted in 20 patients with moderate-to-severe OSA and 20 age- and gender-matched controls. MRI data acquisition including DKI at 3 Tesla and a battery of neurocognitive tests were performed on all patients. DKI data were processed and transformed to a (standard brain) template space to obtain various kurtosis parameters including axial kurtosis (AK), radial kurtosis (RK),

mean kurtosis (MK) and kurtosis fractional anisotropy (KFA) using a 189-region brain atlas in the same template space. Kurtosis metrics obtained from the brain anatomical regions in the patient and control groups were compared, and were associated with data from neurocognitive tests in the patient group using appropriate statistical tests.

Results

Significant differences ($p < 0.05$) were found in AK (54 regions), RK (10 regions), MK (6 regions) and KFA (41 regions) values in patients with OSA as compared to controls. DKI indices, using an atlas-based whole brain analysis approach used in our study, showed widespread involvement of the anatomical regions in patients with OSA.

Conclusions

The kurtosis parameters are more sensitive in demonstrating abnormalities in brain tissue structural organization at the microstructural level, before any detectable changes appear in conventional MRI or other imaging modalities.

eP-48

Extracranial Meningiomas: Report of Two Cases and Review of Literature

F Hirata¹, M Gonçalves², L Lucato³, M Taveira Garcia², a ayres², C da Silva², H Sterman Neto², R Moreno⁴

¹*Universidade de São Paulo, Brazil*, ²*Instituto do Câncer do Estado de São Paulo, Brazil*, ³*Instituto de Radiologia do HC-FMUSP, São Paulo, Brazil*, ⁴*Instituto de Radiologia da Universidade de São Paulo, Brazil*

Purpose

The objective of this retrospective study is to report two cases of our oncology institution, review the largest series to date with extracranial meningiomas, highlighting clinicopathologic and imaging features of these rare lesions.

Materials and Methods

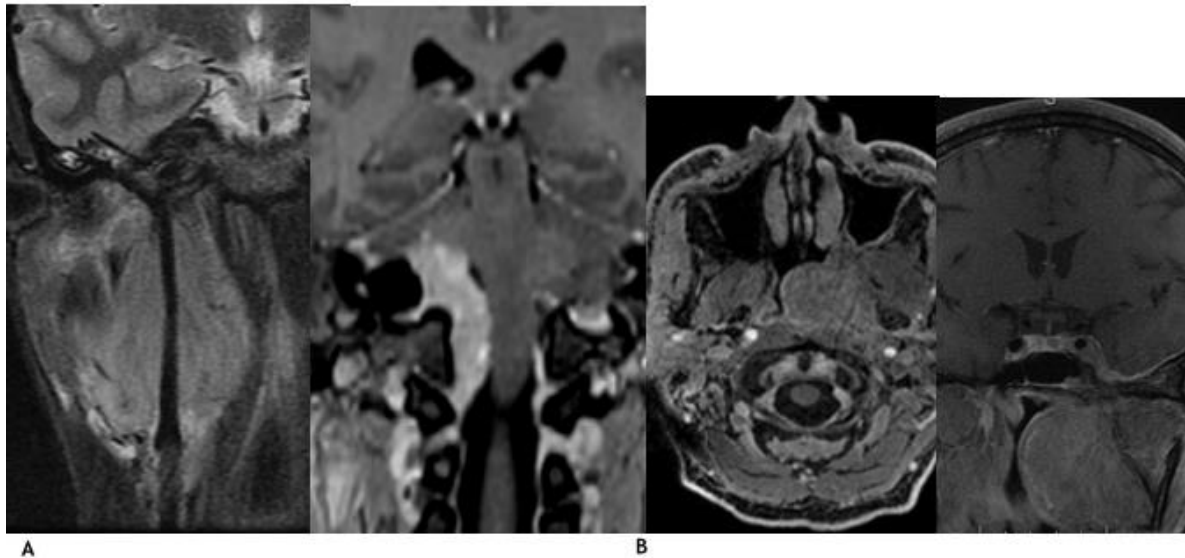
We reviewed the published articles on the subject on PubMed in the last years, with the search words: extracranial meningiomas and MRI. We present two cases from our oncology institution, whose anatomic sites were the posterior cranial fossa (with large cervical extension along the carotid space) and the middle cranial fossa (extending to oropharynx, cavernous sinus, masticatory and parapharyngeal spaces).

Results

Extracranial meningiomas can originate from arachnoid cells in the nerve sheath or in emerging vessels of the skull base, from paquaneal bodies at extracranial sites or from undifferentiated/multipotent mesenchymal cells. Up to 20% of intracranial meningiomas may have extracranial extension to the scalp, orbit, upper airways, oral cavity, and soft tissues. More rarely, these neoplasms may be exclusively extracranial. Differential diagnosis includes paraganglioma, schwannoma, metastatic carcinomas, melanoma and esthesioneuroblastoma. Histological characteristics and immunohistochemical findings aid in this distinction, as well as the imaging methods.

Conclusions

Extracranial meningiomas are rare lesions and imaging is essential for differentiating from other cervical mass lesions, as well as supporting the neurosurgeon in surgical planning.



Case A: ISS, female, 23 years; refers discomfort in the oropharynx, with paresis of the soft palate on the right, deviation and atrophy of the right tongue and bulging of the lateral wall of the pharynx on this side. Intra and predominantly extracranial mass lesion in the posterior fossa on the right, and large extracranial component in the ipsilateral carotid space.

Case B: GSL, male, 63 years; refers a lesion bulging on soft palate on the left for 1 year associated with local pain. Extracranial mass lesion invades the left parapharyngeal space, with compression of the left lateral wall of the nasopharynx, reducing the lumen. Thickening of the dura in the floor of the left middle cranial fossa and invasion of ipsilateral cavernous sinus.

(Filename: TCT_eP-48_ASNR_Leandro2001.jpg)

eP-26

Feasibility of Silent MRA for Depicting Cerebral Arteries in Patients with Cerebrovascular Moyamoya Disease: Comparison with TOF-MRA

N Tomura¹, R Yamakuni¹, Z Watanabe¹

¹*Southern Tohoku Research Institute for Neuroscience, Southern Tohoku General Hospital, Koriyama, Japan*

Purpose

Silent-MRA was compared with time-of-flight (TOF)-MRA for depicting cerebral arteries in patients with cerebrovascular Moyamoya disease.

Materials and Methods

The study was performed in 30 patients (11 males, 19 females; mean age, 44.7 ± 17.8 years) with cerebrovascular Moyamoya disease. All patients had already been diagnosed from intra-arterial DSA. Both silent-MRA and TOF-MRA were simultaneously performed in a single study. Scan parameters for silent-MRA were as follows: flip angle (FA), 5°; bandwidth (BW), 20 kHz; field of view (FOV), 18 cm; resolution, 1.2 mm; spokes per segment, 384; acquisition time, 7:28. Parameters for TOF-MRA were: repetition time, minimum; echo time, minimum; FA, 18°; BW, 31.25 kHz; FOV, 20 cm; slice thickness, 1 mm; overlap, 14; matrix, 416×224; and acquisition time, 4:49. Comparison of silent-MRA with TOF-

Electronic Posters

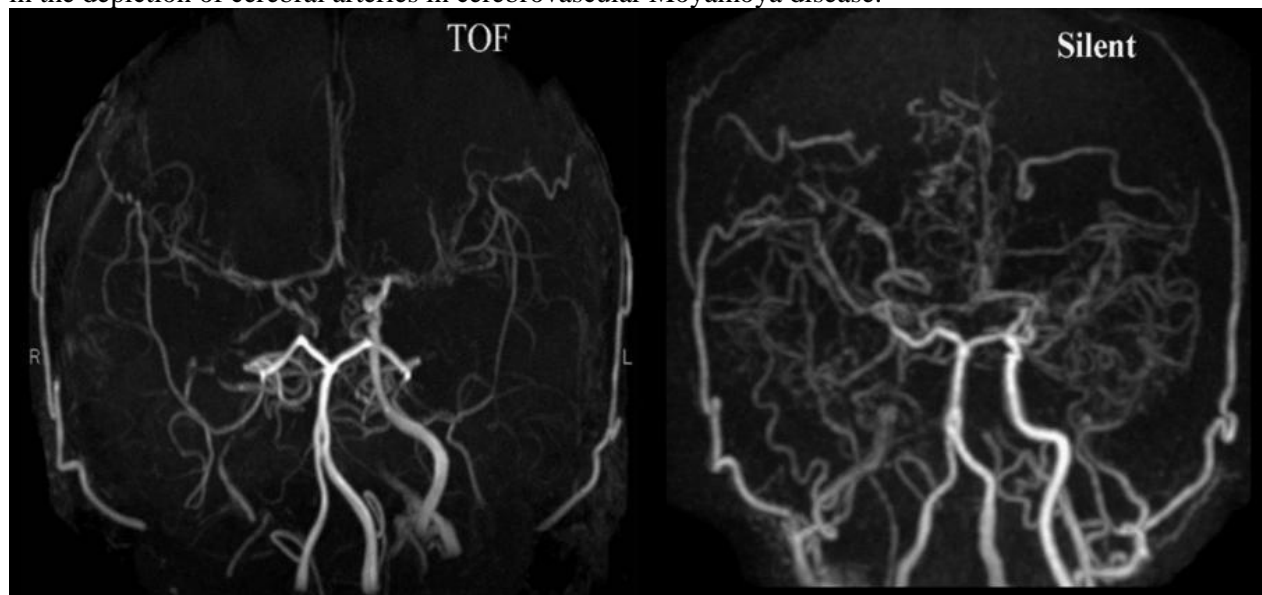
MRA was performed quantitatively and qualitatively. Quantitative analysis was performed by measuring signal-to-noise ratio (SNR) and contrast-to-noise ratio (CNR) using the following equations: $SNR = \frac{\text{signal intensity of the internal carotid artery}}{\text{standard deviation of air}}$; and $CNR = \frac{[(\text{signal intensity of the internal carotid artery}) - (\text{signal intensity of the brain})]}{\text{signal intensity of air}}$. Qualitative analysis was performed using Houkin's MRA grading system (MRA score) for steno-occlusive severity of the main cerebral arteries and grading of Moyamoya vessels. Houkin's MRA grade was defined as the sum of the internal carotid artery, anterior cerebral artery, middle cerebral artery, and posterior cerebral artery scores, as follows: MRA grade 1; total MRA score 2-4, MRA grade 2; total score 5-7, MRA grade 3; and total score 8-10, MRA grade 4. MRA grade 4 is the most severe steno-occlusive lesion of the main cerebral arteries. Grading for Moyamoya vessels was classified as: 1, absolutely negative; 2, probably negative; 3, unclear; 4, probably positive; and 5, absolutely positive. Qualitative analysis was conjointly performed by two radiologists.

Results

In both SNR and CNR, TOF-MRA was significantly superior to silent-MRA ($p < 0.001$, Wilcoxon's signed-rank test). In Houkin's MRA stage for main cerebral arteries, no significant difference was seen between silent-MRA and TOF-MRA in both left and right cerebral hemispheres. In the grading for Moyamoya vessels, silent-MRA was significantly superior to TOF-MRA ($p < 0.001$, Wilcoxon's signed-rank test).

Conclusions

Although TOF-MRA shows higher SNR and CNR than silent-MRA, silent-MRA appears significantly superior to TOF-MRA in the depiction of Moyamoya vessels. Silent-MRA can complement TOF-MRA in the depiction of cerebral arteries in cerebrovascular Moyamoya disease.



(Filename: TCT_eP-26_ASNRFigure.jpg)

eP-67e

Functional and Metabolic Neuroimaging: Multimodal Diagnostic Approach to Regional and Global Brain Changes in Alzheimer's Disease

S Emamzadehfard¹, F Yu², V Eslami³

¹University of Texas Health Science Center, San Antonio, TX, ²Massachusetts General Hospital/Athinoula A. Martinos Center for Biomedical Imaging, Boston, MA, ³University of Texas Medical Branch, Galveston, TX

Purpose

Alzheimer's disease (AD) is the most prevalent form of dementia – the number of individuals afflicted by this debilitating disease continues to increase as the population ages. On histology, it is known that the abnormal accumulation of proteins (tau and A β) lead to amyloid plaques and neurofibrillary tangles. Advances in neuroimaging techniques have made it possible to not only measure the degree of grey-matter atrophy but also assess the changes in connectivity between different brain regions, altered metabolism, as well as the degree of white-matter involvement. The hope is that these imaging biomarkers may help in the diagnosis of AD as well as evaluating disease burden. Herein, we review several imaging findings that have been described on MRI and PET imaging, their potential role in diagnosis, determining prognosis, and monitoring disease progression, as well as present relevant example cases.

Materials and Methods

It can be challenging to distinguish AD from mild cognitive impairment as well as other neurodegenerative diseases on a clinical basis alone, particularly in early disease. A multimodal imaging-based approach may be helpful for diagnosing AD as well as characterizing disease burden. We review the neuroimaging findings on MRI and PET in our patient cohort from 2009-2017, as well as present advanced imaging techniques such as resting-state fMRI and multishell diffusion imaging.

Results

Multimodal neuroimaging approach would be able to determine AD in different stages with various manifestations. Structural MRI showed extensive atrophy within the cortex with gross morphometric changes in the later stages. Voxel based meta-analysis (VBM) shows typical regions of grey-matter atrophy include the precuneus, hippocampus, and posterior cingulate gyrus. VBM show WM atrophy as significant involvement of the cingulum bundle. Atrophied WM regions included the corpus callosum, fornix, and cingulate. Diffusion-based MRI techniques such as diffusion-tensor imaging (DTI) offer increased sensitivity to changes in the gray and particularly the white matter. Decreased WM integrity based on increased demyelination and axonal loss has been associated with grey matter atrophy, particularly in the hippocampus. DTI tractography is a useful tool for detection of WM and GM atrophy, which is linking the hippocampus proper and parahippocampal cortex to the PCC, as well as its relationship with global and hippocampal atrophy. In addition, multishell diffusion imaging methods, such as neurite orientation dispersion and density imaging (NODDI), may represent advancement over DTI in assessing white matter integrity. PET imaging- 8F-FDG PET has been used to assist the diagnosis of Alzheimer's disease. Temporoparietal and posterior cingulate hypometabolism with sparing of subcortical structures and sensorimotor and occipital cortices are characteristic of AD. FDG-PET show hypometabolism GM and WM brain regions, is routinely used in the diagnosis of AD. Pittsburgh Compound-B" or 11C-PIB presumably showing more intense binding to non-AD may potentially be better suited for assessment of e.g. corticobasal degeneration or progressive supranuclear palsy. Tau-PET imaging may allow distinguishing the tauopathy AD from non-tauopathies. Patients with cognitive symptoms but without proof of cerebral tau-pathology are not likely to suffer from AD.

Conclusions

Multimodal neuroimaging diagnostic approach is the main stem of AD detection in any stages, with diverse expressions. Advanced neuroimaging establishes innovative insulted brain regions in AD pathology, including white matter and hippocampus. Familiarity with these imaging tools and their associated findings in AD may help the radiologist make the diagnosis. Future work may help to validate the utility of these biomarkers for assessing disease progression and help to monitor therapeutic efficacy.

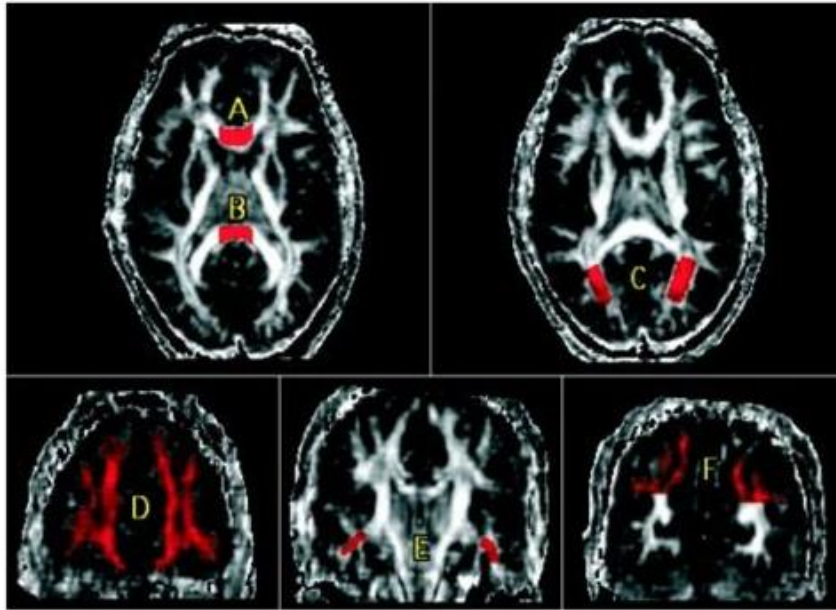


Fig 1. Differential Vulnerability of Anterior White Matter in Nondemented Aging with Minimal Acceleration in Dementia of the Alzheimer Type: Evidence from Diffusion Tensor Imaging Cereb Cortex. 2004;14(4):410-423. doi:10.1093/cercor/bhh003 Cereb Cortex

(Filename: TCT_eP-67e_Slide1.JPG)

eP-01

Hazards of High Flight: The Effects of Hypobaric Exposure Upon the Brain in Aircrew and Astronauts

P Sherman¹

¹USAF School of Aerospace Medicine/San Antonio Military Health System, San Antonio, TX

Purpose

Repeated human exposure to hypobaric conditions is associated with increased white matter hyperintensities, degradation of axonal integrity, and neurocognitive processing decrements. The goal is to characterize the pathophysiologic response of the brain to high altitude and understand its association with white matter injury.

Materials and Methods

Brain MRI FLAIR data from 41 astronauts (ASTR) was quantified for white matter hyperintensity (WMH) volume, subcortical and periependymal. This was compared to previously reported data from 106 U-2 pilots (U2P) and to 320 health matched control subjects (nonparametric group comparisons). Ninety-six U.S. Air Force aircrew trainees were evaluated while undergoing initial occupational hypobaric exposure. Standard USAF procedure is a 30-minute exposure to 25,000 feet (7,620 m). Quantitative ASL and proton MRS data were acquired on subjects at T-24 hours, T+24 hours, and T+72 hours. Voxels were placed in the bilateral frontal white matter (FWM) and anterior cingulate cortex (ACC). Controls were 68 healthy subjects meeting the same physical and physiological criteria minus hypobaric exposure. Brain MRI FLAIR data from 41 astronauts (ASTR) was quantified for white matter hyperintensity (WMH)

Electronic Posters

volume, subcortical and periependymal. This was compared to previously reported data from 106 U-2 pilots (U2P) and 320 health matched control subjects (nonparametric group comparisons).

Results

ASTR mean WMH total volume (mL) was 0.6618 +/- 0.1289 compared to 0.8663 +/- 0.0502 for U-2 pilots and 0.2353 +/- 0.0100 for controls. Both U2P and ASTR have a significantly higher WMH volume compared to controls, with no significant difference between ASTR:U2P. Statistically significant increases in CBF across both white and grey matter in aircrew personnel with hypobaric exposure were observed when using gender and age as covariables (white matter $p < 0.001$, gray matter $p = 0.048$). This difference is dependent upon age as a covariable, although there is no significant difference in age between the exposed and control subjects ($p > 0.10$). ACC sampled areas demonstrated significant single MRS factor differences in all tested metabolites, except GSH, in aircrew personnel with hypobaric exposure: Glu, Cho, NAA, MI $p < 0.05$; Cr, Glu+Gln $p < 0.01$. FWM GSH ($p = 0.029$) demonstrated significant single MRS factor differences in the FWM. Age dependency was a covariant in all single factors.

Conclusions

Astronauts demonstrate similar increased WMH burden to high altitude pilots. Recent demonstration of intracranial fluid shifts and brain plasticity changes in astronauts suggests further analysis of white matter integrity is warranted. There is a highly significant ASL/increased CBF response after a single exposure to hypobaria, with age being a significant contributor, possibly reflecting differences in central nervous system maturation. There was a significant difference in most neurometabolites after exposure to hypobaria. These differences may be representative of changes at a cellular level in response to, or preceding, changes in blood flow versus age-related differences or differing WMH between the two groups.

eP-46

Imaging Assessment of DSC and ASL Perfusion to Differentiate Post-Treatment Changes (PTC) from Recurrent Glioma (RG) in High-grade Glioma

A Garg¹, K Bhullar¹, L Sebastian¹, A Suri¹

¹All India Institute of Medical Sciences, New Delhi, Delhi, India

Purpose

The aim of present study is to compare the diagnostic performance of DSC MR perfusion and ASL perfusion in distinguishing RG from PTC in clinical setting.

Materials and Methods

Twenty-two patients of high-grade gliomas on histopathology who develop enhancing brain lesions on imaging after receiving combination RT and CT were enrolled. DSC perfusion MRI was performed on 3T MR scanner and ASL perfusion was estimated on a 1.5T MR scanner using 3D pseudocontinuous ASL. ROI placement was done on corrected rCBV maps and ASL CBF maps in areas of highest perfusion within the lesion and contralateral normal-appearing white matter and rCBV and ASL CBF ratios were calculated. Six out of 22 underwent surgery and histopathology was used as gold standard. For 16 nonoperated patients, combined clinical and radiologic follow-up was used; lesions were classified as RG if they showed radiologic evidence of progression and as PTC if they remained stable or decrease in size without new treatment or change in therapy for a minimum of three months. Mann-Whitney U statistical test was applied for group significance.

Results

The final diagnosis was RG in 9 (Surgery-6, FU-3) and PTC in 13 (all on FU) patients. In PTC, mean rCBV ratio was 1.16 (range: 0.83- 3.95; median 1.53) and ASL CBF 1.15 (range: 0.42- 1.64; median 1.16). In RG, mean rCBV ratio was 5.0 (range:1.4- 13.3; median 4.23) and ASL CBF was median 2.16

Electronic Posters

(range:0.71- 4.44; median 1.67) Significantly high rCBV (p=0.002) and ASL CBF (p=0.028) was found in RG compared to PTC.

Conclusions

RG has significantly high rCBV using DSC perfusion and high CBF using ASL perfusion.

eP-67g

Imaging Findings of Cancer Immunotherapy Induced Hypophysitis: An Update

G Simmons¹, H Nguyen², D Kaya², S Ahmed², R Dadu², M Cabanillas², K Shah²

¹University of Texas Houston, Houston, TX, ²University of Texas MD Anderson Cancer Center, Houston, TX

Purpose

The use of immune checkpoint inhibitors, such as the anti-CTLA4 agent ipilimumab is associated with autoimmune hypophysitis. We reviewed MRI scans of clinically confirmed immunotherapy-induced hypophysitis (IH) for useful imaging findings.

Materials and Methods

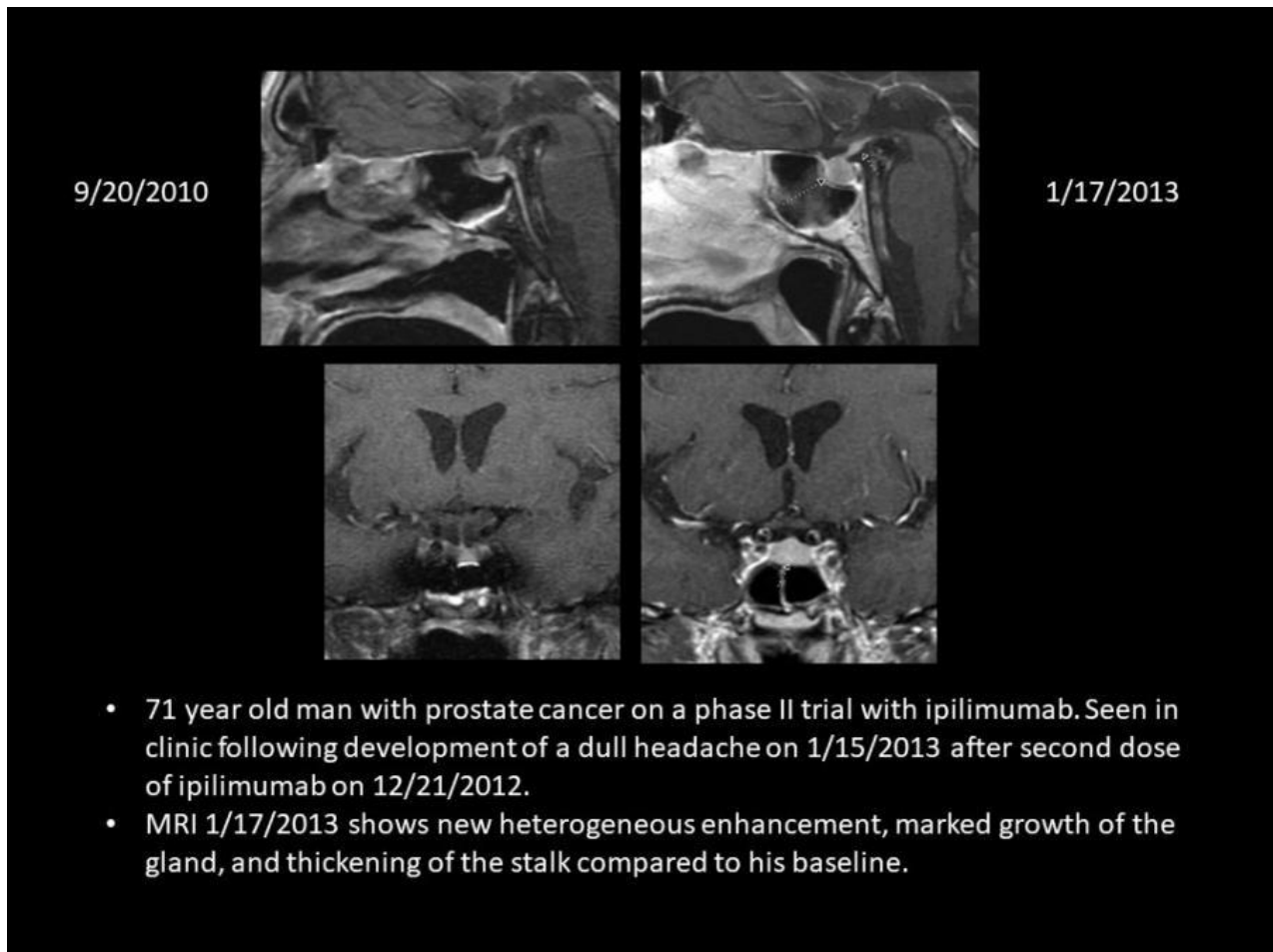
A review of patients treated with immunotherapy since 2005 at MD Anderson Cancer Center yielded 115 cases that were subsequently referred for endocrine consult. Of these, 65 were diagnosed with IH, defined as (1) ≥ 1 pituitary hormonal deficiencies (either adrenocorticotrophic hormone or thyroid stimulating hormone) plus MRI abnormality or (2) ≥ 2 pituitary hormonal deficiencies in patients a) without an MRI or b) with a normal MRI examination. Two CAQ certified neuroradiologists and one trainee with 5 years of experience reviewed all MRIs for abnormalities including suprasellar extension, stalk thickening, heterogeneous enhancement of the pituitary gland, parasellar bulge and enlargement of the gland compared to a prior study. Time to imaging resolution of IH, and presence of brain metastases, were also noted.

Results

Median age at diagnosis of IH was 63 years (38-85); 52/65 (80%) were men, 43 patients had melanoma, 12 had prostate cancer, five had renal cell carcinoma, two had lung cancer and one had thyroid cancer. The 42/65 (64%) IH patients with comparison scan showed increased height of the gland; 35/65 (54%) IH glands showed suprasellar convexity; 34/65 (52%) IH glands demonstrated stalk thickening; 28/65 (43%) IH glands showed heterogeneous enhancement. Mean gland height in patients with IH was 8 mm compared to mean baseline height for the same cases 5 mm. The 54/65 (83%) patients had MRI findings of hypophysitis on MRI interpretation. Of the 11/65 (17%) false negative patients, 8/11 demonstrated none of the above findings on MRI and 2/11 had stalk thickening and heterogeneous enhancement but no growth from baseline. The final case had heterogeneous enhancement in one plane post contrast but not in other planes, no stalk thickening or growth of the gland. At IH diagnosis, MRI scan showed new parenchymal or dural based metastasis in 3/65 (5%) patients. 2/65 (5%) other patients had a history of brain metastasis prior to IH diagnosis.

Conclusions

An updated review of 115 IH cases since 2005 demonstrates MRI changes of hypophysitis in 83%. Baseline MRI scan was often critical in diagnosis through detection of gland growth, given that a small baseline gland size can limit the sensitivity of suprasellar bulge and enhancement changes. Hypophysitis is much more common in the setting of immune checkpoint inhibitor therapy than is metastasis to the pituitary gland. Most cases with follow-up achieved resolution of MRI findings.



(Filename: TCT_eP-67g_PresentationGraphic.jpg)

eP-62

Initial Clinical Experience of Synthetic MRI as Routine Neuroimaging Protocol in the Daily Practice: A Single-center Study

H Baek^{1,2}, K Ryu¹, K Choi²

¹GNU Changwon Hospital, Changwon, Republic of Korea, ²PNU Yangsan Hospital, Yangsan, Republic of Korea

Purpose

Synthetic MR imaging can generate multiple image sequences from a single scan with rapid scan time and additionally quantitative image information. This is the first study to investigate the clinical feasibility of synthetic MRI as routine neuroimaging protocol in the daily practice.

Materials and Methods

We retrospectively reviewed a total of 89 patients who underwent routine brain MR imaging using synthetic MR imaging acquisition from February 2017 to April 2017. Image quality assessments were performed on synthetic T1 FLAIR, T2-weighted, T2 FLAIR and phase-sensitive inversion recovery (PSIR) sequences from multiple-dynamic multiple-echo imaging by two independent readers.

Results

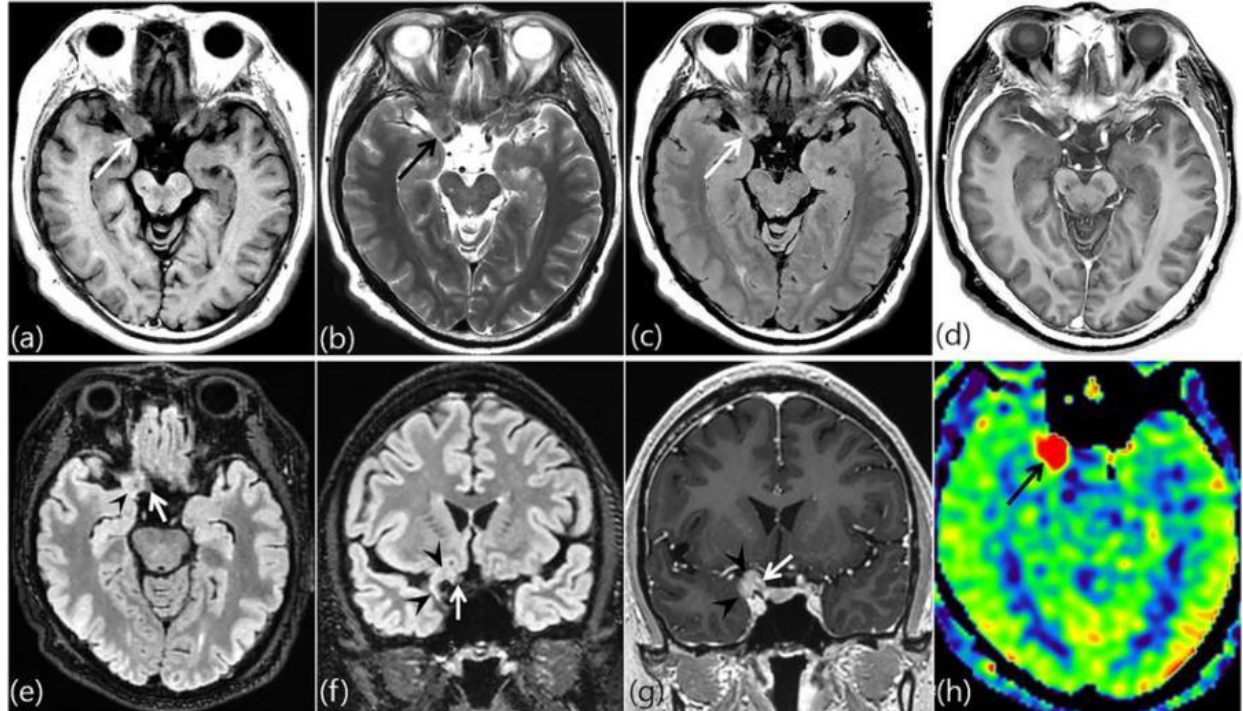
Using a 4-point assessment scale, overall image quality and anatomical delineation of synthetic brain MR imaging were good with more than 3 points, except for T2 FLAIR. Synthetic T2 FLAIR was sufficient,

Electronic Posters

but it showed more pronounced artifacts, especially CSF pulsation artifact and linear hyperintensity along the brain surface. Interobserver agreement for evaluating image quality of all synthetic sequences was good to excellent.

Conclusions

In conclusion, synthetic MRI can be acceptable for clinical use as routine neuroimaging protocol in the daily practice, and it can be used flexibly to set up tailored neuroimaging protocol for each institution.



(Filename: TCT_eP-62_figure.JPG)

eP-67f

Intracranial and Extracranial Atherosclerosis and Cerebral Infarction Patterns with 3T Vessel-Wall Magnetic Resonance Imaging

M Shen¹, B Sui¹, S Chen², C Yuan³, T Hatsukami³, P Gao¹

¹Beijing Tianan Hospital, Capital Medical University, Beijing, China, ²School of Medicine, Tsinghua University, Beijing, China, ³University of Washington, Seattle, WA

Purpose

Large-artery atherosclerosis is an important cause leading to ischemic stroke. Concurrent atherosclerosis is common in Asians. However, research on integrated evaluation of intracranial and extracranial artery is rare. This study aims to investigate relationship between intra and extracranial artery with ischemic stroke pattern.

Materials and Methods

Fifty patients with MCA territory acute ischemic stroke identified on head DWI involving deep perforating artery territory were included in this study, excluding cardiac and other causes. All patients had intracranial 3-D multicontrast vessel wall imaging within two weeks after onset of stroke. Plaque presence of ipsilateral MCA were assessed, and patients were divided into two groups: normal group and group with MCA plaque. Infarct location (identified by lowest layer), volume, maximum area, maximum area location, total layer, multiple infarcts were compared between two groups. In group with MCA

Electronic Posters

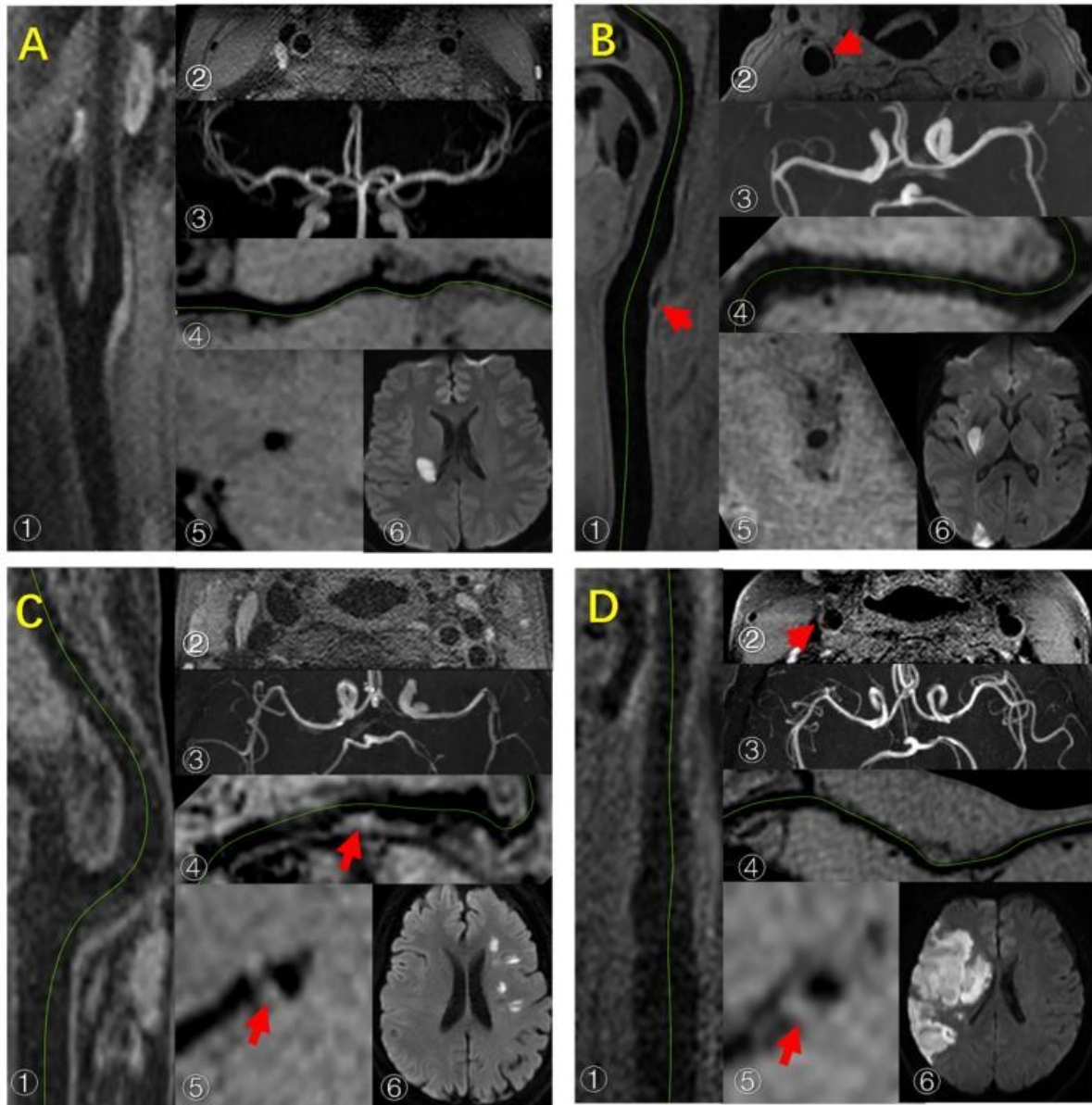
plaque, correlation between plaque characteristics including length, distribution, and maximum wall thickness and infarct characteristics were assessed.

Results

Of 50 patients, 30 (60%) showed MCA plaque, and 20 (40%) showed no plaque. The infarct location for two groups was layer 2.0 (interquartile range: 1.0, 3.3), and 3.0 (2.0, 4.0) respectively, which showed statistically significant difference ($Z=-2.102$, $P=0.036$). MCA plaque group had more patients with multiple infarcts (43.3% versus 0%, $\chi^2=8.983$, $P=0.003$). In MCA plaque group, the lowest layer was negatively correlated with maximum wall thickness ($r=-0.414$, $P=0.023$), total layer was positively correlated with plaque distribution ($r=0.482$, $P=0.037$), and maximum wall thickness ($r=0.451$, $P=0.012$).

Conclusions

Infarct location and multiple infarcts may distinguish MCA atherosclerosis disease and small vessel disease. Concerning patients with MCA atherosclerosis, deep perforating artery infarction correlated with plaque characteristics to a certain extent.



A. Patient without plaque in MCA and CA, and with PAI infarct. **B.** Patient with CA plaque only, and with PAI and BZ infarcts. **C.** Patient with MCA plaque only, and with BZ infarct. **D.** Patient with plaques in CA and MCA, and with PI and PAI infarcts. ①② carotid artery; ③④⑤ MCA; ⑥ Infarct pattern on DWI

(Filename: TCT_eP-67f_Figure.jpg)

eP-06

Is the Neuroradiological Differentiation between M. Fabry and MS Possible?

O Foesleitner¹, J Rath¹, P Rommer¹, L Haider¹, G Sunder-Plassmann¹, D Prayer¹, G Kasprian¹
¹Medical University of Vienna, Vienna, Austria

Purpose

Due to resembling neuroimaging features and often a similar spectrum of clinical symptoms, Morbus Fabry - a rare lysosomal disorder - is frequently misinterpreted as multiple sclerosis (MS). As enzyme replacement therapy (ERT) is currently available, some of the severe sequelae of M. Fabry could be prevented. This study aimed to determine if it is possible to differentiate M. Fabry from MS patients based on their standard neuroimaging features.

Materials and Methods

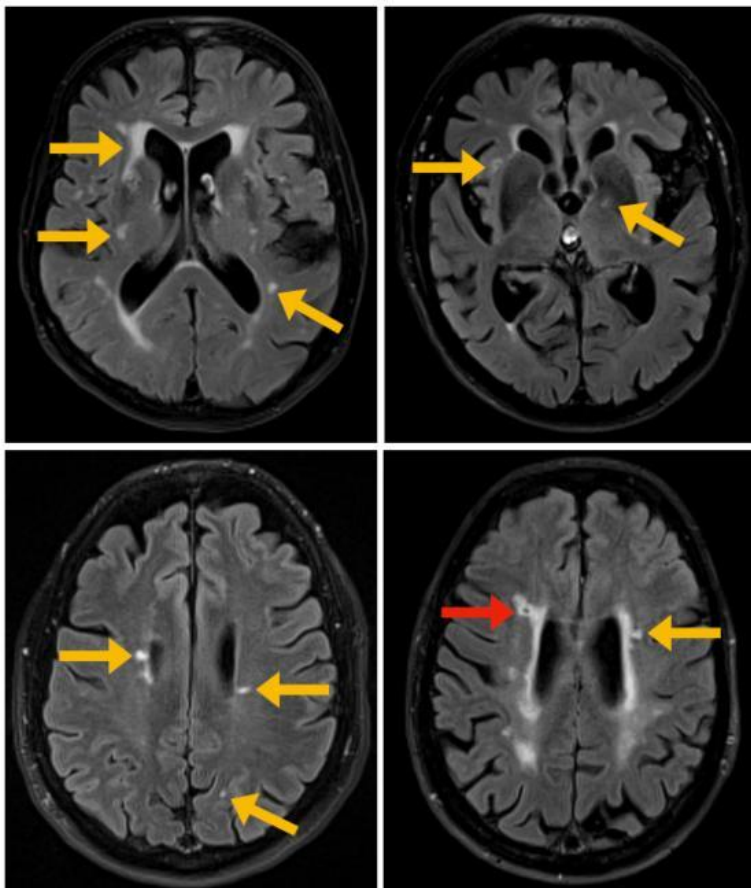
In 24 patients (mean age 46.9y, 10m, 14f) with alpha-galactosidase blood tests and genetical testing positive for M. Fabry underwent 3 Tesla MRI examinations using the recommended MS protocol. 23 MS patients were retrospectively matched based on their sex, age and lesion load. Two blinded raters with different levels of expertise assessed axial FLAIR sequences and attributed the patients to either the MS or the M. Fabry group.

Results

70.8% (17/24) of M. Fabry patients could be correctly identified, 7 M. Fabry patients were misinterpreted as MS. 91.3% (21/23) of MS patients could be correctly identified. The most helpful neuroimaging sign was basal ganglia involvement (presence of lacunar lesions, FLAIR signal alterations). Previously commonly reported signs, such as the pulvinar sign and a megadolicho-basilar artery, were not present in our cohort of M. Fabry patients.

Conclusions

It is difficult to diagnose M. Fabry based on its neuroimaging features alone. However, it is possible to differentiate it from typical MS cases by careful neuroradiological pattern analysis.



Illustrative cases (axial FLAIR images):

Top row: 2 pts. with M. Fabry showing multiple small and/or confluent WM lesions involving the basal ganglia (yellow arrows).

Bottom row: 2 pts. with classic MS signs, flame-shaped periventricular and juxtacortical lesions (yellow arrows) and black holes (red arrow)

(Filename: TCT_eP-06_fabry_ima.jpg)

eP-10

Isolated Seatbelt Sign Does Not Predict Cervical Vascular Injuries Vehicle Accidents

C Tuma Santos¹, D Joyner¹, S Lirette¹

¹*University of Mississippi Medical Center, Jackson, MS*

Purpose

Seatbelts protect the passenger not only by preventing ejection from the vehicle but also by reducing the severity of impact. However, the use of seatbelts has been associated with severe injuries, including trauma to the sternum, ribs, spine, and larynx. Blunt carotid and vertebral artery injury (BCVI) can also occur in restrained passengers and carry devastating consequences. Computed tomography angiography (CTA) has been widely accepted as the screening method of choice. When cerebrovascular symptoms are present, the decision is straightforward. However, screening asymptomatic patients at risk for BCVI remains controversial, as there is no common answer to what is considered a risk factor and which patients should be screened. In the present study, we hypothesize that the seatbelt sign alone is not a reliable predictor of occult BCVI. We propose that a combination of the seatbelt sign with select risk factors may provide a better predictor of BCVI.

Materials and Methods

All patients involved in motor vehicle accidents that had computed tomography angiography (CTA) of the neck over the period between 1st of January 2016 to 31st of December 2016 were included. The medical records of these patients were reviewed for evidence of BCVI. Data for age, sex, neurologic deficits on presentation, GCS, presence of cervical spine injury, skull fractures, facial fractures, rib fractures and intracranial hemorrhage were recorded. Also, we reviewed the type of motor vehicle collision, driver or passenger, type of restraint and presence of seatbelt sign. ROC analysis was performed to assess the utility of seatbelt sign as a predictor of having an abnormal CTA.

Results

Presence of a seatbelt sign provided very little predictive utility with area under the ROC curve (AUC) of 0.29 (95% CI: 0.23-0.36), sensitivity=0.21 (0.11-0.34), specificity=0.37 (0.30-0.45), positive predictive value PPV=0.11 (0.06-0.18), and negative predictive value NPV=0.58 (0.48-0.67). Surprisingly, the presence of a seatbelt sign was associated with over 5 times the odds of having a normal CTA, even after adjusting for GCS (OR=5.11 (2.38-11.0) p<0.001). Results were similar for isolated seatbelt sign (seatbelt sign with no other injuries), AUC=0.26 (0.21-0.32), sensitivity=0.06 (0.01-0.17), specificity=0.46 (0.37-0.55), PPV=0.04 (0.01-0.11), NPV=0.58 (0.48-0.67), OR=14.0 (3.93-50.1) p<0.001.

Conclusions

Presence of the "seatbelt sign" should not be used as an indication for craniocervical CTA in asymptomatic patients after MVC.

eP-12

Local Variance of Diffusion-tensor Imaging to Assess Multi-focal Disease in Individuals

A Hentel¹, S Niogi¹, I Kovanlikaya¹

¹*Weill Cornell Medical Collage, New York, NY*

Purpose

Traumatic axonal injury and focal areas of demyelination are typically under appreciated on conventional magnetic resonance imaging and computed tomography. While diffusion tensor imaging (DTI) is more sensitive to white matter microstructural changes and, therefore, can be used to detect and better quantify the extent of white matter injuries, there are practical challenges to the use of DTI in individuals. Common metrics used as proxies for integrity such as fractional anisotropy (FA) and mean diffusivity

Electronic Posters

(MD) are sensitive to acquisition sequence parameters and hardware necessitating the need for large normative databases for comparison acquired with identical sequence parameters and hardware. Unfortunately, obtaining a large normative database is impractical especially given frequent advances in scanner software and hardware. This paper proposes a new metric to assess DTI that may be relatively insensitive to sequence parameters and scanner hardware, but may be able to identify focal or multifocal changes to white matter.

Materials and Methods

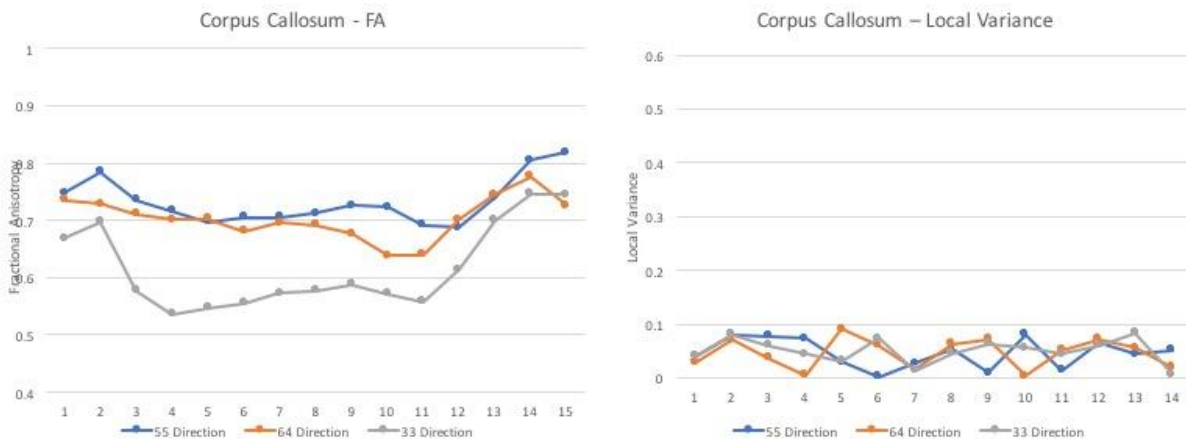
A total of 40 normal healthy adults participated in the study (23 male, 17 female; mean= 40 years; S.D. = 17 years) who underwent scanning on up to three scanners from different vendors (GE and Siemens) and field strength (1.5 Tesla and 3.0 Tesla) running a DTI sequence with varying sequence parameters (alterations in slice thickness, number of gradient directions, and matrix size). Conventional quantitative region of interest (ROI) analysis was completed by measuring fractional anisotropy (FA) of 61 cross-sectional ROIs within 6 white matter tracts (corpus callosum, corticospinal tract, cingulum bundle, superior longitudinal fasciculus, anterior corona radiata, and uncinate fasciculus). The data were measured and statistically analyzed for differences based on scanner/sequence type. An alternative local variance measure was computed for each region of interest (ROI) by measuring the in-plane variance of the FA and averaging it with the out-of-plane variance and a similar statistical analysis was performed assessing for differences based on scanner/sequence type.

Results

Conventional quantitative image analysis demonstrated significant ($p < 0.05$) differences of FA measurement among each scanner/sequence group for each white matter tract. However, no statistically significant differences were found for the local variance measure among the three groups for any cross-sectional ROI within the 6 white matter pathways (i.e. $p > 0.05$ for all ROIs). The attached figure, as an example in one tract, demonstrates the variability of FA measurements in the corpus callosum relative to the homogeneity of a local variance measure.

Conclusions

Our results support existing evidence that it is invalid to combine or compare FA from DTI data sets from different scanners and/or sequence parameters. In contradistinction, the local homogeneity measure appears insensitive to these variations suggesting the possibility to use this approach to either combine DTI data across vendors and sequence types or interpret individual DTI data sets to identify focal or multifocal disease without large comparative normative databases or prior DTI scans.



(Filename: TCT_eP-12_ASNR_graphic.jpg)

eP-18

Longitudinal Quantitative Relationship Between DWI and DTI Parameters in Glioblastoma Following Treatment – An Update

Electronic Posters

K Atsina¹, M Alizadeh², F Mohamed¹, R Nikam³, A Flanders¹, K Talekar¹

¹Thomas Jefferson University Hospital, Philadelphia, PA, ²Temple University, Philadelphia, PA, ³³A I duPont Hospital for Children, Wilmington, DE

Purpose

Diffusion-weighted imaging (DWI) and diffusion-tensor imaging (DTI) provide vital information in assessing microstructural changes due to brain pathology. DWI, which is routinely obtained as part of conventional MR techniques, provides image contrast by utilizing differences in the magnitude of water diffusion. DTI, which employs advanced techniques to DWI, additionally provides information on water anisotropy and the orientation of diffusion. These parameters altogether enable assessment of fiber tracts and tissue cellularity that conventional structural imaging fails to achieve. Apparent diffusion coefficient (ADC) maps are routinely generated from DWI maps and are frequently used as a measure of diffusivity. However, mean diffusivity (MD) derived from DTI is more rotationally invariant and in theory may convey a more robust measure of microstructural change than ADC. Preliminary investigations during a phase I trial, which involved the use of an antisense to the insulin-like growth factor type 1 receptor as an integral part of an autologous tumor cell vaccine, indicated that mean water diffusivity (MD) may provide utility in tracking microstructural changes that may indicate pseudoprogression versus true progression in glioblastoma (GBM) patients. The purpose of this study is to compare DWI (i.e. ADC) with the DTI scalars, including MD, axial diffusivity (AD), radial diffusivity (RD) and fractional anisotropy (FA) in a cohort of GBM patients treated with an immunotherapy regimen at several temporal time points.

Materials and Methods

As part of a phase I-II immunotherapy trial at a single institution, DWI and DTI were acquired using a 3.0T Phillips Achieva scanner in 9 patients (age: 35 - 69) with glioblastoma (GBM). All patients were followed with MR imaging at interval time points for at least 1 year following surgery and immunotherapy as follows: Acute (T < 3 months), Intermediate (T = 3-6 months), and Chronic (T > 6 months). MD, FA, AD and RD maps were computed from raw DTI data with scan specific gradient table and image orientation information, and subsequently preprocessed for magnetic field inhomogeneities and motion induced artifacts using FSL. These DTI maps were coregistered with conventional ADC maps generated from DWI using SPM12. DWI-ADC and DTI indices were calculated by using manually drawn ROIs of suspected area of residual or recurrent tumor in the case of postoperative studies, on fluid attenuated inversion recovery (FLAIR) and contrast enhanced T1 maps coregistered to the same MNI space of the corresponding ADC map.

Results

A very weak or weak positive correlation (Pearson's correlation coefficient) was seen between ADC and three DTI maps (MD, AD, RD) amongst the patients at T < 3 months, whereas strong and moderate positive correlations were seen at T = 3 - 6 months and T > 6 months respectively (see Table 1). Conversely, correlations between ADC and FA were negative and found to be either moderate or strong (see Table 1). Higher coefficient of variance was generally observed in all time frames for ADC (18-30%) and FA values (16-23%), than for MD (11-14%), RD (12-15%), and AD (10-12%) (see Table 2). The ADC value and the DTI indices (MD, AD and RD) were compared between the three time frames (i.e. acute, intermediate and chronic phases) using a one-way ANOVA. Statistically significant increases were seen in AD (p = 0.03) and MD (p = 0.05) between the acute and chronic phases.

Conclusions

Our studies suggest that DTI scalars such as MD, AD and RD are more robust measures of diffusivity compared to ADC and FA as indicated by the lower CV scores in this study population. Additionally, AD and MD are more sensitive at detecting changes in the tissue microenvironment as early as 6 months after initial treatment period. The correlations between mean values for ADC-MD, ADC-AD, and ADC-RD are very weak or weak in the early post-treatment period but improve with time, whereas ADC-FA correlations remain moderate to strong with time. These findings suggest that DTI scalars may be used to tract subtle changes in tissue microenvironment in this given post-treatment setting.

Table 1: Correlation between ADC and DTI scalars (MD, AD, RD)

Time period after therapy (in months)	< 3 months	3-6 months	>6 months
ADC vs MD	0.19	0.77	0.57
ADC vs FA	-0.52	-0.77	-0.68
ADC vs AD	0.08	0.73	0.51
ADC vs RD	0.24	0.78	0.60

Table 2: Mean ADC and DTI scalars (MD, AD, RD, FA) and Coefficients of Variance (CV)

Time period (after therapy)	< 3 months	3-6 months	>6 months
mADC (CV)	1243 (18%)	1432 (30%)	1429 (23%)
mMD (CV)	1269 (14%)	1306 (15%)	1437 (11%)
mFA (CV)	0.19 (23%)	0.19 (19%)	0.17 (16%)
mAD (CV)	1479 (11%)	1526 (12%)	1655 (10%)
mRD (CV)	1163 (15%)	1195 (16%)	1327 (12%)

Table 3: Statistical significance as determined by P<0.05 comparing ADC and DTI scalars amongst different timeframes.

P-Value	ADC	MD	FA	AD	RD
<3m vs 3-6m	0.27	0.17	0.78	0.58	0.72
<3m vs >6m	0.17	0.05	0.28	0.03	0.72
3-6m vs >6m	0.98	0.15	0.366	0.14	0.15

(Filename: TCT_eP-18_ASNRtables.jpg)

eP-35

Management of Small Intracranial Aneurysms: Single Center Experience

L Tu¹, K Seifert², X Wu¹, D Ghandi³, A Malhotra²

¹Yale University School of Medicine, New Haven, CT, ²Yale New Haven Hospital, New Haven, CT, ³University of Maryland School of Medicine, Baltimore, MD

Purpose

Unruptured intracranial aneurysms (UIAs) are relatively common. The majority are small (<7mm). The natural history of small aneurysms is not well known and there is high selection bias in literature. The modality, frequency, and duration of follow-up surveillance imaging are not clearly established. We determine the follow-up and outcome of small (<5 mm) intracranial aneurysms at our institution over the last 15 years.

Materials and Methods

Retrospective review of institutional cases was performed for small (<5mm) UIAs, revealing approximately 450 patients. Pertinent patient and aneurysm-specific data were collected. Subgroup analysis of <3 and 3-5 mm aneurysms was performed. Number of treated aneurysms, reason and method for treatment were noted, as well as follow-up after treatment. For patients undergoing surveillance modality, frequency and duration of follow-up were noted, as well as growth and rupture rates.

Results

Preliminary results indicate a low rate of growth and rupture for UIAs, especially when <3mm. Follow-up imaging is heterogeneous in frequency, duration, and modality. There is poor correlation between growth and rupture rate of small aneurysms.

Conclusions

Imaging surveillance of UIAs is performed frequently - the frequency and duration are not well defined as the natural history is not well known. The growth and rupture rate show relatively poor correlation in small aneurysms.

eP-66

Morphometric Brain Analysis in Retired Soccer Players Exposed to Long-term Mild Traumatic Brain Injuries: A Preliminary Study

M Aranha¹, K Chaim¹, C Carneiro¹, B Pastorello¹, R Anghinah¹, J Ianof¹, A Coutinho¹, C Leite¹

¹*University of São Paulo, São Paulo, Brazil*

Purpose

Chronic traumatic encephalopathy (CTE) can result from exposure to minor traumatic brain injuries, leading to cognitive decline and being presumably related to a progressive tauopathy (1,2) or a disturbance on TDP 43 (3). This condition is mostly described in boxers (4) and football players. Although soccer players are exposed to minor head traumas (mild traumatic brain injury - mTBI) for probably longer periods, the prevalence and effects of CTE on these athletes remains elusive. The purpose of this study is to evaluate the grey matter volume and cortical thickness of retired soccer players' brains, compared to age-matched healthy controls, using voxel-based and surface-based morphometry, respectively.

Materials and Methods

Fifteen retired professional soccer players and 22 age-matched retired healthy controls were included in this preliminary study. Brain magnetic resonance imaging (MRI) with volumetric T1 (3-DT1) sequence was performed in our 3T PET/MR scanner (SIGNA, GE Healthcare) or our 3T MR scanner (Achieva, Phillips Healthcare). Three-DT1 sequences were then processed with the Statistical Parametric Mapping software (SPM8) and FreeSurfer for assessment of gray matter volume and cortical thickness, respectively, and also for statistical analysis (two-sample t-tests).

Results

Voxel-based morphometry analysis revealed statistically significant grey matter volume reduction right orbital gyrus, right precentral gyrus, left middle occipital gyrus, left lingual gyrus, left cuneus, left inferior frontal gyrus and left parahippocampal gyrus ($p < 0.05$, corrected for multiple comparisons - Bonferroni) of soccer players when compared to controls. Surface-based morphometry revealed reduction of cortical thickness in left postcentral gyrus, left rostral middle frontal gyrus, left pars opercularis of frontal lobe and in the right rostral middle frontal gyrus of soccer players when compared to controls, but when corrected for multiple comparisons ($p < 0.05$, FDR), no statistical significant differences were seen between these groups.

Conclusions

Soccer players are exposed to minor head traumas long periods and the effects of mTBI on these athletes remain unclear. This study aims to explore long-term changes on morphometric brain parameters related to mTBI. The results of grey matter volume presented here are in accordance with works in the literature reporting effects of mTBI in football players, fighters or subjects exposed to isolated mTBI event (5). The lack of statistical significance observed in differences of cortical thickness might be due to a small number of subjects. To our knowledge, this is the first study analyzing long-term effects of mTBI in soccer players. This is an ongoing study and we present here its preliminary results.

eP-67c

MRI Assessment of Transverse Sinus Dimensions in Patients with Idiopathic Intracranial Hypertension

J Carlton¹, K Wang¹, K Sweetwood¹, J Schmidgall¹, S Chen¹, C Lincoln¹, T Uribe¹

¹*Baylor College of Medicine, Houston, TX*

Purpose

The use of transverse sinus stenting in treating idiopathic intracranial hypertension (IIH) suggests sinus stenosis may be contributory to the pathogenesis of IIH. We aimed to compare the transverse sinus dimensions on routine sagittal T2-weighted brain MRI sequences of patients with idiopathic intracranial hypertension (IIH) versus normal controls.

Materials and Methods

Brain MRIs of 28 patients with IIH and 37 normal controls were retrospectively reviewed by two blinded board-certified neuroradiologists. IIH cases were defined as having an elevated opening pressure on lumbar puncture and a clinical diagnosis of IIH. Age-gender matched controls were defined as having no diagnosis of IIH and a normal brain MRI. The neuroradiologists measured the AP and CC dimensions of each patient's bilateral transverse sinuses at the narrowest cross-section on sagittal T2-weighted sequences. Mann-Whitney rank-sum test was used to compare sinus dimensions between IIH patients and controls. Receiver operator curve analysis was used to assess discriminatory power of AP and CC sinus dimensions in differentiating IIH patients and controls. Intraclass correlation coefficients (ICC) were used to assess interrater agreement. A p-value <0.05 was considered statistically significant.

Results

No significant differences were found in CC or AP dimension between IIH and controls on either the left or right transverse sinus when measured on sagittal imaging (p=0.23-0.92). CC and AP dimensions were poor discriminators in differentiating healthy controls and IIH patients (area under curve of 0.41-0.55). There was substantial inter-rater agreement (ICC 0.70-0.82) in the sagittal measurements between the two blinded readers.

Conclusions

Transverse sinus dimensions as measured on T2 sagittal brain MRI sequences are not a reliable tool in aiding with diagnosis or discriminating IIH patients. Interobserver agreement of transverse sinus dimensions on sagittal T2 weight MRI is strong.

eP-38

MRI Predictors for the Detection of Brain Invasion, a New Criterion for the Diagnosis of Grade II Atypical Meningioma in Accordance to the 2016 Revised WHO Classification of CNS Tumors

T Ong¹, A Lin², A Bharatha²

¹*University of Toronto, Toronto, Ontario, Canada,* ²*St. Michael's Hospital, University of Toronto, Toronto, Ontario, Canada*

Purpose

As per the 2016 revision of WHO classification of CNS tumors, brain invasion constitutes a histological criterion that suffices by itself to upstage the classification of meningioma to WHO grade II, atypical meningioma. The aim of the study is to determine MR imaging characteristics which could accurately predict brain invasion, consequently impacting tumor grading, patient prognosis and clinical therapy.

Materials and Methods

We retrospectively reviewed 100 preoperative MRI from patients who underwent surgery for resection of meningioma. Histopathologic diagnosis was obtained on specimen. We divided the patients into two

groups according to the histopathologic diagnosis of brain invasion (60 patients) or no brain invasion (40 patients). Histopathologic diagnosis was performed by an experienced neuropathologist mentioning the presence or absence of brain invasion within the specimen. The conventional MR images were evaluated for tumor location, diameter size, contour morphology, perilesional edema, frank brain invasion, peritumoral cleft, tumoral cyst, vascular invasion, bone invasion, surrounding brain parenchymal enhancement, presence or absence of additional meningeal, dural, pial, cortical feeding vessels. Multivariate logistic regression was performed to determine the predictors of histopathologic brain invasion. P-value of less than 0.05 was considered statistically significant.

Results

Volume of peritumoral edema was statistically higher in the brain-invasive meningioma group compared to the non-brain-invasive group (120.81 ± 103.50 cm³ vs 77.3 ± 74.0 , $p=0.02$). The presence of a complete peritumoral cleft was found in 0 (0%) brain invasive meningioma versus 3 (0.8%) non-brain-invasive meningiomas, ($p=0.01$). A complete peritumoral cleft and the presence of meningeal supply alone (OR 3.47, 95%CI 1.42 - 8.49, $p=0.006$) were two independent predictors associated with histopathologic absence of brain invasion. Irregular tumor margins, adjacent brain parenchymal enhancement, peritumoral cyst, dural sinus invasion, bone invasion, hyperostosis, age, and gender, were not significantly different between the two groups.

Conclusions

Through expert opinion, a complete perilesional CSF cleft and the presence of dural supply alone are two independent predictors for the absence of brain invasion in meningiomas. Increased volume of perilesional edema trends towards the presence of brain invasion.

eP-14

MRS Correlates with Beta-amyloid and Tau in CSF

T Tran¹, K Chu¹, K Wei¹, A Fonteh¹, M Harrington¹, K King¹

¹Huntington Medical Research Institutes, Pasadena, CA

Purpose

Alzheimer's disease (AD) is the most common type of dementia and risk factors increase with age. A hallmark of AD is accumulation of amyloid plaques and neurofibrillary tangles (1). MR spectroscopy (MRS) allows us to identify changes in brain chemistry and has been shown to be a sensitive marker for AD diagnosis (2). In recent years, attention has shifted to volume measurements of regions such as the hippocampus to identify evidence of AD but these may not be sensitive markers of preclinical disease. Our study evaluated the diagnostic utility of quantitative MRI and MRS in identifying AD-specific disease pathology (amyloid and tau) in a community based study on nondemented individuals.

Materials and Methods

Forty-seven nondemented subjects (age 65-95) gave their informed consent to participate in the study. All subjects were examined on GE 1.5T clinical scanners and also underwent lumbar punctures for cerebrospinal fluid (CSF) withdrawal (25ml) for evaluation of beta-amyloid and tau. Point-resolved spectroscopy (PRESS) was employed at short TE (35ms) to obtain MRS in the posterior grey matter (PGM) region. MRS data was analyzed using LC Model (Provencher, 2001), hippocampal volume was analyzed using FreeSurfer and JMP was used for statistical analysis.

Results

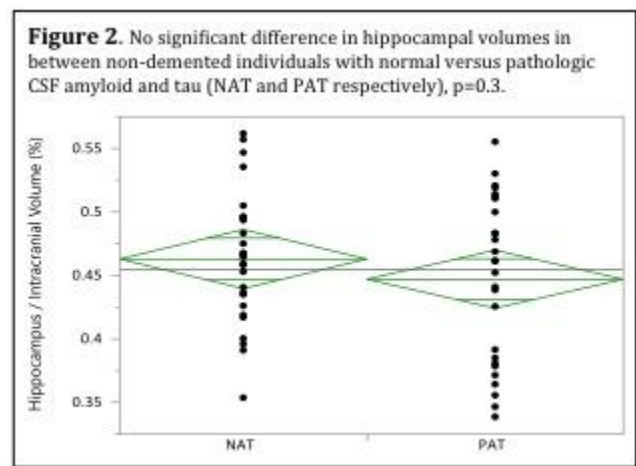
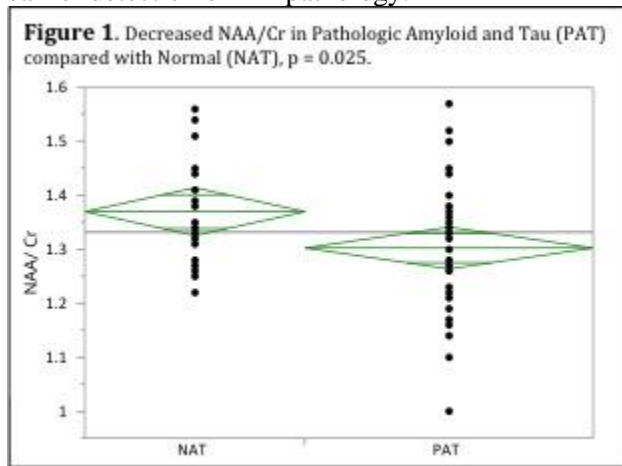
Abnormal amyloid and tau (PAT) are correlated with abnormal NAA/Cr ($p=.04$ and $p=.02$, respectively) (Figure 1). However, hippocampal volume does not differentiate between normal and pathological amyloid and tau (Figure 2).

Conclusions

NAA, an indicator of neuronal integrity, is a useful marker of early pathologic changes associated with Alzheimer's disease prior to onset of hippocampal atrophy. Low NAA/Cr was seen among nondemented

Electronic Posters

participants with abnormal CSF amyloid and Tau (PAT). Therefore, including MRS in studies allows earlier detection of AD pathology.



(Filename: TCT_eP-14_Figures.jpg)

eP-15

MRS is More Sensitive Than MRI to Assess Brain Impact of HIV Severity

K Chu¹, T Tran¹, K Wei¹, A Sondergaard², P Kumar², E Mogadam², K Shriner², K King¹

¹Huntington Medical Research Institutes, Pasadena, CA, ²Phil Simon Clinic, Pasadena, CA

Purpose

Currently, HIV is effectively suppressed with combination antiretroviral therapy but accelerated brain aging may not be clinically apparent. Most studies in HIV were conducted when Autoimmune Deficiency Syndrome was common, and it is uncertain which markers will allow us to best follow brain health in well-controlled HIV. We evaluate N-acetyl-aspartate (NAA), white matter hyperintensities (WMH), and cortical thickness that we hypothesize will identify robust subclinical markers of brain injury related to CD4 nadir, a marker of HIV severity, as well as age-related differences.

Materials and Methods

Thirty-two HIV-positive patients with chronic infection (ages 26-77), with no known HIV central nervous system manifestations, were examined on GE 3T clinical scanners; short echo time point-resolved spectroscopy was obtained and analyzed with LC Model (1) in the posterior and frontal gray matter, parietal and frontal white matter, and basal ganglia over which NAA/Creatine was normalized and averaged. WMH were quantified using Lesion Segmentation Toolbox in SPM with T2 FLAIR and cortical thickness was derived from Freesurfer T1 reconstruction. The three measures were fitted with both CD4 nadir and age in JMP Pro to observe HIV-related markers of brain impact.

Results

Cortical thickness correlated significantly with both age ($-.013 \pm .0017, p < .0001$) and CD4 nadir ($.00019 \pm .000086, p = .048$). WMH correlated only with age ($.079 \pm .021, p = .0009$) and NAA was only significantly fitted with CD4 nadir ($.00089 \pm .00043, p = .048$).

Conclusions

In patients with effectively suppressed HIV, NAA may be used as a reliable, noninvasive measure to assess impact of initial disease severity while cortical thickness and WMH volume are useful to evaluate changes related to aging.

Table 1: NAA was significant marker of HIV severity by association with CD4 Nadir (p=.048).

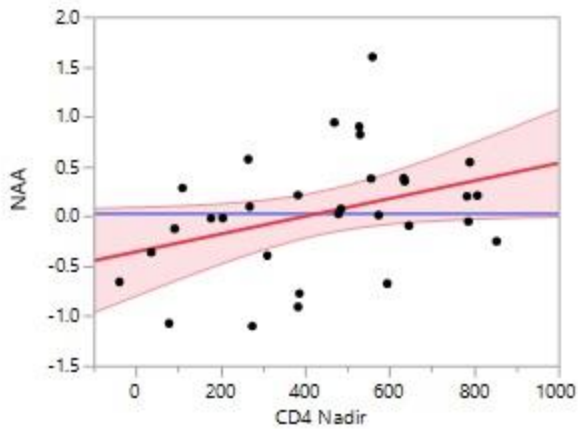


Table 2: WMH shown to be more useful for reflecting brain impact related to aging (p=.0009).

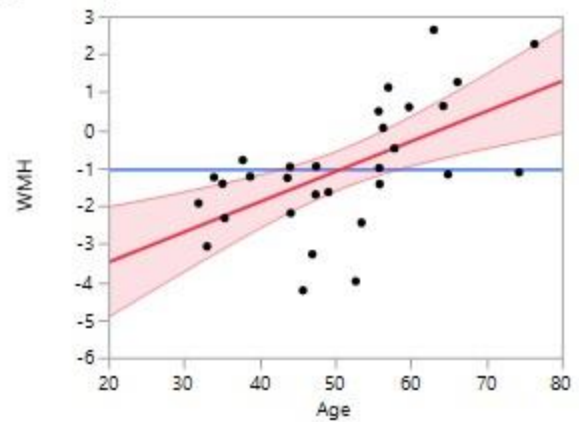
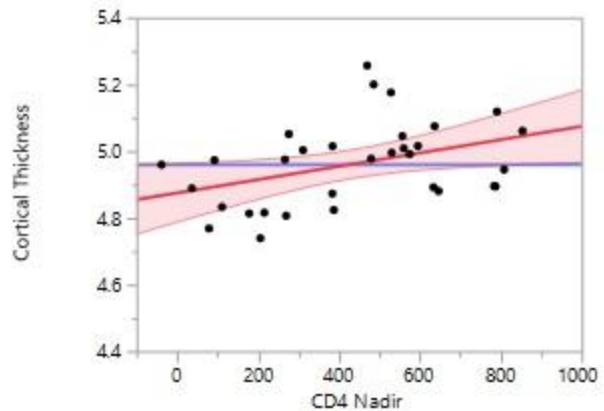
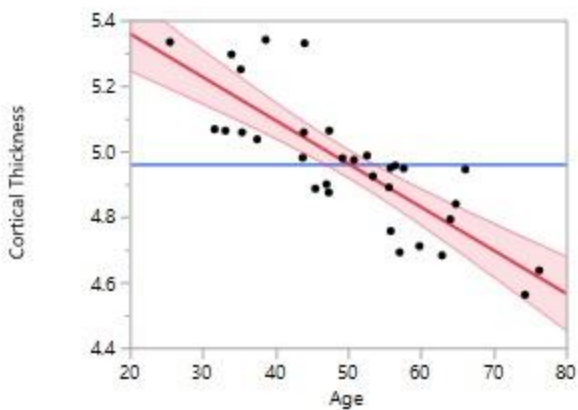


Table 3: Cortical thickness was more impacted by age-related brain changes (p<.0001) rather than HIV severity (p=.048).



(Filename: TCT_eP-15_ASNRAbstract.jpg)

eP-54

Multivariate Analysis of Hemodynamic Stressors on Prediction of Initiation of ICA Intracranial Aneurysms

K Sunderland¹, J Jiang²

¹Michigan Technological University, Houghton, MI, ²Michigan Technical University, Houghton, MI

Purpose

Hemodynamic stressors along the vascular wall and their cardiac cycle changes are thought as useful in predicting the pathological evolution of intracranial aneurysms (IA) [1]. The primary goal of this work is to assess parameters in areas with known eventual IA development and areas lacking IAs, and determine

Electronic Posters

if combining parameters benefits our understanding of the correlation between hemodynamic stressors and IA initiation. To our knowledge, this kind of study has not been done in the past.

Materials and Methods

Based on 3-D DSA data, two groups of vascular geometries were generated: all IAs digitally removed [2] (Model 1), the other with one IA intact (Model 2). In Model 1, preaneurysm geometry was restored using computer modeling, while Model 2 was intended to examine how one IA influences subsequent formation of another closely spaced IA [3]. "Patient-specific" computational fluid dynamic simulations were performed to obtain hemodynamic stressors. Five hemodynamic stressors were investigated among 21 human subjects: aneurysm formation indicator (AFI), oscillatory shear index (OSI), gradient oscillatory number (GON), wall shear stress (WSS), and wall shear stress gradient (WSSG). The occurrence of elevated/lowered parameters was visually assessed within areas of known IA initiation. Additionally, three vessel sections (length equal to vessel diameter) were selected: two proximal to a first aneurysm, and one distal to a last aneurysm (barring proximity to outlet). Sections were divided lengthwise, and parameters assessed, generating six regions (per model) without IAs. Multiple logistic regression determined parameter's impact on IA initiation.

Results

AFI and OSI presence were significantly correlated (0.92, $p < 0.001$), so OSI was excluded from subsequent analysis. WSSG was a significant predictor in both models. AFI improved prediction in Model 1, but not Model 2. GON improved prediction in Model 2. Table 1 shows the overall analysis.

Conclusions

Combining hemodynamic parameters improves the prediction of IA initiation. Future studies will include IAs originated from other locations in the cerebral circulation.

Table 1: Multivariate Odds Ratios of Hemodynamic Assessment Parameters

Variable	Model 1	Model 2
Wall Shear Stress Gradient	1.36 (1.16-1.58)*	1.344 (1.18-1.55)*
Aneurysm Formation Indicator	1.13 (1.01-1.33)*	1.05 (0.91-1.21)
Wall Shear Stress	1.13 (0.97-1.32)	1.10 (0.96-1.26)
Gradient Oscillatory Number	1.04 (0.87-1.23)	1.17 (1.01-1.36)*

Odds Ratios for hemodynamic assessment parameters. Numbers in parentheses indicate 95% confidence interval. Model 1) No aneurysms present. Model 2) One aneurysm present.

* $p < 0.05$

(Filename: TCT_eP-54_ASNJ_Table.JPG)

eP-32

Novel Grading Scheme for Sigmoid Sinus Wall Anomalies in Patients with Venous Pulse Synchronous Tinnitus

J Record¹, D Eisenman¹, R Morales¹, A Steven², M Gharavi¹, A Medina¹, P Raghavan¹

¹University of Maryland Medical Center, Baltimore, MD, ²Ochsner Health System, New Orleans, LA

Purpose

Sigmoid sinus wall anomalies (SSWA) have been implicated in patients with venous pulse synchronous tinnitus (VPST), especially in the setting of idiopathic intracranial hypertension (IIH). We propose a novel grading scheme of SSWA in order to assess correlation with other imaging findings and clinical parameters.

Materials and Methods

Preoperative CT cerebral venograms of 37 patients who underwent sigmoid sinus wall reconstruction for

VPST were reviewed. Four grades of SSWA (9 subgrades) were encountered (table 1). Correlation between grades, body mass index (BMI), and imaging findings supportive of IIH including empty sella and transverse sinus stenosis (TSS) were assessed by linear regressions and differences between groups by Mann-Whitney test.

Results

The mean age of our cohort was 40.5 years (range, 15-70) with a mean BMI of 35.4 kg/m² (range, 17.0-54.2). SSWA were bilateral in 62% of patients. Multifocal dehiscence (grade 2b) was the most common anomaly encountered, occurring in 42% of patients. Notably, 31% of patients demonstrated ectatic appearance of one or both transverse-sigmoid sinus junctions (grade 4, with 25% of patients demonstrating 4b pattern). Of patients 44% had TSS (25% bilateral, 8% unilateral right, and 11% unilateral left). Empty sella was present in 28% of patients. Patients with right TSS demonstrated significantly higher grades of ipsilateral SSWA (p<0.01), and were more likely to be right transverse sinus dominant (58%). No significant association was found between left TSS and ipsilateral grade of SSWA, with only 30% demonstrating left dominance. No correlation was found between SSWA grade and presence of an empty sella. No correlation was found between SSWA grade and BMI.

Conclusions

Multifocal sigmoid sinus wall dehiscence is the most common appearance of SSWA. The presence of right TSS positively correlates with higher grade of ipsilateral SSWA. Notably, 31% of patients demonstrated ectasia of the transverse-sigmoid junction with dehiscence, an entity not previously described in the literature. The role of coexisting stenoses in the genesis or progression of SSWA remains unclear. Our proposed grading scheme may provide the basis for future research to better understand the pathogenesis and clinical implications of SSWA.

Table 1.

SSWA Grade	Imaging Criteria
Grade 1	Sigmoid sinus wall (SSW) thin but intact
Grade 2a	Single SSW dehiscence
Grade 2b	More than one dehiscence
Grade 3a	Sessile diverticulum
Grade 3b	Pedunculated diverticulum
Grade 3c	Multilobulated diverticulum
Grade 4a	Transverse-sigmoid sinus junction (TSSJE) without dehiscence
Grade 4b	TSSJE with dehiscence
Grade 4c	TSSJE with superimposed diverticulum

(Filename: TCT_eP-32_Table1.jpg)

eP-37

O6-Methylguanine-DNA Methyltransferase Promoter Methylation Status in Recurrent Glioblastoma: Correlation Study with DWI and DSC Perfusion MR Imaging Features

H Choi¹, S Choi²

¹Bundang CHA Medical Center, Seongnam-si, Republic of Korea, ²Seoul National University Hospital, Seoul, Republic of Korea

Purpose

To correlate the O6-methylguanine DNA methyltransferase (MGMT) promoter methylation status with DWI and DSC perfusion MRI in the recurrent glioblastomas after standard treatment, which was compared with initial tumors.

Materials and Methods

An institutional review board waiver was obtained for this retrospective study. Between January 2008 and November 2016, forty patients with histologically confirmed recurrent glioblastoma were enrolled, in whom MGMT promoter methylation status were available. Patients were divided into three groups; unchanged MGMT promoter methylation status as methylation (Group MM, n = 13) and unmethylation (Group UU, n = 18), and changed MGMT promoter methylation status from methylation to unmethylation (Group MU, n = 9). Normalized apparent diffusion coefficient (nADC), and normalized relative cerebral blood volume (nrCBV) values were obtained from the both enhancing portion and nonenhancing T2 hyperintense region (NER), of which histogram parameters were calculated. For multiple comparison, ANOVA and Kruskal-Wallis test followed by posthoc test were performed to compare histogram parameters among three groups. T-test, Mann-Whitney U test and multivariable stepwise logistic regression were used to compare parameters between two groups; group MM and group MU. The Kaplan-Meier method was used to estimate survival probabilities. Univariable Cox models were used to assess the impact of imaging and clinical features and on survival.

Results

Group MU showed significantly higher mean, median, the 90th and 95th percentile of cumulative nrCBV values of NER of the initial tumor compared with group MM and group UU (all $P < .05$). Median nrCBV value of NER of the initial tumor was the most excellent predictor for methylation status change ($P < .001$), with a sensitivity of 100%, specificity of 77% at a cutoff value of 1.415. Cox proportional hazards modeling revealed the ratio [nADC_{recurrent}/nADC_{initial}] of the 5th percentile nADC value (hazard ratio, 0.163, 95% CI, 0.053 – 0.503, $P = .002$) of the enhancing portion and the 2nd preoperative KPS (hazard ratio, 0.956, 0.926 – 0.986, $P = .005$) were independent prognostic factors for longer overall survival.

Conclusions

DWI and DSC perfusion MRI may help to predict MGMT methylation status change in the recurrent glioblastoma after treatment, especially from the NER of the initial tumor. Additionally, independent to MGMT methylation status, the 5th percentile of ADC ratio in the enhancing portion and the 2nd preoperative KPS are independent prognostic factors for longer overall survival.

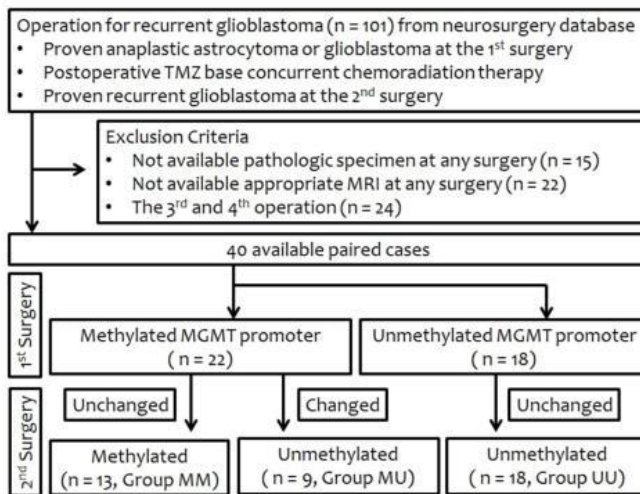


Figure 1: Flowchart shows selection of study population.

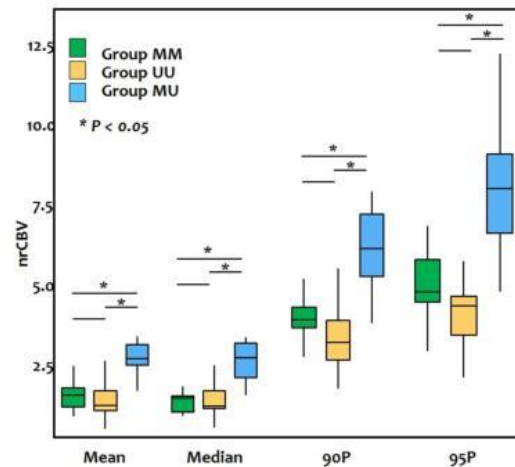


Figure 2. The MU (change of MGMT methylation Status from Methylation to Unmethylation) group showed significantly higher nrCBV values in the Initial non-enhancing FLAIR high SI portion of the Tumors.

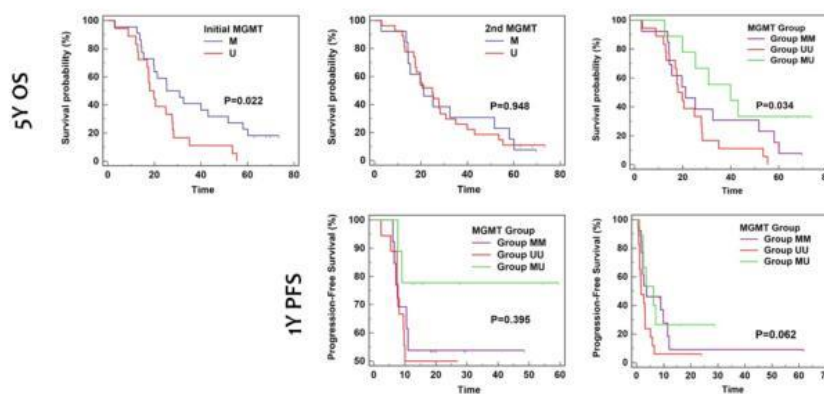


Figure 3. The initial MGMT promoter methylation group showed significantly longer survival than unmethylation group. However, There was no significant difference between two groups, confirmed in the second operation. Among the three groups, the MU group demonstrated longer survival than group UU. There were no significant difference in the 1st and 2nd progression free survival among three groups.

(Filename: TCT_eP-37_figuresasnr.jpg)

eP-39

Perfusion MRI and Diffusion MRI Identify Oligodendroglioma Defined by the 2016 WHO Classification for Brain Tumors: Histogram Analysis Approach

A Latysheva¹, K Emblem¹, A Server¹, J Hald¹

¹Oslo University Hospital - Rikshospitalet, Oslo, Norway

Purpose

The purpose of our study was to assess the value of perfusion and diffusion MRI to characterize oligodendrogliomas and to distinguish them from astrocytomas.

Electronic Posters

Materials and Methods

Seventy-one adult patients with untreated WHO grade II and grade III diffuse infiltrating gliomas and known 1p/19q codeletion status were retrospectively identified and analyzed using relative cerebral blood volume (rCBV) and apparent diffusion coefficient (ADC) maps based on whole-tumor volume histograms. (3, 4) The Mann-Whitney U test and logistic regression were used to assess the ability of rCBV and ADC to differentiate between oligodendroglioma and astrocytoma both independently, but also related to the histopathologic WHO grade. The diagnostic performance was analyzed by the receiver operating characteristic curve (ROC) and optimal cutoff points based upon the Youden index were estimated.

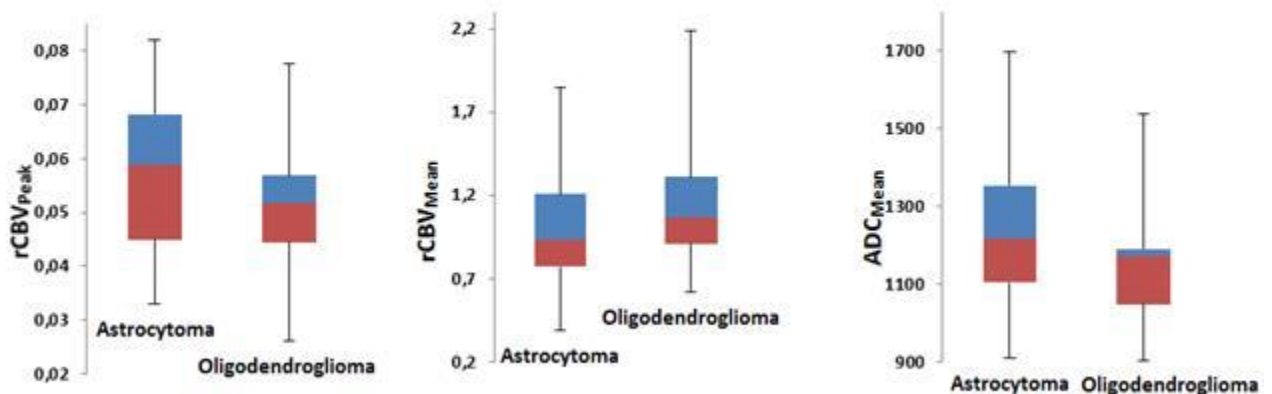
Results

Oligodendrogliomas showed significantly higher microvasculature (higher rCBV_{Mean} ≥ 0.80 , $p=0.003$) and higher vascular heterogeneity (lower rCBV_{Peak} ≤ 0.044 , $p=0.003$) than astrocytomas. Diffuse gliomas with higher cellular density (lower ADC_{Mean} $\leq 1094 \times 10^{-6} \text{mm}^2/\text{s}$, $p=0.009$) were more likely to be oligodendrogliomas than astrocytomas. Histogram analysis of rCBV and ADC were able to differentiate between diffuse astrocytoma (WHO grade II) and anaplastic astrocytoma (WHO grade III), but not between oligodendroglioma (WHO grade II) and anaplastic oligodendroglioma (WHO grade III).

Conclusions

Histogram derived rCBV and ADC parameter may be used as biomarkers for identification of oligodendrogliomas and may help characterize diffuse gliomas based upon their genetic characteristics.

Figure 3. Boxplots with distribution range of rCBV_{Peak}, rCBV_{Mean}, ADC_{Mean} values in different subgroups of diffuse gliomas.



(Filename: TCT_eP-39_Boxplots.jpg)

eP-41

Permeability Surface Area Product (PS) Using Ultra-low kV (70kV) Perfusion Computed Tomography (PCT) in Differentiation of Treatment-induced Necrosis (TIN) from Tumor Recurrence (TR) in Patients Treated for High-grade Glioma

A Garg¹, S Shambanduram¹, L Joseph¹, A Suri¹, V Suri¹

¹All India Institute of Medical Sciences, New Delhi, India

Purpose

Differentiation of treatment-induced necrosis (TIN) from tumor recurrence (TR) in patients treated for

Electronic Posters

high-grade glioma (HGG) is a great challenge in neuro-oncology imaging. The purpose of our study is to determine the role of ultra-low-kV (70kV) perfusion CT scan parameters in differentiation of the two entities.

Materials and Methods

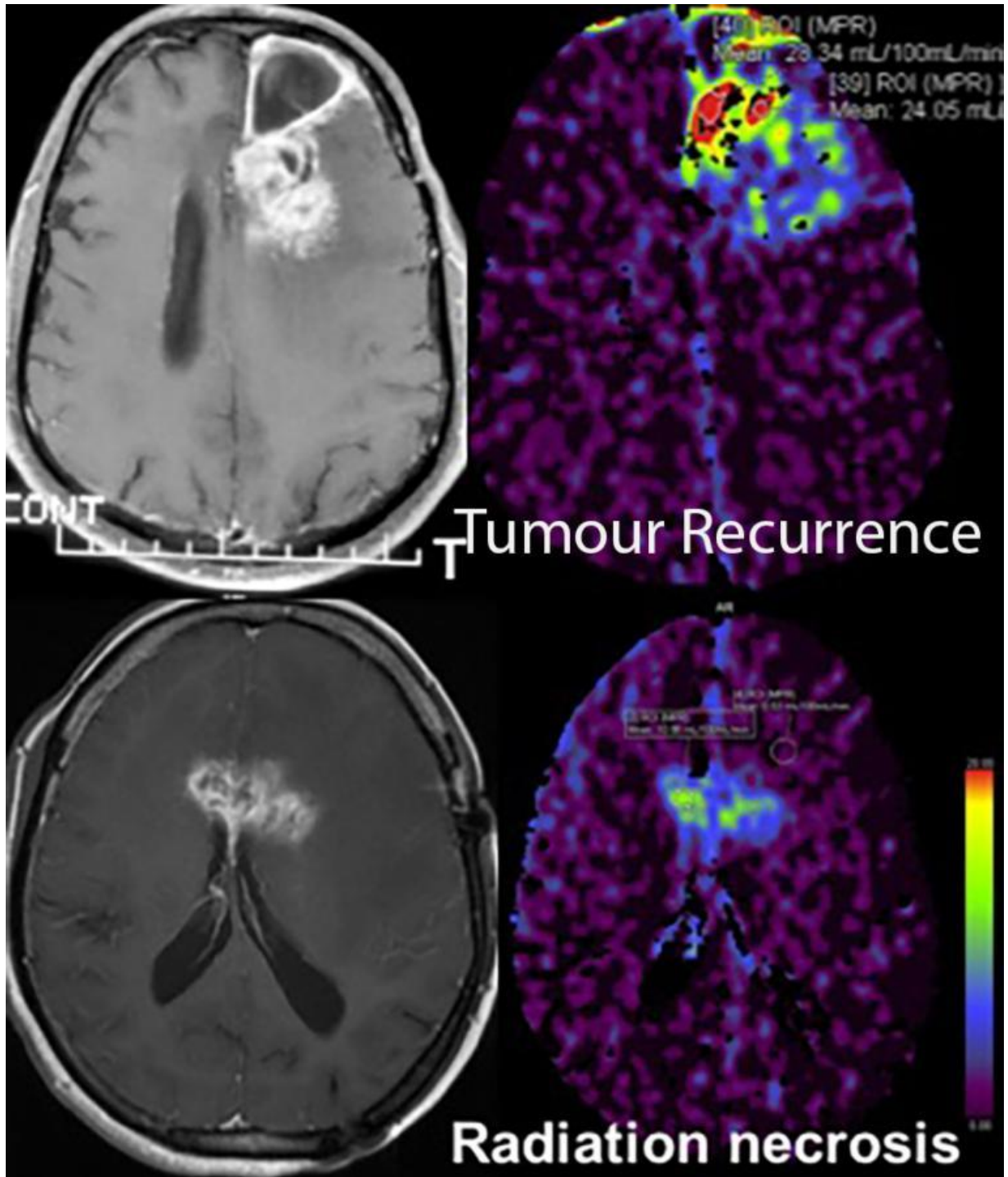
PCT using ultra-low kV (70kV) was done during follow-up period in 33 patients who were treated for high-grade glioma (HGG). From the perfusion parameter maps of CBV, CBF, MTT, TTmax, TTdrain and PS, values from three ROIs drawn in the area of enhancing lesions were analyzed statistically for those with TIN or TR.

Results

Of the total, 25 patients were included for statistical analysis. TR showed significantly higher mean values of CBV, CBF and PS compared to TIN (PS: 20.63 ± 4.7 vs 9.76 ± 2.93 ml/100gm/min, p value 0.00; CBV: 7.97 ± 2.03 vs. $4.41 \pm$ ml/100gm, p value 0.00; and CBF: 75.67 ± 16.51 vs. 47.80 ± 12.26 ml/100gm/min, p value 0.00). For calculating the sensitivity and specificity, the lower limit of 95% confidence interval was taken as the threshold. PS showed the highest accuracy with sensitivity (87.5%) and specificity (100%) and positive predictive value of 95.1% while CBV and CBF revealed 56.2%, 88.9%, 94.4% and 75%, 100%, 93.1% respectively to differentiate TR from TIN.

Conclusions

Vascular permeability calculated as PS using PCT has the highest accuracy in differentiation of TR from TIN in patients who underwent standard treatment for high-grade glioma. PCT with multiple perfusion parameters can be used as a tool to differentiate TR from TIN.



(Filename: TCT_eP-41_Picture1.jpg)

eP-52

Potential Role of MR Fibrography for the Assessment of White Matter Integrity in Acute Ischemic Stroke

V Andreu¹, O Sakai¹, M Chapman¹, M Horn¹, H Jara¹

Electronic Posters

¹*Boston Medical Center, Boston University School of Medicine, Boston, MA*

Purpose

White-matter fibrography (WMF) is a recently developed imaging technique based on Synthetic MRI with which the global brain wiring of the brain, or connectome, can be rendered in three dimensions at high spatial resolution and with the unrivaled anatomic accuracy of the turbo spin echo (TSE) pulse sequence. WMF has not yet been tested in the context of diseases that can alter WM integrity, such as infarct. The purpose of this pilot study was to assess the integrity of WM regions of patients with acute infarct.

Materials and Methods

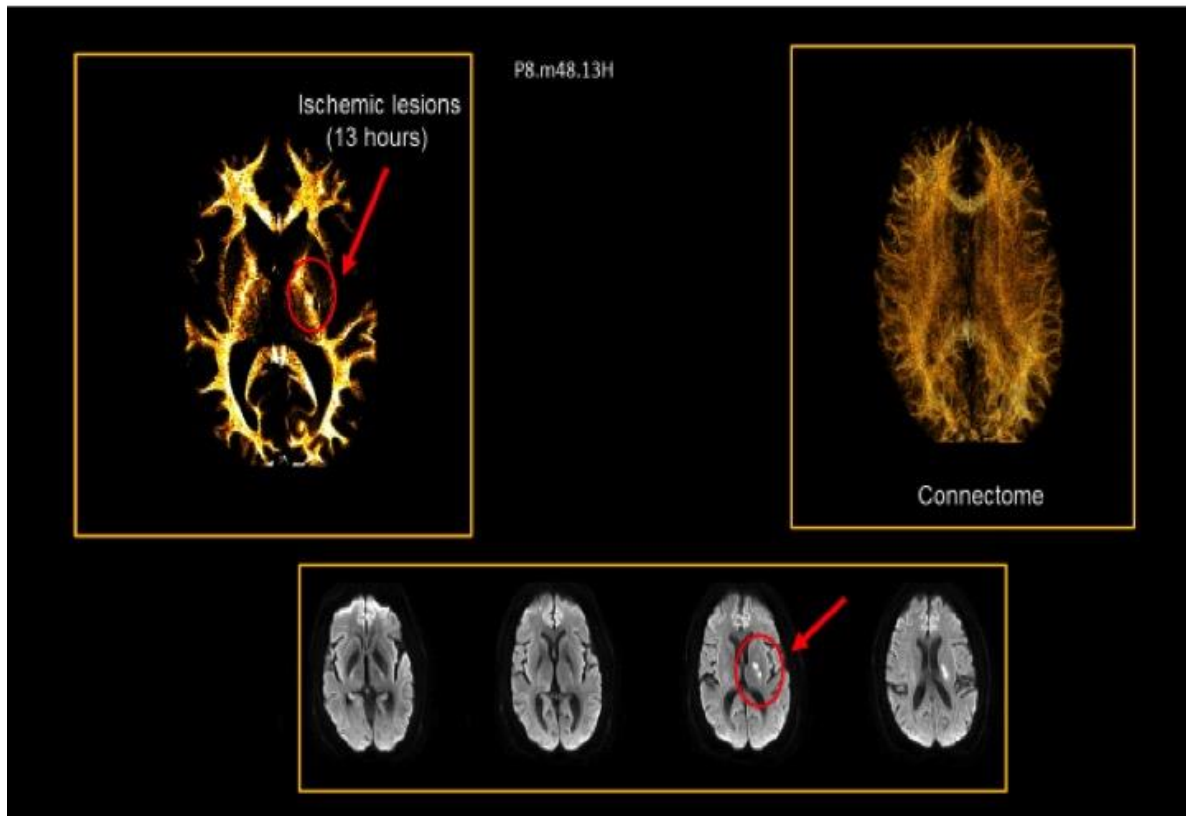
In this IRB approved retrospective study, the Tri-TSE 3T-MRI scans of 15 patients with acute infarct were processed with a synthetic-MRI program that allows for creating weighted images of the four principal qMRI parameters: proton-density (PD), correlation time diffusion coefficient (Dct), T1, and T2. Imaging parameters: 36 contiguous slices, voxel=0.5 x 0.5 x 5 mm³, TRs=475&3500ms, TEs=10&90ms. Areas of acute infarcts were first identified as hyperintensities on diffusion-weighted images and then compared to the raw images of the heavily 1/T1 weighted synthetic images of the connectome.

Results

The connectomes of 10 patients were successfully generated and 5 patients were excluded due to severe motion artifacts. In the 10 included patients, partial or complete loss of WM fibers was observed within the core of the infarct matching the DWI signal abnormality (Figure). For large infarcted territories, partial WM fiber losses were observed.

Conclusions

Using WMF, we were able to demonstrate white matter fiber loss as well as partial damage in ten patients with acute infarct. This early work may have direct treatment decision implications for management in stroke patients.



(Filename: TCT_eP-52_Diapositiva1.jpg)

eP-42

Preoperative MRI Predictors of Hormonal Remission after Pituitary Adenoma Resection

M Braileanu¹, R Hu¹, M Hoch¹, M Mullins¹, A Ioachimescu¹, N Oyesiku², A Pappy¹, A Saindane¹
¹Emory University Hospital, Atlanta, GA, ²Emory University, Atlanta, GA

Purpose

There is limited literature on the use of FIESTA and VIBE for the assessment of postoperative outcomes following pituitary adenoma resection. (1–3) The purpose of this study is to identify imaging predictors of postoperative hormonal remission of functioning pituitary adenomas using conventional and novel MRI sequences.

Materials and Methods

We retrospectively reviewed charts of patients diagnosed with hormonally-active pituitary adenomas who underwent resection at our institution from 2010 to 2016. Patients with preoperative conventional (T1, T2) and novel (FIESTA, VIBE) pituitary MRI sequences were included. Baseline characteristics and postsurgical hormonal outcomes were collected. Three blinded raters independently reviewed randomized coronal postcontrast T1, T2, FIESTA, and VIBE sequences for traditionally assessed adenoma characteristics such as degrees of ICA contact, and Knosp grade.⁴ Intraclass correlation (ICC), chi-squared, and Wilcoxon subgroup analysis were performed. The study was approved by the local IRB.

Results

A total of 34 pituitary adenoma patients were included (average age 39.3±12.2; female n=27).

Electronic Posters

Postoperative diagnoses included ACTH secreting tumor (n=16; 47.1%), prolactinoma (n=13, 38.2%), and growth hormone secreting tumor (n=5; 14.7%). All 34 patients had T1, T2, and FIESTA sequences, while 28 had VIBE. ICC ranged from excellent for mass effect on the chiasm on FIESTA (ICC=0.95, 95% [0.92-0.97], $p < 0.001$) to fair for bony invasion on T1 (ICC=0.48, 95% [0.12-0.72], $p = 0.002$). Postoperative hormone remission was observed in 30 patients (n=34; 88.2%). Decreased degrees of ICA contact were associated with hormone remission on all sequences (T1, $p = 0.01$; T2, $p = 0.02$; FIESTA, $p = 0.01$; VIBE, $p = 0.02$). Hormone remission was associated with smaller Knosp score on T1 ($p = 0.005$), FIESTA ($p = 0.009$), and VIBE ($p = 0.01$), but not T2 sequences ($p = 0.15$). Other imaging characteristics examined were not significantly associated with postoperative endocrine remission.

Conclusions

Extent of cavernous sinus invasion as measured by degrees of ICA contact and Knosp score is associated with postoperative endocrine outcomes. Inclusion of novel sequences may augment presurgical planning.

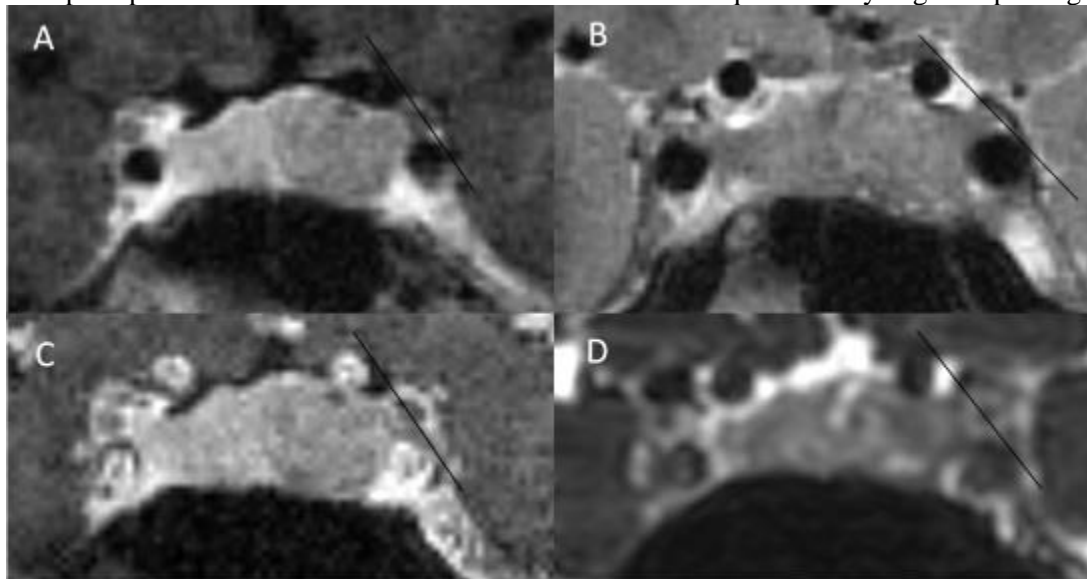


Figure 1: Knosp grade 2 left pituitary prolactinoma that is tangent to the lateral aspects of the intra- and supra-cavernous ICAs (line) on post contrast T1 (A), T2 (B), VIBE (C), and FIESTA (D) sequences. This patient did not have endocrine remission after resection.

(Filename: TCT_eP-42_Figure1-ASNRPituitary.jpg)

eP-40

Primary Intracranial Malignant CNS Neoplasms with Extracranial Osseous Metastasis: Two Original Pathologically Proven Cases

K Patel¹, M Tominna¹, A Wang²

¹Oakland University William Beaumont School of Medicine, Royal Oak, MI, ²Beaumont Health System, Royal Oak, MI

Purpose

Extracranial osseous metastasis of primary malignant intracranial central nervous system neoplasms is extremely rare. We present 2 cases of such metastases. The first case is of a patient with malignant meningioma involving the left frontal lobe who later presented with metastasis to the T7 vertebral body. The second case is of a patient with anaplastic oligodendroglioma involving the right frontotemporal lobe who presented with metastasis to the scapula and later with diffuse metastasis to the spine.

Electronic Posters

Materials and Methods

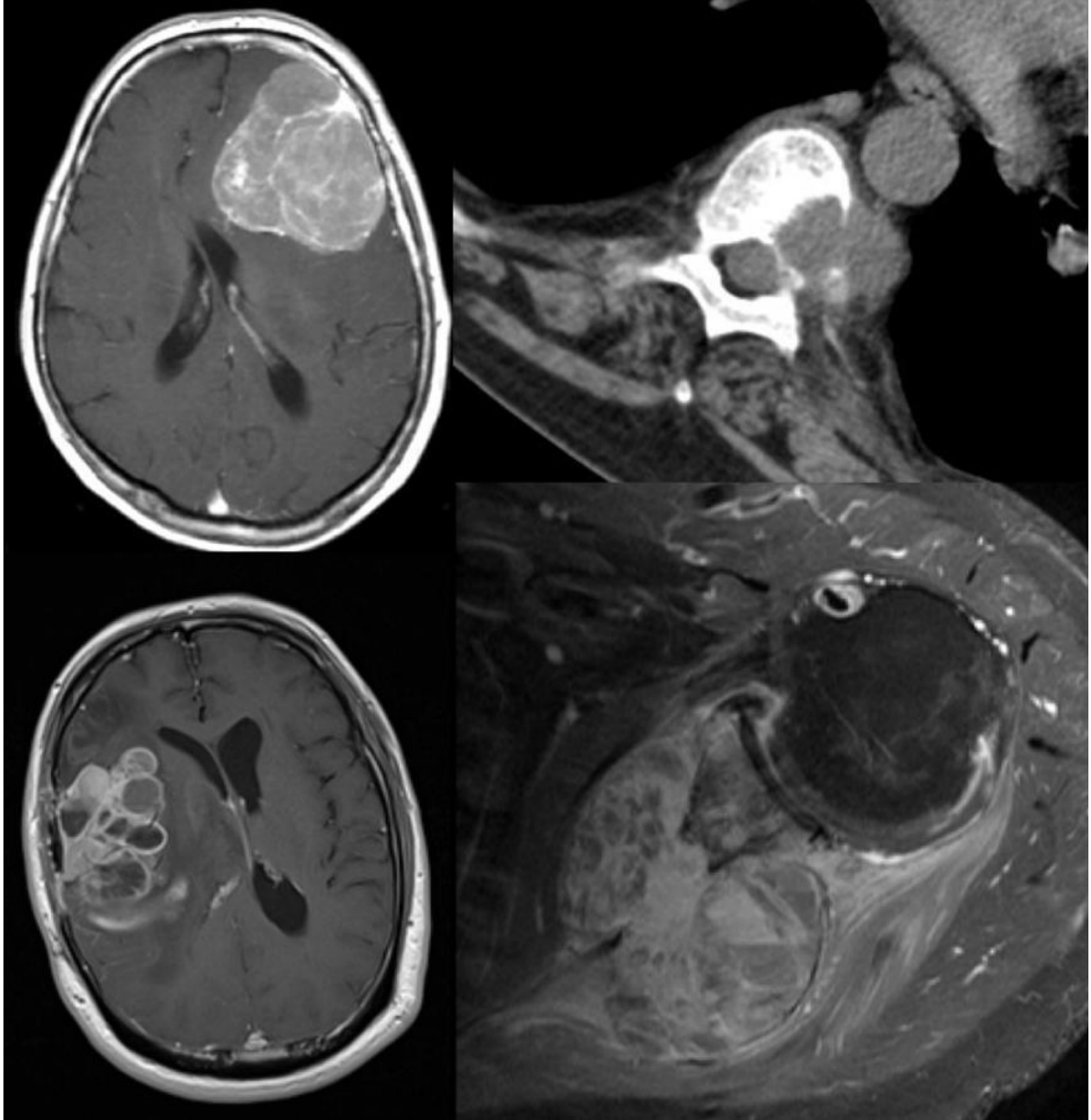
Primary CNS neoplasms rarely metastasize outside the central nervous system. When they do, the lungs and pleura are the most common site of metastasis. Lymph nodes, liver, heart, kidneys, and bones are other sites of spread described in the literature. Extracranial, extra-CNS glioblastoma multiforme (GBM) metastases occur in only about 0.4% to 2.0% of patients with GBM. Extracranial GBM metastases occur most often in the lungs and pleura (60% of patients) but also in the regional lymph nodes (51%), bones (31%), and liver (22%). The reasons why CNS tumors rarely show distant metastases is still not completely understood but many hypotheses have been proposed. It is well known that the blood-brain barrier acts as a barrier to the entry and exit of substances to and from the CNS. Therefore, the tight capillary basement membrane can act as a physical barrier against migration of malignant cells into the bloodstream. In addition, most malignant brain tumors have a poor prognosis with short time of survival after diagnosis which intrinsically reduces the opportunity for distant metastases. For example, GBM (the most common malignant intracranial neoplasm) has a median overall survival of only 14.6 months. Another hypothesized explanation is that the cellular CNS environment prevents the spread of malignant cells because of the lack of extracellular matrix components like collagen and fibronectin overexpressed only in hyperplastic blood vessels. Since extracellular spaces have these glycosaminoglycans, active tumor cells can migrate into the surrounding tissue, but the lack of these substances in the CNS extracellular substrate environment makes hematogenous metastasis to distant organs and viscera rare.

Results

The mechanisms for metastasis outside the CNS are also not well understood but again many theories have been postulated. These include vascular invasion, cranial nerve perineural spread, lymphatic spread, direct invasion, or iatrogenic spread into soft tissue. Given that the most common sites of metastasis are the lungs, liver, and bone, the most common mechanism of metastasis outside the CNS is likely vascular invasion. Surgical damage to the blood-brain barrier has been described as allowing extraneural spread after neurosurgical operation. Tumor cells may have access to the lymphatic or blood circulation through the surgically compromised blood-brain barrier (BBB) and craniotomy with tumor resection is also associated with the opening of brain vessels and consequent spread of tumor cells. In this exhibit, we present 2 original histopathologically proven cases of extracranial osseous metastasis of primary malignant neoplasms. Detailed clinical history will be presented with their clinical presentation, imaging, and pathologic findings. The goal of this exhibit is to illustrate a rare and poorly understood phenomenon of primary CNS tumor metastasis.

Conclusions

In summary, we presented two patients with malignant primary CNS neoplasms who developed distant extracranial osseous metastases. Although the blood-brain barrier and lack of lymphatics reduce the risk of extracranial metastasis of primary malignant CNS neoplasm, risk factors for extraneural metastasis include long survival and iatrogenic procedures. Future studies should aim to better understand the mechanisms of extraneural metastasis. This information could potentially be useful to develop molecular testing with a goal to prospectively provide risk stratification of malignant CNS neoplasms for the development of such metastases on the individual level.



(Filename: TCT_eP-40_Image.jpg)

eP-07

Quantitative Analysis of Cingulate Gyrus Cortical Signal Intensity in Mesial Temporal Sclerosis

S Tumuluru¹, M Parsons¹, A Sharma¹

¹*Mallinckrodt Institute of Radiology, St. Louis, MO*

Purpose

Mesial temporal sclerosis is classically defined as neuronal loss and gliosis in the hippocampus and surrounding structures of the temporal lobe. Additional limbic system structures in the circuit of Papez,

Electronic Posters

such as the mammillary bodies and fornix, can also demonstrate atrophy and gliosis. The purpose of this study was to see if the cingulate gyrus, another component of the circuit of Papez, demonstrates any same-side gliosis in patients with mesial temporal sclerosis.

Materials and Methods

A retrospective, IRB-approved review of brain MRIs of 58 patients with pathology-proven mesial temporal sclerosis from 2012 to 2016 was performed. ROIs were drawn within the cortices of both cingulate gyri and insular cortices at the level of the optic chiasm and within the cortices of both cingulate gyri, insular cortices, and hippocampi at the level of the hypothalamus on coronal T2-weighted sequences. The insular cortices were used as a control as they should not demonstrate any gliosis with mesial temporal sclerosis. The ROIs of the cingulate gyri and insular cortices at each level were analyzed both individually and after averaging together. The statistically significant difference in ROIs between the MTS-side as compared to the non-MTS-side was evaluated with a paired t-test.

Results

The mean (\pm SD) of the ROIs of the MTS-side hippocampus, cingulate gyrus, and insular cortex are 480.28 (\pm 209.86), 427.82 (\pm 190.17), and 443.73 (\pm 192.60) respectively. The mean (\pm SD) of the ROIs of the non-MTS-side hippocampus, cingulate gyrus, and insular cortex are 438.05 (\pm 183.99), 412.39 (\pm 178.65), and 441.91 (\pm 199.81) respectively. The p-value of a statistically significant difference between the ROIs of the hippocampi, cingulate gyri, and insular cortices are 0.0001, 0.0002, and 0.6879 respectively.

Conclusions

The cortex of the cingulate gyrus on the MTS-side demonstrated increased signal intensity that was statistically significant as compared to the non-MTS-side in patients with mesial temporal sclerosis while the insular cortex did not.

Variable	ROI (Mean)	ROI (Std. Dev.)	p-value
Hippocampus (MTS side)	480.28	209.86	0.0001
Hippocampus (non MTS side)	438.05	183.99	
Cingulate gyrus (MTS side)	428.82	190.17	0.002
Cingulate gyrus (non MTS side)	412.39	178.65	
Insular cortex (MTS side)	443.73	192.60	0.6879
Insular cortex (non MTS side)	441.91	199.81	

(Filename: TCT_eP-07_MTSDData.jpg)

eP-57

Reduction of Metallic Coil Artifacts in Cerebral CT Angiography Using a Single Energy Metal Artifact Reduction Technique

M Katsura¹, J Sato¹, M Akahane², T Tajima¹, T Furuta¹, H Mori¹, O Abe¹

¹Graduate School of Medicine, The University of Tokyo, Tokyo, Japan, ²School of Medicine, International University of Health and Welfare, Narita, Chiba, Japan

Purpose

This study aims to evaluate the effect of a novel raw data- and image-based technique for metal artifact

reduction, the single energy metal artifact reduction (SEMAR) algorithm, in cerebral CT angiography after intracranial aneurysm coiling.

Materials and Methods

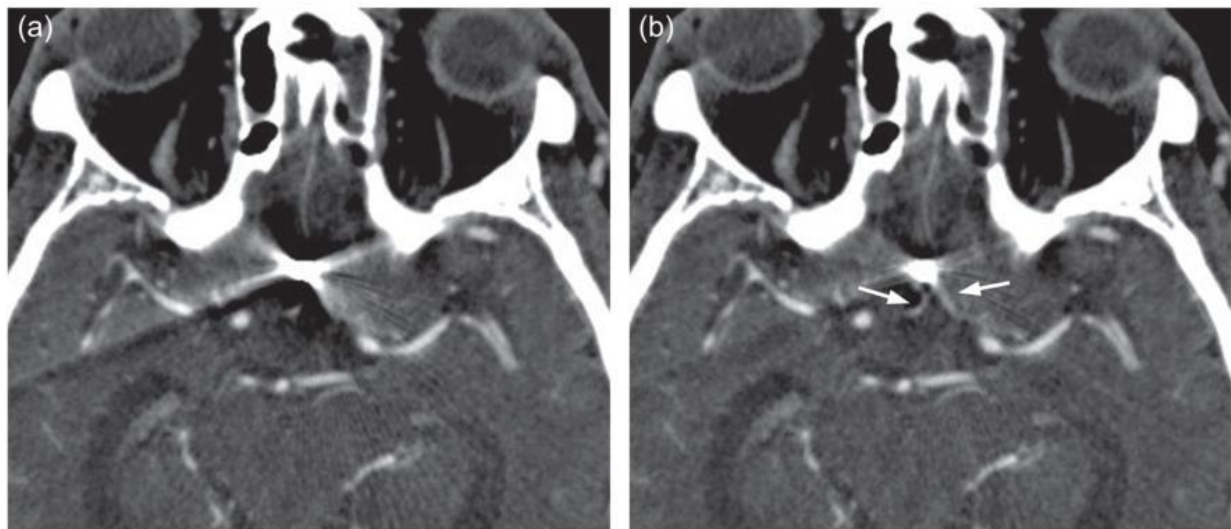
Twenty patients underwent cerebral CT angiography using a 320-detector row CT after intracranial aneurysm coiling. Images were reconstructed with and without applying the SEMAR technique (SEMAR and non-SEMAR images, respectively). The images were qualitatively assessed by two independent radiologists in a blinded manner for the visualization of brain parenchyma and vessels adjacent to the coil, and overall diagnostic acceptability of the exam. Moreover, artifact strength was quantitatively assessed by measuring image noise in the brain parenchyma around the coil. Vessel contrast was also quantitatively assessed by calculating contrast-to-noise ratios (CNRs) from attenuation values in the internal carotid artery (ICA) and middle cerebral artery (MCA).

Results

In the quantitative analysis, SEMAR images offered significantly lower quantitative image noise than non-SEMAR images (26.2 ± 8.4 H.U. vs. 82.6 ± 39.7 H.U., $p < 0.01$, student's t-test). No significant differences were observed between SEMAR and non-SEMAR images for CNR in the ICA (43.3 ± 13.0 vs. 42.4 ± 13.2 , $p > 0.10$) and in the MCA (40.8 ± 12.6 vs. 40.5 ± 12.1 , $p > 0.10$). In the qualitative analysis, SEMAR images yielded significant improvements over non-SEMAR images in visualization of the adjacent brain parenchyma ($p < 0.01$, the sign test), vessels ($p < 0.01$), and overall diagnostic acceptability of the exam ($p < 0.01$).

Conclusions

The SEMAR algorithm improves image quality of cerebral CT angiography by significantly reducing artifacts from metallic coils, while preserving vessel contrast. This technique can potentially enhance the clinical value of standard-of-care cerebral CT angiography examinations for patients who received intracranial aneurysm coiling.



Cerebral CT angiography of a 66-year-old man with a coiled anterior communicating artery aneurysm.

On the non-SEMAR image (a), the details around the metallic coil are not observed due to the dark and bright bands from the platinum coils deposited in the aneurysm.

The dark and bright bands are substantially reduced on the SEMAR image (b), demonstrating improved visibility of the adjacent brain parenchyma and the adjacent anterior cerebral arteries (arrows).

(Filename: TCT_eP-57_Figure.jpg)

eP-36

Repeatability of Dynamic Contrast-enhanced VP Parameter and Its Role in Treatment Response Assessment of Patients with High-grade Glioma

O Aizenstein¹, M Artzi¹, D Blumenthal¹, F Bokstein¹, D Ben Bashat¹, G Liberman¹

¹*Tel Aviv Sourasky Medical Center, Tel Aviv, Israel*

Purpose

MRI is the method of choice for longitudinal assessment of patients with brain tumors. Advanced vascular imaging methods such as dynamic contrast enhancement (DCE) MRI have been shown to provide complementary information regarding various aspects of the lesion vasculature. DCE-based pharmacokinetic (PK) parameters have been suggested as imaging biomarkers for treatment response assessment, providing early indication of treatment efficacy in patients with high grade glial tumors (1-2). However, despite the clinical potential of this method, the practical usage of DCE as an imaging biomarker is currently limited, mainly due to high variation in the estimated parameters, and the lack of reliable criteria to identify significant longitudinal changes (1-2). The aim of this study was to investigate the repeatability of DCE vp values and to define threshold values for significant changes in vp in longitudinal scans for quantitative assessment over time of patients with high-grade glial tumors. Criteria were defined based on test retest data of healthy subjects, and least detected differences (LDD) values were calculated based on mean vp and histogram comparisons.

Materials and Methods

The study was approved by the institutional review board and participants provided informed consent. Eighty-four MRI scans were obtained from 46 subjects: 28 healthy controls, 11 scanned twice, and 18 patients with high-grade-glioma scanned longitudinally. Eight patients were scanned before and approximately two months following bevacizumab. The imaging protocol included high-resolution SPGR/FLASH T1-weighted imaging performed before and after contrast agent injection; FLAIR and DCE data, acquired using multi-phase 3-D T1-weighted SPGR/FLASH imaging alongside contrast agent injection. For the T1 maps, variable flip angle SPGR/FLASH data were acquired with nominal flip angles = 5/10/15/20/30. DCE data were acquired with temporal resolution of six seconds and scan duration of six minutes. A power injector was used to infuse a single dose (0.2cc/kg) of contrast agent (gadolinium 0.5M), followed by a flush of 20cc saline, both at a constant rate of 5cc/sec. The DCE vp parameter was estimated using the DCE Up Sampled Temporal Resolution (DUSTER) tool (3), which is based on the Extended Tofts Model (ETM) and incorporates correction for bolus arrival time (BAT). In patients, histograms of vp values within lesion areas were compared between scans using Earth Mover's Distance (EMD). In healthy subjects, histogram comparisons were performed within the normal appearing brain tissue between and within subjects. Least detected changes (LDD) between and within subjects were calculated for mean vp and EMD. Longitudinal changes in patients were assessed based on RANO criteria, and based on defined threshold values relating to changes in mean vp and histogram comparisons using EMD.

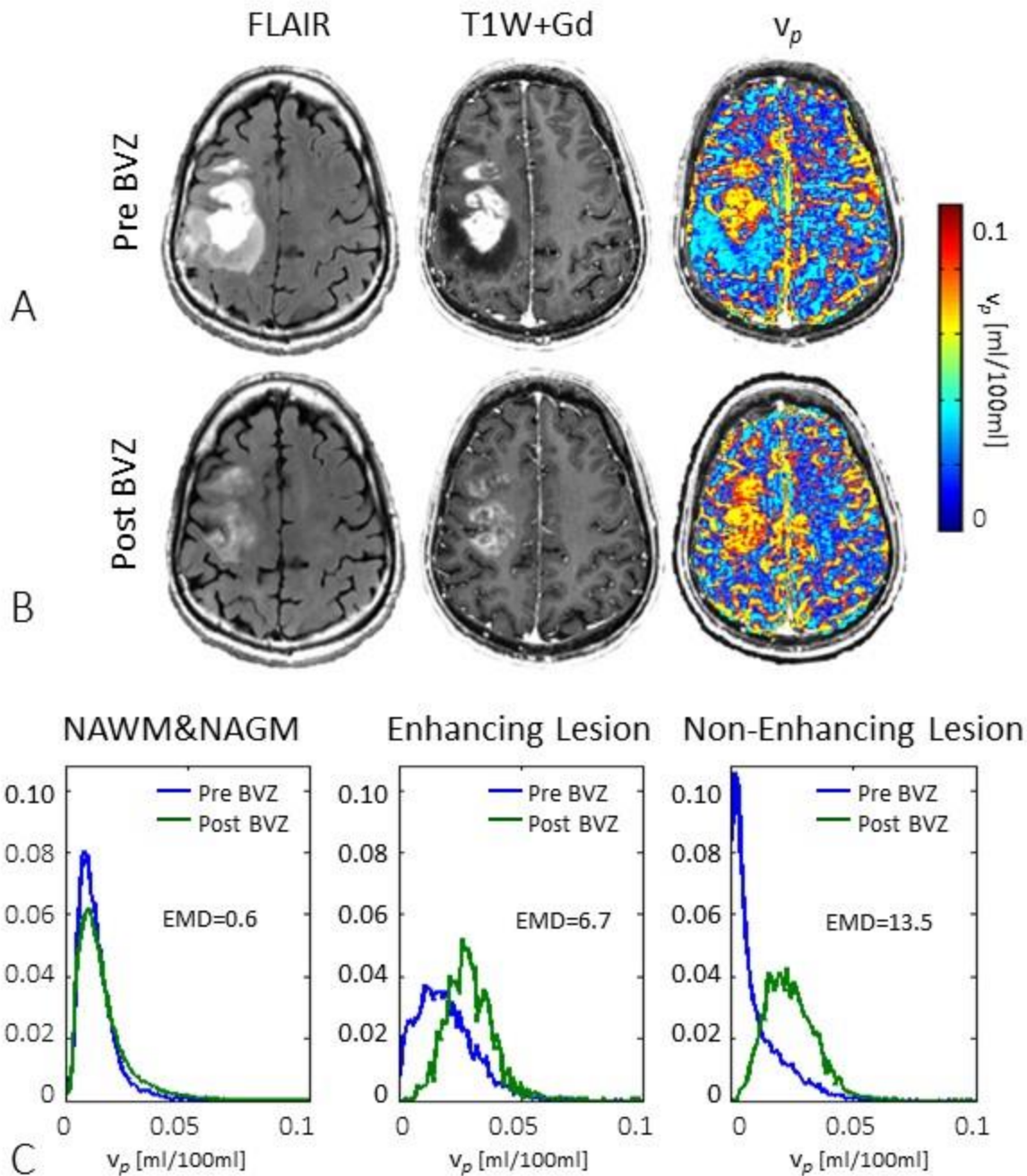
Results

Test-retest in healthy subjects, and between healthy subjects' evaluation resulted in LDD of 0.0027 (24%), 0.0026 (32%)(ml/100ml) for mean vp and values of 2.85, 2.43 for EMD, respectively. In patients, the variability in the vp and EMD values within the normal-appearing brain tissue was similar to that seen in healthy subjects. Based on the defined threshold values of LDD, no significant differences were detected in patients between longitudinal scans within the normal appearing brain tissue for either mean vp or EMD, in most cases. Within the enhancing lesion, concurring results were obtained between changes in lesion volume and vp values and between changes in mean vp and EMD values. Within the nonenhancing lesion, in 33% significant reductions in lesion volume were detected, yet with significant increase in vp values. In two patients who were scanned following bevacizumab and had additional scans, the increase in vp values preceded progression detected at follow-up scans. Figure 1 shows the results obtained in a patient who was scanned before and approximately two months after bevacizumab therapy. This patient was diagnosed with disease response two months following bevacizumab due to substantial reduction in

the volume of both enhancing (61% reduction) and nonenhancing (71% reduction) components of the lesion. However, significant increase in vp and changes according to EMD were noticed at the follow-up scan both in enhancing and nonenhancing components of the lesion, suggesting progression. In this patient, disease progression was diagnosed by RANO criteria at follow-up scans.

Conclusions

The current study demonstrates the repeatability of DCE vp within the normal appearing brain tissue in healthy subjects and patients with brain tumors, based on mean values and histogram comparison using EMD. Criteria for significant changes in vp values were derived based on LDD. Our results suggest the use of vp as an additional parameter to RANO criteria, in order to improve assessment of treatment response in patients with high-grade brain tumors, enabling early prediction of disease progression.



(Filename: TCT_eP-36_Fig1b.jpg)

eP-67d

Revolutionary Roles in the Advanced Imaging of Hypoxia-Induced Brain Oncology: Implications for Patient Care and Management

S Emamzadehfard¹, V Eslami²

Electronic Posters

¹University of Texas Health Science Center, San Antonio, TX, ²University of Texas Medical Branch, San Antonio, TX

Purpose

Circulatory, respiratory, and neuroendocrine systems in human bodies have developed to ensure that oxygen levels are precisely maintained. All nucleated cells in the body sense and respond appropriately to hypoxia through sophisticated mechanisms involving several signal transduction pathways involving gene expression, translation and protein interaction alterations. We sought to determine the importance of hypoxia imaging in oncology and introduction of currently available position emission tomography (PET) imaging tracers for this purpose. Also, we discuss how imaging of hypoxia can become incorporated into patient management.

Materials and Methods

Hypoxia-inducible factor (HIF) is a major regulator of adaptive responses to hypoxia. HIF-1 transcription factor activates transcription of several genes such as erythropoietin, vascular growth factors, and pyruvate dehydrogenase kinase 1, which inhibits the conversion of pyruvate to acetyl coenzyme A for oxidation in the mitochondria. Metabolic-based imaging such as PET is able to accurately assess tumor behavior.

Results

A. It has been recognized that most tumors are highly vascular. The vascularity tumor cells make the tumor very susceptible to developing hypoxia. In solid tumors presence of hypoxic areas is very common and in a wide range of human malignancies acts as an independent prognostic factor. Clonal selection that happens during the adaptation of initial malignant cells to hypoxia drives the tumor toward a more aggressive and therapy-resistant phenotype. B. Applications and impact of hypoxia imaging on patient care. The most important characteristics of tumor microenvironment with possible impact on administered therapeutics are oxygenation and pH. C. Methods for imaging hypoxia . Positron emission tomography (PET) and single-photon emission computed tomography (SPECT) are noninvasive techniques for assessment of hypoxia. An ideal method would also enable measurements of tissue hypoxia to be repeated over time to assess the response to treatment.

Conclusions

As the importance and role of hypoxia in tumor behavior and response to treatment are being discovered, there is growing interest in its detection and imaging.

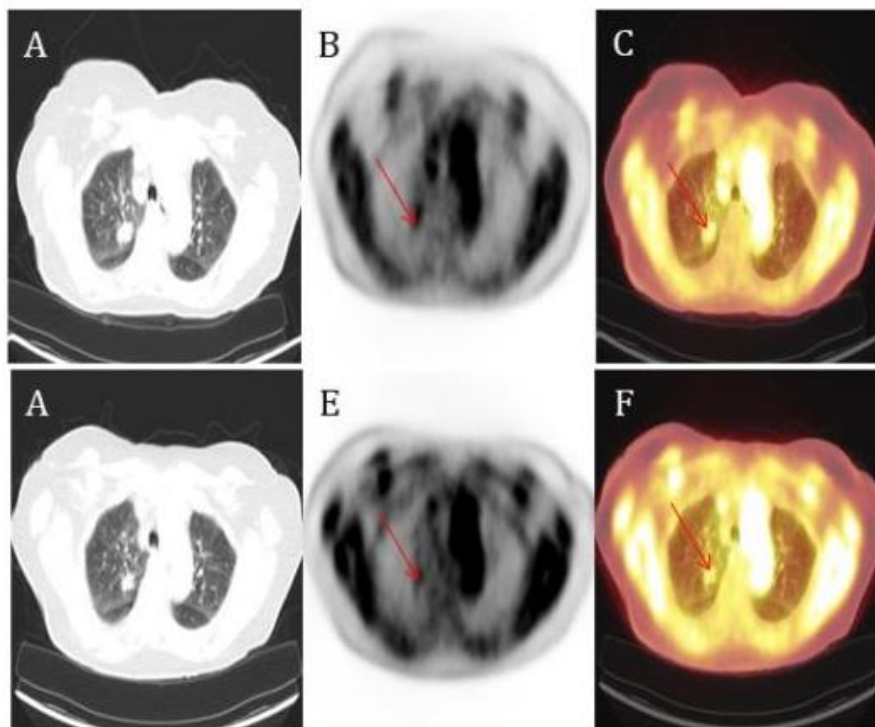


Fig 4. Axial views of CT scan (Panel A, D), ^{18}F -FMISO PET (Panel B, E), overlay of both images (Panel C, F), before (upper row) and after (lower row) receiving Erlotinib treatment. Hypoxia in the tumor decreased after only 2 weeks of treatment.

(Filename: TCT_eP-67d_Slide4.JPG)

eP-55

Small High-signal Lesions Adjacent to the Intracranial Vertebral Artery Incidentally Identified by 3D FLAIR: Analysis of 150 Patients

M Umino¹, R Kogue¹, M Maeda¹, K Tsuchiya², H Sakuma¹

¹Mie University School of Medicine, Tsu, Mie, Japan, ²Saitama Medical Center, Saitama Medical University, Kawagoe, Japan

Purpose

A recent report described a novel benign small high-signal lesion (HSL) posterior to the intracranial vertebral artery (VA) at the foramen magnum in 14 cases using a 3-D FLAIR sequence. However, this entity has not been sufficiently investigated. We aimed to investigate the clinical and MR imaging findings of HSLs adjacent to the intracranial VA that were incidentally found by 3-D FLAIR.

Materials and Methods

We retrospectively evaluated 3,759 consecutive patients using a 3T MR unit. HSLs on 3-D FLAIR were assessed for prevalence, size, anatomical position related to the VA, contact with the VA and spinal accessory nerve (SAN), and size changes on follow-up images.

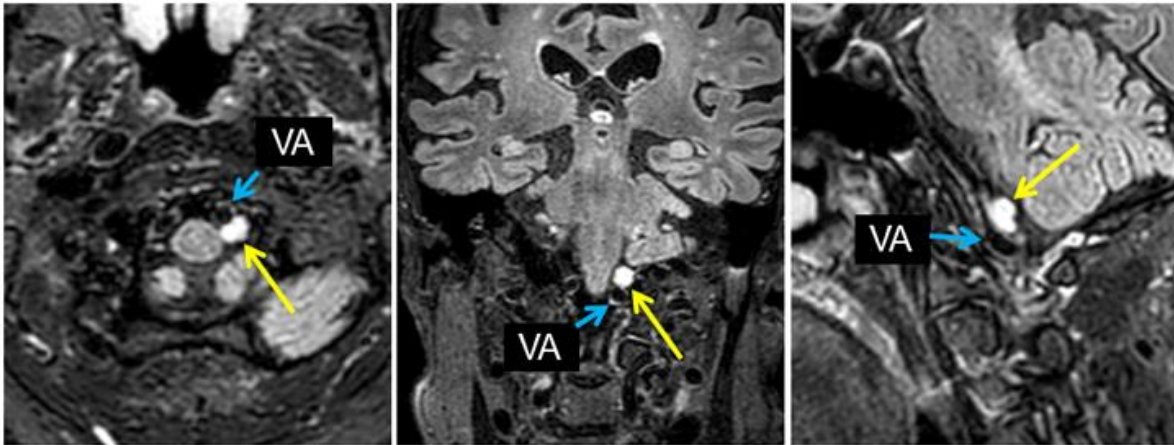
Results

Of 3,759 patients, 150 (4.0%) (72 males and 78 females; age, 60.7 ± 18.8 years) showed 173 HSLs adjacent to the intracranial VA. In total, 131 patients (87.3%) had a single lesion, whereas 19 patients (12.7%) had multiple lesions. The mean size was 3.7 ± 1.5 mm. The majority (87.3%) of HSLs was located posterior to the VA, while the others were either anterior, lateral, or medial to the VA. Of all HSLs, 39.3% showed contact with the VA and 96.4% showed contact with the SAN. Of 80 HSLs that were imaged during follow-up, the size was stable in 91.3% and increased in 8.7%.

Conclusions

HSLs adjacent to the intracranial VA were incidentally found in 4.0% of patients by 3-D FLAIR. Our results suggested a possible association between HSLs and the SAN.

A small high-signal lesion (HSL) adjacent to intracranial vertebral artery (VA) on 3D FLAIR



A small oval high-signal lesion (long arrow) is clearly visible adjacent to the left vertebral artery (VA), which is typically located at a foramen magnum.

(Filename: TCT_eP-55_FigJPEG.jpg)

eP-49

Solitary Fibrous Tumour / Hemangiopericytoma : A New Diagnostic Entity

J Rees¹, M Rivera-Zengotita,¹ I Tuna¹, J Gregory¹, M Rahman¹

¹University of Florida, Gainesville, FL

Purpose

To present examples of the new WHO 2016 diagnostic entity Solitary Fibrous Tumour (SFT) / Hemangiopericytoma (HPC), and to discuss the history of this entity, and the spectrum of both histology and biologic aggressivity which it includes.

Materials and Methods

Imaging and pathologic review of three SFT/HPC cases is performed including two intracranial examples: a cerebellopontine angle tumor and a large frontal transfalcal mass, and a third from the lumbar spine.

Results

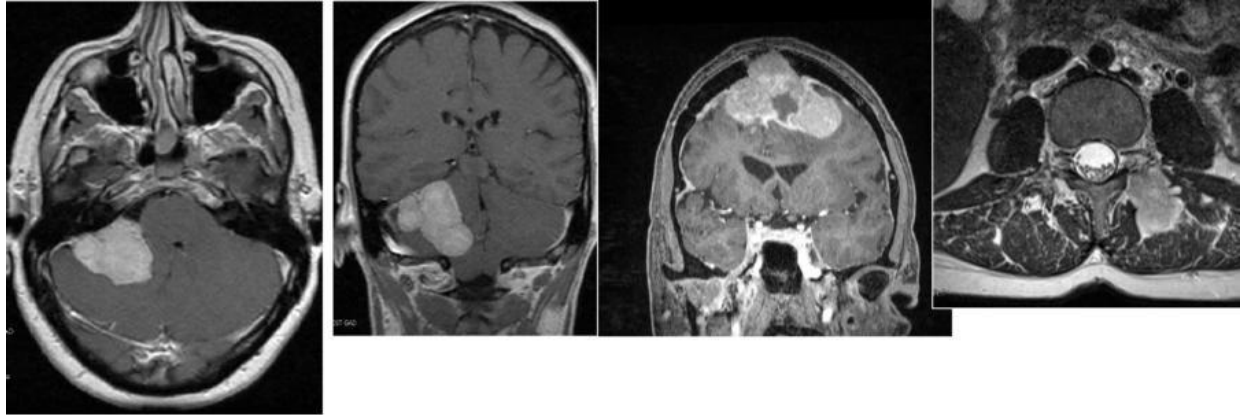
Imaging features show extra axial neoplasms with benign features in the lumbar example and aggressive but nonspecific imaging features in the intracranial examples. Although dural based, they do not show the typical dural tail of meningiomas. On pathologic evaluation, these tumors combine histologic features of

Electronic Posters

the two entities in a spectrum, with typical staghorn vasculature seen in both and varying degrees of cellularity, and hyaline deposition. Mitotic figures are variable from few to greater than 10 per HPF, and there is no invasion of brain parenchyma seen. These features indicate varying degrees of biologic aggressivity and are graded from WHO I (lumbar) - WHO III (both Intracranial). All of these case are positive for STAT 6 on immunohistochemistry.

Conclusions

SFT and HPC had previously been separate entities in the general category of meningioma mimics. In the most recent WHO 2016, they are combined into one diagnostic entity or category based on shared histologic and molecular features. The STAT 6 immunohistochemical marker has become an important unifying diagnostic criterion which links the two. As we learn more about the molecular biology of the neoplasms we deal with, our diagnostic categories and criteria will likely continue to evolve.



(Filename: TCT_eP-49_compositeSFTHPC.jpg)

eP-27

Spectrum of MRI Abnormalities in Idiopathic Intracranial Hypertension and Their Correlation with Clinical Grades of Papilledema

N Ray¹, S Vyas¹, N Khandelwal¹, R Bansal¹

¹*Postgraduate Institute of Medical Education and Research, Chandigarh, India*

Purpose

Multiple MR imaging signs have been described in the literature in cases of idiopathic intracranial hypertension (IIH).(1) We aim to evaluate the correlation between the imaging signs and clinical grading of papilledema in this study.

Materials and Methods

Thirty cases of idiopathic intracranial hypertension (diagnosed according to revised criteria) and same number of age and sex matched control participants were included in this institutional ethic committee approved study. Clinical grading of papilledema was done by fundus examination according to the Modified Frisén scale, by an experienced neuro-ophthalmologist. Contrast enhanced MRI of brain along with CISS and coronal T2 FS sequence for orbits and MR venogram were performed for all patients. Images were evaluated by two experienced neuroradiologists (having 10 years and 5 years experience of evaluating MRI brain) for the presence of established signs of IIH like optic nerve tortuosity, prominent perioptic sheath, intracocular projection of optic nerve papilla, posterior scleral flattening, partially/completely empty sella and stenosis of transverse sinus and relatively newly described sign of optic nerve head (ONH) hyperintensity (2,3) (graded as none, mild and marked) on DWI in presence of papilledema. The correlation between clinical grade of papilledema and the presence or absence of the above-mentioned signs was evaluated by Chi-square test. The sensitivity, specificity, positive and

negative predictive values were calculated for all the signs. Interobserver agreement was calculated by k-statistics.

Results

Statistically significant correlation between clinical grading of IIH was found to exist with transverse sinus stenosis and ONH hyperintensity on DWI, while no significant statistical correlation was found with the rest of the imaging signs and clinical grades of papilledema. The sensitivity, specificity, positive and negative predictive values of each sign and the p values depicting their correlation with clinical grades of papilledema are shown in Table-1. High interobserver agreement was found for all the signs.

Conclusions

Transverse sinus stenosis and DWI hyperintensity at ONH are the only two imaging signs in IIH bearing significant correlation with clinical grading and are having highest sensitivity and specificity amongst all imaging signs. The presence of these two signs should alert the radiologist about the possibility of IIH, even if other imaging signs are absent, in appropriate clinical setting.

TABLE-1- SENSITIVITY, SPECIFICITY, POSITIVE & NEGATIVE PREDICTIVE VALUES OF IMAGING SIGNS IN IIH AND THEIR CORRELATION WITH CLINICAL GRADES OF PAPILLEDEMA						
MRI SIGNS	OBSERVER	SENSITIVITY	SPECIFICITY	POSITIVE PREDICTIVE VALUE	NEGATIVE PREDICTIVE VALUE	CORRELATION WITH CLINICAL GRADE OF PAPILLEDEMA (p value)
OPTIC NERVE TORTUOSITY	1	75 %	80%	78.9%	76.1%	0.626
	2	75 %	80%	78.9%	76.1%	0.626
OPTIC NERVE SHEATH ENLARGEMENT	1	68.3%	83.3%	80.3%	72.4%	0.786
	2	66.7%	85%	81.6%	71.8%	0.792
POSTERIOR FLATTENING OF SCLERA	1	80%	88.3%	87.2%	81.5%	0.691
	2	80%	86.6%	85.7%	81.2%	0.667
INTRAOCULAR PROJECTION OF OPTIC NERVE PAPILLA	1	78.3%	80%	79.6%	78.6%	0.234
	2	78.3%	80%	79.6%	78.6%	0.234
EMPTY/PARTIALLY EMPTY SELLA	1	73.3%	80%	78.6%	75%	0.345
	2	73.3%	80%	78.6%	75%	0.345
OPTIC NERVE HEAD HYPERINTENSITY ON DWI	1	88.3%	96.7%	96.3%	89.2%	0.001
	2	86.6%	98.3%	98.1%	88.1%	0.001
TRANSVERSE SINUS STENOSIS	1	90%	93.3%	93.1%	90.3%	0.001
	2	93.3%	93.3%	93.3%	93.3%	0.001

(Filename: TCT_eP-27_TABLE1.jpg)

eP-20

Structural Abnormalities in Children Patients with Obstructive Sleep Apnea Syndrome: A Voxel-based Morphometry Study

Y Liu¹, w Li¹, H Wen², H He³, Y Peng¹

¹Beijing Children's Hospital, Capital Medical University, National Center for Children's Health, Beijing, China, ²Research Center for Brain-Inspired Intelligence, Institute of Automation, Chinese Academy of Science, Beijing, China, ³The State Key Laboratory of Management and Control for Complex Systems, Institute of Automation, Beijing, China

Purpose

The aim of this study was to use VBM (1) to investigate whether there are gray matter volume changes in untreated OSAS children patients compared to healthy controls (HC). In addition, correlation analysis method was used to assess the impact of OSAS-related variables, including apnea–hypopnea index (AHI), obstructive apnea index (OAI), hypopnea index (HI), intelligence quotient (IQ) and attention on GMV (2).

Materials and Methods

Eleven participants with OSAS (1 female, mean age = 5.18, SD = 2.23, range, 3-10) and 10 healthy controls (5 females, mean age = 7.30, SD = 2.21, range, 4-9) were scanned in a 3.0 T GE Discovery MR750 MRI scanner. A high resolution T1-weighted structural image was scanned for every subject. VBM analysis of T1-weighted images was conducted using the VBM8 toolbox in SPM8. To estimate cortical volume changes between patients and controls, a series of one-tail two sample t-tests were used.

Results

Statistically significant (FDR corrected $p < 0.005$) cortical volume changes were found and shown in Figure 1. Decreased grey matter volume in right supramarginal gyrus and inferior parietal lobule and increased grey matter volume were found in right Rectus gyrus and right pallidum between OSAS patients and HC. Detailed description of cortical regions was listed in Table 1. There were no correlation between GMV and clinical parameters.

Conclusions

In terms of VBM changes in GMV, there is great difference between OSAS children patients and HC. But there were no correlation between GMV and clinical parameters, so we need further study and to include more children patients to find the correlation GMV and clinical parameters.

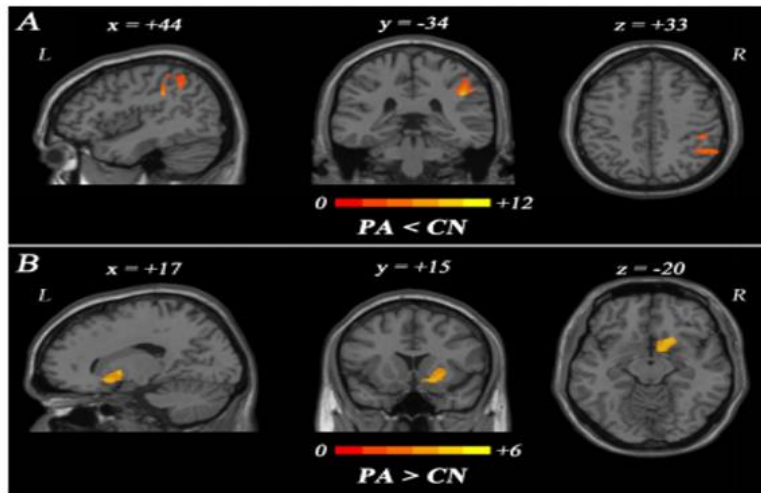


Fig.1 Difference of GWM between patients and controls ($p < 0.005$, topological FDR). Brain regions showing decreased GMV in right supramarginal gyrus and inferior Parietal lobule, and increased GMV in right Rectus gyrus and right pallidum between OSAS children patients and HC.

(A) PA < CN and (B) PA > CN. The color bar was shown as the T value.

Table 1 Brain areas with VBM changes between patients (PA) and controls (CN).

Peak MNI coordinate region	Voxels	Peak MNI coordinate			Peak intensity
		x	y	z	
<i>PA > CN, $p < 0.005$, topological FDR</i>					
Rectus_R	1317	2	6	-20	5.62
Pallidum_R		17	15	-12	4.56
		18	5	-2	4.34
<i>PA < CN, $p < 0.005$, topological FDR</i>					
SupraMarginal_R	1393	44	-34	33	11.86
Parietal_Inf_R		56	-51	42	4.89
		63	-45	27	4.47

MNI, Montreal Neurological Institute

(Filename: TCT_eP-20_Tables.jpg)

eP-13

Structural and Functional Brain Connectivity of Prefrontal Cortex in Sporadic Parkinson's Disease with Executive Dysfunction

A Wada¹, J Kikuta², Y Watanabe³, O Abe³, K Kamagata¹, M Hori¹, M Suzuki¹, R Irie¹, T Takamura¹, K Kumamaru¹, S Aoki¹

¹Juntendo University School of Medicine, Tokyo, Japan, ²Nihon University, Tokyo, Japan, ³The University of Tokyo, Tokyo, Japan

Purpose

Parkinson's disease (PD) patient tends to cause execution dysfunction with higher frequency than healthy

Electronic Posters

subject. The objective of this study is investigation of the relation between execution dysfunction in PD and structural and functional connectivity.

Materials and Methods

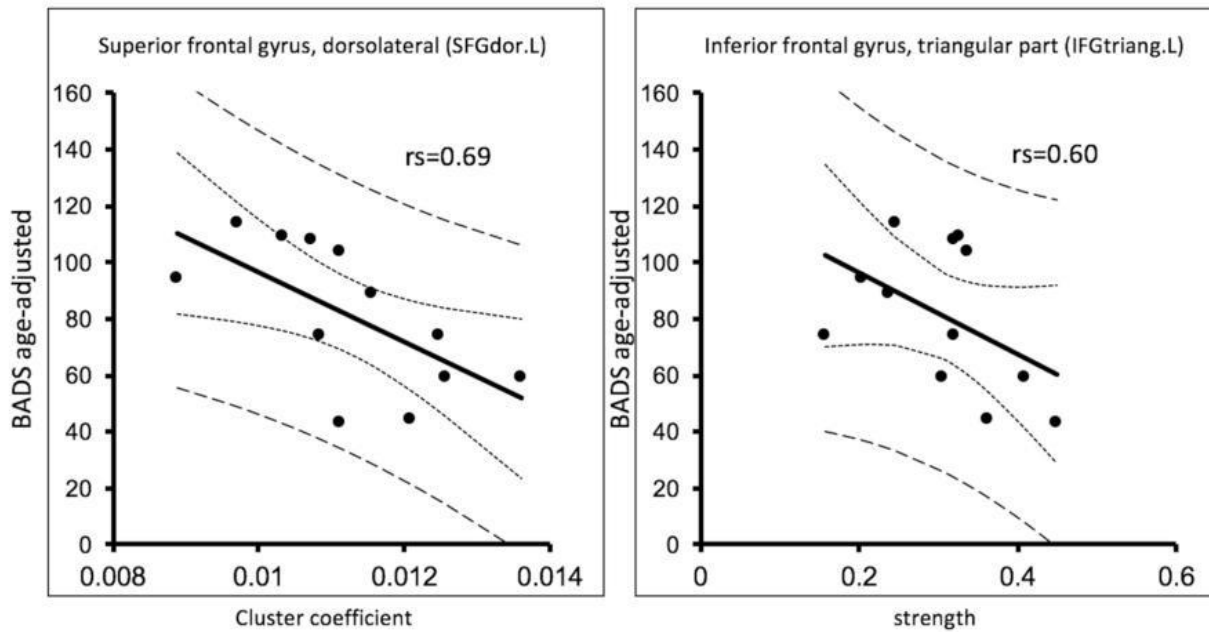
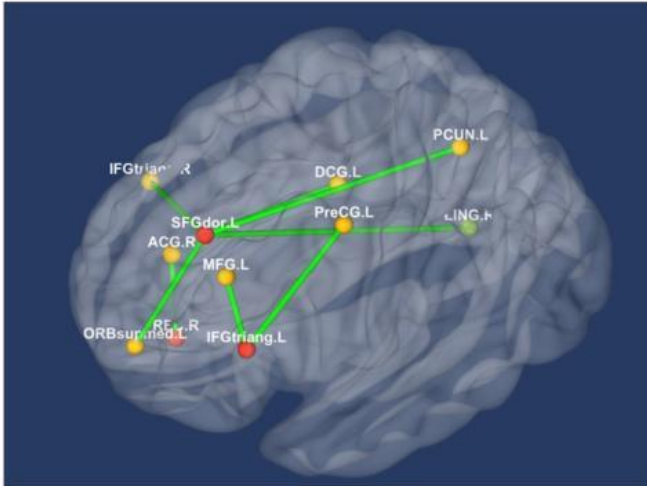
We estimated execution function of 12 PD patients with age adjusted Behavioural Assessment of the Dysexecutive Syndrome (BADS) and divided them into two groups (disability group and nondisability group). We compared the functional connectivity and structural connectivity by using rs-fMRI and probabilistic tractography. All MR imaging was performed by 3.0 T MR unit (Discovery 750w; GE Healthcare) with 32-channel phased-array head coil. Structural and functional connectivity in 90 anatomically defined regions of interest were established by functional connectivity toolbox (CONN) and probtrackx2 in FSL and analyzed by graph theory with brain connectivity toolbox. In graph analysis, we estimated nodal strength, clustering coefficient, local efficacy and betweenness centrality as regional measures and global efficiency, mean strength and clustering coefficient and small worldness as global network measures.

Results

A significant difference was recognized in the functional and structural network of prefrontal cortex between execution the disability group and nondisability group, especially, a significant correlation of cluster coefficient and strength at the prefrontal cortex and execution dysfunction ($p < 0.05$). Clustering coefficient in dorsolateral prefrontal gyrus and strength in inferior frontal gyrus revealed a significant correlation with age adjusted BADS score ($r_s = 0.69$ and 0.60).

Conclusions

Our structural functional network analysis revealed the alteration of prefrontal cortex connectivity associated with the execution dysfunction in Parkinson's disease.



(Filename: TCT_eP-13_ASNR2018_wada_final.jpg)

eP-29

Sulcal Subarachnoid Hemorrhage with Negative Angiogram: Meta-analysis and Management Recommendations

L Tu¹, K Seifert², X Wu¹, D Gandhi³, A Malhotra²

¹Yale University School of Medicine, New Haven, CT, ²Yale New Haven Hospital, New Haven, CT, ³University of Maryland School of Medicine, Baltimore, MD

Purpose

The purpose of this study is to synthesize the current literature into recommendations regarding the management of sulcal/convexity subarachnoid hemorrhage with a negative first angiographic study. We will investigate the utility of additional imaging after an initially negative angiography.

Electronic Posters

Materials and Methods

PUBMED, EMBASE, SCOPUS and research meeting abstracts were searched up to March 2017 for studies of patients with spontaneous subarachnoid hemorrhage (SAH) and an initially negative angiographic study (DSA, CTA, or MRA). Title/abstract and then full-text screening was performed by two independent reviewers. Study quality was assessed via the Cochrane Risk of Bias Tool (CRBT). Meta-analysis was conducted using random and fixed effects models.

Results

A total of 1936 studies were identified, of which 185 underwent full text review; 6 studies were included. Diagnostic methods for initial angiographic as well as follow-up studies were variable. Assessment of study quality by CRBT also showed variability; however, most studies had a low risk of bias. There were no underlying aneurysms among 101 patients in the meta-analysis. The underlying vascular lesions included 21 cases of vasculitis, and single cases of AVF, AVM, among other etiologies. DSA and 3DRA (3-dimensional rotational angiography) were the most sensitivity modalities for detection of these lesions. Further imaging after an additional negative DSA/3DRA was of nearly zero utility.

Conclusions

Spontaneous SAH may be categorized as perimesencephalic, diffuse/aneurysmal, peripheral (convexity, sulcal), or CT-negative (detected only on lumbar puncture) based on the distribution of hemorrhage. The optimal management strategy for sulcal SAH has not been determined, and practice patterns are variable. Our meta-analysis suggests that the etiology of sulcal SAH is non-aneurysmal in cases after a negative initial angiographic study. If there is concern for vasculitis/RCVS, a DSA (preferably with 3DRA) is preferred.

eP-22

Susceptibility-weighted Imaging Provides Complimentary Value to Diffusion-weighted Imaging in the Differentiation Between Pyogenic Brain Abscesses, Necrotic Glioblastomas, and Necrotic Metastatic Brain Tumors

P Lai¹

¹*Kaohsiung Veterans General Hospital, Kaohsiung, Taiwan*

Purpose

Brain abscess can simulate intracranial necrotic glioblastomas multiforme and necrotic metastasis in MRI appearance. The purpose of this study was to investigate the discrimination of abscess and necrotic tumors using susceptibility-weighted (SWI) and the apparent diffusion coefficient (ADC) separately and then combined.

Materials and Methods

Imaging was performed in 26 patients with pyogenic brain abscesses, 31 patients with rim-enhancing glioblastomas, 21 patients with rim-enhancing metastases at 1.5 Tesla. Three observers assessed independently the degree of intralesional susceptibility signal (ILSS). Average ADC was calculated in the cystic cavity. Interobserver agreement on ILSS grading was assessed using the Kendall's coefficient of concordance (KCC). Logistic regression models were used to distinguish between any two diseases. After receiver operating characteristic (ROC) analysis, area under ROC curve was compared among three different analytical models (ILSS, ADC, ILSS and ADC) in any two diseases.

Results

Interobserver agreements for ILSS grading were good for the three reviewers showing a KCC of 0.92. In ILSS analysis, low degree of ILSS (ILSS grade 0, 46.2% and grade 1, 42.3%) was in the majority of abscesses. A high degree of ILSS (ILSS grade 3, 61.3%) was in the majority of glioblastomas. ILSS relatively evenly tended to spread across the four ILSS categories of metastases, and ILSS grade 0 (33.3%) and grade 3 (28.6%) each accounted for about 1/3. The ADC value of the abscess was $0.65 \pm 0.24 \times 10^{-3}$ mm²/s (mean \pm SD), ranged from 0.34 to 1.51×10^{-3} mm²/s. The ADC value of the necrotic

glioblastomas was $2.11 \pm 0.69 \times 10^{-3} \text{ mm}^2/\text{s}$, ranged from 0.83 to $3.03 \times 10^{-3} \text{ mm}^2/\text{s}$. The ADC value of the necrotic metastases was $2.07 \pm 0.80 \times 10^{-3} \text{ mm}^2/\text{s}$, ranged from 0.52 to $2.77 \times 10^{-3} \text{ mm}^2/\text{s}$.

Diagnostic accuracy for differentiating abscess from glioblastoma was 87.7% with the ILSS model; 94.7% with the ADC model; and 100% with the combined ILSS and ADC model. Combined ILSS and ADC model was significantly better than ILSS model in distinguishing abscesses from glioblastomas ($P=0.024$). Diagnostic accuracy for differentiating abscess from metastasis were 70.2% with the ILSS model, 91.5% with the ADC model, and 91.5% with the combined ILSS and ADC model. ADC model ($P=0.006$), combined ILSS and ADC model ($P<0.001$) were significantly better than ILSS model in distinguishing abscesses from metastases. Diagnostic accuracy for differentiating glioblastoma from metastasis were 73.1% with the ILSS model, 67.3% with the ADC, and 75.0% with the combined ILSS and ADC model. ILSS model ($P=0.039$), combined ILSS and ADC model ($P=0.016$) were significantly better than ADC model in distinguishing glioblastomas from metastases.

Conclusions

SWI and ADC are complementary, and the combination of SWI and ADC may improve results compared with the use of only a single technique to differentiate between abscesses, necrotic glioblastomas, and necrotic metastatic brain tumors.

eP-65

The Appearance of Immediate and Delayed Infarct Fogging on CT Perfusion

M Braileanu¹, M Hoch¹, R Hu¹, B Weinberg¹

¹Emory University Hospital, Atlanta, GA

Purpose

The transient iso-dense appearance of a previously hypodense infarct on CT, generally 2-3 weeks after stroke onset, is referred to as the "fogging effect." (1, 2) A similar pseudonormalization of hypodense infarct has also been reported on postinterventional CT after endovascular stroke intervention. (3) We report the appearance of immediate and delayed infarct fogging on CT perfusion.

Materials and Methods

Head CT perfusion radiology reports were queried at two institutions for "fogging." Patient baseline and imaging characteristics, specifically MTT, CBF, and CBV at time of infarct fogging, were collected for this descriptive analysis.

Results

A total of five patients were identified. Average age was 49 years and four patients were female (80%). Two patients initially presented with same-day infarction and subsequent angiographic intervention. Postinterventional noncontrast CT imaging revealed interval decreased conspicuity of infarction, while CT perfusion revealed increased to normal MTT, and normal CBF/CBV. Three cases initially presented with intracranial or subarachnoid hemorrhage, followed by vasospasm and subsequent infarction. Fogging was observed within 6 to 10 days after infarct in this subset of patients. Perfusion CT revealed variable MTT (increased, normal, decreased), with increased to normal CBF/CBV (Figure 1).

Conclusions

CT perfusion imaging is variable in patients with infarct fogging. Perfusion pattern of immediate postinterventional fogging, likely secondary to contrast staining, (3) is similar to normal or acute infarction. (4) In three patients with infarction secondary to vasospasm, fogging occurred within 1 week versus the previously reported 2-3 weeks. (1, 2) A luxury-like perfusion pattern with increased CBV4 was observed in this subset of patients. In both sets of patients, the presence of hyper-dense material (i.e. contrast, increased blood) may have obscured findings of infarction on noncontrast head CT. Recognition of the fogging effect is important to avoid underestimation or misdiagnosis of infarct.

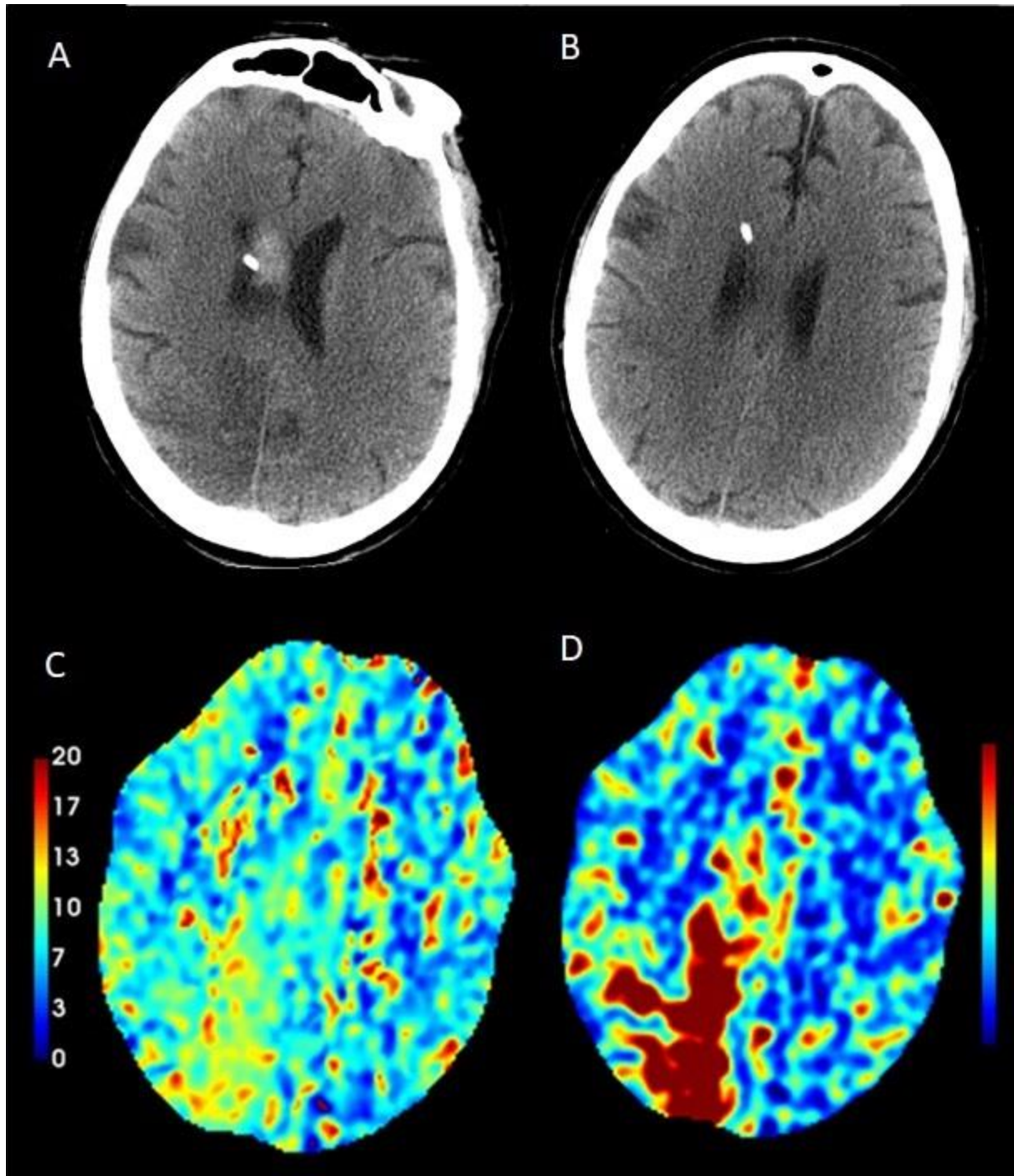


Figure 1: 47yoF initially presented with ICH/IVH secondary to hypertension. A) Patient developed vasospasm and infarction of the right parietal lobe. B) Eight days after infarction, pseudo-normalization, or "fogginess" of the infarct was noted. Corresponding CT perfusion revealed increased C) MTT and D) CBV within areas of fogging.

(Filename: TCT_eP-65_Fig1.jpg)

eP-21

Electronic Posters

The Effect of Tumor Characteristics and Neurovascular Uncoupling on Hand-motor Resting-state Functional Connectivity in Glioma Patients

H Sun¹, B Vachha¹, M Jenabi¹, M Laino², A Holodny¹, K Peck¹

¹Memorial Sloan Kettering Cancer Center, New York, NY, ²Catholic University of Sacred Heart, A Gemelli Hospital, Rome, Italy

Purpose

Motor resting-state networks of healthy human subjects are bilaterally symmetrical. Resting-state fMRI (RSfMRI) has been proposed to identify eloquent areas in preoperative brain tumor patients. We hypothesized that tumor-induced neurovascular uncoupling will affect RSfMRI similarly to task-based fMRI, contributing to the lateralization of bilateral resting-state connectivity.

Materials and Methods

Forty-five preoperative glioma patients and 10 controls performed RSfMRI. Resting-state connectivity maps were generated in AFNI using a seed-based correlation analysis (SCA), seeding based on anatomic landmarks and/or activation-based data. From these maps, voxel activation and average correlation were extracted from ROIs as measures of the degree and strength of connectivity. Plasma volume (Vp) was derived from DCE-perfusion MRI data. Statistical analysis was performed with one-tailed Wilcoxon signed rank tests, Kruskal-Wallis one-way ANOVA and Spearman's ranked correlation ($p=0.05$).

Results

Patients with gliomas exhibited significant lateralization of resting-state motor connectivity compared to controls ($p < 0.05$, all tests), with a significant correlation found between lateralization of resting-state connectivity and the distance of the tumor from the ipsilateral motor area (Voxel activation: $R=0.3752$, $p<0.05$; Average correlation: $R=0.3283$, $p<0.05$). Patients with glioblastomas, <40 mm from the hand-motor region, had a significant correlation between Vp and the strength of the lateralization of resting-state connectivity ($R=0.7364$, $p<0.001$). In patients with tumors <40 mm from the hand-motor region, seeding the nontumor hemisphere yielded differences in resting-state connectivity that were significantly less lateralized than differences derived from seeding in the tumor hemisphere ($p<0.05$ for all tests).

Conclusions

Glioma patients exhibited significant lateralization of resting-state motor connectivity dependent on tumor characteristics. These effects may be explained through a neurovascular uncoupling mechanism in a subset of tumors, and differences in seeding methodology may help compensate for tumor-induced effects on imaging results. These findings have important applications for a scientific understanding of how tumors affect resting-state fMRI dynamics, and how resting-state fMRI can be applied in clinical settings.

eP-11

The Practical External Guide for the Safe Orthogonal Approach

M Seol¹, J Choi¹

¹Presbyterian Medical Center, Jeonju, South Korea

Purpose

The orthogonal approach is a useful route for general neurosurgeries. However, variable courses of venous structures on the lateral surface of cerebral hemisphere sometimes can induce unwanted hemorrhage during the procedure. This study aims to establish dependable window for avoiding the Sylvian vein and vein of Labbé using external landmarks of the head during the orthogonal approach for general neurosurgeries based on normal angiographic studies.

Materials and Methods

Thirty four patients' angiography images were transferred to the image editing software. The Sylvian veins and vein of Labbé in the angiographic images were redrawn together in all patients. Boundaries of the lateral skulls were realigned to fit together, and subsequently venous structures were overlaid (Fig. 1). Midpoint of the line connecting the external auditory canal with the glabella was used to draw the circle (Sylvian circle : SC). Second line connecting the external auditory canal with the coronal suture (Labbé Line:LL) was made to create the zone between LL and SC (Labbé zone:LZ) (Fig. 2,3). Distribution percentage of the Sylvian veins along SC and the vein of Labbé within LZ were measured (Fig. 4). Figure Legends: Fig. 1 Redrawn and summated the Sylvian veins and vein of Labbé from the transferred angiographic images of the 34 patients are shown. The coronal suture (yellow arrowhead) and the pituitary fossa (blue arrowhead) were used as a reference point for summation. Fig. 2 Sylvian circle (SC) starts from midpoint (red arrowhead) of the glabella (pink arrowhead) and external auditory canal (EAC) line (green arrowhead). Line of Labbé (LL) connects the coronal suture (yellow arrowhead) with the EAC. Fig. 3 SC and LL show their positions on the skull lateral view with real courses of the sylvian veins and vein of Labbé. Fig. 4 SC has 79.4% of the Sylvian veins within a 5 mm radius of SC (red curved cylinder-shaped zone). Labbé zone (LZ) is a fan-shaped area which spreads out from EAC up to SC and limited by LL anteriorly and the tentorium cerebelli posteriorly (blue fan-shaped zone). LZ contains the most of the vein of Labbé (95.8%). The triangular zone formed by the 5 mm below of SC superiorly, skull base anteriorly, and LL posteriorly contains less distribution of the veins than the curved cylinder-shaped or fan-shaped zone.

Results

Twenty-seven patients' Sylvian veins (79.4%) were located within a 5 mm radius of SC. Five Sylvian veins (14.7%) were located above SC and two (5.8%) below SC. Most of the vein of Labbé were distributed in LZ (95.8%).

Conclusions

SC and LZ are helpful to avoid damaging the Sylvian vein and vein of Labbé during the orthogonal approach for general neurosurgeries.

Fig.1

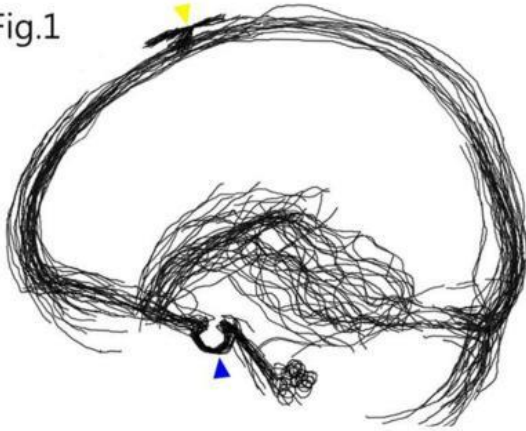


Fig.2

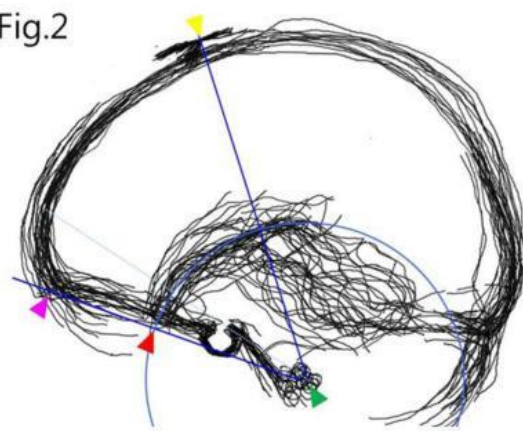


Fig.3

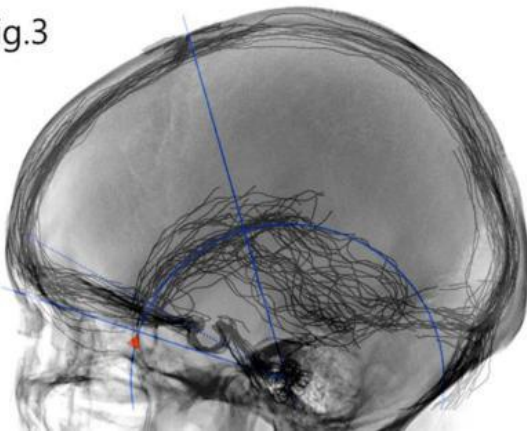
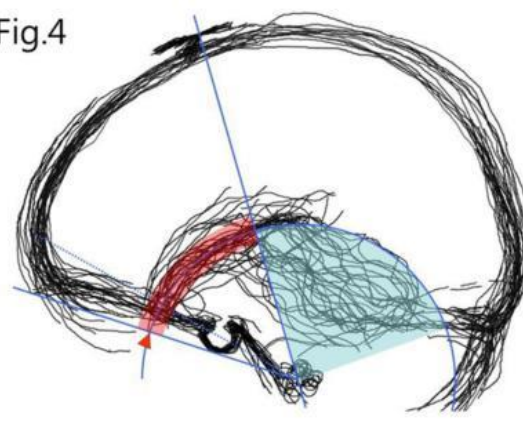


Fig.4



(Filename: TCT_eP-11_Fig1-4.jpg)

eP-51

Toward Routine Clinical Use of Quantitative Susceptibility Mapping – Developing a Fully Automated Inline QSM Pipeline Utilizing GPU Acceleration

J Kim¹, S Bollmann², C Langkammer³, B Bilgic⁴, K O'Brien⁵, M Barth²

¹University of Illinois at Chicago, Chicago, IL, ²Centre for Advanced Imaging, The University of Queensland, Brisbane, QLD, Australia, ³Medical University of Graz, Graz, Austria, ⁴A. A. Martinos Center for Biomedical Imaging, Massachusetts General Hospital, Charlestown, MA, ⁵Siemens Healthcare Pty Ltd, Brisbane, QLD, Australia

Purpose

Quantitative susceptibility mapping (QSM) allows the measurement of tissue magnetic susceptibility variations in-vivo, which are closely linked to iron and myelin content, and oxygenation status (1-4). QSM computation involves multiple processing steps for solving an ill-posed inverse problem. This leads to prohibitively long processing times, impeding its clinical translation. In this work, we introduce a reconstruction pipeline developed on a clinical MRI scanner that can produce fast and reliable QSM images by taking advantage of massively parallelized GPU accelerator.

Materials and Methods

The developed prototype QSM pipeline was written in C++ and CUDA. Our QSM reconstruction steps comprised of atlas-based brain extraction, Laplacian operation on wrapped phase and dipole inversion based on total-generalized variation (TGV) algorithm(5). We employed primal-dual method to solve the

convex optimization problem. The prototype QSM pipeline is compatible with 3D flow-compensated gradient-echo (FC-GRE) and volume interpolated breath-hold examination gradient-echo (FC-VIBE) prototype sequences that utilize GRAPPA and CAIPIRINHA acceleration techniques respectively. We tested the software in 4 participants on a MAGNETOM Prismafit 3T MR scanner with a 64-channel head/neck coil (Siemens Healthcare, Erlangen, Germany). The MRI reconstruction system was equipped with a Tesla K10 GPU accelerator (2x1536 cores, 8GB, NVIDIA). The protocols of tested sequences were; FC-GRE (TR=25ms, TE=20ms, flip angle=12deg, FOV=204x224x160mm³, matrix=204x224x160, GRAPPA=3, TA=4min 52s) and FC-VIBE (TR=25ms, TE=20ms, flip angle=12deg, FOV=204x224x160mm³, matrix=204x224x160, CAIPIRINHA=3x2, TA=2min 43s).

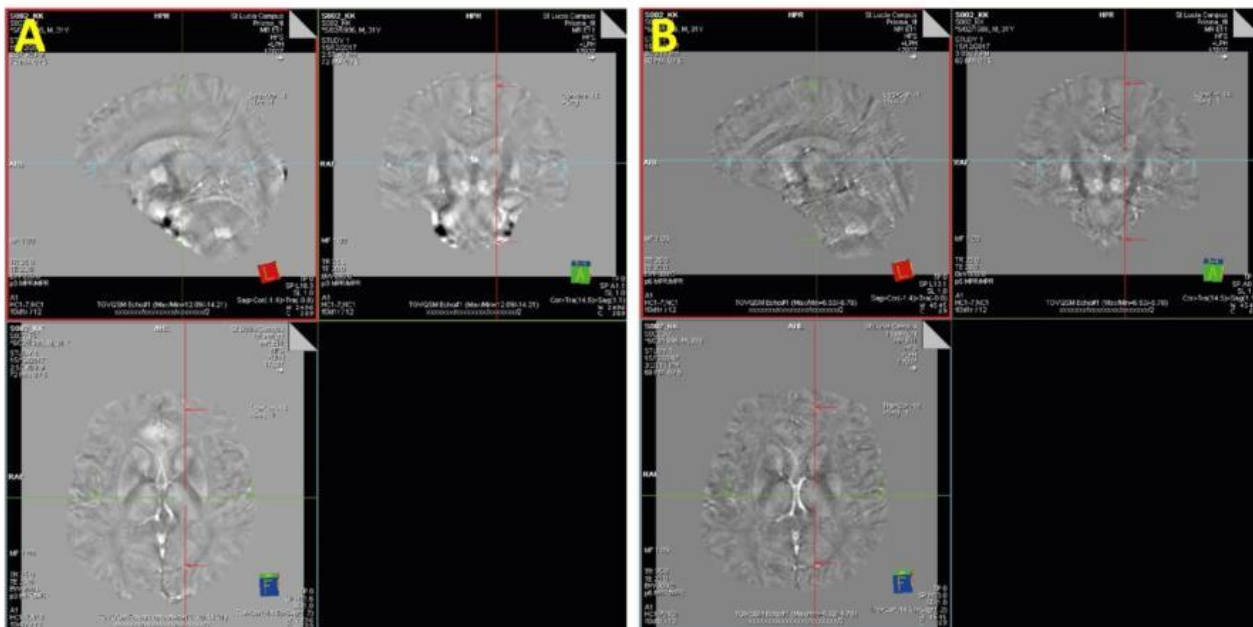
Results

One participant's reconstruction for the standard FC-GRE and FC-VIBE sequence is shown in Figure 1. The total image reconstruction time from raw k-space data to dicom output was 3min 10s for the FC-GRE and 3min 44s for the FC-VIBE. Figure 1 – Results of QSM reconstruction from; (A) FC-GRE (4min 52s acquisition and 3min 10s reconstruction time) and (B) FC-VIBE (2min 43s acquisition and 3min 44s reconstruction time) sequences.

Conclusions

We have developed and tested a prototype of a QSM processing pipeline using TGV optimization capable of producing inline QSM maps at the scanner console that makes this technique available to a large clinical user base. Although our prototype software was optimized for a vendor-specific MRI hardware, our principal concepts demonstrated here are generalizable for different scanner platforms.

Acknowledgements: SB acknowledges funding from UQ Postdoctoral Research Fellowship grant. MB acknowledges funding from ARC Future Fellowship grant FT140100865. The authors acknowledge the facilities of the National Imaging Facility at the Centre for Advanced Imaging, University of Queensland.



(Filename: TCT_eP-51_figure1.jpg)

eP-58

Use of Triple Smart-smoothing Filters for Enhancing Unsupervised Segmentation of Normal and Ischemic Stroke Images with Self-organizing Maps in Brain CT Images

P Mei¹, C Carneiro¹, L Rittner¹, F Reis¹, T Matys²

¹University of Campinas, Campinas, Brazil, ²University of Cambridge, Cambridge, UK

Electronic Posters

Purpose

To investigate the potential of automated clustering of ischemic stroke 2-dimensional (2-D) CT images by self-organizing maps and if preprocessing of the images by smart-smoothing filters could generate more accurate clustering

Materials and Methods

We selected 10 patients that had had an ischemic stroke (later confirmed by either MRI or perfusion-CT) where noncontrast CT was executed within the hyperacute (up to 4.5 hours) or acute (4.5 to 72h) phase after the onset of the clinical symptoms, and nine controls (normal MRI or perfusion-CT). We selected a 2-D slice of either the ganglionic or immediate supraganglionic level of the brain, in the same fashion that ASPECTS is scored. The images were then preprocessed by three different, smart-smoothing filters on ImageJ, a java based app, and then transformed into numerical matrices that were analyzed and segmented by the SOM algorithm on Weka 3, a Java based app. The resulting, postprocessed images were rated by five individuals, either neurologists or radiologists, blinded to the clinical and demographic information, to see if they considered the left and right halves of each image symmetrical or asymmetrical and also compared by a quantitative value, the Structural Similarity Index (SSIM). Statistical analysis of the results was then performed.

Results

The majority of the raters considered eight out of the 10 stroke cases to have an asymmetrical SOM-generated image, as well as 6 out of the 9 controls to have a symmetrical image, which resulted in a sensitivity of 80%, positive predictive value (PPV) of 73%, specificity of 64%, negative predictive value (NPV) of 75% and accuracy of 74%. The SSIM values obtained from stroke patients vs. normal controls did not differ significantly ($p = 0.213$, Wilcoxon signed-rank test).

Conclusions

Our work suggests that a combination of different smoothing filters before SOM analysis performs better than single filtering on avoiding grainy, heterogeneous clusters, and delivering smooth segments with continuous borders. We found acceptable sensitivity, PPV and NPV, suggesting that, even though SOM processing did not show an objective SSIM discrepancy between stroke and normal CTs, qualitative analysis helped a correct diagnosis in the majority of the cases. This method could be furthermore explored and tested in more subjects, especially the ones in the medical field that need more help with diagnosing ischemic lesions on CTs performed early after ictus, like medical students, nurses and other health professionals.

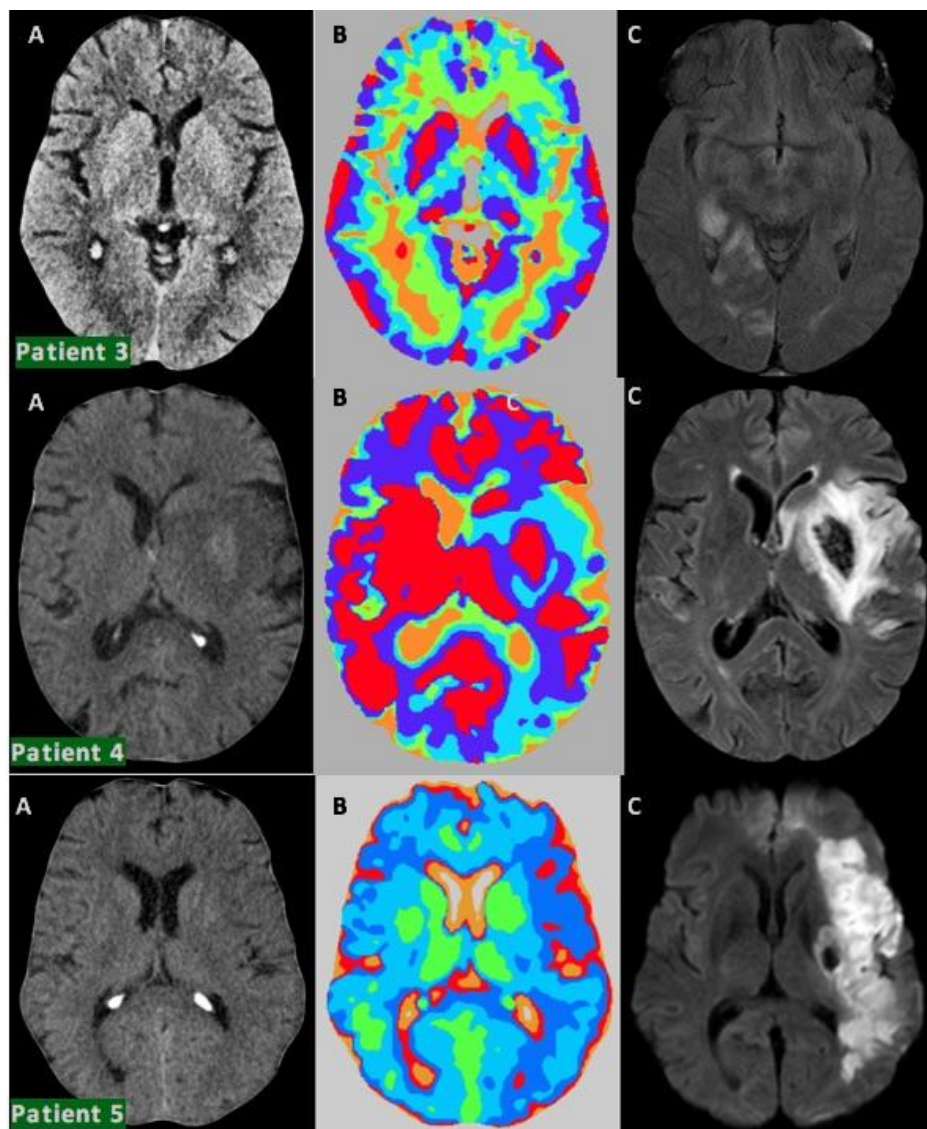


Fig. 3 - Stroke patients 3, 4 and 5, from left to right: A - original CT, B - clustering results after triple filtering and C - FLAIR MRI showing the infarct location

(Filename: TCT_eP-58_CapturadeTela2017-12-11s222651.jpg)

eP-64

Usefulness of Noncontrast CT ASPECTS in the Penumbra in Predicting Functional Outcome After IV Thrombolysis

B Domenech-Ximenes¹, V Cuba¹, G Blasco¹, P Daunis-i-Estadella², C Biarnes¹, M Marti-Navas¹, A Alberich-Bayarri³, S Thio-Henestrosa², J Serena¹, M Terceño¹, Y Silva¹, M Essig⁴, K Nael⁵, C Leiva-Salinas⁶, M Wintermark⁷, S Pedraza¹, J Puig¹

¹Diagnostic Imaging Institute (IDI), IDIBGI, University Hospital Dr Josep Trueta, Girona, Spain, ²University of Girona, Girona, Spain, ³La Fe Health Research Institute, Valencia, IL, ⁴University of Manitoba, Winnipeg, Manitoba, Canada, ⁵Icahn School of Medicine at Mount Sinai, New York, NY, ⁶University of Missouri, Columbia, MO, ⁷Stanford University, Stanford, CA

Purpose

The Alberta Stroke Program Early CT Score (ASPECTS), an imaging-defined measure of ischemic brain injury, is a strong and consistent predictor of clinical outcome. High ASPECTS scores (8–10) favor good clinical outcome after reperfusion; low ASPECTS scores are associated with non-nutritive, futile, or even harmful reperfusion. Although the search for reliable pragmatic imaging biomarkers to select patients for reperfusion continues, preliminary data do not convincingly support the use of noncontrast CT ASPECTS for this purpose. We aimed to assess the ASPECTS on ischemic tissue and in penumbra using perfusion CT (PCT) to predict functional outcome after IV thrombolysis.

Materials and Methods

We evaluated 39 consecutive patients (23 men; age 67 ± 14 years) with middle cerebral artery territory infarcts with noncontrast CT before treatment with fibrinolysis < 4.5 hours of onset, classifying findings as PEN-ASPECTS-positive (penumbra involving ASPECTS area), PEN-ASPECTS-negative (no penumbra involving ASPECTS area), and ASPECTS (nonrecoverable infarcted tissue involving ASPECTS area). Clinical severity was assessed by NIHSS. Infarct volume and ASPECTS at 24h were calculated (Olea Sphere 3.0). Functional outcome was assessed at three months with the modified Rankin scale (mRS) and classified as favorable (≤ 2) or unfavorable (> 2).

Results

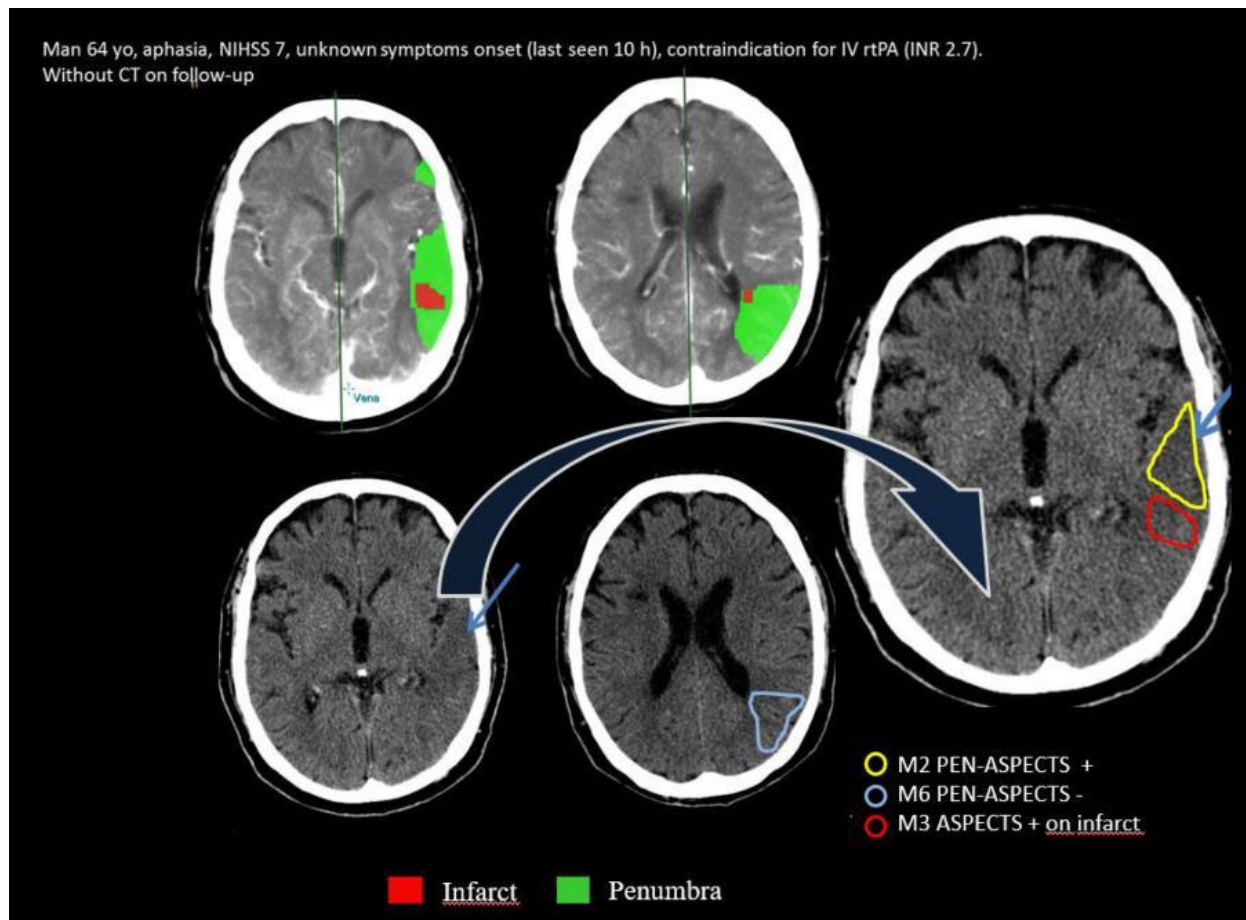
Noncontrast CT findings were classified as PEN-ASPECTS-positive in 22 (58.4%) patients.

Recanalization was successful in 13 (33.3%) patients; four of these were PEN-ASPECTS-positive.

Among patients with PEN-ASPECTS-positive findings, those in whom recanalization was successful were less severe [24h NIHSS 11(8-12) vs. 19(13-21); $p=0.014$], had smaller infarct volumes at 24 h [26.84(20.73-107.64) vs. 189.96(164.4-215.53); $p=0.045$], and had better functional outcome at 3 months [3(1-3) vs. 4(4-5.5)] than those in whom recanalization was unsuccessful.

Conclusions

Assessing PEN-ASPECTS might be useful for identifying patients likely to have favorable outcomes after fibrinolysis.



(Filename: TCT_eP-64_FigurePEN-ASPECTS.jpg)

eP-09

Weight Loss in Obesity: Impact on Carotid Intima-media Thickness and Cardiovascular Risk Factors: A Longitudinal Study

B Domenech-Ximenes¹, G Blasco¹, V Cuba¹, C Biarnes¹, M Marti-Navas¹, P Daunis-i-Estadella², S Thio-Henestrosa², S Pedraza¹, J Fernández-Real³, J Puig¹

¹Diagnostic Imaging Institute (IDI), IDIBGI, University Hospital Dr Josep Trueta, Girona, Spain² University of Girona, Girona, Spain, ³IDIBGI, Girona, Spain

Purpose

Obesity increases the burden of atherosclerosis, and therefore represents a risk factor for clinical cardiovascular disease. Intima-media thickness (IMT) is a noninvasive marker of subclinical atherosclerosis. It remains unclear whether weight loss in obese subjects is accompanied by a reduction in consistent with a lowering of risk of cardiovascular events. We evaluated the effects of bariatric surgery and of a conservative approach (diet and exercise) on carotid IMT and cardiovascular risk factors in obese subjects.

Materials and Methods

We studied 163 individuals [a control group of 75 healthy participants (40 women, age 42 years (31-51), body mass index (BMI) 24.33 (22.23-27.2)) and 88 obese subjects (52 women, age 46 (38-52), BMI 43.37 (40.18-47))]; 22 (25%) obese subjects underwent bariatric surgery. We recorded weight, BMI, blood pressure, cholesterol, triglycerides, fasting glucose, insulin, and insulin resistance index and

Electronic Posters

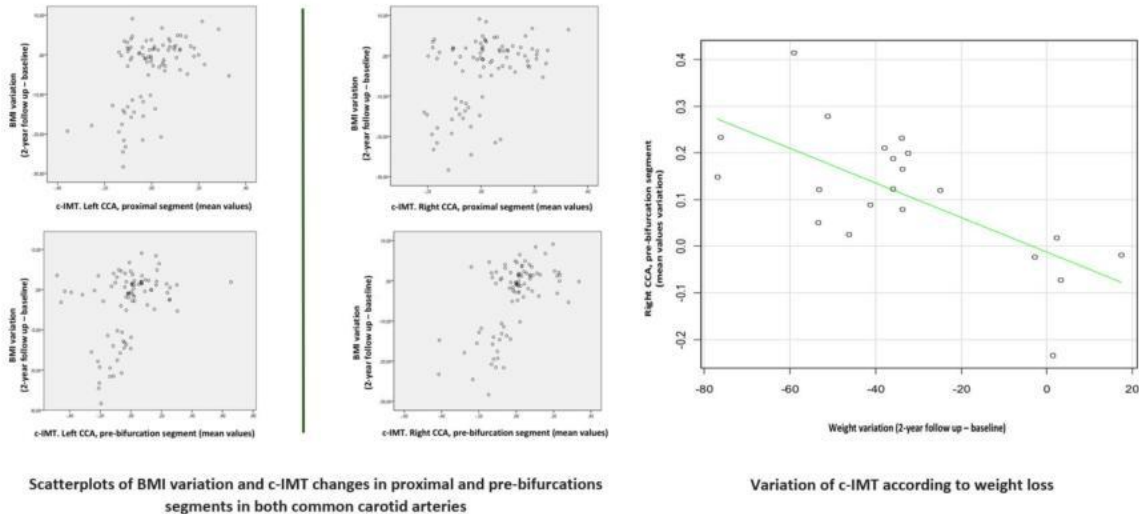
calculated Framingham Risk Scores (FRS). Carotid IMT was evaluated by ultrasound. The impact of weight loss on carotid IMT at two-year follow-up was evaluated with regression models.

Results

At two-year follow-up after bariatric surgery, BMI had decreased from 45.45 to 27.75 kg/m² (p<0.001) and FRS decreased from 15 (10-16) to 13 (8-15) (p=0.035). Mean carotid IMT decreased from 0.85 ± 0.13 mm to 0.65 ± 0.05 mm (p<0.001), a reduction of 0.005 mm per kg. of weight lost. Conservative approach did not impact cardiovascular risk markers.

Conclusions

Weight loss after bariatric surgery substantially reduces carotid IMT values consistent with a lowering in risk of cardiovascular events.



(Filename: TCT_eP-09_FigurecarotidIMTandweightlossobesity.jpg)

Electronic Posters (eP)-Head and Neck

eP-68

Accuracy of MRI in Predicting Extra Capsular Extension of Malignant Lymph Nodes in Oropharyngeal Cancer

A Yepuri¹, H Do¹, N Sadeghi¹, A Joshi², S Barak¹, M Taheri²

¹George Washington University Hospital, Washington, DC, ²The George Washington University, Washington, DC

Purpose

Extracapsular extension (ECE) of metastatic lymph nodes is a high-risk feature for loco-regional recurrence and distant metastasis after surgical resection in patients with oropharyngeal cancer (OPC). Patients with ECE typically require postoperative radiation therapy, which increases patients' morbidity and mortality. MRI has been proposed to play a pivotal role in the detection of ECE in malignant lymph nodes in OPC patients. In this study, we measured the accuracy of previously published and novel MR nodal characteristics suggestive of ECE.

Materials and Methods

In this IRB approved retrospective study, 28 patients with stage III or IV OPC treated in part with selective neck dissection at our institution during the past 10 years were included. All those included in

Electronic Posters

the study were imaged with a preoperative MRI examination. The stored images on PACS were reviewed by an experienced neuroradiologist and a neuroradiology fellow for the: 1) presence of suspicious nodes (SN), 2) the size of the SN, 3) the size of the area of central necrosis within SN, and 4) contour/margin of SN. Pertinent clinical and pathologic data were extracted from an electronic medical record.

Results

Eleven out of 28 patients had pathologically proven ECE. Of the MRI features characterized, presence of necrosis >1 cm in postcontrast MRI was the most sensitive in predicting presence of ECE (sensitivity=72%). The two radiologists differed in their analyses in less than 5% of the MRI findings.

Conclusions

Of the MRI findings characterized in this study, presence of central necrosis >1cm in a SN was the most sensitive MRI marker for the presence of ECE in patients with OPC. The overall accuracy of these MR findings was modest.

eP-75

Clival Chordomas: Evaluation of the Typical and Atypical Radiologic Features

I Mark¹, J Morris¹, C Carr¹

¹Mayo Clinic, Rochester, MN

Purpose

To provide updated information on the spectrum of imaging appearances in clival chordomas at a single institution, with a focus on enhancement pattern

Materials and Methods

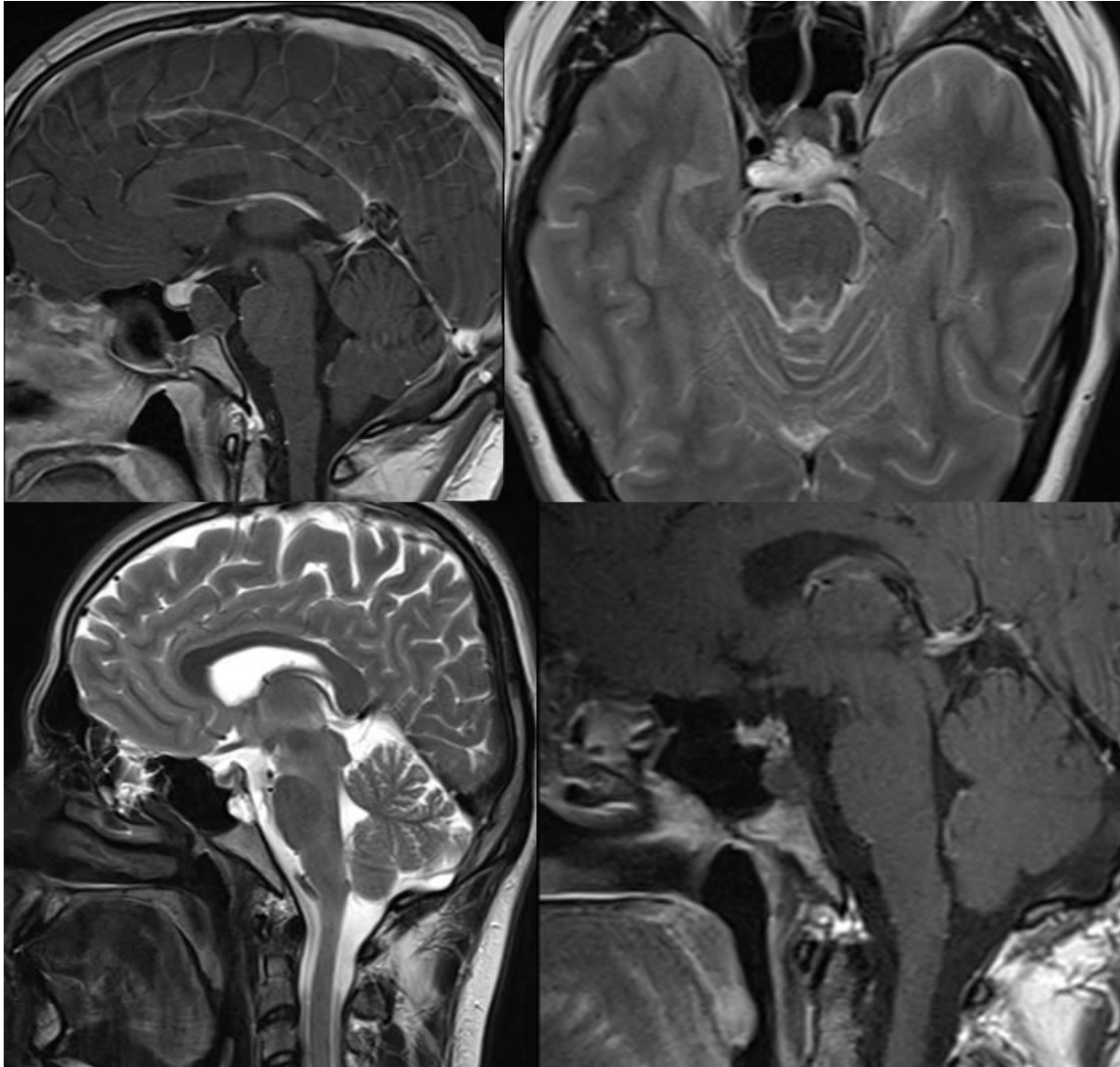
We searched our institutional databases for all patients with pathologically proven clival chordomas from 1997-2017 who had preoperative imaging available. All images were reviewed by a single, fellowship-trained neuroradiologist. The images were evaluated for osseous involvement (osseous, extrasosseous, or both), location (primarily midline vs off midline), aggressiveness of appearance, calcifications (present, absent, or residual), and bony margins (well defined, ill defined, or mixed). Additional MRI characteristics included: degree of T2 hyperintensity, T2 hypointense septations, and T1 hyperintensity. Finally, the degree of contrast enhancement was graded as: marked, moderate, mild, minimal, or absent.

Results

Thirty patients (10 female and 20 male; mean age 27.7 years) were included. Of those, 10 did not have preoperative CT images available. Of the 28 cases with preoperative contrast enhanced MRI the enhancement findings were as follows: 10 (35.7%) had no contrast enhancement, four (14.3%) had mild enhancement, four (14.3%) had moderate, and six (21.4%) had marked enhancement. The chordomas were located off midline in 24.1% (7/29) of patients and primarily midline in 75.9% (22/29) of patients. Aggressive features were noted in 62.5% (15/24) of patients. T2 signal was marked in 48.3% (14/29) and mild in 51.3% (15/29) of patients.

Conclusions

Clival chordomas are classically thought of as slow growing, destructive tumors with local invasion that demonstrate enhancement on MRI, ranging from 95-100% in prior studies. Contrast enhancement has been used as one tool to differentiate from benign entities such as ecchordosis physaliphoras. Our experience finds that up to nearly half of clival chordomas will demonstrate mild or no enhancement at all. Absence of enhancement should not influence the diagnosis of clival chordomas.



(Filename: TCT_eP-75_Picture1.jpg)

eP-73

CT Findings in Angioedema of the Upper Aerodigestive Tract

G Trent¹, L Moreira Vidal², A Medina¹, J Record¹, R Morales³, P Raghavan¹

¹University of Maryland School of Medicine, Baltimore, MD, ²University of Maryland, Baltimore, MD, ³University of Maryland Medical Systems, Baltimore, MD

Purpose

To describe the imaging findings in the upper aerodigestive tract in a cohort of patients with hereditary and drug induced angioedema

Materials and Methods

A retrospective review of the PACS and EMR (01/01/2007 – 01/01/2017) was performed. Thirty patients presenting to the ER with suspected acute angioedema were identified. Contrast-enhanced CT studies of

Electronic Posters

the neck were reviewed by 2 board certified neuroradiologists for the presence of edema in 10 anatomic subsites: perioral subcutaneous soft tissues, lips, oral tongue, base of tongue, floor of mouth, supraglottis, glottis, subglottis, hypopharynx, and retropharyngeal space.

Results

Our cohort included 13 males and 17 females (Age range 8-83, mean 55, median 58). Twenty-six patients (87%) were African American, 4 were Caucasian. Eleven patients had a documented history of recent ACEI/ARB use; 1 had a documented history of hereditary angioedema. The interobserver reliability between the 2 readers for all 10 subsites was poor to modest (Cohen's K 0.02-0.4). However, the most frequently affected subsites, according to at least one reader, were the oral tongue (94%), lips (94%), base of tongue (87%), and oropharynx (72%). The supraglottis was affected in 45%, the glottis in 42%, the subglottis in 13%, and the retropharyngeal space in 34%. In 75% of patients, perioral subcutaneous edema was noted. Two patients demonstrated fluid collections in the lips and tongue necessitating drainage.

Three patients required intubation.

Conclusions

CT may aid in the detection of edema of the aerodigestive tract in patients with angioedema. However, the findings may be subjective and a high degree of clinical vigilance is necessary for timely diagnosis and appropriate airway management for this potentially life-threatening disease.

eP-74

Detection of Loco-regional Recurrence in Head and Neck Malignancy: A Comparison of CT, MRI, and FDG PET-CT

E Kim¹

¹*Hallym University College of Medicine, Anyang, Kyungki-do, Republic of Korea*

Purpose

To compare the diagnostic accuracy of computed tomography (CT), magnetic resonance imaging (MRI), and fluorodeoxyglucose (FDG) positron emission tomography (PET)-CT, alone and in combination, in the detection of loco-regional recurrence of head and neck malignant tumor

Materials and Methods

A total of 101 patients with loco-regional recurrence of head and neck malignant tumor underwent CT, MRI, and PET-CT within 30 days before surgery. In each patient, CT, MRI, and PET-CT were retrospectively reviewed to determine the presence of recurrent tumor in the primary site on a patient-by-patient basis and regional lymph nodes on a level-by-level basis. Imaging results were correlated with the postoperative histopathologic finding or 12-month follow-up as standard of reference. The receiver operating characteristics (ROC) curve was used to compare the diagnostic accuracy of CT, MRI, PET-CT, and their combination.

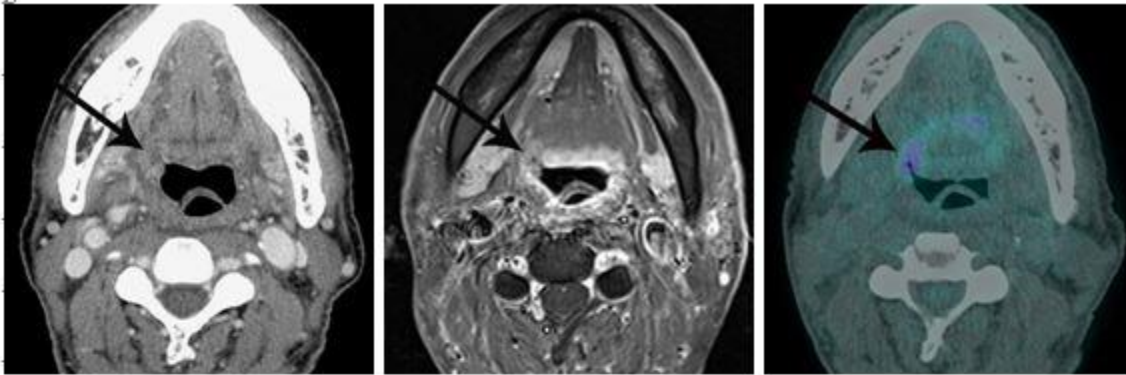
Results

The sensitivity/specificity/accuracy of CT, MRI, and PET-CT for the detection of primary site recurrence was 89.5%/86.7%/89.1%, 94.2%/86.7%/93.1%, and 97.7%/93.3%/97.0%, respectively. The sensitivity/specificity/accuracy of CT, MRI, and PET-CT for the detection of nodal recurrence was 67.1%/99.2%/92.7%, 75.0%/99.2%/94.3%, and 85.2%/94.3%/92.5%, respectively. The area under the curve (Az value) obtained from the ROC curve showed that PET-CT was significantly superior to CT for primary site recurrence (0.955 vs. 0.881, $P < .05$) and MRI and PET-CT were significantly superior to CT for nodal recurrence (0.871 and 0.898 vs. 0.831, $P < .01$ for both). In overall, combination of imaging modalities improved the diagnostic performance, with the highest performance being achieved by MRI plus PET-CT (Az value = 0.961 for primary site recurrence 0.926 for nodal recurrence).

Conclusions

MRI plus PET-CT offered the highest diagnostic performance in the detection of loco-regional recurrence

of head and neck malignant tumor, compared with CT, MRI, PET-CT, and other combinations including CT.



↵

Figure 1: Primary site recurrence in a 65-year-old male patient who had undergone chemoradiotherapy for squamous cell carcinoma on the right side tonsil. **(a)** Primary site recurrence (arrow) in the right tonsil bed is not well seen on axial contrast-enhanced CT (score 1, false-negative). **(b)** Axial contrast-enhanced fat-suppressed T1-weighted MRI demonstrates a small mass-like lesion but without intense enhancement (arrow) in the anterolateral tonsil bed (score 3, true-positive). **(c)** Corresponding ^{18}F -FDG PET/CT image clearly shows a focal area of FDG uptake (arrow, $\text{SUV}_{\text{max}} = 5.6$) in the right tonsil bed, suggesting local recurrence (score 4, true-positive). Histopathological findings obtained after wide excision revealed recurrent tumor. ↵

(Filename: TCT_eP-74_.JPG)

eP-72

Imaging Features of Incomplete Partition Type I (IP1)

D Jamjoom¹, A Zakzouk², F Zawawi¹, S Cushing¹, B Papsin¹, S Blaser¹

¹The Hospital for Sick Children, Toronto, Ontario, Canada, ²King Saud University, Riyadh, Saudi Arabia

Purpose

In IP1, the cochlea lacks the entire modiolus and interscalar septa, resulting in a cystic appearance accompanied by a grossly dilated vestibule (Sennaroglu 2004). The aim of this study is to describe the imaging features of IP1 and correlate these features with the presence or absence of cochlear nerve to determine suitability for cochlear implantation.

Electronic Posters

Materials and Methods

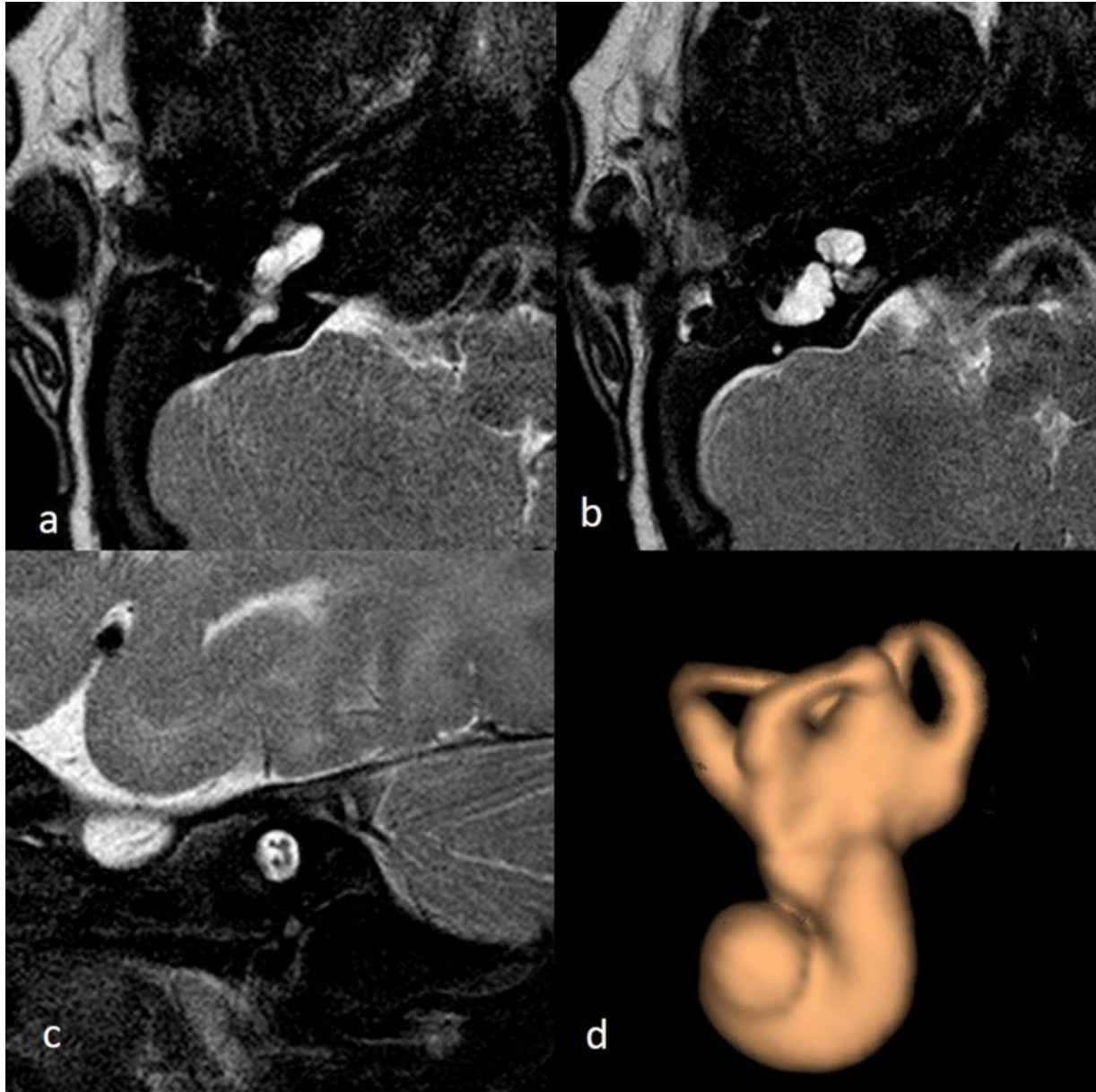
Retrospective analysis of CT and MR images in patients diagnosed with IP1 was carried out. Criteria for Classic IP1 deformity include: dilated basal turn of the cochlea (a) which still maintains a reniform shape on axial imaging, normal sized IAC (c), absent modiolus and internal septa, absent or thin lamina cribrosa (b), dilated ductus reuniens and abnormal posterior labyrinth consisting of a dilated vestibule and absent or small bone islands (d). CT evaluated labyrinthine biometry and presence of a vestibular aqueduct. MRI studies evaluated presence or absence of cranial nerves 7 and 8.

Results

A total of 32 IP1 patients (64 ears) were evaluated. The above criteria for classic IP1 were met in 49 ears (bilateral in 23 patients). Asymmetric bilateral involvement was present in three patients, one each with contralateral common cavity, LSCC dysplasia or hypoplastic cochlea. An associated dilated vestibular aqueduct was found in 12 patients, three which were bilateral. MRI was available in 17 patients, 12 of whom had a full complement of four cranial nerves in each IAC (c). One patient had four nerves on one side and only two on the contralateral side which was lacking a cochlea. One patient had three nerves on one side, two on the other. One patient had three nerves on one side and normal nerves on the other side. One patient had indeterminate number of nerves present bilaterally, another had indeterminate number of nerves present unilaterally. Bilateral CI were placed in six patients. Unilateral CI was placed in nine patients with bilateral involvement. No unilateral involvement patients underwent cochlear implantation.

Conclusions

While patients with imaging features of Classic IP1 are likely to have a cochlear nerve, MRI of the IAC is strongly suggested in order to confirm its presence and allow consideration of cochlear implantation. Presence of VA was seen with both normal and decreased nerve complement. None of the other anatomic anomalies preclude successful implantation.



(Filename: TCT_eP-72_IP1MontageJPEG.jpg)

eP-76

Sellar Tumor Morphology and Risk of Transsphenoidal Surgery Complications

J Reese¹, J Campbell¹, J Han¹, K Lam¹, A Heffernan¹, G Day¹, S DeShields¹

¹*Eastern Virginia Medical School, Norfolk, VA*

Purpose

Endonasal transsphenoidal surgery is becoming the preferred surgical approach for sellar tumors and preoperative imaging is necessary to plan surgical approach. There are a few studies that have evaluated the prospect of tumor volume in predicting the rate of postoperative complications. Data is inconclusive on the relationship between sellar tumor morphology in predicting surgical outcomes. We examine the correlation of tumor morphology and rate of surgical complications.

Electronic Posters

Materials and Methods

Preoperative MRI/CT scans from 138 patients undergoing endonasal transsphenoidal sellar tumor resection from 2007 to 2017 were retrospectively evaluated. Sellar tumors were categorized into 6 morphologies including large lobulated (L), microadenoma (M), round (R), snowman (S), transverse oblong (T), or superior-inferior (V). Anterior-posterior (AP) diameter, transverse diameter, and superior-inferior (SI) diameter were also measured. The rates of postoperative complications were then stratified in relation to the predefined sellar tumor morphology and size. P-values were calculated using a fisher's exact test for morphology association and a two-tailed t-test for tumor diameter association.

Results

The classified morphologies were significantly associated with surgical complication rates with large lobulated at 92%, snowman at 58%, transverse oblong at 53%, superior-inferior oblong at 35%, round at 35%, and microadenoma at 33% (p-value 0.0093). Size dimensions were also significantly associated with complication rate with AP diameter greater than 2.2 cm (p-value 0.0005), transverse diameter greater than 2.7 cm (p-value 0.0001), and SI diameter greater than 2.1 cm (p-value 0.0066).

Conclusions

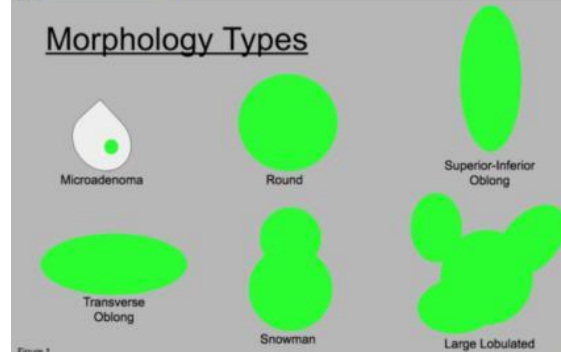
Sellar tumor morphologies classified on preoperative imaging in combination with AP, transverse, and SI diameters can be used to predict the likelihood of postsurgical complications. Each classified morphology is significantly associated with varying probability of surgical complications. In addition, tumor diameter thresholds may also be applied in predicting surgical outcomes. Using tumor morphology and size as predictive measures may help surgeons counsel patients and help surgical planning regarding the extent of resection warranted and need for complex closure.

Variable	Tumor Shape						p-value*
	L	M	R	S	T	V	
Residual, n (%)							<0.0001
Yes	9 (21.4)	0 (0.0)	1 (2.4)	20 (47.6)	8 (19.1)	4 (9.5)	
No	3 (3.1)	9 (9.4)	25 (26.0)	37 (38.5)	9 (9.4)	13 (13.5)	
Recurrence, n (%)							0.1655
Yes	0 (0.0)	0 (0.0)	0 (0.0)	4 (57.1)	0 (0.0)	3 (42.9)	
No	12 (9.2)	9 (9.3)	26 (19.9)	53 (40.0)	17 (13.0)	14 (10.7)	
Re-Op, n (%)							0.1072
Yes	2 (15.4)	1 (7.7)	0 (0.0)	7 (53.9)	0 (0.0)	3 (23.1)	
No	10 (8.0)	8 (8.4)	26 (20.8)	50 (40.0)	17 (13.6)	14 (11.2)	
Adjuvant Tx, n (%)							0.0540
Yes	2 (40.0)	0 (0.0)	0 (0.0)	1 (20.0)	2 (40.0)	0 (0.0)	
No	10 (7.3)	9 (9.8)	26 (19.6)	56 (42.1)	15 (11.3)	17 (12.8)	
Dysosmia, n (%)							1.0000
Yes	0 (0.0)	0 (0.0)	0 (0.0)	1 (100.0)	0 (0.0)	0 (0.0)	
No	12 (8.8)	9 (9.6)	26 (19.0)	56 (40.9)	17 (12.4)	17 (12.4)	
Sinusitis, n (%)							0.9215
Yes	1 (14.3)	0 (0.0)	1 (14.3)	4 (57.1)	0 (0.0)	1 (14.3)	
No	11 (8.4)	9 (9.8)	25 (19.1)	53 (40.5)	17 (13.0)	16 (12.2)	
Meningitis, n (%)							0.1962
Yes	0 (0.0)	1 (14.3)	0 (0.0)	6 (85.7)	0 (0.0)	0 (0.0)	
No	12 (9.2)	8 (8.1)	26 (19.9)	51 (38.5)	17 (13.0)	17 (13.0)	
Vision Disturbance, n (%)							0.9386
Yes	1 (9.1)	0 (0.0)	2 (18.2)	4 (36.4)	2 (18.2)	2 (18.2)	
No	11 (8.7)	9 (7.1)	24 (18.9)	53 (41.7)	15 (11.8)	15 (11.8)	
Diabetes Insipidus, n (%)							0.2128
Yes	3 (10.3)	2 (6.9)	8 (27.6)	14 (48.3)	1 (3.3)	1 (3.3)	
No	9 (8.3)	7 (8.4)	18 (16.5)	43 (39.5)	16 (14.7)	16 (14.7)	
Presence of Complication, n (%)							0.0091
1 or more	11 (15.3)	3 (4.2)	9 (12.7)	33 (46.5)	9 (12.7)	6 (8.3)	
None	1 (1.5)	6 (9.0)	17 (25.4)	24 (35.8)	8 (11.9)	11 (16.4)	

*Fisher's Exact Test used
p < .05

Variable	Tumor Size					
	Length (cm), mean (95% CI)	Width (cm), mean (95% CI)	Height (cm), mean (95% CI)	S Length (cm), mean (95% CI)	S Width (cm), mean (95% CI)	S Height (cm), mean (95% CI)
Residual						
Yes	2.4 (2.1-2.7)	3.0 (2.7-3.4)	2.4 (2.1-2.7)	2.0 (1.6-2.3)	2.1 (1.7-2.5)	1.4 (1.1-1.7)
No	1.8 (1.6-1.9)	2.1 (1.9-2.2)	1.6 (1.5-1.8)	1.6 (1.4-1.8)	1.6 (1.4-1.8)	1.2 (1.0-1.4)
p-values	0.0002	<0.0001	<0.0001	0.0686	0.0143	0.3539
Recurrence						
Yes	2.0 (1.5-2.6)	2.3 (1.6-3.1)	2.2 (1.4-3.0)	2.3 (1.0-3.6)	2.4 (1.4-3.3)	1.5 (1.1-1.9)
No	2.0 (1.8-2.1)	2.4 (2.2-2.6)	1.8 (1.7-2.0)	1.7 (1.5-1.9)	1.8 (1.6-2.0)	1.3 (1.1-1.4)
p-values	0.8138	0.8059	0.3103	0.0871	0.1001	0.5105
Re-Op						
Yes	2.5 (1.8-3.2)	2.8 (2.0-3.6)	2.3 (1.6-3.0)	2.3 (1.5-3.0)	2.3 (1.8-2.8)	1.9 (1.2-2.6)
No	1.9 (1.8-2.1)	2.4 (2.2-2.5)	1.8 (1.7-2.0)	1.7 (1.5-1.9)	1.7 (1.5-1.9)	1.2 (1.1-1.3)
p-values	0.0862	0.1142	0.0954	0.0308	0.0575	0.0028
Adjuvant Tx						
Yes	3.1 (1.8-4.4)	3.6 (2.6-4.6)	2.9 (1.7-4.1)	--	--	--
No	1.9 (1.8-2.1)	2.4 (2.2-2.5)	1.8 (1.7-2.0)	--	--	--
p-values	0.0008	0.0062	0.0065	--*	--*	--*
Sinusitis						
Yes	2.0 (1.3-2.6)	2.6 (1.8-3.4)	1.7 (0.7-2.8)	1.5 (0.8-2.1)	1.4 (0.6-2.2)	1.5 (0.1-2.9)
No	2.0 (1.8-2.1)	2.4 (2.2-2.6)	1.9 (1.7-2.0)	1.8 (1.6-2.0)	1.8 (1.6-2.0)	1.3 (1.1-1.4)
p-values	0.9578	0.5473	0.7068	0.3772	0.2625	0.4567
Meningitis						
Yes	2.7 (1.5-3.8)	3.2 (1.8-4.6)	2.4 (1.6-3.2)	2.3 (1.8-2.9)	2.5 (2.2-2.8)	1.9 (1.1-2.7)
No	1.9 (1.8-2.1)	2.4 (2.2-2.5)	1.8 (1.7-2.0)	1.7 (1.5-1.9)	1.7 (1.5-1.9)	1.2 (1.1-1.4)
p-values	0.0260	0.0421	0.1335	0.0265	0.0160	0.0051
Vision Disturbance						
Yes	2.0 (1.4-2.6)	2.6 (2.0-3.3)	2.2 (1.5-3.0)	2.1 (1.0-3.1)	2.2 (1.4-3.0)	1.4 (0.4-2.3)
No	2.0 (1.8-2.1)	2.4 (2.2-2.6)	1.8 (1.7-2.0)	1.7 (1.6-1.9)	1.8 (1.6-2.0)	1.3 (1.1-1.4)
p-values	0.7555	0.4090	0.1610	0.3608	0.2544	0.8187
Diabetes Insipidus						
Yes	2.2 (1.8-2.7)	2.6 (2.1-3.1)	1.9 (1.5-2.3)	2.2 (1.8-2.7)	2.3 (2.0-2.7)	1.7 (1.3-2.0)
No	1.9 (1.8-2.0)	2.3 (2.2-2.5)	1.9 (1.7-2.0)	1.6 (1.4-1.7)	1.6 (1.4-1.8)	1.1 (1.0-1.3)
p-values	0.2030	0.2856	0.9556	0.0063	0.0007	0.0018
Presence of Complication						
1 or more	2.2 (2.0-2.4)	2.7 (2.5-3.0)	2.1 (1.8-2.3)	2.0 (1.7-2.2)	2.1 (1.8-2.3)	1.4 (1.2-1.6)
None	1.7 (1.6-1.9)	2.0 (1.9-2.2)	1.6 (1.5-1.8)	1.5 (1.3-1.7)	1.4 (1.2-1.7)	1.1 (0.9-1.3)
p-values	0.0005	<0.0001	0.0066	0.0052	0.0006	0.0322

*Two-tailed t-test used
*Sample size too small, unable to perform test
p < .05



(Filename: TCT_eP-76_TableandFigure.jpg)

eP-76a

Ultrasound Differentiation of Benign and Malignant Nodules Originating from the Thyroid Isthmus

L Vu¹, J Debnam², S Ahmed², W Wei³, M Williams⁴, B Edeiken-Monroe⁴, T Vu²

¹N/A, N/A, ²UT MD Anderson Cancer Center, Houston, TX, ³University of Texas MD Anderson Cancer Center, Houston, TX, ⁴The University of Texas MD Anderson Cancer Center, Houston, TX

Purpose

The goal of this study was to determine if there are any ultrasound features that can distinguish a papillary thyroid carcinoma (PTC) originating from the isthmus from a colloid nodule.

Materials and Methods

This IRB approved retrospective study examined patients from our institution from January 2006 to March 2010 with isthmus nodule(s). Thirty consecutive patients were included with the isthmus nodule biopsy proven PTC. The controlled group consists of 30 patients matched to the study patients for age, and sex with biopsy proven isthmus colloid nodule(s) and imaging follow-up. A neuroradiologist blinded to cytologic and histological results reviewed the ultrasound from these 60 patients and characterize the isthmus nodule according to margins, shape, vascular flow, and internal parenchyma characteristics including echotexture, calcification, cystic change or spongiform appearance, and comet tail. Fisher's exact test was used to associate imaging features with lesion status.

Results

The median age at biopsy on patients with isthmus PTC is 57(range 33-89) and the group with colloid nodule had median age of 66.5 (range 39-84). 30/30 PTC and 29/30 colloid had hypoechoic internal echotexture ($p>0.99$). 10/29 PTC and 7/30 colloid had irregular margins ($p=0.052$). 13/27 PTC and 13/29 colloid had no internal vascular flow ($p=0.06$). 18/30 PTC and 10/30 colloid had internal calcification ($p=0.07$). 28/30 PTC and 30/30 colloid have shapes that were wider than tall ($p=0.49$). 27/30 PTC and 26/30 colloid had thyroid capsule abutment more than 25% ($p>0.99$). 0/30 PTC and 8/30 colloid had spongiform appearance and or cystic change ($p=0.005$). 29/30 PTC and 28/30 colloid have no comet tails parenchyma appearance ($p>0.99$).

Conclusions

Spongiform appearance or cystic content within nodules in the thyroid isthmus are reliable ultrasound criteria for benign nodules.

eP-71

Vein of Galen Malformations: An Overview for the Diagnostic Neuroradiologist

S Bukhari¹, F Alsugair¹, J Bhattacharya¹, M Nicolas-Jilwan¹

¹King Faisal Specialist Hospital, Riyadh, Saudi Arabia

Purpose

Vein of Galen malformations are rare developmental vascular anomalies uncommonly encountered by diagnostic neuroradiologists. The purpose of our presentation is to overview the pathogenesis of these malformations and point out the characteristic features to be evaluated on imaging studies of affected patients.

Materials and Methods

A retrospective review of all patients with vein of Galen malformations who presented to our institution between 2002 and 2017 was performed. Twenty-five patients with an age range of 0-16 years were included. We selected various imaging modalities including CT, CT angiograms, MRI, MR venograms, MR arteriograms and conventional angiography images which encompass the full range of imaging manifestations of vein of Galen malformations.

Electronic Posters

Results

We highlight all the pertinent features that should be assessed when interpreting imaging studies on patients with vein of Galen malformations: the anatomy of the vascular malformation including its type (choroidal versus mural), associated persistent arterial and venous embryonic vascular anatomy and patterns of progression. The cerebral sequelae in the form of resultant cerebral ischemia (encephalomalacia, calcifications) or hemorrhagic complications. The hydrodynamic complications including ventriculomegaly, hydrocephalus, venous hypertension and cerebellar tonsillar prolapse

Conclusions
We present a wide range of imaging modalities which illustrate the full spectrum of manifestations of vein of Galen malformations, in an effort to simplify a systematic and comprehensive assessment of the radiologic studies of these patients.

Electronic Posters (eP)-Informatics

eP-77

Effect of Report Template Use on Neuroradiology Report Error Rates

O Kallas¹, C Hawkins², D Siegal³, N Kadom

¹Emory University Hospital, Atlanta, GA, ²Emory University School of Medicine, Atlanta, GA, ³Henry Ford Hospital, Detroit, MI

Purpose

Neuroradiology reports may contain nongrammatical (nonsense, translational, omission, commission) and grammatical errors (typographical, grammatical). Such report errors can alter the meaning of neuroradiology reports and potentially cause patient harm. Recent studies have shown that the use of templates can significantly reduce report error rates. The purpose of this study was to evaluate the effect of using different report types (standard template, structured template, and free text) for noncontrast head CT studies on report error rates at our institution.

Materials and Methods

We searched our institution's radiology information system, A.I. (Analytical Informatics Inc, Baltimore, MD), to obtain 25 free-text, 50 standard template, and 50 structured template noncontrast head CT reports over a 3-year period. Reports were retrospectively reviewed for 11 types of errors, and the numbers and types of errors within each report were recorded. Statistical analysis was performed using Chi square tests (Stata v13) to evaluate for significant differences in error rates between the report types.

Results

All free-text reports contained at least one error (100% error rate), while only 32% of standard and 36% of structured template reports contained errors. Similarly, 96% of free-text reports had nongrammatical errors, while only 16% of standard and 22% of structured template reports contained nongrammatical errors. Error subtype analysis revealed a statistically significant reduction in nonsense, grammatical, punctuation and omission errors ($p < 0.0001$) with either of the two template report types compared to free text reports.

Conclusions

Use of standard or structured report templates can significantly reduce noncontrast CT report errors. The reduction of nongrammatical errors with the use of templates is specifically important because this error type is not captured with dictionary-based correction algorithms. The only other current option for further reducing nongrammatical errors is proofreading; in the future, applications based on Computational Language Understanding (CLU) may be able to detect nongrammatical errors and mark them for correction.

Electronic Posters (eP)-Interventional

eP-81

Outcomes of Pediatric Sclerotherapy in Vascular Malformations

L Walker¹, D Kumari², S Rahim³, M Rajdev², J Curcio², K Blackham⁴, D Nakamoto³, I Patel³
¹University Hospitals Cleveland Medical Center/ Case Western Reserve, Cleveland, OH, ²University Hospitals Cleveland Medical Center, Cleveland, OH, ³University Hospitals Case Medical Center, Cleveland, OH, ⁴University Hospital of Basel, Basel, BS

Purpose

Outcomes of pediatric sclerotherapy in vascular malformations

Materials and Methods

A retrospective chart review of a single institution from 2004-2017 found 28 pediatric patients (16 females: 12 males) who underwent a total of 74 sclerotherapy sessions. These sessions were performed by either US, Fluoroscopy or MRI. Type of malformations, number of sessions, sclerosants, modality, outcomes, and complications were evaluated. Patients were divided into three subgroups by type [low-flow (LF), high-flow (HF) or lymphatic (LM)].

Results

Of the lymphatic malformations (n= 13), 62% had significant response (SR), 23% had partial response (PR), and 15% had no response or worsening (NR/W). Of low flow-malformations (n=14), 42% had significant response, 42% had partial response, and 17% had no response or worsening. Of high-flow (n=1), 100% had partial response. Adjuvant surgery was performed in 5/28 SR patients, 4/28 PR patients, and 2/28 in NR/W patients. The average number of sclerotherapies were three sessions per patient with 7/28 needing four or more (25% of central malformations). Follow-up showed a low percentage of short-term complications (less than six months) including 3.6% with skin ulceration and 1.8% with skin pigmentation. No long-term complications were identified.

Conclusions

Follow-up of pediatric patients with head and neck sclerotherapy demonstrated no long-term complications. However, there were rare short-term complications of skin ulceration and pigmentation.



(Filename: TCT_eP-81_ScreenShot2017-12-15at75839PM.jpg)

eP-78

Single-centre Comparison of Endovascular Treatment of Paraophthalmic-region Aneurysms Using Conventional Coiling, Stent-assisted Coiling, Balloon-assisted Coiling and SILK Flow Diverter Techniques

E Du¹, J Shankar¹

¹*Dalhousie University, Halifax, Nova Scotia, Canada*

Purpose

Intracranial aneurysms affect approximately 5-10% of the general population. Endovascular coil embolization of intracranial aneurysms has become the widely preferred and safer method of treatment. The principle limitation of endovascular coiling methods is aneurysm recurrence, a complication that is being met with the use of vascular reconstructive devices, including balloons and stents. Flow diverting stents, which have only recently been adopted for clinical use in the reconstruction of intracranial vasculature, have shown immense promise, particularly so for the management of paraophthalmic-region aneurysms. These aneurysms are unique due to their proximity to the ophthalmic artery, and subsequently visual symptoms. The various techniques have not been compared for safety and efficacy of treatment of these aneurysms. The purpose of our study was to compare the safety and effectiveness of the various endovascular options (conventional coiling, balloon-assisted coiling, stent-assisted coiling, flow diverter) for the treatment of paraophthalmic-region aneurysms.

Materials and Methods

We retrospectively reviewed 82 consecutive patients with paraophthalmic-region aneurysms treated endovascularly from our interventional neuroradiology database. Six patients were excluded, as we could

Electronic Posters

not access the remote interventional images/reports. Two additional patients were excluded due to premature termination of aneurysm treatment. This left 74 patients and 83 total procedures (including retreatments). We documented demographic, aneurysmal, procedural and outcome characteristics. These characteristics were compared across the four techniques of aneurysm treatment (conventional coiling, balloon-assisted coiling, stent-assisted coiling and SILK flow diverter). We used chi-square tests for the dichotomous variables (longest-to-date Raymond-Roy occlusion, technical complications for each embolization technique, need for retreatment, parent artery stenosis/occlusion).

Results

The mean age for patients was 63 years, and 90% of them were female. Thirty-two percent, 17%, 23% and 13% of patients were treated with conventional coiling, stent-assisted coiling, balloon-assisted coiling and SILK flow diverter, respectively. The mean angiographic follow-up was 56 months (range 3-188 months). Complete aneurysmal occlusion was achieved in 45.8%, 30.8%, 57.1% and 54.6% with conventional coiling, stent-assisted coiling, balloon-assisted coiling and SILK flow diverter ($p=0.557$). The complication rates (both symptomatic and asymptomatic) were 40.6%, 17.6%, 30.4% and 30.7% for conventional coiling, stent-assisted coiling, balloon-assisted coiling and SILK flow diverter ($p=0.015$). Parent artery occlusion was seen in 32%, 17%, 23%, and 13% of conventional coiling, stent-assisted, balloon-assisted and SILK flow diverter procedures, respectively ($p=0.077$).

Conclusions

There was no significant difference across these techniques for paraophthalmic-region aneurysmal occlusion. However, there was a significantly higher risk of complications and higher incidence of parent artery occlusion with conventional coiling for aneurysms at this location. To assess this last point, further study with a larger patient population would be required.

eP-82

Spontaneous Dilatation of Stents After Carotid Artery Stenting, CAS, without Post-CAS Balloon Dilatation for High-signal Lesions on MR Black-blood Images

Y Tanno¹, T Mori¹, N Nakai¹, S Kasakura¹, K Yosioka¹

¹*Shonan Kamakura General Hospital Stroke Center, Kamakura, Japan*

Purpose

Lesions showing MRI-T1WI black-blood high-intensity (T1BBHI) look more vulnerable and softer. Stents spontaneously dilate more significantly in lesions showing T1BBHI than in lesions without T1BBHI, when patients underwent carotid artery stenting (CAS) without post-CAS balloon dilatation.

Materials and Methods

We included in our analysis patients: 1) who underwent elective CAS without post-CAS balloon dilatation from May 2012 to March 2017, and 2) who underwent conventional angiography at 3 months after CAS. Patients' baseline characteristics, the presence or absence of T1WIBBHI, carotid artery % stenosis according to the NASCET criteria before and just after CAS and 3 months after CAS were evaluated. In lesions with and without T1BBHI, we compared percent stenosis before, just after and 3 months after CAS. We performed CAS with distal protection of filter devices, pre-CAS balloon dilatation with a 3.0-mm balloon for lesions with T1BBHI and 4.0-mm balloon for lesions without T1BBHI, 10-mm diameter self-expandable stents of Carotidwallstent, Precise or Protégé.

Results

One-hundred-ten lesions were analyzed. Symptomatic lesions were 62. Carotid artery percent stenosis before, just after CAS, and three months after CAS was 72.7%, 33.2% ($p<0.0001$) and 21.1% ($p<0.0001$). In lesions with and without T1BBHI, carotid artery percent stenosis was 73.3% and 71.7% before CAS (n.s.), 37.1% and 28.3% ($p<0.05$) just after CAS, 24.4% and 21.9% (n.s.) 3 months after CAS, respectively, and change of percent stenosis was -10.39% and -7.76% ($p<0.05$). Stents were dilated spontaneously in both lesions.

Electronic Posters

Conclusions

Stents dilated spontaneously without post-CAS balloon dilatation particularly in lesions showing T1BBHI more significantly.

eP-83

The Halifax Endovascular Thrombectomy for Stroke Effectiveness Study - An Audit

K Virani¹, S Hu¹, S Phillips¹, J Shankar¹

¹*Dalhousie University, Halifax, Nova Scotia, Canada*

Purpose

Endovascular thrombectomy (EVT) treatment for acute ischemic stroke is now recommended as standard of care in several countries, including Canada. However, implementing EVT in routine clinical practice poses many challenges, even in countries with advanced health care systems, because of the specialized and resource-intensive nature of the treatment. While clinical trials rightfully elucidate treatment efficacy, it is also imperative to determine if said treatment can be effective in routine clinical practice. Information about treatment effectiveness can inform decisions about the implementation of new and complex interventions. The Halifax Infirmary (Halifax, Nova Scotia) is the largest neurological centre in Atlantic Canada and the only site capable of delivering EVT in Nova Scotia. The Halifax experience with EVT is of relevance to planning and policy decisions about EVT in Nova Scotia as well as the other Atlantic provinces. The aim of the current study is to delineate if EVT at the Halifax Infirmary (HI) is an effective treatment for acute ischemic stroke.

Materials and Methods

All patients who underwent EVT at the HI between December 2011 and December 2016 were identified from our prospective registry. Demographics (age and sex), process measures (e.g. time from hospital arrival to recanalization), imaging characteristics (Alberta Stroke Program Early CT [ASPECT] score, collateral score, and recanalization score using Thrombolysis in Cerebral Infarction [TICI] score, and functional outcome (modified Rankin score [mRS] at approximately 90 days post-EVT) were derived from the registry, and by review of the patients' imaging studies and hospital records. Effectiveness was assessed by comparing our cohort with patients receiving EVT in the ESCAPE trial.

Results

Ninety-one patients (M:F= 48:43, mean age= 64 yrs; range= 39-91 yrs) presented to our hospital after a mean of 194 min \pm 230 min (median= 97 min) from last seen normal. Of these 58% had an ASPECT score of >7, and 80% of patients had good or intermediate collaterals on their initial CT angiogram. A majority (72% vs. 75% in ESCAPE trial, p= 0.97) also received intravenous alteplase. Retrievable stents only were used for EVT. The mean duration of EVT was 70 min \pm 62 min (median= 58 min). Successful recanalization (\geq TICI 2b) was achieved in 76% (vs. 72.4% in ESCAPE trial, p= 0.97). Among the patients (54 out of 70) in whom recanalization was achieved, mRS scores of 0-2, 3-5 and 6 were seen in 57.4, 24.1 and 14.8% respectively. This compares similar to what was achieved in the ESCAPE trial (53, 37 and 10% respectively, p= 0.96, 0.86 and 0.91 respectively).

Conclusions

An audit of our initial experience with EVT for treatment of acute ischemic stroke yielded results similar to those achieved in the ESCAPE trial. Continuing quality improvement requires ongoing monitoring and feedback of the efficiency and effectiveness of EVT.

eP-79

Transvenous Coil Embolization for a Dural Arteriovenous Fistula with Angiographically Isolated Transverse-sigmoid Sinus: Multiple Microcatheter Technique Via a Modern Triaxial System

T Mine¹, G Benndorf¹, T Stavngaard¹
¹*Rigshospitalet, Copenhagen, Denmark*

Purpose

Dural arteriovenous fistulas (DAVFs) involving an "isolated" transverse-sigmoid sinus (TSS) with direct cortical venous drainage (CVD) have a high risk of intracranial hemorrhage. (1) Optimal endovascular strategy for definitive fistula closure has not been established. Transvenous approach is usually not considered due to expected technical challenges to navigate catheters into the isolated sinus portion. We present a case where transvenous catheter navigation through the "occluded" sinus allowed coil embolization for DAVFs with angiographically isolated TSS using a multiple microcatheter technique via a modern triaxial system.

Materials and Methods

A 69-year-old woman presented pulsatile tinnitus caused by DAVFs with isolated left TSS (Figure 1a). Via transfemoral venous approach, a triaxial system consisting of a 6Fr long sheath advanced into right jugular vein, a 6Fr guiding catheter advanced into the angiographically patent left transverse sinus, and microcatheters was established (Figure 1b). Two microcatheters were navigated through the thrombose segment into the isolated sinus and placed within the proximal and distal portion. Coil embolization was started with the proximal catheter to block the main draining cortical vein, and finalized with the distal catheter to block the drainage towards the deep venous system (Figure 1c).

Results

The affected sinus segment was tightly embolized and the fistula was completely occluded (Figure 1d). Pulsatile tinnitus disappeared immediately after the procedure.

Conclusions

Angiography reflects the main blood stream under the local blood pressure, hence it is not always equal to actual anatomical conditions. If there are potentially patent segments despite invisible in angiography, transvenous penetration could be less struggle and safer than transarterial liquid embolization. Multiple microcatheter approach could reduce the risk of unexpected moving of catheter tip during coil insertion and our triaxial system could provide the stable backup. (2, 3) Our procedure could be accomplished on the basis of the standard concept of the treatment for DAVFs and the new combination of recently advanced modalities.

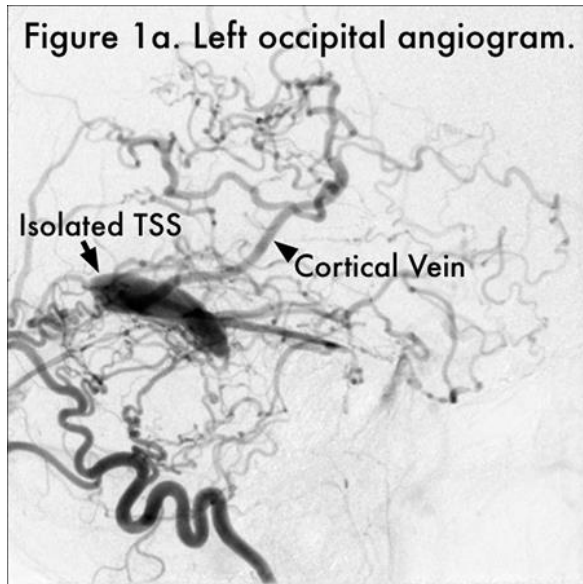
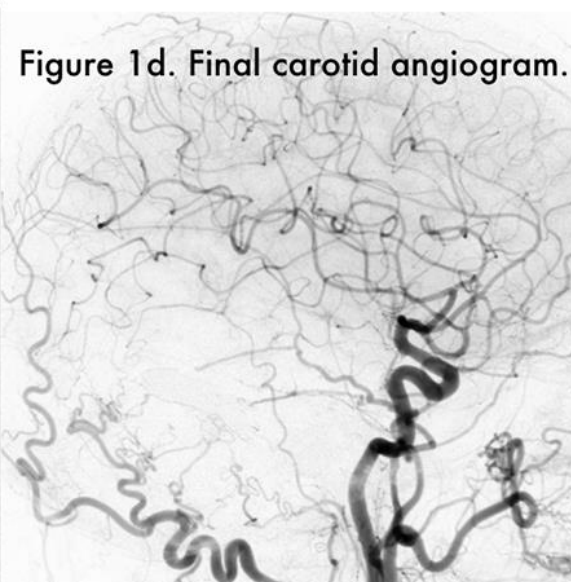
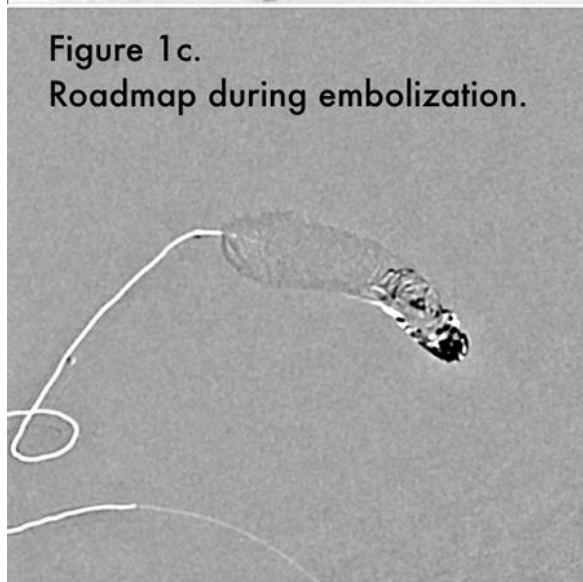
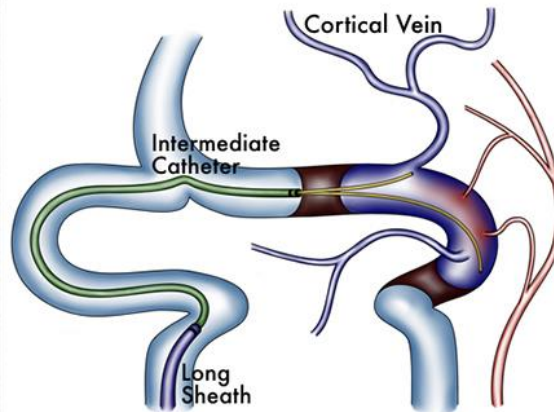


Figure 1b. Scheme of procedure.



(Filename: TCT_eP-79_ASNRfigure1.jpg)

eP-83a

Transvenous Coil Occlusion of Dural Arteriovenous Fistula with Angiographically "Isolated" Transverse-Sigmoid Sinus

T Mine¹, T Stavngaard², J Mason³, G Benndorf⁴

¹Copenhagen Rigshospitalet, København, Denmark, ²Rigshospitalet, Copenhagen Ø, Copenhagen, ³Baylor College of Medicine, Bellaire, TX, ⁴Baylor College of Medicine, Houston, TX

Purpose

Dural arteriovenous fistulas (DAVFs) involving an "isolated" transverse-sigmoid sinus (TSS) portion with direct cortical venous drainage (CVD) have a high risk of intracranial hemorrhage. Optimal endovascular strategy for definitive fistula occlusion has not been fully established. Transvenous occlusion (TVO) of involved sinus is very effective and usually possible without fearing compromise of

normal venous drainage. However, due to expected technical challenges in navigating catheters into thrombosed sinus segments, many operators prefer transarterial embolization (TAE) using liquid embolics. We present a case where catheter navigation through the angiographically "occluded sinus" was straightforward allowing TVO of a DAVF using a multiple microcatheter technique.

Materials and Methods

A 69-year-old woman presented with increasing pulsatile tinnitus caused by a DAVF involving an "isolated" left TSS (Figure 1a). Via transfemoral venous approach, a triaxial catheter system was advanced into the right jugular vein with the intermediate catheter navigated as far as possible into the angiographically patent proximal left transverse sinus. Then a microcatheter was successfully navigated through the angiographically nonpatent transverse sinus portion into the distal portion of the "isolated sinus". As this maneuver turned out to be not technically challenging but rather straightforward, it was immediately repeated with a second microcatheter. Then the two catheters were positioned into the distal and proximal portions of the "isolated sinus" each of which drained into different cerebral venous systems, deep and superficial. First, the more distal sinus portion was packed densely with coils until control runs showed stasis of the superficial CVD. Subsequent coil packing of the remaining sinus compartment through the 2nd microcatheter resulted in complete occlusion of the AV shunting without remaining deep CVD.

Results

Stepwise coil packing of the two "isolated" sinus compartments resulted in complete occlusion of the AV shunting. The patient reported full disappearance of the pulsatile tinnitus immediately after the procedure. DSA FU after 3 months confirmed stable occlusion of the AV shunt and complete resolution of clinical symptoms. No complications were observed.

Conclusions

Angiographic drainage pattern in DAVFs is a reflection of the preferred blood flow, guided by local hemodynamics, such as arterialized venous flow and pressure as well as additional sinus thrombosis. Hence it does not always correspond to actual anatomical arrangements. Similar to dural cavernous sinus fistulas (DCSFs), thrombosed and thus angiographically less or nonopacified sinuses may still be used as efficient endovascular approach, avoiding time consuming transarterial catheter manipulations. As transvenous coil packing allows full control over the positioning of embolic material without potential hazards of untoward liquid migration into distal CVD, this technique still proves a valuable technique. Using dual or multiple catheter techniques provides additional flexibility for the operator to perform targeted occlusion that helps preventing rerouting CVD during the procedure.

Figure 1a. Left occipital angiogram.

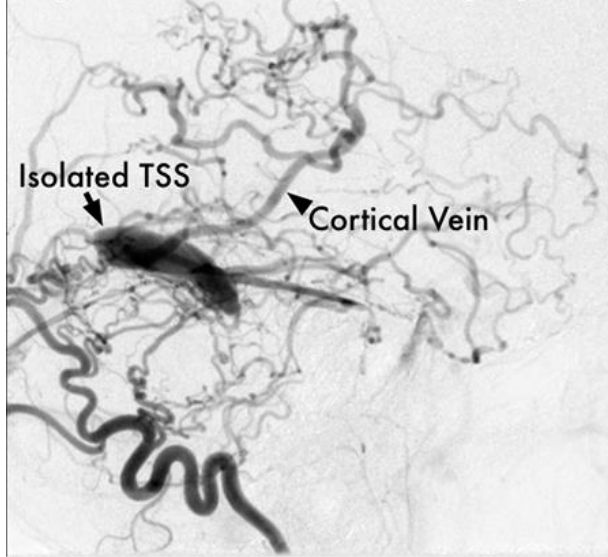


Figure 1b. Scheme of procedure.

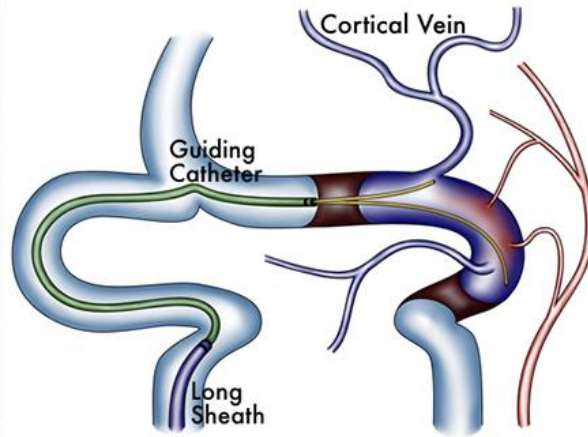


Figure 1c.
Roadmap during embolization.

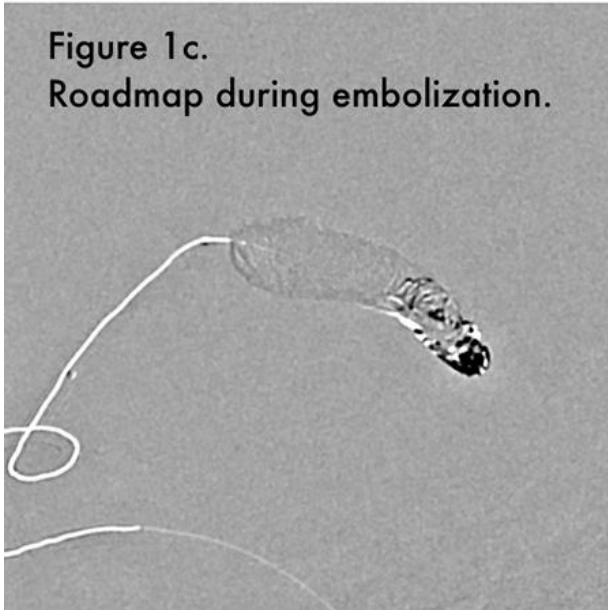
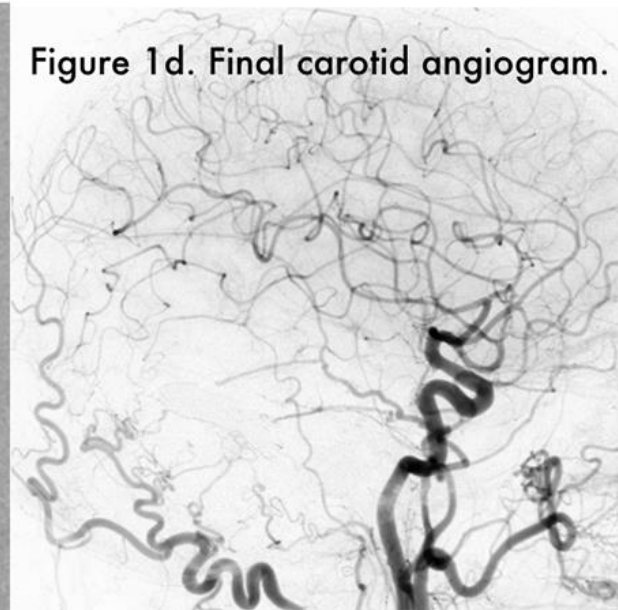


Figure 1d. Final carotid angiogram.



(Filename: TCT_eP-83a_ASNRfigure.jpg)

eP-80

Unilateral PRES Caused by Rapid Fluctuation of BP Secondary to Coronary Air Embolism

K Patel¹, M Tominna¹, J Wilseck²

¹Oakland University William Beaumont School of Medicine, Royal Oak, MI, ²Beaumont Hospital, Royal Oak, MI

Purpose

Unilateral posterior reversible encephalopathy syndrome is extremely rare. We present the case of a 63-year-old female undergoing elective stent-assisted coiling of an unruptured basilar tip aneurysm who

Electronic Posters

developed symptomatic unilateral PRES following inadvertent coronary air embolism following resuscitation with atropine and epinephrine.

Materials and Methods

A 63-year-old female presented for elective stent-assisted coiling of an unruptured enlarging basilar tip aneurysm. The patient had a past medical history significant for coronary artery disease, hypertension, and type 2 diabetes mellitus. Arterial access into the right femoral artery was obtained using a 501 micropuncture set. A 6-F shuttle guide catheter was placed in the descending thoracic aorta-left subclavian artery junction. Through this a 5-F intermediate catheter was advanced into the left vertebral artery. This coaxial system was used to provide stability given the tortuous vertebral anatomy. Angiography of the left vertebral artery demonstrated a wide neck aneurysm of the basilar tip. A stent was carefully deployed from the posterior cerebral artery to the distal basilar artery. Coil embolization of the basilar tip aneurysm sac was performed through the stent interstices without complication. There was adequate occlusion of filling of the aneurysm and microcatheter was removed. The patient suddenly developed bradycardia and hypotension along with inferior lead ST elevation during exchange of the guide catheter arterial infusion bag. Air was visualized within the arterial tubing attached to the proximal shuttle guide catheter. Tubing was immediately disconnected and the catheter was aspirated to obtain blood. The patient's bradycardia and hypotension were managed by the anesthesia department with intravenous .5mg atropine and 1 mg epinephrine and 100% oxygen. Vitals were fluctuating and the patient became hypertensive. Eventually, the blood pressure stabilized in the normal range and ST elevation resolved. A contrast injection through the intermediate catheter was performed. Patency of the left vertebral artery and posterior fossa arterial vasculature was demonstrated without evidence of arterial air emboli. Four vessel diagnostic cerebral angiogram was then performed, which showed no evidence of arterial occlusion or arterial air emboli.

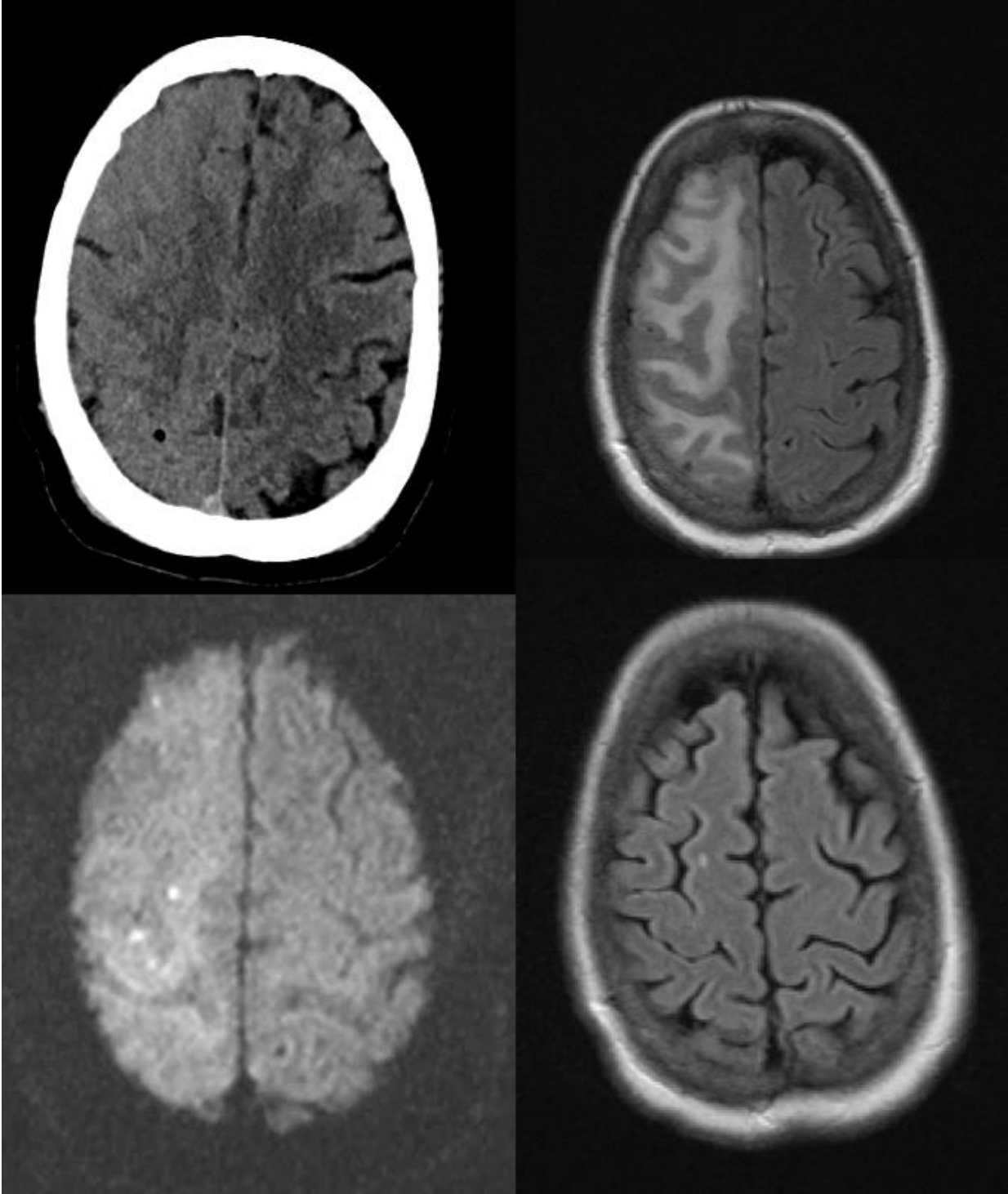
Results

After the procedure, the patient underwent a head CT which demonstrated no acute hemorrhage with two foci of air within the right superior central sulcus. Right hemispheric sulcal effacement with preservation of the grey white differentiation was also visualized, consistent with diffuse right hemispheric vasogenic edema (Figure 1). She was transferred to the ICU for close observation and medical management. Upon extubation, the patient showed signs of left sided hemiparesis and dysarthria with hemi-neglect (NIHSS-8). Repeat head CT the next day showed resolution of the previously seen foci of intracranial air but persistent diffuse vasogenic edema involving the right cerebral hemisphere. MRI of the brain performed 48 hours after the procedure demonstrated vasogenic edema throughout the superior right cerebral hemisphere (Figure 2). Small scattered foci of diffusion restriction were visualized in both cerebral and cerebellar hemispheres, consistent with acute infarcts, but the majority of the white matter did not restrict (Figure 3). The patient remained stable and was subsequently transferred to a regular medical floor. The patient's symptoms of left hemiparesis and neglect slowly improved over six days. The patient was then transferred to inpatient rehabilitation. Her symptoms continued to improve and she was discharged home after two days. (NIHSS-1 at discharge). Repeat MRI performed six weeks after the procedure demonstrated complete resolution of the right cerebral hemispheric vasogenic edema (Figure 4). At the time of her follow up imaging, the patient was asymptomatic and had complete resolution of her neurological symptoms.

Conclusions

Posterior reversible encephalopathy syndrome (PRES) is usually a reversible radiological and clinical entity which presents with a variety of symptoms ranging from headache, seizures, visual disturbances, altered mental status, and loss of consciousness. The most common causes of the syndrome are severe hypertension, eclampsia, bone marrow or solid organ transplantation, immunosuppressive drug toxicity, renal failure, infection, and various autoimmune diseases. Typical imaging manifestations are bilateral symmetric areas of hemispheric edema involving the parieto-occipital cortical and subcortical regions which usually do not enhance or show restricted diffusion. However, atypical imaging findings in terms of location, asymmetry, and unilaterality of the lesions have been described in the literature but are not very common. To the best of our knowledge, there are only a few reported cases of unilateral involvement

by PRES. Here we present a very rare case of unilateral PRES caused by rapid fluctuation of blood pressure secondary to coronary air embolism during cerebral arterial angiography.



(Filename: TCT_eP-80_images.jpg)

Electronic Posters (eP)-Pediatrics

eP-88

A Longitudinal Study of Patients With Morning Glory Disc Anomaly and Intracranial Vascular Abnormalities

S Key¹, S Mansukhani¹, N Kadom¹, P Lenhart¹

¹Emory University, Atlanta, GA

Purpose

Morning glory disc anomaly (MGDA) is a congenital deformity of the optic nerve and disc. The appearance of the optic disc and peripapillary blood vessels resembles the morning glory flower (1). The disease is typically unilateral and presents with poor visual acuity. The etiology of this disease is unknown. Although MGDA can occur in isolation, it is often associated with midfacial malformations, transsphenoidal encephaloceles, and intracranial vascular abnormalities (2). This study focuses on intracranial vascular abnormalities in patients with MGDA. Several studies have demonstrated the increased prevalence of intracranial vascular abnormalities in patients with MGDA. These commonly affect the anterior circulation in the brain, such as moyamoya syndrome and internal carotid artery stenosis (3). Patients are prone to serious and potentially fatal complications including strokes, bleeding, and aneurysms (4, 5). Patients with vascular abnormalities are often followed with imaging to assess for progression of vascular disease. The preferred imaging modality in children is MRI and MRA. There is currently no evidence-based guidance informing the decision regarding which patients with MGDA and intracranial vascular abnormalities need follow up imaging, or how often radiologic exams should be performed. It is also unclear how intracranial vascular abnormalities in MGDA patients progress over time. The purpose of this study is to characterize the clinical course, progression of imaging findings, and treatment outcomes for patients with MGDA and intracranial vascular abnormalities.

Materials and Methods

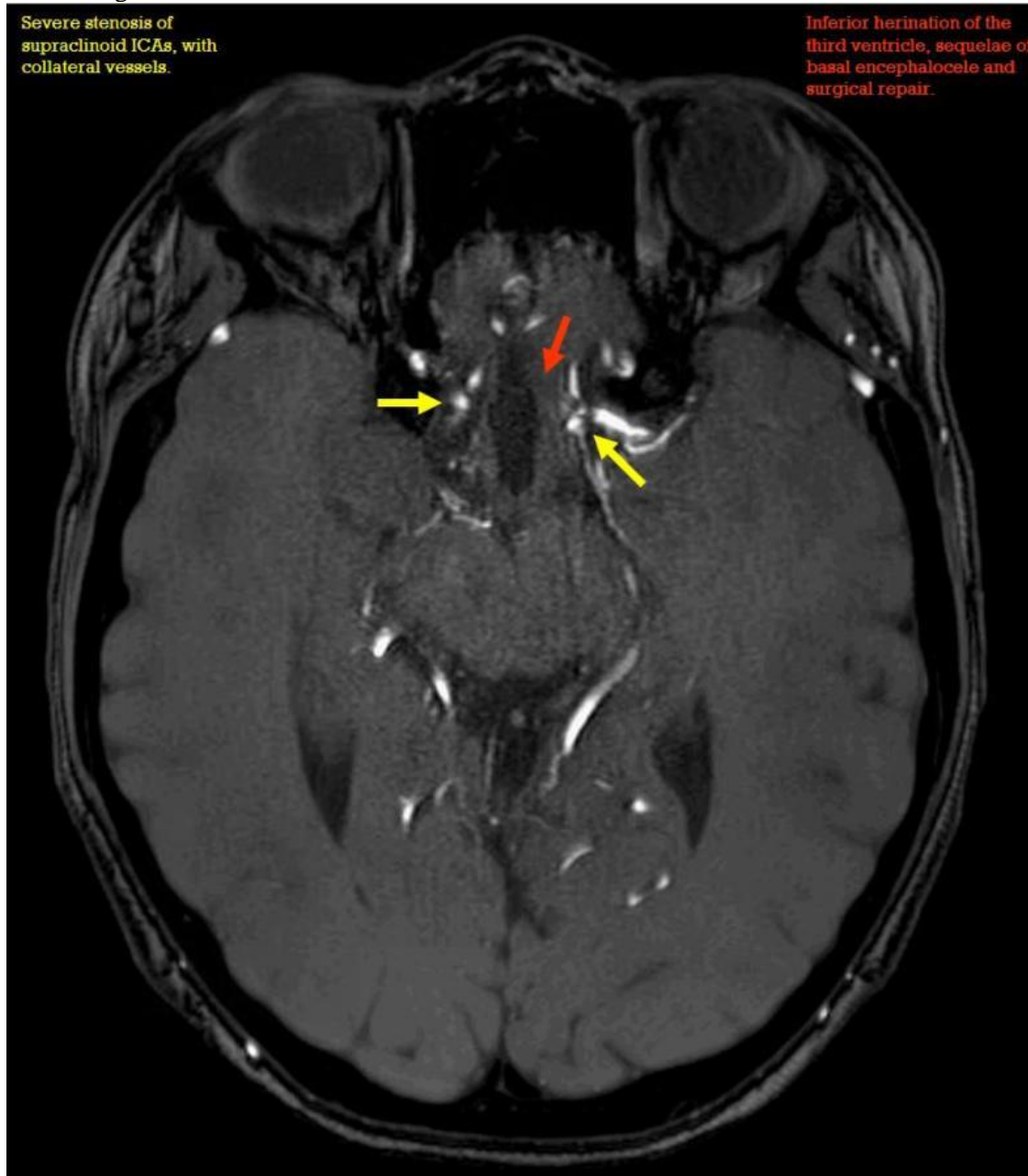
We retrospectively reviewed the medical records of 25 patients at Emory Eye Center and Children's Healthcare of Atlanta (CHOA) between 2001-2017. The study was approved by the Emory and CHOA Institutional Review Board. After IRB approval was obtained, the Emory Clinic Electronic Health Record (EHR), the Children's Healthcare of Atlanta Montage Radiology Database, and the Children's Healthcare of Atlanta EHR were searched using the keywords "morning glory", "other disorders of optic disc", and "congenital malformations of the optic nerve" for examinations performed between 01/01/2001 and 04/01/2017. Patients with MGDA and at least one radiology examination of the intracranial vasculature, including magnetic resonance angiography (MRA), computed tomography angiography (CTA), or catheter angiography were eligible for inclusion. Information from the EHR and/or paper patient medical records was used to ensure patients had a clinical diagnosis of MGDA. Ophthalmologic exam data and imaging exam data was collected and analyzed.

Results

Nineteen of the 25 patients had an abnormality on MRI and/or MRA characteristic for MGDA, including abnormal morphology of the globes or optic nerves (17), intracranial vascular abnormalities (10), colobomas (7), or basal encephaloceles (2). Intracranial vascular abnormalities included: stenosis of one or both internal carotid arteries (ICAs) (6); absence, stenosis, or hypoplasia of one or both A1 segments of the anterior cerebral arteries (5); absence of one ICA (1); and stenosis of the M1 segment of one middle cerebral artery (1). Six of the 25 patients had multiple MRI and/or MRAs performed, including four of the patients with abnormalities. Five of these six patients were stable on follow-up exams. One of these patients had an initial normal MRA of the head, which progressed to slight asymmetry of the supraclinoid ICAs two years later, and severe narrowing of the supraclinoid ICAs six years after the first exam. Catheter angiography then demonstrated bilateral moyamoya syndrome, and the patient underwent bilateral encephaloduroarteriosynangiosis (EDAS).

Conclusions

We found a prevalence of 40% for cerebrovascular abnormalities in 25 patients with MGDA. Not all patients with vascular anomalies underwent follow-up imaging, reflecting the lack of evidence-based guidance regarding screening. Most patients who had serial imaging did not have significant progression of intracranial vascular disease (5/6). One patient progressed from a normal head MRA to moyamoya syndrome over the course of six years, and was treated with bilateral EDAS. Based on our findings, we recommend including MRA imaging in the initial MRI screening for patients with MGDA; follow-up every 2-3 years should be performed to identify progressing vascular changes that may require medical and/or surgical interventions.



(Filename: TCT_eP-88_MRImage.JPG)

eP-84

Asymptomatic Intracranial Aneurysms in Children: 18-years' Experience in a Tertiary Pediatric Center

D Bisson¹, A Amirabadi², M Shroff², T Krings³, V Pereira³, P Muthusami²

¹University of Toronto, Toronto, Ontario, Canada, ²The Hospital for Sick Children, University of Toronto, Toronto, Ontario, Canada, ³Toronto Western Hospital and University Health Network, Toronto, Ontario, Canada

Purpose

There is little data in the literature on the natural history and characteristics of incidental intracranial aneurysms in children. The purpose of this study was to analyze this cohort, to help guide management.

Materials and Methods

An IRB-approved retrospective review was performed of incidental intracranial aneurysms in patients <18 years of age, from 1998-2016 at our Institute. Ruptured and symptomatic aneurysms, and aneurysms flow-related to an arteriovenous shunt, were excluded. Clinical data (age, sex, syndromic association) and radiological data (location, aneurysm type, size, presence of intraluminal/intramural thrombus, mass effect) were recorded. Follow-up imaging data was assessed for temporal changes.

Results

We found 60 intracranial aneurysms in 51 patients (M:F = 36:15; mean age 10.5±0.5 years, range 9 months–17 years). A single aneurysm was found in 45/51 (88.2%) patients, while 2 and 3 aneurysms were found in 3 patients each (5.8%). Syndromic association was found in 22/51 (43.1%) of patients, most frequently Sickle Cell Disease (10/22=45.5%). Aneurysms were saccular in 38/60 (63.3%), the remaining fusiform. Mean size was: saccular 4.8 mm (range 0-30 mm), fusiform 6.5 mm (range 4-15 mm). Aneurysms arose from the internal carotid artery (R:L =1.4) 31/60 (51.7%), most commonly in the cavernous segment (10/31 cases : 32.2%). The average duration of follow-up was 47.2 ± 38.0 months, with a mean size change of -0.61±4.2 mm. Size change/time during follow-up was -0.01±0.08 mm. Only one case showed a significant increase in size (from 4.0 mm to 8.0 mm), and required treatment, which was performed by endovascular sacrifice of the internal carotid artery.

Conclusions

Incidentally discovered intracranial aneurysms are rare in children. They are more likely to be associated with cerebrovascular syndromes, have a male predominance, commonly involve the internal carotid arteries and are often single. They do not show a significant growth or imaging signs of rupture. Most do not necessitate treatment and short-term follow-up intervals are not warranted.

eP-85

Bilateral Hyperintensity of the Central Tegmental Tract in Pediatrics: A Systematic Review

C Mallio¹, J Van Goethem², T De Bondt², L van den Hauwe², P Parizel²

¹Università Campus Bio-Medico di Roma, Rome, Italy, ²University Hospital Antwerp, Antwerp, Belgium

Purpose

The aim of the present study is to provide a comprehensive literature review on central tegmental tract hyperintensity in pediatric patients.

Materials and Methods

The literature search was performed in December 2017 using Medline PubMed (<http://www.ncbi.nlm.nih.gov/sites/entrez/>), Google Scholar (<https://scholar.google.it/>) and Cochrane Central (<http://www.thecochranelibrary.com/view/0/index.html>) databases. The following combinations of keywords were used: "tegmental tract AND hyperintensity" AND "tegmental tract AND MRI". The title and abstract of each study were consulted and discussed by all authors, to define whether each study was matching or not with the topic of our review. The reference list of each selected article was further

Electronic Posters

reviewed to identify additional studies of potential interest. For each of the papers included we evaluated the following features: number of reported patients with central tegmental tract hyperintensity, age at detection, gender, clinical condition, concomitant imaging findings including DWI and imaging follow-up. Statistical analysis of the age distribution was done using a Kolmogorov-Smirnov test.

Results

According to the inclusion criteria, 20 publications relevant to the topic were included. Of these, 11 were retrospective studies and nine were case reports. We found a total of 226 patients with central tegmental tract hyperintensity reported in literature. The age parameter showed a significantly non-Gaussian distribution (KS test; p-value < 0.001). The median age was 1.83 years (range: 7 days – 21years; P25= 1.00years, P75= 3.00years; IQR= 2years). The age of individual patients was not available in 111 cases. Regarding the patients gender, 54 (41%) were females and 78 (59%) were males. Details about the gender of individual patients with central tegmental tract hyperintensity were not available in 94 cases. The most common clinical condition associated with central tegmental tract hyperintensity was cerebral palsy (51 cases; 22,6%), followed by glutaric aciduria type 1 (50 cases; 22,10%). Central tegmental tract hyperintensity was most commonly reported without other concomitant brain MRI abnormalities (32 cases; 21,8%). Data regarding DWI and follow-up were largely unreported.

Conclusions

MRI T2-hyperintensity of the central tegmental tract is a poorly understood and poorly investigated phenomenon. Central tegmental tract hyperintensity was reported in 226 cases. The two most common clinical conditions associated with central tegmental tract hyperintensity were cerebral palsy and glutaric aciduria type 1. Moreover, central tegmental tract hyperintensity was found most commonly in the absence of other concomitant brain MRI abnormalities.

eP-87

Computed Tomographic Findings in Congenital Zika Syndrome: Beyond Microcephaly

A Meoded¹, A Hazin², T Huisman¹

¹The Johns Hopkins University School of Medicine, Baltimore, MD, ²Instituto de Medicina Integral Professor Fernando Figueira Recife, Brazil

Purpose

Starting in May 2015, an outbreak of ZIKV infection has been reported in Brazil in association with an increasing number of neonates with congenital microcephaly in ZIKV-affected regions. The main concern is the causal relationship between prenatal ZIKV infection and congenital microcephaly, which has been confirmed recently. Prenatal ZIKV infection may cause severe brain anomalies that are described as congenital Zika syndrome. In this study, we aim to illustrate the postnatal neuroimaging findings that may be seen in babies with congenital ZIKV infection.

Materials and Methods

We report findings obtained by means of brain CT in 63 infants with congenital microcephaly in which the clinical and epidemiologic data are compatible with congenital ZIKV infection. We performed a detailed semiquantitative analysis of brain abnormalities seen in these babies.

Results

Head CT images were obtained at a mean age of 36 days after birth. Punctate calcifications were seen in all the infants and mainly involved the frontal lobe and the parietal lobe and were located mainly at the corticomedullary junction with a predominately bandlike distribution. Ventriculomegaly was found in all the infants and was rated as severe in the majority. All the infants had global hypogyration of the cerebral cortex that was severe in 78% of the infants. Cerebellar hypoplasia was present in 74% of the infants. In all the infants, there was abnormal hypodensity of the white matter. Associated abnormalities were found such as: polymicrogyria, lissencephaly-pachygyria, agenesis/hypoplasia of the corpus callosum, cerebellar and brainstem hypoplasia.

Electronic Posters

Conclusions

Congenital ZIKV infection may cause several brain abnormalities that can be detected by postnatal neuroimaging. Although, these findings are not pathognomonic, their detailed knowledge in combination with clinical history, other clinical and imaging features, and laboratory studies is important for an early diagnosis, prognosis, and counseling of the affected children and families.

eP-92a

Diffusion Restriction in Subacute Sclerosing Panencephalitis(SSPE)--A Not So Uncommon Finding

M Bhat¹, C Prasad¹

¹*National Institute of Mental Health and Neurosciences, Bangalore, Karnataka, India*

Purpose

To describe the unusual finding of diffusion restriction in four cases of SSPE. SSPE is a progressive encephalitic illness of childhood and early adolescence that occurs due to persistent measles virus infection of the central nervous system. It is characterized by cognitive decline, myoclonic jerks and typical EEG findings. Variable clinical presentations may delay the diagnosis and initiate unnecessary investigations. Imaging plays an important role as an adjunct to CSF antibody titres in definitive diagnosis of SSPE. Multiple studies have described the conventional imaging features of SSPE; however, there are few reports of diffusion weighted imaging (DWI) in SSPE. We herewith describe the imaging findings in four cases of SSPE with special reference to DWI.

Materials and Methods

We reviewed the clinical, EEG and imaging findings in four patients with SSPE that presented to our institute from 2014-2017. The CSF of all patients was positive for anti-measles IgG antibodies and titre was 1:625. MRI brain was performed in all four patients in a Phillips clinical scanner. T1WI pre and postcontrast, T2WI, FLAIR, GRE sequences were obtained along with a six direction DTI. Fever was the initial complaint in all four cases, followed by cognitive decline and myoclonic jerks. The course was rapidly progressive over 2-3 months and all of them presented in a bed-bound state. MRI in case one demonstrated swelling of bilateral putamina with patchy T2/FLAIR hyperintensities in both caudate nuclei and putamina. T2 hyperintensities were also noted in the white matter of both temporoparietal regions. On DWI there was patchy diffusion restriction in the basal ganglia (Fig.1). The second patient had T2/FLAIR hyperintensities in the right parietooccipital grey and white matter which showed peripheral diffusion restriction. The third patient had bilateral frontal and parietooccipital white matter T2 hyperintensities in addition to diffusion restriction in both basal ganglia. The last patient had T2/FLAIR hyperintensities in both middle cerebellar peduncles, pons, midbrain and frontal and parietooccipital white matter. Hot cross bun was also noted in the pons. Diffusion restriction was seen in the MCP's.

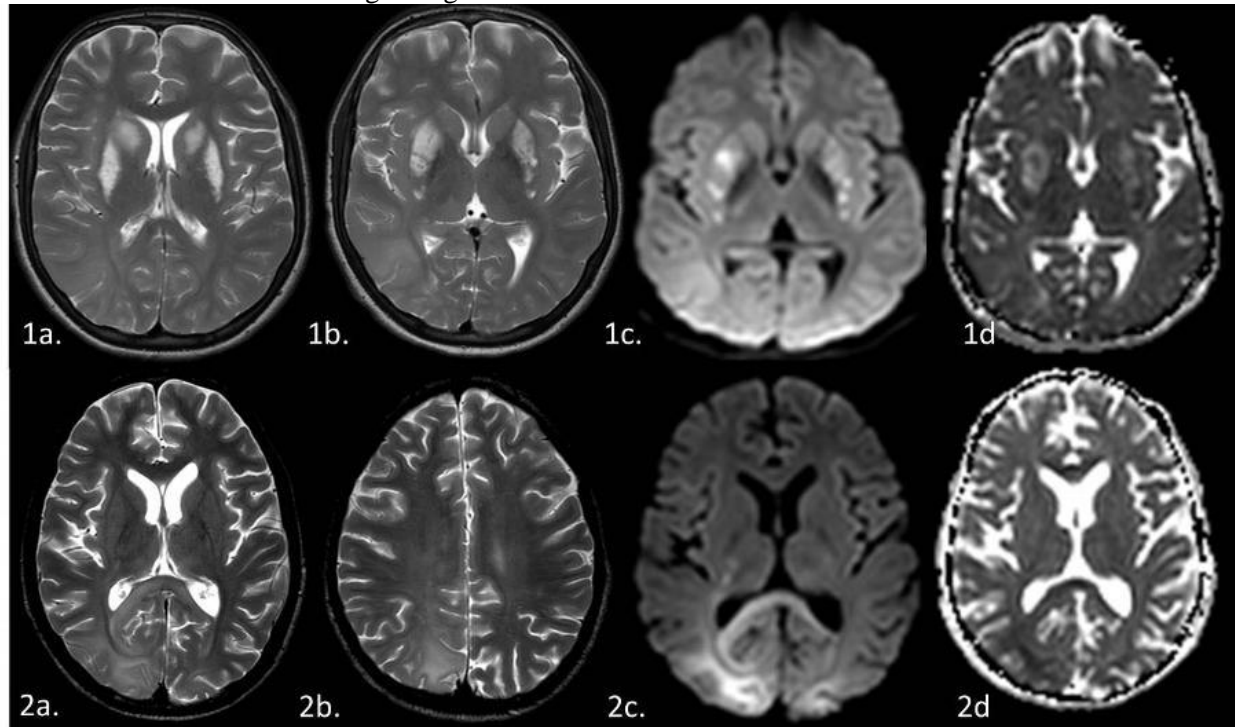
Results

SSPE is a near-fatal neurological condition that begins insidiously and progresses slowly, leading to death within 1-3 years after onset. About 10% of patients may present with a rapidly progressive course with death occurring within six months of onset. All the cases in this series were in bed-bound state at presentation which was 2-3 months from onset and fulfilled the criteria for fulminant SSPE. Their condition worsened during the hospital stay despite treatment. The conventional imaging findings were consistent with the earlier described features. Involvement of basal ganglia and brainstem is uncommon and has been described in two instances previously. Literature on DWI in SSPE is sparse. Most authors have described facilitated diffusion with increased ADC values. Two reports have described diffusion restriction in SSPE. Oguz et al. reported DWI findings in two cases of rapidly progressive SSPE (1). In one of their cases, there was increased diffusion in all the lesions with restricted diffusion in the margins of the lesions. The other case demonstrated restricted diffusion in bilateral middle cerebellar peduncles. In the present series diffusion restriction was noted in the MCP's in case four and margins of lesion in case two. Shah et al. described extensive diffusion restriction in bilateral cerebral hemispheric white matter,

internal capsule, thalami and midbrain in a case of fulminant SSPE and ascribed it to cytotoxic or intramyelinic edema secondary to the necrotizing leukoencephalopathy (2). Cytotoxic edema involving infected oligodendrocytes may contribute to diffusion restriction as is seen in tumefactive demyelination and PML (3, 4).

Conclusions

Diffusion restriction may be seen in fulminant cases of SSPE and its occurrence in unusual locations should not deter us from making a diagnosis of SSPE if clinical criteria are satisfied.



(Filename: TCT_eP-92a_sspe.jpg)

eP-90

Head Trauma, Atrophy and a Tumor: A Fallacy of Interpretation

C Prasad¹, M Bhat¹

¹National Institute of Mental Health and Neurosciences (NIMHANS), Bangalore, Karnataka, India

Purpose

It broadens the imaging phenotype of basal ganglionic germinoma.

Materials and Methods

A 18-year-old boy presented to our OPD with multiple episodes of seizures and occasional headache since past 6 months. He had a past history of loss of consciousness following road traffic accident which happened about 3 years back. In view of trauma, he was evaluated with CT which demonstrated a left temporo-parietal hemorrhagic contusion and was treated conservatively. He was evaluated with MRI brain at our institute.

Results

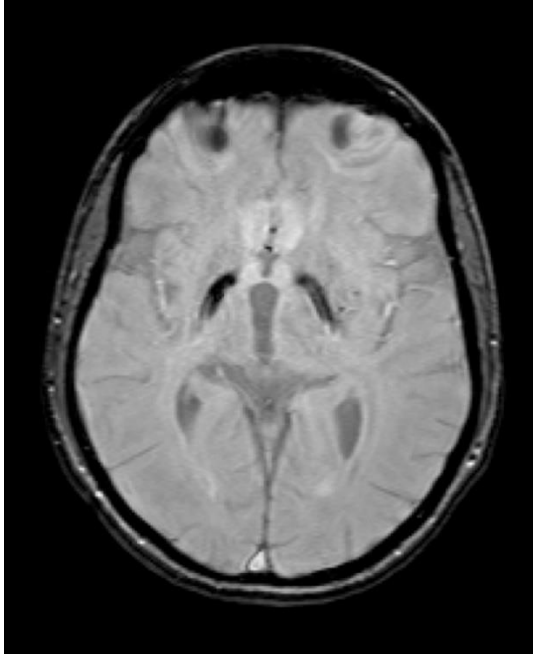
MRI showed T2 and FLAIR hyperintensity involving the bilateral basal ganglia and the adjacent white matter with element of atrophy. Another well-defined CSF intensity lesion noted in the genu of the corpus callosum. Similar lesion was noted in the sellar/suprasellar location with expansion of the sella. These lesions were predominantly T1 hypointense and demonstrated patchy enhancement on postcontrast

Electronic Posters

scan. Gradient images demonstrated mineralization of the bilateral globus pallidi and left substantia nigra. Patient was biopsied and final histopathological diagnosis was germinoma.

Conclusions

Imaging features of basal ganglionic germinoma is typically characterized by mineralization of the basal ganglia with features of atrophy. These features particularly atrophy should not dissuade from the diagnosis of tumor especially when it complicated with past history other CNS affliction as in our case. The presence of sellar/suprasellar and corpus callosum in addition widens the imaging phenotype.



(Filename: TCT_eP-90_SWIjpeg.jpg)

eP-92b

Hemorrhagic Encephalopathy as Fatal Adverse Event to the First Infliximab Infusion in an Adolescent with Ulcerative Colitis

C Agostinis¹, V Casotti¹, L D'antiga¹, G Bonaldi¹

¹*Ospedale Papa Giovanni XXIII - Bergamo, Alzano Lombardo, Italy*

Purpose

We report the radiological findings in a 17-year-old boy affected by steroid-resistant ulcerative colitis who presented devastating cerebral and cord lesions a few hours after infusion of infliximab, a chimeric monoclonal anti-TNF α antibody used to treat Crohn's disease, ulcerative colitis, and rheumatoid arthritis.

Materials and Methods

A 17-year-old Caucasian boy with a three-year history of ulcerative colitis was admitted to the pediatric department to undergo the first infusion of infliximab in last March. He had been treated previously with steroid, 5-ASA and azathioprine and then had been switched to infliximab after a new relapse. Six hours after infusion he complained of abdominal pain, and rapidly developed delirium, quickly followed by unresponsiveness coma, leading to intubation. Immediate CT scan and CT angiography of the head were normal.

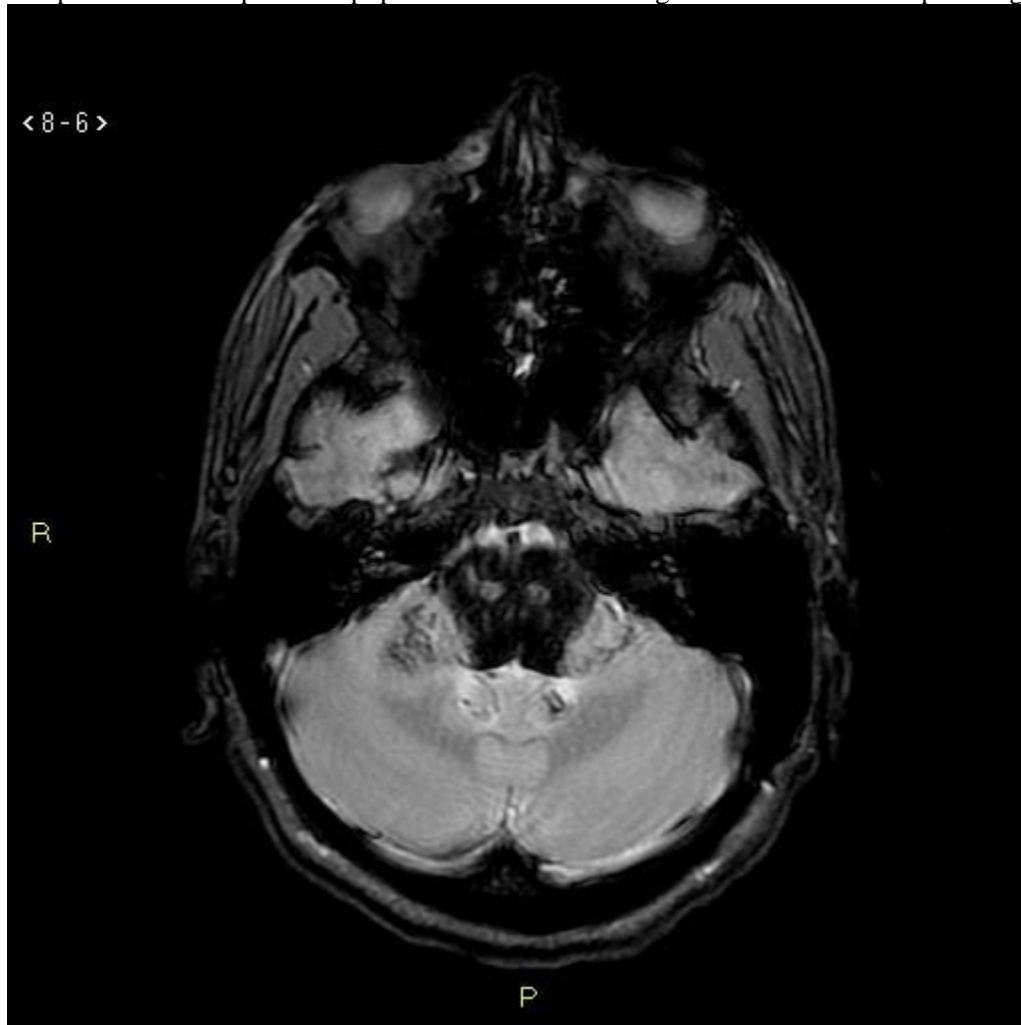
Results

A few hours after coma onset, MRI scan showed multiple, extensive brainstem and supratentorial lesions with predominantly restricted water diffusion. These lesions progressively enlarged during the next few

days, also involving the upper cervical spinal cord, and showed hemorrhagic transformation (Fig. 1). The patient died one month later.

Conclusions

Neurological adverse reactions to infliximab may vary in time of onset, type and severity, ranging from headache, dizziness, seizures, PRES to demyelinating central and peripheral disorders. In our case the strict temporal relationship between drug infusion and neurological deterioration made the diagnosis of iatrogenic damage certain. The nature of the CNS lesions is not completely defined but this case is strikingly similar to one recently described in a seven-year-old child (1), suggesting a not-so-infrequent complication in the pediatric population. We are waiting for the results of the pathological examination.



(Filename: TCT_eP-92b_1.jpg)

eP-92

Intramedullary Neuroenteric Cyst without Associated Vertebral Segmentation Anomalies in Children: Case Series and Literature Review

R Fragomeni¹, R Lakshmanan², M Gundogan³, A Cohen¹, T Huisman¹, B Soares¹

¹Johns Hopkins University School of Medicine, Baltimore, MD, ²Princess Margaret Hospital, Perth, Australia, ³Al Jalila Children's Specialty Hospital, Dubai, United Arab Emirates

Purpose

Neuroenteric cysts are an uncommon entity accounting for approximately 1.3% of spinal tumors and occurring more frequently within the second and third decades of life. The cysts are composed of endodermal origin epithelial lining found along the neural axis, and result from abnormal communication of the embryologic ectoderm and endoderm related to abnormal partitioning of the notochord. For this reason, associated vertebral segmentation anomalies are common. Patients usually present with debilitating neurologic symptoms and pain at the level of the lesion. Magnetic resonance imaging is key to the diagnosis of the lesion. The purpose of our presentation is to review the imaging appearance and clinical course in children with intramedullary neuroenteric cysts without associated vertebral segmentation anomalies.

Materials and Methods

We retrospectively reviewed the clinical course, imaging findings and operative strategies in four children having neuroenteric cysts in an intramedullary location without associated vertebral segmentation anomalies.

Results

All patients presented with pain at or below the location of the lesion with associated extremity weakness. All lesions were located in the anterior aspect of the spinal cord and showed T1WI hypointense and T2WI hyperintense signal with no contrast enhancement. DWI was performed in one case and showed high ADC values (facilitated diffusion). Surgical treatment consisted of biopsy with cyst fenestration, marsupialization, or complete resection. Three of our patients developed symptomatic recurrence with lesions reaching preoperative size in up to 77 months after surgery.

Conclusions

Due to propensity for recurrence, it is important to consider neuroenteric cyst in the differential diagnosis of an intramedullary cystic lesion without associated vertebral segmentation anomalies in children.



(Filename: TCT_eP-92_SagT2.jpg)

eP-89

Qualitative and Quantitative ADC Histogram Analysis of Pediatric Medulloblastomas SHH, WNT and Non-WNT/non-SHH Subgroups

E Tong¹, M Aboian¹, S Cha¹

¹*University of California San Francisco, San Francisco, CA*

Purpose

Identification of molecular subtype of pediatric medulloblastomas is critical for predicting patient outcomes and different molecular subtypes have distinct qualitative imaging characteristics and diffusion patterns. Unfortunately, most clinical practices do not have access to technology to differentiate Group 3 and Group 4 tumors, which have different clinical outcomes. We perform qualitative analysis and ADC histogram analysis of SHH, WNT, and non-WNT/non-SHH tumors to distinguish subgroups and identify imaging biomarkers which may correlate with patient outcomes and/or recurrence.

Materials and Methods

We identified 53 pediatric patients (<18 yrs old) with medulloblastomas with available MRI imaging. Histopathologic subtypes included anaplastic, desmoplastic/nodular, and classic. Molecular subtypes included SHH, WNT, and non-SHH/non-Wnt. We evaluated the qualitative imaging patterns of these medulloblastomas based on their location, enhancement pattern, and necrosis and performed quantitative

Electronic Posters

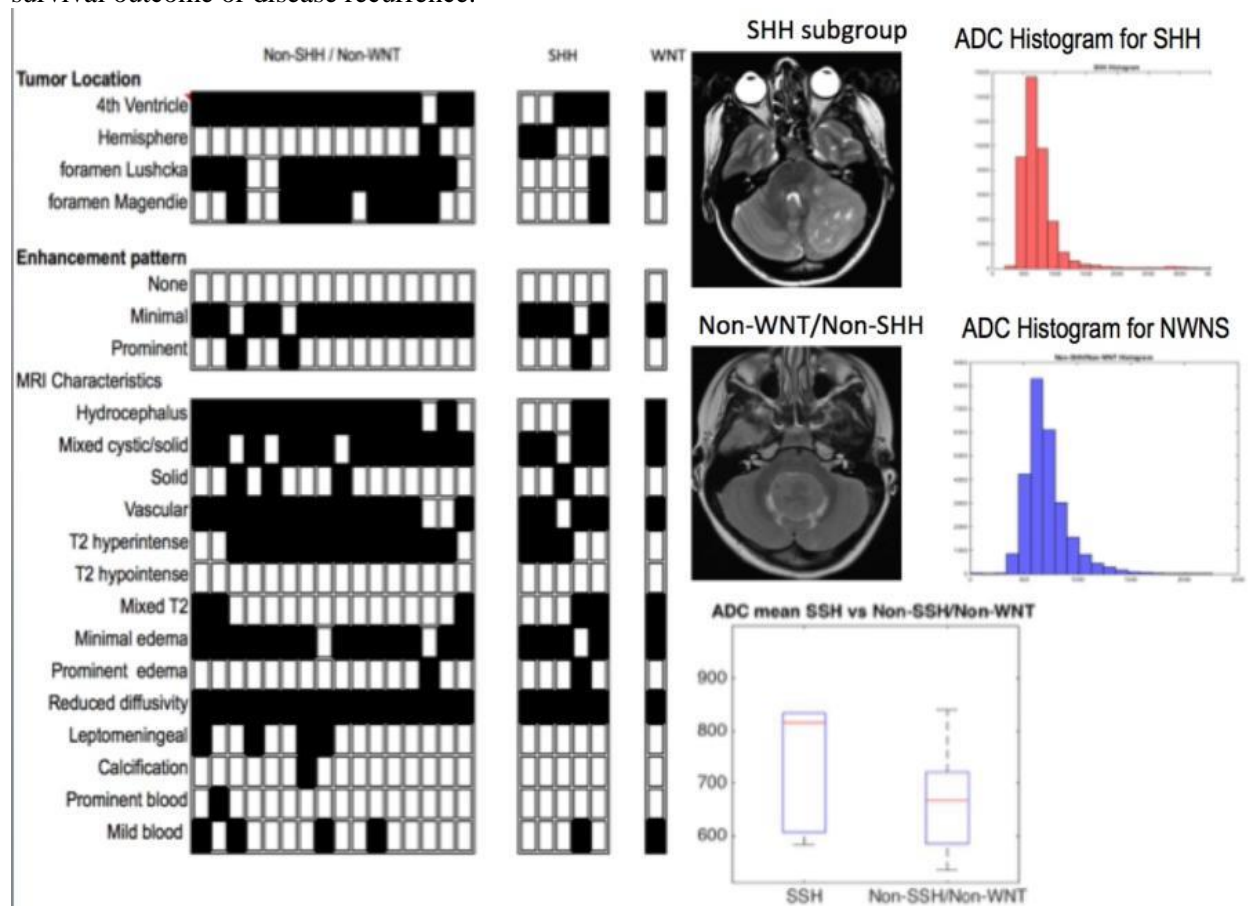
ADC histogram analysis. Correlations to patient outcomes at 1-5 year overall survival and time to recurrence were performed.

Results

On qualitative imaging analysis, non-WNT/non-SHH subgroup tumors are more likely to have leptomeningeal disease spread, intratumoral blood products and calcifications. Although both groups are predominantly found in the fourth ventricle in our cohort, the non-WNT/non-SHH subgroup tumors are more likely to involve the foramen of Luschka and foramen of Magendie. On quantitative analysis, all of the tumors are reduced in diffusion, while the non-WNT/non-SHH subgroup tumors have lower mean and median ADC values (0.702+/-0.114) as compared to SHH group (0.776+/-0.102). Quantitative evaluation of T2 and FLAIR signal within the 3-D tumor demonstrated wide range in T2 and FLAIR signal intensities between different tumors ranging from 119 to 1852 intensity units, with no significant difference between SHH and non-WNT/non-SHH tumor subgroups. Preliminary analysis did not show correlation between the mean ADC and survival outcome or disease recurrence within the non-WNT/non-SHH subgroup.

Conclusions

We performed qualitative imaging characterization and quantitative ADC histogram analysis to distinguish medulloblastoma subgroups. Leptomeningeal disease spread, intratumoral blood products and calcifications are more common in non-WNT/non-SHH subgroup. Non-WNT/non-SHH subgroup tumors have lower mean and median ADC than SHH group; however, there is no definitive correlation with survival outcome or disease recurrence.



(Filename: TCT_eP-89_figure1.jpg)

eP-91

Super-resolution Processing of Fetal Brain MRI and Automated Volumetric Segmentation

J Maffie¹, J Grinband²

¹*New York Presbyterian, New York, NY*, ²*Columbia University, New York, NY*

Purpose

Fetal MRI imaging is greatly complicated by fetal motion, necessitating repeat imaging and limiting the quality of images obtained. Specifically, head and body movements cause large distortions of brain images, making neuroanatomical diagnosis difficult. The typical approach currently employed by many institutions is to acquire multiple scans and to select the one with the least head movement for diagnostic purposes. We developed a technique that utilizes brain imaging information gathered in the multiple suboptimal studies typically acquired during standard fetal body imaging to produce an aggregate image set with greater effective resolution and less artifact than the component studies. We furthermore utilize this volumetric data for automated segmentation and construction of normalized biometric developmental curves of CSF, cerebral, cerebellar and cerebral grey-matter volumes.

Materials and Methods

We retrospectively selected subjects at a range of gestational ages who had prenatal MRI for suspected non-neurologic anomalies based on prenatal ultrasound. In addition, we selected patients with agenesis of the corpus callosum to evaluate how this diagnosis may affect global development. The subjects each had between three and seven independently acquired single-shot fast spin-echo (SSFSE) sequences in all three planes which included the brain. Each sequence was reviewed manually and those deemed to meet minimum quality standards were included for further processing. Interslice registration to correct for movement between slice acquisition was performed using FSL tools FLIRT algorithm applied sequentially to each sequence. An arithmetic, per-voxel average of all corrected sequences was taken to minimize any nonsystematic artifact. Registration and averaging was semiautomated utilizing custom Matlab scripts. The resulting high-resolution brain volumes were then segmented using FSL tools FAST algorithm and these were compared to selected hand-segmented volumes for accuracy. Developmental curves were constructed for the segmented volumes.

Results

The images processed by this super-resolution technique were consistently rated as higher quality compared to unprocessed images by blinded radiologist raters. In addition, developmental brain volume nomograms were constructed to facilitate comparison with individual segmented patient brain volumes.

Conclusions

By allowing for increased effective resolution and minimizing motion artifacts, super-resolution techniques have the potential to expand the availability and diagnostic power of fetal brain imaging, and to make quantitative developmental biometric analysis a practical clinical tool.

eP-86

Utility of Computed Diffusion-weighted Magnetic Resonance Imaging for Acute Pediatric Encephalitis/Encephalopathy

Y Shinohara¹, Y Kamata¹, K Kuya¹, Y Tsubouchi¹, Y Saito², Y Maegaki¹, T Ogawa¹

¹*Tottori University, Faculty of Medicine, Yonago, Tottori, Japan*

Purpose

Computed diffusion-weighted imaging (cDWI) is a mathematical computation technique that calculates a high b-value image from DWI acquired with at least two different lower b-values. This study aimed to explore the utility of cDWI in the diagnosis of acute pediatric encephalitis/encephalopathy.

Materials and Methods

Twenty-two children were enrolled, for whom acquired DWI (aDWI) $b=1000$ and $b=3000$ were examined during the acute phase of febrile encephalitis/encephalopathy. For each patient, cDWI was calculated pixel by pixel from the aDWI $b=0$ and $b=1000$ by using software equipped with a commercially available image viewer (EV Insite; PSP Corporation, Tokyo, Japan). Visual assessment among aDWI $b=1000$, $b=3000$ and cDWI $b=3000$ was performed for each patient by two experienced neuroradiologists. Quantitative assessment was also performed by using a signal intensity (SI) ratio, defined as mean SI at the affected lesion/mean SI at the center of the pons for each image. The Mann-Whitney test was used for statistical analysis of the SI ratios of cDWI $b=3000$ versus aDWI $b=1000$ and cDWI $b=3000$ versus aDWI $b=3000$. A p -value of less than 0.05 was considered statistically significant.

Results

In the visual assessment, the visibility of diffusion-restricted lesions on cDWI $b=3000$ was superior to that on aDWI $b=1000$ and almost equal to that on aDWI $b=3000$ with moderate inter-observer agreement. The SI ratio of cDWI $b=3000$ was significantly higher than that of aDWI $b=1000$ images ($p=0.019$), while the SI ratio of cDWI $b=3000$ was not significantly different from that of aDWI $b=3000$ ($p=0.869$).

Conclusions

cDWI $b=3000$ is useful for detecting diffusion-restricted lesions in acute pediatric encephalitis/encephalopathy. cDWI enables the generation of high b -value images without additional scanning, which would be helpful for sedated pediatric patients in the clinical settings.

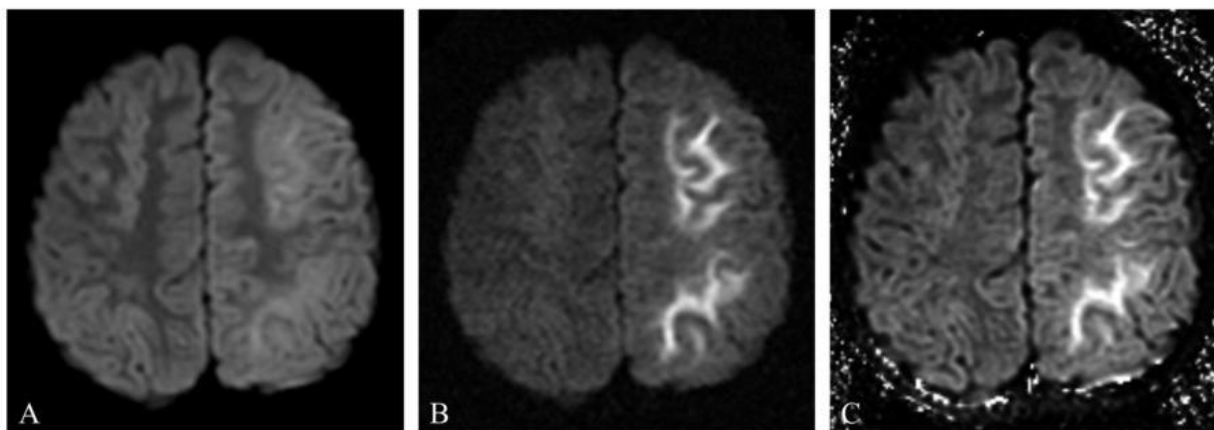


Figure. MRI of a 48-month-old boy with acute encephalopathy with biphasic seizures and late reduced diffusion (AESD) on day 5 of the illness. A: acquired DWI (aDWI) $b=1000$, B: aDWI $b=3000$, C: computed DWI (cDWI) $b=3000$. Restricted diffusion in the left frontal and parietal subcortical white matter can be found with greater clarity on both aDWI $b=3000$ (B) and cDWI $b=3000$ (C) compared to that on aDWI $b=1000$ (A).

(Filename: TCT_eP-86_FigureforASNR2018.jpg)

Electronic Posters (eP)-Socioeconomics

eP-94

24/7/365 Neuroradiologist Coverage Improves Turn Around Times by 75% and Improves Resident Perceptions of Their On-call Educational Experience

R Homer¹, K Spittler², N Salamon²

¹University of California Los Angeles, Santa Monica, CA, ²University of California Los Angeles, Los Angeles, CA

Purpose

To quantitate the effects of 24/7/365 neuroradiologist coverage on turn-around times for neuroimaging studies and to evaluate radiology resident perceptions of their on-call learning experience.

Materials and Methods

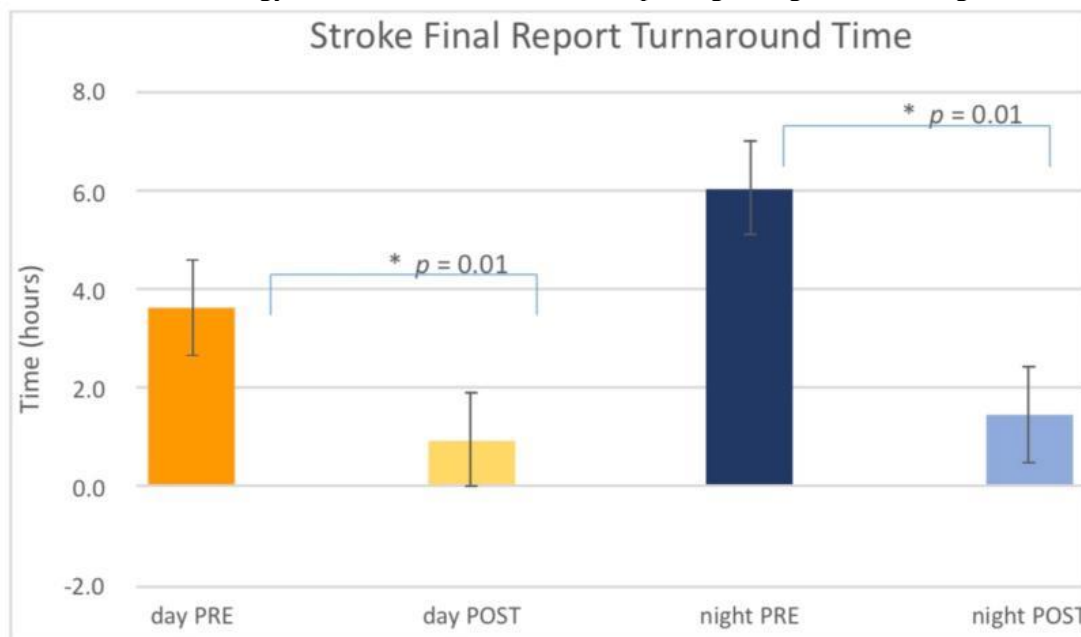
Turn-around time (TAT) for CT brain, CT cervical spine, MRI/MRAs/CTAs head and neck from 10PM-7AM from 10/1/2016-3/1/2017 for the five-month study period post implementation of 24/7/365 coverage vs. before implementation from 10/1/2015- 3/1/2016 was determined. During the experimental period neuroimaging studies were interpreted by a PGY2 or PGY3 radiology resident and a preliminary report was issued and finalized soon after. During the control period, prior to the implementation of 24/7/365 coverage, the studies were similarly interpreted by a radiology resident and a preliminary report was issued. A final report was generated by the neuroradiology attending and fellow the next day. Resident perceptions of the effects of 24/7/365 coverage were assessed by survey.

Results

Emergency Department TAT was decreased from 5.2 hours (962 studies) to 1.3 hours (1759). Inpatient TAT was decreased from 7.6 hours (1357 studies) to 4.2 hours (1263). Daytime TAT was decreased from 1.7 to 1.1 hours for ED and 4.1 to 2.8 hours for inpatients 80% of PGY2 and 90% of PGY3 residents reported improved perception of their neuroradiology education on-call. Resident-perceived changes in autonomy with the addition of the overnight attending were most often felt to be neutral to their educational experience in 50% of PGY2 and 80% of PGY3 residents. Thirty percent and 10% of PGY2 and PGY3 residents felt education was decreased and 20% and 10% of PGY2 and PGY3 residents reported improvement. Of residents 10/12 PGY2 and 11/11 PGY3 completed surveys.

Conclusions

The addition of overnight neuroradiology attendings reduces ED and inpatient TAT by 75% and 44%. ED TAT is similar to daytime. Daytime TAT is improved. Residents report an improved educational experience in neuroradiology on call with most residents reporting no significant change to autonomy.



(Filename: TCT_eP-94_TAT.jpg)

eP-93

Electronic Posters

Evaluating Compliance of MRI Brain Scans to American College of Radiology (ACR) Ordering Guidelines Using Text Mining

P TANG¹, S Liu², X JING³, N Liu³, S LAM³, L Lim⁴, L McAdory⁵, L Chan⁵

¹KK Women's and Children's Hospital, Singapore, Singapore, ²National University of Singapore, Singapore, ³SingHealth Health Services Research Centre, Singapore, Singapore, ⁴Yong Loo Lin School of Medicine, National University of Singapore, Singapore ⁵Singapore General Hospital, Singapore, Singapore

Purpose

Our previous research showed that MRI brain scans with indications following the American College of Radiology (ACR) guidelines show a higher percentage of brain abnormalities compared to scans not following guidelines. The process of manually classifying these indications according to whether or not they are following the ACR guidelines is labor-intensive and time-consuming. The aim of our study is to develop a predictive model using text mining to automate this classification process.

Materials and Methods

Anonymized reports of patients who had MRI brain scans in KK Women's and Children's Hospital (KKH) and Singapore General Hospital (SGH) were collected. These reports were manually categorized by human operators in each hospital as to whether or not they conformed to the ACR ordering guidelines. We randomly selected 80% of all subjects for model derivation and used the remaining 20% subjects for model validation. Both term frequency and term frequency-inverse document frequency were used as the weighting factor in text mining. We adopted three machine learning algorithms to predict whether or not the MRI brain scan is following the ACR guidelines. These algorithms included generalized linear model, random forest and support vector machines (SVM). Area under the receiver operating characteristic curve (AUC) was used to compare the predictive models.

Results

There were 2,911 MRI brain scans done in KKH and SGH of which 2,262 scans were performed according to the given 16 ACR guidelines. The random forest model based on term frequency-inverse document frequency weighting factor achieved the best performance (AUC=0.84) compared to generalized linear model (AUC=0.73) and support vector machines (AUC=0.72).

Conclusions

The discriminatory ability of the predictive models is best using random forest for automated classification of MRI brain scans indications.

ACR category number	ACR criteria	Number of cases in KKH (2006-2013)	Number of cases in SGH (2006-2013)
1	Neoplastic conditions	222	65
2	Vascular	118	200
3	Congenital / Anatomical disorders	142	1
4	Congenital / Acquired neurodegenerative disorders	2	8
5	Congenital or acquired hydrocephalus	45	2
6	Metabolic disorders	15	0
7	Trauma	70	3
8	Hemorrhage	45	9
9	Inflammatory and autoimmune disorders	77	5
10	Infectious disorders	137	12
11	Endocrine disorders	34	0
12	Evaluation of cranial nerves	79	23
13	Epilepsy and movement disorders	414	23
14	Psychiatric disorders	10	5
15	Follow-up of treatment	460	13

(Filename: TCT_eP-93_TableforASNRACR.jpg)

eP-95

Face-to-Face: Resident-led Radiology Medicine Rounds Facilitate Evidence-based Processes for Clinical Decision Support

A Goldman-Yassen¹, S Strauss¹, J Burns¹, J Farinhas¹, J Bello¹

¹Montefiore Medical Center, Albert Einstein College of Medicine, Bronx, NY

Purpose

A weekly resident-led radiology-medicine conference was instituted to bridge the interspecialty gap between clinical teams and the "reclusive radiologist". This project attempts to determine the feasibility and utility of these conferences in clinical practice.

Materials and Methods

Weekly "RadMed" conferences were instituted wherein a senior radiology resident led a teaching session for 30-40 medicine residents and students. Using a case-based structure, medicine residents provided clinical cases for the radiology resident to discuss: 1) resources for clinical decision support, 2) thought process behind imaging interpretation, 3) recommendations based on imaging findings, 4) basic imaging principles, and 5) opportunities for dose and cost reduction. A pilot survey administered after 4 months assessed participants' view of the usefulness of the conference and changes to implement.

Results

Fifteen "RadMed" 30-minute conferences were held over 4 months, after which a pilot survey was

Electronic Posters

administered. Fourteen of 40 medicine residents responded; 13 of the 14 had attended 2 or more conferences, and 71% found rounds useful/highly useful based on positive impact on care, direct interaction with the radiologist, and the thought processes behind image interpretation. Those describing the rounds least useful cited scheduling issues and desiring more discussion on basic image interpretation.

Conclusions

Resident-led "RadMed" conference was easily implemented without disrupting radiology resident workflow. The preliminary survey results suggest a perceived need among the medicine residents for radiology education, but with scheduling as an important obstacle to their learning. Preliminary results suggest that conferences enhanced relationships between specialty residents and promoted using the radiologist for clinical decision support. While data collection continues regarding efficacy, preliminary results demonstrate value in applying evidence-based processes for clinical decision support. Future directions include development of a more structured curriculum, administration of a more detailed survey to assess ACGME clinical milestones and knowledge gaps and use of objective assessment of program impact with measures of clinical performance.

Electronic Posters (eP)-Spine

eP-97

Intraoperative Glue Embolization of Symptomatic Vertebral Haemangiomas

j_saini¹, A HR¹

¹*National Institute of Mental Health and Neuro Sciences, Bengaluru, Karnataka, India*

Purpose

Vertebral hemangiomas account for 12% of benign lesions of the vertebral column. They are usually detected incidentally. (1) Rarely they may enlarge, cause pain and neurological deficit because of spinal cord compression, vertebral body or arch expansion, or pathological fracture. Treatment options for symptomatic vertebral hemangiomas include transarterial embolization, surgical excision, radiotherapy, and percutaneous injection of alcohol or methyl methacrylate. Nowadays, preoperative embolization followed by surgical excision is the preferred treatment modality in many centers. (2) Our purpose is to share our experience in intraoperative embolization of vertebral haemangiomas.

Materials and Methods

We describe four patients with symptomatic vertebral haemangiomas in the cervicodorsal levels who underwent intraoperative glue embolization. After initial laminectomy in these patients, a tumorogram was obtained under fluoroscopic guidance through direct-contrast injection via a spinal needle inserted through the pedicles of the vertebra at the involved level. Fifteen percent glue was injected via the same spinal needle. All these patients underwent surgical decompression of the intraspinal epidural component in the same sitting along with posterior spinal stabilization of the adjacent levels.

Results

In all these four patients, complete embolization of the tumor was possible intraoperatively through the transpedicular approach and the blood loss was significantly less along with adjunctive surgery. Clinical follow-up of these patients at 6 -12 months showed a reduction in the size of the epidural component, relief of cord compression and significant improvement in their neurological deficits.

Conclusions

Intraoperative embolization of vertebral hemangioma is a safe and efficacious adjunctive procedure along with surgical decompression and spinal stabilization for treatment of symptomatic vertebral haemangiomas.

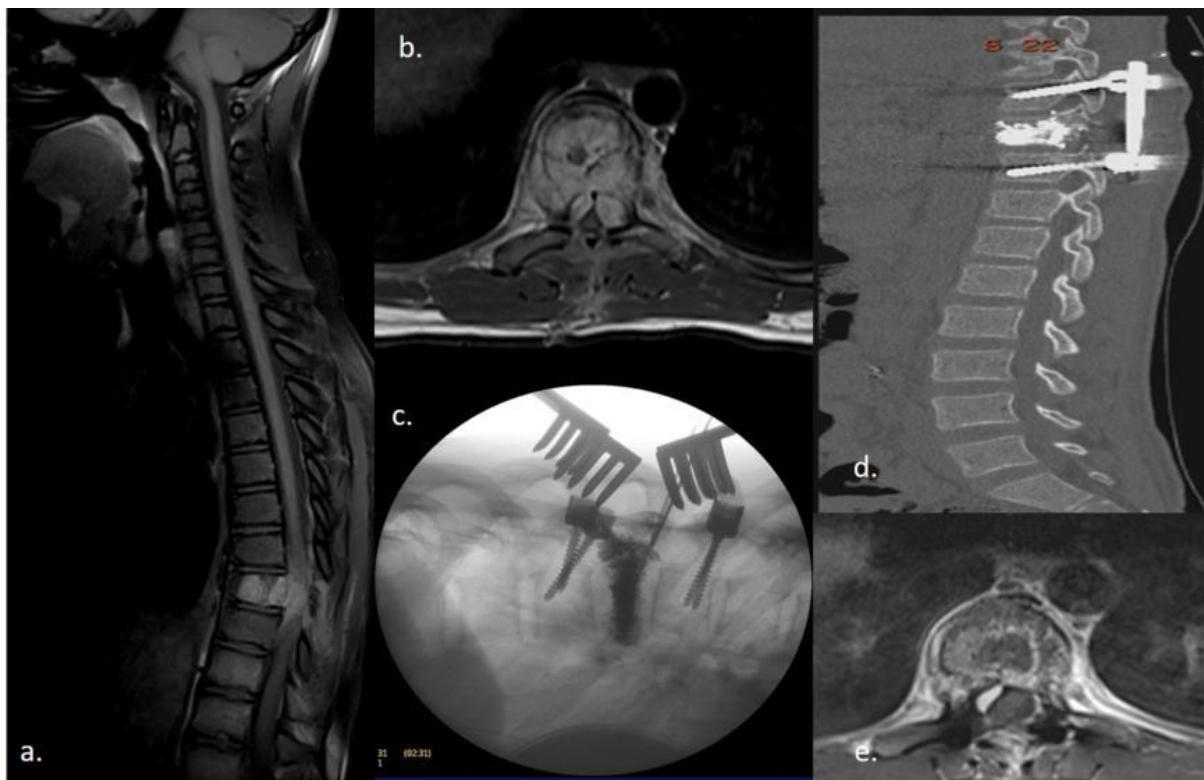


Fig 1:- Sagittal MR (a) and axial (b) images acquired after decompressive laminectomy shows intense enhancement of the D8 vertebral haemangioma with an epidural component. Cord compression is seen at this level. (c) Sagittal fluoroscopic image shows transpedicular screw fixation at D7 and D9 levels and needle placement at D8 vertebral body level with 15 % glue cast insitu. (d) Post procedure sagittal CT reconstruction image shows posterior spinal fixation from D7-9 levels with glue cast insitu at D8 vertebral level.(e) Axial post contrast T1W image shows at D8 vertebral level significant resolution of the enhancement with reduction of the epidural component.

(Filename: TCT_eP-97_asnr2018.jpg)

eP-96

Utility of Spine Biopsy in Antibiotic Selection for Spondylodiscitis

M Folkertsma¹, M Oswood²

¹University of Minnesota, Minneapolis, MN, ²Hennepin County Medical Center, Minneapolis, MN

Purpose

Spondylodiscitis is an infection of the vertebral endplates and adjacent intervertebral disk. Many patients with spondylodiscitis are treated medically with antibiotics based on organism sensitivity defined in blood or tissue biopsy cultures. Image-guided spine biopsy can provide definitive diagnosis in cases where remote cultures reveal no growth or where alternative organisms are suspected. We assessed the utility of image-guided spine biopsy as it relates to the clinical management, specifically by changing the antibiotic regimen.

Materials and Methods

This was a retrospective observational study, in which data were collected from medical charts. Patients were eligible for the study if they had high suspicion of spondylodiscitis based on clinical and MRI findings and had image guided spinal biopsy. Eighty-eight patients were identified at our institution from 1/2000 through 1/2017. Data collected were: initial antibiotics administered, blood or tissue culture results during the admission, spinal biopsy culture results and antibiotics administered after the culture

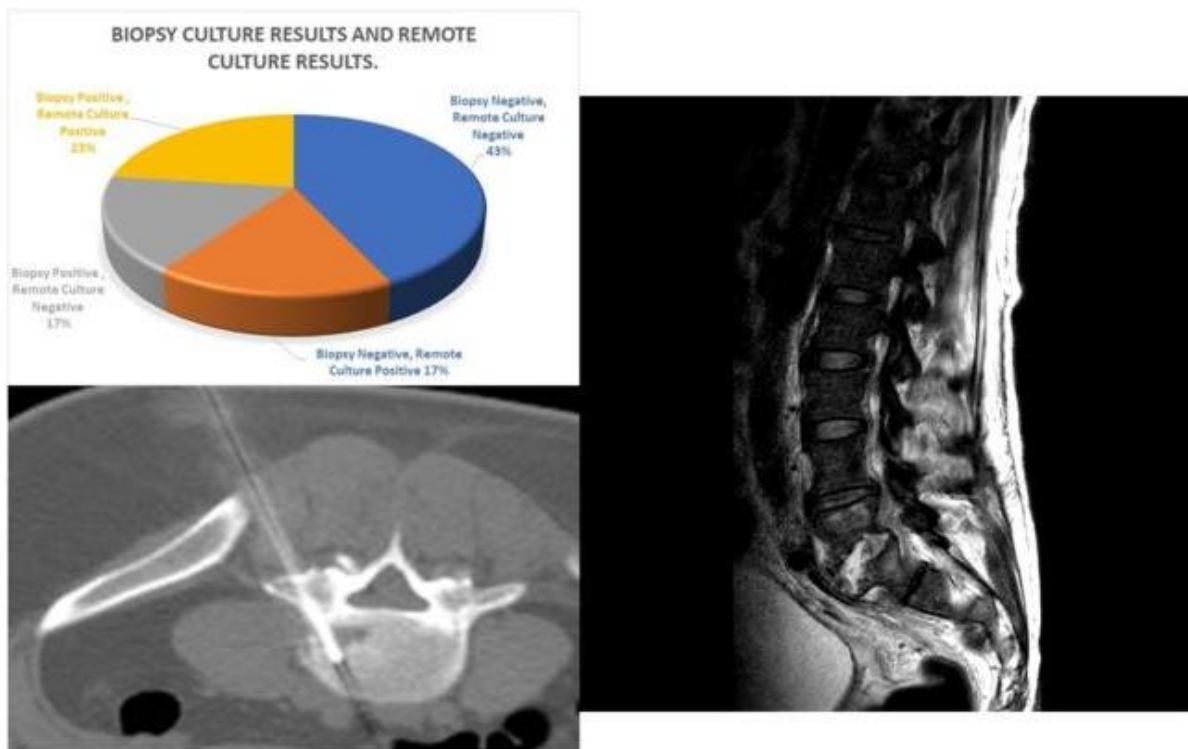
results were finalized. Image-guided biopsies were performed in the radiology department by a radiologist.

Results

Thirty-five (40%) of the biopsies resulted in positive cultures. This result is near the expected yield as described recently in the literature (48%). Fifteen (17%) of the biopsies resulted in growth of pathogens with sensitivities differing from previous cultures or empiric antibiotics coverage and resulted in change of coverage or narrowing of the spectrum. The remaining patients with positive biopsies maintained the same antibiotics as the empiric coverage or treatment instituted from cultures of other sites. Thirty-two (36%) patients had positive blood/tissue/abscess cultures from sites outside of the spine.

Conclusions

Likelihood of culturing a causative organism from image-guided spine biopsy with high clinical and MRI suspicion of spondylodiscitis is 40%. Likelihood of an image-guided spine biopsy altering the antibiotic regimen is 17%.



(Filename: TCT_eP-96_Spinemix.jpg)

Education Exhibits-Adult Brain

EdE-15

'Barbell Sign': A Diagnostic Imaging Finding in Progressive Multifocal Leukoencephalopathy

A Bezuidenhout¹, R Bhadelia¹

¹*Beth Israel Deaconess Medical Center, Boston, MA*

Purpose

The recently proposed diagnostic algorithm for progressive multifocal leukoencephalopathy (PML) underscores the importance of imaging and emphasizes the role of the radiologist in the diagnostic work-up. We describe a case series of patients with visual symptoms and a typical pattern of brain involvement in definite PML for which we have coined the term 'barbell sign'.

Materials and Methods

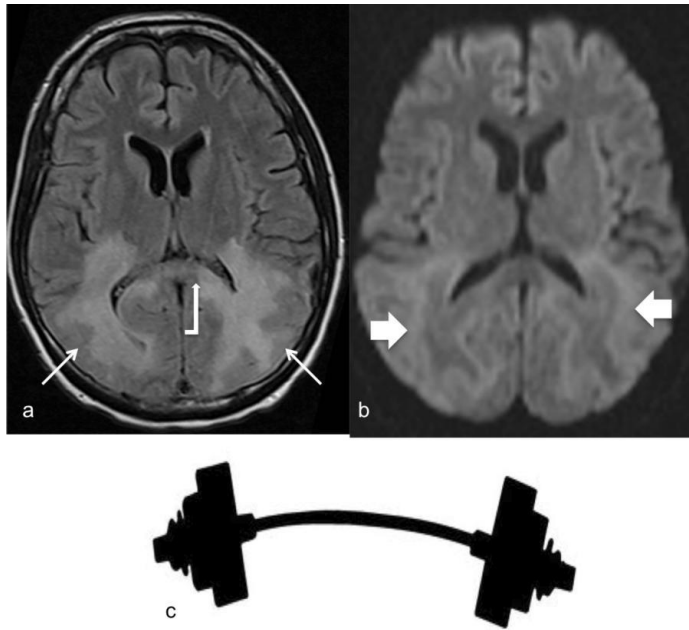
A total of six patients were included over a three-year period. Five patients were from an institution in South Africa and one patient from an institution in North America. All six patients had a diagnosis of definite PML. The hospital records of patients were retrieved and analyzed regarding clinical features, laboratory findings and outcomes. The MR imaging from the two institutions were analyzed by two neuroradiologists for the presence of the 'barbell sign'. The 'barbell sign' was defined as a coalescent bilateral occipitoparietal lesion hyperintense on T2WI and FLAIR images extending across the callosal splenium, and involving the subcortical U-fibers with no or minimal mass effect, no postcontrast enhancement, and a thin rim of peripheral restricted diffusion.

Results

All six patients were immunocompromised with low CD4 counts. All five patients recruited from the African institution were HIV positive with a mean nadir CD4 count of 90 ± 99 cells/ μ L. The patient recruited from North America was on immunosuppressive therapy with a nadir CD4 count of 300 cells/ μ L. Symptoms included visual impairment (n=6), confusion (n=3), focal weakness (n=4), aphasia (n=2) and ataxia (1). Four out of the five patients with HIV associated PML passed away in the month following diagnosis, while the fifth patient with HIV associated PML as well as the non-HIV associated PML patient were discharged to long term care facilities as they were deemed incapable of self care. MRI demonstrated confluent T2WI and FLAIR hyperintensities in bilateral occipito-parietal lobes with involvement of the splenium of corpus callosum in all six patients. FLAIR imaging was found to be the imaging sequence most helpful in characterizing the confluent white matter abnormalities. Ancillary findings were the lack of mass effect, no enhancement and a rim of increased signal on DWI at the margin of the FLAIR hyperintensities. The pattern of brain involvement had the appearance of a barbell.

Conclusions

Radiologists should be familiar with the typical and atypical imaging findings in PML as they are often the first to suggest the diagnosis and in some cases may assist in prognostication. The characteristic 'barbell' imaging appearance of PML described here should help in this regard.



(Filename: TCT_EdE-15_Figure1.jpg)

EdE-02

A Case-based Approach to Abnormalities of the Deep Grey Matter

T Myers¹, J Scott¹

¹*Foothills Medical Centre, Calgary, Alberta, Canada*

Purpose

The deep grey matter of the brain are involved in a wide array of pathological processes and the number of differential considerations for abnormalities in this region is high. Differential considerations include, but are not limited to: metabolic abnormalities, ischemia (arterial and venous), infections, mitochondrial diseases, toxic poisoning, malignancy and neurodegenerative disease. Although many of these entities share similar imaging findings, there are several key imaging characteristics that help narrow the differential diagnoses or are pathognomonic of a particular entity. It is the purpose of this educational exhibit to provide a case-based approach to abnormalities of the deep grey matter using cases from each of the above categories to emphasize the important differentiating features. In addition, the importance of the integration of the imaging appearance with the clinical setting, patient presentation and laboratory data will be discussed.

Materials and Methods

A case-based approach will be used to review the diverse causes of deep grey matter abnormalities that can be seen in clinical practice. Cases containing both CT and MRI images, supplemented by advanced imaging techniques, key laboratory findings and confirmed pathology, when available, will be provided. Cases have been chosen to highlight key imaging features and pertinent negatives that aid diagnosis. Cases from several major categories of causes of deep grey matter abnormalities have been chosen. Common causes of deep grey matter abnormalities such as hypoxic ischemic injury, venous infarct and thalamic glioma will be included. Cases highlighting the imaging and laboratory findings in less common entities such as Neuropathy, Ataxia and Retinitis Pigmentosa, Wilson's Disease, West Nile encephalopathy, Murray Valley encephalopathy, Wernicke's Encephalopathy and Methanol poisoning will also be presented.

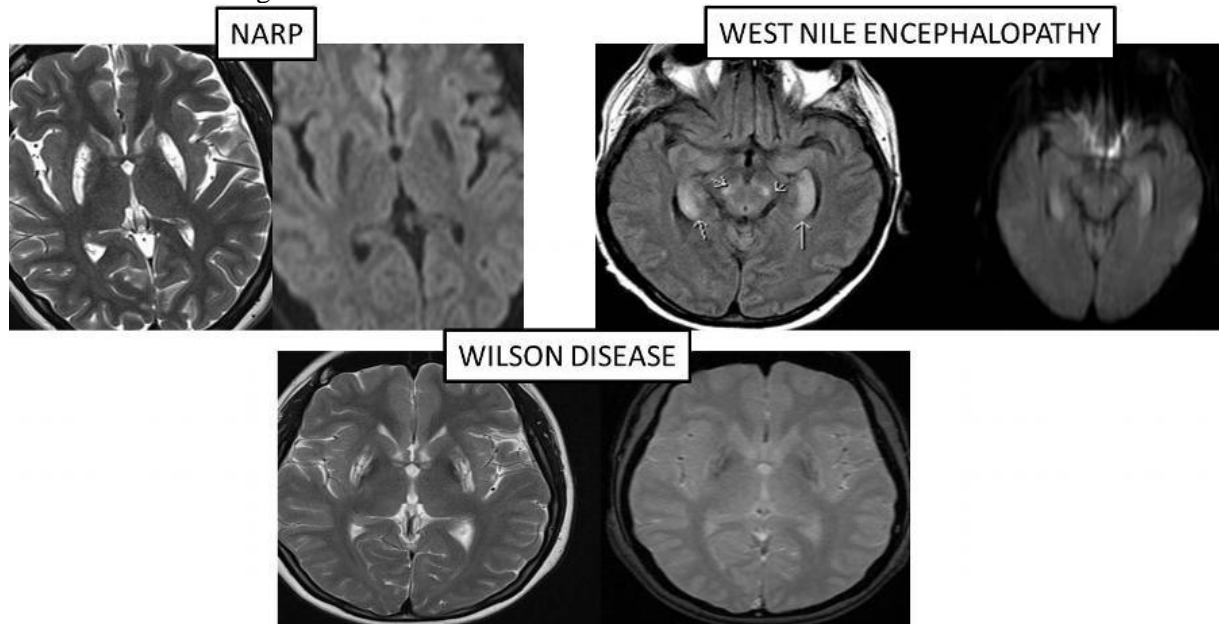
Education Exhibits

Results

The deep grey matter of the brain includes the caudate nuclei, the lentiform nuclei and the thalami. The lentiform nuclei, in particular, are highly metabolically active and are subsequently vulnerable to insult secondary to toxins, ischemia, infections and metabolic disease. The pattern of signal abnormality in the deep grey matter aids in narrowing the number of differential considerations. For example, increased T2 signal can be seen in multiple settings, including ischemia, malignancy, toxic poisoning as well as neurodegenerative, metabolic and mitochondrial disease. Increased T1 signal is seen in hepatic failure, hemorrhage, toxic poisoning and calcium deposition. These primary signal changes should subsequently be evaluated in the context of the corresponding signal change on other MRI sequences such as DWI, SWI, and post-gadolinium T1, in addition to other specialized tests such as spectroscopy, as necessary. The extent of brain involvement, including the deep white matter and cortex, should be evaluated. The imaging findings combined with the patient presentation, laboratory findings and patient medical history significantly narrows the list of differential considerations.

Conclusions

The deep grey nuclei, in particular the lentiform nuclei due to their high metabolic activity and vascular supply, are involved in a multitude of pathological processes. When one is presented with deep grey matter abnormality on CT or MRI the list of differential considerations is long, including: metabolic abnormalities, ischemia, infection, neurodegenerative disease, toxic poisoning, malignancy and mitochondrial disease. A case-based approach, highlighting cases within these major categories, was used to gain an understanding the typical signal changes and distribution of findings in each process. Pathonomonic findings were also identified.



(Filename: TCT_EdE-02_Picture1.jpg)

EdE-22

A Pictorial Review of MRI Brain Findings in Sickle Cell Disease and the Emerging Application of Arterial Spin Labelling Perfusion Imaging

S Culleton¹, M Sokolska², J Markus³, R Jager⁴, K Pegoretti Baruteau¹

¹National Hospital for Neurology and Neurosurgery, London, United Kingdom, ²University College Hospital London Hospitals NHS Foundation Trust, London, United Kingdom, ³University College Hospital London, London, United Kingdom, ⁴ION Institute of Neurology, London, United Kingdom

Education Exhibits

Purpose

Sickle cell disease (SCD) is the most common inherited haemoglobinopathy (1). Cerebral complications can present without overt neurology and they are defined as silent cerebral infarcts (SCI) (2). Recognizing these entities is important as they precede more severe neurological impairment in affected patients. This pictorial review highlights cerebral pathology in SCD on MRI brain imaging. Examples of the application of arterial spin labelling (ASL) perfusion imaging in SCD are also illustrated.

Materials and Methods

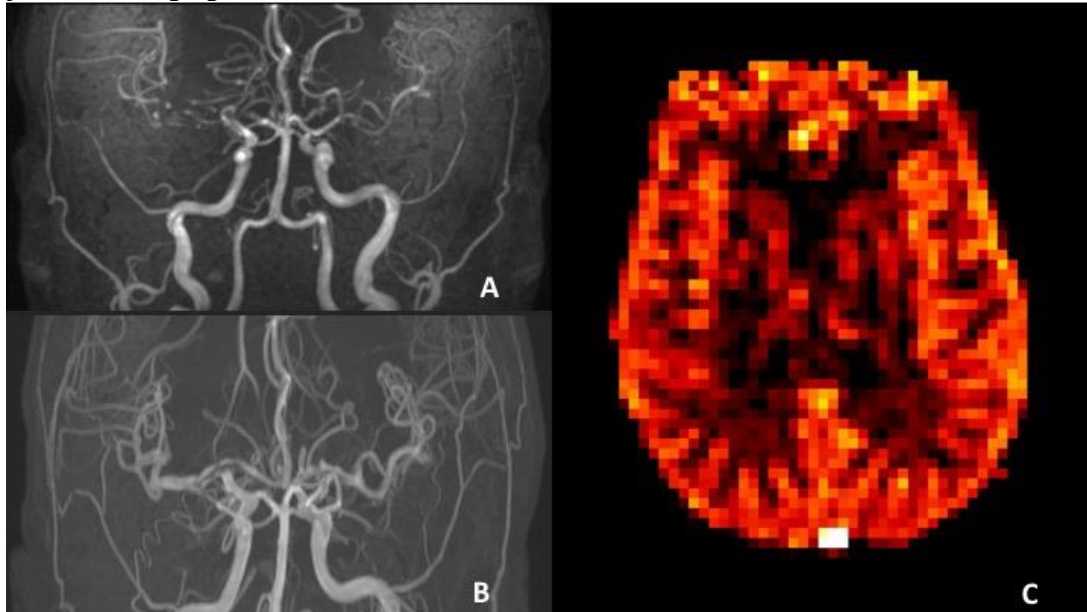
MRI brain imagings of SCD performed at our institution were reviewed from January to November 2017. Studies with evidence of cerebral pathology due to SCD were selected. Cases of ASL perfusion imaging in SCD patients were included.

Results

The spectrum of ischemic events on MRI are shown, ranging from SCI, territorial and watershed infarcts. Vascular manifestations of SCD such as intracranial stenosis, aneurysms and torturous vessels are presented. The applications of ASL perfusion imaging in the setting of SCD are discussed. Figure 1 illustrates: A) TOF MRA 1.5T shows bilateral stenosis of the proximal MCAs. B) TOF MRA 3.0T is of better image quality and shows turbulent flow in the M1 segments bilaterally and that the intracranial stenosis suspected on images at 1.5 T are artifactual and due to turbulent flow. C) ASL perfusion image shows symmetrical perfusion of both hemispheres and no evidence of any regional hypoperfusion.

Conclusions

The cerebral complications of SCD contribute significantly to morbidity and mortality in affected individuals and also plays an important role in the therapeutic management. In this pictorial review we describe the image appearances of these complications and potential pitfalls and the emerging use of ASL perfusion imaging.



(Filename: TCT_EdE-22_Slide1.jpg)

EdE-23

A Review on the Varied Manifestations of Reversible Cerebral Vasoconstriction Syndrome

C Choi¹, S Jain¹, H Sonwalkar¹

¹Royal Preston Hospital, Manchester, England

Education Exhibits

Purpose

To review the clinical presentations and various imaging features of Reversible Cerebral Vasoconstriction Syndrome (RCVS).

Materials and Methods

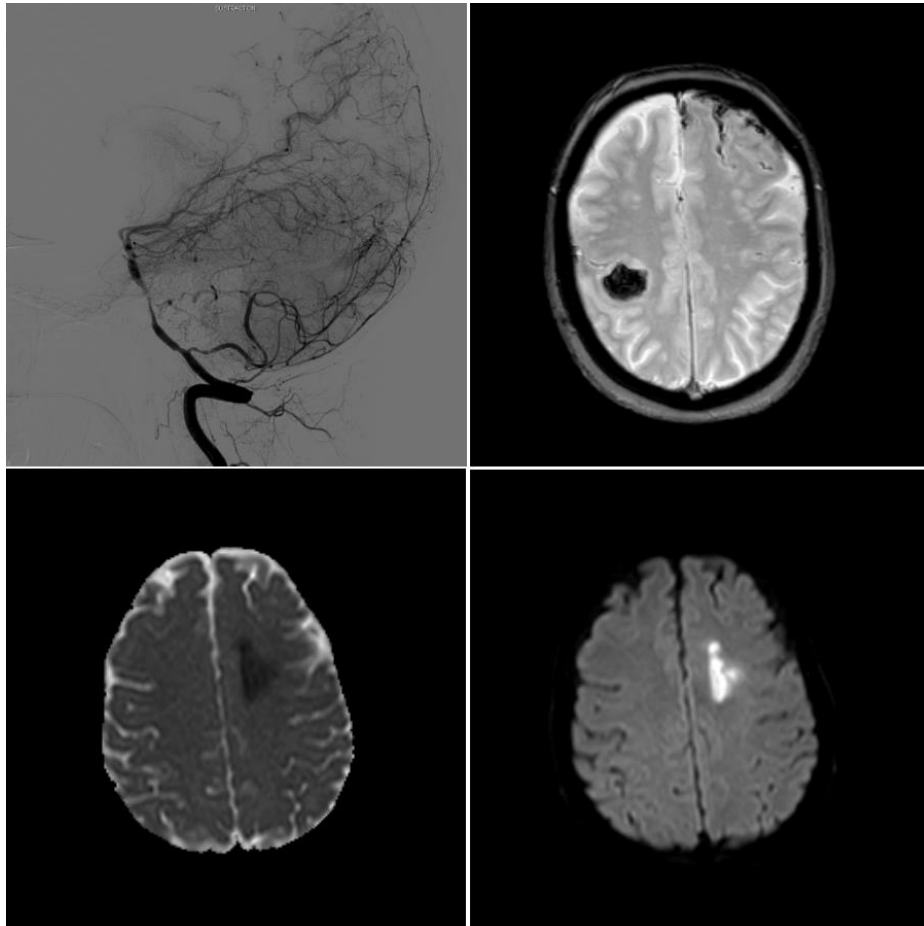
We present multiple cases of RCVS collated from our center to demonstrate the variation in clinical presentation and imaging features.

Results

Reversible Cerebral Vasoconstriction Syndrome (RCVS) is an increasingly recognized condition which may occur spontaneously or secondary to exposure to a precipitating substance or event. Clinically, it presents with sudden severe headache with or without neurological impairment. Multifocal narrowing of the intracranial arteries resulting and a 'string of beads' appearance may be demonstrated on catheter angiography, MR angiography, or CT angiography. These stenosis should be demonstrated to resolve within 12 weeks. There are a number of other associated imaging features which can occur on their own or in combination. These include subarachnoid haemorrhage, parenchymal haemorrhage, cortical infarcts, watershed infarcts, and reversible foci of cerebral oedema. We present multiple example cases to demonstrate the spectrum of this condition.

Conclusions

Reversible cerebral vasoconstriction syndrome is an increasingly recognized entity with a spectrum of possible imaging findings. It is hoped that review of these cases will enhance recognition of the different manifestations of the condition.



(Filename: TCT_EdE-23_RCVS.jpg)

EdE-33

Added Utility of Brain Diffusion Imaging in Extra-cerebral Lesions

M Elsayed¹, S Soman², R Rojas¹, Y Chang¹, R Bhadelia¹

¹Beth Israel Deaconess Medical Center, Boston, MA, ²Harvard Medical School, BIDMC, Boston, MA

Purpose

Diffusion-Weighted Imaging (DWI) has been a well established modality in evaluating cerebral pathology such as ischemia, abscesses and brain tumors. Over recent years, its utility has also generalized to diagnose a myriad of extracranial lesions involving nearly every organ system (1). However, DWI's role in detection of lesions beyond the confines of cerebral parenchyma, but within the scope of a Brain MRI, has not been extensively addressed in an academic setting (2, 3). Oftentimes, radiologists focus on identifying intracerebral lesions when interpreting the Brain DWI sequence and consequently the remaining extracerebral components of the imaging are often unintentionally overlooked. The purpose of this exhibit is to illustrate a series of cases in which extracerebral lesions were detected more readily on diffusion imaging. It is the authors' intention that these cases encourage the radiologic community to implement more emphasis on including extracerebral portions of Brain DWI into routine search patterns.

Materials and Methods

At the authors' institution, numerous cases of extracerebral lesions have been identified on Brain MRI DWI. Subsequently, there has been increasing emphasis in expanding the search pattern of Brain MRI diffusion imaging.

Results

The cases of this exhibit demonstrate diffusion abnormalities in extracerebral entities including the nasopharynx, lacrimal glands, infratemporal masses, parotid glands, and the calvarium. The associated pathologies range from lymphoma to malignant metastases.

Conclusions

Although the most common utilization of DWI concerns intracranial pathology such as ischemia, it is imperative that extracerebral regions of Brain MRIs are assimilated into the routine search pattern of radiologists. The authors propose that DWI possesses great potential in yielding significantly more diagnoses of pathology beyond the brain parenchyma. Lesions involving the meninges, calvarium, glandular tissue, lymphoid tissue, sinuses, orbits and musculature are potentially being overlooked. The cases presented will inspire the radiologic community to systematically broaden the routine search pattern of Brain DWI.

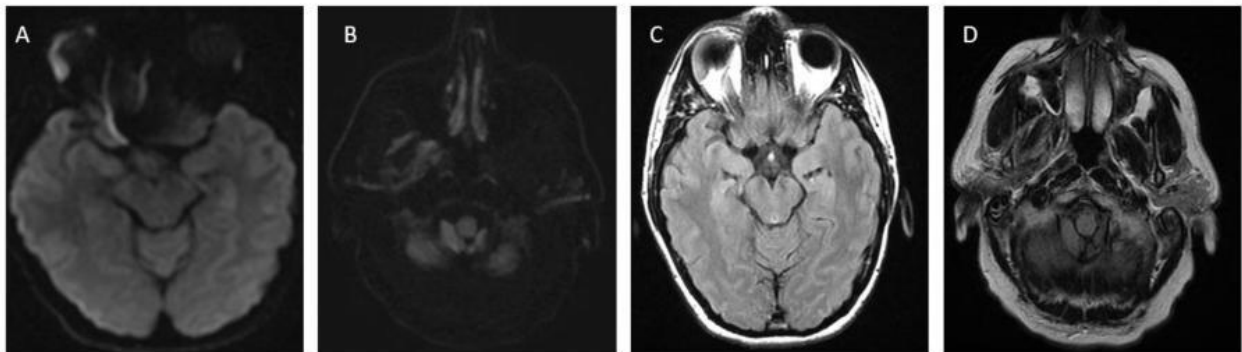


Figure 1. Brain MRI DWI and T2 FLAIR sequences. A&B) Brain DWI demonstrating diffusion abnormalities in the right lacrimal gland and right infratemporal fossa, respectively. C&D) T2 FLAIR Brain MRI sequences demonstrating less conspicuous correlative lesions.

(Filename: TCT_EdE-33_Figure1DWIASNR.JPG)

EdE-25

Adult Posterior Fossa Neoplasms: Imaging and Pathologic Review

A Tsai¹, T Hutchins¹, K Salzman¹

¹*University of Utah, Salt Lake City, UT*

Purpose

The purpose of this exhibit is to review the common, uncommon, and rare posterior fossa neoplasms in an adult with emphasis on imaging criteria for diagnosis and the 2016 WHO Classification of Tumors of the Central Nervous System.

Materials and Methods

All common, uncommon and rare intra-axial and fourth ventricular posterior fossa tumors in the adult will be reviewed. The characteristic imaging features on CT and MR including advanced MR features will be reviewed as well as an imaging differential diagnosis. The latest WHO criteria for these tumors will also be described.

Results

Each adult posterior fossa tumor will be individually reviewed with its own imaging differential diagnosis with emphasis on differentiating features and advanced imaging characteristics. The most common intra-axial posterior fossa tumors in an adult include metastatic disease and hemangioblastoma. Less common posterior fossa tumors in the adult include ependymoma, subependymoma, lymphoma and choroid plexus tumors. Rare tumors in the adult include dysplastic cerebellar gangliocytoma (Lhermitte-Duclos disease), medulloblastoma, astrocytoma, hemangiopericytoma, cerebellar liponeurocytoma and rosette-forming glioneuronal tumor.

Conclusions

This exhibit will display the common, uncommon and rare posterior fossa tumors that occur in the adult population. The goal of the exhibit is to help the radiologist provide an accurate pre-operative diagnosis/differential diagnosis of these adult tumors.

EdE-19

Amyloid Deposition and Angiitis: Spectrum of Imaging Findings

E Portela de Oliveira¹, V Yogendrakumar¹, N Zakhari¹, T Nguyen¹, C Torres¹

¹*University of Ottawa - The Ottawa Hospital, Ottawa, Ontario, Canada*

Purpose

This education exhibit aims to: 1) Discuss the different nomenclature used in the literature for amyloid deposition with angiitis. 2) Provide a concise overview of the prevalence and clinical relevance of amyloid deposition with angiitis. 3) Review the mechanisms and pathogenesis of amyloid beta related angiitis in order to facilitate the imaging approach. 4) Illustrate and discuss the key imaging features with radiological-pathologic correlation.

Materials and Methods

Representative magnetic resonance and computed tomography images will be displayed in a case-based format along with histopathological correlation, illustrating the main features of amyloid deposition associated with angiitis. A brief discussion of the relevant radiological features of the noninflammatory form of cerebral amyloid angiopathy will also be presented.

Results

Cerebral amyloid angiopathy (CAA) involves cerebrovascular amyloid deposition and is classified into several types according to the amyloid protein involved. An uncommon, but clinically striking presentation of CAA is the association with angiitis. Cerebral amyloid angiopathy related inflammation

Education Exhibits

(CAA-I) has been described under various names, also called amyloid β -related (ABRA), primary angiitis of the CNS associated with CAA, amyloid angiopathy and granulomatous angiitis and cerebral amyloid inflammatory vasculopathy. Acute-onset cognitive behavioral abnormalities, focal neurological deficits, seizures, or unusual headaches are the most common clinical presentations. CAA-I shows a spectrum of radiological manifestations, more commonly demonstrating hyperintensities on T2-weighted (T2W) or fluid-attenuation inversion recovery (FLAIR) images with presence of microbleeds on susceptibility weight images (SWI).

Conclusions

Cerebral amyloid angiopathy related inflammation is a rare entity that causes rapid-onset CNS dysfunction in elderly patients. If properly treated with steroids and other immunosuppressive therapy, patients may respond well. After reviewing this presentation, neuroradiologists will be able to recognize the key imaging features of the disease, and understand the clinicoradiological criteria. A proper diagnosis can therefore be suggested in a timely fashion, thus improving patient's outcome and avoiding unnecessary biopsies.

EdE-14

Bilateral Hippocampal Abnormalities Diagnosed on Magnetic Resonance Imaging: A Pictorial Essay

A Fukuda¹, E Punaro¹, F da Graça¹, S Appenzeller¹, F Reis¹

¹*State University of Campinas, São Bernardo do Campo, São Paulo, Brazil*

Purpose

We aim to illustrate typical findings of bilateral hippocampal abnormalities on magnetic resonance imaging (MRI), in a didactic way, in order to facilitate the learning process and memorization of these patterns by radiologists in their clinical practice. The diseases were selected in our archive of images and included: herpes virus type 1 encephalitis, herpes virus type 8 encephalitis, autoimmune encephalitis, tuberous sclerosis, kernicterus, mesial temporal sclerosis, Alzheimer's dementia, bilateral glioma, transient global amnesia, frontotemporal dementia and remaining embryonic cysts of the hippocampal sulcus.

Materials and Methods

All the images and medical data were compiled from patients with hippocampal diseases in the Clinical Hospital of the State University of Campinas – Brazil, without any restriction for sex and age. No intervention was done for research purposes.

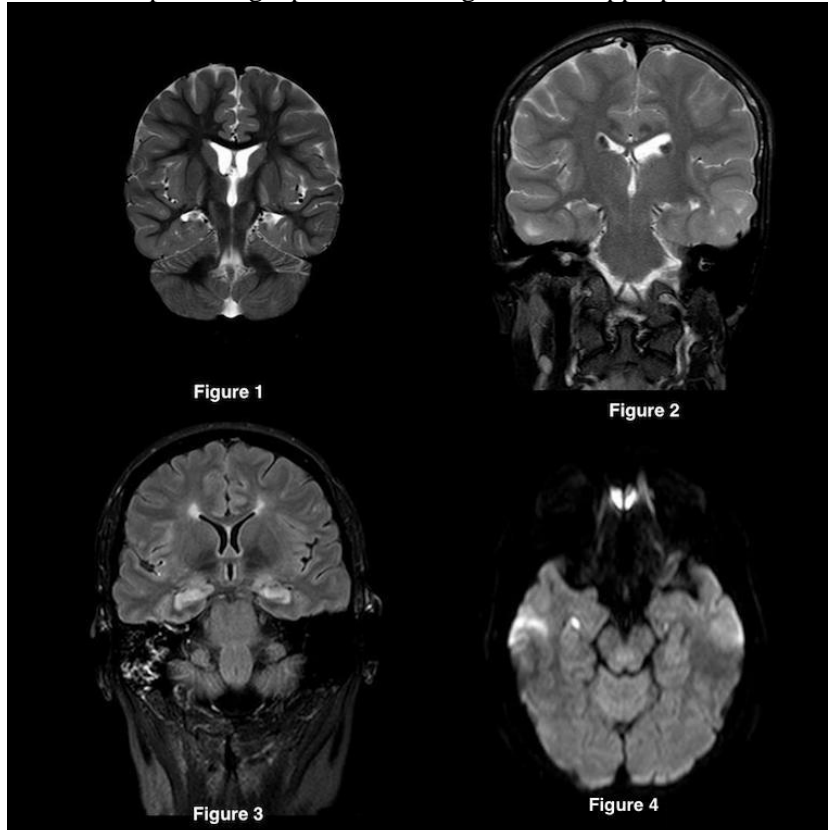
Results

We selected 11 cases with typical MRI findings of temporal lobe disease, described in correlation with anatomopathological data and clinical evolution, four of which we present below. Figure 1. A 3-year-old female patient, presented jaundice, fever, hypoactivity and seizures at seven days of life, being diagnosed with bilirubin encephalopathy. Coronal T2 Weighted-Image fat-sat showing symmetric hyperintensity of the hippocampus, globus pallidus and substantia nigra. Figure 2. A 12-year-old male patient with a medical history of crises since three years old, developmental delay and typical skin changes (angiofibromas and hypomelanotic macules). Coronal T2 Weighted-Image Spair showing small subependymal nodules with hypointensity. There are also cortical tubers in the temporal lobes and hippocampal malrotation with blunter inner architecture. Figure 3. A 26-year-old female patient, with acute myeloid leukemia admitted for hematopoietic stem cell transplantation presented a generalized tonic-clonic seizure and acute onset cognitive impairment. Coronal FLAIR shows hyperintensity and increase in volume in both hippocampus. Figure 4. A 59-year-old female patient, presented with acute onset loss of short-term memory with complete recovery after few hours and normal laboratory investigation. Global transient amnesia was the most probable diagnosis. Diffusion-Weighted Image showed focal restriction in CA1 regions of both hippocampus.

Education Exhibits

Conclusions

Patients with temporal lobe diseases are often with impaired consciousness, confusion and unable to collaborate with the neurological examination. Therefore, MRI may play a key role in the diagnosis. Imaging findings of hippocampal diseases are varied. Additional lesions in other sites, such as globus pallidus and substantia nigra may aid in the identification of the correct etiology and guide the clinical management. Other aspects, as increased or reduction in volume and restricted diffusion are important tools to consider. Once temporal lobe diseases are often severe and life threatening, neuroimaging has a vital role in providing a precocious diagnosis and appropriate medical clinical care for these patients.



(Filename: TCT_EdE-14_Figures1-4.jpg)

EdE-29

Characterizing the Misnomer: Glomus Tumors of Head and Neck

A Naqvi¹, O Islam¹

¹Queen's University, Kingston, Ontario, Canada

Purpose

1. Review head and neck Paragangliomas etiology and types 2. Learn the common anatomical locations where these tumors present 3. Learn the common clinical manifestations of Paragangliomas 4. Review the common imaging characteristics of Paragangliomas and their subtypes

Materials and Methods

1. Introduction to Paragangliomas 2. Anatomy Review with Common Locations 3. Clinical Pearls: Natural History and Clinical Manifestation 4. What the Radiologist Needs to Know: Imaging Characteristics • Carotid Body Tumors • Glomus Jugulare • Glomus Tympanicum • Glomus Jugulotympanicum • Glomus Vagale

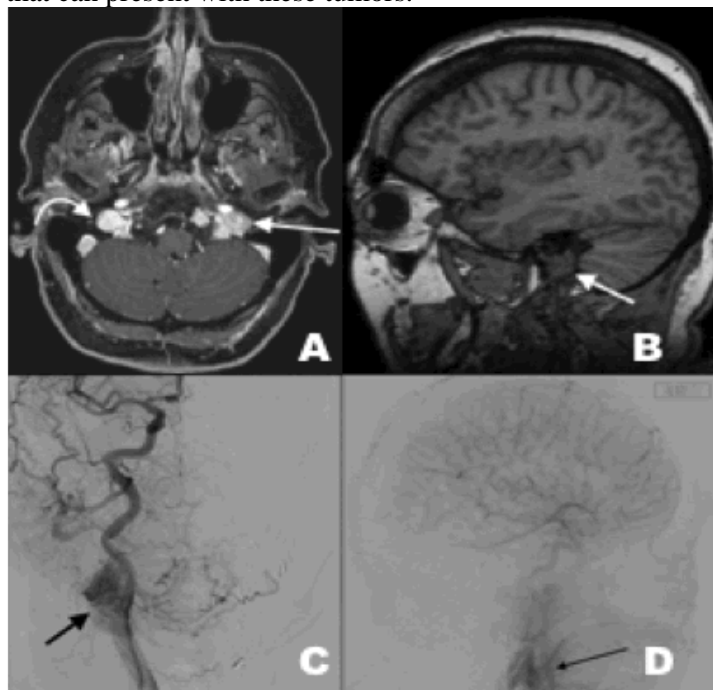
Education Exhibits

Results

Head and Neck Paraganglioma characteristics through a case-based pictorial essay: 1. 59-year-old man with a slow growing left neck mass. Multi-planar contrast enhanced CTA images demonstrate an avidly enhancing mass (white arrow) within the left carotid space, splaying the left ICA and the left ECA. Carotid Body Tumor. 2. Glomus Tympanicum in a 59-year-old woman with left-sided conductive hearing loss, an erythematous tympanic membrane and pulsatile tinnitus. Bone algorithm Axial and Coronal images demonstrate a 7mm lobulated soft tissue mass within the mesotympanum overlying to the cochlear promontory. 3. Glomus Jugulotympanicum in a 62-year-old woman with right-sided pulsatile tinnitus and hearing loss. MR Axial T2W (inset) and Axial T1W post Gad enhanced with fat saturation demonstrate a soft tissue mass with avid enhancement in the jugular foramen with subsequent invasion of the jugular fossa wall and extending towards the hypotympanum. 4. Glomus Vagale in a 75-year-old woman with a slow growing left neck mass. A. T1W MR; B. T2W MR; C. T1W Postgadolinium enhanced MR with Fat Saturation demonstrate a 5cm mass in the carotid space with anterior displacement of the carotid bifurcation, that is low signal on T1 and heterogenous signal on T2 with avid enhancement. The mass contains multiple internal serpentine and punctate low signal foci (in B) compatible with vascular flow voids ("salt and pepper"). 5. Glomus Jugulare in a 50-year-old woman with a prior right side carotid body tumor excision. A. Axial T1W Postgadolinium MR with Fat sat; B. Sagittal T1W MR; C. Early Arterial phase Right carotid Angiogram AP view; D. Late-phase Right carotid Angiogram lateral view. Axial and Sagittal MR images demonstrate a 1.4cm (white arrow) heterogeneously enhancing mass ("salt and pepper"). Angiogram images demonstrate the original hyper-vascular right carotid body tumor with persistent enhancement. Multiple tumors are seen in approximately 10% of cases.

Conclusions

The correct identification of glomus tumors are essential for adequate patient. Our pictorial essay enables us to review different types of glomus tumors and their etiologies. We demonstrate the most common locations of these tumors, that help with reaching the correct diagnosis along with clinical manifestations that present with these tumors. Furthermore, we delve into the imaging characteristics that are unique to the head and neck glomus tumors and their subtypes. Such an approach helps to simplify the complexities that can present with these tumors.



(Filename: TCT_EdE-29_GJ.gif)

EdE-07

Coregistration of fMRI and DTI Data: a Technique for Improving Diffusion-tensor Tractography.

B Petrovic¹, J Meyer¹, D Burman¹

¹*NorthShore University HealthSystem, Evanston, IL*

Purpose

Diffusion tensor imaging (DTI) and diffusion tensor tractography (DTT) are noninvasive tools for assessment of white-matter tracts. These techniques allow for visual representation of major white matter tracts, assessment of the integrity of the tracts, and assessment of their relationship to surrounding structures, including space occupying masses. DTI and DTT are increasingly being employed in routine clinical practice. In particular, these techniques are becoming an important part of preoperative planning for patients with brain tumors where they may provide information that leads to alteration of surgical approach or prognostic information that allows for better preoperative estimation of the likelihood of a postoperative neurological deficit. A major limitation of DTT is difficulty in displaying a relatively complete, useful representation of a white-matter tract of interest because tracts can be artificially truncated. fMRI is a technique frequently used in preoperative evaluation of brain tumor patients to delineate the relationship of eloquent cortex to surgical targets. Combining fMRI data with diffusion tensor imaging data can allow for depiction of more complete tractograms and can overcome some of the frequently encountered artificial truncation of white matter tracts. The purpose of this poster will be to illustrate how coregistration of functional MRI and DTI data can be used in clinical practice as part of the preoperative imaging assessment of brain tumor patients to obtain better, more complete tractograms of the corticospinal tract and arcuate fasciculus.

Materials and Methods

IRB approval was obtained with waiver of informed consent. MR imaging was performed during routine care of patients and was retrospectively reviewed. The electronic medical record was searched to identify patients with primary brain tumors who underwent both fMRI and DTI in the same sitting. Age, gender, and patient diagnosis were recorded. Color FA maps were generated from the DTI data and fused with MPRAGE MR images. Anatomic landmarks on the FA color maps were utilized to identify seed regions of interest (ROIs) for tractography and tractograms of either the corticospinal tract or arcuate fasciculus were generated. The tractograms were fused with FLAIR images. Next, areas of activation on fMRI that would serve as additional seed ROIs were imported after processing with Statistical Parametric Mapping 8. Additional tractograms utilizing seed ROIs based relevant areas of fMRI activation were generated. The two types of tractograms (i.e. those based on seed ROIs derived from FA color maps or from fMRI activation) were differentiated by color coding.

Results

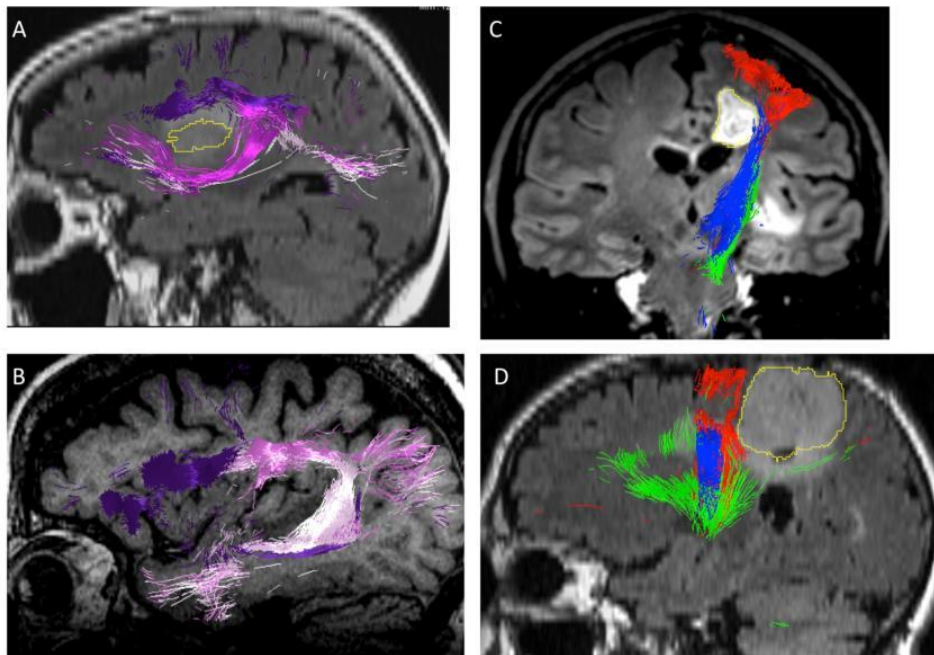
Tractograms of the arcuate fasciculus were improved and made more useful by addition of fMRI data. Figure A is the tractogram of the arcuate fasciculus in a 62-year-old woman with glioblastoma. The yellow circle indicates where enhancing tumor was seen on postcontrast imaging. The pink fibers represent the tractogram generated from seed ROIs selected on the color FA map. The dark purple fibers represent additional fibers generated when selecting an ROI based on an area of activation during a language task. Without addition of the fMRI-based seed ROI, the relationship of the tumor to the arcuate fasciculus would not be adequately defined. Figure B is a tractogram of the arcuate fasciculus in a 62-year-old woman with glioblastoma. In this case, additional fibers from an fMRI-derived seed ROI (dark purple fibers) not only extend the tractogram farther anteriorly but also flesh out the portion of the tractogram in the temporal lobe. This technique is also quite useful with tractography of the corticospinal tract (CST). Figure C is a tractogram of the CST in a 58-year old-woman with brain metastasis from ovarian primary. The yellow circle indicates where enhancing tumor was seen. Fibers generated from FA map-derived seed ROIs are depicted in green and blue. Additional fibers generated from ROI based on area of activation during hand motor task on fMRI are shown in red. Without the fMRI-derived seed ROI,

Education Exhibits

the tractogram is truncated, failing to propagate superiorly near the cortex. Addition of the fMRI-derived seed ROI allows for visualization of the most superior fibers of the CST and better illustrates the relationship of the CST to the mass. Similar findings are seen in figure D, a tractogram of the CST in a 48-year-old man with high grade glioma. Without additional fibers from fMRI-based seed ROI (red), the relationship of the CST to the mass (yellow circle) would be poorly understood.

Conclusions

A major limitation of tractography has been difficulty in achieving a relatively complete representation of a white matter tract of interest as the tracts can be artificially truncated in multiple situations. Presence of crossing fibers in a given voxel, presence of unrelated fibers traveling parallel to the tract of interest, or presence of merging, diverging, or fanning tracts can all interfere with fiber tracking algorithms. Accurate tracking of white matter tracts with tractography becomes even more difficult in the setting of pathology such as brain tumors or significant edema which can alter the fractional anisotropy. Frustratingly, this is frequently the scenario where tractography can be most useful. Coregistration of fMRI and DTI data is a technique that can ameliorate this problem as it allows one to incorporate relevant areas of activation during an fMRI task as additional seed ROIs, resulting in more complete and robust tractograms without having to alter parameters of the fiber tracking algorithm (which might otherwise lead to generation of spurious tracts). Images presented in this poster show how seed ROIs in areas of activation during finger tapping or motor tasks can be used to flesh out the most superior portions of the CST, near the motor cortex, while fMRI activation of Broca's area during language tasks can be used to show the most anterior fibers of the arcuate fasciculus in the frontal lobe.



(Filename: TCT_EdE-07_imagesforASNRsubmission.jpg)

EdE-03

Epilepsy: Overview of Surgical Evaluation and Treatment Options

P Szpakowski¹, K Learned²

Education Exhibits

¹Hospital of Pennsylvania of the University of Pennsylvania, Philadelphia, PA, ²University Pennsylvania Health System, Philadelphia, PA

Purpose

The purpose of this educational exhibit is to familiarize radiologists with the steps in management of patients with epilepsy, surgical options and complications with imaging correlates.

Materials and Methods

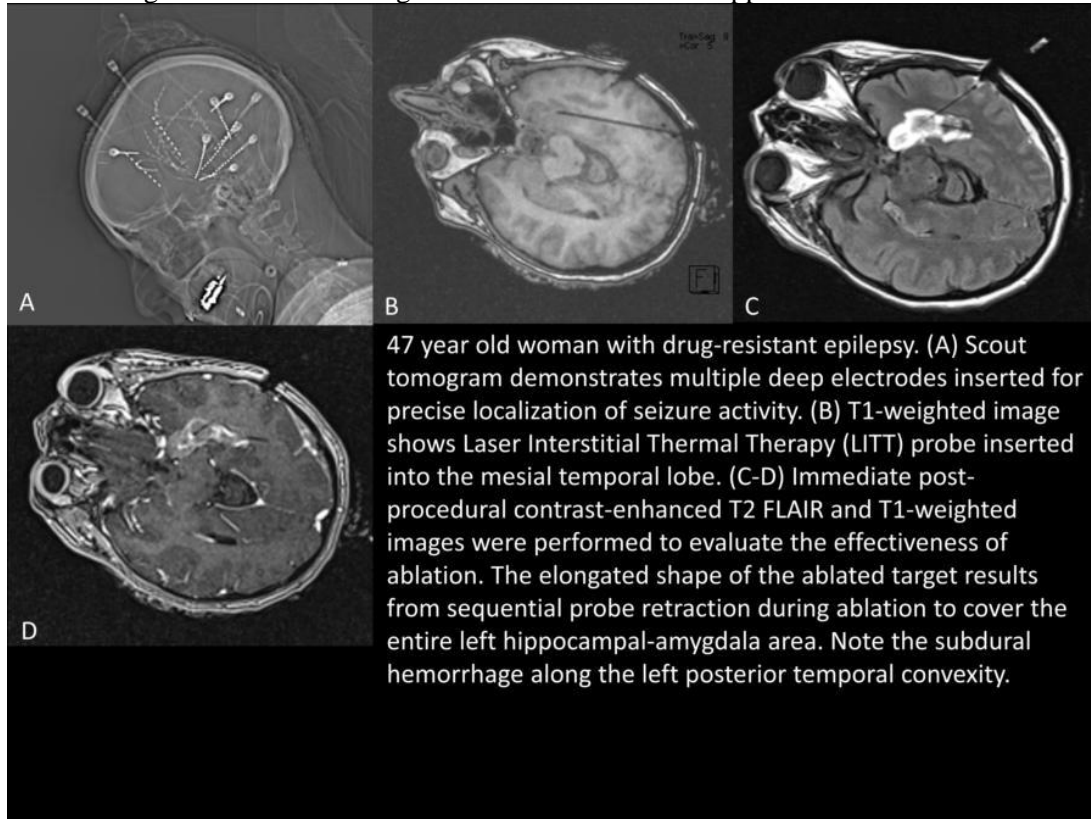
A review of most recent literature of the definition of epilepsy, its causes, clinical workup, and the neurosurgery for epilepsy diagnosis and treatment. A case-based approach illustrates clinical and imaging findings.

Results

Epilepsy is estimated to affect up to 50 million people worldwide with significant proportion who are resistant to treatment. The International League Against Epilepsy has redefined the definitions of seizures, epilepsy, and drug-resistant epilepsy. For patients who are being considered for neurosurgical intervention, each patient undergoes pre-surgical evaluation using EEGs, neuroimaging, and psychological testing. Use of invasive electrodes, such as subdural electrodes and intracerebral deep electrodes, allow neurologists and neurosurgeons to map out potential sources of seizure activity. A subset of drug-resistant patients can have surgically treatable conditions such as mesial temporal sclerosis or tumors. The number of surgical options can include lobectomy, laser ablation, vagal stimulators, and, more recently, response neurostimulators. Reported complication rates vary depending on the type of procedure and include hematomas, empyema, meningitis, abscesses, and neurological deficits.

Conclusions

Epilepsy is a complicated disorder with various surgical treatment options and a variety of complications necessitating the need for radiologists to be familiar with its appearances.



(Filename: TCT_EdE-03_epilepsy.jpg)

EdE-17

Flight of Ideas: A Neuroimaging-based Differential for Secondary Psychosis

D Poletto¹, H Raman¹, R Bucelli¹, D Mamah¹, M Goyal¹

¹*Washington University School of Medicine, St. Louis, MO*

Purpose

Psychosis, according to the Diagnostic and Statistical Manual of Mental Disorders, 5th edition (DSM-5), includes delusions, hallucinations, and disorganized thinking or behavior [1]. Whereas psychosis often heralds a diagnosis of schizophrenia or a related mental illness, it can also be the presenting or primary symptom of other neurological illnesses, including ones that are potentially reversible with appropriate treatment. Neuroimaging is becoming increasingly recognized as a critical tool in identifying these secondary causes of psychosis. Here we review the causes of secondary psychosis and their neuroimaging manifestations to better equip the reader in identifying these important diagnoses.

Materials and Methods

This educational poster will first review the imaging findings of secondary disease processes that most commonly feature psychotic symptoms in their initial presentation, based on a detailed review of the literature. Illustrative cases will be presented. Next, we will discuss imaging features of conditions in which secondary psychosis is unusual yet has been reported, to provide a more thorough compendium for future reference.

Results

The most common secondary causes of psychosis include autoimmune diseases, in particular autoimmune encephalitis [2, 3]; neurodegenerative disorders such as Alzheimer's disease, Lewy body dementia, and Parkinson's disease [4, 5]; traumatic brain injury; medications and substance abuse; and infectious processes. Other less common conditions that may present with psychosis include metabolic or toxic etiologies, ischemic injury, inflammatory conditions, and numerous congenital or hereditary disorders.

Conclusions

Neuroimaging might provide clues to a secondary cause of psychosis. Some of these conditions, such as autoimmune encephalitis, are treatable and often reversible. Thus, this educational poster aims to raise awareness of these important disorders, as the radiologist could have a critical impact in patient outcome by identifying or suggesting the appropriate diagnosis from neuroimaging.

Table 1. Neuroimaging findings of conditions/diseases in which psychotic symptoms are frequently a component of the initial presentation.

Category	Condition/Disease		Neuroimaging findings	Clinical considerations
Autoimmune	Auto-immune limbic encephalitis	Anti-NMDARE [†]	Imaging most often normal. Findings may include T2/FLAIR hyperintensity and enhancement of the mesial temporal lobes, insula, and cingulate gyrus. Regional cortical diffusion restriction possible.	Delusions and hallucinations may be the only presenting features, and misdiagnoses of primary psychiatric illnesses have been reported. ²
		Paraneoplastic and other CNS-directed antibodies	Bilateral T2/FLAIR hyperintensity and edema of the mesial temporal lobes, insula, and cingulate gyrus, +/- enhancement, and +/- involvement of the brainstem, cerebellum, and thalamus.	
	Vasculitis	Susac's Syndrome	Round T2/FLAIR hyperintensities in the central corpus callosum, sparing the callosal-septal interface, that may acutely restrict diffusion; additional punctate foci of diffusion restriction and T2/FLAIR hyperintensity in the deep gray and white matter; leptomeningeal enhancement also possible.	Psychosis may occur at presentation. Screening for hearing loss and retinal artery occlusion is essential. ³
Neurodegenerative Processes	Alzheimer's Disease		Cortical amyloid deposition seen on amyloid-PET. Early hypometabolism on FDG-PET and volume loss on MRI in the mesial temporal lobes and posterior cingulate progressing to diffuse atrophy.	Psychosis typically occurs with hallucinations and delusions, with a median prevalence of 41%. ⁴
	Dementia with Lewy Bodies		Cortical volume loss in the temporal, parietal, and occipital lobes, with relative sparing of the hippocampus on MRI. Reduced uptake in the putamen (+/- caudate) on DAT-SPECT. Hypometabolism preferentially in the occipital cortex on FDG-PET.	Well-formed, visual hallucinations are characteristic, experienced by 76% of patients in one large study. ⁵
	Parkinson's Disease		Loss of the normal layered architecture of the substantia nigra on high resolution MRI, particularly on susceptibility weighted sequences. Reduced uptake on DAT-SPECT, particularly in the posterior putamen.	Hallucinations and delusions are less common than in patients with DLB. ⁵
Traumatic	Chronic TBI/CTE		Encephalomalacia most commonly in the temporal and frontal poles, diffuse atrophy, or sequelae of prior DAI on conventional MRI. Loss of tract integrity and decreased fractional anisotropy in the corpus callosum and corticospinal tracts on advanced imaging.	Psychosis occurs after a long latent period following the initial insult.
Metabolic/ Toxic	Illicit drug use/chronic abuse		Variable depending on drug type: sequelae of hemorrhagic or ischemic infarct in cocaine or amphetamine abuse; leukoencephalopathy with T2 hyperintensity in the cerebral and cerebellar white matter in heroin or inhalant abuse; diffuse atrophy in many types; multifocal or regional areas of vascular narrowing.	Psychosis may be a sign of intoxication or withdrawal. Symptoms tend to be temporary and reversible.
Infectious/ Inflammatory	Neurosyphilis		Thick, nodular leptomeningeal enhancement, enhancing parenchymal nodules or masses, and cortical/subcortical infarcts on MRI; multifocal large vessel stenoses and dilatations on MRA; cortical atrophy.	Typically presents with dementia-like symptoms, but may also present with psychotic features.

Abbreviations: anti-NMDARE = anti-N-methyl-D-aspartate receptor encephalitis; CTE = chronic traumatic encephalopathy; DAI = diffuse axonal injury; DAT = dopamine transporter; DLB = dementia with Lewy Bodies; PD = Parkinson's Disease; TBI = traumatic brain injury.

† Although anti-NMDARE can be associated with ovarian teratoma, a non-paraneoplastic form is now increasingly diagnosed.

(Filename: TCT_EdE-17_Table45abstract.jpg)

EdE-28

Foramen of Monro: A Review of Neuroimaging Anatomy, Morphometry, and a Spectrum of Obstructive Lesions Seen on CT and MRI

Z Chaudhry¹, V Mayercik¹, F Zaccagna², D Barone², S Hashmi¹, T Matys², T Massoud¹

¹Stanford University School of Medicine, Stanford, CA, ²University of Cambridge, Cambridge, United Kingdom

Purpose

The interventricular foramen of Monro (FoM) was named in 1783 after the Scottish physician Alexander Monro secundus. Each FoM connects the lateral ventricle with the third ventricle, and also contains choroid plexus. We review the neuroimaging features of lesions located around FoM with special emphasis on their wide-ranging differential diagnosis.

Materials and Methods

We present the imaging manifestations of a wide spectrum of pathologies at FoM, and categorize them according to patient age.

Results

We first describe the imaging anatomy and morphometry of the FoM. Its mean narrowest width is 2.4mm and each is a short 'canal' rather than a 'foramen'. FoM may be congenitally atretic or may occlude by

Education Exhibits

infection or hemorrhage to cause ventriculomegaly, diagnosed on prenatal sonography. Rarely unilateral ventriculomegaly may manifest in adults due to membranous stenosis of FoM. The differential diagnosis of masses arising from or encroaching on FoM can be considered according to patient age. The commonest pediatric etiology is subependymal giant cell astrocytoma (in 20% of tuberous sclerosis [TS]). Others causes in children include TS subependymal nodules, choroid plexus papilloma, craniopharyngioma, germinoma, glioma, Langerhans cell histiocytosis, neurofibromatosis, pilocytic astrocytoma, and rare congenital intraventricular cysts (arachnoidal, endodermal, or neuroepithelial) that may also manifest in adulthood. In adults the commonest (20%) true mass at FoM is a colloid cyst, a benign lesion several millimeters to 3cm in size attached to the anterosuperior aspect of the third ventricle roof. These are generally asymptomatic but 10% enlarge or cause hydrocephalus. Rapid enlargement has been associated with coma and death. Other masses in adults include neurocytoma, subependymoma, aneurysm (e.g. giant basilar tip), cysticercus cyst, glioma, lymphoma, meningioma, metastasis, pituitary adenoma, choroid plexus cyst, and cavernous malformation.

Conclusions

A thorough appreciation of imaging findings for the wide spectrum of pathologies at FoM is essential for the neuroradiologist and neuroendoscopist.

EdE-08

Glioma 2HG Imaging: Basic Principles, Clinical Implementation, and Interpretation Tips

R Durel¹, A Agarwal¹, J Maldjian¹, C Choi¹, M Pinho¹

¹UT Southwestern, Dallas, TX

Purpose

To present our institutional experience with a fully automated method of 2-hydroxyglutarate (2HG) magnetic resonance spectroscopy (MRS), as a means of noninvasively detecting and quantifying 2HG in isocitrate dehydrogenase (IDH) mutated gliomas. The overarching goal is to provide neuroradiologists with basic principles for acquisition, post processing and interpretation of this novel imaging technique.

Materials and Methods

Clinicians and scientists in our institution have been working in collaboration to translate recent developments in MRS for detection and quantification of 2HG into routine clinical practice. This collaborative effort has resulted in a fully automated processing pipeline. In short, raw spectra are sent from clinical MRI scanners to an XNAT database. Data is then automatically processed through LCModel for creation of metabolite levels and QC plots. A JPEG of the resulting processed spectra, metabolite levels, and QC information is generated, converted to DICOM, and sent back into PACS to reside with the patient data.

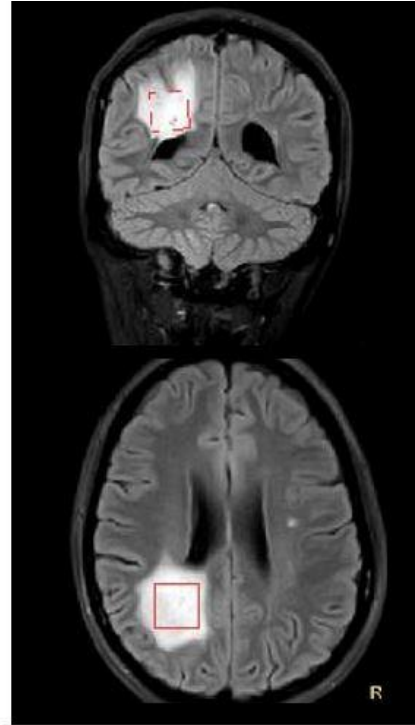
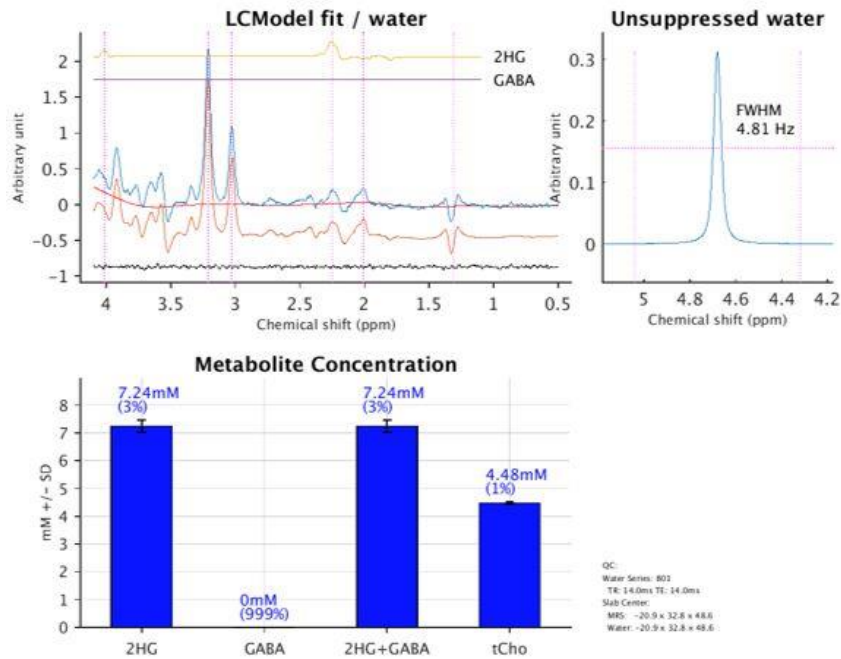
Results

This poster showcases our implemented clinical 2HG imaging workflow organized in the following sections: - Basic principles of IDH mutations and 2HG metabolism - 2HG-optimized long TE point-resolved spectroscopy (PRESS) – clinical implementation, advantages and disadvantages - Guidelines for patient selection and data acquisition in clinically feasible scanning times - Automated off-line postprocessing pipeline with PACS integration - Case-based review of spectral quality assurance, interpretation of LC model results and technical pitfalls.

Conclusions

Noninvasive MRS detection and quantification of 2HG is clinically feasible and will enable the incorporation of this crucial imaging biomarker in routine clinical practice.

Education Exhibits



(Filename: TCT_EdE-08_Normal2HG.JPG)

EdE-37

Image-based Review of Carotid Plaque Features for Stroke Risk Assessment on CT Angiography

E Dou¹, H Patel¹, A Gupta¹, H Baradaran¹

¹New York-Presbyterian Hospital/Weill Cornell Medical Center, New York, NY

Purpose

Stroke risk reduction therapy has largely been guided by the degree of carotid artery stenosis as defined by NASCET criteria; however, there are additional plaque features beyond luminal stenosis that can be identified on routine CT angiography (CTA), that are associated with cerebrovascular ischemia (1-3). Our purpose is to provide an imaging-rich, case-based review of easily identifiable plaque features on CTA that are associated with cerebrovascular ischemia.

Materials and Methods

We reviewed the literature to identify plaque features on CTA that are associated with cerebrovascular ischemia. After reviewing hundreds of CTA examinations, we identified imaging examples illustrating these carotid plaque features for educational purposes.

Results

We identified four carotid plaque features seen on CTA which are associated with cerebrovascular ischemia. First, we will provide an image-heavy review of three plaque features on CTA which are described as "high-risk" features: 1.) The presence of "soft" plaque, defined by low attenuation (HU < 40-50) which may correlate histopathologically with high-risk lipid-rich core and/or intraplaque hemorrhage; 2.) Plaque ulceration, defined as concave irregularities in the contour of the carotid lumen with 1-2mm outpouchings of contrast into the plaque; and 3.) Carotid artery wall thickening. Conversely, we will review imaging examples of carotid plaque features negatively associated with ipsilateral cerebrovascular ischemia, the presence of calcified plaques, defined as HU > 130.

Education Exhibits

Conclusions

Through an image-rich review, we will present multiple easily identifiable carotid plaque features on CTA which can serve as additional imaging markers to identify patients who are more likely to have cerebrovascular ischemia.

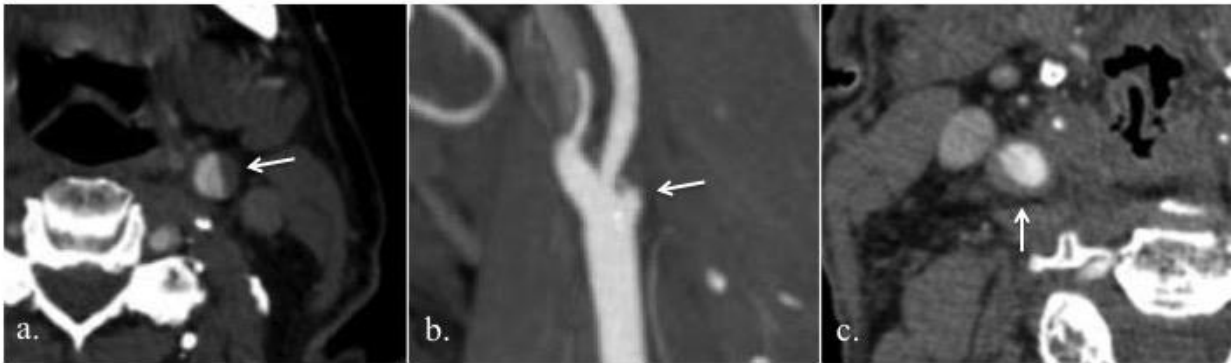


Figure 1: Examples of “high-risk” CTA carotid plaque features. **(a.)** “Soft” plaque, defined as HU< 40-50. **(b.)** Plaque ulceration, defined as outpouchings of contrast into the plaque. **(c.)** Carotid artery wall thickening.

(Filename: TCT_EdE-37_Figure1.jpg)

EdE-38

Imaging Review of Brainstem Stroke Syndromes: Where to Look Out

A Goncalves Filho¹, D Fragoso¹, I Padilha¹, A Pettengill¹, J Gavino², R Rivero², A Massaud², R Hoffmann Nunes², F Pacheco³, A da Rocha¹

¹*Irmandade da Santa Casa de Misericórdia de São Paulo, Sao Paulo, Brazil*, ²*DASA, Sao Paulo, Brazil*, ³*Santa Casa de São Paulo School of Medicine, São Paulo, Brazil*

Purpose

Brainstem stroke syndromes refer to a group of syndromes that usually occur secondary to occlusion of small perforating arteries of the posterior circulation. Because of their location, they often involve impairment both of the cranial nuclei and of the long tracts. The hallmark of most strokes – weakness on one body side – is not always present. Therefore, the diagnosis could be challenging and neuroimaging is essential in this condition. Our purpose is to discuss brainstem stroke syndromes after a brief anatomy review.

Materials and Methods

Patient selection and data collection were performed using our electronic patient's database. After reviewing our institution teaching files, we have selected only cases with acute neurologic symptoms. However, other mimicking lesions were also selected to discuss differential diagnosis. The findings were classified and exposed according with their topography to following a didactic approach. The brainstem anatomy review was done using DTI and tractography.

Results

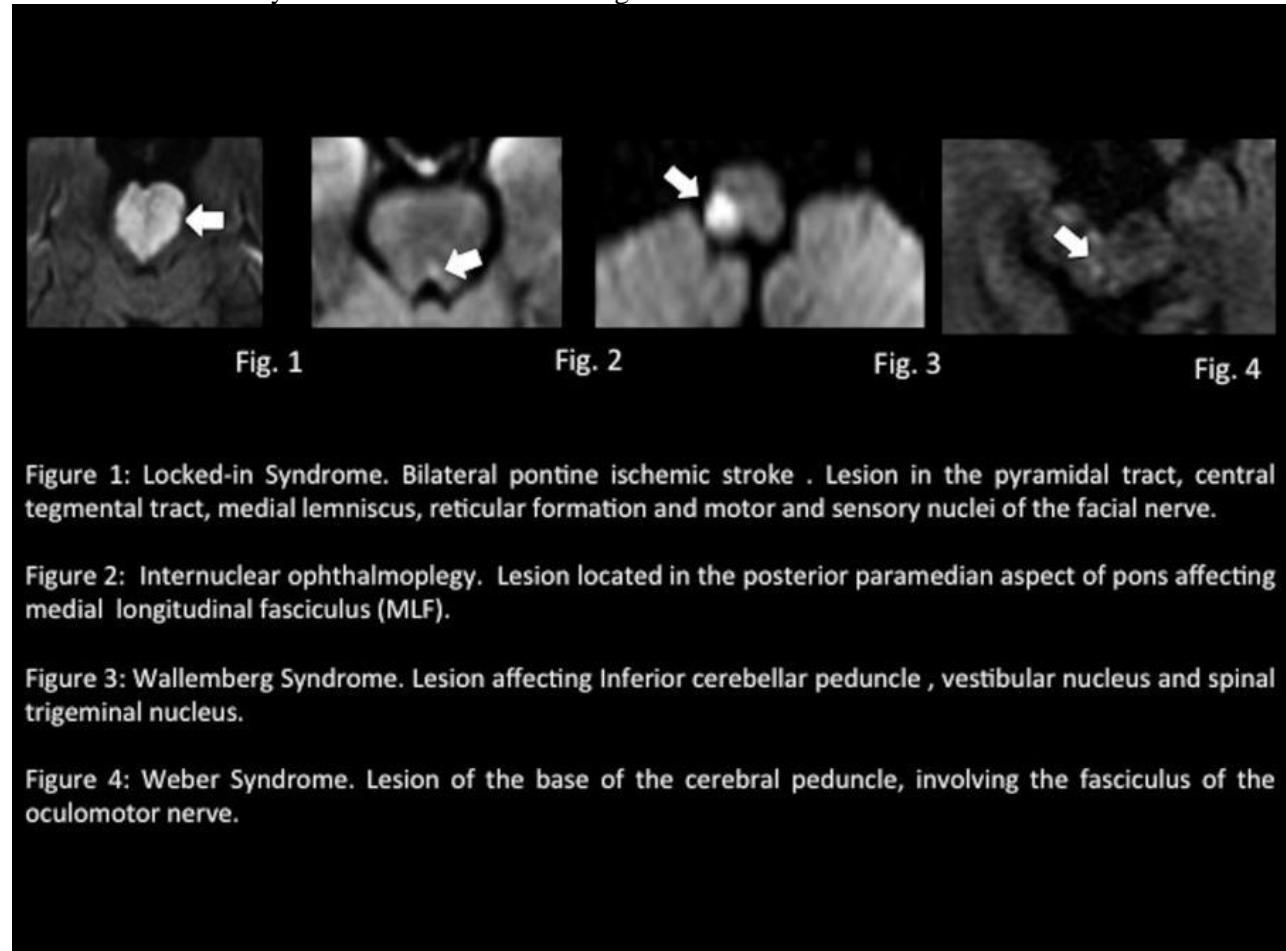
Almost one-third of ischemic strokes affect the vertebrobasilar system, including brainstem. Therefore, DTI was used to demonstrate cranial nuclei and fibers tracts to correlate the regions involved in each syndrome. At the level of the midbrain, Weber, Benedikt and Claude syndromes – all of them involving CN III - were discussed and exemplified. Foville and Millard-Gluber syndromes were highlighted

Education Exhibits

considering pons involvement. One of the most catastrophic neurologic syndromes – locked-in syndrome – was also discussed. Finally, medial and lateral medullary syndromes were reviewed.

Conclusions

The brain stem is a complex structure that contains multiple nuclei and tracts that are vital to our daily activities. Therefore, neurologic symptoms may vary widely and neuroimaging plays an important role to the precise diagnosis. Sometimes, even in the presence of a vast symptomatology, there is just a tiny abnormality that should be recognized. Thus, neuroradiologists must be aware of neurological symptoms and brainstem anatomy to be confident with the diagnosis.



(Filename: TCT_EdE-38_Slide1.jpg)

EdE-18

Intracranial Dural Arteriovenous Fistula After Treatment: The Utility of the Combination of 3D-TOF MRA and ASL

K Noguchi¹

¹University of Toyama, Toyama, Japan

Purpose

The purpose of this educational poster is to show the utility of magnetic resonance imaging in the assessment of the recurrence or worsening of intracranial dural arteriovenous fistula (DAVF) after treatment.

Education Exhibits

Materials and Methods

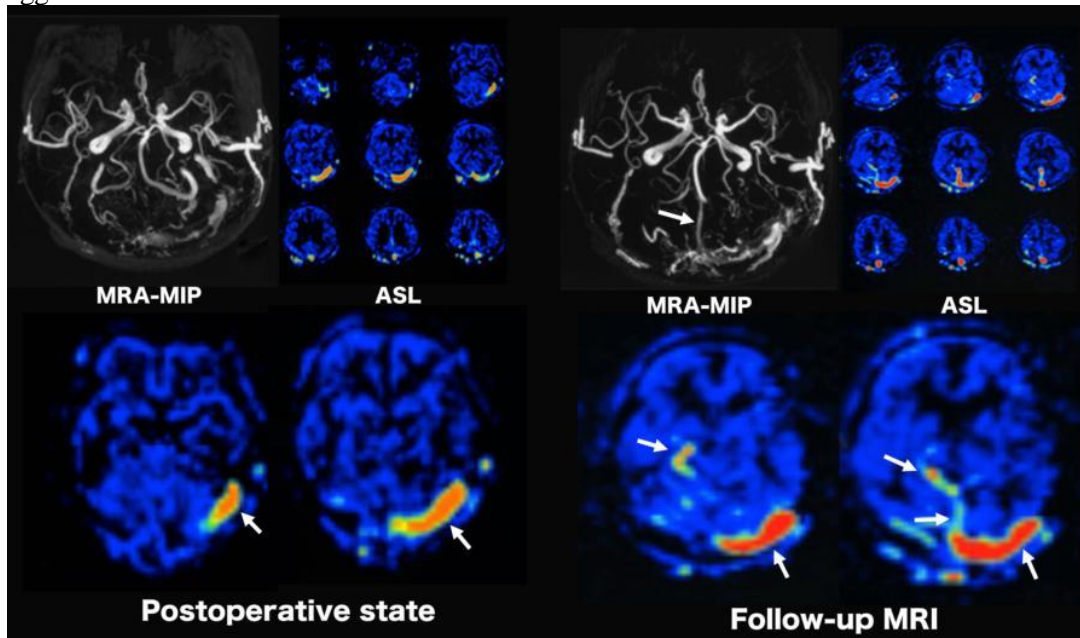
Table Outline: 1. General statement of DAVF 1-1) Etiology, 1-2) Location and Symptom, 1-3) Classification, 1-4) Treatment 2. Review of MRI findings 2-1) Conventional MRI, 2-2) Susceptibility-weighted imaging (SWI), 2-3) 3-D TOF-MRA, 2-4) MR digital subtraction angiography (MRDSA), 2-5) Dynamic susceptibility contrast (DSC), 2-6) Arterial spin labeling (ASL) 3. Sample cases: Preoperative and postoperative follow-up cases 4. Future directions 5. Summary

Results

DSA is considered as a gold standard in the diagnosis of DAVF. However, 3-D TOF MRA is also able to diagnose DAVF accurately in almost all cases. Advanced MRI such as SWI and DSC-rCBV can clearly manifest venous congestion and cortical venous drainage in DAVF. ASL is able to detect arteriovenous shunt and venous drainage. The combination of 3-D TOF MRA and ASL that are noncontrast enhanced methods are able to detect the changes of venous drainage pattern during postoperative follow-up.

Conclusions

The combination of 3-D TOF MRA and ASL gives reliable information as to whether outpatients with DAVF after treatment would require additional DSA. This combination provides accuracy and helps to decrease the number of invasive DSA procedures performed for screening to detect the recurrence or aggravation of DAVF after treatment.



(Filename: TCT_EdE-18_ASNR2018Figure-4.jpg)

EdE-11

Is the Scanner the New Focus Group? Neuroradiology's Role in the Emerging Field of Neuroeconomics

M Gusman¹

¹Brooke Army Medical Center, San Antonio, TX

Purpose

Introduce the emerging field of neuroeconomics to a neuroradiology audience.

Materials and Methods

This poster will: - contextualize neuroeconomics - highlight neuroanatomy involved in decision-making - explore the neuroradiology role in this new field

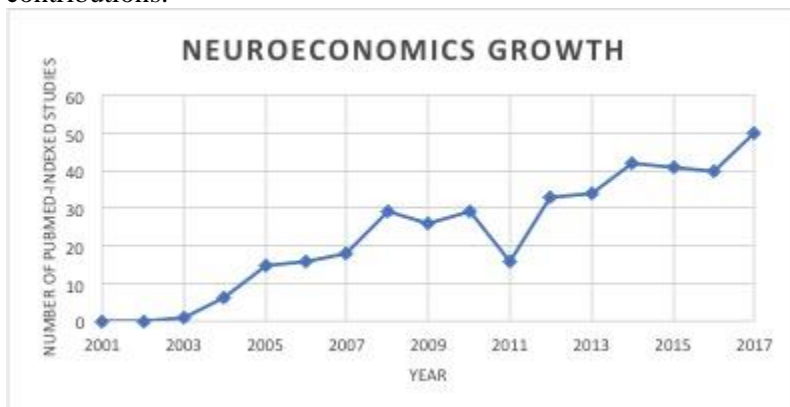
Education Exhibits

Results

It has been over a decade since functional magnetic resonance imaging (fMRI) gained the popular and scientific imagination with articles in which conclusions drawn from small numbers of subjects essentially predicted a future of mind-reading machines. As often true of emerging technology, these early expectations were not met. Yet, as the public moved on and google searches decreased, serious work continued behind the scenes. Radiology and surgery found practical applications for fMRI in pre-operative planning; economists and psychologists found other uses. In recent years, Pubmed-indexed studies tagged with 'neuroeconomics' have been increasing and several universities have established neuroeconomics departments. The 2017 Nobel Prize in Economics, was awarded to Richard Thaler for his work in advancing behavioral economics. Behavioral economics can be defined as the study of factors which affect decision making. Similarly, neuroeconomics attempts to decipher the neural correlates of the same process. The tidbits that this has yielded thus far are fascinating. For example, functional imaging suggests that the dorsolateral prefrontal cortex (DLPFC) is involved in weighing perceptual (how much is here? how much is it worth?) and moral (is this fair?) aspects of decision making. Subsequent studies used transcranial magnetic stimulation (TMS) to temporarily deactivate the DLPFC; this resulted in various changes in the subjects' decision making--for example, in the most recent of these studies, the subjects temporarily became more generous. Beyond research, there is potential to commercialize this technology. Many design teams and marketers are interested in learning which components of a product or its advertising speak to its target audience on the most primal level (what makes a good ad?). Our knowledge of neuroanatomy and imaging technology is becoming increasingly valuable in contributing to research and answering such questions.

Conclusions

As imaging-based research in this field is currently predominantly performed by those with psychology and neuroscience backgrounds, there are many opportunities for neuroradiologists to make meaningful contributions.



(Filename: TCT_EdE-11_Neuroeconomics.jpg)

EdE-06

It's Not All in Your Head! Imaging Findings of Neurovascular Compression Syndromes Around the Cervical Spine

A Condos¹, S Story¹, J Yetto¹, M Cathey¹

¹Naval Medical Center San Diego, San Diego, CA

Purpose

Neurovascular compression (NVC) is the process through which vascular structures, particularly arteries, come into direct conflict with adjacent nerves resulting in cranial nerve displacement and/or indentation. Many different symptomatic presentations have been attributed to neurovascular compression based upon

Education Exhibits

the conflict along the nerve root exit zone or cisternal segment of a cranial nerve. Patients with radiological evidence of neurovascular compression may present along a spectrum from entirely asymptomatic to severe progressive neurological deficit. Thus far, the degree of neurovascular compression has not proven to be directly associated with the severity of symptomology. The most common causes of NVC are of intracranial origin with trigeminal neuralgia being the most frequent presentation. However, extracranial and, more specifically, cervical spine causes of NVC do exist and result in symptomatic conditions such as occipital neuralgia, spasmodic torticollis, and hypoglossal nerve palsy. Additionally, variant vertebral artery anatomy is a common finding and the most frequently implicated vessel associated with cervical spine related NVC. The purpose of this poster is to review cases of neurovascular compression as a potential etiology of several neurological clinical syndromes and the radiographic presentations of such and to identify important anatomical characteristics of NVC and potential NVC mimics.

Materials and Methods

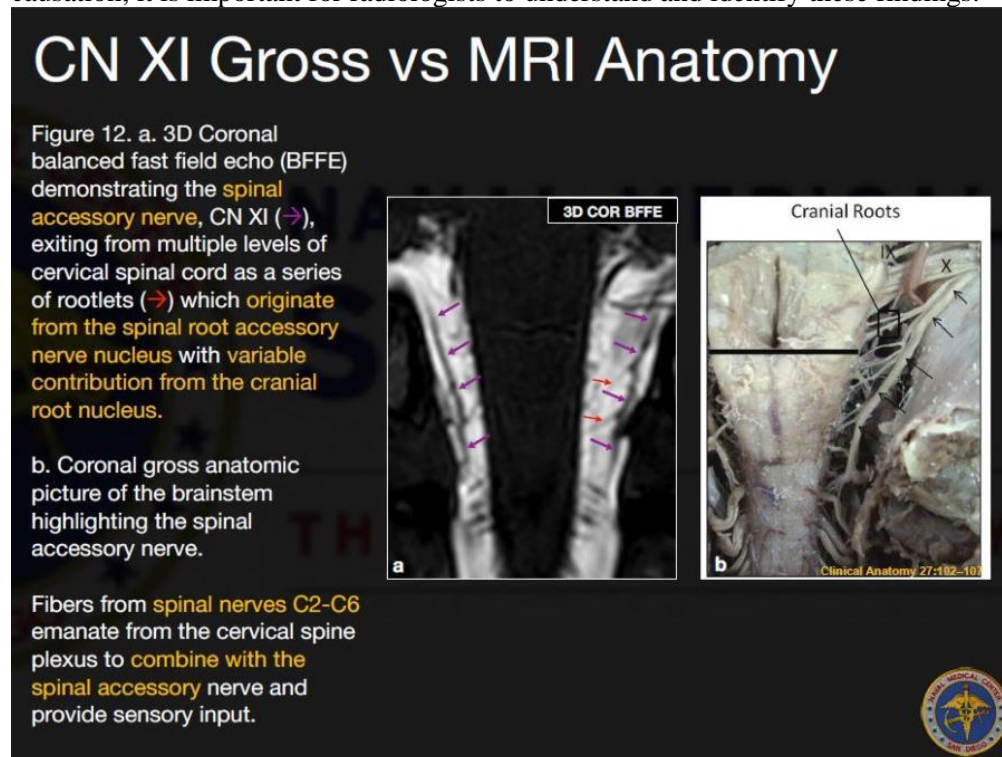
Retrospective review of 3T MR and CT examinations over the past 3 years with NVC within the cervical spine was performed. A variety of extracranial, cervical spine related NVC cases are presented which clearly demonstrate the pertinent imaging findings on high resolution cross-sectional imaging. Relevant anatomy is reviewed. Additionally, a literature review on NVC around the cervical spine was completed.

Results

Divided into: 1. Introduction to NVC. 2. Cervical spine related cases of NVC. 3. Treatment. 4. Imaging Considerations

Conclusions

Neuroradiologists play a critical role in the diagnosis of cervical spine-related NVC and a comprehensive knowledge of these entities as well as potential mimics is critical. Knowledge of operative considerations allows the radiologist to proactively address these concerns and improve diagnostic accuracy in the post-operative setting. Though the presence of these anatomic relationships does not necessarily equate to causation, it is important for radiologists to understand and identify these findings.



(Filename: TCT_EdE-06_cnxi.JPG)

EdE-12

Localization and Lateralization of Memory by BOLD Functional MRI Using Home Town Walking Paradigm for Temporal Lobe Epilepsy Surgery. How I Do It.

V Sawlani¹, K Kawsar¹, J Herbert¹, M Harley¹, N Davies¹, R Flintham¹, A Zisakis¹, D Mccorry¹, R Chelvarajah¹

¹*University Hospitals Birmingham NHS Foundation Trust, Birmingham, United Kingdom*

Purpose

fMRI has substantial potential to lateralize memory functions and predict post-operative memory outcome in epilepsy patients undergoing temporal lobe epilepsy surgery (1, 2). However, fMRI paradigms involving words and pictures encoding and retrieval task often fail to localize and lateralize memory in epilepsy patients in the clinical setting. The aim of our study is to localize and lateralize memory function by using the Home Town Walking Paradigm in epilepsy patients worked up for temporal lobe epilepsy surgery. Practical steps for memory fMRI are described.

Materials and Methods

We performed 55 memory fMRI from January 2014 to December 2016 by using the Home Town Walking Paradigm in temporal lobe epilepsy (n=26), temporal lobe tumours (n= 21) and vascular malformations (n=8). The fMRI is performed on two consecutive days with a block design, requiring mental navigation through one's hometown by using landmarks given by patients themselves. All the patients worked up for temporal lobe surgery undergo neuropsychometric assessment including memory functions before and after the surgery. A robust patient information sheet with examples of an imaginary walk is sent to patients with the appointment letter. A reminder is sent one week before the appointment to practice the mental navigation before coming for an fMRI test. Patients were called 30 minutes before the appointment to provide a written mental navigation task and to practice it before the scan.

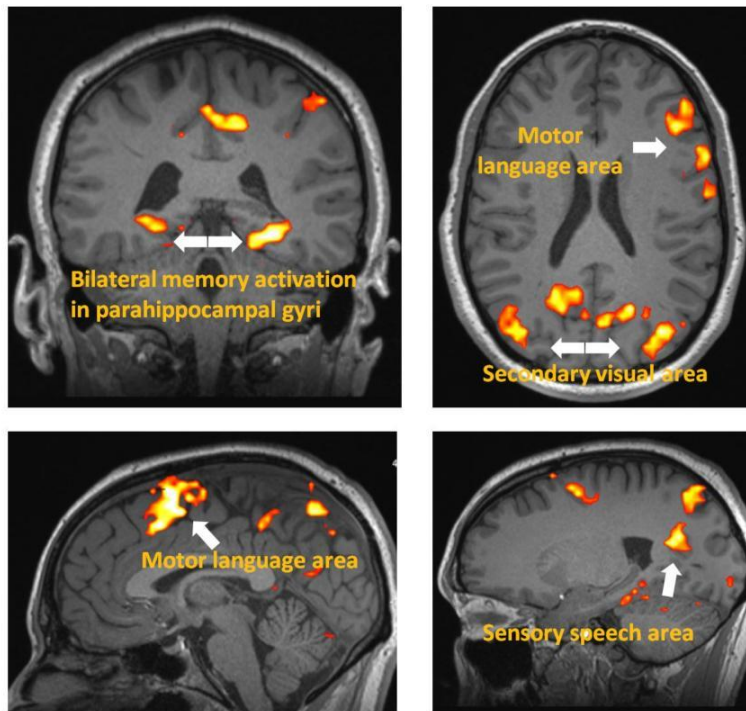
Results

We got successful results in 46/55 patients with less than 10% failure rate. 70% of patients showed good activation on day one and 90% patient showed activation on day two. Home Town Walking Paradigm reflects episodic memory involving deep encoding and retrieval tasks and has both visual and verbal memory components. The greater complexity of the hometown-walking task produced stronger activations in parahippocampal and fusiform gyri, with little activation in the hippocampus (3). Activation in the posterior cingulate is related to visuospatial memory processes and activation in the parietal cortex related to mental navigation and imagination. Activation of the dorsolateral prefrontal cortex probably reflecting the need for sequencing and planning for episodic memory and working memory (Fig. 1). Lateralization of language areas may also correspond to verbal memory.

Conclusions

Memory fMRI using the Home Town Walking Paradigm produced consistent and reproducible results. It has completely replaced the WADA test in our clinical practice.

Image 1. Memory fMRI - Home town walking paradigm showing bilateral activation in Para-hippocampal gyri, language and secondary visual areas



(Filename: TCT_EdE-12_Capture2.JPG)

EdE-04

MRA Imaging Strategies of High-risk Carotid Plaques

H Patel¹, E Dou¹, A Gupta¹, H Baradaran¹

¹*New York-Presbyterian Hospital/Weill Cornell Medical Center, New York, NY*

Purpose

While traditional cerebrovascular risk stratification has been based off luminal measurements of carotid stenosis, recent developments in imaging have shown that MRI imaging of carotid plaque is effective in predicting future embolic events resulting in stroke or TIA(1). Despite the recent innovations in identifying "high-risk" plaque features on MRI, these findings have not been translated to routine clinical practice, likely due to the need for specialized equipment or long scanning times. Some of these high-risk plaque features, however, can be detected using standard TOF sequences or other quickly acquired T1 sequences (2, 3) without the need for specialized equipment or sequences. Our purpose is to review imaging findings of "high-risk" carotid plaque on standard time-of-flight MRA and quickly obtained MRA sequences without a dedicated carotid coil or long scanning times.

Materials and Methods

Since 2015, we have routinely acquired a 3-D fat-suppressed T1 sequence, requiring less than five minutes and without utilizing a dedicated carotid coil, in addition to our standard TOF carotid artery in all MRA neck imaging studies. We reviewed neck MRAs performed at our institution, including both TOF and 3-D fat-suppressed T1 sequences, to identify illustrative examples of high-risk plaque features.

Results

We will review the basic parameters of the 3-D fat-suppressed T1 sequence. Then, through an imaging-rich review, we will review the components of carotid plaque which can be assessed on the 3D fat-

Education Exhibits

suppressed T1 sequence, including high-intensity signal within the plaque which is likely due to intraplaque hemorrhage or lipid-rich necrotic core, both high-risk features. Next, we will review how to identify intraplaque high-intensity signal on standard TOF MRA.

Conclusions

Evaluation of high-risk plaque features, especially intraplaque hemorrhage, can be performed without specialized equipment or lengthy MR sequences. We will provide an imaging-rich review of the scan parameters and imaging features that can be used to identify plaque features associated with higher stroke risk using a quickly acquired 3-D T1 sequence and on routine TOF MRA.

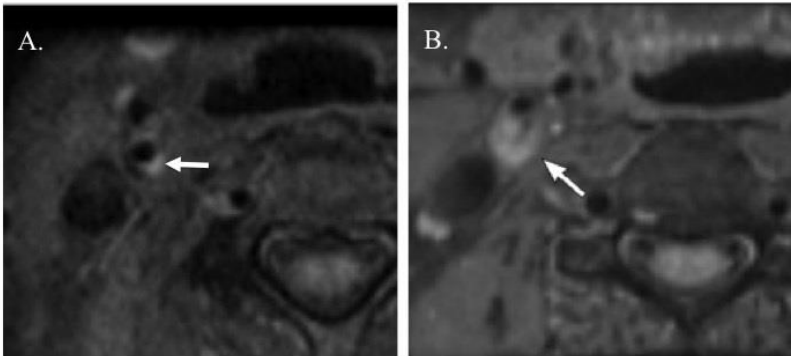


Figure 1. (A.) Intra-plaque hemorrhage of the right internal carotid artery on axial reformatted from a coronal 3D FS T1w image. **(B.)** Intra-plaque hemorrhage of the right internal carotid artery on axial reformatted images from a coronal 3D FS T1w image.

(Filename: TCT_EdE-04_mrimage1.jpg)

EdE-36

MRI Perfusion Changes in Status Epilepticus: ASL Evaluation in a Human Subject

O Ashour¹, P Paul¹, S Moawad¹, M Li¹, K Krugh¹, X Wang¹, M Buehler¹

¹University of Toledo, Toledo, OH

Purpose

Status epilepticus is a serious neurological condition, that is known to cause progressive neuronal damage. Certain associated imaging abnormalities have been previously studied by structural MRI and diffusion-weighted imaging; however, little literature exists on the perfusion changes that accompany status epilepticus in human subjects.

Materials and Methods

We studied a case of status epilepticus using serial MRI imaging at four time points over the course of three months, including diffusion-weighted imaging and Arterial Spin-Labeling (ALS) perfusion. Post processing including spatial registration and noise reduction was performed, followed by quantitative analysis of ASL sequences, with calculation of cerebral blood flow.

Results

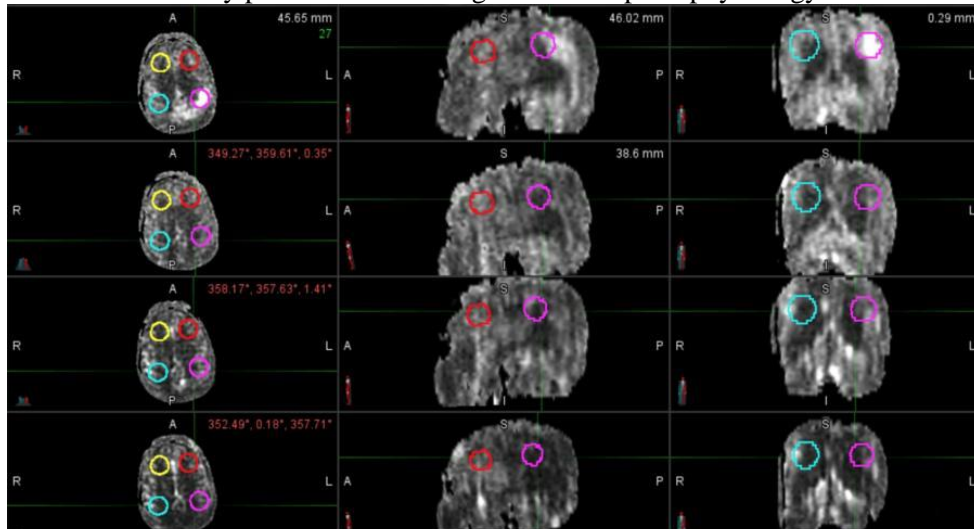
The presented case is a 55-year-old female patient who presented in status epilepticus, secondary to alcohol dependence. She presented initially with altered mental status. However, she had a complicated course, where she experienced multiple episodic nonconvulsive seizures with focal twitching. Her status epilepticus was hard to control using different regimens of sedatives and hypnotics. Serial MRI studies showed transient focal diffusion signal abnormalities corresponding to epileptogenic foci determined on EEGs acquired at simultaneous time points. ASL showed focal hyperperfusion at these regions. ASL also demonstrated generalized cortical hypoperfusion in the non-epileptogenic brain regions that progressively

Education Exhibits

worsened with time. Quantitatively, there was approximately 20% generalized reduction in cerebral blood flow bilaterally over the course of three months.

Conclusions

Perfusion changes have previously been documented at the foci of epileptogenic activity. This case suggests that concomitant generalized decline of cortical blood flow is an under reported phenomenon that can occur with prolonged status epilepticus. The correlation of such a finding with other changes on structural MRI may provide further insights into the pathophysiology of this condition.



(Filename: TCT_EdE-36_ScreenShot2017-12-15at70934PM-down.jpg)

EdE-30

Myelin Water Imaging: Assessment of Myelination with MRI

C Laule¹, I Vavasour¹, S Kolind¹, T Bjarnason¹, J Zhang¹, D Lang¹, H Liu¹, E Ljungberg¹, R Tam¹, E MacMillan¹, J Kramer¹, S Sirrs¹, A Traboulsee¹, L Boyd¹, P Kozlowski¹, A Rauscher¹, W Moore¹, D Li¹, A MacKay¹

¹University of British Columbia, Vancouver, British Columbia, Canada

Purpose

Although conventional MRI can detect pathological changes, it lacks specificity for the type and severity of tissue damage and cannot detect subtle abnormalities in the so-called normal appearing white matter. More sophisticated MRI techniques can provide more specific information about myelin content in the central nervous system (CNS). Accurately measuring myelin in vivo will improve our understanding of development, neurological diseases, injury and aging, as well as aid in diagnosis and management of individuals with demyelinating diseases and enable better assessment of myelin-targeted therapies. Myelin water imaging is an imaging technique which provides quantitative and specific mapping of myelin content in vivo. The purpose of this educational exhibit is to provide an overview of the principles and applications of myelin water imaging in neurological disorders. The specific objectives are to: 1. Explain the structural basis of myelin water imaging. 2. Describe the MRI acquisition and analysis of multiecho T2-relaxation based myelin water imaging. 3. Summarize key myelin water imaging findings

Education Exhibits

in healthy brain and spinal cord tissue. 4. Review myelin water imaging abnormalities in different CNS developmental and acquired pathological conditions. 5. Learn how myelin water imaging findings compare to results from other quantitative neuroimaging MR techniques such as diffusion tensor imaging and magnetization transfer imaging.

Materials and Methods

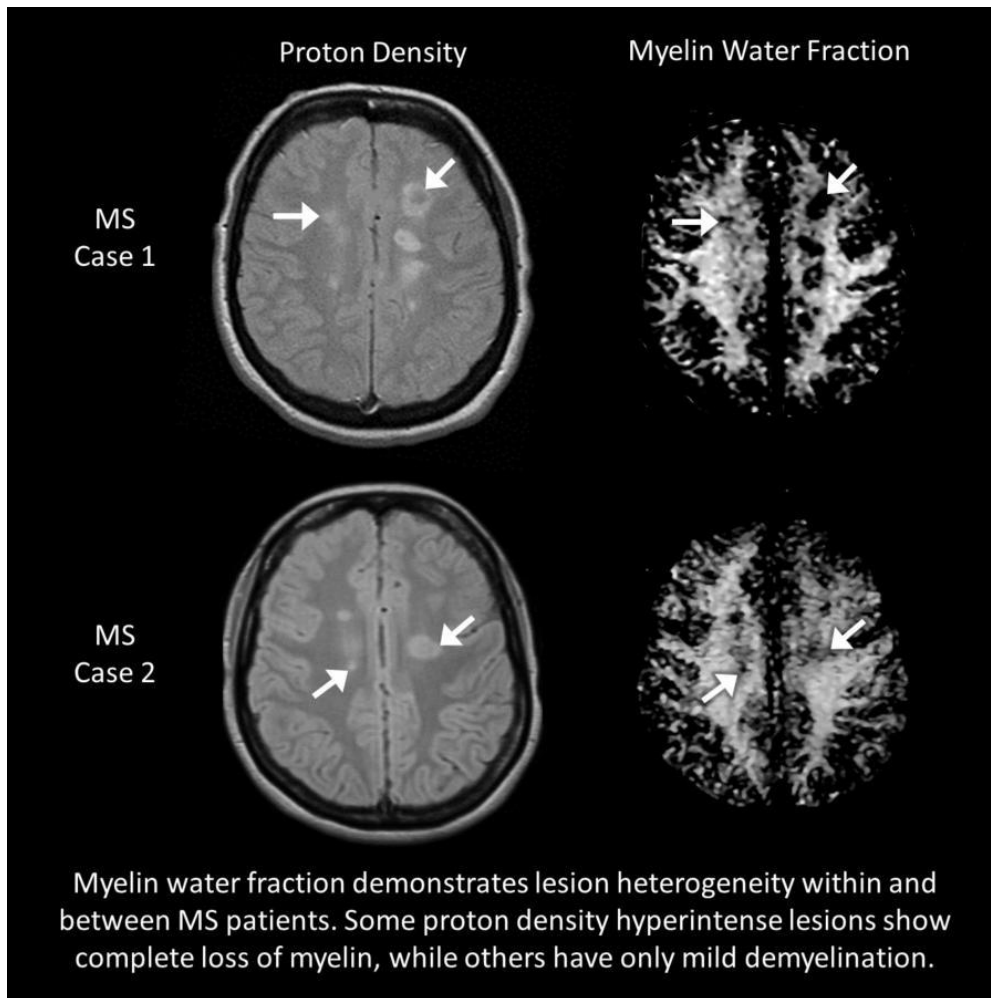
MRI signal in CNS tissue arises almost entirely from water. Water in different physical environments has unique T2 relaxation times [1]. Water trapped between the myelin lipid bilayers (myelin water) has a very short T2, intra/extra-cellular water has an intermediate T2, and cerebrospinal fluid has the longest T2 relaxation time. The key to myelin water imaging is isolation of the signal from the myelin water relative to the rest of the water, providing a quantitative measure directly related to myelin content within each imaging voxel. The gold-standard acquisition technique is a multi-echo spin-echo approach, which samples the MRI signal multiple times during T2 relaxation. A multicomponent fit of the T2 decay curve (signal vs. TE time) determines the relative contribution of the different water environments. The amount of myelin water signal provides a quantitative myelin-related measure and can be expressed as the myelin water fraction, defined as the T2 signal attributed to myelin water relative to the entire signal. The original myelin water imaging acquisition was too slow to be clinically feasible, but more recently, several approaches to accelerate myelin water measurement have developed [2]. For example, a combined gradient and spin echo approach reduces scan time by a factor of 3, enabling whole brain myelin water imaging in less than 10 minutes [3]. Other accelerated approaches such as T2prep, Vista, and mcDESPOT employ different strategies with the same goal of isolating signal from the myelin water. Adoption of these new, faster myelin water imaging acquisition strategies has led to a rapid expansion of accessibility and application of MWI around the world.

Results

Pathology-MRI validation in preclinical models and post-mortem multiple sclerosis CNS tissue show excellent qualitative and quantitative agreement between multi-echo derived myelin water fraction and histological staining for myelin, including an average $R^2=0.74$ for human brain tissue. Myelin water imaging has successfully demonstrated changes with development, and shows regional variations in normal brain and spinal cord that match expectations from post-mortem studies. Myelin water techniques have described in vivo myelin abnormalities in conditions such as multiple sclerosis (Figure), neuromyelitis optica, stroke, schizophrenia, autism, dyslexia, dyscalculia, primary/amyotrophic lateral sclerosis, concussion, brain cancer, phenylketonuria, neurofibromatosis, and Niemann-Pick Disease, in both cross-sectional and longitudinal studies. Myelin water imaging has also been included as an outcome measure in multiple sclerosis clinical trials [4]. Beyond brain imaging, the advent of higher field strength (3T, 7T) has enabled more detailed visualization of spinal cord myelin anatomy and pathology, and applications to study spinal cord injury are growing [5]. Several other quantitative MR methods are also influenced by myelin, including magnetization transfer ratio (MTR), diffusion tensor imaging (DTI) and frequency shift imaging. However, the lack of strong correlation between MTR, DTI, frequency and myelin water suggests that these measures provide complementary information; the correlation between myelin water and brain metabolite concentrations measured using magnetic resonance spectroscopy (MRS) is currently being investigated.

Conclusions

Myelin water is a specific imaging biomarker that provides quantitative mapping of myelin content in vivo. Myelin water imaging has successfully been used to study both the brain and spinal cord where it can increase our understanding of development, aging and disease processes. Clinical application of myelin water imaging may improve accuracy of diagnosis, prognosis and assessment of therapeutic response [4]. Myelin water imaging is beginning to play an important role in the development and monitoring of new treatments targeted at remyelination and neuroprotection. Recent advances in accelerating the acquisition and extending the technique to whole brain coverage have made myelin water imaging potentially useful as a clinical tool to assess myelin in the brain and spinal cord.



(Filename: TCT_EdE-30_MyelinWaterEducationAbstractFigure.jpg)

EdE-01

Neuroimaging Review: Manifestations of Toxicity of the Most Common Over-the-Counter Medications

V Yedavalli¹, V Kuttappan¹, V Pandey¹, P Chowdhry¹, A Patil¹

¹Advocate Illinois Masonic Medical Center, Chicago, IL

Purpose

Over-the-counter medications are widely used and effectively treat the most common of ailments. However, while rare, overdose of these medications can lead to serious neurological consequences. There is a sparsity of literature pertaining to imaging manifestations of such cases. For that reason, we delve into the neuroimaging manifestations of the toxicities of the most commonly consumed over-the-counter medications.

Materials and Methods

The most common over-the-counter medications are cough suppressants, cold and allergy drugs, and painkillers. In this review, we specifically look at potential neuroimaging manifestations of overdose of these drug subtypes. For cough suppressants, we focus on dextromethorphan. For cold and allergy drugs,

Education Exhibits

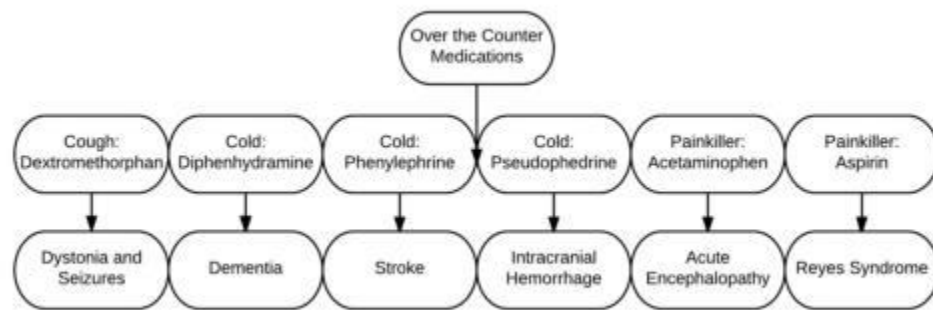
we delve into diphenhydramine, phenylephrine, and pseudophedrine. And for painkillers, we investigate overdoses of acetaminophen and aspirin.

Results

Although over-the-counter drugs are prevalent and overdose is rare, it is essential to be aware of the critical neurological sequelae of overdose of these medications. We specifically focus on the potential neuroimaging presentations of dextromethorphan, diphenhydramine, phenylephrine, pseudophedrine, acetaminophen, and aspirin toxicity. Increasing awareness of toxicity of these commonly consumed drugs is integral in accurate and timely diagnosis.

Conclusions

Over-the-counter drug toxicities and their neuroimaging manifestations are sparse in the literature. The objective of this review is to explore the potential imaging manifestations of overdose of these easily accessible medications. In doing so, we hope to shed light upon a rarely explored topic by correlating these toxicities to their respective neuroimaging presentations.



(Filename: TCT_EdE-01_OvertheCounterMedicationNeuroimaging-Page1.jpg)

EdE-24

Pictorial Review of Melanocytic Tumors of CNS

Z ASSIS¹, L Hamilton², T Myers¹, N Kashani², J Lysack¹, M Joshi²

¹Foothills Medical Centre, University of Calgary, Calgary, Alberta, Canada, ²University of Calgary, Calgary, Alberta, Canada

Purpose

Pigmented lesions of the CNS are a diverse group of pathologies ranging from completely benign to aggressive malignant lesions. These lesions display a spectrum of radiological findings. The purpose of this educational exhibit is to discuss the clinical and imaging features of common as well as relatively rare melanocytic tumors of CNS such as metastatic melanoma, primary CNS melanocytoma, diffuse leptomeningeal melanomatosis and orbital melanoma. A brief radio-pathological correlation will also be presented along with a brief discussion on their management and prognosis.

Materials and Methods

Melanocytic neoplasms of the central nervous system are rare, and most frequently they are metastatic in origin. In this exhibit, we review the clinical, imaging, and histopathological findings of these rare lesions in a case-wise approach. Imaging pearls and teaching points will be discussed for each of the pathologies.

Results

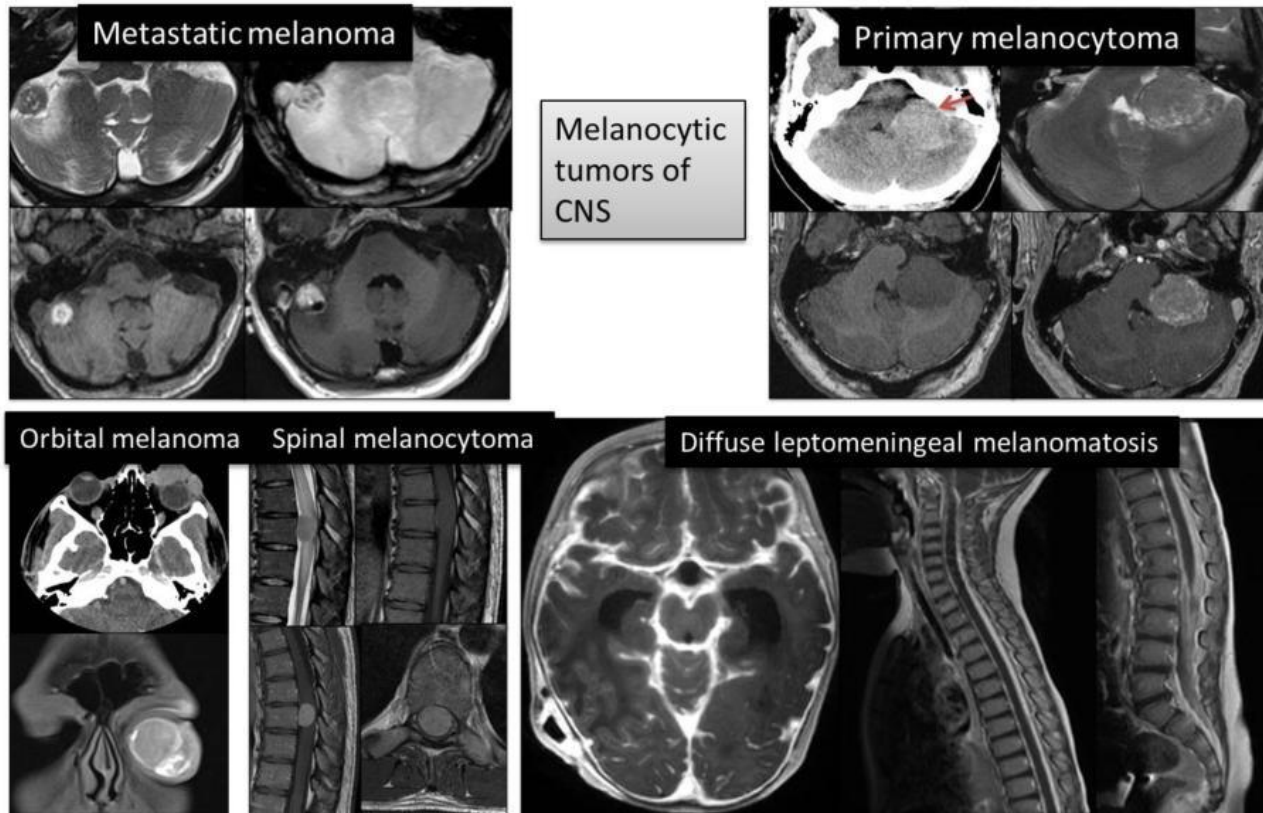
Findings: We present the radiological features of various CNS melanocytic tumors. Key features include:
a. Metastatic melanoma: Primary cutaneous melanoma. Multiple hyperdense parenchymal lesions on CT. May or may not show associated hemorrhage. On MRI, presence of intrinsic T1 hyperintensity is helpful,

Education Exhibits

but may not be always seen. Lesions always enhance on postcontrast studies. b. Primary melanocytoma: Low-grade extra-axial tumors, predominantly located in posterior fossa or spinal canal. May be solitary or multiple at presentation. T1 hyperintensity is a clue, but may not present in all cases. Meningioma and schwannoma are close mimics. c. Diffuse leptomeningeal melanomatosis: Highly malignant pediatric neoplasm showing diffuse leptomeningeal thickening and enhancement. Commonly present with obstructive hydrocephalus. Poor prognosis. d. Orbital and ocular melanoma: Enhancing space occupying lesions, T1 hyperintense. Intra-ocular have typical raised "dome-like or mushroom" appearance. e. Neurocutaneous melanosis: Rare sporadic phakomatosis characterised by multiple congenital cutaneous nevi and meningeal melanocytosis. Leptomeningeal and parenchymal involvement seen. CNS melanosis may progress to malignant form in 50% of cases. Discussion: Melanocytes occur normally within the leptomeninges and are more concentrated at the base of the brain and on the ventral surface of the cervical spinal cord. In these locations, pigmented leptomeninges may be visible macroscopically at surgery or autopsy. Leptomeningeal melanocytes are of neuroectodermal origin. At MR, these pigmented foci frequently demonstrate T1 and T2 shortening, which is believed to be related to the presence of melanin +/- hemorrhage. The imaging characteristics of melanin are thought to be caused by the presence of paramagnetic free radicals (indole semiquinones and semiquinones). Interaction of the unpaired electrons in melanin with water protons results in dipole-dipole interactions.

Conclusions

Although typical MRI signals of melanin (described as T1 hyperintense and T2 hypointense) can help us diagnose these lesions and differentiate them from other nonpigmented lesions, we show that many of these pigmented lesions do not necessarily display such signals. Histopathological examination of primary and secondary melanocytic neoplasms reveals variable degrees of melanin pigmentation and they may be amelanotic. On imaging, they may closely mimic more common entities such as meningioma, schwannoma, meningitis or leptomeningeal carcinomatosis.



(Filename: TCT_EdE-24_Picture1.jpg)

EdE-27

Quite a Slippery Slope: Spectrum of Mass Lesions and Pseudo-lesions of the Clivus

G Curaudeau¹, M Lanfranchi¹, L Chan¹, K Buch², K Hammoud³

¹Tufts Medical Center, Boston, MA, ²UMass Medical Center, Worcester, MA, ³Tufts Medical Center, Cambridge, MA

Purpose

The purpose of this abstract is to illustrate the common lesions and pseudolesions that affect the clivus. Leveraging review and reference articles relating to embryology, anatomy and pathology, we will highlight factors that will facilitate categorization of clival lesions radiographically.

Materials and Methods

We are using established review and reference materials, as well as pathologically confirmed imaging studies obtained at Tufts Medical Center in Boston, to create our educational exhibit. This information will be organized and depicted in a visual manner to enhance absorption and retention.

Results

As a result of its diverse histological make-up, primary clival lesions emanating from the skull base can be derived from residual notochord (e.g: Chordoma, Ecchordosis Physaliphora), cartilaginous (e.g: Chondrosarcoma, Enchondroma), or hematopoietic cells (e.g: Plasmacytoma, Lymphoma). Other pseudo lesions can complicate the differential and include arrested pneumatization/marrow variants, arachnoid granulations, meningocele, fibrous dysplasia and Paget's disease. Due to its central location, secondary tumors infiltrating the clivus can originate superiorly (e.g: invasive pituitary macroadenoma, meningioma, craniopharyngioma), or inferiorly (e.g: nasopharyngeal carcinoma, SCC or rhabdomyosarcoma). Bony metastases are also always a consideration.

Conclusions

Understanding the embryological development of the clivus, as well as its anatomical migration enables more accurate and narrower differentials when confronted with true and pseudo clival lesions radiographically.



(Filename: TCT_EdE-27_image1.jpg)

EdE-16

Review of the Postoperative Cranium: What the Radiologist Should Know

D Bansal¹, T Krewson¹, M Vang¹, V Jain¹

¹*MetroHealth Medical Center/Case Western Reserve University, Cleveland, OH*

Purpose

To review neurosurgical techniques for brain surgeries, expected postoperative imaging findings, and common and uncommon complications seen in the immediate and late postoperative period after neurosurgery.

Materials and Methods

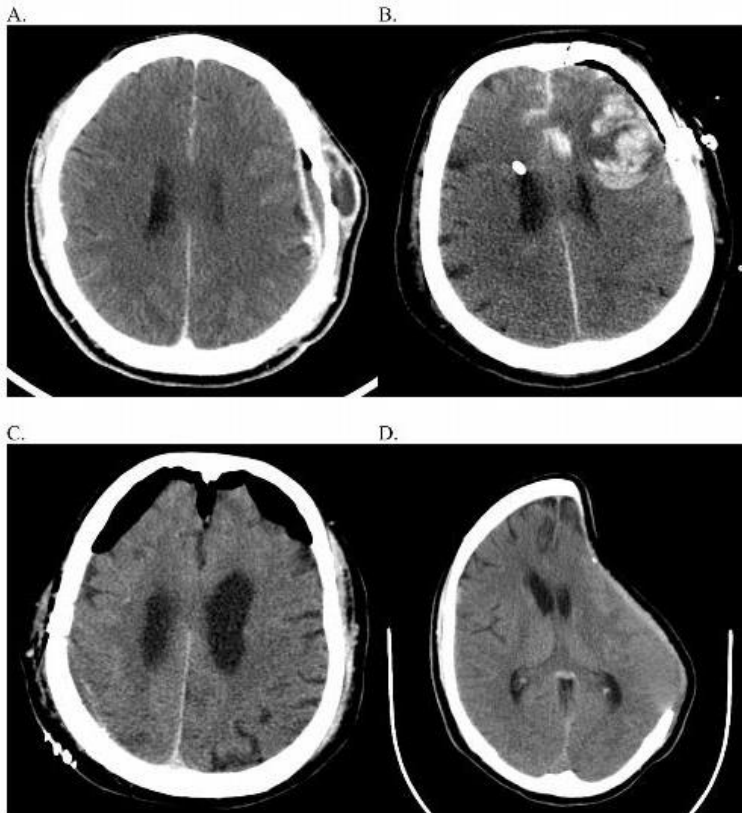
The medical records of all patients who experienced postoperative neurosurgical complications were retrospectively reviewed from June 2012-June 2017. Patients were identified via EPIC's Slicer Dicer program. The patient's imaging and medical charts were evaluated to determine the etiology, type, and extent of the complications.

Results

Many neurosurgical techniques have been established to treat patients with intracranial abnormalities such as tumor, infection, and hemorrhage. Imaging plays a vital role in the routine postoperative care of patients after cranial surgery to monitor treatment response and assess for complications. As radiologists, it is crucial to be familiar with the commonly performed neurosurgical techniques and normal cranial anatomy in order to distinguish between the expected postoperative appearance of the brain and postoperative complications. Computed tomography (CT) is often the imaging modality of choice in the early postoperative period. The widespread use of CT is largely due to its accessibility, cost-effectiveness, and speed as compared to magnetic resonance imaging (MRI). However, MRI is more sensitive for ischemia and infection. This educational exhibit aims to illustrate neurosurgical techniques and normal postoperative imaging appearances of burr holes, craniotomy, craniectomy, and cranioplasty. Complications commonly discovered after neurosurgery will be demonstrated, including infection, abscess, empyema, hemorrhage, and herniation. Lastly, a few uncommon and life-threatening complications will be shown, such as tension pneumocephalus, paradoxical herniation, and trephine syndrome.

Conclusions

Postoperative imaging plays an important role in the follow-up of patients after neurosurgery. An awareness of the normal anatomy, surgical techniques, and potential complications are imperative for an adequate postoperative radiological evaluation. The most important aspect of imaging is to differentiate expected postoperative changes from complications to facilitate early diagnoses and treatments to improve patient outcomes.



A. A 25-year-old male with a left subgaleal and epidural abscess and an infected bone flap 6 months after a left hemi-craniectomy for evacuation of a left convexity subdural hematoma. Axial CT image shows peripheral enhancement of the subgaleal and epidural fluid collections. Bone window images (shown in the educational exhibit) demonstrate erosive changes compatible with osteomyelitis.

B. A 55-year-old male with a large left frontotemporal lobe hematoma and subarachnoid hemorrhage that developed after an elective clipping of an unruptured anterior communicating artery aneurysm via a left frontotemporal approach.

C. A 77-year-old male that developed tension pneumocephalus 7 hours after evacuation of a large right convexity subdural hematoma. This patient also experienced altered mental status that improved after drainage of pneumocephalus. Axial CT demonstrates subdural air separating and compressing the frontal lobes and a widened interhemispheric space (Mount Fuji sign).

D. A 30-year-old male with a sinking skin flap 3 months after craniectomy performed for a large left frontal lobe and basal ganglia hemorrhage.

(Filename: TCT_EdE-16_ASNRpictures-2.jpg)

EdE-09

Role of Resting-state fMRI In Depression

A Chaudhry¹

¹*Johns Hopkins Medicine, Stevensons Ranch, CA*

Purpose

Major depressive disorder (MDD) is a prevalent clinical condition with huge socioeconomic burden on society. Advancement in understanding of pathophysiology and underlying neuromechanisms have led to improved clinical diagnostic criteria and development of a multitude of treatment regimens. Imaging has generally played a secondary role in evaluation of these patients. However, with the rapid evolution of functional magnetic resonance imaging (fMRI), neural systems associated with depression have been uncovered. In this review, we aim to discuss the role of subcortical as well as cortical (particularly

Education Exhibits

prefrontal and cingulate) brain regions (modulated by serotonin and dopamine neurotransmission) as evaluated on restingstate fMRI (rsfMRI).

Materials and Methods

Discuss pathophysiology of MDD, review role of support emotion processing, reward seeking, regulate emotion and its role in MDD. Review principals of rsfMRI as well as common pearls and pitfalls of this imaging technique. Discuss role of default mode network subregions, lateral frontal areas (within a frontoparietal network associated with cognitive control), basal ganglia, hippocampus, frontal lobe (including the orbitofrontal cortex) and less consistently the cingulate cortex and thalamus as well as the insula, and cerebellum.

Results

Role of dopamine and serotonin pathways in depression. Pictorial review of rsfMRI findings within the DMN, frontotemporoparietal lobes, as well as deep gray nuclei and cerebellum. Discuss rsfMRI activation patterns used in evaluation of patients pre and postserotonin reuptake inhibitor therapy.

Conclusions

Resting state fMRI studies in depression can identify pattern of brain regions associated alterations in neuronal connectivity especially within the posterior DMN components (related with selfreferential processing), within the lateral frontal areas (associated with externally directed cognition), insula and basal ganglia. Additionally, rsfMRI can demonstrate alterations in neuronal activity in patients before and after serotonin reuptake inhibitor therapy, which can potentially serve as a guide for monitoring treatment response.

EdE-40

State-of-the-art Diffusion Tensor Imaging in the Assessment of Diffuse Axonal Injury

D Grassi¹, D Da Conceição¹, C Leite²

¹*Faculdade de Medicina da Universidade de São Paulo, São Paulo, Brazil,* ²*University Of São Paulo, São Paulo, Brazil*

Purpose

Traumatic brain injury (TBI) remains as a major public health problem worldwide. Diffuse axonal injury (DAI) is present in nearly 50% of all cases that require hospital admission. However, the DAI findings are frequently under-recognized in conventional neuroimaging studies. In such scenarios, diffusion tensor imaging (DTI) plays an important role because it provides further information on white matter (WM) integrity that is not obtained with standard sequences. [1-3] Herein, we aim to review the current contribution of diverse state-of-the-art DTI analytical methods to the understanding of DAI pathophysiology and prognosis.

Materials and Methods

A comprehensive search in Pubmed was performed using the following keywords: "traumatic brain injury", "diffuse axonal injury", and "diffusion tensor imaging". We discuss the basic principles, advantages and caveats of each main DTI analytical method, along with the relevant findings of recent DTI studies of TBI patients.

Results

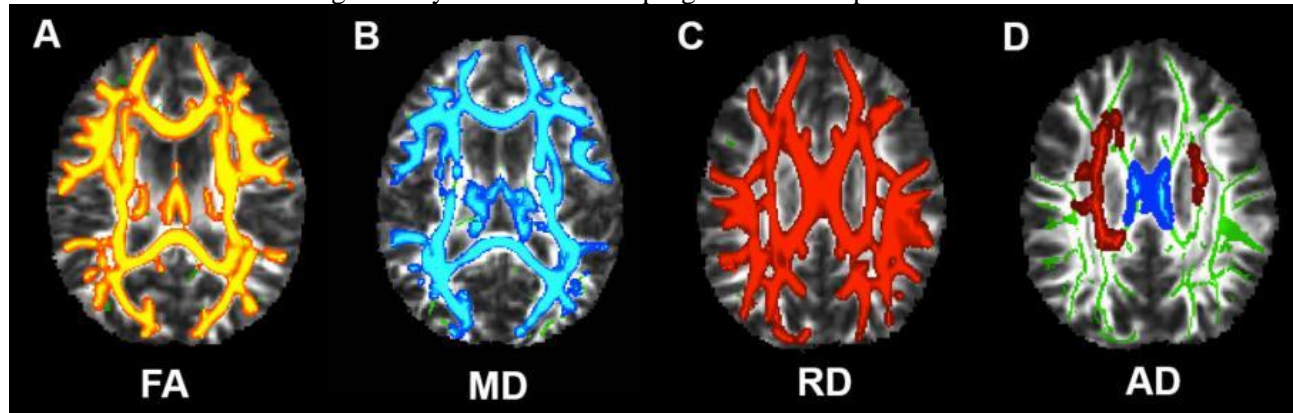
Distinct methods are available to analyze DTI data. In region-of-interest (ROI) analysis, diffusion parameters are obtained from a pre-determined area of the brain. ROI studies indicate that changes in water diffusion anisotropy do occur in DAI, and these changes may be biomarkers for severity of tissue injury and predictors for outcome. Tractography allows the parcelation of WM, and this information may be particularly useful in anatomofunctional studies because WM bundles are linked to specific cognitive, motor, and behavioral domains. Prior investigations demonstrated microstructural abnormalities in distinct projection, association and commissural fibers that are often linked to persistent symptoms in head injury survivors. Voxelwise analysis is suitable for global analyses of brain parenchyma and is

Education Exhibits

particularly useful for large group comparisons of individuals with no significant distortions in brain anatomy. Abnormalities in DTI metrics have been demonstrated in large clusters of WM in patients with moderate to severe TBI in comparison to healthy controls (Figure).

Conclusions

DTI is valuable in indicating severity biomarkers and prognosis in DAI patients.



(Filename: TCT_EdE-40_Figure.jpg)

EdE-13

The Varying Presentations of Neuromyelitis Optica (NMO): A Continually Broadening Clinical Entity

J Kang¹, E Nguyen¹, R Ourfalian¹, J Acharya², A Rajamohan², F Torres¹

¹Kaiser Permanente Los Angeles Medical Center, Los Angeles, CA, ²University of Southern California, Keck School of Medicine, Los Angeles, CA

Purpose

Previously known as Neuromyelitis Optica (NMO), in 2015, the International Panel for NMO Diagnosis (IPND) eliminated use of the term "NMO", and is now referring to the disease as Neuromyelitis Optica Spectrum Disorder (NMOSD). This was partly due to the specificity of Aquaporin-4 Channel-IgG autoantibody (AQP4-IgG) broadening the clinical and neuroimaging spectrum of NMO. In addition, IPND developed a consensus diagnostic criteria for both NMOSD with and without AQP4-IgG-seropositivity. At our institution, we have cared for patients demonstrating dramatically different neuroimaging findings with the diagnostic criteria for NMOSD. The purpose of this paper is to review key neuroimaging findings showcasing the variable appearance of NMOSD.

Materials and Methods

We will present five distinct clinical presentations of NMOSD, both with and without seropositivity, and review the key anatomical landmarks that are affected, such as the hypothalamus, optic chiasm, and the area postrema of the brainstem.

Results

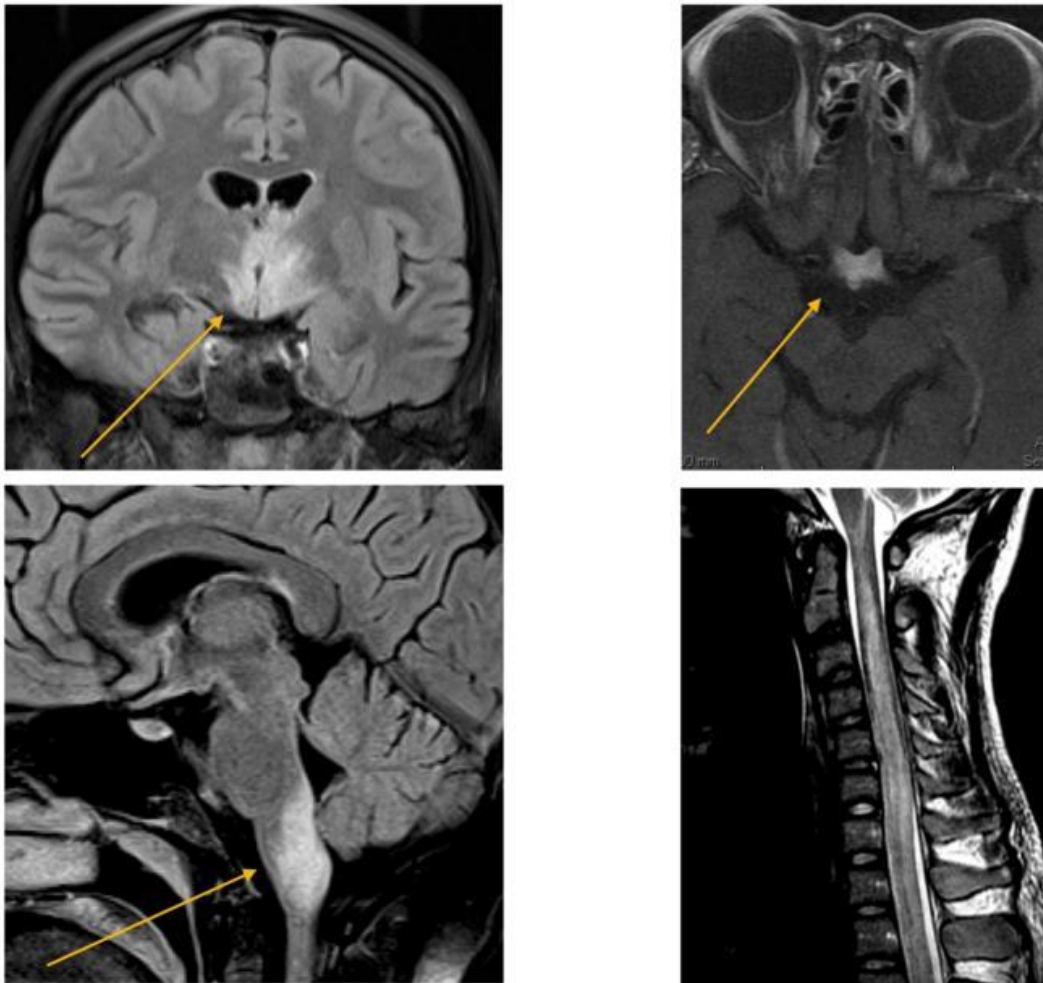
Historically, NMOSD, also known as Devic's disease was thought to be a single acute event involving both the spinal cord and optic nerves. However, with the recently proposed unifying term of NMOSD, and the use of AQP4 antibody biomarker, we now know that the demyelinating disease can be relapsing and can have a wide variety of clinical presentations. Given the location of the AQP4 protein antigen predominantly along the ependymal surfaces, the imaging findings involve regions near the central canal of the spinal cord and the ventricular surfaces.

Conclusions

With the recent proposal of the broadly encompassing NMOSD criteria, we hope to review the diagnostic

Education Exhibits

criteria of both seronegative and seropositive NMOSD, in order to help the neuroradiologist play a key role in diagnosing the disease.



(Filename: TCT_EdE-13_NMOImages.jpg)

EdE-34

Three-dimensional Printing Technology for Neuroradiology

N Kaneko¹, S Tateshima¹, M Loecher¹, D Chen¹, R Chi¹, W Chang¹, J Villablanca¹, D Ennis¹, F Vinuela¹, J Hinman¹, G Duckwiler¹

¹*University of California Los Angeles, Los Angeles, CA*

Purpose

Three-dimensional (3-D) printing technology constitutes a novel manufacturing process that builds layers to create a 3-D solid object from digital image data. An interest in having 3-D printing capability in academic radiology departments has emerged recently as it has a natural synergy in many ways including education, clinical diagnosis and planning, and research. Complex patient-specific structures can be printed with various materials by 3-D printers based on radiographic data. Multiple types of 3-D printers

Education Exhibits

are commercially available and different in terms of mechanism, material, resolution, cost etc. The differences should be recognized before utilizing this emerging technology. The purpose of this review is to summarize the 3-D printing methods and the promising roles in neuroradiology.

Materials and Methods

Digital Imaging and Communication in Medicine (DICOM) data acquired from CT, MRI or 3-D rotational angiography are exported and the 3-D images are reconstructed into volumetric shapes by using image processing software. The 3-D data are then converted to a stereolithography format (.stl) for 3-D printing.

Results

The ability to fabricate accurate 3-D objects based on acquired data set is suitable for educational purposes to patients or medical students. Material jet printers can print the objects with color and good resolution although the cost of the printer and material is relatively high. Plaster bone models by binder jet printing are able to replicate complex cranial deformation or spondylosis which can be used for presurgical simulation. Patient-specific hollow vascular replicas created from plastic mold printed with fused deposition material technique are useful for the simulation of endovascular treatment or for vascular research. We have developed a new research method to analyze gene expression influenced by complex-flow stress on endothelial cells attached on the patient-specific vascular model. By combining flow study such as 4-D Flow MRA, this in vitro model can bridge the gap of biophysical flow phenomenology and the biological impact of complex flow patterns on endothelial cells using patient-derived imaging data.

Conclusions

Three-dimensional printing is a promising technology that enables better understanding of anatomy, preinterventional simulation and personalized, precision medical research. Each type of 3-D printer has advantages and disadvantages, which should be considered and selected depending on the purpose.

EdE-31

To SWI or Not To SWI: That is NOT a Question!

A Gutweiler¹, A Germana¹, J Yetto¹, A Cho¹, D Hawley¹, M Cathey¹

¹*Naval Medical Center San Diego, San Diego, CA*

Purpose

Susceptibility weighted imaging (SWI) is an innovative MRI sequence that exploits the magnetic susceptibility differences of tissues in order to enhance contrast resolution of background tissues from substances like iron, hemorrhage, or calcium. SWI combines both magnitude and phase information to produce this image. As such, it is more sensitive to substances that cause local field inhomogeneity compared to standard T2* sequences. In this poster, we present the basic imaging physics that allow for the unique contrast offered by SWI. We will also present multiple unique cases in which the exquisite sensitivity of SWI at 3T was crucial in arriving at the correct diagnosis.

Materials and Methods

This poster will review the technical aspects of SWI. We will demonstrate the utility of SWI in arriving at the correct diagnosis using a case-based approach, highlighting a wide variety of neuropathologic entities, all at 3T field strength.

Results

Initially, susceptibility weighted imaging was devised to improve the visualization of cerebral veins. With time, the sequence has increasingly been employed in the imaging of cerebral ischemia, neuro-inflammatory processes, tumors and hemorrhagic lesions. While T2* is often (though not ubiquitously) employed in standard brain MRI protocols, it is well established that SWI is more sensitive than T2* for detection of substances like iron, hemorrhage, or calcium, particularly at high field-strength. We will present cases in which SWI was either the primary sequence to highlight imaging abnormalities or at least made more clear the true extent of neuropathology, facilitating arrival at the correct diagnosis.

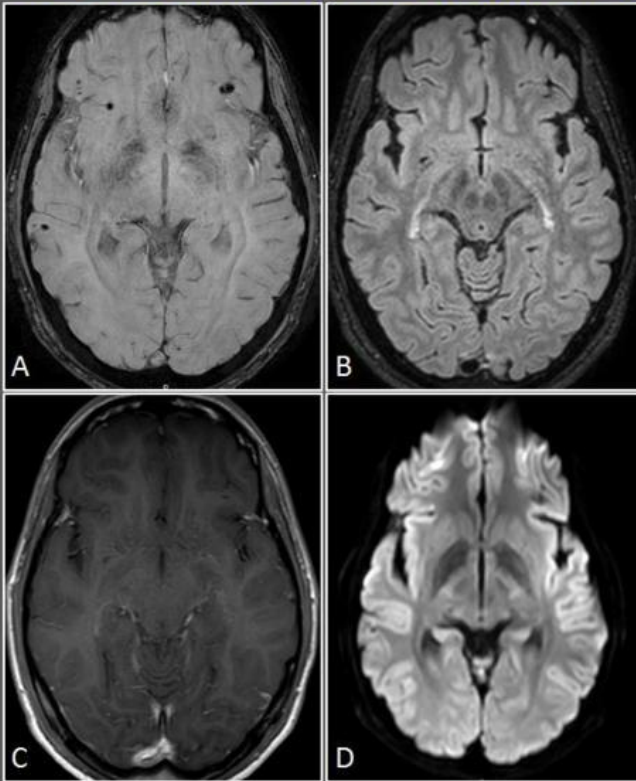
Education Exhibits

Conclusions

We present multiple cases which underscore SWI as an indispensable tool in the neuroradiology imaging armamentarium and suggest its inclusion on all brain imaging protocols. Due to its exquisite sensitivity to blood products, iron, and calcium, this approach allows radiologists to suggest a diagnosis (or differential diagnosis) even as other conventional MRI sequences may be largely unrevealing.

To SWI or Not to SWI: That is NOT a Question!

Adding Value with Susceptibility-Weighted Imaging at 3T



22 year old male with trauma to the left side of his face resulting in a concussion 2 months prior to MR imaging.

The susceptibility weighted image (A) demonstrates multiple foci of blooming susceptibility at the grey-white junction of the cerebrum. Numerous other foci of susceptibility are present throughout the cerebrum (not shown). There is no obvious corresponding signal abnormality on the FLAIR (B) or T1 post (C) images. Subtle foci of hypointense signal abnormality are noted on the DWI (D), which correspond to the known areas of blooming susceptibility in (A). A diagnosis of grade 1 diffuse axonal injury was thus made largely on the SWI image.

(Filename: TCT_EdE-31_SWIASNR.JPG)

EdE-26

Too Much on Your “Plate”? Spectrum of Pathologies Involving the Tectal Plate

N Gandhi¹, R Glikstein², V Tsehmaister Abitbul¹, C Torres¹

¹The Ottawa Hospital, Ottawa, Ontario, Canada, ²University of Ottawa, Ottawa, Ontario, Canada

Purpose

Review the differential diagnosis of tectal plate lesions

Materials and Methods

This pictorial essay will review the anatomy and importance of tectal plate lesions (specifically in the setting of Parinaud syndrome), and look at diverse pathologies involving the tectal plate and/or causing Parinaud syndrome.

Results

The tectal plate (or tectum) forms the posterior aspect of the midbrain, and includes the quadrigeminal plate and additional neural tracts posterior to the cerebral aqueduct. The quadrigeminal cistern is formed

Education Exhibits

by the superior and inferior colliculi, involved in the auditory and visual pathways respectively. Although seen mainly in the pediatric population, brain stem lesions are approximated to represent 10-25% of brain tumors, with 5% being localized to the tectal plate (1). Patients with these tumors usually present with a unique characteristic of aqueductal stenosis, which is late in onset. Due to their locations, consequent hydrocephalus often follows development of the lesion (2). Midbrain pathology can also result in syndromes like Parinaud syndrome, which is a clinical entity created by compression of the dorsal midbrain at the level of the superior colliculus, usually secondary to mass effect from adjacent pathology (3). With respect to tumors of the tectal plate, astrocytomas are the most common type (4). In this pictorial essay, we looked at various tectal plate/Parinaud syndrome causing lesions that have been encountered at The Ottawa Hospital, including glioma, hematoma, demyelinating plaque, Wernicke's encephalopathy, metastasis, Parinaud cavernoma, Parinaud abscess, pineal gland cysts and pineal gland tumors.

Conclusions

As an uncommon pathology, we should be aware of various tectal plate lesions in order to guide patient management decisions. In this pictorial essay, we looked at various lesions involving the tectal plate and/or causing Parinaud's syndrome.

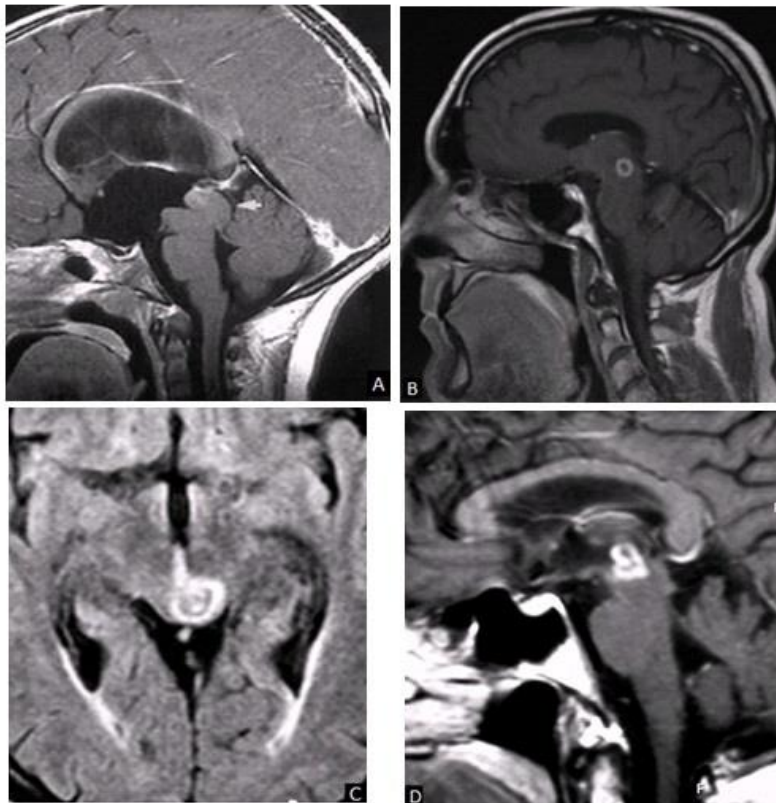


Figure 1: MRI images showing different pathologies. (a) Sagittal T1W post contrast image demonstrates a minimally enhancing mass involving the tectum, proven to be a glioma. (b) Sagittal T1W post contrast image demonstrates a ring enhancing lesion involving the inferior aspect of the tectal plate, proven to be a metastatic focus. (c) Axial T2 FLAIR image demonstrates a predominantly hyperintense mass involving the tectum, proven to be a cavernoma. (d) Sagittal T1W post contrast image demonstrates a peripherally enhancing mass centered at the superior aspect of the tectum and tegmentum, proven to be an abscess.

(Filename: TCT_EdE-26_ASNRabstractimages.jpg)

EdE-20

Twig-like Middle Cerebral Artery Anomaly: A Rare But Important Vascular Finding

J Chudyk¹, F Cabrera Florez¹, R Viso¹, C Parada¹, I Lylyk¹, P Lylyk¹

¹Instituto Médico ENERI - Clínica Sagrada Familia, Buenos Aires, Argentina

Purpose

The twig-like middle cerebral artery (Tw-MCA) or aplastic middle cerebral artery is a rare and misdiagnosed vascular anomaly characterized by a plexiform arterial network that replaces the M1 normal segment. It is secondary to the disruption of the main middle cerebral artery (MCA) trunk, and have usually been associated with vascular events occurred in the prenatal period and other vascular malformations. The initial manifestation is often associated with ischemic or hemorrhagic events. The aim of this study is to report the incidence of Tw-MCA findings in a four year cohort at ENERI Medical Institute in Buenos Aires, Argentina.

Materials and Methods

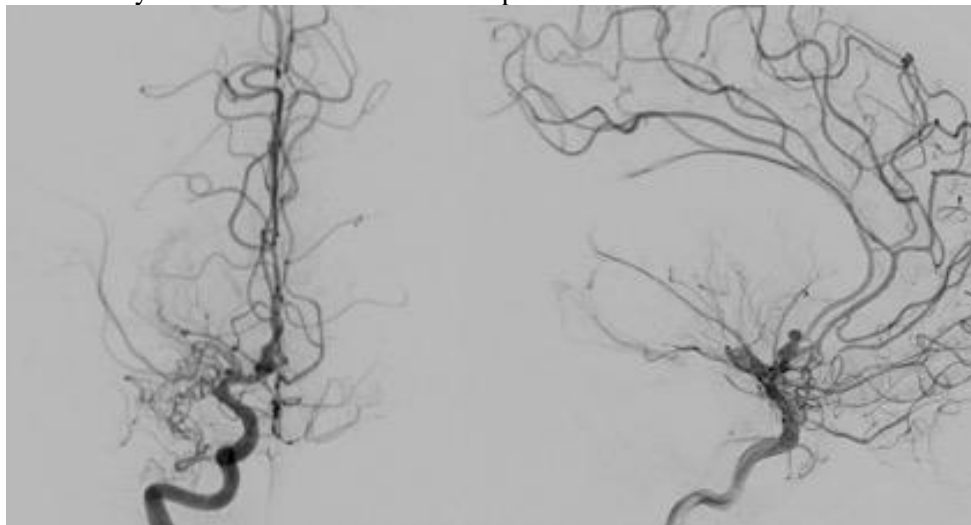
From January 2014 to December 2017, 7800 neuro endovascular procedures (including diagnostic and therapeutic) were analyzed at ENERI Medical Institute in Buenos Aires, Argentina. We describe the patient characteristics, clinical manifestations and angiographic findings, including collateralization pathways.

Results

A total of seven patients (0,1%) presented Tw-MCA angiography pattern. The right side was the most affected (57.1%); mean age was 47.8 years; 57.1% were female. The most common clinical presentation was a hemorrhagic event (57.1%): Two patients with aneurysmal subarachnoid hemorrhage, two patients with intraparenchymal hematomas at the same side of the Tw-MCA. Two contralateral ischemic stroke events (one associated with a contralateral MCA M1 stenosis) and one patient present seizures secondary to contralateral parietal arteriovenous malformation. The vascular collateralization from anterior circulation was observed in 85.7% and vascular collateralization from posterior circulation in 57.1%; no external carotid artery collateralization was observed.

Conclusions

Tw-MCA is a rare vascular anomaly associated with vascular events such as hemorrhagic or ischemic stroke. The knowledge of this anomaly will avoid misdiagnosis, like Moya-Moya disease, and unnecessary endovascular treatment attempts.



(Filename: TCT_EdE-20_twiglikemca.jpg)

EdE-05

Untangling the Carotid Web

S Patel¹, D Guerrero¹, M Gelbman¹, S Lev¹

¹*Nassau University Medical Center, East Meadow, NY*

Purpose

1. Present a case series of carotid webs and its mimickers, with comparative analysis and emphasis on distinguishing radiologic appearances. 2. Discuss theories of pathogenesis and potential clinical implications of carotid webs, which include high grade stenosis and embolic stroke.

Materials and Methods

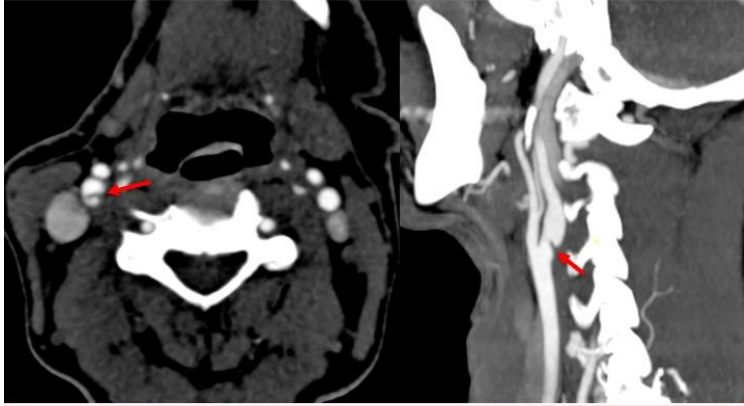
We performed a retrospective case review of patients, at our Level 1 trauma and designated stroke center, who were found to have carotid webs during the past year. The carotid webs were discovered by CTA examination, although workup included additional modalities, such as MRA as well. We compared our cases to an assortment of vascular mimics. Peer reviewed literature research was also conducted as an educational supplementation, including discussion of pathophysiology, management, and clinical implications.

Results

Carotid web is composed of fibrosis and hyperplasia within the intimal layer, which leads to luminal narrowing of the internal carotid artery. Often described as a "shelf-like projection", carotid web appears as a linear intraluminal filling defect at the carotid bulb, often posteriorly. It may mimic dissection, pseudoaneurysm or atherosclerosis. Carotid web is not a modifiable risk factor and may be an occult etiology for patients with recurrent embolic strokes with no clear risk factors. Carotid web is generally accepted as a variant of fibromuscular dysplasia (FMD), an idiopathic angiopathy that most commonly affects females (1). CTA is usually performed first, as part of a trauma or stroke work-up. We emphasize the critical role of 2-D reformatted images as well as 3-D reconstructions for optimal analysis. Digital subtraction angiography (DSA), however, remains the gold standard. Medical management ranges from no intervention to angioplasty, stent grafting, and endarterectomy, depending on the degree of stenosis. Optimal management is not yet established. If left undiagnosed or untreated, blood stasis/pooling at the site of the web can potentially lead to thrombus formation, embolization and ipsilateral stroke.

Conclusions

Carotid web may be a predisposing risk factor for embolic strokes in young to middle aged adults. The ability for the diagnostic radiologist to recognize carotid webs is essential, as the immediate and long term management will be fundamentally different from that of other similar appearing vascular pathologies. Our case series analysis should help untangle some of the difficulties associated with discerning carotid webs.



CTA Neck. 67 year old male status post fall. Axial image (left) just above the level of right carotid bifurcation demonstrates an additional contrast filled “collection” posterior to the left common carotid artery. The appearance may be suspicious for pseudoaneurysm or dissection. Oblique sagittal MIP imaging (right) further characterizes the abnormality as a linear filling defect at the posterior aspect of the proximal left internal carotid artery, consistent with a carotid web.

(Filename: TCT_EdE-05_CarotidWeb.jpg)

EdE-21

Variable Imaging Features of Cavernous Malformations in the Central Nervous System: A Pictorial Essay

S Kamalian¹, M Isikbay², S Kamalian³, A Simeone¹, S Teoh¹, P Sasson¹

¹Mount Auburn Hospital, Cambridge, MA, ²Harvard Medical School, Cambridge, MA, ³Massachusetts General Hospital, Boston, MA

Purpose

Cavernous malformations have variable features on different imaging modalities depending on lesion size and the presence of complications. The purpose of this pictorial essay is to review the epidemiology, pathology, clinical presentation, imaging features on different imaging modalities, natural history of the disease and treatment options.

Materials and Methods

Multiple patients with cavernous malformations who presented to our institution over the last several years were selected. The CT and MRI imaging features of cavernous malformations, associated findings, complications, and the pearls and pitfalls in radiological interpretation are discussed. We performed a review of the literature to discuss the epidemiology, clinical presentation, natural history of the disease and treatment options for cavernous malformation.

Results

There is an increasing number of patients diagnosed with cavernous malformation, largely due to increased availability and use of advanced brain imaging in both emergency department and outpatient settings. While the majority of these lesions remain asymptomatic throughout life, patients may become symptomatic and present with seizure or focal neurological deficit in the setting of bleeding and or mass effect. Cavernous malformations have variable imaging features on different imaging modalities depending on the size and the presence of associated complications.

Conclusions

Imaging plays a crucial role in the assessment of patients with symptomatic cavernous malformation in the central nervous system. Therefore, familiarity with the variable imaging features on different imaging modalities, associated findings and complications is essential to guide the appropriate patient management.

Education Exhibits

EdE-35

Virtual Reality in Neuroradiology: An Overview of Economics, Feasibility, and Its Potential Impact on Patient Care

F Priamo¹, K Kovtun¹, A Aizer¹, C Williams¹, R Huang¹

¹*Brigham and Women's Hospital, Boston, MA*

Purpose

The purpose of this exhibition is to discuss the current state of virtual reality in radiology, including its current applications in radiation oncology, the economics and feasibility of creating a virtual reality workstation, and potential applications of virtual reality in radiology and as a tool for referring physicians. The exhibition also will discuss future directions of virtual reality in radiology and avenues for research in the field.

Materials and Methods

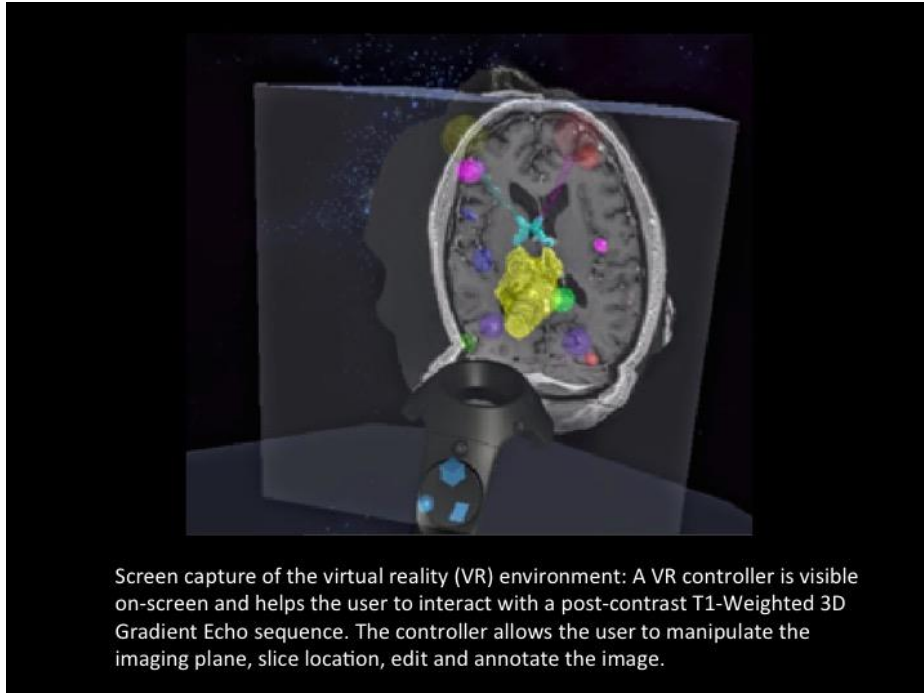
We seek to demonstrate the economics and feasibility of employing virtual reality in radiology by detailing the pricing of individual equipment used. We will discuss what barriers currently exist in the wide-scale implementation of the technology. We will demonstrate its current application in radiation oncology at our institution and detail what knowledge has been gained and is possibly transferrable to the practice of radiology. We will detail current applications specific to neuroradiology. Finally, we will discuss unanswered research questions.

Results

Virtual reality equipment can be acquired at a surprisingly low cost. However, the lack of commercially available software currently limits its scalability. At an institutional level, virtual reality has aided our Radiation Oncology department's ability to plan and shape the radiation field by providing a tactile and immersive experience that not only accounts for factors related to the patient's anatomy but also the radiation equipment itself. In diagnostic radiology, there is a huge potential for the use of virtual reality given the large volume of high-resolution, isotropically acquired imaging that is currently being used routinely. In neuroradiology, such imaging includes MRA and CTA of the head and neck, Balanced Steady-State Gradient Echo sequences in Cranial Nerve Imaging, T1-Weighted 3-D Gradient Echo Sequences for postcontrast imaging and T2-Weighted 3-D Fast Spin Echo Sequences commonly used in evaluating Multiple Sclerosis. In our experimental software, the DICOM data from these studies can be easily imported and viewed in the virtual reality realm. Virtual reality would also provide a platform for referring physicians such as neurosurgeons and interventional neuroradiologists to experience the anatomy in an immersive simulation that would closely mimic the real-world intraoperative environment. Despite its huge potential and promise, there's a lack of data on its actual impact on patient care, ease of use and workflow. Therefore, the field would provide a huge avenue for research.

Conclusions

Virtual reality is an emerging field that provides an immersive experience for radiologists and their referring physicians to better understand both their patients and disease. As it stands, the equipment that can be used is commercially available and relatively low-cost. However, there is currently no commercially available software for viewing studies in the virtual reality environment. Virtual reality lends itself well for neuroimaging given the large volume of studies currently being performed using 3D/Isotropic technique. For these reasons, Virtual reality provides a rich opportunity for future directions in research and in patient care.



(Filename: TCT_EdE-35_Slide1.jpg)

EdE-41

Where Does the Water Come From? A Multi-imaging Approach for Evaluation of CSF Leak

S Li¹, D Hynes²

¹Baystate Medical Center-UMSM, Springfield, MA, ²Baystate Medical Center-UMMS, N/A

Purpose

CSF leakage is a medical condition in which the cerebrospinal fluid (CSF) held in the membranes surrounding the brain and the spinal cord leaks out through a hole in the dural/theal sac into either the epidural spaces or outside the central nervous system (CNS). It is a complex problem that has a diverse etiology, and a variety of clinical presentations. The evaluation of CSF leakage is also complex, requiring the application of different imaging modalities depending on the symptoms and locations of the CSF leaks. The purpose of this exhibit is: to review the clinical and radiological features of the CSF leakage; to determine which imaging modality should be used for each of the conditions in searching for their underlying causes; to understand the pearls and pitfalls of the different imaging techniques. The related treatment plan and the clinical courses will be briefly discussed.

Materials and Methods

All cases have been gathered at Baystate Medical Center between 2008-2017. Examples of different imaging modalities used to search for the origins and locations of the CSF leakage were illustrated and compared. The advantages and disadvantages of each technique were discussed.

Results

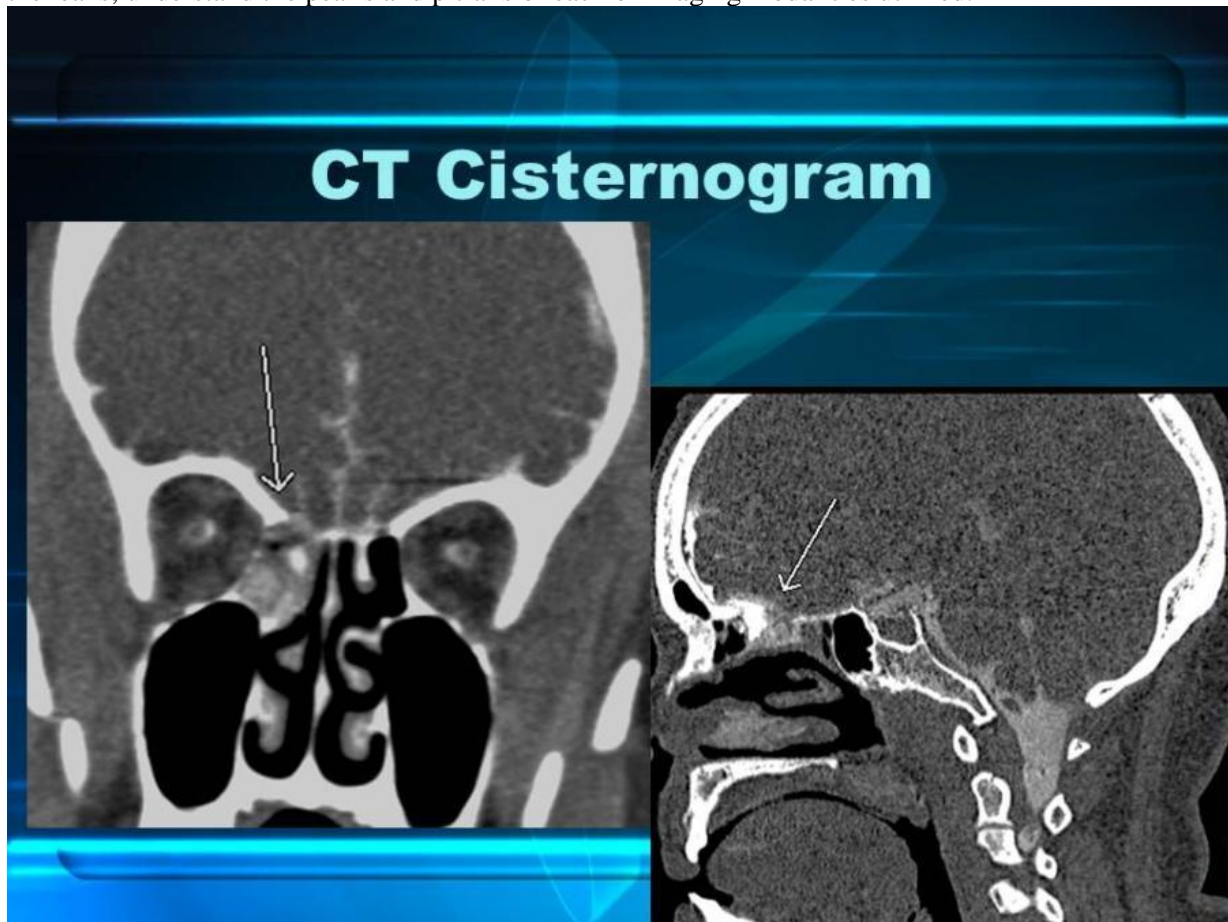
The most common etiology of CSF leak is post-traumatic or postsurgical. When it is post-traumatic, it is often a complication of skull-base fracture. Idiopathic CSF leak is called when no cause could be found and CSF leak is spontaneous. When the leak is iatrogenic, it is often due to sinus surgery or skull-base surgery. They commonly present as otorrhea or rhinorrhea. Erosion of the calvarium or sinus by infection causing CSF leak is rare. The etiology, the presentation and the location are often apparent. In the spine, rupture of the enlarged nerve root sleeves of the thecal sac could also cause CSF leak. Intracranial

Education Exhibits

hypotension (a loss of CSF greater than its rate of production which leads to a decreased volume inside the skull) may be the presenting syndrome. Multiple imaging modalities have been recruited to search for the origin and location of the CSF leak. Traditionally, radionuclide cisternography was used due to its highly sensitivity for detection of CSF leakage but also made it difficult to pinpoint the precise location of the leak. High-resolution CT is very useful for detection of bony defects but the exact location of the leak is aided by additional intra-thecal contrast administration – CT cisternography. Nerve root sleeve enlargement or rupture could be detected by myelography or CT myelography. Both radionuclide cisternography and CT cisternography/myelography require lumbar puncture for intra-thecal installation of either the radionuclide or iodine containing CT contrast.

Conclusions

At the end of this exhibit, the reviewers will: learn the different causes and clinical presentations of CSF leakage; know how to evaluate CSF leaks using different imaging techniques according to the locations of the leaks; understand the pearls and pitfalls of each of imaging modalities utilized.



(Filename: TCT_EdE-41_Slide4.JPG)

EdE-39

“Just Rule It Out!” Differentiating Cytotoxic Edema from Vasogenic Edema on NCHCT in the Acute Setting

A Condos¹, S Story¹, A Germana¹, J Yetto¹, A Cho¹, M Cathey¹

¹Naval Medical Center San Diego, San Diego, CA

Purpose

"Rule out stroke" is a commonly provided clinical indication for a non-contrast head CT (NCHCT) in the setting of acute neurologic symptoms. This "history" combined with a paucity of additional relevant clinical information available at initial interpretation can be problematic to the radiologist who, when faced with a positive study, may experience so-called "confirmation bias" where the tendency is to look for evidence to support the suspected diagnosis rather than to look for evidence that might suggest an alternate diagnosis, despite evidence for the alternate being more definitive. The purpose of this poster is to review the pathophysiology and imaging appearances of cytotoxic and vasogenic edema with the goal of teaching a junior radiology resident how to distinguish between an acute neurological syndrome versus a stroke mimic. Furthermore, accurate characterization of edema location and distribution, along with associated parenchymal abnormalities, is critical for early and accurate diagnosis, workup, and intervention.

Materials and Methods

Retrospective review of CT examinations for presenting symptoms of stroke over the past two years was performed. Studies that demonstrated findings of cytotoxic and vasogenic edema were included with their corresponding follow-up MRI. A variety of cases are presented that clearly demonstrate the pertinent imaging findings, beginning with the initial presentation NCHCT with follow-up 3T MRI to aid in further discussion when appropriate. Relevant anatomy to include vascular territories is reviewed. Finally, a discussion of the various imaging pearls and pitfalls, to include imaging artifacts that may interfere is provided.

Results

On NCHCT, acute ischemia is most commonly associated with cytotoxic edema, whereas other etiologies such as demyelinating processes, infections, and malignancies usually present with vasogenic edema. This poster will highlight the physiologic and pathologic mechanisms differentiating cytotoxic and vasogenic edema using a comprehensive case-based review of NCHCT for "rule out stroke" tailored towards helping trainees in radiology in distinguishing these entities on NCHCT. Divided into: 1. Discussion of cytotoxic edema versus vasogenic edema. 2. Vascular territories and relevant anatomy 3. CT and MRI cases.

Conclusions

Differentiating cytotoxic edema from vasogenic edema can be challenging. Timely and effective characterization of cytotoxic versus vasogenic edema is crucial in the acute setting as it is often a deciding factor in the extent of further work-up as well as the rapidity of further management. With experience, radiologists can confidently distinguish these entities at initial presentation.

Case 1: 63 year-old female with new onset mental status changes and frequent falls after returning from a trip one week prior.

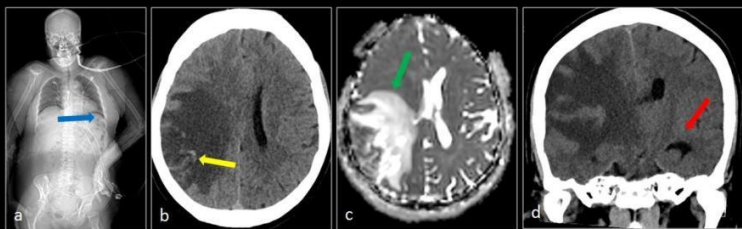


Figure 1. a. Initial scout radiograph demonstrates decerebrate posturing (→). b. Non-contrast head CT in the emergency department reveals confluent cytotoxic and vasogenic edema within the right frontoparietal cortex with associated hemorrhagic conversion (→). At the time of interpretation this was favored to represent hemorrhagic conversion of a sub-acute stroke with progressive vasogenic edema. c. Subsequent MRI demonstrates pseudonormalization of the ADC map (→), concordant with the initial interpretation. d. Repeat non-contrast head CT performed three days later demonstrates increasing vasogenic edema causing subfalcine and uncal herniation and trapped left lateral ventricle (→).

(Filename: TCT_EdE-39_Cerebraledema.JPG)

Education Exhibits

Education Exhibits-Head & Neck

EdE-42

3D Visualization and Printing of Lymph Node Stations in the Head and Neck: A Novel Tool for Patient Visualization

S Johnson¹, E Quigley¹, C Johnson¹, R Wiggins¹, Y Anzai¹, T Hutchins²

¹University of Utah School of Medicine, Salt Lake City, UT, ²University of Utah, Neuroradiology, Salt Lake City, UT

Purpose

The anatomic spaces of the neck can present challenges to the novice interpreter. As imaging plays a crucial role in staging head and neck malignancies, the proper identification of cervical lymph node levels is an important skill to master. Physical and virtual 3-D models can be helpful in learning the relevant anatomy and boundaries for proper lymph node classification.

Materials and Methods

Neck CTs from representative cases of cervical lymphadenopathy were retrospectively reviewed. The anonymized DICOM data was converted into STL format utilizing Materialise Mimics (Materialise, Michigan). The osseous and soft tissues of the head and neck were manually segmented and converted into a fused virtual model. Lymph nodes at anatomic subsites were included. The model was annotated for use in virtual reality and online 3-D rendering. The virtualized multicolor model was utilized in a stereoscopic head-mounted display (Oculus) for demonstrating patient-specific anatomy and pathology. The virtualized model can be viewed in conventional radiographic format, or positioned to replicate surgical positioning. The fully segmented model can be printed in tissue realistic materials (osseous like bone, biomimetic flexible soft tissues, and silicone like lymph nodes) (Whiteclouds, Ogden, UT; Stratasys [Eden Prairie MN]; 3DSystems, Rock Hill, SC).

Results

Physical and virtual models were checked by two neuroradiologists to confirm accurate representation of the original PACS images. The virtual labelled models will be utilized by trainees, and they will be surveyed to compare the perceived utility of the models versus conventional PACS image review alone. Post tests on nodal localization will be performed.

Conclusions

Virtual and biomimetic 3-D printed anatomic models can aid in the instruction of radiology and surgical trainees. Specifically, accurate identification and understanding of cervical lymph node stations can be accelerated through this method. The virtual model allows better definition of the various anatomic borders used by neuroradiologists, surgeons, and pathologists.



(Filename: TCT_EdE-42_vr2.jpg)

EdE-46

A Look at the Eyelids: A Pictorial Review of Pathologic Disorders and Neuroimaging Findings

D Martin¹, J Choi², A Khalaf², B Lanzman³, T Massoud²

¹Stanford University, Stanford, CA, ²Stanford University School of Medicine, Stanford, CA, ³Stanford University Medical Center, Stanford, CA

Purpose

The eyelids are critical to eye health by covering the cornea and aiding in tear distribution. Clinical examination of the eyelids is frequently sufficient, but imaging is extremely helpful in accurate interpretation and staging of infections and malignancies. The eyelids are usually visible on routine neuroimaging, but their specific imaging appearances has received little attention.

Education Exhibits

Materials and Methods

We present the imaging manifestations of a wide spectrum of pathologies originating from or involving the eyelids, and we categorize these entities etiologically.

Results

We first describe the gross and imaging anatomy of the eyelids. Pneumofornix is air trapped under the eyelids. Congenital and developmental eyelid abnormalities can be challenging for the reconstructive surgeon, include epicanthal folds, blepharophimosis, colobomas, cryptophthalmos, and canthal dystopias. Acquired eyelid disorders range from self-resolving ones to malignancies. Benign noninflammatory lesions include seborrheic or actinic keratosis, nevus, xanthelasma, molluscum contagiosum, and hydrocystoma. The swollen red eyelid is common clinically due to benign inflammatory disorders, including nonspecific blepharitis (but also present with herpes zoster ophthalmicus, and contact or atopic dermatitis), chalazion, and hordeolum; or malignancies, most commonly basal cell carcinoma, squamous cell carcinoma, sebaceous carcinoma, and melanoma. Importantly, preseptal and orbital cellulitis must be differentiated both clinically and on imaging. Mechanical eyelid disorders include entropion, ectropion, ptosis, lid retraction, trichiasis, dermatochalasis, facial palsy, and blepharospasm. Eyelid trauma may result from blunt or penetrating injury-isolated or usually occurring in multisystem trauma. We display examples of eyelid venolymphatic and arteriovenous malformations. Also shown are appearances of oculoplastic devices, e.g. eyelid weights and springs, and changes after canthotomy, cantholysis, and canthopexy. Finally, the iron content in eyelid mascara can produce interesting artifacts on CT and MRI.

Conclusions

Accurate diagnosis of eyelid problems is crucial to their proper management. Neuroimaging has an important role, particularly in cellulitis and malignant disorders of the eyelids.

EdE-50

AJCC 8th Edition Head and Neck Cancer Update: Nasopharyngeal Cancer

P Moullet¹, J Yetto¹, A Germana¹, J Foley¹, M Cathey¹

¹*Naval Medical Center San Diego, San Diego, CA*

Purpose

The American Joint Committee on Cancer recently released the 8th Edition Cancer Staging Manual, which is scheduled for implementation on January 1, 2018. Within the 8th edition are significant changes to head and neck cancer staging, particularly with regards to nasopharyngeal cancers. The purpose of this poster is to illustrate the relevant nasopharyngeal cancer staging changes with the goal of providing neuroradiologist a "go-to" for updated head and neck cancer staging.

Materials and Methods

Sequences of 3T MRI imaging were used to identify relevant anatomical landmarks for consideration while staging nasopharyngeal cancers with graphical overlay to demonstrate pertinent regions of tumor involvement. Specific cases were used to illustrate key points. Additionally, a literature review of current understanding and background of tumor staging was performed.

Results

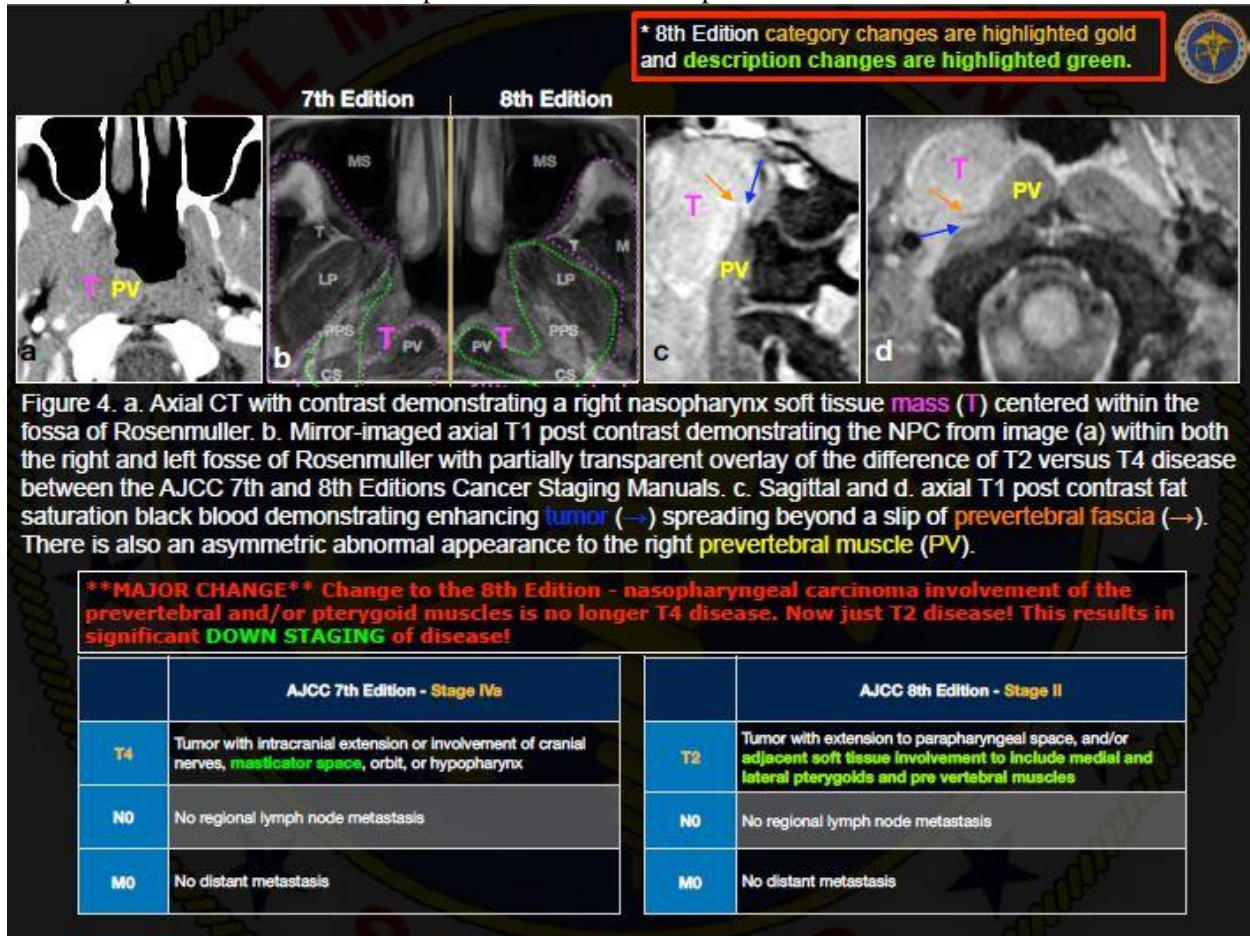
Case-based approach to illustrate relevant nasopharyngeal cancer staging changes as per the AJCC 8th Edition Cancer Staging Manual with an emphasis on staging updates. Divided into: 1. Nasopharyngeal Cancer Epidemiology, 2. Relevant Anatomy for Nasopharyngeal Cancer, 3. Nasopharyngeal Cancer Primary Sites, 4. Nasopharyngeal Cancer Method and Pattern of Spread, 5. AJCC 8th versus 7th Edition Changes for Nasopharyngeal Cancers, 6. Prognostic Stage Groups for Nasopharyngeal Cancers, and 7. Illustrative Cases.

Conclusions

Squamous cell carcinoma, particularly of the nasopharynx, is commonly encountered in daily clinical practice by neuroradiologists. There are significant changes to the staging system for these cancers within

Education Exhibits

the AJCC 8th Edition Cancer Staging Manual. In some cases this actually results in "down-staging" the disease relative to current standards. For example, prior T4 disease involving the medial and/or lateral pterygoid and/or prevertebral muscles will now be T2 disease. This update reflects current prognosis and treatment options for these cancers and has the potential to offer added psychological benefit to afflicted patients at the time of initial diagnosis. The neuroradiologist radiologist plays a critical role in the diagnosis and staging of nasopharyngeal cancer and a detailed knowledge of these staging updates is crucial to provide relevant and comprehensive care for our patients.



(Filename: TCT_EdE-50_NPC.JPG)

EdE-52

AJCC 8th Edition Head and Neck Cancer Update: p16+ Oropharyngeal Cancers

M Landon¹, J Foley¹, P Moullet¹, A Germana¹, J Yetto¹, M Cathey¹

¹Naval Medical Center San Diego, San Diego, CA

Purpose

The American Joint Committee on Cancer recently released the 8th Edition Cancer Staging Manual, which is scheduled for implementation on January 1, 2018. Within the 8th edition are significant changes to head and neck cancer staging, particularly with regards to oropharyngeal cancers, which is now divided into two separate chapters: p16+ versus p16- oropharyngeal cancers. The purpose of this poster is to focus on the new p16+ oropharyngeal chapter with the goal of providing the neuroradiologist a "go-to" guide for updated head and neck cancer staging.

Education Exhibits

Materials and Methods

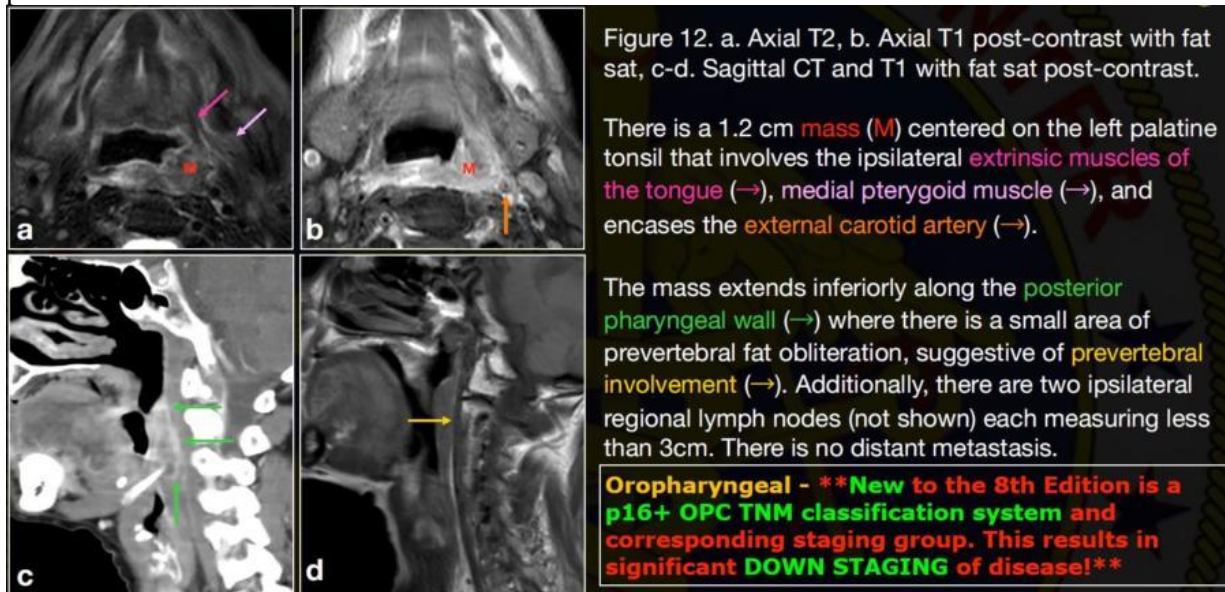
3T MRI imaging sequences were used to identify relevant anatomical landmarks for consideration while staging oropharyngeal cancers, with graphical overlay demonstrating pertinent regions of tumor involvement. Specific cases were selected to illustrate key points. Additionally, a literature review of the current understanding and background of tumor staging was performed.

Results

Case-based approach to illustrate pertinent p16+ oropharyngeal cancer staging criteria divided into: 1. p16+ Oropharyngeal Cancer Epidemiology 2. Relevant Anatomy for Oropharyngeal Cancer 3. Oropharyngeal Cancer Primary Sites 4. Oropharyngeal Cancer Method and Pattern of Spread 5. AJCC 8th Edition p16+ Oropharyngeal Cancer Staging 6. Prognostic Staging Groups for p16+ Oropharyngeal Cancers 7. Comparison Chart (p16+ versus p16- Oropharyngeal Cancers) 8. Illustrative Cases

Conclusions

Squamous cell carcinoma, particularly of the oropharynx, is commonly encountered in daily clinical practice by neuroradiologists. There are significant changes to the staging system for these cancers within the AJCC 8th Edition Cancer Staging Manual. Overall, the new p16+ oropharyngeal cancer staging results in significant "down-staging" of disease compared to the staging of traditional (p16-) oropharyngeal cancers. This update reflects current prognosis and treatment options for these cancers and has the potential to offer added psychological benefit to afflicted patients at the time of initial diagnosis. The neuroradiologist plays a critical role in the diagnosis and staging of oropharyngeal cancer, making a detailed knowledge of these staging updates crucial to providing relevant and comprehensive care for our patients.



(Filename: TCT_EdE-52_OPC.JPG)

EdE-51

AJCC 8th Edition Head and Neck Cancer Update: p16- Oropharyngeal Cancers

J Foley¹, M Landon¹, P Moullet¹, J Yetto¹, A Germana¹, M Cathey¹

¹Naval Medical Center San Diego, San Diego, CA

Purpose

The American Joint Committee on Cancer recently released the 8th Edition Cancer Staging Manual, which is scheduled for implementation on January 1, 2018. Within the 8th edition are significant changes

Education Exhibits

to head and neck cancer staging, particularly with regards to oropharyngeal cancers, which is now divided into two separate chapters: p16+ versus p16- oropharyngeal cancers. The purpose of this poster is to illustrate the AJCC 8th edition changes to traditional or p16- oropharyngeal and hypopharyngeal cancer staging with the goal of providing a neuroradiologist a "go-to" for updated head and neck cancer staging.

Materials and Methods

Sequences of 3T MRI imaging were used to identify relevant anatomical landmarks for consideration while staging oropharyngeal cancers, with graphical overlay demonstrating pertinent regions of tumor involvement. Specific cases were selected to illustrate key points. Additionally, a literature review of the current understanding and background of tumor staging was performed.

Results

Case-based approach to illustrate pertinent p16- oropharyngeal cancer staging criteria. Divided into: 1.

p16- Oropharyngeal Cancer Epidemiology 2. Relevant Anatomy for Oropharyngeal Cancer 3.

Oropharyngeal Cancer Primary Sites 4. Oropharyngeal Cancer Method and Pattern of Spread 5. AJCC 8th

Edition p16- Oropharyngeal Cancer Staging 6. Prognostic Stage Groups for p16- Oropharyngeal Cancers

7. Hypopharyngeal Cancer Epidemiology 8. Relevant Anatomy for Hypopharyngeal Cancer 9. AJCC 8th

Edition Hypopharyngeal Cancer Staging 10. Prognostic Stage Groups for Hypopharyngeal Cancers 11.

Illustrative Cases

Conclusions

Squamous cell carcinoma, particularly of the oropharynx, is commonly encountered in daily practice by neuroradiologists. There are significant changes to the staging system for these cancers within the AJCC 8th Edition Cancer Staging Manual. The most significant change to both p16- oropharyngeal and hypopharyngeal cancer staging is the addition of the N3 description for "extra-nodal extension." When present, this results in Stage IVb disease or greater, independent of any other factors. This update reflects current prognosis and treatment options for these cancers and has the potential to offer added psychological benefit to afflicted patients at the time of initial diagnosis. Neuroradiologists play a critical role in the diagnosis and staging of p16- oropharyngeal and hypopharyngeal cancers and a comprehensive knowledge of these entities is paramount for accurate treatment and prognosis, paving the way for best possible patient outcomes.

Case 5

* 8th Edition category changes are highlighted gold and description changes are highlighted green.

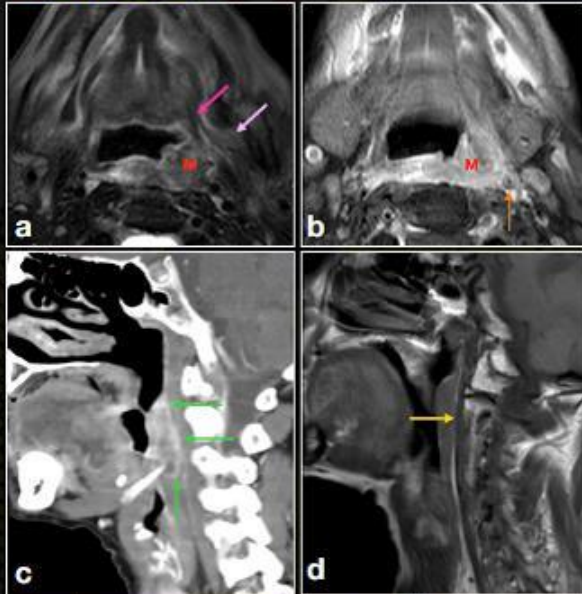


Figure 12. a. Axial T2, b. Axial T1 post-contrast with fat sat, c-d. Sagittal CT and T1 with fat sat post-contrast.

There is a 1.2 cm **mass (M)** centered on the left palatine tonsil that involves the ipsilateral **extrinsic muscles of the tongue (→)**, medial pterygoid muscle (→), and encases the **external carotid artery (→)**.

The mass extends inferiorly along the **posterior pharyngeal wall (→)** where there is a small area of prevertebral fat obliteration, suggestive of **prevertebral involvement (→)**. Additionally, there are two ipsilateral regional lymph nodes (not shown) each measuring less than 3cm. There is no distant metastasis.

Oropharyngeal - **New to the 8th Edition is a p16+ OPC TNM classification system and corresponding staging group. This results in significant DOWN STAGING of disease!**

	AJCC 7th Edition - Stage IVb	NEW	AJCC 8th Edition - Stage III for p16+		AJCC 8th Edition - Stage IVb for p16-
T4b	Tumor invades the lateral pterygoid muscle, pterygoid plates, lateral nasopharynx, skull base, or encases carotid artery	T4	Tumor invades the larynx, extrinsic muscles of the tongue, medial pterygoid muscle, hard palate, or mandible or beyond	T4b	Tumor invades the lateral pterygoid muscle, pterygoid plates, lateral nasopharynx, skull base, or encases carotid artery
N2b	Metastasis in multiple ipsilateral lymph nodes, none larger than 6cm in greatest dimension	N1	Metastasis in one or more ipsilateral lymph nodes, none larger than 6cm in greatest dimension	N2b	Metastasis in multiple ipsilateral lymph nodes, none larger than 6cm in greatest dimension and ENE (-)
M0	No distant metastasis	M0	No distant metastasis	M0	No distant metastasis

(Filename: TCT_EdE-51_p16negslide.jpg)

EdE-44

ASL Alert! Extracranial Findings Ahead

K Hsu¹, G Zaharchuk¹, N Fischbein¹
¹Stanford University, Stanford, CA

Purpose

Arterial spin label (ASL) perfusion is routinely utilized at our institution for evaluation of brain pathology. While areas of extracranial ASL high signal are often normal and related to vascular, mucosal, or scalp perfusion, on occasion, high signal on ASL in the extracranial compartment is a marker of pathology. There is currently limited literature on the utility of ASL in the head and neck. The purpose of this educational exhibit is to showcase a variety of extracranial pathologies included on arterial spin labeling perfusion imaging.

Materials and Methods

We present a selection of images from our PACS system of patients with extracranial pathology in the head and neck that was identified on ASL perfusion imaging of the brain. We also present some of the "expected" findings on extracranial ASL imaging that can be mistaken for pathology. We discuss the etiology ASL findings and review the identified pathology as applicable.

Results

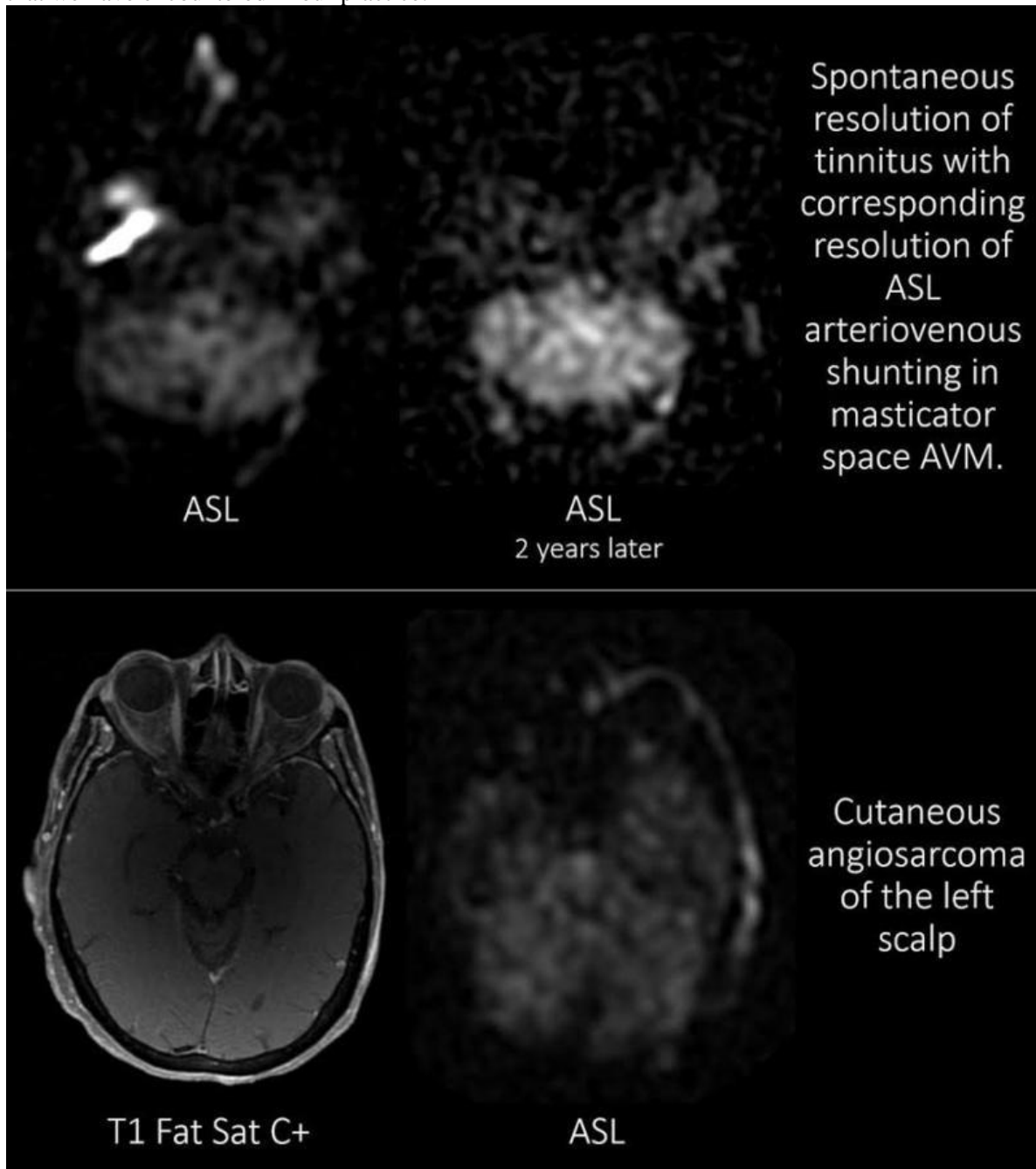
We present multiple examples of normal and pathological extracranial ASL signal. Our exhibit includes

Education Exhibits

examples from the following tissues or anatomical subsites: Normal - Scalp, nose/nasal mucosa, arteries, retrograde venous flow and CSF pulsation Orbit - Meningioma, hypervascular metastasis Temporal bone - Glomus tympanicum, endolymphatic sac tumor Nasal cavity/sinuses - Juvenile angiofibroma, esthesioneuroblastoma Vascular - Extracranial AVMs and AV fistulae. Infantile hemangioma Spine – Paraspinal soft tissue metastasis Bone - Osseous "hemangioma". Skin - Angiosarcoma

Conclusions

Extracranial areas of high signal are not infrequently encountered on ASL perfusion images of the brain. ASL can be a sensitive marker for extracranial pathology, and we present a spectrum of imaging findings that we have encountered in our practice.



(Filename: TCT_EdE-44_ASNRASLfigure.jpg)

EdE-49

Atavistic and Vestigial Structures Observed in Neuroradiology: A Pictorial and Educational Review of Interesting Evolutionary Remnants Seen on Neuroimages

A Patel¹, D Martin², H Dahmouh³, T Massoud¹

¹*Stanford University School of Medicine, Stanford, CA*, ²*Stanford University, Stanford, CA*, ³*Stanford Hospital, Stanford, CA*

Purpose

Organisms may retain nonfunctional anatomical features following natural selection. Atavistic and vestigial organs have long been a source of perplexity. Atavism is when an ancestral trait reappears after loss through evolutionary change in previous generations, whereas vestigial structures are largely or entirely functionless relative to their original roles. Aside from taxonomic purposes, it is useful for neuroradiologists to know if a given structure is atavistic or vestigial to be able to relate this to its function.

Materials and Methods

We studied a list of 86 human vestigial organs compiled by Wiedersheim in 1893, and here describe and illustrate atavistic and vestigial structures that may be seen in neuroimaging.

Results

There are numerous examples of human vestiges in the head, neck, and spine. These include the plica semilunaris of the eye, vomeronasal organ, wisdom teeth, Darwin's tubercle, the mastoid process, and several muscles e.g. orbitalis, external ear muscles, occipitalis minor, platysma, vibrissal capsular muscles, chondroglossus, and levator claviculae in the posterior triangle of the neck. The lumbosacral spine and coccyx may rarely yield human 'tail' abnormalities classified as either vestigial pseudotails or atavistic true tails. Pseudotails may be a few inches long and contain soft tissues, but bone, cartilage, and spinal cord are lacking. They are remnants of the distal unvertebrated mesodermal portions of tails in embryos 31-35 days old. A true tail is an anomalous prolongation of the coccygeal vertebrae by up to five caudal vertebrae, but bone may also be absent. True tails may be familial. Spina bifida most frequently coexists with both pseudotails and true tails.

Conclusions

Humans are walking records of their evolutionary past, and the list of vestigial organs is always a work in progress. Atavistic and vestigial structures may at times be unexpected or puzzling on neuroimaging. This presentation will aid in identifying and understanding them.

EdE-45

Imaging of the Nasolacrimal Drainage System: A Comprehensive Pictorial and Educational Review

V Mayercik¹, Z Chaudhry¹, C Chan², N Fischbein³, T Massoud¹

¹*Stanford University School of Medicine, Stanford, CA*, ²*Stanford University Hospital, Stanford, CA*, ³*Stanford University, Stanford, CA*

Purpose

Most nasolacrimal drainage system (NLDS) abnormalities result in epiphora, and some cause swelling in the area of the lacrimal sac. Imaging is useful to outline the anatomy, function, location and degree of obstruction of the NLDS, or to visualize the tissues extrinsic to it. Scant attention has been paid to comprehensive classification of the neuroimaging manifestations of NLDS abnormalities.

Materials and Methods

We present the imaging manifestations of a wide spectrum of pathologies originating from or involving the NLDS, and we classify these entities according to their etiology and location.

Education Exhibits

Results

We first describe the imaging anatomy of the NLDS on CT, MRI, and both contrast and nuclear dacryocystography (DCG). The valves of Hasner, Taillefer, and Krause are frequently seen in the nasolacrimal ducts (NLD) on DCG. NLDS abnormalities may be congenital, e.g. affecting the lacrimal puncta, or dacryostenosis may lead to dacryocystitis in the newborn. An absent valve of Hasner may result in retrograde pneumatocele of the lacrimal sac. Dacryocystitis may result from stagnation of tear flow, and usually occurs with obstruction of the NLD, either primary acquired nasolacrimal duct obstruction (PANDO) when caused by inflammation or fibrosis without any precipitating cause, or secondary acquired lacrimal drainage obstruction (SALDO) following infectious, inflammatory, neoplastic, traumatic, and mechanical causes. We illustrate numerous imaging examples of these abnormalities, including neoplastic spread from nearby tissues (more common than primary tumors), mostly from eyelid cancers (basal cell carcinoma, squamous cell carcinoma), and from the maxillary antrum. Mechanical obstructions may be due to intraluminal foreign bodies (dacryoliths) caused by long-term administration of topical medications, external compression from nasal foreign bodies, mucoceles, or dentigerous cysts.

Conclusions

Management strategies for lesions involving the NLDS vary substantially, depending on the abnormalities revealed on neuroimaging. We comprehensively review the wide spectrum of pathologies encountered in the NLDS.

EdE-47

Imaging Pediatric Proptosis: From Eye to Brain

M Ho¹, J Chen¹, M Brodsky¹, J Garrity¹

¹Mayo Clinic, Rochester, MN

Purpose

1. Review the pathophysiology and major etiologies of pediatric proptosis 2. Utilize clinical history and appropriate imaging modalities for evaluation 3. Demonstrate pearls and pitfalls of diagnosis

Materials and Methods

Evaluation of the child with proptosis begins with a thorough ophthalmologic history and examination. Multiple modalities are available for clinical assessment, including ocular ultrasound, optical coherence tomography, and angiography. Following initial assessment, additional radiologic evaluation of the orbits and brain may be indicated using CT, MR, and/or cerebral angiography. The following mnemonics are useful for assessment: Location: "4 O's" = Ocular, Optic nerve, Orbit, Outside Etiology: "CT VEIN" = Congenital/CSF, Trauma, Vascular, Endocrine, Inflammation/Infection, Neoplasm

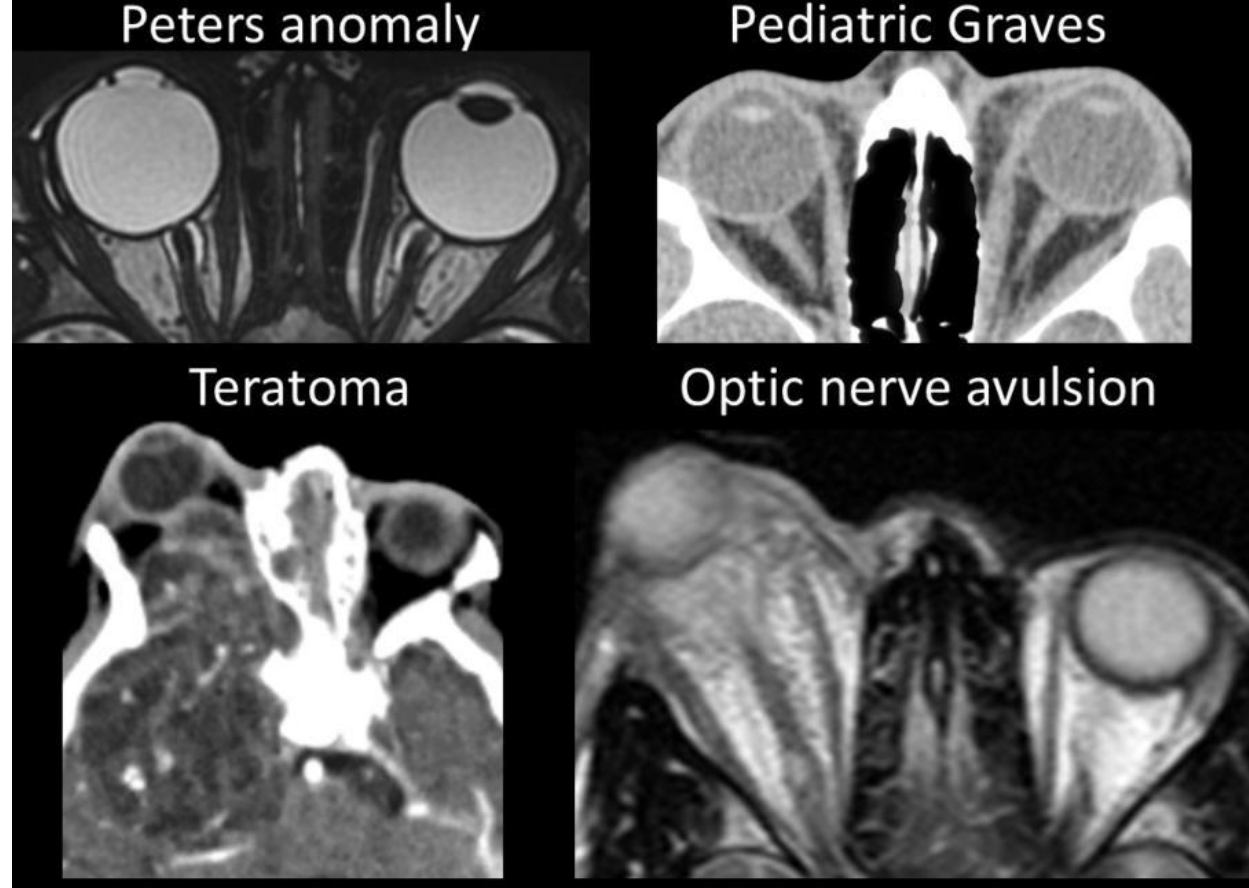
Results

Clinical - Definitions: Proptosis vs. pseudoproptosis, exophthalmos, exorbitism - Symptoms (age, time course, laterality) + 8-point eye examination Imaging Modalities - Ophthalmology: Ultrasound, optical coherence tomography, angiography - Radiology: CT, MR, cerebral angiography Congenital Macrophthalmos - Simple megalocornea, anterior megalophthalmos, buphthalmos Congenital masses - Hamartoma vs. choristoma, ectodermal and endodermal malformations Genetic overgrowth - NF1 (cranio-orbito-temporal), megalencephaly CSF Optic disc edema - Papilledema vs. pseudopapilledema: US, OCT, CT, MRI Optic nerve tortuosity - DDX: normal, papilledema, optic neuritis, optic glioma Syndromic craniosynostosis Trauma Anterior chamber - Corneal laceration, hyphema, lens dislocation, cataract Posterior chamber - Retinal vs. choroidal detachment, vitreous hemorrhage Retrobulbar hematoma - ON stretching, avulsion Pediatric orbital mechanics - "White-eyed" trauma, ligamentous elasticity, craniofacial ratio - Blowin > blowout, greenstick (trapdoor), CSF leak - Midface: Naso-orbito-ethmoid Vascular Vascular anomalies - Malformations vs. tumors - Carotid-cavernous fistula Vascular syndromes - Hemangiomas, PHACES - Sturge-Weber: embryology & temporal evolution, high-risk

Education Exhibits

features - DDx: Parry-Romberg (enophthalmos), Wyburn-Mason (high-flow) Endocrine - Pediatric Graves: Often milder, atypical distribution, auto-decompression Inflammation/Infection Orbital inflammation - Idiopathic (pseudotumor), granulomatous, lymphocytic, histiocytic, autoimmune, demyelinating - Locations: uvea/sclera, intraconal, EOM/lacrimal, brain & multisystem Orbital cellulitis: 1° vs 2° sinusitis, pre- vs. postseptal - Subperiosteal abscess: spreading thrombophlebitis, porous bone Neoplasm Diverse histology and locations; infection mimics - Benign, malignant primary, metastasis - Rb, optic glioma/PNST/meningioma, orbital RMS/lymphoma/NB, bone

Conclusions
Ophthalmologic history and examination are key to the evaluation of pediatric proptosis. Following initial assessment, radiologic imaging can be obtained to further assess orbital and brain pathology. Useful mnemonics include the "4 O's" for location and "CT VEIN" for etiology.



(Filename: TCT_EdE-47_Proptosis.jpg)

EdE-57

Lesions of the Craniocervical Junction: An Imaging Review

S Onderi¹, A Mahajan¹
¹*Yale School of Medicine, New Haven, CT*

Purpose

1. To review the basic anatomy of the craniocervical junction
2. To highlight the importance of a detailed analysis of the craniocervical junction during evaluation of images obtained for head, neck or cervical spine pathology.
3. To present imaging findings of a variety of lesions of the craniocervical junction.

Education Exhibits

Materials and Methods

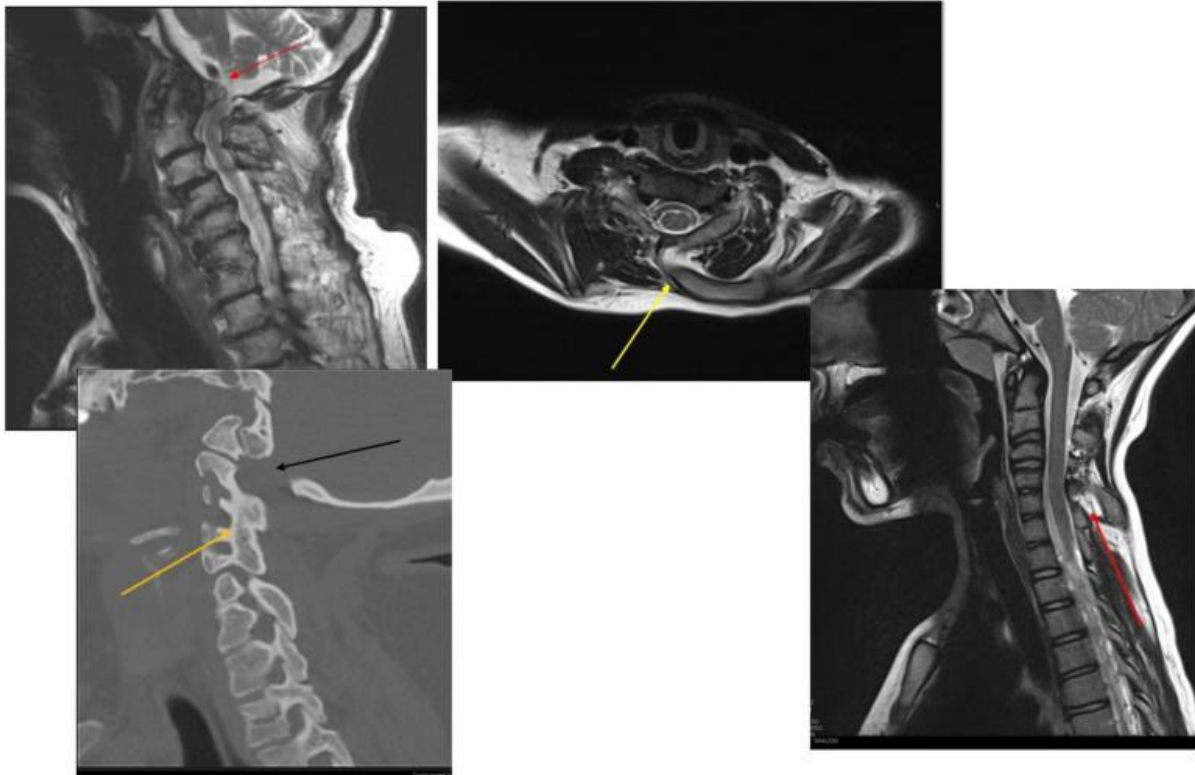
A number of nontraumatic lesions involving the craniocervical junction diagnosed at our institution are presented. Lesions are classified by etiology including congenital, inflammatory, infectious, neoplastic and vascular.

Results

Craniocervical abnormalities are often identified incidentally during analysis of imaging obtained for brain, neck or spine evaluation. The complexity of this region, the protean presentation of many conditions in this location, and its often peripheral location on imaging can render its detailed evaluation suboptimal or incomplete. A number of different etiologies of lesions involving the craniocervical junction is demonstrated including common neoplasms like meningiomas, findings associated with congenital conditions like Klippel Feil, amongst other etiologies.

Conclusions

Craniocervical junction lesions are often incidentally identified during imaging of the head, neck and cervical spine. Familiarity of this region, and knowledge of the differential diagnosis and protean presentation of these findings is crucial to avoid missing pathology, avoid overdiagnosis/misdiagnosis, and to aid in treatment.



(Filename: TCT_EdE-57_ASNRfigures.jpg)

EdE-48

New Historadiologic Classification of Cochlear Malformations: Review of Neuroimaging Diagnostic Criteria and Clinical Implications

S Abdulla¹, F D'Arco²

¹University Health Network, University of Toronto, Ontario, Canada, ²Great Ormond Street Hospital, London, United Kingdom

Education Exhibits

Purpose

This is an educational review of the new combined radiopathologic classification for cochlear hypoplasia (CH) and incomplete partition (IP) by Sonneroglu (2016). We review the MRI and CT diagnostic criteria for the newly described inner ear malformations and their impact on clinical management.

Materials and Methods

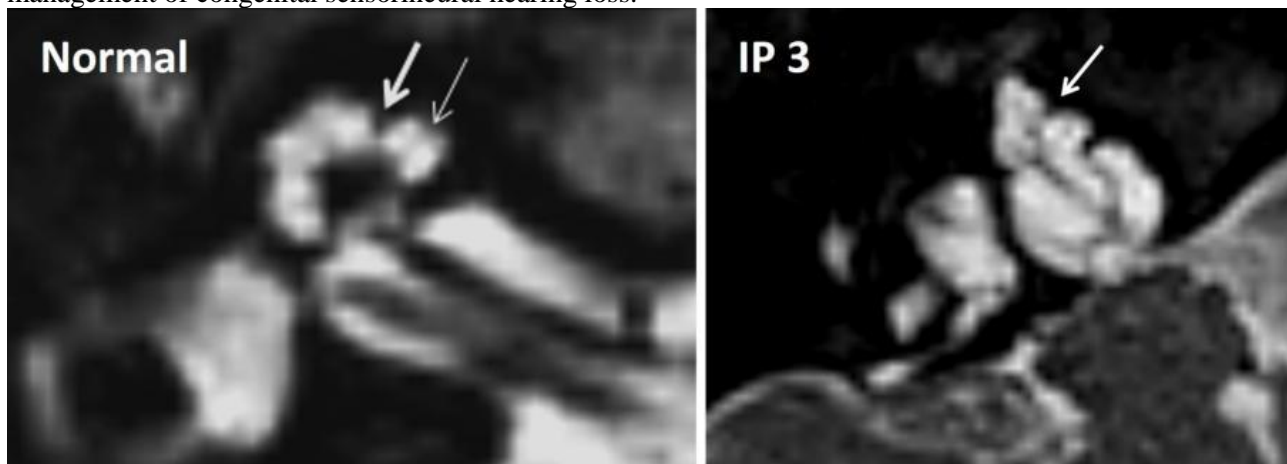
The newly proposed classification of CH and IP by Sennaroglu (2016) is based on histopathologic classification. Four different types of CH as well as a third type of IP have been introduced. We reviewed the high resolution MRI and CT diagnostic criteria for each of the new malformations in this pictorial essay with emphasis on the diagnostic perils for each malformation.

Results

Pertinent MRI features and CT measurement techniques for the four types of CH are as follows. CH 1: Cochlear bud and no internal structure. CH 2: Small cochlea with hypoplasia of modiolar and interscalar septum. CH 3: Cochlea hypoplasia (width <5.4mm, height < 3.3mm) but preserved internal architecture. CH 4: Cochlea hypoplasia, normal basal turn and hypoplastic middle and apical turns. The CH classification impacts management as CH 1 patients have a higher incidence of cochlear nerve aplasia/hypoplasia whilst if cochlear implantation is considered in CH 2-4 a thinner and shorter electrode will be more beneficial. Lastly, the less well-known IP 3 associated with X-linked deafness has a normal external shape but absent internal structure. Recognition of IP 3 is vital for pre-operative planning as both the cochlear aperture and internal auditory canal (IAC) are enlarged without angulation predisposing to electrode misplacement.

Conclusions

The new classification of cochlear malformation based on the historadiologic classification provides a comprehensive framework for neuro-otologic management of congenital sensorineural hearing loss. Awareness of the new criteria is important for practicing neuroradiologists in diagnosis and clinical management of congenital sensorineural hearing loss.



(Filename: TCT_EdE-48_Picture4.jpg)

EdE-43

Nontraumatic Head and Neck Emergencies, Pearls and Pitfalls: A Pictorial Essay

S Kamalian¹, S Teoh¹, P Sasson¹, P Schaefer², M Lev², S Kamalian²

¹Mount Auburn Hospital, Cambridge, MA, ²Massachusetts General Hospital, Boston, MA

Purpose

Imaging, especially CT, has an ever-increasing and crucial role in the evaluation of non-traumatic head and neck emergencies. The complex anatomy and widely diverse causes of these conditions pose special

Education Exhibits

challenges to radiologists. Moreover, the failure or delay in diagnosis can result in serious or life-threatening complications. Therefore, the purpose of this pictorial essay is to briefly review the anatomy and explain imaging findings of the most common and life threatening non-traumatic head and neck emergencies.

Materials and Methods

The important anatomical landmarks, fascial planes and spaces of the head and neck are explained. Several cases with diverse etiologies were selected from the patients admitted to our tertiary care academic institution. The imaging findings, pearls and pitfalls in radiologic interpretation, and the potential complications are discussed. The cases are arranged and presented based on their primary anatomical involvement, including the oral cavity, pharynx, larynx, major cervical vessels, superficial and deep cervical spaces, as well as paranasal sinuses, orbits, and temporal bones.

Results

Non-traumatic head and neck emergencies include a wide variety of infectious, inflammatory and neoplastic pathologies. Although many of these conditions are initially local, they can extend through the fascial planes and involve multiple spaces, including the intracranial compartment and mediastinum with serious or life-threatening complications.

Conclusions

Imaging plays a crucial role in the assessment of non-traumatic head and neck emergencies. Therefore, familiarity with the anatomy, imaging findings of these conditions and their potentially life-threatening complications is essential to ensure accurate and timely diagnosis, and thus guide the appropriate treatment.

EdE-58

Sellar and Juxtapellar Mass Lesions... But Not What You Think!

J Reese¹, F Mihlon¹

¹*Eastern Virginia Medical School, Norfolk, VA*

Purpose

Headaches and vision changes may necessitate imaging often revealing sellar or juxtapellar masses most commonly being adenomas. However, there are uncommon entities the radiologist should be aware of as well as common entities that have unusual appearances. The purpose of this exhibit is to raise awareness of these uncommon sellar and juxtapellar diagnoses through a series of cases.

Materials and Methods

A case series of unusual sellar and juxtapellar diagnoses was compiled. The cases were proven to be rare diagnoses mimicking more common entities or unusual presentations of more common lesions. Imaging features and clinical presentations were reviewed to help raise suspicion for these entities when encountered. Three challenging sellar/juxtapellar cases were selected from the cases and are reviewed here for this abstract. Case 1 Presentation 35-year-old patient presents with severe headache, vision changes, and endocrinologic disturbance for 1.5 months. Imaging Sellar/Suprasellar T1 hyperintense and T2 hypointense nonenhancing mass causing severe compression of the optic chiasm and distortion of the hypothalamus. Report suspected pituitary macroadenoma with chronic blood products/proteinaceous material. Case 2 Presentation 49-year-old woman presented with worsening headaches. Found to have panhypopituitarism and vision changes. History of ventriculoperitoneal shunt since birth and hypopituitary since birth. Patient self-reported a brain mass that had been present for "years." Imaging Large septated left middle cranial fossa arachnoid cyst extending into the optic canal with associated dysplasia of nearby brain. A 3 cm suprasellar mass was located anterior to the infundibulum. The mass was isointense to brain tissue and inseparable from the optic chiasm. Flattening of the pituitary and chronic expansion of the sella was present. Question of hamartoma or glioma extending from the floor of the third ventricle. Case 3 Presentation 66-year-old with remote history of gastric lymphoma with

Education Exhibits

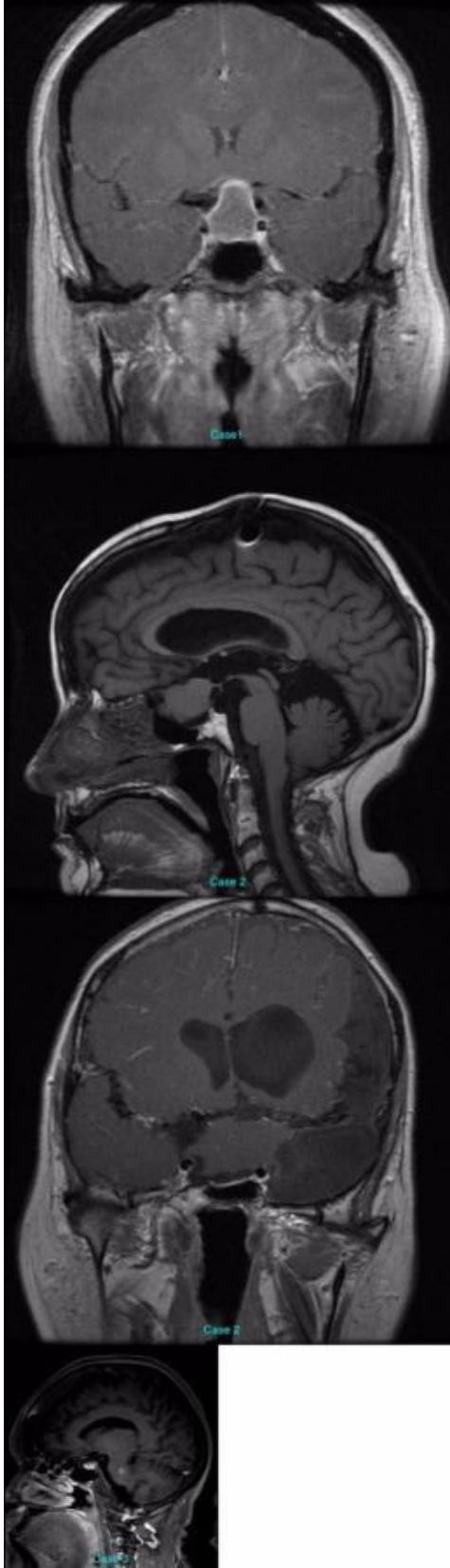
incidentally discovered expansile bone lesion at the sphenoclivial junction cervical MRI done for gait and headaches. Imaging 1.5 cm expansile enhancing mass at the sphenoclivial junction bulging into the sphenoid sinus above and nasopharynx below. Bone margins were sclerotic. Considerations include anterior chordoma, minor salivary gland tumor, and metastasis

Results

Case 1 Resection and pathology results: At transsphenoidal resection, purulent material was seen filling the sella. Subsequent gram stain culture revealed probable pneumococcus. Specimen for pathology revealed acellular eosinophilic material. Diagnosis: Pituitary abscess Discussion: Pituitary abscess is a rare sellar mass with a high mortality accounting for less than 1% of all pituitary disease. Typical imaging features include a single cystic mass that is T1 hypointense and T2 hypointense and shows rim enhancement. Imaging features are not specific and it is highly difficult to diagnose before surgery. The diagnosis should be considered when patients have fever, headache, and signs of pituitary dysfunction, or for patients with sellar lesion presenting with signs of meningeal inflammation. Case 2 Pathology results: Benign brain tissue Diagnosis: Ectopic brain secondary to large arachnoid cyst Discussion: Intracranial arachnoid cysts account for 1% among all intracranial space-occupying lesions and they are typically thought of as incidental findings (2). However, they may fluctuate in size and result in compression of nearby brain tissue. In this case, a large middle cranial fossa arachnoid cyst resulted in ectopic brain tissue displaced to the suprasellar region simulating a suprasellar tumor. Case 3 Pathology results: Pituitary adenoma Diagnosis: Ectopic adenoma Discussion: Ectopic adenomas are rare and are defined as extrasellar pituitary adenomas that show no connection to the normal pituitary gland. The most common location is the sphenoid sinus floor. CT and MRI are complementary. (3) CT provides important information regarding the bony anatomy including the tendency to cause bone expansion with sclerosis helping to differentiate from more aggressive lesions. On MRI, lesions are usually isointense relative to adjacent grey matter, and they show enhancement after the administration of contrast material.

Conclusions

We present a case series that can be used to educate radiologists and raise awareness of uncommon sellar and juxtaseellar diagnoses.



(Filename: TCT_EdE-58_AbstractMergedcopy.jpg)

EdE-56

Stuck in the Middle: Nervus Intermedius Related Neuropathologic Imaging Spectrum

M Landon¹, S Elakkad¹, J Yetto¹, A Germana¹, M Cathey¹

¹*Naval Medical Center San Diego, San Diego, CA*

Purpose

The nervus intermedius (NI), so-named due to the intermediate course it takes between the facial and vestibular nerves within the cerebellopontine angle (CPA), ultimately gives rise to the greater superficial petrosal nerve, chorda tympani, and the lesser known posterior auricular nerve. Primary pathologies of the NI can present as nervus intermedius neuralgia (NIN). Alternatively, pathology in the distribution of any nerves derived from NI can present with symptoms referred to the NI. Advances in imaging technology have improved our ability to see this nerve and its branches, allowing for greater diagnostic accuracy when pathology referable to the NI is suspected. The purpose of this poster is to review the anatomy and function for the NI using case based approach, highlighting the NI neuropathologic spectrum of disease.

Materials and Methods

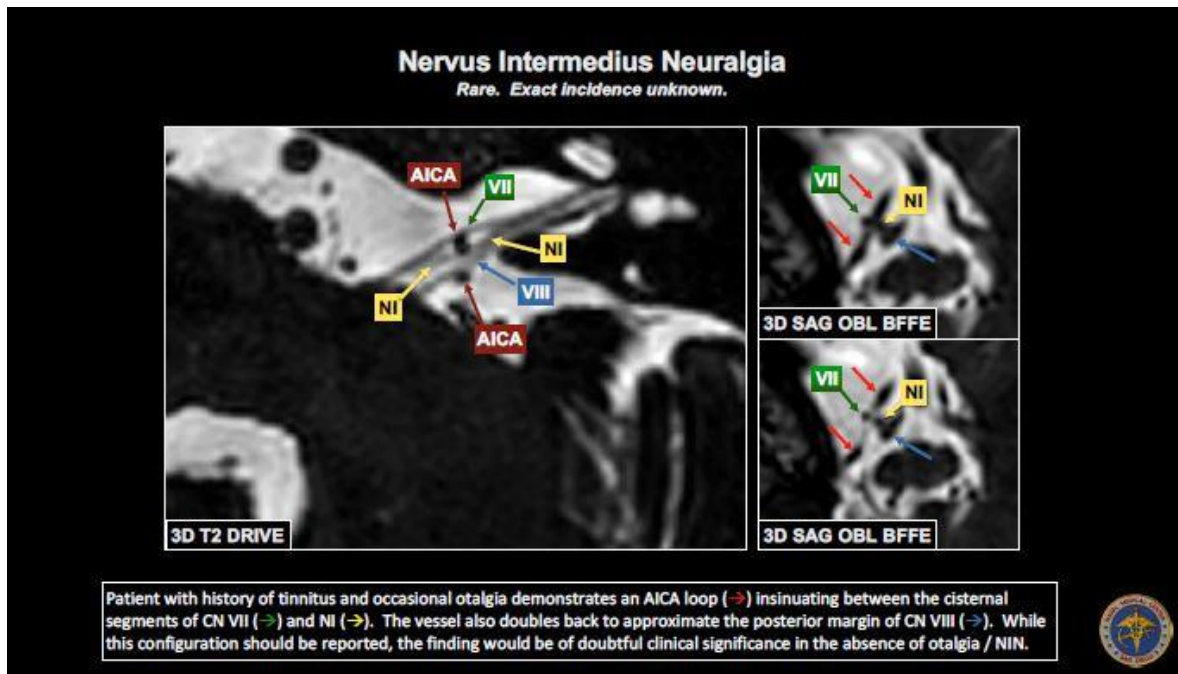
Using images of the temporal bone from our high resolution state-of-the-art CT and 3T MRI, we will illustrate normal anatomy of the NI and its branches. Furthermore, we will show specific imaging examples of a variety of pathologies that involve the NI and its branches.

Results

The NI is involved in a variety of functions including: - Innervating the lacrimal, submandibular, and sublingual glands - Transmitting sensory input from portions of the external auditory canal, paranasal sinuses, and nasal mucosa - Conveying taste input from the anterior two-thirds of the tongue, floor of the mouth, and palate Pathologies either directly involving NI (e.g CPA mass or vascular compression) as well as pathologies involving its branches (e.g. sinonasal tumors, perineural tumor spread, or contact point headaches) may be referable to the NI. Overlapping innervation with branches of the trigeminal, glossopharyngeal, and vagus nerves can confound diagnosis and/or lead to mis-localization, resulting in delayed diagnosis or inappropriate therapy.

Conclusions

Understanding the anatomy of the NI, its branches, and its pathologic spectrum allows radiologists to take a nuanced approach to these complex cases, improving diagnostic accuracy and providing value added to our referring providers and patients.



(Filename: TCT_EdE-56_NIN.JPG)

Education Exhibits-Informatics

EdE-59

How to Perform Radiomic and Radiogenomic Studies in the Clinical Setting Taking Imaging and Biological Factors into Account

M Patel¹, V Sawlani¹

¹University Hospitals Birmingham NHS Foundation Trust, Birmingham, United Kingdom

Purpose

Phenotypic information is routinely being extracted through imaging non-invasively which can be used for precision medicine (1). It is critically important that radiologists lead this artificial intelligence revolution. They have developed clinical skills and experience through generations of accumulated knowledge. Clinically useful, predictive radiomic properties must be clearly linked to meaningful biologic characteristics and qualitative imaging properties familiar to radiologists. Radiomics and radiogenomics incorporates several important disciplines, including radiology (imaging interpretation), computer vision (quantitative feature extraction) and machine learning (classifier evaluation) (2).

Materials and Methods

We provide a practical approach for radiologists to undertake radiomic and radiogenomic studies. The process (Fig. 1) outlines the preliminary steps of: selection of imaging data, pseudonymization, normalisation, registration and tumour segmentation. This is followed by extraction of quantitative intensity, texture, shape and wavelet-based features. Machine-learning analysis of radiomic, genomic, clinical data and multiparametric MRI data is performed, involving feature selection and classification. The trained classifier model then requires testing on an independent dataset for validation (3).

Results

After potential radiomic imaging biomarkers have been identified, radiologists should attempt to correlate with other conventional imaging features and physiological/metabolic information from multiparametric

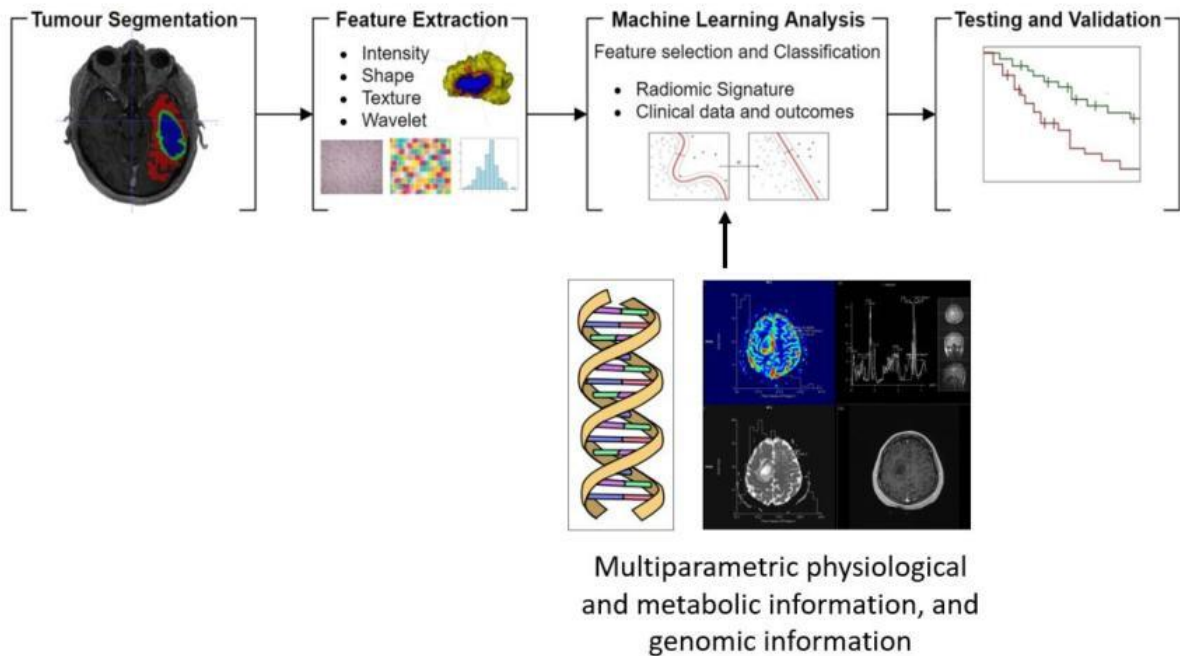
Education Exhibits

MRI, and explain the findings with biological features of disease. This is an important step in the process of radiomic biomarker validation. This newly developing field should form a part of the Radiology Training Programmes.

Conclusions

Through the convergence of radiology, computer vision and machine learning techniques, radiomics provides a mechanism for a multidisciplinary approach in neuroimaging. When radiomic models align well with disease biology, then only radiomic findings maximize their likelihood for clinical utility. Without this, there is the risk of drowning into the plethora of clinically unsupervised informatics.

Image 1. Outline of processes involved in Radiomic and Radiogenomic studies. The complete picture involves the amalgamation of conventional imaging, computer extracted features, physiological and biological features, genomics and clinical data.



(Filename: TCT_EdE-59_Capture.JPG)

EdE-60

None of your Business! Billing in Neuroradiology

A Wyckoff¹, T O'Neill¹

¹UT Southwestern, Dallas, TX

Purpose

Review billing for imaging studies, with an emphasis on MRIs in neuroradiology. Discuss the basics of inpatient and outpatient billing and the conditions to make a claim, Current Procedural Terminology (CPT) codes and their relationship with International Classification of Diseases (ICD) codes, and requirements and qualifiers for MRI exams.

Materials and Methods

Review provided and suggested resources for billing outlined by the American Medical Association (AMA) and Centers for Medicare and Medicaid Services (CMS). Provide hands-on background from

Education Exhibits

medical billers with pearls and pitfalls commonly seen in the billing of neuroradiology imaging studies. Review historical trends in neuroradiology billing and potential challenges for the future.

Results

Billing in radiology is a complex system which is often ignored in training. Knowledge of this system will aid the practicing radiologist in crafting their reports, establishing protocols, and properly directing referring physicians on appropriate orders to place, in order to maximize the payment for work performed and minimize rejected claims. With this understanding, the neuroradiologist is equipped with ways to keep up to date and take a proactive role in their practice.

Conclusions

Understanding radiology billing is a useful knowledge set for any practicing radiologist.

Education Exhibits-Interventional

EdE-61

Current Guidelines and Novel Techniques in the Prevention/Treatment of Spinal Cord Ischemia (SCI) as a Consequence of Thoracic Endovascular Aortic Repair (TEVAR)

J Kang¹, H Dermendjian¹, C Lam¹

¹*Kaiser Permanente Los Angeles Medical Center, Los Angeles, CA*

Purpose

We will illustrate the protocols in spinal drain management for spinal cord ischemia (SCI) in patients undergoing thoracic endovascular aortic repair (TEVAR) through several cases we have encountered at our institution. Additionally, we will discuss advanced techniques that are in the pipeline that can be used as adjuncts for monitoring and preventing spinal cord ischemia. Innovative techniques such as minimally invasive segmental artery coil embolization (MACES) and near-infrared spectroscopy of collateral networks (CnNIRS) have shown promise in recent studies.

Materials and Methods

The major aims of SCI prevention include optimization of spinal cord perfusion, decreasing oxygen demands, early detection of neurologic deficits, and increasing mean arterial pressure (MAP).

Results

The incidence of SCI in patients who undergo TEVAR is reported to be up to 14%. Spinal drains in high-risk individuals have shown to reduce incidence of SCI in open thoracoabdominal aortic repair. High risk patients demonstrate > 20 cm coverage of the aorta, prior abdominal aortic aneurysm repair including embolization of the hypogastric arteries, and/or coverage of the left subclavian artery without revascularization. Target spinal pressure may vary by institution, but often range from below 8 mmHg to 12 mmHg. A MAP target of 90 mmHg is well documented. Moreover, medications such as mannitol, corticosteroids, and naloxone, as well as induced hypothermia to 34 degrees Celsius have been described as possible neuroprotective measures. Innovative techniques such as minimally invasive segmental artery coil embolization (MACES) and near-infrared spectroscopy of collateral networks (CnNIRS) have shown promise in recent studies.

Conclusions

No randomized controlled trials evaluating the benefits of spinal drains for SCI in TEVAR have been published to date. However, this exhibit will present the most current data regarding efficacy of spinal drains in high risk patients undergoing TEVAR.

EdE-62

The Many Faces of Dural Arteriovenous Fistulas: Unmasking Them One at a Time

Z Wilseck¹, J Wilseck², A Srinivasan¹

¹*University of Michigan Health System, Ann Arbor, MI*, ²*Beaumont Hospital, Royal Oak, MI*

Purpose

Intracranial and spinal dural arteriovenous fistula (DAVF) can have variable presentations and clinical symptoms related to lesion location and pattern of venous drainage. The goals of this educational exhibit are to briefly discuss the classification systems for intracranial and spinal DAVFs and highlight imaging features as well as strengths and weaknesses of CT and MR while correlating with angiographic findings based on individual cases. Additionally, management options and outcomes will be discussed.

Materials and Methods

This exhibit will begin with an overview of commonly used classification systems including the Borden and Cognard classification systems. Additionally angiographic examples will be provided with classification grading and the relation to morbidity and mortality. In the next part of the exhibit, imaging examples will be presented of both intracranial and spinal DAVFs focusing on cases with atypical noninvasive imaging findings. The angiographic correlation for these cases will also be shown. Finally, relevant scientific literature will be cited and discussed regarding endovascular treatment options. The modalities that will be discussed will include CT, MRI, MR angiography, MR venography, and catheter angiography.

Results

The diagnosis of intracranial or spinal dural arteriovenous fistulae can be difficult based on clinical symptomatology and initial non-invasive imaging findings. The radiologist must be aware of the limitations of noninvasive imaging in addition to the expected imaging findings, e.g. presence of venous signal on a time of flight MRA can be the only clue towards a DAVF. While the diagnosis of DAVFs can be based upon MR, for complete understanding of the disease as well as therapeutic planning, digital subtraction angiography is necessary. In this exhibit, imaging pearls and pitfalls will be discussed using case examples. This will provide the readers of the educational exhibit with many practical tools in the approach to DAVF diagnosis and management.

Conclusions

Following the review of this exhibit, the reader will gain an increased understanding of the "many faces" of dural arteriovenous fistulae including typical and atypical imaging findings, classification systems, and treatment options.

Education Exhibits-Pediatrics

EdE-69

A Pictorial Review of Pediatric Posterior Fossa Tumors with Molecular Radiological Correlation According to New Classification.

S Culleton¹, J Davila², F D'Arco³

¹*National Hospital for Neurology and Neurosurgery, London, United Kingdom*, ²*University of Ottawa, Ottawa, Ontario, Canada*, ³*Great Ormond Street Hospital for Children, London, United Kingdom*

Purpose

To produce a pictorial essay based on the main radiological-pathological correlations in posterior fossa pediatric tumors based on the most recent WHO classification (2016). The combination of molecular data

Education Exhibits

and imaging characteristics will introduce new tumoral entities that may benefit from alternative treatments to improve outcome. Changing the role of the radiologists as much as the pathologist in the next decade.

Materials and Methods

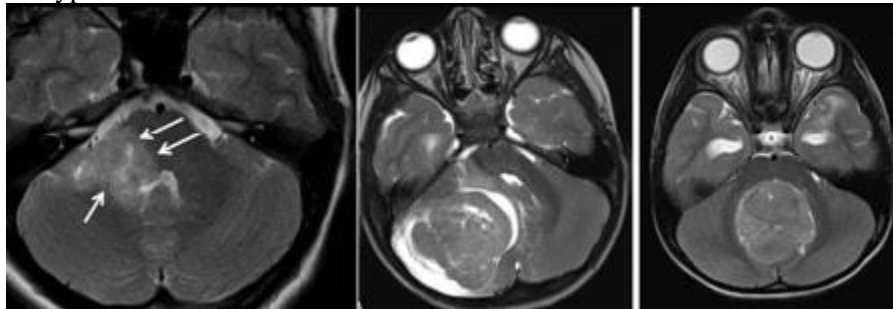
We reviewed pediatric posterior fossa tumors with molecular diagnosis and described main radiological features that allow differentiating them in their respective subtype.

Results

The leading cause of death from solid tumours in children are brain tumours (1-3). The posterior fossa tumours are divided in embryonal and non-embryonal tumors. Main embryonal tumors are medulloblastomas, divided in four main molecular groups (but several subgroups are already being described): WNT, SHH, group 3 and group 4 all with different imaging characteristics (Figure 1). Other embryonal tumors included ATRT and ETMR. Figure 1 shows the different locations described in different types of medulloblastomas. On the left WNT in the ponto-cerebellar angle (arrows), in the middle SHH in peripheral location and on the right a group 3/4 in the midline (i.e. fourth ventricle). Nonembryonal tumors include pilocytic astrocytoma, posterior fossa ependymoma and diffuse midline gliomas (formerly DIPG). Specific imaging features, pitfalls and pearls for differential diagnosis are analyzed.

Conclusions

Our data shows that MRI can be used as a surrogate for molecular diagnosis in the classification of tumors according to 2016 WHO classification. The key findings of both histological and molecular subtypes contribute to this differentiation.



(Filename: TCT_EdE-69_Postfossa.jpg)

EdE-67

Approach to Pediatric Face and Neck Masses

M Ho¹, S Cofer¹, K Balakrishnan¹

¹Mayo Clinic, Rochester, MN

Purpose

1. Develop a systematic framework for assessment of pediatric face and neck masses 2. Integrate basic science and technical concepts in evaluation of pediatric HN 3. Review diagnostic categories of pediatric HN masses, using a case-based approach

Materials and Methods

Approach to the pediatric face/neck mass should include the "5 W's": Age (who/when), Location (where), Composition (what), and Syndromes (why/how). Imaging modalities that can be used for lesion characterization include MR, US, CT, nuclear medicine, and angiography. We will discuss clinical-radiologic features, pathophysiology, and differentials across the spectrum of diagnostic categories: congenital, vascular, inflammatory, soft tissue and bone lesions.

Results

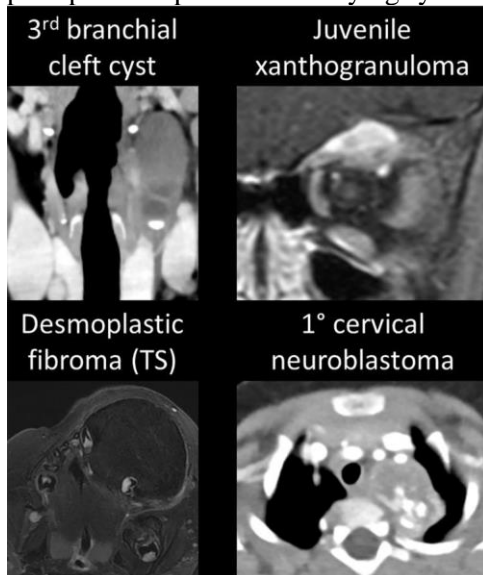
Congenital: Midface: dermal sinus tract, glial heterotopia, sincipital encephalocele Dermal:

Education Exhibits

pilomatricoma, inclusion cyst, abnormal pigmentation/vasculature Branchial arches Embryology and classification, type 1-4 Branchial pouches Thymus: 3rd pouch → thymopharyngeal duct cyst, cervical thymus Parathyroid: 3rd inferior/4th superior → cystic adenoma Thyroid: 4th pouch → suprahyoid, hyoid, infrahyoid TGDC Vascular: Vascular malformations Low-flow syndromes: lymphatic (generalized lymphatic anomaly), venous (blue rubber bleb nevus), capillary (megalencephaly-capillary malformation) High-flow syndromes: HHT, CM-AVM, Wyburn-Mason Vascular tumors Benign: congenital vs. infantile hemangioma, syndromes (hemangiomatosis and PHACES) Borderline: JNA, Kaposiform hemangioendothelioma Inflammatory: Inflammatory: parotitis, dacryocystitis (LADD syndrome), ranula Autoimmune: IgG4, LCH, Sjögren Soft Tissue: Paragangliomas: SDH mutations and neuroendocrine syndromes (NF1, VHL, MEN) Nerve sheath tumors: NF1 (neurofibromas and optic gliomas), NF2 (vestibular schwannomas), NF3 (plexiform schwannomas and rhabdoid tumors) Fibrous lesions: fibromatosis colli, myofibromatosis, leiomyoma, tuberous sclerosis (desmoplastic and nuchal fibromas), Gardner syndrome (desmoid tumors and osteomas) Fat-containing: lipomatosis, lipoblastoma, liposarcoma, teratoma Malignant: sarcomas, neuroblastic tumors (primary vs. secondary), lymphoma (nodal vs. extranodal) Bone: Key features = matrix, zone of transition, periosteal reaction Jaw: cherubism, keratocystic odontogenic tumor (Gorlin syndrome), giant cell granuloma, LCH Skull: leptomeningeal cyst, LCH, Ewing sarcoma Spine: chordoma, aneurysmal bone cyst, osteoid osteoma

Conclusions

1. Evaluation of the pediatric HN mass includes patient age, location, and composition 2. Genetics and embryology provide a framework for understanding pediatric HN pathology 3. Specific lesions can prompt workup for an underlying syndrome



(Filename: TCT_EdE-67_Face-neck.jpg)

EdE-65

Congenital Brain Anomalies: Easy as 1-2-3

M Ho¹

¹Mayo Clinic, Rochester, MN

Purpose

1. Discuss fundamental concepts of brain development 2. Demonstrate key imaging features of various brain malformations 3. Utilize a simplified diagnostic approach for rapid assessment and classification

Education Exhibits

Materials and Methods

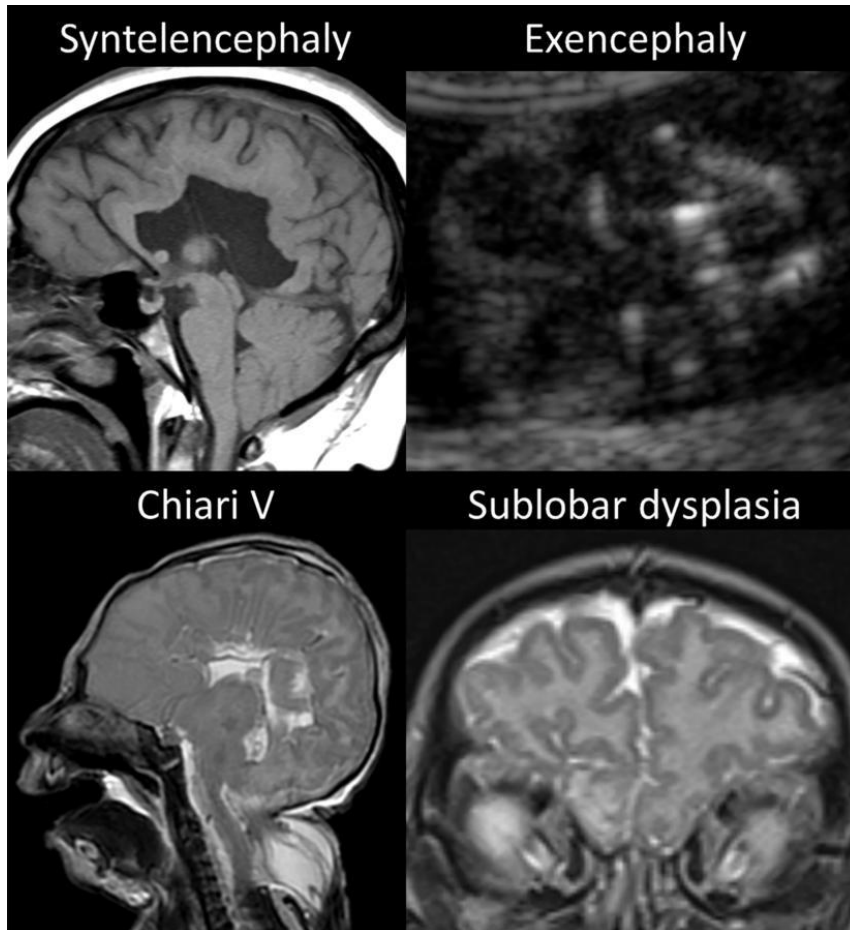
We will review key steps in brain embryology and propose a simplified classification for congenital malformations: (1) formation, (2) destruction, and (3) migration. Multiple radiologic examples will be presented, with correlation of pathogenesis and neuroimaging features.

Results

Part 1: Formation: Midline commissures - Corpus callosum, anterior, posterior, hippocampal, habenular
Callosal dysgenesis - Colpocephaly, Probst and sigmoid bundles Septo-optic dysplasia - Partial, complete, plus Holoprosencephaly - Lobar, semilobar, alobar, middle interhemispheric Chiari malformations - Type 0-5 Dandy-Walker spectrum - D-W malformation, variant, mega cisterna magna, Blake pouch cyst Joubert syndrome - DTI and related syndromes Rhombencephalosynapsis Part 2: Destruction: Acrania - exencephaly - anencephaly sequence Schizencephaly - 1st trimester, closed vs. open-lip Porencephaly - 2nd trimester, minimal astrogliosis Hydranencephaly Maximal hydrocephalus Encephalomalacia - 3rd trimester and postnatal Part 3: Migration: Gray-matter heterotopia - Periventricular/subependymal, subcortical/columnar, band, leptomeningeal Lissencephaly - Type I (classic): Undermigration, agyria/pachygyria variants - Type II (cobblestone): Overmigration, congenital muscular dystrophy Polymicrogyria - Late migration/early cortical organization - Diverse etiologies, morphologies Focal cortical dysplasia - ILAE classification (I-III) Megalencephaly Sublobar dysplasia Compound dysplasias

Conclusions

Congenital brain anomalies can be classified into abnormalities of (1) formation, (2) destruction, and (3) migration. Knowledge of key imaging features and embryologic principles aids in evaluation of complex brain malformations.



(Filename: TCT_EdE-65_Congenitalbrain.jpg)

EdE-64

Magnetic Resonance Imaging of Pediatric CNS Infections

S Kralik¹, N Supakul¹, N Nelson¹, R Radhakrishnan¹, I Wu¹, C Ho¹

¹*Indiana University, Indianapolis, IN*

Purpose

Pediatric central nervous system (CNS) infections can result in significant neurological injury. The purpose of this educational exhibit is to demonstrate the radiological findings and complications caused by pediatric CNS infections.

Materials and Methods

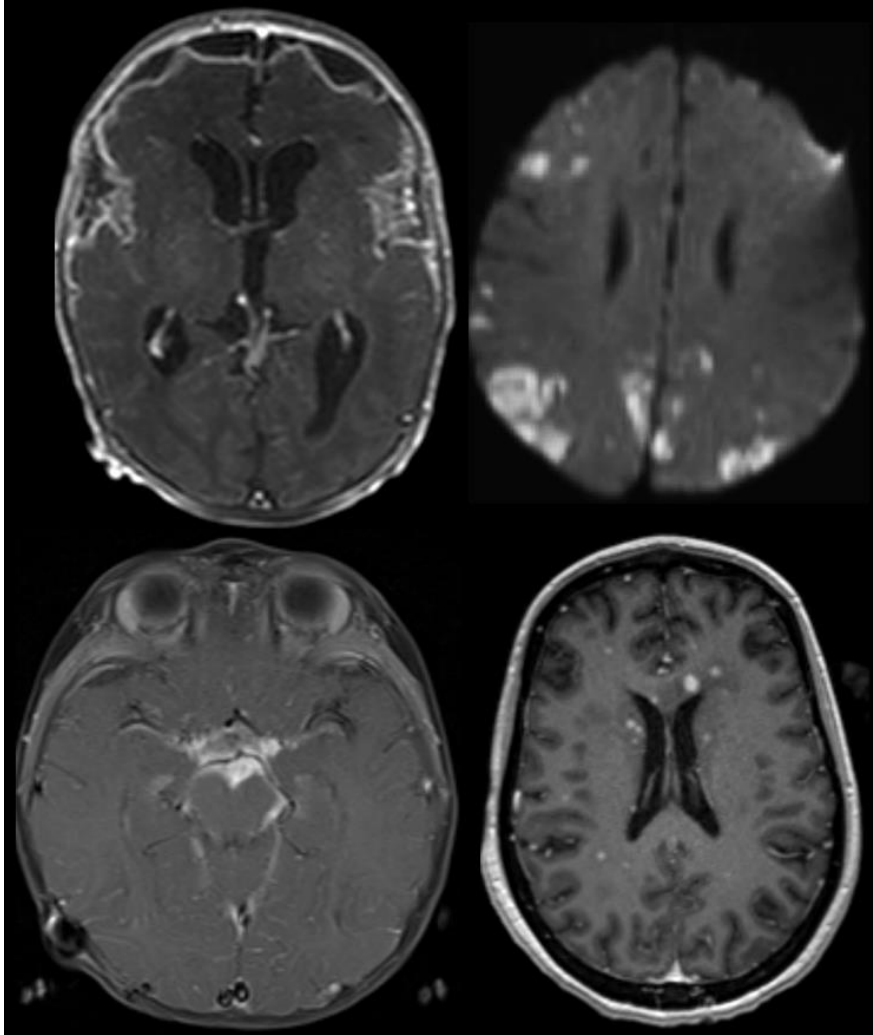
A radiology database search and review of the electronic medical record will be performed to identify pediatric patients (age <18) with clinical confirmation of a specific CNS infection. We will present common and uncommon MRI patterns, findings, and complications caused by CNS bacterial, viral, and atypical infections to demonstrate differences between these broad infectious groups. When appropriate, we will discuss whether specific CNS infections are more prevalent in different pediatric age groups, and highlight potential sources of the CNS infection.

Results

Pediatric CNS bacterial infections lead to MRI findings and complications that are not specific to a particular pathogen but may include leptomenigeal enhancement, cytotoxic edema, hemorrhage, empyema, abscess, ventriculitis, sinus thrombosis, hydrocephalus, and vasculitis. Bacterial pathogens differ between neonates and older children. Pediatric CNS viral infections lead to MRI findings that are dependent on the pathogen and age at time of infection. Several of the MRI findings seen with bacterial infections are uncommon with viral infections. In utero TORCH infection may lead to brain malformations and parenchymal calcifications. Herpes Simplex virus (HSV) type 2 infection may lead to neonatal infection and demonstrate multifocal areas of cytotoxic edema, hemorrhage, and vasculitis. In older children, Enteroviruses and arboviruses constitute the majority of causes of viral encephalitis and MRI findings include parenchymal T2 signal hyperintensity in the brainstem, cerebellum and cervical spinal cord. Influenza and West Nile viruses may manifest with symmetric edema in the thalami, while other viral infections may not have abnormalities detectable with MRI. Atypical CNS infections include fungal, mycobacterial, parasitic and amoebic infections and demonstrate MRI findings more similar to bacterial infections. Potential clues of an atypical infection include basilar leptomenigeal enhancement with tuberculosis, microabscesses with Candida infection, and hemorrhage and infarcts with Aspergillus. Lastly, pediatric CNS infections may be secondary acute sinusitis, otomastoiditis, and ventricular shunt infection. This may lead to surgical interventions to assist in treatment of infection. Importantly, a normal MRI does not exclude a CNS infection and cerebrospinal fluid remains essential for determination of the diagnosis, however, MRI demonstrates the extent of injury and complications from the CNS infection.

Conclusions

Pediatric CNS infections can lead to significant neurologic injury. MRI is the modality of choice in the evaluation of pediatric CNS infections. Although a normal MRI does not exclude a CNS infection, MRI is helpful for assessing the extent of injury, potential source of infection, and need for surgical intervention.



(Filename: TCT_EdE-64_ASNRCNSinfection.jpg)

EdE-68

Neonatal Brain Imaging: Pearls and Pitfalls

M Ho¹

¹Mayo Clinic, Rochester, MN

Purpose

1. Understand applications of various imaging modalities in neonatal brain injury 2. Develop an organized approach to neonatal brain MRI interpretation, with appropriate clinical-imaging correlation and utilization of advanced techniques 3. Distinguish patterns of injury in preterm vs. term neonates, and recognize more complex imaging features requiring additional workup

Materials and Methods

We will discuss the utility of various imaging modalities in neonates (US, CT, MR) and protocol considerations, including scan timing and potential risks of sedation, anesthesia, and gadolinium contrast administration. Following review of the normal neonatal brain, we will investigate the distinct pathophysiology, grading systems, and temporal imaging findings of preterm and term brain injury. More

Education Exhibits

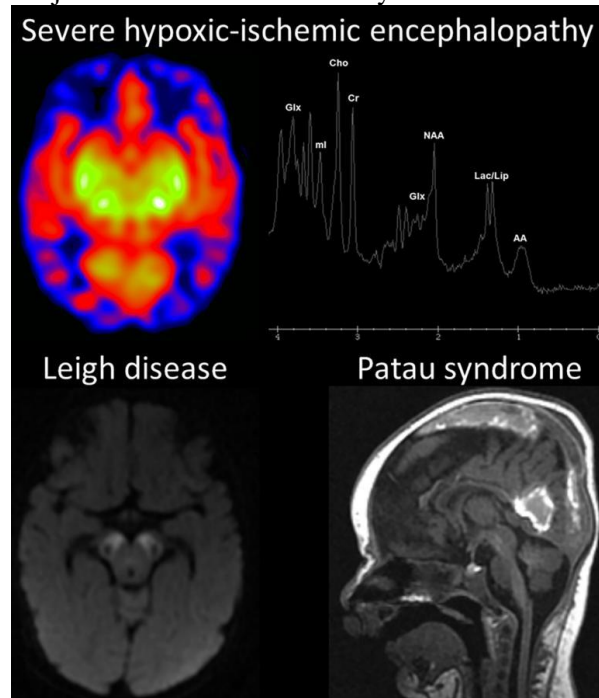
complex etiologies will be presented with clinical-imaging correlation: congenital, infectious, metabolic, migrational, genetic, neoplastic, and traumatic.

Results

Imaging Considerations: - Modalities: NIRS, US, CT, MR - Protocols: feed and swaddle, sedation, anesthesia, gadolinium - Timing of examination: ASAP after injury, F/U at or near-term Normal Neonatal Brain: - DWI: selection of b-value - T1/T2: myelination in PLIC and CST - Arterial spin labeling: mild relative hyperperfusion of CST and BG - MR spectroscopy: short vs. long TE, increasing NAA:Cho, mild Lac < 37 wks Preterm Brain Injury: - Classification: extremely, very, moderate, late preterm - Immature neuroglial tissue, hemodynamic compromise, impaired neurodevelopment US and MRI cases with follow-up - Injury scoring: intraventricular hemorrhage (1-4), white matter injury (1-3), ventriculomegaly (1-3), cerebellar hemorrhage (1-3) Term Brain Injury: - Hypoxic-ischemic encephalopathy: disrupted autoregulation, postanoxic hyperperfusion and secondary metabolic cascade, role of therapeutic hypothermia US and MRI cases with follow-up - Patterns (focal/multifocal, watershed, basal ganglia) and scoring (mild-severe) - Role of ASL (postanoxic hyperperfusion) and MRS (metabolic disruption) - Medullary and cortical vein thrombosis - Ulegyria, "Swiss cheese" brain Complex Cases: Congenital malformations (with fetal correlation) - Chiari II with absent corpus callosum - Dandy-Walker malformation - Vein of Galen malformation - Focal cortical dysplasia IIIc - Polymicrogyria - Syndromic craniosynostosis Infection - Prenatal (TORCH) - Postnatal sepsis Metabolic - Kernicterus - Hypoglycemia - Hyperammonemia - Leigh disease Genetic - Trisomy 13 (Patau) - Trisomy 18 (Edwards) - Oral-facial-digital syndrome - Megalencephaly-capillary malformation - Pontine tegmental cap dysplasia - Linear sebaceous nevus - Median cleft face syndrome Neoplasia - Desmoplastic infantile ganglioglioma - Desmoplastic infantile astrocytoma Trauma - Fetal demise (Spalding sign) - Accidental: ping-pong fracture, leptomenigeal cyst - Stellate fracture

Conclusions

Neonatal imaging modalities and protocol considerations should be tailored to the individual patient. Patterns of injury are highly influenced by gestational age, perinatal history, and scan timing. Brain MRI and advanced sequences aid in patient prognosis and management, and should be evaluated in conjunction with clinical history and labs.



(Filename: TCT_EdE-68_Neonatal.jpg)

EdE-66

New Pediatric Neuroimaging Applications

M Ho¹, N Campeau¹, A Lu¹, J Huston¹, K Welker¹

¹Mayo Clinic, Rochester, MN

Purpose

1. Review principles of cutting-edge anatomic and functional imaging techniques 2. Demonstrate targeted applications of advanced techniques in pediatric neuroimaging 3. Discuss opportunities for implementation in daily clinical practice

Materials and Methods

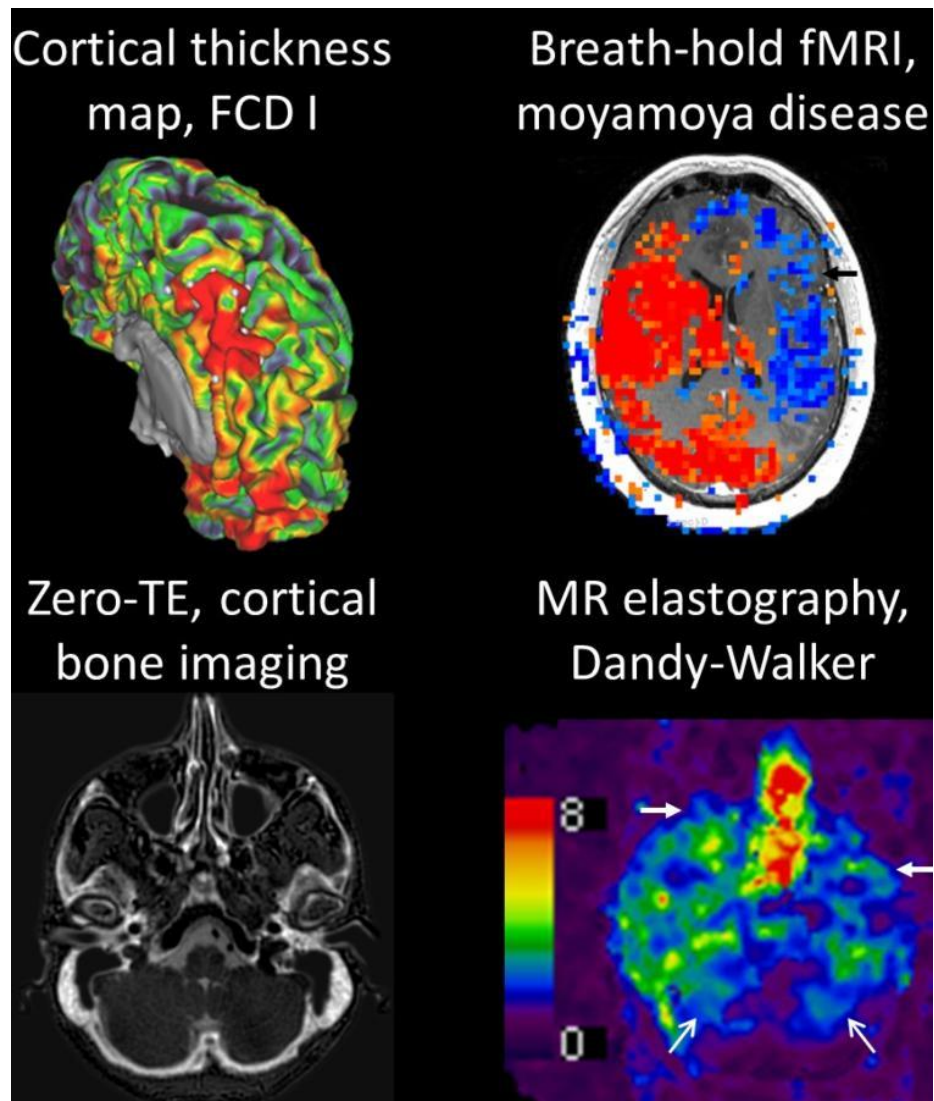
In recent years, a vast array of advanced MRI techniques have become available for clinical utilization in various categories: anatomic, diffusion, perfusion, vascular, functional, and metabolic. Through an intensive case-based review, we will demonstrate the added value of advanced sequences in pediatric neuroimaging. Numerous examples of integrated applications will be provided in the following diagnostic categories: vascular/ischemia, epilepsy/migrational, head & neck, tumor, metabolic, and trauma.

Results

Vascular/Schemia: Perfusion techniques: ASL, DSC, DCE - Neonatal brain injury: preterm vs. term - Acute ischemia: tissue at risk, dissection, focal cerebral arteriopathy - Vasculopathy, moyamoya: breath-hold BOLD for cerebrovascular reserve - Autoregulation and vascular steal - Vascular malformations: hyperperfusion and steal MRA techniques: time-of-flight, phase-contrast, time-resolved, bolus Dual-energy CT: bone subtraction Epilepsy/Migrational: Presurgical epilepsy workup - DIR, ASL, DTI, SISCOM, PET-MRI, ZTE - Cortical malformations and encephaloceles fMRI: cortical reorganization (neuroplasticity) DTI: structural connectivity, congenital brain malformations - Callosal dysgenesis, Joubert, cerebellar dysgenesis MEG: seizure focus propagation and eloquent mapping Clinical 7T and small-bore 3T: high-performance gradients Head and Neck: PET-CT/MRI - HN cancer, whole-body staging Zero-TE - Cortical bone imaging for craniostyostosis, skull base, spine MR elastography - Meningioma, pituitary adenoma, hydrocephalus Phase-contrast - 2-D CSF flow, 3-D vascular imaging 3-D printing/modeling - Craniofacial and skull base surgery DCE-MRI - Transplant vascularity, tumor recurrence Tumor: Supratentorial/infratentorial cases Presurgical mapping - DTI, fMRI, MEG Tumor recurrence - Perfusion and MRS Multinuclear MRI - Na-23: ion homeostasis - P-31: energetics Metabolic: Spectroscopy + anatomic/perfusion findings Metabolic - Mitochondrial, lysosomal, peroxisomal cases Toxic - Acute serotonin syndrome, chronic methylbromide poisoning Trauma: Brain trauma: nonaccidental, accidental, DAI - Perfusion, cortical bone imaging, microstructure Dual-energy CT - Metal artifact reduction Spine tractography - Brachial plexus avulsion, penetrating cord trauma

Conclusions

1. Gaining technical understanding is key to appropriate utilization of advanced techniques 2. Thoughtful integrated protocoling helps maximize imaging yield and efficiency 3. Awareness of emerging technologies will increase opportunities for translation into daily practice



(Filename: TCT_EdE-66_Newtechniques.jpg)

EdE-63

Trasversal and Longitudinal Brain MRI Findings in Infantile Pompe Disease Patients

C Cinnante¹, S Calloni², A Pichiecchio³, F Arrigoni⁴, D Stocchetti⁵, L Lombardi⁵, F Triulzi⁵
¹Fondazione Irccs Ca Granda Ospedale Maggiore Policlinico Milano, Milano, Italy, ²University of Milan, Milan, Italy, ³C. Mondino National Neurological Institute, Pavia, Italy, ⁴Scientific Institute, IRCCS Eugenio Medea, Bosisio Parini, Lecco, Italy, ⁵Ospedale Maggiore Policlinico IRCCS Ca' Granda, Milan, Italy

Purpose

Infantile Pompe Disease (IPD) is a progressive autosomal-recessive disorder caused by a deficiency of the lysosomal enzyme acid alpha-glucosidase (GAA). Pathology studies reported glycogen deposition in the central nervous system. Enzyme replacement therapy (ERT) is the first treatment for IPD. A specific pattern of recognition at MR imaging is still lacking. Our aim is to evaluate the trasversal and longitudinal brain Magnetic Resonance Imaging (MRI) findings in IPD patients treated with ERT.

Education Exhibits

Materials and Methods

Four patients were included in the study (nine MRI, mean age 5.5 years). Conventional brain images were acquired on a 1.5 Tesla Philips scanner; two exams had spectroscopy. A qualitative evaluation of the MR images was made in consensus by two neuroradiologists. Two patients had a longitudinal assessment.

Results

Perinatal MRI (one patient) was unremarkable. MRI of all patients acquired at the same age (3-4 years) showed a diffuse signal alteration of the fronto-parietal periventricular white matter, with sparing of the U-fibers. MRI acquired at subsequent ages (six, eleven and fourteen years, one patient) showed a marked progression of the disease, with appearance of microcysts at the level of the white matter bilaterally, involvement of the external, internal capsulae and the brainstem. Spectroscopy showed a mild decrease of N-Acetyl-Aspartate (NAA). One patients had multiple nodules of heterotopia with epilepsy and mild cognitive impairment. Neurodevelopment assessment was unremarkable for the other two patients.

Conclusions

Brain involvement in IPD is still under acknowledged. Our evaluation demonstrated an extensive white matter involvement, with no significant cognitive decline, thus suggesting that this alteration can be considered not the epiphenomena of a delayed myelination but the result of the glycogen deposition in the microglia. The longitudinal assessment at disposal suggests that a progression of the brain disease may occur despite the treatment.

Education Exhibits-Spine

EdE-72

So Everybody Saw the Fracture. Now What Should the Radiologist Mention in the MRI Report to Make It More Useful?

R Bordia¹, A Ortiz¹

¹*New York University Winthrop Hospital, Mineola, NY*

Purpose

To provide a checklist of features of vertebral compression fractures (VCFs) on MRI that should be reported by radiologists in order to help guide planning of vertebral augmentation procedures.

Materials and Methods

A retrospective review of 40 consecutive MR lumbar spine images was performed by one spine interventional radiologist and one neuroradiologist. Several features of VCFs were identified which are relevant for planning vertebral augmentation procedures.

Results

The following is a checklist of features of VCFs that should be addressed in MRI reports: I. Basic radiology principles a. Clinical history b. Use of prior imaging for comparison c. Number of fractures d. Fracture level(s) and the numbering system used (counting from C2 or L5-S1) II. Overview of the fracture level a. Fracture morphology (wedge, impaction, biconcave) b. Height loss (mild, moderate, severe or % loss of height) c. Kyphosis III. Specific fracture details a. Fracture edema b. Presence of cleft c. Fracture lines (location, orientation, extent) d. Vertebral endplate status IV. Adjacent structures a. Evidence of intervertebral disk injury b. Posterior element injury c. Status of spinal canal d. Paraspinal soft tissue edema

Conclusions

It is not sufficient to simply report the presence or absence of VCFs. A complete description of the fracture pattern and its impact on adjacent structures is necessary to make the MRI reports useful for treatment planning.

Education Exhibits

EdE-71

Spinal Manifestations of Multiple Myeloma on MRI: An Imaging Review of Active, Progressive, and Treated Disease.

M Hanna¹, X Chin¹, B Parnes², A Arneja¹, A Aggarwal¹, A Doshi¹

¹*Icahn School of Medicine at Mount Sinai, New York, NY*, ²*Suny Downstate, Brooklyn, NY*

Purpose

Multiple myeloma (MM) accounts for 1% of all cancers and 10% of all hematological malignancies. It is the most common primary malignant bone neoplasm in adults. Various imaging techniques have been utilized in the evaluation of multiple myeloma including plain radiographs, CT, PET/CT, and MRI. Advanced techniques using whole-body diffusion MRI (DWIBS) and diffusion-weighted imaging (DWI) have led to further refinement of staging in multiple myeloma, providing greater clinical impact.

Materials and Methods

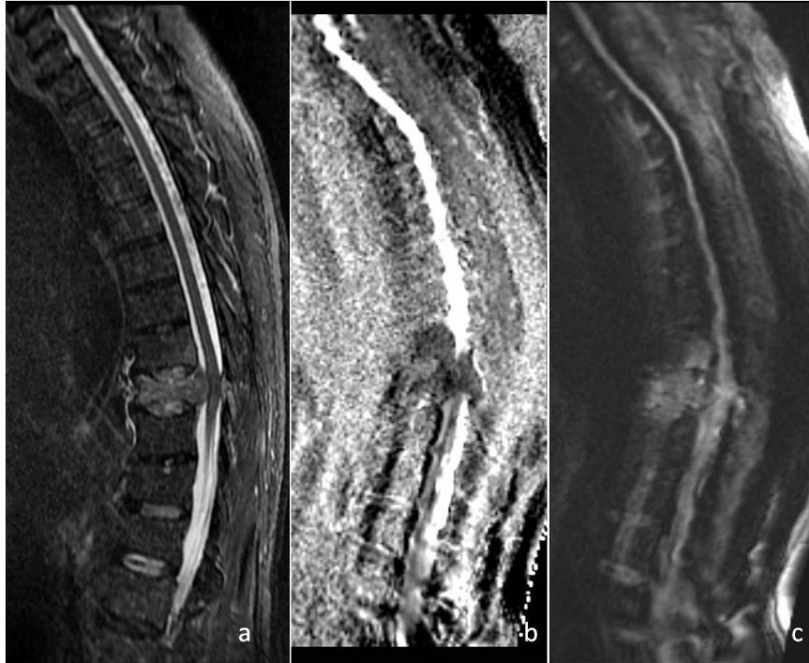
The education exhibit will focus on various manifestation of spinal disease in patients with multiple myeloma. This review will include examples of vertebral marrow changes, focal spinal lesions, pathologic compression fractures, and extravertebral myelomatous involvement. A comprehensive review of imaging findings on CT, PET, and MRI will be presented as well as review of DWI in the evaluation of the spine. In particular, the exhibit will discuss the utility of imaging and DWIBS/DWI in the evaluation of treated, active and progressive myelomatous disease.

Results

Spinal involvement is common in patients with multiple myeloma. Several imaging modalities are currently utilized to evaluate burden of disease and assess for treatment response or activity of disease. The knowledge of common and uncommon imaging manifestation of spinal myelomatous disease on CT, PET, and MRI can allow the radiologist to better evaluate disease burden and activity. DWIBS/DWI evaluation has demonstrated a role in the evaluation of multiple myeloma as it can provide a marker of lesion cellularity in the post treatment setting when morphologic marrow signal changes persist.

Conclusions

Multiple myeloma is a common malignancy affecting the bone marrow. Imaging plays an important role in the evaluation of this disease and knowledge and understanding of the imaging manifestation on various modalities including DWI is helpful in evaluation of disease burden, activity, treatment, and progression.



MRI Thoracic Spine with contrast

a. Sagittal STIR b. Sagittal ADC c. Sagittal DWI; Extensive tumor replacement of the T9 vertebral body with epidural extension and flattening of the cord. The mass demonstrates restricted diffusion suggesting active disease.

(Filename: TCT_EdE-71_MultipleMyelomaASNR121517.jpg)

EdE-70

Utility of Diffusion-weighted MRI in Evaluation of Spinal Metastases

A Chaudhry¹

¹*Johns Hopkins Medicine, Stevensons Ranch, CA*

Purpose

Radiologist frequently encounter tumor and tumor-like lesions as incidental findings on spine MRIs. These can result from a number of processes which can be benign or malignant. Deciphering between the two can be challenging and is critical for patient care as miss of a malignant lesion can prove to be fatal. This educational exhibit will be a case-based presentation of common and uncommon causes of benign and malignant processes that result in lytic and/or sclerotic lesions in the skeletal system on CT and have variable appearance on routine T1 and T2 sequences. We will focus on the utility of diffusion-weighted imaging in these cases in deciphering benign from malignant lesion.

Materials and Methods

1. Case-based presentation will include clinical features, key imaging findings, radiology-pathology correlation, treatment and prognosis of common and uncommon causes of benign and malignant spinal column neoplasms. 2. Case examples include: Fibrous dysplasia, enchondroma, chondrosarcoma, sarcoma, lymphoma, metastasis (carcinoid, prostate, lung, melanoma, etc). 3. Chart of salient features for quick reference.

Results

1. Review physics of diffusion-weighted imaging (B-values: 50, 400, and 800 s/mm²) with ADC

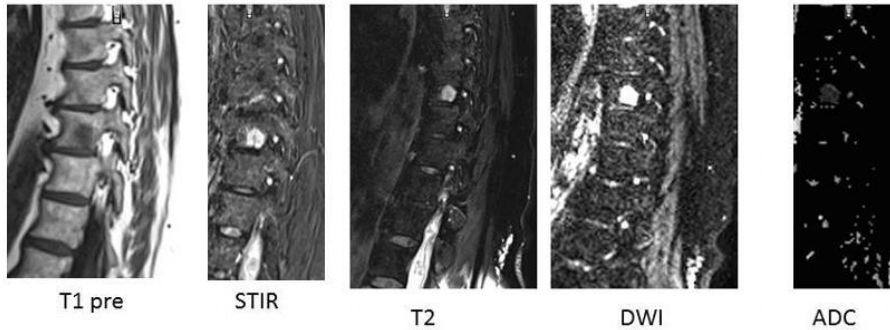
Education Exhibits

mapping 2. Review imaging findings of various spinal tumors 3. Discuss limitations and pitfalls of diffusion-weighted imaging in the musculoskeletal system

Conclusions

Osseous spinal tumors frequently are encountered incidentally on radiologic imaging and nonspecific imaging findings cause a diagnostic dilemma. Being familiar with discriminating imaging findings including diffusion-weighted imaging (DWI) can help characterize a tumor as benign or malignant thus assisting radiologists in guiding clinical management of the lesion.

Case: 59 year old male with worsening back pain, history of CKD



- Unable to give contrast due to low GFR.
- T1 hypo, T2 hyperintense lesion, with restricted diffusion; highly suggestive of neoplasm. Biopsy confirmed metastatic renal cell carcinoma

(Filename: TCT_EdE-70_diffusioncase.jpg)

Electronic Educational Exhibits-Adult Brain

eEde-093

"Journey to the Center of the Senses": Neuronanatomy of Auditory, Visual and Oculomotor Nuclei and Tracts by In Vivo and Post Mortem 7T Images and Histology

R Moreno¹, M Martin², W Rodrigues Fernandes³, L Fajardo², J Takahashi², E Amaro⁴, H Heinsein⁵, A Alho^{N/A}, L Lucato², C Leite⁵

¹Hospital das Clínicas da FM-USP, Sao Paulo, Brazil, ²Instituto de Radiologia do HC-FMUSP, Sao Paulo, Brazil, ³Fleury Medicina e Saúde, São Paulo, Brazil, ⁴Faculdade de Medicina da Universidade de São Paulo, Brazil, ⁵University of São Paulo, São Paulo, Brazil

Purpose

1. Illustrate, detail and nominate auditory, visual and oculomotor nuclei and tracts based on correlation of brain autopsy with 7T MR images, on In vivo and postmortem population, with its histological analysis 2. Delineate 7T MRI accuracy based on comparison of brain autopsy and in vivo images 3. Establish 7T MRI advantages over the usual magnetic fields 4. Briefly discuss potential future uses for 7T MRI to further understand anatomic and pathological mechanisms in some central diseases compromising those systems

Materials and Methods

In this work, we employed 7 Tesla to precisely identify auditory, visual and oculomotor brainstem and diencephalus nuclei and tracts in a fixed brain. Brain processing: Upon autopsy, the brain was fixed in formalin 8%, dehydrated in a graded series of ethanol solutions and embedded in celloidin. The entire brain was serially sectioned on a microtome (Polycut, Cambridge Instruments, UK). Axial, 430- μ m-thick slices were then stained with Nissl staining and mounted as previously described by Heinsen et al.⁵ and Heinsen and Heinsen⁴. It will selectively stain DNA and RNA dark blue. MRI: 7T MRI was acquired from different subjects either in vivo or post mortem (in-situ and ex-situ). In vivo DTI - RESOLVE: 20 dir, 1.5mm thick, TR 6000, TE 72, 0.6mm in plane resolution In vivo 3DSPACE - 1.5mm thick, TR 2000, TE 113, 0.4mm in plane resolution In vivo T2 TSE - 1.5mm thick, TR 7000, TE 60, 0.4mm in plane resolution post mortem in-situ T2 TSE - 2mm thick, TR 5500, TE 9.5, 0.4mm in plane resolution post mortem in-situ SWI - 1.5mm thick, TR 23, TE 14, 0.2mm in plane resolution post mortem ex-situ - 3DGRE, 1mm thick, TR 12, TE 8, 0.4mm in plane resolution Cortex fields are illustrated by resting state functional MRI and DTI tractography. The study was approved by a local Ethics Committee (#09637112.2.0000.0065, Medical School-USP).

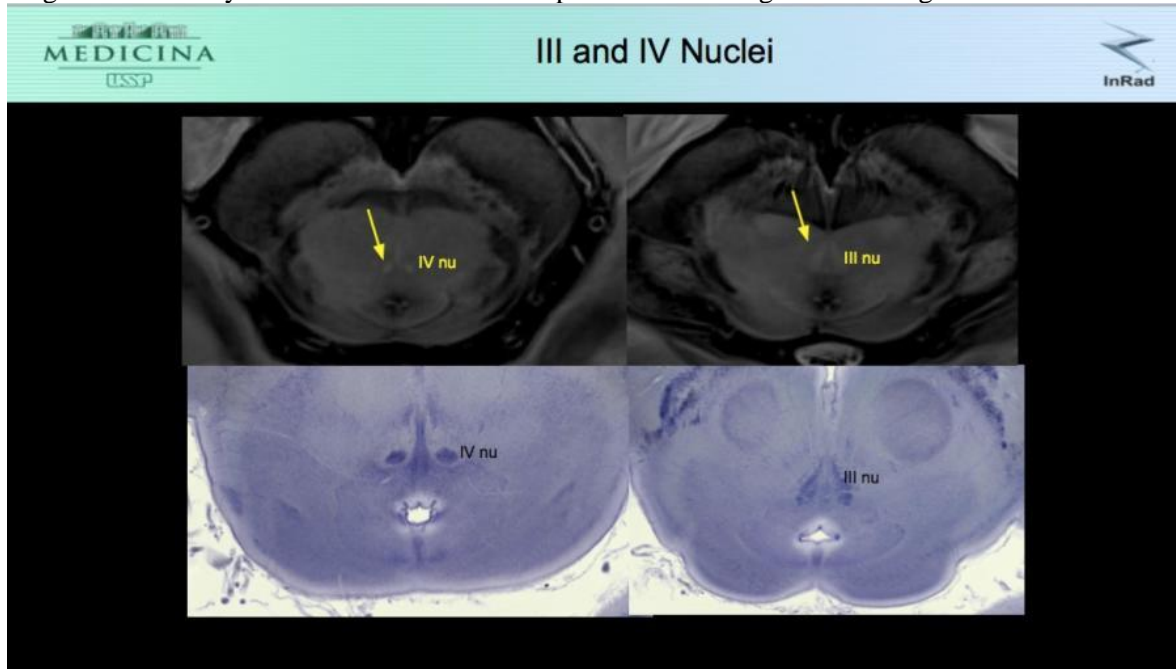
Results

Connections in the central auditory, visual and oculomotor systems are located mostly in tiny and complex structures of the brainstem and diencephalus and, also, in specific areas of cortex. Growing evidence suggest that these pathways are particularly vulnerable to many inflammatory, infectious and neurodegenerative diseases. Recent improvement of neuroimaging methods, in collaboration with another neuroscience advances, has shifted our understanding about pathogenesis of such conditions, encouraging studies to identify brainstem based biomarkers to early diagnosis. We intend to better delineate auditory, visual and oculomotor nuclei and tracts based on correlation of brain autopsy, 7T MR images, resting state functional MRI and tractography. Such understanding is essential to correctly identify initial lesions and enable a precise diagnosis for more targeted investigations and treatments.

Conclusions

Auditory, visual and oculomotor central pathways are for the majority located in tiny structures of brainstem and thalamus, as in specific cortex sites, not well accessed by conventional neuroimaging.

Advances of new techniques, as 7T MRI have the potential to better outline those structures, contributing to better understanding of pathogenesis in hearing and visual diseases, as well as improving their diagnostic accuracy. Future research should explore how to bring these findings from bench to bedside.



(Filename: TCT_eEde-093_terceiro.jpg)

eEde-021

"MR Calling for Voxel Placement": Do's and Don'ts

A Agarwal¹, R Durel², M Pinho¹, J Maldjian²

¹University of Texas Southwestern Medical Center, Dallas, TX, ²University of Texas Southwestern, Dallas, TX

Purpose

1. How to plan a MRS study and understand the affect of voxel placement, TE (echo-time) selection 2. Advantages and disadvantages of single voxel spectroscopy versus chemical shift imaging (CSI) 3. To differentiate between a good quality spectra and a suboptimal study 4. How to avoid interpretation errors

Materials and Methods
The reading room is frequently called by the MRI technical team for planning a MR spectroscopy exam. This includes voxel placement, TE selection and quality assessment. Radiology trainees (residents and fellows) are actively involved in this at most of the centers. We will use cases from our teaching file and PACS to illustrate the role and importance of these parameters. We will also use cases to highlight interpretation errors and show some good quality spectra versus suboptimal studies.

Results

The exhibit will be outlined in the following format: - Basic principles of proton spectroscopy - Planning a MRS study and data acquisition (ROI, TE) - When to use Single voxel versus 2D/3D chemical shift imaging (CSI) - Postprocessing techniques - Examples of good quality spectra and poor quality studies - Common interpretation errors by the neuroradiologist

Conclusions

This exhibit aims to provide a basic outline of the technical aspect or MR spectroscopy without entailing in depth details. Case-based approach will primarily be used to understand the basic physics behind MRS.

Electronic Educational Exhibits

eEde-088

4D Flow MRA for Assessment of Intracranial Pathologic Processes: Discussion of New Techniques and Review of Existing Techniques

W Chang¹, J Chiang¹, M Loecher¹, A Chien¹, N Kaneko¹, D Ennis¹, J Villablanca¹

¹University of California Los Angeles, Los Angeles, CA

Purpose

Four-D Flow MRA is an area of active investigation with numerous new applications that have emerged in recent years. This presentation will investigate the new techniques that have been developed in the last several years and review current applications of 4-D Flow MRA.

Materials and Methods

We will describe: 1. High resolution 4-D Flow MRA, including techniques using radial acquisition. 2. Wall Shear Stress analysis, current theories and applications. 3. Noninvasive pressure measurements within aneurysms and other structures. 4. Advanced postprocessing techniques including particle path traces. 5. Use of 3-D Printing to create aneurysm models from 4-D Flow MRA or DSA. 6. Application of machine learning to 4-D Flow MRA for automatic segmentation. 7. Description of Flow Morphology including streamline analysis and clinical implications.

Results

New advances in 4-D Flow MRA have enabled new novel clinical applications, including 3-D printing of vascular flow phantoms, intra-aneurysmal relative pressure measurements, analysis of flow patterns and wall shear stress trends, and streamline/flow morphology analysis. Further investigation in technology such as machine learning may further automate these techniques, allowing increased clinical utility.

Conclusions

This presentation will summarize new techniques in 4-D Flow MRA, and investigate several novel applications as well as describe areas of active investigation that may yield future techniques.

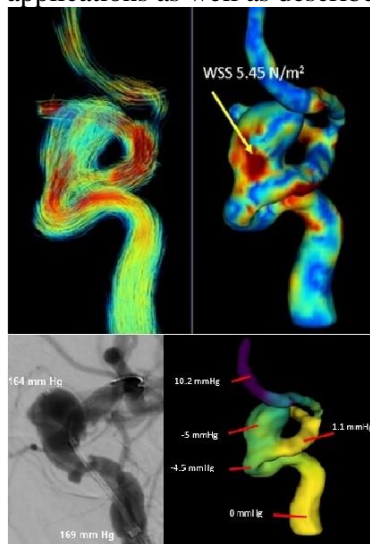


Figure 1: a) top left: streamline map from an ICA aneurysm showing inflow jet morphology. b) top right: WSS map showing focally elevated wall shear stress at the site of the inflow jet. c) bottom right: DSA from the same patient showing 5 mm Hg pressure drop from catheter based measurements. d) bottom left: 4D flow relative pressure map showing 5 mm Hg pressure drop.

(Filename: TCT_eEde-088_4dfab.jpg)

eEde-040

A Case of the Sagging Brain: A Review of Intracranial Hypotension

K Seifert¹, X Wu², L Tu¹, A Malhotra¹

¹*Yale New Haven Hospital, New Haven, CT*, ²*Yale University School of Medicine, New Haven, CT*

Purpose

The purpose of this exhibit is to review the clinical presentation, imaging characteristics, and treatment strategies of intracranial hypotension.

Materials and Methods

Intracranial hypotension is defined as a cerebrospinal fluid pressure <60 mm H₂O. It can present with vague symptoms of postural headache, nausea, vomiting, vertigo, neck pain, back pain, etc. and severity of symptoms varies widely. As it is often caused by a CSF leak, treatment consists of repairing the defect, which is extremely effective in reducing patient symptoms. Intracranial hypotension can be related to procedures, such as lumbar puncture, spinal or cranial surgery, or overshunting of CSF, which is easier to diagnose given presenting symptoms and history. Other times, intracranial hypotension is spontaneous, thus making the collection of ambiguous symptoms harder to diagnose. Patients will often receive imaging based on their unclear neurological symptoms. As imaging characteristics tend to be nonspecific and are still being outlined, diagnosis is often delayed. Thus, it is important to better understand the imaging characteristics associated with intracranial hypotension to ensure prompt diagnosis and treatment.

Results

The clinical presentation of orthostatic hypotension will be reviewed, including characteristic causes. Several key findings are noted in patients with intracranial hypotension and will be reviewed in this exhibit. These include: pachymeningeal enhancement, sagging brain, subdural fluid collections, enlarged venous structures, pituitary swelling, cerebellar tonsillar herniation, effacement of the basal cisterns, and decreased mamillopontine distance.

Conclusions

Intracranial hypotension is an under-diagnosed entity, likely due to vague clinical symptoms and imaging findings. As this diagnosis is effectively treated with repair of the dural defect, better awareness of imaging findings is important. The exhibit learner will be more knowledgeable regarding the presentation, imaging findings, and treatment of intracranial hypotension, thus allowing for prompt diagnosis.

eEde-013

A Hidden Treasure in Epilepsy Imaging: Antero-Inferior Temporal Encephalocele

W Tjong¹, S Cleary¹, A Hussain¹

¹*University of Rochester Medical Center, Rochester, NY*

Purpose

The purpose of this educational exhibit is to review antero-inferior temporal encephalocele.

Materials and Methods

Educational review of antero-inferior temporal encephalocele as an educational exhibit accompanied by different cases to reflect the imaging features of this clinical condition.

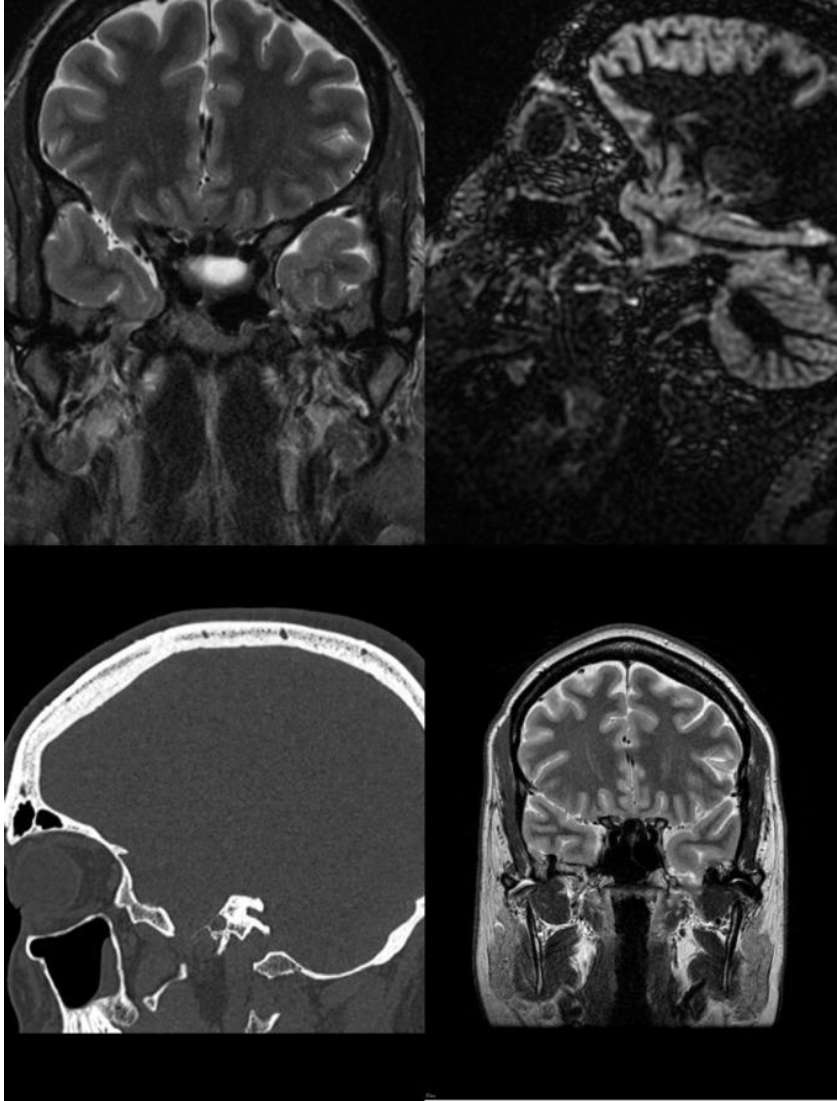
Results

Neuroimaging plays a pivotal role in the management of epilepsy patients. Medically intractable epilepsy patients may benefit from neurosurgical intervention. The surgical success rate is even higher if a structural culprit can be identified. Antero-inferior temporal encephalocele is one of the under-recognized

causes of epilepsy. Familiarity with this condition, its imaging features and variations will positively impact the neuroradiologist's ability to diagnose this condition accurately.

Conclusions

This presentation will provide a simplified approach to antero-inferior temporal encephalocele diagnosis in epilepsy imaging.



(Filename: TCT_eEde-013_ASNRsubmissionacquirecencephaloces.jpg)

eEde-047

A “Tract” Less Traveled: Imaging of Lesions of the Brain Stem

S Pahwa¹, T Richards¹, L Walker², J Curcio¹, M Rajdev¹, V Kondray¹, M Coffey¹, A Nayate¹
¹University Hospitals Cleveland Medical Center, Cleveland, OH, ²University Hospitals Cleveland Medical Center/Case Western Reserve, Cleveland, OH

Purpose

The goal of this exhibit is to present typical and atypical clinical scenarios and associated imaging findings of lesions affecting the brain stem.

Electronic Educational Exhibits

Materials and Methods

Anatomic/functional divisions Radiographic anatomy: cranial nerve nuclei and white-matter tracts
Typical and atypical lesions: - Infectious/Inflammatory: ischemia, osmotic demyelination syndrome, hypertrophic olivary degeneration, inflammatory, infectious, and degenerative lesions - Vascular malformations - Common tumors

Results

This educational exhibit illustrates a wide variety of brainstem lesions and their MRI manifestations. The lesions described are vascular, metabolic, infectious, inflammatory, and neoplastic in etiology. A detailed understanding of cross-sectional brainstem anatomy and normal MRI signal characteristics is critical in detecting subtle lesions. As a radiologist when faced with diagnostic challenges within the brainstem, a combination of pertinent clinical information and knowledge of classic imaging findings will lead to an appropriate and timely diagnosis.

Conclusions

Diagnosis of lesions of the brain stem requires both a familiarity with imaging appearance of common lesions and intimate knowledge of cross-sectional anatomy. The arrangement of gray-matter nuclei and white-matter tracts in the brain stem, and clinical signs and symptoms play a key role in the understanding and diagnosis of clinical syndromes in the brain stem.

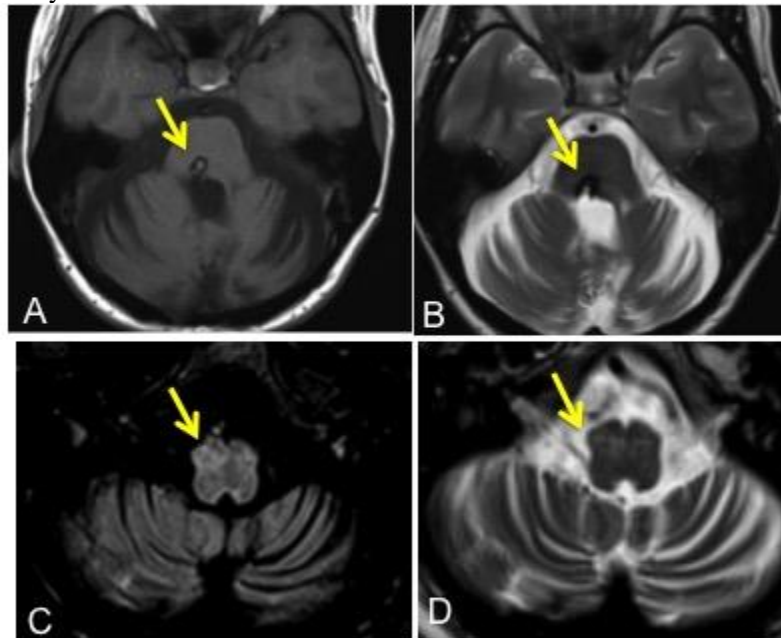


Fig 2. Cavernous Malformation and Hypertrophic Olivary degeneration

31 year old male: Axial T1-weighted (A) and T2-weighted (B) images demonstrate a cavernous malformation in the midbrain with mixed signal intensity "popcorn" appearance. Axial FLAIR (C) and T2-weighted (D) images at the level of medulla reveals asymmetric hyperintense signal and enlargement of right inferior olivary nucleus – classical appearance for hypertrophic olivary degeneration caused by primary lesions in dentate – rubro-olivary pathway.

(Filename: TCT_eEde-047_Fig1.jpg)

eEde-087

Advanced MRI Sequences Used in Neuroimaging: Basic Physics of DSC, DWI, MRS, and SWI with Clinical Applications for Residents and Fellows

A Chan¹, S Baig², B Laughlin², A Iaia², P Moftakhar², S Farooqui²

¹Christiana Care Health System, Bear, DE, ²Christiana Care Health System, Newark, DE

Purpose

The purpose of this electronic educational exhibit is to provide residents and fellows a deeper and intuitive understanding of the physics underlying modern advanced MRI sequences used in neuroimaging, particularly DSC, DWI, MRS, and SWI. In addition, many examples will be used to demonstrate the many applications of these sequences, stand alone and in combination, to help solve the common diagnostic dilemmas in neuroimaging.

Materials and Methods

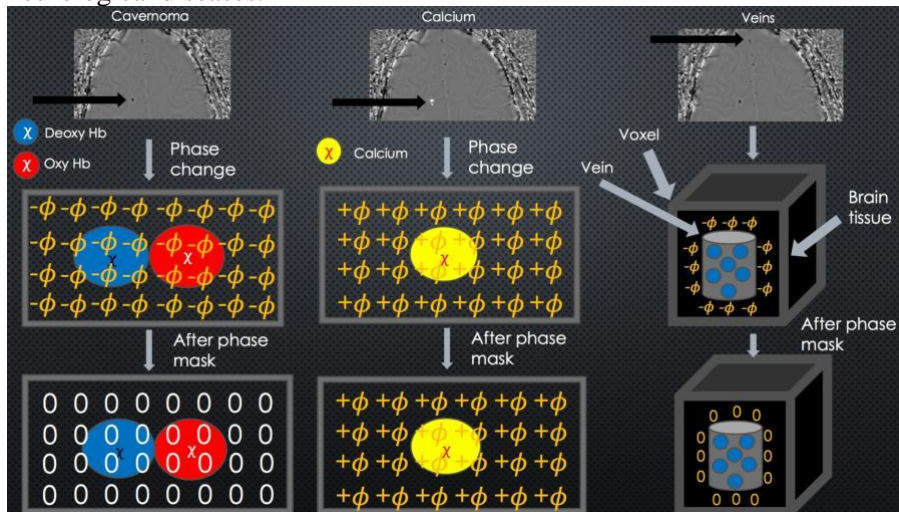
This electronic educational exhibit will utilize MR images and Microsoft PowerPoint animations to provide a graphically heavy presentation.

Results

This electronic educational exhibit will describe four advanced MRI sequences, DSC, DWI, MRS, and SWI. The relevant physiology, sequence physics, image acquisition, and clinical applications of each technique will be discussed in each section. 1. We will discuss DSC. First, we will demonstrate the basics of the central volume principle and cerebral hemodynamics, then show the bolus tracking method and how it is used to derive tissue contrast concentration $C(t)$ through EPI and gamma variate function to achieve first-pass bolus. Following, we will explain how to calculate rCBV, rCBF, and rMTT, and lastly, describe a leakage correction method used in the setting of blood brain barrier disruption. 2. We will discuss DWI. First, we will demonstrate the difference between free moving versus restricted water molecules and show how diffusion sensitive gradients and b-value generates contrast. Following, we will break down the DW-SI formula and show the process of acquiring source (in three orthogonal directions) and trace images. Finally, we illustrate the calculation of the ADC map and demonstrate the effect of T2 blackout. 3. We will discuss MRS. First, we will explain chemical shift and the chemical shift scale, then show an example spectra and explain spectral properties, peak height, and width. Following, we will animate the single (PRESS and STEAM) and multivoxel spectroscopy sequences. Lastly, we will contrast short and long TE spectroscopic studies and illustrate the suppression of unwanted substances to attaining accurate spectra. 4. We will discuss SWI. First, we will explain magnetic susceptibility (diamagnetic and paramagnetic substances) and its effect on phase. Next, we will discuss the acquisition and marriage of the magnitude and phase images to generate SWI images. Lastly, we will discuss the details of study interpretation by explaining why 3-D magnitude and MinIP images are used, how to determine calcium versus hemorrhage.

Conclusions

By the end of this electronic educational exhibit, we hope the audience will apply the basic physiological and physical principles of MRI presented here to their daily work and aid in their diagnosis of neurological diseases.



(Filename: TCT_eEde-087_abstract_2.jpg)

Advances in Mild Traumatic Brain Injury Imaging Biomarkers

R Shah¹, J Allen¹

¹*Emory University, Atlanta, GA*

Purpose

Imaging diagnosis and prognostication of patients with mild traumatic brain injury (mTBI) remains elusive. The goal of this educational exhibit is to highlight recent advancements in MR imaging biomarkers of mTBI.

Materials and Methods

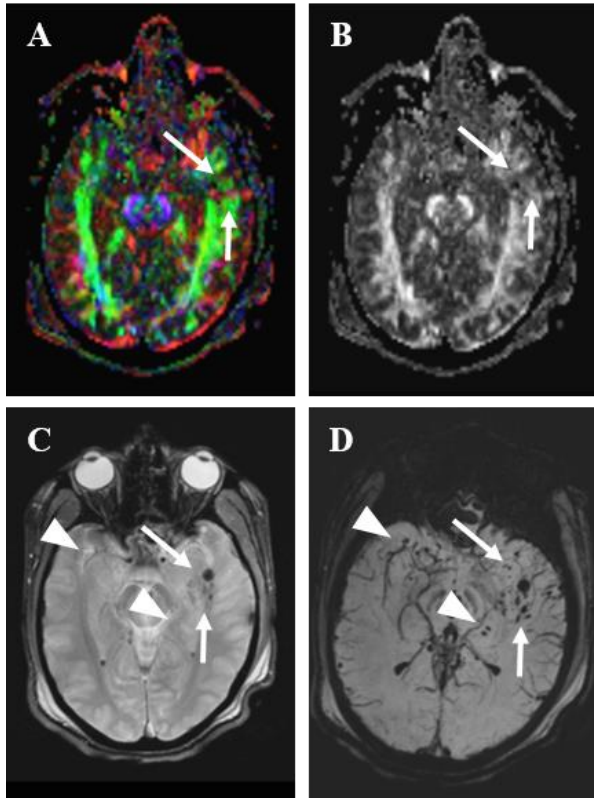
There are many advanced MRI techniques that have shown potential in demonstrating subtle brain injury in mTBI such as susceptibility weighted imaging, diffusion tensor imaging (including diffusion kurtosis), functional MRI (including task-based and resting state), and magnetic resonance spectroscopy. In addition, new statistical models are being applied to mTBI neuroimaging metrics, such as principal component analysis. In this exhibit, we will focus on these methods and their limitations, how they can provide evidence of structural and functional brain damage, and their potential to deliver prognostic information.

Results

Susceptibility weighted imaging and quantitative susceptibility mapping are more sensitive for microhemorrhages than conventional T2* sequences and may allow for semiautomated detection. Alterations in fractional anisotropy in mTBI have been well described; however, recent data suggest a time-dependent directionality to these changes with a pattern similar to cerebral infarction, with a 'pseudonormalization' phase during the subacute time period. Functional MRI (fMRI) studies have recently reported abnormal connectivity following mTBI in both tasked based fMRI as well as in intrinsic connectivity networks in resting-state fMRI. Recent advances in whole-brain MR spectroscopy have allowed the characterization of global metabolic changes in TBI. However, variability in acquisition and analysis has limited inferences and generalizability of results.

Conclusions

Despite great strides in characterizing group differences in patients with TBI using advanced MRI techniques and new statistical methods, translation to clinical practice on an individual patient level has not yet been achieved. Further research into methods of TBI diagnosis and prognostication are needed to guide the development and test the efficacy of novel therapies as well as allow patient-centric clinical care.



(Filename: TCT_eEde-102_Figure1.jpg)

eEde-096

Advantages of Arterial Spin Labeling Perfusion in the Diagnosis and Follow-up of Patients with Glioblastoma

S Omar¹, L Amaral¹, C Campos¹, V Marussi¹, L Freitas¹, A Benine Belezia², B Inada¹, T Vilas Boas³, F Barros¹

¹Hospital Beneficencia Portuguesa de São Paulo, São Paulo, Brazil, ²A Beneficência Portuguesa de São Paulo/Hospital Santa Catarina de São Paulo, São Paulo, Brazil, ³Hospital Beneficência Portuguesa de São Paulo, Campinas, São Paulo, Brazil

Purpose

Demonstrate the usefulness of Arterial Spin Labeling (ASL) compared and associated with other advanced techniques of perfusion, spectroscopy and conventional images in the diagnosis and follow-up of patients with glioblastoma.

Materials and Methods

Discuss several cases from the initial diagnosis to the post-treatment follow-up of patients with glioblastoma. Emphasis will be placed on images and findings related to ASL technique.

Results

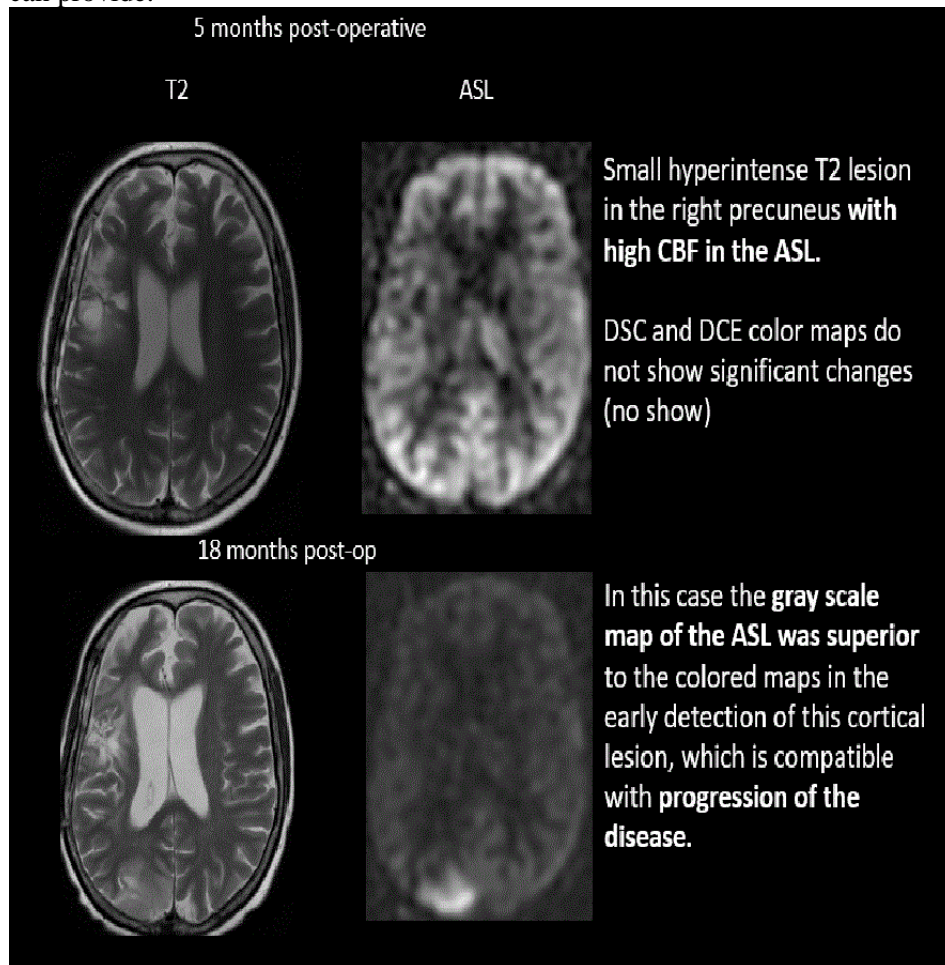
ASL is a non-ionizing and completely noninvasive technique for measuring tissue perfusion (blood flow), which uses magnetically labeled arterial blood water protons as an endogenous tracer. This technique can be used, as in the cases presented, in the first tumor evaluation, in the recent and late postoperative period and in the differentiation between changes related to applied therapy and residual or relapsed lesion.

Conclusions

Glioblastomas are the most deadly primary tumors in the central nervous system. Your accurate diagnosis

Electronic Educational Exhibits

and follow-up are extremely important. The ASL technique allows and helps the other advanced techniques and conventional images in the correct interpretation of the various challenges that this tumor can provide.



(Filename: TCT_eEde-096_GBMAASLdpigif.gif)

eEde-001

ALS or Not? A Neuroimaging, Physiological, and Management Focused Review of Amyotrophic Lateral Sclerosis and Its Motor Neuron Disease Mimics

V Yedavalli¹, A Bogachkov¹, V Pandey¹, V Kuttappan¹, P Chowdhry¹, G Gorelick¹, A Patil¹

¹*Advocate Illinois Masonic Medical Center, Chicago, IL*

Purpose

Amyotrophic Lateral Sclerosis (ALS) is a debilitating neurodegenerative disorder leading to gradual motor impairment without sensory or cognitive deficits. It characteristically affects both upper and lower motor neurons with a clear male predominance. However, ALS has a number of mimics which can present similarly with isolated upper motor neuron disease. In this review, we focus on distinguishing ALS from its mimics systematically utilizing neuroimaging and physiology while also touching upon management of each entity.

Materials and Methods

As ALS has several mimics, we hope to elucidate both ALS and its motor neuro disease mimics. We

Electronic Educational Exhibits

specifically focus on Primary Lateral Sclerosis (PLS), Progressive Muscular Atrophy (PMA), Progressive Bulbar Palsy (PBP), and Supranuclear Palsy (SNP). Because of the nonspecific clinical picture, it is essential to delineate whether the pathology is truly ALS or a mimic as it could alter patient management and timely treatment.

Results

ALS, with its nonspecific clinical features, has a number of mimics which can complicate diagnosis. We focus on the neuroimaging, physiological, and treatment distinctions between ALS and its mimics in this review. We specifically focus on motor neuron diseases which have similar clinical presentations to ALS. In doing so, we hope to create a systematic approach of differentiating each entity for facilitating accurate diagnosis and appropriate management.

Conclusions

In this exhibit, we differentiate ALS from its other motor neuro disease mimics. With the nonspecific clinical picture with which ALS presents, it is integral to include these motor neuron mimics within differential diagnoses by using a systematic approach to distinguish each entity. Given the different treatments and overall patient management based on each entity, timely and accurate diagnosis is essential for potentially improving prognosis.

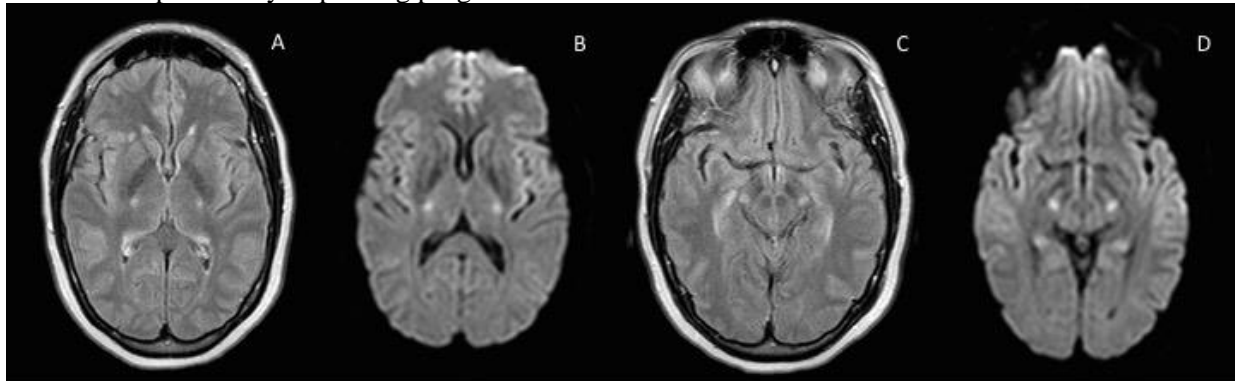


Figure 1. 44 year old female with progressive bilateral arm weakness without sensory or cognitive impairment. Symmetric rounded T2 hyperintensities (A) within the posterior limbs of the internal capsules with associated restricted diffusion (B). These hyperintensities continue into the cerebral peduncles (C) with restricted diffusion again demonstrated (D). These hyperintensities follow the corticospinal tracts and the patient was diagnosed with amyotrophic lateral sclerosis.

(Filename: TCT_eEde-001_ALSanditsMimics.jpg)

eEde-058

An Interactive Vascular Imaging Learning Module

J Cramer¹, J Pelz¹, J Helvey¹, D Poage¹, M White¹, M Keiper¹

¹University of Nebraska Medical Center, Omaha, NE

Purpose

Neuroradiology is a perceptually difficult subspecialty. [1] CTA and MRA are particularly challenging. [2] Learning these modalities is most effective when viewing an entire study as opposed to a single image, but educational resources displaying image stacks are uncommon. Consequently, learning vascular

Electronic Educational Exhibits

imaging largely occurs by chance during rotations. We seek to improve vascular imaging education via a web-based module that allows users to review image stacks in a quiz-based format.

Materials and Methods

Twenty cases were selected with a mix of aneurysms and proximal and distal arterial cutoffs, as well as normal and other confounding cases. The module was implemented via a Wordpress quiz plugin (WatuPro, Kiboko Labs) and a custom HTML image stack viewer. There is one multiple answer question for each study. Upon completion, users receive a score and can view annotated images. The module is currently implemented with internet access, but could be modified to run without internet but with less functionality.

Results

The cases encompass a wide spectrum of findings that will improve a learner's search pattern. Moreover, we include cases with multiple findings to account for satisfaction of search as a confounder. [3]

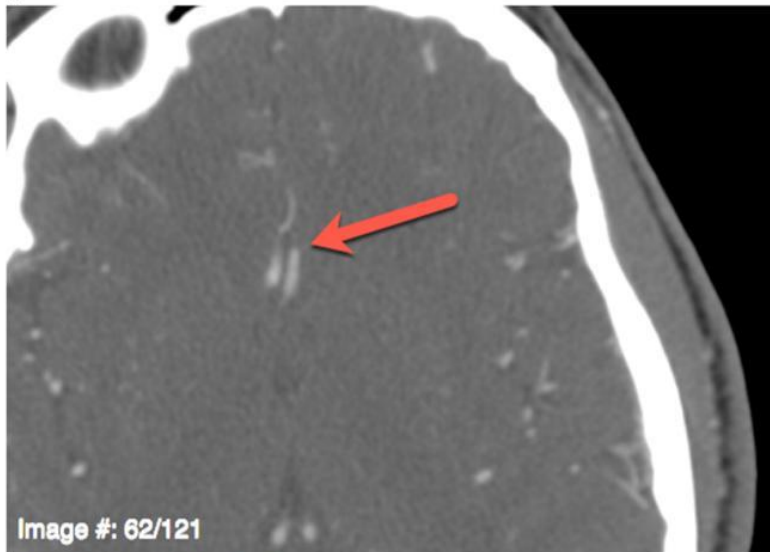
Wordpress was chosen to allow universal access. We created a custom HTML viewer to optimize the user experience for speed and simplicity. The viewer can also be embedded in other webpages allowing for seamless display of both the quiz and viewer.

Conclusions

Perceptual errors are a challenge with vascular imaging studies. We anticipate that a custom quiz-based module displaying entire imaging studies will improve CTA and MRA learning.

Scroll through these studies and identify the finding(s). There are arterial cutoffs, aneurysms, and some with neither.
Double-click/tap to zoom.

1.



What finding(s) are present on [this study](#)? Select all that apply.

- Cutoff - ACA
- Cutoff - MCA
- Cutoff - PCA
- Aneurysm - ICA
- Aneurysm - ACOM
- Aneurysm - PCOM
- Aneurysm - ACA
- Aneurysm - MCA
- Aneurysm - PCA
- None of the above

That's correct! There is an occlusion of the left A2 ACA branch (red arrow) best seen on image #62.

Figure 1: Example question. The user has zoomed in on the viewer and selected the correct answer on the quiz, prompting feedback and annotating the finding.

(Filename: TCT_eEde-058_figure1.jpg)

eEde-085

Applications of 3D Cinematic Rendering in Neuroimaging: Studio Magic Meets Anatomy and Pathology

D Patel¹, S Akunyili¹, M Hoch¹, R Hu¹
¹Emory University Hospital, Atlanta, GA

Purpose

To provide overview of potential applications of 3-D cinematic rendering in neuroimaging and demonstrate its potential value in enhanced visualization, treatment planning, medical education and patient communication

Materials and Methods

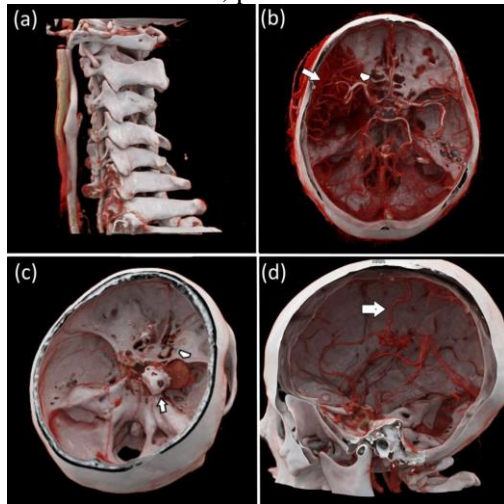
We will review different applications of 3-D cinematic rendering for advanced visualization of various brain and spine pathologies through specific case examples.

Results

Multidetector computed tomography (MDCT) with its high temporal and spatial resolution, allows for acquisition of volume data set [1]. This volume data set can be rendered into life-like 3-D reconstructions to provide enhanced visualization of disease processes that may be difficult to evaluate on 2-D images [2]. Recent advent of cinematic image rendering which utilizes path-tracing method and global illumination model to create photorealistic images, has brought 3-D reconstruction to a new exciting level, with its complex lightening effects to provide improved depth perception and spatial relations [1-4]. There are numerous applications of cinematic rendering. Medical education can be enhanced with cinematic 3-D reconstructions of lifelike anatomy (Figure 1a). Photorealistic imagery of a meningioma displacing adjacent vessels (Figure 1b) and of a large cavernous carotid artery aneurysm (Figure 1c, arrowhead) with a calcified portion (arrow), are more natural for clinicians to understand and can be useful in presurgical/treatment planning [1,2]. It can also play role in describing a complex disease process, such as arteriovenous malformation (Figure 1d), to a patient to facilitate better understanding and informed decision making.

Conclusions

Cinematic 3-D image rendering is an exciting tool that, through its detailed life-like spatial 3-D reconstruction, can play an important role in various aspects of neuroimaging, including but not limited to medical education, patient communication and presurgical/treatment planning.



(Filename: TCT_eEde-085_Figure1_Submitted.jpg)

eEde-071

Arterial Spin-labeled MRI Perfusion in Routine Clinical Neuroimaging Practice: Our Institutional Experience

S Kumar¹, N Soni², U Misra¹, S Behari³, J Kalita³

¹SGPGIMS, Lucknow, Uttar Pradesh, India, ²University of Iowa Health Center, Iowa City, IA

Purpose

ASL is a noninvasive MR perfusion technique, uses magnetically labeled arterial blood water protons as an endogenous tracer to detect changes in cerebral blood flow (CBF). In this educational exhibit we aimed to present: • Basic Principle of ASL • Age dependent CBF variability • Correlation between ASL and DSC MRI perfusion in brain tumors • To distinguish various intra-axial lesions on the basis of the ASL derived CBF

Materials and Methods

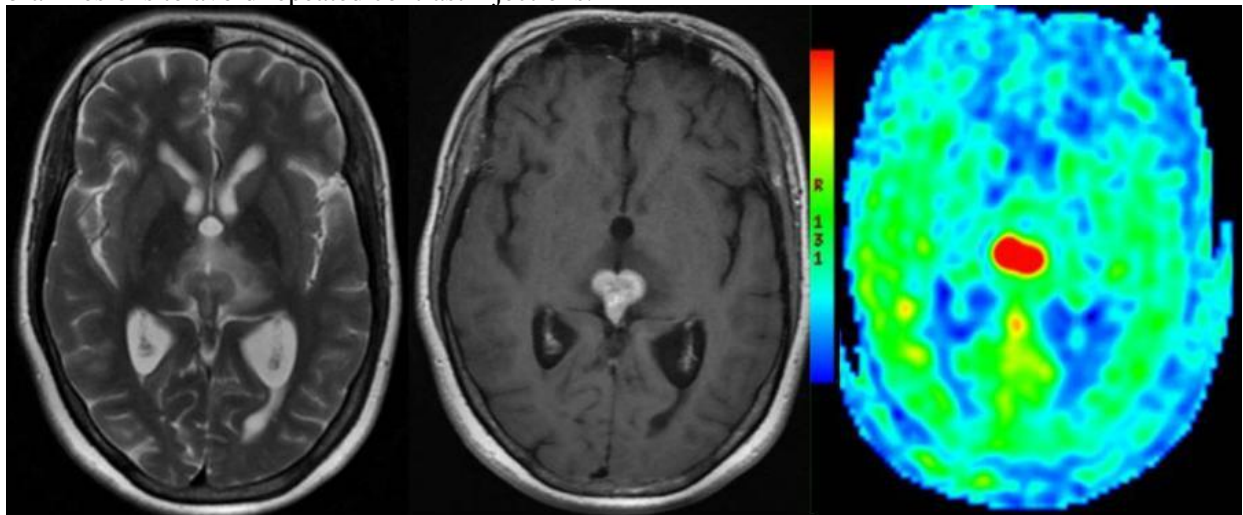
All patients underwent MRI including 3-Dimensional Pseudocontinuous ASL sequence (3-D PCASL) sequence on a 3T GE scanner using a 12-channel head coil. ASL data was transferred to the workstation (ADW4.4, GE, USA) for postprocessing and images were analyzed using Functool Software with automated generation of quantitative CBF perfusion maps. CBF values were calculated by positioning three circular ROIs (5-10 mm²) over region of interest.

Results

Our results demonstrate: 1. A significant age related decline in various regional and global GM and WM CBF values with increasing age. 2. A very strong correlation between 3-D PCASL and DSC perfusion values and support the possibility of ASL as an alternative to DSC MRI. 3. ASL derived CBF is helpful in distinguishing neoplastic from non-neoplastic intra-axial lesions.

Conclusions

Nowadays with more availability of 3T scanners, improved ASL perfusion sequences with background suppression and simpler quantification, 3-D PCASL is a fairly good alternative to invasive contrast perfusion studies (DSC & DCE) and may now be used in everyday clinical practice such as follow-up of brain lesions to avoid repeated contrast injections.



(Filename: TCT_eEde-071_Picture4.jpg)

eEde-073

Astroblastoma: Large Case Series of a Rare CNS Tumor with Clinical, Pathological and Radiological Correlation with Advanced Tumor Imaging

B Wang¹, G Fuller¹, L Ketonen¹

¹MD Anderson Cancer Center, Houston, TX

Purpose

1. To illustrate the CT and MRI findings of astroblastoma, with pathological correlation. To our knowledge this has not been systematically evaluated in the radiological literature. 2. To describe a new imaging feature of astroblastoma 3. Raise radiologists' awareness of this rare CNS tumor

Materials and Methods

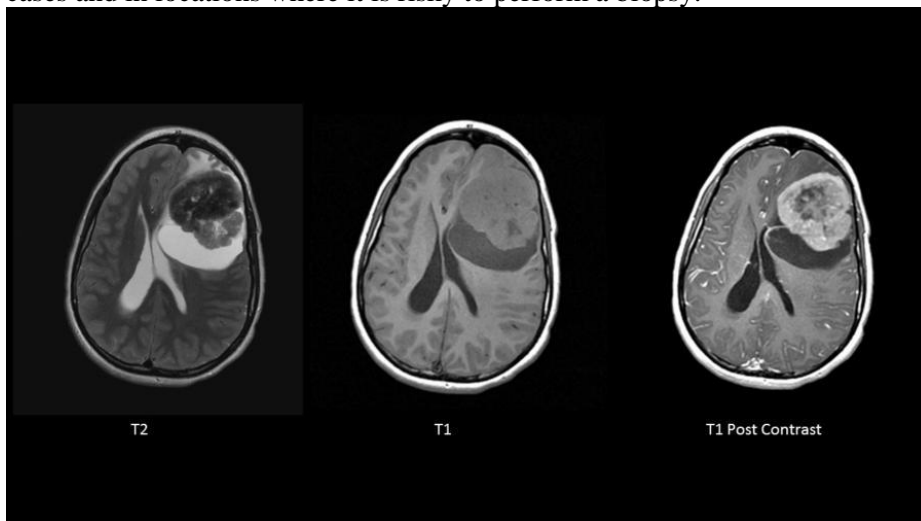
We report here a series of 17 tissue-confirmed cases of astroblastoma seen at our institution. This is a rare glial tumor usually found in the cerebral hemispheres of young adults and children, although it can arise in all age groups. Astroblastoma, along with chordoid glioma of the third ventricle and angiocentric glioma, is grouped under the "Other Neuroepithelial Tumors" rubric in the current (2016) version of the WHO classification of CNS tumors. We present here the spectrum of CT and MR imaging features, including diffusion-weighted imaging (DWI) and diffusion-tensor imaging (DTI), with selected MR spectroscopy (MRS) and perfusion imaging. Radiological and pathological correlation will be discussed.

Results

The patients in our case series ranged from childhood to middle age (3 – 47). A female predilection was seen, with 3 males and 14 females. Astroblastoma frequently presented as a large, peripherally located, supratentorial lobulated solid and cystic mass with little, if any, associated vasogenic edema. Multiple cysts are also common, and conveyed a bubbly appearance. Calcification is common, usually in a punctate pattern. On MR imaging, enhancement is often heterogeneous. A previously unreported feature, T2 hypointensity within the tumor, was found to correlate with collagenous sclerosis on histopathological examination.

Conclusions

We present here a large collection of astroblastomas, a rare CNS tumor. T2 hypointensity within the tumor correlates with collagenous sclerosis on pathology, which has not been previously discussed in the literature. The knowledge gained may potentially impact patient management, especially in inoperable cases and in locations where it is risky to perform a biopsy.



(Filename: TCT_eEde-073_AstroblastomaImage.jpg)

eEde-049

Atypical Encephalitis and its Mimic – Understanding Imaging Features

J Junn¹, A Corey², M Zygmunt¹, A Prater³, R Peterson⁴

¹*Emory University Hospital, Atlanta, GA*, ²*Emory, Fayetteville, GA*, ³*Emory University, Atlanta, GA*, ⁴*Emory University School of Medicine, Atlanta, GA*

Purpose

Describe and discuss radiologic features to differentiate atypical encephalitis and its mimic

Materials and Methods

This educational exhibit will highlight different types of infectious encephalitis and characteristic imaging locations for each offending agent. Examples of atypical encephalitis will include Eastern equine, West Nile, Zika, Herpes simplex virus type 1 (HSV1), Rhomboencephalitis, and St. Louis encephalitis. We shall also review imaging mimics of encephalitis such as CNS changes in specific toxic exposures or metabolic abnormalities including hyperglycemia, carbon monoxide poisoning, heroin inhalation, and CNS vasculitis.

Results

Imaging features of encephalitis are often nonspecific with abnormal T2 hyperintensity of the gray matter, which may or may not involve the white matter or the deep gray nuclei. Understanding of the common locations of imaging abnormalities for different causes of atypical encephalitis is important in aiding diagnosis. For instance, rhomboencephalitis has locational predilection for the brainstem while the West Nile involves the basal ganglia and thalami. In addition, we will discuss other metabolic and vascular causes that mimic encephalitis such as subacute infarction and hyperglycemia.

Conclusions

Understanding of characteristic locations for atypical encephalitis is important for diagnosis.

eEde-095

Atypical Variants of Common Cerebral Lesions with Otherwise Characteristic DWI Patterns

S Ferracioli¹, M Castillo², C Zamora², V Onofri², L Lucato¹, C Leite³, C Alves⁴, F Hirata³, M Aranha³, L Fajardo¹, V Gonçalves³

¹*Instituto de Radiologia do HC-FMUSP, Sao Paulo, Brazil*, ²*University of North Carolina at Chapel Hill, Chapel Hill, NC*, ³*University Of Sao Paulo, Sao Paulo, Brazil*, ⁴*Santa Casa De Sao Paulo, Sao Paulo, Brazil*

Purpose

Our purpose is to review unusual DWI patterns of common cerebral lesions that otherwise present with characteristic features on DWI, elucidate potential reasons for these appearances, and discuss the use of additional sequences and clinical information to achieve the correct diagnosis.

Materials and Methods

We searched the teaching files of two academic institutions for 1) cerebral lesions with DWI findings deemed to be highly characteristic and 2) atypical cases with uncommon DWI patterns including variations in distribution and degree or presence of diffusion restriction. We also discuss the pathophysiology and review the pertinent literature.

Results

DWI is a robust MRI sequence that provides information regarding diffusion of water in tissues, thereby improving characterization of lesions that may have similar appearances on conventional imaging. Many lesions are known to have a highly characteristic DWI pattern which leads to the correct diagnosis. In rare instances lesions can present with an unusual pattern on DWI that may be seen as a lack of expected

diffusion restriction (or vice versa) or an unconventional distribution of restriction. In this exhibit we include common cerebral lesions such as abscesses, neurocysticercosis, toxoplasmosis, ischemic infarct, ADEM, PRES, necrotic tumor (such as glioblastoma and metastasis), lymphoma and radiation necrosis. We describe characteristic and variant patterns on DWI and discuss how other MRI sequences or clinical information may be utilized to suggest the right diagnosis. We also examine the pathophysiology behind characteristic and variant DWI patterns and show key cases.

Conclusions

The pattern of DWI restriction adds valuable information that helps refine the differential diagnosis of common cerebral lesions. However, atypical DWI patterns are rarely seen and may be confusing. Here we show illustrative cases and discuss how other imaging sequences may aid to achieving the correct diagnosis.

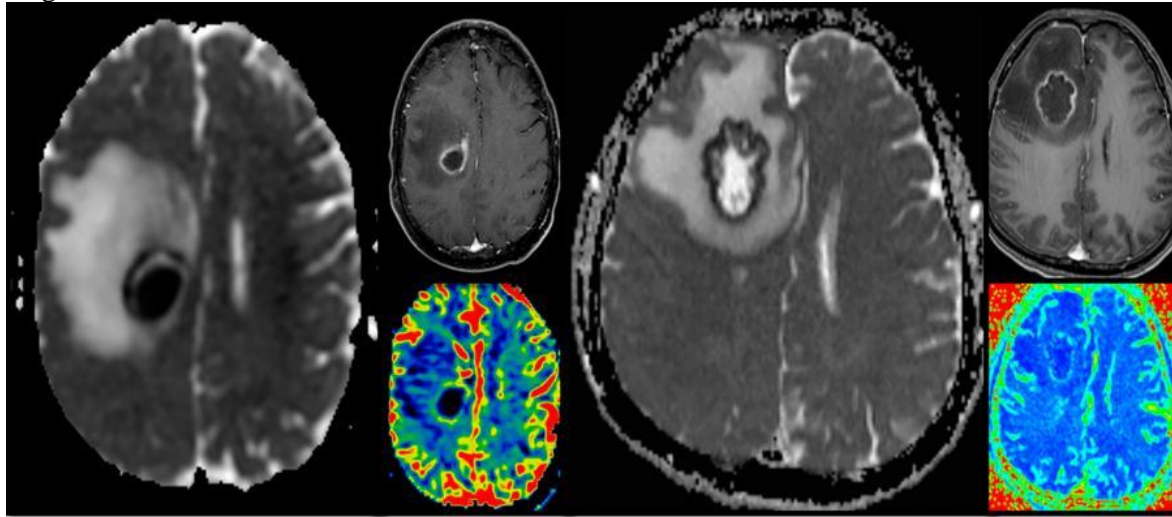


Figure 1.

Case A. Abscess case where post contrast T1 image (A2) was a typical ring enhancing lesion with smooth peripheral margins, but with cold perfusion (as shown in image A3), which is atypical, as abscesses are usually warm. DWI images was an useful aid in the diagnose, as it had the characteristic DWI pattern of central restricted diffusion (A1).

Case B. An atypical abscess case where the post contrast T1 image (B2) had an ring enhancing lesions with thick and irregular margins, with a tumor-like appearance, but with cold perfusion (as shown in image B3). DWI images didn't help in this case, since it had a thick multilayered peripheral restricted diffusion in its margins (B1), different from the usual central diffusion appearance. In this case, DWI pattern may be atypical due to blood products that may result in signal intensity loss. The degree of viscosity, the causative organism and the level of protein in the abscess cavity may affect DW image findings and ADC values.

(Filename: TCT_eEde-095_1010_atypicalDWIpatterns.jpg)

eEde-104

Blunt Cerebrovascular Imaging: A Practical Review for the Neuroradiologist Working in a Busy Trauma Center

A Rizvi¹, D Sadowsky¹, M Tenner¹, S Bobra¹, H Mehta², E Gulko¹

¹Westchester Medical Center, Valhalla, NY, ²New York Medical College-Westchester Medical Center, Valhalla, NY

Purpose

Through a case-based approach, the purpose of this exhibit is to review the imaging findings and classification of blunt cerebrovascular injury (BCVI) across multiple imaging modalities.

Materials and Methods

- Introduction to BCVI including pathomechanisms, clinical manifestations, and common locations •
- Discussion of the Biffel scale • Drawn from a Regional Level I trauma center, present case examples of

Electronic Educational Exhibits

BCVI from each classification and from multiple imaging modalities (CT, MRI, DSA) • Present tips and tricks to aid in diagnosis

Results

BCVI is a complication of blunt trauma to the head and neck, with increased risk for mortality and acute infarcts. Imaging findings can be subtle, with implications for patient management. Firm knowledge of BCVI and its imaging findings will allow the neuroradiologist to confidently and promptly recognize it.

Conclusions

Familiarity and comfort in diagnosing BCVI is required for any radiologist working in a trauma center. The current presentation will provide an educational review of BCVI for direct application for the neuroradiologist.

eEde-020

Build It and They Will Come: Comprehensive Blueprint for Starting a Clinical fMRI Service

F Raslau¹, C Smith¹, A Andersen¹, D Powell¹, E Escott¹

¹*University of Kentucky, Lexington, KY*

Purpose

Functional imaging, consisting of functional MRI (fMRI) and diffusion tensor imaging (DTI), has significantly impacted the standard-of-care in preoperative planning for assessing surgical risk, maximizing tumor resection, and improving patient outcome. However, it may seem daunting to start a clinical fMRI service. We offer a comprehensive overview and practical insights for anyone who is contemplating incorporating presurgical fMRI into their clinical practice. We will review the key relationships between the fMRI team, neurosurgical referral base, as well as the support structure consisting of software companies, local IT and medical center, and wider academia. In due course, we will answer common questions and address typical challenges in order to provide a blueprint for building a clinical fMRI service.

Materials and Methods

We draw upon our experience that spans a decade, as well as published guidelines. Topics of discussion are divided thematically: 1) preliminary questions, 2) building a clinical fMRI service, and 3) challenges and tips.

Results

Preliminary questions: What is a clinical fMRI service? Why is it important? For whom? For what indication? Who is involved? How much time and money? Building a Clinical fMRI Service: fMRI workflow, core fMRI team, neurosurgeons, hardware equipment, post-processing software, IT and billing support, financial support, academic resources, outreach Challenges and tips: Challenging patients, patient compliance, interpretation challenges of fMRI and DTI, misregistration errors

Conclusions

A clinical fMRI service is embedded at numerous intersecting streams and erected on a complex support structure. Attention to these streams and structures is important. We hope that shedding light on these details will bring clarity and motivation for anyone contemplating how to build a clinical fMRI service.

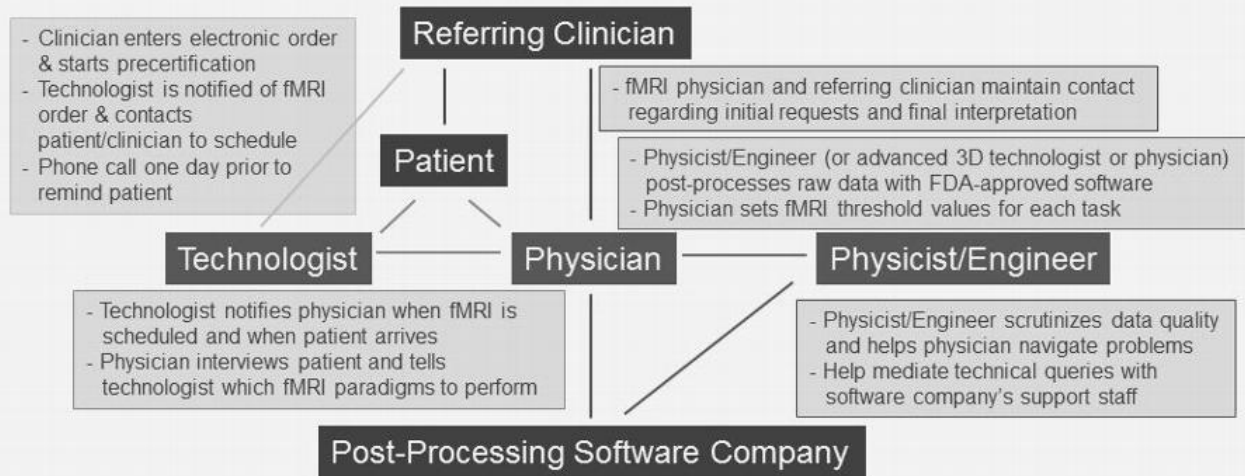


Figure 2. fMRI workflow in terms of personal interactions. A variety of interactions are maintained between the fMRI team members and other professionals and the patient. Main points are summarized for each relationship.

(Filename: TCT_eEde-020_figure.jpg)

eEde-009

Camping Out in the Hippocampus: Imaging Spectrum of Etiologies Affecting the Hippocampi and Tips for Honing the Differential Diagnosis

K Hammoud¹, N Spittler², K Buch³, R Hakimelahi³, J Nguyen⁴, M Lanfranchi¹

¹Tufts Medical Center, Cambridge, MA, ²Tufts University School of Medicine, Boston,

MA, ³Massachusetts General Hospital, Boston, MA, ⁴University of Virginia, Charlottesville, VA

Purpose

1. To illustrate the salient imaging anatomy of the hippocampus and highlight its role in memory, spatial recognition, and emotions 2. To depict the spectrum of entities manifesting with hippocampal abnormalities through illustrative case examples, including but not limited to: - Hippocampal sclerosis - Alzheimer's Disease - Frontotemporal lobar degeneration variants - Ischemic stroke - Illicit-drug associated ischemia and hemorrhage - Transient global amnesia - Herpes simplex virus encephalitis - Mitochondrial encephalopathy, lactic acidosis, and stroke-like episodes (MELAS) - Epileptogenic related cytotoxic edema - Autoimmune and paraneoplastic limbic encephalitis - Infiltrating glioma 3. To provide pearls and pitfalls for using additional imaging and historical features to render a clinically valuable differential diagnosis

Materials and Methods

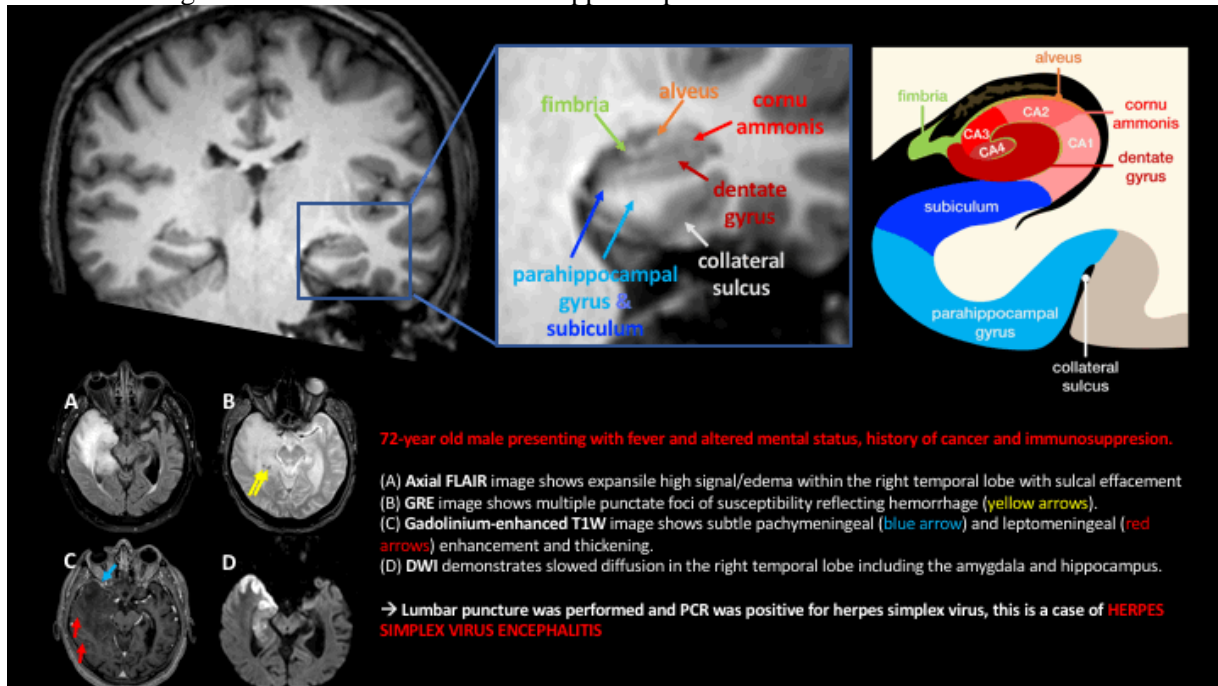
The first portion of the presentation will be dedicated to delineating the complex anatomy and function on the mesial temporal lobe and hippocampus using both volumetric MRI and original anatomic illustrations. The second portion of the presentation will consist of various illustrative case examples using multiple modalities including MRI, CT, PET and SPECT imaging accompanied by detailed clinical histories. Lastly, flowcharts and tables will be used to help consolidate the information presented on the previous slides and propose an algorithm for developing a differential diagnosis in the presence of a hippocampal abnormality on imaging using clinical and imaging findings. There will also be a brief discussion regarding potential pitfalls and variants including sulcal remnant cysts, hippocampal calcifications and incomplete hippocampal inversion

Results

A wide spectrum of disorders may manifest with nonspecific imaging abnormalities in the hippocampi and ancillary imaging findings and clinical history may help to render a clinically relevant differential diagnosis.

Conclusions

The anatomy and function of the hippocampus is complex and highly integrated with the limbic system. A wide spectrum of congenital, degenerative, ischemic, infectious, neoplastic, metabolic/toxic, autoimmune disorders may manifest with nonspecific imaging abnormalities in the hippocampi. Utilization of ancillary imaging findings and clinical history may help to render a clinically relevant differential diagnosis when confronted with a hippocampal lesion.



(Filename: TCT_eEde-009_Slide1.gif)

eEde-011

Cerebral Hemispheric Abnormalities from Birth to Adulthood: Emphasis on Clinical Features, Imaging Findings and Differential Diagnosis

M Alberawi¹, P Minhas¹, S Dua¹, M Jhaveri¹, S Gaddikeri¹, M Nagarajan¹

¹Rush University Medical Center, Chicago, IL

Purpose

Cerebral hemispheric pathologies are diverse and are not frequent in routine radiological encounter. The most common clinical manifestation is seizure. The aim of our presentation is to discuss and educate trainees regarding various pathologic conditions from birth to adulthood with imaging manifestation of hemispheric abnormality.

Materials and Methods

1. To list various pathologic entities that can present as cerebral hemispheric abnormality as the imaging manifestation 2. Discuss systematic approach to these pathologic entities including relevant clinical manifestation, neurological examination and EEG findings 3. Illustrate key imaging findings with

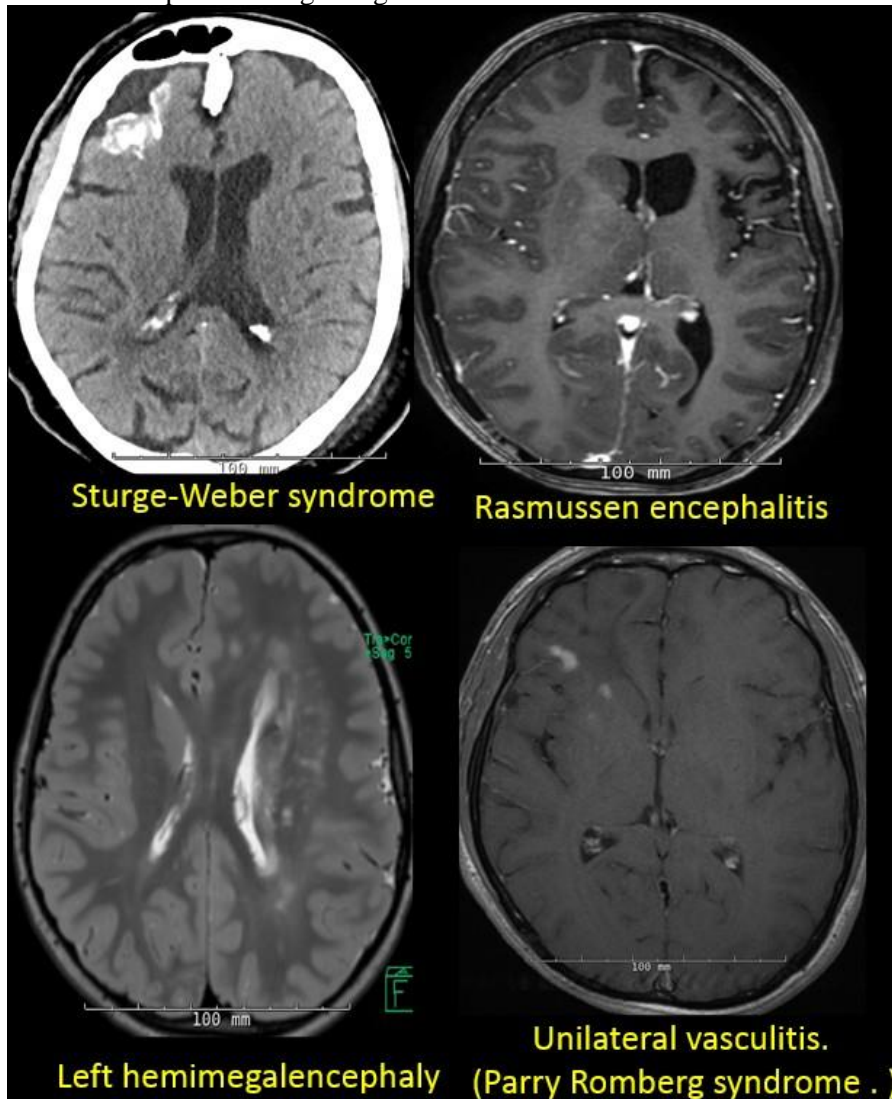
emphasis on most useful MRI sequences that can aid in narrowing the differential diagnosis of these pathological conditions and clinical syndromes

Results

Multifarious pathologic conditions can affect one cerebral hemisphere with relative sparing of the contralateral. Although, most common clinical manifestation is seizure, the differential consideration may vary depending on the age at presentation. Many of these pathologic entities can be suspected considering the clinical and imaging manifestation. Imaging modalities, especially the MRI can be helpful in recognizing these syndromes and guide further management. Various pathology including Sturge-Weber syndrome, hemimegalencephaly, Rasmussen encephalitis, cerebral hyperperfusion, cerebral ischemia, hemiplegic migraine, infection, trauma, unilateral vasculitis, hemiatrophy with multiple developmental venous anomaly, Dyke-Davidoff Masson syndrome, cerebral hemiatrophy with germinoma and gliomatosis will be discussed in this presentation.

Conclusions

At the end of presentation the radiologist would have reviewed: 1. Diverse clinical entities presenting as unilateral cerebral hemispheric abnormalities. 2. Various clinical manifestations and imaging findings which are helpful in recognizing these individual entities.



(Filename: TCT_eEde-011_asnr.jpg)

eEde-084

Clinical Applications and Usefulness of 3D Double Inversion Recovery Imaging in Central Nervous System Diseases

M Umino¹, M Maeda¹, H Sakuma¹

¹Mie University School of Medicine, Tsu, Mie, Japan

Purpose

Double inversion recovery imaging (DIR) provides two different inversion pulses, which attenuate cerebrospinal fluid and normal white matter. The purpose of this exhibition is to understand the principle of the DIR sequence, clinical applications of 3-D DIR in various central nervous system (CNS) diseases, and clinical benefits of the 3-D DIR sequence in comparison with other MR sequences.

Materials and Methods

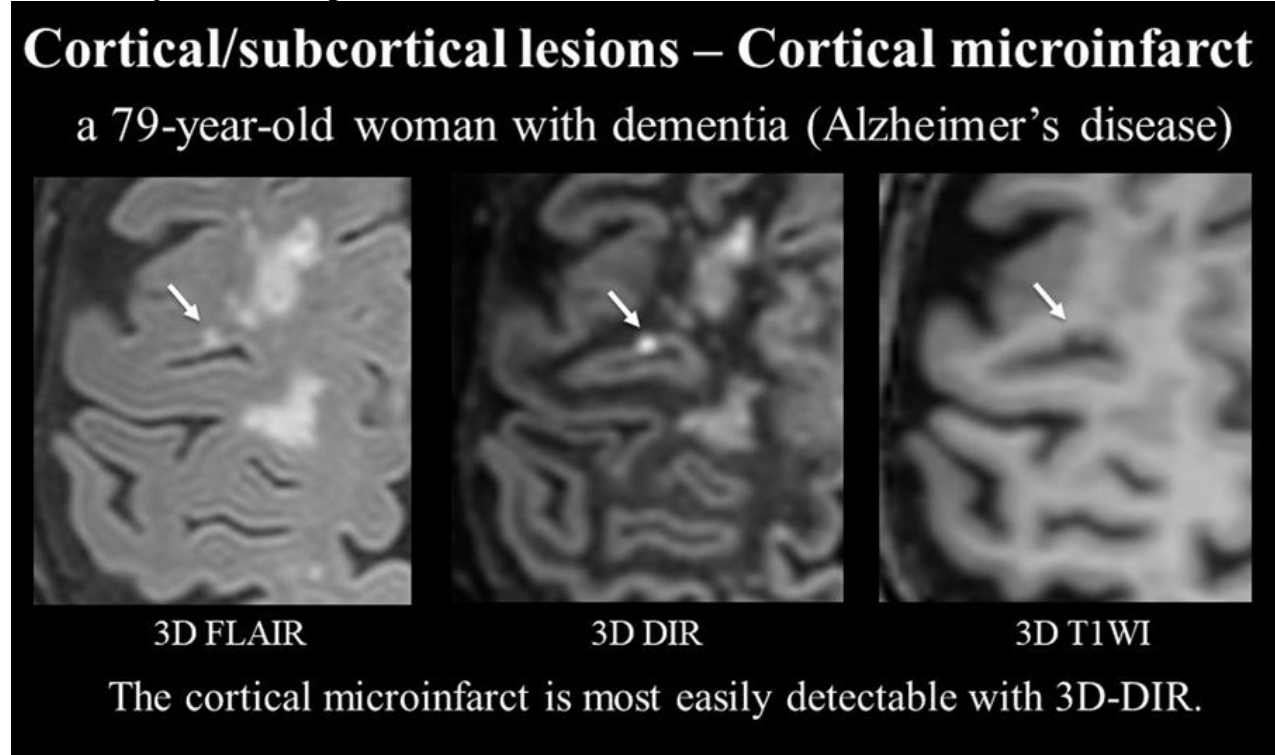
We reviewed numerous brain MR images obtained by 3-D DIR imaging at 3T MRI. The majority of brain lesions were of sulcal abnormalities, cortical and subcortical abnormalities, and optic neuritis.

Results

Three-D DIR can be applicable to the following various disease entities: sulcal abnormalities such as subarachnoid hemorrhage, meningitis, or cortical superficial siderosis, cortical and subcortical abnormalities such as multiple sclerosis, cortical microinfarcts (Fig.), or malformations of cortical development including focal cortical dysplasia and tuberous sclerosis, and optic neuritis caused by multiple sclerosis or neuromyelitis optica. Three-D DIR imaging provides better lesion conspicuity and particularly more accurate delineation of the lesion topography of cortical abnormalities.

Conclusions

Three-D DIR sequence provides useful adjunctive information that is not available from conventional MRI techniques for the diagnosis of various CNS diseases.



(Filename: TCT_eEde-084_FigDIR.jpg)

eEde-036

Cranial Nerve Nuclei Involvement in Multiple Sclerosis: Clinical and Imaging Correlation

M Alkaphoury¹, M Alberawi¹, M Nagarajan¹, M Kontzialis¹, M Kocak¹

¹*Rush University Medical Center, Chicago, IL*

Purpose

Although the cranial nerve nuclei in the brainstem are not directly visualized on imaging, their approximate location may be inferred using imaging landmarks. Demyelinating plaques in the brainstem may involve cranial nerve nuclei and fascicular fibers and, therefore, present with cranial nerve deficits.

Materials and Methods

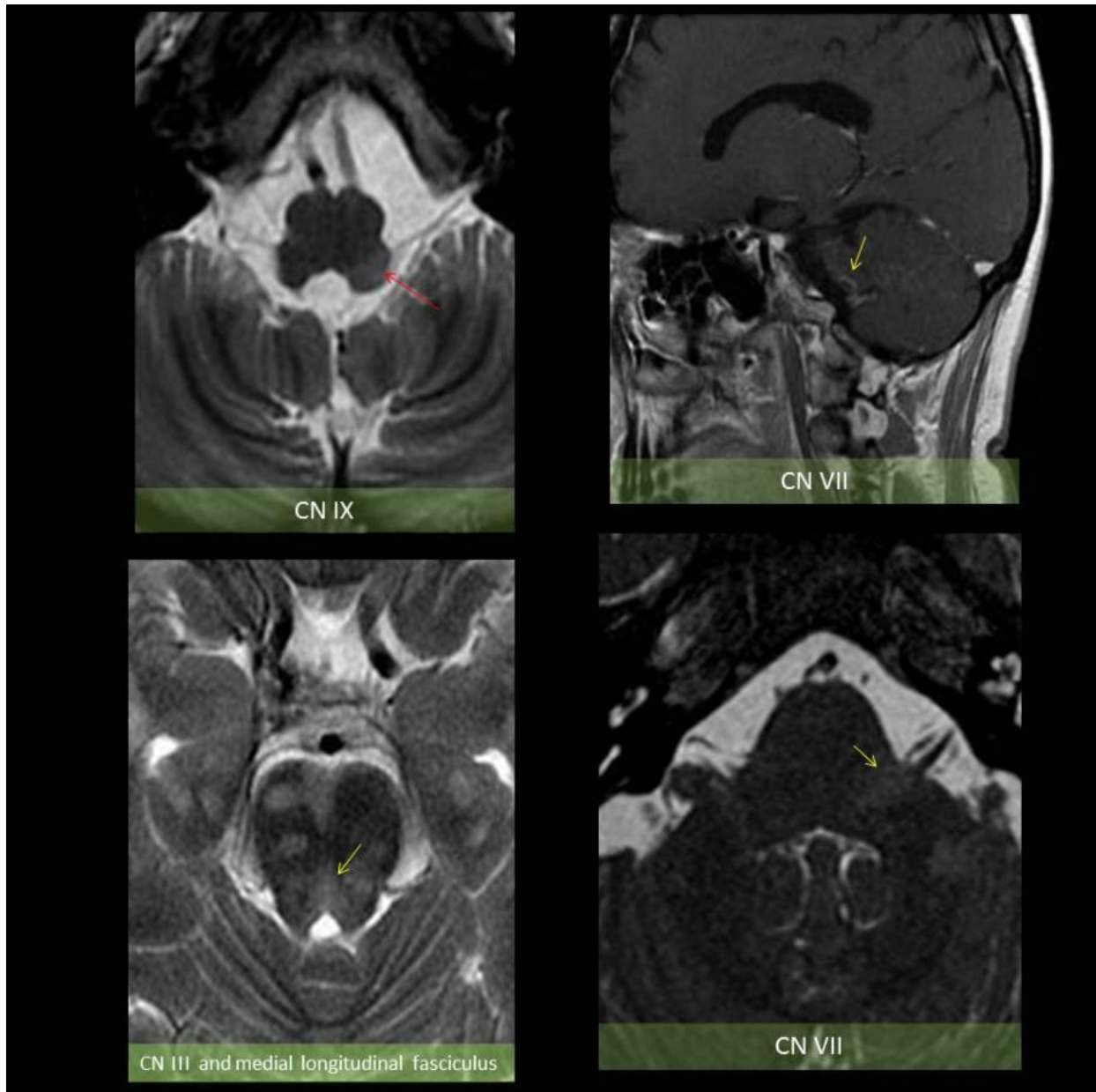
We'll use case images from our neuroradiology department to illustrate cranial nerve nuclei involvement in patients with multiple sclerosis. The clinical information, including presenting symptoms and clinical examination, were obtained from the patients' electronic medical records.

Results

Cranial nerve nuclei in the brainstem are not directly visualized on imaging. However, some imaging landmarks may indirectly infer the approximate location of these nuclei at the midbrain, pons and medulla oblongata levels. In this educational exhibit, we present a variety of cases where the expected locations of different cranial nerve nuclei were involved by demyelinating plaques in multiple sclerosis. Patients presented with typical cranial nerve deficits corresponding to the involved cranial nerve nuclei and/or fascicular fibers within the brainstem. Some lesions involved the nuclei, others involved the fascicular nerve fibers within the brainstem while other lesions involved both the nuclei and the fibers. Some lesions were enhancing in disease activity.

Conclusions

The approximate location of the cranial nerve nuclei in the brainstem may be inferred using imaging landmarks. Patients with multiple sclerosis can present with cranial nerve deficits secondary to involvement of the cranial nerve nuclei and/or fascicular fibers.



(Filename: TCT_eEde-036_CNMS-ASNR.jpg)

eEde-016

Craniocervical Fibromuscular Dysplasia – An Imaging Update

K Schallert¹, S Mukherjee¹

¹University of Virginia Health System, Charlottesville, VA

Purpose

Describe and illustrate the recent updates and advances in the understanding of the pathophysiology, epidemiology, clinical presentations, and imaging manifestations of craniocervical fibromuscular dysplasia (FMD)

Electronic Educational Exhibits

Materials and Methods

Background: Fibromuscular dysplasia (FMD) is a nonatherosclerotic, noninflammatory vascular disease that may result in arterial stenoses and occlusions as well as aneurysms and vessel dissections. FMD can occur in any arterial bed, most commonly involving the renal and extracranial carotid and vertebral arteries. Objectives: • Understand the current developments in FMD including new research as well as dispelling myths • Describe and illustrate the imaging findings in craniocervical FMD beyond "string of beads"

Results

1. Historical background 2. Epidemiology/genetics/etiology 3. Clinical presentations of craniocervical FMD • Hypertension (most common presentation) • Headaches (often recurrent) • Pulsatile or nonpulsatile tinnitus • Dizziness • Neck pain • Chest pain • Abdominal pain • Amaurosis fugax • Aneurysms • Dissections 4. Imaging findings • Multifocal FMD (String of beads) • Focal FMD • S-shaped curve • Intracranial aneurysms • Dissection • Carotid web • Infarcts • Duplex ultrasound findings 5. Management options and surveillance imaging

Conclusions

Craniocervical FMD is almost as common as renal FMD and is associated with more severe complications. Radiologists' recognition of the less common clinical presentations, beyond hypertension, helps to identify craniocervical FMD and direct management. Characteristic vascular loops and "string of beads" are the typical imaging presentations. Arterial dissection, strokes, and aneurysms are potential perilous complications.



(Filename: TCT_eEde-016_CraniocervicalFMDGraphicDPI300FINAL.jpg)

eEde-069

Electronic Educational Exhibits

CT Anatomy of Cranial Nerves

L Daftari Besheli¹, A Eajazi¹, R Tiwari¹, H Rajebi¹, B Tantiwongkosi¹, A Singh¹

¹University of Texas Health San Antonio, San Antonio, TX

Purpose

Cranial nerves (CNs) involvement is seen in heterogeneous groups of diseases, such as inflammatory processes, infectious diseases, and primary neoplasms and secondary neoplasms. Sometimes cranial nerve involvement is the first manifestation of the pathology. Magnetic resonance imaging is the imaging modality of choice to visualize CNs; however, CT has a critical role in detecting possible CN involvement when it is done first to investigate the patient's symptoms. The anatomy of the CNs on CT images can be challenging for radiologists. In this presentation we focused on CT anatomy of cranial nerves in an interactive fashion with the help of 3-D diagrams.

Materials and Methods

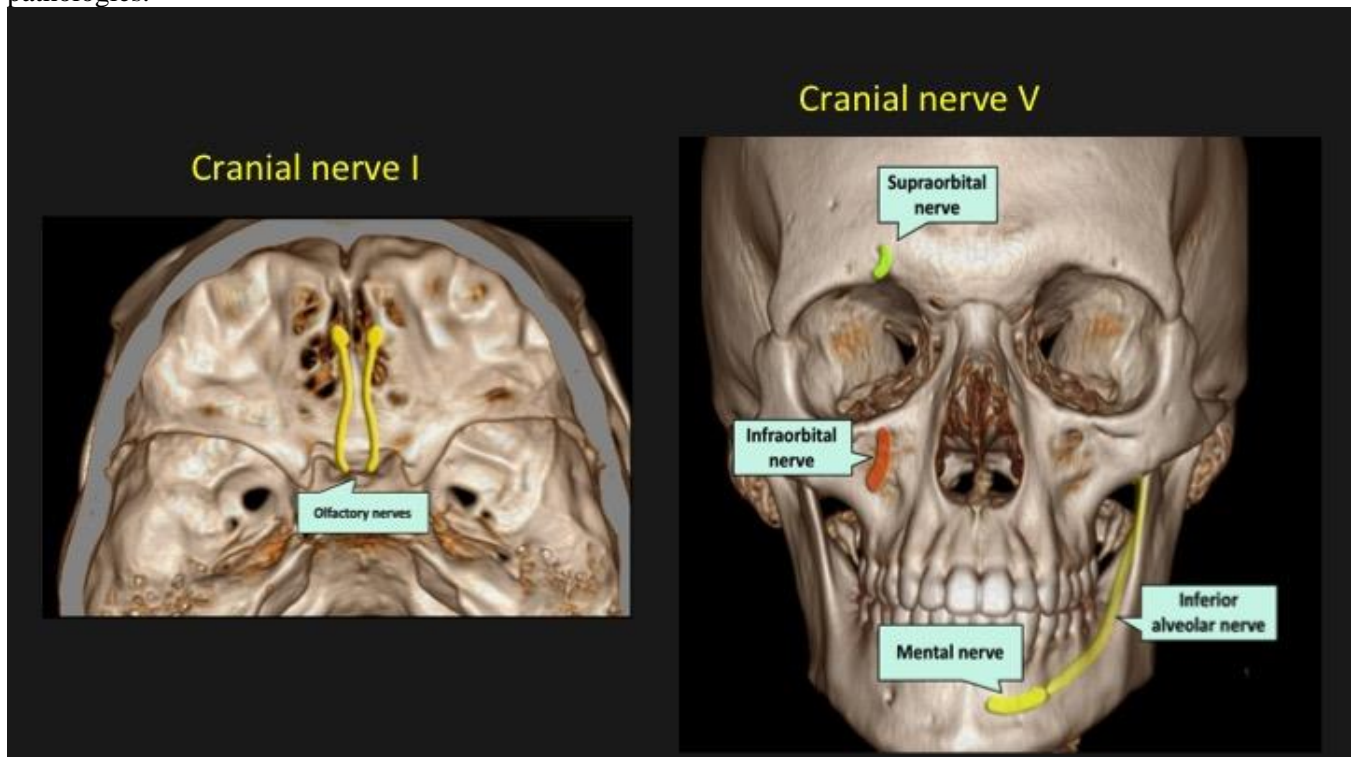
In this presentation the CT anatomy of the cranial nerves I to XII is supplemented with 3-D diagrams, which allows complete visualization of the course within the craniofacial complex.

Results

The cranial nerves I to XII pursue complex courses from their origin in the brain into the skull base and exit the cranium to their branches and/or final destinations. Although CNs are only visualized in detail on magnetic resonance imaging, knowing the detailed CT anatomy of CNs is very important to distinguish CN pathologies particularly when CT is performed first for workup of new presentations of a disease.

Conclusions

Thorough knowledge of the anatomic features of the cranial nerves and detailed clinical information are required to delineate the pathologies associated with cranial nerves. Illustration of the CT anatomy of CNs with the aid of 3-D diagrams enables improved learning of their complex course and helps in detecting pathologies.



(Filename: TCT_eEde-069_JPEG.jpg)

eEde-028

Diamox Challenge: A Case-based Pictorial Review in Evaluation of Chronic Cerebral Ischemia

K Gupta¹, R Jadhav², V Bachhav³, R Prasad¹, A Ali⁴, S Virmani⁵, M Nagarajan¹

¹*Rush University Medical Center, Chicago, IL*, ²*Rush University Medical Centre, Chicago, IL*, ³*Rush university medical center, chicago, IL*, ⁴*RUSH UNIVERSITY MEDICAL CENTER, CHICAGO, IL*, ⁵*Rush University Medical Center, Chicago, Chicago, , IL*

Purpose

Evaluation of cerebrovascular reserve is important in management of patients with TIAs or carotid stenosis. This is important to prevent future risk of ischemic sequela. Acetazolamide (Diamox) is a known vasodilator and Diamox challenge is a simple noninvasive method to assess brain perfusion response/cerebrovascular reserve. Diamox challenge can be performed with either PET, SPECT, CT or MRI; PET being the gold standard. We present a pictorial review of a series of Diamox challenge brain perfusion SPECT studies and their clinical utility performed at our institution. Correlation with other imaging modalities/angiogram is provided where available.

Materials and Methods

Most common diseases evaluated were Moyamoya disease, Encephalomalacia and cerebral artery stenosis. Baseline and post Diamox cerebral brain perfusion SPECT were performed with Tc-99m labelled Ceretec. Studies were assessed for changes in perfusion pattern using semiquantitative methods and visual assessment and results were correlated with postinterventional outcome.

Results

Baseline brain SPECT perfusion studies concurred well with other imaging modalities. However, post Diamox challenge SPECT perfusion studies were more informative about cerebrovascular perfusion reserve. Quantification of baseline and post Diamox SPECT perfusion data can effectively predict cerebral perfusion reserve and had a good correlation with postsurgical outcome in majority of the cases.

Conclusions

Diamox challenge test optimizes the treatment approach for patients with chronic cerebral ischemic disease.

CASE 1: LEFT ANTERIOR AND MIDDLE CEREBRAL ARTERY STENOSIS

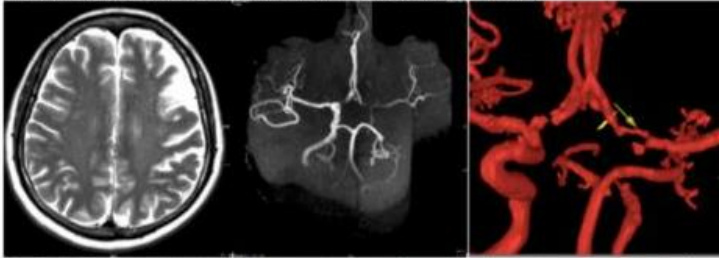


FIG 1A: T2 axial FLAIR demonstrates sulcal prominence in the left frontoparietal region with volume loss consistent with old infarct.
MRI angiogram and 3D MR contrast angiogram demonstrates high-grade stenosis in the left A1 segment anterior cerebral artery and left M1 segment of middle cerebral artery.

PRE AND POST DIAMOX STUDY

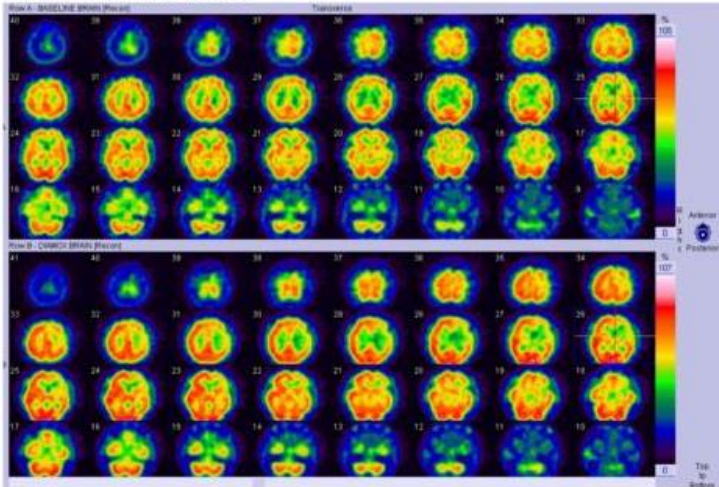


FIG 1B.

FIG 1B Row A: Pre-diamox Tc-99m Ceretec brain SPECT demonstrate mildly reduced perfusion in left frontoparietal region.
FIG 1B Row B: Post-Diamox Tc-99m Ceretec Brain SPECT demonstrate improvement in bilateral cerebral hemisphere perfusion except for left fronto-parietal region, suggesting low perfusion reserve.

(Filename: TCT_eEde-028_Diamoxfinalimage.jpg)

eEde-070

Do You See What I See....Not If It's Bitemporal: A Pictorial Review of Pathology Affecting the Optic Chiasm

P Annigeri¹, J Corrigan¹, S Patel¹, H Marin¹, B Griffith¹
¹Henry Ford Health System, Detroit, MI

Purpose

Disease processes involving the optic chiasm usually present with a fairly specific visual field deficit, bitemporal hemianopsia. However, while clinical findings can localize a lesion to the chiasm region, imaging is required for lesion identification, characterization, and classification. Unfortunately, this can be quite challenging due to both the diverse pathology involving the optic chiasm, as well as the complex surrounding anatomy. The purpose of this exhibit is to provide a pictorial review of the normal anatomy of the optic chiasm and surrounding structures, as well as review the numerous pathologic processes affecting it with emphasis on key differentiating imaging features.

Electronic Educational Exhibits

Materials and Methods

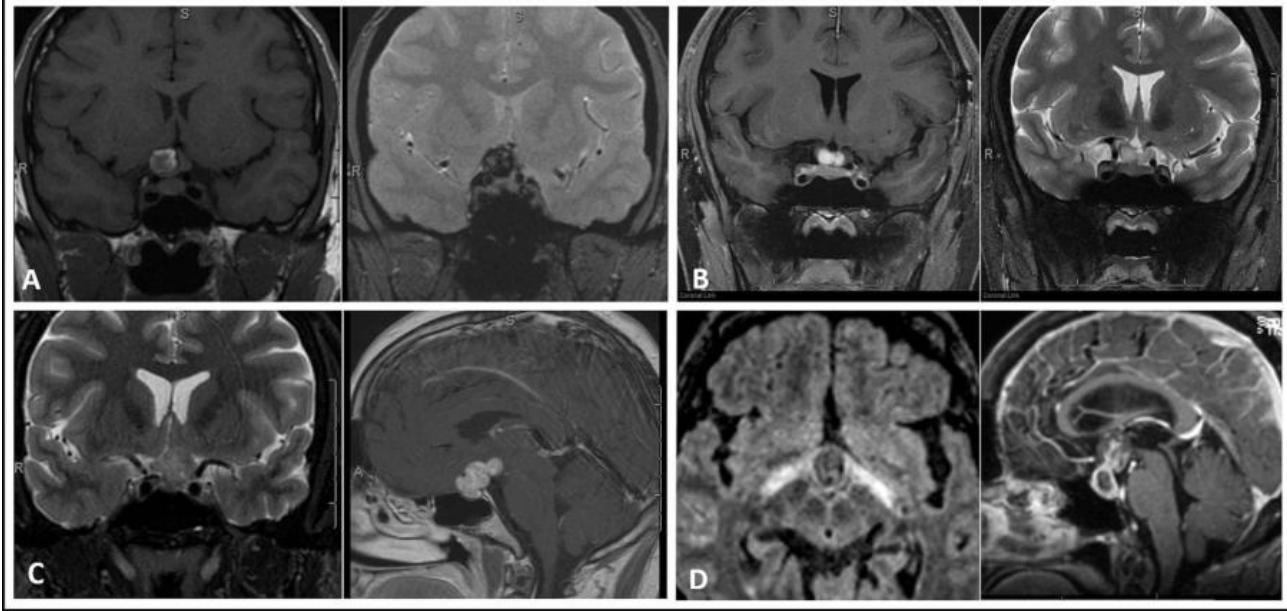
• Using representative case files, we will review the anatomy of the optic chiasm and its relationship to surrounding anatomic structures. • We will review a broad spectrum of pathologies affecting the optic chiasm, including both common and uncommon disease processes, including: optic nerve glioma, cavernous malformation (Fig. 1A), pilocytic astrocytoma (Fig. 1B), neurosarcoidosis, silicone infiltration, lymphoma, germinoma (Fig. 1C), sellar region Atypical Teratoid/Rhabdoid Tumor (Fig. 1D), chiasmatic ganglioglioma.

Results

Using a case-based approach, this exhibit will review various pathologies affecting the optic chiasm, including their clinical presentations and imaging appearance. Normal anatomy of the optic chiasm and its surrounding structures will also be discussed.

Conclusions

Evaluating chiasmatal pathology on imaging requires not only knowledge of potential intrinsic disease processes, but also an understanding of the surrounding anatomy and pathology involving those structures. This exhibit will provide viewers with an in-depth pictorial review of both common and uncommon pathologies affecting the optic chiasm with emphasis on key differentiating imaging features.



(Filename: TCT_eEde-070_Opticchiasm.jpg)

eEde-012

Don't Fear the Amygdala! Review of Anatomy and Pathologic Conditions, with Emphasis on Epileptogenic Disorders

K Buchanan¹, D Cooke², D Spencer², R Bronen²

¹Yale University School of Medicine, Branford, CT, ²Yale University School of Medicine, New Haven, CT

Purpose

The aim of this project is to review the imaging anatomy of the amygdala using Magnetic Resonance and Computed Tomography imaging and to illustrate multiple etiologies of pathological conditions involving this region with a focus on patients with epileptogenic disorders.

Materials and Methods

Imaging anatomy of the amygdala will be illustrated using diagrams, magnetic resonance (MRI) and

computed tomography (CT) images with an emphasis on differentiation from adjacent limbic system structures. MRI and CT will be utilized to demonstrate a wide spectrum of pathologies in the amygdala, including volumetric enlargement and imaging signal abnormalities on Fluid-Attenuation Inversion Recovery (FLAIR) and T1 sequences. The lesions described will represent pathologies predominantly in patients with epilepsy and other seizure disorders also discussing postsurgical imaging findings and clinical outcome.

Results

Imaging of the amygdala can be challenging in case presentations involving subtle findings or non-dedicated temporal lobe imaging, which may be attributed to its amorphous morphology. It is essential to recognize subtle findings in this region as this often significantly impacts patient management and prognosis. This exhibit demonstrates techniques for evaluating pathological lesions using examples including but not limited to: amygdala atrophy, contusion, gliomas, vasculopathy, FLAIR signal abnormality, laser interstitial therapy, dysmorphism/malformation of amygdala, cavernoma, focal cortical dysplasia, autoimmune encephalitis, neurocutaneous melanosis, arteriovenous malformation and lissencephaly.

Conclusions

Demonstrating techniques to evaluate the anatomy and multiple pathologies of the amygdala is vital for discerning lesions in this region. Etiologies for patients with seizure disorders are often undiagnosed as findings are difficult to detect on conventional imaging. Therefore, we believe this review will assist radiologists and clinicians in appropriate diagnosis, ultimately correct management and improved prognosis for these patients.

eEde-006

Dysmyelinating Diseases in Adults

O Eissa¹, T Moritani², S Ramchandren¹, F Syed¹, J Kim¹, A Srinivasan¹, J Bapuraj¹

¹University of Michigan Health System, Ann Arbor, MI, ²University of Michigan, Ann Arbor, MI

Purpose

Dysmyelinating diseases of the central nervous system presenting in adulthood are relatively uncommon. The imaging features seen in this population are distinct from those seen in the pediatric age group. The aim of this exhibit is to highlight these conditions and their imaging features.

Materials and Methods

This is an illustrative review of adult patients with dysmyelinating diseases presenting to the University of Michigan Health System.

Results

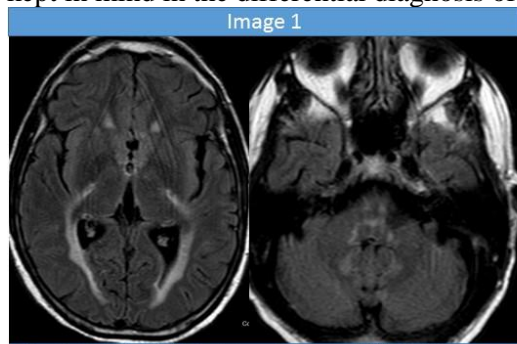
Adult onset dysmyelinating diseases predominantly involve the white matter of the central nervous system. Early recognition of asymptomatic disease is vital given potential for specific treatments. A radiologist plays an important role as part of the multidisciplinary team caring for these patients by recommending appropriate imaging studies and providing their accurate interpretation. Dysmyelinating diseases in adults can be broadly divided into acquired and hereditary conditions. Acquired conditions include infection, vascular disease or exposure to toxins. The hereditary group of conditions however are challenging to diagnose. Recent classification schemes group these conditions into three categories: (1) Diseases which have definitive imaging findings without genetic basis; (2) Diseases caused by genes coding for protein not directly involved in metabolic pathway and for which diagnosis is made by genetic testing, and (3) Diseases in which a genetic basis is directly involved in the enzymatic pathways or protein modulating cellular metabolism. These conditions can be diagnosed by specific biochemical tests (e.g. Metachromatic leukodystrophy). Often specific treatments exist for this third group of conditions (e.g. Inborn errors of metabolism [IEMS]). An alternate classification scheme for dysmyelinating diseases is based on the pattern of brain involvement, specifically grey or white matter predominance or equal

Electronic Educational Exhibits

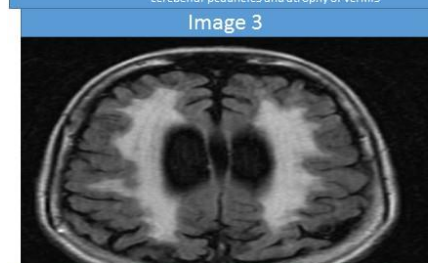
involvement of both. This classification is useful in narrowing the differential to diseases that have predominant distribution in the deep white matter (e.g. Metachromatic leukodystrophy), subcortical white matter (e.g. Kearns-Sayre syndrome) or grey white matter (e.g. MELAS).

Conclusions

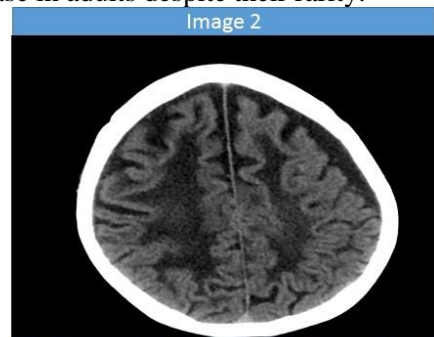
Adult-onset dysmyelinating diseases represent an under-researched area in neuroradiology literature compared to the well-known pediatric dysmyelinating diseases. Early recognition of asymptomatic patients with milder features of the disease is critical, especially given the potential for specific treatment in some of these diseases. Neuroradiologists should have an approach to the detection, diagnosis, and disposition of leukodystrophies in adult patients. These adult onset diseases of dysmyelination should be kept in mind in the differential diagnosis of white matter disease in adults despite their rarity.



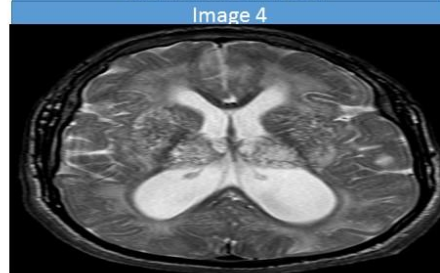
60 yr old patient with APBD (adult polyglucosan body disease). (A,B) FLAIR axial images show hyper intense white matter abnormalities in the periventricular regions, with occipital predominance, the posterior limb of the internal capsule, medial edges of the middle cerebellar peduncles and atrophy of vermis.



25 yr old patient with metachromatic leukodystrophy. MRI brain axial FLAIR image demonstrate extensive periventricular hyperintense white matter.



38 yr old patient with adrenoleukodystrophy. CT image demonstrate diffuse abnormal deep white matter disease.



25 y M enlarged tongue, above average intelligence. MRI axial T2 image demonstrates abnormal periventricular white matter with enlarged perivascular spaces. Dx: Mucopolysaccharidosis Hurler-Scheie compound.

(Filename: TCT_eEde-006_Slide1.JPG)

eEde-055

Enlarged Perivascular Spaces and Perivascular Enhancement Pattern: A Practical Approach for Clinicoradiological Diagnosis

F Scortegagna¹, A Pettengill², I Padilha², R Hoffmann Nunes², F Pacheco³, A Maksoud Piccolo⁴, L Amaral⁴, A da Rocha²

¹Dasa Group, São Paulo, Brazil, ²Irmandade da Santa Casa de Misericórdia de São Paulo, São Paulo, Brazil, ³Santa Casa de São Paulo School of Medicine, São Paulo, Brazil, ⁴Beneficiencia Portuguesa, São Paulo, Brazil

Purpose

To provide an in-depth overview of the MR imaging features of perivascular spaces, including atypical cases, perivascular enhancement pattern and related diseases.

Materials and Methods

We reviewed several confirmed cases of diseases associated with perivascular enlarged spaces and/or perivascular enhancement from our neuroradiology department.

Electronic Educational Exhibits

Results

The perivascular spaces surround the walls of vessels as they course from the subarachnoid space through the brain parenchyma, being commonly seen at magnetic resonance (MR) imaging and may sometimes appear markedly enlarged, cause mass effect, and assume bizarre cystic configurations that may be misinterpreted as other pathologic processes, most often a cystic neoplasm. These findings also have recently been related to small vessels disease, specifically associated with lacunar ischemic stroke and white-matter hyperintensities. In addition, it is known that its prevalence is higher in several diseases, as mucopolysaccharidosis, some muscular dystrophies, traumatic brain injury, as well as hypomelanosis of Ito, Lowe syndrome and Bannayan-Riley-Ruvalcaba syndrome, among others. Another important feature to ponder is that recognizing patterns and enhancement contrast mechanisms helps the differential diagnoses of central nervous system (CNS) lesions. The perivascular pattern is often unspecific, representing a diagnostic challenge and is usually characterized by linear morphology or pitting, distributed predominantly in the territory of the perforating and pial arteries. A large group of diseases can present this pattern, including lymphoproliferative/hematopoietic diseases such as lymphoma and inflammatory idiopathic disease such as sarcoidosis, primary angiitis of CNS, CLIPPERS as well as autoimmune/HIV related conditions or other neoplastic conditions.

Conclusions

Enlarged perivascular spaces and/or perivascular enhancement pattern admits a broad differential diagnosis and should always be assessed in close correlation with clinical and laboratory context.

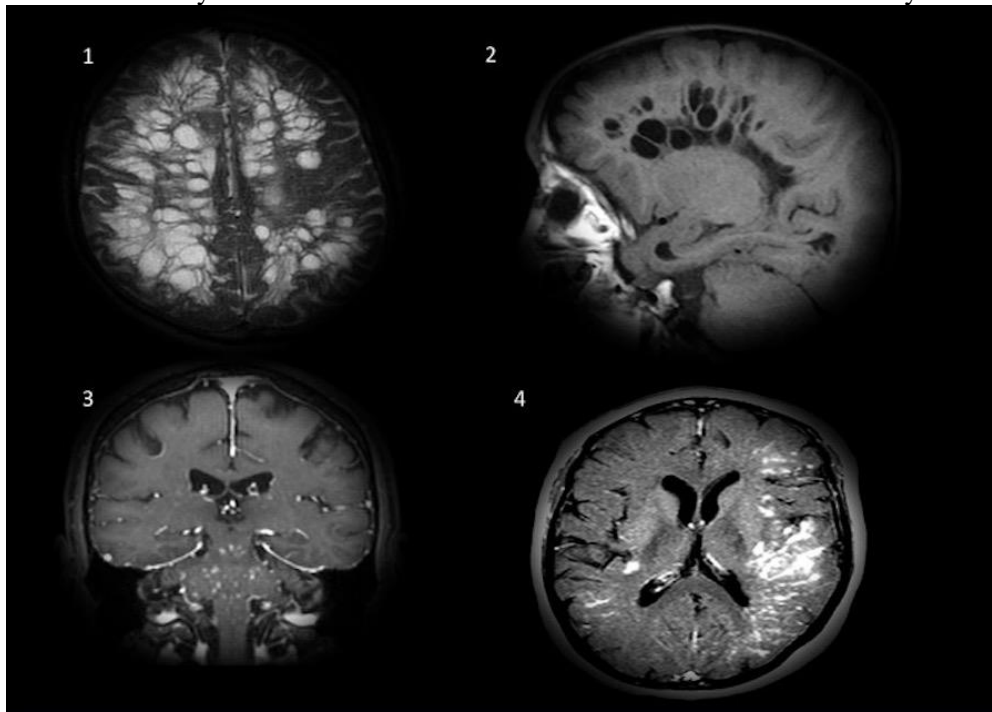


Figure 1: Axial T2WI showing exuberant diffuse enlarged perivascular spaces in a 69 year-old investigating dementia.

Figure 2: Sagittal T1 demonstrates enlarged perivascular spaces in the periventricular/corona radiata white matter in a 10 year-old patient with left eye cataract and renal impairment – Lowe Syndrome.

Figure 3: Coronal T1 post gadolinium evidenciates punctiform perivascular pons enhancement resolved in subsequent control images after steroid therapy – CLIPPERS

Figure 4: Axial T1 post gadolinium demonstrates extensive bilateral perivascular enhancement predominating on the left hemisphere - Sarcoidosis

(Filename: TCT_eEde-055_Slide8.jpg)

eEde-101

Evaluation of Collateral Status in the Acute Stroke Setting: A Primer for the Practicing Neuroradiologist

A Rizvi¹, D Sadowsky¹, M Tenner¹, S Bobra¹, H Mehta², T Miller³, E Gulko¹

¹Westchester Medical Center, Valhalla, NY, ²New York Medical College-Westchester Medical Center, Valhalla, NY, ³Montefiore North Medical Centre, Bronx, NY

Purpose

The purpose of this presentation is to review the evaluation of intracranial arterial collaterals in the setting of acute ischemic stroke. The goal is to allow the neuroradiologist to gain proficiency in assessing collaterals, which may guide management of patients presenting for potential thrombectomy.

Materials and Methods

We aim to review the literature regarding evaluation of collaterals in the setting of anterior circulation large vessel occlusions. We will discuss various classification schemes of collateral assessment, including single and multiphase CTA. Through a case-based approach, we will present cases that highlight and enforce collateral status grading.

Results

Increasing recent literature has demonstrated that functional outcomes in acute ischemic stroke patients undergoing thrombectomy is in part influenced by the robustness of collaterals. Collateral status has clinical implications for penumbral tissue, and may extend the time window for endovascular intervention. Comfort in interpreting the collateral status is of importance for the practicing neuroradiologist. The objective of this presentation is to provide an educational resource that will aid in collateral evaluation.

Conclusions

Status of arterial collaterals in the acute stroke setting influences timing and progression of ischemic tissue to irreversible infarct. Consideration of collateral status is increasing in practice amongst neuroradiologists, and confident evaluation will aid in patient triage for potential thrombectomy.

eEde-056

Finding the Source of Subarachnoid Hemorrhage: Distribution Patterns and Additional Imaging Clues

M Ghuman¹

¹QEII Health Sciences Centre, Dalhousie University, Halifax, Nova Scotia, Canada

Purpose

Subarachnoid hemorrhage (SAH) have different etiologies ranging from trauma (most common), aneurysmal rupture, idiopathic perimesencephalic hemorrhage, arterial dissection, cerebral venous thrombosis, amyloid angiopathy and vasculopathies e.g. reversible cerebral encephalopathy and posterior reversal encephalopathy syndrome. On imaging, the distribution pattern of the subarachnoid blood and additional findings often provide a hint to the underlying cause of the hemorrhage. In this presentation, we aim to discuss clinical examples illustrating the importance of this pattern recognition and additional pointers to the underlying cause.

Materials and Methods

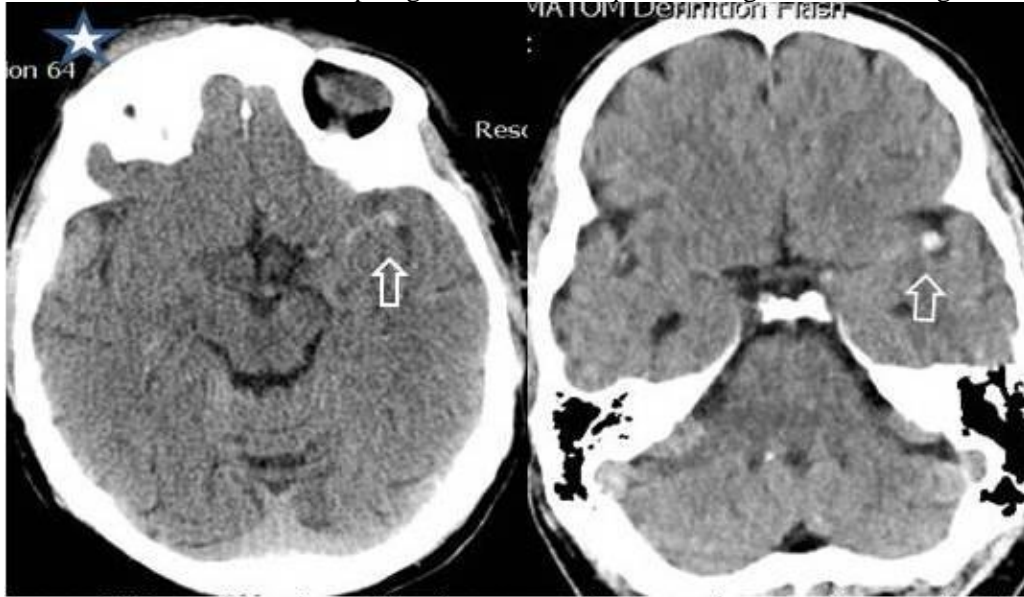
Different etiologies and the corresponding usual pattern of distribution of SAH have been described in the literature. Institutional imaging database was reviewed and selective SAH cases were analyzed. Pertinent clinical information was also reviewed.

Results

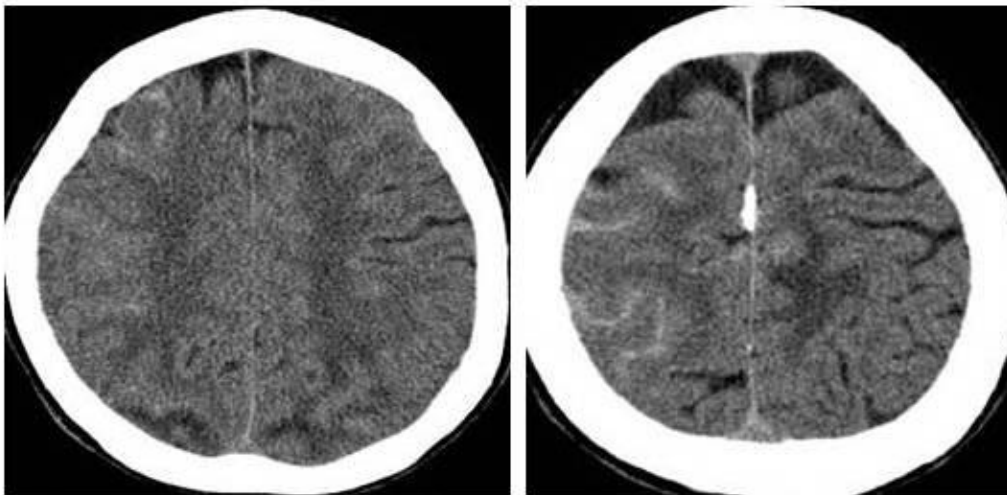
SAH needs to be differentiated from pseudo-SAH. Three distinct patterns by location on initial unenhanced CT have been described which include suprasellar or central basal cisterns, perimesencephalic or low basal cisterns and convexal. Aneurysmal SAH often shows a distinct distribution that point to the particular location of the leaked aneurysm.

Conclusions

Analyzing the information from all findings and different patterns of SAH distribution can help narrow down the differentials and help to guide the next step in investigation and management of these patients.



68 M fell from bicycle and had retrograde amnesia. Focal hyperdensity in left sylvian fissure. CTA was normal. First CT image showed hematoma in the right frontal scalp. **Focal traumatic SAH mimicking MCA aneurysm**



58 F post-op day 8 hemicolectomy for colonic carcinoma, increasing confusion, tingling sensation left hand. CT noncontrast showed convexal SAH with hypodensities in frontoparietal subcortical white matter. **Posterior reversible encephalopathy syndrome (PRES)**

(Filename: TCT_eEde-056_ImageSAH.jpg)

eEde-031

Functional MRI (fMRI) in Presurgical Planning: How We Do It

R Patel¹, A Kamali¹, L Ocasio², S Calle¹, O Arevalo¹, P Rabiei¹, S Khanpara¹, E Bonfante¹, R Riascos¹
¹*The University of Texas Health Science Center at Houston, Houston, TX*, ²*Memorial Hermann Hospital, Texas Medical Center, Houston, TX*

Purpose

1. To discuss the principles and physics of BOLD functional magnetic resonance imaging (fMRI) technique 2. To review the imaging acquisition and standard postprocessing techniques of fMRI 3. To illustrate utilities of fMRI application in day to day practice mainly in the presurgical planning 4. To understand the limitations and challenges of fMRI

Materials and Methods

In routine practice, primary indication for fMRI is evaluation of eloquent areas of the brain in relation to a focal parenchymal brain lesion such as neoplasm, epileptic focus or arteriovenous malformation. This educational exhibit will review all aspects of clinical fMRI from preprocedural patient preparation, selecting correct fMRI paradigms depending on location of focal parenchymal lesion, imaging acquisition, post processing fMRI and interpretation. Relevant cortical neuroanatomy and concepts such as neurovascular coupling/uncoupling, language lateralization, cortical plasticity/reorganization are also included. Over 10 different presurgical cases are presented in a case based format; pathological entities include brain tumors and arteriovenous malformation.

Results

In our practice, BOLD fMRI is employed routinely as part of the preoperative assessment for patients undergoing neurosurgical intervention. Localizing eloquent regions involved in language, motor, visual and auditory function plays a critical role in assessing the risk of developing a postoperative deficit, which can aid in preprocedural discussion with patient and also in presurgical planning. Presurgical fMRI does not completely obviate the need for intraoperative mapping or testing. Presurgical mapping is in fact complimentary to intraoperative mapping strategies, including intraoperative electrical stimulation. There is growing evidence that presurgical fMRI and intraoperative utilization can decrease operative time and improve post-procedural outcome.

Conclusions

For participants, this exhibit will be a good learning module to understand the principles and basic physics of BOLD fMRI technique, how to perform, postprocess as well as interpret the fMRI and also to learn the functional anatomical considerations in neurosurgical candidates prior to surgery. When used effectively, fMRI has an impact on the preservation of language, motor, and vision networks postoperatively which is vital in improving patient care and outcome.

eEde-038

Get SMART: A Radiologic Review of SMART Syndrome

R Hebert¹, J Scheibal¹, R Tramel¹, N Lall², A Steven²
¹*Ochsner Clinic Foundation, New Orleans, LA*, ²*Ochsner Health System, New Orleans, LA*

Purpose

The purpose of this educational exhibit is to review the incidence, clinical presentation, typical disease course, and characteristic imaging findings of SMART syndrome. These characteristic features will be compared to other differential diagnoses to provide contrast between these disease entities. Viewers of the exhibit will benefit from understanding how to correctly identify and differentiate this disease from other similar appearing entities in order to appropriately coordinate therapy.

Materials and Methods

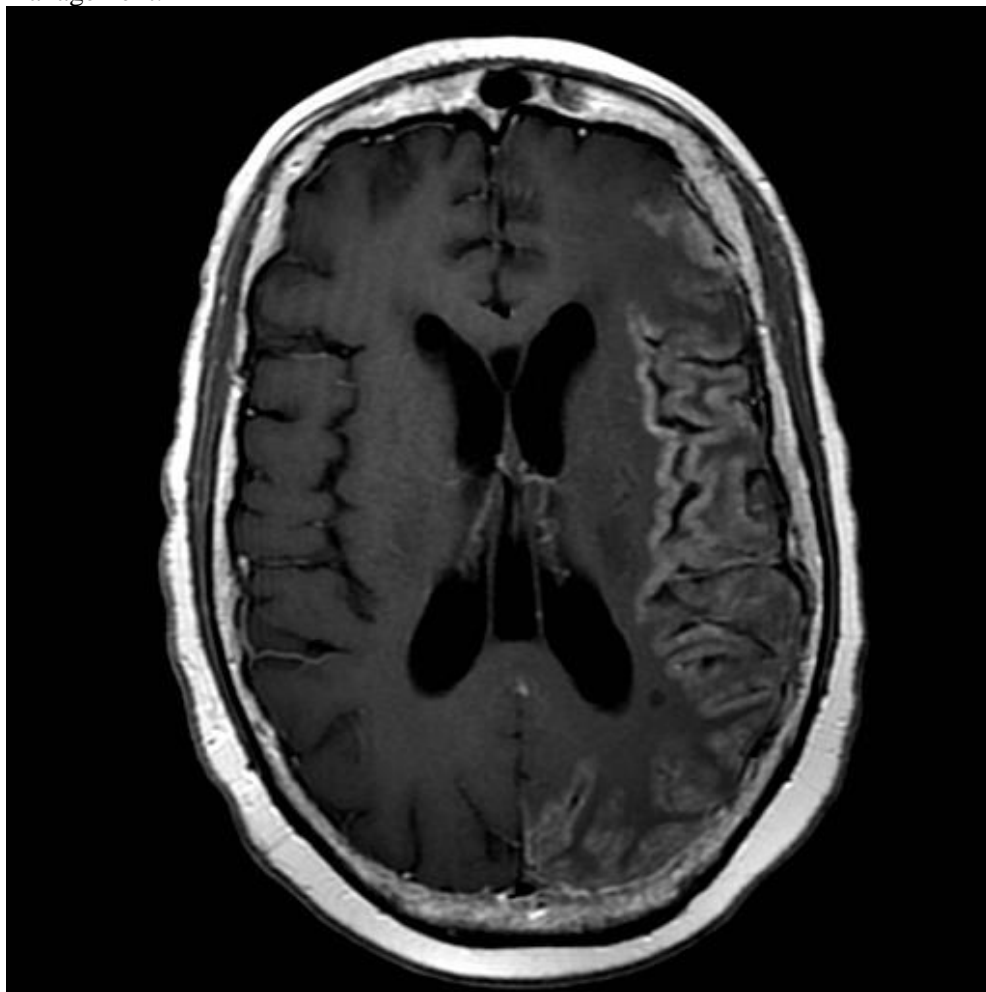
The exhibit will detail the hallmark imaging findings of SMART syndrome and compare and contrast these imaging findings with other similar appearing disease processes. We will also present a small series of cases the authors have encountered.

Results

Stroke-like migraine attacks after radiation therapy (SMART) syndrome is an uncommon condition thought to represent a delayed complication in patients after whole-brain irradiation. The syndrome is characterized by recurrent migraine headaches and complex neurological deficits. Patients may present with seizures and stroke-like symptoms, such as aphasia, hemiplegia, and visual disturbances. The pathogenesis of SMART syndrome remains largely unknown. Characteristic imaging features of SMART syndrome are transient and reversible unilateral, thick gyriform cortical enhancement and associated increased T2/ fluid attenuated inversion recovery (FLAIR) signal. The purpose of this exhibit is to review the clinical presentation and imaging findings of SMART syndrome, as well as discuss key differential diagnoses and management.

Conclusions

SMART syndrome is an uncommon condition that will likely be encountered more frequently in the future as cancer survival rates continue to improve. The complex clinical presentations of this syndrome can pose a difficult challenge to clinicians. Radiologists can play an instrumental role in the proper identification of this syndrome and differentiating from other neurologic disorders to guide clinical management.



(Filename: TCT_eEde-038_1_1.jpg)

eEde-026

Getting Reacquainted with Cranial Nerve Anatomy and Pathology

B White¹, S Castillo¹, F Jeelani¹, T O'Neill²

¹University of Texas Southwestern Medical Center, Dallas, TX, ²University of Texas Southwestern, Dallas, TX

Purpose

The purpose of this electronic exhibit is to provide learners with a self-guided deep review of important cranial nerve (CN) and skull-base anatomy as well as key pathology.

Materials and Methods

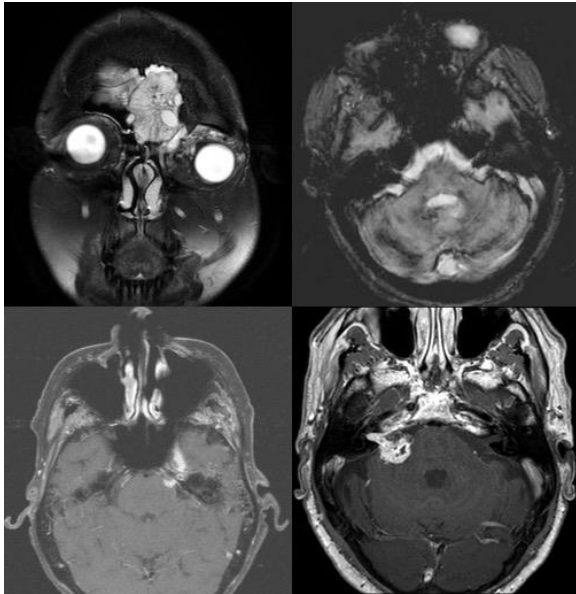
This exhibit will use multiple scrollable CT and MR series including high-resolution heavily-T2-weighted sequences to demonstrate cranial nerve anatomy as well as skull-base foramina, the visual pathway, and routes of perineural spread, etc. The learner will have the opportunity to view images with and without annotations for self-assessment and reinforcement. Examples of high-quality cases including both key images and scrollable image stacks will also be included to illustrate important or common pathologies for each cranial nerve.

Results

In addition to high-yield functional and structural anatomic review, examples of pathologies affecting the cranial nerves will include trauma, meningiomas, schwannomas, aneurysms, vasculitis, esthesioneuroblastoma, optic glioma, optic neuritis, sellar lesions, perineural tumor spread, trigeminal neuralgia, petrous apicitis, cavernous sinus thrombosis, Bell's palsy, Ramsay-Hunt, cholesteatoma, superficial siderosis, glomus tumors, thoracic malignancy resulting in recurrent laryngeal palsy, and others.

Conclusions

The study of cranial nerve anatomy with its complex three-dimensional relationships is best served with annotated interactive scrollable series, which can present the salient features in a high-quality workstation-style format. Combining this robust anatomical review of cranial nerve and skull base anatomy with illustrative pathologic cases will refresh the learner on important and/or common diagnosis and reinforce the foundational material.



(Filename: TCT_eEde-026_ASNRCN.jpg)

eEde-024

Graph Theory: Bare Essentials for The Understanding of Functional Brain Networks

J Nguyen¹, E Palacios², M Yu¹

¹Tulane University School of Medicine, New Orleans, LA, ²Tulane University, New Orleans, LA

Purpose

The aim of this tutorial is to illustrate important concepts of graph theory as applicable to the understanding of resting state fMRI, hence the understanding of brain networks. The reader will learn basic building blocks and properties of graph theory needed for the characterization of brain networks. Important concepts for the understanding of fMRI functional connectivity include clustering-coefficient, characteristic path length, node degree and degree distribution, centrality and modularity will be explained in details. Examples will be given to clarify the learned concepts.

Materials and Methods

- Describe the basic principles of fMRI and resting state fMRI - Describe the functional connectivity of the brain based on resting state fMRI principles - Describe the organization of the brain networks based on functional connectivity - Describe the basic concepts and properties of graph theory such as vertex, edge, graph types, trees, connectivity and transversability, - Describe the applications of some important concepts in graph theory for the analysis of brain networks, including clustering-coefficient, characteristic path length, node degree and degree distribution, centrality and modularity - A post test will be available for self-evaluation of the learned concepts

Results

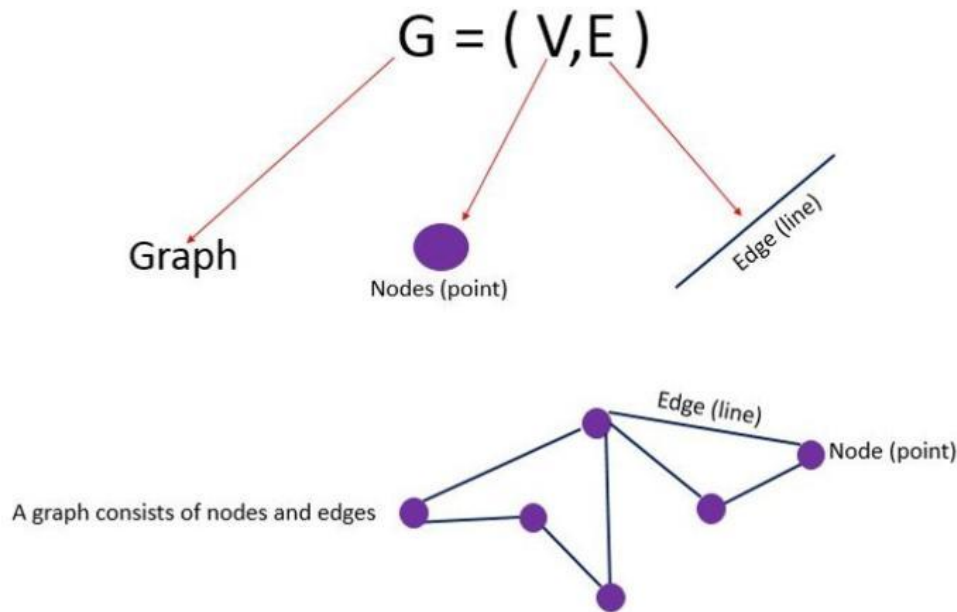
Functional magnetic resonance imaging (fMRI) is a neuroimaging technique using MRI technology that measures brain activity by detecting blood oxygenation and flow that occur in response to neural activity when performing an explicit task. Signal generation of fMRI is based on the blood oxygenation level dependent (BOLD) contrast, which relies on regional differences in cerebral blood flow to delineate regional activity. Resting state functional MRI (R-fMRI) is a relatively new method for evaluating regional interactions that occur when a subject is not performing an explicit task. Human brains are believed to form an integrative network in which information is continuously processed and transferred between structurally and functionally linked brain regions. Using resting state fMRI, pioneering studies have shown that a high level of functional connectivity existing between regions of functional networks, like the primary visual network, auditory network and higher order cognitive networks. Graph theory is branch of mathematics concerned with the relationships of nodes and lines. Functional brain networks can be defined as a graph with the collection of nodes reflecting the brain regions, and lines reflecting the connections between these brain regions. A graph representation of the functional brain network allows for the examination of its organization using graph theory. The aim of this tutorial is to illustrate important concepts of graph theory as applicable to the understanding of resting state fMRI, hence the understanding of brain networks. The reader will learn basic building blocks and properties of graph theory needed for the characterization of brain networks. Important concepts for the understanding of fMRI functional connectivity include clustering-coefficient, characteristic path length, node degree and degree distribution, centrality and modularity will be explained in details. Examples will be given to clarify the learned concepts.

Conclusions

Human brain consists of spatially distributed but functionally linked regions forming multiple interconnected networks, which can be explored using resting-state fMRI. Pioneering studies have shown that functional communication within the human brain is highly organized according to efficient topology. A graph representation allows for the modeling of the interconnectivity of the brain networks using the mathematics of Graph Theory. This can serve as a new platform to further explore the overall structure of local and global functional connectivity in the human brain.

Electronic Educational Exhibits

Graph Definition



(Filename: TCT_eEde-024_graphdef.jpg)

eEde-004

Hemodynamics and Imaging of Intracranial Pressure-Hypertension, -Normotension and -Hypotension

S Kanekar¹, T Zacharia¹

¹Penn State Milton Hershey Medical Center, Hershey, PA

Purpose

1. To discuss the normal hemodynamics of the intracranial pressure 2. To discuss with illustrations the imaging findings and causes of Intracranial -Hypertension, -Normotension and -Hypotension

Materials and Methods

Intracranial pressure (ICP) is defined as the pressure within the craniospinal compartment, a closed system that comprises a fixed volume of neural tissue, blood, and cerebrospinal fluid (CSF). Monro-Kellie doctrine states that an increase in the volume of one intracranial compartment will lead to a rise in ICP unless it is matched by an equal reduction in the volume of another compartment. We retrospectively reviewed the imaging studies from our PACS of 750 patients with neurological complications due to abnormal intracranial pressure, which form the basis of this exhibit. All patients had CT and MRI exams of brain. In addition, 73 patients had advanced imaging that includes perfusion imaging, and diffusion tensor imaging (DTI).

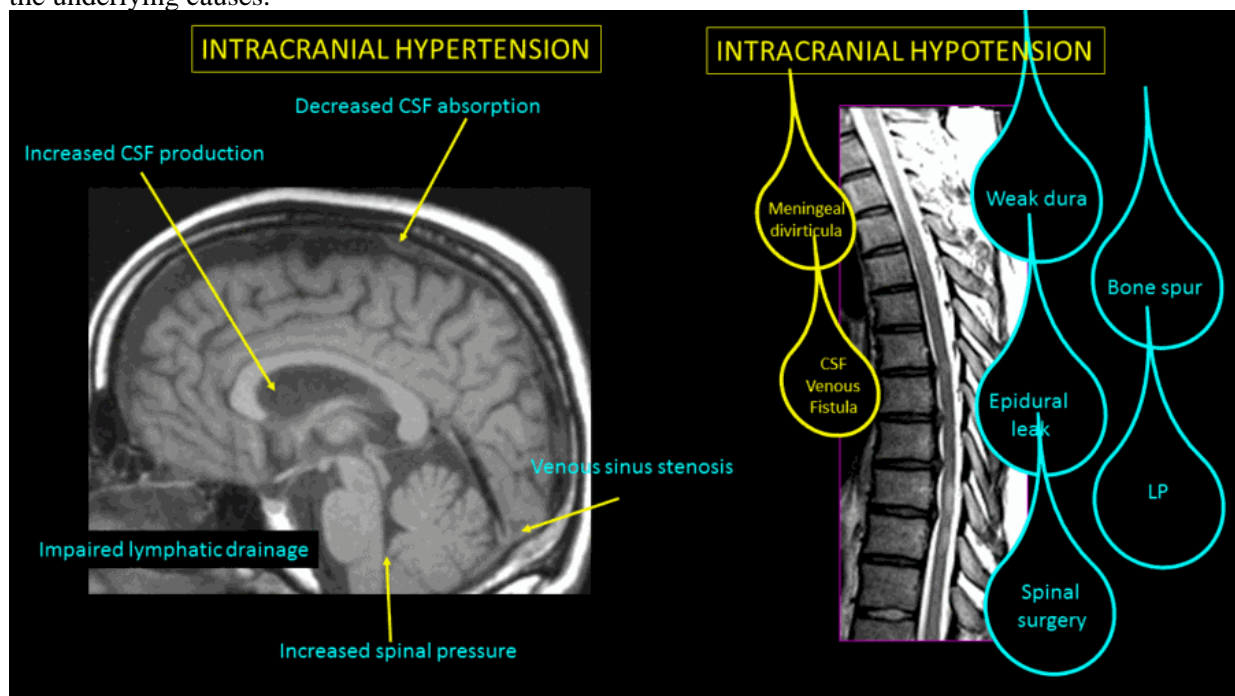
Results

For ease of understanding, this exhibit is reviewed under 3 broad categories of Intracranial pressure (ICP): -IC Hypertension, -IC Normotension and -IC Hypotension. Depending on the specific causes the exhibit has been further categorized into: (A) IC Pressure: Space-Occupying Lesions: Intracerebral Hemorrhage Epidural Hemorrhage Subdural Hemorrhage Tumor Abscess; Diffuse Cerebral Edema Meningitis Encephalitis Hepatic Encephalopathy Reye's Syndrome Acute Liver Failure Electrolyte Shifts Dialysis Hypertensive Encephalopathy Postanoxic Brain Injury Lead Encephalopathy Uncompensated

Hypercarbia Head Trauma Diffuse Axonal injury Hydrocephalus Subarachnoid Hemorrhage Meningitis Aqueductal Stenosis Idiopathic Miscellaneous Pseudotumor Cerebri Craniostylosis Venous Sinus Thrombosis. (B) Normal-Pressure Hydrocephalus. (C) IC Hypotension: 1. True Hypovolemic State 2. Traumatic CSF Leaks a. Definite trauma (MVAs, sports injuries, etc) b. Thecal holes and rents from LPs and epidural catheterizations c. Spinal and cranial surgeries including skull base and some sinus surgeries d. Proximal brachial plexus avulsion injuries, nerve root avulsions 3. CSF shunt over drainage 4. Spontaneous CSF leaks a. Undetermined cause b. Preexisting weakness of the dural sac, surgical anatomical observations i. Meningeal diverticula ii. Disorders of connective tissue matrix 1. Marfan syndrome, c. Trivial trauma in the setting of preexisting dural weakness d. Spondylotic spurs, herniated disc.

Conclusions

1. For participants, this exhibit will be a core learning module to understand the hemodynamics of the intracranial pressure and pathophysiology of intracranial -hyper, -normo and -hypotension. 2. We illustrate the various imaging findings of the intracranial hypo and hypertension and imaging "pearls" to the underlying causes.



(Filename: TCT_eEde-004_123.gif)

eEde-094

High-resolution Vessel Wall MR Imaging and Intracranial Aneurysms: Current Understanding and Potential Clinical Applications

A Lal¹, T Huynh², M Levitt³, G Juric-Sekhar¹, M Mossa-Basha¹

¹University of Washington, Seattle, WA, ²St Michael's Hospital, Toronto, Ontario, Canada, ³University of Washington, Harborview Medical Center, Seattle, WA

Purpose

Intracranial aneurysms are a common but heterogeneous disease entity with potential for high morbidity and mortality. They can vary in many aspects of their intrinsic qualities, including underlying causes, histologies, and imaging characteristics. In recent years, intracranial vessel-wall MR (IVWMR) has

Electronic Educational Exhibits

gained traction in characterization of aneurysms, and in the future, may play an important role in management of intracranial aneurysms.

Materials and Methods

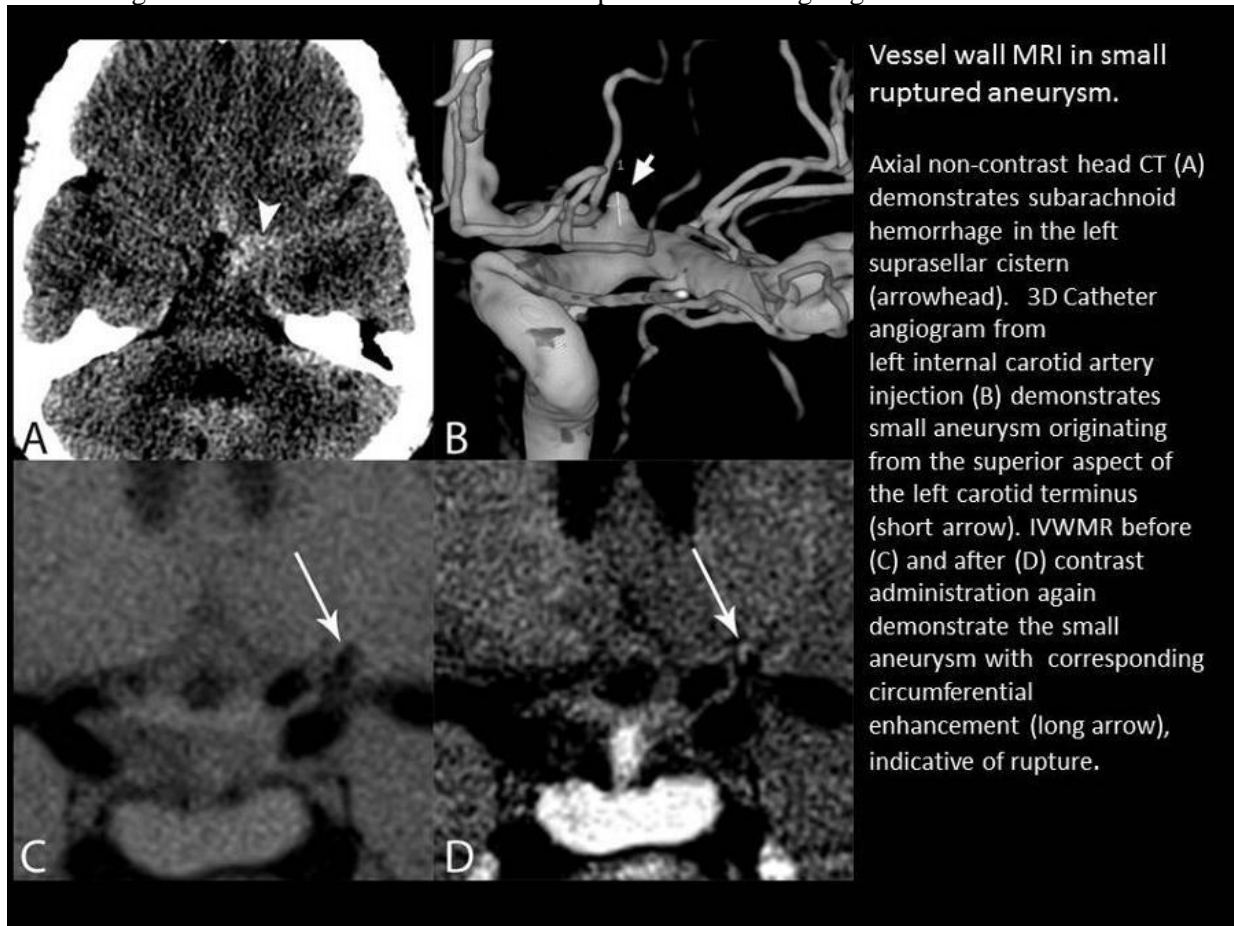
Our institution is involved in research projects that explore the utility of IVWMR in intracranial aneurysm evaluation. We reviewed our imaging archives for patients with intracranial aneurysms who received IVWMR. Cases that highlighted various areas of potential use were selected. In addition, we reviewed the literature on use of IVWMR in intracranial aneurysms. This presentation provides a framework that radiologists can use for understanding pathophysiological processes and IVWMR utilization for intracranial aneurysms.

Results

We highlight cases that illustrate the value of IVWMR in intracranial aneurysm evaluation within a variety of settings, including ruptured and unruptured aneurysms, multiple and treated aneurysms and its ability to predict outcomes. We discuss applications of IVWMR in the evaluation of aneurysms as described in the literature. Mention will also be made of potential pitfalls and limitations of IVWMR when used to evaluate intracranial aneurysms.

Conclusions

The relatively new field of IVWMR and its use in furthering our understanding and characterization of intracranial aneurysms may have significant clinical implications in the future. Therefore, it is important for radiologists to familiarize themselves with the published and ongoing research in this field.



(Filename: TCT_eEde-094_ASNRAbstractGraphics.jpg)

eEde-106

I Don't Want to Miss A Thing: An Overnight Survival Guide of Neuroradiological Emergencies of the Brain for the On-call Resident

A Baig¹, D Guerrero¹, S Mangat¹, S Lev¹

¹*Nassau University Medical Center, East Meadow, NY*

Purpose

To highlight potential pitfalls in the diagnosis of neuroradiological emergencies. To discuss perceptual and cognitive errors and devise strategies to negotiate imaging blind spots.

Materials and Methods

Imaging studies (CT, CTA/CTV, MRI, and MRA/MRV) of emergency cases from our Level I trauma center during the past five years were scrutinized to identify causes of common resident misses and misinterpretations. We categorized these by mechanisms of injury, location and etiology. The viewer of this exhibit is challenged to take each case study as an unknown, and to detect early or subtle signs, much as an on-call resident would.

Results

Vascular emergencies can be ischemic, hemorrhagic or both. While interpreting a "CVA", the resident may be overly biased by clinical history. We present several stroke mimickers, such as a GBM that was misread as an infarct. "Loss of consciousness" (LOC), on the other hand, should prompt one to consider diffuse axonal injury (DAI). Fat embolism, seen in patients with long bone fractures, however, can be a mimic. Subtle contusions can be overlooked or mistaken for artifact. 2-D reformats are essential in detecting subtemporal, convexity and tentorial hematomas. Conversely, partial volume averaging of the skull base can be mistaken for hemorrhage. Contusions can expand and repeat imaging is often indicated. A CTA "spot sign" has high predictive value for hematoma growth. Subdural hematomas (SDH) can be overlooked without appropriate windows. Nonaccidental trauma should be considered in the pediatric population when extra-axial hemorrhages of varying ages are noted. Subarachnoid hemorrhage may indicate a ruptured aneurysm. We demonstrate an unusual case of an MCA aneurysm rupturing superiorly, with an associated intraparenchymal hemorrhage overshadowing the lesser subarachnoid component. Diffuse cerebral edema can produce a "pseudosubarachnoid hemorrhage" appearance. Intraventricular hemorrhage can be extremely subtle, is associated with DAI and has high mortality. Subtle skull base fractures may be associated with pneumocephalus, sinus or mastoid fluid, and even ossicular dislocation. Vascular injury is especially suspect with high velocity and rotational motions, and can cause delayed infarcts. We demonstrate pseudoaneurysms, A-V fistulas, and carotid dissections/occlusions. Assess for depressed calvarial, sphenoid (associated with carotid-cavernous fistulas), and petrous (carotid canal) fractures. Posterior reversible encephalopathy syndrome is a rare condition that can be easily missed and requires prompt identification.

Conclusions

Neuroradiological emergencies comprise a diverse array of conditions. The interpreting radiologist can actively participate in patient management with appropriate imaging recommendations, prompt diagnosis, and timely communication. An imaging approach "checklist" is essential, as is recognition of mimics and artifacts. Failure to recognize can lead to potentially devastating delayed consequences.

eEde-044

I'm Positive That's Not Mold: A Pictorial Review of Neuroradiological Manifestations of Atypical Gram Positive Bacteria Masquerading as Fungi

V Yedavalli¹, V Pandey¹, V Kuttappan¹, A Patil¹

¹*Advocate Illinois Masonic Medical Center, Chicago, IL*

Purpose

Infectious CNS processes can present in a multitude of ways. Fungi and certain gram positive bacteria can have overlapping symptoms and presentations, making diagnosis challenging and timely treatment difficult. Delaying such treatment can lead to increased morbidity. This pictorial review delves into the neuroimaging manifestations of specific atypical gram positive bacteria which present similarly to fungi.

Materials and Methods

Given the diagnostic dilemmas in treating bacterial and fungal CNS infections, accurate diagnosis is of utmost importance. In this review, we focus on subsets of gram positive bacteria which mimic fungi. Specifically, we compare and contrast the neuroimaging manifestations of atypical mycobacteria, actinomyces, nocardia, and streptomyces. We also examine the different neurological presentations in which each type of bacterium can manifest.

Results

We highlight the neuroimaging manifestations of atypical mycobacteria, actinomyces, nocardia, and streptomyces, which are bacteria which mimic fungi. By comparing and contrasting the different neuroimaging presentations of these specific gram positive bacteria, we hope to elucidate the key differentiating factors for accurate diagnosis and treatment.

Conclusions

Differentiating fungi and atypical bacterial infections which can mimic fungi is integral to timely diagnosis. We review imaging characteristics of gram positive bacteria known to have similarities to fungi with the goal of improving diagnostic and therapeutic accuracy.

eEde-008

Imaging Aging Brain: An Update

A Faulkner¹, A Bag¹

¹*University of Alabama at Birmingham, Birmingham, AL*

Purpose

The number of Americans surviving into their 80s and beyond is expected to grow dramatically and it is expected that 72 million older (>65 years of age) Americans will make up to 20% of the total population by 2030. As the number of older Americans grows rapidly, neurodegenerative diseases and brain diseases associated with aging are also expected to rise significantly. It is obvious that there will be a significant increase in imaging of the aging brain, necessitating a structured reporting system. This is particularly true because of the extreme heterogeneity of radiological reports in current radiology practice--both in community and academic settings. Inconsistent imaging protocols across different practices add another layer of complexity to the problem. The purpose of this educational exhibit is to: a) propose a comprehensive imaging protocol for imaging of the aging brain that is simple and currently relevant, b) enumerate different visual rating scales for evaluation of changes associated with aging brain, and c) propose a simple, structured reporting system that encompasses all of the necessary details that a subspecialty neurologist needs to know.

Materials and Methods

Based on current recommendations, an appropriate MRI protocol will be proposed. Rating systems for evaluations of degree of white matter diseases, degree of hippocampal atrophy, parietal lobe atrophy and global brain atrophy will be reviewed (such as the Fazekas scale for white matter lesions and the MR parkinsonism index). A structured reporting system will be proposed for comprehensive evaluations of changes associated with normal aging and changes induced by different neurodegenerative diseases.

Results

The educational exhibit is to propose a homogenous imaging protocol for imaging of aging brain and to propose a structured reporting system that is meaningful to a neurologist treating older patients and patients with different neurodegenerative diseases.

Electronic Educational Exhibits

Conclusions

After review of this educational exhibit, it is expected that the viewer will: a) know the protocol for imaging of aging brain, b) know different rating systems for assessment of aging brain, and c) be educated regarding what to include in a structured radiological report.

eEde-050

Imaging and Pathologic Correlation in Different Tissues in Familial CCM Disease

B Hart¹, T Bocklage², S Tandberg¹, K SantaCruz³, B Zlotoff⁴, M Mabray¹, L Morrison¹, M VonLoh¹
¹University of New Mexico, Albuquerque, NM, ²University of Kentucky, Lexington, KY, ³University of New Mexico Hospital, Albuquerque, NM, ⁴University of Virginia, Charlottesville, VA

Purpose

Familial CCM disease, resulting from mutations in one of three known genes, is a multisystem, indeed, a neurocutaneous disorder. CNS disease is the hallmark. Cavernal malformations of brain and spinal cord give rise to the name CCM and to the most serious complications. However, the results of the mutation extend throughout the body, including retina, skin, adrenal glands, and bone and possibly liver. We present a review of similarities and differences in pathological and imaging findings in lesions occurring in brain, skin, and bone in fCCM patients.

Materials and Methods

We examined histology and immunohistochemical findings in resected or biopsied lesions from our hospital from cerebral cavernous malformations, skin lesions, and bone lesions from different patients, all of whom had familial CCM disease (CCM1-CHM). Standard H&E stains were utilized in all and, in some cases, immunohistochemical stains.

Results

CCMs in the brain show corresponding MRI and pathologic features. They lack the notable venous component of vascular malformations elsewhere. Bone lesions represent combined capillary-venous malformations, according to the 2014 ISSVA classification. They comprised a disorderly mix of thin and thick-walled, small to medium sized blood vessels embedded in a fibrous to focally myxoid stroma, which entirely replaced marrow fat and hematopoietic elements. MRI shows striking absence of fat signal intensity. Skin lesions are angiokeratomas (dilated blood vessels with overlying epidermal hyperkeratosis) or capillary-venous malformations; MRI correlation is presented.

Conclusions

We illustrate pathologic and MRI appearance of vascular malformations arising in brain, skin, and bone in familial CCM disease. Some features show strong correlation with MRI appearance, such as relative absence of marrow fat in bone lesions and the heterogeneous, reticulated appearance on brain MRI. The differences, especially between the CNS and other lesions, raise questions about the mechanism of lesion formation and lesion specificity in different tissues.

eEde-043

Imaging Features of Histiocytosis Syndromes Involving the Central Nervous System

Y Wang¹, A Abdullah², M Ibrahim², H Parmar²
¹Sichuan Provincial People's Hospital; University of Michigan Health System, Chengdu, China; Ann Arbor, MI, ²University of Michigan Health System, Ann Arbor, MI

Purpose

Histiocytosis syndromes are a group of heterogeneous disorders characterized by abnormal accumulation and infiltration of histiocytes, cells derived from hematopoietic cells of monocyte/macrophage lineage.

Electronic Educational Exhibits

While many systems are involved, central nerve system (CNS) is rarely affected. In this educational exhibit, we describe imaging features of histiocytosis syndromes involving the CNS, aiming to increase our understanding of this disorder.

Materials and Methods

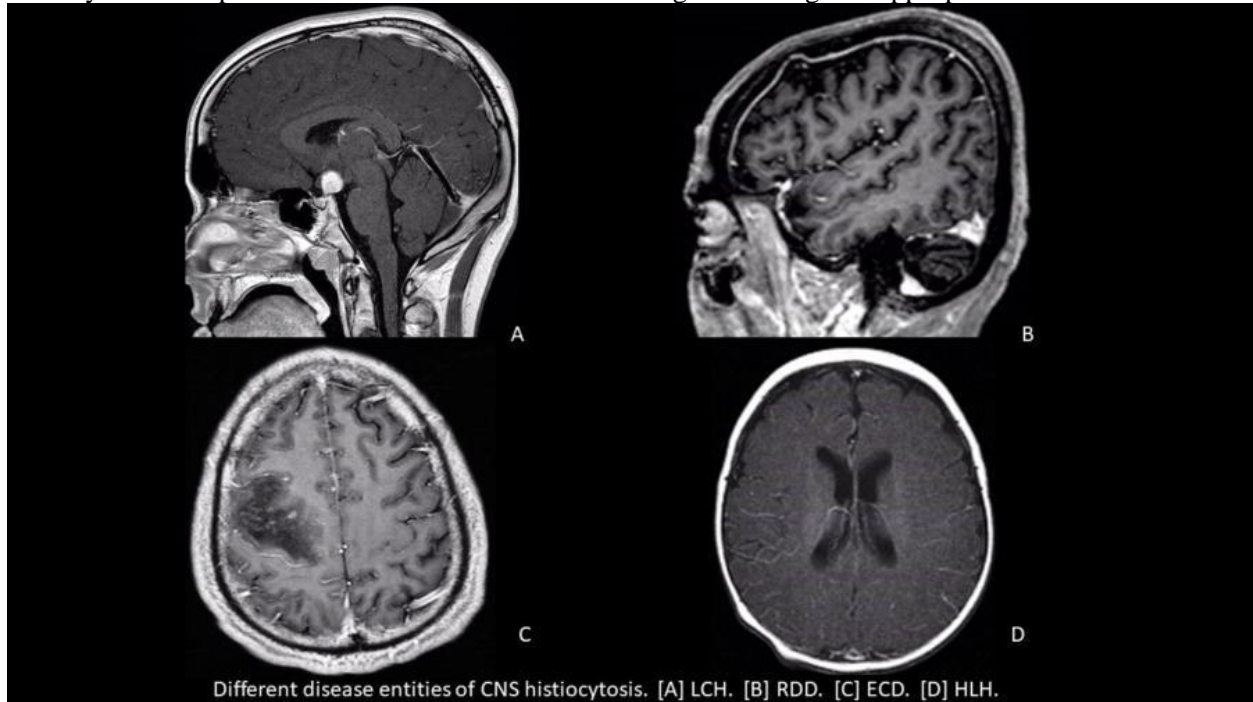
Eight patient records (5 male, 3 female; age range of 0.5 to 70 years) were identified from radiology database and reviewed. Diagnosis was confirmed by pathology in all patients. MRI (n=8) and CT (n=4) were obtained and images were evaluated together by two neuroradiologists.

Results

Histiocytosis syndrome identified included: Langerhans cell histiocytosis (LCH, n=2), Rosai Dorfman Disease (RDD, n=3), Erdheim Chester Disease (ECD, n=1), hemophagocytic lymphohistiocytosis (HLH, n=1), and crystal-storing histiocytosis (CSH, n=1). Findings of LCH presented as enlarged and avidly enhancing suprasellar mass with thick infundibulum (n=1). Extensive pial enhancement over brainstem and spinal cord (n=1) was also noted. RDD manifestations included asymmetric thickening and enhancement of dura with focal nodularity (n=1), aggressive extra-axial mass with destruction of adjacent sphenoid bone (n=1), and enhancing mass centered at the hypothalamus/optic chiasm (n=1). ECD presented as scattered signal abnormality with variable enhancement within white matter, basal ganglia and brainstem (n=1). HLH presented as diffuse and extensive leptomeningeal enhancement (n=1). CSH presented as large areas of signal abnormality with surrounding infiltration and local mass effect (n=1).

Conclusions

CNS manifestations of histiocytosis syndromes are various due to their heterogeneous nature. While imaging findings can provide important clues, diagnosis of this disorder is challenging and definitive diagnosis often necessitates pathologic examination. Awareness of the imaging features of CNS histiocytosis is important to include in the differential diagnosis and guide appropriate treatment.



Different disease entities of CNS histiocytosis. [A] LCH. [B] RDD. [C] ECD. [D] HLH.

(Filename: TCT_eEde-043_ASNRSslide4_jpg300dpi.jpg)

eEde-014

Imaging Giant Cell Arteritis: Vessel Lumen and Vessel Wall

B Kwan¹, T Chen², K Misquitta², A Naheed², D Mikulis², D Mandell²

¹University of Toronto, Toronto, Ontario, Canada, ²Toronto Western Hospital, Toronto, Ontario, Canada

Purpose

To illustrate the existing and emerging roles of neuroimaging in the diagnosis of giant cell arteritis (GCA)

Materials and Methods

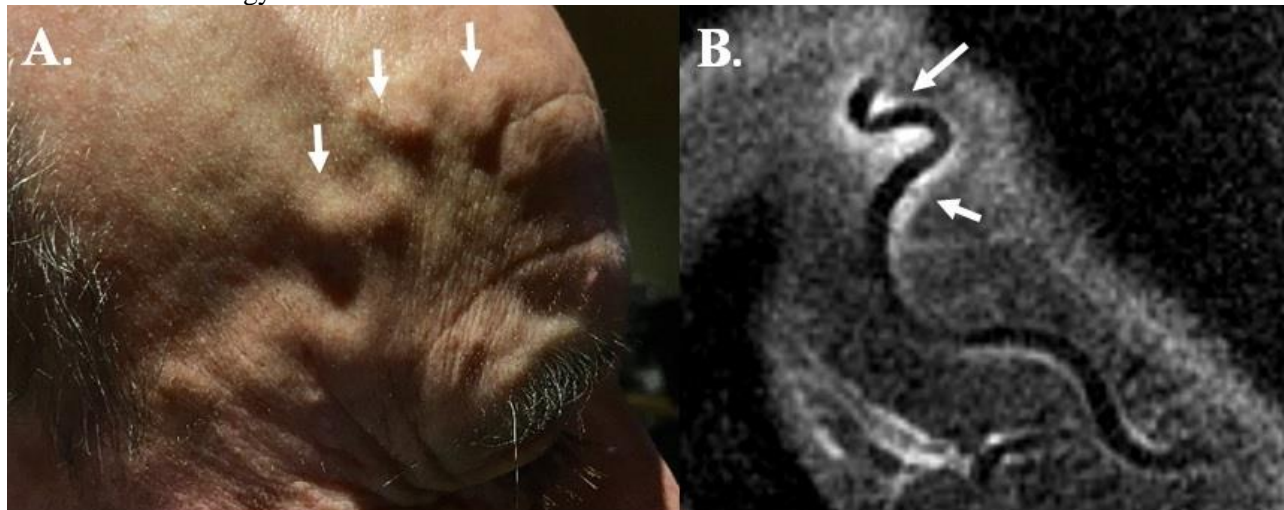
We will discuss the clinical indications for neuroimaging in patients with possible GCA and summarize the existing literature. The technical aspects of high-resolution vessel wall MRI using two-dimensional and three-dimensional pulse sequences will be discussed including differences on tissue weighting (T2 FS and T1 FS pre and postgadolinium). We will illustrate the luminal and vessel wall imaging findings in GCA (in both the external carotid artery branches and intracranial arteries) on both CTA, MRA and MR vessel wall imaging and discuss neuroimaging pitfalls related to this diagnosis. Finally, image guided biopsy of the scalp arteries will be discussed. We will also include clinical images and histopathological correlates of the neuroimaging findings.

Results

Giant cell arteritis is a diagnosis currently suspected based on clinical and laboratory findings, and confirmed by biopsy of the superficial temporal artery. Yet clinical and laboratory findings are often non-specific, and biopsy is invasive and has a high false-negative rate. Emerging neuroimaging techniques can accurately diagnose GCA and guide the physician to potential biopsy sites.

Conclusions

Neuroimaging has an emerging role in the diagnosis of GCA, and newer techniques such as vessel wall MRI may have particular diagnostic utility. Neuroradiologists should be aware of the utility and limitations of neuroimaging for this diagnosis. Image guided biopsy for GCA is also another emerging area in neuroradiology.



A. A case where physical exam revealed marked, cord-like thickening of the right superficial temporal artery (arrows). B. T2 FSE fat suppressed 2D arterial wall imaging demonstrates edema within and surrounding the vessel wall of the right superficial temporal artery (arrows).

(Filename: TCT_eEde-014_Figure1-GCA300dpi.jpg)

eEde-067

Imaging of CNS Lymphoma: What to Expect and How to Avoid Getting Tricked!

G Bathla¹, N Soni¹, P Watal¹, A Capizzano¹, T Moritani²

¹University of Iowa Hospitals and Clinics, Iowa City, IA, ²University of Michigan, Ann Arbor, MI

Purpose

1. To discuss the spectrum of imaging findings in both primary and secondary CNS lymphoma and revisit useful imaging signs 2. To briefly review imaging of various rare manifestations [primary meningeal lymphoma, intravascular lymphoma, lymphomatosis etc] and the pertinent imaging cues 3. To review the common imaging pitfalls and differentials

Materials and Methods

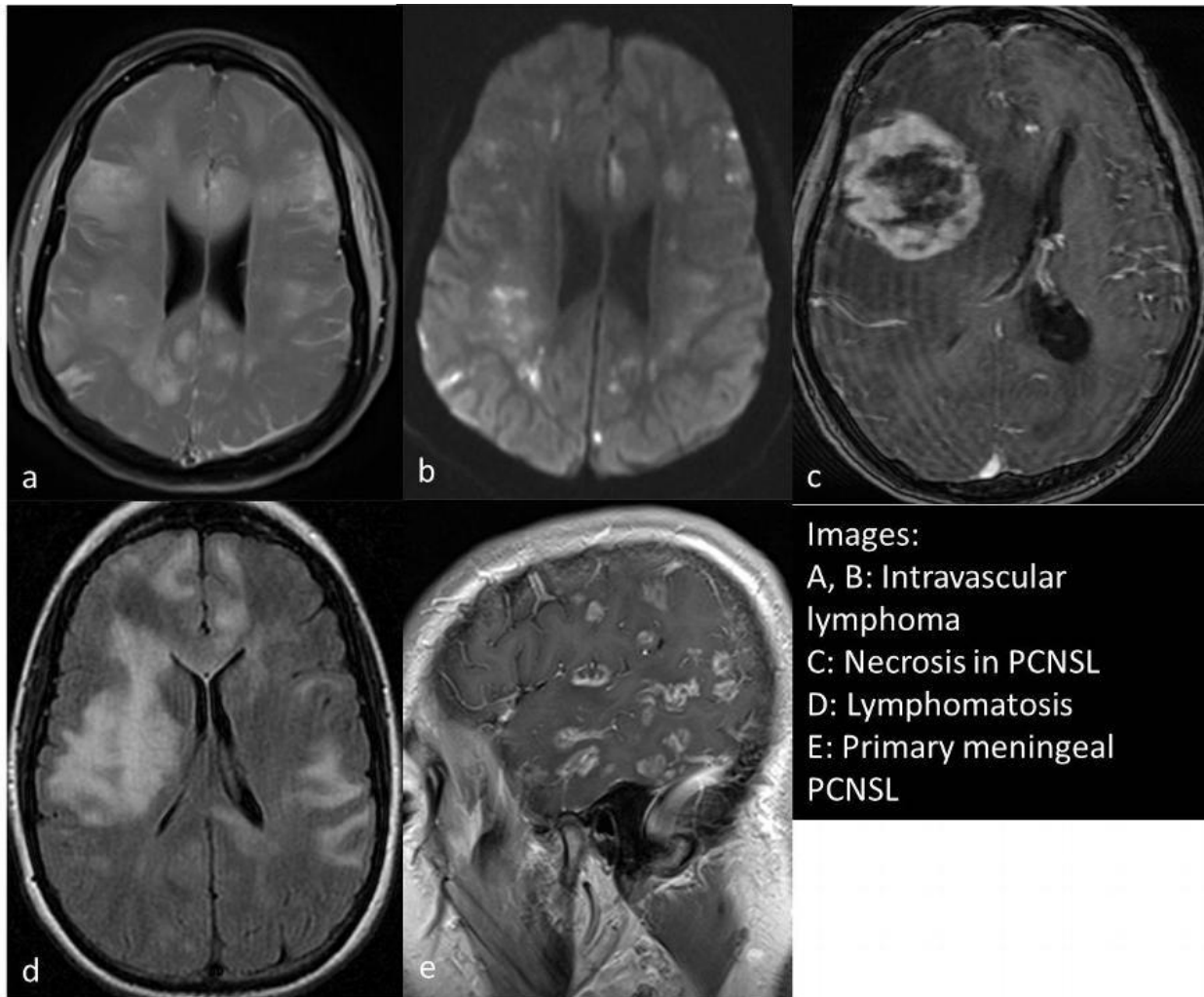
The authors review the common and rare manifestations of CNS lymphoma. This will be a imaging and case-based review, highlighting the pertinent imaging cues and potential pitfalls. The authors will also review the common imaging differentials and discuss the strategies to avoid potential misdiagnosis and pitfalls.

Results

Primary CNS lymphoma [PCNSL] accounts for 1-5% of primary brain neoplasms. PCNSL can have a myriad of appearances although the location, appearance and epidemiology vary between immunocompetent and immunocompromised patients. It may present as a parenchymal, ventricular or meningeal lesion or uncommonly, may mimic infarcts or diffuse parenchymal infiltration. Rare manifestations resulting from primary meningeal involvement, diffuse white matter or intravascular infiltration may again result in considerable diagnostic confusion.

Conclusions

PCNSL can have varying imaging appearance, predominantly dictated by the immune status of the patient. In general, PCNSL in immunocompetent patients generally presents late, is solid, DWI bright and shows uniform enhancement. Contiguity with a CSF surface and perivascular enhancement are useful clues. Immunocompromised patients on the other hand present earlier and often have multiple, necrotic, hemorrhagic lesions with irregular or rim enhancement. Secondary CNS involvement predominantly affects the leptomeninges. Advanced MRI techniques may help with problem solving in atypical cases.



(Filename: TCT_eEde-067_PCNSLabstractimages.jpg)

eEde-082

Imaging of Meckel's Cave Pathology

L Tu¹, K Seifert², X Wu¹, D Gandhi³, A Malhotra²

¹*Yale University School of Medicine, New Haven, CT*, ²*Yale New Haven Hospital, New Haven, CT*, ³*University of Maryland School of Medicine, Baltimore, MD*

Purpose

Meckel's cave is a dura-lined structure connecting the medial portion of the middle cranial fossa with the posterior fossa. The cave houses the trigeminal ganglion and provides channels for the rootlets of the trigeminal nerve. We will review the anatomy of Meckel's cave and discuss the imaging of pathologies arising from or involving this region.

Materials and Methods

A series of illustrative cases will be used to demonstrate the range of pathologies affecting Meckel's cave. A brief review of the relevant literature will be presented.

Results

Schwannomas and meningiomas are among the most frequent pathologies involving the Meckel's cave.

Electronic Educational Exhibits

Metastatic disease including perineural spread of tumor can also be seen, but are less common. Infectious and inflammatory diseases including tuberculosis, nocardia, neurosarcoidosis, and others may involve Meckel's cave. Rare lesions include epidermoid and amyloidoma of the trigeminal nerve.

Conclusions

This review will discuss the complex anatomy of Meckel's cave and surrounding structures, and discuss the imaging findings of related pathologies. This will provide the knowledge needed to devise a more complete imaging strategy for accurate diagnosis and treatment planning.

eEde-034

Imaging of Tumefactive Demyelination: A Comprehensive Review

M Ouyang¹, T Moritani², J Kim², A Capizzano¹, K Jones¹

¹University of Iowa Hospital and Clinics, Iowa City, IA, ²University of Michigan, Ann Arbor, MI

Purpose

Many central nervous system disorders exhibit demyelination. In certain cases, the demyelination presents as a large space-occupying lesion, similar to a tumor, and poses a diagnostic challenge, especially since the clinical symptoms and neuroimaging findings may vary between patients. The purpose of this educational exhibit is to review this topic and describe the definition, history, epidemiology, clinical manifestations, pathology, imaging findings, differential diagnoses, and management of tumefactive demyelination.

Materials and Methods

A literature review of tumefactive demyelination was performed. Multiple representative cases are gathered from the University of Iowa and University of Michigan. The collected cases are incorporated and discussed in the educational exhibit with images from various modalities including CT, MRI, MR spectroscopy, and FDG-PET.

Results

Tumefactive demyelination is uncommon, but can be seen in multiple neurological diseases, including multiple sclerosis, Balo's concentric sclerosis, Balo-like lesions, myelinoclastic diffuse sclerosis (Schilder's disease), Marburg variant, acute hemorrhagic leukoencephalitis (Hurst disease), acute disseminated encephalomyelitis, neuromyelitis optica spectrum disorders, and autoimmune encephalitis. Clinical and imaging presentation of tumefactive demyelination may resemble other entities such as CNS tumors (particularly high-grade gliomas), various infections, progressive multifocal leukoencephalopathy (PML) related immune reconstitution inflammatory syndrome (IRIS), neurosarcoidosis, and immune mediated encephalitides. Therefore, accurately diagnosing tumefactive demyelination remains a challenge. The full clinical picture of each potential case and imaging pattern in multiple modalities including enhancement characteristics (incomplete ring sign) and peripheral diffusion restriction, along with continued follow up imaging may help the radiologist favor tumefactive demyelination over other differential diagnoses.

Conclusions

The detailed discussion and example cases provided in this exhibit will assist the radiologist in understanding and recognizing tumefactive demyelination, an uncommon but important manifestation of multiple neurological diseases. Although accurate diagnosis is often difficult, it has important implications in management decisions, especially as misdiagnosis may lead to treatment modalities such as brain biopsy, resection, or brain irradiation that could exacerbate the demyelination process. Therefore, familiarity with this topic is essential in helping guide the management of patients with tumefactive demyelination.

eEde-002

Immunomodulatory Drugs and Neurotoxicity: Clinical Manifestations and Aspects of Imaging

T Morimoto¹, L Amaral¹, C Campos¹, V Marussi¹, L Freitas¹, A Benine Belezia², b inada¹, T Vilas Boas³, A Maksoud Piccolo⁴, N Dapaixao¹

¹Hospital Beneficência Portuguesa de São Paulo, São Paulo, Brazil, ²A Beneficência Portuguesa de São Paulo/Hospital Santa Catarina de São Paulo, Sao Paulo, Brazil, ³Beneficência Portuguesa de São Paulo, Campinas, Brazil, ⁴Beneficência Portuguesa, São Paulo, Brazil

Purpose

The present study aims to describe clinical manifestations and imaging aspects of induced neurotoxicity by immunomodulatory drugs.

Materials and Methods

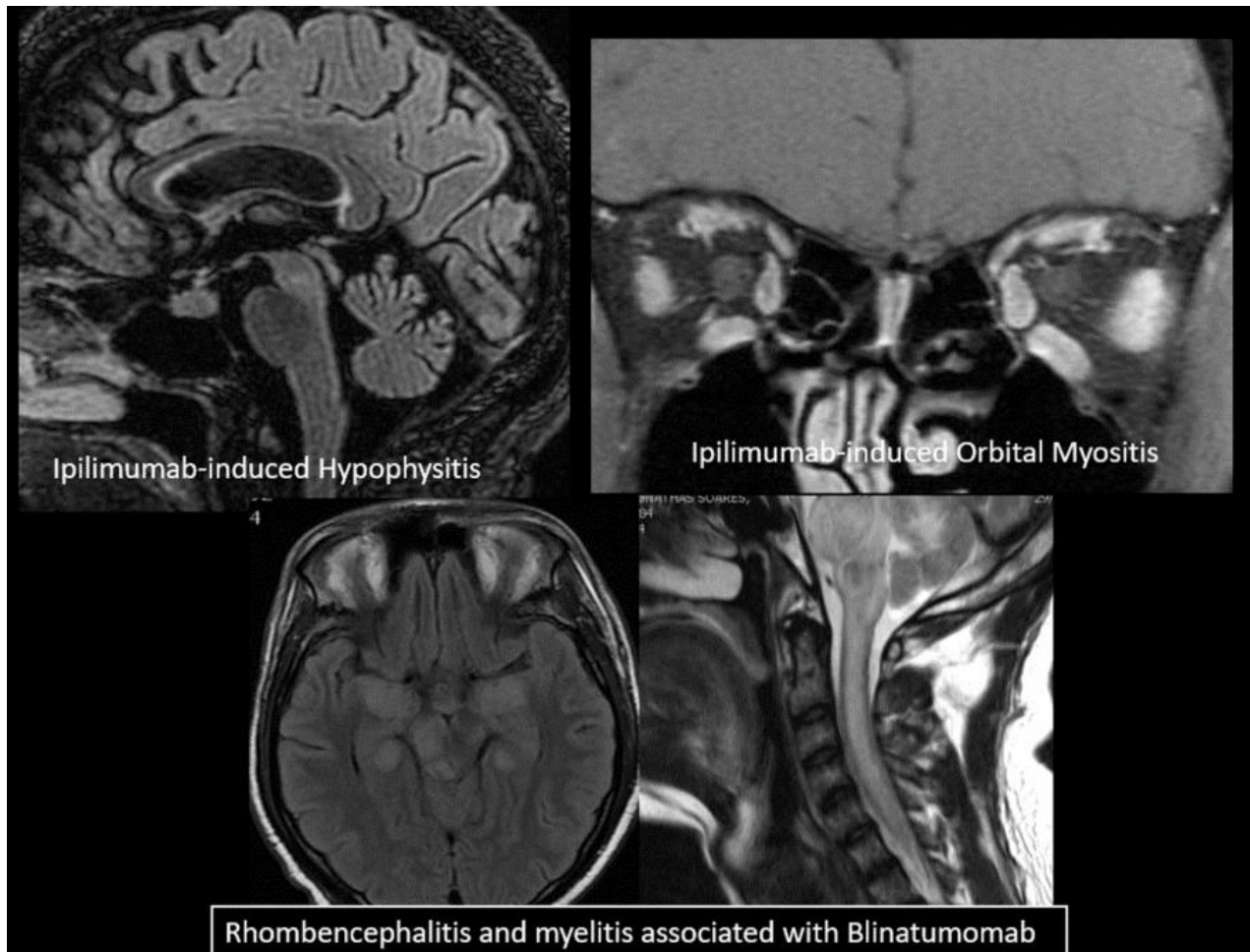
Discuss several cases of patients suffering from neurotoxicity by Immunomodulatory drugs before and after the initiation of the treatment.

Results

Pharmacological and cellular treatment of cancer is changing dramatically with benefits for patient outcome and comfort, but also with new toxicity profiles. Immunomodulatory drugs (IMiDs) are a class of antineoplastic drugs widely used, that can trigger neurotoxicity. Chemotherapy-induced neurotoxicity can affect the peripheral, the autonomic, or the central nervous system. The most common form is peripheral neuropathy, which manifests with hypoesthesia (numbness), paresthesia (tingling, pins and needles, or a limb falling asleep), and hyperesthesia (pain), often in a stocking and glove distribution. Other adverse effects include encephalopathy, cerebellar alteration, disturbed consciousness, seizures, dementia-like amnesia, expressive aphasia, dysarthria, lethargy, reversible coma, intratumoral hemorrhage, bleeding, cerebrovascular events, PRES, radiation necrosis.

Conclusions

During the past years, many new compounds have been introduced in clinical cancer treatment, and cellular therapy is a highly dynamic evolving field. However, physicians have also been faced with new side effects associated with these approaches. An increased awareness of central neurotoxicity as a possible side effect of IMiD therapy, along with early recognition is essential for a better therapeutic planning.



(Filename: TCT_eEde-002_Neurotoxdpigif.gif)

eEde-041

Infections of the Central Nervous System: Atypical Imaging Manifestations and Pathologies

M Walters¹, D Pong¹, A Singh¹, B Tantiwongkosi¹

¹University of Texas Health Science Center San Antonio, San Antonio, TX

Purpose

This education exhibit aims to provide an image rich review of the uncommon imaging findings associated with frequently and infrequently encountered central nervous system (CNS) infectious processes.

Materials and Methods

Radiological images and relevant clinical and pathologic information was extracted from our PACS station and electronic medical record system at our hospital network. Images were retrieved from recent imaging studies to review a spectrum of atypical imaging findings of commonly and uncommonly encountered CNS.

Results

This educational exhibit will illustrate uncommon and rare clinical and imaging manifestations of encountered CNS infections beginning with infectious vasculopathy and infarction with emphasis on Varicella Zoster and Cryptococcal encephalitis. Features of infectious intracranial perineural spread will

then be addressed with illustrative examples including fungal sinusitis. Rhombencephalitis resulting from *Listeria* and coccidiomycosis will be shown. A rare case of *N fowleri* amebic meningoencephalitis is presented. Differentiating characteristics from mimics including thromboembolic cerebral infarction, lymphoma, post-treatment changes and post-traumatic cerebral contusion will also be addressed.

Conclusions

This educational exhibit provides an in-depth review of infrequent imaging findings associated with common and uncommonly encountered CNS infectious pathologies. Proper differentiation among these entities may prove difficult. However, a radiologist's knowledge of these uncommon clinical and imaging CNS findings can assist in timely diagnosis and administration of life-saving timely therapies.

Infections of the CNS: Atypical Imaging Manifestations & Pathologies

- Vasculitis and infarction
 - Cryptococcus
 - Varicella Zoster
- Intracranial perineural spread
 - Invasive fungal sinusitis and cerebritis
- Rhombencephalitis
 - *Listeria*
 - Coccidiomycosis
- Amebic Meningoencephalitis
 - *N fowleri*
- Mimics
 - Thromboembolic cerebral infarction
 - Lymphoma and post-treatment changes
 - Post-traumatic cerebral contusion

Cryptococcal Meningitis

- Ubiquitous unicellular yeast
- most common fungal infection of the CNS
- Rarely results in small vessel intracranial vasculitis resulting in **infarction**
 - Most often unilateral and within the basal ganglia

Varicella Zoster Encephalitis

- Most severe, rare complication of primary or secondary infection
- Results in differing **vacuolopathy** and **infarction** pattern related to immune status:
 - Immunocompromised:
 - Small vessel vasculitis
 - Immunocompetent:
 - Large vessel vasculitis

Amebic Meningoencephalitis

- Result of *N fowleri* infection
 - Intranasal inoculation by contaminated warm fresh bodies of water
- No predilection for the immunocompromised
- Up to 98% mortality rate
- Non-specific imaging findings
 - Cerebral edema
 - **Infarction**
 - **Leptomeningeal enhancement**

(Filename: TCT_eEde-041_braininfectionjpeg.JPG)

eEde-042

Intracranial Manifestations of Cerebral Amyloid Disease

D Patel¹, M Yazdani¹

¹Medical University of South Carolina, Charleston, SC

Purpose

Cerebral amyloid disease (CAD) is a diverse group of CNS disorder with multiple intracranial manifestations. Amyloid deposition in neuritic plaques is also the cause of Alzheimer's disease. Most common manifestation of CAD is cerebral amyloid angiopathy (CAA). This presentation aims to

illustrate underlying pathophysiology of CAD, various intracranial manifestations of this disease, distinguishing imaging features and pertinent imaging based differential diagnostic considerations.

Materials and Methods

Using a series of illustrative Brain MRI cases from our didactic imaging files we will show different manifestations of intracranial amyloid. We will start by describing the pathology and imaging features of cerebral amyloid angiopathy followed by cerebral amyloid angiopathy-related inflammation, intracerebral amyloidoma, leptomeningeal amyloidosis, and amyloid-beta related angiitis (ABRA).

Results

Our cases in conjunction with review of the current literature will enhance the pathophysiology and multiple intracranial manifestations of cerebral amyloid disease.

Conclusions

The herein presentation expects to improve awareness, description, and identification of cerebral amyloid disease to all radiologists with an illustrative and instructive approach.

eEde-063

Intracranial Microbleeds: How to Narrow Your DDx

V Patel¹, T Hinkel², M LeComte¹, D Pastel³, A Mian⁴, R Khan¹

¹University of Arizona Medical Center, Tucson, AZ, ²Midwestern University, Glendale, AZ, ³Dartmouth-Hitchcock Medical Center, Lebanon, NH, ⁴Boston University/Boston Medical Center, Boston, MA

Purpose

To familiarize the reader with multiple patterns and additional imaging features of intracranial microbleeds, using susceptibility-weighted imaging (SWI) and supporting T2* gradient-echo imaging (GRE), through a case-based approach. The pathophysiologic processes behind each entity will be discussed.

Materials and Methods

Electronic educational review

Results

This educational exhibit will review multiple patterns of intracranial microhemorrhages with an emphasis on SWI imaging with supporting GRE imaging, using both 3T and 1.5T MRI. After a brief review of the imaging techniques, a multitude of cases will be used to show the imaging findings, highlight distinguishing features, and provide pertinent pathophysiologic information about each entity. Cases to be presented include: traumatic axonal injury (grades I-III), amyloid angiopathy, multiple cavernous malformations, CADASIL, vasculitis, hemorrhagic metastases, radiation sequela, and hypertensive angiopathy.

Conclusions

After the reader has viewed the exhibit, they will be able to much better identify and distinguish the patterns of intracranial microbleeds and understand the physiologic processes behind them.

eEde-078

Is Rathke Cleft Cyst a Silent and Incidentally Detected Lesion? Various Appearances of Symptomatic Rathke Cleft Cyst

H Jung¹, S Suh¹, I Ryoo¹

¹Korea University Guro Hospital, Korea University College of Medicine, Seoul, Republic of Korea

Purpose

Rathke cleft cyst (RCC) is a non-neoplastic cystic mass that derived early in life as a result of poor

Electronic Educational Exhibits

obliteration of the Rathke pouch. Most RCCs remain asymptomatic throughout life, and the lesions are a common (13–22%) finding at autopsy. However, some RCCs become large, resulting in a mass effect on the pituitary and surrounding structures, leading to headaches or symptoms due to compression of the optic chiasm, cavernous sinus, hypothalamus, or pituitary gland. In recent years, a few cases of hemorrhagic RCC have been reported, and patients with hemorrhage into an RCC experience acute worsening or new onset of symptoms mimicking pituitary apoplexy. RCC can be occasionally symptomatic and the appearance of RCC could be various. Therefore, the aim of this report is to inform various clinical manifestations and MR imaging findings of symptomatic RCCs.

Materials and Methods

Between November 1999 and December 2016, a search of the electronic database of single institute revealed 149 patients who underwent surgical removal of RCCs. We retrospectively evaluated clinical data of them, selected patients with symptomatic RCCs, and reviewed the MR images of the subjects.

Results

Among them, we found 33 patients with symptomatic RCC mimicking pituitary apoplexy. The patients complained of one or more symptoms and signs of headache, nausea, vomiting, decreased visual acuity, visual field defect, cranial nerve palsy, endocrinological abnormality or altered mental status. The MR imaging findings of RCCs mimic those of pituitary adenoma apoplexy. Also infection or inflammation of RCC manifests as meningitis or hypophysitis, and RCC with suprasellar extension can make it difficult to differentiate it from cystic craniopharyngioma. One intracavernous RCC resembled a cystic tumor originated from bony structure.

Conclusions

RCC is occasionally symptomatic and mimics other sellar tumors or infectious/inflammatory conditions. RCC apoplexy is not a rare clinical manifestation of symptomatic RCC.

eEde-091

Is There Hemorrhage? Using Dual Energy CT to Differentiate Intracranial Hemorrhage from Contrast and Calcifications

V Stine¹, T West¹, M Zapadka², C Lack¹

¹Wake Forest School of Medicine, Winston Salem, NC, ²Wake Forest Baptist Health, Winston Salem, NC

Purpose

At the end of this presentation, the audience should understand the physical basis behind dual energy and how to use dual energy CT images to increase the diagnostic confidence in interpreting intracranial hyperdense lesions.

Materials and Methods

Various case examples from our institution of intracranial hemorrhage, calcifications, and iodinated contrast material will be shown. Through a series of case examples, we will demonstrate that by applying material decomposition processing, the causative agent can be identified, leading to a specific diagnosis. An explanation of the physics behind dual-energy CT, including the energies typically used to obtain images and post processing involved, will be provided.

Results

Dual-energy CT (DECT) is a technique with an expanding role in diagnostic imaging. While DECT initially gained traction for abdominal imaging applications, its utility in neuroimaging is being realized and applied on a more frequent basis. During the early implementation of dual energy scanning at our institution, we encountered knowledge gaps in 1) the physical principles of DECT acquisition, 2) understanding terminology of data available with DECT post processing and 3) how to use postprocessing data to aide in interpretation of brain imaging. This presentation will not only address these knowledge gaps we encountered in our practice, but also specifically demonstrate how to improve your confidence in differentiating intracranial hemorrhage from calcification and iodinated contrast.

Electronic Educational Exhibits

Conclusions

Dual-energy CT is well suited for increasing specificity in diagnosing hyperdense intracranial lesions.

eEde-018

It's Not All in Your Head! Imaging Findings of Neurovascular Compression Syndromes Around the Cervical Spine

S Story¹, J Yetto¹, A Condos¹, M Cathey¹

¹*Naval Medical Center San Diego, San Diego, CA*

Purpose

Neurovascular compression (NVC) is the process through which vascular structures, particularly arteries, come into direct conflict with adjacent nerves resulting in cranial nerve displacement and/or indentation. Many different symptomatic presentations have been attributed to neurovascular compression based upon the conflict along the nerve root exit zone or cisternal segment of a cranial nerve. Patient's with radiological evidence of neurovascular compression may present along a spectrum from entirely asymptomatic to severe progressive neurological deficit. Thus far, the degree of neurovascular compression has not proven to be directly associated with the severity of symptomology. The most common causes of NVC are intracranially with trigeminal neuralgia being the most frequent presentation. However, extracranial, and more specifically, cervical spine causes of NVC do exist and result in symptomatic conditions such occipital neuralgia, spasmodic torticollis, and hypoglossal nerve palsy. Additionally, variant vertebral artery anatomy is a common finding and the most frequently implicated vessel associated with cervical spine related NVC. The purpose of this exhibit is to review cases of neurovascular compression as a potential etiology of several neurological clinical syndromes and the radiographic presentations of such and to identify important anatomical characteristics of NVC and potential NVC mimics.

Materials and Methods

Retrospective review of 3T MR and CT examinations over the past three years with NVC within the cervical spine was performed. A variety of extracranial, cervical spine related NVC cases are presented which clearly demonstrate the pertinent imaging findings on high resolution cross-sectional imaging. Relevant anatomy is reviewed. Additionally, a literature review on NVC around the cervical spine was completed.

Results

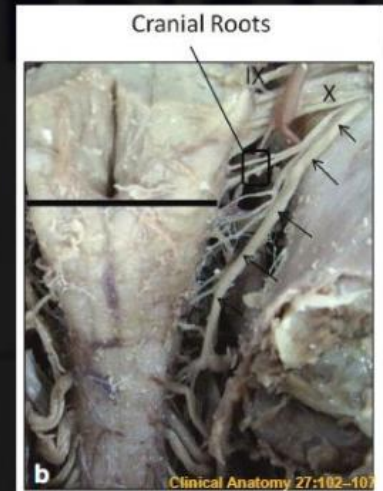
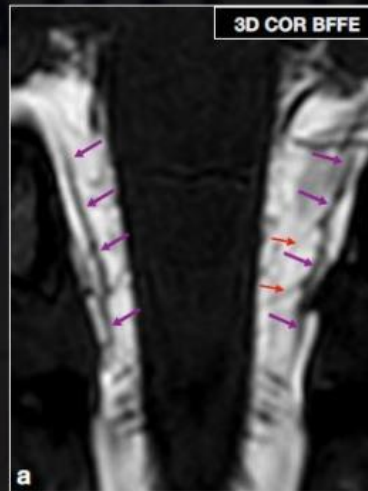
Divided into: 1. Introduction to NVC, 2. Cervical spine related cases of NVC, 3. Treatment, 4. Imaging Considerations

Conclusions

Neuroradiologists play a critical role in the diagnosis of cervical spine related NVC and a comprehensive knowledge of these entities as well as potential mimics is critical. Knowledge of operative considerations allows the radiologist to proactively address these concerns and improve diagnostic accuracy in the post-operative setting. Though the presence of these anatomic relationships does not necessarily equate to causation, it is important for radiologists to understand and identify these findings.

CN XI Gross vs MRI Anatomy

Figure 12. a. 3D Coronal balanced fast field echo (BFFE) demonstrating the **spinal accessory nerve, CN XI** (→), exiting from multiple levels of cervical spinal cord as a series of rootlets (→) which **originate from the spinal root accessory nerve nucleus with variable contribution from the cranial root nucleus.**



b. Coronal gross anatomic picture of the brainstem highlighting the spinal accessory nerve.

Fibers from **spinal nerves C2-C6** emanate from the cervical spine plexus to **combine with the spinal accessory nerve** and provide sensory input.



(Filename: TCT_eEde-018_NVCSlide.JPG)

eEde-052

Last But Not Least, and Perhaps Lost but Not Forgotten: Utility of a Post Contrast Head CT Following Single Phase Arterial CTA

A Thomas¹, D Dunaway¹, S Chen¹, T Huynh¹

¹Baylor College of Medicine, Houston, TX

Purpose

CT angiography protocols at many institutions are currently in flux. Today most institutions' CTA protocols still employ only a single arterial phase CTA. Moreover, multiphase CT angiography is increasingly gaining favor, especially in the context of acute ischemic stroke for the evaluation of leptomeningeal collateral perfusion of the ischemic penumbra. The degree of collateral flow correlates positively with clinical outcomes and may help predict likelihood of hemorrhagic conversion from reperfusion therapy and core infarct volume. Even in the absence of acute ischemic stroke, additional venous phase images may be valuable in evaluating a range of additional pathology, providing utility beyond that of a standard single-phase CTA.

Materials and Methods

We report our institutional experience obtaining additional venous phase images following arterial phase acquisition as part of our standard CTA protocol.

Electronic Educational Exhibits

Results

We present cases in which the venous phase of the CT angiogram provides valuable additional clinical information. For example, we have found it to not only be useful in the setting of acute ischemic stroke and differentiating acute from subacute stroke, but also helpful in revealing occult lesions such as tumors, vascular malformations and small peripheral aneurysms that may have not been visible on the arterial phase, screening noncontrast head CT or obscured by hemorrhage. We also present cases of technical problems that may arise with arterial imaging in which obtaining a "venous" phase may provide sufficient information to preclude the need for immediate repeat CTA imaging and additional IV contrast load. We demonstrate different reconstruction techniques that can be used on the delayed venous phase imaging to maximize the conspicuity of these various pathologies.

Conclusions

Multiphase CT angiography, increasingly described for the evaluation of acute ischemic stroke, can also provide invaluable information in additional clinical settings. We describe our experience where a range of alternative diagnoses were made possible due to the addition of a delayed phase to the standard single phase CTA protocol.

eEde-090

Less Common but Clinically Relevant MR Artifacts and Pitfalls, Easily Remedied

A Malik¹, U Rassner¹

¹*University of Utah, Salt Lake City, UT*

Purpose

- Identify these clinically relevant magnetic resonance (MR) artifacts: venous saturation on post contrast Time-of-Flight (TOF) MR angiography (MRA), silicone oil chemical shift artifact, parallel imaging with a single channel transmit receive coil, failed fat saturation with accidental water saturation, T2 effects on T1 Inversion Recovery (IR), Dixon fat saturation (FS) swap artifact
- Describe basic causes and remedies for these artifacts
- Understand resulting pitfalls in image interpretation

Materials and Methods

Use an image-rich, clinically oriented, interactive approach to educate trainees and practicing radiologists about these MR artifacts, their identification, causes, remedies and how they may effect image interpretation. A pre and post-test will be provided to engage the learner. These examples are based on actual clinical scenarios at our institution and the clinical context will be emphasized. Information will be presented in a graded fashion, to allow for varying background knowledge. Simple text and visual explanations will be used by default. Advanced and interested participants will have access to more detailed explanations and diagrams on separate screens to minimize clutter and information overload.

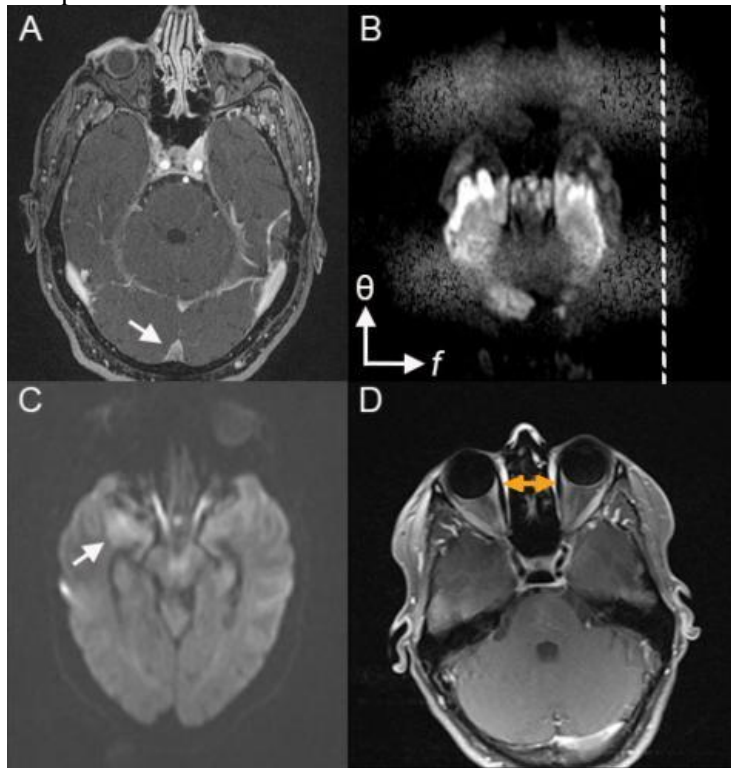
Results

- Venous saturation on postcontrast TOF MRA can mimic sinus thrombosis, remedied by turning off the saturation band.
- Certain medical devices (i.e. vagal nerve stimulators) require a transmit receive head coil (typically single channel). When this coil is accidentally used with parallel imaging, the resulting artifact simulates RF noise. However, while RF noise is aligned with the phase encoding direction and can be difficult to troubleshoot, this artifact is aligned in the frequency encoding direction and is easily removed by disabling parallel imaging.
- Chemical shift artifact from silicon oil in the globe may create a pseudoinfarct on echoplanar diffusion weighted imaging.
- Failed fat saturation can result in water saturation, suppressing contrast enhancement. Changing the isocenter or shimming, or alternate fat suppression techniques are helpful.
- IR T1 sequences can have T2 effects appearing as pseudoenhancement, not seen on other post contrast sequences. Adjustment of TR and TE can resolve this.
- Dixon FS swap artifacts may appear as pseudolesions, not seen with other sequences. Always reconstructing both Dixon fat and water images allows correct interpretation.

Electronic Educational Exhibits

Conclusions

Identifying, managing and resolving these MR artifacts will aid in more efficient and improved image interpretation.



A. Pseudothrombus in the superior sagittal sinus (arrow) due to the venous saturation band on a post contrast TOF MRA (arrow). B. Artifact due to parallel imaging with a single channel transmit receive coil. θ , phase encoding direction; f , frequency encoding direction. Dotted line indicates the expected direction of RF noise, in the phase encoding direction. C. Pseudoinfarct on echoplanar diffusion weighted imaging (arrow) due to chemical shift artifact from silicone oil in the globe. D. Failed fat saturation resulting in water saturation, including loss of normal bilateral medial rectus enhancement (arrow).

(Filename: TCT_eEde-090_mr_artifacts_v02fig.jpg)

eEde-037

More Than Your Typical Small Vessel Ischemic Disease: Understanding White Matter Changes

J Curcio¹, C Lanzieri¹, V Kondray¹, M Rajdev¹

Electronic Educational Exhibits

Purpose

The goal of this study is to become comfortable in distinguishing white matter disease. An emphasis will be placed on using clinical history in correlating white matter findings with the appropriate diagnosis. The vast majority of imaging examples will be using MRI, specifically T2/FLAIR and DWI sequences.

Materials and Methods

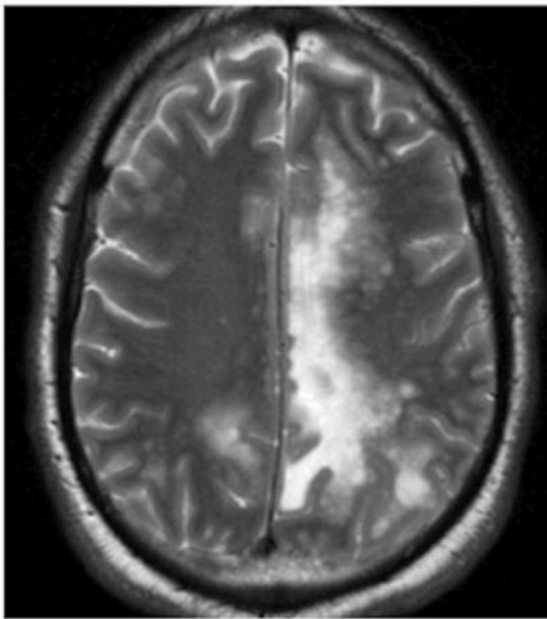
The imaging studies were obtained from teaching files within the University Hospital PACS followed by a chart review of individual cases. T2/FLAIR, T1 post contrast, and DWI sequences with white matter changes were used for teaching purposes.

Results

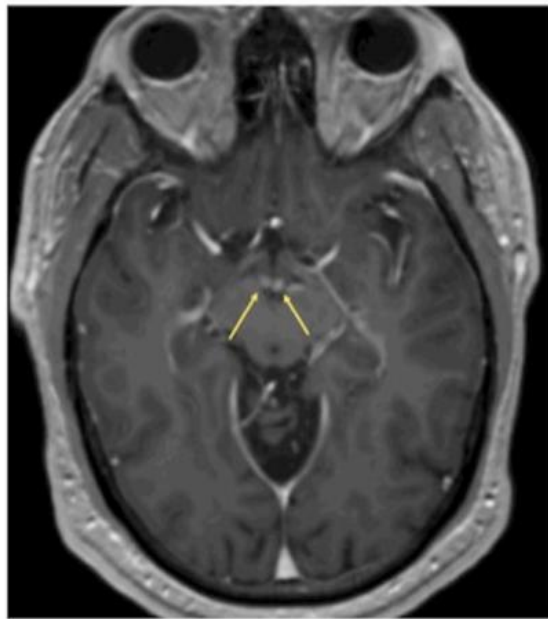
During everyday practice, the radiologist comes across white matter changes in various age groups. The majority of white-matter changes are due to chronic microvascular ischemia, but it is important to be aware of other disease processes that demonstrate white matter change. The role of the radiologist is to recognize the pattern of white-matter change, and to use clinical history in determining the underlying diagnosis, thus leading to appropriate medical care. The categories of white-matter disease discussed in this study include: autoimmune, toxic-metabolic, vascular, infectious and iatrogenic.

Conclusions

The radiologist plays a crucial role in recognizing patterns in white-matter changes, as well as using clinical history to determine the most appropriate diagnoses. Although chronic small vessel ischemic disease is a common finding, making the distinction from other etiologies will drastically alter patient outcomes.



36 y.o. male with a history of AIDS presents with new-onset seizure. Axial T2 weighted images demonstrate asymmetrical hyperintense signal throughout the periventricular and subcortical white matter, predominately within the left hemisphere. Patient tested positive for JC virus.



41 y.o. male with a past medical history of chronic alcohol abuse presents with a seizure. Axial T1 post gad demonstrate enhancement within the bilateral mammillary bodies.

(Filename: TCT_eEde-037_ASNRWMDgraphicfile.jpg)

eEde-057

MRI Clues of Craniocervical Junction Dural Arteriovenous Fistulas: Beware of the Brainstem

M McDonald¹, J Chen², J Handwerker¹

¹*University of California at San Diego, San Diego, CA*, ²*San Diego VA/UCSD Medical Center, La Jolla, CA*

Purpose

The anatomy of the craniocervical junction is complex and can play host to a wide variety of neoplastic, infectious and inflammatory pathologies, making it easy to overlook an underlying vascular malformation when forming a differential diagnosis. Although dural arteriovenous fistulas (DAVFs) can occur anywhere along the neuraxis, it is important to consider the possibility of an underlying craniocervical DAVF in patients who present with lower cranial nerve palsies with or without brain stem dysfunction in the setting of craniocervical parenchymal abnormalities. Even when the index of suspicion is high, the diagnosis of craniocervical DAVFs remains challenging both clinically and radiologically secondary to complex regional anatomy, nonspecific changes on MRI and often small, tortuous vessels that may not be apparent on conventional CT/MR angiographic techniques. This exhibit will present several cases of isolated craniocervical DAVF to highlight common secondary imaging hallmarks that can clue the practicing radiologist into a potential diagnosis of craniocervical DAVF for the purposes of timely treatment guidance.

Materials and Methods

A review of our institutional databases and electronic medical record was performed retrospectively to identify cases of isolated craniocervical DAVF. When available, serial imaging inclusive of both initial presentation and subsequent post-treatment surveillance is included.

Results

By the end of this educational exhibit the attendee will be able to: 1. Describe the classification scheme of DAVFs type I-V 2. Identify common imaging hallmarks suggestive of underlying craniocervical DAVF including: a. Secondary venous congestion b. Abnormal flow voids along the pial surfaces, venous sinuses and basal cisterns 3. Describe basic diagnostic angiography findings related to DAVF and implications for treatment planning and long-term outcome 4. Compare and contrast potential mimics of craniocervical DAVF including infectious (e.g. rhombencephalitis), inflammatory (multiple sclerosis, neuromyelitis optica) and neoplastic etiologies (astrocytoma, ependymoma, etc.)

Conclusions

While rare, DAVFs of the craniocervical junction are clinically important entities that can present a diagnostic dilemma to both the practicing clinician and interpreting radiologist. As these vascular malformations may not be readily detectable via routine MR or CT angiographic techniques, the radiologist must become familiar with secondary signs of an underlying DAVF to facilitate timely and appropriate management with either endovascular or surgical techniques.

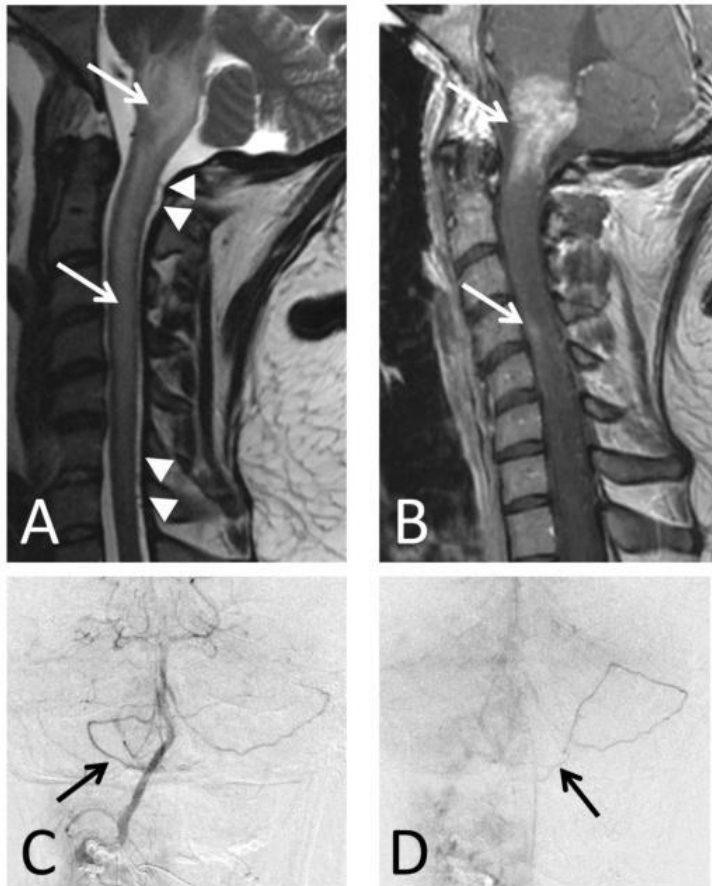


Figure 1. 22 year-old female presenting for admission from an outside hospital for progressive bilateral ascending flaccid paralysis. Marked expansile edema was noted extending from the inferior pons through the visible cervical spinal cord (arrows, A) associated with patchy internal contrast enhancement (arrows, B). Multiple tortuous flows voids along the dorsal surface of the cervicomedullary junction and cervical spinal cord (arrowheads, A) suggested a possible vascular etiology. Subsequent diagnostic angiography revealed a type V DAVF arising from a muscular branch of the right vertebral artery (arrow, C) and draining into a perimedullary vein (arrow, D).

(Filename: TCT_eEde-057_dAVF.jpg)

eEde-092

MRI Physics and Sequences Used in Neuroimaging: Basic Physics of Common MR Sequences with Clinical Applications for Medical Students, Residents, and Fellows

A Chan¹, B Laughlin², S Baig², A Iaia², P Moftakhar², S Farooqui²

¹Christiana Care Health System, Bear, DE, ²Christiana Care Health System, Newark, DE

Purpose

The purpose of this electronic educational exhibit is to provide medical students, residents, and fellows a deeper and intuitive understanding of the physics and clinical applications of common MRI sequences used in neuroimaging.

Materials and Methods

This electronic educational exhibit will utilize MR images and Microsoft PowerPoint animations to provide a graphically heavy presentation.

Results

First, we will first describe how MR signal is generated from biological tissues to produce images. We begin by introducing the properties of the hydrogen atom (H1) and how the main magnetic field induces their precession at the Larmor frequency. Next, we explain how the radiofrequency pulse is used to change their net magnetization and then show their subsequent T1 and T2 relaxation. Following, we will describe how magnetic field gradients aids in localization of protons in the frequency/phase encoding and

slice directions. Lastly, by using the basic spin and gradient echo sequences, we will describe the basic anatomy of the standard MR pulse sequence diagram, and in conjunction with TR and TE, to discuss the process of creating T1-, T2-, and T2*-weighted images. Second, will build on the preceding section to discuss the FLAIR sequence by showing the 180° inversion pulse, T1 relaxation, and choosing the adequate inversion time. In addition, we will discuss gadolinium enhanced T1WI by describing the normal and abnormal blood brain barrier (BBB), then demonstrate the T1 shortening of gadolinium upon interaction with protons in a diseased BBB. Following, we will discuss TOF MRA by demonstrating the usefulness of GRE sequences to saturate background tissue to create bright flowing blood. Next, we will discuss the concept of k-space and how EPI and fast spin-echo images make modern MRI imaging possible by decreasing scan time. Lastly, the physical concepts underlying diffusion weighted imaging will be discussed, followed by a demonstration of how gradients are used to generate contrast by probing molecular motion. In addition, for each of the described MR sequences, we will show their clinical utility by highlighting the different pathologies detected with each sequence.

Conclusions

By the end of this presentation, we hope the audience will understand the basics of MR physics and how these principles are used on a daily basis to diagnose diseases in neuroimaging.

eEde-010

Multimodality Comprehensive Review of Mesial Temporal Sclerosis: A Nuclear Medicine Perspective

V Bachhav¹, K Gupta¹, A Patil², R Prasad¹, A Ali¹, S Virmani¹

¹Rush University Medical Center, Chicago, IL, ²Advocate Illinois Masonic Medical Center, Chicago, IL

Purpose

Mesial temporal sclerosis is one of the common causes of epilepsy with foci localized in the temporal lobes. About 70% of patients undergoing partial temporal lobectomy experience amelioration or eradication of seizures. Hence, early diagnosis is of great clinical significance. The primary evaluation includes MRI and CT Brain. The importance of perfusion brain SPECT (baseline and ictal) and metabolic PET imaging in localization of epileptic focus is also well known.

Materials and Methods

We retrospectively reviewed the usual and unusual multimodality imaging spectrum of challenging cases of mesial temporal sclerosis with their post-surgical correlation wherever applicable.

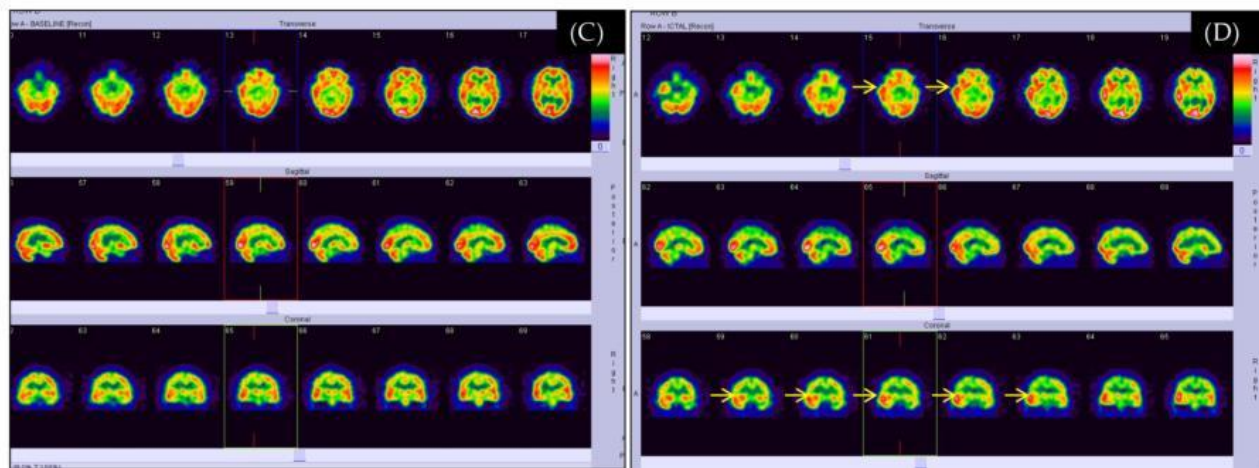
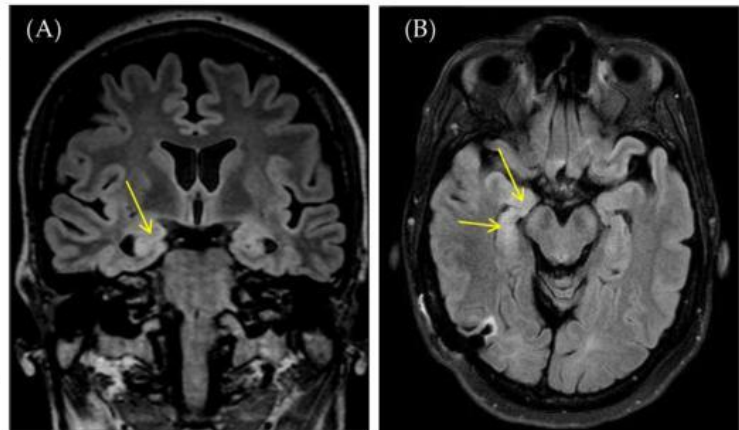
Results

Most illustrative cases were selected to highlight the imaging spectrum of epilepsy. Advantages and limitations of various imaging modalities are also discussed and highlighted in this case based pictorial review.

Conclusions

The above case based pictorial review aims to increase the confidence for seizure focus localization and thus help in better patient management.

Coronal Flair (A) and Axial Flair (B) MRI images demonstrating ill-defined hyperintensity in the right hippocampus and mesial temporal region consistent with Mesial temporal sclerosis. Baseline (C) and ictal (D) SPECT images demonstrating moderate intense uptake in the right temporal region on ictal phase images corresponding to the likely seizure focus.



(Filename: TCT_eEde-010_ep-slide.jpg)

eEde-060

Multimodality Imaging Review of Vertebral Artery Abnormalities

K Patel¹, M Tominna¹, J Wilseck²

¹Oakland University William Beaumont School of Medicine, Royal Oak, MI, ²Beaumont Hospital, Royal Oak, MI

Purpose

Vertebral artery abnormalities are commonly encountered by neuroradiologists during the course of their normal workday. Often times these are incidental findings without any clinical significance. However, occasionally these findings may be the cause of the patient's symptoms and require urgent or emergent treatment. Patients with vertebral artery pathology commonly present with nonspecific symptoms such as neck pain and/or focal neurological deficits. Therefore, imaging is an integral part of the evaluation of the vertebral artery. Common vertebral artery variant anatomy includes hypoplasia, duplication, fenestration, and abnormal site of origin. Common pathologic conditions of the vertebral artery include atherosclerosis, thrombosis, occlusion, vasculitis, dissection, aneurysm, and pseudoaneurysm. It is important to be able to identify normal variants of the vertebral artery and differentiate these variants from pathologic conditions. It is often difficult to distinguish these using conventional imaging techniques such as CT angiography or MR angiography. In such cases, invasive angiography may be required to adequately delineate the

Electronic Educational Exhibits

vascular anatomy and make the diagnosis of a suspected vertebral artery abnormality seen on noninvasive imaging. Endovascular treatment may also be performed at the time of invasive angiography or with repeat angiography at a later time if indicated. Common endovascular treatment procedures performed include embolization, angioplasty and stenting.

Materials and Methods

CT angiography (CTA) is often employed as the first line imaging modality for a suspected abnormality of the vertebral artery due to its widespread availability and superior spatial resolution. MR angiography (MRA) may also be used but higher cost and difficulty to access as well as inferior spatial resolution are limitations to its use. If the abnormality cannot be definitively characterized using these imaging modalities, diagnostic invasive angiography may be performed. Even if the diagnosis can be made using CTA or MRA, invasive angiography may be needed for detailed anatomical characterization of the abnormality and/or potential treatment. In this exhibit, we review the normal anatomy and common variants of the vertebral artery. Several original cases of vertebral artery abnormalities will be presented with their clinical presentation, noninvasive, and invasive imaging. For those cases which underwent endovascular treatment, postintervention images will be provided. The goal of this exhibit is to help neuroradiologists have a better understanding of the imaging features of vertebral artery abnormalities as well as the management of these abnormalities.

Results

After viewing this exhibit, you should have a strong understanding of the normal anatomy of the vertebral artery. You should be able to identify commonly seen anatomical variants and pathological conditions and have an understanding of the specific imaging features of each abnormality on both noninvasive and invasive imaging. Finally, you should also have a general understanding of the appropriate management options for these abnormalities.

Conclusions

Adequately evaluating the vertebral artery with noninvasive imaging remains a challenge for radiologists for many reasons such as artifacts and limited spatial resolution of the vasculature. Cerebral angiography is still the gold standard for evaluation of the intracranial and extracranial arterial vasculature. Although the differentiation of vertebral artery pathology can sometimes be difficult, certain imaging features can be suggestive of a particular diagnosis. Accurate diagnosis is important to help guide management which may include imaging follow-up, medical therapy, endovascular treatment, and/or surgery.

eEde-027

Multimodality Neuroimaging in Dementia

K Gupta¹, R Jadhav², V Bachhav³, R Prasad¹, A Ali⁴, S Virmani⁵, M Nagarajan¹

¹Rush University Medical Center, Chicago, IL, ²Rush University Medical Centre, Chicago, IL, ³Rush university medical center, chicago, IL, ⁴RUSH UNIVERSITY MEDICAL CENTER, CHICAGO, IL, ⁵Rush University Medical Center, Chicago, Chicago, , IL

Purpose

Introduction of biomarkers and advancement in imaging technologies have improved antemortem diagnosis of dementias. Structural imaging is important to rule out treatable causes of cognitive impairment, whereas functional imaging has role in specific diagnosis. In this presentation we review all the specific findings that can be identified with imaging techniques in most frequently encountered dementing disorders.

Materials and Methods

We retrospectively reviewed imaging workup (including CT, MRI, SPECT and PET/CT scans) of patients being evaluated for dementia. The clinical outcomes of these patients were followed and contribution from various imaging towards diagnosis was determined.

Results

Various dementing disorders were analyzed. The most studied Alzheimer's disease is more comprehensively assessed on MR imaging. FDG PET and rCBF SPECT demonstrate defects secondary to brain damage. Specific amyloid ligands, such as PIB (florbetapir), are under research and demonstrate the extent of pathological proteins in neural cells. Frontotemporal dementias were better assessed on FDG-PET and rCBF SPECT to distinguish from AD. Routine structural imaging with CT or MR showed characteristic structural changes such as atrophy in the frontal lobes involving the ventromedial, orbitofrontal, anterior cingulate, anterior insula, and amygdala in established cases. Dementia with Lewy bodies (DLB) shows widespread defects involving visual cortex on FDG PET. Visual and quantitative analysis of I-123 Ioflupane SPECT have high positive predictive values in diagnosis of parkinsonian pathology. T2 FLAIR and diffusion weighted MR images are useful in CJD (Creutzfeldt-Jakob disease) as well as FDG PET, MR angiography and T2 FLAIR MR in vascular dementias.

Conclusions

New imaging techniques revolutionize the diagnosis of neurodegenerative disease so as to obtain a complete molecular, structural, and metabolic characterization. This can be used to improve diagnosis, follow disease progression and response to treatment.

DEMENTIA CASES

CASE 1. Alzheimer's disease

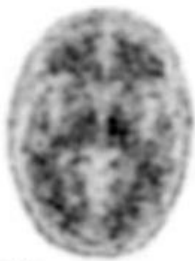


FIG 1A

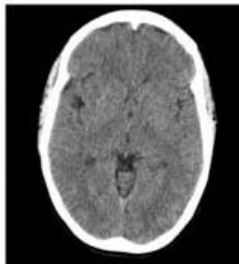


FIG 1B

FIG 1A PET Florbetapir imaging demonstrating moderate degree of amyloid neuritic plaque. FIG 1B CT brain is unremarkable.

CASE 2. Multi-infarct dementia

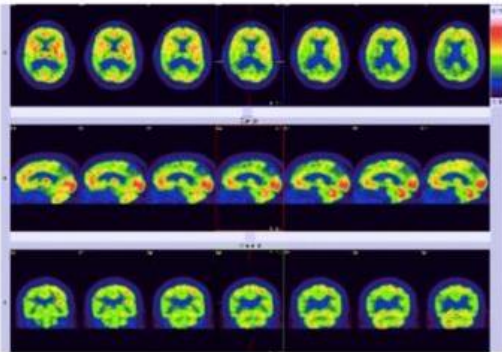


FIG 2A: FDG PET BRAIN demonstrate multiple areas of reduced metabolism consistent with multi-vascular infarcts.

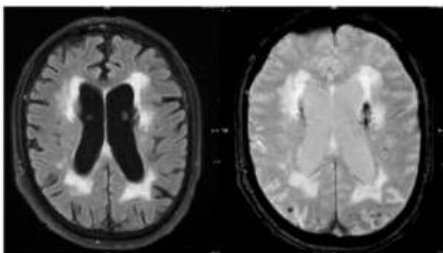


FIG 2B MRI FLAIR

SWI

FIG 2A: FDG PET demonstrate multiple areas of reduced metabolism consistent with multi-vascular infarcts. FIG 2B: MRI SWI images demonstrates punctate acute/subacute infarcts in left superior subcortical frontal lobe. T2 FLAIR hyperintensities represent chronic microvascular ischemic changes.

(Filename: TCT_eEde-027_DEMENTIA.jpg)

Multinodular and Vacuolating Neuronal Tumor of the Cerebrum: Key MR Imaging Features for Diagnosis and Differentiation from Other Cystic Brain Lesions

T Gleason¹, J Villanueva-Meyer¹, S Cha¹

¹University of California San Francisco, San Francisco, CA

Purpose

Multinodular and vacuolating neuronal tumor (MVNT) of the cerebrum is a newly recognized brain lesion, which can mimic dysembryoplastic neuroepithelial tumor (DNET) or other benign cystic brain lesions on imaging. The purpose of this exhibit is to highlight unique imaging features of MVNT, a nonsurgical malformative lesion, that provide insight into differentiating it from other cystic brain lesions.

Materials and Methods

A concise discussion of the underlying pathology and clinical biology of MVNT, followed by a case based discussion of the key imaging features and differential diagnosis of MVNT. Specifically, the discussion focuses on how to distinguish MVNT from DNET, ganglioglioma, gangliocytoma, perivascular spaces, and focal cortical dysplasia.

Results

Histologically, MVNT is composed of small neuroepithelial cells expressing neuronal markers including synaptophysin and the neuronal protein ELAV3/4. MVNT is a hamartomatous or malformative lesion rather than a true neoplasm. Accurate diagnosis of MVNTs is essential for proper management since they are considered incidental lesions not requiring surgical excision. On MR imaging, MVNTs share certain key imaging features: a. Clusters of small cystic lesions in a supratentorial subcortical white matter location b. Minimal to no mass effect c. Subtle, but distinct, internal nodularity d. Homogeneous T2 hyperintensity relative to white matter e. Lack of postcontrast enhancement f. No reduced diffusion or blooming on susceptibility-weighted imaging

Conclusions

MVNTs are a newly defined malformative lesion with distinct MR imaging features, which can avoid unnecessary surgical confirmation and differentiate them from other cystic brain lesions.

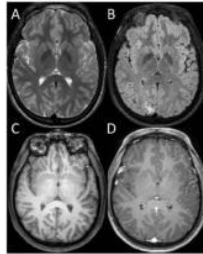


Fig. 1. Right parietal multinodular and vacuolating neuronal tumor. A) Axial T2. B) Axial FLAIR. C) Axial T1. D) Gadolinium enhanced Axial T1.

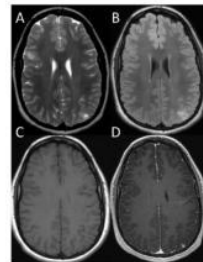


Fig. 3. Left parietal ganglioglioma. A) Axial T2. B) Axial FLAIR. C) Axial T1. D) Gadolinium enhanced Axial T1.

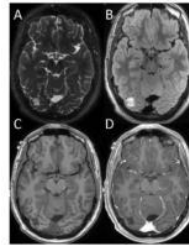


Fig. 2. Right occipital dysembryoplastic neuroepithelial tumor. A) Axial T2. B) Axial FLAIR. C) Axial T1. D) Gadolinium enhanced Axial T1.

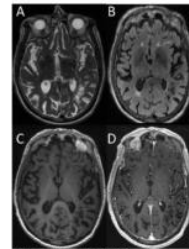


Fig. 4. Left parietal and subcortical perivascular space. A) Axial T2. B) Axial FLAIR. C) Axial T1. D) Gadolinium enhanced Axial T1.

(Filename: TCT_eEde-080_Figures1-4MVNT.jpg)

eEde-032

Neuroimaging Findings in Patients Treated with Biologic Drugs: Will We Know It If We See It?

N Aly¹, M Patel², M Ouyang¹, J Gastala¹, T Moritani³, A Capizzano¹

¹*University of Iowa Hospitals and Clinics, Iowa City, IA*, ²*University of Iowa, Iowa City, IA*, ³*University of Michigan, Ann Arbor, MI*

Purpose

Biologic agents are a rapidly evolving class of drugs including protein or nucleic-based pharmaceuticals, vaccines, and tissue derivatives that are not directly extracted from native sources, but rather manufactured to interact with specific targets. These have unique mechanisms of action and are increasingly used for a plethora of diseases. Thus, related atypical neuroimaging findings are likely to be encountered by radiologists. This educational exhibit will explore the spectrum of associated neuroimaging findings in patients under treatment with biologic agents and their potential significant side effects.

Materials and Methods

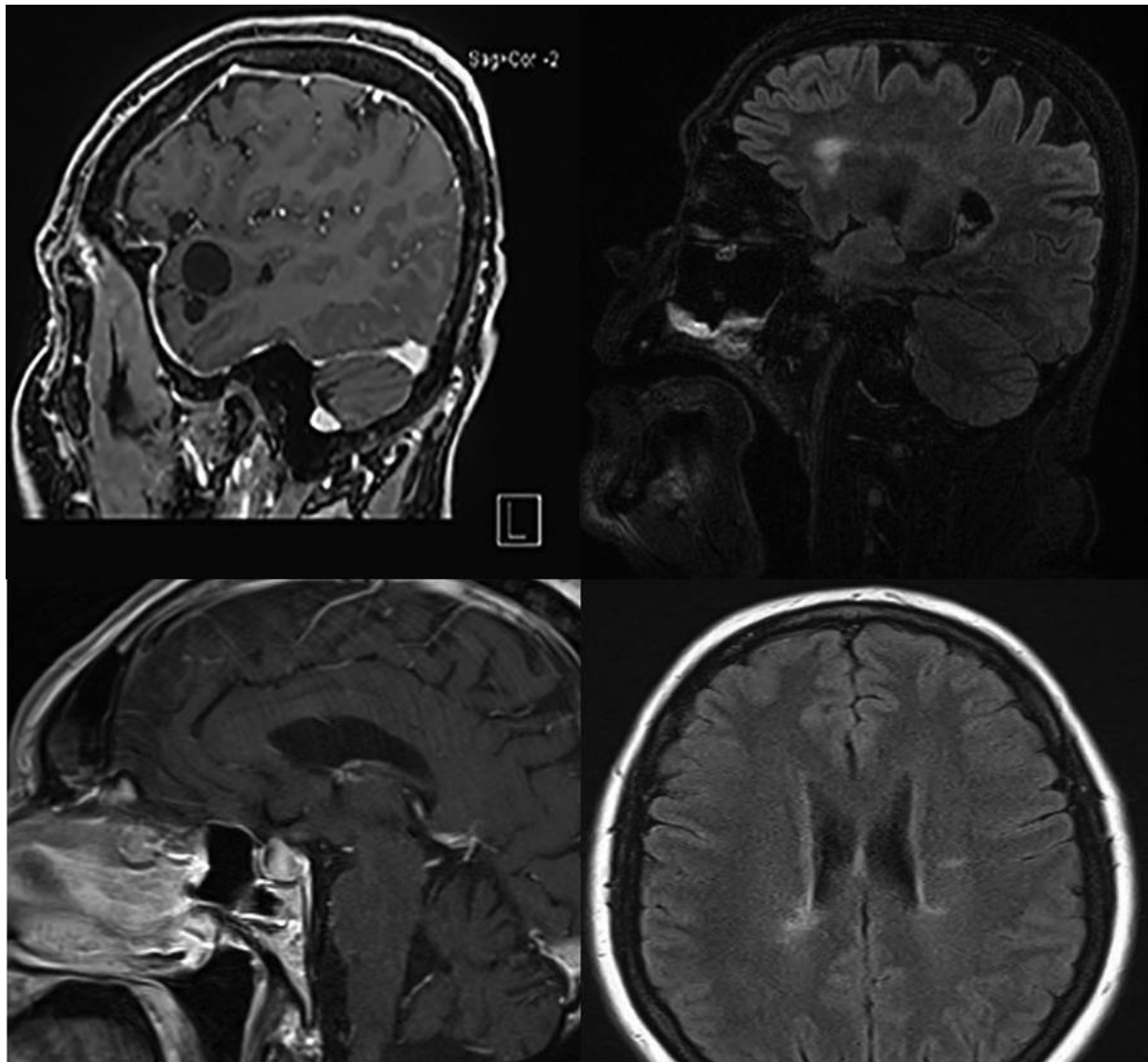
Review of clinical presentations from multiple cases of patients treated with biologics from the University of Iowa Hospital and Clinics with neuroimaging findings, including MRI, deemed secondary to the biologic treatment. Additionally, a literature review of previously documented findings in similar patients and plausible mechanisms for these findings.

Results

Biologic agents are classified according to their mechanism of action, which are ultimately responsible for neuroimaging findings. Some of the discussed cases include: 1. Tumor necrosis factor alpha inhibitors: Adalimumab (Humira ®) showed demyelinating lesions Etanercept (Enbrel ®) was associated with inflammatory changes in the brain. 2. Epidermal growth factor receptor (EGFR) inhibitor Erlotinib (Trevi ®) demonstrated atypical brain metastases that were cystic and nonenhancing. 3. Monoclonal antibodies: Anti CTLA-4 Ipilimumab (Yervoy ®) showed hypophysitis Anti-VEGF Bevacizumab (Avastin ®) exhibited pseudoresponse of GBM, coagulation necrosis, and ischemia Anti-CAM alpha 4 integrin: Natalizumab (Tysabri ®) and anti-CD20: Rituximab (Rituxan®) with findings of progressive multifocal leukoencephalopathy (PML)

Conclusions

Patients on biologic agents may present with a variety of symptoms accompanied by distinct neuroimaging findings. Recognizing the findings and associations requires careful assessment of the clinical presentation, pharmacological history, underlying diagnosis, and imaging findings. Since these drugs are expensive and not without significant side effects, a comprehensive understanding is required to use them safely and efficiently. Knowledge of these agents continues to advance with ongoing research in this field and this case series aims to further educate radiologists in recognizing significant neuroimaging findings in these patients.



Top left: Sagittal T1 post contrast MRI showing multiple non-enhancing cystic metastasis from lung adenocarcinoma in a patient treated with Erlotinib, pathology proven. Top Right: Sagittal FLAIR MRI sequence showing inflammatory lesions in a patient with rheumatoid arthritis on Etanercept. Bottom Left: Sagittal T1 post contrast MRI sequence showing hypophysitis in a patient with metastatic melanoma on Ipilimumab treatment. Bottom Right: Axial FLAIR MRI sequence showing demyelinating lesions in a patient on Adalimumab for Crohn's disease.

(Filename: TCT_eEde-032_300dpiabstractgroupfinalcaption.jpg)

eEde-079

Neuroimaging Findings in Septal Dysembryoplastic Neuroepithelial Tumor (DNET)-like Neoplasms. Why Is It Important to Recognize This Entity?

P Batchala¹, P Darvishi¹, T Eluvathingal Muttikkal¹, S Patel¹, J Donahue¹
¹University of Virginia Health System, Charlottesville, VA

Purpose

Dysembryoplastic neuroepithelial tumor (DNET)-like neoplasm of the septum pellucidum is a rarely reported entity that can be mistaken on imaging for colloid cyst, central neurocytoma or other cystic lesions. On histopathology these tumors can also be mistaken for central neurocytoma or

oligodendroglioma. Here we review three cases of pathology proven DNET-like neoplasms arising from septum pellucidum and review the literature.

Materials and Methods

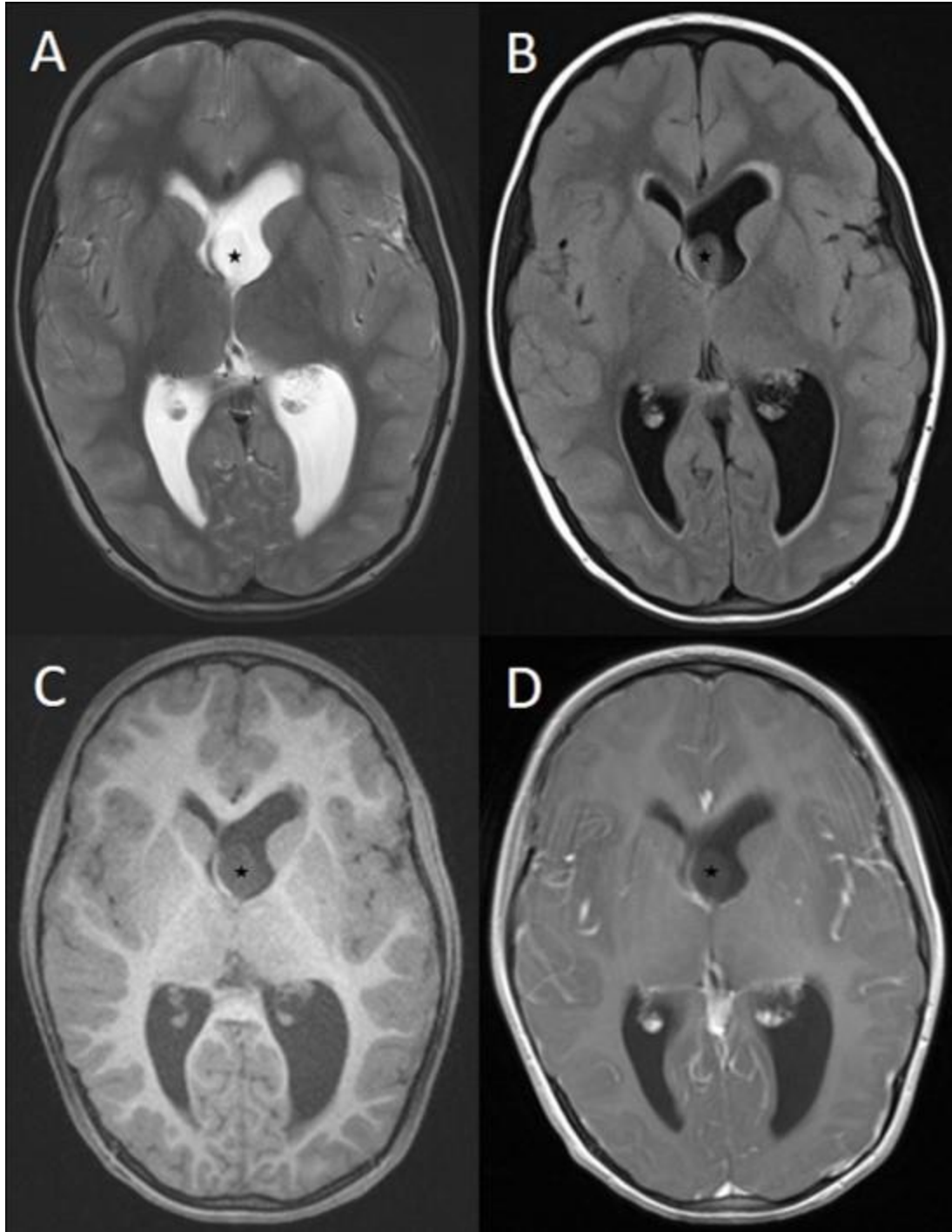
Through a search in our institutional database, three cases of histologically proven septal DNET-like neoplasms were identified.

Results

DNET is typically a cortical tumor with characteristic imaging and histopathological findings [1]. Septum pellucidum or intraventricular location of DNET-like neoplasms is rare, seen in approximately 3.9% of all DNET cases [2]. Unlike cortical DNETs which often present with epilepsy, septal DNET-like neoplasms more often present with symptoms of elevated intracranial pressure due to obstructive hydrocephalus [3]. Very similar to a colloid cyst, the tumor is located close to foramen of Monro in the anterior inferior aspect of septum pellucidum, either attached to the septum or between the leaves, and are usually less than 3cm in size. The CT and MRI signal characteristics resemble cortical DNET. Figure 1 shows a typical septal DNET-like neoplasm (black star) that is homogeneously hyperintense on T2WI (A) and hypointense on FLAIR (B) and T1WI (C). The tumor does not show post contrast enhancement (D). Of our 3 histopathologically proven septal DNET-like tumors, only 1 was prospectively diagnosed preoperatively, while the other two were mistaken for colloid cysts. On histopathology, the tumors typically show oligodendrocyte-like cells (OLC) in a pseudorosette formation, "specific glioneuronal element", and floating neurons in a mucoid background. Differentiating this lesion from oligodendroglioma or central neurocytoma can be challenging with only little help from immunohistochemical stains [3, 4]. Imaging can play a crucial adjunct role in such circumstances.

Conclusions

It is important to include septal DNET-like neoplasm in the differential diagnosis of cystic lesions close to Foramen of Monro. Unlike gliomas, a potential histopathological mimic, these lesions do not require chemoradiation and recurrence is uncommon.



(Filename: TCT_eEde-079_septalDNETlikeneoplasm.jpg)

eEde-081

Neuroimaging of Posterior Fossa Tumors: A Pictorial Review

A Torres¹, A Wolosker¹, L Abreu Jr.¹, M Borri¹

¹*Fleury Group, Hospital Sao Luiz, São Paulo, Brazil*

Purpose

The purpose of this pictorial essay is to demonstrate imaging characteristics of intra-axial and extra-axial posterior fossa tumors, among which astrocytic, ependymal, embryonal, glioneuronal and meningeal neoplasms and tumors of neural sheath.

Materials and Methods

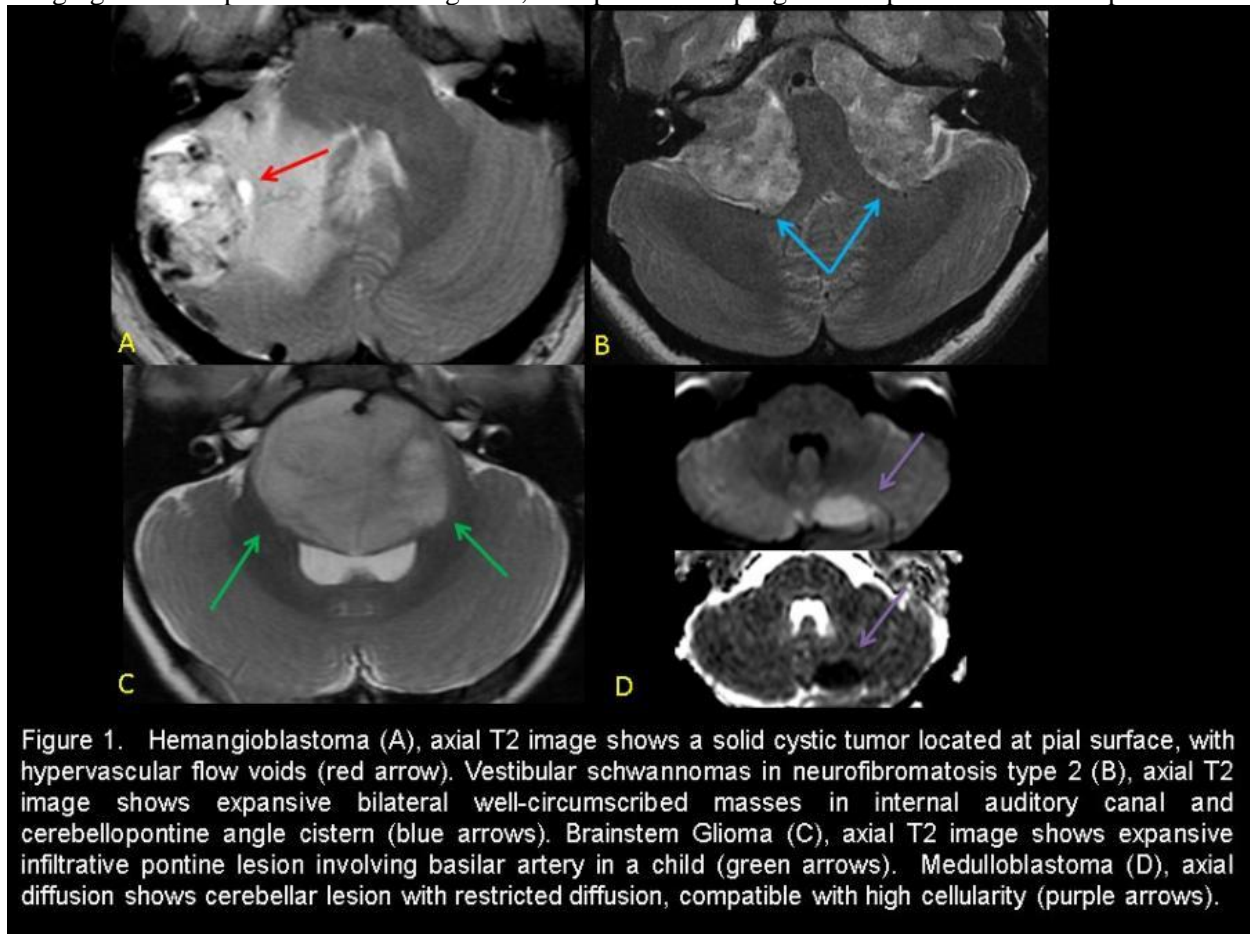
The pictorial essay was performed with images of brain computed tomography (CT) and magnetic resonance (MRI) of patients from our archive, including advanced MRI techniques. We reviewed the literature and correlated our images with described presentation patterns.

Results

The posterior fossa is the infratentorial compartment of cranial vault. It is the site of many types of tumors, with varied grades, intra-axial and extra-axial, primary and metastases. Children and adults are compromised, with peculiar types more frequent in each of age group. Some characteristics of these tumors such as grade, cellularity, plasticity, vascularization, dissemination and compromised anatomical sites are presumed in the image, mainly in MRI studies, assisting the diagnosis (Figure 1).

Conclusions

Imaging has an important role for diagnosis, therapeutics and prognosis of posterior fossa neoplasms.



(Filename: TCT_eEde-081_Posteriorfossatumors.jpg)

eEde-061

Not All Cerebral Strokes Are Arterial: Imaging Evaluation of Cerebral Venous Thrombosis

J Curcio¹, C Lanzieri¹, V Kondray¹, M Rajdev¹

Purpose

The purpose of this study is to diagnose cerebral venous thrombosis and its acute complications with focused imaging techniques. The radiologist should also be comfortable with cerebral venous anatomy and its variants. In addition, diagnostic pitfalls of cerebral venous thrombosis will be reviewed.

Materials and Methods

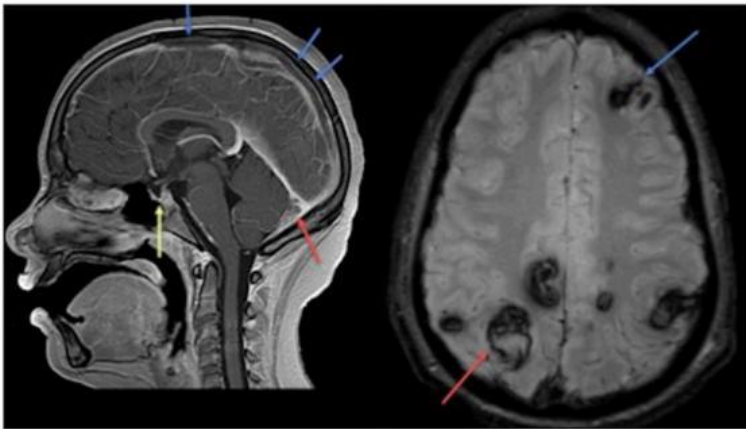
Patients were identified based on positive findings to support a radiographic diagnosis of cerebral venous thrombus. Additional patients with a clinical suspicion for cerebral venous thrombosis were also identified and their images were reviewed.

Results

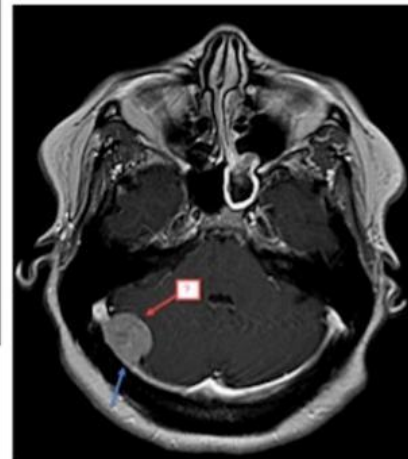
Although cerebral venous thrombosis has a relatively good outcome, it is fairly uncommon and is a great mimicker of other diseases. If left untreated, severe cases can lead to a coma or even death. Cerebral venous thrombosis can occur in the setting of infection, hypercoagulability, malignancy, among other causes. Given the nonspecific clinical manifestations, it is essential to obtain the appropriate imaging techniques given its diagnostic challenges. The preferable imaging modalities used to detect CVT include TOF MR venography, contrast-enhanced MR venography and CT venography. The acute complications that were found include venous hemorrhagic infarction and subarachnoid hemorrhage.

Conclusions

It is important to have a great understanding of normal cerebral venous anatomy and its variants. It is also pertinent to be aware of imaging features of the disease process and its complications. Current imaging modality techniques, including MR and CT angiography, have dramatically increased our ability to make this diagnosis, distinguishing it from pitfalls and prompting medical care in a timely manner.



12 y/o male presenting with headaches and progressive vision loss over two weeks following blunt trauma. Sagittal T1-weighted contrast-enhanced image demonstrate extensive thrombus throughout the superior sagittal and confluence of sinuses. There is an empty sella appearance of the pituitary gland concerning for intracranial hypertension. Gradient-echo axial MRI demonstrates multifocal hemorrhagic venous infarcts. Patient was diagnosed with Heterozygous Factor V Leiden Mutation.



47 y/o woman with a history of obesity and post-coital headaches. Volumetric axial T1 weighted images post contrast demonstrates an extra-axial right posterior fossa mass causing near complete compression of the right transverse sinus with reconstitution distally.

(Filename: TCT_eEde-061_ASNRCVTgraphicfile.jpg)

eEde-045

Pattern of Cerebral Tubercular Vacuities from Autopsy to Modern Imaging: Review of Radiopathological Finding in the Existing Literature and Our Institutional Experience

S Kumar¹, N Soni², J Kalita¹, U Misra¹

¹SGPGIMS, Lucknow, Uttar Pradesh, India, ²University of Iowa Hospitals and Clinics, IA

Purpose

Strokes occur in 15-57% of TBM patients and makes an important prognostic factor. In this exhibit, we aimed to review the cerebral parenchymal and vascular findings in TBM patients on autopsy, CT and MRI reported in the literature along with our institutional experience.

Materials and Methods

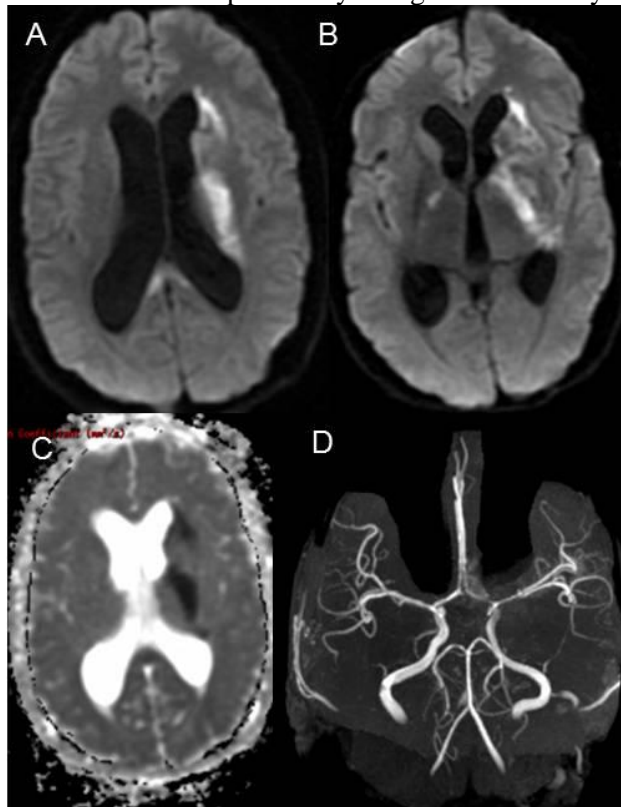
Review of the existing data in the literature and retrospective evaluation of our departmental data

Results

TB vasculitis pattern was initially reported on catheter angiographic, demonstrating narrowing of supraclinoid internal carotid artery, widely sweeping pericallosal artery, and delayed circulation in middle cerebral artery. Incidence of cerebral infarction on CT had been reported in 28-38% of TBM with commonest involvement of the 'tubercular zone' involving caudate head nucleus, anteriomedial thalami, anterior limb and genu of internal capsule. MRI is superior and had shown more infarcts in 40-46% patients of TBM with more detection of brainstem infarcts. On autopsy also, brainstem microscopic infarctions were found more common.

Conclusions

Thus, the overall presence of infarcts in TBM is frequently under reported; brainstem infarction is more common than was previously thought and this may be responsible for the poor prognosis.



(Filename: TCT_eEde-045_Picture1.jpg)

eEde-076

Perfusion-weighted Imaging of High-grade Gliomas Using High Versus Low Flip Angle Dynamic Susceptibility Contrast Imaging

J Gastala¹, A Bryant², T Moritani³, P Kirby¹, A Capizzano¹

¹*University of Iowa Hospitals and Clinics, Iowa City, IA*, ²*University of Iowa, Iowa City, IA*, ³*University of Michigan, Ann Arbor, MI*

Purpose

Treatment related changes and recurrent tumor often have overlapping imaging features on conventional MRI. Dynamic Susceptibility Contrast (DSC) MR imaging is a perfusion technique which can provide complementary information on tumor neoangiogenesis and can help assist in differentiating between post-treatment changes and recurrent tumor using calculated cerebrovascular parameters such as relative cerebral blood volume (rCBV). This educational exhibit will examine differences in the post-treatment assessment of high-grade gliomas (HGGs) using high and low flip angle DSC-MR techniques.

Materials and Methods

A review of the current literature combined with cases and experience from our institutions will be presented. The pathophysiology of HGGs with regard to neovascularity and perfusion characteristics, principles of DSC-MR imaging including how variables such as flip angle affect calculated cerebrovascular parameters, and the current role for DSC-MR in treatment response will be reviewed. Case modules of DSC-MR imaging of treated HGGs along with histopathologic correlation will highlight the spectrum of post-treatment findings. Particularly, differences in assessment by calculated rCBV parameters with low and high flip angles from two different institutions will be presented.

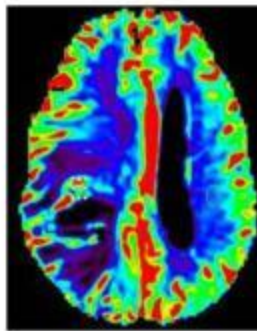
Results

DSC-MR imaging calculates hemodynamic parameters based on the T2* relaxivity of paramagnetic contrast, assuming only intravascular contrast compartmentalization. Within neoplasms, increased vascular permeability causes contrast leakage and confounds those calculated parameters. Changing the flip angle used in DSC-MR imaging modulates the T1- and T2*-weighted effects of contrast leakage and can affect the calculation of rCBV and assessment of treatment response.

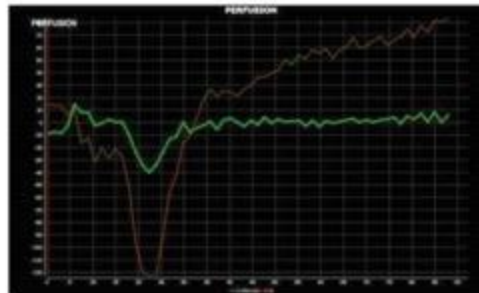
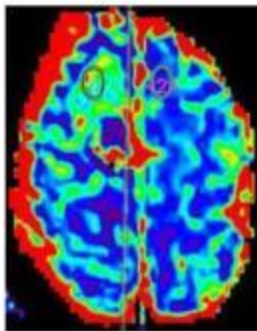
Conclusions

DSC-MR imaging is a useful tool to augment the assessment of treatment response of HGGs by conventional MRI. Differences in DSC-MR technique can affect assessment of treatment response and the radiologist should be aware of how parameters such as flip angle affect this assessment.

GBM Corrected rCBV FA=40 degree



GBM Corrected rCBV FA=90 degree



(Filename: TCT_eEde-076_HGGflipangleimages.jpg)

eEde-033

Perivascular and Paravascular Spaces, an Enigma to Be Understood

R Samant¹, J McCarty¹, m Kumar¹, R Ramakrishnaiah¹, R Van Hemert¹, M Gokden¹

¹University of Arkansas for Medical Sciences, Little Rock, AR

Purpose

1. Summarize the recent concepts in anatomy, physiology and pathophysiology of the perivascular and paravascular spaces which are important lymphatic clearance pathways of the brain 2. Demonstrate the characteristic MRI findings indicating abnormality involving the perivascular/paravascular spaces or surrounding parenchyma 3. Discuss the common and uncommon pathologies which present with characteristic MRI findings indicating perivascular involvement

Materials and Methods

A literature search was performed on PubMed, Ovid and Google Scholar and article titles containing perivascular pathway, paravascular pathway and brain lymphatic drainage were collected. The 15 most cited articles were reviewed and updated concepts regarding anatomy, physiology and pathology of brain lymphatic drainage were identified. These will be presented concisely using illustrative diagrams. Our institution's teaching file from 2011 to 2017 was searched and cases with MRI brain findings indicating

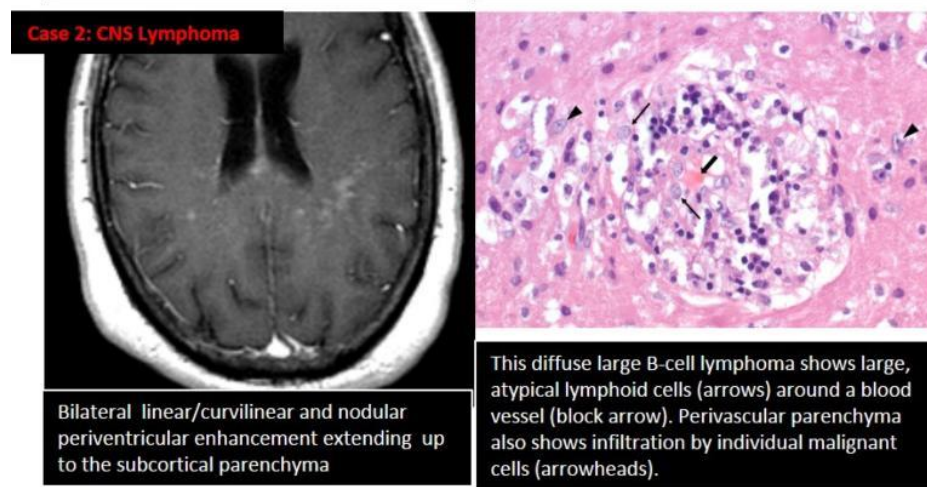
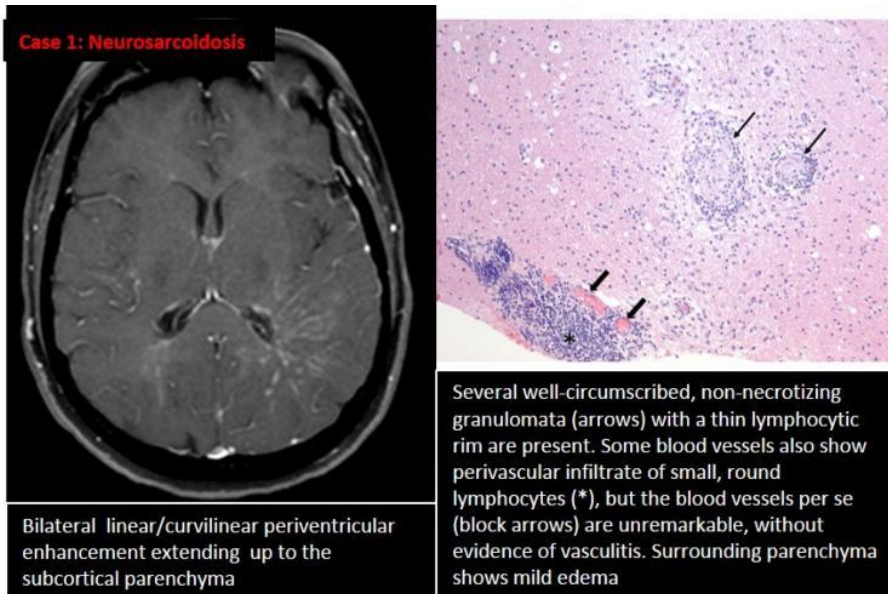
intraparenchymal perivascular abnormality were identified. Relevant cases from this list will be presented in an interactive case based format. Radiopathological correlation in at least three of these cases (CLIPPERS, Lymphoma and Neurosarcoidosis) will be included.

Results

Lymphatic drainage in the brain exists and is composed of perivascular pathway, glymphatic pathway and CSF drainage pathway [1]. The interstitial fluid from brain parenchyma is known to drain to deep upper cervical lymph nodes [2]. Brain lymphatic drainage has established roles in maintaining homeostasis and immune regulation. Dysfunction of this system has been implicated in the pathophysiology of neuroinflammatory, neurodegenerative, neurovascular and neurooncological diseases [1]. It is important that neuroradiologists are up-to-date on their understanding of the brain lymphatic system and its role in pathophysiology. Having a concise list of differential diagnosis for characteristic imaging findings indicating perivascular pathologies will be a high yield practical take away from this exhibit.

Conclusions

Perivascular and paravascular spaces are important brain lymphatic system pathways which play a role in the pathophysiology of CNS disorders. Neuroradiologists should have an up-to-date understanding of these pathways and have a concise differential diagnosis of characteristic perivascular abnormalities on MRI.



(Filename: TCT_eEde-033_PerivascularEnhancement_Final.jpg)

eEde-030

PET-CT of the Brain: A Case-based Review

W Boyce¹, I Gayed¹

¹*University of Texas Houston, Houston, TX*

Purpose

1. Review common indications for functional positron emission tomography (PET-CT) neuroimaging 2. Review normal PET neuroimaging findings and commonly used radiotracers 3. Recognize key imaging features of dementia, epilepsy and brain tumors on PET-CT 4. Discuss newly approved PET radiotracers, such as Amyvid and their emerging role in neuroimaging 5. Avoid pitfalls in performance

Materials and Methods

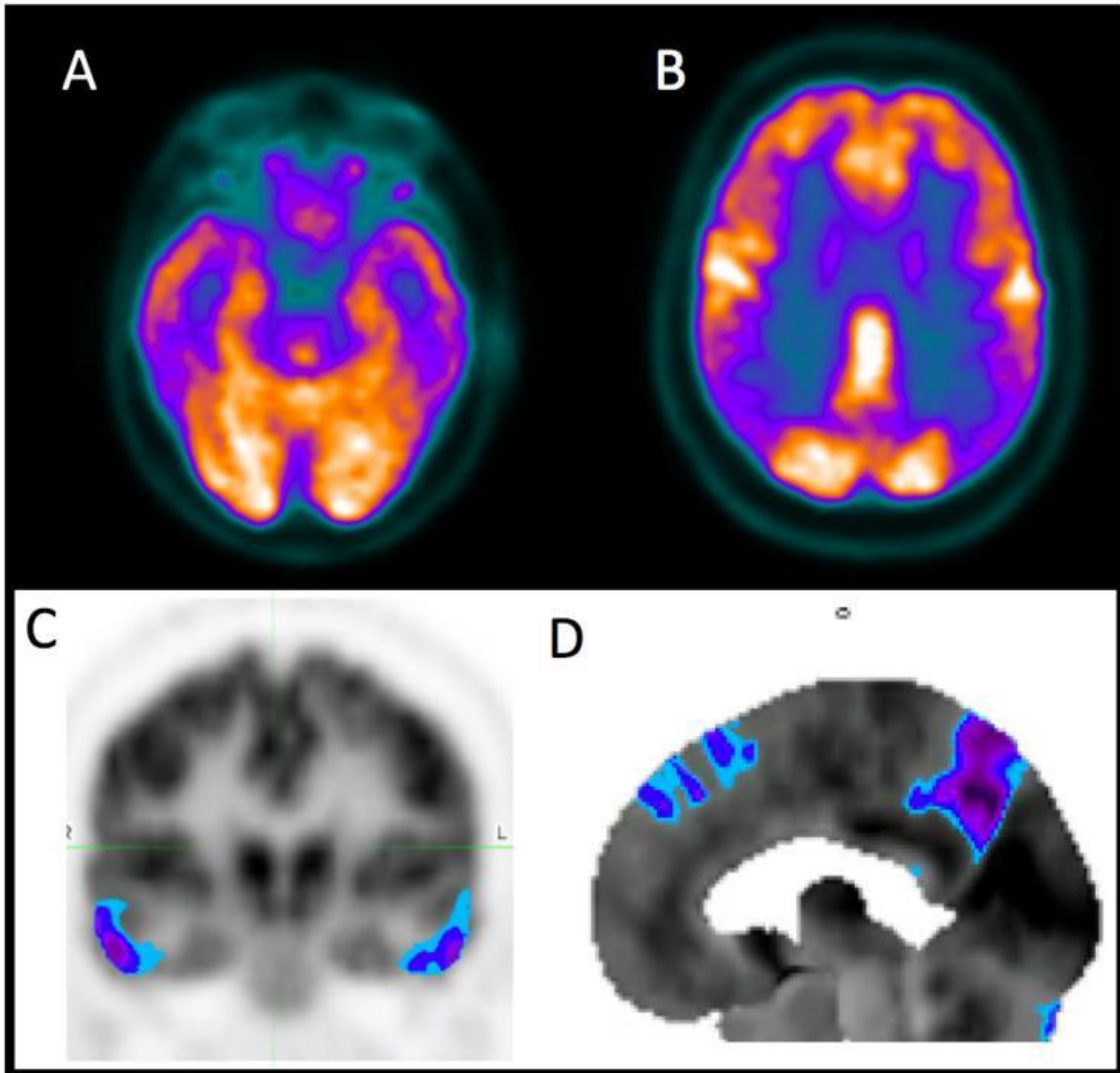
We present a case-based neuroimaging PET-CT review of common and uncommon pathologies encountered in a large academic teaching facility. Examples include various etiologies of dementia (Alzheimer's dementia, front temporal dementia, vascular dementia, Lewy body dementia), seizure foci in epilepsy, and brain tumors. Normal and abnormal examples of our newly approved PET-CT Amyvid scan for detecting beta-amyloid deposition will be presented. Fused PET/CT and PET/MR examples demonstrate both metabolic and anatomic abnormalities.

Results

Functional metabolic imaging is an integral part of evaluating a variety of neurological disorders, such as epilepsy and dementia. PET-CT is used to identify seizure foci in patients with intractable seizures and guide operative planning. PET helps demonstrate metabolic patterns in the brain to identify the underlying etiology of dementia and guide clinicians to the appropriate clinical therapy. PET-CT helps characterize malignant lesions seen on MRI or CT. Characteristics of common neuroimaging PET radiotracers will be discussed. Fusion with MRIs and quantification analysis will help increase the confidence of visual image interpretation and lesion localization.

Conclusions

PET imaging plays a central role in neuroimaging, especially for patients with intractable seizures, dementia and malignancy. It is imperative for the radiologist to recognize key imaging features of PET neuroimaging studies and the normal physiologic features of newly approved radiotracers. PET imaging is rapidly advancing and has bright future, as newly discovered radiotracers emerge.



PET-CT in a patient with dementia shows hypometabolism in the bilateral temporal lobes (image A) and bilateral parietal lobes (B), in a pattern suggestive of Alzheimer's dementia. Quantitative analysis (C, D) is useful for confirming the pattern.

(Filename: TCT_eEde-030_ASNRexamplePET-CT.jpg)

eEde-064

Possible Causes of Convexal Subarachnoid Hemorrhage: More Than Just Trauma or Bleeding Aneurysm

L Koren¹, P Martin¹, A Hilario¹, E Salvador¹, G Ayala¹, F Ballenilla¹, C Fernandez-Cabrera¹, A Ramos¹

¹Hospital 12 de Octubre, Madrid, Spain

Purpose

To evaluate the imaging findings and the etiologic background of convexal subarachnoid hemorrhage (CSAH).

Materials and Methods

We perform a retrospective review of imaging data of patients with spontaneous convexal subarachnoid hemorrhage admitted at our institution over the last four years.

Results

Subarachnoid hemorrhage (SAH) is an extravasation of blood into the subarachnoid or leptomeningeal space. More than 85% of the cases of primary SAH are due to the spontaneous rupture of an aneurysm whose typical distribution is occupying supratentorial cisterns. However, this is not the only pattern of distribution, since in approximately 5% of patients with spontaneous SAH the bleeding is localized into one or few sulci. The term of convexal subarachnoid hemorrhage therefore refers to a spontaneous bleeding located in a sulcus (or several adjacent ones) without involvement of interhemispheric fissures, base cisterns or ventricular system. There are various causes of convexal SAH among which we highlight two entities: the reversible vasoconstriction syndrome and the amyloid angiopathy. Other possibilities to consider, although less frequent, are reversible posterior encephalopathy syndrome, cortical venous thrombosis, endocarditis or dural arteriovenous fistula among others. Computed tomography is the initial diagnostic test due to its high sensitivity for detecting acute subarachnoid hemorrhage and its widespread availability. MRI, and especially the susceptibility-weighted sequence, is the technique of choice to identify the underlying cause.

Conclusions

CSAH is an important subtype of nonaneurysmal SAH that refers to a localized bleeding inside one or several cortical sulci of the brain. Among the different causes, two are particularly common: the reversible vasoconstriction syndrome in young patients and the amyloid angiopathy in older ones. Radiologists should be familiar with these entities to look for key imaging findings that allow establishing a definitive diagnosis.

eEde-025

Presurgical Localization of Eloquent Brain Structures: A Case Based Review

R Patel¹, A Kamali¹, L Ocasio², S Calle¹, O Arevalo¹, P Rabiei¹, S Khanpara¹, E Bonfante¹, R Riascos¹
¹The University of Texas Health Science Center at Houston, Houston, TX, ²Memorial Hermann Hospital, Texas Medical Center, Houston, TX

Purpose

1. To review detailed cortical and functional neuroanatomy 2. To discuss the variety of methods available to localize eloquent portions of the brain such as functional MRI (fMRI) and diffusion tensor imaging (DTI) 3. To illustrate the importance of fMRI and DTI in presurgical planning as a case-based review

Materials and Methods

In our practice, the primary indication for utilizing fMRI, DTI is the evaluation of eloquent areas of the brain in relation to a focal parenchymal brain lesion such as neoplasm, epileptic focus or arteriovenous malformation. This educational exhibit will review all aspects of clinical fMRI, and DTI techniques using over 10 different presurgical cases in a case- based format. Noninvasive imaging techniques included anatomical conventional MRI, BOLD fMRI and DTI.

Results

While performing neurosurgical intervention, electrical cortical stimulation is considered the gold standard for identifying cortical and subcortical areas of eloquence. However, this method has a failure rate up to 15% of cases. Electrical cortical stimulation may also result in seizures and may require the patient to be awake during testing. Anatomical imaging is the most commonly used and precise method

Electronic Educational Exhibits

for preoperative localization of structural lesions. Using certain anatomical landmarks and rules, many of the cortical areas can be localized. However, language dominance and localization of white matter tracts cannot be achieved with conventional MRI. fMRI can be used to localize cortical areas as well as to determine language dominance. Wada testing is useful for determining language dominance in left-handed or ambidextrous patients. DTI can be used to localize white matter tracts.

Conclusions

The goal of this exhibit is to reinforce functional anatomical considerations in brain tumor and epilepsy patients prior to surgery by using conventional MRI, fMRI and DTI. When used effectively, fMRI and DTI have a profound impact on the preservation of motor, language and vision networks and improve postsurgical outcome.

eEde-051

Radiologists' Role in Providing Comprehensive Analysis of CTA, MRI Perfusion, CT Perfusion for Preparation for Neurointerventional Procedures

T Palmer¹, M Lammle¹, D Ro¹, S Cordina¹

¹*University of South Alabama, Mobile, AL*

Purpose

- Familiarize the reader with the different vascular pathologies visible on CTA that are of interest to the neuro-interventionalist
- Provide to the reader a checklist of the details of interest to the neurointerventionalist to include specific standardized measurements to allow for preprocedure planning
- Familiarize the reader with the different vascular pathologies and their practical assessment using representative clinical cases provided in this exhibit

Materials and Methods

Outline Summary: a. Aneurysms and Pseudoaneurysms i. CTA head/neck imaging and postprocessing, MPR, 3D reconstructions, and standardized measurements for preprocedure planning ii. Types of aneurysms iii. Preprocedure planning prior to Conventional Angiography b. Arteriovenous malformations i. CTA head/neck imaging and postprocessing, MPR, 3D reconstructions, and standardized measurements for preprocedure planning ii. Identification of feeding and draining vessels for preprocedure planning prior to Conventional Angiography iii. Spetzler-Martin Classification c. Arterial dissections i. CTA head/neck imaging and postprocessing, MPR, 3D reconstructions ii. Evaluation for management options, stenting, coiling or surgical ligation d. Arterial occlusion/stroke imaging i. CTA head/neck imaging and postprocessing, MPR, 3D reconstructions ii. CT/MRI perfusion imaging

Results

The goal of this educational exhibit is to help clarify common findings that can be communicated to the interventionalist for preprocedure planning.

Conclusions

- Familiarize the reader with the different vascular pathologies visible on CTA that are of interest to the neurointerventionalist
- Provide to the reader a checklist of the details of interest to the neurointerventionalist to include specific standardized measurements to allow for preprocedure planning
- Familiarize the reader with the different vascular pathologies and their practical assessment using representative clinical cases provided in this exhibit

Arteriovenous malformation characterization (AVM)

AVM require a multimodality approach to characterization and typically MRI and CTA are the starting points that most radiologist will encounter them. Often, the lesions are diagnosed serendipitously when the emergency department orders a CT for headache. Since the morphology of AVMs is quite broad, a simpler approach should be employed that involves identification of feeding/draining vessels if possible, determination of the nidus size/location, Spetzler-Martin classification, concomitant hemorrhage, or other incidental findings.

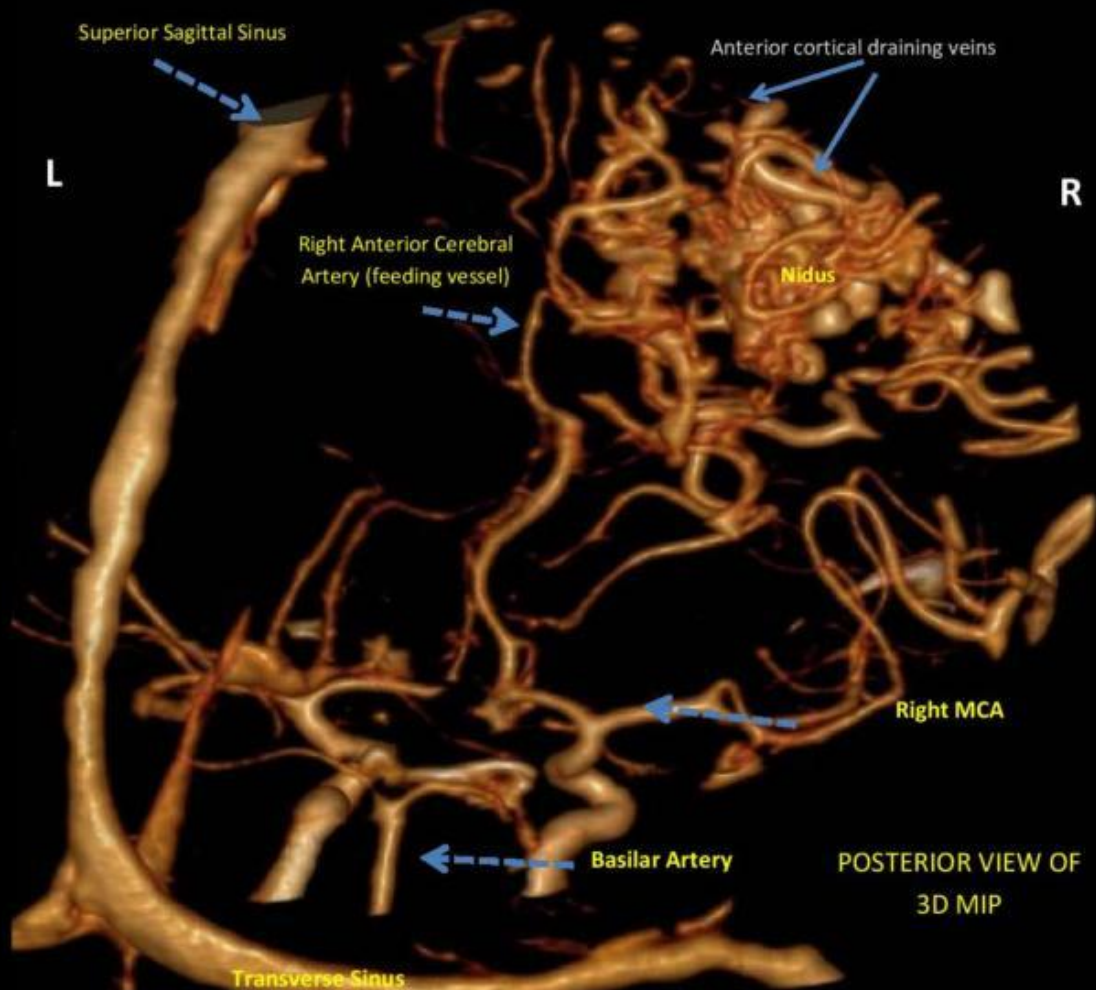


Figure 4: 3D MIP reconstructions of an AVM with the nidus located at the right frontal cortex measuring approximately 30mm x 28mm x 28 mm. The arterial feeding vessel on the 3D reconstruction is the enlarged right Anterior Cerebral Artery which was later confirmed on angiography. The venous outflow is drained primarily through a left frontal anterior cortical vein that drains into the anterior portion of the superior sagittal sinus which demonstrates early contrast filling and appears prominent on this reconstruction secondary to increased flow.

(Filename: TCT_eEde-051_imagesalnewmeasurements-page-004.jpg)

eEde-029

Radionuclide Imaging in Neurology

K Gupta¹, R Jadhav², V Bachhav³, A Ali⁴, S Virmani⁵, M Nagarajan¹

¹*Rush University Medical Center, Chicago, IL*, ²*Rush University Medical Centre, Chicago, IL*, ³*Rush university medical center, chicago, IL*, ⁴*RUSH UNIVERSITY MEDICAL CENTER, CHICAGO, IL*, ⁵*Rush University Medical Center, Chicago, Chicago, , IL*

Purpose

Wide availability of newer radiopharmaceuticals and advancement in system resolution has revolutionized brain imaging methodologies. It is now possible to better understand biochemical changes, determine neurotransmissions, map blood flow and follow pathophysiology of specific neurology and psychiatric diseases. We present a case-based review of common and uncommon radiopharmaceuticals and their imaging spectrum used in neurology.

Materials and Methods

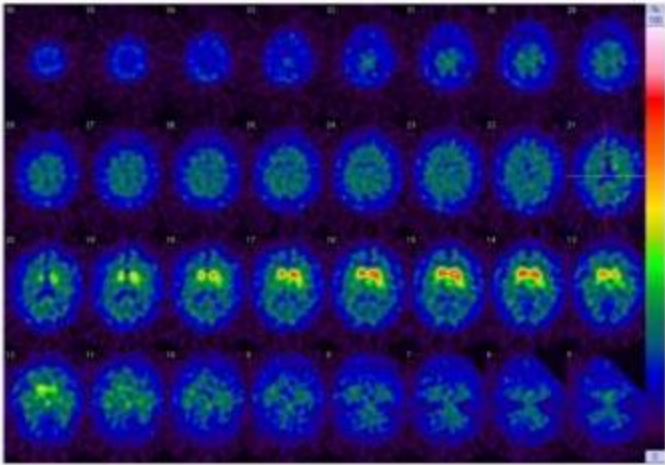
We reviewed cases of radionuclide brain imaging of the last two years including planar imaging, SPECT and PET. We selected interesting cases, common and rare indications as well as newer radionuclide imaging are represented pictorially.

Results

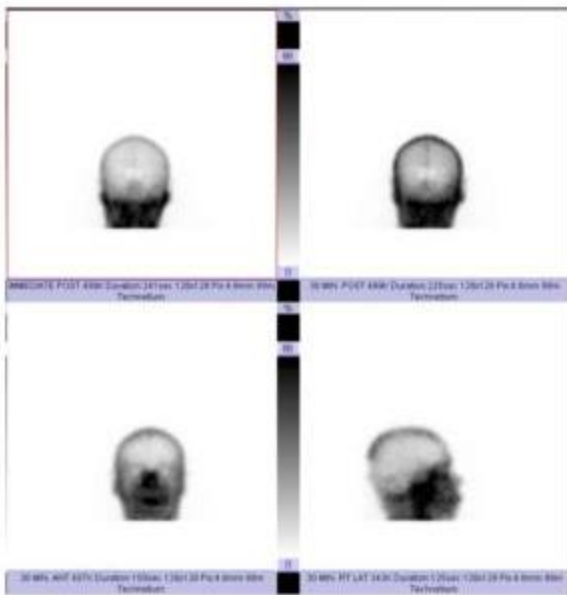
The reviewed cases were divided into the following categories: • Cerebral blood flow for assessment and prognosis of stroke, TIA, Carotid stenosis and trauma • Determination of cerebral flow reserve with Diamox • Epilepsy focus localization • Early assessment of Parkinson's disease and parkinsonian syndromes • Dementia imaging • Amyloid plaque imaging in Alzheimer's disease • Brain death study • Shunt patency • CSF studies for leak and hydrocephalus • PET metabolic imaging for brain tumor, recurrences and radiation necrosis

Conclusions

Nuclear medicine studies are complementary to structural imaging and contribute to clinical diagnosis. Imaging with newer ligands can determine disease pathophysiology in early stages and hence improve prognosis.



CASE 1. I-123 Ioflupane DAT scan: Slightly decreased uptake in the tail portion of right striata suggest possibility of Parkinsonian syndrome. Uptake in the left striata is within normal limits.



CASE 2. Tc-99m DTPA perfusion study demonstrate no radionuclide activity in sagittal and lateral sinuses, consistent with brain death.

(Filename: TCT_eEde-029_CASE1.jpg)

eEde-089

Rapid MRI Brain: Getting it Done Quicker and Better

A Rizvi¹, D Sadowsky¹, M Tenner¹, S Bobra¹, H Mehta², E Gulko¹

¹Westchester Medical Center, Valhalla, NY, ²New York Medical College-Westchester Medical Center, Valhalla, NY

Purpose

Through a case-based approach, the purpose of this exhibit is to highlight the utility of rapid MRI brain techniques in diagnosing and managing patients with various CNS pathologies. Review of the literature and discussion of rapid MRI protocols will be presented. The goal of the exhibit is to familiarize the neuroradiologist with the techniques and applications of rapid MRI brain examinations.

Materials and Methods

1. Introduction of rapid MRI brain with review of the literature 2. Techniques and Protocols of rapid MRI brain, including limitations 3. Presentation of cases, drawn from a Level I trauma center will include: a. Follow-up of intracranial hemorrhage b. Follow-up of known hydrocephalus c. Diagnose of acute stroke d. Immediate follow-up of postoperative tumor resections e. Diagnosis of sinusitis

Results

The rapid MRI brain exam provides the neuroradiologist a dynamic modality to compliment CT and conventional MRI examinations, and may suffice in answering a specific clinical question. As an alternate to ionizing radiation, rapid MRI brain offers the advantages of MR imaging, at the fraction of the time of a conventional full MRI brain exam. Also in patients who may not tolerate a full MRI examination, it prevents immediate deferral to CT imaging.

Conclusions

The rapid MRI brain exam is a unique imaging modality that can aid the neuroradiologist and referring physicians in managing patients in a variety of clinical scenarios. A firm understanding of implementing and interpreting rapid MRI exams will aid the neuroradiologist in providing enhanced patient care.

eEde-054

Recognition of Dural Sinus and Cortical Venous Thrombosis on Non-venographic Imaging in Patients with Malignancy

M Shroads¹, J Bykowski¹

¹*University of California San Diego Health, San Diego, CA*

Purpose

It is well known that patients with malignancy are at increased risk for venous thrombosis. Dural-sinus and cortical-venous thrombosis can be difficult to diagnose in newly symptomatic oncology patients, as the initial imaging study is often not optimized for venous evaluation and findings may overlap or coexist with meningeal involvement of tumor, edema from parenchymal metastases, or new hemorrhagic metastases. It is crucial for radiologists to be aware of the risk of intracranial venous thrombosis in this patient population and to facilitate early detection given the morbidity associated with complications.

Materials and Methods

Multiple cases of intracranial venous thrombosis in oncologic patients are presented in the order in which the imaging was obtained to highlight subtle findings and complications that should prompt suspicion for underlying dural sinus or cortical venous thrombosis on nonvenographic imaging.

Results

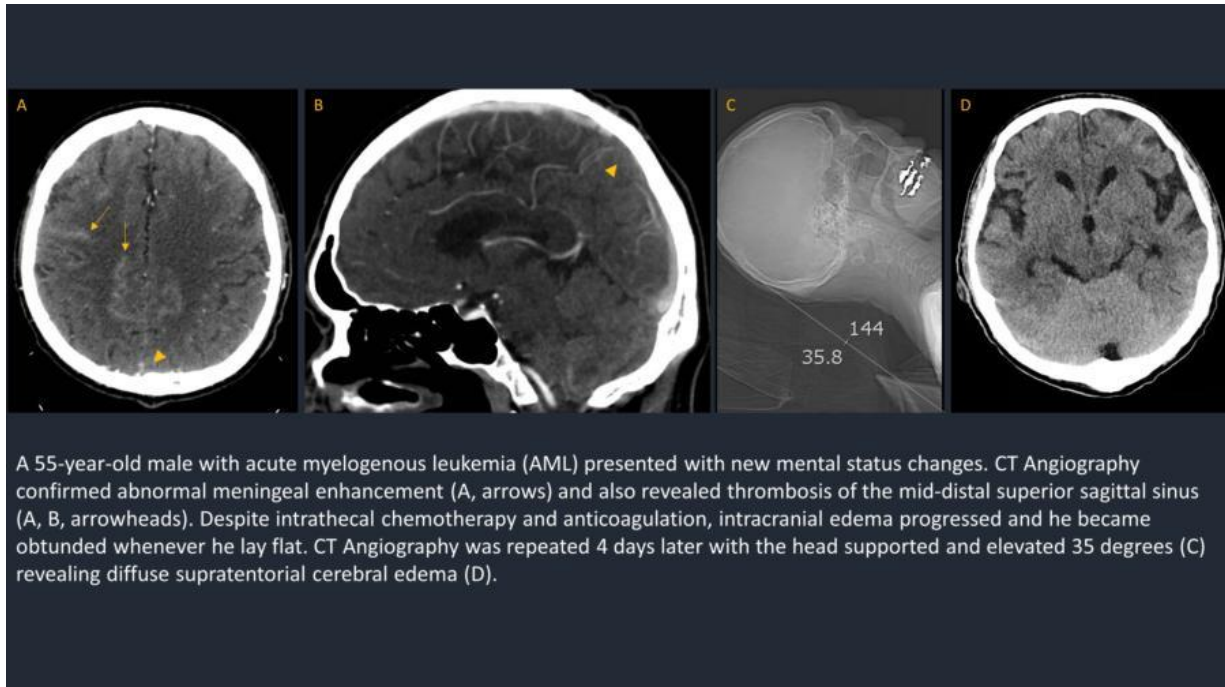
Selected cases demonstrate key imaging features, pitfalls, and mimics, including: - Pattern of gyral edema on opposing sides of a sulcus - Hemorrhagic transformation at presentation - Increased conspicuity of veins on susceptibility weighted imaging - Subtle or absent diffusion restriction in acute venous infarct - Utility of MRI cortical venous mapping for radiation and surgical planning to identify nonenhancing veins - Limitations of CT angiography - Pitfalls of nonocclusive thrombus on time of flight venography - Satisfaction of search

Conclusions

Dural-sinus and cortical-venous thrombosis may elude detection in oncology patients, as initial imaging of new central nervous system symptoms is not tailored for evaluation of the intracranial venous system.

Electronic Educational Exhibits

Pretest suspicion combined with a recognition of subtle signs are helpful to expedite appropriate treatment.



(Filename: TCT_eEde-054_SVTGRAPHIC.jpg)

eEde-023

Role of PET-MRI in Neuro-oncology

A Chaudhry¹

¹Johns Hopkins Medicine, Stevensons Ranch, CA

Purpose

The aim of this exhibit will be to provide a comprehensive overview of the physical principles, techniques and clinical applications of the emerging hybrid modality: positron emission tomography-magnetic resonance imaging (PET-MRI). This hybrid modality attempts to provide the functional imaging obtained from a PET study and detailed structural information obtained from an MRI study.

Materials and Methods

1. Review physical principles and techniques of PET- MRI 2. Clinical applications of PET-MRI including neuro-oncology, neurodegenerative disorders, and inflammatory conditions 3. Role of PET-MRI in evaluation of neurodegenerative and inflammatory conditions 4. Pearls and pitfalls of PET-MRI 5. Future role of PET-MRI in neuroradiology

Results

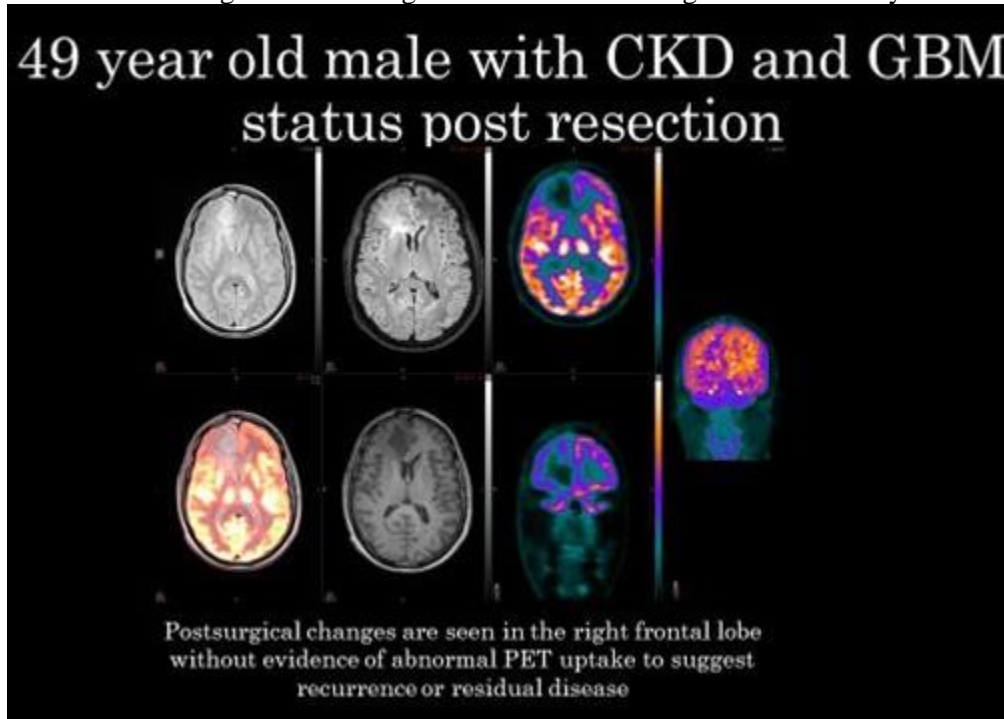
1. Physical principles and techniques of PET-MRI: Relevant concepts involving image acquisition, postprocessing and interpretation will be provided. 2. Overview of clinical applications of PET-MRI in neuro-oncology patients: An overview of initial tumor diagnosis, discussion of tumor biology and its effect on tumor imaging (e.g., tumor metabolism, angiogenesis, cellularity, etc.), post-treatment follow-up imaging evaluation and its role in therapy selection will be provided. 3. Role of PET-MRI in evaluation of neurodegenerative and inflammatory conditions (including MS) 4. Pearls and pitfalls: Common pitfalls and controversies regarding PET-MRI in neuroradiology will be discussed. 5. Future of PET- MRI: A

Electronic Educational Exhibits

discussion of future applications and challenges facing PET- MRI in neuroradiology, specifically neuro-oncology and neurodegenerative disorders will be provided.

Conclusions

PET-MRI is an emerging hybrid imaging modality offering detailed functional and structural imaging with promising clinical applications especially in the field of neuro-oncology, neurodegenerative and inflammatory CNS conditions. This case-based exhibit provides the viewer an in-depth review of the relevant concepts underlying the technical and clinical aspects along with common pearls and pitfalls of PET-MRI allowing for better integration and relevant usage of this modality in clinical practice.



(Filename: TCT_eEde-023_petmricasesess.jpg)

eEde-015

Small Vessel Brutality: Level I Trauma Center Style

E Supsupin¹

¹University of Texas Health Science Center Houston, Houston, TX

Purpose

Small vessel injuries may be serious and potentially life threatening if the diagnosis is missed or delayed. This is a pictorial review of small vessel injuries in a level I trauma center.

Materials and Methods

For purposes of this presentation, traumatic injuries to the external carotid artery (ECA) and its branches are considered "small vessel injuries". The angiographic anatomy of the ECA and its branches is reviewed. The range of small vessel injuries encountered in a level I trauma center are presented. Highlight cases emphasize the potentially serious impact of these injuries on patient outcomes.

Results

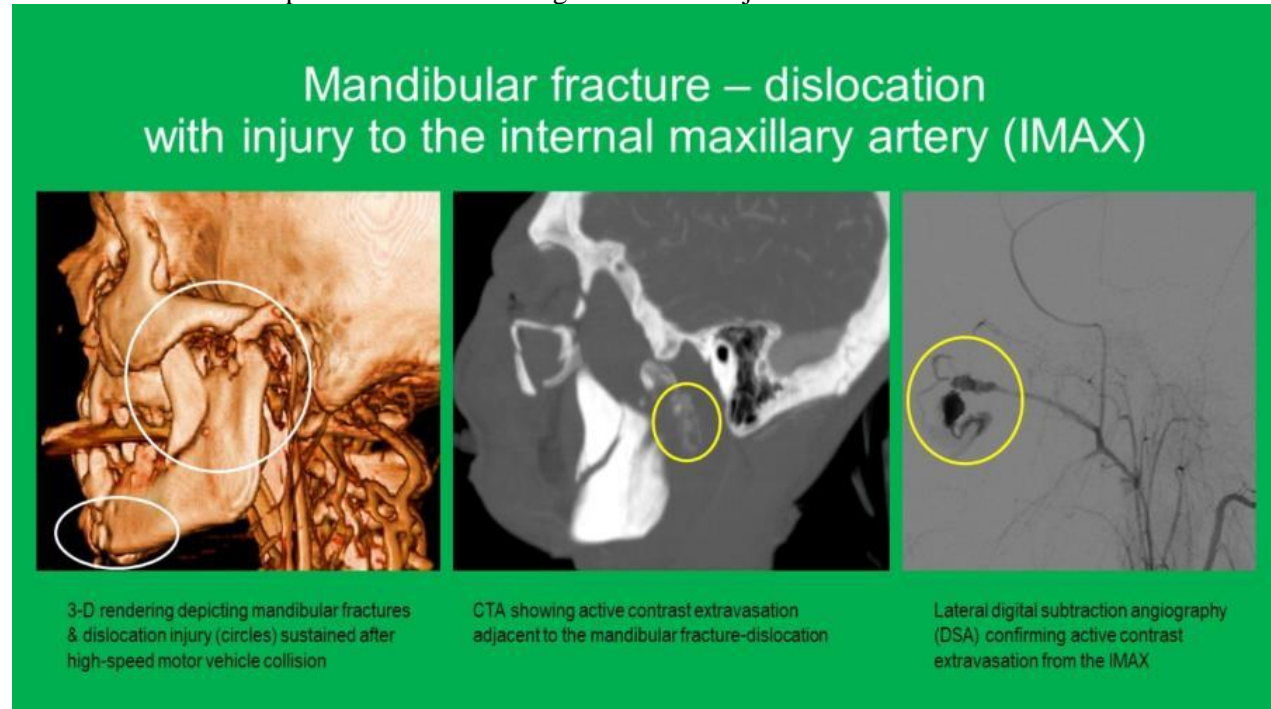
In blunt or penetrating trauma, CT angiogram (CTA) is the initial imaging of choice in the evaluation of head and neck vascular injuries. Traumatic injuries to the ECA (particularly its smaller branches) may be easily overlooked because of sheer small size of these vessels. This is compounded especially in

Electronic Educational Exhibits

multitrauma, by the radiologist's "tunnel vision" and focused attention to large vessels only, specifically the internal carotid or vertebral arteries. Yet small vessel injuries can be just as devastating as large vessel damage, if not timely addressed. Missed or delayed diagnosis may adversely affect patient outcome.

Conclusions

Catastrophic injuries to the ECA and its branches may be easily missed. These small vessels deserve inclusion in our search pattern when evaluating for vascular injuries.



(Filename: TCT_eEde-015_MandibularfracturedislocationwithIMAXinjury.jpg)

eEde-017

Spontaneous Intracranial Hypotension and Idiopathic Intracranial Hypertension: Hunting for The Typical Findings at MRI

A Hilario¹, E Salvador¹, L Koren¹, F Ballenilla¹, G Ayala¹, P Martin¹, A Ramos¹

¹Hospital 12 de Octubre, Madrid, Spain

Purpose

1. To describe imaging findings reported in idiopathic intracranial hypertension (IHH) discussing their possible roles in pathophysiology 2. To illustrate typical imaging findings and diagnostic approaches associated with spontaneous intracranial hypotension (SIH)

Materials and Methods

We have reviewed literature and searched our database for the last five years looking for CT/MRI images of confirmed cases of IHH and SIH.

Results

IHH is a rare disorder occurring more frequently in obese women of childbearing age, resulting in increased intracranial pressure from an unknown cause. Headaches are often the presenting symptom (90%) and papilledema is the hallmark of diagnosis. Traditionally, imaging ruled out secondary causes of elevated CSF pressure but now may reveal findings frequently seen in IHH such as empty sella, flattening of the posterior globes, optic nerve head protrusion, distention of optic nerve sheaths, tortuosity of optic nerve, cerebellar tonsillar herniation, meningoceles, CSF leaks and transverse venous sinus stenosis. In

Electronic Educational Exhibits

cases of SIH, the most common sites of leakage identified were at the cervicothoracic junction/thoracic region of the spinal canal. In the absence of a dural defect, a recent hypothesis proposes increased CSF absorption from negative pressure gradient in the inferior vena cava. The typical feature of SIH is orthostatic headache with at least one feature of meningeal irritation. The MRI appearances are mainly attributed to CSF hypovolemia resulting in venous engorgement, diffuse dural thickening, decreased dimension of the suprasellar cistern, bowing of optic chiasma, flattening of the pons against the clivus, effacement of the perimesencephalic cistern and hindbrain herniation. Subdural hematoma is a late finding and occurs in around 10% of patients.

Conclusions

IHH remains a diagnosis of exclusion, and imaging findings should not prompt invasive procedures, unless other signs of IHH (such as papilledema) are present. MRI depicts imaging markers that allow diagnosis of SIH in any patient presenting with headache and neck pain.

eEde-099

Stroke or Not Stroke?: Imaging Findings of Stroke Mimics

M Prenafeta Moreno¹, V Cheranovskiy¹, V Perez Riverola¹, J Branera¹, A Rovira², A Rovira Gols¹
¹UDIAT-CD, Corporació Sanitària Parc Taulí, Sabadell, Barcelona, Spain, ²Vall d'Hebron University Hospital, Barcelona, Spain

Purpose

The purpose of this exhibit is: 1. To discuss the most common conditions other than stroke that can cause acute focal neurological deficits. 2. To review the imaging findings that can help in the diagnosis of stroke mimics. 3. To explain the usefulness of MRI and particularly of CT and MR perfusion maps in the diagnosis.

Materials and Methods

1. Introduction 2. Clinical factors 3. Role of neuroimaging 4. Pictorial review of stroke mimics 5.

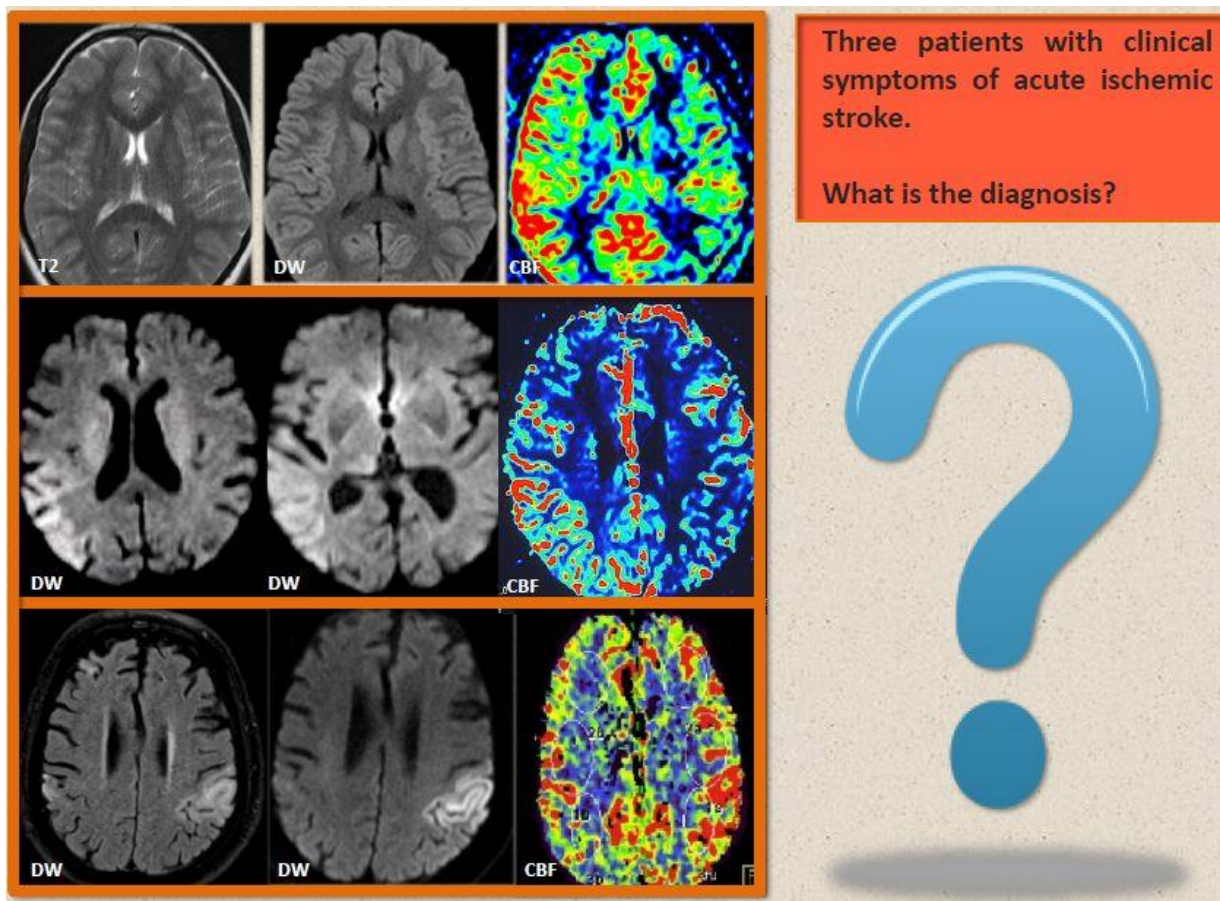
Treatment considerations

Results

Radiological findings of different stroke mimics will be discussed: - Migraine and other less common entities related with headaches - Epilepsy and related diseases - Tumors and pseudotumors - Glycemic disorders and other metabolic disorders

Conclusions

It is important to recognize radiological findings of stroke mimics to avoid unnecessary treatment applied in ischemic stroke and which can cause life-threatening complications.



(Filename: TCT_eEde-099_ImagenABS.jpg)

eEde-019

Subclavian Steal in the Setting of Right-sided Aortic Arch with Mirror Image Branching and Innominate Artery Atresia

B Reznikov¹, B Laughlin¹, T Sivapatham¹, B Nkansah²

¹Christiana Care Health System, Newark, DE, ²Milton Hershey School, New Castle, DE

Purpose

We will present a case report of a patient with a rare vascular anomaly, subclavian steal phenomenon in the setting of a right-sided aortic arch with mirror image branching and atresia of the left innominate artery. We will discuss the clinical presentation and imaging findings. This exhibit will also review the incidence, embryology, and clinical implications of this vascular anomaly. The subclavian steal phenomenon/syndrome will also be reviewed.

Materials and Methods

The patient's records will be reviewed and the clinical presentation will be described. A pictorial review of the pertinent imaging features will be presented. A literature search will be performed targeting this rare vascular anomaly and its incidence, embryology, and clinical implications will be described. We will also review the subclavian steal phenomenon/syndrome.

Results

A 45-year-old woman with history of chronic left upper extremity paresthesias, weakness, and pain presented for an outpatient brain MRI which revealed a markedly decreased caliber of the left internal

carotid artery flow void. Subsequent vascular imaging which included time of flight MRA, CT angiography, and time resolved MRA demonstrated multiple vascular anomalies. There was a right-sided aortic arch with mirror image branching and atresia of the left-sided innominate artery. The right common carotid and internal carotid arteries appeared normal. The right vertebral artery was enlarged and tortuous. There was delayed filling of the left subclavian, vertebral, common carotid, internal carotid, and middle cerebral arteries. There was reversal of flow in the left vertebral artery which was filled across the vertebrobasilar junction and through hypertrophied spinal arteries, muscular branches, and additional collaterals. Subsequent clinical evaluation revealed only minimal variance in blood pressure between the upper extremities. There was no clinical evidence for cerebral hypoperfusion and no signs of infarction on MRI. Revascularization was deferred at this time. Right-sided aortic arch anomalies are estimated to occur in 0.05 - 0.1% of the population. Three types of right-sided aortic arch anomalies have been described: right-sided arch with aberrant left subclavian artery, right-sided arch with mirror image branching, and right-sided arch with isolated left subclavian artery. There have only been a few case reports describing the right sided arch anomaly seen in our patient. Our exhibit will review the embryology of right-sided arch anomalies and discuss the subclavian steal phenomenon/syndrome. Conclusions

We have described an extremely rare anatomic variant, subclavian steal in the setting of a right-sided aortic arch with mirror image branching and atresia of the left innominate artery. The incidence, embryology, and clinical significance of this entity have been described. We have also reviewed the subclavian steal phenomenon/syndrome.



Figure 1. (a) atretic innominate artery stump, (b) collateral vessel (from arch to left common carotid artery), (c) left common carotid artery, (d) left subclavian artery, (e) left vertebral artery.

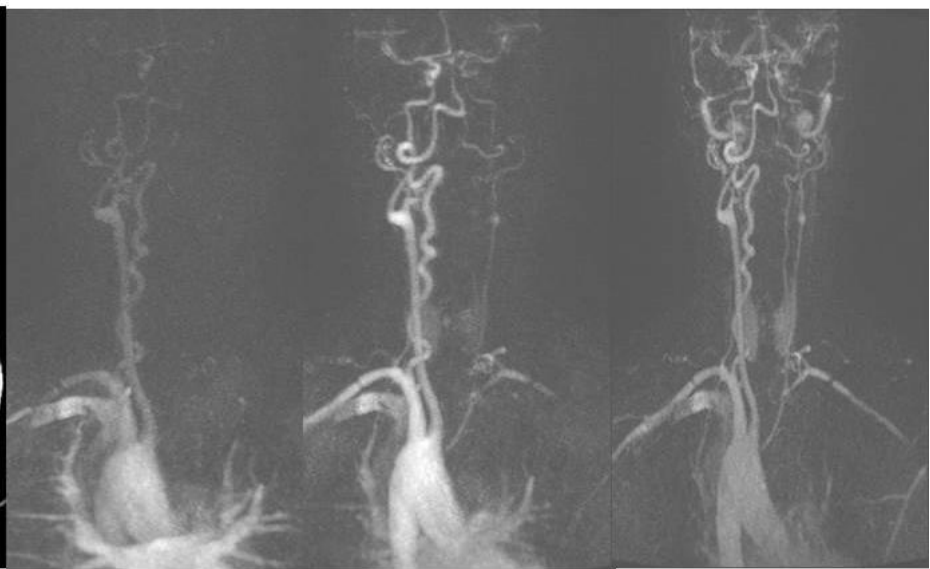


Figure 2a. Early phase image of time resolved MRA demonstrates enhancement of the right sided aortic arch and right carotid and vertebral arteries without enhancement of the left innominate, carotid, subclavian, or vertebral arteries.

Figure 2b. Subsequent image of time resolved MRA demonstrates enhancement of the distal left vertebral artery without enhancement of the proximal left vertebral artery. Delayed enhancement of the left common carotid, internal carotid, and subclavian arteries is evident.

Figure 2c. Additional delayed image demonstrates enhancement of the more proximal portions of the left vertebral artery and progressive enhancement of the left subclavian artery consistent with subclavian steal.

(Filename: TCT_eEde-019_ASNRimagefinal1.jpg)

eEde-007

Swallow, Swallow, Little Swallow. Is it Parkinson's Disease or is it Essential Tremor?

C Besada¹, M Perez Akly¹, J funes¹, A Miquelini¹

¹Hospital Italiano de Buenos Aires, CABA, Argentina

Purpose

1. To depict anatomical and physiopathological features of the nigrosome-1 zone represented by the swallow tail sign 2. To stamp in the memory the images of this radiological sign by evoking the beloved Oscar Wilde's story: The Happy Prince 3. To highlight the importance of the MR SWI sequence as a tool to properly evaluate the presence of this sign 4. To stress the value of this finding in the challenging diagnostic process of movement disorder's diseases 5. To raise awareness on this subject among the radiologic and neurologic community

Materials and Methods

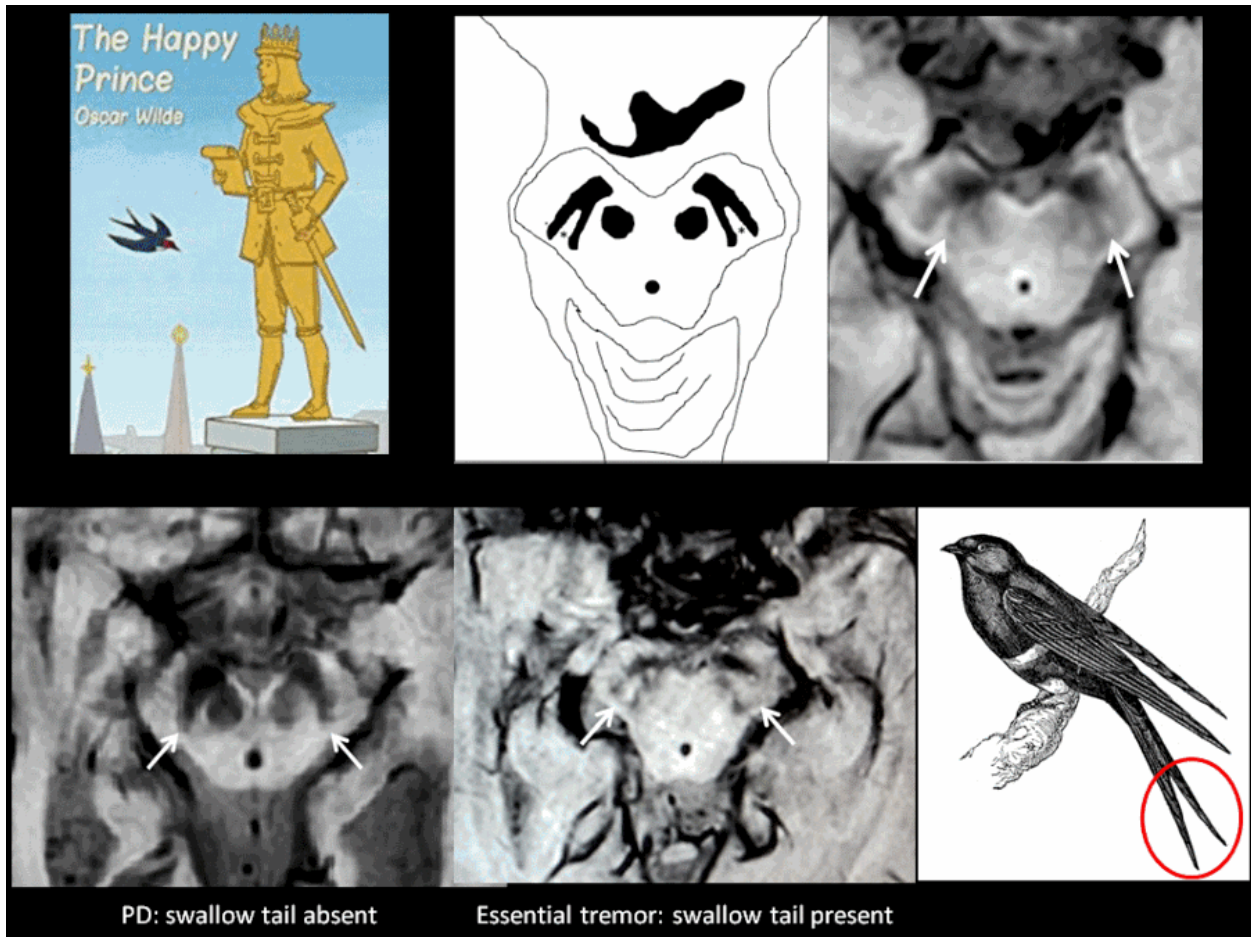
In Oscar Wilde's beautiful tale, the little swallow helps the Happy Prince fulfill his dream of aiding the ones in need. In our study, the "swallow tail" sign may also help us fulfill our hope of aiding patients with movement disorders. Parkinson's disease (PD) and essential tremor (ET) are neurological entities with diagnoses based on clinical findings which may have similar manifestations in initial stages, with an error in clinical diagnosis of up to 29%. The use of magnetic susceptibility sequences (SWI) in MRI of 3T allows detecting the nigrosome-1 area that is an accumulation of dopaminergic neurons located in the dorsal and lateral sector of the pars compacta forming the sign of "the swallow tail". This area groups around 80% of the dopaminergic neurons and degenerates in early stages of PD, which can be detected by the mentioned sequence. The absence of the "swallow tail" sign is proposed to be highly suggestive of PD. A study comparing PD and ET patients was conducted in a 3T MRI scanner to prove the value of the depiction of this radiological sign between these groups of patients. Images were assessed by two neuroradiologists blinded to clinical diagnosis.

Results

Parkinson's disease is the second most common neurodegenerative disease after Alzheimer's disease. There is no definitive biomarker validated for Parkinson's disease. The use of MRI in the diagnosis of PD was classically confined to rule out other causes of parkinsonism. Technological progress including higher magnetic field equipments, and specific high resolution techniques have allowed to describe new features that could be useful specially in the early stages of PD. In this study we compared images of PD patients with ET patients due to the possibility of clinical overlapping between the two entities. Sixteen patients were included in each group. The results obtained showed high sensitivity and specificity for discrimination between the two groups. We also found a good interobserver variability for assessing each side of nigrosome-1 area and an excellent overall assessment of the absence of the nigrosome-1 area.

Conclusions

High resolution SWI sequence is a reliable MR technique to depict the nigrosome-1 area shown by the presence of the "swallow tail" sign. We found high sensitivity, specificity and diagnostic accuracy to differentiate patients with PD from ET, with adequate interobserver variability. Radiologists and neurologists should be aware of this possibility to help in the challenging diagnostic process of these disorders. We thank the little swallow for providing the "swallow tail" sign and continue helping the ones in need as well as it did with the Happy Prince.



(Filename: TCT_eEde-007_Presentacin1.gif)

eEde-086

Synthetic MRI and Quantitative Mapping

D Ginat¹, T Carroll¹

¹University of Chicago, Chicago, IL

Purpose

The goal of this exhibit is to review the physics behind synthetic MRI and quantitative mapping as well as potential applications in neuroimaging.

Materials and Methods

Synthetic MRI is a novel technique that enables reconstruction of various image contrasts from a single scan. The technique allows MRI parameters such as TR, TE, and TI to be modified based on mathematical inferences instead of being predetermined, as with conventional sequences. A single saturation recovery TSE sequence is used to estimate absolute physical properties, proton density, longitudinal relaxation rate, and transverse relaxation rate, including correction for B1-inhomogeneities.

Results

Synthetic MRI can provide multiple contrasts in a single scan, which is acquired in about five minutes, as opposed to conventional MRI, which is relatively time-consuming and redundant. Overall synthetic MRI quality is similar to that of conventional proton-density, STIR, and T1- and T2-weighted contrast views for neuroimaging and some conditions may even be more conspicuous on synthetic MRI. Synthetic

Electronic Educational Exhibits

reconstruction inherently prevents misregistration across synthetic contrast views. The quantitative nature of the method and its ability to probe multiple physical properties in a single sequence make it suitable for volumetric analysis. Parametric maps can be generated using the MR scanner to measure magnetic properties in the tissue. Motion and signal encoding artifacts affect all reconstructed synthetic views if present in the original acquisition. Certain artifacts are more common with synthetic T2 FLAIR than conventional FLAIR. While these are readily recognizable, comparison with conventional T2 FLAIR and DWI may be useful too for elucidating the situation. Synthetic scanning is performed in the axial view only, and commercial 3-D acquisitions are currently unavailable. Additional post processing in order to change the values of TE and TR of the images retrospectively currently requires separate software that is installed on a stand-alone computer.

Conclusions

Synthetic MR imaging makes it possible to reconstruct several different image contrasts from a single acquisition. Scan time can be decreased by up to nearly a factor of 3 with synthetic MRI compared with conventional MRI. Synthetic MRI provides quantitative tissue characterization that enables segmentation and fat suppression. Synthetic images have equal or greater relative contrast and more noise compared to conventional MRI, but overall have similar diagnostic utility for detecting brain lesions.

eEde-048

TB Meningitis: Imaging Features and Their Progression Over Time

N Dobbs¹, D Summers¹, H Nghia², G Thwaites²

¹*Department of Clinical Neuroscience, Edinburgh, United Kingdom,* ²*Hospital for Tropical Diseases, Ho Chi Minh City, Vietnam*

Purpose

In Western populations, tuberculous meningitis (TBM) is a rare disease (1). Despite its rarity, it is the most lethal form of the disease and there can be a long delay from symptom onset to the initiation of treatment (1). This exhibit will increase the reader's familiarity with imaging findings, with the aim of expediting diagnosis and appropriate treatment in TBM.

Materials and Methods

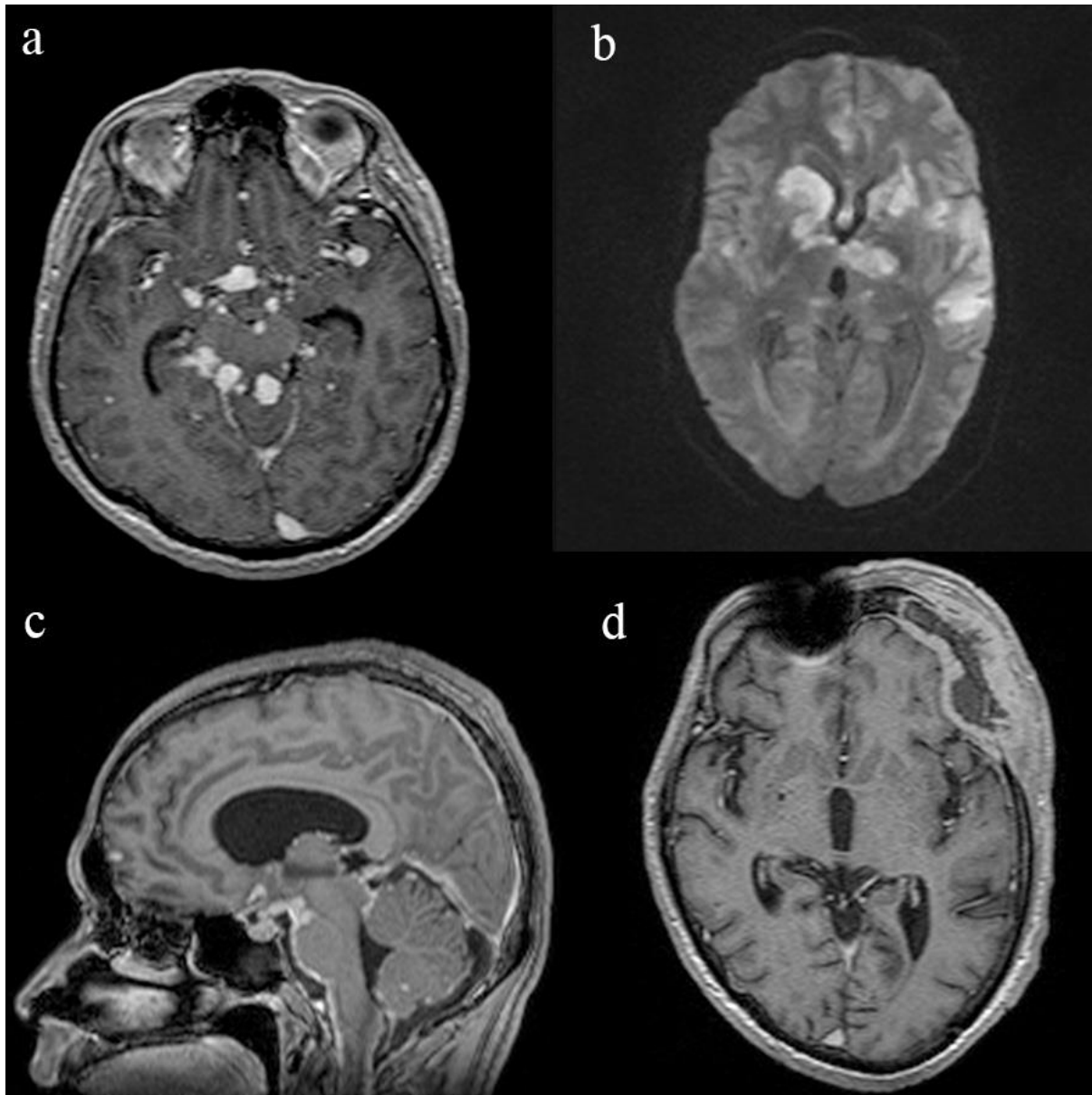
Cases which highlight the imaging findings in TBM have been selected from access to the neuroimaging of 120 patients with TBM in Vietnam, at three time points (0, 60 and 240 days from diagnosis) from a study funded by the Wellcome Trust. This allows the rare opportunity to review the typical and atypical findings in TBM and how they can change over time via multiple imaging case reviews.

Results

Cases which highlight the typical features of TBM are shown, including tuberculomas (image a), infarcts (image b), meningeal enhancement (image c), hydrocephalus, and transient splenic lesions. Unusual complications such as TB osteomyelitis of the skull (image d) are also reviewed.

Conclusions

After using this electronic educational exhibit the reader should be aware of the typical and atypical imaging findings in TBM.



(Filename: TCT_eEde-048_Abstractimage.jpg)

eEde-068

The 2017 WHO Classification of Pituitary Gland Tumors: An Update for the Radiologist

J Aristizabal¹, P Naval Baudin², C Zamora³, M Castillo³

¹University of Antioquia, Medellin, Colombia, ²Hospital Universitari de Bellvitge, L'Hospitalet de Llobregat, Barcelona, Spain ³University of North Carolina, Chapel Hill, NC

Purpose

The recently published 4th edition of the WHO Classification of Tumors of Endocrine Organs introduces significant changes in the designation of adenohypophyseal cell neoplasms, outlines new entities, and redefines old ones. The purpose of this educational exhibit is to summarize and discuss the most relevant changes.

Electronic Educational Exhibits

Materials and Methods

This exhibit is based on a review of the 3rd (2004) and 4th (2017) editions of the WHO Classification of Tumors of Endocrine Organs. Both publications were compared and relevant changes in the classification of pituitary gland tumors are summarized.

Results

Aggressive imaging features in pituitary adenomas do not necessarily correlate with histological subtype or risk of malignancy. The new classification adopts a designation based on cell lineage that relies on hormonal factors, immunohistochemistry for pituitary-specific transcription factors, mitotic count and Ki-67 index. It abandons the concept of hormone-producing adenoma because of its poor specificity and prognostic value. Some definitions have been updated, such as "typical" or "atypical" adenomas, pituitary carcinoma, null-cell adenomas, plurihormonal adenoma, pituitary blastoma and PIT-1 positive adenoma. The new classification also advances the concept of high and low-risk subtypes which may be a relevant factor for radiologists to consider when recommending imaging follow-up.

Conclusions

This exhibit reviews the new WHO classification of pituitary adenomas based on neuroendocrine cell lineage. It also discusses new entities, redefinition of old terms, and new concepts such as tumors with high and low risk of recurrence.

eEde-077

The Many Faces of Lymphoma

M Daun¹, J Pao¹, A Cruz¹, E Kuoy¹, D Chow¹

¹*University of California, Irvine, Orange, CA*

Purpose

The purpose of this presentation is to review the multifaceted presentations of both primary (immunocompetent and immunocompromised) and secondary CNS lymphoma, as well as discuss pitfalls in diagnosis including the various etiologies that can be mimicked by lymphoma.

Materials and Methods

1. Initial review of the imaging characteristics of the various types of CNS lymphoma, including primary lymphoma (in immunocompetent and immunocompromised patients) as well as secondary lymphoma, will illustrate the broad scope of imaging manifestations that can be seen in the disease. 2. An overview of various etiologies that can mimic/be mimicked by lymphoma in the CNS will be provided, including but not limited to: -Primary glioma -Leptomeningeal disease -Meningioma -Infections such as toxoplasmosis -Infarction 3. An overview of the utility of ancillary imaging techniques including MR spectroscopy, perfusion imaging, and nuclear medicine studies will present strategies to identify lymphoma among its vast differential diagnoses. 4. Finally, synthesis will be provided with a case-based review of CNS lymphomas in various presentations, as well as case presentations of mimicking entities.

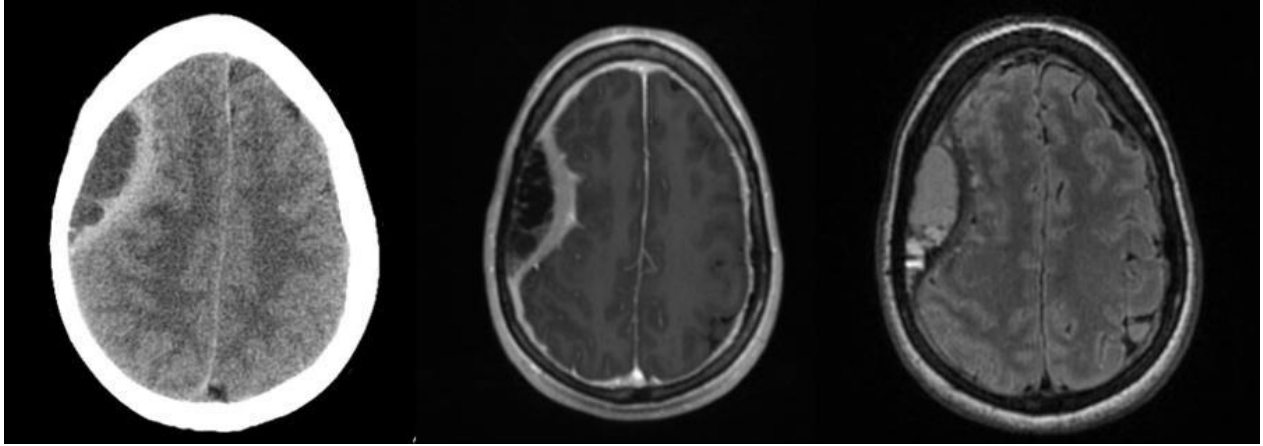
Results

Lymphoma is a nearly omnipresent differential consideration for intracranial lesions that present diagnostic dilemma. Given the heterogeneity of presentation, as well as its reputation as "the great imitator," CNS lymphoma is an entity that requires great consideration and regular review. However, understanding the broad scope of imaging features, knowing the similar appearing pathologic entities, taking into consideration the patient history and risk factors, and utilizing a variety of specialized diagnostic modalities and techniques can lead the radiologist to the correct diagnosis.

Conclusions

CNS lymphoma can present in a multitude of ways and closely mimic a variety of intracranial pathology. It is crucially important that academic neuroradiologists and general community radiologists alike understand and utilize all of their available tools in order to arrive at the correct diagnosis in these notoriously difficult cases.

Electronic Educational Exhibits



(Filename: TCT_eEde-077_FigureCNSLymphomaAbstractASNR.jpg)

eEde-035

The Medulla Oblongata: " The Forgotten Zone"

B Canty¹, C Dani², A Srinivasan³, M Ibrahim¹, J Kim¹

¹University of Michigan, Ann Arbor, MI, ²Michigan State University - Flint Area Medical Education, Flint, MI, ³University of Michigan Health System, Ann Arbor, MI

Purpose

This educational exhibit will revisit the anatomy and some of the most common pathologies involving the medulla oblongata of the brainstem. Large amounts of literature have been devoted to the cerebral hemispheres, cerebellum, midbrain, pons, and spinal cord. However, it seems much of the neuroradiology literature and textbooks only skim over the medulla region. The medulla is a very important region that must be mastered by a practicing radiologist.

Materials and Methods

In this exhibit, general anatomy will be reviewed, including cranial nerve nuclei, boundaries of the medulla, and important tracts coursing to and from the spinal cord and brain. In addition, common and some uncommon pathologies will be reviewed with examples using MRI, CT, and conventional angiography. Cases will be selected from our institution over the past few years.

Results

Both general radiologists and neuroradiologists need to be aware of the many important diagnoses affecting the medulla. Some entities are common such as multiple sclerosis, PICA infarcts (lateral medullary syndrome), and some are unusual variants like vascular impressions, or uncommon entities such as hypertrophic olivary degeneration. Clinical entities such as Horner's syndrome, ALS, and vocal cord paralysis can involve or originate in the medulla. These and other entities, both benign and malignant, vascular and non vascular, will be displayed and discussed with emphasis on anatomic localization of imaging abnormalities.

Conclusions

For whatever reason, perhaps due to its small size, the medulla oblongata does not seem to warrant much attention or discussion in neuroradiology. This exhibit will refresh the students', residents', and practicing radiologists' understanding of a very critical portion of anatomy and review some of the common and not so common entities involving the medulla, so that this anatomy and pathology can be more readily recalled and diagnosed after reviewing the exhibit.

eEde-098

The Post-DAWN Trial: Renaissance of the CT Perfusion

O Kutsenko¹, J Rozell², K Durwas², S Shiraj^{N/A}, R Mangla¹

¹*SUNY Upstate University Hospital, Syracuse, NY*, ²*Upstate Medical University Hospital, Syracuse, NY*

Purpose

The DAWN trial opened new prospects for extended time window for endovascular treatment of the acute ischemic stroke in select patients. The CT perfusion with fast post processing is the primary imaging technique for patient's selection. We discuss practical approach and common pitfalls of the CT perfusion interpretation.

Materials and Methods

We reviewed our clinical database of the fully automated RAPID and semiautomated VITREA software. We compare both methods, discuss common pitfalls and artifacts, and describe various parameters measured by these softwares. Findings will be described with case examples.

Results

CLEAN trial of 2015: effectiveness of the thrombectomy within six-hour 2017 DAWN trial: thrombectomy in patients with presentation at six to 24 hours. Chosen based on "tissue window" rather than standard "time window". Compatible post-thrombectomy functional outcomes. Why CT perfusion is the modality of choice: - distinguishes salvageable brain - widely available - quantitative perfusion metrics - cost effective and faster than MRI RAPID automated software based on machine learning algorithms that identify regions of asymmetry. VITREA semi-automated software based on singular value deconvolution algorithm. Parametric and nonparametric neuroimaging mapping Table 1. CTP mapping Parameter MTT CBF CBV Ischemic penumbra ↑ ↓ Normal or ↑ Infarct core ↑ ↓ ↓ ↓ Other parameters like Tmax, AIF, VOF, FWHM, BAT, FMT or TTP used in different software. Pitfalls: 1. Post-processing software 2. CTP thresholds 3. Arterial input function and venous output function selection 4. Delayed arrival of bolus 5. Penumbra without infarction core 6. Hyperperfusion leading to false positive results 7. False negative studies 8. Oligemia 9. Common artifacts Comparative review of the CTP with collateral imaging.

Conclusions

In patients with delayed stroke presentation skilled interpretation of the CT perfusion may significantly improve functional outcomes. Technical aspects and practical approach to clinical interpretation are presented.

eEde-022

The Supplemental Motor Area: A Review of Its Anatomy, Function, and Clinical Significance on Presurgical Functional MRI

R Holwerda¹, R Hu², A Gore³, B Weinberg², M Hoch²

¹*Emory University, Atlanta, GA*, ²*Emory University Hospital, Atlanta, GA*, ³*Emory University, Norcross, GA*

Purpose

The supplemental motor area (SMA) is an often overlooked region when utilizing functional MRI (fMRI) for preoperative planning. Using real clinical cases, we present an educational series highlighting key aspects of SMA functionality for trainees and neuroradiologists new to fMRI.

Materials and Methods

After IRB approval, a retrospective review was conducted of all fMRI cases performed for preoperative planning over the past three years at our institution. Informative cases were chosen that best illustrate the

Electronic Educational Exhibits

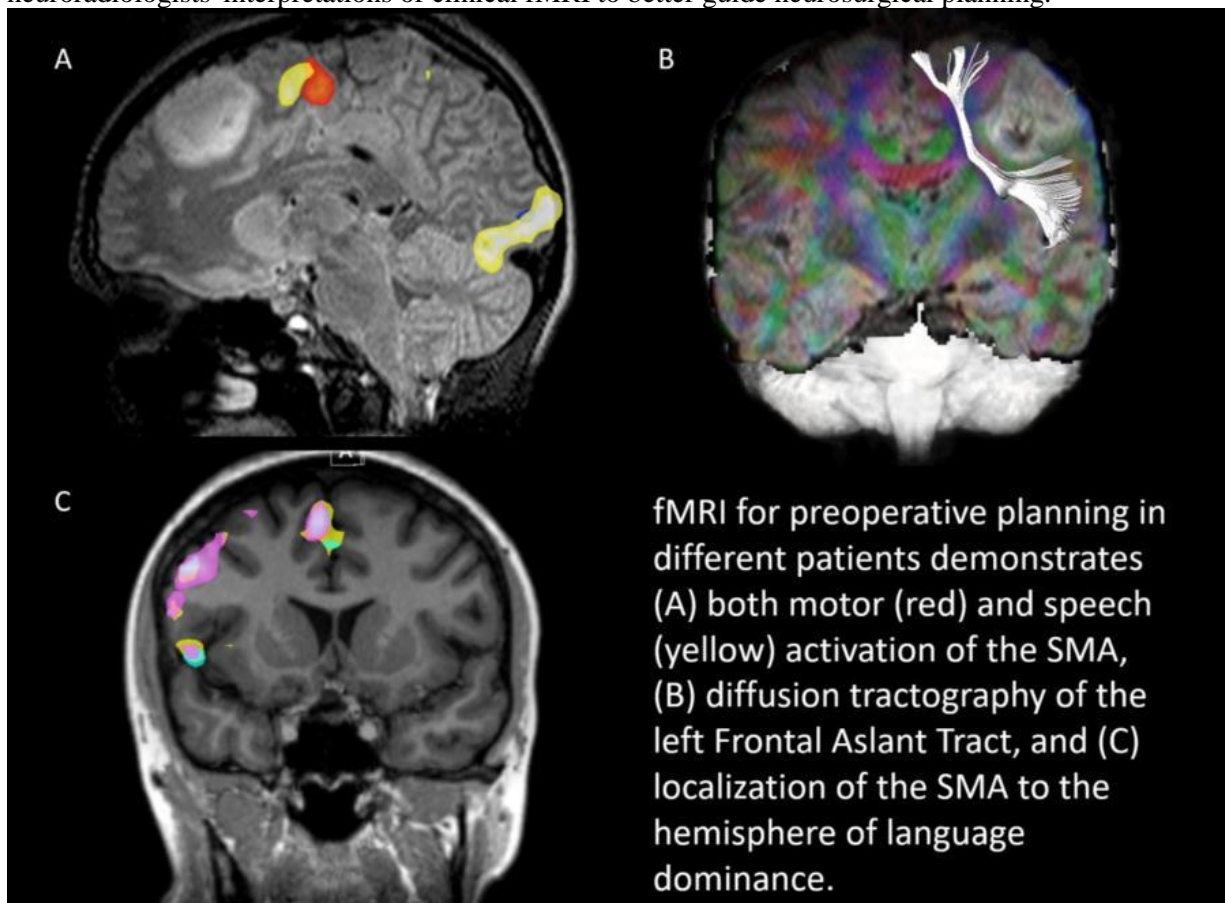
anatomy and function of the SMA with BOLD motor and language tasks. We also demonstrate how to place ROI's to generate consistent diffusion tractography of the Frontal Aslant Tract connecting the SMA to Broca's area. Best interpretation approaches and pitfalls of SMA fMRI are provided.

Results

The SMA plays a key role in higher order cognitive tasks, including both motor and language functionality, which can contribute to postoperative deficits if not planned for accordingly. Simple motor paradigms may not elicit SMA activation. The SMA is located within the superior frontal gyrus and is internally subdivided into the pre-SMA and SMA proper. The pre-SMA is more anteriorly located and involved with complex cognitive and language tasks, while in a more posterior position, the SMA proper deals with motor tasks. Language activation of the SMA is most frequently localized to the side of language dominance, which has implications with resectable lesions involving the SMA, as specific neurological deficits can occur following surgery (i.e. SMA syndrome). The Frontal Aslant Tract is a white-matter pathway that connects Broca's area with the SMA. Interruptions in these fibers can result in an aphasia affecting verbal fluency.

Conclusions

This educational work provides a thorough review of the functionally complex SMA and can improve neuroradiologists' interpretations of clinical fMRI to better guide neurosurgical planning.



(Filename: TCT_eEde-022_abstract1.jpg)

eEde-059

The Unusual Suspect: Variations of the Central Nervous Venous System Mimicking Pathology. A Radiologist's Guide.

C Freeman¹, J Lazor¹, A Nabavizadeh¹

¹*Hospital of the University of Pennsylvania, Philadelphia, PA*

Purpose

The anatomy and imaging appearance of the venous system in the brain and spine are highly variable, and veins can occasionally mimic pathology and obscure a patient's clinical picture. This includes both congenital variations in the venous system and dynamic variations secondary to physiologic or pathologic states. The purpose of this interactive educational exhibit is to demonstrate examples of variations in the central nervous venous system that can mimic more severe pathology.

Materials and Methods

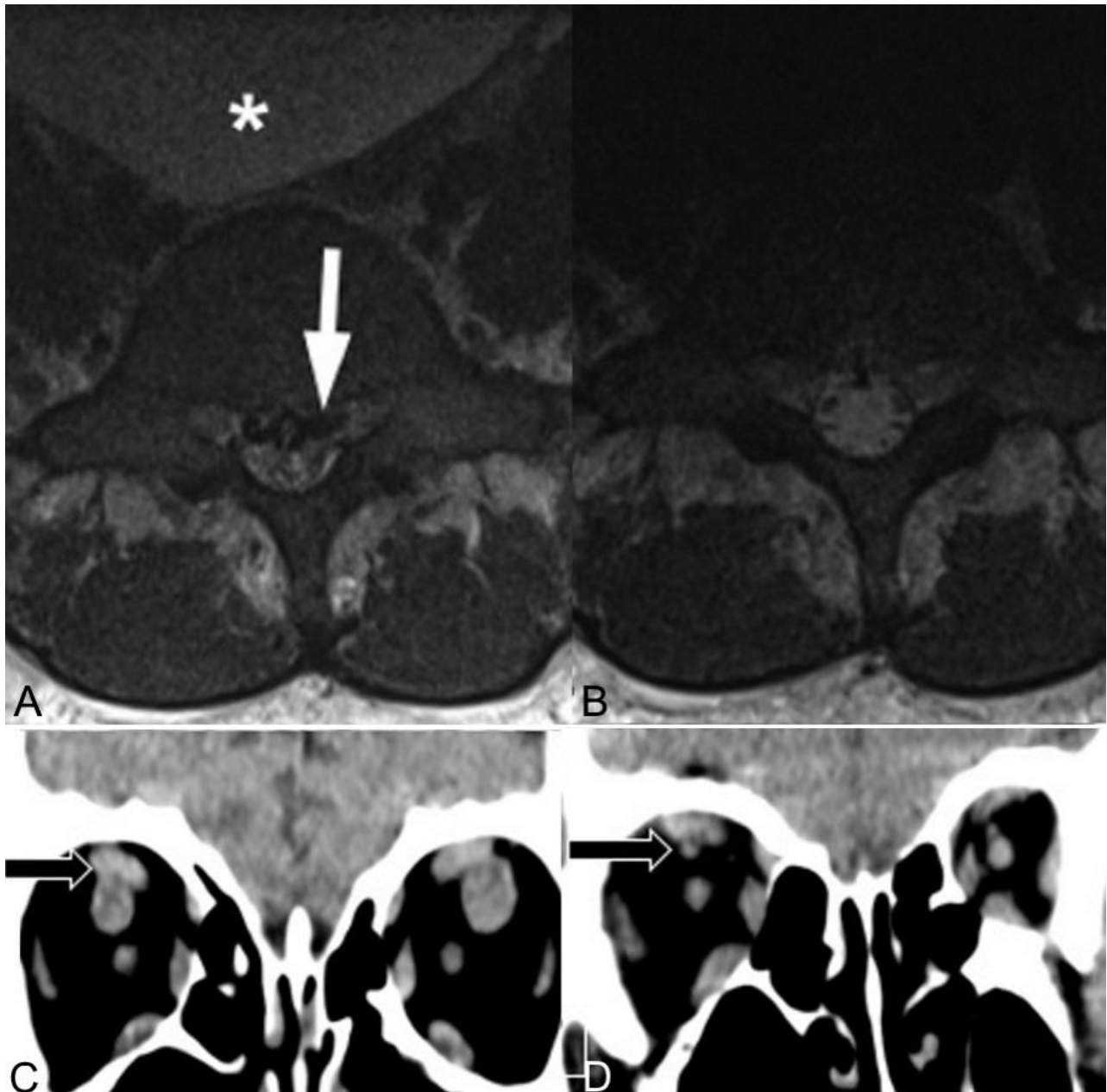
Several cases of variations of the brain and spine venous system will be presented with a review of relevant literature. The imaging features and potential differential diagnoses of these variations will be discussed.

Results

Over a dozen cases seen at the University of Pennsylvania Health System will be included in this exhibit. The cases fall into the following major categories: 1. Dilatation of the epidural venous plexus in the brain and spine-mimicking extra-axial mass or hematoma (Figure 1A and B). 2. Benign entities of the venous system, such as venous varices and giant arachnoid granulation, mimicking more severe pathologies such as venous sinus thrombosis or arteriovenous malformations. 3. Variations of superior ophthalmic veins in response to intubation and positive pressure ventilation, which can mimic more severe pathologies such as carotid-cavernous fistula, especially in the setting of trauma (Figure 1C and D).

Conclusions

Central nervous venous system variations can present a challenge for clinicians and radiologists. Clinically, patients with these variants may present with symptoms mimicking those of more severe pathology, such as mass effect, and radiographically, the appearance of venous variations may imitate other disease processes. Venous variations may be a secondary presenting feature of other, more serious pathology, further compounding these difficulties. Consequently, being able to recognize venous variations and their potential causes is critical for differentiating benign imaging findings from processes requiring further investigation.



(Filename: TCT_eEde-059_Figure1.jpg)

eEde-072

To Cross from Common to Uncommon: MR Imaging of Sellar and Parasellar Lesions

H Rajebi¹

¹*University of Texas Health San Antonio, San Antonio, TX*

Purpose

A diverse group of common and uncommon lesions arises from or around the sellar region, a relatively perplexing area for evaluation. Although MRI plays the key role in characterization and localization of these lesions, given the similarities in signal intensities, complex adjacent anatomic configuration, and

broad-spectrum pathology, accurate diagnosis is usually challenging. In this exhibit, we aim to review, discuss and compare unique imaging findings of the sellar and parasellar lesions, using a patterned approach to narrow differential diagnosis.

Materials and Methods

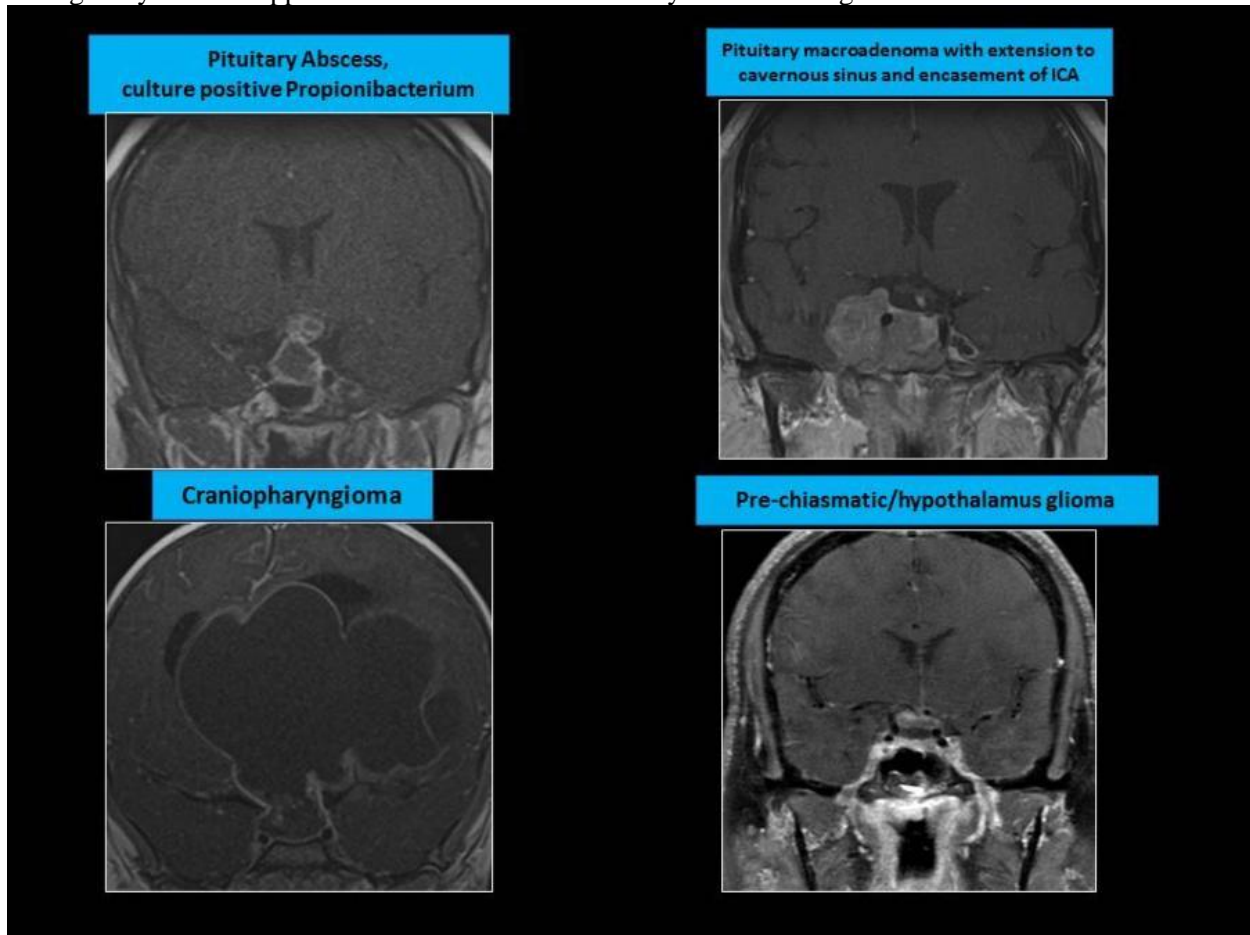
After a brief review of relevant embryology and anatomy, a comprehensive institutional case-based review of the sellar and parasellar lesions will be presented. Diagnostic hints and pitfalls will be illustrated in each case. Finally, a systematic approach to the lesions of this region will be hypothesized.

Results

Cases of pituitary micro and macroadenoma, pituitary germ cell tumor, metastasis, lymphoma, parasellar meningioma, prechiasmatic/hypothalamus glioma, craniopharyngioma, Rathke cleft cyst, cavernous sinus thrombosis, sphenoid sinus mucocele, internal carotid and anterior cerebral artery aneurysms, arachnoid cyst, epidermoid cyst, pituitary apoplexy, pituitary abscess and hypophysitis will be discussed in detail. Different MR sequences, characteristic imaging features, the possible extension of the lesion into the adjacent structures and, patient's demographic and clinical symptomatology for each entity will be described.

Conclusions

Given the wide variety of the lesions involving the sellar region, equivalent imaging patterns and complicated adjacent anatomic structures, a thorough knowledge of the lesions around this location through a systematic approach seems warranted for every neuroradiologist.



(Filename: TCT_eEde-072_ASNRgraph.jpg)

eEde-105

To SWI or Not to SWI: That is NOT a Question! Adding Value with Susceptibility-Weighted Imaging at 3T

A Germana¹, J Yetto¹, A Gutweiler¹, A Cho¹, D Hawley¹, M Cathey¹

¹*Naval Medical Center San Diego, San Diego, CA*

Purpose

Susceptibility weighted imaging (SWI) is an innovative MRI sequence that exploits the magnetic susceptibility differences of tissues in order to enhance contrast resolution of background tissues from substances like iron, hemorrhage, or calcium. SWI combines both magnitude and phase information to produce this image. As such, it is more sensitive to substances that cause local field inhomogeneity compared to standard T2* sequences. In this electronic educational exhibit, we present the basic imaging physics that allow for the unique contrast offered by SWI. We will also present multiple cases in which the exquisite sensitivity of SWI at 3T was crucial in arriving at the correct diagnosis.

Materials and Methods

This educational exhibit reviews the technical aspects of SWI. We will demonstrate the utility of SWI in arriving at the correct diagnosis using a case-based approach, highlighting a wide variety of neuropathologic entities, all at 3T field strength.

Results

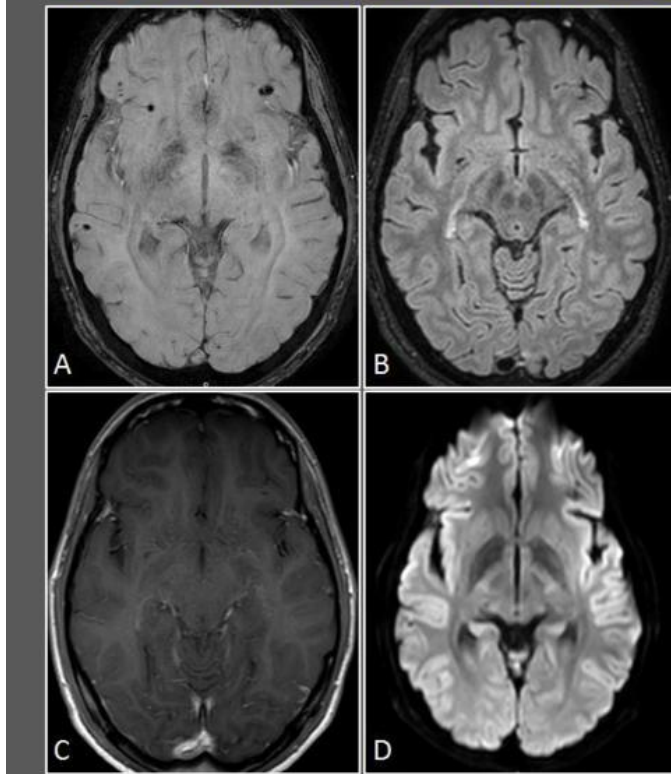
Initially, SWI was devised to improve the visualization of cerebral veins. With time, the sequence has increasingly been employed in the imaging of cerebral ischemia, neuro-inflammatory processes, tumors and hemorrhagic lesions. While T2* is often (though not ubiquitously) employed in standard brain MRI protocols, it is well established that SWI is more sensitive than T2* for detection of substances like iron, hemorrhage, or calcium, particularly at high field-strength. We will present multiple cases in which SWI facilitated determination of the correct diagnosis by either 1) being the primary sequence to highlight imaging abnormalities or 2) demonstrating a broader extent of neuropathology.

Conclusions

We present multiple cases which underscore SWI as an indispensable tool in the neuroradiology imaging armamentarium and suggest its inclusion on all brain imaging protocols. Due to its exquisite sensitivity to blood products, iron, and calcium, this approach allows radiologists to suggest a diagnosis (or more refined differential considerations) even as other conventional MRI sequences may be largely unrevealing.

To SWI or Not to SWI: That is NOT a Question!

Adding Value with Susceptibility-Weighted Imaging at 3T



22 year old male with trauma to the left side of his face resulting in a concussion 2 months prior to MR imaging.

The susceptibility weighted image (A) demonstrates multiple foci of blooming susceptibility at the grey-white junction of the cerebrum. Numerous other foci of susceptibility are present throughout the cerebrum (not shown). There is no obvious corresponding signal abnormality on the FLAIR (B) or T1 post (C) images. Subtle foci of hypointense signal abnormality are noted on the DWI (D), which correspond to the known areas of blooming susceptibility in (A). A diagnosis of grade 1 diffuse axonal injury was thus made largely on the SWI image.

(Filename: TCT_eEde-105_SWI12517.JPG)

eEde-039

Towards a Purer Dura: An Imaging Review of Widespread Pachymeningeal Disease

T Campion¹, A Krishnan¹

¹*Barts Health NHS Trust, London, United Kingdom*

Purpose

The pachymeninges form the outer layer of the meningeal covering of the brain, consisting of two layers, the outer periosteal and inner meningeal (with an underlying dural border cell layer which is inseparable from the arachnoid membrane). Because the vessels within this layer do not produce a blood-brain barrier, contrast enhancement within it may be a normal finding. However, there is also a wide range of pathology that can affect the pachymeninges, and the finding of widespread enhancement can thus lead to a diagnostic dilemma. In this educational exhibit, we will: -Describe the macroscopic and microscopic anatomy of the pachymeninges, and its relevance to imaging. -Discuss appropriate imaging techniques and normal imaging findings. -Review aetiologies for pachymeningeal abnormalities, and identify important associated imaging findings to help in distinguishing these.

Materials and Methods

We performed a RIS search for pachymeningeal pathology supplemented with search for specific pathologies in order to provide a comprehensive imaging overview.

Results

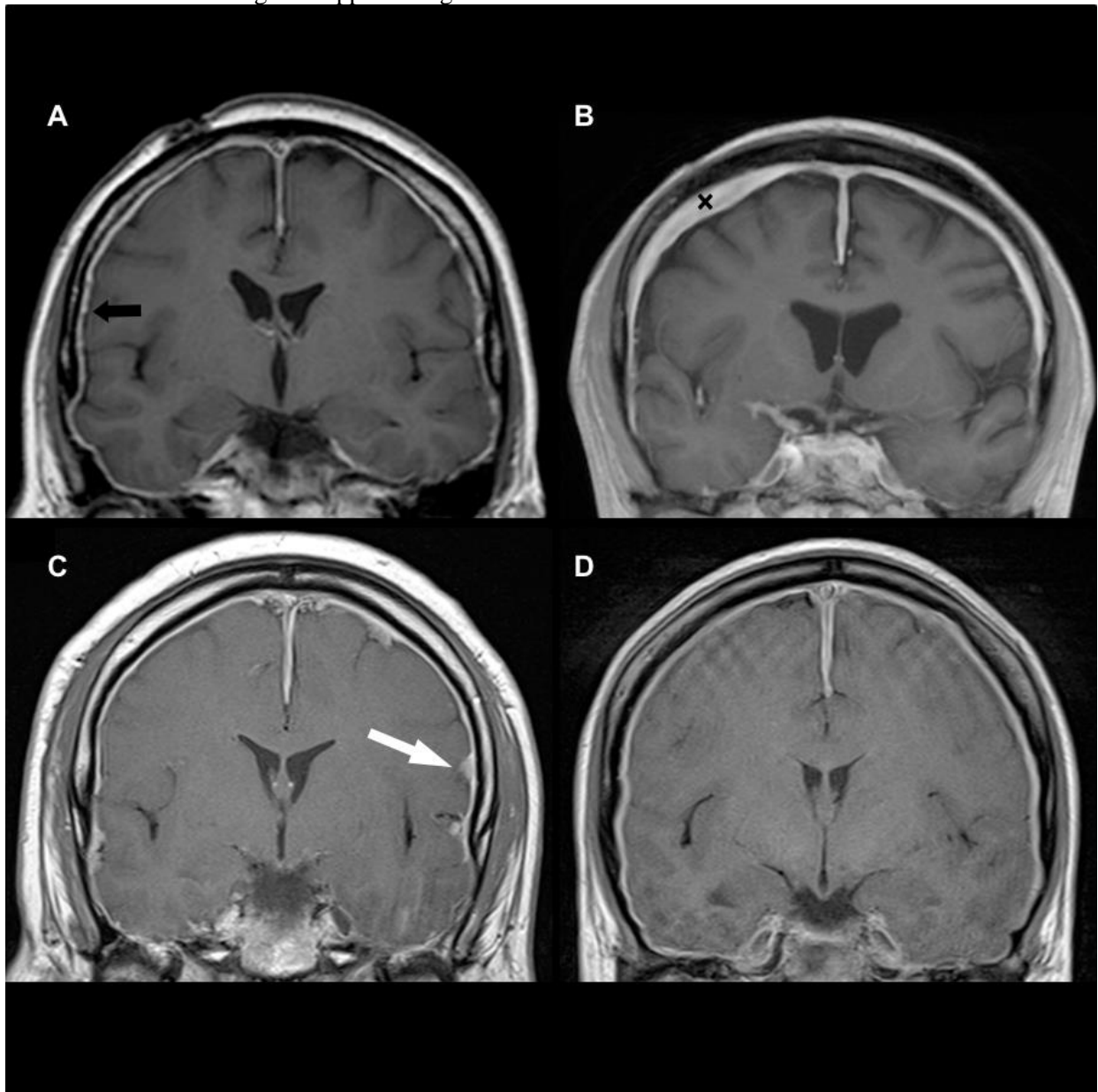
Imaging examples will include: -Normal spectrum of findings on MRI -Intracranial hypotension -

Electronic Educational Exhibits

Iatrogenic causes -Venous sinus thrombosis -Infective causes -Granulomatous and autoimmune causes, including sarcoid and IgG4 disease -Benign and malignant neoplastic causes
Figure legend: Coronal T1 post contrast images at the level of the third ventricle in four patients with pachymeningeal abnormalities. (A) Black arrow demonstrates subtle nodularity on a background of dural thickening and enhancement in a patient with metastatic breast cancer. (B) Thick, asymmetric (X) pachymeningeal disease in a patient with IgG4-related pachymeningitis. (C) White arrow demonstrates broader-based nodularity in a patient with neurosarcoidosis. (D) Smooth, symmetrical pachymeningeal enhancement in a patient with intracranial hypotension.

Conclusions

There are numerous causes for the imaging finding of widespread enhancement of the pachymeninges, and a thorough understanding of the appropriate anatomy and normal and abnormal imaging appearances is crucial for the radiologist in approaching these cases.



(Filename: TCT_eEde-039_duralfigurefinal.jpg)

eEde-107

Traumatic Injuries to the Dural Venous Sinuses

B Perry¹, T Danziger¹, T West¹, J Sachs¹

¹*Wake Forest Baptist Health, Winston-Salem, NC*

Purpose

To provide an image-rich and case-based discussion of traumatic injuries to the dural venous sinuses. After reviewing the exhibit, the reader will be able to recognize noncontrast CT findings of venous hemorrhage or thrombosis which may prompt further evaluation with CT venography.

Materials and Methods

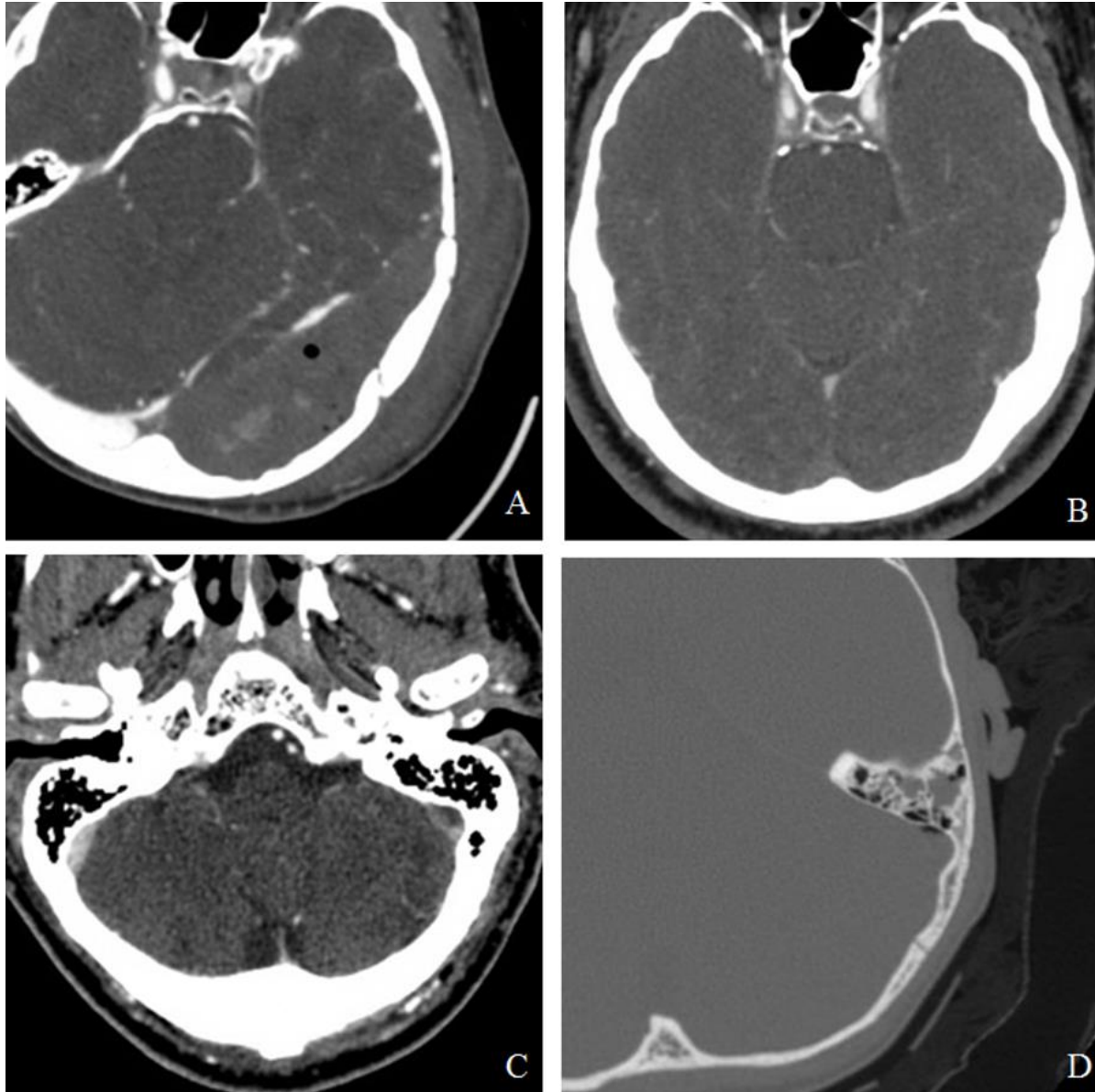
This exhibit will review the anatomy of the dural venous sinuses with an emphasis on identifying structures seen on typical exams performed in the emergency setting. This includes a discussion of modalities used to evaluate the dural venous sinuses and a review of protocols for CT venography. The exhibit will largely represent a case-based discussion of pathology encountered at a large level 1 trauma center, including the entity "benign venous epidural hematoma" and its management.

Results

In patients with blunt head trauma, there is a high prevalence of dural venous sinus injury with calvarial fractures extending to a dural sinus or jugular bulb (1). Because of this increased risk of venous injury, CT venography is indicated in patients with these fracture patterns (1). Common patterns of venous injury include sinus thrombosis, extrinsic sinus compression, and epidural hematomas (2). Figure A: CTA Head in a patient with skull base fractures and a subsequent venous epidural hematoma with displacement of the left transverse sinus and active extravasation. Figure B: CTA Head of a patient with thrombosis of the superior sagittal sinus. Figures C and D: patients with left sided skull base fractures and associated acute thrombus (C) and gas (D) within the left sigmoid sinus. Identification of these injuries leads to difficult management decisions regarding anticoagulation in patients who either already have intracranial hematomas or are at a high risk of bleeding (3).

Conclusions

Dural venous sinus injury is likely underdiagnosed given its strong association with certain fracture patterns (1). Early recognition of these injuries positively affects clinical management and decision making (3).



(Filename: TCT_eEde-107_asnrimage18v2.jpg)

eEde-108

Traumatic Vascular Injury Resulting in Hemorrhagic or Ischemic Stroke: Typical and Usual Mechanisms of Injury

J Vera¹, D Sorte²

¹University of New Mexico Health Sciences Center, Albuquerque, NM, ²University of New Mexico, Albuquerque, NM

Purpose

Review of cross-sectional imaging in unusual and representative cases including blunt or penetrating cervical vascular injury, intracranial dissection and pseudoaneurysm, transection, and embolism. Illustrate

CTA and angiographic imaging findings of traumatic vascular injuries and possible endovascular or surgical treatment.

Materials and Methods

Nine cases of both common injury (dissection) and unusual injuries (e.g. infradiaphragmatic to MCA bullet embolus) which resulted in secondary ischemic or hemorrhagic strokes were reviewed. Pertinent clinical history was obtained from electronic medical record (EMR) and associated imaging studies were retrospectively evaluated. CT head, CTA head and neck, and MRI brain were reviewed. Five of nine cases had cerebral angiograms.

Results

CASE 1, CASE 2, CASE 3, CASE 4, CASE 5, CASE 6, CASE 7, CASE 8, CASE 9

Conclusions

Although the more typical carotid and vertebral injuries in trauma, namely dissection, must be recognized, unusual types of vascular injuries can also occur in blunt and penetrating trauma. Thoughtful evaluation of cross-sectional imaging and judicious recommendation of conventional angiography allows diagnosis and endovascular management of more uncommon vascular injuries in some cases.

eEde-074

True Progression Versus Pseudoprogession: Is It Possible to Differentiate Them or Is It a Lost Battle in Neuro-oncology?

A Hilario¹, P Martin¹, L Koren¹, E Salvador¹, J Sepulveda¹, A Hernandez-Lain¹, A Perez-Nuñez¹, A Lagares¹, A Ramos¹

¹Hospital 12 de Octubre, Madrid, Spain

Purpose

The purpose of this study is to describe tips and tricks of MRI that helps us differentiate true progression (TP) from pseudoprogession (PsP) in the follow-up of treated gliomas.

Materials and Methods

This work has been carried out in a reference center in neuro-oncology. We review DWI, DCE and DSC perfusion MRI, as well as patterns of contrast enhancement in a group of glioblastomas treated surgically and with chemoradiotherapy according to STUPP scheme.

Results

PsP occurs in 20-30% of all patients treated for malignant glioma, and the risk is increased in patients with MGMT promoter methylation. PsP usually appears on MRI within the first three months of completing radiotherapy, but can occur six months after treatment or longer. Confirmation of PsP requires either stability or improvement of enhancement or histological diagnosis. Conventional MRI signs have limited utility, but new enhancement outside the margins of irradiation or subependymal spread are useful MRI markers in identifying TP. Analyzing DSC, longitudinal trends in rCBV may be more useful than absolute rCBV in distinguishing PsP from TP. Although one would expect lower rCBV (≤ 1.75) values in PsP, overlapping rCBV for PsP and TP at initial progressive enhancement has been demonstrated. At DCE, patients with PsP have lower measures of Vp, Ve and Ktrans than patients with TP. Due to the slow and progressive enhancement of post-treatment changes, pseudoprogession shows a smaller initial (iAUC) and higher final (fAUC) area under the time signal-intensity curve at the semiquantitative analysis. On the basis of DWI, the mean ADC has a limited role, but the lower end values (5th percentile point) of the cumulative ADC histograms could help differentiating TP from PsP.

Conclusions

Accurate differentiation between PsP and TP remains challenging for optimal treatment. Diffusion and perfusion imaging parameters may demonstrate different diagnostic values for predicting PsP in treated gliomas.

Tumor or Not Tumor, That's the Question: Brain Tumor Mimicking Infection and Infarction

S KIM¹, Y Lee², B Baek², W Yoon²

¹Chonnam National University Hwasun Hospital, Hwasun-gun, Jeollanam-do, Republic of Korea, ²Chonnam National University Hospital, Gwangju, Chonnam, Republic of Korea

Purpose

To present the main tumor mimicking lesions (focus on infarction and infection) and review the diagnostic key imaging findings

Materials and Methods

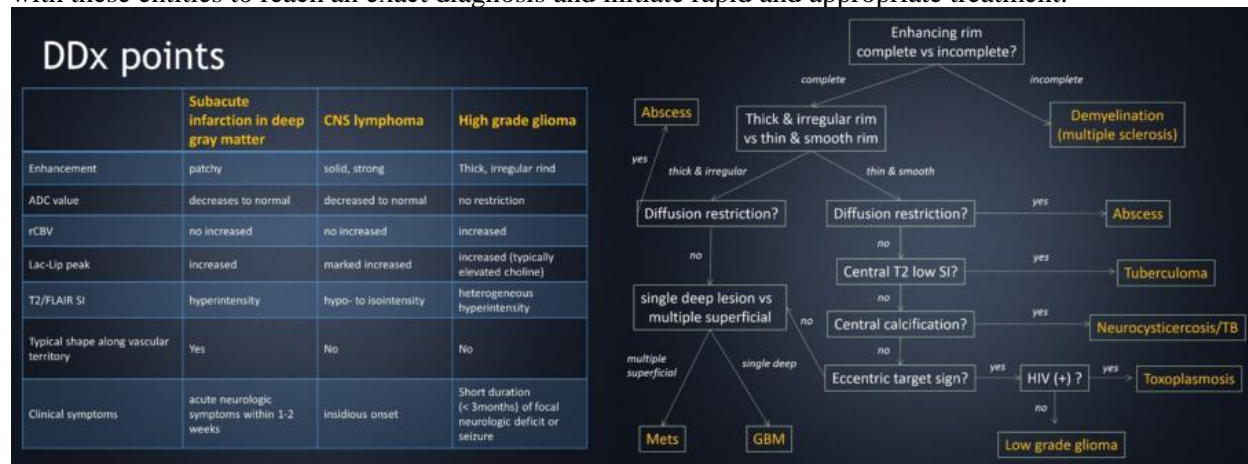
Retrospective analysis of 56 patients during the period 2015 to 2017, presented with clinical and morphological findings suggestive of tumor mimicking infection or infarction with CT and MR imaging. Anatomical location, CT images, conventional and advanced MR images including diffusion-weighted image, susceptibility-weighted image, MR spectroscopy, and clinical information were analyzed. Based on the analyzed information, we present a case-based exhibition.

Results

Subacute infarction in deep gray matter can mimic brain tumor such as CNS lymphoma or high-grade glioma. Typical shape along vascular territory, T2/FLAIR hyperintensity, acute onset neurologic symptoms within 1-2 weeks were key differential diagnostic features. Diagnostic features of subacute infarction involving cerebral cortex were cortical laminar necrosis and gyral enhancement. Postoperative ischemic change also can mimic tumor recurrence. Immediate postoperative MR imaging plays an important role in differential diagnosis. Various intracranial infections can be observed with rim enhancing lesions and also can mimic rim enhancing brain tumor such as GBM and metastasis. By evaluating enhancing wall characteristics, central content, and surrounding edema, pyogenic abscess, tuberculoma, neurocysticercosis, toxoplasmosis can be distinguished from brain tumors.

Conclusions

A variety of non-neoplastic intracranial lesions can mimic brain tumors. Radiologists should be familiar with these entities to reach an exact diagnosis and initiate rapid and appropriate treatment.



(Filename: TCT_eEde-065_fig.jpg)

eEde-053

Uncommon Pediatric Intracranial Vascular Anomalies

P Goyal¹, R Mangla², A Bhatt³

¹*St. Vincents Medical Center, Bridgeport, CT*, ²*SUNY Upstate Medical University, Syracuse, NY*, ³*University of Rochester Medical Center, Rochester, NY*

Purpose

We describe here imaging features of uncommon pediatric intracranial vascular anomalies.

Materials and Methods

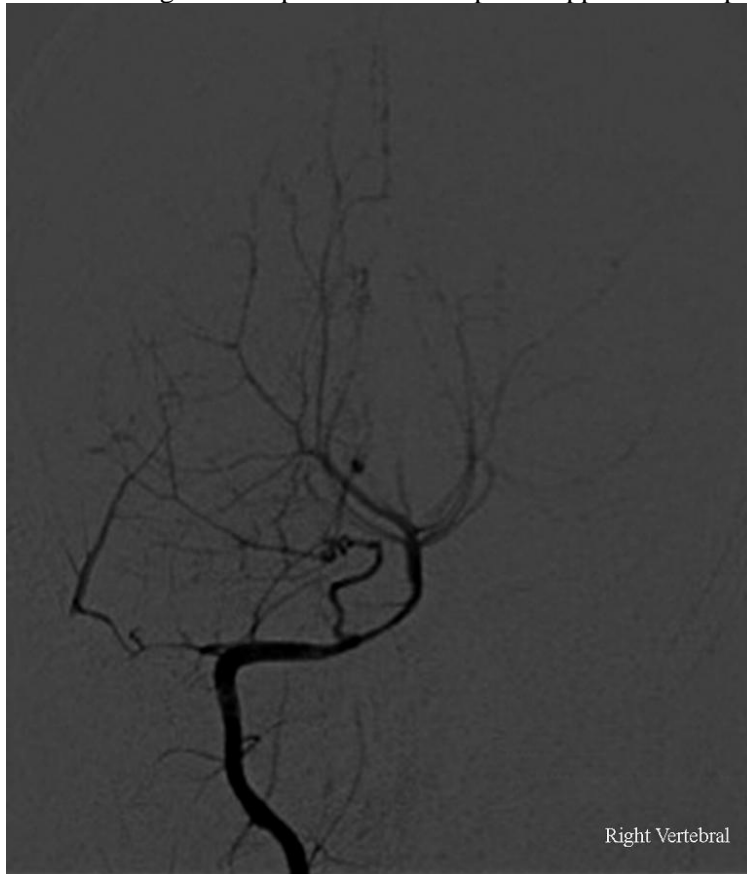
We collected common and uncommon pediatric intracranial vascular anomalies (tumors and malformations) from our database. Then we chose uncommon vascular anomalies.

Results

We describe vascular anomalies which include but are not limited to rapidly involuting congenital hemangioma (RICH), PHACES syndrome, malignant variant of intracranial Kaposiform hemangioendothelioma involving cavernous sinus, vein of Galen malformation, familial cavernous malformation, ACTA2 cerebral arteriopathy, Cerebrofacial Arterio-Venous Metameric Syndrome, capillary malformation-arteriovascular malformation (CM-AVM), Cerebrofacial Venous Metameric Syndrome 2 plus 3, intracerebral venous malformations in blue rubber bleb nevus syndrome (BRBNS).

Conclusions

Knowledge of the imaging features of these anomalies will lead to a more accurate diagnosis that may result in a targeted comprehensive therapeutic approach for optimal patient care.



(Filename: TCT_eEde-053_ACTA2cerebralarteriopathy.jpg)

eEde-066

Unique Imaging Features of IDH-1 Mutant Glioblastomas, a Newly Defined Entity

E Calabrese¹, J Villanueva-Meyer¹, S Cha¹

¹University of California San Francisco, San Francisco, CA

Purpose

Glioblastoma multiforme (GBM) is the most common and most aggressive form of primary central nervous system malignancy and unfortunately carries a dismal prognosis. A recently recognized small subset of GBMs carry mutations in the isocitrate dehydrogenase 1 (IDH-1) gene, which is typically associated with low grade gliomas, and infers a significantly better prognosis. IDH-1 mutant GBMs have characteristic imaging features that can strongly suggest the diagnosis before biopsy. The purpose of our study was to identify unique imaging features of IDH mutant GBM compared to those of IDH wild-type GBM.

Materials and Methods

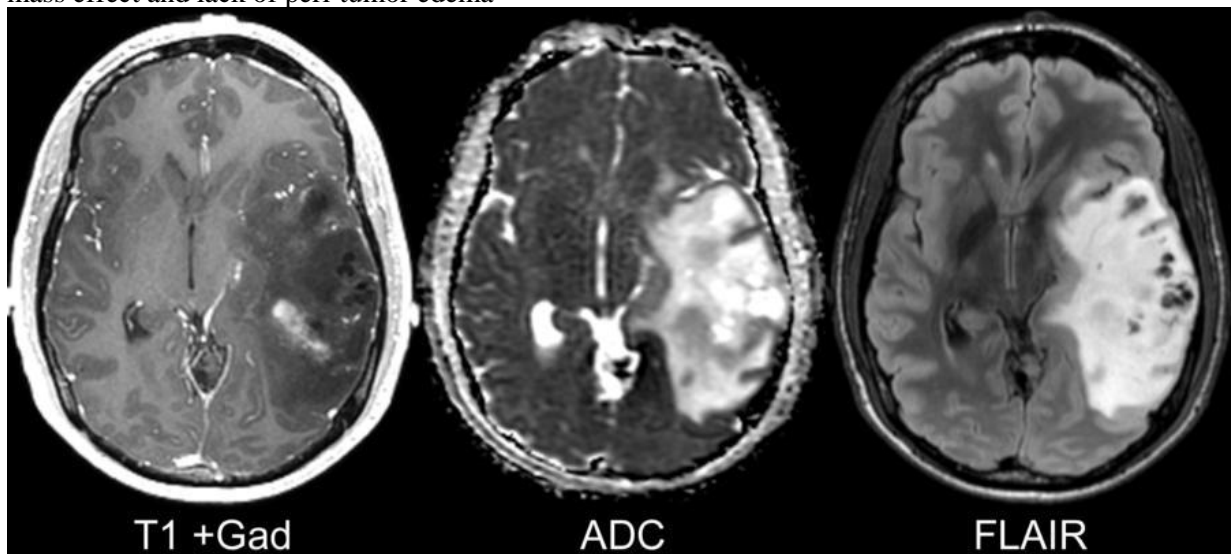
Patients were selected retrospectively from the UCSF neuroradiology database according to IRB-approved protocols. We studied the imaging features of histopathologically and molecularly confirmed IDH-1 mutant GBMs and evaluated for cortical expansion, patterns of gadolinium enhancement, diffusion characteristics, presence of susceptibility, and associated FLAIR signal abnormality. Results were compared with matched IDH-1 wild-type GBMs in similar anatomic locations.

Results

Three unique and key imaging features of IDH-1 mutant GBM were identified: 1) nonenhancing cortical expansion, 2) nondominant enhancement without distinct necrosis within a larger area of nonenhancing infiltrating tumor, and 3) minimal mass effect and lack of peri-tumor edema.

Conclusions

IDH-1 mutant GBMs carry a better prognosis than the more common IDH-1 wild-type GBMs, and can be distinguished by three key features on MRI: 1) Nonenhancing cortical expansion 2) Nondominant enhancement without distinct necrosis within a larger area of nonenhancing infiltrating tumor 3) Minimal mass effect and lack of peri-tumor edema



(Filename: TCT_eEde-066_figure.jpg)

eEde-083

Unusual Appearance of Third Ventricular Colloid Cysts Supporting a Common Embryologic Origin with the Rathke's Cleft Cyst: Case Review Series

S Khanpara¹, R Patel¹, P Rabiei¹, O Arevalo¹, A Kamali¹, E Bonfante¹, R Riascos¹, K Westmark¹

¹*The University of Texas Health Science Center at Houston, Houston, TX*

Purpose

Colloid cysts are benign mucin-containing cysts and account for 0.5%-1% of primary brain tumors and 15%-20% of intraventricular masses. More than 99% are found wedged in the foramen of Monro. The cysts are typically attached to the anterosuperior portion of the third ventricular roof. The purpose of this exhibit is to show a previously unreported appearance of five third ventricular colloid cysts which is reminiscent of the Rathke's cleft cyst.

Materials and Methods

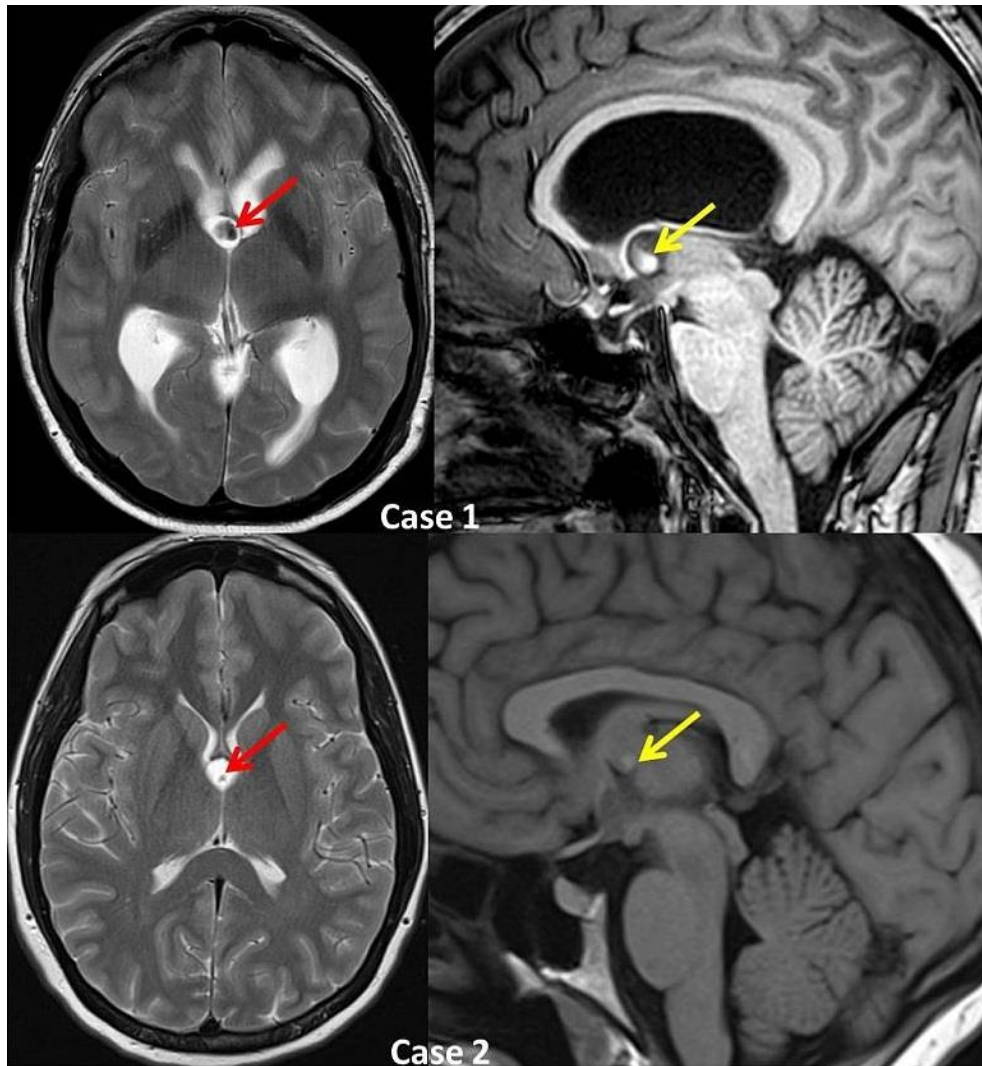
Retrospective review of patients diagnosed with intracranial colloid cysts MR images in the Memorial Hermann System from January 2014 to November 2017. The MR signal characteristics were noted as well as size and location in third ventricle.

Results

Based on retrospective search of key word "colloid cyst" in radiology PACS search engine at our institute, a total of 62 colloid cyst cases were found. On detailed imaging analysis of those 62 colloid cyst cases, five of 62 cysts had a very unusual appearance being either isointense or high in signal on the FLAIR and T2-weighted images, hypointense on T1-weighted image with a nodule within the cyst that was hypointense on the T2-weighted images and hyperintense on the T1-weighted images.

Conclusions

A mural nodule within a pituitary cyst has been reported to be diagnostic of a Rathke's cleft cyst. A remarkably similar appearance was found in five of 62 colloid cysts examined by MRI at our institute and to our knowledge are not published in the literature. This observation is of interest as it has been described in one pathology literature that colloid cysts, neurenteric cyst and Rathke's cleft cyst may constitute the same entity.



Representative two case demonstrate colloid cyst with an internal nodule which is T2 hypointense (red arrow) and T1 hyperintense (yellow arrow)

(Filename: TCT_eEde-083_CC3.jpg)

eEde-062

Unusual Imaging Findings in the Familial Cavernous Malformation Cohort

M VonLoh¹, M Mabray¹, B Hart¹, L Morrison¹

¹University of New Mexico, Albuquerque, NM

Purpose

This educational exhibit will discuss the multitude of findings which patients with familial CCM may demonstrate on imaging, including cerebral, spinal, and systemic manifestations.

Materials and Methods

Familial CCM is an autosomal dominant disease most common in patients of Hispanic American descent traditionally characterized by multiple cerebral cavernous malformations. Our large imaging cohort has revealed several additional imaging manifestations of this heritable condition. This educational exhibit

will review the spectrum of imaging findings in CCM including unusual imaging findings in the CNS and body.

Results

The sporadic cerebral cavernous malformation is a well known vascular malformation to neuroradiologists. These lesions are best evaluated by MRI and demonstrate typical diagnostic signal characteristics. CCMs and associated hemorrhages can result in complications including focal neurological deficits and seizures. Imaging patients with the familial form most commonly demonstrate multiple CCMs; however, several atypical CNS and systemic manifestations can be found including unusual exophytic CCMs, infiltrative appearing lesions, cysts associated with CCMs, CCM development within radiation fields, optic nerve, spinal cord, and spinal nerve root CCMs. Other interesting associated systemic manifestations encountered include atypical vertebral hemangiomas/venous malformations, skin and soft tissue malformations and adrenal calcifications.

Conclusions

A broad spectrum of imaging findings can be seen in patients with familial CCM. Knowledge of these more unusual imaging findings can help guide management and prevent additional unnecessary imaging studies or procedures in their evaluation.



(Filename: TCT_eEde-062_CCMsamplepictures.jpg)

eEde-097

Utility of Arterial Spin-labeling Perfusion in Common Clinical Scenarios

O Ashour¹, S Moawad¹, P Paul¹, X Wang¹, M Li¹, K Krugh¹, M Buehler¹

¹University of Toledo, Toledo, OH

Purpose

Arterial Spin Labeling (ASL) has numerous advantages among perfusion sequences, and is approaching mainstay status in many large clinical centers. This exhibit presents clinical examples of cases where ASL was able to supplement information, either to answer the main clinical question or regarding an incidental finding, that resulted in a significant change in management.

Materials and Methods

Pseudo-continuous ASL was included in stroke protocols in our department for approximately one year. A retrospective chart and PACS review was performed to identify significant cases.

Results

This exhibit includes five cases, which are examples of focal and generalized hypoperfusion and hyperperfusion patterns. The first case shows regional hypoperfusion in the right MCA territory resulting from chronic right ICA occlusion. The second case shows focal hyperperfusion in the parietal lobe in a patient with seizure whose EEG corroborated the same seizure focus. The third case shows hemispheric hyperperfusion, contralateral to the patient's symptoms, during an episode of hemiplegic migraine that occurred during epigastric trigger point injection. The fourth case shows a regional hypoperfusion pattern in both cerebellar lobes secondary to basilar artery stenosis, with a superimposed pontine infarct. The fifth case shows a pronounced focal hyperperfusion pattern in areas of heterogeneous faint enhancement within a right temporo-parietal intermediate grade astrocytoma, which correlated to the presence of oligodendroglioma elements on pathological analysis.

Conclusions

ASL sequences are quick, accurate for quantification of blood flow, and easily repeatable within the same session, with the added advantage of concomitant structural MRI imaging. Although its use is still limited by poor signal to noise ratio and susceptibility artifacts, ASL has proven its ability to complement and provide more direct quantitative measures compared to conventional dynamic susceptibility contrast perfusion and scintigraphic brain imaging.

eEde-100

Utility of the ADC Map in Identification of Diffusion Restriction on a Background of Basal Ganglia Iron Deposition - T2 Gray Out Effect

R Crowder¹, J Karis²

¹Barrow Neurological Institute, Mesa, AZ, ²Barrow Neurological Institute, Phoenix, AZ

Purpose

The purpose of this exhibit is to review T2 signal effects on DWI. More specifically, to introduce the concept of T2 related signal loss masking true diffusion restriction on B1000 images, and highlighting the utility of evaluating the ADC/eADC map in these regions.

Materials and Methods

A total of 15 cases will be reviewed in which basal ganglia diffusion restriction is readily identified on the ADC/eADC map, but secondary to iron deposition is less conspicuous or undetectable on review of the B1000 images.

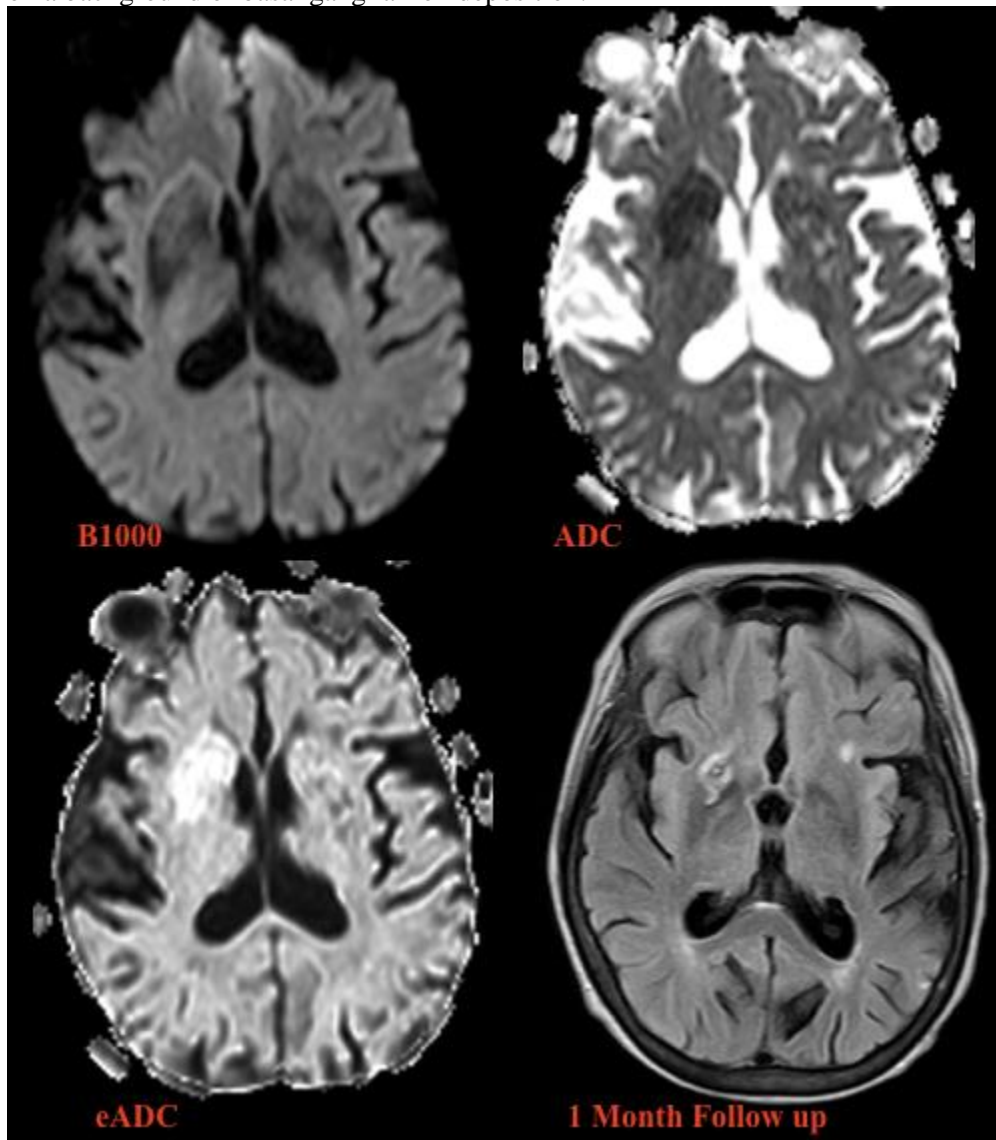
Results

DWI is inherently T2 weighted, and therefore changes in T2 signal intensity directly influence DWI signal, independent of tissue diffusion characteristics. Calculation of an ADC map eliminates the T2 contribution to the image and displays true tissue diffusibility. Pathology that alters T2 signal may complicate accurate interpretation of B1000 images, and the concepts of T2 shine-through, T2 wash-out and T2 black-out have been well described in the literature and are a well known pitfall amongst most neuroradiologists. However, the concept of DWI isointensity in regions where there is a balance between

T2 related signal loss and reduced tissue diffusibility has not yet been described. This case series will demonstrate examples of diffusion restriction identified on the ADC/eADC map in which corresponding hyperintensity was not conspicuous on the B1000 images due to the T2 shortening effect of iron deposition within the basal ganglia.

Conclusions

The contribution of T2 signal to DWI images is a well known potential pitfall. A concept not yet described is the masking of diffusion restriction on B1000 images secondary to iron deposition in the basal ganglia. Review of the ADC/eADC map in this setting is helpful in identifying diffusion restriction on a background of basal ganglia iron deposition.



(Filename: TCT_eEde-100_T2grayout.jpg)

eEde-046

Vessel Wall Imaging in Aneurismatic Pattern of Infectious Vasculitis

R Moreno¹, W Rodrigues Fernandes², J Takahashi³, S Tufik⁴, M Kase⁴, L Fajardo⁵, L Lucato⁶, C Leite⁷, G Titoneli⁸

Electronic Educational Exhibits

¹Hospital das Clínicas da FM-USP, Sao Paulo, Brazil, ²Fleury Medicina e Saúde, São Paulo, São Paulo, ³INRAD, São Paulo, São paulo, ⁴HCFMUSP, São Paulo, SP, ⁵InRad - HCFMUSP, São Paulo, São Paulo, ⁶Instituto de Radiologia do HC-FMUSP, Sao Paulo, Brazil, ⁷University Of Sao Paulo, Sao Paolo, Brazil, ⁸FLEURY, SÃO PAULO, SÃO PAULO

Purpose

1. Demonstrate MR findings of intracranial fusiform and/or saccular aneurysms associated with vasculitis related to definitive or probable central nervous system (CNS) infections of different etiologies, according to clinical and laboratory information 2. Highlight relevant information provided by axial T1 spin echo (T1WI) and high-resolution contrast-enhanced, black-blood T1WI with fat suppression (VWI) on evaluation of vessel wall thickness and enhancement at the dilated segment 3. Show 3D TOF MR alterations of luminal morphology of intracranial arteries on infectious CNS diseases 4. Delineate a take-home message board, by the analysis of representative cases with imaging findings in agreement with those recently described in literature

Materials and Methods

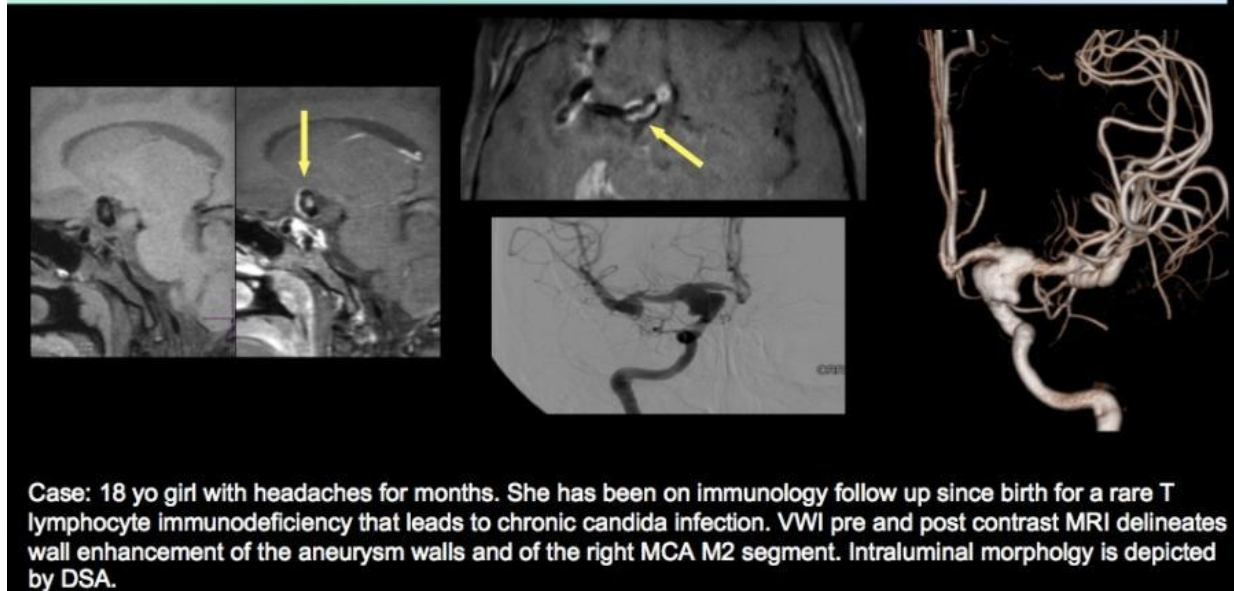
Review imaging particularities of aneurysms related to vasculitis associated with HIV, bacterial or parasitic meningitis, chronic mucocutaneous candidiasis and neurosyphilis. Neuroinfection agent confirmation was made by cerebral spinal fluid analysis, aerobic/ anaerobic cultures, PCR or immunoglobulin tests. Conventional imaging: Computed tomography angiography (CTA) Magnetic resonance angiography (MRA) Digital subtraction angiography (DSA) Vessel wall analysis was made by: 2D T1 weighted MR High-resolution (3D) intracranial vessel wall (VW) MRI Multiplanar 3D acquisitions

Results

Cerebrovascular disease is a known complication in a variety of central nervous system (CNS) infections. Despite advances in prevention and therapy, it remains a frequent cause of morbidity and mortality. Recent theories suggest that such aneurysmatic formations could be secondary to a pro inflammatory state, mediated majority by interleukines, besides the direct vessel wall damage by the infectious agent. In our study we retrospectively analysed neuroimaging findings of aneurysms associated with HIV, bacterial or parasitic meningitis, chronic mucocutaneous candidiasis and neurosyphilis. Conventional imaging (CTA, MRA and DSA) revealed abnormalities of the vessel lumen and contributes to establish aneurysm dimensions, location and local mass effect. Vessel wall thoroughly analysis by 2-D T1 with fat saturation MRI sequences can characterize coarse alterations, but has a limited spatial resolution. New 3-D volumetric T1 high-resolution MRI sequences, with high signal-to-noise ratio, that suppresses MRI signal from neighboring fat, blood and cerebral spinal fluid (VW imaging) can better delineate the wall inflammatory process itself. Vessel wall enhancement probably is related to degree of inflammation, indicating wall fragility.

Conclusions

Clinicians must be alert to the distinctive signs and symptoms that could suggest aneurysmal complications in patients with proven or suspected CNS infections, since they significantly worsen patient prognosis. Aneurysm's intraluminal morphologies can be well demonstrated by conventional imaging, such as MRA, CTA and invasive DSA. However, vessel wall analysis using new techniques, for example high-resolution (3D) intracranial VW- MRI, adds value, contributing to early recognition, resulting in more targeted treatments and better outcomes.



(Filename: TCT_eEde-046_mccaneurysm.jpg)

eEde-003

“CRUMPLED”: An Acronym For The Differential Of Diffuse Cortical Insults On Diffusion-weighted Imaging In Acutely Encephalopathic Patients

Y Koksels¹, J Benson², H Huang³, A McKinney¹

¹University of Minnesota, Minneapolis, MN, ²University of Minnesota, St. Paul, MN, ³University of Minnesota, School of Medicine, Minneapolis, MN

Purpose

Acute encephalopathic syndromes can present a diagnostic challenge due to the wide range of possible etiologies, which also can have vastly different outcomes. The presence of diffuse cortical injury (DCI) on diffusion-weighted imaging (DWI) can help narrow the differential diagnosis. The aim of this exhibit is to categorize the range of possible etiologies of DCI into a useful acronym, "CRUMPLED".

Materials and Methods

A review of the PACS system was completed to find a characteristic example of patients with DCI on DWI from different etiologies. The diagnosis was confirmed for each example via a subsequent review of the electronic medical record used to assess for data such as biopsy results, laboratory values, and clinical correlation. The electronic exhibit intends to demonstrate several sample cases of each letter within the acronym, and to demonstrate which types of DCI are potentially reversible or irreversible.

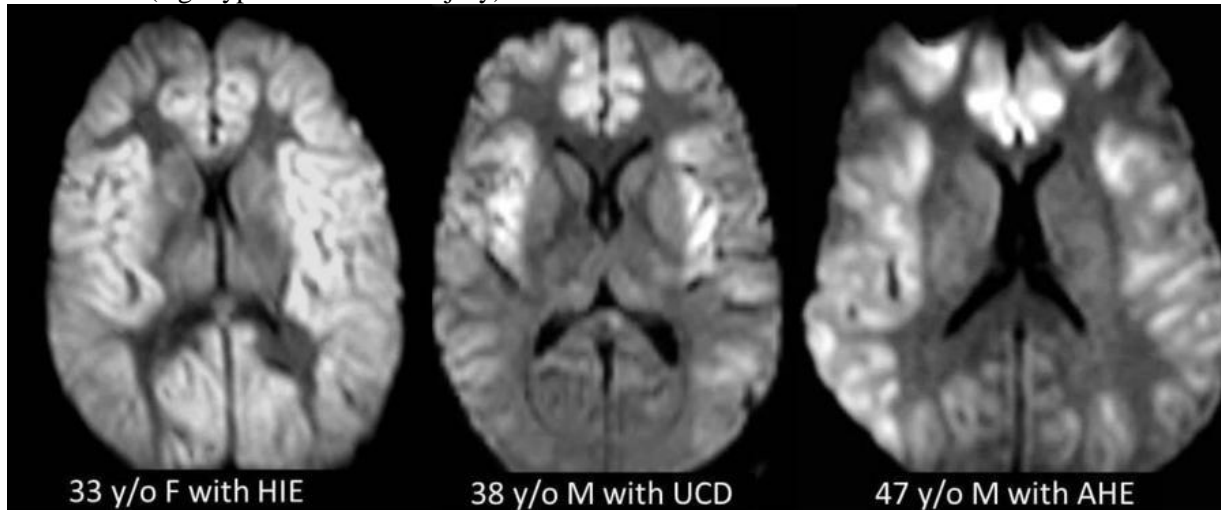
Results

The possible etiologies of DCI on DWI can be organized using the acronym "CRUMPLED": 'CR'= Creutzfeldt-jakob disease, 'U'=urea cycle disorders (hyperammonemia)/Uremia, 'M'= mitochondrial (cytopathy/encephalopathy) , 'P'= prolonged seizure (status epilepticus), 'L'= laminar necrosis (cardiac arrest=HIE [hypoxic-ischemic encephalopathy])/ liver disease (acute hepatic encephalopathy [AHE]), 'E'= encephalitis (e.g. meningoencephalitis from infectious etiologies), 'D'= diabetes mellitus (hyper/hypoglycemia). Other secondary imaging findings (outside of DWI) can be used to help differentiate between the aforementioned etiologies, such as the use of ADC maps, FLAIR imaging,

intravenous contrast, and follow-up imaging (to identify reversibility), examples of which are to be provided in the exhibit.

Conclusions

"CRUMPLED" is proposed as a convenient acronym for the categorization of a diverse range of acute etiologies associated with DCI on DWI, arising from varying degrees of cytotoxic edema. These etiologies can range from being potentially reversible (e.g. hyperammonemia or prolonged seizures) to irreversible (e.g. hypoxic-ischemic injury).



(Filename: TCT_eEde-003_ASNR2018fig.jpg)

Electronic Educational Exhibits-Head & Neck

eEde-145

Acute Invasive Fungal Sinusitis: Raising the Index of Suspicion

A Baheti¹, J Donahue¹, S Mukherjee², S Patel²

¹University of Virginia, Charlottesville, VA, ²University of Virginia Health System, Charlottesville, VA

Purpose

Acute invasive fungal sinusitis (AIFS) is a true otorhinolaryngological emergency. If not recognized early and treated aggressively, the disease can be fatal. This presentation will review the clinical presentation, imaging findings, and complications associated with AIFS.

Materials and Methods

A PACS query was performed on the key search phrase "invasive fungal sinusitis" in CT and MRI of the head, orbits, and face over the past 13 years. Relevant clinical data and representative images of patients with AIFS were identified and collated. A literature review on AIFS and imaging was undertaken.

Results

Imaging for AIFS is usually nonspecific and is often wrongly attributed to more benign pathologies. AIFS has a strong predilection for immunocompromised patients with poorly controlled diabetes mellitus, patients with hematological malignancies, those undergoing chemotherapy and post-transplant patients. Presenting symptoms include fever, facial pain, facial numbness, nasal congestion, discharge, and epistaxis. Although osseous dehiscence, intracranial extension, and orbital invasion are specific imaging findings for AIFS, they are uncommon early in the disease course when timely diagnosis can impact mortality and morbidity. Specific early imaging findings on the initial study (typically CT) that should raise suspicion include severe unilateral nasal cavity mucosal thickening and soft tissue infiltration of the

maxillary periantral fat tissue planes. Most commonly affected areas include the middle turbinates, maxillary sinuses, and ethmoid and sphenoid air cells. Contrast-enhanced MRI may show pathologic nonenhancement of necrosed sinonasal mucosa, and is especially valuable in characterizing intracranial complications such as leptomeningitis, cerebritis, abscess, or infarctions from angio-invasive disease. Detection of these imaging findings helps to direct emergent surgical debridement and rapid initiation of intravenous antifungal therapy.

Conclusions

AIFS is a rapidly progressive, life-threatening disease process with reported mortality rates of 50-80%. Recognizing the early imaging findings and complications of AIFS is critical in directing emergent surgical and medical treatment.

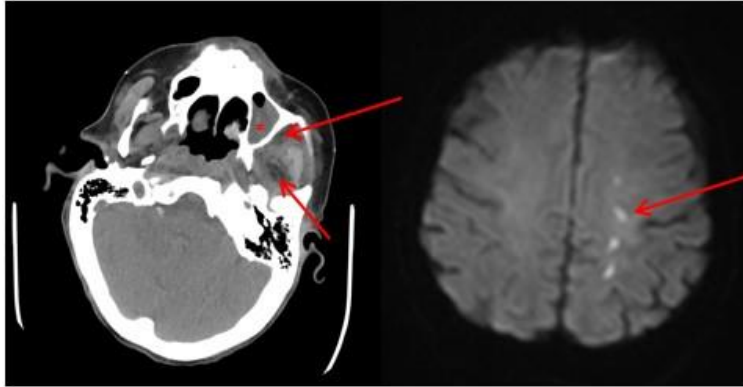


Fig 1a and b: 63 year old female with ovarian cancer on chemotherapy presenting with left sided facial paralysis and numbness. (A) NCT shows air-fluid level in the left maxillary sinus (*). Arrows demonstrate infiltration of the retro-antral fat temporalis muscle. (B) DWI sequence from an MRI demonstrates acute infarcts in the left frontoparietal white matter. The findings were favored to represent angio-invasive fungal sinusitis causing acute infarctions. The patient underwent nasal endoscopy with left sided biopsy of a nasal mass and the hard palate, revealing invasive rhinocerebral mucormycosis. Given the extent of infection and the patient's multiple co-morbidities, she was deemed a poor candidate for surgical debridement. Despite the use of IV antifungals, the patient's condition continued to worsen and she expired as an inpatient.

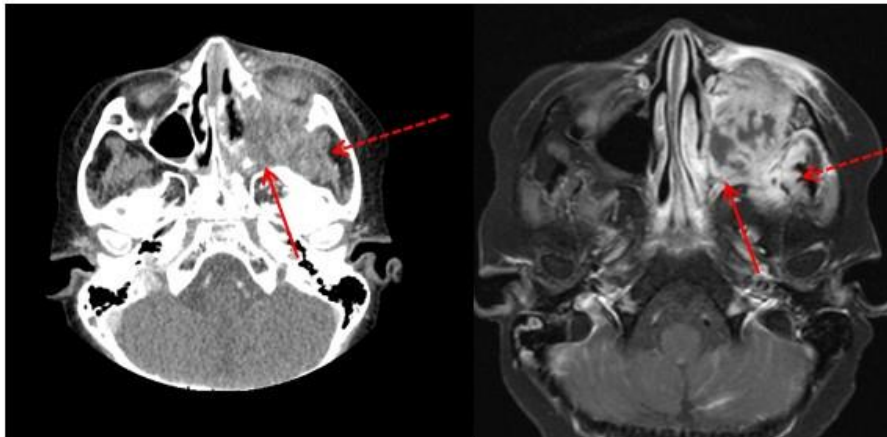


Fig 2a and b: 10 year old male with history of medulloblastoma presenting with persistent epistaxis, facial edema, and orbital edema. (A) Contrast enhanced CT demonstrates heterogeneously enhancing suppurative mass in the left maxillary sinus with osseous erosion and extension to the inferior orbit, pterygopalatine fossa (PPF, solid arrow), and masticator space (dashed arrow). (B) Contrast enhanced MRI better demonstrates involvement of the left masticator space and PPF. Endoscopic biopsy of the nasal component revealed aspergillus fumigates. The patient underwent multiple surgical debridements of the left maxillary sinus, left nasal cavity, and a total left ethmoidectomy. The patient also received IV amphotericin as well as amphotericin sinus rinses. He recovered well without residual effects.

(Filename: TCT_eEde-145_ifpicture.jpg)

eEde-158a

Adult Benign Orbital Mass with Perineural Trigeminal Spread

S Elkhamary¹

¹*Manosura University Faculty of Medicine, Riyadh, Saudi Arabia*

Purpose

To describe orbital and central nervous system imaging findings of retrograde perineural spread of through V1, V2 and V3 branches of the trigeminal nerve, in 10 patients with different benign orbital disease. All diagnosis were proved by biopsy.

Materials and Methods

At two institutions, we identified and reviewed computed tomography and magnetic resonance images of 10 patients who presented with diffuse bilateral-orbital infiltration. Biopsies of the orbital tissues as well of the V2 and V1 affected branches were obtained from all patients.

Results

Four patients had inflammatory IgG4 disease with histiocytic infiltration. Three patients showed typical findings of Rosai-Dorfmann disease (non- Langerhans histiocytosis with emperipolesis), two had eosinophilic granulomatosis with polyangiitis (Churg-Strauss syndrome) and one had Wegner's disease. MR imaging demonstrated postgadolinium enhancement of at least one branch of the trigeminal nerve in all cases. Other findings included abnormal contrast enhancement and soft tissue thickening in orbit, cavernous sinus, Meckel's cave, and/or the cisternal segment of the trigeminal nerve.

Conclusions

Although perineural spread of disease involving the orbit occurs most commonly in malignant tumors, inflammatory and histiocytic disorders must also be included in this differential diagnosis. Similarly, any patient with bilateral orbital mass who undergoes MR imaging should receive an imaging assessment focused on trigeminal perineural spread

eEde-124

Approach to Pediatric Face and Neck Masses

M Ho¹, S Cofer¹, K Balakrishnan¹

¹*Mayo Clinic, Rochester, MN*

Purpose

1. Develop a systematic framework for assessment of pediatric face and neck masses 2. Integrate basic science and technical concepts in evaluation of pediatric HN 3. Review diagnostic categories of pediatric HN masses, using a case-based approach

Materials and Methods

Approach to the pediatric face/neck mass should include the "5 W's": Age (who/when), location (where), composition (what), and syndromes (why/how). Imaging modalities that can be used for lesion characterization include MR, US, CT, nuclear medicine, and angiography. We will discuss clinical-radiologic features, pathophysiology, and differentials across the spectrum of diagnostic categories: congenital, vascular, inflammatory, soft tissue and bone lesions.

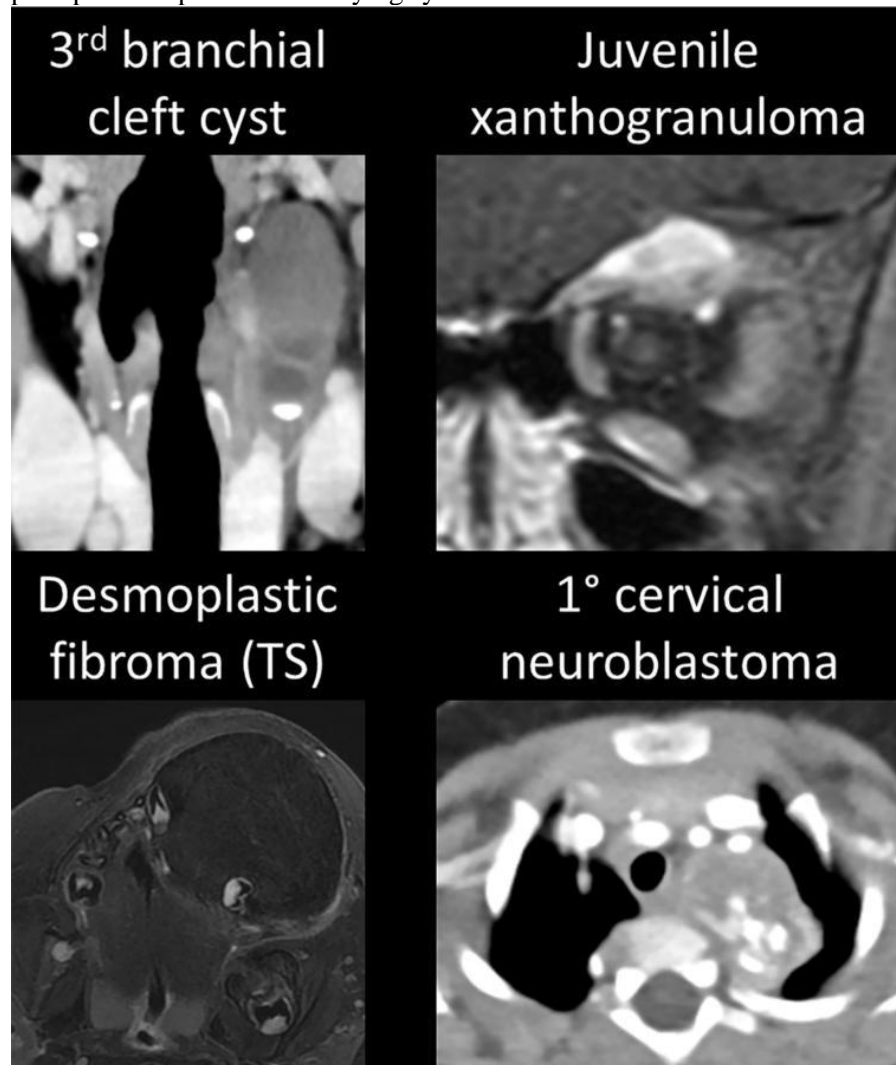
Results

Congenital: Midface: dermal sinus tract, glial heterotopia, sincipital encephalocele **Dermal:** pilomatricoma, inclusion cyst, abnormal pigmentation/vasculature **Branchial arches** Embryology and classification, type 1-4 **Branchial pouches** Thymus: 3rd pouch → thymopharyngeal duct cyst, cervical thymus **Parathyroid:** 3rd inferior/4th superior → cystic adenoma **Thyroid:** 4th pouch → suprahyoid, hyoid, infrahyoid **TGDC** **Vascular:** Vascular malformations **Low-flow syndromes:** lymphatic (generalized

Electronic Educational Exhibits

lymphatic anomaly), venous (blue rubber bleb nevus), capillary (megalencephaly-capillary malformation)
 High-flow syndromes: HHT, CM-AVM, Wyburn-Mason Vascular tumors Benign: congenital vs. infantile hemangioma, syndromes (hemangiomatosis and PHACES) Borderline: JNA, Kaposiform hemangioendothelioma Inflammatory: Inflammatory: parotitis, dacryocystitis (LADD syndrome), ranula Autoimmune: IgG4, LCH, Sjögren Soft Tissue: Parangliomas: SDH mutations and neuroendocrine syndromes (NF1, VHL, MEN) Nerve sheath tumors: NF1 (neurofibromas and optic gliomas), NF2 (vestibular schwannomas), NF3 (plexiform schwannomas and rhabdoid tumors) Fibrous lesions: fibromatosis colli, myofibromatosis, leiomyoma, tuberous sclerosis (desmoplastic and nuchal fibromas), Gardner syndrome (desmoid tumors and osteomas) Fat-containing: lipomatosis, lipoblastoma, liposarcoma, teratoma Malignant: sarcomas, neuroblastic tumors (primary vs. secondary), lymphoma (nodal vs. extranodal) Bone: Key features = matrix, zone of transition, periosteal reaction Jaw: cherubism, keratocystic odontogenic tumor (Gorlin syndrome), giant cell granuloma, LCH Skull: leptomeningeal cyst, LCH, Ewing sarcoma Spine: chordoma, aneurysmal bone cyst, osteoid osteoma

Conclusions
 1. Evaluation of the pediatric HN mass includes patient age, location, and composition. 2. Genetics and embryology provide a framework for understanding pediatric HN pathology. 3. Specific lesions can prompt workup for an underlying syndrome.



(Filename: TCT_eEde-124_Face-neck.jpg)

Beyond the Adenoma: Infectious, Inflammatory and Neoplastic Diseases of the Sellar and Parasellar Regions

M McDonald¹, N Farid²

¹*University of California at San Diego, San Diego, CA*, ²*University of California, San Diego, San Diego, CA*

Purpose

The sella and parasellar region is an anatomically complex area and is the site of a wide variety of neoplastic, infectious/inflammatory, developmental, and vascular pathologies, many of which can mimic the more commonly encountered pituitary adenoma both clinically and radiologically. Using illustrative cases, this exhibit will highlight the imaging findings of the less common conditions affecting the sella/parasellar region and will emphasize a structured search pattern for the evaluation of parasellar disease which may aid in medical and surgical treatment planning.

Materials and Methods

A review of our institutional imaging database and electronic medical record was performed retrospectively to identify cases of both benign and malignant pathology involving the sellar and parasellar regions. When available, serial imaging inclusive of both initial diagnostic imaging and post-treatment surveillance is included.

Results

By the end of this educational exhibit the participant will be able to: 1. Describe in detail the anatomic boundaries and contents of the sella and parasellar regions. 2. Identify the imaging hallmarks of nonadenomatous sellar pathology, including: - congenital variants (ectopic pituitary gland, congenital pituitary duplication) - infectious processes (extension of fungal sinusitis, skull-base osteomyelitis) - inflammatory processes (lymphocytic hypophysitis--both idiopathic and immunotherapy-related, IgG4 disease) - neoplastic processes (Langerhans cell histiocytosis, metastases, local invasion from parasellar, hypothalamic, or sinonasal neoplasms) - vascular pathologies (cavernous-carotid fistulas, parasellar arteriovenous malformations, cavernous sinus venous malformation) 3. Consolidate learning via a brief self-assessment quiz

Conclusions

Although pituitary adenoma is the most common lesion of the sella, it is important for the radiologist to be familiar with other types of pathology affecting the sella and parasellar region to avoid misdiagnoses and to facilitate medical and surgical treatment planning.

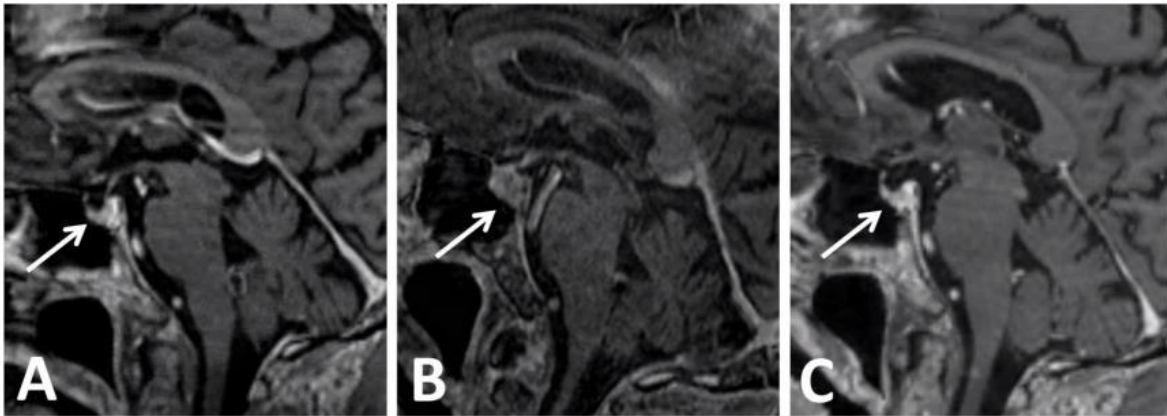


Figure 1. Immunotherapy-related lymphocytic hypophysitis. Surveillance MRI in an 86 year old male with metastatic melanoma demonstrating a normal size and contour of the pituitary gland (A, arrow). 6 weeks after initiating combined immunotherapy with ipilimumab/nivolumab, the patient represented to clinic complaining of new onset headaches, fatigue and weakness. Imaging at that time demonstrated interval enlargement of the pituitary gland (B, arrow) with a convex upward border. Although this finding could be related to interval intrasellar metastasis, serological confirmation of panhypopituitarism and the time course of symptom onset suggested new onset lymphocytic hypophysitis related to immunotherapy. After cessation of immunotherapy and a 6-week course of oral steroids, the patient's symptoms resolved with corresponding decreased pituitary gland size (C, arrow), confirming the diagnosis.

(Filename: TCT_eEde-139_asnrpituitarymcdonald.jpg)

eEde-128

Changes in the AJCC Cancer Staging Manual Eighth Edition For Head and Neck Cancers: A Pictorial Review

C Shaeffer¹, K Schallert¹, S Mukherjee²

¹University of Virginia, Charlottesville, VA, ²University of Virginia Health System, Charlottesville, VA

Purpose

The AJCC Eighth Edition Staging Manual, which is the worldwide standard for staging and managing head and neck cancers, has been updated with significant changes. Given that these guidelines will be implemented for all patients with head and neck cancer effective January 1, 2018, it is essential for all head and neck radiologists to be aware of these changes. The purpose of this educational exhibit is to emphasize the changes in staging head and neck cancers using a case-based approach.

Materials and Methods

Using a pictorial case-based review we will discuss the salient changes to head and neck cancer staging in the eighth edition, particularly with regards to the separate classification of HPV/EBV positive tumors from non-HPV/EBV positive oropharyngeal and nasopharyngeal cancers.

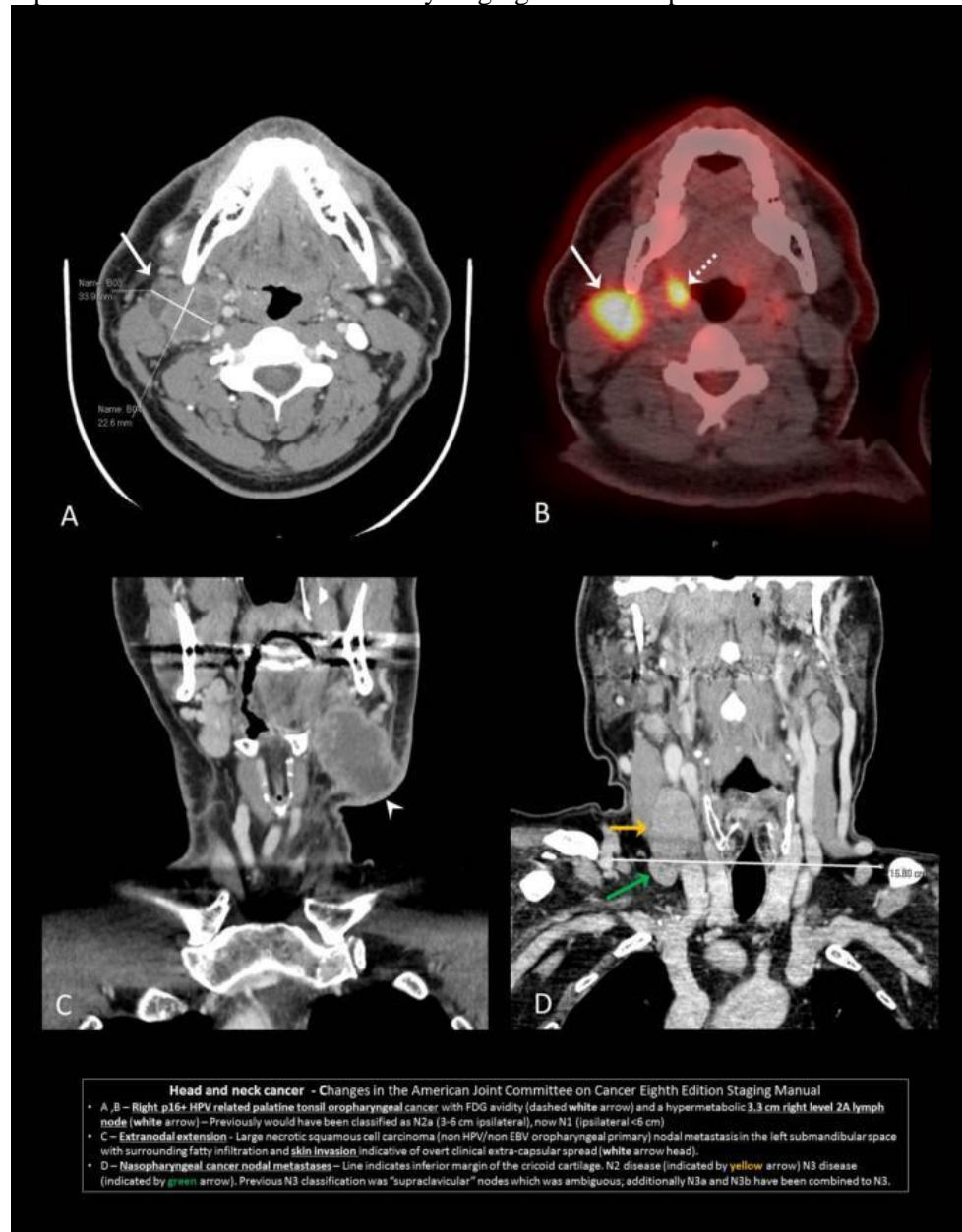
Results

Relevant specific changes which will be reviewed include: • Changes in staging tables for nodal metastasis: - HPV related oropharyngeal squamous cell carcinoma (both clinical and pathologic lymph

node involvement) - N3 staging changes in EBV related nasopharyngeal carcinoma - All other head and neck squamous cell carcinomas (clinical and pathological nodal staging) • New size criteria differentiating N1, N2 and N3 disease in HPV related oropharyngeal cancers. • Updated T staging for EBV associated nasopharyngeal carcinomas with regards to involvement of osseous and masticator structures • Incorporation of overt clinical extra-capsular extension in nodal staging for non-HPV, non-EBV squamous cell carcinoma

Conclusions

The changes in the Eighth Edition of AJCC Cancer Staging Manual will crucially affect staging and management of head and neck cancers. Neuroradiologists, especially head and neck radiologists, need to be familiar with these changes so as to incorporate them in their radiology reports whenever possible as well as multidisciplinary conferences. An important caveat here for radiologists is to search pathology reports when available for accurately staging EBV/HPV/p16 related head and neck cancers.



(Filename: TCT_eEde-128_ASNRHeadandNeckSubmissionGraphicDPI300.jpg)

eEde-121

Clinical and Imaging Correlation of Afferent and Efferent Visual Pathways Defects: A Case Based Review

R Patel¹, C Sitton¹, A Kamali¹, M Syed¹, O Arevalo¹, S Calle¹, E Bonfante¹, R Riascos¹, O Adesina¹

¹*The University of Texas Health Science Center at Houston, Houston, TX*

Purpose

1. To review the gross imaging anatomy of the afferent as well as efferent visual pathways 2. To illustrate spectrum of pathologies involving afferent as well as efferent visual pathways along with discussion of clinical localizing signs and key ophthalmologic/radiologic findings

Materials and Methods

1. Comprehensive clinical evaluation was performed by neuro-ophthalmology attending. 2.

Comprehensive imaging evaluation was performed by neuroradiology attending.

Results

The afferent visual system consists of the retina, optic nerves, optic chiasm, optic tracts, lateral geniculate ganglia, optic radiations, visual cortex and associated cortical areas. Clinical examination may reveal afferent pupillary defects, decreased visual acuity, and visual field deficits. These signs help the clinician to localize anatomical regions of interest for imaging. Imaging locations of these disease processes can involve the prechiasmatic, chiasmatic, and postchiasmatic visual pathways and can be determined based upon the pattern of vision and field loss. The efferent visual system consists of the frontal eye fields, parieto-occipital temporal area, brainstem ocular motor nuclei, interconnecting fiber tracts, cranial nerves (III, IV, V) responsible for innervating the extraocular muscles responsible for ocular movements, the sympathetic and parasympathetic fibers subserving pupillomotor function, and the ciliary ganglion. Clinical examination may reveal cranial nerve palsies causing ocular misalignment, pupillary changes, nystagmus, and gaze palsies. These signs help the clinician to localize anatomical regions of interest for imaging that can include the brainstem, cisternal segment, cavernous sinus and orbit. Representative cases in various disease categories such as vascular, trauma, demyelination, infection/inflammation, and neoplastic were presented in a case-based format.

Conclusions

Neuro-ophthalmology is an interdisciplinary field that utilizes ophthalmology, neurology, and neuroradiology to determine the visual implications of neurologic and systemic disorders. A wide variety of neurologic and systemic conditions can involve the afferent as well as efferent visual pathways and radiologists need a detailed understanding of the anatomy and physiology of the visual system in order to relate imaging abnormalities to patient symptomatology. Multidisciplinary approach for accurate assessment of lesion location, lesion characteristics is crucial in determining patient diagnosis and management.

eEde-143

Differential Diagnosis of Calcified Sinonasal Masses

A Klebba¹, D Shatzkes¹

¹*Lenox Hill Hospital, New York, NY*

Purpose

Sinus wall mucoperiosteal thickening is a frequent finding in chronic rhinosinusitis, but calcification in a discrete sinonasal mass is considerably less common. The goal of this exhibit is to provide a differential diagnosis for calcified sinonasal masses with illustrative cases.

Materials and Methods

The literature on imaging of sinonasal masses was reviewed, and cases of calcified sinonasal masses were compiled by searching through the authors' teaching files. Lesions were categorized based on type of calcification and underlying pathologic process. Illustrative images were chosen, and a brief review of each entity was provided.

Results

I. Types of sinonasal mass calcification were classified as:

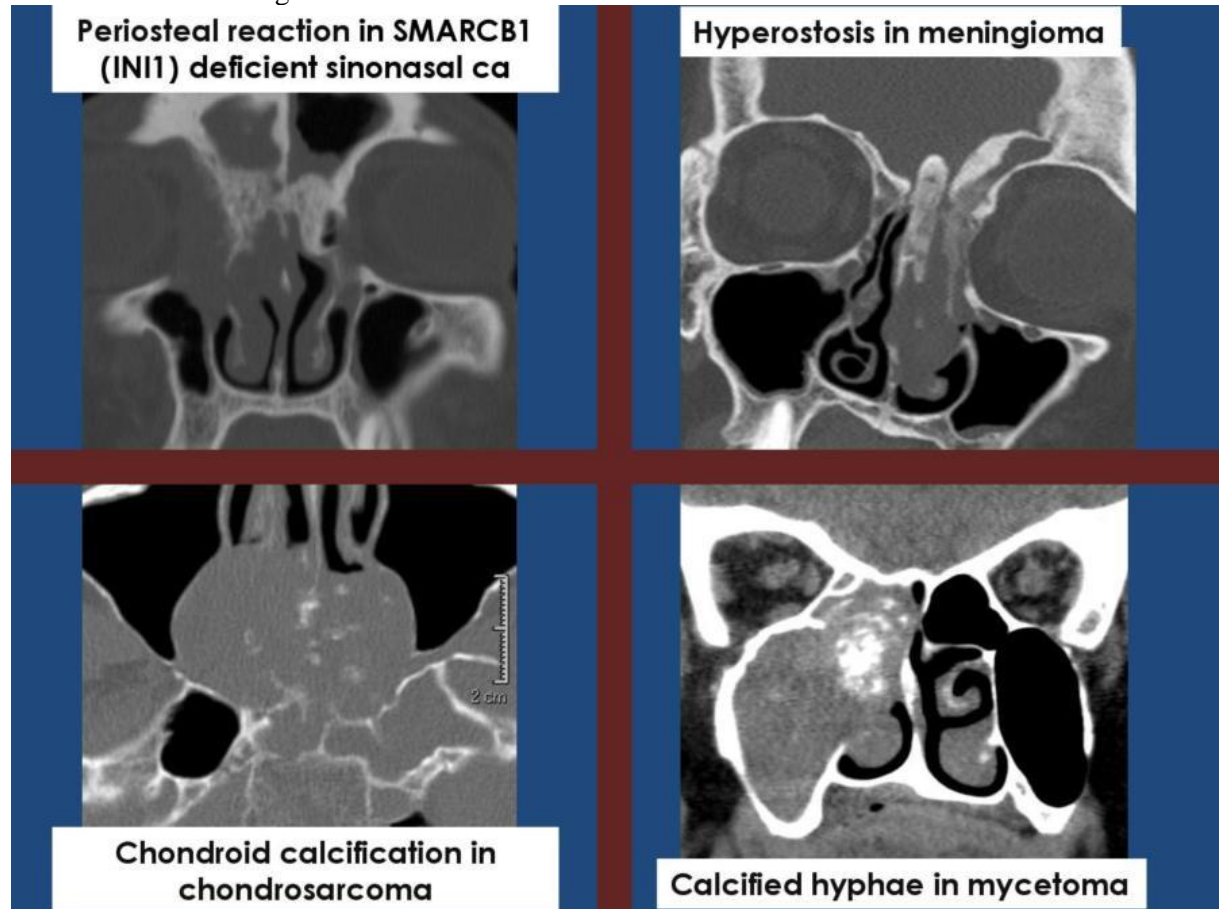
- Intrinsic tumoral matrix production
- Calcification related to impact of tumor on adjacent bone (hyperostosis, residual fragments of destroyed bone)
- Dystrophic calcification within devitalized tissue

II. Calcified sinonasal masses were categorized as:

- Neoplastic
 - o Malignant sinonasal tumors
 - o Esthesioneuroblastoma
 - o Chondrosarcoma
 - o Adenocarcinoma
 - o Osteosarcoma
 - o SMARCB1 (INI1) deficient sinonasal carcinoma
 - o Benign sinonasal tumors
 - o Osteoma
 - o Ossifying fibroma
 - o Inverted papilloma
 - o Meningioma
 - o Juvenile angiofibroma
 - o Odontogenic tumors and dysplasias with secondary sinonasal involvement
 - o Skull base tumors with secondary sinonasal involvement
- Non-neoplastic
 - o Tumefactive
 - Fibrous dysplasia
 - Mycetoma
 - Rhinolith/sinolith
 - Odontogenic cysts and dystrophic calcification

Conclusions

There are a limited number of causes of calcified sinonasal masses that include both neoplastic and non-neoplastic etiologies. Because calcification in a sinonasal mass is uncommon, its presence can help narrow differential diagnosis.



(Filename: TCT_eEde-143_Sinonasalcalcificationsimages_DS-page-0011.jpg)

Don't Get Cheeky - A Multimodality Imaging Review of Parotid Gland Masses

D Thut¹, o atar¹, D Kowal¹

¹*University of Massachusetts Medical School - Baystate, Springfield, MA*

Purpose

The aim of this educational exhibit is to demonstrate the imaging characteristics of various histologic types of parotid gland tumors using CT, MR, US and nuclear medicine including 18FDG PET/CT.

Materials and Methods

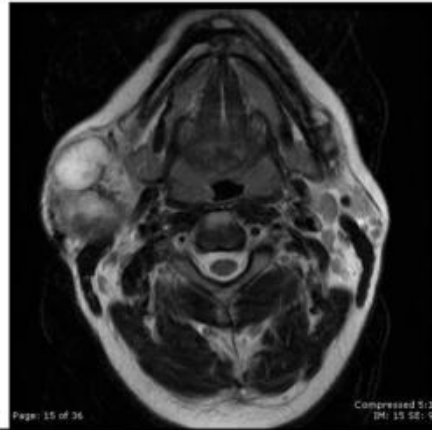
Pearls and pitfalls of diagnostic imaging of parotid gland masses will be provided in a pictorial atlas format. For each of the common tumors and tumor mimics, we will answer the classical six questions of journalism: who (pathology), what (it looks like), when (epidemiology), where (unilateral or bilateral, spread), how (it presents), and why (management).

Results

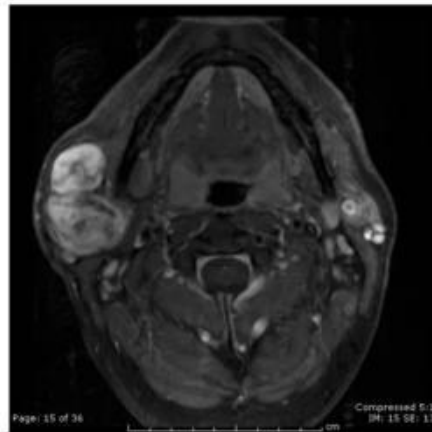
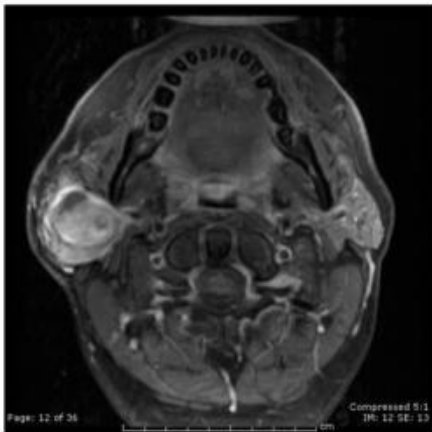
The differential diagnosis for parotid tumors includes pleomorphic adenoma, Warthin tumor, lymphoma, metastasis, mucoepidermoid, adenoid cystic carcinoma, and lymphangioma. Potential mimics of parotid tumors include intraparotid abscess, sarcoidosis, benign intraparotid lymph nodes, and Sjögren disease. Low-grade malignant neoplasms such as mucoepidermoid tumors or acinic cell carcinomas can have the appearance of well circumscribed benign tumors on CT and MRI and may demonstrate no significant FDG uptake on PET. The diagnosis of Warthin tumor should be considered in a solid mass with a cystic component. Although benign, these tumors can be very hypermetabolic on FDG PET and are associated with increased Tc-99m pertechnetate uptake on salivary scintigraphy. Warthin tumors, oncocytomas, and lymphoma often can present as bilateral solid parotid masses. Pleomorphic adenoma is typically a T2 hyperintense, homogeneously enhancing lesion with a smooth, sharp, slightly undulating margin. These benign tumors can also demonstrate FDG avidity. Consider carcinoma ex pleomorphic adenoma if rapidly enlarging, with aggressive/invasive features and new areas of low signal on T2-weighted images. Consider lymphoma or metastatic disease in the setting of concomitant bilateral cervical adenopathy. Metastases to the parotid gland typically arise from primary malignancies of the scalp. An irregular margin or facial paralysis are strong indicators of malignancy. Perineural spread of parotid cancer is a critical factor in treatment strategy, and imaging helps to evaluate this important risk factor. CT and MRI can determine the intrinsic versus extrinsic origin of a parotid-region mass, the extent of a primary parotid tumor, and to help to determine the relationship to the facial nerve. Ultrasound is a versatile, low-cost and widely available modality that can quickly differentiate between solid and cystic lesions including abscesses. It is often used to guide needle biopsy.

Conclusions

It is important for the radiologist to be familiar with common intrinsic parotid masses and their mimics, typical imaging appearances, clinical presentations, and how they are treated or monitored.



T2-weighted images demonstrate a lobulated heterogeneous hyperintense mass in the right parotid gland with areas of low signal intensity, suspicious for malignant components in a patient with known pleomorphic adenoma



Contrast enhanced T1-weighted images with fat saturation demonstrate heterogeneous enhancement of the mass with some focal areas of non-enhancement, possibly representing necrosis or calcifications

- Who?** Carcinoma ex pleomorphic adenoma, also known as malignant mixed tumor (MMT)
- What?** Aggressive and infiltrating, irregular masses extending into the gland parenchyma and beyond. On MRI, T1/T2 heterogeneous, restricted diffusion/low ADC; may have small calcifications; FDG-avid unlike benign mixed tumor
- When?** Older patients (6th to 8th decade), 5-10% of pleomorphic adenoma degrade into MMT after 10-15 years
- How?** Rapid enlargement of parotid mass, may have facial nerve weakness and pain
- Where?** Perineural spread along CN VII and CN V invasion of mastoid and carotid space; high rate of metastasis at the time of diagnosis typically to brain, bone, lungs and local lymph nodes,
- Why?** Treated with surgery, chemotherapy and radiation

(Filename: TCT_eEde-132_Cheekyimages.jpg)

Evaluation of the Many Causes and Appearances of a Retropharyngeal Effusion

T Naney¹, M Mabray¹, J Hallstrom¹, G Lorenzo¹

¹*University of New Mexico, Albuquerque, NM*

Purpose

The deep spaces of the neck and specifically the danger space are a relatively small but very important region in evaluation of the neck, partially visualized on brain imaging, and even included on chest exams. A retropharyngeal effusion expands this space but is not necessarily specific in making a diagnosis in the absence of other factors, such as clinical scenario, laboratory evaluation and adjacent radiographic findings. This educational exhibit will expand on the infectious, malignant, and inflammatory causes of a retropharyngeal effusion, including interesting cases as well as findings and clinical presentations that will help to differentiate.

Materials and Methods

The cases utilized were found through a directed search for retropharyngeal effusions in our PACS database. Specific cases were chosen based off clinical presentation, imaging characteristics and subsequent follow-up. This was followed by correlating imaging features with laboratory results and symptomatology to ascertain the cause of the retropharyngeal effusions.

Results

Retropharyngeal effusions in the absence of other findings are not specific. In one case, a retropharyngeal effusion was detected on an MRI which did not demonstrate osteomyelitis/discitis but was associated with elevated inflammatory markers and 15 days later on a subsequent MRI, cervical spine osteomyelitis/discitis was discovered. A similar appearing retropharyngeal effusion in a younger patient with elevated inflammatory markers was determined to be the result of calcific tendinitis of the longus colli muscle. A retropharyngeal effusion was present in a pediatric patient after foreign body ingestion which caused inflammation to the airway with gas adjacent and possibly within the retropharyngeal space suggesting development of a fistulous tract. In all of these cases, there was a retropharyngeal effusion which appeared similar in attenuation and without enhancement but differences in clinical situation, laboratory evaluation, and associated radiographic findings. These are contrasted with a standard more sinister enhancing retropharyngeal effusion consistent with a retropharyngeal abscess.

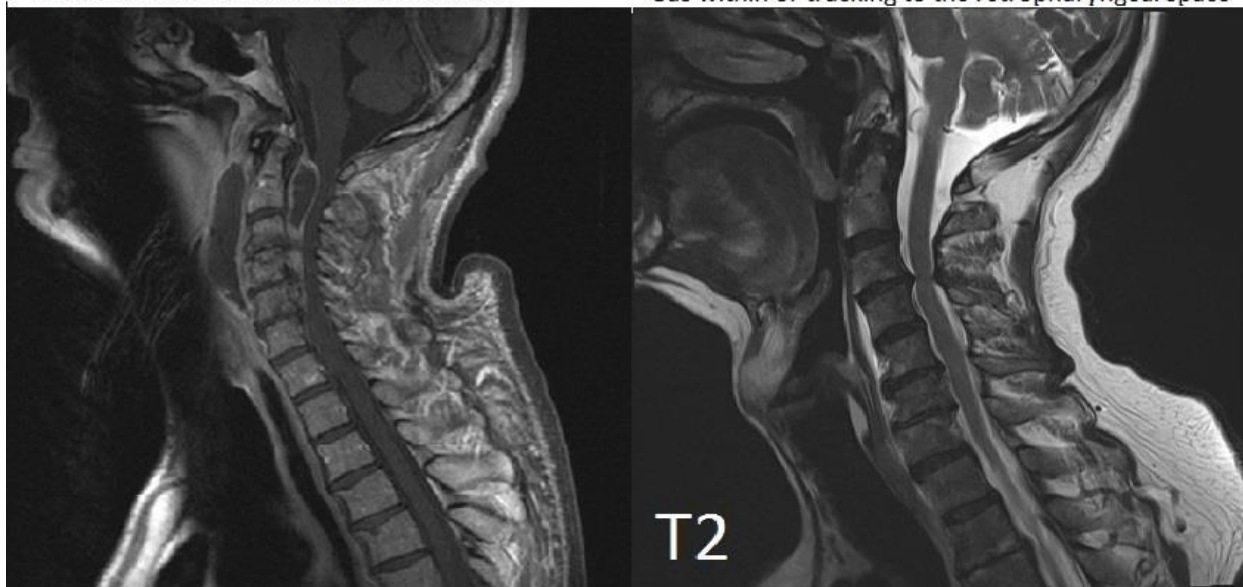
Conclusions

As stated previously, evaluation of the danger space can be difficult to interpret, but this educational exhibit will utilize an interactive demonstration to depict various radiographic appearances and clinical scenarios which will lead a radiologist to determine the nature of a retropharyngeal effusion more accurately.



Calcific tendinitis of the longus colli muscle

Gas within or tracking to the retropharyngeal space



Ventral epidural and retropharyngeal abscesses

15 days prior to osteomyelitis/discitis C6/7

(Filename: TCT_eEde-111_ASNR.jpg)

eEde-149

Expansile and Destructive Lesions of the Skull Base: A Review of Typical and Atypical Features

A Martin¹, D Bleicher², R Bhatia², N Nagornaya²

¹Jackson Memorial Hospital, Miami, FL, ²University of Miami/Jackson Memorial Hospital, Miami Beach, FL

Purpose

A wide variety of lesions may present as masses in and about the bony skull base, with neoplastic, congenital, and postinflammatory etiologies most commonly encountered. Despite the wide array of etiologies, large lesions often share similar imaging characteristics, including bony expansion and erosion, skull-base foraminal invasion, and heterogeneous MR signal.

Materials and Methods

Ten representative cases of large skull-base masses with pathology proven diagnoses are presented, with attention to the unique and shared imaging characteristics.

Results

Large masses of the skull base, regardless of origin, may present with similar imaging characteristics, with bony erosion, foraminal invasion, and heterogeneous MRI signal frequently encountered. Such appearances may require the radiologist to consider a broader differential. Despite this, several lesions demonstrate unique features that can further narrow the differential.

Conclusions

Following this presentation, the learner should appreciate a greater understanding of the variety of manifestations of skull base masses.

eEde-154

Expected Findings and Potential Complications Following Tympanoplasty and Mastoidectomy

J Aristizabal¹, C Zamora², M Castillo²

¹*University of Antioquia, Medellin, Colombia,* ²*University of North Carolina at Chapel Hill, Chapel Hill, NC*

Purpose

The postoperative imaging evaluation of patients who have undergone tympanoplasty and mastoidectomy with or without ossicular reconstruction is often challenging due to variations in technique and implanted materials. The purpose of this review is to familiarize the reader with the normal postoperative CT appearance and potential complications after the procedure.

Materials and Methods

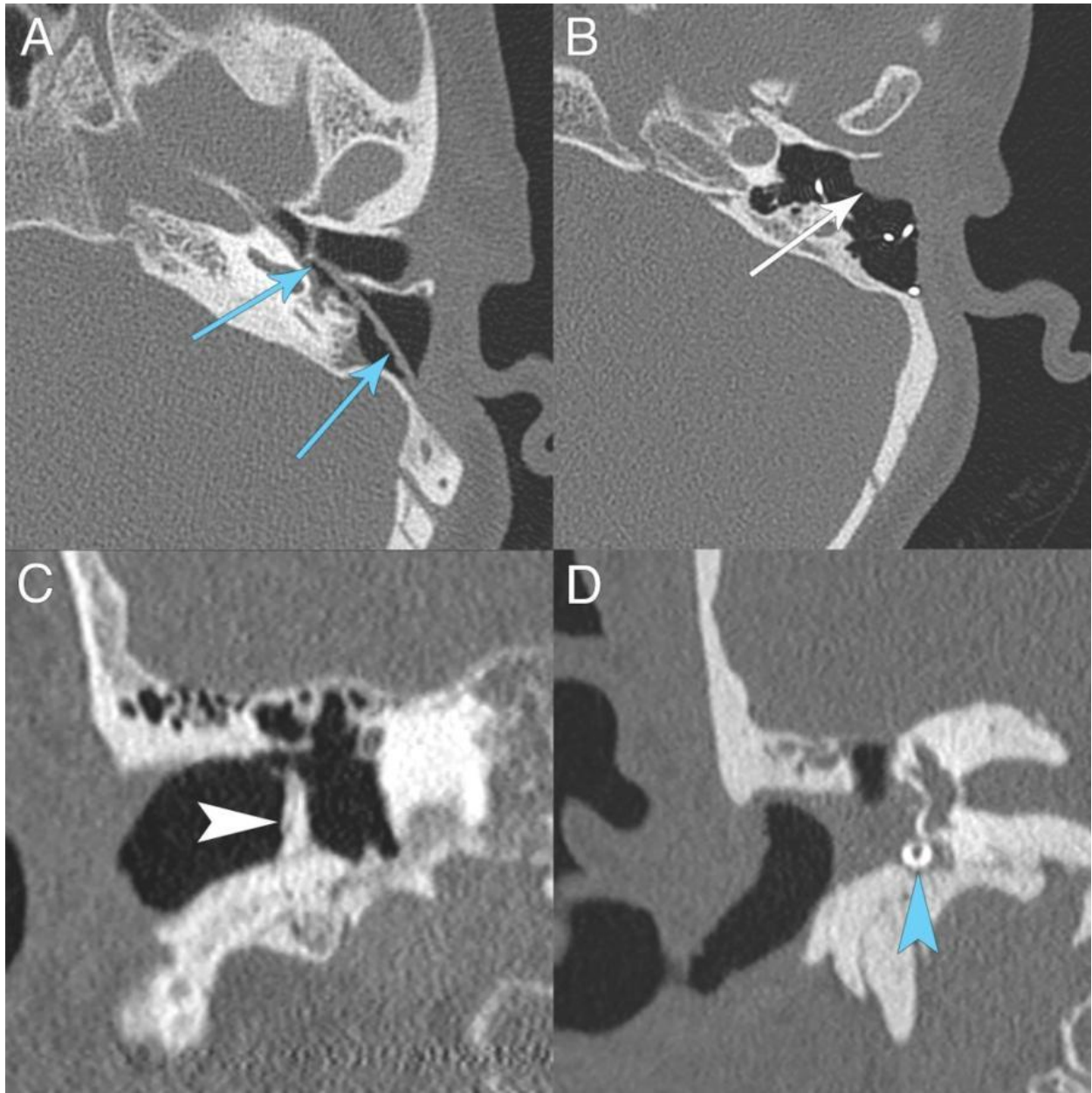
We searched our teaching files for patients who had undergone tympanoplasty and mastoidectomy during the past 10 years and identified cases of patients who had an uneventful clinical course to show the breadth of normal findings. We also collected examples of complications that were encountered during follow-up.

Results

We identified cases that illustrate different types of tympanoplasty with various implanted materials such as cartilage and temporal fascial grafts and silicone rubber sheets. We also found cases with associated ossiculoplasty including incus interposition and different types of total or partial ossicular replacement prostheses. We describe complications such as tympanic membrane thickening, ossification, retraction or perforation, cholesteatoma formation, dehiscence of the facial nerve, lateral semicircular canal, or tegmen tympani, stenosis or enlargement of the auditory canal, erosion, extrusion or dislocation of the prosthesis, formation of granulation tissue and infection. (Figure) Temporal bone CT, Axial. A. Silicon rubber sheet in the mastoidectomy bowl (blue arrows) B. Recurrent cholesteatoma in a different patient after tympanomastoidectomy and cochlear implant (white arrow). Temporal bone CT, Coronal. C. Different patient with ossification of the cartilage graft (white arrowhead) D. In other patient, the ossicles were partially resected and there is dislocation of the cup of a stapes prosthesis.

Conclusions

On this educational exhibit we describe the normal postoperative findings after tympanoplasty and mastoidectomy and illustrate some of the more common complications that we encountered in our practice.



(Filename: TCT_eEde-154_Imagen.jpg)

eEde-112

Extracranial Lumps and Bumps – the Usual and Unusual Suspects from a Radiologist's Point of View

S Ezhapilli¹

¹*SUNY Upstate Medical University, Syracuse, NY*

Purpose

- To review characteristic cross-sectional imaging findings and clinical implications of extracranial cystic lesions of head and neck
- To discuss the utility of CT, MRI and FDG PET CT in differentiating benign

Electronic Educational Exhibits

from malignant cystic lesions of head and neck • To illustrate a systematic approach for categorization of extra cranial cystic lesions which can aid clinicians and radiologists

Materials and Methods

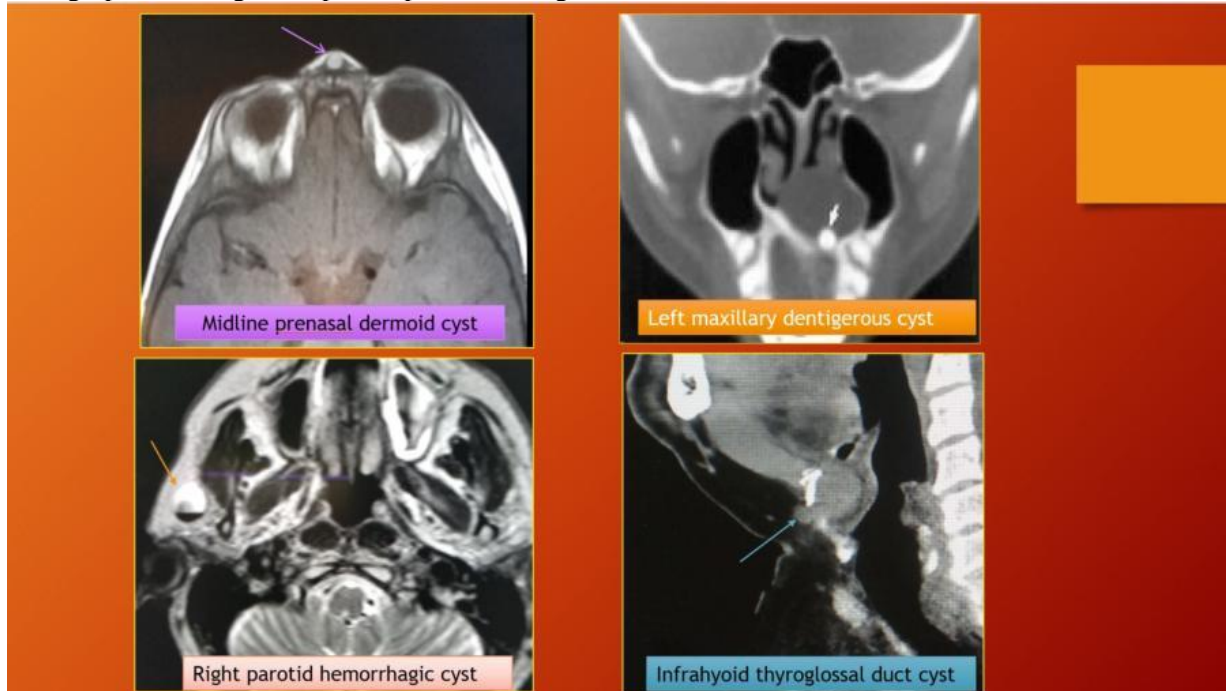
Majority of extracranial cystic lesions of head and neck are either clinically suspected or identified. However, a vast number of these lesions remain unresolved clinically, and require CT/MRI for detailed evaluation. In addition, a number of extracranial cystic lesions are incidentally identified on cross-sectional imaging of head and neck. CT/MRI can be a problem-solving tool for such lesions for appropriate categorization of cystic lesions is crucial in diagnostic and therapeutic options. Extracranial cystic lesions can be broadly classified based on location into lesions of head, face and neck and further subclassified into non-neoplastic and neoplastic categories. The exhibit systematically reviews a variety of common and a few uncommon extracranial cystic lesions encountered in neuroradiology practice.

Results

This pictorial review primarily illustrates the etiology, characteristic imaging features and clinical relevance of extra cranial cystic lesions of head and neck. Extracranial lesions of head include ectodermal inclusion cyst, trichilemmal cyst, sebaceous cyst and cystic metastasis. Examples of extracranial cystic lesions of face include dentigerous cyst, odontogenic keratocyst, parotid cystic lesion, cystic lacrimal adenocarcinoma and first branchial cleft cyst. The cystic lesions involving the neck include thyroglossal duct cyst, laryngocele, ranula, cystic hygroma, necrotic lymph node and thyroid cysts. The review would also include detailed evaluation and literature review will demonstrate prognosis and therapeutic option.

Conclusions

Extracranial cystic lesions of head and neck are required to be adequately categorized with pertinent radiographic findings for optimal patient management and favorable clinical outcome.



(Filename: TCT_eEde-112_extracranialcysts.jpg)

Foregut Anomalies of the Head and Neck

A Portanova¹, M Lu², A Bhatt¹, E Lin¹

¹University of Rochester Medical Center, Rochester, NY, ²University of Rochester, Rochester, NY

Purpose

1. Review the spectrum of foregut anomalies in the head and neck 2. Discuss the normal embryology of the foregut in relation to the head and neck 3. Introduce the different embryological theories of how these foregut anomalies develop in the head and neck to better understand where they may arise and their associated findings

Materials and Methods

A retrospective review of all patients who underwent diagnostic imaging at the University of Rochester Medical Center between the years 2000-2018 was performed. Using a search application built into the RIS, the terms "esophageal duplication," "duplication cyst," "tubular duplication," "esophageal cyst," "bronchogenic cyst," "neurenteric cyst" and "neurenteric fistula" were identified in all radiology reports. Imaging studies and electronic medical records of patients with a foregut anomaly of the head and neck were reviewed. The age, gender, type of foregut anomaly, location and associated findings were compiled.

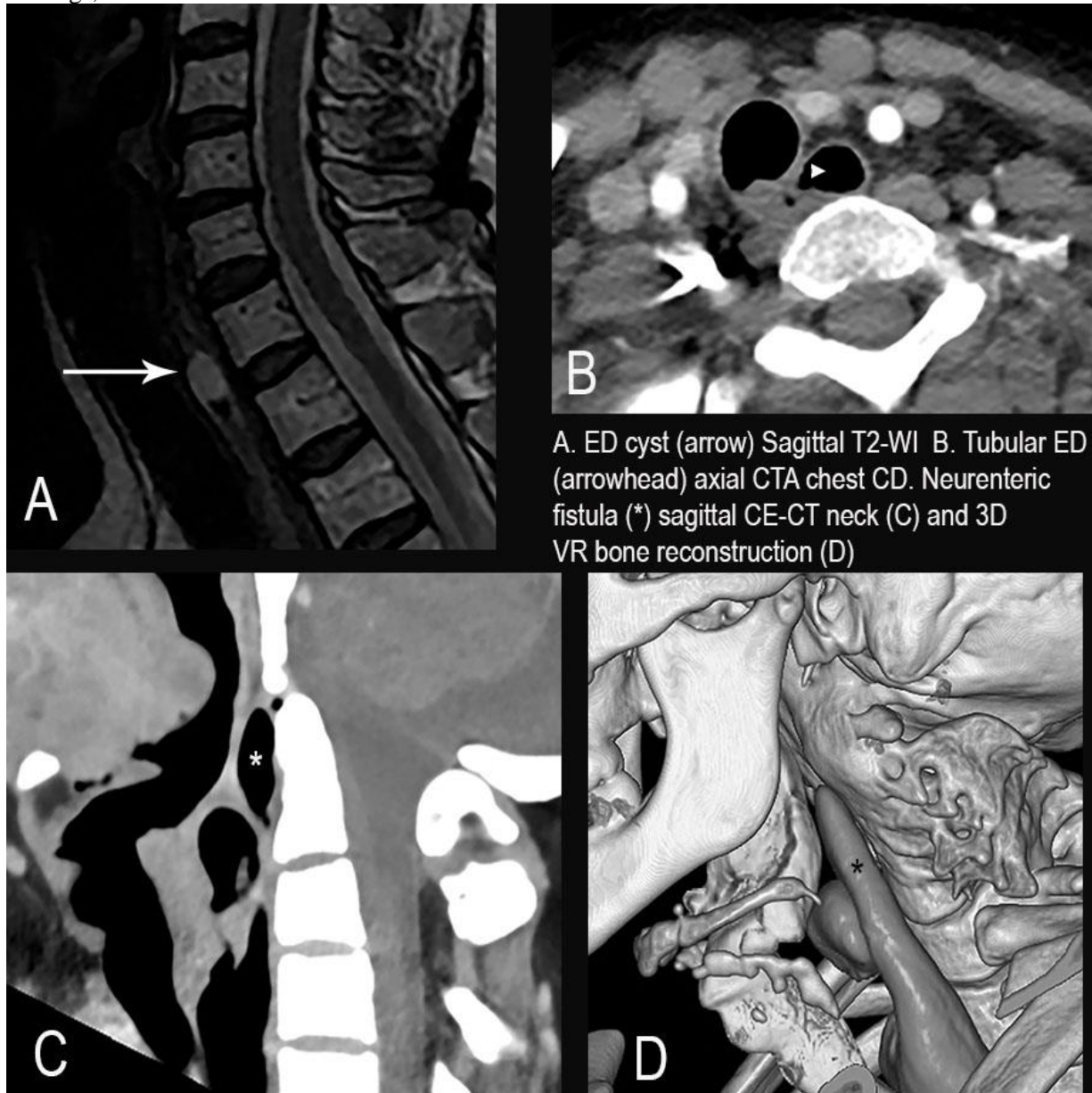
Results

Four cervical foregut anomalies were identified, consisting of two esophageal duplication (ED) cysts, one tubular ED and one neurenteric fistula. The patients' age ranged from 16-68 years with a mean of 32. Three of the four patients were female. The ED cysts (Fig. A) and tubular ED (Fig. B) were located in the cervical esophagus. The tubular ED extended inferiorly into the mediastinum (not shown). The neurenteric fistula (Figs. C and D) extended from the cervical esophagus to the C2 vertebra. Key cross-sectional images will be presented. Alimentary tract anomalies of the head and neck are uncommon and consist of cystic and tubular ED, bronchogenic cysts and neurenteric cysts and fistulas. Foregut duplication cysts can be confirmed pathologically by the presence of alimentary tract mucosa or respiratory epithelium, as well as smooth muscle in the case of alimentary tract anomalies. EDs are typically cystic, with an incidence of 1 in 8200 [1], but can be tubular in rare instances. Bronchogenic cysts are most often found in the thorax, but more than 70 cases have been reported in the head and neck [2]. Neurenteric cysts and fistulas are rare and are associated with vertebral and spinal cord anomalies [3]. Normal embryology and embryological theories of how each of these foregut anomalies will be reviewed. The primitive foregut gives rise to the oropharynx, respiratory system, esophagus, stomach, proximal duodenum, liver, pancreas and biliary tree. Several theories describe how foregut anomalies may arise. Bronchogenic and ED cysts are thought to develop from abnormal budding of the tracheobronchial diverticulum from the primitive foregut during week 5 of embryo development [4]. EDs may also arise from abnormal recanalization of the esophagus during week 10 [4]. Neurenteric cysts and fistulas may develop secondary to a split notochord phenomenon, which occurs around week 3 [5]. Graphic illustrations will be used to complement the description of these theories.

Conclusions

1. Foregut anomalies of the head and neck are rare and consist of bronchogenic cysts, esophageal duplication cysts, tubular esophageal duplications and neurenteric cysts and fistulas. 2. The primitive foregut gives rise to several structures of the normal head and neck aerodigestive tract, including the oropharynx, esophagus and trachea. 3. The various foregut anomalies arise secondary to different aberrations in foregut development. 4. Potential explanations for the development of these foregut anomalies include abnormal budding of the tracheobronchial diverticulum from the primitive foregut, abnormal vacuolization of the primitive esophagus, and the split notochord. 5. Understanding how foregut anomalies arise allows the radiologist to recognize these entities in the head and neck, include them in the

differential when encountering cystic and tubular lesions in the head and neck, and identify associated findings, such as vertebral anomalies.



(Filename: TCT_eEde-125_esophagealduplicationgraphic.jpg)

eEde-151

Fungal Infection of Paranasal Sinus and Their Complications

P Singh¹, V Gupta¹, C Ahuja¹, S Vyas¹, N Khandelwal¹

¹*Postgraduate Institute of Medical Education and Research, Chandigarh, Chandigarh, India*

Purpose

Fungal sinusitis is increasingly reported world over, common pathogens being *Aspergillus*, *Rhizopus*, *Bipolaris* and *Mucor*. Depending upon hyphal invasion of sinus wall and blood vessels, further subtypes

Electronic Educational Exhibits

are noninvasive (fungus ball and allergic fungal rhinosinusitis {AFRS}) and invasive (chronic, granulomatous and acute invasive). In susceptible individuals invasive disease may occur including dreaded orbito-cranial extension. Radiologists should recognize these patterns for early diagnosis.

Materials and Methods

After a short review of literature confirmed cases of fungal infection of paranasal sinuses (PNS) were selected from departmental archives. Illustrative cases of typical computed tomography (CT) and magnetic resonance imaging (MRI) findings are presented. CT and MRI are ideal investigations and show suggestive imaging appearance.

Results

Fungal sinus contents appear as hyperdense polypoidal mucosal thickening on CT and hypointensity on T1 and T2 images on MRI. Other findings are sinus expansion, bony remodelling, sclerosis and erosion. Invasion is denoted by bone destruction, inflammatory changes in maxillofacial region, neck spaces and intraorbital/intracranial soft tissue masses. Invasion of periantral fat, sphenopalatine foramen, pterygopalatine and infratemporal fossae etc. may be seen. Orbital involvement can be through lamina papyracea or orbital fissures and may involve orbital apex (orbital apex syndrome). Intracranial spread may involve skull base, basifrontal region through cribriform plate or middle cranial fossa presenting as extradural or intradural disease with leptomeningitis, cerebritis and abscess. Cavernous sinus lesion may cause thrombosis and cranial nerve palsy. Dreaded complications are arterial thrombosis, mycotic aneurysms, cerebral infarction or hemorrhages. AFRS is an allergic reactive pan-rhinosinusitis, forming eosinophilic mucin, often involving nasal cavity. Mucor infection occurs in diabetic patients mostly with rhino-orbito-cerebral pattern.

Conclusions

Radiologists should recognize imaging signs of fungal colonization of PNS. Diagnosis of invasive disease in predisposed patients is vital for instituting early treatment to prevent protracted illness and dreaded complications.

eEde-123

Head and Neck Findings in Mucopolysaccharidosis

A Riello¹, A Costacurta², D Horovitz³

¹*Fleury Labs a+, Rio de Janeiro, Rio de Janeiro, Brazil,* ²*Clinica Felipe Mattoso, Rio de Janeiro, Brazil,* ³*Instituto Fernandes Figueira, Rio de Janeiro, Brazil*

Purpose

The purpose of this presentation is to show and describe the imaging features of the mucopolysaccharidosis (MPS) in the head and neck that are relevant in the clinical management of those patients, since some of these might pose life-threatening risks, as sleep apnea syndrome. Those head and neck findings in MPS include manifestations in the orbit, oral cavity, pharynx and larynx.

Materials and Methods

We describe the various imaging features in the head and neck of patients with mucopolysaccharidosis, including X-Ray, CT and MRI findings, with special focus on the most common abnormalities in the cervical spine, craniovertebral junction, oral cavity, pharynx and larynx.

Results

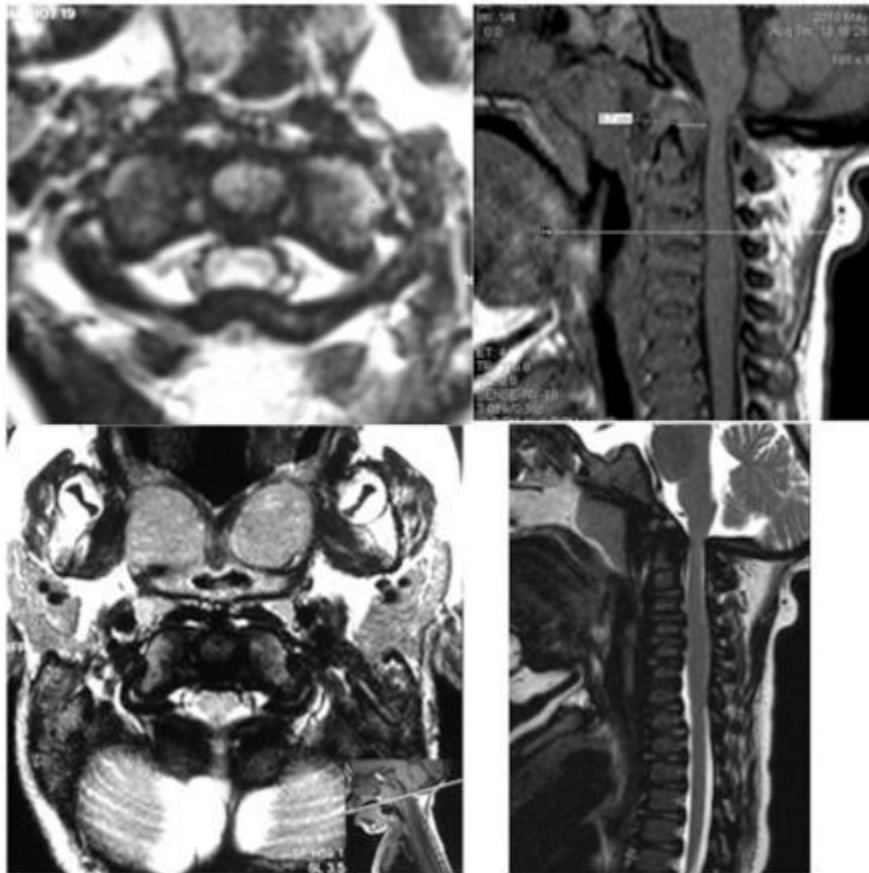
Mucopolysaccharidosis (MPS) is an inherited metabolic disease and a member of the group of lysosomal storage disorders. Its hallmark is a deficiency of lysosomal enzymes involved in the degradation of mucopolysaccharides, the glycosaminoglycans (GAGs), owing to mutations in genes encoding lysosomal hydrolases. Partially degraded GAGs accumulate within lysosomes and in the extracellular space, interfering with the degradation of other macromolecules, which also accumulate. This process leads to chronic degeneration of cells, gradually affecting multiple organs and systems, especially the skeletal system, liver, spleen, heart, eyes, and central nervous system (CNS). There are seven distinct types of

Electronic Educational Exhibits

MPS, which are divided further into subtypes according to the deficient enzyme and severity of the clinical picture. MPS is inherited via an autosomal recessive pattern, the exception being MPS type II, which has X-linked recessive transmission. Clinical manifestations vary considerably among the different types of MPS, including cognitive impairment, delayed psychomotor development or neurologic regression in the first years of life. Some have mild manifestations or no other clinical manifestations, whereas others are accompanied by multisystemic abnormalities, especially skeletal involvement. MPS has characteristic neuroimaging features in the brain and cervical spine, varying according to the type of MPS. Bone abnormalities in the skull and spine (dysostosis multiplex) are often present in these patients. The imaging features of MPS in the head and neck are relevant in the clinical management of those patients, since some of these might pose life-threatening risks, as sleep apnea syndrome. Those head and neck findings in MPS include manifestations in the orbit, oral cavity, pharynx and larynx.

Conclusions

It is important to look for and describe abnormalities in the head and neck beyond the brain and cervical medulla, especially in the oral cavity, in the pharynx and in the larynx, since some pathological findings may influence the clinical management of the patients with MPS and can also pose life-threatening risks, as sleep apnea syndrome.



(Filename: TCT_eEde-123_Apresentacaomps2imagem001-copia.jpg)

Head and Neck Paragangliomas: From Genetics to Radiology

S Kushchayev¹, Y Kushchayeva², M Brooks¹, O Teytelboym¹, K Pacak²

¹Mercy Catholic Medical Center, Darby, PA, ²National Institutes of Health, Bethesda, MD

Purpose

Head and neck paragangliomas (HNPs) are rare tumors arising from neural crest cells. Overall, HNPs represent less than 0.5% of all head and neck neoplasms. About 3% of paragangliomas occur in the head and neck location. HNPs are slowly growing tumors. In contrast to paraganglial tumors of the adrenals, abdomen, and thorax, HNPs seldom release catecholamines and are hence rarely vasoactive. In this presentation, we review the clinical presentation of HNPs, discuss imaging findings and topographical classifications of HNPs, and recent advances in the genetics of HNPs in the context of imaging.

Materials and Methods

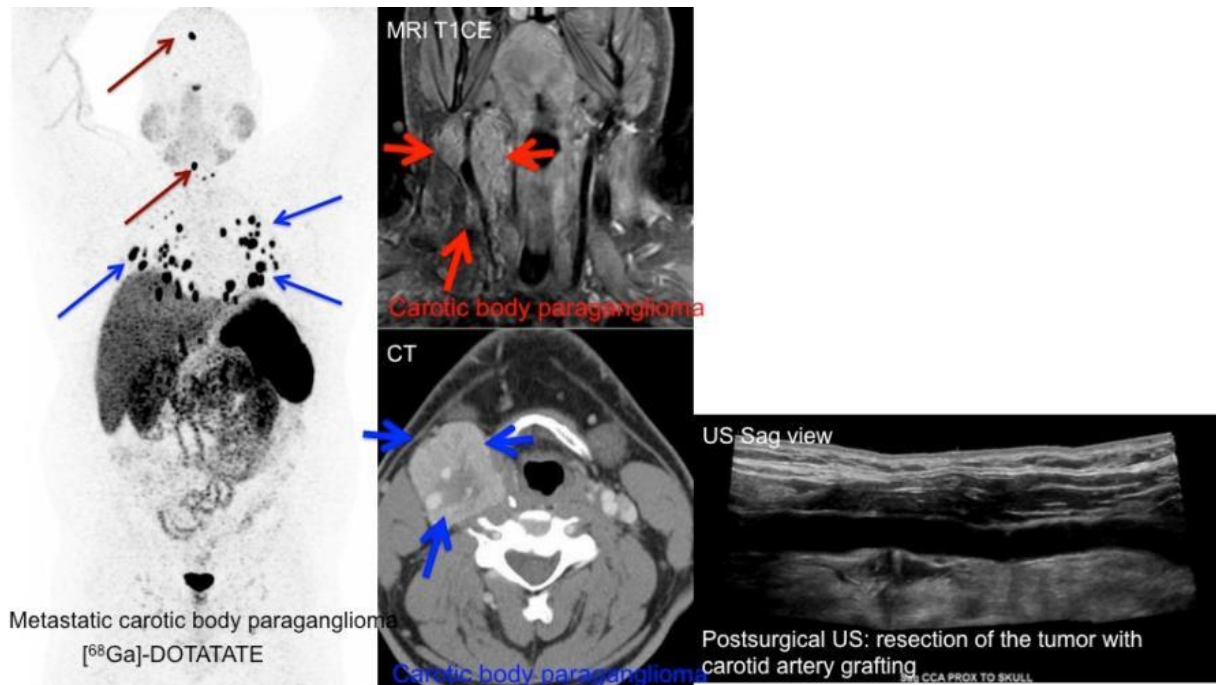
This study summarizes the extensive experience of the observation of patients with HNPs under the protocol Diagnosis of Pheochromocytoma at the National Institutes of Health (Bethesda, Maryland, USA), (Eunice Kennedy Shriver National Institute of Child Health and Human Development, protocol NCT00004847 Principal Investigator Karel Pacak, MD).

Results

In this exhibit, we review clinical and imaging presentations of HNPs depending on genetic variants of the tumors. HNPs have been associated with nine susceptibility genes: NF1, RET, VHL, succinate dehydrogenase (SDH) A, SDH-B, SDH-C, SDH-D, SDH-AF2 (SDH5), and TMEM127. HNPs may be associated with mutations of VHL (in von Hippel-Lindau syndrome), RET (in MEN-2), or NF1 (in neurofibromatosis type 1). Multiple HNPs and malignant tumors are common in patients with SDH-D mutations. Hereditary HNPs are mostly caused by mutations of the SDH-D, SDH-B, and SDH-C genes. The presentation will illustrate the pathologic findings that correspond to specific imaging features. We will review HNPs depending on tumor locations: carotid body paragangliomas, vagal paragangliomas, tympanic and jugular glomus tumors. We will review HNPs arising at other locations, such as the ciliary glomus or laryngic glomus. The study will review the most recent literature and guidelines for the evaluation of HNPs with different radiological modalities, including ultrasound, CT, MRI, and nuclear medicine scans (18-F-FDOPA, 18-F-FDG, 68-GaDOTATE). We will review the clinical classifications of HNPs, including the Shamblin classification of carotid body paragangliomas and Fisch classification for temporal paragangliomas. Our presentation will provide practical algorithms for the diagnosis of HNPs. We will review surgical treatment options for HNPs and postsurgical imaging.

Conclusions

This exhibit provides a comprehensive review of the literature, clinical characteristics, histological types and imaging features of HNPs; summarizes the treatment options, and offers a practical algorithm for clinical translation of radiological finding in HNPs.



(Filename: TCT_eEde-129_HNPs.jpg)

eEde-118

Horner's Syndrome: Where Does a Radiologist Need to Look? A Comprehensive Review of Anatomy, Imaging and Pathologies

P Kochar¹, P Sharma², P Sooin³, H Sawhney¹, G Garg¹, M Rosovsky¹, R Sulaiman¹

¹Yale New Haven Health Bridgeport Hospital, Bridgeport, CT, ²Yale New Haven Health System at Bridgeport Hospital, Milford, CT, ³GLM Hospital, New Delhi, Delhi, India

Purpose

1. Comprehensive review of anatomy of the oculosympathetic chain 2. Understand difference between preganglionic and post ganglionic Horner's syndrome (HS) 3. Using anatomical knowledge to predict location of the lesion/abnormality based on clinical findings (first order, second order or third order neurons) 4. Review pathologies causing Horner' syndrome at various levels along the sympathetic chain

Materials and Methods
HS is caused by a multiple pathologies along the long and complex oculosympathetic chain extending from brain, cervical spine, orbits and the neck. Symptomatology is different at different levels of involvement. In this review, we comprehensively discuss the anatomy of the oculosympathetic pathway and utilize this knowledge along with clinical information to locate the site of expected pathology. This review will enhance the ability of the radiology residents and fellows to follow a targeted approach to make a radiologic diagnosis in patient's with HS.

Results

Classical symptoms of HS ipsilateral ptosis, miosis, and facial anhidrosis. It results from interruption of the oculosympathetic chain, a long, circuit with central, preganglionic, and postganglionic neurons. Depending on the anatomic location of pathology, HS presents with unique clinical findings divided into central, preganglionic, and postganglionic HS. Prior knowledge of the complex circuit of sympathetic chain with correlation of the clinical findings, one can carefully scrutinize the areas to look for the pathologies. This will help in early diagnosis and treatment of this complex disease process.

Conclusions

Multiple pathologies are known to cause HS. In addition to clinical findings, thorough knowledge of the anatomy of complex oculosympathetic pathway will help a neuroradiologist to develop a search pattern for making an early imaging-based diagnosis and ultimately aid in prompt and accurate treatment. Additionally, this knowledge will help us tailor our imaging evaluation for HS patients.

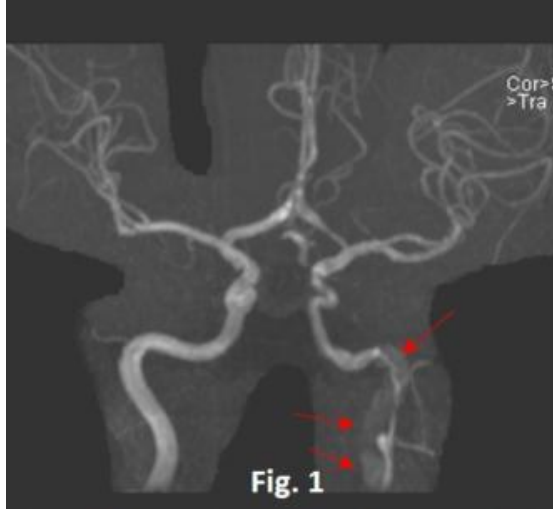


Figure 1: MRA demonstrates dissection of left cervical and petrous carotid artery with minimal flow related enhancement in the pseudolumen (arrows). Patient symptomatology includes left sided headache, left ptosis, left miosis, and anhidrosis of the forehead.

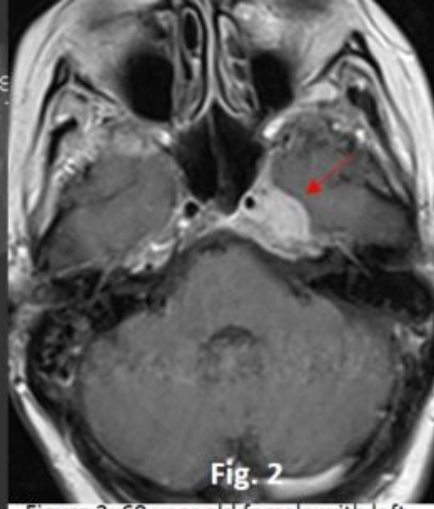


Figure 2: 69 year old female with left miosis, ptosis, and VIth and V1/V2 cranial nerves palsies. Contrast-enhanced axial T1-weighted image shows homogeneous intense enhancement (arrow) of mass representing a meningioma.



71 year old woman with paresthesia of left arm, left ptosis and anhidrosis.
A, Axial contrast-enhanced CT image at level of left thoracic inlet demonstrates infiltrative mass (arrow).
B, Coronal CT image shows mass partly encasing left subclavian artery (arrow) at the left lung apex of. Mass was confirmed to be small cell carcinoma of lung.

(Filename: TCT_eEde-118_final.jpg)

Hyperparathyroidism: A Multimodality Case-based Pictorial Review

V Bachhav¹, K Gupta¹, A Patil², R Prasad¹, A Ali¹, S Virmani¹

¹Rush University Medical Center, Chicago, IL, ²Advocate Illinois Masonic Medical Center, Chicago, IL,

Purpose

Hyperparathyroidism is a common endocrine disorder, with more than 95% of cases attributed to primary hyperparathyroidism (parathyroid adenoma, parathyroid hyperplasia and parathyroid carcinoma). Successful minimally invasive parathyroidectomy depends on accurate preoperative localization. Ultrasound and 99mTc-Sestamibi SPECT/CT are considered the initial imaging modalities. However, there is little consensus regarding the optimal imaging protocol. There is growing support for the use of 4D-CT. Additionally PET-CT or MRI can be used in cases with diagnostic dilemma. We present a case-based pictorial review of common and uncommon imaging spectrum of primary hyperparathyroidism, highlighting the advantages and limitations of various imaging modalities including ultrasound, 99mTc-sestamibi scintigraphy, 4-D CT, MRI and PET CT.

Materials and Methods

We retrospectively reviewed the usual and unusual multimodality imaging spectrum of challenging cases which highlighted the advantages and limitations of various imaging modalities.

Results

Most illustrative cases were selected to highlight the imaging spectrum for the etiology of primary hyperparathyroidism including parathyroid adenoma, parathyroid hyperplasia and parathyroid carcinoma. Advantages and limitations of various imaging modalities are also discussed and highlighted in this case-based pictorial review.

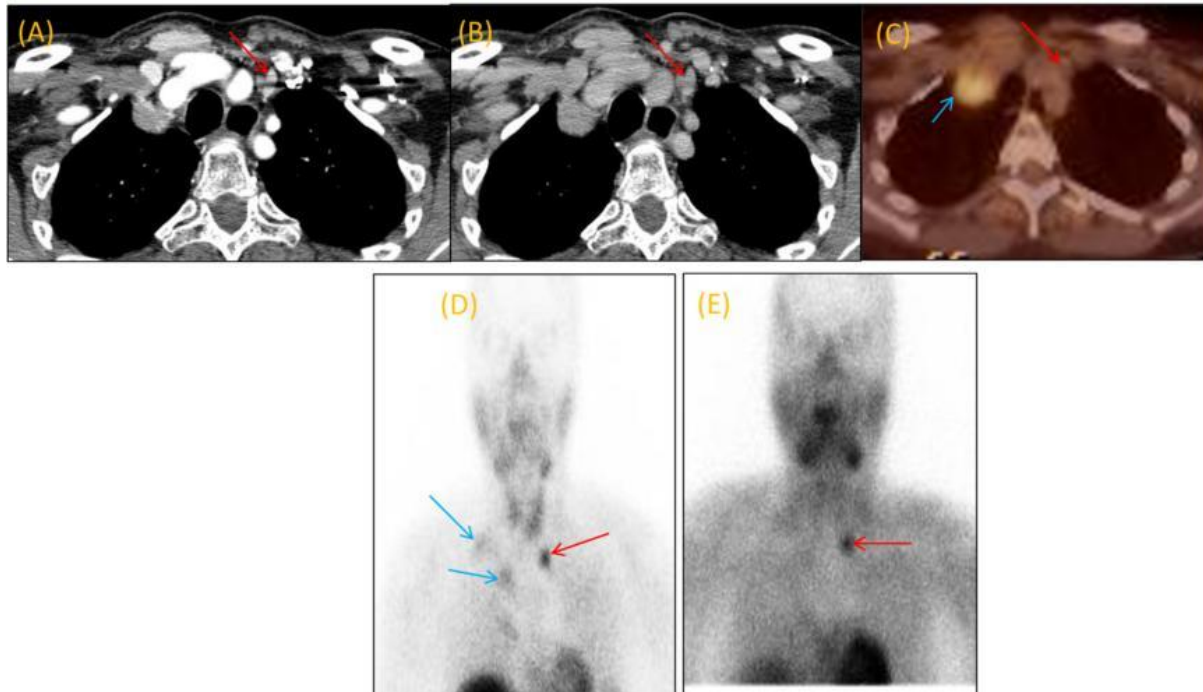
Conclusions

Embryological, anatomical and functional knowledge of the disease is essential for correct clinical interpretation. Equally important is to correlate the findings with various available imaging modalities, clinical symptoms and lab findings. The above case-based pictorial review aims to increase the confidence of the interpreting radiologist and thus help in better patient management.

Small, well-defined enhancing on the arterial phase (A) with washout on the venous phase (B) inferior to the left thyroid lobe in the superior mediastinum.

Sestamibi study initial (D) and delayed images (E) showed persistent uptake in this region concerning for a parathyroid adenoma. Axial PET (C) demonstrating Non FDG avid parathyroid adenoma in the superior mediastinum(→) and Incidental FDG avid soft tissue nodule in the right superior mediastinum(→) representing metastasis from known lymphoma.

Ultrasound neck (Not shown) showed heterogeneous appearance of the thyroid gland with multiple hypodense nodules with non visualization of the aforementioned adenoma.



(Filename: TCT_eEde-157_sss.jpg)

eEde-133

Imaging Findings of Nontumorous Salivary Gland Diseases: What Radiologists Need to Know

H Baek¹, K Ryu¹, K Choi²

¹GNU Changwon Hospital, Changwon, Republic of Korea, ²PNU Yangsan Hospital, Yangsan, Republic of Korea

Purpose

To illustrate the role of imaging for evaluating the various nontumorous diseases in the major salivary glands

Materials and Methods

Various imaging modalities are directed to the major salivary glands for evaluating salivary gland disease. Of these, plain radiography and sialography were commonly used imaging modalities in the past. Recently, high-resolution ultrasonography (HRUS) is being increasingly used for targeted salivary gland investigation. In addition, computed tomography (CT) and magnetic resonance imaging (MRI) provide more useful information about the diseased salivary glands due to the technical advances of cross-sectional imaging techniques. In this educational exhibit, we illustrate the nontumorous salivary gland disease with their imaging findings.

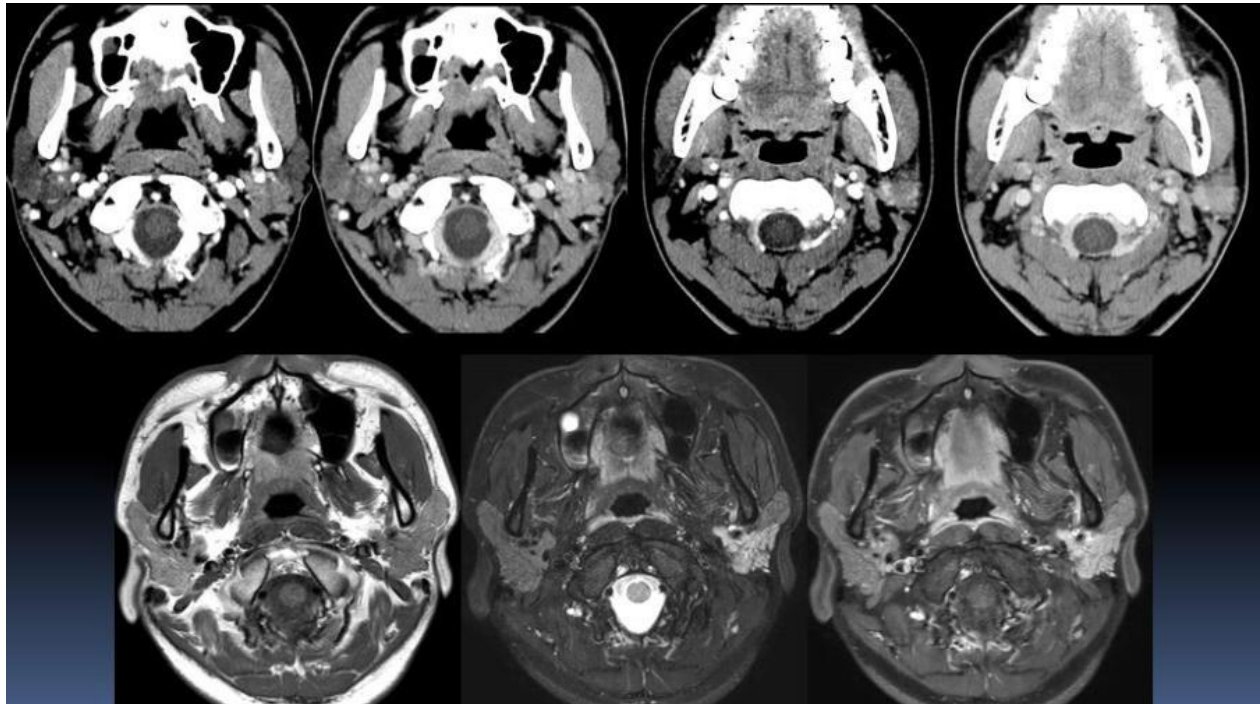
Results

Imaging armamentarium for salivary gland imaging includes plain radiography, sialography, high-

resolution ultrasonography, computed tomography, magnetic resonance imaging and radionuclide scintigraphy. Major cause of nontumorous salivary gland disease is an inflammation which is caused by various causes such as infection, sialolithiasis, systemic autoimmune disease, granulomatous disease etc. In case of sialadenitis, HRUS shows diffuse glandular enlargement with decreased echogenicity and heterogenous echotexture. Diffuse increase in intraglandular vascularity may be shown, and in some cases, abscess formation can occur in acute stage. In chronic stages, the gland may be normal or small in size with reduced echogenicity and vascularity. On CT and MRI show increased enhancement and diffuse enlargement of involved glands with or without abscess formation, and intraparenchymal/regional lymphadenopathy. There is associated soft tissue stranding/thickening of adjacent fat and cervical fascia. Major systemic diseases involving salivary glands are autoimmune processes predominantly including Sjögren's syndrome. Imaging findings reveal diffuse enlargement of the gland in early stages with/without the presence of focal masses, nodules, cysts, nodes, calculi, or calcifications and features of chronic sialadenitis in later stages. Multiple granulomatous diseases including Wegener's disease, tuberculosis, syphilis, and fungal infections may involve salivary glands either diffusely or focally. CT reveals hyperattenuating glandular parenchyma in both acute and chronic stages associated with enlargement in acute and loss of glandular volume in chronic stages. However, on MRI images, the gland is hyperintense on T2W images in acute and relatively hypointense in chronic stages.

Conclusions

A variety of diseases involve the major salivary glands with few characteristic features on imaging. HRUS should be the first screening imaging tool, and CT is the most optimal imaging modality for nontumorous diseases. In addition, MRI can provide additional information for diagnosing salivary gland disease.



(Filename: TCT_eEde-133_Figure3.JPG)

eEde-120

Imaging in Diplopia (Double Vision)

K Kadakia¹, A Agarwal², S Kanekar³, V Nguyen¹, B White¹

¹University of Texas Southwestern, Dallas, TX, ²University of Texas Southwestern Medical Center, Dallas, TX, ³Penn State Milton Hershey Medical Center, Hershey, PA

Purpose

1. To understand the basic clinical aspects of diplopia, demarcate true (binocular) versus monocular diplopia and imaging indications 2. CT and MR protocol for imaging assessment of diplopia 3. Common etiologies of true diplopia and imaging anatomy of the associated cranial nerves (III-VI) and their pathways 4. Illustrate common and interesting cases of various pathological conditions

Materials and Methods

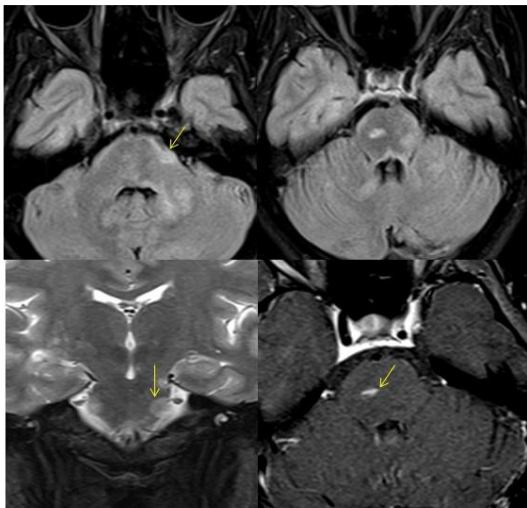
Diplopia is a common imaging indication at most of the centers. This may be acute, when the initial modality is frequently CT or may be long-standing, which is most commonly evaluated through MR. We will use cases from our teaching files and PACS repository to first discuss the MR protocol and then illustrate the imaging anatomy of the III-VI cranial nerves. Common pathological conditions will then be discussed and illustrated through examples. Search pattern using an anatomy based approach and common blind spots will also be discussed.

Results

- Clinical aspects of diplopia
- Common etiologies of binocular (in detail) versus monocular (short discussion) diplopia
- A. Orbital/ocular lesions
- B. Extraocular muscle diseases (e.g., entrapment, thyroid ophthalmopathy)
- C. Cranial nerve dysfunction pathology
 - i - Intraorbital course
 - ii - Superior orbital fissure
 - iii - Cavernous sinus
 - iv - Cisternal segment
 - v - Brainstem and supranuclear (demyelination - see fig. example, stroke, tumor)
- Anatomy of the oculomotor, trochlear and abducens nerves
- MR Imaging protocol
- Case Illustration, search pattern and blind spots
- Conclusion

Conclusions

This exhibit provides a basic outline of the clinical and imaging aspects of diplopia, focusing on how to develop a search pattern and avoid the blind spots.



Lesions within the brainstem: 27 year old female history of MS and acute onset lateral rectus palsy. Axial FLAIR MR, Coronal T2 MR and post-contrast images reveal multiple lesions in the pons including lesions involving the root entry zone of left sixth nerve

(Filename: TCT_eEde-120_Diplopia.jpg)

eEde-113

Imaging Nonmelanoma Cancer of the Head and Neck

A Costacurta¹, A Riello²

¹*Fleury-Felippe Mattoso, Rio de Janeiro, Brazil,* ²*Fleury Labs a+, Rio de Janeiro, Brazil*

Purpose

Skin cancers (most of which are basal and squamous cell) are the most common cancers (5.4 million cancers diagnosed each year) and on the rise. If death is uncommon, significant morbidity with cosmetic deformities can occur if neglected or underestimated. These cancers are easily assessed by the physician. Their depth, however, is another issue. The recent released eighth edition of the American Joint Committee on Cancer (AJCC) dedicates a new chapter to cutaneous squamous cell carcinoma and emphasizes the importance of perineural spread to staging. The aim of this pictorial essay is to provide radiologists with illustrative examples of skin cancer, depicting the relevant superficial anatomy of the head and neck and usual spread pattern and outlining a systematic approach to radiological interpretation.

Materials and Methods

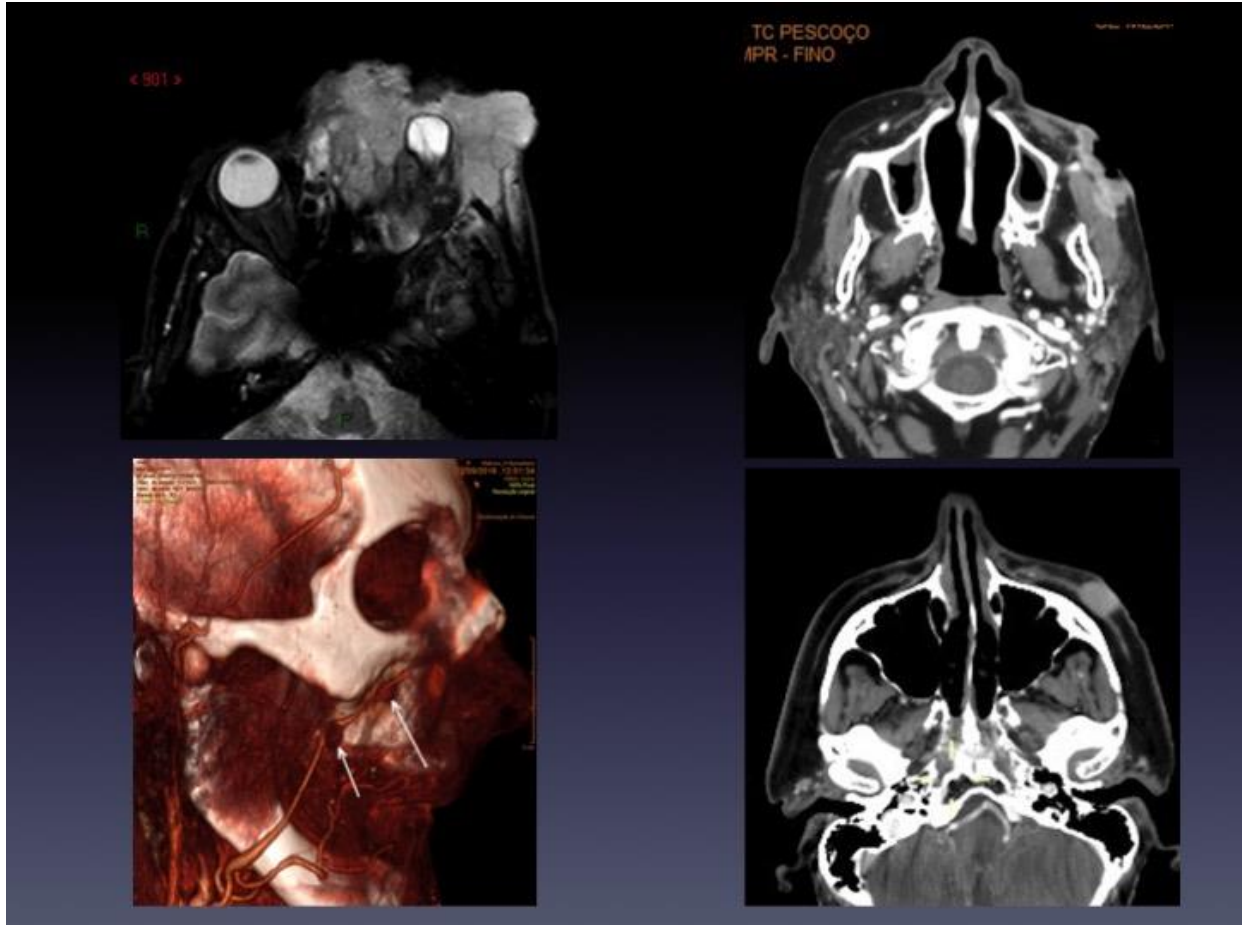
The analysis of a multi-institutional series of skin cancers and literature review

Results

The evaluation of a skin lesion is a step-wise process, having in mind the AJCC staging. Dimensions and depth of the lesion from superficial to deep structures: epidermis/dermis, subcutaneous fat, superficial musculoaponeurotic system of the face, mimetic muscles, bone. Calvarial compromise following galea invasion High-risk features for cancer such as lesion on the ear, lip or around the orbit with extensive and deep invasion Facial innervation, proximity with neural foramina and perineural spread Checking the superficial system and parotid glands for lymph node spread

Conclusions

Imaging has an important role in staging skin cancer. Invasion of the bone or perineural spread upstages the tumor and has therapeutic implications. Awareness of spread patterns and local anatomy and systematic search for signs of deeper invasion can improve patient care.



(Filename: TCT_eEde-113_Slide1.jpg)

eEde-136

Imaging of Otolaryngology Devices and Implants: What the Radiologists Must Know

D Pong¹, M Walters¹, A Singh³, B Tantiwongkosi

¹University of Texas Health Science Center San Antonio, San Antonio, TX

Purpose

This pictorial review discusses and illustrates commonly and uncommonly encountered surgical devices/implants used in otolaryngology.

Materials and Methods

The list of the surgical devices was obtained from otolaryngology preoperative case files from 2009-2017. Images were obtained from the PACS. Correlation of the imaging findings and photography of the devices are emphasized. Some hand drawn diagrams will be presented.

Results

Otolaryngologists perform a wide array of interventions from the orbit to the base of the neck. Knowledge of the types of procedures and implants/devices as well as the expected postoperative imaging appearance can be helpful for avoiding misdiagnoses. In particular, familiarity with the different types of devices and implants utilized in ENT surgery is crucial for accurate assessment of the postoperative patients. Common ENT-related implants include tracheostomy tubes, cochlear implants, facial trauma fixation hardware and myringotomy tubes (in children). Cochlear implants, in particular, have specific imaging features which

Electronic Educational Exhibits

should be commented on and complications to be evaluated. However, there are also several highly subspecialized otolaryngology-related implants and devices to be aware of for the radiologist. Implants utilized in ossicular chain reconstruction have a characteristic appearance. Eyelid gold weights (utilized after parotidectomy) and tracheoesophageal puncture (utilized after total laryngectomy) serve very specific functional and anatomic purposes. The most common postoperative ENT imaging appearances will be highlighted with computed tomography, as CT is the primary modality for follow-up of most ENT surgeries.

Conclusions

Imaging of the ENT patient requires intimate knowledge of common and uncommon ENT devices for accurate assessment and avoidance of misdiagnoses.

Imaging of Devices in Otolaryngology Beyond Lines and Tubes

Organs	Devices
Ear	External: hearing aids, BAHA, myringotomy tubes Middle: PORP, TORP Inner: Cochlear implants
Nose	Nasoplasty implants, nasal airways, nasogastric tubes, maxillary sinus stent
Larynx and trachea	Tracheostomy tubes, T tubes, endotracheal tubes, tracheal stents, silicone, tracheoesophageal puncture (TEP)
Orbits	Gold weight, mesh, mini plates/screws, glaucoma device, scleral bands, silicone, artificial lens, PMMA orbital implants

Tracheoesophageal Puncture (TEP)

A voice prosthesis that is utilized after a total laryngectomy (TL). An iatrogenic fistula is created between the trachea and esophagus after a TL and the device (a one-way valve) is inserted to create a supply of air for esophageal speech via vibration of the pharyngoesophageal sphincter.

Cochlear Implants

- Used for profound sensorineural hearing loss.
- Post-operative imaging considerations include: CSF Fistula, Facial Nerve lesions and Electrode malpositioning.

Partial Ossicular Replacement Prosthesis

- Biocompatible synthetic prosthesis is used to bridge stapes superstructure (capitulum) to TM or malleus
- Intact stapes superstructure necessary

(Filename: TCT_eEde-136_ENTdeviceJPEG.JPG)

eEde-119

Imaging Pediatric Proptosis: From Eye to Brain

M Ho¹, J Chen¹, M Brodsky¹, J Garrity¹

¹Mayo Clinic, Rochester, MN

Purpose

1. Review the pathophysiology and major etiologies of pediatric proptosis 2. Utilize clinical history and appropriate imaging modalities for evaluation 3. Demonstrate pearls and pitfalls of diagnosis

Materials and Methods

Evaluation of the child with proptosis begins with a thorough ophthalmologic history and examination. Multiple modalities are available for clinical assessment, including ocular ultrasound, optical coherence tomography, and angiography. Following initial assessment, additional radiologic evaluation of the orbits and brain may be indicated using CT, MR, and/or cerebral angiography. The following mnemonics are useful for assessment: Location: "4 O's" = Ocular, Optic nerve, Orbit, Outside Etiology: "CT VEIN" = Congenital/CSF, Trauma, Vascular, Endocrine, Inflammation/Infection, Neoplasm

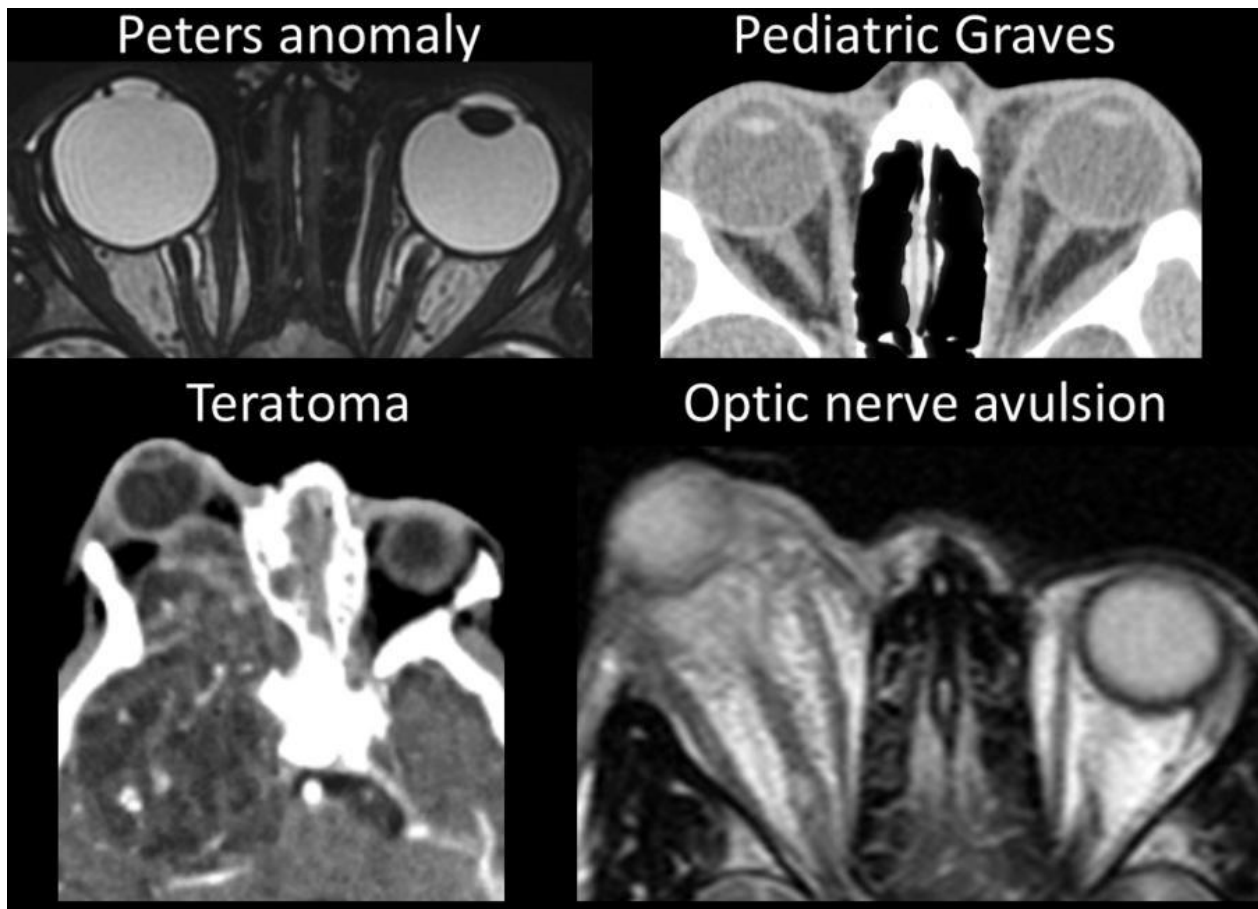
Electronic Educational Exhibits

Results

Clinical: - Definitions: proptosis vs. pseudoproptosis, exophthalmos, exorbitism - Symptoms (age, time course, laterality) + 8-point eye examination Imaging Modalities: - Ophthalmology: ultrasound, optical coherence tomography, angiography - Radiology: CT, MR, cerebral angiography Congenital: Macrophthalmos - Simple megalocornea, anterior megalophthalmos, buphthalmos Congenital masses - Hamartoma vs. choristoma, ectodermal and endodermal malformations Genetic overgrowth - NF1 (cranio-orbito-temporal), megalencephaly CSF: Optic disc edema - Papilledema vs. pseudopapilledema: US, OCT, CT, MRI Optic nerve tortuosity - DDx: normal, papilledema, optic neuritis, optic glioma Syndromic craniosynostosis Trauma: Anterior chamber - Corneal laceration, hyphema, lens dislocation, cataract Posterior chamber - Retinal vs. choroidal detachment, vitreous hemorrhage Retrobulbar hematoma - ON stretching, avulsion Pediatric orbital mechanics - "White-eyed" trauma, ligamentous elasticity, craniofacial ratio - Blowin > blowout, greenstick (trapdoor), CSF leak - Midface: naso-orbito-ethmoid Vascular: Anomalies - Malformations vs. tumors - Carotid-cavernous fistula Syndromes - Hemangiomas, PHACES - Sturge-Weber: embryology and temporal evolution, high-risk features - DDx: Parry-Romberg (enophthalmos), Wyburn-Mason (high-flow) Endocrine: - Pediatric Graves: often milder, atypical distribution, auto-decompression Inflammation/Infection: Orbital inflammation - Idiopathic (pseudotumor), granulomatous, lymphocytic, histiocytic, autoimmune, demyelinating - Locations: uvea/sclera, intraconal, EOM/lacrimal, brain and multisystem Orbital cellulitis: 1° vs 2° sinusitis, pre- vs. postseptal - Subperiosteal abscess: spreading thrombophlebitis, porous bone Neoplasm: Diverse histology and locations; infection mimics - Benign, malignant primary, metastasis - Rb, optic glioma/PNST/meningioma, orbital RMS/lymphoma/NB, bone, brain

Conclusions

Ophthalmologic history and examination are key to the evaluation of pediatric proptosis. Following initial assessment, radiologic imaging can be obtained to further assess orbital and brain pathology. Useful mnemonics include the "4 O's" for location and "CT VEIN" for etiology.



(Filename: TCT_eEde-119_Proptosis.jpg)

eEde-140

Immediate, Delayed, and Latent Complications Following Craniofacial Trauma

J Vera¹, G Lorenzo²

¹University of New Mexico Health Sciences Center, Albuquerque, NM, ²University of New Mexico, Albuquerque, NM

Purpose

The purpose of this educational exhibit is to describe and demonstrate the immediate, delayed and latent complications after severe craniofacial trauma.

Materials and Methods

Clinical history was obtained from electronic medical records (EMR). The nature of trauma included blunt, penetrating and iatrogenic causes. Six cases with associated imaging such as CT, MRI, and nuclear medicine were collected to detail findings at variable times of onset following injury, including immediate, delayed, and latent (i.e. >10 years) periods.

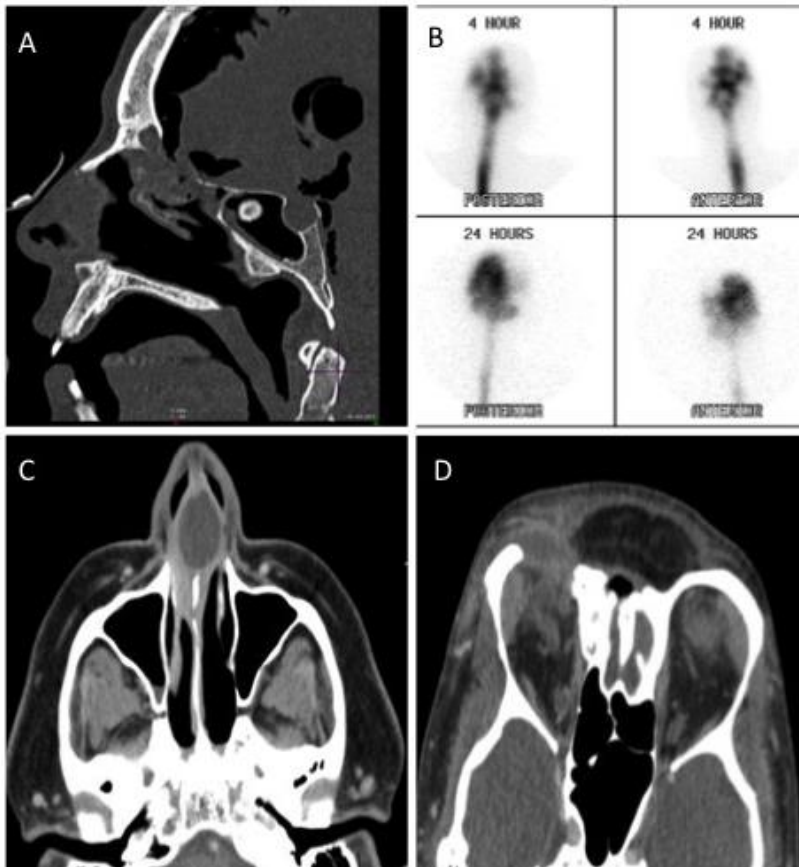
Results

The sequela of craniofacial fractures is responsible for great morbidity and mortality in severely injured patients. Despite advances in surgical management, patients remain at risk for infectious and functional complications after severe craniofacial injury including, CSF leak, meningitis, diplopia, enophthalmos, nasal obstruction, mucocele, mucopyocele, mandibular malunion/nonunion and malocclusion. In order to formulate a meaningful report, the radiologist must be aware of the normal and abnormal postoperative

appearance of craniofacial reconstruction. One must also appreciate the role of imaging in understanding infectious and functional complications secondary to skull base, orbital, sinonasal and mandibular injuries.

Conclusions

The immediate, delayed and latent complications after severe craniofacial injury can have devastating effects on the patient's cosmetic and functional status. The radiologists plays an important role in recognizing the normal and abnormal sequela in this very complex patient population.



(Filename: TCT_eEde-140_Slide1.jpg)

eEde-138

Intraosseous Venous Malformations of the Head and Neck: An Under-recognized but Pathognomonic Imaging Finding

E Yushvayev¹, J Steinklein², D Shatzkes³

¹Lenox Hilll hospital, New york, NY, ²Hofstra Northwell School of Medicine, NEW YORK, NY, ³Lenox Hill Hospital, New York, NY

Purpose

This exhibit serves to educate the viewer on vascular malformations within osseous structures of the head and neck. Throughout history, there has been inconsistent terminology of vascular anomalies in the literature preceding the establishment of the International Society for the Study of Vascular Anomalies

(ISSVA). ISSVA, most recently revised in 2014, provides a practical and simplified approach to organizing vascular lesions based on histology and presence or absence of neoplasia. Intraosseous venous malformations (VM) possess a characteristic appearance on computed tomography (CT) that, to our knowledge, has not been well characterized or described in radiology literature. Similarly, there is limited pathologic literature regarding this diagnosis and often these lesions are biopsied and erroneously classified as arteriovenous malformation or other vascular lesion. This exhibit will provide a comprehensive review of this unique and under-recognized pathologic entity, and will highlight characteristic and pathognomonic imaging findings of intraosseous VM.

Materials and Methods

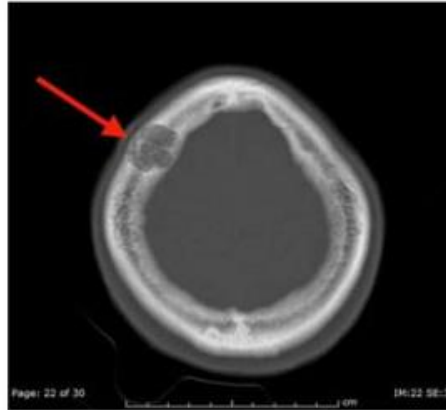
ISSVA classification for vascular anomalies will be addressed. Specifically, terming intraosseous VM as "hemangioma" is incorrect. We review the epidemiology, imaging findings, work up, prognosis, and treatment of facial intraosseous VM. Imaging will be presented for multiple intraosseous VMs of the head and neck. Specifically, VM encountered in the calvarium, skull base, facial bones and cervical spine will be presented. Examples of intraosseous venous anomalies are shown involving nearly every bone of the facial bones, skull base and calvarium.

Results

1) ISSVA classification for vascular anomalies a) Neoplasm: hemangioma, etc. b) Malformation: high-flow (AVM) versus slow-flow (VM or lymphatic malformation) 2) Histopathology 3) Epidemiology of osseous venous malformations 4) Management a) Imaging of a "don't touch" lesion b) Surgical options 5) Imaging technique and findings a) Example cases i) Skull base ii) Zygomatic bone iii) Mandible iv) Temporal bone v) Calvarium vi) Maxillary bone vii) Sphenoid wing viii) Nasal bone

Conclusions

Intraosseous venous malformations of the head and neck are rare, under-recognized and under-reported in both radiology and pathology literature. Prior to the establishment of ISSVA, such lesions of the skeleton were misclassified or mislabeled as hemangiomas, which is now proven to be incorrect. In our experience, the imaging appearance of intraosseous venous malformations is unique. By the end of this exhibit, the reader/viewer will recognize this unique pathologic entity and its pathognomonic imaging appearance. The goal is to avoid suggesting an alternative diagnosis and prevent unnecessary patient stress/anxiety and potential biopsy and/or surgical treatment.



(Filename: TCT_eEde-138_Figures001.jpg)

eEde-142

Isolated Palsy of the Hypoglossal Nerve: An Imaging Update!

A Guarnizo¹, R Glikstein², C Torres¹

¹University of Ottawa - The Ottawa Hospital, Ottawa, Ontario, Canada, ²University of Ottawa, Ottawa, Ontario, Canada

Purpose

1. To review the anatomy and course of the 12th cranial nerve 2. To discuss the common and rare pathologies that affect the hypoglossal nerve along its five segments 3. To review the imaging features of hypoglossal nerve denervation

Materials and Methods

A retrospective review of the imaging findings in patients with isolated hypoglossal nerve palsy was performed. Different disorders affecting the hypoglossal nerve were identified along its course. Detailed CT and MR imaging features of the lesions causing CN 12 palsy and the associated findings that result from hypoglossal denervation were described.

Results

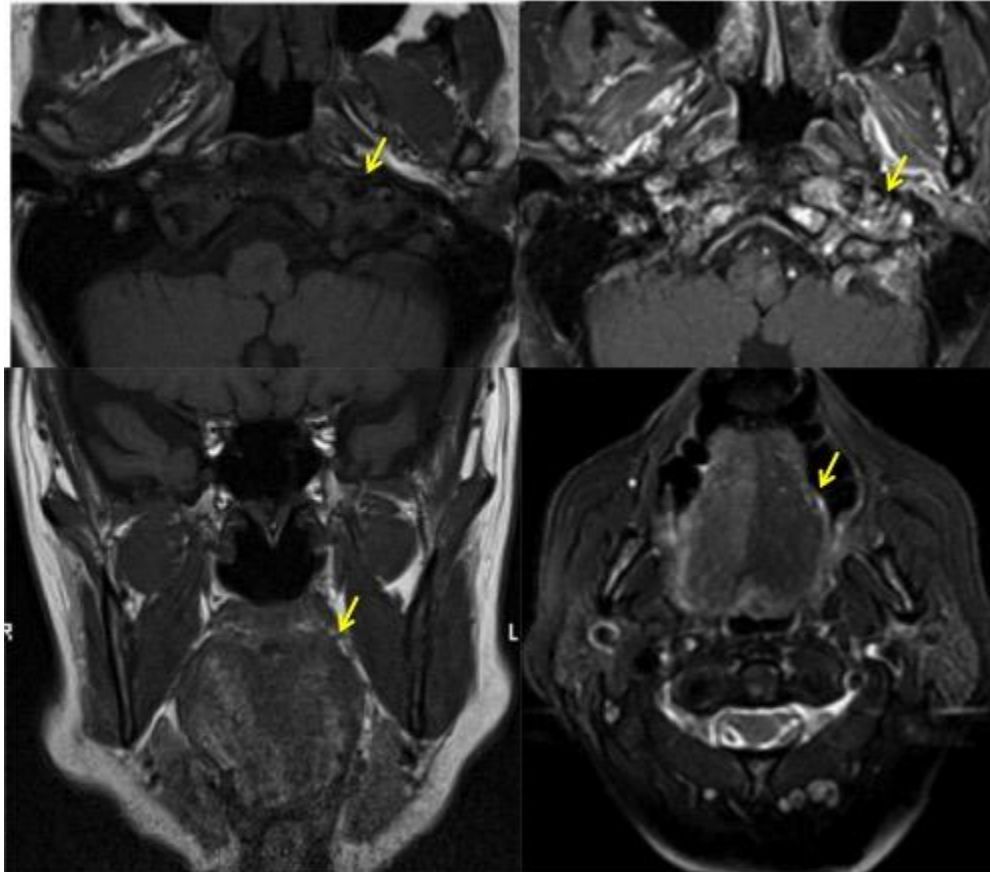
Multiple lesions can affect the hypoglossal nerve along its five segments. Within its medullary segment, we found lesions such as neoplasms, vascular malformations and demyelinating disease. Primary neoplasms, metastatic disease, traumatic injury and vascular pathologies involved the cisternal, skull base

Electronic Educational Exhibits

and the carotid segments. Squamous cell carcinoma was the most common pathology involving the sublingual segment of the nerve. Chronic hypoglossal denervation was seen as atrophy and fatty replacement of the muscles in the affected hemitongue. In addition, a "pseudomass appearance" secondary to posterior bulging could be seen and signal changes vary on MRI depending on the acuity or chronicity of the nerve injury.

Conclusions

The hypoglossal nerve gives motor innervation to the intrinsic and extrinsic muscles of the tongue. Injury to this nerve manifests with particular features that involve the imaging appearance and movement of the tongue. It is important to be familiar with the anatomy and the imaging findings of hypoglossal denervation in order to identify or suspect an underlying pathology.



(Filename: TCT_eEde-142_12CNpalsy.jpg)

eEde-122

Isolated Sixth Nerve Palsy: Anatomy-based Approach for Lesion Localization

A Agarwal¹, V Nguyen², K Raj¹, J Maldjian²

¹University of Texas Southwestern Medical Center, Dallas, TX, ²University of Texas Southwestern, Dallas, TX

Purpose

Teaching Points: 1. Imaging anatomy of the sixth (abducens) nerve 2. Anatomy-based approach to lesion location in isolated sixth nerve palsy (acute and chronic) 3. Common pathologies affecting the sixth nerve

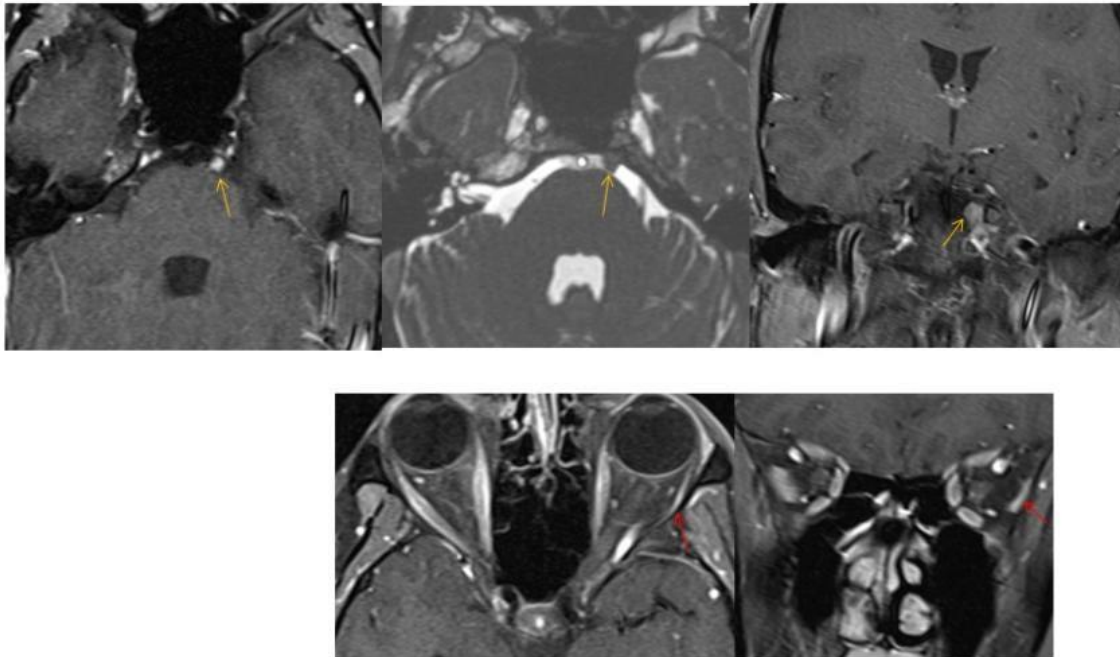
Materials and Methods

We will use our teaching file and case repository to illustrate the anatomy of the sixth nerve and various pathological conditions affecting the nerve. Anatomy-based approach will be used for lesion localization.
Results

1. Anatomy of the sixth (abducens) nerve (CT and MRI based) 2. MR Imaging protocol for evaluation of sixth nerve 3. Clinical presentation: acute and chronic VI nerve lesions 4. Lesions involving the sixth nerve: - Lesions within the brain stem - Lesions involving the root entry zone (REZ) and cisternal segments - Lesions along the Dorello's Canal - Lesions within the cavernous sinus - Lesions within the superior orbital fissure 5. Rare primary lesions of the sixth nerve: neoplasm(Schwannoma) 6. Multiple Cranial Neuropathies: Inflammatory (Sarcoidosis), Carcinomatosis, Lyme's disease 7. Mimics of sixth nerve lesions: - Intraorbital pathologies (orbital apex syndrome and pseudotumor)

Conclusions

This exhibit outlines the imaging anatomy of the sixth (abducens) nerve and provides an imaging spectrum of the different pathological conditions affecting the nerve. The focus of this exhibit will be lesion localization based on an anatomical approach.



Primary lesions of the 6th nerve: Schwannoma of the left 6th nerve in a 37 year old with long-standing lateral rectus palsy. Axial post-contrast, CISS and coronal post-contrast images in the top row reveal the schwannoma involving the cisternal segment of the nerve. Bottom row images reveal severe thinning of the left lateral rectus (red arrows)

(Filename: TCT_eEde-122_Schwannoma.jpg)

Medullary Thyroid Carcinoma

S Kushchayev¹, Y Kushchayeva², K Pacak², O Teytelboym¹

¹*Mercy Catholic Medical Center, Darby, PA*, ²*National Institutes of Health, Bethesda, MD*

Purpose

Medullary thyroid carcinoma (MTC), arising from the parafollicular C cells of the thyroid, accounts for 1–2% of thyroid cancers. MTC is frequently aggressive and metastasizes to the cervical and mediastinal lymph nodes, lungs, liver, and bone. The aim of this exhibit is to perform a comprehensive review of imaging appearance of the primary tumor, the recurrent disease and distant metastases arising from MTC.

Materials and Methods

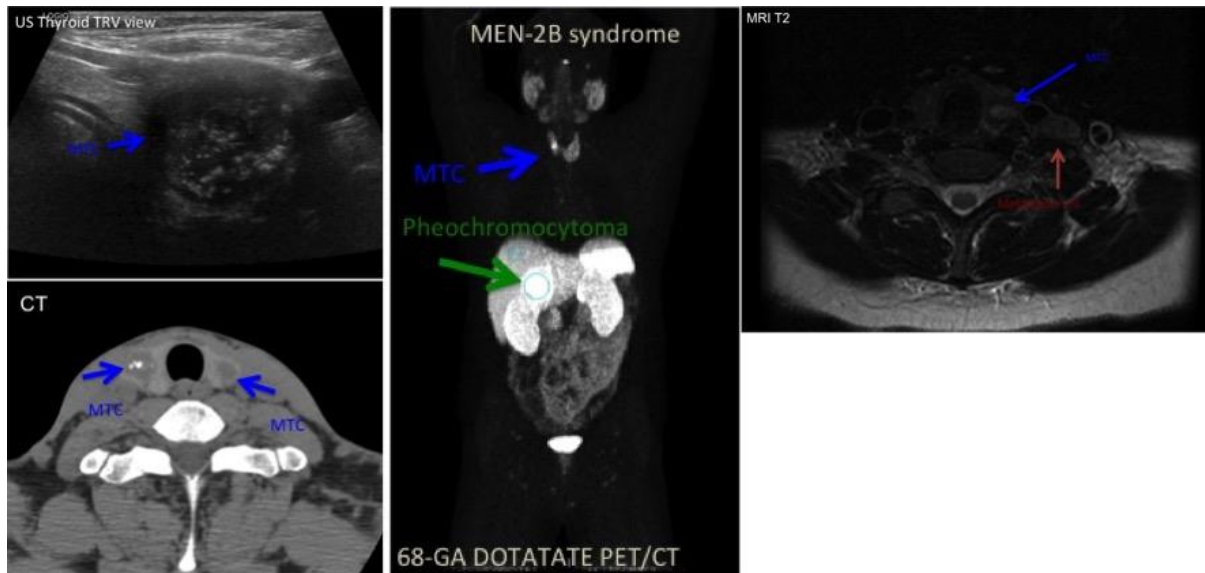
A systematic literature review and an analysis of databases from the National Institutes of Health (Bethesda, MD) and Mercy Catholic Medical Center (Philadelphia, PA) were performed. The biology and molecular aspects of MTC as a background for the current imaging modalities of this malignancy are reviewed. We discuss the modern imaging techniques available--advanced magnetic resonance imaging (MRI)-based techniques such as whole-body MRI, dynamic contrast-enhanced (DCE) technique, diffusion-weighted imaging (DWI), positron emission tomography/computed tomography (PET/CT) with 18-F-DOPA, 18-F-FDG and 68-Ga-DOTADATE, an integrated positron emission tomography/magnetic resonance (PET/MR) hybrid imaging--for the primary MTC tumor, local recurrences, metastatic lymph nodes, and the most common sites of distant metastases: lung, liver, and bones.

Results

Primary MTC is usually a solid neoplasm, round-to-oval in shape with calcifications. Ultrasound (US) is helpful in the evaluation of high-risk patients for occult MTC, assessment for suspected recurrent disease or regional nodal metastases. There two types of US patterns of MTC: B-type (benign) and M-type (malignant, associated with aggressive behavior). MTC usually metastasize to regional lymph nodes, liver, bone, and lungs. Preoperative evaluation of lymph nodes is essential as early nodal metastases in identified in up to 50% of patients. Lung metastases are numerous and associated with mediastinal adenopathy. Neck CT or MRI are used for the evaluation of suspected thyroid nodules > 3 cm, to assess substernal extension and local extent of MTC, and spread to regional lymph nodes. Computed tomography (CT) is the most sensitive imaging procedure for detecting lung and mediastinal lymph node metastases and can be helpful in detection of hepatic and bone metastases. Liver metastases are also numerous and disseminated; they grow slowly, and patients remain asymptomatic for a long time. MRI is superior to CT for the detection and characterization of small liver metastases. Bony metastases are uniformly multifocal with spine and pelvis as the most common sites. MRI is the optimal modality for the characterization of osseous MTC metastases. Molecular imaging (MIBG, Octreoscan, 18-F-DOPA and 68-Ga Dotatate) plays a crucial role in the evaluation and management of recurrent and metastatic MTC. 18-F-DOPA PET/CT is superior to other modalities for the detection of lesions in metastatic disease with the overall detection rate of 72%.

Conclusions

1. MTC is a neuroendocrine tumor which has the distinct presentation, behaviors, imaging appearance and the treatment approach. MTC should be categorized separately from neoplasms arising from thyrocytes (papillary and follicular thyroid carcinomas).
2. Imaging plays a fundamental role in diagnosis and treatment planning of MTC. Molecular imaging, particularly 18-F-DOPA PET/CT plays a crucial role in the evaluation and management of MTC and has proven to be an efficient tool for the detection of local recurrences and distant metastases. In advanced MTC 18-F-FDG and 68-Ga-DOTATATE PET/CT also might be helpful.
3. Knowledge of specific features MTC may help neuroradiologists to plan appropriate radiological workup and follow-up.



(Filename: TCT_eEde-158_ASNR-MTCall.jpg)

eEde-114

MRI-guided Head and Neck Lesion Laser Ablation

D Ginat¹

¹University of Chicago, Chicago, IL

Purpose

To review the use of MRI guidance and mapping sequences for efficient localization of the target, the percutaneous interstitial laser ablation methods, and the use of MR thermography for temperature monitoring during laser ablation, with a focus on applications in the head and neck region, including an illustrated step-by-step sample protocol

Materials and Methods

Laser ablation, which is also known as laser interstitial thermal therapy (LITT) is a minimally-invasive treatment modality that is performed as an outpatient percutaneous procedure. The technique exploits the phenomenon that heat-induced protein denaturation and tissue coagulative necrosis occurs at temperatures above 43 °C, with time to cell death varying exponentially with temperature. This is accomplished through the use of light at wavelengths of 800 nm through 1064 nm from diode or Nd:YAG lasers, which is absorbed by chromophores in the target lesion, leading to the release of thermal energy.

Results

MR thermography is a validated noninvasive imaging technique that can provide accurate temperature monitoring during laser ablation. Several MR thermography methods have been developed, including sequences based on proton resonance frequency (PRF), the diffusion coefficient, T1 and T2 relaxation times, magnetization transfer, proton density, as well as temperature sensitive contrast agents. PRF techniques exploit temperature-induced effects of the chemical shift, in which the temperature difference is directly proportional to the phase difference. The local magnetic field depends on both the main magnetic field and chemical shift. Therefore, PRF changes can be measured with very fast echo-shifted RF spoiled gradient echoes. Since PRF phase mapping gives a linear relationship to temperature and is not influenced by tissue changes, this method provides accurate temperature measurements in the temperature range of interest for thermal ablation. MR thermography guidance can help avoid local complications of treatment effects, such as hemorrhage and necrosis of surrounding normal structures. PRF MR thermography is intended to mitigate image degradation from susceptibility effects, which are

Electronic Educational Exhibits

inherent to many areas of the head and neck region. The presence of lipids is a potential source of artifacts since the PRFs of lipid hydrogen is independent of temperature. Fat can be conveniently suppressed in gradient-echo imaging by frequency-selective slice excitation.

Conclusions

Laser ablation is a minimally invasive procedure that can be used to treat a variety of lesions in the head and neck by using infrared light to induce coagulative necrosis. Lesion targeting with the laser applicator can be facilitated using MRI guidance and navigation software. MR thermography, particular using PRF sequences, is a noninvasive technique that can provide accurate temperature monitoring of the head and neck soft tissues during laser ablation.

eEde-147

Otolaryngologic Manifestations of Systemic Diseases

L Daftari Besheli¹, A Eajazi¹, A Singh¹, B Tantiwongkosi¹

¹*University of Texas Health San Antonio, San Antonio, TX*

Purpose

Heterogenous groups of systemic diseases can involve otolaryngologic system. In some cases it is the first manifestation of a systemic disease. It is important for the neuroradiologists to recognize the imaging findings in order to provide accurate diagnosis or raise the concerns of the underlying systemic causes.

The purpose of this pictorial review is to discuss various systemic diseases with otolaryngologic involvement and spectrums of the imaging findings that the neuroradiologists must know.

Materials and Methods

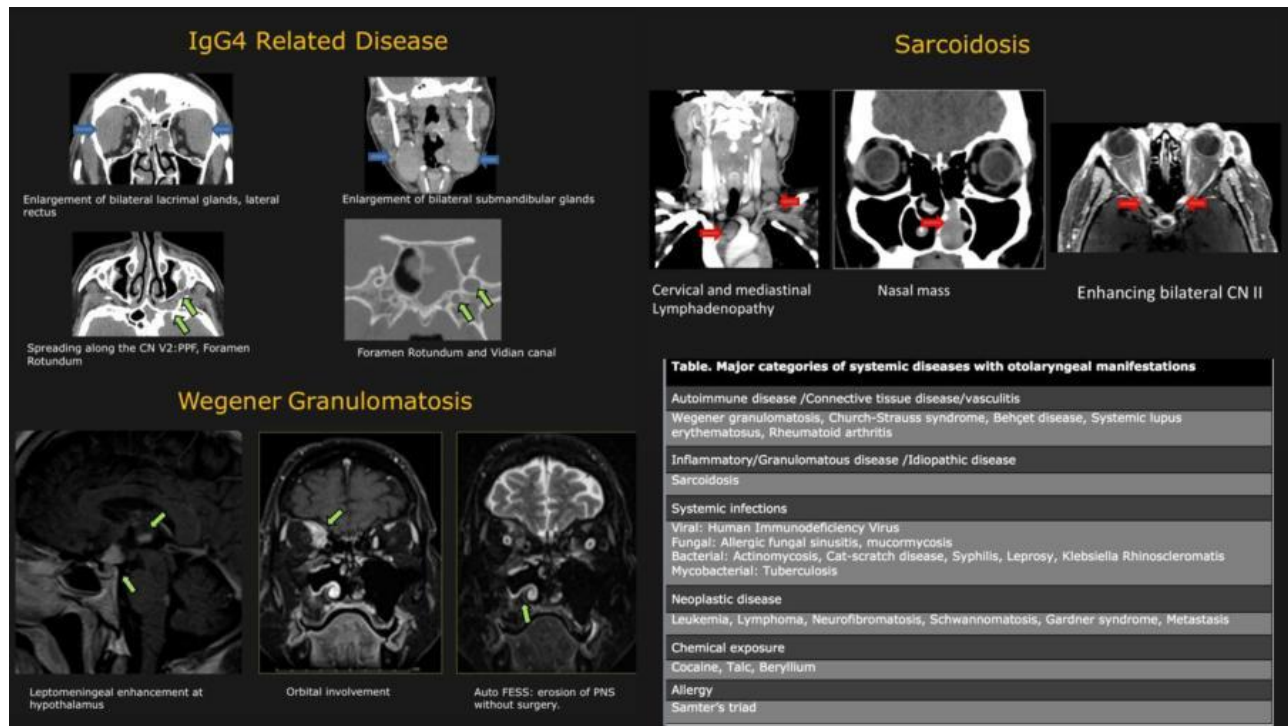
Literature searches showed that this topic was well published in otolaryngology, but not in radiology journals. This inspires us to search our case files from 2009 to 2017 for patients who have head and neck imaging findings and systemic illness. The diseases were classified into six categories: 1) Autoimmune disease/Connective tissue disease/Vasculitis, 2) Inflammatory/Granulomatous disease, 3) Systemic infection, 4) Allergy, 5) Neoplasm, and 6) Chemical/drug toxicity.

Results

Our search revealed heterogeneous groups of systemic conditions with otolaryngeal manifestations classified as above. The imaging findings and distinguishing characteristics of each disease is presented in this pictorial review. Correlation between the radiologic imaging, clinical imaging and histology will be shown upon the availability.

Conclusions

Otolaryngologic abnormalities could be the first manifestations of certain systemic diseases and may have some characteristic imaging findings. Radiologists could be the first physicians who raise the concerns of the possibility, which finally lead to an appropriate management.



(Filename: TCT_eEde-147_Figure.JPG)

eEde-135

Our Paranasal Sinuses – An Epochal Journey

S Patel¹, S Lev¹

¹Nassau University Medical Center, East Meadow, NY

Purpose

1. To review the comparative anatomy, form, and function of the paranasal sinuses of humans, primates, and hominids, utilizing a CT imaging approach 2. To discuss current theories pertaining to the evolutionary pressures that have led to the current configuration of the human paranasal sinuses and review how these changes may have contributed to a predisposition for sinus infections

Materials and Methods

Freely available CT data sets from the online Digital Morphology Museum of the Kyoto University Primate Research Institute (KUPRI) were uploaded into our PACS software. DICOM files of primates were used to create 2-D axial, sagittal, and coronal images, as well as 3-D reconstructions. In addition, we obtained several representative skulls, both authentic and replica, for CT scanning at our institution. A variety of comparative qualitative measurements were obtained. Photographs were taken at regional natural history museums for further illustration.

Results

Originally, the paranasal sinuses developed in mammals primarily as an olfactory aid. In hominids and humans; however, with retraction of maxillofacial prognathism, the sinuses played a key role in the formation of the entire cranium and also acquired new functions. Olfaction became nonessential while reliance on astute stereoscopic vision became more crucial. Changes in climate may have prompted our bipedal ancestors to venture forth onto the African savannah and may also have contributed significantly to variations in sinus morphology, as the sinuses served an important role in cooling and thermoregulation. Indeed, several focal differences in paranasal sinus configuration may be seen in

today's modern humans who inhabit environmental extremes. Progressive maxillofacial anatomical changes from primates to homo sapiens have led to a more vertically oriented paranasal sinus configuration with altered drainage patterns. Notable changes included enlargement of the maxillary sinuses and further development of the ethmoid air cells. As the cranium became more spherical in homo sapiens, as opposed to Neanderthals, craniofacial morphology continued to change and the frontal and sphenoid sinuses expanded accordingly. The evolutionary role of paranasal sinus pneumatization in humans and Neanderthals as an adaptation to extreme cold remains controversial. There are important differences in the paranasal sinuses of primates. The African apes, (gorillas and chimpanzees) have four, while the Asian apes (orangutans and gibbons) have just two, lacking the ethmoid and frontal sinuses. Gorilla and man are the only species that possess large nonolfactory sphenoidal sinuses. Comparative differences such as these, together with a vertical sinus orientation and variations in drainage patterns, may lead to a clearer understanding our well documented predilection to infection.

Conclusions

The modern human paranasal sinuses came about as a result of a changing niche within the environment which favored an upright posture. A comparative anatomical approach applying the unique perspectives provided by radiological imaging can facilitate our understanding of our evolutionary history. Important changes in paranasal sinus configuration and orientation occurred together with progressive maxillofacial development and enlargement of cranial capacity. Alterations in sinus structure, although mostly beneficial to our species, may have incurred several disadvantages as well and contributed to modern sinus ailments.

eEde-126

Overcoming “Stage” Fright: AJCC 8th Edition Head and Neck Cancer Update

J Yetto¹, A Germana¹, P Moullet¹, J Foley¹, M Cathey¹

¹Naval Medical Center San Diego, San Diego, CA

Purpose

The American Joint Committee on Cancer (AJCC) recently released the 8th Edition Cancer Staging Manual which is scheduled for implementation on January 1, 2018. Within the 8th edition are significant changes to head and neck cancer staging, particularly with regards to oropharyngeal and nasopharyngeal cancers. The purpose of this educational exhibit is to illustrate the relevant head and neck cancer staging changes with an emphasis on oropharyngeal and nasopharyngeal cancers using a case-based approach.

Materials and Methods

High resolution CT and 3T MRI imaging sequences were used to identify relevant anatomical landmarks for consideration while staging head and neck cancers with graphical overlays to demonstrate pertinent regions of tumor involvement. Specific cases were used to illustrate key points. Additionally, a literature review of the current understanding and background of tumor staging was performed.

Results

Case-based approach to illustrate relevant nasopharyngeal cancer staging changes as per the AJCC 8th Edition Cancer Staging Manual with an emphasis on staging updates. Divided into: 1. Head and Neck Cancer Epidemiology 2. Relevant Anatomy 3. Head and Neck Cancer Primary Sites 4. Methods and Patterns of Spread 5. AJCC 8th versus 7th Edition Changes 6. Prognostic Stage Groups 7. Illustrative Cases

Conclusions

Squamous cell carcinoma, particularly of the oropharynx and nasopharynx, is commonly encountered in daily clinical practice by neuroradiologists. There are significant changes to the staging system for these cancers within the AJCC 8th Edition Cancer Staging Manual. In some cases this actually results in "down-staging" the disease relative to current standards. For example, prior T4 disease involving the medial and/or lateral pterygoid and/or prevertebral muscles will now be T2 disease. In other cases this

Electronic Educational Exhibits

results in significant upstaging of disease. Specifically, the addition of the N3 description for "extra-nodal extension" with regards to both p16- oropharyngeal and hypopharyngeal cancer staging results in Stage IVb disease or greater independent of any other factors. These updates reflect current prognosis and treatment options for these cancers and has the potential to offer added psychological benefit to afflicted patients at the time of initial diagnosis. The neuroradiologist plays a critical role in the diagnosis and staging of head and neck cancer and a detailed knowledge of these staging updates is crucial to provide relevant and comprehensive care for our patients.

Conclusions - ***MAJOR CHANGES***

- **Nasopharyngeal Carcinoma**
 - With regards to **known primary**
 - Invasion of medial/lateral pterygoid or prevertebral muscles was **previously T4 disease and is now T2 disease**
 - **In the setting of no primary with a squamous cell cancer positive lymph node**
 - If EBV+ lymph node, then it is staged per nasopharyngeal guidelines
- **Oropharyngeal Carcinoma**
 - With regards to **known primary, divided into**
 - **p16+ OPC**
 - Staging Criteria New and Different than p16-
 - **p16- OPC**
 - Extranodal extension results in Stage IVb disease or greater
 - **In the setting of no primary with a squamous cell cancer positive lymph node**
 - If p16+ lymph node, then it is staged per p16+ oropharyngeal guidelines
- **Hypopharyngeal Carcinoma**
 - Extranodal extension results in Stage IVb disease or greater

Figure 14. a. Axial T2 image demonstrating the **MAJOR CHANGE** between T2 (green dots) and T4 (pink dots) nasopharyngeal tumors with regards to the 7th and 8th Edition Cancer Staging Manuals.

Results in DOWN STAGING of disease!

(Filename: TCT_eEde-126_HNStaging.JPG)

eEde-144

Patterns of Perineural Spread: A Pictorial Review

T Ouyang¹, T Zacharia¹, S Kanekar¹

¹Penn State Health Milton-Hershey Medical Center, Hershey, PA

Purpose

1. Review relevant imaging anatomy of cranial nerves 2. Present common and uncommon imaging features of perineural spread in the brain and neck, with a focus on MRI and CT

Materials and Methods

A retrospective, pictorial review of a wide variety of cases of perineural spread from our institution will be presented.

Electronic Educational Exhibits

Results

Perineural spread (PNS) means direct extension from a primary tumor along a nerve or neural sheath. While PNS is most commonly described in head and neck and skin malignancies, other central nervous system and systemic malignancies may also have this pattern of spread. Rarely benign conditions may also spread along nerves mimicking PNS of tumor. Malignant PNS is associated with significantly increase in local recurrence and approximately 30% decrease in five-year survival rate. Perineural spread is now considered an independent prognostic indicator during staging. Moreover, as many as half of patients with PNS may remain asymptomatic or present with only subtle clinical manifestations.

Conclusions

Knowledge of relevant anatomy and myriad appearance of perineural spread is critical for identifying and delineating PNS, which may in turn affect treatment decision-making.

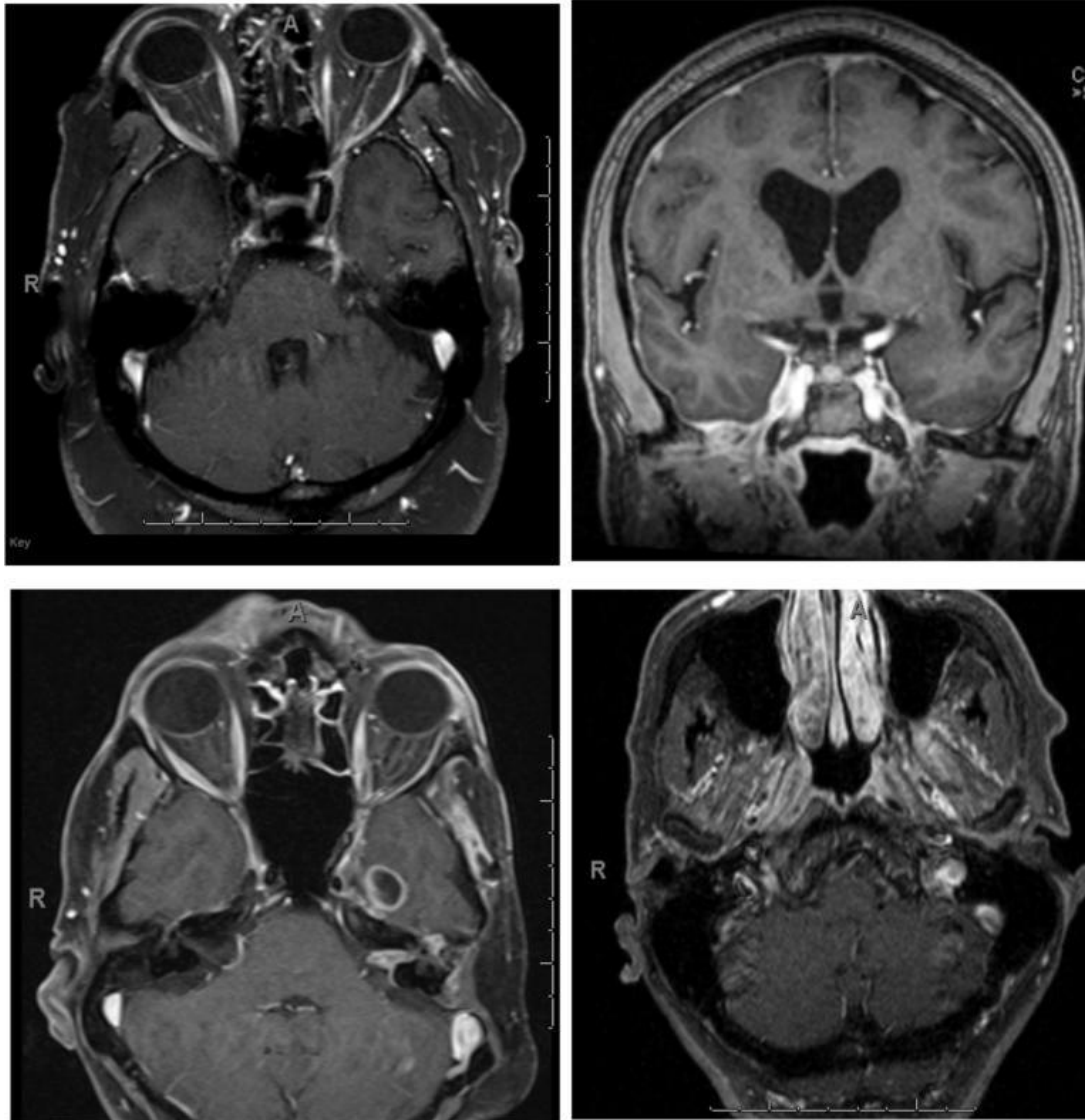


Figure 1. Perineural spread. Abnormal enhancement along the (A) left trigeminal nerve in the cisternal segment, (B) right trigeminal nerve in the foramen ovale, (C) left internal auditory canal, and (D) right hypoglossal nerve in its canal.

(Filename: TCT_eEde-144_PerineuralSpreadFigure.jpg)

Pearls and Pitfalls in Staging of the Laryngeal Cancer

V Jain¹, H Gallagher-Zate¹

¹*MetroHealth Medical Centre, Case Western Reserve University, Cleveland, OH*

Purpose

Laryngeal Cancer is the second most common head and neck cancer. Imaging is extremely beneficial to evaluate the disease extent and staging which guides the management and gives prognostic information. Accurate description of the tumor spread is of paramount importance to cure the disease while minimizing the amount of resection to preserve the functions of the larynx. This exhibit will show cases discussing the key areas of tumor spread which make a huge impact in management of the patients and change the treatment options. Radiologists can improve the quality of patient care by learning about these pearls and pitfalls while interpreting these cases.

Materials and Methods

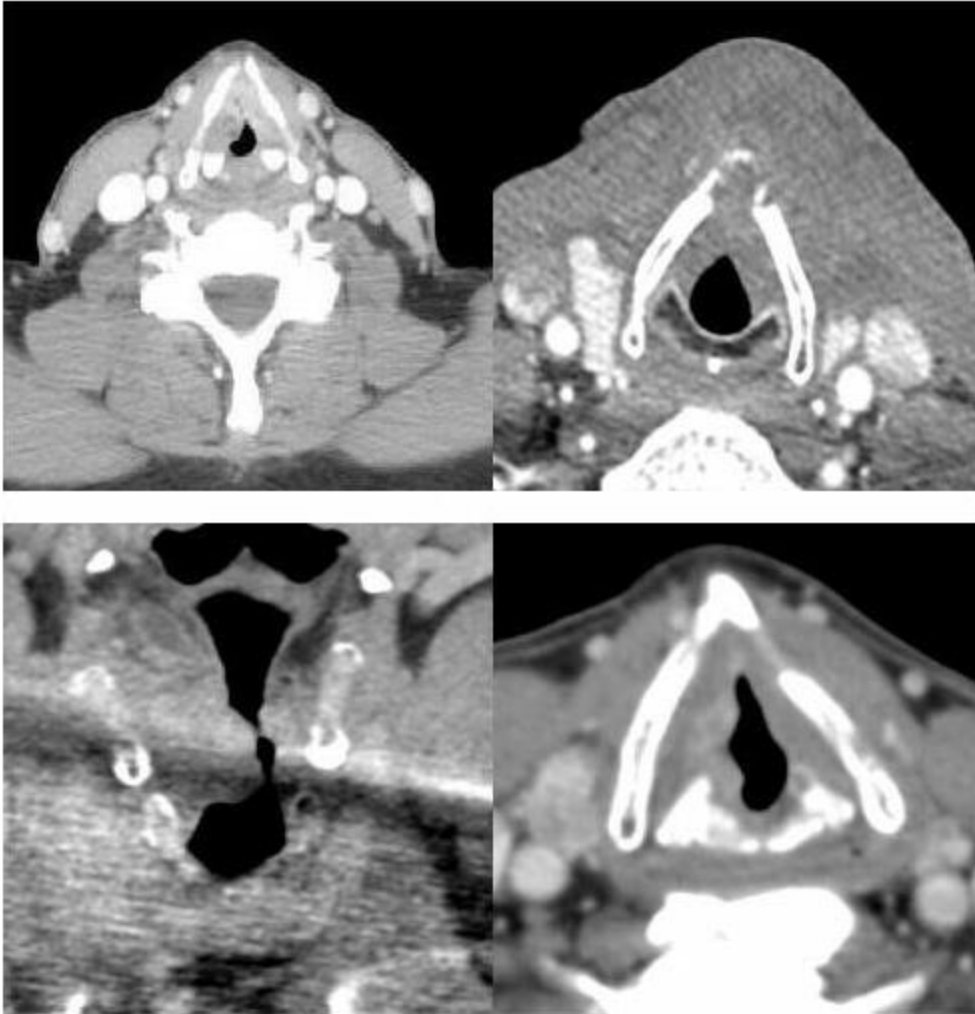
Multiple cases of laryngeal cancers on CT neck performed in past five years were selected from the PACS. The radiology reports, tumor board notes and recommendations and surgical findings during resection were reviewed. Cases were selected which had excellent teaching points to highlight the knowledge of tumor spread and staging.

Results

Diagnosis of laryngeal cancer is usually made by ENT surgeons in their office on laryngoscopy. Imaging, usually CT neck with contrast is performed to look for submucosal tumor spread, loco-regional spread, cartilage invasion and metastatic lymphadenopathy. CT is very useful to see the areas obscured by bulky tumors which limit the field of view on laryngoscopy. CT is excellent in detecting invasion of preepiglottic and paraglottic fat invasion which upstages the tumor to T3 and increases likelihood of metastatic lymphadenopathy. However, CT may over diagnose paraglottic fat invasion in subtle cases due to peritumoral edema. Hypopharynx and larynx are distinct structures but intimately associated, and knowledge of anatomy and careful scrutiny of the tumor spread is crucial to describe extension into the Hypopharynx which will need more extensive surgery. Tumor spread in the commissures, cricoarytenoid region, postcricoid area and subglottic larynx should be diligently evaluated as it changes surgical approach and staging. Tumor involvement in these areas is often subtle and is a perfect example of "you can't see what you don't know". Multiple cases will be shown depicting anatomy of these complex areas, normal appearance, tumor extent and pitfalls. Some cases of pearls and pitfalls in evaluation of metastatic lymphadenopathy such as necrotic nodes mimicking cysts, sub centimeter nodes with abnormal morphology and new N3b staging with extra nodal extension will also be shown. Two cases showing synchronous and metachronous tumors will be shown to highlight importance of careful evaluation of the entire study and corners of the images for unexpected second malignancies.

Conclusions

Laryngeal cancer is very common and CT neck is an excellent tool for staging the cancer in three subsites namely supraglottis, glottis and subglottis which are staged differently. Detailed anatomical knowledge is crucial in accurately describing the disease extent. Familiarity with the pattern of tumor spread in submucosal spaces, adjacent hypopharynx, commissures, cricoarytenoid region, postcricoid region, subglottis, extralaryngeal soft tissues, prevertebral space improves the quality of reporting, accuracy and patient outcome. Radiologists play a crucial role in helping surgeons to cure the disease with smallest possible resection in an attempt to save as much laryngeal function as possible by delivering excellent and accurate description of tumor extent in their reports.



Top Left image: Cancer involving both TVC and anterior commissure. The tumor is extending more than anterior 1/3rd portion of both vocal cords.

Top right Image: Tumor at AC is destroying the thyroid cartilage with extralaryngeal tumor spread. The Broyle's ligament extends from the TVC to the cartilage at AC and there is focal absence of the inner perichondrium at this location creating a weak spot for tumor spread.

Bottom left image: Right sided transglottic mass (involving the supraglottic and glottic larynx) is obstructing the opening of the right ventricle leading to internal fluid filled laryngocele formation. The tumor is also extending in the subglottic space.

Bottom right image: Right TVC mass is extending posteriorly to involve cricoarytenoid joint and posterior commissure. Tumor at cricoarytenoid joint frequently leads to fixation of the TVC (which should be confirmed by laryngoscopy) and upstages to T3.

(Filename: TCT_eEde-131_Images-1.jpg)

Posterior Ischemic Optic Neuropathy: Uncommon Cause of Acute Visual Deficit

S Kim¹, Y Lee², B Baek², W Yoon²

¹Chonnam National University Hwasun Hospital, Hwasun-gun, Jeollanam-do, Republic of Korea, ²Chonnam National University Hospital, Gwangju, Chonnam, Republic of Korea

Purpose

1. To overview the related vascular anatomy and pathophysiologic basis of PION 2. To illustrate the characteristic MR imaging features of PION 3. To determine usefulness of diffusion-weighted imaging (DWI) and apparent diffusion coefficient (ADC) map for differential diagnosis of optic nerve pathology

Materials and Methods

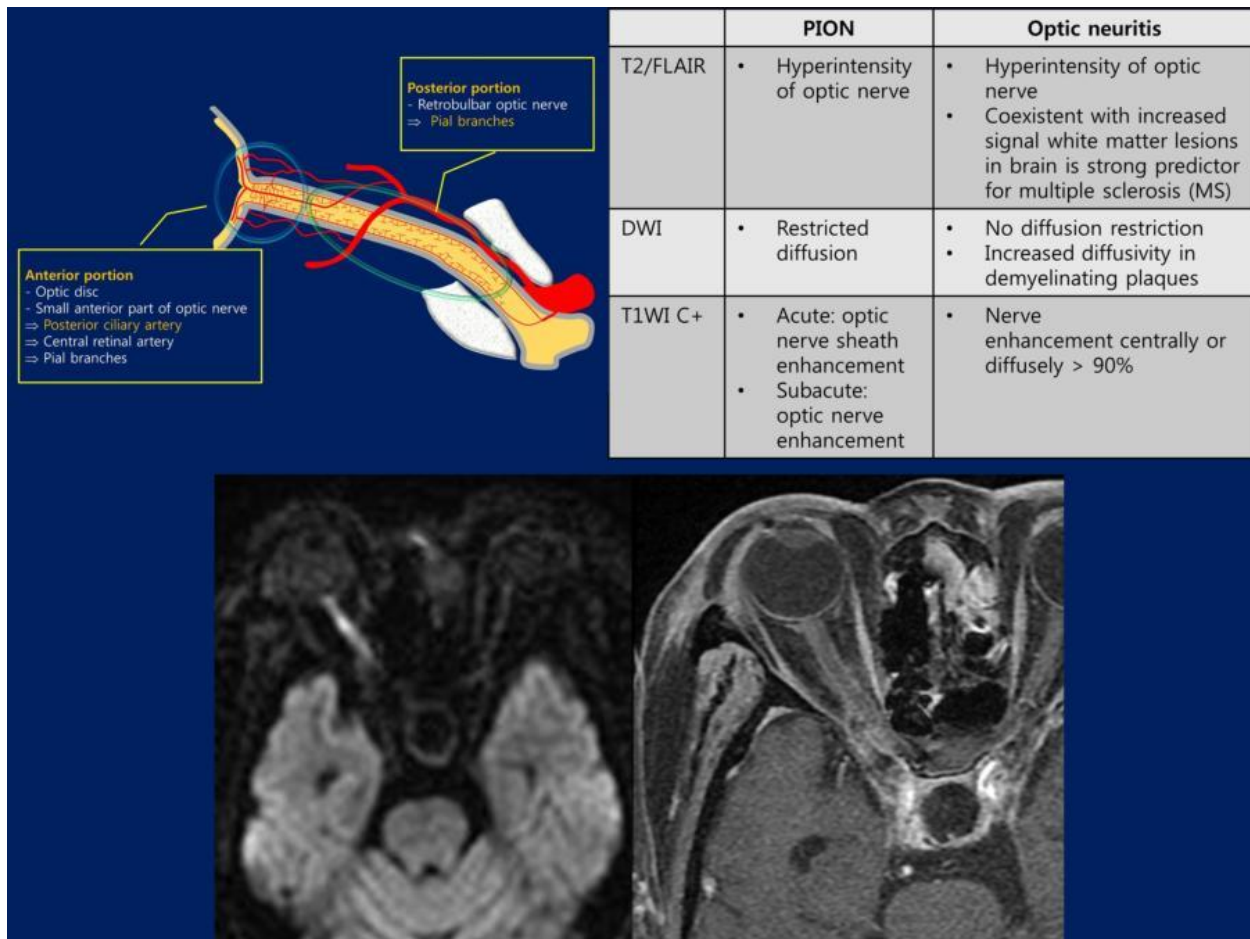
Retrospective analysis of eight patients with a clinical diagnosis of posterior ischemic optic neuropathy during the period 2014 to 2017. MR images including diffusion weighted image and clinical information were analyzed. Based on the analyzed information, we present a case-based exhibition.

Results

1. Overview of related vascular anatomy, etiologies, pathogenesis and clinical presentation 2. Illustrate MR imaging features of PION 3. Case-based review of PION with various etiologies - Invasive aspergillosis - Mucormycosis - ICA occlusion - Post-operative complication - Meningioma - Idiopathic 4. Role of DWI and ADC map for detection and differential diagnosis - Neuromyelitis optica - Infectious optic neuritis

Conclusions

PION characterized by damage to the retrobulbar portion of the optic nerve due to ischemia is uncommon cause of acute visual deficit. Key MR imaging features of PION are restricted diffusion in the optic nerve on DWI and ADC, enhancement of optic nerve sheath without optic nerve enhancement in acute setting, restricted diffusion in acute setting, and diffuse enhancement of optic nerve in subacute setting. Knowing the pathogenesis and MR imaging features can lead to accurate diagnosis and proper patient management.



(Filename: TCT_eEde-117_fig3.jpg)

eEde-115

Pseudocontinuous Arterial Spin Labeling: Clinical Applications and Usefulness in the Evaluation of Head and Neck Lesions

M Umino¹, R Nakayama², K Inoue¹, M Maeda¹, H Sakuma¹

¹Mie University School of Medicine, Tsu, Mie, Japan, ²Ritsumeikan University, Kusatsu, Shiga, Japan

Purpose

Pseudocontinuous arterial spin labeling (pCASL) enables noninvasive quantification of blood flow and is used to evaluate head and neck lesions. This study aimed to investigate the clinical applications and usefulness of pCASL, including the comparison between two pCASL sequences, echo-planar (EP) and turbo spin-echo (TSE), in the diagnosis of head and neck lesions via tumor blood flow (TBF) quantification. We also aimed to evaluate the use of pCASL for detecting changes in the TBF following chemoradiation

Materials and Methods

We reviewed numerous head and neck lesions using pCASL at 3T MRI. A majority of head and neck lesions were of inflammatory type or tumors (benign and malignant, including parotid tumors).

Results

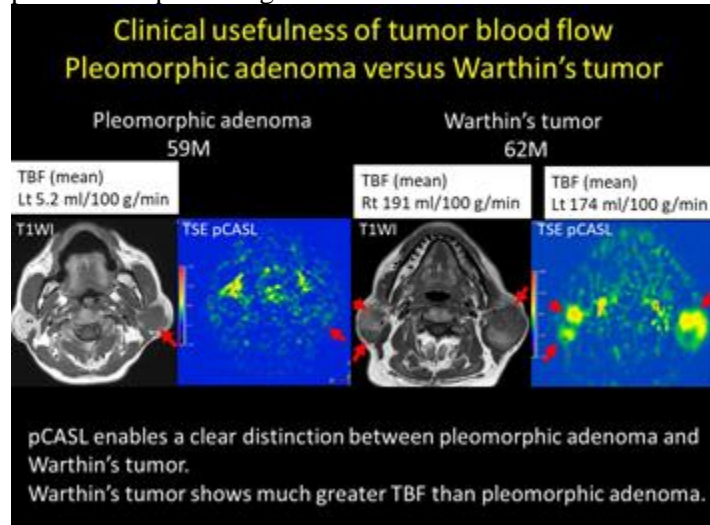
TSE pCASL showed lesser image torsion and better lesion conspicuity than EP pCASL. pCASL can be applicable to the following various disease entities: parotid tumors, such as pleomorphic adenoma and

Electronic Educational Exhibits

Warthin's tumor; inflammatory diseases, such as parotitis and IgG4-related disease; hypervascular head and neck benign tumors, such as paraganglioma and juvenile angiofibroma; and malignant tumors, such as squamous cell carcinoma and adenoid cystic carcinoma. pCASL can provide additional information for the evaluation of tumor/lesion vascularity and is useful for the differentiation of parotid tumors (Fig.). The changes in the TBF in head and neck squamous cell carcinomas in response to chemoradiation were also detected using pCASL.

Conclusions

pCASL is a promising and useful tool in the evaluation of head and neck lesions.



(Filename: TCT_eEde-115_pleomorphicwarthin.jpg)

eEde-134

Radiologic-pathologic Correlation of Parotid Gland Tumors

D Thut¹, o atar¹, M Elsayad¹, D Kowal¹

¹University of Massachusetts Medical School - Baystate, Springfield, MA

Purpose

The aim of this educational exhibit is to correlate imaging findings of benign and malignant parotid tumors with histopathology.

Materials and Methods

Cases were derived from a retrospective review of the imaging of pathology-proven parotid tumors from Baystate Medical Center, from 2012-2017. These patients had at least one imaging study prior to the biopsy, whereas several patients had multiple imaging modalities showing the parotid mass. Imaging findings are correlated with histopathology from core biopsy or gross resection.

Results

Of all salivary gland tumors, 80% are found in the parotid gland. Most (70-85%) of parotid gland tumors are benign. Often parotid gland tumors are found as incidental masses on imaging studies or focal areas of FDG uptake on oncologic PET/CT scans. The following benign and malignant parotid tumors are some of the most commonly encountered masses in clinical practice and will be discussed: Pleomorphic adenoma, Warthin tumor, mucoepidermoid carcinoma, adenoid cystic carcinoma, acinic cell carcinoma, metastatic squamous cell carcinoma, and lymphoma. Conventional imaging with CT, MRI and ultrasound demonstrate tissue characteristics and vascularity that correlate with histopathologic findings. In general, benign tumors tend to be well circumscribed, uniformly enhancing, and with no significant uptake on FDG PET. Malignant tumors tend to have ill-defined or irregular margins, heterogeneous enhancement

Electronic Educational Exhibits

and are usually hypermetabolic on PET. Additional MR findings supportive of malignancy include low signal intensity on T2 weighted images and low ADC values (restricted diffusion). Unlike conventional imaging that is mostly used for defining the anatomy and extent of disease, molecular imaging and diffusion-weighted imaging can predict tumor biology.

Conclusions

Imaging can narrow the differential diagnosis and provide information on the extent of the lesion, which is critical for treatment planning. Molecular imaging and newer MR techniques such as high-resolution diffusion-weighted imaging can predict tumor biology. Although imaging can aid in distinguishing malignant from potentially benign tumors, biopsy or resection is often needed to make the definitive diagnosis.

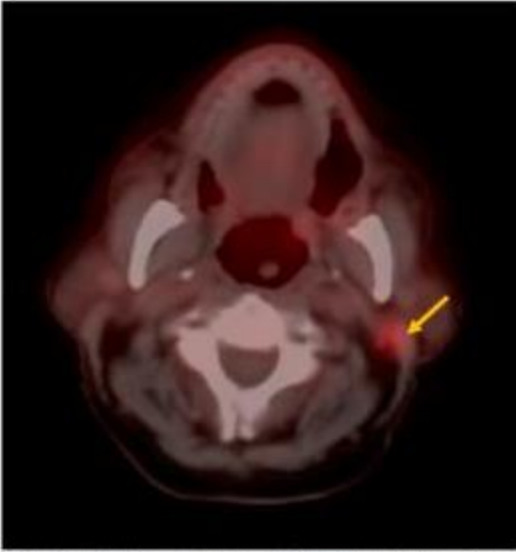


Figure 1A: Warthin tumor. Fused PET/CT images demonstrates a hypermetabolic focus corresponding to a soft tissue nodule in the inferior aspect of the deep lobe of the left parotid gland (arrow)

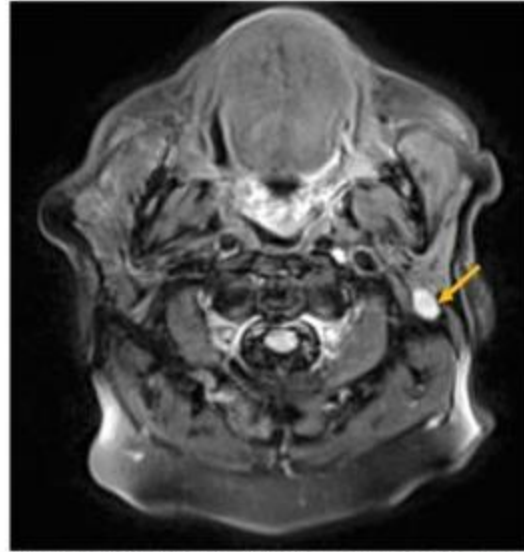


Figure 1B: Warthin tumor. Axial FLAIR images during routine brain MRI shows incidental ovoid hyperintense focus in the posterior aspect of the deep lobe of the left parotid gland (arrow).



Figure 1C: Warthin tumor. High frequency linear array ultrasound at time of biopsy demonstrates an ovoid intraparotid hypoechoic mass with small anechoic spaces (arrow).

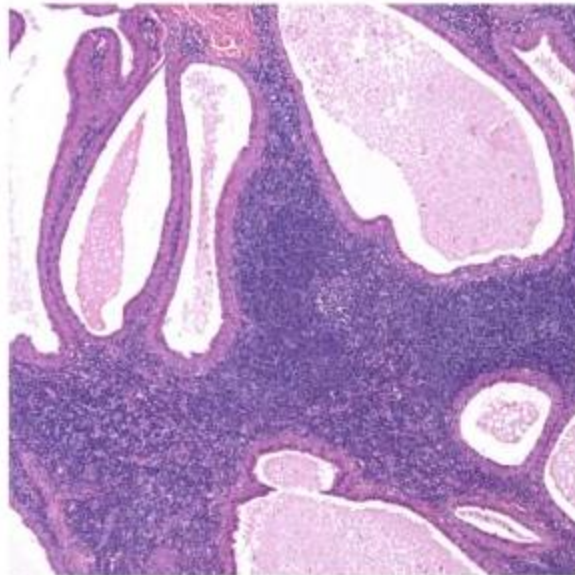


Figure 1D: Warthin tumor. Histological section stained with HE with 10x magnification, demonstrating the Warthin's neoplasm characterized by cystic spaces lined by tall columnar cells with abundant granular and eosinophilic cytoplasm. The stroma is rich in lymphocytes.

(Filename: TCT_eEde-134_Radpathparotidabstractimages.jpg)

eEde-130

Radiologically Important American Joint Committee on Cancer (AJCC) Eighth Edition Head and Neck Cancer Staging Changes

M Daun¹, A Cruz¹, J Pao¹, E Kuoy¹, D Chow¹

¹University of California, Irvine, Orange, CA

Purpose

The purpose of this presentation is to highlight the major changes to head and neck cancer staging in the most recent AJCC Eighth Edition, with emphasis on the materials that pertain to radiologists.

Materials and Methods

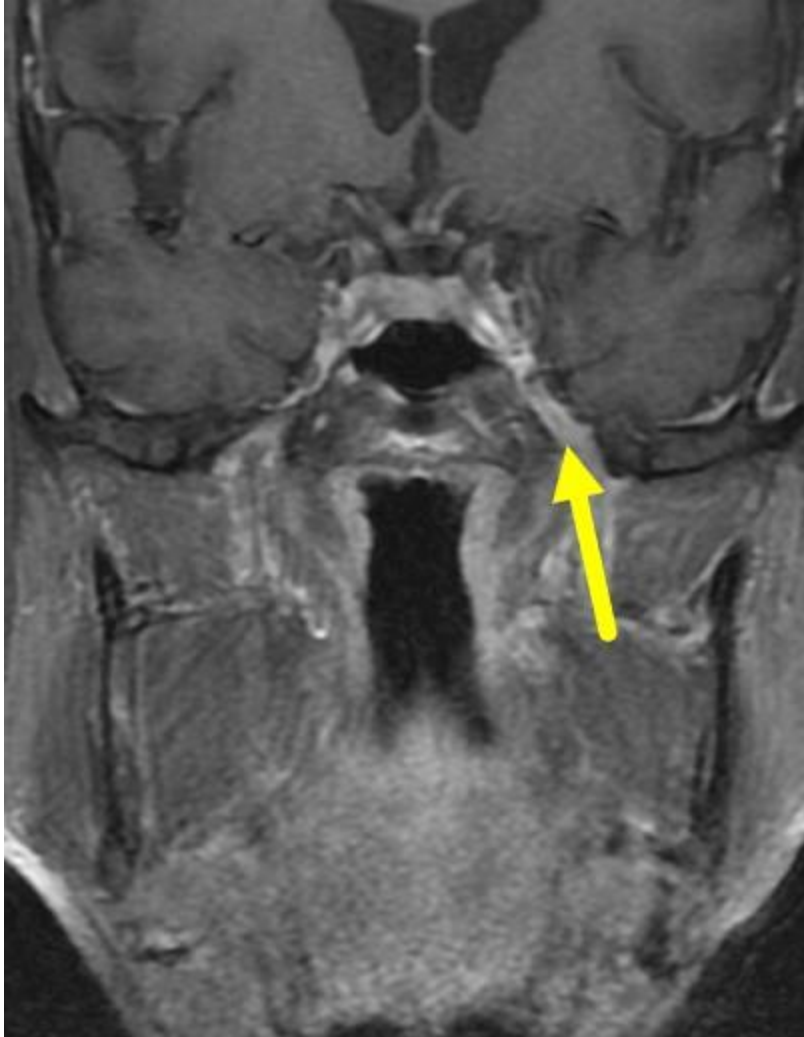
Case presentations will be used to introduce the major changes where an image and relevant clinical findings are first presented, then the major staging changes will be discussed as well as how radiologists should interpret the imaging findings in light of the new cancer staging changes to optimally assist their physician colleagues in managing the patient.

Results

There are two major changes in the head and neck section within the AJCC Eighth Edition. The first is the significance of HPV in the rising incidence and changing landscape of oropharyngeal cancer. The second major change is the significant prognostic indication related to extranodal extension of metastatic cancer. Other changes that will be discussed include: restructuring of pharyngeal cancer with emphasis on nasopharyngeal cancer categorization, changes to T categorization of cutaneous head and neck cancers, and how to stage head and neck cancers when one encounters adenopathy with an unknown primary malignancy.

Conclusions

The recent AJCC Eighth Edition incorporates major changes to the head and neck cancer section with significant prognostic indications. Knowing how these changes manifest on imaging and appropriately reporting these relevant findings will improve the report quality and better assist in the patient's management.



(Filename: TCT_eEde-130_FigureAJCCabstractASNR.jpg)

eEde-109

Review of Cervical Lymph Nodes Not Included in the Numbered Image-based Classification: Imaging and Clinical Significance

H Lin¹, R Ramzi¹, W Smoker², R Holliday³, D Reede¹

¹SUNY Downstate University Hospital, Brooklyn, NY, ²University Of Iowa Hospitals & Clinics, Iowa City, IA, ³NYEE, New York, NY

Purpose

1. Review the location of nodes not included in the numbered image-based classification (NIBC) 2. Learn common etiologies for adenopathy based on imaging features 3. Discuss primary drainage sites and clinical significance of nodes in these locations

Materials and Methods

Selected cases and illustrations are presented in quiz format to demonstrate the location of nodes not in the NIBS (facial, parotid, retropharyngeal, retropharyngeal, occipital, posterior auricular and supraclavicular), and to emphasize how understanding of drainage pathways, imaging appearance

Electronic Educational Exhibits

(enhancement, calcification, cystic changes etc.) with associated clinical information help determine the etiology of nodal enlargement in these locations.

Results

The location and significance of nodes in the NIBC have been extensively reviewed. However, nodes not in NIBC are not well recognized in the radiology literature. Facial nodes are rare and, when present, can suggest malignancies originating in the mucous membranes of the nose, cheek, eyelids or conjunctiva. The parotid gland, the only salivary gland with intraglandular nodes, may be mistaken for a primary parotid tumor when enlarged. These nodes drain parts of the naso-oropharynx, external nasal, auricular and frontotemporal regions. Skin cancer accounts for the majority of metastatic nodes in this location. When bilateral, lymphoma or sarcoidosis should be considered. Occipital nodes are typically due to lymphoma or systemic disease, not head and neck malignancies. Retropharyngeal nodes can suggest cancer in the nasopharynx, pharynx, nasal cavity, paranasal sinuses and, rarely, papillary thyroid cancer. Posterior auricular nodes drain the temporoparietal scalp, posterior auricular surface and posterior external acoustic meatus; often, secondary to local disease process. Supraclavicular nodes may be due to metastasis, infection or systemic disease such as lymphoma.

Conclusions

It is important for radiologists to be familiar with the location of these nodes, their drainage pathways and relevant imaging findings that suggest infection or malignancy in primary drainage sites. Knowledge of the clinical significance of these nodes enables radiologists to play a significant role in patient management.

eEde-150

Sellar and Juxtaseilar Mass Lesions... but Not What You Think!

J Reese¹, F Mihlon¹

¹*Eastern Virginia Medical School, Department of Radiology, Norfolk, VA*

Purpose

Imaging for headaches and/or vision changes sometimes reveals a sellar or juxtaseilar mass as the underlying etiology, most commonly a pituitary adenoma. However, there are uncommon entities the radiologist should be aware of as well as common entities that have unusual appearances. The purpose of this exhibit is to raise awareness of these uncommon sellar and juxtaseilar diagnoses through a series of cases.

Materials and Methods

A case series of unusual sellar and juxtaseilar diagnoses was compiled. The cases were proven to be either rare diagnoses mimicking more common entities or unusual presentations of more common diagnoses. Imaging features and clinical presentations are reviewed to help raise awareness of these entities. Three challenging sellar/juxtaseilar cases are selected from the cases and reviewed for this abstract. Case 1 Presentation: 35 year old with headache, vision changes, endocrinologic disturbance for 1.5 months Imaging: Sellar/suprasellar isointense T1 and slightly hypointense T2 nonenhancing mass causing marked mass effect upon the optic chiasm and hypothalamus. This was initially suspected to reflect a pituitary macroadenoma with chronic blood products/proteinaceous material. Case 2 Presentation: 49 year old with worsening headaches. Found to have panhypopituitarism and vision changes. History of ventriculoperitoneal shunt and hypopituitary since birth. Patient self-reported a brain mass that had been present for "years." Imaging: Large septated left middle cranial fossa arachnoid cyst extending into the optic canal with associated dysplasia of nearby brain. A 3 cm suprasellar mass was located anterior to the infundibulum. The mass was isointense to brain tissue and inseparable from the optic chiasm. Flattening of the pituitary and chronic expansion of the sella were present. Question of hamartoma or glioma extending from the floor of the third ventricle. Case 3 Presentation: 66 year old with history of lymphoma and incidentally discovered expansile bone lesion at the sphenoclivus junction on cervical spine MRI done

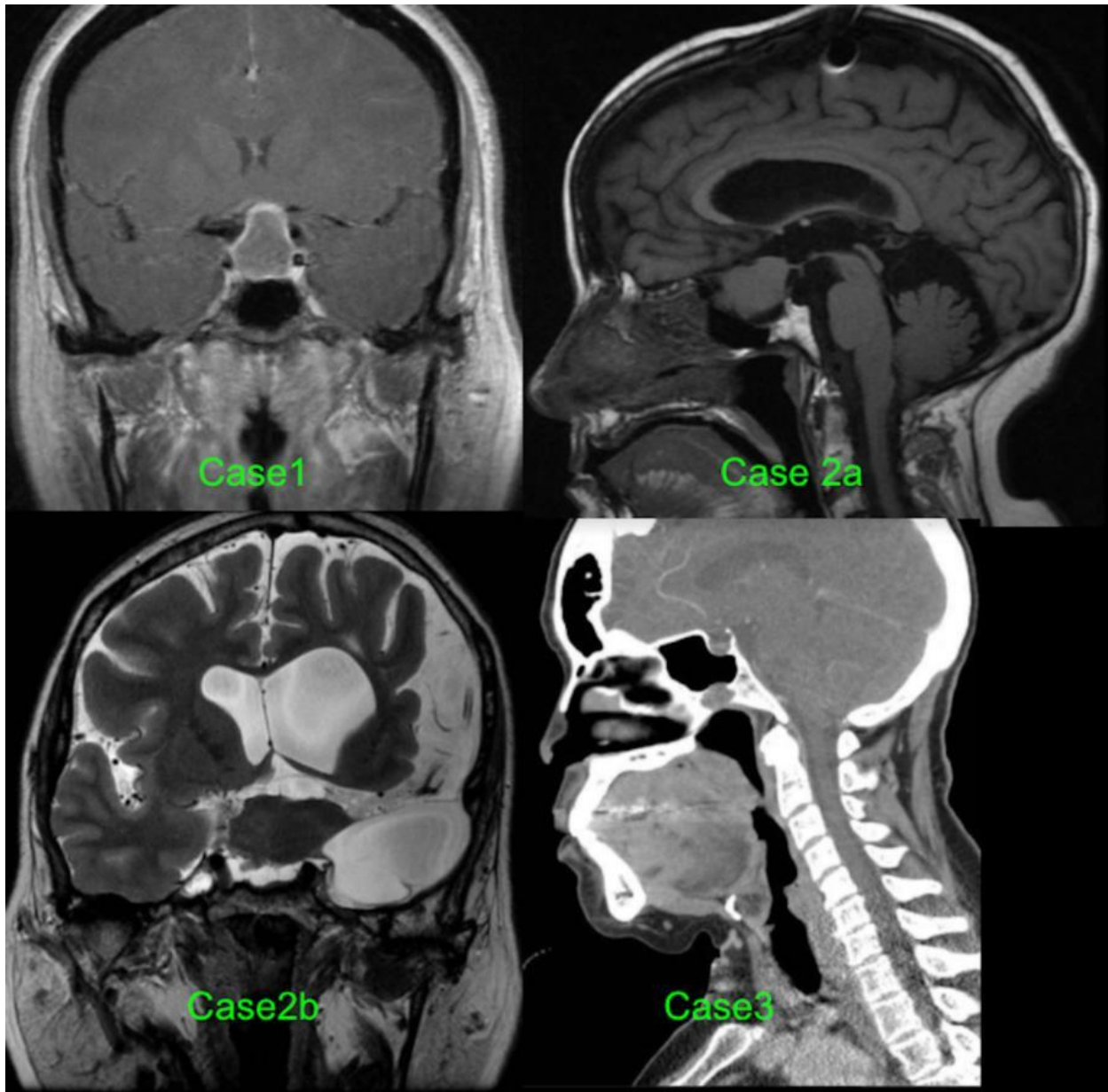
for gait and headaches. Follow-up neck CT was obtained. Imaging: 1.5 cm expansile enhancing mass at the sphenoclivial junction bulging into the sphenoid sinus above and nasopharynx below. Bone margins were sclerotic. Considerations initially included anterior chordoma, minor salivary gland tumor, and metastases.

Results

Case 1 Resection and pathology results: At transsphenoidal resection, purulent material was seen filling the sella. Subsequent gram stain culture revealed probable pneumococcus. Specimen for pathology revealed acellular eosinophilic material. Diagnosis: Pituitary abscess Discussion: Pituitary abscess is a rare sellar mass with a high mortality accounting for less than 1% of all pituitary disease. Typical imaging features include a single cystic mass that is T1 hypointense and T2 hypointense and shows rim enhancement. Imaging features are not specific and it is highly difficult to diagnose before surgery. The diagnosis should be considered when patients have fever, headache, and signs of pituitary dysfunction, or for patients with sellar lesion presenting with signs of meningeal inflammation. Case 2 Pathology results: Benign brain tissue. Diagnosis: Ectopic brain secondary to large arachnoid cyst Discussion: Intracranial arachnoid cysts account for 1% among all intracranial space-occupying lesions and are typically thought of as incidental findings. However, they may fluctuate in size and result in compression of nearby brain tissue. In this case, a large middle cranial fossa arachnoid cyst resulted in ectopic brain tissue displaced to the suprasellar region simulating a suprasellar tumor. Case 3 Pathology results: Pituitary adenoma Diagnosis: Ectopic pituitary adenoma Discussion: Ectopic pituitary adenomas are rare and are defined as extrasellar pituitary adenomas that show no connection to the normal pituitary gland. The most common location is the sphenoid sinus floor. CT and MRI are complementary. CT provides important information regarding the bony anatomy including the tendency to cause bone expansion with sclerosis helping to differentiate from more aggressive lesions. On MRI, lesions are usually isointense relative to adjacent grey matter, and they show enhancement after the administration of contrast material.

Conclusions

We present a case series that can be used to educate radiologists and raise awareness of uncommon sellar and juxtaseellar diagnoses.



(Filename: TCT_eEde-150_EducationalSella.jpg)

eEde-141

Skull Base Neurovascular Foramina: Imaging Anatomy, Variants, and Clinical Significance

J Meldrum¹, G Punch¹

¹*Tripler Army Medical Center, Honolulu, HI*

Purpose

This interactive electronic exhibit reviews anatomy, imaging considerations, and clinical examples of 16 adult skull base neurovascular foramina of the anterior, middle, and posterior cranial fossae. The exhibit discusses common anatomic variations and embryological remnants.

Electronic Educational Exhibits

Materials and Methods

The electronic exhibit functions as an interactive PowerPoint presentation. The user selects from 16 adult skull base neurovascular foramen using a home screen. This directs the user to information and images describing 1) the anatomy and boundaries of the foramen, 2) neural and vascular structures which traverse the foramen, 3) clinical considerations of the foramen such as common pathology or classification systems, 4) imaging considerations for evaluating the foramen, and 5) relevant notes or associations with the foramen. In addition, four variant foramina (such as the canaliculus innominatus and the posterior condylar canal) and five remnant foramina (such as the foramen cecum and median basilar canal) are included.

Results

The electronic exhibit serves as a learning guide and/or review of approximately 25 skull base foramina, simplifying an oft complex and intimidating subject. The interactive, visual nature of the educational exhibit makes for an enjoyable and effective learning experience.

Conclusions

This electronic educational exhibit is an interactive, visual guide to demystify skull base foramen anatomy and offer relevant clinical information to radiologists of various skill levels and experience.

Skullbase Neurovascular Foramina

	Anterior	Middle	Posterior
Normal	Cribriform Plate Anterior Ethmoid Canal Posterior Ethmoid Canal	Optic Foramen Superior Orbital Fissure Inferior Orbital Fissure Foramen Rotundum Foramen Ovale Foramen Spinosum Vidian (Pterygoid) Canal Foramen Lacerum Carotid Canal	Foramen Magnum Jugular Foramen Hypoglossal Canal Internal Auditory Canal
Variant		Canaliculus Innominatus Foramen of Vesalius	Posterior Condylar Canal Mastoid Foramen
Remnant	Fonticulus Frontalis Foramen Cecum	Craniopharyngeal Canal Median Basilar Canal Fossa Navicularis Magnus	

(Filename: TCT_eEde-141_Slide1.JPG)

eEde-116

Spaceflight-associated Neuro-ocular Syndrome: The Role of Cerebral Spinal Fluid Physiology, Microgravity Analogues and Quantitative Magnetic Resonance Imaging (qMRI)

L Kramer¹, K Hasan¹, A Kamali¹, E Bershad²

¹University of Texas, Health Science-Houston, Houston, TX, ²Baylor College of Medicine, Houston, TX

Purpose

Visual acuity changes in astronauts are well documented on short and long duration missions and commonly manifest as acquired hyperopia (farsightedness) (1). This aberration is corrected using glasses that can be continuously adjusted to maintain normal vision. In the last decade, a shuttle astronaut developed choroidal folds which distorts vision beyond correction. This was the premier case in which high resolution MRI of the orbits was used in the field of space medicine. Since this study the role of MRI has evolved into a larger effort to study all visual acuity changes in astronauts now referred as spaceflight associated neuro-ocular syndrome (SANS). This exhibit will review the orbital and intracranial abnormalities related to SANS and the use of microgravity analogues and qMRI to improve understanding of this medical mystery.

Materials and Methods

All MR imaging was performed on a 3T magnet using a 16-channel head coil. High resolution T2-weighted imaging of the orbits were retrospectively reviewed for 27 astronauts exposed to microgravity (2). CINE phase-contrast (CINE-PC) flow quantification of cerebral spinal fluid (CSF) was retrospectively reviewed for 14 astronauts and 6 healthy controls (3). Six healthy controls were analyzed in a prospective microgravity analogue study using cross-over study design (4). Carotid artery flow, CSF aqueductal flow and lateral ventricle volumetry were quantified in supine and HDT positions with and without exposure to elevated levels of carbon dioxide using CINE-PC of the carotid artery and cerebral aqueduct and 3-D T1-weighted imaging of the brain.

Results

Posterior globe flattening, optic nerve protrusion, optic nerve sheath dilatation and optic nerve sheath tortuosity are identified with increasing prevalence and severity in long duration missions. These anatomic changes are also found in patients with idiopathic intracranial hypertension (IIH). Symptomatic astronauts have revealed mildly elevated intrathecal pressures supporting a potential relationship to IIH. qMRI CSF production rate measurements show a postflight increase. This is consistent with animal studies showing that CSF production rate is suppressed in microgravity and rebounds with recovery in normal gravity. A small increase in lateral ventricular volume is shown in the microgravity analogue studies similar to changes reported in astronauts (5). CSF velocity increases when healthy subjects are exposed to brief elevated levels of carbon dioxide following 24 hours of HDT.

Conclusions

Exposure to microgravity has a number of consequences in susceptible individuals: Increased lateral ventricular volume, increased nerve sheath diameter, optic disk protrusion, globe flattening and a hypothesized suppression of CSF production rate. Expansion of lateral ventricular volume likely decreases intracranial compliance. With decreased intracranial compliance increased intracranial blood flow induced by carbon dioxide exposure results in increased CSF pulsatility. Prolonged exposure to increased CSF pulsatility potentially injures the orbital structures via a water hammer effect. This implies that varying elevated levels of carbon dioxide aboard the international space station in conjunction with increased lateral ventricular volume may play a role in SANS.

eEde-148

Structure, Function, and Pathology of the Mandible from Cradle to Grave

M Busch¹, M Matheus¹, P Mullin¹

¹Medical University of South Carolina, Charleston, SC

Purpose

The mandible is a complex bone which makes significant contributions to speech, respiration,

Electronic Educational Exhibits

mastication, as well as facial expression. Diseases of the mandible occur during all stages of life and have the capacity to significantly alter its function and appearance, substantially altering quality of life. Its importance is highlighted by the increasing frequency of complex head and neck surgeries now employed in the treatment of head and neck malignancies. This presentation will address embryology and anatomy of the mandible, leading into a discussion of congenital anomalies, acquired diseases of childhood, acquired diseases of adulthood, and finally, physiologic age related changes of the mandible.

Materials and Methods

Embryology and anatomy will be demonstrated using a combination of illustrations and diagrams as well as medical images from normal patients. Using a large series of illustrative head and neck CT and MRI cases from our didactic imaging files, we will show the continuum of disease related to the mandible extending from in utero to old age. Specific cases to be presented include fetal micrognathia, congenital anomalies, adult micrognathia, trauma, infection, and neoplastic processes of the mandible affecting the pediatric and adult populations.

Results

Understanding the importance of the mandible as a whole and how to evaluate it conveys a significant impact on patient care. Therefore, we will discuss the appropriateness of the existing imaging modalities ranging from fetal MRI to pediatric/adult CT as well as the meaningful imaging characteristics of each pathological process and how it may influence treatment decisions.

Conclusions

The herein presentation expects to improve awareness of the structure and function of the mandible as it relates to the pediatric, adult, and geriatric populations, and to improve description and recognition of pathologic conditions of the mandible which occur throughout life.

eEde-137

Stuck in the Middle: Nervus Intermedius-related Neuropathologic Imaging Spectrum

S Elakkad¹, M Landon², A Germana², J Yetto², M Cathey²

¹Naval Medical Center San Diego, san diego, CA, ²Naval Medical Center San Diego, San Diego, CA

Purpose

The nervus intermedius (NI), so named due to the intermediate course it takes between the facial and vestibular nerves within the cerebellopontine angle (CPA), ultimately gives rise to the greater superficial petrosal nerve, chorda tympani, and the lesser known posterior auricular nerve. Primary pathologies of the NI can present as nervus intermedius neuralgia (NIN). Alternatively, pathology in the distribution of any nerves derived from NI can present with symptoms referred to the NI. Advances in imaging technology have improved our ability to see this nerve and its branches, allowing for greater diagnostic accuracy when pathology referable to the NI is suspected. The purpose of this exhibit is to review the anatomy and function for the NI using case-based approach, highlighting the NI neuropathologic spectrum of disease.

Materials and Methods

Using images of the temporal bone from our high resolution state-of-the-art CT and 3T MRI, we will illustrate normal anatomy of the NI and its branches. Furthermore, we will show specific imaging examples of a variety of pathologies that involve the NI and its branches. Finally, we will provide an updated review of the literature on this topic.

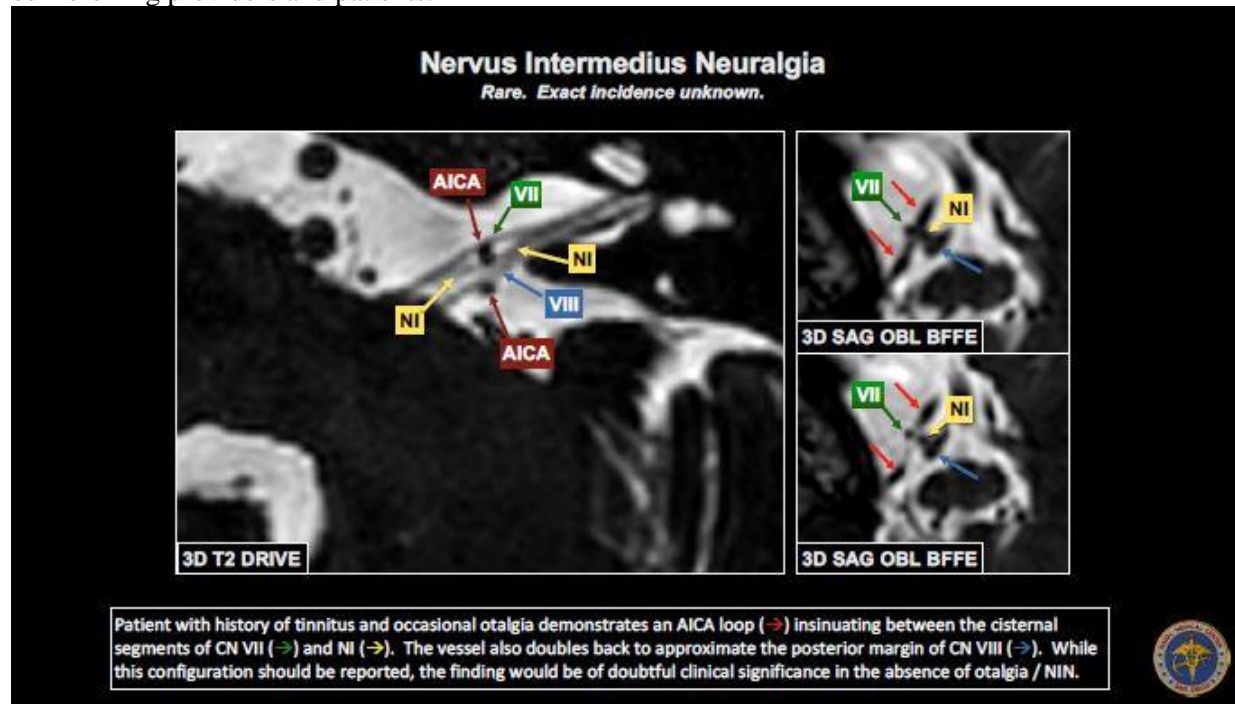
Results

The NI is involved in a variety of functions including: - Innervating the lacrimal, submandibular, and sublingual glands - Transmitting sensory input from portions of the external auditory canal, paranasal sinuses, and nasal mucosa - Conveying taste input from the anterior two-thirds of the tongue, floor of the mouth, and palate Pathologies either directly involving NI (e.g CPA mass or vascular compression) as well as pathologies involving its branches (e.g. sinonasal tumors, perineural tumor spread, or contact point headaches) may be referable to the NI. Overlapping innervation with branches of the trigeminal,

glossopharyngeal, and vagus nerves can confound diagnosis and/or lead to mislocalization, resulting in delayed diagnosis or inappropriate therapy.

Conclusions

Understanding the anatomy of the NI, its branches, and its pathologic spectrum allows radiologists to take a nuanced approach to these complex cases, improving diagnostic accuracy and providing value added to our referring providers and patients.



(Filename: TCT_eEde-137_NIN.JPG)

eEde-152

Systematic Approach to Sellar/Suprasellar Region Lesions: A Case-based Review of Challenging Cases

O Eissa¹, M Bazerbashi², J Kim¹

¹University of Michigan, Ann Arbor, MI, ²University of Toledo, Toledo, OH

Purpose

To review the normal anatomy of the sellar and suprasellar regions and to show a series of challenging cases which will include common and uncommon pathologies. Readers will learn to narrow their differential and generate a reasonable best diagnosis using a systematic approach based on location, age, clinical presentation, blood chemistry, and imaging findings. Readers will also learn to include in their reports the pertinent findings that may affect patient management and surgical approach.

Materials and Methods

We will review the normal sellar anatomy with both illustrations and cross-sectional imaging. Then readers will see our step-by-step approach to dealing with sellar lesions followed by several multimodality case-based examples including pathologically proven common and uncommon cases.

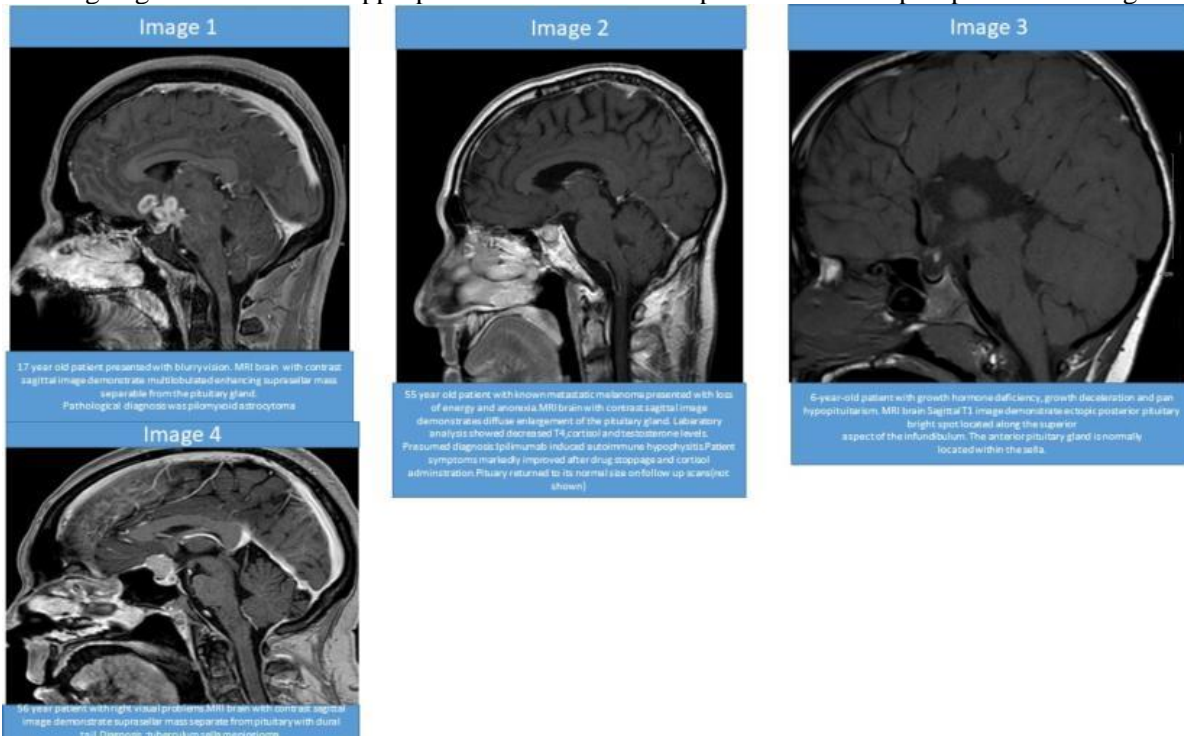
Results

The approach to sellar and suprasellar lesions is a topic which has been discussed many times in the radiology literature; however, these lesions remain challenging to many radiologists particularly with

regards to establishing an appropriate differential and reporting the clinically significant findings with regards to preoperative planning.

Conclusions

Sellar/Suprasellar lesions are commonly encountered in clinical practice. A systematic approach helps the radiologist generate the most appropriate differential and report the relevant preoperative findings.



(Filename: TCT_eEde-152_Slide2.JPG)

eEde-146

The Clivus: Case-based Review of Clival Abnormalities

J Giampa¹, A Mahajan²

¹Yale New Haven Hospital, Franklin Lakes, NJ, ²Yale School of Medicine, New Haven, CT

Purpose

The purpose of this educational exhibit is to review the normal anatomy of the clivus and its relationship to adjacent structures as well as present a case-based review of pathologic processes involving the clivus.

Materials and Methods

Following a review of the normal clival anatomy, a variety of cases will be presented and discussed, as a case-based review.

Results

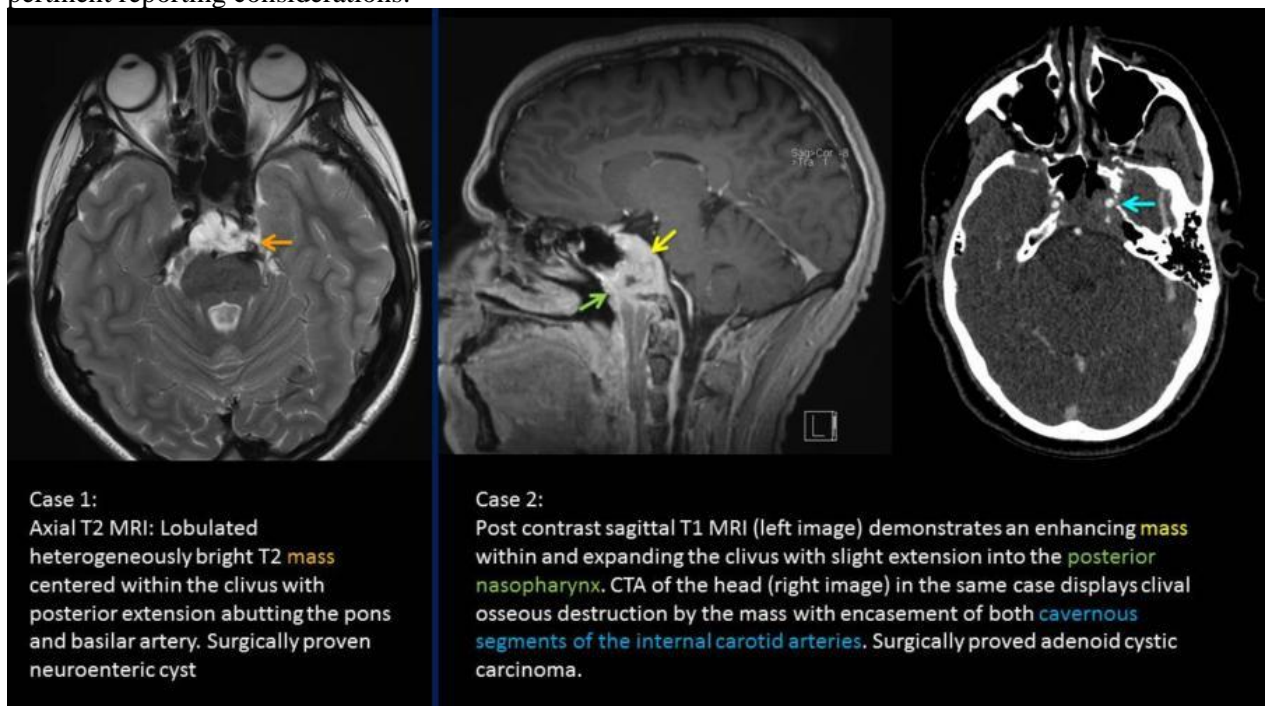
Latin for "slope", the clivus is located behind the dorsum sellae extending inferiorly to the foramen magnum with a downward tilt. The posterior inferior continuation of the clivus termed the basion is the anterior aspect of the foramen magnum opposite the opisthion comprising the posterior border of the foramen magnum. The clivus joins anteriorly with the sphenoid sinus as well as the inferior aspect of the nasopharynx. The petro-occipital fissures provide the lateral margins of the clivus. Posterior to the clivus the basilar artery is located within the prepontine cistern. Lesions involving the clivus may present with headache, cranial nerve palsies (especially the CN6/abducens nerve) or may be found incidentally. MRI is the imaging modality of choice for recognition and characterization with sagittal T1-weighted sequences

Electronic Educational Exhibits

being of use as abnormalities demonstrate loss of normal bright fatty marrow signal intensity. CT also plays a complementary role in providing osseous detail. Knowledge of adjacent anatomical structures is key for image interpretation as involvement of the nasopharynx, pituitary gland, cavernous segments of the carotid arteries, basilar artery, and pons may indicate specific disease processes in addition to having therapeutic and prognostic implications. This exhibit will present a wide range of clival abnormalities covering common and uncommon processes involving the clivus including: chordoma, chondrosarcoma, adenoid cystic carcinoma, plasmacytoma, meningioma, lymphoma, metastatic disease, Paget disease, fibrous dysplasia, avascular necrosis, osteomyelitis, aneurysmal bone cyst, ecchordosis physaliphora, neuroenteric cyst, and hematoma.

Conclusions

As demonstrated in this exhibit, there are a multitude of pathological processes that may be found within the clivus. Familiarity with the cases presented along with patient specific clinical information will aid in the formation of an appropriate differential diagnosis. Review of local anatomy also aids in providing pertinent reporting considerations.



Case 1:
Axial T2 MRI: Lobulated heterogeneously bright T2 mass centered within the clivus with posterior extension abutting the pons and basilar artery. Surgically proven neuroenteric cyst

Case 2:
Post contrast sagittal T1 MRI (left image) demonstrates an enhancing mass within and expanding the clivus with slight extension into the posterior nasopharynx. CTA of the head (right image) in the same case displays clival osseous destruction by the mass with encasement of both cavernous segments of the internal carotid arteries. Surgically proved adenoid cystic carcinoma.

(Filename: TCT_eEde-146_Slide1.JPG)

eEdE-158b

The Essence of the Sense - Taste! The Cranial Nerves, Brainstem and Cortical-subcortical Substrate of the Taste Sensation

D Gandhi¹, P Sooin², P Sharma³, P Kochar³, J Sapire³

¹St. Vincent's Medical Center, Bridgeport, CT, ²GLM Hospital, New Delhi, Delhi, India, ³Yale New Haven Health System at Bridgeport Hospital, Milford, CT

Purpose

The taste sensation is one of the most important special sensory phenomena. It is especially true for people who love tasting all kinds of cuisines. This can truly be understood when one is struggling with upper airway illness with dulling of taste sensations. What makes us like or dislike the taste of food? The aim of this exhibit is to explore the taste sensation pathway and its higher center neural control. The

Electronic Educational Exhibits

exhibit will enable clinicians, trainee radiologists and head and neck radiologists to understand anatomy and neural pathways of taste sensation, one of the special sensory pathways in humans.

Materials and Methods

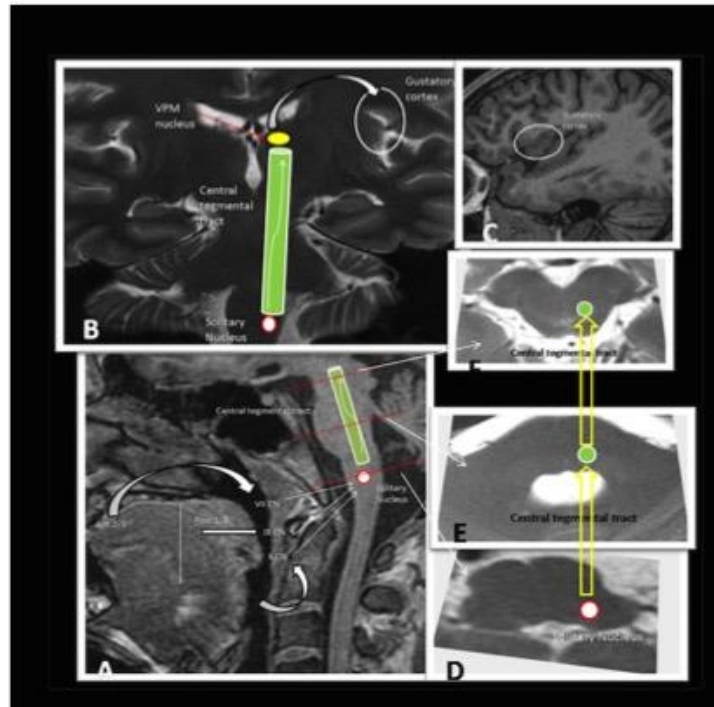
The taste sensation is one of the most important special sensory phenomena. The only thing we understand is that the tongue contains taste buds which make us taste food good or bad. However, very few know the neural pathways and higher center neural control. In this review, we comprehensively discuss neural pathways and cortical and subcortical substrate of cranial nerves involved in taste sensation superimposed on diagrammatic/CT or MRI imaging. This will help the audience to better understand the anatomy and location of the structures inside the body.

Results

The gustatory pathway begins from the tongue. Anterior 2/3 rd of the tongue is innervated by facial nerve and posterior 1/3 rd by glossopharyngeal nerve. The pharynx and epiglottis are innervated by the glossopharyngeal and vagus nerves. The axon of sensory nerves in these 3 cranial nerves terminate in the rostral part of the nucleus of tractus solitarius in the medulla. Second order neurons then travel through the ipsilateral central tegmentum to the ventroposteromedial (VPM) nucleus of the thalamus. The VPM nucleus then projects to ipsilateral gustatory cortex near the postcentral gyrus or insular cortex (Brodmann area 43; insulo-opercular cortex; primary gustatory cortex). The orbitofrontal and anterior insular cortex are the secondary gustatory cortex. The OFC is an area of multisensory integration. It receives inputs from primary gustatory, olfactory, somatosensory, auditory and visual areas and modulates awareness of flavor, taste recognition, and discrimination. Thalamus processes taste sensation along with pain, touch and temperature sensations from intraoral structures. Most of the studies favor left hemispheric dominance for the taste. However, studies have shown ipsilateral, contralateral and bilateral dysgeusia after involvement on the unilateral gustatory cortex.

Conclusions

Taste sensation begins at the tongue and ultimately end in cerebral cortex though relay mechanism by several order neurons. In-depth understanding of these pathways is easier if superimposed on diagrams and neuroimaging. We need to be aware of anatomical and functional relationships beyond our classical teaching and knowledge base. This will not only enhance our readings but also better management of our patients.



Taste sensation pathway: (A) Facial nerve, glossopharyngeal and vagus nerves carry taste sensation from anterior 2/3 of tongue, posterior 1/3 of tongue and pharynx/epiglottis respectively. (A,D) These nerves terminate in medulla at nucleus of tractus solitarius. A,B,D,E,F) From medulla, second order neurons reach to the ipsilateral central tegmentum to the ventroposteromedial (VPM) nucleus of the thalamus. (B, C) Which then projects to Brodmann area 43 - insulo-opercular cortex; primary gustatory cortex.

(Filename: TCT_EdE-54_Taste1.jpg)

eEdE-182d

The Role of Imaging in Penetrating Injuries of the Salivary Ducts: A Pictorial and Educational Review

J Choi¹, A Patel¹, C Chan², M Penta³, T Massoud¹

¹Stanford University School of Medicine, Stanford, CA, ²Stanford University Hospital, Stanford, CA, ³Stanford University, Stanford, CA

Purpose

Most injuries to salivary ducts are iatrogenic and involve Stensen's duct, occurring during drainage of a facial or parotid abscess or following superficial parotidectomy. Other causes include penetrating injuries, suppuration around a calculus, or, rarely, malignancy. Injury is uncommon to the submandibular and sublingual ducts, owing to the protection of the mandible. Laceration of the parotid duct is frequently overlooked especially in multiple trauma settings. Imaging has an important role to play in the challenging management of patients presenting late after a missed duct laceration. Multimodality imaging may be complex, including sialography, ultrasonography, CT and MRI.

Materials and Methods

We review the imaging manifestations of pathologies and traumatic injuries to the main parotid duct.

Results

We first describe the imaging anatomy of the parotid duct. In the acute phase after trauma, diagnosis of

ductal injury is usually clinical. Sialography, ultrasonography, CT and MRI are helpful when such injury has been overlooked or to evaluate duct patency after treatment. Only half of injuries are recognized acutely whereas the rest appear later as sialoceles or fistulas, the most common complications of parotid duct injuries. A sialocele corresponds to an inflammatory pseudocapsule in the soft tissues of the cheek containing salivary secretions with no proper drainage. A salivary fistula is an external drainage of saliva occurring alone or after a sialocele that causes skin rupture. The average delay in presentation is 7 days for fistulas, and 12 days for sialoceles. We describe the Van Sickles classification of injuries to the main parotid duct, and illustrate this with multimodality imaging examples of fistula and sialocele formation.

Conclusions

Salivary duct injuries are distressing both to the patient and the surgeon alike since conservative and operative treatments are challenging. This exhibit will aid in understanding the important role of multimodality imaging in assessing complications following ductal injuries.

eEde-155

The Third-window Syndrome in the Temporal Bone: A Pictorial Assay

A Riello¹, A Costacurta²

¹*Fleury Labs a+, Rio de Janeiro, Rio de Janeiro, Brazil*, ²*Clinica Felipe Mattoso, Rio de Janeiro, Brazil*

Purpose

The aim of this study is to review the pathophysiologic mechanism and the radiological appearance of the many conditions that encompass the Third Window Syndrome (TWS) in the temporal bone, highlighting the most common findings and the atypical features that may occur.

Materials and Methods

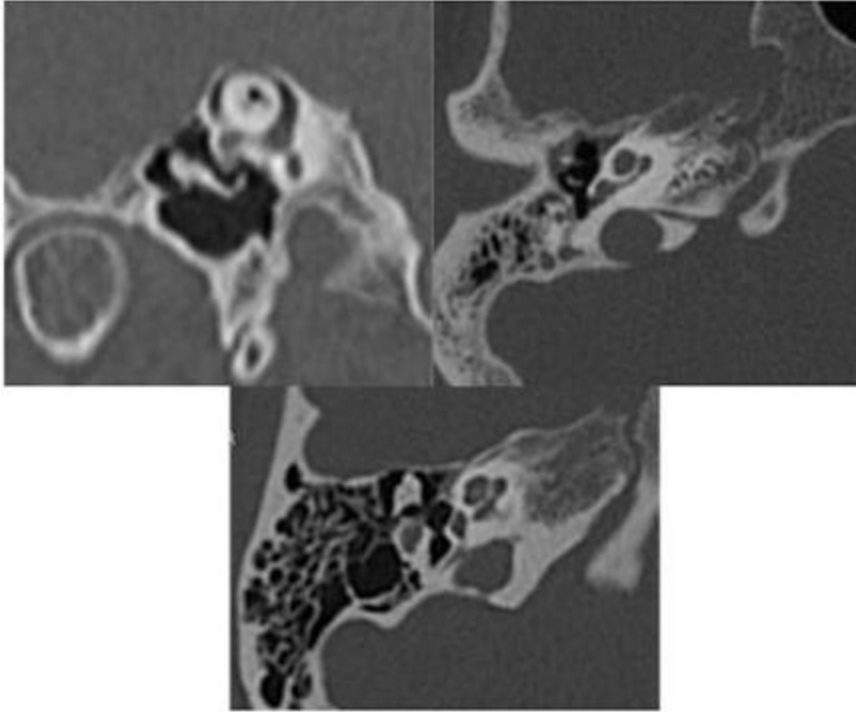
We describe the appearance of the various anatomic findings in the Third Window Syndrome of the temporal bone in high resolution computed tomography (HRCT).

Results

Dehiscence of the otic capsule is increasingly being recognized as an important source of symptomatic otologic pathology. In 1988 Minor et al. described the superior semicircular canal dehiscence (SSCD). In 2008, Merchant and Rosowski proposed a universal theory for the underlying mechanism of hearing loss accompanying these defects. Normal sound conduction is transmitted through the oval and round windows, which serve as fluid interfaces between air in the middle ear and perilymphatic fluid spaces of the inner ear. Various conditions can enlarge existing bony channels or create additional defects in the bony labyrinth, producing hydrodynamic third windows. In Third Window Syndrome middle ear pressure changes or sounds cause a wide range of auditory and vestibular symptoms, including varying degrees of fluctuating progressive hearing loss, autophony, sound induced vertigo, nystagmus and tinnitus. At audiometry, there is a characteristic low-frequency air-bone gap due to decreased air conduction and increased bone conduction. Potential third windows include bony dehiscence of the semicircular canals, enlargement of the opening of the vestibular aqueduct, dehiscence of the scala vestibuli side of the cochlea, abnormal bony thinning between the cochlea or any of the vestibular structures and vascular channels and the recently described unique entity of cochlear-facial dehiscence (CFD).

Conclusions

Third Window Syndrome typically presents with auditory and vestibular symptoms. High-resolution temporal bone computed tomography provides superb anatomical detail of the anatomical variations and pathologies that may present as part of that syndrome, including bony dehiscence of the semicircular canals, enlargement of the opening of the vestibular aqueduct, dehiscence of the scala vestibuli side of the cochlea, abnormal bony thinning between the cochlea or any of the vestibular structures and vascular channels and cochlear-facial dehiscence.



(Filename: TCT_eEde-155_Apresentacao3ajanela001-copia.jpg)

eEde-110

Unilateral Cervical Lymphadenopathy – Evaluation of Imaging Features to Differentiate Different Causes That Mimic Lymphoma

J Junn¹, A Corey², M Zygmunt¹, A Prater³, R Peterson⁴

¹Emory University Hospital, Atlanta, GA, ²Emory University, Fayetteville, GA, ³Emory University, Atlanta, GA, ⁴Emory University School of Medicine, Atlanta, GA

Purpose

Describe and discuss radiologic features to differentiate different causes of unilateral cervical lymphadenopathy

Materials and Methods

This educational exhibit will briefly discuss the different nodal stations for cervical lymph nodes. We shall then highlight different etiologies and characteristic imaging features for unilateral cervical lymphadenopathy that mimic lymphoma including Kakuchi Fujimoto, Castleman's, cervical metastatic disease, Kakuchi Kumara, mononucleosis, Rosai Dorfman, Kimura disease, and tuberculosis.

Results

Cervical lymphadenopathy is a common reason for imaging of the neck for patients presenting with palpable abnormalities. Though imaging features alone could be difficult to identify the exact cause, integration of other imaging findings and clinical history can help delineate the cause of cervical lymphadenopathy. Through this educational exhibit, we will discuss imaging features of different unilateral cervical lymphadenopathy and further highlight accompanying imaging features and techniques/biopsy planning that will aid in diagnosis.

Conclusions

Imaging is important in assessing cervical lymphadenopathy as it provides more comprehensive

assessment, especially areas that not amenable to tactile examination. As there are numerous etiologies for cervical lymphadenopathy, integration of other imaging features can help narrow the diagnosis for proper and timely patient management.

eEde-127

Velopharyngeal Dysfunction: What a Radiologist Must Know

P Batchala¹, N Mecci¹, S Mukherjee¹, S Patel¹, J Donahue¹, T Eluvathingal Muttikkal¹

¹*University of Virginia Health System, Charlottesville, VA*

Purpose

"Velopharyngeal Dysfunction" (VPD), results from inadequate closure of the muscular ring that separates the nasopharynx from the rest of the airway during speech and deglutition. Management of VPD is multidisciplinary and challenging. Imaging plays a crucial role in the evaluation. Comprehensive literature on the subject is sparse. We present an overview of radiological anatomy, advantage and disadvantages of the imaging techniques, and the clinical and surgical perspectives.

Materials and Methods

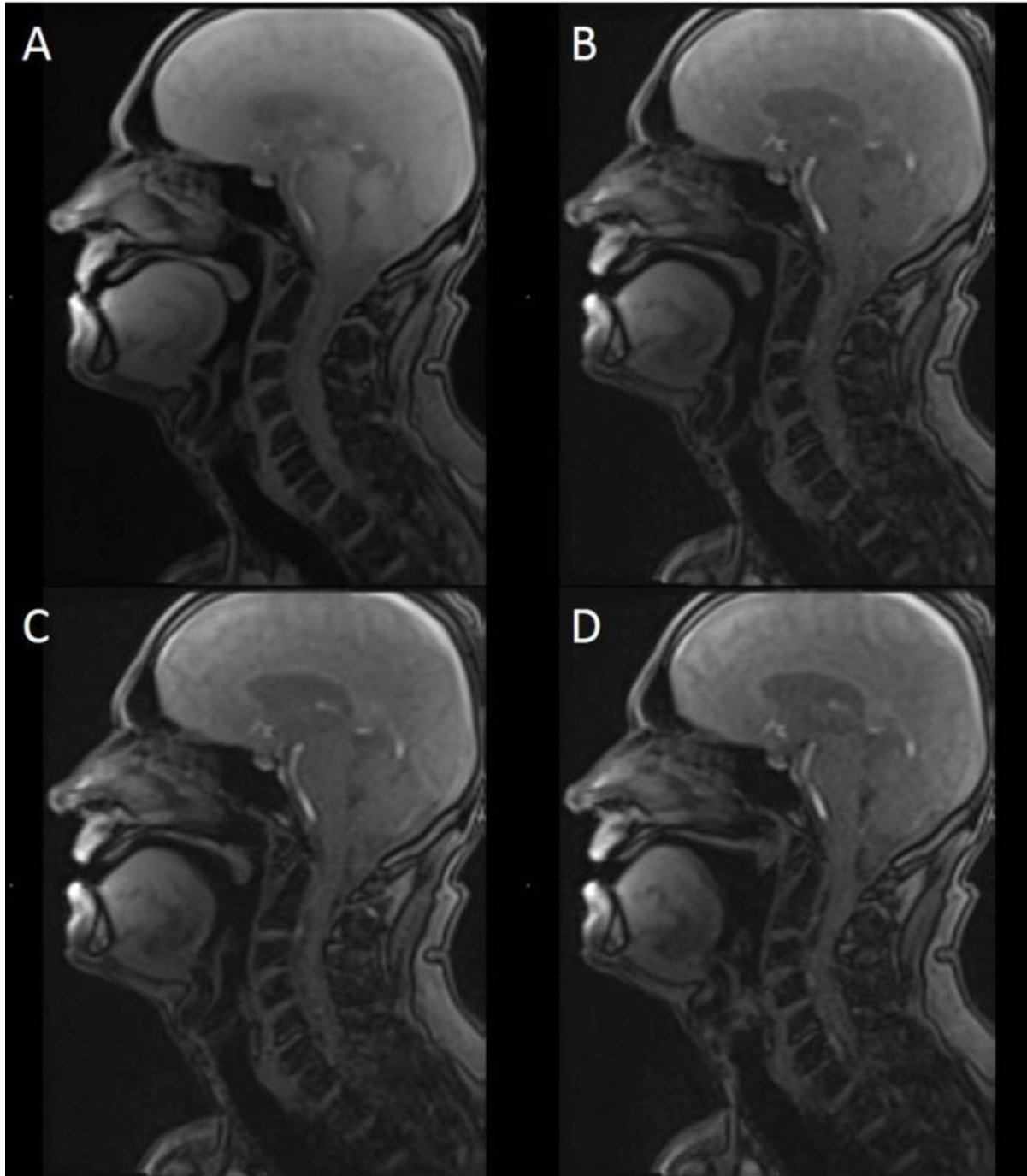
We describe in detail the MRI anatomy of the six muscles that comprise the velopharyngeal sphincter and their function. We briefly touch upon the initial clinical evaluation and also the nonsurgical and surgical options available for management. We enumerate the imaging techniques available for evaluating VPD, in particular the current role of cine MRI, its advantages and disadvantages over video fluoroscopy and nasopharyngoscopy. We also describe the different closure patterns that can be observed on imaging, which are relevant for decision-making (See Figure 1: A - velopharynx at rest; B, C, D - still images from a CINE sequence demonstrating velopharyngeal touch closure pattern during phonation). The postsurgical and post-treatment appearances are also described.

Results

VPD can result from anatomical defects ('insufficiency') or functional disorder ('incompetency') involving the sphincter. Etiologies can be congenital or acquired. VPD can cause social, psychological and emotional problems secondary to speech and deglutition difficulties. Initial clinical evaluation is often followed by imaging, which has a crucial role in the anatomical and functional assessment. Cine MRI with the current advancements in spatial and temporal resolution can provide high quality data of the sphincter. The technique is noninvasive, radiation free, and feasible in both adults and children. The disorder can be managed nonsurgically or surgically depending on the clinical and imaging findings.

Conclusions

Through this exhibit we aspire to create familiarity about VPD among the radiology community. By collating the clinical information with the imaging data, the radiologist can play a key role in VPD management.



(Filename: TCT_eEde-127_Figure1-abstractsubmission.jpg)

Electronic Educational Exhibits-Informatics

eEde-159

A New Centralized Learning Forum: ASNR's Resident Portal

V Yedavalli¹, S Gayen², J Smirniotopoulos³

Electronic Educational Exhibits

¹*Advocate Illinois Masonic Medical Center, Chicago, IL*, ²*MedPix, Bethesda, MD*, ³*George Washington University, Washington, DC*

Purpose

For residents who have a strong interest in neuroradiology, there are scattered websites that are pertinent to their level of training. Most resources tend to be catered to fellows instead. As a solution, we present one of the newest additions to the ASNR website: The ASNR Resident Portal. The objective of the portal is to consolidate the vast amount of neuroradiology related information into one centralized forum for residents and medical students alike.

Materials and Methods

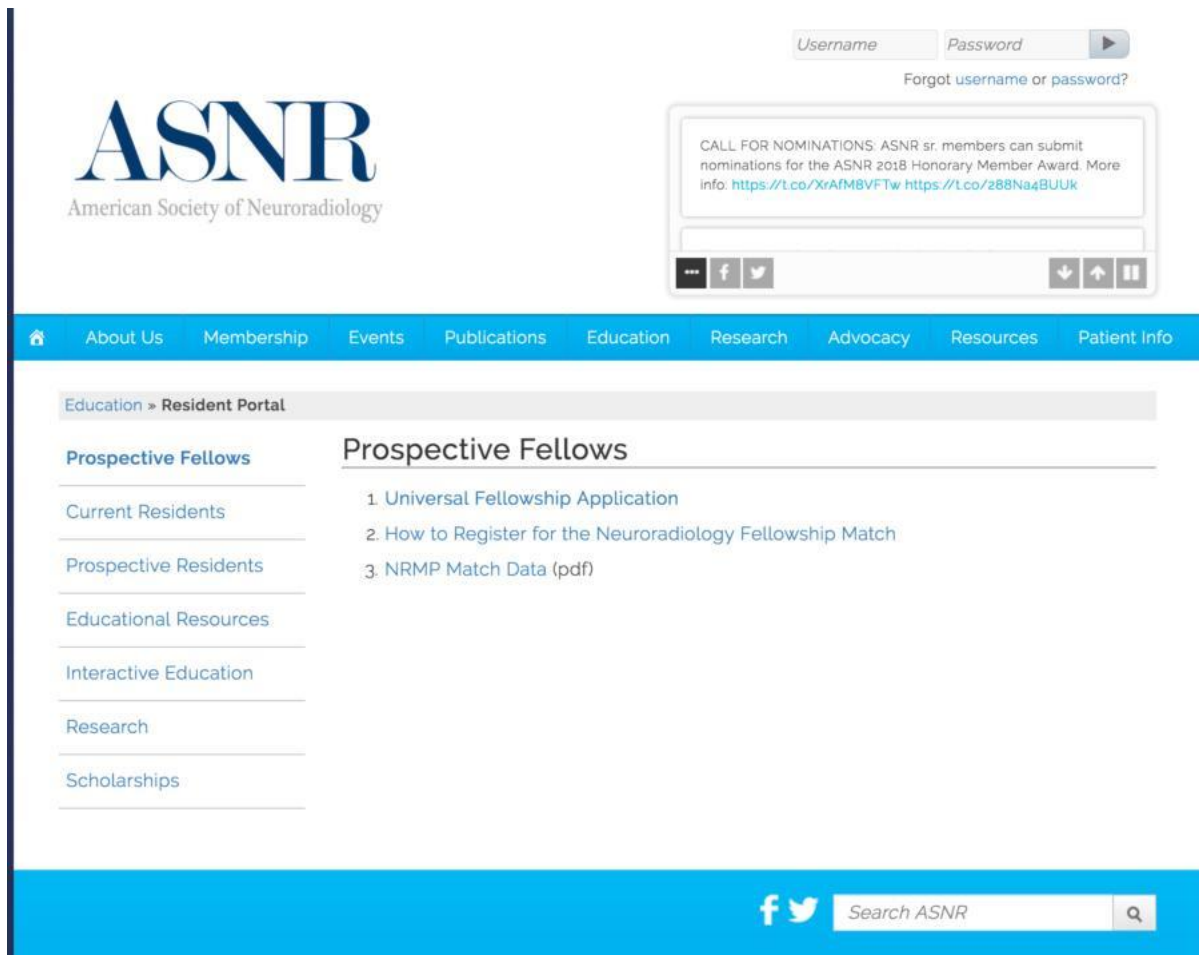
The ASNR Resident Portal was created to be a centralized forum in a tab format for neuroradiology resources pertinent to the resident level. Mirroring ASNR's successful Fellowship Portal, the Resident Portal emphasizes a vast array of topics such as information on the CORE exam, fellowship matching, and a soon to be developed neuroradiology question bank in conjunction with MedPix. Additionally, there are a number of resources which focus on research and potential publishing options. We continually request feedback in the dynamic process of bettering the Resident Portal for increased resident exposure to neuroradiology.

Results

Neuroradiology is a vast field which can be challenging for residents to grasp and master. Many of the online neuroradiology resources catering to residents are scattered and range in level of difficulty. In order to create a centralized forum for neuroradiology resources and a method of increasing exposure and interest in the field of neuroradiology, we created ASNR's Resident Portal. Our goal is to spark interest in the field starting with medical students and junior residents. As only 55% of fellowships filled through the match in the past few years, it is imperative to increase awareness of our great field. Our hope is that the ASNR's Resident Portal in conjunction with MedPix facilitates such endeavors.

Conclusions

ASNR's Resident Portal is a new central forum on ASNR's website for residents and medical students alike. With information of important topics such as the CORE exam, neuroradiology fellowship, the match process, research, and a future neuroradiology question bank in partnership with MedPix, our main objective is facilitating valuable resources, increasing exposure, and increasing interest in the field such that junior residents and medical students consider a career in neuroradiology.



(Filename: TCT_eEde-159_ScreenShot2017-09-19at40845AM.jpg)

eEde-165

Implementation of the Game-based Learning Platform, Kahoot, in Radiology Resident Training

S Calle¹, E Bonfante-Mejia¹, R Riascos¹

¹The University of Texas Health Science Center at Houston, Houston, TX

Purpose

1. Discuss the benefits of competition and gamification in education 2. Illustrate the advantages of implementing Kahoot in the classroom over traditional approaches of teaching 3. Describe what the game-based learning platform, Kahoot, is and the different functions it offers 4. Demonstrate how to design interactive kahoots for the purposes of resident training 5. Explain the term "blind kahoot" and how it can be employed in the teaching of new material

Materials and Methods

Kahoot is a web-based program where the user can easily construct games, nicknamed "kahoots" free of charge. A variety of question formats are available depending on the objective including: quiz, jumble, discussion and survey. The interface is aesthetically pleasing, user-friendly and intuitive. Each case or question can be entered in a couple of minutes, depending on the user's expertise and familiarity with the program. In the quiz setting, the instructor can design a multiple-choice question prompting a diagnosis, finding, sign or anatomic structure. The case can be accompanied by uploadable media files such as images or video. The game itself provides suspenseful game show-type music, countdown timers and a

Electronic Educational Exhibits

gong sound to signal when the time is up. A leaderboard appears at the end of each question and displays the current ranking of the students. The quizzes provide a wide range of customizable options including the allotted time, whether or not to award points for a specific question, and individual vs team-based play, among others. Students can enter their answers using their laptops, tablets or mobile devices either online or directly on the Kahoot application. The jumble feature instructs the players to organize images in a chronological or sequential order. This element has proved particularly useful in explaining processes. We have applied this feature in the teaching of the evolution of infarcts on head CT, varying appearances of blood over time and the stages of neurocysticercosis, to name just a few. Blind kahoot is a term coined by Stephanie Castle and basically references a specific dynamic to a game where new material is introduced. By setting milestones and ordering the questions in a specific fashion, the user can introduce a new concept by slowly layering rules and applying new knowledge to subsequent questions.

Results

It is now well known that the retention rate of traditional lectures is very low. The introduction of interactive teaching and creative activities not only sparks the interest and concentration of the learners, but also creates a more gratifying environment for the interaction between educators and trainees. The need in our neuroradiology section for a novel way to engage our first-year residents in the fundamentals of head CT brought on a search for the new frontier in education. From the start, our priority was set on finding something that was both entertaining and effective. After exploring several game development tools available online, the idea of implementing Kahoot as a platform for interactive training and evaluation arose. Ideas such as the "fun theory" and "gamification" have sprung up worldwide as educators strive to keep young, millennial minds engaged. The fun theory states that a simple way to alter people's behavior is by making it entertaining. Gamification refers to the application of game playing to other activities. The unification of these ideas can be seen in the implementation of Kahoot. Since the implementation of Kahoot in resident training we have noticed a remarkable change in attitude. The trainees now take on an active role in the learning process and appear attentive and awake.

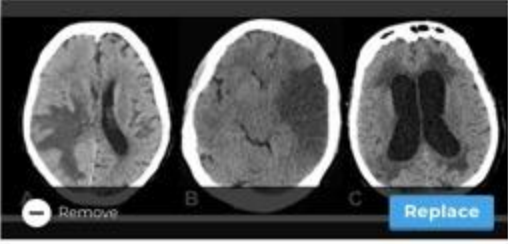
Conclusions

The potential applications of the Kahoot platform as an educational method, as well as its customizable design, integration of mobile devices, and entertainment factor represent a truly innovative take on radiology training.

Close **K! Question 7** Next

Question (required)
In which case would you recommend a CT angiogram?

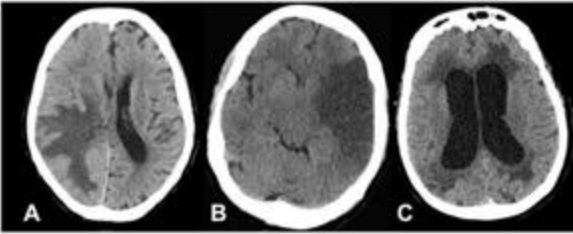
Time limit: 120 sec Award points: YES

Media

 Remove Replace

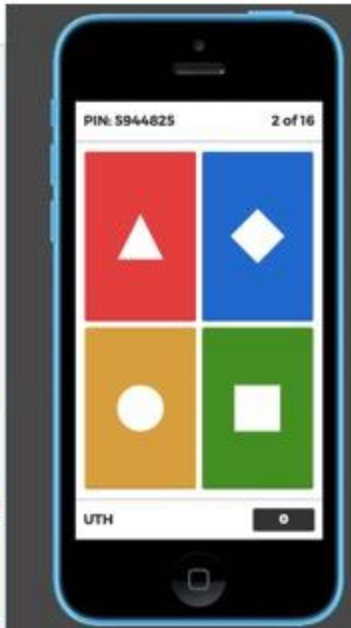
Answer 1 (required): A ✓
 Answer 2 (required): B ✓
 Answer 3: C ✓
 Answer 4: All of the above ✓

In which case would you recommend a CT angiogram?

108


 Skip 0 Answers

A B
 C All of the above



(Filename: TCT_eEde-165_Picture1.jpg)

eEde-163

Innovative Web-based Platform for Trainee On-call Preparation in Neuroradiology: An Interactive Quiz Series

P Sajedi¹, J Hostetter², S Karnezis¹, A Azizyan¹, N Salamon³

¹University of California Los Angeles, Los Angeles, CA, ²University of Maryland Medical Center, Baltimore, MD, ³David Geffen School of Medicine at University of California Los Angeles, Los Angeles, CA

Purpose

To demonstrate the use of a novel cloud-based PACS system with a fully integrated educational assessment tool to prepare trainees for neuroradiology cases on-call

Electronic Educational Exhibits

Materials and Methods

A zero-footprint cloud-based PACS, Pacsbin.com, was created using open web technologies allowing users to acquire de-identified studies onto their personal device for the purpose of imaging sharing and education. This PACS provides a full range of image manipulation tools, including window/leveling, cross-reference, and zoom functions. Quizzes were assembled onto this platform using fundamental adult and pediatric neuroradiology on-call studies from our institutional database encompassing a variety of disease processes. For each case, stepwise multiple choice questions were designed as well as questions requiring participants to mark a particular region of interest. Quizzes were taken prior to and following a flipped classroom session where cases were reviewed and sample search patterns were provided.

Results

Interactive educational web-based programs provide a unique method of learning radiology and have become increasingly popular amongst trainees. While several platforms exist, currently the only standardized means of tracking resident performance include in-service exams and the radiology CORE examination. This cloud-based imaging viewer and educational assessment tool program is novel in its ability to present questions in various ways (multiple choice, free text, mark image, etc.) and store results allowing user performance to be assessed over time. We sought to integrate this platform to improve trainee comprehension and comfort level with common acute neuroradiology cases in preparation for overnight call. Cases assembled from our institutional database were supported with multiple choice and region of interest questions designed to allow trainees to work through each case methodically before arriving at a diagnosis (Figure 1). Participants received immediate score assessments following the completion of the quiz, providing instant feedback with the opportunity for remediation as desired. Detailed assessment results were also automatically sent to the quiz proctor in order to address general deficiencies and monitor changes in user performance over time. The information gathered from these cases was then enriched via a flip classroom experience with the intent of consolidating the material and improving trainee comfort. An additional quiz was taken following the classroom session to ensure the material presented was fully integrated.

Conclusions

We have applied an innovative web-based platform in order to improve comprehension and comfort level with common on-call neuroradiology cases. We believe this fully synthesized cloud-based PACS has potential as a global education assessment tool given its ability to automatically generate and store results, allowing user performance to be analyzed over time. In the short-term future, we foresee several additional applications to this platform, including preparation for the radiology board examination and neuroradiology CAQs.

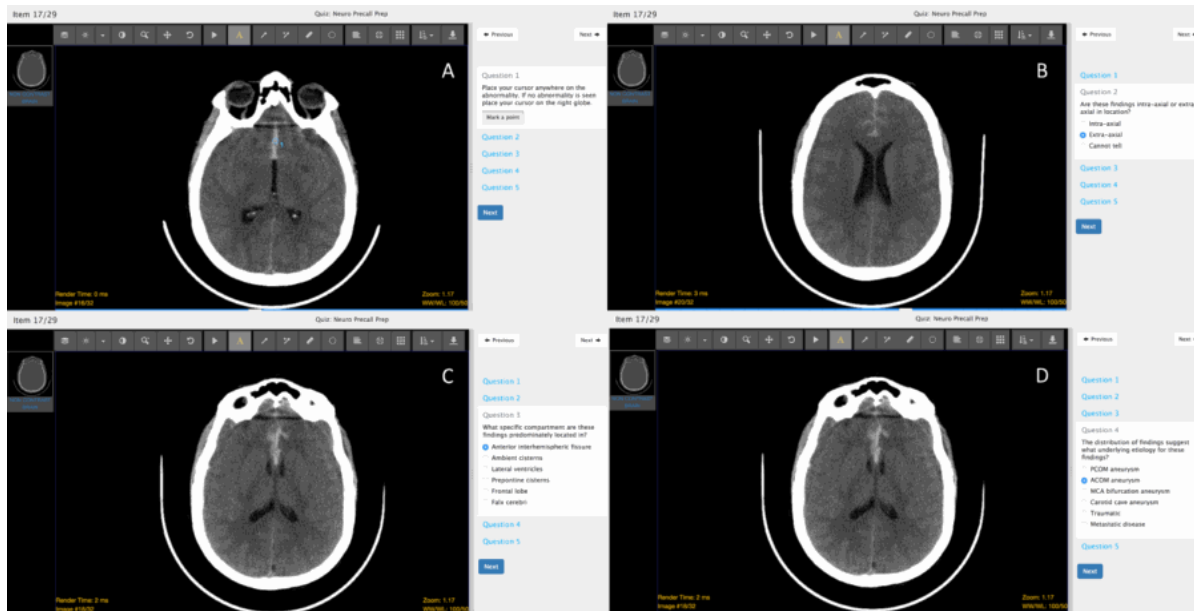


Figure 1: Four select images (A-D) of a specific case with sequential questions designed to train participants to work through a case deliberately while on a fully functional image viewer.

(Filename: TCT_eEde-163_ASNR18.gif)

eEde-164

Joining the Neuroradiology Community on Twitter: Why Bother and How to Do it?

C Atat¹, T Smayra², J Ghauche³, S Yazbek⁴

¹Hotel Dieu de France Hospital, Beirut, na, ²HOTEL DIEU DE FRANCE HOSPITAL, BEIRUT, na, ³HOTEL DIEU DE FRANCE HOSPITAL, BEIRUT, NA, ⁴Hotel Dieu de France Hospital, Beirut, Lebanon

Purpose

Twitter is a powerful #SoMe (social media) tool. It has around 330 million monthly active users and it is gaining popularity in the professional world. Many radiologists have joined and are joining twitter every day for professional purposes. The neuroradiology community on Twitter is growing very fast.

Materials and Methods

We present the many advantages of signing up and using Twitter as a neuroradiologist by reviewing its multiple purposes and applications. We then define the words and actions most commonly used on twitter. We finish by describing the steps required to get online and use twitter effectively.

Results

Twitter has many benefits and applications in #MedEd (medical education) and in academic medicine. It is a great educational tool, with widespread online educational resources. It is fun and permits access to medical information through gaming. Engaging on twitter is an excellent way for a radiologist to step out of the dark room and become visible. It allows sharing medical information related to research, articles and meetings as well as connecting with colleagues nation-wide and internationally. It also permits the spread of information to a wide audience as well as the general public, to become a powerful influencer of opinions regarding medicine, research and health policies. We will give definitions of the words and actions commonly used on Twitter, like tweet, retweet, handle, hashtag, DM (direct message), like, follow and tweet chats. We will next describe the different steps to get started and get online. To start using Twitter professionally, you must first determine your brand, choose a handle and write a concise bio that goes through your title, your area of expertise, optionally your organization and add few hashtags you

Electronic Educational Exhibits

frequently use and follow as #mentoring #FOAMed #FOAMRad #Neurorad #HNrad. The last step, before your first tweet, is to choose different accounts to follow. We will provide a nonexhaustive list of interesting accounts to follow in the neuroradiology community including educational accounts, academic societies' accounts, journals, and neuroradiologists.

Conclusions

Twitter is fun, easy to use and has many benefits and applications in the field of radiology and neuroradiology. Join the neuroradiology community on Twitter today: download the application, take a look yourself and let the journey begin.

eEde-160

Neuroradiology Insider: Development of a Mobile App to Assist the Novice Radiologist

D Guerrero¹, B Heller¹, M Ramchand¹, N Kanth¹, S Lev¹

¹*Nassau University Medical Center, East Meadow, NY*

Purpose

1. To demonstrate how to develop a free, interactive, user-friendly educational neuroradiology assistant for handheld platforms using Google Forms© 2. To help the novice radiologist employ a visual and cognitive approach to navigate through frequently encountered neuroradiology imaging scenarios 3. To simplify and streamline student learning and to assist the instructor's ability to track progress

Materials and Methods

We created a prototype app using Google Forms© titled Neuroradiology Insider. The homepage of our application consists of four categories (Clinical History, Visual Approach, Radiology Differential and Imaging Recommendations), serving as entry portals into the app and reflecting the workflow approach of the neuroradiologist. Selecting an individual portal opens a menu of new options to choose from, each of which leads to a new window of decision points. Many of these are illustrated with radiological images, diagrams and clip art. For example, if one chooses "Radiology Differential", the user embarks on a path which provides the needed skills and information to postulate an astute differential diagnosis. The differential section starts with a list of common locations (e.g. Intra-axial, Extra-axial, Intraventricular). As one progresses, new categories are shown, such as Morphology and Etiology, intended to hone the differential. "Clinical History" contains many common neurological scenarios (e.g. Stroke, Fever) with unique insights and tips. "Visual Approach" offers guidance in detecting subtle lesions and pathology in various regions. "Imaging Recommendations" helps the user to consider the appropriateness of further imaging modalities. The core structure is to demonstrate the most important, key considerations.

Results

Google Forms© is a versatile web-based tool that does not require knowledge of advanced coding and it enables a variety of applications. It enables the developer to continually revise and update, thus creating a dynamic platform for learning. Using Google Forms© we have created an interactive mobile neuroradiology app which takes the user through a stepwise sequence intended to reflect the thought process of the more senior neuroradiologist, an approach not usually encountered in traditional textbooks. One important feature of our app is that an instructor has the option to have the learner electronically submit the completed Insider form. The responses are then automatically recorded into Google Spreadsheets©, which can be used to track and monitor the learner's progress. We anticipate that using this application on mobile devices will transform the student from a passive observer to an active participant, who learns to make tailored observations and incorporates visual findings to develop an accurate differential diagnosis.

Conclusions

We demonstrate how Google Forms© can be used to develop a learning application that can be shared and configured on mobile platforms. An algorithmic approach was applied to create a dynamic step-by-step guide. This intuitive, interactive tool encourages independent thinking and may help the user

cultivate his or her own diagnostic approach. The tool provides the framework for the learner to develop the skills needed to evaluate common neuroradiological scenarios and with modifications can be readily applied to other specialties in radiology.

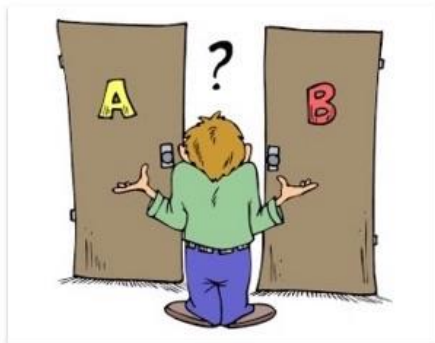
Neuroradiology Insider (Sample Home Screen)



Clinical History



Visual Approach



Radiology Differential



Imaging Recommendations

SUBMIT

(Filename: TCT_eEde-160_SampleHomeScreen.jpg)

eEde-162

Oh My Gad! Gadolinium Deposition Demystified

H Ismail¹, L Wang², A Vagal³

¹University of Cincinnati, Cincinnati, OH, ²University of Cincinnati Medical Center, Cincinnati, OH, ³University Hospital/University Cincinnati College of Medicine, Cincinnati, OH

Electronic Educational Exhibits

Purpose

The extracranial deposition of Gadolinium following the use of Gadolinium-based contrast agents (GBCAs) has historically been well documented. In recent years, an increasing number of studies have demonstrated evidence of intracranial Gadolinium deposition. This educational exhibit aims to provide a review of these findings as well as provide guidance for the proper usage of GBCAs and suggestions for future investigations.

Materials and Methods

Provide an introduction to Gadolinium (Gd) and Gadolinium-based contrast agents (GBCAs). Summarize the current literature on GBCA deposition. Examine the controversies regarding unresolved questions and clinical applications of these findings.

Results

Gd deposition occurs in the brain with highest amount in the dentate nucleus. Degree of deposition corresponds with cumulative dose of GBCAs. Amount of deposition is significantly higher with linear agents. Majority of deposition occurs in the capillary endothelium with some in the neural interstitium, suggesting ability to cross the blood-brain barrier. Deposition occurs even with normal renal function.

Conclusions

Further questions remain regarding: the chelation state of deposited Gd, the capacity for clearance, the clinical significance of these findings, especially in pediatric patients, women of childbearing age, and patients who may require frequent exams. Until then, all radiologists should ensure that contrast is required, select the best possible agent and dose, and document accurately when administering GBCAs.

eEde-166

Tips for Optimizing Workstation Efficiency, Beyond the Basic IT Setup

J Lally¹, C Sitton¹

¹*The University of Texas Health Science Center at Houston, Houston, TX*

Purpose

In the era of ever-increasing study volumes, declining reimbursement, and increased availability of around the clock remote reading, physician productivity and efficiency has emerged as a primary focus in practice management and radiologist performance. While factors upstream and downstream from radiologist interpretation are critically important, the actual acts of navigating the picture archiving and communication software (PACS), utilizing the voice recognition software, and referencing additional resources are highly individual. While most radiologists are content using the standard IT provided software and computer input devices, many additional options are available, at low or no cost, for workflow optimization and personalization. This exhibit will demonstrate how to utilize multiple commercially available input devices, microphones, automation software, and voice recognition, as well as overcoming the obstacles limiting their implementation.

Materials and Methods

Workplace factors: working within the limitations of your system Programmable devices: keyboards, keypads, alternative input devices and mice Hands-free dictation: headsets and table-mounted microphones Automation software: key-binding, remapping, hotkeys, auto-correct, and shortcuts Voice recognition beyond the basic: advanced pick lists, findings mode, and nested macros Putting it all together: designing and customizing your optimal work-flow

Results

Beyond the mouse and keyboard, the use of alternative input devices has been shown to increase radiology efficiency when viewing large CT angiography data sets. While many devices and software programs are available, one must consider the factors unique to their workplace. For example, the individual who switches workstations often and is forbidden to install software, true plug-and-play

Electronic Educational Exhibits

devices are a necessity. In all cases, adopting a hands-free microphone will allow one hand to always remain on the keyboard/keypad. VR and automation software can tremendously augment work-flow.

Conclusions

While the standard PACS workstation is adequate in providing the radiologist with the basic needs of reporting, it is often set up as a one-size-fits-all approach. Use of multiple customizable devices and software provides the greatest gains in efficiency by reducing unnecessary clicks, reduced window navigation, creating shortcuts, and ultimately "keeping the eyes on the images".



(Filename: TCT_eEde-166_Workflow.jpg)

eEde-161

Training and Assessment of First-year Resident Milestones in Neuroradiology Using the Educational Platform Thinkific

S Calle¹, E Bonfante-Mejia¹, R Riascos¹

¹The University of Texas Health Science Center at Houston, Houston, TX

Purpose

1. To examine the difficulties in establishing clear milestones for the first-year resident neuroradiology rotation
2. To discuss the lack of material that highlights fundamental skills required for basic head CT interpretation
3. To propose a method to ensure the rotation milestones are met and a reproducible and objective assessment is carried out

Electronic Educational Exhibits

Materials and Methods

It is our goal to complete an entire online course of fundamental head CT interpretations skills that can reinforce the subjects encountered in the first year neuroradiology rotation. Training modules were created using Microsoft PowerPoint. These presentations led the trainee through the process of approaching a head CT following a simple checklist and a diagnostic algorithm with accompanying images. The idea was to simulate the training process encountered between the attending and the first year-resident in the reading room in an independent self-study manner. Fundamental concepts including cerebral edema, stroke imaging, herniation syndromes and trauma can be introduced in this fashion. The web-based educational platform Thinkific provides an intuitive and user-friendly interface to upload training modules in a variety of formats and create evaluations, free of charge. The quiz setting allows the user to develop multiple choice questions and insert images to test the trainee on the previously presented topics. The evaluations can be modified to require a certain percentage of correct answers to establish that the trainee has understood the material. The results are forwarded to the instructor for review.

Results

A recurrent challenge encountered in academic institutions is to develop radiology rotations that have clearly defined expectations for residents. In particular, in our institution, radiology residents complete one to two months of neuroradiology exposure before beginning to take call in the emergency room during their second year of residency. For this reason, it is crucial that we determine, in an objective manner, that our residents are equipped with sufficient knowledge and understanding of the fundamentals of head CT in the emergency setting to carry out their duties on call. Surprisingly, material that covers basic head CT interpretation skills in a step-by-step manner is scarce. For residency program directors this tool may prove useful in guaranteeing the trainees have met their neuroradiology milestones prior to taking call. For the residents, these modules can be reviewed at any time to refresh fundamental concepts.

Conclusions

The potential applications of utilizing Thinkific as a platform for resident training and evaluation are limitless. Its flexibility of design and customization options can adapt to the individual needs of the section. On-the-go access to the site provides a valuable tool for the education of trainees and the overall academic improvement of the department both in and out of the reading room. Multimedia capabilities allow for the integration of cases, articles, videos, and other files and webpage clips, which further enhance the learning experience. Future projections of this initiative include expanding its accessibility to other users outside our section, possibly initially to other sections in our department and then progressively to other institutions and the general public. As more people become involved, our hope is that ideas for the potential uses and applications of the platform will continue to grow and evolve.

Dashboard
Fundamentals of Neuroradiology

Chapters

Achievements & Progress 0 / 10

Discussion

Search by lesson title

Learning Cerebral Edema

- Part I: General Overview
- Part IIa: Algorithm Introduction
- Part IIb: Fundamentals of Cerebral Edema
- Part IIc: Vasogenic Edema
- Part IId: Cytotoxic Edema
- Part IIe: Transepndymal Edema
- Part IIIf: SPOT the differences and similarities- Case 1
- Part IIg: SPOT the differences and similarities- Case 2

Part IIIf: SPOT the differences and similarities- Case 1

PREV SLIDE Page 3 of 10 NEXT SLIDE

No audio for this slide.

Can you see the differences and similarities between these two cases?

VS.

NEXT

Dashboard
Fundamentals of Neuroradiology

Chapters

Achievements & Progress 1 / 10

Discussion

Search by lesson title

Learning Cerebral Edema

- Part I: General Overview
- Part IIa: Algorithm Introduction
- Part IIb: Fundamentals of Cerebral Edema
- Part IIc: Vasogenic Edema
- Part IId: Cytotoxic Edema
- Part IIe: Transepndymal Edema
- Part IIIf: SPOT the differences and similarities- Case 1
- Part IIg: SPOT the differences and similarities- Case 2

Cerebral Edema Post-Training Assessment

Question 1/1 1 Correct

What type of edema is seen on the following image?

Choose only ONE best answer.

- A Vasogenic edema
- B Cytotoxic edema
- C Transepndymal edema

RETAKE NEXT

(Filename: TCT_eEde-161_Picture1.jpg)

Electronic Educational Exhibits-Interventional

eEde-169

An Update on Programmable CSF Shunt Valves: Identification, MR Safety, and Potential Pitfalls

J Costello¹, U Rassner¹

¹*University of Utah, Salt Lake City, UT*

Purpose

Programmable CSF shunts are commonly used devices for the treatment of complex hydrocephalus [1]. As opposed to traditional fixed CSF shunt valves, programmable devices allow the operator to alter the amount of CSF drainage, depending on the clinical context. This provides for serial intracranial pressure optimization and can ultimately prevent over or underdrainage of CSF, without the need for shunt revision or valve replacement [2]. With their increased use, many different programmable CSF shunt valves have been developed by various manufacturers, each with distinct radiographic appearances, CSF drainage settings, and MR safety considerations. Recognizing, understanding and accurately reporting these devices can be a challenging task, particularly in a typical busy neuroradiology practice. In addition to those discussed by Lollis et.al. [3], there are several other programmable shunt devices that are currently being used and new MRI safety considerations have also been raised. The goal of this education exhibit is to provide an updated resource for radiologists to refer to for the routine imaging interpretation of programmable and fixed pressure CSF shunt valves. We also review updated MR safety considerations regarding each shunt device.

Materials and Methods

Radiographic appearance of each programmable CSF shunt device was obtained using images collected within the University of Utah radiology department and published manufacturer data. Manufacturing brands included were Medtronic, Sophysa, Aesculap AG, and Codman/Johnson & Johnson. Examples of fixed CSF shunt devices are also displayed for each brand. Published manufacturer settings were obtained and depicted for each shunt. Updated MR safety considerations are discussed, based on published guidelines and user experience within the University of Utah radiology department.

Results

Programmable shunt valves are distinguished from fixed valves by the presence of a radiopaque rotatory component, often containing a notch. There may also be a small radiopaque marker used to determine laterality of the device. The radiographic appearance of different programmable valves is unique between different manufacturers. However, if unfamiliar with their appearance, certain valves can be confused, one pair in particular being the Codman Certas Plus (Fig.1 A) and Sophyseal valves (Fig.1 B), which have some analogous imaging features. Some manufacturers have a similar programmable valve setting scheme for all of their valves (all five versions of Medtronic Strata valves), while others have a unique setting scheme for each model produced by the same manufacturer (Codman Hakim and Codman Certas Plus). Furthermore, while some programmable valves have a limited number of distinct settings (Medtronic Strata and Sophysa valves for example), others have a continuously variable range of settings (Codman Hakim). In general, programmable shunt devices have been rated MRI safe or conditional, although, shunt valve settings can potentially be modified or lose the ability to be adjusted after MRI scanning. Due to these potential MRI interactions, the Codman Certas Plus (2013), Strata II (2017), and Strata NSC (2017) shunts have been recalled by their manufacturers. For this reason, all programmable shunt valve settings should be assessed following an MRI study.

Conclusions

Programmable shunt valves are useful devices in the treatment of complex hydrocephalus and their use can prevent unnecessary surgeries for shunt revision or valve replacement. Being able to accurately recognize and interpret programmable shunts is essential for any neuroradiology practice. Due to potential MRI interactions with programmable shunt valves, settings should be assessed following an MRI exam.

Recognition of fixed pressure valves is also important, to avoid unnecessary MRI screening radiographs for patients with these devices in place.

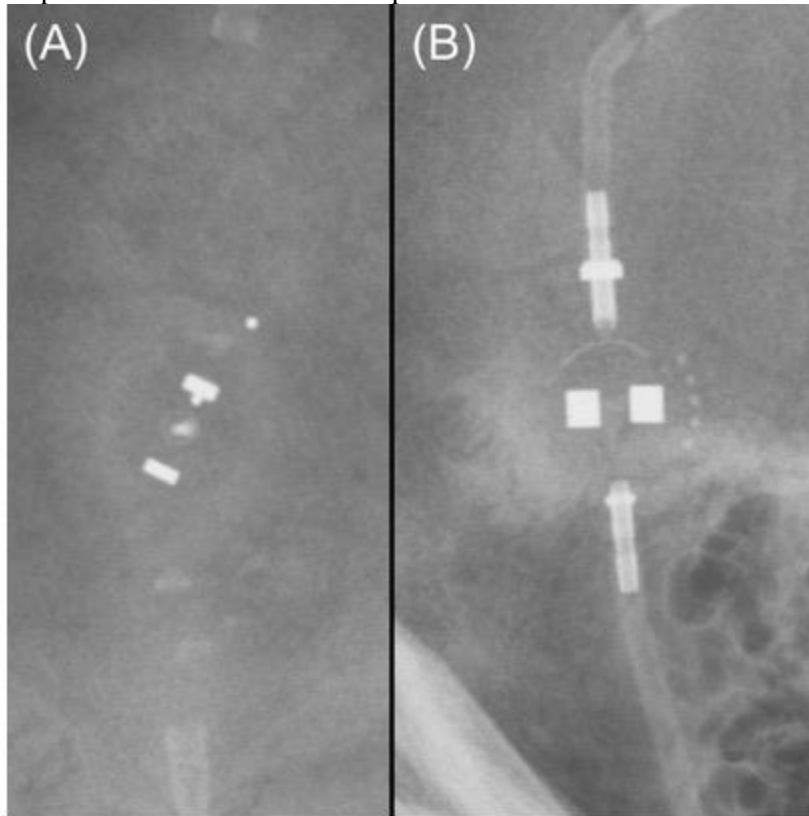


Figure 1 A: Codman Certas Plus valve. Figure 1 B: Sophysa Polaris valve. The Sophysa valves are distinguished by five adjustable positions on the left aspect of the device. The rotatory components of both devices appear similar.

(Filename: TCT_eEde-169_Figure1and2.jpg)

eEde-167

Endovascular Treatment of Adult Galenic Dural Arteriovenous Fistulas: Technical Considerations

I Khan¹, S Swaminathan², T Hui³, F Hui¹

¹National Neuroscience Institute, Singapore, Singapore, ²SingHealth, Singapore, Singapore, ³Tan Tock Seng Hospital, Singapore, Singapore

Purpose

Adult Galenic dural arteriovenous fistulas (DAVFs) represent a rare subgroup of tentorial DAVFs that carries a high risk of hemorrhage and has an aggressive clinical course (1). Treatment is particularly challenging due to their deep location, proximity to crucial structures, associated venous occlusions and multidirectional arterial feeders (2). We present a series of three patients with Galenic DAVFs treated by transarterial Onyx glue injection with varying degrees of shunt closures.

Materials and Methods

Between 1 Jan 2011 and 1 Dec 2016, we retrospectively reviewed all cases of intracranial DAVFs managed endovascularly in the department. The records of three adults with Galenic DAVF were evaluated for the type and number of treatment sessions, degree of penetration of Onyx glue and the angiographic as well as clinical outcomes.

Results

Case 1: 35-year-old male presented with seizures and was treated in a single session. The glue injected intra arterially filled the fistulous site without penetration of the Vein of Galen. The shunt was completely occluded and the patient had no neurological deficits. Case 2: 51-year-old male underwent two sessions of transarterial glue embolization during which glue was injected through the fistula, completely filling the dilated Vein of Galen. Check angiography confirmed complete closure of the DAVF. The patient remained well clinically and seizure free. Case 3: 44-year-old male presented with seizure and dementia and underwent multiple sessions of embolization. After the last session, flow through the DAVF was markedly reduced but still present. His dementia improved and he remained seizure free.

Conclusions

Adult Galenic DAVFs can be treated effectively by transarterial glue embolization. Proper penetration of the liquid embolic agent is a prerequisite for achieving angiographic cure of the fistula, as shown in the results of this case series.

eEde-171

From NINDS till DAWN: A Radiologist's Guide to the Evolving Role of Intravascular Therapy for Acute Ischemic Stroke

M Gelbman¹, S Patel², S Lev²

¹*Nassau University Medical Center, Brooklyn, NY*, ²*Nassau University Medical Center, East Meadow, NY*

Purpose

We perform a comparative analysis of landmark clinical trials regarding the efficacy of various intravascular stroke therapies. We intend to familiarize the radiologist with current evidence-based trends in acute stroke management to aid delivery of timely and appropriate intervention.

Materials and Methods

We review and summarize major findings from large scale randomized clinical trials of intravenous (IV) and intra-arterial (IA) stroke therapy. Clinical outcomes, differences in methodology, types of mechanical devices utilized, patient selection, and differences in therapeutic window are emphasized. We employ a variety of novel graphical representations to improve understanding of complex data.

Results

Diagnostic and interventional algorithms for acute ischemic stroke (AIS) are continuously evolving and can be a source of confusion for radiologists and our clinical colleagues. The landmark NINDS trial, supported by other large scale trials including ECASS II and ECASS III, established improved clinical outcomes in patients that receive IV-tPA administered up to 4.5 hours after symptom onset. Subsequent clinical trials (PROACT I & II) demonstrated the safety and efficacy of local IA delivery of recombinant pro-urokinase (pre-UK), especially in large-vessel MCA occlusion. Early trials utilizing mechanical thrombectomy devices, namely Merci Retriever and PENUMBRA embolectomy device, showed even higher recanalization rates. Second generation devices (e.g. SOLITAIRE and TREVO) demonstrated superiority over Merci Retriever (SWIFT and TREVO II trials). In 2013, three trials (MR RESCUE, SYNTHESIS, and IMSII) showed disappointing results with no significant benefit over IV t-PA. However, critics point to multiple design flaws including limited use of second generation devices. In 2015, five randomized clinical trials (MR CLEAN, EXTEND-IA, ESCAPE, SWIFT-PRIME, and REVASCAT) showed significant benefit of endovascular therapy compared to IV-tPA alone in appropriately selected patients up to 6-12 hours. A major breakthrough occurred in 2017 with the

publication of the DAWN trial showing marked clinical benefit to intra-arterial therapy in appropriately selected patients up to 24 hours after onset of AIS.

Conclusions

Diagnostic and interventional paradigms in stroke management are constantly evolving and the role for endovascular therapy continues to grow. Prompt diagnosis is essential. Awareness of emerging imaging modalities together with knowledge of clinical information relevant for patient selection is paramount. This will help the multidisciplinary team initiate appropriate and timely intervention and significantly reduce mortality and morbidity.

eEde-170

Pediatric MR Cisternography for CSF Leak

C Shah¹, S Davis¹, T Chandra²

¹Nemours, Jacksonville, FL, ²Nemours, Orlando, FL

Purpose

1. To illustrate technique of MR Cisternography in children 2. Demonstrate diagnosis of CSF leak in 2 year old with recurrent meningitis 3. Discuss etiologies of CSF leak in children

Materials and Methods

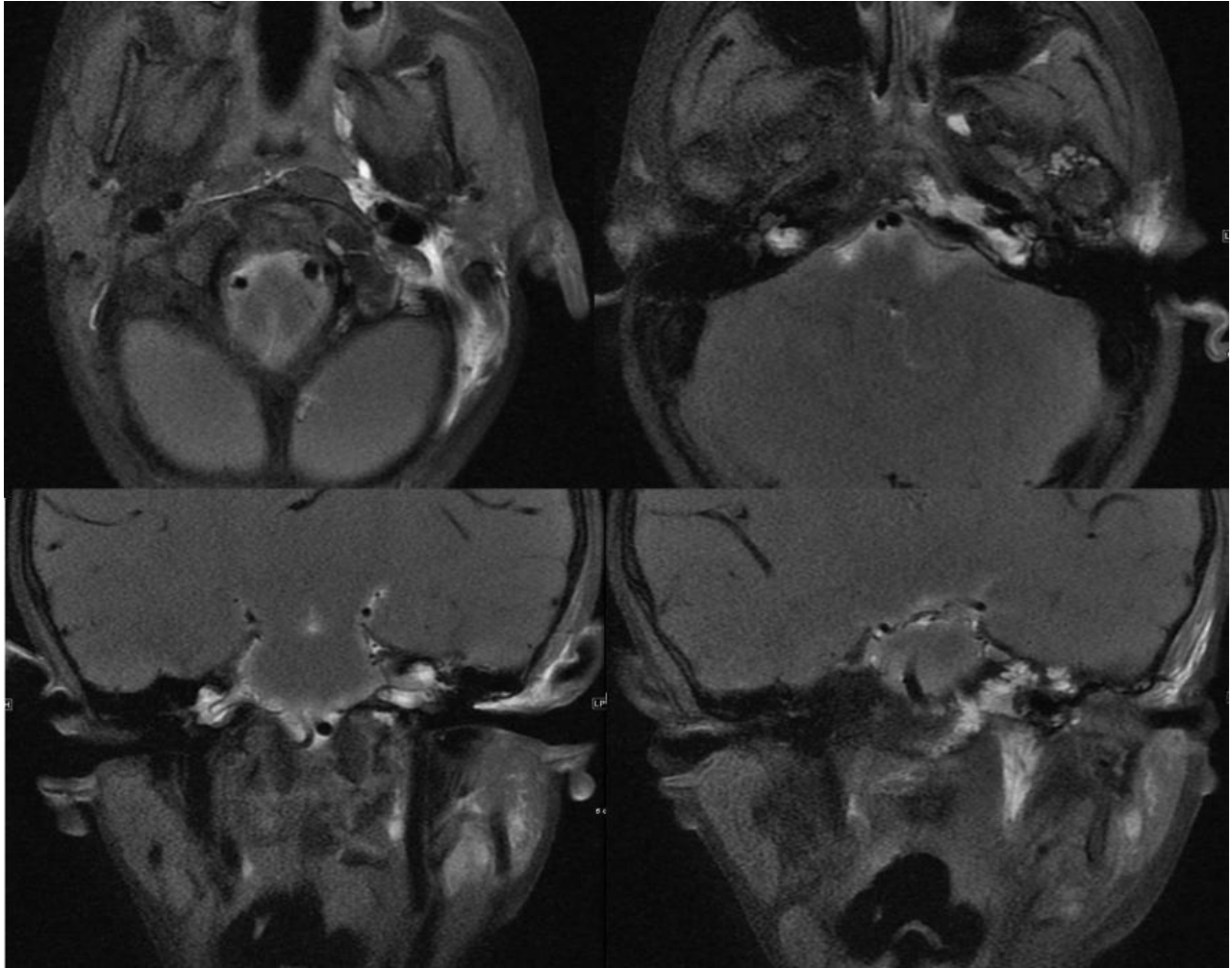
We illustrate the technique of pediatric MR Cisternography used at our tertiary care children hospital. Extensive CSF leak is demonstrated on MR Cisternography in a three-year-old girl.

Results

Technique of Pediatric MR Cisternography: Younger children may require anesthesia/sedation for the procedure. Our patient was three-year-old and required general anesthesia. After informed consent and proper prepping the thecal space was accessed with a 22-gauge spinal needle at the L4-L5 level with fluoroscopic confirmation. Clear CSF returned. CSF was sent for culture and sensitivity. 0.25 mL MultiHance previously mixed with 2.5 mL of sterile saline was gently injected into the intrathecal space over approximately 1 minute. The patient was repositioned supine for PICC placement (IV antibiotics for recurrent meningitis). Approximately 30 minutes after the intrathecal injection the patient was placed on a tilt table and placed in the Trendelenburg position, 25 to 30 degrees with the head tilted to the left for 10 minutes. The patient was then transferred to MRI for further imaging. MRI was performed with patient in supine position as required by anesthesia as the patient was intubated, However, child's head was turned to the left as the defect was suspected on the left side based on prior CT scan and MRI studies performed during prior episodes of meningitis. Findings: On the preintravenous contrast T1 fat-suppressed images, CSF is hyperintense, in keeping with T1 shortening from contrast in the CSF space from the lumbar puncture. However, also noted is T1 hyperintensity along the left petrous apex, which extends along the left parapharyngeal space, surrounding the left common carotid artery as well as the internal jugular vein. T1 hyperintensity is also noted surrounding the left mastoid and extension of this deep soft tissues adjacent to the occipital bone on the left side. On the coronal images, this contrast is also seen surrounding the left parotid gland and along the superior wall of the external auditory canal. This demonstrates extensive CSF leak. Discussion: Various etiologies of CSF leak will be discussed.

Conclusions

Pediatric MR Cisternography is an important diagnostic tool in the setting of recurrent meningitis and CSF leak.



(Filename: TCT_eEde-170_Picture3.jpg)

eEde-168

Radial Access and Neuro Interventions: From the Office to the Recovery Room

N Voutsinas¹, M Cai¹, R De Leacy¹, A Fischman¹

¹*Icahn School of Medicine at Mount Sinai Hospital, New York, NY*

Purpose

Transradial access (TRA) is now considered the default approach in many centers around the world for coronary interventions. Traditional transfemoral access (TFA) continues to be utilized in endovascular neurointerventions; however, TRA is becoming increasingly utilized. Certain clinical management issues need to be considered to ensure optimal patient selection for performing a procedure via TRA.

Interventional neuroradiology offers unique challenges including complex anatomy, severe disease, and time pressure when performing procedures such as stroke intervention via TRA. The purpose of this exhibit is to highlight the TRA technique and clinical concerns as it applies to endovascular neurointervention.

Materials and Methods

Prior to TRA, preprocedural evaluation is critical. Ultrasound is utilized to check for radial and ulnar artery size and anatomic variation. The modified Allen or Barbeau test is routinely performed to check for

ulnar collateral flow via the palmar arches to ensure adequate flow to the digits in the event of a radial artery occlusion post procedure. Barbeau D waveform is considered an absolute contraindication to TRA. Prior to prepping the patient for the procedure, administration of topical nitroglycerine and lidocaine can dilate the radial artery to make access easier (Beyer et al, PRE-DILATE study, 2013). Using ultrasound guidance, the radial artery is accessed with a 21g needle using a single wall technique and a hydrophilic introducer sheath is placed in the artery. A medication solution of heparin, verapamil and nitroglycerin is infused slowly via the sheath to provide vasodilation, decrease risk of radial artery spasm, and prevent thrombus formation around the access sheath. At the end of the procedure, the access sheath is removed and a compression band is placed at the arteriotomy and patent hemostasis is achieved allowing for flow in the radial artery during the compression period of 60-90 minutes.

Results

Most endovascular neurointerventions can be safely performed via TRA including stroke therapy, carotid stenting, thrombectomy, aneurysm and AV malformation embolization, vertebral intervention and angioplasty. Advantages of TRA over TFA include: faster recovery, immediate ambulation after anesthesia, lower risk of access site bleeding, and avoidance of tortuous aortic anatomy in select cases. TRA and TFA can be used simultaneously during complex interventions. Some of the potential complications of TRA, such as stroke or pseudoaneurysm at the access site, are also found with TFA in regards to neurointervention.

Conclusions

TRA is safe and effective in a wide variety of neurologic endovascular interventions including but not limited to: stenosis, aneurysms, AV malformation, and stroke. While TFA remains the traditional mode of access, TRA can be considered in the appropriate patient population. Prior to proceeding with TRA, patients should be assessed to ensure they are candidates. Excluding patients with poor ulnar collateral circulation, small radial artery size, or anatomic variations of the radial artery (ex: radial loop) is paramount to ensure patient safety and optimal patient selection. Complications from the procedure are rare and are mostly related to the unique anatomy of the radial artery and its access site.

Electronic Educational Exhibits-Pediatrics

eEde-179

Acute Pediatric Neurotoxicity: A Review

M Kontzialis¹, T Huisman²

¹Rush University Medical Center, Chicago, IL, ²Johns Hopkins University, Baltimore, MD

Purpose

The purpose of this exhibit is to review the various causes of acute neurotoxicity in children.

Materials and Methods

In acute pediatric neurotoxicity, the clinical information is often limited, and the clinical and imaging findings may be nonspecific. The various causes of pediatric neurotoxicity will be reviewed. Toxins affecting the pediatric brain may be divided in endogenous and exogenous.

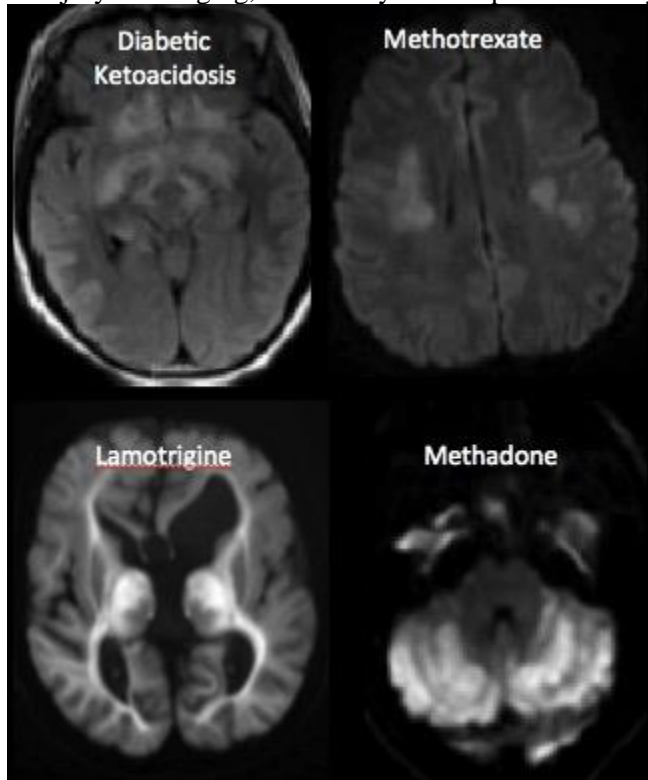
Results

Endogenous toxins include high or low concentration of "normal" metabolites, such as glucose and bilirubin. Endogenous toxins also include accumulation of "abnormal" metabolites, as is the case in inborn errors of metabolism. Exogenous toxins include therapeutic agents (i.e., methotrexate, cyclosporine, tacrolimus, propofol, vigabatrin, lamotrigine), drug overdose (i.e., cocaine, methadone, tricyclic antidepressants), and accidental toxic exposure and ingestions (i.e., carbon monoxide, glue). The status of myelination at the time of injury may determine the pattern of injury, as in maple syrup urine disease. Combined treatments may potentiate neurotoxicity, as is the case with methotrexate and whole

brain radiation. Typical neurotoxic imaging findings in children include posterior reversible encephalopathy syndrome, acute toxic encephalopathy, and reversible splenial lesions. Commonly implicated therapeutic agents include methotrexate, and cyclosporine. Anti-epileptic drugs tend to have a more central pattern of injury. Cerebral edema and stroke may occur in complicated cases of diabetic ketoacidosis. Hypoglycemia tends to involve the parieto-occipital lobes, and may lead to hypoglycemic stroke. The globi pallidi may be involved in hepatic failure, total parenteral nutrition and carbon monoxide poisoning. Methadone overdose may cause cerebellar and watershed infarcts. Tricyclic antidepressant overdose may lead to cerebellar and basal ganglia lesions.

Conclusions

Familiarity with the various causes of toxicity in the pediatric brain is essential. There are various patterns of injury on imaging, which may be nonspecific or they may point towards the correct diagnosis.



(Filename: TCT_eEde-179_pediaticneurotoxicityfigure.jpg)

eEde-181

Adding Insult to Injury: Methotrexate Neurotoxicity in Acute Lymphocytic Leukemia

K Barton¹, J Nickerson¹

¹University of Vermont Medical Center, Burlington, VT

Purpose

The purpose of this educational exhibit is to present a case-based review of the findings of methotrexate-related neurotoxicity in the setting of acute lymphocytic leukemia.

Materials and Methods

Acute lymphocytic leukemia (ALL) is the most common pediatric malignancy, accounting for approximately 25% of all pediatric cancers. ALL can directly affect the CNS via leukemic infiltration of the brain and meninges. Treatment of CNS disease with intrathecal methotrexate can, proverbially, add

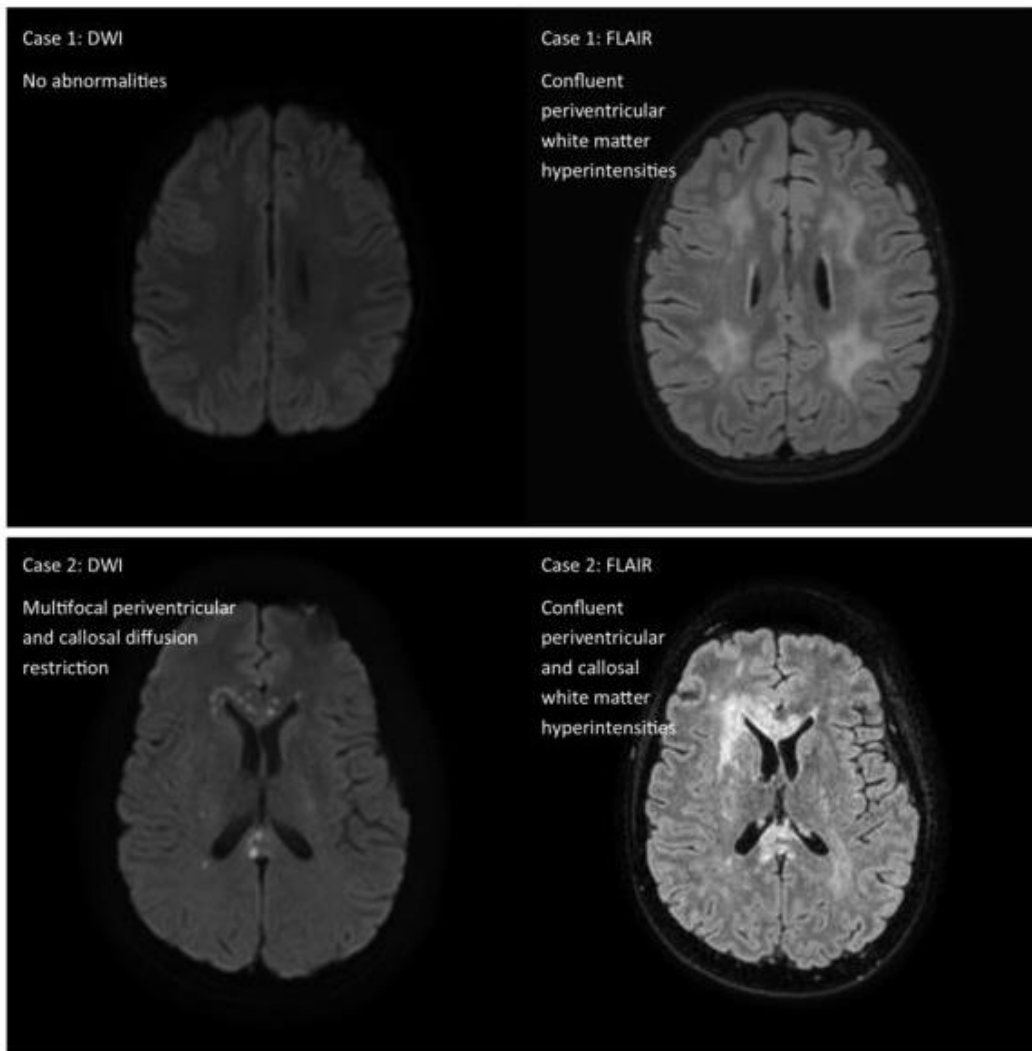
insult to injury resulting in methotrexate-related neurotoxicity. Up to 18% of patients undergoing therapy for ALL can experience acute treatment-related neurotoxicity.

Results

There is a spectrum of MR imaging findings in methotrexate-related neurotoxicity. White-matter hyperintensities on T2 and T2 FLAIR are most common, typically diffusely distributed, particularly involving the centrum semiovale. Associated abnormalities on diffusion-weighted imaging can be present as well, but not in all cases. The T2/FLAIR hyperintensities can progress or can wax and wane over time. In this case-based educational exhibit we will illustrate the spectrum of findings with multiple cases from our institution.

Conclusions

Acute lymphocytic leukemia is the most common childhood malignancy, and neither CNS disease nor symptomatic treatment-related neurotoxicity is rare. The clinical presentation in methotrexate-related neurotoxicity often mimics stroke, with acute-onset sensory, motor, and/or speech deficits. Therefore familiarity with the MR imaging findings of methotrexate-related neurotoxicity is critical to differentiate this diagnosis from acute ischemia and from progression of CNS disease.



(Filename: TCT_eEde-181_ASNRsubmissionimages.jpg)

eEde-177

Brain Tumor Mimics in Alexander Disease

A Vossough¹

¹*Children's Hospital of Philadelphia, University of Pennsylvania, Philadelphia, PA*

Purpose

Alexander disease is a rare leukodystrophy and neurodegenerative disorder. It is an autosomal disorder caused by mutations in the glial fibrillary acidic protein (GFAP) that maps to chromosome 17. The infantile or type I form of the disease is classically depicted as a frontal-predominant leukodystrophy, often with macrocephaly. The type II form of the disease has a more variable imaging appearance. The purpose is familiarize neuroradiologists with cerebral masses mimicking brain tumors occurring in Alexander disease patients.

Materials and Methods

This educational exhibit will depict the spectrum of masses and pseudo-masses in Alexander disease patients. The exhibit will illustrate educational cases of imaging findings of brain masses in this population, which are not true tumors. The potentials for misdiagnosis will be explored. The cases will be selected from an institutional cohort of 30 Alexander disease patients. Relevant cases from the literature will also be included. Diagnostic tips that may be helpful for diagnosis will be provided.

Results

Tumor-like lesions in patients with Alexander disease can be seen in the brainstem, cerebellar peduncles, cerebellum, basal ganglia, olfactory regions, and optic chiasm. Brainstem lesions may occasionally be symmetric. These tumor-like lesions may appear focal, show significant mass effect, and even show contrast enhancement. They can closely mimic true brain tumors. These lesions are typically due to focal aggregation of cells with abnormal GFAP accumulation. Although these tumor-like lesions can slowly grow over time, they ultimately do not behave as typical progressive neoplasms.

Conclusions

Tumor-like brain masses can occur in various areas of the brain in patients with Alexander disease and often mimic serious cerebral neoplasms. Neuroradiologists should be aware of the appearance of these lesions in order to prevent unwarranted treatment and unnecessary invasive procedures in these patients.

eEde-178

Centrum Semiovale Diffusion Restriction: Its Not Just Methotrexate Toxicity

A Krishnan¹, K Tran², A Wang³

¹*Beaumont Health, Royal Oak, MI*, ²*Oakland University William Beaumont School of Medicine, Royal Oak, MI*, ³*Beaumont Hospital, Royal Oak, MI*

Purpose

A number of conditions can affect the centrum semiovale ranging from small vessel ischemia through metabolic derangements and toxicity. Diffusion-weighted abnormalities on the other hand are seen in a smaller group of conditions in this location. In particular, in children, well defined rounded restriction in the centrum semi-ovale has been considered pathognomonic for intrathecal methotrexate neurotoxicity. A few other conditions can, however, mimic these findings and should also be considered in the differential.

Materials and Methods

Cases affecting the centrum semiovale, particularly diffusion restricted lesions, were collected and will be presented with supporting clinical information to assist in the differentiation of the conditions.

Results

In addition to methotrexate toxicity, Charcot-Marie-Tooth Neuropathy X Type 1, post infectious

(influenza), and vascular pathologies such as venous hypertension from dural AvF were found to have a similar but slightly different pattern of imaging findings. Features such as clinical history, treatment, presence of other findings in the brain help separate some of these entities.

Conclusions

This exhibit will attempt to present a select group of conditions causing diffusion restriction in the centrum semi-ovale and, with the help of supporting features, help separate them.

eEde-201

Clival Masses in Children

D Gunda¹, S Jazbeh¹, A Nayab¹, W Green², M Lambert¹

¹*University of Oklahoma Health Sciences Center, Oklahoma City, OK*, ²*N/A, N/A*

Purpose

While clival lesions in the adult population are common and well-described in the literature, pediatric clival lesions are not as commonly encountered and therefore literature is scattered in case reports. The purpose of this exhibit is to discuss some of the frequently encountered and unusual pathologies that one could encounter in the clivus in children. The authors hope to have a single resource for reference to provide a differential diagnosis and differentiating imaging features.

Materials and Methods

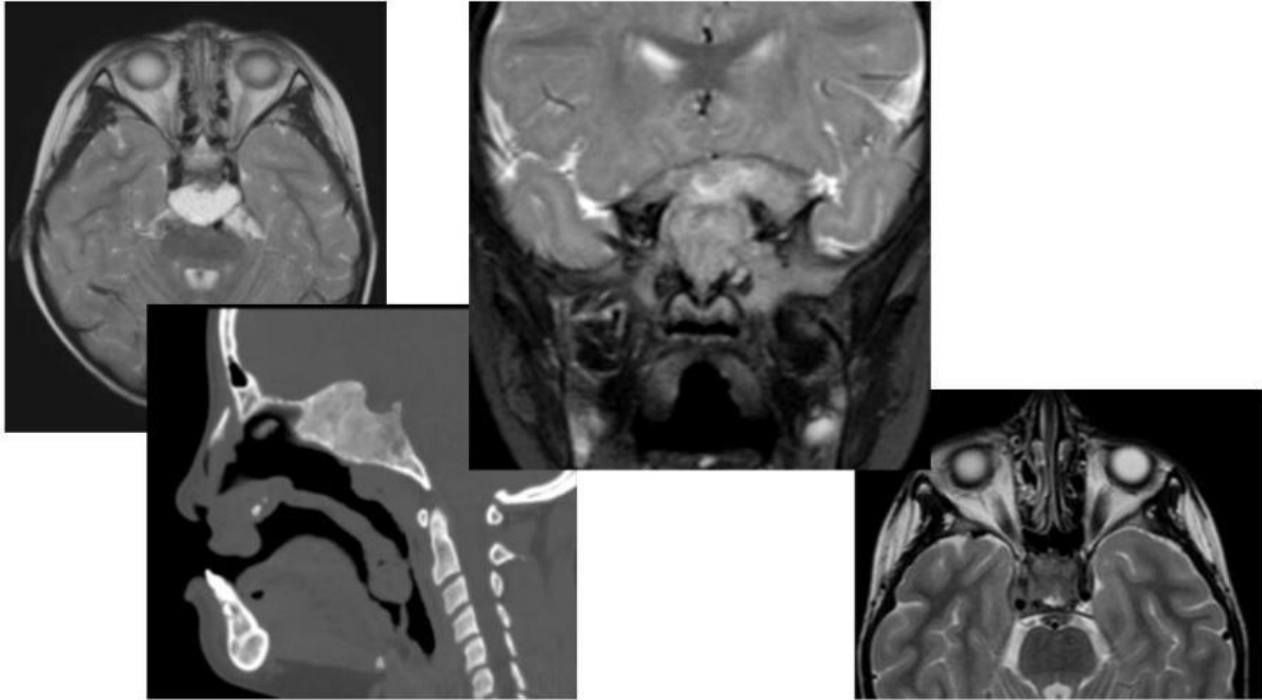
The authors assessed various lesions encountered in the clivus at our institution in pediatric patients. Pathologic confirmation was obtained on operated on lesions. A thorough literature search was performed to assess their incidence and differentiating imaging features.

Results

Because of relatively prominent hematopoietic marrow in children, MRI features of decreased T1 marrow signal in clival pathology is not as reliable. Therefore assessing the CT features and T2/diffusion-weighted images on MRI would be more valuable in children. Furthermore, common clival lesions in adults such as meningioma, pituitary macroadenoma and plasmacytoma should not be considered in children. Common diagnoses such as neuroblastoma metastases, lymphoma, leukemia, rhabdomyosarcoma and langerhan's cell histiocytosis should be the primary diagnoses in children. Some uncommon benign and malignant lesions include chordoma, fibrous dysplasia, ecchordosis physaliphora, arrested pneumatization of the sphenoid sinus, enchondroma and epithelioid hemangioendothelioma. Direct extension of skull base osteomyelitis, nasopharyngeal carcinomas and juvenile nasal angiofibromas should also be considered when assessing clival pathology in children.

Conclusions

It is important to understand that when encountering clival lesions in children, the differential diagnosis in adults does not apply to children. Because several of the lesions are not surgical lesions, it is important to have an understanding of the imaging features of the commonly encountered pediatric clival masses.



(Filename: TCT_eEde-201_ClivalMasses.jpg)

eEde-203

Comprehensive Imaging Review of the Wide Spectrum of Cavernous Sinus Region Pathology in the Pediatric Population

F Lu¹, K Shekdar¹

¹*Children's Hospital of Philadelphia, Philadelphia, PA*

Purpose

Cavernous sinus (CS) is a small but complex structure containing vital neurovascular structures. A wide range of pathologies can affect the CS, either arising from different components within the CS or from adjacent structures and spaces. Although a number of articles have reported cavernous sinus pathologies in adults, comprehensive imaging review of cavernous sinus region pathology in pediatric population is sparse. The purpose of this exhibit is to review the spectrum of cavernous sinus pathologies encountered in the pediatric population on multimodality imaging particularly on computed tomography (CT) and magnetic resonance (MR) imaging, and to highlight specific imaging features of many common and uncommon CS lesions.

Materials and Methods

Following IRB approval we retrospectively reviewed imaging features of CS involvement in pediatric patients affected by various disease processes primarily on CT and MR imaging. All studies were performed on either a 3 Tesla or 1.5 Tesla Siemens MRI scanner utilizing a brain and cavernous sinus protocol MRI without and with gadolinium contrast. Many of the reviewed studies had unenhanced or contrast enhanced CT imaging preceding the MR study, or as the only imaging study.

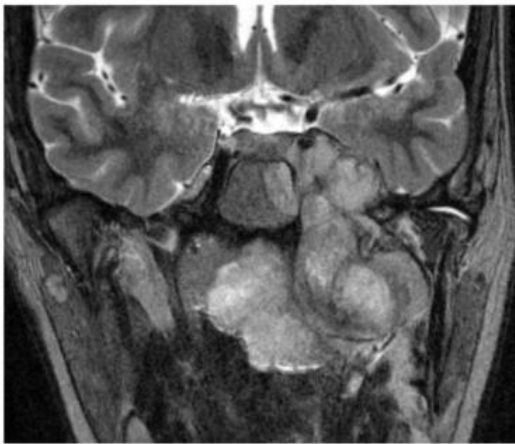
Results

Basic anatomy of the CS will be reviewed with emphasis on imaging anatomy of CS on CT and MR. The imaging protocol on both CT and MR for optimal evaluation of the CS in children of different ages groups will be discussed. The imaging findings of common and uncommon lesions involving the CS will

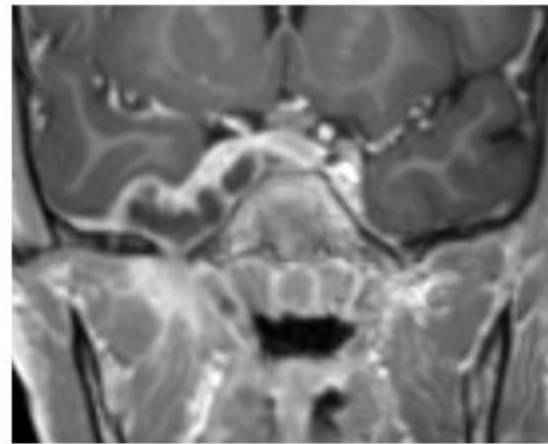
be presented in the following categories: 1. Neoplasms: a) primary tumors arising from contents of the CS, such as neurofibromatosis, schwannoma, meningioma. b) tumors arising from the surrounding structures and spaces and extending into the CS, such as rhabdomyosarcoma, juvenile nasopharyngeal angiofibroma, Langerhans cell histiocytosis, chordoma, pituitary macro-adenoma, atypical teratoid/rhabdoid tumor, teratoma, lymphoma and a rare case of craniopharyngioma extension c) Metastases: from neuroblastoma, osteosarcoma, leukemia/chorioma. 2. Infectious and inflammatory conditions such as abscess extension from the paranasal and oto-mastoid infection, CS thrombosis/thrombophlebitis, meningitis. 3. Vascular: infantile hemangioma and vascular lesions associated with PHACES syndrome, hemangioendolymphoma and 4. Miscellaneous: including but not limited to dermoid/epidermoid, fibrous dysplasia, arachnoid cyst.

Conclusions

CS is a critical anatomic landmark which is surrounded by many structures and spaces. CS can be involved by a wide variety of disease processes some which are unique to the pediatric population. Familiarity with imaging features of these CS disease processes in children can aid the diagnosis and appropriate treatment.



Nasopharyngeal rhabdomyosarcoma



Sphenoid sinusitis with epidural abscess extending to cavernous sinus

(Filename: TCT_eEde-203_ASNRCavernousSinus3.jpg)

eEde-194

Congenital Brain Anomalies: Easy as 1-2-3

M Ho¹

¹Mayo Clinic, Rochester, MN

Purpose

1. Discuss fundamental concepts of brain development 2. Demonstrate key imaging features of various brain malformations 3. Utilize a simplified diagnostic approach for rapid assessment and classification

Materials and Methods

We will review key steps in brain embryology and propose a simplified classification for congenital malformations: (1) formation, (2) destruction, and (3) migration. Multiple radiologic examples will be presented, with correlation of pathogenesis and neuroimaging features.

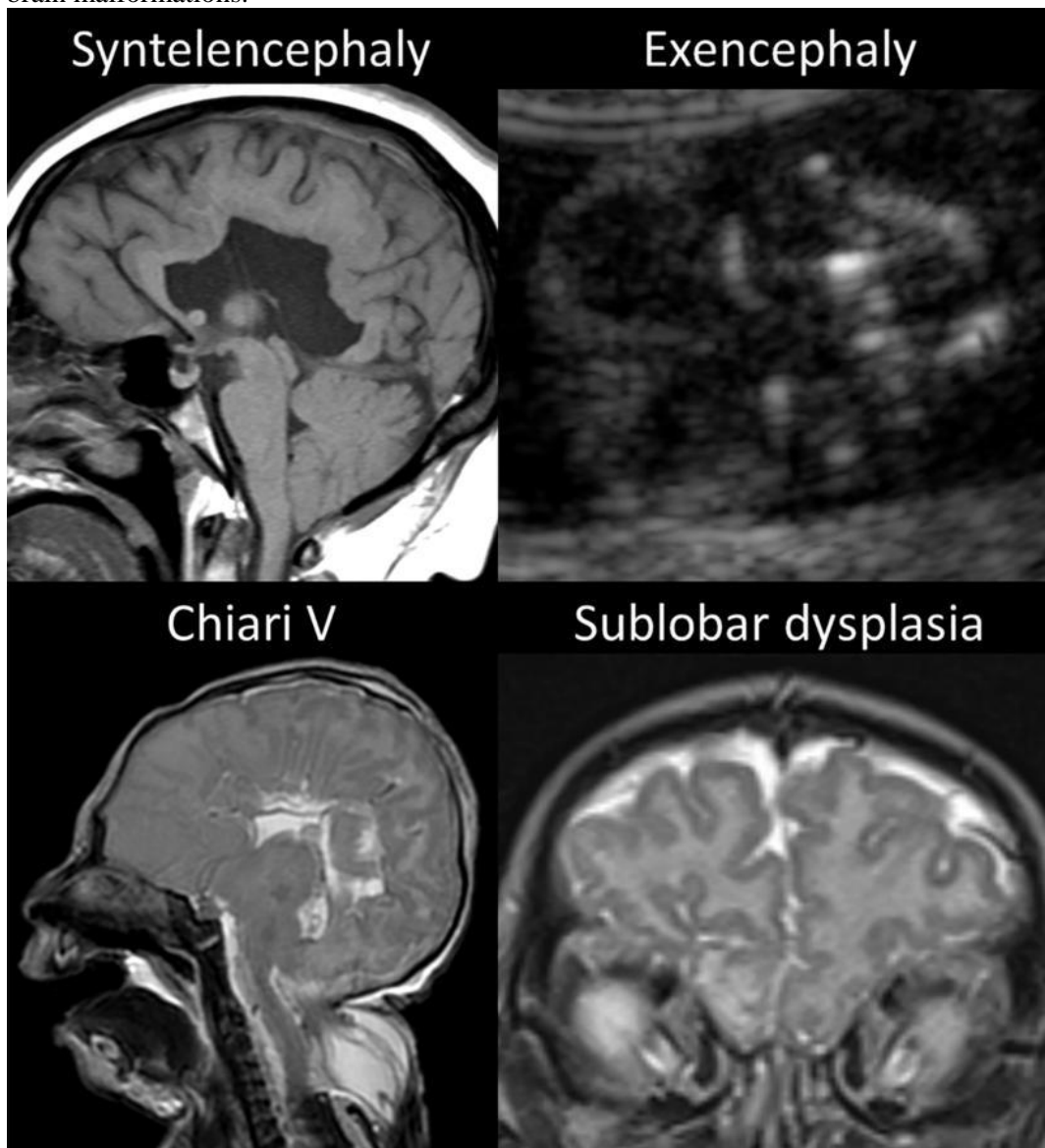
Results

Part 1: Formation Midline commissures - Corpus callosum, anterior, posterior, hippocampal, habenular
Callosal dysgenesis - Colpocephaly, Probst and sigmoid bundles Septo-optic dysplasia - Partial, complete,

Electronic Educational Exhibits

plus Holoprosencephaly - Lobar, semilobar, alobar, middle interhemispheric Chiari malformations - Type 0-5 Dandy-Walker spectrum - D-W malformation, variant, mega cisterna magna, Blake pouch cyst Joubert syndrome - DTI and related syndromes Rhombencephalosynapsis Part 2: Destruction Acrania - exencephaly - anencephaly sequence Schizencephaly - 1st trimester, closed vs. open-lip Porencephaly - 2nd trimester, minimal astrogliosis Hydranencephaly Maximal hydrocephalus Encephalomalacia - 3rd trimester & postnatal Part 3: Migration Gray matter heterotopia - Periventricular/subependymal, subcortical/columnar, band, leptomenigeal Lissencephaly - Type I (classic): undermigration, agyria/pachygyria variants - Type II (cobblestone): overmigration, congenital muscular dystrophy Polymicrogyria - Late migration / early cortical organization - Diverse etiologies, morphologies Focal cortical dysplasia - ILAE classification (I-III) Megalencephaly Sublobar dysplasia Compound dysplasias Conclusions

Congenital brain anomalies can be classified into abnormalities of (1) formation, (2) destruction, and (3) migration. Knowledge of key imaging features and embryologic principles aids in evaluation of complex brain malformations.



(Filename: TCT_eEde-194_Congenitalbrain.jpg)

eEde-191

Congenital Cystic Malformations of the Posterior Fossa: A Review of Pre and Postnatal Imaging

C Scelsi¹, S Nazarian¹, S Forseen¹, M Bajaj¹

¹*Augusta University, Augusta, GA*

Purpose

With recent advances in neuroimaging over the past few decades, congenital posterior fossa abnormalities are being diagnosed with greater frequency and accuracy, especially in the prenatal period. Accurate diagnosis is crucial for prognostic implications and to prompt evaluation for other associated structural anomalies. Congenital malformations of the posterior fossa encompass a wide spectrum of diseases; however, in this education exhibit, we will primarily review cystic malformations of the posterior fossa.

Materials and Methods

Our review will include a brief review of posterior fossa anatomy and basic embryology. Cases will be selected from our case files across multiple imaging modalities and presented with provided clinical history and treatment if available.

Results

Multiple cases will be presented to include the Dandy-Walker spectrum, arachnoid cyst, mega cisterna magna, Blake's pouch cyst, and Joubert syndrome illustrated on fetal MRI, pre and postnatal MRI and cranial ultrasound. Other associated anomalies seen on these cases will also be discussed.

Conclusions

Cystic malformations of the posterior fossa can pose a diagnostic challenge to radiologists. With recent advances in imaging, accurate and early diagnosis is critical to planning therapy and prognostic implications. Here, we review common and uncommon cystic malformations of the posterior fossa and how to distinguish between them.

eEde-186

Craniofacial Fibrous Dysplasia: Beyond Ground Glass Bony Matrix

S Kushchayev¹, Y Kushchayeva², T Glushko¹, K Pen², F Brown¹, O Teytelboym¹, M Collins², A Boyce²

¹*Mercy Catholic Medical Center, Darby, PA*, ²*National Institutes of Health, Bethesda, MD*

Purpose

Fibrous dysplasia (FD) is a congenital non-neoplastic disorder secondary to sporadic mutation of the α -subunit of the Gs stimulatory protein. Osseous changes are characterized by replacement and distortion of the normal bone with poorly organized, structurally unsound, fibrous tissue. The disease process may be localized to single or multiple bones. In McCune-Albright syndrome (MAS), FD is associated with hyperfunction of endocrine organs and overproduction of melanin in the skin. In Mazabraud syndrome, FD is associated with intramuscular myxomas. In radiology, FD is very often unconditionally associated with the term "ground glass matrix." However, FD is a complex disease, and knowledge of its unique pathogenesis and course of the disease is crucial for neuroradiologists to interpret imaging findings and potential complications. This presentation aims to illustrate the spectrum of radiologic findings of osseous and extra-osseous abnormalities associated with craniofacial FD, and review complications related to craniofacial FD.

Materials and Methods

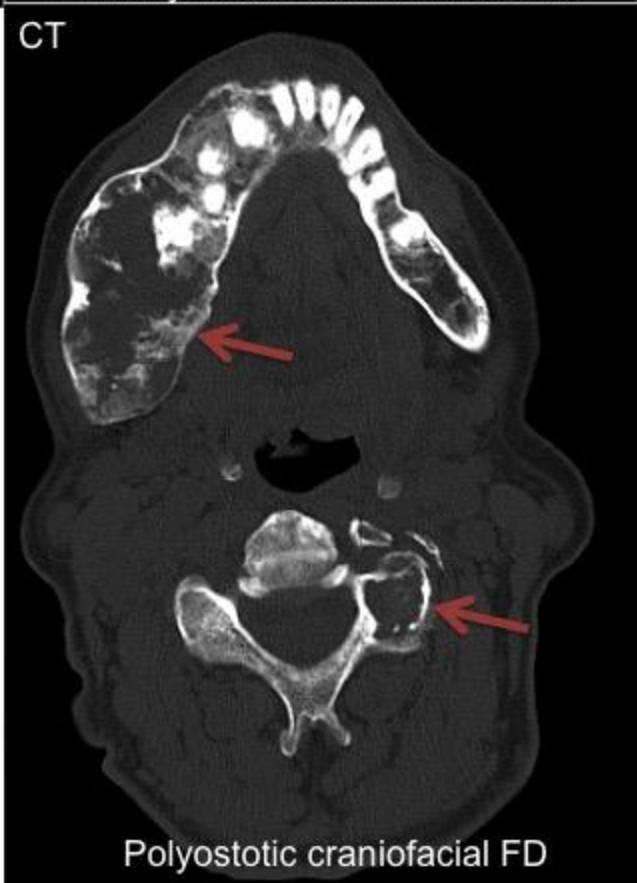
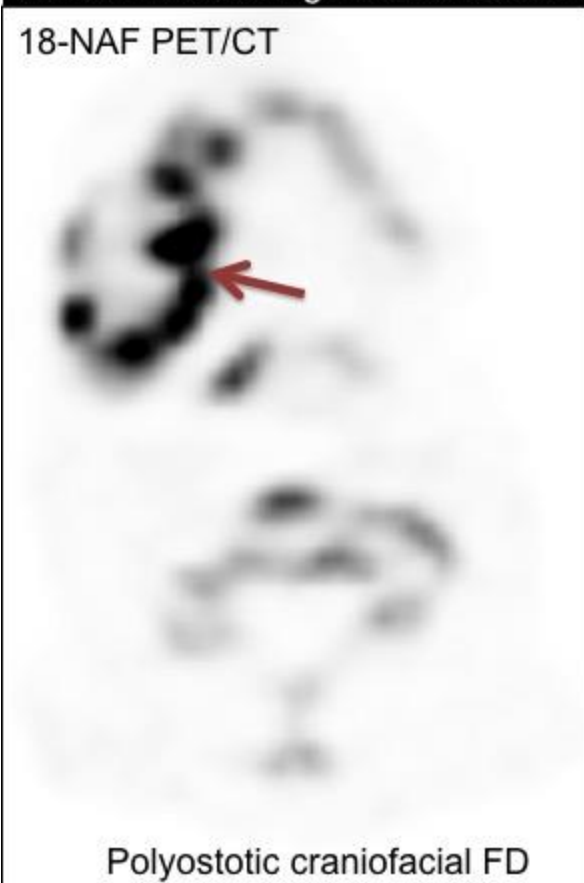
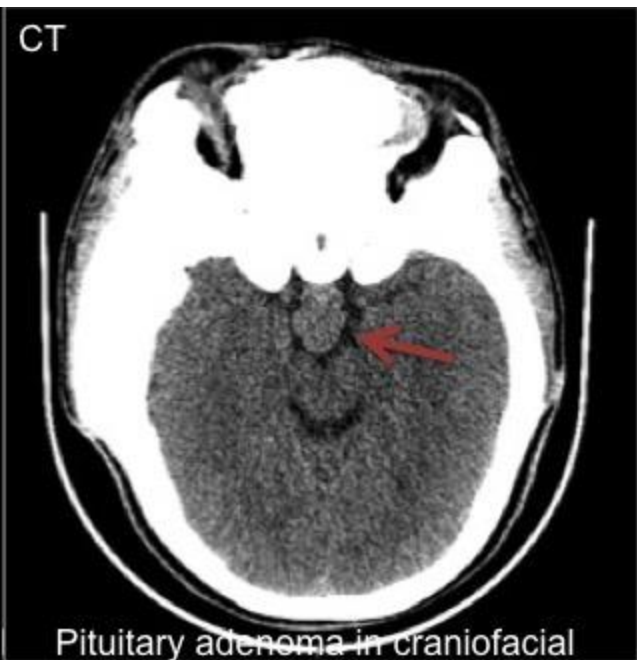
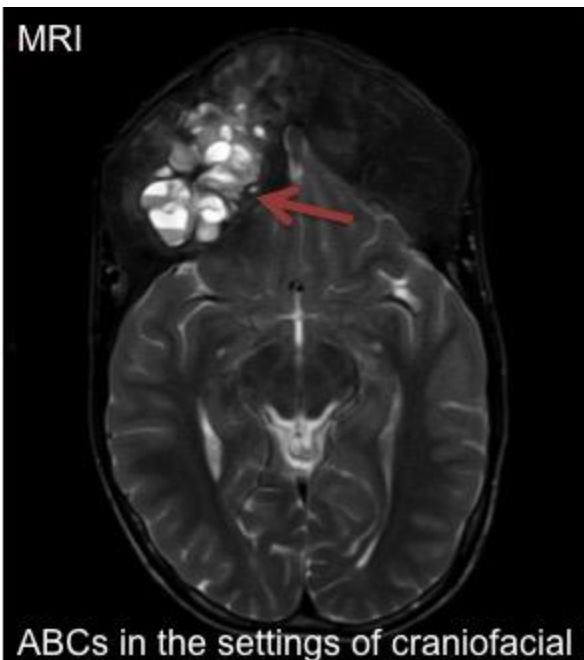
This study summarizes more than 25 years of observation of patients with fibrous dysplasia under the protocol Screening and Natural History Study of Fibrous Dysplasia at the National Institutes of Health (Bethesda, Maryland, USA), (SNHFD, protocol 98-D-0145, Principal Investigator Michael T. Collins, MD).

Results

Craniofacial bones are the most common FD location. Clinical presentation of craniofacial FD is a gradual, painless enlargement of the craniofacial region, facial asymmetry, and deformities that often lead to devastating functional and esthetic consequences for affected individuals. Lesions in this location are not typically well demarcated, may cross sutures, and most commonly affect the zygomatico-maxillary complex and sphenoid bones. From late childhood to puberty, indolent growing mass lesions cause facial deformity and distortion of adjacent structures such as optic and vestibulocochlear nerves, eye/globe, nasal airway, middle ear ossicles, and teeth. Rapid enlargement of FD lesions in children or continued active disease with symptoms in adulthood is uncommon but may occur. Neurologic complications include optic and vestibulocochlear nerve compression, and brain compression. Involvement of the orbit is common in FD. Proptosis, globe dystopia, and hypertelorism may be seen on imaging. Optic nerve encasement is common and usually asymptomatic. Prophylactic surgical optic nerve decompression is not recommended. More than 70% of patients with craniofacial FD have temporal bone involvement. Hearing loss, which is typically mild, typically develops secondary to narrowing of the external auditory canal and fixation of the ossicles within the epitympanum. FD of the skull base may be associated with growth hormone excess. Sinuses may be also be affected in craniofacial FD; however, the incidence of sinusitis is not increased. Pain, deformities, benign and malignant bony matrix transformations may occur. Patients with MAS may develop extraskelatal endocrinological abnormalities, that require followup (pituitary, thyroid, ovarian, testicular disorders).

Conclusions

1. FD is a complex disease involveing not only bone but also numerous endocrine organs.
2. Radiologists play a crucial role in the identification of osseous complications associated with craniofacial FD.
3. Patients with McCune-Albright syndrome have extensive polyostotic FD often involving the craniofacial location and may have different extraskelatal abnormalities (ovarian cysts, testicular changes, pituitary adenoma, or intraductal papillary mucinous neoplasm), which often require follow-up.
4. The craniofacial form of the disease is the most common FD and the most difficult form to manage. "Clinical guidelines for the management of craniofacial fibrous dysplasia," which was published in 2012, provides detailed and comprehensive recommendations for clinical FD management in the craniofacial region.



(Filename: TCT_eEde-186_ASRN-1.jpg)

Demystifying Leukodystrophy: Use of An Interactive Computer-based Learning Tool to Simplify an Infrequently Encountered Entity

J Pack¹, J Branchcomb², B Diegnan², B Tamrazi³, A Rajamohan⁴, J Acharya⁵

¹*Keck School of Medicine USC, Los Angeles, CA*, ²*LAC+USC, Los Angeles, CA*, ⁴*Children's Hospital of Los Angeles, Los Angeles, CA*, ⁴*University of Southern California, Keck School of Medicine, Los Angeles, CA*, ⁵*University of Southern California, Pasadena, CA*

Purpose

Trainees, generalists and neuroradiologists without subspecialty training in pediatric neuroradiology rarely encounter leukodystrophies in routine clinical practice. We intend to provide a computer-based, interactive teaching tool to provide a systematic framework to simplify these diagnoses.

Materials and Methods

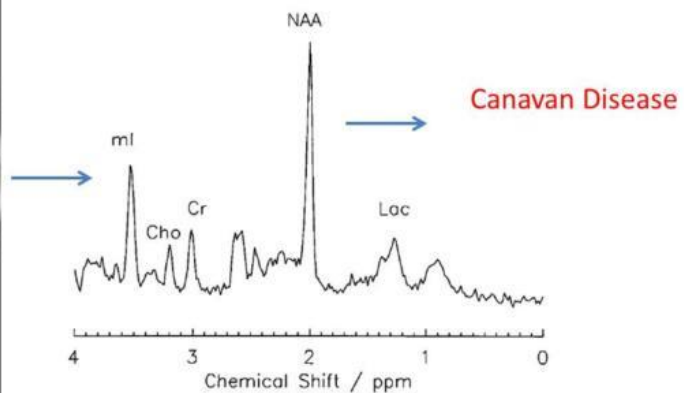
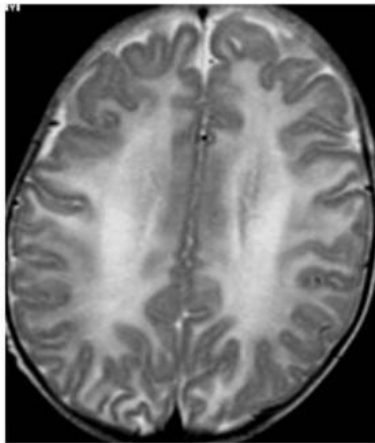
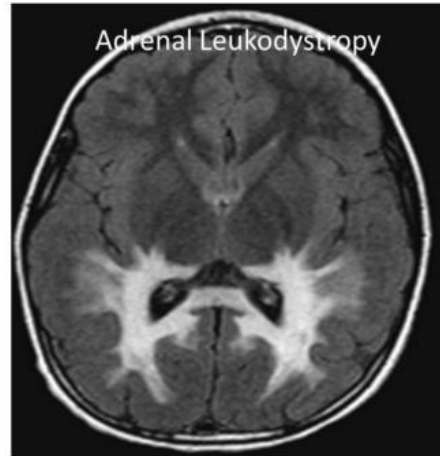
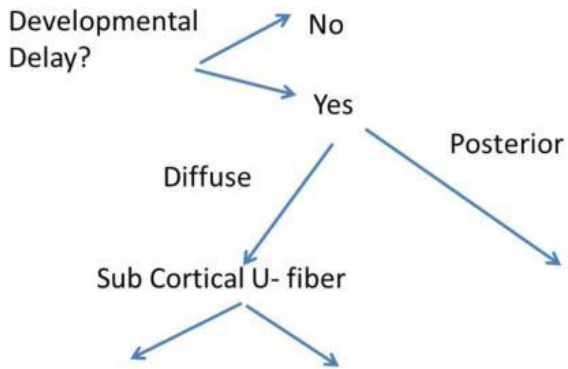
We will incorporate a computer-based, interactive decision tree that users can refer to and utilize as a study tool. The user will select an appropriate clinical scenario. Upon selection of the appropriate clinical scenario (i.e macrocephaly or normocephalic) the user will be directed to a subset of images and an explanation as to why additional diagnoses were excluded. A further decision point will then be made based on the distribution of the imaging findings. A final decision tree would then direct the user to evaluate which of multiple spectroscopy spectra is the most fitting, and would lead to the most likely diagnosis.

Results

While there can be a significant amount of overlap between the multiple leukodystrophies, there are characteristic patterns that when approached systematically can simplify a challenging subject. Repetition and case-based learning have been proven to be among the most effective teaching tools, especially in rare entities which are not frequently encountered. While there are many papers and resources that describe these entities, it is easy for one to get lost in the more subtle details. A simplified, algorithmic approach, as depicted in the schematic of the teaching tool below, can provide an effective means of arriving at a correct diagnosis.

Conclusions

By incorporating an interactive teaching tool designed to provide a systematic approach to leukodystrophies, a general radiologist or nonpediatric neuroradiologist will be able to overcome potential diagnostic pitfalls, improve knowledge base and arrive at an accurate diagnosis in a patient with suspected or even unsuspected leukodystrophy.



(Filename: TCT_eEde-176_Picture8.jpg)

eEde-190

Dysmyelinating Disease in Children with Emphasis on Diffusion-weighted Imaging

F Boucher¹, J Kim¹, L Lai², T Sato³, T Moritani¹

¹University of Michigan, Ann Arbor, MI, ²CHLA, Los Angeles, CA, ³University of Iowa, Iowa City, IA

Purpose

Dysmyelinating disease of the central nervous system is a group of inherited disorders disrupting the production and maintenance of normal myelination, often with the initial manifestations presenting during childhood. These diseases demonstrate overlapping imaging features such that differentiating between these entities is a challenge in daily clinical practice for neuroradiologists. The aim of this exhibit is to highlight these conditions, detail the relevant pathophysiology, describe their imaging features with an emphasis on diffusion-weighted imaging, and cover select management and treatment options.

Materials and Methods

Data of patients presenting to Michigan Medicine Mott's Children's Hospital, The University of Iowa Hospitals and Clinics and Children's Hospital Los Angeles and archived images of dysmyelinating disorders in pediatric patients are presented in this educational exhibit.

Results

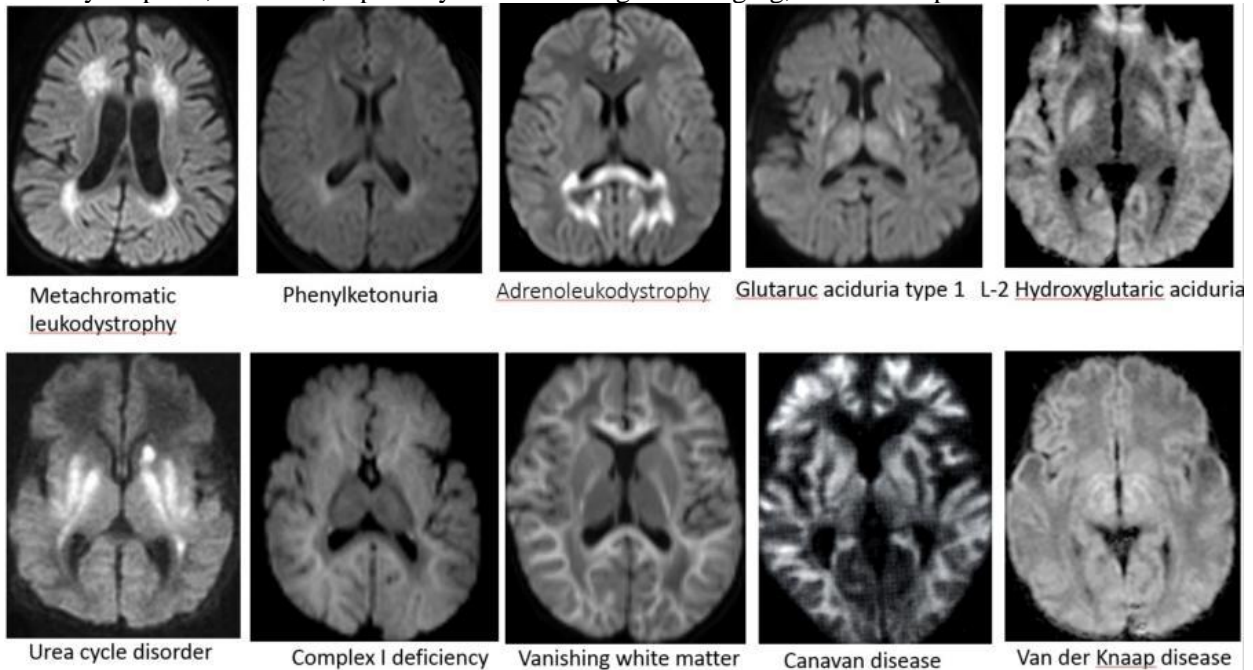
Leukodystrophies, commonly presenting in childhood, are seen to affect the central nervous system with symmetric patterns of predominantly white matter involvement. Classification of these conditions has traditionally been based on the underlying pathophysiology, cellular organelles, and metabolic pathways affected and the accumulating biochemical constituents. These conditions can be diagnosed by specific

Electronic Educational Exhibits

biochemical tests, often from a simple peripheral blood draw (e.g. Metachromatic leukodystrophy). Another helpful classification for these conditions is based on their imaging characteristics on CT/MRI, especially diffusion-weighted imaging, based on the underlying patterns and distribution of brain involvement, such as white matter only or both grey and white matter. This classification is particularly helpful while refining the differential: abnormalities predominantly affecting the periventricular white matter (e.g. Metachromatic leukodystrophy), nonvascular areas of restricted diffusion (eg. MELAS), expansion of sylvian fissures with marked involvement of the globus pallidus (e.g. Glutaric aciduria) or involvement of multiple additional, nonwhite matter, areas, like the basal ganglia and optic nerves (e.g. Krabbe disease).

Conclusions

Leukodystrophies represent a diagnostic difficulty for many practicing neuroradiologists. With advancements in various treatment options, which can forestall disease progression, and with the possibility of cure on the horizon, the importance of accurate and timely diagnosis is more prescient than ever. Neuroradiologists, amongst a multidisciplinary team, have a developing role in guiding the management of these patients who, until recently, had an inescapable outcome. Clinical neuroradiologists should have an approach to the detection, differentiation, diagnosis and disposition of the various leukodystrophies; CT/MRI, especially diffusion weighted imaging, aids in this process.



(Filename: TCT_eEde-190_Imagefordysmyelinatingdisease.jpg)

eEde-188

Imaging of Microcephaly Under the Cloud of Zika Virus

S Kanekar¹, A Agarwal²

¹Penn State MiltonHershey Medical Center, Hershey, PA, ²SouthWestern University Hospital, Dallas, TX

Purpose

1. The purpose of this exhibit is to describe a radiological approach to the evaluation of the patient with microcephaly.
2. To discuss the genetics and role of Zika virus in microcephaly
2. To illustrate with examples varies types of microcephalies on MR and CT

Materials and Methods

Microcephaly is defined as an occipitofrontal head circumference (OFC) <-2 standard deviations (SD) below the mean for sex, age, and ethnicity. The term "true" or "severe" microcephaly is used for an OFC <-3 SD. Microcephaly results from inadequate brain growth at some point during development. The etiology of microcephaly may be congenital (secondary to cerebral malformations or metabolic abnormalities) or acquired, most frequently following an ischemic insult. Microcephaly evident at birth is called primary microcephaly while postnatal is termed as secondary microcephaly. A multidisciplinary approach involving radiologists, pediatric neurologists, geneticists, biochemists and obstetricians is essential in diagnosing the underlying cause of microcephaly, with an obstetrician being particularly important in the case of an antenatal or perinatal discovery of microcephaly.

Results

We retrospectively studied 114 patients with clinical diagnosis of microcephaly from our PACS system data which formed the basis for this exhibit. All the patients had undergone both CT, MRI head examination. In addition 71 patients also had 3D imaging of the head and face. For better understanding of this entity, genetic-based classification was used to classify data and exhibit presentation. They were classified into: 1. Acquired (Intrauterine infection, Irradiation, exposure to drugs/toxins, fetal alcohol syndrome) 2. Metabolic (Serine deficiency, Amish microcephaly) 3. Syndromic 4. Secondary (Rett syndrome, Aicardi-Goutières disease, infantile neuronal ceroid lipofuscinoses) 5. Primary. Primary were further classified into autosomal recessive; with DNA repair deficiency; with disturbances of neuronal migration (lissencephaly/polymicrogyria); with cerebellar and brainstem malformation; disorders of diencephalic and telencephalic cleavage (Holoprosencephaly).

Conclusions

1. Diagnosis of microcephaly is always easy but to pinpoint the cause is very challenging. It is a team approach involving radiologists, pediatric neurologists, geneticists, biochemists and obstetricians.
2. We review the specific pointers on imaging which may help in diagnosing the possible underlying cause.
3. This exhibit discusses the role of genetics and Zika virus in microcephaly.

Primary microcephaly

Microcephaly with disturbance of neuronal migration

Terminology:

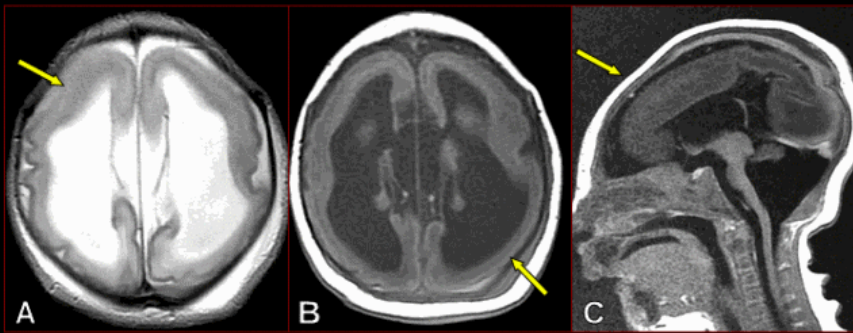
- Complete absence of gyri causes smooth cerebral surface (**lissencephaly**). Referred to as **microlissencephaly** when associated with microcephaly
- No gyri (**agyria**) or broad gyri (**pachygyria**) related terms
- Some neurons accumulate in periventricular white matter (**heterotopia**)
- In some cases one can see neurons that came close to their cortical position form a subcortical band (**band heterotopia**)

Imaging:

- Migration anomalies manifest as abnormally smooth brain surface with thick, smooth cortex, disorganized cortical layering, wide gyri & shallow sulci. Also see broad/triangular Sylvian fissures, gray matter heterotopia, ventriculomegaly (due to fetal stage rather than hydrocephalus), and agenesis of corpus callosum

General features:

- Failure of cerebral cortical development due to defective neuroblast migration towards cortex
- Normal neocortex forms between 12-24 weeks by radial 'waves' of neurons forming 6 separate layers
- 'Inside out' layering normally occurs with subsequent neurons going through established layers. In lissencephaly, deep neurons are unable to pass through overlying established cortical layers and become trapped
- Same factors control neural proliferation and migration thus microcephaly is seen with neural migration anomalies
- Only minority have microcephaly at birth but most become microcephalic during first year of life
- Some forms of lissencephaly are syndromic
- Clinically patients present with mental retardation, epilepsy, spastic quadriplegia, poor feeding, bouts of apnea, and generalized seizures
- Thalamus and basal ganglia are normal as they form via separate pathway



Microlissencephaly – Case 1

Term used to denote presence of lissencephaly in the setting of microcephaly. T2 (A) and T1 (B) weighted MR demonstrate smooth cortex with ventriculomegaly. C. Sagittal T1 weighted MR shows decreased craniofacial ratio with slanted frontal bone. Cerebellar hypoplasia is also present.

(Filename: TCT_eEde-188_Slide2.GIF)

eEde-193

Imaging of Pediatric Hearing Loss

K Ali¹, P Minhas¹, M Nagarajan¹, S Gaddikeri¹, J Raseman¹

¹Rush University Medical Center, Chicago, IL

Purpose

1. To describe the various causes of hearing loss with their imaging characteristics in the pediatric population 2. To highlight relevant embryological and genetic correlates 3. To discuss the importance of imaging findings in surgical management

Materials and Methods

Hearing loss is classified into sensorineural and conductive types with each type having nonsyndromic, syndromic and acquired causes.

Results

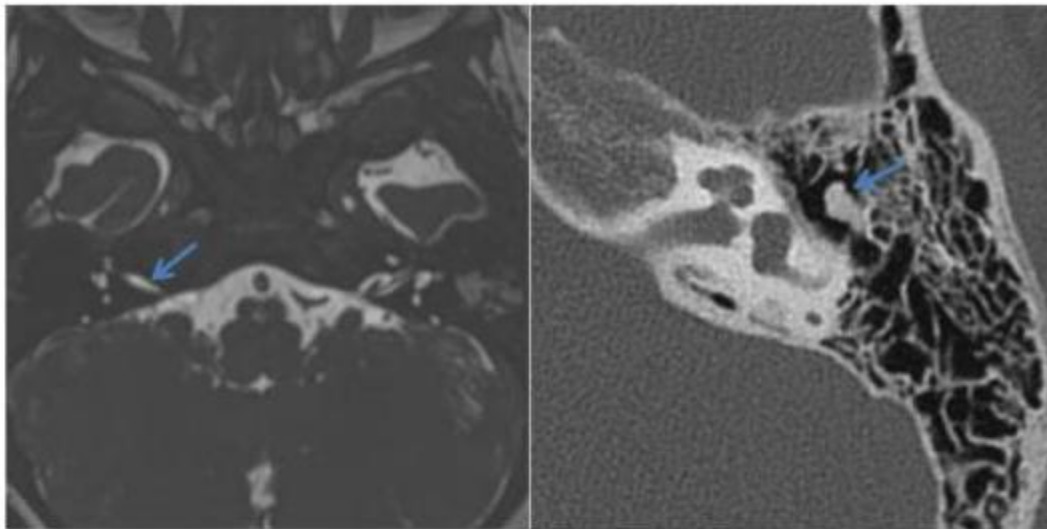
1. Causes of sensorineural hearing loss such as: A. Congenital - cochlear aplasia/hypoplasia, common cavity, cochlear hypoplasia, enlarged vestibular aqueduct, cochlear nerve deficiency B. Syndromic - Branchio-oto-renal syndrome, CHARGE syndrome C. Acquired - labyrinthitis, trauma, posterior fossa tumors 2. Causes of conductive hearing loss such as: A. Congenital malformations of the middle and external ear like EAC atresia, dysplastic ossicles, oval window atresia B. Syndromic – Hemifacial microsomia, Treacher Collins syndrome C. Acquired - chronic serous otitis media, trauma 3. Brief review of important aspects of embryological development 4. Unique advantages of CT and MRI 5. Imaging

Electronic Educational Exhibits

findings pertinent to surgical management: plausibility of cochlear implantation: degree of cochlear hypoplasia, presence of labyrinthitis ossificans etc, abnormal course of facial nerve, high-riding jugular bulb, pointers of CSF gushers etc.

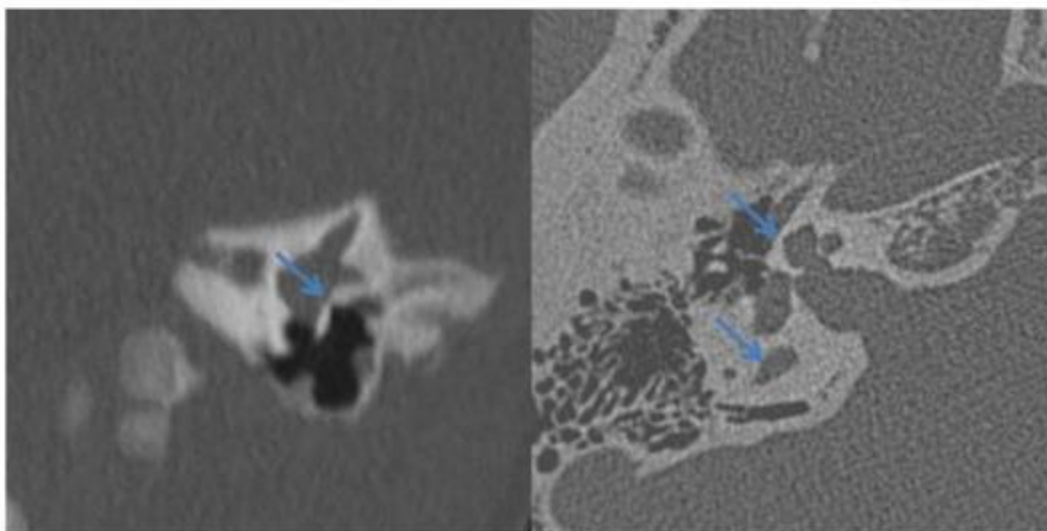
Conclusions

Causes of pediatric hearing loss are varied. Both CT and MR are complementary in imaging work-up. Familiarity with characteristic imaging findings not only aids in diagnosis but also in prompt surgical management.



A. Right IAC atresia with absent 8th nerve

B. Dysplastic and fused left malleus and incus



C. Oval window atresia with absent 7th nerve

D. Incomplete partition II with dilated vestibular aqueduct

(Filename: TCT_eEde-193_ASNR2018-1.jpg)

eEde-175

Imaging of Secondary Degeneration in Pediatric CNS Disease

A Handa¹, A Capizzano¹, J Kim², T Sato³, T Moritani²

¹*University of Iowa Hospitals and Clinics, Iowa City, IA*, ²*University of Michigan, Ann Arbor, MI*, ³*University of Iowa, Iowa City, IA*

Purpose

Secondary degeneration following central nervous system disease is a well known entity among adult patients and can be classified into antegrade (Wallerian), retrograde, and trans-synaptic degeneration. In contrast, secondary degeneration among pediatric patients has not been well described in the literature. The purpose of this educational exhibit is to review the imaging findings of secondary degeneration in pediatric patients. We will review pertinent neuroanatomy, underlying pathophysiology along with imaging findings of secondary degeneration in an interactive format. We will also discuss differential diagnoses and pitfalls.

Materials and Methods

We reviewed cases of pediatric secondary degeneration in our institutions (University of Iowa Hospital and Clinics, University of Michigan) and selected representative cases. The exhibit will consist of a case-based review covering wide spectrum of etiologies including ischemia, neoplasm, demyelination, degeneration, toxic metabolic, congenital, vascular, and others. Various imaging modalities will be presented including CT, MRI (including DWI and DTI), as well as FDG-PET.

Results

Cases will include: 1. Wallerian degeneration (following hypoxic ischemic encephalopathy (HIE), brain infarct etc) 2. Trans-synaptic degeneration (following HIE, brain infarct, hemorrhage, mesial temporal sclerosis, and degeneration of Papez circuit) 3. Crossed cerebellar diaschisis, 4. Noncrossed cerebellar diaschisis 5. Crossed cerebellar atrophy 6. Hypertrophic olivary degeneration (due to posterior fossa syndrome, cavernoma, opsoclonus-myoclonus syndrome with neuroblastoma) 7. Secondary degeneration related to basal ganglia or thalamic hemorrhage The clinical presentation and imaging findings will be reviewed to highlight the approach to reach the correct diagnosis. Pertinent neuroanatomy will also be reviewed.

Conclusions

This educational exhibit will review the imaging features of secondary degeneration in pediatric patients. Familiarity with the imaging features of secondary degeneration and understanding of pertinent neuroanatomy is important in helping the radiologist arrive at the correct diagnosis and ensuring prompt and appropriate treatment strategies.

eEde-204

Imaging Review of Pediatric Skull Abnormalities

L Daftari Besheli¹, A Ejazi¹, H Rajebi¹, B Tantiwongkosi¹, A Singh¹

¹*University of Texas Health San Antonio, San Antonio, TX*

Purpose

Skull abnormalities are apparent clinically as abnormal size and shape or masses under the scalp, or are identified as incidental findings on imaging examinations. Abnormalities in the pediatric skull include a large number of diverse conditions from localized skull pathologies to systemic disorders. The skull abnormalities can yield important clues for diagnosis of focal skull pathology or a systemic disease. In this exhibit, we will review a number of conditions that affect the pediatric skull.

Materials and Methods

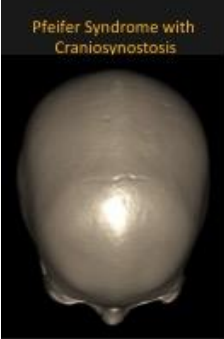
In this review, skull abnormalities are discussed in two major categories including skull lesions and skull anomalies/variants.

Results

Skull lesions include benign and malignant bone tumors as well as systemic diseases causing skull defects. Pediatric skull lesions and skull anomalies/variants are summarized in Tables 1 and 2 respectively. In this review we describe each skull abnormality separately and present imaging criteria for diagnosis of each individual lesion.

Conclusions

Recognition of abnormalities of the skull can assist in diagnosis of variable systemic disease conditions and can help direct further diagnostic work-up. Understanding imaging characteristics of the primary skull lesions and skull anomalies as well as normal variants may assist in diagnosis of diverse congenital and acquired conditions.

 <p>Pfeifer Syndrome with Craniosynostosis</p>	Table 1- Primary skull lesions in pediatric population	Table 2- Skull anomalies
 <p>Atretic Parietal Cephalocele</p>	Malignant tumors Chordoma Chondrosarcoma Ewing sarcoma/pPNET (peripheral primitive neuroectodermal tumor) Langerhan cell histiocytosis Osteosarcoma Intermediate malignant potential Giant cell tumor	Abnormalities of skull size Microcephaly Macrocephaly
	Benign tumors Aneurysmal bone cyst Intraosseous hemangioma Osteoma Osteoid osteoma Ossifying fibroma Fibrous dysplasia Cementoossifying fibroma Epidermoid cyst Dermoid cyst Osteoblastoma Infantile myofibroma	Abnormalities and variants of skull shape Wormian bone Positional plagiocephaly Craniosynostosis Scaphocephaly and Dolichocephaly Brachycephaly Plagiocephaly Parietal foramina Cranium Bifidum Abnormally large fontanelles Cleidocranial dysplasia
	Non-tumoral skull lesions Osteomyelitis Leptomeningeal cyst	Faulty fetal packing Molding

(Filename: TCT_eEde-204_Figure.jpg)

eEde-185

Magnetic Resonance Imaging (MRI) Findings of Central Nervous System (CNS) Infections in Pediatric Patients

R Kiwan¹, A Leung¹, Y Sallam¹

¹Western University/London Health Science, London, Ontario, Canada

Purpose

To investigate the MRI findings in pediatric patients who presented with clinical symptoms and signs of CNS infection

Materials and Methods

We searched our PACS database for pediatric patients (age 0-17 years) with clinical concern for CNS infection who were investigated with MRI brain between January 1, 2015 to November 30, 2017. We used these search terms: meningitis, ventriculitis, abscess, cerebritis, encephalitis and infection. The MRI

Electronic Educational Exhibits

examinations were performed on 1.5 T units. The MRI scans were reviewed by a neuroradiology fellow and consultant, and the MRI findings were tabulated. We also reviewed the electronic medical record (EMR) for clinical presentation, laboratory results and outcome.

Results

Our retrospective search resulted in a cohort of 129 patients (ages ranged from 1 week to 17 years with Female: Male (F: M) ratio 1.2). Sixty five patients (50%) had positive MRI findings including parenchymal changes, leptomeningeal enhancement, and altered cerebrospinal fluid (CSF) signal. Sixteen of these patients had 2 or more findings. Thirty seven of the 65 patients (55%) had positive CSF culture including 15 patients (40%) with common infections (e.g. E.coli, H. influenza and Streptococcus pneumoniae) and 22 patients (60%) with uncommon infections (e.g. Bacillus cereus, Cronobacter sakazakii, HSV, Eosinophilic Baylisascaris, Citrobacter freundii and Pseudomonas aeruginosa). Most patients had a full recovery. Two patients died (from Cronobacter sakazakii and Pseudomonas aeruginosa), one patient required bilateral cochlear implants (from Streptococcus pneumoniae), and one patient developed epilepsy (from HSV encephalitis).

Conclusions

In the pediatric population, CNS infection is a common cause of mortality and long-term morbidity. In this retrospective study, 50% of patients who presented with clinical features of CNS infection had relevant MRI findings. Occasionally, the MRI appearance can be pathognomonic, as with Bacillus cereus infection in preterm infants. Also, MRI can be helpful to detect complications, such as labyrinthitis ossificans from Streptococcus pneumoniae or hippocampal injury from HSV.

eEde-180

More Than Just Holes: What We Should Learn About Leukodystrophies with Cysts or Cavitations

I Padilha¹, A Pettengill², A Araújo³, F Pacheco⁴, R Hoffmann Nunes⁵, F SCORTEGAGNA⁶, A MAIA⁷, A da Rocha⁸

¹*Irmandade da Santa Casa de Misericórdia de São Paulo, São Paulo, São Paulo,* ²*Irmandade da Santa Casa de Misericórdia de São Paulo, São Paulo, Brazil,* ³*Irmandade da santa casa de misericórdia de são paulo, São Paulo, São Paulo,* ⁴*Santa Casa de São Paulo School of Medicine, São Paulo, Brazil,* ⁵*Irmandade Santa Casa de Misericórdia de Sao Paulo, Sao Paulo, Brazil,* ⁶*DASA GROUP, SAO PAULO, São Paulo,* ⁷*SANTA CASA DE SÃO PAULO, SAO PAULO, SAO PAULO,* ⁸*IRMANDADE SANTA CASA DE MISERICORDIA DE SAO PAULO, Sao Paulo, Sao Paulo*

Purpose

There are many different metabolic leukodystrophies (LKD) with distinctive features and, some of them, with established genetic and molecular identity. A small subset is associated with cavitory or cystic lesions that are radiologically defined by the association of a diffuse LKD and hypointensities within large areas of dysmyelination. Our purpose is to review and discuss typical and atypical metabolic LKD with cysts and/or cavitation as well as mimicking disorders on magnetic resonance imaging (MRI) in order to scrutinize a practical approach for the differential diagnosis.

Materials and Methods

After reviewing our institution teaching files, we selected cases demonstrating metabolic LKD with cavitation and/or cysts. Disorders were presented according to specific findings highlighting the contribution of cavitation/cyst occurrences and distribution for specific diagnosis. Patient selection and data collection were performed using the electronic patient's database.

Results

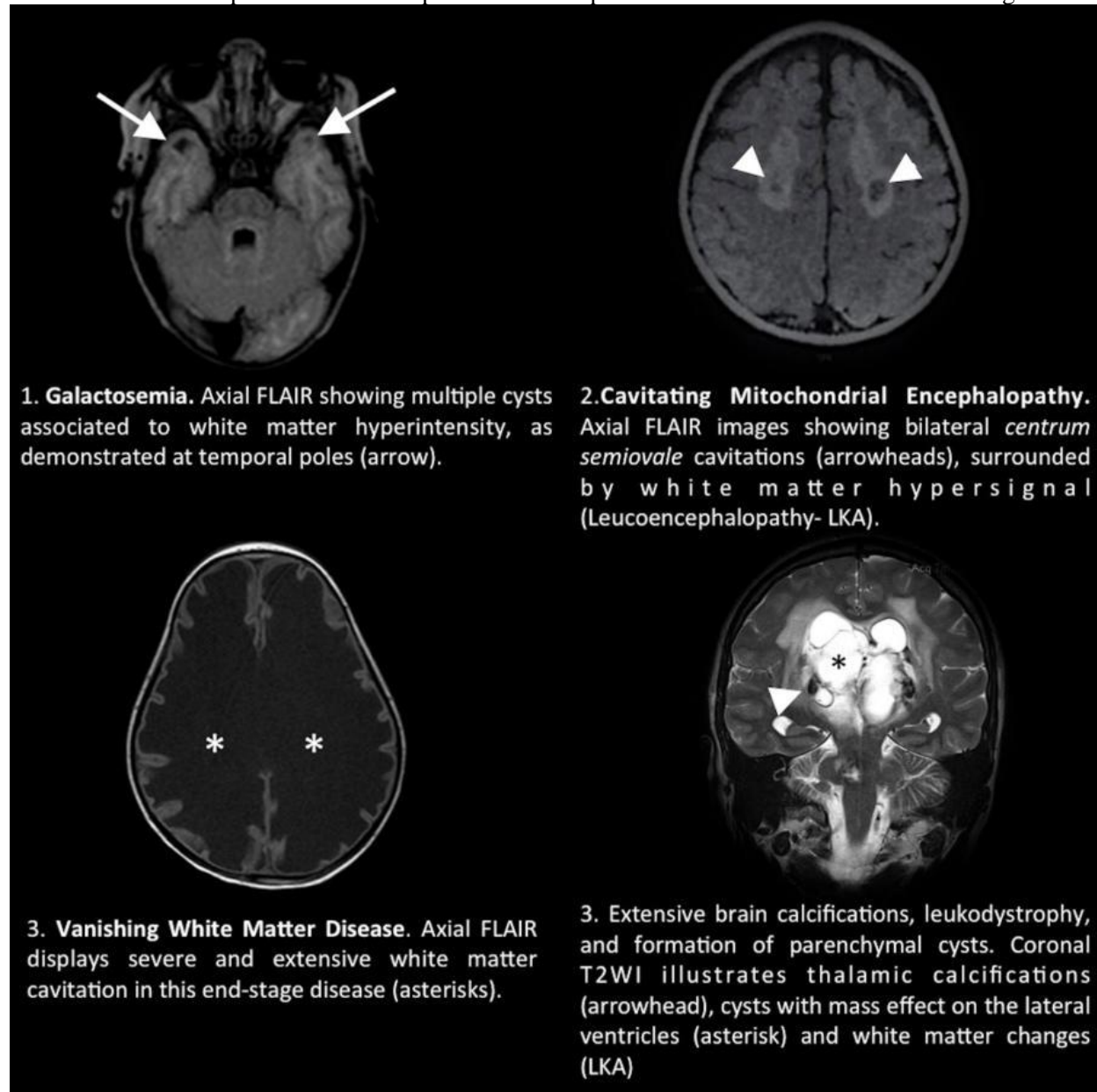
The progressive improvement of magnetic resonance imaging into clinical practice contributed to advances in white-matter diseases comprehension. Some metabolic LKDs with cavitation and/or cysts were found to have a relative specific pattern that could predict differential diagnosis, including lysosomal storage, amino and organic acids, muscle and mitochondrial dysfunction. In this subset, there

Electronic Educational Exhibits

are some disorders already well recognized such as galactosemia and others that have been more recently described: megalencephalic leukoencephalopathy with and without subcortical cysts, vanishing white-matter disease and leukoencephalopathy, cerebral calcification and cysts disease. Furthermore, the main mimicking disorders were also reviewed, including dilated perivascular spaces related to white matter abnormalities, cytomegalovirus congenital infection and periventricular leukomalacia and some neurocutaneous syndromes.

Conclusions

The approach of metabolic LKD with cavitation and/or cysts requires an extensive understanding of specific imaging findings associating to its genetic/molecular identity, distinguishing real cystic/cavitation features and its main pitfalls in order to prevent misinterpretation and to facilitate the correct diagnosis.



(Filename: TCT_eEde-180_ImagesLKD.jpg)

eEde-187

MR Evaluation of Pre- and Postfetoscopic Repair of Open Spina Bifida

B Matos¹, M Dalaqua¹, Y Sameshima¹, D Lapa¹, A Barbosa¹

¹*Hospital Israelita Albert Einstein, São Paulo, São Paulo, Brazil*

Purpose

Since Skin-over-biocellulose for Antenatal Fetoscopic Repair (SAFER) is rising as the treatment of choice for open spina bifida, radiologists must become familiar with prenatal pre and postoperative MR findings in order to provide relevant therapeutic and prognostic information to staff and families.

Materials and Methods

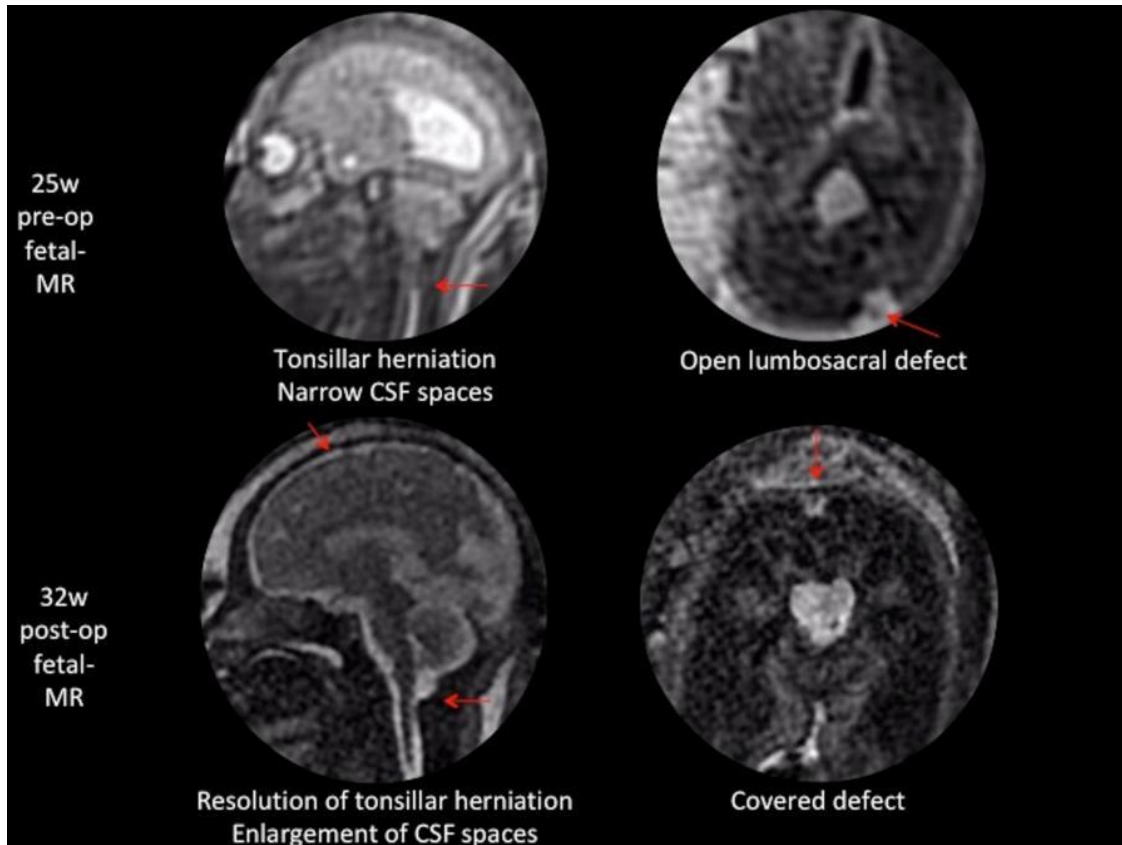
Illustrative follow-up imaging studies of fetal MRI pre and postrepair of open spina bifida were selected from a private institution PACS archive for the last 10 years.

Results

SAFER is a Brazilian technique of minimally invasive fetal surgery for treatment of open spina bifida (OSB), consisting in placement of a cellulose patch underneath the skin, with no duramater primary closure. The patch induces formation of a neoduramater, preventing CSF leak and adhesion of spinal cord. Compared to traditional open fetal surgery techniques, preliminary results demonstrate fetoscopic repair minimizes damage to the uterus, improves motor outcomes and increases reversal of hindbrain herniation. Preoperative MR evaluates posterior fossa and quantifies cerebellar herniation. Postoperative MR shows reversal of hindbrain herniation, opening of encephalic CSF spaces and depicts the patch holding CSF.

Conclusions

Fetal MR is relevant for evaluation of pre and postfetoscopic repair of OSB. Preoperative exam helps plan surgery. Posttreatment findings of reversal of hindbrain herniation and enlargement of encephalic CSF spaces correlate to better neurological outcomes and reduced need for VP shunting.



(Filename: TCT_eEde-187_asnrchiari.jpg)

eEde-198

MR Spectroscopy in Pediatric Neuroimaging: Current indications and Future Implications

R Patel¹, M Syed¹, R Jacob², A Kamali¹, P Rabiei¹, E Bonfante¹, R Riascos¹, N Desai³

¹The University of Texas Health Science Center at Houston, Houston, TX, ²UMC Health System, Lubbock, TX, ³Texas Children's Hospital Baylor College of Medicine, Houston, TX

Purpose

Magnetic resonance (MR) spectroscopy is a known noninvasive imaging tool for a variety of central nervous system (CNS) disorders. Purposes of this educational exhibit are to review basic physics of MR spectroscopy; to describe different methodologies of MR spectroscopy (single vs. multi voxel, short vs. intermediate vs. long TE, PRESS Vs. STEAM techniques); to give overview of normal appearance of MR spectroscopy in various age groups (newborn vs. adolescent) in different parts of brain (cerebral white matter vs. basal ganglia); to describe various artifacts in this technique and briefly give an overview of current clinical and research applications of MR spectroscopy in children.

Materials and Methods

A detailed literature search was performed on current techniques and clinical use of MR spectroscopy with specific reference to children. A series of different cases from three tertiary children medical centers are presented to demonstrate the utilization of MR spectroscopy in various CNS pathologies in a case-based format.

Results

The different cases highlight various metabolic disorders, infectious/inflammatory, neoplastic disorders in

evaluation of hypoxic ischemic encephalopathy. Cases illustrating common artifacts have also been selected.

Conclusions

MR spectroscopy not only plays an important role in diagnosis, differentiating and treatment monitoring of various CNS pathologies when interpreted in association with conventional brain MRI findings, but also can provide neuroradiologists with specific biochemical information. At the end of reviewing this exhibit, the audience should have basic understanding of physics and different methodologies of MRS technique, clinical and research of MRS in neuroimaging.

eEde-174

MR Spectroscopy in the Evaluation of Pediatric White Matter Disorders

L Lai¹, M Nelson¹, M Shiroishi², S Bluml¹

¹*Children's Hospital Los Angeles and University of Southern California Keck School of Medicine, Los Angeles, CA*, ²*University of Southern California Keck School of Medicine, Los Angeles, CA*

Purpose

Leukoencephalopathies encompass a wide spectrum of inherited (leukodystrophies) and acquired neurodegenerative disorders that affect the production and integrity of myelin. The imaging characteristics of these diseases are nonspecific and overlap significantly, as disorders affecting lysosomal, peroxisomal, or mitochondrial function due to different genotypes/enzyme deficiencies can have similar biochemical phenotypes. Our purpose is to highlight the role of Proton MR spectroscopy (MRS) in the evaluation of these disorders. We will also briefly review the pathophysiology, imaging features, and treatment options of these conditions.

Materials and Methods

Retrospective review of imaging with emphasis on MRS of leukodystrophy at our institution

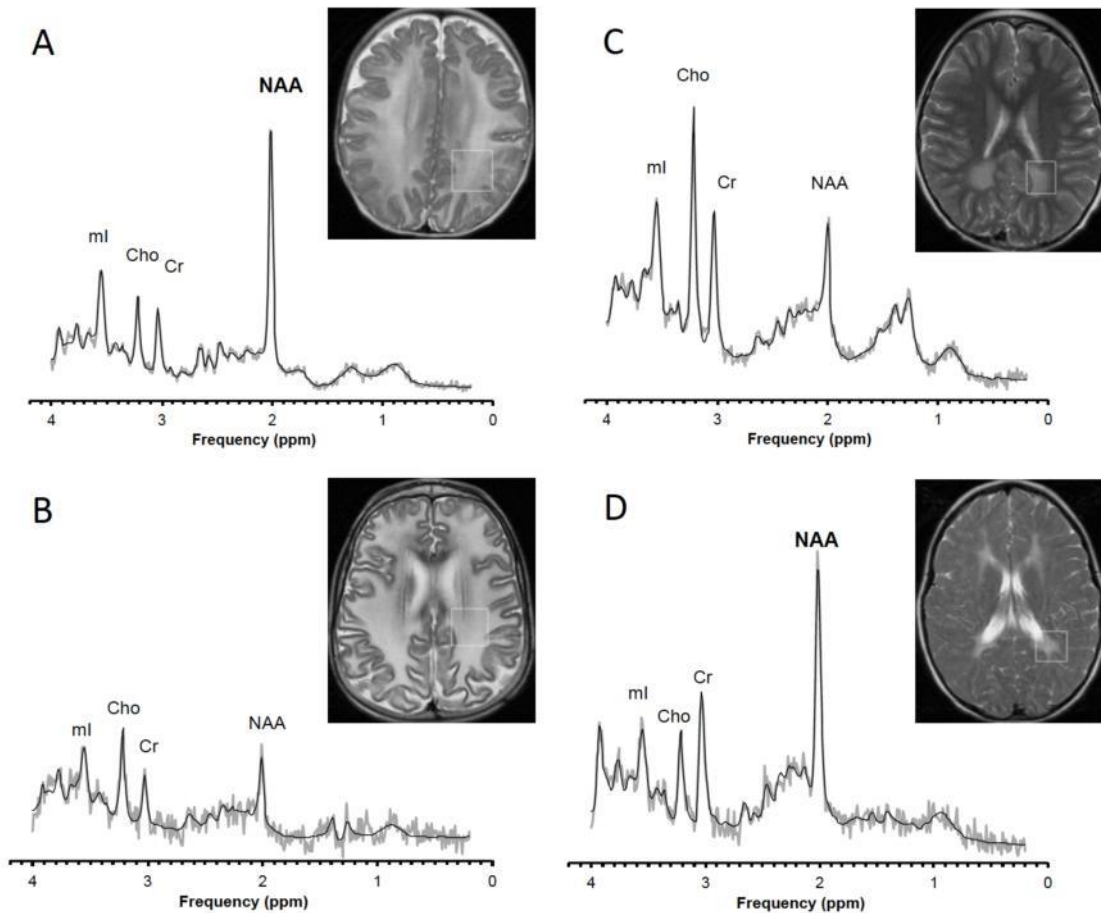
Results

Imaging of leukodystrophies is diagnostically difficult, and up to 60% of children with inborn metabolic errors never receive a specific diagnosis despite extensive clinical, imaging and laboratory investigation. While imaging is still not specific, narrowing the differential using advanced tools can facilitate clinical workup. MRS can sometimes be pathognomonic, as in Canavan disease (elevated N-acetyl aspartate peak). In other cases, it can suggest a disorder of energy metabolism (i.e. elevated lactate in mitochondrial disorders and leukoencephalopathy with brainstem and spinal cord; elevated glycine in nonketotic hyperglycinemia). MRS may also be helpful in differentiating between hypomyelination (deficit in formation of myelin), demyelination (loss or destruction of formed myelin), and white matter rarefaction/myelin vacuolization (reduced white matter and replacement of myelin with CSF, such as with megalencephalopathy with subcortical cysts and leukoencephalopathy vanishing white matter disease). Figure (All spectra: PRESS TE 35ms, TR 2sec, 128 averages, 1.5T. LCModel) A: Canavan disease B: "Vanishing WM" disease C: Adrenoleukodystrophy D: Leukodystrophy with hypomyelination from DARS mutation

Conclusions

With recent advances in genetics and genome editing technologies, more and more knowledge and potential new treatments for leukodystrophies will be uncovered. However, the workup/diagnoses of these conditions remain difficult and the pathophysiology is still unclear. MRS can aid in the imaging diagnosis and understanding of the pathophysiology of these disorders.

FIG: WMD



(Filename: TCT_eEde-174_MRS.jpg)

eEde-189

MRI Surrogates for Tubulinopathies

L Brandao¹, A Rossi²

¹*Clinica Felipe Mattoso- Grupo Fleury, Rio De Janeiro, Brazil,* ²*Istituto Scientifico Giannina Gaslini, Genova, Italy*

Purpose

Tubulin genes play a crucial role in Central Nervous System developmental events such as neuronal migration and axonal guidance (axon outgrowth and maintenance). Recent studies have described malformations of cortical development with mutations of components of microtubules (MT) and microtubule-associated proteins. We aimed to characterize imaging findings associated with disorders of microtubule function.

Materials and Methods

MRI of 12 patients with confirmed tubulin mutations (6 TUBA1A, 3 TUBB2B, and 3 TUBB3) were visually analyzed. MRI studies were performed on 1.5T GE Signa Horizon and 1.5 Tesla (T) General Electric (GE) Excite units. Available sequences included sagittal T1 and T1 3D SPGR, axial T1, T2,

FLAIR, GRE and DWI, as well as coronal T2. Specific note was made of the cortical gyral pattern, cortical thickness, white matter, ventricular and cisternal size, basal ganglia, capsular size, corpus callosum, size and contours of the brainstem, cerebellar hemispheres and vermis. Results were determined by unanimous consensus of the authors.

Results

All patients had abnormal findings on MRI, including: 1. microcephaly 2. reduced white matter 3. ventriculomegaly 4. abnormal gyral and sulcal patterns (predominantly pachygyria and agyria as well as "dysgyria") 5. polymicrogyria-like cortical dysplasia 6. a small or absent corpus callosum 7. partially fused dysmorphic basal ganglia 8. a small and dysmorphic pons 9. a hypoplastic cerebellum

Conclusions

Combinations of findings in malformations of cortical development, when present together, can suggest a disorder of MT function. Dysmorphic basal ganglia with an abnormal internal capsule were the most consistent feature of malformations of MT. Evaluation of MRIs from patients with known mutations of tubulin genes allows the establishment of some early correlations of phenotype with genotype and may assist in identification and diagnosis of these rare disorders.

eEde-200

Neonatal Brain Imaging: Pearls and Pitfalls

M Ho¹

¹Mayo Clinic, Rochester, MN

Purpose

1. Understand applications of various imaging modalities in neonatal brain injury 2. Develop an organized approach to neonatal brain MRI interpretation, with appropriate clinical-imaging correlation and utilization of advanced techniques 3. Distinguish patterns of injury in preterm vs. term neonates, and recognize more complex imaging features requiring additional work-up

Materials and Methods

We will discuss the utility of various imaging modalities in neonates (US, CT, MR) and protocol considerations, including scan timing and potential risks of sedation, anesthesia, and gadolinium contrast administration. Following review of the normal neonatal brain, we will investigate the distinct pathophysiology, grading systems, and temporal imaging findings of preterm and term brain injury. More complex etiologies will be presented with clinical-imaging correlation: congenital, infectious, metabolic, migrational, genetic, neoplastic, and traumatic.

Results

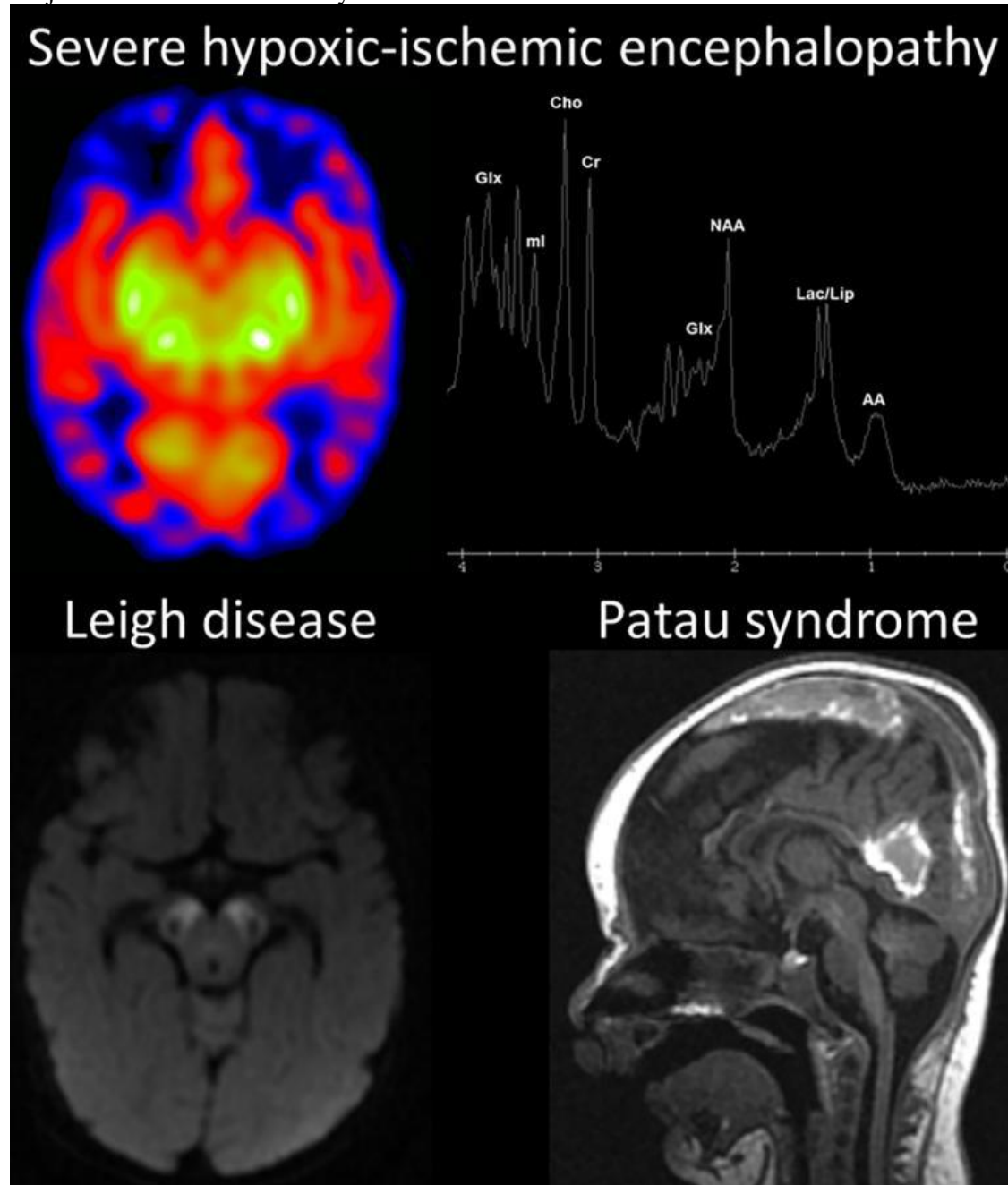
Imaging Considerations: - Modalities: NIRS, US, CT, MR - Protocols: feed and swaddle, sedation, anesthesia, gadolinium - Timing of examination: ASAP after injury, F/U at or near-term
Normal Neonatal Brain: - DWI: selection of b-value - T1/T2: myelination in PLIC, CST - Arterial spin labeling: mild relative hyperperfusion of CST, BG - MR spectroscopy: short vs. long TE, increasing NAA:Cho, mild Lac < 37 wks
Preterm Brain Injury: - Classification: extremely, very, moderate, late preterm - Immature neuroglial tissue, hemodynamic compromise, impaired neurodevelopment
US, MRI cases with follow-up - Injury scoring: intraventricular hemorrhage (1-4), white matter injury (1-3), ventriculomegaly (1-3), cerebellar hemorrhage (1-3)
Term Brain Injury: - Hypoxic-ischemic encephalopathy: disrupted autoregulation, postanoxic hyperperfusion and secondary metabolic cascade, role of therapeutic hypothermia
US, MRI cases with follow-up - Patterns (focal/multifocal, watershed, basal ganglia), scoring (mild-severe) - Role of ASL (postanoxic hyperperfusion), MRS (metabolic disruption) - Medullary, cortical vein thrombosis - Ulegyria, "Swiss cheese" brain
Complex Cases: Congenital malformations (with fetal correlation) - Chiari II with absent corpus callosum - Dandy-Walker malformation - Vein of Galen malformation - Focal cortical dysplasia IIIc - Polymicrogyria - Syndromic craniosynostosis
Infection - Prenatal (TORCH) - Postnatal sepsis
Metabolic - Kernicterus - Hypoglycemia

Electronic Educational Exhibits

- Hyperammonemia - Leigh disease Genetic - Trisomy 13 (Patau) - Trisomy 18 (Edwards) - Oral-facial-digital syndrome - Megalencephaly-capillary malformation - Pontine tegmental cap dysplasia - Linear sebaceous nevus - Median cleft face syndrome Neoplasia - Desmoplastic infantile ganglioglioma - Desmoplastic infantile astrocytoma Trauma - Fetal demise (Spalding sign) - Accidental: ping-pong fracture, leptomenigeal cyst - Nonaccidental: stellate fracture, SDH

Conclusions

Neonatal imaging modalities and protocol considerations should be tailored to the individual patient. Patterns of injury are highly influenced by gestational age, perinatal history, and scan timing. Brain MRI and advanced sequences aid in patient prognosis and management, and should be evaluated in conjunction with clinical history and labs.



(Filename: TCT_eEde-200_Neonatal.jpg)

eEde-196

Neuroimaging of Long-term Epilepsy-associated Brain Tumors

J Rozell¹, R Mangla²

¹*Upstate Medical University Hospital, Syracuse, NY*, ²*SUNY Upstate Medical University, Syracuse, NY*

Purpose

The neuroradiology expert opinion is often needed to clarify the underlying nature of a given long-term epilepsy-associated brain tumor's LEAT. This educational exhibit will describe common and uncommon imaging findings of these lesions.

Materials and Methods

We will describe radiological findings, common differential diagnosis and imaging pearls in patients with GG gangliogliomas, DNET dysembryoplastic neuroepithelial tumors, PXA pleomorphic xantastrocytomas, INET isomorphic astrocytoma variants (analogous to WHO I, SEGA subependymal giant cell astrocytomas, ANET angiocentric gliomas, ASTRO astrocytoma variants, OLIGO oligodendrogliomas including mixed gliomas, PA pilocytic astrocytomas, CYSTS arachnoid, dermoid or epidermoid cysts, MVNT multinodular and vacuolating neuronal tumors of the cerebrum, NOS (not otherwise specified) highly differentiated neuroepithelial tumors

Results

Unlike the most rapid tumor growth seen in adult or elderly patients with brain tumors the tumors belonging to the spectrum of long-term epilepsy-associated brain tumors (LEAT) may not show rapid cell growth and will not require surgical treatment or any adjuvant radiation or chemotherapy. The control of seizure should be the primary choice and should be consulted by a comprehensive and multi-disciplinary epilepsy center. If medical treatment fails surgery may be recommended as primary and in many instances also a curative treatment option.

Conclusions

Knowledge of the imaging features of LEAT will lead to a more accurate diagnosis that may result in a targeted comprehensive therapeutic approach for optimal patient care.

eEde-197

New Pediatric Neuroimaging Applications

M Ho¹, N Campeau¹, A Lu¹, J Huston¹, K Welker¹

¹*Mayo Clinic, Rochester, MN*

Purpose

1. Review principles of cutting-edge anatomic and functional imaging techniques 2. Demonstrate targeted applications of advanced techniques in pediatric neuroimaging 3. Discuss opportunities for implementation in daily clinical practice

Materials and Methods

In recent years, a vast array of advanced MRI techniques have become available for clinical utilization in various categories: anatomic, diffusion, perfusion, vascular, functional, and metabolic. Through an intensive case-based review, we will demonstrate the added value of advanced sequences in pediatric neuroimaging. Numerous examples of integrated applications will be provided in the following diagnostic categories: vascular/ischemia, epilepsy/migrational, head and neck, tumor, metabolic, and trauma.

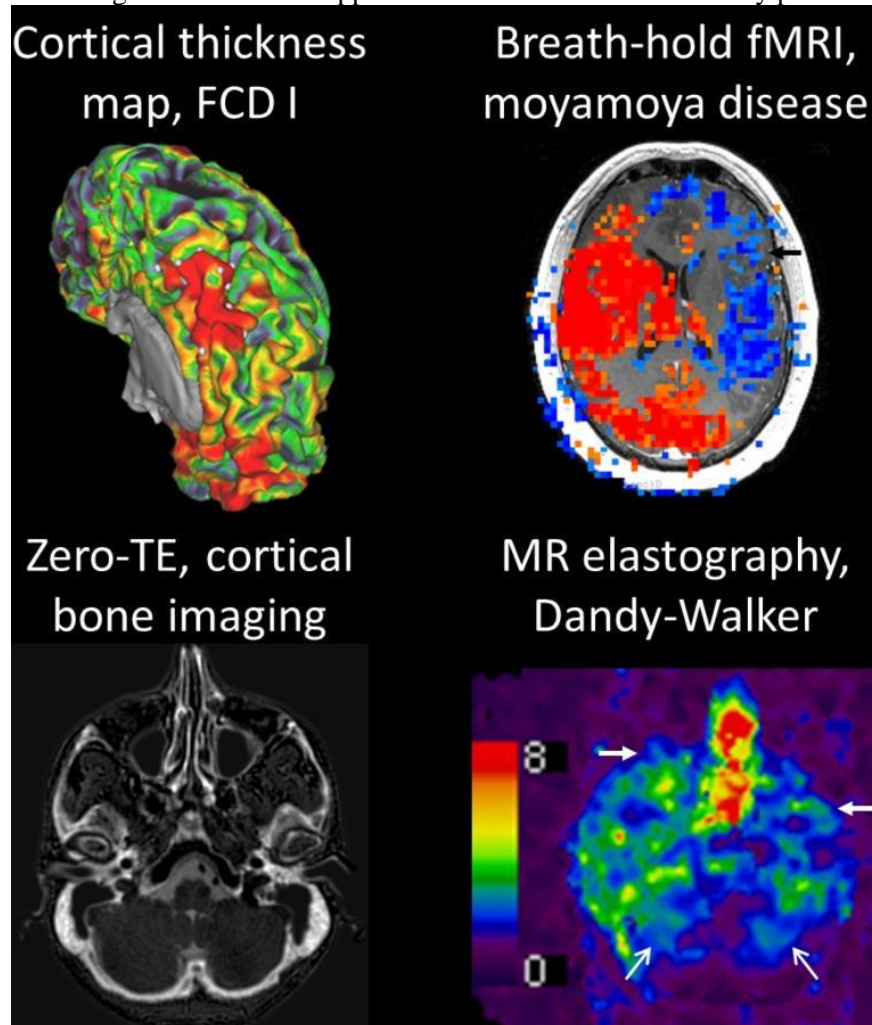
Results

Vascular/Ischemia: Perfusion techniques: ASL, DSC, DCE - Neonatal brain injury: preterm vs. term - Acute ischemia: tissue at risk, dissection, focal cerebral arteriopathy - Vasculopathy, moyamoya: breath-hold BOLD for cerebrovascular reserve - Autoregulation and vascular steal - Vascular malformations:

Electronic Educational Exhibits

hyperperfusion and steal MRA techniques: time-of-flight, phase-contrast, time-resolved, bolus Dual-energy CT: bone subtraction Epilepsy/Mirational: Presurgical epilepsy workup - DIR, ASL, DTI, SISCOM, PET-MRI, ZTE - Cortical malformations and encephaloceles fMRI: cortical reorganization (neuroplasticity) DTI: structural connectivity, congenital brain malformations - Callosal dysgenesis, Joubert, cerebellar dysgenesis MEG: seizure focus propagation and eloquent mapping Clinical 7T and small-bore 3T: high-performance gradients Head and Neck: PET-CT/MRI - HN cancer, whole-body staging Zero-TE - Cortical bone imaging for craniosynostosis, skull base, spine MR elastography - Meningioma, pituitary adenoma, hydrocephalus Phase-contrast - 2-D CSF flow, 3 vascular imaging 3-D printing/modeling - Craniofacial and skull base surgery DCE-MRI - Transplant vascularity, tumor recurrence Tumor: Supratentorial/infratentorial cases Presurgical mapping - DTI, fMRI, MEG Tumor recurrence - Perfusion and MRS Multinuclear MRI - Na-23: ion homeostasis - P-31: energetics Metabolic: Spectroscopy + anatomic/perfusion findings Metabolic - Mitochondrial, lysosomal, peroxisomal cases Toxic - Acute serotonin syndrome, chronic methylbromide poisoning Trauma: Brain trauma: nonaccidental, accidental, DAI - Perfusion, cortical bone imaging, microstructure Dual-energy CT - Metal artifact reduction Spine tractography - Brachial plexus avulsion, penetrating cord trauma Conclusions

1. Gaining technical understanding is key to appropriate utilization of advanced techniques
2. Thoughtful integrated protocoling helps maximize imaging yield and efficiency
3. Awareness of emerging technologies will increase opportunities for translation into daily practice



(Filename: TCT_eEde-197_Newtechniques.jpg)

Olfactory Bulb Hyperplasia in Alexander Disease

M Jurkiewicz¹, P Rodriguez², A Pollock¹

¹Children's Hospital of Philadelphia, Philadelphia, PA, ²University of Pennsylvania, Philadelphia, PA

Purpose

Alexander disease (AxD) is a rare, but well known, leukodystrophy that presents most commonly as an infantile form in the first two years of life with macrocephaly, rapid neurological deterioration, seizures, spasticity, as well as behavioral, feeding, and speech problems, and delayed motor development (1, 2). Mutations in the glial fibrillary acid protein (GFAP) lead to formation of Rosenthal fibers, the histologic hallmark of AxD (1, 2). The later-onset juvenile and adult forms of AxD, which exhibit longer life expectancies and motor and brainstem symptoms instead of cognitive deficits, have also been associated with GFAP mutations (2). MR imaging criteria associated with the diagnosis of juvenile AxD include confluent T1-weighted shortening in the symmetric and confluent signal predominantly in the frontal white matter, T2-weighted shortening or prolongation in the basal ganglia, thalami, and brainstem, and contrast enhancement in the periventricular rim and frontal white matter, midbrain, putamen, and head of caudate. We have noted enlarged olfactory bulbs in patients with infantile AxD using MRI. In this study we report our observations in this patient group.

Materials and Methods

Retrospective review of brain MRI in two patients with genetically confirmed Alexander disease

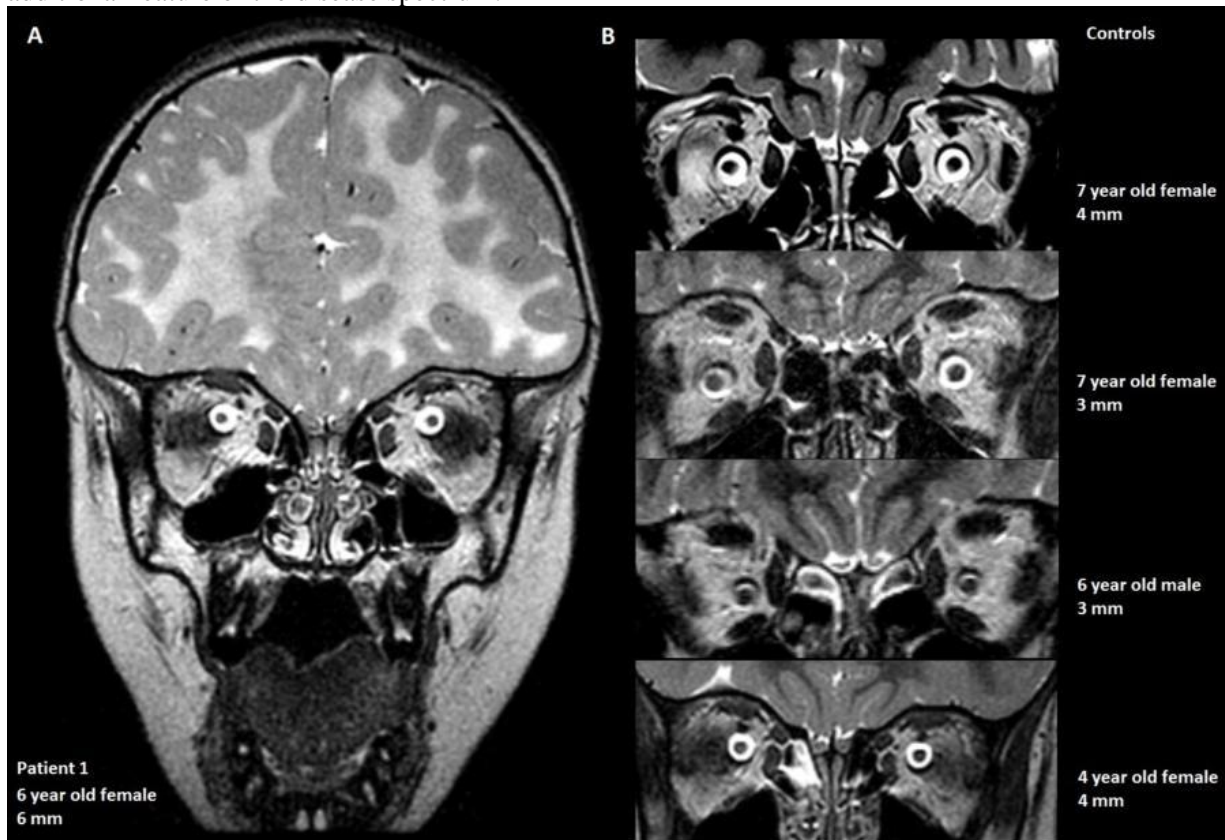
Results

The patient is a 12-year-old boy diagnosed at age 2 with infantile AxD based on a genetic mutation in exon 1 of the GFAP gene. He presented with developmental delays and strong right-hand dominance. On MRI, there was bilateral symmetric, confluent T1 shortening and corresponding T2 prolongation in the cerebral white matter with a frontal predominance, but also involving the parietal lobes, and to a much lesser extent the occipital and temporal lobes. There was T2 prolongation in the medulla and bilateral dentate nuclei, as well as basal ganglia and thalami. There was no associated enhancement following contrast administration. There was prominent global atrophy involving the supratentorial and infratentorial parenchyma with prominent supratentorial ventricles and sulci. There was associated thinning of the dorsal pons and midbrain with prominence of the cerebral aqueduct and fourth ventricle. All of these findings were in keeping with AxD. Additionally, the bilateral olfactory bulbs appeared abnormally enlarged along their entire course, without associated signal abnormality or postcontrast enhancement. The olfactory bulbs measured 6 mm in maximum diameter on the first slice posterior to the posterior sclera (Figure 1A), which was larger than any of the similarly aged-matched healthy control subjects (Figure 1B). Likewise, the olfactory bulbs in a second patient with infantile AxD were also enlarged along their entire course and measured 7 mm in diameter, which was larger than any of the similarly aged-matched healthy subject controls. Compared to controls, AxD patients demonstrated an increased T2 prolongation in the central white matter of the bulbs, and the abnormal olfactory bulbs also had a more ovoid-enlarged morphology compared to J-shaped concave morphology. As a result, there was less cerebrospinal fluid surrounding the enlarged olfactory bulbs in the AxD patients.

Conclusions

AxD patients accumulate among other proteins, GFAP that form rods called Rosenthal fibers, which are ultimately caused by mutations in GFAP (1, 2). Rather than exhibit the full spectrum of infantile AxD, GFAP mutant mice lines with the same mutations found in humans develops a less severe encephalopathy that is more analogous to the adult-onset AxD. Nevertheless, the mutant GFAP mice develop Rosenthal in various brain regions and also in the olfactory bulbs (3). Furthermore, microarray analysis of the olfactory bulbs in a different GFAP mutant mice line at three weeks and four months showed that the olfactory bulbs develop a stress response with up-regulation of genes involves iron homeostasis, glutathione

metabolism, and peroxide detoxification (4). Based on this prior work of GFAP transgenic mice, it is likely that our findings are part of the disease process and carry over to the human infantile AxD. Our understanding of olfactory bulb development also helps explain our findings. The olfactory bulbs and nerves are not cranial nerves, but rather an extension of the telencephalic vesicles that lead to the formation of the forebrain (5). The olfactory bulbs contain central white matter and an external neuronal layer. Therefore, it is not unreasonable to notice the extension of the white matter pathology from the frontal lobes to the olfactory bulbs in AxD. At birth, the olfactory bulbs have a round to oval shape with central T2 prolongation from the unmyelinated white matter (5). By 5.2 years, the olfactory bulbs develop an adult type, which is more J-shaped with more prominent latter than central components and demonstrates minimal central T2 prolongation (6). We suspect that the extension of the same ongoing supratentorial white matter abnormalities in AxD results in abnormal maturation of olfactory bulbs. These findings are of uncertain clinical significance, but there is strong evidence to support that this is an additional feature of the disease spectrum.



(Filename: TCT_eEde-184_AxDFigure.jpg)

eEde-199

Pediatric Brain Networks: Network Measures and Clinical Applications of Connectomics

A Meoded¹, T Huisman²

¹The Johns Hopkins University School of Medicine, Baltimore, MD, ²Johns Hopkins University, Baltimore, MD

Purpose

The structural connectome is a comprehensive description of the network of elements and connections that form the brain. In the last years, this framework has been increasingly used to investigate the

Electronic Educational Exhibits

developing and diseased brain. This educational exhibit aims to discuss the significance of network measures and potential clinical applications of the pediatric structural connectomics.

Materials and Methods

We will describe network measures obtained from connectomics that can be used as diagnostic biomarkers to quantify differences between patients and healthy subjects. We further discuss different clinical applications of connectomics of pediatric CNS disorders.

Results

The brain's structural connectome has features of complex networks--such as small-world topology, highly connected hubs and modularity. The definition of each measure will be discussed. Currently various neurodevelopmental and congenital malformations can be considered as connectopathies or disconnection syndromes, and thus the structural connectome may help us understand the pathogenesis and implication for cognitive and behavioral functions of brain disorders from a network perspective. Connectomics has great potential for elucidating abnormal connectivity in congenital brain malformations, especially axonal pathfinding disorders. For example, patients with agenesis of the corpus callosum may provide us with a unique opportunity to study the response of the brain to an underlying developmental abnormality. We will discuss network based approach to study children with this congenital malformation. In addition, the structural connectome may aid in elucidating the pathomechanism of cognitive impairment in children with tuberous sclerosis complex (TSC). Connectomics of children with TSC with and without autism spectrum disorder will be demonstrated.

Conclusions

Connectomics has emerged as an ideal tool to study structural networks that are implicated in neurocognitive functions and behavioral functions. The measurement of the network topology allows a better understanding of the pathogenesis, implication for cognitive and behavioral functions, and treatment of pediatric brain disorders from a network perspective.

eEde-202

Pediatric Diffuse Gliomas: Insight into the Histone H3 K27M Mutational Status Based on MR Imaging Features

M Manchandia¹, M Aboian¹, D Solomon¹, S Cha¹

¹*University of California, San Francisco, San Francisco, CA*

Purpose

For the first time, the 2016 WHO classification of tumors of the central nervous system (CNS) incorporates molecular parameters to define tumor entities, including a new diagnostic entity known as diffuse midline glioma, H3 K27M mutant that occurs primarily in children and carries a very poor prognosis. We aim to review the imaging characteristics of pediatric diffuse gliomas with respect to their histone H3 K27M mutation status using a case-based approach and highlight limitations of conventional MR imaging in distinguishing H3 K27M mutant and wildtype diffuse gliomas.

Materials and Methods

Imaging characteristics of pediatric diffuse gliomas that contain the histone H3 K27M mutation will be reviewed and contrasted with wildtype tumors, with particular attention given to their primary location within the CNS and patterns of recurrence and metastatic disease.

Results

Diffuse gliomas with histone H3 K27M mutation are located mostly along the midline and are found predominantly within the thalamus, pons, vermis, 4th ventricle, and cervical spinal cord whereas those without the mutation are found predominantly within the cerebral hemispheres. We will present multiple cases of these midline tumors along with description of their recurrence and metastatic patterns. In addition to demonstrating the preferential location and recurrence and metastatic patterns of these tumors based on their H3 K27M mutation status, we will demonstrate the highly variable radiographic features of

Electronic Educational Exhibits

these tumors and lack of any significant correlation with respect to necrosis, enhancement patterns, edema, or infiltrative features.

Conclusions

Although previously grouped with adult high-grade gliomas, pediatric diffuse gliomas have been shown to be molecularly distinct and further subclassified on the presence of the histone H3 K27M mutation, which is a negative predictive factor. We will present a case-based review of imaging characteristics of histone H3 K27M mutant and wildtype diffuse gliomas, which are primarily distinguished based on midline and peripheral location, respectively, and unique recurrence and metastatic patterns seen in the H3 K27M mutant tumors.

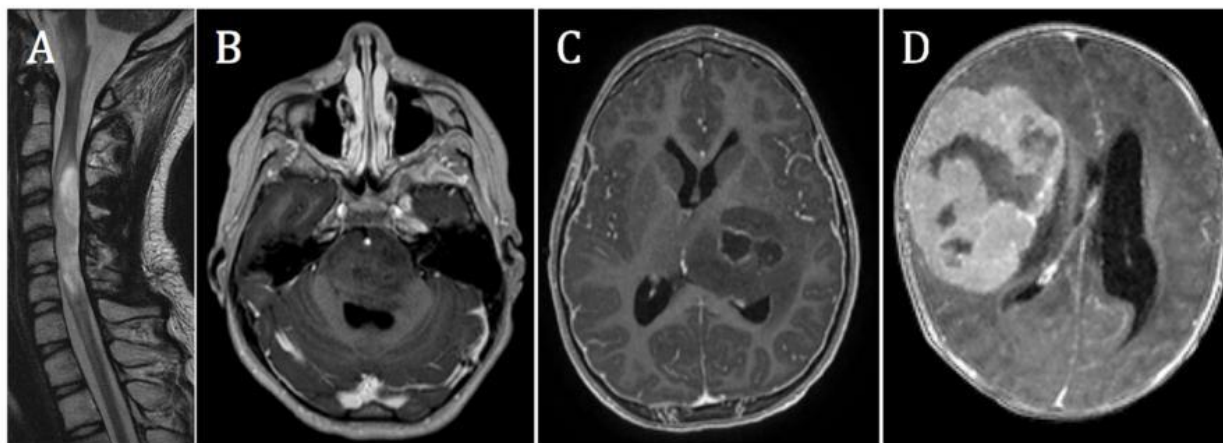


Figure 1: T1-weighted post contrast images of pediatric diffuse gliomas with the H3 K27M mutation (A-C) demonstrating preferential midline location within the cervical spinal cord, pons, and thalamus versus H3 wildtype diffuse glioma (D) demonstrating preferential location within the peripheral right cerebral hemisphere. Noted as well is the variability in contrast enhancement and necrosis among the H3 K27M mutant diffuse gliomas and compared to the wildtype diffuse glioma.

(Filename: TCT_eEde-202_ASNR_2018_asbtract_figure.jpg)

eEde-173

Pediatric Stroke Alert: A Multidisciplinary Team Approach

P Mullin¹, D Patel¹, A Harvin¹, E Mack¹, M Spampinato¹

¹Medical University of South Carolina, Charleston, SC

Purpose

Childhood stroke is a significant cause of morbidity. Acute neurological deficit is under recognized in children, resulting in a delayed stroke diagnosis. Here we review our initial experience with a multidisciplinary protocol to triage, diagnose, and treat pediatric stroke.

Materials and Methods

The pediatric stroke alert system is activated for children (>30 days of age) with new focal neurological deficit, focal seizure, or altered mental status. A multidisciplinary team is notified by pager. Initial work-up includes vital signs, history, neurological exam, pediatric NIH Stroke Scale, and laboratory tests. Once the team determines that imaging is required, the patient is brought to radiology. We utilize a fast brain MRI protocol, including DWI, FLAIR, GRE, and time-resolved MR angiography (scan time = 7 minutes). If MRI is contraindicated, the patient undergoes a noncontrast head CT and head/neck CT angiography.

Electronic Educational Exhibits

Results

To date, the pediatric stroke team has provided care to 6 patients with stroke-like symptoms (3 males, age range 1-17 years). All patients had risk factors for cerebral infarction, such as organ transplant, cerebrovascular pathology, and malignancy. Average stroke alert-to-imaging time was 182.2 minutes (range 38-525 minutes). The imaging work-up consisted of MRI in three cases, and CT in the remaining cases. Final diagnoses included remote cerebellar infarction, brain tumor, encephalitis, post-ictal state, and post-transplant lymphoproliferative disorder.

Conclusions

A single-call activation system and involvement of a multidisciplinary team is essential for the rapid comprehensive management of pediatric stroke. Given the range of diseases presenting with stroke-like symptoms in children, MRI is the most appropriate imaging modality in this patient population. We have developed a fast MRI protocol to limit ionizing radiation exposure and to decrease the need for sedation. An MRI-based approach has the advantage to facilitate the diagnosis of several pathologies that may not be evident on CT.

eEde-208

Phake Outs: Imaging Spectrum of Phakomatoses and Their Mimics and Tips for Narrowing the Differential

K Hammoud¹, P Toskas², N Spittler², N Madan³

¹Tufts Medical Center, Cambridge, MA, ²Tufts University School of Medicine, Boston, MA, ³Tufts Medical Center, Boston, MA

Purpose

1. To illustrate the development of the embryonic ectoderm in order to establish a better understanding and reasoning for the spectrum of neurocutaneous pathology seen in phakomatoses 2. To depict the spectrum of phakomatoses and mimickers through illustrative case examples, including but not limited to: - Neurofibromatosis 1 T2 bright spots vs demyelinating disease and other nonspecific white matter changes - Neurofibromatosis 2 CNS findings vs isolated meningiomas, schwannomas and ependymomas - Tuberous sclerosis vs. heterotopic gray matter and cortical dysplasia - Sturge-Weber syndrome vs. arteriovenous malformations and TORCH infections - Basal cell nevus syndrome vs. other dental cystic lesions such as ameloblastomas and aneurysmal bone cysts - Von Hippel-Lindau with hemangioblastomas vs. other cystic lesions in spine/brain. Also endolymphatic sac tumors vs paragangliomas, petrous apicitis, etc. - Cowden/COLD syndrome (MR 1168235) Lhermitte Duclos vs. demyelinating process, rhombencephalitis - Parry Romberg Syndrome/PFH 3. To provide pearls for using additional imaging and clinical history to help narrow the differential diagnosis

Materials and Methods

The initial portion of the presentation will be dedicated to delineating the development of the ectoderm into the skin and neuroectoderm and eventually the nervous system using original illustrations. The second portion of the presentation will be comprised of various illustrative case examples using multiple modalities accompanied by detailed clinical histories and physical exam findings. Many of these cases will be directly contrasted with cases with mimickers which may have similar imaging appearances. Lastly tables will be provided to help consolidate the information presented on the previous slides and aid in narrowing the differential diagnosis.

Results

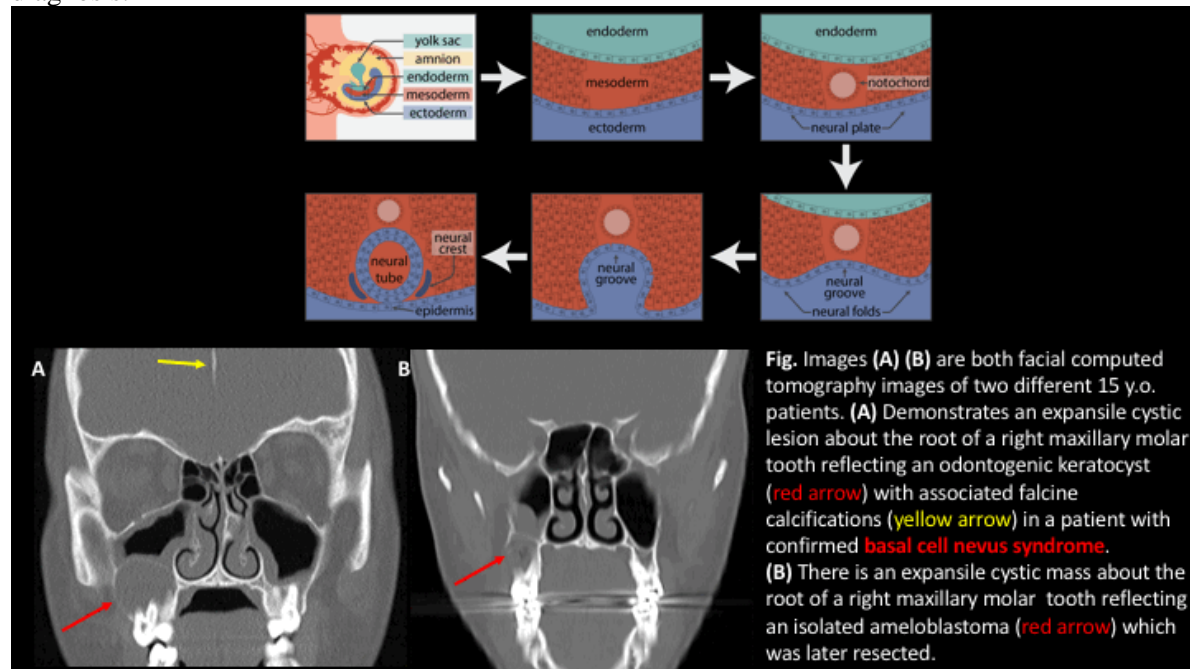
Phakomatoses represent a group of neurocutaneous disorders which involve structures which arise secondary to aberrant migration, formation or differentiation of the embryonic ectoderm which forms the central and peripheral nervous systems and skin. Regarding imaging features in the central nervous system, there is significant overlap between the different neurocutaneous syndromes and other pathologies. It is therefore key to ascertain the patient's clinical history, search for other non-neurologic

Electronic Educational Exhibits

associated findings and correlate the imaging findings with physical exam findings in order to reach a more accurate diagnosis.

Conclusions

The phakomatoses/neurocutaneous disorders represent a group of syndromes with similar embryologic origins which manifest in the central and peripheral nervous systems and skin. It is paramount for the radiologist to have a good understanding of these syndromes so as to recognize them when presented on imaging. Clinical history and physical exam are also vital in helping to mold and narrow the potential diagnosis.



(Filename: TCT_eEde-208_PhakeASNR.gif)

eEde-209

Practice Your Cords: The Song and Dance of Spinal Cord Ultrasound in Neonates

P Craig¹, A Zarchan¹, K McKenna¹

¹University of Kansas-Wichita, Wichita, KS

Purpose

This is intended to review the basics of spinal cord ultrasound in newborns. Goals of presentation include:

1. Briefly discuss the indication for spinal cord ultrasound.
2. Review normal anatomy displayed on a spinal cord ultrasound.
3. Explore benign anatomic variants that can mimic true pathology.
4. Examine spinal cord pathology on ultrasound and in select cases compare additional imaging of the lumbar spine on MR and radiography.

Materials and Methods

Initially, a literature search was carried out to compile a list of target cases we wanted to obtain. We then performed a retrospective review of all spinal cord ultrasounds performed at our institution from Jan 1, 2005 to Dec 1, 2017. This resulted in a total of 834 spinal cord ultrasound exams. We extracted cases that were exemplary of normal anatomy, benign variant anatomy, and true pathology. After compiling the cases, we then looked at additional imaging of the pathology on lumbar spine radiography and MR when available.

Electronic Educational Exhibits

Results

Indications for spinal cord ultrasound in our case series included screening for additional abnormalities when known congenital anomalies exist, sacral dimple, and soft tissue mass in the lumbar region. The most common by far was sacral dimple, which was felt to be over-screened given the number of normal exams. A normal spinal cord ultrasound was reviewed, detailing key anatomy. Cases were successfully obtained that covered the spectrum of variant anatomy, including ventriculus terminalis, prominent filum terminale, filar cyst, and pseudosinus tract. Pathological spinal cord ultrasounds were then compiled. Lipomas resulting in tethered cord, dermal sinus tract, lipomyelocele, lipomyelomeningocele, filum lipoma, and caudal regression syndrome are presented. Additional imaging of these conditions was also reviewed when available.

Conclusions

Ultrasound of the spinal cord is often the initial screening exam in newborns who present with findings suspicious for pathology. A strong knowledge of anatomy and normal variants is key to the radiologists ability to accurately report the findings and add value to patient care.



(Filename: TCT_eEde-209_610final2.jpg)

eEde-192

Preoperative Planning for Cochlear Implants: Assessment of the Cochlear Nerve

Z Zitterkopf¹, A Aly¹, M Ali¹, E Pedersen¹

¹Creighton University Medical Center, Omaha, NE

Purpose

1. Review embryology/anatomy of the inner ear
2. Review the role of cross-sectional imaging in preoperative assessment for cochlear implants
3. Explain the role of computed tomography (CT) and magnetic resonance imaging (MRI) in the assessment of cochlear nerve hypoplasia
4. List new treatment options in cases of congenital cochlear nerve aplasia/hypoplasia

Materials and Methods

The presence of a cochlea along with a cochlear nerve remains an absolute requirement in the clinical

Electronic Educational Exhibits

evaluation for cochlear implantation. A thorough understanding of the embryological development of the Organ of Corti explains why a normal cochlea does not eliminate cochlear nerve dysplasia. The radiologist continues to have greater role in the evaluation of cochlear implantation as increasingly innovative methods for treating profound sensorineural hearing loss (SNHL) develop. Temporal bone CT aids in the diagnosis of cochlear malformation, while MRI of the internal auditory canal (IAC) best assess the cochlear nerve.

Results

Temporal bone CT is adequate for the evaluation of the bony labyrinth and the bony cochlear nerve canal. Cochlear nerve canal stenosis remains an important finding in patients with profound SNHL warranting further evaluation via MRI. T2-weighted sagittal images obtained in an oblique plane perpendicular to the long axis of the IAC is the preferred method for visualizing the 4 major nerves within the IAC.

Conclusions

Cochlear nerve aplasia remains a contraindication to cochlear implantation. Thorough understanding of inner ear anatomy and embryology along with correct interpretation of CT and MRI findings aid in the appropriate selection and improved efficacy of cochlear implantation in those with profound sensorineural deafness.

eEde-206

Radiogenomics of Medulloblastoma: Emphasis on MRI Features

T Gleason¹, M Aboian¹, S Cha¹

¹*University of California San Francisco, San Francisco, CA*

Purpose

Medulloblastoma is a common malignant pediatric tumor of the central nervous system. The purpose of this exhibit is to highlight unique imaging features of different medulloblastoma molecular subtypes.

Materials and Methods

A concise summary of the 2016 WHO classification of medulloblastoma molecular subtypes, followed by a case-based discussion of key imaging characteristics of pediatric medulloblastoma and its molecular subtypes.

Results

The MRI characteristics of the four molecular subtypes of medulloblastoma based on 2016 WHO Classification will be described which include Wnt, Shh (p53 mutant and wildtype), Group 3, and Group 4 tumors. These molecular subtypes will be correlated to the histologic classification of medulloblastomas including classic, large cell/anaplastic, and desmoplastic/nodular types. Literature discussing prognostic information and metastatic recurrence patterns based on molecular subtypes will be highlighted.

Differential diagnosis including cases of ependymoma and pilocytic astrocytoma within the posterior fossa will be included.

Conclusions

Medulloblastomas are a common and devastating pediatric CNS tumor. Key imaging characteristics can help differentiate medulloblastoma from other posterior fossa tumors and help identify the molecular subtype of medulloblastoma, which can be integrated with classic histology patterns to guide treatment and prognosis.

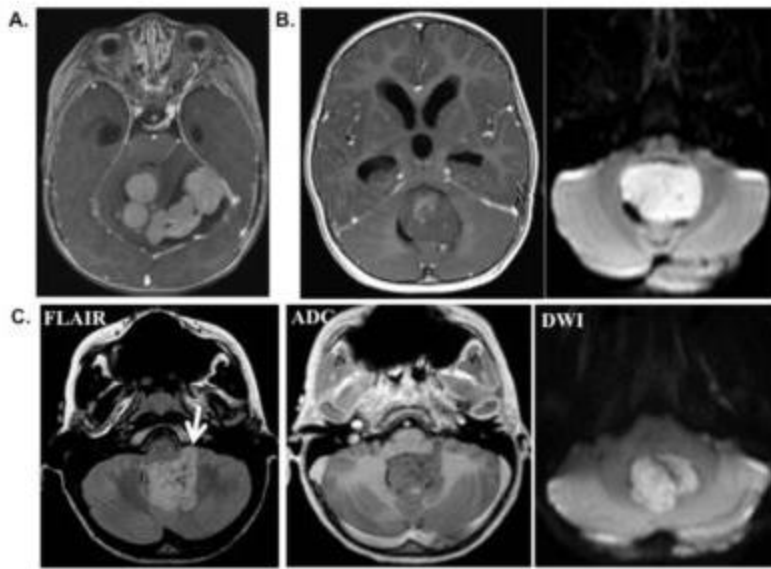


Figure 1: Imaging characteristics of medulloblastomas. (A) Contrast enhanced imaging of Shh subtype medulloblastoma. (B) Contrast enhanced and DWI image of non-Wnt/non-Shh subtype medulloblastoma that is located along the midline and demonstrates only mild contrast enhancement. (C) non-Wnt medulloblastoma demonstrates extension into the left foramen of Luschka.

(Filename: TCT_eEde-206_MedulloblastomaFigure1.jpg)

eEde-195

Simultaneous PET/MRI Neuroimaging in Pediatric Epilepsy: Our Experience at Mallinckrodt Institute of Radiology, St. Louis, Missouri

M Ponisio¹, M Parsons², M Miller-Thomas², M Smyth¹

¹Washington University in Saint Louis, Saint Louis, MO, ²Mallinckrodt Institute of Radiology, Saint Louis, MO

Purpose

Assess the value of simultaneous PET/MRI for pediatric refractory epilepsy by demonstrating how this new hybrid modality provides complementary functional and morphological imaging allowing detection of subtle or no changes on MR images, and the multiple modality imaging required for minimally invasive surgical strategies.

Materials and Methods

A retrospective review of 42 pediatric patients who underwent PET/MRI imaging for epilepsy were compared with conventional imaging, and the impact of PET/MRI on clinical patient management was accessed.

Results

The importance of PET/MRI for presurgical evaluation of pediatric refractory epilepsy is demonstrated, showing how this hybrid modality provides complementary functional and morphological imaging allowing identification of cortical malformation, which is the major cause of seizures in children, by detecting subtle changes on MR images that may initially be reported as normal, when coregistered with 18F-FDG PET interictal images. In addition, PET/MRI provides the multiple modality imaging required

to optimize surgical planning and outcomes for minimally invasive surgical strategies: stereo-electroencephalography (SEEG), laser interstitial thermal-ablation therapy (LITT) and stereotactic radiosurgery, RF ablation.

Conclusions

PET/MRI is the key imaging modality for presurgical evaluation of pediatric refractory epilepsy, providing complementary functional and morphological compared to conventional MRI and PET/CT, and allowing for minimally invasive surgical strategies, more appropriate for this patient population.

eEde-182

The Very Frequent Finding of Enlarged Perivascular Spaces In Children: Why Should We Care?

L Brandao¹

¹*Clinica Felippe Mattoso-Grupo Fleury, Rio De Janeiro, Brazil*

Purpose

Perivascular spaces (PVSs), also referred to as Virchow-Robin spaces, surround both penetrating arteries and emerging veins in the brain. The purpose of this study was to describe the major clinical situations associated with small as well as enlarged PVSs in the brain in children.

Materials and Methods

A retrospective review of the MR brain studies was done over a six-month period from June to November 2017 from children referred for predominantly developmental delay. MRI studies were performed on 1.5T GE Signa Horizon and 1.5 T GE Excite units. Available sequences included sagittal T1 3D SPGR, axial T1, T2, FLAIR, GRE and DWI, as well as coronal T2, to determine the frequency and size (enlarged >3mm and unenlarged < or = 3mm) of PVSs in the supratentorial white matter.

Results

One-hundred-ten children were identified (64 males, 46 females with age range of 20 days to 12 years - median, 6 years). PVSs were demonstrated in the scans of 99% of the children, located mainly in the deep parietal white matter. In 95,5% of the cases the PVSs were small and associated with global developmental delay (60), autism (35) and headaches (10). Large perivascular spaces were demonstrated in 4,5 % of the cases and were associated with Lowe Syndrome (1), mucopolysaccharidosis (2), PTEN mutation (1) and Hypomelanosis of Ito (1). Additional imaging and clinical findings helped distinguish among the different causes of large PVSs.

Conclusions

Large PVSs may be associated with inborn metabolic disorders such as Lowe syndrome and mucopolysaccharidosis, as well as with genetic disorders such as PTEN mutation and Hypomelanosis of Ito. Associated clinical and imaging findings are extremely helpful in the differential.

eEde-207

Usual and Unusual Imaging Findings and the Pathology of Craniopharyngioma

D Shlensky¹, J Kim¹, A Capizzano², T Moritani¹, T Sato³

¹*University of Michigan, Ann Arbor, MI*, ²*University of Iowa Hospitals and Clinics, Iowa City, IA*, ³*University of Iowa, Iowa City, IA*

Purpose

1. To understand the epidemiology, genetic features, clinical symptoms, and treatment paradigms of Craniopharyngioma 2. To review both typical and atypical imaging features of Craniopharyngioma 3. To learn how certain imaging findings may be suggestive of specific Craniopharyngioma subtypes, which have unique genetic patterns

Electronic Educational Exhibits

Materials and Methods

This exhibit will begin by reviewing information regarding the epidemiology, genetics, symptoms, treatment, and pathology of Craniopharyngiomas. It will then provide examples of typical and atypical imaging findings of Craniopharyngiomas, and discuss how these relate to pathologic findings and tumor subtypes.

Results

Craniopharyngiomas are rare epithelial neoplasms that develop from remnants of Rathke's pouch, and account for approximately 3% of all intracranial tumors. They impact pediatric and adult populations, with bimodal peaks at 5-14 and 50-74 years old. Although they are WHO grade I neoplasms, they are associated with significant pretreatment symptoms, most commonly headache, and post-treatment morbidity including visual disturbance, endocrine dysfunction, and cognitive abnormalities. Optimal treatment is controversial, but recent data has shown no difference in tumor control rates or progression free survival when comparing subtotal resection with adjuvant radiotherapy versus gross total resection. The latter option is limited, however, by tumor location, size, and proximity of adjacent structures, with increased risk of long-term endocrine deficits. There are two types of Craniopharyngioma, papillary (pCP) and adamantinomatous (aCP), with distinct genetic features. Papillary tumors have activating mutations in BRAFV600E in 81-100% and tend to only occur in adults. In contrast, aCP have CTNNB1 mutations resulting in Wnt/ β -catenin hyperactivity and can occur in adults or children. On imaging, some characteristics can be used to suggest subtype. For example, calcifications on CT and T1 hyperintensity correlate with aCP subtype. The cystic component's T1 bright signal reflects proteinaceous or cholesterol content, or hemorrhage. Papillary types tend to be solid, rounded, and do not usually have calcifications. Despite the usual description of Craniopharyngiomas as enhancing sellar/suprasellar masses, case reports exist of unusual features such as nasopharyngeal location. Other atypical examples of Craniopharyngiomas will also be provided in this exhibit.

Conclusions

By viewing this exhibit, the reader will enhance their understanding of the clinical aspects of Craniopharyngiomas, their typical imaging features which relate to tumor subtypes with different pathologic findings and genetic underpinnings, and examples of atypical Craniopharyngioma presentations.

eEde-205

Variability of Imaging in the Invariably Midline Diffuse Midline Glioma

J Gastala¹, A Bryant², T Moritani³, P Kirby¹, Y Sato⁴

¹University of Iowa Hospitals and Clinics, Iowa City, IA, ²University of Iowa, Iowa City, IA, ³University of Michigan, Ann Arbor, MI, ⁴University Of Iowa Health Care, Iowa City, IA

Purpose

A new tumor entity, the diffuse midline glioma, histone H3 K27M mutant, was introduced in the 2016 World Health Organization Classification of Tumors. This mutation is present in most adult and pediatric diffuse gliomas arising in midline structures, and includes tumors previously referred to as diffuse intrinsic pontine gliomas (DIPG). This molecularly defined subset of tumors has worse overall survival compared to wildtype tumors, independent of patient age, histologic diagnosis, and grade. The purpose of this exhibit is to highlight the variability of imaging characteristics in this new tumor entity.

Materials and Methods

A review of the current literature including epidemiology, pathophysiology and pathology, and genetics of diffuse midline gliomas will be presented. A spectrum of imaging findings from our institutions with histopathologic and genetic correlation will be presented.

Results

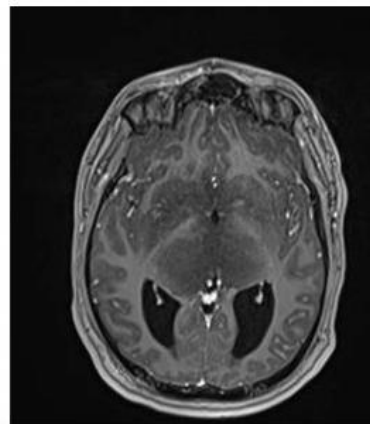
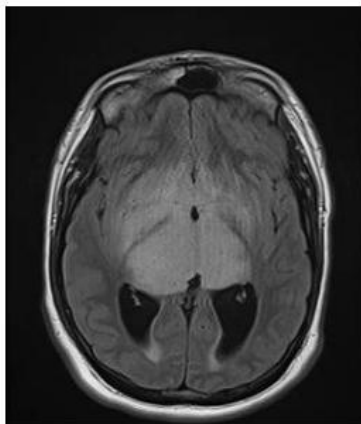
The histone H3 K27M mutation is present in most adult and pediatric diffuse gliomas arising in midline

Electronic Educational Exhibits

CNS structures. These tumors exhibit a diffuse growth pattern and a midline location including the thalamus, pons, brain stem, vermis/cerebellum, and spinal cord. Imaging features are variable and cannot reliably distinguish mutant from wildtype midline tumors. Cervical spine gliomas tend to be uniformly enhancing while gliomas within the thalamus and posterior fossa are more likely to be solid or infiltrative and less frequently necrotic.

Conclusions

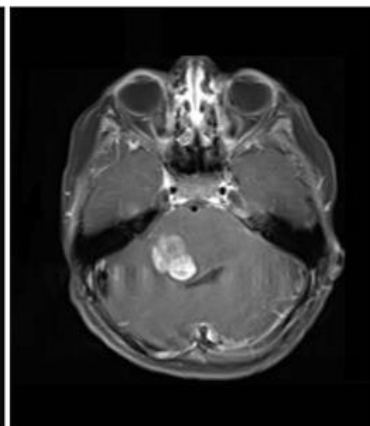
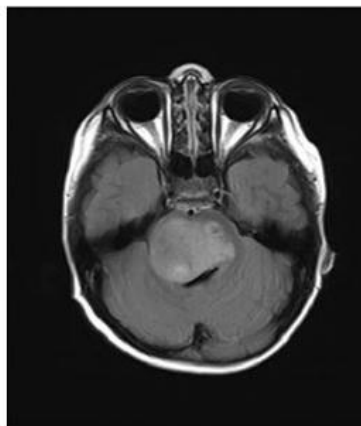
Diffuse midline glioma, histone H3 K27M mutant, is a specific subgroup of diffuse gliomas with worse prognosis regardless of histologic grading. Imaging characteristics of these tumors are variable and the radiologist should be aware of the spectrum of imaging findings.



26y M

Bithalamic diffuse
midline glioma

Axial FLAIR and
postcontrast



6 y M

Diffuse midline glioma of the
pons

Axial FLAIR and postcontrast

(Filename: TCT_eEde-205_ASNRDMGImages.jpg)

eEde-172

Vessel-wall Imaging of Intracranial and Cervical Arteries in Childhood Arteriopathies

D Jamjoom¹, P Muthusami¹, M Shroff¹, M Moharir¹

¹*The Hospital for Sick Children, Toronto, Ontario, Canada*

Purpose

The role of VWI in diagnosis and prognostication of pediatric arteriopathies is not well characterized. In this exhibit we demonstrate vessel wall imaging (VWI) appearances and patterns in children presenting

with stroke. We also discuss technical challenges and limitations of this imaging technique in the pediatric population.

Materials and Methods

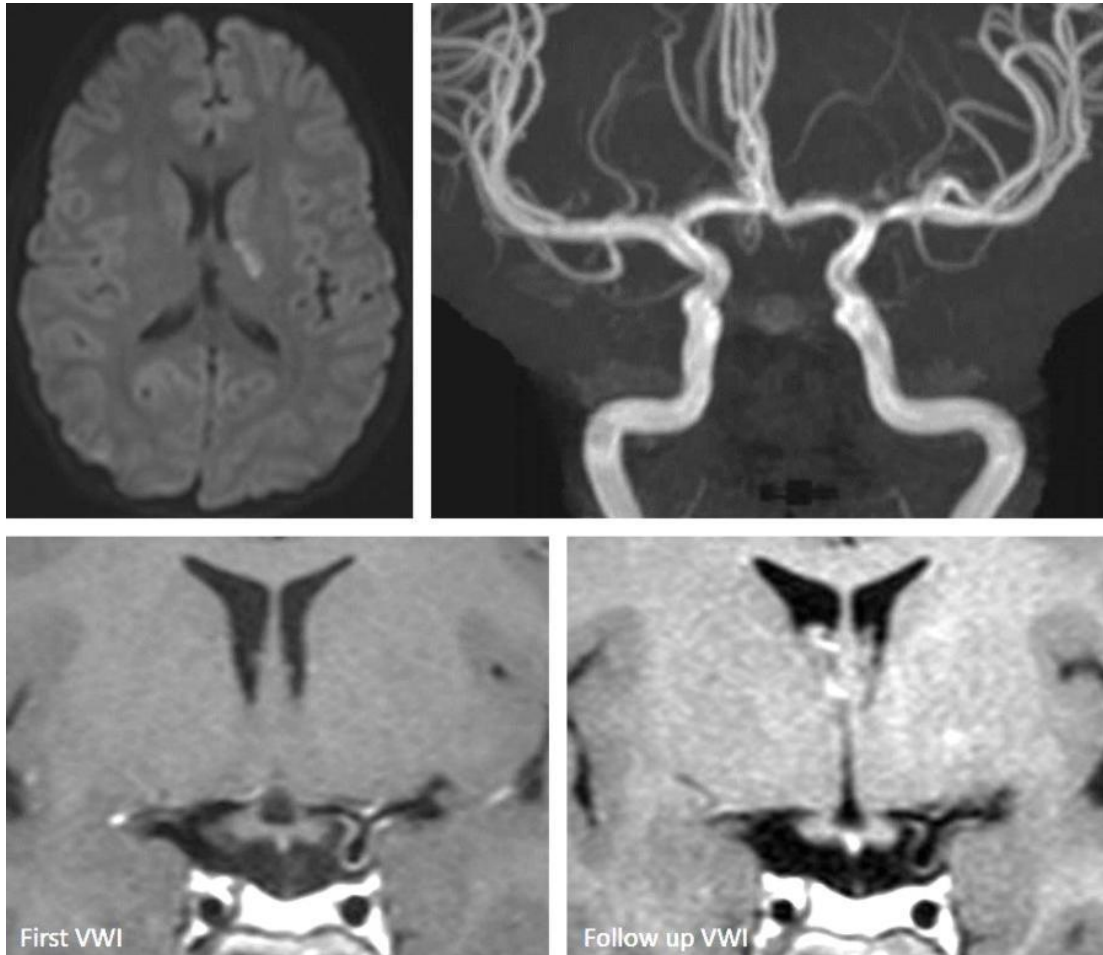
56 VWI examinations were performed on 35 patients (21 male, age: 4 months - 17 years) between January 2010 and July 2017 for patients presenting with acute stroke. The vessels of interest were examined for wall abnormality, including T1-hyperintensity, appearance and pattern of enhancement. Findings on conventional vascular imaging (MRA, CTA, catheter angiography) were also documented. Temporal evolution of VWI change was assessed where follow-up imaging was available. The various types of artifacts and their frequency were documented.

Results

VWI is useful in differentiating various arteriopathies based on the pattern of vessel wall involvement and associated enhancement. In this pictorial exhibit, we demonstrate patterns of vessel wall enhancement in common childhood arteriopathies like transient cerebral arteriopathy, CNS vasculitis (figure), Moyamoya disease and dissection, the temporal evolution of the VWI appearances, and how these correlate with lumenographic information. We also discuss the technique, modifications and challenges of performing VWI in children. We analyze the types and frequency of artifacts commonly encountered while interpreting VWI in children.

Conclusions

Performing and interpreting VWI in children requires specific considerations and technical modifications. Pediatric arteriopathies have VWI appearances which are not always typical but are distinct from findings in adult cerebrovascular disease.



(Filename: TCT_eEde-172_post-varicellavascularitis.jpg)

Electronic Educational Exhibits-Socioeconomics

eEde-211

Revisiting Reinterpretation of Head and Neck Imaging by Neuroradiologists with Subspecialization: Have the Numbers Improved?

Z Royce¹, A Corey², K Baugnon¹, A Aiken³, P Hudgins¹

¹Emory University, Atlanta, GA, ²Emory University, Fayetteville, GA, ³Emory University Hospital, Atlanta, GA

Purpose

Fifteen years have passed since Loevner et. al.[1] published their landmark study showing added value by reinterpretation of outside studies for Head and Neck (H&N) tumor board. The purpose of our study was to assess incidence and impact of interpretation discrepancy of outside contrast enhanced computed tomographic (CECT) studies in patients with H&N cancer.

Materials and Methods

Our quality improvement study included 45 patients H&N cancer referred to our multidisciplinary cancer center with outside CECT examinations submitted for reinterpretation by one of four neuroradiologists with H&N expertise. Patient demographics and technical quality of the CECT were recorded.

Discrepancy with the primary interpretation was assessed using a four-point scale: 1. no discrepancy 2. minor discrepancy, unlikely to change clinical management 3. major discrepancy due to error in interpretation, likely to change management 4. major discrepancy due to error in detection, likely to change management A senior H&N radiologist confirmed the reinterpretation accuracy by pathologic proof or characteristic imaging findings. An online search classified the primary interpreting physician as a neuroradiologist or non-neuroradiologist.

Results

Of the 45 primary interpretations, 14 (31%) were assigned scores of 1 and 3 (6.7%) scored 2. Twenty eight (62.2%) were assigned scores of 3 or 4, indicating major discrepancies likely to change clinical management. Common errors included missing a mass (23.5%), underestimating extent of the tumor (23.5%), and missed metastatic lymph node (20.6%). Neuroradiologists interpreted 66.7% of studies. Major discrepancies were found in 73.3% of reports by non-neuroradiologists and 56.7% by neuroradiologists.

Conclusions

Reinterpretation of outside CECT by H&N radiologists revealed clinically relevant discrepancies in a majority of the primary interpretations performed by both neuroradiologists and non-neuroradiologists. Reinterpretation of outside CECT by a radiologist with H&N expertise continues to be an integral component of H&N tumor boards.

eEde-210

The American Society of Neuroradiology (ASNR)/ACR/RSNA Common Data Elements Project - What It Will Do for the House of Neuroradiology

A Flanders¹, M Kohli², C Kahn³, J Jordan⁴

¹Thomas Jefferson University Hospital, Philadelphia, PA, ²University of California San Francisco, San Francisco, CA, ³University of Pennsylvania, Philadelphia, PA, ⁴Providence Little Company of Mary Medical Center, Torrance, CA

Purpose

The function of this workgroup is to develop a catalog of CDEs for neuroradiology that are both practical and useful for clinical practice with the goal to unify practice standards by improving consistency in reporting, and to develop human and machine interpretable features that can be used to measure quality in our speciality. There are numerous secondary benefits in comparative effectiveness research, precision medicine, radiomics, registry participation, machine learning, communication and public health. A CDE, or common data element, is a question/concept combined with a set of expected responses. CDEs can record properties of imaging findings such as anatomic location, shape, image number, image coordinates, and dimensions, and can store computed values such as texture metrics. Examples might include an ASPECT Score for stroke (integer range: 0 - 10), Pfirman criteria for root compression (integer range: 0 - 4), foraminal stenosis (text: normal, mild, moderate, severe) or machine derived values. There are many examples of CDEs in our literature which correlate to outcomes, therapeutic response and disease state. Many of these published CDEs have been validated through clinical trials research and have reasonable interrater agreement. A clinical report might contain many CDEs or collections of CDEs that are relevant to a specific disease. There are many examples of imaging CDEs in our literature which correlate to outcomes, therapeutic response and disease state. Many of these published CDEs have been validated through clinical trials research and have reasonable interrater agreement. The purpose of this exhibit is to provide context, background and benefits of creating a repository of CDEs for organized neuroradiology and to describe the process for developing this content, how it will be coded and consumed to meet these objectives in the future.

Materials and Methods

The ASNR, in cooperation with the Informatics leadership at the ACR and RSNA has volunteered to be the first subspecialty domain expert group to help produce relevant clinical concepts for our speciality. The goal is to: 1. develop a catalog of the most commonly used concepts in clinical neuroradiology, 2. codify/validate these concepts and responses with a team of experts, 3. encode these into a common schema, 4. catalog and store concepts in a repository (radelement.org) to support multiple use cases. The intent is to develop core concepts that are used commonly in radiology reporting; the minimal number of defined concepts that should be conveyed to the ordering clinician for a particular clinical use case. The important characteristic is that both the concept and the response are consistent whenever it used. Use of a controlled response creates consistency in activities like clinical reporting for the human consumer but it also creates an environment that facilitates computable consumption of concepts that can drive downstream actionable processes. Benefits include: 1. increased acceptance by clinicians, 2. modular authoring and modification of report templates, 3. easier execution of comparative effectiveness research studies, 4. aggregation of data for registries, 5. re-use of clinical reports for research. Initial CDE collections that the group has begun work upon include: CT Stroke, Neck Lymph Nodes staging, Pituitary Mass, Lumbar Degenerative Disease, Laryngeal Cancer Staging, Metastatic Spine Compression and Multiple Sclerosis Brain. The work group utilizes a set of collaborative tools to create, comment, review and maintain the collections. Periodic teleconferences and face-to-face meetings are scheduled at the RSNA and ASNR annual meeting. CDE collections are taking shape and are in various phases of completion.

Results

Many quality and value-based healthcare initiatives serve as motivators for developing CDEs. Healthcare organizations and subspecialty provider organizations are being requested to develop, benchmark and comply with specific quality standards overall and to develop specific ones for each speciality. Pay-for-performance initiatives, meaningful use and PQRS programs are now being wrapped up into the new value-based programs under MIPS/MACRA. The dissemination of electronic medical records (EMR) created by the ARRA stimulus package has facilitated the collection, sharing and dissemination of data which can be used to benchmark practice and quality standards for a speciality. Clinical subspecialties (e.g. cardiology, gastroenterology, pathology, ophthalmology, oncology) have been very active in defining very granular structured data housed in the EMR that they recommend can be used to establish quality parameters by demonstrating value of the services delivered. Adoption of CDEs in clinical practice

fosters participation in data registries which in turn, are being used to set and measure practice standards. While organized radiology has been very active in demonstrating our compliance with healthcare IT, interoperability and exchange of information, we are behind in defining quality parameters of our clinical reports. With the exception of mammography, most of our quality metrics have focused around service delivery times (i.e. turnaround times) and not about the content of our reports. For the most part, all of the requisite technology to use CDEs in clinical reporting exists today on commercial reporting systems. All modern reporting systems support the use of templates, macros and picklists. Picklists in particular are essentially multiple choice responses to a particular question which is the basic schema of a CDE.

Conclusions

The Common Data Elements Work Group activities for the ASNR will form the underpinning of a number of quality, safety, communication and performance initiatives for neuroradiologists. Use of a common set of concepts throughout the "House of Neuroradiology" provides clarity in clinical reporting and can be leveraged by a host of informatics tools to improve secondary processes in the healthcare ecosystem.

Electronic Educational Exhibits-Spine

eEde-218

"When You Have Eliminated the Impossible, Whatever Remains Must Be the Truth" - Investigating Spinal Infections

A Pettengill¹, I Padilha¹, A Araújo¹, F Scortegagna², R Hoffmann Nunes¹, F Pacheco¹, A Maia¹, L Amaral³, A da Rocha¹

¹*Irmandade da Santa Casa de Misericórdia de São Paulo, São Paulo, Brazil*, ²*Dasa Group, São Paulo, Brazil*, ³*Beneficiencia Portuguesa, São Paulo, Brazil*

Purpose

Infection involvement of the spine can occur as a result of a wide range of agents, including bacteria, virus, parasites and fungus. Our purpose is to review the patterns of spinal lesions when infections were the final diagnosis.

Materials and Methods

We reviewed our institution's teaching files and the electronic patients' database in order to demonstrate spinal infections affecting all of its anatomic compartments. The lesions were classified according to the specific structure involved and to the causal agents.

Results

A broad spectrum of infections can affect the spine, involving multiple anatomical compartments. The most common are bacteria, but, although rare, virus, parasites and fungus should not be neglected since appropriate and early treatment can prevent severe sequelae. Clinical and laboratorial data are frequently unspecific and imaging approach might play a fundamental role to confirm diagnosis. The imaging systematic assessment includes the recognition of structure involvement (vertebrae, disc, adjacent soft tissue, epidural or subdural spaces and spinal cord) as well as radiologic distribution and lesion features in different imaging methods. Imaging findings related to some conditions may support the diagnosis; therefore, we explore in this pictorial review the imaging aspects of some rare infectious diseases, such as cryptococcosis, neurocysticercosis, schistosomiasis, brucellosis, echinococcosis, syphilis and others, dividing them according to involved compartment (external - bone and meningeal, internal - spine and nerve roots) in order to explore the differential diagnosis didactically.

Conclusions

Currently, radiologists must be aware that, although improbable, infectious disease remains possible no

matter where you are. This report highlights a suitable and systematic diagnostic approach guiding an appropriate nosological test for early diagnosis and correct treatment.



1. Sagittal T2WI shows **Cryptococcal spondylodiscitis and epidural collection (arrows)** in this patient with non responsive treatment that was submitted to a biopsy. The microscopy smear confirmed *Cryptococcus sp.*

2. **Medullary Blastomycosis.** Sagittal T1WIGD+ demonstrates a rim enhancement lesion (arrow) with T2WI hypointensity (not shown). The chest computed tomography showed extensive air space consolidation with small irregular cavities.

3. **Tuberculous spondylodiscitis with intracanal involvement.** Sagittal T1WIGD+ shows extensive inflammatory abnormalities of more than three vertebral bodies with massive bone destruction, epidural collections and subligamentar spread (arrows).

4. **Medullary Schistosomiasis.** Sagittal T1WIGD+ displays arboriform enhancement of conus medullaris (arrow) in a patient from an endemic region. The cerebrospinal fluid analysis showed a spiculated parasite, typical of a *Schistosoma mansoni*.

(Filename: TCT_eEde-218_Slide1.jpg)

eEde-244

3D Rotational Angiography of Spinal Arteriovenous Malformations – Improving Characterization for Safer and More Effective Treatment

B Kelley¹, H Marin¹, M Kole¹, S Patel¹, B Griffith¹

¹Henry Ford Health System, Detroit, MI

Purpose

Spinal arteriovenous malformations (AVMs) and arteriovenous fistulas (AVFs) are rare but complex neurovascular lesions typically presenting with congestive myelopathy or subarachnoid hemorrhage. Diagnosis and treatment planning for these lesions is challenging due to difficulty fully unveiling their

Electronic Educational Exhibits

complex angioarchitecture on CT, MRI, and conventional digital subtraction angiography (DSA). Two-dimensional (2-D) and three-dimensional (3-D) rotational angiography provide useful information about spinal angioarchitecture and can be particularly helpful in characterizing both the morphology of vascular lesions and their location relative to normal spinal cord vessels and osseous landmarks. The purpose of this exhibit is to introduce this advanced imaging technique with case-based examples of 3-D rotational angiography of spinal AVMs and AVFs.

Materials and Methods

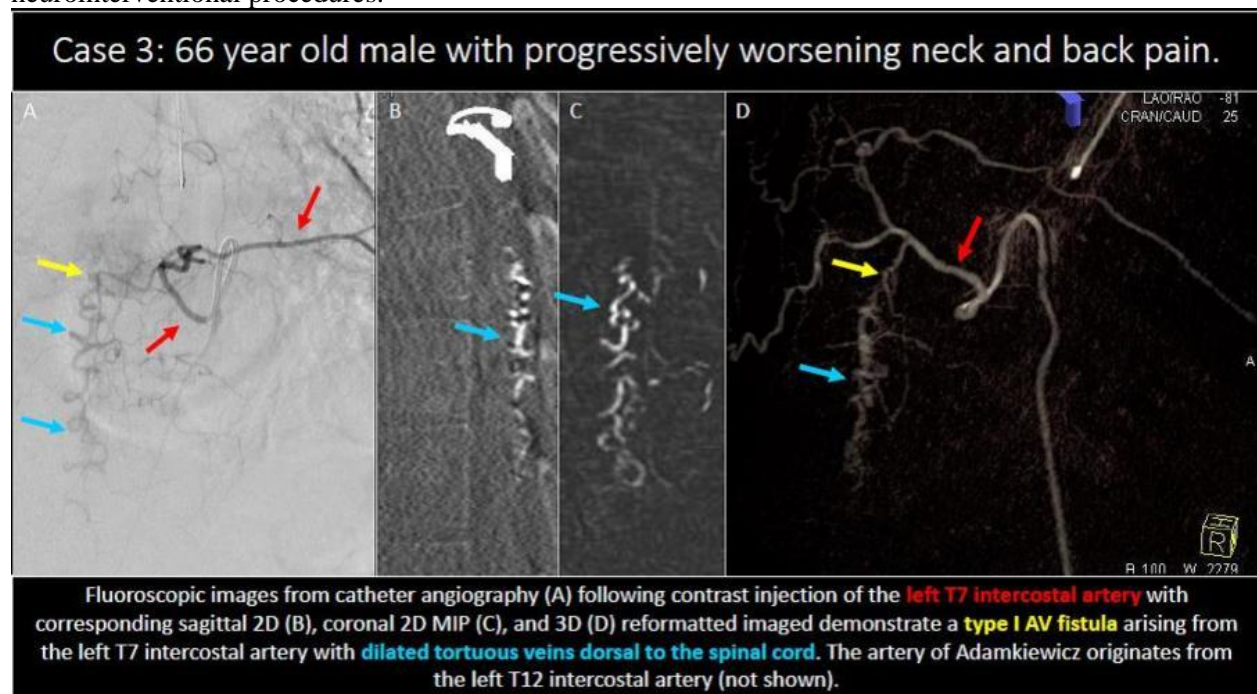
This exhibit will review the acquisition, post processing, and imaging used in 3-D rotational angiography technique. Classification systems for spinal AVMs and AVFs will also be reviewed. Case-based examples will be used to highlight how 3-D rotational angiography can supplement DSA to better visualize the overall morphology of the vascular lesions and their relationship to surrounding structures.

Results

Rotational angiography can demonstrate spinal angioarchitecture in multiple projections with or without anatomical landmarks to facilitate a safe and precise approach for endovascular or surgical treatment. In dural (type 1) AVFs, multiplanar reconstruction (MPR) can allow for precise identification of the arterial feeder, vascular shunt, and arterialized bridging vein (Fig. 1). In the setting of perimedullary, nidal, or conal AVMs, 3-D reformatted images can be used to better appreciate the complete morphology of these complex lesions.

Conclusions

This educational exhibit will highlight how 3-D rotational angiography can be used to better characterize spinal AVMs and AVFs to facilitate more detailed treatment planning prior to surgical or neurointerventional procedures.



(Filename: TCT_eEde-244_3Dangio.jpg)

eEde-229

A Review of Primary Masses of the Posterior Spinal Elements

V Kuttappan¹, V Yedavalli¹, V Pandey¹, P Chowdhry¹, A Bogachkov¹, G Gorelick¹, A Patil¹

¹*Advocate Illinois Masonic Medical Center, Chicago, IL*

Purpose

Primary spinal tumors account for fewer than five percent of all osseous neoplasms. Within this subset, only certain entities directly involve the posterior elements. The purpose of this review is to provide an overview of primary masses specifically involving the posterior elements as these masses can be overlooked.

Materials and Methods

In this review, we provide clinical presentation, demographics, physiology, and imaging characteristics amongst various modalities for masses that involve the posterior elements. We stratify these posterior element masses into benign and malignant categories with clinical examples.

Results

As an area that is often overlooked when interpreting a cross-sectional scan or radiograph, differentiating masses involving the posterior elements can provide significant clinical value. Many benign lesions such as aneurysmal bone cysts, osteoid osteomas, osteochondromas, chondroblastomas, chondromyxoid fibromas, and giant-cell tumors can cause pain and/or pathologic fracture leading to dire neurologic ramifications. Malignant neoplasms as osteosarcoma, chondrosarcoma, and Ewing's sarcoma can be aggressive, exerting locally destructive effects while also potentially propagating systemically via the posterior spinal vasculature. Understanding these clinical and imaging manifestations of these aforementioned pathologies is paramount to arriving at a correct diagnosis for appropriate management.

Conclusions

As primary masses specifically involving the posterior elements can often be overlooked on cross-sectional imaging or radiographs, this review focuses on differentiating both benign and malignant entities of the most common pathologies. In doing so, we hope to elucidate key distinguishing factors of each entity for accurate diagnosis and timely management.

eEde-231

Acute Nontraumatic Myelopathies from ADEM to Zika

D Alden¹, S Alden¹, B Huang¹

¹*University of North Carolina School of Medicine, Chapel Hill, NC*

Purpose

Acute onset extremity weakness and paresthesia are among the most common indications for emergent spinal MRI imaging. The purpose of this exhibit is to broaden the audience's differential diagnostic armamentarium and reporting accuracy in the setting of suspected acute or subacute myelopathy by presenting a review of common and uncommon causes of spinal cord disease with a focus on key distinguishing clinical and imaging findings.

Materials and Methods

Through an illustrative case-based review organized by categories of disease we will cover spinal cord anatomy, discuss typical MRI findings in various nontraumatic etiologies of myelopathy and spinal neuropathy, and examine the imaging, demographic, and clinical factors that can help us condense otherwise nonspecific findings into a focused differential or a single discrete diagnosis. This format allows a collective discussion of the imaging and clinical differentials.

Results

Spinal cord lesions on MRI are sometimes found in patients who present with clinical myelopathies and there can be significant overlap of findings between etiologies. While this can often lead to an impression of "nonspecific myelopathy" we feel that when reported in the context of relevant demographic and clinical information a more narrow and useful differential diagnosis can be offered. Entities with classic imaging and clinical features, including Guillain-Barré syndrome, spinal cord infarction, and dural

Electronic Educational Exhibits

arteriovenous fistula, are discussed both in terms of salient findings but also imaging appropriateness. Specificity enhancing MRI techniques, such as diffusion-weighted imaging, are also reviewed.

Conclusions

The interpretation of spinal cord and radicular abnormalities on MRI can be made more specific and clinically helpful to our referring colleagues when we examine these findings in the broader context of the patient's clinical presentation. This knowledge can increase our confidence in rendering a targeted diagnosis or differential and can make a significant impact on the downstream work-up and treatment of the patient.

Disease Categories	Entities	Disease Categories	Entities
Vascular disease	Ischemic infarction Vasculitis Spontaneous hemorrhage AVM/AVF Cavernous malformations Surfer's myelopathy	Neoplasm	Ependymoma Glioma Metastatic disease Neurofibroma Meningioma Schwannoma Paraneoplastic syndromes
Viral infections	Poliovirus Coxsackievirus HIV HTLV-I Zikavirus	Drugs/Toxic/Metabolic	Radiation Subacute combined degeneration Drugs of abuse Jellyfish toxic myelopathy
Bacterial and atypical infections	Epidural infection Infectious myelitis/arachnoiditis	Demyelinating disease	Multiple sclerosis Neuromyelitis optica Idiopathic transverse myelitis
Postinfectious disease	ADEM Guillain-Barre syndrome	Autoimmune/vasculitic disease	Sjogren disease Systemic lupus erythematosus Antiphospholipid syndrome Neuro-Behçet Syndrome Mixed connective tissue disease Sarcoidosis
Compressive lesions	Acute disc herniation		

(Filename: TCT_eEde-231_Myelopathy.jpg)

eEde-240

An Introduction to AOSpine Classification in Thoracolumbar Trauma

G Simmons¹, R Patel²

¹UT Houston, Houston, TX, ²The University of Texas Health Science Center at Houston, Houston, TX

Purpose

To provide an brief introduction to the state of of spine classification, including the Magerl and TLICS spine classification. To introduce the imaging fundatmentals of the AOSpine classification with a focus on the discriminating imaging morphological features. To provide real world examples of the classification in work. To provide an opportunity to practice classification with several case-based examples.

Materials and Methods

Reproducible and comprehensive classifications of spinal fractures facilitate communication between teams of providers and the selection of optimal treatment protocols. It remains a goal of the spine community. Historically, proposed systems have included a diverse range of characteristics including 1) mechanism of injury 2) bony morphology 3) anatomic determinants of fracture stability and 4) neurological status. One of the traditional systems introduced by Magerl et al. in 1994 uses morphological features to classify fractures. Unfortunately, the Magerl system suffers from being overly complex and it

Electronic Educational Exhibits

does not include neurological status and other clinical factors that may guide surgeon intervention More recently, the thoracolumbar injury classification system (TLICS) assigns points based on 1) neurological status 2) integrity of the posterior ligamentous complex (PLC) and 3) morphology of the fracture. However, evaluation of the PLC is typically performed with MRI, the availability and reproducibility of which is problematic. Moreover, the chosen severity scoring may be culture or region specific, based on available resources. It may not reflect global surgical preferences or the most rational approach to treatment. The AOSpine Trauma Knowledge Forum set out to construct and validate a Forum has constructed a system incorporating fracture morphology and clinical factors essential for surgical decision making. Goals included creating a comprehensive yet simple classification system with clinically acceptable intra- and interobserver reliability incorporating: Morphological evaluation based primarily on features identified by CT examination The extent of neurological deficit The presence and absence of key medical comorbidities Morphological characteristics that can be reliably and reproducibly identified serve as the backbone of this system

Results

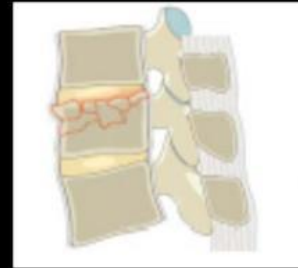
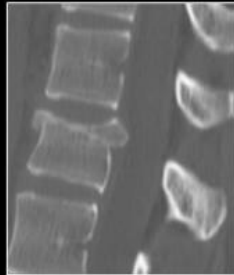
The morphological features of the AOSpine classification represent a simple, hierarchical and comprehensive set of CT features that may become increasingly important to the radiologist's repertoire as the AOSpine criteria become progressively validated. The core morphological features are: Presence of dislocation/translation Tension band injury Vertebral body integrity Vertebral process integrity Timely and accurate communication of the classification system may improve patient outcomes A review of a series of 10 cases incorporating the classification features should help reinforce the classifiers

Conclusions

Given the progressive validation of the AOSpine classification system in Thoracolumbar trauma, a review of the classification system is highly pertinent to daily practice in the emergency department reading room. Increased familiarity of the AOSpine classification system coupled with timely and accurate communication may improve patient outcomes. A review of the history of the classification system as well as an opportunity to review a series of 10 cases incorporating the classification features should help reinforce the classification system.

Example Case #1

54 year old female status post motor vehicle collision.



Patient presentation/CT scan
START !

Is there Displacement / Dislocation?

No

Tension band injury?

No

Vertebral body Fracture?

YES

Posterior wall involved?

Both endplates?

No

Type A3: Incomplete burst

(Filename: TCT_eEde-240_graphic2.jpg)

eEde-235

Common Diagnostic Errors in Spinal Imaging

R Rivera-de Choudens¹, A Srinivasan², F Rivas-Rodríguez¹, C Torres³

¹University of Michigan, Ann Arbor, MI, ²University of Michigan Health System, Ann Arbor, MI, ³The Ottawa Hospital, Ottawa, Ontario, Canada

Purpose

Describe common cognitive errors that lead to misdiagnoses in spinal imaging and some of their causes as well as delineate strategies to reduce misdiagnosis.

Materials and Methods

A thorough review of the literature regarding sources of errors in diagnostic imaging was performed. Cases of known diagnostic errors and/or possible sources of diagnostic errors were retrospectively selected from a large database and presented for educational purposes.

Results

Diagnostic errors in medicine are a major cause of patient harm and are estimated to result in 40-80,000 deaths annually in U.S. hospitals. In radiology, errors are estimated to occur in approximately 2-3% of daily reads. It is therefore of paramount importance that the radiologist is aware of potential sources of error in his/her diagnostic approach. Errors may be divided into cognitive and system errors. Most are cognitive errors which include faulty perception, failed heuristics and biases. These are best explained by

Electronic Educational Exhibits

the theoretic dual-process model of reasoning. This model proposes two general classes of cognitive operations each of which may be a source of error. Once these processes are understood a cognitive strategy may be implemented to reduce and/or mitigate error.

Conclusions

Cognitive and systems errors are a major cause of patient morbidity and mortality. Knowledge of common sources of error and adequate implementation of cognitive strategies designed to reduce them may lead to reduction in misdiagnosis and improved patient care.

eEde-242

Craniocervical Junction Trauma

A Mian¹, F Minja², G Jindal³

¹*Yale University, Old Lyme, CT*, ²*Yale University School of Medicine, New Haven, CT*, ³*Warren Alpert School of Medicine, Brown University, Providence, RI*

Purpose

We will present some common injury patterns in CCJ trauma along with relevant classification systems and degrees of instability.

Materials and Methods

Retrospective review of CCJ trauma cases in our database.

Results

Evaluating craniocervical junction (CCJ) injuries can be challenging due to the unique biomechanics and complex anatomy of this region (Siddiqui et. al., 2017). Specific examples of CCJ injuries which will be highlighted include: atlantooccipital dissociation, fractures of the occipital condyles, C1 ring and dens, avulsion injuries, distraction and rotational injuries with attention to ligamentous disruption, and other nonosseous and vascular injuries (Offiah and Day, 2017). Injuries in the CCJ account for a large portion of cervical spine injuries and can be devastating due to high energy trauma. An estimated that one out of three cervical spine injuries involve the CCJ (Riascos et al., 2015). Below, we will begin with a brief review of practical radiologic and anatomic concepts designed for the emergency clinician or radiologist. The complex biomechanics of the CCJ result from the need to support a relatively heavy calvarium, while achieving the dual function of protecting the spinal cord, cranial nerves and head vessels. The CCJ also needs to allow for marked flexibility and range of motion. This is accomplished via a bony frame with a significant soft tissue contribution to its structural integrity, including synovial joints, muscles and extensive intrinsic and paraspinal ligaments. The radiologic complexity of the CCJ stems from its disparate anatomic makeup and the large number of vital injury-prone structures contained in this small space. For a clear understanding of the following common and devastating injuries to the CCJ, the complex relationships between the osseous and usculoligamentous support structures should be reviewed by the reader. Important reviews can be found by examining the study on anatomy and biomechanics of the CCJ by Menezes et al (Menezes and Traynelis, 2008) and the radiological review by Riascos, et al (Riascos et. al., 2015).

Conclusions

Many common injuries of the CCJ have been described. Unique anatomic and biomechanical considerations in this region contribute to the diagnostic and therapeutic challenges attending CCJ injury. The advent of MDCT and MRI have revolutionized the diagnostic accuracy with the ability to predict instability and need for surgical fixation in patients with CCJ trauma. Moreover, CTA and MRI are increasingly vital to evaluate for vascular and ligamentous/soft tissue damage which can have crucial prognostic and management implications. The ED clinician and ED radiologist is well-served by knowing the anatomy, mechanisms of common injury and clinical presentations unique to the CCJ. The superiority of MDCT for the evaluation of osseous disruption is well established. Nonetheless, in the setting of known fracture, it is often necessary to take the follow-up step of a dedicated trauma protocol MRI to

Electronic Educational Exhibits

exclude superimposed soft tissue damage and exclude cord edema or hemorrhage, vital to accurate prognostication. In order to distinguish typically conservatively managed injuries such as occipital condyle fractures from those which will require traction or surgical intervention such as Jefferson fractures or AOD, it is often necessary for clinicians to take a multidisciplinary approach, which can assist in evaluating complicated CCJ injuries.

Axial and Coronal Schematics of the C1-2 ligaments

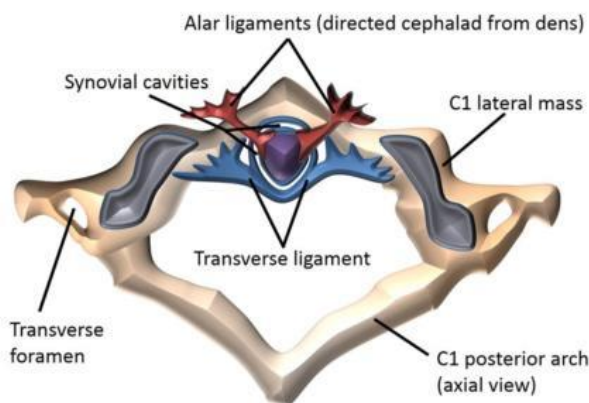


Figure 1. Axial schematic showing obliquely oriented alar ligaments directed cephalad with insertions on the dens inferomedially and occiput superolaterally (not shown). Transverse ligament is oriented horizontally with insertions on the C1 lateral masses and a complex attachment on the dens with synovial cavities which allow a large axial rotatory ROM.

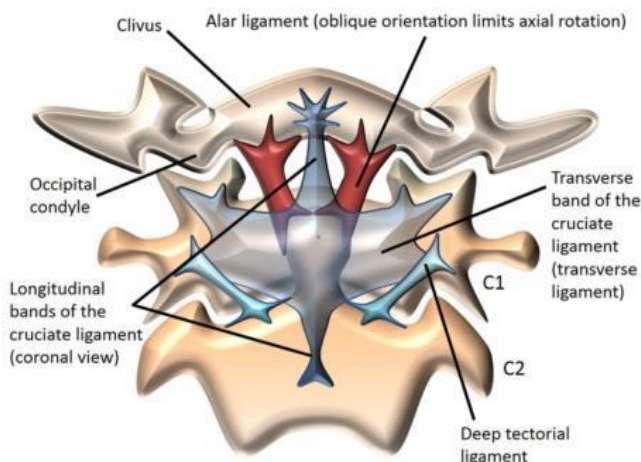


Figure 2. Coronal schematic showing obliquely oriented alar ligaments directed cephalad with insertions on the dens inferomedially and dorsal clivus superolaterally. The transverse ligament is oriented horizontally posterior to the dens with insertions on the C1 lateral masses.

(Filename: TCT_eEde-242_axialcoronalschematicsc.jpg)

eEde-228

Cystic Lesions of the Spinal Channel with Emphasis In “Parameningeal” Location: A Practical Approach

P Martin¹, E Salvador¹, L Koren¹, A Hilario¹, C Fernandez-Cabrera¹, G Ayala¹, A Ramos¹

¹Hospital 12 de Octubre, Madrid, Spain

Purpose

1. To identify the cystic lesions of the spinal channel depending on their location and dependency and provide imaging clues to guide the diagnosis 2. To review and update the classifications for meningeal cystic lesions, taking a close look at the etiopathogenesis and therapeutic implications 3. To evaluate the utility of different imaging techniques and MRI sequences in order to achieve an accurate diagnosis

Materials and Methods

Since the appearance of Magnetic Resonance Imaging (MRI), the diagnostic rates of spinal cystic lesions have increased rapidly. Since Nabor's classification in 1988, several classifications have been proposed in order to understand cystic "parameningeal" lesions, their pathogenesis, prognosis and treatments options.

Results

A variety of cystic lesions may develop in spinal canal. These lesions can be divided into intramedullary, intradural-extramedullary (aracnoid cysts, neuroenteric cysts), extradural meningeal lesions (meningeal diverticula, dural dissection cysts) and extradural not meningeal lesions (sinovial cysts, discal cysts, epidermoid cysts) according to their anatomical presentation. In this article we review the new classifications and diagnostic algorithms, with special emphasis in cystic lesions in parameningeal location, to simplify its comprensión and application to the clinical practice.

Conclusions

An appropriate comprehension about the etiopathogenesis and classification of spinal cystic lesions, specially when the meninges are involved, is essential to guide the diagnosis and to select therapeutical options. Also will be important to keep in mind usefull additional sequences to be performed in these cases.

eEde-215

Degenerative Spine Imaging Primer: Lumbar Disc Nomenclature Version 2.0 and Beyond

B Tantiwongkosi¹, A Singh¹

¹*University of Texas Health Science Center San Antonio, San Antonio, TX*

Purpose

This pictorial review aims to illustrate the relevant imaging anatomy of the lumbar spine and imaging characteristics of lumbar disc degeneration utilizing the most updated version of nomenclature (Lumbar Disc Nomenclature Version 2.0). All levels of trainees, practicing clinicians and radiologists are recommended to use the appropriate terms and nomenclature in order to accurately communicate to one another.

Materials and Methods

The Combined Task Forces of the North American Spine Society (NASS), the American Society of Spine Radiology (ASSR) and the American Society of Neuroradiology (ASNR) published the Lumbar Disc Nomenclature Version 2.0 in the Spine Journal in 2014. The article provides the clear recommendation of nomenclature in normal anatomy and lumbar degenerative diseases. The article also illustrates the complex anatomy using multiple hand draw diagram. We are inspired by the publications and eager to present an educational exhibit utilizing the clinical images of computed tomography (CT), magnetic resonance imaging (MRI) and diagrams to illustrate the complex anatomy and a wide range of lumbar degenerative diseases. Mimickers (infections, trauma, and normal variants), diagnostic pearls, and pitfalls will also be discussed.

Results

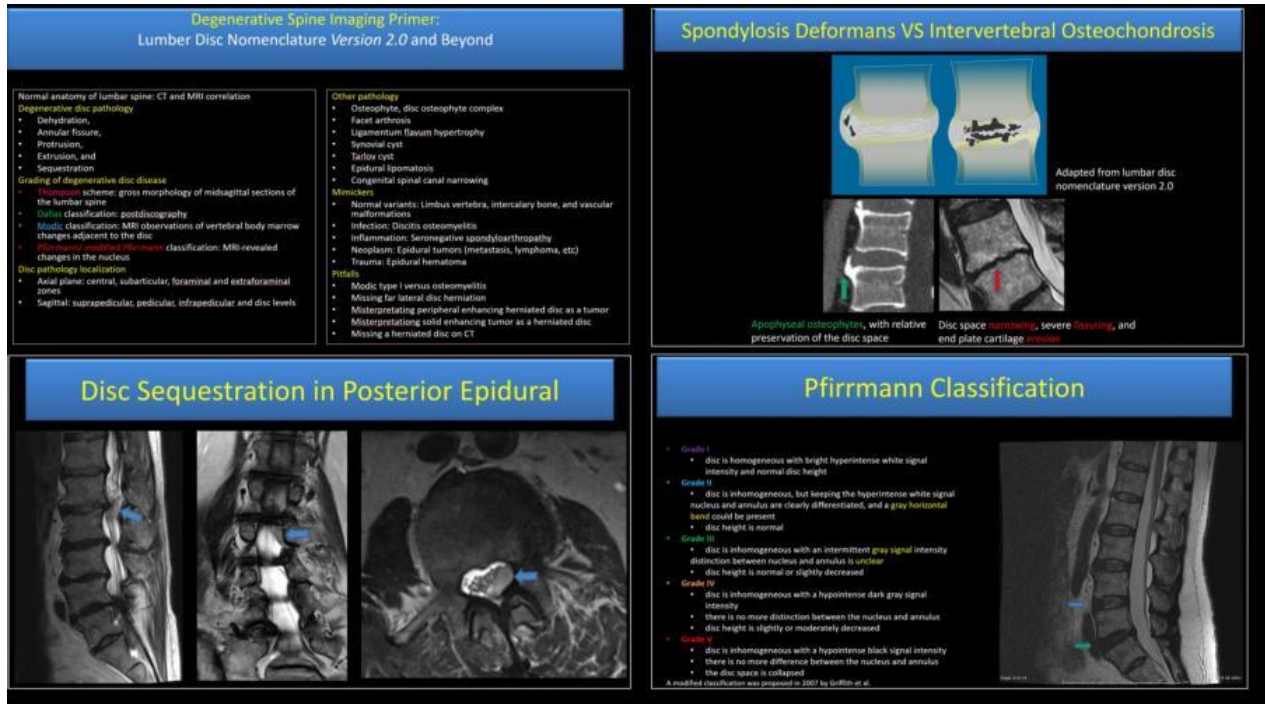
The exhibit will illustrate the imaging anatomy of the lumbar spine on CT and MRI with multiple planes and sequences. Degenerative entities include annular fissures (the term annular tear is inappropriate due to the implication of trauma as the cause of the lesions), disc bulge, protrusion, extrusion, and sequestrations. A rare case of posterior displacement of the sequestered disc fragment is presented. Precise locations of the herniated disc materials are classified into axial (central, subarticular, foraminal and extraforaminal zones) and sagittal planes (suprapedicular, pedicular, infrapedicular and disc levels). Mimickers include normal variants (limbus vertebra, intercalary bone, and vascular malformations), osteomyelitis, seronegative spondyloarthropathy, etc.

Conclusions

Radiologists must be able to communicate with the clinicians accurately as encouraged by the

Electronic Educational Exhibits

international task forces in order to make the diagnosis and localize the disease using the Lumbar Disc Nomenclature Version 2.0.



(Filename: TCT_eEde-215_SpineDJDJPEJG.JPG)

eEde-214

Dynamic Effect of Axial Load on the Lumbar Spinal Canal: Pictorial Essay

E Arruda¹, L Amaral², C Campos², V Marussi², L Freitas², A Benine Belezia³, B Inada², T Vilas Boas⁴, M Costa²

¹Hospital Beneficência Portuguesa de São Paulo, João Pessoa, Paraíba, Brazil, ²Hospital Beneficência Portuguesa, São Paulo, Brazil, ³A Beneficência Portuguesa de São Paulo/Hospital Santa Catarina de São Paulo, Sao Paulo, Brazil, ⁴Beneficência Portuguesa de São Paulo, Campinas, Brazil

Purpose

Illustrate the usefulness and demonstrate the mechanical effect of the axial load on the lumbar vertebral canal during MRI, CT and myelo-CT.

Materials and Methods

The study consisted of a retrospective analysis of the data of MRI and myelo-CT studies with axial load of 68 patients by an experienced neuroradiologist. The main indications for this examination are patients with sciatica and neurogenic claudication and when the conventional imaging does not explain the symptomatology. The absolute contraindications for the MRI are patients with cardiac pacemaker and magnetic aneurysm clips. In these situations, CT or Myelo-CT was performed. Sagittal DP and axial DP images parallel to the disc were acquired with and without load. The axial loading was applied after 5 minutes using a device developed by our service which consists of a jacket of neoprene with straps of nylon connected to a footplate to apply a pressure consisting of 50% of the patient's weight on the trunk against the footplate where there is a digital scale nonmagnetic. Afterwards one neuroradiologist measured the transverse area of the dural sac (TADS) on the disc, with and without load, and then the images were interpreted. We considered relative stenosis when TADS <100mm² and absolute stenosis when TADS <75mm².

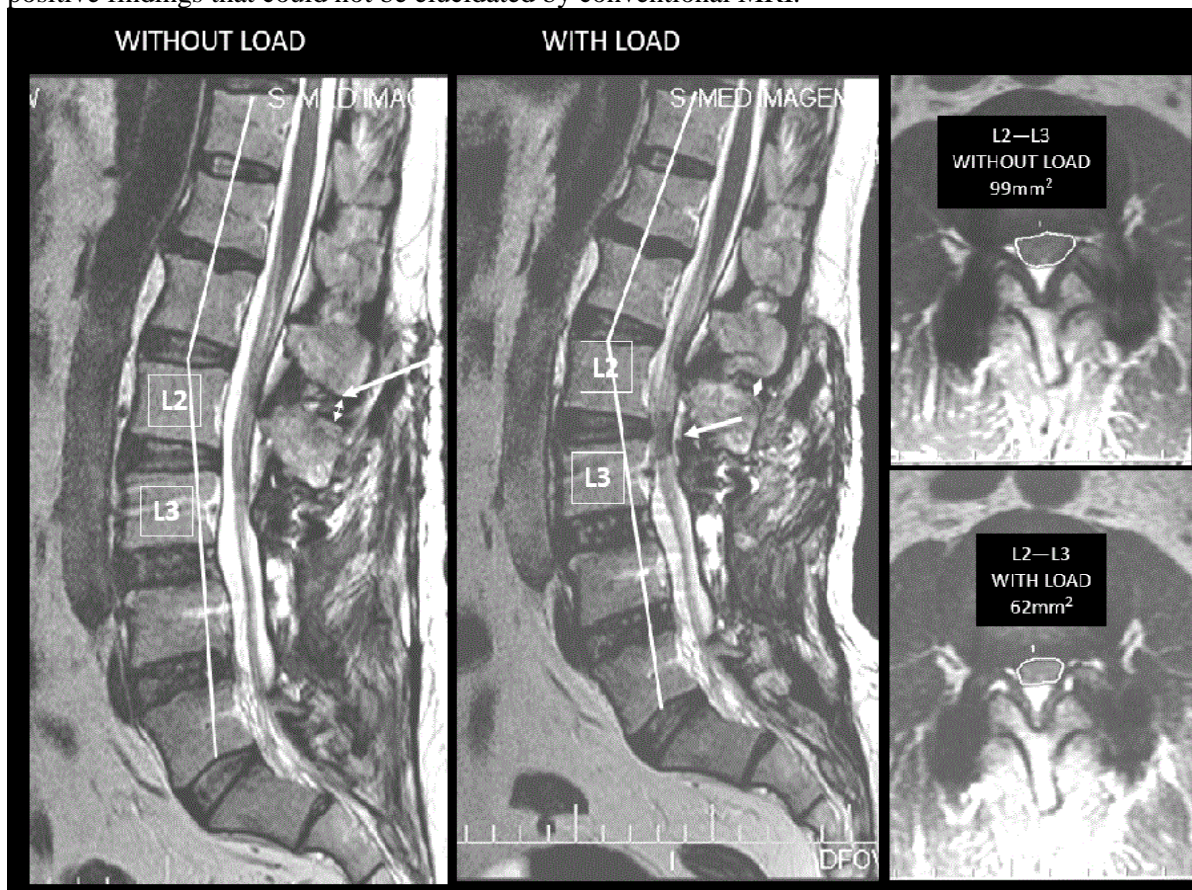
Electronic Educational Exhibits

Results

Axial loading resulted in diverse radiologic findings: changes in total lumbar curvature, disk space height, disk bulge, epidural fat shape, ligamentum flavum thickening, lateral recess and neural foraminal narrowing, evidence of synovial cyst, changes in dural sac dimension, relative stenosis became absolute.

Conclusions

MRI and myelo-CT of the lumbar spine using an axial loading device is a useful tool to test imaging and can add more information to explain patient symptomatology, affect treatment decision and reveal positive findings that could not be elucidated by conventional MRI.



(Filename: TCT_eEde-214_compressoaxialdpigif.gif)

eEde-226

Image-guided Synovial Cyst Rupture for Treatment: A Tutorial

D Lu¹, J Acharya², M Law¹, P Kim³, W Gibbs¹, J Go⁴

¹University of Southern California, Keck School of Medicine, Los Angeles, CA, ²University of Southern California, Pasadena, CA, ³Keck School of Medicine of University of Southern California, La Crescenta, CA, ⁴LAC/USC Medical Center, Los Angeles, CA

Purpose

The purpose of this exhibit is to describe the methodology used to perform image-guided rupture of synovial cysts within the central canal.

Materials and Methods

Patients presenting with intraspinal synovial cysts may have chronic back pain, radiculopathy, or leg

weakness. Percutaneous rupture of these cysts can be easily performed under CT guidance. The purpose of this exhibit is to describe the imaging findings, clinical presentation, and underlying pathophysiology of intraspinal synovial cysts. The CT approaches used to aspirate or rupture these cysts will be described including transfacet rupture, as well as transforaminal, interlaminar, and transosseous approaches to rupture these cysts. The methodology, equipment needed, and injectate used will also be described. Success rates and review of the literature will also be described.

Results

Patients presenting with intraspinal synovial cysts may have chronic back pain, radiculopathy, or leg weakness. Percutaneous rupture of these cysts can be easily performed under CT guidance. The purpose of this exhibit is to describe the imaging findings, clinical presentation, and underlying pathophysiology of intraspinal synovial cysts. The CT approaches used to aspirate or rupture these cysts will be described including transfacet rupture, as well as transforaminal, interlaminar, and transosseous approaches to rupture these cysts. The methodology, equipment needed, and injectate used will also be described. Success rates and review of the literature will also be described.

Conclusions

The imaging features of these extradural cystic lesions arising from the facets is fairly straightforward on both CT and MRI. CT guided treatment of intraspinal synovial cysts is a fairly easy and reproducible technique. Different approaches may be used to access and rupture these cysts based on the location of the lesion within the central canal to relieve the patients' symptoms.

eEde-212

Imaging Spectrum of Physiologic Patterns of Marrow Transformation

M Aftab¹, K Tsuchiya²

¹*Genesys Regional Medical Center, Flushing, MI*, ²*Michigan State University COM, Grand Blanc, MI*

Purpose

The purpose is to provide a pictorial review to understand the various patterns and variations of marrow signal in normal patients. This review will cover physiologic changes associated with aging and degenerative marrow change abnormalities.

Materials and Methods

Case examples and atlas of imaging characteristics of physiologic, benign, and degenerative patterns of marrow changes will be presented. These will include Ricci patterns and Modic type marrow changes as well as characteristics of atypical hemangiomas. Emphasis will be placed on unique characteristics that distinguish these from malignant etiologies.

Results

Bone marrow is a unique organ that constantly changes with age and environment with different health states. Understanding the imaging correlates of these findings is key to categorizing these findings as benign. Alternatively, recognizing the fundamental characteristics that distinguish the etiology as an infectious, or neoplastic process is critical and should raise a red flag.

Conclusions

MR imaging is very sensitive for marrow signal changes and a wide spectrum of marrow signal abnormalities are routinely seen in the neuroradiological practice. It becomes critical to distinguish and differentiate between the benign versus neoplastic marrow replacing processes to prevent unnecessary workup for patients, and to reduce excessive cost utilization while providing clinically relevant information to the referring provider.

Infectious Discitis and Osteomyelitis: A Binary Systematic Approach

C Olivas Chacon¹, F Brown¹, L He¹, D LOPEZ GARCIA², C Pedersen¹

¹*Mercy Catholic Medical Center, Darby, PA*, ²*HAHNEMANN UNIVERSITY HOSPITAL, Philadelphia, PA*

Purpose

1. To compare and contrast the classic imaging features of discitis/osteomyelitis and its mimickers. 2. To teach a step-by-step systematic approach to confusing cases and improve the confidence of readers in diagnosing discitis/osteomyelitis. 3. To demonstrate the use of a binary checklist to arrive at the correct diagnosis with challenging cases.

Materials and Methods

We provide a systematic binary approach to imaging diagnosis of discitis osteomyelitis for radiology trainees. Our aim is to encourage organized thinking by following a check list when approaching challenging cases with a myriad of imaging features. Our target audience are radiology trainees.

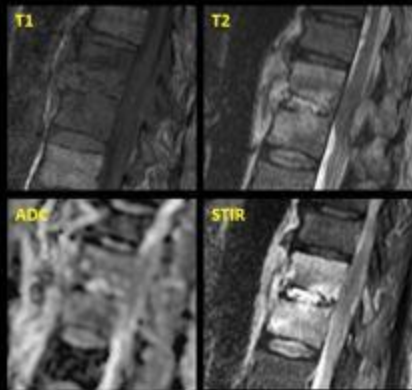
Results

Many different disease processes may mimic infectious spondylitis. Differentiating an infectious etiology as the cause of back pain can be very challenging given the overlapping features of infectious mimickers. For example, endplate degenerative (Modic) changes and neuropathic arthropathy of the spine can be confused with infectious spondylitis. More unusual mimickers such as patients with ankylosing spondylitis can develop pseudoarthrosis, endplate erosions, and subchondral sclerosis; these findings can be easily misinterpreted. In these confusing cases, the absence of highly suggestive imaging findings for discitis osteomyelitis must also be considered in a systematic manner. An organized approach to these overlapping imaging findings requires the radiologist to ask themselves the following questions: 1. Is there soft tissue involvement/abscess formation? 2. Is there nonfocal endplate bone destruction? (if yes, highly suggestive of infection) 3. Is there focal osteopenia/ resorption around trabeculae? 4. Is there high T2 signal in the bone marrow? 5. Is there high T2 signal in the intervertebral disc? 6. Is there vacuum phenomenon? (if yes, highly suggestive of non-infectious process) 7. Is there intervertebral disk enhancement? 8. Is there focal vertebral body height loss?

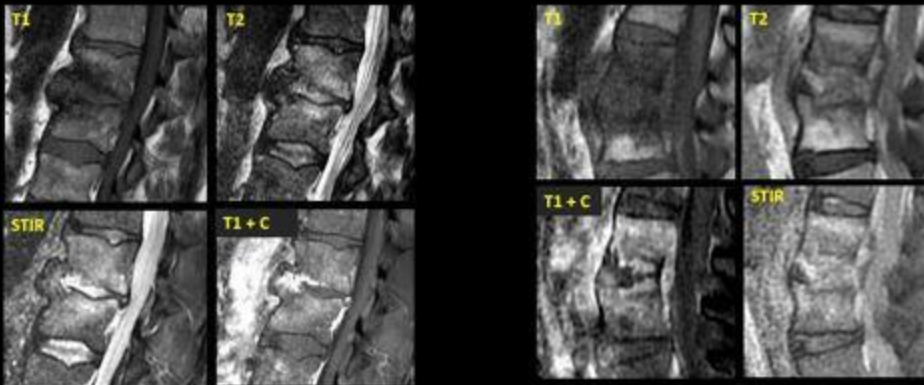
Conclusions

Differentiating infectious etiology as the cause of back pain can be challenging given the subtleties and overlapping features of the infectious mimickers. Following a check list when approaching these cases will help the reader favor an infectious or noninfectious etiology. Having an organized systematic approach will facilitate decision making.

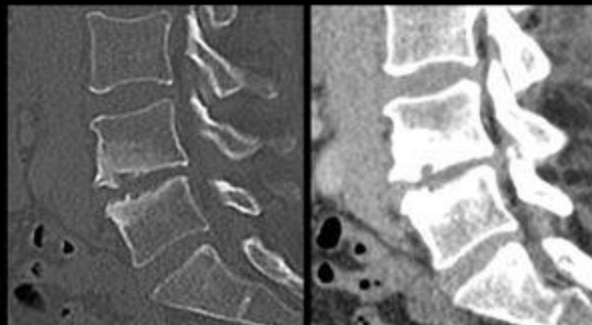
What imaging features are present?



How many characteristics of infection each of these cases have?



- Focal endplate erosions are characteristic of Schmorl's nodules and indicative of degenerative changes.
- The presence of vacuum phenomenon is a negative predictor, usually indicating a degenerative etiology.



(Filename: TCT_eEde-224_figure.JPG)

eEde-239

Keep Your Head on Straight: An Imaging Guide to Craniovertebral Junction Trauma

M Gelbman¹, J Meyer², S Lev²

¹*Nassau University Medical Center, Brooklyn, NY*, ²*Nassau University Medical Center, East Meadow, NY*

Purpose

We aim to provide a comprehensive image-rich review of craniovertebral junction (CVJ) trauma radiology to emphasize key principles and review strategies to effectively evaluate this critical region.

Materials and Methods

Computed tomography (CT), magnetic resonance imaging (MRI), and angiographic anatomy of the bony and soft tissue structures of the CVJ are reviewed along with common anatomic variants which can mimic injury. We utilize cases from our high-volume Level I trauma center to illustrate a broad array of fractures and traumatic soft tissue injuries involving the CVJ.

Results

The interface joining the skull and vertebral column and the brainstem and spinal cord is susceptible to severe injury in the setting of trauma. The effects of acute CVJ trauma can be quite detrimental, with significant morbidity and mortality. Unfortunately, the location of the CVJ at the extreme aspects of cervical spine and brain imaging studies along with the inconspicuous nature of many significant CVJ injuries can make detection of subtle lesions quite challenging. It is imperative for the radiologist to be cognizant of the normal anatomy and common variants which should not be mistaken for traumatic injury. We demonstrate a variety of osseous injuries including occipital condyle fractures (type 1-3), atlas fractures (including Jefferson and "plough" fractures) and axis fractures (including type 1-3 odontoid fractures, burst fractures, lateral mass fractures, and type 1-3 hangman fractures). Relevant classification schemes, mechanisms of injury, epidemiology, and imaging algorithms are outlined. We describe associated central nervous system, peripheral nerve, ligamentous, and vascular injuries. Spinal stability and craniocervical distraction injuries are also addressed.

Conclusions

Given the significant and often subtle nature of CVJ injuries, the radiologist must be thoroughly prepared to evaluate this region. Search patterns should include special focus to this region during the interpretation of brain, spine, and maxillofacial studies. Awareness of the spectrum of common injuries involving the CVJ is imperative.

eEde-217

Low Back Pain: To Image or Not to Image--That is the Question

O Nemer¹, A Hussain¹, C Kondray², N Bekal³

¹*University of Rochester Medical Center, Rochester, NY*, ²*The Metrohealth System, Cleveland, OH*, ³*Medical College of Georgia at Augusta University, Augusta, GA*

Purpose

The purpose of this interactive educational computer exhibit is to review the imaging indications of the low back pain based on the updated American College of Radiology Appropriateness Criteria (ACR AC).

Materials and Methods

Interactive educational computer exhibit to explain the updated American College of Radiology Appropriateness Criteria regarding imaging of low back pain using different clinical scenarios.

Results

Low back pain is a very common medical problem with high impact on the health system, including

Electronic Educational Exhibits

radiology. Better resource utilization is key by identifying proper indications for imaging and what kind of imaging modality used. The updated American College of Radiology Appropriateness Criteria regarding imaging of low back pain is an evidence-based guide that can be used to serve this purpose.

Conclusions

Familiarity with the updated American College of Radiology Appropriateness Criteria regarding imaging of low back pain will help in meaningful, evidence-based imaging utilization.

eEde-216

Lumbosacral Transitional Segments and Associated Rib Anomalies

S Forseen¹, S Forseen¹, B Gilbert², A Wang³, S Nazarian³, A Zahran⁴

¹Augusta university, Augusta, GA, ²Augusta University, Augusta, GA, ³Medical College of Georgia, Augusta, GA, ⁴Baylor College of Medicine, Houston, TX

Purpose

This abstract reviews the prevalence of spinal segment variations, including lumbosacral transitional vertebrae (LSTV), supernumerary ribs, or absence of ribs and their morphological relevance in spinal imaging.

Materials and Methods

We retrospectively reviewed 262 consecutive adults who had received cervical, thoracic and lumbar CTs at our institution between January 2009 and December 2011. Exclusion criteria consisted of any factor that would interfere with evaluation of facet orientation and accurate segmental numbering, such as severe artifacts, displaced fractures, or surgical fusion. Vertebral segments were numbered from craniad to caudad with the assumption of seven cervical and twelve thoracic segments. The positions of the lowest ribs were recorded for each case. The caudal most ribs were determined with criteria adapted from Wigh and Carrino. A rib was defined as a bony structure that slopes from superomedial to inferolateral and maintains a central articulation with the vertebral body. A transverse process was defined as a horizontal bony process that does not centrally articulate with the vertebral body. The total number of lumbosacral transitional segments will be recorded with the use of the Castellvi system. Fisher's exact test was used to compare categorical variables.

Results

Twelve sets of ribs were most commonly observed, with the caudal-most set of ribs associated with the 19th vertebral segment in 235/251 (94%) of cases. Thirteen sets of ribs were observed in 10/251 (4%) of cases and eleven sets of ribs were observed in 6/251 (2%) of cases, with the caudal-most ribs associated with the 20th and 18th vertebrae, respectively. LSTVs were observed in 37/251 (15%) of cases. Castellvi Ia/Ib LSTVs were associated with thirteen sets of ribs (lumbar ribs), $p < 0.01$. Castellvi IIIb LSTVs were associated with eleven sets of ribs, $p < 0.01$.

Conclusions

Lumbar imaging is typically performed without imaging the cervical and thoracic segments. As a result, a set of common assumptions are often made with regard to spine numbering, such as the caudal-most rib bearing vertebra is T12, or the caudal most mobile segment represents L5. Most of the reported errors were attributed to a failure to recognize unconventional spinal anatomy (e.g. supernumerary segments, eleven ribs, thirteen ribs), suboptimal intraoperative x-rays, miscounting, using poor references when counting, and failure to relocalize after exposure. Interestingly, a number of the errors were attributed to faulty methods of counting, such as counting down from the lowest set of ribs or counting up from the sacrum, or miscommunication (e.g. radiologist counting down from the ribs and surgeon counting up from the sacrum). Accurate numbering of the lumbar segments is important in order to prevent wrong level spine surgeries and procedures. Forseen et al. (2015) examined the location of the thoracolumbar facet transition as a potential method of identifying the T12 segment, observing the thoracolumbar facet transition at segment nineteen in only three quarters of the cases. The variation in the location of the

thoracolumbar facet transition precludes its use as a reliable landmark for the T12 segment. As stated in our current study, there is a strong association between lumbosacral transitional vertebrae and supernumerary or absence of ribs. Castellvi Ia/Ib lumbosacral transitions were associated with thirteen sets of ribs (lumbar ribs), while Castellvi IIIb LSTVs were associated with eleven sets of ribs.

eEde-233

Magnetic Resonance Imaging of Spinal Emergencies: A Primer for Radiology Residents in the Emergency Department

V Pargaonkar¹, K Buch², R Peterson³, S Rohatgi¹

¹University of Massachusetts, Worcester, MA, ²University of Massachusetts Medical Center, Worcester, MA, ³Emory University School of Medicine, Atlanta, GA

Purpose

The purpose of this exhibit is to review pertinent neuroimaging findings for an array of spine emergencies. Early diagnosis and familiarity with common features in spine emergencies is crucial to prevent significant morbidity, neurologic deficit and permanent disability.

Materials and Methods

In this exhibit, we will use a case-based approach to discuss imaging features of spine emergencies on MRI. A variety of emergent cases will be discussed by etiologic category including: infectious, traumatic, degenerative, neoplastic and vascular etiologies. Key pertinent differential diagnosis, imaging pearls, pathologic mimics, and pitfalls to avoid in diagnosis as well as treatment and management guidelines will be included.

Results

Spine emergencies often present as diagnostic dilemmas due to lack of clinical familiarity and varied presentations. We recommend a compartment-based approach to these pathologies, to help simplify resident learning. The compartment-based approach to the spinal emergencies and the pathologies are discussed below: 1. Intramedullary - cord contusion, infarction, intramedullary tumors and non-neoplastic cord lesions secondary to inflammatory and autoimmune etiologies 2. Extramedullary Intradural lesions - arachnoiditis, infections, neoplasms causing compression, hemorrhage related to spinal vascular malformations inflammatory/autoimmune conditions 3. Extramedullary Extradural – abscesses and phlegmons secondary to osteomyelitis-diskitis, emergent complications of back surgery, traumatic injuries including pseudomeningoceles, discogenic nerve root compressions, extension of synovial cysts, epidural hemorrhage 4. Bones and surrounding soft tissues - fractures, metastasis, infection, ligamentous injuries, vascular injuries

Conclusions

In the era of increased use of imaging, assessment of emergency room patients MRI plays a crucial role in the evaluation of spinal disorders. Prompt diagnosis of spine emergencies on MR is critical in avoiding and or limiting long-term adverse outcomes. This exhibit is designed to provide a framework by which residents develop a methodical approach to evaluate and interpret MR images, and to work in concert with clinicians to optimize patient care and treatment outcomes.

eEde-234

Magnetic Resonance Imaging of the Brachial Plexus: A Review of Anatomy and Pathology

V Pargaonkar¹, S Rohatgi¹, M Lanfranchi², K Buch³

¹University of Massachusetts, Worcester, MA, ²Tufts Medical Center, Boston, MA, ³University of Massachusetts Medical Center, Worcester, MA

Purpose

Imaging of the brachial plexus can be a technical and diagnostic challenge related to anatomy and a wide variety of pathology affecting the brachial plexus. The purpose of this review is to provide a complete, practical approach to understand the anatomy of brachial plexus with illustration of various pathologies of the brachial plexus on MR Imaging.

Materials and Methods

In this exhibit, we will discuss the MR imaging techniques, protocol, normal anatomy and imaging appearances of various brachial plexus pathologies. The imaging patterns of common brachial plexus pathologies such as traumatic injury and various nontraumatic etiologies such as infectious, inflammatory, neoplastic, radiation induced, vascular and compressive pathologies will be discussed with illustrative examples.

Results

This exhibit will include a detailed anatomic discussion of the brachial plexus. The brachial plexus arises from the ventral rami of the spinal cord at C5-T1 levels and is divided into roots, trunks, divisions, cords and branches. The major anatomic landmarks that aid in the localization of brachial plexopathies are interscalene space, costoclavicular triangle, and relation to the subclavian vessels. A detailed discussion will also focus on standard clinical imaging sequences of the brachial plexus as well as advanced imaging sequences including STIR imaging, diffuse tensor imaging and tractography, MR angiogram and venogram, unilateral versus bilateral imaging, high resolution imaging and use of intravenous contrast. An array of brachial plexus pathology will be presented and discussed in a case review format with etiologies including traumatic injuries, nerve sheath tumors, non-neurogenic tumors involving brachial plexus, radiation induced plexopathy, brachial neuritis, immune mediated neuropathies, compressive lesions and thoracic outlet syndrome.

Conclusions

It is important that the radiologist is aware of the common MR imaging appearances of various brachial plexus pathologies and optimal imaging techniques in order to provide accurate diagnosis and optimize treatment outcomes.

eEde-232

MRI Findings of Compressive Myelopathy: Differential Diagnosis and Pitfalls

A Reddy¹, J Kim², T Moritani², M Patel³

¹*Univ of Iowa Hospitals and Clinics, Iowa city, IA*, ²*University of Michigan, Ann Arbor, MI*, ³*University of Iowa, Iowa City, IA*

Purpose

To demonstrate MRI findings of compressive myelopathy: differential diagnosis and pitfalls

Materials and Methods

Review MRI findings with compressive myelopathy of the cervical and thoracic spinal cord from various etiologies including trauma, stenosis from chronic degenerative disease, compression from bone tumors, primary cord tumors and myelitis. MR findings were reviewed with special attention to DWI and ADC signal abnormalities.

Results

Compressive myelopathy can be caused by various etiology including severe spinal trauma, chronic degenerative disease and extra and intradural neoplasms. Furthermore, these surgically treatable conditions should be promptly distinguished from neurological conditions like spinal cord infarction, demyelinating disease and transverse myelitis where operative interference may be detrimental. Each of these disease processes has their own specific presentations and unique variable MR findings including snake eye pattern, central round lesion patten and asymmetric mutiple cord lesions with or without mass effect or edema, and with or without contrast enhancement. DWI usually shows no restriction with

increased ADC in compressive myelopathy. However, DWI can show restricted diffusion in the acute phase.

Conclusions

Various patterns of MR findings along with DWI/ADC can be used to identify compressive myelopathy amenable for surgical decompression from clinical mimics like ischemia, infection or demyelinating disease.

eEde-219

Multifocal and Diffuse Spinal Bone Marrow Lesions Mimicking Metastases: A Pictorial Review

H Sa e Silva¹, P Naval Baudin², J Aristizabal³, V Onofrij⁴, C Zamora⁴, M Castillo⁴

¹*Hospital Pedro Hispano, ULSM, Matosinhos, Porto, Portugal*, ²*Hospital Universitari de Bellvitge, L'Hospitalet de Llobregat, Barcelona, Spain*, ³*University of Antioquia, Medellin, Colombia*, ⁴*University of North Carolina Hospitals, Chapel Hill, NC*

Purpose

There are numerous benign entities that can radiographically mimic spinal bone metastases and pose a diagnostic challenge. The purpose of this review is to present a spectrum of lesions focusing on the imaging characteristics of unusual diseases as well as potential mimics and pitfalls for diagnosis.

Materials and Methods

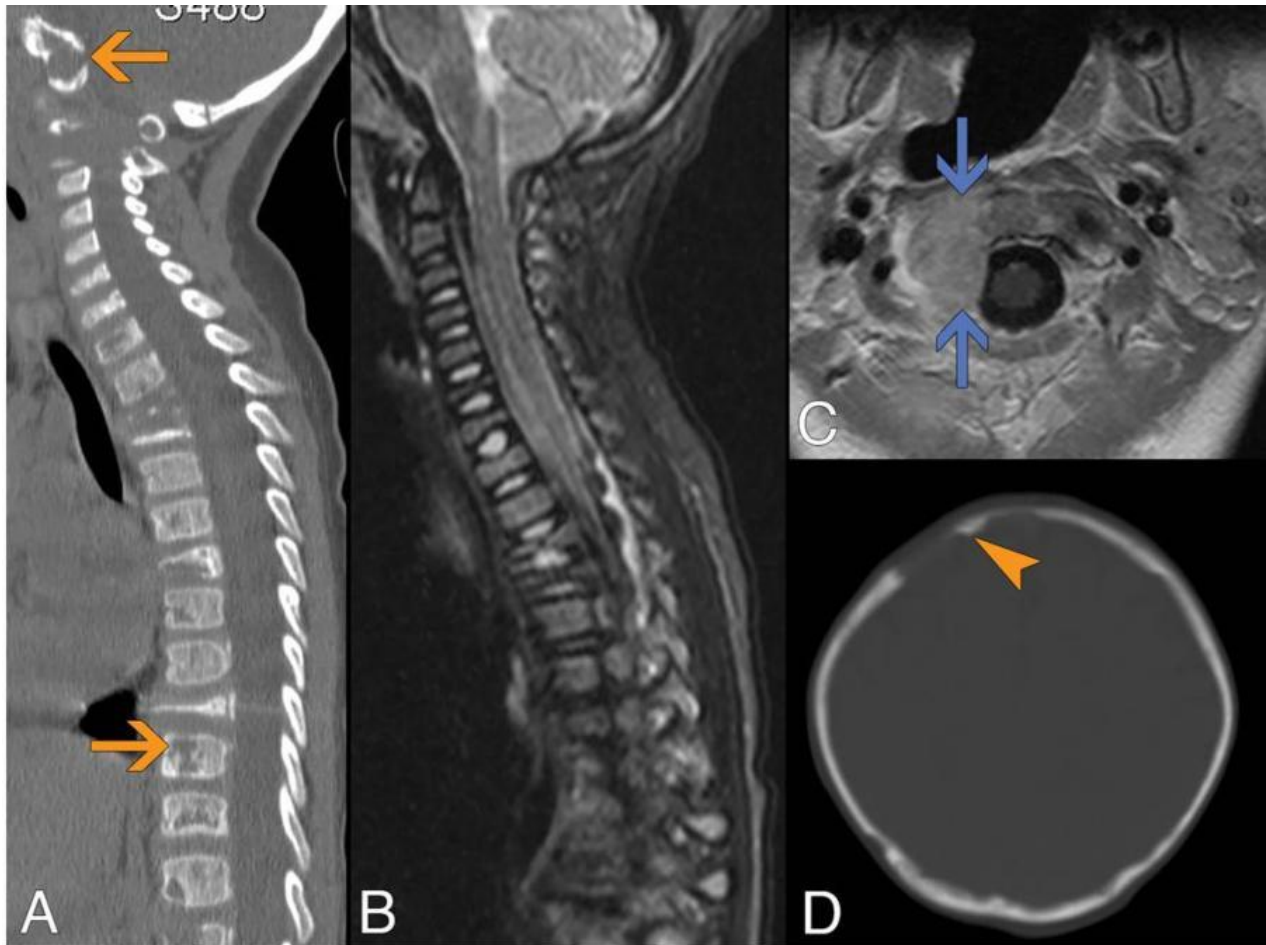
We searched our teaching files over the past 12 years and collected illustrative cases of patients who presented with multifocal or diffuse spinal bone marrow lesions that posed a diagnostic challenge that had overlapping characteristics with metastases. In this exhibit we will describe which additional imaging and clinical features may suggest the correct diagnosis.

Results

We identified normal variants (heterogeneous bone marrow), benign vascular neoplasms (atypical hemangiomas), inflammatory diseases (sarcoidosis, Langerhans cell histiocytosis, spondylarthropathies), hemoglobinopathies (thalassemia, sickle cell disease), various syndromic entities (osteopoikilosis in tuberous sclerosis), melorheostosis (Gorham vanishing bone syndrome) and metabolic disorders (Brown tumor, amyloid and renal osteodystrophy). Bone infarcts, post radiation changes, and lymphangiomatosis were also identified as potential pitfalls for diagnosis.

Conclusions

Outside metastases, the differential diagnosis of multifocal and diffuse spinal bone marrow lesions is broad. Familiarity with this variability and knowledge of characteristic disease patterns will help narrow the differential diagnosis.



19-month-old boy with multifocal Langerhans cell histiocytosis. **(A)** Sagittal CT shows widespread lytic lesions throughout the spine and base of skull (orange arrows) and several vertebrae plana. Sagittal fat-saturated T2 image **(B)** shows relative preservation of the bone marrow signal. Axial post-contrast T1 image **(C)** shows enhancement of a solid lesion in the right lateral mass of C1 (blue arrows). **(D)** Axial CT image shows lytic lesions in the right parietal and frontal bones, the latter showing a beveled margin (arrowhead).

(Filename: TCT_eEde-219_Picture1.jpg)

eEde-243

Newer AOSpine Subaxial Cervical Spine Traumatic Injury Classification: What Neuroradiologists Need To Know - A Case-based Review

R Patel¹, N Chinapuvvula¹, P Bawa¹, A Kamali¹, S Khanpara¹, E Bonfante¹, R Riascos¹

¹*The University of Texas Health Science Center at Houston, Houston, TX*

Purpose

Subaxial cervical spine injury is one of the most frequent and serious encounters in emergency departments and trauma centers worldwide. Greater than 50% of all cervical spine fractures and

approximately 75% of the dislocations are subaxial in nature. It is an important diagnosis to identify and communicate appropriately with emergency physicians and trauma surgeons. Treatment decision-making is based on imaging findings and can be challenging; therefore, it is essential for radiologists to provide accurate and consistent reports. Several classification systems have been used in an attempt to provide standardized nomenclature. Most recently proposed The AOSpine subaxial cervical spine injury classification system has demonstrated substantial reliability in its initial assessment, and could be a valuable tool for communication, patient care and for research purposes. Purpose of this exhibit is to review cross-sectional CT and MRI anatomy of cervical spine pertinent to trauma and to describe a morphology-based AOSpine subaxial cervical spine traumatic injury classification system as case-based format.

Materials and Methods

Illustrative subaxial cervical spine injury case examples with most recent AOSpine classification system will be presented from one of the busiest level 1 trauma institutions.

Results

AOSpine subaxial cervical spine injury classification system is based on three injury morphology: compression injuries (A), tension band injuries (B), and translational injuries (C), with additional descriptions for facet injuries, as well as patient-specific modifiers and neurologic status. With most recent literature based on this classification system supports that it is an accurate, reliable, and validated scoring system that incorporates radiologic assessment of injury morphology and disco-ligamentous integrity along with clinical assessment of neurologic status to help guide surgical management. Familiarity with this classification system and its radiologic constituent findings is critical for the accurate communication of injury severity between the neuroradiologist and attending trauma/spine surgeon.

Conclusions

AOSpine subaxial cervical spine traumatic injury classification system is an accurate, reliable and validated tool for the assessment of subaxial cervical spine injury severity. After reviewing this exhibit, the reader will understand the newer AOSpine subaxial cervical spine traumatic injury classification and be able to quickly and accurately diagnose as well as classify subaxial cervical spine injuries, and efficiently aid the trauma team in clinical management decisions.

eEde-238

Role of Imaging in the Diagnosis and Management of Vascular Injuries and Complications in Craniospinal Trauma

G Jindal¹, R Rojas², N Peri³

¹Warren Alpert School of Medicine, Brown University, Providence, RI, ²Beth Israel Deaconess Medical Center, Boston, MA, ³VA Medical Center, Boston, MA, Newton, MA

Purpose

Vascular injuries are an important component of trauma involving head, face and spine. The aim of this exhibit is to describe the different types of vascular injuries and the role of different imaging modalities in diagnosis and management.

Materials and Methods

The exhibit would be discussed under the following sections: 1. Introduction 2. Types of vascular injuries 3. Role of Imaging in diagnosis and management - CT, MR, CTA/MRA, conventional angiogram, etc.

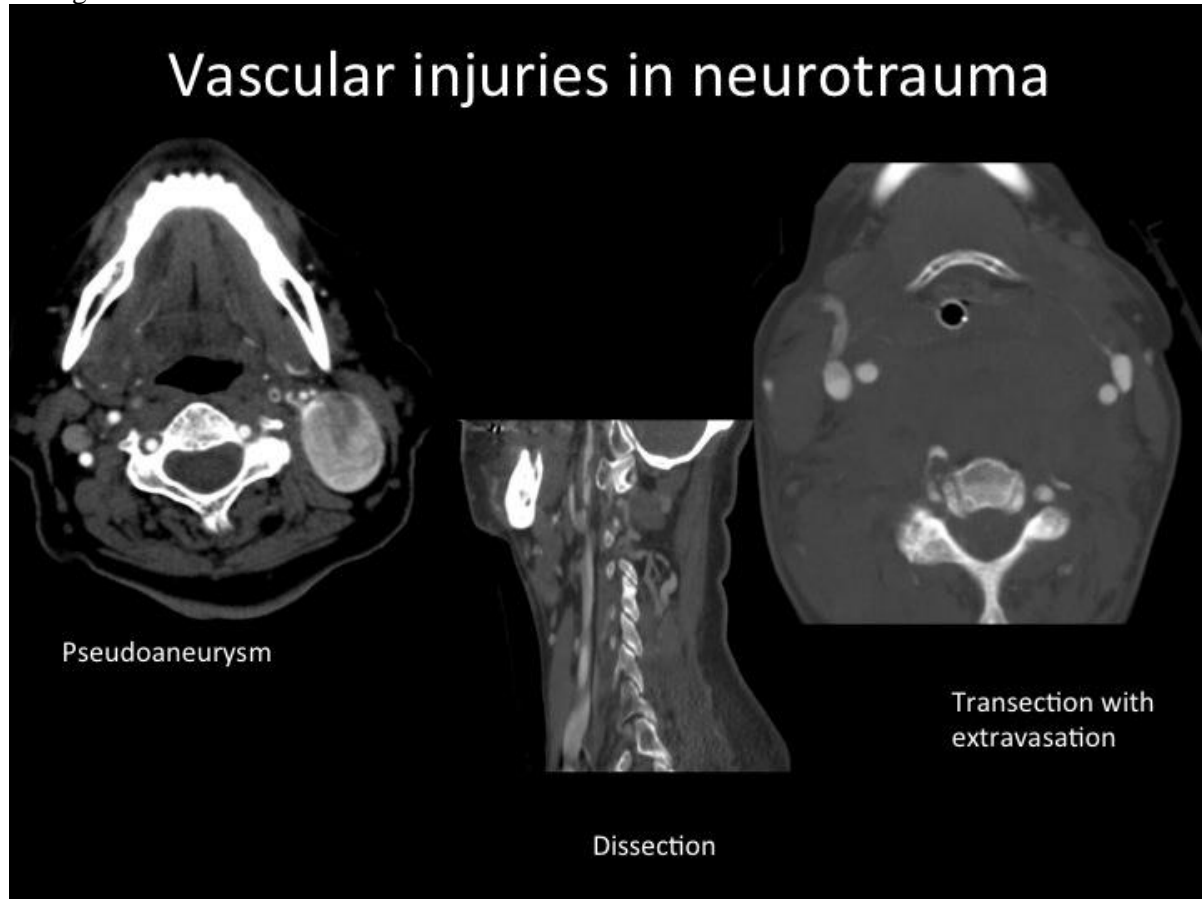
Results

Vascular injuries are an important component of trauma involving head, face and spine with serious consequences. Vascular injuries can be arterial or venous and arterial injuries include minimal intimal irregularity or intimal flap, dissection with intramural hematoma, occlusion, pseudoaneurysm, transection, arteriovenous fistula, etc. (1). It is very important to suspect and diagnose these on routine CT and MR

studies in order to recommend advanced vascular imaging studies for further evaluation. Treatment includes conservative medical, endovascular or surgical therapy.

Conclusions

Vascular injuries are an important component of craniospinal trauma with serious consequences. The different imaging modalities have an important role and complement each other in their diagnosis and management.



(Filename: TCT_eEde-238_Slide1.jpg)

eEde-222

Spectrum of Imaging Findings and Complications in Facet Joint Infection

V Onofrij¹, C Zamora¹, M Castillo¹, P Puac Polanco²

¹University of North Carolina at Chapel Hill, Chapel Hill, NC, ²Sanatorio el Pilar, Guatemala, Guatemala

Purpose

Facet joint infections are increasingly recognized and may constitute a significant source of morbidity particularly in patients who are immunocompromised. They can result from hematogenous dissemination from a distant source or arise primarily as a complication of minimally invasive spinal procedures such as facet joint injections. The purpose of this review is to present a spectrum of imaging findings and complications related to infectious facetitis.

Materials and Methods

This pictorial exhibit is based on a query of our teaching files encompassing the last 10 years. We

Electronic Educational Exhibits

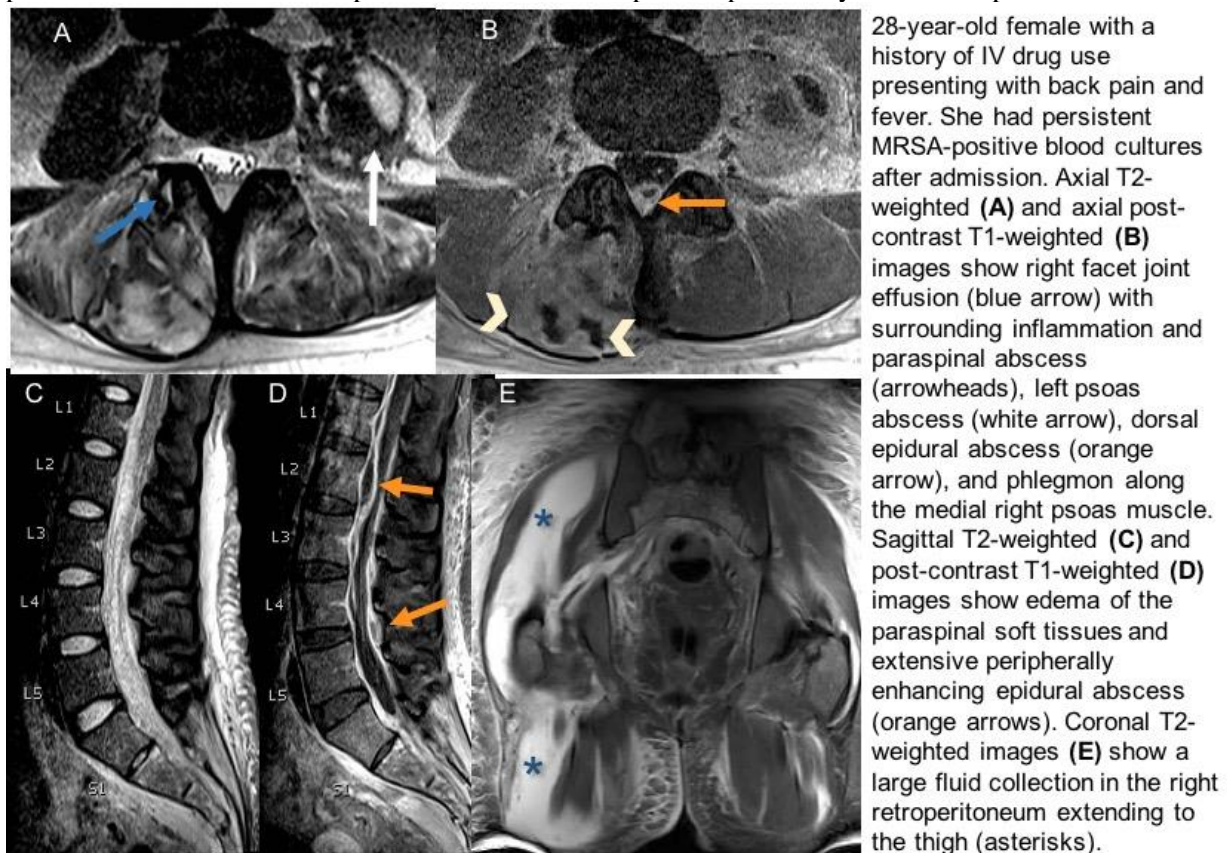
identified patients who presented with facet joint infections and characterized the type and extent of disease and imaging manifestations as well as associated complications.

Results

The extent of abnormalities in patients with facet joint infections varied from mild facet and perifacet inflammation to extensive disease spreading to the neural axis. Complications presented in the form of perifacet abscess (one or more levels), contralateral infection (presumably through the retrodural space of Okada), epidural abscess, epidural phlegmon, pyomyositis (paraspinal or iliopsoas), sacral perineural abscess, infection extending to the sacroiliac joints or pelvic organs, listhesis due to ligamentous disruption and/or laxity, spondylodiscitis, and spinal leptomeningitis with intracranial spread of pus and ventriculitis.

Conclusions

The spectrum of disease in facet infections is varied. Early recognition and a high index of suspicion in patients who are immunocompromised are critical to prevent potentially severe complications.



(Filename: TCT_eEde-222_Facetitis.jpg)

eEde-221

Spinal Cord Hyperintensity: What to Expect? A Pattern-based Approach

C Ahuja¹, N Khandelwal¹

¹Post Graduate Institute of Medical Education and Research, Chandigarh, India

Purpose

Spinal cord signal change signifies an alteration in the internal milieu of the involved segment of the cord secondary to disturbances in the protons within the neuronal components. A number of disorders mimic

Electronic Educational Exhibits

one another in imaging appearance which leads to a diagnostic dilemma. The present illustration describes a pattern-based approach to spinal cord T2 hyperintensity which would aid in the diagnosis of cord pathology.

Materials and Methods

Retrospective data evaluation of all cord pathologies detected on MRI over the last 5 years was done. The pathology/lesion was classified based on its: a. location (cervical, dorsal, lumbar or multisegmental), b. axial extent (anterior/motor dominant, posterior/sensory dominant, central or transaxial/complete), c. longitudinal extent (short segment vs long segment), d. number (single/multiple), e. nature (discrete/well defined, fluffy, expansile) f. Adjoining changes (e.g. prominent intradural vascular channels, skeletal changes, etc.). Subsequent confirmation was sought for by looking at the operative notes (wherever available), assessing response to drugs, or following systemic evaluation of the pathology. Classical MRI appearance of certain lesions was taken to be diagnostic.

Results

Ventral motor involvement was noticed in motor neuron disease. Dorsal predominant lesions were noted in subacute combined degeneration. Central fluid indicates hydromyelia. Short segment lesion extent was seen with multiple sclerosis while long segment involvement was diagnostic of neuromyelitis optica in an appropriate clinical setting. Expansile lesions indicated presence of neoplasm although oedematous cord also shows expansion to a limited extent.

Conclusions

A pattern based approach helps in narrowing down the differentials of altered cord signal so that prompt and appropriate management can be followed.

eEde-237

Spinal Cord Intramedullary Tumors: Rule of 'Four' a Radiologist Should Know

S Vyas¹, A Kumar¹, N Khandelwal¹

¹*Postgraduate Institute of Medical Education and Research, Chandigarh, India*

Purpose

Spinal cord intramedullary tumors are rare, constitute 4-10% of all CNS tumors and 20% of all intraspinal tumors. They have varied clinical presentations and complex radiographic appearance. Since these are rare and infrequently encountered in our clinical practice we tried to simplify radiological approach by rule of 'four' a radiologist should know about the spinal cord intramedullary tumors.

Materials and Methods

We comprehensively reviewed the various types (classifications), clinical presentations, imaging modalities, imaging characteristics, imaging pattern and differential diagnosis of the spinal cord intramedullary tumors.

Results

There are four common types of spinal cord intramedullary tumors which constitute about 98% of tumors namely ependymoma (60%), astrocytoma (30%), hemangioblastoma (6-8%) and ganglioglioma (1%). Four common clinical presentations viz. back/neck pain, weakness/paraesthesia, gait disturbance, and bowel/bladder dysfunction. Four imaging modalities namely MRI (imaging modality of choice), CT Myelography, conventional X-rays and Myelography. Four imaging pattern viz. cord lesion with solid enhancement, cord lesion with heterogeneous/patchy enhancement, cord lesion with no enhancement and cord lesion with lepto-meningeal enhancement. Four important imaging characteristics viz. cord enlargement, enhancement, cysts and Syringohydromyelia, and haemorrhages. Four important imaging differential diagnosis of the tumors which includes inflammatory lesions (tuberculoma/neurocysticercosis), vascular lesions (cavernous malformations, dural arterio-venous fistulas and infarction), demyelinating lesions (neuromyelitis optica, multiple sclerosis and acute disseminated encephalomyelitis) and spinal cord contusions.

Conclusions

Rule of 'four' in cases of spinal intramedullary lesions helps in characterizing intramedullary spinal cord tumors as these are rare and have bizarre clinical and radiological spectrum.

eEde-230

Spinal Subdural Collections and Injections: Improving Detection and Diagnosis

B Diegnan¹, A Rajamohan¹, J Pack¹, W Gibbs¹, E Velez²

¹University of Southern California, Keck School of Medicine, Los Angeles, CA, ²LAC+USC, Los Angeles, CA

Purpose

1. Discuss the potential causes of spinal subdural collections and injections 2. Learn how to recognize spinal subdural pathology on multiple imaging modalities

Materials and Methods

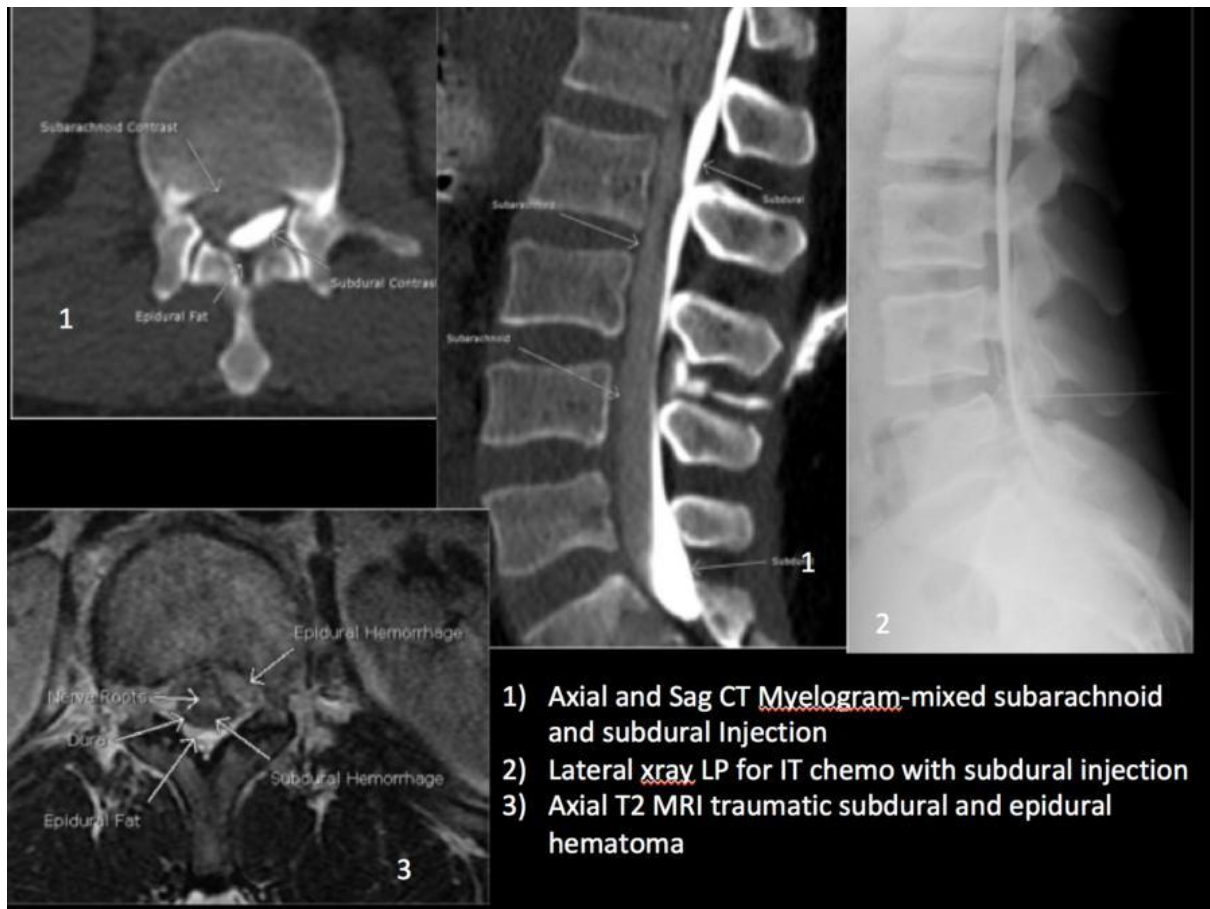
Illustration of the pertinent spinal meningeal anatomy that creates the potential subdural space, review the causes for pathologic and iatrogenic introduction of fluid into the subdural space, characterize imaging findings of subdural collections and injections on CT, fluoroscopy and MRI with distinction between epidural and subarachnoid collections.

Results

Spinal subdural collections and injections are rare and often unrecognized as they can be difficult to diagnosis. Spinal subdural collections can be spontaneous in a setting of coagulopathy, subsequent to trauma, or a result of a procedure that separates the dura from the arachnoid mater. Spinal subdural injections can result from a multitude of procedures. We will discuss a variety of settings in which one may encounter subdural fluid, blood, or contrast in the context of diagnostic imaging, lumbar puncture, myelography, intrathecal chemotherapy, and lumbar drain placement. There are key imaging findings to distinguish subdural collections from epidural and subarachnoid collections that can be identified on multiple imaging modalities.

Conclusions

Recognizing the presence of fluid or contrast in the subdural space and distinguishing it from epidural and subarachnoid collections can be a diagnostic dilemma. The radiologist needs a thorough understanding of the anatomy and imaging characteristics to make an accurate diagnosis to allow for proper management or correction of an unintended procedural collection.



(Filename: TCT_eEde-230_Images1.jpg)

eEde-220

Spine Infections: What the Radiologist Needs to Know

M Walters¹, D Pong¹, A Singh¹, B Tantiwongkosi¹

¹University of Texas Health Science Center San Antonio, San Antonio, TX

Purpose

This pictorial review aims to illustrate the relevant imaging findings of typical and atypical infections of the spine with emphasis placed on clinically important details and how they affect management.

Materials and Methods

Radiological images as well as relevant clinical and pathologic information were extracted from our PACS station and electronic medical record system at our hospital network. Images were retrieved from recent imaging studies to review a spectrum of infections of the spine and frequently encountered mimics.

Results

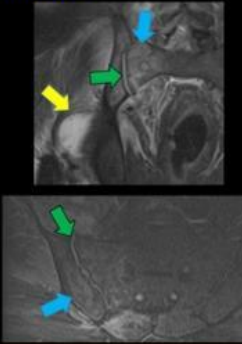
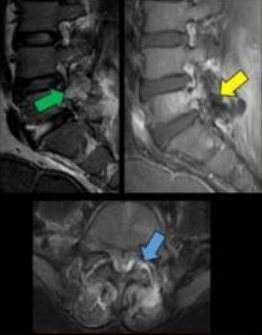
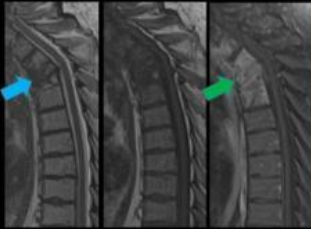
The exhibit begins with illustration of pertinent anatomic imaging of the spine and adjacent structures. Next, the classic imaging findings of pyogenic spine infections will be reviewed. Imaging of infrequently encountered nonpyogenic etiologies such as mycobacterial, fungal, viral, and parasitic organisms will then be presented. Infectious spread within (epidural, intramedullary, cerebrospinal fluid) and outside the spine will be reviewed including how these processes change management. Then imaging of the complications of advanced osteomyelitis diskitis including focal kyphosis will be reviewed. Recent data on the yield of image guided biopsy of bone, intervertebral disk, and soft tissue will be addressed. The

Electronic Educational Exhibits

exhibit will conclude with noninfectious processes with imaging findings that can simulate infection including trauma, malignancy, Modic type changes, acute cartilaginous nodes, and seronegative spondylarthropathy.

Conclusions

This educational exhibit provides an in-depth review of infectious processes of the spine and their mimics with emphasis on differentiating imaging features and clinical relevance.

<h3>Spine Infections: What the Radiologist needs to know</h3> <ul style="list-style-type: none"> • Typical and atypical imaging findings: <ul style="list-style-type: none"> • Pyogenic • Non-pyogenic <ul style="list-style-type: none"> • Mycobacterial • Fungal • Parasitic • Viral • Yield of biopsy <ul style="list-style-type: none"> • Osseous • Intervertebral Disk • Soft tissue • Extension <ul style="list-style-type: none"> • Intraspinal <ul style="list-style-type: none"> • Epidural <ul style="list-style-type: none"> • Anterior and posterior • Intradural extra-medullary • Intra-medullary • Extraspinal <ul style="list-style-type: none"> • Septic facet arthritis • Paraspinal abscess • Sacroiliitis • Mimics <ul style="list-style-type: none"> • Modic type changes • Trauma • Ankylosing Spondylitis 	<h3>Septic Sacroiliitis</h3> <ul style="list-style-type: none"> • Infrequent complication of lumbosacral osteomyelitis <ul style="list-style-type: none"> • more commonly hematogenous in etiology • Osseous edema & erosion surround frequently widened and fluid joint space • Adjacent soft tissue inflammation with intramuscular abscesses differentiate from non-infectious processes such as ankylosing spondylitis 
<h3>Septic facet arthritis</h3> <ul style="list-style-type: none"> • Frequently result of infectious contiguous spread • Non-specific fluid within facet joints • Adjacent osseous erosion and edema are more specific imaging findings • Frequent adjacent soft tissue phlegmon and abscess formation • Can result in posterior epidural abscess 	<h3>Candida Osteomyelitis</h3> <ul style="list-style-type: none"> • Clinical and imaging findings of fungal osteomyelitis diskitis are often non-specific <ul style="list-style-type: none"> • Osseous destruction • T1 hypointense marrow infiltration & enhancement • May spare disk spaces • Frequently spans multiple vertebral levels with resultant focal kyphosis & gibbus deformity 

(Filename: TCT_eEde-220_spineinfectionjpeg.JPG)

eEde-213

The Mechanisms and Origins of Spinal Pain, from Molecules to Anatomy, Pathology, and the Imaging Findings

M Connolly¹, J Kim¹, A Srinivasan², T Moritani¹

¹University of Michigan, Ann Arbor, MI, ²University of Michigan Health System, Ann Arbor, MI

Purpose

Effective spinal pain treatment lies in identifying the underlying source. Incidental imaging findings can complicate the diagnosis. This exhibit will discuss current knowledge of spinal pain from the biochemical through gross anatomical and pathological levels.

Materials and Methods

We will begin the exhibit with theorized initial causes of spinal pain using many schemas: - Trauma, endplate calcification, and altered disc loading initiate inflammation; exposing disc to bone.

Electronic Educational Exhibits

Neovascularization allows transient bacteremia to cause chronic discitis. - Neurogenic and angiogenic factors lead to vascularization and innervation of discs. - Specific cytokines which amplify inflammation and those which trigger Modic changes. - Modic type 1 changes are symptomatic. Type 2 is less associated with pain. Type 3 symptoms and outcomes are not well defined. - High intensity zones (HIZ) on T2 indicate disc disruption. STIR and postcontrast hyperintensity reflect inflammation. - Annular fibrosis (AF) T1 and T2 HIZ may reflect bony endplates or AF calcification. T2 hyperintensity reflects isolated annular fissure. - Inflammation on MR does not necessarily correlate with clinical symptoms of disc herniation and is often asymptomatic, even with persistent herniation and inflammation. - Association of cytokines in lumbar facet joints and sciatic pain, secondary to cytokine release from degenerating joint. - Pathologic pain sensitivity - Inappropriate cytokine production

Results

We will explain the clinical significance of imaging findings and give examples of when imaging findings and clinical symptoms were, and were not, well correlated. Etiologies of spinal pain are both microscopic and macroscopic; intervention may correct the abnormality, but occult sources of pain may persist. Conversely, imaging abnormalities can correlate with benign clinical findings. Growing evidence questions the long-term benefits of spine surgery, highlighting the need for precise pain source identification. We will discuss management and treatment of spinal lesions based on the mechanisms.

Conclusions

Knowledge of causes and underlying mechanisms of spinal pain aid proper diagnosis and management.

eEde-236

The Value of Diffusion Imaging and Apparent Diffusion Coefficient in the Diagnosis of Myxopapillary Ependymomas, with Summary of the Clinicoradiopathologic Spectrum and Literature Review of Future Treatment Aims

J Guan¹, M Ouyang², T Moritani³, J Kademian¹, T Sasaki⁴, P Kirby¹

¹University of Iowa Hospitals and Clinics, Iowa City, IA, ²University of Iowa Hospital and Clinics, Iowa City, IA, ³University of Michigan, Ann Arbor, MI, ⁴University of Iowa, Iowa City, IA

Purpose

Myxopapillary ependymoma (MPE) is an uncommon, slow-growing spinal cord tumor that is histologically and morphologically distinct from other groups of ependymomas. While overall survival is good, MPE is plagued with high rates of recurrence and dissemination likely because of its affinity for early seeding along the neuroaxis. Due to MPE's resistance to conventional chemotherapy, surgical resection with or without radiation remains the only viable treatment option, thus differentiating MPEs from other CNS tumor mimics is crucial as it accentuates the need for complete surgical resection. The purposes of this educational exhibit are to present the radiopathologic spectrum and tumor mimics of MPE; offer recommendations for the use of diffusion imaging, especially ADC values; for accurate differentiation of MPE from tumor mimics, and based on literature review, provide the most current developments in the future treatment aims of MPE.

Materials and Methods

After obtaining IRB approval, a medical record search was performed for all patients from our institution from 2011 through 2016 who were either diagnosed on pathology to have MPE or who had MPE included as a differential on MRI imaging reports. The clinical presentation and overall clinical course during and after treatment for each of these patients were noted. For patients who had biopsy-proven MPE, their MRI images were reviewed to characterize the tumor appearance on T1WI, T2WI, postcontrast T1WI, as well as diffusion-weighted imaging, recording the corresponding ADC values. In a similar fashion, the MRI images for patients who had a different tumor diagnosed on pathology but had MPE mentioned as a differential on MRI imaging report were reviewed. The histopathology slides from the biopsies of the

MPE cases were obtained for pathologic correlation. Finally, a literature search was performed for the most current developments on future treatment aims of MPE.

Results

The mean age at presentation was 38.7 years (range, 19-81). Survival rate is 95% at a mean follow-up time of 13.1 years (range, 1-26), with mean survival time of 8 years (range, 1-26). The most common presenting symptom(s) is back and lower extremity pain with or without motor/sensory deficits or bladder/bowel dysfunction. Pathologic characteristics include pseudopapillary arrangements of monomorphic, cuboidal cells with hyalinized fibrovascular core (perivascular pseudorosettes), often with myxoid change. Immunohistochemistry is positive for GFAP, Vimentin, and S-100 proteins, and is negative for cytokeratin and epithelial membrane antigen. MRI characteristics include a well-circumscribed mass in the lumbosacral spine that is hypo- to isointense on T1WI and hyperintense on T2WI, with homogeneous enhancement. Common differentials of MPE due to similar MRI appearances include spinal metastases, chordoma, schwannoma, meningioma, hemangioma, paraganglioma, and anaplastic ependymoma, but in retrospect, diffusion imaging was able to differentiate MPE from these tumor mimics due to higher ADC values ranging from $1.35 \times 10^{-3} \text{mm}^2/\text{s}$ to $2.0 \times 10^{-3} \text{mm}^2/\text{s}$, compared to non-MPE lesions showing ADC values below $1.3 \times 10^{-3} \text{mm}^2/\text{s}$. From recent genomic and transcriptional medicine research, MPE has been found to express protein patterns consistent with the "Warburg" phenotype. Increased expression of pyruvate dehydrogenase lipoamide kinase isozyme 1 (PDK1) and hexokinase 1 (HK1) leads to a shift towards glycolysis and lactate accumulation, and increased expression of pyruvate kinase muscle isozyme isoform M2 (PKM2) compared to total PKM levels allows cells to accumulate metabolites for cellular growth and division. Based on these findings, potential future avenues for drug therapy include use of small molecule inhibitors and activators like the HK inhibitor Lonidamine, the PDK1 inhibitor Dichloroacetate, and PKM activators such as TEPP46 and DASA58.

Conclusions

MPE is an uncommon CNS tumor with a wide clinicoradiopathologic spectrum. Although its prognosis is good, MPE is plagued with high rates of recurrence and dissemination, thus early differentiation of MPE from tumor mimics and effective therapy are paramount for disease control. Diffusion imaging offers a highly accurate way to differentiate MPE from its tumor mimics. While the current treatment algorithm for MPE consists of solely surgical resection with or without radiation therapy, current attempts to characterize the genomic and transcriptional landscape of MPEs have opened new avenues in future targeted drug therapies for MPE.

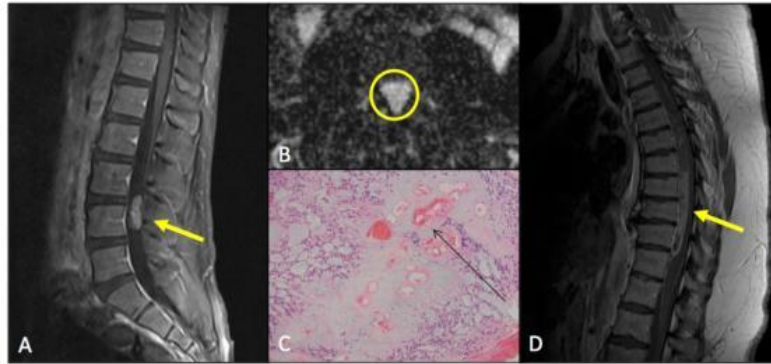


Figure 1. MRI and pathologic characteristics of a typical myxopapillary ependymoma as compared to a tumor mimic. **(A)** Post-contrast sagittal MRI of myxopapillary ependymoma diagnosed in a 17 year-old male who presented with intermittent back pain for 2 years. Note the well-circumscribed lumbar mass showing avid homogeneous enhancement. **(B)** Associated ADC in the same patient showed increased signal ($2.0 \times 10^{-3} \text{mm}^2/\text{s}$). **(C)** Histopathology of the resected tumor shows hyalinized vessels surrounded by a basophilic myxoid matrix, the nuclear free zone (aka perivascular pseudorosettes). **(D)** Post-contrast sagittal MRI of a case of exophytic anaplastic ependymoma that mimicked a benign extra-medullary tumor such as MPE. During surgical resection, the superior and inferior portions of the mass were easily removed with blunt dissection, however the mid section of the mass appeared tightly adherent to the spinal cord and a dissection plane between the mass and the spinal cord could not be discerned.

(Filename: TCT_eEde-236_ASNR2018Images.jpg)

eEde-241

Trauma and the Fused Spine

M Gelbman¹, H Hunt², S Lev²

¹Nassau University Medical Center, Brooklyn, NY, ²Nassau University Medical Center, East Meadow, NY

Purpose

1. Assorted primary injuries with critical imaging findings are demonstrated to illustrate how the rigid ankylosed spine is especially susceptible to trauma. 2. We review both mechanisms/patterns of injury and the role of various imaging modalities in the radiologic work-up and clinical management. 3. Emphasis will be placed on crucial differences between the ankylosed and nonankylosed spine.

Materials and Methods

We provide a case-based discussion of traumatic findings seen in the ankylosed spine utilizing CT, MR and myelography cases from our high volume level 1 trauma center. We review the current literature highlighting important radiologic findings and clinical outcomes. We describe common disorders causing spinal ankylosis with attention to pathophysiology, epidemiology and biomechanics. We also review the current ACR appropriateness criteria pertaining to suspected fracture in the setting of spinal ankylosis.

Results

Structural and biomechanical alterations in the fused spine have been implicated in the pathogenesis of spinal fractures. This phenomenon is recognized in patients with Ankylosing spondylitis (AS), Diffuse Idiopathic Skeletal Hyperostosis (DISH), Degenerative Spondyloarthropathy (DS), Ossification of the Posterior Longitudinal Ligament (OPLL), and surgical fusion of the spine. Associated fractures are often of high morbidity even in the setting of low-energy trauma. Abnormal spinal rigidity is associated with an increase in transverse fractures and hyperextension injuries. The cervicothoracic junction as well as the regions between the rigid and nonrigid segments are especially vulnerable due to increased stressor forces. Many of these patients have multiple noncontiguous fractures throughout the entire spine. These fractures must be carefully searched for as the radiologic appearance can be quite inconspicuous. We

Electronic Educational Exhibits

encourage special attention to the fused spine with the use of proper window settings as well as 2D/3D multiplanar reformats to improve detection. MR is especially valuable to evaluate for associated soft tissue injuries, such as epidural hematomas and ligamentous injury. Fractures of the ankylosed spine are often unstable and delayed diagnosis can lead to further potentially devastating complications.

Conclusions

Given the significant clinical impact and often subtle imaging findings of trauma to the ankylosed spine, it is imperative for the radiologist to promptly recognize this special category of injury. Awareness of the spectrum of associated radiologic findings and of the predisposition to unstable fractures, even after minor trauma, is paramount. Unfortunately, uncommon injury mechanisms, misleading physical exam findings and equivocal radiographs often delay diagnosis.

eEde-223

Tuberculosis: MRI Manifestations within the Spine and Brain

D Bleicher¹, J Post¹, A Ruiz¹, G Saigal¹, N Nagornaya¹

¹*University of Miami/Jackson Memorial Hospital, Miami, FL*

Purpose

A review of the multiple imaging manifestations of Central Nervous System Tuberculosis (CNS TB), a well recognized global pandemic, was done to aide in the timely diagnosis and therapy of this treatable infectious disease.

Materials and Methods

A retrospective review of patients with pathologically proven tuberculosis who presented to a large public hospital serving a predominantly indigent population was performed, which included both immunosuppressed and immunocompetent persons. Classical and atypical imaging findings on MRI in the spine and brain were identified which allowed for an earlier diagnosis of TB to be made.

Results

CNS TB can present with many imaging manifestations. In the spine these include findings related to osteomyelitis-discitis, epidural and paraspinal abscesses, meningitis, and spinal cord tuberculomas. In the brain these include meningitis with or without parenchymal involvement, parenchymal tuberculomas (such as caseating, noncaseating, and liquefactive), TB abscesses, vasculitis, infarcts, and CNS-IRIS. The sequelae of spine and brain involvement include such entities as arachnoiditis and communicating hydrocephalus. Although the imaging characteristics may overlap with several other pathologies, attention will be drawn to certain features that are both unique and classical, such as avid leptomeningeal enhancement.

Conclusions

Although there have been improvements in both diagnosis and treatment, TB remains a leading cause of global pandemics. Furthermore, in the United States, the incidence has not declined since 2013-2015. Prompt recognition of both typical and atypical imaging patterns in both the spine and brain is therefore crucial to avoid the severe associated morbidity and mortality that can follow a delay in diagnosis and treatment.

eEde-225

Understanding the Imaging of Spine Infection

J Ovalle¹

¹*Medicadiz, Ibagué - Eje Cafetero, Tolima, Colombia*

Purpose

To show the main findings in spinal infection, bacterial, fungal, granulomatous disease through educational cases and schemes to main patterns on MR imaging.

Materials and Methods

Magnetic resonance (MR) is the most sensitive and specific modality for spine infection. Pyogenic spondylodiscitis is a bacterial infection of the bony spinal columns, the intervertebral discs, and/or the ligaments of the extradural spine. The most common cause is hematogenous spread of infection from remote site. Urinary tract infections are the most frequent culprit. Other etiologies include direct inoculation, such as in the postoperative setting, discography, therapeutic spinal injections, and contiguous spread from adjacent infected sites. Staphylococcus aureus is the most frequent causative organism. Predisposition to spine infections includes disease such as diabetic patients, renal failure, cirrhosis, immunosuppressed states, and intravenous drug use. Clinically these patients present with focal low back pain, fever and muscle spasm. Laboratory shows elevated erythrocyte sedimentation rate and elevated C-reactive protein, leukocytosis less commonly.

Results

Regarding MR protocol, fat-suppressed T2 WI are useful, and post gadolinium T1 fat suppressed to increase conspicuity of the findings. T1 hypointensity, T2 hyperintensity, and enhancement after gadolinium on bone marrow, disc space T2 hyperintensity and disc space enhancement. Epidural abscesses have relatively high associated morbidity and mortality. Pyogenic spondylodiscitis have classic imaging findings on MR, regarding disc space T2 hyperintensity, enhancement, height loss, in adjacent vertebral bodies we can see endplate destruction, T1 hypo, T2 hyper intensity and enhancement, in paraspinal soft tissue we can see ill-defined inflammation/swelling, abscess. In epidural space we could see reactive enhancement/venous plexus distention and abscesses.

Conclusions

In our exhibit we are going to show cases and schemes with the main findings of spine infections using MR techniques.

eEde-227

You're In My Space! A Pictorial Review of Anatomy and Pathological Processes Involving the Spaces of the Spinal Canal

J Joshua¹, J Corrigan¹, S Patel¹, H Marin¹, B Griffith¹

¹*Henry Ford Health System, Detroit, MI*

Purpose

Accurately localizing pathology within the spinal canal and its contents, specifically the meningeal layers and dural spaces can be challenging. Lesions within the subdural space, in particular, can be mistakenly localized to the subarachnoid or epidural space by the untrained eye. This exhibit will discuss the normal anatomy and imaging of the spinal canal, emphasizing the meningeal layers and dural spaces, as well as key imaging features of various pathological conditions involving them.

Materials and Methods

1. Using diagrams, MRI, and myelography, we will discuss the normal anatomy of the spinal canal, specifically the subarachnoid, subdural, and epidural spaces, emphasizing imaging features that allow for

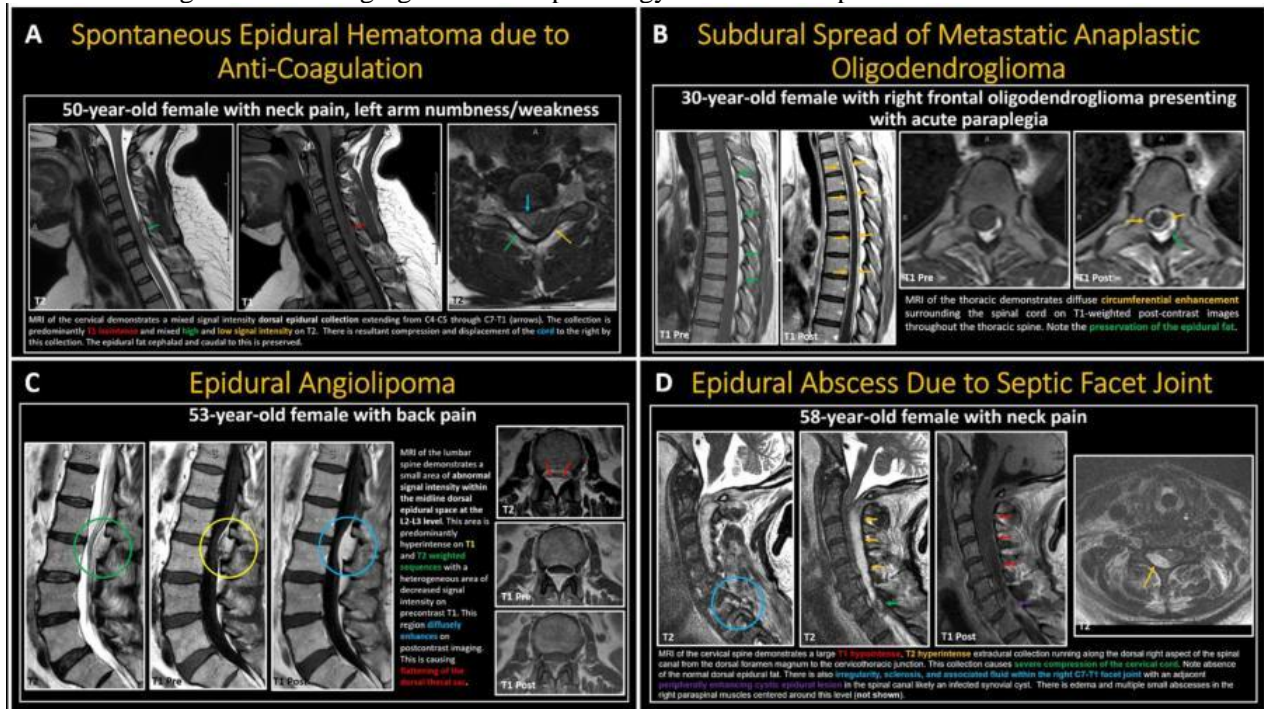
accurate differentiation. 2. Using our teaching files, we will show a variety of pathologic processes involving these spaces, emphasizing the subdural and epidural spaces, including: hemorrhage (Fig 1A), tumors (e.g., metastases (Fig 1B), angioliopoma (Fig 1C), nerve sheath, lymphoma), abscess (Fig 1D), lipomatosis, and pseudomeningocele. 3. We will discuss imaging features that can help in differentiating the pathology within these spaces and in formulating an appropriate differential diagnosis.

Results

Key Learning Points: 1. Discussion of spinal canal and meningeal anatomy, emphasizing key means of differentiating the various spaces on imaging 2. Differential diagnoses and features of pathology found in these spaces, emphasizing subdural and epidural pathology

Conclusions

Familiarity with the normal anatomy and appearance of the spinal canal, meninges and dural spaces is important for the neuroradiologist. Correctly localizing a lesion to its appropriate space within the spinal canal is essential as it is necessary for formulating a differential diagnosis and determining appropriate management. At the conclusion of this exhibit, viewers should be familiar with the normal anatomy of the spinal canal and its spaces, how to differentiate lesions within those spaces on imaging, as well as the differential diagnoses and imaging features of pathology within these spaces.



(Filename: TCT_eEde-227_Spineall.jpg)